

Fraunhofer Institut
Chemische Technologie

Energetic Materials

Ignition, Combustion and Detonation

32nd International Annual Conference of ICT
July 3 - July 6, 2001
Karlsruhe, Federal Republic of Germany

REPORT DOCUMENTATION PAGE

Form Approved OMB No. 0704-0188

Public reporting burden for this collection of information is estimated to average 1 hour per response, including the time for reviewing instructions, searching existing data sources, gathering and maintaining the data needed, and completing and reviewing the collection of information. Send comments regarding this burden estimate or any other aspect of this collection of information, including suggestions for reducing this burden to Washington Headquarters Services, Directorate for Information Operations and Reports, 1215 Jefferson Davis Highway, Suite 1204, Arlington, VA 22202-4302, and to the Office of Management and Budget, Paperwork Reduction Project (0704-0188), Washington, DC 20503.

1. AGENCY USE ONLY (Leave blank)	2. REPORT DATE	3. REPORT TYPE AND DATES COVERED
	July 2001	3-6 July 2001 Final Report

4. TITLE AND SUBTITLE
International Annual Conference (32nd) of ICT Held in Karlsruhe, Federal Republic of Germany on July 3-July 6, 2001. Energetic Materials: Ignition, Combustion and Detonation.

5. FUNDING NUMBERS
N000-

6. AUTHOR(S)

7. PERFORMING ORGANIZATION NAME(S) AND ADDRESS(ES)
Fraunhofer-Institut fur Chemische Technologie (ICT)
Joseph-von-Frauhofer-Strasse
Postfach 12 40
D-76318 Pfinztal (Berghausen)

8. PERFORMING ORGANIZATION REPORT NUMBER
ISSN 0722-4807

9. SPONSORING/MONITORING AGENCY NAME(S) AND ADDRESS(ES)
Office of Naval Research,
European Office
PSC 802 Box 39
FPO AE 09499-0039

10. SPONSORING/MONITORING AGENCY REPORT NUMBER

11. SUPPLEMENTARY NOTES
Text in German and English; abstract in English.
This work relates to Department of the Navy Grant issued by the Office of Naval Research International Field Office. The United States has a royalty free license throughout the world in all copyrightable material contained herein.
.

12a. DISTRIBUTION/AVAILABILITY STATEMENT
Approved for Public Release; Distribution Unlimited.
U.S. Government Rights License. All other rights reserved by the copyright holder.

12b. DISTRIBUTION CODE
A

12. ABSTRACT (Maximum 200 words)
These are presentation and poster session papers presented at the 32nd International Annual Conference of ICT held in Karlsruhe, Germany, onJuly 3-6, 2001.

The main topic concerning energetic materials is the formulation and synthesis of new components. Their characterization is based on experimental research of ignition, combustion and detonation phenomena.

Conference objectives include experimental and theoretical activities on: initiation and ignition processes; investigation of combustion and detonation phenomena, plume signature, and improved diagnostics and measurement techniques.
.

13. SUBJECT TERMS
Chemistry, Foreign reports, Conference proceedings, German language, Combustion

15. NUMBER OF PAGES

16. PRICE CODE

17. SECURITY CLASSIFICATION OF REPORT	18. SECURITY CLASSIFICATION OF THIS PAGE	19. SECURITY CLASSIFICATION OF ABSTRACT	20. LIMITATION OF ABSTRACT
UNCLASSIFIED	UNCLASSIFIED	UNCLASSIFIED	UL

Herrn Dr. Axel Homburg,

Vorsitzender des Kuratoriums des Fraunhofer ICT,

zu seinem 65. Geburtstag am 5. Juli 2001

gewidmet.

Dedicated to Dr. Axel Homburg,

Chairman of the Kuratorium of Fraunhofer ICT

on the occasion of his 65th Birthday

on July 5th, 2001

Herausgeber / Editor:

Fraunhofer-Institut
für Chemische Technologie (ICT)
Joseph-von-Fraunhofer-Straße
Postfach 12 40
D-76318 Pfinztal (Berghausen)

Bundesrepublik Deutschland

Telefon (07 21) 46 40 - 0
Telefax (07 21) 46 40 - 111

Herstellung:

DWS Werbeagentur und Verlag GmbH, Karlsruhe
Printed in Germany

ISSN 0722-4087



Fraunhofer Institut
Chemische Technologie

Energetic Materials

Ignition, Combustion and Detonation

20011130 073

32nd International Annual Conference of ICT
July 3 - July 6, 2001
Karlsruhe, Federal Republic of Germany

U.S. Government Rights License
This work relates to Department of the Navy Grant or Contract issued by Office of Naval Research (ONR) International Field Office-Europe. The United States Government has a royalty-free license throughout the world in all copyrightable material contained herein.

AQ F02-02-0262

32nd International
Annual Conference of ICT

Energetic Materials -
Ignition, Combustion
and Detonation

A main topic concerning energetic materials is the formulation and synthesis of new components. Their characterization is based on experimental research of ignition, combustion and detonation phenomena.

Detailed knowledge of new energetic materials is based on investigations of transport phenomena of heat and species, fluid dynamics and chemical reaction mechanisms supported by advanced measurement techniques. Combination with innovative modeling tools will lead to faster developments.

Conference objectives include experimental and theoretical activities on

- initiation and ignition processes
- investigation of combustion and detonation phenomena
- plume signature
- improved diagnostics and measurement techniques

The 32nd International ICT Annual Conference will act as a forum to review the state of the art, to present new methods and results and to improve comprehension of energetic materials.

Chairman of the Conference

Dr. Lukas Deimling
Fraunhofer ICT, Pfinztal, D

July 3 - July 6, 2001
Karlsruhe, Congress Center
Stadthalle, Weinbrenner-Saal

Federal Republic of Germany

Vorbemerkung

Die Themen unserer Jahrestagung haben wieder ein breites internationales Echo gefunden. Die große Anzahl von eingegangenen Beiträgen machte, wie in den vergangenen Jahren, eine Einteilung in Vorträge und Poster notwendig. Poster ermöglichen eine intensive Diskussion und eine direkte Rückkoppelung von interessierten Tagungsteilnehmern.

Der vorliegende Tagungsband erscheint zu Konferenzbeginn und enthält die schriftlichen Fassungen der Vorträge und Poster. Aus zeitlichen Gründen mußte die Drucklegung vor Eingang sämtlicher Beiträge erfolgen. Nachträglich eingegangene Manuskripte finden sich im Anhang oder wurden durch die Kurzfassung ersetzt.

Prelimentary Remark

The subjects of the annual ICT-Conference have again found wide international response. The vast number of contributions necessitated - as in previous years - a division into oral presentations and posters. Posters enable an intensive discussion and direct feedback from interested conference participants.

The Conference Proceedings are published at the beginning of the conference and contain the written versions of the presentations and posters. Due to the shortage of time, printing had to commence prior to receipt of all contributions. Subsequently received manuscripts are either included in the Annex or the abstract is printed instead.

TABLE OF CONTENTS

LECTURES

V1
Neuer Oxidator für spezielle pyrotechnische Anwendungen
New Oxidizer for Special Applications in Pyrotechnics

B. Berger, P. Folly, G. Wilfing, R. Kresse

V2
Ignition of a Pyrotechnic Powder by "Hot-Spots" and Ordinary Adiabatic Compression

J.F. Moxnes, G. Odegardstuen

V3
Laser Diode Ignition of the Iron/$KclO_4$ Pyrotechnic Mixture: Experimental and Parametrical Study

F. Opdebeck, P. Gillard, E. Radenac

V4
Plasma Ignition and Combustion

A. Koleczko, W. Ehrhardt, S. Kelzenberg, N. Eisenreich

V5
Plasma Ignition Experiments with a Single-Base Propellant: Comparison between Plasma Jet and Current Injection Configuration

B. Baschung, D. Grune

V6
Gasification of Solid Propellants and Propellant Ingredients under Influence of Thermal Radiation

B.N. Kondrikov, S. Cristoforetti, I.V. Grebenyuk, L.T. DeLuca

V7
The Combustion Mechanism of AP Based Propellant Containing Magnalium

Hiroto Habu, Keiichi Hori, Takeo Saito, Masahiro Kohno

V8
Physics of Combustion of HTPB/Nitramine Compositions

A.A. Zenin, S.V. Finjakov

V9
The Synthesis and Combustion of High Energy Thermoplastic Elastomer Binders

P. Braithwaite, W. Edwards, A.J. Sanderson, R.B. Wardle

V10
Ballistic Testing of Clean Solid Rocket Propellants

L.T. DeLuca, F. Cozzi, S. Manenti, A. Olivani, B. D´Andrea, F. Lillo

V11
The Application of Gel Permeation Chromatography to the Investigation of the Ageing Processes of Nitrocellulose

P.R. Deacon, G.R.A. Kennedy, A.L. Lewis, A.F. Macdonald

V12
Stability Analyses of Double Base Propellants Containing New Stabilisers – Part II –

S. Wilker, U. Ticmanis, G. Pantel, M. Stottmeister, J. Petrzilek, J. Skladal

V13
Formal Kinetics of the Thermal Decomposition of Hexanitrostilbene by Thermal Analysis and Multivariate Regression

T. Rieckmann, L. Lichtblau, R. Schirra, S. Völker

V14
Pyrolysis of Energetic Materials in Inert vs. Reactive Atmospheres

T.B. Brill, R.I. Hiyoshi

V15
Combustion Mechanism of Nitramine Based Solid Rocket Propellants

H. Singh

V16
Analytical Characterization of Insensitive RDX

C. Spyckerelle, L. Donnio, J. Aviles, A. Freche

V17
Review on Safety Aspects of Gun Propellants

A.C. Hordijk, W. Groenewegen, C.A. van Driel, H.W.R. Sabel

V18
The Advantages of Environmental Monitoring for Munition Life Assessment

J. Theobald, C.E. Hobman, D.A. Tod

V19
Shock to Detonation Transition in a PBX Based on RDX

R. Mendes, J. Campos, I. Plaksin, J. Ribeiro

V20
Initiation of High Explosives with Shaped Charge Jets

M. Held

V21
Tandem Warheads with Non-Initiating Effect against Explosive Reactive Armor

R. Gagnaux, F. Häller, M. Bär, B. Gisler, O. Rickli

V22
Ablative Acceleration of Thin Flyer Plates

Y. Haas, S. Cogan

V23
Performance Testing of Percussion Caps

T.T. Griffiths, R.J. Duncombe, C.J. Hutchinson

V24
Hexanitrostilbene (HNS) Development for Modern Slapper Detonators

S.M. Harris, S.E. Klassen, W.T. Quinlan, D.M. Cates, R. Thorpe

V25
Thermal Decomposition of Trinitrotoluene (TNT) with a new one-dimensional Time to Explosion (ODTX) Apparatus

T.D. Tran, L.R. Simpson, J. Maienschein, C. Tarver

V26
2,2-Dinitro-ethene-1,1-diamine (FOX-7) – Properties, Analysis and Scale Up

H. Östmark, H. Bergman, U.Bemm, P. Goede, E. Holmgren, M. Johansson, A. Langlet, N.V. Latypov, A. Pettersson, M.-L. Pettersson, N. Wingborg, C. Vörde, H. Stenmark, L. Karlsson, M. Hihkiö

V27
Evaluation of Crystal Defects by the Shock Sensitivity of Energetic Crystals suspended in a Density-Matched Liquid

R.H.B. Bouma, A.E.D.M. van der Heijden

V28
Development of a Practical Reduced Sensitivity Composition B Replacement

J. Niles, D. Doll

V29
Measurement Techniques in Cook-Off Research at the TNO Prins Maurits Laboratory

G. Scholtes, N. van der Meer, R. Bouma, J. Makkus, F. Jacobs, R. van Esveld, A. van der Steen, L. Cheng

V30
Cook off Verhalten von Sprengstoffen

R. Wild, T. Eich

V31
Irregularities of Detonation Wave Structure and Propagation in PBX

I. Plaksin, J. Campos, J. Ribeiro, R. Mendes

V32
Characterization of Coating for Energetic Materials

M. Mezger, S. Nicolich, R. Yacizi, D. Kalyon

V33
Evaluation of Modified JP-10 Fuels for Pulse Detonation Engine

C. Dubois, S. Ringuette, R. Stowe

V34
Ignition and Burning Behaviour of Propellants induced by Nanoparticles

V. Weiser, N. Eisenreich, S. Kelzenberg

V35
An Investigation on Submicron Metal Particles Influence on Burning Rate of Porous Composite Fuels

A.N. Ischenko, Y.P. Khomenko, Y.A. Biryukov, A.T. Roslyak, N.M. Samorokova, N.N. Parfenov

V36
Expertise of Nanometric Aluminium Powder on the Detonation Efficiency of Explosives

A. Lefrancois, C. Le Gallic

V37
The Effect of Ultrafine Aluminium Powder on the Detonation Properties of Various Explosives

P. Brousseau, M.D. Cliff

V38
Rheologische Eigenschaften nanoskaliger Aluminium-Suspensionen
Rheology of nano-scaled Aluminium Suspensions

U. Teipel, U. Förter-Barth

V39
IRSIM (IR-Signatur-Modell) – Ein neues Programm zur Berechnung von Abgasstrahl-Signaturen
IRSIM (IR-Signature-Model) – A new Computational Model for Calculating Exhaust Plume Singnatures

H. Benk

V40
IR-Signatures of Rocket Exhaust Plumes

L. Deimling

V41
Modern Measurement Techniques for Energetic Materials

Y.M. Timnat

V42
Combustion Characteristics and Screening Capability of Red Phosphorus-Based Mixtures

S. Cudzilo

V43
Designing Advanced Gun Propellants with Improved Energy Release

R.L. Simmons, C.M. Walsh

POSTER PRESENTATIONS

P44
Explosive Characteristics of Aluminized Plastic Bonded Explosives based on Octogen and Polyurethane Binder

M.A. Radwan

P45
Stress Strain Properties of Nitramine Composite Rocket Propellants

M.A. Radwan

P46
Effect of Copper Chromite Particle Size on the Combustion Process of a Plastisol Propellant Part I: Thermal Investigations by DSC

A. Mouloud, M.A. Benmahamed

P47
The Final State and Intermediate Steps in Conjugate Detonation Theory

Shaoming Hu

P48
Supercritical Fluid Technology: A New Process on Formation of Energetic Materials

H. Kröber, W. Reinhard, U. Teipel

P49
Zur Kristallisation von Ammoniumdinitramid (ADN)
On the Crystallization of Ammonium Dinitramide (ADN)

U. Teipel, T. Heintz

P50
A Convenient Method for Preparation of Pentaerythritol Diazido Dinitrate (PDADN)

Zhang Lijie, Guo Shaojun, Su Tianduo, He Guoshu

P51
Dynamic Vapour Sorption Studies of Pyrotechnics

T.T. Griffiths, R.J. Duncombe, J. Hutchinson

P52
Inflation of Elastic Airbag under Water – Experiment and Calculations

A.B. Vorozhtsov, S.S. Bondarchuk, A.E. Salko, V.P. Zima

P53
Zerkleinerung energetischer Materialien in wässrigen Suspensionen
Size Reduction of Energetic Materials in Aqueous Phase

I. Mikonsaari, U. Teipel

P54
Production of Commercial Naphtylamine Explosives

Jianlan Cui, Duanlin Cao, Jingcai Cheng, Yajun Xing

P55
Production of High-Detonation Nitro-Compositions from Waste Polystyrene

Duanlin Cao, Jianlan Cui, Jianwen Guo, Jingcai Cheng, Chunlei Xuan

P56
Studies on Crystal Conversion of α-HMX into β-HMX and its Separation

Duanlin Cao, Jianlan Cui, Jingcai Cheng

P57
The Influence of Fluorine-Containing and Fast Burning Additives on Combustion of Highly Metallized Mixtures

V.E. Zarko, V.N. Simonenko, A.B. Kiskin, S.V. Larionov, Z.A. Savelyeva

P58
Anomalous Combustion of NEPE Propellant with Defects

Du Lei, He Guoqiang, Cai Timin, Liu Peijin, Wang Guohui

P59
Study on Combustion of New Energetic Nitramines

V.P. Sinditskii, V.Y. Egorshev, M.V. Berezin

P60
Heat-Mass Transfer and Ignition in Ring Vortex

V.P. Samsonov, M.V. Alekseev

P61
About some Singularities Laminar Diffusion Dust Flames in Co-Flowing Oxidizer

N.I. Poletaev, J.I. Vovchuk, A.V. Florko

P62
Radiation Heat Exchange in Burning Dispersive Systems

I.A. Florko, A.V. Florko, N.I. Poletaev, V.G. Shevchuk

P63
Investigations of GAP Prepolymers with NMR and MALDI-TOF Mass Spectrometry

M. Kaiser, B. Ditz, C. Völkl

P64
Use of a Cylinder Test for Determining some Characteristics of Explosives

W.A. Trzcinski

P65
The Study and Caculate of Output of Carbon on Burning Surface of DB and CMDB propellants

Wang Jiang-Ning, Wang Bai-Cheng, Zhang Rui-e

P66
Accumulation of Catalysts on the Surface of Solid Strands in the Course of Burning

N.N. Bakhman

P67
Study and Optimization of Aerozol Fire-Extinguishing Propellants Based on the Modified Phenol-Formaldehyde Resin

D.L. Rusin, A.P. Denisjuk, Y.G. Shepelev, D.B. Mikhalev

P68
Characterization of a Canadian Unexploded Ordnance Impacted Range for Potential Contamination by Energetic Materials

S. Thiboutot, G. Ampleman, A. Gagnon, A. Marois

P69
Thermodynamic TDS Code: Application to Detonation Properties of Condensed Explosives

S.B. Victorov, S.A. Gubin, I.V. Maklashova, I.I. Revyakin

P70
A Study on Friability Test to Assess the Impact Sensitivity of Insensitive Explosives

Sung-Ho Kim, Jung-Su Park, Jeong-Kwan Lee, Jeong-Kook Kim

P71
Structural Characterization and Thermal Decomposition Mechanism of some Lanthanide-NTO Complexes

Jae-Kyung Kim, Bang-Sam Park, Chong-Hyeak Kim, Sock-Sung Yun

P72
Catalytic Combustion of Liquid Rocket Fuel 1,1 Dimethylhydrazine

Z.R. Ismagilov, M.A. Kerzentsev, I.Z. Ismagilov, V.A. Sazonov, V.N. Parmon, G.L. Elizarova, O.P. Pestunova, V.A. Shandakov, Y.L. Zuev, L.N. Rolin, V.N. Eryomin, N.V. Pestereva

P73
About some Features of Synthesis NTO

A.R. Basal, V.L. Zbarsky, V.F. Zhilin

P74
Particular Features of Aromatic Acid and Aldehyde Nitration

N.V. Yudin, V.L. Zbarsky

P75
A New Method of Preparation of Nitro Derivatives of Octahydro-2H-Imidazo(4,5-b)Pirazin-2-One

G.F. Rudakov, V.F. Zhilin, E.V. Veselova, A.G. Moiseev

P76
Impact Sensitivity and Explosion Heat of HMX/META-Carborane Compositions

V.A. Teselkin, M.N. Makhov

P77
Explosive Performance of Aluminised NQ-Based Compositions

M.F. Gogulya, A.Y. Dolgoborodov, M.A. Brazhnikov, M.N. Makhov, V.I. Arkhipov

P78
Sensitivity and Properties of Energetic Materials Database

V.P. Sinditskii, V.V. Serushkin, V.Y. Egorshev, G.V. Belov

P79
Investigation of Chemical and Catalytical Activity of Fine Metal Powders

E.E. Sirotkina, N.S. Kobotaeva, N.V. Svarovskaya, T.S. Skorohodova, V.S. Sedoi

P80
Characterization of Ultra-Fine Powders Produced by the Exploding Wire Method

V.S. Sedoi, V.V. Valevich

P81
Detonation Behavior of Emulsion Explosives

Yoshikazu Hirosaki, Kenji Murata, Yukio Kato, Shigeru Itoh

P82
Mathematical Modeling of the Long Tubular Solid-Propellant Element Anomalous Ignition in the Semi-Closed Volume

A.N. Lukin

P83
New Method of Prevention of the Anomalous Combustion Regimes Development in the Large-Sized SPRM

A.N. Lukin

P84
Ignition and Combustion Studies on Formalazine

M. Varma, R.K. Singh

P85
Structure Investigation of Energetic Substances by $^{14}N/^{15}N$ NMR Spectroscopy

Y.A. Strelenko

P86
withdrawn

P87
Computer Modeling of Decomposition Reactions of Hexanitrohexaazaisowurtzitane (CL-20)

A. Porollo, T. Petukhova, V. Ivshin, T. Pivina, B. Korsunskii, O. Golovanov

P88
Burn Rate Studies of Composite Propellants Containing Ultra-Fine Metals

P. Lessard, F. Beaupre, P. Brousseau

P89
New Melt-Cast Explosives based on Energetic Thermoplastic Elastomers

P. Brousseau, G. Ampleman, S. Thiboutot, E. Diaz

P90
Laboratory Testing of TNAZ Mixtures

P. Marecek, K. Dudek, P. Vavra

P91
Relationship between Crystal Shape and Explosive Properties of K-6

H. Ritter, S. Braun, M. Schäfer, H.R. Aerni, H.R. Bircher, B. Berger, J. Mathieu, A. Gupta

P92
Determination of New Values of Enthalpies of Formation of Nitrogen-Containing Organic Radicals

Y.D. Orlov

P93
The Modern Database on Enthalpies of Formation of Nitrogen-Containing Organic Radicals

Y.D. Orlov

P94
Catalytic Oxidation of UDMH for Solution of Environmental Problems of Missilery

O.P. Pestunova, G.L. Elizarova, M.A. Kerzhentsev, Z.R. Ismagilov, V.N. Parmon

P95
Mono- and Bisdiaziridines with High Formation Enthalpy

N.N. Makhova, N.Z. Kamalova, T.V. Chabina, V.Y. Petukhova, T.S. Pivina

P96
Solid Propellant Combustion under Shock Wave Loading

A.Y. Dolgoborodov, V.N. Marshakov

P97
Explosion Heat and Metal Acceleration Ability of High Explosives

M.N. Makhov

P98
Peculiarities of Solid Propellants Ignition by CO_2-Laser Radiation

B.N. Kondrikov, S. Cristoforetti, L.T. DeLuca

P99
Thermal Decomposition of Liquid Polynitroesters in a Broad Range of Temperatures and Pressures

B.N. Kondrikov, E.K. Alyoshkina

P100
Unconventional Properties of Ultrafine Energetic Materials

M.J. Gifford, A. Chakravarty, M.W. Greenaway, S. Watson, W.G. Proud, J.E. Field

P101
Phase Transformations in Hexanitrohexaazaisowurtzitane

N.V. Chukanov, N.I. Golovina, V.V. Nedelko, V.V. Dubikhin, S.A. Voschikova, O.A. Ananina, T.S. Larikova, G.M. Nazin, S.M. Aldoshin, B.L. Korsounskii, F. Volk

P102
The Energy Properties of the Nitro- and Nitratederivatives Adamantanes

Y.N. Matyushin, V.P. Lebedev, E.A. Miroshnichenko, L.M. Kostikova, Y.O. Inosemzev

P103
Enthalpy Characteristics of the Polynitroamines

E.A. Miroshnichenko, L.M. Kostikova, J.O. Inozemtcev, Y.N. Matyushin

P104
Efficient Energies of Interaction of Functional Groups and Energies of Dissociation Bonds in Alkylnitrates

L.M. Kostikova, E.A. Miroshnichenko, J.O. Inozemtcev, Y.N. Matyushin

P105
Thermochemical Characteristics of Salts MEDINA and EDNA

Y.N. Matyushin, T.S. Konkova, E.A. Miroshnichenko

P106
Damage Models for Service Life Prediction

C. Hobman, B. Downes, D. Tod

P107
Development of Very Energetic Binder System Ingredients (PGN and DGTN)

A.J. Sanderson, L.F. Cannizzo, R.M. Hajik, T.K. Highsmith, L.J. Martins

P108
Development of an Alternate Process for the Synthesis of CL-20

L. Cannizzo, S. Hamilton, A. Sanderson, R. Wardle, S. White

P109
Cook-Off Research at the TNO Prins Maurits Laboratory, Part II

G. Scholtes, R. Bouma, J. Makkus, M. Boers, A. van der Steen

P110
EXPLO5 – Computer Program for Calculation of Detonation Parameters

M. Suceska

P111
Luminosity of Shock Waves in Perfluoroalkanes, Perfluoroalkylamines and Perfluorotoluene

I.M. Voskoboinikov

P112
The Limits of Shock-Initiated Explosion in liquid Bisfluorodinitroethylformal (FEFO) and 1,6-Diazido-2-Acetoxyhexane – Critical Diameters of Detonation of Bisfluorodinitroethylformal Solutions

I.M. Voskoboinikov, S.A. Dushenok, A.A. Kotomin

P113
The Temperatures of Shock Fronts at some Liquid Hydrocarbons with Chemical Composition C_5H_8

I.M. Voskoboinikov, M.F. Gogulya

P114
The Ignition of Ethanol Azide Individual Drops

V.V. Golovko, A.K. Kopeyka, E.A. Nikitina

P115
Study of the Effect of Polymer Coating on Aluminium Agglomeration

O.G. Glotov, V.E. Zarko, V.A. Shandakov, D.A. Yagodnikov

P116
Thermische Charakterisierung von Treibladungspulver
Thermal Characterization of Propellants

P. Mäder, H.R. Bircher, B. Berger, P. Folly

P117
Thermal Decomposition and Combustion of 2-Methyl-5-Nitrotetrazole

V.I. Kolesov, V.P. Sinditskii, V.Y. Egorshev, B.A. Lurie, M.Y. Soloviev

P118
Instability in Propellant Channel Inflammation

I.G. Assovskii, O.A. Kudryavtsev

P119
Porous Graphitic Carbon (PGC) – A Convenient Column Packing Material for the HPLC Analysis of FOX-7

E. Holmgren, P. Goede, N. Latypov, C. Crescenzi, H. Carlsson

P120
2,2-Dinitro-1,3-Bis-Nitrooxy-Propane (NPN): A New Energetic Plasticiser

N. Wingborg, C. Eldsäter

P121
Some Characteristics of the Potassium 4,6-Dinitrobenzofuroxan Thermal Decomposition

B. Lurie, M. Dobbagh

P122
Effect of Alex and Boron Additives on Ignition and Combustion of Al-KNO_3 Mixture

V.N. Simonenko, V.E. Zarko, A.B. Kiskin, V.S. Sedoi, Y.A. Biryukov

P123
Study of Combustion Characteristics of the ADN-Based Propellants

O.P. Korobeinichev, A.A. Paletsky, A.G. Tereshenko, E.N. Volkov,
J.M. Lyon, J.G. Carver, R.L. Stanley

P124
Microparticle Formation of 1,3,5,7-tetranitro-1,3,5,7-tetraazacyclooctane by Crystallizations with Ultrasound

Kwang-Joo Kim, Kap-Mo Kim, Jung-Min Lee

P125
Seeded Batch Cooling Crystallization of 3-Nitro-1,2,4-Triazol-5-one

Kwang-Joo Kim, Jung-Min Lee, Hyoun-Soo Kim, Bang-Sam Park

P126
Obtaining of Submicron Particles of Silicon and Study of their Interaction with Nitrogen and Carbon

Y.A. Biryukov, A.T. Roslyak, L.N. Bogdanov

P127
Analysis of Reaction Products of Centralite I in Propellants

J. Petrzilek , J. Skladal, F. Zrcek, M. Prazak, L. Janouskova

P128
Thermal Decomposition of Cellulose Nitro Ethers in Ultra-Thin Layers on Metal Surfaces

V.A. Malchevsky, O.F. Pozdnyakov

P129
Effect of Aging on Thermal Decomposition of Ammonium Perchlorate

M.A. Sadek, M.H. Moeen, M.A. Radwan, H.H. Ameen

P130
The Development of Environmental Logging Devices for Munition Life Assessment

J. Theobald, D.A. Tod, S. Kilvington

P131
Feasibility Study to Use a Laser System for an Insensitive Munition Deflagration Test

M. van Rooijen, E. Lapebie, F. Peugeot, F. Opdebeck, P. Gillard

P132
Sensitivity of Ammonium Perchlorate and AP-Based Mixture to Mechanical Action

G.T. Afanasev, V.M. Makharinskiy, S.M. Muratov, D.P. Trebunskikh

P133
Ballistic Properties of HNF/Al/HTPB Based Propellants

A.E.D.M. van der Heijden, H.L.J. Keizers, L.D. van Vliet, M. van Zelst, W. Groenewegen, F. Lillo, G. Marcelli

P134
Explosive and Ballistic Deactivating Techniques for Neutralizing of Military Ordnance and High Explosive Devices in the Typical IEDD Scenario

S. Al Ketbi, A. Barshaid, S. Alsaabi

P135
Precision required for Parameters in Thermal Safety Simulations

U. Ticmanis, G. Pantel, S. Wilker, M. Kaiser

P136
Formation of Structural and Physicochemical Characteristics of Cellulose Nitrates

V.I. Kovalenko, E.A. Matukhin, G.M. Khrapkovskii

P137
Theoretical Study of the Mechanism of Nitroalkane Gas-Phase Monomolecular Decomposition

G.M. Khrapkovskii, E.V. Nikolaeva, D.V. Chachkov, A.G. Shamov

P138
Synthesis and Characterization of Hydrazinium Azide Hydrazinate

A. Hammerl, T.M. Klapötke, H. Piotrowski, G. Holl, M. Kaiser

P139
New 1,2,4-Triazolyl and Tetrazolyl Derivatives of Nitroguanidine

A.M. Astachov, I.V. Gelemurzina, A.A. Nefedov, L.A. Kruglyakova, R.S. Stepanov, A.D. Vasiliev

P140
Heats of Formation of Energetic Oxetane Monomers and Polymers

R.D. Schmidt, G.E. Manser

P141
Molecular Mechanics Force Field Calculation to Predict Explosive Properties of Organic Nitrocompounds

M. Karthikeyan, P.N. Gadhikar, M.B. Talawar

P142
High Energy Propellants Sintered Boron Based

J.M. Mota, M.A. Martinez, F. Velasco, A.J. Criado

P143
Destruction of TNT by Oxidation with Ozone

M.E. Rabanal, B. Oquillas, M.A. Martinez, A.J. Criado, N. Braojos, A. Perez de Diego

P144
Foamed Propellants with Energetic Binders: Burning Characteristics

A. Meßmer, T.S. Fischer

P145
Thermal Analysis of Hydrazinium Nitroformate (HNF)

S. Löbbecke, H. Schuppler, W. Schweikert

P146
Application of Microreactors for the Nitration of Ureas

J. Antes, T. Türcke, J. Kerth, F. Schnürer, H.H. Krause, S. Löbbecke

P147
WinMOPAC - A helpful Tool for the Simulation of New Energetic Molecules

P.B. Kempa, J. Kerth

P148
Kinetic Model for the Polymerization Reaction of Toluene Diisocyanate with HTPB

S.A. Shokry

P149
About the Burning Behaviour and other Properties of Smoke Reduced Composite Propellants based on AP/CL20/GAP

S. Eisele, K. Menke

P150
New Aspects for Determination of Aging Behaviour of Energetic Materials

E. Geißler, N. Eisenreich, A. Geißler, C. Hübner

P151
Erzeugung schneller gerichteter Ringwirbel für den Impulstransport über mittlere Distanzen
Generation of Fast Directional Vortex Rings for Middlerange Impulse Transport

J. Backhaus

P152
Alterungs- und Nutzungsdauerbewertung von neuartigen Festtreibstoff-Formulierungen mit CL 20, AP und energetischen Weichmachern
Ageing and Service Time Period Assessment of Novel Solid Rocket Propellant Formulations containing CL20, AP and Energetic Plasticizers

M.A. Bohn, S. Eisele

P153
Abbrand von Sandwich-Strukturen mit wechselweise angeordneten Oxidator-Brennstoff-Paaren
Combustion of Oxidizor-Fuel Sandwiches

S. Poller, V. Weiser, S. Hötzeldt, S. Kelzenberg, F. Hidalgo

P154
Modellierung und Experiment von gefrorenen H_2O_2/Methanol-Mischungen
Modelling and Experiments of frozen H_2O_2/Methanol Mixtures

V. Weiser, C. Besnard, S. Kelzenberg, S. Poller

P155
Modellierung des Einflusses thermischer Stoffeigenschaften auf das Abbrandverhalten fester Treibstoffe
Modelling of the Influence of Thermal Properties on the Burning Behaviour of Solid Propellants

V. Weiser, S. Kelzenberg, N. Eisenreich, C. Moya

P156
withdrawn

P157
Solvent Effects on the Morphology of ε-CL-20 Crystals

V. Thome, P.B. Kempa, M. Herrmann

P158
High Speed Mechanical Testing of Solid Polymeric Materials

O. Jedicke, C. Hübner, A. Moreno Martin, N. Eisenreich, A. Herzog, K. Zilly

P159
Thermo-mechanical Properties of Special Polymeric Materials

O. Jedicke, A. Moreno Martin, N. Eisenreich

P160
Characterization and Development of Gas Generators for Fire Extinguishing Systems

J. Neutz, T. Fischer, H. Ebeling, M. Klemenz, V. Weiser

P161
The Effects of Color Changing on Thermal Stability and Compatibility of TATB

Huang Yi-gang, Wang Xiao-chuan, Li Guang-lai, Wang Lin

P162
The Contacted Compatibility of PBX and Polyurethane

Luo Xuemei, Zuo Yufen, Xu Ruijuan

P163
Emissionsspektren brennender Metalle
Emissionsspektra of Burning Metals

E. Roth, Y. Plitzko, V. Weiser, W. Eckl, H. Poth, M. Klemenz

P164
Abbranduntersuchungen an flüssigen und gelförmigen Mischungen von Nitromethan und H_2O_2
Combustion of Liquid and Gelled Mixtures with Nitromethan and H_2O_2

V. Weiser, F. Hidalgo, Y. Plitzko

P165
Verbrennungsmodellierung mit Hot Spots
Combustion Modelling with Hot Spots

S. Kelzenberg, N. Eisenreich, T. Fischer, A. Koleczko

P166
Synthesis and Characterization of 2,6-Diamino-3,5-Dinitropyrazine-1-Oxide (NPEX-1)

J. Kerth, W. Kuglstatter

NEUER OXIDATOR FÜR SPEZIELLE PYROTECHNISCHE ANWENDUNGEN

New Oxidizer for Special Applications in Pyrotechnics

B. Berger, P. Folly
Gruppe Rüstung. Fachabteilung Waffensysteme und Munition
Feuerwerkerstrasse 39, CH-3602 Thun

G. Wilfing, R. Kresse
Chemetall GMBH
Trakehner Strasse 3, D-60487 Frankfurt am Main

Kurzfassung

Das Oxidationsmittel Cesiumnitrat wird u.a. in pyrotechnischen Mischungen zur Erzeugung von IR-Licht verwendet. Es weist jedoch hygroskopische Eigenschaften auf. Als Ersatz für diesen Oxidator wurde das, gegenüber Feuchtigkeitseinflüssen unempfindliche, Cesiumperchlorat synthetisiert. Die aus dem durchgeführten Synthese-Prozess hervorgehende Korngrössenverteilung sowie weitere physikalisch-chemische Daten wurden bestimmt und mit den Literaturwerten verglichen.

Zur Untersuchung der Verwendungsmöglichkeit von Cesiumperchlorat in pyrotechnischen Redoxsystemen wurden Mischungen mit positiver, ausgeglichener und negativer Sauerstoffbilanz von Titan/Cesiumperchlorat hergestellt und bezüglich Umsetzungsgeschwindigkeit, Reaktionswärme, Empfindlichkeit gegenüber mechanischen und thermischen Einflüssen untersucht. Die Resultate sind, bis auf die Reaktionswärme, mit den Werten des gut dokumentierten pyrotechnischen Redoxsystems Titan/Kaliumperchlorat vergleichbar.

Abstract

The oxidizer cesium nitrate is used in military pyrotechnics to produce IR radiation. However it shows slight hygroscopic effects. As a substitute cesium perchlorate, which shows less hygroscopic properties, could be used. Cesium perchlorate was synthesized by using cesium hydroxide or cesium carbonate and perchloric acid. Physical and chemical data of the new oxidizer were determined and compared with available data from literature.

In a next step compositions with negative, balanced and positive oxygen ratio of the redox system titanium/cesium perchlorate were mixed and some of the most important pyrotechnical parameters of this compositions were determined. The results show that the burning rate, the handling safety as well as the thermal stability are comparable to the values of the well documented pyrotechnic redox system titanium / potassium perchlorate.

1. Einleitung

Seit Jahrzehnten werden sowohl in der militärischen wie auch in der zivilen Pyrotechnik stets die gleichen Reduktions– und Oxidationsmittel verwendet. Unterschiedlichste Leistungen und Effekte werden durch Änderung der Sauerstoffbilanz, durch Verwendung verschiedener Korngrössen des Reduktions- und/oder Oxidationsmittels, durch Variation der hergestellten Granulatgrösse, durch Zugabe von Hilfssubstanzen, durch Variation der Menge an pyrotechnischer Mischung und durch verschiedenartiges Design der Umhüllung erreicht.

Die in der militärischen Pyrotechnik häufig verwendeten Reduktionsmittel sind fein-körnige Pulver (Partikeldurchmesser 3-20µm) von Zirkonium, Titan, Magnesium, Bor, Silizium, sowie verschiedene Legierungen davon.

Die wichtigsten Oxidatoren sind anorganische Salze wie Natrium-, Kalium- oder Bariumnitrat, Kaliumperchlorat, Bleioxide, Mangandioxid und Strontiumperoxid. Viele dieser Oxidationsmittel sind giftig. Eines der Ziele der Forschungstätigkeit auf dem Gebiet der Pyrotechnik ist die Suche nach neuen, möglichst ungiftigen Oxidationsmitteln. Derartige Untersuchungen haben vor allem für die Airbag-Technologie grosse Bedeutung [1].

Im Rahmen von Studien bezüglich Tarnen von Wärmequellen gegenüber der Detektion durch Wärmebildkameras wurde u.a. in den Nebel / Rauchmischungen das Oxidationsmittel Cesiumnitrat verwendet. Die Reaktion dieses Oxidators bewirkt eine kurzzeitige Störung der Wärmebilder. Dieser Effekt ist auf die anlässlich der Umsetzungsreaktion von Cesiumnitrat entstehenden Reaktionsprodukte sowie auf anschliessend stattfindende Reaktionen zurückzuführen [2]. So wird Cesiumnitrat bei der Reaktion mit dem Energieträger über mehrere Zwischenstufen zu Di-Cesiumoxid umgewandelt, das danach seinerseits in einer stark exothermen Reaktion zu Cesiumhydroxid weiter reagiert.

$$CsNO_3 \xrightarrow{O_2} Cs_2O \xrightarrow{H_2O} CsOH$$

Die beschriebenen Effekte der Reaktion von Cesiumnitrat mit einem Reduktionsmittel beziehungsweise der nachfolgend ablaufenden Reaktionen werden auch in der modernen Gefechtsfeldbeleuchtung genutzt. Das Gefechtsfeld wird dabei mit Licht im nahen IR-Bereich (700 bis 1000nm) beleuchtet [3]. Cesiumnitrat weist jedoch hygroskopische Eigenschaften auf.

Die Problematik von ungiftigen, nicht hygroskopischen und trotzdem leistungsstarken Oxidatoren ist natürlich auch dem europäischen Hersteller vieler Reduktionsmittel für die militärische Pyrotechnik, der Firma Chemetall, bekannt. Auf Grund diesbezüglicher Dis-

kussionen erklärte sich Chemetall bereit, das bisher auf dem Markt nicht erhältliche Cesiumperchlorat zu synthetisieren. Die Fachgruppe Pyrotechnik der Gruppe Rüstung untersuchte anschliessend die Verwendbarkeit von Cesiumperchlorat in der militärischen Pyrotechnik. Dazu wurden einige pyrotechnisch relevante Leistungsparameter von Cesiumperchlorat enthaltenden Mischungen ermittelt.

2. Ausgangssubstanzen

2.1 Cesiumperchlorat ($CsClO_4$)

Es ist an dieser Stelle nicht möglich, die vollständige Synthese bekannt zugeben. Nachfolgend ist jedoch eine allgemeine Beschreibung des Herstellungsprozesses aufgeführt.
Cesiumhydroxid oder Cesiumcarbonat wird mittels Perchlorsäure neutralisiert. Auf Grund seiner schlechten Löslichkeit in Wasser fällt das entstehende Cesiumperchlorat sofort aus der Lösung aus. Das Reaktionsprodukt wird anschliessend in einem Trockenschrank auf Gewichtskonstanz getrocknet [4].

$$CsOH + HClO_4 \text{ ----------> } Cs\,ClO_4 + H_2O \qquad (1)$$

Das anfallende Reaktionsprodukt weist folgende Korneigenschaften auf:
Mittlere Korngrösse (gemessen nach dem Verfahren von Malvern[1]): 34.9 µm
Spezifische Oberfläche gemäss dem Verfahren von Malvern: 0.1 m^2/g

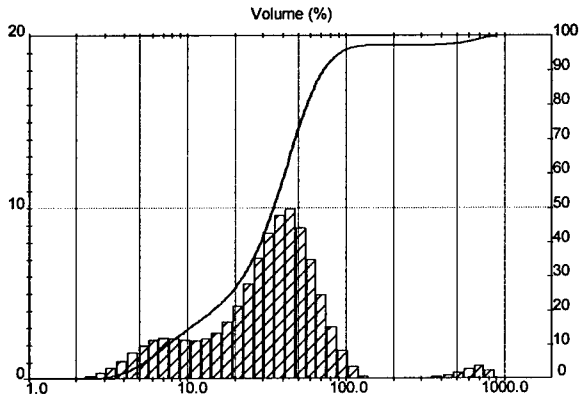


Abbildung 1: Korngrössenverteilung des $CsClO_4$

[1] Verfahren nach Malvern: Laserbeugungsinterferrometrie zur Bestimmung der Korngrösse

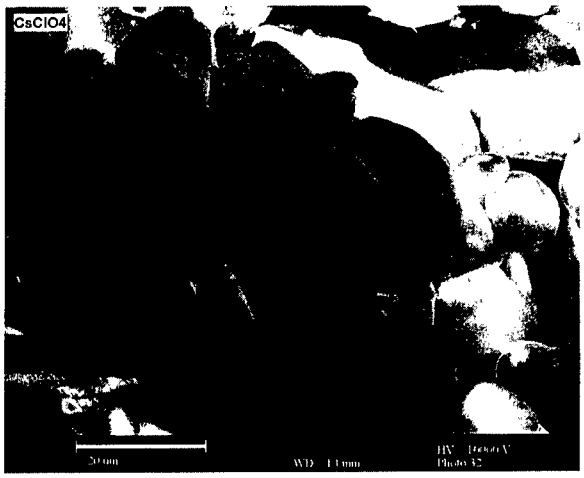


Abbildung 2: Rasterelektronenmikroskop - Aufnahme von $CsClO_4$-Kristallen

Das thermische Verhalten von Cesiumperchlorat zeigt die nachfolgende Abbildung.

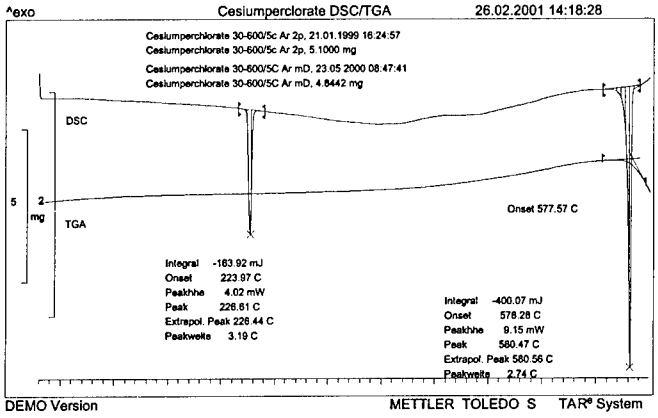


Abbildung 3: DSC[2] / TGA[3] Ausdruck von Cesiumperchlorat

Die DSC–Aufzeichnung zeigt, analog wie bei Kaliumperchlorat, bei 226°C eine Endothermie. Diese ist auf die Umwandlung der kubischen Cesiumkristalle in die rhombische Form zurückzuführen [5]. Die zweite Endothermie bei 580°C wird vom Schmelzvorgang der Substanz hervorgerufen. In der TGA–Aufzeichnung ist bei einer Onset–Temperatur[4]

[2] DSC: Differential Scanning Calorimetry
[3] TGA: Thermal Gravimetry
[4] Onset-Temperatur: Begriff für die Temperatur bei der ein thermischer Effekt beginnt. Es ist der Schnittpunkt der extrapolierten Basislinie vor dem Effekt mit einer Tangente an die durch den Effekt verursachten Kurve.

von 577°C der Beginn eines Gewichtsverlustes sichtbar. Dieser Vorgang weist auf eine Zersetzung des Cesiumperchlorates hin. Der Vergleich der Onset–Temperatur des Schmelzvorganges (DSC–Aufzeichnung) von 580°C mit derjenigen des Zersetzungsvorganges von 577°C zeigt, dass praktisch mit Beginn des Schmelzvorganges auch die Zersetzung des Cesiumperchlorates beginnt.

2.2 Das Reduktionsmittel: Titanmetallpulver (Ti), Typ E

Das verwendete Titanmetallpulver wurde ebenfalls von der Firma Chemetall Gmbh in Frankfurt hergestellt. Eine detaillierte Spezifikation befindet sich im Anhang.

Das Reduktionsmittel weist die folgenden Korneigenschaften auf:

Korngrösse (gemessen nach dem Verfahren von Blaine) :	3.0 µm
Korngrösse (gemessen nach dem Verfahren von Malvern) :	9.5 µm
Spezifische Oberfläche gemäss dem BET - Verfahren :	3.2 m^2/g
Spezifische Oberfläche gemäss dem Verfahren von Malvern:	1.2 m^2/g

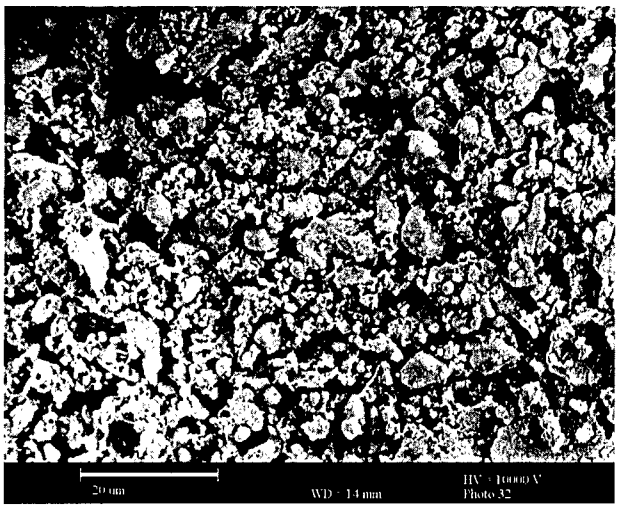


Abbildung 4: REM[5] – Aufnahme des verwendeten Titanmetallpulvers

Neben einem Grossteil Titanpartikel mit einem kleinen Korndurchmesser sind auf der REM - Aufnahme auch einige Körner mit einem Durchmesser von 15 bis 20 µm feststellbar. Praktisch keiner der hier abgebildeten Partikel weist eine ideale Kugelform auf.

Das Verhalten von Titanmetallpulver Typ E bei thermischer Einwirkung zeigt die folgende Abbildung

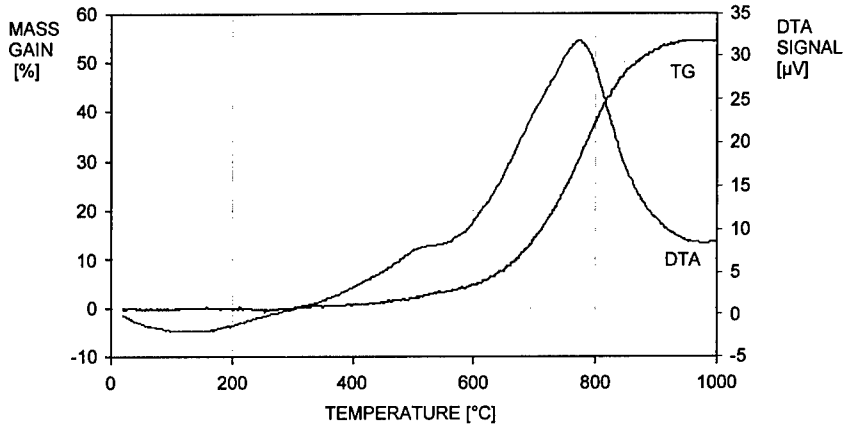


Abbildung 5: DTA[6] und TGA Kurve von Titanmetallpulver

Auf der TGA-Kurve ist deutlich zu erkennen, dass ab einer Temperatur von 400°C langsam die Oxidationsreaktion des Titanpulvers beginnt. Im Temperaturbereich von 600 bis 800°C wird anschliessend der Grossteil des Titanpulvers oxidiert. Die gleiche Aussage liefert die DTA-Kurve. Auch hier ist zwischen 400 und 500°C ein schwacher exothermer Vorgang sichtbar, der ab 600°C in eine starke Exothermie mit einem Maximum bei ca. 760°C übergeht.

Als Binder wird Nitrocellulose (NC), Typ 220 E mit einem N–Gehalt von 13.2 %, hergestellt durch die Firma WASAG Nitrochemie, verwendet.

3. Hergestellte und untersuchte Mischungen

Das Titan- und das Cesiumperchloratpulver wird in einem Turbulamischer während zweier Mischsequenzen gemischt. Anschliessend erfolgt die Zugabe der, in einem Aceton / Ethanol - Gemisch gelösten Nitrocellulose. Sie wird als Binder zum Granulieren der feinpulverigen Mischung verwendet. Die vorgetrocknete Mischungsmasse wird mittels Sieben der Maschenweite 0.75 und 0.5 mm granuliert. In einem Vakuumofen erfolgt bei 60°C die Entfernung der noch vorhandenen Lösungsmittelreste.

Tabelle 1: Zusammensetzung der untersuchten Mischungen

Substanz	Zusammensetzung [Gew.%]											
Ti	10	20	25	29*	30	35	40	50	60	70	80	90
$CsClO_4$	89	79	74	70	69	64	59	49	39	29	19	9
NC	1	1	1	1	1	1	1	1	1	1	1	1

[5] Raster – Elektronen - Mikroskop
[6] Differential Thermal Analysis

Für das vorliegende Redoxsystem wird üblicherweise die folgende Reaktionsgleichung postuliert:

$$2Ti + CsClO_4 \text{ -------> } 2TiO_2 + CsCl \quad (2)$$

Gemäss dieser Reaktionsgleichung enthält die Mischung mit ausgeglichener Sauerstoffbilanz 29.2 Gew.% Titan*.

Einige Daten der Ausgangssubstanzen sowie möglicher Reaktionsprodukte sind in der nachfolgenden Tabelle zusammengestellt.

Tabelle 2: Schmelz- und Siedetemperaturen der Verbindungen des Redoxsystems [5,6]

Substanz	Schmelzpunkt [°C]	Siedepunkt [°C]
Titan (Ti)	1660	>3000
Titan-II-oxid (TiO)	1750	>3000
Titan-IV-oxid (TiO_2	1850	>3000
Titan-III-oxid (Ti_2O_3)	1900-2130[d]	---
Cesiumperchlorat ($CsClO_4$)	zersetzt[7]	---
Cesium (Cs)	28.5	690
Cesiumchlorid (CsCl)	642	1300

[d]) decomposition

4. Untersuchte Reaktionsparameter

In diesem Abschnitt sind einige wichtige Parameter von militärischen Pyrotechnika aufgeführt und die zu ihrer Bestimmung verwendeten Messverfahren kurz beschrieben. Weitergehende Informationen zu den einzelnen Messverfahren sind in der zitierten Literatur zu finden [7, 8].

- ***Umsetzungsgeschwindigkeit*** (Standardmessverfahren der FG Pyrotechnik)
  Sie wird in einer Brennschiene über eine Messstrecke von 20 cm gemessen. Die Detektion der Flammfront erfolgt über Lichtleiter. Die Mischungen werden mittels eines elektrischen Glühdrahtes angefeuert.

- ***Reaktionswärme***
  Die während der Redoxreaktion freigesetzte Reaktionswärme wird in einem adiabatischen Kalorimeter des Typs IKA C 4000 unter 30 bar Helium gemessen.

- ***Brisanz*** (vergl. Anzündverzögerung)

- ***Max. Gasdruck*** (vergl. Anzündverzögerung)

[7] Siehe DSC - und TGA - Aufzeichnungen im Anhang.

- Anzündverzögerung

Die Bestimmung dieser drei Grössen erfolgt mittels einer modifizierten Differenzgasdruckmessanlage von Diehl [7]. Die dazu verwendete Druckbombe hat ein Volumen von 20 cm^3, die Ladedichte beträgt 0.15 g/cm^3. Die Anzündung der pyrotechnischen Mischung wird mittels eines normierten Glühbrückenelementes der Fa. Ems–Patvag durchgeführt.

- Sicherheitskenndaten

Unter dem Ausdruck **"**Sicherheitskenndaten**"** wird die Empfindlichkeit pyrotechnischer Mischungen gegenüber Schlag, Reibung und elektrostatischen Entladungen verstanden.

Die Schlag- und Reibempfindlichkeit wird gemäss den Prüfverfahren nach BAM (Bundesanstalt für Materialprüfung, Berlin) bestimmt, die Empfindlichkeit gegenüber elektrostatischen Entladungen mit einer selbstentwickelten Prüfmethode [10].

Die Untersuchung der thermischen Stabilität bzw. des thermischen Verhaltens der Mischungen erfolgt mittels Differential-Scanning-Calorimetry (DSC) und Thermal Gravimetry Analysis (TGA). Dazu wird das "Star System" der Firma METTLER TOLEDO eingesetzt.

5. Resultate

5.1 Umsetzungsgeschwindigkeit (Abbrandgeschwindigkeit)

Die Messung der Umsetzungsgeschwindigkeit erfolgt mit dem unter Abschnitt 4 beschriebenen Messaufbau. Die in der nachfolgenden Graphik eingetragenen Werte sind Mittelwerte aus mindestens 3 Messwerten.

Die grösste Umsetzungsgeschwindigkeit des Redoxsystems Ti / $CsClO_4$ beträgt 1.1 m/s und wird bei der Umsetzung der Mischung mit einem Titananteil von 60 Gew.% auf, dh. die Mischung mit einem Reduktionsmittelüberschuss von rund 31 Gew.% bezogen auf die Mischung mit ausgeglichener Sauerstoffbilanz gemäss der Reaktionsgleichung (2) gemessen. Die Umsetzungsgeschwindigkeiten des Redox-systems bewegen sich je nach Zusammensetzung, bzw. nach Sauerstoffbilanz, in einem Bereich von 0.03 m/s (Mischung mit einem Titananteil von 20 Gew.%) bis 1.1 m/s (Mischung mit einem Titananteil von 60 Gew.%). Der Höchstwert von 1.1 m/s ist ca. 0.2 m/s tiefer als derjenige des Redoxsystems Titan Typ E, (gleicher Titantyp wie bei dem hier beschriebenen System) und Kaliumperchlorat.

Die Streuung der Umsetzungsgeschwindigkeitswerte ist, ausser im Bereich des Höchstwertes, klein. Sie liegt zwischen 0.2 m/s (Mischung mit einem Titananteil von 60 Gew.%) und 0.01 m/s (Mischung mit einem Titanteil von 29 Gew.%)

Tabelle 3: Gemessene Umsetzungsgeschwindigkeiten

Anteil Ti [Gew.%]	v_U – Mittelwert [m/s]	v_U – Minimalwert [m/s]	v_U – Maximalwert [m/s]
10	--------[1]		
20	0.034	--------[2]	--------[2]
25	0.167	0.149	0.180
29	0.261	0.256	0.266
30	0.323	0.305	0.337
35	0.420	0.408	0.426
40	0.617	0.599	0.635
50	0.878	0.830	0.943
60	1.140	1.042	1.274
70	0.984	0.948	1.020
80	0.549	0.480	0.613
90	0.102	0.095	0.111

[1]) Die Mischung konnte nicht zur Reaktion gebracht werden.
[2]) Die Mischung konnte nur einmal angefeuert werden.

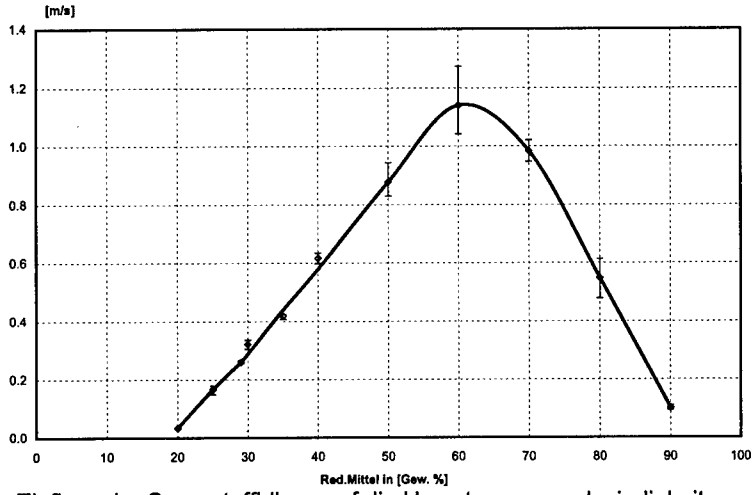


Abbildung 6: Einfluss der Sauerstoffbilanz auf die Umsetzungsgeschwindigkeit

5.2 Reaktionswärme (Verbrennungswärme)

In der nachfolgenden Graphik sind die gemessenen Reaktionswärmen eingezeichnet. Das dazu verwendete Messverfahren ist ebenfalls in Kapitel 4 beschrieben. Zur Zeit ist eine Berechnung der theoretischen Reaktionswärmen nicht möglich, da über Cesiumperchlorat keine ausreichenden thermodynamischen Daten in der Literatur zu finden sind. Es ist jedoch geplant, zusammen mit dem Chemischen Institut der Universität Uppsala die benötigten Daten zu ermitteln und anschliessend mit dem Computer-Code EKVI die

theoretischen Reaktionswärmen und Reaktionstemperaturen der verschiedenen Mischungen zu berechnen.

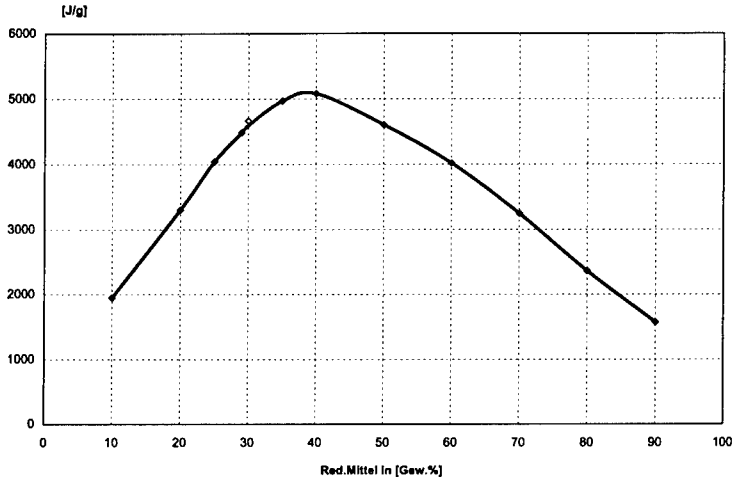


Abbildung 7: Einfluss der Sauerstoffbilanz auf die Reaktionswärme

Die gemessenen Reaktionswärmen liegen, abhängig von der Sauerstoffbilanz der Mischungen, in einem Bereich von 1500 bis 5100 J/g. In Abbildung 7 ist ersichtlich, dass die Werte bis zu einem Titananteil von 30 Gew.% praktisch linear ansteigen. Bei der Mischung mit einem Titananteil von 40 Gew.% wird der Höchstwert des untersuchten Redoxsystems (5080 J/g) gemessen. Bisherige Untersuchungen an pyrotechnischen Redoxsystemen ergaben, dass die Zusammensetzung mit der grössten Reaktionsenthalpie gut mit derjenigen mit ausgeglichener Sauerstoffbilanz gemäss der klassischen Reaktionsgleichung übereinstimmt. Beim vorliegenden Redoxsystem ist dies jedoch nicht der Fall. Gemäss Reaktionsgleichung (2) müsste die Mischung mit einem Titananteil von rund 29 Gew.% die grösste Reaktionswärme liefern. Für diesen Artefakt gibt es zwei mögliche Erklärungen, nämlich dass die Reaktion nicht gemäss der klassischen Reaktionsgleichung (2) abläuft oder aber dass das verwendete Cesiumperchlorat einen grossen Anteil an Verunreinigungen aufweist. Eine diesbezügliche Untersuchung hat ergeben, dass dies nicht der Fall ist.

Im Vergleich zu den bisher untersuchten Redoxsysteme für pyrotechnische Anwendungen, liegen die gemessenen Reaktionswärmen der verschiedenen Mischungen in einem mittleren Wärmebereich. Sie eignen sich kaum als Anzündmischungen für unempfindliche Treibmittel.

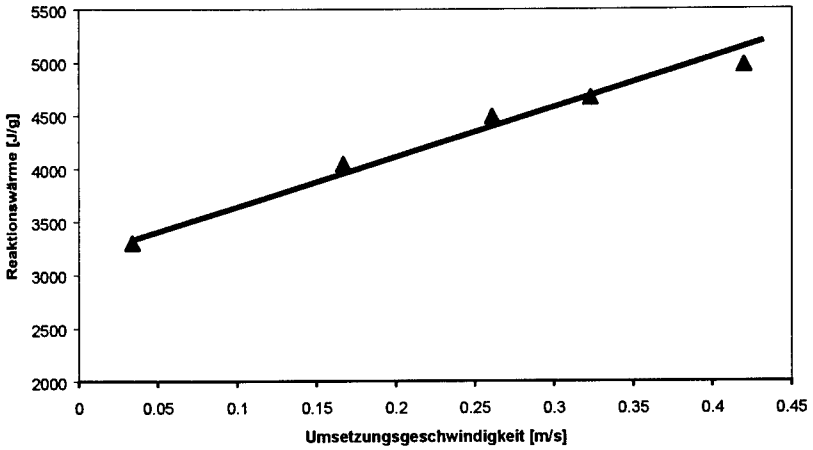


Abbildung 8: Reaktionswärme als Funktion der Umsetzungsgeschwindigkeit für Mischungen mit einem Titananteil von 20 bis 35%.

5.3 Anzündverzögerung

Die Anzündverzögerungszeiten wurden mit dem unter Abschnitt 4 beschriebenen Messverfahren ermittelt. Der Mittelwert basiert auf mindestens drei Messungen.

Tabelle 4: Anzündverzögerungszeit als Funktion der Sauerstoffbilanz

Anteil Ti [Gew.%]	Mittelwert [ms]	Minimalwert [ms]	Maximalwert [ms]
10	-------[1]	-------[1]	-------[1]
20	-------[1]	-------[1]	-------[1]
25	-------[1]	-------[1]	-------[1]
29	112.5	106.7	118.2
30	193.2	157.5	228.9
35	117.1	95.6	138.6
40	45.4	44.0	46.7
50	30.3	30.2	30.4
60	23.2	23.0	23.4
70	23.0	22.4	23.6
80	36.7	32.8	40.5
90	115.8	109.3	121.2

[1]) Die Mischungen liessen sich nur mittels eines Anzündverstärkers anfeuern, die erhaltenen Messwerte liefern deshalb keine Aussage bezüglich Anzündverzögerung.

Die Mischungen mit einem Titananteil von 10, 20 und 25 Gew.% mussten mittels einer empfindlicheren Anzündmischung zur Reaktion gebracht werden. Es konnte deshalb von diesen Mischungen keine gültigen Anzündverzögerungen bestimmt werden. Der Kurvenverlauf der restlichen Messwerte zeigt ein ähnliches Bild wie schon die Brisanz und der

maximale Gasdruck. Die Mischung mit einem Anteil von 30 Gew.% Titan weist ein Maximum auf. Die gemessene Anzündverzögerungszeit beträgt 193 ms. Anschliessend fallen die Werte mit zunehmender negativer Sauerstoffbilanz (zunehmendem Titananteil) bis auf einen Wert von 23 ms. Ab einem Titananteil > 70 Gew.% steigen die Anzündverzögerungswerte wieder an. Die gemessenen Werte liegen etwa im Bereich ähnlicher pyrotechnischer Redoxsysteme wie beispielsweise Titan (E) / Eisen-III-oxid.

5.4 Sicherheitskenndaten

Zur Ermittlung der Schlag- und Reibempfindlichkeit wurden die Prüfverfahren des BAM eingesetzt, die Bestimmung der Empfindlichkeit gegnüber elektrostatischen Ladungen erfolgte mittels einer selbstentwickelten Prüfmethode [8].

Tabelle 5: Reib- und Schlagempfindlichkeit als Funktion der Sauerstoffbilanz

Anteil Ti [Gew.%]	Schlagempfindlichkeit [J]	Reibempfindlichkeit [N]	Empfindlichkeit auf elektrostatische Entladungen [mJ]
10	>20	288	>5600
20	>20	360	>5600
25	>20	240	180
29	20	160	5.6
30	19	192	5.6
35	>20	120	10
40	>20	120	0.56
50	>20	120	1
60	>20	144	1
70	>20	360	1
80	>20	324	0.56
90	>20	360	1

Empfindlichkeit bezüglich Schlageinwirkung

Die Proben wurden auf dem BAM Fallhammer unter Verwendung eines 2 kg Fallgewichtes (ohne Verdämmungsring) auf ihre Empfindlichkeit gegenüber Schlageinwirkung geprüft. Bis auf zwei Ausnahmen zeigen die untersuchten Mischungen bei einer Schlageinwirkung von 20J keine Reaktion, bei den Mischungen mit einem Titananteil von 29 Gew.% (Mischung mit ausgeglichener Sauerstoffbilanz) bzw. 30 Gew.% ist von den 6 untersuchten Proben mindestens bei einer bei 20 bzw. 19.5 J eine Reaktion feststellbar. Diese Resultate bedeuten nach den von uns definierten Einteilungskriterien, dass die Mischungen wenig bis nicht schlagempfindlich sind.

Empfindlichkeit bezüglich Reibung

Die Reibempfindlichkeit der verschiedenen Mischungen wurde mit einem BAM Reibapparat untersucht. Dabei wird die maximale Reibstiftbelastung ermittelt, bei der bei 6 Proben keine Reaktion auftritt, sowie diejenige Stiftbelastung, bei der bei 6 Versuchen mindestens eine Reaktion feststellbar ist.

Mit ansteigendem Titananteil bis 35 Gew.% nimmt die Reibempfindlichkeit der Mischungen zu (120N), bleibt dann bis zu einem Titananteil von 50 Gew.% auf diesem Wert stehen und nimmt anschliessend mit weiter ansteigendem Titananteil wieder ab. Die Mischungen können gemäss unseren Einteilungskriterien als wenig bis mittel empfindlich bezüglich Reibung eingestuft werden. Die maximale Reibempfindlichkeit des Systems Titan E / Kaliumperchlorat beträgt vergleichsweise 20N.

***Empfindlichkeit gegenüber elektrostatischen Entladungen** [8]*

Die Methode zur Bestimmung der Empfindlichkeit von Explosivstoffen ist unter Absatz 4 erwähnt. Zur Ermittlung des kritischen Wertes werden bei jeder Entladungsenergiestufe 6 Messungen durchgeführt. Die kritische Entladungsenergie liegt vor, wenn von den 6 Proben mindestens eine reagiert.

Die maximale elektrostatische Aufladung die ein Mensch unter idealen Bedingungen aufweisen kann, beträgt ca. 50 mJ [9], unter extremen Bedingungen 90 mJ [9].

Mischungen des untersuchten Redoxsystems mit kleinen Titananteilen sind gegenüber ESD unempfindlich (>5600mJ), mit zunehmendem Titananteil (bis 40 Gew.%) werden sie jedoch zunehmend empfindlicher. Mischungen mit Titananteilen grösser 40 Gew.% weisen ESD-Werte im Bereich von 1mJ auf.

Der Vergleich mit anderen pyrotechnischen Redoxsystemen wie zum Beispiel Titan / Kaliumperchlorat lässt eine Einstufung der Mischungen des Systems Titan / Cesiumperchlorat in den Bereich "mittlere Empfindlichkeit" zu.

Empfindlichkeit bezüglich thermischer Belastung

Die Empfindlichkeit der verschiedenen Mischungen auf thermische Belastung wird mit einem DSC / TGA-Gerät untersucht. Die dabei verwendete Aufheizgeschwindigkeit beträgt stets 5°C / min.

Die DSC–Aufzeichnung zeigt bei 229°C eine schwache Endothermie. Sie ist auf die Umwandlung der Cesiumkristalle von der kubischen in die rhombische Form zurückzuführen. Bei 422°C ist eine starke Exothermie sichtbar die von der Redoxreaktion des Titans mit dem Cesiumperchlorat herrührt. Der Ursprung der permanenten Exothermie im

Temperaturbereich von 420 bis 520°C ist wahrscheinlich eine Weiterreaktion der, anlässlich der Hauptreaktion, angefallenen Reaktionsprodukte.

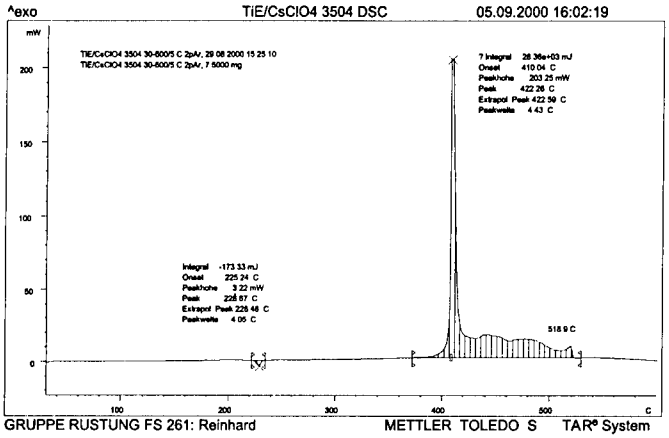


Abbildung 9: DSC–Aufzeichnung der Mischung mit ausgeglichener Sauerstoffbilanz (29 Gew.% Ti / 71 Gew.% $CsClO_4$)

Die SDTA Aufzeichnung zeigt bei einer Temperatur von 231,7°C eine schwache Endothermie. Es handelt sich dabei um die in Abschnitt 2 beschriebene Umwandlung der Cesiumperchloratkristalle von der kubischen in die rhombische Form. Eine starke Exothermie ist bei 406.5°C sichtbar. Es muss sich dabei um die topochemische Redoxreaktion des Titans mit dem Cesiumperchlorat handeln, wobei ein Teil des dabei freigesetzten Sauerstoffes gemäss der TGA–Aufzeichnung unverbraucht das System verlässt (die Zersetzungstemperatur von Cesiumperchlorat liegt bei 580.5°C, vergl. Abschnitt 2). Ab einer Temperatur von rund 650°C bis hin zu 960°C ist auf der TGA–Aufzeichnung ein weiterer Gewichtsverlust von 63% sichtbar. Es könnte sich hier um das Verdampfen von Cesium handeln, das gemäss Literatur einen Siedepunkt von 690°C aufweist.

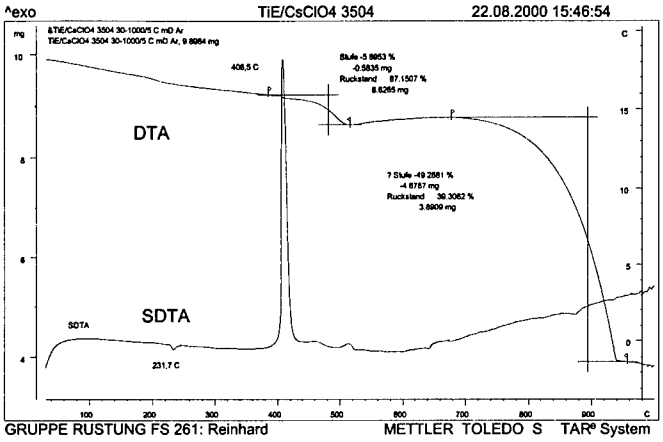


Abbildung 10: TGA / SDTA Aufzeichnung der Mischung mit ausgeglichener Sauerstoffbilanz (29 Gew.% Ti / 71 Gew.% $CsClO_4$)

6. Zusammenfassung / Folgerungen

Die Synthese des neuen Oxidators Cesiumperchlorat wurde beschrieben und verschiedene seiner chemisch-physikalische Parameter bestimmt. Cesiumperchlorat zeigt, ähnlich Kaliumperchlorat, bei 226°C eine Kristallumwandlung von der kubischen in die rhombische Form [5], bei 580°C beginnt es unter Zersetzung zu schmelzen.

Mischungen mit positiver und negativer Sauerstoffbilanz sowie die Mischung mit ausgeglichener Sauerstoffbilanz gemäss der klassischen Reaktionsgleichung des Redoxsystems Titan/Cesiumperchlorat wurden hergestellt und bezüglich ihrer Leistungs- und Sicherheitskenndaten charakterisiert.

Die gemessenen Reaktionswärmen der Mischungen mit positiver oder negativer Sauerstoffbilanz sowie der Mischung mit ausgeglichener Sauerstoffbilanz sind rund 23% kleiner als diejenigen des Redoxsystems Titan / Kaliumperchlorat. Sie liegen jedoch in einem üblichen Reaktionswärmebereich (3000 bis 5000 J/g).

Die Umsetzungsgeschwindigkeiten der verschiedenen Mischungen sind in der gleichen Grössenordnung wie diejenigen entsprechender Mischungen des Redoxsystems Titan / Kaliumperchlorat.

Dies gilt auch für den maximalen Gasdruck und die Sicherheitskenndaten. Einzig die Mischung mit einem Titananteil von 29 Gew.% weist eine geringe Empfindlichkeit gegenüber Schlageinwirkung auf. Die Empfindlichkeiten gegenüber Reibung und elektrostatischen Entladungen liegen in einem für derartige Mischungen typischen Bereich.

Bis zur exothermen Hauptreaktion ist das Verhalten der verschiedenen Mischungen unter thermischer Einwirkung ähnlich derjenigen des Systems Titan / Kaliumperchlorat. Beim Aufheizen der Proben wird zuerst, analog dem Kaliumperchlorat, die endotherme Umwandlung der Cesiumperchloratkristalle von der kubischen in die rhombische Form beobachtet. Ab einer Temperatur von 400°C beginnt die topochemische Redoxreaktion zwischen Titan und Cesiumperchlorat. Das dabei entstehende Cesiumchlorid bildet mit dem noch im Überschuss vorhandenen Cesiumperchlorat ein eutektisches Gemisch, dessen Schmelzpunkt im Bereich von 400 bis 500°C liegt. Diese Schmelzpunktserniedrigung löst die stark exotherme Hauptreaktion aus (Titanpartikel in flüssigem Oxidator). Beim Redoxsystem Titan / Cesiumperchlorat finden anschliessend an die Hauptreaktion weitere exotherme Reaktionen statt. Ob ein Zusammenhang zwischen diesen detektierten exothermen Nachreaktionen und der IR-Strahlung besteht, wird das Thema einer zukünftigen Untersuchung sein.
Cesiumperchlorat ist auf Grund seiner kaum vorhandenen Hygroskopizität ein interessantes Oxidationsmittel für pyrotechnische Mischungen zur Erzeugung von IR-Strahlung im nahen Infrarotbereich. Mischungen bestehend aus Titan und Cesiumperchlorat weisen im Vergleich zu Mischungen des Redoxsystems Titan / Kaliumperchlorat ebenfalls günstige pyrotechnische Leistungs- und Sicherheitsparameter auf.

Verdankungen:
Die Herstellung der Mischungen sowie die Bestimmung verschiedener Parameter wird an dieser Stelle Herrn B. Haas (Gruppe Rüstung, FS 261) verdankt. Ein weiterer Dank geht an Herr G. Reinhard (Gruppe Rüstung, FS 261) für die DSC Untersuchungen.

7. Literatur

[1] Atlantic Research Corporation
Improved Gas Generating Composition
Patent PCT/US99/16154, 1999

[2] Piepenbrock Pyrotechnik GmbH
"PPT IR/RP – Nebelstoffe"
Göllheim; D; 1997

[3] U. Krone, K. Basse
"Pyrotechnic IR Illumination"
IPS Symposium; Grand Junction; USA; 2000; p 141-143

[4] R. Kresse
"Synthese von Cesiumperchlorat"
Chemetall; Persönliche Mitteilung; Thun; 1998

[5] R. C. Weast
"Handbook of Chemistry and Physics"
Chemical Rubber Company; 53rd Edition; Cleveland; USA; 1972

[6] Gmelins Handbuch der anorg. Chemie
"Cesiumperchlorat"
8. Auflage; Berlin; D; 1937; p 168-170

[7] B. Berger; J. Gyseler; B. Haas
"Untersuchung der Leistungscharakteristika von Pyrotechnischen Mischungen"
19. Internationale Jahrestagung des ICT; Karlsruhe; D; 1988

[8] B. Berger; J. Gyseler
"Methode zur Prüfung der Empfindlichkeit von Explosivstoffen gegenüber elektrostatischen Ladungen"
18. Internationale Jahrestagung des ICT; Karlsruhe; D; 1987

[9] W. Kronenberg
Persönliche Mitteilung; GR; Thun; 1982

8. Anhang

Spezifikation

Titanium metal powder (Ti), Grade E

Typical Analysis	Auto Ignition Temperature	> 315°C
	Combustion Rate	40 ± 10 sec/50 cm
	Particle Size	99.9% < 45 µm
	Average Particle Size	3 ± 1 µm
	Apparent Density	Approx.1.4 g/cm^3
	Gain on Ignition	56.0 ± 1.5 %
	Ti total	93.5 ± 1.0 %
	Ti active	84 ± 2.5 %
	Ca	max. 1 %
	N	max. 1 %
	C	max. 0.3 %
	Si	max. 2.5 %
	Mg	max. 0.05 %
	Al	max. 1.5 %
	Cl	max. 0.1 %

Recommended Test Methods Determination of average particle size, particle size distribution, combustion properties and gain on ignition. Gravimetric or colorimetric analysis of titanium and accompanying substances.

Handling Keep away from flames, sparks and heat sources. Use ground connected metallic apparatus to prevent electrostatic charges causing self ignition. Vacuum drying of suspensions is not recommended. Wear gloves and protective goggles. In case of fire cover with dry sand or dry chemical/dolomite (powdered limestone). Never extinguish with water, carbon dioxide or halocarbon.

See our material safety data sheet and special precautionary advice for more information on safety.

Packaging As dry powder in tin cans. Ti content 1.0 kg, 2.5 kg or 5.0 kg. Other packaging quanties on request.

Transport Classification GGVE, GGVS, RID, ADR: class 4.2, fig. 12a
IMDG-code: class 4.2 UN-No. 2546, PG. I
ICAO: air transport prohibited

Edition: December 2000

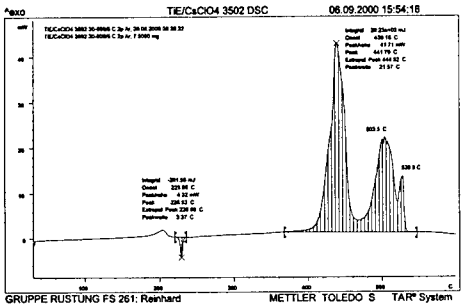


Abbildung 11: DSC-Plot einer Ti / $CsClO_4$-Mischung mit positiver Sauerstoffbilanz

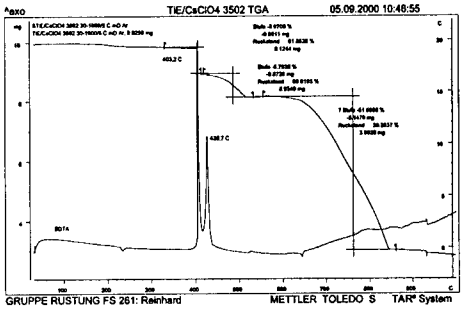


Abbildung 12: TGA/SDTA-Plot einer Ti / $CsClO_4$ - Mischung mit positiver Sauerstoffbilanz

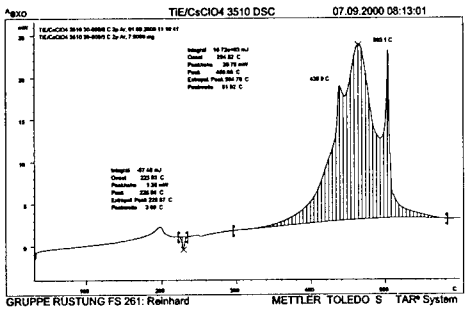


Abbildung13: DSC-Plot einer Ti/$CsClO_4$-Mischung mit negativer Sauerstoffbilanz

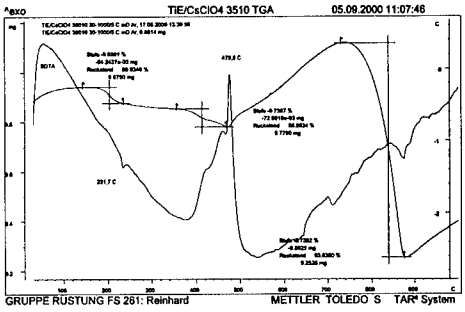


Abbildung 14: TGA/SDTA-Plot einer Ti / $CsClO_4$ - Mischung mit negativer Sauerstoffbilanz

32nd International Annual Conference of ICT
July 3 – July 6, 2001
Karlsruhe Federal Republic of Germany

IGNITION OF A PYROTECHNIC POWDER BY «HOT-SPOTS» AND ORDINARY ADIABATIC COMPRESSION

Dr. John F. Moxnes (1), MSc. Gard Ødegårdstuen (2)

(1) FFI (Norwegian Defense Research Establishment)
P.O. Box 25, N-2007 Kjeller, NORWAY
Telephone: + 47 63 807514, Fax.: + 47 63 807509

(2) Nammo Raufoss AS
P.O. Box 162, N-2831 Raufoss, NORWAY
Telephone: + 47 61 152757, Fax.: + 47 61 152250

In this article we are studying the ignition threshold of an incendiary charge (pyrotechnic powder) by using numerical simulations, a hot-spot theory and experiments at the firing range and in the laboratory.

Three different loading conditions were studied; Piston Driven Compaction (PDC), firing of Multipurpose (MP) projectiles at the firing range, and drop tests.

In the PDC experiments a high-speed piston with an impact velocity up to ~300m/s was fired against the incendiary charge bedded in a lexan tube, and the ignition threshold was observed by using a high-speed camera.

Next we studied the ignition when firing Multipurpose projectiles at the firing range. Different targets and different impact velocities were used to find the ignition threshold.

At last a drop test situation was studied where a free falling steel bar impacted the powder at a low velocity in the order of 10m/s.

By using the hydrocode Autodyn and the hot-spot model, we found that inter-granular friction lead to ignition for the PDC- and the firing experiments, while ignition was caused by ordinary adiabatic compression in the drop tests. The theoretical and experimental ignition threshold was for all three different cases in good agreement.

INTRODUCTION

In this article we present a hot-spot ignition model for a granular material consisting of a mixture of powdered Al/Mg alloy, $KClO_4$ and a small amount of calcium resinate. By assuming that a major part of the energy created during compression is fluxed into the particles through the particle surface, we were able to foresee the ignition of the powder in three different loading conditions.

In the Piston Driven Compaction (PDC) experiment, a high-speed piston, with an impact velocity up to ~300m/s, was fired against the powder bedded in a tube. The piston and the tube were made of lexan (Polycarbonate), which makes it possible to observe the ignition threshold by using a high-speed camera (~30μs between each frame, and an aperture of ~5μs). By using calculations from the Autodyn-2D code as input to the hot-spot model we found that the theoretical and experimental ignition level was in good agreement.

In the second experiment the MP-ammunition was fired at the firing range. Different targets and different impact velocities were used to find the ignition threshold and again, by using theoretical calculations and the Autodyn-2D code[1], good agreement with the experimental results was achieved.

In the drop test experiment different masses and different velocities (by varying the dropp height) were used to find the ignition threshold and also in this very different situation we were able to foresee the ignition level.

EXPERIMENTAL PROCEDURE

The three different experiments used in this study are presented in figure 1

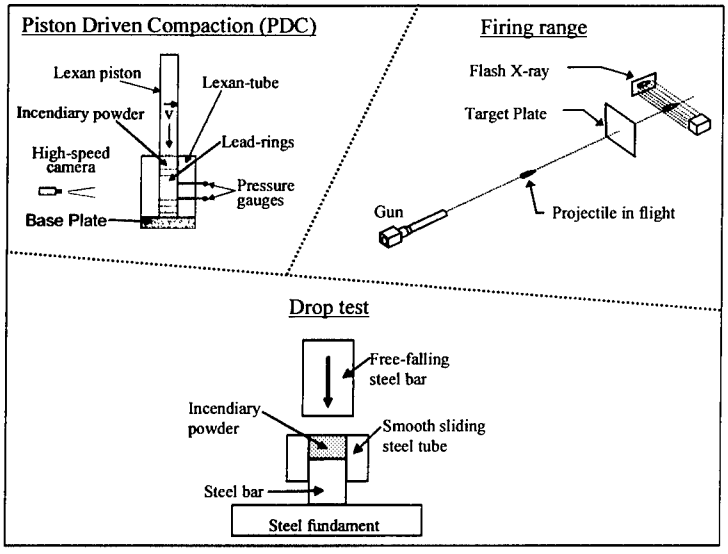


Figure 1 Setup of Piston Driven Compaction (PDC), Firing test at the firing range & Drop test

THE HOT-SPOT MODEL

During compression the average size of the contact area between the granular particles changes. The contact area is directly related to the density of the granular material. A granular material becomes stiffer as the density increases, and the average contact-surface between the particles is directly related to this stiffness. The following relation is then used for the contact surface area[2][3],

$$A(\rho) = 4\pi a^2 \left(\frac{K(\rho)}{K(\rho_{TMD})} \right) \tag{1}$$

ρ = *Density of the powder*
ρ_{TMD} = *Theoretical Maximum Density (TMD) of the powder (no space between the particles)*
$K(\rho)$ = *Elastic bulk modulus for the powder*
a = *radius of particles*

For large deformations, the granular particles are definitively not spheres, and the relation (1) is probable not good enough.

Letting $R(\rho)$ be the average distance between the granular particles. For "identical" spherical particles, we have

$$\frac{4}{3}\pi R^3 = \frac{V}{N} \tag{2}$$

R = *Distance (for identical particles)* , V = *Volume*
N = *Number of particles in the actual volume*

We also have

$$N = \frac{total\ mass}{mass\ of\ a\ particle} = \frac{\rho V}{\frac{4}{3}\pi a^3 \rho_{TMD}} \tag{3}$$

then

$$R(\rho) = a \left(\frac{\rho_{TMD}}{\rho} \right)^{1/3} \tag{4}$$

During compression of the powder the Autodyn simulations give history files for the internal energy pr. mass-unit, $e(n)$, and the density, $\rho(n)$, where n is the cell number, and to find the hot-spot temperature we solve the heat equation.

$$\rho_p c_v^p \dot{u}^p(n,x,t) = \kappa^p \nabla^2 u^p(n,x,t) + \dot{e}_v(n,t)\rho^p \tag{5}$$

The boundary condition at the surface of a particle in cell n is given by

$$\kappa^p \nabla u^p(n,x,t)\bar{n} = e_s(n,x,t)\rho^p \frac{V^p}{A(\rho(n,t))} \tag{6}$$

$\bar{n}$:	Vector, perpendicular to the particle surface
V^p:	Particle volume
κ^p:	Particle conductivity
ρ^p:	Particle density
c_v^p:	Specific heat capacity of the particle
$u^p(n,x,t)$:	The temperature in a particle (grid), n = all the grids, x = position in granular particle, t = time
$e_v(n,t)$:	The energy versus time and versus mass, as output from the Autodyn simulations assumed to be plastic and fluxed into the particle
$\rho(n,t)$:	Density of the granular (powder) material
$e_s(n,x,t)$:	The energy versus time and versus mass, as output from the Autodyn simulations assumed to be plastic and fluxed into the particle through the surface
$A(\rho)$:	Contact area as a function of the density of the granular powder
V^p:	Volume of particle

We observe that the energy is fluxed into a density dependent surface during the compression.

Bu using spherical coordinates and a θ dependency (suppressing the index n) the following boundary condition is used

$$\frac{\partial u}{\partial r}(a,\theta,t) = \frac{\dot{e}_s \rho^p \frac{4}{3}\pi a^3}{A(\rho)\kappa^p}, \qquad \theta \le \theta_c(\rho) \tag{7}$$

The angle θ_c, is given from the density by

$$A(\rho) = \int_0^{\theta_c} \sin\theta d\theta \cdot 2\pi a^2 \tag{8}$$

Then

$$\theta_c(\rho) = \arccos\left[1 - \frac{2A(\rho)}{4\pi a^2}\right] \tag{9}$$

We assume the following relation between the surface energy and the total energy

$$\dot{e}_s = \left(1 - A_{rel}(\rho)\right)\dot{e} \qquad \dot{e}_v = A_{rel}\dot{e}, \qquad A_{rel} = A/(4\pi a^2) \tag{10}$$

The hot-spot model needs as input the time history of the density and energy. During shock compression Autodyn gives, due to coarse gridding, not the correct time history of the density, particle velocity and the total energy through the shock. For the density and the particle velocity we have found that behind the shock [4] Autodyn calculations are in good agreement with theoretical shock calculations, but the energy values in Autodyn are much larger than values from theoretical shock calculations. We believe that this phenomenon is caused by the artificial viscosity used to stabilize the numerical scheme in Autodyn.

We let $v(\rho)$ be the particle velocity as a function of the density through the shock. Consider particle number i and let S_i be its position in the x-direction at the time t where $S_i(0) = 0$ and the time starts when the particle number i starts to move forward in the x-direction caused by the shock. We let the position of the particle number $i\text{-}1$ be $S_{i-1}(t)$, where:

$$S_{i-1}(t) = -S_0 + v(\rho_{max})t, \qquad v = \textit{particle velocity} \tag{11}$$

It is just so the shock has passed the particle $i\text{-}1$, and it will continue to move with the particle velocity $v(\rho_{max})$, where ρ_{max} is the density after the shock has passed. Particle number i would now be accelerated, and it has the position

$$S_i(t) = \int_{t=t_0}^{t} v(\rho(u))du \tag{12}$$

We have that relative velocity between particle number i and $i\text{-}1$ is

$$\frac{d}{dt}\left[S_i(t) - S_{i-1}(t)\right] = v(\rho(t)) - v(\rho_{max}) = \dot{R}(\rho(t)) \tag{13}$$

A time derivation of $R(\rho(t))$ give us the following relation for the density through the shock.

$$\dot{\rho} = \frac{3\rho^{1/3}}{a(\rho_{TMD})^{1/3}}\rho(v(\rho_{max}) - v(\rho)) \tag{14}$$

Notice that the typical time scale for the rising time of the shock is proportional with the particle radius a. We have found that Autodyn simulations and theoretical shock calculations give the same relation between the particle velocity and the density also when the grid is coarse. We therefore use this relation from Autodyn as input to equation (14), and the only missing quantity for the hot-spot model is then the energy e(t).

The energy as a function of the density can be found from Autodyn by writing a numerical routine that calculates energy as a function of the density, without taking into account the

stresses caused by the artificial viscosity. We have not done that so far, and instead we have used the following relation from shock theory

$$e(\rho) = e_0 + \frac{1}{2}\left(v^2(\rho)\right) \tag{15}$$

This energy, e together with the density ρ calculated from equation (14) are input functions to the heat transfer equations 5 and 6 presented earlier.

One dimensional shock theory gives the following relation between the velocity and the density where P is the axial stress

$$v^2(\rho)\rho_0 = \left(P(\rho)\left(1 - \rho_0/\rho\right)\right) \tag{16}$$

Inserting into (14) we get

$$\dot{\rho} = \frac{3\rho^{4/3}}{a\left(\rho_{TMD}\right)^{1/3}\rho_0^{1/2}}\left[\left(P(\rho_{max})\left(1-\rho_0/\rho_{max}\right)\right)^{1/2} - \left(P(\rho)\left(1-\rho_0/\rho\right)\right)^{1/2}\right] \tag{17}$$

RESULTS

In this chapter we present simulation with the Autodyn code together with calculations using the hot-spot model. The history plots represent areas (cells) in the Autodyn simulations where we found the highest impact impulse for the different experiments.

Piston Driven Compaction (PDC)

The PDC experiment setup was shown in figure 1. Three different initial densities for the powder are chosen for hot-spot calculations.

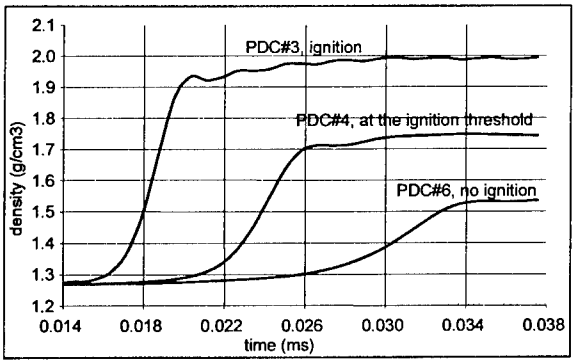


Figure 2
Piston Driven Compaction (PDC)
Loading density = 1.3g/cm³
Density versus time

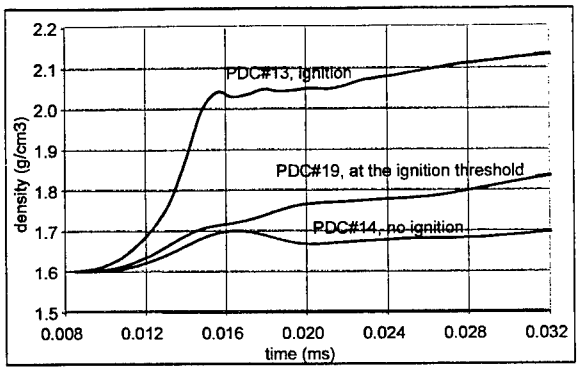


Figure 3
Piston Driven Compaction (PDC)
Loading density = 1.6g/cm^3
Density versus time

In figures 2 and 3 we see Autodyn simulations of different PDC shots. The initial loading density of the incendiary powder was 1.3g/cm^3 and 1.6g/cm^3.

The hot-spot curve shown in figure 4 shows a maximum temperature of ~920K, which is very close to and above the temperature needed to obtain an ignition (800K). In figure 5 we see the density as a function of time calculated by using equation 14. A close study of the two figures shows that the maximum hot-spot temperature was obtained before the compaction of the incendiary charge was completed. We have seen that this phenomenon is not unique for PDC#4.

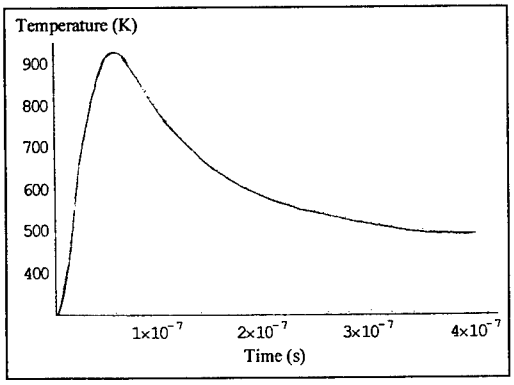


Figure 4
Hot- spot temperature versus time for PDC#4, which is at the ignition threshold, and where the input densities were 1.3g/cm^3 before, and 1.75g/cm^3 after the shock wave

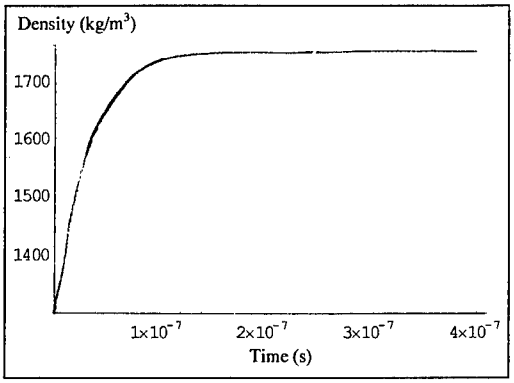


Figure 5
Density versus time of the shock wave for PDC#4

In figure *6* we see PDC #6, which did not ignite and had an initial loading density of 1.3g/cm^3. Observe that the hot-spot curve shows a maximum temperature of ~480K, which is too low to ignite the incendiary charge.

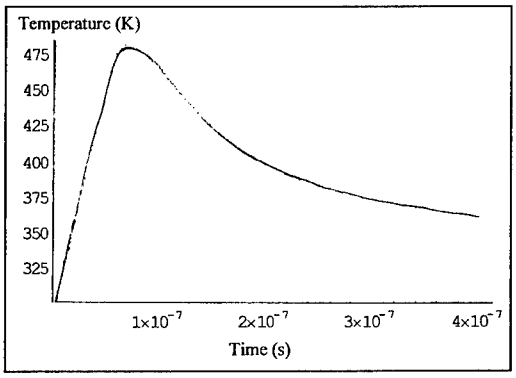


Figure 6
Hot- spot temperature versus time for PDC#6, which gave no ignition, and with an input density of 1.3g/cm^3 before, and 1.54g/cm^3 after the shock

MP, with and without void in the nose tip

The firing experiment setup was shown in figure 1. Nose caps with and without a void within the tip were studied. The nose cap press-loading together with setback and spin forces during launching cause a void within the nose cap for some of the rounds. The experimental matrix of the firing tests is presented in table 1 below

firing expr #	Number of Nose cap Loading increments	Firing range (m)	Nose tip Remarks	V_o / V_{impact} (m/s)	Target giving 50% ignition	Simulated density before and after the shock (kg/m^3)
1	2	100	Void (~5mm)	1100 / 1050	0.9mmAl	1300 / 1900
4	5	100	Gap (~0.3mm)	1100 / 1048	0.40mmAl	1500 / 2050

Table 1 Firing experiments performed

As an introduction to the firing experiments we observe in figure 7 the density gradients of the incendiary along the center-line of the nose cap before and after impact for experiment #1.

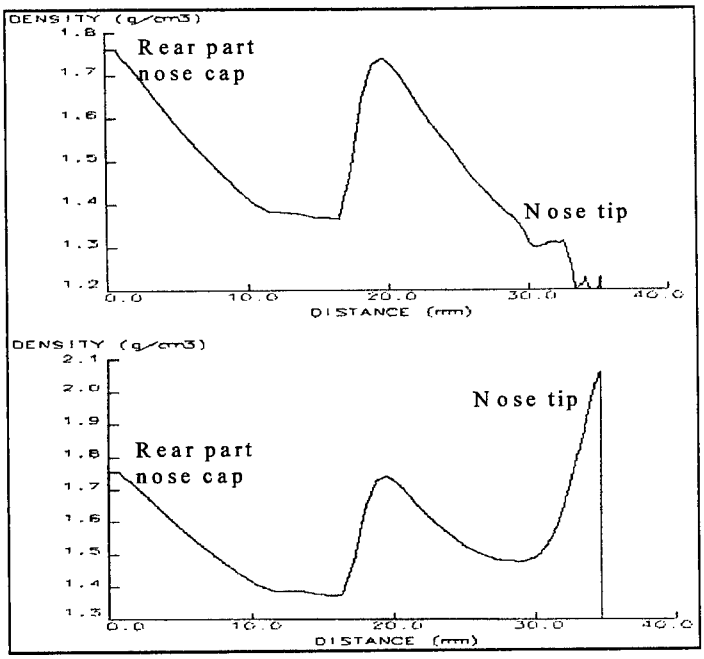


Figure 7
Experiment #1, density gradient of the incendiary charge, along the nose cap center line, before and after impact

In figure 8 we show Autodyn calculations of the density as a function of the time for test #1 and test #4. For test #1 we show curves at the ignition threshold (50% ignition) and below. For test #4 we only look at the ignition threshold (50% ignition).

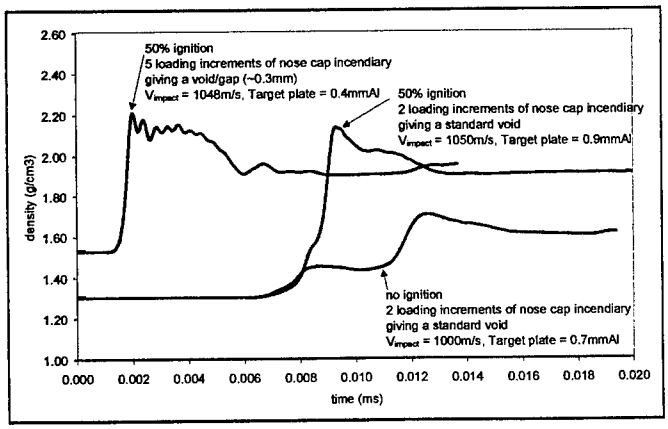


Figure 8
Firing test #1 and #4, density versus time

The curves presented above in figure 8 are not realistic due to the coarse grid. The firing experiments are simulated with a grid resolution of ~0.2mm in the impacting area of the incendiary charge, and this is too coarse to resolve the shock waves. In figure 9 and 10 we see the hot-spot calculations for firing test#1 and #4.We observe that the theoretical hot-spot temperatures for the two cases are very close to the ignition temperature at ~800K.

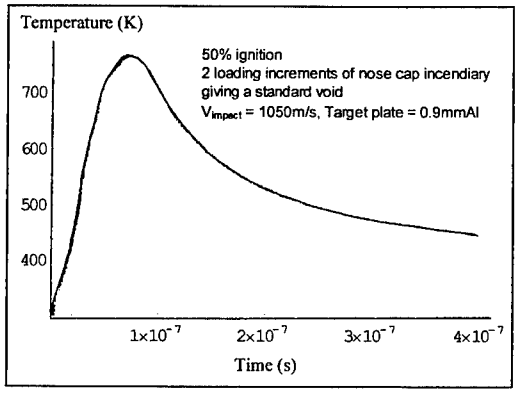


Figure 9
Hot- spot temperature versus time for the firing experiment #1, with 2 loading increments of the nose cap incendiary giving a standard void in the tip, giving 50% ignition. The input densities were 1.3g/cm^3 before, and 1.90g/cm^3 after the shock

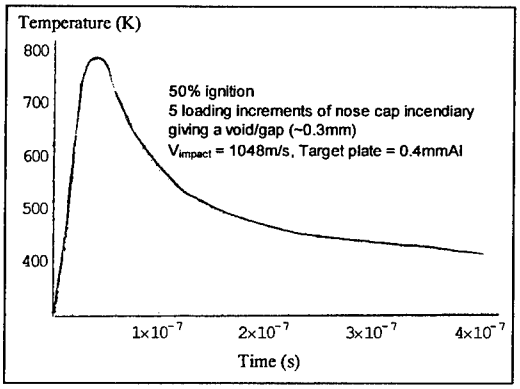


Figure 10
Hot -spot temperature versus time for the firing experiment #4, with 5 loading increments of the nose cap incendiary giving a void/gap (~0.3mm) in the tip, giving 50% ignition. The input densities were 1.54g/cm^3 before, and 1.90g/cm^3 after the shock

If we compare the hot-spot calculations of the firing test figure 9 with the hot-spot calculations of PDC #4 in figure 2, we observe that the ignition threshold is obtained with identical densities before the shock, but with different densities behind the shock. In the PDC experiments a plane shock impacts the whole surface and there were no free surfaces. This gave increased deviatoric stresses and increased internal energy. For the firing test, with the standard void, there was an oblique impact with free surfaces, which gave less deviatoric stresses and less internal energy. This we believe is the explanation of the differences in the density behind the shock. For the firing test with the small gap in the nose tip, shown in figure 10, there was almost the same situation as for the PDC experiments, with higher deviatoric stresses and higher internal energy.

Drop test

The drop test experimental set-up was shown in figure 1. There were no shock waves, and we could resolve the dynamic situation by using Autodyn. In figure 11 we see the internal energy (temperature) versus time from the Autodyn simulations. Two cases are shown, one which ignited (50%) and one which did not ignite.

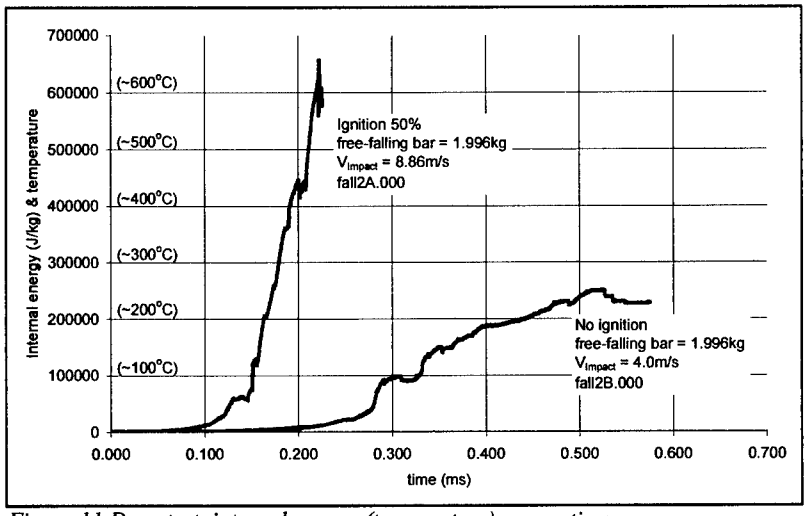


Figure 11 Drop test, internal energy (temperature) versus time

As input to the hot-spot calculations we used the energy time history presented in figure 11, and the density-time curve from Autodyn (not shown her). During this slow compression we did not theoretically find any hot-spots. The internal energy history at all points of the granular particles were the same as shown in figure 11. Approximately 600°C (873K) was obtained at the 50% ignition threshold, which was quite close to the 800K needed to start an ignition.
The curve in figure 12 gives a rough overview based on a general impact / crush up occasion.

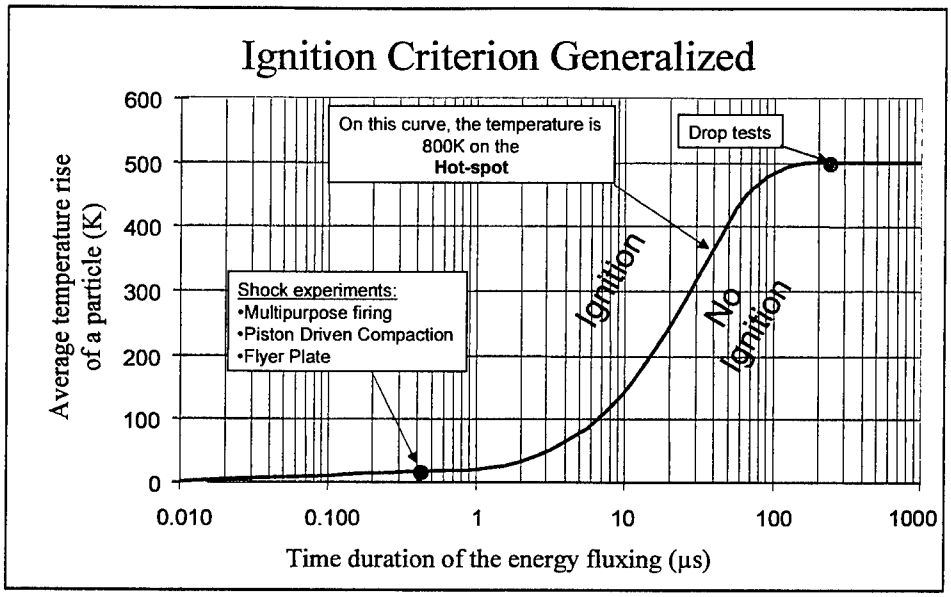


Figure 12 *A generalized presentation of the Ignition Criterion*

CONCLUSIONS

In this paper we present a hot-spot ignition model for a granular material consisting of a mixture of powdered Al/Mg alloy, $KClO_4$ and a small amount of calcium resinate. By assuming that a major part of the energy created during compression is fluxed into the particle surface, we were able to foresee the ignition of the powder in three very different loading conditions.

The model gives an explanation of the mechanisms taking place during ignition. By using the model together with the Autodyn simulations it is possible to estimate ignition sensitivity of the MP round both regarding functioning and safety.

REFERENCES

[1] AUTODYN-2D user manual

[2] Mechanical properties of a porous material studied in a high speed
Piston Driven Compaction experiment,
John F. Moxnes, FFI (Norwegian Defense Research Establishment)
Gard Ødegårdstuen, Nammo Raufoss AS
Alice Atwood and Pat Curran,
Naval Air Warfare Center Weapons Division, China Lake, CA, USA
30th International Annual Conference of ICT

[3] Karlsruhe, Federal Republic of Germany, June 29 – July 2, 1999
Predicting ignition stimuli of press filled projectile nose caps,
John F. Moxnes, FFI (Norwegian Defense Research Establishment)
Gard Ødegårdstuen, Raufoss Technology AS, (today, Nammo Raufoss AS)
28th International Annual Conference of ICT, Combustion and Detonation
Karlsruhe, Federal Republic of Germany, 24-27 June, 1997

[4] Simulations of shock velocity using Autodyn-2D (In press)

Laser diode ignition of the Iron/$KClO_4$ pyrotechnic mixture: Experimental and parametrical study.

Frédéric Opdebeck*, Erwann Radenac** and Philippe Gillard*

*Laboratoire Energétique Explosions et Structures de l'université d'Orléans

63 Boulevard de Lattre de Tassigny

18020 Bourges Cedex France

** Laboratoire de Combustion et de Détonique,

ENSMA, BP 109

86960 Futuroscope Cedex, France

Abstract:

This paper deals with the thermal ignition of Fe/$KClO_4$ pyrotechnic mixture by means of a laser diode. This mixture has been made in laboratory. The average size of iron grains is close to 1.6 μm : this powder has been provided as it is by an industrial company (Eckart Poudmet). Concerning the $KClO_4$, the final average grain size is about 24 μm. Both components are mixed by means of an orbital motion mixer. Afterwards, the mixture is placed in a mould where it is compacted in order to obtain pellets. The laser beam is focused on the pyrotechnic pellet using an optical device (composed by a first lens which colimates the divergent laser beam and a second one which refocuses it) and an optical fibber. A sapphire window has been placed between the last lens and the pyrotechnic mixture in order to avoid optical equipment injuring. The laser diode can provide an outgoing power of 7 W and a maximal pulse of 300 ms.

This work is devoted to the influence of some experimental parameters (laser power, laser beam diameter, the porosity ε, the carbon black powder proportion and the iron/KClO4 proportions) on the ignition threshold energies E_{50} and the ignition delay time t_i. The whole investigation has been carried out with a constant laser power density (2.2 kW/cm²). The result of the study has shown that all these parameters increasing leads to a t_i and E_{50} decreasing. It can be mentioned that a minimum energy lead to ignition was found for a given spot diameter.

Keywords : Energetic materials ; Pyrotechnics ; Laser ; Ignition Experiments

1 Introduction

Ignition, by laser, of explosive reactions, on pyrotechnic mixtures, is currently the object of many works [1], [2], [3], [4], [5], [7], [8], [9], [12], [13]. The laser diodes are a mean particularly interesting because of the very great reliability of these devices like for their exceptional energetic efficiencies and their small size. But its better advantages are: the not sensitive to magnetic disruption and the laid power is perfectly well known. Laser diode can be used with an optical fiber to drive the energy to the explosives. It is also possible to use lenses in order to concentrate energy on the explosive surface. This is the last one which is used here in order to ignite pyrotechnic mixtures *Fe/KClO4* and to characterise ignition properties (ignition delay time t_i and ignition threshold energy E_{50}).

Pyrotechnic mixture is composed of iron and $KClO_4$ (FK). The average granulometry of iron Fe used is 1.6 µm whereas $KClO_4$ is 24 µm. This mixture is packed under various pressure, which give a tablet whom the porosity depends of chosen pressure. As pellets are reactive heterogeneous materials, the Bruceton statistic method [5] is to use in order to calculate the energy thresholds E_{50} and ignition delay time t_i.

This work is devoted to determinate ignition properties (E_{50} and t_i) of the Fe/$KClO_4$ pellet. The influence of some experimental parameters (laser power, laser beam diameter, the porosity ε, the carbon black powder proportion and the iron/KClO4 proportions) on the ignition threshold energies E_{50} and the ignition delay time t_i. The most of the investigation has been carried out with a constant laser power density (2.2 kW/cm²).

2 Experimental set up

The device used here is the same than Radenac [5], but the principle will be recalled quickly. A system of lenses assembled on an optical board is used (Figure 1) for concentrating laser beam on the surface of pyrotechnic composition. Laser spot diameter can be easily modified by changing the lens L_1, in this way, various spot sizes on the pellet were obtained. This apparatus provides a power 4 W on the pellet surface and a maximum pulse time 300ms with spot diameter on the surface tablet ranges from 155 to 400 µm.

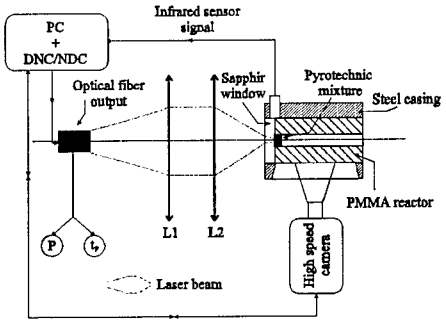


Figure 1: Experimental set-up.

3 Influence of laser power

The results presented on the Figure 2, were obtained on the pyrotechnic composition FK whose percentage oxidant/reductor is 38/62. This composition was ignited in the form of pastilles of low porosity $\varepsilon = 25.9$ % on the initiation board by refocalisation whose principle was presented Figure 1; the diameter of spot chosen for this study is 186 µm.

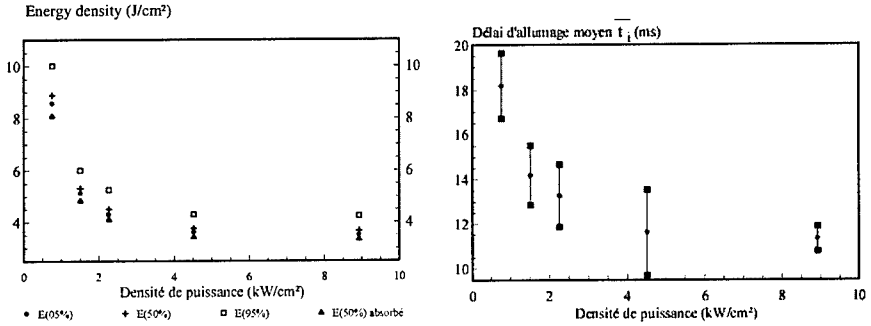


Figure 2: Evolution of value and dispersion of E_{50} and t_i according to the power.

The Figure 2 shows the power density influences of the values of E_{50} and t_i. We can note a decrease in threshold ignition energy and t_i when the power density increases. For the energy threshold E_{50}, one notes that an increase of power P causes to decrease the difference between the zone of E_{95} ignition and non-ignition E_{05} (Figure 2). Working with high power density allows to decrease problems link with the heterogeneity of studied material.

For the time of lighting t_i, the dispersion of this value tends to decrease when the power increases. It is necessary all the same to reach powers densities higher than 8 kW/cm² so that

this reduction in dispersion is sensitive. For low densities of power, no variation of the dispersion for the lighting time t_i is observable.

These results on the influence of the laser power lead us to the conclusion that it is possible to obtain reproducible measurements by working with high density power laser. It is interesting to work with high density of laser power, owing to invariance of the ignition parameters E_{50} and t_i. The reduction in the dispersion of the results is obtained by this way.

4 Influence of laser spot diameter

The study of the spot diameter influence was undertaken on the composition *FK*. The mixture used is still the same (38/62), the lens L_1 was changed for each new value of the diameter of spot. The various shootings were carried out with density of constant power, 2.2 kW/cm².

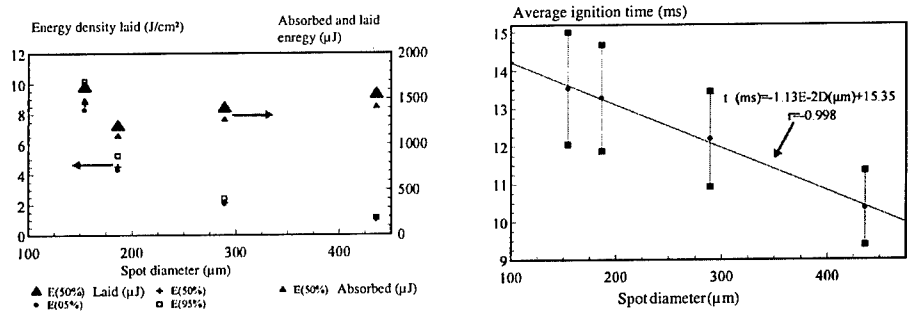


Figure 3: Effect of spot diameter on the energy thresholds and ignition times properties.

The analysis of the results of the Figure 3 shows that the spot diameter initially implies a reduction in the quantity of energy deposited on the pastille from 1700 to 1200 mJ (scale of right-hand side Figure 3) for the low diameters of spot. After having passed by a minimum being located around 180 mµ (Figure 3), this quantity of energy increases slightly up to 1500 mJ as the laser beam diameter increases. This result concerning the influence of D_{spot} (Figure 3) agrees with the evolutions described in work of Baoren [7], Holy and Girmann [8], Alexandrov [9]. Those many work highlight the existence of a critical diameter of lighting, corresponding to a minimum of threshold of the E_{50} initiation. The initiation becomes difficult for the lowest spot diameter.

The influence of the laser spot diameter D_{spot} on the density of deposited energy is shown on Figure 3 (scale of left-hand side). This decreases from 9 to 1 J/cm² when the diameter of the laser beam varies from 154 to 436 µm. As it shows on the Figure 4, the whole of these

results is certainly to correlate with an increase in the diameter of laser spot D_{spot} which induces an increase in the number of active sites (likely to cause ignition) in the zone heated by the laser beam.

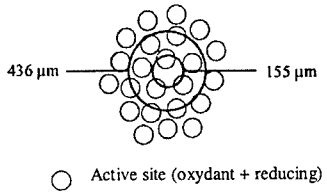


Figure 4: Effect of beam diameter on the ignition process.

By examining the influence of the diameter of spot on the lighting time t_i, it can be said that an increase of the term D_{spot} causes a reduction in t_i, and this reduction follows the equation of a line of the type: $t_i = -1.13 \cdot 10^{-2} D(m\mu) + 15.35$.

An interpretation of this result can be given. It is possible that the increase in the lighting time t_i is controlled by the diffusion time of heat for the ignition of an active site (small D_{spot}). On the contrary for the large diameters of laser spot D_{spot}, several active sites are concerned with the laser heating; in this case the decrease of the lighting time t_i of composition FK come from the synergy between the various active sites of the zone heated by the laser.

5 Influence of porosity

The Figure 5 shows the influence of the porosity on the lighting time and the threshold energy of initiation for two different powers of the laser, P=0.6 W and P=2.372 W.

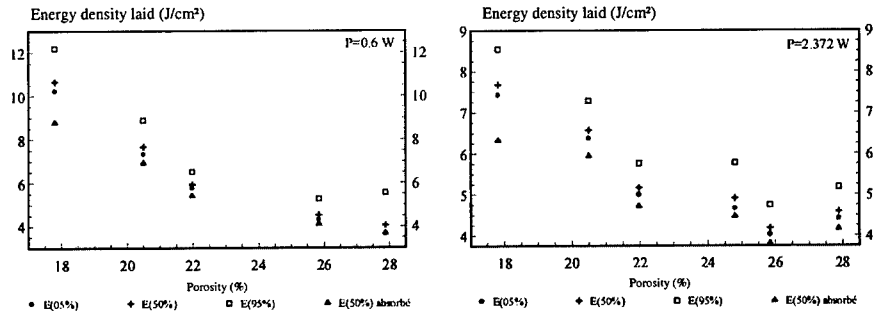


Figure 5: Effect of the porosity on the thresholds and ignition times.

A variation of the laser power does not change the variation of E_{50}, according to porosity ε, but that a reduction in the laser power amplifies the effect of porosity on the energy

threshold E_{50}. The Figure 5 shows that on a same interval of porosity, E_{50} varies from 7.75 to 4 J/cm² for a laser power of 2.372 W, whereas for a power of the laser of 0.6 W, the thresholds of initiation vary from 10.4 to 4 kW/cm².

The quantity of energy absorbed by the pyrotechnic composition and leading to ignition according to porosity is also represented on the Figure 5; this quantity of energy is calculated by multiplying the energy deposited by the absortivity (determined experimentally) of the pellet's surface (Figure 6). It is noted that the emissivity of the surface of pyrotechnic composition grows overall when the porosity increases; this passes by a maximum located around 22 %. Beyond 22 %, the emissivity of surface decreases very slightly, which is confirmed by the results Sainte Catherine [10] and Adorjan and Wierum [11]. This observation is confirmed in experiments by Brochier [12] which shows this optical parameter should not be neglected in the interpretation of the results on the porosity effect.

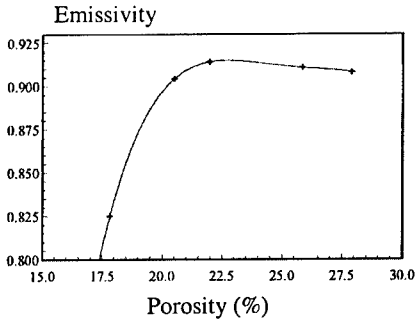


Figure 6 : Variation of the emissivity according to the porosity.

The Figure 7 shows that a variation of the laser power, does not have any significant consequence on the value of the times of lighting determined according to the porosity. Thus for both powers, the lighting time t_i is a decreasing function of porosity. This ignition time seems to be stabilised with a value finished for strongest porosities.

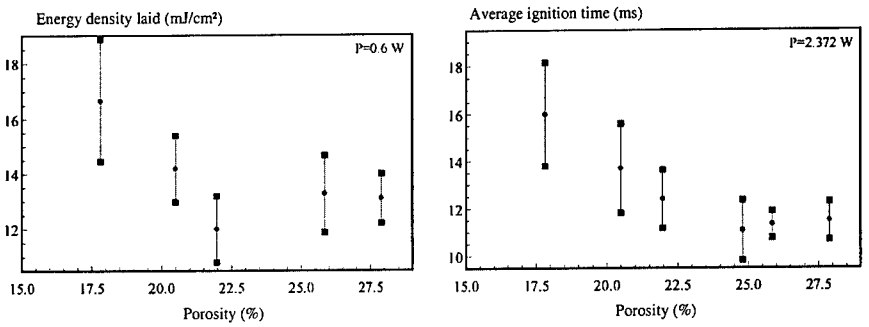


Figure 7 :

6 Influence of carbon amount.

The influence of the carbon black addition on the mixture will be observed. For these tests, the composition used has got the same ratio than $Fe/KClO_4$ (ie 62/38), black carbon was added from 0.75 % to 2.5 % in mass. The pellets porosity varies from 17.8 % to 25.8 %. The spot diameter is keeping at 186 µm. Initially we have seek the influence of the black carbon amount on the emissivity value of the pellet surface.

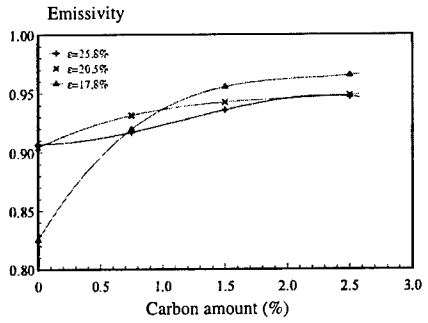


Figure 8: Variation of emissivity according to carbon amount.

The Figure 8 shows the emissivity value according the carbon ratio for three porosities. The black carbon favours an increase of the emissivity of the surface tablet. A more precise analysis of the results of the Figure 9 shows that a reduction of the tablet porosity amplifies the effect of the carbon black addition on the increase in emissivity. In order to give an example, the pellet emissivity (for ε=17.8 %) increase from 0.825 to 0.97 when the carbon ratio varies from 0 % to 2.5 %, whereas the pellet emissivity (for ε=25.8 %) increase from 0.91 to 0.94.

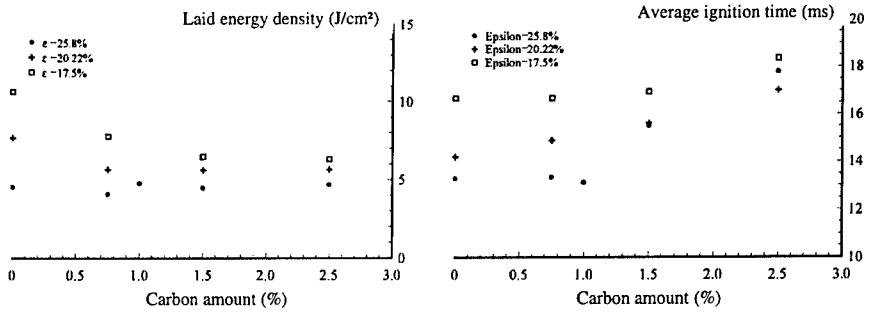


Figure 9: Effect of the carbon amount on thresholds and ignition times.

Curves presented in Figure 9 underline the influence of porosity on the effectiveness of the carbon black addition in the pyrotechnic composition FK. We carried out measurements of the parameters E_{50} and t_i for three different porosities 25.8 %, 20.5 % and 17.8 %. The Figure 9 illustrates the porosity effects on the controls of the efficiency of the adding of the carbon black on the decreasing of thresholds. According to these paces, the greater porosity is, the less influence the carbon black has, it can even become unperceivable. By example for ε=17.5 %, thresholds decrease from 11 to 6.5 J/cm² when carbon ratio varies from 0 % to 2.5 %, whereas they are not changed for the case where ε=25.8 %.

It is possible to specify this tendency by noting that an increase of porosity accelerates the growth of the lighting time t_i according to the content of carbon black. It is interesting to note, a content of carbon black higher than 2.5 % makes than the times of lighting of composition FK are almost identical, whatever the porosity. This effect seems to be similar to the threshold energy dependency.

The influence of the carbon black on the time of lighting that we highlighted in this work does not agree with that established numerically by Gillard and Roux [13]. Indeed, those showed that an increase in the coefficient absorption (i.e. an increase in the content of carbon black) led to a reduction in the time of lighting t_i. The comparison between this numerical study and our experimental results shows that the influence of the addition of opacifier agent on the lighting time is not only optical, assumption which was made in the work undertaken by Gillard and Roux [13]. In fact, the influence of the effective absorbed energy is lower than the previous effect.

7 Influence of iron amount

In this part, the composition FK is conditioned as pastilles which the porosity equal to ε=25.8 %. The power ignition is 2.37 W and the spot diameter laser is D_{spot}= 186 µm.

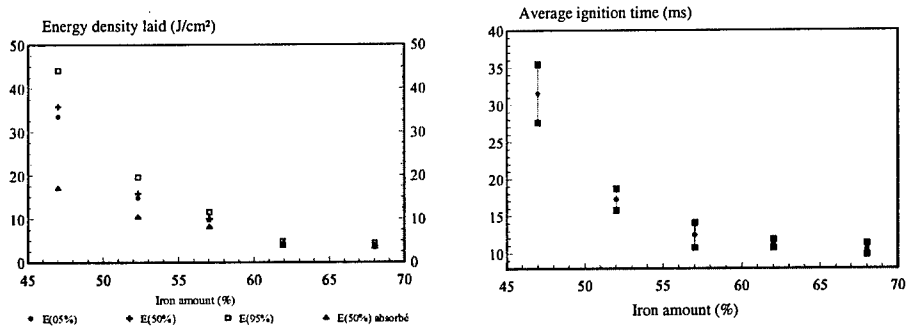


Figure 10: Effect of the iron amount on threshold and ignition delay.

The Figure 10 shows a very great influence of the ratio of iron in the pyrotechnic mixture on the ignition threshold E_{50} and the lighting time t_i. the Figure 10 highlights an increase of iron percentage of mixture FK causes a considerable reduction in the value of E_{50} and t_i. It is noted that the values of the ignition threshold and the lighting time are minimal for the strong contents of iron.

The dispersion obtained on t_i and E_{50} is very largely modified by the iron ratio. The results presented in the Figure 10 show that an increase of the iron amount, under the test conditions chosen, causes a reduction of t_i and E_{50} dispersion. That thus means, in the case of iron, that the reducer acts like a promoter of the ignition. There is a stabilisation of ignition, when iron percentage increase, linked to the reduction of the dispersion. This result concerning the stability of initiation comes to confirm the assumptions that we previously made within the framework of the study of the power influence (strong density of power) and of the spot diameter. Indeed, for these cases, we suppose the ignition is favoured by a great number of hot points localised near the reducing metal, which explains, the reduction of the lighting time, the ignition threshold and their associated dispersions: the increasing of iron amount supports the formation of hot points, which increases the probability of initiating a site active.

Heterogeneous is not the only parameters that may changes thresholds and ignition times. They can come from three other characteristics:

1. Figure 10 shows the absorbed energy (in which the emissivity can be deduced), when the iron amount is 47 %, the pellet's surface absorbs only 48 % of the laser power

whereas at 68 % of iron the laser absorption is near 92 %. Thus the emissivity plays a significant role in ignition, but it cannot describe, itself, the results from the Figure 10.

2. Thermal properties induce, in thermal transfer inside pellet, different behaviours. Indeed, thermal diffusivity grows from $2\ 10^{-5}$ to $2\ 10^{-7}$ m^2/s when decreasing the iron percentage. By changing the iron amount, the diffusity is modified in a significant way, which can induces different value of E_{50} and t_i.
3. The mixture reactivity; Variation of the stoechiometry change the reaction kinetic **Erreur! Source du renvoi introuvable.**].

8 Conclusion

This study has highlighted the influence of several parameters on the energy thresholds and ignition delay times. The analysis of these results shows variations of the parameters E_{50} and t_i hide influence of physic phenomenon like:

- The thermal influence;
- The chemical kinetic;
- The laser absorption of pellet's surface;
- The heterogeneous, especially highlighted at spot diameter study.

All these characteristics are able to change the pyrotechnic mixture response to laser heating, particularly the iron amount that can multiply by ten thresholds. This work shows, in order to optimise the ignition of pyrotechnic composition, it is necessary to chose high porosity, mixture that contents a lot of reductor, thus the dispersion and the energy thresholds are the smallest. To avoid radial loss and decrease the heterogeneous effect, the optimal spot diameter is to about 180 μm.

[1] A.A. BRICH, I.A. GALEEVE, B.N. ZAITSEV, E.A. SBITNEV, L.V. TARARINSTEV. "Mechanism of Initiation of Condensed Explosives by Laser Iradiation". Fizica Goreniya Vzryva, volume 5, number 4, pages 457, 1969.

[2] V.J. MENICHELLI, L.C YANG. "Detonation of Insensitive High Explosives by a Q-Switched Ruby Laser". Appl. Phys. Lett., volume 19, pages 473-475, 1971.

[3] H. OSTMARK." Laser ignition of explosives : Ignition Energy dependence of particle size". Colloque G.T.P.S. Juan-Les-Pins. pages 241-245, 1987.

[4] G. KRASSOULIA, FX THINAT. "Un initiateur optopyrotechnique d'allumeur et d'application spatiale". Colloque GTPS la Grande-Motte, pages 27-37, 1989.

[5] E. RADENAC, Ph. GILLARD, M. ROUX. "Laser Diode ignition of the combustion of pyrotechnic mixtures. Experimental study of the ignition of $Zr/KClO_4$ and $Zr/PbCrO_4$". 29th International Annual Conference of ICT, pages 40.1-40.14, 1997.

[6] E. RADENAC. "Etude expérimentale et numérique de l'allumage de composition pyrotechniques par une diode laser". Thèse de l'université de Poitiers, 1998.

[7] J. BAOREN, C. DANMING, W. ZUONI, L. YULIAN, Z. KEXING, L. XUFA, L. YIDE. "Experimental sudies on {PETN} detonators initiated by laser radiation". Technical report, Southwest Institute of Fluid Physics, 569-579, address "P.O.Box 523 Chengdu, China".

[8] J.A. HOLY and T.C. GIRMANN. "The effect of pressure on the laser initiation of $TiH_x/KClO_4$ and others pyrotechnics". Technical report, Monsanto research corporation for the US - Department of energy, address "Miamisburg, Ohio 45342-0032".

[9] V.E. ALEKSANDROV, A.V. DOLGOLAPTEV, V.B. IOFFE, and B.V. LEVIN. "Inflammation of porous systems by monopulse laser radiation". Combustion, Explosion and shock wave, volume 21, number 1, pages 54-57, 1985.

[10] C. SAINTE-CATHERINE. "Etude des possibilités d'applications des lasers ND-YAG". Thèse de l'Ecole nationnale supérieure des Mines de Paris, 1990.

[11] A.S. ADORJAN and F.A. WIERUM. "Radiative properties of rough surfaces". AIAA journal, volume 9, number 11, pages 2172-2179, 1971.

[12] M. BROCHIER. "Contribution à l'étude de l'initiation de substances pyrotechniques par laser". 19th International Annual Conference of ICT, publisher S.N.C. Davey Bickford, pages 78-89, 1988.

[13] Ph. GILLARD and M. ROUX. "Ignition of pyrotechnic mixture by means of a laser diode Part I: Numerical modelling". Propellants, Explosives, Pyrotechnics, volume 22, pages 256-262, 1997.

Plasma Ignition and Combustion

Andreas Koleczko, Walter Ehrhardt, Stefan Kelzenberg, Norbert Eisenreich*

Fraunhofer-Institut für Chemische Technologie, 76327 Pfinztal, Germany

Summary

Electro-thermal-chemical (ETC) initiation and combustion offers the possibility to increase the performance of guns substantially as new propellant formulations and high loading densities (HLD) can be safely ignited and burnt in an augmented way. This paper reports investigations of burning phenomena in the low pressure region for JA2 and the effects of plasma interaction on ignition and study its influence on the burning rate. The comparison of transparent and opaque versions of the propellant is of special interest. Electrically produced plasma can strongly influence the ignition and combustion of solid propellants. Predominantly, plasma arcs influence strongly the burning of propellants by its radiation. The high intensity of the radiation initiates burning with short time delays in the µs-range and high conversion during exposure also in the case of a stable burning. Radiation can penetrate into the propellant interior and partially fragment at absorbing structures which could be artificially introduced or be inherently present as in the case of a JA2 propellant. Simplified approaches based on the heat flow equation and radiation absorption can explain these effects at least on a qualitative scale. Dynamic effects are understood by more sophisticated models.

1. Introduction

Electro-thermal-chemical (ETC) initiation and combustion[1-8] offers to increase the performance of guns substantially as new propellant formulations and high loading densities (HLD) can be safely ignited and burnt in an augmented way. In basic research, the phenomena are studied in closed vessels. The propellant is ignited with plasma either introduced by a jet[1-4] from a capillary or a cavity or by an arc from an exploding wire inside the propellant charge[1,6-10]. Measurements record current and voltage across the capillary, cavity or wire and pressure-time history in the chamber. The propellant burning rates versus the pressure are calculated by analysing the pressure-time history using standard interior ballistic codes. These regression rates have indicated ETC augmentation of the burning rate of solid propellants[7,9-14]. Solid propellant ETC guns achieved performance increases that could not only be explained by the added electrical energy[1]. The augmentation can result from a modification in the inherent burning rate of the propellant caused by the plasma interaction, or by grain fragmentation resulting in an increase of the burning surface area. Recent results of experimental and theoretical investigations indicated that both concepts could be realised. The conventionally used burning rate descriptions like Vieille's law do not describe sufficiently the effects found in ETC ignition and combustion. Especially, radiation emitted from a plasma arc can strongly reduce ignition delay times and augment burning rates[11-14].

It is the objective of this paper to report on investigations of burning phenomena in the low pressure region for JA2, the effects of plasma interaction on ignition and its influence on the burning rate. The comparison of transparent and opaque versions of the propellant is of special interest.

* Corresponding author; e-mail: Norbert.Eisenreich@ict.fhg.de

2. Simplified Theoretical Approach for Radiation Interaction

The explanation of important phenomena of plasma interaction on the ignition and combustion of solid propellants bases on the approach that the transition of the condensed phase to the gaseous phase dominates the ignition and burning of solid energetic materials. The non-affected solid heats up to the temperature of the burning surface caused by the energy transfer from the flame or other energy sources like radiation. The conversion to the gaseous phase can occur by endothermic evaporation, exothermic pyrolysis or heterogeneous reactions induced by some unspecified energy flux from the gaseous phase. The effects can be described by the heat flow equation whereas diffusion of species can be neglected. A detailed outline of this approach is published elsewhere[15-17]. In the following, a radiative energy transfer Q_R is assumed in addition to the energy flux from the flame by conduction Q_0.

In the case of an absorption of the total energy flux on the propellant surface which pyrolyses at a temperature T_p, an approximation for the ignition delay time t_{ign} can be found:

$$t_{ign} \approx \frac{\pi \lambda \rho \, c_p \left(T_p - T_0\right)^2}{4 Q_R^2} \tag{1}$$

For a semi-transparent propellant with a unique absorption coefficient, a more complicated solution can be obtained. If the energy transfer is constant the following relation for the burning rate r can be derived where the conductive heat from the flame Q_0 is supposed to represent Vieille's law.

$$r = \frac{A \cdot p^n + \dot{Q}_R}{\rho\left(c_p \cdot \left(T_s - T_0\right)\right)} \tag{2}$$

Eq. (2) shows that conductive and radiative heat transfer affect the burning rate in the same way. Eq. (2) enables to analyse the influence of physical and chemical parameters of solid propellants on ignition delay and linear burning rate. It was found that Eq. (2) represents the temperature dependence of the linear burning rate of many solid propellants very well[11,15]. The fit parameter T_s lies systematically higher than the pyrolysis temperature obtained in thermal analytical experiments (e.g. TG or DSC). For JA2 T_s was found to be rather constant and close to 675 K[15], and the conductive heat flux from the flame to the propellant surface increased from 6000 W/cm^2 to 15000 W/cm^2 at pressures from 70 to 175 MPa.

Ignition, burning rates and their pressure dependence were calculated also by the method of Zarko and Rychkov[19,20]. They developed a one-dimensional computer code CTEM (Combustion Transients of Energetic Materials) which takes into account time-dependent phenomena of condensed propellants subjected to the time-variable heat flux.

The mass conversion of porous propellants deviates from Vieille's law. A 3-dimensional hot spot model has been developed to calculate conversion rates, temperature profiles and normalized pressure. The model is described in reference 18.

3. Experiments

For the experiments a transparent version of standard JA2 composition but without carbon was used.

The propellants were investigated in two types of chambers:

(1) A closed vessel was used with a volume of 100 ml, enabling the registration of the pressure-time behaviour at different loading densities. The plasma initiation was performed by a wire explosion in the axis of the bomb (Figure 1).

(2) An "optical" bomb is equipped with windows and can withstand pressures up to 13 MPa. It was used for photographic studies of the burning zones and spectroscopic investigations. The experimental set-up is described in detail in other publications[24, 25].

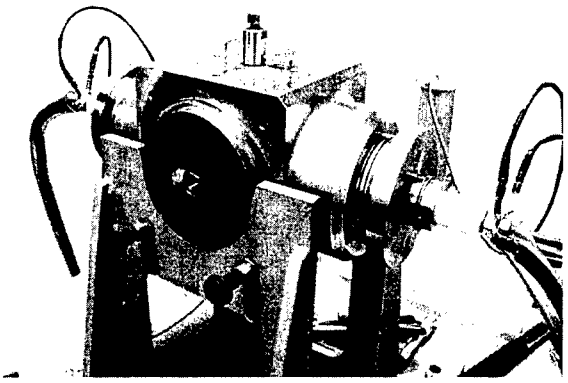


Figure 1: Closed vessel for the plasma interaction studies.

The burning rates were calculated from the pressure time-curves according to the procedures described in Refs. 26-27. In the case of the simple geometry of the plates the burning rates or apparent burning rates were estimated from the pressure maximum which was related to the thickness of the JA2 and the first derivative of the pressure time curve ignoring the influence of the boundaries of the propellant stripe, the true equation of state of the gases and the cooling by energy loss to the bomb volume.

In addition, the JA2 plates were pre-treated applying "open" conditions which means that the same plastic tubes were prepared with the propellant stripes outside the closed vessel and then the plasma arc initiated by the wire explosion.

The vessel was equipped with one fiber optical system pressure transducer. For interrupted-burning tests, a special closed chamber was used with a plug containing a stainless steel rupture disc. In this chamber propellants were investigated which were pre-treated in the "open" experiments.

4. Comparison of the Ignition of Transparent and Black JA2

In preliminary experiments it was found that the burning rates of black and transparent JA2 are equal if they are not ignited by plasma or pre-treated by plasma in an open experiment.

Figure 2 shows the pressure time curves of experiments where black and transparent JA2 were subjected to a plasma arc of 2 kJ and where transparent JA2 was initiated by 1 g B/KNO_3. The ignition delay indicated by an initial pressure rise is similar for both cases of plasma ignition and essentially faster than that of the conventional ignition. The pressure increase is similar for the black JA2 ignited by plasma and the JA2 ignited by B/KNO_3 resulting in similar burning rates. The conversion of the solid material is accordingly higher on the plasma pulse. The ignition delay decreases with increasing electrical energy fed to the arc. The pressure increase which is roughly proprtional to the apparent burning rate in the setup used is strongly enhanced for transparent JA2.

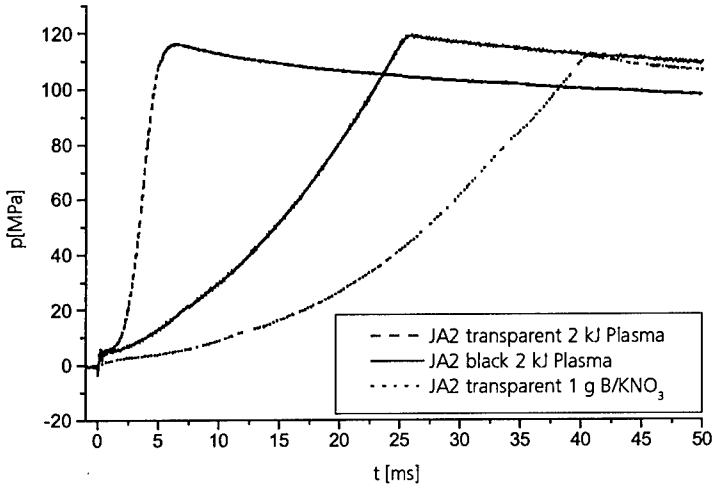


Figure 2. Comparison of plasma and pyrotechnic ignition of black and transparent JA2.

Results of discharged energies of 1 kJ, 2 kJ and 6 kJ applied to transparent JA2 are plotted in Figure3. Using the lowest energy of 1 kJ, a long time period occurs where JA2 burns with the normal low pressure burning rate after the end of the electrical pulse (see also Figure 5). When reaching a pressure of 6 to 8 MPa a strong increase of the apparent burning rate is found. The pressure of 6 to 8 MPa is reached fast with an electrical energy of 2 kJ and the period of normal burning is short. After a discharge of 6 kJ only a strongly enhanced burning is observed.

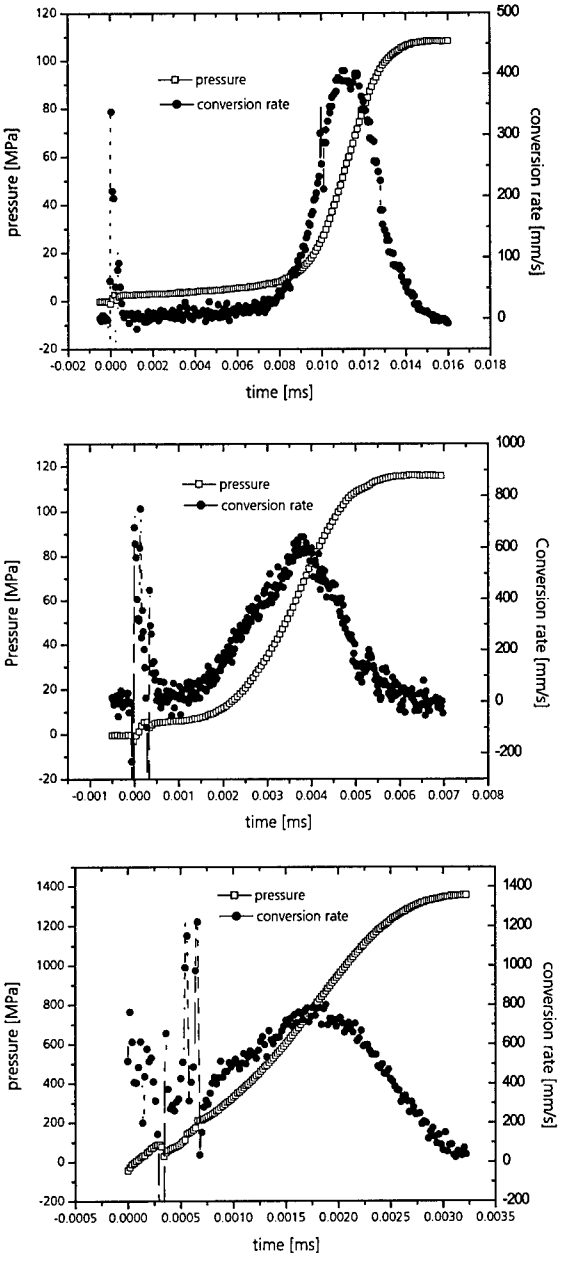


Figure 3. Comparison of the pressure-time-curves and conversion rates of the ignition of transparent JA2 with various electric energies 1 kJ (top), 2 kJ (mid), 6 kJ (bottom).

The following hypothesis on plasma ignition of JA2 is proposed:

- Black JA2: a short ignition time is obtained, only at high radiant fluxes in depth effects could be observed
- Transparent JA2: a short ignition time is obtained, plasma radiation forms a porous structure in the interior of the propellant causing a successive porous combustion characteristics
- Ignition delay times and burning rate enhancement follow at least qualitatively the theoretical approaches described above

5. Pre-Treatment of Transparent JA2

JA2 was pre-treated by plasma discharge after wire explosion in open experiments where 0.8 or 1.5 kJ energy were applied. Black JA2 ignited and burned under these conditions.

The transparent pre-treated JA2 plates show effects of fragmentation in the interior which are lens shaped crazes of a diameter of 2 mm or less. They are orientated parallel to the rolling direction during the production of the JA2 plates (possible due to the orientation of the nitrocellulose fibres. The following experiments were performed with the pre-treated JA2 plates:

1. Observation of the burning behaviour by a camera and measurement of the burning rate in the optical bomb: The frames which are shown in Figure 4 indicate that the flame front is not linear but penetrates into the crazes forming a broad flame zone still in the solid at higher pressures. The depth increases when the pressure increases. The apparent burning rate is higher than that of non-treated JA2 at 4 and 7 MPa. The apparent burning rate obtained from the experiment in the plasma bomb shown in Figure 3 using 1 kJ electrical energy agrees well with the (apparent) burning rate measured in the optical bomb (see Figure 5).
2. A detailed analysis of the pressure-time curves obtained by 1 and 2 kJ plasma arc ignition in the closed vessel results in a similar behaviour of the burning rate depending on pressure. There is an increase of the apparent burning rate (or conversion rate) after 4 MPa and dramatically after 7 MPa above that of black JA2.
3. If ignited by 1 g B/KNO_3 the pre-treated transparent JA2 exhibits the same burning behaviour as if ignited untreated by a plasma arc.
4. Experiments with burning interruption were performed. They indicate that the burning takes place in the lens shaped crazes and voids whereas the solid keeps its outer shape

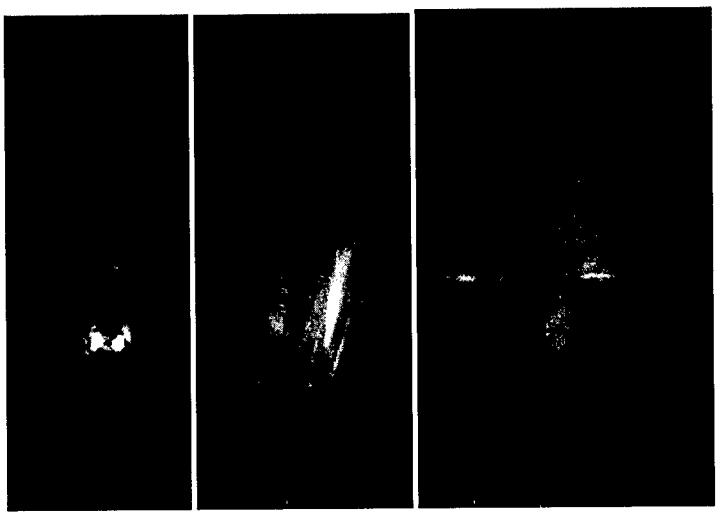


Figure 4. Pre-treated transparent JA2 (1,8 kJ) studies in an optical bomb at pressures of 20, 40 and 100 MPa (from left to right). Burning occurs in the volume of the not yet fully pyrolysed propellant.

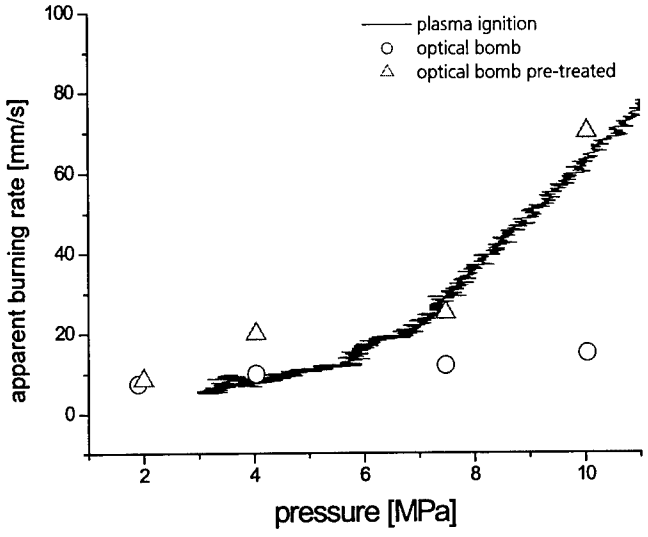


Figure 5. Apparent burning rate of transparent JA2 ignited by a 1 kJ electrical pulse: obtained from ignition in the plasma vessel compared to the burning rate of transparent JA2, pre-treated by a 1 kJ plasma and without plasma pre-treatment measured in an optical bomb.

6. Modelling the Porous Burning of Transparent JA2

The burning rate dependence of transparent JA2 with plasma treatment is qualitatively described by the following model:

1. The plasma pulse (as pre-treatment or in the ignition phase) causes crazes and voids in the interior of the propellant which later act as hot spot centres of burning.

2. If the initial pulse does not cause a pressure increase above 2 to 3 MPa then a "normal" linear burning begins including hot spots at the surface. The burning rate does not exceed the burning rate of normal JA2.

3. The pressure gradient between the propellant interior and the closed volume drives hot reaction products into the porous structure which cause conversion and burning in the case that the flame quenching distance or the flame stand-off distance is below the size of the pores (crazes, voids).

4. This case is realised above 4 to 7 MPa and the burning occurs within a volume between the surface and a depth where the hot gases can penetrate into pores. At pressures of 4 to 7 MPa the flame stand-off distance decreased already below 1 mm.

The hot spot mechanism above can describe this behaviour on a qualitative scale, physical and chemical data of JA2 and the kinetics of nitrocellulose decomposition were used[21-23]. The experimental data of Figure 3 indicate that the enhanced burning occurs immediately in the case of 6 kJ electrical energy applied and shortly after the end of the pulse on 2 kJ. On 1 kJ a long normal burning is found till a pressure of 4 to 7 MPa is reached.

The ignition is initiated by hot spots which could be pores on the surface. At the beginning shortly a stable burning with a constant burning rate is obtained. After an amount of material conversion to be chosen a hot spot array is set in front of the burning surface in the non-reacted propellant where the individual hot spots spherically enlarge by conversion. At increasing total conversion (pressure) the rate of setting further hot spot arrays increases. The consequence is that at higher total conversion (pressure) a broader volume of the propellant contributes to the burning progress and the pressure increase.

The results of numerical calculations studying a linear progression of the porous burning in a solid energetic material with a grid of 50x50x500 points are shown in Figures 13 and 14. In Figure 13 the pressure initially increases slowly according to the normal linear burning rate. After a certain conversion (in this case a fraction of 0.2 of the total volume) hot spots are set in the interior of the solid propellant ahead of the burning surface. The conversion of the propellant then increases strongly with time. In Figure 14 hotspots are initiated directly after the ignition and form peaks in the curve of the apparent burning rate curve (conversion rate). These peaks emerge to a strong peak at high (up to 2 orders of magnitude) total conversion (pressure) when the hot spots are set faster. This indicates the simultaneous burning of hot spot arrays at different individual conversion. The results are similar, at a qualitative level, to the experimental findings of apparent burning rates depending on time and pressure.

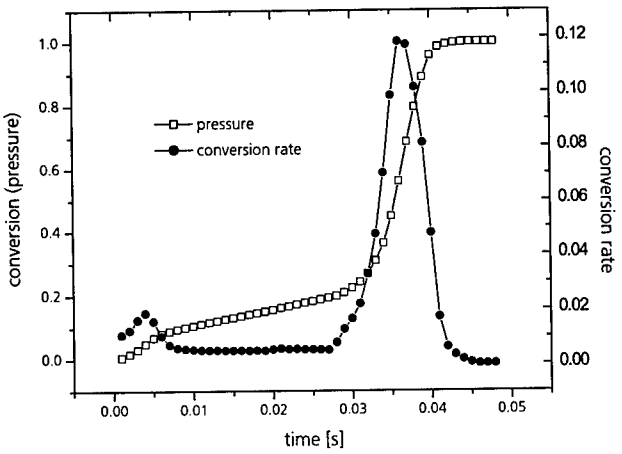


Figure 6. Conversion which corresponds to a normalised pressure calculated by the hot spot model of porous propellants: up to 0.03 s (0.2 conversion) a normal linear burning occurs, at a conversion of 0.2 hot gases penetrate into the solid material to fill the crazes and void in the interior and therefore form hotspots.

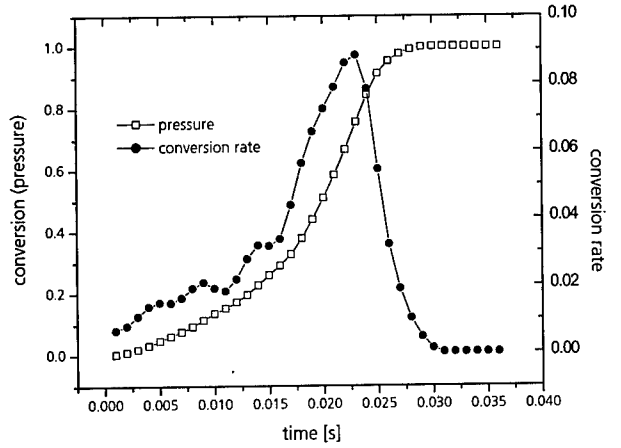


Figure 7. Conversion which corresponds to a normalised pressure calculated by the hot spot model of porous propellants: penetration of hot gases into the solid material without a delay.

7. Conclusion

Plasma can influence the ignition and combustion of solid propellants. Especially, plasma arcs interact strongly by their radiation with propellants. The high intensity of the radiation initiates burning with short time delays in the µs-range and high conversion during exposure also in the case of a stable burning. If the radiation can penetrate into the propellant interior partial fragmentation by absorbing structures occurs which could be artificially introduced or be inherently present as in the case of a double base propellant.

Simplified approaches based on the heat flow equation and radiation absorption can explain these effects at least on a qualitative level. Dynamic effects are understood by more sophisticated models.

8. References

(1) Th. H. G. G. Weise, "German Nation Overview", *10th Electromagnetic Launch Symposium,* San Francisco, California, 25-28 April 2000.

(2) C. R. Woodley and S. Fuller, "Apparent Enhanced Burn Rates of Solid Propellants Due to Plasmas", *16th International Symposium on Ballistics*, San Francisco, CA, USA, September 23-28, 1996, pp. 153-162.

(3) W. G. Proud. and N. K. Bourne, "The Electrothermal Enhancement of Propellant Burning by Plasma Injection", *Propellants, Explosives, Pyrotechnics. 22*, 212-217 (1997).

(4) A. Bach, N. Eisenreich, and M. Neiger, "Charakterisierung eines Plasma-Jets mit optischen und spektroskopischen Methoden", *22nd Int. Ann. Conf. of ICT, Karlsruhe*, Germany July 2-5, 1991, pp 98.1-10.

(5) M. J. Taylor, "Measurement of the Properties of Plasma from ETC Capillary Plasma Generators," *10th Electromagnetic Launch Symposium,* San Francisco, California, 25-28 April 2000.

(6) P. J. Kaste et al., "ETC Plasma-Propellant Interactions", *29th Int. Annual Conference of ICT*, Karlsruhe, Germany, June 30 – July 3, 1998, Germany, pp. 125.1-14.

(7) H. K. Haak, A. M. Voronov, and Th. H. G. G. Weise, "The Interaction of Electrothermally Supplied Energy with Compact Solid Propellants", *9th EML Symposium*, Edinburgh Scotland, UK, May 13-15, 1998.

(8) W. F. Oberle and G. P. Wren, "Radiative and Convective Heat Loss in Electrothermal-Chemical (ETC) Closed Chambers", *35th JANNAF Combustion Subcommittee Meeting*, Tucson, AZ, USA, December 1998, Vol. I, pp. 229-236.

(9) D. E. Kooker, "Burning Rate Deduced from ETC Closed-Chamber Experiments: Implications for Temperature Sensitivity of Gun Systems", *35th JANNAF Combustion Subcommittee Meeting*, Tucson, AZ, December 1998, Vol. II, , pp. 201-217.

(10) A. Birk, M. Del Guercio, A. Kinkennon, D. E. Kooker, and P.J. Kaste, "Interrupted-Burning Tests of Plasma-Ignited JA2 and M30 Grains in a Closed Chamber", *Propellants, Explosives, Pyrotechnics 25*, 133-142 (2000).

(11) A.Koleczko, W. Eckl, and T. Rohe, "Untersuchungen zur Einkopplung elektrischer Energie in flüssige Energieträger und deren Verbrennungsprodukte", *27th International Annual Conference of ICT*, Karlsruhe, Germany, June 25-28, 1996, 142.1-21.

(12) A. Voronov, A, Koleczko, H. Haak, Th. Weise, N. Eisenreich,"Energy Criteria for Combustion control in a large caliber gun", *IEEE Trans. on Magn.* (in press).

(13) A. Voronov, et al. "The Interaction of Electrothermally Supplied Energy with Compact Solid Propellants", *IEEE Trans. on Magn. 35*, No.1, 224-227, (1999).

(14) N. Eisenreich, W. Ehrhard, S. Kelzenberg, A. Koleczko, and H. Schmid, "Strahlungsbeeinflussung der Anzündung und Verbrennung von festen Treibstoffen", *31st Int. Annual Conference of ICT*, Karlsruhe, Germany, June 27-30, 2000, 139.1-19.

(15) N. Eisenreich, "*Vergleich theoretischer und experimenteller Untersuchungen über die Anfangstemperaturabhängigkeit von Festtreibstoffen*", ICT-Bericht 8/77, Fraunhofer-Institut für Chemische Technologie (ICT), Pfinztal, Germany, (1977).

(16) W. Eckl, S. Kelzenberg, V. Weiser, and N. Eisenreich, "Einfache Modelle der Anzündung von Festreibstoffen", *29th Int. Annual Conference of ICT*, Karlsruhe, Germany, June 30 – July 3, 1998, 154.1-20.

(17) N. Eisenreich, T. S. Fischer, and G. Langer,"Burning Rate Models of Gun Propellants", *European Forum on Ballistics of Projectiles*, Saint Louis, France, April 11-14, 2000, pp. 117-127.

(18) Koleczko, A,Ehrhardt,W., Kelzenberg,S., Eisenreich,N., "Plasma Ignition and Combustion" *Propelent, Explosives, Pyrotechnics 26*, 75-83 (2001)

(19) V. E. Zarko, L. K. Gusachenko, and A. D. Rychkov, "Simulation of Combustion of Melting Energetic Materials", *Defence Science Journal 46*, No. 5, pp. 425-433, (1996).

(20) L. K. Gusachenko, V. E. Zarko, and A. D. Rychkov, "Modeling of Gasification of Evaporated Energetic Materials under Irradiation", *INTAS Workshop*, Milan, Italy, July 1996.

(21) T. S. Fischer , W. Koppenhöfer, G. Langer, and M. Weindel, "Modellierung von Abbrandphänomenen bei porösen Ladungen", *30th International Annual Conference of ICT*, Karlsruhe, Germany, June 29-July 2, 1999, 98.1-13.

(22) N. Eisenreich and A. Pfeil, "Pyrolysis Craters Produced by Laser Pulse Irradiation on Propellant Solids", *Appl. Phys. 15*, 47 (1978).

(23) N. Eisenreich, "Successively Initiated Arrays of Hot Spot in a Reactive Medium", *Proc. Physics of Explosives*, Berchtesgaden, September 29-October 1, 1997

(24) N. Eisenreich, H. P. Kugler, and F. Sinn, "An Optical System for Measuring the Burning Rate of Propellant Strands", *Propellants, Explosives, Pyrotechnics 12*, 78-80 (1987).

(25) W. Eckl, V. Weiser, G. Langer, and N. Eisenreich, "Burning Behaviour of Nitramine Model Formulations", *Propellants, Explosives, Pyrotechnics 22*, 148-151 (1997).

(26) H. Krier and S. A. Shimpi, "*Predicting Uniform Gun Interior Ballistics Part I: An Analysis Of Closed Bomb Testing*", Technical Report AAE 74-5, (1974), Aeronautical and Astronautical Engineering Department University of Illinois at Urbana-Champaign, USA (1974).

(27) M. Hund, N. Eisenreich, and F. Volk, "Determination of Interior Ballistic Parameters of Solid Propellants by Different Methods", *Proc. 6th Int. Symp. on Ballistics*, Orlando, USA, 1981, pp. 77-84.

Plasma Ignition Experiments with a Single-Base Propellant: Comparison between Plasma Jet and Current Injection Configuration

B. Baschung, D. Grune

French-German Research Institute of Saint Louis
5, rue du Général Cassagnou- BP 34 – 68301 Saint Louis - FRANCE

Abstract: During the last years a lot of experiments concerning launchers have been performed in order to increase the muzzle velocity by controlling the ignition and the burning of solid propellants with a hot plasma. The plasma generation is built up by wire explosion at high voltage and by further discharge of a high-voltage capacitor bank. There are two different methods for the ignition of the solid propellant by means of the generated hot plasma: with a plasma jet through a nozzle, or directly in the propellant bed, the so-called current injection configuration.

This paper presents burning experiments performed with a granulated and a compacted single-base propellant without graphitization in a closed vessel and their results. The propellant was ignited by a conventional method and by the two above-mentioned plasma ignition methods. The histories of current and voltage in the plasma generator, and the gas pressure in the combustion chamber were measured during the burning experiment.

The following results are obtained and discussed:

1. Plasma jet leads to the fastest burning of the propellant for a constant electrical energy injected into the plasma. This behavior is apparently correct, and can be explained by the different electrical power histories of both plasma ignition methods. Consequently, the spatial burning rate depends on the electrical power history at constant injected plasma energy.
2. At low plasma energy in the current injection configuration, there are no differences in the dynamic vivacities between conventional and plasma ignition. Only the ignition delay time is reduced, but the spatial burning rate increases. Consequently, the dynamic vivacity is no longer a characteristic value under plasma ignition conditions.
3. The investigation method with a plasma closed vessel presents the possibility of defining a substitute form function of a compacted propellant with a prescribed ignition, especially plasma ignition. The knowledge of this function is necessary for interior ballistics cycle calculations.

In conclusion, the question is discussed whether the burning behavior by plasma ignition obtained for this single-base propellant is restricted to this type of propellant or whether it is also valid for other propellants.

1. INTRODUCTION

During the last years a lot of experiments concerning launchers have been performed in order to increase the destruction probability by controlling the ignition and the burning of solid propellants with a hot plasma. The goal of this kind of ignition is a reduction of the ignition delay time and an increase of the muzzle velocity. The plasma generation is built up by wire explosion at high voltage and by further discharge of a high-voltage capacitor bank. There are different methods of igniting a solid propellant by means of the generated hot plasma [1, 2]. In particular, for this paper two ignition methods in a closed vessel, namely plasma jet and current injection, were chosen in order to look in a more detailed way into the burning process of solid propellants under these ignition conditions. The burning experiments in the closed vessel are performed with a granular and a compacted single-base propellant without graphitization. The results of the different burning behaviors between the two ignition methods, on the one hand, and the two different propellants in geometry, on the other hand, are discussed and compared with conventional ignition.

2. EXPERIMENTS

2.1 Closed vessel

To study the burning phenomena a multifunction closed vessel for both the plasma jet and the current injection configurations is used. This closed vessel also allows conventional ignition by the hot-wire method. The closed vessel has a volume of 460 cm^3 and operates up to a maximum pressure of 400 MPa. Fig. 1 represents a cross-sectional view of the closed vessel in the plasma jet configuration. In this case, the plasma is generated in the plasma generator (on the left-hand side; 10 mm internal diameter) and expands through a nozzle into the combustion chamber where the propellant is located [3].

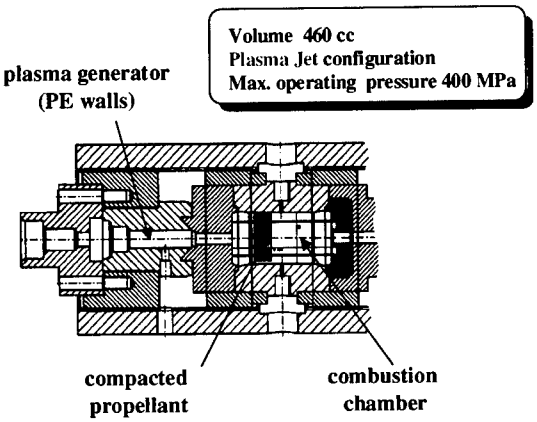


Figure 1: Closed vessel in plasma jet configuration

In the current injection configuration (Fig. 2) the plasma is directly generated in the propellant bed of the combustion chamber. The electrodes, one on each side of the cylindrical chamber, are connected with two exploding wires surrounded by a very thin multi-slotted polyethylene cannula (9.4 mm of internal diameter). The characteristic of this cannula is to provide protection against a spark discharge towards the vessel walls during the ignition process.

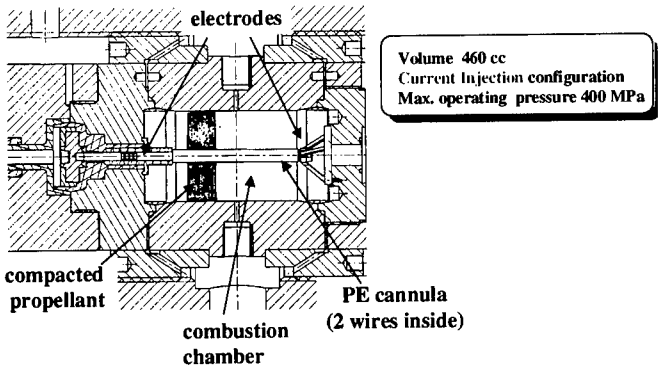


Figure 2: Closed vessel in current injection configuration

The distance between both electrodes is 80 mm in both configurations, i.e. plasma jet and current injection.

The location of the compacted propellant is sketched in both figures and shows that it is fixed in such a way that the pressure gage ports remain open during the combustion process. Therefore, the pressure history and the pressure maximum are recorded without any disturbance with a piezoelectric gage.

2.2 Electrical energy source

The high-voltage capacitor bank in use consists of two 50 kJ modules (865 μF/10 kV). During the discharge the history of the voltage is measured with a high-voltage detector, while the intensity of the current is measured by means of Rogowsky coils. These measurements allow to calculate both the resistance and the electrical power of the plasma, and consequently, the plasma energy injected into the closed vessel.

2.3 Energetic materials

For this investigation a 7-hole single-base propellant is used in two different shapes; first, as a granular propellant and secondly, the same propellant compacted to a cylindrical disc with a 10 mm hole in its center. The dimensions of the 7-hole single-base propellant and its density are listed in table 1. Table 2 presents the data for the compacted propellant.

	7-hole single-base propellant
Dimensions of the grains [mm]	L = 2.00, D = 2.15, d = 0.17
Density [g/cm^3]	1.65

Table 1: Granular propellant data

	Compacted propellant
Coating	3% binder
Dimensions of the cylindrical disc [mm]	L = 22, D = 50, d = 10
Density of the cylindrical disc [g/cm^3]	1.45
Mass of a disc [g]	60

Table 2: Compacted propellant data

2.4 Experimental conditions

Table 3 gives a summary of the experimental conditions.

The loading densities of the granular and the compacted propellants differ because the final weight of the compacted propellant discs after production is lower.

The electrical data of each experiment are also contained in the table. Especially the value of the electrical energy stored in the capacitor bank is given in the last column. The electrical energy injected into the plasma is given for each experiment in the corresponding figure.

The conventional ignition was achieved with the hot-wire method and a small amount of igniter material.

Experiment	Solid propellant	Loading density Δ [g/cm^3]	Configuration	Number of capacitors [C=865µF]	Voltage [kV]	El. energy stored in the bank [kJ]
G0	granular	0.15	Plasma jet	conventional ignition		
G1	granular	0.15	Plasma jet	1	8	27.7
C0	compacted	0.13	Plasma jet	conventional ignition		
C1	compacted	0.13	Plasma jet	1	8	27.7
C2	compacted	0.13	Current injection	1	8	27.7
C3	compacted	0.13	Current injection	2	7	42.4

Table 3: Experimental conditions

3. RESULTS AND DISCUSSION

In the first part of this discussion the different pressure histories observed are discussed as the expression of the different burning behaviors under the different ignition conditions. In addition, to look in a more detailed way into the burning process, the calculated dynamic vivacities and the spatial burning rates are presented and discussed. The decomposition of the compacted propellant is the object of the second part of the discussion.

3.1 Phenomenological specifications of the burning processes

In Fig. 3 the burning behaviors between conventional ignition and ignition with a 20 kJ plasma jet are compared. The upper part of this figure shows the pressure histories with the

granular propellant. This graph explains unequivocally the reduced ignition delay time with the plasma jet (curve G1). The pressure maximum is reached six times faster with the plasma jet compared with hot-wire ignition (curve G0), although both pressure slopes are quite similar. It seems that the plasma causes a faster building-up of the necessary temperature gradient in the propellant for stationary burning. On the lower part of Fig. 3 the pressure histories with the compacted propellant are compared under the same conditions as with the granular propellant. Here also the ignition delay time is reduced with plasma jet ignition (curve C1), but the maximum pressure is reached only three times faster compared with the conventional ignition (curve C0). The maximum pressure with the compacted propellant is lower than with the granular propellant. This behavior can be explained by a smaller loading density of the compacted propellant disc (see table 3) and additionally, by energy losses of the propellant due to an adhesive product.

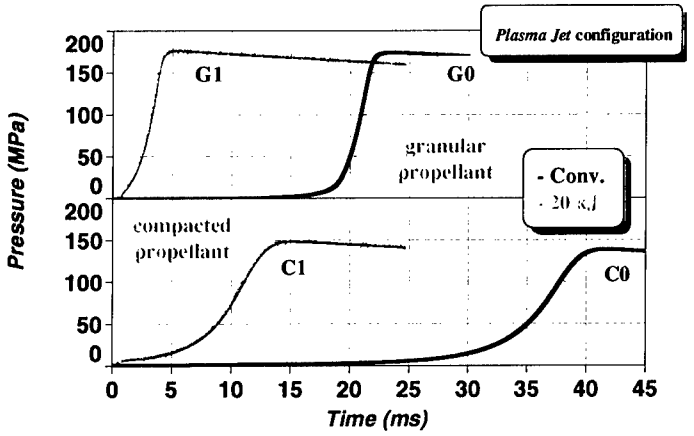


Figure 3: Influence of plasma ignition on the burning behavior

The calculated dynamic vivacities versus the fraction of the burnt mass of the above-mentioned burning tests are represented in Fig. 4. Whether the propellant is granular or compacted, this graph shows that the differences between conventional (curves G0 and C0) and plasma jet ignition (curves G1 and C1) are very small. It seems that the plasma ignition leads to a somewhat quicker burning. With both ignition methods, the granular propellant burns like a porous untreated single-base propellant, whereas the compacted propellant acts like small fragments of an unknown number of 7-hole propellant grains.

Some comments about dynamic vivacity $D = A\varphi(z)$ are now presented. The dynamic vivacity is a characteristic value corresponding for the quality control of a propellant (A is a constant and varies with the chemical ingredients; $\varphi(z)$ is the form function and describes the variation of the propellant surface during the burning). The dynamic vivacity is independent of the pressure, if the exponent α is equal to 1 in VIEILLE's burning law $r = \beta p^{\alpha}$. Because of a high plasma pressure, produced by high temperature and mass ablation, the dynamic vivacity also depends on the manner of the plasma formation and becomes very complex. Therefore, it is useful to look at the spatial burning rates dz/dt (CHARBONNIER's law: $dz/dt = A\varphi(z)p^{k}$).

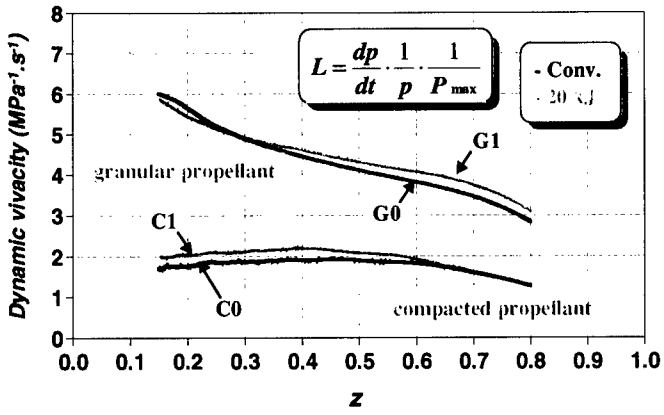


Figure 4: Dynamic vivacity versus the fraction of the burnt mass z

Fig. 5 shows the calculated spatial burning rates versus the fraction of the burnt mass of the burning tests mentioned above. As shown with the granular propellant, the spatial burning rate with plasma ignition (curve G1) starts at a high level. This also predicts CHARBONNIER's burning law. In both cases, conventional (curve G0) and plasma ignition (curve G1), the maximum of dz/dt is close to 70% of the burnt mass. It means that in this case plasma ignition also leads to an impeccable and reasonable ignition. For the compacted propellant the spatial burning rate with plasma ignition (curve C1) is also always higher than with hot-wire ignition (curve C0), corresponding to the plasma pressure. The maximum dz/dt with plasma ignition at 60% of the burnt mass is distinctly lower than with conventional ignition. The reason for this may be that the compacted propellant disk is split into different

mass fractions dependent on the ignition method. In the case discussed here, the differences are low.

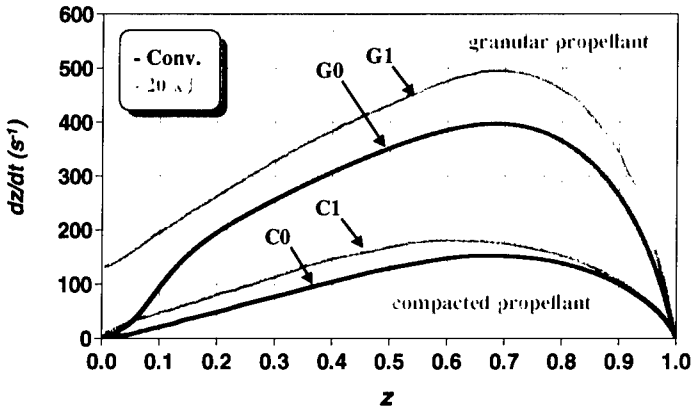


Figure 5: Spatial burning rate *dz/dt* versus fraction of the burnt mass *z*

The next paragraphs describe the burning behavior of the compacted propellant with plasma ignition under current injection conditions in comparison with plasma jet injection.

The graph in Fig. 6 presents measured pressure histories with the current injection configuration (C2 and C3) compared with the plasma jet configuration (C1).

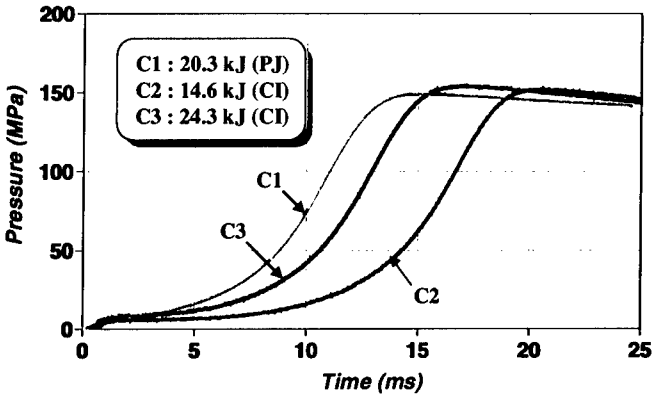


Figure 6: Influence of the plasma ignition method on the burning behavior of the compacted propellant

The ignition delay time is also shortened with current injection. But it seems that plasma jet ignition is more effective, because in this case the burning duration is shorter with 20.3 kJ of energy injected into the plasma compared to 24.3 kJ for the current injection method. This statement is only apparently true and can be refuted by the different electrical power histories recorded during the ignition period shown in Fig. 7. The experimental arrangement used for the plasma generation with current injection leads to different electrical power histories (curves C2 and C3) from those with the generator for the jet configuration (curve C1). The duration of the energy injection is 50% longer in the burning experiments with current injection. As mentioned later by means of the spatial burning behavior, the differences between jet injection and current injection are small. These differences may disappear or even be reversed with the use of an optimally adapted plasma generator for current injection. This difference between current injection and jet injection is very important. It explains that the ignition delay time and the spatial burning rate of solid propellants depend on the electrical power history at constant plasma energy. Consequently, the burning behavior can be adapted by adjusting the plasma energy injection into the propellant bed.

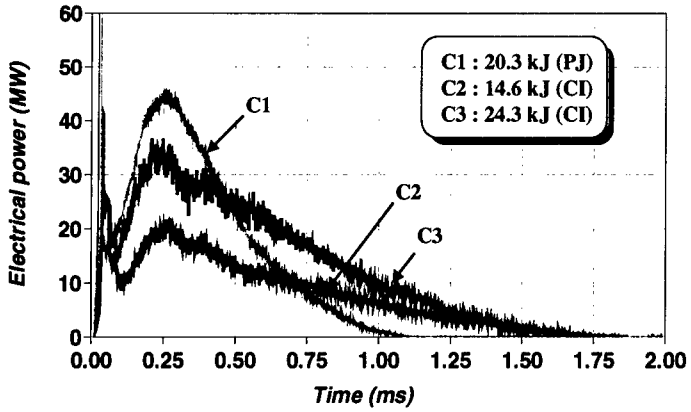


Figure 7: Electrical power histories recorded during the experiments

Fig. 8 shows the spatial burning rates *dz/dt* versus the fraction of the burnt mass *z* of the compacted propellant with the different ignition methods. The conventional ignition (curve C0) yields the lowest spatial burning rates. The fastest spatial burning rate is observed with the plasma jet generator (curve C1) for these experiments. This ignition method results in a shift of the *dz/dt* maximum from 70% to 60% of the burnt mass. For the current injection

experiments (C2 and C3), the spatial burning rates are lower but with 24.3 kJ of injected energy the data of jet injection are almost reached. It is possible that the differences disappear with a well-adapted energy injection.

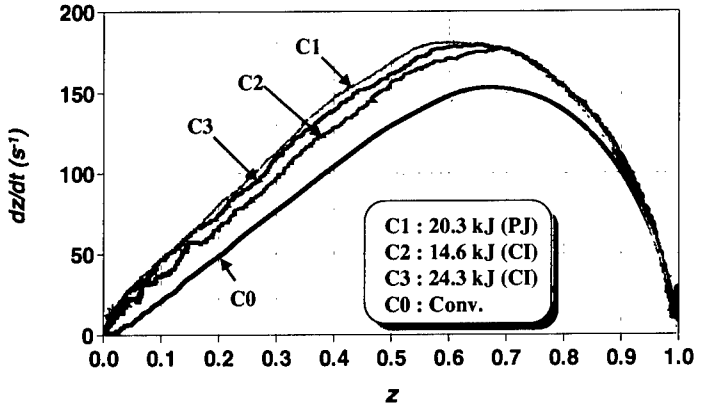


Figure 8: Spatial burning rates *dz/dt* versus the fraction of the burnt mass *z* of the compacted propellant with the different ignition methods

3.2 Decomposition of the compacted propellant

The aim of using a compacted propellant is to increase the muzzle velocity by increasing the chemical energy in the propellant bed with a high loading density Δ ($\Delta > 1 g/cm^3$). For this kind of loading it is necessary to decompose the compacted propellant quickly in order to avoid deflagration in the weapon.

To look into the mechanism of the decomposition of the compacted propellant, the burning rate of the 7-hole granular propellant (curve G0) and the fictive burning rates of the compacted propellant (curves C0 and C1) are calculated and shown in Fig. 9. The fictive burning rates are calculated using the form function of the 7-hole propellant.

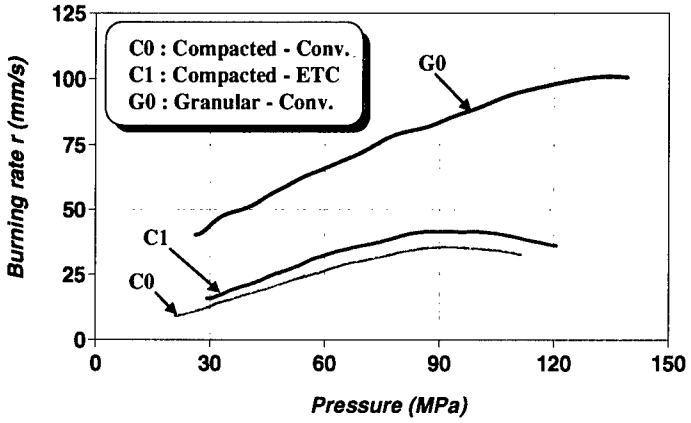


Figure 9: Burning rates of the granular and compacted propellants

For both the conventional and the plasma ignition, the fictive burning rates are lower than the real burning rate. It means that the compacted propellant burning surface is decomposed into fragments in such a way that the burning surface remains always smaller compared to the granular propellant. The decomposition by plasma ignition is certainly more effective, because in this case the fictive burning rate at the same pressure is higher than with conventional ignition.

It is possible to calculate the burning surface related to the form function of the 7-hole propellant using the fictive burning rate. The results of these calculations are shown in Fig. 10.

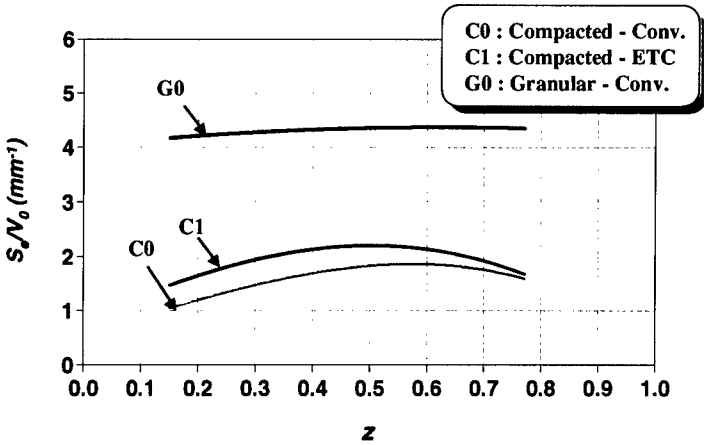


Figure 10: Burning surface versus the fraction of the burnt mass z

They describe the relationship between the form function S_e/V_0 and the fraction of the burnt mass z. The curve G0 presents the form function of the progressive 7-hole grain. During the combustion the progressivity of this propellant decreases, because the grain diameter is greater than the grain length and in addition the grain has a large web.

With the compacted propellant these free surfaces during burning are not reached either with conventional ignition (curve C0) or with plasma jet ignition (curve C1). The hot plasma causes a decomposition of the compacted propellant into an unknown number of compacted pieces. The outer grains of these pieces ignite early and quickly before the flame front works its way deeper and deeper into these pieces. During this burning phase we state an increase of the propellant surface up to 50% of its burnt mass z. In this burnt mass area, an equilibrium is reached between the burning-down of propellant grains, on the one hand, and the progressivity of the burning of the 7-hole grains in addition to new ignited free surfaces, on the other hand. In this burnt mass area the burning surface runs up to 50% of the granular propellant. Later on a decrease of the burning surface can be observed.

With conventional ignition the burning phenomena are very similar. Here the decomposition of the compacted propellant takes place in such a way that the compacted cracked pieces are larger. Therefore the burning surface is always smaller and the equilibrium of degressive and progressive burning is reached later at about 60% of the burnt mass z. In this burnt area the burning surface runs up only to 40% of the granular propellant.

This investigation method presents the possibility of defining a form function of a compacted propellant with a prescribed ignition, especially plasma ignition.

4. CONCLUSION

The burning experiments in a closed vessel under two different plasma ignition conditions with a compacted single-base propellant have shown that plasma injection seems more effective than current injection. It has been shown that the spatial burning rate depends on the electrical power history for constant plasma energy injected into the propellant bed. This statement explains unequivocally the measured differences in the ignition delay time between current and jet injection of the hot plasma. Therefore, it is important to measure not only its injected energy, but also its electrical power history in order to compare the results of burning investigations with different plasma generators and different plasma ignition methods.

Is this result restricted only to the single-base propellant? The single-base propellant used here seems to be very insensitive to the radiation of the hot plasma, because the differences in the burning rate between conventional and plasma ignition are small. But there are propellant formulations which seem to be highly sensitive to plasma radiation. Taking this characteristic into account, the plasma ignition pulse has to act in an adapted time in order to prevent or to take advantage of a gas layer around the propellant surface, which absorbs the radiation. In this case a well-adapted electrical power history is also important, indeed of great importance. A last important result concerns interior ballistics cycle calculations. For these calculations the gas production can only be calculated by using a form function of the propellant. It is very difficult to predict a form function for the compacted agglomeration of a grained multihole propellant, especially under plasma ignition conditions. As shown in Fig 10, the closed vessel equipment for plasma generation yields a usable substitute form function. However, this result has to be confirmed by further experiments.

5. REFERENCES

[1] A. Chaboki, S. Zelenak, B. Isle, "Recent Advances in Electrothermal-Chemical Gun Propulsion at United Defense, L.P.", *IEEE Transactions on Magnetics*, Vol. 33, NO. 1, January 1997.

[2] C. R. Woodley, S. Fuller, "Apparent Enhanced Burn Rates of Solid Propellants Due to Plasmas", in Proceedings of the *16th International Symposium on Ballistics San Francisco*, CA, 23-28 September 1996.

[3] B. Baschung, D. Grune, "Abbrandverhalten von Treibladungspulvern bei Plasmaanzündung", *Wegrtechnisches Symposium "Innenballistik der Rohrwaffen" BAkWVT, Mannheim, BRD, 25.-27.05.99*, ISL Report PU 326/99.

GASIFICATION OF SOLID PROPELLANTS AND PROPELLANT INGREDIENTS UNDER INFLUENCE OF THERMAL RADIATION

B.N. Kondrikov, S. Cristoforetti, I.V. Grebenyuk

Mendeleev University of Chemical Technology, Moscow, Russia

L.T. DeLuca

Politecnico di Milano, Milano, Italy

Abstract

Gasification of several propellants and propellant ingredients under the influence of external thermal radiation was studied. Detailed analysis of the solutions of the Fourier equation confirmed the overall model developed some thirty years ago in the Solid Propellant Group of the Guggenheim Laboratory of Princeton University. The model is used for treatment of experimental results of gasification of four double-base propellants, RDX, HMX and HTPB published earlier. The results have shown that the mechanism of gasification and the regression rate strongly depend not only on the external heat flux but also on the relation between energy generation in condensed phase and heat supply from gas phase. When this ratio becomes sufficiently big, the steady state gasification process gets unstable and a very small increase in the external heat flux can be followed by a drastic change of heat generated both in gas and in condensed phases. The first one is abruptly enhanced whereas the second one is essentially reduced. The derivative of the gasification rate on external heat flux becomes smaller and the overall influence of the external heat flux on the regression rate diminishes.

1. Introduction

About three decades ago two papers [1,2] were published, both in English [1] and Russian [2]. They described results of the experiments carried out by one of the authors of this presentation (BNK) during his three-month-long scientific visit at Prof. M. Summerfield's SP Laboratory of Princeton University. Ignition of N-5 double-base propellant under the influence of a 100W CO_2-laser radiation was studied. Peculiarities of behavior of different double base and composite propellants in the preignition period were extensively studied afterwards in the same Laboratory by another co-author of this paper (LDL) [3-6].

The following conclusions were drawn about the behavior of the tested propellants under thermal radiation for different pressures and radiant flux intensities:

1. A period of induced gasification precedes the moment of ignition at low and elevated pressures (0.1 to about 1 MPa) (Fig.1).
2. The regression rate, u, versus intensity of flux, q, during the period of induced gasification is a piece-wise function consisting of two straight lines, with a distinctly smaller slope at high fluxes (Fig.2). It was speculated that the controlling process is a condensed phase exothermic thermal decomposition in the low flux branch, but an overall endothermic process in the high flux branch.
3. The gasification is an auto-inhibiting process. The condensed products of the propellant decomposition form a layer of carbonaceous particles on the irradiated surface. This layer reduces the intensity of the impinging heat flux by absorption, and at the same time becomes the essential factor leading to ignition after gasification. Correspondingly, the regression rate depends on gasification time, decreasing when the time is increased (Fig.3).

These conclusions were unfortunately ignored in many of the following investigations. The main objective of this presentation consists in clarification of the physico-chemical mechanisms related to induced gasification of organic solid materials under the influence of externally applied thermal radiation. We intend to provide a detailed description of the preignition period peculiarities for different propellants. In this presentation we would like to focus our attention on the gasification process per se. It would be necessary to stress that the main objective of this paper is in no case restoration of the historical justice but only detailed and thorough description of the data appeared after our works [1-6] in terms of a model developed in our early investigations.

Three groups of solid materials described in this respect in recent publications are considered.

(1) Double-base propellants: the US compositions N-5, 1040 and 1041, and the Russian composition N.

(2) Nitramines: RDX and HMX.

(3) The widely used binder of composite propellants: HTPB.

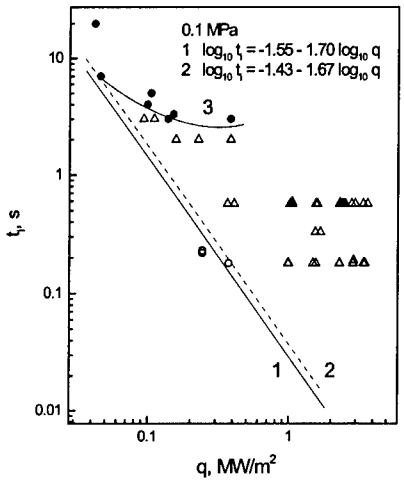


Fig. 1: Ignition and gasification of N-5 propellant at 0.1 MPa. Triangles are gasifications, solid circles are ignitions (steady state burning occurs after cessation of the heat flux), open circles correspond to runs with no visible changes of the irradiated surface. The straight line 1 is the continuation of the $t_i(q)$ dependence at higher fluxes for 2 MPa. An approximation for 0.1 MPa pressure is represented by the dashed line 2.

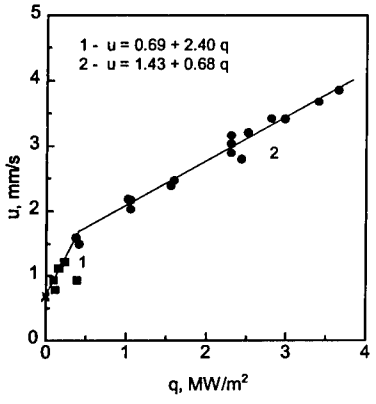


Fig. 2: Gasification of N5 propellant at 0.1 MPa. Irradiation time: solid circles - 0.57 s; solid squares - 1-2 s. Propellant burning per se is denoted by crosses on the vertical axis, q = 0.

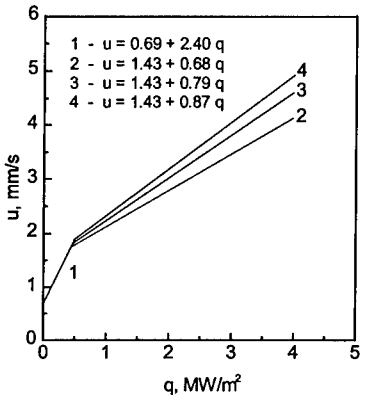


Fig. 3: Influence of gasification time on burning rate of N5 propellant after the break point (0.1 MPa.). Irradiation time: 2 - 0.57 s; 3 - 0.18 s; 4 - 0 (extrapolation). Line 1 corresponds to line 1 in Fig. 2.

2. Theory

Treatment of the results of the type presented in Figs.2 and 3 was originally carried out [1,2] using the simple expression:

$$m[c(T_s - T_0) - Q_s] = q_g + q \tag{1}$$

where m is the mass burning rate, $m = u\rho$;
u is the linear burning rate;
ρ is the initial density of the burning substance;
c is the mean specific heat in the temperature interval included between T_0 and T_s;
T_s is the surface temperature;
T_0 is the initial temperature;
Q_s is the heat evolved/absorbed as a result of physico-chemical transformations in condensed phase, per unit of mass;
q_g is the heat feedback to condensed phase due to gas phase reactions, $q_g = -\lambda_g (dT/dx)_s$;
λ_g is the heat conductivity of gas phase near the gas/liquid interface;
$(dT/dx)_s$ is the temperature gradient in gas phase at the burning surface;
q is the radiant flux.

Generally speaking, q is the sum of the external flux and the radiant flux, q_r^0, generated by the second flame. Of course, these fluxes have different spectral characteristics and can be hardly summated, but usually $q_r^0 << q$ and the difference in spectra can be neglected. In the case of self-sustained burning with no external radiant flux, q_r^0 is explicitly added to q_g or implicitly included in it. Accordingly, $Q_r^0 = q_r^0 / m$ can be defined.

Eqn. (1) eventually is an abridged form of the heat conservation equation:

$$c(T_s - T_0) - Q_m - \eta Q - (1-\eta) Q_e = Q_g + Q_r \tag{2}$$

where Q_m is the sum of the latent heat of fusion and enthalpies of polymorph transformations of the burning substance;
Q_e is the latent heat of vaporization of the burning substance;
Q is the enthalpy of condensed phase chemical reactions taken with the inverse sign;
η is the depth of condensed phase reaction, i.e. mass fraction of the burning substance that undergoes chemical transformations in the reaction layer of the condensed phase;
$Q_g = q_g/m$;
$Q_r = q/m$.

In all cases the heats Q_i are enthalpies of the corresponding physico-chemical processes taken, as usual, with the inverse sign (say, enthalpy of vaporization, $\Delta H_{vap} > 0$, whereas $Q_e = -\Delta H_{vap} < 0$, etc.), corresponding to positive or negative contribution into the heat balance of the burning wave.

Comparing Eqns. (1) and (2) the value of Q_s can be determined:

$$Q_s = \eta Q + (1-\eta) Q_e + Q_m \tag{3}$$

In some works a different combination of the heats is used:

$$Q_\Sigma = c(T_s - T_0) - Q_g - Q_r - Q_m = \eta Q + (1-\eta) Q_e = Q_s - Q_m \tag{4}$$

A more sophisticated physical model of the process is based on the solution of Fourier equation in Lagrangian coordinates bound to the interface. Introducing the dimensionless spatial coordinate $\xi=x/\delta$, the Fourier equation is:

$$\theta''-\theta'+a_0+a_1e^{a_2\xi}=0 \tag{5}$$

where $\theta=T(x)-T_0$ is the temperature difference with respect to the initial temperature;
$\theta'=dT/d\xi$ and $\theta''=d^2T/d\xi^2$;
$a_0=\Phi\delta^2/\lambda$;
$a_1=\alpha q\delta^2/\lambda$;
$a_2=\alpha\delta$;
κ is the thermal diffusivity of condensed phase;
$\Phi=Q\rho k(T_s)$ is the velocity of heat evolution/absorption in condensed phase per unit volume, with $k(T_s)$ indicating the reaction rate constant;
α is the absorbivity coefficient of the substance;
$\delta=\kappa/u$ is the conductive thermal layer thickness.

The boundary conditions are formulated comprising temperatures and heats of phase transformations and chemical reactions inside the interval $-\infty<\xi<0$ in such a way that the conservation equation (2) is satisfied at $\xi=0$.

As usual the half-infinite space of condensed phase is divided into two essentially unequal parts. The first one, at $-\infty<\xi<\xi_1$, is the preheated zone in the condensed phase where heat evolution at the expense of chemical reaction is neglected, only the enthalpies of phase transformations in condensed phase are considered. The second one, located at $\xi_1<\xi<0$, is the reaction zone where the reaction heat is generated with a constant speed Φ.

In zone 1: $-\infty<\xi<\xi_1$ $\quad a_0=0$

In zone 2: $\xi_1\le\xi<0$ $\quad a_0=const$,

$$\eta Q=-\Phi\xi_1\delta/m \tag{6}$$

The overall solution of Eqn. (5) has the form:

$$\theta=C_1+C_2e^{\xi}+a_0\xi+\frac{a_1}{a_2(1-a_2)}e^{a_2\xi} \tag{7}$$

where C_1 and C_2 are integration constants to be determined by means of the boundary conditions.

The partial solution related to the reaction zone, expressed in terms of temperature interval in the reaction zone, ΔT, is:

$$\Delta T=\left(\frac{\delta q_g}{\lambda}-a_0-\frac{a_1}{1-a_2}\right)\left(1-e^{\xi_1}\right)-a_0\xi_1+\frac{a_1\left(1-e^{a_2\xi_1}\right)}{a_2(1-a_2)} \tag{8}$$

This particular result is of special interest. Predicting a value of ΔT on the base of an accepted chemical kinetic model one may determine the thickness of the reaction zone, $x_1=\xi_1\delta$. Then, employing the heat conservation equation (2), and following from that Eqns. (3) and (4), the values of η and Q, or η and k or $q_g+q_r^0$ can be determined. The three equations (2), (6) and (8) allow estimation of three numbers, once all of the others have been properly defined. The corresponding

computer code was written by Dr. A.I. Sumin in C+. Similar results have been published in a row of papers beginning presumably from work [7].

Approximate solutions of Eqn. (8) were also obtained in the asymptotic cases. One may note, however, that Eqn. (9) perhaps was not previously published. It is written for the case $\alpha|x_1|<1$:

$$x_1 = -\frac{2\lambda\Delta T}{q_g + \sqrt{q_g^2 + 2\lambda\Delta T\left(\Phi + \alpha q - q_g/\delta\right)}} \tag{9}$$

Bearing in mind Eqns. (2) and (9) one may present the result in the form of Eqn. (1)

$$m[c(T_s - T_0) - Q_s] = m[c(T_s - T_0) - Q_m - (1-\eta)Q_e - \eta Q] = q_g + q \tag{10}$$

where

$$m\eta Q = -\Phi x_1 = \frac{2\lambda\Phi\Delta T}{q_g + \sqrt{q_g^2 + 2\lambda\Delta T\left(\Phi + \alpha q - q_g/\delta\right)}}$$

Here, q_r^0, is simply introduced into q_g. The variables in the square brackets of Eqn. (10) are not affected directly by radiation flux change. Only the expression for $m\eta Q$ contains q in the denominator, but in such an environment that eventually should prevent its real influence on the $m\eta Q$ product and correspondingly on the $u(q)$ dependence. The small increase of T_s at q augmentation is compensated by the decrease of the reaction layer thickness, the time of reaction in the condensed phase and the depth of reaction η.

Bearing in mind these circumstances, the use of Eqn. (11) as a main tool for elaboration of the $u(q)$ experimental data, as chosen by the authors of [1,2], seems to be well grounded.

$$u = a + bq \tag{11}$$

From Eqns. (10) and (11) follows that

$$a = \frac{q_g}{\rho[c(T_s - T_0) - Q_s]} \quad \text{and} \quad b = \frac{1}{\rho[c(T_s - T_0) - Q_s]}$$

One may say that in general a and b are functions of q and to determine q_g and Q_s the value of du/dq, da/dq, db/dq should be calculated from experimental results. This is in fact a rather complex procedure because the derivatives of the variables on q, included in a and b, are usually not known. When, however, the function $u = u(a,b,q)$ is approximated by the straight line (11) the problem is drastically simplified, since a, b, and $q_g=a/b$ are constants. Then Q_s and T_s are connected to each other with the relation:

$$Q_s = c(T_s - T_0) - 1/\rho b$$

The sharp transition from one part of the piece-wise function to the other at a small change of the radiant flux should be ascribed to the development of a new form of burning instability, investigation of which may also provide useful data concerning the burning mechanisms.

One may conclude that measuring the $u(q)$ dependence is a powerful method of condensed substance burning characteristics estimation. We employ this technique in Section 3 for the analysis of some experimental results of our own and some of the others.

3. Analysis of experimental data.

3.1 Double-base propellants

Experimental information on gasification of double-base propellants under the influence of external heat flux is taken from works [1,2,7,8]. The propellants of the types N-5, N, 1040 and 1041 were studied. The first two propellants were investigated at 1 atm (0.1 MPa), the third and fourth ones at 14.6 atm (1.49 MPa).

The functions of u versus q from the works [1,2,7,8] are presented in Figs.2-4. In all cases the form of $u(q)$ dependence given by Eqn. (11) is chosen. Experimental measurements of T_s at different q were not implemented in these works. Fortunately, it is known that surface temperatures of double-base propellants in many cases are close to each other at the same pressure, on the one hand, and tightly connected with the corresponding burning rates, on the other hand [9]. More recently the data of [9] and results of some other works were collected in [10]. Relation (12) following from [10]:

$$T_s = \frac{3547}{6.18 - \log_{10} u}, K \qquad (u, \text{ in mm/s}) \qquad (12)$$

is assumed to be more reliable than the original compilation of [9]. Particularly, the kinetic constants derived from Eqn.(12) (see Eqn. (13)) are in good agreement with most of the available data on chemical kinetics of double base propellants decomposition [7,13,14,17]. In this presentation formula (12) is used.

A.P. Denisyuk et al. pointed out [11] that double-base propellants with a catalyst have about the same surface temperature as a similar propellant with no catalyst. Correspondingly, for the catalyzed 1040 propellant one may suggest about the same surface temperature as for the uncatalyzed 1041 propellant at a given pressure. At u=2.15 mm/s (1041 propellant, with no catalyst) Eqn. (12) yields T_s≅607 K. The same surface temperature is accepted for 1040 propellant with a catalyst.

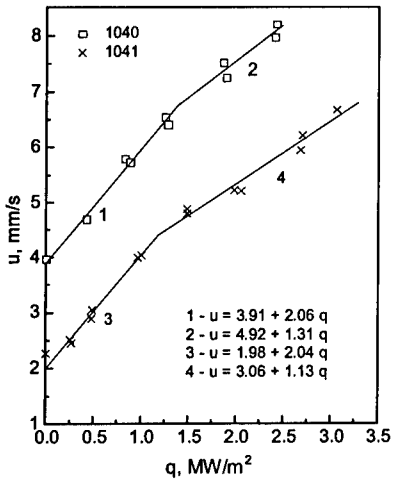


Fig. 4: Burning rate of propellants 1040 and 1041 at 1.49 MPa. The experimental points taken from [8] are approximated by a piece-wise function according to the proposed model.

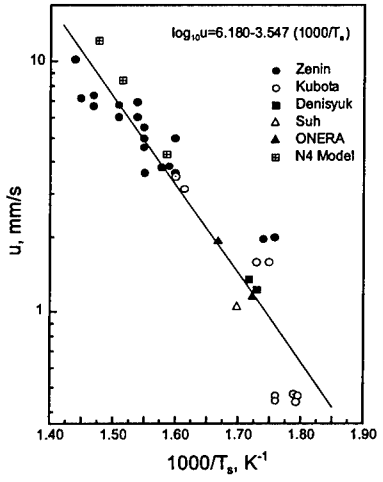


Fig. 5: Dependence of burning rate on surface temperature, from [10].

Temperature T_s of the N propellant was measured in works [12-14]. At T_0 = 293 K, values of 492 K [12], 523 K [13], 553 K (formula (12)) and 548 K [14] are extracted from the experimental results there obtained. The last one (See also Fig.3 of the work [14]) seems to be the most reliable result and was taken here as the reference value for calculations with N and N-5 formulations at p=1 atm, in spite of the fact that they have slightly different compositions. The first one contains diethylftalate as a carbon-rich additive, whereas the second one contains dinitrotoluene.

All of the other characteristics of the propellants are taken from the corresponding publications [1,2,7,8,12-15,17] and given in Table 1. The values Q=1.5 MJ/kg and Q_e=-200 kJ/kg are accepted based on the works [13,15]. Moreover, a small negative heat of melting was assumed to be compensated by the small positive heat evolution due to reaction of nitric esters with a stabilizer [13], therefor the approximation Q_m=0 was introduced. Values of a and b of Eqn.(11) were taken from the graphs represented in Figs.2-4. The heats q_g, Q_g, Q_s were calculated using a and b coefficients of Eqn. (11) experimentally estimated. The values of Φ, κ, η and $-x_1 = -\xi_1\delta$, given in Table 1, were calculated employing Eqns. (2), (6) and (8). At last, temperature sensitivity coefficients σ_p^o in the (1041) and (N) columns were taken from experimentally measured results [8,13], whereas the similar σ_p numbers were calculated by means of the approximation $\sigma_p = bc\rho$, corresponding to the approach of [16].

It is of interest to note some correlations in Table 1. The heat evolution in the gas phase, Q_g, and in the condensed phase, Q_s, are very close, in pairs, for 1040 and 1041 propellants, whereas the values of q_g differ essentially leading to different burning rates. About the same situation for Q_s is observed in the case of N-5 and N propellants. Heats Q_s are about the same for N and N-5 propellants, but both are one and a half times more than the Q_s values for 1040 and 1041 propellants.

Table 1: Characteristics of DB propellants, first part of the *u(q)* dependence (at q = 0). Designations in the upper line correspond to the name of the propellant in the text

Parameter	1040	1041	N5	N
$\bar{c}$, kJ/kgK	1.42	1.42	1.88	1.46
ρ, g/cm^3	1.54	1.54	1.48	1.6
λ, W/m K	0.23	0.23	0.25	0.23
T_0, K	298	298	293	293
u_o, mm/s	3.9	2.15	0.69	0.58
m, kg/m^{2}s	6.0	3.3	1.02	0.96
T_s, K	607	607	548	548
a, mm/s	3.9	1.98	0.69	0.55
b, m^3/GJ	2.06	2.04	2.4	3.26
Q_g, MJ/kg	0.32	0.32	0.28	0.19
q_g, MW/m^2	1.9	0.97	0.29	0.17
Q_s, MJ/kg	0.12	0.12	0.20	0.18
σ_p*10^3, 1/K	4.76	4.76	6.7	7.6
σ^o_p *10^3, 1/K		4.6		7.2
η	0.18	0.19	0.23	0.22
-x_1, μm	1.95	3.83	10.2	13.2
Φ, TW/m^3	0.88	0.23	0.035	0.021
k, s^{-1}	366	96.4	15.8	8.87
k_o, s^{-1}	137	137	7.6	7.6

Again, there is a difference between the values of q_g that is reflected for N-5 and N propellants also in the Q_g values. One may assume that a catalyst works not only in condensed phase but also in gas phase, or in the fizz-zone, over the interface, and that the burning rate augmentation due to pressure increase may be followed by heat evolution decrease in condensed phase at the double-base propellants burning

Temperature sensitivity coefficients σ_p calculated from *u(q)* data for 1041 and N propellants, where the corresponding characteristics σ_p of the propellants are directly measured, almost coincide, in pairs, being essentially different for these propellants, separately.

The data of Φ calculated using Eqns. (2), (6) and (8) allow to assess the overall reaction rate constants for processes going on in condensed phase. The constants are shown in the penultimate line of Table 1. The rate constants given in the last line were calculated assuming the validity of the generalized Arrenius expression we derived from the data collected in [10] (Fig.5):

$$k = 10^{13,8} \exp\left(-\frac{32400}{RT}\right) \tag{13}$$

One may note that propellants 1041 and N without catalysts relate very well to the general expression (13). On the other hand, the catalyzed formulations are characterized by a faster reaction in the condensed phase than the expression (13) may account for, obviously because of acceleration of the reaction by the catalysts.

Table 2: Characteristics of 1041 propellant burning near the break point of the *u(q)* dependence

Parameter	First part of *u (q)* dependence	Second part of *u (q)* dependence
q, MW/m^2	1.19	1.19
u, mm/s	4.42	4.42
m, kg/m^2s	6.81	6.81
T_s, K	641	641
a, mm/s	1.98	3.06
b, m^3/GJ	2.04	1.13
Q_g, MJ/kg	0.14	0.40
q_g, MW/m^2	0.97	2.71
Q_s, MJ/kg	0.17	- 0.09
Q, MJ/kg	1.5	0.56
σ_p*10^3, 1/K	4.5	4.5
η	0.22	0.15
$-x_1$, μm	2.90	2.01
Φ, TW/m^3	0.77	0.285
k, s^{-1}	330	330
k_o, s^{-1}	568	568

Calculations of the burning characteristics on the left and right sides of the dog-leg point of the *u(q)* function (Table 2) are implemented for the 1041 formulation with no catalyst. In fact, for uncatalyzed propellants T_s may be determined in a more reliable way than for catalyzed ones. Assuming that the surface temperature in the vicinity of the break point is a constant, the main characteristics of the burning wave change essentially at a negligibly small augmentation of the radiant flux.

3.2 RDX

Reaction of RDX on external thermal radiation is described in the paper [18]. Parameters of the burning wave with no external radiation are given in [19,20]. Using the model of Section 2 one may correlate the results of these investigations.

Authors of [18] employed several methods of specimens irradiation: CO_2-laser, ND:YAG-laser and Xenon arc lamp. Because of considerable deviation of burning rate data upon application of ND:YAG-laser and Xenon arc lamp to irradiate neat RDX, only CO_2-laser data for neat RDX are presented in Fig.6.

The long experience of operation with different sources of radiation [3-6] demonstrates that CO_2-laser is the most reliable source of heat in the sense of reproducibility of results and possibly little influence of scattering and reflection of light at irradiated surface on burning rate. Addition of carbon black to RDX (0.5% and 2% CB) leads to a diminished scatter of points. Accordingly, the ND:YAG and Xenon arc lamp burning rate data for RDX containing 0.5% and 2% CB are also included into the graph of Fig.6. Burning characteristics of RDX are presented in Table 3. Data of the corresponding tables both from [19] and [20] are used. In Table 2 the values of a and b estimated by means of Eqns. (10),(11) are juxtaposed to the data following from elaboration of the experimental points of the work [18] (Fig. 6).

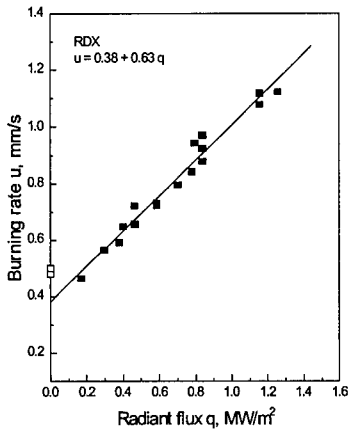


Fig. 6: Gasification of RDX at 0.1 MPa. Points at q=0 are taken from works [19,20]

Table 3: Burning characteristics of RDX. Numbers in brackets in the upper line correspond to the list of references

RDX	[19]	[20]	[18]
ρ, g/cm^3	1.67	1.67	1.7
u, mm/s	0.5	0.48	
m, kg/m^{2}s	0.83	0.80	
T_0, K	293	300	293
T_s, K	593	593	593
Q_g, MJ/kg	0.80	0.63	
Q_r^0, MJ/kg	0.059	0.11	
$Q_g + Q_r^0$, MJ/kg	0.85	0.74	0.93
q_g, MW/m^2	0.66	0.50	
q_r^0, MW/m^2	0.049	0.090	
$q_g + q_r^0$, MW/m^2	0.71	0.59	0.60
Q_s, kJ/kg	-0.41	-0.31	-0.49
a, mm/s	0.50	0.48	0.38
b, m^3/GJ	0.70	0.81	0.63

Values of λ = 0.25 W/(m K), α= $1{\cdot}10^3$ mm^{-1}, Q_m = 161 kJ/kg [22], Q = 0.8 MJ/kg, are accepted. Specific heat in [19] is taken as $\bar{c}$ = 1.31 kJ/(kg K). In a work [20] the relation of [21] is quoted: $\bar{c} = 0.605 + 1.47{\cdot}10^{-3}\, T_s$, with $\bar{c}$ in kJ/(kg K). It yields the value of $\bar{c}$ = 1.48 kJ/(kgK) at T_s = 593 K [19,20], the boiling point of RDX subjected to partial thermal decomposition. In spite of this fact in Table 2 of the paper [20] the more traditional lower value 1.30 kJ/(kg K) was chosen. Considering the detailed analysis performed by the late Yu. Maximov [22] the latent heat of evaporation is Q_e = 415 kJ/kg. In Table 3 all calculations of [19,20] including those containing c = 1.30 kJ/(kg K) are preserved, but treatment of the results of [18] (the last column of Table 3) is implemented using the value of $\bar{c}$ = 1.48 kJ/(kg K).

A relatively good correlation between these three sets of independent measurements is found in Table 3.

3.3. HMX

Physico-chemical and burning characteristics of HMX at atmospheric pressure taken from works [19,23] are collected in Table 4. Experimental results on burning rate of irradiated HMX from [18] are presented in Fig.7. The experimental points in u vs q plane (Fig.7) are suggested to be situated along the straight line intersecting the vertical axis in the point $u(q=0)$=0.65 mm/s. With the density indicated in [18] as 0.95 of TMD, i.e. approximately 1.8 g/cm^3, this corresponds to a mass burning rate of 1.15 kg/m^{2}s. Such value is about 1.5 times higher than the one usually accepted for pressed HMX at atmospheric pressure and room temperature. In work [19] the linear burning rate appears to be 0.35 mm/s, in [23] 0.41 mm/s. The generalized $u(p)$ line combining results of seven experimental works [24] in the pressure interval of 0.1 to 100 MPa evaluates this dependence in the form of Vieille's law:

$$m = 4.34 p^{0.85} \qquad (m \text{ in kg/(m}^2\text{s)}, p \text{ in MPa}).$$

At p=0.102 MPa it leads to m=0.623 kg/(m^{2}s), which corresponds to u=0.35 mm/s for a sample density of 1.8 g/cm^3.

This makes it very probable that in the case of HMX the line in the u vs q plane shown in the corresponding figure of work [18] (the line 2 in our Fig.7) should be supplemented with a line 1, forming in general the piece-wise function of the type found for the double base propellants.

The low flux branch (line 1 of Fig.7) can be easily constructed by means of Eqns. (10) and (11) on the basis of the experimental data on self-sustained burning of HMX [19,23] given in Table 4. The specific heat c= 1.3 kJ/(kg K) based on [19,23] and the heat of melting Q_m =236 kJ/kg from [22] were employed.

The high flux branch (line 2 of Fig.7) can not be predicted on the basis of burning characteristics determined at q=0. It is a least mean squares approximation of the experimental points of [18]:

$$u = 0.65 + 0.46\, q \qquad (14)$$

with u in mm/s at q in MW/m^2.

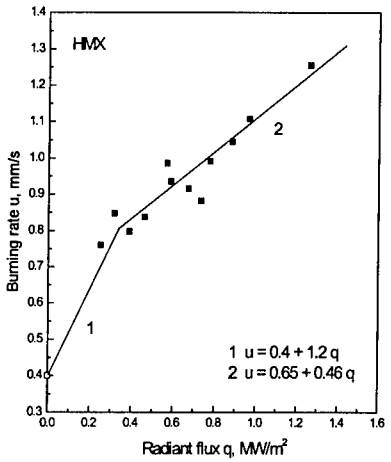


Fig. 7: Gasification of HMX at 0.1 MPa. Line 1 is constructed on the base of the burning characteristics determined at q=0 (Table 4). Line 2 is a least mean squares approximation of the experimental points taken from [18].

It does not coincide with the straight line in Fig.6 for RDX. Presumably the uniform elemental chemical composition of both substances does not result in the same behavior under thermal irradiation. The differences in physical habitude and chemical kinetics are still essential. On the basis of the experimental line the main characteristics of the burning wave, Q_s, Q_Σ and q_g are calculated. The data obtained by elaboration of the experimental dependence $u(q)$ (Fig. 7) are given in the third and fourth column of Table 4.

Table 4: Burning characteristics of HMX. Numbers in brackets in the upper line correspond to the list of references

HMX	[19]	[23]	[18] (Line 1 of Fig. 7)	[18] (Line 2 of Fig. 7)
ρ, g/cm^3	1.7	1.7	1.77	1.77
u, mm/s	0.35	0.4	0.40	
m, kg/m^{2}s	0.6	0.7	0.71	
T_s, K	633	593	613	630
Q_g, MJ/kg	0.56	0.54		
Q_r^0, MJ/kg	0.046	0.13		
$Q_g + Q_r^0$, MJ/kg	0.60	0.66	0.47	1.24
q_g, MW/m^2	0.33	0.38		
q_r^0, MW/m^2	0.028	0.090		
$q_g + q_r^0$, MW/m^2	0.36	0.46	0.33	1.43
Q_Σ, MJ/kg	0.08	-0.04	0.18	-0.57
Q_s, kJ/kg	-0.16	-0.27	-0.05	-0.80
a, mm/s	0.35	0.4	0.4	0.65
b, m^3/GJ	0.98	0.88	1.2	0.46

It should be noted that authors of [25,26] give the regression rate of HMX at q = 337 cal/cm^{2}s = 14.10 MW/m^2 close to 1.8 mm/s, i.e. about two times less than the regression rate of inert material, HTPB, at these fluxes (see next Section). Meanwhile extrapolation of line 2 of Fig.7 (Eqn. (14)) at q = 14.1 MW/m^2 gives a rate of 7.1 mm/s, i.e. a value about 4 times greater than experimentally assessed in [26] and calculated in [25]. The calculations of [25] provided also the regression rates at 70%, 80%, 90% and 100% of the incident flux absorbed (14.10 MW/m^2). They are 1,35, 1,52, 1,65 and 1.82 mm/s, respectively. From these data a straight line of the type of Eqn. (11) can be constructed. It is:

$$u = 0.234 + 0.1125q \qquad (15)$$

This immediately yields, q_g = 2.1 MW/m^2 and $Q_s \approx$ -4.5 MJ/kg, for c = 1.3 kJ/(kg K), T_s = 660 K [25], T_0 = 293 K, ρ = 1.8 g/cm^3. The first result, q_g, is noticeably higher than the data of Table 4. The second, Q_s, is fantastically low. It is 2.5 times lower than decomposition heat of HTPB, -1.8 MJ/kg (see next Section).

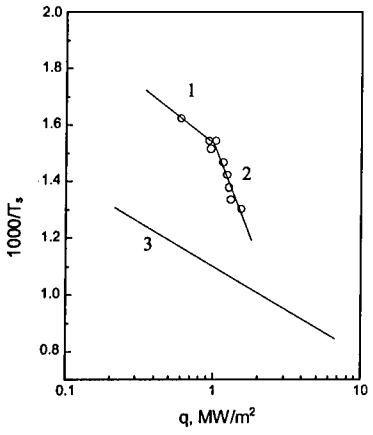
3.4 HTPB

The pyrolysis of HTPB and various other solid propellant binders was investigated by N.S. Cohen et al. [27], using a focused xenon arc image radiant source. Carbon black powder (3%) was added to the HTPB to increase its absorption coefficient. The steady-state regression rate, u, was measured by weighing the sample before and after the test and the surface temperature was measured using an optical pyrometer. These data were used to construct Arrhenius plots from which energy activation (33.8 kcal/mole) was extracted. The heat flux reached 12 MW/m^2 and the regression rate in inert gas atmosphere ranged from 0.4 to 4 mm/s.

D.R. Esker and M.Q. Brewster [28] investigated pyrolysis of HTPB cross-linked with IPD/(90/10) under the influence of a powerful CO_2-laser radiation. HTPB is sufficiently opaque at 10.6 μm and an opacifier is not necessary for CO_2-laser processing. The carbon black however was used in some of the experiments. Regression rate, plume transmission, and surface temperature (by means of microthermocouples method) were measured. Regression rate tests were conducted in a partially sealed chamber that was flushed with argon and helium before each test and maintained usually at a slight positive pressure during the test to reduce oxygen infiltration. A weak flame was still observed in the gas phase, but for most conditions (all steady regression tests) the standoff distance of the flame (>2 cm) was such that conductive heat feedback from the flame to the sample was negligible. This was verified with thermocouple measurements.

Dependence of the surface temperature of HTPB sample on absorbed laser flux is presented in Fig.8. The $1/T_s$ vs q dependence from work [27] is also shown in Fig.8 with the straight line 3. Curve 2 in Fig.8 corresponds to an activation energy of about 8 kcal/mole, coinciding with the data of [29] obtained by FTIR method.

Results of the authors of [28] concerning dependence of the regression rate on the absorbed flux are presented in Fig. 9. The points taken from figures 4, 5 and 8 of [28] corresponding to the usual experimental conditions (the most essential among these is probably the elevated pressure precluding penetration of air in the bomb) are used. The straight line in Fig.9 is drawn at Q_s=-430 cal/g= -1.8 MJ/kg [27] and T_s=654 K [28] at q=1 MW/m^2 (from Fig.8). Only four points out of 28, at high fluxes, deviate from the line in Fig.9. The properties of HTPB were assumed to be ρ_c=0.92 g/cm^3, c = 0.6 cal/(g·K) = 2.5 kJ/(kg·K), κ= 10^{-3} cm^2/s, T_0=300 K, and α = 500 cm^{-1} [28].



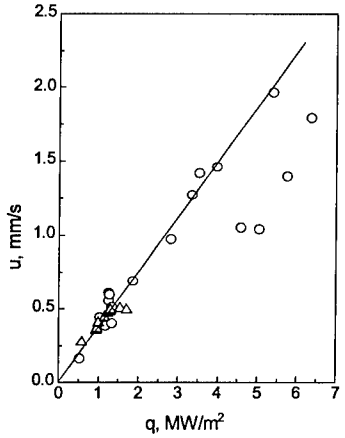


Fig. 8: Dependence of surface temperature on absorbed laser flux. The experimental points approximated by the lines 1 and 2 are from work [28]. Line 3 is taken from work [27].

Fig. 9: Gasification of HTPB. The experimental points are from Fig.8 (circles) and Figs.4,5 (triangles) of work [28]. Line is calculated on the basis of the proposed model.

It is of interest to note that there are two other groups of points taken from [28] that form a different straight line in *q-u* coordinates, corresponding to Q_s=-0.5 MJ/kg. One group is presented in Fig.2 of work [28] (the points for HTPB without carbon black), the other one in Fig.8 of [28] (the points at slightly different conditions of ambient atmosphere suction in the bomb). However, differences in experimental conditions between the two groups of points are expressed rather foggy in paper [28]. Accordingly, it would be difficult to explain now this difference in the *u(q)* dependence.

4. Conclusions

Gasification of several propellants and propellant ingredients under the influence of external thermal radiation was studied. Detailed analysis of the solutions of the Fourier equation confirmed the overall model developed some thirty years ago in the Solid Propellant Group of the Guggenheim Laboratory of Princeton University. The model is used for treatment of experimental results of gasification of four double-base propellants, RDX, HMX and HTPB published earlier. The results have shown that the mechanism of gasification and the regression rate strongly depend not only on the external heat flux but also on the relation between energy generation in condensed phase and heat supply from gas phase. When this ratio becomes sufficiently big, the steady state gasification process gets unstable and a very small increase in the external heat flux can be followed by a drastic change of heat generated both in gas and in condensed phases. The first one is abruptly enhanced whereas the second one is essentially reduced. The derivative of the gasification rate on external heat flux becomes smaller and the overall influence of the external heat flux on the regression rate diminishes. This overall picture, two straight lines representing the *u(q)* dependence, is observed in the experiments with three double-base propellants out of four (the Russian N propellant was studied only at fluxes below the break point on the *u(q)* dependence), and for HMX where the heat evolution in the condensed phase at burning with no external flux is sufficient to generate the first part of the piece-wise function. Heat evolution at RDX self-sustained burning is relatively small, the value of Q_s is essentially negative, and the first part of the overall dog-leg line is eliminated. In the case of HTPB the feedback from gas phase reactions is absent and the *u(q)* dependence corresponds to Eqn. (11) with the first term equal to zero and very big heat absorption contained in the second term.

Acknowledgements

The great contribution of Prof. Martin Summerfield and Dr. Thomas Ohlemiller at the first stages of implementation of this project some thirty years ago in America is highly appreciated. The part of this presentation fulfilled in Russia was supported by Russian Foundation of Basic Research (Grant 01-03-32610).

References

1. B.N. Kondrikov, M. Summerfield, T. Ohlemiller, "Ignition and gasification of a double-base propellant induced by CO2 laser radiation," Thirteenth Int. Symposium on Combustion, Paper №129, Aug.23-29, 1970, Univ. of Utah, Salt Lake City, Utah.
2. B.N. Kondrikov, T. Ohlemiller, M. Summerfield, "Ignition and gasification of double-base propellant subjected to radiation of CO2 laser", Voprosy teorii vzryvchatykh vestchestv (Problems of theory of explosives)," Proceedings of Mendeleev Institute of Chemical Technology, Moscow, 1974, Vol. 83, pp. 67-78.
3. L. DeLuca, L.H. Caveny, T.J. Ohlemiller, M. Summerfield, "Radiative ignition of double-base propellants: I. Some formulation effects", AIAA Journal, 1976, Vol.14, №7, pp. 940-946.
4. L. DeLuca, L.H. Caveny, T.J. Ohlemiller, M. Summerfield, "Radiative ignition of double-base propellants: II. Pre-ignition events and source effects", AIAA Journal, 1976, Vol.14, №. 8, pp. 1111-1117.
5. L. De Luca, T.J. Ohlemiller, L.H. Caveny, M. Summerfield, "Solid propellant ignition and other unsteady combustion phenomena induced by radiation," Technical Report, Department of Aerospace and Mechanical Sciences, Princeton University, Princeton, New Jersey, 1976.

6. T.J. Ohlemiller, L.H. Caveny, L.T. De Luca, M. Summerfield, "Dynamic effects of ignitability limits of solid propellants subjected to radiative heating", in 14th Symposium (International) on Combustion, The Combustion Institute, Pittsburgh, PA, USA, pp. 1297-1307.
7. E.V. Konev, S.S. Khlevnoi, "Burning of a powder in the presence of luminous radiation", Fiz. Goreniya Vzryva, 1966, Vol. 2, №. 4, pp.33-41.
8. L.H. Caveny, T.J. Ohlemiller, M. Summerfield, "Influence of thermal radiation on solid propellant burning rate", AIAA Journal, 1975, Vol. 13, pp. 202-205.
9. A. Zenin, B. Novozhilov, "Unequivocal dependence of surface temperature of double-base propellants on burning rate", Fiz. Goreniya Vzryva, 1973, Vol.9, № 1, pp. 246-249.
10. Q. Brewster, S.F. Son, "Quasi-steady combustion modeling of homogeneous solid propellants", Combustion and Flame, 1995, Vol. 103, pp. 11-26.
11. A.P. Denisyuk, A.G. Arkhipova, I.V. Kalashnikov, "Surface temperature of a burning propellant", Fiz. Goreniya Vzryva, 1983, Vol.19, № 2, p. 136.
12. A.A. Zenin, O.I. Nefedova, "Burning of double-base propellants in a broad interval of initial temperatures", Fiz. Goreniya Vzryva, 1967, Vol.3, № 1, pp. 45-53.
13. A.A. Kovalskii, E.V. Konev, B.V. Krasilnikov, "Combustion of nitroglycerin powder", Fiz. Goreniya Vzryva, 1967, Vol.3, № 4, pp.547-554.
14. V.V. Alexandrov, E.V. Konev, V.F. Micheev, S.S. Khlevnoy, "Surface temperature of nitroglycerine powder in burning conditions", Fiz. Goreniya Vzryva, 1966, Vol.2, № 1, pp. 68-73.
15. V.V. Alexandrov, N.S. Bufetov, "Thermal decomposition of nitroglycerine propellant in vacuum", Fiz. Goreniya Vzryva, 1971, Vol.7, № 2, pp. 306-308.
16. M.M. Ibiricu, F.A. Williams, "Influence of externally applied thermal radiation on the burning rates of homogeneous solid propellants", Combustion and Flame, 1975, Vol.24, pp. 185-198.
17. S.S. Khlevnoy, V.F. Micheev, "Influence of initial temperature and transparency of a nitroglycerine propellant on ignition by means of irradiation", Fiz. Goreniya Vzryva, 1968, Vol.4, № 4, pp. 579-583.
18. V.N. Simonenko, V.E. Zarko, A.B. Kiskin, "Characterization of self-sustaining combustion of cyclic nitramines", Energetic Materials: Production, Processing and Characterization, 29th Annual Conference of ICT, 1998, Karlsruhe, Germany.
19. A. Zenin, HMX and RDX: Combustion Mechanism and Influence on Modern Double-Base Propellant Combustion, Journal of Propulsion and Power, 1995, Vol.11, pp. 752-758.
20. L.T. DeLuca, F. Cozzi, G. Germinasi, I. Ley, A.A. Zenin, "Combustion mechanism of an RDX-based composite propellant", Combustion and Flame, 1999, Vol.118, pp. 248-261.
21. Encyclopedia of Chemical Technology, ed. Kirk, R.E., Othmer, D.E., New York, 1951, Vol. 6, p. 40.
22. Yu.Ya. Maximov, "Boiling point and enthalpy of evaporation of liquid RDX and HMX", Journal of Physical Chemistry (Russ.), 1992, Vol. 66, pp. 540-542.
23. A.A. Zenin, V.M. Puchkov, S.V. Finiakov, "Characteristics of the combustion wave of HMX at different pressures and initial temperatures", Fiz. Goreniya Vzryva, 1998, Vol. 34, №. 2, pp. 59-65.
24. A.E. Fogel'zang et al., Database "Flame", RCTU, Moscow, 1998.
25. K. Prasad, R. Yetter, M.D. Smooke, An eigenvalue method for computing the burning rates of HMX propellants, Combustion and Flame, 1998, Vol.115, pp. 406-416.
26. D. Hanson-Parr, T. Parr, Twenty-fifth (Int.) Symposium on Combustion, The Combustion Institute, 1994, pp. 1281-1287.
27. N.S. Cohen, R.W. Fleming, R.L. Derr, Role of binders in solid propellant combustion, AIAA Journal, Vol. 12, №2, 1974, pp. 212-218.
28. D.R. Esker, M.Q. Brewster, Laser pyrolisis of hydroxyl-terminated polybutadiene, Journal of Propulsion and Power, 1996, Vol.12, pp. 296-301.
29. J. K. Chen, T. B. Brill, Chemistry and kinetics of Hydroxyl-Terminated Polybutadiene (HTPB), and Diisocyanate-HTPB polymers during slow decomposition and combustion-like conditions, Combustion and Flame, 1991, Vol.87, pp. 217-232.

THE COMBUSTION MECHANISM OF AP BASED PROPELLANT CONTAINING MAGNALIUM

Hiroto HABU, Keiichi HORI, Takeo SAITO and Masahiro KOHNO
The Institute of Space & Astronautical Science (ISAS), Ministry of Education, Culture, Sports & Technology, JAPAN
3-1-1,Yoshinodai, Sagamihara, Kanagawa 229-8510, JAPAN

Abstract

Suppression of HCl in the combustion gas of AP based solid propellants is preferable for the environment. Neutralized propellant which includes magnesium (Mg) as a metallic fuel is one of the candidates, however, Mg has unsuitable characteristics such as hazard in handling and relatively high reactivity with AP. These led us to use magnalium (Mg/Al) which is the alloy of Mg and aluminum (Al) instead of Mg. The acid suppression effect of Mg/Al was investigated in the previous study and it was found that the concentration of HCl was approximately one-fifth of conventional propellants.

The combustion characteristics and mechanism of Mg/Al have been studied in detail by several investigators. It was described that Mg/Al particle has two-stage combustion mechanism in the oxidative atmosphere, and burns rapidly compared with Al particles. However, reports on the combustion mechanism of the propellant with Mg/Al have not been published to date. Therefore, it is necessary to investigate the combustion characteristics of Mg/Al propellants.

It was shown that Mg/Al enhances the burning rates of AP based propellants by 40% in the range from 1.0MPa to 7.0MPa. To clarify the cause of the high burning rate, the temperature profile of burning propellant was measured with fine thermocouple, type S (Pt-Pt/Rh10%, 5□m). In addition, flames of each propellant were photographed in pressurized N2 atmosphere with a camera which mounted a special optical filter. From these experimental results, it is suggested that there is the difference on the combustion mechanism between the propellant with Mg/Al and that with Al.

The present paper discusses the combustion mechanism of the AP based propellant with Mg/Al including the chemical properties of Mg/Al itself.

1. Introduction

Many investigators have estimated the environmental impacts of HCl [1~4], and they consider that it will be necessary to develop the "clean" propellant system in the future although the effect of the diffused HCl on the environment is negligible at present.

Several techniques to suppress HCl were proposed as follows,

□(a) Replacement of Al by Mg

□(b) Replacement of AP by alkali metal nitrate such as NaNO3 or KNO3.

□(c) Replacement of AP by high energy non-chlorine oxidizer.

Although type (c) is ideal, high energy non-chlorine oxidizers are expensive at present, furthermore, characteristics of the propellants with them are under investigation. Though the acid suppression effect of type (b) which is called as scavenged propellant is relatively high, the propellant with these salts has low combustibility and shows relatively low performance. Type (a) is feasible because Mg has a high affinity to chlorine, however, Mg has following disadvantages for application to the propellant ingredient,

□(1) Low Isp.

□(2) Low density and low heat of oxidation compared with Al.

□(3) High sensitivity to mechanical friction.

These led us to use magnalium (Mg/Al) which is the alloy of Mg and Al instead of Mg. Mg/Al is the material used widely for pyrotechnics and is well known to have the peculiar properties different from general metals. For example, the melting point (eutectic point) of Mg/Al containing Mg from 35 to 65 % by mass is lower than that of Al and Mg, and the difference reaches approximately 200K. Higher Mg in Mg/Al lowers Isp and enhances the HCl suppression effect on numerical calculation, and 50 mass % of Mg seems to be feasible considering the both aspects of suppressing HCl and keeping the performance. It was shown in our previous study [5] that the AP based propellant with Mg/Al is as stable as the conventional propellants, and the concentration of HCl in the combustion gas was approximately one-fifth of conventional propellants (@50 mass% of Mg in Mg/Al). Mg/Al containing 50% Mg by mass was selected in this work for the above reasons.

It is widely recognized that the Al particle have to be small to achieve a high filling factor in the propellant. Generally, fine Al particle is manufactured by the gas atomizing method, thus, the particle is almost spherical. However, Mg/Al particle is usually manufactured by milling method and its shape is irregular. As fine Mg/Al particles such as Al are not commercially available, it is necessary in this work to prepare them by ourselves and to estimate the combustion property of the propellant with them including the properties of Mg/Al itself.

Gordon et al. [6] investigated the Mg/Al combustion, and they suggested that Mg/Al particles have the two-stage combustion mechanism and explained that Mg burns initially with particle fragmentation and later residual Al burns gradually. Takeno and Yuasa [7] also studied the combustion mechanism of Mg/Al particles in oxidative atmosphere in

detail, and their experimental results confirmed the suggestion of Gordon. Blackman et al. [8] estimated the combustion mechanism of various kind of metal particle in air, and they found that the burning rate of Mg/Al particle is ten times as high as that of Al with photographic observations.

Willoughby et al. [9] investigated the combustion mechanism of various kinds of metal particles in AP based propellants. In their report, it was mentioned that Mg/Al hardly agglomerates even at 100G, thus, it is considered that the propellant with Mg/Al has a particular combustion mechanism.

The object of the present study is to estimate several properties of Mg/Al itself and to investigate the combustion mechanism of the propellant with Mg/Al.

2. Experimental Procedures

2.1 Estimation of Mg/Al Properties

In this work, as-received Mg/Al particles were sieved with #440mesh (32μm). The sieved mother particles were milled for 30 hours in nitrogen atmosphere with the ball-mill to be broken into fine particles. The milled particles were observed and photographed by SEM. The heat of combustion of Mg/Al, Mg and Al were measured with a bomb calorimeter in 2.5MPa oxygen. DTA was used to estimate the thermal properties of Mg/Al, Mg and Al. Samples were heated in air, and the heating rate was 10K per minute.

2.2 Burning Rate Measurement

The compositions of propellant samples are listed in Table 1, and the burning rate was measured in pressurized nitrogen gas from approximately 1MPa to 7MPa with a strand burner. The size of strand samples was 7×7×70mm.

Table 1 Composition of Propellants (mass%)

HTPB&IPDI	AP	Al (MDX-65)	Mg/Al (50/50mass%)
15	65	20	-
15	65	-	20

2.3 Photographic Flame Structure Observations

The flames of propellants with Al or Mg/Al were photographed in the pressurized burner (approximately 2.0MPa) through a transparent window. As the flame emits strong lights, the camera mounted special optical filter transmitting the light of blue was employed.

2.4 Measurement of Temperature Profile

The Temperature profile of the burning propellant was measured with fine thermocouples in nitrogen pressurized strand burner. The thermocouples were Type S, Pt-Pt/Rh 10 percent of 5μm in diameter. As fine thermocouple wires are initially covered with silver

(resulting in 75μm in diameter), the sheath was dissolved in nitric acid (Photo.1). The thermocouple wires were welded with a micro-torch and the junction bead diameter was less than twice of a thermocouple wire (Photo.2).

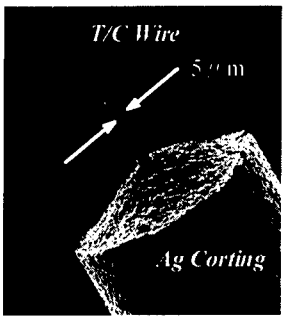


Photo.1 Thermocouple Wire

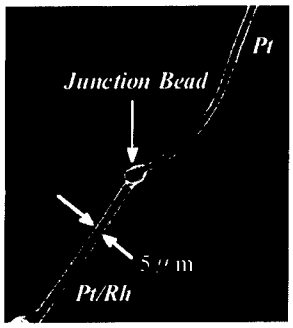


Photo.2 Thermocouple

Generally, the thermocouple is embedded in cured propellant with adhesives, however, it is undesirable to use other materials such as adhesives for temperature measurement. Summerfield et al. [10] studied the temperature profile with fine thermocouples, and their technique is that the fine thermocouple is embedded directly into uncured propellant.

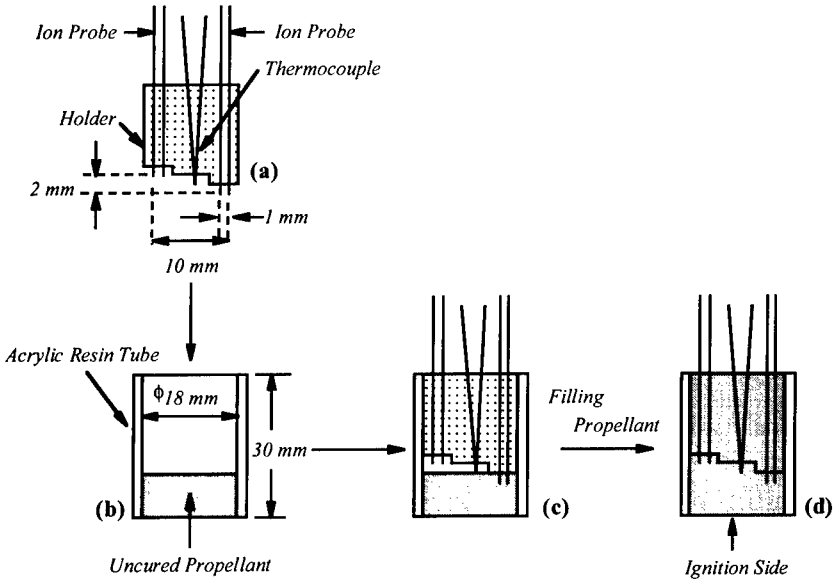


Fig.1 Sample Preparation Procedure

The present study adopted theirs to accurately measure the temperature profile of burning propellants. Moreover, to measure the local burning rate around the thermocouple bead and decide the accurate combustion wave thickness, two pairs of ion probes were embedded with a thermocouple. The sample preparation procedure is shown in Fig.1. The thermocouple and two pairs of ion probes were fixed on the acrylic resin plate as a holder with a double-coated tape, and their relative position is shown in Fig.1 (a). The size of sample case is ϕ18mm×30mm. The case was partially filled with the uncured propellant, which was evacuated enough [Fig.1 (b)]. After that, the holder was put in the case carefully [Fig.1(c)] and the rooms of the case were filled with uncured propellant [Fig.1 (d)]. The propellant was cured and uniform throughout the sample case.

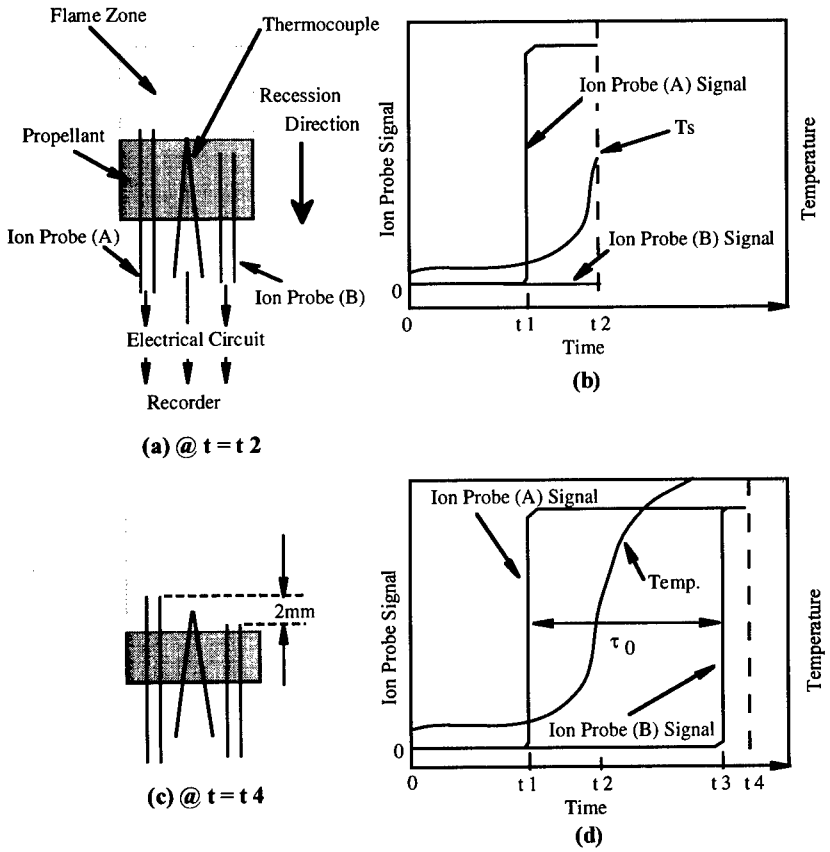


Fig.2 The Principle of Burning Rate Measurement with Ion Probes

The role of ion probes as signal generators is explained as follows. As shown in Fig.2, each pairs of ion probes were connected with the electrical circuit and put on the voltage. When each pairs of ion probes are under the burning surface, the signals are not output. When the tips of the ion probe (A) emerged just above the burning surface [@ t = t 1], the signal is output because the weak current flows in the circuit as the flame is filled with many kinds of ions. Further, the combustion wave proceeds, and a thermocouple reaches the burning surface, surface temperature (Ts) is observed (t = t 2). After that, ion probe (B) also signaled at t = t 3. The burning rate is estimated with the interval,τ_0 [Fig.2(d)].

3.Results

3.1 Several Properties of Fine Mg/Al Particles

SEM photographs of Mg/Al and Al particles are shown in Photos.3~4. To smash Mg/Al into fine particles, the ball-mill had to be operated for more than 30 hours. The milled particle size was measured with the apparatus which employed the laser diffraction scattering and it was found that the average size was approximately 10μm.

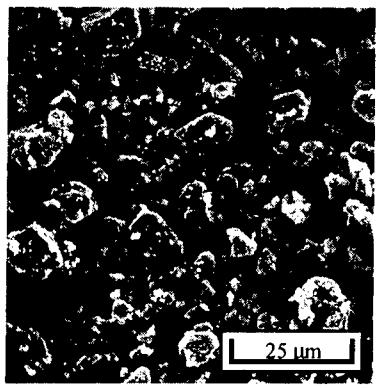


Photo.3 SEM Photograph of Mg/Al Particles

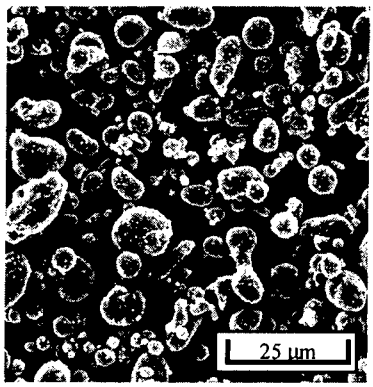


Photo.4 SEM Photograph of Al particles

The heat of combustion of metals is shown in Fig.3. Solid line shows the arithmetic mean and coincides with the results. It is found that the heat of Mg/Al combustion decreases with increasing the concentration of Mg, and it is shown that there is no difference in the heat of combustion between the alloy and the arithmetic mean.

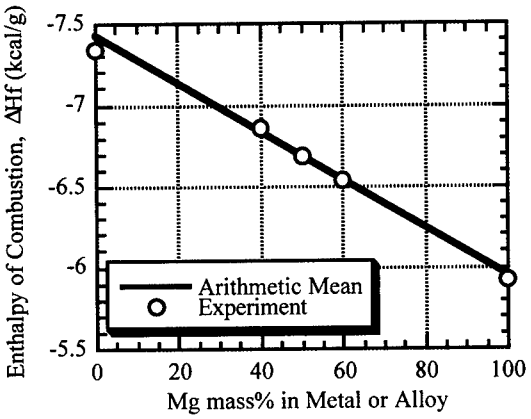


Fig.3 Heat of Combustion of Metals

From the result of DTA analysis shown in Fig.4, Mg/Al is rapidly oxidized at approximately 810K although Al is not oxidized up to 1400K. The results show that the chemical properties of Mg/Al are similar to Mg, being quite different from Al. As for the difference in the property between Mg/Al and Mg, it is pointed out that the endothermic property at the melting point, which emerges for the former does not appear apparently for the latter. Anyway, this analysis shows that Mg/Al is oxidized easily at relatively low temperature.

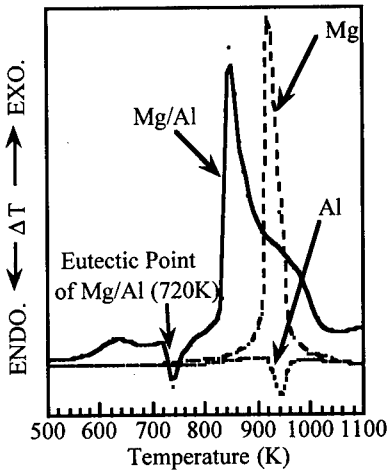


Fig.4 DTA curves in AIR

3.2 Linear Burning Rate and Flame Observation

The results of the burning rate measurement are shown in Fig.5. The burning rate of the propellant with Mg/Al was found to be approximately 1.4 times as high as that with Al. Moreover, the pressure exponent of each propellant was almost the same, 0.45~0.46. These tendency is always observed between the propellant with Mg/Al and that with Al at the different propellant composition, for example AP/HTPB/Metal = 60/20/20 (% by

mass).

The flame of the propellant containing Al or Mg/Al is shown in Photos.5 and 6. In Photo.5, lots of clear traces of large burning Al particles are observed and several hundreds μm, and they seem to be agglomerates. On the other hand, in Photo.6, such clear traces is not evidently shown, and it is found that there is a strong luminous zone above the burning surface.

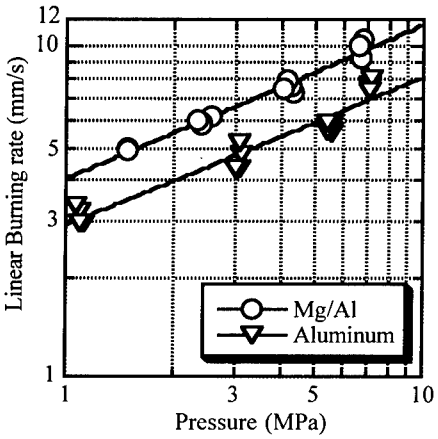


Fig.5 Linear Burning Rate of Propellants

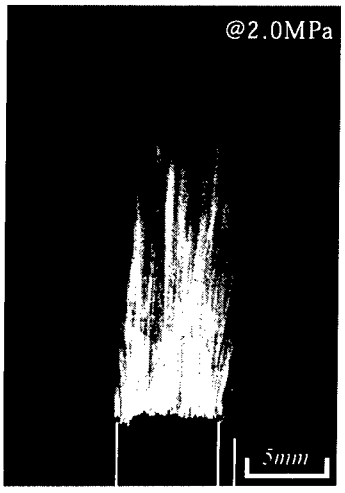


Photo.5 Flame of Al Propellant

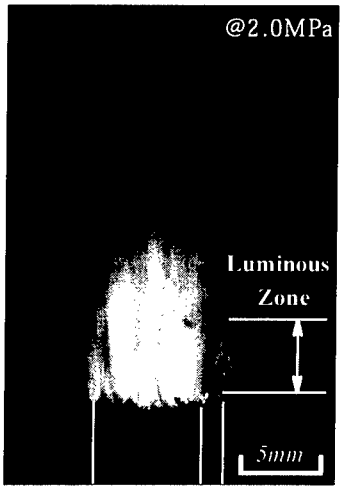


Photo.6 Flame of Mg/Al Propellant

3.3 Measurement of Temperature Profile

Figure 6 illustrates the typical result of a temperature profile of the burning propellants and ion probe signals, and the typical temperature profiles of the propellant with Al and Mg/Al are shown in Fig.7. The burning surface temperature was identified as the point that changes the slope of temperature in a logarithm plot, and it was suggested that each propellant shows almost the same value, 823~883K. Based on the measured temperature profiles, the temperature gradient $(dT/dx)_{s+}$ was calculated, the average values of each propellant being shown in Table 2. The temperature gradient of the propellant with Mg/Al was 1.74 times as steep as that with Al.

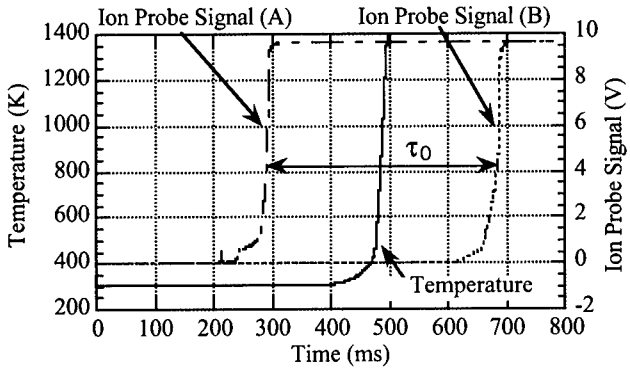


Fig.6 Data Sample of Temperature Measurement

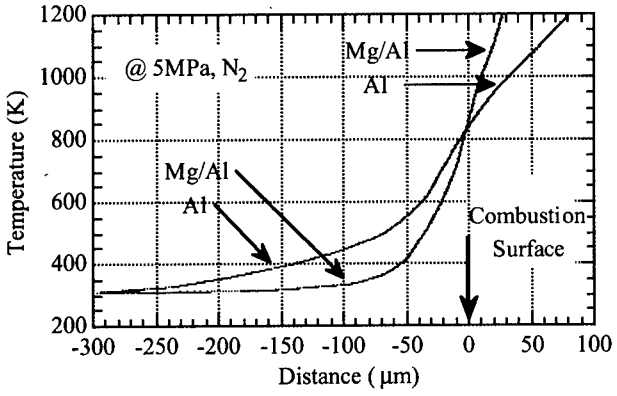


Fig.7 Temperature Profiles of Burning Propellants

Table 2 Temperature Gradient in the gas phase

	Al Propellant	Mg/Al Propellant
$(dT/dx)_{s+}$ ($\times 10^3$K/mm)	6.37	11.1

4. Flame Structure

It is generally explained that Al particles are accumulated on the burning surface, and the agglomerates are ignited in some distance from the burning surface, and burns gradually. It seems in our observation that Al particle burns with the above mechanism (Photo.5).

However, the combustion behavior of Mg/Al is sure to be different from that of Al. Boiling point of Mg is relatively low (1376K @0.1MPa), and this point seems to exist within the distance of 50μm from the combustion surface (Fig.7). Therefore, Mg/Al may start to spout Mg vapors just above the combustion surface, which may prevent Mg/Al to agglomerate. In fact, from the flame observation and Ref.[9], Mg/Al particle may not agglomerate in their combustion process. Ejected Mg vapor would be oxidized at first and this oxidation step may correspond to the luminous zone above the combustion surface. This idea is supported by DTA result that Mg/Al is easily oxidized at relatively low temperature. That is, the two-stage combust ion mechanism for Mg/Al itself is maintained even in the propellant combustion, and Mg/Al enhances the burning rates of AP based propellants by 40%.

Bomb calorimeter experiment shows that heat of Mg/Al combustion is lower than Al, therefore, heat of metal combustion is not responsible for the high burning rate of Mg/Al propellant. As described above, gas phase reaction zone of Mg/Al propellants is closer to the combustion surface, and the temperature gradient on the side of the gas phase at the burning surface is steeper (Table 2). It seems that higher burning rate is due to the larger heat flux to the burning surface.

5. Conclusion

The chemical properties of Mg/Al and the combustion mechanism of the AP based propellant with Mg/Al are discussed. It is found that the heat of Mg/Al combustion decreases with increasing the concentration of Mg, and DTA analysis showed that Mg/Al is oxidized easily in air at low temperature compared with Al. From the photographic observations and temperature measurement, it seems that Mg/Al particles burn with the two-stage mechanism even in the propellant.

It is considered that the high burning rate of the propellant with Mg/Al depends mainly on the high temperature gradient in the gas phase at the burning surface.

References

[1] Andrew E. Potter, Environmental Effects of the Space Shuttle , The Journal of Environmental Sciences, March/April, 1978, pp15~21

[2] Allan J. McDonald, Robert R. Bennett, Jerry C. Hinshaw and Michael W. Barnes, Chemical Rockets and the Environment, Aerospace America , May, 1991, pp32~36

[3] J. Anderson and Vernon W. Keller, A Field Study of Solid Rocket Exhaust Impacts on the Near-Field Environment , NASA Technical Memorandom, TM-4172, 1990

[4] B. D'Andrea, F. Lillo, A. Volpi, C. Zanotti and P. Giuliani, Advanced Solid Propellant Combustion For Low Environmental Impact and Negligible Erosive Effect , Proceedings of the 21st International Symposium on ISTS 98-a-1-12, 1998, pp68~73

[5] Hiroto Habu, Keiichi Hori, Takeo Saito and Masahiro Kohno, The Combustion of Magnalium (Mg/Al alloy)-AP based Propellants , Proceedings of the 22st International Symposium on ISTS, 00-a-27, 2000

[6] Derck A. Gordon, Combustion Characteristics of Metal Particles , Solid Propellant Rocket Research, Academic Press, New York, 1960, pp271

[7] Tadao Takeno and Saburo Yuasa, Ignition of Magnesium and Magnesium-Aluminum Alloy by Impinging Hot-Air Stream , Combustion Science and Technology, Vol.21, 1980, pp109~121

[8] A. W. Blackman and D. K. Kuehl Use of Binary Light Metal Mixtures and Alloy as Additives for Solid Propellants , ARS Journal, September, 1961, pp1265~1272

[9] P.G.Willoughby, K.L.Baker and R.W.Hermsen, Photographic Study of Solid Propellants Burning in an Acceleration Environment , Thirteenth, Symposium (International) on Combustion, The Combustion Institute, 1970, pp1033~1045

[10] A.J.Sabadell, J.Wenograd and M.Summerfield, Measurement of Temperature Profiles Through Solid Propellant Flames Using Fine Thermocouples , AIAA Journal, Vol.3, No.9, 1965, pp1580~1584

PHYSICS OF COMBUSTION OF HTPB/NITRAMINE COMPOSITIONS

Anatoli A.Zenin, and Sergej V.Finjakov
Semenov Institute of Chemical Physics, Russian Academy of Sciences.
Moscow 117977, Kosygin Str. 4. Russia. 5195.g23@g23.relcom.ru

ABSTRACT

Burning wave structure of compositions of HTPB/HMX and HTPB/RDX have been studied by microthermocouple techniques and by data processing. Temperature profiles of the burning waves were received. The following burning wave parameters were found: burning rates, burning surface temperatures, heat feedback from gas to solid, heat release in solid, thickness of heat layer in solid, conductive sizes of combustion zones in gas and solid. Temperature and pressure sensitivities of the burning rate and the surface temperature were estimated. The main features of physics of the composition combustion were described. Burning rate control regions were determined, macrokinetics of the chemical processes in the solid reaction layer and gasification laws in the burning waves were established. Criteria of stable combustion were found. Burning rate response functions to acoustic pulsations were obtained by the burning rate und surface temperature sensitivities. It was established that HTPB addition to HMX can increase or decrease the response functions depending on amount of the addition.
The obtained data can be useful in modelling of various regimes of HTPB/nitramines composition combustion.

1. INTRODUCTION

Cyclic nitramines RDX and HMX offer many advantages for modern propulsion: better performances (high energy and specific impulse), safety (low sensitivity in open air) and environments friendliness (smokeless and nontoxic). Pure nitramines and nitramine-based propellant compositions have been under intense experimental and theoretical studies for more than 30 years [1-12]. Complete reviews of works were suggested by Boggs [13], and by authors [14-20]. A set of works suggests important investigations devoted to the problem of these propellant behaviour in field of time-varying external parameters [21-32]. The main attension focusses here on pressure driven burning rate response functions - see recently published [33-38]. The response functions are necessary for simulation of propellant combustion behaviour inside rocket motors [39-43].

The objective of this paper is to study physical characteristics of combustion of RDX/HTPB and HMX/HTPB compositions and to use these characteristics for determination of pressure driven burning rate response functions of the compositions. The work continues investigations of physics of combustion of various solids by microthermocouple techniques performed in [44-55], and study, based on these results, burning rate behaviour of the solids in field of acoustic pulsations [56, 57].

2. OBJECT OF INVESTIGATIONS

Investigations were performed for the following mixtures:
No.1: RDX:HTPB1, 80:20 (%, by weight), mixture density ρ=1,35g/cm^3; nitramine particle sizes (nps) were<100mkm; chemical brutto-formula: $O_{21.76}H_{43.72}N_{21.72}C_{25.27}$;

No.2: HMX:HTPB1, 80:20 (%, by weight), density ρ=1,5g/cm^3; (nps) were: <30mkm/315mkm (50%/50%); chemical brutto-formula: $O_{21.76}H_{43.72}N_{21.72}C_{25.27}$;
No.3: RDX:HTPB1, 87:13 (%, by weight), ρ=1,42g/cm^3; (nps) were<100mkm; chemical brutto-formula: $O_{23.6}H_{37.87}N_{23.57}C_{21.16}$;
No.4: HMX:HTPB1, 87:13 (%, by weight), density ρ=1,59g/cm^3; (nps) were: <30mkm/315mkm (50%/50%); chemical brutto-formula: $O_{23.6}H_{37.87}N_{23.57}C_{21.16}$;
HTPB1 - it is slighly modified HTPB-binder.
Cylindrical samples of diameters 5-15mm and 20-30 mm long were protected by thin layer of polymer glue.

3. METHODS OF EXPERIMENTAL INVESTIGATIONS

Temperature profiles and surface temperatures were obtained for indicated above mixtures at pressures 0.1(0.5), 1.0, 2.0 5.0 and 8.0 MPa and at sample temperatures T_o=+20 and +100°C. Stable combustion waves at T_o between -150 and -100°C were not observed at all.
Temperature profiles of the combustion waves and the burning surface temperatures were received experimentally by microthermocouple methods, by microthermocouples imbedded into solid. Thermocouples went through combustion waves when the waves propagated through the solid samples and registered temperature profiles. The ribbon U-shaped thermocouples made of alloys W+5%Re/W+20%Re of 2-7 μm thick were used. Every sample had inside 2-3 thermocouples placed one above the other. Distances between the junctions were 2-4 mm. The samples were burned in a bomb of constant pressure in atmosphere of nitrogen. In experiments at elevated sample temperatures the sample was placed into a small thermostat inside the bomb. The sample heating was controlled by thermocouples. Samples were ignited by electrically heated wire. Thermocouple signals were recorded by amplifier and oscillograph. Burning rate was measured by time delay between the thermocouple signals, by photoregistrations of sample combustion and by pressure increase during the sample combustion. Photoregistration of sample combustion allows also the type of combustion to be established. Burning surface temperatures were measured by thermocouples that are being pressed to the surface during sample combustion and by establishing the locations of slope breaks on temperature profiles recorded by thermocouples (see below). As a rule, temperature gradient close to the burning surface has a very high value. It implies that thermocouple measurements can give temperature profiles with significant errors due to thermocouple heat inertia. Because of that it is necessary to find conditions under which thermocouple measurements in combustion waves will introduce small errors. These conditions have been found by numerical simulations [44]. The thermocouple partially absorbs the heat of the thermal layer and decreases the temperature at the point of the measurement. The requirement of small temperature error (less than 10%) of the thermocouple is indicated by the following formula :

$$h<0.2\ \chi/r_b;$$

Here: h - thermocouple thickness (in cm), χ- heat diffusivity of the solid (in cm^2/s), r_b - linear burning rate (in cm/s). $\chi/r_b=l_t$ where l_t is the thickness of the thermal layer of the condensed phase. There is another requirement for correct measurements by thermocouples in combustion waves: the thermocouples have to have U-shape form. It is necessary because of a very high difference between heat conductivity coefficients of metallic thermocouple wire and that of solid or gas. The junctions of U-shaped thermocouples do not experience large temperature decrease. Modelling experiments and numerical simulations show that the decrease of junction temperature will be small (≤3%) if the

horizontal part of the U-shaped thermocouple is about one hundred times more than thermocouple thickness h [44]. Thermal inertia of the thermocouple in the gas phase can be taken into consideration and eliminated by a correction procedure. The procedure implies the use of the following equation:

$$dT_{ex}/dx=(r_b\tau_o)^{-1}\cdot(T - T_{ex});$$

Here: T - the real temperature of gas in the combustion wave; T_{ex} - the temperature registrated by thermocouple; τ_o - time response of the thermocouple in gas. Time response depends on mass burning rate m ($m=\rho\cdot r_b$) and on T. The temperature profiles in gas were corrected by this equation. The theory of thermocouple measurements in combustion waves of solids was created and confirmed by measurements of combustion wave temperature profiles by thermocouples with sequentially decreased thickness (method of "zero diameter"). All the above mentioned requirements have been met in the investigations. Different types of metal wires for thermocouples were used (We,Re and Pt,Rh) to test the catalytic effect on thermocouples. The catalytic effect was not observed. The method of burning surface temperature measurement by determining locations of slope breaks on temperature profiles registered by thermocouples (method of "slope break") is based on the existence of the delay ($r_b\tau_o$) on the temperature profiles when thermocouples go through the burning surface. The delay is due to the change of heat exchange between environment and thermocouple: contact heat exchange in solid is replaced by convective heat exchange in gas.

4. RESULTS OF EXPERIMENTAL MEASUREMENTS AND PROCESSING

Figs.1-12 show averaged temperature profiles of the studied mixtures. Averaging was performed for 6-10 temperature curves for every regime of combustion of mixtures 2-4. Mixture 1 had elevated scattering of temperature profiles at elevated pressures and because of that about 15 temperature curves were used here for the averaging. Tables 1-4 show the averaged burning wave parameters obtained by experiments and by processing experimental data (see below).

4.1. Carbon Residue After Combustion.

A porous black carbon residue on the burning surface of the mixtures 20:80 (No.1. and No.2.) was observed. The residue of the mixtures holds the shape of sample after combustion at 0.1-2.0 MPa. The measured density of carbon residue for the mixtures 20:80 comprises about 0.1g/cm^3 at 0.1 MPa, about 0.01g/cm^3 at 2.0 MPa and less than 0.01g/cm^3 at 5.0 MPa.
The mixtures 13:87 (No.3. and No.4.) practically have no carbon residue.

4.2. Mass Burning Rates.

It can be seen that mass burning rate m increases when pressure increases, when sample temperature T_o increases and, as a rule, when amount of oxidizer increases (exclusion for RDX-mixtures with ratio 80:20 at T_o=+100°C is connected, presumably, with especially low mixture density and, may be, with not very good sample side protection from the flame penetration). Mass burning rate of RDX-mixtures are always higher than that of HMX-mixtures. Values of m for the studied mixtures comprise values from 0.05 to 0.4-1.2g/cm^{2}s. Standard deviation of mass burning rate measurement is $\vartheta m=\pm 5\%$.

4.3. Burning Surface Temperatures.

It can be seen that burning surface temperature T_s always increases when m increases. Because of that the same conclusions can be made for T_s: burning surface temperature increases when pressure increases, when sample temperature T_o increases and, as a rule, when amount of oxidizer increases.

Values of T_s change from 305 to 485°C. Standard deviation of burning surface temperature measurement is $\vartheta T_s=\pm 5\%$.

4.4. Characteristics of Temperature Profiles.

Figs.1-12 show that at pressures 1.0-2.0 (5.0) MPa the gas phase of the combustion waves has two-zone structure: the first zone with mean zone temperatures T_1 and the second zone (flame zone) with the final zone temperatures T_f. Both zones merge at 5.0 (8.0) MPa. At 0.1 MPa exists only the first zone with the zone temperature T_1. Values of T_1 comprise values from 800°C to 1150°C for mixtures 20:80, and from 900°C to 1550-1660°C - for mixtures 13:87. Thermodynamically calculated values of T_f are achieved at 5.0-8.0 MPa. Standard deviation of the first zone temperature (T_1) measurement is $\vartheta T_1=\pm 10\%$ and that of the flame zone is $\vartheta T_f=\pm 5\%$.

Distances L_1 between the burning surface and the beginning of the flame zone (in fact, L_1 is the length of the first flame) change from 3.5-4 mm at 0.1 MPa to 0.5-1mm at 5.0 MPa for mixtures 20:80, and from 1.3-3 mm at 0.5 MPa to 0.35-0.8 mm at 5.0 MPa - for mixtures 13:87. Distances L between the burning surface and the flame (up to $0.95T_f$, in fact, L is the length of the gas phase reaction zone) change from 2.5-3 mm at 1.0 MPa to 1-1.6 mm at 8.0 MPa for mixtures 20:80, and - from 2.5-3 mm at 0.5 MPa to 0.6-1 mm at 8.0 MPa - for mixtures 13:87. Standard deviations of L_1 and L are ±15%.

4.4.1. Characteristic sizes in gas and solid, and heat diffusivity of heat layer in solid.

Characteristic thickness l_t and l_m (of heat layer and melted layer) in the solid phase were obtained by temperature distributions in solid - see Tables 1-4. Experimentally obtained thickness of heat layer in solid l_t is the distance between the burning surface and the section in solid with temperature $T^*=(T_s-T_o)/e - T_o$ (e is the base of natural logarithm). It was assumed here that the section of heat release in solid resides close to the surface in a thin layer and practically all the thickness of the region of temperature curve in solid is the heat layer. The assumption was based on the results of the measurements of temperature profile in solid which show that the heat diffusivity obtained by formula $\chi=l_t \cdot r_b$ is equal to the value obtained for the solid by other methods [44]. The values l_t obtained by temperature profiles (see Tables 1-4) allow the mean values of the heat diffusivity of heat layer in solid to be estimated. As a rule, at 0.1-0.5 MPa ($T_s\approx 300$-350°C) the heat diffusivity of all mixtures is equal to $\chi=1\cdot 10^{-3}$cm^2/s, at 1.0-2.0 MPa ($T_s\approx 360$-400°C) - to $\chi=(1.5\text{-}2)\cdot 10^{-3}$cm^2/s and at 2.0-8.0 MPa ($T_s\approx 410$-480°C) - to $\chi=(2\text{-}3)\cdot 10^{-3}$cm^2/s. Thickness of melted layer in solid l_m was obtained by nitramine melting temperatures T_m which are equal to 200°C for RDX and 280°C for HMX. Tables 1-4 show that l_m decreases for RDX-mixture (20:80) from 150-170 μm at 0.1 MPa to 50-60 μm at 8.0 MPa, for HMX-mixture (20:80) from 50 μm at 0.1 MPa to 35-40 μm at 8.0 MPa, for RDX-mixture (13:87) from 95-100 μm at 0.5 MPa to 33-45 μm at 8.0 MPa, for HMX-mixture (13:87) from 45-42 μm at 0.5 MPa to 22-25 μm at 8.0 MPa. The temperature profile in solid at 0.1 MPa has thick melted layer l_m=170 μm which can be seen even by the shape of this profile (see Fig.1 and Fig.6).

Characteristic size of the gas phase l_g on the temperature profiles was determined as the thickness at which the temperature gradient φ decreases e-times beginning from the burning surface. Tables 1-4 show the obtained values of l_g. It can be seen that at 1atm l_g are equal to 1.4-1.8 mm and at the elevated pressures l_g comprise values from 260-420 μm at 1.0 MPa up to 100-200 μm at 8.0 MPa for mixtures 20:80, and values from 250-350 μm at 0.5 MPa up to 120-160 μm at 8.0 MPa - for mixtures 13:87. These are very large values for the scale of burning waves.

4.4.2. Conductive sizes in gas .

For detailed analysis of the physics of combustion of these mixtures it is important to estimate the conductive size ψ of the gas phase of the investigated combustion waves. The conductive size ψ can

be obtained by the following formula: $\psi=\lambda_1/mc_p$; where λ_1 is the heat conductivity of the gas phase and c_p is the specific heat of the gas phase. Tables 1-4 show the obtained values ψ. It can be seen that values ψ decrease from 63-72 μm at 0.1 MPa to 4.2-7.1 μm at 8.0 MPa for RDX-mixture 20:80, from 74-91 μm at 0.1 MPa to 6.8-11.3 μm at 8.0 MPa - for HMX-mixture 20:80, from 32-48 μm at 0.5 MPa to 4.9-5.1 μm at 8.0 MPa - for RDX-mixture 13:87, and from 22.7-25.5 μm at 0.5 MPa to 4.4-4.9 μm at 8.0 MPa - for HMX-mixture 13:87. It is obvious that $\psi<<l_g$.

4.5. Heat Manifestations in Zones of Combustion Waves.

The obtained temperature profiles and burning surface temperatures allow various heat manifestations in zones of the combustion waves to be estimated.

4.5.1. Heat release in solid and heat feedback from gas to solid.

Heat flux from gas to solid q·m by heat conductivity is as follows:

$$q\cdot m=-\lambda_1(T)\cdot(dT/dx)_o;$$

Here: λ_1 is coefficient of heat conductivity of the gas phase, $(dT/dx)_o=\varphi$ is the temperature gradient in gas close to the burning surface. Heat feedback from gas into solid by heat conductivity q is as follows:

$$q=-\lambda_1(T)\cdot\varphi/m;$$

Heat release in the reaction layer of the condensed phase (or on the burning surface) Q is as follows:

$$Q=c\cdot(T_s-T_o)-q+q_m;$$

Where c is coefficient of solid specific heat and q_m is the heat of nitramine melting: $q_m=28x0.8cal/g$ for mixtures 20:80 and $q_m=28x0.87cal/g$ for mixtures 13:87. The standard deviations of Q and q are equal to ±10% and 20%, correspondingly. Table 5 shows the used functions $\lambda_1(T)$, c(T) and $c_p(T)$. Tables 1-4 show that the temperature gradient φ in gas close to the burning surface has very large values especially in mixtures 13:87: it can be as much as 10^5 K/cm. The general conclusion about the heat release in solid and the heat feedback from gas to solid in combustion waves of the studied polymer-nitramine mixtures is as follows: large heat release in solid and small heat feedback from gas to solid are observed for all of the studied regimes. Indeed Q is equal to 81-159cal/g and q is equal to 5.3-21.5cal/g. It is important to stress that Q increases when pressure and m increase. And q can decrease when pressure and m increase (at p>2.0-5.0 MPa). Values Q and q increase when amount of oxidizer (nitramine) in mixture content increases. Q decreases when T_o increases. The mixtures on the base of RDX have the higher values Q than that of the mixtures on the base of HMX.

4.5.2. Heat release rate in gas close to the burning surface.

The temperature profiles and burning surface temperature allow heat release rates Φ_o in gas close to the surface to be estimated. Values of Φ_o show, obviously, the intensity of chemical reactions in gas. Values of Φ_o were obtained from the heat conductivity equation and the temperature profiles. The heat conductivity equation, connected with the burning surface, for the gas phase of stable propagated combustion wave is as follows:

$$d/dx\cdot(\lambda_1 dT/dx)-m\cdot c_p\cdot dT/dx+\Phi(x)=0;$$

Here $\Phi(x)$ is the distribution of the heat release rate in the gas phase of the combustion wave. The first term of the equation at $x\approx0$ is small and thus the following expression for $\Phi(x\approx0)=\Phi_o$ is valid:

$$\Phi_o=c_p\cdot m\cdot\varphi;$$

The standard deviation of Φ_o is equal, as a rule, to 20-30%. Tables 1-4 show that the values Φ_o are very high and can comprise $33{,}8\cdot K cal/cm^3 s$. Φ_o increases when pressure, amount of nitramine and T_o increase. The mixtures with RDX have, as a rule, higher values Φ_o than those of the mixtures with HMX.

Table 1: Burning wave parameters of mixture No.1 (RDX:HTPB1, 80:20)

	p, MPa	0.1		1.0		2.0		5.0		8.0	
	T_o,°C	20	+100	20	+100	20	+100	20	+100	20	+100
1	m,g/cm²s	0.05	0.06	0.18	0.42	0.27	0.62	0.48	0.97	0.65	1.16
2	T_s,°C	305	310	350	410	370	440	430	475	445	486
3	$\varphi \cdot 10^{-4}$,K/cm	0.4	0.3	2.4	1.9	4.0	3.0	6.8	3.6	4.0	4.5
4	q, cal/g	8.0	5.3	15.0	5.3	17.5	6.5	18.8	5.3	8.4	5.7
5	Q, cal/g	101	81	109	113	113	123	132	136	148	139
6	l_t, μm	260	220	120	70	90	55	70	40	70	40
7	l_m, μm	170	150	80	80	75	75	50	60	60	50
8	L_1, mm	4.0	4.0	1.3	1.8	0.75	1.0	-	0.6	-	-
9	T_1,°C	800	820	900	950	950	1000	-	1100	-	-
10	L, mm	-	-	2.5	3.0	2.0	2.5	1.2	2.0	1.0	1.5
11	T_f,°C	-	-	1480	1500	1500	1600	1500	1600	1500	1600
12	l_g, μm	1400	1800	260	260	230	250	220	140	200	120
13	ψ, μm	72	63	22.6	10.7	15.6	7.4	9.3	5.0	7.1	4.2
14	Ω	20	28	12	24	15	34	24	28	28	29
15	Φ_o,Kcal/cm³s	0.055	0.05	1.2	2.3	3.1	5.4	9.5	10.3	7.6	15.6

Note: the thick frame includes data obtained by averaging unstably profiles.

Table 2: Burning wave parameters of mixture No.2 (HMX:HTPB1, 80:20)

	p, MPa	0.1		1.0		2.0		5.0		8.0	
	T_o,°C	20	+100	20	+100	20	+100	20	+100	20	+100
1	m,g/cm²s	0.04	0.05	0.10	0.15	0.16	0.24	0.29	0.53	0.38	0.70
2	T_s,°C	300	305	325	340	340	370	380	440	400	455
3	$\varphi \cdot 10^{-4}$,K/cm	0.55	0.55	1.7	1.8	2.6	2.8	4.5	3.5	6.0	4.4
4	q, cal/g	13.8	11.0	18.4	13.2	18.0	13.5	18.6	8.9	19.8	7.8
5	Q, cal/g	94	77	98	83	103	93	115	120	121	127
6	l_t, μm	270	200	160	160	140	120	95	60	90	50
7	l_m, μm	50	50	40	60	40	50	30	35	40	35
8	L_1, mm	3.5	3.5	1.2	1.5	0.80	1.0	0.5	1.0	-	-
9	T_1,°C	800	850	880	950	950	1050	1050	1150	-	-
10	L, mm	-	-	2.5	3.0	1.8	2.5	1.3	2.0	1.2	1.6
11	T_f,°C	-	-	1470	1540	1480	1580	1490	1590	1500	1600
12	l_g, μm	1400	1600	400	420	320	250	160	200	100	120
13	ψ, μm	91	74	37.8	26.2	24.0	17.5	14.5	8.7	11.3	6.8
14	Ω	15	22	11	16	13	14	11	23	9	18
15	Φ_o,Kcal/cm³s	0.06	0.076	0.47	0.76	1.16	1.92	3.75	5.5	6.6	9.1

Table 3: Burning wave parameters of mixture No.3 (RDX:HTPB1, 87:13)

	p, MPa	0.5		1.0		2.0		5.0		8.0	
	T_o,°C	20	+100	20	+100	20	+100	20	+100	20	+100
1	m,g/cm²s	0.10	0.14	0.15	0.23	0.27	0.42	0.63	0.74	0.95	0.99
2	T_s,°C	325	350	350	365	375	410	445	460	475	477
3	φ·10⁻⁴,K/cm	1.9	3.0	2.8	3.6	5.0	5.2	8.0	8.5	10.5	11.5
4	q, cal/g	20.5	24.6	21.5	18.5	22.0	16.0	16.5	16.0	16.6	16.8
5	Q, cal/g	98	77	105	88	112	105	142	122	152	127
6	l_t, μm	145	100	140	93	80	65	50	42	37	36
7	l_m, μm	100	95	92	90	60	75	40	50	33	45
8	L_1, mm	1.8	2.0	1.3	1.6	0.8	1.2	0.6	0.8	-	-
9	T_1,°C	900	960	1000	1040	1100	1150	1600	1660	-	-
10	L, mm	2.8	3.0	2.0	2.6	1.7	2.0	1.0	1.1	0.6	0.7
11	T_f,°C	1350	1450	1600	1650	1800	1850	1900	1950	1900	1950
12	l_g, μm	300	250	220	200	180	170	180	140	130	120
13	ψ, μm	40.8	32	29.3	18.3	15.5	10.6	7.0	6.4	5.1	4.9
14	Ω	7.3	8.0	7.5	11	12	16	26	22	25	24
15	Φ_o,Kcal/cm³s	0.5	1.2	1.2	2.4	3.8	6.3	14.8	18.6	29.6	33.8

Table 4: Burning wave parameters of mixture No.4 (HMX:HTPB1, 87:13)

	p, MPa	0.5		1.0		2.0		5.0		8.0	
	T_o,°C	20	+100	20	+100	20	+100	20	+100	20	+100
1	m,g/cm²s	0.16	0.18	0.20	0.24	0.27	0.32	0.48	0.56	1.00	1.10
2	T_s,°C	350	355	360	370	375	390	420	435	480	485
3	φ·10⁻⁴,K/cm	3.0	2.0	3.6	3.5	4.4	5.0	6.4	7.6	8.0	9.2
4	q, cal/g	21.5	12.8	21.0	17.5	19.6	19.5	17.3	18.3	11.6	12.0
5	Q, cal/g	104	90	108	91	115	95	133	112	159	135
6	l_t, μm	150	100	120	95	90	86	66	58	45	40
7	l_m, μm	45	42	42	40	38	36	30	28	25	22
8	L_1, mm	1.3	2.0	1.0	1.4	0.6	1.0	0.35	0.8	-	-
9	T_1,°C	880	920	970	1050	1080	1180	1450	1550	-	-
10	L, mm	2.5	3.0	2.5	2.6	1.6	2.0	1.2	1.2	1.0	0.9
11	T_f,°C	1300	1350	1500	1600	1700	1780	1860	1900	1870	1900
12	l_g, μm	250	350	220	240	200	200	150	130	160	120
13	ψ, μm	25.5	22.7	20.0	17.7	15.5	13.0	9.3	8.0	4.9	4.4
14	Ω	10	15	11	14	13	17	16	16	33	27
15	Φ_o,Kcal/cm³s	1.35	1.0	2.0	2.4	3.4	4.6	9.0	12.5	23.8	30.1

Table 5: Thermophysical coefficients of nitramine-polymer mixtures

T,°C	300	350	400	450	500	550	600
c, cal/g·K	0.305	0.308	0.312	0.316	0.320	0.322	0.325
$\lambda_1 \cdot 10^4$,cal/cm·s·K	1.00	1.15	1.25	1.38	1.50	1.62	1.75
c_p cal/g·K	0.275	0.282	0.290	0.295	0.300	0.305	0.310

5. DISCUSSIONS

5.1. Burning Rate Control Regions in Combustion Waves.

The results of measurements q and Q show that the main factor of the creation of the burning rate of the studied mixtures is heat release in solid (or on solid surface) and, in a smaller degree, heat feedback from the gas layer adjacent to the surface. The following conclusion can be made from the analyses of the obtained data: the high temperature region of the burning waves cannot affect the burning rate. Indeed the influence of the heat release in the gas phase of the burning wave on the burning rate can be estimated by the following formula obtained as a solution of the heat conductivity equation:

$$m \cdot q = \int_0^\infty \Phi(x) \cdot \exp(-x/\psi) \cdot dx;$$

Here $\Phi(x)$ is the distribution of the heat release rate in the gas phase of the burning wave (see above). This equation shows that the influence of the heat release in gas on the burning rate decreases very quickly when x exceeds ψ. It implies that the heat release in gas does not affect the burning rate beginning from $x>\psi$. Tables 1-4 show that the values ψ are very small and they are much smaller than the characteristic size of the gas phase l_g - see values Ω in the Tables ($\Omega=l_g/\psi$). It can be seen that Ω is equal to 7-33. It implies that only a very thin layer in the gas phase close to the burning surface can be responsible for the burning rate.

Thus the obtained results show that the burning rate control region in the studied combustion waves for all the regimes of combustion is the region of heat release in solid just under the burning surface (or immediately on the burning surface) and a very thin low-temperature gas layer close to the burning surface which has the thickness $\sim\psi$. High temperature gas regions cannot influence the burning rate because of a very large heat resistance of the main volume of the gas phase.

5.2. Macrokinetics of Solid Gasification in Combustion Waves.

The following equation connects burning rate of solid with burning surface temperature and with macrokinetic characteristics of solid gasification:

$$m^2 = \lambda\rho/Q^2 \cdot \Re T_s^2/E \cdot Q^* k_o \cdot 1/N \cdot \exp(-E/\Re T_s);$$

Here $N=1/\eta_s + (1-\eta_s)/\eta_s \cdot \ln(1-\eta_s) - (q/Q) \cdot [\ln(1-\eta_s)]/\eta_s$; $\eta_s=Q/Q^*$; Q^* is the maximum heat release in solid (for polymer-nitramine mixture combustion waves $N\cong 1$); λ is solid heat conductivity, E is activation energy of limiting stage of the gasification process.

This expression was obtained by the solution of the system of two equations for the steady propagated burning wave: the heat conductivity equation for solid phase and the equation of diffusion of reagents. The burning wave propagates due to heat release in solid Q and heat feedback from gas to solid q. Function of the volumetric heat release rate Φ_c in solid was assumed as follows:

$$\Phi_c(\eta, T)=Q^*k_o\cdot\rho\cdot(1-\eta)\cdot\exp(-E/\Re T);$$

Here η is the reaction completeness ($\eta=\eta_s$ on the burning surface), k_o is the preexponent multiplier. Calculations show that the simplified macrokinetic laws of gasification in the combustion waves of the studied mixtures have the following forms:

No.1. RDX:HTPB1, 80:20; $m=5.78\cdot10^3\cdot\exp(-25{,}800/2\Re T_s)$, g/cm^{2}s;
No.2. HMX:HTPB1, 80:20; $m=4.47\cdot10^3\cdot\exp(-25{,}500/2\Re T_s)$, g/cm^{2}s;
No.3. RDX:HTPB1, 87:13; $m=7.24\cdot10^3\cdot\exp(-26{,}600/2\Re T_s)$, g/cm^{2}s;
No.4. HMX:HTPB1, 87:13; $m=6.26\cdot10^3\cdot\exp(-26{,}300/2\Re T_s)$, g/cm^{2}s;

Here T_s in K, m in g/cm^{2}s; $\Re$ is the gas constant.
One of the merits of these laws are the possibility of estimations of values T_s under different conditions by using experimentally obtained values of mass burning rates m.

5.3. Nitramine Gasification Controls Gasification of the Mixtures in Combustion Waves.
It can be seen that the obtained macrokinetic laws of solid gasification in combustion waves for the studied mixtures are close each other. It is interesting to compare the dependensies of mass burning rates on burning surface temperatures for investigated mixtures and unified dependense $T_s(m)$ for pure nitramines (HMX, RDX, dimer - see [48, 49]). Fig. 13 demonstrates this comparison. It can be seen that practically all points of the investigated mixtures fit the unified dependense $T_s(m)$ for pure nitramines. It is very impostant result. It implies that, inspite of liquid-phase mixing between molten HTPB-binder and molten nitramines, the process of nitramine gasification controls gasification of the investigated mixtures in combustion waves. Similar result was obtained for mixture RDX/HTPB, 84:16, in work [50].

5.4. Pressure and Temperature Sensitivities of Burning Rate and Surface Temperature.
Pressure and temperature sensitivities of burning rate and surface temperature are important characteristics of solid combustion. The following sensitivities were found:

$\beta=(\partial\ln m/\partial T_o)_{p\text{-const}}$, - sensitivity of mass burning rate to initial temperature;
$r=(\partial T_s/\partial T_o)_{p\text{-const}}$, - sensitivity of burning surface temperature to initial temperature;
$\nu=(\partial\ln m/\partial\ln p)_{To\text{-const}}$, - pressure sensitivity of mass burning rate;
$\mu=(T_s-T_o)^{-1}\cdot(\partial T_s/\partial\ln p)_{To\text{-const}}$, - pressure sensitivity of burning surface temperature.

Table 6 shows the sensitivity of mass burning rate to initial temperature β.

Table 6: Temperature sensitivities of burning rate, β, %/K (interval T_o=+20- +100°C).

	p, MPa					
No. mixture	0.1	0.5	1.0	2.0	5.0	8.0
1	0.228		1.06	1.04	0.88	0.72
2	0.275		0.507	0.507	0.754	0.764
3		0.42	0.534	0.552	0.2	0.051
4		0.147	0.228	0.212	0.193	0.119

Note: empty sell implies that under these conditions the value was not determined.

Table 6 shows that oxidizer content increasing leads to significant β decreasing especially at elevated pressures. It can be seen also that HMX-based mixtures have decreased values of β in comparison with β of RDX-based mixtures. As a rule, typical dependence of β(p) is increasing β at low pressures, maximum of β at 0.5-2.0 MPa and decreasing β at elevated pressures. Table 6 shows that this type of functions β(p) takes place for mixtures 1, 2 and 4.
Below, instead of sensitivity β, the parameter $k=\beta\cdot(T_s-T_o)$ will be used. Table 7 shows the obtained values of ν, r, μ and k for mixtures No.1-4. The temperature interval was +20°C - +100°C.

Table 7: Values of parameters: ν, r, μ, and k.

	p, MPa	0.1		0.5		1.0		2.0		5.0		8.0	
mixture	T_o,°C	20	100	20	100	20	100	20	100	20	100	20	100
No.1	ν	0.64	0.6	0.64	0.6	0.64	0.6	0.64	0.6	0.64	0.6	0.64	0.6
	r	0.06	0.06	0.3	0.3	0.75	0.75	0.88	0.88	0.56	0.56	0.52	0.52
	μ	0.063	0.21	0.07	0.17	0.076	0.14	0.114	0.124	0.122	0.085	0.06	0.05
	k	0.65	0.48	1.5	2.0	3.5	3.28	3.64	3.54	3.6	3.3	2.95	2.7
No.2	ν	0.61	0.76	0.61	0.76	0.61	0.76	0.61	0.76	0.61	0.76	0.61	0.76
	r	0.06	0.06	0.13	0.13	0.19	0.19	0.38	0.38	0.75	0.75	0.69	0.69
	μ	0.036	0.05	0.046	0.08	0.056	0.11	0.08	0.185	0.12	0.19	0.12	0.05
	k	0.77	0.56	1.2	0.85	1.54	1.22	1.62	1.36	2.65	2.56	2.9	2.7
No.3	ν			0.6	0.72	0.8	0.72	0.82	0.56	0.83	0.56	0.9	0.56
	r			0.3	0.3	0.19	0.19	0.44	0.44	0.3	0.3	0.3	0.3
	μ			0.118	0.08	0.11	0.13	0.127	0.21	0.165	0.125	0.132	0.08
	k			1.28	1.05	1.76	1.42	1.96	1.71	0.85	0.72	0.23	0.19
No.4	ν			0.3	0.4	0.4	0.42	0.5	0.5	0.6	0.6	1.5	1.4
	r			0.06	0.06	0.13	0.13	0.19	0.19	0.19	0.19	0.06	0.06
	μ			0.03	0.078	0.06	0.09	0.104	0.11	0.23	0.21	0.24	0.22
	k			0.49	0.37	0.78	0.62	0.75	0.62	0.77	0.65	0.55	0.46

Note: empty sell implies that under these conditions the value was not determined.

Table 7 shows that burning rate pressure sensitivities ν are normal. They are equal to ν=0.6-0.64 for No.1, 0.6-0.76 for No.2, 0.56-0.83 for No.3, and 0.3-0.6 for No.4 (large values of ν at 8.0 MPa for

No.4 are abnormal). Values of μ are equal to 0.03- 0.2, and of r - 0.06-0.8. Parameter k, as a rule, exceed 1, and only mixture 4 has low values of k.

5.5. Criteria of Stable Combustion.

Zel'dovich's criterium of stable combustion is as follows: $k<1$ [58]. However, when $k>1$, combustion can be also stable if $k^*<1$, where k^* is Novozhilov's criterion of stable combustion: $k^*=(k-1)^2/(k+1)r$; [22, 27, 30]. Table 8 shows the obtained values of k^*

Table 8: Values of Novozhilov's criterion k^*

p, MPa	0.5		1.0		2.0		5.0		8.0	
T_o°C	20	100	20	100	20	100	20	100	20	100
mixt. 1	0.33	1.11	1.85	1.6	1.7	1.6	2.6	2.2	185	1.5
mixt. 2	0.14	-	0.6	0.11	0.38	0.06	0.99	0.91	1.34	1.14
mixt. 3	0.11	-	0.96	0.38	0.7	0.42	-	-	-	-

It can be seen that combustion of mixture 1 has unstable character at elevated pressures. Only at 0.5 MPa, To=20'C, the combustion is stable. It corresponds to increased scatter of the temperature profiles. Possibly, the main reason of the unstable combustion of mixture 1 is low density (less than 1,4 g/cm^3). Table 8 also shows that: 1) mixtures of (87:13) has significantly more stable combustion than mixtures of (80:20); 2) HMX provides more stable mixture combustion than RDX;

5.6. Pressure-Drived Burn-Rate Response Functions.

5.6.1. Theory of Burn-Rate Response Functions.

A description of propellant burning rate behavior in a pressure field having low amplitude pulsations, which was made in the framework of the ZN theory [27, 30, 37], is used in this work. Let the pressure have harmonic dependence on time t according to the expression

$$p=p_o+p_1\cos\varpi t$$

where $p_1<<p_o$. Then the burning rate in the linear approximation will have the following form:

$$r_b=r_{bo}+r_1\cos\varpi t$$

where $r_1<<r_b$. Novozhilov obtained [27, 30, 37], using the complex amplitude method, the following expression for the burning rate response to oscillatory pressure:

$$U=[\nu+(\nu\cdot r-\mu\cdot k)\cdot(z-1)]/[1+r\cdot(z-1)-k\cdot(z-1)/z];$$

Here $z=(1+\sqrt{1+4i\omega}\,)/2$; $U=V_1/\eta_1$, where V_1 is complex amplitude of burning rate fluctuation, $\eta_1=p_1/p_o$, and ω is a nondimensional frequency what is equal to cyclic frequency ϖ, in 1/s, multiplied by time of solid heat layer relaxation χ/r_b^2. Values of ν, μ, k and r are based on the mean pressure p_o. It is convenient to have the equation for the response function in traditional form:

$$U=(A+B\cdot i)/(C-D\cdot i)=(A\cdot C-B\cdot D)/(C^2+D^2)+(A\cdot D+B\cdot C)\cdot i/(C^2+D^2)$$

Thus:

$$\text{Re}\{U\}=(A\cdot C-B\cdot D)/(C^2+D^2) \quad \text{and} \quad \text{Im}\{U\}=(A\cdot D+B\cdot C)/(C^2+D^2)$$

Where:
$$A=\nu+\delta\cdot(R_1-0.5);\quad B=\delta\cdot(R_1^2-0.25)^{0.5}$$
$$C=1+r\cdot(R_1-0.5)-k\cdot(1-1/2R_1);\quad \delta=\nu\cdot r-\mu\cdot k$$
$$D=(k/2R_1)\cdot[(2R_1-0.5)/(2R_1+0.5)]^{0.5}-r\cdot(R_1^2-0.25)^{0.5}$$

The theory is based on the supposition that the relaxation time for the solid heat layer is much longer those for the leading part of the gas phase and reaction layer of the solid. Estimations show that for the investigated mixtures this supposition is valid. Indeed, values of χ/r_b^2 are at least 10-20 times higher than other relaxation times. This implies that results of the calculations are the real response functions. Estimations also show that the standard deviations of these calculations for Re{U}, Im{U} are equal to 20-50% for the studied propellant mixtures.

5.6.2. Results of Calculations of Burn-Rate Response Functions.

As it well kniwn, the real part of the response function, Re{U}, is amplitude of burning rate response on pressure pulcations and the imaginery part, Im{U}, is the change of phase of the burning rate response. Figures 14-19 demonstrate examples of the obtained functions Re{U(ω)} and Im{U(ω)} for mixtures No. 1-4. It can be seen that functions of Re{U(ω)} are positive and have maximum at resonance frequency ω_{n1}. It is natural that functions of Im{U(ω)} which present phase of oscillations, change the sign close to resonance frequency (at ω_{n2}).

Table 9 shows the dimensionless characteristics of the obtained burning rate response functions. Here $\text{Re}\{U_{max}\}$ is maximal values of Re{U}, $\sqrt{k}/r \approx \omega_{n,th}$ is a theoretical expression of resonance frequency, ω_{n1} is nondimensional frequency corresponding to $\text{Re}\{U_{max}\}$, ω_{n2} is nondimensional frequency corresponding to Im{U}=0 (generally $\omega_{n1}\neq\omega_{n2}$), $\text{Im}\{U_{max(+)}\}$ is maximal values of Im{U} in the positive region of Im{U(ω)}, and $\text{Im}\{U_{max(-)}\}$ is maximal absolute values of Im{U} in the negative region of the functions. When functions of Im{U(ω)} are monotonically decrease with ω increasing in the negative part of these curves (see for example Im{U(ω)} for mixture 1), values of $\text{Im}\{U_{max(-)}\}$ can be at ω>20. Table 9 indicates in these cases that $\text{Im}\{U_{max(-)}\} < \text{Im}\{U(\omega=20)\}$. The value of ω_m is a nondimensional frequency corresponding to $\text{Im}\{U_{max(-)}\}$.

The obtained response functions conventionally can be devided into three groups: normal (N), viscous (V) and exclusively large (L) functions. The first group, presented by Figs. 15, 16, and 18 (20°C), has normal values of $\text{Re}\{U_{max}\}$, equal to 1.2-2(3). As a rule, maximal numbers of pulsating combustion regimes have normal values of $\text{Re}\{U_{max}\}$. For the investigated mixtures the number of normal regimes is equal to 14 (among 32). The second group, presented by Figs.14, 18 (100°C), and 19, has gently sloping curves with a smoothing maximum of low values: $\text{Re}\{U_{max}\}<1.2$. The burning rate response have a viscous character in this case. For the investigated mixtures 13 regimes have the viscous character. The third group, presented, partly, by Fig. 17, has a sharp change of the response curves and large values of maximum of Re{U} at resonance frequency: $\text{Re}\{U_{max}\}>3$. It is obvious that close to this frequency any small perturbations can significantly affect the response functions. This pulsating combustion takes place close to the boundary of combustion stability. Five combustion regimes have exclusively large values of $\text{Re}\{U_{max}\}$ (see Table 9).

Table 9 shows that mixture 1, having stable combustion only at 0.1 MPa, has at this pressure viscous pulsating combustion. Mixture 2 burns in the field of pulsating pressure, as a rule, normally. Mixture 3 has normal pulsating combustion for 5 regimes, viscous - for 3 regimes and large - for 2 regimes. Mixture 4 burns in the field of pulsating pressure, as a rule, viscously.

Thus the most weak reaction on the pressure pulsations has mixture HMX/HTPB1, 87:13.

From the point of view of theory of oscillations, mixtures of nitramines with inert binder like HTPB have pulsating combustion behaviour of low quality. The low quality of the behaviour is a very positive characteristic of rocket fuels.

Table 9: Dimensionless characteristics of response functions of mixtures 1-4.

			Property							
mixture	p, MPa	T_o, °C	Re $\{U_{max}\}$ mixtures	Re $\{U_{max}\}$ HMX	$\sqrt{k}/r$	ω_{n1}	ω_{n2}	Im $\{U_{max(+)}\}$	Im $\{U_{max(-)}\}$	ω_m
No.1	0.1	20	1.06		13.4	10	8.5	0.166	<-0.18	
		100	0.7		11.5	3	2	0.048	<-0.35	
No.2	0.1	20	1.25		14.6	12	11.5	0.25	<-0.15	
		100	1.18		12.5	10	10	1.17	<-0.11	
	0.5	20	2.2		8.4	8	8	0.675	<-0.81	
		100	1.44		7.1	6	6	0.28	<-0.38	
	1.0	20	4.8	1.35	6.5	6	6.25	1.875	-2.2	10
		100	2.07	1.12	5.8	5	4.75	0.54	-0.85	12
	2.0	20	2.24	0.93	3.3	3.5	3.25	0.73	-0.87	6
		100	1.65	1.14	3.0	3	2.5	0.37	-0.67	6
	5.0	20	3.22	0.88	2.2	2	2.25	14.6	-8.5	2.5
		100	11.1	0.97	2.1	2	2.25	4	-6.6	2.5
No.3	0.5	20	1.38		3.8	3.5	3.25	0.32	-0.53	8
		100	1.55		3.4	4.5	4.6	0.39	-0.29	15
	1.0	20	39.5	1.35	6.9	6.5	6.5	20.1	-15	8
		100	2.9	1.12	6.3	6	5	0.82	-1.63	10
	2.0	20	6.1	0.93	3.18	3	3.25	2.3	-2.85	4.5
		100	1.5	1.14	3	2.5	2	0.3	-1.07	4
	5.0	20	1.27	0.88	3.1	3	2.75	0.19	-0.315	10
		100	0.77	0.97	2.8	2.5	2.25	0.09	-0.17	12
	8.0	20	1.03		16	6	5	0.05	<-0.083	
		100	0.6		13	5.5	5	0.025	<-0.04	
No.4	0.5	20	0.42		11.6	8	7.5	0.048	<-0.05	
		100	0.48		10.1	4.5	4	0.034	<-0.09	
	1.0	20	0.67	1.35	6.8	5	4.75	0.1	<-0.20	
		100	0.58	1.12	6	4	3.5	0.065	<-0.17	
	2.0	20	0.75	0.93	4.6	3.5	3	0.1	<-0.22	
		100	0.67	1.14	4.1	3	2.7	0.07	<-0.17	
	5.0	20	0.82	0.88	4.6	2.5	2	0.078	<-0.39	
		100	0.77	0.97	4.2	2	1.75	0.066	<-0.29	
	8.0	20	2.12		12.3	6	5.5	0.248	<-0.50	
		100	1.84		11.3	6	5	0.18	<-0.35	

It is interesting to note (see Table 9), that mixture HMX/HTPB1, 80:20, has higher values of $Re\{U_{max}\}$ than values of $Re\{U_{max}\}$ for pure HMX under corresponding conditions (see Table 9). However mixture HMX/HTPB1, 87:13 has lower values of $Re\{U_{max}\}$ than corresponding values of $Re\{U_{max}\}$ for pure HMX. It implies that 20% of inert binder addition to HMX increases burning rate response functions, but 13% of HTPB1 addition decreases this response.

6. CONCLUSIONS

Burning wave structure of compositions of HTPB/HMX and HTPB/RDX have been studied by microthermocouple techniques and by data processing. Temperature profiles of the propellant compositions were obtained for oxidizer/nitramine mixtures of content 80:20 and 87:13 at pressures 0.1 - 8.0 MPa and at initial temperatures 20 - 100°C. The following burning wave parameters were found: burning rates, burning surface temperatures, heat feedback from gas to solid, heat release in solid, thickness of heat layer in solid, conductive sizes in gas and solid. Temperature and pressure sensitivities of the burning rate and the surface temperature were obtained. Burning rate control regions in the combustion waves of the studied compositions were found. Macrokinetics of the chemical processes in the solid reaction layer and gasification laws were established. Criteria of stable combustion for all investigated regimes were found. The main features of physics of the composition combustions are as follows: significant carbon residue on the burning surface at low pressures (when portion of nitramines are 20%), elevated temperature sensitivities of burning rates, significant heat release in solid which increases with pressure, relatively small heat feedback from gas to solid, two-zone structure in the gas phase, wide reaction zone in the gas phase, burning rate control regions are placed on the burning surface and in a thin low-temperature gas layer close to surface. It was established that process of nitramine gasification controls gasification of the investigated mixtures in combustion waves.

Burning rate response functions to acoustic pulsations were obtained. It was shown that HTPB addition to HMX can increase or decrease the response functions depending on amount of the addition. The response functions of the mixture increase when HTPB addition is equal to 20% and decrease when it is equal to 13%, in comparison with the response functions of pure HMX.

ACKNOWLEDGMENT

This work was sponsored by the European Research Office of the U.S.Army,
contract N68171-97-M-5771. This support is much appreciated.

REFERENCES

1. Zimmer-Galler, R., *AIAA J.* 6:2107-2110 (1968).
2.BenReuven, Caveny, L., Vichnevetsky, R., and Summerfield, M., *16th Symp. (Intern.) on Combustion*, The Comb. Institute, Pittsburgh, 1976, pp. 1223-1233.
3.Cohen, N., and Price, C. (1981). AIAA Paper 81-1582.
4. Cohen-Nir, E., *18th Symp. (Intern.) on Combustion*, The Comb. Institute, Pittsburgh, 1981, pp. 195-206.
5. Kubota, N., *18th Symp. (Intern.) on Combustion*, The Comb. Institute, Pittsburgh, 1981, pp. 187-194.
6. Kubota, N., *19th Symp. (Intern.) on Combustion*, The Comb. Institute, Pittsburgh, 1982, pp. 777-785.
7. Kuwahara, T., and Kubota, N., *J. Spacecraft Rockets.* 21:502-507 (1984).
8. Beckstead, M., *18th Symp. (Intern.) on Combustion*, The Comb. Institute, Pittsburgh, 1981, pp. 175-185.

9. Beckstead, M., *26th JANNAF Combustion Meeting*, Pasadena , CA, USA, vol. CPIA No. 529, Vol.IV, 1989, pp. 255-268.
10. Davidson, J., and Beckstead, M., (1996). AIAA Paper 96-0885.
11. Li, S., and Wlliams, F., *J. Propuls. Power* 12:302-309 (1996).
12. Botcher, T., and Wight, C., *J Phys. Chem.* 97:9149-9153 (1993).
13. Boggs, T., *The Thermal Behaviour of RDX and HMX*, Vol.90, *AIAA, Progress in Astronautics and Aeronautics*, AIAA, Washington, DC, 1984, pp. 121-175.
14 Fifer, R., *Chemistry of Nitrate Ester and Nitramine Propellants*, Vol.90, *AIAA, Progress in Astronautics and Aeronautics*, AIAA, Washington, DC, 1984, pp. 177-237.
15. Yetter, R., Dryer, F., Allen, M., and Gatto, J., *J. Propuls. Power* 11:683-697 (1995).
16. Litzinger, T.,Fetherolf, B., Lee, Y., and Tang, C., *J. Propuls. Power* 11:698-703 (1995).
17. Liau, Y., and Yang, V., *J. Propuls. Power* 11:729-739 (1995).
18. Brill, T., *J. Propuls. Power* 11:740-751 (1995).
19. Margolis. S., and Williams, F., *J. Propuls. Power* 11:759-768 (1995).
20. Singh, H., *J. Propuls. Power* 11:848-855 (1995).
21. Hart, R. W., and McClure, F. T., *J. Chem.Phys.*30:1501-1514 (1959).
22. Novozhilov, B. V., *J. Appl. Mech. Techn.Phys.* 6:10-106 (1965). (in Russian)
23. Hart, R. W., Farrell, R. A., and Cantrell, R. H., *Comb.Flame* 10:365-380 (1966).
24. Horton, M. D., and Price, E. W., *9th Symp. (Intern.) on Combustion*, Academic Press, N.Y., 1963, pp. 303-310.
25. Culick, F. E. C., *AIAA J.* 9 (12):2241-2255 (1968).
26. Milfeith, C. M., Baer, A. D., and Ryan, N. W., *AIAA J.* 10 (10):1280-1285 (1972).
27. Novozhilov, B. V., *Nonstationary Combustion of Solid Rocket Fuels*, Nauka, Moscow, 1973, (Translation AFSC FTD-MD-24-317-74)
28. King, M. K., AIAA Paper 80-1124 (1080), *Joint Propulsion Conference*, Hartford, CN.
29. Kuo, K. K., Gore, G. P., and Summerfield, M., *Transient Burning in Solid Combustion*, Vol. 90, *AIAA, Progress in Astronautics and Aeronautics*, AIAA, Washington, DC, 1984, Chap. 11.
30. Novozhilov, B. V., *Theory of Nonsteady Burning and Combustion Stability of Solid Propellants by Zel'dovich-Novozhilov Method*, Vol. 143, *AIAA, Progress in Astronautics and Aeronautics*, Washington, DC, 1992, 601-641.
31. Zarko, V. E., Simonenko, V. N., and Kiskin, A. B., *Radiation Driven Transient Burning*, Vol. 143, *AIAA, Progress in Astronautics and Aeronautics*, AIAA, Washington, DC, 1992, 363-396.
32. De Luca, L., *Theory of Nonsteady Burning and Combustion Stability of Solid Propellants by Flame Model*, Vol. 143, *AIAA, Progress in Astronautics and Aeronautics*, Washington, DC, 1992, 519-600.
33. Erikson, W. W., and Beckstead, M. W., (Jan.1998), AIAA Paper 98-0804.
34. Finlinson, J. C., and Stalnaker, R. A., *Pure Oxidizer T-Burner Pressure Coupled Response for AP, HMX, RDX, from 200 to 1000 PSI*, 1997 JANNAF Combustion Meeting. FL.
35. Finlinson, J. C., Stalnaker, R. A., and Blomshield, F. S., (Jan.1998), AIAA Paper 98-0556.
36. Hickman, S. R., and Brewster, M. Q., (Jan.1998), AIAA Paper 98-0557.
37. Novozhilov, B. V., Kohno, M., Maruzumi, H., and Shimara, T., *Solid Propellant Burning Rate Response Functions of Higher Orders*, The Institute of Space and Astronautical Sciences, Report No.661, Kanagava, Japan, 1996.
38. Brewster, M. Q., *Solid Propellant Combustion Response: Qusi-Steady Theory Development and Validation*, Vol. 185, *AIAA, Progress in Astronautics and Aeronautics*, Reston, VA, July 2000. Chap. 2-16.
39. Culick F. E. C., and Yang, V., *Prediction of the Stability of Nonsteady Motion in Solid-Propellant Rocket Motor*, Vol. 143, *AIAA, Progress in Astronautics and Aeronautics*, Washington, DC, 1992, pp. 719-780.
40. Roh, T. S., Tseng, I. S., and Yang, V., *J. Propuls. Power* 11 (4):640-650 (1995).
41. Pivkin, N. M., and Pelykn, N. M., *J. Propuls. Power* 11 (4):651-656 (1995).
42. Culick F. E. C., Burnley, V., and Swenson, G., *J. Propuls. Power* 11 (4):657-665 (1995).

43. Blomshield, F. S., Bicker, C. J., and Stalnaker, R. A., *High Pressure Pulsed Motor Firing Combustion Instability Investigations,* 33rd AIAA/ASME/SAE/ASEE *Joint Propuls.Conference &Exh.* Seattle, 1997.
44. Zenin, A. A., *Experimental Investigations of Solid Propellant Burning Mechanisms and Flow of Combustion Products,* D.Sc.Thesis, Inst.of Chem.Phys., USSA Acad.of Sciences, Moscow, 1976, (in Russian).
45. Zenin, A. A., *Processes in Zones of Double Base Propellant Combustions,* in book *Physical Processes in Combustion and Explosion,* Atomizdat, Nauka, 1980, Moscow, pp. 68-104 (in Russian).
46. Zenin, A. A., *Thermophysics of Stable Combustion of Solid Propellants,* Vol. 143, *AIAA, Progress in Astronautics and Aeronautics,* Washington, DC, 1992, pp. 197-231.
47. Zenin, A. A., *J. Propuls. Power,* 11 (4):752-758 (1995).
48. Zenin, A. A., Puchkov, V. M., Finjakov, S. V., and Kusnezov, G. P., *Burning Wave Parameters and Nitramine Combustion Mechanism, 26th Symp. (Intern.) on Combustion,* The Comb. Institute, Pittsburgh, 1996.
49. Zenin, A. A., Puchkov, V. M., and Finjakov, S. V., *Characteristics of HMX Combustion Waves at Various Pressures and Initial Temperatures, Combustion, Explosion and Shock Waves* 34 (No.2):170-176 (1998).
50. De Luca, L., Cozzi, F., Germinasi, G., Ley, I., and Zenin, A. A., *Comb. Flame* 118:248-261 (1999).
51. Zenin, A. A., and Finjakov, S. V., (Jan. 1999), AIAA Paper 99-0595.
52. Zenin, A. A., Finjakov, S. V., Puchkov, V. M., and Ibragimov, N. G., *J. Propuls. Power* 15 (No.6):753-758 (1999).
53. Zenin, A. A., Finjakov, S. V., Puchkov, V. M., and Ibragimov, N. G., *Physics of Nitrosoamine Combustion: As a Monopropellant and As an Ingredient of Modern Propellants,* Energetic Materials, *30th Intern.Annual Conference of ICT,* FRG, pp. 51-1, 51-13 (1999).
54. Zenin, A. A., and Finjakov, S. V., (Jan.2000) AIAA Paper 2000-1032.
55. Zenin, A. A., Finjakov, S. V., Puchkov, V. M., and Ibragimov, N. G., *Chem. Phys. Reports,* 2000, 18(9), pp. 1721-1737.
56. Zenin, A. A., and Finjakov, S. V., *Burning Rate Response Functions of Nitramine-Containing Propellants and HMX Due to Data of Microthermocouple Measurements, Fizika Gorenija i Vzriva* 36(1): 12-22 (2000) (in Russian)
57. Zenin, A. A., and Finjakov, S. V., *Burning Rate Response Functions of Composite-Modified Double-Base Propellants and HMX,* Vol. 185, *AIAA, Progress in Astronautics and Aeronautics,* Reston, VA, July 2000. Chap. 2-17.
58. Zel'dovich, Y. B., *Zhurn. Experim. Teor. Fiz.* 12(11-12): 498-524 (1942) (in Russian)

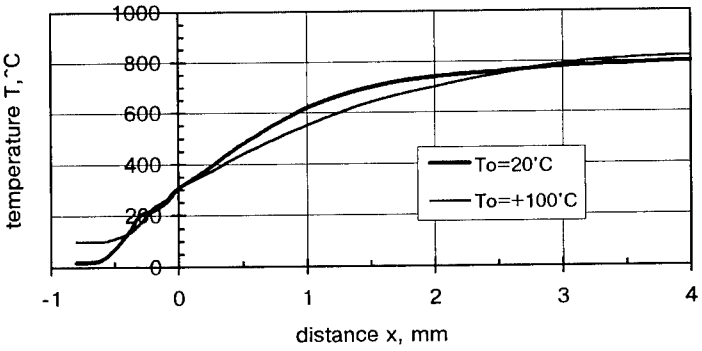


Figure 1: Averaged temperature profiles T(x).
RDX/HTPB1, 80:20. p=0.1 MPa.

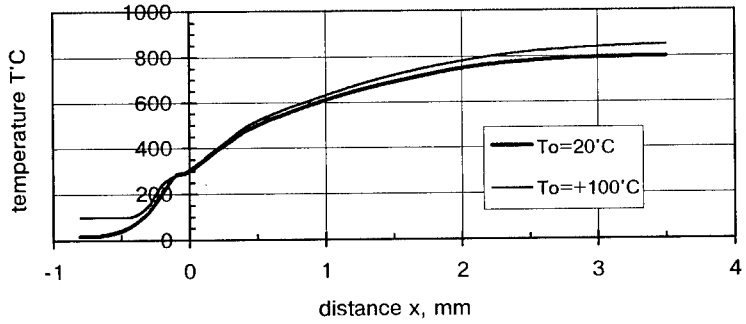


Figure 2: Averaged temperature profiles T(x).
HMX/HTPB1, 80:20. p=0.1 MPa

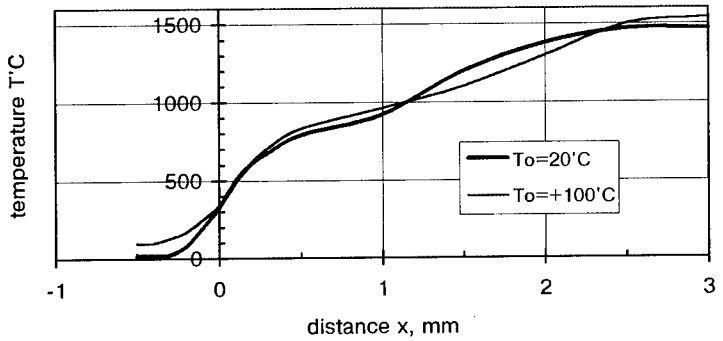


Figure 3: Averaged temperature profiles T(x).
HMX/HTPB1, 80:20. p=1.0 MPa

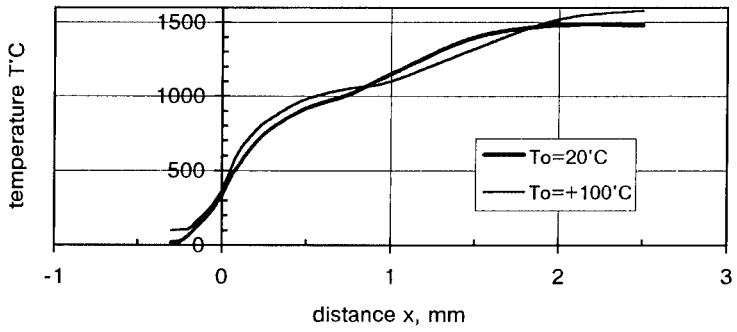


Figure 4: Averaged temperature profiles T(x).
HMX/HTPB1, 80:20. p=2.0 MPa

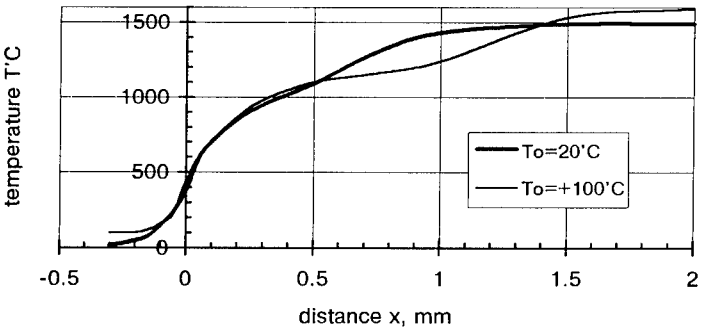


Figure 5: Averaged temperature profiles T(x).
HMX/HTPB1, 80:20. p=5.0 MPa

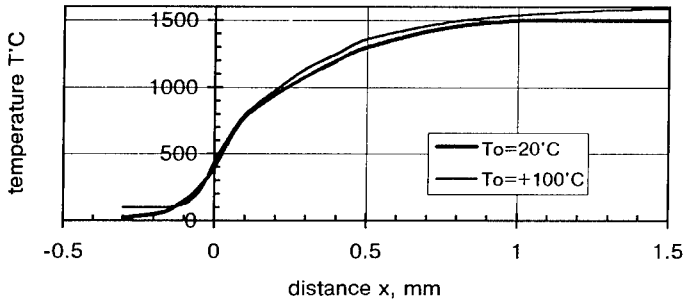


Figure 6: Averaged temperature profiles T(x).
HMX/HTPB1, 80:20. p=8.0 MPa

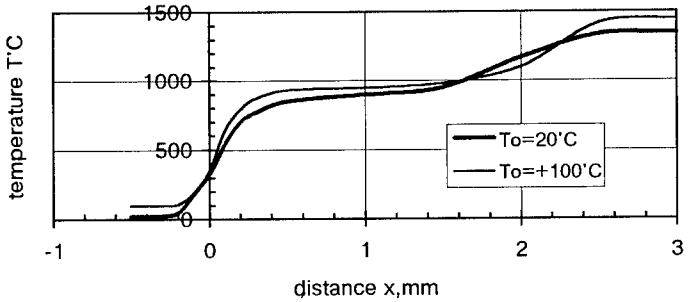


Figure 7: Averaged temperature profiles T(x).
RDX/HTPB1, 87:13. p=0.5 MPa

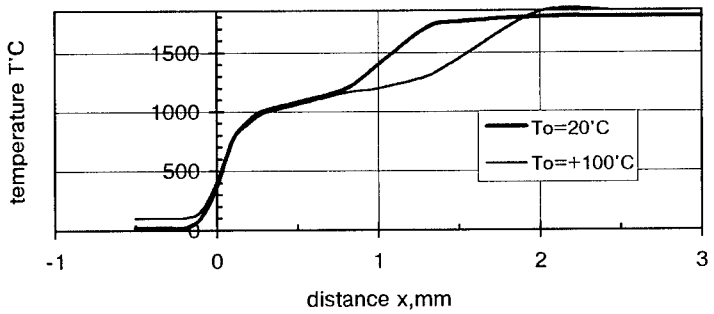


Figure 8: Averaged temperature profiles T(x).
RDX/HTPB1, 87:13. p=2.0 MPa

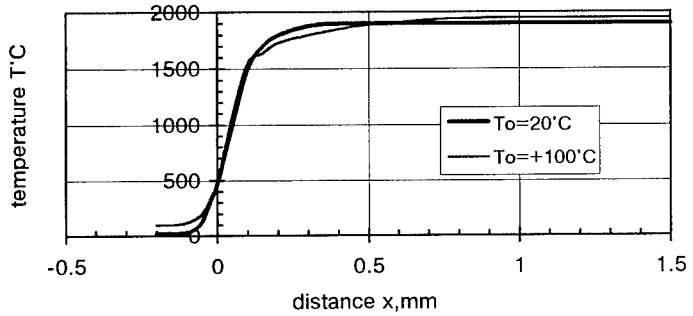


Figure 9: Averaged temperature profiles T(x).
RDX/HTPB1, 87:13. p=8.0 MPa

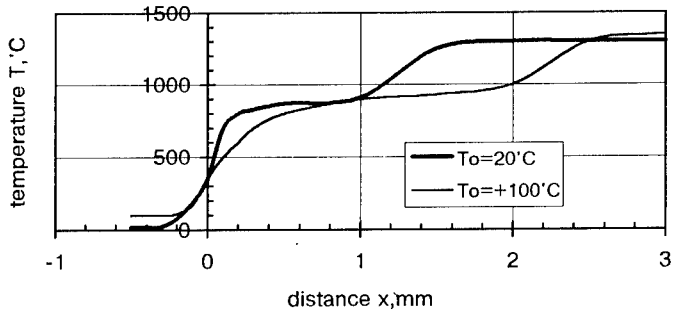


Figure 10: Averaged temperature profiles T(x).
HMX/HTPB1, 87:13. p=0.5 MPa

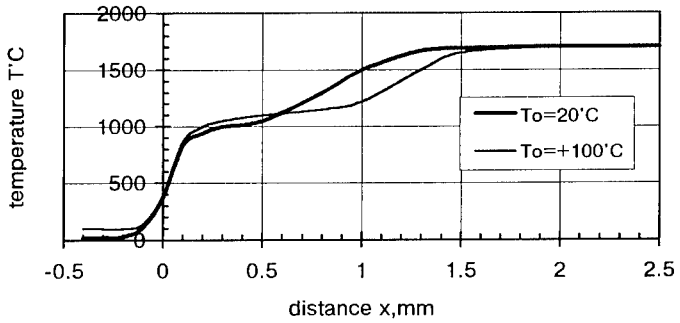


Figure 11: Averaged temperature profiles.
HMX/HTPB1, 87:13. p=2.0 MPa

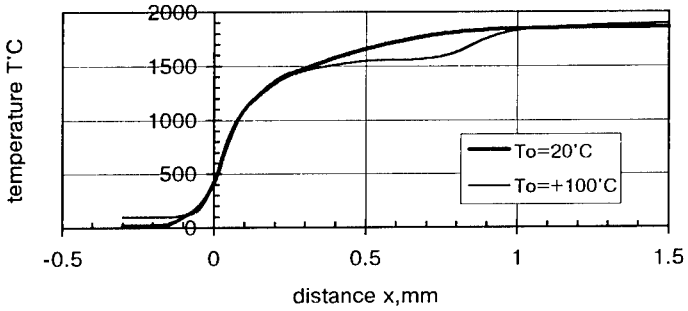


Figure 12: Averaged temperature profiles.
HMX/HTPB1, 87:13. p=5.0 MPa

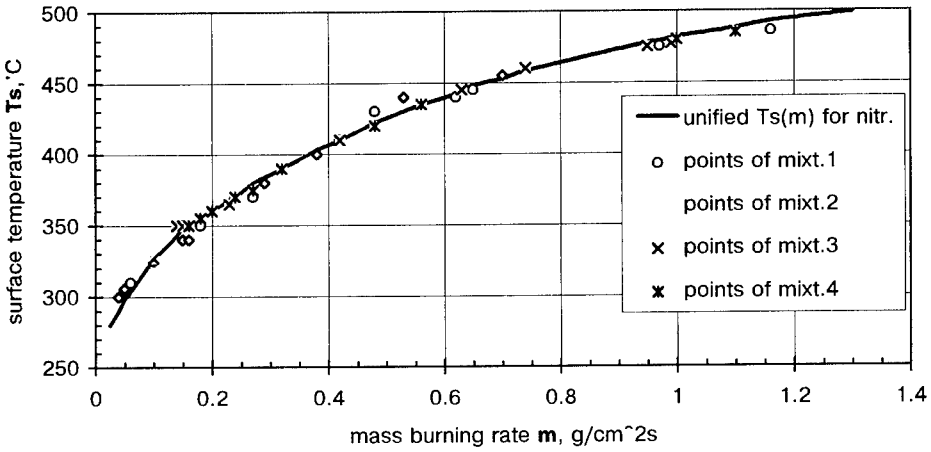


Figure 13: Unified gasification law Ts(m) for pure nitramines and points for nitramine-based propellant mixtures

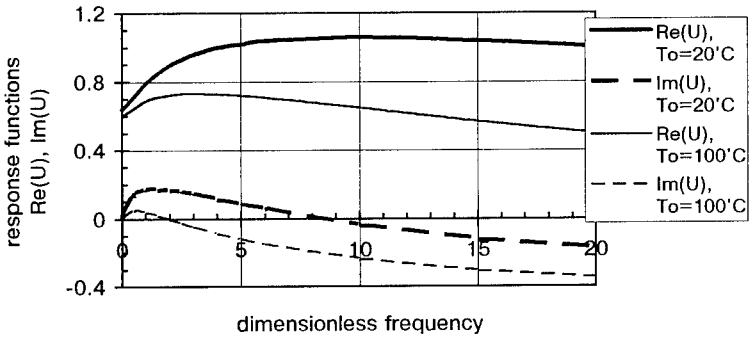


Figure 14: Burn-rate response functions of mixture 1. 0.1 MPa.

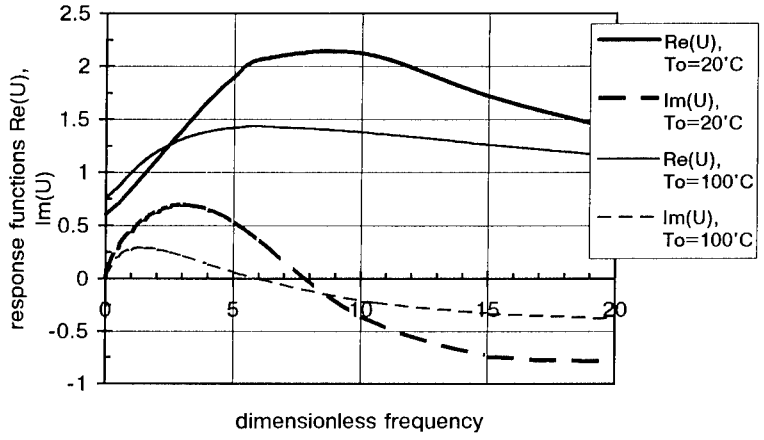


Figure 15: Burn-rate response functions of mixture 2.
0.5 MPa.

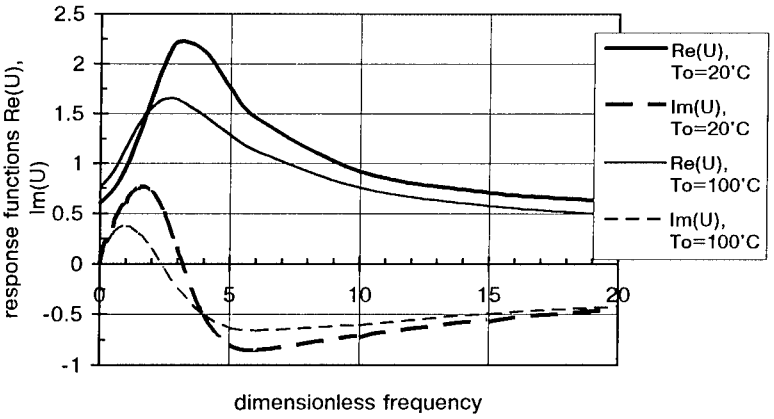


Figure 16: Burn-rate response functions of mixture 2.
2.0 MPa.

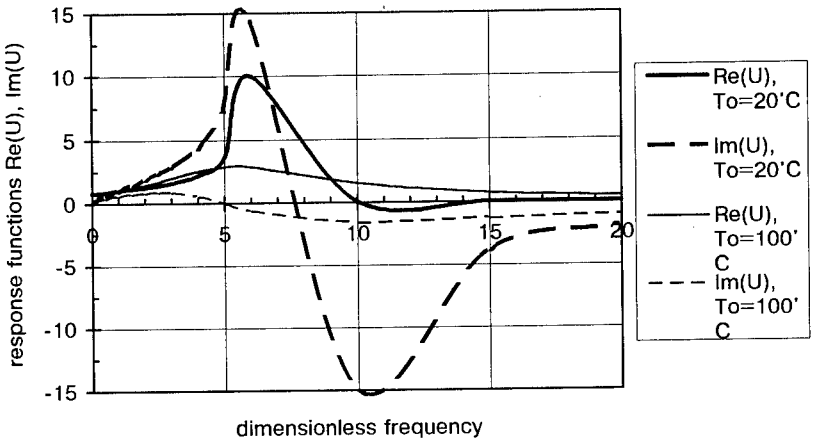


Figure 17: Burn-rate response functions of mixture 3.
1.0 MPa.

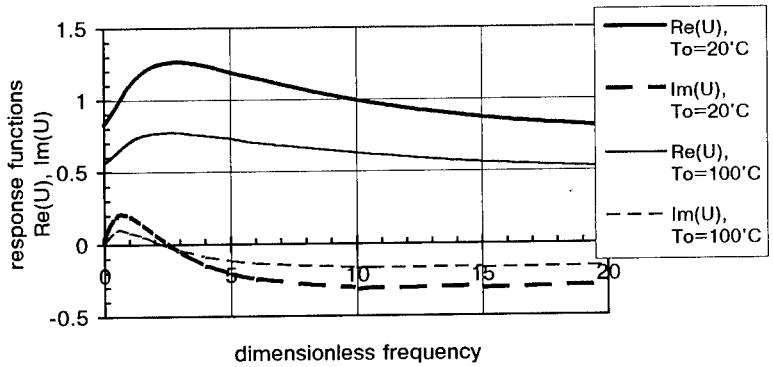


Figure 18: Burn-rate response functions of mixture 3.
5.0 MPa.

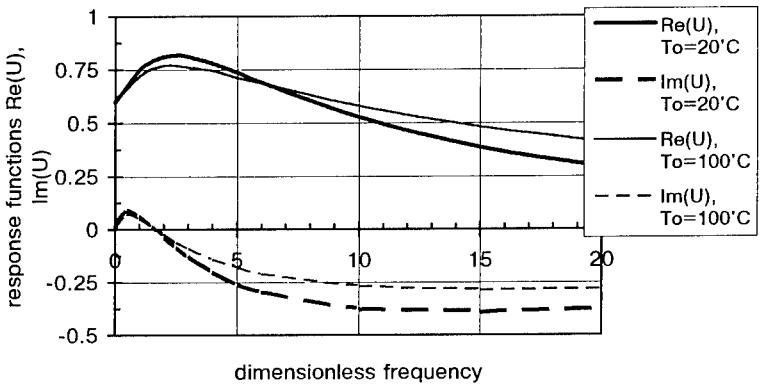


Figure 19: Burn-rate response functions of mixture 4.
5.0 MPa.

The Synthesis and Combustion of High Energy Thermoplastic Elastomer Binders

P. Braithwaite, W. Edwards, A. J. Sanderson, and R. B. Wardle
Thiokol Propulsion
P.O. Box 707, M/S 244
Brigham City, Utah 84302-0707

ABSTRACT

For nearly twenty years' researchers at Thiokol have been actively involved in the synthesis, development and characterization of a wide range of energetic thermoplastic elastomers (ETPE's) and energetic thermoplastics (ETP's). These polymers have been evaluated as neat materials and as binder systems for a wide variety of energetic formulations. The hard block of choice for the majority of these polymers is BAMO, while several different materials have been utilized in the soft block including AMMO, BAMO-AMMO, GAP, NMMO, and PGN. Recently considerable work has been performed with chain extended BAMO (CE-BAMO), BAMO-GAP and BAMO-PGN. CE-BAMO and BAMO-GAP have moderately high densities, and high heats of formation. BAMO-PGN has a very high density, a favorable oxygen balance and a reasonable heat of formation. These properties make CE-BAMO, BAMO-PGN and BAMO-GAP ideally suited as binders for high performance energetic compositions. This paper discusses initial characterization data for these promising new polymer systems.

INTRODUCTION

When formulating new explosives, rocket propellants, gun propellants and pyrotechnics, selection of the proper binder system is essential. The binder system is principally responsible for a compositions structural integrity and processing characteristics, it also can have a very significant impact on the response of a composition to unplanned stimuli such as those found in common insensitive munitions tests. Additionally the binder has a direct effect on explosives detonation properties, propellants burning rate and a pyrotechnics reactivity.

Among the more interesting and promising emerging binder systems are ETPE's and ETP's comprising of energetic oxetanes and oxiranes. A considerable amount of work has been performed using BAMO-AMMO and other similar ETPE's as binder system for new gun propellants, high explosives and rocket propellants.[1,2,3,4,5] More recently studies have been performed to evaluate three new energetic polymer systems, BAMO-GAP, BAMO-PGN and CE-BAMO. Because GAP, PGN, and BAMO are all more energetic than AMMO the resulting polymers are more energetic than BAMO-AMMO. Because of their highly energetic nature their use provides the formulator greater flexibility in developing compositions which meet specific system needs.

Approved for public release, unlimited distribution.

©2001 Thiokol Propulsion, a division of Cordant Technologies, Inc.

TECHNICAL DISCUSSION

There are many requirements that need to be met by a new binder if it is to be useful. This paper will discuss several aspects of CE-BAMO, BAMO-PGN and BAMO-GAP primarily relating to their potential utility in gun propellants and explosives including their synthesis, density, heat of formation, calculated performance in explosives and gun propellants and individual burning rates.

Synthesis

The polymers discussed in this paper are all made using isocyanate chain linking/extension chemistry. Mixtures of suitable crystalline and amorphous hydroxyl terminated difunctional polyethers are end-capped with 2,4-toluene diisoscyanate. The polymers are then linked and chain extended with a suitable glycol, normally butane diol. The synthesis of the polyether prepolymers - pBAMO, pAMMO, pNMMO, PGN, and GAP – by standard techniques is well known[6]. The linking/extension chemistry is carried out in a solvent with a tin catalyst at ambient temperatures.

This chemistry is extremely flexible in that any ratio of two or more prepolymer blocks can easily be prepared. We have made thermoplastic materials with as little as 10% hard block and up to 100% hard block. In addition, we have found that the urethane rich linking segments can be selected to optimize mechanical properties. For example, chain extension with glycols made by reacting a controlled excess of a diol with and isocyanate, effectively a urethane oligomer, give tougher TPEs at the expense of energy.

A typical synthetic procedure for 25%GAP-75%pAMMO block copolymer is as follows.

18.75g of GAP diol and 6.25g of pBAMO were dissolved in 80ml of dry methylene chloride. To this mixture, 0.12ml of dibutyltin dilaurate and 3.11g of 2,4-toluene diisocyanate was added and the reaction stirred at ambient for 4 hours. 0.805g of butane-1,4-diol was then added and the reaction was left overnight. The crude product solution was then precipitated with 500ml of methanol and washed with more methanol to give a rubbery granular product. The polymer was analysed by GPC to give Mn = 28440, Mw = 219500 (vs polystyrene standards). Tensile strain properties at ambient and 0.6 in/min were εm = 251%, σm(corrected)= 702psi. The shore A was 52 and the density 1.31g/ml. The polymer melted to a viscous liquid above 80°C. When cooled over several hours it give a rubbery solid, that was soluble in organic solvents such as methylene chloride, ethyl acetate and acetone.

Basic Characterization and Theoretical Evaluation

The density and heat of formation of BAMO, CE-BAMO, GAP, and PGN are summarized in Table I. Also shown in Table I for comparative purposes are the density and heat of formation for AMMO and NMMO.

Table I. Density and Heat of Formation of Selected Ingredients.			
Component	ρ (g/cc)	ΔH_f (kcal/mole)	Composition
AMMO	1.17	10.5	C 5, H 9, N 3, O 1
BAMO	1.30	100.3	C 5, H 8, N 6, O 1
CE-BAMO	1.29	103.5	C 5, H 7.831, N 5.396, O 1.063
GAP	1.293	33.9	C 3, H 5, N 3, O 1
NMMO	1.31	-79.67	C 5, H 9, N 1, O 4
PGN	1.47	-73.6	C 3, H 5, N 1, O 4

As shown in Table I AMMO has the lowest density of all materials considered in this paper. It has a lower heat of formation than GAP and a less favorable oxygen balance than NMMO or PGN. When comparing NMMO and PGN it is clear that PGN is more energetic as it has more oxygen and considerably higher density. CE-BAMO and BAMO have similar properties and are both very energetic. The data shown in Table I were obtained from two principal sources, Cheetah 2.0 and experimental measurements at Thiokol Propulsion.

To compare the theoretical performance of BAMO-GAP, CE-BAMO, and BAMO-PGN with BAMO-AMMO and BAMO-NMMO a series of calculations were performed. In the first series of calculations the performance of high explosives using the selected TPE and HMX were made. All explosives considered in these calculations contained 85% HMX and 15% energetic polymer. With the exception of CE-BAMO all polymers contained 25% BAMO and 75% soft block. The results of these calculations are shown in Table II. Also shown in Table II are calculated performance parameters for the well-known HMX based explosive, PAX-2A.

Table II. Calculated Detonation Properties Of Model Explosives					
Composition	***Solids (%)***	***ρ (g/cc)***	***P_{cj} (Gpa)***	***V_{cj} (mm/μ sec)***	***ΔE @ V/Vo = 6.5 (kJ/cc)***
PAX-2A	85	1.780	31.71	8.428	7.87
BAMO-AMMO/HMX	85	1.751	29.71	8.308	7.74
BAMO-GAP/HMX	85	1.779	31.81	8.539	8.15
CE-BAMO/HMX	85	1.779	32.02	8.549	8.22
BAMO-NMMO/HMX	85	1.783	31.46	8.488	8.09
BAMO-PGN/HMX	85	1.813	33.36	8.704	8.44

As shown in Table II the explosives formulated using BAMO-GAP and CE-BAMO have higher detonation pressures, detonation velocity and energy than the composition that utilized BAMO-AMMO. The explosive that utilized BAMO-PGN is predicted to significantly out perform the composition that used BAMO-NMMO. Each of the explosives which use the new polymer systems are predicted to have higher performance than PAX-2A with the BAMO-PGN/HMX composition having the highest performance of all explosives shown in Table II. The relatively high performance of the BAMO-PGN/HMX explosive is clearly the result of PGN's high density and relatively high oxygen content. All calculations shown in Table II were performed using Cheetah 2.0.

A similar series of calculations were performed to evaluate the performance of model gun propellants containing the same energetic polymer systems. In this case RDX was

selected as the energetic solid filler and all compositions were evaluated at 75% solids. The results of the gun propellant calculations are shown in Table III. Included in this table are calculated performance parameters for JA2.

Table III. Calculated Properties Of Model Gun Propellants					
Composition	***Solids (%)***	***ρ (g/cc)***	***I (J/g)***	***T_f (K)***	***Gamma***
JA2	0	1.57	1151	3423	1.227
BAMO-AMMO/RDX	75	1.604	1167	2776	1.275
BAMO-GAP/RDX	75	1.644	1289	3229	1.264
CE-BAMO/RDX	75	1.643	1320	3287	1.266
BAMO-NMMO/RDX	75	1.649	1258	3180	1.259
BAMO-PGN/RDX	75	1.692	1307	3538	1.245

As shown in Table III model propellants using BAMO-GAP and CE-BAMO have very high impetus values at moderate flame temperatures. These propellants are predicted to have considerably more energy than the similar composition utilizing BAMO-AMMO as the binder. As in the case of high explosives, BAMO-PGN was found to be more energetic than BAMO-NMMO in gun propellants. The influence of additional oxygen in BAMO-PGN is observed in a higher flame temperature and lower gamma when compared with other TPE (or TP)/RDX propellants. All propellants considered in Table III have calculated impetus values much higher than that of JA2. Additionally the density of these new model propellants is much higher than that of JA2.

The unfilled mechanical properties of several different polymers have been measured and are summarized in Table I. As shown by these data all materials have excellent mechanical properties.

Table IV. Mechanical Properties Of Selected TPE and TP's.						
Material	**BAMO (%)**	**Modulus (psi)**	**Max. Stress (psi)**	**Strain @ max. stress (%)**	**Strain @ failure (%)**	**Shore A**
BAMO-GAP	25	534	165	220	241	51
BAMO-GAP	35	1243	248	228	252	64
CE-BAMO	100	14900	893	609	609	-
BAMO-PGN	25	581	182	325	358	58

Burning Rate Data

The burning rate of several different energetic polymers has been measured using a strand burner. Samples for the burning rate tests were prepared by making sheets of material approximately 0.125-inches in thickness and cutting them into strands approximately 0.25-inches in width and 1 inch in length. Care was taken to minimize the number of voids present in all samples. These samples were then tested in a standard strand burner at pressures ranging from approximately 100 psi to 14,000 psi. The burning rate data are summarized in Table V and are shown graphically in Figure 1.

Table V. Measured Burning Rates Of Energetic Polymers.						
	Burning Rate (in/sec) @ (psi)					
Polymer	*500*	*1000*	*2000*	*3000*	*6000*	*9000*
BAMO-AMMO (25% BAMO)	0.182	0.259	0.358	0.381		
BAMO/BAMO-AMMO (62.5% BAMO)	0.220	0.355	0.611	0.749		
BAMO-GAP (25% BAMO)	0.463	0.760	0.986	1.120	1.433	1.294
BAMO-GAP (35% BAMO)	0.410	0.758		1.294	1.460	1.492
BAMO-PGN (25% BAMO)	0.235	0.329		0.654	0.800	1.078

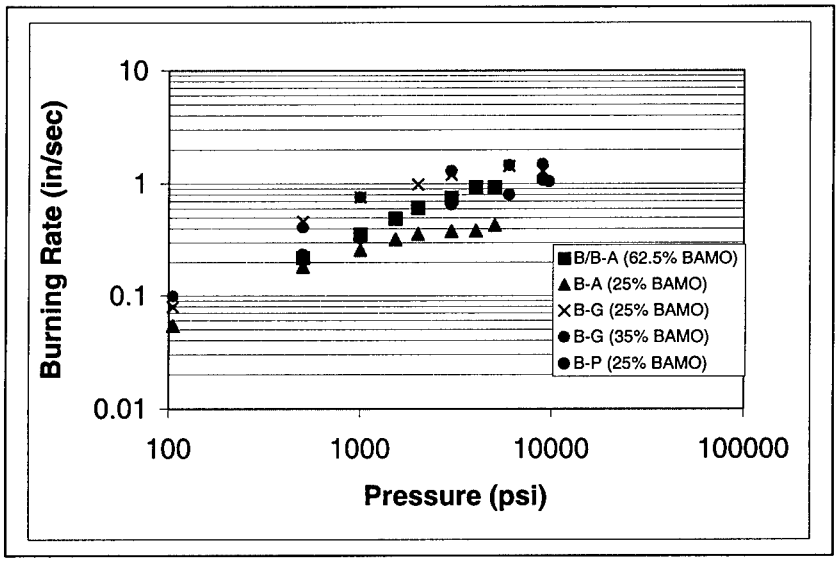


Figure 1. Strand burning rate data for energetic polymers.

While there is some data scatter, it is clear that BAMO-GAP TPE has a higher burning rate than BAMO-PGN or either of the BAMO-AMMO polymer systems. (In the case of CE-BAMO it is interesting to note that its burning rate was measured at three to five times higher than BAMO-AMMO (25% BAMO)). The burning rate of BAMO-PGN was found to be similar to that of BAMO/BAMO-AMMO while the lowest burning rate polymer was clearly BAMO-AMMO (25% BAMO). In related studies the burning rate of CE-BAMO has been found to be at the high end of the data shown in Figure 1.

The differences in burning rate followed the trend that would be expected for these materials. That is, azide based materials such as GAP and BAMO have been found to have higher burning rates than nitrate esters such as PGN. Additionally since AMMO has much less energy than any of the other polymers in this study TPE's which contain AMMO would be expected to have lower burning rates. The relatively wide range of

burning rates available make these polymers very useful for formulators tasked with producing propellants with a wide range of burning rates.

It should be noted that none of the polymers were able to sustain combustion at near ambient pressures. At 100 psi sporadic data were obtained for some of the polymers; however, combustion did not become steady until the pressure approached 500 psi. Some carbonaceous residue was found after burning the BAMO-PGN strands while the BAMO-GAP and CE-BAMO strands tended to burn quite cleanly. No observations regarding residue were made when testing the BAMO-AMMO and BAMO/BAMO-AMMO.

CONCLUSIONS

Several new energetic polymer systems have been discussed in this paper, namely, CE-BAMO, BAMO-GAP and BAMO-PGN. These polymers were compared with BAMO-AMMO and other energetic TPE's. These polymers are readily synthesized and may ultimately be lower in cost than existing energetic TPE's. Each of the new polymers were found to have excellent mechanical properties and are considerably more energetic than BAMO-AMMO. BAMO-PGN is expected to be particularly useful in new explosives while CE-BAMO and BAMO-GAP were found to have an excellent balance of impetus and flame temperature in gun propellant calculations. Additionally the relatively high burning rates of CE-BAMO and BAMO-GAP should make them attractive in applications requiring high burning rate compositions.

References:

[1] P. Braithwaite, J. Widener, S. Peters, "The Influence Of Reprocessing On The Characteristics Of EX-101 Propellant," Proceedings of the NDIA Insensitive Munitions and Energetics Technology Symposium, San Antonio, Texas, November 27-30, 2000.

[2] P. Braithwaite, D. Backes, A. Haaland, R. Wardle, T. Manning, L. Harris, K. Klingaman, "Characterization of Thermoplastic-Elastomer (TPE) Gun Propellants," Proceedings of the NDIA Insensitive Munitions and Energetics Technology Symposium, Tampa, Florida, Nov-Dec 1999, NDIA Meeting #055.

[3] I. A. Wallace, P. C. Braithwaite, A. C. Haaland, M. R. Rose, R. B. Wardle, "Evaluation of a Homologous Series of High Energy Oxetane Thermoplastic Elastomer Gun Propellants," Proceedings of the 29th International Annual Conference of ICT, Karlsruhe, Germany, June 30 - July 3, 1998.

[4] M. Michienzi, "Continuous Processing of Green Energetic Material (GEM) Rocket Propellant." Proceedings of the NDIA Insensitive Munitions and Energetics Technology Symposium, Tampa, Florida, Nov-Dec 1999, NDIA Meeting #055.

[5] K. E. Newman, R. A. Hardy, "Formulation and Characterization of Polyoxetane Molding Powders with Virgin and Reclaimed Nitramines," Proceedings of the NDIA Insensitive Munitions and Energetics Technology Symposium, Tampa, Florida, Nov-Dec 1999, NDIA Meeting #055.

[6] a) R.B. Wardle and J.C. Hinshaw, US Patent 4,988,797, 1991. b) A. P. Manzara and B Johannessen, US Patent 5,164,521, 1992. c) G. Bagg, H. Desai, W. B. H. Leeming, N. C. Paul, D. H. Paterson, and P. F. Swinton "Scale-up od polyGLYN Manufacture" Proc. ADPA Int. Symp. On Energetic Materials Technology, New Orleans, 1992.

BALLISTIC TESTING OF CLEAN SOLID ROCKET PROPELLANTS

Luigi T. DeLuca, Fabio Cozzi, Stefano Manenti, Andrea Olivani
Laboratorio di Propulsione, Dipartimento di Energetica
Politecnico di Milano, 20133 Milan, Mi, Italy

Bruno D'Andrea, Francesca Lillo
FiatAvio - Comprensorio BPD, Colleferro, Rm, Italy

Abstract

Ignition, steady burning, and flame structure of innovative ammonium perchlorate NH_4ClO_4 (AP)-based composite solid rocket propellants were experimentally investigated at the Propulsion Laboratory of Politecnico di Milano (by a variety of strand burners) and at Colleferro plants of FiatAvio (by strand burners and small-scale test motors). The unusual ignition behavior of some of these compositions, tailored for burning at low burning rates and relatively low chamber pressures (11 to 35 atm), was found to be associated with a peculiar multiphase flame structure. The presence of a scattered liquid film and formation of large spherical particles at the reacting surface layer hinder a smooth flame development. In turn, this induces low average burning rates under steady operations while increasing the pressure exponent and pressure deflagration limit markedly above the usual values. Although acceptable, a reduced specific impulse was correspondingly observed in small-scale motor testing under similar operating conditions. Difficulties may be overcome by decreasing the residence time in the reacting surface layer and thus affecting the nature of the issuing combustion products.

BACKGROUND

Although the environmental impact of chemical rocket propulsion is overall negligible[1], during last years attention has focused on AP-based propellants with the intent of improving performance while reducing the hydrogen chloride *HCl* fraction in the exhaust products. New strategies in the development of "energetic" and "clean" solid compositions include a variety of options spanning from propellants containing chlorine scavengers to chlorine neutralizers to energetic oxidizers. Chlorine scavenging formulations, whereby AP is partially replaced by sodium nitrate $NaNO_3$, are the closest to the relatively well-known class of conventional AP/HTPB composite propellants for longtime used by propulsive industries. This technique, leading to a large fraction of *HCl* scavenged directly in the combustion chamber to form the common *NaCl* salt, allows a good compromise between performances, costs, safety, reliability, and enhanced environmental protection.

For many years FiatAvio has been investigating several innovative classes of propellants[2,3]. Up to-date new formulations were developed and fully characterized to be addressed to solid rocket motors for different applications. In particular, compositions containing different amounts of aluminum, binder, and AP/$NaNO_3$ were qualified at laboratory and motor firing levels. Excellent results were achieved for propellant compositions burning at relatively high pressures (say, above 40 atm), leading to small-scale and full-scale motors with improved performance and scavenging effect[4] in the range 50 to 75% (see Table 1). Several motor configurations have been tested. Most runs were performed in a standard 2 inches small-scale test motor; MTM is a special small-scale motor used to test propellants, thermal protections, and nozzles; E00 data concern a full-scale motor. Combustion chamber pressures cover a range from 45 to 200 atm (from E-2"-2012 to E00) and related burning rates could be tailored for the proper motor requirements. Burning rates higher than 0.6 cm/s were obtained with high gas flows in side-burning motor configurations; only one end-burning propellant grain, E-MTM-2, was fired. All of the tested motors ignited regularly and burned uniformly featuring a pressure/time plot in agreement with the corresponding motors using conventional propellants (see Fig. 1).

Table 1 - Motor configurations and propellant formulations

Propellant	Al (%)	Binder (%)	Scavenging Effect* (%)	Chamber Pressure (atm)	Burning rate** (cm/s)	Propellant mass (kg)
E-2"-2012	20	12	70	45	0.743	0.4
E-2"-2013	20	13	70	50	0.875	0.4
E93	1	14	75	100	2.13	0.4
E93	1	14	75	200	3.138	0.4
E91	1	14	55	100	2.180	0.4
E91	1	14	55	200	3.172	0.4
E-MTM-1	20	12	50	45	0.780	6.5
E-MTM-2	20	12	50	45	0.810	7.0***
E-81	1	14	75	100	2.20	≈ 8.0
E00	5	14	-	100	2.00	≈ 60
E101	4	14	75	15	0.530	0.4
E125	4	14	75	15	0.460	0.4

* Reduction of *HCl*, at nozzle exit with p = 1 atm, wrt the corresponding conventional propellant.
** Burning rate suitably tuned within the required range at the operating pressure.
*** Motor configuration is end-burning, while all other configurations are side-burning.

However, reduced aluminum content compositions tailored for burning at low burning rate and chamber pressure, say in the range 11 – 35 atm, showed some anomalies in terms of ignition and burning behavior under small-scale motor testing. All propellant formulations are trimodal in AP and monomodal in the scavenging agent. Two of these specific compositions, respectively called E101 and E125, are reported as last entries in Table 1. The corresponding strand samples, tested in a Crawford

burner at Fiat Avio, evidenced (under simple visual observation) some ignition delays but regular regression of the surface. At the motor level, unconventional pressure/time combustion profiles were detected. A detailed testing of transient and steady burning of E101 and E125 was then carried out, over the same range of operating conditions, at the Propulsion Laboratory of Politecnico di Milano. For a better understanding, the related experimental results were contrasted to those from a reference composition called E00 (a conventional AP/HTPB composite propellant containing about the same *Al* fraction), even if the combustion requirements of E00 (high burning rate and high pressure) are drastically different from those of E101 and E125.

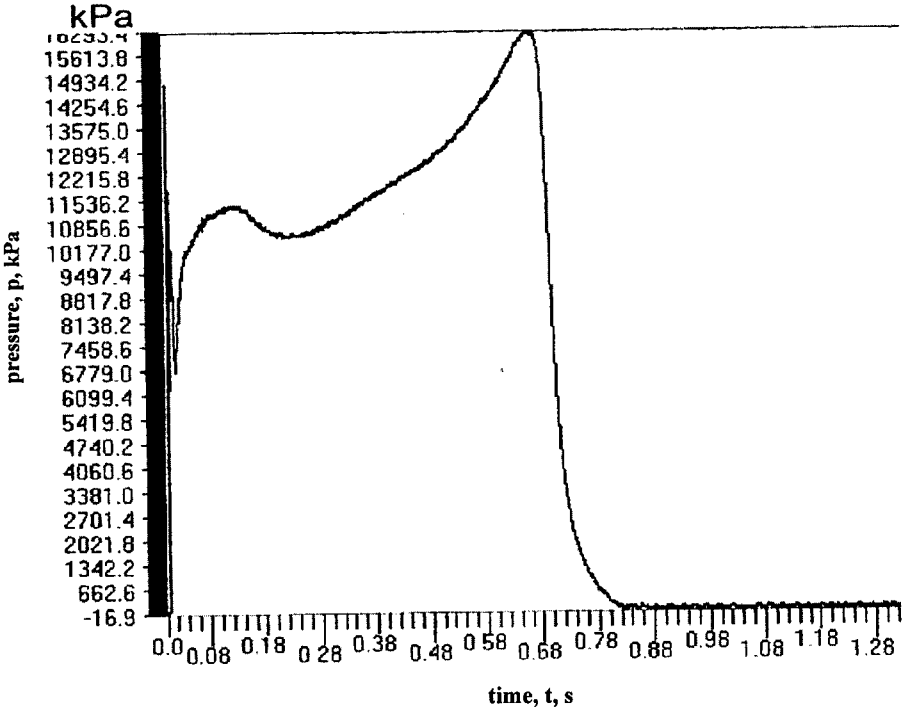


Figure 1 - Pressure history of E-81, fired at +21 °C, in good agreement with the wanted mission profile.

Objective of this paper is to report the findings of the above experimental campaign about transient and steady burning. Measured densities of the three composite propellants under examination are:

- 1.679 ± 0.009 g/cm^3 for E00;
- 1.743 ± 0.024 g/cm^3 for E101;
- 1.740 ± 0.009 g/cm^3 for E125.

LABORATORY EXPERIMENTAL TECHNIQUES

Radiative ignition was performed by means of a water-cooled, CO_2 laser providing a continuous emission at 10.6 μm with 200 W maximum output and 11 mm beam diameter ($1/e^2$ Gaussian beam). Full opening of the mechanical shutter required about 3 ms. The thermal flux actually impinging on the surface samples was in the range 100 to 500 W/cm^2. Testing was performed in the combustion chamber sketched in Fig. 2, having an internal volume of 4 lt, over the range 11 to 35 atm of nitrogen.

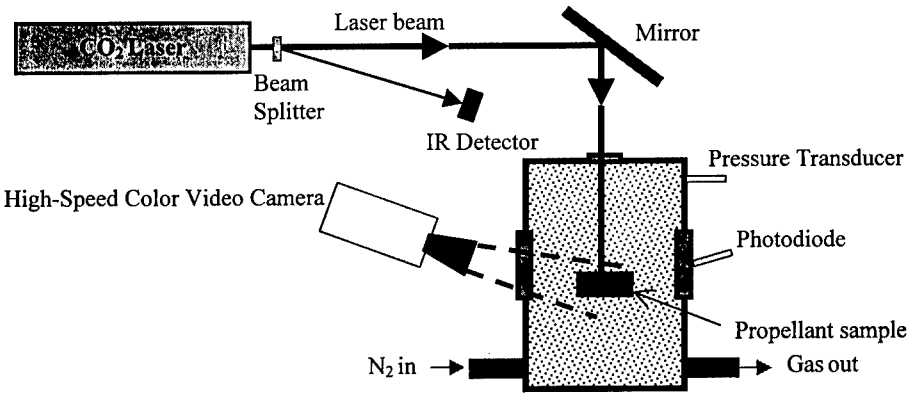


Figure 2 – Sketch of the ignition apparatus.

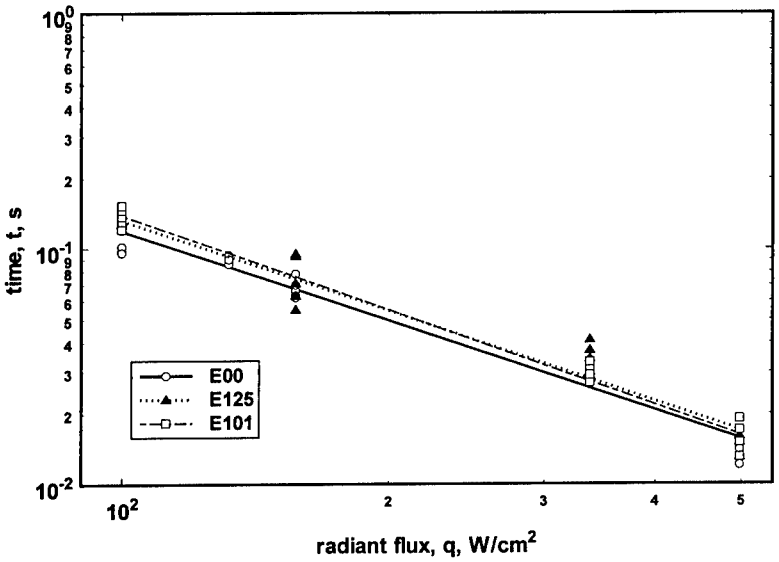


Figure 3 - Ignition of tested propellants under 11 atm of N_2.

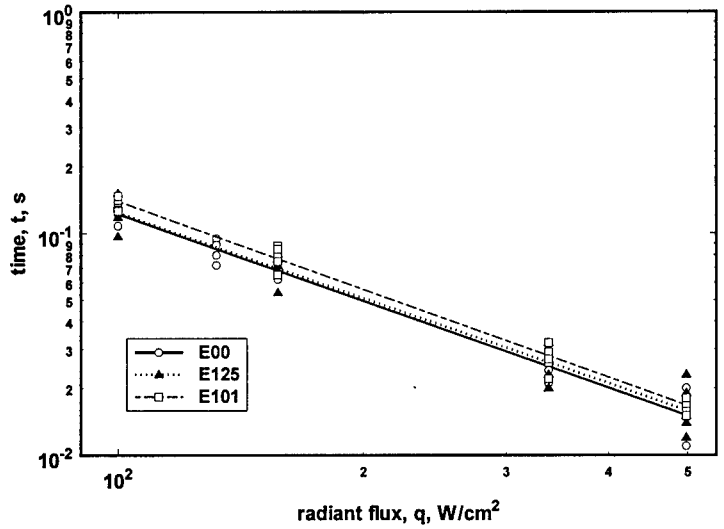


Figure 4 - Ignition of tested propellants under 25 atm of N_2.

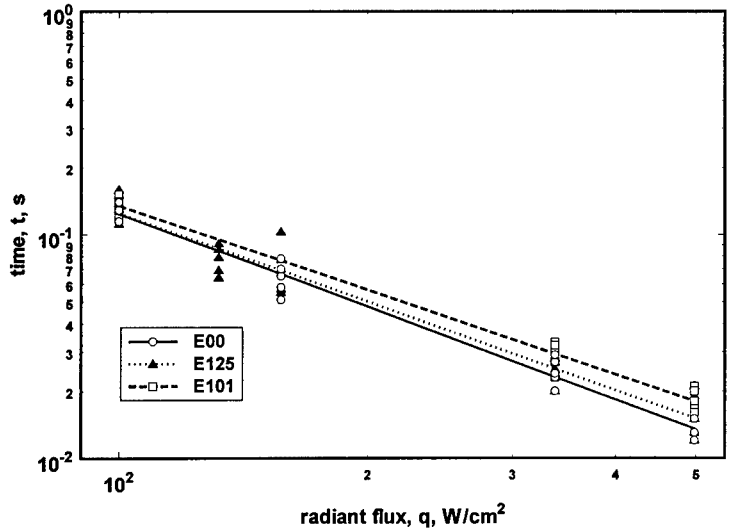


Figure 5 - Ignition of tested propellants under 35 atm of N_2.

This kind of apparatus[5,6,7] has become today rather common thanks to its easy control of the ignition stimulus (in terms both of energy flux and exposure time). Data concerning first flame appearance and flame development were systematically collected with a standard infrared (IR) photodiode having a view angle of 30° and spectral sensitivity in the range 0.35-1.1 μm with maximum response at 0.8 μm.

The photodiode, 5 mm^2 active surface, was placed in front of the combustion chamber at a distance of about 70 mm from the propellant sample. In addition, a high-speed color video camera (up to 2000 frames/s) was systematically used to supplement or corroborate the IR photodiode information. Pressure was monitored/controlled with a piezoresistive transducer, 20 kHz natural frequency and 68 atm full scale, calibrated before testing and mounted flush with the chamber wall. Propellant samples were parallelepipeds about 3.5 x 3.5 mm^2 cross-section and 5 mm long, with fresh-cut burning surface and no lateral surface inhibitor. All runs were performed in nitrogen atmosphere and ambient temperature. The measured ignition delay, defined as first flame appearance from the shutter opening, was reported in a standard time (t) vs. radiant flux intensity (q) bilogarithmic plot.

Ignition testing, with at least five runs at each investigated point, was performed under both continuous and go/no-go radiation. As expected[8,9], no difference could be detected as far as first flame appearance is concerned. However, experimental results point out a sensible scattering of data probably due to the heterogeneity of the propellant samples and multiphase effects at the burning surface layer (see below for details). The results obtained for the investigated compositions at 11, 25, 35 atm are respectively shown in Figs. 3, 4, 5. Best linear fitting laws found for the associated *log t* vs. *log q* plots by a least squares method are reported below, along with the correlation factor R and total number of experimental points N. For all tested compositions, the slope of the straight lines *log t* vs. *log q* is much larger than the theoretical –2 value[10], as commonly found for AP-based composite propellants under CO_2 laser essentially due to radiation penetration.[5,7] In summary, the following results were obtained for first flame appearance (t being in s and q in W/cm^2):

at 11 atm	E00	$t_{ign} = (39.79 \pm 9.870) \cdot q^{-1.262 \pm 0.046}$	R^2=0.969 N=50
	E101	$t_{ign} = (65.29 \pm 18.42) \cdot q^{-1.336 \pm 0.050}$	R^2=0.980 N=15
	E125	$t_{ign} = (46.04 \pm 16.27) \cdot q^{-1.271 \pm 0.065}$	R^2=0.953 N=20
at 25 atm	E00	$t_{ign} = (43.21 \pm 10.80) \cdot q^{-1.282 \pm 0.047}$	R^2=0.969 N=25
	E101	$t_{ign} = (58.72 \pm 12.17) \cdot q^{-1.314 \pm 0.037}$	R^2=0.989 N=15
	E125	$t_{ign} = (45.19 \pm 16.10) \cdot q^{-1.281 \pm 0.065}$	R^2=0.953 N=40
at 35 atm	E00	$t_{ign} = (71.83 \pm 17.58) \cdot q^{-1.381 \pm 0.045}$	R^2=0.980 N=20
	E101	$t_{ign} = (42.96 \pm 10.48) \cdot q^{-1.252 \pm 0.044}$	R^2=0.983 N=15
	E125	$t_{ign} = (51.31 \pm 17.16) \cdot q^{-1.308 \pm 0.063}$	R^2=0.948 N=25

How much is the measurement accuracy? Ignition delay was measured as the time difference between the opening of laser shutter, as detected with an IR detector (rise time about 8 μs), and the first flame

appearance as detected by a video camera. The detection of first flame appearance is erroneous at most by a full frame, since flame appearance may occur in general between two consecutive frames; this error is at most 1 ms at 1000 frames/s. Being the IR detector very fast, the total error in measuring the ignition delay can also be estimated as 1 ms; thus, the true ignition delay is less than the measured value. Based on this error size estimate and the results obtained in Figs. 3-5, the observed ignition delay times (in terms of first flame appearance) can be considered similar for all tested compositions; only slightly shorter for the reference composition E00.

The effect of pressure is illustrated in Figs. 6 and 7 respectively for E00 and E101, pointing out a negligible influence; a similar negligible influence was found for E125 as well. Likewise, ignitability is similar for all tested compositions and only slightly easier for the reference composition E00; see Figs. 8 and 9 respectively for propellants E00 and E125. In summary, ignition delay (in terms of first flame appearance) and ignitability feature common trends for all tested compositions and therefore are unable to explain the poor performances under small-scale motor testing manifested by E101 and E125 with respect to E00. What are, then, the reasons of the observed difference?

A second series of tests was carried out in the same ignition apparatus, see Fig. 2, trying to elucidate transient flame development from the first flamelet to full flame rather than just detect first flame appearance. Although it is known since long time that flame development during ignition transients can follow a wide range of patterns leading to all sorts of combustion pathologies[5-9,11,12], this usually is not a problem for motor applications due to implementation of well-behaved propellants under well-controlled operating conditions. However, in this instance, detailed visual analyses immediately confirmed a scattered occurrence of the first flame on hot spots of the burning surface, likely due to the combined effect of nonuniform laser heating and heterogeneous mixture composition, as clearly manifest from the experimental results reported in Figs. 3-5. Surprisingly, both the high-speed color video camera and IR photodiode also revealed a flame development sluggish in time and erratic in space for E101 and E125 as compared to the reference composition E00. Results obtained under continuous irradiation at 11 and 35 atm are respectively reported in Figs. 10 and 11; flame development is obviously much slower under go/no-go testing (see E125 at 11 atm in Fig. 10). The overall flame structure appears that typical of little aluminized compositions for E00, but strongly irregular chaotic and heterogeneous for E101 and E125.

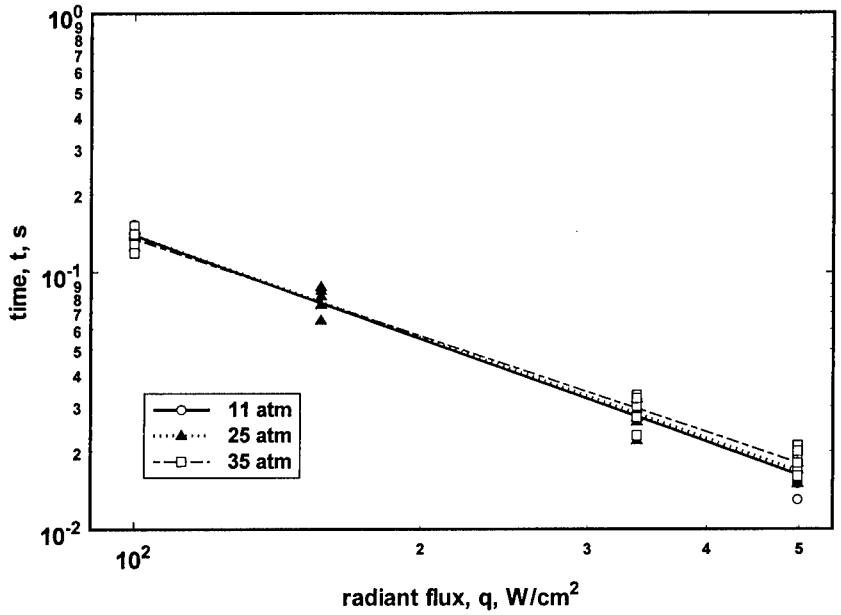


Figure 6 - Ignition of propellant E00 under 11, 25, 35 atm of N_2.

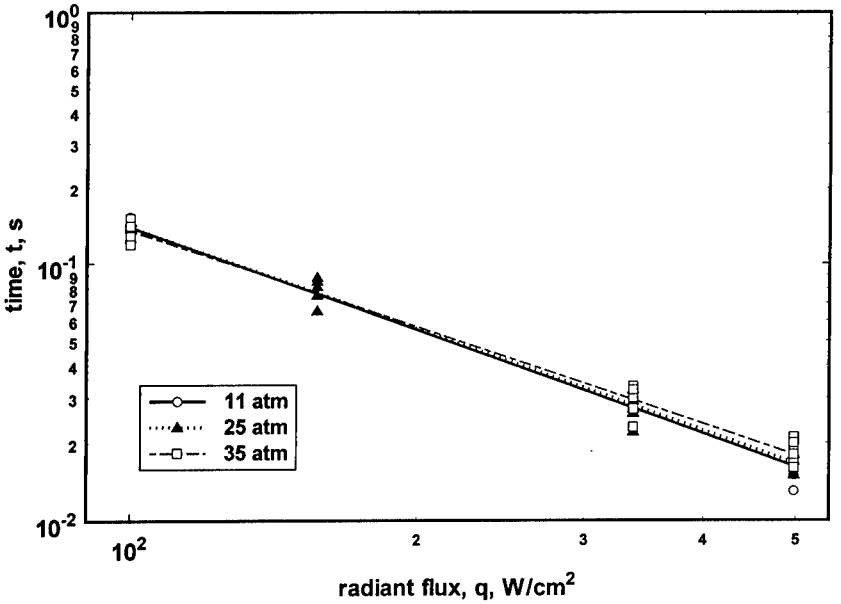


Figure 7 - Ignition of propellant E101 under 11, 25, 35 atm of N_2.

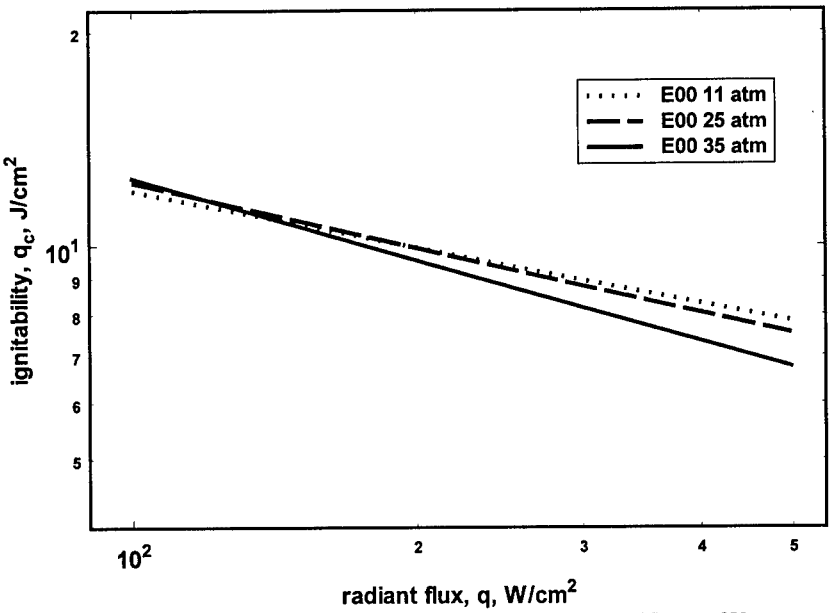


Figure 8 – Ignitability of propellant E00 under 11-35 atm of N_2.

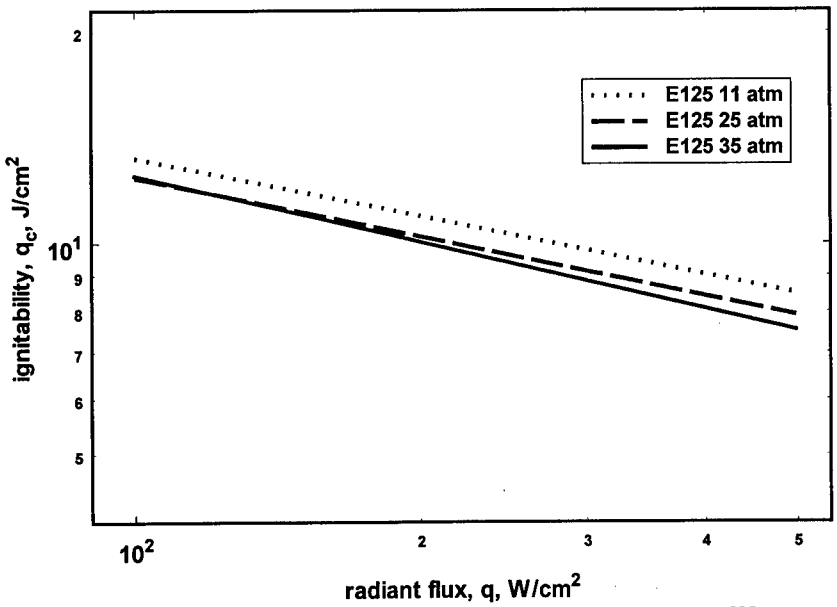


Figure 9 – Ignitability of propellant E125 under 11-35 atm of N_2.

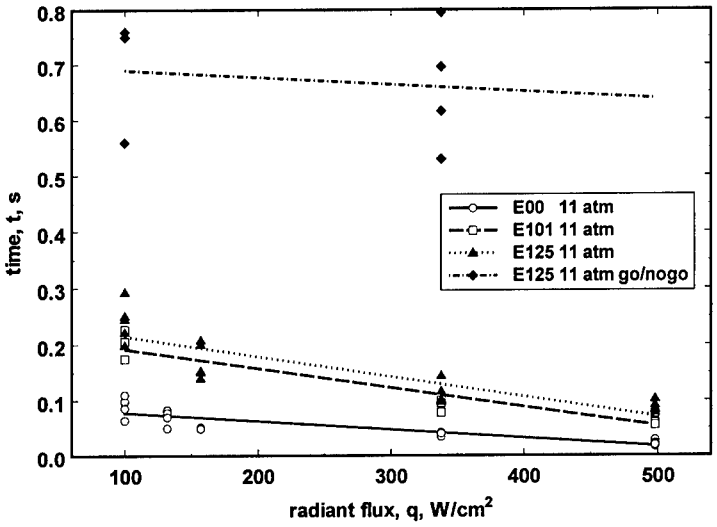


Figure 10 – Sluggish flame development for E101 (continuous irradiation) and E125 (continuous and go/no-go irradiation) at 11 atm over the whole range of radiant flux.

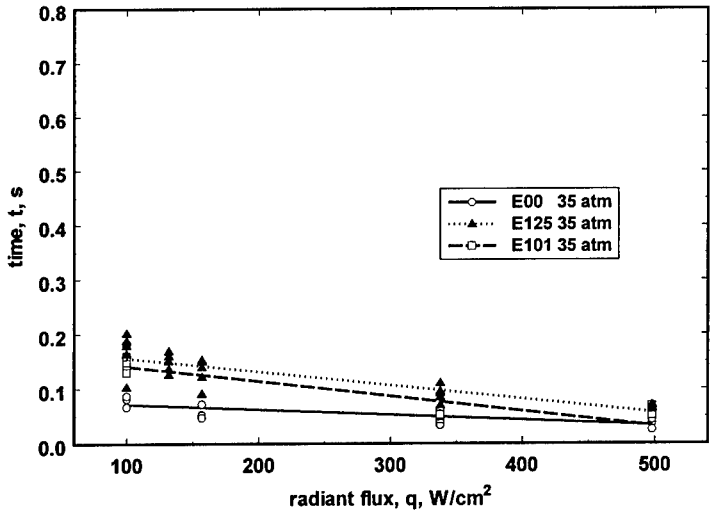


Figure 11 – Sluggish flame development for E101 and E125 under low radiant flux at 35 atm.

A third series of experiments was then conducted, under steady operating conditions, in a windowed Crawford burner to verify if and how the sluggish flame development observed for compositions E101 and E125 under radiant ignition would affect steady burning. Testing was performed in a different combustion chamber, 2 lt of internal volume, under a low nitrogen flow and at ambient temperature.

Pressure was controlled by a pneumatic feedback system. At least three runs were performed at each investigated point and five readings effected at each run. Propellant samples were parallelepipeds about 3.5 x 3.5 mm^2 cross-section and 30 mm long, with fresh-cut burning surface and a lateral surface inhibitor. Ignition was given by a hot Nichrome wire. While it was possible to burn steadily the reference composition E00 from 35 atm down to 1 atm, E101 and E125 could not be burn steadily below respectively about 9 and 7 atm. In addition, as shown in Fig. 12, steady burning rates of compositions E101 and E125 were systematically lower with respect to the reference composition E00, while exhibiting a sensibly larger pressure exponent. Similar trends were observed for steady burning under external radiation or under water. In summary, the following results were obtained for steady burning rates (r_b being in cm/s and p in atm):

E00	$r_b = (0.150 \pm 0.004) \cdot p^{0.473 \pm 0.010}$	R^2=0.991 N=15 p= 1-35 atm
E101	$r_b = (0.031 \pm 0.002) \cdot p^{0.835 \pm 0.020}$	R^2=0.993 N= 9 p=11-35 atm
E125	$r_b = (0.029 \pm 0.002) \cdot p^{0.809 \pm 0.020}$	R^2=0.994 N= 9 p=11-35 atm

How much is the measurement accuracy? Burning rate was obtained by the time required for burning surface to travel across a fixed distance (15 mm). This measurement was deduced from the digital recording of the burning sample by a video camera, thanks to special software that allows a frame-by-frame analysis and directly provides burning rates. The length measurement requires a calibration in order to convert the pixel width into millimetres; the error associated with this process was estimated around 0.4%, while a further 0.7% is due to uncertainty in the spatial position of the burning surface. An additional error of about 0.4% is due to time measurements; this value was obtained as the ratio of half of the video camera exposure time (about 0.8 ms) to the average measured time interval (about 2 s). The total error, assuming uncorrelated and random error sources, is[13]

$$\frac{\varepsilon_{\bar{r}_b}}{\bar{r}_b} = \sqrt{\varepsilon^2_{calibration} + 2*\varepsilon^2_{position} + 2*\varepsilon^2_{time}} =$$

$$= \sqrt{(0.004)^2 + 2*(0.007)^2 + 2*(0.004)^2} = 0.012$$

In order to get the time and space interval, both the burning surface position and time are measured twice. Thus, a factor 2 appears in the computation of the total error. Five readings are taken for each test and averaged to yield one measurement, reducing the total error to about $1.2\% / 5^{0.5} = 0.5\%$.

DISCUSSION OF RESULTS

For the investigated set of operating conditions, the effects of pressure and *Al* presence are negligible. Overall, ignition delays of the tested compositions fall in the general class of AP-based composite

propellants[6,7,14,15,16]. However, this may be misleading for practical applications. Detailed visual observations and testing under a variety of operating conditions revealed a slow time development and nonuniform space propagation of E101 and E125 flames with respect to the baseline E00. Likewise steady burning rates of E101 and E125, with and without laser radiation assistance, are sensibly decreased with respect to the baseline E00.

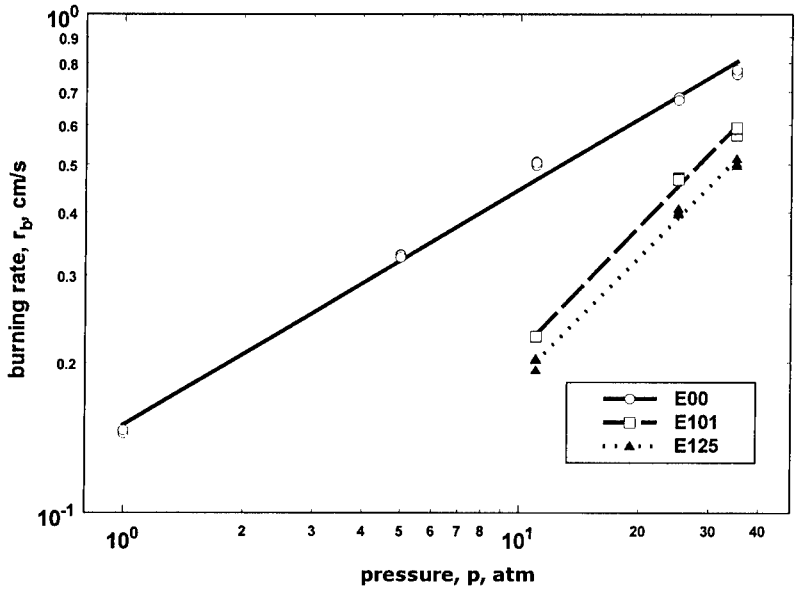


Figure 12 – Steady burning rates of tested propellants.

Why these poor ballistic properties? Very likely, this is due to the poor flame structure of E101 and E125. For these compositions, a liquid layer is observed to flow over the burning surface in a disordered way, making even more complex the burning surface heterogeneity. Exceedingly long residence times in the reacting surface layer induce the formation of large spherical particles (of the order of several 100 μm) among the combustion products inhibiting a smooth flame development. Both factors, liquid layer flowing and solid particle formation, disrupt the regular gas flow from the burning surface; see Fig. 13 contrasting flame development for E125 vs. E00 propellants. Experiments with standard small-scale test motors indicated similar difficulties. A reduced specific impulse was correspondingly observed, testifying the need of improving the flame structure of the new compositions in view of the intended applications.

This interpretation of the results is confirmed by steady burning runs, revealing a markedly decreased burning rate of compositions E101 and E125 with respect to the reference E00 both with and without radiation assistance. Under adiabatic burning, this difference decreases with increasing pressure due to reduced residence time in the reacting surface layer, leading to an anomalous large pressure exponent. Under radiation, this difference decreases with increasing radiant flux due to the combined effect of reduced reacting surface layer residence time and progressive changing of the combustion wave into an ablation wave[17]. A further confirmation was offered by the much larger value of the pressure deflagration limit (PDL)[18] of compositions E101 and E125 with respect to the reference E00. Thus, liquid layer flowing and formation (with subsequent evolution) of spherical combustion products particles hinder flame propagation by lowering the average burning rate while increasing the pressure exponent and PDL markedly above the usual values[19].

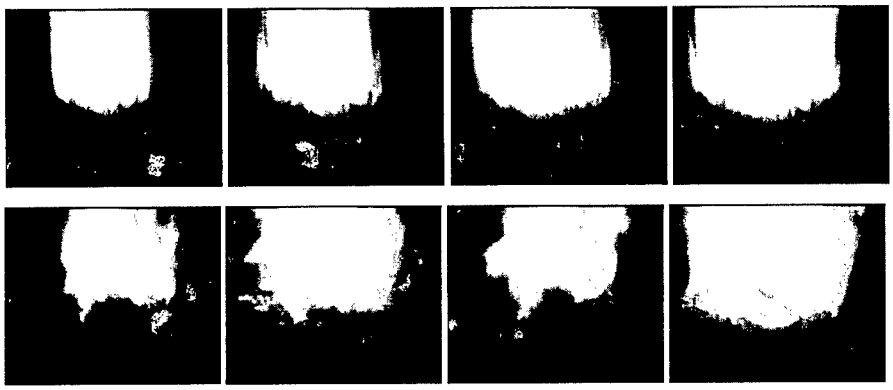


Figure 13 – Flame Development of E00 (top) and E125 (bottom) compositions

CONCLUSIONS AND FUTURE WORK

Liquid layer flowing and solid particle formation disrupt the regular gas flow from the burning surface, hindering flame propagation under both laboratory burners and small-scale test motors of E101 and E125 with respect to E00. Difficulties may be overcome by decreasing the reacting surface layer residence time and thus the multiphase nature of the issuing combustion products. This can be obtained by appropriate operating conditions (for example, increasing combustion pressure and/or impinging radiant flux) or other means. Further data are being collected in a windowed strand burner and under water strand burner with the intent of better understanding the peculiar ballistic effects observed during this experimental program.

REFERENCES

1 "Environmental Aspects of Rocket and Gun Propulsion", AGARD Conference Proceedings No. 559, Paris, France, February 1995.

2 B. D'Andrea and F. Lillo, "Industrial Constraints as Evaluation Criteria in Developing Solid Space Propellants Using Alternative Energetic Materials", AIAA Paper 97-2795.

3 B. D'Andrea, F. Lillo, A. Faure, and C. Perut, "A New Generation of Solid Propellants for Space Launchers", IAF Paper 99-S.3.01.

4 B. D'Andrea, F. Lillo, and R. Massimi, "Performance Investigation of Advanced Solid Propellant Formulations by Conventional and Innovative Methodologies", ICT Paper P94, 1996.

5 B.N. Kondrikov, M. Summerfield, and T.J. Ohlemiller, "Ignition and Gasification of a Double-Base Propellant Induced by CO2 Laser Radiation," Thirteenth International Symposium on Combustion, Paper № 129, 23-29 Aug 1970, University of Utah, Salt Lake City, Utah.

6 L.T. De Luca, T.J. Ohlemiller, L.H. Caveny, M. Summerfield, "Solid propellant ignition and other unsteady combustion phenomena induced by radiation," Technical Report No. 1192-T, Department of Aerospace and Mechanical Sciences, Princeton University, Princeton, New Jersey, 1976.

7 C.E. Hermance, "Solid-Propellant Ignition Theories and Experiments", in "Fundamentals of Solid Propellant Combustion", edited by K.K. Kuo and M. Summerfield, AIAA Progress in Astronautics and Aeronautics, 1984, Vol. 90, chapter 5, pp. 239-304, AIAA, Washington, DC, USA.

8 L.T. DeLuca, L.H. Caveny, T.J. Ohlemiller, M. Summerfield, "Radiative ignition of double-base propellants: I. Some formulation effects", AIAA Journal, 1976, Vol. 14, No. 7, pp. 940-946.

9 L.T. DeLuca, T.J. Ohlemiller, L.H. Caveny, M. Summerfield, "Radiative ignition of double-base propellants: II. Pre-ignition events and source effects", AIAA Journal, 1976, Vol. 14, No. 8, pp. 1111-1117.

10 H.S. Carslaw and J.C. Jaeger, "Conduction of Heat in Solids", Oxford University Press, London, UK, 2nd edition, 1971.

11 T.J. Ohlemiller, L.H. Caveny, L.T. De Luca, M. Summerfield, "Dynamic effects of ignitability limits of solid propellants subjected to radiative heating", in 14th Symposium (International) on Combustion, The Combustion Institute, Pittsburgh, PA, USA, 1972, pp. 1297-1307.

12 B.N. Kondrikov, S. Cristoforetti, I.V. Grebenyuk, and L.T. DeLuca , "Gasification of Solid Propellants and Propellant Ingredients under Influence of Thermal Radiation", 32nd International ICT Conference, 03–06 July 2001, Karlsruhe, Germany.

13 J.R. Taylor, " An Introduction to Error Analysis. The Study of Uncertainties in Physical Measurements ", 2nd edition, University Science Books, 1997, pp. 150-152.

14 A.D. Baer and N.W. Ryan, "Ignition of Composite Propellants by Low Radiant Fluxes", AIAA Journal, 1965, Vol. 3, No. 5, pp. 884-889.

15 E.W. Price, H.H.Jr. Bradley, G.L. Dehority, and M.M. Ibiricu, "Theory of Ignition of Solid Propellants", AIAA Journal, 1966, Vol. 4, No. 7, pp. 1153-1181.

16 G. Lengellé, A. Bizot, J. Duterque, and J.C. Amiot, "Ignition of Solid Propellants", La Recherche Aérospatiale, 1991, pp. 1-20, No. 1991-2.

17 L.T. DeLuca, M. Verri, and A. Jalongo, "Intrinsic Stability of Energetic Solids Burning under Thermal Radiation", in 'Progress in Combustion Science -- in Honor of Ya.B. Zel'dovich', Edited by W.A. Sirignano, A.G. Merzhanov, and L.T. DeLuca, 1997, Volume 173 of AIAA Progress in Astronautics and Aeronautics, Chapter 12, pp. 195-218, AIAA, Reston, VA, USA.

18 C. Bruno, G. Riva, C. Zanotti, R. Dondé, C. Grimaldi, and L.T. DeLuca, "Experimental and Theoretical Burning of Solid Rocket Propellants Near the Pressure Deflagration Limit", Acta Astronautica, 1985, Vol. 12, No. 5, pp. 351-360. See also IAF Paper 83-367, 1983.

19 J.A. Steinz. and M. Summerfield, "Low Pressure Burning of Composite Solid Propellants", in "Propellants Manufacture, Hazards, and Testing", edited by C. Boyars and K. Klager, Advances in Chemistry Series, 1969, Vol. 88, chapter 9, pp. 244-295, American Chemical Society, Washington, DC, USA.

The application of Gel Permeation Chromatography to the Investigation of the Ageing Processes of Nitrocellulose.

Authors: P R Deacon, G R A Kennedy, A L Lewis and A F Macdonald

Chemistry Research Division
AWE plc, Aldermaston, Reading RG7 4PR, UK.

Nitrocellulose (NC) is used as the binder in many polymer bonded explosives (PBXs) and its degradation with time is of ongoing interest to the explosives community. Conventional gel permeation chromatography (GPC) has been used to follow the reduction in molecular weight distribution (mwd) of NC extracted from PBX formulations aged at elevated temperatures. This molecular weight information has been used to investigate the reaction kinetics of depolymerisation. The obtained data is presented and used to validate a random chain scission decomposition model, exhibiting linear Arrhenius-type behaviour over the temperature range of 36-66°C. A methodology for consistent analysis is outlined, and consideration is given to alternative molecular weight distribution measurement techniques as a way of validating the GPC information.

The addition of Right Angle Laser Light Scattering (RALLS) and viscometry detection (triple detector GPC) has identified chromatographic features in both pristine and extracted material which are apparently related to the NC feed stock and time in solution. A high molecular weight 'pre-peak' was observed to merge into the main peak concurrently with changes in the specific refractive index increment (dn/dc) and viscosity with time in solution. Mark-Houwink plots of intrinsic viscosity vs. molecular weight also have been investigated in an attempt to reveal the possible conformational changes that may exist in NCs of different molecular weights.

Key Words:

Nitrocellulose
GPC Triple Detection
PBX
Kinetics
Mark-Houwink

STABILITY ANALYSES OF DOUBLE BASE PROPELLANTS CONTAINING NEW STABILISERS

– PART II –

Jan Petržílek[□], Stephan Wilker[•], Uldis Ticmanis[•], Gabriele Pantel[•], Lutz Stottmeister[•], Jan Skládal[□]

[□] AliaChem a.s., Div. Synthesia, Research Institute for Industrial Chemistry, CZ-532 17 Pardubice-Semtín, Czech Republic

[•] Wehrwissenschaftliches Institut für Werk-, Explosiv- und Betriebsstoffe, Großes Cent, D-53913 Swisttal, Germany

Abstract

This work – which is the second part of a series of publications – deals with the influence of different stabilisers on the decomposition behaviour of DB propellants. By systematically varying stabiliser types and concentrations and by using and combining different analytical methods an overview on the reactivity and reactions of different types of stabilisers and their decomposition products was obtained.

This work shows the effect of changes of the electron density of DPA derivatives on the reactivity towards nitric oxides and nitroglycerin. DPA was substituted by electron withdrawing groups (-NO_2, -Cl) in positions 3 and 4 and with electron donating groups (-CH_3, -OCH_3, -OH) in positions 2, 3 and 4.

The ageing was performed at different temperatures and observed by different techniques such as heat flow calorimetry, vacuum stability and weight loss. The combination of the results gives clear evidence that the electron density at the nitrogen atom and the ability of DPA to form stable radicals are the main parameters which describe their stabilising reactions. The results are compared with the Hammett constants of the substituents. A clear linear relationship between the Hammett constants and the reactivity of each stabiliser was detected.

Kurzfassung

Diese Arbeit – die den zweiten Teil einer Publikationsserie darstellt – behandelt die Einflüsse verschiedener Stabilisatoren auf das Zersetzungsverhalten zweibasiger Treibladungspulver. Die systematische Variation von Stabilisatortypen und -konzentrationen und die Verwendung kombinierter Analyseverfahren erlaubt einen Überblick über die Reaktivität und Reaktionsweisen der verschiedenen Stabilisatoren und deren Abbauprodukte.

In diesem Teil der Arbeit werden die Einflüsse der Änderung der Elektronendichte von DPA-Abkömmlingen gegenüber nitrosen Gasen und Nitroglycerin untersucht. DPA wurde mit elektronenziehenden (-NO_2, -Cl) in *meta*- und *para*-Position sowie mit elektronenschiebenden Gruppen (-CH_3, -OCH_3, -OH) in *ortho*-, *meta*- und *para*-Position substituiert.

Die Alterung erfolgte bei verschiedenen Temperaturen und wurde mit verschiedenen Techniken (Vakuumstabilität, Wärmeflusskalorimetrie und Gewichtsverlust) untersucht. Die

Kombination der Versuchsergebnisse ergibt klare Schlüsse darauf, dass die Elektronendichte am Stickstoffatom und die Fähigkeit von (substituierten) DPA, stabile Radikale zu bilden, die beiden wichtigsten Größen sind, die die stabilisierende Wirkung beschreiben. Die Ergebnisse wurden mit den Hammett-Konstanten der Substituenten verglichen. Dabei wurde ein linearer Zusammenhang zwischen diesen und der Reaktivität der einzelnen Stabilisatoren ermittelt.

1. Introduction

A set of model experimental spherical propellants stabilized by different concentrations of common stabilizers (diphenylamine, 2-nitrodiphenylamine, Centralite I or Akardite II) was prepared. The chemical stability of the samples was tested by different methods (heat test at 100 °C, Bergmann-Junk test, Weight loss test, Methylviolet test, Vacuum stability test and Heat flow calorimetry). The results were presented and discussed in Part I of this work[1]. The clear conclusion was that all the tested stabilizers are able to prevent propellants effectively from autocatalysis, but at the same time, stabilizers or their reaction products are initiating decomposition reactions of nitrate esters. This decomposition leads to undesirable manifestations as are higher heat flow, gas evolution or weight loss in comparison with propellants without stabilizer in the period before autocatalysis starts. The results of most stability tests are thus governed by two factors: the "chemical stability" declared as the time of safe storage and by the chemical incompatibility. An interpretation of the stability tests must therefore be done under considerations of this fact. An other conclusion was that chemical reactions strongly depend on the amount of oxygen above the sample[1-9].

The theory explaining the reaction mechanisms of diphenylamine type stabilizers was developed which assumes formation of free radicals from diphenylamine as the key step of the reaction chain. The theory explains the difference between the highly incompatible diphenylamine and 2-nitrodiphenylamine, which was the only stabilizer studied without explicit incompatibility problems. Different ability of free radical formation can explain the different results better than differences in basicities.

This second part of the work continues with diphenylamine type stabilizers by studying model experimental spherical propellants stabilized by diphenylamines with different substituents. The aim is to see the substituent effect on the stabilization effectiveness and the extent of incompatibility. These results might be important for better understanding of the reaction mechanisms and could possibly make suggestions of such chemical structures, which will maximize the stabilization effectiveness and minimize the incompatibility effects.

2. Experimental part

Model experimental spherical propellants were prepared in the same way as it was mentioned in the Part I of this work[1]. The only differences between particular samples of the set was the concentration and sort of stabilizer. The samples contained approximately 14 % of nitroglycerine. The stabilizers 3-chlorodiphenylamine, 3-hydroxydiphenylamine, 4-hydroxydiphenylamine, 2-methyl-4-methoxydiphenylamine were purchased from Tokyo Kasei Kogyo CO., LTD (6-15-9 Toshima, Kita-Ku, Tokyo, Japan). 3-Methyldiphenylamine, 3-methoxydiphenylamine and 4-nitrodiphenylamine were purchased from Aldrich Chemicals. 3-Nitrodiphenylamine was prepared by the University of Pardubice according to ref.[10].

The testing procedures were carried out at the conditions described in Part I of this work[1], heat flow measurements and weight loss tests were performed at the same temperature (89 °C), vacuum stability both at 89 °C and 115 °C. A list of discussed samples is presented in Tables I and II. Additional heat flow measurements of selected samples were performed at 70 °C.

3. Results and Discussion

3.1 Relations between the type of substituent of DPA and its initial concentration and results of heat flows and gas evolution

General relations

Results of heat flow measurement (HFC) and vacuum stability test (VST) for samples stabilized by diphenylamines up to the concentration 25 $\mu mol.g^{-1}$ are presented graphically in Figures 1 and 2. Figures 3 and 4 show results of samples with higher concentration of diphenylamines and Figures 5 and 6 results measured for samples stabilized by DPA and nitrated diphenylamines. It is clearly seen that the results for most of stabilized samples show the nearly similar pattern:

- "First maximum" of heat flow which is caused by oxidation by oxygen above the sample (this reactions are missing in the case of VST where no air is present in the measuring ampoule)
- "First minimum" or "induction period" characterized by low heat flow and very low or no gas evolution. The diphenylamine concentration decreases to zero during this period and as the main reaction product N-NO-DPA was found and in much less extent N-nitro-DPA's[7,9,11]. According to the theory presented in Part I of this work[1] DPA blocks oxidation reactions of aldehydes to carboxylic acids and formation of gaseous products, terminates radical reactions by formation of stable radicals and causes accumulation of unknown compounds with high enthalpy of formation[2]. DPA is capable of effective functioning also as an antioxidant in a propellant. On the other hand, DPA is responsible for the nitrate esters decomposition during this period[1,2,12].
- The beginning of high heat flow and fast gas generation is observed just after the first minimum. This raise of exothermic reactions was explained in Part I of this work by a change of the conditions in the propellant into oxidative after the DPA had been depleted. This conditions enable highly exothermic oxidation of previously accumulated compounds (mostly aldehydes) and consequent decomposition of the reaction products – mainly alpha carbonyl carboxylic acids[1,2] to gases. Local maximum (so called "second maximum") of heat flow and rate of gas evolution is observed just after the first minimum which is believed to be caused by vigorous decomposition of some compound accumulated in the sample during the first minimum. It is highly probable that such exothermic reactions are accompanied by higher extent of radical chain reactions.
- "Second minimum" is characterized by decrease of heat flow and gas evolution rate after second maximum, but both parameters remain high for relatively long time. The main reactions in the propellant are C-nitration of N-NO-diphenylamine, oxidation reactions of previously accumulated aldehydes and decomposition of such oxidation products.

Two major types of departures from the above pattern were observed – a significant increase of heat flow during the induction period (in the case of 3-methoxy and 3-hydroxy-diphenylamines) and lack of second maximum and second minimum (in the case of diphenylamines substituted by a nitro group in *ortho* position).

There are estimates of main parameters describing the HFC results in Table II and the results of VST measurements in Table I. For that samples exhibiting the induction period, second maximum and minimum it is possible to put several general conclusions:

- The duration of the induction period is proportional to the initial concentration of diphenylamine (or one of its derivatives) in the sample (This is only valid if the DPA concnetration is below 1-2%. If it exceeds 4-5%, a reduction of the length of the induction period is observed. For details see ref. [12]).
- The induction period is longer for diphenylamines with electron-acceptor substituents and shorter for diphenylamines with electron-donating substituents.
- Heat flow intensities grow with electron-donating capability of substituents and with initial concentration of the stabilizer. The same relation was observed for rates of gas evolution. Such effects are most remarkable when the initial concentrations of diphenylamine were higher than 1 %. Heat flows in second maximum (and in many cases also in first minimum) were higher than that measured for the unstabilized sample. Gas evolution rates after first minima (or the induction period) are higher than for not stabilized sample.

Table I Results of vacuum stability tests at 89 and 115 °C

Sample	Subst.	C	VST 89 °C			VST 115 °C	
			time	Max rate	rate	time	Max rate	rate
		[%]	[days]	[$cm^3.g^{-1}.day^{-1}$]		[days]	[$cm^3.g^{-1}.day^{-1}$]	
STAB-319	H	0.38	2.2	0.31	0.28	0.069	9.94	7.91
STAB-225	H	0.79	3.2	0.35	0.29	0.099	12.82	10.53
STAB-282	H	2.77	3.6	0.79	0.70	0.108	13.93	10.84
STAB-303	3-CH_3	0.34	2.6	0.32	0.32	0.076	11.16	8.20
STAB-291	3-CH_3	0.92	3.5	0.43	0.40	0.163	21.40	17.06
STAB-292	3-CH_3	3.11	4.3	0.75	0.72	0.172	20.66	18.45
STAB-302	3-OCH_3	0.43	1.5	0.78	0.78	0.073	12.32	14.63
STAB-289	3-OCH_3	0.80	1.9	0.94	0.94	0.076	17.56	16.20
STAB-290	3-OCH_3	2.95	2.1	2.50	2.38	0.115	46.66	38.39
STAB-315	3-OH	0.27	1.3	0.42	0.39	0.066	10.33	9.49
STAB-316	3-OH	0.59	2.1	0.60	0.60	0.083	15.66	13.61
STAB-317	3-Cl	0.46	3.1	0.26	0.26	0.080	8.62	7.90
STAB-318	3-Cl	1.08	5.2	0.34	0.33	0.139	11.06	10.21
STAB-304	3-NO_2	0.48	3.2	0.26	0.26	0.097	8.90	8.87
STAB-293	3-NO_2	1.07	6.7	0.30	0.31	0.191	9.60	9.36
STAB-311	2-CH_3-4-OCH_3	0.24	0.8	0.43	0.38	0.044	13.39	11.48
STAB-312	2-CH_3-4-OCH_3	0.75	0.9	0.74	0.57	0.049	20.64	15.08
STAB-320	4-NO_2	0.53	3.6	0.21	0.21	0.115	7.16	7.16
STAB-226	2-NO_2	0.97	--	0.17	0.17	--	7.14	7.14
STAB-187	2-NO_2	3.00	--	0.13	0.13	--	4.94	4.94
STAB-238	2-NO_2-4-NO_2	0.90	--	0.14	0.14	--	7.43	7.43

Table II List of samples and results of heat flow measurement at 89 °C

Sample	Substituent			1. Minimum				2. Maximum			2. Minimum		
				START		END							
		C	C	P	P	time	Q	P	time	Q	P	time	Q
		[%]	[μmol.g^{-1}]	[μW.g^{-1}]		[days]	[J.g^{-1}]	[μW.g^{-1}]	[days]	[J.g^{-1}]	[μW.g^{-1}]	[days]	[J.g^{-1}]
STAB-319	H	0.38	22.3	44.1	55.3	1.48	7.5	155.5	2.78	21.0	116.3	4.11	36.7
STAB-225	H	0.79	46.6	45.0	61.1	2.56	22.3	156.1	4.44	31.4	92.0	6.25	53.9
STAB-282	H	2.77	163.7	105.5	127.8	3.74	32.7	275.1	5.42	65.8	n.a.	n.a.	n.a.
STAB-303	3-CH_3	0.34	18.7	38.8	51.2	1.45	6.3	124.1	2.82	18.8	106.0	4.86	39.1
STAB-291	3-CH_3	0.92	50.0	91.6	108.7	2.36	22.0	272.8	4.01	54.3	230.5	6.17	103.1
STAB-292	3-CH_3	3.11	169.7	111.1	120.9	4.17	37.4	277.8	5.78	67.3	n.a.	n.a.	n.a.
STAB-302	3-OCH_3	0.43	21.5	53.8	83.0	1.22	5.4	228.7	2.58	16.2	218.7	3.61	27.0
STAB-289	3-OCH_3	0.80	40.0	36.6	77.2	1.48	7.1	170.7	1.73	10.0	169.6	1.85	11.8
STAB-290	3-OCH_3	2.95	148.3	144.3	394.1	2.08	37.8	970.9	2.23	45.3	n.a.	n.a.	n.a.
STAB-315	3-OH	0.27	14.5	63.7	79.6	0.89	6.5	172.8	2.74	28.8	133.3	4.34	50.3
STAB-316	3-OH	0.59	31.6	83.5	120.1	1.22	11.4	220.4	3.45	49.1	181.8	n.a.	n.a.
STAB-317	3-Cl	0.46	22.7	36.8	47.0	1.68	6.7	112.5	3.24	18.6	92.5	4.98	34.2
STAB-318	3-Cl	1.08	52.9	41.2	58.3	3.59	14.1	124.7	5.44	28.0	n.a.	n.a.	n.a.
STAB-304	3-NO_2	0.48	22.6	36.4	43.7	2.15	8.0	101.9	4.10	21.2	87.6	5.67	34.2
STAB-293	3-NO_2	1.07	49.9	30.6	54.6	5.03	17.9	125.0	7.52	36.5	112.1	9.26	54.5
STAB-311	2-CH_3-4-OCH_3	0.24	11.4	67.2	67.2	0.71	5.2	180.5	2.18	24.7	176.4	2.89	35.8
STAB-312	2-CH_3-4-OCH_3	0.75	35.0	103.7	115.5	0.91	11.2	298.2	2.73	54.4	297.9	3.00	61.3
STAB-320	4-NO_2	0.53	24.5	55.3	53.4	1.91	9.4	91.2	4.30	23.3	86.0	5.32	33.3
STAB-226	2-NO_2	0.97	46.7	48.5	--	--	--	--	--	--	106.0	--	--
STAB-187	2-NO_2	3.00	140.2	49.1	--	--	--	--	--	--	54.0	--	--
STAB-238	2-NO_2-4-NO_2	0.90	34.8	77.0	--	--	--	--	--	--	77.0	--	--

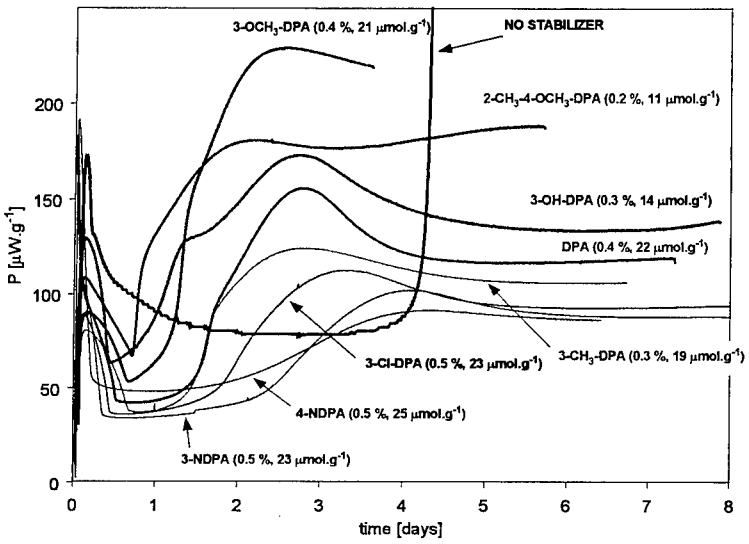


Figure 1 Heat flow results at 89 °C for low amount of stabilizers

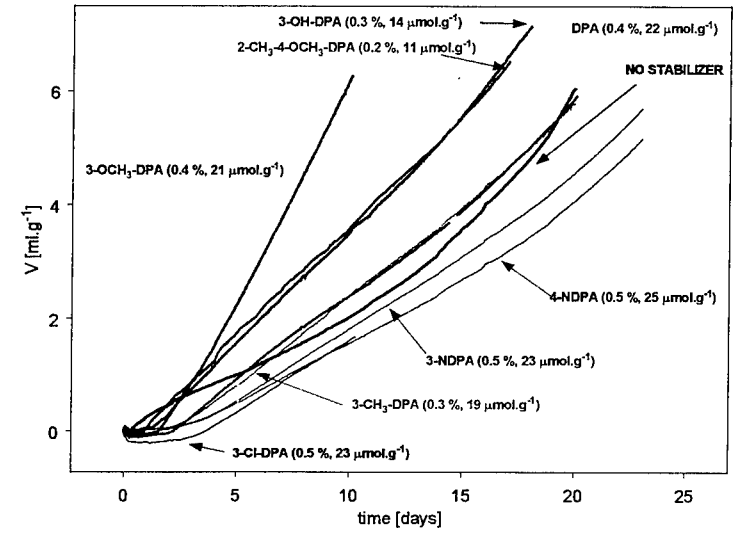


Figure 2 Results of vacuum stability test at 89 °C for low amount of stabilizers

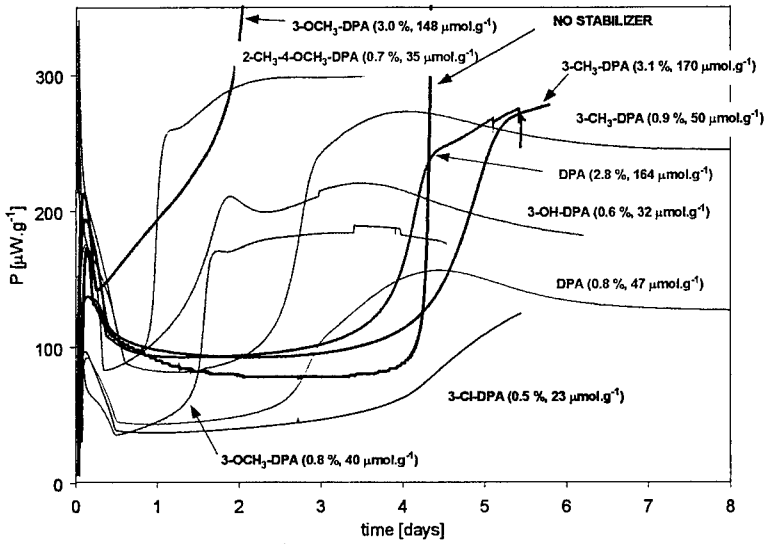


Figure 3 Heat flow results at 89 °C for high amount of stabilizers

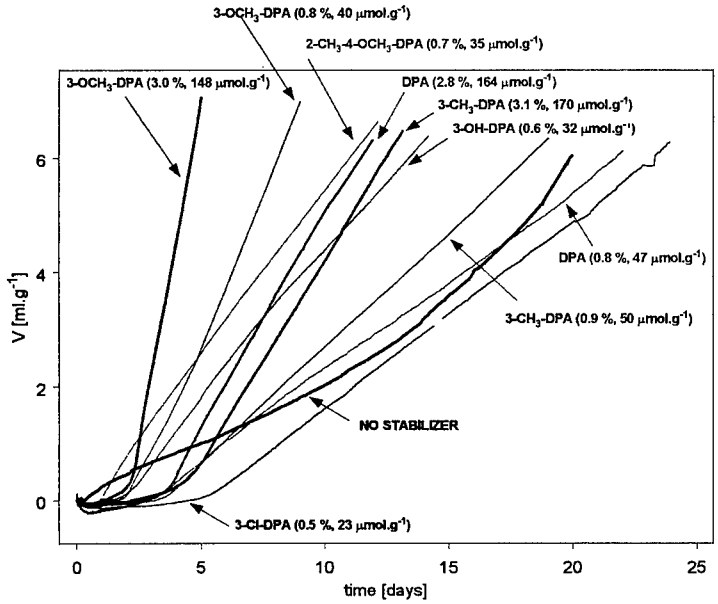


Figure 4 Results of vacuum stability test at 89 °C for high amount of stabilizers

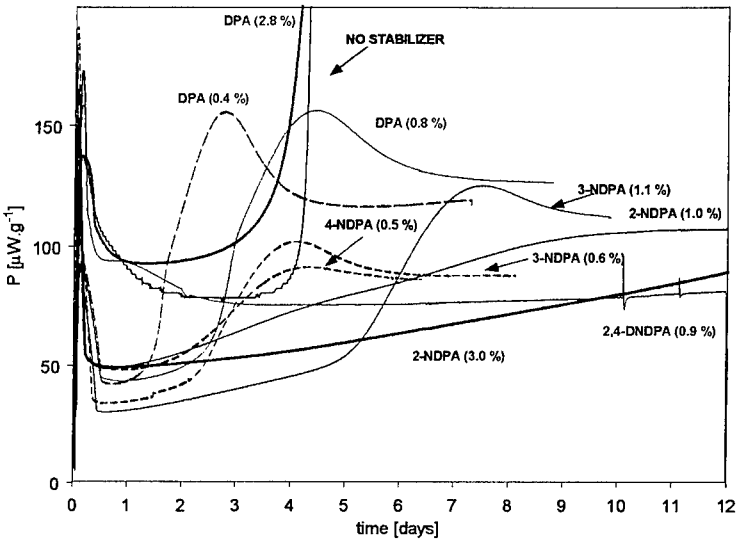


Figure 5 Heat flow results at 89 °C for nitrated diphenylamines

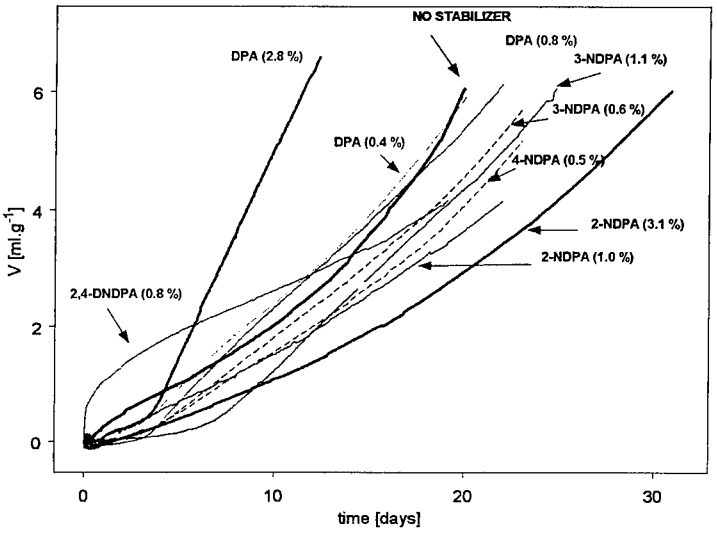


Figure 6 Results of vacuum stability test at 89 °C for nitrated diphenylamines

Quantification of relations between substitution and duration of first minimum

The time of the end of the first minimum is the time to DPA depletion[7,9,11]. Also it was proven in ref.[2,13] that the reaction order of DPA depletion is of zero order. The above mentioned presumptions make us possible to calculate rate constants of DPA depletion using the time to end of first minimum (t_{END}):

$$\frac{dc}{dt} = k \tag{1}$$

$$c = c_0 - k.t \tag{2}$$

$$0 = c_0 - k.t_{END} \tag{3}$$

$$k = \frac{c_0}{t_{END}} \tag{4}.$$

Logarithms of rate constants calculated using HFC or VST times to end of first minimum and initial concentrations of DPA's determined by HPLC are presented in Table III. It is obvious from the results that the rate constants do not have the same values for the same diphenylamine, but are raising with its initial concentration in the sample. This conclusion had been previously published by Blay[14] based on kinetics of DPA depletion in pure nitroglycerine and by us[2,13]. But it is clearly seen from our results that electron-donating substituents are increasing the slope of dependence of k on c_0 (Figure 7). Therefore interpolation for k was done for each substituted DPA at c_0 = 24.507 μmol.g^{-1} (the only concentration for 4-NDPA which was available). Logarithms of interpolated results are also presented in Table III.

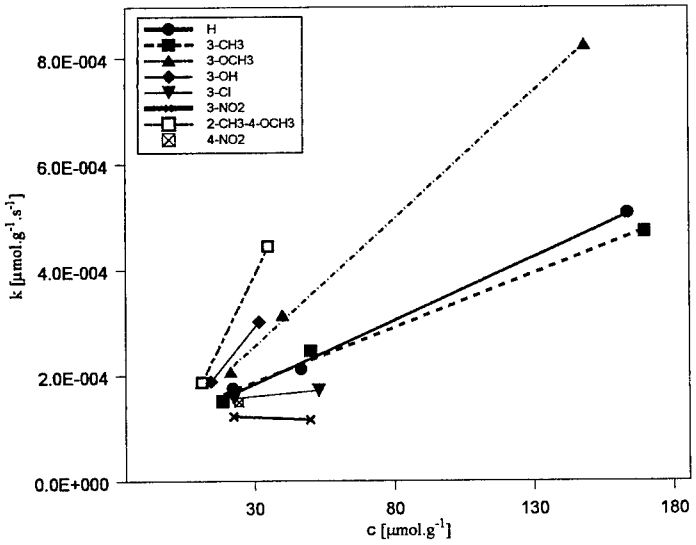


Figure 7 Relation between initial concentration and rate constant of DPA depletion

Table III Rate constants of DPA depletion calculated from HFC and VST results

Sample	Subst.	C	Log(k) calaculated from			Log(k) interpolated to C_0 = 24.5 μmol.g^{-1} calaculated from		
		[%]	HFC 89	VST 89	VST 115	HFC 89	VST 89	VST 115
STAB-319	H	0.38	-3.76	-3.93	-2.43	-3.75	-3.92	-2.42
STAB-225	H	0.79	-3.68	-3.77	-2.26			
STAB-282	H	2.77	-3.30	-3.28	-1.75			
STAB-303	3-CH_3	0.34	-3.82	-4.08	-2.55	-3.79	-4.02	-2.53
STAB-291	3-CH_3	0.92	-3.61	-3.78	-2.45			
STAB-292	3-CH_3	3.11	-3.33	-3.34	-1.94			
STAB-302	3-OCH_3	0.43	-3.69	-3.78	-2.47	-3.66	-3.75	-2.43
STAB-289	3-OCH_3	0.80	-3.51	-3.61	-2.22			
STAB-290	3-OCH_3	2.95	-3.08	-3.09	-1.82			
STAB-315	3-OH	0.27	-3.73	-3.89	-2.60	-3.61	-3.81	-2.46
STAB-316	3-OH	0.59	-3.52	-3.75	-2.36			
STAB-317	3-Cl	0.46	-3.81	-4.07	-2.48	-3.80	-4.06	-2.48
STAB-318	3-Cl	1.08	-3.77	-3.93	-2.36			
STAB-304	3-NO_2	0.48	-3.92	-4.09	-2.57	-3.92	-4.09	-2.57
STAB-293	3-NO_2	1.07	-3.94	-4.06	-2.52			
STAB-311	2-CH_3-4-OCH_3	0.24	-3.73	-3.78	-2.52	-3.52	-3.54	-2.28
STAB-312	2-CH_3-4-OCH_3	0.75	-3.35	-3.35	-2.08			
STAB-320	4-NO_2	0.53	-3.83	-4.10	-2.61	-3.83	-4.10	-2.61

In Part I of this work a radical reaction mechanism of DPA reactions has been suggested as probable. It generally holds for reactions of such type that their rate constant is little dependent on substitution of the aromatic ring of the substrate. To measure this dependence it is possible to use Hammett's equation[15]. For the rate constants of reactions of substituted diphenylamines with peroxidic radicals the value of reaction constant of Hammett's equation $\rho = -0.847 \pm 0.079$ follows from literature[16], with σ^+ constant being used as explanatory variable. On the contrary, for the dependence of logarithms of equilibrium constants values of protonation of substituted diphenylamines (provided the protonated form is on the right side of the equation) on substitution constants σ^- the value is given[10] $\rho = -2.543 \pm 0.110$. The quantification of substituent effect is performed by using the Hammett equation. By means of linear regression the value of reaction constant $\rho = -0.18 \pm 0.05$ (N = 7, R = 0.82, residual standard deviation = 0.080) for HFC, $\rho = -0.16 \pm 0.03$ (N = 7, R = 0.91, residual standard deviation = 0.049) for VST at 115 °C, $\rho = -0.29 \pm 0.07$ (N = 7, R = 0.86, residual standard deviation = 0.108) for VST at 89 °C has been estimated of the dependence of rate constant logarithm on Hammett's constant σ^+ for substituted DPA derivatives. The fact that the dependencies are explained by σ^+ Hammett's constants is possible to be interpreted as formation of positive charge on the reaction centre and its conjugation with an electron-donor substituent in *para* position. Negative value of reaction constant ρ means the acceleration of reactions by electron-donor substituents. It holds for the absolute value of reaction constant that its value decreases with the distance of the substituent from the reaction centre and further that it decreases with decrease of size of change of the charge in the reaction centre. A very low absolute value of reaction constants found can be explained by a small change of charge in the reaction centre. The reactions leading to nitrosation of diphenylamine are relatively little dependent on the kind of substitution of the aromatic ring of diphenylamine.

Missing first minimum, second maximum and second minimum in the case of ortho nitrosubstituted diphenylamines

The conclusion was brought in Part I of this work that the explanation made on the basis of low basicity of 2-NO_2-DPA is very unlikely. Our new results obtained for 4-NO_2-DPA exhibiting all the common periods are in accordance with that conclusion. Our explanation was that 2-NO_2-DPA will not almost stabilise a possible radical due to steric hindrances. This will result in the fact that this stabiliser will not cause acceleration of the decomposition of nitrate esters and also it is not able to terminate radical reactions. This reflects itself in the absence of induction and accelerated periods.

We used computer modeling of the diphenylamines and its radicals formed by breaking the N-H bond. The geometry of the molecules was optimized by minimizing energy using molecular mechanic followed by semi-empirical quantum mechanic model with an AM1 set of parameters. Thus heats of formations (for compounds in gas state) were calculated and presented in Table IV.

Table IV Heats of formation calculated by empirical quantum mechanic model with AM1 set of parameters

Substituent X	$\Delta H_{F\,(X\text{-}DPA)}$ [kJ.mol^{-1}]	$\Delta H_{F\,(NO\text{-}X\text{-}DPA)}$ [kJ.mol^{-1}]	$\Delta H_{F\,(X\text{-}DPA\bullet)}$ [kJ.mol^{-1}]	$\Delta(\Delta H_F)^a$ [kJ.mol^{-1}]	$\Delta(\Delta H_F)^b$ [kJ.mol^{-1}]	$\Delta(\Delta H_F)^c$ [kJ.mol^{-1}]
H	236.8	320.1	398.0	-161.2	-77.8	-83.4
2-NO_2	246.2	349.3	421.3	**-175.1**	-72.0	**-103.0**
3-NO_2	253.8	343.3	415.7	-161.9	-72.5	-89.4
4-NO_2	243.9	337.7	411.8	-167.9	-74.1	-93.8
3-CH_3	205.3	288.6	366.7	-161.4	-78.1	-83.3
3-OCH_3	78.6	162.9	241.4	-162.8	-78.6	-84.2
3-Cl	207.3	293.5	370.6	-163.3	-77.2	-86.1
3-OH	51.6	137.0	214.3	-162.7	-77.3	-85.4
2-CH_3-4-OCH_3	52.2	136.1	201.6	-149.4	-65.4	-83.9
2-NO_2-4- NO_2	263.8	382.0	449.8	**-186.1**	-67.8	**-118.3**

a $\Delta(\Delta H_{F(X\text{-}DPA)} - \Delta H_{F(X\text{-}DPA\bullet)}$

b $\Delta(\Delta H_{F(X\text{-}NO\text{-}DPA)} - \Delta H_{F(X\text{-}DPA\bullet)}$

c $\Delta(\Delta H_{F(X\text{-}DPA)} - \Delta H_{F(X\text{-}NO\text{-}DPA)}$

From the results it is apparent that nitro-substitution in position *ortho* causes significantly higher energy necessary for free radical formation, but also significantly higher energy consumption during formation of the N-nitrosated compound. Breaking the N–NO bond requires an energy comparable or just little less than other diphenylamines. From the thermodynamic point of view thus it is more demanding to break an N-H bond of an *ortho* nitrosubstituted DPA compared to the other DPA's, but it is easier to break an N-NO bond of an *ortho* nitrosubstituted N-NO-DPA then in case of the other DPA's.

Fast increase of heat flow during the first minimum in the cases of 3-methoxy and 3-hydroxydiphenylamines

It follows from HFC results that some other exothermic reactions are running during the first minimum in the case of samples stabilized by 3-methoxy or 3-hydroxydiphenylamines. Heat flow increases gradually and such fact leads us to the conclusion that some consequent reaction is the cause of it. It is known from earlier results[6-9] that the main product during the first minimum in the case of DPA stabilized propellants is N-nitrosodiphenylamine which is nitrated after the second maximum in *para* position (under the conditions of HFC measure-

ment, where no air oxygen can access the sample). An accumulation of 4-nitro-N-nitroso-diphenylamine is observed during second minimum.

The 3-methoxy and 3-hydroxy substituents cannot activate the aminic reaction centre by mesomeric effect, but can activate the aromatic ring of diphenylamine to electrophilic attack. Thus the nitration can proceed at the same time as nitrosation. To perform all the further necessary experimental research covering preparation of chromatographic standards and performing HPLC analyses exceeded our possibilities. Thus computer simulation was done which estimated relative susceptibility to the electrophilic attack at different positions of DPA skeleton substituted by different substituents. As the measure of the susceptibility of the molecule to attack by an electrophile the HOMO density was calculated. The HOMO density reveals reactive sites based on the distribution of electrons in the highest occupied molecular orbital. Regions of the molecule with high values of HOMO density have loosely bound electrons which are reactive to electrophilic attack. Also the electrophilic frontier density was computed which is also a measure of the susceptibility of the substrate to attack by an electrophile. Electrophilic frontier density reveals reactive sites based on the electron distribution of a set of active orbitals near the HOMO. It is especially useful for large molecules where several orbitals may have energies nearly equal to the HOMO. Because of the fact that both calculated parameters were well correlated for calculated molecules, only HOMO density was taken into account. The parameters were calculated using semi-empirical quantum mechanic using MOPAC with AM1 parameter set. The geometry of molecules had been optimised by molecular mechanic and quantum mechanic with AM1 parameters before calculation of HOMO or electrophilic densities. Results calculated for DPA, 3-COH_3-DPA and 3-OH-DPA are presented in Table V.

Table V Relative densities of HOMO at certain reaction centers

Substituent	**X-diphenylamine**			**X-N-nitrosodiphenylamine**	
X	**N**	**C4**	**C4'**	**C4**	**C4'**
H	0.281	0.079	0.142	0.103	0.112
3-CH_3	0.279	0.088	0.135	0.147	0.076
3-OCH_3	**0.256**	0.164	0.079	**0.193**	0.046
3-OH	**0.273**	0.130	0.110	**0.195**	0.046

It is apparent from the results that the most reactive center for an electrophilic attack is the aminic nitrogen in all cases (what is in compliance with our assumption of N-nitrosation as the most important reaction of DPA). The highest density of HOMO for N-nitroso-diphenylamines is at C4 position, but in the case of 3-OCH_3 and 3-OH substituted diphenylamines the reactivity in that position raises after N-nitrosation and then is comparable by the value with N-nitrosation. This can explain the observed significant increase of heat flow during first minimum – both N-nitrosation and consequent exothermic nitration of N-nitroso-diphenylamines in position C4 takes place.

3.2 Results of weight loss tests

The most important difference between this method and HFC or VST is the possibility of air resp. oxygen to come into contact with the sample. Two major informations can be revealed from weight loss measurements – the time to accelerated decomposition (which is related to the heat tests and says how efficiently the sample is protected from severe autocatalysis and

also is related to the duration of safe storage). The other information is the rate of weight loss, which is related to the extent of reactions in the sample which can lead to volatile products. Three parameters were used for description of the weight loss results – time to accelerated decomposition ($WL.NO_X$), weight loss just before the accelerated decomposition (WL) and the relative rate of weight loss (WL.p1). To achieve the last mentioned parameter all measured curves were processed by principal component analysis (PCA) rather than computing linear regression for each measurement. Each measurement was taken as one column of the resource matrix and the result of PCA was explanation of 98.8 % of total variability by one score factor and 99.8 % by two factors. First loading vector was used as a measure of weight loss rate. This approach is more correct than simple computation of slopes for each curve, because the measured curves are not strictly linear and the least square regression would be task with autocorrelation error. Also PCA leads to the results with much less effort. Each measured curve can be restored from the first score vector by multiplying the corresponding loadings coefficient. Such coefficients (WL.p1) correspond with relative rate of weight loss and for substituted DPA's are mentioned in Table VI.

$$WL89 = (-0.261\pm0.104) + (0.439\pm0.024)WL{\cdot}p1 + (0.0252\pm0.0025)WL{\cdot}NO_X \qquad (5)$$

(N = 21; R = 0.994; residual standard error 0.161 %).

Table VI Results of weight loss at 89 °C and score vectors obtained by PCA for all parameters measured by HFC, VST and weight loss

Sample	Subst.	C [%]	WL.p1 [-]	$WL.NO_X$ [days]	WL89 [%]	t1 [a)] [-]	t2 [a)] [-]
STAB-319	**H**	0.38	3.849	14	1.771	0.095	0.103
STAB-225	**H**	0.79	2.852	27	1.674	0.082	0.254
STAB-282	**H**	2.77	4.826	47	3.368	0.323	0.387
STAB-303	**3-CH_3**	0.34	2.597	15	1.258	0.068	0.114
STAB-291	**3-CH_3**	0.92	3.266	23	1.817	0.238	0.289
STAB-292	**3-CH_3**	3.11	5.220	40	3.278	0.378	0.469
STAB-302	**3-OCH_3**	0.43	2.477	10	0.958	0.190	0.051
STAB-289	**3-OCH_3**	0.80	3.639	12	1.573	0.191	0.065
STAB-290	**3-OCH_3**	2.95	8.500	17	3.592	1.000	0.143
STAB-315	**3-OH**	0.27	1.996	10	0.775	0.096	0.034
STAB-316	**3-OH**	0.59	2.618	13	1.186	0.183	0.105
STAB-317	**3-Cl**	0.46	2.077	16	1.069	0.042	0.148
STAB-318	**3-Cl**	1.08	2.760	24	1.605	0.091	0.391
STAB-304	**3-NO_2**	0.48	3.057	15	1.472	0.055	0.207
STAB-293	**3-NO_2**	1.07	2.425	30	1.585	0.072	0.585
STAB-311	**2-CH_3-4-OCH_3**	0.24	2.965	15	1.472	0.150	0.000
STAB-312	**2-CH_3-4-OCH_3**	0.75	3.174	17	1.565	0.290	0.027
STAB-320	**4-NO_2**	0.53	2.686	17	1.330	0.048	0.231
STAB-226	**2-NO_2**	0.97	2.296	30	1.647	0.054	0.380
STAB-187	**2-NO_2**	3.00	1.633	70	1.832	0.000	1.000
STAB-238	**2-NO_2-4-NO_2**	0.90	3.020	16	1.502	0.038	0.164

[a)] score vectors referred in chapter 3.3, calculated by PCA from all data using all parameters obtained by HFC, VST and weight loss

3.3 Relations between all measured results

Results obtained by three different methods (HFC, VST and weight loss) for the set of samples are available. It was shown earlier in this work that the parameters obtained by different methods are correlated. In fact it means that it is possible to reduce the number of such parameters without significant loss of information. The question is how many independent (orthogonal) parameters can describe the measured data and what will be the relation between them and the original parameters. To answer the question PCA analysis was performed which proceeds the source matrix consisting of rows represented by each sample and columns represented by 15 parameters mentioned in Tables I and II (times to end of first minimum measured by HFC or VST at both temperatures, time to second maximum, heat flows at the start end the end of first minimum, rates of gas evolution in the second maximum and second minimum at both temperatures, time to accelerated decomposition during the weight loss test, rates of weight loss and the parameter WL.p1). The result of PCA was the possibility to reduce the number of parameters (so called "score vectors") to two, which can describe 95.6 % of overall variability (all the information given by source matrix). The resulting score vectors are mentioned in the Table VI as *t1* and *t2*. It is clear from the data, that sample STAB-290 is highly influential – rates of heat flow, gas evolution and weight loss are much higher compared to the other samples, so the suspicion that the sample can change the results significantly was expressed. The principal component analysis performed for all the data except the sample STAB-290 resulted in comparable two score vectors which explained 95.3 % of overall variability. Thus the sample STAB-290 is not an outlier.

The results of PCA mean that there are just two major informations given by all the used methods – the first score vector correlates well with heat flows, rates of gas evolution and rate of weight loss (parameter WL.p1). The second score vector (which is linearly independent on the first one) represents well times to end of first minimum or to second maximum (measured by HFC or VST). The second score vector is well correlated with time to accelerated decomposition. The weight loss just before the accelerated decomposition is a linear combination of both score vectors. Using the computed score vector in further evaluation is more convenient than working with original measured parameters because of two reasons – the scores are built from results obtained by four independent tests based on three principles (HFC, VST and weight loss) so they are more robust and are not much afflicted by measurement errors. The second advantage is the extracting factors which are standing behind the measured parameters are orthogonal.

The first score vector can be interpreted as the measure of unwanted reactions – the extent of exothermic reactions leading to the gas evolution and thus the weight loss. These reactions are caused mainly by incompatibility of the discussed stabilisers with nitrate esters. Except for 2-NDPA this property grows with the stabiliser's concentration and also grows with the substituent's electron-donating ability. Because of the fact that in most cases the incompatibility exhibits after the second maximum when all DPA is almost transformed to N-NO-DPA and its nitration takes place, we can expect higher reactivity of aromatic rings activated by electron-donating substituents (especially with M+ effect) like OH or OCH_3. Otherwise, in the case of electron-acceptor substituents (deactivating the aromatic ring to the electrophilic attack) will proceed nitration rather to the unsubstituted ring than to that already substituted. To make quantification of such dependency σ^+ constants were used as the explanatory variable (sum of all σ^+ constants for substituents in one ring was used for electron-donating substituents which are activating the ring; in the case of electron-acceptor substituents nitration to the unsubstituted ring was expected, thus $\sigma^+ = 0$ was used). We can think of the first score factor as it was heat flow. Heat flow is proportional to the reaction heat, concentration (in the case of first order reaction) and rate constant of reaction. If we

accept the presumption that the reaction heat depends only little on substitution and interpolate the first score vector to the same concentration (24.507 $\mu mol.g^{-1}$), we can use such parameter as some rate constant of the incompatibility reaction. A correlation between logarithms of such parameter and Hammett σ^+ constants obtained as mentioned above in this paragraph is shown on the Figure 8. The correlation is quite good (correlation coefficient 0.938).

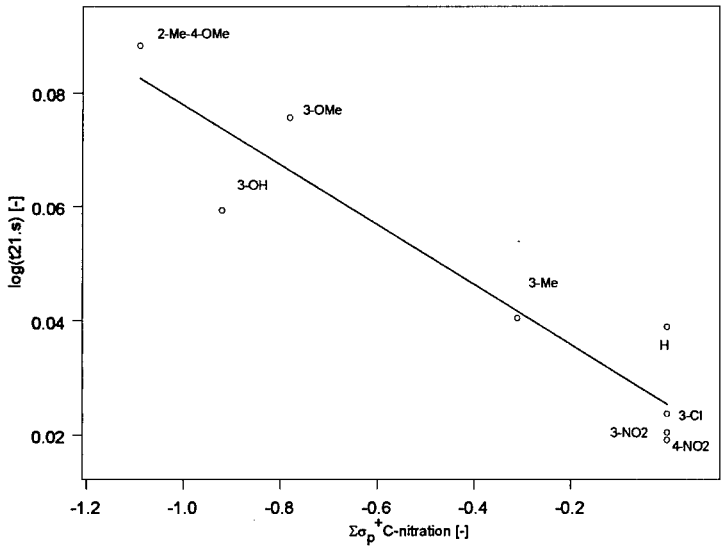


Figure 8 Dependency of logarithms of first score vector on sum of Hammett σ^+ constants

The second score vector can be identified with the long term chemical stability of the sample. It is clear that it grows with initial amount of stabilizer, but the slope of grows decreases with electron-donating ability of substituent of DPA. The best results were achieved in case of 2-NDPA and 3-NDPA. The worst results were obtained for 2-methyl-4-methoxydiphenylamine.

4. Conclusions

Results of three independent methods (HFC, VST and weight loss) can be described by two independent factors – the first of it is responsible for intensity of chemical reactions which are manifested by heat flow, rate of gas evolution and rate of weight loss. The second factor represents the time to accelerated decomposition. Each individual method brings both of the independent information, the methods are interchangeable at least in the cases of propellants stabilized by diphenylamine based stabilizers. The results are correlated, but in the absolute scale there are differences caused mainly by the possibility of air oxygen access to the sample. Oxygen causes directly or via oxidation of nitrogen oxide to nitrogen dioxide oxidation of stabiliser, changes the pathways of chemical reactions and thus decreases time to accelerated decomposition[1-9,12]. A clear difference between the methods can also be seen in the case of the unstabilized sample which (at the same temperature of 89 °C) exhibited severe

decomposition after one day under conditions of weight loss (ampoule is not tightly closed), after 4.5 days under standard conditions of HFC, and after eight hours during HFC measurement with a not fully loaded ampoule. No severe decomposition was observed under VST conditions within 20 days.

All studied diphenylamines (with exception of substitution by nitro group in position *ortho*) showed a chemical incompatibility with nitrate esters – the intensity of unwanted reactivity increased with the initial concentration of stabilizer and in most cases exceeded the levels reached by unstabilized sample. The extent of undesirable reactions also grows with electron-donating capability of substituent regardless whether the substituent could conjugate with the reaction centre of the amine nitrogen atom or not, because the most intensive reactions appear after the original DPA had been transformed to N-nitrosodiphenylamine. It was proven by quantum mechanical calculations, that aromatic rings of N-nitrosodiphenylamine substituted by methoxy or hydroxy group in *meta* position are susceptible to the electrophilic attack by the similar extent as nitrogen of appropriate diphenylamine.

On the other hand the effectiveness of a stabilizer – expressed by time to accelerated decomposition – is proportional to the time when DPA is depleted. This time is shorter for the substituents with electron-donating effect and the shortest for that case where such substituent can conjugate with the aminic reaction centre. However the dependency expressed by Hammett reaction constant is so small, that it is most probable, that the reaction mechanism is of radical nature and hence conclusions brought in the Part I of this work are supported by these results.

Such conclusions are also supported by results of the recent work[17], where it was proven by measuring a set of N-nitrosodiphenylamines that homolysis of N-NO bonds is much more likely than the corresponding heterolysis. The gap between heterolysis and homolysis gets broader for electron-donating groups and narrower for an electron-withdrawing group. Also it was proven that much lower energy is required for homolytical breaking of the N-NO bond than the N-H bond (the same result was obtained by quantum mechanical computations - see Table IV). Based on these results we can expect such reactions in the propellant, where diphenylamine will react with NO+ forming N-nitrosodiphenylamine, which can then easily form NO• and DPA• radicals by homolytical cleavage. These radicals will be responsible for further propagation of chain reactions. In the case of substituents with +M effect in *ortho* or *para* position (e.g. 4-methoxydiphenylamine) the formation of a stable DPA• radical will be the most easy and thus the depletion of the diphenylamine will proceed by the highest rate.

5. References

1. S. Wilker, J. Petržílek, J. Skládal, G. Pantel, L. Stottmeister: "Stability analyses of propellants containing new stabilisers – Part I –", *Int. Annu. Conf. ICT* 31, 61 **(2000)**.
2. J. Petržílek, *Annotations to Doctoral Thesis*, Pardubice **(2000)**.
3. J. Petržílek, J Skládal, "Vliv podmínek urychleného stárnutí na reakce difenylaminu v bezdýmném prachu", *New Trends in Research of Energetic Materials, Pardubice* 3, **(2000)**, University of Pardubice.
4. J. Petržílek, J Skládal, "Vliv podmínek urychleného stárnutí na reakce Centralitu I v bezdýmném prachu", *New Trends in Research of Energetic Materials, Pardubice* 3, **(2000)**, University of Pardubice.
5. J. Skládal, J. Petržílek, F. Zrcek, M. Pražák, L. Janoušková: "Analysis of Reaction Products of Centralite I in Propellants", *Int. Annu. Conf. ICT* 32, 132, **(2001)**.
6. S. Wilker, P. Guillaume, "International Round Robin Test to Determine the Stability of DB Ball Propellants by HFC", *Int. Annu. Conf. ICT* 29, 132, **(1998)**.
7. P. Guillaume, M. Rat, G. Pantel, S. Wilker, "Microcalorimetric and Chemical Studies of Propellants", *Int. Annu. Conf. ICT* 27, 133 **(1998)**.
8. U. Ticmanis, G. Pantel, L. Stottmeister, "Stabilitätsuntersuchungen einbasiger Treibladungspulver- Mikrokalorimetrie im Grenzbereich", *Int. Annu. Conf. ICT* 29, 27 **(1998)**.
9. P. Guillaume, M. Rat, G. Pantel, S. Wilker, "Heat flow calorimetry of propellants – Effects of sample preparation and measuring conditions", *Propellants, Explosives, Pyrotechnics* 26, 1-7, **(2001)**.
10. O. Pytela, P. Vetešník, "Dissociation constants of monosubstituted diphenylamines and optimized construction of acidity function", *Collect. Czech. Chem. Commun.*, 48, 2363 **(1983)**.
11. J. Petržílek, "Vacuum Stability Test of Aged Spherical Propellants", *Symp. Chem. Probl. Connected Stab. Explos.* 11th, 323-336 **(1998)**.
12. S. Wilker, J. Petržílek, J. Skládal, U. Ticmanis, G. Pantel, L. Stottmeister, "Stability analyses of double base propellants in dependence of their DPA and NG content", *New Trends in Research of Energetic Materials, Pardubice* 4 **(2001)**, University of Pardubice.
13. J. Petržílek, "Kinetic Study of Stabilizer Consumption in Spherical Propellants", *2nd Workshop on Thermal Analysis and Stability of Propellants, WIWEB, Germany* **(1999)**, 84.
14. N.J. Blay, „Some Relationships Between the Stability of Nitrate Esters and the Stability of Propellants", *Symp. Chem. Probl. Connected Stab. Explos.* 3, 61-85 **(1973).**
15. O. Exner, "Korelační vztahy v organické chemii", *SNTL Praha* **(1981)**.
16. V.T. Varlamov, E.T. Denisov, "Kinetika reakcii 2,4,6-tri-tretbutilfenoksilnogo radikala s aromatičeskimi aminami v kvaziravnovesnom režime i energii dissociacii N-H sviazi v aromatičeskich aminach", *Izv. Akad. Nauk SSSR, Ser.Khim.* 4, 743 **(1990)**.
17. Xiao-Qing Zhu, Jia-Qi, Qian Li, Ming Xian, Jianming Lu, Jin-Pei Cheng: "N-NO Bond Dissociation Energies of N-Nitroso Diphenylamine Derivatives (Or Analogues) and Their Radical Anions: Implications for the Effect of Reductive Electron Transfer on N-NO Bond Activation and for the Mechanisms of NO Transfer to Nitranions", *J. Org Chem.* 65, 6729-6735 **(2000)**.

FORMAL KINETICS OF THE THERMAL DECOMPOSITION OF HEXANITROSTILBENE BY THERMAL ANALYSIS AND MULTIVARIATE REGRESSION

Thomas Rieckmann[1], Leonard Lichtblau[2], Rainer Schirra[2], Susanne Völker[3]

[1]*University of Applied Sciences Cologne, Department of Chemical Engineering and Plant Design, Betzdorfer Str. 2, D-50679 Cologne*

[2]*Dynamit Nobel GmbH, Kaiserstraße 1, D-53839 Troisdorf*

[3]*42 Engineering, von-Behring-Str. 9, D-34260 Kaufungen*

Abstract

The thermal decomposition of hexanitrostilbene (HNS) has been investigated by simultaneous TGA/DTA and DSC at constant heating rates between 0.05 and 40 °C/min and in isothermal experiments. Depending on the temperature time history, the reaction takes place either in the solid phase or in the liquid phase after melting of the sample. To observe the solid phase reaction, isothermal experiments below the melting temperature or experiments with constant heating rates well below 2.5 °C/min have to be performed. It is thus impossible to judge the thermal stability of solid HNS using formal kinetic models derived from DSC experiments at heating rates of 10 – 20 °C/min, corresponding with the standard procedure. Therefore, separate formal kinetic models have been developed for the thermal decomposition of high bulk density HNS in the solid, respectively in the liquid phase by application of the non linear multivariate regression technique. The solid phase model is based on data from isothermal and non-isothermal TGA experiments to ensure its validity for different heating modes.

Keywords: Explosives; Hexanitrostilbene (HNS); Thermal stability; Formal kinetics; Modelling; TGA; DSC; Thermolysis; Pyrolysis; Multivariate regression

1 Introduction

Hexanitrostilbene (HNS, Fig. 1) is a common example for a heat resistant explosive [1].

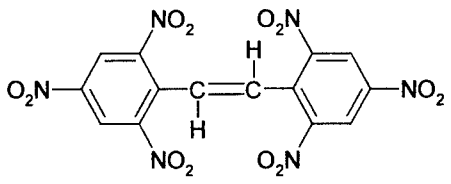


Fig. 1. Hexanitrostilbene, HNS.

HNS is a nitro aromatic compound with very low vapour pressure [2], high vacuum stability and a melting temperature documented between 316 and 321 °C [3, 4]. The high decomposition stability of HNS enables its application for perforating the source rocks in gas and petroleum wells [3]. As the average depths of the wells and, as a consequence the ambient temperatures in the wells are increasing, knowledge about the thermal stability at temperatures up to 260 °C is required. Of special interest is the fraction of a HNS perforator filling which will decompose during stand still times of the drill lasting for some hours.

The thermal stability of heat resistant explosives is usually investigated by differential scanning calorimetry (DSC) under non-isothermal conditions. Standard experiments are performed at constant heating rates of 10; 15; or 20 °C/min. Under these conditions, HNS is showing a strong exothermic peak at temperatures between 300 and 350 °C, depending upon the initial mass, the particle size, the composition and the modification of the sample, as well as the heating rate. Previously, the thermal decomposition of HNS has been investigated by this method and has been described as a single reaction with first order kinetics. The kinetic parameters which are necessary to model the decomposition rate at a specific temperature were calculated separately for every experimental heating rate [5].

Our own tests on the stability of HNS with a combined TGA/DTA (STA) system indicated three prominent findings: 1) at standard heating rates of 10; 15; and 20 °C/min, HNS is melting before its decomposition starts, 2) melting and decomposition are separated and separable events, and 3) it is impossible to model the thermal decomposition by a single reaction of first or zero order, which was shown by a Friedman analysis [6] and a formal kinetic analysis by multivariate regression [7, 8]. The obvious problem associated with describing the decomposition of a solid at temperatures below its melting point using kinetic data obtained from molten samples stimulated us to investigate HNS under conditions which allowed the separation of solid and liquid phase decomposition. Two different formal kinetic models have been developed for the solid and liquid phase decomposition by applying the multivariate regression technique to experiments at very low and high constant heating rates, respectively [8, 9].

Essential for the correct prediction of the thermal stability of HNS in wells is a formal kinetic model with validity for the expected temperature time histories. The kinetic model has to be applicable for conditions with constant as well as with varying temperatures. Recent experiments investigating the isothermal decomposition of HNS showed that our formal kinetic model for the solid phase decomposition has to be modified to describe results gained at constant temperatures. Therefore, isothermal experiments as well as experiments with low constant heating rates have been evaluated simultaneously to develop a formal kinetic model with maximum validity for the possible conditions in gas and petroleum wells.

2 Experimental

All experiments have been performed with HNS HBD, an HNS modification with a high bulk density of 800 kg/m^3 prepared by Dynamit Nobel GmbH, Troisdorf. The sample consisted of spherical particles with diameters between 0.5 and 1.5 mm. Initial tests with particles of uniform size indicated no dependency of the experimental results on the particle diameter.

2.1 Differential scanning calorimetry

A Netzsch DSC 200 instrument has been used for the DSC measurements. High purity nitrogen was used as purge gas with a gas flow rate of 0.9 L/h. The experiments entailed variation of the heating rate and the initial sample mass. Initial sample masses of 1; 2; and 5 mg have been investigated in closed crucibles made from aluminium with a pinhole in the cap. The experiments have been performed under non-isothermal conditions with constant heating rates of 2.5; 5; 10; 15; and 20 °C/min.

2.2 Thermogravimetric Analysis

Combined TGA/DTA experiments have been performed using an STA 503 (Bähr GmbH, Altendorfer Str. 12, D-32609 Hüllhorst). The maximum load of the STA is 1000 mg, and mass variations of ± 200 mg can be detected. The mass resolution is 1 µg. The STA apparatus has a horizontal weighing beam which generates an unusually low drag in the weighing direction, and the effect of drag was further reduced by using high purity helium (99.999 %, Linde) as a low viscosity purge gas with a gas flow rate of 1.7 L/h. Open crucibles made from Al_2O_3 have been used in all experiments. The thermocouples measuring the sample temperature and the reference temperature, respectively are integrated in the sample holder and are located directly beneath the platinum plates under the crucibles. This configuration provides an intense and reproducible thermal coupling to the sample. A temperature calibration has been done by analyzing the DTA signal from the melting peak of the pure substances In (T_m = 156.6 °C), $KClO_4$ (T_m = 299.4 °C), Ag_2SO_4 (T_m = 426.4 °C), and K_2SO_4 (T_m = 583.0 °C).

Initial sample masses of 5 mg have been investigated under three different heating conditions: 1) high constant heating rates of 2.5; 5; 10; 15; 20; and 40 °C/min, 2) very low constant heating rates of 0.05; 0.2; and 0.4 °C/min, and 3) fast heating up with a constant heating rate of 57 °C/min followed by an isothermal section at 254; 264; 274; 284; 289; 294; 299; and 304 °C, respectively. The linearity of the T(t) curves was excellent for all constant heating rates. During the isothermal sections of the experiments, the temperature varied no more than 0.1 °C.

2.3 Formal Kinetic Models

Formal kinetic models have been calculated to describe the total mass loss of the TGA experiments. The material balance of the crucible contents is described as a dynamic system with concentrated parameters which results in a single respectively in a set of ordinary differential equations (ODE). The simultaneous numerical solution of the ODE system and the estimation of the kinetic parameters by the least squares (LSQ) method were performed using the software Thermokinetics (Netzsch GmbH, Germany).

Netzsch Thermokinetics is a software module for the evaluation of thermokinetic experiments. The differential equations are calculated using a 5th-degree Runge-Kutta embedding method with automatic optimization of the interpolation nodes for numerical solution of the reaction equations (Prince-Dormand method). To minimize the deviance LSQ, an improved version of the hybrid procedure described in [10] is used. This is a combination of a derivation-free, regularized Gauss-Newton procedure (Marquardt procedure) with a step-length optimization [11].

The kinetic parameters have been fitted by simultaneously running the optimization routine and the ODE solver according to the technique of multivariate regression [7]. The task of non-linear regression is the iterative calculation of the minimum sum of least squares. In case the multivariate regression technique is applied, the total LSQ yields into a sum of LSQ calculated with data from the n different experimental runs

$$LSQ = \sum_{k=1}^{m} \sum_{i=1}^{n} (y_{exp\,k,i} - y_{mod\,k,i})^2 .$$

The experimental values $y_{exp,k,i}$ are the normalized mass, $y = m(T)/m_0(t=0)$ from STA. Data from all experiments at high heating rates have been used simultaneously for the liquid phase decomposition model. For the solid phase decomposition model, data from all experiments at low heating rates as well as from all isothermal experiments have been used simultaneously. The model values $y_{mod,k,i}$ result from the numerical solution of the respective ODEs. The multivariate analysis is based on the assumption that the kinetic parameters have to be identical for all experimental conditions in the modelled parameter range. This constraint facilitates the choice of an appropriate model considerably and improves the model validity.

The kinetic analyses of this work is based on formal kinetic models. Those models include one or multi-step processes, in which the individual steps are linked as parallel, competitive, or consecutive reactions. The intermediate and final products are to be viewed as pseudo components and may comprise a whole variety of chemical species. Arrhenius equations were used for the temperature dependent rate constants. The following irreversible reaction types and corresponding reaction equations [12] turned out to be applicable for the kinetic description of the decomposition of HNS HBD (Table 1): $de/dt = - k_0 \cdot \exp(-E_a/RT) \cdot f(e,p)$

Table 1. Code and reaction types used for the kinetic description

Code	*f(e,p)*	*reaction type*
Fn	e^n	reaction of n^{th} order
R3	$3\ e^{2/3}$	3D phase boundary reaction
Cn-x	$e^n\ (1+ k_{cat}\ x)$	autocatalytic reaction of n^{th} order with catalysis by x

3 Results and Discussion

3.1 Differential Scanning Calorimetry

DSC runs have been performed at constant heating rates of 2.5; 5; 10; 15; and 20 °C/min. At all heating rates, the sample melted around 320 °C, indicated by an endothermic heat flow signal and started decomposing at higher temperatures with a strong exothermic heat flow signal. With varying heating rate, the melting temperature kept constant while the decomposition peak was shifted according to theory. The DSC measurements showed no dependency of the decomposition temperature on sample mass.

Due to insufficient reproducibility of the DSC signals, the heating rate could not be lowered to less than 2.5 °C/min. Therefore, we decided to use the mass loss information from a combined TGA/DTA (STA) for the detailed investigations. The advantages of using the mass signal for kinetic modelling compared to the heat flow signal lie in its higher validity and resolution and its accessibility over a broad range of experimental conditions. Furthermore, the mass signal is directly proportional to the extent of reaction, even if the process contains endothermic and exothermic steps simultaneously. The performance of the STA was checked by comparing heat flow measurements of HNS from STA and DSC. The curves from the two devices showed excellent agreement regarding the melting peaks. The maximum of the decomposition peaks was slightly shifted to higher temperatures in the STA measurement, most probably due to different heat balances of the two systems. As we intended to use the heat flow signals from STA only for qualitative interpretation, the performance of the instrument is regarded as very satisfactory.

3.2 Thermogravimetric Analysis

As a basis for kinetic modelling, dynamic and isothermal STA experiments have been performed. The results of the thermogravimetric experiments at constant heating rates of 0.05; 0.2; 0.4; 2.5; 5; 10; 15; 20; and 40 °C/min are shown in Fig. 2.

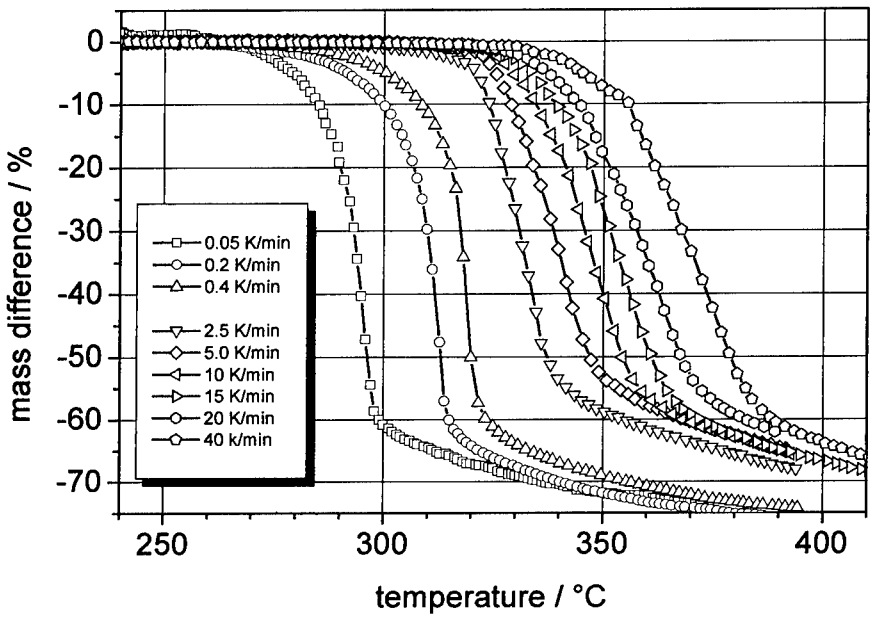


Fig. 2. Mass loss as function of temperature for all TGA experiments performed with constant heating rates.

The normalized mass loss is depicted as function of temperature and a distinctive division between experiments with low (0.05; 0.2; 0.4 °C/min) and high (2.5; 5; 10; 15; 20; 40 °C/min) heating rates is visible regarding the curve form as well as the attained final mass. This behaviour could be interpreted with help of the DTA signals. At a heating rate of 40 °C/min, the melting peak was well separated from the reaction peak and the sample melted completely, before significant mass loss occurred. By lowering the heating rate, the reaction peak approached the melting peak. At a heating rate of 2.5 °C/min, the melting peak was still observable and the vast majority of the sample reacted in the molten state. At a heating rate of 0.4 °C/min (or less), the melting peak disappeared and the sample reacted completely in the solid state before the melting temperature was reached [8]. Inspection of the crucible contents after the experiments confirmed the fact that the reactions took place in solid respectively liquid phase. The residues from samples exposed to low heating rates retained the initial spherical shape and diameter of the virgin material, whereas the residues from samples decomposed at high heating rates formed an even layer at the bottom of the crucible.

Under all conditions, the decomposition of HNS is a multi reaction process. The experimental curves for low heating rates are characterized by a slow mass loss at low temperatures which is

gradually accelerated with rising temperature as a fast exothermal reaction comes into control. This is followed by a slow reaction over a broad temperature range, most probably a secondary pyrolysis of solid reaction products. The experimental curves for high heating rates show almost no mass loss at temperatures below the melting point. The fast decomposition of the molten samples takes place via at least two reactions with different heat release and is also followed by a slow reaction, comparable to the last reaction of the solid state process.

The solid phase decomposition has additionally been investigated in isothermal experiments at temperatures of 254; 264; 274; 284; 289; 294; 299; and 304 °C. The mass loss as function of time is depicted in Fig. 3.

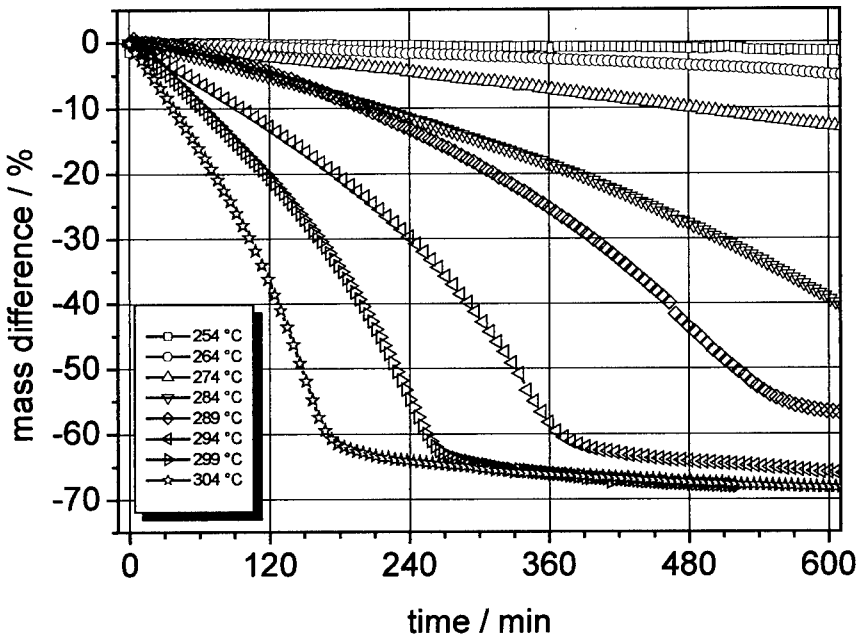


Fig. 3. Mass loss as function of time for all TGA experiments performed with constant temperatures.

Corresponding to the results from the dynamic experiments, the mass loss occurs in at least two steps. A faster, accelerating reaction phase leads to a mass loss of around 60 % and is followed by a slow reaction with a mass loss of less than 10 %.

3.3 Formal Kinetic Models

Separate formal kinetic models have been derived for the decomposition in the solid and the liquid phase. For the liquid phase model, experiments with constant heating rates between 2.5 and 40 °C have been evaluated by multivariate regression. The best description of the experimental mass loss was attained with a formal kinetic model which consists of four consecutive reactions $A \rightarrow B \rightarrow C \rightarrow D \rightarrow E$ of the type Fn, Fn, Cn, and Fn [9]. The best fit model is shown in Fig. 4 together with the data from the dynamic TGA experiments. The kinetic parameters are summarized in Tab. 2.

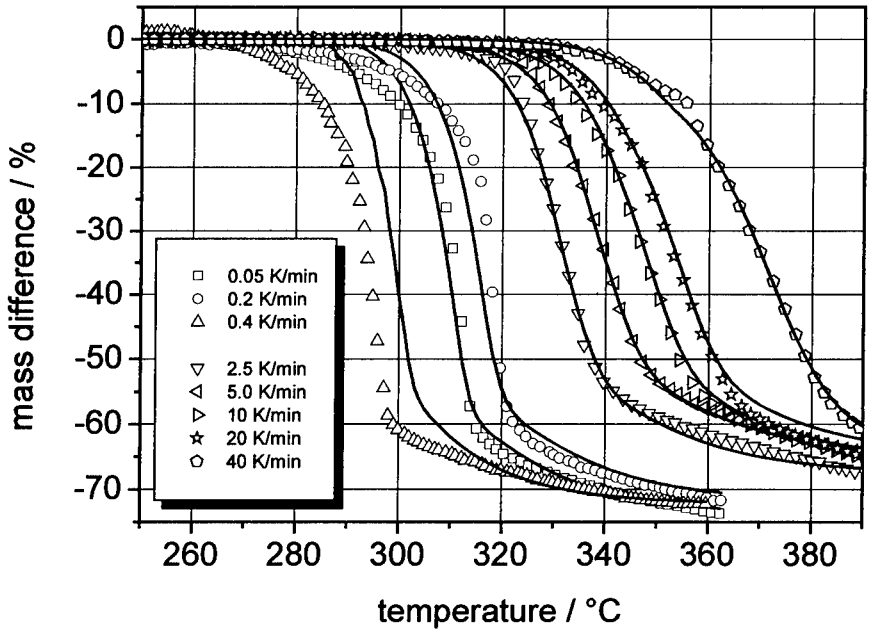


Fig. 4. Best fit formal kinetic model for the liquid phase decomposition. Comparison of the mass loss as function of temperature to TGA results at low and high constant heating rates. The model comprises four consecutive reactions $A \rightarrow B \rightarrow C \rightarrow D \rightarrow E$ of the type Fn, Fn, Cn, and Fn.

The formal kinetic model for the liquid phase decomposition fits the experiments with constant heating rates of 2.5 - 40 min very well. As expected, the solid phase decomposition at heating rates of 0.05 - 0.4 °C/min can not be described by this model.

Solid phase decompositions are often described by one formal reaction of either zero or first order. Our previous investigations demonstrated that these models are inadequate for the

description of TGA results gained with constant heating rates [8]. The results of our isothermal TGA experiments verify this conclusion. The mass losses depicted in Fig. 3 do neither follow a straight line as would be expected for a zero order reaction nor an exponential decay as would be expected for a first order reaction.

With the data from the non-isothermal TGA experiments, we previously developed a formal kinetic model comprising three consecutive reactions A → B → C → D of the type R3, Cn, and Fn [9]. This kinetic model is compared to results from isothermal and non-isothermal TGA experiments in Fig. 5.

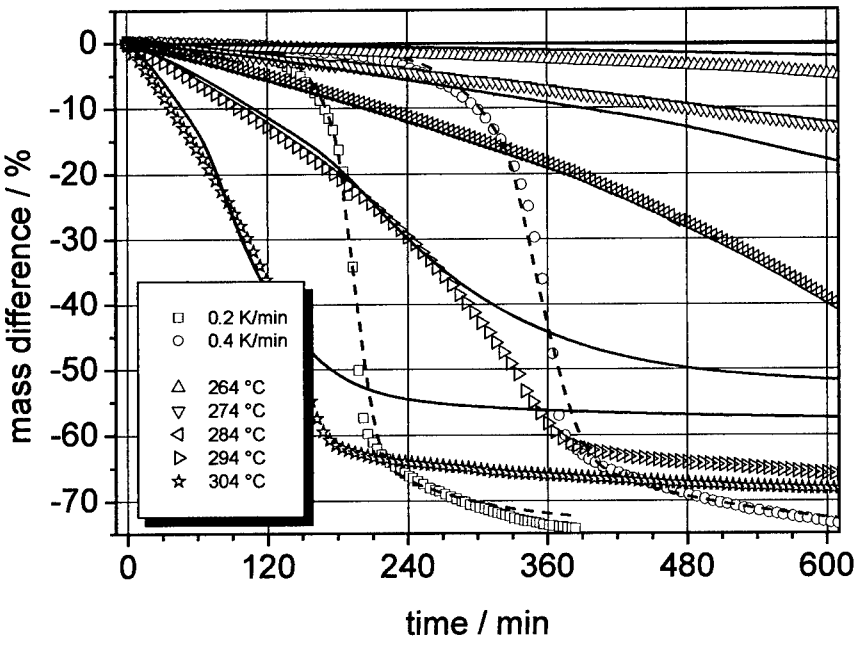


Fig. 5. Previous best fit formal kinetic model for the solid phase decomposition. Comparison of the mass loss as function of time to experimental TGA results at low constant heating rates and at isothermal conditions. The model comprises three consecutive reactions A → B → C → D of the type R3, Cn, and Fn.

The model describes the experimental mass loss under non-isothermal conditions quite well but the description of the mass loss under isothermal conditions is not satisfactory. Therefore, we have revised the formal kinetic model for the solid phase decomposition. The model was fitted by multivariate regression using data from isothermal and non-isothermal TGA experiments simultaneously. Best results were gained by varying the kinetic parameters for the reaction

mechanism already used in the previous modelling. The modified formal kinetic model is shown in Fig. 6 and the kinetic parameters are summarized in Tab. 2.

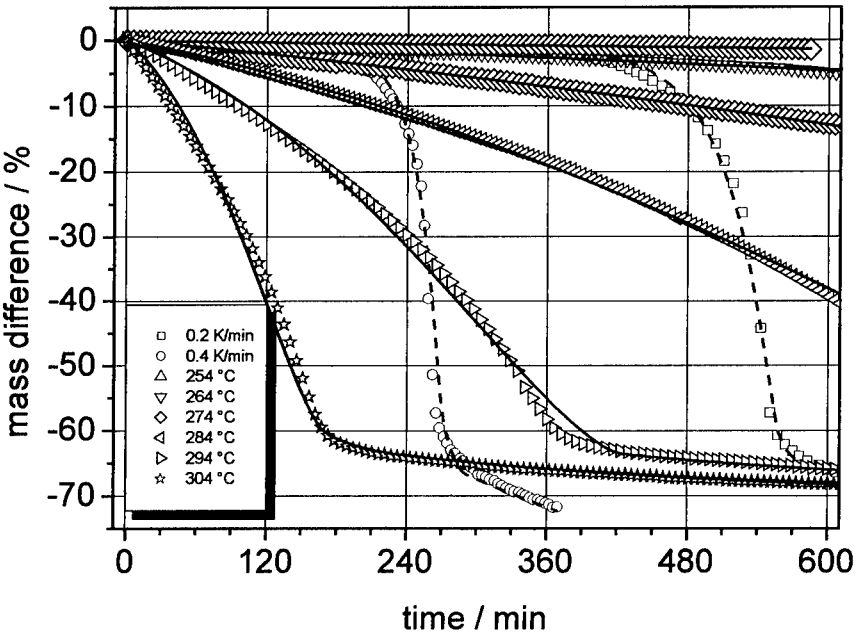


Fig. 6. Modified best fit formal kinetic model for the solid phase decomposition. Comparison of the mass loss as function of time to experimental TGA results at low constant heating rates and at isothermal conditions. The model comprises three consecutive reactions $A \rightarrow B \rightarrow C \rightarrow D$ of the type R3, Cn, and Fn.

For all heating conditions, the correspondence between experimental and calculated mass loss is very good. The first reaction step R3, a three dimensional phase boundary reaction, has an activation energy of 176 kJ/mol. It can be interpreted as being dominated by a mass transfer limited sublimation of the virgin solid. The calculated activation energy of this reaction step is very close to the sublimation enthalpy of the sublimation of HNS which was measured to be 180 kJ/mol between 160 and 205 °C [3]. The second reaction step Cn was modelled as an autocatalytic reaction with autocatalysis by the intermediate pseudo component C. Autocatalysis during decomposition of nitro compounds is known to be caused by NO_x [13, 14]. Whether the active species are NO, a main product of this reaction step as detected by mass spectrometry, or highly activated NO_2 which dissociates to NO and O, can not be determined by this investigation. The calculated activation energy of the second reaction step is 262 kJ/mol and the reaction order is 0.35. In a condensed phase reaction, a reaction order of $n < 1$ is typical for a mass transfer limited

reaction [15]. The third reaction step Fn, supposedly a secondary pyrolysis of the complex primary product, has a low formal activation energy of 108 kJ/mol and a reaction order of 1.64. A reaction order above 1.0 is a possibility to include a great number of individual reactions with distributed activation energies into one formal reaction [15].

Table 2. Kinetic parameters of the formal reaction models for the decomposition of HNS in the liquid phase and the solid phase, respectively.

	liquid phase decomposition	solid phase decomposition
	$A \xrightarrow[Fn]{1} B \xrightarrow[Fn]{2} C \xrightarrow[Cn]{3} D \xrightarrow[Fn]{4} E$	$A \xrightarrow[R3]{1} B \xrightarrow[Cn]{2} C \xrightarrow[Fn]{3} D$
log ($k_{0,1}/s^{-1}$)	31.62	11.75
$E_{a,1}$ / kJ/mol	389.6	175.9
n_1	0.40	
log ($k_{0,2}/s^{-1}$)	0.79	19.53
$E_{a,2}$ / kJ/mol	28.4	261.7
n_2	0.55	0.35
log ($k_{cat,2}/s^{-1}$)		0.61
log ($k_{0,3}/s^{-1}$)	17.78	5.39
$E_{a,3}$ / kJ/mol	233.8	108.3
n_3	0.91	1.64
log ($k_{cat,3}/s^{-1}$)	0.028	
log ($k_{0,4}/s^{-1}$)	22.50	
$E_{a,4}$ / kJ/mol	296.0	
n_4	2.46	
mass loss by step 1	0.073	0.078
mass loss by step 2	0.118	0.742
mass loss by step 3	0.600	

The quality of the fit for non-isothermal conditions is additionally shown in Fig. 7 where the modelled mass loss as function of temperature is compared to data from TGA experiments with constant heating rates between 0.05 and 0.4 °C/min. The correspondence between experimental and calculated mass loss is excellent.

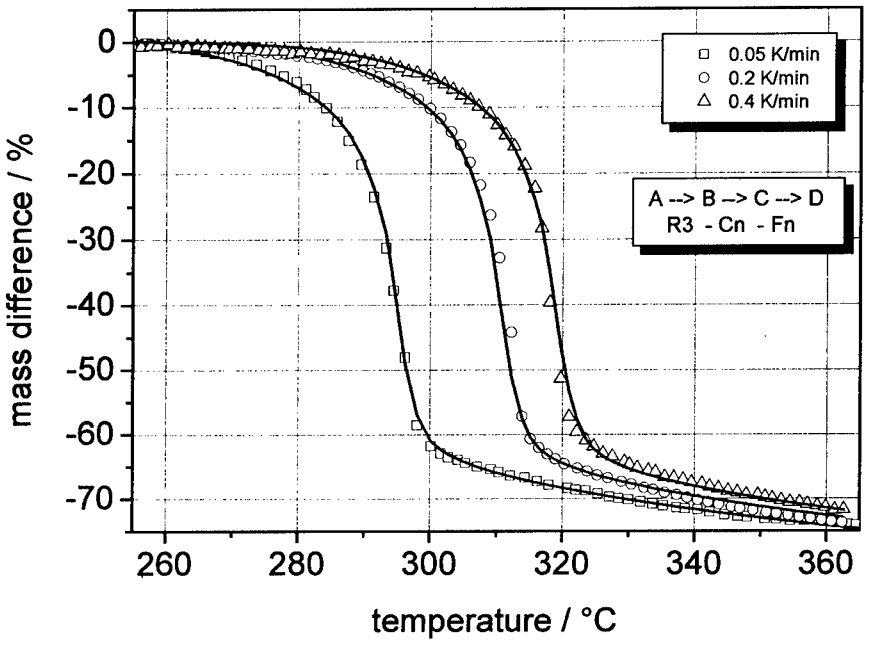


Fig. 7 Modified best fit formal kinetic model for the solid phase decomposition. Comparison of the mass loss as function of temperature to TGA results at low constant heating rates.

Conclusions

To predict the thermal decomposition of HNS successfully, care must be taken if the reaction will take place in the crystalline or molten state. The liquid and the solid phase decomposition of HNS have to be described by different formal kinetic models. Both models comprise multiple steps to simulate physical and chemical processes adequately.

STA measurements are less restricted compared to DSC measurements and turned out to provide a much better basis for our kinetic investigation. The non-linear multivariate regression is an indispensable method to derive formal kinetic models. This technique is the only way to decide between different reaction models and receive a formal model which gives reliable results for the whole parameter range.

Using the formal kinetic models developed in this work, the validity of predictions of the thermal stability of HNS under all heating conditions should be very good.

References

[1] Singh, B. and Malhorta, R. K.: Hexanitrostilbene and its properties. *Def. Sci. J.*, 33(2) (1983) 165-176.

[2] Rosen, J. M. and Dickinson, C.: Vapour pressure and heats of sublimation of some high melting organic explosives. *Journal of Chemical and Engineering Data* 14(1) (1969) 120-124.

[3] Gessel, U. and Zöllner, H.; Einsatz von HNS in der Erdölexplorationstechnik. Proceedings of the 27th International Annual Conference of ICT. Fraunhofer Institut Chemische Technologie, Karlsruhe, Germany (1996)

[4] Aziz, A., Cartwright, M., and Hill, C.J.: Thermal stability of the crystallisation nucleant 2,4,6 trinitrotoluene, TNT, and 2,2',4,4',6,6' hexanitrostilbene, HNS. *J. Thermal Analysis* 47 (1996) 1617-1628.

[5] Kony, M., Dagley, I., and Whelan, D.: Deuterium kinetic isotope effects in the thermal decomposition of HNS. Proceedings of the 22th International Annual Conference of ICT. Frauenhofer Institut Chemische Technologie, Karlsruhe, Germany, 1991.

[6] Friedman, H.L., *J. Polymer Lett.* 4 (1966) 323.

[7] Opfermann, J.: Kinetic analysis using multivariate non-linear regression. I. Basic concepts. J. Therm. Anal.Cal. 60 (2000) 641-658.

[8] Rieckmann, Th., Völker, S., Lichtblau, L. and Schirra, R.: Thermal decomposition of hexanitrostilbene at low temperatures. *J. Anal. Appl. Pyrolysis* 58-59 (2001), 569-588

[9] Rieckmann, Th., Völker, S., Lichtblau, L. and Schirra, R.: Investigation on the thermal stability of hexanitrostilbene by thermal analysis and multivariate regression. *Chem. Eng. Sci.* 56 (4) (2001), 1327-1335

[10] Marquardt, D.: *SIAM J. Appl. Math.* 11 (1963) 431.

[11] Opfermann, J.: Nichtlineare Ausgleichsrechnung für den Mikrorechner MC80. *Rechentechnik/Datenverarbeitung* 22.3 (1985) 26.

[12] Brown, M. E., Dollimore, D., and Gallway A. K. in Bamford, C.H. and Tipper, C.F., (Ed.): Comprehensive Chemical Kinetics Volume 22, (Reactions in Solid State), Amsterdam, 1980, p. 57

[13] Falbe, J. (Ed.): Römpp-Chemie-Lexikon CD ROM, version 1.5. Georg Thieme Verlag, Stuttgart, 1998.

[14] Bohn, M.: Modeling of stabilizer reaction for improved prediction and extension of service lifetime. Proceedings of the 2. Internationaler Workshop Mikrokalorimetrie, Swisttal, Germany, 1999.

[15] Burnham, A.K. and Braun, R.L.:Global kinetic analysis of complex materials. *Energy Fuels* 13 (1999) 1-22.

PYROLYSIS OF ENERGETIC MATERIALS IN INERT *vs.* REACTIVE ATMOSPHERES

Thomas B. Brill and Reiko I. Hiyoshi

Department of Chemistry and Biochemistry

University of Delaware

Newark, DE 19716 USA

ABSTRACT

Flash pyrolysis of NG, NC, PETN, RDX, and HMX was conducted in an air atmosphere for comparison with an argon atmosphere. T-Jump/FTIR spectroscopy was employed. The difference roughly correlates with the extent of condensed phase vs. gas phase decomposition. That is, if condensed phase decomposition dominates, the dependence on the atmosphere is weak; if the gas phase dominates the dependence is strong (i.e. NG>PETN≅RDX>NC≅HMX). The main reactions in air are CO with O_2, which is fast, and NO with O_2, which is slow. However the effects for nitrate esters are different from nitramines. Differences in the relative humidity had little effect except in the case of HMX.

1. INTRODUCTION

During combustion or explosion of an energetic compound, the primary decomposition chemistry occurs in the atmosphere of the formed gases. Secondary reactions involving these products are frequently responsible for the violent exothermicity of the combustion and explosion. The $NO_2 + CH_2O$ reaction of HMX and RDX is a good example.[1] After a longer period of time however diffusion and turbulent mixing of these gases with the surrounding atmosphere of air. Tertiary reactions that may be of concern in air pollution can result from this final stage of the process.

An extensive amount of research has been conducted on the flash pyrolysis of energetic compounds in an argon atmosphere to define the primary and secondary reaction chemistry.[2,3] The tertiary reaction chemistry of the products with the components of air is, of course, not addressed by this work. The products that will be detected in the atmosphere are important to regulatory agencies responsible for evaluating the risks and certifying the safety of the participants and nearby civilian communities during training exercises, mission activities, and the disposal of hazardous materials.[4]

This paper highlights recent findings on the behavior of nitroglycerin (NG), pentaerythritol tetranitrate (PETN), nitrocellulose (NC), RDX, and HMX when pyrolysis in air is compared to an inert Ar atmosphere. The technique of T-jump/FTIR spectroscopy was used with simulated air (i.e. CO_2 was eliminated and the humidity was controlled) to compare the concentration and time evolution of the products with those generated in an inert Ar atmosphere.

2. EXPERIMENTAL

In terms of control the fast heating event, T-jump/FTIR spectroscopy[5-7] is perhaps the most developed technique. Figure 1 shows the essential features. The concept is to use a film-like sample of small mass to optimize the heat transfer from the Pt ribbon heater filament. The control circuit enables flash heating of the sample at a controlled rate up to 20,000°C/sec to a chosen temperature inside of a closed cell. Simultaneously, rapid scan (4 Hz) IR spectra are recorded of the species leaving the filament surface. All except one of these studies[8] have previously been performed in an Ar atmosphere. They can, however, be performed in any surrounding atmosphere and with a chosen pressure in the 0.1-100 atm range. The goal of this work is to identify and quantify the evolved gaseous products and to measure thermochemical and kinetic events where possible in the most controlled, but qualitatively relevant, conditions.

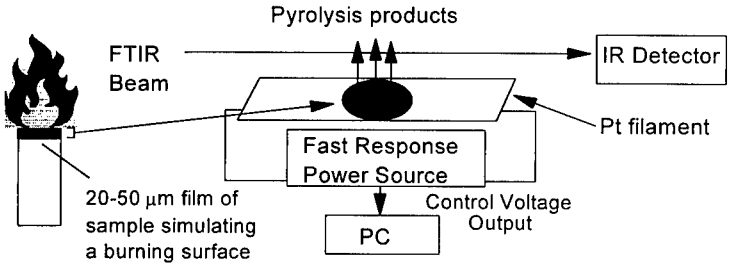


Figure 1. Essential features of the T-Jump/FTIR method

A simulated atmosphere containing 80% N_2 - 20% O_2 was used because of the need to remove the strongly IR-absorbing CO_2 component of air. CO_2 is a potentially useful diagnostic product of reactions of gases with air and its natural presence in air confuses the analysis. The air humidity is a possible variable in the identity and quantity of certain products in the plume. Thus several values of the relative humidity (e.g., 0%, 20%, and 60%) and a matrix of temperatures and pressures were employed in this work.

Figure 2 shows how the simulated air atmosphere was created. A commercial gas mixture of 80%N_2-20%O_2 was purchased to pressurize a storage reservoir up to 10 atm. Trays of aqueous H_2O inside the vessel provided different chosen values of the relative humidity when the pressure was changed. The true relative humidity was measured with an in-line hygrometer. The spectroscopy cell containing the sample and Pt filament was swept with this simulated air atmosphere. The flash pyrolysis results were compared at the same conditions with an Ar atmosphere. The spectra were corrected with the background of the same atmosphere.

The concentrations of the products were determined by first-order spectral resolution with least-squares optimization using quadratic programming constraints.[9] Equation 1 summarizes the method in terms of the matrix manipulation, where **R** is the spectral matrix (m x p), **C** is the sought after concentration matrix (m x n), and **K** is the previously developed calibration matrices (n x p) for each gaseous product.

$$\mathbf{R} = \mathbf{C}\,\mathbf{K} \qquad (1)$$

The n is the number of components, the m is the number of spectra, and the p is the wavenumber scale. The concentrations of all of the species in the calibration matrix are obtained by minimizing the residual of **R**. Figure 3 compares the spectrum of the gaseous products from NC to the residual after fitting the products with the calculated spectrum. No species remain above the noise level.

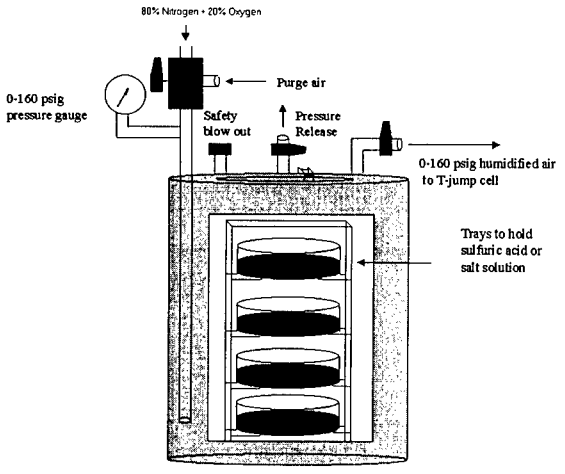


Figure 2. The device to create the simulated air atmosphere with chosen relative humidity.

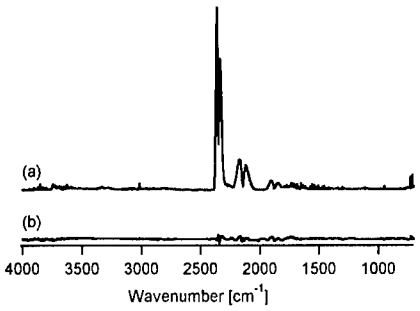


Fig. 3 (a) IR spectrum of decomposition products of NC in Ar (pressure: 5atm),
(b) Residual spectrum after subtraction of products

3. RESULTS

Several categories of reactions might be expected to occur between the more reactive products from energetic materials and the more reactive components of air, namely O_2 and H_2O. Reactions 2 and 3 are especially noteworthy. In addition the water gas shift reaction 4 may occur if the temperature becomes high enough.

$$2NO + O_2 \rightleftarrows 2NO_2 \quad (2)$$

$$2CO + O_2 \rightarrow 2CO_2 \quad (3)$$

$$CO + H_2O \rightleftarrows CO_2 + H_2 \quad (4)$$

The findings to date on NG, PETN, NC, RDX and HMX are summarized in the sections below in the order of complexity; that is, the easiest to understand is described first.

3.1 Nitroglycerin (NG)

Figure 4 compares the IR-active gaseous products from flash pyrolysis of NG at a set temperature of 350°C under 5 atm of Ar [species preseent but not shown are HCN (<1%), H_2CO (<1%), and HONO (<1%)] and 5 atm of air at 0% relative humidity [species not shown are H_2CO (<2%) and H_2O (<7%)]. The atmospheric moisture content up to 60%RH had no effect on the pyrolysis products. Likewise the pyrolysis temperature of 400°C and pressures of 1 atm or 8 atm had no effect. On the other hand, the effect of the surrounding atmosphere profoundly influenced the results. The reaction stoichometry in Ar based on quantitation of the IR spectra and completion with IR inactive products (H_2 and N_2) is given by reaction 5:

$$C_3H_5N_3O_9 \rightarrow 2.11NO + 1.94CO + 1CO_2 + 0.33H_2O + 0.167NO_2 + 0.11HCN + 2.11H_2 + 0.33N_2 \quad (5)$$

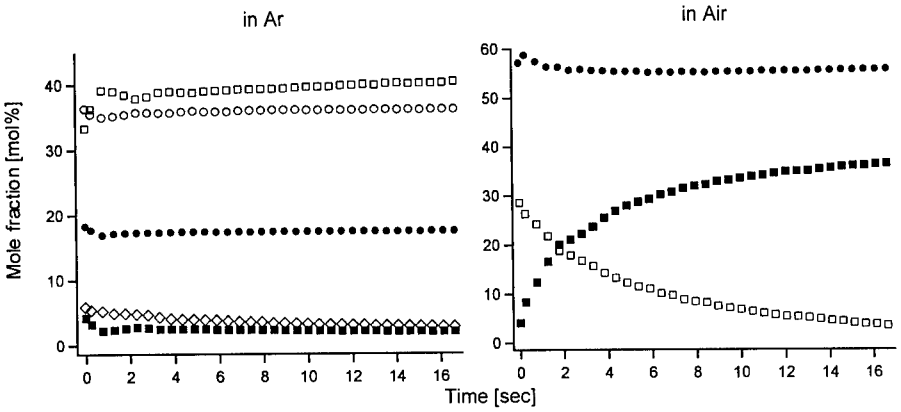


Fig. 4 Decomposition products of NG (pressure: 5atm)
○:CO, ●:CO_2, □:NO, ■:NO_2, ◇:H_2O

Under the same conditions except with a simulated air atmosphere, all of the CO is instantly converted to CO_2 by reaction 3, and NO is slowly converted to NO_2 by reaction 2. The H_2O content remains essentially constant, which indicates that reaction 4 is not occurring at these conditions.

3.2 Pentaerythritol tetranitrate, PETN

PETN has the molecular formula $C_5H_8N_4O_{12}$ and thus has proportionally more carbon and hydrogen than NG. In accordance with this fact, Figure 5 shows that flash pyrolysis at 350°C under 5 atm of Ar produces more CO than NO compared to NG and also small amounts of the species not shown: CH_4 (3%), C_2H_4 (1%), C_2H_2 (3%), HCN (3%), CH_2O (<1.5%), and H_2O (<4%). The same results were obtained at 1 atm and 8 atm, except that the hydrocarbons are not found at higher pressure. When the pyrolysis is conducted at 350°C under 5 atm of simulated air with 0% RH, Figure 5 shows that CO_2 is formed in place of CO (reaction 3), that all of the hydrocarbons are oxidized, and that the initial amount of NO is greatly reduced. The latter difference can only be ascribed to the conversion of more of the nitrogen in PETN to N_2. The H atoms of PETN result in the formation of more H_2O (10%) compared to an Ar atmosphere. Figure 5 shows that as time progresses after primary decomposition occurs, reaction 2 takes place. Changing the RH in the 0-60% range in air had no effect on the product concentrations. Overall, the behavior of NG and PETN is similar.

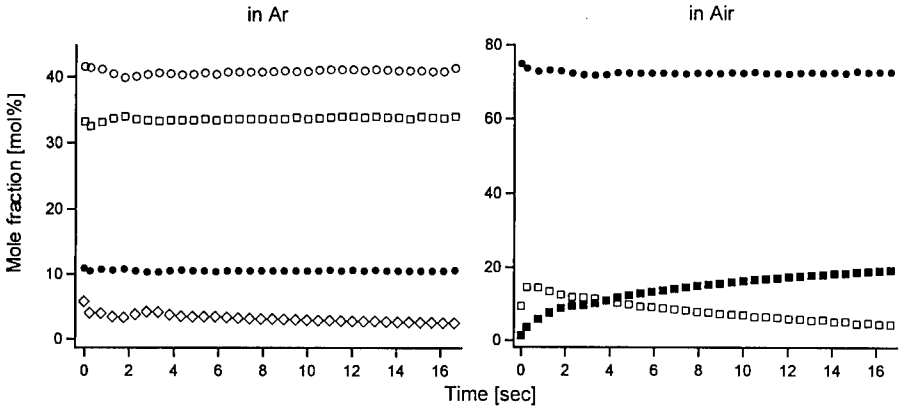


Fig. 5 Decomposition products of PETN (pressure: 5atm)

○:CO, ●:CO_2, □:NO, ■:NO_2, ◇:H_2O

3.3 Nitrocellulose, NC

Nitrocellulose (13% N) was flash pyrolyzed at 300°C under 1 atm of Ar and simulated air with 0%RH. The results are shown in Figure 6. In contrast to NG and PETN, it is remarkable that the gaseous products are initially the same under these two atmospheres, although like PETN, small amounts of the hydrocarbons CH_4 (1%), C_2H_4 (2%) and C_2H_2 (4%) form in the Ar atmosphere. Reaction 2 slowly takes place with time converting NO to NO_2. At higher pressures in air, but not in Ar, NC appears to combust on the filament leading to CO_2 as the dominant product.

A possible explanation for the stark difference between the pyrolysis behaviors of the NG-PETN class and NC is the fact that the vapor pressure[10] of NG (0.31 mbar at 90°C) and PETN (0.0011 mbar at 100°C) is significant at these pyrolysis conditions, whereas NC essentially has no measurable vapor pressure. Hence, NC decomposes primarily in the condensed phase and the products thus formed are relatively independent of the surrounding atmosphere. The products of NG and PETN, on the other hand, exhibit much greater dependence on the surrounding atmosphere because of greater mixing during the decomposition process.

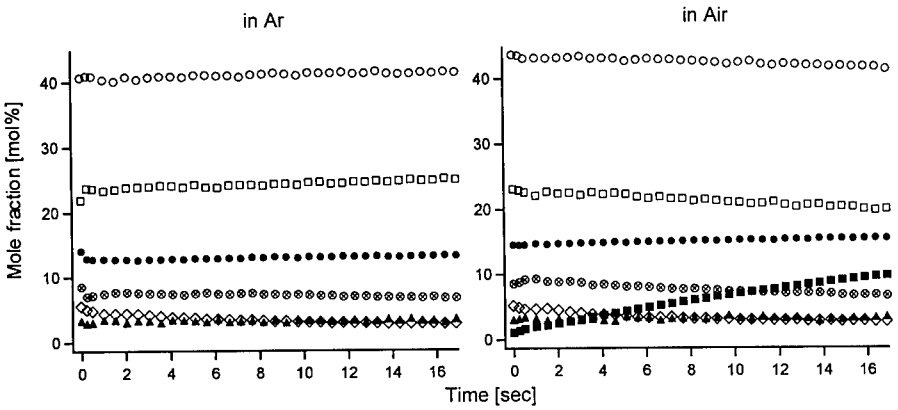


Fig. 6 Decomposition products of NC (pressure: 1atm)
○:CO, ●:CO_2, □:NO, ■:NO_2, ▲:HCN, ⊗:H_2CO, ◇:H_2O

3.4 RDX

Comparison of the flash pyrolysis of RDX at 350°C under 5 atm of Ar and air with 0%RH is shown in Figure 7. In the Ar atmosphere the gaseous products are essentially consistent with those reported previously at these conditions,[1] including the previously identified minor species[11] s-triazine, mono-nitrosoRDX, and hydroxylmethyl formamide all in <3% mole fraction. The gaseous products in the air atmosphere are, on the other hand, very different and are suggestive of ignition of the sample. The minor species just mentioned occur in less than 1% mole fraction. These results are consistent with the fact that RDX has an appreciable vapor pressure, being about 15 times less than that of PETN at 100°C. As a result the RDX and its gaseous products can mix with and ignite in air. Relatively little NO and NO_2 remains after ignition so that reaction 2 has little role. An interesting result is found when RDX is flash pyrolyzed at 1 atm in air. The reverse of reaction 2 might be occurring to some extent, or possibly reaction 6 may take place to some extent. The evidence for the latter is the fact that NO_2 and CH_2O decrease in concentration, while NO increases with time. The concentration behavior of CO and CO_2 as a function of time are not always consistent, perhaps suggesting that reaction 3 plays a competitive role.

$$NO_2 + CH_2O \rightarrow NO + CO + H_2O \qquad (6)$$

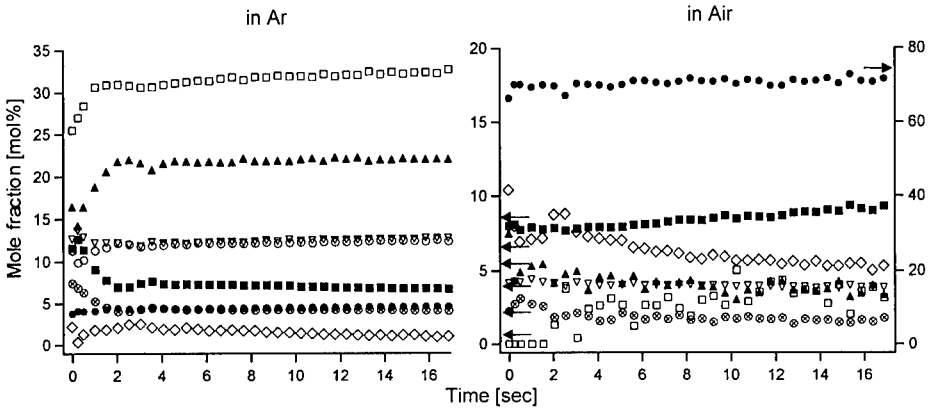


Fig. 7 Decomposition products of RDX (pressure: 5atm)
○:CO, ●:CO_2, □:NO, ■:NO_2, ▽:N_2O, ▲:HCN, ⊗:H_2CO, ◇:H_2O

3.5 HMX

The behavior of HMX somewhat resembles NC because of the strong role of condensed-phase chemistry, but in other ways it is quite different and resembles RDX. Consistent with the greater role of the condensed phase, the vapor pressure of HMX is about 10^5 less than that of PETN at 100°C.[10] Figure 8 shows the result of flash pyrolysis of HMX in 1 atm Ar at 400°C compared to that at 350°C in 1 atm air with 0%RH. HNCO, HONO and hydroxylmethyl formamide are present in <1% in Ar, and HNCO and HONO are present at <1% in air. Notice that the only significant differences are in the CH_2O concentration, which is somewhat lower in Ar compared to air, and the H_2O concentration, which is higher in Ar. The most remarkable feature is that NO is not converted to NO_2 in air, i.e. in contrast to the nitrate esters, the forward reaction 2 does not affect the results. The same behavior has been found in a higher O_2 concentration.[8] In fact the NO concentration *increases* slightly with time in both air and Ar. Consequently, a buffering or inhibition action exists in the HMX decomposition process or among the gaseous products.

A possible, although not too likely, explanation is that a combination of reactions takes place that gives the appearance of inhibition. For example, reactions 2 and 3 might occur along with reaction 6. Reactions 2 and 6 are off-setting in that 2 lowers the NO concentration and raises NO_2, while reaction 6 raises NO and lowers NO_2. Similarly, reaction 3 lowers the CO

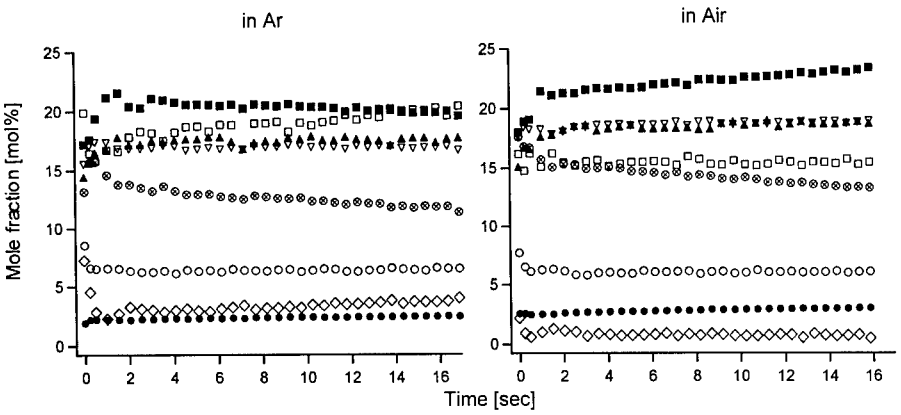


Fig. 8 Decomposition products of HMX (pressure: 1atm)
○:CO, ●:CO_2, □:NO, ■:NO_2, ▽:N_2O, ▲:HCN, ⊗:H_2CO, ◇:H_2O

concentration, while reaction 6 raises it. What makes this scenario less than satisfying is the fact that the H_2O and CO_2 concentrations should increase with time, which they do not. On the other hand, CH_2O decreases with time, which it should according to reaction 6. Alternatively, it may be simply that the extra O_2 might be responsible for the behavior of the NO and NO_2 concentration trend when reaction 2 is attempting to shift to the left and is inhibited from doing so.

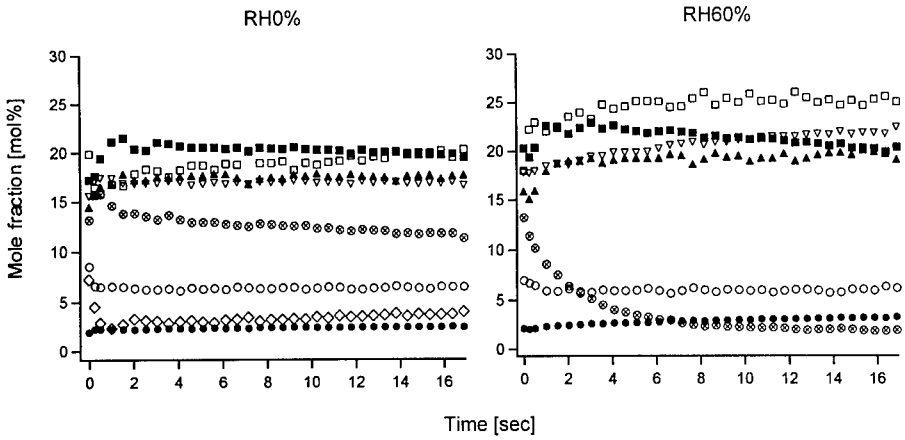


Fig.9 Decomposition products of HMX (pressure: 1atm)
○:CO, ●:CO_2, □:NO, ■:NO_2, ▽:N_2O, ▲:HCN, ⊗:H_2CO, ◇:H_2O

HMX is the only compound studied to date in which the humidity has a pronounced effect on any of the decomposition products. Figure 9 shows that the CH_2O concentration drops dramatically with time when the humidity is large. A possible explanation is simply that the CH_2O is aggregating the H_2O molecules and the solution of CH_2O-$H_2O$is condensing on the cell walls.

4. RATE OF THE FORWARD REACTION OF 2

The forward step of 2 is a termolecular reaction whose rate constant has been evaluated to be 2.0×10^{-38} cm^6 $molecule^{-2}$ s^{-1} at 25°C.[12] Figure 10 shows however that in the present work a first order rate expression fits the decrease in NO concentration rather well in NG, PETN and NC. This does not mean that the reaction is first order, but merely that the practical process, which includes reaction, mixing, and a temperature gradient combine together to give the appearance of a first order process whose average rate constant is about 0.07 s^{-1} at 5 atm. The conversion of the third order rate constant[12] given above into first order units using the approximate initial NO concentration in Figure 10 yields a rate that is about 33 times slower than the average of those in Figure 10. This difference may be the result of the fact that the O_2 concentration is much larger than that of NO which produces the faster overall rate. If the reaction is treated instead as a psuedo-second order process instead of third order and the units adjusted accordingly, then the calculated rate is about 56 times faster than that observed. The observed rate intermediate between a second and third order process. Hence, it is plausible that the excess O_2 is responsible by accelerating the forward reaction of 2 in this system.

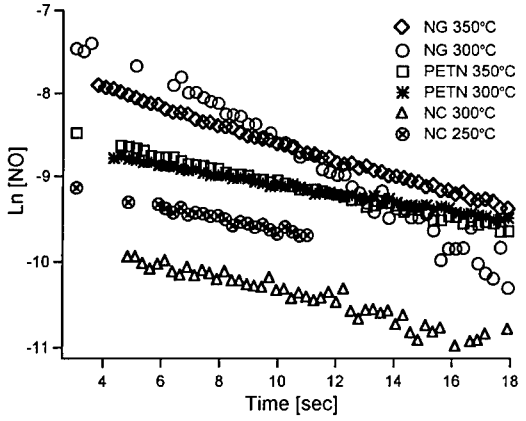


Fig. 10 First order rate plots for NO decomposition in Air (5atm) by reaction 2.

Alternatively, it may be that the higher pressure (5 atm) used in this work accelerates the apparent rate of the forward reaction of 2. We are checking on this possible explanation.

5. DISCUSSION

The gaseous products from the flash pyrolysis of the nitrate esters NG, PETN, and NC and the nitramines RDX and HMX are compared in an inert Ar atmosphere and a reactive atmosphere of simulated air (80%N_2-20%O_2). NG and PETN behave in a straightforwardly understandable fashion, which is consistent with vaporization-decomposition in which the air mixes and reacts with the products. NC differs mainly in the fact that decomposition occurs in the condensed phase and so the reaction with air occurs to a lesser extent.

The results are unexpectedly complex in the cases of the nitramines. RDX appears to have more gas phase decomposition and reaction with air than HMX, which is consistent with the higher vapor pressure of RDX. However, both RDX and HMX do not exhibit the decrease in NO and increase in NO_2 concentrations, which are expected in the air atmosphere and found for the nitrate esters. One or more inhibiting species or reactions in these nitramines appear to effectively stop or disguise this reaction. It is possible that the high NO_2 concentration produced by pyrolysis causes NO + O_2 to form by the reverse of reaction 2 but that equilibrium nearly exists because of the excess O_2 in the atmosphere. The kinetics of the forward reaction 2 are faster than the literature rate possibly because of the excess O_2 in the atmosphere.

6. ACKNOWLEDGMENTS

RIH thanks the Ministry of Education, Culture, Sports, Science and Technology for financial support. TBB thanks the Strategic Environmental Research and Development Program for support on CP1193.

7. REFERENCES

1. T. B. Brill and P. J. Brush, Phil. Trans. Roy. Soc. London, A, **339**, 377 (1992).
2. T. B. Brill, Prog. Energy Comb. Sci. **18**, 91 (1992).
3. T. B. Brill, H. Arisawa, P. J. Brush, P. E. Gongwer, and G. K. Williams, J. Phys. Chem. **99**, 1384 (1995).
4. W. J. Mitchell, Amer. Acad. Envir. Eng., Book Chapter (www.enviro-engrs.org, Online Publications, 2000).
5. T. B. Brill, P. D. Brush, K. J. James, J. E. Shepherd, and K. J. Pfeiffer, Appl. Spectrosc. **46**, 900 (1992).

6. J. E. Shepherd and T. B. Brill, 10th Int. Symp. Detonation, NSWC, White Oak, MD, 1993, p. 849.
7. S. T. Thynell, P. E. Gongwer, and T. B. Brill, J. Propuls. Power, **12**, 933 (1996).
8. S. F. Palopoli and T. B. Brill, Combust. Flame, **87**, 45 (1991).
9. H. Arisawa and T. B. Brill, Combust. Flame, **109**, 87 (1997).
10. R. Meyer, Explosives, 3rd Ed. VCH Publishers, Weinheim, Germany, 1987.
11. P. E. Gongwer and T. B. Brill, Combust. Flame, **115**, 417 (1998).
12. R. Atkinson, D. L. Baulch, R. A. Cox, R. F. Hampson, Jr., J. A. Kerr, M. J. Rossi, and J. Troe, J. Phys. Chem. Ref. Data, **26**, 521 (1997).

COMBUSTION MECHANISM OF NITRAMINE BASED SOLID ROCKET PROPELLANTS

Haridwar Singh
High Energy Materials Research Laboratory. Pune. INDIA

Recently developed nitramine based solid propellants along with energetic binders, plasticizers and high energy ballistic modifiers have great potential to offer increased energy (Isp ~ 300 s) with plume signature advantages over the state-of-the-art propellants for various applications and hence there has been considerable research over the years attempting to elucidate the combustion mechanism of nitramines involving both ignition and burning. Central to the combustion process is the decomposition of nitramines. A number of researchers have provided reviews of the kinetics and proposed mechanisms for the decomposition process (1-10). However, considerable controversy and uncertainity exists as to the initial decomposition pathways. Various mechanisms have been proposed which occur under differing temperature and pressure conditions. Due to the short lived nature of highly reactive decomposition intermediates as well as of the nitramines themselves, it is difficult to experimentally observe in a quantitative way, many of the proposed decomposition intermediates.

Part of the difficulty in postulating decomposition mechanisms lies in the lack of thermochemical data regarding the various bond strengths involved in the nitramines and their potential decomposition products (5,6,10,11). Melius et.al (11) have applied sophisticated quantum chemistry to calculate the heat of formation and free energies of prototype nitramines and their resulting intermediate decomposition products. The bond energies and dissociation energies obtained from these calculations were used to determine decomposition pathways of HMX and RDX. Since the combustion products of RDX and Double base propellants (DBP) are fuel rich, no exothermic chemical reactions are possible between their combustion products. Thus, the flame temperature and specific impulse of the RDX-CMDB propellant are approximately equal to the weight averaged values of those of each component. The flame structure of RDX-CMDB (Composite Modified Double Base) propellants is similar to that of DBP (homogenous) and is significantly different from that of AP(Ammonium Perchlorate)-

CMDB propellants (heterogeneous). The crystalline RDX particles mixed with the base matrix of DBP, melt, decompose and gasify at the burning surface of the propellant. The decomposed RDX gas diffuses into the decomposed gas of the base matrix at and just above the burning surface (12-14). This diffusion process occurs before the RDX particles produce their monopropellant flamelets above the burning surface. Thus, a homogeneous reactive gas of the mixtures of the RDX and the base matrix decomposed gases is formed at the burning surface and produces the luminous flame at some distance above the burning surface. The burn rate of RDX-CMDB propellant decreases with the increase in concentration of RDX, despite an increase in the energy contained per unit mass of propellant.

It has been reported that the mole fraction of NO_2 produced by the initial decomposition of HMX is less than that of NO_2 produced by the initial decomposition of DBP (16). Thus, the ratio of NO_2/aldehydes of DBP (the initial decomposition products) is decreased by the addition of HMX. This indicates that the addition of HMX shifts the equivalence ratio of NO_2/aldehydes towards fuel rich. Thus, the reaction rate in the fizz zone decreases and the heat feedback from the gas phase to the burning surface decreases when HMX is mixed within DBP matrix(14). Consequently, the burn rate of HMX-CMDB propellants decreases, when compared with DBP which is used as the base matrix in HMX-CMDB.

Several studies on the combustion of CMDB propellants have shown that the addition of HMX to DB matrix leads to a reduction of the burn rates with a slight increase in the pressure exponent. It has been suggested that diffusion control effects are not introduced by the presence of HMX, as they are in the case of AP. Kubota (15) found that the flame structure was not altered by the addition of HMX particles. They were not active at the burning surface and thus the burn rates of CMDB propellants do not appear to differ significantly from the burn rate of DB matrix. Yount and Musso (17) using high speed motion pictures found that HMX did not ignite at the burning surface of CMDB propellants, but rather ignited and burned in the gas stream above the surface and therefore concluded that HMX could be considered as a diluent. Its decomposition occurs at a sufficient distance from the burning surface so that the heat feedback to the surface is not involved in rate control. In their studies, Cohen et.al (18) have found that there exists a burn rate-exponent shift in nitramine propellants, which has been attributed to the difference in the burn rates and decomposition behaviour between RDX and

its binders. The reason that the high pressure exponent appears is that the burn rate of the nitramine powder exceeds that of the binder. Other explanations for the phenomenon include physical effects, burning surface structure changes (from melt layer to cratered surface) and the ignition delay for the nitramine crystals. Nevertheless, due to the difficulties in experimental investigations, the high pressure combustion mechanism of nitramine based propellants is not yet fully understood.

Over low pressure range, several studies have shown that addition of RDX to DBP leads to decrease of the burn rate with a slight increase in pressure exponent. The burn rate appears weakly dependent upon the nitamine particle size but the use of fine nitramine powder helps to remove the slope break phenomenon to higher pressure.

The gas phase flame chemistry of an RDX flame was studied theoretically using a steady laminar, one-dimensional, premixed flame model by Melius (19). Their results provide a new description of the chemistry of a nitramine flame. There is a primary flame zone composed of a very endothermic pyrolysis region, followed by a combustion region. The primary flame zone is separate from the luminous flame zone. Although the luminous flame zone does not stand off from the primary flame, it maintains a spatial separation. Melius (19) found that it is not the primary flame chemistry near the surface but rather the secondary, luminous flame chemistry that couples with the overall heat and mass transport to control the burn velocity. Zenin (20) is of the view that in the condensed phase of combustion wave of nitramines, evaporation and thermal decomposition occur simultaneously with negative het release at pressures less than 5-10 atm. Howeever, heat release becomes positive beyond the threshold of low pressure. He found that gasification law and heat release law in solid propellants do not change but dark zone laws and dependence on temperature sensitivity change significantly with inclusion of HMX.

Although several models of nitramine combustion have been developed (21-24), controversy remains concerning the relative importance of condensed phase and gas phase processes in deflagration.

A large number of studies have been carried out at HEMRL on the combustion mechanism of nitramine based propellants (RDX based cast double base (CDB), extruded

double base (EDB), and composite modified double base (CMDB)) including the effect of various burn rate modifiers, platonisers, high energy additives, high energy plasticizers etc (25-32). This paper discusses the combustion behaviour on the basis of the findings from these experiments and proposes a mechanism based on the data obtained in addition to reviewing the different mechanisms that have already been proposed for the combustion behaviour of DBP, CMDB and Nitramine CMDB class of propellants.

Our studies on energetic plasticizer and nitramine based propellants have indicated that the combustion zones of energetic plasticizer (Glycidyl Azide Polymer - GAP) propellants containing AP are not homogeneous due to the heterogeneous structure of the propellant. Since the decomposition gas of the GAP-DBP is fuel rich and that of AP oxidizer rich, it is possible that the diffusion between the products of AP and GAP-DBP shifts the equivalence ratio towards stoichiometry, which results in increased reaction rates and flame temperature. Since the combustion products of RDX and DBP are fuel rich no exothermic reactions are possible between their combustion products. The flame temperature and specific impulse of the RDX-CMDB propellants are approximately weight averaged value of each of these components. Unlike AP, the addition of nitramines does not alter the flame structure of DBP. No diffusion like luminous streams are observed which indicate that fully developed monopropellant flame of nitramines are produced at the burning surface. The luminous flame appears downstream in the gas phase of the GAP/nitramine propellant and is caused by the exothermic gas phase reaction of nitramines. When the concentration is low, nitramine particles probably sublime endothermally at the burning surface and reduce the overall heat of reaction generated at the burning surface. This reaction is responsible for the reduced burn rate of GAP/nitramine propellants. As the concentration is increased the luminous flame zone produced above the burning surface approaches it and the heat transferred back from the gas phase to the burning surface increases, resulting in increases in burn rates. Differential Scanning Calorimetry (DSC) studies on RDX based compositions with epoxy as well as GAP matrix indicated no change in the decomposition pattern of either the base matrix or RDX. Lower flame temperature of RDX-binder premixed flame than that of AP-binder diffusion flame was the reason for the lower burn rates observed in nitramine composite formulations. In extruded DBP, inclusion of nitramines upto 30% in both high and low cal-val compositions reduced burn rates by 10-25% with marginal decrease in pressure exponent values. Inclusion of energetic plasticizer GAP increased burn rates by 27-68%.

Theories for lead catalysis proposed over the years cover almost every conceivable possibility. The results from a host of lead and copper compounds studies lend no support to other theories. Catalysis and platonization appear to depend on the availability of carbon to catalyze the reactions mainly with NO. Plateau effects observed may be due to the reduction in the effect of carbon or due to the carbon consumption as fast as it is produced. The search for an effective catalyst of nitramine propellants is still under way. Burn rate increase of the order of 10-20% is generally observed at low pressure regions, with nitramine DBP, EDB, CP and CMDB with marginal decrease/increase in pressure index values. At pressures above the slope break region, where nitramine controls the propellant burn rate, confirmed cases of catalysis are not available. In view of the uncertainity on the mechanism of action of ballistic modifier in the combustion of nitramine based propellants, most of the research for effective catalysts/platonizers is either by trial and error method or by selecting a modifier which decomposes exothermally at the burning surface.

By and large our experimental results bring out that burning surface temperature and condensed phase reactions donot change significantly when RDX and ballistic modifiers are included in the formulations. It seems in the low pressure regime, the condensed phase (fizz zone) reactions dominate, whereas at higher pressure, when luminous flame zone is very close to the burning surface, gas phase reactions dominate with less importance of the dark zone.

References :

1. Kubota, N., J. Propulsion and Power, 15(6), Nov-Dec 1999 and references 1-19 contained therein.
2. Fifer, R.A., Fundamentals of Solid Rocket Propellant Combustion, Kuo, KK and Summerfield, M (Eds.), 90, 177 (1984).
3. BenReuven, M, Caveny, L.H., Vichnevetsky and Summerfield, M., 16th Symposium (Intl.) on Combustion, The Combustion Institute, 1223 (1976).
4. Flanagan, D.A., "Nitramine Combustion", AFRPL.TR-84-004 (1984).
5. Schroeder, M.A., BRL Technical Report BRL-TR-2659 and references reported therein (1985).
6. Boggs, T.L., "Fundamentals of Solid Rocket Propellants", Kuo, KK and Summerfield, M. (Eds.), 90, 121 (1984).

7. Schroeder, M.A., BRL-TR-2673 (1985)
8. Dubovitskii, F.I., and Korunskii, B.L., Russ. Chem. Revs., 50, 958 (1981).
9. Shaw, R., and Walker, F.E., J. Phys. Chem. 81, 2572 (1977).
10. McMillen, D.F., Borker, J.R., Lewis, K.E., Trevor, P.L., Golden, D.M., Final Report on SRI Project PYU 5787 AD-A039019 (1979).
11. Melius, C.F., and Binkley, J.S., 21st Symposium (Intl.) on Combustion, The Combustion Institute 1953-1963 (1986).
12. Musso, R.C. and Grigor, A.F., AIAA paper 68-495 (1968)
13. Cohen-Nir, E., 18th Symp. (Intl.) on Combustion. The Combustion Institute, 195-206 (1981).
14. Yano, Y and Kubota, N., Propellants Explosives and Pyrotechnics, 10, 192-196 (1985).
15. Kubota, N. and Masamoto, T., 16th Symp (Intl) on Combustion, The Combustion Institute. 1201 (1977).
16. Suryanarayana, B., Graybush, R.J., Antera, J.R., Chemistry and Industry, 2177 (1967).
17. Yount, R.A., Musso, R.C., 9th JANNAF Combustion Meeting, 2,231 (1972).
18. Cohen, N.S., "Nitramine Smokeless Propellant Research", ADA-054311 (1977).
19. Melius C.F., JANNAF Propulsion Meeting, 1(503), 177 (1988).
20. Zenin, A, J. Propulsion and Power, 11(4), 752-758 (Jul-Aug 1995)
21. Beckstead, M.W., Derr, R.L., and Price, C.F., 13th Symposium (Intl.) on Combustion , 1047 (1970).
22. Price, C.F., Boggs, T.L., Derr, R.L., AIAA Paper 79-0164 (1979).
23. BenReuven, M., and Caveny, L.H., AIAA J., 19(10), 1276 (1981).
24. Cohen. N.S., Lo, G.A. and Crowley, J.C., AIAA J., 23(2), 276 (1985).
25. K.V. Raman, Haridwar Singh, Prop. Expl. Pyro., 13(1988), 149-151.
26. S.N. Asthana, M.V. Vaidya, P.G. Shrotri and Haridwar Singh, J.Energ. Materials, 10(1992), 1-16.
27. S.S. Dhar, Ph.D Thesis submitted to Pune University, India, 1993.
28. S.S. Dhar and Haridwar Singh, 31st AIAA Seminar, 1995.
29. H.Singh, J.Propulsion and Power, 11(4), 849-855, 1995.
30. A.N. Nazare, Ph.D Thesis submitted to Pune University, 1997.
31. G.K. Gautam, Ph.D Thesis submitted to Pune University, 1998.
32. C.N. Divekar, S.N. Asthana and Haridwar Singh, J.Propulsion and Power, 2000 (accepted).

ICT
32nd International Annual Conference of ICT
July 3-July 6, 2001

Analytical Characterization of Insensitive RDX

Author(s)
C. SPYCKERELLE, L. DONNIO, J. AVILES*, A. FRECHE*
SNPE DPE Sorgues
*SNPE DPE Paris

Abstract:

Many countries and especially most of NATO countries have now adopted IM (Insensitive munitions) policies for their armament in order to save live and material plus enhance military capabilities.
The best way to obtain such IM is to reduce and master both reactivity (or sensitivity) and violence of reaction, in trying to alter the energetic materials.
Such a goal has been attained (reduction of shock sensitivity) with SNPE I-RDX in the case of inert binder cast PBXs; some exemples of evidence of this improvment are given.
The shock sensitivity of an energetic ingredient is related either to its chemical nature (TATB or NTO are less shock sensitive ingredients than RDX or HMX) or for a same ingredient, supposedly to different intrinsic parameters such as shape, size, internal defects of RDX crystals...
In order to determine if the origin of the insensitivness of I-RDX shown in cast PBX charge may be related to one peculiar characteristic of the crystal itself, extensive physico-chemical characterization such as:
Chemical purity (HMX content, search for other impurities...)
Internal defects determination (solvent content, water content, density, matching refractive index microscopy ...)
Thermal stability (DSC, TGA, ...)
Morphology...
has been performed.
Results relative to this comparative work between I-RDX and other RDX are presented.

32nd International Annual Conference of ICT

Review on safety aspects of gun propellants

A.C. Hordijk, W. Groenewegen, C.A. van Driel and R. Sabel

TNO Prins Maurits Laboratory, Research Group Pyrotechnics and Energetic Materials,
P.O. Box 45, 2280 AA Rijswijk, The Netherlands

ABSTRACT

In the development of gun propellants over the years a number of aspects are very important. Apart from the performance requirements - higher specific impulse and a lower flame temperature – also safety requirements for safer production, use, storage and extended storage life time can be mentioned.

A number of gun propellant generations have been investigated and developed over the years. This presentation reviews these generations with special attention to the processing safety, LOVA and to a small extent IM properties because of TNO' s interest in gun propellant research and testing. TNO has produced and tested a first generation LOVA gun propellant and is currently producing a 3rd generation one.

With regard to the processing safety, small scale testing as friction and impact sensitivity (level 1), followed by shock sensitivity determination of the product is mostly carried out. Furthermore the rheological and thermal properties are very important in relation to its thermal stability because of heating during processing of the pastes.

Further testing of the LOVA and IM properties of (candidate) gun propellants is as well on substance level (level 2) using either the substance as such or in a test vehicle. IM tests are article tests (level 3 tests). An overview is presented of the data found in literature on these 3 level tests of (candidate) gun propellants. Data are presented as well from TNO developments.

Keywords
Gun propellants, safety, sensitivity, LOVA, IM, processing, internal ballistics.

1. INTRODUCTION

In the development of gun propellants over the years a number of aspects are very important. Apart from the performance requirements - higher specific impulse and a relatively low flame temperature – also safety requirements for safer production, use, storage and extended storage life time can be mentioned. The product price is important as well from the view point of becoming a commercial successful product

The first gun propellants produced were single base propellants, using Nitro-cellulose lateron followed by double and triple base propellants. These propellants are mostly processed by ram extrusion techniques using a lot of solvent. The solvent is needed to swell and partly dissolve the NC making it possible to mix the swollen mass with the other ingredients.

There were several reasons to look for alternatives:

- the thermal stability is relatively poor because of the nitrate esters present
- the use of much solvent which has to be recycled in favour of the environment and cost reduction
- an increase in performance without an increase in vulnerability [1]
- an increase in safety both under processing conditions as in operations – in other words – less sensitive or more LOVA.

Now, what is LOVA? This term is not so well defined. The criteria for LSP or LOVA propellants were not internationally agreed upon. One could say, that there are less sensitive propellants (LSP) and when applied in ammunition you get LOVA (low vulnerability ammunition – ammo filled with LSP) [2].
From about 1970 you find in literature two major directions of research:

1. the search for LSP and LOVA
2. the international search for LOVA acceptance test set ups and result interpretation

In the search for LSP, for the first generation LOVA, one replaced all the nitrate esters by a cured HTPB or GAP binder [3] and with NQ and /or RDX as a filler. Nitro-glycerine was eliminated as the most dangerous component.

In the second generation CAB was used as a binder, mostly replacing all the nitrate esters. In most cases some NC was left (about 4 wt %) (see table 1).
The third generation is characterised by the use of TPE's. A number of TPE's were tested for their filled properties, such as Katron (a di or triblock copolymer of polystyrene and polybutadiene), Hytrel and some polyacrylates [4, 5]. In most cases some small-scale batches were produced and tested for processability and mechanical characteristics.

The other research route is characterised by a rather intense exchange of information e.g. by means of publications in which a company presented its ideas about LOVA and the specific tests used to find out whether their candidate propellant possesses LOVA characteristics [6]. Meetings as the Gun and Propulsion Symposia played an important role in the exchange of information. New developments on propellants and test set ups and test interpretations met each other. Discussions inside NATO and its NIMIC centre lead to the design of tests and to agreement on result interpretation.

TNO has the research capabilities for processing and testing of LOVA gun propellants [7, 8]. TNO 's first generation LOVA gun propellant has been tested in part according to UN test series 7 and to IM tests with a M 1 propellant as a reference [9]. The production of a 3rd generation propellant will take place this year. TNO is interested in the status with respect to other LOVA gun propellants, which is a major reason for this overview.

In this paper an overview is presented on the various types and generations of gun propellants and their properties (2nd chapter). In the 3rd Chapter an overview is presented about the test and test procedures for safety characterisation ranging from processing to transportation. In the 4th Chapter the various 3rd generation gun propellants are presented and their test results as far as known. This paper closes with a discussion and some conclusions.

2. GUN PROPELLANTS

In this chapter a limited overview is presented of types and major performances of types and generations of LOVA gun propellants.

2.1 Overview of types and generations

In table 1 an overview of the various propellant types and generations are presented including some remarks. For the single, double and triple based propellants investigations have been performed on the rheological behaviour as function of the solvent content. This could be done because capillary extrusion rheometers became available. It appeared that above solvent content levels of about 15 wt % the effect on rheological properties was very small [10, 11]. Of course the solvent content has strong influence on safety properties, like impact, friction and shock sensitivity.

Propellants	**Remarks**
Single, double and triple based propellants	• a lot of solvent had to be used and recycled • a stabiliser is needed because of the nitrate esters present
First generation LOVA propellants • fluid energy milled HMX and RDX comp. in PU cured • highly filled	• processing problems
Second generation LOVA propellants • CAB based (+ NC) binders, using solvents • low burning rate and energy • safety prop. OK	
Third generation LOVA propellants • Non solvent processed, TPE binder • Energetic TPE's - demo in 1989	• expensive, but affordable • very expensive – for very special applications only

Table 1 Overview of the various propellant types and generations

2.2 Performance overview of types and generations

In table 2 an overview is given of the developments in impetus and flame temperature over the years due to changes in formulation.

	propellant	Impetus (J/g)	T_f (K)	gun (mm)	v_0 (m/s)	P (max) (MPa)
single base	M 1	923	2508			
triple base	M 30	1065	3040	**155**	828	318.8
	JA 2 (tank)	1142	3417	**120**	1550	400
PML 3rd gen.		1046	2560	**155**	823	322.0

Table 2 Some typical results for a gun application

In figure 1 the impetus and flame temperature are plotted thereby demonstrating the gain in performance but also the effect thereof on barrel erosion, which is proportional to the flame temperature.

The impact of the use of high explosives, like RDX can be clearly seen in this figure. The use of energetic TPE's leads to a shift towards the upper right corner, thus an increase both in flame temperature and in impetus.

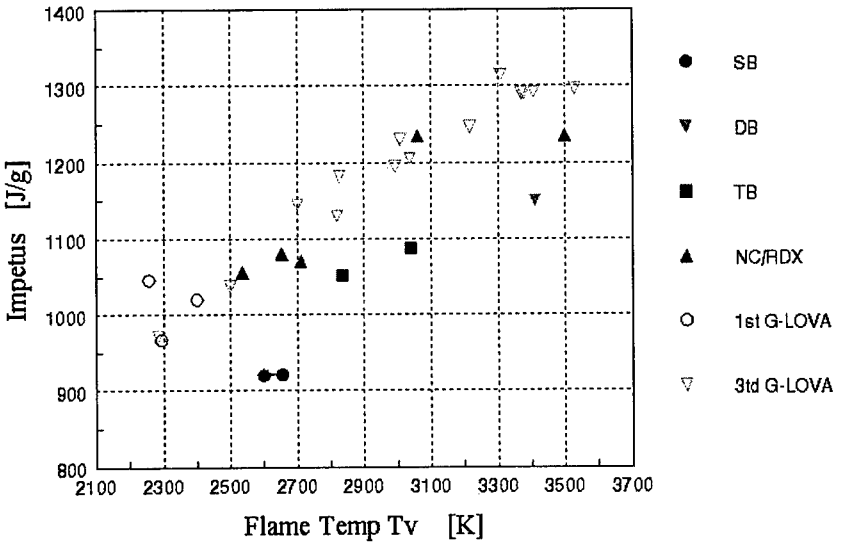


Fig 1 Impetus versus Flame temperature for various generations of gun propellants

3. SAFETY PROPERTIES

Safety issues concern the whole route from formulation via processing to transportation, storage and use. This also means that various parties are involved in the thinking about and the formulation of regulations. This chapter deals with the safety aspects as applied in product development, furthermore with those in the Transport and Storage sector (UN regulations) and those in the Military world (IM testing).

3.1 Processing safety (level 1 tests)

In the R&D one uses generally a protocol to determine whether it is useful to proceed with a certain compound or formulation. Knowing the safety features of the various ingredients a small scale batch is enough to obtain processing (rheological) data and enough material to perform small scale tests on: impact and friction sensitivity, thermal stability (DSC) and compatibility (VTS) [12].
When satisfying answers have been obtained, the next step is a level 2 test or tests – especially the determination of the shock sensitivity –either by a small scale test, like the MAP test (sample mass of about 30 g) or by a larger scale test like the GAP test (sample mass hundreds of grams)

3.2 Transportation - UN Tests (level 2 and 3 tests) [13]

Some years ago within the UN one agrees upon the Test Series 7 for Extremely Insensitive Detonating Substances (EIDS). The only compatibility group applicable to this division, is N; "ammunition containing only extremely insensitive detonating substances (EIDS)". Testing is a prerequisite for assigning this compatibility group. The question "when is an explosive article extremely insensitive?" is answered by conducting UN test series 7 (Appendix A). This test series consists of ten tests; the first six types of test are tests on the **substance** (the candidate EIDS), the remaining four are tests on **articles** containing an EIDS(s). In order for a substance to be classified as an EIDS, a substance must pass (negative response) all substance tests in Test series 7. The tests are conducted on the substance in the form in which it is to be used in the article. For an article to be classified as Hazard Division 1.6, it must contain only EIDS and pass all article tests in Test Series 7; this means that a candidate 1.6 article may not undergo article tests until after its explosive load has been classified as an EIDS (has undergone the substance tests). The article tests are

applied to the articles in the condition and form in which they are offered for transport.

3.3 IM article tests (level 3 tests)

The IM tests [14] are article tests: Fast and slow cook-off, bullet and fragment impact, shaped charge and sympatic detonation. They are considered to be more realistic for the Insensitive Munitions community so that these tests became more important than the UN series 7. Although for the selection of substances which may lead to IM articles mostly the tests are applied as described in the UN test series 7 (b, c, d, f) (see Appendix A for a short description of the tests).

In table 3 a comparison is made between the UN test series 7 and IM tests.

	UN test no	**Test Description**	**IM**
Substances	7 (a)	Cap test	
	7 (b)	Gap test	Gap test
	7 (c)	Friability test	friability test
	7 (d)	bullet impact	bullet impact
	7 (e)	external fire	
	7 (f)	slow cook-off	slow cook-off
Article tests	7 (g)	art. external fire	art. external fire (fast cook-off)
	7 (h)	art. slow cook-off	art. slow cook-off
	7 (j)	art. bullet impact	art. bullet impact
	7 (k)	art. stack test	
			article fragment impact
			article shaped charge
			sympatic detonation of article

Table 3 Comparison of tests – UN series 7 and IM tests

The data in table 3 show that the various sectors benefit from each other efforts. Furthermore, there is continuing search for generic tests, the development of tests and test vehicles that may give a representative result for the larger article. As an example the MAP test may be considered: a small scale shock sensitivity test applying a higher shock pulse with a shorter duration than applied in the larger GAP test. The results however, give an excellent ranking of the shock sensitivity of the substances under investigation.

Another example is the friability test with a relative simple test set up. It was shown that the test results gave a good screening for the bullet impact test.

4. TEST RESULTS

In the search for new developed gun propellants and how far their development has been proceeded we found a number of interesting publications and test results presented therein. They have been summarised in table 4. In this table the calculated Impetus and flame temperature are presented as well as the level 1 (the processing level) and level 2 (larger scale substances tests) results.
As may be noticed the results on level 3 tests are very scarce – article tests have not been carried out to now.

From this table may be concluded that the TNO first generation LOVA gun propellant is definitely a more LSP (less sensitive propellant) than the reference M1 as are e.g. the 3rd generation propellants based on Poly NIMMO. It is clearly demonstrated that the testing methodology indeed focus on IM tests taking the expertise build up in the UN testing into account.
The 3rd generation TNO propellant is developed, produced and tested within a CEPA collaboration program. The test results will be available at the end of this year.

	Single	Triple base	1st gen.	2nd gen.	3rd gen.	3rd gen.	3rd gen.	3rd gen.
			TNO		TNO	Thiok.	DREV	DERA
	M1	JA 2	LCG	XM 39		A/B + RDX	GAP	pNim
Impetus (J/g)	995	1156	1045	1070	1046	1037	1310	1230
flame temp. (K)	2846	3451	2400	2671	2560	2445	3500	3037
density (g/cc)					1.61	1.618		
Level 1								
impact (Nm)	3	< 2.5	7.5	9.6	@	+	+	
friction (N)	192		252		@	+	+	
ESD (J)	4.5		4.5		@	> 8		
VST (ml/g)	2.27		0.26		@			
DSC – T_0 (C)	177		190	192	@	151		
TGA/DTA	153		200		@			
HoExpl. (cal/g)	855	1110	± 760	812	@			
Level 2								
Ballistic	+		+		+	+	+	+
Mech. E (MPa)	2900	310	40	6200	@	4700	+	+
σ_m (MPa)	74	30	4.8	92		12.9		
ε_m (%)	6	48	37	2.7		1		
GAP test [3]	8%		3%		@			+
friability								
slow cook-off								
SCB	strong		mild		@			
crit. diam. (mm)	> 73	25	> 73	30	@			
bullet attack	+		+		@			+
EIDS extern fire	+		+		@			
Shaped charge	+		+		@			+
Level 3 [2]								
sympatic det.					@			+
lit.	9		9	5	-	15	16	1, 17
	M1	JA 2	TNO [1]	XM 39	TNO	Thiok.	DREV	DERA

Table 4 *Safety of GUN PROPELLANTS*

[1] The experiments were carried out with M 1 propellant as a reference. The results of the various tests were in most cases expressed as better than and sometimes worse than the M 1 results.

[2] The 3rd generation gun propellants presented in this table are in the process of being scaled up. Therefore the article tests have not been performed.

[3] GAP test – given is the EIDS test result in 100 %*(L_0 –L)/L_0

@ to be determined this year

5. DISCUSSION and CONCLUSIONS

In composing this table, it appears that Europe and the USA use some different tests, especially for the level 1 tests, like the BAM test set up for impact and friction sensitivity (in Europe) and the corresponding BRL tests in the USA.

It may be concluded that the single, double and triple base gun propellants score less on the level 1 test results: the impact and friction data are considerably better for the newer generations of gun propellants. In processing, however, it must be remembered that NC based propellants are wet and thus are safer, except for the danger of fire.
Level 2 tests results, as far as available, lead to about the same conclusions as above.
Level 3 tests are hardly carried out yet.
TNO' s first generation LOVA gun propellant is definitely a more LSP (less sensitive propellant) than the reference M1.

Acronyms

A/B	AMMO / BAMO – an energetic TPE
EIDS	Extremely Insensitive Detonating Substances
GAP	an energetic curable binder
HTPB	a curable binder
IM	Insensitive Munitions
LOVA	Low Vulnerability Ammunitions
LSP	Less Sensitive Propellants
NC	Nitro Cellulose
NQ	Nitro Quanidine
NGl	Nitro Glycerine
pNim	Poly NIMMO – an energetic TPE
RDX	high explosive
TPE	Thermoplastic elastomer
UN	United Nations
NATO	North Atlantic

Acknowledgement
The authors would like to acknowledge the support of Mr. Jan van Gool and the contributions of John Koman and Rudie Krämer in extrusion work and of Caspar Schoolderman for his rheology measurements. Furthermore Louis Broekhuijsen, Wim de Klerk and Ellen la Haye for carrying out the level 1 tests and the group EM for carrying out the level 2 tests.

LITERATURE

[1]	Leach, C Kermarrec, J-Y.	Co-operation between the UK and France on the assessment of gun propellants ICT 2000, V 1
[2]	Stein, W.W.	Results of different vulnerability tests for propellants ADPA symposium on Energetic Materials Technology 1992
[3]	Schedlbauer, F.	LOVA Gun propellants with GAP binder Prop., Expl., Pyrotechnics 17, 164-171 (1992)
[4]	Kaste, P.J. Willer, R.L.	Ballistic evaluation of a TPE based LOVA propellant 5th International Gun propellant & Prop. Symposium, 1991
[5]	Willer, R.L. Biddle, R.A.	Semicommercial TPE binders for LOVA Gun Propellants 5th International Gun propellant & Prop. Symposium, 1991
[6]	Degano Goliger	Gun propellants for Low Vulnerability Ammunitions 22nd DOD Explosive safety Seminars August 1986
[7]	Sabel, H.W.R. Schonewille, E.	Extrusion trials with the TSK 045 Twin screw extruder ICT 1998
[8]	Hordijk, A.C. Velde, I. v.d.	Capillary extrusion rheometry and extrusion of propellants and propellant simulants - ICT 2000
[9]	Meer, B.J. van der	Safety tests on seven new LOVA formulations (PML 1994)
[10]	Baker, F.S. Carter, R..E.	Processing characteristics of Gun Propellants Prop. Expl. Pyrotechnics 7, 139 – 147 (1982)
[11]	Baker, F.S. Carter, R..E.	The rheological assessment of Propellants Rheology, Vol 3, 1980, Plenum Publishers
[12]	Heijden, A. Driel, C. van	PE - Protocol for initial assessment of Performance and sensitivity (TNO protocol)
[13]	NN	UN test series 7
[14]	NATO	IM STANAG 4439
[15]	Braithwaite, P. et al	Characterisation of TPE Gun propellants EM & IM Technology Symposium '99
[16]	Beaupré, F. Ampleman, G.	Processing and Characterisation of gun propellant formulations containing ETPEs – ICT '98, V 36
[17]	Leach, Ch. Kelly, J.	Factors affecting the vulnerability of composite LOVA gun propellants - EM Techn. Symp. 1995

APPENDIX A

Table A.1: UN 7 test series on substances

	Name of the test	Aggression	Sample and Procedure	Criteria for positive response, i.e.: not an EIDS
7 (a)	EIDS cap test	Shock of a standard detonator or blasting cap	A cardboard tube casing (80 mm ID, 200 mm H) is placed on a steel witness plate on a lead cylinder. A standard detonator is inserted coaxially to a depth equal to its length. Three samples are tested unless a detonation occurs earlier.	1. detonation 2. compression of lead cylinder by 3.18 mm 3. total penetration of witness plate
7 (b)	EIDS gap test	Specified shock level, i.e., specified donor charge and gap	A 1.077 kg pentolite charge and a candidate EIDS sample contained in seamless steel tube (73 mm ID, 280 mm H), are separated by a PMMA gap of 70 mm. The total is placed on a witness plate with an air gap of 1.6 mm.	1. detonation 2. penetration of witness plate
7 (c) (i)	Susan test	Impact under conditions of high velocity	The EIDS candidate is loaded into standardised projectile (5.4 kg, 81.3 mm OD) and fired at target plate with impact velocity of 333 m/s. The air shock blast overpressure is measured at 3.05 m	Average airblast pressure (10 records) is greater than 27 kPa
7 (c) (ii)*	Friability test	Impact at specified velocity	A bare sample is fired at 150 m/s at steel plate. The fragments after impact are collected and ignited in a closed vessel; the dp/dt is recorded	Average dp/dt is 15 MPa/ms or greater
7 (d) (i)*	EIDS bullet impact test	Kinetic energy transfer by impact of a standard 12.7 mm bullet	A standard 12.7 mm bullet is fired at 820 m/s at the EIDS capped in a steel pipe (53 mm ID, 200 mm H). Three tests are performed with the long axis of the article perpendicular to the line of flight, and three with the articles long axis oriented parallel to the line of flight	1. explosion 2. detonation
7 (d) (ii)	Friability test	see 7 (c) (ii)		
7 (e)	EIDS external fire test	External fire	The effect on an external fire on confined samples is tested by placing a minimum of five confined samples (casing: 7 (d) (i)), stacked horizontally and banded together in a fire, a minimum of 15 samples are tested.	1. detonation 2. fragment mass exceeding 1 gr 3. range of fragments more than 15 m
7 (f)	EIDS slow cook-off test	Gradually increasing air temperature	The sample (casing: 7 (d) (i)) is placed in an oven over a 40°C to 365°C range, at 3.5°C an hour until a reaction occurs.	1. fragmentation of one or two end caps (detonation) 2. fragmentation of the tube into more than 3 pieces (detonation)

* Recommended test

Table A.2: UN 7 test series on articles

	Name of the test	Aggression	Sample and Procedure	Criteria for positive response, i.e.: not Hazard Division 1.6
7 (g)	1.6 article external fire test	External fire	The experimental set-up is the same as for test 6 (c): The test is applied to a stack of packages of the explosive or articles in the condition and form as they are offered for transport. A minimum volume of 150 l, or a minimum of 3 packages are stacked together. Three 0.2 mm thick aluminium witness plates are placed at 4 m from the firewood.	Events requiring 1.1, 1.2 or 1,3 classification: mass explosion, fragmentation or intense heat radiation and range of fragments more than 15 m, resp.
7 (h)	1.6 article slow cook-off test	Gradually increasing air temperature	The temperature range tested is the same as for test 7 (f). The test is conducted on two separate articles as presented for transport.	A reaction more severe than burning
7 (j)	1.6 article bullet impact test	Kinetic energy transfer associated with the impact and penetration by a standard 12.7 mm bullet	An all-up complete EIDS loaded item is subjected to a three-round burst fired at 856 m/s velocity with an equivalent 600 rounds/min rate of fire, and impacting within a circular target area of 50 mm diameter. The test is repeated in three different orientations. The degree of reaction is tested by post-test inspection of test film and hardware.	1. detonation 2. explosion
7 (k)	1.6 article stack test	Initiation by propagation	The test is performed with two or more articles (in the condition and form in which they are offered for transport); one of the articles should be provided with their normal means of initiation or be caused to function in its designed mode (donor). The test is conducted three times, unless a detonation of an acceptor occurs earlier. The first test is conducted without confinement, the next two tests are conducted with confinement as with test 6 (b): the test packages or articles are placed on a steel witness plate and are completely covered earth or sand. A minimum thickness of confinement of 1 m in every direction is created.	1. propagation (detonation of acceptor): determined by fragment size and number of acceptor article fragments, crater dimensions and/or witness plate damage.

THE ADVANTAGES OF ENVIRONMENTAL MONITORING FOR MUNITION LIFE ASSESSMENT

John Theobald, Claire E. Hobman & David A. Tod
DERA, Fort Halstead, Sevenoaks, Kent, TN14 7BP, UK

ABSTRACT

DERA started monitoring the real environmental conditions, such as temperature and relative humidity, experienced by munitions approximately 10 years ago, as a means improving the prediction and extension of available service life.

The philosophy behind this approach is discussed together with a brief review of the development of monitoring devices and procedures. As an illustration of the concept, the results obtained for one particular munition system are presented, together with the extension to service life that has been achieved.

One of the main advantages of this approach is the reduction in the level of surveillance that needs to be carried out. This leads to both savings in time and also a reduction in the number of expensive assets that must be destroyed, either for test firing or breakdown.

Keywords:
Environment
Temperature
Humidity
Service life
Surveillance

1 INTRODUCTION

The Rocketry and Lifeing group at DERA, Fort Halstead first started monitoring the environmental conditions experienced by munitions more than 10 years ago(1), (2). At this time, munitions that had been designed for a Northern European war, were suddenly and unexpectedly being deployed to the Gulf, under very different climatic conditions. Important and urgent questions regarding the safety and suitability of these munitions were being asked.

It was clear at this time that there were two approaches that could be taken to answer the important questions regarding life assessment.

The first alternative approach was to carry out a major surveillance programme, involving test firings together with breakdown of munitions followed by a detailed examination including chemical and mechanical analysis. This would destroy a significant number of assets and therefore be potentially very expensive.

The second alternative approach was to adopt a predictive methodology requiring an understanding of the critical ageing mechanism for each munition. It would then be possible to carry out artificial ageing of the critical components, together with mathematical modelling of the process. However, this would require the precise characterisation of the real environmental factors experienced by the munitions. The process would be time consuming, but only destroy the relatively small number of assets needed to validate the model and therefore be less expensive overall.

The climatic zones defined in NATO STANAG 2895 (3) were considered as a possible source of the environmental data, but it was decided that these were inadequate for a number of reasons:

- A limited number of zones are used to define the temperature and humidity conditions experienced throughout the world and they must therefore be a generalisation.
- By definition, the zones reflect the average climate over a number of years rather than specific weather conditions.
- Munitions are moved between zones for logistic reasons and it can be difficult to track the exact time spent in each zone.

For these reasons, it was concluded that the actual environment experienced by the munitions was needed.

2 DEVELOPMENT OF MONITORING DEVICES

There are a number of factors that ideally should be measured in order to characterise the environment experienced by munitions. Clearly temperature can affect the chemical and mechanical degradation of energetic materials. Humidity can have a significant affect on chemical degradation, which may be the simple corrosion of mechanical parts. Shock and vibration can lead to mechanical failure, with vibration being particularly important for air launched weapons. Less obviously, atmospheric pressure may of importance to air launched weapons, where rapid changes in pressure can cause failure of environmental seals.

Initial work on environmental monitoring devices has focussed on the development of units for temperature and humidity. There are a number of key requirements that need to be satisfied:

- The devices should be highly automated, self-contained and of small size.
- The systems need to be rugged to withstand the military environment and fully comply with the local explosives regulation. For this reason, commercial systems are unsuitable.
- They should contain standard electronics for the best reliability, availability and cost effectiveness.

Many commercial units have been tested over the last 10 years, but none have been found to be ideal in their standard form. Some commercial logging systems are specified as being intrinsically safe and have been tested under one or more certification schemes. In Europe, such loggers carry the Ex symbol, but as with all intrinsically safe devices, this refers to their suitability for use in explosive gas atmospheres. They are therefore eminently suitable for use on oil production platforms and chemical works, but unfortunately, the regulations have no relevance to their use in proximity to explosives.

With the limitations of commercial temperature and humidity loggers, the Rocketry and Lifeing group at DERA developed units designed for the specific purpose of deployment within explosive magazines and even within munitions. These units are shown in figure 1. They are based on a die-cast aluminium box, 50 x 40 x 30 mm, which provides a very robust construction. Further, more detailed, information on the development of

environmental monitoring devices is the subject of an accompanying poster presentation.

These loggers have been deployed in many magazines throughout the world and for a number of munition specific trials. This has included embedding the devices within some of the larger munitions and monitoring of the temperature transfer function of munition containers.

3 EXPERIENCE WITH A SPECIFIC MISSILE SYSTEM

The concept of using environmental monitoring to assess and extend munition life can be illustrated by an example using a missile system based on an elastomer modified cast double base propellant (EMCDB).

The propellant grain of this rocket motor is cast in a two stage process with the boost and sustain running concentrically down the full length of the motor. The boost propellant has soft elastic properties, typical of an EMCDB whereas the sustain is much harder, with mechanical properties more like a CDB propellant.

The motor was designed for a storage life of 10 years under A3 storage conditions (3), specifically 20°C. The missiles have been deployed world-wide in a variety of climatic zones for varying periods of time. For logistic reasons, units have also been moved between various climatic zones. The real storage life may therefore be very different to those specified in the design criteria.

Accelerated ageing was conducted to establish the critical ageing mechanism for the rocket motor, as this was considered to be the most

important critical factor for the missile system as a whole. It was found that ageing complete sections of motor, i.e. boost and sustain propellant in contact, caused a significant change in the mechanical properties of the boost propellant. On accelerated ageing, the strain energy of the boost propellant decreased, indicating an increased tendency for cracking. This cracking would lead to a larger burning surface and hence increased pressure on firing, with the potential for catastrophic failure.

Chemical analysis of the samples showed that the change in mechanical properties was as a direct consequence of migration of plasticicer from the boost to the sustain propellant, caused by a higher level of plasticiser in the boost.

A more detailed accelerated ageing trial was conducted at four temperatures, 40, 50, 60 and 70°C, with measurement of strain energy for up to 20 weeks. The data displayed considerable scatter, which caused problems when trying to fit the data using the Arrhenius equation (figure 2). In order to derive an activation energy for the diffusion process, a scheme based on interpolation was adopted. A series of graphs were plotted where the data was shifted to a common axis using various assumed activation energies. Examples of these graphs are given in figures 3 and 4. The common axis used for the graphs was based on the equivalent time at 70°C, the highest ageing temperature used. If the principle of superposition is valid, the lines for the four temperatures should overlay for the correct activation energy. From a visual examination of the graphs, the best superposition occurred for an activation energy of 75KJ/mole (figure 5).

A temperature graph for the deep storage facility used in the UK for this particular missile system is shown in figure 6. This graph covers the period for 1996, but detailed logging has been carried out in this magazine for the last 10 years. This cumulative data has been collated and expressed in histographic form, for the total time for each two degree temperature interval, figure 7. Using the Arrhenius equation with the activation energy for the critical ageing mechanism (75KJ/mole), the equivalent time at 20°C for each temperature interval has been calculated. Summation for these individual times for each temperature interval provides the effective time experienced by the missile equivalent to storage at 20°C.

From the activation energy and magazine temperature data, the design storage life of 10 years can be extended up to 15 years providing the missiles remain in deep storage. This proposition has been confirmed by surveillance testing.

4 CONCLUSIONS

Experience has shown that the use of environmental monitoring, together with an understanding of the critical failure mechanisms and modelling can lead to a more accurate service life prediction. There is still a need to conduct surveillance test, although to a lesser extent, with a consequent saving in expensive assets.

Conventional service life prediction based on climatic zones tends to be conservative in nature and there is considerable scope for life extension based on a true understanding of the environment experienced by munitions, leading to further cost savings.

5 REFERENCES

1 Environmental data logging for weapon life assessment, J S Dodds, D A Tod, J Theobald in Sensors for the Detection & Analysis of Energetics, Explosives & Pyrotechnics Symposium, Washington January 25 –26, 1999.

2 Environmental data logging, J Theobald in TEEMAC Open Workshop on Prediction of Life and Life Extension for Munitions, RMCS Shrivenham, 30 – 31st October 2000.

3 NATO STANNAG 2895, Extreme climatic conditions and derived conditions for use in defining design/test criteria for NATO forces materiel, February 1990.

Figure 1

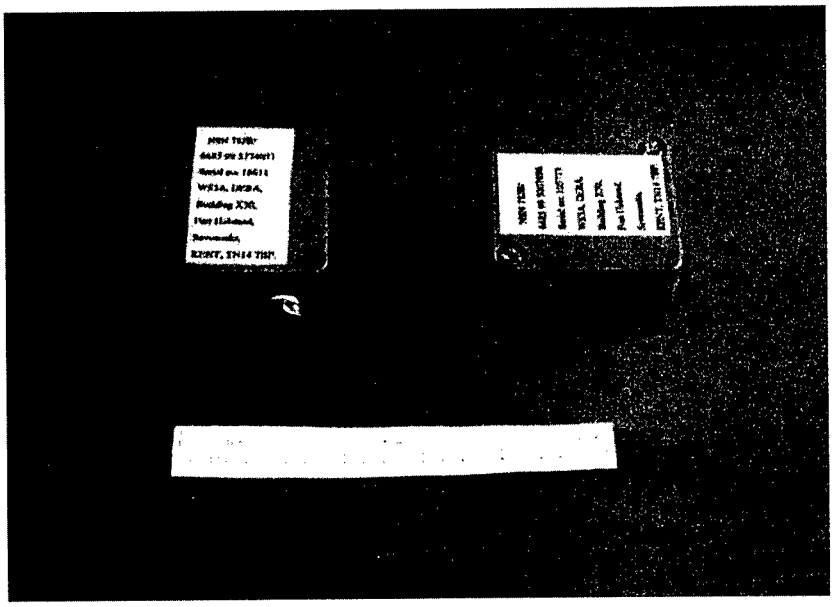


Figure 2

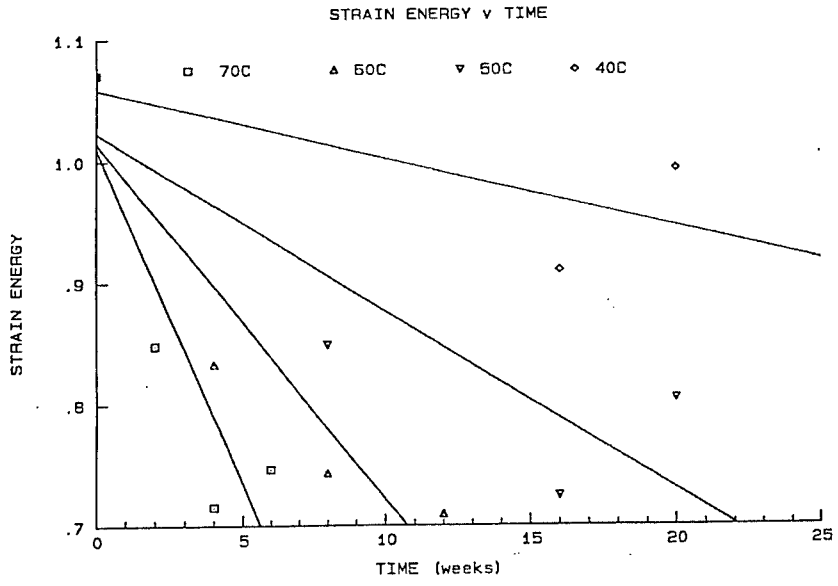


Figure 3

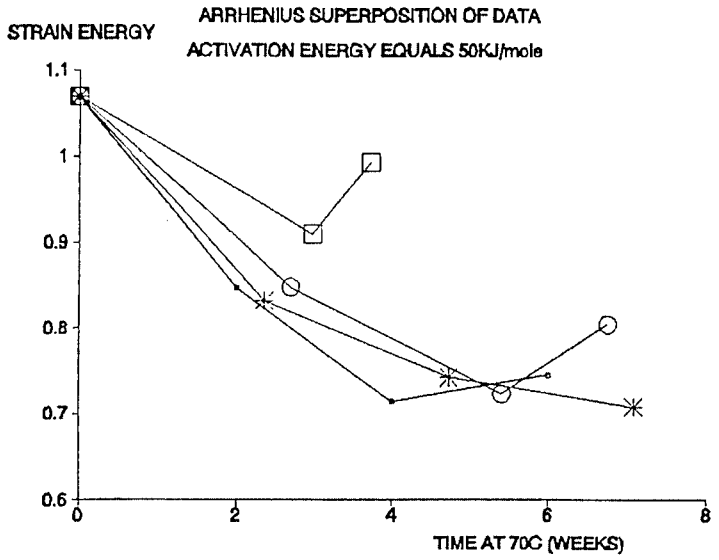


Figure 4

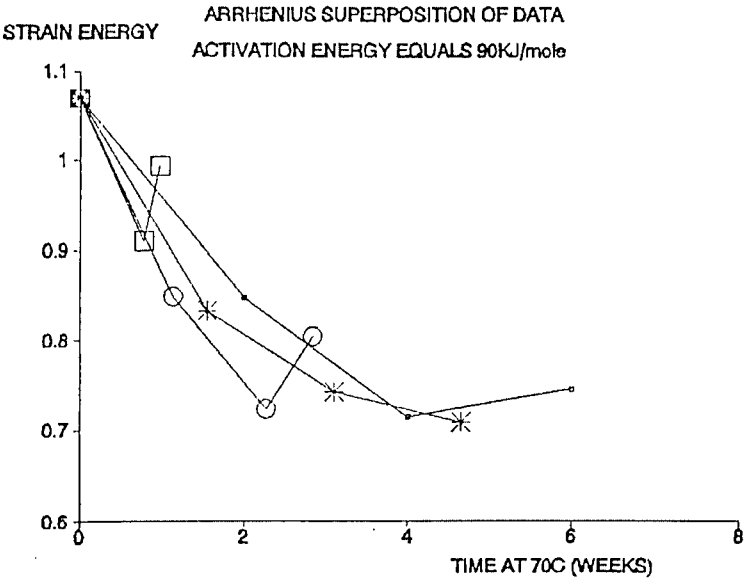


Figure 5

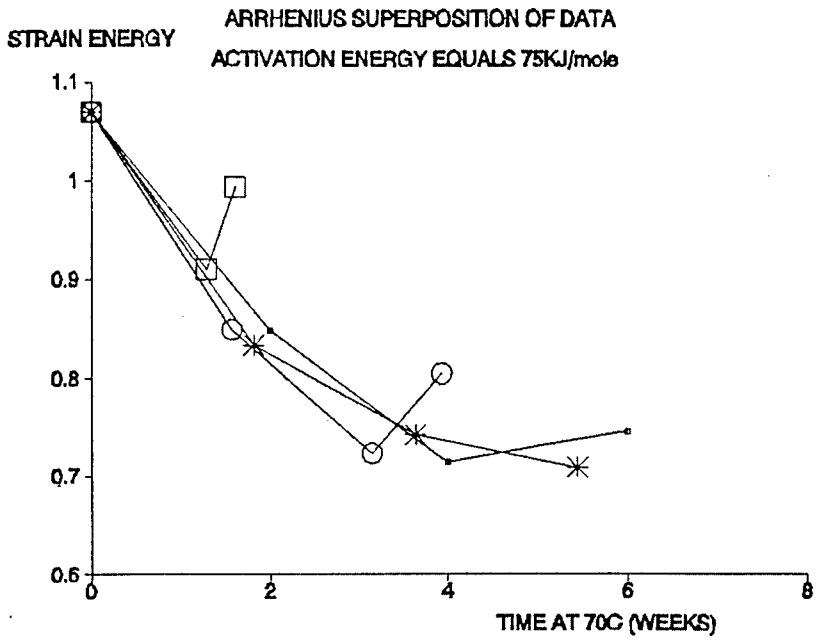


Figure 6

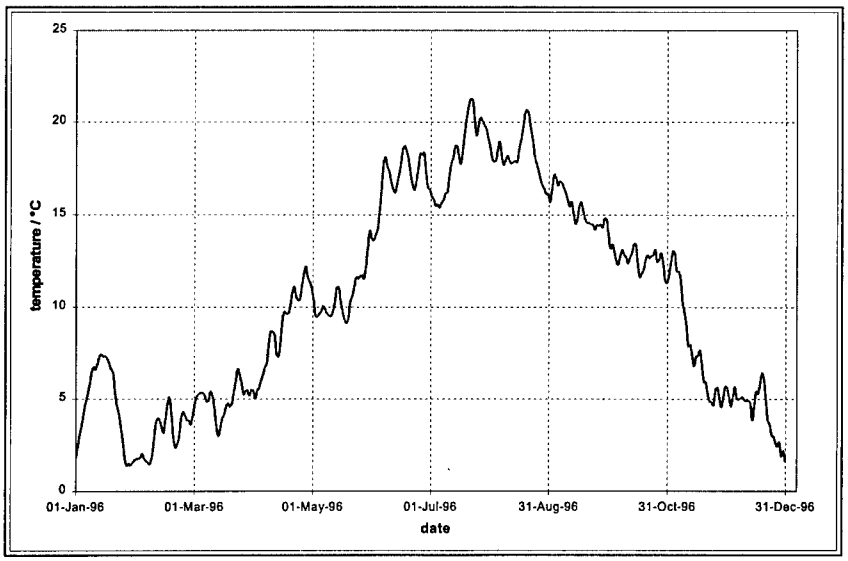
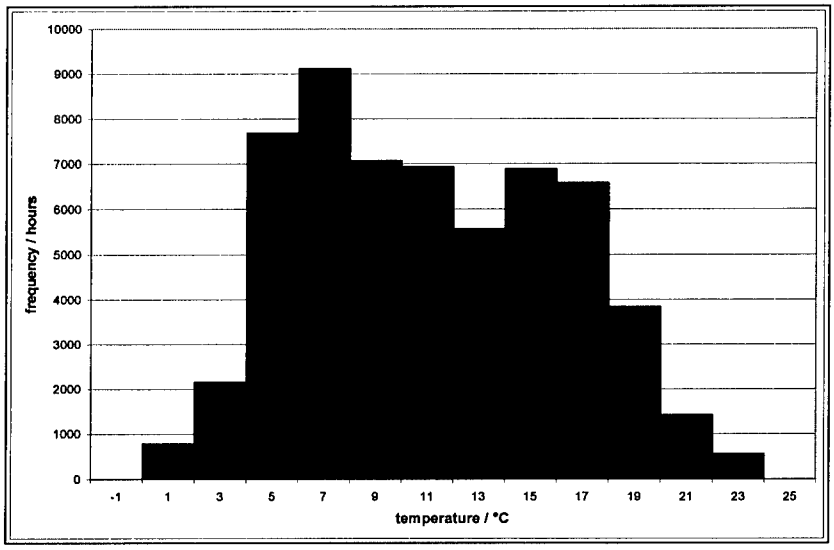


Figure 7


10000
9000
8000
7000
6000
5000
4000
3000
2000
1000
0
frequency / hours
-1
1
3
5
7
9
11
13
15
17
19
21
23
25
temperature / °C

SHOCK TO DETONATION TRANSITION IN A PBX BASED ON RDX

R. Mendes, J. Campos, I. Plaksin and J. Ribeiro

LEDAP - Lab. of Energetics and Detonics,
Mechanical Eng. Dept., Fac. of Sciences and Technology of the University of Coimbra
Polo II, 3030-201 Coimbra, Portugal

ABSTRACT

The shock transition to Detonation Wave (DW) in a PBX based on RDX, by flyer plate impact, using an electric gun, is presented. The electric gun has a capacitor bank with 25.4 μF of capacity that can works at 40 kV of maximum voltage. It is able to accelerate Polyester flyer plates, of 350 μm of thickness and 25 mm of diameter, to velocities ranging from 2.4 to 4.5 km/s. The tested PBX is composed by 85 wt% (bimodal particle distribution, 75 wt% of d_{50} = 96μm and 25 wt% of d_{50} = 22μm) and 15 wt% of binder based on HTPB, presenting an effective density of 1.574 g/cm^3, (> 99 % TMD) and detonation velocity of 7.9 km/s.

The cylindrical PBX sample was placed under a PMMA barrier, in order to evaluate the detonation pressure on the PMMA interface. An optical method based on 64 optical fibbers ribbon (250μm of diameter each fibber) connected to a fast electronic streak camera, allows to measure, not only the detonation velocity in PBX but also the shock velocity trough the PMMA target.

The obtained results, presented as a space-time diagram with 1 ns resolution, show continuously the transition from shock to detonation regime. In that regime, DW propagation presents irregularities of local velocity values, around a mean detonation velocity. The results show also the effects of flyer plate velocity on the Shock to Detonation Transition (SDT) distance and on the DW irregularities.

KEYWORDS: SDT-shock to detonation transition, Irregularities on DW; flyer plate impact; PBX.

1 - INTRODUCTION

The development of new insensitive energetic materials implies the existence of strong shock initiating devices and new accurate experimental measurement methods, in order to characterise the initiation of this kind of explosives. The explosive samples were initiated by flyer plate impact using an electric gun. When the flyer plate strikes the target, the collision process generates a pressure pulse of high intensity, having its amplitude and time duration controlled respectively by the velocity and thickness of the flyer plate. When a pressure pulse has an enough intensity to initiate the PBX, the shock wave, inside the explosive, accelerates continuously until to be converted in a DW. It was also verified that a strong pressure pulse generates a short shock to detonation transition (SDT) in the explosive, allowing the use of small samples. The registration optical method, developed in LEDAP during 1996-2000, based on 64 optical fibbers ribbon (250μm of diameter each fibber), connected to a fast electronic streak camera (vd Mendes, R. et al., 1996, and Plaksin, I. et. al., 1997). This method allows the simultaneous registration of several detonation parameters in one experiment. Until now it was used to characterise the DW velocity, detonation pressure, detonation front curvature, shock to detonation transition SDT and collisions of DW (Mach wave formation/ and relaxation process) (vd Mendes, R., et al., 1997 and 1998 and Plaksin, I. et. al., 2000). Using now this optical method to characterise the SDT in small explosive samples, with the resolution capability of the mesoscale level, we can perform measurements and observation of velocity oscillation behaviour in the detonation front. These oscillations seem to be originated by the kinetics instabilities in chemical reaction zone and by the initial heterogeneities of the explosive, that are a function of the explosive particle sizes in PBX, (vd. Plaksin, I. et. al., 1997, 1999, 2001).

2 - THE MEGA AMPERE PULSE-MAP AND FLYER PLATE GENERATOR

The used thin polymeric flyer plate was accelerated by a high voltage discharge across the metal bridge foil, placed under the flyer plate. Depending on the bridge dimensions, the bridge vaporises in a very short time and generates a very high pressure. The generated metallic plasma, confined by the barrel and tamper material allows to pushes out a section of the polymeric film, above the bridge, to form the flyer plate. The pressure from the burst bridge material is high enough to accelerate the plate to velocities higher than 1 km/s. Generally the plate is allowed to travel across a barrel, which has at the end the target where we wish to apply the high pressure. The pressure into the target is dependent of the flyer plate velocity and of the shock properties of both, flyer plate and target material. The duration of the pressure pulse, into the target, is mainly a function of the flyer plate thickness and of the shock velocity in the flyer plate material. In Figure 1 is presented a typical arrangement scheme of our electric gun, sometimes called slapper, LED-MAP.

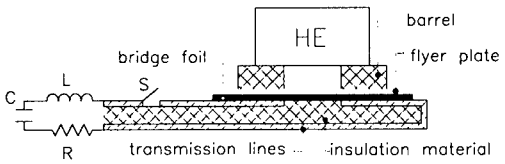


Figure 1. Typical scheme of electric gun, slapper, arrangement.

Typically an underdamped RLC circuit (vd. Figure 1) can describe the electric circuit of the electric gun, where R is the constant resistance, L is the inductance of the electric circuit and C is the capacity of the capacitor bank. The main properties of the LED-MAP and flyer plate are presented in Table 1 and Table 2.

Table 1. Electric parameters of the capacitor bank.

C	R	$\mathscr{L}$	V_{max}	ω	$(dI/dt)_{max}$
[μF]	[mΩ]	[nH]	[kV]	[Mrad/s]	[TA/s]
25.4	4.2	31.5	40	1.1	1.3

Table 2. Main characteristics of the Flyer Plate.

Material	Kapton; Mylar
Thickness	50 – 700 μm
Diameter	5 – 35 mm
Velocity	9 – 2.5 km/s
Pressure[1]	53 – 7.9 GPa

[1] Pressure induced on a kapton target induced by a Kapton flyer

2.1 - FLYER PLATE VELOCITY

2.1.1 - Singular optic fibber method

To measure the flyer plate velocity it was used two methods. The first one uses the singular optic fibbers to measure the time of flight of the flyer plate from the rest position until the top of each fibber. Several fibbers at different known distances from the flyer plate are positioned inside the barrel as present in Figure 2. When the flyer plate arrives close to the optical fibber the air between the flyer and the fibber is compressed up to the ionisation,

emitting a strong light pulse, after that, the flyer impacts the fibber and the light transmitted decrease very sharp, defining a narrow light. The light seen by the optical fibbers is then converted by a fast photo diode in a voltage signal, which is recorded in a digital signal analyser.

Making a fit of the experimental points (Z,t) to one displacement equation, the velocity of the flyer plate is achieved by differentiating the displacement equation (vd. Mendes, 1994).

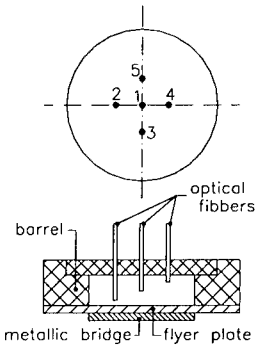


Figure 2. Experimental set-up for velocity measurement using singular optical fibbers.

2.1.2 - Optical fibber ribbon method

The experimental method uses 64 optical fibbers ribbon with 250 μm of diameter each one, to measure continuously the time of flight of the flyer plate. The optical fibber ribbon is placed inside the barrel and the top of the optical fibbers is cut with a known wedge (vd. Figure 3). Then, when the flyer plate crosses the barrel, it will impact successively each optic fibber, generating a light pulse, which is recorded with a fast electronic streak camera. In order to avoid the input of parasite light, from the aluminium burst, a non-transparent film isolates the fibbers, also the dihedral shape of the cut fibbers reduces the light transmitted to the streak camera by the Snell's law of transmission ray. On the top the fibbers are isolated also with an air gap, with 0.1mm of thickness between the top of fibbers and the cover (vd. Mendes, R. et. al. 1996). A typical record is present in Figure 3. knowing the wedge angle between the fibbers top and the flyer surface, it can be estimated the (Z,t) diagram of the flyer movement inside the barrel. To find the flyer velocity the same procedure as described to the sigular fiber method was used. A typical (Z,t) diagram of the displacement curve, fitted to the experimental points, and the flyer velocity curve are presented in Figure 4.

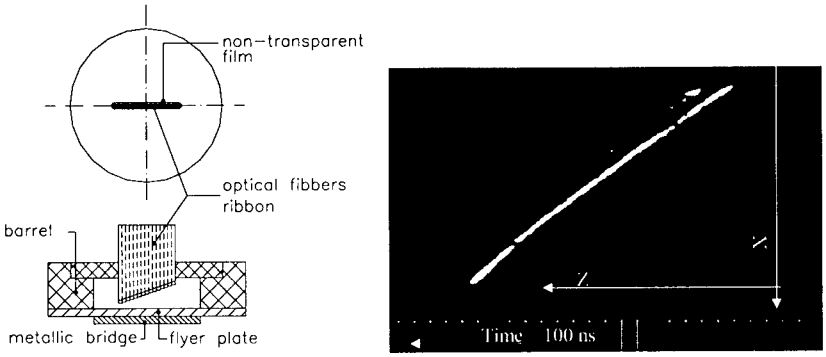


Figure 3. Experimental set-up and typical recorded signal of the flyer plate evolution inside the barrel.

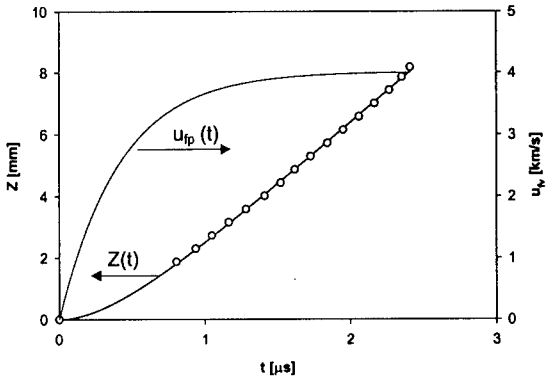


Figure 4. Experimental points (Z,t); curve fitting of displacement *Z(t)* and velocity u_{fp} *(t)*.

3 - EXPLOSIVE CHARACTERISTICS

The used PBX (85% wt RDX, 11.5% HTPB and 3.5% DOS) has a density of 1.574 g/cm^3, which corresponds to a more than 99% TMD. The RDX has a bimodal particle distribution (75 wt% of d_{50} = 96μm and 25 wt% of d_{50} = 22μm). The detonation velocity is 7.90 km/s, measured in cylindrical charges of 25 mm of diameter initiated by flyer plate impact. The detonation pressure is 24.4 GPa, measured by the shock attenuation method in PMMA barrier. The measured critical diameter, ϕ_c, in PVC confinement, is between 3.5 and 3.75mm.

4 - SHOCK TO DETONATION TRANSITION EXPERIMENTS

When a pressure pulse stresses the heterogeneous explosive sample, a shock wave travels inside the explosive. If the pressure pulse has an enough intensity to initiate the explosive, the shock wave accelerates until to be converted in a detonation wave, to support the acceleration of the shock wave, a chemical reaction start immediately as the pressure pulse strikes the sample. Generally the distance and the delay time needed for the shock wave to be converted in a detonation wave are dependent of the intensity and duration of the pressure pulse. Consequently the experimental effort of the SDT work is to characterise input pressure pulse and the shock to detonation distance Z_{SDT} and the detonation induction time t_d.

In our experiments a thin flyer plate, with a known velocity, shocks an explosive sample. To measure the initiation distance the optical fibber ribbon is placed, in a normal direction relatively to the detonation wave propagation, inside the explosive, that experimental arrangement is presented in Figure 5. As the front of the shock/detonation waves cross the optical fibber a light pulse is generated and is recorded with a fast electronic streak camera.

A cylindrical PVC tube with 10 or 20 mm of height and 25 mm of internal diameter confines the explosive samples. In the explosive top was attached PMMA barrier, inside of which was also put the optical fibber ribbon. The fibbers inside the PMMA barrier measure the velocity of the shock wave induced by the detonation wave. The flyer plate is Mylar with 0.350 mm of thickness and 25 mm of diameter.

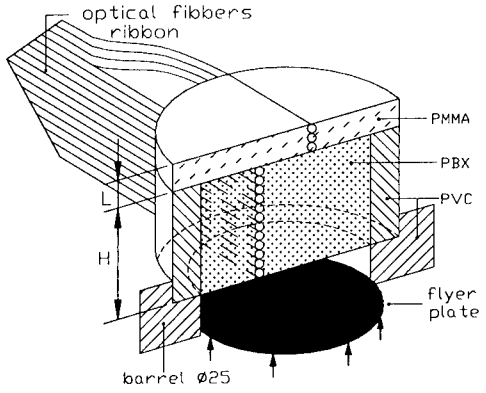


Figure 5. Experimental set-up to characterise the SDT.

A typical fotocronogram recorded is presented in Figure 6, in that figure it can be seen the initial shock wave velocity, the transition to the detonation wave and the normal detonation wave, also is presented the shock wave attenuation inside the PMMA barrier. With that

experimental method it can be recorded "continuously" the evolution process of the detonation wave front in a space-time diagram. In Figure 7 is presented the (Z,t) diagram for two experiments showing clearly the effect of different flyer plate velocities in the initiation process of PBX.

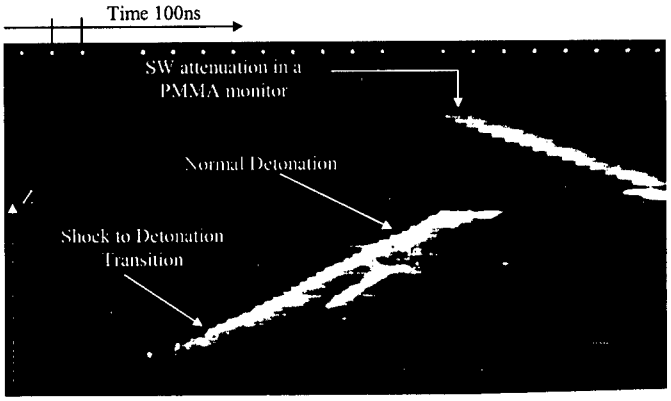


Figure 6. Typical fotocronogram of the SDT, and the SW attenuation in an inert monitor.

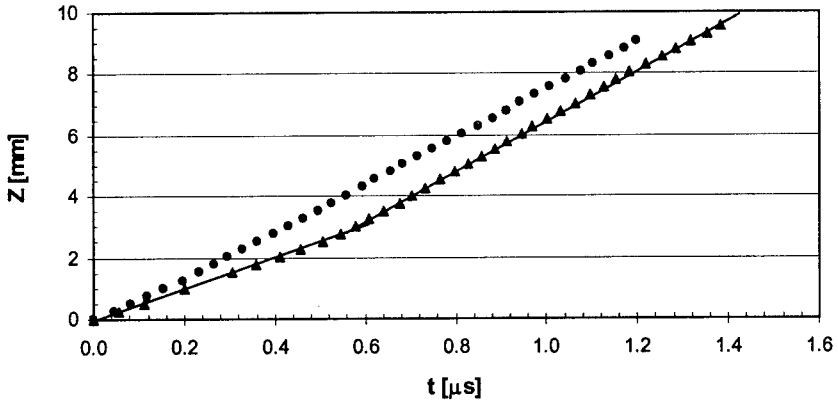


Figure 7. Diagram (Z,t) of the DW front propagation.

The typical approach to find the SDT distance, has been applied in this paper, based on the intersection of two linear trend lines, drawn over the experimental (Z,t) points.

The determination of the DW mean velocity was obtained by the linear fitting, applied to the experimental (Z,t) points. The local detonation velocity was calculated by eq. 1 and a (D,Z) diagram is presented in Figure 8.

$$D_i = \frac{z_{i+1} - z_{i-1}}{t_{i+1} - t_{i-1}} \qquad (1)$$

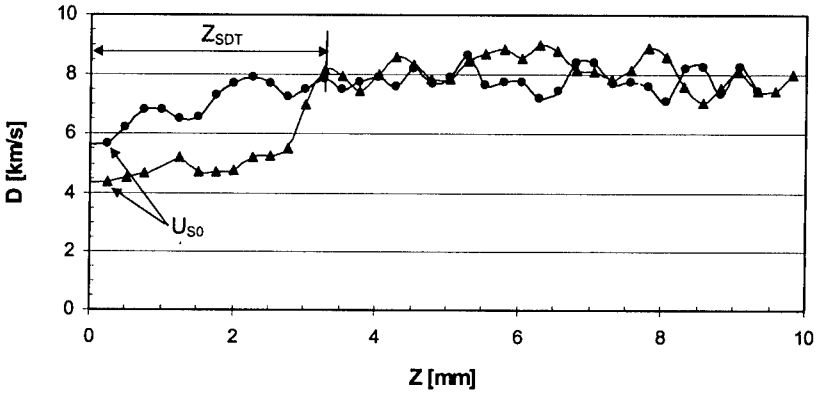


Figure 8. DW front velocity.

Therefore, with our high-resolution method at the mesoscale level, the shock to detonation transition point, as well the oscillations of the DW front propagation are clearly observed. The SDT zone is characterized by the initial shock wave accelerated, on its run equal to $\approx 10 x d_{50}$ of coarse particles, followed by one or two irregular oscillations of shock reaction front. The quasi–regular DW characterised by spatial scale of $10\text{-}11 x d_{50}$ of coarse particles with the temporal period about to 120 ns follows the SDT zone. The obtained results are confirming and adding the results obtained in the long charges tests, of the same PBX (vd. Plaksin, I. et. al. 1997, 1998 and 2001), they are showing a significant evidence that the detonation wave in PBX, at the mesoscale level, has a quasi-regular structure characterized by spatial temporal oscillations of velocity and pressure. In that zone, the oscillations are related to the local oscillations of the energy release, which is due to the local changes of pressure and temperature. Nevertheless the global energy release keeps constant, which is seen by a constant mean velocity at macroscopic level.

Considering the Hugoniot characteristics of the flyer plate material (Mylar) given by eq. (2) (vd. LASL, 1980 (1)) and the shock impedance of the PBX, in the initial zone of the shock wave propagation, by the generally used mismatch method was possible the build up of the Hugoniot characteristics of the PBX (vd. Figure 9). Using four experimental points, the U_s-u_p relationship for our explosive is presented in eq (3). The measured initiation distance, as a function of the flyer plate velocity is presented in Table 3.

$U_s = 2.356 + 1.601\ u_p$ [km/s] for $u_p < 2.62$ km/s (2)

$U_s = 2.070 + 2.081\ u_p$ [km/s] for $u_p < 1.70$ km/s (3)

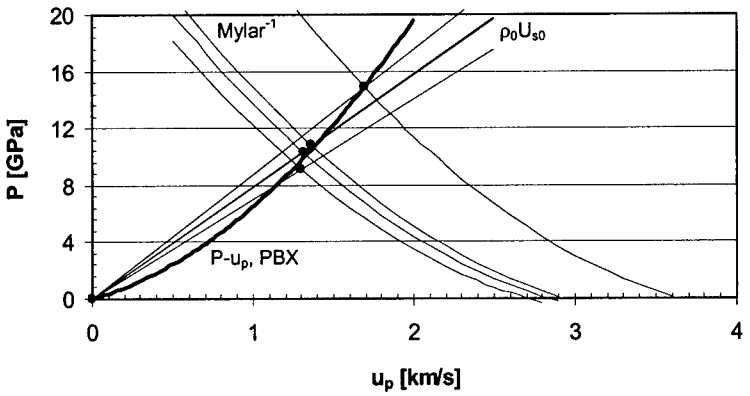


Figure 9. Classical mismatch method for PBX Hugoniot evaluation.

Table 3. Flyer plate velocity and detonation distance Z_{SDT}.

u_{fp} [km/s]	P_{ind} [GPa]	Z_{SDT} [mm]
2.71	9.1	3.25
2.84	10.3	2.25
2.84	10.3	3.00
2.94	10.8	2.50
3.64	14.9	1.50

The correlation of the sensitivity between our explosive and others PBX, based on RDX, obtained from bibliography, is presented in Figure 10 showing the pressure values as a function of SDT distance in a logarithmic scale. The results of the explosive 84-16 (84% RDX-16% binder based on HTPB) with 1.55 g/cm^3 of density were obtained by Bélanger, C. et. al., 1985, and the explosive sample was initiated by aluminium flyer plates. The experimental data for the PBX 9407 with 1.60 g/cm^3, 9405 with 1.761 g/cm^3 and 95-05 with 1.711 g/cm^3 were obtained from LASL, 1980. The sensitivity tests for that explosives were obtained by Gap test, which induces in the explosive sample a different pressure pulse profile compared to the flyer plate test.

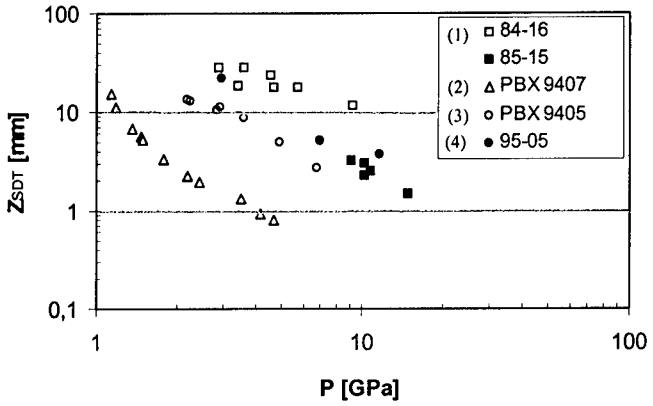


Figure 10. Correlation of the shock to detonation distance as a function of pressure pulse intensity for several PBX based on RDX, (1- Bélanger, C. et. al., 1985 and 2, 3, 4 - LASL, 1980-(2)).

Observing the results in Figure 10 the difference between our explosive 85-15 and the 84-16 explosive may be due to the experimental method used by Belanger et. al. 1985, to find the Z_{SDT}, that monitored only two events. Also the coarse particles (d_{50} about 650μm) used in the explosive 84-16 can explain the less sensitivity of this explosive compared to the 85-15. The explosive PBX 9407, formed by fine particles (between 10-50 μm) and the high porosity of that explosive, compared to the others, can also explain its high sensitivity. At last, our experimental results seems to be in agreement with the results of PBX 9407 and PBX 9405 due to the less mass content of RDX that induces less sensitivity.

5 - Conclusions

The high pressure, generated by flyer plate impact induces, in very short distances, a detonation wave in PBX explosives. This initiation method, coupled to a high-resolution optical method, allows testing small explosive samples, in the mesoscale level, without losses of information.

The shock to detonation transition point, as well the oscillations of the DW front propagation, are clearly observed. At the mesoscopic level, were observed velocity oscillations in the DW front, nevertheless the mean detonation velocity still constant.

The sensitivity results of our explosive seem to be in relative agreement when compared to others PBX based on RDX and inert binders.

REFERENCES

BELANGER, C., PELLETIER, P. e DROLET, J.F., "Shock sensitivity study of the curable plastic bonded explosives", in 8th *International Symposium on Detonation*, pp. 361-368, Albuquerque, NM, USA, 15-19 July, 1985.

LASL, Shock Hugoniot Data, 1980 (1), ed. by S. P. Marsh, Univ. California Press, Berkley.

LASL, Explosive Property Data, 1980 (2), ed. by T.R. Gibbs and A. Popolato, Univ. California Press, Berkley.

MENDES, R., 1994, "Contribuição para o estudo da geração e caracterização de ondas de choque", Master thesis, DEM-FCTUC, Coimbra.

MENDES, R., PLAKSIN, I. AND CAMPOS, J., 1997, "Single and two initiation points of PBX," *10th Biennial International Conference of the American Physical Society Topical Group* on Shock Compression in Condensed Matter, edited by S. C. Schmidt et al., AIP CP 429, NY, 1998, pp. 715-718.

MENDES, R., CAMPOS, J. AND PLAKSIN, I., 1998 "Double initiation and Mach formation in PBX," in *eleventh International Symposium* on *Detonation*, Aspen, CO, Aug 29- Set 4.

MENDES, R., PLAKSIN, I., RIBEIRO, J., AND CAMPOS, J., 1996 "Electrical explosion of the aluminium foil behaviour of explosions products in the process of flyer plate launch," in *Shock Waves in Condensed Matter*, St Petersburg, Russia, Set. 2-6.

MENDES, R., 2000, "Iniciação e detonação de explosivo plástico de RDX", Phd. thesis, DEM-FCTUC, Coimbra.

PLAKSIN, I., MENDES, R., CAMPOS, J. AND GOIS, J., 1997 "Interaction of double corner turning effect in PBX," *10th Biennial International Conference of the American Physical Society Topical Group* on Shock Compression of Condensed Matter, edited by S. C. Schmidt et al., AIP CP 429, NY, 1998, pp. 755-758.

PLAKSIN, I., CAMPOS,J., MENDES, R., RIBEIRO, J. AND GÓIS, J., 1999, "Mechanism of detonation wave propagation in PBX with energetic binder"; *11th Biennial International Conference of the American Physical Society Topical Group on Shock Compression of Condensed Matter, Co, USA,* edited by M. D. Furnish et al., AIP CP 505, NY, *2000, pg, 817-820.*

PLAKSIN, I., CAMPOS, J., RIBEIRO, J., MENDES, R. AND PORTUGAL, A., 2000, "Detonation Study of PBX Micro-samples", in *Shock Waves in Condensed Matter*, St Petersburg, Russia, Oct. 2-6.

PLAKSIN, I., CAMPOS, J., RIBEIRO, J., AND MENDES, R., 2001, "Irregularities of Detonation Wave Structure and propagation in PBX", in *this proceeding of ICT.*

ICT 2001

INITIATION OF HIGH EXPLOSIVES WITH SHAPED CHARGE JETS

Prof. Dr. Manfred Held
EADS-TDW, 86523 Schrobenhausen, Germany

ABSTRACT

The initiation phenomena of high explosive charges are manifold, especially if they come from loads of jets or projectiles with diameters less than the critical detonation diameter of the explosives themselves. Covered high explosives are changing the initiation threshold because of a number of different effects:

- „preshocking" of the HE by the faster running shock wave
- „precompression" of the HE by the cover material, pushed in front of the penetrating shaped charge jet or projectile
- „load history" is drastically changed for covered to uncovered explosives
- „loaded area" on the high explosive is also different by the spread angle of the secondary fragments, ejected from the cover material.

On a large number of test results under various configurations together with sophisticated diagnostic techniques, the different phenomena are presented and interpreted.

Besides the fascinating phenomena the thumb rules is given for the prediction of the initiation threshold of a number of high explosive charges with v^2d, where v is the impact velocity and d the jet or projectile diameter, or with u^2d, where u is the cratering velocity in the high explosive charge, when different jet or projectile materials are investigated.

COVERED HIGH EXPLOSIVE CHARGES

On tests of covered high explosive charges Chick and Hatt[1] found interesting phenomena. High explosive charges with an air gap between the cover plate and the acceptor charge behave more sensitively or can be initiated with lower jet velocities compared to tests, where the high explosive charge is in direct contact to the cover plate. These results are confirmed with many tests by the author[[2], [3] and [4]] The two typically used test set-ups are presented in Fig. 1 The detonation breakthrough for the arrangement in a direct contact with a 50 mm barrier is around 30 mm while the buildup distance with a 15 mm air gap to the 50 mm barrier is only around 7 mm.

A high explosive charge in contact to a 100 mm barrier is not more initiated by this shaped charge jet. This is also the case of a 0,5 mm air gap, where no earlier shock wave load can influence the charge. With 1 mm air gap the high explosive charge is detonating with 70 mm buildup distance. From 5 mm air gap on the buildup distances are nearly constant in the range of 20 mm to 25 mm (Fig. 2).

By splitting the barrier, but in sum always 100 mm, and now changing the plate in direct contact to the acceptor charge from 1 mm to 6 mm, it was found that with a 6 mm thick plate no detonation occurred anymore (Fig 3) Detonation starts with a 4 mm plate in 75 mm buildup distance, with a 2 mm plate in 50 mm and with a 1 mm plate only in 5 mm buildup distance. But by using the same total length of the 100 mm barrier, the $v^2 \cdot d$ load remains constant.

The buildup distances Δs and delay times Δt for the breakthrough of the detonation waves are summarized for both test conditions as functions of the jet velocities after the different barrier thickness in Fig. 4 The acceptor charge is initiated by the jet in the axis. The detonation wave needs 3.1 µs to come from the axis to the side wall where it is recorded by the frame and streak camera (24 mm/7,8 mm/µs = 3,1 µs). If the detonation time Δt of 3.1 µs is subtracted from the delay time the initiation times t_i are achieved, which are more scattering for the data where the acceptor charge is in

contact to the barrier, but which are well fitted by a straight line in the case with an air gap (see Fig. 4, lower lines).

The diameters of the particulized jet $d_{jp}(v_j)$ and the particulation times $t_p(v_j)$ along their velocity gradient are known. Therefore the diameter $d_j(v_j)$ of the continuously stretching jet can be calculated with the arrival time t_a of the jet on the high explosive charge surface by $d_j(v_j) = d_{jp}(v_j) \cdot \sqrt{t_p(v_j) / t_a(v_j)}$. Therefore the buildup distances Δs, delay times Δt and initiation times t_i can be presented over the $v_j^2 \cdot d_j$ values (Fig. 5).

A further interesting and surprising result was found by Chick et. all[5] what was also confirmed by the author[3]. The detonation starts in the second portion of a split acceptor charge after the air gap (Fig. 6). The first already perforated and radially a little expanding high explosive charge starts to detonate delayed in a so-called retonation wave which is clearly demonstrated by the simultaneously achieved frame and streak records.

EXPLANATIONS

In explosive reactive armour sandwiches it is also well known and in practice used to install gaps, voids etc. in different shapes and forms to sensitize the arrangements to get also initiations not only by the very fast shaped charge jets, but also by KE rounds with moderate velocities. Few people have explained that the air is compressed to high temperatures by the deformation of bulge of the front plate or jets are formed like at explosive welding which is now radially initiating the explosive layer (Fig. 7). But this is no explanation for the „axial symmetrical events" of covered high explosives without and with air gaps or on the split high explosives with internal air gaps. What are the physical differences on these two arrangements?

- Preshocking of the high explosive charge by a shock wave which is definitely running faster in steel than the craterground-velocity of the penetrating jet and is therefore arriving earlier on the acceptor charge than the jet

- Precompression of the acceptor charge by the bulge of the cover material in front of the shaped charge jet or KE rod
- Different shock load histories; in the case of contact the pressure load is slowly increasing in a ramp wave in microseconds time-scale before the jet is penetrating in the high explosive acceptor charge, whereas in the case of an air gap the impacting jet creates an one-dimensional much higher shock pressure, but only for a fracture time of microseconds.
- Different loaded area in the case where the high explosive charge is in contact to the barrier.
- Debris clouds in the case of an air gap in the high explosive charge.

The possible different stimuli for the high explosive charge arranged in contact, respectively with an air gap to a casing, a cover plate or barrier should be discussed in more details.

1. Preshocking

The jet impacting and penetrating the barrier is definitely creating shock waves which are running faster in steel with 6 mm/µs as the longitudinal velocity and therefore arrive earlier on the interface between the barrier and the high explosive charge than the penetrating shaped charge jet. But these shock waves are on one hand not very strong and second they are drastically attenuated by the shock impedance mismatch between the barrier material and the high explosive charge. After the author's opinion this will not remarkably influence the behavior of the acceptor charge. As shown in the Figure 2, an air gap of 0.5 mm, where no shock wave can be definitely transferred from the barrier to the acceptor charge, has also fully desensitised the high explosive charge, or in Fig. 3 also a cover plate thickness of only 6 mm was enough to reduce the sensitivity to get no initiation more. Therefore shock waves are not really desensitising the acceptor charge after the author´s opinion.

2. Precompression

To demonstrate the precompression of the acceptor charge by the bulge of the barrier through the perforating shaped charge jet a block of plexiglass of 70 x 70

mm^2 cross section and of 100 mm length instead of the high explosive charge with an internally installed grid was observed with the streak and framing camera. In a test with the standard shaped charge and a 100 mm mild steel barrier thickness small fringes were observed in the streak record which are created by very weak shock waves on the contact surface in the plexiglassblock. But before the jet is arriving the steel block starts to bulge which is precompressing the block of plexiglass in a depth of about 10 to 15 mm and starting about 5 µs before the jet arrives. This time difference is analyzed between the start of the movement of the end surface of the barrier or of the bulge and the extrapolation of the constant penetration line of the jet into the plexiglass back to the original boundary of the steel barrier and the plexiglass block (Fig. 8).

Stilp and Hohler[7] measured the perforation of a KE round through a steel plate and photographed the exit side in detail and summarized 4 firings in Fig. 9. Ruby laser stroboscope flashes have visualized the weak shock waves in air behind the steel plate and also the bulging of the steel plate on the rear surface. The analysis of these tests gives clearly also the slowly increasing velocity of the rear surface of the steel plate and demonstrates the precompression effect if a layer of high explosive were in contact to the rear plate.

In the time distance plot of Fig. 10 these effects are schematically illustrated with the impact of the shaped charge jet with a velocity of 8 mm/µs, which gives a cratering velocity of around 4 mm/µs in the steel barrier. The impacting jet creates weak shock waves in the range of nearly 6 mm/µs. But the penetrating shaped charge jet is deforming the layers in front of the crater bottom in the range of 10 mm up to 20 mm which gives the bulge on the end-surface of the barrier. The bulging barrier material is compressing the high explosive charge.

It is well known that higher compressed high explosive charges with less voids or hot spots are much less sensitive. Therefore the jet is not able to initiate the high explosive charge in this compressed zones. The high explosive charge is initiated as soon as the jet is penetrating the „not influenced" or compressed high explosive charge. This explains also the large buildup distances and the long time delays.

This is after the author's opinion the main reason for the much larger buildup distances or the longer delay times with the high explosive charge in contact or that the jet is no more able to initiate the high explosive charge at all.

3. Pressure time history

The precompression of the steel barrier against the high explosive charge is working along a time scale of about 3 µs to 5 µs in the case of contact. In the end-phase the bulging material is achieving the cratering velocity which can be calculated after Bernoulli with the steel material or density ρ_t = 7,85 g/cm^3. As soon as the copper jet with its density of 8,9 g/cm^3 is penetrating into the high explosive charge, a small jump is created in the pressure load by the Bernoulli equation (Fig. 11, top left). In the case of an air gap the impacting jet creates an one-dimensional pressure which is predicted by the shock wave equation $p_s = \rho_0 \cdot U \cdot u$ but only in a fracture time of microseconds for the given jet diameters. The load is then continuing with the further penetrating jet. This pressure can be calculated with the Bernoulli equation $p_B = 0{,}5 \cdot \rho_j \cdot (v_j - u)^2 = 0{,}5 \cdot \rho_{HE} \cdot u^2 = 0{,}5\ \rho_{HE} \cdot v_j^2 / (1+\sqrt{\rho_{HE} / \rho_j})^2$ (Fig.11, top right).

4. Impacted area

The impacted area is also different in the case where the acceptor charge is in contact to the barrier or it is arranged with an air gap. In the second case the spall-ring can extend and hit the acceptor charge over a larger surface area which is also influencing the reactivity (Fig. 11 down). But it is expected by the author that this has a minor effect because the area A goes in the initiation threshold equation only with the exponent of ¼ compared to the velocity v ($I_{cr} = v \cdot A^{¼}$).

5. Split acceptor charge

The initiation of the second portion of a split acceptor charge can have an additional reason beside the other discussed possibilities. The second portion cannot be desensitised by a preshocking or precompressing process. The loaded area should

also be not much larger. But the different time load histories exist and there is one additional effect. It was found by Finnigan[8] that tubular propellant charges are ignited, if the fragment has perforated the first tube wall and the ejected propellant debris cloud of the first layer is impacting on the other side where the reaction is now starting (Fig. 12). Haskins[9] found by impacts of fragments only on unconfined high explosive charges that radial and/or axial dispersed high explosives, now pulverized, are starting to react and to detonate on surrounding fixtures or structures. The velocities of the ejected explosive material are measured to impact the support beam or back-plate with ca. 200 m/s - 400 m/s, if XDT is yielding. The shaped charge jet, perforating the high explosive charge, will also eject explosive material from the free surface with much higher velocities which is now impacting the second high explosive part, passing the air gap. The powdered material starts to react and to detonate by this high velocity impact. Definitely pulverized high explosives are much more sensitive compared to solid cast or pressed charges.

CONCLUSIONS

The initiation of high explosive charges with impacts of fragments, projectiles or shaped charge jets is not at all an easy task. If the high explosive charge is covered, without or with an air gap between cover plate and high explosive charge, different threshold values are found. The reasons for this are shortly summarized:

- „Preshocking" has, if at all, a minor effect
- „Loaded area" should have a small contribution
- „Load history" is drastically different for covered to uncovered explosives and can have, depending on the type of high explosive etc., a great influence on the threshold values
- „Precompression" by bulging has the greatest influence in the desensitation of high explosive charges in direct contact or very short distance to the cover plate, after the author's opinion

- The initiation mechanism is partially different in split acceptor charges by the with high velocities ejected and dispersed explosive material, which is much more sensitive

To get a better ranking for the different types of high explosive charges and for better understanding of the different phenomena and also better designing the layout of less sensitive high explosives or to get the right initiation levels for explosive reactive armours, more tests with different types of high explosive charges as acceptor charges and cover plate materials and configurations should be conducted.

REFERENCES

(1) M. C. Chick & D.J. Hatt, „The Initiation of Covered Composition B by a Metal Jet", Propellants, Explosives, Pyrotechnics 8, 121-126, 1983

(2) M. Held, „Experiments of Initiation of Covered but Unconfined High Explosive Charges by Means of Shaped Charge Jets", Propellants, Explosives, Pyrotechnics 12, 35-40, 1987

(3) M. Held, „Experiments of Initiation of Covered but Unconfined High Explosive Charges under Different Test Conditions by Shaped Charge Jets", Propellants, Explosives, Pyrotechnics 12, 97-100, 1987

(4) M. Held, „Discussion of the Experimental Findings from the Initiation of Covered but Unconfined High Explosive Charges with Shaped Charge Jets", Propellants, Explosives, Pyrotechnics 12, 167-174, 1987

(5) M.C. Chick, I.D. Macintyre and R.B. Frey, „The Jet Initiation of Solid Explosives", 8th Symposium (International) on Detonation 318-327, 1985

(6) M. Held, „Analysis of the Shaped Charge Jet Induced Reaction of High Explosives", Propellants, Explosives, Pyrotechnics 14, 245-249, 1989

(7) A.J. Stilp and V. Hohler, „Aeroballistic and Impact Physics Research at EMI - an Historical Overview", Distinguished Scientist Award - HVIS 1992

(8) S.A. Finnigan, J.C. Schulz and J.K. Pringle, „Planar Motor Test Model", AGARD-CP-511, 20:10-14, 1992

(9) P.J. Haskins and M.D. Cook, „Studies of XDT Produced by Projectile Impact of Secondary Explosives", 28th Int. Annual Conference of ICT, 36:1-9, 1997

Setups for SC Jet Initiation Tests

TDW

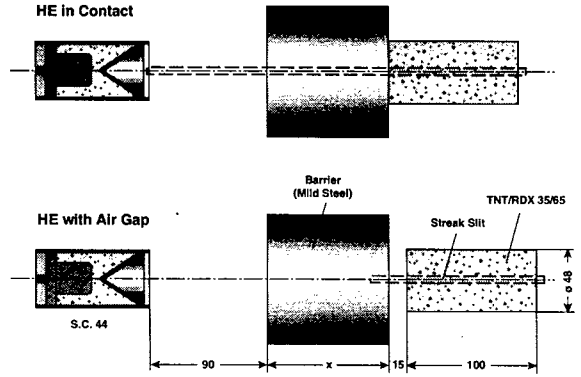


Fig. 1

Δs = f (Width of Air Gap)

TDW

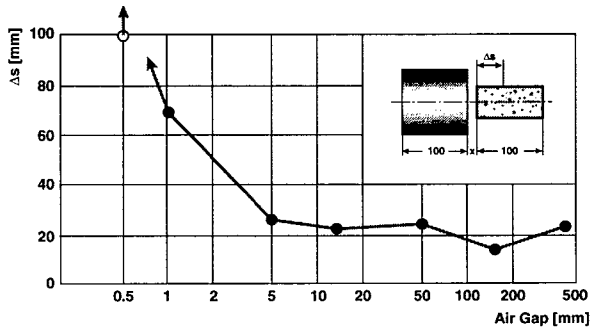


Fig. 2

Spaced Barrier

TDW

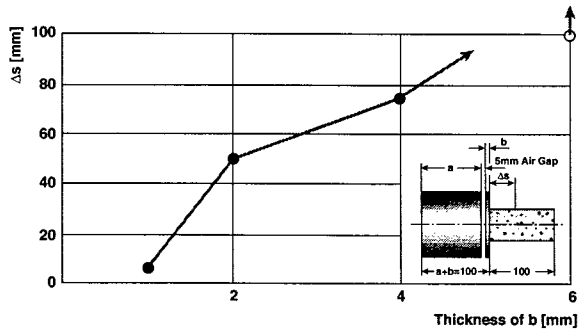


Fig. 3

Δs, Δt, t_i = f (v_j)

TDW

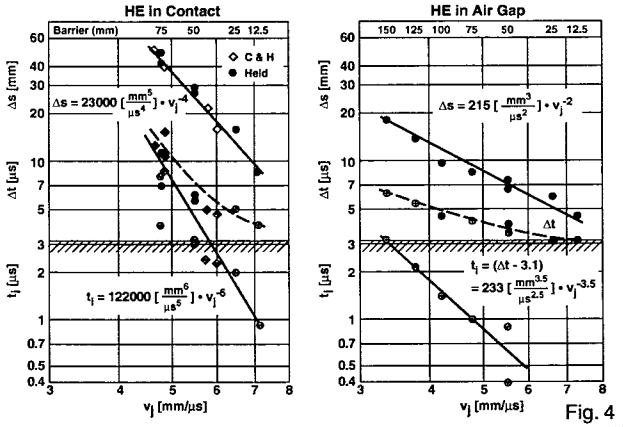


Fig. 4

Setups for SC Jet Initiation Tests

TDW

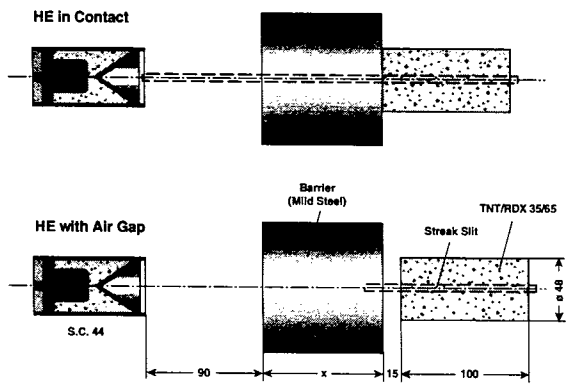


Fig. 1

TDW • Schrobenhausen — Chck & Hatt/1998

Δs = f (Width of Air Gap)

TDW

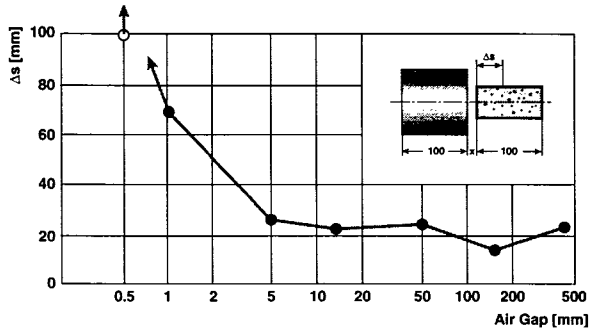


Fig. 2

TDW • Schrobenhausen — Chck & Hatt/1998

Spaced Barrier

TDW

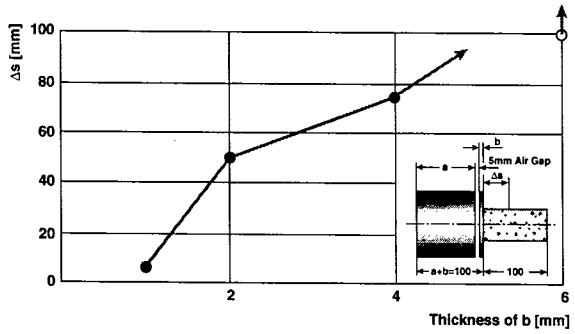


Fig. 3

TDW • Schrobenhausen — Chck & Hatt/1998

Δs, Δt, t_i = f (v_j)

TDW

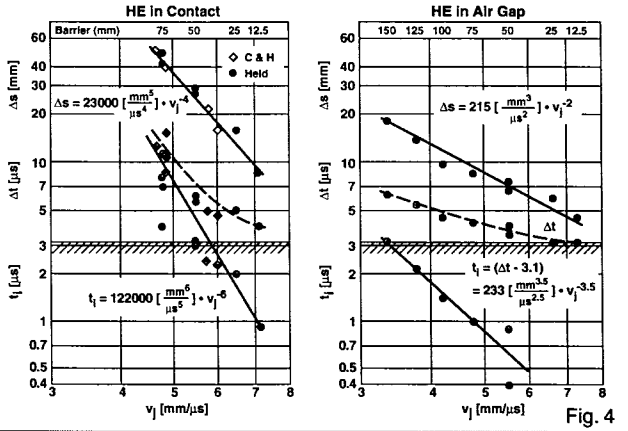


Fig. 4

TDW • Schrobenhausen — Chck & Hatt/1998

$\Delta s, \Delta t, t_i = f(v_j^2 \cdot d_j)$

TDW

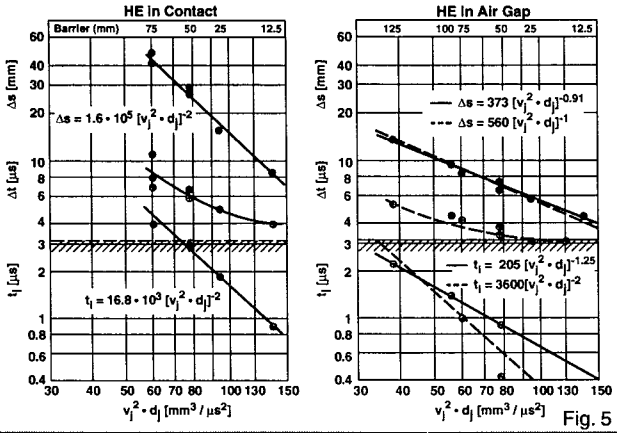


Fig. 5

TDW • Schrobenhausen Chick & Hatt/1996

Jet Initiation of a Split HE - Charge

TDW

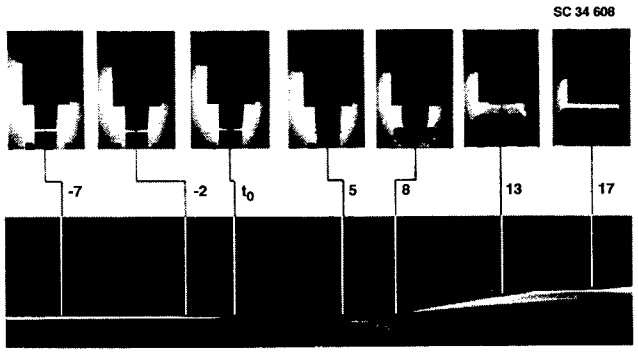
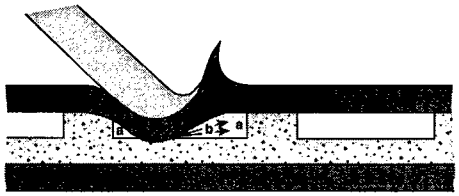


Fig. 6

TDW • Schrobenhausen Chick & Hatt/1996

Easier Initiation of the HE by Grooves

TDW



a Compressed and heated air

b Jetting

Fig. 7

TDW • Schrobenhausen Chick & Hatt/1996

Jet Load against Plexiglass after 100mm M.S. Barrier

TDW

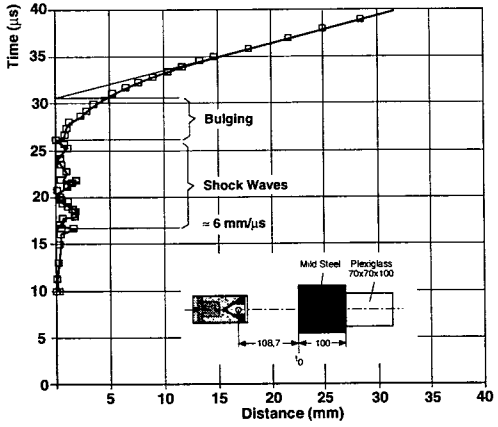


Fig. 8

TDW • Schrobenhausen Chick & Hatt/1996

$\Delta s, \Delta t, t_i = f(v_j^2 \cdot d_j)$

TDW

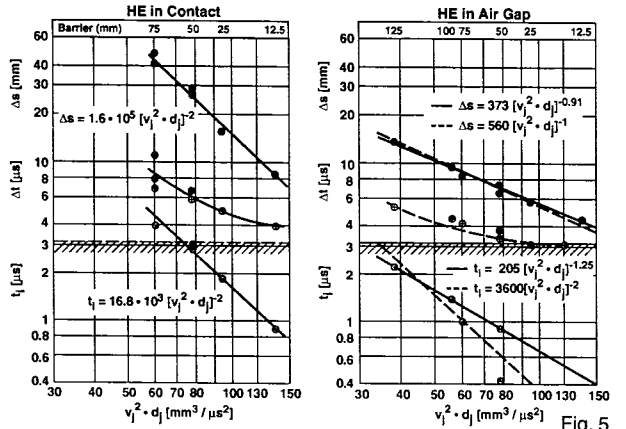


Fig. 5

Jet Initiation of a Split HE - Charge

TDW

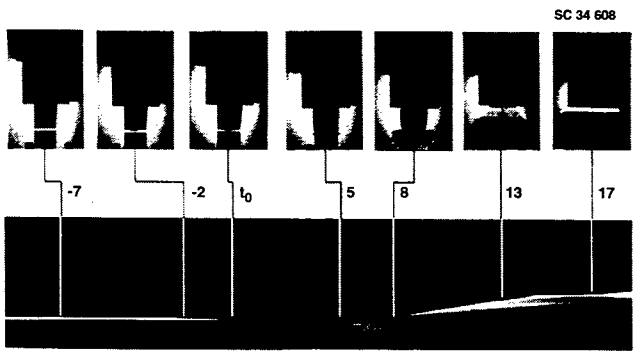
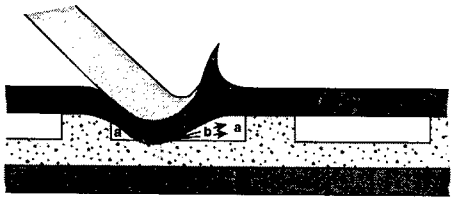


Fig. 6

Easier Initiation of the HE by Grooves

TDW



a Compressed and heated air

b Jetting

Fig. 7

Jet Load against Plexiglass after 100mm M.S. Barrier

TDW

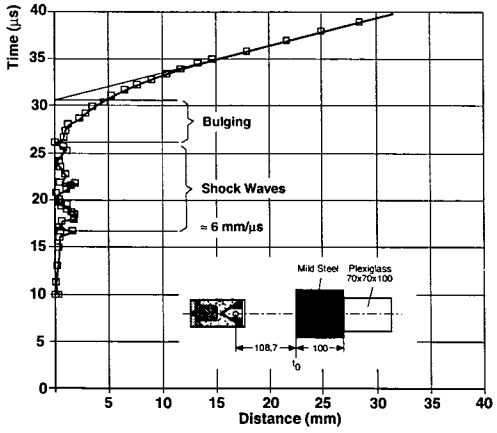
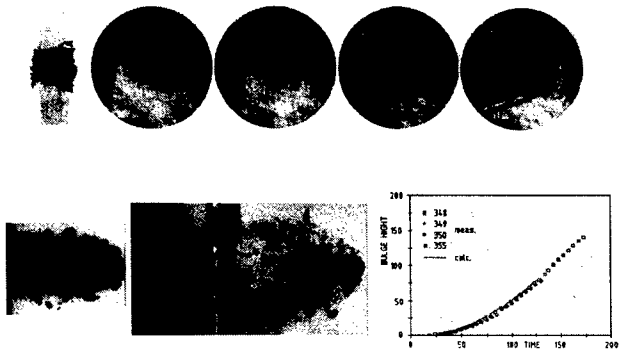


Fig. 8

TDW

30 Rear side bulging and debris cloud expansion behind a RHA plate perforated by a tungsten sinter alloy penetrator



A. Stilp and V. Hohler, HVIS 1992

Fig. 9

Time - Distance - Plot

TDW

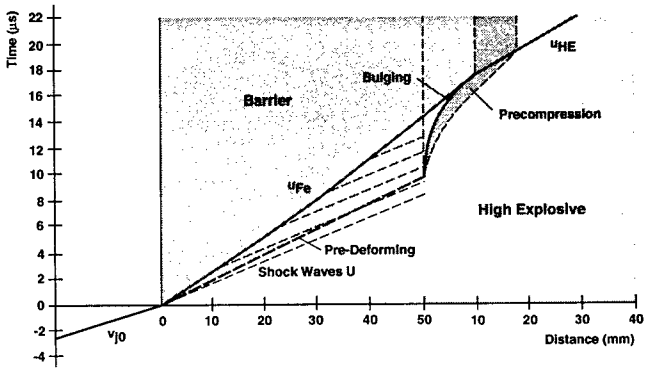


Fig. 10

Different Loads

TDW

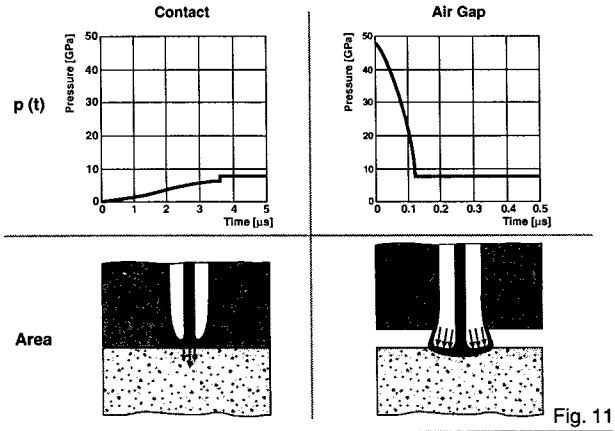
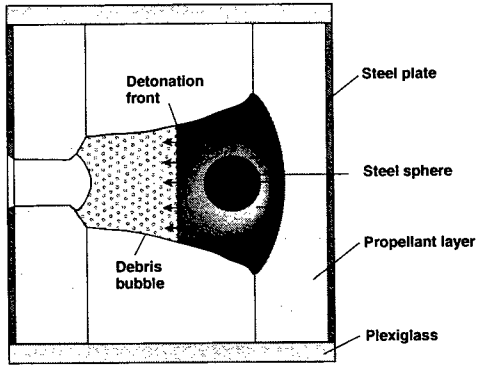


Fig. 11

Delayed Detonation Process

TDW

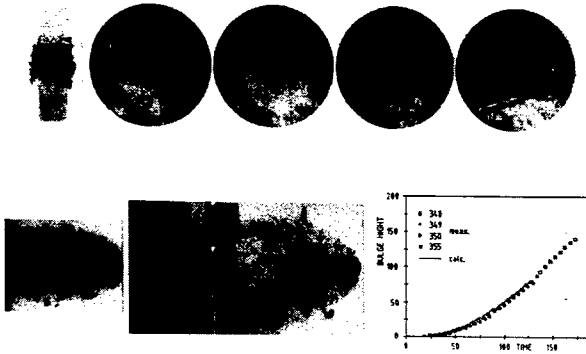


S.A. Finnigan, AGARD CP-511, 1992

Fig. 12

TDW

30 Rear side bulging and debris cloud expansion behind a RHA plate perforated by a tungsten sinter alloy penetrator



A. Stilp and V. Hohler, HVIS 1992

Fig. 9

TDW + Schrobenhausen Chick & Hart/1996

Time - Distance - Plot

TDW

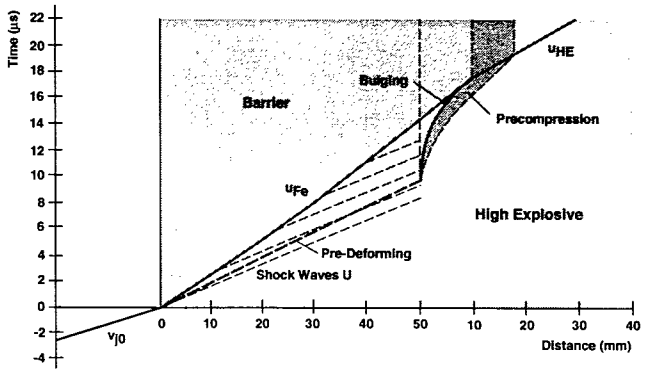


Fig. 10

TDW + Schrobenhausen Chick & Hart/1996

Different Loads

TDW

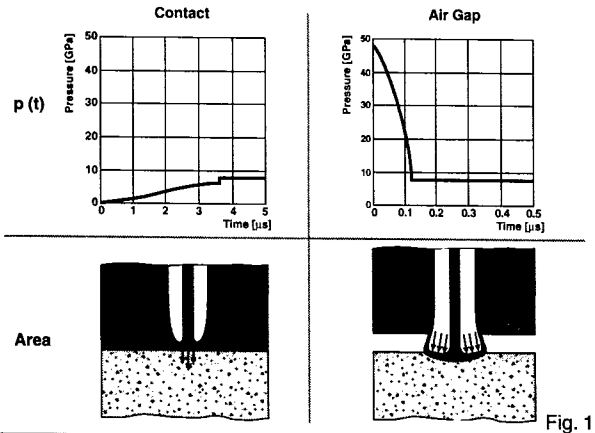
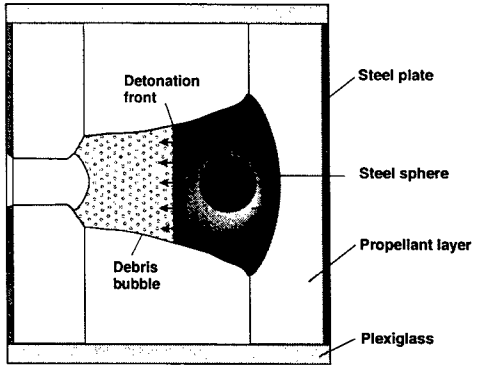


Fig. 11

TDW + Schrobenhausen Chick & Hart/1996

Delayed Detonation Process

TDW



S.A. Finnigan, AGARD CP-511, 1992

Fig. 12

TDW + Schrobenhausen Chick & Hart/1996

TANDEMHOHLLADUNGEN ZUR NICHTDETONATIVEN RÄUMUNG VON REAKTIVPANZERUNGEN (TANDEM WARHEADS WITH NON-INITIATING EFFECT AGAINST EXPLOSIVE REACTIVE ARMOR)

René Gagnaux [¥], Franz Häller [¥¥], Max Bär [¥], Bruno Gisler [¥], Oskar Rickli [¥]

Swiss Ammunition Enterprise Corporation

[¥] Warhead Division, Research & Development, CH 6460 Altdorf

[¥¥] Warhead Division, Research & Development, Allmendstr. 74, CH 3602 Thun

ABSTRACT

The penetration performance of shaped charge jets - or of kinetic energy (KE) penetrators - may be effectively reduced by covering the conventional armor with single, double or heavy explosive reactive armor (ERA). These ERA-modules consist primarily of steel-plates surrounding layers of explosive. The impact of a shaped charge jet rapidly initiates the explosive. Thereby the surrounding plates are accelerated, which in turn will damage or disturb the rest of the incoming jet.

This add-on protection concept has led to the development of so-called Tandem warheads where a precursor charge has to neutralize the ERA protection. This may be done in two principal manners: Either the precursor removes the ERA simply by its initiation, or it has to clear a path for the following main charge jet through the ERA, without leading to detonation. The first case has some conceptual disadvantages: The initiation of the main charge has to be delayed until the main part of the fragments of the ERA are out of the way for the jet. Whereas the loss of standoff is secondary, the major problem for a compact warhead is the risk of damaging the main charge by the fragments of the initiated ERA-Box. The non-detonative clearing however has the advantage, that it bypasses entirely the driving force of the defense mechanism – the detonation of the ERA.

Hence we focused our efforts on the development of a Tandem-warhead with a non-initiating precursor charge. The tested ERA-Box was composed of two C4-explosive filled ERA-sandwiches, at 65° NATO-angle.

In a first phase the effects of different liner geometries, explosives and caliber were modeled. The liner material was fixed to be copper, as the influence of liner density on the initiation sensitivity showed only a minor contribution. Then some of the promising variants were tested.

An exact fitting of caliber, liner geometry and explosive was necessary to obtain a non-initiating precursor in a satisfactorily wide operational range. After extensive test series an optimal liner geometry was established. As expected the cavity size is growing with the caliber of the precursor. We noticed further, that there is an optimal standoff for the precursor charge in order to get a maximal cavity geometry in the ERA-Box. A comparison of the penetration performance of the main charge in different configurations and on different targets will be presented.

1 Einleitung und Veranlassung

Mit sogenannten Reaktivpanzerungen[i] ist es möglich geworden, die Penetrationswirkung von Wucht- und Hohlladungsgeschossen erheblich einzuschränken. Damit konnte der Kampfwert von gepanzerten Fahrzeugen deutlich erhöht werden. Bei dieser Schutzart verwendet man Module aus Stahlplatten mit einer dazwischenliegenden Sprengstoffschicht, die auf der konventionellen Panzerung aufgesetzt werden (*Abbildung 1*). Durch den Aufschlag eines Hohlladungsstachels - oder allgemeiner eines Penetrators - kommt es zu einer Detonation der Sprengstoffschicht. Durch die wegfliegenden Metallteile wird der anfliegende Penetrator dann empfindlich in seiner Wirkung gestört.

Solche Reaktivpanzerungen können mit sogenannten Tandemgefechtsköpfen auf zwei Arten bekämpft werden. Entweder man bringt die Reaktivpanzerung mit der Vorladung gezielt zur Detonation und zündet dann die Hauptladung mit einer genügend grossen Verzögerung (wie zum Beispiel bei der Panzerfaust), oder man bohrt die Reaktivpanzerung mit einer geeigneten Vorladung nichtdetonativ auf. Der Hauptladungsstachel kann unmittelbar danach weitgehend unbehindert angreifen.

Mit einer nichtdetonativen Räumung hat man den grossen Vorteil, dass die treibende Kraft des Abwehrmechanismus - die Detonation der Reaktivpanzerung - übergangen wird. Bei kompakten Geschossbauweisen hat man ohnehin kaum eine andere Wahl, denn eine durch die Vorladung initiierte Detonation würde die nahestehende Hauptladung beschädigen oder sogar zerstören. Darum haben wir uns für eine Systemkonfiguration mit einem nichtdetonativen Räumungskonzept entschlossen.

Die Hauptzielsetzung unseres Entwicklungsvorhabens bestand also darin, einen Tandemgefechtskopf so zu konzipieren, dass die Reaktivpanzerung von der Vorladung nichtdetonativ durchbohrt wird, und somit der darauf folgende Hauptladungsstrahl die Hauptpanzerung unbehindert angreifen kann.

[i] Reaktivpanzerung = Explosive Reactive Armor (ERA) = blindage réactif explosif

2 Rahmenbedingungen und Versuchsdurchführung

2.1 Reaktivpanzerung

Die untersuchte Reaktivpanzerung gehört zur leichteren Bauart (*Abbildung 1*). Sie besteht im wesentlichen aus zwei sandwichartig aufgebauten Plattenmodulen (*Abbildung 2*), die mit dem Sprengstoff C4[i] gefüllt sind (etwa 0.3 kg Sprengstoff pro Modul). Die Neigung zur Angriffsrichtung wurde den Standards entsprechend auf 65° NATO, bezogen auf die ERA-Box, festgelegt. Der Winkel zwischen unterem und oberem Plattenmodul liegt bei 9°. Bei den Stahlteilen handelt es sich um 2 mm (Modulplatten) bzw. 3 mm (Box) dicke Stahlbleche. Eine solche ERA-Box schützt eine Fläche von 0.04 m^2 und wiegt 5.6 kg. Der Zielaufbau hinter der Reaktivpanzerung besteht aus Panzerstahlplatten (Rolled Homogeneous Armor, RHA).

2.2 Sprengstoffe

Für unsere Untersuchungen haben wir uns auf industriell eingeführte Formulierungen mit Oktogen beschränkt, und zwar auf PBXN-5 (plastic-bonded explosive, pressed, MIL-E-81111B), PBXN-110 (plastic-bonded explosive, cast cured, MIL-E-82901), PBXW-11(Q) (plastic-bonded explosive, pressed, WS-33500) und LX-14[1]. Zwei Formgebungsverfahren kamen zur Anwendung, das Druckgiessen[2] und das isostatische Pressen[3]. Das letztgenannte Verfahren wurde mit der Methode der Schrumpfmontage[4] kombiniert. Der druckgegossene PBXN-110 besitzt den Vorteil einer niedrigen Verwundbarkeit[5]. In einem etwas geringeren Ausmass gilt dies auch für den gepressten PBXW-11(Q). Dafür hat dieser eine noch etwas höhere endballistische Leistung[6].

2.3 Einlagewerkstoff

Alle Versuche wurden mit Kupfer höchster Reinheit als Einlagewerkstoff durchgeführt. Dieser Werkstoff wurde nicht variiert, da die Arbeiten von A.J. Koch und F. Häller[7] einen nur geringen Einfluss der Werkstoffdichte auf das Detonationsverhalten eines Sprengstoffmoduls gezeigt hatten.

[i] C4, MIL-C-45010A(AR) Amendment 4, 02 march 90, 91 % Hexogen (RDX)

2.4 Tandemgefechtskopf

Der untersuchte Tandemgefechtskopf setzt sich aus einer Vorladung und einer Hauptladung zusammen (*Abbildung 3*). Bei der Hauptladung handelt es sich um eine Hohlladung kompakter Bauart mit Detonationsumlenker. Ein typischer Sprengaufbau ist in der *Abbildung 4* zu sehen.

3 Auswahl von Einlagegeometrie und Sprengstoff der Vorladung

In der Konzeptphase wurden die Auswirkungen von verschiedenen Einlagegeometrien (*Abbildung 5*) und Sprengstoffarten (PBXN-5, PBXW-11(Q) und PBXN-110) simuliert. Die so ausgewählten Einlagegeometrien wurden zunächst mit dem Kaliber 50 mm beim eingebauten Sprengabstand (Built In Stand-Off, BISO) experimentell erprobt.

Es stellte sich schnell heraus, dass nur die FAETSCH-Geometrie zum Erfolg führen konnte. In *Abbildung 6* ist ersichtlich, dass die Einlagegeometrien ETZLI und HOLDEN immer zu einer Detonation des Reaktivzieles führten. Dies hängt mit Ausformung und Geschwindigkeit des Stachels (*Abbildung 7*) über die bekannte Beziehung für die Sensitivität $I_{crit} = v^2 d$ zusammen (wobei v die Geschwindigkeit der Strahlspitze und d deren Durchmesser ist).

Auch bei einer Vergrösserung des Sprengabstandes (was zu Änderungen von Stachelgeometrie und Stachelgeschwindigkeit führen kann) konnte im untersuchten Bereich keine Änderung des Verhaltens (ETZLI), bzw. nur eine schwache Änderung (HOLDEN) festgestellt werden (*Abbildung 8*).

Ein Vergleich der bei der FAETSCH-Vorladung eingesetzten Sprengstoffarten PBXN-5 (FAETSCH_Px) und PBXN-110 (FAETSCH_Gx) (*Abbildung 6*) zeigt, dass unsere Zielsetzung bei dieser Einlagegeometrie mit dem Sprengstoff PBXN-110 erfüllt ist. Dieser ist auch insensitiv, was bei heutigen Systemen wichtig ist.

4 Einfluss des Kalibers der Vorladung

Um die Ausmasse des im Reaktivziel durchgeschlagenen Loches zu optimieren, wurde auch der Einfluss des Kalibers der Vorladung untersucht. Da der Stacheldurchmesser in direktem Zusammenhang mit der Grösse der Vorladung steht, nimmt die Ausdehnung des durchbohrten Querschnittes mit deren Kaliber deutlich zu (*Abbildung 9*).

Wie aus der Beziehung $I_{crit} = v^2 d$ zu erwarten ist, ändert sich aber leider auch das Detonationsverhalten des Reaktivzieles (*Abbildung 10*). Mit zunehmendem Kaliber - bei gleichbleibendem BISO - nimmt die Detonationshäufigkeit zu. Um nichtdetonativ Räumen zu können, müsste der Sprengabstand also erhöht werden (*Abbildung 10, rechts*).

5 Optimierung der Vorladung

Durch eine sorgfältige Abstimmung von Kaliber und Einlagegeometrie konnten die Parameter des Vorladungsstrahles so verändert werden, dass die Reaktivpanzerung in einem genügend weiten Abstandsbereich nichtdetonativ durchbohrt werden konnte (*Abbildungen 11 und 12*). Erst dann konnten wir nachweisen, dass es bei der Vorladung eine optimale Einsatzdistanz gibt, analog zur bekannten Stand-Off-Kurve für die Eindringtiefe eines Hohlladungsstrahles[6].

In der *Abbildung 13* nimmt der Sprengabstand von oben nach unten zu. Bei sehr kleinen Sprengabständen – oberste Reihe in *Abbildung 13* - wurden nur wenige Ladungen gesprengt, da dort sofort klar war, dass die ERA-Box nicht vollständig durchbohrt werden kann. Die dritte Reihe von oben zeigt das Ergebnis beim optimalen Sprengabstand.

Dies lässt sich mit der zeitlichen Ausbildung des Vorladungsstrahles erklären. Einerseits nimmt dessen Länge mit der Zeit - also auch mit dem Sprengabstand - zu (*Abbildung 15*), andererseits nimmt aber der maximale Strahldurchmesser ab (*Abbildung 14*). Dies bedeutet, dass bei kurzen Sprengabständen die Strahllänge zum vollständigen Durchschlagen des Reaktivzieles nicht ausreicht (siehe z.B. oberste Reihe in *Abbildung 13*). Mit zunehmendem Sprengabstand - sprich zunehmender Strahllänge - wird das Reaktivziel dann vollständig durchbohrt, der Austrittsquerschnitt nimmt zu. Bei noch grösseren Sprengabständen nimmt die Grösse des Austrittsquerschnittes aber wieder ab, da der maximale Strahldurchmesser asymptotisch abnimmt (*Abbildung 14*).

6 Tandemleistung

Mit diesen Erkenntnissen konnte die endballistische Leistung des Tandemgefechtskopfes BADUS ganz wesentlich gesteigert werden. In *Abbildung 16* sind einige typische Durchschlagsleistungen mit dem Sprengstoff LX-14[1] in der Hauptladung einander gegenübergestellt. Als Vergleichsbasis dient die Bohrleistung der alleinigen Hauptladung gegen ein gewöhnliches RHA-Ziel ohne Reaktivpanzerung (Fall 1). In der Tandemkonfiguration von Fall 2 - gegen das gleiche Panzerstahlziel - liegt die Leistung um 8 bis 13 % niedriger. Die

Ursache dieses Verlustes liegt hauptsächlich im Problem der Abschirmung der Hauptladung. Das Anbringen der Reaktivpanzerung führt im Falle einer nichtdetonativen Räumung zu einem nur leicht höheren Verlust (Fall 3). Würde die nichtdetonative Räumung versagen, dann wäre der Leistungsverlust natürlich sehr hoch (Fall 4).

7 Ausblick

Mit diesem Konzept der nichtdetonativen Räumung konnten wir eine Reaktivpanzerung leichter Bauart mit doppeltem Sprengstoffsandwich ausser Gefecht setzen. Ziel der Weiterentwicklung wird es sein, eine Reaktivpanzerung schwerer Bauart ebenfalls nichtdetonativ zu räumen.

---

[1] J.R. Humphrey, LX-14 - A new high-energy plastic-bonded explosive, November 21, 1977, LLL, UCRL-52350, MIL-H-48358

[2] R. Gagnaux, O. Rickli, H.R. Bircher, J. Mathieu, Unempfindliche Hohlladungen, Design, Herstellverfahren, Leistung, 28. Internationale ICT-Jahrestagung 1997

[3] J. Meister, R. Kaeser, Neueres industrielles Verfahren zur Herstellung von Hochleistungshohlladungen, 27. Internationale ICT-Jahrestagung 1996

[4] R. Kaeser, Verfahren zum Zusammenbau eines Hohlladungsgeschosses, Europäische Patentschrift, O 494 469 B1

[5] H.R. Bircher, J. Mathieu, R. Gagnaux, M. Bär, Unempfindliche Hohlladungen - Verwundbarkeit, Prüfmethoden und Ergebnisse, 28. Internationale ICT-Jahrestagung 1997

[6] R. Gagnaux et H.R. Bircher , Vulnérabilité et performances – Un choix d'explosifs pour charges creuses, EuroPyro 99, 25th international pyrotechnics seminar, Brest 1999

[7] A.J. Koch und F. Häller, Sensitivity of ERA-Boxes initiated by shaped charge jets, 19th International Symposium on Ballistics, 2001, Interlaken

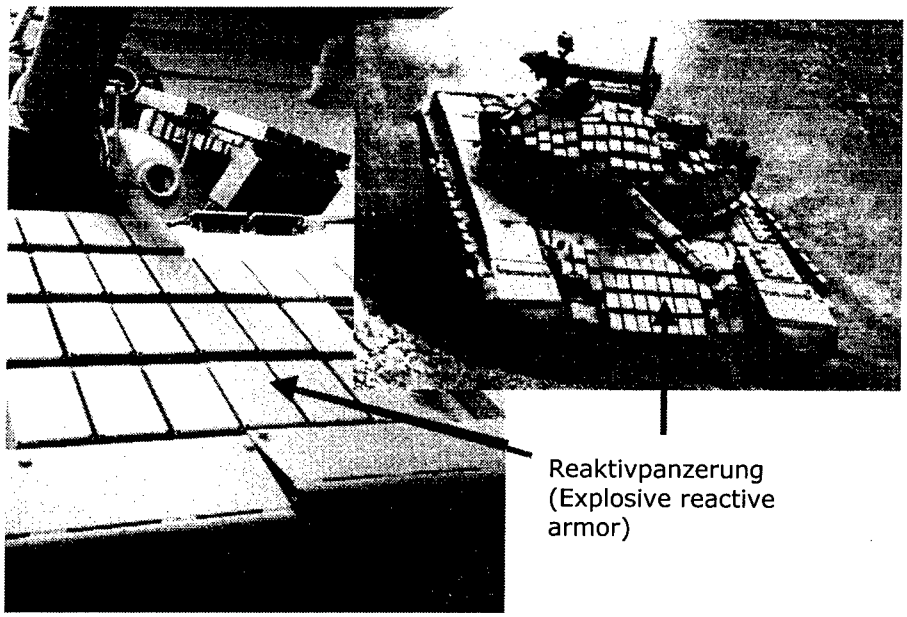


Abb. 1 - Beispiele von Reaktivpanzerungen leichter Bauart

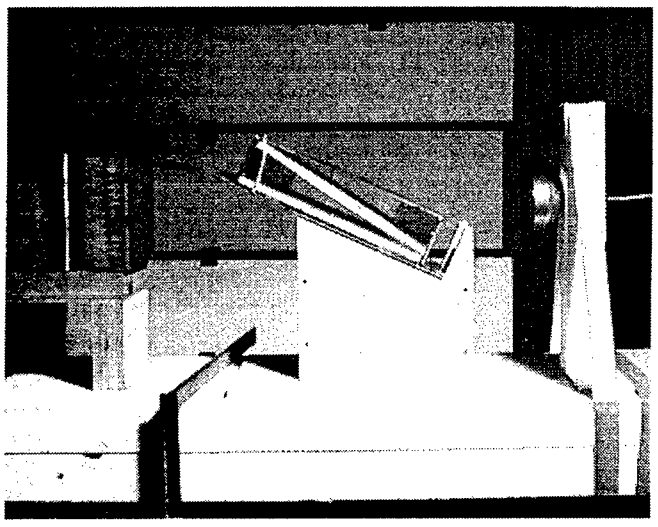


Abb. 2 - Ein typisches Versuchsdispositiv. Von links nach rechts: Zielblöcke, untersuchte Reaktivpanzerung, Vorladung

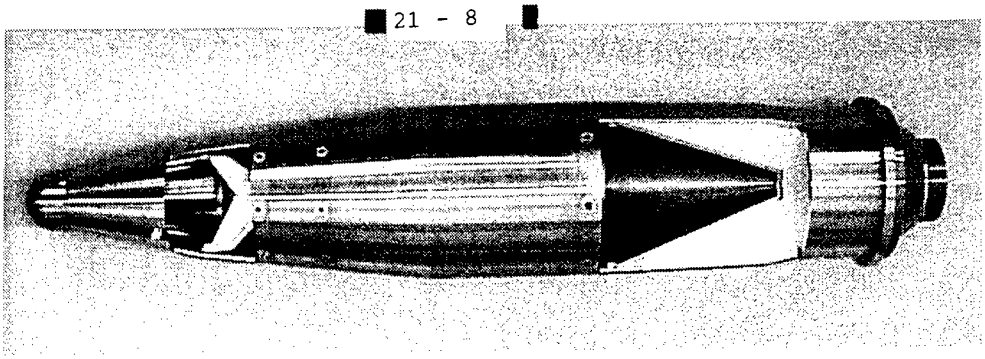


Abb. 3 - Der Tandemgefechtskopf BADUS
(aufgeschnittenes Modell, ohne Antrieb)

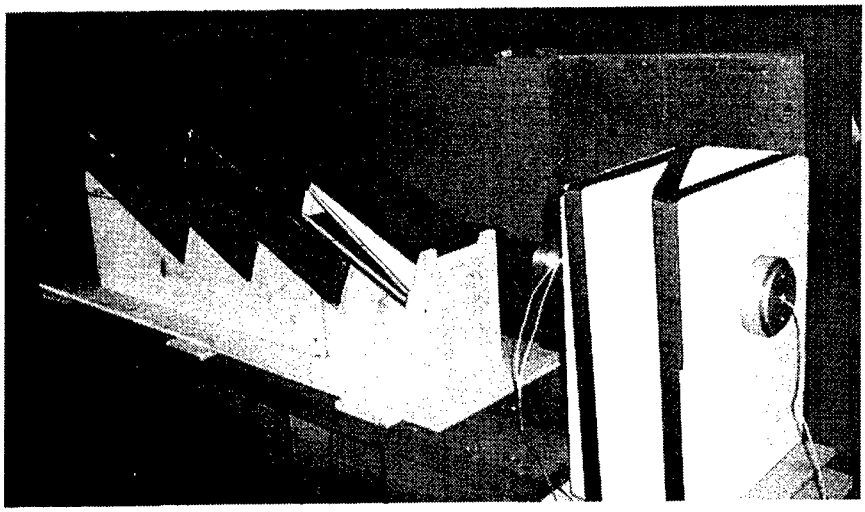


Abb. 4 - Der statische Tandem-Sprengaufbau

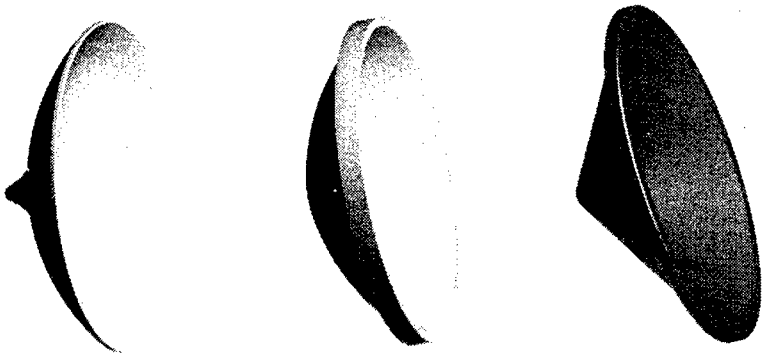


Abb. 5 - Die untersuchten Einlagegeometrien
(Von links nach rechts: ETZLI, HOLDEN und FAETSCH)

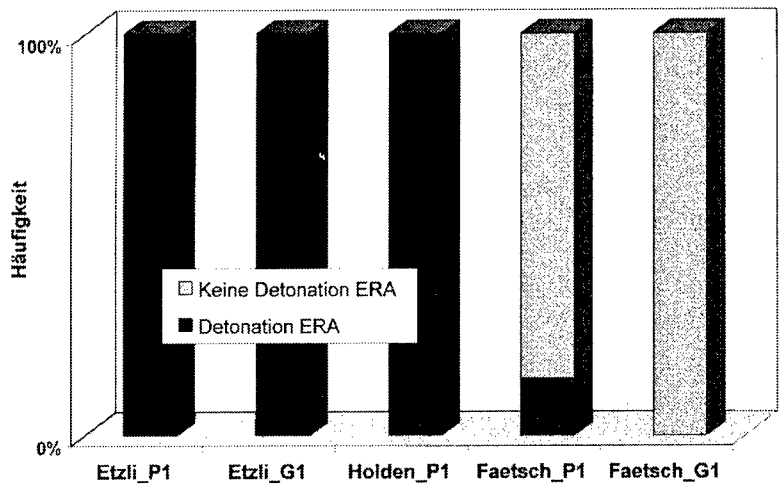


Abb. 6 - Verhalten des Reaktivzieles beim eingebauten Stand-Off
Einfluss von Einlagegeometrie und Sprengstoffart

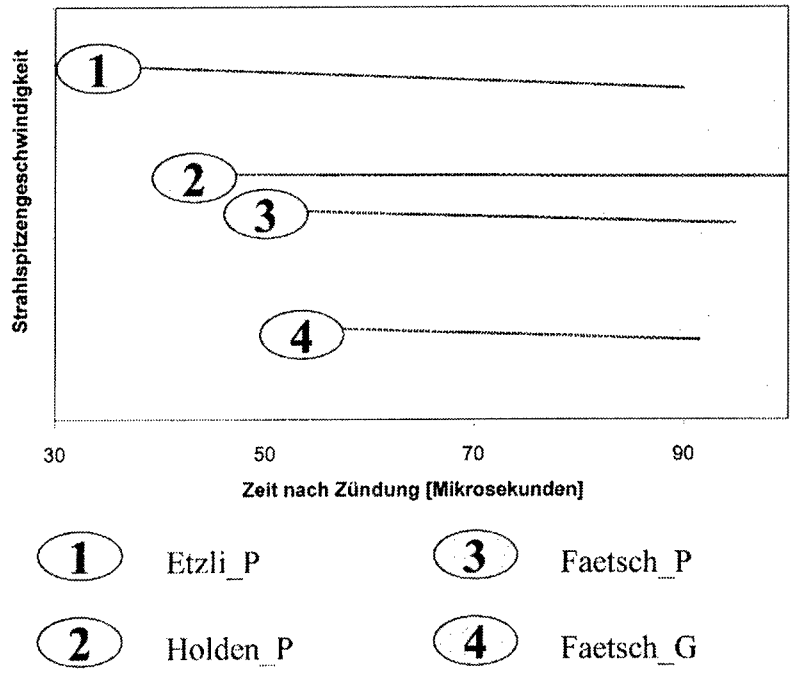


Abb. 7 - Strahlspitzengeschwindigkeit
Einfluss von Einlagegeometrie und Sprengstoffart

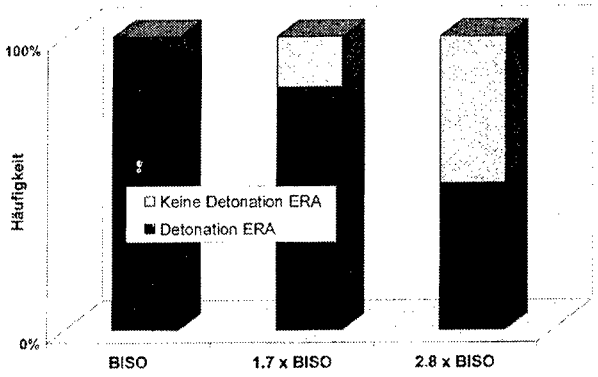


Abb. 8 - Verhalten des Reaktivzieles bei der Einlagegeometrie HOLDEN
Einfluss des Sprengabstandes Vorladung zur ERA-Box

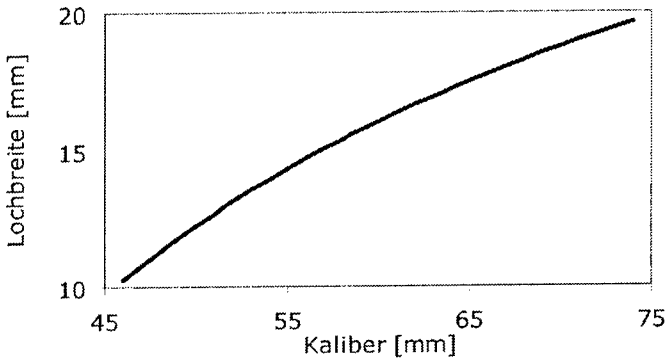


Abb. 9 - Grösse der Durchbohrung im Deckblech der ERA-Box
Einlagegeometrie FAETSCH, Einfluss vom Kaliber der Vorladung

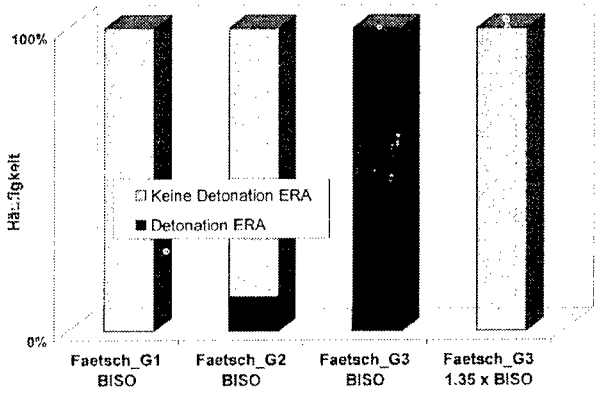


Abb. 10 - Verhalten des Reaktivzieles
Einfluss des Kalibers der Vorladung, von links nach rechts zunehmend

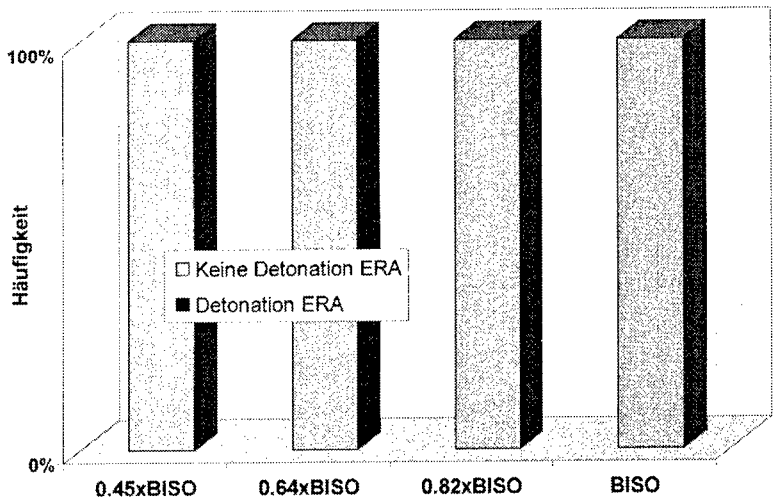


Abb. 11 - Einlagegeometrie FAETSCH_G2E1 bei verschiedenen Sprengabständen
Keine Detonation der ERA-Boxen

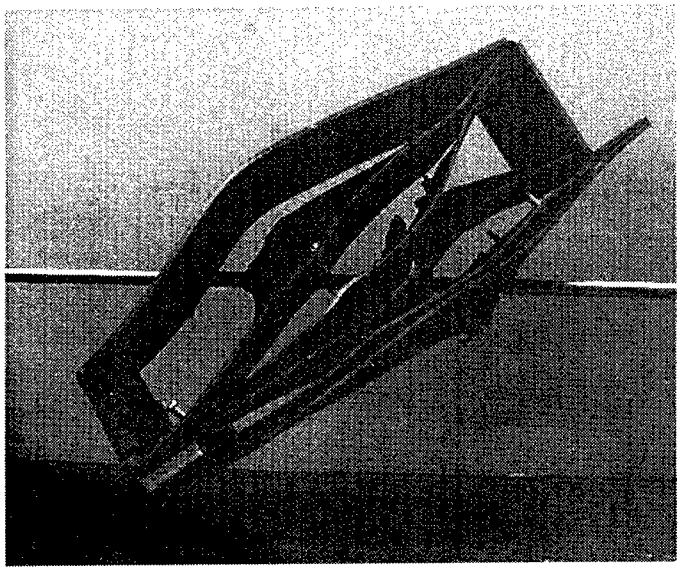


Abb. 12 - Reaktivziel, nichtdetonativ aufgebohrt

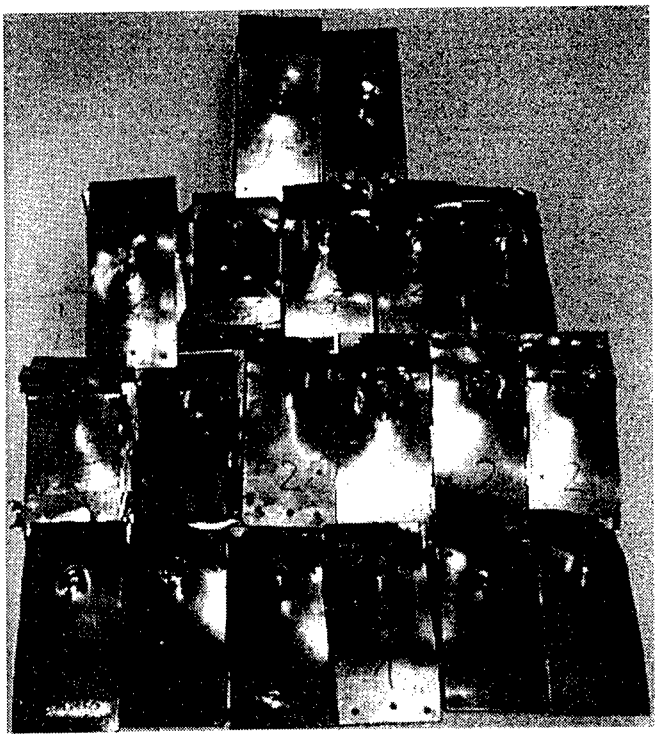


Abb. 13 - Rückseite der nichtdetonativ durchbohrten ERA-Boxen, bei von oben nach unten zunehmenden Sprengabständen

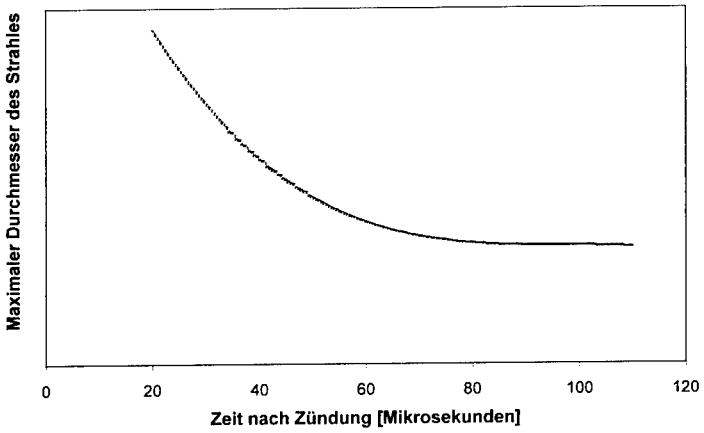


Abb. 14 - Maximaler Durchmesser des Vorladungsstrahles (FAETSCH_G2E1)

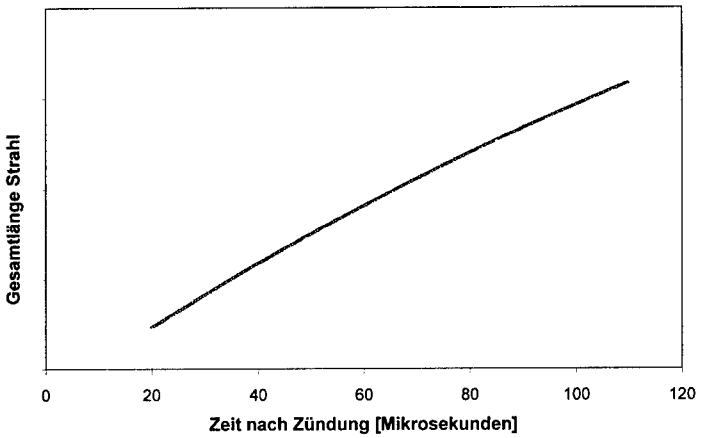
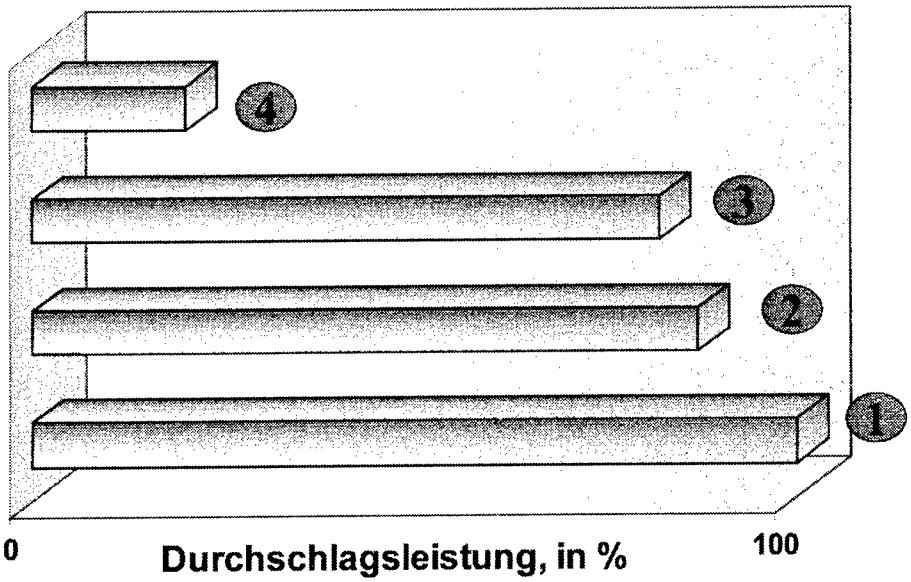


Abb. 15 - Gesamtlänge des Vorladungsstrahles (FAETSCH_G2E1)



1 Hauptladung allein (100%)

2 Tandem BADUS 2, Ziel ohne Reaktivpanzerung

3 Tandem BADUS 2, Ziel mit Reaktivpanzerung, nicht detonativ geräumt

4 Zum Vergleich: Tandem BADUS 1, bei einer Detonation der Reaktivpanzerung

Abb. 16 - Leistungsvergleich (Zielmaterial: Panzerstahl)

Ablative Accelaration of Thin Flyer Plates

Yehuda Haas and Semion Cogan

Department of Physical Chemistry and the Farkas Center for Light Induced Processes, The Hebrew University of Jerusalem, Jerusalem, Israel

Fax: +972-2-5618033, e-mail: yehuda@chem.ch.huji.ac.il

Abstract

Explosives may be initiated by the impact of a high velocity metal flyer. High velocity aluminum flyers were formed by laser ablation a thin layer of aluminum off a glass substrate. A Q-switched Nd:YAG laser (1.064 nm) was used to initiate the ablation, operated at moderate pulse energies (20-80 mJ). The flyer's velocity was measured directly by a time-of-flight (TOF) method, and found to be 1-4 km/s, depending on the flyer's thickness and the laser energy. The pressure of the flyer on impact with a solid target was also measured, using a piezoelectric gauge. It was concluded that up to 70% of the initiating laser energy was converted to the flyer's kinetic energy. A threshold energy of about 10 mJ is required to initiate the ablation, setting a lower limit to laser power requirements.

Introduction

Thin metal flyer plates can be accelarated to high velocities and be used for explosive initiation [1,2,4]. Lasers have been used for this purpose, and it was shown that the flyers attained the energy and momentum required to initiate explosions of secondary explosives. The usual method is to coat a transparent substrate (glass or quartz) by a thin (a few micrometers) layer of metal, and irradiate the metal form the glass side by a focussed, pulsed laser beam. The mechanism of the flyer formation is still under investigation. It is believed that the process is initiated by multiphoton absorption of the laser energy by the metal, creating a plasma at the glass-metal interface. The plasma pushes the metal away from the substrate, forming the flyer. The flyer attains a velocity of a few km/s almost instantly. The impact of the flyer on a solid surface can create pressures of up to 10GPa, sufficiently high to initiate explosion [1].

In this work we aimed at a better characterization of the flyer formation , by a systematic study of several parameters that may affect the process. These include the laser pulse's energy, metal layer thickness and ambient pressure. The velocity of the flyer was directly measured using a time-of-flight method, and the flyer's impact was estimated by using a sensitive piezoelectric gauge.

Experimental

The experimental setup for measuring the flyer's velocity is schematically displayed in **Figure 1**. The substrate was a microscope slide, on which a thin aluminum coating was deposited using either a sputtering method (for thicknesses up to 3.5 microns, or vapour deposition). The substrate was mounted on a translation stage, whose position could be controlled to 1 mm. It was irradiated from the uncoated side by Nd:YAG laser pulse at 1.064m (the initiating laser). The laser (Continuum model YG681-10) was operated at the Q-switch mode, creating 10 ns pulses of up to 700 mJ. The beam was attenuated in a contiuous manner to the desired energy using a polarizer cube, and focussed unto the target with a lens system. The area of the irradiated zone was about 1 mm^2. The flyer moved away from the microscope slide and crossed a cw He-Ne laser beam (632.8 nm), which was focussed to a waist of 100 micron (the probe laser). The distance between the substrate's surface and the and the probe laser's beam could be determined to within 5 μ. The intensity of the probe laser's beam was measured by a phoptomultiplier tube (Hamamatsu R928),

attached to a monochromator. Background signal level was negligible. The phoptomultiplier (PM) signal was recorded by a 500MHz digital oscilloscope (Tektronix TDS 620B), interfaced to a personal computer. The trigger was provided by a photodiode, sensing the laser pulse. The time response of the system was estimated to be 2 ns.

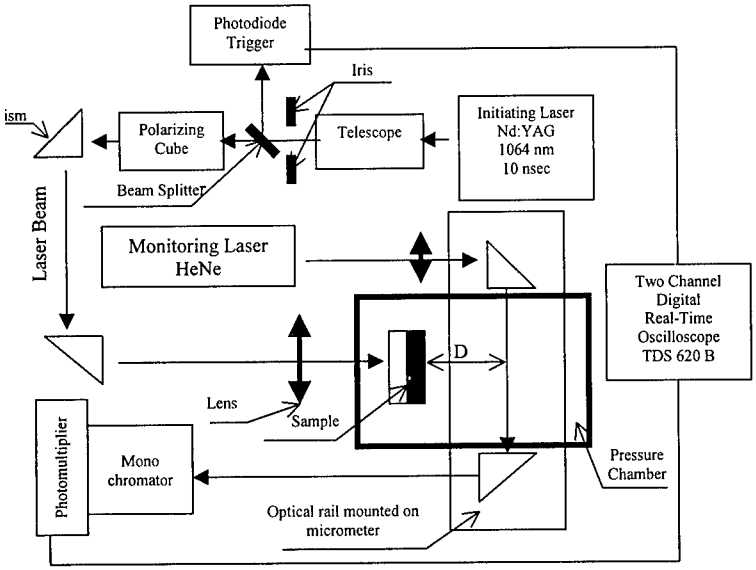


Fig. 1: Time of flight experimental setup

The mass of the flyer was estimated by measuring the ablated area under a microscope, and assuming that the all of the ablated mass was contained in the flyer. The density of aluminum for the present experiments was assumed to be the bulk densit (2.7 g/cm3). **Figure 2** shows the holes created on the microscope slide by the ablation of a 3 μ aluminum layer. Reproducibilty is seen to be quite reasonable. The measured area was 0.83 mm^2, leading to a flyer's mass of 6.7 ng.

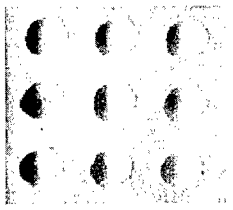


Fig. 2: Holes created on microscope slide by ablation The laser's energy was 73.3 mJ.

The pressure created by the flyer was measured using a PVDF piezoelectric gauge (Piezotech Model S-25-01). **Figure 3** shows a scheme of the experimental setup. The microscope slide was rigidly clamped to the PVDF gauge, with an accurate spacer ring between them. The spacer's width was accurate to 5 μ. To avoid excessive damage to the sensitive gauge, a mylar sheet (100 μ thick) was placed in front of it. The PVDF gauge's signal was monitored by the same oscilloscope used for the TOF measurements.

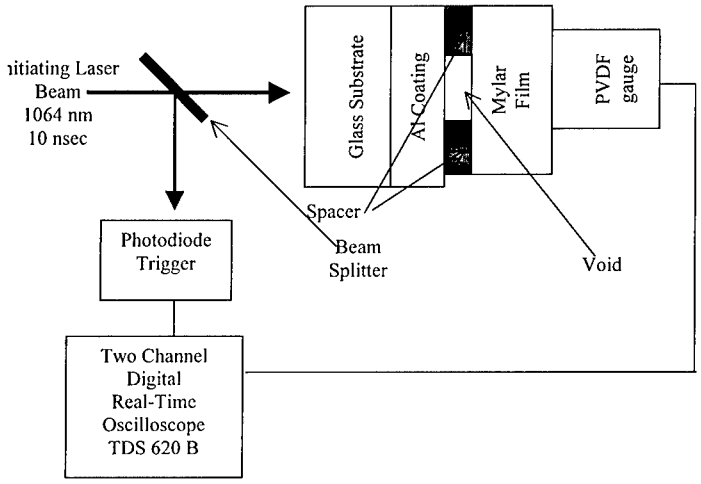


Fig. 3: Pressure measurement experimental setup

Experimental results

Flyer's velocity

A typical oscilloscope trace of the PM's output is shown in **Figure 4**. The time of flight was determined, as shown in the figure, from the beginning of the attenuation of the probe laser beam. Some ambiguity is introduced if the attenuation is not instaneous. We used the time to reach maximum change in the signal as time of flight, as explained in the figure caption.

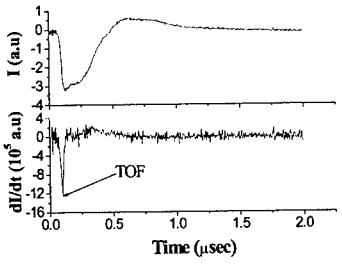


Fig. 4: Typical signal and the TOF determination. Top trace, real time PM signal; bottom trace, its time derivative. The time of flight is the time interval from the trigger signal to the maximum value of the derivative.

Figure 5 shows the results of typical series of measurements. Data were collected at 0.1 mm intervals between 0.2 and 1.1 mm. It is seen that the time of flight increases approximately linearly with distance (a small levelling-off is observable at the long distance end).

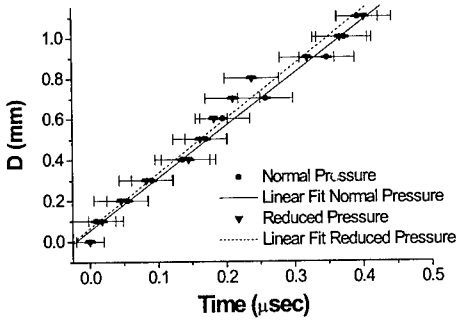


Fig. 5: Time vs. distance of flight 9 μm thick aluminium layer at reduced (dashed line) and normal (solid line) pressures.

The results of experiments with a 9 μ thick aluminium layer are summarized in **Table 1**. It is seen that the velocity increases with the initiating laser pulse energy from about 1.35 km/s at 23 mJ to about 2.6 km/s at 73.3 mJ. There is only a negligible difference between the velocities measures at atmospheric pressure (about 700 torr) to those measured at 2 torr. When thinner coatings were used, a larger difference was measured, the velocities were higher under vacuum conditions.

Table 1: The flyer velocities measured for 9μm in thickness coatings at different initiating laser energies and pressures

Coating Thickness (μm)	Pressure (torr)	Initiating Laser Energy (mJ)	Flyer velocity ($*10^3$ m/sec)
		25.6	1.36 ± 0.06

		37.5	1.8 ± 0.1
		49	2.07 ± 0.03
		57.8	2.27 ± 0.04
		67.1	2.46 ± 0.07
		73.3	2.57 ± 0.07
	2	23	1.36 ± 0.06
		41.1	1.85 ± 0.05
		48.1	1.91 ± 0.07
		53	2.45 ± 0.06
		67.1	2.47 ± 0.08
		73.3	2.7 ± 0.1

Figure 6 shows that the squared velocity of the flyer is linearly proportinal to the initiating laser energy. It is seen that the velocity is somewhat greater under vacuum than when the flyer travels at atmospheric pressure. The difference is larger for the thinner flyer.

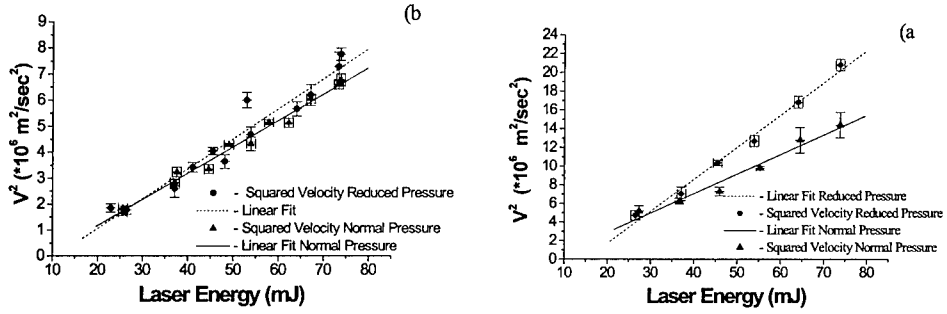


Fig. 6: Squared flyer velocity vs. initiating laser energy

a) 3.5 μ Al coating

b) 9.0 μ Al coating

Pressure measurements

Figure 7 shows typical PVDF gauge signal recorded by oscilloscope and its numerical integration. The PVDF signal S_{PVDF} is proportional to the instantaneous pressure change. The total impact pressure P_{TOT} is therefore obtained by numerical integration of the signal over the time interval of the PVDF response:

$$P_{TOT} = \frac{C}{AR}\int_0^t S_{PVDF}dt$$

Where A is the flyer's area, R the resistor across which the voltage is read, C a conversion constant and t the duration of the signal. We define t_c as a typical time interval over which the

gauge's signal is observed. The intrinsic time constant of the gauge is about 1 ns. The observed response of a few microseconds is therefore due to system parameters. The constant C is typical for each gauge and is provided by the manufacturer.

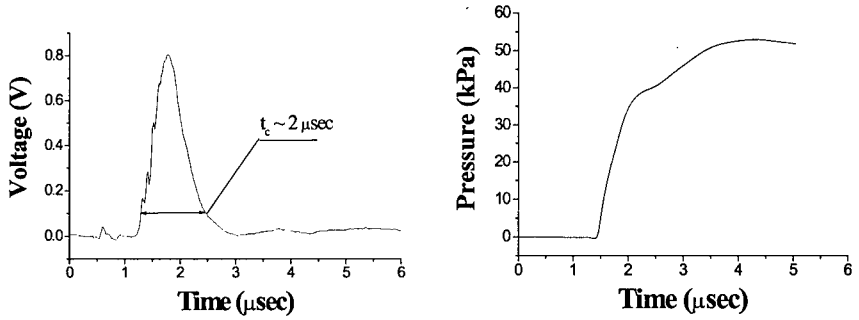


Fig. 7: Typcal PVDF signal recorded by osciloscope (on the left) and pressure determined by its numarical integration (on the right).

Discussion

It was found experimentally, that the squared velocity (V_{FLYER}^2) of the flyer is proportional to the initiating laser's energy. Assuming that the flyer remains intact during the first 1 mm of its travel, and that its mass m_{FLYER} is determined as explained in the experimental part, the kinetic energy EK_{FLYER} may be calculated from the relation

$$EK_{FLYER} = 1/2 m_{FLYER} V_{FLYER}^2$$

The initiation laser energy is required to separate the flyer from the substrate, create the plasma, and provide the kinetic energy of the flyer. In addition, it may be assumed that the flyer is heated to a temperature higher than ambient, which was not measured. Only the kinetic energy is useful in initiation of explosives, we therefore, define as the conversion efficiency α, the fraction of the laser's energy that is converted to kinetic energy:

$$\alpha = EK_{FLYER} / E_{LASER}$$

α was determined experimentally for a variety of conditions. The results are collected in Table 2. It was found that the efficiency increased as the laser energy was increased, and reached approximately 70% at E_{LASER}= 73.3 mJ.

At low laser energies, a flyer was not formed. This was attributed to the need to separate the flyer from the glass substrate and the rest of the metal layer. Exact determination of the threshold

energy required to separate a flyer is difficult, apparently due to the multiphoton nature of the process. We estimate it to be about 10 mJ, under our experimental conditions.

Table 2: Energy Coversion Efficiency culculated for different aluminium coatings at different conditions.

Coating Thickness (μm)	Initiating Laser Energy (mJ)	Pressure (torr)	Energy Conversion Efficiency
3.5	73.8	2	0.65
	64.0		0.61
	53.9		0.54
	45.5		0.53
	37.1		0.44
	26.5		0.41
	73.7	700	0.44
	64.5		0.45
	55.2		0.40
	45.9		0.36
	36.7		0.38
	27.4		0.43
9.0	73.8	2	0.69
	64.0		0.58
	53.9		0.57
	45.5		0.59
	37.1		0.46
	26.5		0.44
	73.8	700	0.69
	62.3		0.62
	53.9		0.61
	44.6		0.57
	37.1		0.58
	25.6		0.50

The linear relation between the kinetic energy of the flyer and the laser's energy indicates that after the initial multiphoton process, most of the energy conversion is due to monophotonic absorption processes. The nature of these processes is not known at this point: it may be due to absorption by the plasma or by the neutral gases formed between the flyer and the substrate after its departure from the substrate. Watson and Field [2] showed that the glass substrate is ablated to a depth of 280- 1100 nm. The material released in this process is trapped between the rest of the substrate and the flyer, and may absorb the later part of the laser pulse energy.

The measured pressures in our experiments (of the order of 50 - 100 kPa), are much lower than expected based on previous reports of the order of GPa [3]. This may be accounted for by the following reasons:

1) The flyer collides with a Mylar sheet and not directly with the gauge. The force of the impact is spread in the plastic, and some of it is converted to plastic deformation.

2) As seen from Figure 7, the pressure signal builds up over a relatively long time. The collision time of a thin flyer (3m thick) travelling at 3 km/s with a rigid body is of the order of 1 ns. The actual time response was of the order of microseconds; Since the pressure created is proportional to the interaction time, the reading is lower by 3 or 4 orders of magnitude than that expected for direct impact on the gauge. The long response time is probably due to the slow response of the mylar. Some measurements were taken without the protecting Mylar layer, resulting in destruction of the gauge. The signal rise-time in these experiments was limited by the time constant of the system (2 ns).

Watson and Field [4] reported that the plasma can penetrate the flyer, and interpreted this as indicating the disintegration of the flyer. Their laser energies were somewhat higher than used in this study, but some plasma penetration was reported also for 56 mJ pulses. Our results show that even if the flyer allowed plasma penetration, its impact on a target is not affected. One might surmarise, that some loosening of the metal lattice allows plasma penetration, but the total mass of the flyer remains unchanged over the flight distances used here. In particular, we cannot rule out melting of the flyer.

Conclusions

The main conclusions from this work are:

A Nd:Yag laser pulse of 1.064 μ and 10 ns duration can be used to form an aluminum flyer by laser ablation of a thin layer of the metal from a glass substrate. Metal layer thicknesses of up to 9 μ were used. The initiating laser energy can be converted to kinetic energy of the flyer with an efficiency of up to 70%.

There is a threshold energy required to initiate the creation of the flyer. In our experiments it was of the order of 10 mJ. This energy is required for the initial ablation process, which is multiphoton absorption. It is also required to create the initial plasma and gaseous cloud that drives the flyer away from the substrate.

The linear relationship between the laser's energy and the kinetic energy of the flyer indicates that most of the laser's energy is transferred to the flyer by monophotonic processes, probably absorption by the gaseous cloud.

The flyer attains its final velocity within 0.1 mm from the substrate. The velocity of the flyer, and therefore its impact on a target, remains fairly constant over the first mm of its travel. The velocity is barely affected by the ambient pressure, particularly for thick flyers.

The flyers produced in this study attained kinetic energies of the order required for explosive initiation [1, 3].

References

1) S. Watson, J. E. Field, J. Appl. Phys. 88, 65 (2000).

2) S. Watson, J. E. Field, J. Phys. D. 33, 170 (2000).

3) R. C. Weingart, R. S. Lee, R. K. Jackson, N. L. Parker, Proc. 6th Symposium (Int) on Detonation (San Diego, Ca. 1976) p. 201.

4) S. Watson, J. E. Field, J. Appl. Phys. 88, 3859 (2000).

PERFORMANCE TESTING OF PERCUSSION CAPS

Trevor T Griffiths and Richard J Duncombe
Defence Evaluation and Research Agency,
Fort Halstead, Sevenoaks, Kent, UK

Colin J Hutchinson
Defence Evaluation and Research Agency,
Bishopton, Renfrewshire, UK

ABSTRACT

The performance of primary explosives incorporated into initiatory devices has been measured by closed vessel testing. Thermal analysis and chemical analysis of the initiatory compositions was also undertaken.

The effect of charge weight on the pressure-time curves of the percussion caps was investigated. Percussion caps filled with reduced charge weights were found to have lower peak pressures.

Sensitivity measurements were made on caps containing 0%, 0.5%, 1.0%, 1.5% and the normal 2% tetrazene. A similar pressure-time performance was observed but the incidence of failure increased as the amount of tetrazene present decreased. When no tetrazene was present, all of the caps failed to function.

Percussion caps were examined before and after accelerated ageing. When exposed to 100% relative humidity (RH) leaching of the lead styphnate was observed and none of the caps functioned, corrosion of the brass cap casings was evident. Under slightly less harsh conditions of 79% RH a gradual deterioration in the performance of the caps was observed. After B3 diurnal cycling the time to maximum pressure, maximum pressure and duration of the pressure pulse were found to be similar for each set of data but the area under the pressure-time curve increased as the time of ageing increased.

Thermal analysis by differential scanning calorimetry confirmed that changes had occurred to the initiatory composition after ageing. The peak decomposition temperature had decreased from 287°C to 270°C. However, chemical analysis did not show any significant change in the composition.

INTRODUCTION

The aim of this research was to investigate if performance testing should be introduced into the Routine Periodic Inspection (RPI) procedures of initiatory devices. Performance testing would ensure that they were 'fit for purpose' but would reduce the amount of chemical analysis that needed to be undertaken.

Additionally, specification test methods are satisfactory for assessing new material but it is often difficult to obtain sufficiently large samples of aged initiatory materials to undertake a full chemical analysis.

When a primary explosive is initiated, a chemical reaction occurs to produce a high temperature reaction and gaseous products. The rapid release of these gaseous reaction products results in a rapid pressure rise which gradually decreases as the reaction is completed and the temperature drops. This pressure/time dependence has been used to assess the performance of primary explosive compositions used in percussion caps. Changes in performance were indicated by a lengthening of initiation time, reduction in the peak pressure, lengthening of the time to peak pressure and changes in slope or shape of the pressure/time curves.

EXPERIMENTAL

A closed vessel test, which allowed a quantitative assessment of the performance of small explosive devices, was used for the research. The programme of work involved:

- Commissioning and optimisation of firing apparatus and data recording equipment,
- Measurement of the percussion cap performance parameters,
- Performance measurements of percussion caps containing aged material.

A schematic of the apparatus used for testing the percussion caps is shown in figure 1. The volume of the closed vessel can be varied from 1 to 5cm^3 in 0.5cm^3 increments. The percussion cap was initiated by a spring-loaded firing pin.

The pressure/time dependence was measured using a Kistler Type 6215 piezo electric transducer fitted in the side of the closed vessel. The output was fed via a charge amplifier into one channel of a Nicolet 440, four channel, 12 bit, 10 mega samples/second digital storage oscilloscope. A sweep time of 120μs was used and 5% of the signal was recorded prior to firing. The sampling rate used was 500μs/point. The system was filtered to remove acoustic ringing.

A typical trace showing the first 30ms is shown in Figure 2. In general, the maximum pressure (P_{max}), time to maximum pressure, and area under the pressure-time curve for the positive impulse were determined. The mean value for each parameter was calculated from the results of 30 firings.

In some experiments the time to initial pressure rise was determined. This was a summation of time to compress the spring of the firing pin and the time to initiate the chemical reaction. Firings performed with the firing pin in direct contact with the cap showed that the time to compress the spring in the firing pin assembly was around 1.2ms.

Percussion caps

The percussion caps used for this investigation were 5.56mm in size. This type of percussion cap is often used for the initiation of small arms munitions. They contain a nominal 25mg of VH2 composition, which is a mixture of lead styphnate, barium nitrate, tetrazene, lead dioxide, antimony sulphide and calcium silicide.

Initial experiments

Experiments were conducted to identify the critical parameters of the pressure vessel (volume) and recording system (transducer sensitivity, scaling factor, filtering frequencies). Sixty caps were then tested using a volume of $3cm^3$ to establish baseline data for the P_{max} and the area under the pressure curve.

Effect of reduced charge weight on performance

Caps filled with three different charge weights were used to investigate the effect of reduced charge weight on performance. One lot contained the full charge weight (25.3mg), the remaining two lots contained either 22.5mg or 19.5mg of VH2 composition. The caps were manufactured by direct weighing of the composition into the cap before sealing. Thirty caps were tested to establish mean values for the time to initial pressure rise, P_{max}, the time to P_{max}, and area under the pressure curve.

Effect of reduced tetrazene content on performance

Tetrazene is normally present in VH2 composition at the 2% level; it is incorporated as a sensitiser. Caps were manufactured with VH2 composition containing 1.5%, 1.0%, 0.5% or 0% tetrazene. For each composition, the pressure-time curves of thirty caps were measured and the change to the sensitivity of the modified VH2 compositions was assessed.

Ageing studies

The percussion caps were aged in a variety of ways, in each case they were stored in open boxes.

ISAT A conditions

The caps were ageing for 4 weeks under ISAT A conditions. Details of ISAT A environmental conditions are given in Table 1.

High relative humidity

Caps were aged at ambient temperature under high humidity conditions. They were conditioned at either 100% RH for two months, or 79% RH for 6 months. Thirty caps were removed from the environmental chamber held at 79% RH every 2 months and tested.

B3 diurnal cycling

The percussion caps were aged under B3 diurnal cycling conditions for four months. The details of B3 temperature cycling are given in Table 2.

Chemical analysis

Thermal analysis

Some of the cap compositions were examined using differential scanning calorimetry (DSC). Samples were heated from 30°C to 350°C at 5°C min^{-1} under a nitrogen atmosphere using a Mettler DSC 20 differential scanning calorimeter. The three compositions examined were the unaged material, a sample from caps which had been subjected to the high humidity trial (79% RH) for six months and composition removed from caps after four months B3 diurnal cycling.

Quantitative chemical analysis

The unaged composition and sample removed from the percussion caps in the two high humidity trials were analysed to establish if any significant changes to the composition had occurred.

RESULTS AND DISCUSSION

Initial experiments

Experiments performed without acoustic filtering displayed relatively high levels of ringing, which affected the measurement of functioning times and pressure. The frequency of the ringing was determined to be about 15kHz with an amplitude of about 1V peak to peak.

Filtering of signals >10kHz was found to be essential to remove these acoustic vibrations appearing on signals. However, too much filtering, < 1kHz resulted in too much smoothing of signals and detail such as peak pressures were incorrectly measured. Filtering in the range 3kHz - 10kHz gave a good compromise of the two effects.

The effect of changing closed vessel volume was investigated by testing thirty caps in volumes of 3, 4 and 5cm^3; the results are summarised in Table 3. A linear relationship between P_{max} and volume of the closed vessel was observed over the range of volumes studied. The transducer output signal was saturated for volumes of the closed vessel of less than 3cm^3. A transducer scaling factor of 300kPa/V and a closed vessel volume of 3cm^3 were used for subsequent firings.

Effect of reduced charge weight on performance

The relationship between pressure output and VH2 charge weight was determined by testing 30 caps containing three charge weights 25.3mg, 22.5mg and 19.5mg. The time to initial pressure rise, P_{max}, time to P_{max} and the area beneath the pressure curve are given in Table 4.

Both P_{max} and area under the pressure curve showed only a small increase as the charge weight increased from 19.5mg to 22.5mg, but at 25.3mg a large increase in value was observed. The time to initial pressure rise and the time to P_{max} appeared to be unchanged by the change in charge weight.

Effect of reduced tetrazene content on performance

The pressure-time results are given in Table 5, they showed only small variations in time to initial pressure, P_{max}, time to P_{max} and the area under the pressure-time curve. However, the ease of initiation dropped significantly as the quantity of tetrazene present was reduced. A high incidence of failure, approaching 30% was observed as the quantity of tetrazene reached 0.5%. The composition where all of the tetrazene had been removed failed to initiate.

Accelerated ageing

ISAT A conditions.

The performance characteristics of the caps aged for 4 weeks under ISAT A conditions were very similar to those of unaged caps, the results are shown in Table 6. There was a small decrease in peak pressure after ageing but the areas under the curves were similar. However, the results have a large standard deviation and further work would be required to confirm if the decrease in peak pressure was as a result of ageing.

High relative humidity

The thirty caps exposed to 100% RH for 8 weeks failed to function. There were yellow crystalline formations on the external surfaces of the caps, which suggested leaching of lead styphnate from the composition. Due to the environment in which they were being aged, there was considerable corrosion of the brass casing of the caps, The results of the tests on the caps aged at 79% RH of 2, 3 and 4 months are given in Table 7. The peak pressure results are shown in figure 3.

The P_{max} results indicate a decrease in performance of the caps after ageing at 25°C and 79% RH. However, the area measured under the pressure/time curves remained relatively constant. As the ageing period increased the time to initial pressure rise and the time to peak pressure decreased. This suggests that the sensitivity of the composition was increasing. The pressure pulse duration remained relatively unchanged.

B3 Diurnal cycling

The pressure-time results for the caps tested after diurnal cycling are given in Table 8. No significant drop in the value of P_{max} was observed and the duration of the pressure pulse was found to be similar. However, there was a decrease in the time to initial pressure rise and the time to P_{max} as the period of ageing increased. Additionally, the area under the pressure–time curve increased as the ageing period increased.

Chemical analysis

Thermal analysis

The results of the DSC analysis are summarised in Table 9.

The thermograms show that the peak temperature of decomposition (287°C) given by the unaged material, Figure 4, reduces to approximately 269°C for the samples aged at 79% RH for 6 months, as shown in Figure 5. The peak at 287°C is still apparent but is much smaller. For the VH2 samples removed from the caps aged under B3 diurnal conditions a shoulder is apparent, on the main exotherm, at 269°C, Figure 6.

The presence and increasing peak size of the peak at 269°C may indicate a measure of degradation in the composition and could consequently be used as an early indication of degradation and/or failure of the composition in service.

Quantitative chemical analysis

Quantitative chemical analysis was unable to show any difference between the unaged and the aged VH2 composition.

CONCLUSIONS

The performance of percussion caps can be determined from their pressure /time profile. Percussion caps that contained less than the specified quantity of VH2 had a considerably lower peak pressure.

Tetrazene is extremely important for sensitisation of the VH2 composition. A high incidence of failure was observed in caps when the relative quantity of tetrazene was decreased. When tetrazene was absent, none of the caps functioned.

Performance testing of percussion caps aged under ISAT A conditions indicated no significant change in performance.

Ageing the caps under 100% RH conditions at ambient temperature for 8 weeks caused leaching of the lead styphnate and failure to initiate. Ageing under 79% RH conditions at ambient temperature for six months showed a drop in performance.

The percussion caps aged under B3 Diurnal conditions for 4 months showed no significant drop in pressure performance but the composition appeared to be more sensitive.

DSC of the compositions removed from caps aged at high humidity confirmed that a change had occurred as a result of ageing. The presence of a shoulder on the main exotherm of those aged under B3 conditions suggests that they had also started to age.

Quantitative chemical analysis of VH2 composition that no longer initiated did not show any differences from unaged material.

As a means of assessing percussion caps and fuseheads for the purposes of RPI and proof, the measurement of their pressure-time profile is unsuitable. Although, evidence can be obtained on degradation, the large number of samples required for a valid statistical assessment is difficult and expensive to obtain.

DSC appears to be more suitable for assessing degradation in cap compositions and would therefore be more suited to RPI of stores. Assessment of compositions could be made on fewer samples in a much shorter time-scale making thermal analysis a cost-effective technique.

TABLES

ISAT A Ageing Conditions		
Duration	Temperature (°C)	Relative Humidity (%)
3 days	46±2	95±2
1 day	Cooling	
1 day	46±2	95±2
1 day	60±2	95±2
1 day	Cooling	

Table 1; ISAT A conditions

B3 Storage conditions		
Local time (hours)	Ambient air temperature (°C)	Relative humidity (%)
0100	35	67
0200	34	72
0300	34	75
0400	34	77
0500	33	79
0600	33	80
0700	36	70
0800	40	54
0900	44	42
1000	51	31
1100	57	24
1200	62	17
1300	66	16
1400	69	15
1500	71	14
1600	69	16
1700	66	18
1800	63	21
1900	58	29
2000	50	41
2100	41	53
2200	39	58
2300	37	62
2400	35	63

Table 2; B3 diurnal cycling conditions

Volume of closed vessel (cm^3)	Transducer output (V)	P max (kPa)
3.0	9.3 σ 0.4	2790 σ 120
4.0	7.8 σ 0.7	2340 σ 210
5.0	6.0 σ 0.2	1800 σ 60

Table 3; Transducer output as a function of closed vessel volume

Mean charge weight (mg)	Time to Initial pressure rise (ms)	Time to P_{max} (ms)	P_{max} (kPa)	Area under pressure curve (mVs)
19.5	3.1 σ 0.2	3.3 σ 0.3	1875 σ 208	21.5 σ 1.3
22.5	2.8 σ 0.2	2.9 σ 0.2	1974 σ 240	21.8 σ 1.0
25.3	3.0 σ 0.2	3.1 σ 0.2	2787 σ 120	29.8 σ 2.0

Table 4; Results for different VH2 charge weights

Tetrazene amount (%)	Time to initial pressure rise (ms)	Mean time to P_{max} (ms)	P_{max} (kPa)	Area under pressure curve (mVs)	Comments
0	-	-		-	All failed
0.5	2.9 σ 0.2	3.0 σ 0.3	2545 σ302	25.8 σ 1.4	29 % failure rate
1.0	3.0 σ 0.2	3.2 σ 0.2	2488 σ 284	23.2 σ 1.1	19 % failure rate
1.5	Not measured	Not measured	2712 σ 343	22.2 σ 2.8	10 % failure rate
2.0	3.0	3.2	2730 σ 210	22.3 σ 2.3	All fired

Table 5; Effect of reduced tetrazene levels on performance

Sample	P_{max} (kPa)	Area under pressure curve (nVs)
Control	2730 σ 210	22.3 σ 2.3
Aged 4 weeks	2460 σ 330	23.0 σ 1.7

Table 6; Results for caps aged under ISAT A conditions.

Sample	Time to initial pressure rise (ms)	Time to Pmax (ms)	Pmax (kPa)	Duration (ms)	Area under pressure curve (mVs)
Control	3.0 σ 0.3	3.2 σ 0.3	2730 σ 210	19.9 σ 1.3	22.3 σ 2.3
2 months	2.5 σ 2.2	2.9 σ 2.1	2190 σ 480	23.3 σ 2.4	23.8 σ 1.4
4 months	1.7 σ 0.2	2.0 σ 0.2	2250 σ 600	21.6 σ 2.4	25.1 σ 2.4
6 months	1.5 σ 0.1	2.0 σ 0.2	1650 σ 510	21.4 σ 2.7	24.8 σ 3.9

Table 7; Results for caps aged at 25°C and 79% RH.

Sample	Time to initial pressure rise (ms)	Time to P_{max} (ms)	P_{max} (kPa)	Duration (ms)	Area under pressure curve (mVs)
Control	3.0 σ 0.3	3.2 σ 0.3	2730 σ 210	19.9 σ 1.3	22.3 σ 2.3
2 months	1.7 σ 0.1	1.9 σ 0.1	2430 σ 150	22.0 σ 0.9	22.8 σ 1.2
3 months	1.6 σ 0.1	1.8 σ 0.2	2760 σ 330	17.6 σ 0.3	26.7 σ1.8
4 months	1.5 σ 0.1	1.7 σ 0.1	2910 σ 300	18.3 σ 0.7	30.9 σ 1.9

Table 8; Results for caps aged under B3 diurnal cycling conditions

Sample	1st peak temp (°C)	2nd peak temp (°C)	3rd peak temp (°C)	Heat of decomposition ($J\ g^{-1}$)
Unaged	139.6 ± 0.0	287.3 ± 0.0	None	747 ± 15
79 % RH for 6 months	138.3 ± 0.1	269.3 ± 0.1	288.5 ± 0.6	498 ± 82
4m B3 diurnal cycling	138.2 ± 0.0	288.5 ± 0.2	None	640 ±28

Table 9; Thermal analysis of unaged and aged cap compositions

FIGURES

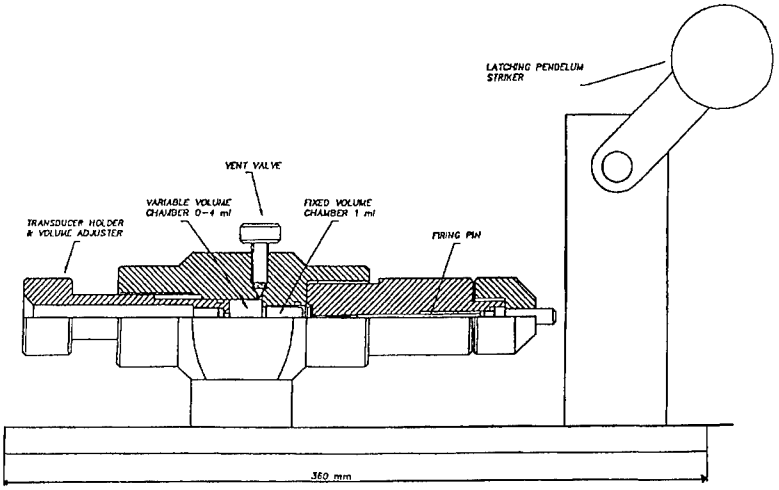


Figure 1; Schematic of the firing apparatus

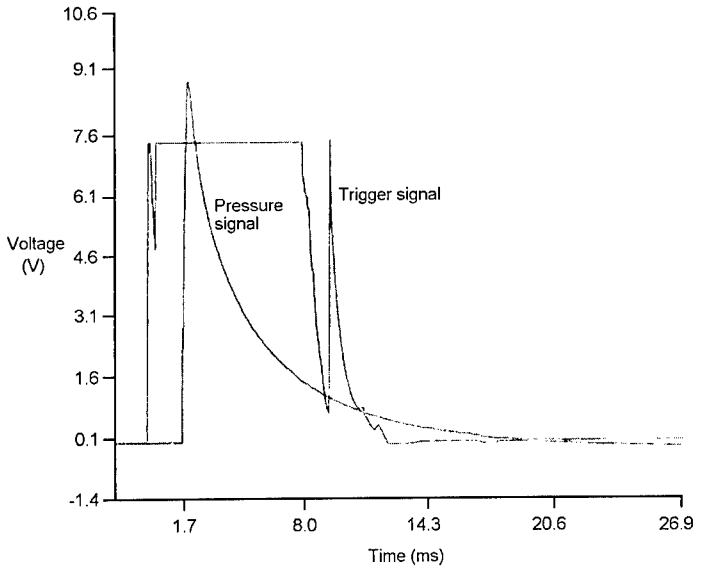


Figure 2; Results from a Percussion Cap Firing

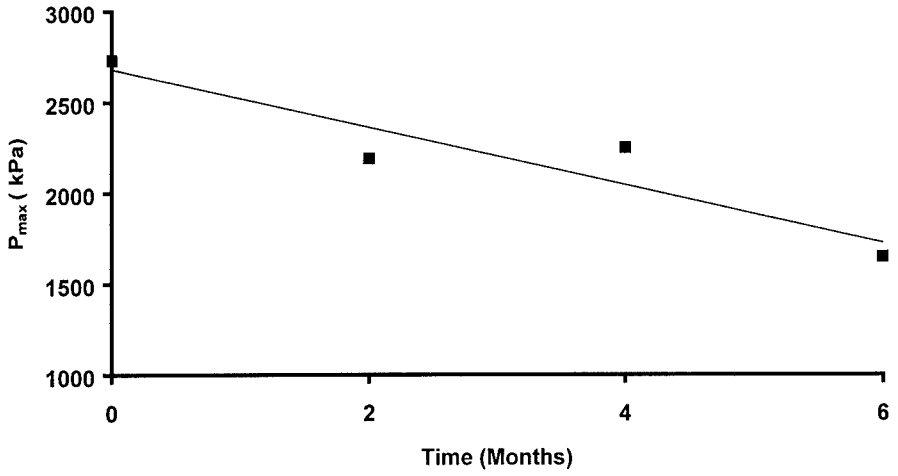


Figure 3; Mean peak pressure after ageing at 25°C and 79% RH.

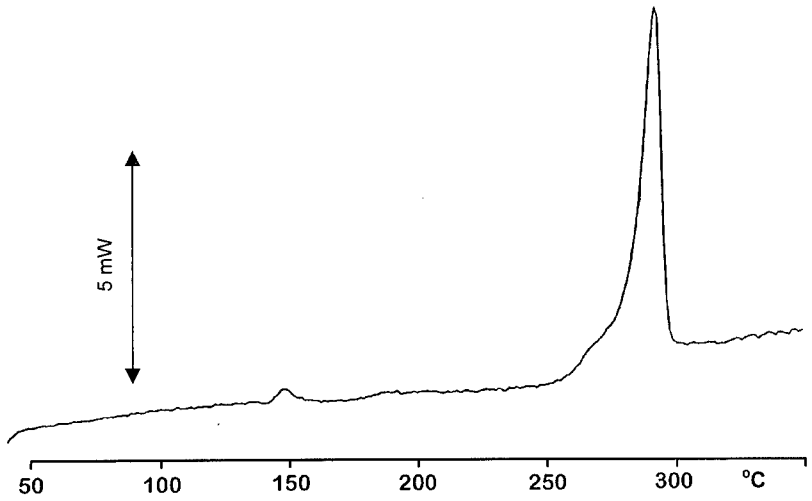


Figure 4; DSC thermogram of unaged VH2 composition

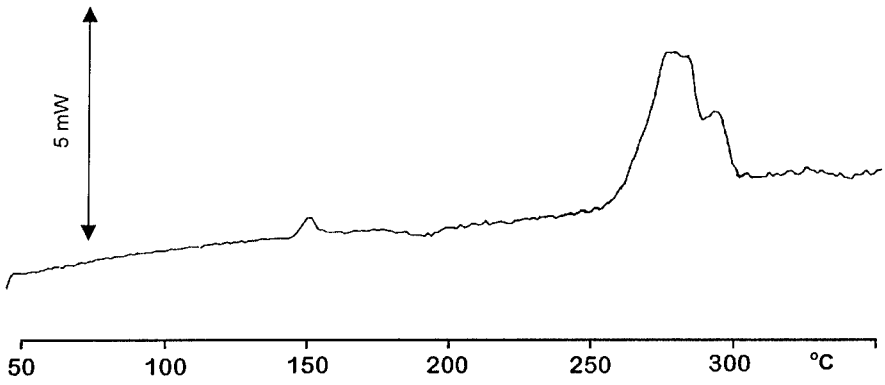


Figure 5; DSC thermogram of VH2 composition aged at 79%RH for 6 months

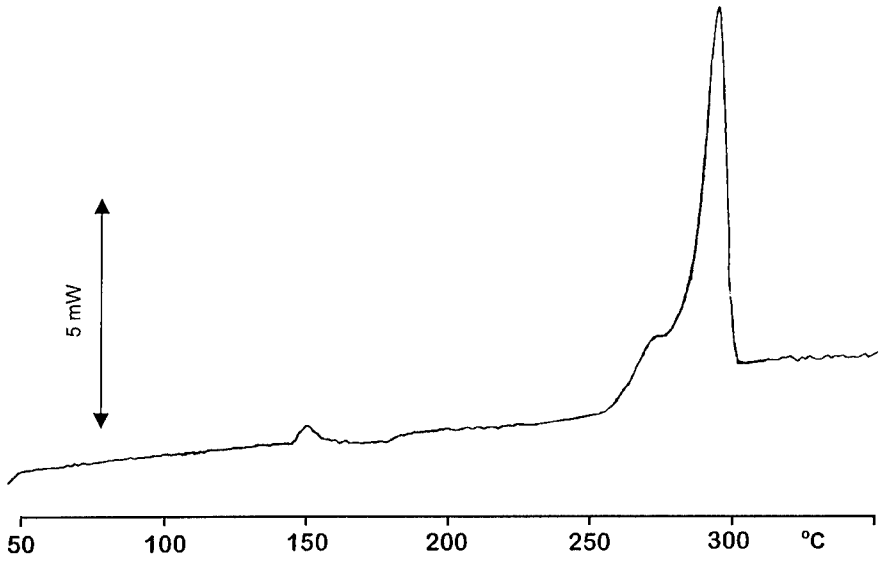


Figure 6; DSC thermogram of VH2 composition aged under B3 diurnal cycling conditions for 4 months

Hexanitrostilbene (HNS) Development for Modern Slapper Detonators

Steven M. Harris and Sandra E. Klassen
Sandia National Laboratories, MS 1453
P. O. Box 5800
Albuquerque, New Mexico 87185-1453

W. Tim Quinlin, Dillard M. Cates, and Ray Thorpe
BWXT Pantex, P.O. Box 30020
Amarillo, Texas 79120-0020

Abstract: The Explosive Technologies Group at Sandia National Laboratories in Albuquerque, NM, USA, has spent the last eight years working with personnel at BWTX Pantex Plant, Amarillo, TX, USA, to develop a hexanitrostilbene (HNS) material with high purity, high specific surface area (SSA), and low residual solvent content specifically for use with modern slapper detonators. The basic approach involves crash precipitation of a solution of HNS to water. Variations include different solvents such as acetonitrile, dimethylformamide (DMF), N-methylpyrolidinone (NMP), and tetrahydrofuran (THF); different water temperatures; and the addition of precipitation modifiers to the water. Solvent washes were also applied to precipitated materials with various results. This paper discusses the morphological and chemical analysis results that were obtained. Several batches of HNS with acceptable properties have been produced and tested with modern detonators to ascertain their initiation characteristics. We are currently working to correlate chemical and morphological data with detonator initiation levels, and we are also working to scale up our production processes to 1 kg or larger batch sizes.

Introduction

New designs for modern slapper detonators have provided the opportunity to develop a new grade of HNS that is optimized for initiation with these detonators. The Explosives Technology Group at Sandia National Laboratories in Albuquerque, New Mexico, USA, has been working with the US Department of Energy's Pantex Plant in Amarillo, Texas, USA, on this development project for about 8 years now. The goals of the project are to provide a reproducible process for a material of high surface area, high purity, and stable

Sandia is a multiprogram laboratory operated by Sandia Corporation, a Lockheed Martin Company, for the United Ststes Department of Energy under contract DE-AC04-94-AL85000.

morphology that also handles well. We would also like to understand how material characteristics, such as particle morphology and purity levels, influence the initiation threshold. This paper provides the status of this work.

Currently HNS is available in four grades: HNS-I, HNS-II, HNS-FP, and HNS-IV. HNS-I is the result of the reaction of trinitrotoluene (TNT) with aqueous sodium hypochlorite in tetrahydrofuran (THF) and methanol (MeOH).[1] The product is washed with water several times and dried. HNS-I made to Sandia specifications[2] must be 98.5% HNS at a minimum and often contains dipicrylethane (DPE) as the major impurity. The SSA is typically 1.5 – 2.0 m^2/g. HNS-II is the result of the recrystallization of HNS-I, and therefore, is a more pure material than HNS-I. The SSA is also lower than HNS-I. The exact amounts of impurities will vary with the manufacturer since recrystallization procedures differ. HNS-II made at Pantex will typically have a surface area of 0.3 – 0.7 m^2/g and contain only trace impurities. The surface areas of both HNS-I and HNS-II are too low to be usable in slapper detonator designs. The FP in HNS-FP represents fine particle, and HNS-FP is a material that is made by crash precipitation of a DMF solution of HNS into water.[3] This process typically yields a material that is 6-9 m^2/g and contains 0.5 – 1% of DMF solvent trapped in the particles. Because of concerns about compatibility and morphological stability during long term storage, the trapped DMF solvent is removed by washing the particles with dioxane followed by MeOH. The final product is usually about 6 m^2/g. Tests have been conducted with HNS-FP in the new slapper detonator designs, but the results were inconsistent. Some lots performed well, but others did not, and an explanation for this inconsistency has not been determined. HNS-IV is crash precipitated material with surface areas in the range of 10-15 m^2/g. A solvent content of up to 0.5% of DMF is allowed by Department of Defense specification.[5] This material has also been tested in the new detonator designs, but the performance was only deemed adequate. The same concerns that exist for HNS-FP before the solvent washes can also be expressed for HNS-IV. The amount of DPE in HNS-FP or HNS-IV is determined by the amount of DPE in the HNS that is used as the starting material.

New Solvents for Crash Precipitation Methods

HNS is a fairly insoluble material in most organic solvents. HNS is soluble in DMF, and DMF is commonly used to bring HNS into solution for crash precipitation. HNS is also soluble in a few other organic solvents, such as NMP, acetonitrile, and THF, and so crash precipitation experiments were also conducted using these solvents to determine if any of them offered advantages over DMF. Typical SSA and % solvent results are shown in Table 1. Representative micrographs taken with a scanning electron microscope (SEM) are shown in Figures 1 – 4. All of the solvents yield materials of fairly high specific surface area. Materials produced using the amide solvents (DMF and NMP) tend to retain the most solvent in the particles. Materials produced from NMP and THF tend to contain large particles as well as many very small particles, as shown in Figures 2 and 4. Particles produced from DMF and acetonitrile are more evenly distributed, as shown in Figures 1 and 3. Acetonitrile tends to produce a smooth, well-formed particle, whereas DMF can produce particles that are either smooth or irregular.

Table 1. Typical Specific Surface Area Ranges Resulting From Crash Precipitation Into Water of Solutions of HNS With Various Solvents.

Crash Precipitation Solvent	Specific Surface Area, m^2/g	Solvent Content, Wt%
Dimethylformamide (DMF)	9 - 19	0.2 – 1.2
N-Methylpyrolidinone (NMP)	16 - 21	0.6 – 0.9
Acetonitrile	6 - 12	0.1
Tetrahydrofuran (THF)	16 - 20	0.2 – 0.3

Comparison of Threshold Results to Bulk Powder Characteristics

Initiation threshold testing was performed on selected lots of materials to determine if correlations could be drawn between the threshold value and the characteristics of the powders.[5] The results in one test vehicle are shown in Table 2. These data show no clear correlation between high SSA and low threshold. If anything, it appears that the lower SSA powders have a lower threshold except in one case. The data also show no clear correlation between low solvent content and low threshold. The two powders with the

Figure 1. Crash Precipitated HNS From a DMF Solution. Original Magnification is 3,000X.

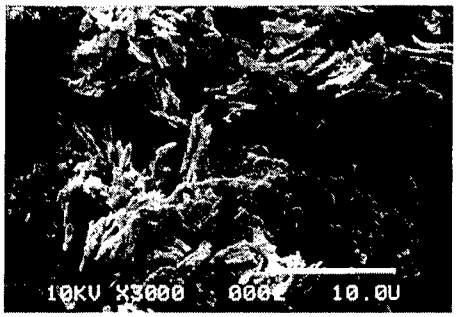


Figure 2. Crash Precipitated HNS From an NMP Solution. Original Magnification is 5,000X.

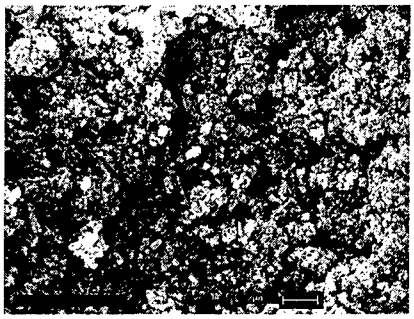
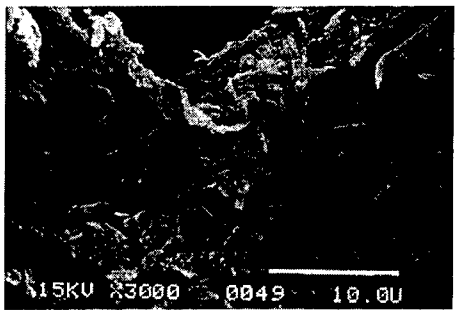


Figure 3. Crash Precipitated HNS From an Acetonitrile Solution. Original Magnification is 3,000X.



Figure 4. Crash Precipitated HNS From a THF Solution. Original Magnification is 3,000X.



lowest solvent content do show the lowest thresholds, but one powder of higher solvent content is also among the lower thresholds. Two powders with either no solvent or reasonably low (0.34%) solvent are among the highest thresholds. It also appears that a low level of DPE does not lower threshold as the powder with the most DPE also has the lowest threshold.

Table 2. Normalized Threshold Energy and Powder Characteristics. Test Vehicle 1.

Crash Precipitation Solvent	Normalized Threshold Energy	Specific Surface Area m^2/g	HNS Content Wt %	DPE Content Wt %	Solvent Content Wt %
DMF with dioxane wash	> 0.75	6.2	99.96	Trace	--
DMF – no wash	> 0.70	16.8	95.76	0.46	1.12
DMF – no wash	0.51	10.4	98.39	Trace	0.82
Acetonitrile	0.40	10.1	97.98	1.87	0.04
Acetonitrile	0.44	8.2	99.30	Trace	0.10
THF	> 0.76	20.0	99.03	Trace	0.34

Threshold results in a different test vehicle with a different set of powders are shown in Table 3. Some of these runs also included precipitation modifiers such as KCl and polyvinylalcohol (PVA). In general, it was found that lower surface area materials were obtained using KCl and NaCl. Higher surface area materials tended to result when PVA and substances like sugar were used. As before, it does not appear that very high surface area or the absence of solvent in the particles is necessary to obtain lower threshold initiation values. To further confuse the issue, materials made from similar processes and with similar surface areas, as shown in Figure 5, do not necessarily show similar thresholds. Very different morphologies, however, can sometimes perform quite similarly

Table 3. Normalized Threshold Energy and Powder Characteristics. Test Vehicle 2.

Crash Precipitation Solvent	Normalized Threshold Energy	Specific Surface Area m^2/g	HNS Content Wt %	Solvent Content Wt%
DMF with dioxane wash	1.00	6.1	99.4	0.03
Acetonitrile/PVA	1.01	9.2	99.3	0.08
NMP	1.13	21.4	97.8	0.6
Acetonitrile	1.20	8.1	99.3	0.06
DMF with dioxane wash	1.30	6.1	99.9	0.013
DMF – no wash	1.34	16	98.0	0.5
DMF – no wash	1.81	9.4	95.9	1.2
Acetonitrile/KCl	3.20	4.1	99.3	0.13

in contrast to expectations as shown in Figure 6. A plot of SSA versus normalized threshold energy for twelve different lots of material, as shown in Figure 7, shows that threshold can not be predicted based on SSA alone. Particle size data for eight lots showed no correlation to threshold either. Intuitively, one expects particle morphology to play a role in initiation, but any link to bulk powder properties is not obvious. Future work will focus on characterization of particle morphology and pore size in pressed pellets.

Figure 5. HNS-FP of Similar Morphology But Different Performance. Original Magnification is 3,000X. Both materials have an SSA of 6.1 m^2/g. The normalized threshold energy of the material on the left is 1.00 and on the right is 1.30.

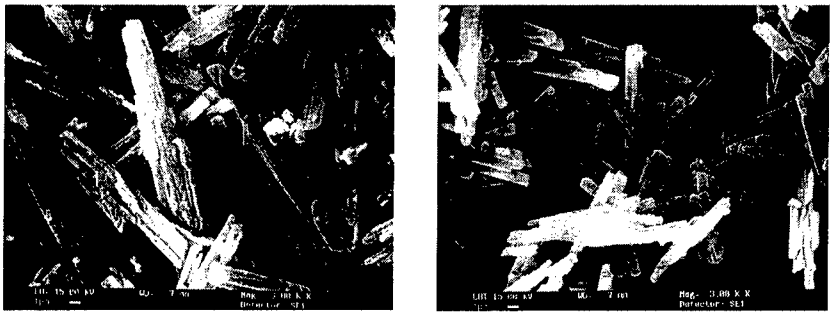


Figure 6. HNS-FP of Different Morphology But Similar Performance. Original Magnification is 5,000X. The material on the left has a surface area of 8.1 m^2/g and a normalized threshold energy of 1.20. The values for the material on the right are 21.4 and 1.18, respectively.

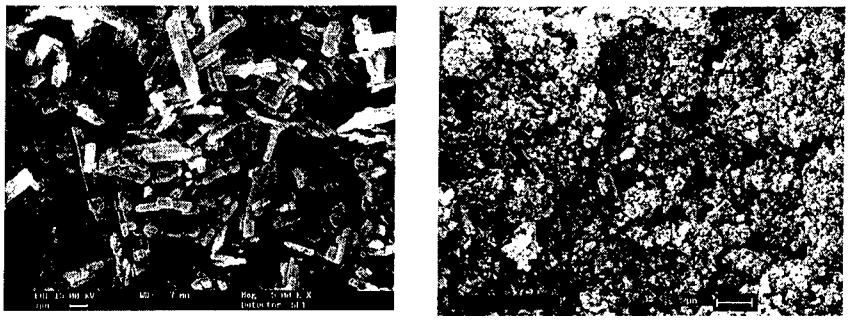
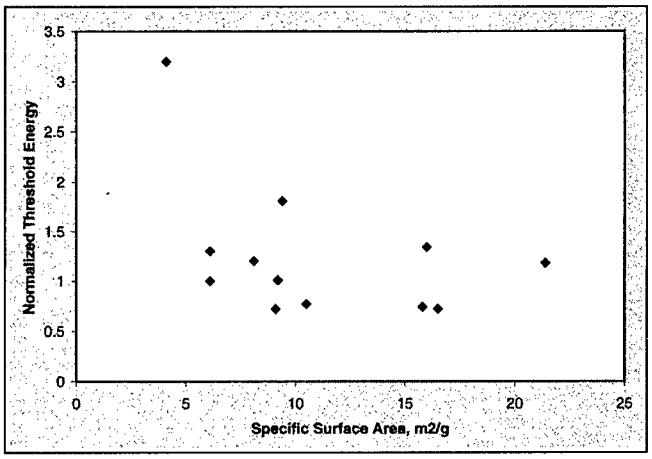


Figure 7. Specific Surface Area vs Normalized Threshold Energy for Twelve Different Lots of HNS Material.



Methods to Reduce Residual Solvent Content

Purity of the HNS material remained a concern. The main sources of impurities are synthetic byproducts and residual solvent. The main byproduct that has been found is dipicrylethane (DPE). The amount of DPE in the materials being developed for modern slapper detonators is directly related to the amount of DPE in the HNS that is used for crash precipitation. A few percent or less of DPE does not appear to affect the threshold value, but DPE can be easily eliminated from the product by using HNS-II as a starting material. Even though the threshold results that have been obtained thus far indicate it is not necessary to eliminate the solvent to get good threshold values, work continued to obtain a material that was solvent free because of concern about the stability of the particle morphology over time. Table 4 shows loss of SSA over time for two high surface area materials that were stored at ambient conditions. Compatibility of solvents with device materials is also a concern that can be eliminated if the materials contain no solvent.

Table 4. Loss of SSA Over Time for Two High Surface Area HNS Materials.

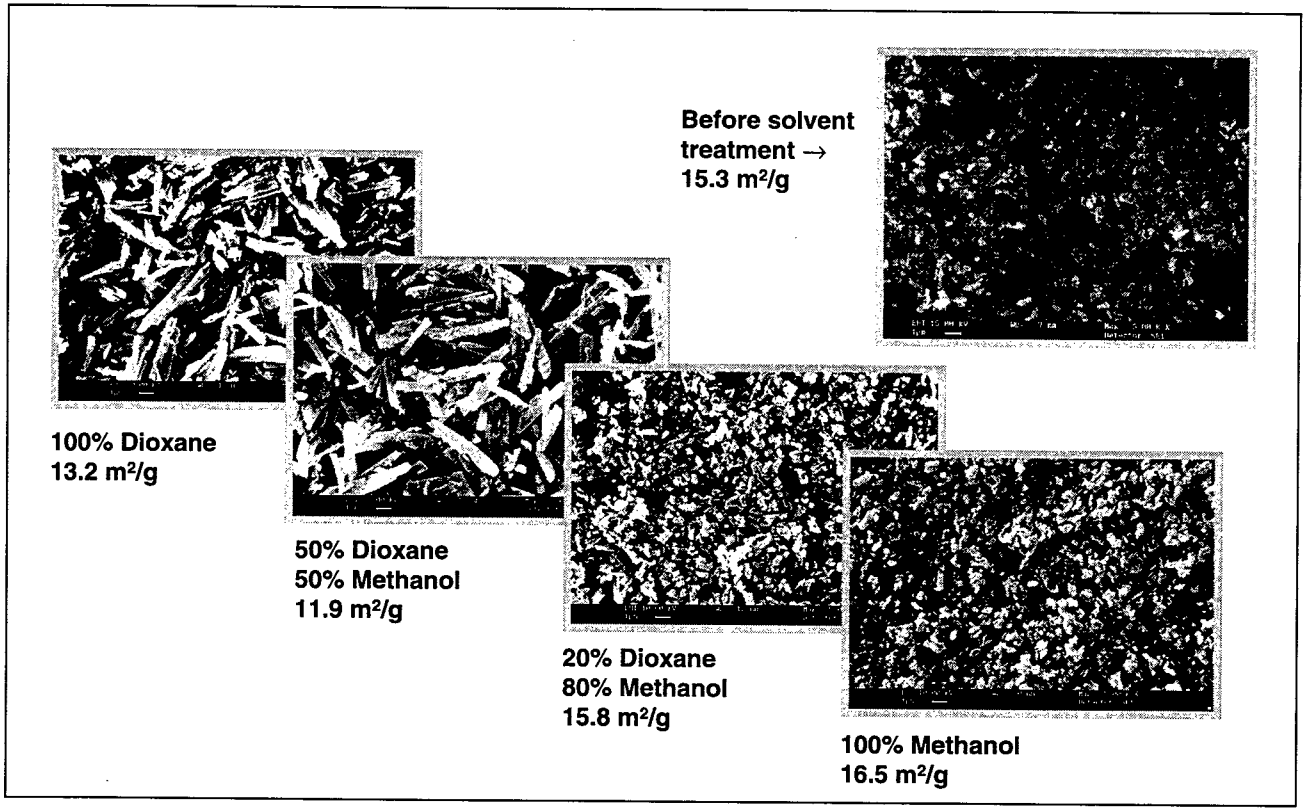
Precipitation Solvent	Specific Surface Area, m^2/g			
	1997	1998	1999	2000
NMP (0.6% NMP)	21.4		17.8	
DMF (0.5% DMF)		16.0	15.3	13.2

One method that is known to remove solvent is washing the particles with dioxane followed by MeOH as is done to produce HNS-FP.[3] Past experience, however, showed that the SSA of these materials always tended to be about 6 m^2/g for materials of starting SSA from 6 – 9 m^2/g. Past work also showed that MeOH could be used to slow the action of dioxane,[6] and so a series of washes with differing ratios of dioxane and MeOH were performed using the DMF material in Table 4 as the starting material. The experiments were done on a lab scale, and the results are shown in Table 5 as well as Figure 8. All of the solvent washes did remove DMF, and presumably the dioxane that was incorporated into two of the batches could be removed with a MeOH wash. Dioxane alone or dioxane rich solvent mixture lowered the surface area and completely changed the morphology of the starting material. The MeOH rich wash retained the characteristics of the starting material while removing the DMF, and MeOH alone raised the surface area of the starting material slightly. Threshold tests of the two higher surface area batches showed the lowest threshold initiation values to date.

Table 5. Results From Solvent Washes of a High Surface Area DMF Precipitated Material. Test Vehicle 2.

Preparation	Specific Surface Area m^2/g	HNS Wt %	DMF Wt %	MeOH Wt %	Dioxane Wt %	Normalized Threshold Energy
Starting Material	15.3	98.0	0.5	--	--	1.34
100% Dioxane	13.2	95.9	< 0.05	< 0.05	2.34	No Data
50% Dioxane/50% MeOH	11.9	96.1	< 0.05	< 0.05	2.02	No Data
20% Dioxane/80% MeOH	15.8	98.0	< 0.05	< 0.05	< 0.05	0.74
100 % MeOH	16.5	97.1	< 0.05	< 0.05	< 0.05	0.72

Figure 8. Scanning Electron Micrographs of an HNS Material That Was Treated With a Variety of Solvent Washes. Original Magnification is 5,000X For All Micrographs.

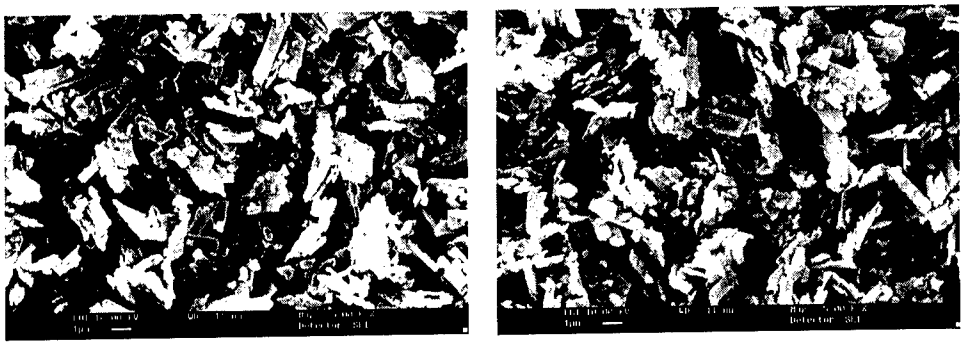


Past experience also indicated that the temperature of the water may have an effect on how much DMF is retained in the particles.[7] The concern was that warm water may also lower the SSA of the product. Two runs were made on a pilot plant scale where a solution of HNS in DMF was added to ambient temperature water instead of chilled water. Results are shown in Table 6. The surface areas of each batch were mid-range, but the materials were both solvent free. Threshold testing of these two batches produced materials that were both similar to the MeOH washed materials in the previous paragraph. Thus it was demonstrated that material with no solvent and low threshold could be produced at a pilot plant scale. The two batches were produced within two days of each other and reproduced reasonably well with respect to surface area and also particle morphology as shown in Figure 9. The challenge now is to reproduce it a year later and to see if higher surface areas can be achieved without incorporating solvent into the particles.

Table 6. Results From Pilot Plant Runs With Ambient Temperature Water for Crash Precipitation. Test Vehicle 2.

Preparation	Specific Surface Area m^2/g	HNS Wt %	DPE Wt %	DMF Wt %	Normalized Threshold Energy
A standard solution of HNS was quenched in ambient temperature water.	10.46	100.6	< 0.05	< 0.05	0.77
	9.09	99.67	0.27	< 0.05	0.72

Figure 9. Scanning Electron Micrographs of Two Pilot Plant Lots. The SSA of the material on the left is 10.46 m^2/g, and on the right 9.09 m^2/g. Original Magnification is 5,000X.



Because of such promising results, DMF is the solvent under the greatest consideration at this time. THF and NMP give particles with a bimodal size distribution that may be difficult to reproduce from lot to lot. Not enough is known about initiation to be sure that the large particles will not provide a source of threshold variability. Materials produced with acetonitrile are quite attractive in that they generally have low initiation thresholds, the process is fairly reproducible, and they handle well. Materials made using other solvents generally have a static problem. Nevertheless, the solubility of HNS in acetonitrile is low enough that only lab batches have been made at this time. The process is too solvent intensive to scale up without also incorporating a solvent recovery system. Binders are also being considered to improve handling in the DMF materials and also pellet strength in some applications. In these cases the high surface areas that were achieved in the solvent washed process may be needed since surface area may be lost during formulation of the material. This, however, remains to be seen.

Conclusion and Future Work

The ability to make a new high purity grade of HNS with high surface area, low solvent content, and low initiation threshold for modern slapper detonator designs has been demonstrated at a pilot plant scale. We are in the process of determining reproducibility and capability of the process to produce materials of higher surface area in the event this is necessary to prevent a low SSA product when binders are added. Many questions remain concerning the link between the morphology of the material and its performance. Future efforts will focus on the characterization of the material after it has been pressed into pellets. Once we are satisfied that we have a reproducible process in place, we plan to conduct a long term aging study to determine compatibility and morphological stability.

Acknowledgements

The authors gratefully acknowledge the excellent contributions of the following individuals.

Bill Brigham, Sandia National Laboratories Threshold Testing

Elaine Boespflug, Sandia National Laboratories	Sample Logistics
Melissa Moore, BWXT Pantex	Scanning Electron Microscopy, Specific Surface Area and Particle Size Determinations

References

1. K G. Shipp and L. A. Kaplan, *Reactions of α-Substituted Polynitrotoluenes. II. The Generation and Reactions of 2,4,6-Trinitrobenzyl Anion,* Journal of Organic Chemistry, **31**, 857, 1966.
2. Sandia Specification, SS710123, *Process Specification, Pantex Manufactured HNS.*
3. S. E. Klassen and R. G. Jungst, *Production and Characterization of Fine Particle Hexanitrostilbene Explosive for Slapper Detonator Applications,* Sandia Report, SAND85-1471, August, 1985. Specified External Distribution Only
4. Military Specification, *Explosive, HNS-IV,* MIL-E-82903(OS), 30 December 1994, Superseding WS 32972A 23 February 1990.

THERMAL DECOMPOSITION OF TRINITROTOLUENE (TNT) WITH A NEW ONE-DIMENSIONAL TIME TO EXPLOSION (ODTX) APPARATUS

T. D. Tran, L. R. Simpson, J. Maienschein and C. Tarver

Energetic Materials Center
Lawrence Livermore National Laboratory
P. O. Box 808, Livermore, CA 94551

ABSTRACT

The thermal explosion of trinitrotoluene (TNT) is used as a basis for evaluating the performance of a new One-Dimensional-Time-to-Explosion (ODTX) apparatus. The ODTX experiment involves holding a 12.7 mm-diameter spherical explosive sample under confinement (150 MPa) at a constant elevated temperature until the confining pressure is exceeded by the evolution of gases during chemical decomposition. The resulting time to explosion as a function of temperature provides valuable decomposition kinetic information. A comparative analysis of the measurements obtained from the new unit and an older system is presented. Discussion on selected performance aspects of the new unit will also be presented.

The thermal explosion of TNT is highly dependent on the material. Analysis of the time to explosion is complicated by historical and experimental factors such as material variability, sample preparation, temperature measurement and system errors. Many of these factors will be addressed. Finally, a kinetic model using a coupled thermal and heat transport code (chemical TOPAZ) was used to match the experimental data.

INTRODUCTION

The thermal explosions of a wide variety of high explosives (HE) have been investigated using the One-Dimensional-Time-to-Explosion (ODTX) apparatus at Lawrence Livermore National Laboratory. Such experiments involved holding at constant elevated temperature a small spherical (12.7 mm-diameter) HE sample in two identical aluminum anvils that are confined at 150 MPa. The time to explosion is the elapsed time between the sample insertion (and anvil closure) and the rupture of containment. The time to explosion as a function of the temperature provides useful kinetic information on the material decomposition. The system was first reported in 1976 by Catalano et al. (1). The thermal decomposition of trinitrotoluene (TNT) was one of the first reactions studied in this original work. Multi-step chemical kinetic decomposition modeling of TNT was first reported by Tarver et al. (2) and McGuire and Tarver (3).

We have recently built a new apparatus as a replacement. It incorporates new components, modern equipment and expanded diagnostic capabilities. Basic experimental design parameters such as sample size, anvil materials and dimension remain unchanged to facilitate comparison with previous

work. The upgrades and new features include in-situ temperature sensing and control, faster sample loading, external (hydraulic) pressure sensor, and computer-controlled operation and data collection as well as provisions for additional diagnostics. The new system was designed to provide very accurate determination of the temperature and the time to explosion. A high level of accuracy in time to explosion is needed to investigate effects of factors such as sample heterogeneity, impurity, and confinement pressure on the decomposition kinetics. Such a study is now possible using the new ODTX unit.

The thermal decomposition of trinitrotoluene (TNT) was used to verify the performance of the new ODTX apparatus. It was chosen because of available historical ODTX data, its common use and its useful physical properties. TNT, for example, has a low melting point (~ 80°C). Since explosive thermal reactions occur at significantly higher temperatures (> 170°C), the behavior of a liquid explosive can eliminate complexities in kinetics derived from heterogeneity associated with porosity and particle size in pressed plastic bonded materials such as HMX-based composites. We expected that the molten TNT reaction would provide a higher resolution of any difference in the explosion times and temperature measurements inherent in the two systems. A comparative analysis of the measurements obtained from both the new and existing apparatuses is presented. This serves as a basis for reconciling the existing database with results from the new apparatus.

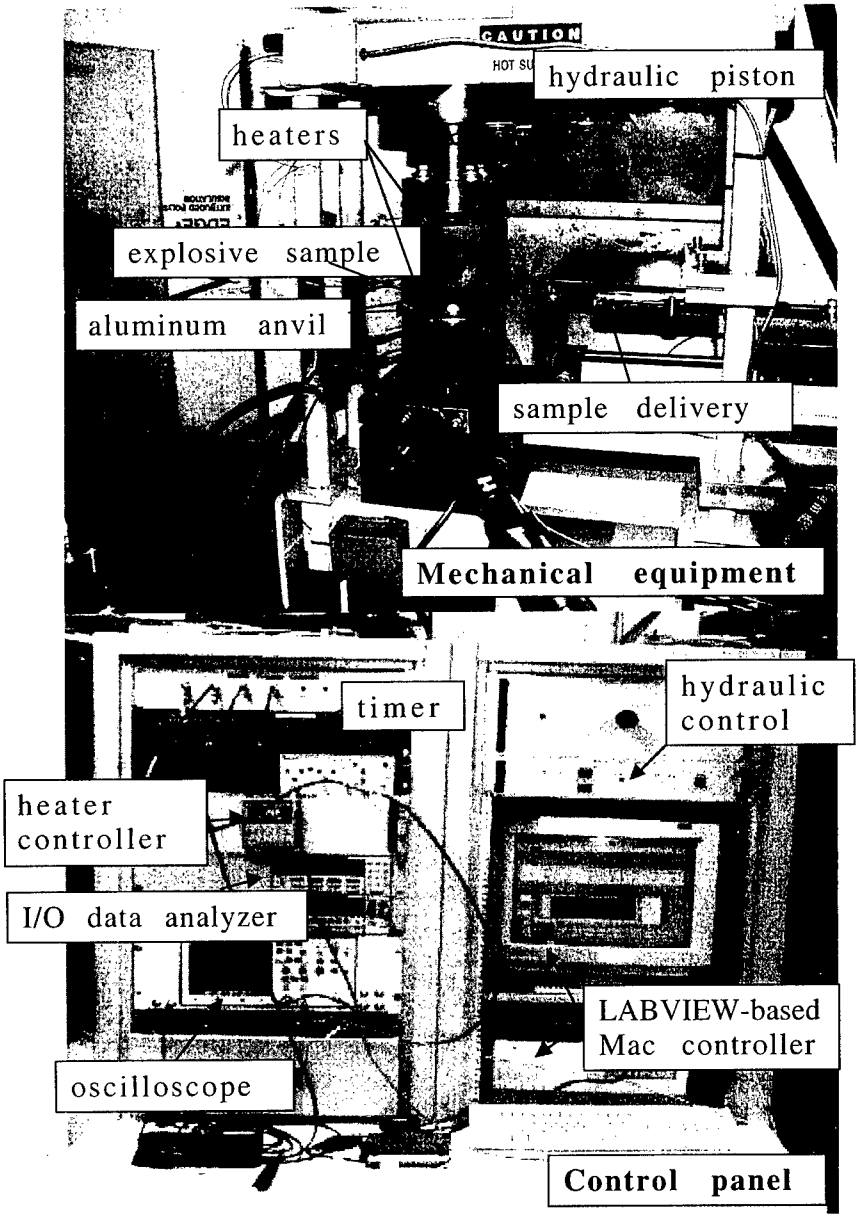
EXPERIMENTAL

The thermal explosion experiments were conducted on two similarly designed ODTX apparatuses. The old unit was identical to the one described by Catalano et al. (1). The new system was designed to perform identical experiments but contained upgrades, modern equipment and new capabilities. A short description of the experiment and features of the new apparatus is presented below. Any similarity with the old unit will be noted. A picture of the new apparatus is shown in Figure 1.

Anvils/sample holder - The anvil design is identical for both systems. The sample holder/confinement components consist of two identical cylindrical aluminum anvils (75-mm diameter x 50 mm long, 6061 T6 Al). Each anvil contains a 12.7 mm-diameter hemispherical cavity and a 18.5 mm-diameter circular groove with a knife-edge bottom to accommodate a copper O-ring seal (3 mm-wide, Vacuum Products Corp., GK-075, P/N 191000). A circular copper ring clamped between the two knife-edges provides a gas-tight seal when two anvils are pressed together. The upper anvil is mounted to the piston surface of a hydraulic piston. The confinement pressure is calculated based on the cross-sectional area confined by the knife-edge. The anvil temperature is controlled by a calibrated resistive thermal devices (RTD) inserted into a 3 mm-diameter x 32 mm deep well at 3 mm below the anvil surface.

Hydraulic system – The new system uses a high throughput two-stage hydraulic pump (Power Team, Model D) for the opening and closing of the top anvil. A 16-ton double-acting hydraulic cylinder (RD-166, Enerpac) is used to move the top anvil (and the encased heater) and applies the closing (confinement) force. The bottom anvil, held in the heating block, is mounted rigidly. The standard operating hydraulic pressure is 20.5 MPa (giving a 150 MPa confinement pressure). This hydraulic

Figure 1. Picture of the One-Dimensional-Time-to-eXplosion System (ODTX)



pressure can be adjusted up to 35 MPa. A dynamic pressure gauge (Iomega, PX613) is mounted at the cylinder inlet to monitor the closing pressure as well as the relief pressure pulse immediately after the explosion.

Heating blocks - The heaters are brass cylindrical cups with encased heating elements (230V, 500-watt, Tempco Electric Co.) around the sidewall. The anvils fit tightly in the heaters. The heating is controlled *in-situ* through a temperature controller (OMEGA model CN300). The heater temperature is controlled by a resistive thermal device (RTD) located in the anvil. Typically, the RTDs are calibrated to within 0.3°C of a standard calibration probe.

Sample Delivery – The HE sample is delivered automatically by a pivoted mechanical jaw that grips the sample and then opens to release the sample when it is positioned above the sample cavity. The jaw is guided by a double-acting pneumatic piston (Tendra model 1) powered by 200 KPa compressed air. This new design is significantly faster than the swing-arm, vacuum suction/pressure release holder in the old unit. The new loading mechanism requires less than 1 second while the old system requires a total of about 10 seconds.

System control/data collection - The new system is fully automated and is interfaced with a computer. The operating software is LABVIEW. The control system consists of a Macintosh computer (Power PC 7600, Apple Co.) and interfaced temperature/pressure data collection modules (multimeters 2010, Keithley Instruments), temperature controller (CN3000, OMEGA Corp.), hydraulic pressure transducer (PX613, Omega Engineering) and pressure-data-processing oscilloscope (PCB 482R4, Hewlett-Packard Co.). The standard set-up has provision for 20 channels of input/output data, if additional diagnostics are used.

Time measurements - A digital timer (Model. 776, Keithley Instruments) records the time to explosion. The time is activated by a Reflective Optical Switch (Opto Switch No. R-280-A-W, Steven Engineering) mounted at the sample delivery arm. The explosive event is measured acoustically by a sensor embedded in the mounting assembly of the bottom anvil. Mechanical and optical position switches are located at various positions to monitor the locations of other moving parts.

Temperature measurements – Temperatures in the new system are measured with 4-wired RTDs (resistive thermal devices, 100 Ohm Platinum RTD with 3.2 mm-diameter ceramic end, P/N29229-T01, RdF Corporation). Most RTDs are accurate to within the manufacturer's suggested range of ± 0.3°C when calibrated against a known probe in our laboratory.

Sample preparation – The samples are 12.7 mm diameter spheres. Samples from previous work (2,3) were machined from pressed billets at 135 MPa and ambient temperature. They were pre-coated with a thin layer (0.025 mm) of parylene N. Recent samples (from various sources) were pressed directly to shape in a die at 200 MPa under room temperature. Samples at various densities were made by varying the weight prior to pressing. Specimens at densities below about 1.20 g/cc contain loosely bounded particles that can flake off easily during handling.

Experiments involved materials from four separate TNT batches. Table 1 summarizes the four types of TNT and their characteristics. The first 3 batches (B-180, B-569 and C-175) were either military grade or from a commercial vendor. The recrystallized pure material was fine crystal that was crash-precipitated from a dissolved TNT/acetone solution. This material was first made in 1975.

EXPERIMENTAL RESULTS AND DISCUSSION

Initially, the temperature profile of the heated anvils was recorded to calibrate the heaters and verify the system operation. The new apparatus was then tested with TNT. A comparison of the operation of the two systems was done by investigating the thermal profile of the heated anvils and the time to explosion curves generated with the same materials.

Temperature measurements in old and new apparatuses - The anvil temperatures were measured differently in the two systems. In the old system, the temperature was recorded by a thermocouple (TC Type J, Omega Inc.) inserted in a 5 mm-thick disc sandwiched between the heated anvils. The tip of the TC was located about 19 mm from the center of the sample cavity. The temperature was recorded and this disc was manually removed before HE samples delivery. This transition took about 20 seconds before the heated anvils were reclosed. A small temperature reduction (about 1-2°C) was observed but was not corrected for in the measurement. This brief "cooling" period, however, is fairly consistent between tests, resulting in good reproducibility in the time to explosion measurements as observed over several years.

Table 1. Characteristics of historical and recent TNT samples

Variables/batch	**B-180**	**B-569**	**C-175**	**Recrystallized**
Source	MH VOL 7-654	MH VOL 7-654	HOLSTON C1B91 D003-040	Work ID. 75-166
ODTX date	1974	2000	2000	2000
Purity*	96 ± 2 %	94 ± 2.0 %	90 ± 3.4 %	100 ± 1%
Sample preparation	Pressed at 135 MPa & ambient temp. Machined to shape. Coated w/ 0.025 mm thick parylene-N	Pressed to shape at 200 MPa & ambient temp.	Pressed to shape at 200 MPa & ambient temp.	Pressed to shape at 200 MPa & ambient temp.
Sample weight, g	1.77	1.70	1.23 – 1.70	1.70
Sample density, g/cc	1.66	1.59	1.160-1.59	1.59

* Analysis for batch B-180 was done by Liquid Chromatography (previously unpublished data). Analysis for batches B-569, C-175 and recrystallized TNT was done by Liquid Chromatography/Mass Spectroscopy.

The reported temperature in the new ODTX unit is the average of two controlling RTDs inserted in the top and bottom anvils (one for each anvil). The controlling RTD is located in a well (3 mm–diameter x 32 mm deep) drilled into the side of the anvil, at 6.5 mm below its flat surface. Under well-controlled conditions, the calibrated controlling RTDs are found to be within 0.2 °C of the measured sample temperature (from another calibrated RTD placed at the center of the cavity). The fast sample delivery and anvil closure mechanisms in the new unit resulted in a significantly smaller heat loss (less than 0.5°C) during sample loading.

The difference in the reported temperatures for the old and new systems was quantified in a series in heating experiments, The disc used for the old apparatus was modified to accept a Cu ball (simulating the HE sample) fitted with a calibrated RTD in the center. This disc was placed in both systems and the temperatures were measured in the range between 200 and 300°C. Figure 2 compares the readings for the two systems. The TC readings, i.e., old ODTX temperatures, were consistently 2-4°C higher than that recorded from the calibrated RTD at the cavity center. We attribute this difference to systematic error, possibly from the uncalibrated TC or the meter or the TC placement or a combination of these factors. On the other hand, the controlled RTDs at the top and bottom anvils in the new unit were within 0.3°C of the Cu ball value. This difference could be reduced to less than 0.2°C by accounting for a slight offset between top and bottom anvil temperature due to their difference in thermal environment due to convective heat transfer to the top anvil (i.e., top anvil needed slightly less heat input). This is the limit of the new system temperature measurement accuracy. The temperature variance between the systems is consistent with an observed shift in the time-to-explosion recorded for the two apparatuses. We discuss this later in this paper.

Time measurement between the two apparatuses – The largest source of error in the time measurement in the old ODTX was attributed to the analog timer reading. It is precise to within 0.005 minute or about 0.3 seconds. The precision in the time measurement meter in the new ODTX is significantly higher (±1 μs). In repetitive time measurement tests in which timer was deliberately terminated by an electronic signal, the new system time measurement accuracy (reproducibility) is greater than 1 ms. Relative to other system errors, time measurement was not expected to significantly affect the variance in the explosion time.

Comparison of TNT decomposition with two ODTX units – Two series of TNT decomposition experiments were conducted to compare the relative performance of the two systems. Identical conditions were maintained between the two sets of tests. The TNT samples (from batch C-175) were pressed at a density of 1.355 g/cc to account for volume increase due to melting and thermal expansion (see discussion in next section). The times to explosion on the two apparatuses are compared in Figure 3. The uncorrected data for the old system show slightly longer times when plotted with the results from the new system. We have determined earlier that the recorded thermocouple temperatures from the older unit ranges between 2°C and 3°C higher than those measured at the cavity center. If we corrected for this offset, the corrected time to explosion curves for the two systems show good reproducibility. Similar observations were also observed in ODTX experiments with another material

(PBX-9501.) The results for both TNT and PBX-9501 (not discussed) provide adequate calibration for the new ODTX apparatus. We continue to conduct additional experiments to gain more working knowledge of the new system.

Thermal explosion of TNT at various densities – Because of large expansion of TNT upon melting, it was of interest to investigate this effect on the thermal decomposition kinetics. This can be studied simply by varying the density and hence mass of the pressed sample. Samples at varying masses can be conveniently pressed to a constant-volume (1.073 cm^3) spherical size for ODTX experiments. Sample density was varied by changing the pre-weight amount prior to pressing. Low-density materials such as those at 1.15 g/cc have visible pores and contained loosely packed particles.

We have found recently that tests with nominal densities (~1.6 g/cc) TNT samples produced large amount of smoke prior to explosion. Controlled heating experiments showed TNT flowing from between anvils, indicating leakage. This was likely due to the large volume expansion (~ 14%) associated with TNT melting at about 80°C (4). In addition, molten TNT would continue to expand at a rate equivalent to as much as 0.7% volume increase per 10°C (reference 5 for data between 85-120°C). An analysis of the heat flow in a 12.7 mm TNT sphere with a constant surface temperature was done using the solution provide by Carslaw and Jaeger (5). An isothermal condition (i.e., center temperature approaching 96% of surface temperature) in the solid sphere would be achieved after 179 s. This approximation is consistent with our experimental observations where explosion times in most tests were significantly longer than this value. It is interesting to note that the thermal decomposition behavior is remarkably reproducible even in the events that leaking was observed. This is consistent with rather reproducible kinetics observed by previous workers (in ref. 2,3) with full-density samples.

Experiments with TNT at lower densities (less than liquid TNT density) produced little smoking prior to explosive events in contrast to those at nominal densities where significant discharge of smoke was evident. For example, materials pressed at 1.355 g/cc (~ 82% TMD) were found to be mechanically robust for handling and produced well confined conditions during the ODTX tests until thermal runaway. In addition, the faster new system showed no observable smoking prior to explosion event while the old system still showed occasional evident of leaking (i.e., smoking). We, however, can not directly correlate any effect between leakage and time to explosion.

The thermal explosion curves of TNT at a range of density between 1.15-1.60 g/cc are shown in Figure 4. Corrected data from the old unit and those from the new system were combined. The data were complicated by scatter in the measured times. While there appears to be a slight dependence on the times to explosion with sample density, the statistical significance of the results has not been analyzed. Experiments to investigate the new system reproducibility could be used to delineate the variances in the observed data, and are underway.

Effects of batch-to-batch variance – Four batches of TNT with various purity levels were included in this work to investigate the differences in the time to explosion that were noted in the early stage of this project. Recent results were from two available type-1 TNT flakes (B-569 and C-175). Historical data reported by previous workers (1, 2) were from a different batch of TNT (B-180). All

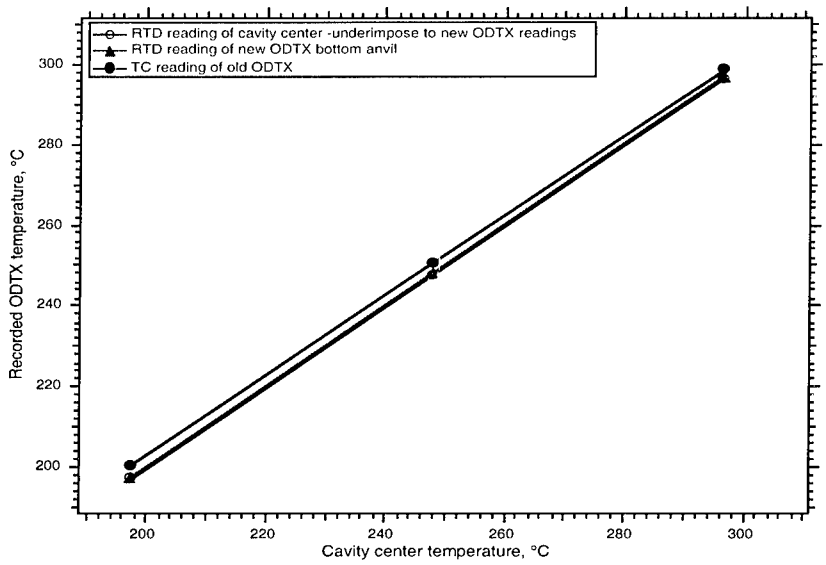


Figure 2. Comparison between temperature readings for the two systems. The values for the cavity center superimpose on those for new ODTX in this plot (within 0.2°C).

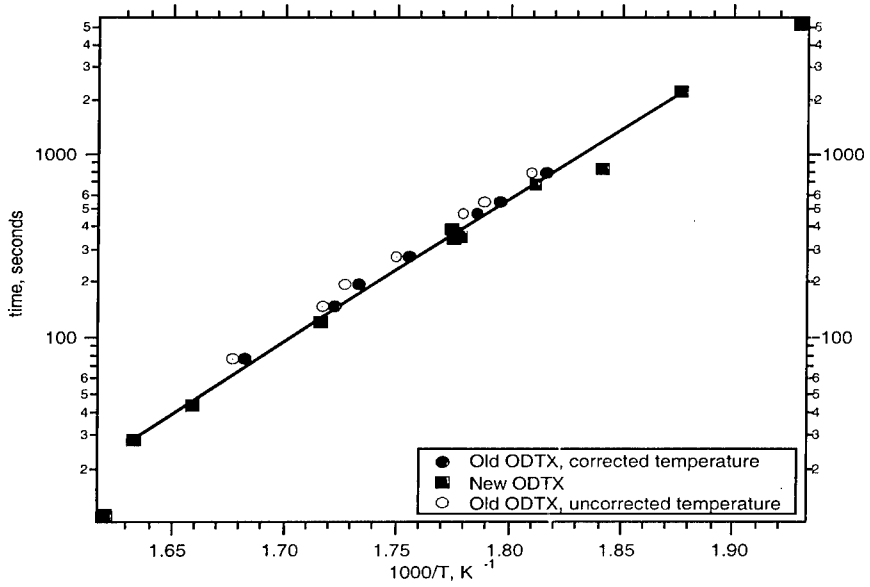


Figure 3 – Comparison of time to explosion for TNT (batch C-175) obtained with two ODTX apparatus. Thermocouple temperatures from the old ODTX were recorded 'as is' and corrected for offset between old and cavity temperature. RTD readings are from new system. TNT was pressed to 1.355 g/cc (~ 82% of solid TMD). Solid line is best-fit line of the new ODTX data in the range indicated to serve as a visual guide.

these experiments were conducted with the old ODTX unit. Recently, pure (recrystallized) TNT samples were studied with the new ODTX units. Characteristics and history of the four types of TNT are summarized in Table 1. The time to explosion of four batches of TNT versus anvil temperatures was presented in Figure 5. All temperature data were presented as is without correction for any temperature difference between the two systems because of uncertainty involved in the use of several thermocouples and RTDs over the course of many years. Temperature variance, however, is expected to be about 2°C.

In addition to the difference in apparatus and TNT sources, the samples were pressed and prepared in different procedures. The current samples (batch B569, C-175 and recrystallized materials) were pressed to 1.355 g/cc to accommodate a large expansion associated with TNT melting and subsequent liquid expansion prior to explosion. Samples from the earlier work (batch B-180, reference 1), on the other hand, had density around 1.66g/cc. Another variance noted from the historical TNT samples (from Ref. 2) is that the pressed parts (i.e., at 1.66 g/cc) were coated with 0.0254 mm thick Parylene N. While we do not understand the original purpose for this application, we speculate that this was used to retard the melting of TNT upon contact with the hot anvils. Our recent experience showed that the sample sizzled immediately after contacting the hot anvil. Some materials could be seen spilling out of the cavity prior to anvil closure. An insulating coat with Parylene N (melting point ~420°C, Parylene Technical data, Paratronix Inc.) could temporarily protect the sample before the anvils closure. Recent tests with samples (without coating) pressed at a lower density (i.e., less than liquid density) was found to emit much less smoke prior to anvil closure. Experiments with the new system, with a faster closing speed, gave a clean closure and produced no observable smoking prior to explosive events.

The large difference in the times to explosion is clearly attributed to sample purity associated with the batch-to-batch variances. While we did not study the effects of the parylene N coating, this thin and inert insulation layer is expected to produce a relatively small change to explosion time. Such an effect could be predicted with our model but this has not been determined.

The results suggest that impurity play a large role in the thermal decomposition chemistry of TNT. The pure recrystallized TNT shows the fastest time to explosion over the whole temperature region. The times to explosion appear to increase with impurity level associated with various batches. An increase of at least 10-fold is observed with increasing impurity from 0 to 10%. Additional analysis is underway to determine the composition and chemical nature of the impurities.

KINETIC MODELING OF TNT DECOMPOSITION USING CHEMICAL TOPAZ

Multi-step chemical kinetic decomposition modeling of TNT was first reported by Tarver et al. (2) and McGuire and Tarver (3). That TNT model was based on the ODTX data for Batch B-180, which is now known to contain approximately 4% impurities. These impurities are currently being analyzed, but most likely consist mainly of mono- and dinitrotoluenes that were not completely nitrated to trinitrotoluene during synthesis. The data (Fig. 5) show that the times to thermal explosion increase greatly with the percentage of impurities present from 100% recrystallized TNT to Batch B-180 (4%

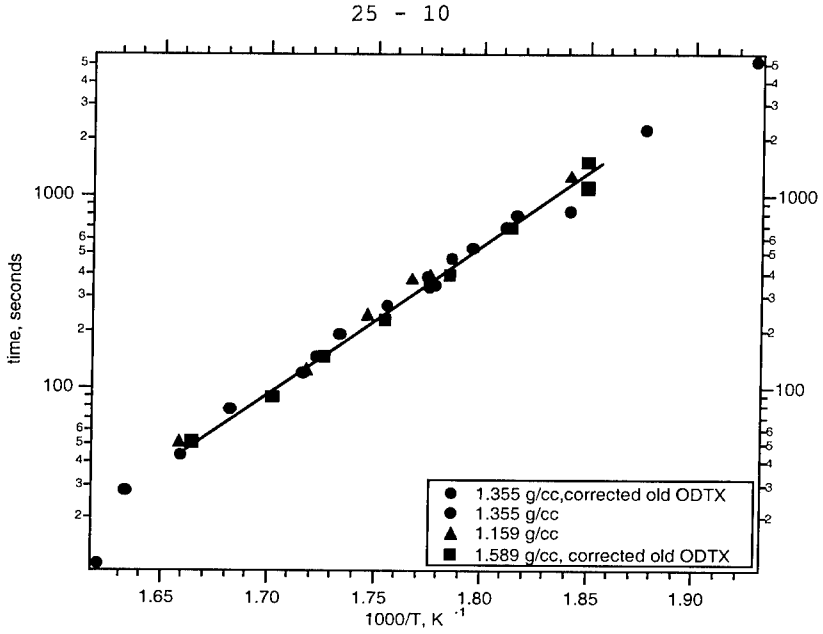


Figure 4. Effects of sample density on time to explosion. Densities were varied between 1.159 g/cc to 1.589 g/cc. Materials are from batch C-175. Solid line is best-fit line drawn through the linear region of the data at 1.589g/cc as visual guide.

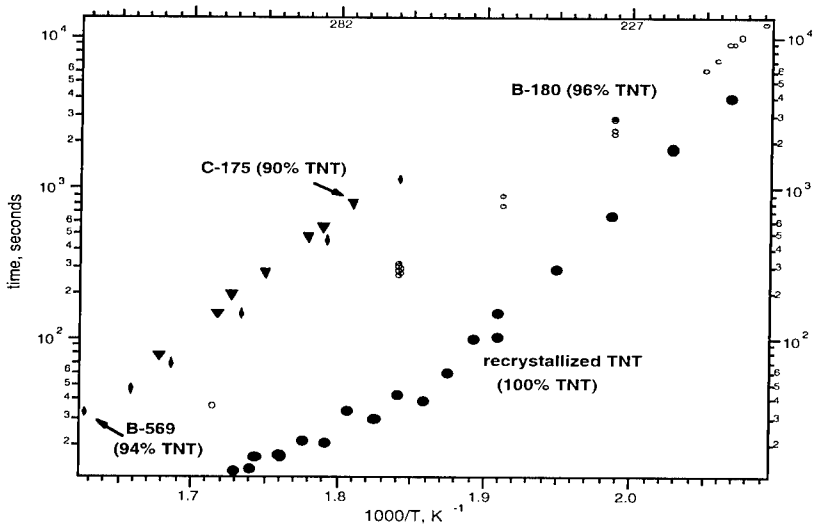


Figure 5. Effects of batch-to-batch variances on TNT decomposition kinetics. Recrystallized TNT was done on the new ODTX and other data were from the old ODTX. Temperature data were not corrected for a small offset between the two systems. See text for other details.

impurities) to Batches B-569 and C-175 (about 10% impurities). The previous decomposition model for TNT (2,3), which assumed an autocatalytic reaction based on very meager experimental kinetic information, was not adequate in simulating pure TNT decomposition.

We propose here a simple decomposition model for pure TNT that includes provisions to account for impurity decomposition. It also incorporates a Chemical TOPAZ code (7) that is a greatly improved version of the heat transfer codes used in the previous studies. Some differences are also expected due to improved numerical algorithms. The model consists of three chemical reactions to simulate the pure TNT ODTX data and an additional reaction to describe the effects of impurity. The four-species, three-reaction rate model for pure TNT uses the form:

$$\text{TNT} \rightarrow \text{Intermediate 1} \rightarrow \text{Intermediate 2} \rightarrow \text{Gaseous Products} \qquad \text{(A)}$$

which the reactions are:

$$A \rightarrow B \qquad (1)$$

$$B \rightarrow C \qquad (2)$$

$$C + C \rightarrow D \qquad (3)$$

where A is TNT, B is intermediate 1, C is intermediate 2 and D represents product gases. There are not sufficient experimental data to determine whether TNT exhibits any autocatalytic behavior. The heat of fusion of TNT, 93.3 J/g, is included in the heat transfer calculations at its melting point of 80.9°C. The first two reactions in Equations (1) and (2) are endothermic since TNT has to break down into smaller, more reactive species before the exothermic processes can occur and cause thermal explosion (runaway reaction). Table 2 lists the thermal and chemical kinetics parameters used in the new model.

Figure 6 contains the comparison of the calculated times to explosion at various initial temperatures using the new TNT model with the ODTX results for pure recrystallized TNT. Also shown in Fig. 6 are the ODTX results for TNT with approximately 4% and 10% impurity levels. The differences in explosion times for these TNT batches are much greater than those measured for plastic bonded explosives (PBX) HE's containing various amounts of endothermic binders. For example, LX-10 (95% HMX and 5% Viton) and LX-04 (85% HMX and 15 % Viton) exhibit parallel lines separated by only a small percentage of the total times to explosion in the ODTX apparatus (3). This is also true for TATB-based explosives, which have similar energies to TNT-based explosives (8). Therefore it is unlikely that the large time differences shown in Figs. 5 and 6 for the 90% TNT and 96% TNT batches are due to simple endothermic breakdown of non-reactive impurities. It appears likely that these impurities react with the intermediate products of TNT decomposition before the exothermic reactions

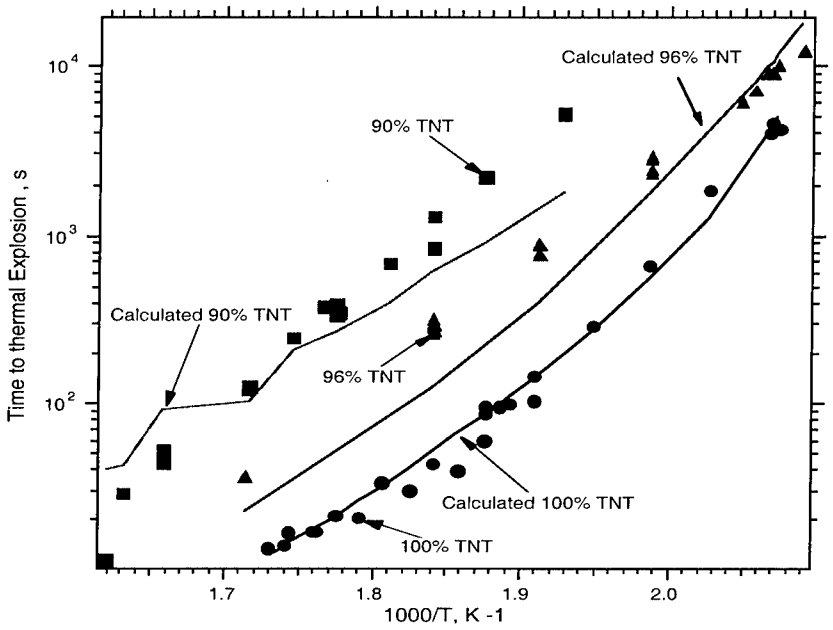


Figure 6. Comparison of experimental data and modeling results for various TNT samples. Kinetics model is based on 5-species,4-reaction with parameters given in Table 2. Pure TNT decomposition doesn't activate reaction 4.

Table 2. Thermal and Kinetic Parameters used in the TNT decomposition model

Properties	TNT	Reaction 1	Reaction 2	Reaction 3	Reaction 4
Heat of fusion, J/g	99.3				
Melting point, °C	80.9				
Thermal conductivity, J/cm s °C	2.59×10^{-3}				
Heat capacity J/g°C	1.1297				
Heat of reaction, J/g		209.2	209.2	- 3765	8368
Ln Z		57	52.8	37.5	40
Activation energy, 1/K		32500	30000	22142	20000
Reaction order		1	1	2	3 for Intermediate 2 1 for Impurity

can occur and thus delay the onset of thermal explosion until the impurities are decomposed. Figure 6 contains calculated curves for 96% TNT and 90% TNT assuming the reaction

$$\text{Intermediate 2} + \text{Impurity} \rightarrow \text{Impurity Products} \qquad (4)$$

occurs before the third (exothermic) reaction in Eq. (3) can proceed. Table 2 also lists the parameters used for this reaction, which assumed that three moles of Intermediate 2 react with each impurity mole in a highly endothermic process. These calculations underestimate most of the measured increases in time to explosion, especially for the 90% TNT batches, and are included as a first approximate description of the complex chemistry that is occurring. More detailed chemical kinetic modeling can be developed when additional data on the nature of the impurities and their effects on TNT decomposition rates are obtained.

ACKNOWLEDGMENT

We gratefully acknowledge Greg Sykora, Kent Montgomery, Dan Greenwood and Barry Levine for their assistance in the development of the new system. We thank Jerry Dow for providing funding. This work was performed under the auspices of the U.S. Department of Energy by Lawrence Livermore National Laboratory under contract No. W-7405-ENG-48.

REFERENCES

1. E. Catalano, R. McGuire, E. L. Lee, E. Wrenn, D. Ornellas, and J. Walton, *Sixth International Symposium on Detonation Proceedings*, p. 214, Office of Naval Research, ACR-221, Coronado, CA (1976).
2. C. M. Tarver, R. R. McGuire, E. L. Lee, E. W. Wrenn, and K. R. Brein, *Seventeenth Symposium (International) on Combustion*, Leeds, UK, p. 1407 (1978).
3. R. R. McGuire and C. M. Tarver, *Seventh International Symposium on Detonation*, Naval Surface Weapons Center, Annapolis, MD, p. 56 (1981).
4. W. A. Gey et al. *J. Amer. Chem. Soc.*, **78**, 1803 (1956).
5. H. S. Carslaw and J. C. Jaeger, *Conduction of Heat in Solids*, Second Edition, Oxford University Press, p. 233 (1959).
6. H. H. Cady and W. H. Rogers, Report LA-2696, US Atomic Energy Commision (1962).
7. A. L. Nichols III and K. W. Westerberg, Numerical Heat Transfer, Part B, **23**, 489 (1993).
8. S. K. Chidester, C. M. Tarver, L. G. Green, and P. A. Urtiew, *Combustion and Flame* **110**, 264 (1997).

2,2-Dinitro-ethene-1,1-diamine (FOX-7) – Properties, Analysis and Scale-up

Henric Östmark, Helena Bergman, Ulf Bemm, Patrick Goede, Erik Holmgren, Martin Johansson, Abraham Langlet, Nikolaj V. Latypov, Anna Pettersson, Marja-Liisa Pettersson and Niklas Wingborg
Swedish Defence Research Agency, FOI, Department of Energetic Materials,
SE-147 25 Tumba, Sweden.

Carin Vörde, Helen Stenmark and Lars Karlsson
NEXPLO-Bofors AB, SE-691 86 Karlskoga, Sweden

Maija Hihkiö
Explosives Technology, Defence Forces Research Institute of Technology
P.O. Box 5, FIN-341 11 Lakiala, Finland

Summary

The properties and possible production scale-up of 2,2-Dinitro-ethene-1,1-diamine (FOX-7) have been studied. The Koenen test gave a type "F" reaction at 6 mm nozzle diameter. The activation energy (E_a = 56 kcal/mole) was measured with Differential Scanning Calorimetry (DSC). The ignition temperature was determined by Wood's metal bath to 215°C. Accelerated Rate Calorimetry (ARC) showed that FOX-7 has a runaway reaction around 230°C. A relationship between the particle size of FOX-7 and the decomposition temperature in DSC has been found. Four phases of FOX-7 have been established, these have been named FOX-7(α), FOX-7(β), FOX-7(γ) and FOX-7(δ). Time to ignition measurements with a CO_2-laser showed that FOX-7 is more difficult to ignite than RDX. Mass spectroscopic studies showed that FOX-7 is a very stable molecule compared to RDX and HMX. An HPLC method based on the porous graphite carbon (PGC) column packing material has been developed for the analysis of FOX-7. FOX-7 was found to be compatible with a variety of materials that might be used in propellants or explosives. The synthesis of 2,2-dinitro-ethene-1,1-diamine (FOX-7) has been studied and the process has been scaled up to 7 kg batches.

Calculations based on reaction calorimeter show the flow of energy in the process and this study has contributed to a safe and convenient pilot scale process

Introduction

The purpose of the ongoing research on energetic materials in Sweden is to produce more powerful, safer and environmentally friendlier explosives that fit into the new action plan of the defence forces. This directs the research towards compositions with lower sensitivity, which improves the ammunition safety and might find use in international operations. A problem with lower sensitivity energetic materials in munition has been that insensitivity almost always has meant lower performance. With new energetic substances and energetic plasticizers and binders it might not be so difficult to manufacture charges with low sensitivity and high performance.

FOX-7 is an explosive that has rendered much interest. The interest in the substance lies in its applicability in several areas thanks to its low sensitivity combined with its relatively high performance (slightly lower than for RDX). The single crystal *X-ray* diffraction density (1) was determined to be 1.878 g / cm^3 whereas the density determined by powder diffraction was found to be 1.885 g / cm^3. The activation energy for the substance has been measured to 56 kcal/mole which if compared to RDX (40 kcal/mole) and HMX (35 kcal/mole) represents an advantage for FOX-7(2). FOX-7 has a very interesting herringbone crystal structure, see figure 1. The crystal packing explains some of the physico-chemical properties of the compound like the absence of a melting point, its low solubility, and its low sensitivity to friction and impact compared to RDX(3).



Figure 1. Molecular packing of FOX-7 in the crystal structure. The view is along the X-axis with the Y-axis down and the Z-axis across the paper.

This paper presents data on the properties and thermal stability of FOX-7, some parts of this material have been published before in another conference contribution [4]. Furthermore, advances in the scale-up of FOX-7 are presented.

Synthesis

All the material used for the studies presented in this paper was produced by the synthesis group at FOA [5]. Identification of the substance was done by FT/IR, NMR and X-ray analysis. Purity was checked by HPLC and DSC.

Sensitivity and Thermal Decomposition

Sensitivity

The sensitivity to impact and friction for FOX-7 is 126 cm (2 kg, BAM) and > 35 kp (Julius-Petri), respectively [5]. The data for RDX is shown as a comparison between the materials.

Table 1. Drop weight and friction data for RDX and FOX-7 measured in the same apparatus

	RDX	FOX-7
Dropweight test (cm)	38	126
Friction test (N)	120	>350

Koenen Test

The Koenen test was performed according to the UN recommendations [6]. The test is designed to determine the sensitiveness of solid or liquid substances to the effect of intense heat under high confinement. The heat sensitivity is expressed as the largest diameter of the nozzle plate hole at which at least one explosion occurs out of three consecutive tests. For FOX-7 the diameter is 6 mm, the first reaction damaging the confinement occurs at the nozzle diameter 6 mm (type "F" effect). RDX of the same particle size explodes at 8 mm.

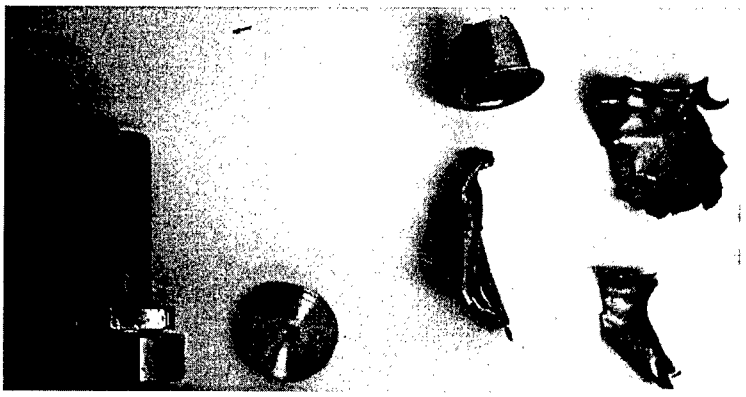


Figure 2. Koenen test on FOX-7: Type "F" reaction at nozzle plate diameter 6 mm

Wood's Metal Bath

Results from Wood's metal bath have earlier been published at the 11Th Symposium (international) on Detonations(1) they are here given purely as a comparison. In the ignition test the time to ignition was measured as a function of the temperature. This was done by immersing a test tube with the sample in a bath of Wood's metal at a certain temperature. Wood's metal bath gave for FOX-7 an ignition temperature of 215 °C. RDX measured under the same conditions gave an ignition temperature of 220°C.

DSC Measurements

The DSC used was a Mettler DSC 30 with a ceramic sensor. Every experiment as well as the calibration was performed in a nitrogen atmosphere. The flow of nitrogen was approximately 50 ml/minute. The DSC was calibrated with indium (Mettler Calibration Standard) and evaluated according to Mettler's recommendations (7). The samples were put in aluminium cups with pierced lids. The samples were heated from room temperature with a heating rate of 0.5 – 10°C/min. The DSC spectrum of FOX-7 shows a complex structure with two exothermal peaks, one at 238 °C/min and another one at 281 °C/min. In table 2 a comparison of the activation energies for RDX and FOX-7 is presented. The activities were calculated using the ASTM method E 698-79 by plotting $-\ln(\beta/T^2)$ versus 1000/T were β is the heating rate in °C/minute and T is

the peak temperature in K, The activation energy was then calculated by fitting a straight line to the data and by using equation 1.

$$E_a = R\frac{d - \ln(\beta / T^2)}{d\,(1/T)} \qquad \textbf{Equation 1}$$

As table 2 shows the activation energy for FOX-7 is larger than that of RDX. The DSC of FOX-7 can differ quite a lot, something which is discussed further on in this paper.

Table 2. Activation energies from DSC experiments in the temperature interval 210 – 250°C

Explosive	E_a (kcal/mole)
FOX-7	56
RDX	48

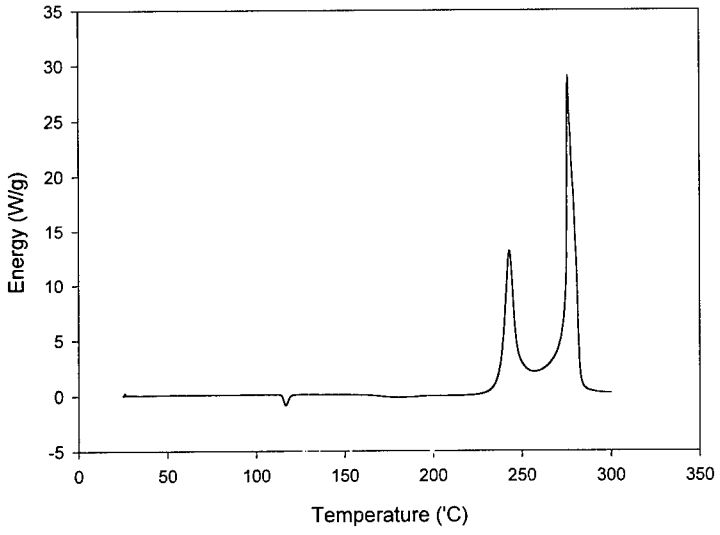


Figure 3. The DSC spectrum of FOX-7 at a heating rate of 10°C/min.

TG Measurements

The TG used was a Mettler TGA 850. The test was performed in a nitrogen atmosphere at a heating rate of 10 °C/minute. The samples were put in alumina cups and the flow of nitrogen was approximately 80 ml/minute. Prior to the testing, the TG was calibrated according to Mettler's recommendations [7]. The TG spectrum shows at least two steps (figure 4). This gives an indication that a two step process characterises the initial decomposition of FOX-7, where the initial intermediate has a low thermal stability. This process also explains the two peaks in the DSC curve.

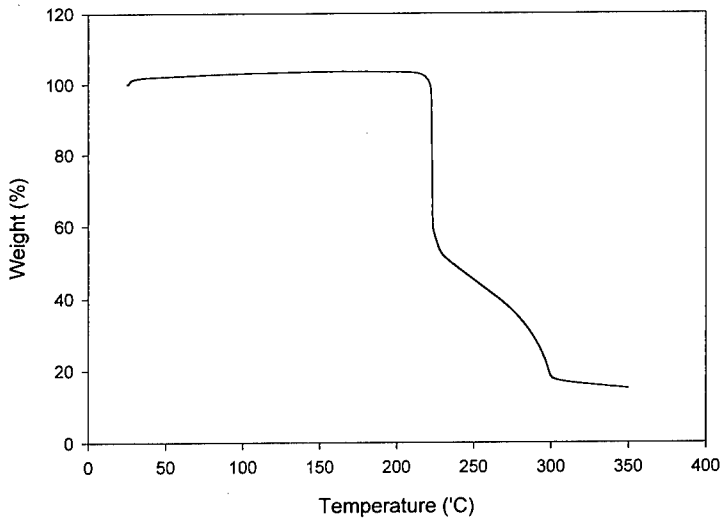


Figure 4. TG plot of FOX-7 at a heating rate of 10 °C/min.

ARC Measurements

The ARC measurements were performed on a Columbia Scientific Accelerating Rate Calorimeter (CSI-ARC-851) in a temperature range of 150 - 400°C. The instrument operated in a heat – wait – search mode where the heating rate was set to 3°/min, the

wait time was varied between 5 and 15 minutes and the slope sensitivity set to 0.01°C/min. As a reference RDX 99/1 was tested in the apparatus under the same conditions. When starting at 150°C the onset was found to be 199°C and the runaway 202°C. When the starting temperature was set to 180°C the onset was 195°C and the runaway found at 201°C. In table 3 and figure 5 below a summary of the onset and runaway temperatures for FOX-7 is given.

Table 3. The onset and runaway temperatures for FOX-7 at 150 and 180 degrees respectively.

FOX-7	Wait time 5 min		Wait time 10 min		Wait time 15 min	
Start temp (°C)	150	180	150	180	150	180
Onset (°C)	222	222	222	219	223	223
Runaway (°C)	230	231	230	229	230	230

The results from the ARC measurements show that the onsets and the runaways in all cases come earlier for RDX 99/1 than for FOX-7. It is also interesting to see that RDX 99/1 goes from onset to runaway much faster than FOX-7.

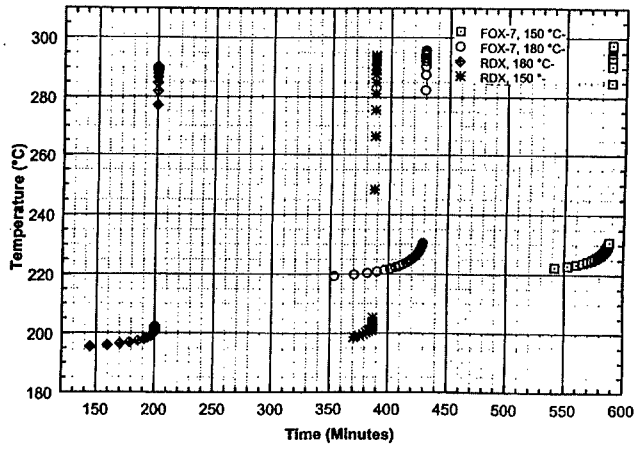


Figure 5. Onset and runaway temperatures for FOX-7 and RDX at 150 and 180 degrees respectively

The Relationship Between Particle Size and Decomposition Temperature in DSC.

There has for a long period of time been problems to understand why the DSC curve of FOX-7 can differ so much between different batches etc. The two decomposition peaks at ~235° C and ~280° C usually differ rather much in the relationship between the areas of the two peaks and at what temperature they occur, when comparing FOX-7 from different sources such as different synthesis routes, different batches, different solvents in recrystallisation processes, different techniques in synthesis and crystallisation and so on. We have often seen confusing examples; such as only one peak at ~235° C, or only one peak at ~280° C or two peaks with equally large areas.
From ur investigations we can conclude that particle size is important – hence, to compare FOX-7 from different sources, it is important that they have the same particle size. Since most processes give FOX-7 of different particle sizes we have experienced that the DSC-curves don't match when we compare the region above 200° C.

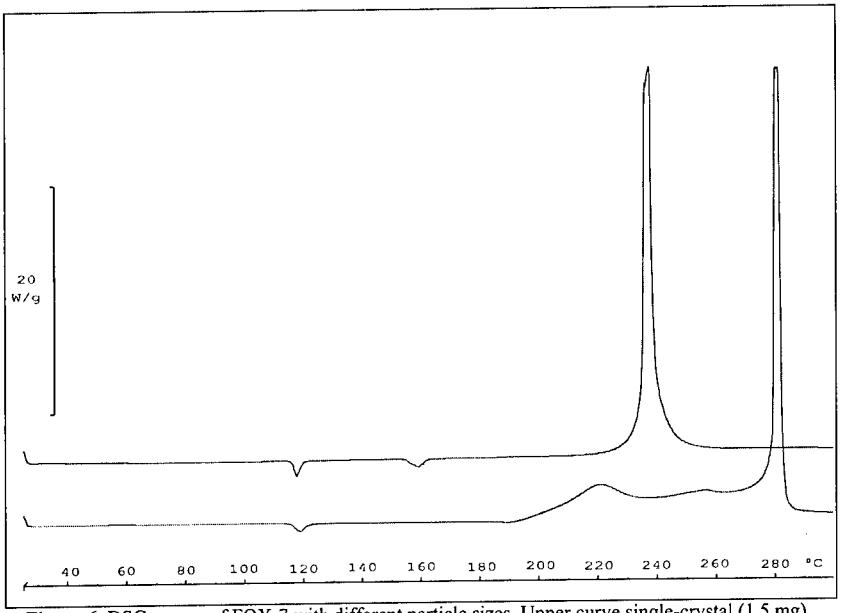


Figure 6. DSC-curves of FOX-7 with different particle sizes. Upper curve single-crystal (1.5 mg). Lower curve very fine powder (1.5 mg).

Figure 6 shows two DSC-curves from the same batch with large differences in the decomposition region above 200° C. It's important to notice that in the lower curve (fine particles) the phase-transition at 158° C has disappeared. Ongoing studies will look further into this and the complete investigation concerning the influence of particle size on the shape of the DSC curves will be published later on this year.

Temperature dependent phase transitions of FOX-7.

It is commonly known that FOX-7 has got phase transitions at higher temperatures. However, investigations of FOX-7 using temperature controlled X-ray powder diffraction methods (XPD) and Differential Scanning Calorimetry (DSC) shows that there exists an high-temperature phase which was previously unknown.

As mentioned above, the DSC curve of FOX-7 exhibits two endothermic peaks at 116° C and 158° C both indicating phase-transitions (figure 6). But XPD in the temperature range of 25° - 140° C shows that there is also a phase-transition at about 80° C. Combining XPD and DSC data therefore tells us that there are three temperature dependent phase-transitions present in FOX-7 (table 4), of which the two phase transitions at 115° C and 156° C are of the first-order type and the newly found phase-transition at ~80° C is of the second-order type.

The particle size of FOX-7 strongly affects the temperature in the XPD investigations at which the transition is observed. The first phase-transition (α <--> β) is observed to take place at about 78° C for very fine particles and can vary up to 95 ° C for larger particles. It takes about 3 hours for the phase-transition to be complete and the time is independent of particle size. The first phase-transition is fully reversible. The second phase-transition (β <--> γ) is observed to take place at about 116° C and the transition temperature is not influenced by the particle size. However, the particle size influences the transition time and the transition time varies from 10 hours for very fine particles to 14 hours for larger particles. The second phase transition is very slow kinetically on its way back and it takes up to 3-4 weeks for the FOX-7(γ)-phase to transform back into the FOX-7(α)-phase

The complete investigation of the different phases with crystallographic data and the phases properties is going to be presented later on this year at IM/EM konference in Bordeaux(8).

To simplify discussions concerning FOX-7 the investigation has led to the renaming of FOX-7 to include an Greek letter for each phase i.e. FOX-7(α), FOX-7(β), FOX-7(γ) and FOX-7(δ).

Table 4[XPD]. Table with data on the four phase-transitions of FOX-7. The (α) phase is stable from -150°C to 80°C, while the (γ) phase decomposes above 225°C.

	~80°C		115°C		156°C		225°C
FOX-7 (α)	<⟶>	**FOX-7 (β)**	<⟶>	**FOX-7 (γ)**	<⟶>	**FOX-7 (δ)**	⟶>

Time To Ignition Measurements

The time to ignition measurements were conducted using a 180 W CW CO_2 laser (Edinburgh PL6), an electronic shutter for producing pulses in the interval 1 ms – CW, a photo diode for measuring the reaction light and an explosive chamber. A more detailed description of the set-up can be found in the literature(9).

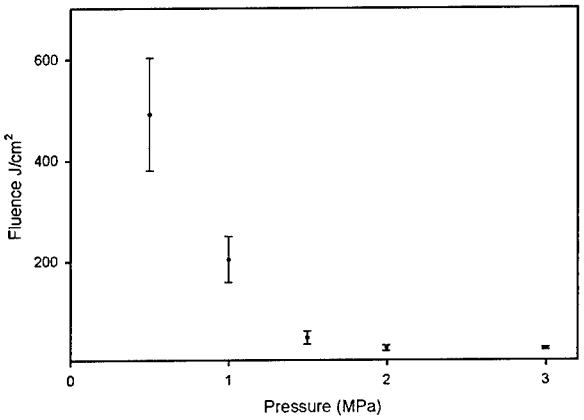


Figure 7. Fluence needed to achieve ignition as a function of pressure for FOX-7.

The measurements shown in figure 7 were conducted with the following parameters: laser power 48 W, spot size 1.5 mm in diameter and the pellets were pressed to 95% TMD. The measurements were conducted in air at elevated pressures. A few experiments were done with RDX, these indicate that RDX ignites much easier than FOX-7. Please note that the data has not been corrected for reflectivity or absorption.

Mass Spectroscopic Data

It has been shown that the thermal fragmentation path of RDX shows similarities to its mass spectral fragmentation[10]. A mass spectroscopic study is thus a natural starting point for acquiring new information about the decomposition mechanism.

The mass spectroscopic study was conducted on a JEOL 300D double-focusing magnetic sector instrument equipped with a PC-based computer system utilising Technivent Vector/2 software for analysis. All mass spectra were obtained by using the solid sample inlet and the heating rates were varied. Both 20 eV, 70 eV and CI spectra were acquired.

One significant observation is that even at 70 eV FOX-7 exhibits a very strong molecular peak (*m/z* 148). This indicates that the molecule is very stable compared to RDX. It has earlier been reported that NTO[11] and TNT[12] show small molecular peaks at 70eV. The mass spectrum at 70 eV was also confirmed by measurements at DFRIT.

Both at 20 eV and 70 eV we observe *m/z* 148, 130 and 18. This indicates the elimination of water in the same fashion as Sharma et al[13] described for TATB. Whether this is due to decomposition in the mass spectrometer or by thermal decomposition remains to be determined. Other interesting *m/z* that are found in the spectra is one group at *m/z* 42, 43, 44, one group at *m/z* 53, 55 and peaks at 69, 72 and 86. In the 20 eV spectra the peaks at *m/z* 53 and *m/z* 69 diminish indicating that the production of these *m/z* is due to electron bombardment. In both the 20eV and the 70 eV spectra trace amounts of *m/z* 102 (M – 46) can be observed. This decomposition was predicted by Karle et al[2]. Further research is needed to confirm this

decomposition. Identification of these peaks is ongoing. In figure 8 and 9 typical spectra of FOX-7 at 20 eV and 70 eV are showed.

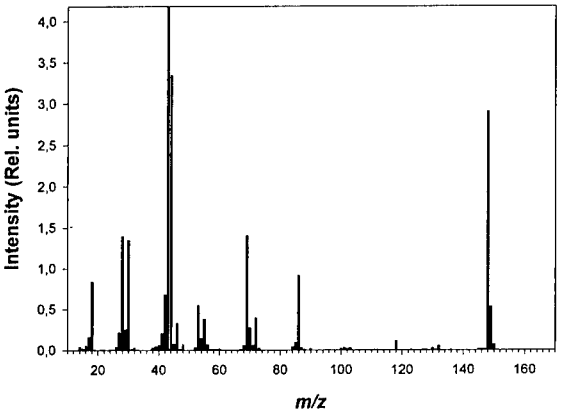


Figure 8. Spectra of FOX-7 recorded at 70 eV using the solid sample inlet and a heating rate of approximately 20 °C /min.

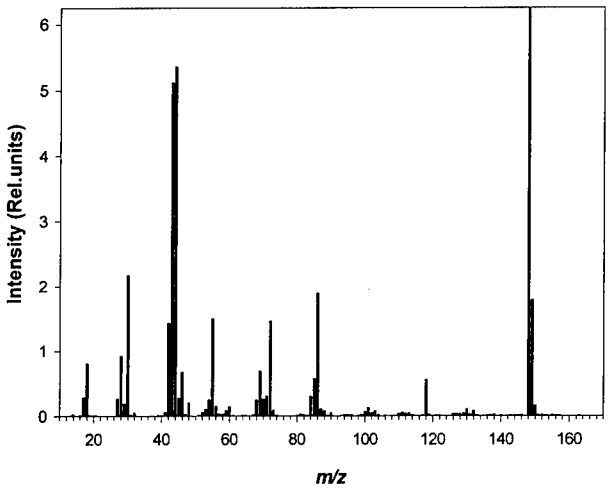


Figure 9. Spectrum of FOX-7 recorded at 20 eV using the solid sample inlet and a heating rate of approximately 20 ° /min.

The CI spectrum was recorded using isobutane as reagent gas and introducing FOX-7 through the solid sample inlet with a heating rate of approximately 20 °C/min (figure 10). In the CI spectrum one can observe the mass peak (m/z+1) and an adduct or dimere at (2m/z+1). A similar spectrum was observed on a mass spectrometer equipped with electro spray ionization, we can at this point not state if this is an adduct or a dimer.

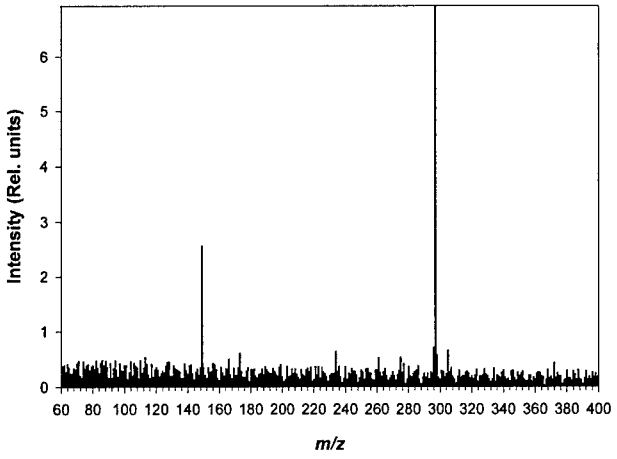


Figure 10. A CI spectrum of FOX-7 using the solid sample inlet and isobutane as reagent gas.

HPLC Analysis of FOX-7

FOX-7 is an extremely polar compound these are normally very difficult to chromatograph on reversed phase as they tend to follow the solvent front. As expected, when using a C18 column under standard conditions FOX-7 eluted with the front (figure 11). It was however possible to analyze the compound on a porous graphitic carbon column (PGC) under acidic (figure 12) and basic conditions. The HPLC analysis showed no detectable impurities.

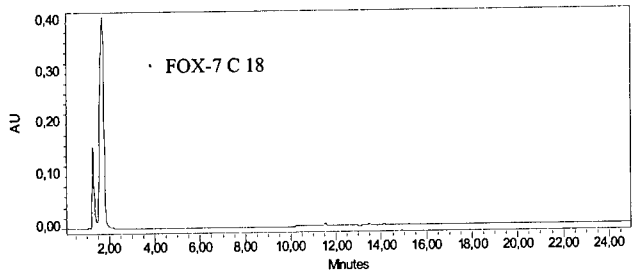


Figure 11. FOX-7 on a C 18 column

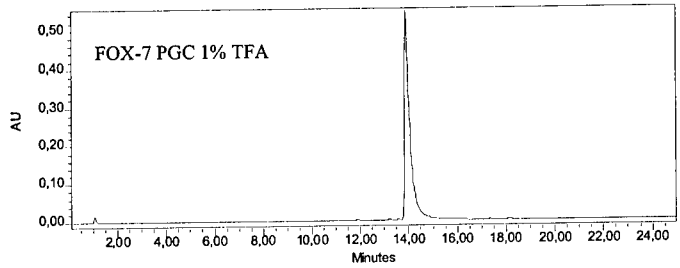


Figure 12. FOX-7 on a PGC column

Experimental: Column: Hypercarb 100x3 mm ,5 um particles (Thermo Hypersil), Gradient System: A : water 99%/1% TFA, (V/V). B : acetonitrile 99%/1% TFA, (V/V). Gradient range: 3 min 0% B, 0-100% B in 7 min, 100% B in 12 min. Flow rate 0.8ml/min.

FOX-7 compatibility

Methods

The compatibility between FOX-7 and different compounds were determined by measuring the heat flow from each pure sample, and from a mixture of the two at a one to one weight ratio in a microcalorimeter. The samples where put in 3 ml glass ampoules, purged with nitrogen prior and hermetically sealed. The weight of the sample was approximately one gram.

The heat flow was measured with a Thermal Activity Monitor, TAM 2277, microcalorimeter, during one week at 65 °C. The total energy evolved by the sample, E, is calculated by integrating the heat flow with respect of time. If the energy

evolution from a pure sample is low, then the sample is said to have a high thermal stability. The compatibility, C, is then calculated as:

$$C_{ab} = E_{ab} - \frac{E_a + E_b}{2}$$

were the subscripts a and b refer to respective pure substance, and the subscript ab refers to the mixture of a and b. If the compatibility is good, then C is low.

If the measured energy evolution of the mixture exceeds the theoretical, calculated from the energy evolution of the pure substances, then the mixture is incompatible. The incompatibility can however be of different magnitudes. If C is higher than 10 J/g during one week at 65 °C, then the compounds has a minor incompatibility. Above 20 J/g, the compounds are incompatible. The accuracy of the microcalorimeter is better than ±0.5 J/g, during one week.

Results and Discussion

As a start, the thermal stability of FOX-7 was measured. It was found to be 0.37 J/g which is considered to be very stable.

The thermal stability and compatibility between the polymers in table 5 and FOX-7 was measured.

Table 5. Thermal stability and compatibility with FOX-7 for different polymers.

Polymer	*Origin/Manufacturer*	E_b *(J/g)*	C_{ab} *(J/g)*
CAB (BF 900)	Supplied by Bofors	0.38	-0.38
ESTANE	Supplied by Bofors	0.27	-0.26
GAP	SNPE, France, 1996	2.57	-0.44
HTPB (R-45 HT)	ARCO, USA	1.89	3.89
Krasol LBH	Kaucuk a.s., Czech Republic	0.24	0.13
VITON	Supplied by Bofors	0.10	0.03

All polymers but HTPB (R-45 HT) and GAP have an excellent thermal stability. The thermal stability of HTPB (R-45 HT) and GAP is still good and should not be any major concern. The compatibility with FOX-7 is excellent for all polymers but HTPB (R-45 HT). The compatibility between HTPB (R-45 HT) and FOX-7 is slightly worse, but the amount of energy produced is still very low.

Compatibility with Isocyanates.

Polymers as HTPB and GAP are usually cured with isocyanates to yield solid rubbery materials. Isocyanates are very reactive and thus one might suspect incompatibility between isocyanates and a variety of materials. In this case the compatibility was measured between FOX-7 and dicyclohexylmethane 4,4′-diisocyanate or HMDI.

Table 6. Thermal stability and compatibility with FOX-7 and a diisocyanate.

Isocyanate	*Origin*	E_b *(J/g)*	C_{ab} *(J/g)*
HMDI	Bayer, Germany	0.70	0.41

As can be seen in table 6, HMDI has a high thermal stability and a excellent compatibility with FOX-7. It should thus be possible to cure a FOX-7 containing polymer with diisocyanate.

Compatibility with Energetic Plasticizers.

To decrease the glass transition temperature and to increase the energy it is beneficial to use energetic plasticizers. The energetic plasticizers used in this study are, n-butyl-2-nitratoethyl-nitramine or butyl-NENA, and dinitroethylbenzene or K-10.

Table 7. Thermal stability and compatibility with FOX-7 and different plasticizers.

plasticizer	*Origin/Manufacturer*	E_b *(J/g)*	C_{ab} *(J/g)*
Butyl-NENA	Dyno, Norway	1.07	0.16
K-10	Synthesised at FOA	0.41	0.44

The two energetic plasticizers have an excellent compatibility with FOX-7. K-10 has a better thermal stability than butyl-NENA, but E_b for butyl-NENA is still very low.

Scaling-Up the Production of FOX-7

The synthesis of FOX-7 was first published in 1998[5]. FOX-7 was first produced at FOI in 200-gram batches and together with NEXPLO BOFORS AB (NEB) in 1,5 kg batches. NEB has now scaled up the process to a 7-kg batch scale in its own pilot plant. Before the production the synthesis was studied in a reaction calorimeter. The result from this thermal study has been used to establish the process values with the purpose to obtain safe process conditions.

Synthesis

The starting material was first dissolved in sulfuric acid. The next step was the addition of nitric acid at a reaction temperature of about +25°C. As the reaction is strongly exothermic the reaction energy had to be cooled away. The addition of nitric acid took about 30 minutes of the total reaction time, which was found to be 2 hours. During the reaction a nitrated intermediate was formed. Normally this intermediate started falling out as a precipitate when half of the nitric acid had been added. After two hours the reaction mixture was added to water while stirring. In this water-sulfuric acid solution, the nitrated intermediate was hydrolyzed to FOX-7 and carbon dioxide. FOX-7 formed as a yellow precipitate as carbon dioxide bubbled away from the slurry. The produced FOX-7 was then filtered washed and dried. The yield was found to be around 80%. The manufactured product is a small-granular raw-product with an average particle size of about 25 μm.

Pilot Production Equipment

For the scale-up of FOX-7, NEB used a 600-liter reaction vessel for the production of the starting material. The reactor is equipped with a jacket and inside coil for cooling and heating and an overhead cooler to condense vapors. About 15 kg of starting material could be produced in a normal batch. The same vessel was used to dissolve the starting material in sulfuric acid. The starting material was then nitrated in a 50-liter reactor equipped with a jacket and an inside coil for cooling. The cooling capacity of the nitration reactor is very large and it is also possible to do nitrations at temperatures below 0°C. The nitration reactor is situated upon a 500-liter vessel and it can only be emptied into the. In the production of FOX 7 the 500-liter vessel contained water for the hydrolysis. About 7 kg of FOX-7 could be produced in a normal batch. It's possible to produce two batches a day. The process for producing FOX 7 can in the future be scaled up to commercial scale in NEB's multi-purpose plant for explosives.

Production Risks and Their Solutions

The reaction mixture decomposes exothermically at 100°C (determined by a DSC-analysis of the reaction mixture). The exothermic decomposition reaction has the capacity to cause a runaway reaction and in worst case a deflagration. Normal temperature of nitration is +25°C and the generated heat of nitration reaction is cooled away. If all the heat produced in the nitration reaction stays in the reaction mixture and is not cooled away, the temperature will increase 120°C. If this temperature rise is added to the starting temperature of +25°C, it will reach 145°C, which is more than enough for the exothermic decomposition reaction to start.

The dosing pump for the nitric acid stops automatically if the process temperature goes above +35°C. However, However, the highest probability for a single accident to occur is if the stirrer isn't on when the nitric acid is added. If all the nitric acid is added and the stirrer is started after this, the reaction will surely runaway. However, also this scenario is impossible, as the dosing pump isn't able to start if the stirrer isn't running. These phenomena are well known and therefore easy to prevent.

A more complicated problem is the risk of high accumulation of nitric acid in the reaction mixture. If the nitration reaction is too slow, the nitric acid isn't consumed fast enough, instead it's accumulated in the reaction mixture. The reaction conditions, which cause accumulation, are low temperature combined with high dosing speed of nitric acid. High accumulation of nitric acid doesn't give any problems during normal process conditions, but if the reaction temperature for some reason rises a few degrees, the reaction speed increases and thereby also the heat generation. If the cooling system isn't powerful enough, the temperature will increase without control until the nitric acid is consumed. Under unfortunate circumstances a temperature will be reached when the formed explosive will start to decompose exothermically. In our case dealing with the synthesis of FOX-7 we will have a runaway if the temperature reaches 100°C.

The worst incident is an unexpected loss of cooling combined with high amount of accumulated nitric acid. Dosing of nitric acid stops immediately if temperature rises to more than +35°C and in the case of an electric power failure. However, if the

accumulation of nitric acid is too large these measures won't be enough. The amount of accumulated energy could in the worst case increase the temperature above 100°C even if the dosing of nitric acid was immediately stopped.

To prevent damage caused by a loss of cooling the reaction temperature must be high enough and the dosing speed of the nitric acid mustn't be too fast. If these conditions are met, a runaway reaction can't occur as a consequence of a loss of cooling. To investigate these conditions properly a study of the reaction has been done in a reaction calorimeter at NEB.

Reaction Calorimetry

The reaction calorimetry studies were performed on a ChemiSens reaction calorimeter. The heart in the calorimeter is a reaction cell, which contains about 200 ml of a test mixture. The reaction cell is totally submerged into a bath of water (or any other heat- or cooling media). Powerful heating- and cooling equipment always keep the surrounding media at the same temperature as the test mixture in the reaction cell. This setup generates totally adiabatic conditions. All heat transfer goes through a peltier-element in the bottom of the reactor. Sensitive thermocouples in the bottom of the reactor cell register the heat flow in- or out of the reaction cell. The information is collected and treated in a computer. The computer also collects data from the temperature in the reactor and from a connected balance. On the balance the nitric acid is weighed out and pumped through a laboratory-dosing pump. The measuring could be done both at isothermal conditions and on a thermal slope. The result is generated power, which can be integrated to reaction energy. Further calculations give information of the accumulation in every step of the nitration reaction.

Temperature and dosing speed of nitric acid have been determined so that a runaway reaction caused by an unexpected loss of cooling can not occur. The nitration temperature is kept at +25°C and the dosing speed for the nitric acid is 30 minutes. Under these conditions the maximum accumulation of nitric acid was found to be 18%. This accumulation can cause an adiabatic rise of temperature of 22°C. This

could cause a maximum temperature of 25 + 22 = 47°C, i.e. far away from the dangerous 100°C[14].

Conclusions

The following conclusions can be drawn from the measurements presented in this paper:

- FOX-7 is thermally more stable than RDX.
- FOX-7 is less sensitive than RDX in the following tests: friction, drop weight, SSGT and Koenen test it can thus be considered to be a low sensitivity explosive
- FOX-7 has an excellent compatibility with a variety of materials that might be used in propellants or explosives, including different polymers, energetic plasticizers and diisocyanate.
- FOX-7 can easily be formulated
- FOX-7 can easily be scaled up to production scale
- FOX-7 is hereby a prime candidate as a component in fillings for IM applications.

Acknowledgements

The authors would like to thank the Swedish Defence Forces and the Swedish Defence Materiel Administration for giving financial support to this project. The authors would also like to thank J. Pettersson for valuable input in the time to ignition measurements.

References

(1) H. Östmark, A. Langlet, H. Bergman, N. Wingborg, U. Wellmar, U. Bemm, "FOX-7 A New Explosive with Low Sensitivity and High Performance" *11Th Symposium (international) on Detonations* Snow Mass Co, 1998.

(2) J. Karle, L. Massa, A. Gindulytè, "Proposed Mechanism of 1,1-Diamino-Dinitroethylene Decomposition: A Density Functional Theory Study": Journal of Physical Chemistry 103, 110045-11051, (1999).

(3) U. Bemm, H. Östmark, "1,1-Diamino-2,2-dinitroethylene: a Novel Energetic Material with Infinite Layers in Two Dimensions": Acta Cryst C54, 1997-1999, (1998).

(4) H. Bergman, H. Östmark, A. Pettersson, M.-L. Pettersson, U. Bemm, M. Hihkiö, "Some Initial Properties and Thermal Stability of FOX-7" *1999 Insensitive Munitions and Energetic Materials Technology Symposium* Tampa, 1999.

(5) N. V. Latypov, J. Bergman, A. Langlet, U. Wellmar, U. Bemm, "Synthesis and Reactions of 1,1-Diamino-2,2-dinitroethylene": Tetrahedron 54, 11525-11536, (1998).

(6) *United Nations: Recommendations on the Transport of Dangerous Goods. Manual of Tests and Criteria ST/SG/AC.10/11/Rev.2.* 2nd revised ed.; United Nations, New York and Geneva, 1995 .

(7) *Mettler Toledo Operating Instructions STAR^e Software, Version 5.0* , 1997, pp 10-1 - 10-24.

(8) U. Bemm, "to be published" *Insensitive Munitions and Energetic Materials Technology Symposium* Bordeaux, France, 2001.

(9) H. Östmark, R. Gräns, "Laser Ignition of Explosives: Effects of Gas Pressure on the Threshold Ignition Energy.": Journal of Energetic materials 8, 308-322, (1990).

(10) J. Stals, : Transactions of the Faraday Society 6, 67, (1971).

(11) H. Östmark, H. Bergman, G. Åqvist, "The chemistry of 3-nitro-1,2,4-triazol-5-one (NTO): Thermal Decomposition.": Thermochimica Acta 213, 165-175, (1993).

(12) A. Alm, O. Dalman, Frölén-Lindgren, F. Hultén, T. Karlsson, M. Kowalska "Analyses of Explosives. Physical-chemical data, chromatograms, mass-, IR- and NMR-spectra. Colour reactions and thin layer chromatography" FOA Rep. C 20276-D1 1978, FOA, .

(13) J. Sharma, J. W. Forbes, C. S. Coffey, T. P. Liddard, "The Physical and Chemical Nature of Sensitization Centers Left from Hot Spots Caused in Triaminotrinitrobenzene by Shock or Impact": Journal of Physical Chemistry 91, 5139 - 5144, (1987).

EVALUATION OF CRYSTAL DEFECTS BY THE SHOCK SENSITIVITY OF ENERGETIC CRYSTALS SUSPENDED IN A DENSITY-MATCHED LIQUID

Richard Bouma, Antoine van der Heijden

TNO Prins Maurits Laboratory, P.O. Box 45, 2280 AA Rijswijk, The Netherlands

Abstract

This paper focuses on a method to study shock sensitivity which excludes effects on shock sensitivity of the binder/crystal interface, binder porosity, crystal shape, and shock impedance mismatch, and which studies exclusively the effect of crystal internal defects on shock sensitivity.

The effect of crystal quality on the shock initiation threshold has been demonstrated in earlier work where HMX has been recrystallized to various qualities, the crystals dispersed in a polyurethane binder, and where the shock initiation threshold of the resulting Polymer Bonded eXplosive has been determined with the water gap test.

In this paper the HMX is recrystallized again to various qualities, but this time the crystals are suspended in a liquid which has the same density as the crystals, instead of a polymeric binder. Eventual defects in the binder system and at the binder/HMX interface are removed, and furthermore, shock impedance mismatch between dispersed and continuous phase is minimized. The shock initiation threshold is determined by the flyer impact initiation technique instead of the water gap test. The same drastic change of crystal quality on shock initiation threshold is observed. This is attributed to the crystal density, which is shown to be a very important parameter.

In the shock initiation experiments with CL-20 the effect of crystal quality is not investigated, but a comparison is made between initiation of CL-20 crystals immersed in a density matching liquid and the same CL-20 crystals dispersed in a polymeric binder.

Introduction

A parameter that influences the shock sensitivity is the defect structure of the energetic filler in an explosive composition. This has been demonstrated with HMX-based Polymer Bonded eXplosives (70 wt.% HMX), applying the BICT water gap test[1,2]. The shock initiation pressure increased from 4.1 to 6.8 GPa, by increasing the HMX crystal density by careful recrystallization from 1.886 to 1.902 g/cm^3, in this particular example.

The HMX crystals were crystallized by means of cooling crystallization from a mixture of acetone and γ-butyrolactone. The crystals have been characterized with regard to density, defects, mean size and shape with help of different analytical techniques and these results have also been reported earlier[3,4].

Encouraged by the significant improvements in decreased shock sensitivity, a similar type of study is presented here in order to prove the concept that the minimization of crystal defects will decrease the sensitivity towards shock of an energetic composition. The HMX is again recrystallized under well-controlled conditions to obtain different crystal qualities, the polymeric binder is replaced by a liquid and the water gap test is replaced by a flyer impact test, to support the general validity of the concept.

Experimental

HMX samples

HMX (supplied by Dyno AS, Norway) has been has been recrystallized to obtain batches with different qualities. All HMX batches have been sieved and the 355 – 425 μm fraction is retained for the shock initiation experiments. The as-received and sieved fraction is referred to as TL 106/95, the two recrystallized and sieved fractions are referred to as TL 633/99 and 635/99. The crystal densities of the batches TL 106/95, TL 633/99 and TL 635/99 are 1.885, 1.900 and 1.895 gcm^{-3} respectively, see also reference 5.

HMX suspensions are made with a 63 % volume / 63 % mass percentage of HMX by carefully selecting a solvent mixture with a density equal to the HMX density, based on the crystal density measured with liquid pycnometry. The samples for flyer impact initiation are confined by a thick-walled PVC cup with internal diameter of 20 mm and a length of 25 mm, and sealed by a 25 μm thick polyimide foil at the flyer impact side.

CL-20 samples

A commercial grade CL-20 (hexanitro-hexaaza-isowurtzitane) with a specified particle size range of 100-150 μm has been procured from SNPE, and is applied without further recrystallization. Various physical properties of the molecule have been reported earlier[6]. The measured tapdensity of this batch is 0.874-0.877 g/cm^3. The value is relatively low and due to the irregular shape of the crystal agglomerates, see figure 1, and limits the amount of CL-20 in an explosive composition based on this grade of CL-20 only.

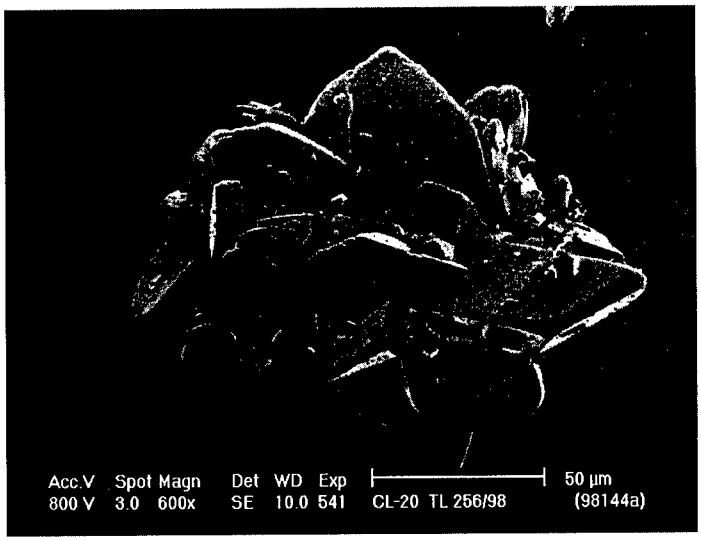


Figure 1: Detailed SEM picture of a single CL-20 agglomerate.

As no liquid with a density similar to the density of CL-20 was available at the time, a liquid with 1.95 gcm^{-3} density has been used to make a suspension of the CL-20 crystals. Shock initiation results of this CL-20 suspension will be compared to corresponding results of a Polymer Bonded eXplosive with the same CL-20. In both samples the volume fraction of CL-20 is the same, nl. 42 %, yielding a CL-20 suspension with 43 wt.% CL-20 and an HTPB based PBX with 62 wt.% CL-20.

The liquid-suspended CL-20 samples are confined by a thick-walled PVC cup with internal diameter of 10 or 20 mm, and length of 10 or 20 mm, and are sealed by a 25 µm thick Kapton foil at the flyer impact side. The CL-20 PBXs are tested without confinement, and samples have a diameter and length of 20 mm.

Flyer impact initiation

Flyer impact initiation has been studied with the TNO MegaAmpere Pulser. A 250 µm Kapton polyimide flyer with a diameter of 21.4 mm will impact the explosive samples over their full diameter. The impact velocities are varied to obtain the threshold corresponding to the Shock-to-Detonation Transition. A Fiber Optic Probe[7] is placed at the central axis to monitor the Shock-to-Detonation Transition or decay of input shock wave, as function of the impact velocity. A schematic drawing of the flyer impact configuration is given below.

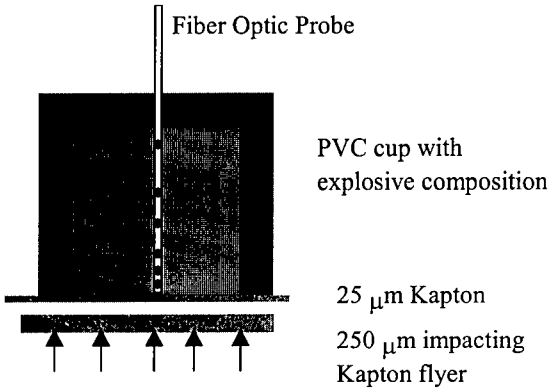


Figure 2: Flyer impact configuration for the solvent dispersed energetic crystals.

Flyer impact initiation results for the HMX samples are given in figures 3, 4 and 5. In these figures the shock wave velocity is plotted as function of distance from the impact/explosive interface. In the legend the flyer impact velocity is indicated.

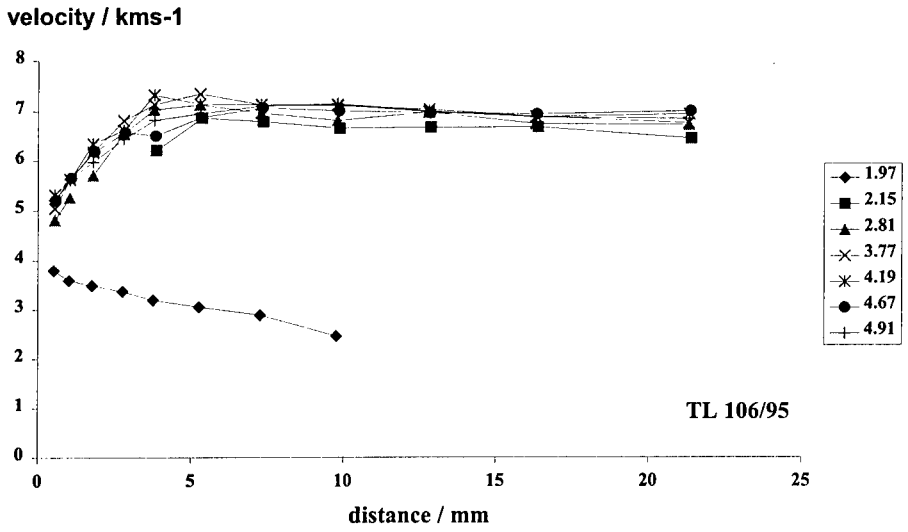


Figure 3: Shock wave velocity vs. distance in 63% HMX suspension at indicated flyer impact velocities in km/s, and with HMX originating from batch TL 106/95.

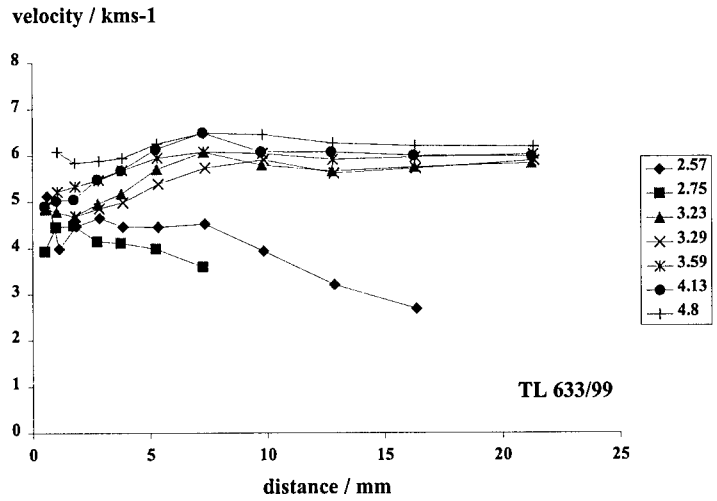


Figure 4: Shock wave velocity vs. distance in 63% HMX suspension at indicated flyer impact velocities in km/s and with HMX originating from batch TL 633/99.

In figure 4, the experiment with a flyer impact velocity of 3.05 km/s is not represented as no good signal with the Fiber Optic Probe is obtained. Post inspection of the flyer plate assembly indicates a Shock-to-Detonation Transion (SDT), but certainly not all material has detonated.

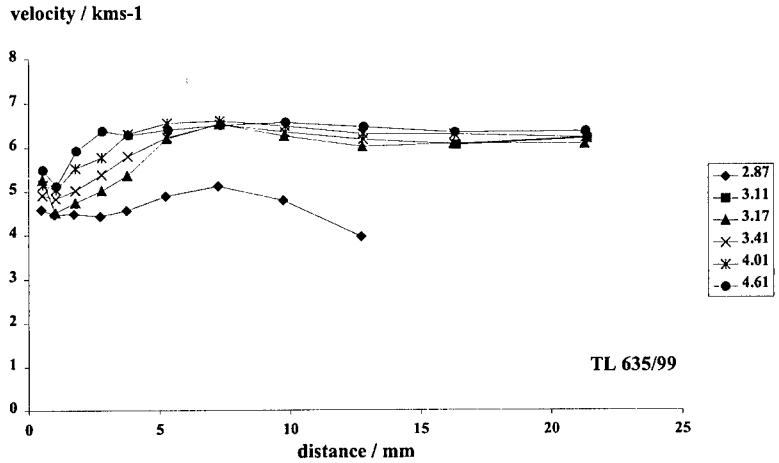


Figure 5: Shock wave velocity vs. distance in 63% HMX suspension at indicated flyer impact velocities in km/s, and with HMX originating from batch TL 635/99.

In figure 5 the experiment at a flyer impact velocity of 2.93 km/s is not given, as no good Fiber Optic Probe signal is obtained. No detonation has occurred as parts of the explosive sample have been found after the experiment.

The flyer impact initiation results of the liquid suspended CL-20 are summarized in table 1, and the results of the CL-20 PBXs are represented graphically in figure 6.

Table 1: Experimental results of Kapton flyer impact on a 42 vol.% CL-20 suspension, indicating flyer impact velocity, sample configuration and maximum of measured shock wave velocity.

flyer impact velocity km/s	Sample diameter Mm	sample length mm	maximum shock wave velocity km/s
2.06	10	20	no initiation
2.59	10	20	5.9*
2.66	10	20	6.1*
3.16	20	20	6.3**
3.31	10	10	6.3*

** Maximum shock wave velocity observed at about 5 mm from the flyer/CL-20 interface.*
*** Maximum shock wave velocity observed near end of explosive charge.*

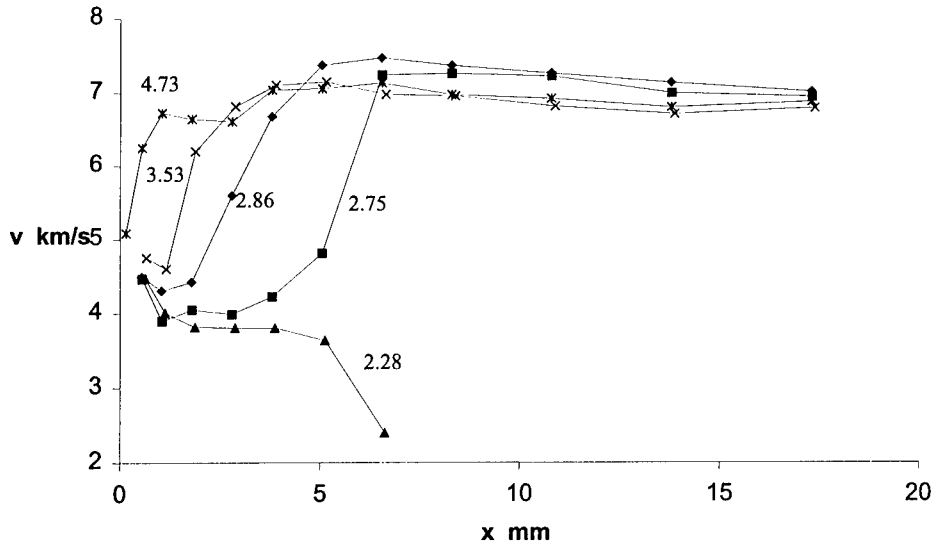


Figure 6: Shock wave velocity versus distance in PBX with 62 wt.% CL-20 after flyer impact at indicated velocities.

The analysis of shock wave and release waves in flyer impact given in reference 6 shows that the plateau observed in the shock wave velocity vs. distance, at the impact velocities 2.28 and 2.75 km/s, is intrinsic material behaviour and is not attributed to the geometry of the experiment.

Discussion and Conclusions

With the flyer impact initiation experiments relative small samples have been tested. Furthermore, the application of a density-matched liquid is a convenient method to obtain an explosive composition without "binder" imperfections and settling of the crystals. The capability to distinguish between the shock initiation sensitivity of different qualities of HMX crystals is shown in table 2, where the experimental results of figures 3, 4 and 5 are summarized.

Table 2: Experimental results of Kapton flyer impact on 63 % HMX suspension, indicating crystal density, threshold flyer impact velocity, and detonation velocity (measured at the end of explosive charge and averaged over positive experiments).

HMX batch	HMX crystal density g/cm3	threshold flyer impact velocity km/s	detonation velocity km/s
TL 106/95	1.885	2.0-2.2	6.8
TL 633/99	1.900	2.8-3.2	6.0
TL 635/99	1.895	2.9-3.1	6.2

From table 2 it is clear that the crystal density has a major influence on shock sensitivity. It seems that the crystal density also has a significant but negative influence on the detonation velocity, as measured at the end of the explosive sample. This effect still needs an explanation. At first sight one may argue that because of the lack of crystal defects the critical diameter of the explosive sample will raise and become comparable to the sample diameter of 20 mm. It is known that close to the critical diameter the detonation velocity will be less than the ideal detonation velocity in 1-dimensional geometry. However, the input shock wave is a planar one, and the effect of the finite dimensions will be noticed on the symmetry-axis only through release waves coming from the outer diameter. The signal of the Fiber Optic Probe, placed on this symmetry-axis, will not be influenced in the first $\approx$ 10 mm by radial release waves. In some of the experiments, a steady-state velocity is obtained within 5 mm, contradicting the hypothesis of the critical diameter effects.

Even though flyer impact initiation is aimed at inducing a well-defined and 1-dimensional shock wave in an explosive sample, a more thorough 2-dimensional analysis is needed to clarify or negate the forementioned argument. Other effects that may influence the detonation velocity are the strong release wave coming from the rear of the impacting flyer, when interfering with the finite reaction zone, and an eventual partial decompostion at the CJ-plane.

In the experiments with the CL-20 suspension it is clear that no stable detonation is possible in 10 mm diameter charges, see table 1 and especially the notes. The maximum in shock wave velocity is observed at about 5 mm from the impact side, a distance at which the effect of radial release waves is expected to be noticed on the central axis of the sample. Assuming that the radial release waves have prevented a stable detonation, one may conclude that the threshold flyer impact velocity for shock initiation is somewhere between 2.1 and 2.6 km/s. The detonation velocity of the CL-20 suspension will be about 6.3 km/s, but for the moment only one positive experiment above the critical diameter has been obtained. The experimental results for the CL-20 suspension and PBX are summarized in table 2.

Table 2: Experimental results of Kapton flyer impact on two different energetic samples containing both 42 vol. % CL-20, indicating threshold flyer impact velocity, and detonation velocity.

sample	threshold flyer impact velocity km/s	detonation velocity km/s
CL-20 suspension	2.1-2.6	ca. 6.3
CL-20 PBX	2.5-2.7	6.9

The concentration of the nitramine CL-20 is relatively low. Therefore, the detonation velocity as measured at the end of the small sample will be compared with a predicted detonation velocity. With the program Cheetah, the detonation velocity and CJ-pressure have been calculated applying the BKW-S product library because of the suspension liquid. For comparison, the detonation properties of the CL-20 PBX have been calculated as well with the BKW-C product library.

Table 3: Detonation velocity D and CJ-pressure P of CL-20 compositions, calculated with Cheetah.

sample	density g/cm3	D (BKW-C) km/s	P (BKW-C) GPa	D (BKW-S) km/s	P (BKW-S) GPa
CL-20 suspension	1.954	-	-	5.50	15.69
CL-20 PBX	1.377	6.06	12.06	6.66	14.47

Both CL-20 compositions have the same CL-20 concentration on volume basis. The calculated detonation velocity however, is varying largely. The CL-20 PBX has the highest detonation velocity, but the lowest pressure. The detonation velocity when calculated with the BKW-S product library is closer to the experimental value in table 3, but is still lower. A relatively large difference (~10%) is observed when comparing the calculated detonation velocities with the BKW-C and BKW-S libraries. Both the discrepancy between experimental detonation velocity, and the discrepancy between the two different libraries ask for explanation.

The use of a density-matched liquid to prepare an energetic composition has shown to be a very simple technique, avoiding for example the work and time needed to be make a castable composition when preparing a PBX, and avoiding the settling of crystals. A significant change in shock sensitivity is measured and attributed to crystal defects. The amount of defects is characterized by the crystal density as with liquid pycnometry. Differences in crystal density as small as 0.8% can make all the difference between a shock sensitive and insensitive composition.

Acknowledgements

The authors acknowledge the Dutch MoD for financial support of a part of the work presented here.

References

1 Shock sensitivity of HMX/HTPB PBX's: Relation with HMX crystal density, A.E.D.M. van der Heijden, R.H.B. Bouma, 29th International Annual Conference of ICT, Karlsruhe, 1998.

2 Formation of HMX crystals with high internal quality by cooling crystallization, H. Kröber, U. Teipel, K. Leisinger, H. Krause, , 29th International Annual Conference of ICT, Karlsruhe, 1998.

3 Characterization of the internal quality of HMX crystals, A.E.D.M. van der Heijden, W. Duvalois, 27th International Annual Conference of ICT, Karlsruhe, 1996.

4 Micro-inclusions in HMX crystals, A.E.D.M. van der Heijden, W. Duvalois, 30st International Annual Conference of ICT, Karlsruhe, 1999.

5 Shock sensitivity of HMX based compositions, A.E.D.M. van der Heijden, R.H.B. Bouma, R.J. van Esveld, 31st International Annual Conference of ICT, Karlsruhe, 2000.

6 Characterization of a commercial grade CL-20: morphology, crystal shape, sensitivity and shock initiation testing by flyer impact, R.H.B. Bouma, W. Duvalois, A.E.D.M. van der Heijden, A.C. van der Steen, 31st International Annual Conference of ICT, Karlsruhe, 2000.

7 Shock sensitivity and the TNO Mega Ampere Pulser, W.C. Prinse, M.P. van Rooijen, J.Mul, 25th International Annual Conference of ICT, Karlsruhe, 1994.

Development of a Practical Reduced Sensitivity Composition B Replacement

John Niles
US ARMY
TACOM-ARDEC
Picatinny Arsenal, NJ

Daniel Doll
Thiokol Propulsion
Brigham City, Utah, 84302

Abstract

An insensitive explosive fill, known as PAX-21, has been developed for the M720E1/60mm mortar and is a "drop-in" melt/pour replacement for the existing fill, COMP B. PAX-21 was formulated to exhibit a significant reduction shock and thermal sensitivity without compromising lethality. Reducing the shock and thermal sensitivity was critical in order to reduce the vulnerability of the M720E1/60mm mortar. The composition of PAX-21, along with its physical, chemical, sensitivity and explosive properties are reported.

Background

The main objective was to achieve a significant reduction in sensitivity with a minimal reduction in performance and no reduction in lethality. An additional objective was to replace the TNT melt phase used in COMP B. Since there is no U.S. domestic source for TNT, an alternative melt phase that is based on a commercially available material is desirable. There are numerous candidate materials that exhibit the same physical properties as TNT, but the challenge was to select a material that exhibited adequate explosive energy and density. This lead to the selection of 2,4-dinitroanisole (DNANs), which contains two energetic nitro groups instead of the three-nitro groups of TNT. This was significant because dinitro aromatic compounds can be produced commercially and are generally not subjected to the explosive manufacturing infrastructure required to produce the more energetic compounds that contain three or more nitro groups. DNANs was an ideal material to replace TNT. It contains two nitro groups so the energy and density loss was minimal relative to TNT. MNA is used at low concentrations so that the melting point can be reduced slightly to approximate TNT's through the formation of a low melting binary DNANs/MNA mixture. The rational for selecting these two materials is shown in figure 1. Using DNANs/MNA as the melt phase, other key ingredients in PAX-21 include AP and RDX.

Ammonium perchlorate (AP) oxidizer is used to compensate for the slight reduction in energy and density when substituting DNANs/MNA for TNT. Since this binary melt/phase is under oxidized, the addition of AP provides a low cost, dense source of oxygen as shown in figure 2. RDX was retained as a key ingredient in PAX-21. Although the theoretical explosive predictions suggest that DNANs/MNA/AP can perform equally to COMP B, RDX was considered necessary to for explosive brisance. The particle size of RDX was carefully controlled to achieve significant improvements in shock sensitivity while maintaining the required pour properties.

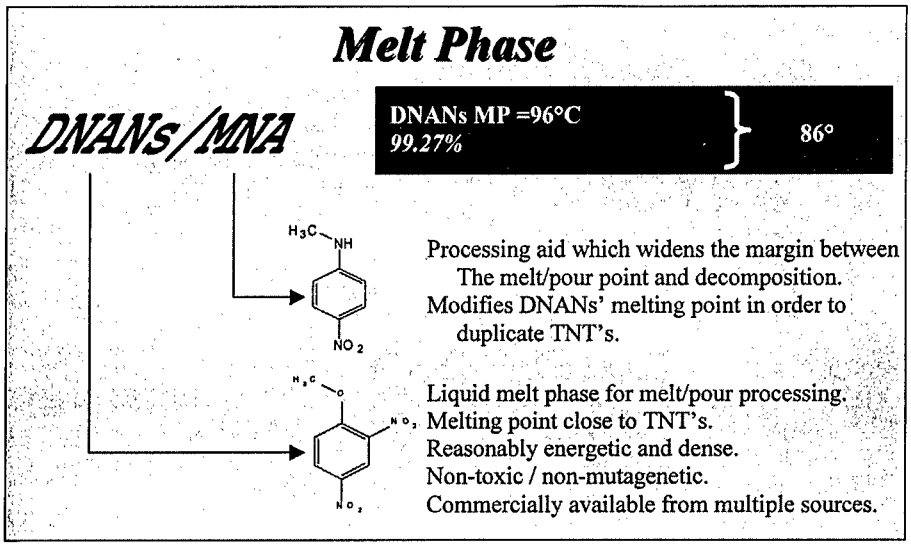


Figure 1. The PAX-21 melt phase that replaced TNT and Wax.

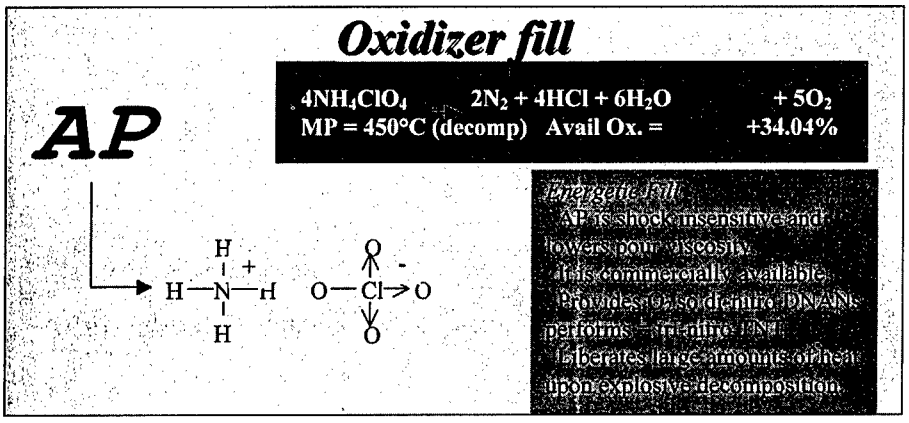


Figure 2. The rational for using AP oxidizer in PAX-21.

A comparison of the properties of PAX-21 is shown in Table I along with COMP B. Several characteristics distinguish PAX-21 from COMP B. Most notable is the significant reduction in shock sensitivity, as measure by NOL card gap, with only a minor reduction in performance, as measured by subscale dent depths against rolled homogenous armor witness plate.

The shrinkage of PAX-21 is approximately half that of COMP B and as a result articles loaded with this new explosive have fewer defects than those loaded with COMP B. Additionally since the viscosity of

PAX-21 is very low it is possible to use the same melt pour equipment currently used for COMP B. One of the most significant technical achievements was the improvement in lethality. The M720E1/60mm mortar uses high fragmenting steel (HF-1). Despite the fact that PAX-21 exhibits a slight reduction in subscale dent depth, it was demonstrated that the lethality was increased 25% over the based line 60mm cartridge containing COMP B.[1]

Table I. The properties of PAX-21 compared to COMP B.

Property	COMP B	PAX-21
Viscosity, kP@195°F	0.16	0.32
Shrinkage (%)	10%	5.0
Theoretical density (g/cc)	1.72	1.75
Measured density (g/cc)	1.69	1.735
Dent depth	0.41	0.393 (hardness 88)
NOL Card Gap (# cards)	203	140
Melting Point (°F)	182	196
SBAT onset (°F)	324	334
DSC onset (°F)	405	449
ARC onset (°F)	347	320
ABL impact (cm)	80	21
TC impact (in)	>46	30.64
ABL friction (lb)	800@ 8'/sec	800 @ 8'/sec
TC friction (lb)	64	61.67
TC ESD confined (J)	0.16	1.28
Thermal Conductivity (BTU/ft. hr. deg F)		0.138
C-J pressure (Mbar)	270.5	295
Theoretical Temperature (K)	3978	3786
Theoretical Cylinder expansion (kJ/cc / 6.5x)	7.23	7.67
Theoretical Shock velocity (mm/ms)	7.94	8.12
Theoretical Total energy of detonation (kJ/cc)	9.10	9.21
DOT hazards classification	1.1	1.3

Technical Discussion

The two most significant features of the PAX-21 composition are 1) the replacement of TNT with DNANs/AP and 2) the use of the correct RDX particle size to optimize the balance between processibility and shock sensitivity. Figure 3 illustrates the technical features of DNANs/AP relative to TNT and how DNANs/AP works to equal TNT in performance. Basically, AP provides oxygen and density to the formulation which compensates for the under oxidized, less dense DNANs. The combination of DNANs and AP exhibit a higher density than TNT but a lower heat of formation. However, when allowed to form

theoretical detonation products, using the CHEETAH 1.40 thermochemical program, equivalent total energy of detonation is achieved.

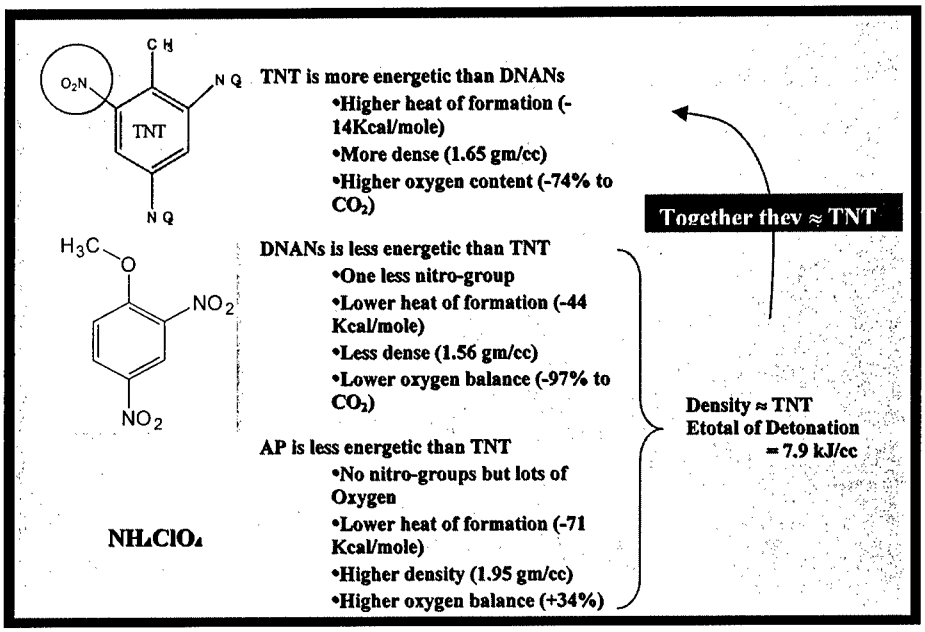


Figure 3. The chemical explanation of how DNANs/AP equals TNT performance.

During the development of PAX-21, the detonation rate was evaluated as function of the relative ratio of AP to RDX. As expected as AP is replaced with RDX the detonation velocity increases. This allows the brisance of the formulation to be tailored for any given explosive containing DNANs/AP as the TNT replacement.

The thermal properties of PAX-21 were evaluated unconfined and confined using simulated bulk auto ignition tests (SBAT) and variable confined cook-off tests (VCCT) under 0.120-inch confinement, respectively. As shown in figure 4, the pour point for COMP B as indicated by the departure of the endotherm from the baseline is 165°F and for PAX-21 is 195°F. The exothermic temperature of decomposition is 325° F for COMP B and 334°F for PAX-21. The temperature delta between the pour point is 140°F for COMP B and 139°F for PAX-21 indicating that the margin of safety during the pour process is essentially the same as COMP B.

The VCCT reaction violence during fast cook-off (40°/min) was considerably less for PAX-21 relative to COMP B. Figure 5 shows that there were numerous fragments collected for COMP B relative to PAX-21. The bolts and the witness plates were damaged considerably relative to COMP B. This was considered a

good indication that the reaction violence of the M720E1/60mm mortar containing PAX-21 would also exhibit less reaction violence during cook-off and the results are shown in figure 6.

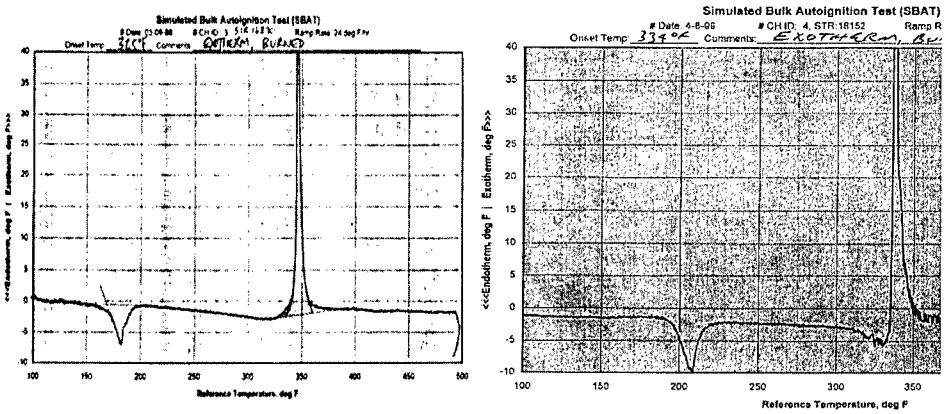


Figure 4. The thermal profile of COMP B and PAX-21 using simulated auto-ignition tests (SBAT).

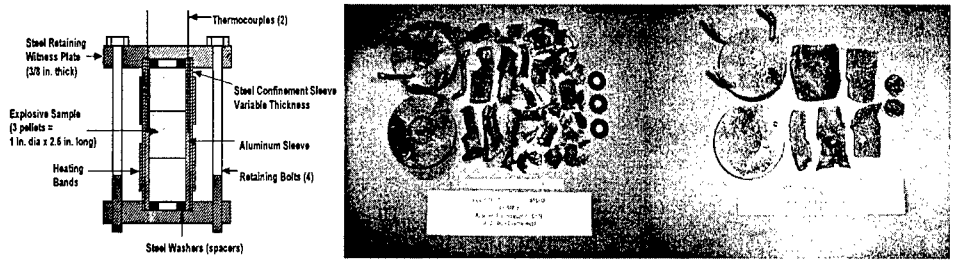


Figure 5. Fast VCCT tests results for COMP B and PAX-21.



Figure 6. The fast cook-off results of the M720E1/60mm mortar containing PAX-21.

The dent depth, detonation rate and shock sensitivity was evaluated from –65°F to 165°F for PAX-21. The results, shown in figure 7 suggested that there was relatively little change in performance over the entire temperature similar to COMP B. The shock sensitivity also remained relatively unchanged. The dent depths, detonation velocity and shock sensitivity values are different than those reported earlier and are from a PAX-21 composition made during a process optimization program which had an objective of defining the significant process parameters which effect PAX-21 properties. The significance of this data shows that the performance and shock sensitivity do not change significantly over the entire temperature range.

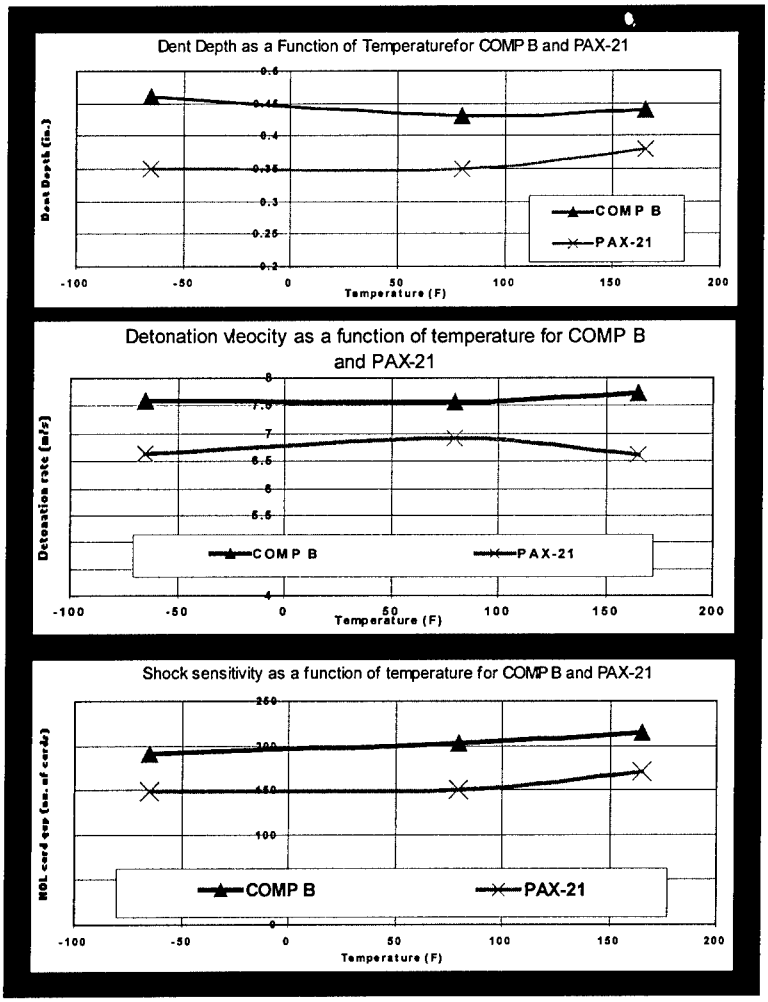


Figure 7. The performance and shock sensitivity for COMP B and PAX-21 from –65°F to 165°F.

One of the most attractive features of PAX-21 is that it exhibits the same processing characteristics of COMP B. The pour point is within 10°F and the pour viscosity is nearly equivalent to COMP B. Consequently, the same melt pour processing methods can be used to load PAX-21 as those currently used to load COMP B. Figure 8 illustrates the "water-like" viscosity of PAX-21, which allows for standard flaking methods to be used. As noted earlier this excellent pour behavior and the reduction in shrinkage make it possible to load articles with PAX-21 that have fewer cracks and voids than identical articles loaded with COMP B.

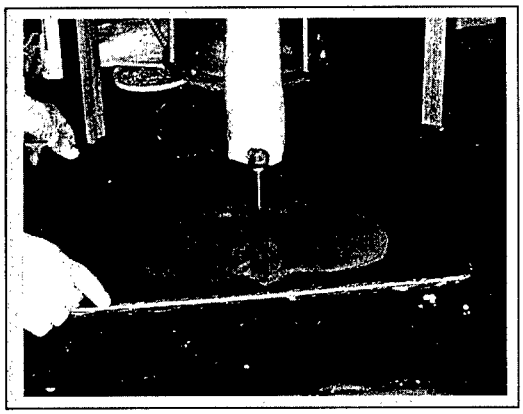


Figure 8. A photographic representation of the processing characteristics of PAX-21.

Summary

PAX-21 was developed to replace COMP B in the M720E1/60mm mortar. The characteristics of PAX-21 relative to COMP B are shown in Table II. PAX-21 is a drop-in melt pour replacement, which exhibits significantly less shock and cook-off sensitivity relative to COMP B with minimal compromise in performance. It uses DNANs/MNA and AP to replace the TNT melt phase of COMP B. Finer RDX sizes were used to maintain relatively high performance but without compromising shock sensitivity. PAX-21 is based on commercially available materials and is available in flaked form in large quantities.

Table II. The important characteristics of PAX-21 compared to COMP B.

	COMP B	PAX-21
Processing	Melt/pour (0.16 kP)	Melt/pour (0.32kP)
Shrinkage	≈ 10%	≈ 4%
Performance Dent Depth	Baseline	95%
Performance Velocity	Baseline	91%
Lethality	Baseline	125% with HF steel/M720E1
Toxicity	Baseline	Same as COMP B
Cost	Baseline	$6.80 / lb for raw materials
Availability FY'02	From Demil	> 300,000 lbs
Subscale Cook-off	Detonation	b/w deflagration-explosion
Shock Sensitivity	203 cards	140 cards

[1]: P. Ferlazzo, J. Niles, R. Wong, "Development of an Insensitive Mortar Cartridge," 2000 NDIA IM/EM International Symposium, San Antonio, TX, November 2000.

MEASUREMENT TECHNIQUES IN COOK-OFF RESEARCH AT THE TNO PRINS MAURITS LABORATORY,

Gert Scholtes, Niels van der Meer, Lun Cheng[1], Richard Bouma, John Makkus, Frans Jacobs, Rene van Esveld and Albert van der Steen
TNO Prins Maurits Laboratory, P.O. Box 45, 2280 AA Rijswijk, The Netherlands
[1]TNO Institute of Applied Physics, P.O. Box 155, 2600 AD Delft, The Netherlands

ABSTRACT

At the TNO Prins Maurits Laboratory, considerable effort has been put into the research of energetic materials and their responses to a thermal stimulus (Cook-off). Instrumented tests have been performed with several explosives to explore the mechanisms controlling the cook-off response. Besides the temperature, pressure and strain of the wall during the expansion of the tube are measured as a function of time. Several techniques have been used to measure the strain. One technique is based on the fibre optic interferometer. This system includes a Sagnac and a Mach-Zehnder interferometer. Another technique is based on the electrical resistance changes of a wire as a function of the expansion. Besides the conventional strain gauges which measure local strains, a resistance wire technique is used to measure the average radial expansion of the tube. All techniques have been used in real cook-off experiments. The results of these experiments and a comparison of these techniques together with the accompanying pressure measurements, will be presented in this paper.

INTRODUCTION

TNO-PML started the development of a midsize cook-off test around the start of the nineties. At this time, the temperature distribution could be measured as a function of time, in a system with well-defined boundary and initial conditions. However, as a result of the discussion during a "Cook-off and XDT mechanisms" Workshop in China Lake, March 1996 [4, 5], where the Cook-off phenomenon was discussed in several working groups, the main research was more changed in the direction of measuring the response of a cook-off reaction. The main outcome of the workshop can be described as the following. The goal desired from attempts to understand Cook-off mechanisms is a validated predictive capability. Besides mechanistic understanding of the Cook-off processes, repeatable and controllable experiments, to investigate the phenomena during the Cook-off process and fundamental property definitions of values for materials (constitutive models), are necessary. Together with some additional conditions, this philosophy is summarised in Figure 1. The following paragraphs will

emphasise on controllable repeatable Cook-off test vehicles and especially on the test equipment and instrumentation techniques.

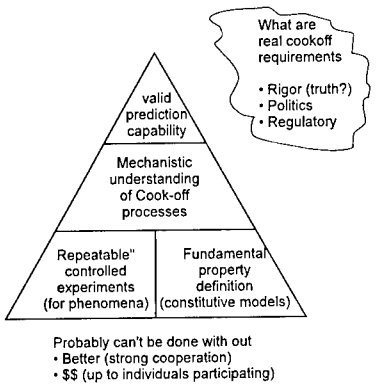


Figure 1. A summary of a philosophy about the Cook-off phenomenon during a workshop session in China Lake, 1996.

THE TNO-PML COOK-OFF TEST VEHICLE

After a brainstorm session, during this NIMIC workshop, it was stated that it would be sufficient, if an experiment would be controllable with known boundary conditions, with characterised materials and geometry. Further attributes of the experiments that are truly useful were outlined:

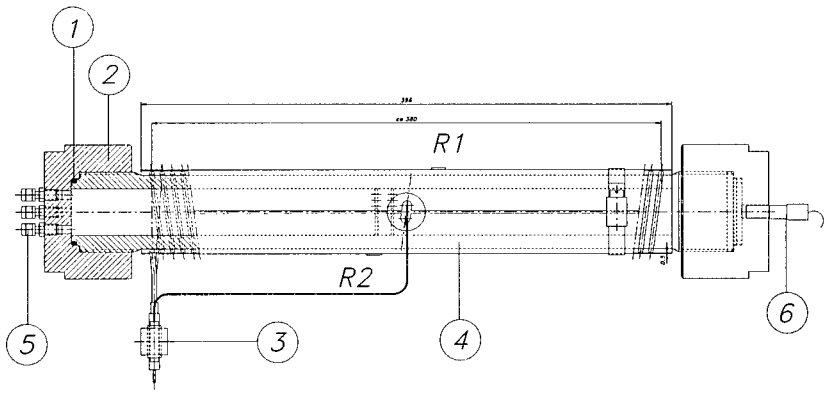
a. Variable and reliable confinement
b. Complete non-interfering diagnostics
c. In situ pressure measurement
d. Internal temperature distribution measurement
e. Strain measurement (temperature compensated techniques)
f. Wall velocity measurement
g. Fragments/debris map (capture and analysis)
h. Known boundary temperature/heating rates
i. Visual observation (during experiment and post mortal assessment)
j. Material state definition (porosity/specific surface area)

Some additional assumptions have to be made. The experiments should really cover the full spectrum of accident threats. That is to say fast and slow heating and different heating profiles including ramping to a constant temperature. In addition a wide range of energetic materials and a range of responses should be covered for the validation purposes of the models.

In report [6], a full description of the latest version of the Cook-off test is given. In Figure 2, the design of the cook-off test tube is shown. A steel cylinder is used with a wall thickness of 10 mm over the total length of 500 mm and with an inner diameter of 35 mm (outer diameter

55 mm). The tube has an inner volume of 480 cm^3 and is closed at both ends with specially constructed steel end-caps. In the construction of the end-caps, a ring is included to ensure the confinement of the explosive substance during the experiment; the ring is deformed into its plastic region with a specially constructed torque wrench. With this cap construction, the cylinder can withstand internal pressures up to 240 MPa (quasi-static).

For heating, a long heating wire, connected to the temperature controller, is wrapped along the total length of the cylinder. A heat-conducting sealant is added between the helical loops to improve the distribution of heat flow from the heating wire to the steel cylinder.



1) Sealing ring
2) Cap
3) Heater connections
R1, R2) Strain gauges
4) Steel cylinder
5) thermocouple feed-through
6) Pressure transducer

Figure 2. The TNO-PML Cook-off test tube.

MEASURING TECHNIQUES

Temperature and Pressure

One end-cap is provided with four thermocouple (TC) feed-throughs. The end-tips of the (k-type) TCs are positioned halfway along the cylinder at different positions in the radial direction. Normally, five TCs are used for measuring the temperature distribution. Four are positioned in the interior of the cylinder and one is positioned outside the cylinder, on the tube wall. A sixth TC is used for controlling purposes and is also positioned outside the cylinder. Sometimes, a seventh thermocouple is located at the outer corner of one end-cap.

The pressure is measured by means of a piezo resistive pressure transducer. This type has the advantage that the pressure can be measured during the whole heating process of the cook-off

experiment, up to the moment just before the response. The actual and total pressure rise of the response can not be measured by means of a conventional pressure transducer and should be measured indirectly by means of strain measurement techniques or other techniques. The conventional pressure transducer is mounted in the second end cap. It is preferable to use a piezo resistive transducer like the HEM-375M from Kulite which is temperature compensated up to 232°C and is capable to operate up to temperatures of 260°C and pressures up to 240 MPa. Because of its high natural frequency of 395KHz the bandwidth of this transducer is sufficient to measure the processes in the "pre-ignition" phase.

STRAIN MEASURING TECHNIQUES

Strain Gauges

Three different techniques of strain measurement have been developed at TNO-PML. The first technique is a conventional strain gauge. The type has been used successfully in repeatedly real-time Cook-off and DDT experiments. For the Cook-off experiments, special strain gauges were used. This type of strain gauge can be mounted locally in between the heating wire. It has an operating temperature range from -269 °C to 290 °C and is still operational for temperatures up to 370 °C for short-term exposure. Besides the extreme operating temperature range, this type has an internal temperature compensation, minimising the temperature dependency of the strain measurement. The disadvantage of this technique is that it only measures the strain in a limited region of the tube.

OPTICAL TECHNIQUES

Other ways to measure the strain are the optical techniques using an interferometric system. Two different interferometer techniques have been developed, the Mach-Zehnder and the Sagnac. In an interferometer, the optical path length of (in general) two light beams are compared to each other. The optical path of one beam is constant and is indicated as the reference beam. Therefore the optical path (change) of the other beam, which is indicated as the sensing beam, can be detected by the interferometer.

An optical interferometer is an extremely sensitive measuring system and can be used to detect changes of less than *nm* in the optical path. For vibration measurements, even amplitudes down to tens of *pm* can be detected using suitable signal processing techniques. An interferometer can also be constructed using fiber optic components. The optical path length of an optical fiber is defined as the product of the effective refractive index N_{eff} of the fiber and the physical length of the fiber. In a Fiber Optic (FO) interferometer sensor, the measurand introduces a change in the optical path length of the sensing fiber.

In the TNO FO interferometer system for Cook-off experiments, a FO Mach-Zehnder interferometer and a FO Sagnac interferometer are incorporated. In the Mach-Zehnder interferometer, the phase of the interferometric signal is proportional to the length of the sensing fiber. In the Sagnac interferometer system, the phase of the interferometric signal is proportional to the rate of the change of the length of the sensing fiber.

Mach-Zehnder interferometer

The Mach-Zehnder [8] is a conventional technique and inexpensive. It consists of two optical fibres providing for two optical pathways. One of the fibres is wrapped around the Cook-off tube, the other one is the reference.

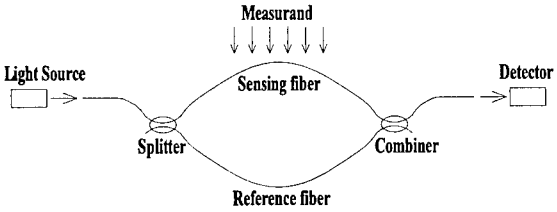


Figure3. Schematic principle of Mach Zehnder interferometer

As shown in Figure 3, input laser light is split into two waves being combined again at the other end of the interferometer resulting in an interference signal. One loop is the reference L_r, in the other loop the phase disturbance L_s is induced along its path around the cook-off tube. An optical coupler combines the two output light waves and this signal is focused onto a photo diode that gives a voltage signal oscillating with the same frequency as the light signal. As the laser wavelength is known, counting the fringes or using a calibrated frequency-to-voltage converter results directly in the elongation of the fibre as a function of time. As the time interval of the phenomena is also recorded, the velocity of the case expansion can be calculated. More precisely, the general expression of the interferometric signal can be described by the following equation:

$$V = V_0 \left[1 + A\cos(\Phi)\right]. \qquad (1)$$

Where V_0 is the signal amplitude when interference is absent, A is the contrast of the interferometric signal and Φ is the phase of the interferometric signal.

For the Mach-Zehnder (MZ) interferometer, the phase Φ_{MZ} is a function of the difference between the length of the sensing fiber (L_S) and that of the reference fiber (L_R):

$$\Phi_{MZ} = \frac{N_{eff}\,2\pi}{\lambda}(L_S - L_R)\,. \qquad (2)$$

Where N_{eff} is the effective refractive index of the fiber and λ is the wavelength of the light. During the expansion of the tube, the change of the length of the sensing fiber is faster than the change in length caused by other parameters. Therefore, L_S-L_R can be divided into a quasi-static part L_0 and a time dependent part L(t), which represents the change in the length of the sensing fiber as function of time. The velocity v(t) is calculated as the time derivative of L(t). The quasi-static part L_0 causes a constant term C in Equation (3). For λ = 1.55 μm and N_{eff} = 1.55, Equation (1) can be rewritten as:

$$V = V_0\left[1 + A\cos\left(C + \frac{2\pi}{10^{-6}}L(t)\right)\right]. \qquad (3)$$

According to Equation (3), a change of 1 μm in L(t) will cause a phase change of 2π and is denoted as a fringe. Therefore, a velocity of 1 m/s is equal to 10^6 fringes per second. To measure the expansion process, a high-speed detector is required. In the TNO system, a Newport detector with a -3dB bandwidth of 1.5 GHz is used to detect the interferometric signal.

Sagnac interferometer

The FO Sagnac interferometer can be used for the detection of fast varying parameters [1, 2]. One of the well-developed applications of the Sagnac interferometer is the optical gyroscope to measure the rotation speed [3]. A FO Sagnac interferometer consists of a light source, a FO coupler and a fiber loop configured as in Figure 4.

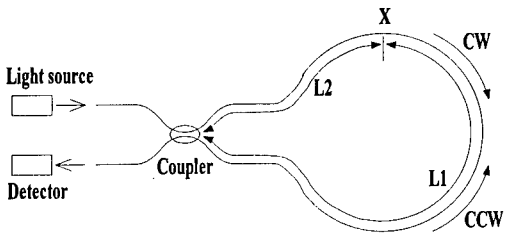


Figure 4. The Sagnac loop interferometer

The coupler splits the light into a clockwise (CW) and a counterclockwise (CCW) beam. The output signal of the FO Sagnac interferometer has the same expression as in Equation [1]. In the absence of a perturbation to the fiber loop, the phase Φ_S is equal to zero because the

optical path of the CW beam and the CCW beam is the same. For a time varying change in length L(t) at location X as sketched in Figure 4, Φ_S can be expressed as:

$$\Phi_S(t) = \frac{2\pi N_{eff}\,\Delta L}{\lambda c}\frac{\partial L(t)}{\partial t} = \frac{2\pi N_{eff}\,\Delta L}{\lambda c} v(t)\,, \qquad (4)$$

where $\Delta L(= L_1\text{-}L_2)$ is the length of the delay fiber and c is the speed of light.

In the Sagnac interferometer signal we can define the fringe constant F as the *velocity* change which causes a phase change of 2π. The fringe constant F ($= \lambda c/N_{eff}\Delta L$) is found to be inversely proportional to the length of the delay fiber. So, the fringe constant can be altered to adapt for the expected velocities of the experiment. In our system, 3 different delay fibers (10 m, 25 m and 50 m) are incorporated in the TNO Sagnac interferometer system. The corresponding fringe constants are 31 m/s, 12.4 m/s and 6.2 m/s. The Sagnac signal can be processed using the fringe counting method.

Resistance wire technique

The resistance wire has a calibrated resistance per unit length and is wrapped around the tube. The changing resistance is measured with an appropriate electronic circuit. In this circuit the current is maintained at a constant value I_C which results in a changing voltage V(t) due to a changing resistance R(t). So, as a result of the elongation of the wire, due to the expansion of the tube, a changing voltage is measured as a function of time.

The change in resistance due to a change in length is given by formula (5), with R the resistance, R_0 the initial resistance, l the length and l_0 the initial length. The parameters *a*, is a material depending constant and has the value of 1.76463, for the material used.

$$\frac{R}{R_0} = a\frac{l}{l_0} + (1-a) \qquad (5)$$

with

$$V = I\ R \qquad and \qquad V_0 = I_C\ R_0 \qquad (6)$$

The Elongation E as a function of time is given by:

$$Elongation(t) = l(t) - l_0 = \frac{l_0}{a}\left(\frac{V(t)}{R_0\ I_C} - 1\right) \qquad (7)$$

EXPERIMENTAL RESULTS

Several series of cook-off experiments have been performed, the last few years. Most of them have been performed with the instrumentation described in the previous paragraphs. In the

following paragraphs some interesting and even unique results will be presented, discussed and even compared with each other.

Temperature measurements

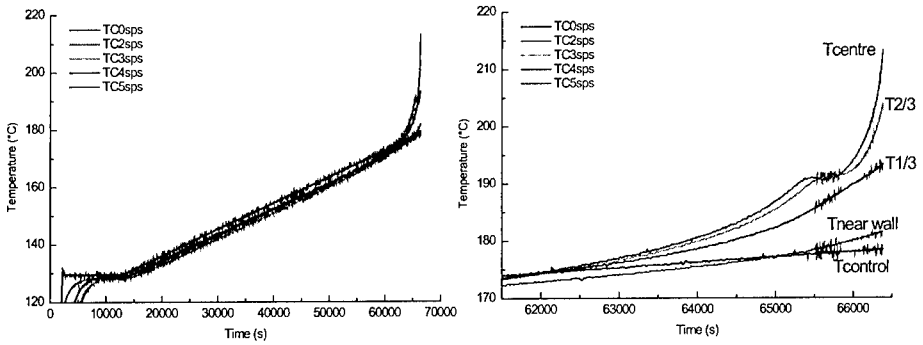


Figure 5. Temperature distribution in a slow cook-off experiment with HMX-PBX, with a magnification of the runaway phase on the right-hand side.

In Figure 5, an example of the temperature distribution, measured in a slow cook-off experiment with a HMX-PBX, is shown. In the left-hand side graph, the interesting part of the heating process is shown while on the right-hand side the last hour of this experiment is shown. In the left-hand side graph it is shown that the tube is preheated until 130°C and kept at this temperature for about 3 hours. After preheating, the tube is heated with the well-known slow cook-off heating rate of 3.3°C/hour. Around 55000 seconds, heat is produced in the internal of the tube due to the decomposition reactions of the explosive substance. At about 62000 seconds most of the explosive substance has the same temperature as the wall (Tcontrol). At a temperature a little over 190°C, the internal thermocouples Tcentre and T2/3 indicate a kind of endothermal reaction. Probably due to the large amounts of energy dissipated from the decomposition reactions, this is not indicated by thermocouple T1/3 and the thermocouple near the wall. This kind of information is essential for the verification of the kinetics in computer simulation. It gives information about endo- and exothermal reactions, phase changes and other thermal processes occurring during cook-off process.

Pressure measurements

Also, the pressure has been measured during several cook-off experiments. In Figure 6, the result of a pressure measurement of an experiment with composition B is shown. The time scale is given in seconds. The whole pressure build-up takes about 10 ms which is quite slow for cook-off reaction with composition B. But looking at the fragmentation in the photograph this is not very surprising.

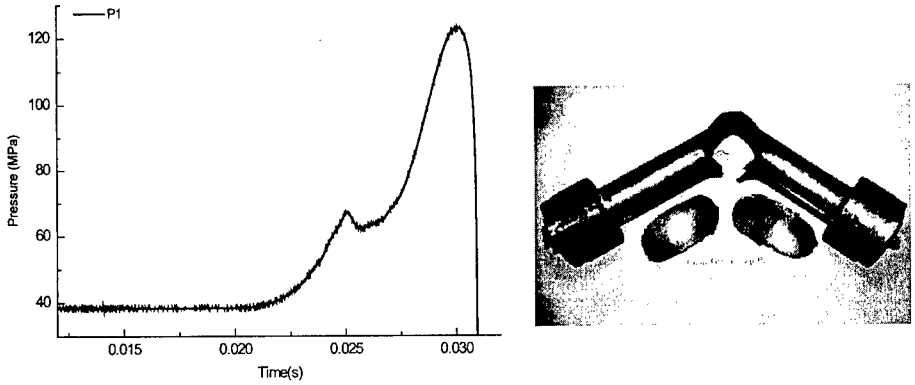


Figure 6. The result of a pressure measurement in a composition B experiment in comparison with the fragmentation pattern.

In Figure 7 and 8, the results of a pressure measurement in another composition B experiment is shown but this time with a free volume of 30%. The heating rate of this experiment was 0.5°C/minute. In Figure 7, the pressure build-up of the whole experiment is shown up to the start of the runaway.

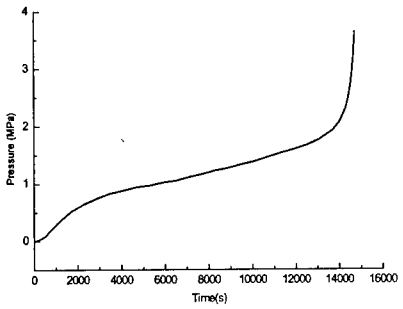


Figure 7. Pressure curve of a composition B experiment with a heating rate of 0.5C/min

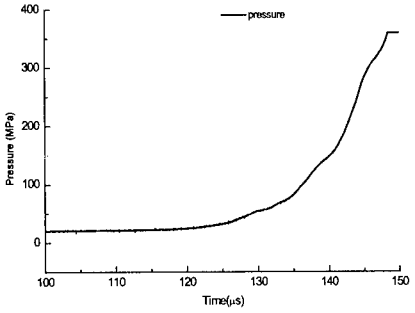


Figure 8. Last phase of the pressure rise in the composition B experiment

The fast pressure rise at the end up to a pressure of 350MPa is shown in Figure 8. The rise time up to a pressure of about 120 MPa in this experiment is about 20 μs, about a factor 500 faster than in the first example. A comparison of the maximum pressure derivatives gives are a difference of a factor more than 1 10^4. A closer look at the end phase of the pressure rise, reveals a pressure wave super-positioned on the pressure curve.

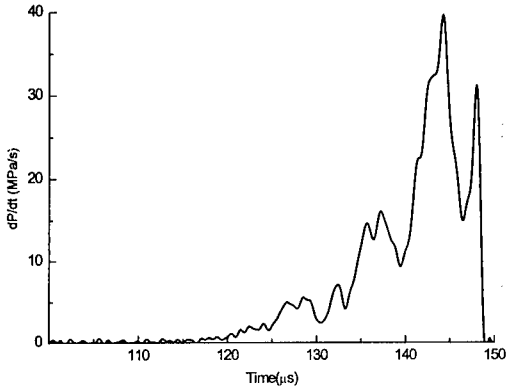


Figure9. The pressure derivative of cook-off experiment with composition B.



Figure 10 Fragmentation of the composition B experiment with a free volume of 30 %

This is even more clear in Figure 9, the pressure derivative as a function of time of this experiment. The fragmentation pattern of the response of this experiment is shown in Figure 11. Small fragments indicate that a near-to-detonation reaction occurred, which was also indicated by the fast pressure rise. Like the information on the temperature of the cook-off process, also the information on the pressure, pressure rise and pressure waves contribute to the insight in the cook-off mechanism in general and can be used the verification of cook-off computer codes.

Strain measurement results

Conventional strain gauge

Many examples have been given in the past on the conventional strain gauges. An example of a strain measurement with a conventional temperature compensated strain gauge is shown in Figure 11. This is the strain measured in the first composition B example in the paragraph on pressure measurement, in which the pressure rate was extremely low. With this type of strain gauge strains up to 1-2% can be measured. The advantage of this technique is that it can be mounted in between the heater because its size of about 10x 5 mm. On the other hand, because of this size it only measures a local strain.

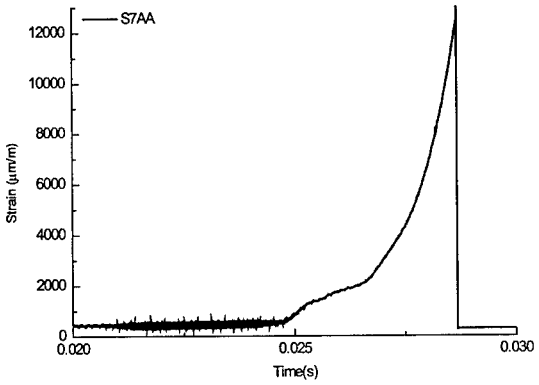


Figure 11. The strain measured with a conventional strain gauge.

Resistance wire and optical strain gauge techniques

The resistance wire technique has two advantages compared to the conventional temperature compensated strain gauges. Firstly, the strain limit is about 5%, compared to the 1-2% and secondly, it measures an average strain instead of the local strain. The second point is also applicable for the optical techniques but like the strain gauge technique is the maximum strain limited to about 1-2% for the temperature resistive fibres.

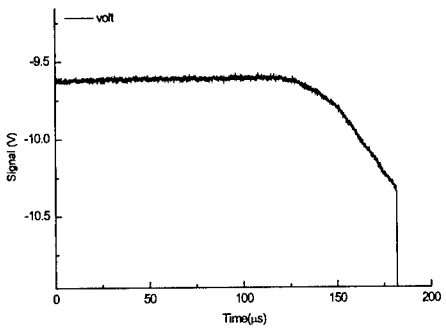


Figure12. The signal measured by means of a resistance wire.

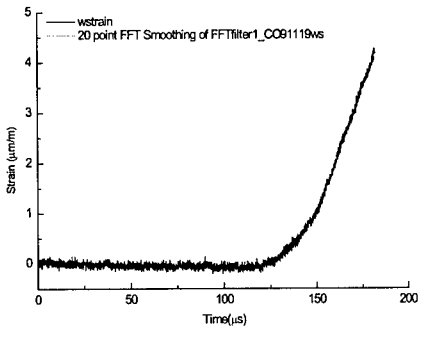


Figure 13 The accompanying strain as a function of time measured with a resistance wire

In Figure 12, an example of a resistance wire strain technique is given. The accompanying strain as a function of time is shown in Figure 13. In this example a maximum strain over 4 % was reached with a linear velocity of about 150 m/s, at the end. The noise in this signal makes the calculation of the velocity more complex because the noise is amplified in the calculation of the derivative. The difficulties in the analyses of this kind of signal are mostly filtering of

the noise. But for future use, the noise on this signal can be reduced by means of a differential amplifier.

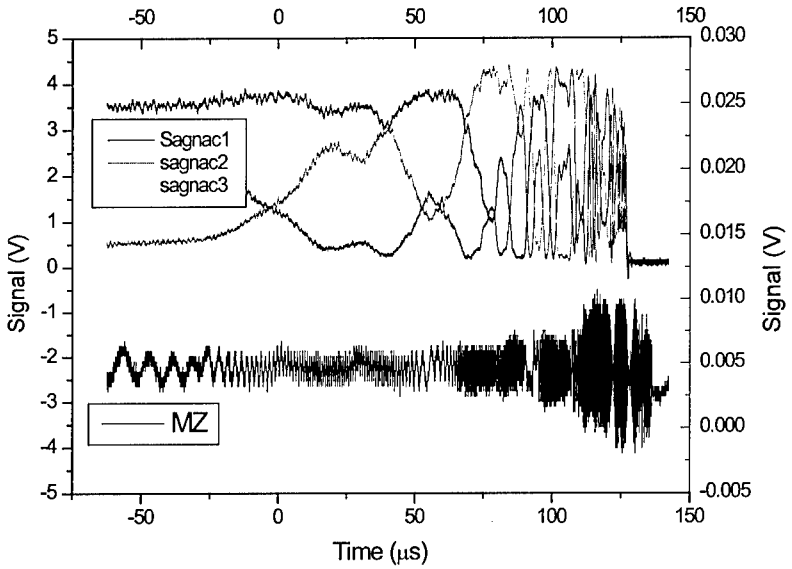


Figure 14. The Original signals from the Mach-Zehnder and Sagnac interferometers as a function of time.

In Figure 14, the Original signals of the Mach-Zehnder and Sagnac interferometers are given as a function of time. The three signals from Sagnac are the three signals from the different directions of polarisation. From these signals it is obvious that the analyses of these signals is not just a strait forward operation. Because of the high frequency of the Mach-Zehnder signal compared to the sagnac signal it contains detailed information in the lower velocity range.

Although the phenomena of aliasing arises quite fast, depending on the sample rate of the oscilloscope, it is possible to make an estimate of the velocity in the Mach-Zehnder by counting the number of times aliasing arises. A comparison with the Sagnac is therefore also possible in the high velocity range. In Figure 15, an example of the aliasing analyses is shown. For the lower velocities up to 25 m/s the velocity can by estimated by simple smoothing. After the velocity of 25 m/s it looks like the velocity decreases but actually it is still increasing. At a velocity of 50 m/s the Mach-Zehnder frequency equals the sample frequency of the oscilloscope. This is shown by the minimum in the signal. As long as the velocity increases the velocity of the higher velocity range can be estimated by simply counting the number of minima and increase the velocity adding 50 m/s for every minimum. In Figure 16, the result of the analyses of velocity measurement are shown in one graph for

the two optical techniques. Because the velocity was measured by two independent fibres at a somewhat different location and the offset of the Sagnac is not fully clear, a small variation between the two signals is shown.

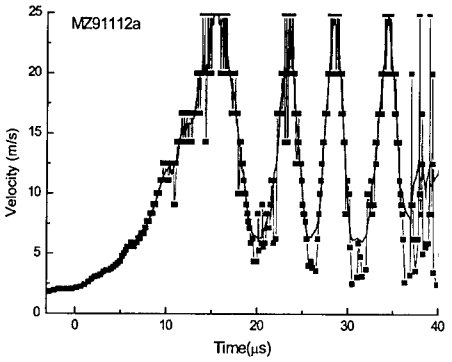


Figure15. An example of the aliasing effect in the Mach-Zehnder velocity calculation.

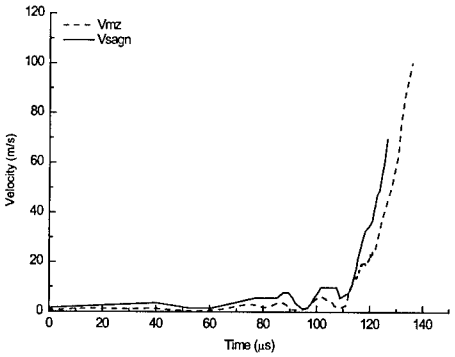


Figure 16 A comparison between the velocity measurements of with the Mach-Zehnder and the Sagnac interferometer.

In Figure 17 a magnification of the low velocity range, at the start of the elongation of fibre, is shown. As in pressure graph in Figure 8, fluctuations in velocity are shown indicating pressure waves inside the tube. A one on one comparison whit the pressures graph is not yet possible due to the difference in location of the strain measurement, in the middle of the tube and the pressure measurement in one of the end caps.

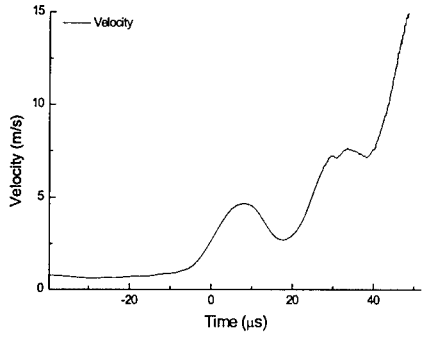


Figure17. The fluctuations of the velocity in a Mach-Zehnder signal in the cook-off strain measurement indicating pressure fluctuations.

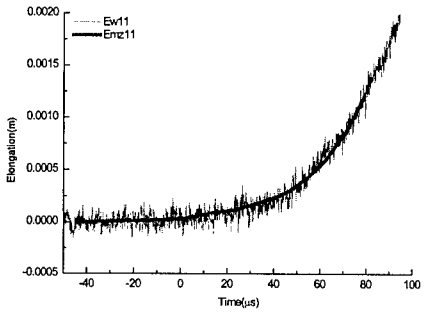


Figure 18 A comparison between elongation with the Mach-Zehnder interferometer and the resistance wire technique

The last example is a comparison between the resistance wire technique and the optical Mach-Zehnder technique. The signals were not triggered at the same moment. For comparison reasons one of the signal was translated in time. The results are shown in Figure 18. This result is surely not a one-time coincidence. The velocities at a strain of 1mm, of four different experiments in which both techniques were used, have been compared. The results are shown in table 1. Except for one experiment, values were comparable within the experimental error due to noise in the resistance wire technique as shown in Figure 18.

Table 1. A comparison in the velocities measured with the resistance wire and the Mach-Zehnder interferometer.

Experiment	Mach-Zehnder velocity at 1mm strain (m/s)	Resistance wire velocity at 1 mm strain (m/s)
Co91111	41	40
Co91112	130	160
Co91117	105	100
Co91119	90	85-95

CONCLUSIONS

TNO-PML has developed a cook-off tube with a reliable confinement with well-known boundary temperatures and heating rates and several measurement techniques. The different techniques, like temperature, pressure measurement and strain/velocity of the wall, have been demonstrated.

A comparison between the different techniques gave some very similar values indicating that these techniques work properly. Also a comparison between strain rates and the fragmentation confirm these results in a qualitative way. An increased strain rate can be correlated to a increase of the fragmentation.

Although visual/sound observation have been carried out by means of a normal video camera, during several cook-off experiments, nothing really could be seen. On the other hand the different techniques can be used as a trigger for a digital camera in future.

If the list of capabilities/measuring techniques demonstrated is compared with the list from the NIMIC workshop, mentioned in the beginning of this paper, it can be concluded that only the last item, "material state definition" is not yet demonstrated. In spite of this fact, we have demonstrated that a "repeatable controlled cook-off experiment" is possible to obtain data to

understand the cook-off phenomena better and to validate our "prediction capabilities now and in the future.

REFERENCES

[1] E.J. Post, "Sagnac effect", Reviews of Modern Physics, Vol. **39**, No. 2, p. 475, 1967.

[2] K. Blotekjaer, "Sagnac interferometry for reciprocal measurands", advances in Optical fiber sensors, Ed. B. Culshaw, p. 53, SPIE Press, 1992.

[3] R.A. Bergh et al., "All-single-mode fiber-optic gyroscope", Optics Letters, Vol. **6**, No. 4, p. 198, 1981

[4] "Cook-off and XDT Mechanisms", The presentations of the Joint NIMIC/KTA 4-20 workshop held at NAWC, China Lake, USA on 12-15 March 1996 (NIMIC-S-172-96).

[5] "Cook-off and XDT Mechanisms", Group discussions, conclusions and annexes of the Joint NIMIC/KTA 4-20 workshop held at NAWC, China Lake, USA on 12-15 March 1996 (NIMIC-S-172-96).

[6] J.H.G. Scholtes and B.J. van der Meer, "The improvement of the TNO-PML Cook-off test", report PML 1994-A56, TNO Prins Maurits Laboratory, The Netherlands.

[7] Gert Scholtes, Niels van der Meer and John Makkus, "Cook-off research at the TNO Prins Maurits Laboratory", presented at the 1998 Insensitive Munitions & Energetic Materials Technology Symposium, November 16-19, 1998, San Diego, CA

[8] W. Demtroder, "Laser Spectroscopy", Springer-Verlag, Chemical Physics vol 5, 1982.

[9] D. Harvey, R. McBride, J. S. Barton, J.D.C. Jones, "A velocymeter based on the fibre optic Sagnac Interferometer", Meas. Sci. Technol. 1077, 1992.

Cook Off Verhalten von Sprengstoffen

Roland Wild , Thomas Eich
WIWEB, Grosses Cent D-53913 Swisttal

Juli 2001

Zusammenfassung

In the Cook Off Test it is sometimes difficult to distinguish between reaction type 4 (deflagration) and reaction type 5 (burning) because both reaction types allow rupture of the confinement. By means of a low cost pressure gauge(carbon resistor) it is possible to measure the pressure time history inside the confinement. An upper limit of the peak pressure for reaction type 5 could be determined.

1 Einleitung

In moderner Munition werden immer häufiger sogenannte unempfindliche Sprengstoffe verwendet. Diese Sprengstoffe zeichnen sich dadurch aus, dass sie bei bestimmten Belastungen nicht detonieren sondern höchstens abbrennen. Eine dieser Belastungen ist ansteigendes Erhitzen (z. B. in einem Feuer) in einem Einschluss. Das Verhalten bei dieser Belastung wird in Cook Off Tests überprüft. Hierbei wird der Sprengstoff von aussen in einem Einschluss mit einer ansteigenden Temperatur, normalerweise ca. 90 K pro Minute, bis zu einer Reaktion erhitzt. Als Diagnostik dient das Splitterbild des Einschlusses nach der Reaktion. Dies ist allerdings nicht immer eindeutig, so dass Fehlinterpretationen durchaus möglich sind. Im folgenden wird ein Verfahren beschrieben mit dem solche Fehlinterpretationen vermieden werden können.

2 Testaufbau und Versuchsdurchführung

Beschreibung der Cook Off Apperatur Die Cook Off Apperatur besteht aus einem Stahlrohr von 100 mm Länge, 50 mm Durch-

messer und einer Wandstärke von 5 mm, das beidseitig mit einem 4 mm starken Schraubdeckel verschlossen wird. Zwei ca. 30 mm breite Ringheizkörper mit einer Leistung von je 430 Watt werden um das Rohr gespannt. Mit diesen Ringheizkörpern wird eine Aufheizrate von $\approx 90\frac{K}{min}$ erreicht. Die Abbildung 1 zeigt eine Aufnahme der Apperatur.

Diagnostik Die Ergebnisse werden analog MilStd 2105B in 5 Kategorien (Reaktionstypen) eingeteilt.

- **Typ 1, Detonation**
  Der Stoff detoniert, die Hülle ist in kleine Splitter zerlegt.
- **Typ 2, Teilweise Detonation**
  Ein Teil des Stoffes reagiert detonativ, ein Teil der Hülle ist in kleine Splitter zerlegt, unter Umständen wird nicht reagiertes Material gefunden.
- **Typ 3, Explosion**
  Der Stoff wird entzündet und brennt progressiv ab, es werden große Splitter erzeugt.
- **Typ 4, Deflagration**
  Der Stoff wird entzündet und brennt ab. Die Hülle wird aufgerissen, es werden aber keine Splitter erzeugt.
- **Typ 5, Abbrand**
  Der Stoff wird entzündet und brennt nicht progressiv ab. Die Hülle bleibt erhalten, lediglich Schwachstellen z. B. die Verschlusskappen werden abgesprengt.

Probleme bei der Bewertung Um als unempfindlicher Sprengstoff zu gelten darf beim Cook Off Versuch keine heftigere Reaktion als im Reaktionstyp 5 beschrieben auftreten[2]. Die Bewertung der Versuchsergebnisse ist für die Reaktionstypen 1 bis 3 kein Problem zumal eine Fehlinterpretation keine Auswirkungen hat, da diese Reaktionstypen für unempfindliche Sprengstoffe nicht zugelassen sind. Schwierigkeiten können allerdings bei der Unterscheidung zwischen Reaktiontyp 4 und 5 auftreten, da in beiden Fällen Beschädigungen an der Hülle (absprengen der Kappen) auftreten können. Ein Aufreissen des Versuchsgefäßes gilt in der Regel als Indikator für mindestens Reaktiontyp 4. Wegen der nicht immer gleichen Festigkeitseigenschaften des Einschlussmaterials können Fehlinterpretationen auftreten. Dies würde dann dazu führen, dass einem Sprengstoff unberechtigterweise die Unempfindlichkeit nicht zugesprochen wird. Um dieses Dilemma zu umgehen wurde der oben beschriebene Aufbau so abgeändert,

dass der im Einschluss, bei der Reaktion entstehende Druck gemessen werden kann. Hierzu wurde unter einem Deckel ein Kohlemassewiderstand als Drucksensor eingebaut, die Zuleitungen zu dem Widerstand wurden hierbei isoliert durch zwei kleine in den Deckel gebohrte Löcher geführt. Die Abbildung 2 zeigt eine Verschlusskappe mit eingebautem Drucksensor.

3 Ergebnisse

Festigkeit der Hülle Um Aussagen über die Festigkeit der Hülle zu erhalten wurde des Behältnis durch Abbrand eines porösen Treibladungspulvers im Innern mit einem dynamischen Druck belastet. Durch Variation der Pulvermenge konnten Drücke zwischen 0.17 GPa und 0.52 GPa erzielt werden, die Druckanstiegsraten lagen bei $\approx 0.4\frac{GPa}{\mu s}$. Die erhaltenen Splitterbilder sind zusammen mit Spitzenwerten des ereichten Druckes[1] in den Abbildungen 3, 4 und 5 dargestellt und in der folgenden Tabelle zusammengefasst.

Druck[GPa]	Splitterbild
0.17	Deckel abgesprengt
0.25	Deckel abgesprengt und Hülle aufgebaucht
0.52	Hülle in grobe Splitter zerlegt

Druckmessungen Die Versuche wurden insgesamt mit vier verschiedenen Sprengstoffen (durchweg kunststoffgebundene Sprengstoffe, einer war gießbar, die anderen pressbar) durchgeführt. Ein typisches Ergebnis wie es bei den Messungen erhalten wurde zeigt die Abbildung 6. Die Abbildungen 7, 8, 9 und 10 zeigen die erhaltenen Splitterbilder zusammen mit den gemessenen Drücken. Die folgende Tabelle fasst die Ergebnisse noch einmal zusammen.

Stoff	Druck[GPa]	Splitterbild
HX 271	0.1	Kappen abgesprengt
PBX N 9	0.2	Kappen abgesprengt
PBX W 11	0.5	Versuchsgefäß aufgerissen
P 11	0.72	Versuchsgefäß in Splitter zerlegt

[1]der Druck wurde mit einer von *M. Ginsberg* und *B. Asay*[1]angegebenen Beziehung berechnet

4 Diskussion der Ergebnisse

Wie man aus den Ergebnissen zur Festigkeitsbestimmung der Versuchsgefäße entnehmen kann, liegt der Spitzenwert des Druckimpulses beim Absprengen der Kappen bei ≈ 0.17 GPa, eine Aufbauchung findet bei 0.25 GPa statt, während ab 0.5 GPa das Versuchsgefäß in grobe Splitter zerlegt wird. Dies bedeutet, dass bei einem Splitterbild "Kappen abgesprengt"der Spitzendruck bei ≈ 0.17 GPa lag. Da dieses Splitterbild, als *ein* Kriterium, beim Reaktionstyp 5 zugelassen ist (das *zweite* Kriterium ist ein nicht progressives Abbrennen) folgt im Umkehrschluss daraus, dass beim Überschreiten dieses Grenzwertes, unabhängig vom aktuellen Splitterbild, der Reaktionstyp 5 nicht mehr anzunehmen ist. Die Messunsicherheit liegt bei $\approx 10\%$, so dass ein Spitzendruck von 0.2 GPa als oberste Grenze für Reaktionstyp 5 anzusetzen ist. Ein Vergleich der Versuche zur Ermittlung der Festigkeit der Versuchsgefäße mit den Ergebnissen aus den Untersuchungen der vier Sprengstoffe zeigt hinsichtlich der Splitterbilder eine brauchbare Übereinstimmung. Entsprechend dem oben aufgestellten Kriterium ist bei den Stoffen HX 271 und PBX N 9 der Reaktionstyp 5 anzunehmen.

5 Zusammenfassung

Es wurde ein Verfahren zur Beurteilung der Reaktionstypen beim Cook Off Test beschrieben. Ziel des Verfahrens war es den Druck im Innern des Versuchsgefäßes während der Reaktion zu messen. Dies konnte mit Hilfe von Kohlemassewiderstände als Drucksensoren erreicht werden. In einer ersten Versuchsreihe wurde zunächst die Festigkeit der Versuchsgefäße untersucht und die gefundenen Druckwerte (Spitzendruck) mit mit den Splitterbildern korreliert. Die mit vier verschiedenen Sprengstoffen durchgeführten Experimente zeigten hinsichtlich des Splitterbildes eine brauchbare Übereinstimmung. Es konnte eine obere Grenze von 0.2 GPa Spitzeninnendruck für Reaktionstyp 5 festgelegt werden.

Literatur

[1] M. Ginsberg, B. Asay, Rev. Sci. Instr. 62 (9) 1991

[2] Technische Lieferbedingung TL 1376-0800

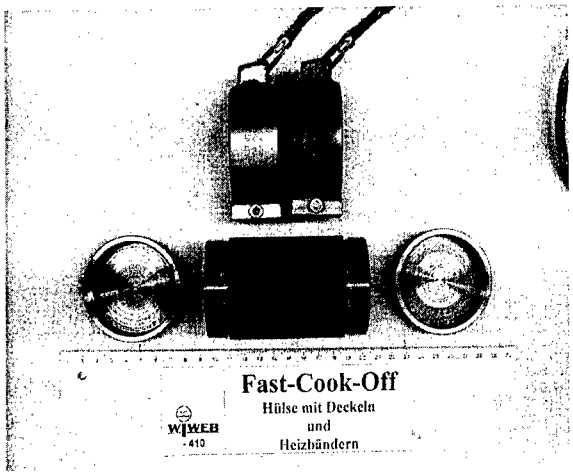


Abbildung 1: Versuchsgefäß

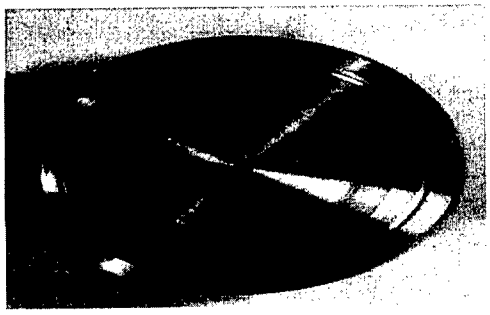


Abbildung 2: Verschlußkappe mit eingebautem Drucksensor

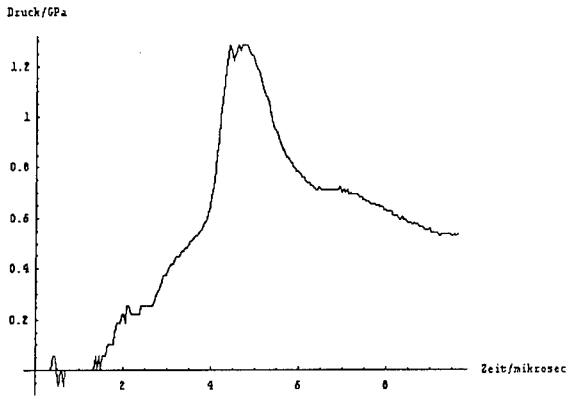


Abbildung 3: Drucksignal

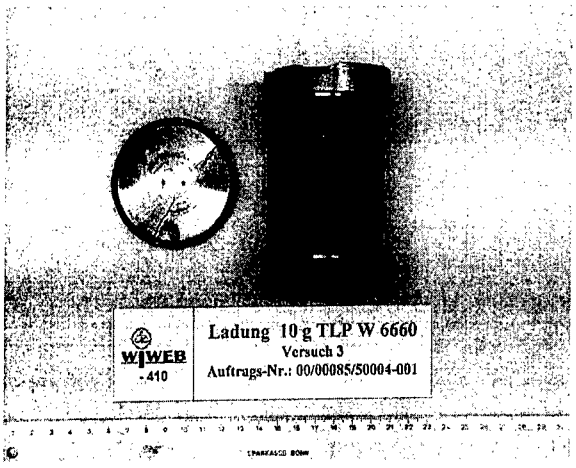


Abbildung 4: Versuchsgefäß nach Belastung mit 0.1 GPa

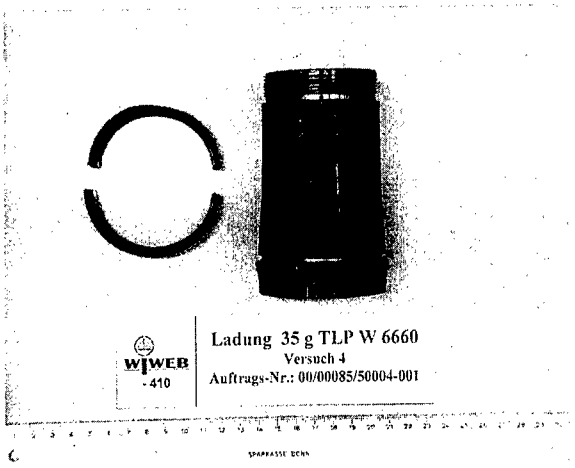


Abbildung 5: Versuchsgefäß nach Belastung mit 0.25 GPa

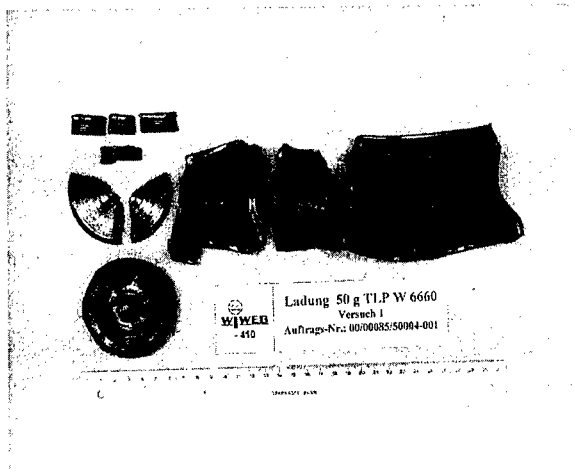


Abbildung 6: Versuchsgefäß nach Belastung mit 0.5 GPa

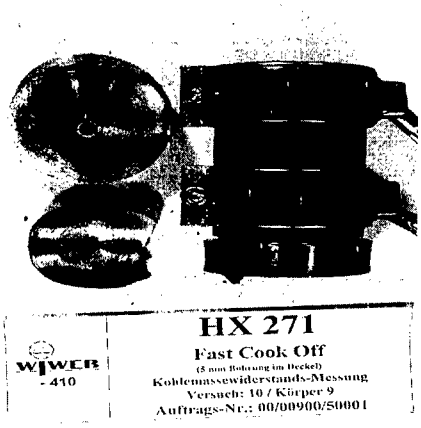


Abbildung 7: HX 271, kunststoffgebunden, gegossen, 0.12 GPa

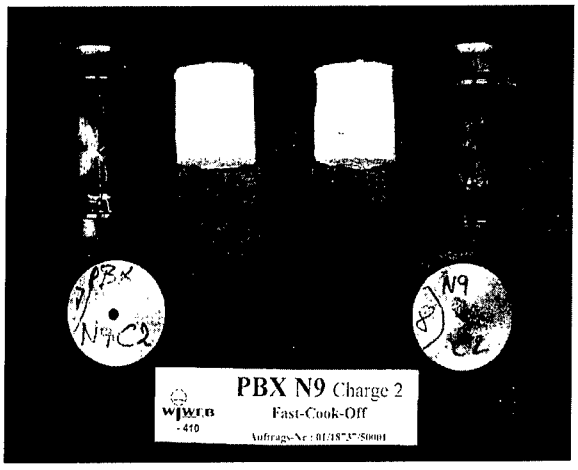


Abbildung 8: PBX N 9, kunststoffgebunden, gepresst, 0.2 GPa

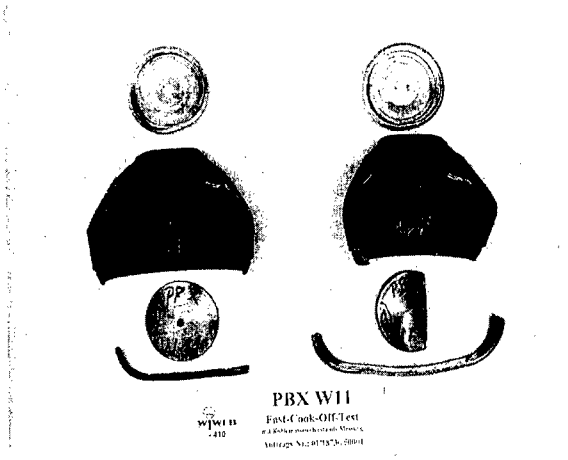


Abbildung 9: PBX W 11, kunststoffgebunden, gepresst, 0.5 GPa

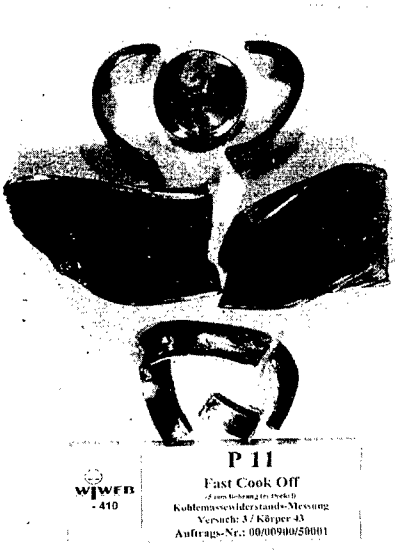


Abbildung 10: P 11, kunststoffgebunden, gepresst, 0.72 GPa

IRREGULARITIES OF DETONATION WAVE STRUCTURE AND PROPAGATION IN PBX

I. Plaksin, J. Campos, J. Ribeiro and R. Mendes

LEDAP - Laboratory of Energetics and Detonics

Mech. Eng. Dep. – Fac. of Sciences and Technology - Polo II -University of Coimbra

3030 – 201 Coimbra - PORTUGAL

ABSTRACT

The detonation of a plastic bonded explosive (PBX) is globally assumed as a steady regime. However, a PBX is a composite material. Increasing the scale of resolution, the detonation reaction includes local strong non-equilibrium reactions and dissipative structures that can be observed as micro-irregularities of Detonation Wave (DW) propagation. The presented fluctuations and irregularities were analysed in PBX slab and rod charges, of different cross-sections, confined by cooper, steel, PMMA or PVC. The PBX compositions were based on RDX or HMX, with HTPB or epoxy resin binders. The registration, with 1 ns resolution, of DW unstable propagation and their spatial-temporal fluctuations were performed using an high-resolution optical method, based on 64 optical fibbers strip, connected to a fast electronic streak camera. This method allows not only the observation of the DF irregularities, but also the measurement of its detonation pressure, using an interface barrier of Kapton. The obtained experimental results show the evidence of self-organisation establishment, in detonation of PBX, where the small micro fluctuations due to the initial PBX heterogeneities, generates a bigger scale unstable DW propagation, included in a global quasi stable propagation.

Keywords: Detonation wave irregularities and fluctuations; Detonation wave structure; PBX heterogeneities; self-organisation of detonation.

1. INTRODUCTION

The problem of the criteria of DW stability of heterogeneous explosives, in meso-scale (scale of the crystal sizes), remains very important for explosive charges of small size, close to its critical diameter. The main studies of DW stability phenomena were developed for the detonation in gases, proving the existing of pulsing front

(Shchelkin, 1959, 1963) and cellular structures of DF, originated in the reaction zone. Also, near close to the detonation limits (critical diameter), the DW presents simultaneously rotating and translating motion - spin detonation (Shchelkin, 1959, 1963, Voitsekhovsky et al., 1963).

Shchelkin, 1959, clarified the concept of unstable detonation in gaseous, due to the kinetic instability of DW - the explosion reaction begins non-simultaneously (in space and in time) over the detonation shock front, but at triple-shock interactions, due to double collisions at discrete sites. These interactions appear over the entire surface of the detonation shock front as a result of the complex instability of the shock wave (SW) chemical reaction.

The study of pulsing front of DW in the homogeneous liquid explosives was started in 1961 (vd. Dremin et al., 1970, 1989). The unstable DW propagation in solid (cast) explosives was presented latter in experimental studies of Howe et al., 1976, and Kozakh et al., 1989. The unstable (pulsing) front, in the heterogeneous condensed explosives, such as suspensions and slurry, as well as the existing of cellular structures in DW reaction zones were presented by Daniljenko et al., 1978, 1980. It was also proved experimentally, in the process of formation of pulsing DW, presenting a cellular structure in the DW reaction zone, the significant role taken by the phenomena of energy and mass transfer and its fluctuations (Daniljenko et al., 1978, 1980).

The phenomena of unstable (pulsing) detonation in powerful PBX explosives, based on RDX and HMX, have been studied (Plaksin et al., 1997, Mendes et al., 1997) applying a new non-intrusive high-resolution optical metrology procedures, using a multi-fibber strip (Plaksin et al., 1997, 1998, 2000). The obtained experimental results show the evidence of self-organisation establishment in detonation of PBX, behind the DF, where the small (micro) fluctuations due to the initial PBX heterogeneities generate a new regime of unstable DW propagation with a bigger scale of fluctuations. The clear explanation, of the experimentally presented phenomena in DW, was not yet concluded, even to the gases (vd. Gavrikov et al., 2000) due to the complex mechanism of the cellular structure formation, in the pulsing front. Nevertheless there was a big progress in the numeric simulation of this phenomenon in the past recent years (Baer, 1999).

The presented study concerns the experimental analysis of the unstable detonation behaviour of PBX, based on RDX and HMX, as a function of DW curvature,

explosive particle size and distribution, and explosive/binder mass ratio. The main efforts in this study were taken to correlate the experimentally observed DW instabilities with the phenomenology of their self-organisation. It implies the identification of main rules of conversion of the preceding unstable regime in the next one. The factor of divergence, in reaction zone, with and between particles, behind the divergent DF, (specified by its curvature) was found to be the main parameter determining the regime of DW instability in PBX.

2. PBX COMPOSITIONS

The tested six different BPX compositions differing in the nature of explosive particles (RDX, HMX), their sizes and value of their mass fractions, type of binder (HTPB, epoxy resin) and explosive/binder mass ratio, are represented in Table 1.

Table 1. *Tested PBX*

PBX composition	Content, % (wt)					Initial density [g/cm^3]
	RDX coarse fraction d_{50}=96μm (class A)	RDX fine fraction d_{50}=22μm (class E)	HMX coarse fraction d_{50}=204μm	HMX fine fraction d_{50}=17μm	Binder	
PE-4A	85				Elastomer 15	1.57
PBX-R	63.75	21.25	-	-	HTPB 11.5 DOS 3.5	1.59
PBX-A	85.00	-	-	-	HTPB 11.5 DOS 3.5	1.58
PBX-E	-	85.00	-	-	HTPB 11.5 DOS 3.5	1.56
PBX-F	70	-	-	-	Epoxy resin 30	1.60
PBX-W	-	-	65.60	16.40	HTPB 13 DOS 5	1.575

The detonation properties and parameters of the studied PBX compositions were presented in previous work (Mendes et al., 1997).

3. EXPERIMENTAL APPARATUS AND TESTS

3.1. Recording Optical System

A high resolution optical method (Plaksin et al., 1997, 1998,1999, 2000) based on 64-90 fibbers strip, with the diameter of each fibber (as well as the inter-axis distance between two adjacent fibbers) equal to 250±1μm, connected directly to a fast electronic streak camera (THOMSON-TSN 506 N) has been used for registration, with a maximum temporal resolution of 0.6 ns, of the DW propagation in PBX mini and macro samples.

The light associated to the DW or shock wave (SW) is transmitted through the optical fibber line to the streak camera, and recorded directly, without any intermediate optics. A few variants of Multi-Fibber Optical Probes (MFOP) were developed for the direct view registration of light, consisting in several bands placed in predefined positions. An example of MFOP is shown on Figure 1, showing two-joined fibber mini-bands.



Figure 1. Micro-photo of MFOP of linear matrix type

The MFOP allow the characterisation of 2D shock and detonation waves in PBX, within a few mm of the propagation, before touching the optical probe. This non-shocked layer of PBX (2~2.5 mm of thickness) is partially transparent for the DF light emission. Placing a Kapton (Polyimide) film, between the PBX sample and MFOP operating surface, allows the sharp attenuation of transmitted light, when the SW crosses the sample/Kapton interface, due to the shock destruction of the polyimide layer. Placing of a set of Kapton films, with μ-gaps between two or more adjacent surfaces, filled by a heavy inert gas (Argon) allows a set of sub-nanosecond successive flashes in the process of SW run through the multi-layer barrier.

The registration of (z-t) diagram using the MFOP (z is the geometrical axis of the explosive charge) of SW propagation into the Kapton multi-layer barrier, provides the way of 2D measurements of SW velocity and pressure fields (for measurements of shock pressure we have used the very well defined shock Hugoniot characteristics of Kapton).

3.2. Experimental test configuration

3.2.1. Long Charge

The experiments were performed to record the (z-t) diagrams of the DW simultaneously with the DF curvature, inside the channels of PBX, confined by Cu and PMMA plates (Figure 2) or in long cylindrical charges confined by PVC or steel. The charge length is 5 to 16 times bigger than the characteristic dimension of the cross section.

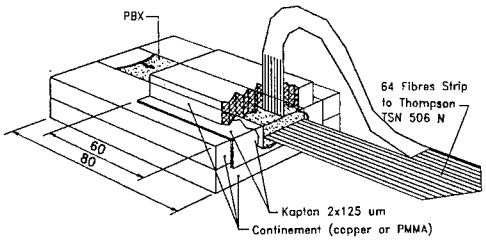


Figure 2. Experimental set-up for Long Charge tests.

The photochronograms obtained with the experimental set-up shown in Figure 2, with a square section (5×5 mm and 10×10 mm) configuration with PMMA confinement, for PBX-R, are presented in Figure 3.

DF curvature can be significantly decreased, for the long PBX charges of the same cross sections, increasing the shock impedance of the confinement. The photochronograms obtained in the experiments with the same experimental set-up, but now using Cu in the confinement, are presented in Figure 4.

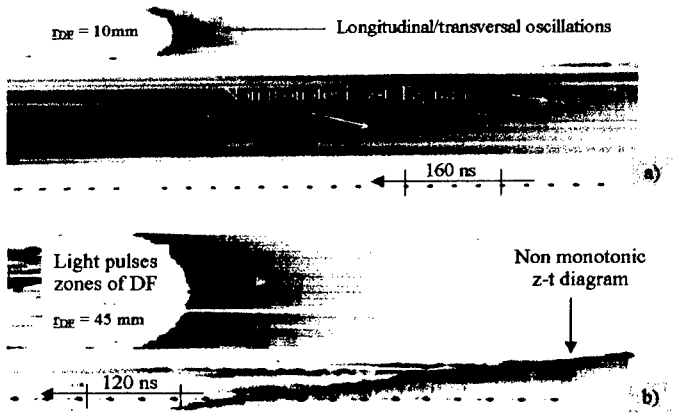


Figure 3. Photochronograms obtained in Long Charge Tests of PBX-R with a square cross section (5×5 mm **a)** and 10×10 mm **b)**) confined by PMMA plates.

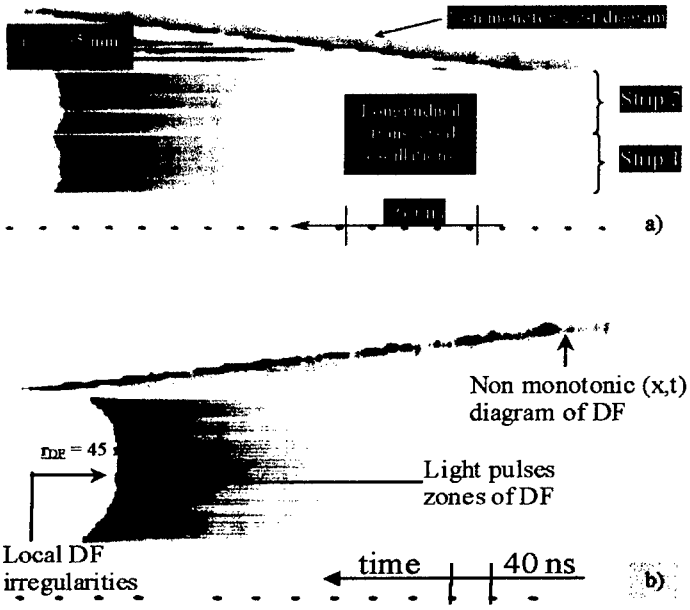


Figure 4. Photochronograms obtained in Long Charge Tests of PBX-R with a square cross section (5×5 mm **a)** and 10×10 mm **b)**) confined by Cu plates.

The decrease of the mean DF curvature implies the characteristic sizes of the DF cells increase where as the mean period of the local DF oscillations changes

insignificantly. The observed irregularities have almost identical spatial temporal scale as the spots on DF light emission. The alternative zones of acceleration and slowing down are recorded on the DF z-t diagrams, for a mean constant detonation velocity.

In order to evaluate the formation and evolution of DF heterogeneities, connected to the irregular DF propagation, a matrix of stratified 5 fibber strips was placed at normal position to DW propagation (vd. Fig. 5 a)). The registration of the light emitted by DW, before touching these parallels optical probes (vd. Fig 5 b)), shows the formation of front irregularities with 40 ns of period, which, if correlated to the mean DF velocity, evaluated in this experiment (7.1 mm/μs), suggests that the dimension of this irregular formations is larger than 5 mean coarse particle diameters.

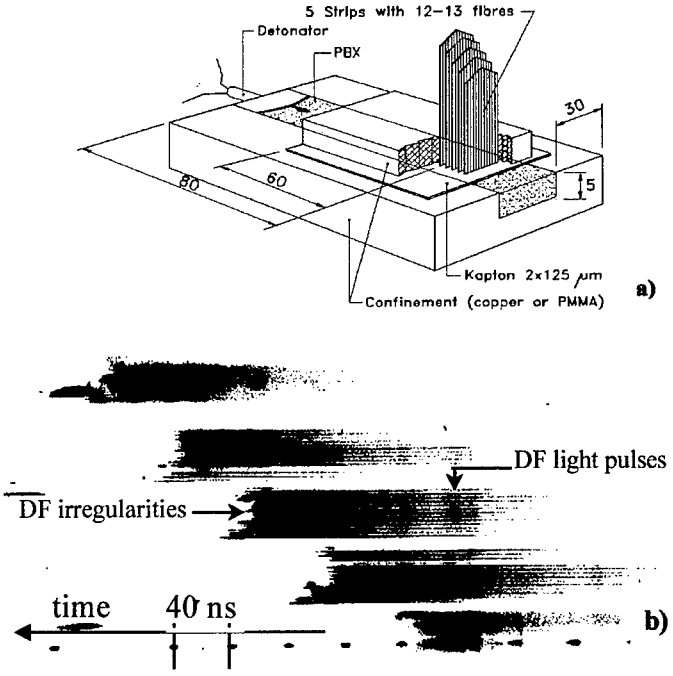


Figure 5. Experimental set-up a) and DF light records b) obtained by MFOP built-up with five multi-fibber strips (channel of PBX-R with a cross section of 5×5 mm, confined by PMMA) (Plaksin et al., 1998).

Experiments have also been performed with simultaneous registration of DF in two PBX channels, confined by Cu, with a length of 80 mm and a cross section of

5×10 mm, initiated synchronously. One of the channels was filled by PBX-A and the other one by PBX-E. The obtained results show not only a smaller DF curvature but also a smaller scale of irregular formation in PBX-E (with small particles) compared with PBX-A (vd. Fig. 6), proving the existing of a cooperative phenomena between reacting particles, behind DF.

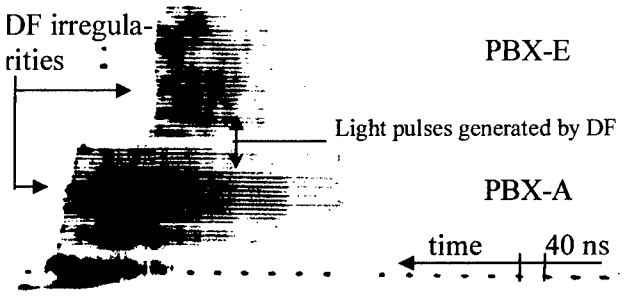


Figure 6. The DF light records of detonation in PBX-E and PBX-A long channels (Plaksin et al., 1998).

The light witness print, from detonation reaction zone, can be obtained covering the PBX channel walls with the optical fibber strip. The patterns of the light emitted by DF, shown in Figure 7, show clearly its cellular structure.

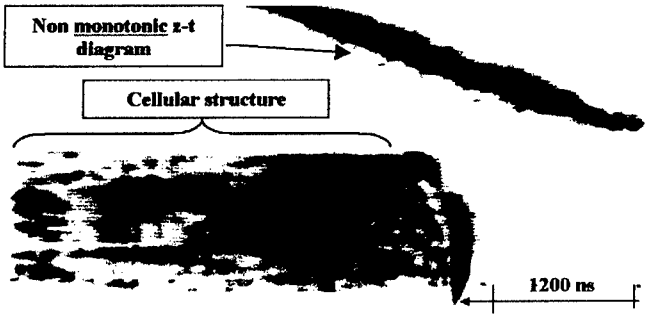


Figure 7. Unstable DW propagation (1.2 μs between marks) in channel of PE-4A with rectangular section of 20×10 mm (PVC confinement).

The curvature of DF can be decreased (up to "zero") using, for the initiation of PBX charges, a plane wave generator. Experimental set-up for the registration of the quasi-plane DW is shown in Figure 8. The photochronogram of DW propagation in

PBX-W explosive charge, of slab configuration; and the shock to detonation transition [SDT], after 1.27 mm of Kapton barrier, is also shown in Figure 8.

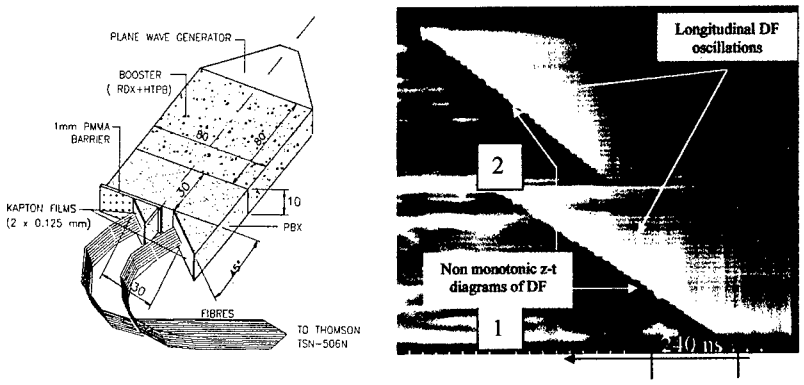


Figure 8. Experimental set-up for PBX long charge test of quasi plane geometry of DF and typical (z-t) diagram showing the non monotonic DW propagation (1) and its transmission through the 1.27 mm Kapton barrier (2) in PBX-W.

For the DW of plane geometry, the quasi-periodical longitudinal light oscillations and the non-monotonic z-t diagram of DF can be observed clearly. The mean period of DF longitudinal oscillation, in PBX-W, is equal to 35±5 ns. This period of time, for the measured mean detonation velocity (D = 7.89 mm/μs), corresponds to a DW run of 280 μm, equivalent to the thickness of an elementary layer of more than one coarse HMX particle. Registration of SDT shows the origin of the longitudinal oscillations in donor PBX-W charge, immediately after the shock run equal to the mean size of the coarse explosive particle.

In order to evaluate the simultaneous effects of the explosive particle size and explosive/binder mass ratio, on the spatial temporal instability, the experiment has been done with the composition PBX-F and compared with the results obtained with the composition PBX-R, using long cylindrical charges confined by PVC (PBX-R) or steel (PBX – F). The obtained photochronogram, for the PBX-F (vd. Figure 9) shows, for similar values of DF curvature in both experiments, relatively different regime of DW instabilities when compared with PBX-R (vd. Figure 10). The longitudinal/transversal DW oscillations as well as the non regular cellular structure, and the fluctuations of pressure on its interface with Kapton barrier, can be seen in the detonation process of PBX-F (vd. Figure 9). Consequently, increasing particle size

and its inter-particle distance (decreasing the ratio explosive/binder) we are increasing the scale of the instabilities.

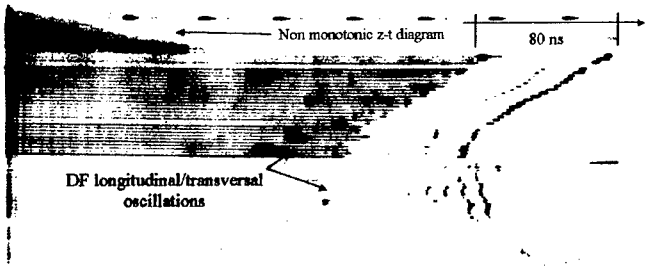


Figure 9. DW unstable propagation in long cylindrical charge of PBX-F with 20 mm of diameter (steel confinement) and fluctuations of pressure on the front surface of SW propagated in 500 μm thick Kapton barrier (four layers of 125 μm of thickness in the upper part and ten layers of 50 μm of thickness in the lower part).

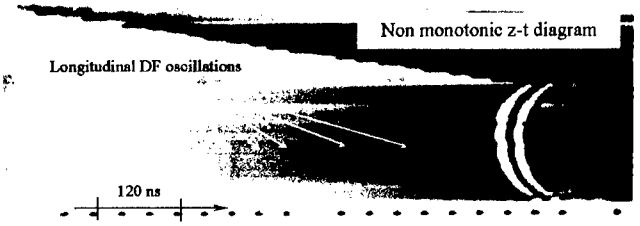


Figure 10. DW unstable propagation in long cylindrical charge of PBX-R with 10 mm of diameter (steel confinement)

It can be concluded, by the meso-scale analysis of DW records, the existence of DF instabilities and irregularities. The scale of these DF fluctuations exceeds the values of the characteristic PBX heterogeneities, defined by its coarse and fine crystals. This proves the existence of a process of self-organisation, behind the DF, where the micro-fluctuations, through the characteristic PBX heterogeneities, generate a new regime of unstable DF propagation with dissipative structures (cell reaction spots) under a bigger scale of irregularities. The obtained results show the change of the dimension of cells and the regime of DF oscillations, with the DF curvature with an increasing values of $R_{DF,}$ beginning from its critical diameter of detonation. It can be also observed the change of DW oscillation regimes, from detonation with longitudinal/transversal modes and then, the detonation with main longitudinal

oscillations of DF. The changing of the instability regimes seems to be influenced by the divergence effect of reacting particles flow influenced by the inter-action rate between particles, in a complex relaxation process (involving pressure, temperature and kinetics of chemical reactions). Therefore, the energy release rate, obtained by the registration the explosive particles flow, can clarify the nature of the observed DF instabilities.

3.2.2. Micro Gap Test

The direct observation of the energy release, by coarse particles, under shock wave, can be done performing μ-Gap Test. The micro-gap test (vd Figure 11) consists of individual coarse HMX crystals, confined by HTPB binder, initiated by PBX donor charge, through a kapton barrier.

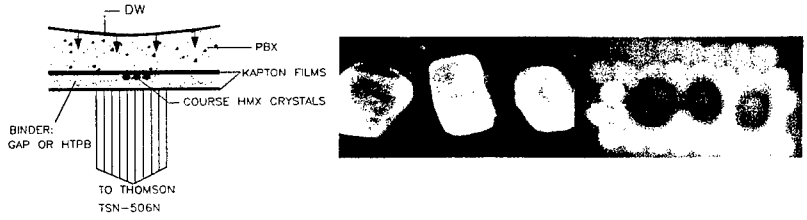


Figure 11. Micro-Gap Test configuration and the view of the matrix of MFOP with the clusters of coarse HMX crystals.

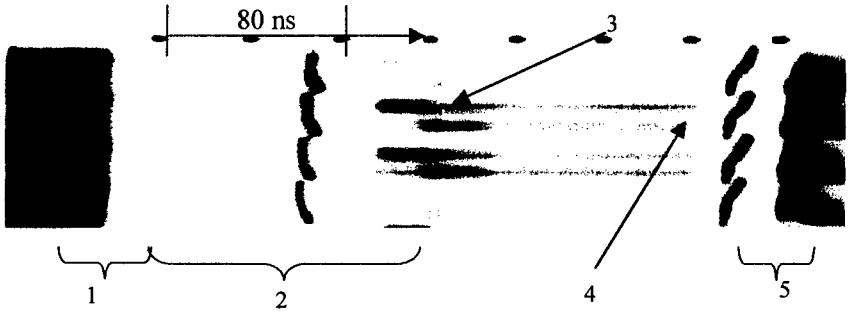


Figure 12. Streak record of Micro-Gap Test with clusters of coarse HMX crystals in HTPB binder: 1 – DW in PBX donor charge; 2 – SW propagation through the upper 5×125 μm Kapton film barrier; 3 – Shock reaction of HMX particles; 4 – SW propagation into 1.00 mm thick HTPB media, attended by the prolonged irradiation from non completed reacted HMX crystals; 5 – propagation of the output SW through the lower Kapton barriers 2×50 μm.

The obtained streak record shown in Figure 12, allows the observation of the particle reaction, inside the binder, and the shape of shock front, propagated into the

binder confinement. It can be measured the input SW pressure, on the upper Kapton multi-layer barrier – in this particular case it is equal to 25 GPa. The results show two phases of reaction, one inside particles and the other in the interface particle-binder. This seems to show that a part of the energy of individual crystals is released, behind the initial front, with significant delay. Duration of the second phase is, at least, four times more than time propagation throughout crystal. In this case, the tangential SW interaction needs to be occurred between the hot-spots formatted by coarse explosive particles, behind the initial front.

4. PHENOMENOLOGY OF SELF-ORGANISATION OF PBX DETONATION

Detonation front heterogeneities are consequence of irregularities of fresh explosive material. They generates unstable kinetics of shock reaction, of coarse and fine particles, and particles and binder. Consequently, front irregularities in PBX are initially governed by its own heterogeneity. On the initial phase, of high explosive crystals ignition, the characteristic dimension of front irregularity is the order of HE crystal size. In the process of DW propagation, the scale of irregularity can be increased as a result of an inter-influence of different parameters of micro-cellular chemical reaction zones, namely, characteristic times of heat/mass transfer and stress relaxation, and synchronisation inside interaction phenomena. In this case, in the crystals superposition layer, a significant energy release takes place behind the initial front, as a consequence of repetitive interactions of the transverse shock waves induced by shock reaction of individual crystals.

In the next phase of the DW propagation, the phenomena of synchronisation arise by a dissipative structure, formed behind of the front. Phenomena of synchronisation, according to Daniljenko et al., 1983, describes the cooperation effect of a multitude of individual reaction spots, where the energy is releasing non monotonically and generating a assynchrone pulsing regime. The individual reaction spots, enhanced by the interactions between them, start to oscillate in a synchronous or resonating modes, increasing its size by coalescence. This coalescence process of the individual explosion spots (consisting in 5-6 coarse particles, as it was shown in the Long Charge Tests) depends of the divergence process of the reacting flow behind the DF. When the DF is significantly curved (high order of divergence) the time of relaxation

increases, the rate of exchange of energy between neighbour hot spots decreases and the conditions for the coalescence, of adjacent elementary cells, are not attained. In this case DW propagates in the regime of triple shock interactions (DF longitudinal/transversal pulsing behaviour similar to the Shchelkin's mechanism of gas detonation). When the order of divergence is small (low DF curvature) the elementary cells are able to join into a bigger one.

5. CONCLUSIONS

The registration, with 1 ns resolution, of DW unstable propagation and their spatial-temporal fluctuations, were performed using an high-resolution optical method, that allows not only the observation of the DF irregularities, but also the measurement of its detonation pressure, using an interface with a Kapton barrier. The obtained experimental results show the evidence of self-organisation establishment, in detonation of PBX, where the small scale (micro) of fluctuations, through the initial PBX heterogeneities, generates local DF irregularities of bigger scale and an unstable DW propagation, that it is converted in a global quasi-stable DW propagation. Models, describing this class of phenomena for the reactive homogeneous and heterogeneous materials were reviewed and it was discussed its appliance to the detonation of PBX. The proposed phenomenological model of the mechanism of DW in PBX, based on the phenomena of instability of energy release of the individual particles and clusters, and its cooperative effect of interaction including synchronisation, was presented and discussed.

REFERENCES

Baer, M. R., 1999, *Computation Modeling of Heterogeneous Reactive Materials at the Mesoscale*", Proceedings of the Conf. of the American Phys. Soc., Topical Group on Shock Compression of Condensed Matter, Snowbird, Utah, June 27-July 2, pp. 27-33.

Daniljenko, V. A., Afanasenkov, A. N., Pis'ma v Zhur. Teor. Fiz., 1978, n° 4, vip. 1, pp. 35-38.

Daniljenko, V. A., Kudinov, V. M. Fizika Gorenija I Vzriva, 1980, n° 5, pp. 56-63.

Dremin, A. N. Savrov, S. D., Trofimov, V. S. and Shvedov, K. K., 1970, *Detonatsionnie Volni v Kondensirovannikh Sredakh,* Nauka, Moskva, URSS.

Dremin, A. V., Klimenko, V. Yu. Davidova, O. N. and Zholudeva, T. A., 1989, *Multiprocess Detonation Model.* Proceedings of the Ninth Symposium (Int.) on Detonation, Portland, Oregon, pp. 724-729.

Gavrikov, A. I., A. A. Efimenko, and S. B. Dorofeev, 2000, *A Model for Detonation Cell Size Prediction from Chemical Kinetics*, Combustion and Flame, vol. 120, pp. 19-33.

Howe, P. Frey, R. and Melani, G., 1976, *Combustion Science and Technology*, Vol. 14, N. 1, 2 3, p.p. 63-74.

Kozakh, G. D., Kondrikov, B. N., Oblomskii, V. B., 1989, *Spinning Detonation in Solid Explosives*, Fizika Gorenija i Vzriva, N. 4, Vol. 25, pp. 86-91.

Mendes, R, Plaksin, I. and Campos, J., 1997, *Single and Two Initiation Points of PBX* Proceedings of the Conf. of the American Phys. Soc. Topical Group on Shock Compression of Condensed Matter, Amherst, Massachusetts, July 27-August 1, pp. 715-718.

Plaksin, J. Campos, R. Mendes and J. Góis, 1997, *Interaction of Double Corner Turning Effect in PBX*, Proceedings of the Conf. on the American Phys. Soc. Topical Group on Shock Compression of Condensed Matter, Amherst, Massachusetts, July 27-August 1, pp. 755-758.

Plaksin, I., Campos, J., Mendes, R., Ribeiro, J. and Góis, J., 1998, *Pulsing Behaviour and Corner Turning Effect in PBX*, Proceedings of the 11th Detonation Symposium, Aspen, CO, Aug. 29 – Set. 4, pp. 658-664.

Plaksin, I., Campos, J., Mendes, R., Ribeiro, J. and Góis, J., 1999, *Mechanism of Detonation Wave Propagation in PBX with Energetic Binder*, Proceedings of the Conf. of the American Phys. Soc. Topical Group on Shock Compression of Condensed Matter, Snowbird, Utah, June 27-July 2, pp. 817-820.

Plaksin, A. Portugal, L. Pedroso, P. Simões and J. Campos, 2000, *Detonation Properties of HMX-DNAM-GAP Compositions*, International Conference in Shock Waves in Condensed Matter, St Petersburg, September 8-13, (to be published in Chem. Phys. Reports).

Plaksin, J. Campos, J. Ribeiro, R. Mendes and A. Portugal, 2000, *Detonation Study of the PBX Micro-samples,* International Conference in Shock Waves in Condensed Matter, St Petersburg, September 8-13, (to be published in Chem. Phys. Reports).

Shchelkin, K. I., 1959, *Two Kinds of Unstable Burning.* Zhur. Experim. i Teor. Fiz. Vol. 36, pp. 600-606.

Shchelkin, K. I. and Troshin, Ya. K., 1963, *Gazodinamika Goernija*, Akademia Nauk, Moskva, URSS.

Voitsekhovsky, B. V. Mitrofanov, V. V.and Toptchijan, M. E. 1963, *Detonation Front Structure in Gases.* Akademia Nauk, Novosibirsk, URSS.

Characterization of Coating for Energetic Materials

By

Mark Mezger TACOM-ARDEC
Steven Nicolich TACOM-ARDEC
Rhami Yacizi Stevens Institute of Technology
Dilhan Kalyon Stevens Institute of Technology

Abstract

The "goodness of mix" and coating quality of energetic materials are key parameters in the reliability of the sensitivity and performance of energetic materials. Historically these characteristics were evaluated qualitatively using microscopy. Recent efforts have been undertaken by TACOM-ARDEC and the Stevens Institute of Technology to develop quantitative techniques for determining coating quality and goodness of mix. The intent of these studies is to develop methods that can be implemented online for statistical process control at a manufacturing facility. In this report wide angle x-ray scattering techniques will be described that can be used to determine both the coating quality and degree of mixedness for energetic materials.

Introduction

Many energetic materials consist of highly filled composite materials of nitramine crystalline solids contained in a polymer/plasticiser matrix. The uniformity, quality of mix, and thickness of coating is critical to the sensitivity and performance of energetic materials. Poorly-coated material, with exposed bare crystals, shows higher sensitivity, especially to friction, than properly coated material.

Conventional water-slurry techniques, twin screw extrusion and other techniques have been employed in the preparation of these coated explosive particles also called "molding powders." Molding powders are used as starting materials for further processing such as pressing, machining, and twin-screw extrusion operations.

The typical microstructures observed in these materials are shown in Figs. 1 and 2. As can be seen in these photomicrographs, the energetic particles are agglomerated to 100 to 500 micron "grains" and only qualitative estimates can be made by electron microscopy.

Traditionally the only method used to determine coating quality is to make qualitative assessments from micrographs like those shown in Figures 1 and 2. The subject of this report is the development of a quantitative process that can be used on a manufacturing line for statistical process control.

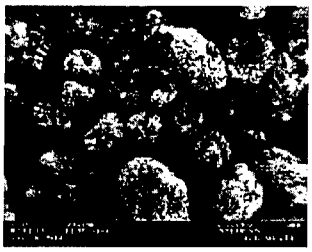


Fig. 1.. Typical molding powder "grains" of coated nitramines 20 simulant with 10% CAB /BDN A/F, 50x



Fig. 2 Fractured cross-section of a nitramine molding powder "grain" with BAMO/AMMO binder2,000x

Approach

For quantitative assessment of the "goodness of coating" in the molding powders, x-ray diffraction based measurement methods were developed and applied. The techniques included wide-angle x-ray diffraction (XRD), low-glancing-angle XRD and x-ray absorbance supplemented by electron microscopy. The specific properties measured quantitatively included a) relative weight fraction of the ingredients, i.e., coating/Nitramine crystal ratio, its variability and the mean value, b) thickness and completeness of the coating, its variability and mean value and c) type and completeness of the coating, i.e., agglomerations of coated crystals vs. coating of agglomerated crystals. These microstructural features that are measured to fully evaluate the goodness of coating are schematically shown in Fig. 3.

The two x-ray diffraction techniques applied wide-angle XRD, low-glancing-angle XRD, which also yields x-ray absorbance measurements, and the coating parameters measured are schematically shown in Fig. 4.

Here the overall distribution binder material, i.e., its volume fraction ϕ is quantitatively determined from the intensity of the diffracted x-rays emanating from the binder versus the filler, i.e., nitramine. This is a "goodness of mixing" analysis which is based on "symmetric diffraction," developed at Stevens and successfully applied to numerous energetic formulations, PEPs and other industrial products (Yazici and Kalyon, 1993, 1996, 1997). A basic measure of the homogeneity of a mixture is the extent to which the concentration values of the ingredients of the formulation found at various regions of the volume of the mixture differ from their mean concentration c. The variance arising from the individual concentration measurements provides such an index to quantitatively assess the quality of mixing. Relative variability is defined with coefficient of varia-

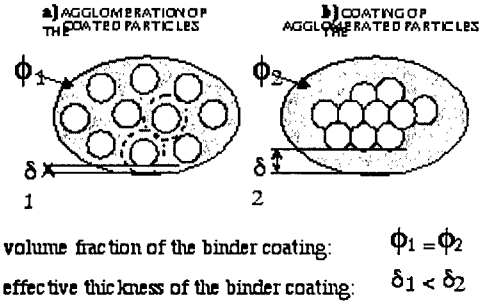


Fig. 3. Microstructural features that are measured to fully evaluate the goodness of coating in molding powders.

tion, which is the ratio of standard deviation to the mean.

The goodness of mixing analysis are an essential part of the goodness of coating evaluation, as they reveal the mean and variation of the binder content in the 1 to 100 cubic millimeter scales. These measurements are highly efficient to evaluate large amount of molding powder and quantitatively determine the problematic variations in the binder distribution. However, the goodness of mixing measurements do not reveal, in the few hundred micron scale, the distribution of the ingredients, i.e., the presence of "agglomeration of particles versus coating of agglomerated particles. As shown in Fig. 3, for the same volume fraction of binder the thickness of the coating on the molding powder grain could vary:

$$\phi_1 = \phi_2 \qquad but \qquad \delta_1 < \delta_2$$

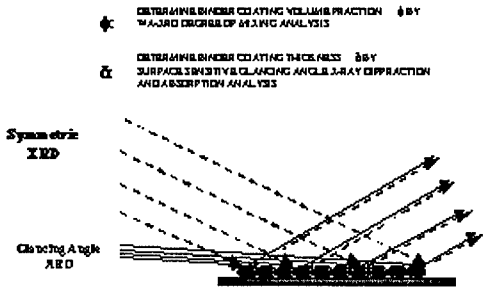


Fig. 4 The working principles of the wide-angle XRD and low-glancing-angle XRD techniques and the coating parameters measured.

In order to differentiate these coating thickness differences the "low-glancing angle" XRD measurements are being developed and applied. As shown in Fig. 4 this measurement is surface sensitive and amplifies the presence of the surface coating on the particles and makes it possible to do high resolution "coating thickness" measurements. Coating thicknesses which are as small as hundred nanometers (see Fig. 5) were measured by this technique.

Such "high-resolution" measurements become an absolute necessity when the binder content is below 10%, the coating is uniform and the surface area of the energetic powder is large due to small particle size. A computer model/program (coat-a-powder) has been developed at Stevens to calculate the coating thickness for a given formulation with specific i) powder material, ii) particle size distribution (PSD) of the powder, iii) binder material, iv) weight fractions of the binder/powder ingredients, and v) the grain-size distribution



Fig. 5 Slurry processed molding powder: CL-20 simulant powder coated with 10 wt.% CAB. Typical coating thickness: 100 - 200nanometer (0.1 - 0.2 m)

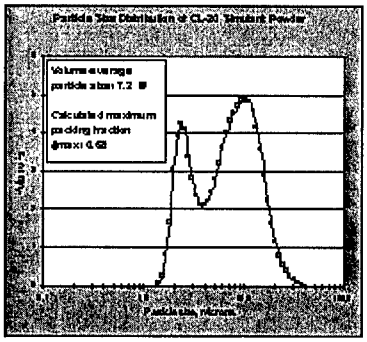


Fig. 6 Particle size distribution of the CL-20 simulant shown in Fig. 5.

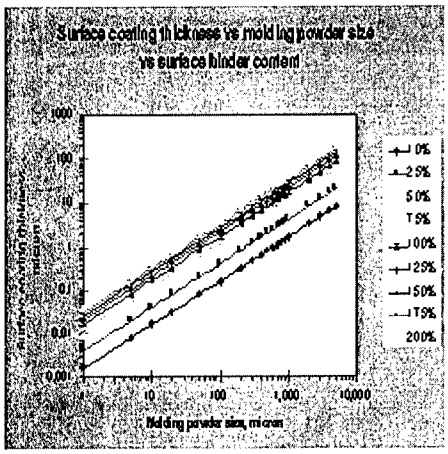


Fig.7 Results of the coat-a-powder calculations for a typical molding powder system

of the molding powder. The program can calculate the expected coating thickness for an ideally uniform coating-thickness-distribution, as in the case of "agglomeration of coated particles shown in Fig. 3; and for non-ideal coating-thickness-distribution, as in the case of "coating of agglomerated particles also shown in Fig. 3, as well as in-between cases. A typical output of the program is given in Fig. 7.

Experimental Procedure

To establish and validate the 'Goodness of Mix" Technique a series of inert simulants and a live energetic material were tested with varying concentrations of binder. Several inert simulants were coated with a polymer matrix at different concentrations and then subjected to high and glancing angle X-Ray diffraction analysis. From the X-Ray data both the binder conenctraion Φ and the surface coating thickness δ were obtained. The data obtained from these experiments is illustrated in Fig. 8. The filler materials were tested for particle size and distribution using a microtrak particle size analyzer and are plotted in Fig. 9. The theoretical binder thickness was then calculated for varying degress of particle agglomeration. A scanning electron micrograph of the energetic sample was also taken and used to varify the accuracy of the methodology. The micrograph is illustrated in Fig. 10.

Discussion

COMPARISON OF THE DEGREE OF MIXING

These techniques were further tested on various sets of LOVA propelant samples collected upon mixing in twin screw extruders, batch mixers and a solvent based crash precipitation process. The materials were the same as those indicated earlier, but the mixing conditions in the processors were altered. The results are summarized in Figure11. Such results were sufficient to explain the changes in the burning rates observed with these samples and provide for the first time the facility to quantitatively characterize the degree of mixedness of energetic materials. The average par-

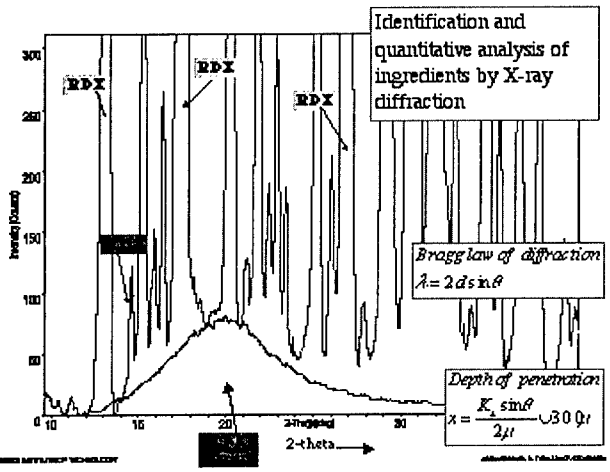


Fig. 8 X-Ray analysis data of a nitramine filled composite. From the data the binder volume fraction and chemical composition can be determined.

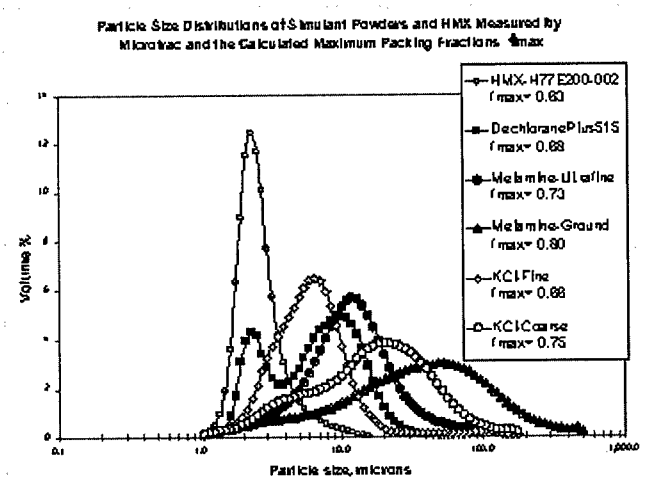


Fig. 9 Particile size distribution of HMX and inert simulants

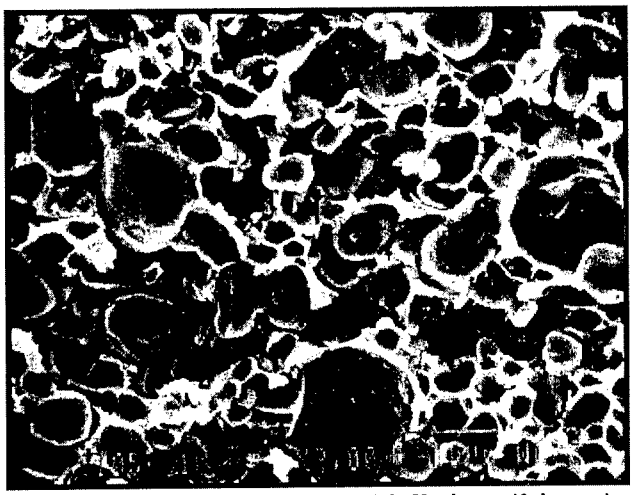


***Fig 10** Micrograph of an energetic material. Used to verifythe coating anlayisis data.*

ticle size and distribution for these materials was also measured using a microtrak analyser and the ideal coating thickness for this distribution was calculated and plotted in Fig. 12. The final coating thickness calculation is compared to the measured values from the micrograph and the result is tabulated in Fig. 13. This indicates that for the method as tested so far is feasible for conducting a quantitative assessment of mixing and coating quality.

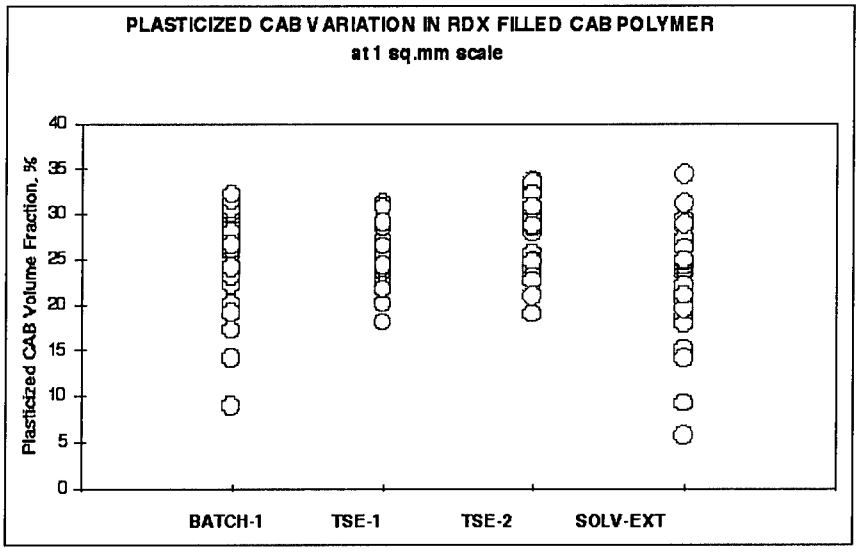


Fig. 11 Goodnes of mix measurements for several RDX filled energetic materials

PlasticizedCAB statistical parameters at 1 sq.mm scale

Volume Fraction Parameters	Batch 1	multi-feed TSE-1	multi feed TSE-2	solvate TSE-3
mean	24.7	25.5	27.2	22.6
standard deviation	6.32	3.44	4.19	5.80
coefficient of variation	.26	.13	.15	.26
mixing index	.85	.92	.90	.86

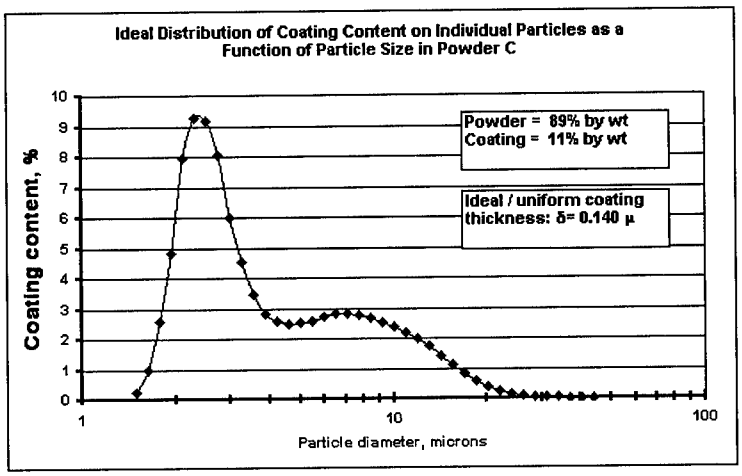


Fig 12. Ideal coating thickness for typical prarticle size distribution of nitramine in an energetic material

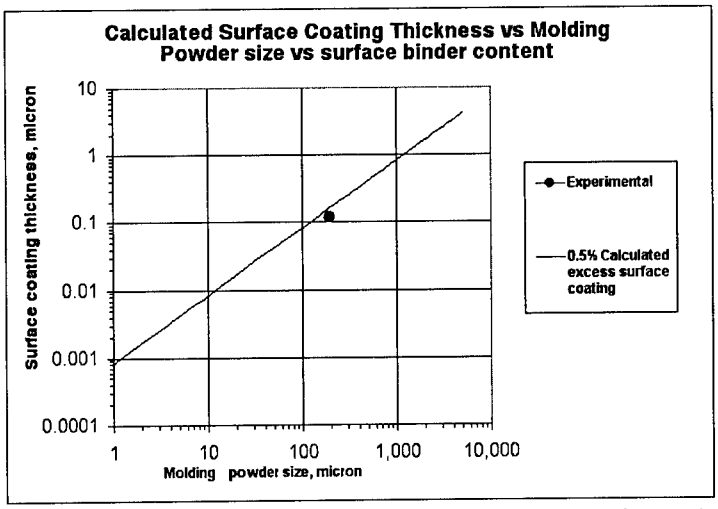


Fig. 13 Calculated vs measured binder thickness for a nitramine filled energetic material

Evaluation of modified JP-10 fuels for Pulse Detonation Engine

Charles Dubois, Sophie Ringuette and Robert Stowe

Defence Research Establishment Valcartier
2459 Pie-XI Blvd North, Val-Bélair, Québec
Canada, G3J 1X5

The Pulse Detonation Engine (PDE) concept is applicable both to rocket and airbreathing cycles. The airbreathing PDE cycle involves four major transient processes, including the filling of the combustion chamber with the fuel/air mixture, the initiation of a detonation in the mixture, the propagation of the detonation wave through the mixture, and the scavenging of the combustion products. The faster these processes can be completed, the higher the cycle frequency and average thrust output of the engine. The majority of studies on PDE-powered vehicle have been based on gaseous fuel systems, including hydrogen and ethylene. Given the mass limitations and storability and safety issues involved in the use of gaseous fuel systems however, it is doubtful, that they would be used in actual flight systems, and liquid fuels or solid propellant gas generators would be preferable. Because of physical properties such as latent heat of vaporisation, heat of combustion and density, JP-10 fuel (exo-tetrahydrodicyclopentadiene) is a good candidate for operating a pulse detonation engine. However, one of the problems that may arise in using such a fuel comes from its lack of detonability. As a first step, we have investigated the autoignition temperature, obtained with the ASTM E659-78 procedure, of JP-10 fuels with and without small amounts of chemical sensitisers such as 2-ethylhexyl nitrate. After discussing the results and the effect of the modifiers, we have attempted to correlate the changes observed in autoignition temperatures with actual detonability tests conducted in a detonation cell.

Introduction

The majority of in-service tactical missiles are powered either by solid propellant rocket motors and/or turbojets. In addition, ramjet powered systems do exist and are expected to be used more and more to increase stand-off distance and the average velocity to target. In spite of the major differences between these propulsion technologies, all are steady flow and are considered as constant pressure combustion devices. Since 1986, renewed interest has been shown in transient flow propulsion technology and in particular the

pulse detonation engine (PDE). Unlike steady flow devices, the PDE has been characterised by an efficiency that is comparable to that produced by a constant volume process. If this is true, it translates into increased thermal efficiency (approximately 30%) and specific impulse compared to an engine that relies on a less efficient constant pressure process. This potential increase in specific impulse has been the primary advantage driving the study of PDEs. In addition, PDEs offer the significant advantages of rapid variable thrust control, no moving parts and the potential for low cost manufacturing. Finally, unlike a ramjet, an airbreathing PDE can be operated from a stand still.

The PDE concept is applicable both to rocket and airbreathing cycles. While, the airbreathing cycle promises the best performance in terms of increased stand-off distance and average velocity-to-target, it also involves the most complex physical interactions. The airbreathing PDE cycle involves four major transient processes, including the filling of the combustion chamber with the fuel/air mixture, the initiation of a detonation in the mixture, the propagation of the detonation wave through the mixture, and the scavenging of combustion products. A simple schematic of such a process is shown in Figure 1. The faster this cycle can be completed, the higher the average thrust output of the engine.

The work done since 1986 in the area of PDEs has demonstrated its viability even if no PDE-powered vehicle has ever flown. The majority of studies interested in PDE fuels has been based on gaseous systems, including hydrogen and ethylene. However, it is questionable, given the mass limitations and storability and safety issues involved in the use of gaseous fuel systems, that they will be implemented in actual flight systems. Rather, liquid fuels or solid propellant gas generators would be preferable. In the area of liquid fuels, only one experimental study has been published, that by the Naval Postgraduate School. This study, which had limited success, investigated the detonability of JP-10, or exo-tetrahydrodicyclopentadiene. One of the main conclusions of this preliminary work was that the detonation properties of this fuel when mixed with air were not sufficient to ensure the design of a PDE motor within an acceptable tube length. In

order to use this fuel in such an engine, its detonability would have to be enhanced by (most likely) chemical modifiers or thermal cracking.

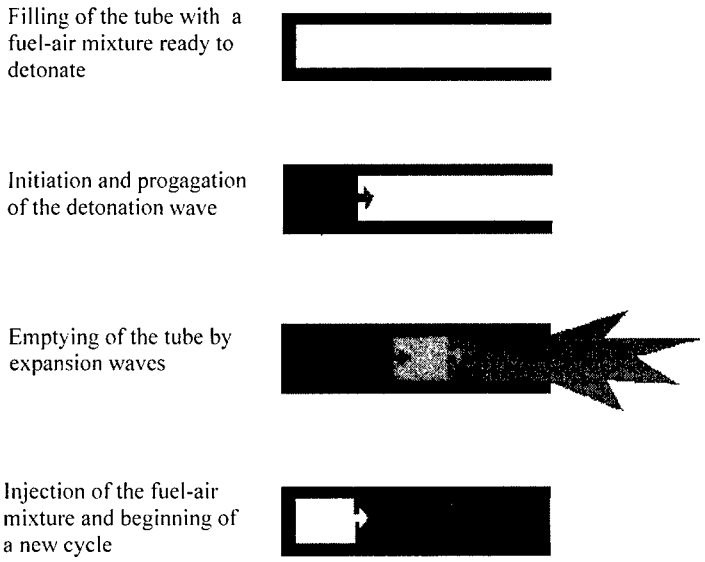


Figure 1: Schematic of a Pulse Detonation Engine operating cycle

The traditional mean of evaluating the detonability of a particular mixture is to use a cylindrical detonation cell. While the procedure and apparatus to conduct such experiments are well known, they require a fairly complex installation in order to guarantee the safety of the operation. In this paper we want to investigate the use of the autoignition temperature as a mean of studying the detonability of a fuel-air mixture. By using the procedure described in the ASTM E 659-78 method, this property of a liquid can be measured in a simple apparatus. Because the amount of fuel needed to conduct an autoignition experiment is very small (less than one tenth of a cm^3), the test is intrinsically safe. The ignition behaviour of the exo-tetrahydrodicyclopentadiene fuel was investigated either as a pure product or when modified by a small amount of 2-ethyl-

hexyl-nitrate (2-EHN). This chemical sensitiser was chosen for this work because data on its effect on other hydrocarbons, as evaluated in a detonation cell, were available from a research group at McGill University (Montreal, Canada) .

Experimental

Autoignition is, by its very nature, dependent on the chemical and physical properties of the material tested as well as the method and apparatus employed for its determination. The autoignition temperature as measured by a given method does not necessarily represent the minimum temperature at which a given material will self-ignite in air. The volume of the vessel used for the test is particularly important as well as other variables such as vessel materials and heat transfer phenomena. The American Society for Testing and Materials has approved procedure E 659-78 "Standard Test Method for Autoignition Temperature of Liquid Chemicals" for determining the hot- and cool-flame autoignition temperature of liquids in air under atmospheric pressure. The hot-flame autoignition temperature (AIT) is defined as the lowest temperature at which a substance will produce hot-flame ignition in air without an external source of energy such as spark or flame, within an ignition delay of ten minutes. A hot flame reaction characterises itself by a sharp temperature raise in the vessel (more than 100 °C) and bright colour flames. For fuel-air mixtures of hydrocarbons and oxygenated hydrocarbons, a faint, pale blue luminescence or flame often occurs below the autoignition temperature. The temperature at which this phenomenon takes place is the cool flame ignition temperature (CIT). The cool flame process generates a single or multiple steps temperature rise of less than 100 °C. At temperatures below the CIT of a compound, some nonluminous reactions may also happen and reveal themselves by a gradual temperature rise which then falls off to the base temperature. The lowest flask temperature at which these reactions are observed is the reaction threshold temperature (RTT).

The ASTM procedure gives details about the configuration of an Autoignition Temperature Apparatus (ATA) as shown in Figure 2. We have built our own version of this apparatus using a cylindrical furnace heated by a 2000 W ceramic heater and a forced convection air flow around the flask. An external computer was used for furnace control

and data acquisition purposes. The reader is invited to consult the ASTM text for a complete description of the apparatus. Each test was recorded on a digital camera for cross-analysing the temperature trace with a visual observation of the flask. The correctness of the experimental set-up was first evaluated by investigating the autoignition behaviour of cyclohexane, a chemical for which AIT data were available in the literature. In this study, four different sample sizes were used in to order to vary the fuel-air ratio in the flask. Once the ATA data proved to be reliable, the AIT, CIT and RTT values of JP-10 were obtained using samples of 100 µl and 200 µl and finally, the ignition of fuel-air mixtures of JP-10/0.1% w/w 2-EHN was investigated.

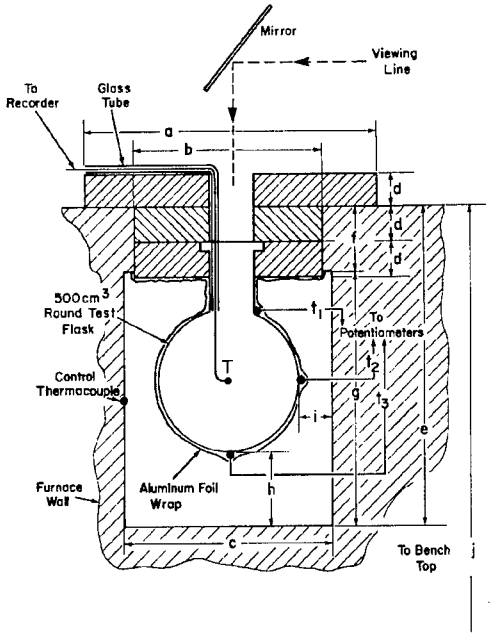


Figure 2: Schematic of the Autoignition apparatus

Results

The first part of this work was devoted to evaluating our ATA by experimentally determining the AIT of cyclohexane in order to compare it with published data. The autoignition behaviour of this liquid chemical has been extensively studied by Snee and Griffiths (1989) because of the need to assess potential spontaneous ignition hazards associated with the batch chemical processes used in the resin manufacturing industry. The stoichiometry for complete combustion of cyclohexane in air corresponds to:

$$c\text{-}C_6H_{12} + 9\ O_2 + 36\ N_2 \text{ --> } 6\ CO_2 + 6\ H_2O + 36\ N_2$$

Figure 3 presents the results of several ignition tests conducted over a temperature range of about 20 °C. Only tests with positive identification of an ignition event are shown. Four different sample sizes were used: 70, 100, 150, and 200 µl. Usually, increasing the sample size will reduce the observe ignition temperature, up to a point where changes in the fuel-air ratio into the flask will have no effect. The injected volumes of cyclohexane produced fuel-rich mixtures with oxygen/fuel ratios ranging from 2.7 to 0.85 to 1.0. This is well below the stoichiometric value of 9:1. For each of the runs, a fairly large temperature increase (60-80 °C) in the flask (0.5 dm^3) was observed together with bright yellow and orange flames. These ignitions were all identified as hot-flame events even if the temperature rise was less than 100 °C. We attributed the lower than expected temperature raise to the fact that the inside thermocouple was larger than the suggested gage size of the ASTM procedure (18 awg instead of 36 awg) and to the timescale of the event compare to the data acquisition frequency. Here, the analysis of Figure 3 shows that data obtained at 70 µl are clear outliers of the remaining points. Accordingly, we concluded that beyond 100 µl, the sample size has no effect on the ignition behaviour and all data collected at 100, 150, and 200 µl were used together to estimate the AIT.

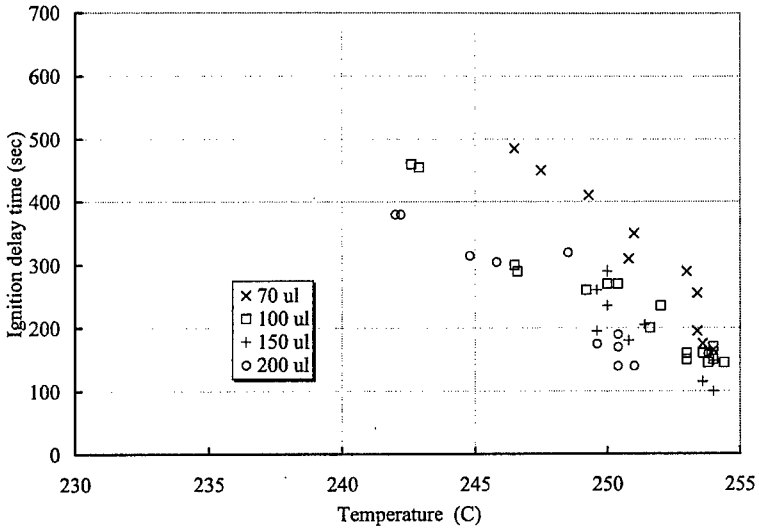


Figure 3: Autoignition time for cyclohexane

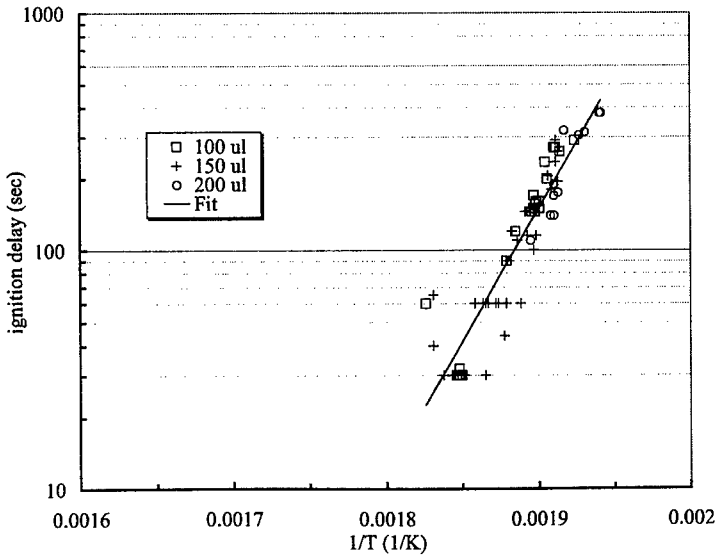


Figure 4: Energy of activation for cyclohexane ignition

The energy of activation for the ignition process can be determined by a plot of the ignition delay versus the reciprocal of the ignition temperature, as shown on Figure 4. While fairly high data dispersion is observed, a linear trend is found by the following relations:

$$\tau = Ae^{(\frac{E}{RT})}$$

$$\ln \tau = \ln A + \frac{E}{RT}$$

The straight line fitted to data does not extend up to the 600 secs limit in the ignition delay. An AIT value of 240 °C and an activation energy of 212 kJ mol^{-1} are found. The published values for cyclohexane are 245, 259 and 270 °C (Colossman (1987), Mullins (1955)), with no mention of the type of ignition observed (RTT, CIT, or AIT). Accordingly, the AIT determined within our apparatus appears to be somewhat lower than other reported data but not unrealistic considering that the AIT is volume dependent and that our tests were conducted in a 0.5 dm^3 flask rather than the 0.2 dm^3 vessel of many published data. The calculated energy of activation is within the range reported by Snee and Griffiths (1989) which goes from 216 to 160 kJ mol^{-1} in vessels of 0.2 to 5.0 dm^3 in size. Globally, these results confirm that our autoignition apparatus behaves within the expected capabilities required by the ASTM E 659-78.

The tests conducted on JP10 and 2-EHN doped JP-10 are shown on Figure 5. Unlike experiments done on cyclohexane, RTT, CIT and AIT were all observed but, generally speaking, not during a same run. As depicted from the graph, the CIT was the most frequent ignition event, mainly because of the temperature range selected for the runs. The effect of 2-EHN on the auto-ignition characteristics is easily observable even though the data are significantly dispersed along the ignition delay direction, particularly for the CIT events. One important observation is that very few tests reported the CIT and AIT process consecutively. The AIT event with hot flames generally occurred only for high

temperature experiments with very short autoignition delays. In spite of this dispersion in the data points, it is found by two fitted straight lines, running parallel, that the pure and the modified jet fuel have about the same energy of activation for their ignition characteristics, respectively at 180 kJ/mol and 195 kJ/mol. The line fitted to JP-10-EHN data being below the JP-10 regression line, it is concluded that adding 2-EHN to JP10 reduces the ignition delay by a factor of 2. However, the net impact of this additive on the respective ignition temperatures is more difficult to evaluate. Our results show that JP-10 and JP-10-2-EHN samples had respectively an AIT of 262 °C and 253 °C. However, for both compositions, CIT and RTT were determined at 248 °C and 227 °C respectively, unchanged by the presence of 2-EHN. This compares well to the reported value of 245 °C (CRC report 1986) for pure JP-10.

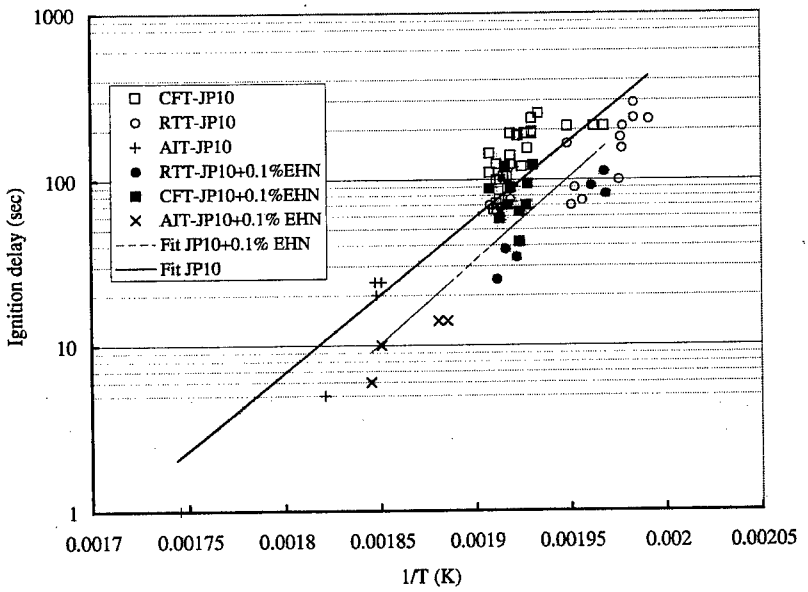


Figure 5: Autoignition of JP-10 fuels

The analysis of data gathered for JP10 shows the frequent occurrence of the cool flame process in the autoignition of this fuel, something that was not observed during the cyclohexane testing program. Recently, Romano *et al* (2001) reported the cool flame reaction as a means of sensitising a hydrocarbon-oxygen mixture to DDT from their observations of the pentane-oxygen mixtures. Because JP-10 seems to pass by this process most of the time before the hot-flame autoignition, this opens an opportunity to investigate how this cool flame reaction can be tailored to enhance the detonation properties of the fuel. In the case of our work, we have shown that addition of 2-EHN cut in half the ignition delay for cool flame ignition. In their work on chemical sensitisation, Higgins *et al* (2000) found that the addition of an amount of 0.025% 2-EHN to a propane-air mixture reduces the run up distance to DDT. Hence, this correlates well with the observed effect of 2-EHN on the autoignition behaviour of exo-tetrahydrodicyclopentadiene.

Conclusion

The aim of this exploratory work was to assess if a chemical additive modifying the detonation properties of a fuel can also be a modifying agent for the autoignition temperature. The experiments conducted confirmed that 2-EHN, known to decrease the tube length for transition to detonation in detonation cell experiments also produces a reduction of the autoignition temperature. Even though the cool flame ignition temperature and reaction threshold temperature were unaffected by the additive, the time required to achieve ignition decreased. When 2-ethyl-hexyl nitrate was used as an additive to the JP10 fuel, the ignition process was governed by the same energy of activation as the pure JP10 component, but with a lower pre-exponential factor, which translates by reducing by a factor of two the ignition delay time.

References

1-Handbook of Aviation Fuel Properties, Coordinating Research Council CRC Report No 530, 1986.

2- I. Colossman, Combustion , 2nd ed, Academic Press, 1987.

3- B. P. Mullins, Spontaneous Ignition of Liquid Fuels, Butterworths, London, 1955.

4-"Standard Test Method for Autoignition Temperature of Liquid Chemicals", ASTM E 659 – 78 (Reapproved 1994) American Society for Testing and Materials, Reprinted from the Annual Book of ASTM Standards.

5- T. J. Snee and J. F. Griffiths, "Criteria for Spontaneous Ignition in Exothermic, Autocatalytic Reactions: Chain Branching and Self-Heating in the Oxidation of Cyclohexane in Closed Vessels", Combustion and Flame, **75**, p381-395

6- J. Odgers and D. Kretschmer, Gas Turbine Fuels and Their Influence on Combustion, Abacus Press, Cambridge, USA, 1986.

7- M. P. Romano, A. J. Higgins, J. H. S. Lee and S. B. Murray, "Sensitization of Hydrocarbon-Oxygen Mixtures to DDT via Cool Flame Oxidation", Proceedings of the Combustion Institute/Canadian Section Spring Technical Meeting, May 2001, Montreal, Canada.

8- A. J. Higgins and J. H. S. Lee, "Internal reporting-Canadian Pulse Detonation Engine Program", McGill University, Canada, 2000.

EINFLUß DER GRÖßE VON METALLPARTIKELN AUF DIE ANZÜNDUNG UND VERBRENNUNG VON ENERGETISCHEN MATERIALIEN

Volker Weiser, Norbert Eisenreich, Stefan Kelzenberg
Fraunhofer-Institut für Chemische Technologie (ICT), Pfinztal, Germany
vw@ict.fhg.de

Zusammenfassung
Eine theoretische Studie zur Partikelanzündung nutzt ein Hot-Spot Model, das die Temperaturentwicklungen einzelner Hot-Spots in einem energetischen Material berechnet. Die Rechnungen ergeben eine besonders effektive Anzündung, wenn eine Vielzahl heißer Feinstpartikel auf einen Festtreibstoff trifft und eindringt. Es wurden Anzündmischungen mit Nanopartikeln aus Titan hergestellt. Sie reagieren schneller als Standartmischungen von B/KNO_3 und Schwarzpulver. Allerdings scheinen die feinen Titanpartikel oxidiert und verdampft zu werden noch bevor sie die Oberfläche des Energetischen Materials erreichen, so daß im Vergleich zu Mischungen mit gröberen Ti-Partikeln die Anzündverzugszeit größer ist. Eine optimierte Mischung aus groben und feinen Partikeln könnte eine Verkürzung der Anzündverzugszeit ergeben.
Eine vorläufige Studie mit Nano-Partikeln aus Aluminium ergab einen stark abbrandbeschleunigenden Effekt.

Abstract
INFLUENCE OF THE METAL PARTICLE SIZE ON IGNITION AND COMBUSTION OF ENERGETIC MATERIALS
A theoretical study of multi-particle ignition uses a hot spot model which calculates the temperature evolution of individual hotspots in an energetic material. It indicates that ultra-fine hot particles would be very effective in igniting energetic materials if impinging and penetrating the solid propellant. Igniting mixtures were prepared containing ultra-fine Ti particles which react fastest comparable to coarse particle mixtures, standard B/KNO_3 and black powder. The ultra-fine particles, however, are obviously oxidised or vaporised too fast for reaching the energetic material to be initiated and longer ignition delays are found comparable to coarse particle mixtures. An optimised mixture of coarse and ultra-fine particles could give an improvement of ignition delay times. A preliminary study on the effect of ultra-fine Al particles in the combustion of a model composite shows strongly increased burning rates.

1 Einleitung

Langjährige Erfahrungen bei der Anzündung von Treibladungspulvern und Raketenfesttreibstoffen zeigen, dass Anzündmischungen neben heißen Gasenschwaden auch heiße Partikel erzeugen sollten [1, 28,29]. Die Gasschwaden erzeugen einen Vordruck über dem Treibstoffkorn [2-10]. Dies begünstigt den konduktiven und konvektiven Wärmetransport und stabilisiert die Gasphasenreaktion. Die heißen Partikel sollen die Anzündenergie effektiv auf den Treibstoff übertragen. Versuche die Anzündung zu beschreiben basieren meist auf der Lösung der Wärmetransportgleichung in einem reagierendem Feststoff [11,12]. Dabei wird der Energieeintrag des Anzünders als zeitlich veränderlicher Wärmefluß angenommen. Er simuliert den Kontakt der heißen Gase [20,24],

der Strahlung [13] und das Auftreffen von Partikeln [14]. Die theoretische Beschreibung der Anzündung durch eine unterschiedliche Anzahl einzelner Partikel ist schwieriger. Der Einsatz eines gemittelten Energieübertrags auf oder nahe der Oberfläche ist eine Möglichkeit. Sie kann aber nicht zwischen einzelnen Partikeln unterscheiden und deren Charakteristika berücksichtigen. Dagegen ist ein Hot-Spot-Modell in der Lage die Größe der Partikel, deren Energieeintrag und deren zufällig verteilte Eindringtiefe in den Treibstoff zu berücksichtigen [15-17].
Dieser Artikel untersucht qualitativ die Partikelanzündung durch ein Hot-Spot-Modell in der festen Phase eines energetischen Materials. Daneben werden praktische Versuche mit Anzündmischungen unterschiedlich großer Metallpartikel im Nano- und Mikromaßstab beschrieben. Untersucht wurde der auf einen Kupferblock auftreffende Schwadenstrahl und der zeitliche Druckaufbau in einer Minibombe. Daneben wurden Hochgeschwindigkeitskameras, Pyrometer und Spektrometer eingesetzt.

2 Beschreibung der Partikelanzündung mit einem Hot-Spot-Modell

Eine vereinfachte Beschreibung der grundlegenden Phenomäne bei der Anzündung fester Treibstoffe nutzt die Wärmeleitungsgleichung im Feststoff mit einem Wärmefluß Q[x,t] aus einer externen Quelle. Der wichtige Parameter der Anzündverzugszeit wird durch die Zeit der Oberflächenaufheizung auf Pyrolyse- oder Vergasungstemperatur dominiert. Der Effekt eindringender, heißer Partikel, der wesentlich zur Anzündung beiträgt, ist schwieriger zu berücksichtigen. Im folgenden wird ein 3D-Modell beschrieben, das reagierende Hot-Spots und der Wärmequelle einer vereinfachten chemischen Reaktion $q_i\, \partial c/\partial t$ [2-6] nutzt.

$$\rho c_p \frac{\partial T}{\partial t} - \lambda \cdot \Delta T = \dot{Q}[\vec{x}, t] + \sum_i q_i \frac{\partial c_i}{\partial t}$$

(ρ - Dichte, λ - Wärmeleitfähigkeit, q_i - Enthalpie der i-th Reaktion, c_i – Konzentration der Komponenten i, c_p – spezifische Wärmekapazität).

Zur Lösung der Differentialgleichung wird eine Greensche Funktion benutzt. Dabei wird die Temperaturabhängigkeit der physikalischen und chemischen Konstanten vernachlässigt:

$$T[\vec{x}, t] = \int_0^{\tau} \int_{-\infty}^{\infty} \left(\frac{\rho c_p}{4\pi\lambda(t - t')} \right)^{3/2} \cdot e^{\frac{\rho c_p (\vec{x} - \vec{x}')^2}{4\lambda(t - t')}} \cdot \frac{\dot{Q}[\vec{x}', t']}{\rho c_p} d^3x' dt'$$

Die heißen Anzündpartikel werden als Wärmequellen an willkürlichen Stellen des energetischen Material eingeführt [16,17] und durch dirac'sche Delta- oder Gaussfunktionen beschrieben:

$$\dot{Q}[\vec{x}', t'] = \sum_i Q_i \cdot \delta[\vec{x}' - \vec{x}_i] \cdot \delta[t' - t_i]$$

In diesem Fall berechnet sich die Lösung zu:

$$T_{hs}[\vec{x}, t] = \sum_i \left(\frac{\rho c_p}{4\pi\lambda(t - t_i)} \right)^{3/2} \cdot \frac{Q_i \cdot e^{\frac{\rho c_p (\vec{x} - \vec{x}_i)^2}{4\lambda(t - t_i)}}}{\rho c_p}$$

Im Falle einer chemischen Reaktion vom Arrheniustyp im Feststoff gilt:

$$\frac{\partial c_i}{\partial t} = -\sum_j A_{i,j} \cdot e^{\frac{E_{i,j}}{RT}} f[c_i, c_j]$$

($A_{i,j}$ – Vorfaktor der Reaktion, $E_{i,j}$ –Aktivierungsenergie).

Eingesetzt als Wärmequelle ergeben sich Integrale, die nur noch numerisch lösbar sind. Dazu wird die zeitliche Entwicklung in viele kleine Zeitschritte zerlegt und für jeden Zeitschritt die räumliche Temperaturverteilung errechnet.

$$T_0(\vec{x},0) \Rightarrow Q_0(\vec{x})\delta(t)$$

$$T_1(\vec{x},t_1) = \int_{-\infty}^{\infty} \frac{e^{\frac{(\vec{x}-\vec{x}')^2}{4\Delta t_1}}}{\sqrt{4\pi\Delta t_1}} \left(Q_0(\vec{x}') + \Delta t_1 \sum_i q_i \frac{\partial c_i\left(T_0(\vec{x}',0)\right)}{\partial t} \right) d\vec{x}'$$

$$T_{n-1}(\vec{x},0) + \sum Q_{i,j,k} \Rightarrow Q_{n-1}(\vec{x})\delta(t)$$

$$T_n(\vec{x},t_n) = \int_{-\infty}^{\infty} \frac{e^{\frac{(\vec{x}-\vec{x}')^2}{4\Delta t_n}}}{\sqrt{4\pi\Delta t_n}} \left(Q_{n-1}(\vec{x}') + \Delta t_n \sum_i q_i \frac{\partial c_i\left(T_{n-1}(\vec{x}',t_{n-1})\right)}{\partial t} \right) d\vec{x}' \qquad (2)$$

Die chemische Reaktion endet mit dem vollständigen Umsatz des energetischen Materials. Abbildung 1 zeigt die Temperaturverteilung in einem energetischen Material ausgehend von einzelnen, anfänglich generierten Hot-Spots und der sich daraus entwickelnden Reaktionsfront. Sie entwickelt sich in einigem Abstand von den anfänglichen Hot-Spots zu einer mehr oder weniger ebenen Reaktionsfront. Der Anzündeffekt wie z.B. der Druckanstieg in einem geschlossenen Volumen, kann durch die Integration des bereits durchreagierten Volumens charakterisiert werden. Abbildung 2 zeigt die Entwicklung des Druckanstiegs oder der entsprechenden Umsetzung. Dargestellt ist die Anzündung durch viele kleine und wenige große Partikel mit jeweils dem gleichen Gesamtenergieeintrag. Für das energetische Material wurden die chemischen und physikalischen Daten von Nitrocellulose eingesetzt. Bei feinen Partikeln wird schneller eine stabile Reaktionsfront und dadurch ein früherer konstanter Druckanstieg beobachtet, als bei größeren Partikeln. Die Druckabhängigkeit des Umsatzes wurde dabei vernachlässigt.

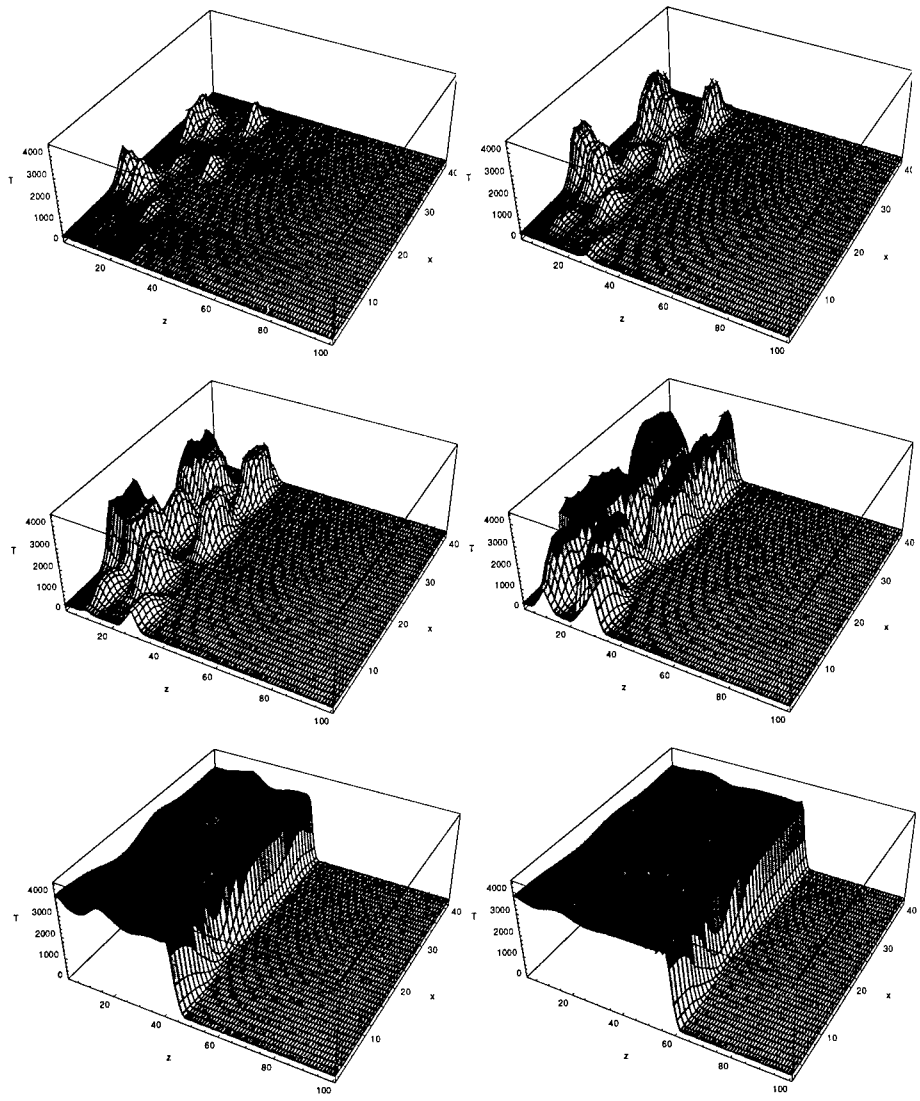


Abbildung 1 Temperaturverteilung in einer x-z-Ebene berechnet mit dem 3D-Hot-Spot-Modell mit aufeinanderfolgenden Zeitschritten.

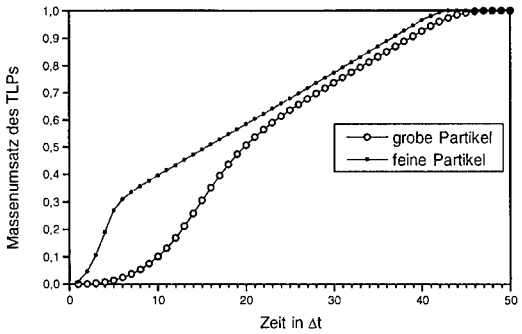


Abbildung 2 Qualitative Beschreibung der Umsetzung eines energetischen Materials bei der Anzündung mit wenig groben Partikeln (große Punkte) und vielen Feinstpartikeln (kleine Punkte)

3 Experimente mit Anzündmischungen unterschiedlich großer Titan Partikel

Die praktische Konsequenz dieser Ergebnisse könnte der Einsatz kleiner Nanopartikel für die Anzündung eines festen energetischen Materials sein. Effektive Metallkomponenten für Anzünder sind Bor, Titan oder Zirkonium. Abbildung 3 zeigt eine Rasterelektronenmikroskopaufnahme ultrafeiner Ti-Partikel. Ihre Größenverteilung liegt zwischen 0.1 und 10 µm.
Zur Untersuchung des Größeneinflusses der Metallpartikel auf die Anzündung wurden verschiedene pyrotechnische Mischungen hergestellt. Dazu wurden jeweils feines oder gröberes Titan mit KNO_3 und GAP kombiniert (40% Ti; 45% KNO_3; 15% GAP/N100). Die Proben wurden wurden mit B/KNO_3 und Schwarzpulver (SP) verglichen.

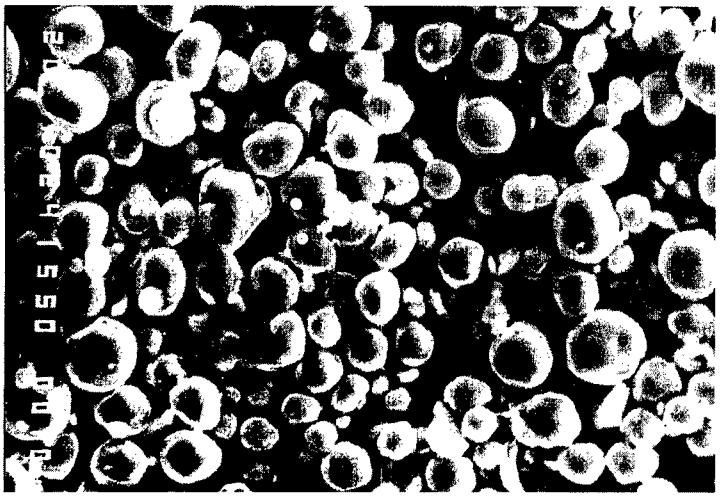
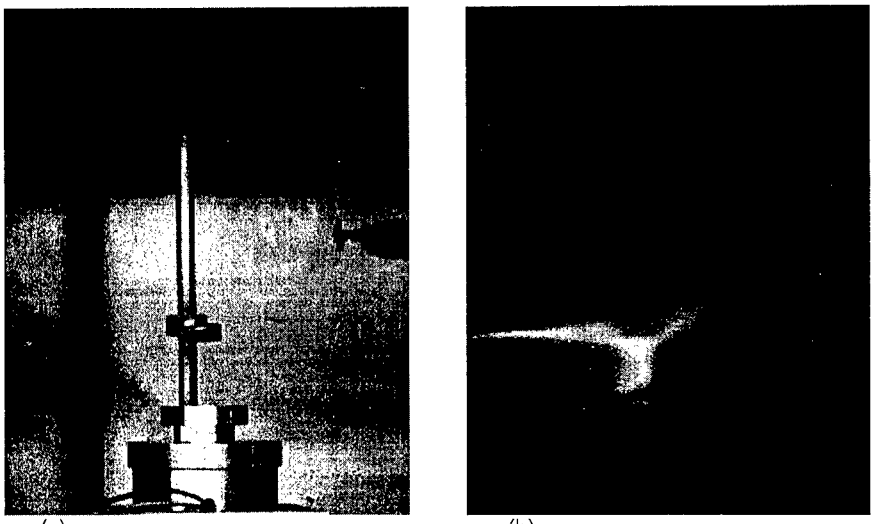
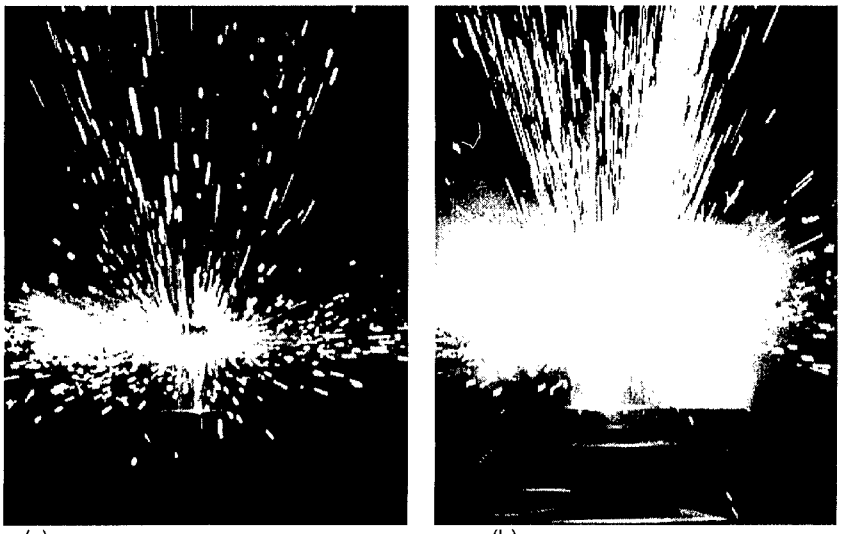


Abbildung 3 REM-Bilder von ultrafeinen Titanpartikeln 100 bis 10000 nm.



(a) (b)

Abbildung 4 (a) Versuchsaufbau zur Untersuchung der Anzündstrahlen der Anzündmischungen, (b) anfänglicher Gasschwadenstrahl



(a) (b)

Abbildung 5 (a) Schwadenstrahl der Anzündmischungen mit Feinsttitan und (b) gröberen Partikeln

500 mg dieser pyrotechnischen Mischungen wurden in ein Bombenvolumen von 2 cm^3 eingefüllt und elektrisch gezündet. Der Auswurf der Reaktionsprodukte aus diesem Hohlraum durch eine Öffnung von 2 mm Druchmesser wurde mit einer Videokamera (50 Bilder/s) und einem 2-Farbenpyrometer mit einer Abtastrate bis 1 MHz untersucht.

Anfänglich ist die Öffnung mit einer 0.5 mm starken Aluminiumfolie verschlossen. Die Einzelbilder der Videoaufnahmen zeigen mehr hellstrahlende Partikelspuren der pyrotechnischen Mischungen mit groben Ti-Partikeln.

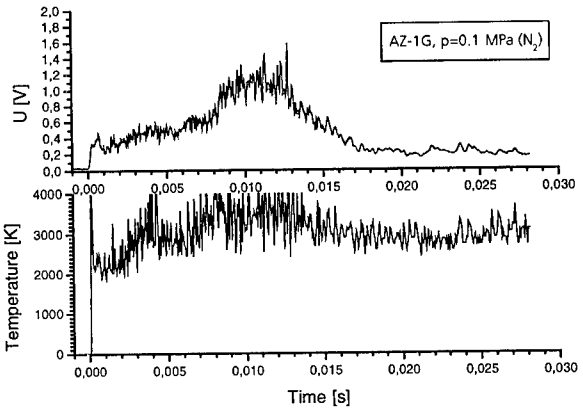


Abbildung 6 Temperaturentwicklung im Anzündstrahl mit groben Ti-Partikeln; gemessen mit einem 2-Farbenpyrometer

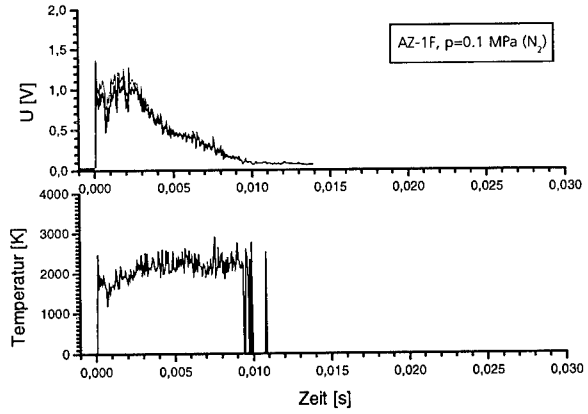


Abbildung 7 Temperaturentwicklung im Anzündstrahl mit groben Ti-Partikeln; gemessen mit einem 2-Farbenpyrometer

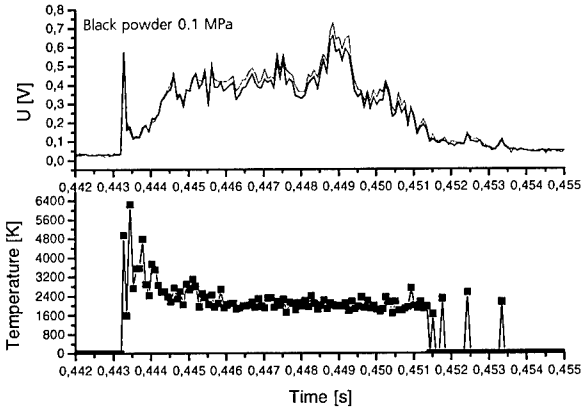


Abbildung 8 Temperaturentwicklung im Anzündstrahls von Schwarzpulver; gemessen mit einem 2-Farbenpyrometer

Die vom 2-Farbenpyrometer aufgenommenen Signale sind in den Abbildung 6 bis 9 dargestellt. Es werden die Spannungen der Ge/Si-Sandwichdiode und der daraus ermittelte zeitliche Temperaturverlauf gezeigt. Sie bestätigen die insgesamt niedrigere Lichtabgabe. Jedoch weisen die Ergebnisse darauf hin, daß die Anzündmischungen mit Feinsttitan schneller ausströmen als die der anderen Proben. Die Reaktion startet früher und ist schneller abgeschlossen. Die Pyrometertemperaturen liegen zwischen 2000 und 3000 K. Wie Emissionsspektren der Anzündstrahlen im UV/Vis-Bereich zeigen wird die graue Kontinuumsstrahlung der Partikel von der Strahlung gasförmiger Verbrennungsprodukte beeinflußt [1,33]. Besonders Kaliumdampf (770 nm), Oxide und Verunreinigungen von Natrium (589 nm) absorbieren stark die Kontinuumsstrahlung der heißen Partikel [31]. Als Beispiel ist in Abbildung 10 ein Vis/NIR-Spektrum aus dem Anzündstrahl der Mischung mit Feinsttitan wiedergegeben. So müssen die Pyrometertemperaturen von Anzündmischungen grundsätzlich als vornehmlich qualitative Informationen zur Größenordnung interpretiert werden.

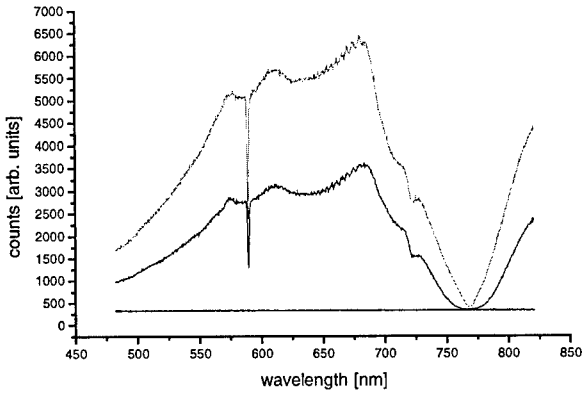


Abbildung 10 Vis/NIR-Spektrum aus dem Anzündstrahl der Mischung mit Feinsttitan. Die Kalium- und Natrium-Linie sind über die gesamte Strahlungsdauer sehr intensiv.

Die Anzündmischungen wurden auch in einer Bombe mit 2 durch Düsen (∅ 1mm) verbundenen Kammern (Anzündkammer 1 ml, TLP-Kammer 30 ml) untersucht. Gemessen wurde der Druckaufbau der reinen Anzündmischungen (350 mg) und gemeinsam mit Treibladungspulver (3 g). Abbildung 12 zeigt die Bombe mit räumlich getrennten Reaktionskammern für die Anzündmischung und das Treibladungspulver. Die Druck-Zeit-Kurven sind in Abbildung 13 und 11 dargestellt. Die Anzündmischung mit Feinstpartikeln reagiert am schnellsten. Die Reaktion startet früher nach etwa 0.8 ms mit einem steilerem Druckanstieg von 7200 MPa/s und ist nach 0.25 ms großteils abgeschlossen (Abbildung 13). Dies ist in guter qualitativer Übereinstimmung mit den oben beschriebenen Pyrometerergebnissen. Jedoch arbeitet die Anzündung mit gröberen Partikeln effektiver. Beim Abbrand der Treibladungspulver wird das Maximum der Druck-Zeit-Kurven bei Einwirkung der Anzündungmischung mit den Feinstpartikeln später erreicht als bei den Anzündmischungen mit gröberem Titan (Abbildung 14). Dabei wurden 4 Treibladungspulver untersucht (JA2, ein Semi-Nitraminpulver, NENA-Pulver, GAP-pulver). Bei allen Pulvern zündet die Mischung mit Feinsttitan langsamer an. Anscheinend sind die feinen Metallpartikel schon oxidiert und verdampft bevor sie auf die Treibstoffoberfläche auftreffen. Dies zeigen auch REM-Aufnahmen der mit den Anzündstrahlen beschossenen Kupferblöcke.
Aus diesen Untersuchungen folgt der Vorschlag bimodale Metallpartikelverteilungen mit einer definierten Feinst- und Grobfraktion einzusetzen, um den Effekt der schnelleren Reaktion bei gleichzeitig guter Anzündung durch heiße Partikel zu kombinieren.

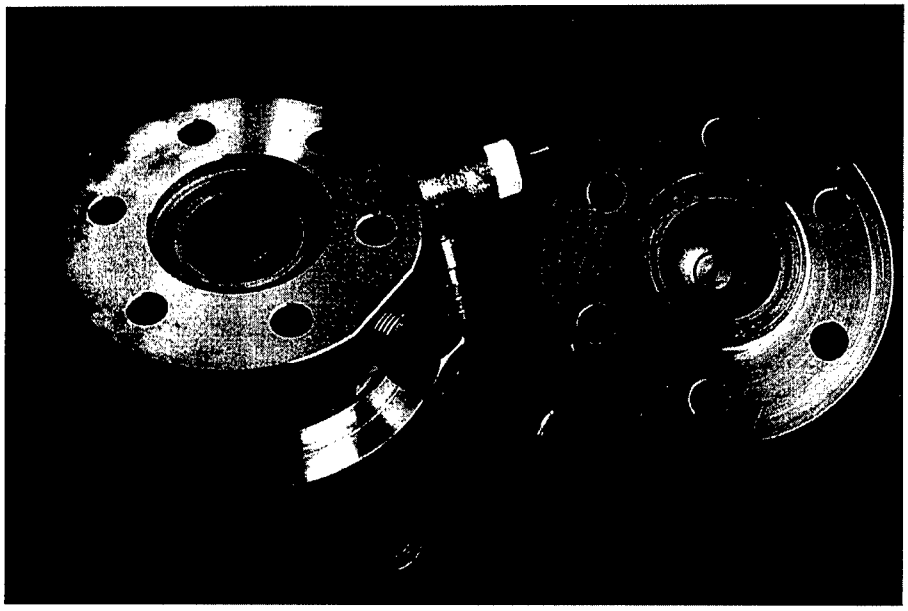


Abbildung 12 Minibombe zur Untersuchung der Anzündphenomäne von Festtreibstoffen

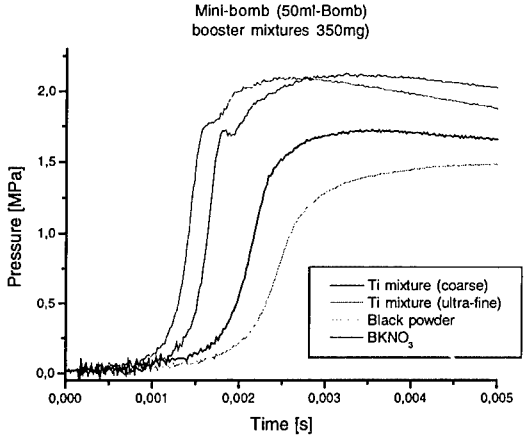


Abbildung 13 Druck-Zeit-Kurven beim Umsatz der Anzündmischungen mit groben und feinen Ti-Partikeln im Vergleich zu B/KNO_3 und Schwarzpulver.

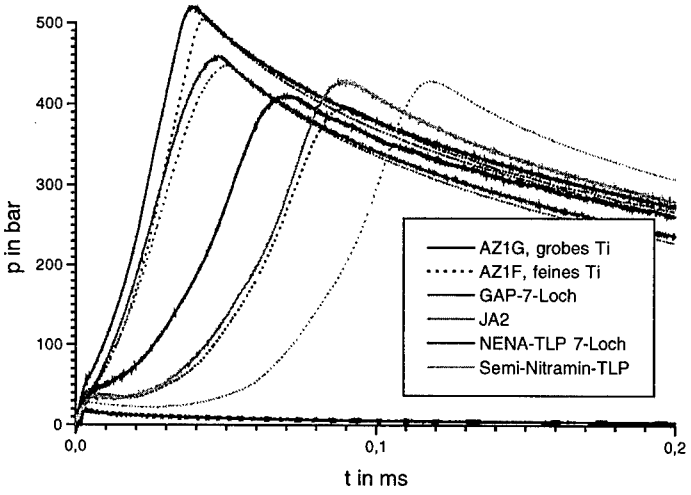


Abbildung 14 Druck-Zeit-Kurven bei der Anzündung verschiedener Treibladungspulver durch Anzündmischungen mit grobem oder feinstem Titan.

4 Abbrand eines Komposittreibstoffes mit Nano-Aluminium

Zur Untersuchung des Einflußes von ultrafeinem Aluminum auf den Abbrand eines Komposittreibstoffs wurden zwei Testtreibstoffe formuliert. Die Zusammensetzung war:

- 75% AP
- 8% Al
- 12% HTPB
- 5% DOA

Die Testtreibstoffe unterschieden sich in der Partikelgröße des Aluminiums:

- HTPB 1090: Al / ALEX
- HTPB 1091: Al / 5 µm

Die Abbrandraten der Testtreibstoffe wurden in einer Crawfordbombe gemessen. Abbildung 15 zeigt Aufnahmen der Testtreibstoffe von Strands gleicher Querschnitte beim Abbrand in einer Optischen Bombe und Abbildung 16 die Ergebnisse der Abbrandratenmessung. Die Mischungen mit ALEX haben eine um über 40% höhere Abbrandrate. Allerdings weisen sie mit 0.56 gebenüber 0.49 auch einen etwas höheren Druckexponten auf. Die gesteigerte Abbrandrate könnte durch die bei den Anzündmitteln beobachtete schnellere Oxidation und Verdampfung der Feinstpartikel nahe der Feststoffoberfläche erklärt werden. Sie führt zu einem steileren Temperaturprofil in der Gasphase und damit einem höheren Wärmeübertrag auf den Treibstoff. Dieser Effekt und auch der Einfluß auf den Druckexponenten soll allerdings noch genauer untersucht werden.



(a) (b)

Abbildung 15 Abbrand eines Komposittreibstoffes mit groben Al-Partikeln (a) und ALEX (b) bei 4 MPa in einer Optischen Bombe.

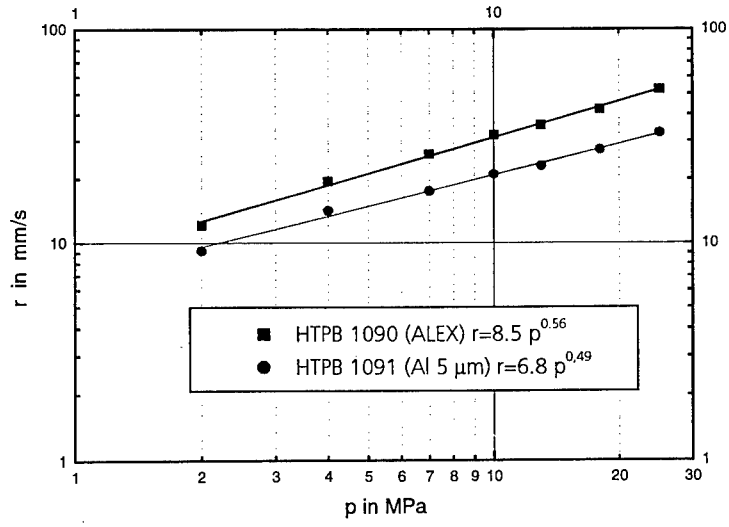


Abbildung 16 Abbrandraten der Testtreibstoffe gemessen in einer Crawfordbombe

5 Literatur

(1) Weiser, V.; Koleczko, A.; Kelzenberg, St.; Eisenreich, N; Müller, D.; Ti-Nanopartikel zur Anzündung von Rohrwaffentreibmitteln; 31th International Annual Conference of ICT, June 27-30, 2000, Karlsruhe, pp. 146-(1-7)

(2) B. N. Kondrikov, T. Ohlemiller, M. Summerfield, "Ignition and gasification of double-base propellant induced by CO_2-laser irradiation", Problems of Theory of High Explosive 83, 67-78 (1974).

(3) C. Zanotti and P. Giuliani, "Composite propellant Ignition and extinction by CO_2 laser at subatmospheric pressure", Propellants, Explosives, Pyrotechnics 23, 254-259 (1998).

(4) B.V. Novozhilov, "Nonsteady Burning and Combustion Stability of Solid Propellants", AIAA Progress in Astronautics and Aeronautics, Vol 143, Washington 1992, pp. 601-641.

(5) A. Zenin, "Nonsteady Burning and Combustion Stability of Solid Propellants", AIAA Progress in Astronautics and Aeronautics, Vol. 143, Washington 1992, pp. 197-231.

(6) C. Zanotti, and Al., "Nonsteady Burning and Combustion Stability of Solid Propellants", AIAA Progress in Astronautics and Aeronautics, Vol 143, Washington 1992, pp. 399-439.

(7) C. Zanotti and Al., "Nonsteady Burning and Combustion Stability of Solid Propellants", AIAA Progress in Astronautics and Aeronautics, Vol 143, Washington 1992, pp.145-196.

(8) Carslaw, H.S. and Jaeger,J.C.; Conduction of Heat in Solids, 2. Edition, Oxford University Press, London 1973.

(9) Frank-Kamenetskii D.A.; Diffusion and Heat Exchange in Chemical Kinetics; Princeton University Press, Princeton 1955.

(10) Warnatz, J.; Maas, U.;Technische Verbrennung; Springer, Berlin 1993.

(11) N. Eisenreich, "*Vergleich theoretischer und experimenteller Untersuchungen über die Anfangstemperaturabhängigkeit von Festtreibstoffen*", ICT-Bericht 8/77, Fraunhofer-Institut für Chemische Technologie (ICT), Pfinztal, Germany, (1977).

(12) W. Eckl, S. Kelzenberg, V. Weiser, and N. Eisenreich, "Einfache Modelle der Anzündung von Festreibstoffen", *29th Int. Annual Conference of ICT*, Karlsruhe, Germany, June 30 – July 3, 1998, 154.1-20.

(13) N. Eisenreich, W. Ehrhard, S. Kelzenberg, A. Koleczko, and H. Schmid, "Strahlungsbeeinflussung der Anzündung und Verbrennung von festen Treibstoffen", *31st Int. Annual Conference of ICT*, Karlsruhe, Germany, June 27-30, 2000, 139.1-19.

(14) N. Eisenreich, A. Pfeil, "Pyrolysis Craters Produced by Laser Pulse Irradiation on Propellant Solids", *Appl. Phys. 15*, 47 (1978).

(15) N. Eisenreich, "Successively Initiated Arrays of Hot Spot in a Reactive Medium", in: BMVg-FBWT 98-1, FIZBw, Bonn,(1998), 69; *Proceedings: Physics of Explosives*, Berchtesgaden, September 29-October 1, 1997

(16) G. Langer, N. Eisenreich, "Entwicklung von Hotspots in energetischen Materialien", *29th International Annual Conference of ICT*, Karlsruhe, Germany, June 30-July 3, 1998, 157.1-9.

(17) G. Langer, N. Eisenreich, "Hot Spots in Energetic Materials", *Propellants, Explosives, Pyrotechnics 24*, 113-118 (1999).

(18) N. Eisenreich and A. Pfeil, "Thermal Analysis of Doublebase Propellants by Pressure DSC" In: D. Dollimore (Ed.), *Proceedings of the 1st Europ. Symp. on Thermal Analysis,* London, Heyden, 1976, pp. 452-454.

(19) N. Eisenreich, A. Pfeil, "The Influence of Copper and Lead Compounds on the Thermal Decomposition of Nitrocellulose in Solid Propellants", *Thermochim. Acta 27*, 339-346 (1978).

(20) N. Eisenreich, V. Weiser; Phenomena of Energy Transport in Pool Fires; 1st Internet Conference on Process Safety, 27.-29. January 1998, Hamm, Germany

(21) Zarko, V.E.; Gusachenko, L.K. and Rychkov, A.D.;Simulation of Combustion of Melting Energetic Materials; Defence Science Journal; 46 No.5, pp425-433, 1996.

(22) Gusachenko, L.K.; Zarko, V.E. and Rychkov, A.D.;Modeling of Gasification of Evaporated Energetic Materials under Irradiation; INTAS Workshop, Milan, July 1996.

(23) Gusachenko, L.K.; Zarko, V.E. and Rychkov, A.D.;Instability of a Combustion Model with Evaporation on a Surface and Overheat in the Condensed Phase; Combustion, Explosion and Shock Waves, 33 No.1, 1997.

(24) Eisenreich N.; Theoretische Untersuchungen über den Abbrand von Festtreibstoffen ICT-Bericht 5/76

(25) DeLuca L. Pagani C.D., Verri M.; A Review of Solid Rocket Propellant Combustion, ISTS paper No 94-a-30v, Int. Symp. Space Techn. Sci. Yokohama, Japan 15-24 may 1994

(26) G.V. Ivanov, F. Tepper; Activated Aluminium as a Stored Energy Source for Propellants, In: Challanges in Propellants and Combustion 100 Years after Nobel, ed.: K.K. Kuo et al. Begell House, 1997, pp 636-645

(27) V. N. Simonenko, V.E. Zarko; Comparative Studying the Combustion Behavior of Composite Propellants Containing Ultra Fine Aluminium, In: Energetic Materials 30th Int. Annual Conf. of ICT, Karlsruhe, Germany, p 21.1

(28) 8. Symposium Innenballistische Leistungssteigerung von Rohrwaffen (BAL 21); Swisttal - Heimerzheim 1982

(29) Rochat, E.; Berger, B.; Unempfindliche Anzündmittel für moderne Treibladungspulver; 30th International Annual Conference of ICT, 1999, Energetic Materials; Karlsruhe, pp. 24-1 - 75-15

(30) V. Weiser, D. Kuhn, R. Ludwig, H. Poth; Einfluß der Partikelgröße auf das Abbrandverhalten von B/KNO_3-Anzündmischungen; 29th International Annual Conference of ICT, 1998, Energetic Materials; Karlsruhe, pp. 75-1 - 75-12

(31) Baier, A.; Weiser, V.; Eisenreich, N.; Halbrock, A.; IR-Emissionsspektroskopie bei Verbrennungsvorgängen von Treibstoffen und Anzündmitteln; 27th International Annual Conference of ICT, 1996, Karlsruhe, pp. 84-(1-12)

(32) Berger, B.; Haas, B.; Reinhard, G.; Einfluss der Korngrösse des Reduktionsmittels auf die Reaktionsparameter pyrotechnischer Systeme; ICT-Jahrestagung 1996; 13-(1-16)

(33) Volker Weiser, Wilhelm Eckl, Evelin Roth, Norbert Eisenreich, Jochen Neutz; High speed methods for temperature measurements in hot gases; 5th International Symposium and Exhibition on Sophisticated Car Occupant Safety Systems – Airbag 2000+; Karlsruhe (Germany), 2000/Dec/4-6; pp. 36-(1-6)

AN INVESTIGATION OF SUBMICRON METAL PARTICLES INFLUENCE ON BURNING RATE OF POROUS COMPOSITE FUELS

A.N. ISCHENKO, Y.P. KHOMENKO, Y.A. BIRYUKOV, A.T. ROSLYAK,
N.M. SAMOROKOVA, N.N. PARFENOV*

Institute of Applied Mathematics and Mechanics of the Tomsk State University
36 Lenin pr., Tomsk, 634050, RUSSIA
*Federative Center of Double Technologies "SOYUZ"
6, Sovetskaya st., Dzerdjinskiy, 140056, RUSSIA

The combustion of composite low-porous model monoblock fuel with aluminium particles is investigated. The results obtained in conditions of a closed bomb, bomb with the nozzle are described, the mathematical model for calculation of monoblock charge combustion is suggested and the data on obtaining submicron metal particles which enter into the structure of fuel are presented

INTRODUCTION

The increase of initial projectile speed in barrel high-speed systems requires increasing the general power of a launching charge. Thus to be within the framework of adopted limitations on maximum pressure (600-700 MPa), it is necessary to supply a progressive regime of fuel combustion accompanied with increase of gas-generation in accordance with increase of working volume in a barrel system.

One from the most perspective directions permitting to decide this complex of problems is the application of high-density monoblock charges with density more than 1 g/cm^3. As the sizes of monoblocks are greater than characteristic burning layer thickness of usual artillery powders, they should burn down with higher rate. It is provided by the availability in monoblocks of a developed porous structure and convective regime of heat transfer inside porous fuel. The porous matrix can be formed technologically on a fabrication stage of a charge, or to arise during combustion because of an inhomogeneous structure, different characteristics of burn-out and deformation of its constituents. The combustion of porous fuel is accompanied by a copious dispersion of condensed phase on separate particles. For good reproducibility of experimental results the individual differences of particles should be very small.

For creation of progressive gas-generation regime various methods can be used: change of porous structure and surface, change of fuel structure on length of the charge, introduction in fuel of ultra dispersible metal particles. The last way is widely applied to change of parameters of combustion of solid rocket fuels /1/, and in artillery charges it has not found yet significant distribution. In the given article the researches of influence of fine aluminium particles (2 - 10 μm) on the gas-generation characteristics in model monoblock fuels are conducted. The results obtained in conditions of a closed bomb, bomb with a nozzle are described, a mathematical model for calculation of monoblock charge combustion is suggested and the data on obtaining submicron metal particles which enter into the structure of fuel are adduced

THE COMBUSTION OF MODEL MONOBLOCK FUEL

The combustion of composite monoblock fuel including in its structure the plasticized nitrocellulose and fast-burning crystalline explosive substance (ES) is investigated. The general view of this structure is presented on Fig.1. Aluminium particles obtained by pneumocirculation technology are shown on the Fig.2. Fig.3 gives a general view of composite fuel with metal particles in it structure. The mass share of particles in experiments did not exceed 5 %, the fuel in the initial state has not a gas-permeable porosity, volumetric share of closed pores, arising at it manufacturing is 3-4%. In combustion of these fuels the two various, pronounced stages are stand out. At first they burn in a slow "level-by-level" regime, which is provided with a molecular heat-transfer mechanism in k-phase. The surface of combustion is not flat, but depths of irregularities does not exceed the characteristic sizes of ES crystals. At reaching of the certain level of pressure (~ 50 MPa) in a near-surface layer of fuel the mass formation of gas-permeable pores begins on account of irregular burn-out of components and disturbance of their adhesive-connections. The leading role passes to a convective regime of the heat transfer connected with the filtration in pores of hot products. The rate of fuel ignition and the combustion surface increases in tens and hundreds times. The stage of convective combustion is accompanied by a copious dispersion of a porous matrix on separate particles. The combustion wave including a zone of pores formation, the front of ignition, the zone of pores combustion, the front of fuel dispersion, and the zone of particles burning out, is located in enough narrow area, which moves along the charge with rate up to 10 cm/ms. That allows to use the described fuels in artillery systems. The metal particles can be used both for regulation of "level-by-level" rate combustion and pressure of transition in a convective regime, and for change of formed pore surface. The investigations developed in ICP RAS /2 /, have shown, that a major factor determining a picture of combustion of such fuel, is the mass contents of crystalline ES. The replacement of ES



Fig.1. The general view of composite fuel without aluminium particles

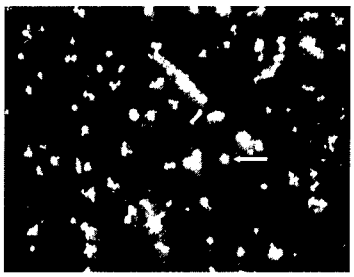


Fig.2. The general view of single aluminium particles

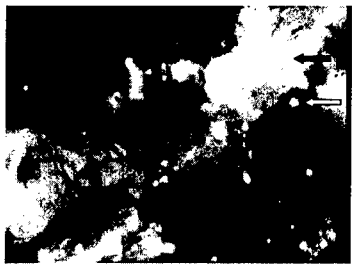


Fig.3. The general view of composite fuel with aluminium particles.
⬅ - crystals of explosive substance;
⇦ - Al particles

part on aluminium particles results in sharp decrease of convective ignition rate W_{ci}. On Fig.4 the relation W_{ci} (P) is shown, it can be described by the law $W_{ci} = AP^{\nu}$, and ν is essential smaller

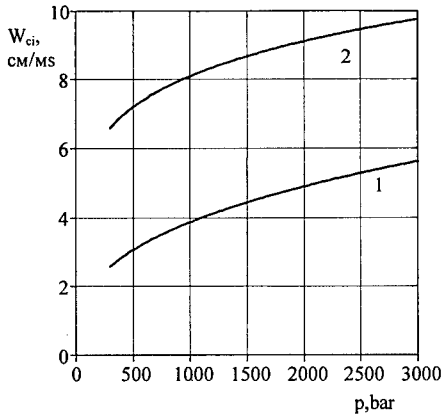


Fig. 4. The convective ignition rate in composite fuel in function pressure.
1 - fuel with Al; 2 - fuel without Al

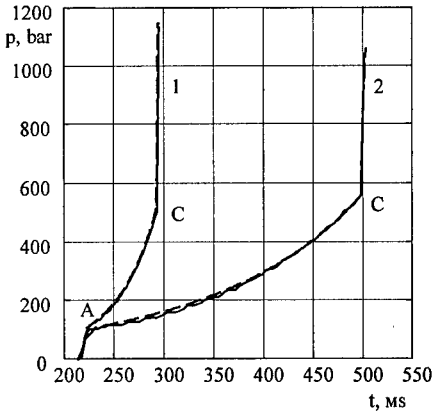


Fig. 5. Time dependence of the pressure in closed bomb from time. 1 - fuel with Al; 2 - fuel without Al;
—— - experiment; ---- - calculation

than unit ($\nu < 0.4$). The introduction of aluminium owing to decrease ES percentage reduces W_{ci} approximately twice. If the contents of ES remains constant, and the aluminium is added owing to reduction of binder quantity, the character of influence is reversed. On Fig.5 the computational and experimental curves of pressure variations in the closed volume of a manometric bomb for fuel with the component of aluminium and without it at the identical contents of ES and identical burning conditions are presented. The experiments were conducted with cylindrical charges armoured on a lateral area, located in a metal cover (Fig.6). The initial recompression in a bomb up to a level 10 MPa (the point A) was provided on account of fast-burning igniter. The moment of a convective regime beginning is marked by a point C.

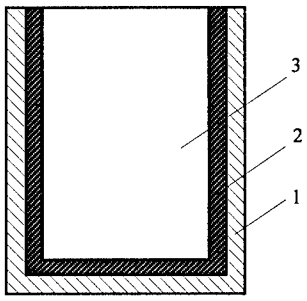


Fig. 6. The general view and loading scheme of the monoblock charge: 1 –the metal cartridge clip; 2 - the armour protection; 3 – the charge

The comparison shows, that period of "level-by-level" combustion and period of convective combustion in fuel with aluminium are considerably reduced, and also the pressure of transition decreases.

Computational curves on Fig.5 are obtained with use of a known technique of manometric results processing /3/ and under the assumption, that the dispersion of fuel is absent completely:

$$\frac{d\psi}{dt} = \frac{S_0}{\Lambda_0}\sigma(\psi)U_{comb}^{eff}(P) \qquad (1)$$

$$P = \frac{Q\psi\Delta(\gamma-1)}{1-\frac{\Delta}{\delta}(1-\psi)-\alpha\psi\Delta}, \qquad (2)$$

Here $= \omega_{comb}/\omega_0$ is the relative share of the burned down fuel; ω_{comb} is the mass of the burned down fuel; ω_0 is the initial mass of fuel; S_0, Λ_0 are the initial surface and volume of fuel, accordingly; σ = S_{comb}/S_0 is the relative combustion surface; S_{comb} is the current combustion surface; U_{comb}^{eff} is the effective face combustion rate; Q is the caloricity of fuel; γ is the isentropic exponent; $\Delta = \omega_0/W_b$ is the loading density; W_b is the volume of manometric bomb; δ is the fuel density; α is the covolum of combustion products.

It was considered, that at convective combustion stage the charge burns on the surface of cross section ($\sigma(\psi)=1$) with increased effective rate. The introduction of such rate is convenient at use single-phase gas-dynamics models for the description of the charge activity in an artillery system. The dependence of effective combustion rate from the pressure is shown on Fig.7. The presence of aluminium particles increases its value at a convective regime by a factor of three times. At a stage of "level-by-level" combustion U_{comb}^{eff} will also increase essentially. The explanation is the following: the aluminium particles have higher heat conduction and play a role of thermal knifes, which increase combustion surface of the charge end face. Besides their presence can result in inhomogeneous heating, destruction and accelerated burn-out of ES crystals. The noted effects promote more fast origin of pores in fuel with aluminium in comparison with a structure without metal particles.

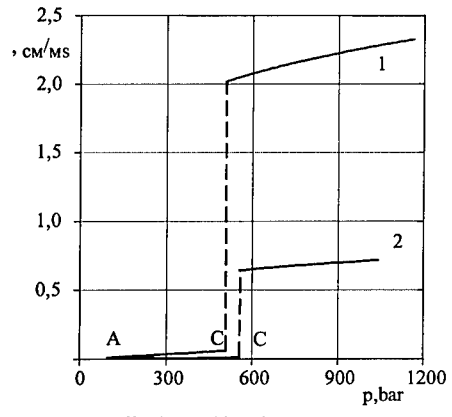


Fig. 7. The effective end burning rate versus pressure: 1 - fuel with Al; 2 - fuel without Al

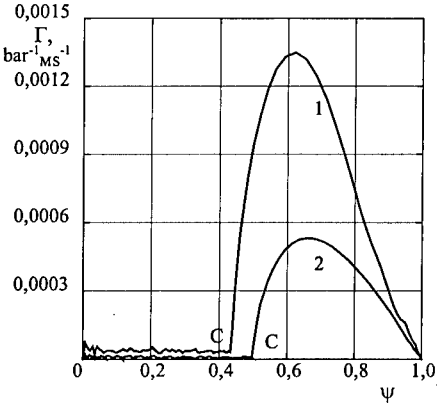


Fig.8. The specific mass combustion rate versus degree of burn-out. 1 - fuel with Al; 2 - fuel without Al

On Fig.8 the relation of specific mass combustion rate /3/

$$\Gamma = \frac{1}{P}\frac{d\psi}{dt}$$

from burn-out degree for considered experiments is shown. At metalized fuel it is higher for both periods of combustion, and at a convective stage the difference on maximum values reaches

more than 100%. It is necessary to mark, that from 45 up to 50 % of mass charges burns down in a "level-by-level" regime, and the progressive increase of gas-generation, connected with ignition of pores surface, their burning out and destruction, corresponds to combustion 15-20 % of mass charges. About 30 % of mass is burning down in degressive mode in the kind of dispersive conglomerates of composite fuel.

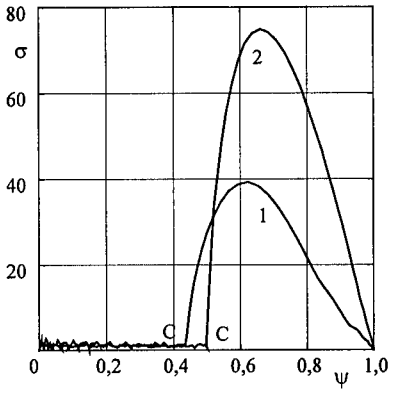


Fig. 9. Relative burning surface versus burn-out degree: 1 - fuel with Al; 2 - fuel without Al

If we assume for both fuels, that in a convective regime the laws, being available up to transition, of "level-by-level" combustion rate (curves AC on Fig.7, accordingly) are saved, than from (1) it is possible to find change of a combustion surface. (Fig.9). It grows from 40 up to 75 times in a comparison with the area of a charge end face, and in metalized fuel this increase is less. Obviously, in this fuel larger pores will be formed. This result in appearance of larger dispersive fragments, including ES crystals, binding and aluminium particles. The fragments is burning out with increased combustion rate on the described mechanism.

The presented data demonstrate broad capabilities of regulation gas-generation characteristics of model monoblock charges. However manometric tests do not allow to reproduce all conditions of an artillery shot and to investigate dynamics and real features of burning out for a formed dispersive mixture. Manometric bomb are characterized by the following parameters: low loading density (0.25 g/cm^3), rather low level of operating pressures (P_{max} <3000 bars), and also absence of a pressure decrease period. For reproduction of the indicated parameters close todiapazone typical for the barrel systems ($\Delta \sim$ 0,6-0,8 g/cm^3; $P_{max} \leq 6000$ bars), the special bomb was developed. Its common scheme is adduced on the Fig.10. To produce initial pressure and convert combustion to the convective regime we used a fast burning igniter and a cap charge (projectile),

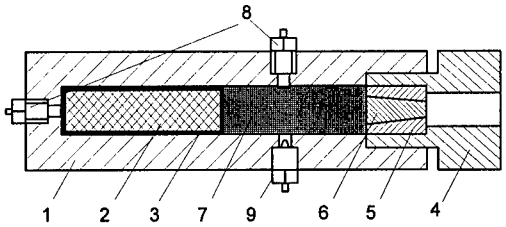


Fig.10. The common scheme of nozzle bomb.
1 – the nozzle bomb hull; *2* – the fuel monoblock; *3* – armour protection; *4* – the nozzle unit; *5* – nozzle; *6* – projectile; *7* - igniter; *8* – pressure gauge; *9* – the ignition device

which was placed in the nozzle unit. Changing the nozzle diameter and mass of monoblock, it is possible to realize different loading densities and pressures in the working bomb volume.

It is possible to describe the combustion and dispersion of monoblock fuel, combustion and motion of igniter charge by the mathematical model based on the following assumptions. Gas-powder mixture in the working volume includes igniter grains, dispersive monoblock particles and their common combustion products. Volumetric concentration of aluminium particles in the mixture is negligible small and their effective influence is taken into account through increase of fuel caloricity and covolum of combustion products. In addition it is supposed, that at dispersion of the monoblock a single fraction of particles will be generated and the exchange of particles between other fractions is absent.

Using a phenomenological approach and the conventional algorithm for deriving equations /4/, we can describe the dynamics of motion of the 3-component (gas, igniter, particles of the monoblock) mixture by the following system:

$$\frac{\partial(\Phi\rho S)}{\partial t}+\frac{\partial(\Phi\rho uS)}{\partial x}=\sum_{j=1}^{2}G_jS; \tag{3}$$

$$\frac{\partial(\Phi\rho uS)}{\partial t}+\frac{\partial(\Phi\rho u^2S)}{\partial x}=-\Phi S\frac{\partial P}{\partial x}+S\sum_{j=1}^{2}(G_ju_j-F_j); \tag{4}$$

$$\frac{\partial(\Phi\rho ES)}{\partial t}+\frac{\partial(\Phi\rho uES)}{\partial x}+\frac{\partial}{\partial x}\left(\frac{\Phi PuS}{\partial x}\right)=S\sum_{j=1}^{2}\left[G_j\left(Q_j+\frac{u_j^2}{2}\right)-F_ju_j\right]-$$
$$-P\sum_{j=1}^{2}\frac{\partial(\Phi_ju_jS)}{\partial x},\quad E=e+\frac{u^2}{2} \tag{5}$$

$$\frac{\partial(\Phi_jS)}{\partial t}+\frac{\partial(\Phi_ju_jS)}{\partial x}=-\frac{G_j}{\delta_j}S,\quad j=1,2; \tag{6}$$

$$\frac{\partial(\Phi_ju_jS)}{\partial t}+\frac{\partial(\Phi_ju_j^2S)}{\partial x}=\frac{S}{\delta_j}\left(F_j-\Phi_j\frac{\partial P}{\partial x}-G_ju_j\right),\quad j=1,2; \tag{7}$$

$$\delta_j=const,\quad j=1,2; \tag{8}$$

$$\frac{\partial z_j}{\partial t}+u_j\frac{\partial z_j}{\partial x}=\frac{P}{I_{kj}},\quad z_j=\frac{h_j}{h_{0j}},\quad j=1,2; \tag{9}$$

$$\Phi_j=\Lambda_j^0(1-\psi_j)N_j,\quad j=1,2; \tag{10}$$

$$\Phi+\sum_{j=1}^{2}\Phi_j=1; \tag{11}$$

$$\psi_j=k_{1j}z_j(1+k_{2j}z_j+k_{3j}z_j^2),\quad j=1,2; \tag{12}$$

$$e = \frac{P(1-\alpha\rho)}{\rho(\gamma-1)}; \tag{13}$$

$$G_j = S_j^0 \sigma_j N_j \delta_j u_G, \quad u_G = \frac{h_{0j}}{I_{kj}} P; \tag{14}$$

$$\sigma_j = 1 + 2k_{2j} z_j^2; \tag{15}$$

$$F_j = \frac{\pi d_{3j}^2}{4} \cdot N_j C_{xj} \cdot \frac{\rho(u-u_j)|u-u_j|}{2}; \tag{16}$$

$$d_{3j} = \left(\frac{6\Lambda_j^0(1-\psi_j)}{\pi} \right)^{1/3}; \tag{17}$$

$$C_{xj} = \begin{cases} C_1 = \dfrac{24}{\mathrm{Re}_j} + \dfrac{4.4}{\mathrm{Re}_j^{0.5}} + 0.42, & \Phi \geq 0.92 \\ C_2 = \dfrac{4}{3}\left(1.75 + \dfrac{150(1-\Phi)}{\Phi \mathrm{Re}_j} \right), & \Phi \leq 0.55 \\ C_3 = \dfrac{(0.92-\Phi)C_2 + (\Phi-0.55)C_1}{0.37}, & 0.55 < \Phi < 0.92 \end{cases} \tag{18}$$

$$\mathrm{Re}_j = \frac{\rho|u-u_j| d_{eff\,j}}{\eta}$$

Here: Φ is the volume fraction of the phase, G_j is the source of mass for combustion of the jth sort of particles, N_j is the number of particles per unit volume, F_j is the interphase-friction force, Λ_j^0 is the initial volume of a particle, $d_{eff,j}$ is the diameter of a sphere with equivalent volume, η is the dynamic viscosity of the gas. The index j indicates that the parameter belongs to particles of the jth fraction. 1 is the grains of igniter, 2 is the dispersive particles of the monoblock.

The equations (3) - (5) express the laws of conservation of mass, momentum and energy for the gas phase, and equation (6), (7), which are repeated 2 times, - the laws of conservation of mass and momentum for each fraction of particles; (8) – is the incompressibility condition; (9) is the combustion equation, and expressions (10), (12), (15) define the interrelation of the different characteristics inside a fraction. Relation (13) is used as the equation of state, and expression (14) is written for the source of mass. Since, in the calculations the porosity does not decrease below the gravimetric value, the interphase-interaction force is described by the well-known /5/ relation (16)-(18).

In describing the conversion of the monoblock fuel into gaseous product, we assume that the fuel partly burns in the end regime and is partly dispersed into particles that completely burn in the working volume of the bomb. If we now replace the burning front by a gas-dynamic discontinu-

ity surface, the dispersed particles will penetrate through this surface together with the products. Tentative estimates show that in convective combustion of a low-porosity charge at the moment of dispersion of its skeleton, the velocities of the gas and the particles formed are approximately identical. We assume, therefore, that on the discontinuity surface on the side of the working volume, the products and the condensed phase move with identical velocities. In the region adjacent directly to the burning front there is only the dispersed fraction present, and particles of the igniting charge are absent. Then, the dynamic compatibility conditions for the introduced gas-dynamic discontinuity have the form /5/:

$$\rho_{MK} u_G = \bar{\rho}_g \left(u_G - u_g\right);$$

$$P_{MK} + \rho_{MK} u_G^2 = P_g + \bar{\rho}_g \left(u_G - u_g\right)^2;$$

$$\frac{u_G^2}{2} + \frac{P_{MK}}{\rho_{MK}} + Q_{MK} = \frac{\left(u_G - u_1\right)^2}{2} + \frac{P_g}{\rho_g} + \\ + \frac{\rho_g \Phi}{\bar{\rho}_g} \frac{P_g}{(\gamma - 1)} \left(\frac{1}{\rho_g} - \alpha\right) + \frac{\rho_{MK} \Phi_2}{\bar{\rho}_g} Q_{MK}; \qquad (19)$$

$$\bar{\rho}_g = \rho_g \Phi + \rho_{MK} \Phi_2;$$

$$\Phi + \Phi_2 = 1.$$

Here u_G it is meaningful rates of "level-by-level" convective combustion and simultaneous dispersion of monoblock fuel. The index *MK* designates parameters of a monoblock charge, *g* - parameters of combustion products.

The boundary conditions in the flow field will look like:

at the combustion front of a charge

$$x = x_T^{MK}: \quad u = u_1 = u_2 = u_g;$$

at the bottom of projectile

$$x = x_{pr}: \quad u = u_1 = u_2 = u_{pr}.$$

The speed of the projectile calculated from the equation of its motion

$$q \frac{du_{pr}}{dt} = SP_{pr} - F_r, \qquad (20)$$

Here q is the mass of the projectile; P_{pr} is the pressure on the bottom of the projectile; F_r is the force of projectile interaction with walls of the nozzle.

After departure of the projectile from the nozzle, the critical flow conditions were specified in the minimum cross-section of the nozzle. The system (3) - (20) was used for processing of experimental relations $P_{\exp}(t)$, obtained on the lateral pressure transducer of a nozzle bomb.

In the solution of system (19), the quantity u_G is considered known and serves as a matching parameter for calculated and experimental results. Furthermore, because dispersion of the monoblock does not occur until transition of combustion to the connective regime, for u_G in this period we use a relation from Fig.7. After the beginning of convective regime u_G was determined from the relation

$$u_G = BP^{\nu} \tag{21}$$

by minimization of a functional

$$J = \left(\int_{t_z}^{t_k} \left(P_{\exp} - P_{cal} \right)^2 dt \right)^{1/2} \tag{22}$$

Here t_z is the time of the convective regime beginning; t_k is the end of combustion; P_{cal} is the computational value of pressure in working bomb volume.

Since the parameters of the dispersed fraction are not known beforehand, they are also obtained by matching the numerical and experimental pressures. In the calculations, we examined the possibility of dispersion of the fuel with formation of particles of various shares: spheres, cylinders, plates, etc., with the corresponding laws of variation in the burning surface after dispersion. Results showed that good agreement with experiment can be achieved if the particle shape is considered nearly spherical. The minimum of the functional in the multidimensional space was sought by an exhaustive method. The velocity u_{comb}^{eff} from the Fig.7 was used as the initial approximation of the dispersion law, and the initial particle parameters were specified with allowance for the monoblock fuel composition.

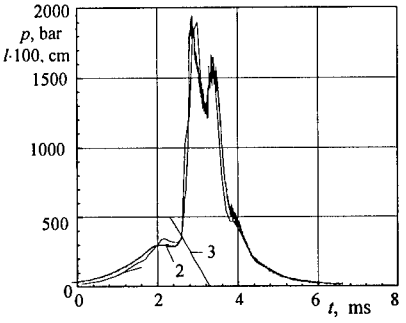


Fig.11. Calculated and experimental pressures in the working bomb volume versus time for the model with dispersion: 1 - p (t), calculation; 2 - p (t), experiment; 3 – l_{MK} (t), calculation

For comparison, Fig.11 shows the calculated curve of $P_{cal}(t)$, obtained for model (3) - (20) upon reaching the minimum of functional (22), and the experimental curve of $P_{\exp}(t)$. It turns out that with such agreement of the curves, the monoblock burns and is dispersed under the law

$$u_G\,(\text{cm/мс}) = 0.8 \left(\frac{P}{P_0} \right)^{0.17}, \quad P_0 = 1 \ bar \tag{23}$$

In this case, up to 70 % of the fuel mass burns at the front and 30 % of the charge enters into the working volume as particles with an effective diameter of 200 microns. Comparison of curves of

p(t) obtained under other conditions shows that for the fuel studied, relation (23) is universal and can be used in calculations of the internal ballistic parameters of an artillery shot.

The dynamics of the second fraction of dispersed particles formed at the burning front is illustrated in Fig.12, which shows the trajectories of the burning front of the monoblock and the afterburning front of the particles. Motion proceeds from right to left, and the nozzle exit limiting the chamber corresponds to x=0. From analysis of the data in Fig.12, it follows that the particles formed fill a region 10-15 cm wide, whose boundaries move in accordance to the wave character of the flow. All dispersed particles have time to burn in the bomb chamber.

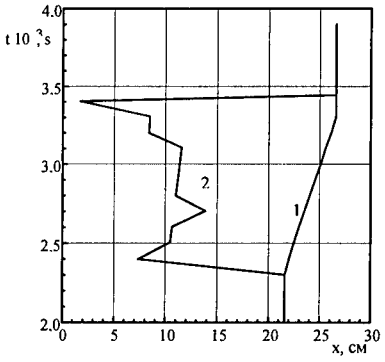


Fig.12. Trajectories of the burning front of monoblock fuel and afterburning front of dispersed particles: curve 1 refers to combustion and dispersion front of monoblock fuel and curve 2 refers to afterburning front of dispersed particles

Thus, suggested experimental techniques of composite monoblock fuels combustion research and mathematical model of interior-chamber processes allow to determine the laws of combustion and dispersion of investigated charges.

THE PROCESSING OF ULTRAFINE METAL PARTICLES

It is known /1 /, that the sizes of aluminium particles, their fractional composition and percentage in fuel have an important bearing on the characteristics of solid propellants combustion. The most interesting results should be expected at application strictly fractionated powders in range about and less than 1 μm. The problem of producing of such powders in quantities, necessary for experimental researches, remains a difficult technological problem.

For producing of submicron powders of metals, alloys, organic and inorganic compounds the authors devised a pneumatic circulation unit combining processes of size reduction, classification, drying, mixing, and granulation of powders. The design and principle of an operation of the unit has been detailed in /6/. Here we can do no more than describe some advantages of our method over other related methods for powder processing /7/.

Intensity of size reduction in complex pneumatic units in the first place is determined by working pressure, parameters of speedup chamber and nozzles, intensity of circulating motion, physical and mechanical properties of feed powders and product size of particles. Our study show that the process of inter particles abrasion is deciding whereas the nozzles design and installation of obstacles did not influence noticeably the process outcome. The high purity of end product after size reduction of hard and super hard materials (carbides, nitrides, oxides of some metals) is also explained by domination of particles interaction (inter particle abrasion), instead of interaction of particles with working surfaces /8/.

Fig. 13 gives the results of size reduction for aluminium of an average dispersibility at the working gas pressure of 7-8 kg /cm2, rotation speed of the rotor 7000 rpm. The fact of size reduction is confirmed by availability in the small-sized product of aluminium particles , absent in initial material. This conclusion is confirmed also by computer images of aluminium particles, obtained with use of optical microscope and TV camera (fig.14, 15).

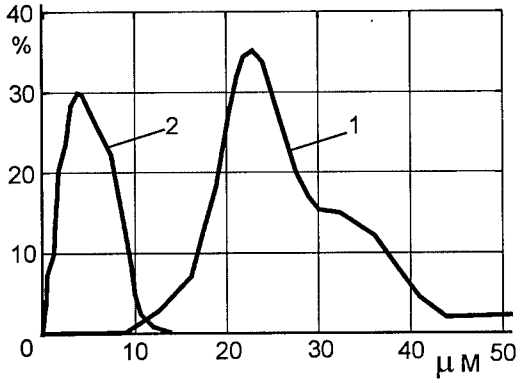


Fig 13. Differential function of size distribution for (1) initial powder of aluminium, and for (2) grinded one.

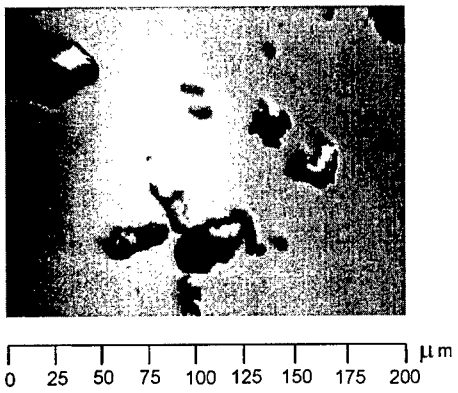


Fig. 14. Initial material ASD-4:
The maximal size of particles is 50 μm, the average one is 25 μm.

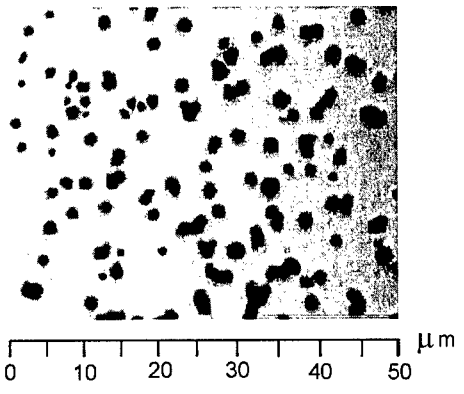


Fig.15. Fine fraction ASD-4 with sizes average, maximal and minimal correspondingly 3, 7 and 2 μm

Integrated theoretical and experimental investigations in the field of aeromechanics of high concentrated heterogeneous flows has already formed a new line of the powder technology on the base of controlled circulating movement of the flow of "gas-solid particles" in closed volumes with the help of gas jets. The result reported in the work shows that with the help of described procedure essentially all processes of powder technology (grinding, classification, blending, drying, granulation etc.), as well as production of submicron powders of aluminium and other materials, including powders with special properties, can be realized.

The experimental and theoretical techniques of research for processes of monoblock fuel combustion, proposed in this article, as well as developed technology for producing of ultra dispersive fractionated metal powders provide capabilities for creation of a new class of fuels with adjustable rate of combustion for a pulse power installations.

This work was supported by Russian Foundation for Fundamental Researches (Grant № 00-01-00857) and by NATO Science Program (Collaborative Linkage Grant No.976783)

REFERENCES

1. L.K. Gusachenko, V.E. Zarko, V.Ya. Ziryanov, V.P. Bobrishev The modeling of solid fuels combustion processes. [in Russian], Nauka, Novosibirsk (1985)
2. A.F. Belyaev, V. K. Bobolev, A.B. Korotkov, A.A. Sulimov The Transition from Combustion to Explosion in Condensed Systems [in Russian], Nauka, Moscow (1973).
3. M.E. Serebryakov Internal ballistics of barrel systems and powder rockets. [in Russian], Oborongiz, Moscow (1962).
4. Y.P. Khomenko, A.N. Ischenko, V.Z. Kasimov Mathematical modeling of interior ballistic processes in barrel systems. [in Russian], Publishing House of SB RAS, Novosibirsk (1999)
5. R.I. Nigmatulin, Dynamics of multiphase media, Part 1, Hemisphere Publ., New York (1991)
6. Yuri Biryukov, Alexander Vorozhsov, Leonid Bogdanov «Obtaining Submicron Abrasive Powders by Pneumatic Processing of Electric Corundum and Products of Solid Rocket Propellants Combustion",29th International Annual Conference of ICT "Energetic Materials, Production, Processing and Characterization", Karlsruhe, 1998.
7. Peter M. Silverberg, Stephen Miranda Sharon, Homing In On the Best Size Reduction Method, Chemical Engineering, November,1998, v. 105, No.12; P.102.
8. Yu. Biryukov, V. Perkov A. Roslyak, L. Bogdanov. Experience on Obtaining of Nano and Submicron Powders of Organic and Inorganic Materials. 4th Korea-Russia International Symposium on Science and Technology / KORUS 2000/ June 26-30, 2000, University of Ulsan, Ulsan, Korea, p. 291-294.

Expertise of nanometric aluminium powder on the detonation efficiency of explosives

LEFRANCOIS Alexandre, LE GALLIC Christian

French Ministry of Defense DGA/DCE/CEG
Centre d'Etudes de Gramat
F-46500 GRAMAT

The interest of nanometric aluminum powder as an efficient additive to energetic materials was demonstrated by many authors in the field of propulsion with the increase of the combustion velocity. The contribution of nanometric aluminum powder to high explosives efficiency is still in question.

CEG has investigated the detonation efficiency of nanometric aluminum, compared to micronic aluminum, in explosives by using cylinder tests with classical velocity measurements and new temperature measurements techniques. Air blasts tests have also been conducted with classical pressure measurements.

These experimental results allow to investigate the effects of nanometric aluminum powder in explosives. They are presented in this paper and compared to other published data.

INTRODUCTION

The use of aluminum particles in high explosives is well known to improve their efficiency. The influence of different parameters such as the weight contents, the particle size, the particle distribution and the particle morphology has been the scope of many experimental and numerical studies.

For micronic aluminum powders, many experimental studies have shown the interest of decreasing the aluminum particle diameter. Plate push test technique has been used by Tao et al [1] to demonstrate that PETN/Al 95/5 charges with 5 µm Al accelerated the plate more than the same charges with 18 µm Al.

Moreover under a critical size close to 1 µm the detonation velocity decreases. For HMX/Al compositions with various aluminum weight contents from 5 to 25 %, Gogulya et al [2] demonstrated that the detonation velocities were decreasing respectively from 0.7 % to 4.2 % for charges with 0.5 µm Al compared to the same charges with 20 µm Al.

The ballistic efficiency also decreases under a critical size close to 1 µm. For the same HMX/Al compositions, the plate push tests and cylinder tests used by Gogulya et al [2] have shown that the cylinder expansion was lower for charges with 0.5 µm Al compared to the same charges with 20 µm Al.

Moreover the aluminum contents by oxidation does not totally contribute to the ballistic efficiency. For 16 µm aluminum particles, Baudin et al. [3] have demonstrated that the aluminum to alumina conversion rate was limited to 30 wt. % in the first 20 µs for HMX/Energetic binder/Al compositions, with the assumption that aluminum did not react in the detonation front.

However, the micronic aluminum particle size has no influence on longer effects such as underwater and blast effects. Happ et al. [4] have shown that the bubble energy in underwater tests was quite equal with Al particules, which granulometry was decreasing from 150 µm to 5 µm, for RDX/Energetic binder/Al compositions.

So all the aluminum contents could oxidize for longer effects. Happ et al. [4] have also demonstrated that in an argon atmosphere of a detonation chamber Al contents of detonation products residues were lower than 1 % from RDX/AP/Al/GAP binder formulations up to 30 wt. % Al.

In this paper, the efficiency of nanometric aluminium powder additives to high explosives is investigated compared to micronic Al powder additives in their sensitivity assessment and in three ways of improvement : ballistic effects, blast effects and underwater effects.

Particle size distribution measurements and Differential Scanning Calorimetry (DSC) of many studies have shown the interest of nanometric Al powder itself [5]:

- Increase surface area and so the heat transfert
- Increase the oxidation rate
- Increase the oxidation energy

Hence the nanometric Al powder is expected to give a potential interest in explosives to release additional oxidation energy in the detonation front and/or detonation product expansion.

BALLISTIC EFFECTS

Explosives compositions

The solid explosive compositions chosen for the ballistic experiments are RDX/AP/wax formulations with powder additives. The compositions have been manufactured at CEG. The formulations densities are listed in table 1. The standard error of the mean density is 0.48 % for the pressed compositions A11 to A13, and only 0.29 % for the pressed compositions A81 to A83. Three types of energetic or inert powder additives are used separately :

- Alex nanophase Al (mean diameter 100 nm) delivered by Argonide
- A 2002 aluminum (mean diameter 5 µm) delivered by Neyco
- LiF (mean diameter 5 µm) delivered by Sigma-Aldrich

A 2002 Neyco Aluminum and Aldrich lithium fluoride are two standard micrometric powders, which are used here as references. Alex nanophase Aluminum is obtained by electroexploded wire technology in argon environment. The mean particle diameter is about 100 nm, only few particle diameter are up to 1 µm.

X-ray fluoroscopy and diffractometry, Transmission Electron Microscopy (TEM), Scanning Electron Microscopy (SEM), Differential Scanning Calorimetry (DSC) and Thermogravimetry (TG) were previously performed on aluminum powders [5].

A samples preparation technique has been precisely set up to perform reliable microstructural analysis. The polished sections are observed with scanning electron microscopy. Pictures 1 and 2 respectively present the microstructure of the explosive compositions A11 and A12.

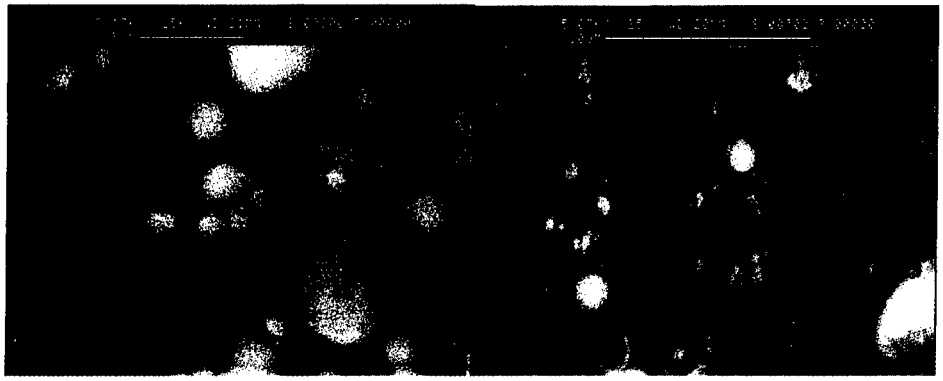
The two different aluminum size distributions are confirmed. Also the aluminum distribution in the composition is controlled as being homogeneous. For the compositions with the highest aluminum content, the matrix is very dense, aluminum particles are connected to each other. For the compositions with the lowest aluminum content, aluminum is more disperse. The Al nanophase particles are still linked to the other, compared to the 5 µm Al powder.

For the impact sensitivity test, also called fallhammer test, Al nanophase based compositions A11 and A81 are much more sensitive than 5 µm Al based compositions A12 and A82. For the friction sensitivity test, it is the same trend between the compositions A11 and A12. However the inversed trend is observed between the compositions A81 and A82.

Table 1 : Explosives compositions

Name	Compositions	Density (g/cm3)	Fallhammer (J)	Friction (N)
A11	RDX / AP / Al 100 nm / wax 20/43/25/12	1.805	5.83	95
A12	RDX / AP / Al 5 µm / wax 20/43/25/12	1.793	14.96	143
A13	RDX / AP / LiF 5 µm / wax 20/43/25/12	1.789	-	-
A81	RDX / AP / Al 100 nm / wax 50/24/12/14	1.664	5.95	140
A82	RDX / AP / Al 5 µm / wax 50/24/12/14	1.654	9.66	115
A83	RDX / AP / LiF 5 µm/ wax 50/24/12/14	1.659	-	-

Picture 1 : Microstructure of A12 **Picture 2 : Microstructure of A11**



Experimental set up

The detonation efficiency of the tested explosive compositions is usually investigated using cylinder tests (figure 1). In this case, the 3-inch cylinder tests is needed for non ideal explosive compositions. The metrology chosen for the experiments is : piezoelectric pins, interferometry VISAR, streak camera, fluxmeter and pyrometer.

Metrology

The detonation velocity of the compositions is measured by lateral piezoelectric pins.

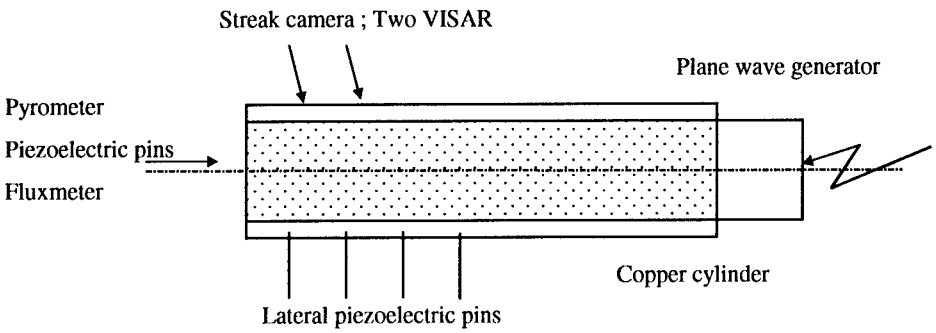
The copper liner velocity is measured for a better accuracy with two interferometers VISAR set up at two different points from the back of the cylinder. The cylinder radius expansion is recorded with a streak camera during a longer time period. The derivation of this streak camera measurements could be compared to the Visar interferometry profiles.

At the back of the cylinder, the curvature of the detonation front is measured with piezoelectric pins.

Still at the back of the cylinder, a low cost fluxmeter developed at CEG collects the thermal flux in a single spectral range [850 nm - 1700 nm] by a specific optical head and fiber with a rise-time less than 20 ns. The fluxmeter has to be preliminarily calibrated to get a conversion between the voltage output and the radiance temperature of the detonation products over the range 1500 K-5000K [6]. The conversion to obtain the true temperature is achieved by assuming the knowledge of the material emissivity. If the fluxmeter is not calibrated, the measurement is only qualitative.

At the back of the cylinder, the true temperature in detonation products is determined with a time-resolved six wavelength UV-visible pyrometer developed at CEG [7, 8]. The thermal radiation is also collected from the emitting surface with a specific optical head, fiber and filters on photoelectric detectors. This apparatus after a calibration allows to determine a true surface temperature over the range 1500 K - 6000 K with a rise-time of 5 ns.

Figure 1 : experimental set-up



Results

Velocity and curvature of the detonation front

The distance vs. time diagram obtained with the lateral piezoelectric pins shows a linear propagation of the detonation front, confirming that the detonation is stationary. The calculated and measured detonation velocities are given in table 2. Thermochemical calculations are performed using CHEETAH code [9] and BKWC with inert Al. We assume that 5 µm Al does not react in the detonation front. For the compositions A11 to A12, the calculated D_{CJ} is much higher than the measured one. The reason of these differences is identified as being firstly related to the correct detonation products identification and calculation [10]. The measured velocity decreases of 2 % for the composition A11 compared to A12, but increase of 0.8 % for the A81 composition compared to A82. The detonation velocities of the compositions A13 and A83 with LiF inert additive are close respectively to the compositions A11 and A81 values. The level of nanophase Al content in the compositions plays a contradictory role on the detonation velocity.

The curvatures of the detonation fronts at the back of the cylinder are given in figures 2 and 3. The curvature of compositions A11 and A12 are similar. The curvature of A13 is slightly higher. The curvatures of compositions A81 and A82 are also similar. The curvature of A83 is clearly lower. The Al nanophase additive in the compositions has the same influence as the 5 µm aluminum additive on the detonation front curvature. For a low aluminum content, the curvature increases compared to LiF inert additive. For a high aluminum content, the curvature slightly decreases compared to LiF inert additive.

Table 2 : Detonation velocity

Compositions	Calculated D_{CJ} (m/s)	Measured D_{CJ} (m/s)
A11	7151**	5634
A12	7204*	5748
A13	--	5664
A81	7167**	7350
A82	7212*	7309
A83	--	7350

* Al inert reactant ; ** Al reactive reactant.

Cylinder expansion

The registration time, depending upon the time resolution and the cylinder expansion, is about 20 µs for the VISAR interferometry measurements, shorter than for the streak camera measurement. Nevertheless, the VISAR could precisely measure the phases of the HE driven shock loading of the copper cylinder : first shock waves, Taylor release waves and next shock and release phases.

The two VISAR measurements did not show any difference for each cylinder test, confirming that the detonation is steady.

The cylinder velocities of compositions A11 to A13 obtained with the VISAR interferometer are presented figure 4. The composition A12 with 5 µm aluminum additive shows the best ballistic efficiency. Compared to composition A11, the velocity gap is about 10 % at 10 µs. The cylinder velocity increases for composition A13 is in between.

The cylinder velocities of compositions A81 to A83 obtained with the VISAR interferometer are presented figure 5. The measurements are similar for the three compositions.

From the streak camera film, the cylinder radius expansion R(t) is recorded. This result is fitted to one branch of hyperbola (1). The criterion of best fit is that the sum of the squares of the deviation in t be a minimum [11]. The fitted curve is then differentiated to obtain the velocity.

$$t^2 + t \,.\, (C_1 \,.\, R(t) + C_2) + C_3 \,.\, R(t) + C_4 = 0 \qquad (1)$$

Figure 2 : Front Curvature of A11 to A13

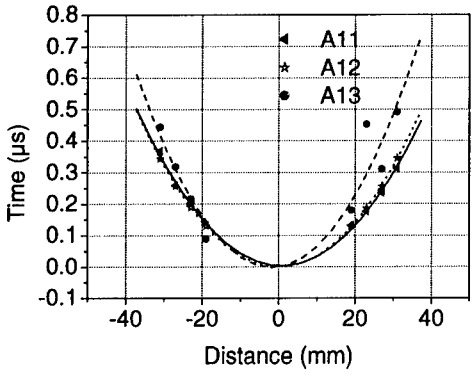


Figure 3 : Front Curvature of A81 to A83

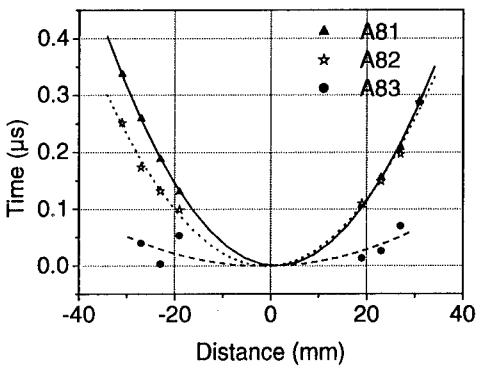


Figure 4 : Cylinder velocity for A11 to A13

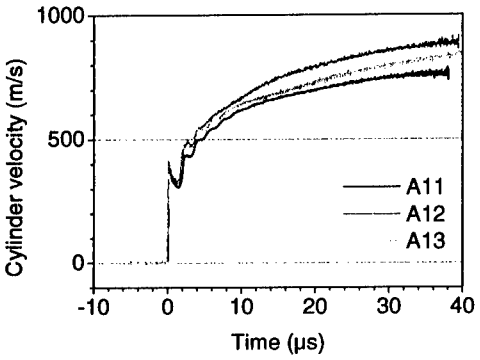


Figure 5 : Cylinder velocity for A81 to A83

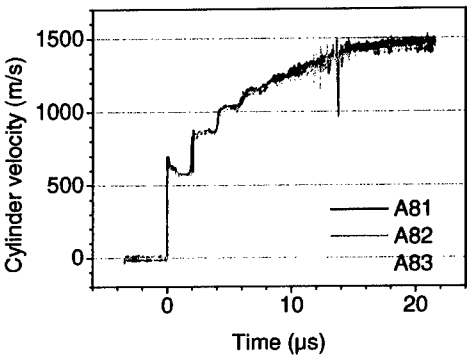
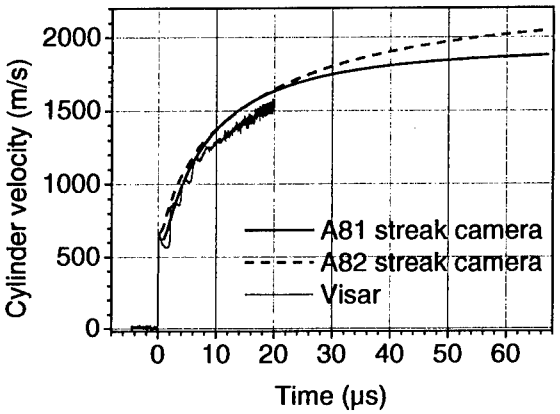


Figure 6 : Streak camera and Visar interferometry measurements comparison



This streak camera processing is compared in figure 6 to the Visar interferometry measurements. The cylinder velocities obtained with the streak camera are slightly higher than the Visar velocities during the first 10 µs. The gap is increasing up to 10 % at 20 µs. The difference observed could be related to the use of the Visar and streak camera.

During the first 20 µs, the streak camera cylinder velocities are similar for compositions A81 and A82. After 20 µs, the cylinder velocity of the composition A82 with 5 µm aluminum is higher than for the composition A81 with 100 nm Al. At 55 µs, the gap is about 10 %.

For a given expansion rate, the Gurney constants are calculated with the Gurney formula (2) by the Visar and also the Streak camera measurements. They are presented in table 3.

The composition A12 with 5µm aluminum has the highest Gurney constant for a low expansion rate, with a maximum gap about 10 % compared to the composition A11.

The composition A82 with 5 µm aluminum has also the highest Gurney constant for a high expansion rate, with a maximum gap of about 10 % compared to the composition A81 with 100 nm aluminum. For a low expansion rate, the Gurney constants of the compositions A81, A82 and A83 are quite similar.

$$V(t) = \frac{\sqrt{2.E}}{\sqrt{\mu + \frac{1}{2}}} \qquad (2)$$

V(t), Cylinder expansion velocity at a given time.
µ, Copper cylinder weight / explosive weight
$\sqrt{2.E}$, Gurney constant.

Table 3 : Gurney Constant

Name	Metrology	Gurney constant G (m/s)			
		V/V0=2.1	V/V0=2.36	V/V0=6.83	V/V0=12.25
A11	Visar	1028	1055	--	--
A12	Visar	1140	1163	--	--
A13	Visar	1085	1115	--	--
A81	Visar	2035	2075	--	--
	Streak Camera	2177	2260	2643	2735
A82	Visar	2020	2102	--	--
	Streak Camera	2125	2212	2734	2901
A83	Visar	1991	2051	--	--

Temperature measurements

Figure 7 : Radiance for composition A81

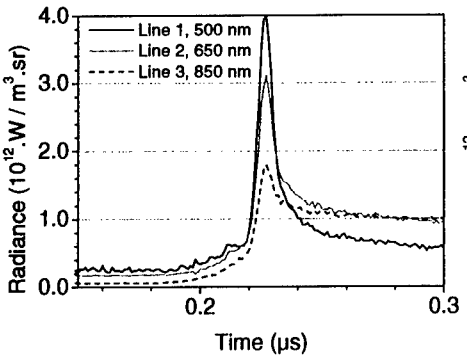


Figure 8 : Radiance for composition A82

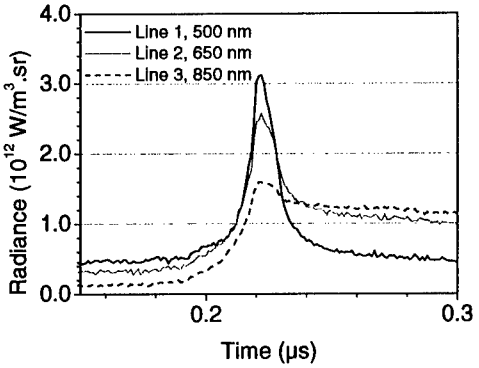
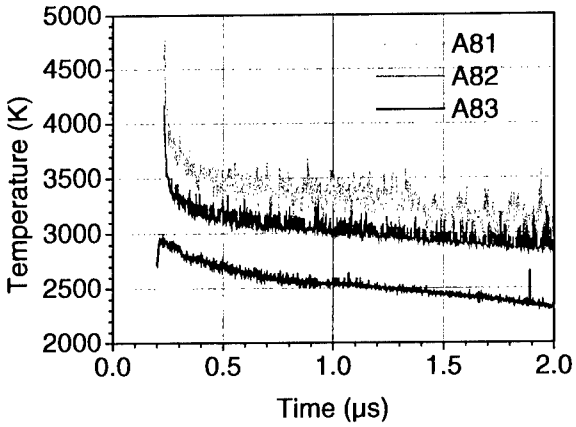


Figure 8 : Temperature for compositions A81, A82 and A83



The fluxmeter is not calibrated in these tests, the measurements are only qualitative and have been recorded at different points of the cylinder back. The thermal flux emitted by the detonation products of the compositions A81 and A11 with 100 nm Al is higher than for other compositions. These results are confirmed by pyrometer measurements.

The UV-visible pyrometer is also used at the back of the cylinder. The voltage results are converted into radiances using the calibration with a black body source, then into radiance temperatures using the Planck law, and finally into emissivity and true temperature using a specific sofware. The radiances for the first three wavelengths and true temperature results are presented figures 7, 8 and 9.

The detonation front radiances are higher for the composition A81. Then appears the detonation products release with a duration of about 2 µs related to the optical window between the explosive and the optical head collector of the pyrometer.

Compared to the composition A83, the temperature of the detonation products is about 30 % higher for composition A81 and 20 % higher for composition A82.

BLAST EFFECTS

Explosive compositions

The solid explosive compositions chosen for the blast experiments are Al-powder 20 wt. % and TNT 80 wt. %. Two types of Al powder additives are used separately :

- Alex nanophase Al (mean diameter 100 nm) delivered by Argonide
- A 2002 aluminum (mean diameter 5 µm) delivered by Neyco

130 g cylindrical charges are tested in this small scale reflected blast test [12]. The main reflected blast wave parameters are compared here : peak overpressure P_r, positive impulse I_{r+} and arrival time of the shock wave.

Experimental set up

The charges are detonated in front of a metallic plate, instrumented with six piezo-electric gages. The reflected blast waves histories (P, t) are then recorded. The charge axis is set up perpendicularly or parallel to the plate, as shown in figures 9 and 10. Tests are performed twice.

figure 9 : Perpendicular experimental set-up

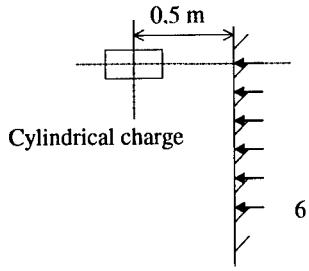


figure 10 : Parallel experimental set-up

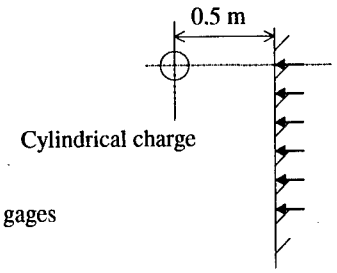


figure 11 : Reflected peak pressure

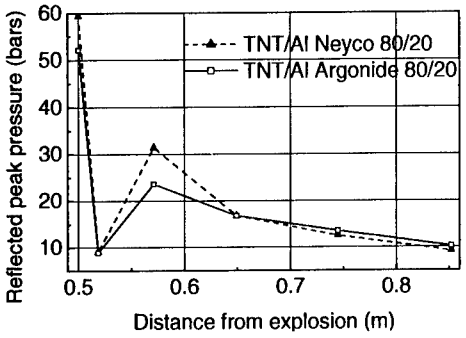
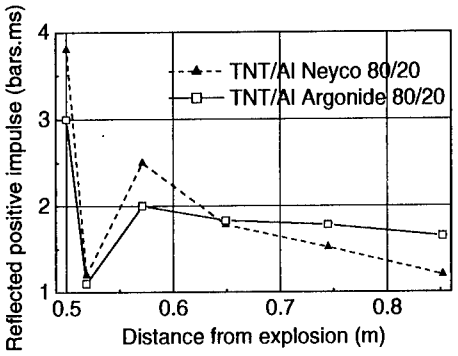


figure 12 : Reflected positive impulse



Results

For the perpendicular configuration, the time of arrival of the shock wave is shorter for the composition with nanometric aluminum. However, the shock wave velocity gaps are less than 100 m/s. The reflected peak pressure and reflected positive impulse, presented in figures 11 and 12, are lower for the first three gages, respectively about 12 % and 20 % for the first gage

at 0.5 m. The reflected peak pressures are slightly higher of about 10 % after the third gages for the composition with nanophase Al. The reflected positive impulse is also higher after the third gages, of about 32 % for the last gage at 0.85 m.

For the parallel configuration and between the two compositions, the gaps are lower for the reflected waves parameters, except for the arrival time.

UNDERWATER EFFECTS

The solid explosive compositions chosen for the underwater experiments are the same compositions as for the ballistic tests. Only the compositions with the highest aluminum or lithium fluoride contents are studied.

Charges of 12 kg with central booster are prepared. The underwater experiments have not been performed yet and results will be available next year.

CONCLUSION AND DISCUSSION

The efficiency of 100 nm diameter aluminum additive for RDX/AP and TNT compositions, compared to 5 µm diameter aluminum additive, has been investigated in their sensitivity assessment and in three ways of improvement : ballistic effects, blast effects and underwater effects.

For the fallhammer sensitivity test, 100 nm aluminum based RDX/AP/Al compositions are more sensitive. For the friction sensitivity test, the same effect is observed between compositions with the high Al contents. However the inverse trend is observed between compositions with the low Al contents.

The ballistic effects decrease for the compositions RDX/AP/Al with 100 nm aluminum contents. This observation needs complementary instrumentation : Visar interferometry measurements for a short time range and Streak camera for a longer one.

A slight decrease of detonation velocity has also been observed for the composition with 100 nm aluminum 25 wt. % content. However the inverse trend is observed for the lower aluminum content compositions.

For a given composition containing aluminum powder, detonation wave curvature increases with aluminum contents and the granulometry itself has no influence on this parameter. When LiF is replaced by Al powder and taking as reference the LiF inert additive for a given composition, the detonation wave curvature depends upon the oxidation rate of aluminum in the detonation front.

The lower the granulometry is the higher the detonation products temperature is and the higher the aluminum oxidation rate is (still compared to the LiF inert additive). These measurements are performed during a short time range after the detonation front. Concerning the oxidation rate, this result is less obvious (even inversed) for longer time during the cylinder expansion.

The small scale reflected blast test has shown the behaviour of aluminized compositions with TNT. Compositions with nanophase aluminum have an interest in a higher shock wave velocity and reflected positive impulse for longer distances.

For underwater tests, results are not still available. They will assess the influence of the charge environment.

In a preliminary literature review [13], the main identified effects of nanometric aluminum particle have been listed among very few unclassified international papers.

Small scale detonation velocity and plate-push tests have been performed by Miller et al. [10] to assess the influence of varying the particle size between 50 nm and 60 µm in ADN/Al, HMX/Al and CL20/Al compositions. The compositions with 3 µm diameter aluminum contents have been taken as references. For the ADN/Al composition with nanophase aluminum contents, the detonation velocity drastically increases. However the detonation velocity decreases for CL20/Al composition containing nanophase aluminum. The ballistic effects also decrease for ADN/Al and HMX/Al compositions.

NM/Al and TNT/Al compositions have been tested by using Cylinder expansion tests [5]. The compositions with 5 µm diameter aluminum contents have been taken as references. The detonation velocities decrease and the ballistic effects is quite similar for the compositions with 100 nm aluminum content than the reference compositions. A reduction of the first release in the projected metallic material related to internal stresses has been observed with the compositions with 100 nm aluminum content.

Ritter et al. [14] have also investigated HMX/Al and BTNNA/Al compositions on cylinder tests. HMX, BTNNA compositions or BTNNA/Al flakes are taken as references. The sensitivities to impact and friction decrease for the compositions with 100 nm aluminum contents. The detonation velocity and the ballistic effects don't increase for the compositions with 100 nm aluminum contents.

To assess more precisely the influence of nanometric aluminum, further investigations should be performed, connected in particular to the nature of the explosive itself (oxidizing environment for the Al particles) combined with the nanometric Al quality (size distribution, morphology, presence of alumina).

REFERENCES

[1] TAO W.C., TARVER M.C., BREITHAUPT D., ORNELLAS D.L., Understanding composite explosive energetics : II Particle size effets and reaction modelling development, 27 th JANNAF Combustion Meeting, November 1990

[2] GOGULYA M.F., DOLGOBORODOV A.Yu., BRAZHNIKOV M.A., BAUDIN G., Detonation waves in HMX/Al mixtures, 11th International Symposium on detonation, Snowmass village, Colorado, 1998

[3] BAUDIN G., BERGUES D., A reaction model for aluminized PBX applied to underwater explosion calculations, 10th International Detonation Symposium, Boston, July 12-16, 1993

[4] HAPP A., KRETSCHMER, MEYER U., KEICHER T., SIRRINGHAUS U., WILD R., Underwater explosives - Influence of aluminum and ammoniumperchlorate on the performance, 29 th International Annual conference of ICT, Karlsruhe, FRG, June 30-July 3, 1998

[5] LEFRANCOIS A., BAUDIN G., BERGUES D., Evaluation des performances detoniques d'explosifs dopes par des charges de particules d'aluminium nanometriques, rapport technique CEG T98-0055.

[6] LEFRANCOIS A., GROUFFAL J-Y, Mesures de température par pyromètre spectrique ultra-rapide sur gels explosifs civils, rapport technique DCE/Centre d'études de Gramat T 2001/CEG/NC.

[7] LEAL-CROUZET B., BAUDIN G., GOUTELLE J-C, BOURIANNES J-C, Ultra-fast optical pyrometry for the measurement of detonating explosive temperature, European Physical Journal - EJP - Applied Physics, Vol. 8, n°2, pp. 189-194, Novembre 1999.

[8] LE GALLIC C., MABIRE C., BOUINOT P., BAUDIN G., Temperature measurement in materials submitted to plate impacts : infrared optical pyrometer, 51st ARA Meeting, Madrid Spain, Spetember 18-21, 2000.

[9] FRIED L.E., CHEETAH User's manual 1.39, Lawrence Livermore National Laboratory UCRL-MA-117541 Rev. 2, 1996.

[10] MILLER P.J., BEDFORD C.D., DAVIS J.J., Effect of metal particle size on the detonation properties of various metallized explosives, 11th International Symposium on detonation, Snowmass village, Colorado, 1998

[11] BELANGER C., WALKER G.R., Standard cylinder test : the hyperbola as a fit of time distance measurements for TNT, 1983, CRDV M-2623/83

[12] LEFRANCOIS A., DELCOR P., BERTHUMEYRIE E., LABRUNIE M., Apport des podres d'aluminium nanométriques dans le domaine des explosifs, rapport technique CEG T 1999-N°00057/CEG/NC, Septembre 1999.

[13] LE GALLIC C., BAUDIN G., LEFRANCOIS A., Nanomatériaux métalliques dans les explosifs : un état de l'art, rapport technique CEG T2000-00130/CEG/NC, August 2000

[14] RITTER H., BRAUN S., High explosives containing ultrafine aluminum ALEX, Réunion de la comission du CCRE chargée de l'axe 2.11, Perforation, protection, detonique à l'ISL du 16 et 17/01/01

The Effect of Ultrafine Aluminium Powder on the Detonation Properties of Various Explosives

Patrick Brousseau
Defence Research Establishment Valcartier
2459 Pie-XI Blvd. North, Val-Belair, Québec
Canada, G3J 1X5

Matthew D. Cliff
Weapons Systems Division
Defence Science and Technology Organisation
PO Box 1500, Salisbury, 5108, South Australia

ABSTRACT

Ultrafine (nanometric) aluminium powder is known to react more rapidly than conventional, micron-size aluminium grades in propellant and explosive compositions. In certain explosive formulations, ultrafine aluminium has been reported to enhance the velocity of detonation (VoD). Defence Research Establishment Valcartier (DREV) and the Defence Science and Technology Organisation (DSTO) are collaborating to assess the potential of nanometric aluminium powders in explosive compositions. Various plastic-bonded explosives (PBXs) and TNT-based formulations have been developed to compare ultrafine and conventional micron-sized aluminium. High loadings of ultrafine aluminium have been achieved (20-30%) for all formulations and good casting quality were observed in most cases. Explosive performance was determined by VoD measurements, plate dent depth tests to obtain an estimation of the relative detonation pressure and detonation calorimetry to determine the heat of detonation and the composition of the gases.

For PBX compositions, no significant differences were observed between formulations containing micron-sized and nanometric aluminium. For mixes of TNT and aluminium, an improvement was noted in the velocity of detonation and in plate dent depths using ultrafine aluminium. Very little additional energy release, however, was measured by the detonation calorimeter for these compositions. Formulations were tested at various diameters with a range of aluminium loadings in an attempt to explain this behaviour. The charge diameter seems to have an effect on performance, indicating that the critical diameter of the TNT/Al mixes is

reduced by the ultrafine aluminium powder. More tests have to be performed to confirm this explanation.

INTRODUCTION

Aluminium powder is commonly added to explosive compositions to improve their performance. Aluminium is known to add energy to the reaction and to enhance the blast effect, as well as the underwater performance. It is generally recognised that the aluminium reacts behind the reaction front, during the expansion of the detonation products. In the reaction zone, aluminium behaves more or less as an inert material and contributes very little to enhancing the detonation front.

Conventional weapons-grade aluminium powder is typically micron-sized. However, advances in metal processing technology have allowed submicron particles to become commercially available. One such type of particle is the aluminium powder Alex, produced by electroexploded wire technology and sold by the Argonide Corporation in the USA [1]. Argonide sells spherical aluminium powder originating from Siberia with a particle size in the 100-200 nm range. The Alex powder has an odd behaviour in thermal tests (DSC, DTA and TGA) under air [1-9]. It exhibits a strong exothermic peak at a temperature that is 100-200 °C below the melting point of aluminium, a phenomenon only observed with nanoscale powders. It was originally claimed that this peak was related to some "structural energy" [1] due to defects in the crystal lattice. However, a number of studies have shown that this internal energy is not present in Alex [2, 3, 5, 10]. Instead, the liberation of energy is caused by an oxidation of the particles at low temperatures (400-500 °C). The large surface area of the particles is certainly a factor in explaining this exothermic peak. Nevertheless, a recent study reports an observation of "stored" energy in another nanometric aluminium powder [9]. It remains to be proven if this is truly stored energy.

Because of its large surface area, Alex can produce dramatic improvements of the performance of some energetic materials. Incorporation in propellants has already shown burn rate improvements [1, 3, 11, 12]. On the other hand, the effect into explosive compositions is less readily apparent. Some researchers have reported enhancements in detonations using aluminium nanopowders [1, 13, 14, 15]. It seems obvious that the replacement of conventional

aluminium with nanometric aluminium will influence late-time events by reacting more rapidly with reaction products. However, it is unclear if the reaction of nanoaluminium will be rapid enough to influence the parameters in the reaction zone and enhance the velocity of detonation and the detonation pressure. The objective of this study to investigate the potential of nanometric aluminium powders in explosives. The study is part of a joint effort between Australia (DSTO) and Canada (DREV) to understand the mechanisms of reaction of nanoscale aluminium in energetic materials.

EXPERIMENTAL

Aluminium

Alex was obtained from the Argonide Corporation in the USA. DSTO and DREV procured two different batches of Alex. DSTO showed that their lot of aluminium contained 9 % of AlN by X-ray diffraction analysis, while DREV did not perform this test. The particle size for both the DSTO and DREV lots was between 100-200 nm. The reference aluminium for DSTO was Cap45a, from Comalco Aluminium Powders, with an average particle size of 17 μm [16]. The reference aluminium for DREV was Valimet H-15, with an average particle size of 12 μm. DREV also used Valimet H-2 (spherical, 2 μm) and MDX-75 from Alcan (spherical, 21 μm). Scanning electron microscopy (SEM) pictures of Alex, Cap45a and H-15 are presented in Figure 1.

Plastic-Bonded Explosives

DSTO cast RDX-based plastic-bonded explosives compositions containing aluminium powder. The binder included hydroxyl-terminated polybutadiene (HTPB) as the prepolymer, was plasticised with IDP and cured with IPDI/DBTDL. Table I presents the range of formulations studied. A number of hazard tests were performed on the formulations: Rotter Impact, Electrostatic Discharge, Temperature of Ignition, BAM friction and Vacuum Stability. All the tests showed acceptable values for the formulations. The mixes with Alex demonstrated

higher viscosities than their Cap45a counterparts. The explosives were cast into mild steel cylindrical tubes (51 mm ID x 297 mm long) of 6 mm wall thickness for subsequent testing.

TNT-Based Compositions

Both DSTO and DREV produced TNT-based compositions. DSTO processed a Tritonal variant with 20 % by weight aluminium and 80% TNT. This composition was cast into 41 mm cylindrical moulds. The charges were 250 mm in length. DSTO also tested melt-cast mixes with TNT, RDX and aluminium. The proportion of aluminium was kept at 20%, with 50% of TNT and 30% of RDX. Various diameters were tested, from 25.4 mm to 50.4 mm.

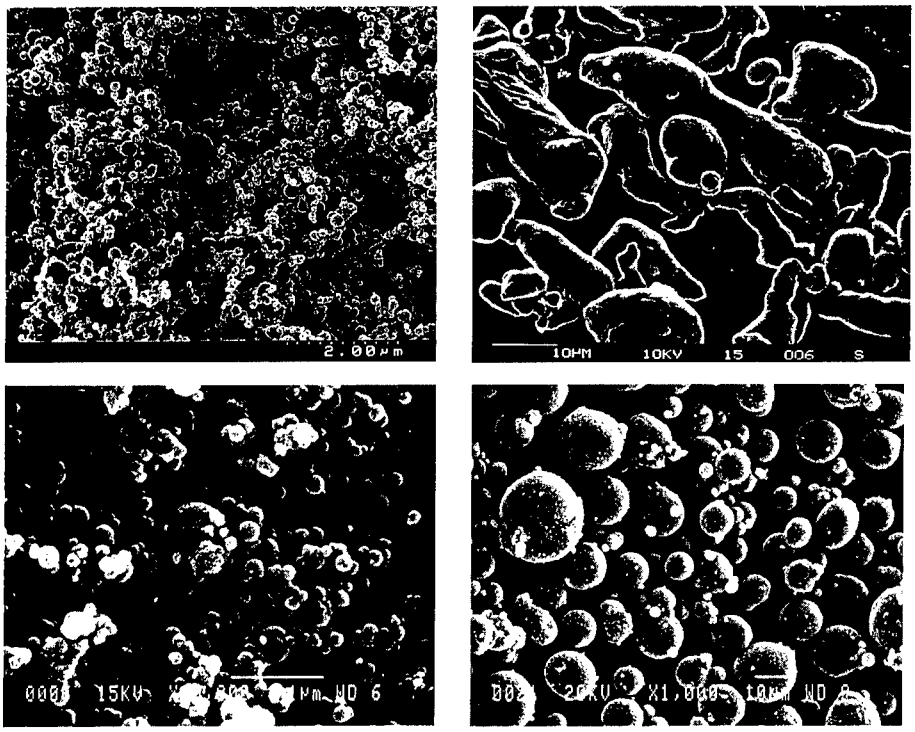


FIGURE 1: SEM pictures of aluminium powders used. Top left: Australian Alex; bottom left: Canadian Alex; top right: Cap45a; bottom right: H-15.

DREV added Alex aluminium to TNT until the limit of processability was reached. The maximum was found at 30% Al. This formulation was then used as the basis for the testing. Aluminium was also added at 20% and 10% to compare with DSTO results and to verify if the trends observed were seen at other percentages. Various diameters were cast from 25.4 mm to 57.8 mm. The length of the cylinders depended on the diameter of the charge. DREV also tested formulations containing RDX, through addition of aluminium to Composition B (RDX/TNT, 60/40). Less than 15 % Al could be added to Comp. B before it became impossible to cast. It was decided to put 10% in the mix, creating a composition TNT/RDX/Al in proportions 54/36/10. Only one diameter of charge was cast, 25.4 mm.

TABLE I: PBX Compositions Used by DSTO in Alex Assessment

Composition	% RDX	% AP	% Binder	% Al	Al Type
ARX-2002	61	-	19	20	Cap45a
ARX-2003	61	-	19	20	Alex
ARX-2004	50	-	20	30	Cap45a
ARX-2005	50	-	20	30	Alex
ARX-2008	41	20	19	20	Cap45a
ARX-2009	41	20	19	20	Alex
ARX-2010	41	20	19	20	Cap45a
ARX-2011	41	20	19	20	Alex

Performance Assessment

DSTO measured the velocity of detonation (VoD) and performed plate dent tests on the experimental explosives. Their compositions were fired in triplicate and average performance results presented. PBX and TNT-based charges were boosted with 51 and 41 mm diameter pentolite right cylinders respectively and initiated from RISI 501 EBW detonators. Velocity of detonation was measured by ten capacitor discharge ionisation probes aligned perpendicular to the charge casing for the PBX series, and side-on piezoelectric pins for TNT-based charges.

Charges were fired in triplicate stacks of 51 mm thick, mild steel witness plates to record dent depths (Figure 2). The upper test plate was removed after each firing for dent depth measurements and the middle and base backing plates discarded. Dent depths only are reported between composition types and give an indication of the relative P_{CJ} between Alex and Cap45a. The details of the set-up can be found in reference 16.

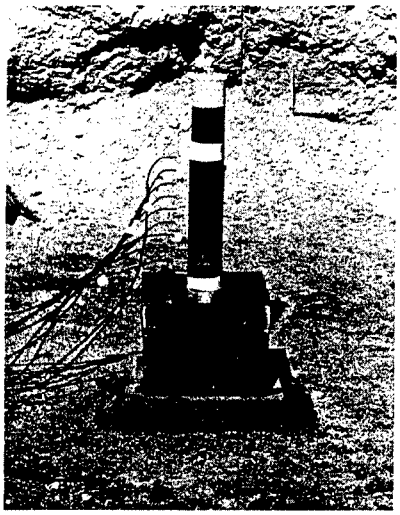


FIGURE 2: Experimental setup for dent test and VoD firings.

DREV evaluated the velocity and the heat of detonation of the experimental explosives. They fired cylinders using an explosive chain composed of a Reynolds RP-83 detonator and a 31.8 mm diameter by 15.2 mm long RDX/Wax booster. Three ionisation probes were used separated by 51 mm from each other, giving two values of detonation velocity. A length of at least two diameters was left at the top to allow for the development of the detonation wave. The charges were fired in the upright position and a steel witness plate was placed underneath the explosive cylinders to confirm a full-order detonation.

The heat of detonation of a number of formulations was also evaluated using a detonation calorimeter. The calorimeter was developed for DREV a few years ago and the design was inspired by the principles of the combustion calorimeter and the detonation calorimeter used by

Ornellas at LANL [17]. Its design is detailed elsewhere [18, 19]. All the explosives were confined in annealed copper (99.9% purity) having a length of 12 cm and a diameter of 3.2 cm. The diameter of each explosive charge was 1.23 cm and the length of the charge was nominally 9.3 cm. Each charge was suspended in the middle of the steel bomb using copper wire and fired using a Reynolds RP-1 exploding bridge wire detonator. Detonation gases were collected and then analysed using a Carlo Erba Mega Gas Chromatograph. The detonation calorimeter was seen as an effective way of measuring any additional "stored" energy liberated by the aluminium during an actual detonation. In addition, the analysis of the detonation gases should provide an explanation to any differences observed in the performance of explosives containing nanopowders.

RESULTS AND DISCUSSION

Plastic-Bonded Explosives

The confined PBX charges containing Alex did not demonstrate any improvements on the detonation velocity and the plate dents (Table II) compared to the PBXs containing Cap45a . In fact, they showed a small decrease in the detonation velocity for all cases and a slight increase in the dent for only one case (ARX-2011). It was concluded that Alex has a negligible effect on the VoD and P_{CJ} for PBXs based on inert binders. It was assumed that the HTPB matrix prevents Alex from reacting rapidly with the detonation gases, and any effect would be observed in the Taylor region, as for conventional aluminium. The use of an energetic binder may solve that problem and allow Alex to react more rapidly. This hypothesis will be investigated in future work at DREV and DSTO. The small reduction of the performance may be related to the fact that Alex contains less active aluminium than the Cap45a because of its large percentage of aluminium oxide (the oxide layer is around 4 nm for a particle that is 75-100 nm in radius). The percentage of AlN may also be a contributing factor.

TNT-Based Explosives

TNT/Al

The first reported results from DSTO on Tritonal variants including Alex indicated a significant improvement on the detonation velocity and the dent depth (see Table III). The detonation velocity was enhanced by 300 m/s while the average witness plate dent depth was increased by 21 %. The results from DREV also showed a similar improvement in the detonation velocity using Alex. DREV originally tested at a smaller diameter than DSTO (25.4 mm instead of 41.1 mm). DREV also found a very small increase in the heat of detonation, much less than the other parameters under study. DSTO sent some of the Cap45a powder to DREV. It was mixed with TNT and the composition was tested in the detonation calorimeter. The results are reported in Table III.

Table II: Performance Results for PBXs

Composition	Aluminium Type	Density (g/cm^3)	VoD (m/s)	Dent Depth (mm)
ARX-2002	Cap45a	1.65	7273	14.67
ARX-2003	Alex	1.61	7266	13.66
ARX-2004	Cap45a	1.64	6976	12.22
ARX-2005	Alex	1.64	6911	11.91
ARX-2008	Cap45a	1.62	6471	11.91
ARX-2009	Alex	1.63	6422	11.76
ARX-2010	Cap45a	1.64	6724	14.01
ARX2011	Alex	1.63	6667	14.15

Clearly, there seemed to be an effect of the type of aluminium on the detonation parameters. The results from Australia and Canada agreed very well on the detonation velocity. The 300 m/s increase was observed with all the formulations. DREV tested formulations of TNT with two other types of aluminium, MDX-75 and H-2. The results are presented in Table IV. From these results, it is obvious that the size of the aluminium has an effect on the detonation

velocity of TNT/Al mixes. The smaller particles caused the mix to have a higher detonation velocity. The amount of heat produced was also greater, probably because the detonation calorimeter charges were small and detonated more easily with smaller aluminium. The very small aluminium is also likely to react more completely than regular aluminium in those oxygen-deficient mixes.

TABLE III: Performance Results of TNT/Al Mixes

Tester	TNT (%)	Al (%)	Al Type	Density (g/cm^3)	Diam. of the charge (mm)	VoD (m/s)	Dent Depth (mm)	Heat of detonation (cal/g)
AUS	80	20	Cap45a	1.71	41.1	6427	5.95	1412
AUS	80	20	Alex	1.76	41.1	6722	7.20	1438
CAN	70	30	H-15	1.82	25.4	6228	-	1536
CAN	70	30	Alex	1.82	25.4	6628	-	1593
CAN	80	20	H-15	1.74	25.4	6182	-	-
CAN	80	20	Alex	1.74	25.4	6598	-	-
CAN	80	20	H-15	1.72	31.8	6456	-	-
CAN	80	20	Alex	1.74	31.8	6724	-	-
CAN	90	10	H-15	1.67	25.4	5718(*)	-	-
CAN	90	10	Alex	1.67	25.4	6507	-	-

(*) One of the two charges failed to detonate.

TABLE IV: TNT/Al Mixes with Four Different Aluminium Types

TNT (%)	Al (%)	Al Type	Density (g/cm^3)	Diam. Of the charge (mm)	VoD (m/s)	Heat of detonation (cal/g)
70	30	MDX-75	1.83	25.4	5740(*)	1478
70	30	H-15	1.82	25.4	6228	1536
70	30	H-2	1.83	25.4	6462	1570
70	30	Alex	1.82	25.4	6628	1593

(*) One of the two charges failed to detonate.

The diameter of the charges was near the critical diameter for all those experiments. For Tritonal, the critical diameter is listed as 18.3 mm [20]. In Table III, the charges were tested in a region where the detonation velocity still increases with the diameter. The hypothesis is that the nanometric aluminium decreases the critical diameter. However, this decrease was not associated with a significant increase in the friction and impact sensitivities. Various diameters of the charges were then evaluated. The results are presented in Table V. Because of instrumentation problems, the VoD results from DSTO are not included. There was a difference in performance even at large diameters. The Canadian results indicated that the difference in VoD was decreased at larger diameters. However, the DSTO dent test results showed a 27.0 % improvement in P_{CJ} at a diameter of 50.4 mm. It then decreased to 20.9% at 60.1 mm. It is very surprising to observe an effect at such large diameters (more than three times the critical diameter). Figure 3 presents a graphical representation of some of the results of Table V. It suggests that the velocities of detonation will be the same at some large diameter (> 100 mm). This reduction in the critical diameter must be accompanied with a change in the energy release rates. In the case of TNT, the Alex seems to be able to react in the detonation front and contribute to the reaction.

TNT/RDX/Al

Mixes with TNT, RDX and aluminium were produced both in Australia (DSTO) and Canada (DREV). DREV tested only one diameter (25.4 mm) while DSTO tried four different diameters. The compositions of the mixes are different and are detailed in Table VI. The results from this table indicate that, as for the PBXs, the VoD is decreased with Alex. However, the Australian measurements of the plate dents show an increase of P_{CJ} even at large diameters. The detonation calorimeter tests showed a little less energy with H-15 compared to Alex (1390 cal/g vs 1416 cal/g). The reaction rate much be such that Alex reacts just fast enough to enhance the brisance and not the reaction front (velocity of detonation). A better analysis of the energy-release mechanisms in the near-field should provide an explanation to this phenomenon.

TABLE V: Effect of the Charge Diameter on the Performance

Tester	TNT (%)	Al (%)	Al Type	Density (g/cm^3)	Diam. of the charge (mm)	VoD (m/s)	Dent Depth (mm)	Increase (%)
CAN	70	30	H-15	1.82	25.4	6228	-	-
CAN	70	30	Alex	1.82	25.4	6628	-	6.4
CAN	70	30	H-15	1.80	31.8	6428	-	-
CAN	70	30	Alex	1.84	31.8	6708	-	4.4
CAN	70	30	H-15	1.81	57.9	6591	-	-
CAN	70	30	Alex	1.84	57.9	6742	-	2.3
AUS	80	20	Cap45a	1.76	31.5	-	4.59	-
AUS	80	20	Alex	1.78	31.5	-	5.00	8.9
AUS	80	20	Cap45a	1.71	41.1	6427	5.95	-
AUS	80	20	Alex	1.76	41.1	6722	7.20	21.0
AUS	80	20	Cap45a	1.70	50.4	-	7.74	-
AUS	80	20	Alex	1.69	50.4	-	9.83	27.0
AUS	80	20	Cap45a	1.70	60.1	-	9.89	-
AUS	80	20	Alex	1.69	60.1	-	11.96	20.9

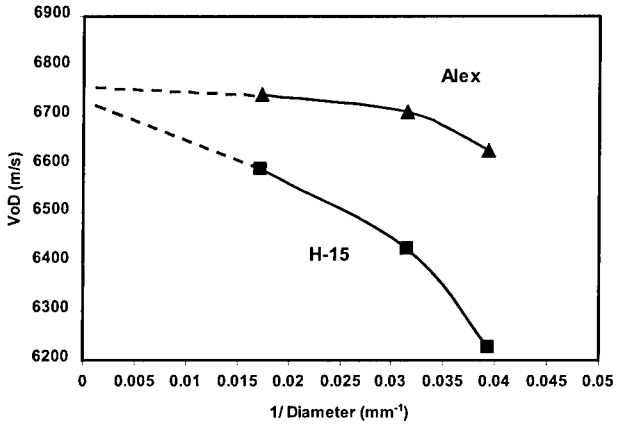


FIGURE 3: Effect of the Charge Diameter on the VoD for Unconfined 70/30 TNT/Al Explosives.

TABLE VI: Performance of TNT/RDX/Al Mixes

Tester	TNT (%)	RDX (%)	Al (%)	Al Type	Density (g/cm^3)	Diam. of the charge (mm)	VoD (m/s)	Dent Depth (mm)	Incr. (%)
CAN	54	36	10	H-15	1.74	25.4	7744	-	-
CAN	54	36	10	Alex	1.74	25.4	7598	-	(1.9)
AUS	50	30	20	Cap45a	1.81	25.5	7047	4.34	-
AUS	50	30	20	Alex	1.82	25.5	6806	4.62	6.50
AUS	50	30	20	Cap45a	1.80	31.6	7042	5.47	-
AUS	50	30	20	Alex	1.80	31.6	6754	6.08	11.3
AUS	50	30	20	Cap45a	1.80	41.1	7111	7.25	-
AUS	50	30	20	Alex	1.82	41.1	6855	8.12	12.0
AUS	50	30	20	Cap45a	1.77	50.5	7039	9.50	-
AUS	50	30	20	Alex	1.76	50.5	6665	10.04	5.6

CONCLUSIONS

Alex was found to enhance the velocity of detonation and the detonation pressure of TNT/Al mixes compared to micrometric aluminium. This effect is attributed partly to a reduction in the critical diameter, which is seen with other types of aluminium. However, even at large diameters (60 mm), Alex seems to give better results than a typical micron-sized aluminium. A small decrease of performance was seen in PBXs containing Alex. For TNT/RDX/Al mixes, the velocity of detonation was decreased with Alex while the plate dent test results indicated an increase in detonation pressure. More work is needed to study the energy release mechanisms in those explosives.

REFERENCES

1. Ivanov, G.V. and Tepper, F., *Activated Aluminium as a Stored Energy Source for Propellants*, Fourth International Symposium on Special Topics in Chemical Propulsion, Challenges in Propellants and Combustion 100 Years after Nobel, 27-28 May 1996, Stockholm, Sweden.
2. Mench, M.M., Kuo, K.K., Yeh, C.L. and Lu, Y.C., *Comparison of Thermal Behvior of Regular and Ultra-Fine Aluminum Powders (Alex) Made from Plasma Explosion Process*, Comb. Sci. and Tech., Vol. 135, 1998, pp. 269-292.
3. Mench, M.M., Yeh, C.L. and Kuo, K.K., *Propellant Burning Rate Enhancement and Thermal Behavior of Ultra-Fine Aluminium Powders (Alex)*, Proceedings of the 29th International Annual Conference of ICT: Energetic Materials, Production, Processing and Characterisation , June 30-July 3, 1998, Karlsruhe, Germany, pp. 30-1,15.
4. Sandén, R., *Characterisation of Electro-Exploded Aluminium*, Proceedings of the 29th International Annual Conference of ICT: Energetic Materials, Production, Processing and Characterisation , June 30-July 3, 1998, Karlsruhe, Germany, pp. 77-1,10.
5. Cliff, M.D., de Yong, L., Edwards, D.P. and Watt, D.S., *Characterisation of Electroexploded Aluminium (Alex)*, DSTO-TR-0818 (Limited Release), DSTO Aeronautical and Maritime Research Laboratory, Melbourne, Australia, 1999.
6. Brousseau, P., Côté, S., Lessard, P., and Beaupré, F., *Thermal Analysis of Aluminium Nanopowders*, Paper presented at the TTCP WTP-4 Workshop, held at Indian Head, MD, USA, April 1999.
7. Hooton, I.E. and Pagotto, J., *Characterisation of Metal Powders*, DRES-TR-1999-192 (Limited Release), Defence Research Establishment Suffield, Canada, 1999.

8. Jones, D.E.G., Brousseau, P., Fouchard, R.C., Turcotte, A.M. and Kwok, Q.S.M., *Thermal Characterization of Passivated Nanometer Size Aluminium Powders*, Journal of Thermal Analysis and Calorimetry, Vol. 61, 2000, pp. 805-818.

9. Pranda, P., Prandova, K. and Hlavacek, V., *Particle Size and Reactivity of Aluminum Powders*, Comb. Sci. and Tech., Vol. 156, 2000, pp. 81-96.

10. DeSena, J.T. and Kuo,K.K., *Evaluation of Stored Energy in Ultrafine Aluminum Powder Produced by Plasma Explosion*, Journal of Propulsion and Power, Vol. 15, No 6, Nov.-Dec. 1999, pp. 794-800.

11. Simonenko, V.N. and Zarko, V.E., *Comparative Studying the Combustion Behavior of Composite Propellants Containing Ultra Fine Aluminium*, Proceedings of the 30th International Conference of ICT, Energetic Materials: Modeling of Phenomena, Experimental Characterization, Environmental Engineering, June 29 - July 2, 1999, pp. 21-1, 14.

12. Bashung, B., Grune, D., Licht, H.H. and Samirant, M., *Combustion Phenomena of a Solid Propellant Based on Aluminum Powder*, 5th International Symposium on Special Topics in Chemical Propulsion (5-ISICP)- Stresa, Italy, June 19-22, 2000.

13. Reshetov, A.A., Shneider, V.B., and Yavorovsky, N.A., *Ultra Dispersed Aluminium's Influence on the Speed of Detonation of Hexagen*, First All-Union Symposium on Macroscopic Kinetic and Chemical Gas-Dynamics, Vol. 1, October 1984, Chernogolovka, Russia.

14. Tulis, A.J., Sumida, W.K., Dillon, J., Comeyne, W. and Heberlein, D.C., *Submicron Aluminum Particle Size Influence on Detonation of Dispersed Fuel-Oxidizer Powders*, Arch. Comb., Vol. 18, No. 1-4, 1998, pp. 157-164.

15. Miller, P.J., Bedford, C.D. and Davis, J.J., *Effect of Metal Particle Size on the Detonation Properties of Various Metallized Explosives*, Proceedings of the Eleventh International Symposium on Detonation, ONR 33300-5, held in Snowmass, Colorado, August 30 – Sept. 4, 1998, pp. 214-220.

16. Cliff, M.D., Dexter, R.M. and Watt, D.S., *The Effect of Electroexploded Aluminium (Alex) on Detonation Velocity and Pressure*, DSTO-TR-0999 (Limited Release), DSTO Aeronautical and Maritime Research Laboratory, Melbourne, Australia, 2000.

17. Ornella, D., *Calorimetric Determinations of the Heat and Products of Detonation for Explosives*, Lawrence Livermore National Laboratory Report # UCRL-52821, 1982.

18. Katsabanis, P., *Development of a Detonation Calorimeter to Measure the Energy Outputof High Explosives*, Final report, Prepared for Defence Research Establishment Valcartier, April 1993.

19. Anderson, C.J. and Katsabanis, P., *Evaluation of Heats of Detonation*, Final report from Mining Resource Engineering Limited, Kingston, Ontario, Prepared for Defence Research Establishment Valcartier, April 2000.

20. Hall, T.N. and Holden, J.R., *Navy Explosives Handbook*, NSWC MP 88-116, Naval Surface Warfare Center, Dalhgren, Virginia, October 2000.

Rheology of nano - scaled aluminium suspensions

Rheologische Eigenschaften nanoskaliger Aluminium - Suspensionen

Ulrich Teipel, Ulrich Förter-Barth

Fraunhofer Institut für Chemische Technologie (ICT)
Joseph-von-Fraunhofer-Straße 7
D - 76327 Pfinztal, Germany

Abstract

Nano-scaled aluminium particles are innovative materials which are more and more used in energetic formulations. In this contribution, the rheological behaviour of suspensions with paraffin oil as well as HTPB as the matrix fluid and nano-scaled aluminium (ALEX) as the disperse phase is introduced and discussed. The paraffin oil/aluminium suspensions show non-Newtonian flow behaviour in dependence on the shear stress over a wide range of concentration, whereas the HTPB/aluminium suspensions exhibit Newtonian behaviour, i.e. there is no dependence of the viscosity on the shear stress up to a concentration of 50 vol.% aluminium content. Both systems have distinct viscoelastic material properties, with elastic moduli not showing any dependence on the solid concentration.

1. Einleitung

Aluminiumpartikel sind ein seit langem bekannter Bestandteil von energetischen Materialien. Die typische Partikelgröße des in Sprengstoffen und Raketenfesttreibstoffen eingesetzten Aluminiums liegt im Bereich von ca. 30 µm [1]. Um die Reaktion des Aluminiums z.B. bei der Verbrennung von Festtreibstoffen zu erhöhen, ist es vorteilhaft, Partikel mit einer größeren spezifischen Oberfläche, d.h. mit kleinerer mittlerer Partikelgröße zu verwenden. Durch die Verdampfung und anschließende Kondensation von Aluminium in Argon oder durch eine Elekroexplosion eines Aluminiumdrahtes ist es möglich, Aluminiumpartikel im Nanometerbereich herzustellen [2,3]. Partikel in diesem Größenbereich weisen aber im Vergleich zu denen im Mikrobereich unterschiedliche physikalische Eigenschaften auf. Aufgrund der geringeren Partikelgröße sind die im System auftretenden interpartikulären Wechselwirkungen wesentlich dominanter, so daß z. B. die Agglomerationsneigung dieser nanoskaligen Partikel wesentlich ausgeprägter ist [4]. Des weiteren können aufgrund des veränderten Materialverhaltens von Nanopartikeln Schwierigkeiten bei der Verarbeitung der Partikel in eine fluide Polymermatrix auftreten.

Im Rahmen dieser Arbeit wird das rheologische Verhalten von Suspensionen mit nanoskaligen Aluminiumpartikeln in stationärer Scherströmung und bei oszillatorischer Scherbeanspruchung untersucht und diskutiert.

2. Meßmethoden

Die Untersuchungen zum rheologischen Verhalten von nanoskaligen Aluminium-Suspensionen wurden in stationärer Scherströmung und bei oszillatorischer Scherbeanspruchung mit dem Rotationsrheometer UDS 200 der Firma Physica Meßtechnik GmbH durchgeführt. Als Meßsysteme wurden ein modifiziertes koaxiales Zylindersystem (Mooney-Ewart-System) und ein Kegel-Platte-System verwendet.

Bei stationärer Scherströmung kann die charakteristische Materialfunktion wie folgt beschrieben werden:

$$\tau(\dot{\gamma}) = \eta(\dot{\gamma}) \cdot \dot{\gamma} \qquad (1)$$

Dabei ist $\eta(\dot{\gamma})$ eine für das jeweils betrachtete Fluid charakteristische Materialfunktion, welche die bei einer rheometrischen Strömung auftretenden Fließeigenschaften beschreibt.

Bei oszillatorischer Scherbeanspruchung wird die Suspension durch eine periodische (z.B. sinusförmige) Deformation $\gamma(t)$ mit der Amplitude $\hat{\gamma}$ und der Kreisfrequenz $\omega = 2\,\pi\,f$ beansprucht [5]:

$$\gamma(t) = \hat{\gamma}\sin(\omega t) \qquad (2)$$

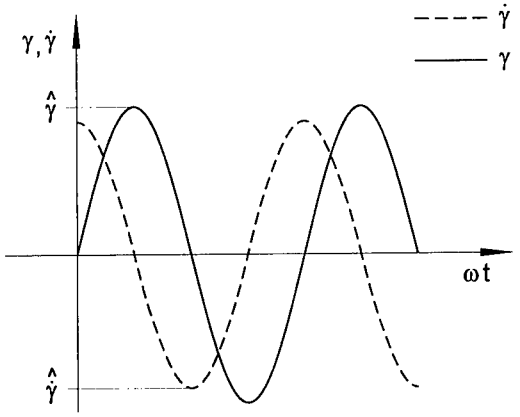


Abb. 1: Deformations- und Schergeschwindigkeitsverlauf bei oszillierender Scherbeanspruchung

Bei hinreichend kleiner Amplitude –im linear-viskoelastischen Bereich– resultiert aus einer oszillatorischen (sinusförmigen) Scherbeanspruchung ein ebenfalls sinusförmiger Schubspannungsverlauf $\tau(t)$. Bei viskoelastischem Materialverhalten ergibt sich für den Schubspannungsverlauf $\tau(t)$ und den Deformationsverlauf $\gamma(t)$ eine Phasenverschiebung δ:

$$\tau(t) = \hat{\tau}\cdot\sin(\omega t + \delta) \qquad (3)$$

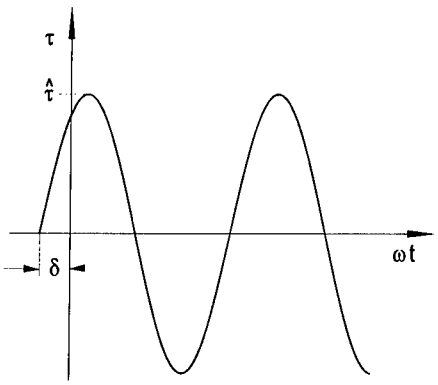


Abb. 2: Schubspannungsverlauf eines viskoelastischen Fluids bei oszillierender Scherbeanpruchung

Während für rein elastische Fluide $\delta = 0°$ und für rein viskose Fluide $\delta = \pi/2$ ist, gilt für viskoelastische Fluide $0° \leq \delta \leq \pi/2$.

Der Schubspannungsverlauf kann unter Verwendung des frequenzabhängigen komplexen Schubmoduls $G^*(\omega)$ wie folgt dargestellt werden:

$$\tau(t) = \hat{\gamma}\left|G^*(\omega)\right| \cdot \sin\left(\omega t + \delta(\omega)\right) \qquad (4)$$

Für den Betrag des komplexen Schubmoduls gilt :

$$\left|G^*(\omega)\right| = \frac{\hat{\tau}(\omega)}{\hat{\gamma}} \qquad (5)$$

Der komplexe Schubmodul $G^*(\omega)$ einer viskoelastischen Substanz wird in einen Real- und Imaginärteil –zwei Materialfunktionen, den Speichermodul $G'(\omega)$ und den Verlustmodul $G''(\omega)$– aufgeteilt. Der Speichermodul $G'(\omega)$ ist ein Maß für die reversibel im Material gespeicherte Deformationsenergie (elastischer Anteil), während der Verlustmodul $G''(\omega)$ ein Maß für die in der Probe dissipierte Energie (viskoser Anteil) darstellt.

$$|G^*(\omega)| = \sqrt{G'(\omega)^2 + G''(\omega)^2} \qquad (6)$$

Oszillatorische Scherversuche müssen im linear-viskoelastischen Bereich des Materialverhaltens durchgeführt werden. In diesem Bereich sind bei konstanter Kreisfrequenz ω die Deformationsamplitude $\hat{\gamma}$ und die sich einstellende Schubspannungsamplitude $\hat{\tau}$ proportional ($\hat{\tau} \sim \hat{\gamma}$). Dies gilt nur bei hinreichend kleinen Schwingungsamplituden. Charakterisiert wird der linear-viskoelastische Bereich einer Substanz dadurch, daß die Moduli $G'(\omega)$, $G''(\omega)$ oder $G^*(\omega)$ bei konstanter Frequenz keine Abhängigkeit von der Deformationsamplitude zeigen.

Die mittlere Größe und die Größenverteilung der Aluminiumpartikel wurde mittels Laserbeugungsspektrometrie bzw. Photonenkorrelationsspektroskopie ermittelt. Außerdem wurden Rasterelektronenmikroskopaufnahmen angefertigt.

3. Materialien

Die untersuchten Suspensionen bestanden aus Paraffinöl oder hydroxyterminiertem Polybutadien (HTPB) als kontinuierliche Phase und nanoskaligen Aluminiumpartikeln als disperse Phase.

Das ausgewählte Paraffinöl besitzt Newtonsches Fließverhalten mit einer dynamischen Viskosität von $\eta(20°C) = 198$ mPas. Die Dichte des Paraffinöls beträgt $\rho = 874{,}7$ kg/m^3 und die Oberflächenspannung $\sigma = 30{,}5$ mN/m.

Das verwendete hydroxyterminierte Polybutadien HTPB R 45-M zeigt ebenfalls Newtonsches Fließverhalten bei einer dynamische Viskosität von $\eta(20°C) = 9300$ mPas.

Die disperse Phase der untersuchten Suspensionen bestand aus nanoskaligem Aluminium (Alex) von der Argonide Corporation, Stanford, Florida/USA. Die mittels Gaspyknometrie ermittelte Dichte der Aluminiumpartikel beträgt $\rho = 2{,}4$ g/m^3 und die spezfische Oberfläche (Gasadsorption) $S = 11{,}2$ m^2/g. Abbildung 3 zeigt eine REM – Aufnahme des Aluminiumpulvers.

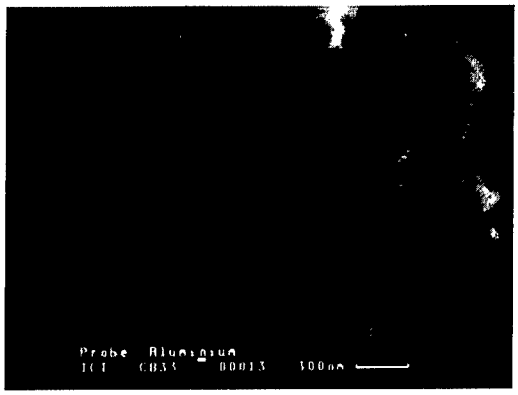


Abb.3: Nanoskaliges Aluminiumpulver

4. Ergebnisse

4.1 Fließverhalten der Paraffinöl/Aluminium - Suspensionen

Vor der rheologischen Charakterisierung der Paraffinöl/Aluminium–Suspensionen wurden diese zur Desagglomeration der Aluminiumpartikel und zur Homogenisierung der Suspensionen mehrere Stunden gerührt und mittels Ultraschallhomogenisator dispergiert. Das Materialverhalten dieser Suspensionen wurde danach in stationärer Scherströmung untersucht. Abbildung 4 zeigt die relative Viskosität in Abhängigkeit der Schergeschwindigkeit. Die Konzentration der dispersen Phase wurde im Bereich von 2 vol.% bis 45 vol.% variiert. Des weiteren ist in Abbildung 4 die Viskositäts-funktion von reinem Paraffinöl dargestellt.

Die relative Viskosität η_{rel} ist definiert als Verhältnis der Viskosität der Suspensionen zur Viskosität der Matrixflüssigkeit bei konstanter Schergeschwindigkeit $\dot{\gamma}$.

$$\eta_{rel} = \frac{\eta_{Suspension}|\dot{\gamma}}{\eta_{Paraffinoel}} \qquad (7)$$

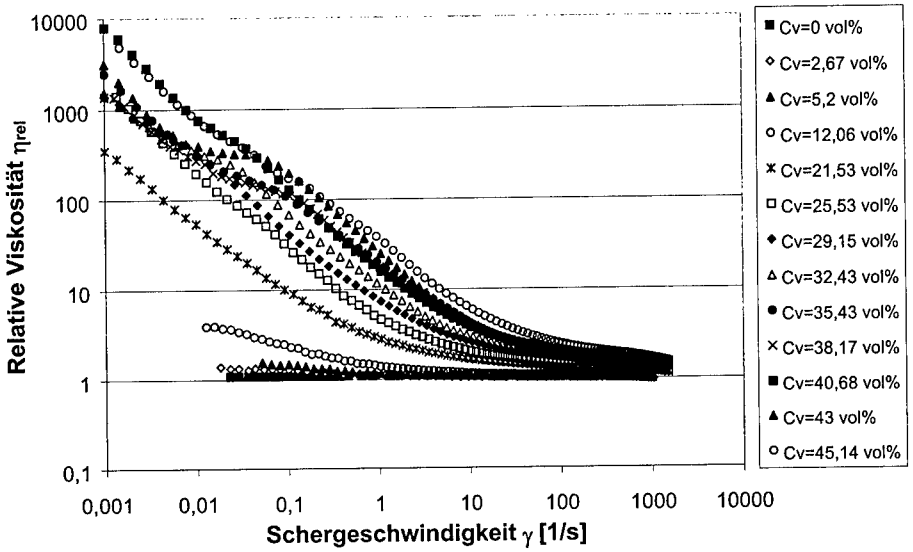


Abb. 4: Relative Viskosität der Paraffinöl/Aluminium–Suspensionen als Funktion der Schergeschwindigkeit; ϑ = 20 °C

Mit zunehmender Aluminiumpartikelkonzentration ist –bei NEWTONschem Fließverhalten der Matrixflüssigkeit– ein immer ausgeprägteres strukturviskoses Fließverhalten der Suspensionen zu beobachten. Dieses Nicht-Newtonsche Verhalten der Suspensionen ist durch die im System auftretenden Partikel/Partikel-Wechselwirkungen und durch, gegenüber einphasigen Fluiden, veränderten hydrodynamischen Verhältnissen bedingt. Bei kleinen Schergeschwindigkeiten ist der Viskositätsanstieg in Abhängigkeit der Konzentration besonders deutlich. In diesem Schergeschwindigkeitsbereich konkurrieren die interpartikulären Kräfte mit den in diesem Bereich wesentlich geringeren hydrodynamischen Kräften, so daß das rheologische Verhalten der Suspensionen sehr stark von der Konzentration und den die Suspension strukturierenden Wechselwirkungen abhängig ist. Durch eine Erhöhung der Schergeschwindigkeit, die eine Vergrößerung der hydrodynamischen Kräfte zur Folge hat, kommt es zu einer strömungsinduzierten Strukturierung der nanoskaligen Partikel und somit zur Abnahme der Viskosität bei gleicher Konzentration. Der Viskositätsunterschied in Abhängigkeit der Konzentration ist aufgrund der hydrodynamischen

Strukturierung des Systems bei größeren Schergeschwindigkeiten wesentlich geringer als im Bereich kleiner Schergeschwindigkeiten.
In Abbildung 5 ist die Abhängigkeit der relativen Viskosität der Suspensionen von der Konzentration der dispersen Phase für die Nullviskosität ($\dot{\gamma} \to 0$) und für eine Schergeschwindigkeit $\dot{\gamma}$ = 1000 s^{-1} dargestellt.

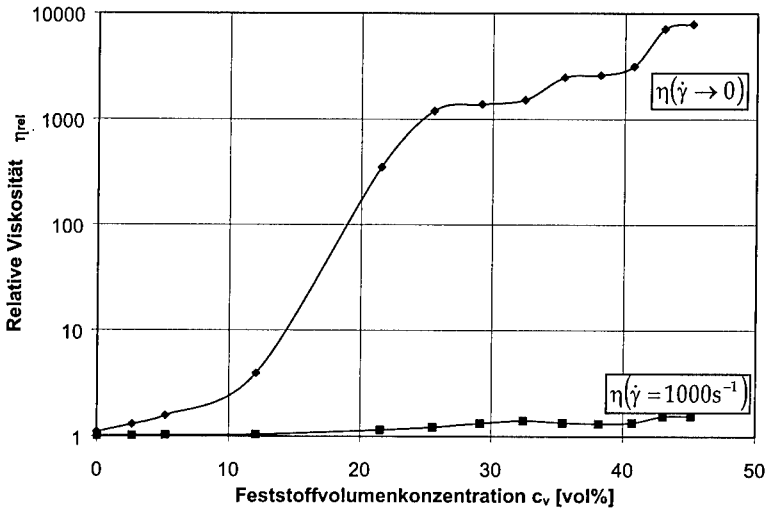


Abb. 5: Relative Viskosität der Paraffinöl/Aluminium–Suspensionen als Funktion der Partikelkonzentration

Bei maximaler Schergeschwindigkeit erfolgt bis zu einer Konzentration von $c_V \approx 25$ vol.% eine lineare Erhöhung der relativen Viskosität mit der Partikelkonzentration. Im unteren Konzentrationsbereich besteht zwischen der relativen Viskosität bei maximaler und minimaler Schergeschwindigkeit nur ein geringer Unterschied, da in diesem Bereich aufgrund des vorhandenen freien Volumens der Matrixflüssigkeit hinreichend großer Abstand der Partikel zueinander besteht und somit wenig Wechselwirkungen auftreten und auch die strömungsbedingte Orientierung der Partikel nicht zu einer wesentlich geringeren Viskosität als der Nullviskosität führt. Durch eine Vergrößerung der Konzentration kommt es zur Erhöhung der Anzahldichte der Partikel, so daß sich die Wahrscheinlichkeit der Partikelwechselwirkungen erhöht. Die sich ausbildende Ruhestruktur des Mehr-

phasensystems hat die in Abbildung 5 dargestellte Nullviskosität zur Folge, welche mit Erhöhung der Konzentration stetig steigt. Bei höherer Schergeschwindigkeit bildet sich eine strömungsinduzierte Struktur aus, so daß eine wesentlich geringere relative Viskosität bei gleicher Konzentration beobachtet wird. Der Unterschied der beiden Viskositätsfunktionen für $\dot{\gamma} \to 0$ und $\dot{\gamma}$ = 1000 s^{-1} , der sich mit steigender Partikelkonzentration vergrößert, resultiert insbesondere aus dem Verhalten der Partikel in der Couette-Strömung. Bei einer Konzentration von 45 vol.% ist ein Viskositätsunterschied von nahezu 10^4 zu beobachten.

4.2 Fließverhalten der HTPB/Aluminium - Suspensionen

In Abbildung 6 ist die relative Viskosität der HTPB/Aluminium–Suspensionen in Abhängigkeit der Schergeschwindigkeit für den Konzentrationsbereich 0 vol.% ≤ c_V ≤ 47 vol.% dargestellt.

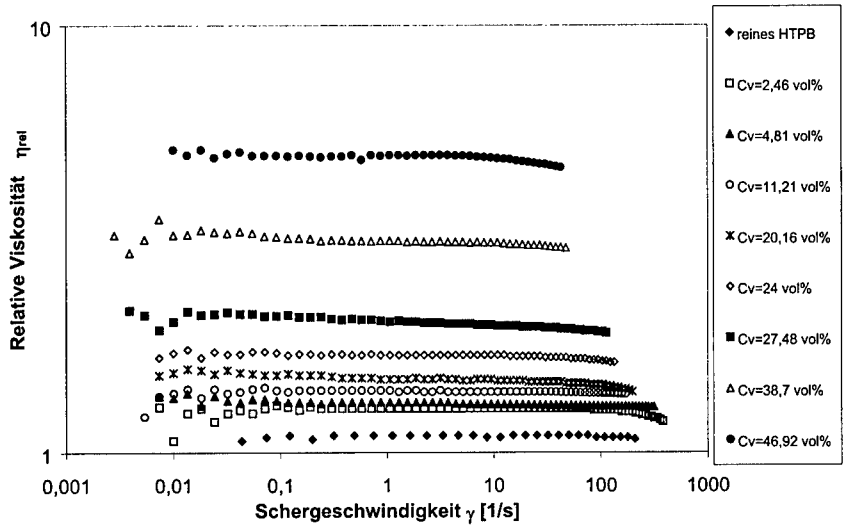


Abb. 6: Relative Viskosität der HTPBl/Aluminium–Suspensionen als Funktion der Schergeschwindigkeit; ϑ = 20 °C

Hydroxyterminiertes Polybutadien HTPB R 45-M ohne Zusatzstoffe zeigt Newtonsches Fließverhalten (siehe Abb 6 oder [6,7]). Im Gegensatz zu den Paraffin-

öl/Aluminium–Suspensionen zeigen die Suspensionen mit HTPB als kontinuierliche Phase über einen weiten Schergeschwindigkeitsbereich bis zu einer Konzentration der dispersen Phase von ca. 50 vol.% Newtonsches Fließverhalten. Mit zunehmender Konzentration erhöht sich nur die relative Viskosität der Suspensionen. Das lineare Fließverhalten bleibt aber erhalten. Abbildung 7 zeigt die relative Viskosität der Suspensionen in Abhängigkeit der Konzentration der dispersen Phase.

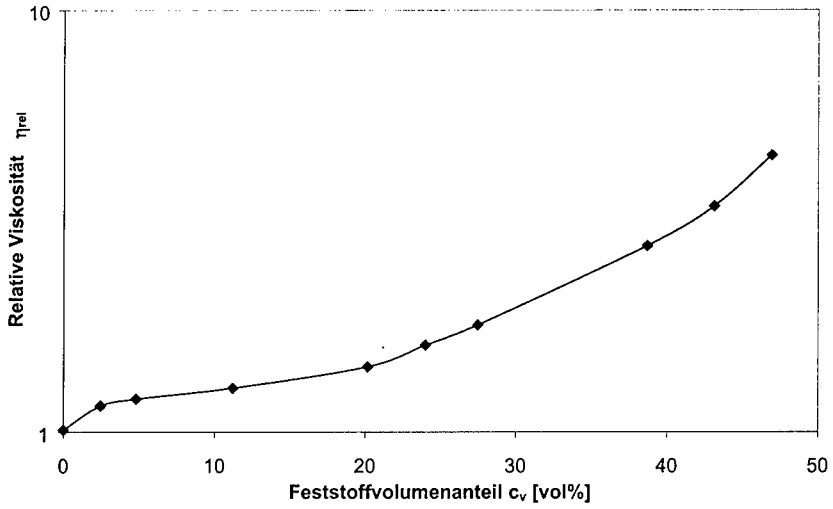


Abb. 7: Relative Viskosität der HTPB/Aluminium–Suspensionen als Funktion der Feststoffkonzentration

Basierend auf den Ergebnissen der Charakterisierung des rheologischen Verhaltens der Suspensionen mit HTPB als Matrixflüssigkeit und nanoskaligen Aluminiumpartikeln ergibt sich folgende Abhängigkeit der relativen Viskosität von der Feststoffvolumenkonzentration:

$$\eta_{rel,S} = \frac{\eta_{Suspension}}{\eta_{HTPB}} = 1 + 5{,}5 \cdot C_V - 31{,}4 \cdot C_V^2 + 74{,}5 \cdot C_V^3 \qquad (8)$$

Mit Gleichung (8) kann somit die Viskosität von Suspensionen, die aus HTPB und nanoskaligen Aluminiumpartikeln bestehen, bis zu Volumenkonzentrationen von $C_V \leq 50$ vol.% beschrieben werden.

4.3 Viskoelastische Eigenschaften der Suspensionen

Die viskoelastischen Materialeigenschaften können durch Experimente in oszillatorischer Scherung ermittelt werden. Der durch Schwingversuche im linear-viskoelastischen Bereich des Materialverhaltens ermittelte komplexe Schubmodul kann gemäß Gleichung (6) in zwei Materialfunktionen, den Speichermodul $G'(\omega)$ und den Verlustmodul $G''(\omega)$, aufgeteilt werden.

Abbildung 8 zeigt die Speicher- und Verlustmodulfunktionen der Paraffinöl/Aluminium-Suspensionen für verschiedene Konzentrationen. Bei niedrigen Kreisfrequenzen weist der Speichermodul kleinere Funktionswerte als der Verlustmodul auf. In diesem Bereich der Kreisfrequenzen überwiegen somit die viskosen Eigenschaften der Suspensionen. Beide Funktionen steigen mit wachsender Kreisfrequenz stetig. Die Speichermodulfunktion besitzt eine größere Steigung als die Funktion des Verlustmoduls, so daß der Speichermodul mit zunehmender Kreisfrequenz stärker wächst als der Verlustmodul und sich beide Funktionen bei einer für die jeweilige Suspension charakteristischen Kreisfrequenz ω_i schneiden. Oberhalb dieser Kreisfrequenz dominieren die elastischen Eigenschaften der Suspension. Im Schnittpunkt ist die Strukturrelaxationszeit λ gleich der reziproken Kreisfrequenz. Es gilt:

$$\omega_i \cdot \lambda = 1 \qquad (9)$$

Somit ergeben sich für die Paraffinöl/Aluminium-Suspensionen in dem Konzentrationsbereich bis $c_V \leq 40$ vol.% Strukturrelaxationszeiten von $0{,}24\ s \leq \lambda \leq 0{,}37\ s$. Des weiteren konnte beobachtet werden, daß der Speichermodul $G'(\omega)$ unabhängig von der Aluminiumkonzentration ist. Somit ist bei Suspensionen mit nanoskaligen Partikeln als disperse Phase die reversible, elastisch in dem Material gespeicherte Deformationsenergie unabhängig von der Partikelkonzentration.

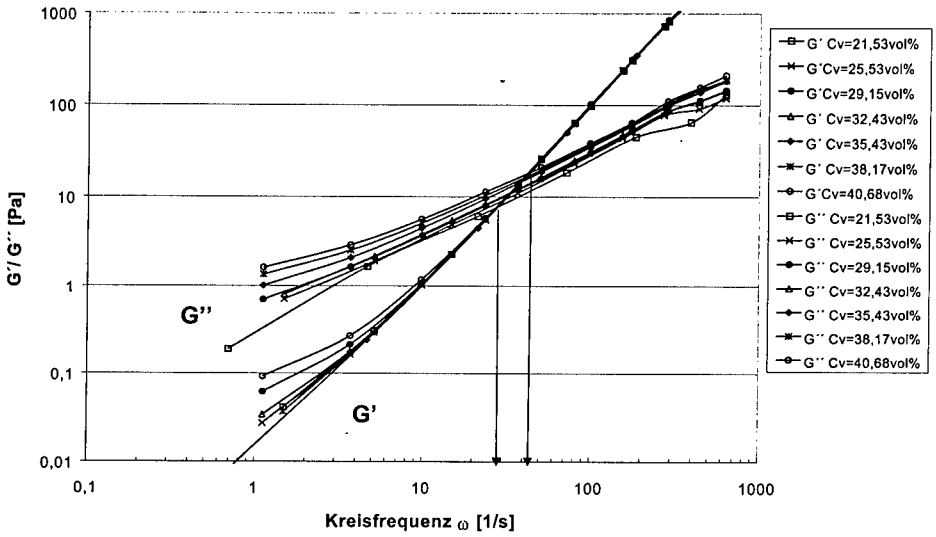


Abb. 8: Speicher- und Verlustmodulfunktion der Paraffinöl/Aluminium-Suspensionen

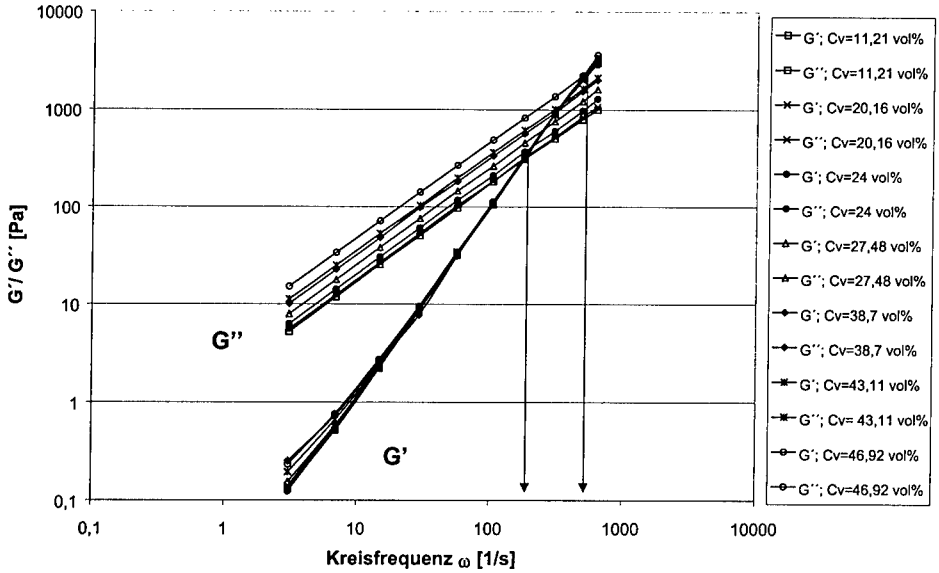


Abb. 9: Speicher- und Verlustmodulfunktion der HTPB /Aluminium-Suspensionen

In Abbildung 9 sind die Speicher- und Verlustmodulfunktionen der HTPB/Aluminium-Suspensionen für verschiedene Konzentrationen dargestellt. Auch hier ist die Konzentrationsunabhängigkeit des Speichermodul $G'(\omega)$ zu erkennen. Die Strukturrelaxationszeiten sind bei diesen Supensionen aber wesentlich geringer. In dem untersuchten Konzentrationsbereich ergeben sich Strukturrelaxationszeiten im Millisekundenbereich ($0{,}0021\ s \leq \lambda \leq 0{,}0062\ s$).

5. Literatur

[1] R. R. Miller, E. Lee, R. L. Powell:
Rheology of solid propellant dispersion
Journal of Rheology 35 (1991) 5, 901 - 920

[2] G. V. Ivanov, F. Tepper:
Activated Aluminum as a Stored Energy Source for Propellants
in: Challenges in Propellants and Combustion, 100 Years after Nobel
(Ed. K.K. Kuo) Begell House, 1997, 636- 645

[3] F. Tepper, G. V. Ivanov, M. Lerner, V. Davidovich:
Energetic formulations from nanosize Metal Powders
Proceedings of the 24th Intern. Pyrotechnics Seminar, 1998, Monterey,
California, USA, 519 – 530

[4] O. G. Glotov, V. E. Zarko, M. W. Beckstead:
Agglomerate and oxide particles generated in combustion of alex containing solid propellants
Proceedings 31th International Conference of ICT, Karlsruhe, 2000,
pp. 130/1 - 130/15

[5] U. Teipel:
Rheologisches Verhalten von Emulsionen und Tensidlösungen
Dissertation, Universität Bayreuth, 1999
Wissenschaftliche Schriftenreihe des Fraunhofer ICT, Band 22

[6] A. C. Hordijk, H. W. R. Sabel, L. Schonewille, J. J. Meulenbrugge:
The application of rheological equipment for improved processing of HTPB based PBXes
Proceedings 27th International Conference of ICT, Karlsruhe, 1996,
pp. 3/1 - 3/11

[7] R. Muthiah, V. N. Krishnamrthy, B. R. Gupts:
Rheology of HTPB propellant: Development of generalized correlation and evaluation of pot life
Propellants, Explosives, Pyrotechnics 21 (1996), 186 - 192

IRSIM (IR-SIGNATURE-MODEL)

A New Computational Model For Calculating Exhaust Plume Signatures

Dr.Hartmut Benk
EADS-LFK, VME 12
P.O.Box 1661
D - 85705 Unterschleißheim / Germany

e-mail –address: hartmut.benk@lfk.eads.net

SUMMARY:

The computer program **IRSIM** allows the simulation of missile exhaust plumes (temperature distribution) and their IR/UV-signatures by means of semi-empirical equations which contain four adjustable parameters at the most. Two of them describe the spatial distribution (I_{core}, σ), the remaining parameters the radiant properties of the exhaust plume (α, γ). These parameters are determined during a single IR- or UV-signature measurement on a missile exhaust plume and are characteristic for certain classes of missile engines. As soon as these four parameters of a specified engine class are known, the IR-or UV-signature of a missile plume of this class under different operating and flight conditions can be predicted by means of **IRSIM**. Vice versa we can conclude from a measured missile plume signature to the corresponding engine class (type of propellant, nozzle geometry etc.) (first step in a missile identification process). The missile plume signatures are described by spatial radiant distributions (thermal images), spectral radiant intensities and total radiant intensities over well defined spectral ranges for different aspect angles. **IRSIM** delivers input data for the design of sensors and decoys. It predicts IR/UV-signatures under realistic tactical situations with sufficient accuracy (according to the state of the art of the experimental recording technique and seeker resolution) and can be integrated in real time scenario simulations in an inexpensive manner.

Key words:

Missile exhaust plume signature, engine classes, signature prediction, missile detection, missile identification, sensors, missile approach warners, decoys.

Literatur:

(1) K.Beier, "*Infrared Radiation Model NIRATAM(NATO Infra Red Air TArget Model), Description of* Program (1993) ", DLR, D-82230 Oberpfaffenhofen, Germany.

(2) L.Deimling, W.Liehmann, N.Eisenreich, M.Weindel, W.Eckl, *"Radiation Emitted from Rocket Plumes "*, Propellants,Explosives,Pyrotechnics 22, 152-155 (1997).

(3) W.Eckl, V.Weiser, M.Weindel, N.Eisenreich, *"Models for the determination of tem- perature and molecule distribution in solid propellant flames* ", Proceedings of the 30th International Annual Conference of ICT - No.112(1999), Fraunhofer-Institut für Chemische Technologie(ICT), P.O.Box 1240, D -76318 Pfinztal, Germany.

(4) H.Benk, L.Deimling, W.Eckl, N.Eisenreich, *"Simulation of Spectral Exhaust Plume Signatures by means of the Combined Computer Model IRSIM/BAM* " (in preparation).

(5) G.N.Abramowitsch, "*Angewandte Gasdynamik* ",VEB Verlag Technik, Berlin,1958

(6) G.N.Abramovich, "*The Theory of Turbulent Jets* ",MIT Press, Cambridge, Mass.,1963

(7) H.Reichardt, "*Gesetzmäßigkeiten der freien Turbulenz*", VDI – Forschungsheft 414, Düsseldorf (1942).

(8) H.Schlichting, "*Grenzschicht -Theorie*", Verlag G.Braun, Karlsruhe, 1965.

(9) C.Donaldson, K.E.Gray, "*Theoretical and Experimental Investigation of the Com -pressible Free Mixing of Two Dissimilar* Gases ", AIAA Journal 4, 2017-2025 (1966).

(10) E.U.Schlünder, "*Über die Ausbreitung turbulenter Freistrahlen* ", Zeitschrift für Flugwissenschaften 19, 108-113 (1971).

IR-Signaturen von Raketenabgasstrahlen
IR-Signatures of Rocket Exhaust Plumes

L. Deimling

Fraunhofer-Institut für Chemische Technologie (ICT)
76318 Pfinztal, P.O. Box 1240

Abstract

This paper deals with the importance of IR-signatures of rocket exhaust plumes concerning detection, identification and tracking of missiles. The employed spectral radiometer in the range of 1,25 to 14 µm is introduced and the experimental setup to detect head-on signatures is sketched. By comparison of IR-signatures of rocket motors with different velocities the influence of surrounding flow to signature is shown.

Kurzfassung

Der vorliegende Beitrag beschäftigt sich mit der Bedeutung der IR-Signatur des Raketenabgasstrahls für die Erfassung, Identifikation und Verfolgung von Raketenflugkörper. In diesem Zusammenhang wird das im Spektralbereich von 1,25 bis 14µm verwendete Spektralradiometer vorgestellt und die Versuchsanordnung zur Signaturmessung aus dem Head-on-Aspekt bei den durchgeführten Schlittenbahnexperimenten skizziert. Durch den Vergleich der IR-Signaturen, die an Raketenmotoren mit unterschiedlicher Geschwindigkeit gewonnen wurden, wird der Einfluss der Relativströmung der Umgebungsluft auf die IR-Signatur aufgezeigt.

1 Einleitung

Der Abgasstrahl ist, bedingt durch seine teilweise sehr intensive Emission von elektromagnetischer Strahlung, besonders zur passiven Erfassung und Identifikation

eines im Anflug befindlichen Flugkörpers geeignet. Die Strahlungsemissionen erstrecken sich dabei vom Ultraviolett über das Sichtbare und das Infrarot bis in den Radarbereich.

Aus verbrennungstechnischer Sicht ist speziell der Infrarotbereich von besonderem Interesse, da hier die spektrale Verteilung vielfältige Auskünfte über die Reaktionsabläufe enthält. Des weiteren weisen Teile des IR-Bereichs eine gute Transmission durch die Atmosphäre auf. Somit sind intensive IR-Strahler auch über große Distanzen detektierbar. Aus diesem Grund wird der IR-Bereich von einer Vielzahl von Such- und Warnsystemen genutzt. Darüber hinaus ist dieser Bereich auch für die optische Fernlenkung von Flugkörpern sehr interessant.

Bedingt durch Störeffekte und Hintergrundstrahlung treten bei den integral arbeitenden Infrarotsystemen Probleme hinsichtlich der Identifikationssicherheit auf. Hier kann durch eine spektrale Zerlegung der IR-Strahlung eine erhebliche Reduzierung der Fehlerrate erreicht werden. Auch im Bereich der Zielverfolgung können eingeleitete Gegenmaßnahmen, wie das Aussetzen von Täuschkörpern, durch spektral auflösende Suchköpfe als solche erkannt und ignoriert werden. Mit Rücksicht auf die teilweise sehr geringen Intensitäten, die es noch zu erfassen gilt, wird dies zunächst durch Unterteilung in wenige relativ breite Spektralbereiche erfolgen. Als langfristiges Ziel ist der Einsatz von hyperspektral auflösenden Sensoren zu sehen. Dies eröffnet dann auch Möglichkeiten die spektralen Eigenheiten bestimmter Flugkörperantriebe zu unterscheiden, und diese bereits im Anflug zur Identifizierung des Flugkörpertyps zu nutzen. Eine frühzeitige Beurteilung der Bedrohung ermöglicht wiederum das Einleiten gezielter Gegenmaßnahmen.

Mit dem Ziel motorspezifische Eigenheiten unterschiedlicher Flugkörperantriebe zu erarbeiten, wurde eine Vielzahl von unterschiedlichen Raketenmotoren hinsichtlich ihrer Abgasstrahlsignatur auf stationären Prüfständen vermessen. Die Ergebnisse werden derzeit in einer Signaturdatenbank zusammengefasst. Im Hinblick auf den Bedrohungsfall gilt das primäre Interesse den Signaturen aus dem Frontaspekt. Für die Modellierung des Abgasstrahls stehen die Signaturen aus dem Seitenaspekts im Vordergrund.

Die Untersuchung gefesselter Abbrände hat jedoch den Nachteil, dass mit der fehlenden Relativströmung der Umgebungsluft erhebliche Änderungen im Abgasstrahl einhergehen, die einen starken Einfluss auf die Strahlungsemission haben.

Stationär brennende Antriebe besitzen eine erheblich breitere Nachreaktionszone, da sich die Abgase aufstauen. Weiterhin treten im stationären Fall größere

Geschwindigkeitsgradienten auf, die sich auf die Durchmischung der Reaktionsprodukte mit der Umgebungsluft auswirken. Daher ist sowohl mit Veränderungen der spektralen Verteilung als auch der Gesamtintensität zu rechnen.

Um diesen Einfluss abzuschätzen, werden die bisherigen Abbranduntersuchungen durch dynamische Abbrände auf einer Schlittenbahn ergänzt. Das Ziel der Schlittenbahnversuche ist es, Gesetzmäßigkeiten zu finden, um die Messergebnisse von gefesselten Antrieben auf frei fliegende Motoren zu übertragen.

2 Das IR-Spektralradiometer

Das verwendete IR-Spektralradiometer ist eine Eigenentwicklung des ICTs und wurde bereits mehrfach bei Emissions- und Transmissionsmessungen an Raketenabgasstrahlen erfolgreich eingesetzt /1,2/.

Die Abbildung 1 zeigt eine Skizze zur Verdeutlichung des Funktionsprinzips des im folgenden beschriebenen IR-Spektralradiometers. Der Monochromator dieses IR-Messsystems besteht aus einer viersegmentigen zirkularen Verlaufsfilterscheibe.

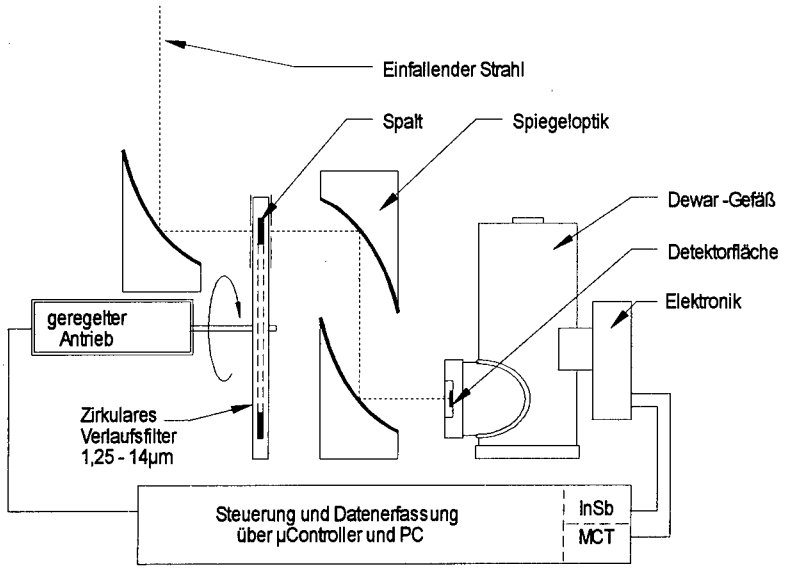


Abbildung 1: Prinzipskizze des verwendeten IR-Spektralradiometer

Bei der Betrachtung einer Strahlungsquelle durch einen mittels eines schmalen radialen Spalts begrenzten Ausschnitts dieser Verlaufsfilterscheibe, ergibt sich in Abhängigkeit der Winkelstellung die Transmission einer definierten Spektrallinie.

Durch Rotation der Verlaufsfilterscheibe kann durch diesen Spalt der gesamte Spektralbereich der Verlaufsfiltersegmente aufgezeichnet werden. Dieser erstreckt sich von 1,25 bis14 µm (8000 bis 700 cm^{-1}). Aufgrund der großen Spektralbreite, der hohen Signalgeschwindigkeit und der geforderten hohen Detektivität kommt ein schneller stickstoffgekühlter InSb-HgCdTe-Sandwich-Detektor zum Einsatz. Die maximale Drehzahl der Verlaufsfilterscheibe beträgt derzeit 6000 U/min. Mit dieser Einstellung liefert das Spektralradiometer in 10 ms ein komplettes Spektrum. Die spektrale Auflösung beträgt 1% der selektierten Wellenlänge.

Zur Vermeidung der chromatischen Abberation finden im gesamten Messsystem lediglich Spiegeloptiken Verwendung. Durch ihre kompakte Bauweise bieten sich Off-Axis-Parabolspiegel als Erfassungsoptik an. Die geräteinterne Abbildung des Monochromatorspalts auf den Detektor erfolgt ebenfalls mittels zweier Off-Axis-Parabolspiegel. Eine absolute Brennweite kann für diesen Spiegeltyp nicht angegeben werden, da sie in Abhängigkeit der Position auf der Spiegelfläche variiert. Entsprechend kompliziert ist die Bestimmung der Abbildungsverhältnisse und des Beobachtungsbereichs (FOV), die für eine präzise Intensitätskalibrierung sehr wichtig sind.

Die Speichertechnik der IR-Spektralradiometer ist elektronisch triggerbar und verfügt darüber hinaus über eine Pretriggerfunktion, sodass zur Offsetkorrektur auch Spektren direkt vor Abbrandbeginn aufgezeichnet werden.

3 Versuchsaufbau

Die dynamischen Abbrände fanden auf der 800-Meter Schlittenbahn der WTD 91 in Meppen statt. Die Aufbauskizze in Abbildung 2 gibt den experimentellen Aufbau wieder.

Die dynamischen Versuche auf der Schlittenbahn können durch das stationär eingerichtete Spektralradiometer lediglich in einem Teilbereich der Bahn zwischen

100 m und 400 m erfasst werden. Der Aspektwinkel zur Abgasstrahlachse variiert dabei zwischen 1° und 5°.

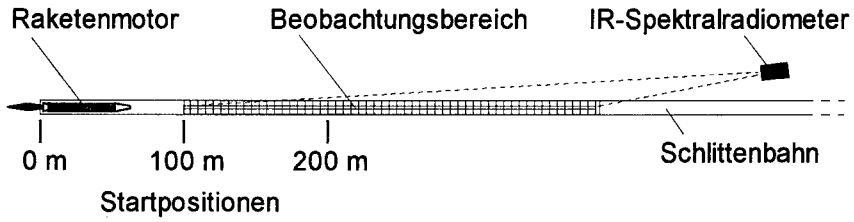


Abbildung 2: Versuchsanordnung der dynamischen Abbrände auf der Schlittenbahn

Zur Beurteilung der Signatur bei unterschiedlichen Geschwindigkeiten, werden Abbrände mit vorgezogenen Startpositionen bei 100 m und 200 m durchgeführt.

4 Ergebnisse

Die Vermessung der IR-Signatur von Raketenmotoren auf dem gleitenden Schlitten liefert entfernungsbedingt erheblich geringere Strahlungsintensitäten als bei den stationären Abbränden. Abbildung 3 zeigt einen Zeitverlauf der versetzt aufgetragenen Einzelspektren eines Raketenmotors (RM 2, Start bei 100 m).

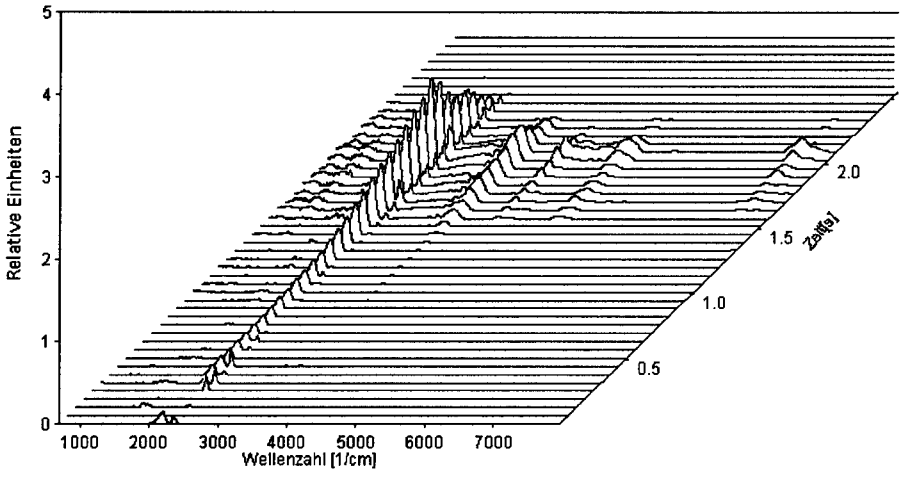


Abbildung 3: Spektrenverlauf eines bewegten Flugkörperantriebs aus dem Frontaspekt

Die Änderungen der Entfernung und der Atmosphäre, die mit der Bewegung des Motors einhergehen, sind nicht korrigiert. Der Spektrenverlauf zeigt bei t = 0 den Startpuls (Eject), eine kurze Totphase und ab t = 0,3 s den Beginn des Triebwerkabbrands. Die empfangene Intensität steigt mit abnehmender Distanz an, bis der Schlitten bei ca. t = 2,1 s das Beobachtungsfeld des Spektralradiometers verlässt.

Die Messungen bei unterschiedlichen Startpositionen auf der Schlittenbahn verdeutlichen den Einfluss der Relativströmung auf den Abgasstrahl. In Abbildung 4 sind drei Zeitverläufe der intensiven CO_2-Emissionslinie bei 4,5 µm eines Raketenmotors mit den Startpositionen 0 m, 100 m und 200 m in einem Diagramm gegenübergestellt.

Der hierfür verwendete Motor (RM 3) hat den Vorteil, dass er abgesehen vom Startpuls über die gesamte Abbranddauer einen relativ gleichbleibenden Schub liefert. Dies zeigt sich auch dadurch, dass beim stationären Abbrand die Strahlungsintensität über den Abbrand annähernd konstant bleibt.

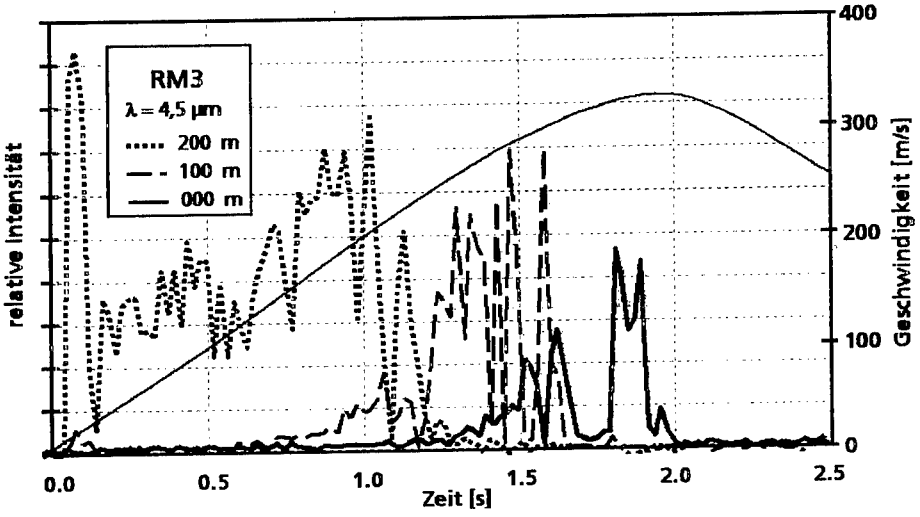


Abbildung 4: Vergleich der im Frontaspekt erfassten Strahlungsintensitäten über der Zeit

Mit zunehmender Vorverlagerung der Startposition bei den Testversuchen erreichen und verlassen die Antriebe den Beobachtungsbereich des Messsystems früher. Somit fehlt den Antrieben mit vorverlegtem Start ein Teil der Beschleunigungsstrecke, so dass sie beim Durchqueren des Messfeldes eine geringere Geschwindigkeit besitzen. Zur Verdeutlichung ist die momentane Geschwindigkeit des Motors über der Zeit in Abbildung 4 als graue durchgezogene Kurve hinterlegt. Der Intensitätsabfall am Ende

jeder Kurve markiert nicht das Ende des Abbrands, sondern das Austreten des Motors aus dem Beobachtungsbereich des Messsystems.

Bei der Betrachtung der maximalen Strahlungsintensitäten, die kurz vor dem Verlassen des Beobachtungsbereichs gemessen werden, können vergleichbare Abbildungsverhältnisse angenommen werden. Anhand der gemessenen Werte kann für den untersuchten Feststoffmotor im Geschwindigkeitsbereich von 150 bis 350 m/s eine Abschätzung des Geschwindigkeitseinflusses auf die Strahlungsintensität erfolgen. Diese Betrachtung ergibt folgende Abhängigkeit der Intensität von der Geschwindigkeit:

$$I_{(V)} \approx 1 - \frac{V^2}{\text{Const.}} \qquad \text{für: } 150\text{m/s} < V < 350\text{m/s}$$

Es wird somit deutlich, dass die Strahlungsintensität im Frontaspekt bei hohen Geschwindigkeiten des Antriebs erheblich geringer wird. Des weiteren nehmen mit der Relativgeschwindigkeit der Umgebungsluft die Fluktuationen im Abgasstrahl zu. Die Versuche zeigen, dass die Intensität der IR-Strahlungsemission zeitweise einbricht und anschließend wieder aufflackert. Diese Erkenntnis wird durch die High-Speed-Videoaufzeichnungen in Abbildung 5 bestätigt.

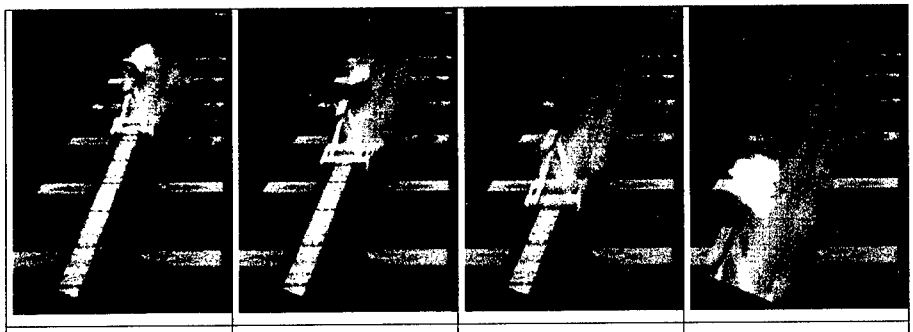


Abbildung 5: High-Speed-Sequenz der Abgasstrahlfluktuationen

Zu den Auswirkungen der Relativgeschwindigkeit auf die spektralen Eigenheiten des Abgasstrahls kann derzeit keine Aussage gemacht werden. Diesbezüglich sind weiterführende Untersuchungen aus dem Front- und Seitenaspekt auf der Schlittenbahn in Meppen vorgesehen.

5 Literatur

/1/ A. Blanc, L. Deimling, „Transmissionsmessungen an Raketenabgasstrahlen" BMVg-Auftrag T/RF11/O 0001/O 1100, Bericht 12/94, ICT Eigenverlag, 1994.

/2/ A. Blanc, L. Deimling, „Abgasstrahltransmission von LAR- und Sidewinder-Motoren mit Composite- und Double-Base-Treibstoffen", BMVg-Auftrag T/RF11/P ooo1/P 1100, Bericht 10/95, ICT-Eigenverlag, 1995.

Modern Measurement Techniques for Energetic Materials

Prof. Y.M. Timnat
Faculty of Aerospace Engineering
Technion – Israel Institute of Technology
Haifa 32000, Israel.

Abstract

After a brief introduction specifying the main modern techniques for investigating energetic materials a number of those is described. A computational procedure developed is dealt with in some detail and the results obtained are compared with the predictions, showing good agreement. Finally the influence of geometric and kinematic factors is studied.

Introduction

By introducing swirl into flames an adverse pressure field is set up. This pressure field changes the velocity distribution at the burner exit and causes a faster decay of the axial velocity in comparison to a non-swirling flame. Measurements of velocity and temperature were carried out in swirling Butane-Propane air flames, which emerged from a round orifice with exit velocities of 75 to 100 m/s. The flame was unconfined over a distance of 2 m where the measurements were taken.

We showed that due to a faster decay of the velocity and more favourable conditions at the exit, flames with swirl can be stabilized closer to the burner exist at higher values of maximum velocity. The length of the flame decreased markedly with increasing degree of swirl. A certain increase in the temperature maximum with the degree of swirl is also observed (Chervinsky and Timnat 1967). Isotherms of the flame, which show the variation in its shape are presented graphically in Fig. 1 for 3 different flames.

In continuation to these studies we investigated a liquid petroleum gas (LPG) flame consisting of 15% ethane, 50% propane and 35% butane percent by volume, which flowed through copper coils immersed in a bath of 12 mm boiling water (Chervinsky and Timnat 1969). The liquid fuel was thus evaporated and injected in gaseous form into the surrounding atmosphere via a 16 mm diameter pipe. The fuel jet was ignited by an oxyacetylene pilot flame and an annular flame front was stabilized in the boundaries of the jet some ten diameters from the orifice. Velocities were measured with a 12 mm diameter Pitot probe mounted on a traversing mechanism; total and static pressure were read on an alcohol manometer inclined at 45°. Velocities were measured along the axis up to 140 orifice diameters. Temperature measurements were performed with a bare Pt/Pt - 13% Rh thermo-couple; traverses in the radial direction were performed at x/d = 0/2, 0.4, 0.6, 0.8, 1 and 1.2

Introduction

By introducing swirl into flames an adverse pressure field is set up. This pressure field changes the velocity distribution at the burner exit and causes a faster decay of the axial velocity in comparison to a non-swirling flame. Measurements of velocity and temperature were carried out in swirling Butane-Propane air flames, which emerged from a round orifice with exit velocities of 75 to 100 m/s. The flame was unconfined over a distance of 2 m where the measurements were taken.

We showed that due to a faster decay of the velocity and more favourable conditions at the exit, flames with swirl can be stabilized closer to the burner exist at higher values of maximum velocity. The length of the flame decreased markedly with increasing degree of swirl. A certain increase in the temperature maximum with the degree of swirl is also observed (Chervinsky and Timnat 1967). Isotherms of the flame, which show the variation in its shape are presented graphically in Fig. 1 for 3 different flames.

In continuation to these studies we investigated a liquid petroleum gas (LPG) flame consisting of 15% ethane, 50% propane and 35% butane percent by volume, which flowed through copper coils immersed in a bath of 12 mm boiling water (Chervinsky and Timnat 1969). The liquid fuel was thus evaporated and injected in gaseous form into the surrounding atmosphere via a 16 mm diameter pipe. The fuel jet was ignited by an oxyacetylene pilot flame and an annular flame front was stabilized in the boundaries of the jet some ten diameters from the orifice. Velocities were measured with a 12 mm diameter Pitot probe mounted on a traversing mechanism; total and static pressure were read on an alcohol manometer inclined at 45°. Velocities were measured along the axis up to 140 orifice diameters. Temperature measurements were performed with a bare Pt/Pt - 13% Rh thermo-couple; traverses in the radial direction were performed at x/d = 0/2, 0.4, 0.6, 0.8, 1 and 1.2

m. Buoyancy effects appeared at a distance of 140 orifice diameters, after which no measurements were taken.

Measured distributions of axial velocity and temperature at x/R-80 are presented in Fig. 2a and b and compared with analytical predictions. The velocity profiles show an increase from the flame axis to the flame front and then a sharp drop towards the boundaries of the flame. An analysis we developed then, based on a phenomenological approach for the definition of turbulent momentum and heat transfer coefficients, gave a reasonably good agreement with the experimental results. The flame surface calculated for different fuel/air ratios is shown in Fig. 3.

The Influence of Unmixedness

Some years later (Spiegler et al. 1976) we developed a model for unmixedness for turbulent reacting flows. The phenomenon of unmixedness is caused by turbulent fluctuations leading to a situation, in which the instantaneous value of fuel or oxidizer concentration, and, therefore, the instantaneous chemical reaction rate vanishes. We presented a qualitative and quantitative analysis, and developed a simple model, that made it possible to evaluate the decrease in the overall reaction rates, without incurring a serious penalty in computer time and memory. The assumptions made led to a mixing length type relation connecting the local value of the r.m.s. fluctuating concentration of a given species to the local gradient of the mean concentration and to the length scale of the turbulent motion. A computational procedure was developed for the general case involving N elementary, reversible, simultaneous reactions in which N species appear. We also built an experimental rig with the aid of which we compared the predictions with experiments and obtained satisfactory agreement (see Fig. 4). To do this we introduced the concept of a decay function, the basic idea being to divide the flow field into cells and to obtain algebraic relations between the

values of the local quantities in one cell and the surrounding ones. The cell properties were not kept constant, so that the concentration variation was described approximately by a family of decay functions that satisfy the initial conditions and yield the equilibrium conditions at infinite time.

The Influence of Geometric and Kinematic Factors

Later we studied the influence of geometric and kinematic factors on changing the flame configuration in liquid fuel burners (Arbib et al. 1978, Arbib et al. 1980). The factors examined were change in the spray angle, swirl number and burner tunnel configuration. We found that these variables allow better control of the flame shape and more effective utilization of the combustion. This work included an experimental effort, in which we examined the influence of pressure in the range between 0.3 and 1.5 MPa on combustion intensity. We used a medium size rig, measured temperatures by a number of thermocouple techniques, such as bare thermocouples, a suction pyrometer and sheathed thermocouples applying appropriate corrections in each case. Composition was monitored by sampling the flow and performing gas chromatograph measurements. In parallel theoretical work we developed a comprehensive code, which allowed to solve the relevant set of elliptical non-linear partial differential equations, taking into account turbulent, reacting, recirculating flow conditions. Agreement between calculations and experiments was satisfactory.

References

Chervinsky, A. and Timnat, Y.M. (1967). *Israel J. Technol.* **5**, 36-46.

Chervinsky, A. and Timnat, Y.M. (1969). *Combustion and Flame*, **13**, 157-165.

Arbib, H.A., Goldman, Y. and Timnat, Y.M. (1978). *Acta Astronautics*, **5**, 1221-1230.

Arbib, H.A., Goldman, Y. and Greenberg, J.B. and Timnat, Y.M. (1980). *Combustion and Flame*, **38**, 259-270.

List of Figures

Fig. 1: Tunnel wall temperature along combustion chamber for conical tunnel, S=0, T_{AD}=2153°C, d=160 mm.

Fig. 2: Heat flux to furnace wall along combustion chamber for conical tunnel, S=0, d=160 mm.

Fig. 3: Flame temperature and CO_2 concentration (at flame axis) along combustion chamber for conical tunnel, regular burner, T_{AD}=2153°C, CO_{2max}=15.3%, d=160 mm.

Fig. 4: Tunnel wall temperature along combustion chamber for conical tunnel, regular burner, T_{AD}=2153°C, d=160 mm.

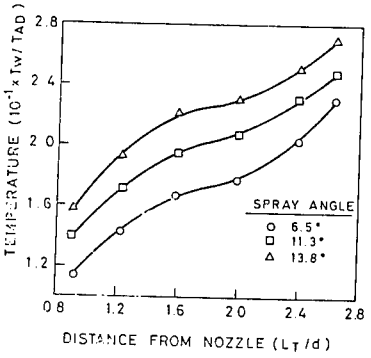


FIG. 1 - Tunnel wall temperature along combustion chamber for conical tunnel, S=0, T_{AD} = 2153 °C, d = = 160 mm.

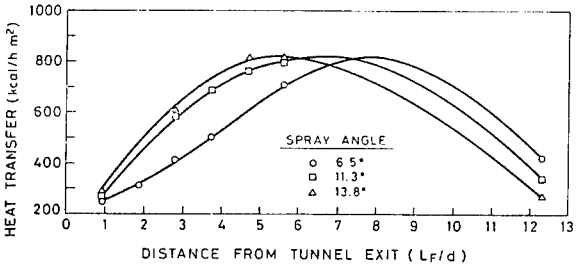


FIG. 2 - Heat flux to furnace wall along combustion chamber for conical tunnel, S=0, d = 160 mm.

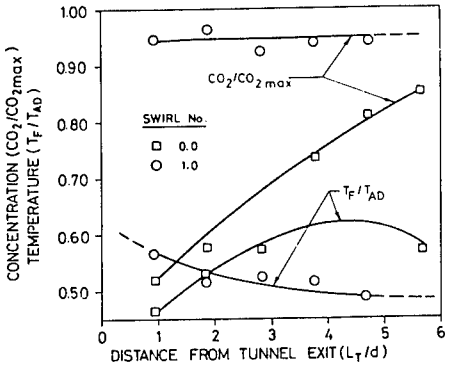


FIG. 3 - Flame temperature and CO_2 concentration (at flame axis) along combustion chamber for conical tunnel, regular burner, T_{AD} = 2153 °C, CO_{2max} = 15.3%, d = 160 mm.

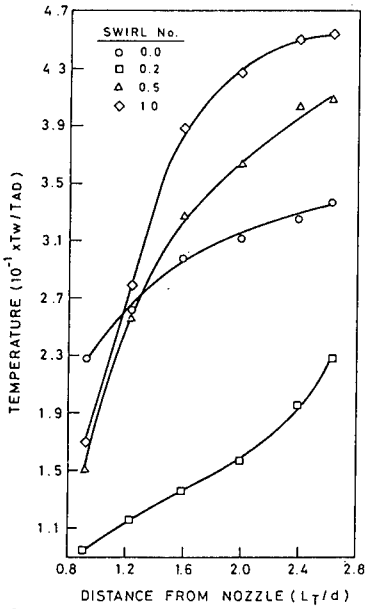


FIG. 4 - Tunnel wall temperature along combustion chamber for conical tunnel, regular burner, T_{AD} = 2153 °C, d = 160 mm.

COMBUSTION CHARACTERISTICS AND SCREENING CAPABILITY OF RED PHOSPHORUS-BASED MIXTURES

Stanisław Cudziło
Military University of Technology
Kaliskiego 2, 00-908 Warsaw 49, Poland
Email: cudzilo@wul.wat.waw.pl

Abstract: Smoke generating mixtures, containing red phosphorus, have better screening capabilities than other types of smoke producing compositions. This is a result of the ability of some ingredients of phosphorus-derived initial clouds to combine with atmosphere components. Thanks to this they are perfectly suitable for generation of warm clouds that are an effective countermeasure for thermal imaging systems and can act as three-dimensional, low-temperature infrared decoys as well. However the high chemical activity of red phosphorus, especially towards oxidisers, is a cause for comparatively rare practical application of the mixtures. In this work, red phosphorus-based and oxygen-free formulates were researched. As a system supporting combustion of the final compositions, mixtures of powdered Al-Mg alloy and polytetrafluoroethylene were used. Some links between composition of mixtures tested and the heat and velocity of combustion were determined. Screening capability in specific infrared bands (0.4÷1.1 μm, 3÷5 μm and 8÷12 μm) of clouds generated by the compositions was also measured.

1. Introduction

Typical smoke-generating, red phosphorus based formulations contain mainly red phosphorus (50÷70 %), oxidisers (most often metal oxides or nitrates) and up to 10 % of a polymeric binder [1-4]. Phosphorus usually acts a double role: as a fuel and as a thermosublimating component. The part of phosphorus acting as a fuel is oxidised in the combustion wave in reactions with oxygen liberated during the oxidiser decomposition. The energy released as a result of the reactions is next exploit to introduce the phosphorus oxides formed and the remaining phosphorus into the initial cloud in which it burns fixing oxygen from air.

The presence of chemically active oxygen carriers in pyrotechnic mixtures containing red phosphorus is a cause for their comparatively high sensitivity to mechanical stimuli, rather poor stability and their undesirable explosive properties [2, 3]. For these reasons, production and application of the compositions is quite dangerous. As a result they are not practically used in Poland, despite their numerous advantages like high screening capability in visible and infrared bands, generation of warm clouds due to afterburning and hydrolysis processes proceeding inside the clouds, and a high degree of IR emission from the clouds themselves.

This study is devoted to some oxygen-free, red phosphorus based compositions in which mixtures of powdered aluminium and magnesium alloy (Al-Mg) with polytetrafluoroethylene (PTFE) were used as a system powering combustion [5-7]. Some links between the ingredient contents and the basic characteristics of combustion processes of the formulations

were established. Next an effect of the composition changes on the attenuation of infrared radiation in the clouds generated by the formulations in a smoke chamber was determined.

2. Mixture composition and manufacture

The mixtures tested were prepared in a two-stage process providing the final compositions in a form of granules. Their interiors contained fast-burning mixture of Al-Mg alloy and polytetrafluoroethylene (G1 or G2) and surroundings included red phosphorus (P) linked by polystyrene (PS). Granules of Al-Mg/PTFE mixtures were formed in the first stage by mixing the substance powders in an acetone solution of chlorinated polyvinyl chloride (SPVC) combined with evaporation of acetone. After drying, the pellets were introduced into a suspension of red phosphorus in a tetrachloromethane solution of PS. Then the solvent was evaporated during continuos stirring. Consequently phosphorus coated the fuel/oxidiser pellets. The application of two kinds of binders and different solvents ensured stability of the Al-Mg/PTFE granules during the second stage of the manufacture process (because of SPVC insolubility in CCl_4). Simultaneously, the use of partly phlegmatised oxidiser and non-combustible CCl_4 improved the safety of the hazardous operation of red phosphorus mixing with the other ingredients. The mixtures were prepared in kilogram batches and pressed into charges with various mass used in next experiments.

The composition of the mixtures supporting combustion (Al-Mg/PTFE/SPVC) and the final smoke generating formulations are presented in Table 1.

Table 1. Symbols and compositions of the mixtures tested

Mixture Symbol	Composition [wt. %]
G1	Al-Mg/PTFE/SPVC = 47/48/5
G2	Al-Mg/PTFE/SPVC = 66/29/5
F1a	G1/P/PS = 35/60/5
F1b	G1/P/PS = 45/50/5
F1c	G1/P/PS = 50/45/5
F1d	G1/P/PS = 55/40/5
F1e	G1/P/PS = 65/30/5
F2a	G2/P/PS = 35/60/5
F2b	G2/P/PS = 45/50/5
F2c	G2/P/PS = 50/45/5
F2d	G2/P/PS = 55/40/5
F2e	G2/P/PS = 65/30/5

Mixtures supporting combustion (Al-Mg/PTFE/SPVC) were deliberately rich in metal in order to obtain high burning rates in the final formulations. Without any additives and at

the density of 1.5 g/cm^3 mixtures G1 and G2 burn at rates of about 1.5 mm/s and 10 mm/s, respectively [8].

3. Heat of combustion

The heat of combustion (Q) was measured with a water calorimetric set in a bomb filled with argon at 0.5 MPa. The samples were prepared in a form of about 5-gram pellets pressed at a density of 1.3 g/cm^3. The combustion processes were initiated with an electrically heated igniter (0.2 g in mass). Its heat of combustion had exactly been known. For each formulation, three calorimetric measurements were done. Their average results are presented in Figure 1 in the form of dependence of combustion heat effects on red phosphorus content in the formulations.

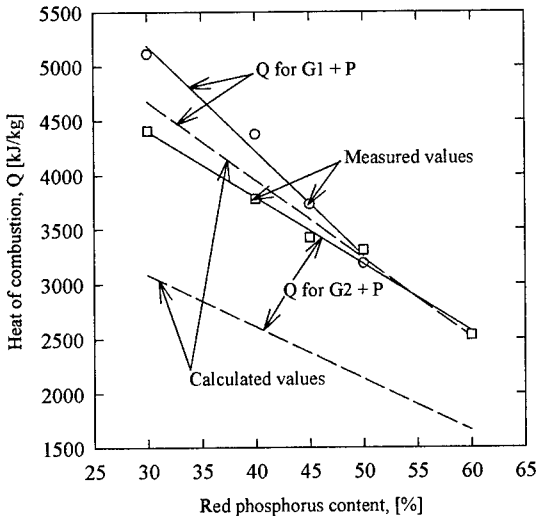


Fig.1. Heat of combustion versus phosphorus content; the dashed lines depict theoretical dependence calculated with an assumption of chemical inertness of phosphorus in combustion wave

With increasing phosphorus content, a monotonous decrease in heat values is observed. The rate of the fall is higher when G1 mixture is used as a system supporting combustion. Moreover for these compositions, the measured values (points and solid lines) only insignificantly differ from the theoretical ones that were calculated from an experimental value of the combustion heat of pure G1 mixture, with an assumption of phosphorus chemical inertness in the combustion wave (dashed lines). In the case of formulations containing mixture G2, the measured heat effects are considerably higher (by 900÷1300 kJ/kg) than the calculated ones. This fact implies that red phosphorus exothermically reacts with the other ingredients and that

Al-Mg alloy is the reacting substance because only its fraction increases when mixture G1 is replaced with mixture G2.

In additional tests, it was also found that a mixture containing 50 % of red phosphorus and 50 % of Al-Mg alloy could burn stably both in air and in argon. Its heat of combustion in argon was about 2600 kJ/kg. The reaction in the mixture proceeded probably according to equation:

$$3Al_3Mg_4 + 17P = 9AlP + 4Mg_3P_2 \quad (1)$$

The molecular formulas of magnesium and aluminium phosphides were drawn from hydrogen phosphide, PH_3 [9].

Since the compositions containing mixture G2 include more Al-Mg alloy, the influence of the heat effects accompanying reaction (1) on the global heat of combustion of the compositions is higher (Figure 1). The reaction contributes also to widening the concentration limits of combustion. Formulations based on G2 mixture burn stably up to 60 % of red phosphorus whereas mixture G1 supports combustion of compositions containing a maximum of 50 % of red phosphorus.

4. Burning rate

The burning rate (m`) was calculated as a ratio of the mass of a cylindrical sample to the time of its combustion multiplied by the burning surface. The samples had densities of 1.3 g/cm^3 or 1.7 g/cm^3 and they were 50 g in mass and 30 mm in diameter. Their combustion was initiated at the top surface with an electrically heated igniter. The lateral surface of the samples was inhibited. The measurements of the combustion time were carried out under room conditions.

The values of the burning rate obtained are presented in Figure 2 as a function of phosphorus content. The results are from single batches of compositions, with each point being an average of three experimental results. The average error for any one datum was ±5 %.

As expected, an increase in weight fraction of red phosphorus causes a decrease in burning rate. In the case of samples containing 60 % of P, the burning rate depends on neither their density nor the composition of the mixture supporting combustion. This indicates that the phosphorus layers coating granules G1 or G2 in the samples are too thick, and therefore, the burning rate is controlled by heterogeneous combustion of red phosphorus in oxygen from air.

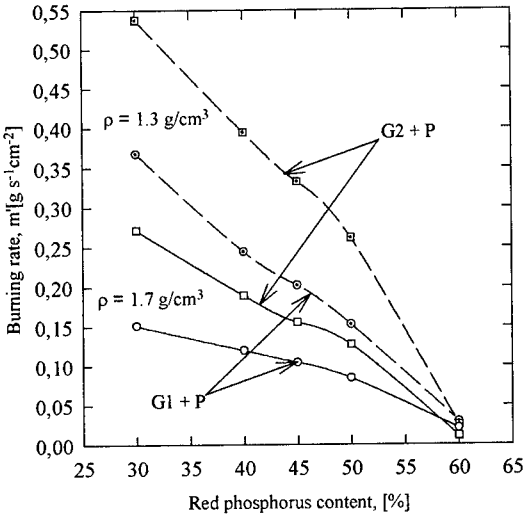


Fig.2. Burning rate as a function of phosphorus content for compositions containing mixtures G1 or G2 at densities of 1.3 g/cm^3 (dashed lines) or 1.7 g/cm^3 (solid lines)

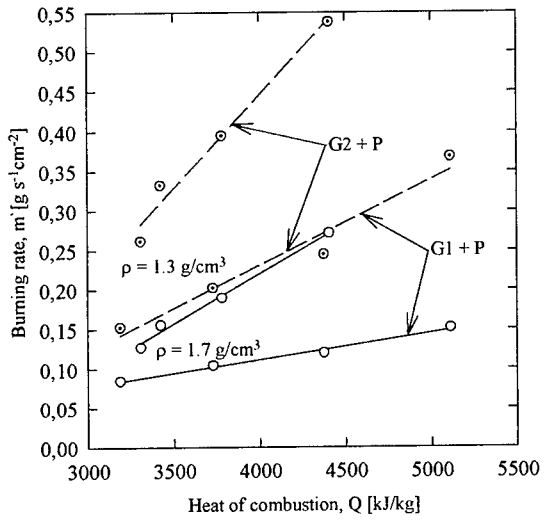


Fig.3. Burning rates versus the heat of combustion

In the range of low and medium contents of red phosphorus, the burning rate increases with decreasing density and rising amount of Al-Mg alloy in the mixture. Thus it can be supposed that in these formulations the transfer of combustion between the fast burning regions

(granules G1 or G2) proceeds without clear stoppage at the phosphorus layers. Then the velocity of combustion wave propagation in the compositions becomes practically a linear function of their heat of combustion, Figure 3.

5. Extinction capability

The transmittance of radiation in 0.4÷1.1 μm, 3÷5 μm and 8÷12 μm wavelength bands through smoke clouds generated by the compositions tested was measured in a chamber of 37.8 m^3 in volume, Figure 4.

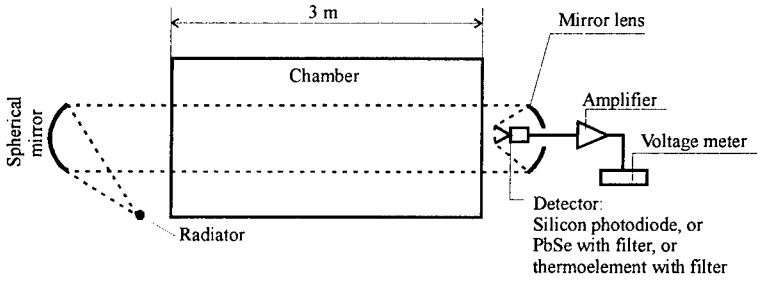


Fig.4. Experimental setup for transmittance measurements

The chamber was equipped with windows on opposite walls through which a beam of radiation generated by a small radiator and reflected with a spherical mirror was passed. After traversing the chamber (3 m in length) the radiation beam was focused on a detector with a Cassegrain mirror lens. For measurements in the visible and near IR bands a silicon photodiode with a peak sensitivity in the range of 0.4÷1.1 μm was applied. In 3÷5 μm and 8÷12 μm bands a PbSe detector and a thermoelement were used, respectively, with suitable filters mounted in front of them. The detector output signals were amplified and measured with a voltage meter. The transmittance was calculated as a ratio of the signal recorded in the presence of smoke to the signal measured without smoke in the chamber. During all experiments the climate in the chamber was the same – temperature of 20 °C and humidity of 50 % RH. The samples had different mass to change the smoke concentration.

After a sample had burnt up, the smoke was agitated for two minutes with two axial fans to ensure its uniform dispersion. Next the detector output signal was recorded and used to calculate the transmittance. Each measurement was repeated three times. Their results did not differ from each other more than 5 %. The average values of transmittance, obtained in this way, are given in Table 2.

As could be expected, the transmittance decreases with increasing phosphorus content in the compositions (Table 2, Figure 5). It should be pointed out that mixtures containing 50 % of red phosphorus provide quite good extinction in the far IR region. Even for low smoke concentration (samples of 10 g or 20 g) the transmittance does not exceed 50 % and it is not far worse than in 0.4÷1.1 μm band. It is quite a surprise because, usually, the values of mass extinction coefficients of short and long wave IR radiation differ from each other more than by an order [2, 10]. In the mid wave IR range, however, the clouds tested have rather low activity. This implies that the particle dispersion in the smoke is especially conducive to good attenuation of the long wave IR radiation.

Table 2. Results of transmittance measurements

Formulation	Sample mass [g]	Transmittance [%] in bands:		
		0,4÷1,1 μm	3÷5 μm	8÷12 μm
F1b 50 % P 45 % G1 5 % PS	10.0	40.0	75.0	47.0
	20.0	**22.0**	55.0	31.0
	30.0	-	**42.5**	26.4
	40.0	-	-	**10.8**
F2b 50 % P 45 % G2 5 % PS	20.0	23.9	-	-
	30.0	-	48.7	-
	40.0	-	-	12.2
F1d 40 % P 55 % G1 5 % PS	20.0	55.5	-	-
	30.0	-	26.5	-
	40.0	-	-	14.2
F2d 40 % P 55 % G2 5 % PS	20.0	58.7	-	-
	30.0	-	73.5	-
	40.0	-	-	23.8
F1e 30 % P 35 % G1 5 % PS	20.0	69.9	-	-
	30.0	-	74.0	-
	40.0	-	-	31.1
F2e 30 % P 65 % G2 5 % PS	20.0	75.0	-	-
	30.0	-	76.6	-
	40.0	-	-	46.0

The transmittance measurements also showed that, the clouds generated by the formulations containing mixture G2, i.e. rich in Al-Mg alloy, are worse at extinction of IR radiation than the other ones. This is shown in Figure 5 in the form of dependence of transmittance on red phosphorus content.

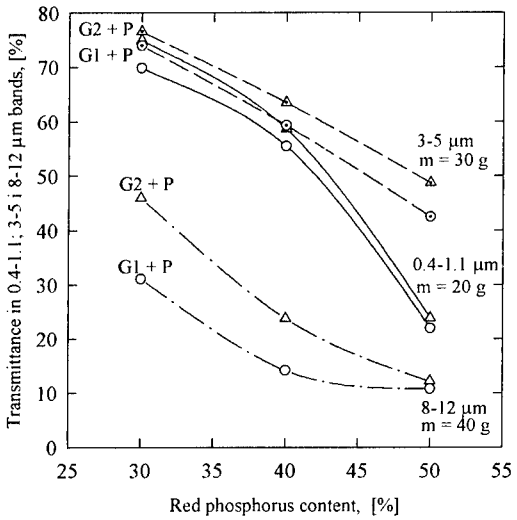


Fig.5. Transmittance of IR radiation versus red phosphorus content

The transmittance in 8÷12 μm, 3÷5 μm and 0.4÷1.1 μm bands was measured in clouds generated by samples of 40 g, 30 g and 20 g in mass, respectively, containing granulates G1 or G2 and 50 %, 40 % or 30 % of red phosphorus.

6. Conclusions

Summing up the results of measurements of combustion characteristics, it can be stated that it is possible to prepare smoke-generating, oxygen-free, red phosphorus based compositions that stably burn at burning rates of about 0.2 $gs^{-1}cm^{-2}$. They can contain 40÷50 % of red phosphorus and 50÷60 % of high energetic mixture of Al-Mg alloy and PTFE as a system powering their combustion process. An increase in the heat of combustion and in the burning rate can be gained by using mixtures rich in metal because red phosphorus can exothermically react with the alloy forming aluminium and magnesium phosphides.

The compositions containing 40÷50 % of red phosphorus generate smoke screens providing quite good attenuation of the long wave IR radiation. At the same smoke concentration, the transmittance in the 0.4÷1.1-μm band is only slightly lower than in the far infrared range. However they have rather poor screening capability in the range of mid wave IR radiation. Although the extinction in each band increases with increasing red phosphorus content, the necessity to ensure the ability of the formulations to burn smoothly at reasonable rates requires the mass fraction of red phosphorus not to exceed 50 %. The use of the mixture pow-

ering combustion, which is rich in Al-Mg alloy, does not solve the problem. As a matter of fact, it enhances the burning rate of the compositions but at the same time it deteriorates the screening capability of the clouds generated by the compositions.

References

[1] J. H. MC LAIN, *Pyrotechnics*, The Franklin Institute Press, Philadelphia, 1980.

[2] P. J. D. COLLINS, *Overview on Red Phosphorus – An International Perspective*, 27th International Pyrotechnics Seminar, Grand Junction, Colorado, USA, 16-21.07.2000.

[3] G. HUA, J. LI, W. GUANG, *Research on Red Phosphorous Anti-Infrared Smoke Composition and its Manufacturing Process*, ibid.

[4] A. I SIDOROV, W. l. STIENKOVOJ, N. A. SILIN, O. A. KIRILOVA, B. A. KORSZUNOV, *Pyrotechnic Aerosol-Generating Mixture and Method of it Preparation* (in Russian) Russian Patent, RU 2083539, 10.107.1997.

[5] S. CUDZIŁO, A. PAPLIŃSKI, E. WŁODARCZYK, *Pyrotechnic Compositions Based on Red Phosphorus* (in Polish), Polish Patent, P 317311, 2.12.1996.

[6] S. CUDZIŁO, W. A. TRZCIŃSKI, *Comparison Investigations of Camouflage Capability of Different Pyrotechnic Smoke Compositions in IR Region*, 25th International Pyrotechnic Seminar, Brest, France, 7-11.06.1999.

[7] S. CUDZIŁO, *Studies of IR-Screening Smoke Clouds*, Propellants, Explosives, Pyrotechnics, **26**, 1-5, (2001).

[8] S. CUDZIŁO, W. A. TRZCIŃSKI, *Studies of High Energy Composites Containing Polytetrafluoroethylene*, 29th International Annual Conference of ICT, Karlsrue, Germany, 30.06-3.07.1998.

[9] L. KOLDITZ, *Inorganic chemistry* (in Polish), PWN, Warsaw, 1994.

[10] S. CUDZIŁO, A. PAPLIŃSKI, *An Influence of the Chemical Structure of Smoke Generating Mixtures on Laser Radiation Attenuation at 1.06 and 10.6 μm Wavelengths*, Propellants, Explosives, Pyrotechnics, **24**, 242-245, (1999).

Designing Advanced Gun Propellants with Improved Energy Release

Mr. Ronald L. Simmons and Dr. Christine M. Walsh
Naval Surface Warfare Center
Indian Head, MD 20640

Abstract

As the need for higher performance gun propulsion increases, it is clear that greater improvements in progressive burning charges are needed. Progressivity means a progressively increasing mass burning rate, which can come from either grain geometry (increasing surface area) or chemistry of the propellant (increasing linear burning rate). This paper is a summary discussion of the many compounds available that are known to have substantial differences in linear burning rate. The burning rate of 22 compounds, representing an overall difference in burning rate of 55x, is discussed. These range from TATB (burning at 2 mm/sec at 100 atm) to 5-nitraminotetrazole (burning at 110 mm/sec at 100 atm).

Introduction

Chemical routes to change the burning rate of gun propellants traditionally have been limited to a surface deterrent coating (which provides a gradient of compositions with increasing linear burning rate as the burning surface recedes), and layered or sandwich propellants, with an initial slow burning outer layer transitioning to a fast burning core. Neither concept is new. Deterrents evolved shortly after the introduction of NC-based smokeless powders in the 1880s, and "fast core" layered propellants were first described a few years later. It has long been recognized that the initial burning (immediately after ignition) has to be slow, followed by gradually faster burning to fill the rapidly expanding volume behind the accelerating projectile.

Traditionally, deterrent coatings consist of centralites, phthalates, organic resins, and high molecular weight polymers in concentrations of 1 to 5% (or more) to produce a gradient of burning rates. These have a disadvantage in that the coatings have little or no energy, and therefore detract from the overall impetus. In recent years, a number of compounds have been identified which burn substantially slower than conventional propellants ... and which have moderate energy such that the penalty in total propellant impetus is minimal.

Other energetic compounds exist which burn substantially faster than conventional propellants. Combinations of these fast-burning and slow-burning compounds offer potential routes to co-layered or multi-layered propellant concepts where each layer is progressively faster burning than the previous layer, and an overall difference in linear burning rate of 20x (or more) could be realized.

Discussion

Conventional NC-based propellants burn at a rate which is directly proportional to flame temperature (Tv) and heat of explosion (Qex), i.e., high Tv and Qex produce fast burning and vice versa (Ref 1,2,3). At current gun operating pressures of 4000 atmospheres, conventional NC-based propellants burn at 250-300 mm/sec. Nitramine and LOVA-type propellants burn at about the same rate. Some are slightly slower and some are slightly faster, however, in general they behave about the same as conventional NC-based propellants, depending on Tv and Qex.

There are a number of energetic compounds that are known to have large differences in linear burning rate. Some of the more recent ones, such as HzTz, FOX-7, and TAGZT, were discussed by C. Knott (Ref 4) in May 2000 at the NDIA Gun & Ammunition Symposium (see Figure 1 where the effects of replacing 20% RDX in the nitramine propellant EX-99 are shown). Note that at 1000 atm, TAGZT burns about 260 mm/sec while HzTz burns about 20 mm/sec, for an overall difference in burning rate of about 13x. The present paper is an expansion of that paper to include other energetic compounds to show that there is a wider diversity in burning rates that can be exploited.

Some of the compounds known to burn faster than NC are TAGN and the linear nitramines DADNH, DANPE, DINA, and DMMD. These compounds were studied in concentrations of 35-60% by weight in NC. TAGN, DADNH, and DANPE are perhaps three of the most intriguing fast burning compounds that have been known for several decades (Ref 5,6,7,8). In Figure 2, it can be seen that 35% DADNH (in NC) burns at 100 mm/sec at 100 atm, 60% TAGN burns at about 150 mm/sec at 1000 atm, while 40% DANPE burns at 120 mm/sec, 40% DINA burns at 80 mm/sec, 50% DMMD burns at 70 mm/sec, and neat NC (12.6%N) burns at 50 mm/sec at 1000 atm, and 7 mm/sec at 100 atm. These compounds represent an overall difference in burning rate of about 14x.

Studied at a higher concentration (75%) in NC are the linear nitramines DATH, DMDTH, and DMED (Ref 5,9). In Figure 3, it can be seen that at 100 atm, DATH burns at 22 mm/sec (at 100 atm), while DMDTH burns at 7 mm/sec, and DMED burns at 2.2 mm/sec. At this pressure, NC burns at 7 mm/sec. DMDTH appears to have a lower pressure exponent than NC and thus burns slower than NC at pressures > 100 atm. DMED is among the slowest burning energetic compounds known. Overall, this group of compounds represent a difference in burning rate of about 20x.

In examining the burning rate of several neat compounds (no binder), the literature reveals the behavior shown in Figure 4 (Ref 10,11,12,13,14,15,16). At 100 atm, BTATZ burns at 50

mm/sec, HMX burns at 17 mm/sec, GUDN (also known as FOX-12) burns at 10 mm/sec, DAAF burns at 8 mm/sec, NC burns at 7 mm/sec, and TATB burns at 2 mm/sec. TATB is perhaps the slowest burning energetic compound known. HzTz may eventually prove to be even slower burning when examined at higher concentrations.

The FLAME database compiled by Fogelzang and his researchers at Mendeleef University shows many interesting possibilities (Ref 10,12,13). For example, a very wide difference in burning rate (at 100 atm) is exhibited by the following compounds (see Figure 5):

Compound	Rate - mm/sec
5-Nitraminotetrazole	110
5-Nitrotetrazole	110
5-Cyanotetrazole	45
Tetrazole	20
5-Aminotetrazole	5

These represent an overall difference in burning rate of 22x.

In Figure 7 is shown the burning rate of a popular high energy double-base propellant JA-2, compared to the fastest burning compound found (5-nitraminotetrazole) and the slowest burning compound known (TATB). At 100 atm, there is a difference in burning rate of 55x, and at 400 atm, the difference is 42x. Current gun propellants typically burn at 10-15 mm/sec at 100 atm, or about 100 mm/sec at 1,000 atm. Thus routes to substantially faster and slower burning propellants for co-layered applications are clearly indicated.

Summary

There are a large number of fast-burning and slow-burning compounds available for use as deterrents or layered concepts. Combinations of these compounds could offer overall differences in propellant linear burning rate of perhaps 20x, or more. Hopefully this possibility will stimulate more research into compounds that potentially burn even slower or faster, and add to a better understanding of the relationship between burning rate and molecular structure. Also research into novel layered propelling charges could offer additional improvements in gun ballistic performance.

Acknowledgements

The authors would like to thank the following for their helpful advice:

Randy Cramer, Susan Peters, and Christine Knott of NSWC/Indian Head; Arpad Juhasz formerly of ARL/Aberdeen; Jim Northrup and Woody Waesche of SAIC; Joe Flanagan formerly of Rocketdyne; Hays Zeigler of Alliant/Radford; Richard S. Miller formerly of ONR, Richard R. Miller formerly of CSD/Pratt & Whitney; Gerry Manser of Aerojet/Sacramento, Paul Braithwaite and Bob Wardle of Thiokol/Wasatch; Tom Brill of

University of Delaware, Vaslav Egorshef and Valery Sanditskii of the Mendeleef University, and Anatoli Zenin of the Semenov Institute of Chemical Physics.

Chemical Glossary

Term	Name
BTATZ	Bis-(1H-1,2,3,4-tetrazole-5-ylamino)-1,2,4,5-tetrazine
DAAF	4,4'-Diamino-3-3'-azoxyfurazan
DADNH	1,6-Diazido-2,5-dinitraza hexane
DANPE	1,5-Diazido-3-nitraza pentane
DATB	Diamino trinitro benzene
DATH	1,7-Diazido-2,4,6-trinitraza heptane
DINA	1,5-Dinitrato-3-nitraza pentane
DMDTH	1,7-Dimethyl-3,5-dinitraza heptane
DMED	Dimethyl ethylene dinitramine
DMMD	Dimethyl methylene dinitramine
EX-99	Nitramine propellant containing 76% RDX
FOX	Acronym for Swedish FOA explosive
FOX-7	Diamino dinitro ethylene
GUDN	Guanylurea dinitramine (FOX-12)
HMX	Cyclotetramethylene tetranitramine
HzTz	Dihyrazino tetrazene
NC	Nitrocellulose
RDX	Cyclotrimethylene trinitramine
TATB	Triamino trinitrato benzene
TAGN	Triamino guanidine nitrate
TAGZT	Bis-triaminoguanidinium-5-5'-azotetrazolate

References

Ref 1) R. E. Gibson, *Rocket Fundamentals*, ABL-SR4, OSRD-3992, The George Washington University, Allegany Ballistics Laboratory, Cumberland, MD, 1944.

Ref 2) H. Muraour, *Relationship Between Temperature of Explosion and Burning Rate*, Comptes Rendu, 1928.

Ref 3) B. L. Crawford, C. Huggett, and J. J. Brady, *The Mechanism of the Burning of Double-Base Propellants*, J. Physical Chemistry, **54**, 854 (1950).

Ref 4) C. Knott, C. Walsh, S. Peters, R. Simmons, and R. Cramer, *Advanced Gun Propellant Formulations and Technology*, NDIA 35th Annual Guns and Ammunition Symposium, Williamsburg, VA, 1-4 May 2000.

Ref 5) R. L. Simmons, *Linear Nitramines for Gun Propellant Applications*, Tri-Service Gun Propellant Symposium, Picatinny Arsenal, NJ, October 1972.

Ref 6) R. L. Simmons, US Patent #4,450,110, *Azido Nitramines*, 22 May 1984.

Ref 7) R. L. Simmons, *Effect of Molecular Structure on Burning Rate*, 26th Annual International Conference of ICT, Karlsruhe, Germany, 4-7 July 1995.

Ref 8) R. L. Simmons, *Unusual Combustion Behavior of Nitramines and Azides*, International Symposium on Special Topics in Chemical Propulsion – 100 Years After Nobel, Stockholm, Sweden, May 1996.

Ref 9) J. E. Flanagan, personal observations at Rocketdyne, Canoga Park, CA 1970-1995.

Ref 10) V. P. Sanditskii, A. E. Fogelzang, V. Y. Egorshef, V. V. Serushkin, and V.I. Kolesov, *Chapter 1.4 Effect of Molecular Structure on Combustion of Polynitrogen Energetic Materials*, AIAA Progress in Astronautics and Aeronautics Volume 185, Solid Propellant Chemistry, Combustion, and Motor Interior Ballistics, 2000.

Ref 11) Nordic Explosives (Bofors) Data Sheet for Guanylurea Dinitramide – FOX-12, Karlskoga, Sweden.

Ref 12) FLAME Database, Mendeleef University of Chemical technology, Russian Academy of Sciences, Moscow, Russia.

Ref 13) V. P. Sanditskii, A. E. Fogelzang, V. Y. Egorshef, V. V. Serushkin, and V. I. Kolesov, *Combustion Behavior and Flame Structure of Tetrazole Derivatives*, 29th International Annual Conference of ICT, Karlsruhe, Germany, 30 June-3 July 1998.

Ref 14) T. L. Boggs, in Fundamentals of Solid Propellant Combustion, AIAA Progress in Astronautics and Aeronautics Volume 90, 1984.

Ref 15) S. F. Son, H. L. Berghout, C. A. Bolme, D. E. Chavez, D. Naud, and M. A. Hiskey, *Burn Rate Measurements of HMX, TATB, DHT, DAAF and BTATZ,* Los Alamos National Laboratory Report P37, Paper 639, July 2000.

Ref 16) M. A. Hiskey, A. Goldman, and J. R. Stine, Journal of Energetic Materials, Volume 16, 1998.

* * * * *

Figure 1 - Additives in EX-99

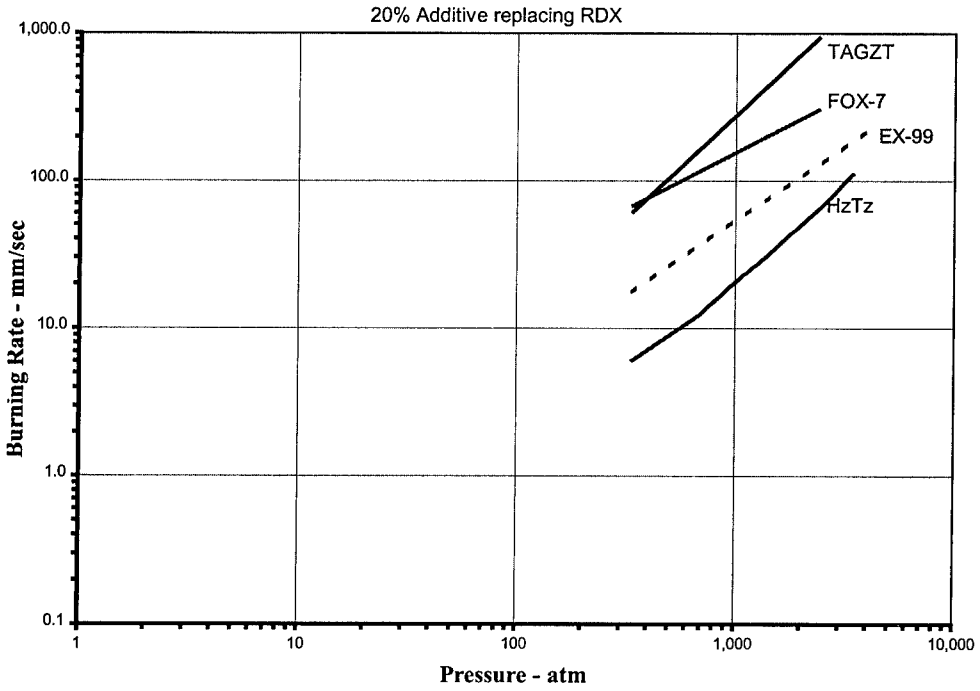


Figure 2 TAGN & Linear Nitramines in NC

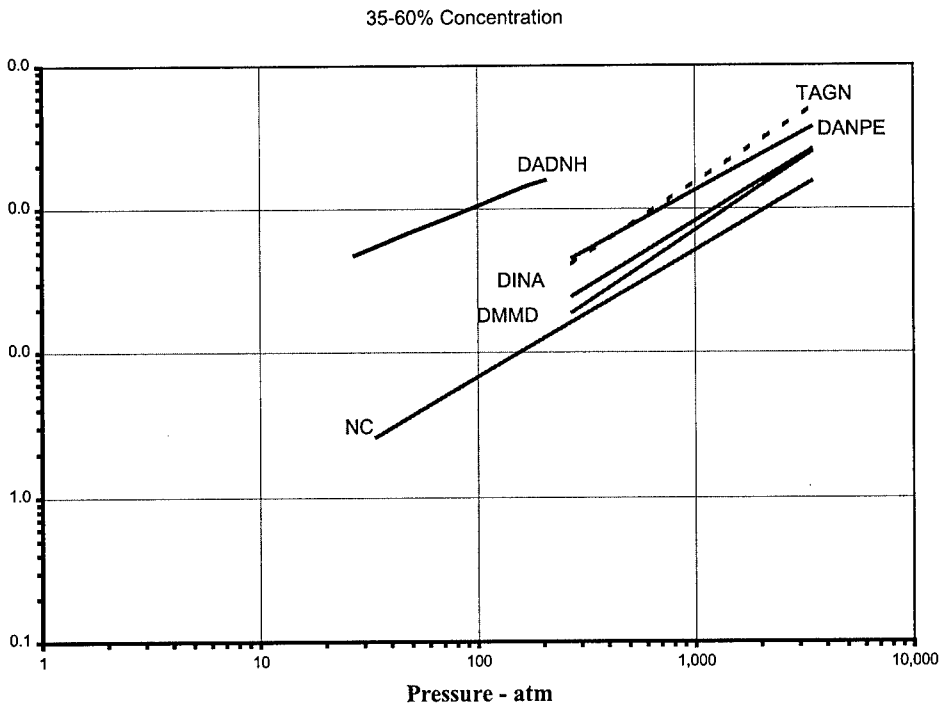


Figure 3 Linear Nitramines in NC

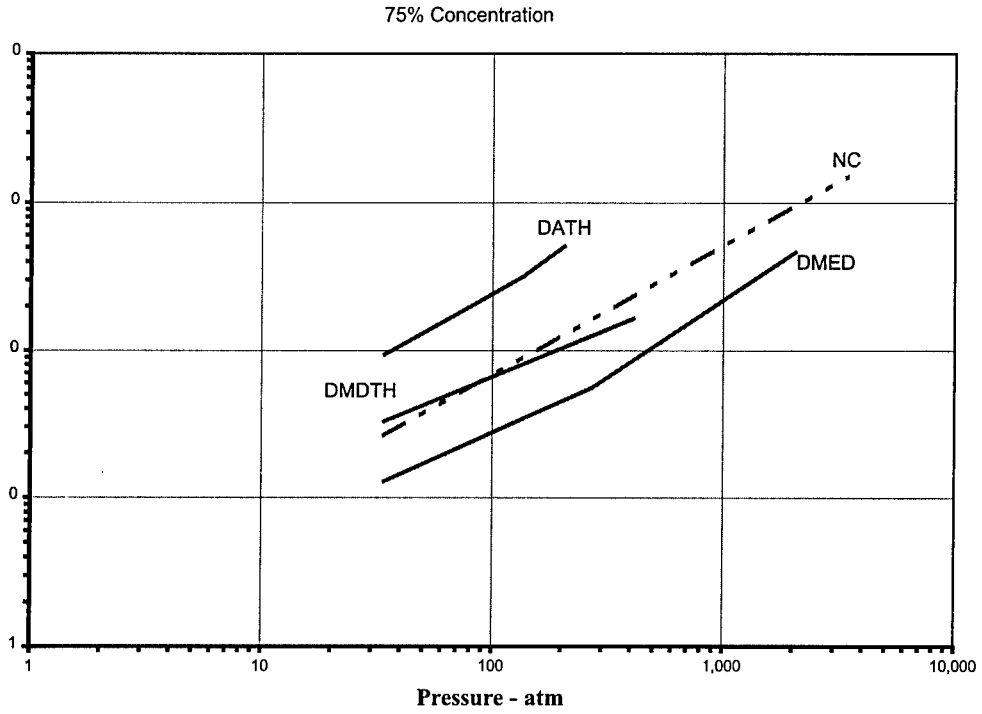


Figure 4 Burning Behavior of Neat Compounds

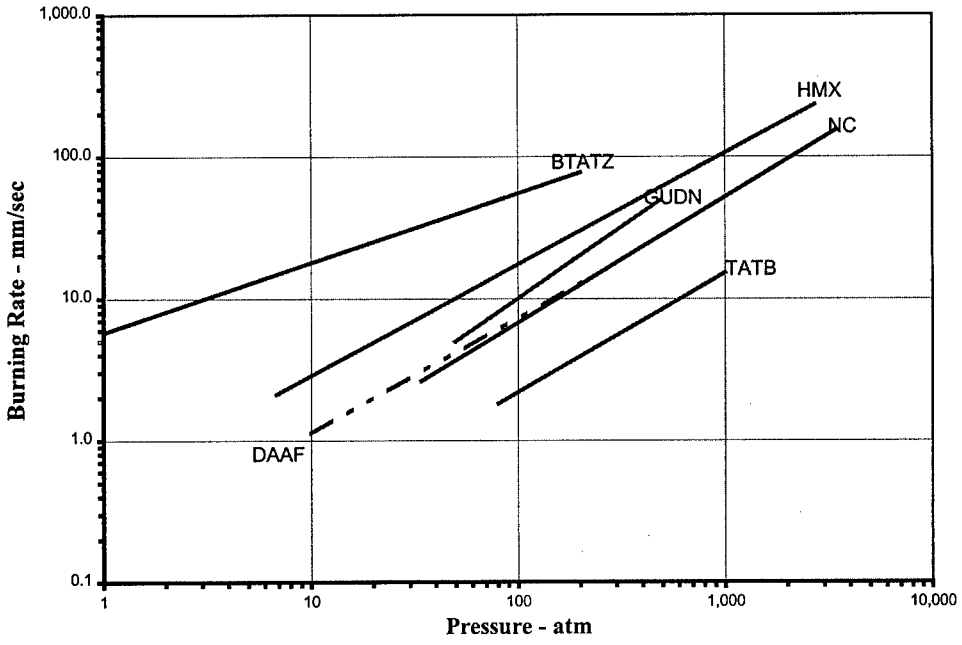


Figure 5 From Russian FLAME Database

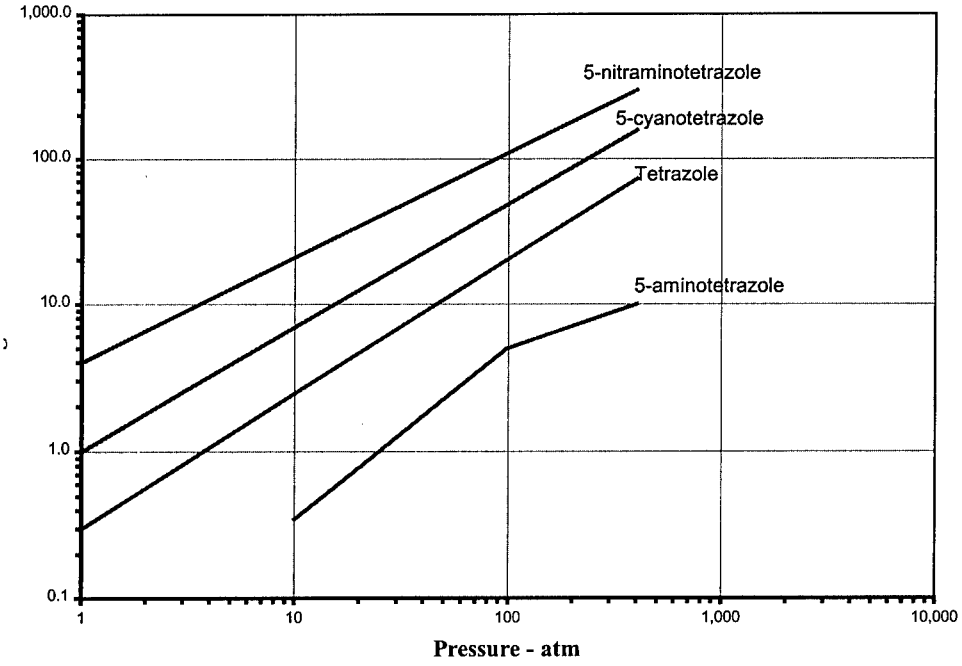
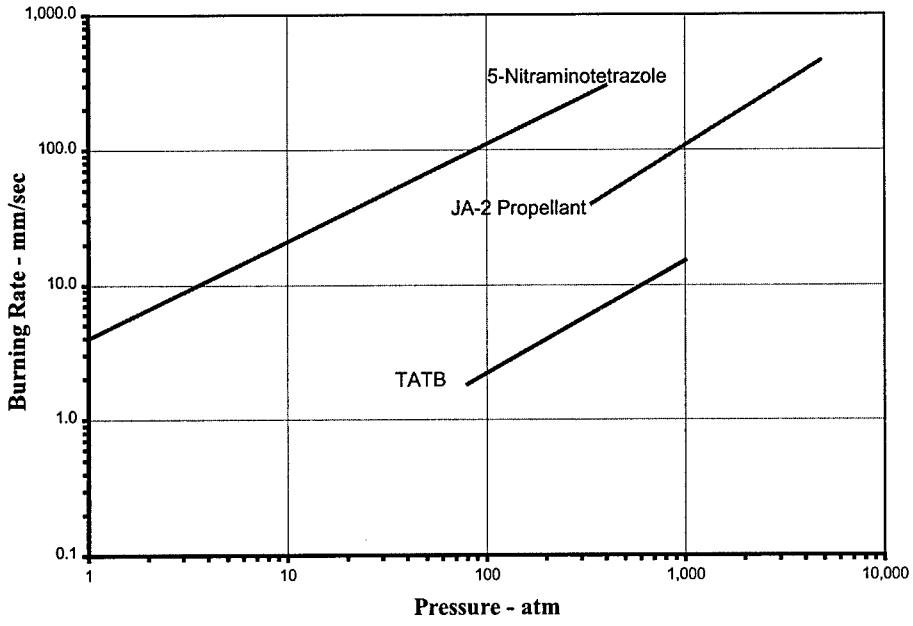


Figure 6 Diverse Burning Rates



EXPLOSIVE CHARACTERISTICS OF ALUMINIZED PLASTIC BONDED EXPLOSIVES BASED ON OCTOGEN AND POLYURETHANE BINDER

MOSTAFA A. RADWAN
Egyptian Armed Forces

ABSTRACT

Different samples of aluminized plastic bonded explosives based on octogen as high brisant explosive and polyurethane as energetic binder were prepared to study the effect of aluminium powder content on the explosive properties. The aluminium content was increased in the reference composition, containing 84% octogen and 16% polyurethane, from zero up to 30% by weight (by decreasing the content of octogen). For the composition containing 15% aluminium the brisance and detonation velocity were slightly decreased by 2.13% and 2.75% respectively while in the other direction the heat, temperature and force of explosion were markedly increased by 58%, 37 % and 8 % respectively. The sensitivity to impact of the prepared explosive compositions were also investigated and markedly decreased by increasing the aluminium content but all the compositions were sensitive to detonator number eight.

KEY WORDS

Plastic bonded explosives, Octogen, Polyurethane, Aluminium, Explosive characteristics.

INTRODUCTION

Plastic bonded explosives (PBXs) are widely used in different warheads due to their capacity of withstanding high levels of mechanical and thermal stresses.

Castable PBXs of relatively low viscosity were developed recently based on RDX and HMX to achieve better mechanical and explosive characteristics (1,2). Energetic PBX based on polyurethane was prepared by Humphrey (3) and PBX with good mechanical and thermal properties based on polystyrene was prepared by Achuthan (4). PBXs based on thermoplastic elastomers which do not require curing or crosslinking agents were prepared by Johnson (5). Other PBXs formulations based on polytetrafluoroethylene and HMX (6), RDX (7) and nitropenta (8) were prepared to improve processing, mechanical properties and other characteristics. The addition of aluminium to the high explosives and PBXs formulations has a marked effect on the explosive properties and sensitivity of these formulations, and the explosive properties of some aluminized high explosives were found in literature (9) but very few researches were focused on aluminized PBXs.

EXPERIMENTAL

Materials

All the chemicals used in this work , Hydroxy terminated polybutadiene (HTPB), Isophoron diisocyanate (IPDI), Dioctylazelate (DOZ), Octogen (HMX), and Aluminium powder (Al) were of high purity.

PROCEDURE

Number of milligram equivalent of OH/gram HTPB and that of NCO/gram IPDI were determined as before (10,11).

The preparation of PBXs formulations was carried out by thoroughly mixing of the different ingredients (HTPB, DOZ, HMX, and Al) with adding of the IPDI at the end, then pouring in a special cardboard tubes to measure detonation velocity and other explosive characteristics. Finally the curing of these compositions was carried out at 55°C for two weeks.

Sensitivity to impact of the prepared samples were determined by employing Julius Peters KG (Germany made) apparatus, using 2 kg falling weight, according to the standard technique (12). Detonation velocity was measured by using the Explomet-FO-Multichannel apparatus supplied by Kontiniro AG. (Swiss made). The tested explosive charges pressed to 1.5 g/cm^3 density and filled into a 300 mm long card board tubes of a 30 mm inside diameter. The time interval needed by the detonation wave to travel a known distance between two fiber optic probes placed at 150 mm distance from each other in explosive charge was determined very accurately (micro second) and the detonation velocity in (m/sec) was displayed.

The brisance of the prepared alluminized PBXs was measured according to Kast method (12). The explosive charge (2.0 gm) was prepared by pressing it to 1.55 g/cm^3 density into an alluminium tube of 30 mm high, 12 mm inside diameter and 4.0 mm wall thickness. The decrease of the copper crusher height was converted into force units according to the calibration chart for copper crusher static compression force test supplied by PHYWE System GMBH, Germany.

Model Calculations

The explosive gaseous products of the prepared alluminized PBXs were calculated according to Springail Roberts rules (9) and the explosion heat, temperature and force were calculated from the thermochemical equations (13).

RESULTS AND DISCUSSION

The measured values of the brisance, detonation velocity, sensitivity to impact and the calculated explosive properties (specific volume, heat, force and temperature of explosion) of the prepared compositions are listed in Table (1). The dependence of these values on the content of Al is represented in figure (1).

The detonation velocity (D) was measured for the reference composition containing zero % aluminium and for those compositions containing 15% and 30% aluminium. The detonation velocity was slightly decreased by 2.75% for the PBX composition containing 15% aluminium and sharply decreased by 19.67 % for that composition containing 30 % aluminium when compared with the detonation velocity of the reference composition due to the decrease of the energetic high explosive content and the increase of the aluminium content which is classified as a non-explosive ingredient.

It is clear from figure (1) that , specific volume V_o of the prepared compositions was linearly decreased by increasing the aluminium content due to the increase of the number of solid carbon atoms as the oxygen balance becomes more negative.

It is noticed from Table (1) and figure (1) that both heat of explosion Q_v and temperature of explosion T_v are markedly increased with the proportion of aluminium. For the composition containing 15 % Al, Q_v and T_v increased by 58% and 37 % respectively while for the composition containing 30% Al, Q_v and T_v increased by 101 % and 64 % when compared with the reference composition. The great increase in Q_v and T_v is due to the highly exothermic process of oxidation of aluminium which offers a useful heat of combustion of 30.9 kJ for gram. It is found in literature (9), that percentage of increase of the

Table (1) : The Measured And Calculated Characteristics of the Aluminized PBXs

No.	Content of Al (Weight percentage)	Detonation Velocity D (m/s)	Brisance B (KP)	Specific volume V_o (Cm^3/g)	Heat of explosion Q_v (kJ/kg)	Temperature of explosion T_v (K)	Upper limit of sensitivity to impact (H/cm)	Force of explosion F (kJ/g)	$V_o x Q_v x 10^{-4}$ $\left(\frac{cm^3}{g} \bullet \frac{kJ}{kg}\right)$
1	Zero	7009	1073	1030	3974	2970	50	1.145	409
2	05 %	--	1070	972	4694	3320	53	1.197	456
3	10 %	--	1059	902	5500	3715	56	1.244	496
4	15 %	6818	1050	831	6286	4070	60	1.237	522
5	20 %	--	972	760	7072	4410	66	1.184	537
6	25 %	--	948	689	7858	4730	71	1.027	541
7	30 %	5639	868	631	8013	4870	74	0.964	506

values of Q_v for TNT and Amatol (50/50) containing 30% Al is 80 % and 100 % respectively which is close to that (101 %) for the studied PBX composition , octogen/ polyurethane (54/16) containing also 30 % Al, when comparing the values of Q_v with that of the reference compositions.

The power of the explosives depends on the values of the characteristic product (Q_v x V_o), also on force of explosion and brisance. With respect to the product Q_v x V_o, Table (1) shows that this product reached a maximum at 25 % of aluminium and then began to decrease when the content of aluminium exceeded this value.

The force of explosion F which is one of the parameters on which the power of explosives depends directly proportional with T_v and V_o and it is noticed from Table (1) and figure (1) that the addition of increasing proportions of aluminium to the reference composition increased the values of F and reached a maximum value between 10 and 15 % of aluminium and then decreased beyond 15 % aluminium content.

The effect of an explosive on the surrounding greatly depends on the value of the brisance which is directly proportional with the values of F, D and density of explosive ρ. For this reason similar behaviour to that of D and F was observed for the values of the brisance of the different compositions due to the decrease of the octogen content and the increase of the aluminium content. For the composition containing 15 % aluminium the value of B was slightly decreased by 2.15 % and for that composition containing 30 % aluminium the markedly decrease in the value of B was 19.1 %.

One of the important effects of adding increasing proportions of aluminium to the reference composition is to decrease the sensitivity of the explosive to impact, represented by the upper limit (H/cm), as shown in Table (1). For the

composition containing 15 % of the non explosive ingredient (aluminium) the sensitivity to impact decreased by 20 % and for that composition containing 30% aluminium the sensitivity to impact decreased by 48 %.

The sensitivity of the prepared compositions to detonation wave was investigated by using detonator number eight and all the compositions completely exploded.

CONCLUSION

The addition of aluminium to the PBXs compositions has great effect on their explosive characteristics. The suitable aluminium content should be in order of 15% to have a considerable increase in the incendiary effect represented by Q_v and T_v which markedly increased by 58 % and 37 % respectively, and in the same time to minimize the fall-off in power beyond 15 % aluminium. For the same composition containing 15 % aluminium the detonation velocity and the brisance were slightly, decreased by 2.75 % and 2.13 % only while the force was increased by about 8 %. In the same time the sensitivity to impact was decreased by 20 % for that composition.

REFERENCE

1- L. R. Rothstein ; " Plastic Bonded Explosive Past, Present and Future", Fraunhofer Ins. , 245-253, 1983.

2- M. J. Stosz; "Development of New Explosive For the U.S. Navy", Fraunhofer Ins. , 45-53, 1983.

3- J.R.Humphrey; "LX-14: A New High Energy Plastic Bonded Explosives ", Lawrence Livermore Laboratory, November 21, 1977.

4- C. P. Achuthan; "Desensitisation of Plastic Bonded Explosives Based on RDX, HMX and Polystyrene", J. Armt. Studies, Vol XXI, No. 1. 1985.

5- N.C. Johnson; "Melt Cast Elastomeric PBX Processing and Properties Overview", J. Hazardous Material, 9, 41-45, 1984.

6- S. B. Wright; "Explosive Molding and Method for Preparation", U.S. Patent, 4, 482, 405, 1984.

7- K. J. Scribner; "Extrusion cast Explosive", U.S. Patent, 4, 555, 277, 1985.

8- H. D. Stanton; "Extrudable PBX Molding Powder", U.S. Patent 4, 952, 255, 1990.

9- J.H. Turnbull and K. Walter ; In the Thermochemistry of High Explosives, The Royal Military College of Science, UK. 1982.

10- V. I. Lyubomilov and T.D. Usevich; "Plast Massay", 2,67,1961.

11- D. J. David and H.B. Staley; In High Polymers, Vol. XVI, Analytical Chemistry of the Polyurethane, Part III, Wiley-Inter Science Publication, New York, 1969.

12- M. Suceska; In Test Methods for Explosives, Springer – Verlaga Publication, New York, 1995.

13- J. Kohler and R. Mayer; In Explosives, 4th edition, VCH Publishers, New York, 1993.

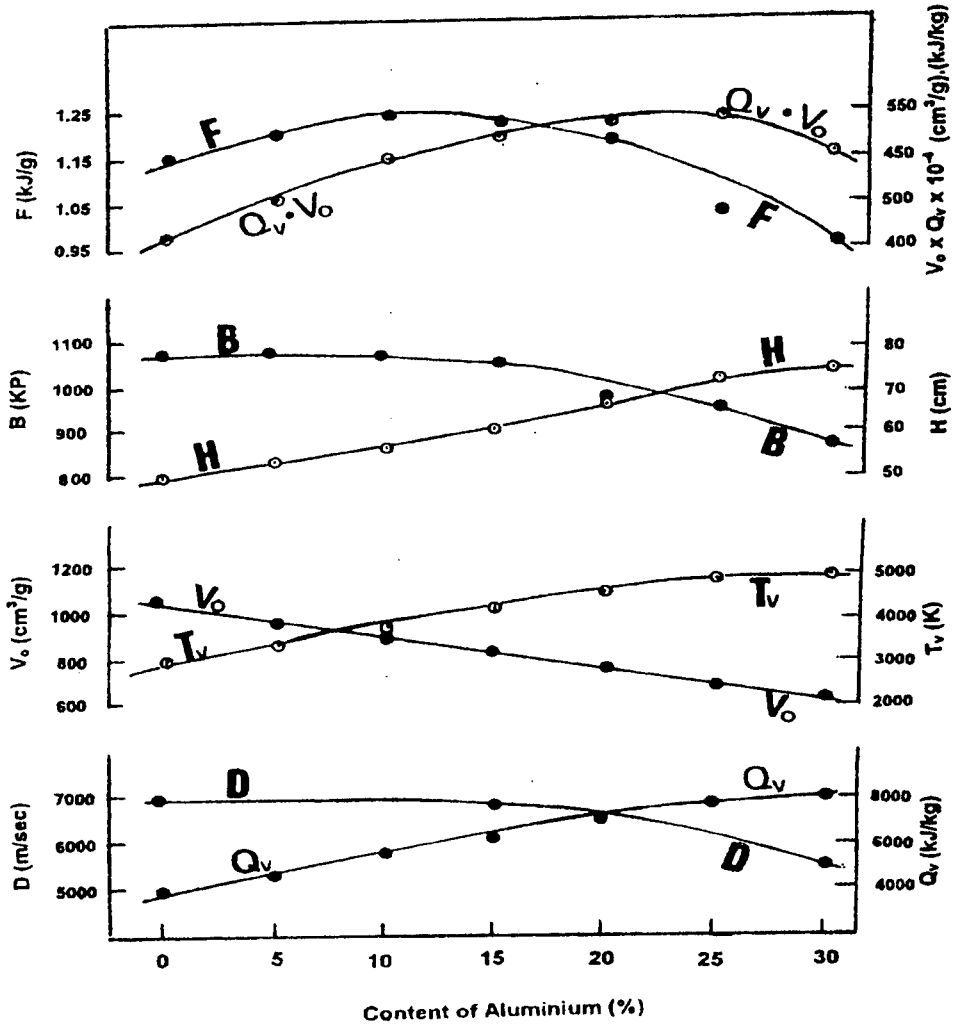


Figure (1) : Dependence of Explosive Properties on Aluminium Content

STRESS STRAIN PROPERTIES OF NITRAMINE COMPOSITE ROCKET PROPELLANTS

MOSTAFA A. RADWAN
Egyptian Armed Forces

ABSTRACT

Polyurethane based on hydroxy terminated polybutadiene prepolymer was selected as an energetic binder in the preparation of different nitramine composite rocket propellant formulations to investigate the effect of various factors on the values of stress and strain of these compositions. The effect of binder content, type and ratio of NCO/OH on the tensile properties was studied. The optimum binder content was found to be 15% weight percent, the best cure ratio (NCO/OH) was 0.9 and samples containing isophoron diisocyanate exhibited better mechanical properties than those based on hexamethylene diisocyanate. The effect of content and crystal size distribution of both oxidizers employed in this work (ammonium perchlorate and octogen) on the values of the stress and strain of the prepared formulations was also investigated.

The dependence of the values of stress and strain of nitramine composite rocket propellant formulations on the bonding agent and plasticiser content was studied and the optimum values were obtained at 25% weight percent plasticiser based on the weight of prepolymer and at 0.15 % of methyl aziridinyl phosphine oxide (bonding agent) based on total weight. Heavy duty mixer was employed to prepare nitramine composite rocket propellant samples with composition based on the previous studies and good values of the stress (7.75 kg/cm^2), strain (34%) and modulus (48 kg/cm^2) were obtained.

KEY WORDS

Stress- strain, Nitramine Rocket propellants, Octogen and Specific impulse.

INTRODUCTION

Nitramine composite rocket propellants (NCRP) are considered as one of the advanced families of conventional composite rocket propellants and of considerable interest for solid rocket propulsions due to their high calorific potential, high density, smokeless combustion products and low adiabatic flame temperature which minimize the insulation problem. These propellants have wide spectrum, low vulnerability, flame and infrared emission (1).

Most of the researche which have been carried out concerning NCRP cared with the effect of nitramine content on rate of burning and pressure exponent (2,3).

A great deal of attention was also focused on the burning rate and combustion mechanism and flame structure of NCRP (4-9).

Although stress and strain values of any composite rocket propellant are decisive parameters for the acceptance of the propellant, prediction of useful storage time and resistance of all possible stresses (10), very few researche on nitramine rocket propellants were dealing with the tensile properties and factors affecting them.

EXPERIMENTAL

Materials

All the chemicals used in this work, Hydroxy terminated polybutadiene (HTPB), Hexamethylene diisocyanate (HNDI), Isophoron diisocyanate (IPDI), Dioctylazelate (DOZ), Methyl aziridinyl phosphine oxide (MAPO), Carbon black (Cb), Dimethyl sulphoxide (DMS), Ammonium perchlorate (APC) and Octogen (HMX) were of high purity.

PROCEDURE

Number of milligram equivalent of OH/gram HTPB and that of NCO/gram HMDI or of NCO/gram IPDI were determined as before (11, 12).
Recrystallization of HMX was carried by dissolving 60.0 g. of HMX in 120 ml of DMS at room temperature. Precipitation was then accomplished by using 1200 ml of distilled water. Filtration, drying and sieve analysis were carried out for the obtained fine crystals of HMX.

Preparation of NCRP formulations was carried out by thoroughly mixing of the different ingredients (HTPB, DOZ, APC, HMX, Cb, MAPO) with adding HMDI or IPDI (in the last step) , then degassing of the obtained slurry by employing special degassing unit to get rid of any air bubbles before pouring it in a special mold. Finally curing of these compositions at 55°C for two weeks. The composition of some of these formulations are given in Table (1).

Stress-strain values for the prepared NCRP and their modulus of elasticity were measured by employing the LRX-5K material testing machine supplied by LLOYD INSTRUMENT, UK. The tensile test was carried out for at least three samples for each prepared formulation and the mean value of the obtained results was recorded. These dumbbell shape samples had the American standard dimensions.

RESULTS AND DISCUSSION

1- Dependence of Stress-Strain Values of NCRP on the Binder Content

Four different formulations (F1 : F4) were prepared and their compositions are listed in Table (1).

TABLE (1) CHEMICAL COMPOSITION OF DIFFERENT NCRP FORMULATIONS (F1 – F9)

No.	Ingredients \ Formulation	F1	F2	F3	F4	F5	F6	F7	F8	F9
1	HTPB (%)	26.46	22.65	18.84	15.04	15.04	15.04	15.04	15.04	11.05
2	HMDI (%)	01.67	01.44	01.20	00.95	00.95	00.95	00.95	00.95	00.76
3	DOZ (%)	06.62	05.66	04.71	03.76	03.76	03.76	03.76	03.76	02.94
4	MAPO (%)	00.15	00.15	00.15	00.15	00.15	00.15	00.15	00.15	00.15
5	Cb (%)	00.10	00.10	00.10	00.10	00.10	00.10	00.10	00.10	00.10
6	HMX (30-50 μm) (%)	19.50	21.00	22.50	24.00	24.00	16.00	20.00	28.00	25.50
7	APC 400 μm (%)	18.20	19.60	21.00	22.40	30.40	34.75	32.58	28.24	32.30
8	APC 200 μm (%)	13.65	14.70	15.75	16.80	12.80	14.63	13.71	11.88	13.60
9	APC 7-11 μm (%)	13.65	14.70	15.75	16.80	12.80	14.63	13.71	11.88	13.60

In these compositions the content of binder (HTPB, HMDI, DOZ, MAPO and Cb) was decreased from 35% down to 20% weight percent to examine the processing without heavy duty mixer, casting and tensile properties. By employing a heavy duly mixer it was possible to decrease the binder content to 15 % (F9). The values of the stress and strain at rapture of samples of the previous formulations, were illustrated against the content of binder and are shown in Figure (1).

The values of the stress were significantly increased by increasing the solid content while the values of the strain were decreased due to the decrease of the binder and plasticizer content.

2- Effect of Curing Ratio (NCO/OH) and Diisocyanate Type on the Values of Stress and Strain of NCRP

The curing ratio of the binder (NCO/OH) was gradually increased from 0.8 to 1.2 in the formulation F4 containing 20% binder and 80% solid ingredients.

The dependence of the stress and strain of the NCRP on the curing ratio (NCO/OH) is represented in Figure (2) which shows a linearly increase in the values of the stress and decrease in the values of the strain respectively by increasing the cure ratio from 0.8 to 1.2.

By replacing the IPDI instead of the HMDI in the formulation F5 , given in Table (1), which contained 20% binder and curing ratio 0.9 the value of the stress was increased by 10.5 % and that of the strain was slightly increased by 2% due to the cyclic structure of IPDI.

3- Dependence of Tensile Properties of NCRP on the APC Crystal Size Distribution

The crystal size distribution of APC has a great effect on the tensile properties of conventional and nitramine composite rocket propellants.

Different formulations were prepared in which the crystal size distribution of APC was altered by changing the content of the coarse grains against that of fine grains employing the composition containing 20% binder of curing ratio 0.9 (F4).

The best values of stress (6.1 kg/cm^2) and strain (38.2%) were obtained for the formulation F5 which is shown in Table (1).

The relatively high content of the coarse grains in this composition may be explained by the presence of relatively high content of the fine crystals of HMX (30-60 um) which together give the maximum loading density of this matrix.

4- Effect of HMX Content and HMX Crystal Size on the Values of the Stress and Strain of NCRP

To complete the study of the effect of crystal size distribution of solid ingredients on the tensile properties of NCRP , the effect of crystal size of HMX was also examined by preparation of different formulations based on F5 in which the crystal size of HMX was increased from (50 μm) up to (350 μm). Figure (3) represents the dependence of the values of stress and strain on the crystal size of HMX. The values of the stress markedly decrease while that of the strain slightly increased by increasing the crystal size of HMX. This behavior may be explained by the increase of the solid loading density and hence the stress when using fine grains of HMX which compensate the coarse

grains of APC. Also the coarse grains of HMX (> 100 μm) absorb considerable amount of the liquids (HTPB and plasticizer) which leads to a decrease in the stress of the compositions containing these coarse grains.

To investigate the effect of HMX content on the tensile properties of NCRP some new compositions (F6 , F7 and F8) were prepared beside the formulation F5 and listed in Table (1) in which the content of HMX was increased from 16 to 28 % on the expense of APC. The results are shown in Figure (4). This figure shows a linear increase in the values of the stress and some decrease in the values of the strain. The accepted values of the stress and strain together which are close to those of conventional composite rocket propellant were obtained from formulation F5 containing 24% HMX.

5- Dependence of Tensile Properties of NCRP on the Plasticizer (DOZ) Content

The plasticizer content was changed from 25 % as in formulation (F5) to 20% and to 30% of weight of prepolymer to study the effect of the plasticizer content on the values of the stress and strain. By decreasing the content of DOZ from 25 % to 20 % of weight of prepolymer or by increasing it from 25 % to 30% the values of the stress were decreased in both cases which may be explained that the optimum wetting ability of the plasticizer to the solid ingredients occurs at 25% content based on prepolymer weight.

The values of the strain were significantly increased (22%), by increasing the plasticizer content from 20% to 25% and then slightly increased (3 %) by increasing it to 30% based on prepolymer weight.

6- Effect of Bonding Agent (MAPO) Content on the Values of Stress and Strain of NCRP

Although the bonding agents are used in all composite propellants with very low percentage (< 0.3 %) based on total weight of the propellant, yet it has a marked effect on the tensile properties of the propellants because its main function is to prevent the settling of the solid ingredients in the propellant formulation.

To examine the effect of bonding agent content on the values of the stress and strain of NCRP , the content of MAPO in formulation F5 (0.15 %) based on total weight) was changed to 0.1, 0.2 and 0.25% .
The results are illustrated in Table (2).

Table (2) : Effect of MAPO Content on The Values of Stress and Strain of NCRP

Content of MAPO in formulation F5 (%)	Stress (kg/cm2)	Strain (%)
0.1	4.90	41.96
0.15	6.63	37.66
0.2	6.42	33.25
0.25	5.52	32.68

The values of the stress show a maximum value for the formulation containing 0.15% MAPO but the values of the strain exhibiting a continuous decrease by increasing the bonding agent content .

This seems to be an expected behavior due to the increase of the physical adhesion and chemical bonds created between the bonding agent and the propellant ingredients.

7- Preparation of NCRP By Employing Heavy Duty Mixer

On the basis of the previous studies and the values of stress and strain of different formulations, a heavy duty mixer was employed to prepare a new formulation F9 , listed in Table (1) , containing 15 % binder. The casting of this sample was successful and the values of the stress were significantly increased to (7.8 kg/cm^2) and the values of strain and young's modulus were 34.1% and 48 kg/cm^2 respectively. These values are higher than the necessary minimum accepted values of stress and strain for composite propellants (7 kg/cm^2 and 30% respectively)

CONCLUSION

NCRP contains polyurethane fuel binder based on HTPB and isophoron diisocyanate with curing ratio (NCO/OH) = 0.9 and has the same formulation as F9 exhibits excellent tensile properties. NCRP formulations containing IPDI improved the tensile properties than those containing HMDI. The content of HMX, DOZ, and MAPO should be in the order of 25 %, 3.0 % and 0.15 % respectively, which gave good values of the stress and the strain of the NCRP samples.

The crystal size distribution of HMX (30- 50 μm) and that of APC (30.4% of 400 μm , 12.8 % of 200 μm and 12.8% of 7-11 μm) exhibited very good tensile properties.

REFERENCES

1. M.K. Hadhoud, M. A. Radwan, M. A. Sadek and S. M. Abdel Karim ; "Performance Characteristics of Nitramine Rocket Propellants", 24th ICT Conference, Karlsruhe, Germany, 1993.

2. W. Beihai ; "Effect of Additives HMX Upon Burning Rate Behaviour of APC/HTPB Composite Propellants", 19th ICT Conference Karlsruhe, Germany, 1988.
3. N. Kubota and H. Ockuhara ; "Burning Rate Temperature Sensitivity of HMX Propellants" , J. Propulsion, 5(4), 406-10, 1989.
4. Y.M. Timat ; In Advanced Chemical Rocket Propulsion, Academic Press, New York, 1987 ,Chapter 2.
5. Y. Yano and N. Kubota, "Combustion of HMX-CMDB Propellants (I)"; J. Propellants, Explosives, Pyrotechnics, 10, (192-196), 1985.
6. N.S. Cohen and C.F. Price; " Combustion of Nitramine Propellants", J.Space Craft, 12(10), (608-12), 1975.
7. M.W. Seckstead and K.P. McCarty ; "Modeling Calculations for HMX Composite Propellants", ATAA, 20 (1), (106-15), 1982.
8. H Maruizumi, D. Fukma,.K.Shirota and N. Kubota; "Thermal Decomposition of RDX Composite Propellants", J. Propellant, Explosives Pyrotechnics, 7, (40-54), 1982.
9. Y.Yano and N. Kubota, "Combustion of HMX-CMDB Propellants (II)", J. Propellants, Explosives, Pyrotechnics, 2, (1-5), 1986.
10. K. Kishore and N.Kubota; In Fundamental of Solid Propellant, Vol. 9. The American Institute of Aeronautics, Astronautico, New York, 1987.
11. V.I. Lyubomilov and T.D. Usevich ; "Plast Massay", 2, 67, 1961.
12. D. J. David and H.B. Staley' In High Polymers Vol. XVI, Analytical Chemistry of the Polyurethanes, Part III, Wiley- Inter Science Publication, New York, 1969.

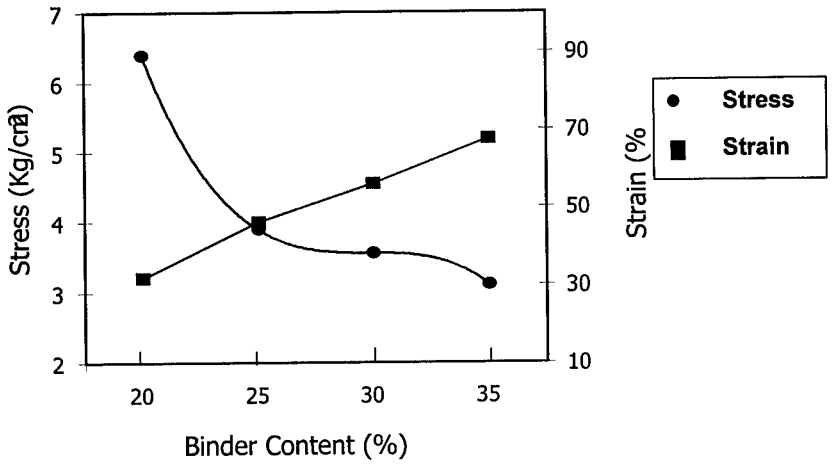


Figure (1) The Effect of Binder on The Stress and Strain Values of The Prepared Ncrp Samples.

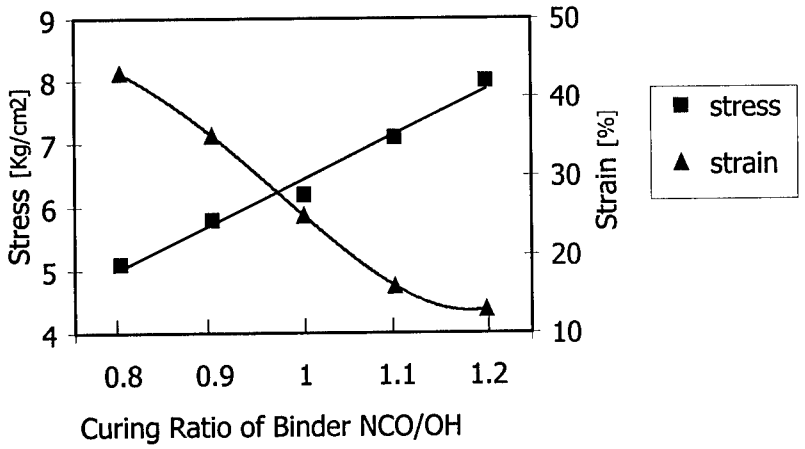


Figure (2) Dependence of The Stress and Strain Values of The Prepared NCRP Samples on The Curing Ratio (NCO / OH).

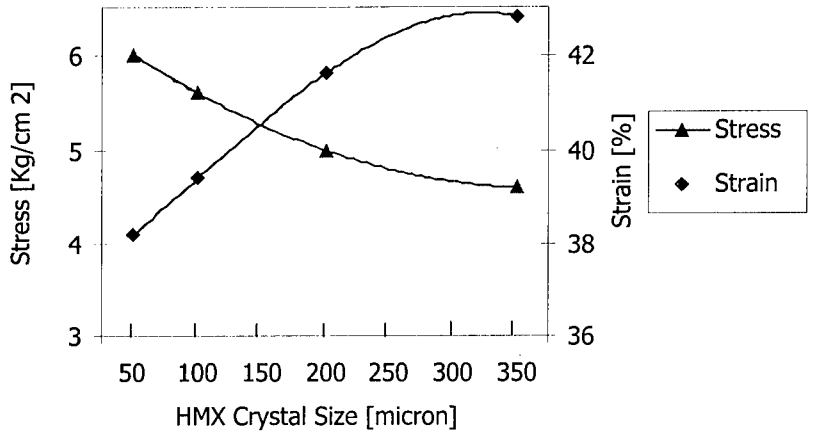


Figure (3) Dependence of The Stress and Strain Values of The Prepared NCRP Samples on The Crystal Size of HMX

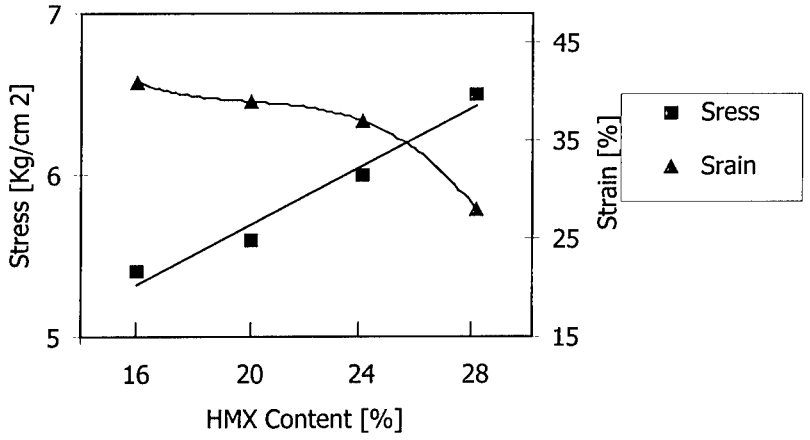


Figure (4) Effect of HMX Content on The Stress and Strain Values of The Prepared Samples

EFFECT OF COPPER CHROMITE PARTICLE SIZE ON THE COMBUSTION PROCESS OF A PLASTISOL PROPELLANT
PART I: Thermal Investigations by DSC

A. Mouloud & M.A. Benmahamed
Laboratoire des Systèmes Pyrotechniques, UER de Chimie Appliquée,
EMP, BP17c, Bordj-El-Bahri, Algiers, Algeria

Keywords: DSC, Plastisol, Copper chromite, Kinetic parameters, Combustion, Ozawa and Kissinger methods.

ABSTRACT

The present work consists in study the effect of the particle size of copper chromite used as combustion catalyst, on thermoanalytical properties of PVC-plasticised propellants, and also the determination of reaction kinetics data from thermodynamic measurements: temperatures and heats of the different transitions, by using kinetic methods of Ozawa and Kissinger. They allow the determination of the activation energy and the pre-exponential factor.
The appropriate apparatus for these analyses is the Differential Scanning Calorimeter (DSC).

The chemical reaction of interest is measured with several heating rates β. The sample temperature at the peak tip is determined for every curve. The activation energy can be obtained from the slope of the graph of log β versus $1 / T_{peak}$ (Ozawa) or $\ln \beta / (T_{peak})^2$ versus $1 / T_{peak}$ (Kissinger).

The determination of kinetic parameters of thermally hazardous materials, by Ozawa and Kissinger methods, allows finally to define the mechanism of the reaction.

1. Introduction

Propellants consist of an inorganic oxidizer (Ammonium perchlorate) which decompose at elevated temperature to give oxygen as one of the major products and a polymer binder (Polyvinylchloride).
The steady-state combustion process is controlled by both condensed phase and gas phase reactions. The thermal decomposition reactions of oxidizer and binder are main reactions in condensed phase [1].

In this report, we study the effect of the particle size of copper chromite, which play the rôle of burning catalyst, on the thermal behaviour of AP/PVC binder propellants and the determination of thermal properties by DSC (Differential Scanning Calorimeter), using Ozawa and Kissinger methods.

Whenever a peak is observed on a DSC trace as the sample is subjected to a controlled temperature ramp, it can be assumed that there has been a conversion, which we can represent as: $A \xrightarrow{k} B + \Delta H$ (1)

where A is the material before conversion, B is the material after conversion, ΔH is the heat of physical transition or heat of chemical reaction, and k is the reaction rate.

In differential scanning calorimetry, the temperature change is controlled to be approximately proportional to the time change:

$$\beta t = T - T_0 \quad (2)$$

$$dT = \beta.dt \quad (3)$$

where t is the time, T is the current temperature, T_0 is the initial temperature and β is the heating rate (°C/mn).

Combining the above equations with the following expression:

$$\frac{d\alpha}{dt} = k_0 \exp(-E / RT)(1 - \alpha)^n \quad [2] \quad (4)$$

(for chemical reactions the rate equation often is assumed to have the form:

$$\frac{d\alpha}{dt} = k(1 - \alpha)^n), \text{ yields: } \frac{d\alpha}{dT} = \frac{k_o}{\beta} \exp(-E / RT)(1 - \alpha)^n \quad (5)$$

where α is the degree of chemical conversion, n is the reaction order, k_0 is the pre-exponential factor, E is the activation energy of the reaction and R is the rate constant.

The equation (5) represents the theoretical shape of the DSC curve, for the kinetic analysis [3].

The mathematical treatment of kinetic equations makes use of the approximate methods, which consists to find a solution for the integrated form of equation (5) by an approximation using the temperature, T_m, corresponding to the maximum rate of decomposition. This method was used by Ozawa and Kissinger, and gave thus the activation energy E and the pre-exponential factor k_0.

1.1. Ozawa method [4]

From the expression (5), we can write:

$$\frac{d\alpha}{dT} = \frac{k_o}{\beta} \exp(-E / RT)\, f(\alpha) \quad (6)$$

where $f(\alpha) = (1 - \alpha)^n$.

By integration, $\int_{\alpha_0}^{\alpha} \frac{d\alpha}{f(\alpha)} = \frac{k_0}{\beta} \int_{T_0}^{T} \exp(-E/RT)\, dT$ (7)

Where α_0 is the value of α and T_0 of T, at $t = t_0$.

The value of the left-hand side is expressed by:

$$\int_{\alpha_0}^{\alpha} \frac{d\alpha}{f(\alpha)} = F(\alpha), \text{ for a given fraction } \alpha, F(\alpha) = \text{constant.}$$

$F(\alpha)$ is independent of temperature and still invariable all of the reaction.

The value of the right-hand side is expressed and tabulated by Doyle [4] as the polynomial function, p :

$$\int_{T_0}^{T} \exp(-E/RT)\, dT = \frac{E}{R}\, p\left(\frac{E}{RT}\right) \quad (8)$$

For largest values of E / RT, p (E / RT) can be approximated by

$$\log p\left(\frac{E}{RT}\right) = -2.135 - 0.4567\, \frac{E}{RT} \quad (9)$$

As the Ozawa method is based on the exploitation of temperature, T_1, for a heating rate of β_1, at T_2 for β_2, and so on (to a given fraction α), the equation obtained is:

$$\frac{k_0}{\beta_1} \frac{E}{R}\, p\left(\frac{E}{RT_1}\right) = \frac{k_0}{\beta_2} \frac{E}{R}\, p\left(\frac{E}{RT_2}\right) = \text{-------} \quad (10)$$

By taking the decimal logarithm of the expression (10), we obtain:

$$-\log \beta_1 + \log p\,(E / RT_1) = -\log \beta_2 + \log p\,(E / RT_2) = \text{------} \quad (11)$$

Combining the equations (9) and (11):

$$-\log \beta_1 - 0.4567\, \frac{E}{RT_1} = -\log \beta_2 - 0.4567\, \frac{E}{RT_2} = \text{------} \quad (12)$$

Finally, we obtain for the activation energy E:

$$E = \left[\left(-\frac{R}{0.4567} \right) \frac{d \log \beta}{d(1/T)} \right] \quad (13)$$

It results therefore that the plot of log heating rate (β) versus 1 / T (T is the temperature, in K, of maximum reaction rate), for a given fraction α, is a straight line. Its slope allows the determination of the approximate activation energy E (Kcal/mole) and so the pre-exponential factor k_0 (s^{-1}), using a (β,Tmax) data pair.

R is the gas constant (1.987 Cal/mol.K).

1.2. Kissinger method [5]

The Kissinger method stipulates that when the reaction rate is maximum, corresponding to the temperature of the top of the decomposition peak,

$$\frac{d}{dt}\left(\frac{d\alpha}{dt}\right) = 0 \qquad (14)$$

The general relation used by Kissinger is:

$$\frac{d\alpha}{dt} = k_0 (1 - \alpha)^n \exp(- E / RT) \qquad (15)$$

(α and T are measured to the same time t).

When equations (14) and (15) are combined:

$$\frac{d}{dt}\left(\frac{d\alpha}{dt}\right) = \frac{d\alpha}{dt}\left[\frac{E}{RT^2}\frac{dT}{dt} - k_0 \exp(- E / RT)\right] \qquad (16)$$

The maximum value for $\frac{d\alpha}{dt}$ is reached at T = Tmax and we have:

$$k_0 \exp(- E / RTm) = \frac{E}{RT_m^2}\frac{dT}{dt}$$

or
$$k_0 \exp(- E / RTm) = \beta \frac{E}{RT_m^2} \qquad (17)$$

where $\beta = \frac{dT}{dt}$.

By taking the logarithm form of the relationship (17), we obtain:

$$\mathrm{Ln}\left(\frac{\beta}{T_m^2}\right) = - \frac{E}{R}\frac{1}{T_m} + \mathrm{Ln}\, k_0 - \mathrm{Ln}\left(\frac{E}{R}\right) \qquad (18)$$

Or also:
$$\frac{d[Ln(\beta / T_m^2)]}{d(1/T_m)} = - \frac{E}{R} \qquad (19)$$

A plot of $\mathrm{Ln}\left(\frac{\beta}{T_m^2}\right)$ versus $\frac{1}{T_m}$ should yield a curve whose slope is E / R and so the pre-exponential factor k_0, from the relationship (17) for (βi, Ti).

Kissinger has shown that the T_m temperature is dependent on the heating rate, according to the expression (19).

2. Experimental Procedure

In a first stage, we will determine the thermodynamic parameters: exothermic onset temperatures and heats of decomposition, for each particle size, at different heating rates, then we deduce their influence on the combustion mode of the considered composite propellants. In a second stage, we will calculate the kinetic parameters of these same materials by using Ozawa and Kissinger methods.

These methods are based on the exploitation of the top of the decomposition peaks, corresponding to the plot of the different DSC traces, studied at a variety of heating rates, from 1.3 to 10 °C/mn.

2.1. Materials

The chemicals used in this study were catalysed composite propellants constituted with an oxidizer charge: ammonium perchlorate, a PVC-binder and specific additives, 75/24/1 by weight. As combustion catalyst, we have chosen: Copper chromite ($Cu_2Cr_2O_5$), at a rate of 1 % [6].

Some characteristics of this catalyst are regrouped in table 1:

Table 1: Characteristics of the used catalyst

Nature of catalyst	Chemical formula	Purity	Molecular weight	Uses
Copper chromite	$Cu_2Cr_2O_5$	Pure	311.08	Combustion catalyst

2.2. Apparatus and procedure

The differential scanning calorimeter apparatus used in this work is a PERKIN-ELMER Model DSC7 operating in the non-isothermal mode [7].

Its technical specifications [3], [7] are as follows:

- DSC type: power compensated temperature null principle. Measures energy directly, not differential temperature,
- DSC cell: independent dual furnaces constructed of platinum-iridium alloy with independent platinum resistance heaters and temperature sensors,
- Calorimetric precision: better than ± 0.1 %,
- Temperature precision: ± 0.1 °C,
- Temperature sensors: distributed, platinum resistance thermometers.

However, the experimental conditions are:

i) Variety of heating rates: from 1.3 to 10 °C/mn,

ii) Sample mass: 1.0 – 1.6 mg,

iii) Sample cell: sealed stainless-steel high-pressure capsules (150 bars and 400 °C),

iv) Atmosphere: nitrogen purge gas with flow rate of 20 cc/mn (1.4 bars),

v) Temperature range: it depends on the sample and the type of experiment. In this case, the samples are analysed from temperature of 50 °C to 400 °C.

3. Results

3.1. Thermodynamical parameters

The plot of DSC curves, seen in fig.1, yields temperatures and heats of decomposition, for each particle size of copper chromite; their values are given in table 2:

Table 2: Temperatures and heats of decomposition of used propellants

Sample n°	Copper chromite particle size (μm)	Sample mass (mg)	Heating rate (°C/mn)	Thermodynamical parameters	
				Onset temperatures (°C)	Heats of decomposition (J/g)
1	G1 ≤ 45	1.6	1.3	275.84	4692.01
2	45 ≤ G2 ≤ 63	1.4		279.29	4930.76
3	63 ≤ G3 ≤ 90	1.5		272.07	5781.87
4	90 ≤ G4 ≤ 125	1.4		270.54	4253.83
5	G1 ≤ 45	1.1	2.5	297.49	4006.75
6	45 ≤ G2 ≤ 63	1.3		288.70	4421.54
7	63 ≤ G3 ≤ 90	1.0		270.87	4712.20
8	90 ≤ G4 ≤ 125	1.3		281.03	4708.74
9	G1 ≤ 45	1.1	5.0	296.04	5136.17
10	45 ≤ G2 ≤ 63	1.4		293.71	3720.17
11	63 ≤ G3 ≤ 90	1.4		293.18	4843.04
12	90 ≤ G4 ≤ 125	1.3		282.77	5528.70
13	G1 ≤ 45	1.0	10	398.66	2619.59
14	45 ≤ G2 ≤ 63	1.0		328.59	4049.59
15	63 ≤ G3 ≤ 90	1.0		316.44	5431.52
16	90 ≤ G4 ≤ 125	1.0		294.71	4845.47

3.2. Kinetic parameters

The methods for determining the Arrhenius kinetic constants for the screening of potentially hazardous materials are based on that of Ozawa and Kissinger. The approximate activation energy can be obtained as proportional to the slope of a plot of log heating rate (β) versus $1/T_m$ (Ozawa method), and a plot of Ln (β/T_m^2) versus $1/T_m$ (Kissinger method), where T_m is the temperature of maximum reaction rate. The two methods assume that the maximum of the reaction rate corresponds to the top of the peaks.

3.2.1. Determination of Arrhenius kinetic constants : Ozawa method

Figure 1 superimposes fourth DSC traces of analyses of the different catalysed composite propellants at heating rates from 1.3 to 10 °C/mn.

The main results are regrouped in table 3:

Table 3: Values of activation energies, using Ozawa method.

Copper chromite particle size (µm)	β (°C/mn)	T_m (°C)	log β	1000 / T_m (K^{-1})	E (Kcal/mole) (*)
G1 ≤ 45	10	392.32	1.000	1.503	10.96
	5.0	301.42	0.699	1.740	
	2.5	303.77	0.398	1.733	
	1.3	277.72	0.114	1.815	
45 ≤ G2 ≤ 63	10	329.34	1.000	1.660	24.90
	5.0	294.18	0.699	1.763	
	2.5	292.36	0.398	1.768	
	1.3	282.87	0.114	1.798	
63 ≤ G3 ≤ 90	10	317.15	1.000	1.694	28.80
	5.0	293.78	0.699	1.764	
	2.5	282.03	0.398	1.801	
	1.3	275.95	0.114	1.821	
90 ≤ G4 ≤ 125	10	295.44	1.000	1.759	49.99
	5.0	287.73	0.699	1.783	
	2.5	284.28	0.398	1.794	
	1.3	271.43	0.114	1.836	

(*): activation energy values are calculated from the relationship (13).

In figure 2, it can be seen the plot of log β versus 1/Tm which should give a straight line of slope E / 4.351.

3.2.2. Determination of Arrhenius kinetic constants: Kissinger method

The main results, obtained from experimental data of figure 1, are given in table 4 :

Table 4: Values of kinetic constants, using Kissinger method.

Copper chromite particle size (μm)	β (°C/mn)	T_m (°C)	$-Ln[\beta / T_m^2]$	$1000/T_m$ (K^{-1})	E (Kcal/mole) (*)	Ln k_0 (s^{-1})
G1 ≤ 45	10	392.32	10.698	1.503	9.10	11.97
	5.0	301.42	11.098	1.740		
	2.5	303.77	11.799	1.733		
	1.3	277.72	12.361	1.815		
45 ≤ G2 ≤ 63	10	329.34	10.499	1.660	23.87	12.70
	5.0	294.18	11.072	1.763		
	2.5	292.36	11.759	1.768		
	1.3	282.87	12.379	1.798		
63 ≤ G3 ≤ 90	10	317.15	10.459	1.694	28.01	12.81
	5.0	293.78	11.071	1.764		
	2.5	282.03	11.722	1.801		
	1.3	275.95	12.354	1.821		
90 ≤ G4 ≤ 125	10	295.44	10.384	1.759	50.35	13.54
	5.0	287.73	11.049	1.783		
	2.5	284.28	11.730	1.794		
	1.3	271.43	12.338	1.836		

(*): activation energy values are calculated from the relationship (19).

In figure 3, it can be seen the plot of Ln $[\beta / T_m^2]$ versus $1 / T_m$. The slope of the line, graphically, gives the activation energy.

4. Discussion

Results of DSC measurements, found in the first part of this work, yields temperatures and heats of decomposition. From the obtained results, it emerges that the burning catalysts favour the decomposition of the oxidizer and therefore increase the calorimetric potential of the considered propellant. It is well known that the energetic performance of the propellants gets better when the value of the calorimetric potential increases.

Copper chromite tends to increase energetic performances of the propellant. Indeed the presence of a high rate of this catalyst makes combustion more and more complete and gives a low combustion products molecular weight which acts positively on the combustion temperature, by increasing it.

In the second part, kinetic constants were calculated by graphical solution, using Ozawa and Kissinger methods.

The following can be generally observed in all the thermograms: an endothermic peak, appeared at around 240 – 250 °C and has been assigned to the allotropic transformation of crystal structure of ammonium perchlorate from orthorhombic to cubic, and a maximum exothermic peak appearing at differents temperatures above 270 °C, resulting from the high temperature decomposition reaction of oxidizer / binder.

The principal parameter in these thermograms is the maximum exothermic decomposition peak temperature (T_m), for a given value of heating rate β.

In view of experimental results, given by the two methods, it emerges that:

- when the heating rate β increases, this yields for a given particle size of copper chromite, a positive displacement of the onset as well as an increase of the maximum decomposition peak temperature (temperature at which the reaction will proceed to completion), see figure 1.
- for the given heating rate, a clear negative displacement of the onset and the maximum decomposition peak temperature, when the particle size of copper chromite changes from the small sizes to the big ones (G1 to G4).

The values of activation energies, by using the two methods Ozawa and Kissinger, were practically the same and varies between 9 and 50 Kcal/mole, when the particle size of copper chromite changes from G1 to G4; the decomposition of the oxidizer becomes more easy , copper chromite particles reduce the energetic level barrier. It is well known that the oxides and some other compounds of transition metals facilitate the ammonium perchlorate decomposition in the combustion process [8,9].

For the value of the pre-exponential factor Ln k_0 , it varies between 12 to 13.5 s^{-1} when the particle size of copper chromite changes from G1 to G4, its increase is not very important as the case with the activation energy.

It's important to mention that the factors responsible for the size, shape, and position of the resulting peaks are not well understood. Often the temperature of maximum deflection, or peak temperature, is considerably higher than the known transition or decomposition temperature of the substance.

The peak temperature is also markedly affected by changes in technique. Only in the case of crystalline inversions (transitions occurring instantaneously at a fixed temperature), has there been a satisfactory explanation of the DSC peaks..

5. Conclusion

Being based on the experimental results obtained from the present work:

- operative conditions must be correctly fixed during the analysis of samples : sample size, range of temperature, heating rate β, flow rate of the purge gas, nature of the sample cell, calibration of the apparatus and the adjustment of the baseline. Indeed the variation of these conditions can give incorrect results interpretation.
- kinetically, the big size of copper chromite particles (for the considered intervall), delivers a highest activation energy (and a highest pre-exponential factor), and then a high calorimetric potential which is directly in relation with the energetic level of the propellant, it corresponds to the measure of calories produced during the combustion.
- Ozawa and Kissinger are quite good methods for determining the Arrhenius kinetic constants of catalysed composite propellants to predict the reaction rate. The results of this study show the effect of copper chromite particle size on thermal decomposition behaviour of ammonium perchlorate.

DSC measurements yield sufficient information for the investigation of decomposition mechanisms of reactive chemicals.

Therefore, the detailed mechanism would be an interest article to be investigated.

6. Nomenclature

β (°C/mn): heating rate

E (Kcal/mol): activation energy of the reaction

K_0 (s^{-1}): pre-exponential factor

α : degree of chemical conversion

mp (g) : weight of substance to be determined

n : reaction order

R (Cal/mol.K) : ideal gas constant, and is equal to 1.987

ΔT (K): measured temperature increase

T (K): absolute temperature

T_0 (K): initial temperature

t (s) : time

AP : Ammonium Perchlorate

PVC : Polyvinylchloride

7. References

[1] A. Davenas and Coll, Technologie des propergols solides, Masson, 1989.

[2] G. Widmann and R. Riesen, Thermal Analysis, HUTHIG, Heidelberg 1987.

[3] DSC 7 thermal analysis system, Users manual Rev.B, Perkin-Elmer, USA 1993.

[4] C. D. Doyle, J.Appl.Polym.Sc, 1961.

[5] W. Wendlant, Thermal Analysis, Vol.19, third edition, John Wiley and Sons, 1986.

[6] M. L. Gueroui & A. Mansour, Utilisation de la DSC pour la Caractérisation Thermique des Propergols Composites Catalysés, EMP/Algiers 1997.

[7] T.L. Mc Naughton and C.T. Mortimer, Differential Scanning Calorimeter, PE 1975.

[8] J. Quinchon, La Fabrication et les Propriétés des Substances Explosives, T3 Les Propergols, ENSTA 1975.

[9] E. Cohen-Nir, La Propulsion par Fusée, E.N.S.I.E.T.A 1988.

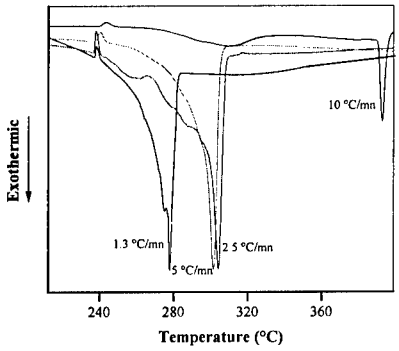


Fig. 1.1 : G1 ≤ 45 µm

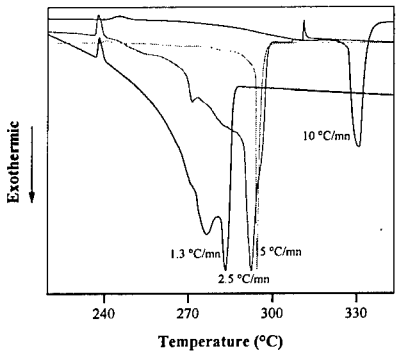


Fig. 1.2 : 45 ≤ G2 ≤ 63 µm

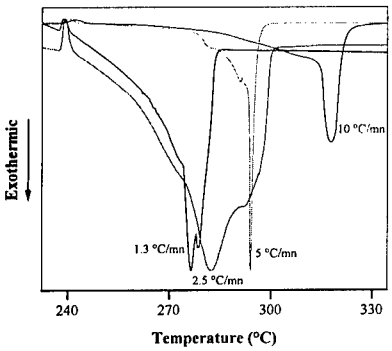


Fig. 1.3 : 63 ≤ G3 ≤ 90 µm

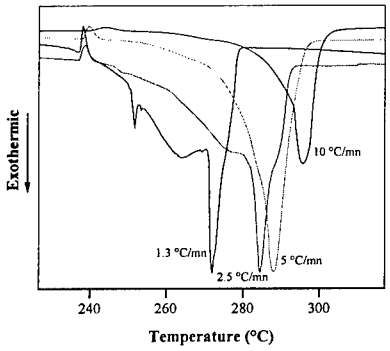


Fig. 1.4 : 90 ≤ G4 ≤ 125 µm

Figure 1: Superimposition of DSC traces of the different composite propellants catalysed with copper chromite

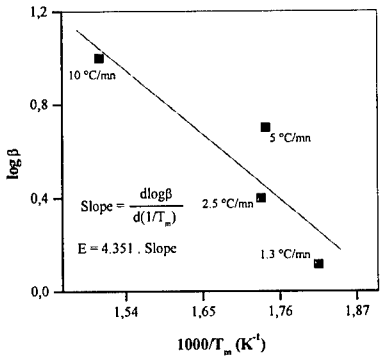


Fig. 2.1 : G1 ≤ 45 μm

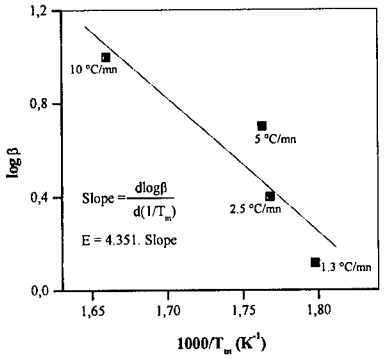


Fig. 2.2 : 45 ≤ G2 ≤ 63 μm

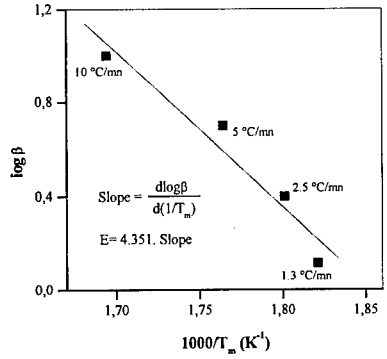


Fig. 2.3 : 63 ≤ G3 ≤ 90 μm

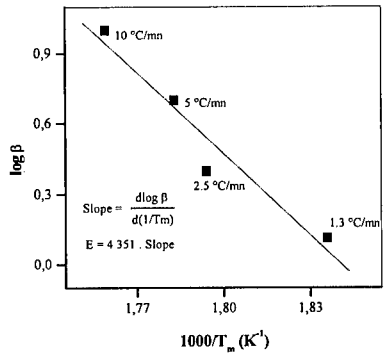


Fig. 2.4 : 90 ≤ G4 ≤ 125 μm

Figure 2: Determination of activation energy for thermal decomposition (Ozawa method)

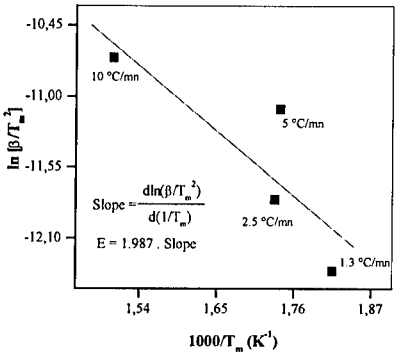


Fig. 3.1 : G1 ≤ 45 μm

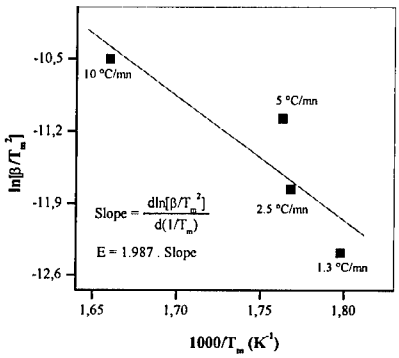


Fig. 3.2 : 45 ≤ G2 ≤ 63 μm

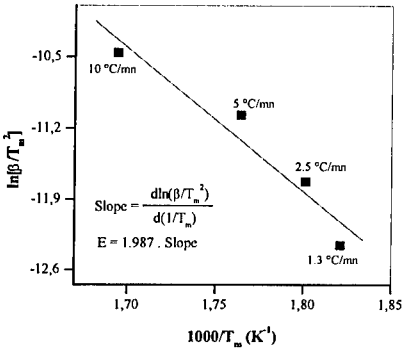


Fig. 3.3 : 63 ≤ G3 ≤ 90 μm

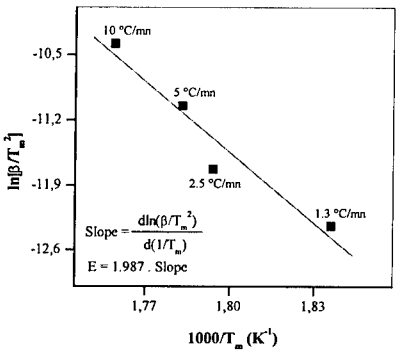


Fig. 3.4 : 90 ≤ G4 ≤ 125 μm

Figure 3: Determination of activation energy for thermal decomposition (Kissinger method)

THE FINAL STATE AND INTERMEDIATE STEPS IN CONJUGATE DETONATION THEORY

Hu, Shaoming
Xian Modern Chemistry Research Institute
Xian 710065, People's Republic of China
E-mail: hushaoming @ hotmail.com

ABSTRACT

According to conjugate detonation theory, the final state of detonation products and the intermediate steps through which the detonation products achieve the final state are discussed in this paper.

The final state P is defined as the stable equilibrium state of explosion products after detonation wave sweeps over. Hypothesizing that the original explosive element explodes into an intermediate state composed of two parts (conjugate pair B+P), conjugate detonation theory considers this final state is achieved at finite detonation velocity through a series of intermediate steps. In conjugate theory, detonation goes according to the mode O→Z→F→(B+P)→P, among which O→Z→F is exactly the same one as in ZND model in CJ theory, and F→(B+P)→P is the process of conjugate pairs produced in micro-explosion and annihilated in expansion.

Key words: Detonation Conjugate detonation theory
Final state Intermediate states

1. Introduction about conjugate detonation theory

A new detonation theory, called conjugate detonation theory, has been proposed by the author at the 29th and 31st ICT. According to conjugate detonation theory, the detonation process is composed of shock wave

front, turbulence zone of conjugate pairs produced by element micro-explosion, and final products zone.

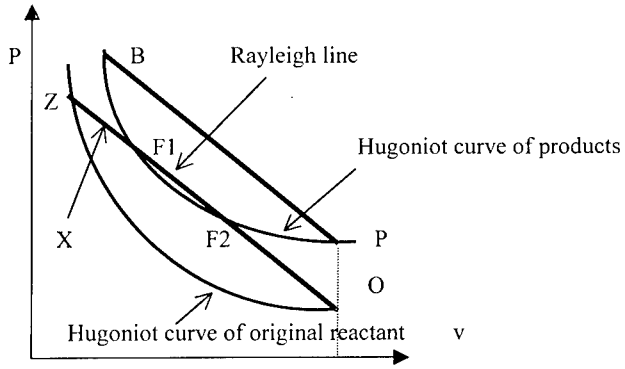
Conjugate detonation theory is deduced from conservation laws, which describes the whole process from the original explosion reactants to the final products.

Comparing with CJ theory, conjugate detonation theory gives a definite final state P, and shows how the explosion materials achieves this final state through a series of intermediate steps.

CJ hypothesis (D=U+C) is a special solution of conjugate detonation theory.

2. The final state

The state of system in detonation propagation is as shown by following Fig..



Hugoniot curve and Rayleigh line in p-v plane

In conjugate detonation theory, the final state is defined as the stable equilibrium state of explosion products after detonation wave sweeps over, as point P shows. It is obvious that the specific volume of original explosive and final products is the same (V_O=V_P), and particles' velocity is zero.

State P is a "real final state", i.e. in this after-detonation system, detonation propagation is thoroughly over. On the contrary, in CJ theory,

between the "final state" (CJ point) and the rear boundary is a time dependent rarefaction wave.

In outward form, state P is the same one as the state of constant volume detonation in CJ theory. In essence, constant volume detonation propagates at infinite detonation velocity, but in conjugate detonation theory state P is achieved at finite detonation velocity through a series of intermediate steps.

3. The intermediate steps

Conjugate theory considers the final state P is achieved through a series of intermediate steps as following:

----Compressed by strong shock, the state of original explosive jumps instantly from point O to point Z.

----Chemical reaction is triggered by high temperature and high pressure in point Z. Exothermic chemical reaction goes down Rayleigh line ZO.

----At a certain point (all of the points at Rayleigh line are equivalent in the view of conservation), chemical reaction reaches peak and element micro-explosion happens that makes the element itself divide into two parts: conjugate pairs p and b (in state P and B correspondingly).

----Being part of the stable detonation wave, this conjugate pairs zone also propagates at detonation velocity D. Part b (in state B) expands instantly into the final state P, i.e. conjugate pairs are annihilated in expansion, at last the whole system returns back to uniform state and achieves final state P.

All of above mentioned steps are stable and meet the requirement of mass/momentum/energy conservation.

In this way, conjugate theory considers detonation process goes according to the mode $O \rightarrow Z \rightarrow F \rightarrow (B+P) \rightarrow P$, among which $O \rightarrow Z \rightarrow F$ is exactly the same as in ZND model in current detonation theory, and $F \rightarrow (B+P) \rightarrow P$ is the process of conjugate pairs produced in

micro-explosion and annihilated in expansion.

4. Mathematical model of conjugate detonation theory

Following is the mathematical model of conjugate detonation theory: (See the Proceedings of the 31st ICT)

Energy equation:

$$e_p = e_0 + Q_V$$

Conservation of original explosion materials:

$$(D-U_0)/V_0 = (D-U\ )/V$$

$$P_0 + (D-U_0)^2/V_0 = P\ + (D-U\ )^2/V$$

$$\frac{(D-U_0)^2}{2} + E_0 + P_0V_0 = \frac{(D-U)^2}{2} + E\ + PV$$

Conservation of explosion products:

$$(D-U_P)/V_P = (D-U_B)/V_B$$

$$P_P + (D-U_P)^2/V_P = P_B + (D-U_B)^2/V_B$$

$$\frac{(D-U_P)^2}{2} + E_P + P_PV_P = \frac{(D-U_B)^2}{2} + E_B + P_BV_B$$

Momentum conservation before/after conjugate mutation:

$$P_F + (D-U_F)^2/V_F = (X_B \cdot P_B + X_P \cdot P_P) + \left[Y_B \cdot (D-U_B)^2/V_B + Y_P \cdot (D-U_P)^2/V_P\right]$$

In this equations, average values is taken for conjugate pairs zone because it is a mixing region composed with part p and part b. The average value of pressure is calculated with respect to corresponding volume fraction as follows:

$$X_B = V_B/(V_B + V_P)$$

$$X_P = V_P/(V_B + V_P)$$

The average value of momentum is calculated with respect to

corresponding mass fraction as follows:

$$Y_B = \frac{(D-U_B)/V_B}{(D-U_B)/V_B + (D-U_P)/V_P}$$
$$Y_P = \frac{(D-U_P)/V_P}{(D-U_B)/V_B + (D-U_P)/V_P}$$

And three state equations:

$$f_P(P_P, V_P, T_P) = 0$$
$$f_F(P_F, V_F, T_F) = 0$$
$$f_B(P_B, V_B, T_B) = 0$$

Therefore all eleven unknown variables (detonation parameters)

$$P_P, T_P, P_F, V_F, T_F, U_F, P_B, V_B, T_B, U_B, D$$

can be found from these eleven equations.

5. Conclusion

State P of is a unique state for detonation products after detonation wave sweeps over. Conjugate detonation theory describes all of the intermediate steps from original state O to final state P.

Supercritical Fluid Technology: A New Process on Formation of Energetic Materials

H. Kröber, W. Reinhard, U. Teipel

Fraunhofer Institut für Chemische Technologie (ICT), Postfach 1240, D-76318 Pfinztal,

e-mail: hkr@ict.fhg.de

Abstract

A new field of applications of compressed gases is the formation of solid particles with well-defined properties, e.g. the particle size, the particle size distribution, the particle shape, the specific surface area and free of solvent inclusions. It is possible to process moderately solids like energetic materials which are difficult to comminute due to their sensitivity to mechanical or thermal stress. The characteristics of compressed gases allow to vary the morphology of solid particles in a wide range.

The RESS - process (Rapid Expansion of Supercritical Solutions) is one of these new techniques generating crystalline uniform particles in the submicron range. During the process, a loaded supercritical fluid is expanded through a nozzle, creating high supersaturation in the jet. Fast nucleation and growth of the crystalline particle occurs. This technique offers advantages compared with conventional size reduction methods. Especially heat sensitive products can be generated by choosing mild process conditions.

Solids which are insoluble in a compressed gas can be processed by applying the PCA-process (Precipitation with a Compressed Antisolvent). For this, a solution consisting of an organic solvent which has to be miscible completely with the compressed gas and a solid material dissolved in this solvent is sprayed through a nozzle into a high-pressure vessel filled with a compressed gas. The formation of the particles is based on two mechanisms which take place simultaneously. On the one hand the solvent evaporates in the compressed gas and on the other hand the compressed gas penetrates into the droplets where it acts as an antisolvent for the dissolved material so that a precipitation occurs.

A pilot plant is presented, which has been built to prepare fine particles by the Rapid Expansion of Supercritical Solutions (RESS-process) and Precipitation by a Compressed Fluid Antisolvent (PCA-process). These techniques offer interesting applications for products, which are produced in small amounts, as certain energetic materials. In this contribution the micronization of different energetic materials by the RESS and PCA process will be under investigation.

1 Introduction

Many product properties that are of relevance in the industrial use can be adjusted by changing the particle size and particle size distribution of the powder. This statement is valid in several fields ranging from polymers to pharmaceutical and inorganic powders.

In the case of solid explosives and propellants small particles are as a rule required to improve the combustion process. Indeed, the attainment of the highest energy from the detonation of a solid explosive (ideal detonation) strongly depends on the particle size of the material.

Grinding and crystallization from solutions are largely used as micronization processes in the industry. However, these processes suffer some limitations: it is difficult to control particle size and particle size distribution of powders, especially when very small (micronic) particles are required. Liquid crystallization, also suffers the problem of solvent contamination of the precipitate (crystal inclusions) and jet milling is not suitable for the treatment of shock sensitive substances like energetic materials.

As an alternative to the traditional techniques, various supercritical fluid based precipitation processes have recently been proposed. These techniques can potentially overcome all the previously described limitations of the classical micronization processes. Supercritical fluids are compressed gases that are used at temperatures and pressures higher than their critical point. They, in principle, do not give problems of solvent contamination since when the decompression occurs they are completely released from the solute. The supercritical fluid of election is CO_2 since it has relatively low critical parameters (ϑ_c = 31.1 °C and p_c = 7.38 MPa), it is not toxic, non flammable and cheap. The operating conditions for supercritical fluids processing are generally mild, thus giving no problem to process "heat sensitive" materials. Also, the control of particle size and particle size distribution of the micronized material promises to be relatively simple to be obtained by continuously modulating the process conditions.

Various supercritical fluid based precipitation processes have been proposed. In this contribution two processes which complement one another will be discussed and results will be presented.

The first micronization process based on supercritical fluids that has been proposed is the Rapid Expansion of Supercritical Solutions (RESS) [1, 2, 3]. In this process the solvent power of the supercritical fluid is used to solubilize the compound to be micronized by fluxing the supercritical fluid in a fixed bed formed by the particles of the starting material. Then, the formed solution is depressurized down to atmospheric pressure in an atomization nozzle. The

fast expansion of the supercritical solution reduces to near to zero the solvent power of the fluid and the solute precipitates in the expansion chamber. After the process the solvent (CO_2) is in the gaseous phase so that solvent free and dry products can be achieved and an additional wash and drying process is not necessary.

Using this technique it is possible to obtain very high supersaturation ratios that can result in the production of very small particles. Some studies on RESS were devoted to the identification of the process parameters that control the precipitation of particles [3]. The main parameters that control RESS are pre-expansion temperature and pressure, and expansion chamber temperature and pressure.

It is difficult to propose a systematic description of the investigated substances and morphologies obtained by RESS since a large variety of particle shapes and sizes has been observed and very different experimental arrangements have been used. Moreover many different substances were investigated (organic and inorganic materials, polymers and biopolymers and biodegradable materials) which differed in their physical and chemical properties so that a comparison is difficult. Kröber et al. micronized benzoic acid and cholesterol as model substances for pharmaceuticals at different process conditions [4]. In contrast to the experimental work of other groups the investigations presented in this paper were carried out with nozzles up to three-times larger than normally used so that an industrial application is simulated more realistic. The first theoretical descriptions demonstrate the complexity of the process, but only provide a rough, qualitative interpretation of experimental results. Türk showed the calculated temperature, pressure, and supersaturation profiles as a function of capillary length for various experimental conditions [5].

Precipitation with a Compressed Fluid Antisolvent (PCA) is the most promising supercritical technique since it has been demonstrated that it is capable to produce controlled micronic and sub-micronic particles [6]. The description of this process departs from liquid crystallization of which it is the homologous in supercritical form. Indeed, in PCA the supercritical fluid substitutes the liquid antisolvent and causes the precipitation of solute since it forms a solution with the primary solvent. Therefore, a pre-requisite to perform PCA is that the process is performed at temperature and pressure conditions at which complete miscibility exists between the primary liquid solvent and the supercritical antisolvent. A distinctive characteristic of supercritical fluids is the diffusivity that can be up to two orders of magnitude higher than those of liquids. Therefore, the diffusion of the supercritical fluid into a liquid solvent can produce a

fast supersaturation of solute dissolved in the liquid and its precipitation in micronized particles.

PCA has been performed using different process arrangements and apparatuses. Since the results can be heavily influenced by the process arrangement, a short description of the two main techniques is presented. When the precipitation vessel is loaded with a given quantity of the liquid solution and then the supercritical antisolvent is added until the final pressure is reached, a batch antisolvent precipitation is performed. This mode of operation can be referred to as liquid batch. It is also possible to charge the precipitation chamber with the antisolvent and then to perform a discontinuous injection of the liquid solution. This mode of operation can be termed gas batch. The difference between these two operation modes is that in the first case the precipitation occurs in a liquid rich phase, whereas, in the second case it occurs in a supercritical fluid rich phase. A semi-continuous PCA processing is performed when a spray of the liquid solution is continuously produced in the precipitation chamber in which supercritical CO_2 is also flowing, added from another inlet point. An injector is used to produce liquid jet break-up to form small micronic droplets that expand in the precipitator. Various injection devices have been proposed in the literature. Yeo et al. proposed the adoption of nozzles and tested various nozzle diameters ranging from 5 to 50 μm [7]. Other authors used small internal diameter capillaries [8, 9], or vibrating orifices [8]. This last apparatus produces a spray by superimposing a high frequency vibration on the liquid jet that exits from an orifice. Coaxial devices have also been proposed in which two capillary tubes continuously deliver the liquid solution and the supercritical antisolvent [10, 11]. The formation of small droplets in this case depends on the turbulent mixing of the two flows. Complex geometries formed by more than two capillaries and different disposition of the liquid and supercritical fluid (inside-outside) have also been tested [10].

The formation of the particles is based on two mechanisms which take place simultaneously. On the one hand the solvent evaporates in the compressed gas and on the other hand the compressed gas penetrates into the droplets where it acts as an antisolvent for the dissolved material so that precipitation occurs. The key operating parameters are pressure, temperature, solution flow rate and initial concentration. These parameters control product quality through their effects on thermodynamics, hydrodynamics and kinetics on mass transfer and precipitation [6, 12, 13]. The washing step with pure supercritical antisolvent at the end of the precipitation process, either batch or semi-continuous, is fundamental to avoid the condensation of the liquid phase that otherwise rains on the precipitated powder modifying its characteristics.

The objective of this study is to generate fine divided particles either by the RESS- and PCA-process. Investigating the RESS-process the effects of nozzle diameter and conditions (pressure, temperature and concentration) before the nozzle on the quality (e.g. particle size and morphology) of the solid product is described using trinitotoluene (TNT) and 3-nitro-1,2,4-triazole-5-one (NTO). Investigating the PCA-process the effects of process conditions (pressure, temperature, flow rates and concentration) on the quality of the solid product is described. Cyclotrimethylene trinitramine (RDX), cyclotetramethylene tetranitramine (HMX) and hexanitrostilben (HNS) dissolved in cyclohexanone, acetone and N-N-dimethyl formamide (DMF), respectively are precipitated with compressed carbon dioxide as antisolvent. In contrast to the experimental work of other groups the investigations presented in this paper were carried out with nozzles and mass flow rates up to three-times larger than normally used.

2 The RESS process

2.1 Experimental Setup

The experimental measurements were performed in a pilot plant which consists of three sections (as shown in Fig 1, schematically): the CO_2-supply unit, the extractor and the precipitation vessel including the nozzle. The extractor is closed with two sintered metal filters (pore size 0.1 µm) to avoid discharging of the solid material. The maximum pressure in the plant is limited to 30 MPa, the extraction temperature to 353 K.

Liquid carbon dioxide is cooled down (W1 and W2) to avoid cavitation in the membrane pump (P). After the compression to pre-expansion pressure, the fluid is heated to the extraction temperature (W3). In the extractor (V = 0.6 l), the supercritical fluid is charged with the solute. To avoid blockages in the nozzle and dropwise condensation of carbon dioxide during the expansion it is necessary to overheat the solution in an additional heat exchanger (W4). The supercritical solution is expanded through a nozzle into the precipitation vessel. The particle formation can be observed through sapphire windows which are placed on different positions in the separation vessel. The expanded gas will be condensed (W1) and recompressed or let off.

After the experiment, the separation vessel is opened and the particles were collected and characterised by SEM-pictures, gas adsorption measurements (BET surface area, Nova 2200, Quantachrome) and laser light diffraction (particle size distribution, Mastersizer S, Malvern).

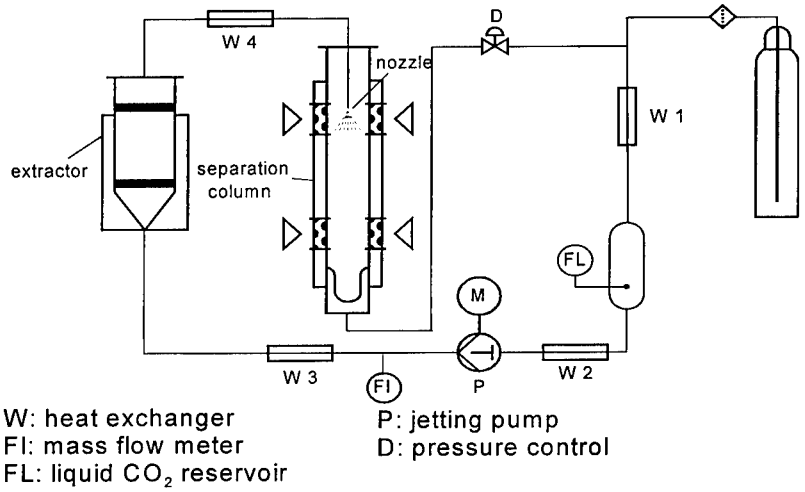


Fig. 1: Flow sheet of the experimental setup (RESS process)

2.2 Results

Trinitrotoluene (TNT)

The extractor was charged with raw material which was extracted by the CO_2 flowing through the extractor. The extraction pressure $p_{extr.}$ and temperature $T_{extr.}$ was 22 MPa and 348 K, respectively. The supercritical solution was overheated up to 458 K and through a Laval nozzle expanded from pre-expansion pressure ($p_{pre\text{-}exp.}$ = 22 MPa) to atmospheric pressure and room temperature. Two Laval nozzles which differ in the smallest diameter (50 µm and 100 µm) were used in these experiments. In Table 1 the parameter and results are summarized.

Run		1	2
Extractor:	p [MPa]	22	22
	T [K]	348	348
Nozzle:	d [µm]	50	100
	T [K]	458	458
Column:	p [MPa]	0.1	0.1
	T [K]	305	305
Mean particle size $x_{50,3}$ [µm]		14.2	10.0

Table 1: Experimental conditions and results of the precipitation of TNT

At these conditions it was possible to micronize TNT by the RESS process. A slight influence of the nozzle diameter on the product quality can be seen from these experiments. The morphology of the precipitated particles can be seen in Fig. 2 from a SEM picture.

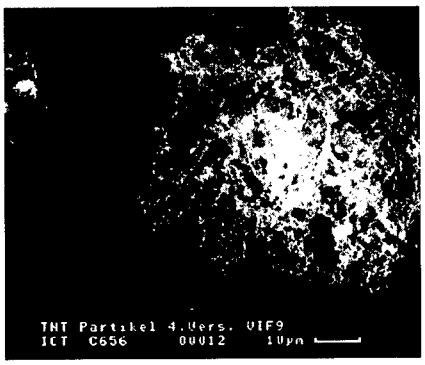


Fig. 2: SEM picture of precipitated TNT particles (Run 2)

In this picture an agglomerate of about 50 µm is shown which contains of many primary needle-like shaped particles.

1,2,4-Triazole-5-one (NTO)

Due to the very low solubility of NTO in pure supercritical carbon dioxide the precipitation of NTO was carried out using a modifier which is mixed into the supercritical CO_2 just before the CO_2 flows through the extractor. The modifier increases the solvent power of the CO_2 because by changing the polarity of the solvent. The modifier has to be complete miscible in the supercritical fluid and has to be evaporated behind the nozzle into the gaseous fluid. For this reason acetone was used as modifier in this study.

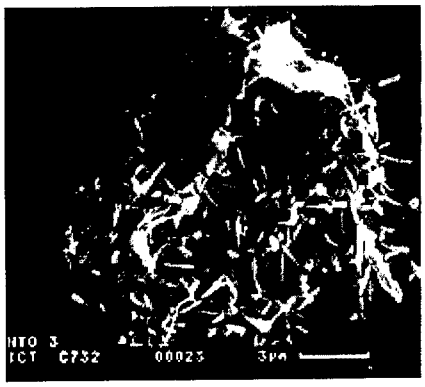


Fig. 3: SEM picture of precipitated NTO particles

The ratio between the flow rates of CO_2 and modifier was 2 000. The extraction was carried out at 333 K and 20 MPa. Before the solution is expanded through the Laval nozzle (diameter: 150 µm) it was heated up to 436 K to prevent blockages in the nozzle and occurrence of liquid or solid carbon dioxide in the spray jet behind the nozzle due to the Joule-Thomson effect. Additional the walls of the precipitation column were heated (323 K) to prevent that liquid droplets of acetone were formed in the column which would result in a dissolution of the precipitated particles in the acetone. In Fig. 3 precipitated particles of NTO are presented, exemplary. The shown agglomerate is very loose and consists of needle-like particles. The measurement of the particle size distribution by laser light diffraction show a mean particle size of x = 540 nn.

3 The PCA process

3.1 Experimental Setup

The experimental work was performed in the same high-pressure pilot-plant, as described above, consisting of the CO_2 supply unit including membrane pump and heat exchanger, the precipitation vessel with sinter metal filter and the membrane pump connected with the nozzle

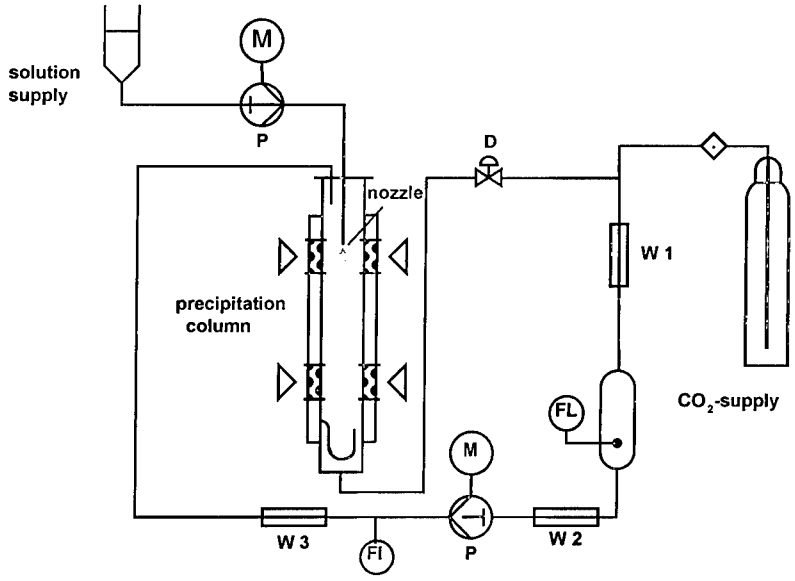


Fig. 4: Flow sheet of the experimental setup (PCA process), W: heat exchanger, P: membrane pump, FI: mass flow meter, FL: liquid CO_2 reservoir, D: pressure control

placed at the top of the precipitation vessel (see Fig. 4, schematically). The inlet of the anti-solvent (CO_2) was either at the top of the vessel or at the bottom, so that co-current flow as well as counter-current flow is possible. The maximum pressure in the plant is limited to 30 MPa, the precipitation temperature to 353 K. The mass flow rate of the CO_2 is limited to 30 kg/h, the maximum volume flow of the solution is 600 ml/h.

At the beginning of the continuous PCA process, CO_2 is fed to the precipitation vessel until the desired pressure is reached. Then a steady antisolvent flow is set, the flow rate of which is controlled at a designated value. After the steady state is maintained for 10 minutes the solution is sprayed into the precipitation vessel through a Laval-nozzle. The particle formation can be observed through sapphire windows which are placed on different positions in the separation vessel. Nucleation occurs as a cloud formation after leaving the nozzle exit, where the droplets of the solution expand and dissolve into the CO_2 phase. Simultaneously, the antisolvent diffused into the solution droplets which leads to a swelling of the droplets and precipitation occurs in the droplets. The particles produced are collected on a sinter metal filter (pore size: 100 nm) placed on the bottom of the precipitation vessel. In order to remove any residual organic solvent from the particles pure CO_2 continues to flow for at least 30 minutes through the precipitation vessel before starting the depressurization of the precipitator. If this purging step with pure CO_2 is not done, organic solvent condenses during the depressurazation and partly solubilizes the powder modifying its morphology and lowering the yield. The fluid mixture (mainly CO_2 and some organic solvent) leaves the precipitation vessel and is depressurized in the separator where solvent is separated from the CO_2. The CO_2 can be recompressed and fed into the CO_2 cycle or let off. Sample of powder precipitated are characterized by scanning electronic microscopy (SEM), laser light diffraction (particle size distribution, Mastersizer S, Malvern) and BET absorption measurement (specific surface area, Nova 2200, Quantachrome).

3.2 Results

The PCA process shares many similarities with classical spray-drying techniques. The major differences lies in spraying the solution into a compressed gas instead of into heated air as the external phase. Compressed CO_2 is quite miscible with the organic solvent under supercritical conditions, however it is nonsolvent for the solute.

During the spray process the particle size and morphology are dependent on many factors, such as the jet breakup, mass transfer rates between the droplet and antisolvent phase, nuclea-

tion kinetics, and particle growth rates. Especially the jet breakup is in the compressed gas phase different from the normal breakup in atmospheric spray processes.

Cyclotrimethylene trinitramine (RDX)

The precipitation of RDX was carried out from acetone solution in which the solute concentration was 5 wt.-%. The precipitation pressure was 15 MPa at a precipitation temperature of 323 K. The solution was atomized through a capillary nozzle with a diameter of 100 µm and a length of 1000 µm. The flow rate of the solution was 480 ml/h whereas the CO_2 flow rate was 6 kg/h. The mean particle size of the precipitated RDX was x = 32.3 µm with a specific surface area of $S_m = 0.34$ m^2/g.The morphology of the particles can be seen from SEM pictures (see Fig. 5). The particles are plate-like with distinct edges and seem to be crystalline.

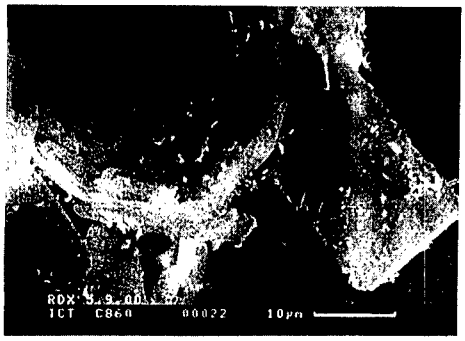


Fig. 5: SEM picture of precipitated RDX particles

The influence of the nozzle type on the product quality was demonstrated by carrying out the same experiment with a two-flow nozzle which consists of an capillary nozzle with a diameter of 2.2 mm and a 1/16" capillary which is inserted co-axial into the larger nozzle. The solution flows through the inner capillary, the CO_2 through the outer one. The result of this comparison is shown in Fig. 6.

The atomization through the two-flow nozzle results in a particle size distribution which is more narrow in comparison to the distribution generated by the capillary nozzle. Additional the mean particle size decreases from x = 32.3 µm to x = 16.6 µm.

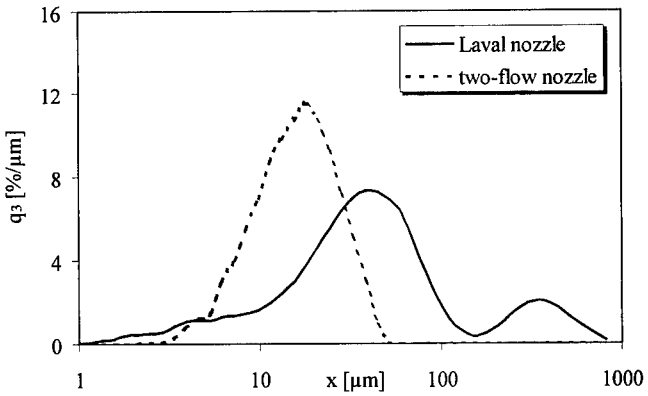


Fig. 6: Comparison between a capillary and a two-flow nozzle

Cyclotetramethylene tetranitramine (HMX)

The precipitation of HMX was carried out from cyclohexanone solution in which the solute concentration was 4 wt.-%. The precipitation pressure was 20 MPa at a precipitation temperature of 313 K. The solution was atomized through a two-flow nozzle which consists of an capillary nozzle with a diameter of 2.2 mm and a 1/16" capillary which is inserted co-axial into the larger nozzle. The solution flows through the inner capillary, the CO_2 through the outer one. The flow rate of the solution was 600 ml/h whereas the CO_2 flow rate was 8 kg/h. The mean particle size of the precipitated HMX was x = 2.3 µm with a specific surface area of S_m = 5.5 m^2/g.The morphology of the particles can be seen from SEM pictures (see Fig. 7).

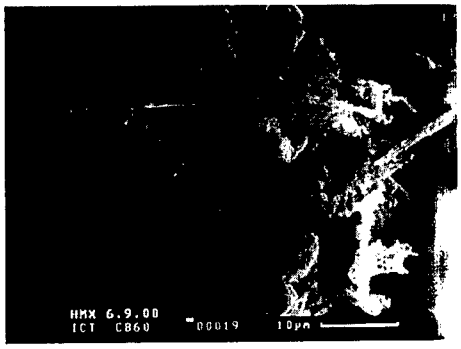


Fig. 7: SEM picture of precipitated HMX particles

The morphology of the HMX particles differs fro· the morphology seen in Fig. 5. The HMX particles seem to be not as crystalline as the RDX ·articles and the shape is more needle-like.

Hexanitrostilben (HNS)

The precipitation of HNS was carried out from N-N-dimethyl formamide solution in which the solute concentration was 1 wt.-%. The precipitation pressure was 10 MPa at a precipitation temperature of 323 K. The solution was atomized through a two-flow nozzle which consists of an capillary nozzle with a diameter of 2.2 mm and a 1/16" capillary which is inserted co-axial into the larger nozzle. The solution flows through the inner capillary, the CO_2 through the outer one. The flow rate of the solution was 600 ml/h whereas the CO_2 flow rate was 8 kg/h. The mean particle size of the precipitated HMX was $x = 3.5$ µm with a specific surface area of $S_m = 6.8$ m^2/g.The morphology of the particles can be seen from SEM pictures (see Fig. 8).

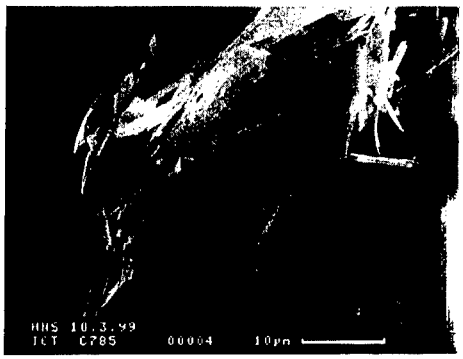


Fig. 8: SEM picture of precipitated HNS particles

4 Summary

Crystallization with compressed gases is still at the very early stages of development. Fundamental studies are required on phase behaviour, mass and heat transfer; experimental information is also required to obtain a reliable picture of the processes.

The special properties of compressed gases make them suitable for processing sensitive substances due to the moderate operation conditions. It is possible to produce crystalline particles with a small size and narrow size distribution without spots, i.e. free of solvent inclusions. However especially PCA is very promising in energetic materials processing. First results show the potential of this technique. It was shown that TNT and NTO can be micronized by the RESS process and that the precipitation of RDX, HMX and HNS by the PCA process is possible. The influence of process parameter on the product quality has to be investigated in further studies.

5 References

[1] Matson DW, Fulton JL, Petersen RC, Smith RD, (1987) Rapid expansion of supercritical fluid solutions: solute foration of powders, thin films and fibers, *Ind. Eng. Chem. Res.*, 26, 2298-2306

[2] Mohamed RS, Halverson DS, Debenedetti PG, Prud'homme RK, (1989) Solids formation after the expansion of supercritical mixtures, In K.P. Johnston and J.M.L. Penninger (Eds.) Supercritical fluid science and technology, *ACS Symp. Ser. 406*, 355-378

[3] Reverchon E, Donsì G, Gorgoglione D, (1993) Salicylic acid solubilization in supercritical CO_2 and its micronization by RESS, *J. Supercrit. Fluids*, 6, 241-248

[4] Kröber H, Teipel U, Krause H, (2000) Manufacture of Submicron Particles via Expansion of Superceritical Fluids, *Chem. Eng. Technol.*, 23, 763-765

[5] Türk M, (1999) Formation of small organic particles by RESS: experimental and theoretical investigations, *J. Supercrit. Fluids*, 15, 79-89

[6] Reverchon E, (1999) Supercritical antisolvent precipitation of micro and nano particles, *J. Supercrit. Fluids*, 15. 1-21

[7] Yeo SD, Lim GB, Debenedetti PG, Bernstein H, (1993) Formation of microparticulate protein powders using a supercritical fluid antisolvent, *Biotech. Bioeng*, 41, 341-345

[8] Randolph TW, Randolph AD, Mebes M, Yeung S, (1993) Sub-micrometer-sized biodegradable particles of poly(l-lactic acid) via the gas antisolvent spray precipitation process, *Biotech. Progress*, 9, 429-435

[9] Dixon DJ, Johnston KP, Bodmeier RA, (1993) Polymeric Materials Formed by Precipitation with a Compressed Fluid Antisolvent, *AIChE J.*, 39, 127

[10] York P, Hanna M, (1994) World Patent 95/01324 Salmeterol xinafoatewith controlled particle size

[11] Jaarmo S, Rantakyla M, Aaltonen O, (1997) Particle tailoring with supercritical fluids: production of amorphous pharmaceutical particles, in: Ed. K. Arai, Proceedings of the 4th Internat. Symp. on Supercritical Fluids, 263-267

[12] Subramaniam B, Rajewski RA, Snavely K, (1997) Pharmaceutical processing with supercritical carbon dioxide, *J. Pharm. Sci.*, 86, 885-890

[13] Palakodaty S, York P, (1999) Phase behavior effects on particle formation processes using supercritical fluids, *Pharm. Res.*, 16, 976-985

ON THE CRYSTALLIZATION OF AMMONIUM DINITRAMIDE
ZUR KRISTALLISATION VON AMMONIUMDINITRAMID

U. Teipel, T. Heintz

Fraunhofer-Institut für Chemische Technologie (ICT)
Joseph-von-Fraunhofer-Str. 7, 76327 Pfinztal
Germany

Abstract

Several properties of Ammonium Dinitramide (ADN) concerning the recrystallization process from melting were investigated. The surface tension of molten ADN at 97 °C was measured to 89 mN/m.
The wetting-angles between molten ADN and different solid surfaces (polytetrafluor ethylene, glass, steel and aluminium) were determined. The wettability depends on the surface tension of molten ADN, the free surface energy of the solid surfaces and the interfacial tension between solid and liquid.
Observations of the recrystallization behaviour of molten ADN showed that there is no nucleation even at supercooling rates of 70 K. It is possible to start crystallisation by the application of seed crystals.

1 Einleitung

Zur Kristallisation von sphärischen Ammoniumdinitramid (ADN)-Partikeln aus der geschmolzenen Phase eignen sich grundsätzlich sowohl die Emulsionskristallisation [1] als auch die Zerstäubungs- bzw. Sprühkristallisation. Die Kristallisationskinetik, bestehend aus Keimbildung und Kristallwachstum, von Ammoniumdinitramid (ADN) ist hierbei ein prozeßbestimmendes Kriterium. Die Problematik liegt in der verzögerten Keimbildung von flüssigem ADN. Zusätzlich zur Unterkühlung der Schmelze ist noch eine weitere Aktivierung z.B. in Form von mechanischer Energie und/oder dem Einsatz von Impfkeimen erforderlich. Nach der Keimbildung muß der Tropfen hinreichend lange vor starken äußeren Einwirkungen geschützt bleiben um seine Kugelform bis zum kompletten Erstarren beizubehalten.
Soll aus einem in der Flüssigkeit oder im Gasstrom dispergierten ADN-Schmelzetropfen ein festes kugelförmiges Partikel erzeugt werden sind Verfahren erforderlich, die es ermöglichen diesen Kristallisationsprozeß auf jedes diskrete Partikel zu übertragen. Hierzu sind grundlegende Untersuchungen der Eigenschaften von geschmolzenem ADN aus dem Bereich der Grenzflächenphänomenologie und der Kristallisation notwendig.
Bei der Zerkleinerung einer flüssigen Phase (ADN-Schmelze) muß zur Erzeugung von Tropfen die Oberflächen- bzw. Grenzfächenspannung durch Energieeintrag überwunden werden. Als Konsequenz bewirkt die Oberflächen- bzw. Grenzfächenspannung bei den dispergierten Tropfen die gewünschte Kugelform, da diese für einen isolierten Tropfen einen Zustand minimaler Energie darstellt.
Das Benetzungsverhalten wird mittels Kontaktwinkelmessung zwischen ADN-Schmelze und verschiedenen Feststoffoberflächen charakterisiert und dient u.a. zur Ermittlung geeigneter Materialien für Kristallisationsanlagen. Hierbei sind insbesondere Anlagenteile von Interesse, die direkten Kontakt zum ADN haben, z.B. Rührer, Reaktionsgefäse und Heiz- oder Kühlflächen.
Zur Optimierung von Kristallisationsverfahren für ADN ist die Untersuchung von Kristallisationseigenschaften wie Keimbildung und Kristallwachstum notwendig. Bei der Emulsionskristallisation kann z.B. durch die Veränderung der rheologischen Eigenschaften der kontinuierlichen Phase die Wechselwirkung der darin dispergierten Partikel gesteuert werden [2].

2 Oberflächenenergie von ADN-Schmelze

2.1 Allgemeine Grundlagen

Während sich bei einem Molekül inmitten einer Flüssigkeit die nach allen Seiten gleich großen Kohäsionskräfte aufheben, bleibt bei Molekülen in der Nähe der Oberfläche eine nach innen gerichtete Restkraft erhalten. Unter der Oberflächenspannung σ versteht man die zur Vergrößerung der Oberfläche erforderlichen Arbeit ΔW im Verhältnis zur Oberflächenänderung ΔA [3]:

$$\sigma = \frac{\Delta W}{\Delta A} \qquad (1)$$

Die Oberflächenspannung σ und die Grenzflächenspannung γ sind wichtige Stoffparameter bei der Dispergierung flüssiger Medien in der Gasphase (Zerstäubungsprozesse) und in der flüssigen Phase (Emulgierprozesse). Die Oberflächenspannung wird abgeleitet aus der Oberflächenenergie einer Flüssigkeit gegenüber einem Gas während die Grenzflächenspannung ein Maß für die Grenzflächenenergie zweier nicht-mischbarer Flüssigkeiten darstellt. Die Grenzflächenspannung ist nicht der Mittelwert aus den beiden Oberflächenspannungen der Flüssigkeiten, welche die Grenzfläche bilden. Der Zusammenhang läßt sich aus den beteiligten Oberflächenspannungen nach folgender halbempirischen Beziehung beschreiben [4]:

$$\gamma = \sigma_1 + \sigma_2 - 2 \cdot \left(\sigma_1^d \cdot \sigma_2^d\right)^{1/2} \qquad (2)$$

hierin sind:
γ = Grenflächenspannung
$\sigma_{1,2}$ = Oberflächenspannung von Flüssigkeit 1 bzw. 2
$\sigma_{1,2}^d$ = Dispersionskräfte an der Grenzfläche

Soll eine flüssige Phase in feine Tropfen zerteilt werden, muß deren spezifische Oberfläche vergrößert werden, wobei die Oberflächen- bzw. Grenzflächenspannung des Fluids (gegenüber der umgebenden kontinuierlichen Phase) überwunden werden muß. Demnach ist bei großer Oberflächen- bzw. Grenzflächenspannung der zur Zerstäubung bzw. zum Emulgieren notwendige Energiebedarf ebenfalls höher.

2.2 Blasendrucktensiometrie

Die Messung der Oberflächenspannung von geschmolzenem ADN erfolgte mittels der Methode des maximalen Blasendrucks. Hierzu wurde das Blasendrucktensionmeter MPT2 der Firma Lauda verwendet.
Bei diesem Verfahren zur Messung der dynamischen Oberflächenspannug strömt ein kontinuierlicher Luftstrom durch eine Kapillare in die zu untersuchende, temperierbare Flüssigkeit. Der Radius der Kapillare r_{kap}, die Eintauchtiefe H und der maximale Blasenradius R sind konstant (Abb. 1).

Die Meßgrößen sind:
- Druck am Eingang der Meßkapillare
- Volumenstrom der Luft durch die Meßkapillare
- Erforderliche Zeit zur Blasenbildung

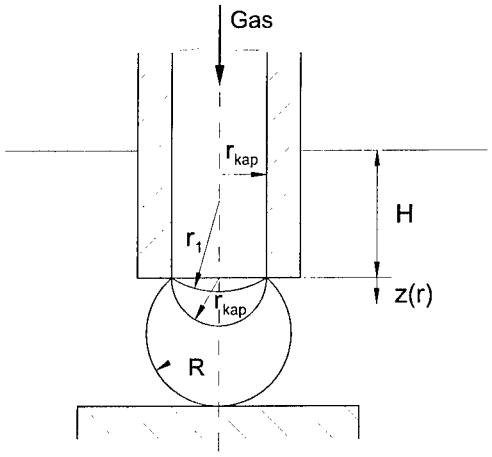


Abb. 1: Meßprinzip des Blasendrucktensiometers

Bildet sich am Ausgang der Kapillare eine Luftblase erreicht der Druck einen Maximalwert wenn der Radius der Blase gleich dem Radius der Kapillare r_{kap} ist. Der Druck fällt wieder auf einen minimalen Wert ab, wenn die Blase den Radius R erreicht und konstruktiv bedingt abreißt. Aus dem maximalen Blasendruck wird in Verbindung mit dem variablen Luftvolumenstrom die Oberflächenspannung für das jeweilige Alter der Blasenoberfläche berechnet. Hierfür wird der physikalische Zusammenhang zwischen dem Blasendruck p_B und der Oberflächenspannung σ verwendet:

$$p_B = \frac{2 \cdot \sigma}{r} + \rho \cdot g \cdot (H + z(r)) \qquad (3)$$

mit:
r = Blasenradius
ρ = Dichte der zu messenden Flüssigkeit
g = Erdbschleunigung
H+z(r) = Eintauchtiefe

2.3 Meßergebnisse

Aus der gemessenen Abhängigkeit des Kapillarendrucks vom Volumenstrom, können folgende Funktionen abgeleitet werden:

- Oberflächenspannung in Abhängigkeit vom Oberflächenalter
- Oberflächenspannung in Abhängigkeit von der Temperatur

Untersucht wurde die Oberflächenspannung von geschmolzenem ADN bei 97 °C. Es wurden Meßreihen von reinem ADN und von ADN mit 2 wt.% MgO als Stabilisator aufgenommen. Außerdem wurde die Oberflächenspannung des bei der Emulsionskristallisation von ADN [2] verwendeten Paraffin ermittelt. Zum Vergleich wurde eine Meßreihen von Wasser in das Diagramm (Abb. 2) aufgenommen.
Reines ADN hat eine Oberflächenspannung von 89 mN/m und weist keine Abhängigkeit vom Oberflächenalter auf. Die leichte Verringerung der Oberflächenspannung

bei ADN mit MgO im Bereich größerer Zeiten (älterer Oberflächen) deutet auf geringe oberflächenaktive Eigenschaften hin. Da während der Messungen keine Durchmischung der Probe möglich ist, können auch lokale Anhäufungen der suspendierten Magnesiumoxidpartikel die Veränderung des Meßwerts für große Meßzeiten hervorrufen.

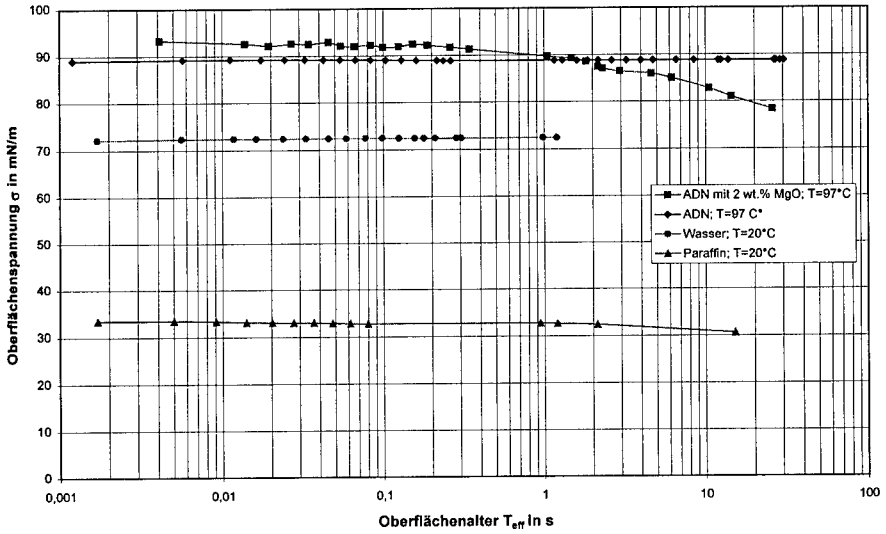


Abb. 2: Oberflächenspannung von ADN-Schmelze

ADN-Schmelze hat mit 89 mN/m eine vergleichsweisehohen Oberflächenspannung. Ursache hierfür ist die Molekülstruktur und die Art der zwischenmolekularen Wechselwirkungskräfte (Ionen-Ionen-Wechselwirkung, Ionen-Dipol-Wechselwirkung, Metallbindungskräfte etc.) in Salz- und Metallschmelzen [4]. Paraffin zeigt eine für organische Flüssigkeiten typische Oberflächenspannung von ca. 32 mN/m. Anorganische und organische Flüssigkeiten mit ausgeprägten H-Brückenbildungen verfügen ebenfalls über relativ hohe Oberflächenspannungen (z.B. Wasser: σ = 72,4 mN/m).

3 Ermittlung des Kontaktwinkes gegenüber Festkörperoberflächen

3.1 Allgemeine Grundlagen

Die Benetzung eines Festkörpers läßt sich durch den Kontaktwinkel, den die Flüssigkeit mit einer festen Oberfläche bildet, beschreiben. Ein Kontaktwinkel von 0° bedeutet vollständige Benetzung. Man spricht dann vom spreiten der Flüssigkeit auf dem Festkörper. Je größer der Kontaktwinkel ist, desto schlechter ist die Benetzung.

Der Grad der Benetzung ist von der freien Oberflächenenergie des Festkörpers abhängig. Bei flüssig-gasförmig und flüssig-flüssig Systemen entspricht die freie Ober- bzw. Grenzflächenenergie der Ober- bzw. Grenzflächenspannung, die als Kraft pro Längeneinheit (mN/m) definiert ist. Während die Oberflächenspannung von Flüssigkeiten direkt gemessen werden kann, bedarf es zur Bestimmung der freien Oberflächenenergie von Festkörpern der Kenntnis der Kontaktwinkel, die unterschiedliche Flüssigkeiten bekannter Oberflächenspannung mit der Festkörperoberfläche bilden. Die Grundlage für die Berechnung der freien Grenzflächenenergie stellt die Gleichung von YOUNG dar [5]:

$$\sigma_{sv} = \sigma_{sl} + \sigma_{lv} \cdot \cos\theta \qquad (4)$$

mit:
σ_{sv} = Grenzflächenspannung fest/gasförmig
σ_{sl} = Grenzflächenspannung fest/flüssig
σ_{lv} = Grenzflächenspannung flüssig/gasförmig
θ = Kontaktwinkel

3.2 Methode der Kontaktwinkelmessung

Die Methode des liegenden Tropfens ist ein optisches Verfahren, bei dem ein Tropfen einer Flüssigkeit mit bekannter Oberfächenspannung σ auf eine zu charakterisierende Festkörperoberfläche aufgebracht wird. Der Durchmesser des Tropfens sollte im Bereich von 2 – 6 mm liegen, da innerhalb dieser Größenordnung der Kontaktwinkel unabhängig vom Durchmesser ist [5]. Den Kontaktwinkel θ erhält man durch Anlegen einer Tangente an den Tropfen im Berührungspunkt fest-flüssig-gasförmig (Abb. 3).

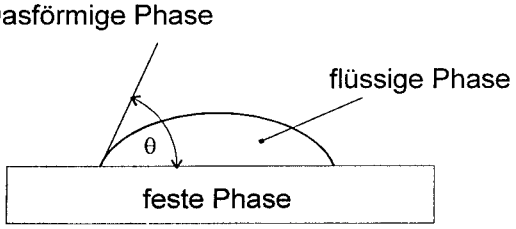


Abb. 3: Kontaktwinkel an liegendem Tropfen

3.3 Meßergebnisse

Im Rahmen dieser Arbeit wurden die Kontaktwinkel zwischen geschmolzenem ADN (als flüssige Phase) und den Feststoffen Glas, Teflon (Polytetrafluorethylen, PTFE), poliertem Stahl und polierten Aluminium gemessen. Die Abbildungen 4 – 7 zeigen beispielhaft Makroskopaufnahmen der liegenden Schmelzetropfen, wobei die eingezeichneten Kontaktwinkel Durchschnittswerte für das jeweilige Stoffsystem darstellen. Die Betrachtung der Tropfen erfolgt aus seitlicher Richtung parallel zur untersuchenden Feststoffoberfläche.

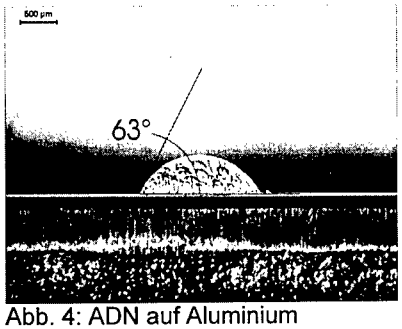


Abb. 4: ADN auf Aluminium

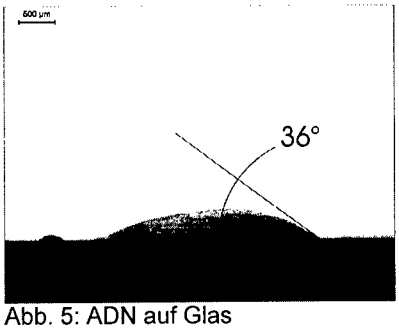


Abb. 5: ADN auf Glas

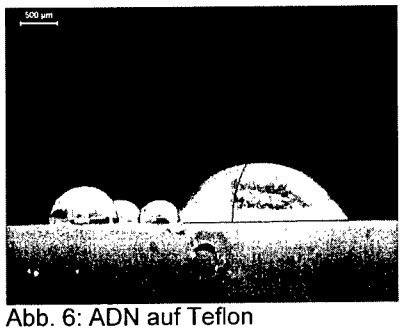


Abb. 6: ADN auf Teflon

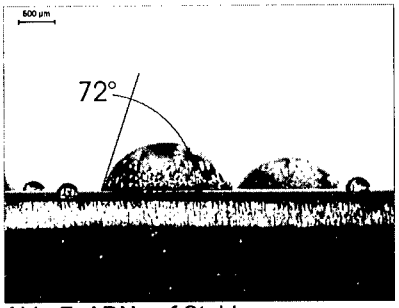


Abb. 7: ADN auf Stahl

Die Grenzflächenspannung setz sich aus dispersen und polaren Anteilen zusammen. Bei der Benetzung sind nur Wechselwirkungen von Bedeutung, die von beiden Phasen ausgehen. Das bedeutet, daß es bei einem Kontakt von einem Festkörper und einer Flüssigkeit an der Phasengrenzfläche nur zu einer Wechselwirkung der beiden polaren und der beiden dispersen Anteile der Grenzflächenspannung der beteiligten Phasen kommt. Ist eine der in Kontakt stehenden Phasen unpolar (z.B. PTFE), so sind nur Dispersionskräfte möglich [5].
Die Benetzung beliebiger Oberflächen ist somit u.a. von deren Polarität abhängig. Man unterscheidet hydrophile und hydrophobe Oberflächen. Bei hydrophilen (polaren) Oberflächen, wie Glas und Metall, neigt z.B. ein Wassertropfen zum spreiten, d.h. er bildet einen spitzen Randwinkel. Bei hydrophoben (unpolaren), also wasserabweisenden Oberflächen, insbesondere bei Kunststoffoberflächen, ergibt sich mit einem Wassertropfen ein stumpfer Randwinkel. Hydrophile Oberflächen haben eine hohe Oberflächenenergie, während hydrophobe Oberflächen niedrige Oberflächenenergien besitzen [6].

Für die Benetzungsversuche wurde kristallines ADN bei Temperaturen oberhalb 93 °C geschmolzen und auf die Prüfkörper aufgebracht. Durch die polare Struktur des ADN-Moleküls (Abb. 8), ergibt sich in Kombination mit verschiedenen Feststoffoberflächen (Abb. 4 bis 7) ein ähnliches Benetzungsverhalten wie im vorherigen Abschnitt für Wasser beschrieben wurde.

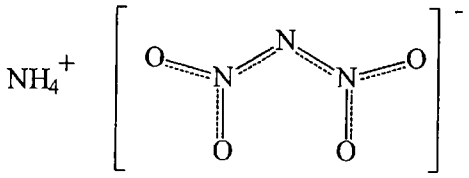


Abb.: 8: Molekularer Aufbau von ADN

Der Randwinkel ist gemäß der Gleichung (4) abhängig von der Oberflächenspannung der Flüssigkeit, des Festkörpers und der Grenzflächenspannung zwischen der Flüssigkeit und dem Festkörper. Außerdem wird das Benetzungsverhalten von der Rauhigkeit der Feststoffoberfläche beeinflußt. Im allgemeinen bewirkt eine rauhere Oberfläche eine Reduzierung des Kontaktwinkels. Glatte Oberflächen neigen zu großen Kontaktwinkeln, wobei bei einer Rauhtiefe von weniger als 0,5 µm die Rauhigkeit keinen Einfluß mehr besitzt. Der Einfluß der Oberflächenrauhigkeit ist bei Flüssigkeiten mit großen Oberflächenspannungen, z.B. Wasser, ausgeprägter als bei organischen Lösungsmitteln mit geringeren Oberflächenspannungen [7]. Diese Einflüsse erklären den in Abb. 6 gemessenen Kontaktwinkel zwischen ADN-Schmelze und Teflon von nur 55°. Die hydrophoben Eigenschaften von Teflon müßten bei der Benetzung mit ADN zu einem größeren Kontaktwinkel als zwischen ADN und Stahl ($\theta \approx 72°$) sowie ADN und Aluminium ($\theta \approx 63°$) führen. Da die Teflonoberfläche eine größere Rauhigkeit als die polierten Metalloberflächen hat und zusätzlich ADN-Schmelze mit σ = 89 mN/m eine sehr große Oberflächenspannung besitzt, bewirkt die rauhe Teflonoberfläche eine Verringerung des Kontaktwinkels.

4 Rekristallisationseigenschaften von ADN-Schmelze

Bei der Emulsionskristallisation von ADN [1] hat sich gezeigt, daß der Phasenübergang von flüssigem ADN zu festen Partikeln den entscheidenden Prozeßschritt darstellt. Die Unterkühlung der Schmelze reicht nicht als treibendes Potential zum Auslösen der Kristallisation, bzw. der Keimbildung aus. Die Abbildungen 9 bis 12 zeigen das Verhalten eines ADN-Schmelzetropfens auf einer dünnen Glasplatte, der mit Umgebungstemperatur von ϑ = 20 °C beaufschlagt wurde. Die Zeitspanne der Unterkühlung t wurde vom Abschalten der Heizung an gemessen. Nach 2 h sind noch keine Anzeichen einer Keimbildung zu beobachten. Die Bildreihe zeigt außerdem die durch thermische Belastung, z.B. Schmelzen, entstehenden Zersetzungsgase in Form von eingeschlossenen Gasbläschen.

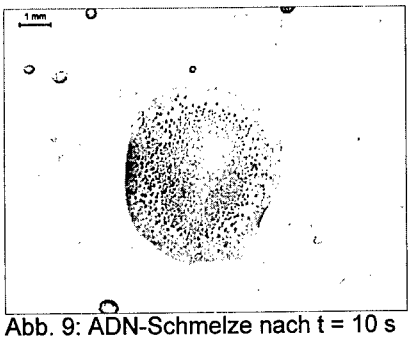


Abb. 9: ADN-Schmelze nach t = 10 s

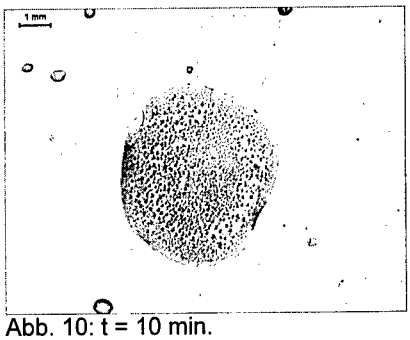


Abb. 10: t = 10 min.

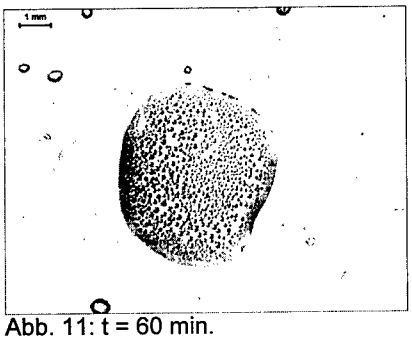


Abb. 11: t = 60 min.

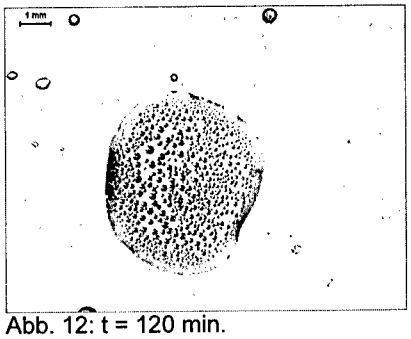


Abb. 12: t = 120 min.

4.1 Kristallisation durch Saatkristalle

Eine Möglichkeit zur Anregung der Kristallisation eines ADN-Schmeltzetropfens ist der gezielte Einsatz von Saatkristallen. Bei diesen Versuchen wurde kristallines ADN so erhitzt, daß eine geringe Menge festes Material als Saatkristall erhalten bleibt (Abb. 13). Danach wurde der Heizvorgang beendet und die Probe mit Umgebungstemperatur beaufschlagt. Die Abbildungen 14 bis 19 zeigen das von den Saatkristallen ausgehende Kristallwachstum, welches innerhalb einer Abkühlzeit von 3 Minuten zum vollständigen Phasenübergang flüssig-fest eines mehrere Millimeter großen ADN-Tropfens führt.

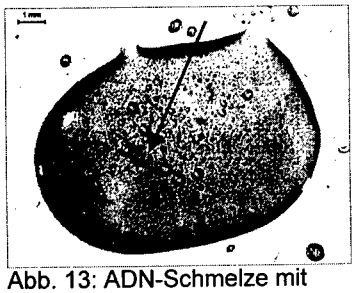


Abb. 13: ADN-Schmelze mit Saatkristallen

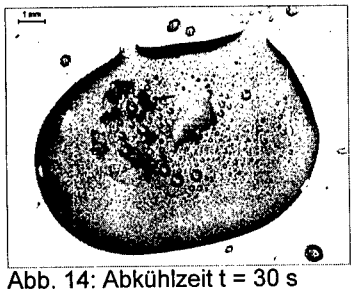


Abb. 14: Abkühlzeit t = 30 s

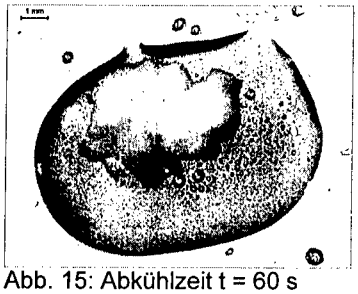


Abb. 15: Abkühlzeit t = 60 s

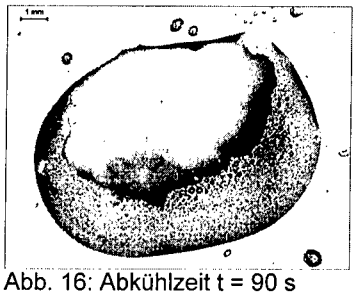


Abb. 16: Abkühlzeit t = 90 s

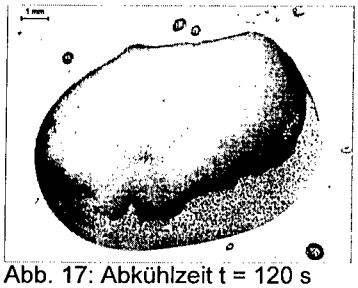


Abb. 17: Abkühlzeit t = 120 s

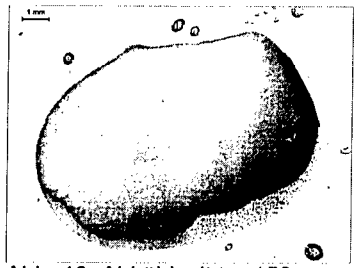


Abb. 18: Abkühlzeit t = 150 s

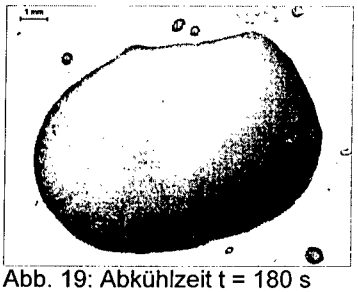


Abb. 19: Abkühlzeit t = 180 s

4.2 Kristallisation durch Impfkeime

Bei einem Tropfen aus ADN-Schmelze erfolgt durch Aufbringen eines Tempereaturgradienten in einem weiten Temperaturbereich keine Keimbildung (siehe Abb. 20). Durch Einbringen von Impfkeimen in das geschmolzene ADN-Kontinuum wird, wie in Abb. 21 dargestellt der Kristallisationsprozeß ausgelöst. Abb. 21 – 23 zeigen den zeitabhängigen Verlauf der Kristallfront. Ein einige Millimeter großer ADN-Tropfen ist in einem Zeitbereich von ca. 90 s vollständig zu einem Feststoffpartikel kristallisiert.

Die Auslösung der Kristallisation durch Impfkeime kann z.B. bei der Emulsionskrisallisation [2] genutzt werden. Der Kristallisationsvorgang wird hierbei durch das Einbringen von Strömungsenergie bzw. durch Partikel-Partikel-Wechselwirkung unterstützt. Abb. 24 zeigt beispielhaft eine Momentaufnahme aus dem Emulsionskristallisations-Prozeß, in der sowohl Tropfen als auch fest ADN-Partikel erkennbar sind.

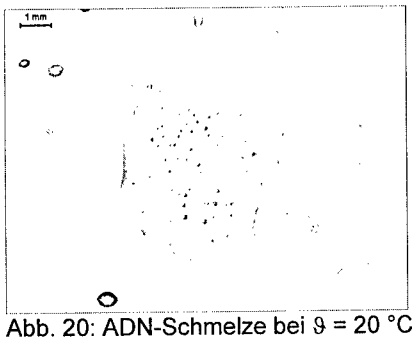


Abb. 20: ADN-Schmelze bei ϑ = 20 °C

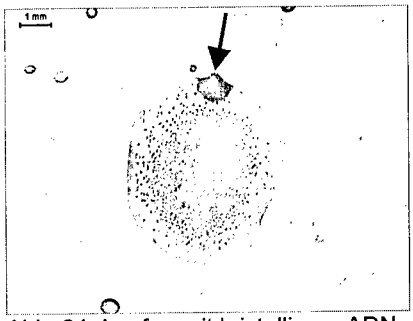


Abb. 21: Impfen mit kristallinem ADN

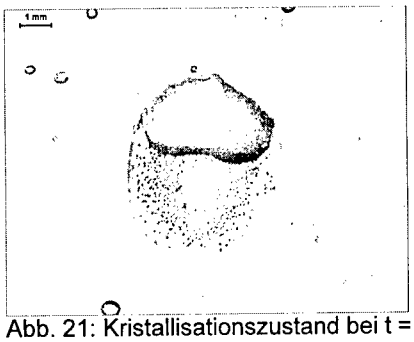


Abb. 21: Kristallisationszustand bei t = 30 s

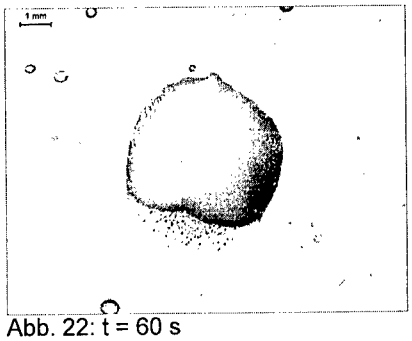


Abb. 22: t = 60 s

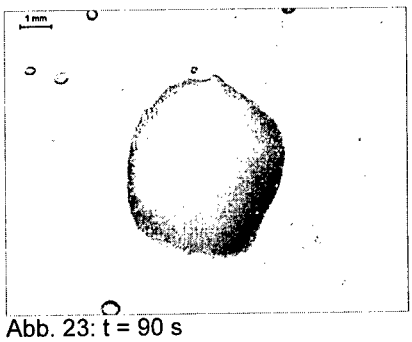


Abb. 23: t = 90 s

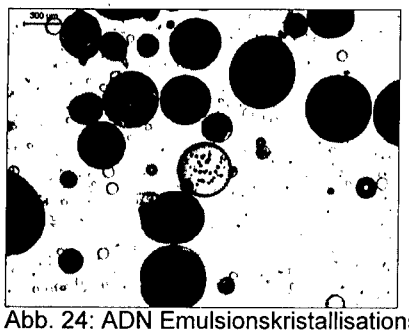


Abb. 24: ADN Emulsionskristallisations-Prozeß

Wie gezeigt werden konnte, ist das Verhalten beim Phasenübergang von ADN von der flüssigen in die feste Phase von verschiedenen Einflußfaktoren, wie z.B. der Oberflächenspannung, der Oberflächenenergie bezogen auf verschiedene Festkörperoberflächen und der verschiedenen Mechanismen bei der Kristallisation abhängig. Das geringe Keimbildungspotential von ADN erfordert Prozeßführungen, die einen Eingriff durch Impfen oder Partikel-Partikel-Wechselwirkung ermöglichen. Vorteilhaft sind daher Verfahren, wie z.B. die Emulsionskristallisation, bei denen der Zeitraum für den Phasenübergang fest-flüssig variabel gestaltet werden kann.
Bei Prozessen in der Gasphase bestehen sich aufgrund der im Gegensatz zu Flüssigkeiten anderen Kraftfelder wesentlich größere Schwierigkeiten für die Keimbildung bzw. Kristallisation.

5 Literatur

[1] U. Teipel, T. Heintz., K. Leisinger, H. Krause: Verfahren zur Herstellung von Partikeln schmelzfähiger Treib- und Explosivstoffe, DE 198 16 853 A1, 1999

[2] U. Teipel, T. Heintz., H. Krause: Crystallization of spherical Ammonium Dinitramide, Propellants, Explosives, Pyrotechnics 25 (2000), 81 - 85

[3] Kuchling, Horst: Taschenbuch der Physik, Verlag Harri Deutsch Thun und Frankfurt/Main 1978

[4] H.-D. Dörfler: Grenzflächen- und Kolloidchemie, VCH Verlag, Weinheim, 1994

[5] H. Lechner: Die Kontaktwinkelmessung: Ein Verfahren zur Bestimmung der freien Grenzflächenenergie von Festkörpern, Seminar Grenzflächenspannungs- und Kontaktwinkelmessung, Universität Leipzig, 1996

[6] H. G. Hauthal: Grenzflächenspannung an der Phasengrenze fest/flüssig, Seminar Grenzflächenspannungs- und Kontaktwinkelmessung, Universität Leipzig, 1996

[7] K. T. Hong, H. Imadojemu, R. L. Webb: Effects of Oxidation and Surface Roughness on Contact Angle, Experimental Thermal and Fluid Science 8 (1994), 279-285

A CONVENIENT METHOD FOR PREPARATION OF PENTAERYTHRITOL DIAZIDO DINITRATE (PDADN)

Zhang Lijie, Guo Shaojun Su Tianduo and He Guoshu
(Xi'an Modern Chemistry Research Institute, China 710065)

ABSTRACT

PDADN was first reported by M.B.Frankel in 1987 with a procedure of chloration , cyclization, azidonation, nitrolysis and nitration using pentaerythritol as starting substrate only to obtain 1.0 g colorless oiliness liquid. We had published a paper which described a new group of energetic materials□azidonitrates (AZN) on 23rd IPS conference in 1997. However, PDADN is a typical representative of AZN and an excellent plasticizer in propellants.

During our further research, a convenient method of preparing PDADN was investigated using pentaerythritol as starting material via bromization, azidonation and nitration. The advantage of this method is not only in a short pathway, but also in high yield.

1. INTRODUCTION

Pentaerythritol diazido dinitrate, also named as 2,2-diazido methyl-1,3-propylene-glycol dinitrate, is a new kind of azido nitrate plasticizer with $-N_3$ group and $-ONO_2$ group, its structure as shown on Figure 1.

Utilization of azido plasticizers has become reality during last several years. These azido plasticizers impart additional energy to propellants, since each group present adds approximately 85 kcal/mol of energy to the system.

Because nitrates have a good plasticization ability with main ingredients of propellants, and plasticizer with $-ONO_2$ possesses good property of the work into shape and can improve the mechanical behavior of propellants, the plasticizer with $-N_3$ and $-ONO_2$ group can not only increase the energy of propellant, but also improve mechanical behavior of propellants, and can also reduce the characteristic signal of propellants.

It was reported from U.S.P 4683086 that the general synthesis method of PDADN with pentaerythritol as starting material, via chloration , cyclization, azidonation, nitrolysis,nitration and purification. A more convenient method than that above mentioned is present in this paper. The chloration reaction is replaced by bromination reaction in this paper, but nitrolysis and nitration to be finished in one step. The reaction time is reduced from 70 hours to 5□6 hours.

2. EXPERIMENT

2.1 Principle and Reaction Formula

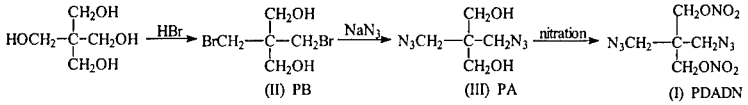


Figure 1

2.2 Apparatus

Convention glass apparatus in laboratory;

Nicolet 60SXR-FTIR Spectrometer, KB_r tablet;

Nuclear magnetic resonance spectrum FX-90Q (Japan);

capillary tube melting point apparatus.

2.3 Synthesis Method

2.3.1 Preparation of PB

0.2 mol pentaerythritol, 0.56mol HB_r aqueous solution (40%), 0.025mol acetic anhydride were added into three necks flask with stirrer , condenser and thermometer. The mixture was stirred and heated to 120^{0}C under atmosphere pressure for about 8.5 hours. The reaction was being carried out, while the water was distilled out. The reaction mixture was cooled to room temperature and was neutralized by adding alkali. Then the reaction mixture was reacted at 50 ^{0}C for addition 15 minute and cooled to10^{0}C. After filtration, Precipitate was washed by water and toluene, and dried , obtained 30g of PB.

2.3.2 Azidonation – the Preparation of PA

Added 0.05mol 2,2-bromomethyl-1, 3-propandiol (PB) and 0.11 mol NaN_3, 175 ml DMF into three necks flask with stirrer and thermometer, then the mixture was stirred and heated to 120^{0}C for 3-4 hours. After the reaction was finished, the mixture was distilled under vacuum until no distillate. CH_2Cl_2 was added into flask, then filtrated and collected filtrating solution. The filtrating solution was not separated and used as next step raw materials.

2.3.3 Nitration – the Preparation of PDADN

The excessive nitric acid was dropped into above mentioned CH_2Cl_2 solution of PA at between 15 ^{0}C -20^{0}C. Let the mixture react for 10 minutes, then it was poured into ice water and organic layer was separated, washing two times with water, then one time with 2% aqueous solution of $NaHCO_3$, washing again with water to neutral. CH_2Cl_2 layer was separated and distilled off the CH_2Cl_2 to obtain a white solid. The yield is 82%. The product is white and low melting point solid, m.p 39^{0}C -41 ^{0}C.

3. RESULTS AND DISCUSSIONS

3.1 The influence of the ratio of pentaerythriol□HBr to PB (mol/mol):

It could be separately produced one-, two-, three-, four- bromo-replaced products with the change of mol ratio of two raw materials. But according to the method of this paper, it should be mainly produced dibromo-replaced product and little tribromo-replaced product. Because three-bromo replaced product can be dissolved in toluene, it can be washed out by cold toluene. Finally, pure PB was obtained. Melting point of PB is 108°C - 110°C, after it was recrystallized. Its infrared spectrum (Figure 2) is in accordance with standard spectrum (Figure 3).

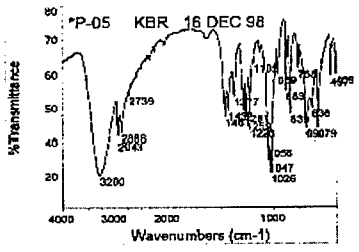


Figure 2 Spectrum of PB

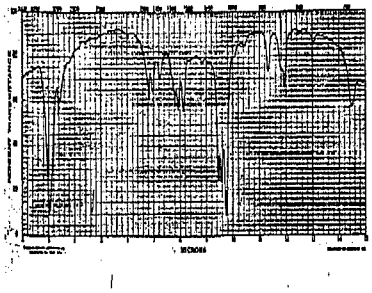


Figure 3 Standard spectrum

3.2 The influence of PA or CH_2Cl_2 solution of PA on product of nitriation

It was found that there is not difference when pure PA or CH_2CL_2 solution of PA was nitrated. Therefore the CH_2Cl_2 solution of PA is not necessary separate and directly used as next step raw material.

Infrared spectrum of PA is shown in Figure 4, it can be seen from Figure 4 that there is $-N_3$ and -OH characteristic absorption peak separately at 2104 cm^{-1} and 3389 cm^{-1} without -Br absorption peak.

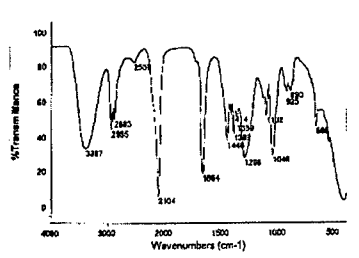


Figure 4 Spectrum of PA

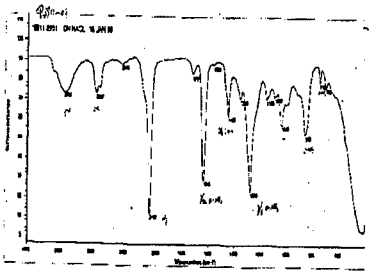


Figure 5 Spectrum of PDADN

3.3 Calculated the yield of PDADN is 82% from the amount of PA employed. The product is white and low melting point solid, m.p. 39^{0}C -41 ^{0}C.

The infrared spectrum of PDADN is shown in Figure 5.

The identifiable bands are as follows: There are -N_3 and -ONO_2 strong absorption peaks, separately at 2107 cm^{-1} and 1641 cm^{-1}. It is in accordance with the results of reference 2.

The Nuclear magnetic resonance spectrum (^{1}H) showed: There are □CH_2N_3□and –CH_2ONO_2□ strong absorption peak separately at δ(ppm) 3.52 andδ(ppm) 4.43. It is in accordance with the results of reference 2.

4. CONCLUTIONS

a) When pentaerythritol took place chloration reaction, generally, only difference replaced mixture was obtained and not was easy separated. But pentaerythritol took place bromization reaction and separated by the method of this paper, pure PB can be obtained.

b) The method of preparation PDADN in this paper has not only a short period of synthesis and high yield, but also is easily produced in large scale.

References:

1) Milton B. Frankel et al. U.S.P 4683086;

2) Gou Shaojun et al. Chinese patent 98109992.0

DYNAMIC VAPOUR SORPTION STUDIES OF PYROTECHNICS

Trevor T Griffiths and Richard J Duncombe
Defence Evaluation and Research Agency,
Fort Halstead, Sevenoaks, Kent, UK

Colin J Hutchinson
Defence Evaluation and Research Agency,
Bishopton, Renfrewshire, UK.

ABSTRACT

Virtually all materials interact with moisture or water vapour. This interaction can be absorption, surface adsorption, capillary condensation or chemical reaction. A new technique that allows these interactions to be measured with a high degree of accuracy is Dynamic Vapour Sorption (DVS). The technique allows kinetic data for both sorption and chemical reactions to be determined.

Experiments have been performed on a range of pyrotechnic ingredients and compositions to investigate the effect of changing the temperature, water concentration and sample mass on the interactions. The studies were conducted in an atmosphere of nitrogen or air.

This preliminary study shows that DVS is more suited to study the interactions of moisture with individual ingredients rather than pyrotechnic compositions. Using the technique it is also possible to study the amount of protection given to magnesium powder by a binder.

INTRODUCTION

Dynamic Vapour Sorption (DVS) was developed to provide basic information on the interaction of moisture with materials, particularly in the food and pharmaceutical industries. It is used primarily to generate kinetic data for sorption/chemical reactions but it can also be used to study diffusion of moisture into and through packaging materials.

This paper describes a preliminary study, using DVS, on a range of pyrotechnic ingredients and compositions.

DYNAMIC VAPOUR SORPTION

The modified DVS-1 Dynamic Vapour Sorption instrument was purchased from Surface Measurement Systems. A schematic of the DVS is shown in Figure 1.

Dynamic vapour sorption occurs when a sample is exposed to a continuous flow of gas with a predetermined and constant relative humidity (RH). A zone of constant moisture concentration and RH is established around the sample. This zone allows the rapid establishment of water sorption or desorption equilibrium by maximising the mass transport of water vapour in and out of the sample. The mass change experienced by a sample due to water sorption/desorption in gas streams of 0% to 98% RH, across the temperature range -10°C to 80°C can be investigated. Sample size can range from 1 to 500mg. Weight changes of up to 150mg can be monitored.

The sample is weighed into a glass crucible fitted to one arm of a Cahn microbalance in the sample channel. A reference material is placed in a second glass crucible to act as a counterbalance. The crucibles are hemispherical with a diameter of 1cm and have a capacity of around 600μl. The balance hangdowns are encapsulated in glassware which also contains the temperature and RH sensors. The microbalance is enclosed in an incubator that operates in the range -10°C to 80°C. Dry gas enters the instrument where it is split into two equal flows via mass flow controllers. One flow passes through a glass bottle containing water, the "wet" channel. The other flow is designated the "dry" channel. In the wet channel the gas bubbles through the water where it becomes saturated. The wet flow and dry flow are mixed in a chamber before again being split between the sample and reference channels. By altering the "dry" and "wet" flow rates, the humidity in the system can be adjusted from 0% to 98% RH. Dry gas is used to purge the top of the balance and hang down regions to prevent the moist gas from entering the balance region and giving condensation problems.

Humidity and temperature are monitored using combined sensors, positioned close to the sample and reference crucibles. Mass changes to the sample due to interaction with moisture as a function of time/humidity are recorded directly.

In some materials, the water molecules are held at the surface. Adsorption can occur by two processes, physical adsorption and chemisorption. Physical adsorption holds the molecules to the surface of the material by non-specific Van der Waals forces and may be mono or multilayer

adsorption. Chemisorption may involve strong specific forces similar to chemical bonding and is always monolayer adsorption. Physical adsorption is generally reversible, whereas chemisorption may result in a permanent weight increase.

Other materials undergo chemical reaction where the chemical form of the material is changed permanently. This usually occurs for metals such as magnesium.

By examining the change in mass as a function of time at several RH values, kinetic data on the rates of adsorption, absorption or chemical reaction can be generated.

EXPERIMENTAL

Experiments can only be performed under isothermal conditions. It is possible to alter the RH of the system in two ways. When the RH is changed as a function of time (typically about 0.1% RH), the sample has time to respond to the change. This technique is primarily used for calibration but it also allows the RH level at which the onsets of degradation or deliquescence occurs to be determined. Alternatively the RH can be changed in discrete steps and weight change monitored as the adsorption/reaction processes occur.

In general, the sample was weighed into the sample pan with the RH set close to ambient, typically 30%. The RH was then reduced to 0%, to dry the sample. When the weight of the sample reached a plateau, and no more drying occurred, the RH was increased, usually in increments of 20%. Sorption processes immediately occurred and a weight increase was observed. The RH was kept constant and the weight monitored until a plateau was reached again. If reaction was still occurring, the experiment was halted after a specified time had elapsed. The RH was then increased in 20% increments up to 80% and then a final step of 15% to achieve 95% RH. This type of run is called a half-cycle. Similar step like functions where the RH was reduced were used to bring the sample environment back to 0% RH. This is a full cycle experiment.

Full cycle experiments were generally carried out on the pyrotechnic ingredients and compositions at temperatures of either 25°C, 40°C or 60°C. The residual weight gain for the samples was calculated. The effects of sample mass, purge gas flow rate, temperature and RH on the kinetics of magnesium degradation were investigated. The effect of ageing magnesium powder in nitrogen for an extended period at 60°C and 95% was also studied. The activation

energy for the reaction of magnesium powder in nitrogen and air was determined. The deliquescence point of the oxidants at 25°C was measured.

The samples examined during this study were as follows:

Magnesium

Grade 4 cut magnesium powder to specification CS5035A, which is often used in pyrotechnic compositions, was used for the experiments.

Acaroid resin coated magnesium

This sample consisted of 84% grade 4 cut magnesium powder coated with 16% acaroid resin. This is the premix used in the preparation of the pyrotechnic composition SR371.

Pyrotechnic oxidants

Samples of the common oxidants found in pyrotechnic compositions barium nitrate, strontium nitrate, potassium perchlorate were examined.

Pyrotechnic compositions

Three pyrotechnic compositions based on a binary mixture of fuel and oxidant, containing magnesium fuel and either strontium nitrate, potassium nitrate or potassium chlorate oxidants were examined. These were SR371, SR800 and SR91. The formulation of each composition is detailed in Table 1.

RESULTS

Magnesium

Effect of temperature

Magnesium powder was examined using the step conditions described, at temperatures of 25°C, 40°C and 60°C and a flow rate of 150cm^3 min^{-1}, using nitrogen as the carrier gas. At all three temperatures very little interaction with moisture occurred until the RH exceeded 60%. As the RH was raised in steps of 20%, small, rapid weight increases were observed. Adsorption at the surface was the most likely interaction occurring. As the RH increased above 60%, chemical reaction started to occur and the rate of weight increase, particularly at 40°C and 60°C, rose sharply. As the RH decreased on the downward cycle, the sample began to show weight loss

due to the desorption of water, but there was a net increase in weight due to degradation of the magnesium. The RH and change in mass plots as a function of time for the sample at 40°C is shown in Figures 2. The isotherms at all three temperatures are shown in Figures 3, 4 and 5.

Magnesium was also examined under similar conditions to those used with a nitrogen purge, but using an air purge instead. The rates of reaction and the levels of degradation were higher in air than in nitrogen. The increase in the rate of reaction was more noticeable at the lower temperatures. This is probably because there is five times as much water present at 60°C than at 25°C, therefore oxygen has less effect at the higher temperature.

The residual weight increases for both nitrogen and air purge are given in Table 2 and shown in Figure 6.

Effect of water concentration

A plot of reaction rate against water concentration is shown in Figure 7. The temperature, flow rate and sample weight were kept constant at 60°C, 150cm^3 min^{-1} and 50mg respectively. The rates were determined by measuring the slope of the weight change as a function of time at 60%, 80% and 95%RH. The results show that the reaction rate was directly proportional to the water concentration. The rate of weight change at 25°C and 40°C was extremely low and could not be measured with sufficient accuracy for similar graphs to be drawn.

Effect of sample mass

Experiments performed under similar experimental conditions, but using different sample weights, showed that the rate of reaction changed with the mass of magnesium. Figure 8 shows a linear relationship exists between the reaction rate and the reciprocal of magnesium concentration. This suggests the reaction is not first order and depends on both water and magnesium concentrations. Thus, the sample geometry and sample size become important parameters in the interaction between water vapour and magnesium.

Extended ageing of magnesium

The sample of magnesium aged at 60°C and 95% RH in nitrogen for 16 hours showed that after the initial rapid weight gain a more linear increase in weight occurred. The rate of reaction then increased slightly and a second linear weight increase was observed. The change in mass against time curve is shown in Figure 9.

Activation energy determination

The rate of reaction in nitrogen at 25°C, 40°C and 60°C with a 95% RH was determined from the slope of the weight gain curves. A linear fit (Figure 10) for the plot of the natural logarithm of the reaction rate against 1/T gave an activation energy of 115 kJ mol^{-1}.

The activation energy was also determined from the experiments performed in air. The linear fit (Figure 10) gave an activation energy of 60kJ mol^{-1}, which is almost half that observed in a nitrogen atmosphere.

Acaroid resin coated magnesium

This sample was subjected to full cycle RH step analysis, at 25°C, 40°C and 60°C using a nitrogen purge of 150cm^3 min^{-1}.

Typical full cycle data for an experiment performed at 40°C is shown in Figure 11. After initial drying, water was adsorbed at each 20% RH step. The amount of water absorbed at each step was greater than that for the uncoated magnesium. On the desorption cycle adsorbed water was lost at each RH step. The residual weight increase due to reaction of water with magnesium are given in Table 2 along with the value corrected for the magnesium content of the sample.

The results show that the acaroid resin readily absorbs moisture. At 25°C the acaroid resin appears to offer some protection to the magnesium as the residual weight was lower for the coated sample. At 40°C almost twice as much water was taken up during the experiment by the coated sample but a similar extent of reaction was observed for the samples. However at 60°C almost three times as much magnesium reacted when acaroid resin was present.

Pyrotechnic oxidants

Some of the commonly used oxidants were selected to examine their behaviour in humid conditions.

In all cases, the materials display little interaction with moisture until a point is reached where absorption occurs and deliquescence is displayed. The samples continued to absorb moisture until a saturated solution was formed. From the plots, the deliquescence point for each of the oxidants was determined, these are given in Table 3.

The results show that all of the oxidants have the ability to absorb substantial quantities of water especially strontium nitrate. However, all of the oxidants examined have high deliquescence points (% RH) so will not absorb significant amount of moisture until high RH levels have been reached.

When examined using the RH step methods at 25°C, each oxidant absorbs virtually no moisture until the step from 80% to 95% RH, at which point large quantities of moisture are absorbed as the sample deliquesces. Barium nitrate absorbs moisture readily as the RH is raised to 95%. On the downward cycle, the absorbed moisture is readily lost at 80% RH. There is virtually no retention of moisture at the end of the experiment. A similar result was found for potassium perchlorate although the RH ranges over which moisture was absorbed and desorbed were different. For each of these oxidants the retained moisture at the end of the experiment was found to be < 0.005%.

Strontium nitrate on the other hand behaved quite differently. Moisture was absorbed from about 80% RH and was readily lost on the downward cycle. However, as the RH was reduced from 60% to 0%, the remaining 12% of moisture was retained. A hydrated form of strontium nitrate was produced. A similar result was found when an experimental temperature of 60°C was used.

Pyrotechnic compositions

SR 371

This sample was examined using an air purge of 200cm^3 min^{-1} and full cycle step method at a temperature of 25°C. The experimental results are shown in Figure 12. After initial drying, the sample adsorbed surface moisture at each RH step. For the 80% and 95% steps, part of the weight change was due to deliquescence of the potassium nitrate. The isotherm showed that a residual weight increase of about 0.04% had occurred. This small increase in weight confirms that the acaroid resin protects the magnesium at 25°C.

SR800

This composition is similar to SR371 except that it contains a different oxidant. When examined under the same conditions as used for SR371, very similar data was produced (Figure 13). The main difference was that less water was adsorbed at the lower RH values. The residual weight gain was also higher at 0.26%.

SR91

This sample was examined using the same conditions as used for the other pyrotechnic samples but at temperatures of both 25°C and 60°C.

The characteristics of the weight change were similar. Both showed absorption ofwater by the oxidant over the range 80% to 95% RH. The magnitude of the weight change was higher at 60°C because of the greater concentration of water present. The isotherms show that moisture was more easily lost at the higher temperature as the RH was reduced on the downward cycle, but both samples showed a residual weight increase of about 4%, mainly due to hydration of the strontium nitrate. This prevented the extent of the moisture interaction with the metal fuel from being determined. The curve for the reaction at 25°C is shown in Figure 14. The presence of strontium nitrate caused a large amount of water to be adsorbed by the composition.

CONCLUSIONS

DVS is suitable for the investigation of moisture interaction with pyrotechnic ingredients but it has limited use for the study of pyrotechnic compositions.

The technique allowed kinetic information on the degradation of magnesium to be generated. It was found that the rate of magnesium degradation was dependent upon a number of factors including water concentration (RH), temperature, particle size, sample size, sample coating and prevailing gas atmosphere.

DVS allowed the moisture interaction of magnesium samples with different surface coatings to be studied. Acaroid resin was found to absorbed moisture and, except at 25°C, did not prevent degradation of magnesium.

TABLES

Composition	Ingredient	Content (%)
SR371	Magnesium	42
	Potassium nitrate	50
	Acaroid resin	8
SR800	Magnesium	42
	Potassium perchlorate	50
	Acaroid resin	8
SR91	Magnesium	35
	Boiled linseed oil	4
	Strontium nitrate	41
	Chlorinated rubber	20

Table 1; Pyrotechnic compositions studied using DVS

Temperature (°C)	Residual weight increase (%)			
	Magnesium		Magnesium coated with acaroid resin	
	Nitrogen	Air	Nitrogen	Nitrogen#
25	0.23	0.32	0.14	0.17
40	0.35	0.54	0.29	0.35
60	0.54	0.80	1.26	1.50

 # Corrected for magnesium content

Table 2; Residual weight gain for magnesium in nitrogen and air

Sample	Deliquescence point (% relative humidity)
Barium nitrate	86
Strontium nitrate	85
Potassium perchlorate	88

Table 3; Deliquescence point under dynamic RH conditioning

FIGURES

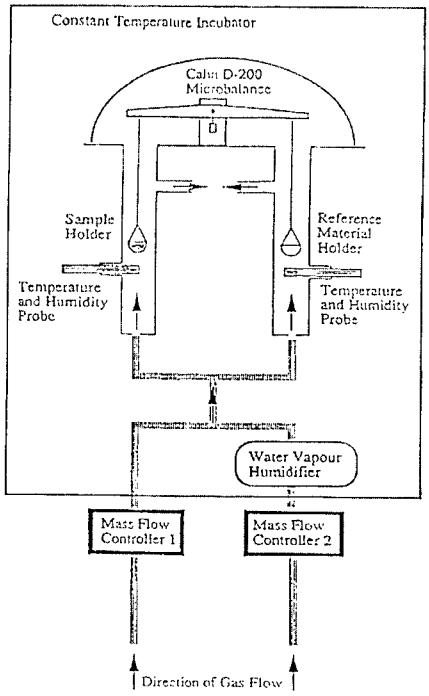


Figure 1; Schematic of DVS apparatus

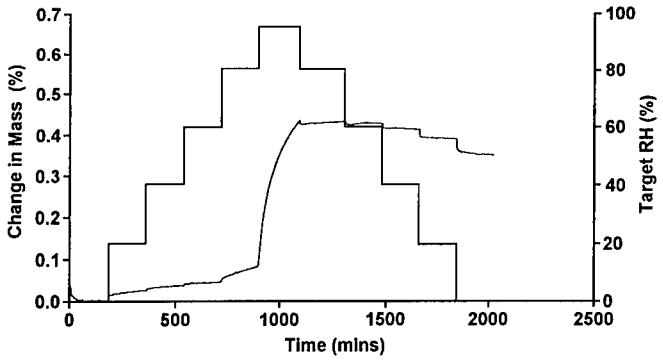


Figure 2; DVS for Magnesium Powder at 40°C in Nitrogen

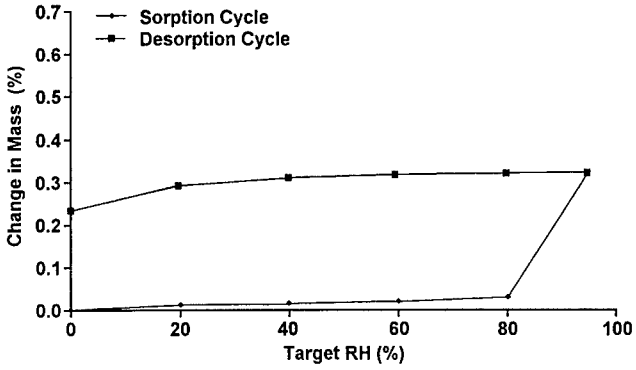


Figure 3; Isotherm for Magnesium Powder at 25°C in Nitrogen

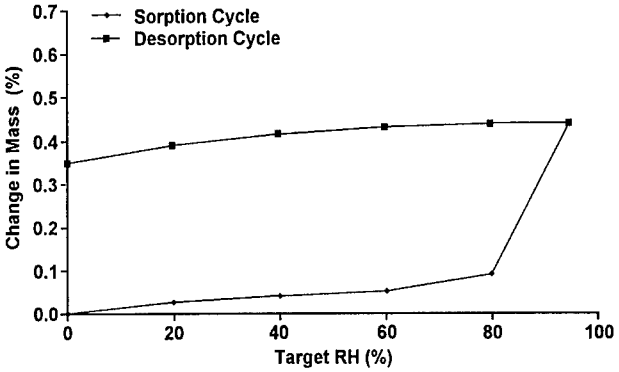


Figure 4; Isotherm for Magnesium Powder at 40°C in Nitrogen

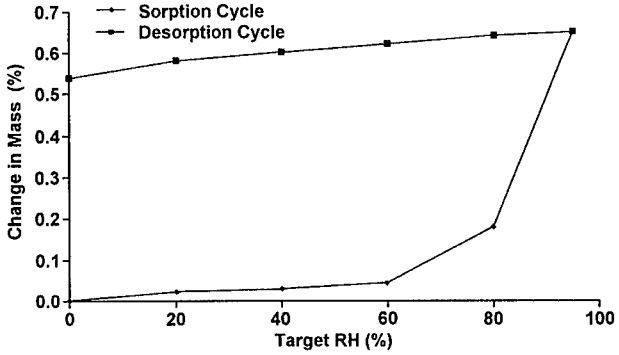


Figure 5; Isotherm for Magnesium Powder at 60°C in Nitrogen

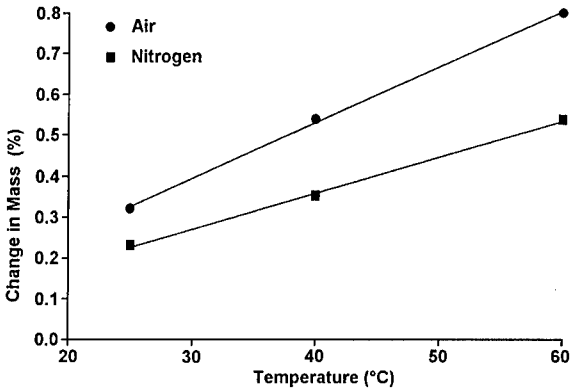


Figure 6; Residual Mass Change for Magnesium Powder in Air and Nitrogen

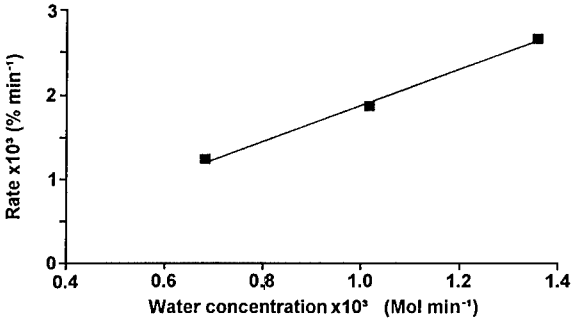


Figure 7; Reaction Rate Against Water Concentration for Magnesium at 60°C in Nitrogen

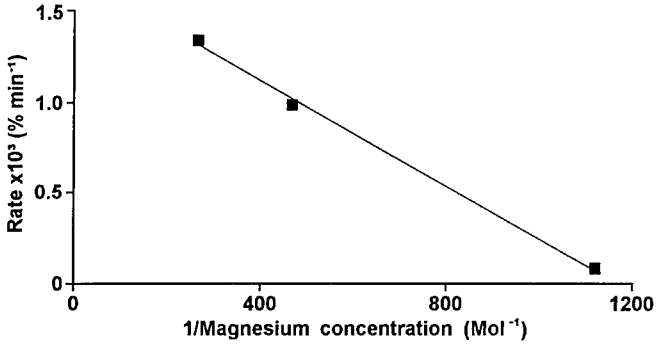


Figure 8; Reaction Rate Against 1/Magnesium Concentration at 60°C in Nitrogen

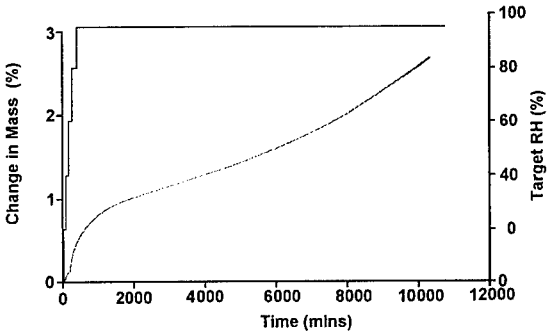


Figure 9; DVS for Magnesium Powder aged at 60°C in Nitrogen for 10000 mins

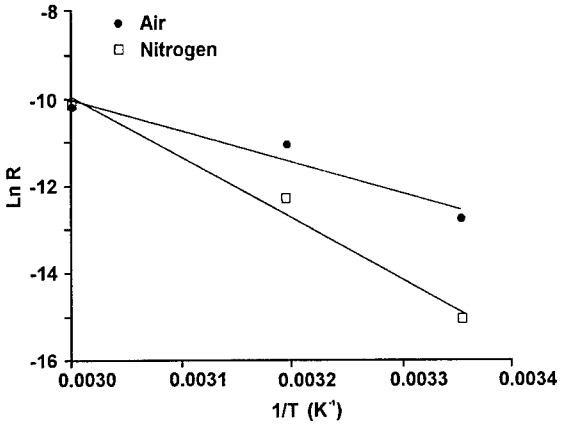


Figure 10 Arrhenius plots for magnesium powder

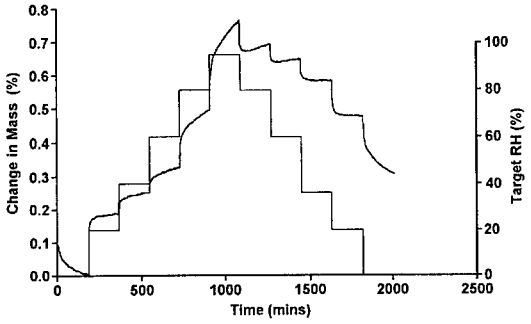


Figure 11; DVS at 40°C in Nitrogen for Magnesium Powder coated with Acaroid Resin

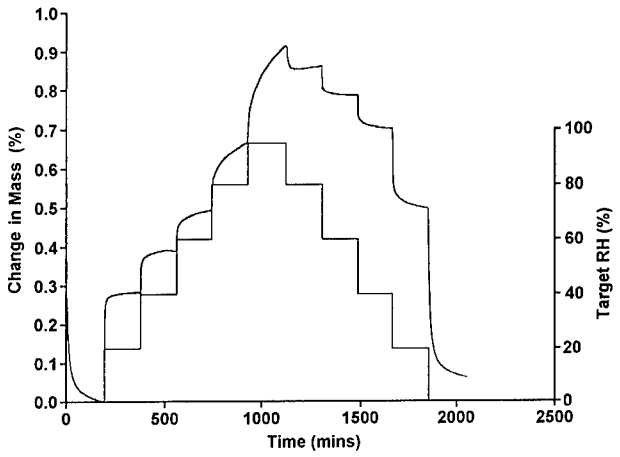


Figure 12; DVS at 25°C in Air for SR371

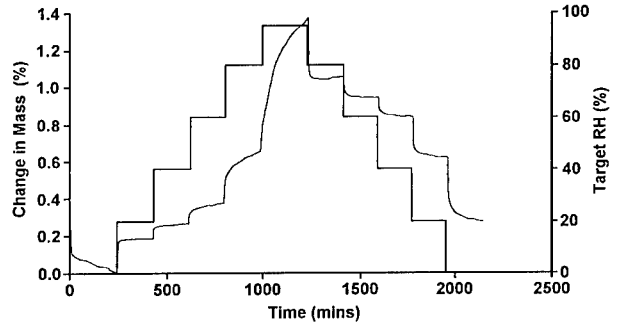


Figure 13; DVS at 25°C in Air for SR800

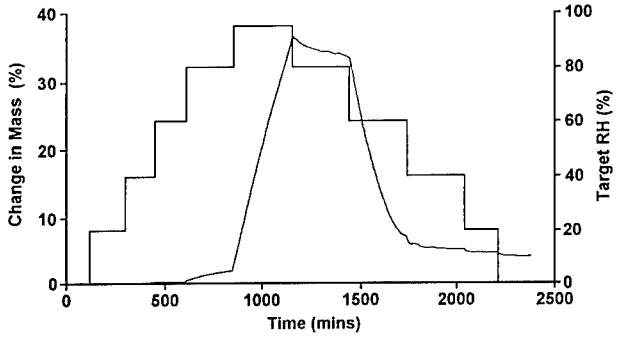


Figure 14; DVS at 25°C in Air for SR91

INFLATION OF ELASTIC AIRBAG UNDER WATER – EXPERIMENT AND CALCULATIONS

Alexander B. Vorozhtsov, Sergei S. Bondarchuk, Andrew E. Salko and Vladislav P. Zima

Tomsk State University, Belynsky str., 54, Tomsk, Russia

Summary

In the present paper the mathematical model, the technique of calculation and results of an experimental research on supercharge and filling of a soft elastic airbag by combustion products of solid propellant at their cooling by means of bubbling in water is shown. The device consists from permeable case. The case contains a double-based solid propellant channel charge, armoured on an outside surface and with plug above of channel. The ignition of a charge, filled with water, implemented on an original technique by a wire spiral from an external source of an electric current.

1. Introduction

Elastic soft airbag inflation by combustion products is studied. Airbag is submerged under water. Such processes can find in the time of elastic pontoons supercharge for submerged objects lifting. For experimental study of underwater unfolding and inflation of soft airbag by combustion products we had model from rubber fabric with drop form. The airbag had such parameters: maximum diameter D_{max}=20 sm, height H_{max}=30 sm, internal volume of cavity under total lifting W_s=2.4 dm^3, weight of cavity 30 g. Inflation of airbag was carried out from case-less solid propellant gas generator directly under water. In this case combustion products bubbling across the water became cold and entered into the airbag with

temperature less than temperature of airbag thermal decomposition. Process of airbag unfolding and inflation fixed with help of filming.

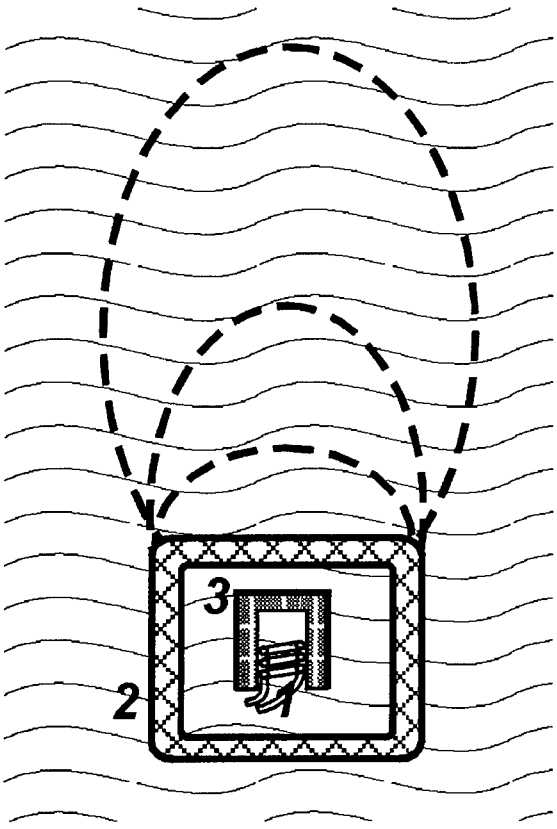
Analysis of films shows that cavity unfolded on the all height in≈1.5s, after it airbag was filled. Time of total inflation is≈6s. Dependencies of airbag volume from time are shown. Calculation of elastic airbag inflation is carried out on the base of mathematical model and software[1]. Calculated data corresponded to experimental ones.

For various purposes and in the various technical devices the supercharge of elastic airbags by combustion products of the solid rocket propellants[2-6] is enough widely used. One from key features of a design of such devices is the availability of the unit ensuring cooling of combustion products up to temperature of functionality of an airbag. It can be the refrigerators - heat exchangers, chemical substances, where the cooling of combustion products is made by means of endothermic reactions. For devices intended for the submerged objects lifting in the water, the cooling of gases is possible effectively to execute by bubbling through water.

In the present paper the mathematical model, the technique of calculation and results of an experimental research on supercharge and filling of a soft elastic airbag by combustion products of solid propellant at their cooling by means of bubbling in water is shown. The scheme of the considered device is submitted on Figure 1. The device consists from permeable (for water) case 2, containing a channel charge of double-based propellant 3, armoured on an outside surface and with plug above of channel. The ignition of a charge, filled with water, implemented on an original technique[3-6] by a wire spiral 1 from an external source of an electric current.

Theoretical study of the ignition system under consideration is based on the following: starting from the zero point of time when cylindrical volume of the channel is filled with water we consider heating of the water due to the discharge of heat from the spiral at the electric current running to the temperature of boiling. Appearing bubbles of steam rise to the top of the volume because of the Archimedes force where the capacity free of the water is being formed. Characteris-

tics of the steam and of the propellants combustion products mixture condition coming further into this capacity are described in the average parameters with account of the different origin of the components. The pressure formed in this capacity determines (due to the hydrostatic correlation) ousting of the water from the channel.



2. Mathematical model

The mathematical statement of a calculation problem of ignition process in the flowing channel in case of absence of a mode of critical boiling is based on homogeneous model of gas - steam - liquid mixture flow in the assumption of an instantaneous exchange of momentum, heat and mass between phases[1,6,7].

Figure 1. The scheme of device.

The following set and gradation of correlative physical phenomena is considered: 1) heating up of a liquid in the channel due to the heat exchange with the heated up by an electric current wire; 2) heating up and gradual ignition of elements of the solid propellant surface due to the heat exchange with the heated up spiral; 3) change of the temperature of a spiral's wire.

Taking into account this consideration dissipation effects, caused by the friction and heat exchange at the bounding flow surfaces are accepted by introduc-

tion of the special members of the source terms. The system of the equations is applied to a reference volume V, bounded by the closed surface, comprised of gas-permeable A and gas-impermeable S materials where heat and mass exchange between a flow, solid propellant and metal wire of a hot spiral occurs. The change of mass, momentum and energy in the control reference volume is connected with 3-D interactions, with influence of the external environment on each of the specified quantity and with transfer through a surface A. The system of equations for the principal laws of conservation is written in the integral form in generalised coordinate systems. The equation of mass conservation is,

$$\frac{\partial}{\partial t}\int_V \rho \cdot dV + \int_A \rho \cdot N \cdot dA = \int_S M \cdot dS \quad . \tag{1}$$

The equation of a change of the local thermodynamic characteristics of a mixture is,

$$\frac{\partial}{\partial t}\int_V \rho \cdot R \cdot dV + \int_A \rho \cdot R \cdot N \cdot dA = \int_S R_o M \cdot dS \tag{2}$$

$$\frac{\partial}{\partial t}\int_V \rho \cdot C_p \cdot dV + \int_A \rho \cdot C_p \cdot N \cdot dA = \int_S C_{po} \cdot M \cdot dS \quad . \tag{3}$$

The equation of conservation of momentum is,

$$\frac{\partial}{\partial t}\int_V \rho \cdot \boldsymbol{u} \cdot dV + \int_A \boldsymbol{\Pi} \cdot dA + \int_S \boldsymbol{\Pi} \cdot dS + \int_S \rho \cdot \boldsymbol{f} \cdot dS = \int_V \rho \cdot \boldsymbol{g} \cdot dV \quad . \tag{4}$$

The equation of conservation of energy is,

$$\frac{\partial}{\partial t}\int_V E \cdot dV + \int_A (E+p) \cdot N \cdot dA + \int_S q \cdot dS = \int_S H_0 \cdot M \cdot dS + \int_V \rho \cdot g \cdot u \cdot dV \quad . \tag{5}$$

Parity for total energy : $$E = \frac{p}{\gamma - 1} + \frac{\rho \cdot |\boldsymbol{u}|^2}{2} \quad . \tag{6}$$

Local values of the specific heats ratio and of the temperature T_g are set by parities

$$\gamma = \frac{C_p}{C_p - R}, \quad T_g = \frac{p}{\rho \cdot R} \quad . \tag{7}$$

The surface S that is impermeable for a flow, formed by the joined coils of a wire is considered to be described by the following scheme (Figure 2).

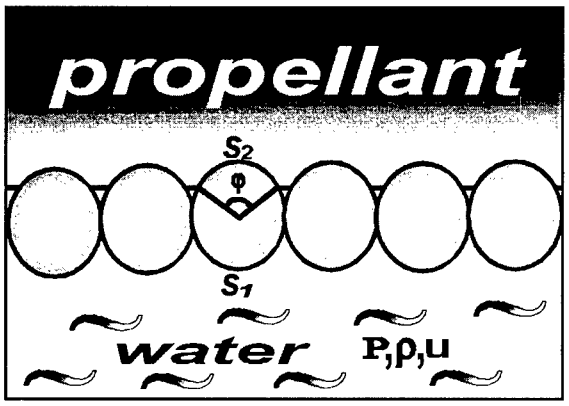


Figure 2. The ignition scheme.

The linear burning rate of solid propellant is determined by a traditional way as a power function of pressure[1,6,7].

For Eqs. (1) - (7) initial conditions are

$$R=R_H,\quad C_p=C_{pH},$$

$$E_H=(C_{pH}/R_H-1)\cdot p_H,$$

$$\rho=p_H/(R_H\cdot T_{gH}),\quad \boldsymbol{u}=0.$$

At the system of Eqs. (1)-(7) is system of a hyperbolic kind, the boundary conditions on the open end of the channel are determined by a direction of a velocity vector of flow. In case of flowing out of a gas-liquid mixture from the channel d_k the conditions of pressure equality on the channel end and external environment are used.

The problem of heating up and ignition of the surface elements of solid propellant in the reference volume V considering absence of the heat transfer along a surface of a change if solved separately for elements of a surface which are heated up through S_1; the site of the propellant is considered inflammable completely if the critical conditions of ignition were generated for it. The valuesS_1 and S_2 are defined from elementary geometrical parties for given channel's geometry, diameters and length of a wire and spiral, "loading" of a wire into the surface of a charge.

The ignition time is calculated in terms of the condensed-phase ignition theory developed by Vilyunov and other authors[8,9]. It is assumed that the ignition of the surface element occurs instantaneously with the surface temperature rise up to a critical value, at which point the heat flux generated in the propellant surface

layer becomes larger than the incident heat flux. The mathematical problem in the ignition of a condensed substance (solid propellant) involves the equation of thermal conductivity taking into account the heat release term and the equation of chemical kinetics:

$$\frac{\partial T}{\partial t} = \chi_0 \cdot \frac{\partial^2 T}{\partial y^2} + Q_0 \cdot F(a,T), \tag{8}$$

$$\frac{\partial a}{\partial t} = -F(a,T).$$

The warming up of a solid propellant charge in a place of contact with wire of a spiral is described by boundary conditions of the first kind (Equality of temperature of the propellant surface to temperature of a wire T_W):

$$y = 0: \quad T(0,t)=T_W; \quad q_1 = -\lambda_0 \cdot \frac{\partial T}{\partial y} \ . \tag{9}$$

Condition at infinity is established for heat flux to be zero:

$$y \to \infty: \quad -\lambda_0 \cdot \frac{\partial T}{\partial y} = 0 \ . \tag{10}$$

For a problem characterized by Eqs. (8)-(10) the following one the initial conditions $T(x,0) = T_H$ and $a(x,0) = 1$.

The change of average on the section temperature of a wire T_W is calculated by the equation, expressing balance of energy for a part of a spiral, referring to the considered reference volume V, submitted by a parity (scheme Figure 2)

$$C_W \rho_W \cdot \frac{\partial T_W}{\partial t} = I^2 \cdot \Omega(T_W) - \frac{\varphi}{\pi} \cdot \frac{q_1}{r} - \frac{q_2}{r} \ . \tag{11}$$

Dependence $\Omega=\Omega(T_W)$ of resistance of a wire of its temperature is considered known. The value of current I is determined through voltage of a source and total value of resistance on all length, of a conductor according to the Ohm law.

The thermal influence on a spiral from a flow is reproduced by statement of boundary conditions of the third kind (rules of Newton – Richman) on a surface of contact "wire – liquid"[5]:

$$y = 0: \quad q_2 = \alpha_2 \left[T_g - T_W \right] \ . \tag{12}$$

Thus, the system of the Eqs.(1)-(12) within the framework of the chosen model describes the basic processes connected with gradual ignition of solid propellant surface elements due to the heat exchange with a heated up spiral and liquid filling the channel.

In the calculations the geometry of an airbag was determined by the shape truncated from below of rotational symmetric ellipsoid and two stages of the process were considered. It was considered, that at the first stage of supercharge the increase of volume of an airbag was caused, mainly, increase of a vertical axis up to it of the maximum size. At the second stage the increase of volume was determined by increase of a horizontal axis of an ellipsoid up to the maximum size, appropriate it, then volume was considered constant. The running value *Ws (t)* of volume during a deployment of a cavity is determined accumulated to a the present situation of time of gas mass located at the temperature of and pressure of external environment (it is supposed, that at bubbling combustion products up to temperature of a water is cooled):

$$W_s(t) = \pi \frac{R \cdot T_{gH}}{P_H} \int_0^t \rho \cdot u \cdot d_k^2 dt .$$

3. Results of researches

Theoretical and the experimental researches were conducted for the gas generator with channel (d_k = 1.2 sm) charge of double-based solid propellant of weight 20 g. The first research concerned comparison computational and experimental relations of a combustion surface development. For the underwater ignition the nickel-chrome wire of diameter 0.5 mm of length 20 sm was used.

For 40 w power, dispersed on a spiral, on Figure 3 the separate frames of tests are adduced. The first copy of frame corresponds to basis before supply of an electrosignal on a spiral (t = 0). Through t = 0.3 s from a moment of supply of a signal the centres of vaporisation on a surface of a spiral, their separation and rise because of the Archimedes force to blocked end (plug) are marked. Further,

through t = 0.7 s at this end steam-gas cavity is formed. The volume of cavity grows from the supply of new portions steam bubbles. Through t = 2 s cavity above a spiral and spiral completely are released from a water, which is only under a spiral. Finally channel is released through t= 3.5 s; full ignition of a channel surface visually is marked.

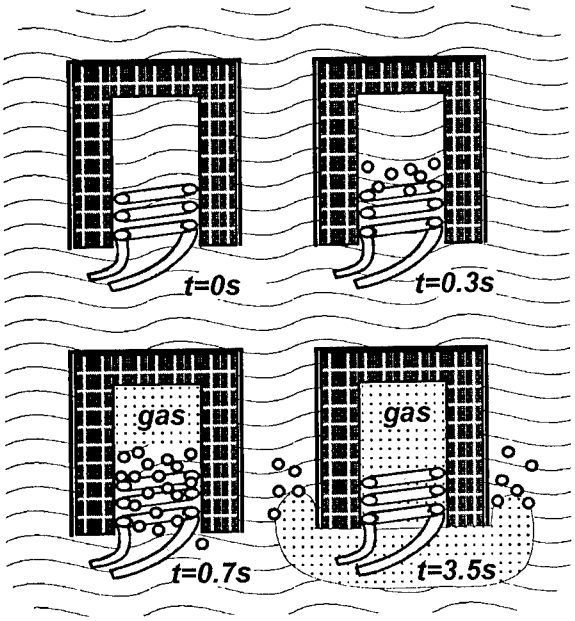


Figure 3. The separate frames of tests.

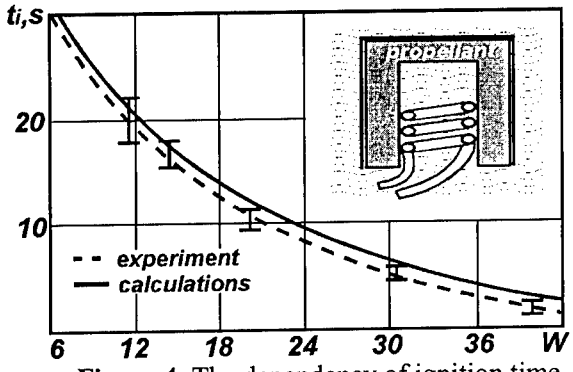


Figure 4. The dependency of ignition time.

On Figure 4 the generalised results of dependency of ignition time t_i from power W, dispersed on a spiral are shown. A solid line - results of calculations, dashed – processing of experimental data.

It is visible, that the time of ignition t_i is nonlinearly reduced with increase of power of a spiral. The comparative analysis of results has shown that in the range ofcapacities 6÷24 w concurrence of experimental and calculated data a rather satisfactory, maximal distinction makes ≈7%. In area of higher capacities the divergence is increased, reaching the greatest values in ≈9.5%.

It is possible to explain similar view of dependencies to that in mathematical model there are no members,

describing the mechanism of heat exchange reduction in the system a wire – a liquid in case of increase of vaporisation.

The second part of researches concerned pressurisation of a cavity on the set-up shown on Figure 1. After supply of voltage on a spiral and ignition of a charge channel surface a bubbling through a water the combustion products began to go in an envelope originally packed on a surface of a case 2. In accordance with supply of gas the envelope begins to be expanded and under act of the Archimedes force to be drawed out up to its maximum altitude. The continuous supply of combustion products hereinafter provides development of an envelope up to full volume. Overall height made H_{max}=30 sm, maximum diameter – D_{max}=20 sm. The development of process was fixed by the videocamera.

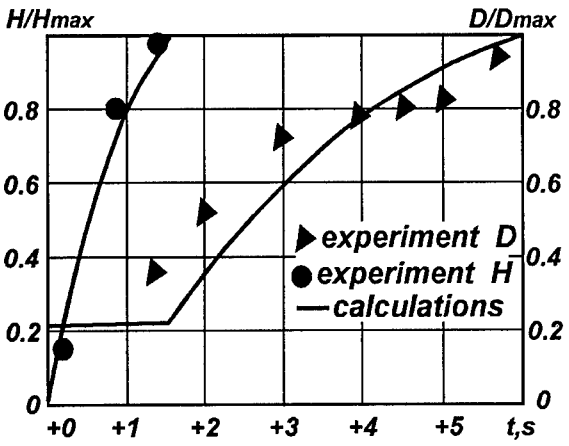


Figure 5. The dependency of relative height and diameter.

On Figure 5 comparison of relative height and diameter of an envelope from time is adduced. From Figure 5 it is visible, that after the end of ignition in the time of +1.5s the envelope is drawed out on height completely, then begins more heavily begins to be increased it diameter.

To t = +6s the filling is completed, volume reaches a maximum level (Figure 6). On this figures the solid lines designate results of calculation, circles and triangles - results of treated experimental data. The difference of dependencies is connected, in our opinion, mainly to physical non-uniformity of deployment of an envelope and inaccuracy of the description of its shape by an ellipsoid. Besides we

shall mark, that of weight of a charge of solid propellant for filling of a cavity of indicated geometry has appeared excessive.

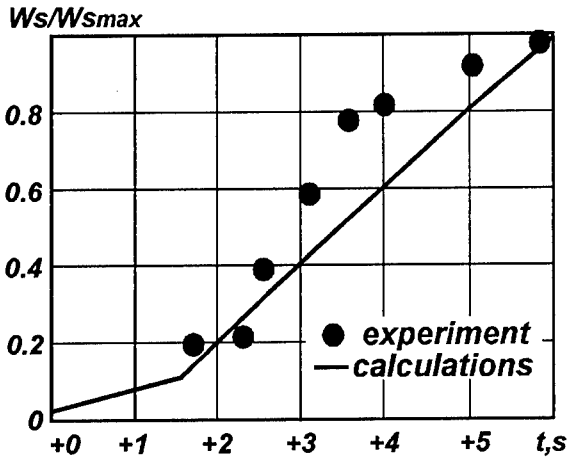


Figure 6. The dependency of relative volume.

Thus, in the paper the technique of calculation of process and parameters of the device for submerged objects lifting in the water. The device differs by a design simplicity and capability of application for a broad band of depths. The comparison of results of calculation with experimental data has shown them rather satisfactory conformity.

The work is supported by NATO Science Program (Collaborative Linkage Grant No976783).

4. References

(1) A. Vorozhtsov, S. Bondarchuk, A. Salko, O. Kondratova. "Mathematical Simulation of Airbag Inflation by Low Temperature Gas Generator Products", *An International Journal Propellants, Explosives, Pyrotechnics*, Vol. 25, Issue 5, –pp.220-223 (2000).

(2) I.V.Tishunin (ed.), *"Auxiliary Systems of Rocket Engineering" (Russian translation), Mir, Moscow, 1970.*

(3) V.P.Zima, N.L. Rybasova, V.D.Barsukov, et.al., Inventor's Certificate No. 1729905 SSSR, MKJ 5 V 63 V 22/08, V 63 S 7/04, "Device to lift a sunken object", Declaration No. 4805775, Appl. 02.01.90, Publ. 04.30.92; Bull. No.16.

(4) A.B. Vorozhtsov, and V.P. Zima, "Research on Solid Propellant Ignition Under Water", *Proceeding of the International Workshop on Combustion Instability of Solid Propellants and Rocket Motors*, Politecnico di Milano, Milano, Italy, June 16-18, 1997.

(5) A.B. Vorozhtsov, and V.P. Zima, "Experimental Investigation of the Underwater Ignition of the Solid Rocket Propellant",*36th Aerospace Sciences Meeting and Exhibit*, Reno, WV, January 12-15, 1998.

(6) Bondarchuk, S.S., Vorozhtsov, A.B., Zima V.P. "Solid Propellant Underwater Ignition Modelling",*AIAA Paper 99-0864 (A99-16700), AIAA, 37th Aerospace Sciences Meeting and Exhibit,* Reno, NV, Jan.11-14, 1999.

(7) S.S. Bondarchuk, A.B. Vorozhtsov, N.A.Obukhov "Ignition Pressure Transient in Solid Rockets Initially Filled with Water", *Journal of Propulsion and Power*, Vol.15, No.6, November-December, pp.861-865 (1999).

(8) V.N. Vilyunov, and V.E. Zarko, *Ignition of Solids*, *Elsevier, Amsterdam, 1989.*

(9) Borovskoy, I.G., Bondarchuk, S.S., Kozlov E.A., and Vilunov, V.N., "Solution of the Problem of Condensed System Ignition Based on a Difference Scheme with Time-Dependent Grid",*Fizika Gorenia i Vzryva*, Vol. 22, No. 3, pp.14-19 (1986).

ZERKLEINERUNG ENERGETISCHER MATERIALIEN IN WÄßRIGEN SUSPENSIONEN

SIZE REDUCTION OF ENERGETIC MATERIALS IN AQUEOUS PHASE

Irma Mikonsaari*, Ulrich Teipel
Fraunhofer Institut für Chemische Technologie
P.O. Box 12 40, 76318 Pfinztal, Germany
*e-mail:miko@ict.fhg.de

ABSTRACT:

Four different size reduction methods were used for the communition of energetic materials in aqueous phase; size reduction by ultrasonic, size reduction by a rotor-stator-system, communition in an annular gap mill and in a colloid mill. Size reduction of HMX, RDX and CL 20 was investigated. Rotor –stator – equipment, e.g. a colloid mill turned out to be suitable for a pre-treatment before fine grinding. The annular gap mill was found to be most effective for producing particles in the submicron range.

KURZFASSUNG:

Zur Zerkleinerung energetischer Materialien wurden vier verschiedene Methoden erprobt; die Zerkleinerung durch Ultraschall, ein Zahnkranzdispergierer, eine Scherspaltkugelmühle und eine Kolloidmühle. Untersucht wurde die Zerkleinerung von HMX, RDX und CL 20. Die Kolloidmühle erwies sich als geeignet zur Vorzerkleinerung für eine anschließende Feinzerkleinerung. Die Scherspaltkugelmühle eignete sich sehr gut für eine Feinzerkleinerung im Submikron-Bereich.

1. Einleitung

Wenn in der Feststoffverfahrenstechnik für folgende Prozeßschritte ein gewünschter Dispersionsgrad erzielt werden soll, ist Zerkleinerung eine häufig eingesetzte Unit Operation.

Zur Verarbeitung von partikulären energetischen Materialien in Raketenfesttreibstoffen, Treibladungspulvern und Explosivstoffen werden Partikeln z.B. im Größenbereich $1\ \mu m \leq x \leq 10$, $50\ \mu m \leq x \leq 150\ \mu m$ und $150\ \mu m \leq x \leq 250\ \mu m$ gefordert. Werden bi- oder trimodal verteilte Partikeln eingesetzt, so können sehr hohe Packungsdichten mit geringen Bindermengen erreicht werden. Außerdem werden wegen ihrer großen reaktiven Oberfläche sowie für z.B. eine verbesserte Abbrandcharakteristik Partikeln im Submikron – Bereich gefordert.

Energetische Materialien mit größerer Korngröße werden in der Regel durch Kristallisation hergestellt [1]. Für die Herstellung sehr feiner Partikeln ist jedoch zur Zeit die Zerkleinerung der wirtschaftlich günstigere Weg.

Bei der Auswahl eines Zerkleinerungsprozesses für energetische Materialien müssen spezielle Forderungen erfüllt sein. Empfindliche Stoffe wie z.B. *RDX* (*Cyclo-1,3,5-trimethylene-2,4,6-trinitramine; Cyclonite; Hexogen*), *HMX* (*Cyclotetramethylene tetranitramine; Octogen*) oder *CL 20* (*HNIW ; Hexanitrohexaazaisowurtzitan*; *2,4,6,8,10,12-hexanitro-hexaaza-tetracyclo-dodecan*) werden mittels Naßverfahren zerkleinert, wobei die kontinuierliche Phase das Material phlegmatisiert. Weiterhin muß beachtet werden, daß Suspensionen mit hohen Konzentrationen hochempfindlichem Sprengstoff (über 20 w.-%) detonationsfähig sein können [2].

In diesem Beitrag werden Ergebnisse zur Naßzerkleinerung von energetischen Materialien in wäßriger Phase vorgestellt, wobei vier verschiedene Verfahren verglichen werden.

2. Grundlagen der Zerkleinerung

Das Zerkleinerungsverhalten von Feststoffen hängt vor allem von ihrem mechanischen Materialverhalten ab. Damit Partikel zerkleinert werden, müssen im Feststoff Brüche entstehen und diese müssen sich durch den Feststoff ausbreiten, d.h. das Bruchverhalten muß günstig sein. Zur Entstehung von Brüchen muß das Partikel von außen durch das Zerkleinerungswerkzeug oder durch benachbarte Teilchen beansprucht werden, und es muß eine Verformung des Partikels und ein Aufbau eines Spannungsfeldes stattfinden. Das Vorhandensein von Materialfehlern, wie z.B. Rissen, im Feststoffgefüge sind zur Entstehung von Brüchen vorteilhaft.

Das zu zerkleinernde Material kann in seinem Materialverhalten durch seine Härte charakterisiert werden. So werden die Zerkleinerungsprozesse in Abhängigkeit der Mohr-Härte der zu verkleinernden Produkte in Hart-, Mittelhart-, und Weichzerkleinerung eingeteilt. Die kristal-

linen energetischen Materialien fallen nach dieser Einordnung in die Gruppe der „Mittelhartzerkleinerung".

Die Zerkleinerungprozesse können außerdem nach ihrem Beanspruchungsmechanismus eingeteilt werden. Dabei unterscheidet man nach Rumpf [3] zwischen den in der Tabelle 1 dargestellten Beanspruchungen.

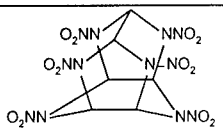
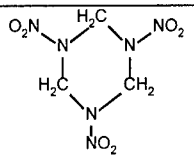
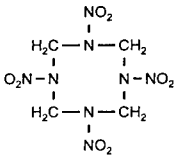
Bei den untersuchten Verfahren wurde das Zerkleinerungsgut vor allem zwischen mehreren Zerkleinerungswerkzeugen sowie durch das umgebende Fluid beansprucht.

Beanspruchung zwischen mehreren Zerkleinerungswerkzeugen	Druck- und Schubbelastung, Beanspruchungen durch Scheren und Schneiden, erzwungene Verformung durch das Werkzeug, geringe Beanspruchungsgeschwindigkeiten, Backen- und Rundbrecher, Walzen- und Wälzzerkleinerungsmaschinen, Kugelmühlen, Reibschalen
Beanspruchung an einem Zerkleinerungswerkzeug	Prallbeanspruchung, Energie- und Impulsübertragung durch Stoß, ohne Formzwang, hohe Beanspruchungsgeschwindigkeiten, Prallbrecher und Strahlmühlen
Beanspruchung durch das umgebende Fluid	Druck- und Zugbelastung, Druckstöße, Kavitation, geringe Kräfte, Zerteilung von wenig festen Partikeln und Agglomeraten, Flocken, Tropfen und Blasen Walzenmühlen, Dispergiermaschienen, Hochdruckhomogenisatoren, Rührmaschinen
Beanspruchung durch nicht mechanische Energieeinleitung	Verformung durch thermische, elektromagnetische, chemische oder detonative Beanspruchung

Tab. 1: Beanspruchungsarten nach Rumpf [3]

3. Materialien

Die untersuchten kristallinen energetischen Materialien und ihre Eigenschaften sind in Tabelle 2 dargestellt.

Material	CL 20	Hexogen	Oktogen
Summenformel	$C_6H_6N_{12}O_{12}$	$C_3H_6N_6O_6$	$C_4H_8N_8O_8$
Strukturformel			
Dichte	2,04 g/cm³	1,82 g/cm³	1,96 g/cm³
Korngröße des Rohmaterials	125 µm	18 – 177 µm	20 µm

Tab. 2: Eingesetzte energetische Materialien

4. Verwendete Zerkleinerungsprozesse

4.1 Kolloidmühle

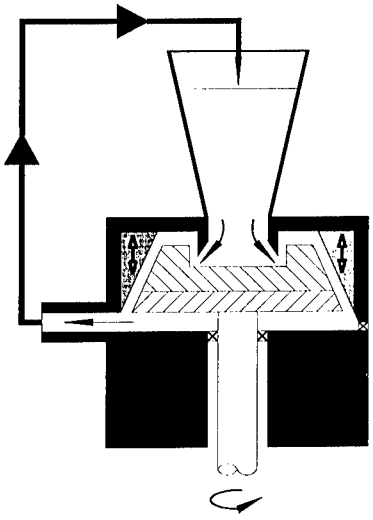


Abb. 1: Kolloidmühle

Kolloidmühlen werden häufig zur Homogenisierung, zum Aufbrechen von Agglomeraten und zur Herstellung von Pasten, Suspensionen und Emulsionen sowie zur Zerkleinerung von weichen, nicht abrasiven Stoffen genutzt. Dies sind Zerkleinerungsapparate zur Feinstzerkleinerung bis zu einer Endfeinheit um 1 µm. Die Eingangsgröße beträgt näherungsweise 100 µm. Die Wirkungsweise ist ein Rotor-Stator-System mit einem konusförmigen Rotor und dem Gehäuse als Stator (Abb. 1). Der Spalt zwischen Rotor und Stator ist verstellbar, um die Endfeinheit des Produktes einstellen zu können. Abbildung 1 zeigt eine schematische Darstellung der Kolloidmühle.

4.2 Ultraschallzerkleinerung

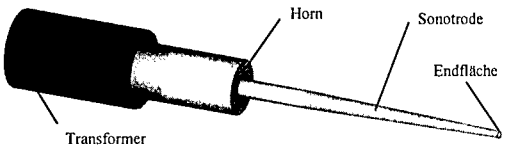


Abb. 2: Ultraschallsonotrode zur Zerkleinerung

Bei der Ultraschallzerkleinerung wird die Kavitation, welche durch den Eintrag von Ultraschall in eine Suspension verursacht wird, zur Zerkleinerung von kristallinem Material ausgenutzt. Die verwendeten Ultraschalldispergierer werden häufig bei der Suspensions- und Emulsionsherstellung sowie zur Probenvorbeitung verwendet und besitzen hohe Energien [4]. Abbildung 2 zeigt eine solche Ultraschallsonotrode.

4.3 Zahnkranzdispergierer

Der Zahnkranzdispergierer besteht aus einem Stator mit schrägen Schlitzen und einem Rotor mit Zähnen (Abb. 3). Seine Rotordrehzahl kann im Bereich von 3 000 min^{-1} bis20 000 min^{-1} variiert werden, so daß maximale Umfangsgeschwindigkeiten von 16,8 m/s realisiert werden können. Die Partikel und die kontinuierliche Phase der Suspension strömen zentral in den Zahnkranzdispergierer ein und werden radial nach außen gefördert.

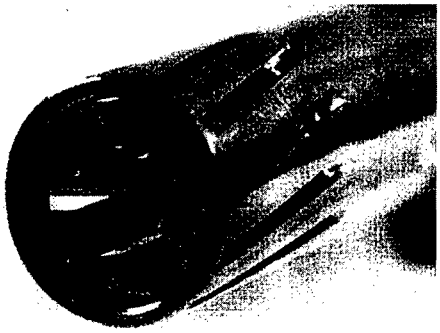


Abb. 3: Zahnkranzdispergierer

4.4 Scherspaltkugelmühle

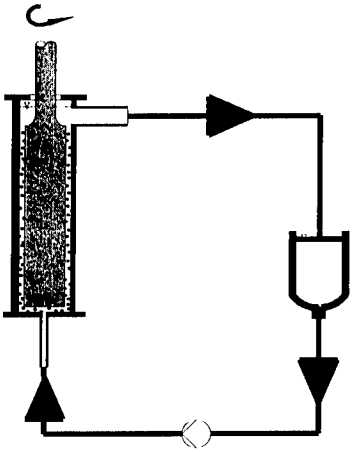


Abb. 4: Scherspaltkugelmühle

Die Scherspaltkugelmühle (Abb. 4) bietet die Möglichkeit, kristalline Stoffe bis zu einer Endfeinheit von 1 µm zu zerkleinern. Sie besteht aus einem zylindrischen Rotor – Stator - System. Im Zwischenraum zwischen Stator und Rotor befinden sich Mahlkugeln. Durch diese Kugelpackung wird die zu zerkleinernde Suspension geführt und in einer Scherströmung zerkleinert. Die erreichbare Endfeinheit hängt außer vom Materialverhalten auch von der Mahlkugelart und –größe sowie von der Rotordrehzahl ab.

5. Experimentelle Ergebnisse

5.1 Kolloidmühle

Zur Untersuchung der Zerkleinerung von RDX in einer Kolloidmühle kam eine Mühle der Firma Probst & Glass, Type PUC 0/100 zum Einsatz. Dieser Apparat erlaubt Durchflüsse von 100 – 2500 kg/h, der Rotor hat einen Durchmesser von 100 mm und eine Drehzahl von 3 000 min^{-1}. Die Spaltweite der Mühle ist variabel und beträgt minimal 0,04 mm.

Abbildung 5 zeigt die Partikelgrößenverteilung der eingesetzten Kornfraktion und die der zerkleinerten Fraktion. In Abbildung 6 ist der Zerkleinerungserfolg als Funktion der Zeit dargestellt. Es ist zu erkennen, daß die Zerkleinerung bereits in den ersten 10 Minuten erfolgt, in denen sich die mittlere Korngröße von x_α=177 µm auf ca. x_ω=20 µm verringert. Die Partikelgrößenverteilung ist durch den Zerkleinerungsprozeß breiter geworden.

Abbildung 7 zeigt das Ausgangsmaterial und die zerkleinerte Fraktion in REM – Aufnahmen.

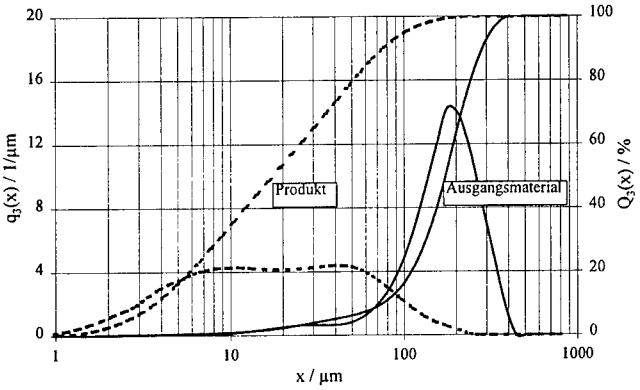


Abb. 5: Partikelgrößenverteilungen des Ausgangmaterials und des zerkleinerten Materials

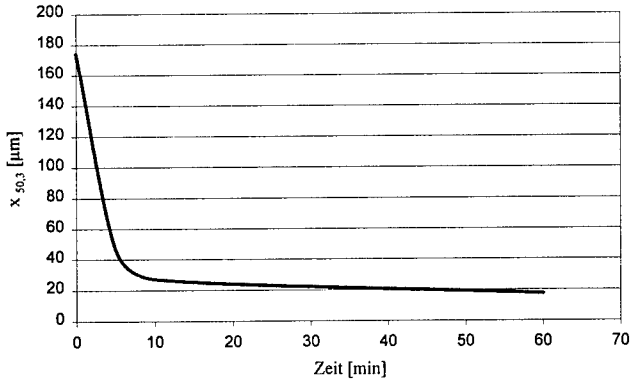
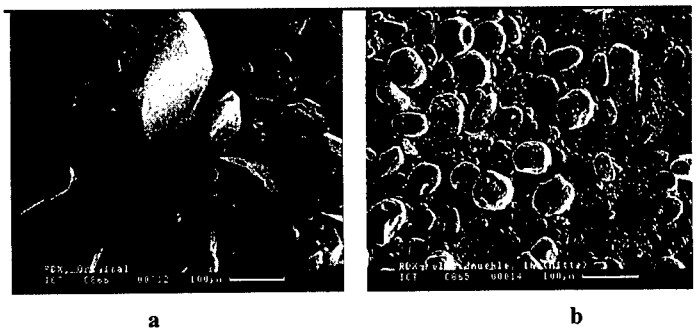


Abb. 6: Mittlere Partikelgröße als Funktion der Zeit



a **b**

Abb. 7: REM – Aufnahmen der verschiedenen RDX-Fraktionen
(a: Rohmaterial, b: zerkleinerte Fraktion)

5.2 Ultraschallzerkleinerung

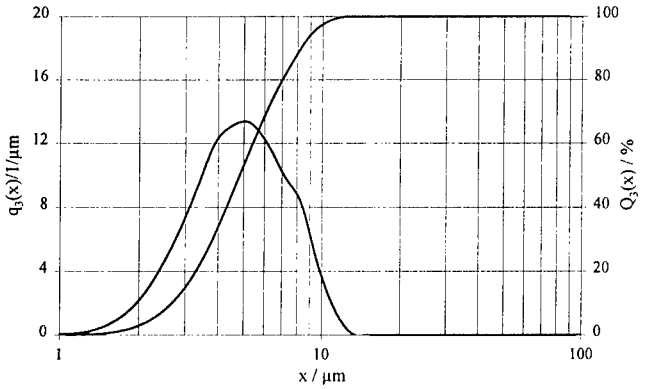


Abb. 8: Zerkleinerung von HMX durch Ultraschall

Bei der Zerkleinerung von HMX mit Hilfe von Ultraschall kam der Desintegrator HD 60 der Firma Bandelin mit einer Eingangsleistung von 60 W und einer Frequenz von 20 kHz zum Einsatz. Die Ultraschallsonotrode besitzt eine effektive Endfläche von 113 mm². In Abbildung 8 ist die Verteilung des zerkleinerten Materials dargestellt, die sehr enge Verteilung mit einer mittleren Partikelgröße von x_{50}=5 µm nach einer Zerkleinerungsdauer von 30 min aufweist.

5.3 Zahnkranzdispergierer

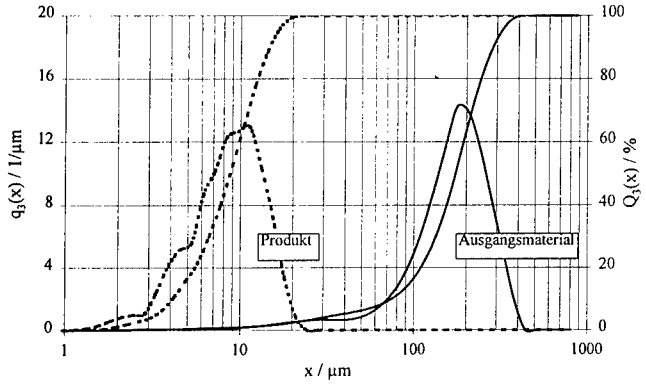


Abb. 9: Zerkleinerung von RDX mit dem Zahnkranzdispergierer

Die Zerkleinerung von RDX und CL 20 wurde mit Hilfe eines diskontinuierlichen Zahnkranzdispergierers der Firma Ystral (Typ X40) untersucht, welcher für Volumen von 1 l verwendet wurde. Die Abbildungen 9 und 10 zeigen die Verteilungen des Ausgangsmaterials sowie des zerkleinerten Produktes für RDX und CL 20. In Tabelle 3 sind die mittleren Partikelgrößen sowie die Verteilungskoeffizienten dargestellt, woraus eine engere Partikelverteilung beim RDX, aber im Mittel feinere Partikel beim CL 20 ersichtlich sind.

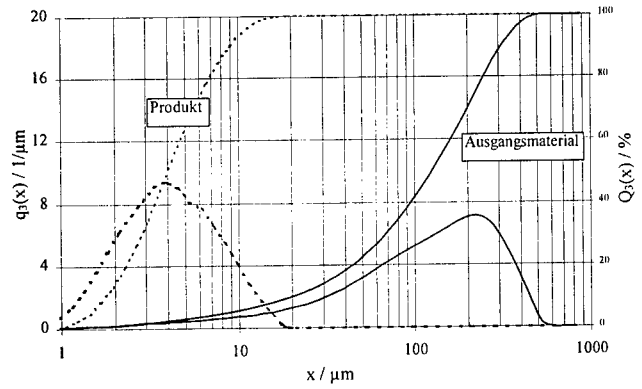
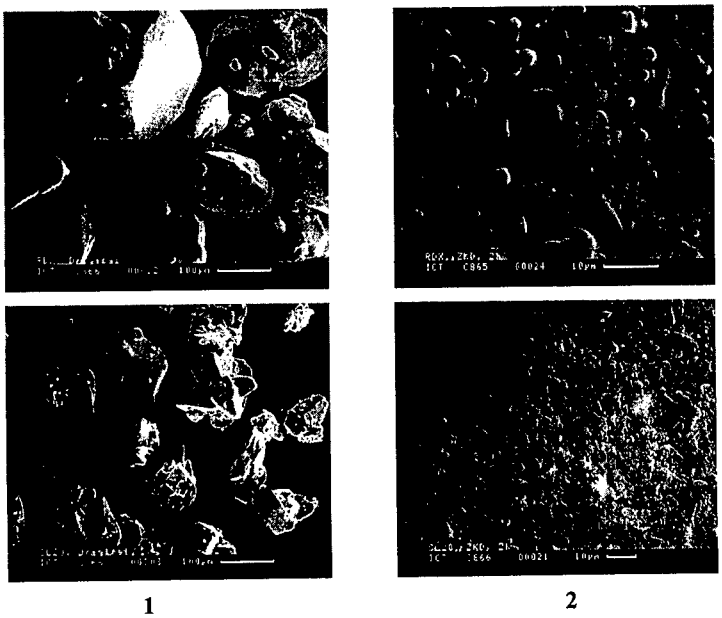


Abb. 10: Zerkleinerung von CL 20 mit dem Zahnkranzdispergierer

Material	Ausgangsmaterial $x_{50,3}$ [µm]	Produkt $x_{50,3}$ [µm]	Distribution $\frac{x_{84,3} - x_{16,3}}{2 \cdot x_{50,3}}$
RDX	174	8,73	0,477
CL 20	125	3,96	0,689

Tab.3: Zahnkranzdispergierung von RDX und CL 20

Abbildung 11 zeigt das Ausgangsmaterial sowie die zerkleinerten Fraktionen in REM – Aufnahmen



a) RDX

b) CL 20

1 2

Abb. 11: Ausgangs (1)- und Endfraktionen (2) in REM – Aufnahme

5.4 Scherspaltkugelmühle

Für die folgenden Versuche zur Zerkleinerung von RDX wurde eine Scherspaltkugelmühle (s. Abb. 4) verwendet. Der Durchfluß betrug 25 l/h, die Batchgröße war 1 l. Es wurden Mahlkugeln aus Zirkoniumoxid verwendet. Abbildung 12 stellt den Zerkleinerungserfolg als Funktion der Zeit dar.

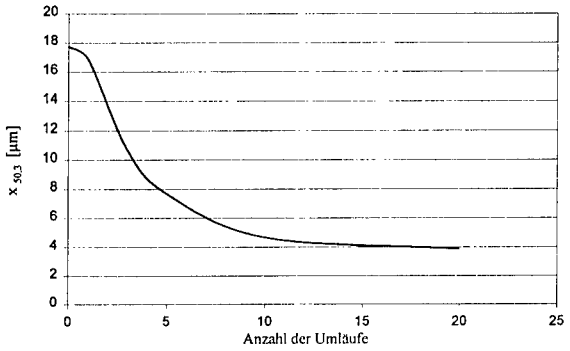


Abb. 12: Zerkleinerung in einer Scherspaltkugelmühle aus Funktion der Zeit

Die mittlere Partikelgröße des Ausgangsmaterials betrug x_α=18 µm. Die effektivste Zerkleinerung erfolgt wie bei der Kolloidmühle in den ersten 10 Minuten. Das Produkt besitzt eine mittlere Partikelgröße von x_ω=4 µm und weist eine sehr enge Verteilung auf (Abb. 13).

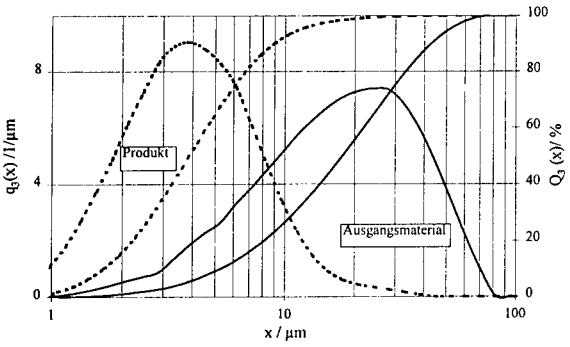


Abb. 13: Zerkleinerung in der Scherspaltkugelmühle

Abbildung 14 zeigt REM – Aufnahmen von dem Ausgangs- und dem Produktmaterial.



a **b**

Abb. 14: REM – Aufnahmen von der Zerkleinerung durch die Scherspaltkugelmühle
a: Ausgangsfraktion, b: Produktfraktion

5.5 Zerkleinerungsprozeß für energetische Materialien

Aufgrund der erzielten Ergebnisse schlagen wir für die Zerkleinerung von energtischen Materialien einen zweistufigen Prozeß vor. Hierbei können Materialien mit einer Ausgangsmaterialgröße von x_α = 200 µm auf eine Endfeinheit $x_\omega \leq$ 5 µm zerkleinert werden. In einer ersten Stufe wird das Material auf eine mittlere Partikelgröße von ungefähr 20 µm in einer Kolloidmühle zerkleinert. Danach erfolgt die Feinstzerkleinerung in einer Scherspaltkugelmühle, wobei unter optimierten Bedingungen Endfeinheiten um 2 µm mit einer sehr engen Partikelgrößenverteilung erreicht werden können.

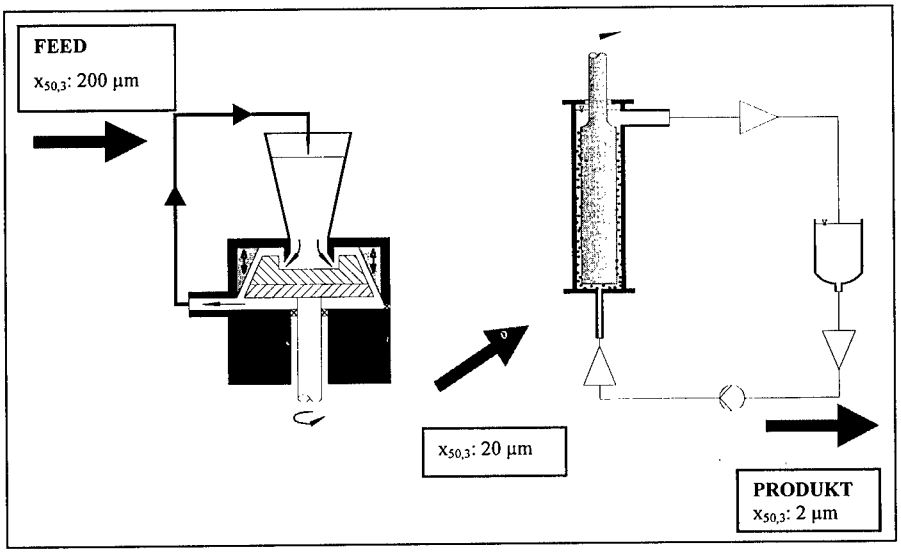


Abb. 15: Zerkleinerungprozeß für energetische Materialien

6. Zusammenfassung

Für die Feinzerkleinerung von kristallinen energetischen Materialien scheint die Scherspaltkugelmühle sehr gut geeignet zu sein. Bei RDX erreicht man Endfeinheiten unter 4 µm, wobei die Versuchsbedingungen weiter optimiert werden können. Auch die Partikelgrößenverteilung ist bei dem Produkt sehr eng, was auf die geringe Rückvermischung der Strömung in der Mühle zurückzuführen ist. Der Zahnkranzdispergierer liefert im Vergleich etwas gröberes

Zerkleinerungsverfahren	*Material*	*Ausgangskorngröße* $x_{50,3}$ *[µm]*	*Produktkorngröße* $x_{50,3}$ *[µm]*
Kolloidmühle	RDX	177	20
Ultraschallzerkleinerung	HMX	20	5
Zahnkranzdispergierer	RDX,	174	9
	CL 20	125	4
Scherspaltkugelmühle	RDX	18	4

Tab. 4: Zerkleinerung von energetischen Materialien

Material, das vor allem breiter verteilt ist. Die Ultraschallzerkleinerung ermöglicht ebenfalls ein feines Produkt; sie ist jedoch sehr energieintensiv und daher für größere Mengen schlecht anwendbar. Die Kolloidmühle ist eine sehr gute Lösung für eine Vorzerkleinerung. So können grobe Fraktionen auf die optimale Korngröße für eine Eingangsfraktion in die Scherspaltkugelmühle vermahlen werden. Tabelle 4 faßt die Zerkleinerungsergebnisse zusammen.

7. Literatur

[1] Teipel, U.: *Production of Particles of Explosives*, Propellants, Explosives, Pyrotechnics (24) 1999

[2] Hommel, H.: *Verfahrenstechnik der Herstellung von Hexogen (RDX) feinst, granuliert*, ICT-Bericht 7/80, Frauhofer Institut für Chemische Technologie

[3] Rumpf, H.: *Die Einzelkornzerkleinerung als Grundlage einer technischen Zerkleinerungswissenschaft*, Chem.-Ing.-Tech. 37, 3, 1965

[4] Teipel, U.: *Rheologisches Verhalten von Emulsionen und Tensidlösungen*, Dissertation, Universität Bayreuth, 1999, Wissenschaftliche Schriftenreihe des Fraunhofer ICT, Band 22

Production of Commercial Naphthylamine Explosives

CUI Jianlan, CAO Duanlin, CHENG Jingcai, XING Yajun

Dept. of Chemical Engineering, North China Institute of Technology, *Taiyuan* 030051, *Shanxi*,

P. R. China

Abstract: This paper proposing two (2) formulas to produce commercial naphthylamine explosives using ammonium nitrate, dinitronaphthalene, and wood-flour and basing on the principle of oxygen equilibrium and the principle of energy optimality, has determined the temperature, option of charge mixture as well as the fineness and density of the explosives. It has also tested the explosion rate, lead cylinder compression value, explosion heat, and explosion temperature of the explosives. Experimental results show that, at 45°C and at 1.00 ~ 1.20 $g \cdot cm^{-3}$, the commercial naphthylamine explosive produced from the mixture of ammonium nitrate, dinitronaphthalene, and wood-flour is of a steady performance, its moisture-proof property and anti-caking property being much better than those of rock explosive No. 2. This explosive can be applied as a substitute for rock explosive No. 2.

Keywords: commercial naphthylamine explosive; dinitronaphthalene; process; explosion properties

1. Preface

Every country has been engaged in explosive improvement research, one of which is about Naphthylamine explosives. It points out one way to elimiate the shortcomings of Nitrammine explosives including the grave hygroscopicity, caking and lack of water resistance. with a great toxicity of TNT, human organs can be damaged contacting it for a long time. Naphthylamine explosives consist of dinitronaphthalene as sensitizer, ammonium nitrate as oxidant, and other components. the moisture-proof property and anti-caking property are much better than those of rock explosive No2. Reducing damage to human body for not using TNT, this kind of explosives can be applied as a substitute for rock explosive No2.

2.Tests and Results

2.1 Experimental methods

(1). Prepare raw material

a. Ammonium nitrate

Appropriate ammonium nitrate is taken , dried in oven from 3 to 4 hours at 30℃and crushed from 20 to 30 minutes in a ball mill, and sifted with 60 mesh sifters.

b. Dinitronaphthalene

self-made dinitronaphthalene is taken and grinded in mortar until it reach desired degree of fineness. Dinitronaphthalene belonging to dangerous articles, and not easy to carry about and purchase, it is self-made in this experiment. People know little about it. So the properties of dinitronaphthalene are illustrated later by experimental results.

Dinitronaphthalene is gray yellow powder, and has two main structure: 1.8-(dinitronaphthalene) and 1.5-(dinitronaphthalene). molar mass 218.2, content of nitrogen 12.84%, oxygen balance -1.39, melting point 150 ~ 160℃, easily dissolving in benzene, dimethylbenzene and acetone, explosion heat 4204 ~ 4210KJ.Kg^{-1} , very low hygroscopicity small, hardly dissolving in water, no act on metal, very safe to heat, when slowly heating to 318℃, decomposed into foam, without explosion, mechanical sensitivity very small, explosion occurs after drop hammer of 2kg strike from over 1.5m, its explosion point 300 ~ 310℃, explosive rate 1150ms^{-1} the density of 1 g/cm^3 lead cylinder compression value 0.9 ~ 4mm, explosive temperature 2807K, explosion volume 488l.Kg^{-1}.

c. Wood-flour

Take fresh wood-flour from carpentering room and sift ready for use.

d. Diesel oil

Industrial Diesel oil.

(2). Mix each component

According to the formula, add ammonium, nitrate dinitronaphthalene and wood-flour to get them well mixed up, next diesel oil is added into ball mill to mix for appropriate time,

(3). Charge

Slowly add the mixture into rolled kraft paper; calculate the charge volume, be sure that the density is within 1.05 ~ 1.19g/cm^3.

(4). Measure properties

2.2 Results

According to the principle of oxygen equilibrium approaching zero and the principle of energy optimality, take three factors—content of dinitrophthalene, mixture temperature and time, (they determine explosive fineness and homogeneity), and three levels for the content of dinitrophthalene 8%, 10%, 12%, temperature 40℃,45℃,50℃, time for mixture 3mins, 5mins, 8mins. Conduct positive cross-link test, on the basis of optimal result, determine the best formula.

(experimental results see table 2—1)

Table 2-1 Formula and properties

Formula and properties	Commercial naphthylamine No1	Commercial Naphthylamine No2
Ammonium nitrate (%)	88	85
Dinitronaphaline (%)	10	10
Wood-flour (%)	2	0
Diesel oil (%)	0	5
Density (g/cm^3)	1.00 ~ 1.05	0.90 ~ 1.00
Oxygen equilibrium	0.009	−0.13
Explosion rate (m/s^1)	3225	2564
Lead cylinder compression value (mm)	13	7
Specific volume (L/Kg^1)	916	921
Explosion heat (kg/kg^1)	3881	3560
Explosion temperature(℃)	2600	2500

3. Discussion

3.1 Fineness

Generally speaking, the finer grinding , the greater surface square the particles, the better mixed up, but the higher the cost of production. So according to demand determine fineness.

3.2 Density

Explosive rate vary with density, according to demand, it is better to control the density within 1.00 ~ 1.20 g/cm^3.

3.3 The manner of mixture

In order to be safe, every component should be processed in advance until granularity reach the desired demand. Adding ammonium nitrate, dinitronaphthalene, and wood-flour in turn.

3.4 Temperature

High temperature for explosive mixture is dangerous. Low temperature may hinder uniform mixture. According to demand appropriate control temperature is about 45℃.

4. Conclusion

On the basis of strictly designed technological experiments, above two formulas are proposed in this paper. The above commercial Naphthylamine explosives are of a steady performance, their moisture-proof property and anti-caking property being much better than those of rock explosive No2. This kind of explosives can be used to cut the mountain for a road and build water conservancy projects and replace rock explosive No2.

Reference

1. Urbanski T. chemistry and technology of explosive, (vol, 3) Oxford:Pergamn press 1967.

2. Bailey Ac, sponggord RJ. CA 1984,101.630017g.

Production of High-Detonation Nitro-Compositions from Waste Polystyrene

CAO Duanlin, CUI Jianlan, GUO Jianwen, CHENG Jingcai, XUAN Chunlei

Dept. of Chemical Engineering, North China Institute of Technology, *Taiyuan* 030051, *Shanxi*, P. R. China

Abstract: Abandoned polystyrene is one of serious pollutants arousing global wide attention. This paper suggesting a method to produce high detonation nitro-compositions using waste polystyrene as raw material and dense nitric acid as nitrating agent, has determined the process conditions such as reaction temperature, reaction duration, and nitric acid to polystyrene ratio. It also identifies that the addition of a composite addictive into the nitrating liquor can effectively diminish the erosion of the nitric acid residue after reaction thus making it possible to put the explosive into direct and safety application. Performance tests of the explosive show that the detonation rate is 9,100 $m \cdot s^{-1}$, brisance is 26 mm (lead cylinder compression test) and explosion heat 6,008 $kJ \cdot kg^{-1}$. Tests also prove that the explosive has a higher explosion property than RDX and a lower mechanical sensitivity than TNT. Explosive produced in this way is a new member of the family of high detonation compositions.

Keywords: waste polystyrene; high detonation composite explosive; composite additive; explosive properties

Preface

In recent years, the demand of polystyrene polyfoam increased greatly with rapid development of packing and food industries. According to the statistics of China Plastic Association in 1999, about one minion tons of waste white polyfoam is discarded every year, which is seen here and there. One say the white waste pollution has been doing harm to our own living surroundings and endangered man's living. Leaders of different countries and the world Environment Organizations have declared clearly that white waste pollution is a global problem.

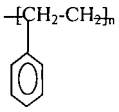
After several years of investigation, it is found that some domestic factories use degraded waste polystyrene to manufacture distance piece against heat, furnishing and decorating plant, flower vase, ruler, furniture, glutinous cement agent, etc. While, the second contamination of the traditional ways of degradation and whether the by-product after degradation can undertake the market competition, need to be considered, for instance, production of some resolving smearing

agent made of waste polystyrene is also endangered. There are some foreign countries ways of manufacturing smearing agent are very strict in degradation technology and resolving agent. Also some foreign countries use polystyrene to produce explosive while the high cost is a problem. The method to produce industrial explosive by nitrated waste polystyrene avoided the second contamination and lowered the cost and solve the problem of white waste pollution, waste reclamations and the high cost of industrial explosive once and for all and add new types of domestic nitro-polystyrene explosive with great value of environmental protection and manufacturing.

1 Experiment principle

1.1 Constitution and structure of waste polystyrene

Waste polystyrene is a kind of industrial packing material waste, which is called formable polystyrene (FPS), whose average formula weight is 295 thousand, structure formula is



1.2 Nitrating theory

With methylene (methane) and phenyl in the structure of waste polystyrene, methylene in phenyl is equal to the provided group making increased the density of para- and ortho- in phenyl electron cloud, but orth-phenyl has space effect, reducing the impact of positive nitro-ion toward ortho-. While in para-phenyl, without obstruction in space, it is advantageous for the movement of positive nitro-ion. In theory, under certain nitrating conditions, the nitrating rate of para-phenyl is grater than that of ortho-phenyl. From the new point of common nitrating theory, such as the nitration of phenyl methane, methyl in phenyl can not be nitrated. Consequently, methylene chain in waste polystyrene cannot be nitrated unless in the strong nitrating system methylene nitration can occur as to form the compound C-NO_2.

The purpose of this design is to manufacture nitro-mixed power by waste polystyrene, while dense nitric is explosive and a nitrating agent. Hence dense nitric to make waste polystyrene nitrated. When the nitrating system is rigorous enough, major nitration of para-methyl happens as to form para-nitrated material; when the nitrating ability of the system becomes weak or even the system completely lost the ability to nitration, the remaining waste nitric with absorbent or

thickening agent will become a kind of thick-nitrated mixture. Waste polystyrene can also be nitrated according to the theory of nitrating phenyl with dense nitric. When the density of nitric is over 85%, waste polystyrene can be nitrated. When the density of nitric is over 95%, it may start fire. Thus the density of nitric in this design is suggested between 85% and 95%.

1.3 Thickening agent

After waste polystyrene is nitrated by density nitric, some waste nitric and water is produced. To make the mixed powder used in industry, some acid resistant and nitric-absorbing addictive are needed. The absorbing theory is on the basis of physical or chemical absorbing, and selecting absorbent addictives, to make minimized the amount of refuse acid on the surface of the mixed powder.

2 Experiment

2.1 Materials and agents

waste polystyrene (foam grade); dense nitric acid; thickener;

2.1 apparatus

① nitrating reactor

② electric agitator

③ thermometers

2.2 operating program

At first, put 1kg 89% dense nitric acid prepared into a reactor, about 190g waste polystyrene that has already been comminuted, in batches added to the reactor. At the same time, reactive temperature is controlled no more than 50℃, in order to prevent the explosion accident. If the temperature is over, the cooling water can cool it. This experiment needs one or two hours or so,. When the reaction carries through, 50g thickener is in batches added into the reactor. After adding these agents, reactive products start flowing out, and be wrapped an sealed.

3 Results and Discussion

3.1 Test results.

Use waste polystyrene as the raw material, experiment with nitric makes its density between 85% and 95%, select highly absorb agent addictives for waste nitric, make the temperature of nitrating reaction between 45℃—50℃ with reacting time limit from one to two hours. Through orthogonal experiment, with exploding rate and brisance as the standards, the preferable

technological datum of using waste polystyrene to make mixed powder are as follows:

Nitric density: 89%

Nitrating temperature: 45℃—50℃

Nitrating time: 1.5 hour

Thickening agent: 5%

The test results are listed below:

Result of waste polystyrene property test

Number	Property (Parameter)	Test mean value
1	Detonation velocity (m/s)	9100
2	Lead cylinder value (cm)	26
3	Gap distance (mm)	10
4	Impact sensitivity (%)	0
5	Density (g/cm^3)	1.2
6	Calorific value (kJ/kg)	100

It shows that the detonation velocity of this mixed powder is greater than that of TNT for mtilitarian use and RDX. With its greater lead cylinder value and calorific value, and shorter gap distance and lower mechanic sensitivity, greater detonation velocity and lower sensitivity feature this industrial mixed powder, which can be used in various blasting, such as hard rock blasting.

3.2 Discussion

3.2.1 Particle size of waste polystyrene

The particle size of waste polystyrene affects nitrating thoroughness and explosive strength. Bigger particle size may lead to incomplete nitration, while smaller particle size raises a higher demand for comminatory. In these conditions, it is concluded that proper particle size is about one mm in diameter.

3.2.2 Nitric density

Higher the nitric density, greater the nitrating ability. In experiment with nitric whose density is over 95%, it is found that waste polystyrene becomes black and because of overheat in part. With nitric density below 95%, no above-mentioned phenomenon with nitric density below 85%, nitrating reaction is very faint, and large amount of water affects the actual explosion. After sufficient experiment, it is found that nitric density around 89% is best.

3.2.3 Time limit of nitration

Because the density of waste polystyrene is very small, and its relative volume is bigger, the addictive rate should not be too fast and not too slow. Add materials step by step while stirring in nitration.

Weak nitrating ability causes long time nitration, hence nitrating time had better control in 1.5 hour.

3.2.4 Addictive

Over nitrating, definite addictive must be added to the reactor, or the present nitric acid will limit the apply of this explosive. So how to select a kind of proper addictive is the key to industrial use.

But with the increasing of addictive, the system's viscosity becomes increased. It demands sufficient stirring strength, which is essential to experiments and industrialization.

4 Conclusion

The better technological condition of prepare for nitro-explosive from waste polystyrene has been found through experiments. The detonation velocity and the brisance of this explosive are better than that of TNT and the mechanical sensitivity is very blow. This technology will form the foundation of eliminating white contamination and increasing new types of explosive.

Studies on Crystal Conversion of α-HMX into β-HMX & Its Separation

CAO Duanlin, CUI Jianlan, CHENG Jingcai

Dept. of Chemical Engineering, North China Institute of Technology,

Taiyuan 030051, *Shanxi*, P. R. China

Abstract: HMX is nowadays one of the high-energetic explosives with excellent comprehensive properties, the popular preparation of which was by means of acetic anhydride to convert α-HMX into β-HMX. Such conversion, however, involved the use of organic solvent deteriorating the working condition and was usually of low output and high cost. In addition, the method failed to synchronize the conversion of α-HMX crystal with the separation of prepared β-HMX particles. This paper proposes a new technological process in which α-HMX prepared by means of acetic anhydride is processed in nitric-acid solvent so that α-HMX in the solvent converts into β-HMX and that foreign matters as in α-HMX can be removed by activated oxidation. Simultaneously, different sizes of the β-HMX as in the solvent can be separated by precipitation. The results illustrate six (6) categories of β-HMX particles with acid value less than 0.02% can be achieved, which conform to the U.S. military standards. This process performs much better than that involving organic solvent; this method is of high output and low cost.

Keywords: HMX, nitric acid, activated oxidization, crystal conversion, gradation

Preface

HMX is nowadays one of the high-energetic explosives with excellent comprehensive properties. For its feature such as high explosion rate, high power and better stability to heat. It is widely used as high-energetic arm combat departments and is becoming basic powder charge.

There are many methods to produce HMX, and its conventional preparation was by means of acetic anhydride to convert α –HMX into β –HMX, because α –HMX made by this method is unstable. The conversion can become true by solvent or nitric acid process .The technology of this crystal conversion by the nitric acid process is studied in this paper, in the same time granularity grade is done, By-products nitrified can be oxidized and decomposed in high nitric acid solvent. After the decomposition of the by-products is almost accomplished, the aims of the crystallizing conversion and the granularity grade can be achieved by controlling some conditions such as the crystalline temperature, the time of keeping the temperature and the rate of stirring, etc.

1 Experiment principle

1.1 The component of the by-products

In general, in the technology of HMX prepared by the means of acetic anhydride, the by-products of HMX contain HADN, PHX, BSX, TAX, AcAn and SEX, etc. HADN can be easily dissolved in water, DPT can be easily decomposed and easily dissolved in low nitric acid, BXS can be easily decomposed in 70% hot nitric acid, the related research indicated that the other by-products can be also decomposed by means of exciting and oxidation. Of course, the little amount of HMX may be also decomposed at the same time.

1.2 Crystal conversion

If there are many types of crystals in a kind of chemical substance, the transition occurs among crystal shapes, that is crystal conversion issue. HMX has four kinds of crystal forms between the room temperature and melting point, but the β-crystal form is the best stable structure in the room temperature and has the highest density. The product is made up with most of α-HMX and a little of γ-HMX by means of acetic anhydride, so they need to be transited to β-HMX by way of crystal conversion.

The crystal conversion in organic solvent may be that solvent molecules pile up in crystal cell again, and then form new crystal shape. While in fact the transition in nitric acid is a re-crystallizing process, in this way of crystal conversion and crystallizing can be reached in the meantime.

1.3 Exciting oxidation

When the temperature is suddenly raised, many organic chemical compounds may be violently decomposed. On the base of this principle, the by-products, which are produced in the technology of the preparation of HMX by the means of acetic anhydride, may be carried on the rapid decomposition reaction in order to rid of it.

1.4 Crystallizing and grade principle

Solution state is the main theoretical basis of the principle of crystallizing and grade, and it generally has three states: unsaturated state, saturated state and super saturated state. They divide T-S chart into unsaturated zone and supersaturated zone.

According to the different supersaturated degree, the whole supersaturated zone is divided into the first sub-stable zone, the second sub-stable zone and unstable zone. In the first sub-stable zone the solution don't spontaneously form crystal core, if the crystal seeds are placed in the zone, the crystal will grow on the crystal seeds; In the second sub-stable zone, unlike the immediate crystallization in the unstable zone, crystallization can occur spontaneously with certain intervals, which are called delay zone. In the unstable zone the solute can be immediately crystallized in the solution and spontaneously form crystal core.

When one substance is separated out of the solution, there are usually two clear steps, at the first, the fine crystal core forms which is the center of crystal, then the core gradually grows up and becomes crystal, but the usual rate of crystallizing is regarded as both the formation rate of crystal core and the growing rate of crystal.

Supposed r_c and r_g are the formation rate of crystal core and the growing rate of crystal, there are the two formulae:

$$r_c = \frac{dN}{dt} = k_c \Delta c^m \qquad r_g = \frac{dl}{dt} = k_g \Delta c^l$$

where: $\frac{dN}{dt}$ describes the number of the crystal core per time unit and volume.

$\frac{dl}{dt}$ refers to the growing of crystal size.

Δc refers to supersaturated degree.

k_c and k_g are the constants of the producing rate of the crystal core and of the growing rate of the constants.

$$r_c / r_g = k_c / k_g \cdot \Delta c^{m-1} = k \cdot \Delta c^{m-1}$$

From the above, the greater Δc, the faster r_c, which is beneficial to the preparation of small grains; the smaller Δc, the faster r_g, which is beneficial to the producing of large grains; if Δc is controlled between r_c and r_g, this is advantage to preparation of appreciate grains. In this paper the granularity grade is designed on the base of basic crystallizing principle that is just described.

2. Experiment

2.1 Materials and Agent

α –HMX(made by oneself)、industrial nitric acid

2.2 Apparatus

① 500 ml three-mouth-beaker

② electric mixer with no-grade adjusting volt

③ transformer with adjusting volt

④ temperature meter

⑤ constant temperature water trough

⑥ standard mesh

2.3 Operating program

At first, 10g α –HMX is put in three-mouth-beaker; the second, it is dissolved by 72% nitric acid under the

stirring condition; the third, the solution is slowly heated to 56 ^{0}C and then rapidly to 67 ^{0}C. When yellowish-brown mist gives off, stopped heating the solution immediately in order to make some by-product decomposed for 1~2 minutes. The solution becomes clear. There are some crystals separating out of the solution. When the temperature of the solution cools down about 48 ^{0}C. According to the different demand of the grade, granularity grade is carried on by controlling appropriate crystalline temperature、crystalline time and stirring velocity. After all of crystals are elementarily separated out, the solution is cooled to below 30 ^{0}C, filtered with quartz funnel, washed three times in cold water, dried and then analyzed and examined.

3. Results and Discussion

3.1 Experimental results of six categories of β -HMX particles (see 1—6 respectively)

Table 1 Results of grade 1

Number	α -HMX /g	78%HNO_3 /ml	Crystalline temperature/℃	Crystalline time/min	Stirring speed /r · min^{-1}	Yield /%
1	10	140	51	40	200	70.2
2	10	140	52	42	180	71.0
3	10	140	51	37	190	72.1
4	10	140	51	36	200	72.6
5	10	140	52	38	190	71.8
6	10	140	51	39	200	71.9

Table 2 Results of grade 2

Number	α -HMX /g	78%HNO_3 /ml	Crystalline temperature/℃	Crystalline time/min	Stirring speed /r · min^{-1}	Melting point/℃	Yield /%
1	10	120	18-20	<1	380	284.5	73.4
2	10	120	18-20	<1	400	284	73.8
3	10	120	18-20	<1	500	285	73.6
4	10	120	18-20	<1	500	285	73.5

Table 3 Results of grade 3

Number	α -HMX /g	78%HNO_3 /ml	Crystalline temperature/℃	Crystalline time/min	Stirring speed /r · min^{-1}	Melting point/℃	Yield /%
1	10	140	50	156	120	283.2	69.6
2	10	140	51	153	120	287	70
3	10	140	51	149	130	282	69.8
4	10	140	52	156	130	282	70.1
5	10	140	51	152	125	283	70
6	10	140	51	156	125	283	70.2

Table 4 Results of grade 4

Number	α -HMX /g	78%HNO_3 /ml	Crystalline temperature/℃	Crystalline time/min	Stirring speed /r · min^{-1}	Melting point/℃	Yield /%
1	10	130	48	106	100	281.5	72
2	10	130	47	114	105	281	71.4
3	10	130	47	112	100	281	72
4	10	130	48	107	100	282	71.6
5	10	130	47	106	100	281	71.7
6	10	130	47	108	100	282	71.8

Table 5 Results of grade 5

Number	α -HMX /g	78%HNO_3 /ml	Crystalline temperature/℃	Crystalline time/min	Stirring speed/r · min^{-1}	Melting point/℃	Yield /%
1	10	150	15-18	<1	600	286.5	75
2	10	150	15-18	<1	600	285.5	75.4
3	10	150	15-18	<1	600	285.6	74.2

Table 6 Results of grade 6

Number	α -HMX /g	78%HNO_3 /ml	Crystalline temperature/℃	Crystalline time/min	Stirring speed/r · min^{-1}	Melting point/℃	Yield /%
1	10	140	51	15	260	282.5	76.1
2	10	140	51	15	260	283	76
3	10	140	52	13	260	283.5	76
4	10	140	51	14	260	283	75.8

Data in table 1—6 show that average yield of crystal conversion is about 73%. The yield of HMX by this technology is lower than that of HMX by the solvent process, but it can obtain the products with the different particles size. So the technology has good industrial prospects.

3.2 Discussion

3.2.1 Oxidation of by-products

The crude product α –HMX, prepared by the means of acetic anhydride, contains about 10% by-products. Before crystal conversion and granularity grade, the by-products must be oxidized and got rid of. Though the yield of HMX by exciting oxidized method in the rapidly heating condition is higher than that of HMX by the slowly oxidizing and decomposing method, its relative safety is worse than the later; in addition, through many experiments, there is no the phenomenon of the violet reaction with abrupt explosion in the former.

3.2.2 Crystalline temperature

Under the serious control of crystalline temperature, knowing of the homogeneous primary nucleation is one of necessary conditions. To get big grains, crystalline temperature must be not more than 45 ^{0}C, when the temperature is no less than 30 ^{0}C, small grains will be obtained.

3.2.3 Crystalline time

The long crystalline time is advantage to the preparation of grade 3 HMX, the short time benefit to the preparation of grade 2 and grade 5 HMX.

3.2.4 Stirring velocity

The rate of stirring is not above 150 $r \cdot min^{-1}$ in the process of the preparation of grade 3 and 4 HMX; when grade 5 HMX is produced, the faster rate of stirring, the better effect; the preparation of the other grade of HMX desires the proper rate of stirring.

4. Conclusion

Products of six categories of HMX, with acid value, melting point and crystal shape conforming to the U.S. military standards, average yield above 73%, are prepared by means of decomposing rapidly impurities as in α –HMX and controlling different crystalline conditions.

References:

1. Michael L. Levinthal, Crystallization of Beta HMX, USP 4785094, Sep.26, 1987
2. Rothrock.M.D, DSMO Recrystallization of HMX and RDX, AD-A 096096, 1987
3. Balwant Singh, L.K.Chaturvedi & P.N.Gadhikar, A Survey of the Cyclotetramethylene tetranitramine, 22 Feb.1997
4. W.K. Burton, N. Cabrera, and F.C. Frank, Crystal Growth and the equilibrium structure of its surface, Phil. Trans.Rou.Soc.A243, P229~385,1950
5. Cao Duanlin etc. Acta Armamentarri (Fascicule of Explosives and Propellants), A study on the Improvement of process of HMX by the Means of Acetic Anhydride. 1996(2)

The Influence of Fluorine-Containing and Fast Burning Additives on the Combustion of Highly Metallized Mixtures

V.E. Zarko, V.N. Simonenko, A.B. Kiskin, S.V. Larionov* and Z.A. Savelyeva*

*Institute of Chemical Kinetics and Combustion, * Institute of Inorganic Chemistry*

Russian Academy of Sciences, Novosibirsk 630090, Russia

ABSTRACT

The effect of fluorine-containing and fast burning additives on the combustion behavior of highly metallized pyrotechnic mixtures (PM) based on Mg, Al, and B has been studied. Differential thermal analysis has been conducted of the mixtures Me+Ox and Me+Ox+fluorine-containing additive. The fluorine-containing additives seem to be most effective in the Al-based mixtures. In this case the early heat release peaks (DTA) are recorded, ignition temperature decreases, the pressure exponent is modified in the burning law. The fast burning additives (complex compounds) affect the combustion of PM containing Mg, Al, or B and the result depends on the additive properties and its decomposition temperature. Thus, the introduction of fluorine-containing and fast burning additives into highly metallized PM at a rate of 5% in excess of 100% allows substantial modification of the burning law, ignition temperature and dispersion extent.

1. INTRODUCTION

Heterogeneous metallized pyrotechnic mixtures (PM) are widely used in various technical applications. The use of metallic fuel in the combustible mixtures results in a high energy release in the combustion wave. Of great utility are Mg, Al, and B as fairly energetic, safe and nontoxic materials [1,2]. Either ammonium and potassium perchlorates or the nitrates of sodium, potassium, strontium, etc. serve as their oxidizers. The variety of conditions for the application of pyrotechnic mixtures determines the number of scientific problems in studying their combustion and ignition characteristics. The goal of the present work was to analyze the influence of fluorine-containing and fast burning additives on the combustion behavior of highly metallized compositions containing Mg, Al or B and inorganic oxidizers. The results of DTA as well as data on the burning rate and dispersion extent are presented.

2. INSTRUMENTATION AND EXPERIMENTAL

Differential thermographic analysis was carried out using OD-103 derivatograph (Hungary). The heating rate was 10^0C/min; the sample weight equaled 20 mg. The samples for the radiative ignition tests were manufactured by pressing at P= 5000 atm. In this case the density approached about 90% of the theoretical maximum one. The samples were 5 and 10 mm in diameter and 7 to 15 mm in length. As a binder, we used iditol added at a rate of 3.8%. The samples were ignited at P=1 atm by either the radiant flux of a Xenon lamp DKSR-10000 or radiation of Nd-YAG laser LTN-101 (λ =1.06 μm, 150 W).

In experiments at atmospheric pressure we recorded simultaneously the signals of reactive force (as described in [3]), photodiode (total flame radiation) and thermocouple. In experiments at P>1 atm we recorded the time of sample combustion by processing the signal of pressure in a constant-volume bomb (68 cm^3). Burning rate was determined as a product of division of the sample length by the combustion time. The ignition of samples at P >1 atm was carried out using a surface igniter layer initiated by electrically heated wire. In addition, condensed combustion products were collected on the bottom of bomb and examined.

3. SYNTHESIS OF FAST BURNING ADDITIVE

At present time fast burning substances (FBS), as components of rocket propellants and pyrotechnic mixtures, are widely used in practice. The general principles of the FBS synthesis [4] and some concrete methods [5] are described in literature. The method of preparation of novel complex compound $Ni(OD)_2(ClO_4)_2 \cdot 4H_2O$ (OD = oxalyldihydrazide) is described first in the present work.

1.2 g (0.01 mole) of oxalyldihydrazide was added to the solution of $Ni(ClO_4)_2 \cdot 6H_2O$ (2.3 g, 0.006 mole) in 10 ml of 0,1M $HClO_4$. The oxalyldihydrazide was dissolved by heating this mixture to 50-60 °C, and then the solution was filtered. 5 ml of 2M $HClO_4$-ethanol (1:1) mixture was added to the filtered solution and the mixture was left to stay in room conditions. After 5 h the resulting blue precipitate (residue) was filtered with suction, washed with water-ethanol mixture (1:1), and dried in air.

Available yield equals 0,85g, which is 30 % of expected. Elemental analysis of the residue gave the following (%): C 9.0; H 3.0; N 19.0; Ni 10.9. At the same time calculations for $C_4H_{20}N_8O_{16}Cl_2$ Ni produced (%): C 8.5; H 3.6; N 19.8; Ni 10.4.

According to the TG analysis data the weight loss in the temperature range 60-120°C equals 12% while the calculated content of water in $Ni(OD)_2(ClO_4)_2 \cdot 4H_2O$ is 12.7%. Under further heating the exothermic decomposition takes place at 290°C.

IR spectrum consists of the following bands (ν, cm^{-1}): 3600, 3535, 3323, 3266, 3225, 3050, 1660, 1607, 1520, 1500, 1250, 1180, 1085wide, 965, 840, 625. The Ni content was found by complexonometric titration with Trilon B solution; analysis for C, H, and N was performed at the Analytical Laboratory of the Institute of Inorganic Chemistry. IR spectrum was recorded by Specord 75 IR spectrophotometer. The thermal analysis was performed using the Paulik, Paulik and Erdey (Hungary) derivatograph.

4. RESULTS AND DISCUSSION

4.1. Components

To prepare pyrotechnic mixtures, Mg (70 - 340 μm), Al (50 - 350 μm) and B (amorphous) were used as fuels, and $NaNO_3$ (melting temperature T_m = 308°C and decomposition temperature T_d = 600 - 700° C) or $KClO_4$ (T_m = 617° C, T_d = 650° C) were used as oxidizers. As additives, we employed fluorine-containing substances NaF, BaF_2, NH_4BF_4, $C_4F{\cdot}O$ and $5ClF_3$ as well as fast burning substances that included AG (aminoguanidine), $Ni(OD)_2(ClO4)_2 \cdot 4H_2O$ and $Cu(AG)_2(ClO_4)_2$. The last compound was produced as described in Ref. [5]. The method described above in Section 3 was used to synthesize the $Ni(OD)_2(ClO_4)_2 \cdot 4H_2O$ complex. Characteristic temperatures for melting, boiling and decomposition of the additives employed are given below.

NaF	T_m - 996° C, T_b - 1704° C
BaF_2	T_m - 1280°C, T_b - 2260° C
NH_4F	T_d = 168° C
NH_4BF_4	T_d = 354° C
$C_4F{\cdot}0{,}5ClF_3$	T_{flush} ~ 400° C
$Cu(AG)_2(ClO_4)_2$	T_{flush} ~ 270° C
$Ni(OD)_2(ClO_4)_2 \cdot 4H_2O$	T_{flush}~ 290° C

Here T_b is the boiling temperature and T_{flush} is the thermal explosion temperature.

4.2. Differential thermal analysis

Differential thermal analysis (DTA) has been carried out of the basic mixture fuel/oxidizer and of the mixtures containing fluorine-containing additives. The content of fluorine-containing additives in all cases was 5% in excess of 100%. The mechanisms of Mg, Al, and B oxidation are presented in Refs.[1,6]. It is known that the magnesium oxide film is porous (Pilling-Bedworth coefficient β = 0.81) and weakly prevents the oxygen diffusion to the metal

surface. The Al oxide film has highly protective properties, β=1.28. It is commonly assumed that the Al oxidation could become vigorous only above the point of the metal melting (660^{0}C). Protective properties of B oxide are worse than those of Al oxide (β = 4.1, thick oxide layer). The amorphous boron is slowly oxidized in the air at room temperature.

Table 1 summarizes some thermophysical properties of metals and their compounds with oxygen, chlorine, and fluorine. The characteristic temperatures of heat release peaks for all mixtures studied are given in Table 2. Figures 1 and 2 exemplify the records of DTA curves for the mixtures of 25% $NaNO_3$ and 75% Al or 75% B.

Table 1. Thermophysical properties of metals and their compounds.

Substance	β	T_m, ^{0}C	T_b, ^{0}C	Refs.
Mg	-	650	1093	11
MgO	0,81	2807	3157	6,10
$MgCl_2$	2,82	710	1420	
MgF_2	1,39	1246	2240	
Al		660	2518	11
Al_2O_3	1,28	2477	3727	6,10
$AlCl_3$	5,45	190	1000(sublimation)	
AlF_3	2,74	800	1000(sublimation)	
B		2027	3866	11
B_2O_3	4,01	455	2067	6,10
BCl_3		-80		
BF_3		-127		

The analysis of DTA results and the data on the thermophysical properties of metal fluoride compounds allows assumption that the formation of fluoride film on the metal surface mostly prevents the Mg oxidation (it starts at higher temperatures). On the contrary, in the same conditions the oxidation temperature for Al and B decreases.

When observing data in Fig.1 and Table 2, it is seen that the first stage of Al (without additives) oxidation in pure $NaNO_3$ melt starts after metal melting. Thereafter the Al oxidation continues at higher temperature. If the mixture contains the fluorine-containing additives, they decompose under heating and the products of their decomposition react with the Al oxide film. The possible ways for interaction of Al and Al_2O_3 with F-additives decomposing at a relatively low temperature are shown below. The product of this interaction AlF3 has no protective properties and it sublimates at T $\geq$ 1000^{0}C.

$$NH_4F \overset{168^oC}{\rightleftharpoons} NH_3 + HF$$

$$NH_4BF_4 \overset{354^oC}{\rightleftharpoons} NH_3 + HBF_4$$

$$HBF_4 \overset{t^oC}{\rightleftharpoons} BF_3 + HF$$

$$6HF + Al_2O_3 \xrightarrow{t^oC} 2AlF_3 + 3H_2O$$

$$6HF + 2Al \longrightarrow 2AlF_3 + 3H_2$$

The above mentioned decomposition and melting temperatures for oxidizers and fluorine-compounds are valid only for pure substances. The mixtures have, as a rule, lower temperatures of phase transition. To determine this temperature, we performed experiments on heating the mixtures containing 50% of oxidizer and 50% of F-additive. The components mixing was carried out with the help of a rubber plug on a tracing paper during 10 - 12 min. Thereafter, the sample was placed on a heating plate and heated up to 360^0C at a rate of 10 - 25^0C/min. The visual observation was performed with a microscope. Decomposition temperature of fluorine-containing compounds was recorded by the appearance of vapors and their condensation on a cover glass located 6.5 mm above the sample. Oxidizer melting was recorded by changes in the crystal shape. Experimental observations for different mixtures are given below.

1. $NaNO_3$ +NaF; fusion of $NaNO_3$ at ~ 300^0C, further heating up to 360^0C proceeds without changes. The residue contains the NaF grains and $NaNO_3$ melt.
2. $NaNO_3$ +NH_4F; at the temperature ~ 120^0C simultaneous decomposition of NH_4F and complete melting of the mixture occurs.
3. $NaNO_3$+NH_4BF_4 ; at the temperature ~ 180^0C decomposition of NH_4BF_4 and complete melting of the mixture occurs.
4. $KClO_4$+NH_4F; at the temperature ~ 160^0C decomposition of NH_4F starts, no mixture melting up to 360^0C.
5. $KClO_4$+NH_4BF_4; at the temperature ~ 300^0C decomposition starts, no mixture melting up to 360^0C.

According to DTA data (Fig. 1, Table 2), the first stage of Al reaction in the mixture of $NaNO_3$ and fluorine-containing additives starts at 300 - 400^0C. The second stage begins at the temperature about 600^0 C, i.e. before Al melting. Presumably, the products of F-additive decomposition react with Al oxide film, destroy it and accelerate Al oxidation. The action of NaF seems to have no effect on Al oxidation because this substance does not decompose at the temperatures of oxidizer melting and melts at higher temperature (996^0 C). Probably, the interaction of NaF with Al and its oxide occurs within the melted oxidizer layer.

The first stage of B oxidation (Fig. 2, Table 2) in melted $NaNO_3$ is recorded at 460^0 C. Introduction of NH_4F and NH_4BF_4 additives shifts the first peak of heat release towards the temperature $\approx 250^0$ C. If $NaNO_3$ is substituted by $KClO_4$, the fluorine-containing additive has no noticeable effect on the process of B oxidation under heating. This can be assigned to the difference in the temperatures of $NaNO_3$ (308^0 C) and $KClO_4$ (617^0 C) melting. When the Ox /B/fluorine - additive mixture contains Mg, the interaction may follow the scheme:

$$Mg + 2B \rightarrow MgB_2$$

$$MgB_2 + HF \rightarrow MgF_2 + H_2 + \text{boranes mixture } (B_4H_{10}, B_4H_6, \ldots)$$

Mg and MgO can react with HF according to:

$$Mg + 2HF \rightarrow MgF_2 + H_2$$

$$MgO + 2HF \rightarrow MgF_2 + H_2O$$

Table 2 indicates that the beginning of Mg oxidation in the presence of NH_4F is shifted from 550^0 C to 400^0 C. However, such an effect is not observed for NH_4BF_4 and NaF.

Table 2. Characteristic temperatures of heat release peaks on DTA curves

Composition (% mass)	Basic	Additive 5% in excess of 100%				
		NaF	BaF_2	NH_4F	$C_4F{\cdot}0.5ClF_3$	NH_4BF_4
75Mg + 25$NaNO_3$	530	530, 680	570, 620	400 ,530 610	480 ,660	710
75Mg + 25$KClO_4$	530 ,590	590	---	---	520 ,710	710
75Al + 25$NaNO_3$ endo-660	690	300,450 600	320,460,600	250, 380 580	450, 580	250, 580, 700
75Al + 25 $KClO_4$ endo-660	690	530, 700	580, 700	---	480, 630	480
75B + 25$NaNO_3$	460, 700	450,650	450, 700	250,680	450, 700	250, 680
75B + 25 $KClO_4$	500, 680	480, 650	550, 730	-----	510, 710	510, 710
Mg+AI+$NaNO_3$	530, 690	530,630	-------	-------	500,710	250,600
Mg+B+$NaNO_3$	460,530 700	420,550 650	-------	------	---------	250,800

Thus, according to DTA data the influence of fluorine-containing compounds seems to be most pronounced upon combustion of the mixtures containing Al and B.

4.3. Combustion of basic PM at P=1 atm

Experiments on the determination of the burning rate and qualitative characteristics of the dispersion extent upon combustion of (Mg+Al+oxidizer) and (Mg+B+oxidizer) mixtures were carried out in the air. Burning rate was determined on the basis of the sample burning time and geometrical characteristics of the combustion product residue were evaluated. Figure 3 shows that for the samples containing two metals (20% Mg+Al or 20%Mg+B) the maximum of the burning rate is achieved at a total metal concentration of about 40-60 %.

To classify the combustion product residue by geometrical size, we distinguish four groups of carcass-formation:

I – skeleton carcass is formed that resembles the shape of the initial sample;

II - scales of 2-4 mm thickness are formed over the sample diameter;

III – scales of 3-5 mm size are formed;

IV - scales less than 2-3 mm in size are formed.

Examination of the combustion residues shows that a dispersion extent decreases in the mixtures with $NaNO_3$ when the metal content exceeds 50%. In this case the scales are formed of the size equal to the sample diameter and 2-4 mm thickness (II group). After combustion of the mixtures containing more than 70% of metal the large slag pieces or a skeleton carcass resembling the initial charge are left (I group).

The samples with $KClO_4$ have a broader dispersion extent range. When the metal content does not exceed 50-60%, the metal dispersion is observed in the form of large droplets and scales of 2-4 mm in size. When the metal content is higher than 60%, the scales become larger with characteristic size of the sample diameter and thickness of 2-4 mm.

Similar results are reported in Refs. [7-9], where the combustion characteristics of PM with the different content of metal (Mg, Al) have been studied. It has been shown that in the mixtures with $NaNO_3$ [7] the maximum of the burning rate and heat release are realized with the Mg and Al contents reaching 35-50% (depending on the component grain size and oxidizer type). With further increase in the metal content, the gas release and metal dispersion extent decrease and the process of carcass-formation starts.

Of practical interest are the combustion of PM containing more than 50% of metal and the possibility of controlling dispersion extent and the burning law for such formulations.

4.4. Combustion of PM with additives at P=1 atm.

The dependence of the burning rate on the metal content (combustion of sample with L=10-15 mm, ∅10mm) and geometrical characteristics of the residues have been studied. Figure 4 shows the dependence of the burning rate on additive concentration for PM containing 75% of

metal. It is seen that the influence of additive on the burning rate becomes noticeable already with 2-3% additive content. The diagram (Fig. 5) shows changes in the burning rate and dispersion extent in dependence on the additive type for the same PM, containing 5% of additive. Pure fluorine-containing additives have rather high melting temperature 800-1300^{0}C which is higher than that of the burning mixture surface. It is expected that in the mixtures under study the melting temperature of these additives exceeds that of the metal. Their influence on the process of PM combustion is likely to be weak and the interaction with metal is possible only in oxidizer melt. The additives that decompose at the burning surface temperature or the lower one have the greatest effect on the burning rate and dispersion extent. These additives include (see Fig. 5) all studied FBS as well as fluorine-containing additives NH_4F, NH_4BF_4 and compound $CuF{\cdot}0.5\ ClF_3$ that decomposes exothermally at about 400°C. For subsequent experiments at elevated pressures the additives have been chosen that considerably affect the PM burning rate and decrease the degree of metal agglomeration. As follows from Fig. 5, these substances decrease the PM burning rate by 20-40% and increase the dispersion extent at atmospheric pressure.

4.5. Combustion of PM at elevated pressure.

Experiments were carried out in a constant-volume bomb. The pressure and time of sample combustion were recorded. Figures 6 and 7 show the dependence of the burning rate on pressure for the mixtures containing 20% of Mg and different amount of Al and B. Total content of metal varied from 20% to 80%. The mixtures had as additive either NH_4BF_4 or complex FBS in amount of 5% in excess of 100% (the complex FBS contained 30% of $Ni(OD)_2ClO_4{\cdot}4H_2O$ and 70% of $Cu(AG)_2(ClO_4)_2$). It is seen that as the metal content in the mixture increases, the mean level of the burning rate and the pressure exponent decrease. Figure 8 presents the dependence of the burning rate on pressure for PM containing 25% of $NaNO_3$ + 25% of Mg + 50% of Al and 5% of the additive of different type in excess of total 100%. The introduction of fluorine-containing and fast burning additives decreases pressure exponent by a factor of 1.2-1.5. In this case the size of metal agglomerates decreases and the dispersion extent converts from group I to groups III-IV.

6. CONCLUSIONS

The results of the present work show that the fluorine-containing additives with decomposition temperature below than that of the PM burning surface affect the combustion

characteristics of highly metallized PM. It is proposed that the action of the additives of this type can be assigned to the interaction of the metal and its oxide with products of the additive decomposition in the condensed phase of the combustion wave. According to DTA data, the greatest effect is reached in the mixture based on Al. The AlF_3 compound is not the protective cover and Al oxidation starts before Al melting.

The FBS action depends on the thermophysical properties of the compound, decomposition temperature and the level of heat and gas release in the reaction zone of the condensed phase. Decomposition in the high-temperature zone of condensed phase resulting in the release of heat and gaseous products leads to destruction of the carcass on the burning surface of highly metallized PM. Totally, the introduction of studied fluorine-containing and fast burning additives leads to the following:

- decrease in the mean level of PM burning rate;
- decrease in the pressure exponent by 20-50%;
- increase in the dispersion extent of the burning surface.

The authors are grateful to L.G. Lavreneva for the synthesis of $Cu(AG)_2(ClO_4)_2$ and O.N.Zhitnitskaya for assistance in preparing the manuscript. Partial support of the NATO Linkage Grant # 976783 is acknowledged.

REFERENCES

1. P.G.Pokhil. A.F.Belyaev, Yu.V.Frolov, et al., Combustion of powder metals in active media. Moscow, Nauka, 1972.
2. A.A. Shidlovskii. Foundations of pyrotechnics. Moscow, Mashinostroenie, 1973.
3. V.N.Simonenko, and V.E.Zarko. Reactive force of combustion products as a measure of nonstationary combustion rate of powder. *Combustion, Explosion, and Shock Waves*, vol.17, No.3, pp.129-132 (1981).
4. V.P.Sinditskii and A.E.Fogelzang. Energetic materials based on coordination compounds. *Russian Chemical Journal*, vol. 41, No.4, pp.74-80 (1997).
5. A.V.Nikolaev, S.V.Larionov, L.G.Lavrenova, T.G.Leonova. Complexes of perchlorates and nitrates in Ni(II) and Cu(II) with aminoguanidine. *Izvest.SO RAN SSSR, Ser. Khim.Nauk*, vyp.1, pp.38-40 (1977).
6. A.L.Breiter, V.M.Maltzev, and E.I.Popov. Models of metal ignition. *Combustion, Explosion, and Shock Waves*, vol.13, No.4, pp.558-570 (1977).
7. Yu.F.Frolov, B.E.Nikolskii. Regularities of combustion of metallized mixtures. *Combustion, Explosion, and Shock Waves*, vol.19, No.5, pp.101-104 (1983).

8. L.Ya.Kashporov, Yu.V.Frolov, G.A.Ostretsov, V.N.Stepanov. Study of agglomeration and dispersion of condensed phase upon combustion of model compositions with a large content of powder metals. *Combustion, Explosion, and Shock Waves*, vol.11, No.1, pp.33-43 (1975).

9. R. Bhaskara Rao, P. Srinivasa Rao, and Harihar Singh. Agglomeration of magnesium particles in magnesium-sodium nitrate combustion. *Propellants, Explosives, Pyrotechnics*, 21, pp.319-324 (1996).

10. J. Glassman. Combustion, 3rd edition, Academic Press, San Diego, London, 1996.

11. E.W. Price. Combustion of metalized propellant. In "Fundamentals of Solid-Propellant Combustion" (ed. by K.K.Kuo and M.Summerfield), Progress in Aeronautics and Astronautics, vol. 90, ch. 9, pp. 479-513 (1984).

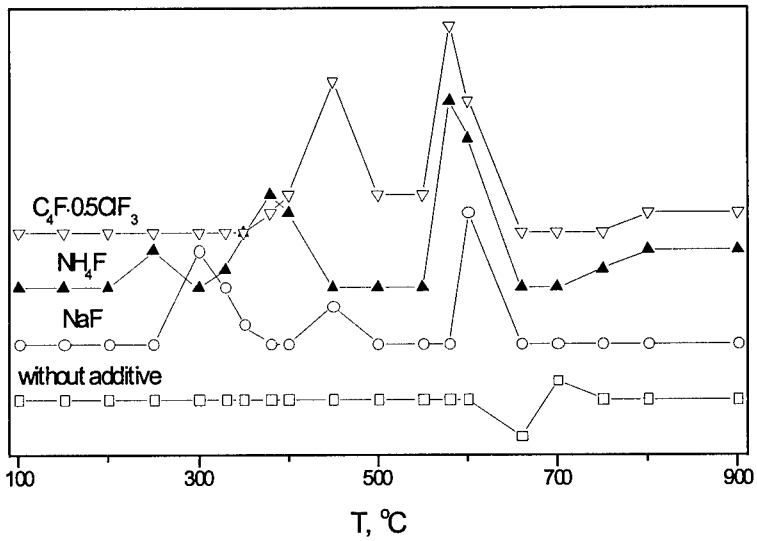


Fig. 1. DTA data for the mixture 25% $NaNO_3$+75% Al + additive (5% in excess of 100%).
Additives: ∇ - $C_4F{\cdot}0.5ClF_3$; ▲ - NH_4F; O – NaF; □ - without additive.

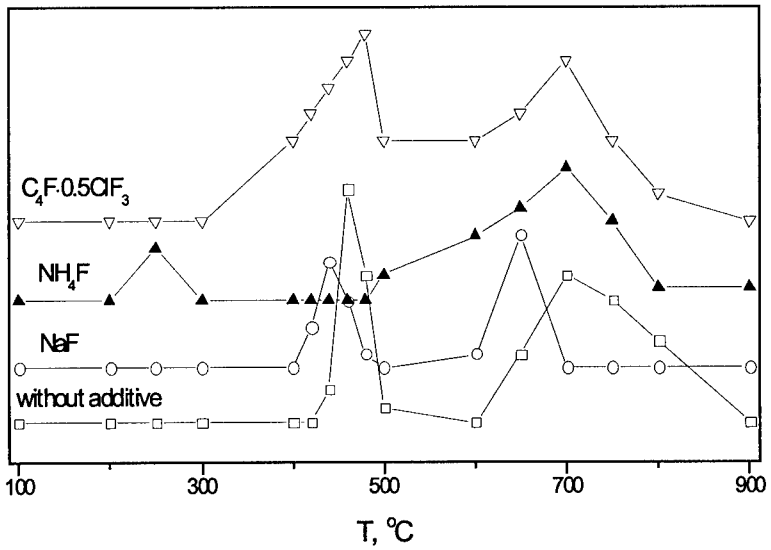


Fig. 2. DTA data for the mixture 25% $NaNO_3$+75% B + additive (5% in excess of 100%).
Additives: ∇ - $C_4F{\cdot}0.5ClF_3$; ▲ - NH_4F; O – NaF; □ - without additive.

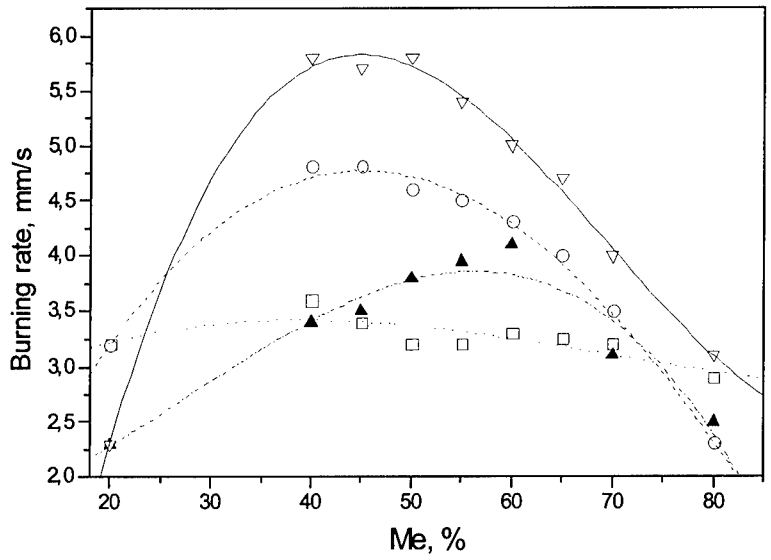


Fig. 3. Burning rate in air vs total metal content for the mixtures: □ - 20% Mg + $NaNO_3$ + Al; O - 20% Mg + $NaNO_3$ + B; ▲ - 20% Mg + $KClO_4$ + Al; ∇ - 20% Mg + $KClO_4$ + B.

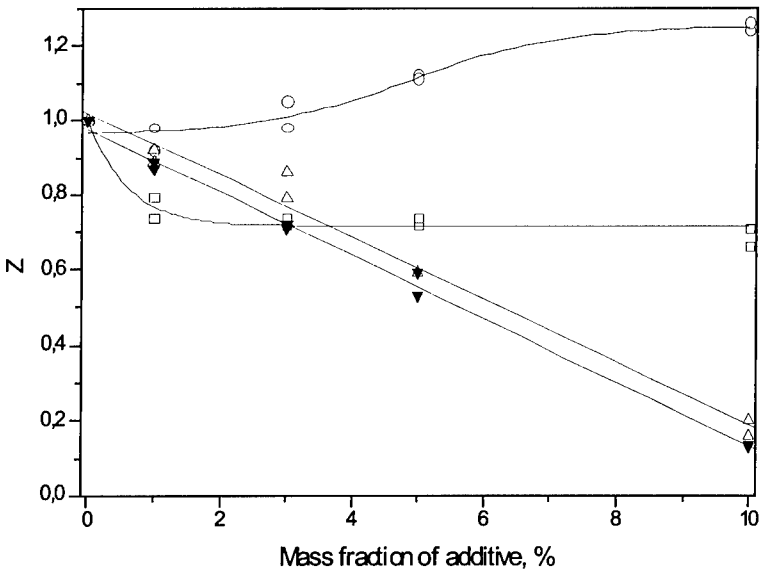


Fig. 4. Relative burning rate Z vs mass fraction of additive (in excess of 100%) for mixture 25% $NaNO_3$ + 25% Mg + 50% Al. Additives: ▼ - $C_4F{\cdot}0.5ClF_3$; Δ - NH_4F; O – NaF; □ - NH_4BF_4. Z = r (with additive)/r (without additive)

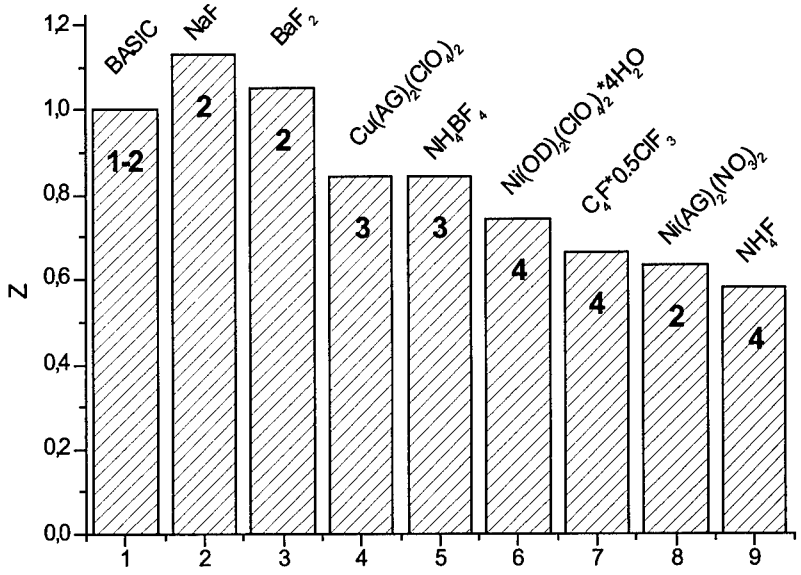


Fig. 5. Diagram of the relative burning rate Z and the degree of carcass-formation for the mixtures 25% $NaNO_3$ + 25% Mg + 50% Al + additive (5% in excess of 100%).

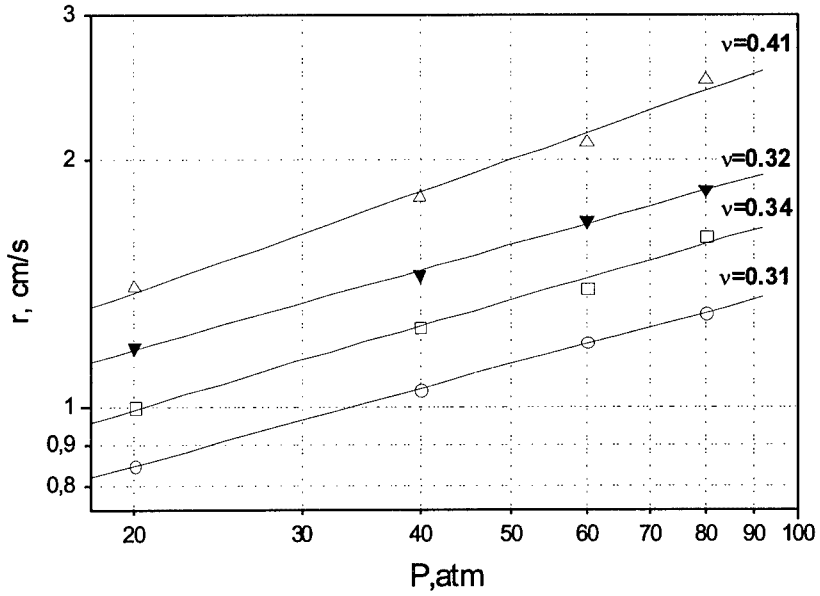


Fig. 6. Dependence of the burning rate on pressure for the mixture 20% Mg + $NaNO_3$ + Al + additive (5% in excess of 100%) with varying content of Al and additive type: O - 60% Al + NH_4BF_4; □ - 40% Al + NH_4BF_4; ▼ - 60% Al + complex FBS; Δ - 40% Al + complex FBS. Complex FBS: [30% $Ni(OD)_2(ClO_4)\cdot 4H_2O$ + 70% $Cu(AG)_2(ClO_4)_2$]

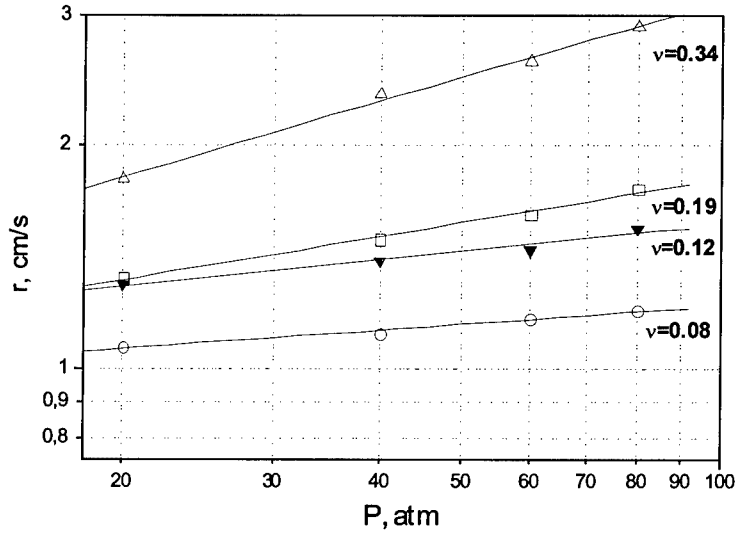


Fig. 7. Dependence of the burning rate on pressure for the mixture 20% Mg + $NaNO_3$ + B + additive (5% in excess of 100%) with varying content of B and additive type: O - 60% B + NH_4BF_4; ▼ - 60% B + complex FBS; □ - 40%B + NH_4BF_4; Δ - 40% B + complex FBS. Complex FBS: [30% $Ni(OD)_2(ClO_4)\cdot 4H_2O$ + 70% $Cu(AG)_2(ClO_4)_2$]

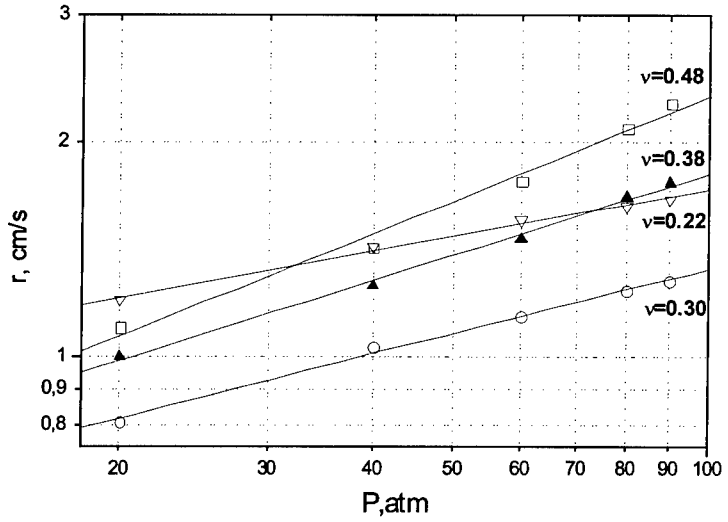


Fig. 8. Dependence of the burning rate on pressure in the mixture: 25% $NaNO_3$ + 25%Mg + 50% Al + additive (5% in excess of 100%) with varying additive type: □ - without additive; O - NH_4BF_4; ∇ - complex FBS [30% $Ni(OD)_2(ClO_4)\cdot 4H_2O$ + 70% $Cu(AG)_2(ClO_4)_2$]; ▲ - $C_4F\cdot 0.5ClF_3$.

Anomalous Combustion of NEPE Propellant with Defects

Du Lei
(Shanghai Astronautics Bureau of CASC, Shanghai, P.R.China, 200000)

He Guoqiang, Cai Timin, Liu Peijin, Wang Guohui
(Northwestern Polytechnical Univ., Xi'an, P.R.China, 710072)

Abstract : Combustion induced crack and gas cavity propagation in solid grain is of practical concerns to many rocket motor designers, as these defect propagations are the main reasons of combustion transition to detonation and of anomalous internal ballistic property during the motor firing. This paper presents the experimental research results from some recent test motor firings. A real-time X-ray radiography (RTR) system was used in this study. And some main factors of affecting crack propagation were researched, anomalous combustion and structural destroy of NEPE propellant sample with gas cavities were analyzed. The results provide some experimental bases and study ways of evaluating combustion safety of solid propellant grain with defects. Some conclusions in the paper had been applied to fault diagnosis of some full-scale motors firing test.

Subject terms: Solid Rocket Motor Defect Combustion NEPE Propellant

Introduction

During the development of SRM(solid rocket motor) grain, some defects such as cracks and gas cavities can always be the normal phenomenon. And while firing and combustion, gas with high-temperature and high-pressure will penetrate into these defect slots, which may be lead to convective burning and structural deformation. With the local pressure and stress increasing in the slots, the possibility of DDT (Deflagration to Detonation Transition) and grain destruction will increase. Even if not all of these abnormal conditions can result in rocket failure, they may cause internal ballistic performance of rocket to deviate significantly from the expected value. So, the research on combustion reliability of grain with defects has become the focus of rocket propulsion engineering. This paper presents some research results about three types of defects' effects on NEPE solid propellant combustion performance, which were got from a lot of experiments on propagation conditions of cracks and gas cavities, and describes the mechanism of anomalous combustion induced defects and destruction of the grain.

Analysis on Crack Propagation Process of Propellant

In terms of flow-dynamics and mechanics, the interface debond and gas cavity can be concluded into crack problems. It is possible that weak-bond turns into interface debond. And some actions such as gas filling in debond slots, surface burning of the slots, and coupling of mechanics and combustion etc., may lead to local grain destruction and debond propagation. This physical process is similar to the crack propagation in the propellant surface except for some differences in restrict conditions and propagation directions. For example, propagation

resulted from weak-bond is always extended along the interface, but crack propagation is always in a random way, even with some branches. When gas cavities expose to the combustion surface entirely, most of them will be pressed closely by high-pressure, then be filled up with hot gases. The maximum pressure and maximum stress in the cavities are relevant with exit condition and connection of the cavities. It is believed that although there are some differences in combustion behavior between on the internal surface of cavities and in the narrow slots, hydromechanics and structural mechanics behaviors of them are same. Thereby, the processes of gas filling, convective burning, defects propagation and stress-strain in the crack are studied using theoretical analysis and experiments methodology, which this paper mainly deals with.

Physical process of propellant crack propagation can be concluded as follows. With the action of ignition flame and pressurization gradient, hot gas may overcome structural obstacle and surface friction, and get into the crack slot to ignite the propellant on the crack internal surface, which leads to higher gas density and pressure in the slot subsequently. At the same time, the deformation of propellant crack will appear because of high-pressure action on the slot, which always results in redistribution of pressure. So, transient pressure distribution in the crack slot is decided by couple action of propellant deformation and pressure reconstruction. It has been indicated in the experiments that high-temperature and high-pressure gas can penetrate into macro-crack with various dimensions, and the depth into the crack is affected by many factors. When the pressure in the crack slot is greater than that on the crack exit, filling process stops and gas begins to flow out from crack. And when gas flow is bared or choked, the pressure on the crack tip will increase dramatically, and crack propagation will appear. As a result, propagation phenomenon takes place easily in the propellant crack flow path which is difficult to generate geometric deformation, just because crack propagation process is related not only to restrict condition, but also to gas flow condition.

Different propellant has different crack propagation mode. It is difficult for cracks to propagate and branch in NEPE propellant, since this propellant has high deformation ability. When higher pressure is produced in the crack, the exit and gas flow path will expand promptly which then will lead to rapid decrease of the pressure. Generally, this kind of propellant will not generate crack propagation during of ignition and gas filling, because the pressure in the crack slot is lower than that on the crack exit. However, when the flow in the crack is choked, the slot in NEPE propellant will deform in a violent manner. And as soon as deformation energy gets above of the fracture energy, the crack will be propagated further. According to this analysis, NEPE propellant crack destruction is a class of slit mode.

Experimental Research on Crack Propagation Condition

In order to study propagation conditions and relative effect factors of crack in the propellant, high-speed real-time X-ray radiograghy system was employed with which instantaneous combustion phenomenon can be observed. A schematic diagram of this system is shown in Fig.1. The X-rays are produced in the X-ray head, then pass through the test motor and finally are intercepted by the image intensifier that can transform the X-ray image into a visible-light image with a time constant of less than 1 microsecond. The visible-light image is then recorded by a high-speed video camera (up to 12,000 pps) and later analyzed by the image processing system (Kodak Ektapro Hi-Spec EM 1012/2 Motion Analyzer System). With this system, video tape is

not needed, and the data and images can be stored in electronic memory directly. So, after experiment, the digital images can be displayed repeatedly with required speed and can be input to the computer to be processed. Pressure signal, which will be used to build up the corresponding relationship between image and pressure, can be recorded by CS2092 data acquisition system. Rectangular cross-section test motor configuration is shown in fig.2.

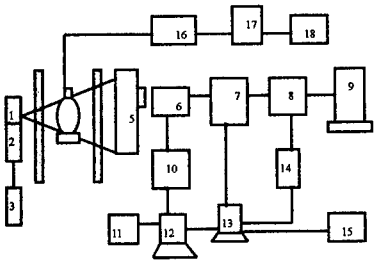


Fig. 1. Layout of the Real-Time X-Ray Radiography System

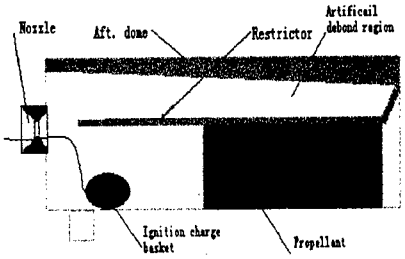


Fig.2 The sketch of test motor

NOTE: 1.X-ray tube head 2. High voltage generator 3. X-ray controller 4.Test chamber 5. X-ray image intensifier 6. Imager 7.High speed motion analysis 8.Video deck 9.TV monitor 10.Controller 11.Laser Driver 12. Computer 13.Image processing work station 14.TV card 15.Laser printer 16. Amplifier 17. Date acquisition & processing system 18. Printer

NEPE propellant has excellent viscoelasticity, and the basic conditions of it's crack propagation are that there are enough deformation and higher tip-slit force in the crack slot. After several effect analyses of restrict condition on the crack propagation, the limit-slit tests were conducted. Fig.3 shows a propagation process that with the pressure action induced by round grain combustion. It undergoes more serious geometric deformation, and it's crack propagates when deformation energy is greater than fracture energy.



Fig.3 The propagation images of NEPE propellant with crack in round sample

From the tests with rectangular and round cross-section sample of NEPE propellant, it is clear that the necessary condition for crack slit of this propellant is that there exists a higher pressure difference between crack tip and other parts. During the period of gas filling into crack, a dynamic load acts on the crack tip, which will produce a stress gradient before it. The higher pressurization gradient is, the higher pressure difference is. So, when the pressurization gradient is high enough, the crack maybe propagate, which is displayed in Fig.4. In addition, crack combustion can make the pressure of its tip higher than chamber stagnation pressure, which can generate a higher stress region around the crack tip. It is believed that the longer crack is, the higher pressure is, and the more serious stress concentration becomes. While a crack length is more than the critical length, the pressure difference at crack tip will exceed the slit pressure difference of the propellant, and then the crack will propagate. Under the condition of constant pressurization gradient and crack height, there exists a critical depth of the crack into which gas

can get. And as long as the crack depth is less than this critical one, high temperature gases enter the crack immediately and then ignite the internal surface.



Fig4 The propagation images of NEPE propellant sample with crack under the ignition shock

It is also be observed from experiment that macro-cracks with various dimensions and shapes can all take part in the combustion, and because of the impingement of ignition, flame can get into crack slot. Fig.5 shows some combustion figures when the crack is I shape, V shape and Y shape on the propellant surface respectively. And more violate convective combustion in the Y shape crack was found.



Fig. 5 The images of ignition and combustion on propellant surface crack

Experimental Research on Anomalous Combustion and Destruction of NEPE Propellant with Gas Cavities

These tests were also conducted with rectangular cross-section motor, and propellant samples with various dimensions and connection-ship of cavities were used (shown in Fig.6). Destruction process of propellant and effects on the internal ballistic performance are shown in Fig.7 and Fig.8.

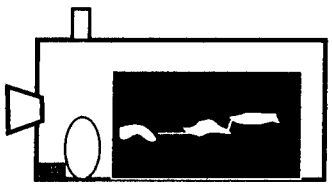


Fig. 6 The sketch of gas cavity propagation test motor

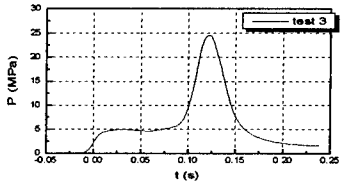


Fig. 7 Pressure-time trace of gas cavity propagation process

With these performance analysis and simulation tests about gas cavity combustion, some results can be described as follows. Cavities can be impressed together during ignition, and they will not be extended. To the single cavity, burning cannot lead to edge extent, and internal surface burning only affects internal ballistic performance. Insular multi-perforated cannot produce connective combustion phenomenon. Connective multi-perforated may cause edge extent, because gases can ignite internal surface of cavities through connective flow hole. When the ratio of burning surface to port area is greater than 400, the enough pressure difference is produced which will result into destruction of propellant grain structure.

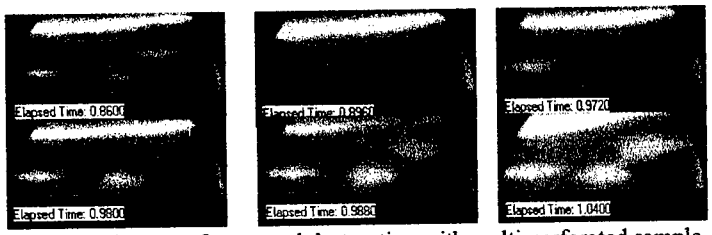


Fig.8 The images of structural destruction with multi-perforated sample

Conclusion

To the rocket motor with grain defects, there exists more significant relationship between the operating reliability and combustion mechanic of the propellant. The cracks and gas cavities of grain are main effect factors on the burning safety and internal ballistic performance. In some cases, these defects do not propagate, and they just only affect the rocket performance in some extent. However, in some other cases, they can lead to the propagation conditions and destruction of propellant, even to DDT failure. The defects with different propellant types, characteristic dimensions, shapes and boundary conditions have different behaviors of combustion-mechanic, propagation condition and mode. Defects propagation phenomenon presented in this paper was setup under special conditions, so a great deal of theoretical and experimental research works should be onset to build up efficient quality control system and evaluation rules of SRM grain.

Reference

1 Wu,S.R. ,Lu,Y.C. ,Kuo,K.K. and Yang,V., Anomalous Combustion of Solid Propellant in a Propagating Debond Cavity, AIAA 92-0770

2 Lu,Y.C. Wu,S.R., Yang,V. and Kuo,K.K., Modeling and Numerical Simulation of Combustion Process Inside a Solid-Propellant Crack Cavity, AIAA 92-0102

3 Wu,S.R., Lu,Y.C., Kuo,K.K. and Yang,V., Combustion-Induced Crack/Debond Propagation in a Metalized Propellant, AIAA 92-3506

4 Lu,Y.C., Kuo,K.K. and Wu,S.R., Crack Propagation Process in a Burning AP-Based Composite Solid Propellant, AIAA 93-2168

5 Nottin,J.P., Gondouin,B. and Lucas,M., Experimental Investigation of Cracks Growth in Composite Propellants, AIAA 85-!437

6 Liu,C.T., Crack Growth Behavior in a Composite Propellant with Strain Gradients—Part II, J. Spacecraft, Vol.27, No.6, 1990

7 R. A.Frederick Jr., Prediction and Analyzing X-Rays to Measure Propellant Crack Propagation Speed, J. of Propulsion and Power,Vol.12, No. 2, March-April 1996

STUDY ON COMBUSTION OF NEW ENERGETIC NITRAMINES

Valery P.Sinditskii, Viacheslav Y.Egorshev, Maxim V. Berezin

Mendeleev University of Chemical Technology, 9 Miusskaya Square, 125047, Moscow, Russia

ABSTRACT

The paper focuses on the combustion behavior of new energetic cyclic nitramines which are mainly the products of condensation chemistry of glyoxal and appropriate amines. Burning rate characteristics of the nitramines were studied in a window constant-pressure bomb at pressures up to 36 MPa. Temperature distributions in the combustion wave of HMX and its structural analog, bicyclo-HMX were measured using thin tungsten-rhenium thermocouples embedded in the pressed samples. An analysis of the nitramine burning characteristics shows that for the most part variations in the nitramine molecular structure which lead to an increase in the thermal decomposition rate result in a simultaneous increase in the burning rate.

INTRODUCTION

Cyclic nitramines such as 1,3,5-trinitro-1,3,5-triazacyclohexane (RDX) and 1,3,5,7-tetranitro-1,3,5,7-tetraazacyclooctane (HMX) are of considerable interest as primary energetic ingredients in solid propellant formulations. However, the combustion behavior of nitramine-containing propellants is not always comply with requirements of the concerned specialists. This is particularly true of high values of the pressure exponent observed for combustion of such propellants, a weak dependence of the burning rate on the nitramine particle size, and difficulties associated with attainment of effective combustion catalysis. These shortcomings have given an impetus to detailed study of combustion mechanisms of RDX and HMX, on the one hand, and an active search for new energetic nitramines, on the other hand. At the present time, a wide range of new energetic nitramines, from keto-analog of RDX to highly promising hexanitrohexazaisowurtzitane (CL-20) and trinitroazetidine (TNAZ) [1,2,3], have been synthesized. While combustion mechanisms and flame structures for RDX and HMX have been well studied, the new energetic nitramines remain to be investigated. Only data of Atwood et al. [4] on burning of CL-20 were published recently. It is obvious therefore that a comprehensive study of combustion of such compounds is essential, first, to predict its performance in practical use, and second, to allow a better understanding of nitramine combustion mechanism. In this connection the main goal of the present work was to study burn rate characteristics of several new energetic cyclic nitramines of related structures, aimed at discovering the combustion

mechanism and influence of the molecular structure. The following compounds containing both five- and six-membered cycles were chosen for the investigation as structural analogs of RDX and HMX: 1,3,5-trinitro-1,3,5-triazacyclohexane-2-one (K6, keto-RDX), 2,4,6,8-tetranitro-2,4,6,8-tetraazabicyclo[3.3.0]octane (bicyclo-HMX), 2,4,6,8-tetranitro-2,4,6,8-tetraaza-bicyclo[3.3.0]-octane-3-one (TN550), 2,4,6,8-tetranitro-2,4,6,8-tetraazabicyclo[3.3.0]octane-3,7-dione (Sorguyl), 2,6-dinitro-2,4,6,8-tetraazabicyclo[3.3.0]octane-3,7-dione (Dingu), and 2,5,7,9-tetranitro-2,5,7,9-tetraazabicyclo[4.3.0]nonane-8-one (TN650).

EXPERIMENTAL

Preparation. The nitramines were synthesized by methods published elsewhere [2,3,5,6,7] and identified by IR- and NMR-spectroscopy analysis. Physicochemical properties of the substances corresponded to literature ones. The molecular structures of the nitramines and some of their properties are given in Table 1.

Combustion Study. Burn rate characteristics of the nitramines were studied in a window constant-pressure bomb of 1.5 liter volume pressurized with nitrogen. Samples to test were prepared as pressed cylinders of relative density of 0.77-0.95 (Table 2) confined in transparent acrylic tubes of 4 mm or 7 mm i.d. A slit camera was used to photograph flame propagation and measure the burning rate. The pressure range studied was 0.1-36 MPa. Besides, the burning rate of bicyclo-HMX was measured in the sub-atmospheric pressure region in a vacuum chamber of 40 liter volume. Temperature profiles were measured using thin tungsten-rhenium thermocouples embedded in the pressed strands. The thermocouples were welded from 25 μm diameter tungsten—5% rhenium and tungsten—20% rhenium wires and rolled in bands to obtain 5-7 μm bead size. A Tektronix TDS-210 digital oscilloscope was used to record the thermocouple signal.

RESULTS AND DISCUSSION

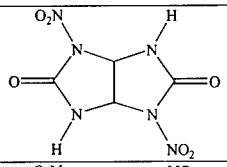
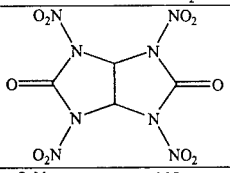
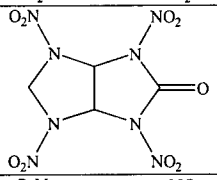
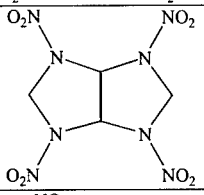
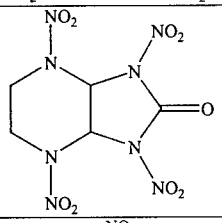
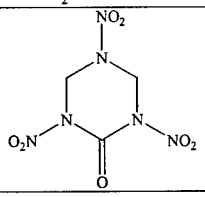
Burning behavior

Burning rate characteristics of the nitramines are presented in Table 2 and Fig. 1-Fig. 3. The table also includes literature data on combustion of RDX [8, 4] and CL-20 [4]. Burning rates of HMX were taken from [9] and augmented with data obtained in this work at low pressures.

Energetics of most of the nitramines may be noted to vary only slightly. The calculated adiabatic flame temperatures vary in a fairly narrow interval from approximately 3300 K to 3470 K, with

the exception of CL-20 having the temperature of more than 3600 K and Dingu with the flame temperature a thousand degrees less.

Table 1. Molecular structure and physicochemical properties of cyclic nitramines

Chemical name (abbreviation)	Molecular structure	Density g/cm^3	ΔH°_f, kJ/mole
2,6-Dinitro-2,4,6,8-tetraazabicyclo[3.3.0]octane-3,7-dione (Dingu)		1.992 [2]	-177.0 [10]
2,4,6,8-Tetranitro-2,4,6,8-tetraazabicyclo[3.3.0]octane-3,7-dione (Sorguyl)		2.04[2] 2.01[3]	-33.5 [11]
2,4,6,8-Tetranitro-2,4,6,8-tetraazabicyclo[3.3.0]octane-3-one (TN550)		1.954 [12] 1.91 [2]	23.0 [11]
2,4,6,8-Tetranitro-2,4,6,8-tetraazabicyclo[3.3.0]octane (Bicyclo-HMX)		1.92[11]	206.3 *)
2,5,7,9-Tetranitro-2,5,7,9-tetraazabicyclo[4.3.0]nonane-8-one (TN650)		1.969 [2]	71.1 [11]
1,3,5-Trinitro-1,3,5-triazacyclohexane-2-one (Keto-RDX)		1.932 [2]	-41.8 [7]

*) The enthalpy of bicyclo-HMX formation was determined in the Institute of Chemical Physics of Russia

Most of the new energetic cyclic nitramines appear to burn faster than conventional and much studied RDX and HMX. A comparison of the nitramine burning rates and adiabatic flame temperatures (see Table 2) shows that there is no obvious correlation between these two parameters at least in the studied pressure range. To take an example, Dingu burns faster than HMX while having the flame temperature almost 700 degrees less.

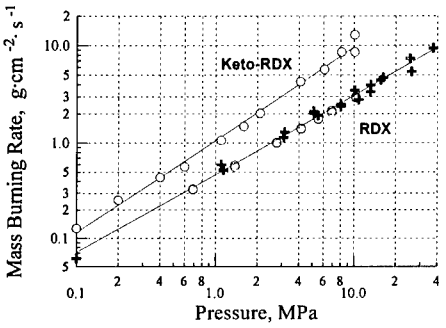


Fig. 1. Comparison of the combustion behavior of RDX (black crosses [8] and open circles [4]) and keto-RDX (light circles).

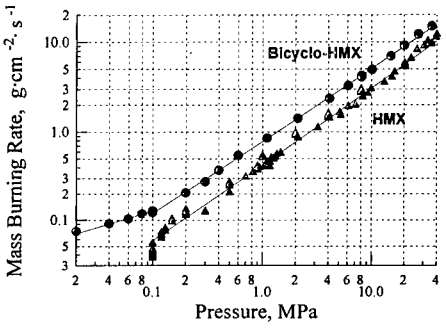


Fig. 2. Comparison of the combustion behavior of HMX (black crosses) and bicyclo-HMX (light triangles).

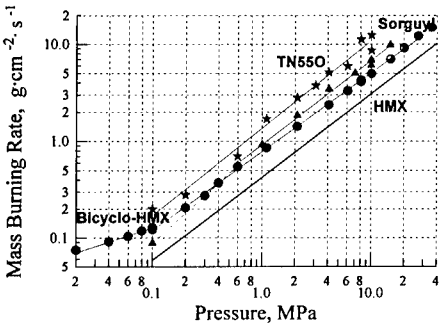


Fig. 3. Comparison of the combustion behavior of bicyclo-HMX (light circles), Sorguyl (triangles) and TN550 (stars). The line without points relates to HMX

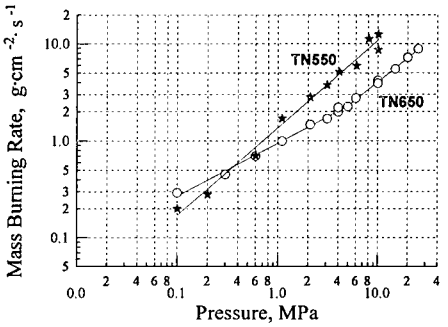


Fig. 4. Comparison of the combustion behavior of TN650 (light circles) and TN550 (stars).

Burning rate *vs.* pressure dependencies for new cyclic nitramines are conveniently grouped together in pairs or threes by similarity in their molecular structures. The first such a pair is RDX/keto-RDX (Fig. 1). The ketone group introduced into the RDX molecule leads to an appreciable growth of the burning rate, with the pressure exponent, n, noticeably increased.

An additional transannular C-C bond in the eight-membered HMX cycle breaks it down into two five-membered cycles, thus forming the molecule of bicyclo-HMX. The latter compound

demonstrates higher burning rates than HMX does, almost reaching CL-20, but having somewhat increased pressure exponent (Fig. 2 and Table 2). Bicyclo-HMX is able to burn in sub-atmospheric pressure region (starting from 0.02 MPa), whereas HMX when pressed into 7 mm i.d. acrylic tubes, showed the low-pressure limit of sustained burning as high as 0.1 MPa.

Table 2. Burn rate characteristics of cyclic nitramines

Nitramine	Pressure interval, MPa	Pressure exponent	Burning rate at 10MPa, mm/s	Strand density, g/cc	Adiabatic flame temperature at 10 MPa, K
Dingu	1-20	0.745	21.8	1.53	2610
Sorguyl	0.6-15	0.867	44.4	1.58	3395
TN550	0.1-10.1	0.901	63.1	1.72	3469
TN650	0.1-4 4-25.5	0.547 0.782	26.5	1.55	3413
Bicyclo-HMX	0.02-0.11 0.11-36	0.354 0.812	27.9	1.82	3530
Keto-RDX	0.1-10.1	0.961	55.6	1.74	3419
RDX	0.1-102	0.825	17.8	1.75	3318
HMX	0.3-40.1	0.861	18.1	1.72	3295
CL-20	0.69-10.3	0.745	30.1	1.96	3636

As in the case of RDX, changing a CH_2 group of the bicyclo-HMX molecule to the C=O group to form TN550 compound results in further increase in burning rates (Fig. 3). The pressure exponent rises from 0.81 to 0.87. However, the replacement of the second CH_2 group with C=O group (Sorguyl) did not appear to result in the expected further growth of the burning rate. The burn rate *vs.* pressure curve for Sorguyl is intermediate between the curves for bicyclo-HMX and TN550 that may be a result of a slight decrease in the energetics of the substance on the second CH_2-group replacement.

The modification of TN550 molecule in TN650 by replacing a five-membered cycle with the less strained six-membered one causes the burning rate to perceptibly decrease in the pressure interval from 0.1 to 10 MPa (Fig. 4).

On the basis of the obtained results, it can be noted that the burning rate characteristics of the studied nitramines depend largely on the molecular structure, despite high similarity in the structural building blocks. It is obvious that the molecular structure of this series of cyclic nitramines can exert primary influence on physicochemical properties and decomposition kinetics of the materials rather than kinetics of redox reactions occurring in the decomposition

products in the flame. The thermal decomposition of secondary nitramines is known to begin with N-NO_2 bond rupture. This bond, however, is a rather conservative one and is not readily susceptible to inductive influence of different substituents. [13]. Nevertheless, an estimation can be made of the decomposition rate constant of linear nitramines of general formula $R_1N(NO_2)R_2$ if using the correlation equation taken from Refs [14, 13]:

$$\lg k_{200} = 0.495(\sigma^*_{R1} + \sigma^*_{R2} - 4.34),$$

where σ^* is the inductive constant of a substituent.

It follows from the equation that substitution of CH_2-fragment ($\sigma^* \sim -0.1$) by CO-fragment ($\sigma^* \sim 1.65$) in even non-strained linear nitramines can result in a quite significant increase in the decomposition rate constant (in ~7 times at 200°C). The geometrical configuration of the nitramine group, pyramidal or planar, is also important. Nitramine groups in α- and β-modifications of HMX are known to have the planar configuration, with the sum of angles at the amine nitrogen approximated to 360°[15]. Because of steric strains in the cycle, RDX has apparently one planar and two pyramidal nitramine groups [16]. As estimated in [17], the average energy of the N-N bond is 40.5 kcal/mole for planar and only 37.7 kcal/mole for the pyramidal nitramine group configuration. This difference may lead to significant variations in the nitramine decomposition rate. As a result, RDX decomposes approximately ten times faster than HMX in solutions [17]. Under all other conditions being equal, at a temperature of 400°C, a compound with the pyramidal configuration of nitramine groups will decompose more than seven times faster than a compound with the planar configuration.

Therefore, for most nitramines studied in this work, the molecular structure influence on the burning rate may be correlated with the structure effect on the thermal decomposition rate. To draw a more specific conclusion it is essential to take account of temperatures at which the decomposition reactions occur. For this purpose the temperature distribution in the combustion wave of bicyclo-HMX has been measured and compared with that of HMX. Since temperature parameters of the HMX combustion wave obtained previously in several works [18,19,20,21,22] had showed considerable inconsistency, thermocouple-aided measurements of HMX temperature profiles were the aim of the present study as well.

Temperature profiles

Typical temperature profiles on combustion of bicyclo-HMX and HMX at low pressures are shown in a comparative manner in Fig. 5 and Fig. 6. The surface temperatures for both compounds are given as a function of pressure in Table 3 and Fig. 7. Also in Table 3 are given the temperature gradients above the surface and the maximum flame temperatures. These temperatures are listed as recorded by the thermocouple, without any correction for radiation heat loss, and therefore may be essentially lower than the real ones. The temperature gradient was found to be subjected to considerable variations in parallel runs because of probable adhesion of the surface molten layer to the thermocouple. The range of the variations is given in the Table.

Although being quite close together, the surface temperatures for HMX are somewhat higher than for bicyclo-HMX. Experimental points for HMX appeared to fall close to data of Mitani and Williams [21] and Lengelle, Duterque, and Trubert [22] and lie along the HMX vapor pressure *vs.* temperature dependence extrapolated from the low-pressure region [23,24]. Deviation of the experimental data from the vapor pressure line as the pressure exceeds 1 MPa, may be caused by very thin, comparable to the thermocouple thickness, flame zone sizes, resulting in overstated surface temperatures.

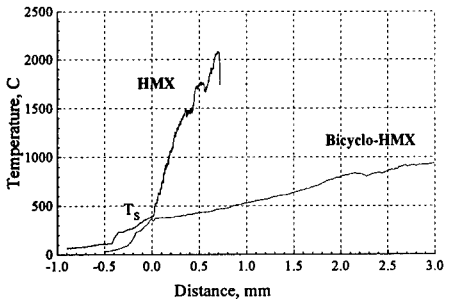


Fig. 5. Temperature profiles for HMX and bicyclo-HMX at atmospheric pressure.

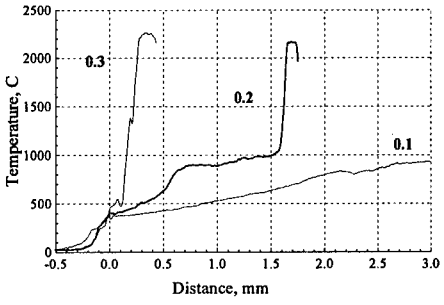


Fig. 6. Comparison of temperature profiles for bicyclo-HMX recorded at 0.1, 0.2, and 0.3 MPa.

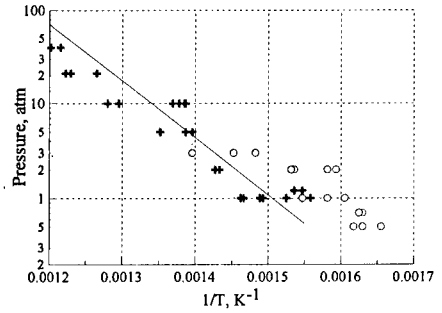


Fig. 7 Plot of pressure *vs* reciprocal surface temperature for HMX (crosses) and bicyclo-HMX (circles). The solid line is the extrapolated temperature dependence of HMX vapor pressure.

The burning behavior of bicyclo-HMX at low pressures is of particular interest. Its burning rate *vs.* pressure dependence was found to reveal a break at approximately 0.1 MPa (see Fig. 2). Below this pressure, the substance burns without a visible flame, evolving copious white fumes. The maximum combustion temperature recorded by a thermocouple barely exceeds 900°C, whereas the combustion temperature of HMX under the same conditions is higher than 2000°C (Fig. 5).

The temperature gradient above the bicyclo-HMX burning surface is negligible (Table 3), thirty times less than that of HMX, suggesting practically no heat feed back from the gas to the condensed phase. However, as pressure increases by an atmosphere, the combustion pattern drastically changes. There appears a luminous flame on combustion of bicyclo-HMX, and the maximum flame temperature reaches 2200-2300°C, i.e. as high as HMX flame temperature (Fig. 6). Thus it is obvious that the break on the burning rate *vs.* pressure curve for bicyclo-HMX is connected with initiation of the luminous high-temperature secondary flame. It appears at 0.2 MPa and stands about 1.5-2 mm off the burning surface. The distance decreases rapidly with pressure and is only 0.2-0.3 mm at 0.3 MPa. The width of the first flame zone (the zone within which the temperature gradually rises from the surface temperature to its maximum value) at low pressures is abnormally large. It is ten to twenty times more than for the normal Michelson profile. Under atmospheric pressure and in the sub-atmospheric pressure region, the combustion process propagates at the expense of condensed-phase decomposition reactions only. The combustion, in this instance, is known to be accompanied by dispersion of the surface layer and formation of an anomalous wide reacting zone above the surface, as, for example, in the case of double base propellants [25].

Table 3. Results of temperature measurements in the combustion wave of HMX and bicyclo-HMX

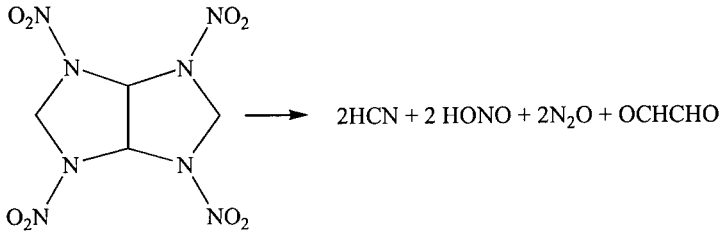
Pressure, MPa	HMX	Bicyclo-HMX

	Surface temperature, °C	Temperature gradient range, 10^{-4} K/cm	Average maximum flame temperature, °C	Surface temperature, °C	Temperature gradient range, 10^{-4} K/cm	Average maximum flame temperature, °C
0.05	-	-	-	358±10	0.015-0.02	490
0.07	-	-	-	360±10	0.065-0.075	660
0.1	414±18	3.5-3.6	2080	381±13	0.11-0.12	960
0.2	445±10	4-8	2180	389±13	0.38-0.40	2170
0.3	-	-	-	445±23	5.5-13	2270
0.5	480±13	11-19	2270	-	-	-
1	498±29	14-30	2290	-	-	2300
2	568±16	-	2320	-	-	-
4	590±10	-	2370	-	-	-

The combustion of nitramines of practical interest, HMX and RDX, has been a subject of many researches for many years [26]. Several models of nitramine combustion have been developed, and although disagreement in the relative importance of gas or condensed phase remains, most of researchers are agreed now that combustion of HMX is controlled by exothermic processes in both the condensed phase and the adjacent gas zone [20, 21, 24, 26, 27, 28]. According to Ref. [21] and Ref. [28], 30% to 48% of HMX undergoes decomposition in the condensed phase on combustion at atmospheric pressure and normal ambient temperature, with the remainder evaporated and reacted in the gas phase. Heat balance calculations based on the data of Table 3 gave about 54% of HMX decomposed in the condensed phase at atmospheric pressure, assuming the rest of HMX evaporated. In the calculations, evaporation heat was taken to be 93.6 cal/g [21], heat of melting 37.5 cal/g [21], heat of HMX decomposition in the condensed phase 140 cal/g [29], and heat transferred back through radiation 30.6 cal/g [19].

Appearance of the C-C bond in the HMX molecule to form the more strained molecule of bicyclo-HMX, by analogy with the transition from RDX to HMX, will most likely be accompanied by changing in the nitramine group configuration from planar to pyramidal one. As mentioned above, this transformation decreases the $N\text{-}NO_2$ bond strength. The thermocouple measurements show that the surface temperatures for both HMX and bicyclo-HMX are quite close together, so changing in the nitramine group configuration may increase the rate of bicyclo-HMX decomposition several times, resulting in its faster burning as compared to HMX. The higher decomposition rate of the bicyclic compound permits of its steady-state combustion at low pressures when contribution of the gas phase is negligible and when more stable HMX fails to demonstrate self-sustained burning.

In parallel with known decomposition pathways of such secondary nitramines as RDX and HMX, which initial stage is N-NO_2 bond rupture, the following scheme of two-stage conversion of bicyclo-HMX in the flame may be proposed:



$$HONO + OCHCHO \longrightarrow CO_2,\ CO,\ H_2O,\ NO$$

REAL code calculations [30] of bicyclo-HMX combustion temperatures assuming the above products frozen in the flame, give 450°C and 875°C for the first and the second stage, respectively. The latter is close to the experimental temperature of the first flame clearly defined at low pressures. It can be concluded therefore that condensed-phase and first flame chemistry of bicyclo-HMX combustion involves its exothermic decomposition and aldehyde oxidation by HONO. In the second flame, HCN, CO, NO and N_2O are consumed to complete oxidation reactions.

CONCLUSION

An important role of kinetics of thermal decomposition in the combustion of cyclic nitramines can be revealed from the analysis of burning rate data and thermocouple-aided measurements. In most cases, the observed effect of the nitramine molecular structure on the burning rate may be explained by the influence of the structure on the thermal decomposition parameters. A lack of any correlation between the burning rate and adiabatic flame temperature along with the above findings suggests that the heat release in the condensed phase and in the adjacent-to-surface gas zone makes a primary contribution to the burning rate. This behavior also suggests that the studied cyclic nitramines will not be susceptible to burning catalysis as is the case of HMX.

ACKNOWLEDGEMENT

The authors are grateful to Dr. G.F. Rudakov and Mrs. E.V. Veselova for synthesizing the nitramines to test, Dr.V.I. Kolesov and Dr. A.I. Levshenkov for their assistance in burn rate

measurements. The authors gratefully acknowledge support from Russian Fund for Fundamental Research (grant 00-03-32075).

REFERENCES

1. Bottaro J.C. "Recent Advances in Explosives and Solid Propellants," *Chem. Ind.*, 1996, No.7, pp.249-252.
2. Pagoria P.F., Mitchell A.R., Jessop E.S. "Nitroureas II. Synthesis of Bicyclic Mono- and Dinitrourea Compounds," *Propellants, Explosives, Pyrotechnics,* 1996, Vol.21, pp.14-18.
3. Boileau J., Wimmer E., Carail M., Gallo R. "Methodes de Preparation de Derives Nitres et Nitroacetyles du glycolurile (I)," *Bull.Soc. Chim. France*, 1986, No.3, pp.465-469.
4. Atwood A.I., Boggs T.L., Curran P.O., Parr T.P., Hanson-Parr D.M., Price C.F., and Wiknich J. "Burning Rate of Solid Propellant Ingredients, Part 1: Pressure and Initial Temperature Effects," *Journal of Propulsion and Power*, 1999, Vol. 14, No.6, pp.740-747.
5. Esk G., Piteau M. "Process for the synthesis of 2,4,6,8-tetranitro-2,4,6,8-tetra-azabicyclo[3.3.0]octane," US Patent 5659032, Aug. 19, 1997.
6. Rudakov G.F., Zhilin V.F., Veselova E.V., Moiseev A.G. "A New Method of Preparation of Nitroderivatives of Octahydro-2H-imidazo[4.5-b]pirazine-2-one," *Proceedings of 32nd Inter. Conference of ICT*, July 3-6, 2001.
7. Mitchell A.R., Pagoria P.F., Coon C.L., Jessop E.S. et al. "Nitroureas 1. Synthesis, Scale-up and Characterization of K-6," *Propellants, Explosives, Pyrotechnics*, 1994, Vol.19, pp.232-239.
8. Glazkova A.P. Combustion Catalysis of Explosives. Moscow, Nauka, 1976, 264 p.
9. Fogelzang A.E., Sinditskii V.P., Serushkin V.V., Egorshev V.Yu., Schipin Y.K, Tropynin V.K. Database Flame - Combustion of Energetic Materials, ver. 2.52, 1990-1999.
10. Stinecipher M.M., Stretz L.A. "Sensitivity and Performance Characterization of DINGU," *Proceedings of 8th Symposium (Intl.) on Detonation*, 1985, pp.351-356.
11. Wu Xiong, Sun Jian, Xiao Lianjie "The Detonation Parameters of New Powerful Explosive Compounds Predicted with a Revised VLW Equation of State," *Proceedings of 9th Symposium (Intl.) on Detonation*, Portland, Oregon, August 28 - September 1, 1989, p.190.
12. Xinping L., Xiong Wu, Xiaohua J. "The Detonation Parameters of High Energy Density Explosive Predicted with a New Revised VLW EOS," *Proceedings of 6 Congres International de Pyrotechnie (Europyro 95)*, Tours, 1995, pp. 221-227.

13. Manelis G.B., Nazin G.M., Rybzov Yu.I., Strunin V.A. Thermal Decomposition and Combustion of Explosives and Propellants, Moscow, Nauka, 1996, 223 p.

14. Stepanov R.S., Shan'ko V.N., Medvetskaya I.P., Gorodetskaya V.M. Chemical Physics of Combustion and Explosion. A Kinetics of Chemical Reactions. Chernogolovka, Branch of Chem. Physic Institute, 1977, pp.56-58.

15. Cady H.H., Larson A.C., Cromer D.T. "The Crystal Structure of α-HMX and Refinement of the Structure of β-HMX," *Acta Crystallogr.*, 1963, Vol.16, p.617.

16. Choi C.S. "The Crystal Structure of Cyclotrimethelenetrinitramine," *Acta Crystallogr.*, 1972, Vol. B28, p.2857.

17. Byrov Yu.M., Nazin G.M. "Effect of Structure on Decomposition Rate of Secondary Nitramines in Gas Phase," *Kinetika i katalyz*, 1982, Vol. 23, pp.12-17.

18. Zenin A.A. "HMX and RDX: Combustion Mechanism and Influence on Modern Double-Base Propellant Combustion," *J. Propulsion and Power*, 1995, v.11, No.4, pp.752-758.

19. Zenin A.A., Puchkov V.M., Finaikov S.V. "The Characteristics of the Combustion Waves of HMX at Various Pressure and Initial Temperatures," *Fizika gorenia i vzryva*, 1998, Vol. 34, No.2, pp.59-66.

20. Kubota N., Sakamoto S. "Combustion Mechanism of HMX," *Proceedings of 19th Inter. Conference of ICT*, 1988, paper 65, pp.1-12.

21. Mitani A., Williams F.A. "A Model for the Deflagration of Nitramines," *Proceedings of 21st Symposium (Int.) on Combustion*, Pittsburgh, 1986, pp.1965-1974.

22. Lengelle, G., Duterque, J. and Trubert, J.F. "Physico-Chemical Mechanisms of Solid Propellant Combustion," in Solid Propellant Chemistry, Combustion, and Motor Interior Ballistics, edited by V. Yang, T. B. Brill, and W. Z. Ren, Vol. 185, Progress in Astronautics and Aeronautics, American Institute of Aeronautics and Astronautics, Reston, VA, 2000, pp. 287-334.

23. Taylor J.W., Crookes R.J. "Vapour Pressure and Enthalpy of Sublimation of 1,3,5,7-Tetra-nitro-1,3,5,7-tetraazacyclooctane (HMX)," *J.Chem.Soc., Trans I*, 1976, Vol.72, pp.723-729.

24. Li S.C., Williams F.A. "Effect of Two-Phase Flow in a Model for Nitramine Deflagration," *Combustion and Flame*, 1990, Vol.80, pp.329-349.

25. Zenin A.A. "Processes in Burning Zones of Double-base Propellants," in Physical Processes in Combustion and Explosion, Moscow, Atomizdat, 1980, pp.68-104.

26. Boggs T.L. "The Thermal Behavior of Cyclotrimethylenetrinitramine (RDX) and Cyclotetramethylenetetranitramine (HMX)," in K.K. Kuo, M. Summerfield (Eds.), Fundamentals of Solid-Propellant Combustion, AIAA Progress in Astronautics and Aeronautics, Vol.90, AIAA, Washington, DC, 1984. pp. 121-175.

27. Ben-Reuven M., Caveny L.H. "Nitramine Flame Chemistry and Deflagration Interpreted in Terms of a Flame Model", *AIAA Journal,* 1979, Vol. 19, pp.1276-1285.

28. Davidson J.E., Beckstead M.W. "A Three-phase Model of HMX Combustion," *Proceedings of 26th Symposium (Int.) on Combustion*, 1996, pp.1989-1996.

29. Korobeinochev O.P., Kuibida L.V., Madirbaev V.Zh. "The Study of Chemical Structure of Octogen Flames," *Fizika gorenia i vzryva*, 1984, Vol.20, No. 3, pp.43-46.

30. G.V. Belov, "REAL - Thermodynamic Examination of Combustion Products Under High Pressure," *Proceeding of 28th International Annual Conference of ICT*, Karlsruhe, FRG, 24-27 June, 1997, paper 70, pp.1-12.

HEAT-MASS TRANSFER AND IGNITION IN RING VORTEX

Victor P. Samsonov, Mikhail V. Alekseev

Surgut State University,
Energetikov st. 14, 628400, Surgut of Tumen region, RUSSIA

The ignition of the decomposition products of the condensed fuel in the ring vortex is studied by the experimental methods and numerical simulation. The ring vortex was created by the powerful force of the laser radiation on the acrylic plastic flat surface. The energy density in the laser beam was $2 \cdot 10^5$-10^6 Wt/m^2.

It was discovered in the experiments that the energy density in the laser beam and the duration of the radiation influence determine the laws of the ignition in the ring vortex.

The main condition of the ignition is the existence of the combustible composition of the fuel vaporous and the oxygen in the air. The temperature mixture must be greater than the ignition one.

The numerical simulation was based on the system of the not stationary, differential equations of a free convection and diffusion, written in the cylindrical coordinates. The comparison of the experimental and numerical results has been made.

The importance of the heat energy and substance transfer by the ring vortex was formulated still earlier [1]. The examples of the vortex flows like these are the whirlwinds forming after the shot of the large gauge gun or the start of the rocket out off the underground mine, or the thermic flows after the explosions and fires. The heat energy transfer in the whirlwind is connected with the ignition dynamics in the flow allows to determine the power of the phenomenon which caused this ring vortex.

The velocity and temperature fields which are forming in the vortex flow on the impulse laser action to the acrylic plastic surface are investigated in the present work. Only the combined application of the two methods – the physical experiment and numerical simulation can allow to supply the complete information about heat and hydrodynamic situation in the ring vortex at the presence of the chemical reactions.

The experiments were carried out in the air atmosphere at the pressure and temperature $P=10^5$ Pa, T=293 K in the closed camera $0,1\times0,1\times0,3$ m^3. The camera was supplied by the windows for the observation and the entrance of the laser radiation. The continuous laser beam was through into focus on the fuel surface by the spherical mirror. The radiation wave length was $\lambda=10,6\cdot10^{-6}$ m (or $\lambda=10,6\cdot10^{-7}$ m). The diameter of the radiation spot was changed in the interval $(1-4)\cdot10^{-3}$ m. The duration of the radiation impulse was given by the mechanic shutter. The time resolution of the radiation energy was controlled in the interval $2\cdot10^5$-10^6 Wt/m^2 by changing the outlet laser power or the diameter of the radiation spot.

The visualization of the destruction products in the flow was carried out by the "laser blade" method [2] in stroboscopic regime. The helium-neon laser beam was transformed to plane-parallel one by the system of the cylinder lenses and was interrupted by the obturator under the given frequency. The suspension of magnesium oxide was prepared for the observation of the atmosphere motion in the camera. The velocity of the destruction products motion was calculated by using the stroboscopic photographs.

The evolution of the radiation process begins at the local heating of the fuel surface. The destruction products and vaporization those escape off the local heating of the fuel surface at the destruction temperature. They are the basic material of the vortex ring. The vortex ring is forming at the definite relation between the time of the radiation action and its power. The large time of the radiation at any its power forms only the continuos, laminar or turbulent jet of the

destruction products. The stable vortex ring is forming at the laser radiation power $q > 10^6$ Wt/m^2. And the time of the laser radiation $\tau < 0{,}1$ s.

The fragments of the film are presented in Fig. 1. The fuel surface is horizontal.

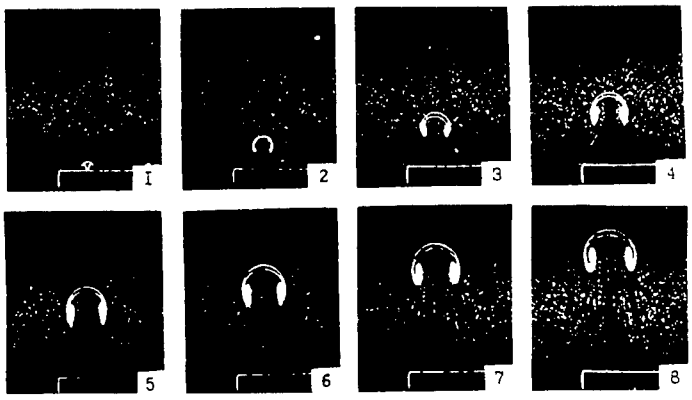


Fig. 1

The laser beam is directed vertically down to the fuel surface. It can be see that the destruction products forms the vortex ring. The formation of the vortex ring is accompanied with the second induced vortex behind the basic one. The experiments with changing the angle of the fuel surface relatively the direction of the gravity acceleration show that the influence of the convection is great. It is obviously because the induction period is approximately 0,1 s and the motion time of the vortex ring is 0,25 s. This influence determines the velocity and temperature fields at the ignition of the destruction products.

Fig. 2 demonstrates the ignition process. At the presented fragments of the film beginning of the ignition and the end of the radiation action are in synchronism. The flame in gas is disposed in the center of the vortex front. The vortex is rather far from the fuel surface. Then the flame front is spreading forward and backward the vortex ring. The period from the inflammation to the

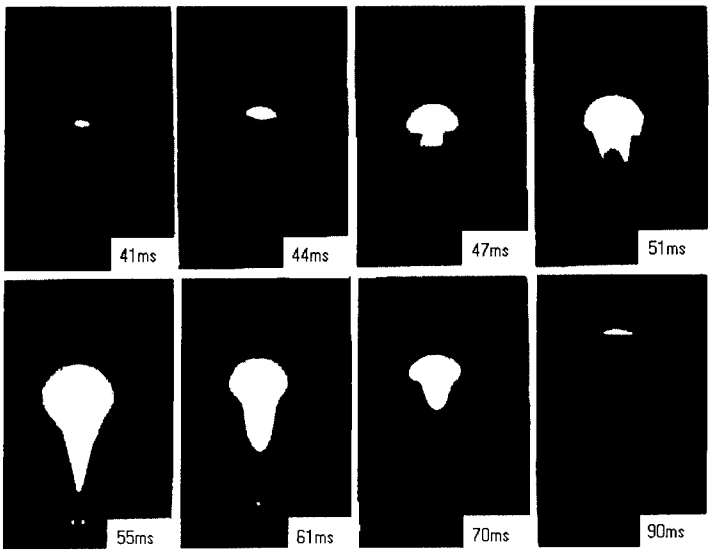


Fig. 2

extinction is of the order 2,3 τ. Here τ is the inflammation time after beginning of the laser radiation action. An increase of the laser action time does not provide the stable regime of the combustion. Obviously, the value 0,4 τ determines the period of the fuel vaporization that is being involved later in the vortex motion. The value 2,3 τ is the burn-out time of the fuel in gas phase.

It was possible in the experiments to achieve the simultaneous inflammation of the destruction products in the front of the vortex ring and far behind it. Thus, the laws of the ignition are completely defined by the distributions of the temperature and concentration in the vortex ring.

The investigation of the dimensional temperature and concentration distributions in the vortex ring by the experimental methods is rather difficult because the photographs give only the integral information. The contact methods are impossible in this situation at all. In this connection the numerical model describing hydrodynamics of the vortex ring at the presence of the chemical reactions in the gas atmosphere was developed. It is based on the system of the free convection equations, including the diffusion one. It can be written in form:

$$\frac{1}{Sh}\cdot\frac{\partial u}{\partial t}+u\frac{\partial u}{\partial r}+w\frac{\partial u}{\partial z}=-\frac{1}{Eu}\frac{1}{\rho}\frac{\partial P}{\partial r}+\frac{1}{\mathrm{Re}}\left(\frac{\partial^2 u}{\partial r^2}+\frac{1}{r}\frac{\partial u}{\partial r}-\frac{u}{r^2}+\frac{\partial^2 u}{\partial z^2}\right)+ \\ +\frac{Gr}{\mathrm{Re}^2}\cdot\Theta\cdot\cos\alpha \tag{1}$$

$$\frac{1}{Sh}\cdot\frac{\partial w}{\partial t}+u\frac{\partial w}{\partial r}+w\frac{\partial w}{\partial z}=-\frac{1}{Eu}\frac{1}{\rho}\frac{\partial P}{\partial z}+\frac{1}{\mathrm{Re}}\left(\frac{\partial^2 w}{\partial r^2}+\frac{1}{r}\frac{\partial w}{\partial r}+\frac{\partial^2 w}{\partial z^2}\right)+ \\ +\frac{Gr}{\mathrm{Re}^2}\cdot\Theta\cdot\sin\alpha \tag{2}$$

$$\frac{1}{Sh}\cdot\frac{\partial \theta}{\partial t}+u\frac{\partial \theta}{\partial r}+v\frac{\partial \theta}{\partial z}=\frac{1}{Pe}\left(\frac{\partial^2 \theta}{\partial r^2}+\frac{1}{r}\frac{\partial \theta}{\partial r}+\frac{\partial^2 \theta}{\partial z^2}\right)+ \\ +\frac{Q}{c_p\cdot T_0}\cdot\frac{C}{Dm}\cdot\exp\left(-\frac{\overline{E}}{\theta}\right) \tag{3}$$

$$\frac{1}{Sh}\cdot\frac{\partial C}{\partial t}+u\frac{\partial C}{\partial r}+v\frac{\partial C}{\partial z}=\frac{Sc}{\mathrm{Re}}\left(\frac{\partial^2 C}{\partial r^2}+\frac{1}{r}\frac{\partial C}{\partial r}+\frac{\partial^2 C}{\partial z^2}\right)-\frac{C}{Dm}\cdot\exp\left(-\frac{\overline{E}}{\theta}\right) \tag{4}$$

$$\frac{\partial \rho}{\partial t}+\frac{\partial(\rho\cdot u)}{\partial r}+\frac{(p\cdot u)}{r}+\frac{\partial(\rho\cdot w)}{\partial z}=0 \tag{5}$$

$$\rho=\frac{\alpha\cdot P}{1+\beta\cdot\theta} \tag{6}$$

The equations (1)-(6) are written in the dimensionless form. Here *Sh, Eu, Dm, Sc, Re, Pe, Gr* are Struhal, Damkeller, Schmidt, Reynolds, Peclet, Grashof numbers relatively, $\overline{E}$ - activation energy, R – universal gas constant, D, ν - diffusion, viscosity coefficients, Q – heat reaction effect, c_p – heat capacity at constant pressure, Θ and C – dimensionless temperature and concentration, a - thermal diffusivity, β - thermal coefficient of expansion, w, u – components of the velocity vector. It was assumed that there was a chemical one-study reaction of the first order. The diameter of the heat spot on the fuel surface and the initial gas velocity were taken as a scales. The laser action time was the time scale.

The results of the calculations are shown in Fig. 3-4. The isolines of the stream-functions represented in Fig.3 show that the secondary induced vortex ring is formed behind the basic vortex ring. This flow determines a character of the

fuel and air concentrations change, also heat loss rate from the vortex ring into the air atmosphere. The secondary induced vortex can be the reason of the nucleation

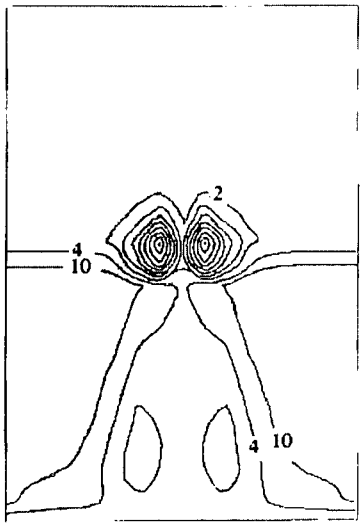


Fig. 3

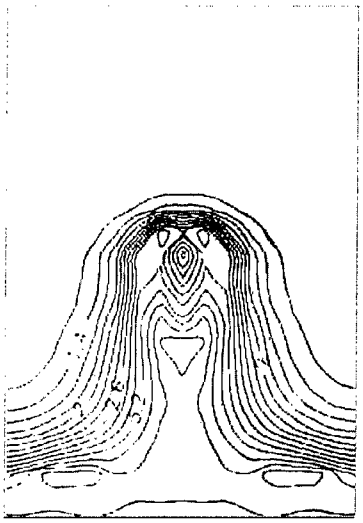


Fig. 4

site for ignition. The temperature field, represented in Fig.4, can explain the shape of the nucleation site for the inflammability in the vortex ring which was observed experimentally.

Thus the experimental and numerical results are in the sufficient compatibility. The vortex ring can transfer only limited volume of the destruction products which are able to enter into the chemical reaction. The amount of the reacting gas is determined by the laser radiation power. The further ignition process completely depends on the hydrodynamics of the vortex ring.

REFERENCES

1. Lavrentev M.A., Shabat D.V. Problems of hydrodynamics and their mathematical models. Moscow, Nauka, 1973. (In Russian)
2. Alhimov A.P., Boyko V.M., Papirin A.N. Optical diagnostics methods of high-velocity two-phase flows // Gas dynamics of disbalanced processes. Novosibirsk: Nauka, 1981. P.20-29. (In Russian)

ABOUT SOME SINGULARITIES LAMINAR DIFFUSION DUST FLAMES IN CO- FLOWING OXIDIZER.

N.I. Poletaev, J. I. Vovchuk, A. V. Florko

Institute of Combustion of the Odessa National University, Odessa, Ukraine

The outcomes of theoretical and experimental researches of combustion of inert gas/metal particles mixtures in a laminar diffusion flame are described. It is shown that, unlike diffusion flames of gaseous reactants, laminar diffusion dust flames in has essential singularities stipulated, in first, by lacking of particles diffusion and, in - second, by discrete character of oxidizer consumption and heat release (microflames). Due to the first singularity metal concentration in a dust remains practically constant from the burner nuzzle up to the top of the flame, but a dust temperature increases as a result of heat transmission from combustion zone. Therefore, the theoretical temperature in combustion zone of two-phase flame may increase upwards the flow up to a value of $2T_{ad}$, (T_{ad} - adiabatic flame temperature of the stoichiometric mixture), whereas for the gas flame burning temperature remains constant along a flame. For the same reason heat release in combustion zone of a dust laminar flame decreases much more feebly than for gas flames. Such integral performances of a dust flame as its height and form also differ from the gas flame ones.

It is known that in laminar diffusion gas flames the oxidizing agent practically does not penetrate through the combustion zone. For a dust flame the oxygen consumption in combustion zone occurs on the surface of microflames surrounding each burning metal particle. As a distance between particles usually considerably exceeds the sizes of individual microflames, there is a principal possibility of oxidizer penetration through the combustion zone. This effect was experimentally acknowledged for diffusion combustion of aluminum dusts.

RADIATION HEAT EXCHANGE IN BURNING DISPERSIVE SYSTEMS

I. A. Florko, A. V. Florko, N. I. Poletaev, V.G. Shevchuk

Institute of Combustion of the Odessa National University, Odessa, Ukraine.

In this work studies contribution of thermal radiation in heat exchange of single submicron oxide particles of metals and their dusts. The absorption and scattering factors are measured and calculated on the basis Mi theory at burning temperatures. The received information is initial for the solving of tasks of reactive heat transfer in dispersed systems. The appropriate calculations for real dusts of Mg and Al have carried out. The results are in satisfactory consent with experimental data.

INTRODUCTION

The interest to researches the radiation characteristics of dust flames is coursed by the importance of the processes of radiation heat transfer for problems of safety in fire-explosion of air-dust mixtures and also some technological aspects of solid fuels combustion, for example, synthesis of oxide nanopowders by combustion methods (Ageev at al. 1993, Zolotko at al. 1996). This work carries out the analysis of researches of the radiation influence on the heat exchange of burning single particles and metallic dusts with an environment. In examined processes the basic sources of radiation are: 1) submicron oxide particles (diameter less than 0.1 μm), which are formed at vapor or gaseous phase burning of a metal particle; 2) an individual burning metal particle; 3) burning dust clouds of metal particles. It is obvious, that for dust the radiation heat flux will be determined both by properties of an individual radiator (oxide particle and metal particle) and their collective effect dependents on particles size and concentration in a dust cloud.

The purpose of researches is the reveal the role of radiation in the thermal balance of a burning single metal particle and their dusts in the process of formation of condensed phase of combustion products and to determine the radiation characteristics of combustion zone and combustion products particles.

TECHNIQUE OF THE EXPERIMENTAL INVESTIGATIONS

The spectral and electrophisical research methods for Mg and Al single particles and dust combustion process have been used. In order to determine the temperature of the condensed phase in a burning zone and the effective emissive ability of a flame, the polychromatic method (Belinsky at al. 1984) and optical radiometer on a basis of pyroelectrical ceramic receiver was used. The researches were carried out in a range of wavelength $\lambda = 0.25 - 20$ μm. The technique of electrophysical researches of a burning single magnesium particle is described Zolotko at al. (1985). A stationary laminar two-phase torch was used as object for researches of burning Mg and Al dusts (Ageev at al. 1990). With the help of specified techniques the following initial information was received: spectral and integral radiance, radial distribution of radiation flux extinction of radiation, current saturation initiated by burning particle in external electrical field, photos of objects. The calculations of extinction coefficient, effective absorption and scattering factors were carried out on the basis of Mi theory on a technique (Bohren and Huffman 1983).

EXPERIMENTAL RESULTS

1. Submicron oxide particles of metals

Optical characteristics of individual submicron particles formed at burning are the initial information for the calculation of radiation fluxes of burning dusts. The most important parameters are the factors of scattering efficiency Q_s and absorption Q_a. They represent the ratio of sections of the appropriate processes to the geometrical section of particle and can be calculated on the basis of Mi theory. For submicron particles in infrared range (diffraction parameter Raleigh $2\pi/\lambda<0.6/n$, where n is the refraction parameter) as will be shown bellow, is possible to use Raleigh approach. Factor Q_s depends on the real part of n and Q_a - on the imaginary part χ. It is known, that n poorly depends on temperature that essentially raising the reliability of calculated values of Q_s. The value χ for particles is an exponential strong depend function of temperature. For this reason now there is no reliable databank for an imaginary part of n at high temperatures. Let's note, by the way, that according to Kirchgofs law Q_s is equal to a

spectral emissive ability. Already this circumstance causes importance of the similar information.

In works (Florko 1989, Florko 1993) the measuring and calculations of the value Q_a in visual and short-range infrared wavelengths ($\lambda \approx 0.6$ μm) for particles MgO and Al_2O_3 were carried out, which have allowed to receive for submicron particles MgO:

$$Q_a=1.5\cdot10^9\, l \exp(-37700/T) \qquad (1)$$

where l is the size of cubic particles MgO, cm.

In view of dependence Q_a from a wavelength (in Raleigh approach $Q_a \sim \lambda^{-1}$) we have:

$$Q_a=10^5\, l\, \lambda^{-1} \exp(-37700/T) \qquad (2)$$

l and λ - are measured in cm. The expression (2) is correct for $\lambda \geq 0.8$ μm (see fig. 1,2) and in approach of a weak dependence of an imaginary part of refraction index from a wavelength.

For particles Al_2O_3:

$$Q_a=500\, d \qquad (3)$$

where d - diameter of a particle, cm (the temperature dependence for particles Al_2O_3 was not explored).

Having substituted in (1) $l = 0.1\ 10^{-4}$ cm., T=2600 K and in (3) diameters of particles Al_2O_3, $d = 0.1\ 10^{-4}$ cm, we shall receive for comparison: MgO – $Q_a = 0.01$ and for Al_2O_3 – $Q_a = 0.005$.

As the dust cloud of metal particles is polydispersive system, the actual interest is represented with calculating the middle value on the distribution functions. Such calculation of the middle value was carried out for sections of impairment (σ_e), scattering (σ_s) and absorption (σ_a). The calculations were carried out according to a relation:

$$\sigma_{e,s,a} = \int Q_{e,s,a}(d)\cdot f(d)\cdot \pi \cdot \frac{d^2}{4} dd \qquad (4)$$

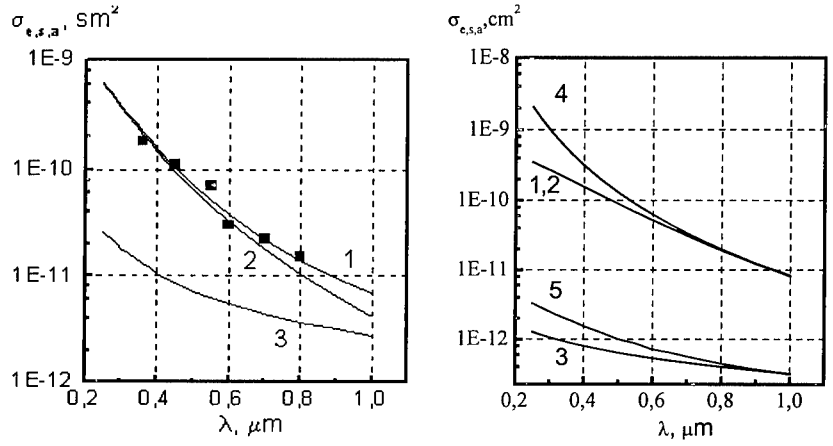


Fig. 1 Averaged on a distribution function of particles MgO on the sizes of section: 1- extinction σ_e; 2- scattering σ_s; 3-absorption σ_a; the points - experiment (are counted under the formula (6)).

Fig. 2 Averaged on a distribution function of particles Al_2O_3 on the sizes of section of processes: 1- extinction σ_e; 2, 4 - scattering σ_s ; 3, 5 - absorption σ_a ; 1, 2, 3 - calculations on the basis of the Mi theory; 4, 5 - in Raleigh approach

The distribution functions *f(d)* was obtained as a result of the disperse analysis of oxide particles (on photos received with the help of an electronic microscope). It has been estimated, that the oxide particles size distribution follows the lognormal distribution:

$$f(d) = \frac{1}{\sqrt{2 \cdot \pi} \cdot d \cdot \sigma_0} \cdot \exp\left[- \frac{\left(\ln(d) - \ln(d_0)\right)^2}{2\sigma_0^2} \right] \qquad (5)$$

It was shown (Zolotko at al. 1996) that the conditions of burning of metal particles (single particles, dust clouds in a wide range of change of dust parameters) practically do not influence on disperse composition of combustion products. Both for MgO and Al_2O_3 particles the value of d_0 and σ_0 are equal accordingly: (0.075 μm, 0.35)

and (0.08 μm, 0.48). The factors of efficiency of processes were calculated on the basis of the Mi theory. The results of calculations of the averaged sections show, that with decrease of a wavelength the sections of processes are sharply incremented (fig. 1 and 2). The determining role in an extinction of radiation plays a scattering and only in infrared range for particles MgO efficiency of a scattering and absorption become comparable. For particles Al_2O_3 the role of the absorption is incidental due to small value of an imaginary part of refraction index. This led to merging of the dependencies from a wavelength of sections of impairment and scattering (see fig. 2). The curves 4, 5 (fig. 2) are obtained in Raleigh approach and illustrate conditions of its applicability. The experimental values of the impairment sections (fig. 1) have been obtained by measuring of the optical densities (βL) combustion zone of single particles Mg according to a relation:

$$\sigma_e = \frac{(\beta \cdot L)}{N_c \cdot L} \tag{6}$$

Where L-combustion zone width, N_c-concentration of c-phase particles (Florko and Golovko 1991).

The experimental study of a radiance of combustion zone of a particle Mg have allowed to reveal a role of radiation in the heat balance of an oxide particles during time of their growth. It is possible to show, that the energy fraction radiated by the particle during condensation up to cubic middlesize ($< l^3 >$) in relation to the energy, allocated at it, is determined by a relation:

$$\eta_e = \frac{16\pi R r_c^2}{\frac{dn_c}{dt} < l^3 > \rho q_c} \tag{7}$$

Where ρ - MgO density, kg/m^3, q_c- specific condensation heat, J/kg, R - integrated radiance, w/m^2, r_c - radius of condensation zone, m, dn_c/dt - velocity of generation of c – particles s^{-1}.

The radiuses of condensation zone r_c and of metal particle r_0 are linked by a relation that was set experimentally:

$$r_c = r_0 \left(\mathrm{P} \cdot 10^{-5}\right)^{1/3} \tag{8}$$

The velocity of generation was determined on saturation currents (Zolotko at al. 1984). The integrated radiance was measured in pressure range $P = 10^4 \div 10^5$ Pa and $\lambda =$ 0,3 ÷ 20 μm (see table 1).

The expression (7) has allowed to establish, that the share of radiation in the heat balance for submicron particles is rather essential and grows with a pressure decreasing from 0.5 up to 0.8 (see tab. 1; some diminution η_e at $P=10^4$ Pa, on our sight, results from the errors of experiments, instead of the physical features). Nevertheless, at an early stage of growth of particles, when $Q_a \sim l \to 0$, the role of molecular heat exchange in the heat balance of a growing particle is leading (for all pressures). The lack of the effective mechanism of heat exchange (molecular or radiation) is one of the reasons that at reduced pressures ($P < 3000$ Pa) the flame becomes transparent. There are difficulties with "dumping" of the energy that released at condensation, the particles overheat and practically cease to grow.

Table 1. Experimental and calculated data for single magnesium particle

P, Pa	10^4	$2 \cdot 10^4$	$5 \cdot 10^4$	10^5	Experimental error, %
$\frac{dn_c}{dt}$, s^{-1}	10^{11}	$2 \cdot 10^{11}$	$4 \cdot 10^{11}$	10^{12}	30
R, W/cm^2	O,14	0,7	3	9	10
η_e	0,5	0,8	0,7	0,5	40
N_c, cm^{-3}	10^9	10^{10}	10^{11}	$5 \cdot 10^{11}$	50
α	0,04	0,08	0,23	0,4	15
γ	6	2	0,8	0,4	20

2. Single particles of magnesium

The radiation of a burning magnesium particle has two components. This radiation of the dust cloud of submicron particles generated due to vapors of magnesium oxide condensation and radiation of the drop of magnesium, covered oxydic coating. The measuring of luminous fluxes from a zone of condensation and times of burning of single magnesium particles of mass 0.2 g (diameter of particles about 4 mm) at various pressures have shown, that the share of radiation in common heat liberation is directly proportional to pressure (see tab. 1). As it is visible from the table at atmospheric pressure ($P = 10^5$ Pa) a particle of magnesium radiates 40 % of energy of condensation. At $P = 10^4$ Pa this quantity decreases up to $\alpha = 4$ %. Meantime, the time of burning τ (to

be more exact quantity τ/d^2) for explored particles Mg is rather feeble function P (Otsisik 1976). This mean that the radiation from a zone of condensation of combustion products is not essential (for maintenance of burning) in the heat balance of a burning particle of magnesium and its role is reduced to heat loses. For particles with a diameter about several millimeters the contribution to a common flux of radiation from an oxidic coating on a surface of a metal drops, has appeared rather considerable and incremented with a pressure pumped down. Temperature of an oxidic coating is rather small ($T \approx$ 1400 K), but because of the advanced surface the emissive ability ($\varepsilon \approx 0.3$) is great that provides its rather high radiance. In the table 1 are set out the ratios of luminous fluxes from an oxydic coating and the condensation zone (γ) calculated according to a relation:

$$\gamma = \frac{\varepsilon \cdot \sigma \cdot T^4 \cdot r_o^2}{R \cdot r_c^2} \qquad (9)$$

The contribution to a common luminous flux of oxidic coating increases with pressure and at $P=10^4$ Pa becomes determining (table 1). It is similarly possible to show that the energy, which is radiated oxidic coating, exceeds energy, which particles obtain from a zone of condensation. Therefore, the radiation of this zone does not render essential influencing on a thermal mode vaporization of a drop of metal. It means, that the vapour -phase combustion regime of a particle Mg is supported as at the expense of heat of condensation of a part of the gaseous monoxide, which condensed on a surface of metal, and at the expense of heat conduction. Let's mark also, that for large particle of Mg the role of radiation of oxidic coating increases with the course of time because of increase of its size and approaching to it of a combustion zone resulting in to temperature rise.

Thus, the role of both components of heat radiation from the metal particle which burn in the vapour -phase regime is reduced to heat loses.

3. Laminar two phase flames of Mg and Al.

To execute researches similar above reduced, for a single aluminum particles is technically complex because of very high temperatures of their ignition and combustion. For study of aluminum particles combustion it is possible to use dust flames this metal -

laminar diffusion (dust/inert gas mixture in co flowing oxidizer) or previously premixed two phase flames (Ageev at al. 1990). The measured values of radiance R of a combustion zone of laminar diffusion dust flame of aluminum (for various mass concentration of the dispersed fuel C_f, kg/m^3) are shown in the table 2. For comparison, radiance of the combustion zone of laminar premixed dust flame of Mg is shown too. In table 2 - T_c - c-phase temperature in combustion zone, d_p - mean diameter of the metal particles.

Table 2. Characteristics of the combustion zone of the Al and Mg dust flames

C_f, kg/m^3	0,2(Al)	0,4 (Al)	0,6 (Al)	0,6 (Al)	0,4 (Mg)	Error, %
T_c, K	2850	3100	3000	3080	2600	3
d_p, μm	5	5	5	14	5	-
R, W/cm^2	0,75	5,2	4,2	3.9	6	10
η_e	0.12	0.35	0.25	0.2	0.43	20

Let's mark, that the integral radiance of a flame Mg is higher, than flame Al, though temperature first on 400 ÷ 500 K is less, than second. It is connected that the efficiency factors of absorption for fragments MgO in 2-3 times exceed those for Al_2O_3. It is easy to be convinced of it, outgoing from relations (1, 3). Radiation heat lose were determined on a measured radiance and geometrical parameters of a flame obtained photographically and from radial distributions of luminous fluxes.

For dust flames of investigated scales 5-10 cm (dust burner, tubes, clouds of small diameter) the role of radiation also is reduced mainly to heat lose. For a combustion zone as depth of 1-2 mm it is possible to consider flame front optically by transparent and radiate heat lose easily estimate on the basis of a Stefan-Boltzmann law and outcomes of measurement or calculations of an emissive ability. The analysis of radiance of flames allows to draw a conclusion, that basically monoxide particles radiate. Therefore, in adiabatic conditions temperature of a condensed phase would be stabilized near to temperature of phase change (liquid - gas), however presence of heat lose by radiation results to essentially lower temperatures c - phase (3200K for aluminum and 2600K for magnesium instead of 3900K and 3300K accordingly).

THE ANALYSIS OF OUTCOMES OF EXPERIMENTS

The outcomes of measurement and calculation extinction of radiation have shown, that the attenuation of radiation is determined practically by scattering (see fig. 1,2), i.e. efficiency factors of scattering (Q_s) and c- phase particles concentration. The values Q_s depend on a real part of refractive index and are weakly change with temperature. Actually it means, that parameter at calculation of extinction, is only concentration N_k. The good consent between outcomes of calculations and measurements, both on an absolute value, and on relation from λ takes place (see fig. 1). It guarantees reliability of outcomes of measurement of concentration of c- particles on absorption of radiation. Value N_k together with efficiency factors of absorption determines a spectral emissive ability of a flame as a whole. The calculations were conducted with usage of the theory Mi taking into account particle size distribution function. The calculations were carrying out for single magnesium particles and for laminar diffusion dust flame of aluminum. The obtained outcomes were used at calculations of a spectral emissive ability ε_λ according to a ratio (Petrov 1982):

$$\varepsilon_\lambda = \frac{K}{K + 1.5 ctg(0.5 K \beta l)} \qquad (10)$$

where $K = \sqrt{\frac{3\beta_0}{\beta_a + \beta_s}}$, β - coefficient of impairment of the radiation, β_a , β_s - coefficients of the impairment of the radiation by absorption and scattering of the energy accordingly.

From a figure 3 it is shown, that in a visible band of lengths it surges that the results are in good consent. In ultraviolet the considerable divergence of the data takes place. One of explanations - size effect (Petrov 1982). Let's remind, that the outcomes of calculations based on applicability of the laws of heat radiation, in particular, it was supposed, pursuant to Kirchhoff's law, equaling of efficiency factors of absorption and spectral emissive ability of particles. Thus, there are no bases to put in question applicability of conventional methods of the description of radiation transmission in

disperse systems. It's understandable as well that, what is it only approximation can be satisfying or not in the limits of experiment errors.

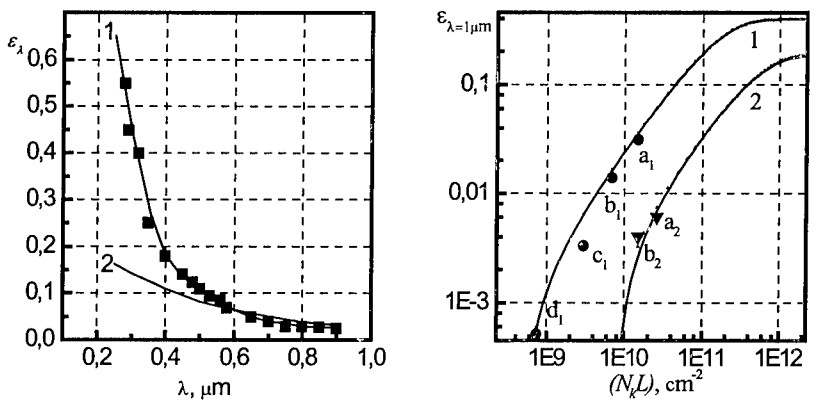


Fig. 3 The spectral emissive ability of a combustion zone of a single magnesium particle at atmospheric pressure:1-outcomes of experiments; 2-calculation according to expression (8).

Fig. 4. The emissive ability dependence of a product of concentration submicron metal oxide particles (N_k) and size of the radiant zone L: 1- dust cloud of the radiant submicron MgO particles; 2 - dust cloud of the radiant submicron Al_2O_3 particles. Points outcomes: a_1, b_1, c_1, d_1- an emissive ability of a zone of condensation of submicron MgO particles at pressure P = 10^5; $5\cdot10^4$; $2\cdot10^4$; 10^4 Pa, accordingly; a_2, b_2- an emissive ability of front of laminar diffusion flame of Al for concentrations combustible 0.6 and 0.4 Kg /m^3, accordingly.

In a fig. 4 according to ratio (10) the calculations of a spectral emissive ability for λ=1 μm (near Wien's maximum) are conducted depending on product of concentration of particles and combustion zone width N_kL (actually from optical density). The obtained value can be used for the estimation of integral radiance. On same figure, the measurement results of ε for Mg particles are shown at different pressure and laminar dispersive diffusion flame of Al for different fuel concentrations. For calculating the efficiency factor, the previously computed scattering and the absorption factors were used. As shown in the fig. 4 results of calculations and measurements are in the satisfactory consent that testifies the applicability of the heat

radiation laws and Mi theory for the radiation transmission in disseminating, absorptive and radiative environments. On fig. 4 it is demonstrated, that for large absorbencies of gas mixtures of particles MgO and Al_2O_3 the value ε is on levels 0.4 and 0.2, accordingly. Consequently at $\beta \cdot L \to \infty$, $\varepsilon \to K \cdot (K+1,5)^{-1}$ and at small absorbencies: $\varepsilon \sim \beta_a \cdot L$.

CONCLUSION

The experimental and calculated investigation allowed one to conclude:

1. The radiation plays essential a role in a heat balance of burning systems and has nature of heat losing and the efficiency depends on the environmental conditions and parameters of the system.

2. Submicron metal oxide particles with 50 % - 80 % of energy discharging at condensation of gas-like combustion products, is transmitted in environment at the expense of radiation. Nevertheless, at early stadium of condensed particles growth the role of radiation is not essential, that slows processes of condensation at lower pressures.

3. The Mi theory allows to receive a relevant data about efficiency factors of scattering dissipation and absorption energy at combustion temperatures.

4. In visible and IR - wave diapasons the radiation is thermal, and is well described on the basis of a known equation of radiation transmission in burning dispersive systems.

REFERENCES

N. D. Ageev, J. I. Vovchuk, S. V. Goroshin, A. N. Zolotko and al. (1993) A patent of USSR № 1822397 "A way of obtaining of a ultra dispersed powder of metal oxide" (*Report " Discoverings, invention "№22*)

A.N. Zolotko, J.I. Vovchuk, N.I. Poletaev, A.V. Florko, I.S. Al'tman, (1996) Nanooxides Synthesis in Two Phase Laminar Flames, *Fizika gorenya i vzryva* , 32(3), 24-33.

A.V. Belinsky, S. V. Kozitsky, A. V. Florko, (1985) The Spectral Device for Research of the Radiant Characteristics of Dispersed Combustion Products, in *Physics of aerodispersed system,* 28, 88-92.

A. N. Zolotko, S. V. Kozitsky, A. V. Florko, (1984) A pulse method of testing of the electrical characteristics of charged particles of combustion products, *in Physics of aerodispersed system*, 26, 79-83.

N. D. Ageev, J. I. Vovchuk, S. V. Goroshin, A. N. Zolotko, N. I. Poletaev, (1990) Steady Combustion of Solid Fuel Gas -Suspentions - Laminar Diffusion Two-Phase Flame, *Fizika gorenya i vzryva,* 26(6), 54-62.

Bohren, C. F. and Huffman, D. R. (1983) *Absorption and Scattering of Light by Small Particles*, Wiley, New York

Florko A. V., Golovko V. V. and Skogarev V. G. (1989) Efficiency Coefficients of the Scattering and Absorption of MgO Particles at Combustion Temperatures, *Fizika Goreniya i Vzryva*, 25(3), 28-32.

A. V. Florko and I. V. Sharf (1993) The Optical Characteristics Al_2O_3 Submicron Particles at Combustion Temperatures in Visible and Infrared Wave Bands. *XVI conference of NIS countries on vaporization, combustion and gas dynamics of disperse systems*, Book of Abstracts, p. 131

A. V. Florko and V. V. Golovko (1991) Features of a Germing and Growth of a C - phase at Combustion of a Single Particle of Magnesium, *Reophysics and thermal physics of non-equilibrium systems,* Proceedings of an International school - seminar, (2), 103 - 107.

Florko A. V., Kozitski, S. V., Pisarenko, A. N. and Matsko A. M. (1986) Investigation of Single Magnesium Particle Combustion at Low Pressures, *Fizika Goreniya i Vzryva*, 22(2), 35-40

M. M. Otsisik (1976) *Composite heat exchange,* Moskow.

Yu. P. Petrov (1982) *Physics of small articles,* Moskow.

Investigations of GAP Prepolymers with NMR and MALDI-TOF mass spectrometry

M. Kaiser, B. Ditz, Wehrwissenschaftliches Institut für Werk-, Explosiv- und Betriebsstoffe, Aussenstelle Swisttal-Heimerzheim, Großes Cent, 53913 Swisttal, Germany
C. Völkl, Wehrwissenschaftliches Institut für Werk-, Explosiv- und Betriebsstoffe, Landshuter Str. 70, 85435 Erding, Germany

Summary

Technical products of polyepichlorhydrin (PECH) and glycidyl azide ploymer (GAP) were investigated by high resolution NMR spectroscopy and MALDI-TOF mass spectrometry. The measurements were carried out using a NMR spectrometer with 400.13 MHz proton resonance frequency. One dimensional ^{1}H and ^{13}C NMR spectra were recorded and the signals were evaluated. After acetylation of the samples and with the help of ^{13}C DEPT NMR spectroscopy functional groups were identified. The mean molecular weights were determined by quantitative INVERSE GATED ^{13}C NMR spectroscopy and MALDI-TOF mass spectrometry. The PECH and the GAP specimen could be identified as polymers of the diol type (PECH-1,2-ethanediol-PECH, respectively GAP-1,2-ethanediol-GAP) with mean molecular weights between 1900 and 2300. It could also be shown that one of the GAP samples contained PECH-1,2-ethanediol-PECH.

Introduction

Glycidyl azide polymer (GAP) is an energetic binder and plasticizer system. It is intended for use in propulsion and explosives formulations [1]. For characterization of mechanical properties of propulsion and explosives formulations containing GAP, it is neccessary to know the alcohol used in GAP ("starting molecule"), to determine the chain length, to characterize the molecular weight distribution and to get information about impurities based on the synthesis route. In this poster presentation the topics mentioned above were investigated.

Synthesis of GAP

The synthesis of GAP is a process consisting of two or more steps [2]. Epichlorhydrin - see figure 1.1, „1" - reacts with an alcohol (HTPB, TMP or 1,2-ethanediol) under formation of an intermediate (figure 1.1, „2"). The product is obtained after addition of sodium azide (see figure 1.1 „3"). The product, consisting of two GAP chains bound to a diol molecule, is often called „GAP" although this is not correct: It should be called „GAP-[alcohol name]-GAP". In the following „GAP-[alcohol name]-GAP" and „PECH-[alcohol name]-PECH" are often called „GAP" or „PECH" for simplification.

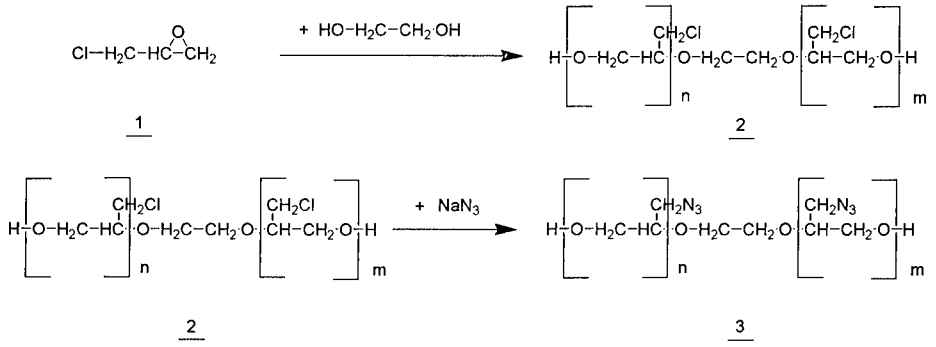


Figure 1.1: Synthesis of „GAP"

Experimental

NMR investigations were accomplished using a Bruker DMX 400WB NMR spectrometer with a proton resonance frequency of 400.13 MHz. The resonance frequency of the ^{13}C nucleus was at 100.62 MHz. The substances were dissolved in chloroform d_1 and examined at ambient temperature. A 5 mm multinuclear high resolution probe was used for the measurements. The number of data points typically totaled 32 K, 64 K or 128 K. Different one-dimensional spectra like ^{1}H, ^{13}C INVERSE GATED or ^{13}C DEPT spectra [3] were recorded. The spectra were calibrated taking ^{1}H and ^{13}C spectra in relation to tetramethyl silane (TMS), where the proton signal of the solvent (choroform) was set to 7.24 and the ^{13}C signal was set to 77.0 (^{13}C INVERSE GATED) and to 77.2 (^{13}C DEPT). Since the carbon atom of a ^{13}C INVERSE GATED signal is bound to ^{2}H, while the one of a ^{13}C DEPT signal is bound to ^{1}H, there is a slight difference between the chemical shifts.

MALDI-TOF MS (matrix-assisted laser desorption/ionisation time-of-flight mass spectrometry) was developed in 1988 and is widely used for the fast and precize determination of the molecular mass of synthetic polymers as well as biopolymeres (peptides, proteins, carbohydrates nucleic acids ...)[4,5]. Due to the very mild desorpion and ionisation the quasi molecular ions, formed with the kations added to the sample as acids, sodium or silver salts, e.g. $[M+Na]^+$, have very little excess energy and even the labile biopolymeres usually show only a neglegable amount of fragmentation.

The MALDI mass spectra were obtained using a BIFLEX™ III time-of-flight mass spectrometer (Bruker Daltonics, Bremen, D), equipped with a nitrogen laser (337 nm). The mass spectra were recorded with delayed ion-extracton at an acceleation voltage of 19 kV operating in positive ion- and reflection-mode (reflector voltage 20 kV). Small ions (up to 600 Da) were excluded by deflection. With Dithranol (1,8,9-Anthacenetriole) used as UV-absorbing matrix and NaTFA (sodium-trifuoroacetate) as cationizing agent the quasi molecular ions [M+Na] of the GAP-polymeres were observed in the mass range beween 800 and 4500 Da. The sample preparation was similar to the procedure described in [6].

Results

A characterization of the samples based on ^1H NMR spectra was almost impossible. There was a difference between acetylated and non-acetylated samples, but there were also overlappings of signals which made it impossible to integrate the peaks and to determine the mean molecular weights.

Since CH_3 and CH groups appear as positive signals in ^{13}C DEPT spectra and CH_2 carbon atoms can be seen as negative peaks, structure elements could be identified.

Acetylation of the sample was another help for structure elucidation. It led to strong shifts of the glycidylazid carbon atoms which were near the acetyl groups („$GA_{end\ group}$“) while there was almost no shift of the glycidylazid carbon atoms which were near the alcohol („GA_{chain}“) [7,8].

Specimen „GAP-Diol sample A“

Since there were no other alcohol signals visible in the spectra, the sample must be a GAP-diol-GAP. Because of no significant overlappings, it was possible to integrate the carbon signals (see table 2.2). The signal at $\delta = 70.4$ was caused by 2 carbon atoms, so the starting molecule was identified as 1,2-ethanediol. The mean molecular weight could be calculated as follows:

60 ($=M_{1,2\text{-ethanediol fragment}}$) + (22±1) * 99 ($=M_{GA\ element}$) + 2 ($M_{H\ end\ group}$) = 2240 ± 99.

Table 2.1: Chemical shifts and related carbon atoms of the specimen „GAP-Diol sample A"

Group:	H_2C	HC	H_2C	H_2C	H_2C	HC	H_2C	H_3C
Neighbour:	OH	O	N_3		N_3		O	
Position:	End group	End group	End group		Chain	Chain	Chain	
Group:	GA	GA	GA	Diol	GA	GA	GA	Acetyl
Spectrum	non-acetylated specimen							
^{13}C (INVERSE GATED):	72.0 – 70.8	69.6	53.2 – 52.6	70.4	51.3	78.3	69.2	-
^{13}C DEPT):	71.9 – 70.9	69.5	53.1 – 52.7	70.4	51.3	78.3	69.2	-
Spectrum	Acetylated specimen							
^{13}C (INVERSE GATED):	68.4 – 68.1	70.9	50.6 – 50.2	70.5	51.4	78.4	69.2	20.6
^{13}C DEPT):	68.4 – 68.1	70.9	50.5 – 50.2	70.5	51.4	78.4	69.2	20.6

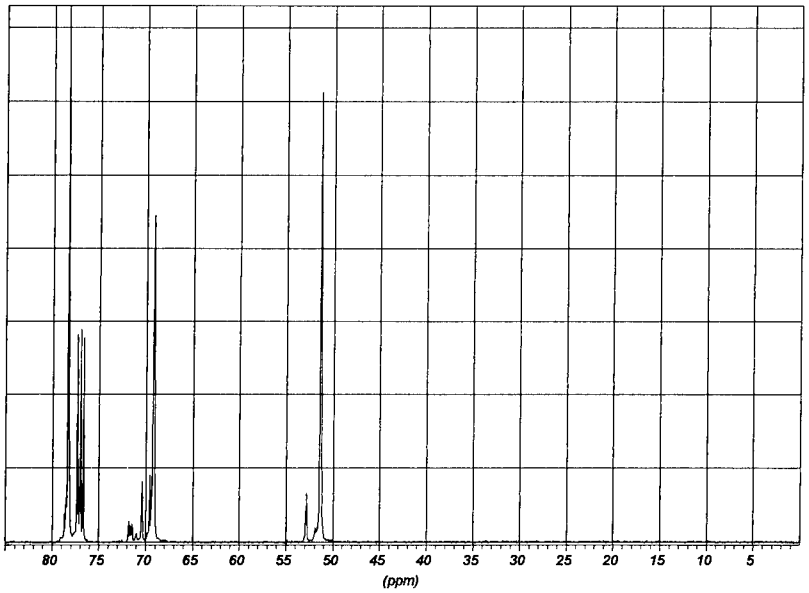


Figure 2.1: Part of ^{13}C INVERSE GATED spectrum of the non-acetylated specimen „GAP-Diol sample A"

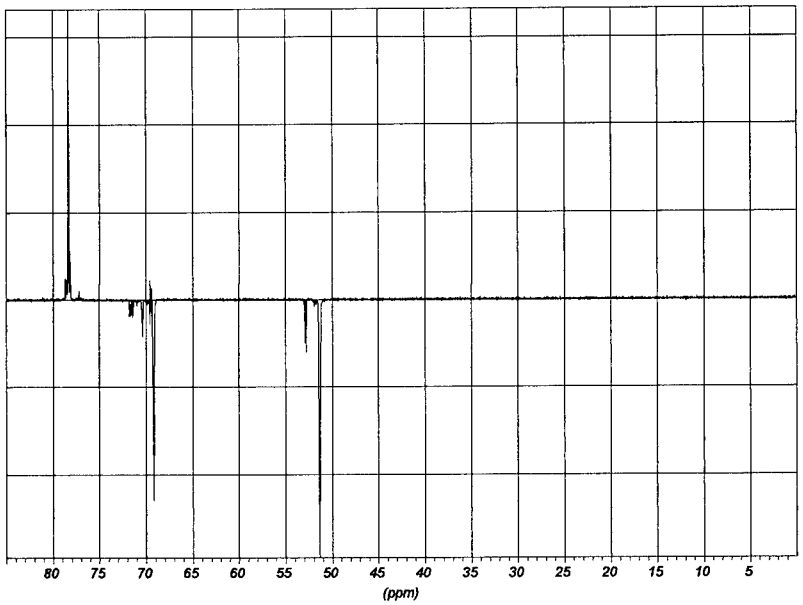


Figure 2.2: Part of ^{13}C DEPT spectrum of the non-acetylated specimen „GAP-Diol sample A"

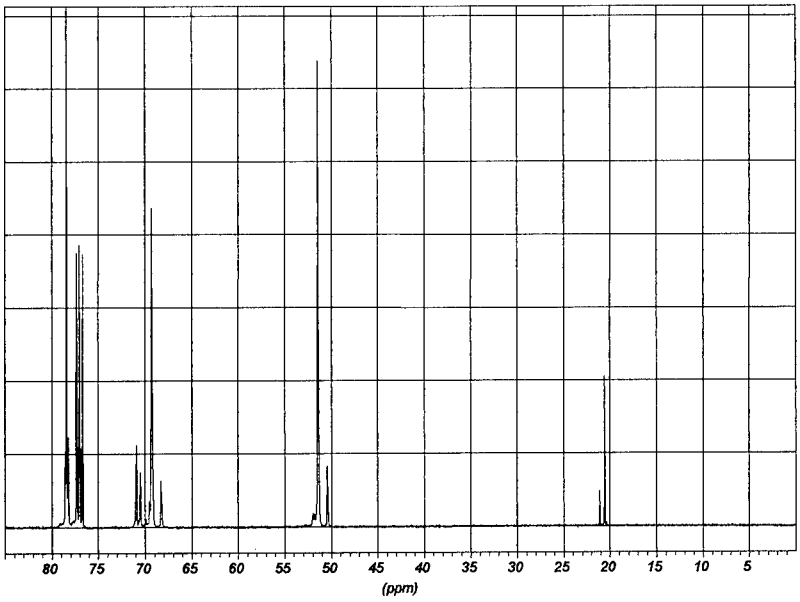


Figure 2.3: Part of ^{13}C INVERSE GATED spectrum of the acetylated specimen „GAP-Diol sample A"

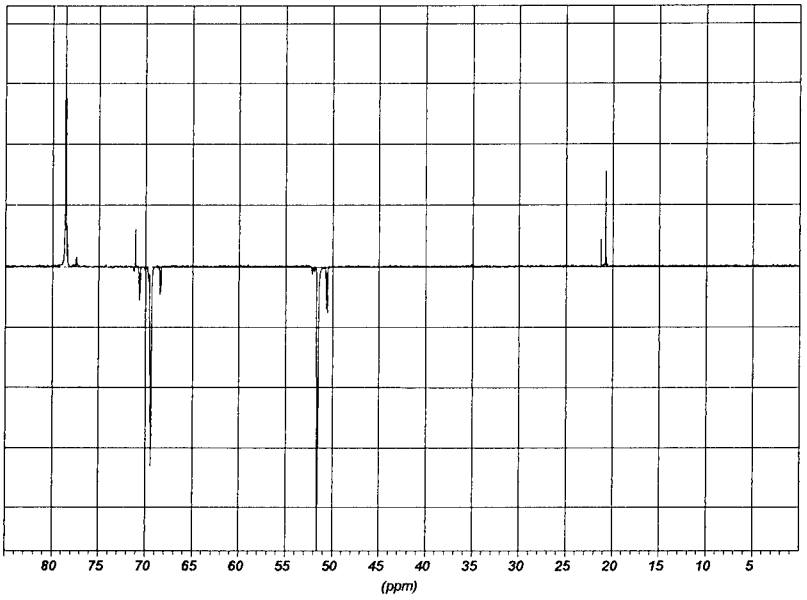


Figure 2.4: Part of ^{13}C DEPT spectrum of the acetylated specimen „GAP-Diol sample A"

Table 2.2: Integration of carbon signals of the specimen „GAP-Diol sample A"

Group:	H_2C	HC	H_2C	H_2C	H_2C	HC	H_2C	H_3C
Neighbour:	OH	O	N_3		N_3		O	
Position:	End group	End group	End group		Chain	Chain	Chain	
Group:	GA	GA	GA	Diol	GA	GA	GA	Acetyl
Integral								
acetylated:	2.337	2.299	1.948	2.306	20.894	20.288	19.305	-
non acetylated:	1.854	2.274	1.866	2.404	21.502	21.691	19.369	2.00
mean:	2.096	2.287	1.907	2.355	21.198	20.990	19.337	2.00

MALDI-TOF mass spectrometry showed four different series of signals. Series 1 was based on structure elements which have a molecular weight of 99 Da (mass difference between each signal of this series). This value was typical for glycidyl azide elements. The difference between a signal of series 2 and the following peak of series 1 was 28 Da. This could be interpreted as an emission of molecular nitrogen, perhaps due to fragmentation. The other two series were very weak. The maximum of the mass distribution (series 1)

was reached at approximate 2300 Da. The distribution of the signals of series 1 between 1328,9 and 3410,1 Da was a Gaussian distibution.

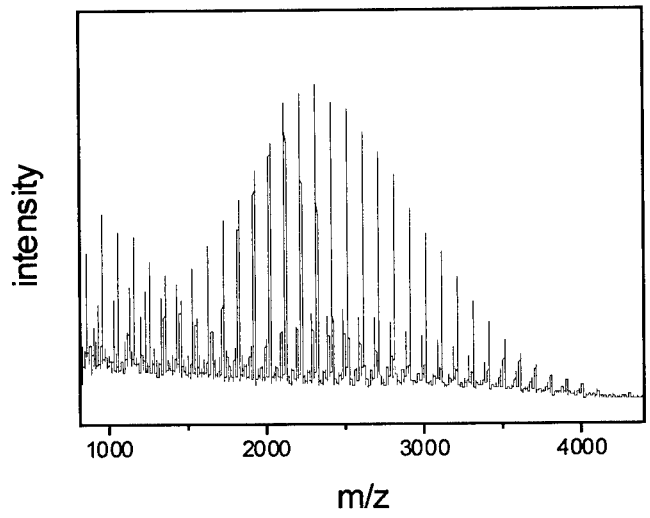


Figure 2.5: MALDI-TOF mass spectrum of the specimen „GAP-Diol sample A non acetylated"

Sample „PECH 2200"

There was a similarity between this specimen and the previous one. Since there were signals at $\delta = 43,3$ and between $\delta = 45,6$ and $\delta = 45,2$ the presence of azide groups was improbable. The existence of a halogen atom, e.g. chlorine was more likely.
Since there were no other alcohol signals visible in the spectra the specimen must be a PECH-diol-PECH. Integration of the significant signals led to 1,2-ethanediol as starting molecule and to a mean molecular weight of

$60\ (=M_{1,2\text{-ethanediol fragment}}) + (23\pm1) * 92.5\ (=M_{\text{PECH element}}) + 2\ (M_{\text{H end group}}) = 2189.5 \pm 92.5$

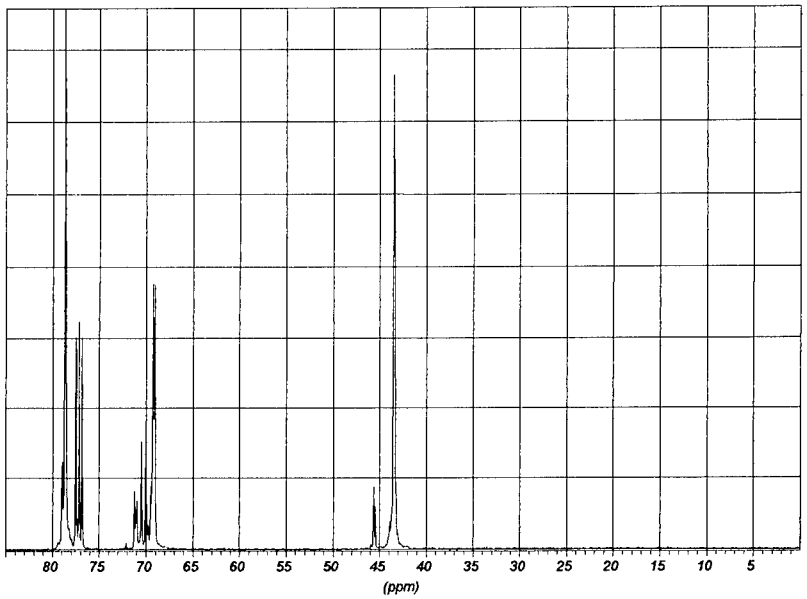


Figure 3.1: Part of ^{13}C INVERSE GATED spectrum of the non acetylated sample „PECH 2200"

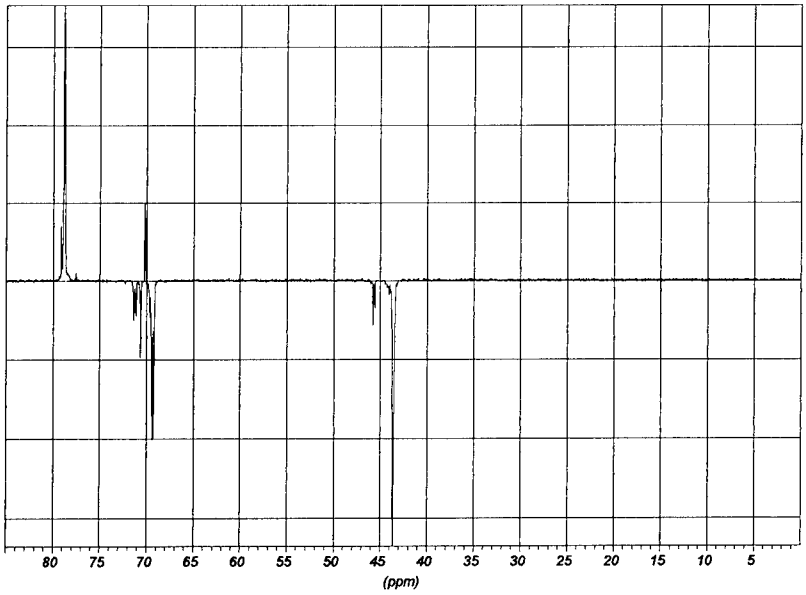


Figure 3.2: Part of ^{13}C DEPT spectrum of the non acetylated sample „PECH 2200"

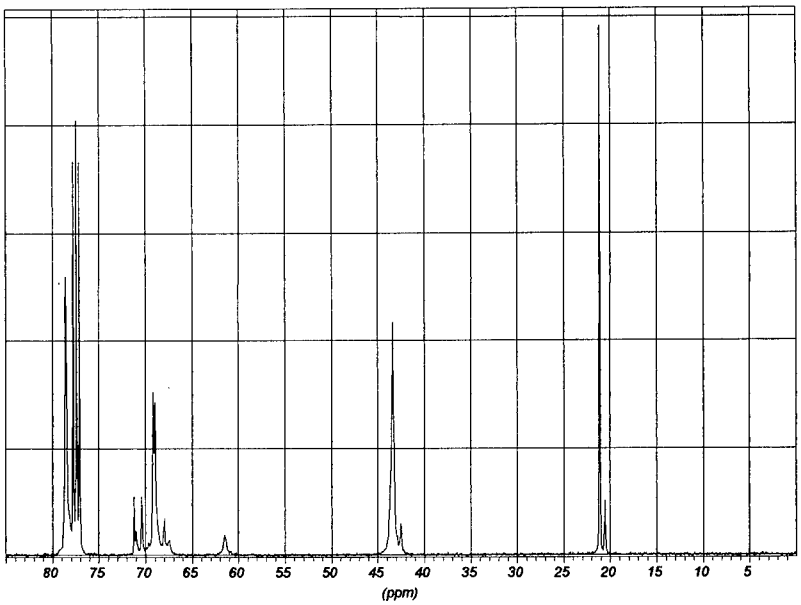


Figure 3.3: Part of ^{13}C INVERSE GATED spectrum of the acetylated sample „PECH 2200"

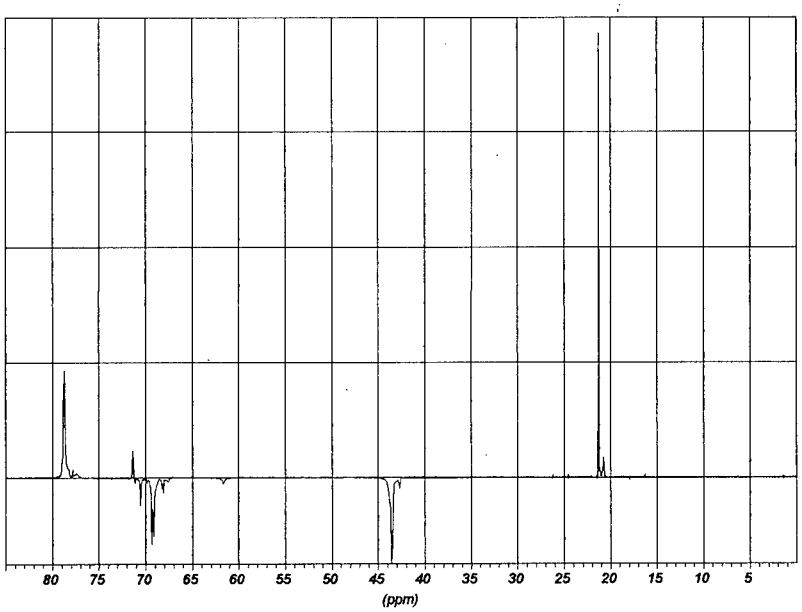


Figure 3.4: Part of ^{13}C DEPT spectrum of the acetylated sample „PECH 2200"

Table 3.1: chemical shifts and related carbon atoms of the specimen „PECH 2200"

Group:	H_2C	HC	H_2C	H_2C	H_2C	HC	H_2C
Neighbour:	OH	O	Cl		Cl		O
Position:	End group	End group	End group		Chain	Chain	Chain
Group:	PECH	PECH	PECH	Diol	PECH	PECH	PECH
Spectrum	non acetylated specimen						
^{13}C (INVERSE GATED):	71.3–70.6 (overlapped)	70.0-69.7	45.6–45.2	70.3	43.3	78.5	69.0
^{13}C DEPT):	71.2–70.7	69.9-69.7	45.5–45.2	70.3	43.3	78.5	69.0
Spectrum	acetylated specimen						
^{13}C (INVERSE GATED):	67.9–66.8 (overlapped)	71.0–70.3 (overlapped)	42.3-41.6	70.0	43.0	78.2	68,7
^{13}C DEPT):	67.8–67.4	70.8	42.3-41.9	69.9	42.9	78.1	68,6

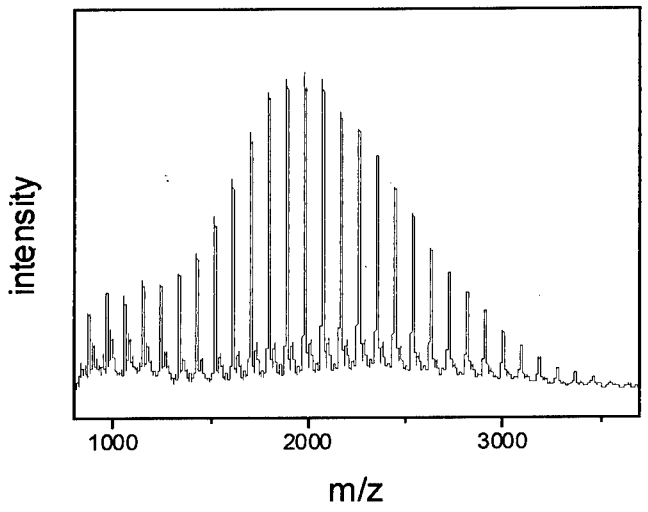


Figure 3.5: MALDI-TOF mass spectrum of the specimen „PECH2200 non acetylated"

The spectrum showed two different series of signals. Series 1 was based on structure elements which have a molecular weight of 92.5 Da (mass difference between each signal of this series), which was typical for PECH elements. The complex isotopic pattern in the mass spectrum is typical for molecules containing a large number of Chlorine atoms. The

maximum of the mass distribution (series 1) was reached at approximate 2000 Da. The distribution of the signals of series 1 between 1243.5 and 3094.3 Da was almost a Gaussian distibution.

Specimen „GAP sample B"

The acetylated sample was similar to the specimen „GAP sample A", but the Signal at δ = 42,9 was typical for methylene groups bound to chlorine as in „PECH".
Integration of the signals led to a relation between „PECH", end groups and „GAP"$_{polymer}$ of 1 : 4: 17. Because of overlappings, calculation of the mean molecular weight was not as simple as in previous cases. 1,2-ethanediol as starting molecule was assumed, but could not be identified. The mean molecular weight of the non acetylated specimen calculated was

60 (=$M_{1,2\text{-ethanediol fragment}}$) + (19±1) * 99 (=$M_{GA\ element}$) + 2 ($M_{H\ end\ group}$) = 1943 ± 99.

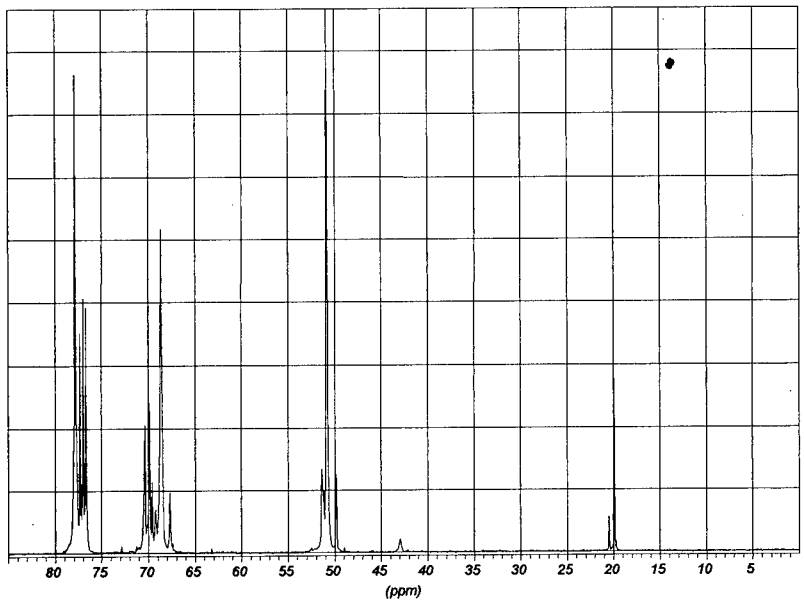


Figure 4.1: Part of ^{13}C INVERSE GATED spectrum of the acetylated specimen „GAP sample B"

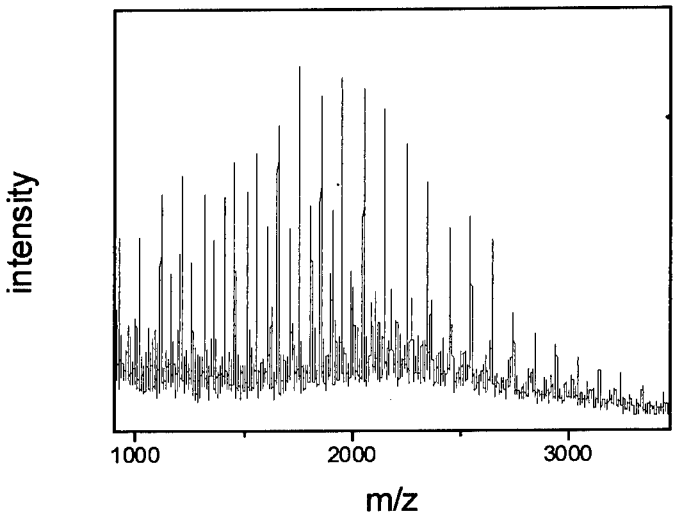


Figure 4.2: Part of MALDI-TOF spectrum of the acetylated specimen „GAP sample B"

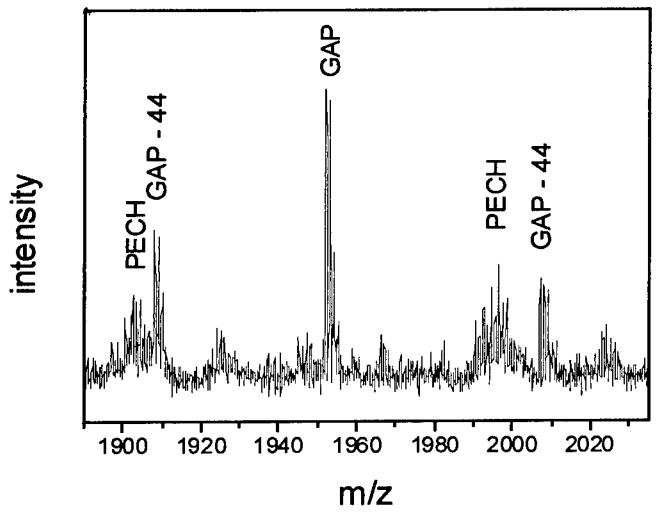


Figure 4.3: Detailed clipping of the acetylated specimen „GAP sample B"

The spectrum of the sample (figure 4.2) was characteristic for a double acetylated specimen. The maximum of the mass distribution was at approximate 1800 Da. A more detailed clipping between 1890 and 2035 Da (figure 4.3) showed that the specimen contained PECH. The difference between the group of signals between 1900 and 1906 Da and those between 1990 and 1998 Da was 92 or 94 Da respectively.

Table 5: Comparison of the mean molecular weights of „GAP" and analogous samples calculated by NMR spectrocopy and MALDI/TOS mass spectrometry

Specimen	Mean molecular weight calculated by NMR	Mean molecular weight calculated by MALDI-TOF
„GAP-Diol sample A non acetylated"	2240 ± 99	approx. 2300
„GAP-Diol sample A acetylated"	2240 ± 99	approx. 2100
„PECH 2200 non acetylated"	2189,5 ± 92,5	approx. 2000
„PECH 2200 acetylated"	2189,5 ± 92,5	approx. 1900
„GAP sample B non acetylated"	1943 ± 99	approx. 1900
„GAP Probe B acetylated"	1943 ± 99	approx. 1800

Literature

[1] R. A. Nissan et. Al.: „GAP Analyses: NMR Methods", NAWCWPNS Technical Publication 8127 (September 1993)

[2] V. Vasudevan, G. Sundararajan: „Synthesis of GAP-PB-GAP Triblock Coploymer and Application as Modifier in AP/HTPB Composite Propellant", Propellants, Explosives, Pyrotechnics 24, 295-300 (1999)

[3] S. Braun, H.-O. Kalinowski, S. Berger: „150 and More Basic NMR Experiments", Wiley-VCH 1998

[4] M. Karas, F. Hillenkamp, „Laser Desorption Ionisation of Proteins with Molecular Masses Exceeding 10,000 Daltons", Anal. Chem. 60 (1988) 2299.

[5] H. Rashiadeh, B. Guo, „Use of MALD-TOF to Measure Molecular Weight Distributions of Polydisperse Poly(metylmethacrylate)", Anal. Chem. , 70 (1998) 131

[6] P. Bartl, Ch. Völkl, „The Application of Matrix-Assisted Laser Desorption/Ionisation Time-of.Flight Mass Spectrometry (MALDI-TOF MS) to the Analysis of Lubricants. Part 1. Polyol Ester Aviation Turbine Engine Oils", J. Synth. Lubr. 15 (1998) 83.

[7] S. Désilets: „Precise Equivalent Weight Determination of Branched Glycidyl Azide Polymers by NMR Spectroscopy", DREV R-4740/94 (March 1994)

[8] M. Kaiser, B. Ditz, Untersuchung von neuen energetischen Bindern (GAP), WIWEB Report Nr.: 98/Y0038/50007 (2000)

USE OF A CYLINDER TEST FOR DETERMINING SOME CHARACTERISTICS OF EXPLOSIVES

Waldemar A. Trzciński
Military University of Technology
Kaliskiego 2, 00-908 Warsaw, POLAND
twa@wul.wat.waw.pl

ABSTRACT

In the paper, the explosive system used in the cylinder test is presented. The method of working out the test results is described and the procedures of determination of the Gurney energy and detonation energy of explosives are given. The semi-empirical methods for determining the effective exponent of isentrope and the coefficients of the JWL equation of state are described. Most of the methods presented in the work have been developed in Military University of Technology. Some results of application of these methods for evaluation of characteristics of high explosives are presented.

1. INTRODUCTION

Recording of the process of acceleration of a metal tube (*the so-called cylinder test*) by the gaseous detonation products of a charge located inside the tube can give us a great deal of data being necessary for solving some problems connected with delivery of energy from an explosive charge to a projectile or a cumulative jet, as well with acting of explosion on surroundings. The acceleration of a metal tube is recorded by precise methods of measurements of the quick-changing processes, such as streak photography [Refs. 1, 2], laser interferometry [Ref. 3] or X-ray photography [Refs. 4, 5]. Results of registration can be used for determining *acceleration abilities of explosive* (*the so-called Gurney energy*), evaluation of *the detonation energy*, and estimation of *the effective exponent of isentrope* and *the equation of state* for the detonation products. In this work the methods of determination of the detonation and energetic characteristics are presented. These methods have been developed in Military University of Technology (MUT).

2. CYLINDER TEST

The cylinder test consists in monitoring the process of launching a metal cylindrical envelope by the products of detonation grazing along the internal surface of the envelope. The scheme of a charge and a metal tube used in the cylinder test is presented in Fig. 1 [Ref. 4].

Tubes of size shown in Fig. 1 are used in MUT. They differ slightly from those having standard size [Ref. 6], i.e. 304.8 mm in length, 12.7-mm internal radius and 15.306-mm external radius. The expansion of the tube is monitored with precise devices for measurement of quick-changing processes. When a streak camera or a laser interferometer is used then the motion of a section of external surface of the tube is observed. In this case, the dependence of the radius of tube surface on time is a result of measurement. When an impulse X-ray apparatus is applied, a shape of whole tube is recorded. X-ray picture of expanding tube and the value of detonation velocity are the results of the test. An exemplary radiograph of a copper tube driven by the detonation products of Octogen (HMX) is shown in Fig. 2 [Ref. 7]. The dependence of the radius of external surface of the tube on the axis co-ordinate is obtained due to computer working out of the X-ray picture.

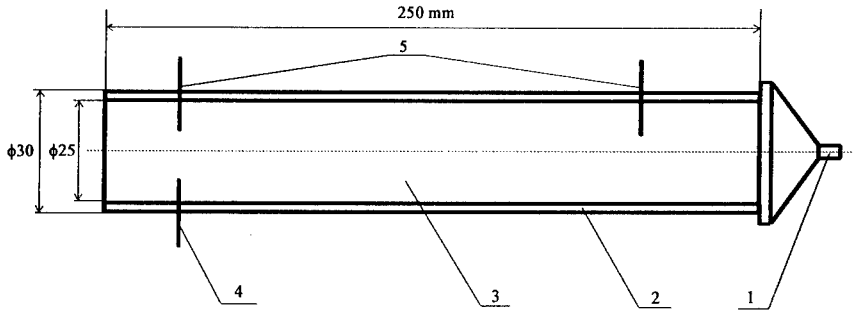


Fig. 1. Diagram of the system prepared for the cylinder test 1 – plane-wave detonator, 2 – copper tube, 3 – charge of the explosive tested, 4 – short-circuit sensor releasing X-ray apparatus, 5 – short-circuit sensors for the measurement of detonation velocity

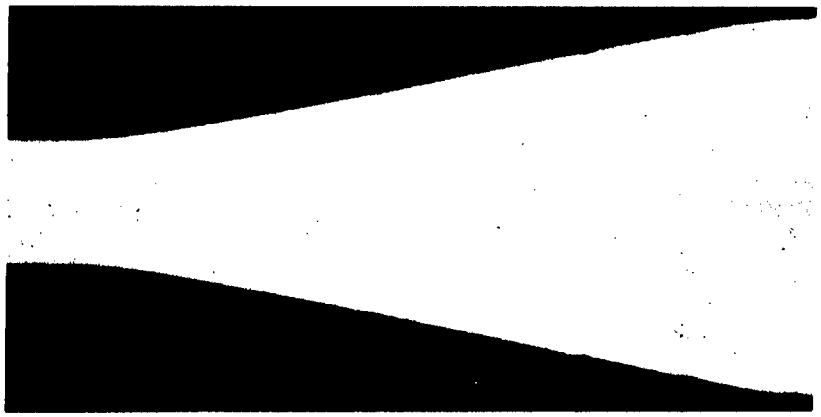


Fig. 2. X-ray photograph of a cooper tube driven by the detonation products of Octogen (HMX)

3. DETERMINATION OF ACCELERATION ABILITIES OF EXPLOSIVES

A diagram of a copper tube accelerated by the detonation products is shown in Fig. 3. A plane detonation wave propagates at a velocity D in a cylindrical charge of explosive. The gaseous detonation products expand, thus driving the tube. It is assumed that the time of detonation wave propagation is long enough to neglect the influence of the initiation of detonation. Then the motion of the detonation products and the tube material may be treated as stationary. Therefore, the axis co-ordinate and time are associated by the following relation

$$x = D \cdot t. \tag{3.1}$$

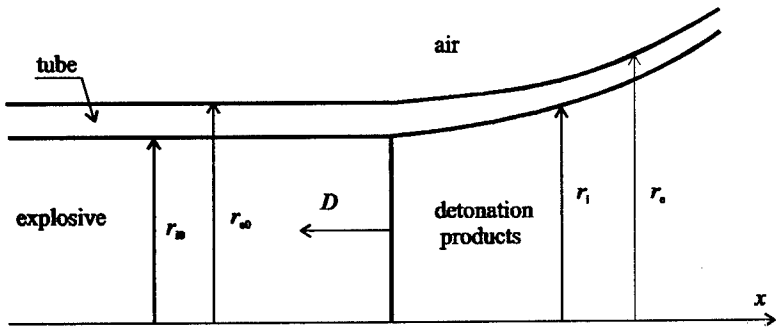


Fig. 3. Diagram of copper tube accelerated by the detonation products

To determine the radial velocity of a copper tube, data of the cylindrical test are recalculated in an appropriate manner [Ref. 8]. First, the position of the central cylinder surface is determined. Assuming a complete incompressibility of the tube material, this position can be established from the relation

$$r_m = \sqrt{r_e^2 - \frac{1}{2}\left(r_{e0}^2 - r_{i0}^2\right)}, \tag{3.2}$$

where r_{e0} and r_{i0} denote the initial radii of external and internal surfaces of the tube, respectively, r_e, and r_m mean the radii of external and central surfaces of the tube for given value of co-ordinate x, respectively.

By using the relation (3.1) we can replace the dependence of the tube radius on axis co-ordinate by the time function of this radius. The time dependence of central position of the tube is approximated by the following function

$$r_m = r_{m0} + \sum_i a_i \{b_i (t - t_0) - [1 - \exp(-b_i (t - t_0))]\}, \tag{3.3}$$

where a_i, b_i, t_0 are parameters. In Ref. [8] it was proved that sufficient accuracy of approximation of the experimental results was achieved by assuming $i = 2$ in (3.3).

Thus, the radial velocity of the central part of the tube is expressed by the relation

$$u_{\mathrm{m}} \equiv \frac{d r_{\mathrm{m}}}{d t} = \sum_i a_i b_i \left[1 - \exp\left(-b_i \left(t - t_0\right)\right)\right] . \tag{3.4}$$

To calculate the kinetic energy of the tube, the total velocity of the tube element must be determined. From geometrical relations it follows that the deflection angle Θ (the angle between the line being tangential to the trajectory of the central surface of the tube and the x-axis) are specified by the relation:

$$\Theta = \operatorname{arc\,tg}\left(\frac{u_{\mathrm{m}}}{D}\right). \tag{3.5}$$

Therefore, the velocity of the central part of the tube is expressed by the equation

$$u_{\mathrm{L}} = 2 D \sin\left(\frac{\Theta}{2}\right). \tag{3.6}$$

We assume that the kinetic energy of the tube is determined by the velocity u_{L}.

The acceleration ability of explosive can be described by *the Gurney energy*, which is defined as a sum of kinetic energies of driven tube and detonation products related to unit mass of explosive. For cylindrical envelopes, the Gurney energy is expressed by the following relation [Ref. 8]

$$E_{\mathrm{G}} = \left(\mu + \frac{1}{2}\right)\frac{u_{\mathrm{L}}^2}{2}, \tag{3.7}$$

where μ denotes a ratio of the metal and explosive masses. The quantity E_{G} estimated for the given degree of expansion characterizes *the acceleration ability* of the detonation products of the explosive. The Gurney energy is determined on the basis of the measured velocities of metal plates and cylindrical tubes driven by the detonation products. The measurements are performed at distances for which the driven metals are not ruptured yet. In the case of copper tubes, the tube material is still ductile when the volume bounded by the tube increases from 7 to10 times.

The Gurney energy was calculated for 17 explosives for which the cylinder test results were collected in Ref. [6]. The time-dependence of the central surface of the copper tube was approximated by the function (3.3), and the tube velocity was calculated from Eqs. (3.4)÷(3.6). Characteristics of the explosives and values of the Gurney energy and Gurney velocity calculated for tenfold expansion of the tube are presented in Table 1.

Table 1. Characteristics of explosives collected in Ref. [6] and calculated Gurney energy and velocity

Explosive	Composition	ρ_0 [kg/m^3]	D [m/s]	p_{CJ} [GPa]	E_G [kJ/kg]	v_G [m/s]
PETN	PETN 100	1770	8300	32,0	**4479**	**2993**
Comp. B	RDX/TNT 64/36	1717	7980	29,5	**3895**	**2791**
Cyclotol	RDX/TNT 77/23	1754	8250	32,0	**4151**	**2881**
HMX	HMX 100	1891	9110	42,0	**4669**	**3056**
LX-04	HMX/Viton 85/15	1865	8470	34,0	**3985**	**2823**
LX-07	HMX/Viton 90/10	1865	8640	37,0	**4256**	**2918**
LX-09	HMX/DNPA+FEFO 93/7	1840	8840	37,5	**4604**	**3034**
LX-10	HMX/Viton 94,5/5,5	1864	8820	37,5	**4453**	**2984**
LX-14	HMX/Estane 95,5/4,5	1835	8800	37,0	**4439**	**2980**
PBX-9011	HMX/Estane 90/10	1770	8500	34,0	**4116**	**2869**
PBX-9004	HMX/NC/CEF 94/3/3	1840	8800	37,0	**4440**	**2980**
TNT	TNT 100	1630	6930	21,0	**3044**	**2467**
Nitromethane	Nitromethane 100	1128	6287	12,5	**3150**	**2510**
Aquanal		1430	3700	5,5	**1494**	**1729**
Pourvex		1360	6100	13,0	**2226**	**2110**
ANFO	NH_4NO_3/oil 94/6	782	5080	5,5	**2226**	**2110**
Unigel		1294	5477	12,0	**2456**	**2216**

NC – nitrocellulose, Viton, Estane, DNFA, FEFO, CEF – binders and plasticizers, Pourvex – slurry explosive, Aquanal – aluminized slurry explosive, Unigel – dynamite.

The result of the cylinder test enable us to investigate changes in the Gurney energy, described by equation (3.7), during expansion of the tube. This way is very useful for explosives containing components, for example aluminium, magnesium, which react with gaseous detonation products behind the detonation wave front. The dependence of the Gurney energy on the relative volume of detonation products is presented in Fig. 4 for explosives tested in MUT (Ref. [7]). Characteristics of explosives are given in Table 2.

Table 2. Explosives tested in MUT [Ref. 7]

Explosive	ρ_0 [kg/m^3]	D [m/s]
TNT	1590	6910
Hexogen phlegmatized* (RDX_{phl})	1650	8390
TNT/RDX 50/50	1640	7610
TNT/Al 85/15	1670	6690
TNT/RDX/Al 42,5/42,5/15	1710	7210
PETN*	1710	8080

*) about 5% of organic phlegmatizer

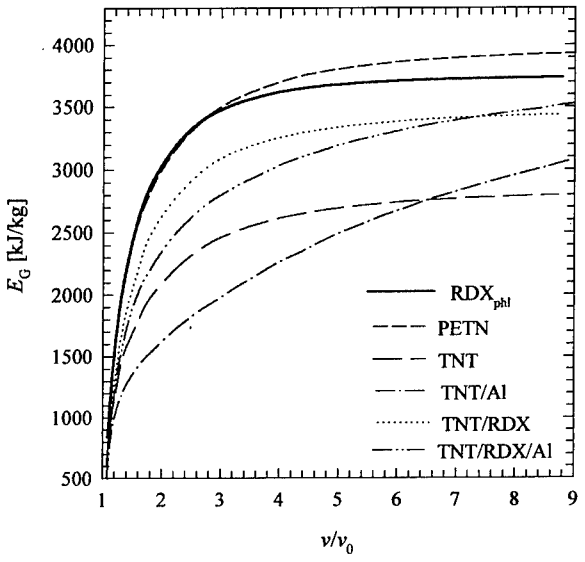


Fig. 4. Dependence of the Gurney energy on the relative volume of detonation products

4. ESTIMATION OF THE DETONATION ENERGY

During the process of tube acceleration, the work done by the detonation products is converted to the kinetic energy of the tube, detonation products and air surrounding the tube, and to the internal energy of tube material and air. If the kinetic energy of air and the heat losses in tube material and air are neglected, then the energy released during detonation (*the detonation energy*), e_0, can be divided in the following way (Ref. [8])

$$e_0 = e_{kL}(v) + e_{kDP}(v) + \int_v^\infty p_i dv, \tag{4.1}$$

where e_{kL} i e_{kDP} denote the kinetic energy of the tube and detonation products, respectively, p_i is the pressure on the isentrope of the latter. All quantities in Eq. (4.1) are related to unit mass of the explosive.

For the volume of detonation products increasing to infinity, the integral in (4.1) is null. Thus, for the given and standard explosives, the following relations are true:

$$e_0 = e_{kL} + e_{kDP}\ , \tag{4.2}$$

$$e_0^{st} = e_{kL}^{st} + e_{kDP}^{st}\ . \tag{4.3}$$

Taking into account the dependence (3.7), the following equation can be obtained from (4.2) and (4.3)

$$\frac{e_0}{e_0^{st}} = \frac{\left(\mu + \frac{1}{2}\right)}{\left(\mu^{st} + \frac{1}{2}\right)} \left(\frac{u_L}{u_L^{st}}\right)^2, \tag{4.4}$$

where u_L i $u_L{}^{st}$ are velocities of the driven tubes determined for infinite volume of the detonation products of the given and standard explosives, respectively.

If the detonation energy is related to unit volume of explosive, then Eq. (4.4) has the form

$$\frac{E_0}{E_0^{st}} = \frac{\left(\mu + \frac{1}{2}\right)\rho_0}{\left(\mu^{st} + \frac{1}{2}\right)\rho_0^{st}} \left(\frac{u_L}{u_L^{st}}\right)^2. \tag{4.5}$$

From Eqs. (4.4) or (4.5) the detonation energy of the given explosive can be estimated, if the detonation energy of standard explosive and the results of cylinder test for both explosives are known. The method for determining the tube velocity at infinite volume of the detonation products is as follows. Velocity of the tube is determined from the results of cylinder test, and the dependence of the square of velocity on the reciprocal volume of the detonation products is constructed. This dependence is extrapolated for reciprocal volume equal to null and in this way the velocity corresponding to infinite volume is found.

To verify the method of determining the detonation energy, the experimental results of the cylinder test given in Ref. [6] are used. After approximation of the time-dependence of radius of the central surface of the tube by the function (3.3), the velocity of the tube is calculated from Eqs. (3.4)÷(3.6). Dependence of the square of velocity on the reciprocal volume of the detonation products is presented in Fig. 5 for some explosives taken from Table 1. The functions are approximated by straight lines and the values of velocity square are found for $v_0/v = 0$ ($v \to \infty$). Pentryt (PETN) is chosen as a standard explosive. PETN has a narrow zone of chemical reactions and solid carbon is absent from its detonation products. It is assumed that the detonation energy of PETN is equal to the energy E_0 from the JWL equation of state [Ref. 6]. The detonation energies of explosives from Ref. [6] calculated by using relation (4.5) are presented in Table 3. The energy is related to unit volume of the explosive.

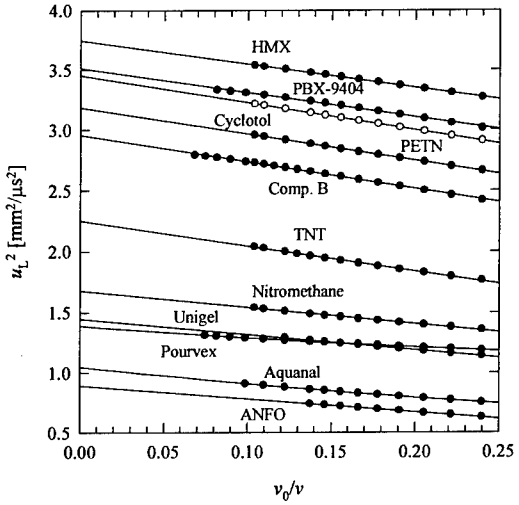


Fig. 5. Dependence of velocity square of the copper tube on reciprocal volume of the detonation products

Table 3. Comparison of the detonation energy calculated from the cylinder test data, E_0^{cal}, with the detonation energy given in literature, E_0 - [Ref. 6], $R_w = [(E_0^{cal}-E_0)/E_0]\cdot 100$ %

Explosive	E_0 [GPa]	E_0^{cal} [GPa]	R_w [%]
PETN	10,1	-	-
Comp. B	8,5	**8,71**	+2,5
Cyclotol	9,2	**9,30**	+1,1
HMX	10,5	**11,09**	+5,6
LX-04	9,5	**9,46**	-0,4
LX-07	9,6	**10,00**	+4,2
LX-09	10,5	**10,71**	+3,0
LX-10	10,4	**10,50**	+1,0
LX-14	10,2	**10,30**	+1,0
PBX-9011	8,9	**9,25**	+3,9
PBX-9004	10,2	**10,35**	+1,5
TNT	7,0	**6,50**	-7,1
Nitromethane	5,1	**4,59**	-10,0
Aquanal	5,5	**2,96**	-46,2
Pourvex	4,5	**3,85**	-14,4
ANFO	2,9	**2,36**	-18,6
Unigel	5,1	**4,01**	-21,4

From Table 3 it follows that, for high explosives, differences between the detonation energies calculated by the method proposed and those given in the literature do not exceed 10 %. The highest one is for nitromethane (-10 %). For TNT, the difference is -7,1 %. The detonation energy of TNT estimated from the cylinder test data is 3988 kJ/kg and that given in Ref. [6] is 4297 kJ/kg. Also the values of the calorimetric heat of detonation of TNT given in literature differ significantly from each other and, in reality, they depend on the measurement conditions.

The method proposed can not be applied for nonideal explosives. From Table 3 it follows that the discrepancy R_w exceeds considerably 10 % for these explosives (last 4 explosives in Table 4). Such a high disagreement may be caused by the fact that heat releasing in nonideal explosives takes place also far behind the detonation zone. Probably, this energy is ineffectively transferred to the tube during later stage of the acceleration.

5. DETERMINATION OF THE EFFECTIVE EXPONENT OF ISENTROPE

The so-called effective exponent of isentrope is often used to calculate the detonation parameters of explosives or some characteristics of the detonation products. The value of the effective exponent is not determined from the parameters in the Chapman-Jouget point but on the basis of the isentrope of the detonation products [Ref. 10]. The effective exponent of isentrope can be estimated from results of the cylinder test. In Ref. [11] the effective exponent is determined by comparing the experimental profile of the copper tube with that obtained from numerical modelling of the process of tube expansion by the detonation products described by the constant-γ equation of state.

The theoretical models proposed in Refs. [12-13] are used for numerical simulation of the process of tube driving. It is assumed that the time of detonation wave propagation is long enough to neglect the influence of the initial conditions. Then the motion of the detonation products and the tube material may be treated as stationary in the frame of reference fixed at the detonation front. It is assumed that the thermodynamic properties of the detonation products are described by the politropic-gas model with the constant-γ equation. As regards the tube material, it is treated as incompressible liquid [Ref. 12] or described by the barotropic model [Ref. 13]. To describe the motion of the detonation products and the tube material use is made of the integral form of the equations of stationary axially symmetric gas-dynamic flow. These equations with appropriate boundary conditions are solved employing Godunov's difference scheme. Dependence of the position of the outer surface of tube on the axial co-ordinate is obtained as a result of computer simulation.

The algorithm used to determine the effective isentropic exponent is as follows. The problem of driving the cylindrical liner is solved numerically for n values of the exponent γ_i ($i = 1, n$). For each γ_i a discrete dependence of the outer tube radius on the axial co-ordinate is derived. This dependence is interpolated by spline functions and the values of $r_{ej}(\gamma_i)$ at chosen points x_j ($j = 1, m$) are calculated. The effective exponent γ_{ef} is determined by minimizing the function

$$f(\gamma) = \sum_{j=1}^{m} \left[r_{ej} - r_{cj}(\gamma) \right]^2 , \tag{5.1}$$

where r_{ej} is the experimental dependence obtained from the cylinder test.

This method is applied in MUT to estimate the effective exponent of isentrope for chosen explosives. The explosives and the values of γ_{ef} are shown in Table 4 ([Ref. 5]).

Table 4. Characteristics of explosives tested in Ref. [5]

Symbol and composition of explosive [%]	ρ [kg/m^3]	D [m/s]	γ_{ef}
HMX [95 HMX, 5 $(CH_2)_n$]	1770	8650	3,03
RDX [95 RDX, 5 $(CH_2)_n$]	1660	8150	3,03
PE [80 RDX, 17 FDB, 3 NC]	1470	7260	2,80
PE/Mg [50 RDX, 30 Mg, 17 FDB, 3 NC]	1520	6680	3,23
PE/P [50 RDX, 30 P_4, 17 FDB, 3 NC]	1550	5850	3,01

FDP is dibutylphthalate $C_{16}H_{22}O_4$, NC is nitrocellulose, ~ 13,3% N, P_4 is red phosphorus

6. DETERMINATION OF THE JWL ISENTROPE

Jones, Wilkins and Lee proposed the equation of the isentrope for the detonation products of explosives in the following form [Refs. 1, 3]

$$p = Ae^{-R_1 V} + Be^{-R_2 V} + CV^{(-1-\omega)} \tag{6.1}$$

where $V=v/v_0$. The following equation of state (JWL EOS) corresponds to this isentrope

$$p = A\left(1 - \frac{\omega}{R_1 V}\right)e^{-R_1 V} + B\left(1 - \frac{\omega}{R_2 V}\right)e^{-R_2 V} + \frac{\omega E}{V} \tag{6.2}$$

where A, B, C, R_1, R_2 and ω are being constant for given explosive. The results of the cylinder test are the basic of the method of determination of these coefficients. Besides them, some connections between coefficients following from the conservation laws, written for the CJ point, are used in this method. Parameters A, B, C are expressed as functions of R_1, R_2, ω, and

ρ_0, D, E_0 and p_{CJ} - Ref. [14]. Density of explosive ρ_0 as well values of detonation velocity D, detonation energy E_0 and pressure at the CJ point are established experimentally. Thus, only the constants R_1, R_2 and ω remain to be determined.

The accuracy of determination of parameters in the JWL EOS depends in a significant manner on correctness of a computer simulation of the process of driving a tube by the products of detonation grazing along the internal surface of the tube. The non-stationary two-dimensional numerical code is applied in the Lawrence Livermore National Laboratory (LLNL) in USA [Refs. 1, 15]. However, the procedure of deducing the JWL constants is time-consuming. Hence, attempts were undertaken to make use of simpler theoretical models describing the process of driving the rube. In Refs. [6, 16] the process of accelerating a metal tube is considered to be the motion of a cylindrical layer of incompressible material as a result of action of the pressure of the detonation products on the internal surface of the layer. Homogeneity of the pressure over the cross-section of the detonation products and the isentropic flow are also assumed. The constants of the JWL isentrope obtained by making use of this model differ insignificantly from those used in LLNL. In Ref. [17] a modification is made in the calculation method by taking a metal strength into consideration to reduce the deviation at the low-pressure region.

In Ref. [14] the method is proposed in which the experimental dependence of radial displacement of the outer tube wall on the axial co-ordinate is compared with that obtained from simulation by the code. The set of JWL constants is chosen for which the experimental and simulated displacements are sufficiently close to each other. The R_1, R_2 and ω are obtained from comparison of the experimental and calculated radial position of the tube wall at chosen m values of the axial co-ordinate x_j. So, the values of these parameters are determined by minimizing the function

$$f(R_1, R_2, \omega) = \sum_{j=1}^{m} \left[r_{ej} - r_{ej}(R_1, R_2, \omega) \right]^2 , \qquad (6.3)$$

where r_{ej} i $r_{ej}(R_1, R_2, \omega)$ are the experimental and calculated positions of external surface of the tube, respectively.

In Ref. [14] a comparison of JWL isentropes determined by different methods on the basis of the same cylinder test results are performed. For example, the JWL isentropes of the detonation products of Composition B are presented in Fig. 6. From analysis made in Ref. [14] it follows that the JWL isentropes determined by the method describe in this reference lie close to the isentropes obtained in LLNL (Ref. [15]) by using the complex non-stationary

hydrocode for simulation of the process of driving the tube. Discrepancies between them are much lower than between the LLNL isentropes and those obtained by using simpler models (Hornberg - Ref. [6], Ijsselstein - Ref. [16], I-Feng Lan –Ref. [17]).

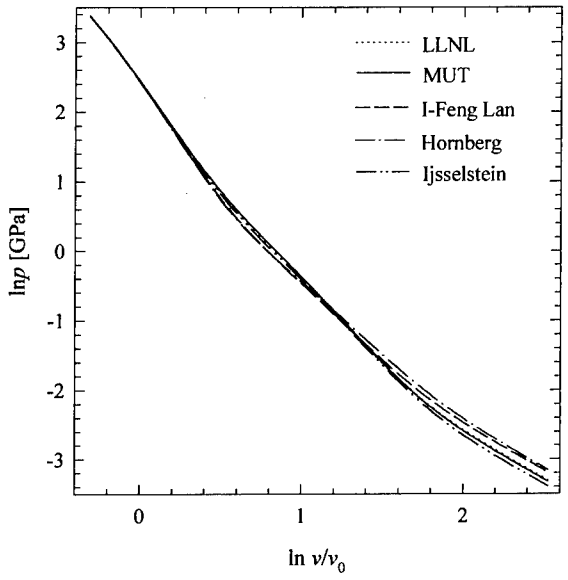


Fig. 6. JWL isentropes for the detonation products of Composition B

An expansion work of detonation products, w, is defined as the work done by the detonation products expanding from the CJ volume to the volume v less the energy of explosive compression - Refs. [18-19],

$$w(v) = -e_c + \int_{v_{CJ}}^{v} p_i dv, \tag{6.4}$$

where $e_c = (p_{CJ} - p_0)(v_0 - v_{CJ})/2$ is the energy of compression of explosive at the detonation front, p_i is the pressure on the isentrope starting from the CJ point.

If the JWL isentrope is known, the expansion work of detonation products may be calculated from equation (6.4). The dependence of the expansion work on the volume of detonation products is presented in Fig. 7 for chosen high explosives. The JWL coefficients for LX-10 and PBX-9404 are taken from Ref. [6]. The JWL isentropes for other explosives are determined by the method described in Ref. [14] in which results of the cylinder test performed in MUT are used.

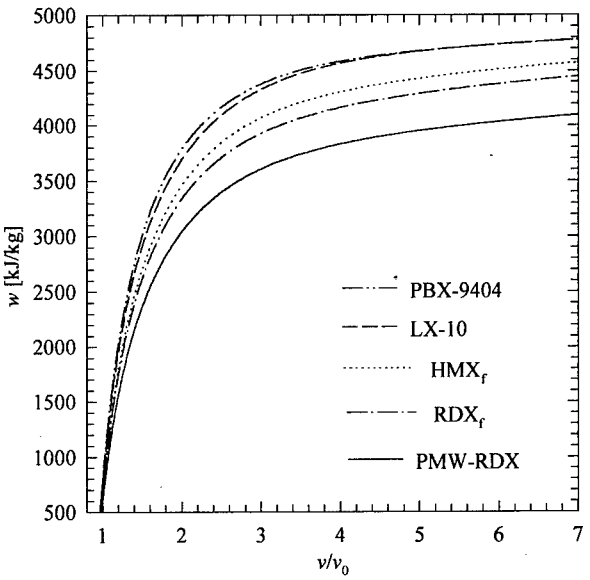


Fig. 7. Expansion work as a function of the volume of detonation products of chosen high explosives: HMX_f (HMX/Teflon/Viton/DBS 96,0/0,5/3,0/0,5; ρ_0 = 1814 kg/m^3), RDX_f (RDX/ Teflon/Viton/DBS 96,0/0,5/3,0/0,5, ρ_0 = 1743 kg/m^3), PMW-RDX (RDX/Teflon/Viton/DBS 90,0/0,4/3,9/5,7; ρ_0 = 1994 kg/m^3), PBX-9404 i LX-10.

7. SUMMARY

In the paper, new semi-empirical methods are proposed for determining the acceleration ability of detonation products and the detonation energy of explosives on the basis of the results of a cylinder test. The procedures of applying the cylinder test data for determination of the acceleration ability (the Gurney energy) and the detonation energy are described. The methods proposed are verified by using the cylinder test data given in the literature. The Gurney energy and detonation energy are computed. For high explosives, the differences between the calculated detonation energies and those taken from literature do not exceed 10 %. The semi-empirical methods for determining the effective exponent of isentrope and the coefficients of the JWL equation of state on the basis of the cylinder test results are also presented.

REFERENCES

[1] Kury J. W., Horning H. C., Lee E. L., McDonnel J. L., Ornellas D. L., Finger M., Strange F. M., Wilkins M. L.: *Metal acceleration by chemical explosives,* Fourth Symposium (International) on Detonation, White Oak 1965.

[2] Bjarnholt G.: *Effects of aluminium and lithium flouride admixtures on metal acceleration ability of Comp. B,* Sixth Symposium (International) on Detonation, White Oak 1976.

[3] Lee E. L., Breithaupt D.; McMillan C., Parker N., Kury J., Tarver C., Quirk W., Walton J.: *The motion of thin metal walls and the equation of state of detonation products*, Eighth Symposium (International) on Detonation, Albuquergue 1985.

[4] Cudziło S., Trzciński W. A.: *Use of a cylinder test for determination of some characteristics of explosives* (in Polish), Biul WAT, **47**, 5, 1997.

[5] Cudziło S., Trębiński R., Trzciński W.: *Determination of the effective exponent of isentrope for the detonation products of high explosives*, Chemical Physics Reports, **16**, 9, 1997.

[6] Hornberg H.: *Determination of fume state parameters from expansion measurements of metal tubes*, Propellants, Explosives, Pyrotechnics, 11, 1986, 23-31.

[7] Trzciński W. A., Cudziło S.: *Determination of the acceleration ability and detonation energy of explosives from a cylinder test* (in Polish), Biul. WAT, **49**, 12, 2000.

[8] Trzciński W. A.: *Use of a cylinder test for determining energetic characteristics of explosives* (in Polish), Biul. WAT, **49**, 12, 2000.

[9] Persson P A., Hornberg R., Lee J.: *Rock blasting and explosive engineering*, Boca Raton, Florida 1994.

[10] Włodarczyk E.: *Introduction into mechanics of explosion* (in Polish), PWN, Warszawa 1994.

[11] Trębiński R., Trzciński W.: *A method of determination of the effective exponent of isentrope for detonation products of condensed explosives* (in Polish), Biul. WAT, **45**, 3, 1996.

[12] Trębiński R., Trzciński W., Włodarczyk E.: *Theoretical analysis of the process of driving a cylindrical liner by the products of grazing detonation*, Journal of. Technical Physics, **29**, 3-4, 1988.

[13] Trębiński R., Trzciński W., Włodarczyk E.: *Theoretical analysis of the influence of material compressibility of a cylindrical liner on the process of launching by products of grazing detonation*, Journal of. Technical Physics, **34**, 3, 1993.

[14] Trębiński R., Trzciński W. A.: *Determination of an expansion isentrope for detonation products of condensed explosives*, Journal of Technical Physics, **40**, 4, 1999.

[15] Horning H. C., Lee E. L., Finger M.: *Equation of state of detonation products*, Fifth Symposium (International) on Detonation, Pasadena 1970.

[16] Ijsselstein R. R.: *On the expansion of high-explosive loaded cylinders and JWL equation of state*, 9th International Symposium on Ballistics, Shrivenham 1986.

[17] I-Feng S.-C., Hung, Chen C.-Y., Niu Y.-M., Shinan J.-H.: *An improved simple method of deducing JWL parameters from cylinder expansion test*, Propellants, Explosives, Pyrotechnics, 1993, 18, 18-24.

[18] Souers P. C., Kury J. W.: *Comparison of cylinder data and code calculations for homogeneous explosives*, Propellants, Explosives, Pyrotechnics, 18 (1993), 175.

[19] Lee E. L., Horning H. C., Kury J. W.: *Adiabatic expansion of high explosive detonation products*, Lawrence Livermore National Laboratory Report UCRL-50422, 1968.

THE STUDY AND CALCULATE OF OUTPUT OF CARBON ON BURNING SURFACE OF DB AND CMDB PROPELLANTS

Wang Jiang-Ning, Wang Bai-Cheng, Zhang Rui-e
Xian Modern Chemistry Research Institute
P.O.Box 18
Xian 710065
P.R. CHINA

ABSTRACT

This paper studied the regularity of produced and calculated of the output of carbon on burning surface with the component in common use of DB and CMDB propellants. This calculated method can programme and predict or analysis the burning property, and also can form the specialist analyst system.

1. INTRODUCTION

Carbon or carbon black is the necessary catalyst carrier for catalytic DB and CMDB propellants. There would be produced some carbon in burning surface whether catalytic or noncatalytic propellants[1]. The effecting for burning property of carbon which born in burning surface was always comply with the rules that the more of the carbon in burning, the higher of the burning rate, at same time the plateau region would move to high pressure.

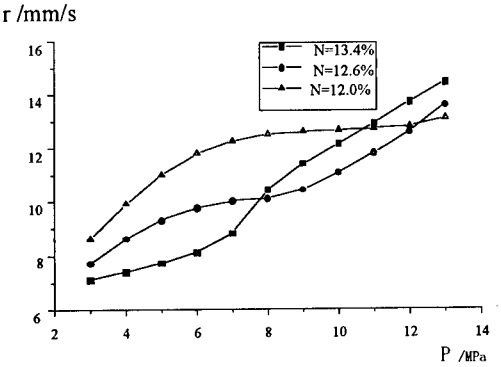


Fig.1. The changing of burning rate and plateau region in the control formulation

In fig.1, with the increased of N=12%, 12.6%, 13.4%, the burning rate also increased higher than 11MPa, but the burning rate dropped before 11MPa. How could explain the opposite experiment phenomenon? Because with the increase of N contained in NC, the density of NO_2 in gas phase is increased, the reaction rate of NO_2+R-CHO→N_2+....is also increased, this could explaining the experiment phenomenon higher than 11MPa, before 11MPa where is the plateau region, the catalytic reaction occurred there. According to the Carbon-unit Theory[1] that carbon in burning surface is catalyst carrier, the burning rate depend on the active weight of catalyst carrier in burning surface. The more of the active weight of catalyst carrier, the higher of the burning rater, with the increased of N contained in NC where the active weight of catalyst carrier is decreased in

the burning surface of the formulation, this is the reason to caused the catalysis reaction rate dropped, at the same time the burning rate also dropped.

This paper will calculate the output of carbon in the burning surface of DB and CMDB propellants in order to use computer to research and forward the burning rate or other burning property.

2. CALCULATE THE WEIGHT OF CARBON IN THE SURFACE OF DB AND CMDB PROPELLANTS

The calculate method of the weight of carbon is N in the formulation is reacted to N_2, H is reacted to H_2O, Some C is reacted to CO_2, some C fly away from burning surface with gas compound, another ports C is reacted to carbon.

2.1 Calculate the Weight of Carbon of NC and NG

Because that NG ($C_3H_5O_9N_9$) is positive bulance of oxygen, it doesn't produced carbon in burning surface. NC{$[C_6H_{10-r}O_{5-r}(ONO_2)_r]_n$} is that N is reacted to N_2, H is reacted to H_2O, some C is reacted to CO_2 by surplus oxygen, and surplus C is produced to carbon. The output of carbon of NC is in table 1 by sued above method.

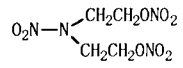
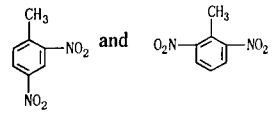
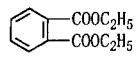
Table 1. The output of carbon per unit weight of NC

Molecular formula	N/%	Output of Carbon/%
$[C_6H_{7.74}O_{9.52}N_{2.26}]_n$	12.0	14.45
$[C_6H_{7.55}O_{9.9}N_{2.45}]_n$	12.6	12.95
$[C_6H_{7.28}O_{10.44}N_{2.72}]_n$	13.4	10.97

2.2 The Output of Carbon of DINA, DNT and DEP

DINA, DNT and DEP not only are a good plasticizer for NC, but also is one of the decisive factor for pressure exponent and plateau region[2]. The output of carbon of calculated and estimated of DINA, DNT and DEP is in table 2.

Table 2. The output of carbon of three plasticizers

Name	Molecular structure	Calculated output/%	Estimated output /%
DINA		10.80	10.80
DNT	 and	42.82	13.18
DEP		59.96	29.98

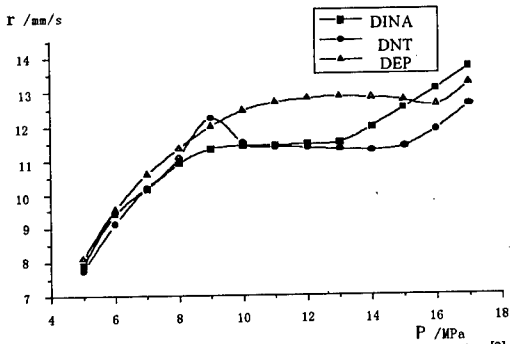
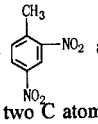
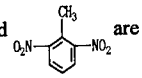


Fig.2 burning rate-pressure curve of control formulation[2].

Thus it can be seen from table 2 on the calculated output that the burning rate is raised with order of DINA, DNT and DEP which is same percent weight in control formulation, but it is found from the date of fig.2 and reference [2] that the DINA's plateau burning rate is same as DNT's, and DEP's is higher than DINA and DNT's. This reason is relation to big or small of the molecular pieces that the DINA, DNT and DEP decomposed. The place of $-NO_2$ on benzene wheels of DNT is varied, It is a mixture with six disstructures.  and  are the great majority, the biggest molecular pieces of the former is two C atom and the later is three C atom, in this paper think that DNT only have two C atom produced carbon in the six disstructures. Therefore the DNT's output of estimated of carbon in burning surface is 13.1%.

The DINA's calculated and estimated output of carbon is same as.

The group of $-C_2H_5$ and $-\overset{O}{\overset{\|}{C}}-O-$ in DEP molecule is not produced carbon because that the $-C_2H_5$ and $-\overset{O}{\overset{\|}{C}}-O-$ easily formed a gas molecule and go away from the burning surface.

2.3 RDX, HMX, DNP et al. Did Not Produced Carbon in Burning Surface

The burning rate is dropped with the increased of RDX's percent in CMDB propellants, fig.3 and fig.4 is the control formulation burning rate-pressure curve.

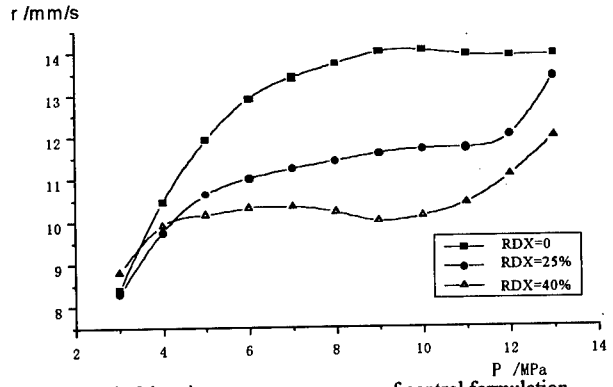


Fig.3 burning rate-pressure curve of control formulation

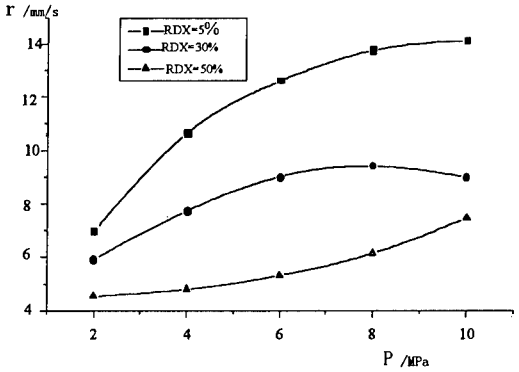


Fig.4 burning rate-pressure curve of control formulation

It was studied that the burning regular of varied percent of RDX in CMDB propellants. And proved that NC and NG et al. Double base additive was firstly decomposed in the burning process of CMDB propellants, and RDX was melted and gasified in burning surface, and decomposed in gas phase. It did not join the catalytic reaction in burning surface, therefore, the RDX did not produced carbon in burning surface.

2.4 Catalyst

The common catalyst is some organic and inorganic metal compound; they are all decomposed to metal oxide. As same as the decomposed of NC and NG et al., the functional group of organic compounds is important to output of carbon produced in burning surface, this subject will be discussed in next paper.

2.5 Other Composition

Additive of C_2, C_1, V et al. is also produced carbon, as in table 3.

Table 3. other composition

Name	Diethyl diphenyl urea (C_1)	1,3-dimethyl-1,3 diphenyl urea (C_2)	V
The output of carbon/%	53.60	59.93	84.88

3 THE CALCULATED OF CARBON OF FORMULATION

Table 4 is a typical example formulation.

Table 4. Typical example formulation

Name	NC(N=12.0%)	NG	RDX	C_2	V	DINA	Ct
Per cent/%	35	28	30	2.0	0.5	2	2.5

The output of carbon was produced in burning surface is 35%×14.45%+28%×0%+2.0%×59.93%+2%×10.80%=6.47%.

4. REFERENCES

(1) Wang Jiang-Ning, Carbon-Unit Theory Hypothesis on Combustion Surface of Double Base Propellant (Physical Model. I), 22nd International Annual Conference of ICT, 1991, P59.

(2) Wang Jiang-Ning, Xu Yu, Wang Ning-Fei, The Burning Property of Double Base Propellant By Using Three kinds of Common Plasticizer and the Prospect for the New Type Plasticizer, 31st International Annual Conference of ICT, 2000.

(3) Wang Jiang-Ning, Zhang Xiao-Hong, Wang Bai-Cheng, Zou Wei-Wu, The Model of DB and RDX (HMX)-CMDB Propellant Combustion, 28th International Annual Conference of ICT, 1997, P45.

ACCUMULATION OF CATALYSTS ON THE SURFACE OF SOLID STRANDS IN THE COURSE OF BURNING.

Nikolai N. Bakhman

Institute of Chemical Physics, Russian Academy of Sciences
117977 GSP-1, Kosygin str. 4, Moscow, Russia

FAX(007 095) 9382156; e-mail: bakhman@center.chph.ras.ru

Keywords: condensed systems; catalyst; burning; quenching; accumulation.

ABSTRACT

Experiments carried out with AP-PMMA-Fe_2O_3 pressed specimens have demonstrated that concentration of catalyst (Fe_2O_3) in the surface layer of extinguished strands can be considerably (up to four times) high than that in the fresh strands. The effect of pressure, oxidizer-fuel coefficient, and length of strands was investigated. Advantages and shortages of methods of quenching and analyses of specimens are examined. The meaning of experimental results is discussed.

INTRODUCTION

For proper understanding the mechanism of action of catalysts on the burning rate of condensed systems it is important to know the real catalysts concentration, m_{ct}, in the flame velocity controlling zone (FVC-zone). This is a rather difficult problem as catalysts can act both in condensed and gas phases (c-phase and g-phase). Some complicated effect can also take place, for example, accumulation of catalysts in the surface layer of specimens and catalysts particles aggregation in this layer. It is difficult also to investigate the action of heterogeneous catalysts in two-phase flow over the surface of specimen. To attain the velocity equal to that of gas the small enough catalysts particles (≤ 1 mcm) need time smaller than that of stay of particles in the FVC-zone. Therefore, the volume concentration of such particles is much smaller

than that in c-phase. In contrast, large enough particles (≥ 100 mcm) are almost motionless in the laboratory coordinates and their volume concentration in the two-phase flow is practical equal to that in c-phase [1].

EXPERIMENTAL

In this work the burning of specimens (10*10*10 mm) pressed from AP (~9mcm)+PMMA(3-5 mcm)+Fe_2O_3(~1.7 mcm) mixtures was investigated in Crawford-type bomb in nitrogen atmosphere (at p=1-30 atm). The specimens were extinguished using two following methods: 1) quenching on a cold copper underlay (cu-method); 2) rapid (10^4-$4*10^5$ atm/s) depressurization method (rd-method). The measurements of m_{ct} were accomplished also by two different methods: 1) by colorimetric (col-method); 2) by optical microscope (om-method). Col-method allow to determine the mass concentration, m_{ct}, of Fe_2O_3 in the surface layer of quenched specimen whereas om-method permit, in principle, to estimate the number and dimension of Fe_2O_3 particles on the surface of specimen. However, in the frame of om-method it is very hard to distinguish individual particles from their aggregates. So, the overwhelming majority of experiments in this work was accomplished by col-method.

RESULTS

1. Quenching on a cold underlay.

1.1 Effect of pressure in the course of burning.

The extent of accumulation of catalyst in the course of burning can be described by the ratio $m_{ct}/(m_{ct})_0$ where $(m_{ct})_0$ and m_{ct} are mass concentration of catalyst in fresh and quenched specimen. It follows from Table 1 that the value m_{ct} can be at least four times high as $(m_{ct})_0$. Further, it is important to note that the ratio $m_{ct}/(m_{ct})_0$ increases with decreasing of mass, M, of condensed residue on the copper undelay. The reduction of M is due to the increase of pressure of nitrogen and hence the rise of burning velocity, u, of strands. In its turn, the increase of u results in decrease of length of temperature wave in the specimen. Accordingly, decreases the critical distance, l_{cr}, between the surface of strand and copper underlay at which the burning fails. Diminution of l_{cr} leads to decrease of mass, M, of condensed residue.

Table 1.

P Atm	$(m_{ct})_0$=1%		$(m_{ct})_0$=5%		$(m_{ct})_0$=10%	
	M, mg	$m_{ct}/(m_{ct})_0$	M, mg	$m_{ct}/(m_{ct})_0$	M, mg	$m_{ct}/(m_{ct})_0$
30	2.0	4.2	2.4	3.5	3.5	3.1
20	2.0	3.8	3.6	3.0	3.5	2.6
10	2.4	3.1	3.9	3.0	6.1	2.0
5	15.7	2.8	11.0	2.3	10.3	1.7
1	23.8	2.5	21.2	1.8	27.0	1.3

Note: quenching was fulfilled by cu-method and measurements of mean values M and m_{ct} by col-method;

$\alpha=(m_{ox}/m_f)/(m_{ox}/m_f)_{st}=0.6$ where α is oxidizer-fuel coefficient (index st means stoichiometric).

The data listed in Table 1 show that in all cases the ratio $m_{ct}/(m_{ct})_0$ decreases with $(m_{ct})_0$ rise. At p=30; 20; and 10 atm this dependence can be explained as a consequence an increase of M with $(m_{ct})_0$. But at p=5 atm (and partly at 1 atm) the value M does not augment but diminishes with $(m_{ct})_0$ increasing. This point needs further investigation.

1.2. Effect of oxidizer-fuel coefficient

The data relevant to the dependence of mean values of mass, M, of condensed residue and ratio $m_{ct}/(m_{ct})_0$ on the oxidizer-fuel coefficient, α, are presented in Table2.

Table 2

α	$(m_{ct})_0$=1%		$(m_{ct})_0$=5%		$(m_{ct})_0$=10%	
	M, mg	$m_{ct}/(m_{ct})_0$	M, mg	$m_{ct}/(m_{ct})_0$	M, mg	$m_{ct}/(m_{ct})_0$
0.6	23.8	2.5	21.2	1.8	27.0	1.3
0.8	25.0	2.2	21.2	1.3	27.2	1.2
1.0	26.7	2.0	21.7	1.2	27.3	1.1
1.5	32.6	2.0	32.0	1.2	37.5	1.1
2.0	36.3	2.5	43.0	1.7	46.6	1.3

Note: quenching by cu-method; measurements of M and m_{ct} by col-method; p=1 atm

It is worth mention that value $m_{ct}/(m_{ct})_0$ has minimum at α=1.0-1.5 and increases both with increasing of excess of oxidizer or fuel. Position of $[m_{ct}/(m_{ct})_0]_{min}$ is roughly

coincides with position of maximum on the curve u(α) where u is burning velocity. Further, value M increases with α (slow at $\alpha \leq 1$ and fast at $\alpha > 1$)

The effect of oxidizer-fuel coefficient on accumulation of catalyst in the surface layer of specimen was studied also by om-method. The measurements were fulfilled on the surface of extinguished specimens using square gauze 350*350 mcm (i.e. 122500 mcm^2 area). It was determined the part of the surface occupied by catalyst, S_{ct}, and ratio S_{ct}/S_Σ where S_Σ=122500 mcm^2. The data listed in Table 3 show that the dependence S_{ct} (and S_{ct}/S_Σ) on α has minimum at α=1.5 (in accordance with corresponding result of Table 2). However, the dependence $S_{ct}(\alpha)$ is rather weak.

Table 3

α		0.6	0.8	1.0	1.5	2.0
P=1 atm						
S_{ct} Mcm^2	$(m_{ct})_0$=1%	857	823	789	755	789
	$(m_{ct})_0$=5%	3300	3085	3040	2990	2990
	$(m_{ct})_0$=10%	8600	8300	8080	7350	8080
$\frac{S_{ct}}{S_\Sigma}$,%	$(m_{ct})_0$=1%	0.70	0.67	0.64	0.62	0.64
	$(m_{ct})_0$=5%	2.69	2.52	2.48	2.40	2.44
	$(m_{ct})_0$=10%	7.02	6.78	6.60	6.00	6.60
p=20 atm						
S_{ct} Mcm^2	$(m_{ct})_0$=1%	1058	1014	970	925	970
	$(m_{ct})_0$=5%	5420	5220	5075	4930	5075
	$(m_{ct})_0$=10%	11520	11050	10580	10350	10580
$\frac{S_{ct}}{S_\Sigma}$,%	$(m_{ct})_0$=1%	0.86	0.83	0.79	0.75	0.79
	$(m_{ct})_0$=5%	4.42	4.26	4.14	4.02	4.14
	$(m_{ct})_0$=10%	9.40	9.02	8.64	8.45	8.64

Note: quenching by cu-method, measurements by om-method.

In all the cases the value S_{ct} increases with pressure:

$(m_{ct})_0$, %	1	5	10
$(S_{ct})_{20atm}/(S_{ct})_{1atm}$	1.23-1.26	1.64-1.70	1.31-1.41

The values S_{ct} and S_{ct}/S_{Σ} are nearly proportional to $(m_{ct})_0$ – Table 4. This result is rather surprising. Indeed, the value S_{ct} can be called "surface concentration" of catalyst but not "volume concentration" and not "mass concentration". Really, om-method does not permit to measure the thickness of layer of catalyst. Further, areas occupied by Fe_2O_3 are not monolithic and om-method could not allow to determine the density of catalyst in these areas.

Table 4.

α	0.6	0.8	1.0	1.5	2.0
P=1 atm					
$(S_{ct})_{(m_{ct})_0=5\%} / (S_{ct})_{(m_{ct})_0=1\%}$	3.85	3.75	3.85	3.89	3.79
$(S_{ct})_{(m_{ct})_0=10\%} / (S_{ct})_{(m_{ct})_0=1\%}$	10.04	10.09	10.24	9.74	10.24
p=20 atm					
$(S_{ct})_{(m_{ct})_0=5\%} / (S_{ct})_{(m_{ct})_0=1\%}$	5.12	5.15	5.23	5.33	5.23
$(S_{ct})_{(m_{ct})_0=10\%} / (S_{ct})_{(m_{ct})_0=1\%}$	10.89	10.90	10.91	11.19	10.91

Note: extinguished by cu-method; measurements by om-method.

1.2 Effect of length of specimen.

The data relevant to influence of total length of several specimens joint together are listed in Table 5.

Table 5.

l	$(m_{ct})_0$=1%		$(m_{ct})_0$=5%		$(m_{ct})_0$=10%	
mm	M, mg	$m_{ct}/(m_{ct})_0$	M, mg	$m_{ct}/(m_{ct})_0$	M, mg	$m_{ct}/(m_{ct})_0$
1	9.5	2.4	11.2	2.1	12.5	1.5
2	9.6	2.6	13.2	2.5	13.6	1.7
4	9.1	3.0	11.6	2.8	14.5	2.1
6	9.0	3.2	12.1	2.9	13.1	2.2
8	9.6	3.4	10	3.1	13	2.3
10	9.8	3.6	13	3.2	12.8	2.4

Note: quenching by cu-method, measurements by col-method; α=0.6; p=10 atm

As it shown in Table 5 the value M practically does not depended on length, l, of specimens. Indeed, in the course of burning a stationary temperature wave spreads downwards the specimen so what amount of heat in this wave and the value M remain constant. However the extent of accumulation of catalyst, $m_{ct}/(m_{ct})_0$, increases with l.

2. Quenching by rapid depressurization method.

Experimental results concerned to quenching of specimens by rd-method are shown in Table 6.

Table 6.

l	$(m_{ct})_0$=1%		$(m_{ct})_0$=5%		$(m_{ct})_0$=10%	
mm	M, mg	$m_{ct}/(m_{ct})_0$	M, mg	$m_{ct}/(m_{ct})_0$	M, mg	$m_{ct}/(m_{ct})_0$
1	62.3	1.0	78	1.05	85.6	1.0
2	51.2	1.07	80	1.08	81.7	1.03
4	52.1	1.13	71.3	1.10	91.8	1.05
6	64.8	1.15	74.5	1.12	81.3	1.09
8	59.7	1.17	79.6	1.14	82.5	1.14
10	58.3	1.20	80.1	1.17	81.1	1.20

Note: extinguishment by rd-method (from 10 to 1 atm)

Measurements by col-method; α=0.6

The following conclusions can be made from the comparison of data presented in Table 6 and Table 5 :

- in both cases the value M practically does not depended on l
- the values M in Table 6 were 5 to 8 times greater than those in Table 5 as surface of specimens quenched by rd-method was not so flat than that quenched by cu-method
- the values $m_{ct}/(m_{ct})_0$ in Table 6 were 1.5-3 times smaller than those in Table 5 (as the ratio $m_{ct}/(m_{ct})_0$ diminished with M increasing)
- both in Table 6 and Table 5 the ratio $m_{ct}/(m_{ct})_0$ increases with l: rather slightly in the case of Table 6 (1.1-1.2 times) and significantly in the case of Table 5 (1.5-1.6 times)

REFERENCE

1. N.N. Bakhman and A.F. Belyaev – Gorenie geterogennykh condensirovannykh sistem. Moscow, Nauka, 1967. English translation: Combustion of Heterogeneous Condensed Systems, Rocket Propulsion Establishment, Westcott, England, RPE-Trans-19,1967.

STUDY AND OPTIMIZATION OF AEROSOL FIRE-EXTINGUISHING PROPELLANTS BASED ON THE MODIFIED PHENOL-FORMALDEHYDE RESIN

Dmitry L. Rusin, Anatoly P. Denisjuk, Yuri G. Shepelev, Dmitry B. Mikhalev

D.Mendeleyev University of Chemical Technology, 9, Miusskaya sq., 125047 Moscow, Russia

ABSTRACT

The researches of the aerosol fire-extinguishing propellants (AFP) are carried out. The propellants with use binder, consisting of modified phenol-formaldehyde resin were composed. Its combustion is steady-state at atmospheric pressure. At that they fully evolve energy, have 2-3% CO and H_2 in the combustion products and possess high mean of the fire-suppressing ability (10-15 g/m^3). Compositions have improved physico-mechanical and technological characteristics (single-axis stretching durability up to 6.5 MPa, break deformation up to 55%, cutting durability 1.5-3.5 MPa, external friction $\leq$ 0.5 MPa). These propellants have a wide range of the burning rate (1.5-7.5 mm/s) without using of special burning catalysts. The products based on these compositions are manufacturing by a through-passage pressing method.

The mathematical models of a type "structure-property" are obtained permitting to predict the deformation-strengthening and rheological properties of propellants, its burning rate and fire-suppressing efficiency.

INTRODUCTION

The iditol is widely used as individual combustive-binder, and it is one of the components of multicomponent combustive-binders of various aerosol fire-extinguishing propellants (AFP) [1-3]. The products on iditol basis are formed by mold pressing exclusively and are characterized by small deformability, increased fragility and porosity.

At manufacturing of products based on known compositions by a method of through-passage pressing these compositions contain, along with iditol, from 8% up to 15% of various rubbers or others polymeric binder. It does not allow to ensure high (more than 0.8) excess oxidizer coefficient values (α) of compositions for decreasing of toxic and fire-explosive components (CO and H_2) content in combustion products of AFP.

The purpose of the present work is the development of compositions on the plasticized iditol basis, the products of which are moulded by a method of through-passage pressing and are characterized with high fire-suppresing ability (FSA), improved physico-mechanical and

technological characteristics as well as wide range of burning rates without application of burning catalysts.

EXPERIMENTAL SECTION

As a polymeric base of compositions the thermoplastic plasticized phenol-formaldehyde resin (iditol, ID) was used. The compositions contained 80-84% wt. a potassium nitrate or its mixtures with potassium perchlorate and technological additives also.

The thermodynamic calculation results show the possibility of composing AFP on plasticized iditol basis, burning products of which practically is not contained a carbon oxide. The burning temperature of such materials was lower than, for example, for compositions on nitroester basis having value α close to 1, by 500-700 K.

Especially it is necessary to emphasize, maximum amount of potassic substances content in the combustion products $\Sigma K = KOH + K + KF + K_2CO_3 + K_2F_2 + K_2O_2H_2 + KCl + K_2FCl + K_2Cl_2$ corresponds to compositions based on inactive binder with low burning temperature and practical absence CO in the combustion products. The part of a potassium perchlorate in this case should not exceed 40% of a total content of oxidizer.

V.G. Korostelev [5] by a design-experiment way the influence to efficiency of an operation of aerosol-forming fire-suppresing compositions of burning products chemical structure is appreciated and is shown, that the best parameters have the hydroxides of a potassium both natrium and chlorides of a potassium, natrium and calcium.

It is visible (fig. 1-3), the full replacement KNO_3 by $KClO_4$ results in increase of burning temperature approximately by 700 K, the value of content ΣK passes through a maximum at the potassium perchlorate contents in structure of an oxidizer of 20-30%. The increase of a part of perchlorate more than 0.4 results in magnification of the contents in burning products of an carbon oxide and at smaller amount of perchlorate - a quantity of CO is insignificant.

During combustion of AFP the aerosol is formed, particles of which terminate combustion of various organic substances in air. The inhibition effect of aerosols usually link either with recombination of generated in the flame radicals on the particles surface, or with a power waste from gas zone on the heating and phase transitions of aerosol particles [4].

Taking into account a high degree of filling of compositions, for maintenance necessary structure-mechanical properties a modifier was added to all samples. As shown earlier [6-11], different modifiers improve rheological, physico-mechanical and ballistic properties of various energetic compositions. It is established, the structure-mechanical and rheological properties of AFP on the iditol basis are essentially improved also as a result of modification.

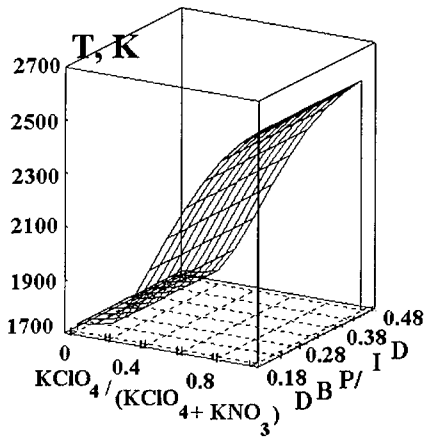


Fig. 1. The influence of $KClO_4$ content in the composition of an oxidizer and ratio DBP/ID on the value of calculated burning temperature of AFP. Samples contain 84% wt. oxidizers

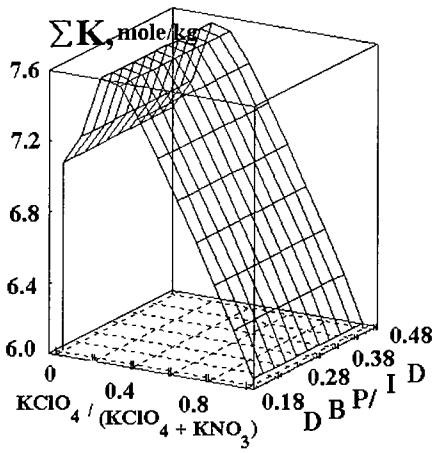


Fig. 2. The influence of oxidizer and binder contents on the value of calculated content of ΣK in the combustion products of AFP

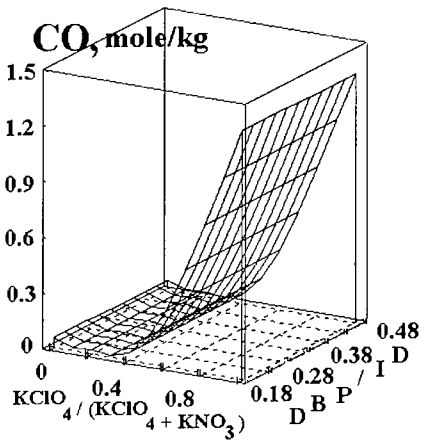


Fig. 3. The influence of oxidizer and binder contents on the value of calculated content of CO in the combustion products of AFP

The variation of plasticizer type, the ratio DOS/(DOS+DBP) and the ratio plasticizer/ID results in an extreme variation of deformation-strengthening (fig. 4) and rheological properties of compositions (fig. 6).

The samples containing mix plasticizer with the ratio DOS/(DOS+DBP) = 0.3-0.7 and ratio plasticizer/polymer, equal to 0.3-0.4, are characterized by the best structure-mechanical parameters. It is important to emphasize, samples, despite of a high filling degree (80-84% wt.), have high values of stretching durability (σ_b) and break deformation (ε_b), reaching accordingly 6.5 MPa and 55%.

The samples of AFP are characterized by essential improved rheological properties (fig. 5).

The mathematical models of a type "structure-property", permitting to predict the rheological properties of compositions, are obtained:

$$\sigma_{cut}=\exp[-67.5489+13124.675/T+0.0205T(DOS/ID)+13.1811(DOS/ID)^3+0.0476T^{1.1}-$$
$$-17.987(DOS/ID)^2];$$
$$\tau_\mu=\exp[-17.903+0.2789\ln V-0.0536T(DOS/ID)+14.8407(DOS/ID)^2+23.0465(DOS/ID)^{0.1}].$$

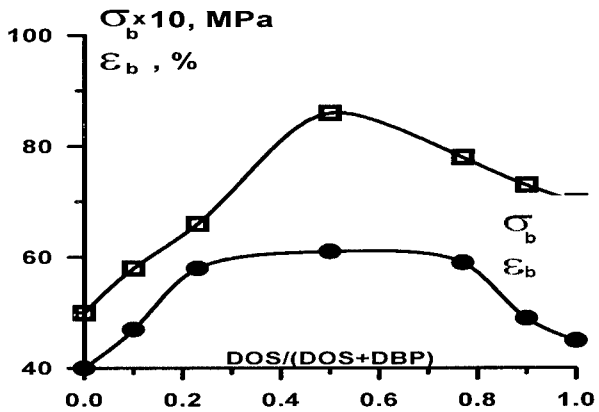


Fig. 4. The dependence of single-axis stretching durability (σ_b) and break deformation (ε_b) of compositions upon plasticizer quality (all samples contain 80% KNO_3, 10.15% ID, 6.45% plasticizer and 3.4% additives)

The graphic interpretation of these functions is represented on a fig. 6.

The variation of compositions formulation results in a variation not only is structure-mechanical (fig. 4-6), but also ballistic and fire-suppressing properties (fig. 7, table 1). For example, the burning rate of such compositions at atmospheric pressure can be changed without use of a burning catalysts in limits from 1.5 up to 7.5 mm/s both by variation of a potassium perclorate content in mix oxidizer and ratio DBP/ID (fig. 7).

The values of the burning rate and FSA of compositions containing 84% oxidizers can be calculated, using analytical dependence:

$$\mathbf{U_{0.1}=\exp(2.572+3.072K-4.8977D-10.2748K^2+6.7656DK),\ mm/s}$$

$$\mathbf{FSA=\exp(1.7135-1.6718K+3.3531K^2+2.8132D^{0.7}-3.1113KD),\ g/m^3,}$$

where $K = KClO_4/(KClO_4+KNO_3)$; D=DBP/ID.

Taking into account the mechanism of a flame suppressing at the presence of an aerosol [2-5], it is logical to assume that the increasing of fire-suppresing efficiency of AFP, which corresponds to decrease of FSA value, with other things being equal, should be observed under rising of potassium-containing compounds concentration in the burning products (and especially hydroxide, chloride and fluoride of a potassium), as well as at increasing of a particles dispersion degree of an aerosol, i.e. at the large values of rate and temperature of combustion. Really, the experimental researches have confirmed the expressed suppositions.

The analysis of obtained results has shown, the maximum efficiency of fire suppression is observed on those compositions which are characterized by maximum values ΣK in the burning products and by maximum values of burning rate at atmospheric pressure.

The high fire-suppressing efficiency of the composition on plasticized iditol basis, containing 20% $KClO_4$ and 64% KNO_3, is confirmed by researches with use of testing boxes having capacities of 0.069 m^3, 0.22 m^3 and 2.2 m^3 - the FSA values were about 10 g/m^3 in all cases.

Most of aerosol-forming fire-suppressing generators operate at pressure close to atmospheric. It is established, the compositions on plasticized iditol basis are characterized by small dependence of a burning rate on pressure (table 1) – the value of exponent ν in the burning rate law comes to 0,10–0,16.

It is interesting, that the experimental composition of gaseous burning products estimated by means of chromatography, has appeared practically identical to thermodynamically calculated, i.e. the absence CO and H_2 in the burning products is characteristic for the developed compositions.

The analysis of gaseous burning products of fire-suppressing compositions was carried out using the gas chromatograph LHM-8MD.

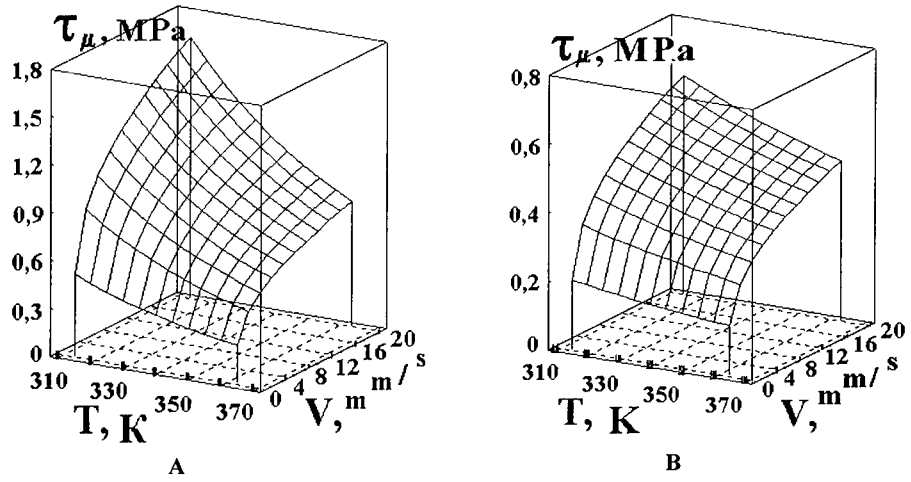


Fig. 5. The temperature-velosity dependences of external friction of AFP containing 64% KNO_3 and 20% $KClO_4$ (DBP/ID = 0.5): **A** – without modifier; **B** – with modifier.

Investigated samples 7 mm in diameter were tested in a closed bomb with capacity of 300 cm^3, previously vacuumized and filled in by argon. The argon atmosphere was used insted of traditionally used helium to increasing of chromatograph sensitivity at analysing of hydrogen.

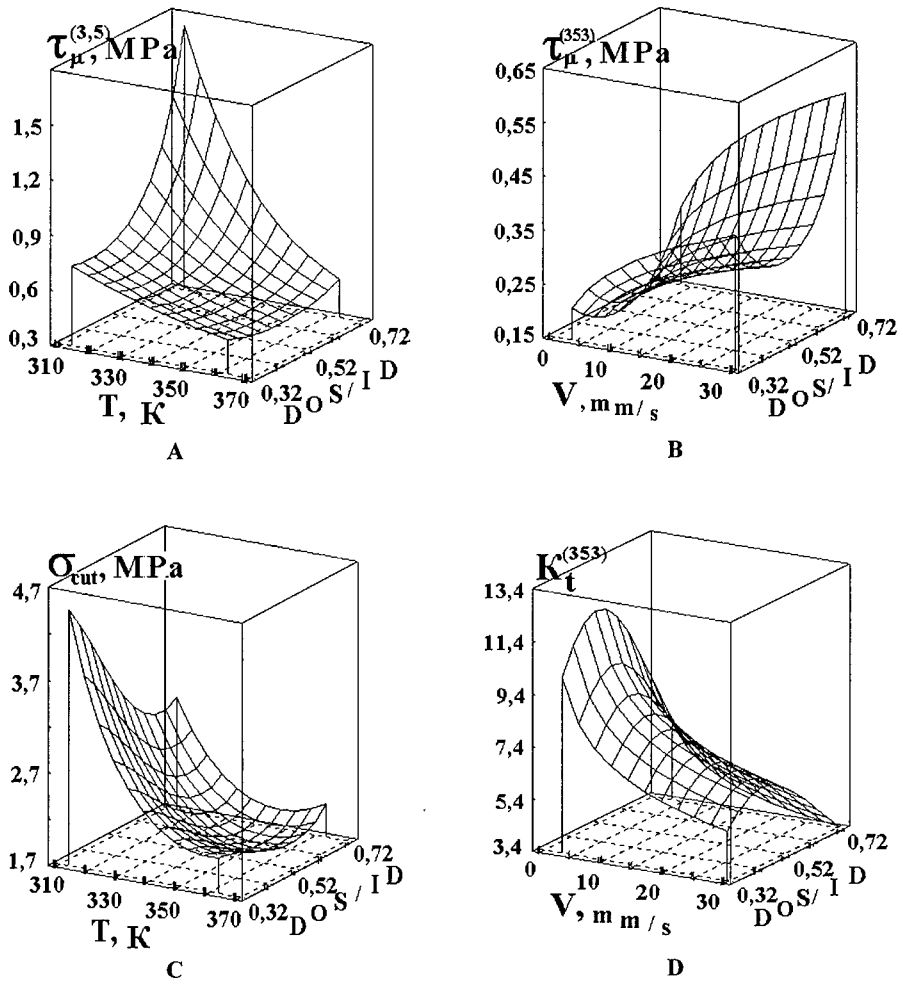


Fig. 7. The dependence of external friction (**A, B**), cutting durability (**C**) and the factor of adaptability (**D**) of compositions upon temperature (**A, C**), slide velocity (**B, D**) and DOS/ID ratio

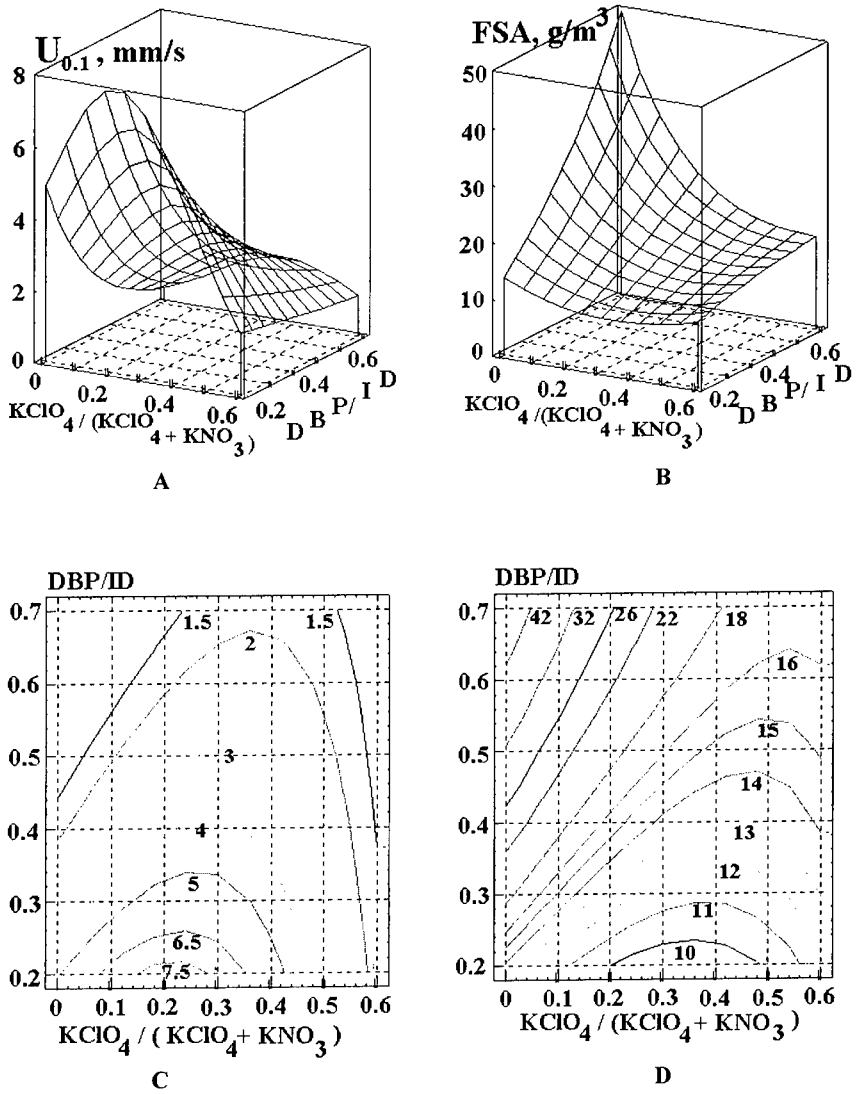


Fig. 8. The influence of ratio DBP/ID and oxidizers formulation on the value of burning rate (**A, C**) and FSA (**B, D**) of AFP (figures at curves: $U_{0.1}$, mm /s (**C**); FSA, g/m^3 (**D**)

The weight of charge was selected so that average pressure, at which the combustion happens, did not exceed 0.2 MPa. The chromatograph was modified so that at the single probe introduction could be divided both two-atomic and three-atomic gases. Previously the calibrating graphic were constructed for each gas and the calibration factors are obtained.

Table 1

The influence of fire-suppressing composition details on its burning rate

Base components	$U = BP^{\nu}$		Interval P, MPa
	B, [mm/(s·MPa)]	ν	
11.1% ID; 2.5% DBP; 84% KNO_3	4.7	0.16	0.1-0.8
11.1% ID; 2.5% DBP; 64% KNO_3 20% $KClO_4$	6.0	0.14	0.1-0.4
11.1% ID; 2.5% DOS; 84% KNO_3	5.0	0.14	0.1-3.0
11.1% ID; 2.5% DOS; 64% KNO_3 20% $KClO_4$	8.1	0.10	0.1-0.8

It is necessary to mean, that after the burning products cooling the condensation of water and interaction vaporous KOH and CO_2 with formation $KHCO_3$ happened. Therefore in the gases the content of stayed CO_2 is determined only and H_2O is not determined. Taking into account of it the recalculation of thermodynamic composition of the burning products was carried out and then it was compared with experimental data (table 2).

Table 2

The comparison of calculated and experimental compositions of gaseous burning products of the AFP containing 64% KNO_3 and 20% $KClO_4$ (DBP/ID=0.225)

P, MPa	Data	The content of gaseous burning products, % (vol.)						
		CO_2	CO	H_2	N_2	NO	NO_2	O_2
0.1	Calculated	42.5	2.7	1.2	53.6	-	-	-
	Experimental	55.0	0.2	-	42.1	0.10	-	2.60
0.5	Calculated	40.9	0.1	0.4	58.42	-	-	0.18
	Experimental	57.5	0.4	0.03	39.6	0.15		2.32

The sample on iditol binder basis, of which oxidizer consists of potassium nitrate and perchlorate, has actual composition of the burning products a little differing from calculated even at atmospheric pressure and total amount CO and H_2 makes about 4%, that fulfil international ecological requirements. The increasing of pressure up to 0.5 MPa the content of indicated above gases does not exceed 1%. Thus, for investigated propellant the completeness of combustion is reached at the pressure close to atmospheric. It generally rare case for combustion of condensed energetic systems.

CONCLUSIONS

The complex researches for structure-mechanical, ballistic properties and fire-suppressing efficiency of compositions on iditol basis, plasticized by DBP, DOS and its mixtures are carried out.

It is established, the structure-mechanical properties of compositions are essentially improved.

The products made from modified compositions are moulded by through-passage pressing method, stady-state burn at atmospheric pressure without application of special burning rate catalysts with rate from 1.5 up to 7.5 mm/s and practically full energy evolving, contain in the burning products 2-3% CO and H_2, have high fire-suppressing ability (10-15 g/m^3) as well as improved physico-mechanical and technological characteristics (single-axis stretching durability up to 6.5 MPa, break deformation up to 55%, cutting durability 1,5-3,5 MPa, external friction $\leq$ 0,5 MPa).

REFERENCES

1. Shidlovsky A.A. Fundamental of pyrotechnics. M.: Mashinostroenie, 1973.
2. Alikin V.N., Kuzmitsky G.E., Stepanov A.E. Autonomous systems of aerosol fire-suppressing propellants. Perm, 1998, 148 p.
3. Agaphonov V.V., Kopylov N.P. Aerosol fire-suppressing plants. M.: VNIIPO, 1999, 168 p.
4. Ewing C.T., Hughes J.T., Carhart H.W. Fire and materials, 1984, v.8, No. 3.
5. Korostelev V.G. Fire suppression of C-H flames by aerosol fire-suppressing compositions. 21th Intern. Sem. on Pyrotechnics. M., 1995, p. 444-458.
6. Rusin D.L., Kozhuch M.S., Mikhalev D.B., et al. Pyrotechnical cord and composition for its processing. Patent of Russian Federation No. RU 2026277 C1, 1995.
7. Zhukov B.P., Denisjuk A.P., Shepelev Yu.G., Rusin D.L. Highly effective fire- extinguishing propellant. 21th Intern. Sem. on Pyrotechnics. M.,1995, p. 1018-1032.
8. Zhukov B.P., Denisjuk A.P., Rusin D.L. , Shepelev Yu.G. Development of solid propellants for effective fire-extinguishing systems. Conversion Concepts for Commercial Applications and Disposal Technologies of Energenic Systems, NATO ASI Series. Series 1: Disarmament Technologies, Vol.14, Kluwer Academic Publishers, Dordrecht/Boston/London, 1997, p. 99-112.
9. Rusin D.L., Mikhalev D.B., Vetrov D.V. Fireconductive cords on a polymeric basis. Proc. of the 25th Intern. Pyrotechnic Seminar Europyro-99, Brest, France, 1999.
10. Zhukov B.P., Zhukov V.B., Rusin D.L., Denisjuk A.P., Shepelev Yu.G., Mikhalev D.B. Highly effective plasma fuel for MHD-generators. Double technologies, 1999, No. 2, p. 22-25.
11. Rusin D.L., Mikhalev D.B., Vetrov D.V. High-elastic fireconductive cords. Proc. of the 31th Intern. Annual Conference of ICT. Karlsruhe, 2000, p.p. 116-1 - 116-10.

CHARACTERIZATION OF A CANADIAN UNEXPLODED ORDNANCE IMPACTED RANGE FOR POTENTIAL CONTAMINATION BY ENERGETIC MATERIALS

Thiboutot, Sonia, Ampleman, Guy, Gagnon, Annie and Marois André

32nd International ICT Conference, June 2001

DEFENCE RESEARCH ESTABLISHMENT VALCARTIER
Emerging Energetic Materials Section
2459, Pie XI Blvd. North, Val-Bélair
Québec, Canada, G3J 1X5
sonia.thiboutot@drev.dnd.ca

ABSTRACT

Operational activities of the Armed Forces such as firing practice may cause the dispersion of Unexploded Ordnances (UXO) and contaminants in the environment. The release of energetic compounds and other contaminants in the environment can be immediate if the ammunition casing is broken upon firing, or the contaminant may be released slowly from leaching out of the UXO. Little is known about the environmental fate of energetic compounds in relation with the presence of UXO's in former training ranges. By their nature, unexploded ordnances pose a safety hazard to personnel and they present also the potential of being a source for energetic materials contamination. The characterization of a UXO contaminated area was undertaken following the decision of closing an important training range located in Eastern Canada. Our efforts were axed toward two objectives: To ascertain that the contamination of soil or biomass did not represent a threat to human health nor to the environment and to assess the environmental impact of UXO's and of their open detonation in range clearance operations. This paper describes the characterization of the unexploded ordnance contaminated Tracadie Range, located in Tracadie, New-Brunswick. The site dynamic, the sampling strategy of soils and biomass are described along with the analytical procedures. The results obtained demonstrated that

in this particular range and at the time the work was accomplished, the presence of UXO's did not lead to the accumulation of energetic materials neither in the environment nor in the biomass. The peculiar geology and hydrogeology of the range may contribute to this fact. This paper represents one of the first published study on the environmental impact of the presence of UXO's in former training ranges. UXO's represent a worldwide problem as they are found in many sites following either training or combat.

INTRODUCTION

The international context with the end of the Cold War has resulted in the closing of many military bases worldwide. At the same time, a growing awareness in potential negative environmental impacts of operational military activities has led many countries to integrate R&D programs related to the environmental impacts of energetic materials (EM). Over the last ten years, efforts have been dedicated on the characterization of the extent of explosives contamination of a great number of ammunition plants and military depots. A large body of information exists on explosives concentrations at sites impacted by manufacturing operations (1-4) where the contaminants most often observed are TNT (2,4,6-trinitrotoluene), RDX (1,3,5-hexahydro-1,3,5-trinitrotriazine), their manufacturing impurities and environmental transformation products (5). In order to support the Canadian Forces in the establishment of the environmental impact of their operational activities, we published a detailed protocol for the characterization of sites contaminated by explosives (6). EM are of concern because of their chemical, physical and toxicological properties. They are known to be both carcinogenic and mutagenic. One of the highest potential sources of contamination by EM in the environment is the presence of a very large amount of Unexploded Ordnance (UXO) on most of the active and non-active firing ranges. UXO are military munitions that have been prepared for action, fired, dropped, or buried, and remains undetonated, posing a hazard to operations, personnel or material. It is estimated that millions of acres throughout the United States, including 1900 formerly used defence sites and 130 bases realignment and closure installations are impacted with UXO's (7). UXO's are also known to be spread in huge tracks of lands in Europe. This represents an international problem, which has not been covered extensively yet. Limited research has

been conducted in the area of fate and transport of explosive from UXO's and processes controlling their fate and transport are poorly understood. Once explosives from UXO move beyond the confinement of the delivery system (mortal shell, artillery shell, rocket, etc.) the process affecting fate and transport should be similar to those associated with explosive contamination from other sources (8,9).

The problematic of potential leaching of EM from UXO's was of high importance for the old Canadian Force Training Range located in Tracadie, New Brunswick. In 1995, a decision was made to return the property to the province of New Brunswick, following the decision of closing CFB Chatham. It was imperative to clear the range from UXO's prior the release of the land to the public. A private firm was hired (Dillon Inc.) to screen the overall range for the presence of UXO's and afterward to clear their presence by open detonation. The firm also proposed to sample soils for potential contamination by EM or their degradation products. The sampling plan proposed involved the sampling of less than 0.1 % of the range. DREV was involved as a DND consultant to review the sampling plan proposed by the industry. The proposed plan was approved but it was also decided to send a DREV's team at the Tracadie Range in order to evaluate the situation in parallel. Moreover, a potential high threat to human health was identified at Tracadie Range related with the biomass present on the range. Blueberry picking has been conducted for years on the range, even on an industrial scale, and this activity was planned to continue after the release of the land to the province. This sensitive food source could represent a receptor of energetic materials should these compounds be present in the soils/water surrounding the plants. Phytoaccumulation of explosives in plants/roots/leaves and fruits has been documented (10-12). In the case of Tracadie, it was imperative to prove that the potential of bioaccumulation of explosives by blueberry plants was not present and that the picking of these fruits did not represent a threat to human life.

RANGE HISTORIC

The Tracadie Range was one of the largest Canadian Forces training range in eastern Canada with some 18 088 hectares (ha) in surface and a perimeter of 60 km. It is located

approximately 8 km west of Tracadie in northeastern New Brunswick. The Range has been used for various military purposes from 1919 until the present time. Early use of the area was as an Army firing range with artillery, gun and mortar ammunition being fired. The area is reported to have continued to be used for live firing and other Army training activities up until its closure in 1994 (13). The Range was also used by the Air Force as an air-to-ground target area from the 1950s to 1992. From 1939 to 1992, the primary use of the Tracadie Range was the training of military personnel in the use of ordnance. Other uses were permitted in conjunction with this primary role under special arrangements and included blueberry picking, commercial forestry, woodcutting, fishing, hunting, and trapping. From 1951 to 1985 an area covering 486 hectares was leased for blueberry cultivation. Industrial cultivation came to an end in 1985 when DND determined that it was not advisable to permit blueberry operations because of the perceived risk from UXO. However, blueberries grow wild in many locations on the Range, and many local residents still access the Range for berry picking. An overall consensus concerning future land use can be summarized as follows: Reserve all lands within one kilometer of either side of the Big Tracadie River for tourism and recreation-related use. Permit traditional activities on the balance of the lands (i.e., hunting, fishing, trapping) in conjunction with forestry and blueberry cultivation.

SAMPLING STRATEGY

The fate and transport processes that act upon UXO's depend upon the environment in which the UXO exists and the manner in which it has breached its delivery containment system. The fate and transport of explosives from corroded, leaking of ruptured UXO munitions in surface soils will be affected by various processes (8). Once the UXO containment system has been breached, then dissolution of the explosive occurs. In the case of rupture of certain UXO types, the explosives may exist as free product in the soil due to spillage or may be partially contained within the delivery system. After dissolution of the explosive has begun, fate and transport processes interact with the dissolved contaminant. The fate is a complex phenomenon, which might involve plant root uptake, which was of high concern at the Tracadie Range. As soon as the EM are free and available in the soil system, they may end up in the blueberry plants and fruits.

The geology and hydrogeology of the range was taken into account, since the fate of the explosives is directly related to these aspects. The Tracadie geological and hydrogeological settings are very particular. The uppermost bedrock strata of the Pennsylvanian sandstone tend to be highly fractured and permeable. Groundwater well yields of 15 up to 22 liters per second are known to occur in the general area. The nature of the soil is highly sandy and the underlying bedrock is 10 feet deep at the most. The site is almost at the sea level and therefore it is washed each spring when the water table is high after the snow melting. Based on these facts and on the potential slow release from discrete UXO's located randomly in a given area, we did not anticipate high concentrations of explosives. Sandy soils are known not to retain EM (8), as opposed to high organic content or clay type soils.

As described earlier, the Tracadie Range is very wide and the systematic sampling of the overall range would not have been achievable. We decided to use a worst case scenario and to sample the areas where the highest levels of EM contamination were suspected. If contamination were not found in these sites, the probability of finding accumulation in other sites would be very low. The worst cases scenarios were defined by using three factors: 1- historical data on the use of the various ranges, 2- visual inspection and 3- UXO electromagnetic screening data from Dillon Inc. Firstly, the historical data pointed out in the direction of area # 1 and #3 which were the two mostly heavily used ranges in the past 25 years. All the soil samples collected were composite samples collected in a wheel pattern in accordance with Ref. 6. Due to the presence of UXO's on the range, we were not allowed to collect sub-surface samples. The collected composite samples consisted of the top 10 cm of surface soil. Soil samples were field screened using immunoassay type test kits for RDX and nitroaromatics. When the field screening tests indicated contamination, additional samples were collected for further analysis.

The first area sampled was area 1. Two distinct sectors were sampled in this area based on historical data, visual inspection and electromagnetic survey. The first one was around the principal target, which was located on a small mound in the center of the area. A total of

18 composite samples were collected in a spiral pattern with the beginning of the spiral starting at the target. Each sample was collected at 10m distance intervals in a spiral by ending up at a distance of 25 m from the target. Samples 1.1 to 1.8 were located in the mound while samples 1.9 to 1.18 were located at the ground level. By using this spiral pattern, all directions were equally sampled. These samples were named 1.1 to 1.18. The results obtained with the field analytical method are presented in table I. The second sector sampled in area 1 was a rectangular field located inside a triangle formed by the access roads, northwest of the observation tower. This field was visited thoroughly by ammunition specialists for the clearance of unexploded ordnance. Many holes from the open detonation were still present on the rectangular field. These samples were taken in a cross pattern with 10 samples vertically and 10 horizontally. 18 other samples were collected in the northwest quadrant of the rectangular field since numerous detonation holes were observed in that area. These samples were named 1.19 to 1.37 (Table I).

Table I

Field analytical method results for soils

Samples	RDX test Kit	TNT test Kit
1.1 to 1.11	Low	Low
1.12	6 %	Low
1.13	Low	Low
1.14	6 %	Low
1.15	20%	Low
1.16 to 1.37	Low	Low
Res.	5 %	7 %
3.1 to 3.11	Low	Low
3.12	5 %	9 %
3.12-3.50	Low	Low

Low: less than 0.1 ppm

On area 3, three main targets were still present. There were two target tanks and many cars piled up as targets. Samples were collected at zero, one and two meters of each target in all directions: north, west, east and south. This strategy was taken in a former study on other active antitank ranges and has proven to be successful (14). Samples 3.1 to 3.4 were collected around the farthest target at the end of the range starting in the north position and going clockwise. Samples 3.5 to 3.8 were collected at one meter and 3.9 to 3.12 at two meters. Samples 3.14 to 3.25 were collected around the other target tank, following the same pattern and samples 3.26 to 3.37 were collected around the target cars with the same strategy. Samples 3.37 to 3.50 were collected randomly on the range in OD holes. In area 3, an open 500-pound bombshell was found after it had been open detonated by the EOD specialists. Burned residues (res) were still present inside the delivery system. These residues were collected and analyzed by both field and lab method to verify if the reaction was complete and if there were still explosive traces in these residues.

The precise location of the collection of blueberries was not possible due to the nature of the dispersion of these samples in the environment. However, the strategy employed was to sample the fruits that presented the highest probability of EM contamination. We sampled 10 jars in area 1 and 6 jars in area 3, mainly near targets and near shrapnel. We also sampled other blueberry growing areas, not based on the worst case scenario but based on the past and future use of the area. Firstly, 6 jars were collected in a region southwest of area 3, where commercial picking of blueberries was conducted for years. Secondly, 7 jars were collected in an area southest of the river that is now transferred to the province of New Brunswick. Finally, two blueberry plants, including the roots were collected in the worst UXO/shrapnel contaminated site in area 1. All biomass samples were frozen and brought back to DREV for analysis. Fresh blueberries were bought in the Quebec region and were used as blanks or spiked for quality control. A total of 32 biomass samples was then treated and analyzed at DREV.

Before transferring the Tracadie range to the province, intensive open detonation (OD) of UXO's was conducted by Explosive Ordnance Disposal (EOD) specialists, from Dillon Inc. In order to verify the impact of this intensive OD operation, the soils were sampled

before and after the open detonation of UXO's. This was done twice (A and B trials). We sampled at distances of 0 m, 1m, 2m, 3m, 4m, 5m and 10m from the UXO's in all directions before and after the detonation. The 0 to 3 m samples were collected directly in the hole created by the detonation. These samples were named OD-A-0 to 10 and OD-B-0 to 10. All field analyses revealed a "Low" response both for TNT and RDX, meaning that less than 0.1 ppm was detected. Samples were still brought back to the laboratory to confirm these results. All analyses confirmed the field results showing no detection of any explosive residues.

EXPERIMENTAL

DREV's team collected samples during a five-day period in August 1996. Soils samples were analyzed on site with an immunoassay field screening method and samples that showed positive response to the test kits were brought back at DREV for HPLC analysis. Blueberries were collected in glass jars (1l) and brought back to DREV for extraction and analysis. Soils extraction and analysis were performed following the EPA 8330 method (15) while the extraction and analysis of blueberries was done in accordance with Ref. 19-. All standards for explosives analytes were obtained from Accustandard. This method allows the quantitative determination of explosives and their related metabolites or impurities. The acetone used for soil extraction, homogenization of soil samples and glassware cleaning was reagent grade and was obtained from Anachemia. The methanol used in the laboratory for preparation of HPLC eluents was Sigma-Aldrich HPLC grade. Deionized water was used in the field for cleaning and for addition in acetone extracts. Laboratory grade water used for preparation of HPLC eluents was obtained from a Millipore Milli-Q Type 1 reagent grade water system. HPLC laboratory analyses performed at DREV were done with a HP Model 1090 equipped with a diode array UV detector HP Model 1100. Elution was done with 1:1 methanol-water at 1.2 ml/min and absorbance was recorded at 254 nm on a spectra-physics Model 8490 variable wavelength detector and peaks were recorded on a Hewlett-Packard 3396 Digital integrator operated in the peak height mode. Field screening immunoassay test kits used for RDX and TNT were obtained from Strategic Diagnosis Inc. Lyophylization of biomass samples was done with LABCONCO freeze dryer system Lypl-Lock 4.5. For all sampling campaigns, every soil

sample that led to a positive response with the test kits were kept cold (4°C) and frozen on the same day. They were kept frozen and in the dark until processed. The processing was conducted the following week at DREV. Individual soil samples in Ziploc bags were shaken and kneaded and then emptied in aluminum pans. The soils were further homogenized by breaking up clumps with gloved hands and stirring. Further homogenization with acetone was achieved, as described in Ref. 6. Soils were extracted with acetonitrile by sonication.

Blueberry samples were sampled in 1L Masson Jars, kept cold, in the dark and frozen at the end of each sampling day. They were brought back to DREV where they were kept frozen until processed. The extraction of the blueberries was done according to Ref. 16. Samples were homogenized using a kitchen blender. Plant samples were cut in fine parts before lyophylization. The second step was to remove the aqueous content of the fruits by extensive lyophylization of the samples. Lyophylized dry fruit solids were then extracted with acetonitrile (ACN). The proportion of extracts-to-solvent was modified in order to improve the detection limits. By doing so, we were able to obtain a detection limit of 0.1 ppm in the dry fruit. A matrix spike was prepared by adding 0.1 ml of an ACN solution containing 100mg of HMX, RDX and TNT. No negative interference was caused by the fruit matrix which would have jeopardized the quantitative evaluation of explosives concentrations in fruits. All main TNT metabolites such as 2-amino-4,6-dinitrotoluene (2-ADNT), 4-amino-2,6-dinitrotoluene, (4-ADNT), 2,4-diamino-6-nitrotoluene (2,4-DANT) and 2,6-diamino-4-nitrotoluene (2,6-DANT) were included in the HPLC standards since they would be the first ones to be suspected in a bio-transformation scenario within the biomass.

Immunoassay field screening method was selected for this sampling campaign based on the user-friendly nature of this test. All field tests were conducted directly in the rear cabin of the rental vehicles. Both RDX and TNT test kits were performed leading to an efficient screening for both nitramines and nitroaromatics. Results that may be obtained with this method range from Low to Hi, Low being equivalent to less than 0.1 ppm and Hi being equivalent to more than 5 ppm. A program of quality assurance and quality control was

conducted within all the sampling campaign. Field blanks were collected on each site, in the surrounding area representative of the ranges sampled. All field blanks showed no contamination by energetic compounds. In general, all the analyses were performed at least in duplicates or triplicates, whenever possible. For the analytical work performed at DREV, 20% of the samples were sent to an external laboratory for confirmation. A ratio of 10% of spiked and surrogates were included in the analytical work.

RESULTS

A total of 87 composite samples were collected according to a worst case scenario pattern. From these samples, 6 reacted positively to the RDX test while 3 reacted to the TNT test kit (Table I). All positive responses were lower than 10% on the test kit scale except for sample 1.15. Analysis by HPLC in triplicates of all samples that reacted positively to the field test revealed no explosive residues. The HPLC results indicated that we had 9 false positive for both TNT and RDX field tests. This represents about 10 % of false positive, which is considered acceptable. The results that we obtained are totally in agreement with recently published data on a similar site sampled in Albuquerque (18). In the New Mexico study, explosives tests areas having the greatest potential for containing soils contaminants were identified using geophysical survey methods. From this survey, five areas were identified as heavily impacted with UXO's. A total of 310 soil samples were collected from the five respective areas. The samples were screened for many contaminants among which EM. No explosive and degradation products were detected in any of the 310 samples. Consequently, it was concluded that it is highly unlikely that significant contamination exists on that range by EM or any other contaminants. In the Dillon study (13) forty-eight soil samples were collected and analyzed for RDX and TNT in the field using field screening kits. Upon completion of the TNT/RDX field screening program, 10 soil samples were selected from the 48 samples which reflected the greatest variation in field screening results and were sent to the laboratory for confirmation of the field test kit results. Laboratory results report the presence of RDX in only one sample at a concentration of 9 mg/kg. No other explosive parameters were detected for the same

sample. All other soil samples were reported as having non-detectable concentrations of explosive.

Results obtained for the biomass collected proved that all samples were free of explosive residues. All analyses were conducted in triplicates and no chromatogram showed the presence of any energetic materials. Spiked samples proved that the extraction/analysis process led to quantitative evaluation of EM without any interference from the blueberry matrix. The two OD performed by the Tracadie EOD team monitored before and after OD did not show any spreading of EM in the environment. Even the ashes found in the incomplete OD of a 500-pound bomb did not show measurable traces of EM. Finally, soil samples from OD holes collected at various depths were free of explosive residues. These results confirm results obtained in a previous study on the impact of large scale OD (18).

CONCLUSION AND RECOMMENDATIONS

In our study, none out of 87 soil samples collected showed contamination by any explosive residues. In the Dillon study, only one sample out of 48 showed the presence of RDX at a concentration of 9 mg/kg (13). Globally, two independent groups found that one sample collected out of 135 composite samples showed the presence of RDX. This represents a positive result for less than 1.0 % of collected samples. There are no standard threshold levels for explosive residues. However, based on our expertise, RDX found at a concentration lower than 10 mg/kg does not represent a problem or a threat. The presence of a large quantity of UXOs on the Tracadie Range and especially in the regions where the soil sampling took place, confirmed that for that particular range, UXO's do not lead to the accumulation of explosive residues and therefore to soil contamination by explosives. The particular hydrogeologic situation with high soil drainage, the sandy nature of the soils and the dispersion pattern of UXO'S probably all contribute to this fact. Another study conducted on an old USA training range also showed the same trend (17). It might be proven in the future that the presence of UXO does not lead to detectable traces of energetic residues in the environment. Other sampling surveys in various conditions will have to be achieved before such general assumption could be made. Even if the number of

samples collected on the Tracadie Range does not represent a systematic characterization of the overall range, we are highly confident that there is no risk associated with the presence of energetic residues neither in the soil nor in the biomass. The dispersion of UXO's over the site, combined with the way in which the explosives are released from the delivery systems can explain in large part the results obtained at Tracadie. In the scenario where explosives are released in the environment from the delivery systems, natural attenuation can take place through biotic and abiotic processes and can contribute to the degradation of explosive contaminants. Natural attenuation has already been demonstrated on large scale and it is known that it can be observed even when high concentrations of explosives (over 100 mg/kg of TNT) are present in the soils. (19). This process would likely be involved in the situation where low levels of explosives would be released in the environment trough the leakage of a UXO delivery system.

The results found at the Tracadie Range proved that there was no risk associated with the presence of energetic materials residues neither in the soils nor in the biomass present on the range. This study also contributed to the overall knowledge on the environmental impact caused by UXO's on training ranges. However, it should be noted that the long-term impact of UXO presence still has to be evaluated. The slow corrosion of UXO casings could lead to the release of explosives in the environment and therefore, UXO's corrosion studies and sampling of more training ranges have to be conducted.

ACKNOLEDGEMENTS

The authors thank Infrastructure management program and Tracadie Range staffs for their help. They also express their thanks to the Director General Environment, National Defence Head Quarters, Ottawa for the support funding.

REFERENCES

1. "Approaches for the Remediation of Federal Facility Sites Contaminated with Explosives or Radioactive Wastes", EPA Handbook # EPA/625/R-93/013 (1993).
2. J. Cragin, D.C. Legget, B.T. Folet, and P.W. Schumacher, "TNT, RDX and HMX Explosives in Soils and Sediments, Analysis Techniques and Drying Losses", U.S.A.T.H.M.A. Report # AMX-TH-TE-FR-85038 (1985).
3. T.F. Jenkins, C.L. Grant, G.S. Brar, P.G. Thorne, P.W. Schumeache, and T.A. Ranney, Field Analytical Chemistry and Technology, 1, 151-162 (1997).
4. M.E. Walsh, T.F. Jenkins, and P.G. Thorne, "Laboratory and Field Analytical Methods for Explosives Residues in Soil", Proceedings of the Symposium on Alternatives to Incineration for Disposal of Chemical Munitions and Energetic, Vol. 2, p. 17, (1995).
5. M.E. Walsh, T.F. Jenkins, and M.H. Stutz, CRREL Report # 93-5, Hanover, NH, (1993).
6. S. Thiboutot, G. Ampleman, G., P. Dubé, T.F. Jenkins, M.E. Walsh, J., Hawari, B Spencer, and L. Paquet, "Protocol for the Charact. of Explosives Cont. Sites", DREV R-9721, (1998).
7. J.M. Brannon, P.Deliman, C. Ruiz, C. Price, and M. Quasim, " Conceptual Model and Process Descriptor Formulations for Fate and Transport of UXO", Army Engineer Waterways Experiment Station Vicksburg Report # WES-IRRP-99-1, (February 1999).
8. J.M. Brannon, T.E. and Myers, T.E., "Review of Fate and Transport Processes of Explosives", Technical report # IRRP-97-2, US Army Engineers Waterways Experiment Station, Vicksburg, Mississippi (April 1997).
9. D.M. Townsend, and T.E Myers, " Recent Developments in Formulating Model Descriptors for Subsurface Transformation and Sorption of TNT, RDX and HMX", Report IRRP-96-1, US Army Engineer Waterways Experiment Station, Vicksburg, Mississippi (June 1996).

10. S.D. Harvey, R.J. Fellows, D.A. Cataldo, and R. Bean, Environmental, Toxicology and Chemistry, Vol. 10, PP. 845-855 (1991).

11. M. Peterson, G. Horst, and P. Shea, Environmental pollution, Vol. 99, pp. 53-59 (1998).

12. P. Thomson, L. Ramer, and L. Shnoor, Environ. Sci. Technol., Vol. 32, pp. 975-980 (1998).

13. Dillon Consulting Firm, Unexploded Ordance Survey & Clearance Plan, Tracadie Range New Brunswick, Stage I/II Report, Volume I-III, February 1997.

14. S. Thiboutot, G. Ampleman, A. Gagnon, and A. Marois, T.F. Jenkins, M.E. Walsh, P.Gé. Thorne, and T.A. Ranney, "Characterization of Antitank Firing Ranges at CFB Valcartier, WATC Wainwright and CFAD Dundurn", DREV-R-9809, (October 1998)

15. EPA, Nitroaromatics and Nitramines by HPLC, Second Update SW 846, 8330 (Sept 1994).

16. S.L. Larson, A.B. Strong, and S.Yost, "Analsysis of Explosives in Plant Tissues: Modification to Method 8330 for Soil", Technical Report IRRP-98-5, US Army Engineer Waterways Experiment Station, Vicksburg, Mississippi, (May 1998).

17. H. Grace, J. Johnson, and P. Middlebrooks, "Phase II. Environmental Baseline Survey of McCormick Ranch Kitland Air Force Base, New Mexico, Part 1-3." Report # 427248, GRAM Albuquerque, New Mexico, 198pp, 211pp and 215pp (January 1996).

18. G. Ampleman, S. Thiboutot, A. Gagnon, A. Marois, R.,Martel, and R. Lefebvre, "Study of the Impacts of OB/OD Activity on Soils and Groundwater, at the Destruction Area in CFAD Dundurn", DREV Report R-9809, (Dec 1998).

19. J. Pennington, P. Miyares, D. Ringelberg, M. Zakikhani, M. Reynolds, D. Felt, R. Coffin, D. Gunnisson, L. Cifuentes, H. Fredrickson, and T. Jenkins, "Natural Attenuation of Explosives in Soil and Water Systems at Department of Defense Sites: Final Report", US Army Corps of engineers, Wateways Experiment Station, Report # ACE-WES-TR-EL-9901 (July 1999).

Thermodynamic TDS code: Application to detonation properties of condensed explosives

S.B.Victorov, S.A.Gubin, I.V.Maklashova, I.I.Revyakin

Moscow State Engineering Physics Institute (Technical University), Russia

E-mail: sb_victorov@mail.ru, gubin@kaf04.mephi.ru

The detonation properties of several explosives are computed by using a theoretical equation of state (EOS) of fluid detonation products based on accurate thermodynamic perturbation theory and intermolecular potentials. The results of detonation experiments were not used to determine the potential parameters, however, the predictions are in excellent agreement with measured detonation properties. The predictions of two versions of the semi-empirical BKW EOS are found to be significantly poorer, although their parameters were calibrated by matching detonation experiments.

1. Introduction

There are many situations where accurate thermodynamic equations of state (EOS) for fluid and solid mixtures are desirable. In particular, such equations are needed in the high pressure areas which are of interest in geophysics, in astrophysics (e.g., planetary interiors), and in other fields of science. In the chemistry and physics of shocks and detonation the knowledge of thermodynamic properties of the detonation products allows one to solve a series of practically important problems, including evaluation of high explosive (HE) performance, generation of tabulated EOS for hydrodynamic simulations, and so on.

Thermodynamic (thermochemical) codes handling the problems of HE detonation are mostly based on semi-empirical EOS of the detonation products, whose parameters are adjusted on measurements of detonation properties for a collection of explosives. As an example, the Becker-Kistiakowsky-Wilson (BKW) EOS has been used in such well-known codes as FORTRAN–BKW, RUBY, LA MINEUR, ARPEGE, TIGER, and CHEETAH. A semi-empirical EOS allows one to calculate accurately those detonation properties that were used for the EOS calibration (e.g., the detonation velocity). That is why such EOS are useful in practical applications and were extensively used during many years. However, these EOS have no strong theoretical background, and they may give wrong values for those detonation parameters that were not employed for the calibration (e.g., for the CJ temperature, the concentrations of detonation products, etc.). Thus, the semi-empirical EOS can not be considered as reliable source of data on thermodynamic properties of the detonation products; there are applications where the accuracy of these EOS is insufficient.

There is an alternative more sophisticated approach based on a theoretical EOS which (a) is derived from first principles of statistical mechanics, (b) relies on realistic potentials of molecular interactions, and (c) accurately replicates the results of Monte Carlo (MC) and molecular dynamics simulations.

In 1962 Fickett made a first attempt in this approach. He tried to describe the detonation properties using the Lennard-Jones-Devonshire (LJD) cell theory and an effective one-component treatment for mixtures of the detonation products. Fair agreement with experiment was made possible by adjusting the pair potentials. Fickett concluded that any significant improvements in his calculated results would require a major advance in the EOS theory and more information about the pair potentials.

Such an advance in the EOS theory took place several years after Fickett's work. But when it did, it came through different workers by different theoretical techniques within a relatively short period of time. The techniques are: the perturbation theories of Barker and Henderson, and of Weeks, Chandler, and Anderson (WCA), and the variational theories of Mansoori and Canfield, and Rasaiah and Steel (MCRS). All of these theories make use of van der Waals's idea that the steeply varying portion of an intermolecular potential mainly determines the equilibrium structure of fluids. This idea was formulated into a mathematically rigorous framework that uses a hard-sphere potential to replace the steep part of the potential. All these theories deal with a classical one-component fluid composed of identical spherical particles. However, detonation products represent a complex mixture because the molecules of the mixture can interact with different intermolecular potentials and they may consist of more than one mixture in more than one phase. Furthermore, concentrations of different molecules depend on pressure and temperature. It is difficult to handle such complex systems within the statistical mechanical theory developed for one-component fluid. Fortunately, advances in mixture theories soon followed the development of the one-component theories. Furthermore, experimental Hugoniot data for many species, which may occur in detonation products, became also available. Availability of the aforementioned theoretical and experimental information motivated the scientific community to renew a fundamental study of behaviour of detonation products.

In France, Chirat and Pittion-Rossillon have developed the ETARC code [1] using an approximate WCA theory. They extended the WCA method to the case of multicomponent fluid with the use of techniques [2,3]. Although their approach yielded reasonable results for

many explosives, there are serious difficulties in solving the detonation problems with ETARC. The main of them is that the WCA theory itself becomes poor at high densities and high temperatures relevant to detonation problems, e.g. this theory may give the values of the compressibility factor that are 15 or even more percent higher than the «exact» Monte Carlo results. Theoretical EOS were further investigated thanks to the progress made in the 1970s and 1980s in the thermodynamic perturbation theories and gave rise to such codes as CHEQ [4], the code of Jones and Zerilli [5], IDeX [6], CARTE [7].

The purpose of this work is to demonstrate that the predictive ability of a theoretical EOS of fluid detonation products, whose parameters were determined without the use of experimental HE detonation properties, is higher than that of the semi-empirical BKW EOS, although parameters of the latter are calibrated directly by matching the results of detonation experiments. All the calculations based on both theoretical and semi-empirical EOS are done by our thermodynamic code TDS.

2. Theoretical formulation

A. General description of the TDS code

The TDS code is designed to perform thermodynamic calculations of compositions and properties of complex chemically reacting or inert systems described by various equations of state under conditions of equilibrium and non-equilibrium. Initial reactants, as well as products, form multicomponent and/or multiphase systems that include a wide variety of elements and compounds. The thermodynamic computation is based on the fundamental Gibbs extremum principle. TDS solves thermodynamic equations for product species and unknown thermodynamic parameters of the system in chemical equilibrium. The program searches for conditional extremum of multivariable function, by solving a system of non-linear equations, for a given chemical system (i.e., a number of chemical elements, reaction products, etc.). Computations can be performed both under the condition of complete equilibrium and under prescribed chemical, thermal, or mechanical non-equilibrium conditions. In chemically non-equilibrium problems, frozen concentrations of one or more product species are preset as initial data. For the case of thermal non-equilibrium, products may include phases with different temperatures. For the case of a mechanical non-equilibrium, which may occur in stationary gas flows, phases may have different velocities. The TDS code has a wide range of applications because it allows a user to perform

non-equilibrium calculations. In particular, chemical non-equilibrium computations can be performed to effectively simulate real low-temperature processes in which detonation products have not reached the equilibrium state. TDS treats the following types of products: multicomponent and/or multiphase chemical systems, including solid and liquid components; systems with fluid phase separation (gas–gas equilibria); ionized species; nanodisperse condensed systems. Unlike other well-known thermodynamic codes, that require the presence of a gaseous phase in products, TDS can treat the entire chemical system composed only of condensed species and successfully solves the problems with the simultaneous presence of gases and a high content of condensed species. The TDS code calculates combustion characteristics of any fuel, including pollutant characteristics; equilibrium characteristics of vapor–liquid systems; phase diagrams for single- and multicomponent systems; characteristics of basic processes for various engines, power plants, and chemical apparatus; synthesis of high-melting compounds; and properties of nanodispersed substances. The TDS code is PC-based program. It has a multiple-window user interface, which makes it much easier to run the code, particularly for users that are familiar with the Microsoft Excel spreadsheet (since the TDS and Excel shells are outwardly very similar). TDS provides the user with online help, warnings, and error messages. The TDS code can be effectively used as an up-to-date, versatile toolkit for analyzing diverse physical and chemical processes and thermodynamic properties of real chemical compounds, and also as educational tool for colleges and technical universities.

In particular, the TDS code allows one to compute high explosive performances including the parameters of the Chapman–Jouguet (CJ) detonation. In solving the detonation problem, the code uses a special technique that guarantees correct determination of the phase composition of detonation products even for the explosives, whose reactive Hugoniots have discontinuities in thermodynamic derivatives due to phase transitions. Thus, the TDS code is the main computer tool we employ in this work to perform theoretical calculations of the CJ detonation.

B. EOS expressions

TDS supports a variety of semi-empirical and theoretical EOS for rare and dense gases, liquids, and solids. Here we describe only EOS relevant to typical detonation problems,

namely, semi-empirical EOS for solid phases of carbon (graphite and diamond) and theoretical EOS for fluid detonation products.

B.1) EOS for solid graphite and diamond

The detonation products of typical HE may contain graphite or diamond nanoparticles. Therefore, there is a need to determine the EOS of these phases of solid carbon. In this work we use the Gruneisen EOS for graphite and diamond [8] with our correction that takes into account the influence of the small size of carbon particles on their thermodynamic properties.

The EOS correction consists of the use of both the increased heats of formation (4.8 kcal/mol for the graphite and 6.75 kcal/mol for the diamond instead of the standard values of 0 and 0.453 kcal/mol, respectively) and the slightly changed densities at the standard (room) state (2.32 g/cm^3 for the graphite and 3.3 g/cm^3 for the diamond instead of the standard values of 2.27 and 3.515 g/cm^3). The specified values of the heat of formation and of the standard state density of carbon nanoparticles were determined to provide the best agreement between the calculated and measured detonation parameters for a series of carbon-rich explosives. For example, such graphite and diamond EOS lead to a break in the slope of the TNT detonation velocity vs. initial TNT density due to the graphite–diamond transition that occurs at $\rho_0 = 1.55$ g/cm^3 in exact agreement with the experiments.

The absolute values of the heat of formation of graphite and diamond that we use here are consistent with the available measurements for the heat of formation of carbon recovered from detonation calorimetry experiments. The difference between the heat of formation of the diamond nanoparticles and the same parameter of the graphite nanoparticles is within the range 1.55–2.38 kcal/mol which was predicted by van Thiel and Ree [9]. They employ an increased value for the standard state density of graphite too, but their magnitude (2.48 g/cm^3) more strongly deviates from the standard value than our one. The reduced value for the standard state density of diamond nanoparticles is due to some physical–chemical surface effects (porous structure etc.). Vereshchagin et al. [10] have measured pycnometric densities of the diamond nanoparticles obtained by processing detonation residues. Their results lie within the range 3.05–3.21 g/cm^3. The value of pycnometric density of the detonation diamonds determined in the recent experimental data of Komanschek and Pfeil [11] is equal to 3.1 g/cm^3. Our value is reasonably consistent with both the results of Vereshchagin et al. and the data of Komanschek and Pfeil.

B.2) One-component EOS of non-ideal fluids

We assume that the actual pair potentials of molecules i and j of the fluid phase of detonation products have an exponential-six (Exp-6) form

$$\varphi_{ij}(r) = \frac{\varepsilon_{ij}}{\alpha_{ij} - 6} \{ 6 \exp[\alpha_{ij}(1 - r/r_{m,ij})] - \alpha_{ij}(r_{m,ij} / r)^6 \}, \quad (1)$$

where r is the intermolecular separation, ε_{ij} is the depth of the attractive well, $r_{m,ij}$ is the position of the potential well minimum, and α_{ij} controls the stiffness of the repulsive part of the potential. Such spherical potentials have been successfully used to describe intermolecular interactions for many materials over a wide range of pressure and temperature including high pressures relevant to detonation problems.

In this work the thermodynamic properties of one-component fluid, whose N identical molecules interact with the Exp-6 potential with parameters ε, r_m, and α, are computed at a given temperature T and volume V from the version [13] of the KLRR perturbation theory [14], which is very successful extension of the WCA theory to the case of high densities and is as accurate as MC simulations. The KLRR perturbation theory divides the pair potential $\varphi(r)$ into a short-range reference potential $\varphi_0(r)$ and a long-range perturbing potential $\varphi_1(r)$ specified in a particular form:

$$\begin{aligned} &\varphi_0(r) = 0, \quad \varphi_1(r) = \varphi(r), \quad \text{for } r > \lambda, \\ &\varphi_0(r) = \varphi(r) - \varphi_\lambda(r), \quad \varphi_1(r) = \varphi_\lambda(r), \quad \text{for } r < \lambda, \end{aligned} \quad (2)$$

where $\varphi_\lambda(r) = \varphi(\lambda) - \varphi'(\lambda)\,[\lambda - r]$ is the smoothing potential and λ is the potential break-point defined [13] by $\lambda = r_m\,[\,1 + (\,2^{-1/2}\,\rho_*\,)^{n/3}\,]^{-1/n}$, where $n = 120$ and $\rho_* = N r_m^3/V$ is a reduced density.

A straightforward computer implementation of a perturbation theory would be rather slow for application in a chemical equilibrium code especially if a large number of product species is to be considered. For this reason, we take the THEOSTAR method [15] of constructing Tchebysev approximants to the excess Helmholtz free energy in terms of transformed thermodynamic variables. The EOS, that we have generated in such a way, decomposes state

space into separate domains and includes about 2000 coefficients. It is as accurate as the original perturbation theory. An appropriate acronym for this EOS is KLRR/C. Fried and Howard [16] have used the same approach to obtain an analytical EOS for the HMSA integral equations for pair distribution functions. We find that the KLRR perturbation theory replicates MC simulations for Exp-6 fluids slightly better than the HMSA integral theory, and KLRR is much easier to compute. That is why the KLRR theory was chosen for this work. Our KLRR/C EOS covers wider range of thermodynamic states than the HMSA/C and HMSA/MC EOS of Fried and Howard. This allows us to use the KLRR/C EOS also in some applications other than shock waves and detonations. The HMSA/MC EOS includes a semi-empirical correcting term that brings the calculated excess thermodynamic properties to very accurate agreement with MC simulations. It is our experience, however, that such semi-empirical term may lead to poorer results for some thermodynamic states that were not used to calibrate the correcting term. For this reason, we do not use semi-empirical terms in our KLRR/C EOS. Some results calculated with the KLRR/C and HMSA/C EOS for the Exp-6 potential with $\alpha = 15.5$ are plotted in Fig. 1 and compared with MC simulation results.

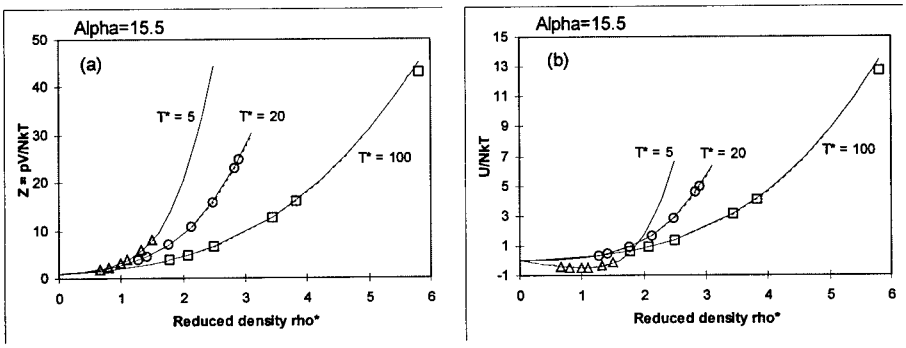


Fig. 1. Reduced temperature $T* = kT/\varepsilon$ isotherms of the compressibility factor $Z = PV/NkT$ (Fig. 1a) and of the excess internal energy factor $E = U_{ex}/NkT$ (Fig. 1b) as a function of reduced density $\rho*$ for the Exp-6 potential with $\alpha = 15.5$. Solid and dashed lines are computed with the KLRR/C and HMSA/C EOS, respectively. Symbols are MC simulations. Note, that the upper point (at $\rho* = 5.802$) lies outside the domain of the HMSA/C EOS.

C. Intermolecular potentials and mixture model

We assume that detonation of a typical HE containing C, H, N, and O atoms produces 13 gaseous (fluid) species, namely N_2, N, H_2O, CO_2, CO, NH_3, NO, CH_4, O_2, O, H_2, H, and OH. Their intermolecular interactions are described by the Exp-6 potentials (1). For strongly

attracting molecules (e.g., H_2O or NH_3), we use Exp-6 potentials with a temperature-dependent well depth

$$\varepsilon_{ii}(T) = \varepsilon_{0,ii}(1 + \lambda_{ii} / T), \tag{3}$$

where T is the temperature, and $\varepsilon_{0,ii}$ and λ_{ii} are the constants (for non-polar molecules $\lambda_{ii} = 0$). The dependence (3) was suggested by Ree [4] to simulate the average electrostatic effects of orientation on the intermolecular potential. The like-pair Exp-6 parameters α_{ii}, $r_{m,ii}$, $\varepsilon_{0,ii}$, and λ_{ii} for the gaseous products listed above were determined mostly by matching experimental Hugoniot data and available results of static experiments. Unlike-pair ($i \neq j$) Exp-6 parameters are assumed to follow extended Lorentz–Berthelot combination rules:

$$\begin{aligned} r_{m,ij} &= k_{ij}(r_{m,ii} + r_{m,jj}) / 2, \\ \varepsilon_{ij} &= l_{ij}(\varepsilon_{ii}\, \varepsilon_{jj})^{1/2}, \\ \alpha_{ij} &= m_{ij}(\alpha_{ii}\, \alpha_{jj})^{1/2}, \end{aligned} \tag{4}$$

where k_{ij}, l_{ij}, and m_{ij} are expected to be close to unity. In this work the parameters k_{ij}, l_{ij}, and m_{ij} are taken as equal to unity for all pairs except for $H_2O - N_2$ and $H_2O - CO_2$. The Exp-6 parameters used in this work are listed in Table 1.

Table 1. The Exp-6 parameters. ($k_{H2O–N2} = 1.02$; $k_{H2O-CO2} = 0.95$.)

Species	$\varepsilon_{0,ii}$, K	$r_{m,ii}$, m $^{-10}$	α_{ii}	λ_{ii}, K	Species	$\varepsilon_{0,ii}$, K	$r_{m,ii}$, m $^{-10}$	α_{ii}	λ_{ii}, K
N_2	100.6	4.25	12.3	0 [a]	H_2	37.0	3.55	10.8	0 [b]
N	120.0	2.65	10.4	0 [a]	H	20.0	1.40	13.0	0
O_2	96.2	3.79	14.7	0 [a]	OH	80.0	3.29	13.0	0 [c]
O	277.0	2.57	11.5	0 [a]	H_2O	188.0	3.24	13.3	496.0 [b]
NO	182.9	3.70	13.0	0 [a]	CH_4	109.0	4.49	12.9	0 [b]
CO_2	247.2	4.26	13.4	0 [a]	NH_3	96.7	3.95	12.9	117.0 [b]
CO	99.5	4.13	14.0	0 [a]					

[a], This work. [b], Ref. 7. [c], Ref. 17.

The post-detonation products are hot reactive mixtures. To calculate properties of such mixtures, we employ a simplifying assumption, the improved vdW1f model [18], in which all

molecules in the mixture are assumed to be identical and to interact with an effective Exp-6 potential. High reliability of this model in predicting the excess thermodynamic properties of multicomponent fluids has been shown by Ree [18], who is the author of the α-mixing rule. Furthermore, there are several theoretical research results partially justifying the vdW1f model.

Since parameters of an effective Exp-6 potential may depend on temperature due to the use of (3), we have extended the original Byers-Brown's THEOSTAR expressions to the case that all the Exp-6 parameters (or any of them) may depend on temperature. A convenient acronym for this extended version is THEOSTAR-T. The TDS code supports the THEOSTAR-T model in its extended form. A widely used form of the Exp-6 potential with the temperature-dependent well depth (3) has been incorporated into the TDS code as a standard tool.

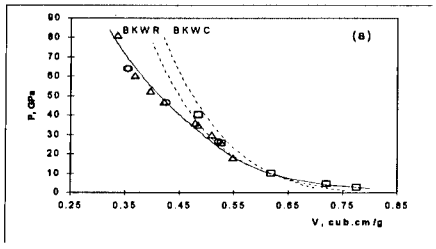
The theoretical approach applied here implies that all thermodynamic quantities at a given temperature T and volume V can be represented as the sum of an ideal contribution (which is equal to the corresponding quantity of the ideal gas at the same T and V) and of an excess contribution (which depends on intermolecular interactions only and is computed from the THEOSTAR-T model). The TDS code is supplied with several large databases to calculate the ideal contribution. In this work we employ the polynomial fits that approximate the JANAF tables [12].

Figure 2 shows a comparison between measured shock Hugoniots and predicted shock Hugoniots for a few typical detonation products using the THEOSTAR-T model with the KLRR/C EOS and Exp-6 parameters from Table 1, and two versions of the BKW EOS, namely, BKWR [19] of Finger et al. and recent BKWC [20] of Fried and Souers. Table 2 gives the initial density and enthalpy used for each of the Hugoniot calculations in Fig. 2. One can see that the results produced by the theoretical KLRR/C EOS are in good agreement with experimental Hugoniot data, the BKW predictions are significantly poorer. The BKWC prediction of the H_2O, NH_3, and H_2 Hugoniots is inadequate.

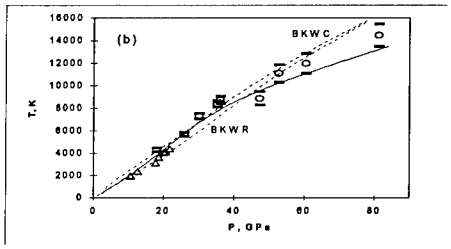
Table 2. Initial conditions for Hugoniot calculations in Figure 2

Species	T_0, K	ρ_0, g/cm^3	H_0, kcal/mol	Species	T_0, K	ρ_0, g/cm^3	H_0, kcal/mol
N_2	77	0.808	–2.84	NH_3	230	0.693	–17.4
H_2O	293	0.998	–68.3	H_2	20.5	0.071	–2.02
CO_2	218	1.173	–98.5	O_2	77	1.202	–1.41

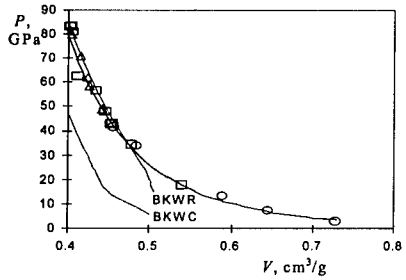
(a)


BKWR
BKWC
(a)
P, GPa
V, cub.cm/g

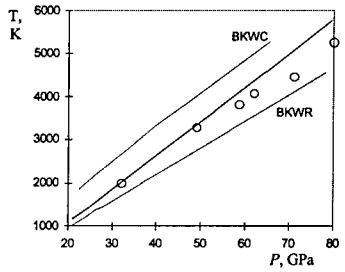
(b)


(b)
BKWC
BKWR
T, K
P, GPa

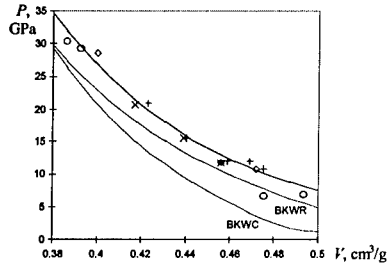
(c)


P, GPa
BKWR
BKWC
V, cm³/g

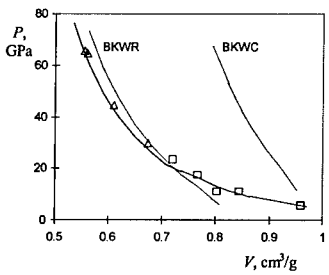
(d)


T, K
BKWC
BKWR
P, GPa

(e)

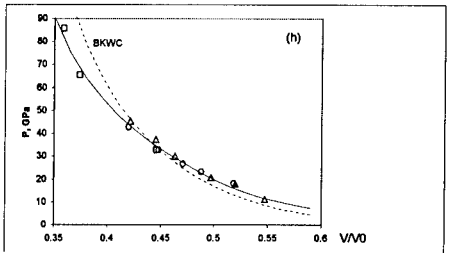

P, GPa
BKWR
BKWC
V, cm³/g

(d)


P, GPa
BKWR
BKWC
V, cm³/g

(f)

(h)


BKWC
(h)
P, GPa
V/V0

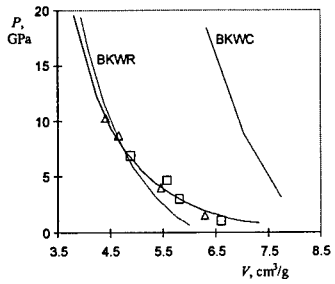


Fig. 2. Predicted (lines) and measured (symbols) Hugoniots for liquids: N_2 (a,b), H_2O (c,d), CO_2 (e), NH_3 (f), H_2 (g), and O_2 (h). The predicted Hugoniots were computed by TDS with the KLRR/C EOS and Exp-6 potentials from Table 1 (solid line), with the BKWR EOS (dashed line labeled BKWR), and with the BKWC EOS (dashed line labeled BKWC).

3. Explosive performance

Table 3 shows a comparison between measured and predicted detonation properties for a few typical HE using the THEOSTAR-T model with the KLRR/C EOS and Exp-6 parameters from Table 1, and the BKWC and BKWR EOS. In Table 3 D is the detonation velocity, P_{CJ} and T_{CJ} are the CJ pressure and temperature, respectively. Although the results of detonation experiments were not used to calibrate Exp-6 parameters of the theoretical EOS, its predictions are in good agreement with measured detonation properties and are much better than those of both semi-empirical BKW models. The BKWC EOS yields better results for the detonation velocity than BKWR, but inadequate Hugoniot replication does not allow us to use the BKWC EOS to obtain reliable predictions for new explosives. The computations of detonation properties of RDX and HMX based on the theoretical EOS predict that their fluid detonation products separate into two fluid phases.

Table 3. Measured and predicted detonation properties of explosives

HE ΔH_f, kcal/mol; ρ_0, g/cm^3	D, km/s experiment klrr-c / bkwc / bkwr	P_{CJ}, GPa experiment klrr-c / bkwc / bkwr	T_{CJ}, K experiment klrr-c / bkwc / bkwr
NO	5.62	10	–
21.0; 1.30	5.61 / 5.84 / 5.77	9.9 / 10.5 / 11.2	3058 / 3414 / 2891
C_3N_{12}	5.60	–	–
218.6; 1.15	5.65 / 5.96 / 5.98	8.9 / 9.7 / 10.5	3954 / 4072 / 3628
CN_4O_8 (TNM)	6.45	15.5	–
8.8; 1.65	6.46 / 6.26 / 6.18	15.1 / 13.8 / 14.8	2222 / 2651 / 2112
$C_2N_6O_{12}$	7.58	–	–
28.6; 1.86	7.59 / 7.48 / 7.20	24.0 / 22.0 / 22.6	2509 / 3154 / 2463
$C_6N_6O_{12}$ (HNB)	9.34	43	–

15.7; 1.965	9.41 / 9.16 / 8.83	39.3 / 37.0 / 37.8	4942 / 5297 / 4422
CH_3NO_2 (NM)	6.35	12.5	3400
−27.0; 1.13	6.35 / 6.28 / 6.67	12.6 / 12.1 / 13.5	3456 / 3451 / 3138
$C_5H_8N_4O_{12}$	8.30	31.7	4200
(PETN)	8.45 / 8.67 / 8.70	30.6 / 31.7 / 32.9	4145 / 4298 / 3528
−125.5; 1.77			
$C_3H_6N_6O_6$ (RDX)	8.64	33.8	–
14.7; 1.77	8.64 a) / 8.97 / 8.99	32.3 a) / 32.2 / 34.0	3938 a) / 4129 / 3349
$C_4H_8N_8O_8$	9.15	–	–
(HMX)	9.17 b) / 9.54 / 9.54	36.9 b) / 37.6 / 39.9	3755 b) / 4045 / 3192
17.9; 1.90			
$C_7H_5N_3O_6$ (TNT)	6.95	22	–
−15.0; 1.64	6.96 c) / 7.00 c) / 7.09 c)	22.3 c) / 22.9 c) / 19.4 c)	3593 c) / 3711 c) / 3048 c)
	7.20 d) / 7.18 d) / 7.48 d)	19.0 d) / 19.0 d) / 21.3 d)	3425 d) / 3474 d) / 3066 d)
	6.80 e) / 6.82 e) / 7.09 e)	17.2 e) / 17.3 e) / 19.0 e)	3373 e) / 3404 e) / 3034 e)

a), b), TDS predicts that the fluid detonation products separate into two (N_2-rich and N_2-poor) fluid phases. If this fluid phase separation is not taken into account, the CJ parameters are: a) $D = 9.02$ km/s, $P_{CJ} = 33.8$ GPa, $T_{CJ} = 3682$ K; b) $D = 9.67$ km/s, $P_{CJ} = 41.0$ GPa, and $T_{CJ} = 3450$ K.

c), TDS predicts that detonation occurs in the anomalous mode due to the diamond-to-graphite phase transition behind the detonation front (see the text).

d), e), The phenomenon of the anomalous detonation was not taken into account. d), Graphite nanoparticles are assumed to be present in products. e), Diamond nanoparticles are assumed to be present in products.

Figure 3 shows predicted and measured detonation velocities for two carbon-rich explosives, TNT and HNS, over a wide initial density range. TDS predicts that there is an initial density range where detonation of these explosives occurs in the anomalous mode [21,22] due to the diamond-to-graphite phase transition in detonation products, namely, at $\rho_0 > 1.55$ g/cm^3 for TNT and at $\rho_0 > 1.60$ g/cm^3 for HNS. In the case of the anomalous detonation, the detonation wave has an unusual two-front structure. The first front (i.e. the detonation front), as it usually is, corresponds to the end of the reaction zone, but in distinction to the usual (CJ) mode of detonation the CJ condition of the equality between the sound velocity and the local particle velocity is not satisfied here. Nevertheless, the first front propagates stably and its velocity is measured as the detonation velocity. The detonation products contain the diamond nanoparticles, there are no graphite nanoparticles here. The diamond-to-graphite transition begins immediately behind the detonation front. A rarefaction wave behind the detonation front contains the sonic surface (the second front), where the sound velocity is equal to the local particle velocity. The diamond-to-graphite transition is finished before the second front and at the sonic surface the detonation products contain the

graphite nanoparticles, there are no diamond nanoparticles here. It is appropriate to mention here that in some experiments on the CJ pressure the sound surface is mistakenly considered as the end of the reaction zone (i.e. as the CJ plane) and this leads to reduced values of the particle velocity and of the CJ pressure. Thus, the two-front structure of the detonation wave takes place for TNT and HMX at the aforementioned values of the initial density. The predicted detonation velocities of TNT are in excellent agreement with the measured values over entire range of the initial density. The theoretical curve for HNS lies slightly above the experimental results, however, its shape exactly replicates that of the measured dependence whose D vs. ρ_0 slope has a break at $\rho_0 = 1.6$ g/cm^3.

4. Conclusion

We have developed a numerically efficient multicomponent EOS model based on accurate thermodynamic perturbation theory. The model employs temperature-dependent Exp-6 potentials that can reliably reproduce (a) experimental shock wave data for many chemical species at temperatures and pressures relevant to detonation conditions and (b) thermodynamic properties of some species measured in static experiments. As a test case of the present model, we computed detonation properties of several explosives by means of our thermochemical TDS code using both the theoretical EOS of fluid detonation products obtained in this work and two versions of the semi-empirical BKW EOS. The predictions of the theoretical model are in good agreement with measured detonation properties, although the results of detonation experiments were not used to determine the potential parameters. The predictions of both tested BKW are poorer, although their parameters were calibrated using experimental detonation properties. We conclude that the computation of explosive performances with theoretical EOS is more reliable and such EOS should be used to predict the detonation properties of new explosives. Further improvements of predictions of HE performance can be realized by using a more fundamental theoretical model based on an explicit multicomponent EOS rather than on one-component fluid theory.

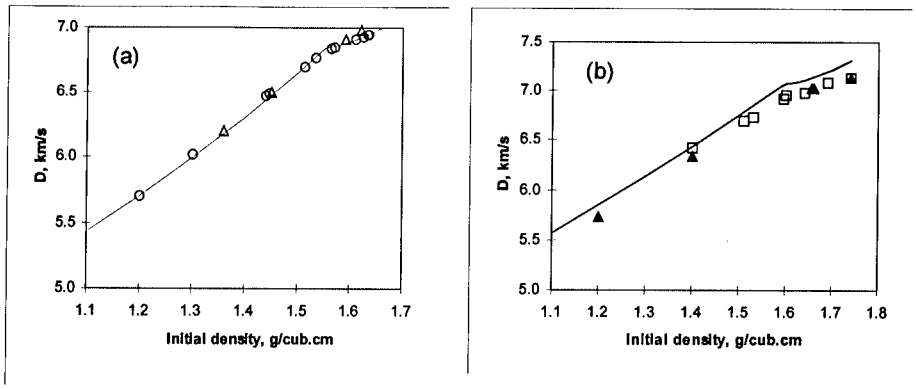


Fig. 3. Comparison between predicted (solid line, the KLRR/C EOS with Exp-6 potentials from Table 1) and measured (symbols) detonation velocities for (a) TNT and (b) HNS ($C_{14}H_6N_6O_{12}$, ΔH_f= 18.7 kcal/mol).

References

1. *Chirat R., Pittion-Rossillon G.* // J. Chem. Phys. 1981. V. 74. No. 8. P. 4634.
2. *Lee L.L., Levesque D.* // Mol. Phys. 1973. V. 26. P. 1351.
3. *Mansoori G.A., Carnahan N.F., Starling K.E., Leland T.W., Jr.* // J. Chem. Phys. 1971. V. 54. P. 1523.
4. *Ree F.H.* // J. Chem. Phys. 1984. V. 81. No. 3. P. 1251.
5. *Jones H.D., Zerilli F.J.* // J. Appl. Phys. 1991. V. 69. No. 7. P. 3893.
6. *Freeman T.L., Gladwell I., Braithwaite M., Byers-Brown W., et. al.* // Math. Engng. Ind. 1991. V. 3. No. 2. P. 97.
7. *Charlet F., Turkel M.L., Danel J.F., Kazandjian L.* // J. Appl. Phys. 1998. V. 84. No. 8. P. 4227.
8. *Van Thiel M., Ree F.H.* // Int. J. Thermophysics. 1989. V.10. P. 227.
9. *Van Thiel M., Ree F.H.* // J. Appl. Phys. 1987. V. 62. P. 1761.
10. *Vereshchagin A.L., Sakovich G.V., Komarov V.F., Petrov E.A.* // Diamond and Related Materials. 1993. V. 3. P. 160.
11. *Komanschek V., Pfeil A.* Nanostructured diamond: Synthesis Characterization and Applications. In: Energetic Materials Production, Processing and Characterization. 29th Int. Annu. Conf. of ICT, 30 June – 3 July 1998, Karlsruhe, Germany, p. 70.
12. *JANAF Thermochemical Tables* (1970), 2nd ed., U.S. Dept. Commerce, National Bureau of Standards, Washington, DC
13. *Byers-Brown W., Horton T.V.* // Mol. Phys. 1988. V. 63. No. 1. P. 125.

14.*Kang H.S., Lee C.S., Ree T., Ree F.H.* // J. Chem. Phys. 1985. V. 82. No. 1. P. 414.

15.*Byers-Brown W.* // J. Chem. Phys. 1987. V. 87. No. 1. P. 566.

16.*Fried L.E., Howard W.M.* // J. Chem. Phys. 1998. V. 109. No. 17. P. 7338.

17.*Hobbs M.L., Baer M.R., McGee B.C.* // Propellants, Explos., Pyrotech. 1999. V.24. P. 269.

18.*Ree F.H.* // J. Chem. Phys. 1983. V. 78. P. 409.

19.*Finger M. et al.* // Sixth Symposium (International) on Detonation. 1976. ACR-221. P. 710.

20.*Fried L.E., Souers P.C.* // Propellants, Explos., Pyrotech. 1996. V. 21. P. 215.

21.*Victorov S.B., Gubin S.A.* Influence of solid carbon phase transitions on detonation parameters of high explosives: anomalous mode of detonation. Int. Conf. «Shock Waves in Condensed Matter», 12–17 July 1998, St.Petersburg, Russia, P. 94.

22.*Victorov S.B., Gubin S.A., Maklashova I.V., Sumskoi S.I.* Structure of rarefaction wave for TNT detonation products. 12th Symp. Combustion and Explosion, 11–15 September 2000, Chernogolovka, Russia, Part 2, P. 88.

A STUDY ON FRIABILITY TEST TO ASSESS THE IMPACT SENSITIVITY OF INSENSITIVE EXPLOSIVES

Sung-ho Kim, Jung-su Park, Jeong-kwan Lee and Jeong-kook Kim

High Explosives Team, Agency for Defense Development (ADD), P. O. Box 35-5, Yuseong, Taejon, 305-600(Korea)

Abstract

We recently developed a friability test procedure, which will be used as one of substance tests for Extremely Insensitive Detonating Substances (EIDSs) in Test Series 7 of the United Nations. This test intended to assess the susceptibility of insensitive explosives to the break-up due to high strain rate and subsequent ignition characteristics of the deformed material. We designed an air gun system by using the hydro code simulation. The projectile velocities of the gun were in good agreement with those predicted by the hydro code with an inert material. Three different types of explosives, melt castable Comp B, castable plastic bonded explosives (PBXs), and pressable PBXs were tested during the development of the test procedure. Two castable PBXs, i.e. DXD-09 and DXD-10, which are currently under development as candidate formulations of EIDS were classified as EIDS, since test results with these formulations were far better than the criterion of the UN Test Series 7.

1. Introduction

In recent development of novel explosive materials, large efforts have been given to minimize hazards from shock, impact and thermal stimuli that happened accidentally. The explosive materials developed to fulfill this purpose are called Insensitive Munitions (IM). UN also recommended a series of tests in order to classify explosive materials as an Extremely Insensitive Detonating Substances (EIDSs).[1][2] UN Test Series 7 is a series of tests introduced newly for this purpose. In the UN Test Series 7, one has to perform many kinds of test methods to establish whether the explosive material is an EIDS or not. Friability test is one of those test methods that can be performed in the laboratory with relatively cheap. It also requires only a few numbers of tests. In addition, it may be carried out as an alternative to the SUSAN and the bullet impact test.

In this paper, we will describe the system and procedures of friability test briefly,

which is followed by the test results about several explosives, i.e. Comp B, castable and pressable PBXs. Our results from friability tests will be compared with those from SUSAN impact tests.

2. Friability Test [3][4]

In accordance with the UN Test Series 7, the friability test is known to be an alternative test to the SUSAN and Bullet impact tests. This test is used to establish the tendency of EIDS candidates to deteriorate dangerously under the effect of a high strain impact.

In this test, a bare cylindrical sample with a diameter of 18 mm, 9 g of EIDS candidate explosive material was impacted against a steel plate with 20 mm thickness at a velocity of 150 m/s. The fragmented sample were collected and weighed. The weight of collected sample must be greater than or equal to 8.8 g. Then the fragmented samples were burnt in a closed bomb with a volume of 108 cc. Based on the closed bomb test, the pressure-time profile was obtained, and the maximum pressure rise rate $(dP/dt)_{max}$ was calculated. In order to pass the criterion for EIDS in the friability test, the tested explosive material has the maximum pressure rise rate not greater than 15 MPa/ms at the velocity of 150 m/s.

3. Test System

In performing the friability test of EIDS candidate explosives, test system consists of two main elements, i.e. air gun test system and combustion test system. Followings are descriptions for each element of the test systems.

3. 1 Air Gun Test System

The air gun test system is used for hard target impacting of the sample explosives. The test sample with sabot is accelerated through the air gun barrel, passes through the screen measuring the velocity, and impacts against the hard target plate. The impacted samples are collected in a catch box. The sabot should be separated before entering the screen measuring the velocity. We recently designed a test system that fulfills the requirements of UN Test Series 7c(ii) and 7d(ii), and successfully made it in our institute. Our test system consists of air gun system, velocity measuring system, and a steel hard target surrounded by a sample catch box. Fig. 1 is a schematic diagram which depicts the air gun test system made recently by us.

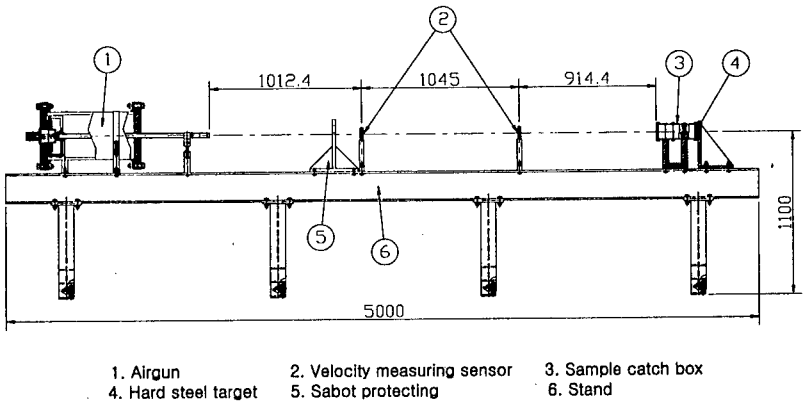


Fig. 1. Air gun test system for the friability test

(1) Air gun

The sample velocity was estimated by using one-dimensional Lagrangian hydro code program. The estimated result reveals that the impact pulse generated by 5 bar compressed air can accelerate the sample of which the velocity reaches 150 m/s at the position 1100 mm apart from start position and the flight time to here is 134.4 ms. This result suggests that 1000 mm length of barrel is enough to obtain the sample velocity 150 m/s with 5 bar compressed air pressure. Comparison of the sample velocities between estimation and experiment is shown in Fig. 2 as a function of compressed air pressure.

Air gun consists of an air chamber of 30 L, a barrel of 1000 mm length and a pilot operated valve. A pressure transducer is mounted onto the chamber to measure the compressed air pressure during the air filling process. Before shooting, the sample is inserted into a sabot. The sabot is made of high-density polyethylene, which we feel a good material for the stability during the flight, and an easy separation of the sample and processability. Fig. 3 illustrates the shape of the sabot.

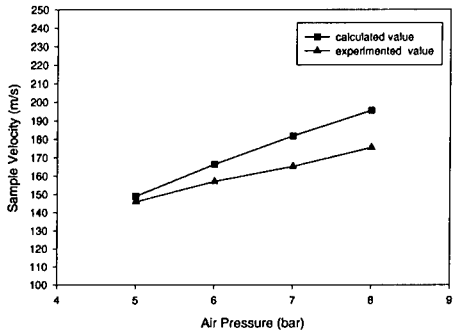


Fig. 2. Comparison of the sample velocities between estimation and experiment.

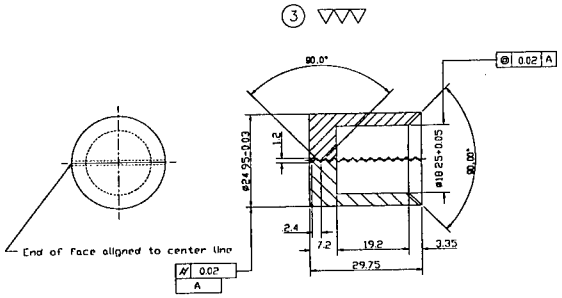


Fig. 3. The shape of the sabot

(2) Velocity measuring system

The velocity of the sample is measured before it enters a catch box. To measure the velocity, a time counter and two photo sensors are utilized. A short electrical pulse is generated during the sample passes the photo sensors, and the time counter measures the time interval between the pulses. The distance between photo sensors in our system is 104.5 cm.

(3) Sample catch box and steel impact plate

To collect the fragmented samples after the impact effectively, three cylindrical

types of catch boxes and a steel plate of 25 mm thickness are clamped together. During the test, the sample enters the catch box with a hole of 30 mm and impacts against the steel plate. Fig. 4 shows the sample catch box and impact steel plate.

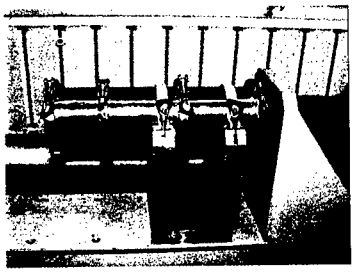


Fig. 4. The sample catch box

3. 2 A Closed Bomb System

After each test, the tested sample is collected and is weighed. If the weight loss in the collected sample is greater than 0.2 g, it cannot proceed to a closed bomb. The successfully collected samples are burnt in a closed bomb to acquire the maximum pressure rise rate, $(dP/dt)_{max}$. The closed bomb consists of (1) a combustion chamber of 108 cubic centimeters, (2)an ignition system that composed of M-100 electric match and 0.5 g black powder, and (3) a pressure measuring system. We used Kistler Model 6221 piezo-type pressure transducer to measure the pressure. Fig. 5 is a schematic diagram of the combustion test system.

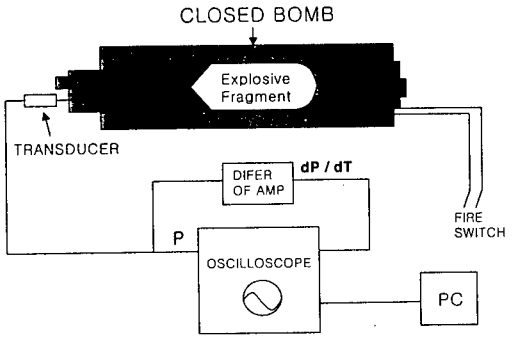


Fig. 5. The schematic diagram of the combustion test system

4. Friability Test of Explosives

As mentioned previously, the procedure of the friability test is mainly divided into two steps. At the first step, a test sample of 9 g is projected against a steel plate at a velocity of 150 m/s, while, at the second step, the transformed sample is burnt in a closed bomb to determine the maximum pressure rise rate, $(dP/dt)_{max.}$

Friability tests were carried out with three different types of explosives of which the mechanical properties are obviously different. The explosives with which we investigated (1) Comp B, a melt castable explosive, (2) castable PBXs, i.e. DXD-09 and DXD-10, and (3) pressable PBXs, i.e. DXD-57 and DXD-59. We summarized compositions and mechanical properties of explosives we tested in this study in Table 1.

Table 1. Compositions and properties of explosives we tested in this study.

Explosives	Compositions	Density (g/cc)	Young's Modulus(MPa)	Elongation (%)	Yield strength(MPa)
Comp B	RDX, TNT	1.672	12.7	1.5	0.833
DXD-09	HMX, NTO Al, U.B	1.72	5	20	0.52
DXD-10	HMX, NTO, AP, Al, U.B	1.76	3.2	27	0.47
DXD-57	HMX, ESTANE	1.81	709.9	2.77	15.85
DXD-59	HMX, Hytemp DOA	1.76	50.3	4.12	1.26

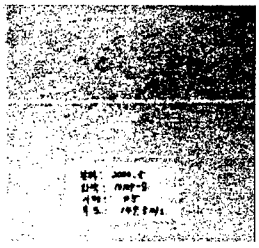
5. Test Results of Explosives

5.1 Impact Test

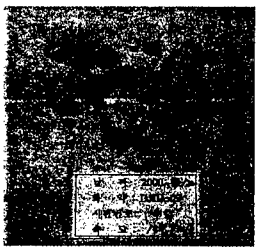
During the impact tests, we noticed that the velocities of samples are quite stable, if the compressed air pressure is the same. The errors of velocities are usually less than ±3 m/s. For instance, with the compressed air pressure of 5 bar, the average velocities of samples made with Comp B, castable PBX and pressable PBX are 151, 151.2, and 149.8 m/s, respectively. Fig. 6 shows fragmented explosive samples after the hard target impact with the sample velocity of 150 m/s. In Fig. 6, one may observe that Comp B samples are deformed more easily at lower impact velocities and pulverized to very small particles. On the other hand, castable PBXs, more specifically DXD-09 and DXD-

10, with low Young's modulus and high elongation rate are hardly deformed at the same impact stress. Deformation of pressable PBXs, i.e. DXD-57 and DXD-59, is a middle range between castable PBXs and Comp B. Based on these results, we may be convinced that melt castable explosive, Comp B, is generally more friable and more sensitive to crumble under a high impact stress than either castable or pressable PBXs.

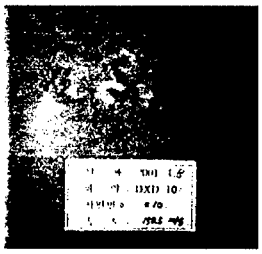
The test results are known to be significantly dependent upon the mechanical properties of the explosives. In general, since the materials with large Young's modulus are quite stiffened to be brittle, they are deformed plastically. On the other hand, since the materials with low Young's modulus and high elongation rate, for example castable PBXs, are easily softened, they have a very low plastic deformation by absorbing impact energies by themselves. We illustrated the recovery rates of the explosives tested in this study due to the change of projected impact velocities in Fig. 7. In Fig. 7, we may observe that the recovery rates of samples get lower, as the velocities become higher. The recovery rates of tested samples after the impact are usually greater than 98.3% (> 8.8g weight).



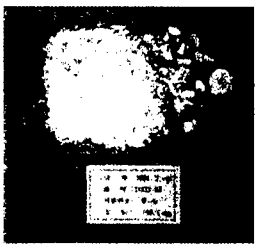
(a) Comp B, 149.5 m/s



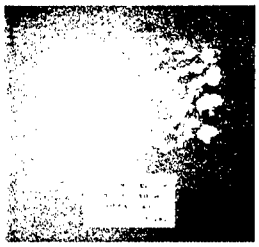
(b) DXD-09, 149.9 m/s



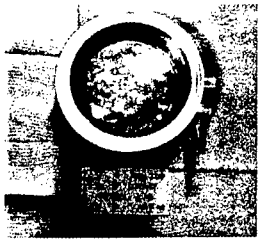
(c) DXD-10, 150.5 m/s



(d) DXD-57, 150.6 m/s



(e) DXD-59, 150.4 m/s



(f) DXD-59 fragment in catch box

Fig. 6. Fragmented explosives samples after the impact test.

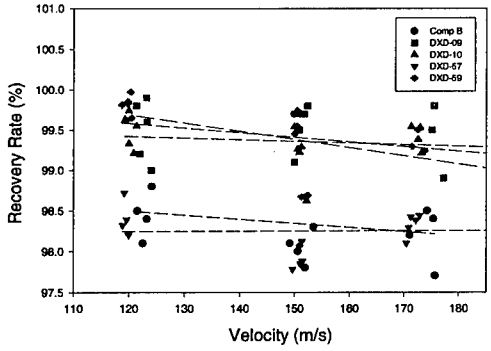
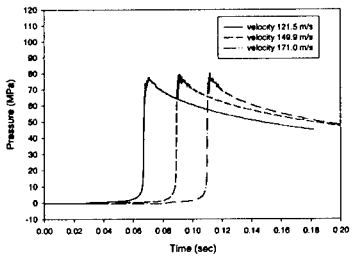


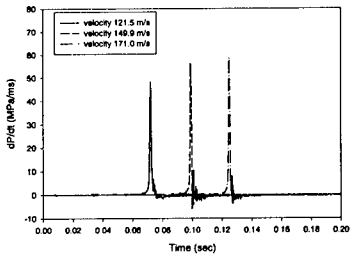
Fig. 7. The recovery rates of tested explosives

5.2 A Closed Bomb Test

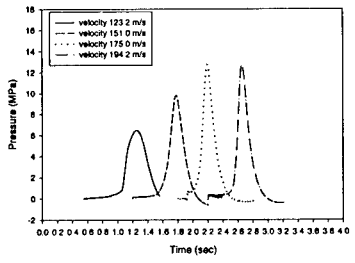
A closed bomb test was performed with test samples collected after the impact. Fig.8 depicts typical pressure profiles and pressure rise rates, (dP/dt), for Comp B, catable PBXs and pressable PBXs. Due to the poor mechanical properties of Comp B, it broke into small pieces which are almost like a powder after the impact test. Since these samples have a large burning surface, the maximum pressure rise rate, $(dP/dt)_{max}$, at a velocity of 150.8 m/s is recorded to be 56.73 MPa/ms. This value is much greater than



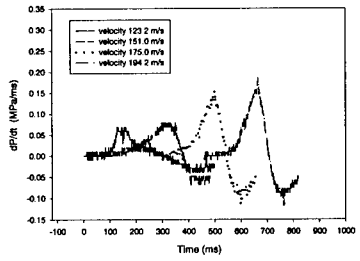
(a)



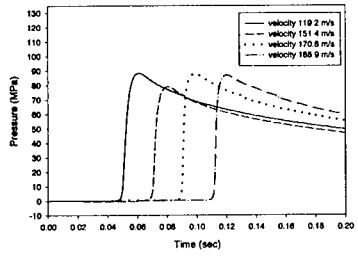
(b)



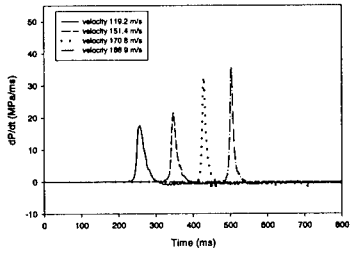
(b)



(d)



(e)



(f)

Fig. 8. Typical pressure and pressure rise rate profile of Comp B (a,b)
Castable PBXs (c,d) and Pressable PBXs (e,f)

that of passing criterion of EIDS, 15 MPa/ms. Since castable PBXs are disintegrated into lumps, their burning surfaces are relatively smaller than those from either Comp B or pressable PBX. Our analysis shows that the maximum pressure rise rates of DXD-09 and DXD-10 are 0.085 MPa/ms and 0.77 MPa/ms, respectively, at the velocity of 151 m/s. Thus, we conclude that both DXD-09 and DXD-10 are indeed an EIDS. We also measured that the maximum pressure rise rates of DXD-57 and DXD-59 are to be 21.56 and 53.45 MPa/ms, respectively, at the velocity of 150.8 m/s. Unfortunately, our pressable PBXs failed to pass the criterion of EIDS. We made a summary regarding the results of the closed bomb test in Table 2, and provide typical pressure and pressure rise rates for three types of explosive samples in Fig. 9.

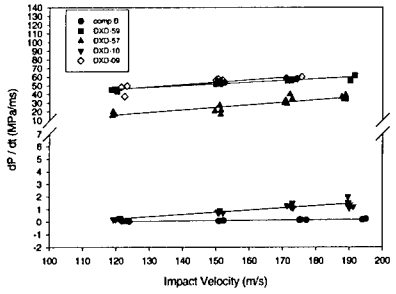


Fig. 9. Maximum pressure rise rate vs projected velocities of samples

Table. 2 Combustion Test Results of Explosive Samples

Explosives	Impact Velocity (m/s)	Sampling rate (ms^{-1})	Maximum Pressure (MPa)	Maximum Pressure rise rate (MPa/ms)
Comp B	122.4	0.2	77.71	45.16
	150.8	0.2	79.41	56.73
	173.6	0.2	80.45	58.83
DXD-09	123.0	1	6.38	0.055
	151.4	1	9.96	0.085
	175.8	1	12.42	0.156
	194.4	1	12.54	0.187
DXD-10	120.2	1	16.54	0.242
	151.1	1	29.75	0.770
	172.4	1	32.73	1.259
	190.0	1	36.88	1.420
DXD-57	119.1	0.2	88.88	17.46
	150.8	0.2	79.61	21.56
	171.5	0.2	87.57	33.09
	188.5	0.2	86.87	35.82
DXD-59	119.5	0.2	85.75	44.87
	150.8	0.2	85.85	53.45
	172.5	0.2	86.77	56.18
	190.0	0.2	87.82	58.71

5.3 SUSAN Test Result

We also performed the SUSAN test in order to compare with results from the friability test result. The SUSAN test results are shown in Fig. 11. At the SUSAN test, pressures are recorded at a function of time at the projectile velocity of 333 m/s. This recording should be repeated at least 5 times. After finished tests, if the average pressure obtained from tests is greater than or equal to 27 Kpa (≅3.92psi), the explosives are not an EIDS. Our results clearly indicate that castable PBXs pass the EIDS criterion, but Comp B and pressable PBXs do not.

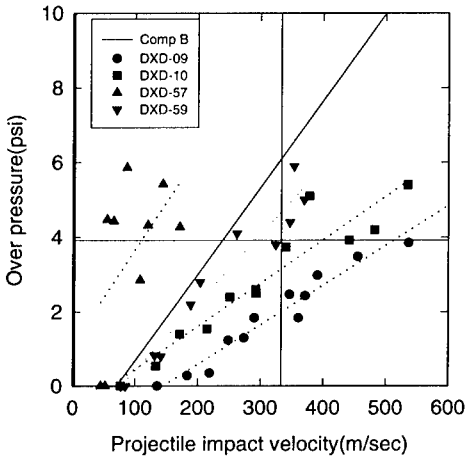


Fig. 10. SUSAN impact test results

6. Conclusion

We designed a friability test system in order to evaluate the sensitivity of insensitive explosives against a high impact strain rate. By performing a few experiments, we found the system constructed newly worked with quite satisfaction. We carried out the friability test with several explosives which were potential EIDS candidates. Melt castable Comp B, and pressable PBXs, DXD-57 and DXD-59, were crushed to be very small fine particles after the impact at the velocity of 150 m/s. In the closed bomb, they

burnt very severely, and the pressure rise rates were substantially greater than the criterion of EIDS. Conclusively, these explosives are not EIDS. In contrast, castable PBXs, DXD-09 and DXD-10, were broken into clumps after the impact, and displayed moderately burning results in the closed bomb. These castable PBXs surely passed the EIDS criterion. Further, we also compared the results from the friability test with those obtained from the SUSAN impact test. According to the analyses of results from these two tests, we feel confident that these two tests are closely related. We are currently conducting more studies relevant to these tests.

Reference

1. Derk Soon Ham, Bo Young Park, Jeong Kwan Lee, "Hazard classification of explosives/ammunitions and Hazard Class/Division 1.6", ADD. TR. GWSD-519-950527, 1995

2. Michael, M., Swisdak, Jr., "Hazard Class/Division 1.6:Extremely Insensitive Detonating Substance (EIDS)", NSWC TR 89-356

3. Gibson, P. W., 'Friability and Critical Diameter Tests on the Maneuver Propulsion Assembly Propellants", AFRPL, TR 85-089, January, 1986

4. Isler, J., "Classification Tests for Assignment to Hazard Class/Division 1.6:SNPE two year experience"

STRUCTURAL CHARACTERIZATION AND THERMAL DECOMPOSITION MECHANISM OF $[Pr(NTO)_3(H_2O)_5]NTO{\cdot}3H_2O$ AND $[Gd(NTO)_2(H_2O)_6]{\cdot}NO_3{\cdot}2H_2O$

Jae-Kyung Kim[(1)], Bang-Sam Park[(1)], Chong-Hyeak Kim[(2)] and Sock-Sung Yun[(3)]

(1) High Explosives Team, Agency for Defense Development(ADD), P.O.Box 35-5, Yuseong, Taejon, 305-600(Korea)
(2) Chemical Analysis Laboratory, Korea Research Institute of Chemical Technology, Yuseong, Taejon, 305-600(Korea)
(3) Department of Chemistry, Chungnam National University, Yuseong, Taejon, 305-764(Korea)

Abstract : 3-Nitro-1,2,4-triazol-5-one (NTO) has been attracted as a candidate for high energetic insensitive explosive material. NTO, which is white crystalline solid, and relatively acidic (pKa=3.67) in aqueous solution, is known to have an ability to form stable complexes with various metal ions. We investigated thermal stability and decomposition mechanism of praseodymium and gadolinium-NTO complexes by thermal analysis methods (TG-DTG and DSC). We synthesized $[Pr(NTO)_3(H_2O)_5]NTO{\cdot}3H_2O$ and $[Gd(NTO)_2(H_2O)_6]{\cdot}NO_3{\cdot}2H_2O$ complexes and found a unique coordination behavior of these NTO complexes determined by single-crystal X-ray diffraction method. The complex $[Pr(NTO)_3(H_2O)_5]NTO{\cdot}3H_2O$ crystallized in the monoclinic *Pc* space group and was revealed to be a novel infinite one dimensional coordination polymer. The crystal structure of $[Gd(NTO)_2(H_2O)_6]{\cdot}NO_3{\cdot}2H_2O$ showed to be a triclinic $P\ \bar{1}$ space group. The thermal decomposition processes of $[Pr(NTO)_3(H_2O)_5]$ $NTO{\cdot}3H_2O$ complex were analyzed to have three distinctive stages, i.e. the dehydration, ring cleavage, and metal oxide formation, while thermal decomposition reaction of the single crystal of $[Gd(NTO)_2(H_2O)_6]{\cdot}NO_3{\cdot}2H_2O$ was proceeded through four stages.

1. Introduction

3-Nitro-1,2,4-triazol-5-one (NTO) is a thermally stable, high energetic explosive, but less sensitive than 1,3,5-trinitrohexahydro-s-triazine (RDX) and octahydro-1,3,5,7-tetranitro-1,3,5,7-tetrazocine (HMX), which are the mostly common nitramine explosives.[1] The metal complexes of NTO are also interesting novel compounds probably used for catalysts in the combustion of propellants. With the our continuing interests in NTO-metal complexes, we recently succeeded in preparing the single crystals of $[Pr(NTO)_2(H_2O)_5]NTO{\cdot}3H_2O$ and $[Gd(NTO)_2(H_2O)_6]{\cdot}NO_3$

·$2H_2O$, and measuring their structures by a four-circle x-ray diffractometer. In addition, we examined thermal decomposition mechanisms by thermal and FT-IR techniques.

2 Experimental

2. 1 Materials

The NTO used in this experiment was synthesized in 450 gram batch sizes through two steps using a reaction calorimeter (Mettler-Toledo GmbH, Switzerland). The synthesized NTO was recrystallized twice in the distilled water. $[Pr(NTO)_2(H_2O)_5]NTO{\cdot}3H_2O$ and $[Gd(NTO)_2(H_2O)_6]{\cdot}NO_3{\cdot}2H_2O$ were synthesized by similar methods in preparing other NTO salts published earlier.[2, 3] The synthesized powder NTO-metal complexes were recrystallized with distilled water at the room temperature for six months to obtain the single crystals for X-ray measurement.

2. 2 Experimental equipment and condition

The single crystals of titled compounds were coated with epoxy resin to prevent spontaneous liberation of water molecules from the specimen under ambient condition. The intensity data were collected at room temperature on a Siemens P4 four-circle X-ray diffractometer with graphite-monochromated Mo K α radiation(λ= 0.71073 Å). Accurate unit cell dimensions were refined using 48 reflections with 2θ ranges 2.05 to 27.50° for $[Pr(NTO)_2(H_2O)_5]NTO{\cdot}3H_2O$ and 1.77 to 27.50° for $[Gd(NTO)_2(H_2O)_6]{\cdot}NO_3{\cdot}2H_2O$. Three standard reflections were measured every 97 reflections : no remarkable decays were observed. The reflections used with the intensities $|I| > 2\sigma|I|$ were Lorentz and polarization corrected ; a semi-empirical absorption corrected based on the psi-scans were applied. A total 6373 reflections ware corrected in the 2θ range 4.10 ~ 55° using 2θ-θ scan mode[4] for $[Pr(NTO)_2(H_2O)_5]NTO{\cdot}3H_2O$ and 6373 reflections in the 2θ range 3.50 ~ 55° for $[Gd(NTO)_2(H_2O)_6]{\cdot}NO_3{\cdot}2H_2O$ respectively.

All calibration in the structure solution and refinement was performed using the Siemens SHELXTL crystallographic software package on a Silicon Graphic system. Space group was assigned based on the systematic absences and intensity statistics, and was confirmed by successful refinements. The structure was solved by the direct method[5] and refined by successive full-matrix least-squares method followed by difference Fourier map. All the non-hydrogen atoms were refined anisotropically; all the hydrogen atoms fixed at the calculated positions with the isotropic thermal parameters were included in the finial structure factor calculation. Final difference of electron density maps contained no significant features.

The thermal decomposition mechanism was investigated with a TGA 50 (Mettler-Toledo GmbH. Switzerland). The conditions of TG were as follows: sample mass, about 1 mg; heating rate, 10 ℃min^{-1}; nitrogen atmosphere. The DSC experiments were carried out with a model 821[e]

(Mettler-Toledo GmbH. Switzerland) differential scanning calorimeter with a standard aluminum sample pan, whose side was rolled up. The conditions of DSC were as follows: sample mass, about 1 mg; heating rate, 10℃ min^{-1}; atmosphere, static air; reference sample: indium. The infrared spectra of the complexes and their decomposition residue were recorded in KBr discs methods on a IFS 88 FT-IR spectrometer (Bruker, U.S.A) at 4 cm^{-1} resolution. Elemental contents of C, H and N were determined with MOD 1108 elemental analyzer (Carlo Erba Co., Italy).

3. Results and discussion

3.1 Crystal structure of $[Pr(NTO)_2(H_2O)_5]NTO{\cdot}3H_2O$

The crystal structure was founded to be monoclinic, which belong to space group *Pc* with crystallographic parameters of a =12.034(3), b = 9.9555(12), c = 18.611(3)Å, β = 102.008(12), V = 2182.6(6)$Å^3$, Z = 4, μ = 2.034 nm^{-1} , $F(000)$ = 1336, Dc=2.046 g/cm^3. The finial R=0.0380, R(all data)=0.0396.

The atomic coordinates and thermal parameter are summarized in Tables 1. The asymmetric unit and atom labeling are shown in Fig. 1, the perspective view of the unit cell of the molecule in the crystal lattice along the a axis and the coordination polyhedron of Pr(1) and Pr(2) ions are illustrated in Fig. 2 and 3. If one wants to obtain the detailed crystal data and structure refinement, including bond lengths and angles, hydrogen bond lengths and angles, perspective views of the above crystal, it may be possible upon request to one of authors (J.-K. Kim, ADD).

As shown in Fig. 1, the two Pr atoms have different coordinate numbers. Pr(1) has 10 coordination numbers, while Pr(2) has 7. Besides chelating with six water molecules from the hydrated cation, the Pr(1) atom forms two chelate rings by combining two different NTO rings. Each chelate ring is formed by interacting the Pr(1) atom with N atom in the NTO ring and O atom of nitro group on the same side of the NTO ring. Two chelate rings are posed to be a trans orientation. On the other hand, the Pr(2) atom combines with three carbonyl O atoms from three different NTO rings and four O atoms of water molecules. According to Fig. 1, there are two free NTO molecules and six crystalline water molecules in the crystal lattice. The empirical formula for each Pr atom is $[Pr(NTO)_2(H_2O)_5]{\cdot}NTO{\cdot}H_2O$, which is in good agreement with our elemental analysis (calculated value: C 10.73 %, H 2.85 %, N 25.04 %, Pr 20.86 %, experimental value: C 10.58 %, H 2.33 %, N 24.34 %, Pr 21.24 %).

The coordinated bond lengths are observed in a range of 2.366 and 2.971 Å. The Pr(1)–O(41) bond is the shortest one, 2.366 Å, while the Pr(1)-O(22) bond is the longest one, 2.971Å. The bond lengths in three NTO rings are observed to be 1.307-1.392 Å. The bond length C(11)-O(11), i.e. 1.241 Å, is significantly shorter than other bonds inside the NTO ring, i.e. 1.2601-1.261 Å due to the characteristics of the double bond.

The bond lengths inside the NTO ring are in good agreement with the calculated ones by Ritchie[6,7] and by others[8]. In the two chelate-rings, the Pr(1)-N(13) (2.694Å) and Pr(1)-O(22) (2.971Å) bonds, are much longer than other bond lengths, which means that strength of these bonds are significantly weak.

Table 1. Atomic coordinates (x 10^4) and equivalent isotropic displacement parameters (x 10^3) for $[Pr(NTO)_2(H_2O)_5]\cdot NTO\cdot 3H_2O$.

	x	*y*	*z*	*U(eq)*/Å^2
Pr(1)	4755(1)	931(1)	3273(1)	24(1)
Pr(2)	9739(1)	2394(1)	3210(1)	21(1)
O(1w)	6507(6)	170(6)	2878(3)	38(1)
O(2w)	2982(5)	245(7)	3650(3)	40(1)
O(3w)	5224(6)	-1095(6)	4044(3)	41(1)
O(4w)	4227(6)	-1126(6)	2506(3)	41(1)
O(5w)	5657(6)	3037(6)	2920(3)	41(1)
O(6w)	3890(7)	2958(7)	3657(3)	43(2)
O(7w)	8776(6)	4416(6)	3581(3)	43(1)
O(8w)	9920(7)	-114(5)	3361(3)	44(2)
O(9w)	11119(6)	4319(7)	3486(3)	49(2)
O(10w)	9662(5)	3925(5)	2122(3)	37(1)
O(21w)	3937(8)	5511(12)	-171(4)	84(3)
O(22w)	1743(8)	-1660(10)	4305(4)	72(2)
O(23w)	7448(7)	-2166(9)	2222(4)	62(2)
O(24w)	9526(8)	6869(6)	3272(5)	72(3)
O(25w)	3591(7)	3025(7)	9042(3)	59(2)
O(26w)	5604(5)	-3391(6)	2654(3)	43(1)
O(11)	1330(6)	1662(7)	2694(3)	36(1)
C(11)	1823(6)	1625(7)	2159(3)	24(1)
N(11)	1255(5)	1662(7)	1442(3)	27(1)
N(12)	2032(6)	1636(7)	983(3)	31(2)
C(12)	2970(7)	1594(8)	1464(4)	26(2)
N(13)	2975(6)	1569(6)	2192(3)	25(1)
N(14)	4036(6)	1500(8)	1224(3)	37(2)
O(12)	4040(6)	1516(11)	575(3)	66(2)

O(13)	4894(5)	1354(7)	1721(3)	41(1)
O(21)	8161(5)	1711(6)	3813(3)	30(1)
C(21)	7680(6)	1764(7)	4352(3)	24(1)
N(21)	8193(5)	1952(7)	5068(3)	30(1)
N(22)	7457(6)	1936(8)	5526(3)	30(1)
C(22)	6507(7)	1722(8)	5055(4)	26(2)
N(23)	6553(5)	1589(6)	4340(3)	23(1)
N(24)	5462(6)	1546(8)	5305(4)	36(2)
O(22)	4612(5)	1286(8)	4837(3)	44(2)
O(23)	5475(6)	1728(12)	5956(3)	75(3)
O(31)	11037(6)	1961(7)	4348(3)	45(1)
C(31)	11292(7)	1866(8)	5028(4)	31(2)
N(31)	12345(6)	1598(8)	5417(3)	32(2)
N(32)	12368(6)	1544(7)	6154(3)	33(1)
C(32)	11323(6)	1789(7)	6162(4)	27(1)
N(33)	10600(5)	1991(7)	5504(3)	32(1)
N(34)	10951(7)	1828(9)	6848(4)	49(2)
O(32)	11610(7)	1761(10)	7407(3)	64(2)
O(33)	9898(8)	1919(18)	6793(5)	121(5)
C(41)	8160(6)	1320(8)	1558(4)	28(1)
O(41)	8407(6)	1382(6)	2249(3)	42(1)
N(41)	7057(6)	1251(8)	1152(4)	33(2)
N(42)	7053(6)	1293(7)	413(3)	31(1)
C(42)	8139(6)	1351(7)	433(4)	28(1)
N(43)	8862(6)	1392(6)	1085(3)	30(1)
N(44)	8548(7)	1475(8)	-245(4)	41(2)
O(42)	9557(7)	1462(13)	-193(4)	80(3)
O(43)	7846(8)	1569(9)	-817(3)	62(2)
O(51)	6718(5)	5062(6)	-1119(3)	39(1)
C(51)	6901(7)	4876(7)	-437(4)	32(2)
N(51)	7973(6)	4704(7)	2(3)	37(1)
N(52)	7925(6)	4528(7)	718(4)	38(1)
C(52)	6837(8)	4594(8)	680(4)	37(2)
N(53)	6150(7)	4803(8)	13(4)	42(2)
N(54)	6403(8)	4380(9)	1341(4)	50(2)
O(52)	7049(7)	4168(8)	1901(4)	67(2)

O(53)	5398(8)	4359(12)	1274(5)	88(3)
O(61)	2920(5)	4814(6)	7958(3)	40(1)
C(61)	2716(7)	4833(7)	7270(4)	28(1)
N(61)	3499(6)	4565(7)	6857(3)	36(1)
N(62)	3038(6)	4713(7)	6127(4)	38(2)
C(62)	2012(6)	5076(7)	6145(4)	29(1)
N(63)	1725(6)	5138(7)	6805(3)	35(1)
N(64)	1216(6)	5333(7)	5474(3)	40(2)
O(62)	1545(8)	5275(10)	4914(4)	72(2)
O(63)	264(7)	5621(10)	5522(4)	71(2)

Note : *U(eq)* is defined as one third of the trace of the orthogonalized *Uij* tensor.

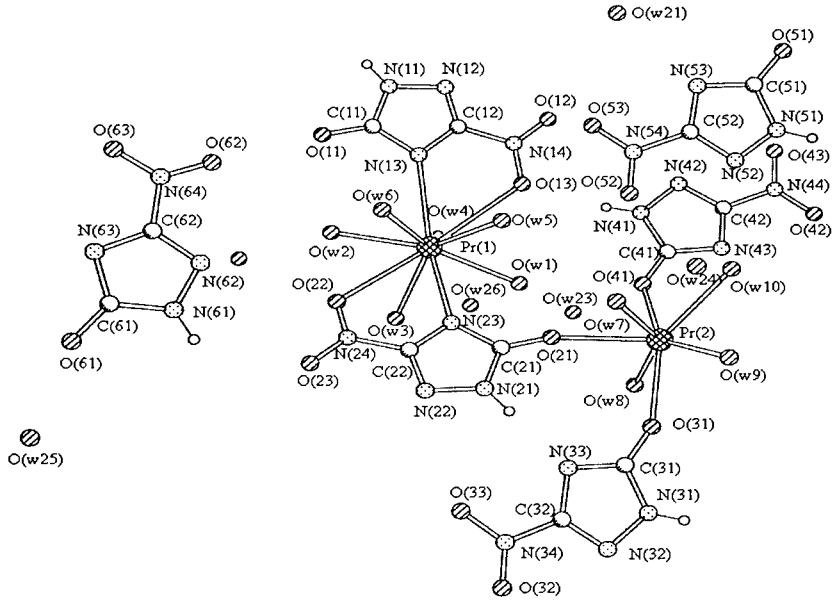


Fig. 1. Asymmetric unit of $[Pr(NTO)_2(H_2O)_5] \cdot NTO \cdot 3H_2O$ showing the atomic notations

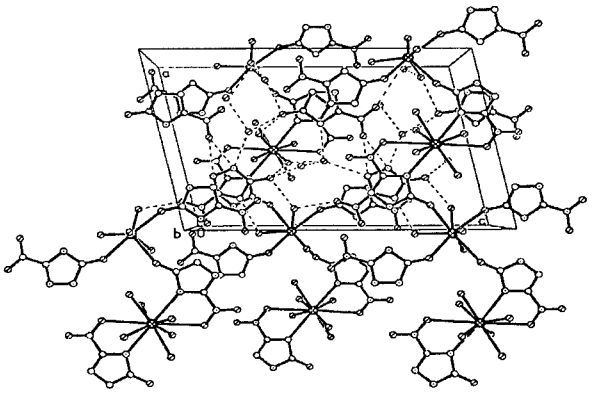


Fig. 2. Packing of molecules $[Pr(NTO)_2(H_2O)_5]\cdot NTO\cdot 3H_2O$ in the crystal lattice

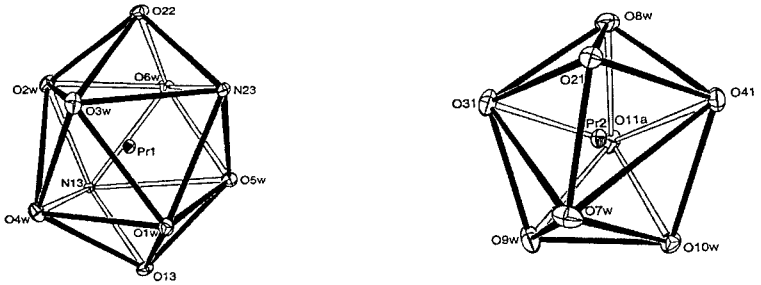


Fig.3. Coordination polyhedron of Pr(1) and Pr(2) ions in $[Pr(NTO)_2(H_2O)_5]\cdot NTO\cdot 3H_2O$.

3.2 Crystal structure of $[Gd(NTO)_2(H_2O)_6]\cdot NO_3\cdot 2H_2O$

The crystal structure was founded to be triclinic, which belongs to the $P\ \bar{1}$ space group with crystallographic parameters of a = 6.1505(13), b = 11.618(3), c = 25.958(8) Å, α= 90.01(1), β = 90.02(2), γ= 90.06(2)°, V = 1838.4(8) Å^3, Z = 4, μ = 3.718 nm^{-1}, $F(000)$ = 1220, Dc=2.246 g/cm^3. The finial R=0.0545, R(all data)=0.0546.

The atomic coordinates and thermal parameter are summarized in Tables 2. The asymmetric unit and atomic notations are shown in Fig. 4, the perspective view of the unit cell of the molecule in the crystal lattice along the a axis and the coordination polyhedron of Gd ion are

illustrated in Fig. 5 and 6. As mentioned previously, the detailed crystal data of this crystal may also be available upon request to J.-K. Kim, ADD.

As shown in Fig.4, two Gd atoms have 8 coordinate number. Each Gd atom combines with the two carbonyl O atoms of two different NTO rings and six water molecules. Thus, there are two NO_3 ions and four water molecules of crystallization in the crystal lattice. The empirical formula is $[Gd(NTO)_2(H_2O)_6]\cdot NO_3\cdot 2H_2O$, which is also in good agreement with our elemental analysis (calculated value : C 7.51 %, H 3.15 %, N 19.71 %, Gd 24.58%, experimental value : C 7.71 %, H 2.67 %, N 19.85 %, Gd 24.99 %).

The NO_3 ions may come from dilute nitric acid, which was used to dissolve the gadolinium oxide. We can notice a similar case of $[Y(NTO)_2NO_3(H_2O)_5]\cdot 2H_2O$ published by Song et al.[9] However, our crystal differs from theirs, where the NO_3 ions directly bond to the Y atom.

The bond lengths between Gd and the O atoms of coordinated water are 2.380 Å in Gd(2)-O(8w), and 2.251 Å in Gd(2)-O(10w), respectively. The bond lengths between Gd and the carbonyl O atoms of NTO are observed to be 2.241 and 2.333 Å in Gd(2)-O(41) and Gd(2)-O(31), respectively. In the NTO rings, the bond length of N(22)-C(22), 1.310 Å, is shorter than those of N(21)-N(22) (1.360 Å), N(21)-C(21) (1.359 Å), C(21)-N(23) (1.338 Å), and N(23)-C22) (1.344 Å) due to the nature of double bond.

We can observe eight hydrogen bonds between H atoms and the N atom of NTO, the O atom of NO_3 ion. The hydrogen bond lengths are 2.882 Å in N(11)-H(11)---O(51) and 3.484 Å in N(31)-H(31)---N(61), and the angles in those hydrogen bonds are observed to be 134.0° and 165.6°, respectively.

Table 2. Atomic coordinates (x 10^4) and equivalent isotropic displacement parameters ($Å^2$ x 10^3) for $[Gd(NTO)_2(H_2O)_6]\cdot NO_3\cdot 2H_2O$

	x	*y*	*z*	*U(eq)*/ $Å^2$
Gd(1)	2157(1)	6073(1)	6056(1)	14(1)
Gd(2)	-2845(1)	1071(1)	8944(1)	14(1)
O(1w)	-1072(16)	6278(7)	5476(3)	23(2)
O(2w)	3557(18)	6644(8)	6896(4)	32(3)
O(3w)	5060(16)	4964(6)	6220(4)	25(3)
O(4w)	3038(16)	5758(7)	5156(3)	25(2)
O(5w)	797(15)	4062(6)	5857(4)	26(3)
O(6w)	878(18)	7912(7)	6245(4)	30(3)

O(7w)	-1469(15)	1670(7)	8102(3)	25(2)
O(8w)	40(15)	-47(6)	8778(4)	24(2)
O(9w)	-1964(17)	769(7)	9849(3)	28(3)
O(10w)	-6073(15)	1294(7)	9528(3)	21(2)
O(11w)	-4125(16)	2911(7)	8755(4)	24(2)
O(12w)	-4186(18)	-942(7)	9143(4)	33(3)
O(13w)	-7952(16)	7715(6)	8731(4)	25(3)
O(14w)	-2973(19)	2718(7)	6267(4)	34(3)
O(15w)	6070(17)	7175(7)	4523(4)	31(3)
O(16w)	-1075(17)	-2160(7)	9533(4)	31(3)
O(11)	-789(15)	5484(7)	6596(3)	22(2)
C(11)	-1170(20)	5413(9)	7083(5)	17(3)
N(11)	28(19)	4893(8)	7435(4)	29(3)
N(12)	-810(20)	4984(9)	7913(4)	30(3)
C(12)	-2460(20)	5534(8)	7814(5)	17(3)
N(13)	-2808(18)	5823(7)	7327(4)	18(3)
N(14)	-3900(20)	5846(9)	8223(4)	26(3)
O(12)	-3380(20)	5634(11)	8667(4)	53(4)
O(13)	-5501(19)	6278(10)	8095(4)	45(4)
O(21)	5288(15)	7343(6)	5836(3)	22(2)
C(21)	5937(18)	8430(8)	5754(4)	13(3)
N(21)	5926(19)	9297(7)	6105(4)	21(3)
N(22)	6718(17)	10341(7)	5893(4)	17(3)
C(22)	7145(19)	10019(8)	5426(4)	13(3)
N(23)	6727(17)	8882(7)	5308(4)	15(2)
N(24)	8060(20)	10881(8)	5054(4)	28(3)
O(22)	8223(18)	10532(8)	4609(4)	36(3)
O(23)	8561(18)	11881(7)	5198(4)	35(3)
O(31)	-5782(16)	483(7)	8405(3)	20(2)
C(31)	-6200(20)	421(9)	7914(5)	18(3)
N(31)	-4988(18)	-96(8)	7568(4)	20(3)
N(32)	-5820(20)	-24(9)	7088(4)	23(3)
C(32)	-7510(20)	539(9)	7181(4)	17(3)
N(33)	-7827(18)	826(8)	7674(4)	18(3)
N(34)	-8880(20)	836(8)	6777(4)	25(3)
O(32)	-10510(20)	1278(9)	6896(4)	40(3)

O(33)	-8430(20)	615(11)	6330(4)	50(4)
O(41)	293(16)	2345(6)	9164(3)	22(2)
C(41)	920(20)	3431(9)	9246(5)	20(3)
N(41)	889(19)	4287(8)	8891(4)	21(3)
N(42)	1672(18)	5340(7)	9106(4)	19(3)
C(42)	2150(20)	5031(8)	9568(5)	17(3)
N(43)	1737(18)	3886(7)	9694(4)	19(3)
N(44)	3048(19)	5863(8)	9940(4)	21(3)
O(42)	3260(18)	5527(8)	10390(4)	31(3)
O(43)	3590(20)	6893(7)	9802(4)	34(3)
N(51)	-5620(20)	3287(7)	7445(4)	22(3)
O(51)	-6713(19)	3540(8)	7064(4)	30(3)
O(52)	-6224(18)	3508(8)	7885(4)	31(3)
O(53)	-3934(17)	2814(8)	7373(4)	32(3)
N(61)	-620(20)	8296(8)	7554(4)	26(3)
O(61)	-1220(20)	8509(8)	7115(4)	33(3)
O(62)	1097(17)	7830(8)	7631(4)	33(3)
O(63)	-1714(18)	8530(8)	7932(4)	36(3)

U(eq) is defined as one third of the trace of the orthogonalized *Uij* tensor

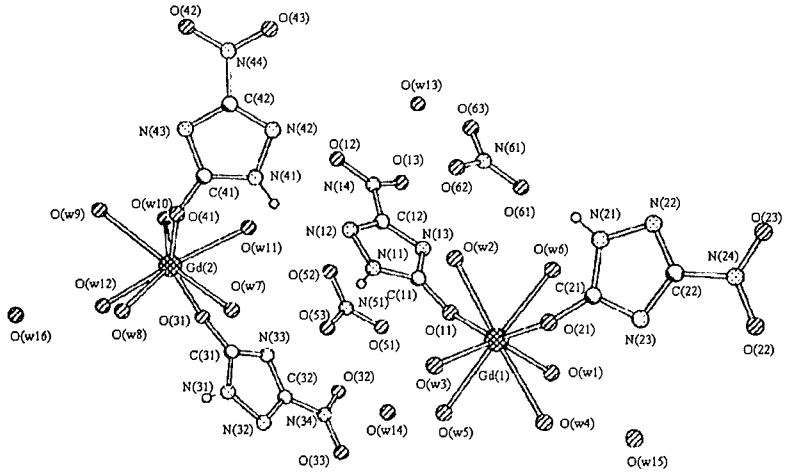


Fig. 4. Asymmetric unit of $[Gd(NTO)_2(H_2O)_6]\cdot NO_3\cdot 2H_2O$ showing the atomic notations.

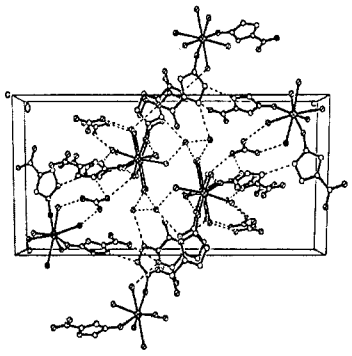


Fig. 5. Perspective view of the unit cell of $[Gd(NTO)_2(H_2O)_6]\cdot NO_3\cdot 2H_2O$ along the *a* axis.

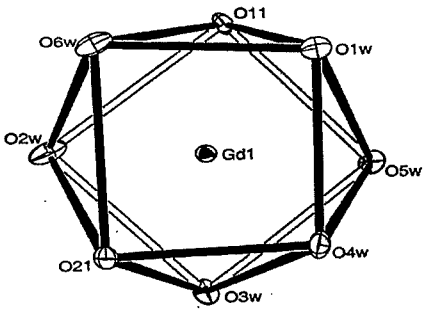


Fig. 6. Coordination polyhedron of Gd ion in $[Gd(NTO)_2(H_2O)_6]\cdot NO_3\cdot 2H_2O$

3.3 Thermal decomposition mechanism of $[Pr(NTO)_2(H_2O)_5]NTO\cdot 3H_2O$

The DSC and TG-DTG curves of the $[Pr(NTO)_2(H_2O)_5]\cdot NTO\cdot 3H_2O$ were obtained under the conditions of linear temperature increase, and are shown in Fig. 7 and 8. As can be seen in Fig. 7 and 8, the thermal decomposition process of the $[Pr(NTO)_2(H_2O)_5]\cdot NTO\cdot 3H_2O$ show three distinctive stages under our experimental condition: dehydration, the NTO ring cleavage and the formation of metal oxide. Our results concur with decomposition patterns reported by Xie *et al* in their studies with Pr, Nd and Sm-NTO complexes previously.[10] The DSC curve in Fig. 7 appears to indicate that dehydration process is composed of three steps, but we have to overcome difficulties in distinguishing those clearly from TG-DTG curves because of the crystalline properties of sample. The first step of dehydration is the loss of three crystalline water molecules in the temperature range of 30.0-60.5 ℃. The mass loss of 8.0 % exactly matches with the theoretical calculation for the loss of three water molecules from $[Pr(NTO)_2(H_2O)_5]\cdot NTO\cdot 3H_2O$. The second step occurs from 60.5℃ to 120.6℃ with the peak maximum temperature of 77.9 ℃. The weight loss from the TG-DTG curves is 10.6 %, which is also in excellent agreement with the calculated value of 10.7 % for the loss of four coordinated water molecules from $[Pr(NTO)_2(H_2O)_5]\cdot NTO$. The last dehydration step begins at 120.6 ℃ and ends at 180.7 ℃. The weight loss for this step is 2.7%. We believe that this result is from the loss of one coordinated water molecules form the $[Pr(NTO)_2(H_2O)]\cdot NTO$.

The cleavage of the NTO ring occurs from 180.7 ℃ to 351.8 ℃. The weight loss for this stage is 29.2%, which is substantially less than that of calculated value, 44.2%, if we follows the reaction mechanism proposed by Xie *el al.*[10] The decomposition residue after this stage are

proposed to be mixtures of $Pr(OCN)_3$, $Pr_2(CO_3)_3$ and polymer materials.

$$2Pr(NTO)_3 \rightarrow Pr_2(CO_3)_3 + \text{mixture}$$

After the cleavage of the NTO ring, the characteristic IR absorption bands of the –C-NO2 group at 1514.5 and 1301.6 cm^{-1} disappears and new absorption bands of the -CO-NH- group come out at 2335.6, 2187.0 and 1506.3 cm^{-1}.

The finial stage is the metal oxide formation of Pr_2O_3 in the temperature range of 351.8-593.1 ℃. The weight loss of this stage is 24.6%. The absorption band of 561 cm^{-1} indicates that the metal oxide is formed.

The total weight loss of the three decomposition stages is 75.2 %, which is in excellent agreement with the calculated value of 75.4 %. The weight percentage of metal oxide is 24.8 % and the weight fraction of Pr in the metal oxide is 21.20 %. These values also concur with the weight fraction of Pr in single crystal of $[Pr(NTO)_2(H_2O)_5]\cdot NTO\cdot 3H_2O$. The various analytical data corresponding to the thermal decomposition are summarized in Table 3.

Table 3. Data on the thermal decomposition of $[Pr(NTO)_2(H_2O)_5]\cdot NTO\cdot 3H_2O$

Temperature( )	Mass loss(%)		No. of lost H_2O
	Obs.	Calc.	
30.0 - 47.3 - 60.5	8.0	8.0	3
60.5 - 77.9 - 120.6	10.7	10.7	4
120.6 - 160.3 - 180.7	2.7	2.7	1
180.7 - 240.8 - 351.8	29.2	44.2	
351.8 - 464.8 - 593.1	24.6	9.8`	
total	75.2	75.4	

3.4. Thermal decomposition mechanism of $[Gd(NTO)_2(H_2O)_6]\cdot NO_3\cdot 2H_2O$

The DSC and TG-DTG curves of the $[Gd(NTO)_2(H_2O)_6]\cdot NO_3\cdot 2H_2O$ are shown in Fig. 9 and 10. Based on the curves in Fig. 9 and 10, we may divide the thermal decomposition processes of the $[Gd(NTO)_2(H_2O)_6]\cdot NO_3\cdot 2H_2O$ into four steps: dehydration, the cleavage of the NTO ring, the decomposition of NO_3 ion and the formation of metal oxide. The DSC curve of Fig. 9 shows that dehydration processes may also be divided into three steps. The three dehydration stages occur in the temperature range of 30.0 and 200 ℃. The total weight loss for these three dehydration steps is 23.2% due to the weight loss of two crystalline and six coordinated water molecules. The NTO ring cleavage occurs between 200.0 and 340.6 ℃ in TG-DTG curves. The observed weight loss for this stage is 27.9 %, which is in excellent accord with the theoretical value of 27.7 %.

At the end of the NTO ring cleavage, as in the Pr-NTO, the characteristic IR absorption bands of the –C-NO2 group at 1515.8 and 1301.7 cm^{-1} disappear and new absorption bands of the -CO-NH- group grow at 2340.8, 1652.7, 2200.4, and 1506.1 cm^{-1}. The third stage, the NO_3 ion decomposition stage of the $Gd_2(CO_3)_3 \cdot 2NO_3$, begins at 340.6 ℃ and ends at 432.2 ℃. The weight loss of 10.1% at this stage is in good agreement with the calculated value of 10.0 %. At the end of this stage, the characteristic band of NO_3, 1384.2 cm^{-1}, exists no longer.

The finial stage is the metal oxide formation of Gd_2O_3 in the temperature range of 432.2 and 592.1 ℃. The observed weight loss of 10.1 % also agrees with the calculated value of 10.6 %.

The total weight loss of the four decomposition stages is 71.3 %, which is in good agreement with the calculated value of 71.5 %. The various analytical data corresponding to the thermal decomposition are summarized in Table 4.

Table 4. Data on the thermal decomposition of $[Gd(NTO)_2(H_2O)_6]\cdot NO_3\cdot 2H_2O$.

Temperature( )	Mass loss(%)		No. of lost H_2O
	Obs.	Calc.	
30.0- 84.0 - 92.1	5.8	5.8	2
92.1- 122.7 - 162.4	12.1	11.6	4
162.4-184.4 - 200.0	5.3	5.3	2
200.0-243.8 - 340.6	27.9	27.7	
340.6-396.6 - 432.2	10.1	10.0	
432.2-484.1- 592.1	10.1	10.6	
total	71.3	71.5	

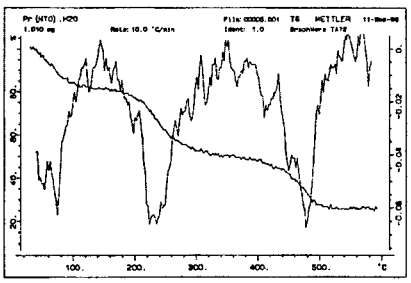


Fig. 7. TG-DTG curves of $[Pr(NTO)_2(H_2O)_5]\cdot NTO\cdot 3H_2O$.

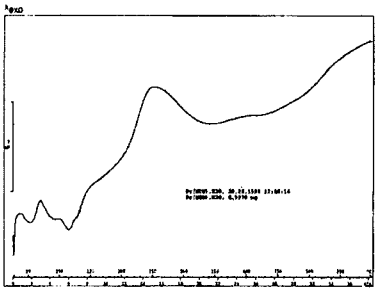


Fig. 8. DSC curve of $[Pr(NTO)_2(H_2O)_5]\cdot NTO\cdot 3H_2O$.

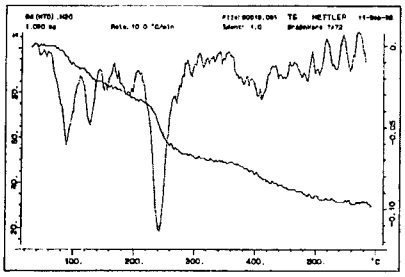


Fig. 9. TG-DTG curves of $[Gd(NTO)_2(H_2O)_6]\cdot NO_3\cdot 2H_2O$.

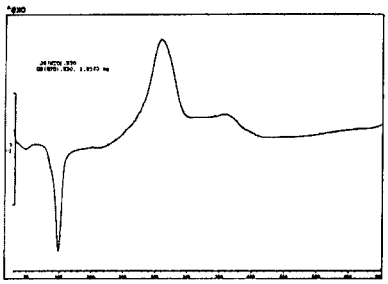


Fig. 10. DSC curve of $[Gd(NTO)_2(H_2O)_6]\cdot NO_3\cdot 2H_2O$.

Reference

1. Lee, K.Y.; Coburn,M.D. LA-10302-MS, Los Alamos National laboratory, Los Alamos, NM 87545, 1985.
2. Hu.R.; Song, J.; Li, F.; Kang, B. *Thermochimica Acta* . **1997**, *299*, 87-93.
3. Song, J.; Hu,R ; Li, F.; Mao, Z.; Zhou, Z. *Energetic materials*, **1996**, *4*, 150-156
4. Siemens, *XSCANS Data Collection Package*, Siemens; Karlsruhe, Germany, 1996
5. Sheldrick, G.M. *Acta Cryst.* **1990**, *A46*, 467
6. Ritchie, J.P.; Kober, E. M. *Proceeding of the9-th International Symposium on Detonation*, Portland, Oregon, 1989, 528-536.
7. Ritchie,J.P. *J. Organic Chem.* **1989**, 54, 3553
8. Sorescu, D,C.; Teressa,R.L.; Thompson,D.L. *J. Molecular Structure*, **1996**, *384*, 87-99.
9. Song ,J.; Hu, R.; Li, F.; Mao, Z.; Zhou, Z.; Hong,Z. *Chemical J. of Chinese Universities.* **1997**, *18*, 676-679.
10. Xie, R.; Hu, R.; Zhang,T.; Li, F. *J.Thermal Analysis*, **1993**, *29*, pp 41-51.

CATALYTIC COMBUSTION OF LIQUID ROCKET FUEL 1,1 DIMETHYLHYDRAZINE

Zinfer R.Ismagilov*[a], Mikhail A.Kerzhentsev[a], Ilias Z.Ismagilov[a], Vladimir A.Sazonov[a], Valentin N.Parmon[a], Galina L.Elizarova[a], Oxana P.Pestunova[a], Vladimir A.Shandakov[b], Yurii L.Zuev[c], Lev N.Rolin[c], Valentin N.Eryomin[c], Natalia V.Pestereva[c]

[a]Boreskov Institute of Catalysis Prospekt Ak. Lavrentieva, 5, Novosibirsk 630090, Russia
E-mail:zri@catalysis.nsk.su
[b]Federal Research and Production Center "ALTAI", Biysk, Russia
[c]State Rocket Center " Makeyev Design Bureau", Miass, Russia

Introduction

Reduction and conversion of weapons production in Russia have made extremely urgent the problems of development and implementation of environmentally safe and efficient processes of disposal of rocket fuel components (RFC). One of the most pressing problems is the development of a disposal process for extremely toxic 1,1-dymethylhydrazine (unsymmetrical dimethylhydrazine -UDMH). There are no industrial facilities for UDMH treatment in Russia and CIS, as well as no reliable treatment technologies that meet economical and environmental requirements. Therefore, solution of problems of utilization of off-specification UDMH and other RFC, industrial wastes containing RFC, spills of RFC on soil, etc., is a very urgent task

Conventional thermal methods: incineration in flame and plasma method consume much energy and lead to the formation of large amounts of secondary pollutants. The need of additional purification of exhaust gas from NO_x and other pollutants complicates these methods for practical application.

Methods of processing of UDMH and other toxic fuels to useful products are not yet promoted to the state of industrial application and cannot solve the problem of UDMH utilization due to the lack of interest of enterprises to deal with such hazardous, toxic and flammable chemicals.

The problem of UDMH utilization can be solved by creation of a treatment plant based on UDMH oxidation in a fluidized catalyst bed [1, 2]. The unique feature of this method is the possibility of flameless total oxidation of organic compounds in near stoichiometric ratio

with oxygen at relatively low temperatures (500-750°C), which suppresses formation of "thermal" and "fuel" nitrogen oxides. This is achieved by the use of highly active catalysts in a fluidized bed that is characterized by rather high heat transfer coefficients and thus allows the efficient removal of reaction heat. Pilot and industrial plant tests in combustion and processing of different types of organic wastes have shown high efficiency and environmental safety of this technology/1-6/.

An important advantage of the technology of catalytic fluidized bed waste destruction is small size of apparatus. A compact installation designed as a mobile unit will allow UDMH treatment at distant locations, navy bases, and thus will exclude hazardous (and sometimes impossible) transportation of rockets or rocket fuels to centralized treatment facilities.

Catalytic oxidation of UDMH.

A laboratory setup for study of UDMH catalytic destruction has been fabricated.

The setup is intended for investigation of reaction of catalytic oxidation of UDMH, and it allows to study composition of reaction mixtures and dependencies of the reaction rate on temperature, space velocity and UDMH concentration.

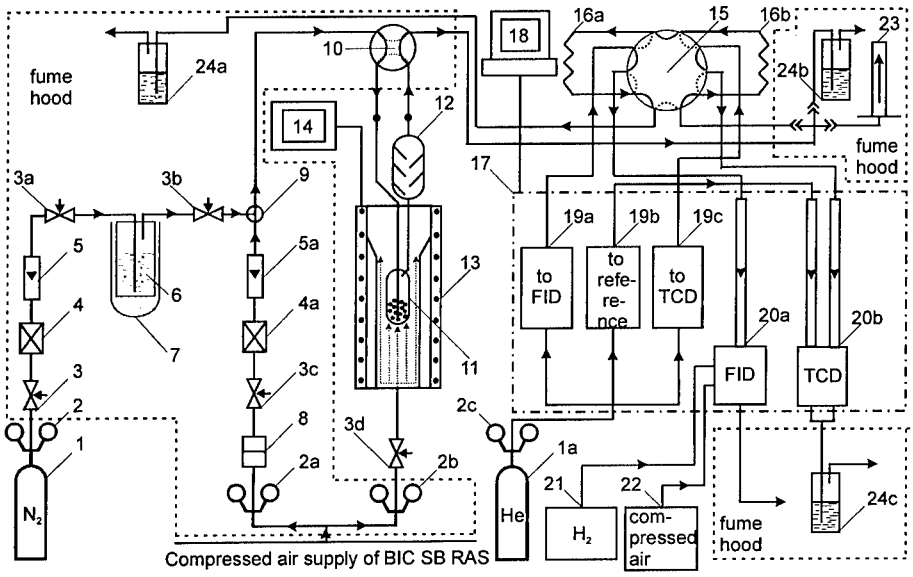


Fig.1. Principal scheme of the laboratory setup

The scheme of the setup is given in Fig. 1 and comprises:

1. System of gas supply, containing cylinders with nitrogen and air (1); devices for gas flow control and measurement – pressure reducers (2), valves (3), gas flow controllers (4) and rotameters (5).
2. System of UDMH supply. The dosage of small amounts of fuel is provided by the saturation of nitrogen flow with UDMH vapor in a saturator (6) kept at 0°C in a Dewar flask (7) with ice and water. This system ensures necessary gas tightness and safety, providing the supply of UDMH in the range of 0.1-5 g/h.
3. Flow mixer for mixing gas-vapor flow with air flow (9).
4. Catalytic reactor (11) with catalyst. We used a gradientless quartz reactor with a vibro-fluidized catalyst bed. Vibro-fluidization of the catalyst was accomplished by connecting reactor to an electromagnetic vibrator, operated with 50 hz frequency. Reactor was placed into the furnace with a fluidized bed of quartz sand (13), providing effective heat removal from the reactor and constant preset catalyst temperature.
5. Electric power supply and temperature measurement devices (14)
6. System of gas analysis (18-20) based on Gas Chromatograph Kristall-2000M. Separation and analysis of UDMH and organic reaction products was done in a Teflon column 1,5 m long, 2mm in diameter, with polymer sorbent HayeSep C modified by 10% KOH, using FID and He as carrier gas at a temperature of 155°C. Air and CO_2 were separated in a stainless steel carbon SKT column (1.5 m long, 0.3 mm diameter, carrier gas He, 30 ml/min, temperature 155°C) and detected with TCD.

Kinetic experiments were conducted at following parameters:

Catalyst temperature	20-500°C
Concentration of UDMH in the initial reaction mixture	0.1-2 mmol/l (0.2-4 vol/%)
Space velocity	5000-40000 h^{-1}
Reaction mixture flow rate	10-100 l/h
Catalyst loading	0,1-2 cm^3

The first series of studies were conducted using the $Cu_xMg_{1-x}Cr_2O_4/\gamma\text{-}Al_2O_3$ catalyst (fraction of 0,25-0,5 mm), developed for catalytic combustion in the fluidized bed. It was found that a noticeable increase of conversion to CO_2 begins at a temperature of 200°C (Fig.2), and at temperatures above 300°C practically complete UDMH oxidation into the deep oxidation products CO_2, H_2O and N_2 is observed.

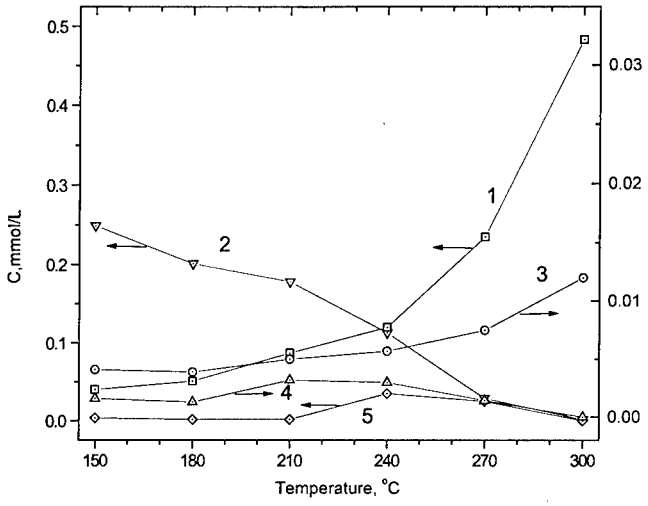


Fig.2. Temperature dependencies of concentrations of UDMH oxidation products over $Cu_xMg_{1-x}Cr_2O_4/\gamma$-$Al_2O_3$ catalyst at initial UDMH concentration 0.26 mmol/L, and space velocity of 6000 h^{-1}: 1 – CO_2, 2 - MDMH, 3 – CH_4, 4- UDMH, 5- DMA

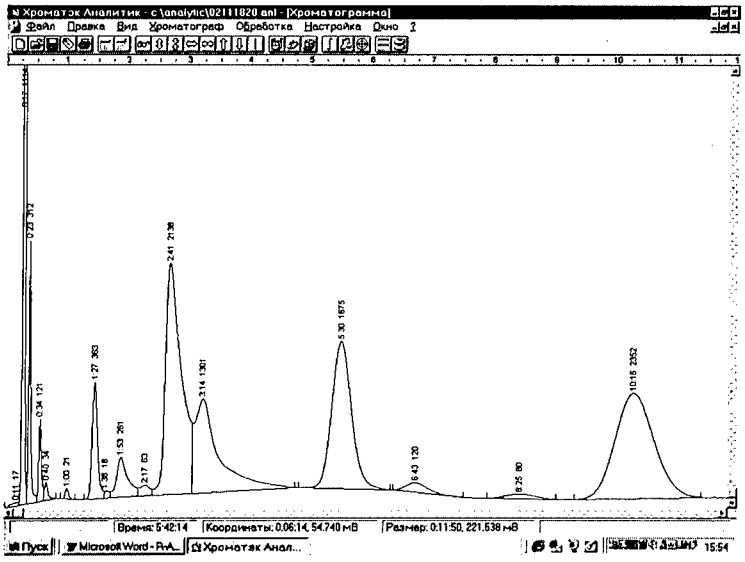


Fig.3. Typical chromatogram of UDMH oxidation products.

Among the reaction products in the temperature range of 200-300°C, along with the products of deep oxidation, 14 peaks corresponding to various intermediate compounds forming from UDMH, were revealed on the chromatograms. Typical GC analysis example of UDMH oxidation products over catalyst $Cu_xMg_{1-x}Cr_2O_4/Al_2O_3$ at 270°C is given on Fig.3

The compounds identified are: methane (17 s), dimethylamine - DMA (2 min 40 s), formaldehyde 1,1-dimethylhydrazone (alias methylenedimethylhydrazine - MDMH) (10 min 16 s), residual UDMH (8 min 25 s). The remaining peaks are not definitely identified at the moment, but preliminary data show that small quantities of ethane, methanol, formaldehyde and other organic compounds could be present among the products.

The influence of the initial UDMH concentration on the composition of oxidation products is shown in Fig.4. It can be seen that at 300°C in the UDMH concentration interval of 0-0,7 mmol/l, practically complete UDMH conversion following the deep oxidation route takes place, and the CO_2 concentration grows proportionally to UDMH concentration. Upon further UDMH concentration increase (over 0,7 mmol/l), the efficiency of UDMH oxidation into the products of deep oxidation is decreased, and substantial quantities of the partial oxidation products appear at the reactor outlet.

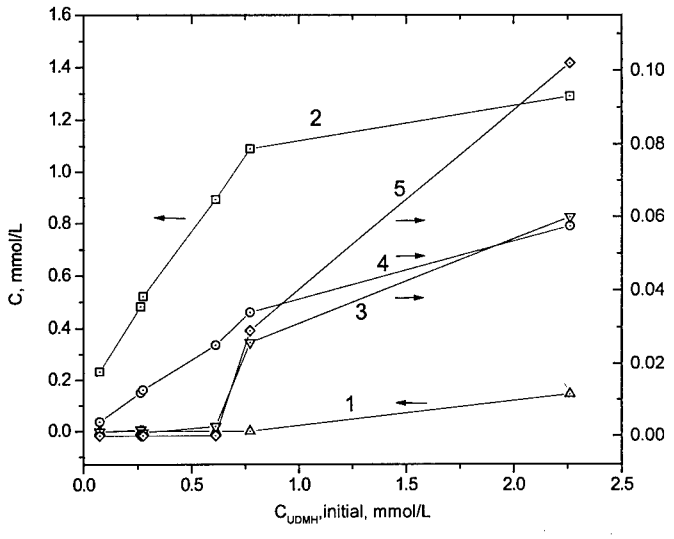


Fig. 4. Dependencies of concentrations of oxidation products 1 – UDMH, 2 – CO_2, 3 - MDMH, 4 – CH_4, 5- DMA over $Cu_xMg_{1-x}Cr_2O_4/\gamma$-$Al_2O_3$ at 300°C

Among intermediate reaction products in a wide range of temperatures 1,1-formaldehyde dimethylhydrazone and methane are present (Fig. 3, 4). These products are already formed in significant quantities at the temperature of 150°C. At the current stage of studies, based on the presence of these compounds among the intermediate products, it is possible to suggest probable mechanism of UDMH oxidation, proceeding via the following principal steps:

$$(CH_3)_2NNH_2 + [\ \ ] \rightarrow [(CH_3)_2NNH_2\ ]_{ads} \quad (1)$$

$$[(CH_3)_2NNH_2\ ]_{ads} + [\ O\ ]_{ads} \rightarrow [(CH_3)_2\ N{=}N]_{ads} + [H_2O]_{ads} \quad (2)$$

$$[(CH_3)_2\ N{=}N]_{ads} + [(CH_3)_2\ N{=}N]_{ads} \rightarrow [(CH_3)_2\ N\text{-}N{=}CH_2]_{ads} + [CH_3N{=}NH\ ]_{ads} \quad (3)$$

$$[(CH_3)_2\ N\text{-}N{=}CH_2]_{ads} \rightarrow (CH_3)_2\ N\text{-}N{=}CH_2 + [\ \ ] \quad (4)$$

$$[(CH_3)_2\ N\text{-}N{=}CH_2] + [O] \rightarrow \text{(intermediate products)} \rightarrow CO_2 + H_2O + N_2 \quad (6)$$

$$[CH_3NNH]_{ads} \rightarrow CH_4 + N_2 \quad (4)$$

$$[CH_3NNH] + [O] \rightarrow \text{(intermediate products)} \rightarrow CO_2 + H_2O + N_2 \quad (7)$$

Proof of this mechanism and it's specification requires additional research.

. It is well known that Ir/γ-Al_2O_3 is one of the principal catalysts used in spacecraft engines for decomposition of liquid propellant – hydrazine [7,8]. There is also information in literature that this catalyst is active in the reaction of UDMH oxidation with ozone [9]. Therefore it was of interest to study particular dependencies of UDMH oxidation with air over 32.9% Ir/γ-Al_2O_3 and compare these data with the results obtained previously for Pt/γ-Al_2O_3 and Pd/γ-Al_2O_3 catalysts.

Recently, it was reported that the activity of nitrides and carbides of some metals, e.g. Mo and W, in hydrazine decomposition is comparable to that of Ir/γ-Al_2O_3 [10]. Since our results with Ir/γ-Al_2O_3 showed that this catalyst is very active in UDMH oxidation, it was decided to study regularities of UDMH oxidation over nitrides. The catalyst chosen was Si_3N_4, because it is known from literature that silicon nitride is active in UDMH decomposition [11].

The experimental temperature dependencies of the concentration of various UDMH oxidation products over the Ir/γ-Al_2O_3 and Si_3N_4 catalysts are presented in Fig.5 and 6. Table 1 gives the comparison of N_2O and NO concentrations and corresponding selectivities for these two catalysts.

It can be seen from Fig. 5 that at temperatures (340-400°C) and high space velocity (72000 h^{-1}) practically total UDMH oxidation to CO_2 takes place over Ir/γ-Al_2O_3 (at initial conc. of UDMH 0.35 mmol/l the predicted conc. of CO_2 is 0.7 mmol/l and the experimental values are 0.68-0.70 mmol/l). Out of the intermediate products only methylene-

dimethylhydrazine (MDMH) has substantial concentration (curve 3) at temperatures below 280°C.

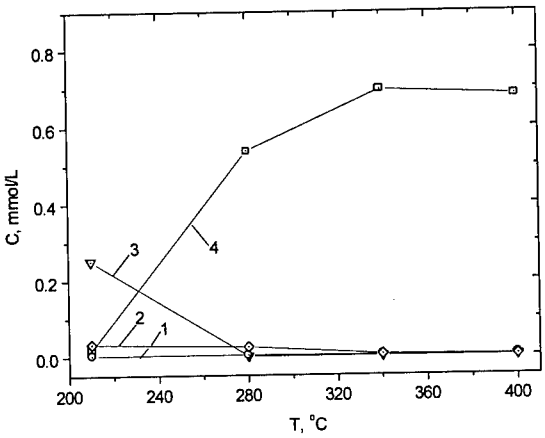


Fig. 5. Temperature dependencies of the UDMH oxidation products concentrations on the $Ir/\gamma\text{-}Al_2O_3$ catalyst for UDMH initial concentration of 0.35 ± 0.05 mmol/l and space velocity 72000 h^{-1}: 1 - CH_4, 2 - DMA, 3 –MDMH, 4 - CO_2.

As follows from Fig. 6, UDMH conversion to CO_2 over Si_3N_4 (curve 4) attains only 70% at 400°C (UDMH with conc. 0.60 mmol/L gives 0.84 mmol/L CO_2, as compared to 1.2 mmol/L calculated for total UDMH oxidation). Among intermediates, MDMH predominates (curve 3). It is interesting to note that methane concentrations in reaction products for both catalysts are ca. 0.005 mmol/L, which is substantially lower that CH_4 concentration found for other catalysts previously studied. In case of $Ir/\gamma\text{-}Al_2O_3$ this can be explained by its high activity sufficient for methane oxidation in temperature range studied.

In case of Si_3N_4 lower selectivity to methane may be explained by predominance in the reaction intermediates of molecules retaining two methyl groups at nitrogen atom – dimethylamine (DMA) and MDMH.

Table 1 shows that the increase of NO и N_2O concentrations with the rise of the temperature correlates with the increase of UDMH conversion to CO_2 (Fig. 5 and 6). Concentrations of NO on the products of the reaction over $Ir/\gamma\text{-}Al_2O_3$ (2000-3000 ppm) in the range of total UDMH oxidation is comparable to the data obtained previously for $Pt/\gamma\text{-}Al_2O_3$ и $Pd/\gamma\text{-}Al_2O_3$ (1600-3000 ppm), but substantially higher than NO concentration over oxide catalyst $Cu_xMg_{1-x}Cr_2O_4/\gamma\text{-}Al_2O_3$ (30-470 ppm).

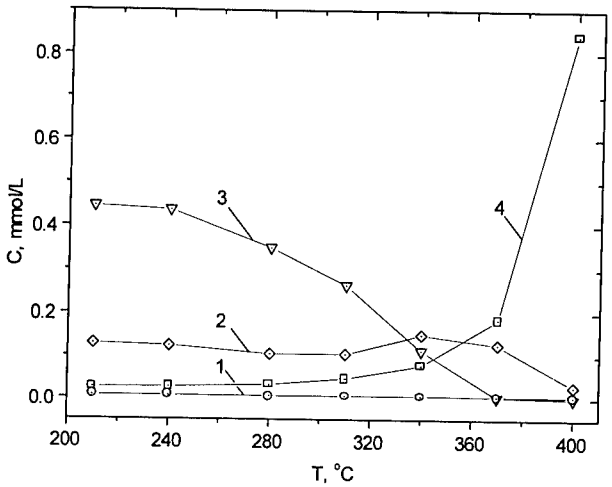


Fig. 6. Temperature dependencies of the UDMH oxidation products concentrations on the Si_3N_4 catalyst for UDMH initial concentration of 0.60± 0.05 mmol/l and space velocity 7200 h^{-1}: 1 - CH_4, 2 - DMA, 3 –MDMH, 4 - CO_2.

Table 1.

Temperature dependencies of NO and N_2O concentrations and selectivity of NO and N_2O formation on Ir/γ-Al_2O_3 и Si_3N_4 catalysts

	Ir/γ-Al_2O_3				Si_3N_4			
***T*, ℃**	C(NO), ppm	X(NO), %	C(N_2O), ppm	X(N_2O), %	C(NO), ppm	X(NO), %	C(N_2O), ppm	X(N_2O), %
400	2890	17.16	238	2.82	2263	8.40	303	2.25
370	2670	15.86	-	-	170	0.63	142	1.05
340	1948	11.57	242	2.87	108	0.40	91	0.68
310	880	5.23	-	-	153	0.57	33	0.24

Pilot scale experiments

Pilot plant was designed and built for fluidized bed UDMH destruction experiments. The schematic diagram of this installation is shown in Fig. 7.

The mixture to be treated (e.g. mixture of water and UDMH or pure UDMH) is supplied from the tank (10) to the catalytic fluidized bed reactor (1). The compressed air is fed to the reactor in a quantity necessary for the complete oxidation UDMH in the catalyst bed at temperatures 500-700 °C. The electric heater - nichrome wire coiling around the reactor wall is used for preheating the catalyst bed to start the process of catalytic oxidation. The gases leaving the reactor may contain small quantities of nitrogen oxides (NO and NO_2), trace amount of unburned UDMH, and dust of variable size resulting from catalyst attrition and mineral part of treated wastes. The temperature of the gases at the exit of the reactor is lowered to 250-350 °C using the heat exchanger immersed in the catalyst bed. From the reactor the gas enters the cyclone (3) where large-sized dust particles (>30 μ) are separated and the gas temperature is decreased to 350-500 °C.

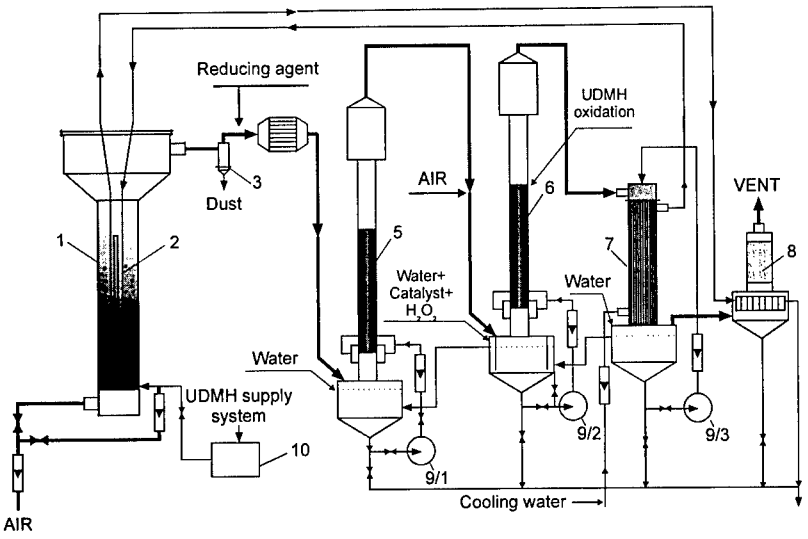


Fig. 7. Scheme of the process of UDMH catalytic destruction:
1 – catalytic fluidized bed reactor; 2 –water heat exchanger; 3 – cyclone; 4 – SCR reactor; 5, 6 – jet scrubber, 7 –absorber-condenser; 8 – aerosol filter; 9/1-9/3 – pump, 10 - tank for UDMH

At the second stage the gas passes through the reactor with monolithic honeycomb catalysts (4) used for the reduction of nitrogen oxides and destruction of residual UDMH in the gas stream. For further purification of the gas from UDMH and medium-sized dust particles a foam jet scrubber No 1 (5) is used which acts both as a gas and dust trap and as a regenerative heat exchanger. Here, in the highly turbulent foam layer with a constantly refreshed surface, separation of the gas from medium-sized particles (3-30 μ) and other toxic admixtures occur, with concomitant gas cooling to 70-90 °C. For further treatment the gas is directed to the jet scrubber No 2 (6) in which complete destruction of traces of UDMH is conducted over powder catalysts for liquid phase UDMH oxidation added to the scrubber liquid. If necessary additional air or hydrogen peroxide can be fed into to the scrubber.

After this scrubber, the gas saturated with water vapor enters the absorber-condenser (7) where its purification from low-sized particles (0,1-3 μ) takes place with final removal of trace amounts of UDMH and gas cooling to 30-40°C. The UDMH accumulated in the absorber-condenser will be oxidized in the scrubber liquid using catalysts for liquid phase UDMH oxidation.

The series of pilot experiments were accomplished in two stages – testing of the main catalytic reactor with fluidized catalyst bed (experiments 1-5) and testing during the simultaneous operation of the main reactor and off-gas treatment system: reactor for the selective catalytic reduction of nitrogen oxides (SCR) and wet gas cleaning units (experiments 6-9).

The main results of testing are given in Tables 2-4. In experiments 1-5, process parameters providing the most total UDMH oxidation were determined. In experiments 6-9, the process parameters in the main reactor were specially chosen to provide the presence of some residual UDMH in the exhaust gas. That was done in order to study the efficiency of UDMH removal from the gas stream by the units of the off gas treatment system.

Table 2

Results of testing of the main reactor with fluidized catalyst bed

No	Main air flow, m^3/h	Air flow through injectors, m^3/h	UDMH flow rate, L/h	Oxidizer excess coeff. α	T in the reactor, °C	Composition of the gas at the outlet of the main reactor		
						NO_x mg/m^3	CO mg/m^3	UDMH mg/m^3
1	16.2	1.6	1.08	2.7	630	6000	< 5	<0.05
2	16.2	1.6	2.24	1.31	675	6000	< 5	<0.05
3	16.2	1.6	2.56	1.14	735	6000	< 5	0.075

Table 3

Results of testing of the SCR reactor

No	T in the SCR reactor °C	NH_3 flow rate, m^3/h	Conc. of NH_3 (init.), g/m^3	Conc. of NO_x (init.), mg/m^3	Composition of the gas at the outlet of the SCR reactor			
					NO_x mg/m^3	CO mg/m^3	NH_3 mg/m^3	UDMH mg/m^3
6	420	0.20	7,86	2000	80	< 5	< 5	0.095

Table 4

Result of outlet gas and scrubbing liquid analysis in the scrubbers

Gas					Water			
No	Scrubber No	NO_x mg/m^3	NH_3 mg/m^3	UDMH mg/m^3	pH	NO_2^- mg/L	NO_3^- mg/L	UDMH mg/L
6	1	80	< 5	0.10	6.55	150	9.60	1.62
	2	80	< 5	0.17	3.85	240	36.5	1.94
	Absorber-condenser	-	-	-	3.20	423	11.5	2.16

Based on the results obtained /12,13/, the following conclusions can be made:

1. In the temperature interval of 600-720°C practically complete UDMH oxidation takes place. Concentration of CO in the exhaust gas from the main reactor does not exceed the detection limit - 5 mg/m^3.
2. During the catalytic oxidation of UDMH in the fluidized catalyst bed at temperature 630-735°C and at optimum regimes with oxygen excess coefficient α>1, UDMH concentration at the reactor outlet does not exceed 0,1 mg/m^3, which corresponds to the UDMH oxidation efficiency of not less than 99,9998%.
3. During the catalytic oxidation of UDMH, concentrations of nitrogen oxides at the outlet of main catalytic reactor constituted 2000-6000 mg/m^3 with NO_2 to NO ratio ca. 2:1.
4. The SCR catalyst provides no less than 90% efficiency of gas purification from nitrogen oxides at the temperature of 405-420°C and in the excess of ammonia. Ammonia was not detected at the reactor outlet.
5. Monolithic afterburning catalyst, placed after the SCR catalyst in the SCR reactor, provides oxidation of excess ammonia with the efficiency of no less than 99,9% and UDMH oxidation at low concentrations (2 mg/m^3) with the efficiency ca 80%.

References:

1. Z.R.Ismagilov, M.A.Kerzhentsev, - Catal.Rev., Sci &Eng.,1990, vol32, 51-103.
2. Z.R.Ismagilov, M.A.Kerzhentsev, Catal. Today, 1999, vol.47, 339-346.
3. Z.R.Ismagilov, N.A.Koryabkina, R.A.Shkrabina,V.A.Ushakov. Catalysis Today, 29, 1996, p. 427-431
4. Z.R.Ismagilov, React. Kinet. Catal. Lett., v. 60, N 2, 1997, P. 215-218
5. Z.R.Ismagilov. Second World Congress on Environmental Catalysis, November 15-20, 1998, Miami Beach, Florida, USA, AIChE, 1998, p.94-96.
6. Z.R.Ismagilov, R.A.Shkrabina, N.A. Koryabkina, New technology for production of spherical alumina supports for fluidized bed combustion, Catal. Tod., 1999, **47,** p. 51-71
7. 3. T.P. Gaidei, V.N. Novgorodov, I.Ya. Tiuryaev, Zh. Prikl. Khim. (in Russian), 1997, vol.70, No 7, 1125-1132.
8. 4. T.P. Gaidei, I.Ya. Tiuryaev, Zh. Prikl. Khim. (in Russian), 1997, vol. 70 No 8, 1319-1322.
9. 5. L.Ye. Gorelenko, B.V. Strakhov, G.I. Yemelyanova, Vestn. Mosk. Un-ta, series 2 (in Russian), 1987, vol. 28, No 4, 359-362

10. 6. J.A.J. Rodrigues, G.M. Cruz, G. Bugli, M. Boudart, G. Djega-Mariadassou, Catal. Lett., 1997, vol. 45, 1-3.
11. J.L. Armstrong, Y.-M. Sun, J.M. White, Appl. Surf. Sci., 1997, vol. 120, 299-305.
12. Z.R.Ismagilov, M.A.Kerzhentsev, Catalysis for solving environmental problems of disarmament, Abstracts of Fourth European Congress on Catalysis, Rimini, Italy, 4-9 September, 1999, p.93.
13. Z.R.Ismagilov, V.N.Parmon, M.A.Kerzhentsev, V.A.Sazonov, I.Z.Ismagilov, G.L.Elizarova, O.P.Pestunova, L.N.Rolin, V.N.Eryomin, Yu.L.Zuev, N.V.Pestereva, G.V.Sakovich. «Environmentally friendly treatment method of unsymmetrical dimethylhydrazine and wastes containing it», submitted for publication in the «Proceedings of the Scientific-Technical Seminar "Problems in Methodology of Utilization of Solid Propellants, Production Wastes, and Liquid Fuel Residues in Missilery Objects" Research&Production Corporation "ALTAI", Biysk, 16-17 November, 1999.

Acknowledgment: to the International Science and Technology Center (ISTC Project #959)
Key words: rocket fuel, UDMH, catalytic combustion, fluidized bed

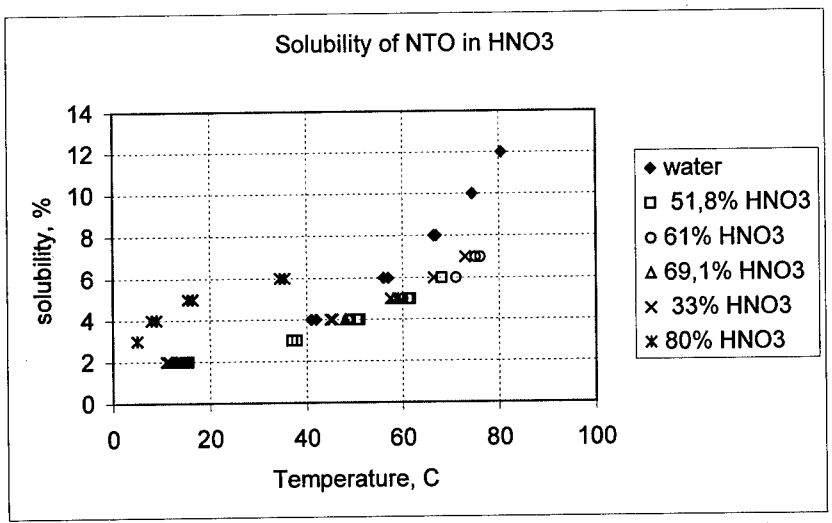
About some features of synthesis NTO

A.R. Basal, V.L. Zbarsky, V.F. Zhilin
Mendeleyev University of Chemical Technology of Russia.

In the last years 5–Nitro–2,4–dihydro–3 H–1,2,4-triazol–3–on (NTO) has attracted steadfast attention of the experts in energetic materials. It is stipulated by its low shock sensitivity of NTO and, therefore, possibility of creation of low vulnerability ammunition on its basis.

However, a rather high price of initial raw material (semicarbazide) and a lot of waste formed during its manufacturing make an existing method of NTO production ecological "dirty" and uneconomical. In this work literary data on stages of NTO production (synthesis of semihydrazide, triazolon and NTO) have bin analised[1-3] and possibilities of improvement of its technology have been considered.

The special attention is given to reduction of waste. The solubility of triazolon in water and water formic acid and the solubility of NTO in water and diluted nitrogen acid have bin studied. The results are presented in the figure 1.



The mechanisms of formation of triazolon and NTO are updated. The obtained data allow offering paths of development for more ecological pure technology of triazolon and NTO.

G.I. Chipen, R.P. Bocalder, V.Ya. Greenshtein. //Chemistry of heterocyclic compounds, 1966. № I, p. 110-116.
A. Becuwe, A. Delclos. // Propellants, Explosivs, Pyrotechnics, 1993. V. 18, p. 1-10.
Unated States Patent N 4,733,610.

PARTICULAR FEATURES OF AROMATIC ACID AND ALDEHEDE NITRATION

Nikolai V. Yudin, Vitold L. Zbarsky
Mendeleyev University of Chemical Technology of Russia

The content of an o-isomer in the reaction products with a growth of the acidity decreases from 26.5 to 17.5% at nitration of benzaldehyde in acidic mixture containing 79.1-98.6 % H_2SO_4. Rate constants of nitration for benzaldehyde, benzoic acid, 2- and 4- halogenbenzoic acid at 23^0 C are defined. A considerable difference in constant rates of nitration of o- and p-substituted benzoic acid (120-140 for fluoro- and 25-35 in the case of chloro-derivatives) is observed.

Earlier [1,2] we studied the influence of sulfuric acid concentration in nitrating mixture on ratio of isomeric nitrobenzoic acids and found a considerable fall in the o-isomer yield with increasing medium acidity. We explain that the protonated form of acid and acyl cation take part in nitration together with the free base. Such an approach can be applied generally at considering nitrating processes of substance containing oxygen connecting to α-carbon atom of side chain.

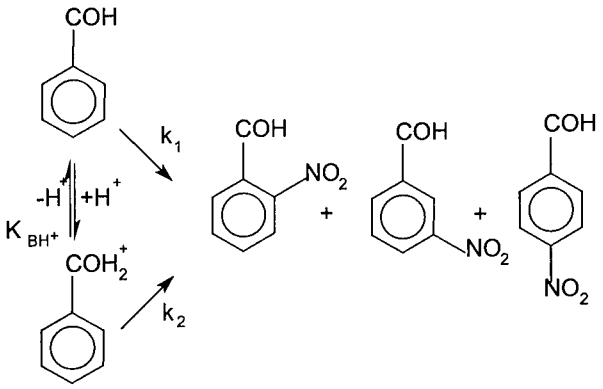
This work is result of study of nitrating benzaldehyde, benzoic acid, 2-fluoro-, 4-fluoro- , 2,6-difluoro-, 2-chloro-, 4-chlorobenzoic acid which together with benzoic acid serve as initial materials for a big amount of chemical products. The composition of nitration products was defined by the HPLC method (using an UV-detector), the kinetic measurement was conducted with help of "Specord M40" spectrophotometer. Reaction rate for benzaldehyde in nitric acid and sulfuric acid mixture containing 76-99.6 % H_2SO_4 and 0.013-1.5 mol/l (0.1-5% mass.) HNO_3 at several temperatures are measured and the ratio of isomeric products is defined. The concentration of benzaldehyde in the reaction mixture was 0.005-0.03 mol/l (0.03-0.2 % mass.) allowing neglect the change in the acidic mixture composition during the experiment. For benzoic and halogenbenzoic acids constant rates k_2 are defined at 23^0 C in 74-106% sulfuric acid with range of the nitric acid concentration from 0.08 to 0.004 mol/l and range of the compound concentrations from $4*10^{-5}$ to $12*10^{-5}$ mol/l.

It is estimated that the yield of o-nitrobenzaldehyde decreases while the concentration of sulfuric acid increases and reaches 17.5% in 99.6 % H_2SO_4 vs. 26.5% in 76.1 % H_2SO_4, the data are given in Table 1. This effect do not connect with a course of secondary reaction as the o-/m- ratio reaming invariable during the whole

process. The total yield of nitrobenzaldehydes changes from 71 to 97% having maximum at 88-92% H_2SO_4 due to oxidation reaction which was proved by the HPLC method according to the presence of nitrobenzoic acid.

Reaction temperature lowering results in a decrease in the o-isomer content in the mixture (See Table 2) and 4-6% increase in the total yield in all acids. Here as well as in the case of benzoic acid such a dependence can be explained by nitrating the substance in two forms: free base and protonated (Figure 1). For benzaldehyde a only single sigmoid is observed that confirms the correctness of the suggested reaction mechanism.

Figure 1



Proportion of isomers formed in the nitration of benzaldehyde (25^0 C).

Table 1

H_2SO_4 % mass.	HNO_3 % mass.	yield % mass.	o-nitrobenzaldehyde		p-nitrobenzaldehyde	
			% mass.	confidence interval	% mass.	confidence interval
76,08	5,30	80	26,9	0,5	2,44	0,08
79,08	5,10	80	26,8	0,7	2,41	0,14
82,98	0,44	91	26,4	0,7	2,41	0,14
85,12	0,40	87	24,7	0,8	1,88	0,16
87,55	0,10	95	22,9	0,5	1,88	0,09

Dependence of the content o-nitrobenzaldehyde (%) in a mixture from temperature.

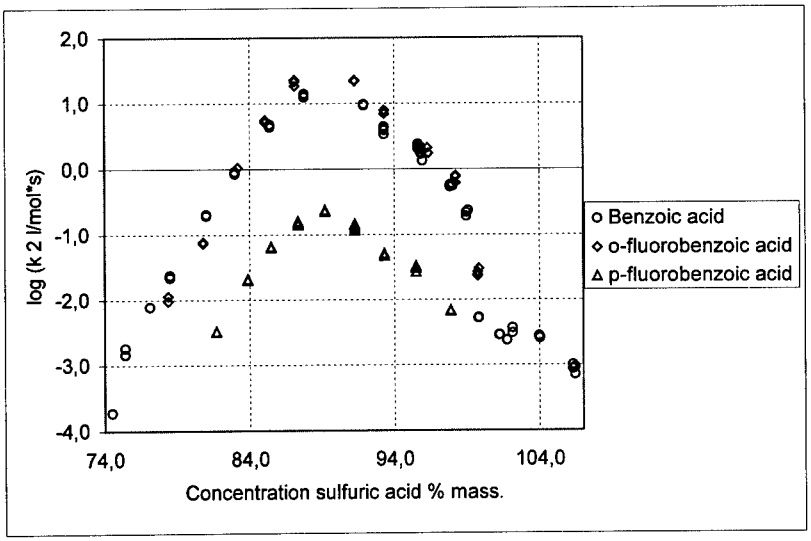
Table 1

H_2SO_4 % mass.	Temperature ^{0}C.											
	-20,5	-9,0	2,5	13,0	17,0	23,0	25,0	30,0	35,0	40,0	45,0	51,0
74,8								24,6	24,9	25,5	26,0	26,4
86,4			19,1	19,4	21,0	21,4		23,0	23,2			
93,5	15,1	15,4	15,7	16,0		17,1		17,7				

For more profound study of these effects we measured the constant of nitration rate for benzaldehyde, benzoic acid and halogenbenzoic acids at nitration by mixture of nitric and sulfuric acid. Some data are given at Figure 2. Big difference between k_2 nitration for o- and p-isomers was unexpected. It was 120-140 for fluorobenzoic acid and 25-30 for chlorobenzoic acid. The nitration rate of 2-fluorobenzoic and 2-chlorobenzoic acids turned out to be higher that of benzoic acid. The obtained data were analyzed in coordinates k_2 *vs.* $-(H_R - \log a_{H2O})$. In all cases except of 2,6-difluorobenzoic acid the tg(α) angular coefficient come out far under 1. We observed the correlation between tg(α) and pK_{BH+} (Table 3). pK_{BH+} for o-isomers were calculated according to the Ates-Maclleland method.

Variation of the rate of nitration from concentration H_2SO_4.

Figure 2



Angular coefficients (tg(α)) in dependence k_2 from $-(H_R - \log a_{H2O})$.

Table 3

№	Substance	tg(α)	pK_{BH+}
1	benzoic acid	0,78	7,82
2	2-fluorobenzoic acid	0,89	8,41
3	4-fluorobenzoic acid	0,66	7,88
4	2-chlorobenzoic acid	0,88	8,53
5	2.6-difluorobenzoic acid	0,98	9,22
7	Benzaldehyde	0,68	7,72

Thus we demonstrated a common character of the mechanism of nitrating aromatic acids and aldehydes in high acidity system.

1. V.Zbarsky, N.Yudin, V.Zhilin Proc. 29-International Conference of ICT "Energetic Materials", 30.06-3.07, 1998, Karlsruhe, Deutschland, paper 53, pp.1-2.

2. V.Zbarsky, N.Yudin, V.Zhilin. Khimicheskaya Promyshlennost' (Chemical Industry), 1997, No. 10, pp. 668- 672 (in Russian).

3. V. A. Ostrovsky, G. I. Koldobsky. Weak organic bases. Leningrad, Publishing house of the Leningrad University, 1990, 145 p. (in Russian).

A NEW METHOD OF PREPARATION OF NITRO DERIVATIVES OF OCTAHYDRO-2H-IMIDAZO[4,5-b]PYRAZIN-2-ONE

Gennady F.Rudakov, Victor F.Zhilin, Ekaterina V.Veselova, Andrei G.Moiseev.
Mendeleev University of Chemical Technology, 9 Miusskaya Square, 125047, Moskow, Russia

Abstract

A new fusion reaction of nitro derivatives of octahydro-2H-imidazo[4,5-b]pyrazin-2-one from 4,5-diazidotetrahydro-2H-imidazol-2-one is proposed and the 4,7-dinitro-, 1,4,7-trinitro- и 1,3,4,7-tetranitro- derivatives of octahydro-2H-imidazo[4,5-b]pyrazin-2-one are obtained thanks to the presented method.

1. Introduction.

At present syntheses of effective high-density and high-energy compounds are carried out by scientists of many countries including Russia. In our opinion the most progress in these investigations has been achieved in the group of polycyclic nitramines[1,2] and nitramides[3,4,5], which include nitro derivatives of octahydro-2H-imidazo[4,5-b]pyrazin-2-one.

1,3,4,7-tetranitrooctahydro-2H-imidazo[4,5-b]pyrazine-2-one (K56) can be generated through nitrolyse of mono- and diacetyl derivatives of 4,7-dinitrooctahydro-2H-imidazo[4,5-b]pyrazin-2-one [5], which is produced by condensation of 1,3-diacetyl-4,5-dibromotetrahydro-2H-imidazol-2-one with ethylenedinitramine in the presence of triethylamine. A mixture of nitric anhydride in a concentrated nitric acid with trifluoromethanesulfonic acid anhydride is required as a nitrating system.

The generating scheme of 1,3,4,6-tetranitrohexahydroimidazo[4,5-d]imidazol-2(1H)-one can be used to produce of nitro derivatives of octahydro-2H-imidazo[4,5-b]pyrazin-2-one.

2. Results

2.1 Synthesis of 4,7-dinitrooctahydro-2H-imidazo[4,5-b]pyrazin-2-one.

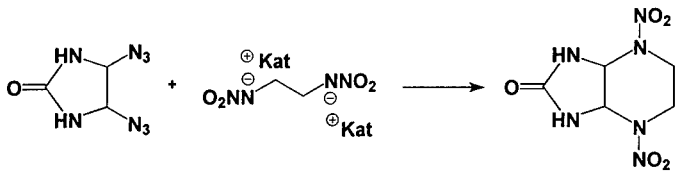
It has been shown recently that 4,5- derivatives of tetrahydro-2H-imidazol-2-one can be obtained from 4,5-diazidotetrahydro-2H-imidazol-2-one (DAZ) which displays a high activity in the reaction with C- and O-nucleophiles. This substance appeared to react easily with N-nucleophiles, nitramine salts in particular, being a suitable precursor in the synthesis of nitro derivatives of octahydro-2H-imidazo[4,5-b]pyrazin-2-one.

The amidoalkilation reaction between salts of ethylenedinitramine (EDNA) and 4,5-diazidotetrahydro-2H-imidazol-2-one takes place, resulting in a high output of 4,7-dinitrooctahydro-2H-imidazo[4,5-b]pyrazin-2-one, which is independent of the solvent polarity, practically (Table 1).

Table 1. The yields of 4,7-dinitrooctahydro-2H-imidazo[4,5-b]pyrazin-2-one in different solvents

Solvent	ε	Yield %
1,4-Dioxane	2,2	80
2-Propanol	18,3	90
Acetone	20,7	79
DMFA	36,7	74
Acetonitrile	37,5	75
DMSO	48,9	76
2-Propanol--Water	72,8	80

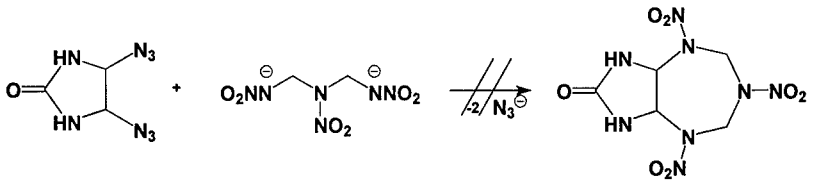
The reaction will not change its course when passing from alkaline metal salts to EDNA organic salts (Kat^+=Na^+, K^+, $C_6H_5N^+H$, Et_3N^+H ...).



The best reagent is triethylamine salt of ethylendinitramine, which has a good solubility in different organic solvents. This reaction can also be carried out with no

prior salt extraction at room temperature (20°C). The reaction is accomplished in 1,5-2 hours.

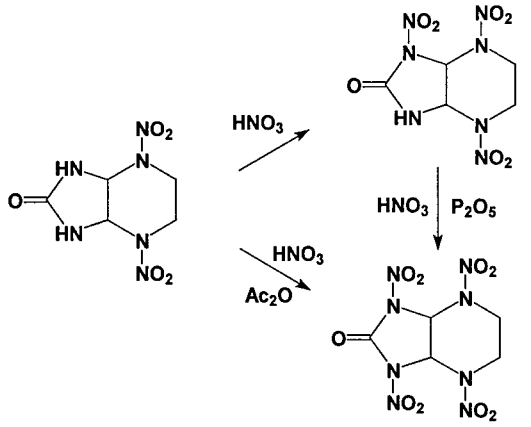
The investigation of dependence of nitramine nature on the route of amidoalkilation reaction has shown that bicyclic structures are not formed at the interaction between DAZ and salts of methylendinitramine and of 1,3,5-trinitro-1,3,5-triazapentane. This reaction is accompanied by evolution of N_2O and formation of compounds of polymeric nature which are insoluble in DMFA.



It is interesting to note that the same situation is observed when using 1,4-di(nitramino)butane and methylnitramine which can not form cyclic products.

2.2 Nitration of 4,7-dinitrooctahydro-2H-imidazo[4,5-b]pyrazin-2-one

The course of nitration of 4,7-dinitrooctahydro-2H-imidazo[4,5-b]pyrazin-2-one depends on the nature of the nitrating agent and leads to formation of tri- and tetranitro derivatives of octahydro-2H-imidazo[4,5-b]pyrazin-2-one.



The maximum yield of 1,3,4,7-tetranitrooctahydro-2H-imidazo[4,5-b]pyrazin-2-one is 98 % and can be obtained by using a mixture of acetic anhydride and nitric acid in the ratio 1:5.

A pure (TLC) substance is formed in this condition and further purification is not required. The decrease in nitric acid content in the nitrating mixture caused a significant increase in the amount of trinitro derivative in the final product.

Table 2. Effect of nitrating agent on yields of nitro derivatives of octahydro-2H-imidazo[4,5-b]pyrazin-2-one.

Yield, %	HNO_3 (98,5%)	Ac_2O/ HNO_3, mol/mol			H_2SO_4/ HNO_3 1:1,6	P_2O_5/ HNO_3 1:4
		1:1	1:3	1:5		
1,4,7-trinitro-	46 (60)*	47	<5	—	<3	—
1,3,4,7-tetranitro-	—	53	92	98	92	83

*) temperature 50°C.

The use of concentrated nitric acid as a nitrating agent does not lead to tetranitro derivative formation even at 50°C. In turn, 1,4,7-trinitrooctahydro-2H-imidazo[4,5-b]pyrazin-2-one can be easily transformed into 1,3,4,7-tetranitrooctahydro-2H-imidazo[4,5-b]pyrazin-2-one by using the mixtures HNO_3-H_2SO_4 or HNO_3-P_2O_5, that is significantly more available than nitric anhydride.

3. Resume

As a result of this investigation, a new fusion reaction of nitro derivatives of octahydro-2H-imidazo[4,5-b]pyrazin-2-one was proposed and production conditions of 4,7-dinitro-, 1,4,7-trinitro- и 1,3,4,7-tetranitro- derivatives of octahydro-2H-imidazo[4,5-b]pyrazin-2-one were optimized. The influence of the nitrating mixture composition on the yield and on the ratio of products at the nitration of 4,7-dinitrooctahydro-2H-imidazo[4,5-b]pyrazin-2-one has been studied in details. It has been shown that the output of K56 is approaches a quantitative yield of 98% when a mixture of acetic and nitric acid in the ratio 1:5 is used. The compound formed does not require specific purification.

4. Acknowledgements

The authors would like to thank the Russian Fund for Fundamental Research (grant 00-03-32075) for giving financial support to this project.

5. References

1. Borman, S., "Advanced Energetic Materials Emerge for Military and Space Applications"; Chem. and Eng. News, 18 (Jan.17, 1994).
2. Eck, G., Piteau, M., "Process for the synthesis of 2,4,6,8-tetranitro-2,4,6,8-tetraazabicyclo(3.3.0)octane"; US Patent 5659032, August 19, 1997.
3. Boileau, J., Wimmer, E., Carail, M., Gallo, R., "Methodes de preparation de derives nitres et nitroacetyles du glycolurile"; Bull. Soc. Chim. de France, 3, 1986, pp.465-469.
4. Vedachalam, M., Ramakrishnan, V.T., Boyer, J.H., "Facile Synthesis and Nitration of cis-syn-cis-2,6-Dioxodecahydro-1H,5H-diimidazo[4,5-b:4',5'-e]pyrazine"; J.Org.Chem., 56, 1991, pp.3413-3419.
5. Pagoria, P.F., Mitchell, A.R., Jessop, E.S., "Nitroureas II. Synthesis of Bicyclic Mono- and Dinitrourea Compounds";Propellants, Explosives, Pyrotechnics, 21,14-18,1996, pp.14-18.
6. Shutalev, A.D., "Synthesis of 4,5- derivatives of tetrahydro-2H-imidazol-2-one"; Khim.Het.S., 12, 1993, pp.1645-1649.

IMPACT SENSITIVITY AND EXPLOSION HEAT OF HMX/META-CARBORANE COMPOSITIONS

V.A. Teselkin, M.N. Makhov

Semenov Institute of Chemical Physics RAS.
Kosygin Str., 4, 117977, Moscow, Russia

Experimental results of impact sensitivity and explosion heat (EH) in binary compositions HMX/meta-carborane depending on additive content are presented. It is shown that carborane addition to HMX results in increase of both impact sensitivity and EH of compositions. The obtained results are explained in terms of chemical interaction between oxygen-containing HMX decomposition products and carborane additive.

Introduction

Composite explosives are widely used in practice and are investigated in many aspects, including their sensitivity to mechanical impact as well. Using solid HE mixture with inert additive as an example [1-3] it was shown that the sensitivity of these compositions was strongly depended on additives' nature, especially on their physical-mechanical and thermal-physical properties. Depending on additives' properties it may result either to retarding or sensitising on solid HE. So, when adding low-strength paraffin-type component to solid HE, one would observe decrease in composite explosive sensitivity to mechanical action. According to [1] these additives not only affect the stage of explosion initiation blocking it progress, but make the conditions of explosion spreading from the initiation point worse acting as a some kind of thermal barrier. If inert additive is of abrasive nature, the increase of composition sensitivity would take place, even if its content is very small [2]. Sensitising action of hard additives is explained by their heating up to temperatures ensuring ignition of explosives caused by additives' parts friction either in between or friction with casing restricting the charge. When inert additives without retarding or sensitising properties are used, their influence on initiation and explosive spreading of compositions is limited by the role of 'heat diluent' only [3]. Thus, one can see that additives properties' influence on impact sensitivity of solid HE mixtures can be explained by physical interaction of components at the stage of 'hot points' formation. It is obvious that solid HE is responsible for initiation of explosion in binary compositions, containing an inert additive, under mechanical impact. However, when considering explosion initiation in compositions of fuel/oxidiser type, besides physical interaction of the components one should also bear in mind their chemical inter-

action as well, since it plays the most important role at the stage of hot spot formation under impact.

In works [3,4] the mechanism of explosion initiation for binary compositions AP/fuel was suggested. According to the proposed mechanism, chemical interaction of fuel with products of low-temperature AP decomposition (e.g., chlorine acid, chlorine oxides) play the main role in the process of hot spot formation. Investigating of AP/HMX sensitivity to impact [3], it was shown that the explosion initiation could be explained by aforementioned mechanism. It should be noted that in this case HMX manifests itself, mainly, as a fuel additive. However under the initiation of explosive mixtures, HMX can exhibit not only the properties of fuel or explosive additive, but also the properties of oxidiser.

Data on HMX thermal decomposition are presented in [5]. In accordance with them the HMX decomposition proceeds by a radical mechanism with the breakage of N-NO_2 bond at the first stage of reaction followed by the formation of NO_2 radical. It should be natural to make a suggestion that under initiation of some HMX-based compositions, radical NO_2 can take part not only in thermal decomposition of HE itself, but, under certain conditions, it can also take part in reduction-oxidation reactions with fuel additive or with the products of its thermal decomposition. The probability of the last-mentioned process may considerably increase, if NO_2 meets highly chemically active additives as a partner. For example, carboranes can be considered as such active additives with high caloricity and reducing capacity [6,7]. High chemical activity of carboranes was proved by the data on extremely high impact sensitivity of compositions containing inorganic oxidiser with boron-organic additives [8].

At present work for checking up the above-mentioned assumption on the possible HMX role under initiation as an oxidiser, the sensitivity of HMX/meta-carborane mixtures were tested.

The use of fuel additives is generally recognized way of increasing the energy content of HE. One of such additives is Al. The addition of Al powders to HE is known to enhance considerably EH. Explosive compositions containing meta-carborane should also have large EH (due to high heat effect of interaction between boron and EP). Therefore it is of interest to investigate the influence of meta-carborane additive on EH of HMX and to determine the value of meta-carborane content, corresponding to the maximum value of EH.

Results

The experiments on impact sensitivity were performed with the help of critical tensions' method described in [9]. The tests were carried out with the aid of drop-weight machine K-44-II (10-kg hammer; drop height – 0.25 m). Thin pressed pellets of tested HE were placed between

10-mm diameter rolls. Roll apparatus was designed in such a way that it ensured free scattering of the fracture products under impact.

Pressure in the sample was measured with the help of strain gauge. Simultaneously the instant of explosion initiation was fixed by photo-diode. Critical pressure of explosion initiation P_{cr} was determined at these experiments. P_{cr} is defined as the pressure, at which the non-explosive samples fracture under impact transforms into the fracture followed by explosion. The value of P_{cr} is the characteristic of HE sensitivity. It is considered that lower value of P_{cr} corresponds to higher HE sensitivity.

In experiments coarse HMX with fractions 160-315 μm was used. Taking into account that meta-carborane is a material of wax-like type, meta-carborane-containing compositions were prepared in the following way. Preliminary it was dissolved in ethanol/acetone mixture with volume ratio 1:3. Appropriate amount of HMX was added into the given solution with continual mixing up to the instant of full liquid evaporation. For comparison, there were performed the experiments on explosion initiation of HMX-based compositions with another chemically active additive, i.e. ferrocene. Since ferrocene is a powder material, the preparation of its compositions with HMX was made in a normal fashion.

The obtained experimental data on P_{cr} versus additive content for both HMX-containing mixtures are given in Table 1 (see also Fig. 1)

Analysing the obtained data, one can see that the addition of both additives results in P_{cr} decrease in comparison with that for HMX. This result can be explained by the following reasons. On the one hand, the decrease P_{cr} for the mixtures can be caused by strong change in physical-mechanical properties of the tested material followed by the long persistence of sample fracture. Larger times of sample disintegration provide better conditions for hot spot formation and its growth. On another hand, it seems to us more likely, the reason of P_{cr} decrease is in chemical components' interaction.

In order to analyse the possibilities of P_{cr} decrease for the cost of the change in physical-mechanical properties of the compositions, the value dP/dt was applied. It shows the rate of the pressure decay at charge disintegration. As it was shown in [10], P_{cr} value can be influenced by dP/dt because the decrease of dP/dt would result in increase of disintegration time. Pressure records handling gives the dP/dt values listed in Table 1. It was obtained at critical conditions of initiations.

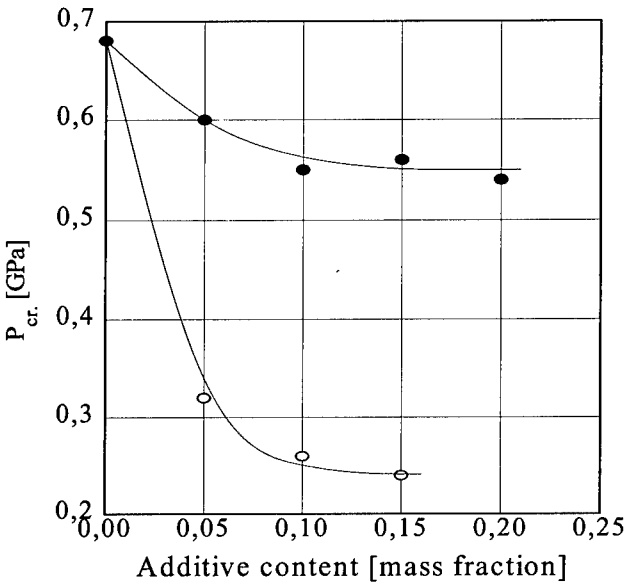


Fig. 1. Dependence of P_{cr} on the additive content for HMX/meta-carborane compositions (o) and for HMX/ferrocene compositions (•).

Table 1. Parameters of explosion initiation for compositions: HMX/meta-carborane and HMX/ferrocene.

Composition	P_{cr}, GPa	σ_{cr}, MPa	dP/dt, GPa/μs
HMX	0.68	180	0.053
HMX/meta-carb. (95/5)	0.32	114	0.024
HMX/meta-carb. (90/10)	0.26	97	0.020
HMX/meta-carb. (85/15)	0.24	92	0.023
HMX/ferrocene (95/5)	0.60	140	0.022
HMX/ ferrocene (90/10)	0.55	110	0.020
HMX/ ferrocene (85/15)	0.56	100	0.020
HMX/ ferrocene (80/20)	0.54	90	0.025

One can see that the values of P_{cr} in compositions are varied in a wide range when dP/dt is at one and the same level of (0.02 – 0.03) GPa/μs. Besides, the effect of P_{cr} decrease in compo-

sitions with meta-carborane is more evident, than in ferrocene-containing compositions. So, this value (dP/dt) could not uniquely explain the differences in mixtures' sensitivity.

The picture of explosion initiation becomes clear, if analysing this process one involves the mechanism of components' chemical interaction [3,4]. According to this mechanism, the decrease of P_{cr} is caused by additional heat release at chemical interaction of fuel additive with oxygen-containing agents (NO_2) formed at HMX thermal decomposition. The higher sensitivity of the HMX/meta-carborane compositions in comparison with ferrocene-containg compositions can be explained by higher caloricity of meta-carborane. Calculated caloricity values for meta-carborane and ferrocene are 58 and 32 MJ/kg respectively.

Powerful explosions followed by intensive volume luminosity can be taken as one more bright proof of chemical interactions. Such things were noticed in experiments on impact loading HMX/carborane (both meta- and orto-carborane) systems. Powerful explosions and luminosity took place due to volume ignition of the part of the product exhausted from the compression zone into environment. The HMX is exploded in these conditions with the less sound effect and luminosity. One can explain observed facts as following. Hot products of explosion decomposition of the sample, which are produced in the compression zone, ignite aerosuspension adjacent to peripheral charge zone. This aerosuspension consists of non-reacted products of sample fracture mixed with surrounding air.

It seems that not HMX products of thermal decomposition (their content is not enough for volume explosion) but the oxygen of surrounding air plays great role in the volume explosion growth. Volume explosions were not observed when the tests had been performed in argon atmosphere.

Chemical interactions of oxygen-containing HMX products of thermal decomposition with meta-carborane can explain the results of experiments on heat explosion measurement.

The values of EH were measured using the calorimeter with the bomb of 5 liters internal volume. The charge diameter and the thickness of the stainless casing were 20 and 7 mm respectively. The mass of the charge was 35 - 40 grams. Prior to a test the bomb was blown out with argon and pumped out. The bomb with a charge was placed in a vessel with a calorimetric liquid (distilled water). The calorimeter temperature was monitored by the measuring system with a resistor thermometer. Energy equivalent of the calorimeter was measured in special runs in which benzoic acid was burned in excess of oxygen. The EH value of the detonator used was also measured. The error of EH measurements was 1 %.

The results obtained are presented in Table 2. Figure 2 illustrates the dependence of EH on carborane content. In Table 2: β is the content of meta-carborane; ρ is the initial charge den-

sity, Q is the explosion heat (H_2O - gaseous); N is the number of moles of gaseous products. The calculation method, developed for aluminized high explosives [11], was used for evaluating EP compositions of HMX/carborane mixtures.

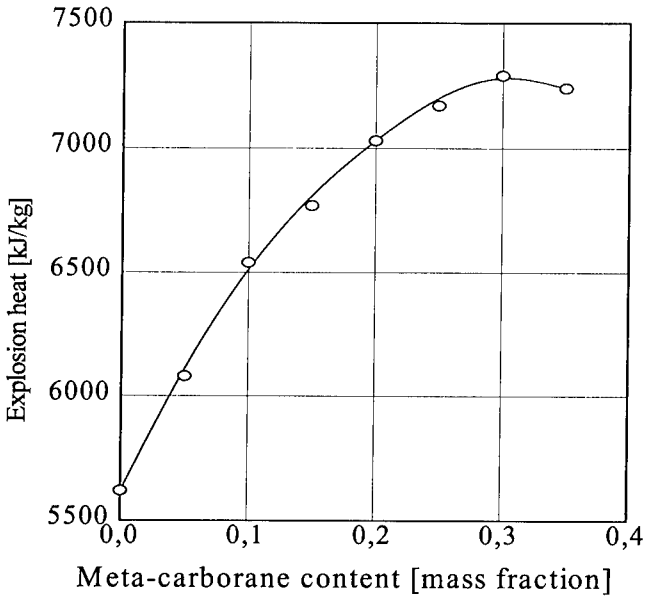


Figure 2. Dependence of EH on the meta-carborane content for HMX/meta-carborane compositions.

Table 2. EH and the number of moles of gaseous EP for HMX/meta-carborane compositions.

β		0.05	0.10	0.15	0.20	0.25	0.30	0.35
ρ, g/cm3	1.80	1.71	1.65	1.58	1.52	1.47	1.43	1.38
Q, kJ/kg	5610	6150	6550	6820	7030	7180	7280	7240
N, mol/kg	37.40	36.42	35.45	34.58	33.67	32.79	30.63	28.25

The results of calorimetric measurements show that meta-carborane addition to HMX significantly increases EH. Meta-carborane concentration, corresponding to the maximum EH value, lies in the region of 30 %. Unfortunately, meta-carborane has a negative enthalpy of formation, which contributes negative effect to EH. HMX has a negative oxygen balance. There-

fore, in contrast to boron, carbon and hydrogen of carborane act as ballast and decrease EH. In the case of compositions, containing oxidisers (e.g., inorganic oxidisers or organic explosives with positive oxygen balances), carbon and hydrogen of carborane could be considered as fuel. Carborane addition to HMX results in decreasing of the number of moles of gaseous EP. However, hydrogen of carborane retards a reduction of N.

Conclusion

The results obtained for HMX-based compositions show the increase of both mechanical sensitivity and heat of explosion when carboranes are added. It should be noted that in these mixtures HMX exhibits oxidising properties. Chemical interaction of carboranes with HMX products formed under thermal decomposition is followed by additional energy release that results to increase of both mixtures' sensitivity and heat of explosion. HMX/meta-carborabe compositions with addition of 10-15% are extremely dengerously explosive and as per level of sensitivily are equal to primary explosives, such as lead azide.

The values of P_{cr} for lead azide and HMX/meta-carborane systems are 0.26 [9] and 0.24 GPa relatively.

References

1. I.A. Karpukhin, V.K. Bobolev. Fiz. Gorenia i Vzryva, 1976, V. 3, No. 4, p. 485. (in Russian).
2. F.P. Bowden and A.D. Jofffe. Initiation and Growth of Explosion in Liquids and Solids, Cambridge at the University Press, 1952.
3. I.A. Karpukhin, V.K. Bobolev, V.A. Teselkin. Fiz. Gorenia i Vzryva, 1979, V. 15, No. 2, p. 140 (in Russian).
4. I.A. Karpukhin, V.K. Bobolev, V.A. Teselkin. Fiz. Gorenia i Vzryva, 1971, V. 7, No. 2, p.261. (in Russian).
5. F.I. Dubovitskiy, B.L. Korsunskiy. Successes in Chemistry, 1981, V. L, issue 10, p. 1828-1871. (in Russian).
6. Russel N. Grimes. Carboranes. Academic Press. N-Y & L 1970.
7. B.M. Mikhajlov. Chemistry of Boron-H, 'Science', M., 1967 (in Russian).
8. V.A. Teselkin, A.V. Dubovik. The Effect of Fuel's Caloricity on Impact Sensitiveness of Binary Oxidizer-Fuel Compositions. Proc. 31th Intern. Annual Confer. of ICT. Karlsruhe. FRG. 2000. P. 74 (1 – 3).
9. G.T. Afanasjev, V.K. Bobolev. Sensitiveness of Solid Explosives to Impact. M., Nauka, 1968

10. V.G.Schetinin. DAN USSR, 1981, V. 258, No. 4, p. 865 (in Russian).

11. M.N. Makhov M.N. The Heat and Products of Explosion of Aluminized High Explosives. Proc. 31th Intern. Annual Confer. of ICT. Karlsruhe. FRG. 2000. P. 42 (1 – 11).

EXPLOSIVE PERFORMANCE OF ALUMINISED NQ-BASED COMPOSITIONS

Michael F. Gogulya, Alexander Yu. Dolgoborodov, Michael A. Brazhnikov,
Michael N. Makhov, and Vitaliy I. Arkhipov

N. Semenov Institute of Chemical Physics RAS,
Kosygin st. 4, Moscow, Russia

Abstract

Nitroguanidine (NQ) is of particular interest both in theory (as an explosive with high hydrogen content) and in practice (as a possible energetic component of non-ideal explosive producing large number of moles of gaseous products under explosion decomposition). In this connection, there were performed experiments on explosion properties of NQ and NQ mixtures with Al, which is much used fuel. There were experimentally measured the following parameters: detonation velocity, pressure time histories and temperature time histories, velocity of accelerated metal plate, explosion heat. The aforementioned parameters characterise the dynamics of energy release at different stages of the explosion processes. The tested compositions contain Al (15% wt.) of different particle size and particle shape (spherical Al particles with mean size < 0.1, 15 μm and flaked Al (≈1×20×20 μm)). The obtained data show that Al addition to NQ practically does not result in detonation velocity decrease in comparison with that of pure HE. For pure NQ, it was observed von Neuman spike; C-J pressure was also determined. Introduction of ultra-fine and flake Al results in pressure increase. Temperatures of Al-containing mixtures as well as the velocities of accelerated metal plates are higher than those of pure NQ. The most marked positive effect of Al introduction was observed for explosion heat values.

Introduction

Aluminium is widely used as an additive enhancing detonation characteristics of HE. However the mechanism of aluminium oxidation in and behind detonation waves is not well understood. This problem attracted new interest after nanoparticles of aluminium became available. We present here the results of the investigations directed to solution of the problems on search and realisation of new ways providing significant increase of detonation performance and metal acceleration ability of HE/Al mixtures. Our previous studies into detonation of aluminium/RDX and aluminium/HMX compositions [1,2] revealed that the interaction between aluminium and HE detonation decomposition products occurs about a few fractions of microsecond behind detonation front but the oxidation degree seems to be too

low. Nitroguanidine (NQ) is an explosive with oxygen balance of – 30.8%. Molecule of NQ comprises significantly less carbon, e.g. in contrast to HMX, and we expected that the detonation decomposition products of this HE are more favourable for realisation of high energetic potential of the aluminium additive.

Experimental Techniques

Detonation velocity was measured with the aid of a set of contact foil gauges. The gauges were manufactured from 0.03-mm thick copper foil. The gauges designed for compositions with aluminium additive were insulated with a plastic film, so that the total thickness of gauges did not exceed 0.1 mm. The time interval of detonation front travel along the measurement base was recorded by the frequency meter ChZ-43A with an accuracy of 0.01 μs. The experimental error of detonation velocity measurements does not exceed 40 m/s. It was measured simultaneously with pressure profiles. Experimental assembly for detonation velocity measurements is shown in Fig 1. HE samples were initiated with a plane wave generator made of RDX-wax composition supplemented by an intermediate 10-mm-high pellet of RDX (ρ_0 = 1.68 g/cm^3) and an intermediate pellet made of exactly the same explosive material as the studied NQ or NQ/Al sample (thickness of this intermediate pellet was 11-15 mm). This was done in order to facilitate formation of steady detonation wave because of low shock sensitivity of NQ [3,4]. Detonation velocity was measured when detonation front propagates between first and second foil gauges (first measurement distance L_1 and corresponding velocity – D_1) and when it propagates between second and third gauges (second measurement distance L_2 and corresponding velocity – D_2), see Fig. 1, $L_1 \approx L_2 \approx 25$ mm.

Temperature and pressure profiles were measured with the aid of dual-channel optical pyrometer (λ = 420 and 627 nm). Resolution time of the experimental set-up was about 10 ns. Temperature measurements in condensed HE could be performed employing the so-called window technique. Apart from that, optical pyrometry allows one to measure pressure profiles with a high resolution both in time and amplitude. This is attained employing the so-called indicator technique [5,6].

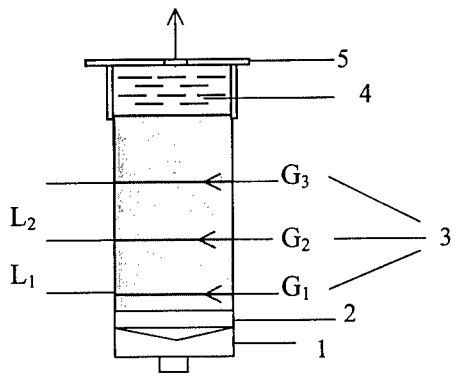


Fig.1. Experimental assembly for optical pyrometry and detonation velocity measurements: 1 - plane wave generator made of RDX - wax composition; 2 - intermediate 10-mm high RDX pellet (ρ_0 = 1.68 g/cm^3); 3 – copper foil gauges; 4 – indicator (bromoform) or window material (LiF + Glycerol); 5 - diaphragm (5 mm in diameter).

Indicator technique is based on the property of some liquids to lose their transparency just after a shock front. Shock front radiation in these materials (indicators) may serve as a fast-response pressure gauge capable of monitoring pressure variations at the sample - indicator interface. The intensity of shock front radiation follows pressure variations at the boundary with the studied sample, extending the signal in time. Bromoform was used as indicator. Pressure variation in the shock wave front propagating through bromoform are directly related to change of parameters at the HE - bromoform interface which, in turn, depends on the detonation wave profile. Using indicator Hugoniot and its acoustic velocity, one can transform pressure profile measured at the shock front in indicator consequently to the contact boundary between indicator and explosive charge and than to the detonation products [5]. Bromoform shock Hugoniot as well as shock front temperatures were measured in [7-11]. The pressure dependence of the shock front temperature for bromoform between 11 and 44 GPa can be written as $T = (237 \pm 26) + (112 \pm 1)p$, here p is in GPa and T - in K. The available data on the acoustic velocity [9,11] behind shock wave with an amplitude in the range 15 - 45 GPa are described by the equation: $C = 0.981 + 0.204p - 2.36\ 10^{-3}p^2$. Experimental assembly is shown in Fig. 1. The layer of the bromoform was about 20 mm thick.

Temperature measurements are often performed by means of the technique in which radiation is monitored through another material ("window") that retains its transparency within the range of pressures of interest. Radiation is recorded from the interface between the material tested and window. LiF plate about 8 mm thick served as a window material. To increase the time of recording the signal from the HE - window interface, a glycerol 12-mm thick layer was poured on LiF plate.

The Plate Acceleration Technique described in [12] consists in measurements of the velocity of a metal plate accelerated by detonation products in the direction of detonation wave propagation (Fig. 2).

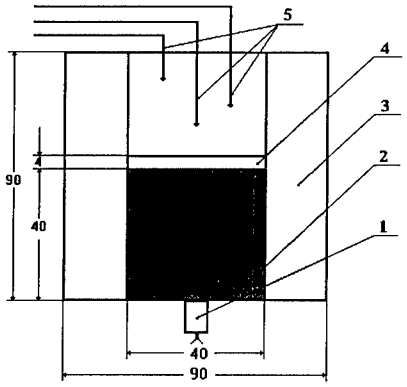


Fig. 2. Scheme of metal plate acceleration technique: 1 - detonator cap, 2 - HE charge, 3 - steel cylindrical casing, 4 - steel disk, 5 - contact pins (all sizes are in mm).

HE charge 40 mm in diameter with a 4-mm thick steel plate of the same diameter attached to the charge end are placed in a steel cylindrical 40-mm i.d. casing with length of 90 mm and wall thickness of 25 mm. In the interior of the casing eight contact pins are mounted at different distances along its axis; they are faced the accelerated plate. The basic charge of the tested NQ was 35-mm long. We used an additional intermediate pellet (a 10-mm thick layer of pressed RDX at density 1.68 g/cm^3) in order to reinforce the initiation impulse and avoid any problems related with low shock sensitivity of NQ. As the plate travels, it touches the pins, which is recorded by an oscilloscope. The plate velocity along its trajectory was determined from time intervals between subsequent touching of the pins and known spacing between them.

Several runs were performed for each explosive composition; the measurement results were averaged and approximated by an analytical function of the velocity of the plate versus distance or time of its flight. Distance L = 40 mm from the initial position of the free surface of accelerated plate was used as the standard base for comparing the plate velocity. The plate velocity was measured to within ~1%.

Explosion heats are measured in a bomb calorimeter schematically shown in Fig. 3.

The calorimeter is made of a strong steel vessel 5 litre in volume with a self-tightening cover. The vessel is placed in a compartment with a calorimetric liquid (distilled water). The energetic equivalent of the calorimeter was measured in special runs in which a reference material, benzoic acid, was burned in oxygen.

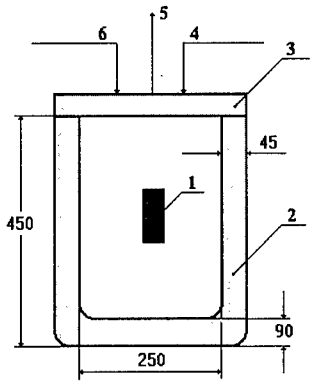


Fig. 3. Calorimetric bomb (1- HE confined charge, 2 – bomb casing, 3 – bomb cover, 4 – electric wire, 5 – gas exhaust orifice, 6 – gas inlet orifice).

Explosion of tested HE charges was initiated with an electric detonator whose explosion heat was measured in calibration runs. The pure NQ and NQ/Al (85/15) mixtures for calorimetric measurements were pressed in charges of 30 mm in diameter and 50-60 g in weight and placed into the 10-mm thick casing. To initiate detonation we used an additional intermediate detonator (a 10-mm thick pellet of pressed RDX). Naturally, the heavier the casing at the given charge diameter, the closer would be the detonation velocity to the ideal values. Prior to a test the bomb was purged with helium and pumped out to 1 or 2 Torr. After HE charge explosion the calorimeter temperature was monitored continuously with a resistor thermometer. The measurement error was ~1%.

Preparation of NQ/Aluminium Charges

Three various batches of aluminium powder were tested including spherical particles with size <0.1{0.9}; 15{0.99} μm and flake aluminium with size ≈1 x 20 x 20 μm {0.85}. Here figures in parentheses indicate content of active aluminium (the higher it is the smaller is the amount of aluminium oxide film). The aforementioned aluminium powder batches are referred to below as Al(0.1), Al(15) with mean particle size in micrometers indicated in the parentheses and Al(fl) for flaked aluminium. Weight content of aluminium in mixtures with HE was 15% in all experiments. The aluminium powder with mean particle size of 15 μm was prepared by sieving technical powder manufactured by atomising melted aluminium in an inert compressive gas (industrial technique is described in [13]. The particles are of drop-like, almost spherical shape. The technique of production of nanophase (nanoparticle) powders of metals, alloys and some compounds using the condensation of vapours levitating in the electromagnetic field drop is described in [14]. Nanophase aluminium particles manifest pyrophoric properties when exposed to air. When this powder is passivated by air, the powder loses its pyrophoric properties but the content of aluminium in the particles drops to about 90% due to oxidation of aluminium and formation of Al_2O_3 film. As flaked aluminium we applied the technical-grade aluminium pigment powder specified as PAP-2 and manufactured by an industrial technique described in [13]. This product consists of 85% or more of aluminium, 3.8% or less of stearine covering the aluminium flakes and other components. Finally, content of Al_2O_3 in the powder is nearly 10%. The standard flake size is less than 45 μm. Microscopic observations show that the flake thickness is about 1 μm or less and flake transverse size is about 10 - 30 μm (20 μm in average).

NQ crystals have needle-like shape; their sizes together with the loose-packed density depend on the crystallisation way of the crystals. The theoretical maximum density (TMD) of NQ is 1.78 - 1.80 g/cm^3 [3,4]. Here we used technical-grade powder with loose-packed density of 0.4 g/cm^3, produced by means of crystallisation with small amount of gelatine as a surface-active agent. Original batch consists of needle-like particles of about 25 - 50 μm in thickness and up to 500 μm in length. To decrease particle size, we used for this purpose recrystallisation of original NQ from aqueous solution. The recrystallisation also results in additional purification of the product. After recrystallisation the needle particles were of

about 5 - 10 μm in thickness and about 50 μm in length. These sizes are consistent with those described earlier [4]; this batch has a low loose-packed density of 0.2 g/cm^3. Detonation performance of this low-bulk density NQ differs significantly from that of high-bulk density product consisting of coarse cylinder particles [4]. The components of the mixtures were mixed in a rotating drum with porcelain balls during 8 hours. For safety the drum was filled with liquid hexane, which later was evaporated at 70°C from the prepared mixture during 4 hours. Size of NQ was not practically changed under mixing. To avoid deformation of flaked particles during the mixing process with NQ grains, we have used the following procedure: aluminium particles were added to HE particles merged in hexane and manual mixing was done until full evaporation of liquid. Microscopic observations show that all tested mixtures have quite uniform structure. NQ/Al(0.1) composition consists of the needle NQ particles uniformly covered by a layer of nanophase aluminium particles. Charges were manufactured by cold pressing of the premixed components. Density of pressed charges was about 0.90 - 0.95 TMD. For NQ we use single crystal density of 1.78 g/cm^3 in accordance to [3].

Experimental Results

Data on detonation velocity are listed in Table 1, where ρ_0 and η are the absolute and relative charge density, D_1 and D_2 are the detonation velocity measured at distance L_1 and L_2 respectively. For comparison the Table lists the density of HE in mixture, ρ_{0HE}. This density can be defined as mass of HE containing in the charge divided by the difference between the charge volume and that occupied by metal additive, this means that whole charge porosity is attributed to HE. One need to compare the obtained results on detonation velocity in equivalent conditions, but the tested charges differed in their porosity. Thus taking into account the relationship $D = 1.44 + 4.015\rho_{0HE}$ proposed in [15], it is possible to recalculate detonation velocities (D_2) measured at different charge density to those (D^*) would be measured at the same HE density in the mixture: $D^* = D_2 - 4.015(\rho_{0HE} - 1.635)$.

Because of low shock sensitivity of NQ, we have used quite powerful initiator to be sure that NQ detonation can be achieved within firing set-up. Hence, one can expect that the overdriven detonation should propagate in the first tested pellet. Indeed, excess in the detonation velocity at the first measurement base D_1 relative to the second base has been

observed in all the tested compositions except for the mixture with Al(0.1). Indeed, in this case D_1 is slightly higher than. D_2 (except NQ/Al(0.1) mixture).

TABLE 1 Characteristics of Tested NQ and NQ/Al Charges

ρ_0, g/cm^3	Al	η	D_1, km/s	D_2, km/s	ρ_{0HE}, g/cm^3	$D^*(\rho_{0HE} = 1.635)$, km/s
1.635	-	0.918	8.25	7.94	1.635	7.94
1.743	Al(15)	0.929	8.02	7.94	1.640	7.92
1.720	Al(fl)	0.916	8.17	7.78	1.616	7.86
1.785	Al(0.1)	0.951	7.99	8.13	1.684	7.93

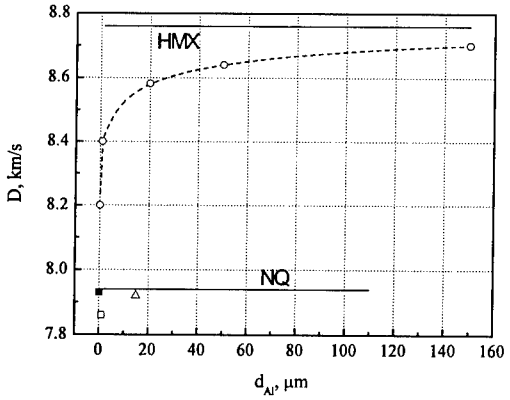


Fig. 4. Detonation velocity versus Al particle size: o - HMX/Al [16]; □ - NQ/Al(fl); ■ – NQ/Al(0.1); Δ - NQ/Al(15).

The detonation velocity of pure NQ registered at the second base agrees well with the data available in literature for close values of charge diameter [3,4]. Besides, the value we obtained agrees with that calculated by using the relation between ideal detonation velocity and HE density in the charge mentioned above. Those are the reasons to believe that the detonation in NQ initiated by our strong initiation system reaches its steady state after 35-40 mm of propagation, and the 40-mm charge diameter is close to the infinite detonation diameter for NQ of given density and particle size.

The data on detonation velocity versus particle size for NQ/Al and HMX/Al are plotted in Fig. 4 in order to illustrate the effect of Al introduction on detonation velocity of explosive mixtures. For NQ/Al, there are plotted D* values (for D* calculation ρ_{0HE} was chosen to be equal to the density of pure NQ). It is seen that addition of ultra-fine Al to HMX (HE with negative OB) results to significant detonation velocity decrease. It can be explained by two causes: decrease of HE amount in the mixture and decrease of mole number of gaseous products. The losses of mole number of gaseous products caused by replacement of apart of HE by Al as well as Al reaction with oxygen containing in carbon oxides are not compensated by supplement energy release in detonation zone. Quite opposite situation is seen when analysing the results on NQ/Al compositions. Decrease of detonation velocity D* is minor in comparison with pure NQ; in case of NQ/Al(fl), it is less than 100 m/s. NQ detonation products contain much more water than HMX does, thus Al oxidation is not followed by diminishing of the amount of gaseous products and energy release practically compensate the loss of HE in the mixture.

Pressure profiles obtained in pure NQ and NQ/Al(0.1), NQ/Al(15) and NQ/Al(fl) mixtures are shown in Fig. 5(a,b). In experiments, there are measured pressure variations at the front of shock wave spreading in bromoform that are directly related with pressure changes at the HE – bromoform interface which, in turn, depend on the detonation wave profile. In [5], it is described the procedure of pressure profile transformation from shock wave front to detonation products. In Fig. 5(a,b) there are given pressure time histories at the interface and in detonation products respectively.

The experimental value of the detonation pressure for pure NQ at density of 1.72 g/cm^3 cited in [17] is 24.5 GPa. The values calculated in [18] for NQ at density of 1.629 g/cm^3 equal 25.6 and 23.8 GPa depending on the equation of state used for calculation of CJ parameters. In [18] there are also the experimental and calculated values of the detonation pressure for the mixture NQ/estane (95/5) at density 1.705 g/cm^3. The experimental pressure equals 26.8 GPa and calculated one 28.8 or 27.1 GPa depending on the NQ equation of state.

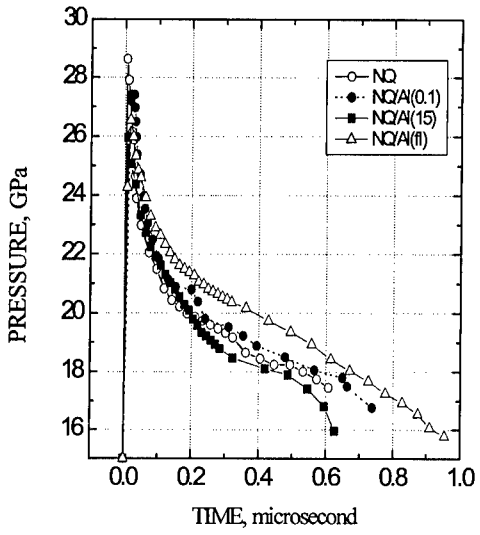


Fig. 5a. Pressure time histories at the DP/ bromoform interface.

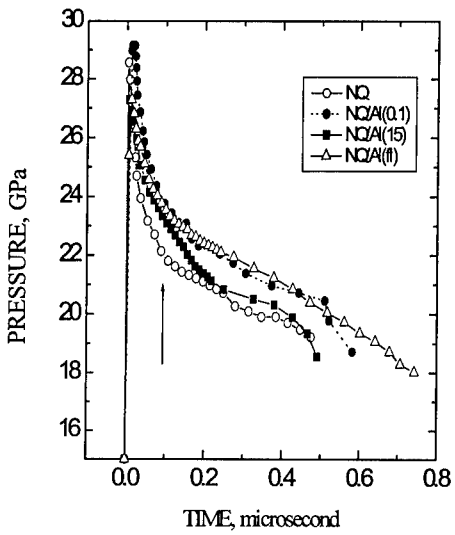


Fig. 5b. Pressure time histories in the DP. The arrow shows C-J point for NQ.

Let us discuss the data on pressure profiles in pure NQ in details. For pure NQ, Fig.5b clearly demonstrates the region of elevated pressures attributed to exothermic chemical reactions (so-called "chemical spike" or von Neumann spike). Selection of the inflection or break point on pressure profiles, which corresponds to the termination of chemical reaction (the C-J point of a detonation) is a quite subjective task and introduces some discrepancy [6]. For pure NQ, the CJ pressure would fall in pressure interval of (22.14÷21.62) GPa, which corresponds to the polytrope index of (3.66÷3.77) and the detonation reaction zone of (0.7÷1) mm or (90÷125) ns. This estimation of the CJ pressure is in a good agreement with the experimental value of 24.5 GPa cited in [17] for pure NQ at density 1.72 g/cm^3 and markedly less than the calculated ones. Thus, pure NQ have quite high detonation velocity and relatively low detonation pressure typical of HE with high hydrogen content.

There is some discrepancy in comparison of the pressure profiles obtained for NQ/Al charges differed slightly in the initial density and measured detonation velocity. It is of interest to have the information on the pressure profile in the detonation products. Both values (detonation velocity and initial charge density) should be involved for the pressure profile

transformation from the shock front in the bromoform into detonation products. Experimentally measured detonation velocities (D_2 see Table 1) were used for pressure profile transformation. Considering Figs 5a and 5b, one can see that relative position of the pressure profiles occurring in the inert media can be slightly influenced by the media shock impedance. Basing on the obtained pressure profiles, it is difficult to say which of aluminium, flake or ultra-fine, is more effective; we believe that both powders start react with detonation products in detonation zone and this interaction results in positive effect within monitoring time.

Detonation product temperatures measured for NQ and NQ/Al(0.1) also corroborate aforementioned conclusion on the chemical reaction between Al and detonation products. The brightness temperature time histories for pure NQ and NQ/Al(0.1) mixture are shown in the Fig. 6. The calculated thermodynamic temperatures differ significantly depending on the equation of state for detonation products and equal either 1581 K or 2533 K [17].

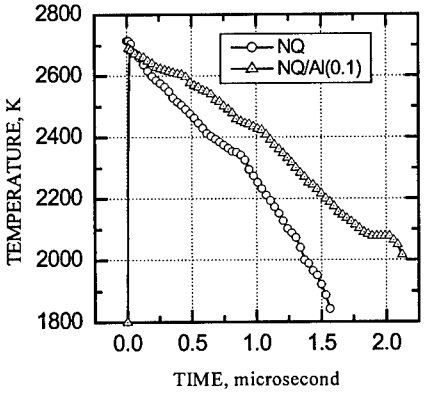


Fig. 6. Brightness temperature time histories for NQ and NQ/Al(0.1) with LiF used as the window (λ = 627 nm).

For pure NQ, the temperature of detonation products recorded at the interface with the window material turns out to be higher than that expected in accordance with [3,17]. Temperatures measured at the contact interface with LiF for pure NQ and NQ/Al(0.1) mixture are practically equal. However, as time goes on, the excess of temperature of the detonation products of the NQ/Al(0.1) mixture over pure NQ temperature becomes higher and higher. This

effect can be attributed to the arising of chemical interaction between detonation products and Al.

Plate acceleration tests were performed for NQ-charges at two densities as well as for NQ/Al-charges; the obtained data on metal plate acceleration (W) are listed in Table 2. Comparing the data one can conclude that the increase of NQ charge density by 0.1 g/cm^3 results in the increase of the plate velocity by ~90 m/s at all measurement positions. The acceleration trajectories shown in Fig. 7 for NQ/Al mixtures were recalculated from the experimental data to one and the same NQ porosity in the charge of ~ 8% basing on the plate velocity – density relation obtained for pure NQ. The data on metal plate acceleration correlate with all data described above. The most noticeable positive effect is achieved when ultra-fine or flake Al is added. This inference follows from the fact that trajectories for Al-containing compositions lie higher than the trajectory for pure NQ in W-L plane. It was clearly seen from the pressure and temperature measurements that effectiveness of Al introduction is more evident when considering pressure and temperature profiles at larger times. The conclusion on the growth of the reaction between Al and detonation products is supported by surpass in W measured for NQ/Al mixtures over that of pure NQ; it increases at larger distances (see Fig. 7).

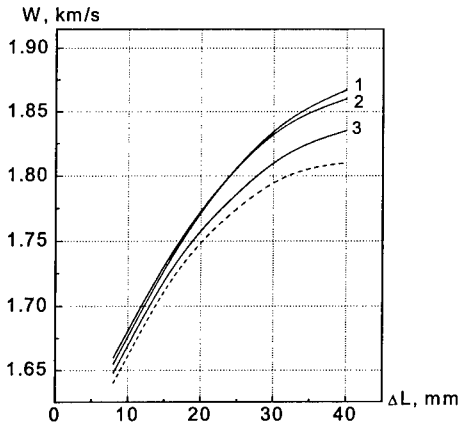


Fig. 7. Acceleration trajectories for NQ и NQ/Al. 1 - Al(fl); 2 – Al(0.1); 3 – Al(15); Dash - pure NQ.

Explosion heat data are also given in Table 2. One can see that the introduction of Al into the NQ results in the more significant increase of the explosion heat comparing with the effect observed in HMX/Al mixtures [19]. Besides, the finer Al particles are the higher the value of the explosion heat is. The effect of Al particle size on the explosion heat is in qualitative agreement with trends revealed in experiments on the metal plate acceleration ability. On the condition of the complete Al oxidation in explosion products, one can estimate the explosion heat as 5580 kJ/kg at given Al content (15%). Comparing this value with experimental ones, one can see that there is no complete Al oxidation in NQ detonation products expanding in calorimetric bomb.

Table 2. Detonation Performance of NQ and NQ/Al (85/15) Mixtures

Composition	NQ	NQ	NQ/Al(0.1)	NQ/Al(fl)	NQ/Al(15)
ρ, g/cm^3	1.58	1.635	1.785	1.720	1.743
Q, kJ/kg	--	3480	4960	4930	4820
W, km/s					
ΔL(mm) = 8	1.57	1.62	1.67	1.62	1.63
16	1.65	1.7	1.76	1.70	1.71
24	1.70	1.75	1.82	1.76	1.77
32	1.72	1.77	1.86	1.81	1.80
40	1.73	1.78	1.88	1.83	1.82

Conclusion

- In contrast to the majority of HE, addition of Al to NQ does not result to significant decrease in detonation velocity in NQ/Al in comparison with pure NQ, except for NQ/Al(fl) mixture, which demonstrates weak deficit in detonation velocity after addition of Al.
- Recorded pressure in NQ/Al mixtures exceeds that in pure NQ.
- Temperatures recorded in NQ/Al(0.1) are higher than those in pure NQ.
- The introduction of the tested Al powders results in the increase of the final plate velocity. The maximum gain in casing velocity is about 3.1% for NQ/Al over pure NQ.
- The introduction of Al into the NQ results in significant increase of the explosion heat besides, the finer the Al particles are the higher the value of the explosion heat is.

Acknowledgement

We would like to thank Dr. I.O. Leipunskiy and all staff of the Laboratory headed by academician Tal'rose V.L. (Institute of Energetic Problems of Chemical Physics, Russian Academy of Sciences) for producing of nanophase Al and photomicrography.

References

1. M.F. Gogulya, M.A. Brazhnikov // HDP - 95. Tours, France. 1995, p. 299.
2. M.F. Gogulya, A.Yu. Dolgoborodov, M.A. Brazhnikov, G. Baudin. // The Eleventh Int. Detonation Symposium. Colorado, USA. ed. by J. Short. 2000, p. 979-987.
3. L.I. Khmelnitski. Handbook of High Explosives. Part II. Moscow. Dzerzhinski Military Ordnance Engineering Academy, 1962. (in Russian).
4. Donna Price and A.R. Clairmont. // Proc. Twelfth Symp. (Intern.) on Combustion. Poitiers, France, July 14 to 20, 1968. The Combustion Institute, 1969, p. 761.
5. M.F Gogulya and A.Yu. Dolgoborodov // Chem. Phys. Rep. 1995, V. 13, No 12, p. 2059.
6. I.M. Voskoboinikov and M.F. Gogulya // Sov. J. Chem. Phys. 1985, V. 3, No 7, p. 1623-1632.
7. J.B. Ramsay. LASL Shock Hugoniot Data. // S.P. Marsh, Ed, Univ. of California Press, Berkeley, 1980, p. 552.
8. I.M. Voskoboinikov and A.Yu. Dolgoborodov // Detonatsiya, Chernogolovka, 1989, p. 91 (in Russian).
9. R.G. McQueen and D.G. Isaak // Shock Compression in Condensed Matter, S.C. Schmidt, J.N. Johnson, and L.W. Davidson, Eds, Elsevier, Berlin, 1990, p. 125.
10. M.F. Gogulya and M.I. Voskoboinikov // Fiz. Goreniya i Vzryva 1988, V. 24, No 6, p. 127 (in Russian).
11. A.Yu. Dolgoborodov, I.M. Voskoboinikov, and I.K. Tolstov // Khim. Fiz. 1991, V. 10, No 5, p. 679 (in Russian).
12. V.I. Arkhipov, M.N. Makhov, V.I. Pepekin // Chemical Physics Reports. 1993, V. 12, No 12, p. 1640.
13. Powders of Non-Ferrous Metals. Handbook. Ed. by S.S. Naboichenko. Moscow. Metallurgiya. 1997 and see also L.V. Dubnov, N.S. Bakharevich, A.I. Romanov. Industrial High Explosives. Moscow. Nedra. 1988. (in Russian).
14. M. Ya. Gen and A. V. Miller. Patents of USSR, No 814432 and No 967029.
15. M.D. Hurwitz // OSRD 1945, p. 5611.
16. Unpublished data by the authors.
17. M.L. Hobs and M.R. Baer. // Proceedings of the Tenth Intern. Detonation Symposium, July 12 - 16, 1993, p. 409-418.
18. Charles L. Mader. Numerical Modeling of Detonations. University of California Press. Berkely, Los Angelos, London, 1979.
19. V.I. Arkhipov, M.N. Makhov, V.I. Pepekin, V.G. Schetinin. // Khim. Fiz. 1999, V. 18, No 12, p. 53-57 (in Russian).

SENSITIVITY AND PROPERTIES OF ENERGETIC MATERIALS DATABASE

Valery P. Sinditskii, Valery V. Serushkin, Viacheslav Yu. Egorshev
Department of Chemical Engineering, Mendeleev University of Chemical Technology, 9 Miusskaya Sq., 125047, Moscow, Russia
and
Gleb V. Belov
Glushko Thermocenter, IVTAN Association of RAS, 13/19 Izhorskaya Street, Moscow, Russia

ABSTRACT

The sensitivity of energetic materials database HAZARD has been created to provide specialists with extensive information on sensitivity characteristics of individual explosives, explosive mixtures, propellants, and pyrotechnic compositions to different types of mechanical and electrostatic stimulus. The general conception, contents and key features of the database are described. The potentialities of the database for solving scientific and practical problems are discussed.

INTRODUCTION

The success in the design and development of rocket motors, gun systems, various gas-generators, pyrotechnic devices, percussion, igniting, delaying compositions, etc. depends significantly on the knowledge of sensitivity characteristics of selected energetic materials (EM) under various conditions. However, at the present time most of sensitivity data have not been gathered and arranged that requires a considerable preparative work. The are numerous and various data on sensitivity of explosives, propellants, pyrotechnics, explosive mixtures, etc. in the world's scientific literature. Along with these known data, there exist also many unpublished experimental results collected by various scientific and research organizations. To colligate this extensive information in convenient-in-use form, the computer database HAZARD possessing wide analytical possibilities has been developed by scientists of Mendeleev University of Chemical Technology and Glushko Thermocenter. The development of this database continues efforts of Mendeleev University on evolution of the information infrastructure in the field of energetic materials started with issue of the database FLAME [1] on steady-state combustion of EM.

GENERAL CONCEPTION AND CONTENTS OF THE DATABASE

HAZARD database is designed for collecting, storing, and reviewing properties and sensitivity data of energetic materials. The conception of the database implies identification and classification of EM by their assignment, chemical and hazard classes and incorporates both

general properties and special sensitivity data. The main groups of energetic materials are following: individual explosives of different chemical classes, propellants, pyrotechnics, and mixtures. The general properties are subdivided into three groups: Physicochemical, Thermodynamic, Detonation & Combustion properties. Data on sensitivity of EM include the following: Impact sensitivity, Friction sensitivity, Shock sensitivity, Electrostatic discharge sensitivity. Each type of sensitivity data combines data obtained by different experimental methods, with a brief description of the methods and references included. Data are presented in the form of interconnected tables as shown in **Fig. 1**.

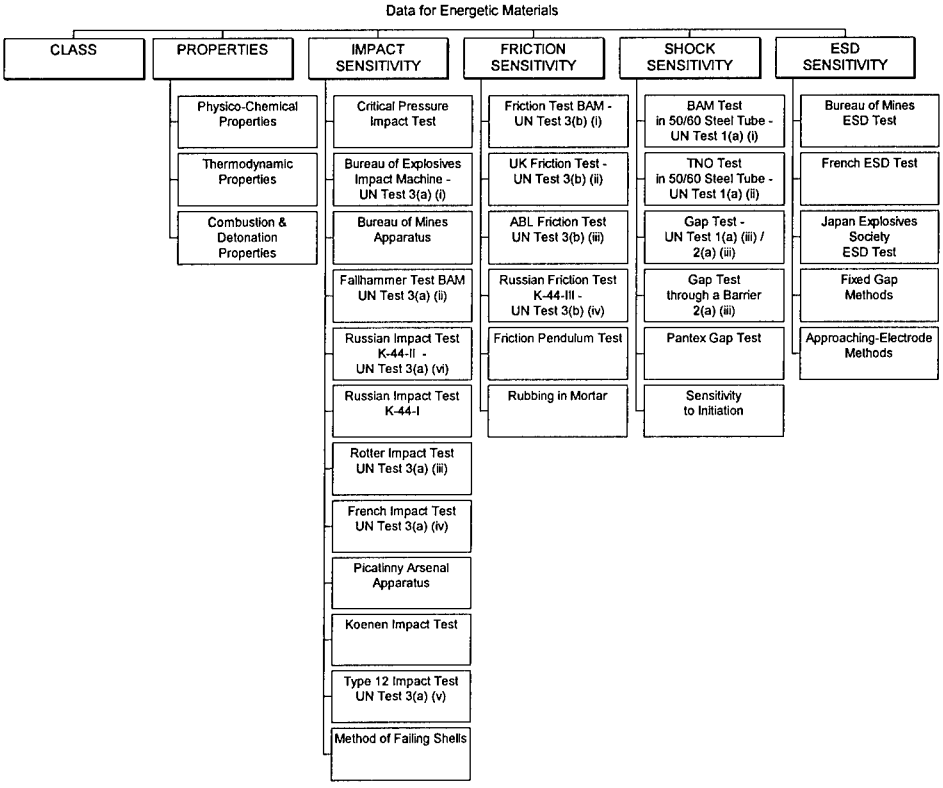


Fig. 1. Database HAZARD table structure

The conception also implies a possibility of adding database with new materials, calculation of their thermodynamic parameters, editing data, searching for EM by a single or complex parameter, analyzing information, and creating reports.

Now HAZARD contains data for over 300 individual explosives from both traditional classes (such as C-nitro-, N-nitro- and O-nitrocompounds) and specific classes (tetrazoles, furoxans,

coordination compounds, etc.).

General Properties

The database contains many general properties (**Fig. 2, Fig. 3**) for each included energetic material. For convenience sake all properties are subdivided into three separate tables: Physicochemical, Thermodynamic, Detonation & Combustion properties. Some of the thermodynamic properties such as Oxidizer-Fuel Ratio, Oxygen Balance, Heat of Combustion in Oxygen, Adiabatic Flame Temperature, Powder Force, Specific Impulse are calculated ones and filled up automatically at adding data in the Brutto Formula and Enthalpy of Formation fields. A built-in module of the thermodynamic code REAL [2] is used for the calculations.

Sensitivity Properties

The main complexity of creating such a database is in a significant number of experimental techniques commonly used to determine sensitivity of energetic materials, resulting in the problems associated with comparison of the data obtained by different methods. In this connection the conception of the database implies presentation as much information as possible. There are four kinds of sensitivity data: Impact, Friction, Shock, and ESD (electrostatic discharge). The corresponding sensitivity data windows (**Fig. 4-Fig. 6**) have a common structure that generally includes test **Method**, **Method description, Reference, Test Conditions**, test **Results**, and **Special Conditions/Notes** boxes. **Test Conditions** and test **Results** boxes for different types of sensitivity (Impact, Friction, Shock and ESD) contain fields which cover test conditions and results of the test methods. **Method description** button allows reviewing of the detailed description for the chosen test method. The detailed information on test results is kept in the **Results** boxes for Impact, Friction and ESD sensitivity data windows. This information can be presented and analyzed in the graphic form. **Special Condition/Notes** field in the sensitivity data windows serves for storing of additional information about test conditions and results.

If an energetic material has been tested for one type of sensitivity (impact, friction, shock, or electrostatic discharge) but through different test techniques, or by different authors, or under different conditions, all the results will be presented as different records.

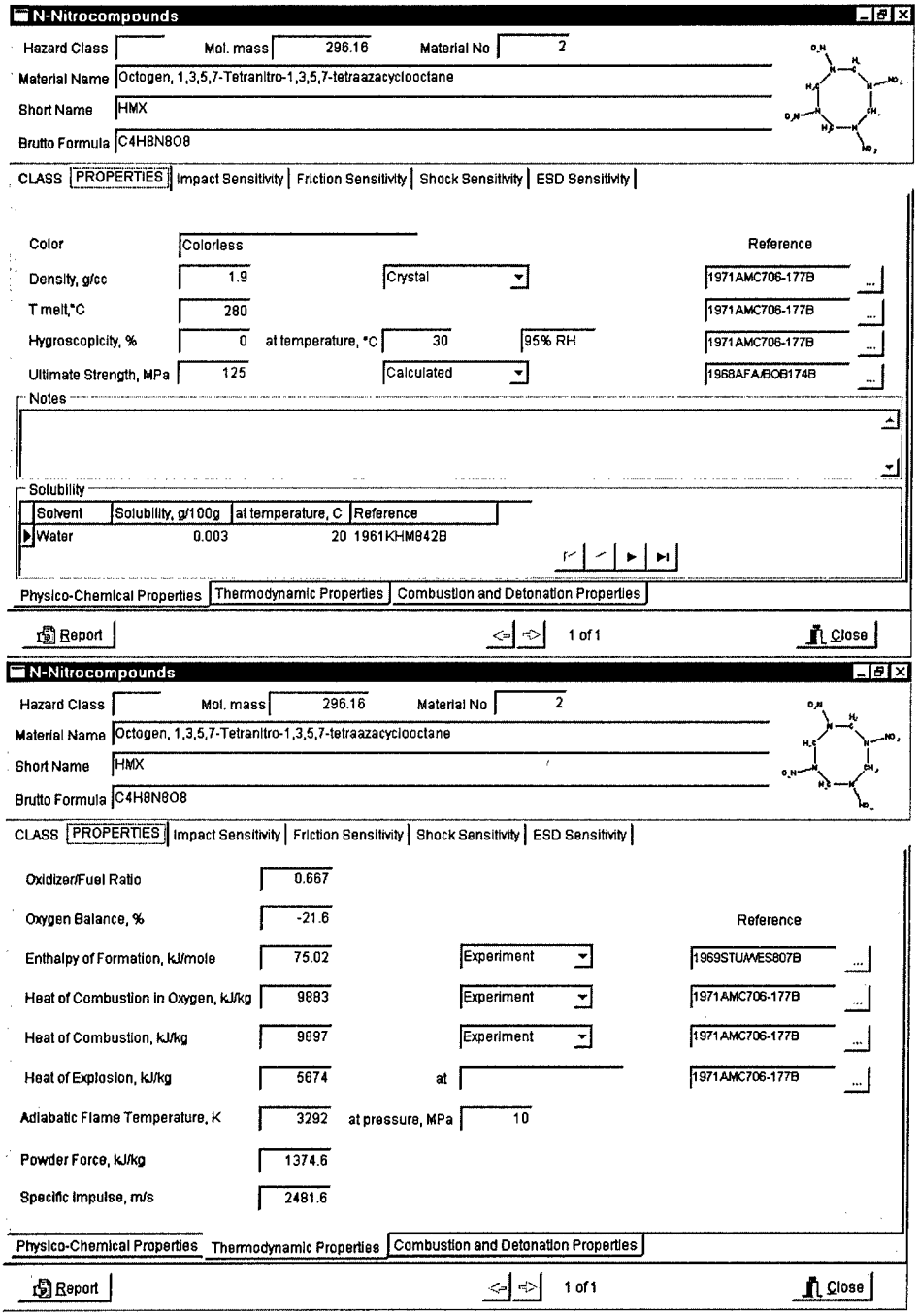


Fig. 2. General properties tables: Physicochemical and Thermodynamic Properties bookmarks.

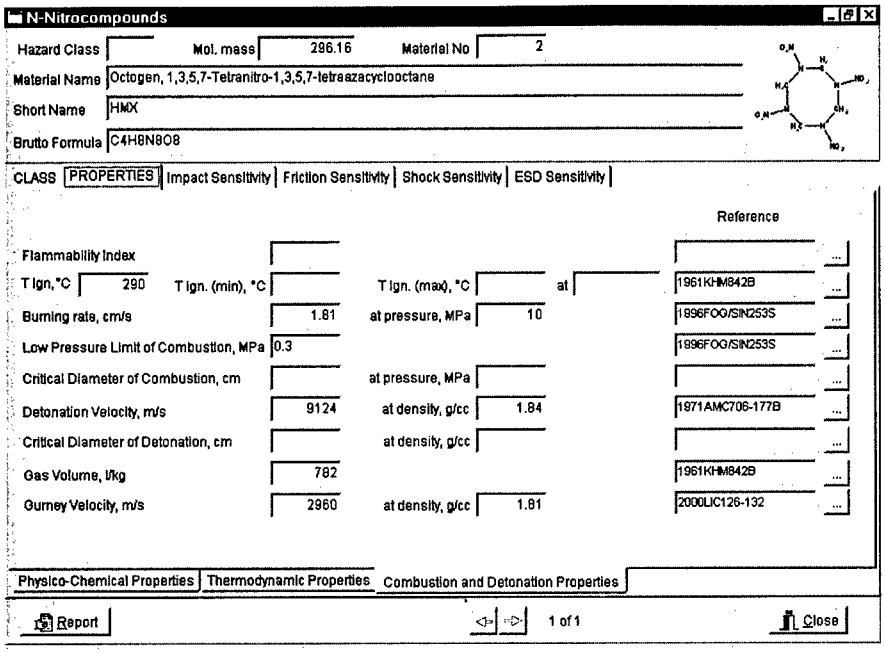


Fig. 3. General properties tables: Combustion and Detonation Properties bookmark

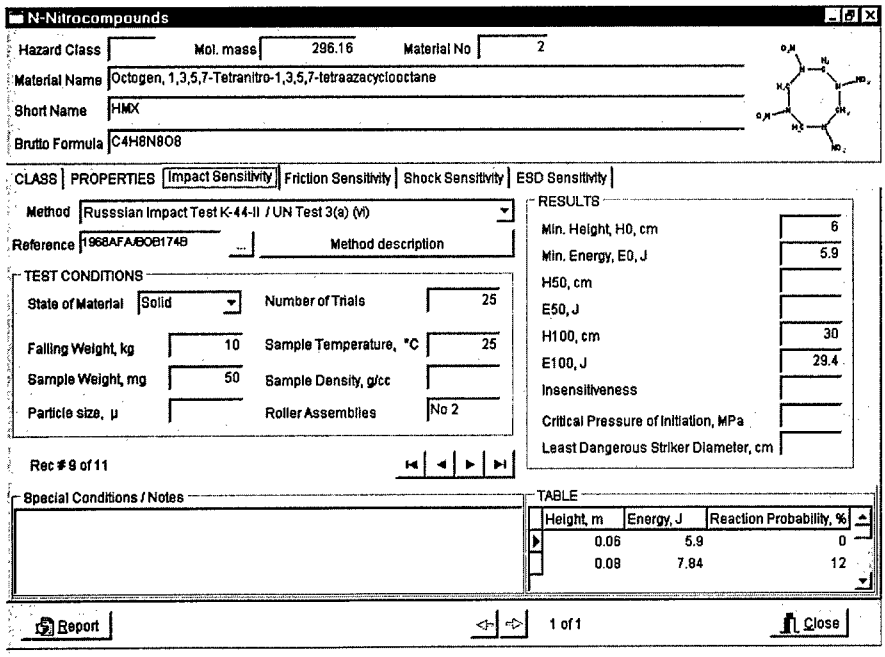


Fig. 4 Sensitivity tables: Impact Sensitivity bookmark

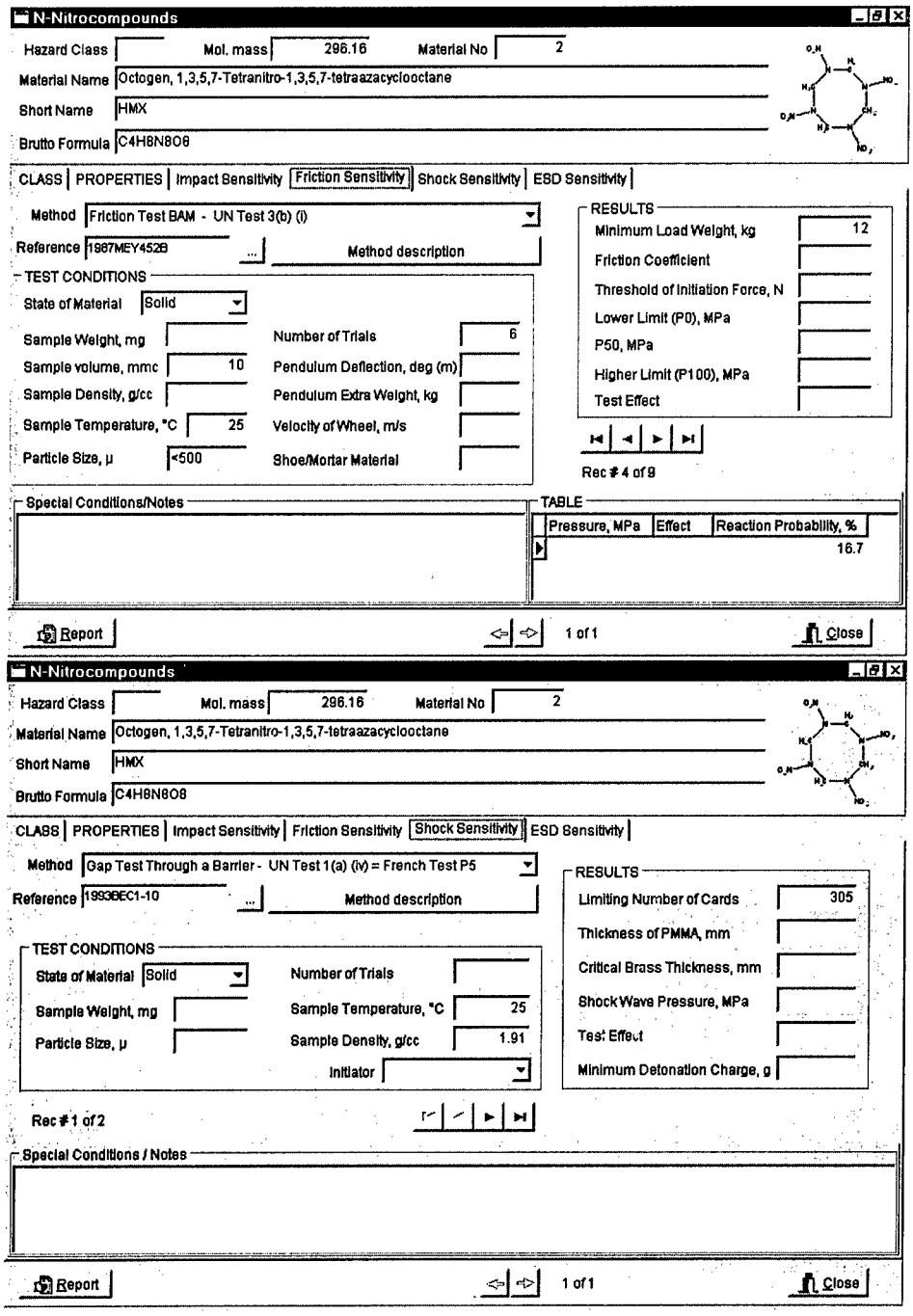


Fig. 5. Sensitivity tables: Friction and Shock Sensitivity bookmarks

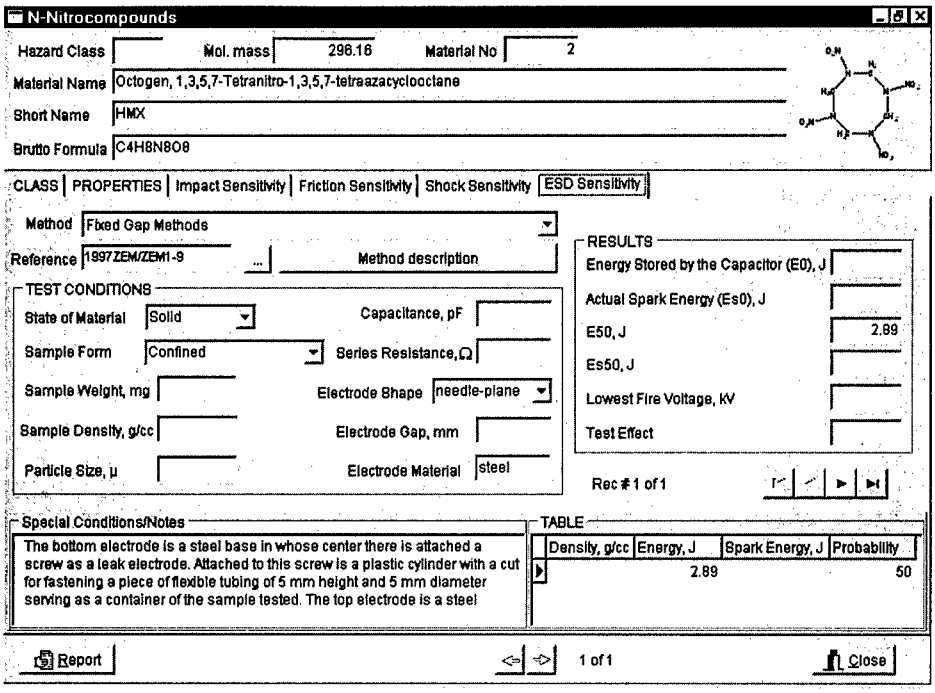


Fig. 6. Sensitivity tables: ESD Sensitivity bookmark

KEY FEATURES

Database HAZARD provide the user with wide opportunities to search, review, compare, analyze, add, export and import data on properties and sensitivity of energetic materials. A more detailed description of database key features is given below.

Classification

The general conception of the database implies classification of EM by their chemical classes. Each energetic material to be introduced will be stored in the database under a particular class according to its chemical or arrangement belonging. The Classifier is intended for structurization of information, simplification of searching, and selection of necessary data. It serves for visual search for an EM by choosing it from the corresponding class in the Classifier tree with the mouse (**Fig. 7**).

Classes have their interior structure and may be composed of constituent parts, **Fragments**, which, in turn, can be also subdivided into **Elements**. Such subdivision facilitates arranging energetic materials in the database as well as searching and selecting materials by their chemical or linkage features.

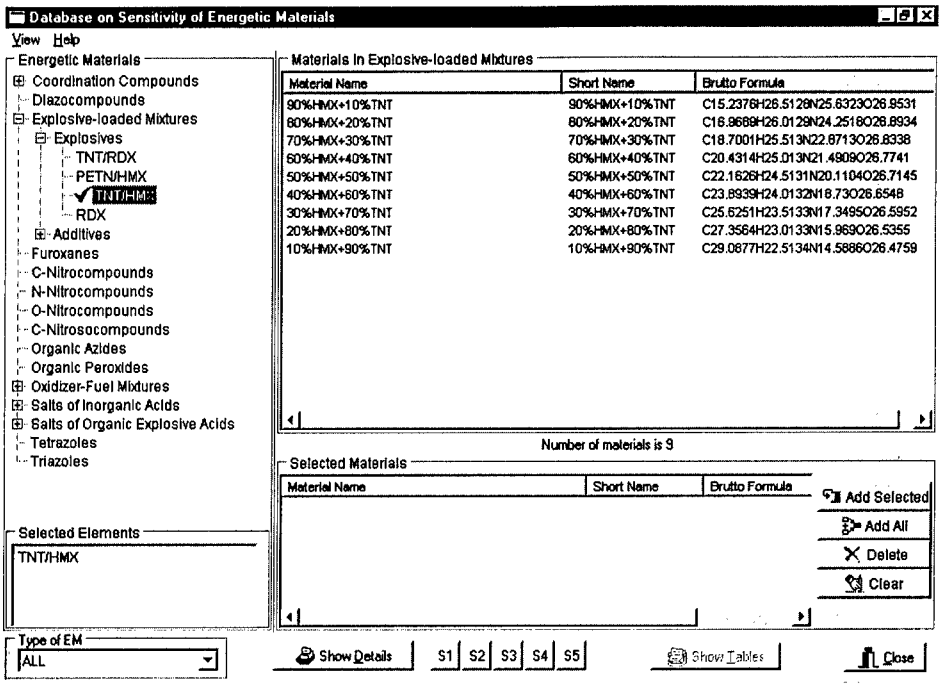


Fig. 7. View database Window with Classifier tree

Reviewing, Searching and Comparing Energetic Materials in DataBase

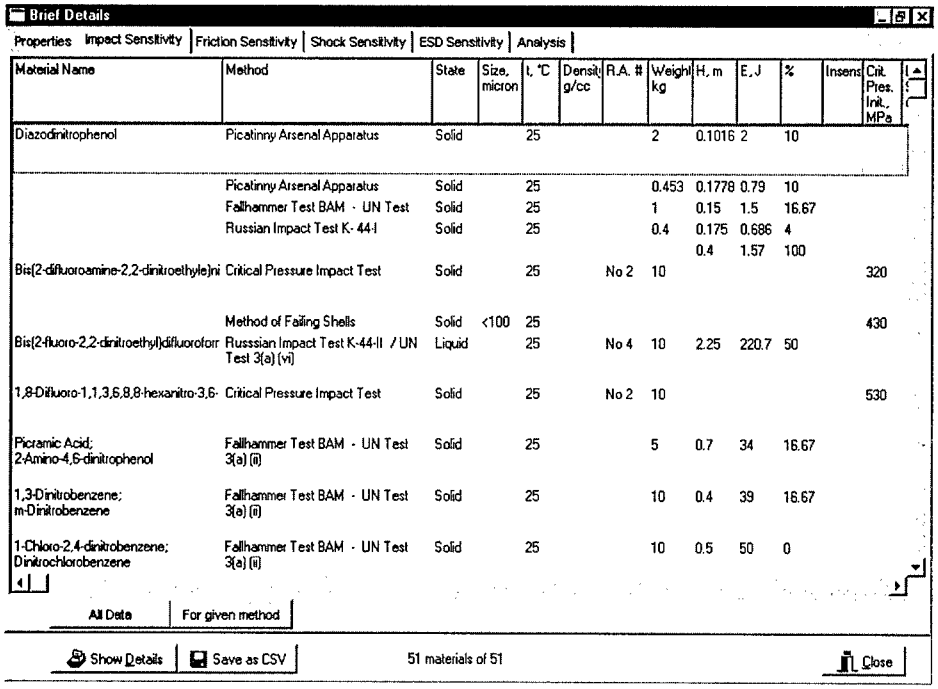
A set of standard means to find EM by its full, short, or part of name, or chemical composition is realized in the HAZARD database. The **View database** window (see **Fig. 7**) allows searching for an energetic material by **Short Name**, **Material Name**, or **Brutto Formula**, respectively. Furthermore, it is easy to search for compositions and mixtures which contain a desired energetic ingredient or materials having a given reference in the database.

All materials that correspond to the inquiry will appear in the **Selected Materials** Table located at the bottom of the window (**Fig. 7**). The list of the selected materials can be easily modified with **Add One, Add All, Delete, and Clear** buttons.

The **Brief Details** window contains a comparative table of main properties and sensitivity data for the selected materials. It comprises **Properties, Impact Sensitivity, Friction Sensitivity, Shock Sensitivity, ESD Sensitivity** Tables and **Analysis** bookmark (**Fig. 8**). There is an opportunity to compare selected energetic materials within a particular method of sensitivity measurements.

Data analysis

Database HAZARD has build-in opportunities for data analyzing. There are three approaches realized in the database. The first one (**Sensitivity vs. Material**) allows the user to compare selected materials in graphic form by its sensitivity to different types of mechanical and electrostatic stimulus determined by any one of methods available in the database. The second one (**Sensitivity vs. Properties**) gives an opportunity to analyze the influence of any material property on any type of sensitivity for selected materials. The third method (**Sensitivity vs. Sensitivity**) is intended to ascertain a possible correlation between different types of sensitivities. Choosing the desired method of analysis is realized by means of clicking the corresponding bookmark in the **Analysis** window – **Fig. 9**.



Material Name	Method	State	Size, micron	t, °C	Densit g/cc	R.A. #	Weigh kg	H, m	E, J	%	Insens	Crit. Pres. Init., MPa
Diazodinitrophenol	Picatinny Arsenal Apparatus	Solid		25			2	0.1016	2	10		
	Picatinny Arsenal Apparatus	Solid		25			0.453	0.1778	0.79	10		
	Fallhammer Test BAM - UN Test	Solid		25			1	0.15	1.5	16.67		
	Russian Impact Test K- 44-I	Solid		25			0.4	0.175	0.686	4		
								0.4	1.57	100		
Bis(2-difluoroamine-2,2-dinitroethyle)ni	Critical Pressure Impact Test	Solid		25		No 2	10					320
	Method of Failing Shells	Solid	<100	25								430
Bis(2-fluoro-2,2-dinitroethyl)difluoroforr	Russsian Impact Test K-44-II / UN Test 3(a) (vi)	Liquid		25		No 4	10	2.25	220.7	50		
1,8-Difluoro-1,1,3,6,8,8-hexanitro-3,6-	Critical Pressure Impact Test	Solid		25		No 2	10					530
Picramic Acid; 2-Amino-4,6-dinitrophenol	Fallhammer Test BAM - UN Test 3(a) (ii)	Solid		25			5	0.7	34	16.67		
1,3-Dinitrobenzene; m-Dinitrobenzene	Fallhammer Test BAM - UN Test 3(a) (ii)	Solid		25			10	0.4	39	16.67		
1-Chloro-2,4-dinitrobenzene; Dinitrochlorobenzene	Fallhammer Test BAM - UN Test 3(a) (ii)	Solid		25			10	0.5	50	0		

Fig. 8. Brief Details Window

Report generation, data export and import

Database HAZARD is equipped with special tools for exporting and importing data. Besides, flexible opportunities to generate reports on the results of database session are the build-in implement of the DB. The report may contain information selected by the user and is saved to hard disk as an html-format file.

APPLICATIONS

Database HAZARD may be used as a manual on sensitivity characteristics and properties of individual explosives, double-base and composite propellants, explosive mixtures, as well as a powerful analytical tool for solving different problems on designing devices that use EM. It may be also very useful in educational and scientific areas.

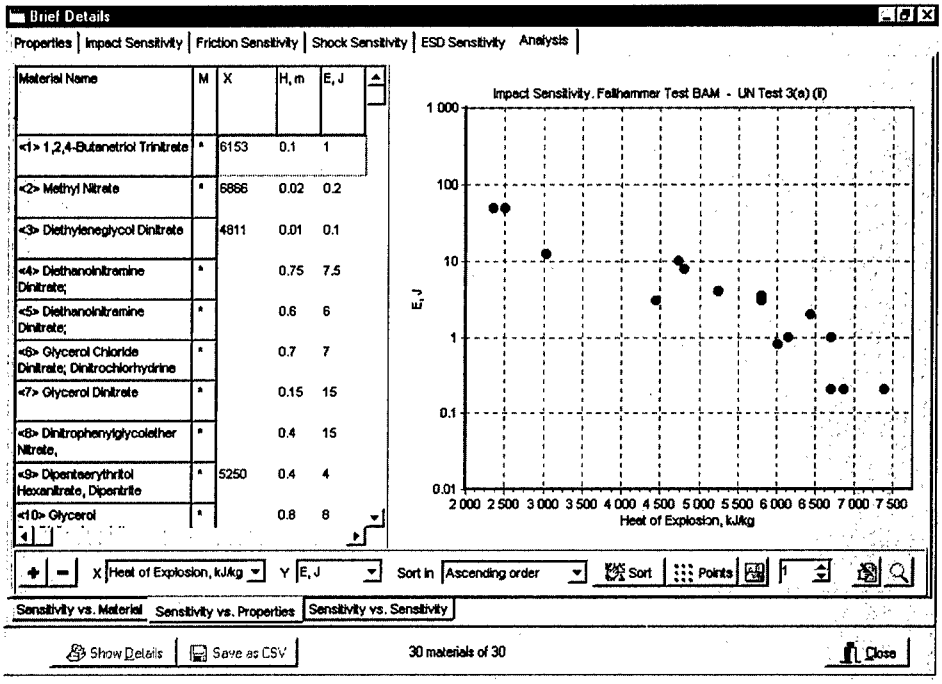


Fig. 9. Analysis Window

ACKNOWLEDGEMENT

This work was performed under contract No DAAD17-99-M-0020. Dr. Rose Pecse-Rodriguez is greatly acknowledged for coordinating the work.

REFERENCES

1. A.E.Fogelzang, V.V.Serushkin, V.P.Sinditskii, V.Y.Egorshev, Yu.K.Shchipin, V.A.Tropynin, Combustion and Properties of Energetic Materials Database - the Second Issue, AIAA Paper 98-0451, 1998.

2. G.V. Belov, "REAL - Thermodynamic Examination of Combustion Products Under High Pressure," *Proceeding of 28th International Annual Conference of ICT*, Karlsruhe, FRG, 24-27 June, 1997, paper 70, pp.1-12.

INVESTIGATION OF CHEMICAL AND CATALYTICAL ACTIVITY OF FINE METAL POWDERS

E.E. SIROTKINA, N.S. KOBOTAEVA, N.V. SVAROVSKAYA,
AND T.S. SKOROHODOVA

Institute of Petroleum Chemistry, Russian Academy of Science, 634055, Tomsk, Russia

V.S. SEDOI

Institute of High Current Electronics, Russian Academy of Science, 634055 Tomsk, Russia,

Abstract

It is known that fine metal powders produced by the method of exploding wires have enhanced activity. This aspect has received attention. The present paper is aimed to study physicochemical properties and reactivity of the copper, cobalt, and indium powders produced by the exploding wire and evaporation-condensation methods.

The chemical activity was studied in reactions: synthesis of metals acetylacetonates, synthesis of metal phthalocyanines, synthesis of metal tetraphenylporphins.

Oxidation of isopropylbenzene with a metal powder was used to determine the catalytic activity of powders.

The following research methods were applied: electron paramagnetic resonance, chromatography, and microcalorimetry.

It has been shown that the chemical reactions no observed previously for materials in compact form are implemented:

Interaction between the indium nanopowder and boiling acetic acid. In this case indium acetate is formed in 3-5 min. yielding up to 100 %.

The copper nanopowders produced in surroundings of nitrogen, argon, and xenon react easy with boiling acetylacetone (137 °C) yielding copper acetylacetonate of 90–95 %. A powder produced by evaporation – condensation method (yield reaches 63 %) was the less active.

1. Introduction

It is known that nanosized powders (NP) produced by the method of electrical explosion of wires in inert environment have enhanced activity. Thus synthesis of complex compounds (phthalocyanines and tetraphenylporphines) with NP of copper and indium proceeds under

milder conditions (at room temperature and atmospheric pressure) compared to traditional synthesis using metal salts [1, 2].

Reasonable ordinary chemical reactions allowed to control the course of reaction by the use of physicochemical methods (microcalorimetry, electron spectroscopy) are necessary for estimation of the reactivity of metal NP and its accordance to the NP production methods and conditions. It is desirable also that the reaction courses have great distinctions both for various NP and for coarse metal powders.

2. Synthesis of metal acetilacetonates

Following a number of experiments the reactions of copper with mild organic acids (acetic acid, acetylacetone) were chosen as ones of this kind. It is known [3] that acetic acid interacts with metallic copper in the presence of oxidizers or atmospheric oxygen and forms base acetate with the equation (1):

$$2\ Cu + 2\ CH_3COOH + O_2 \rightarrow Cu(CH_3COO)_2 \cdot Cu(OH)_2. \qquad (1)$$

The reaction is rather ordinary and proceeds up to completion under mild heat. Formed based copper acetate (II) has well-defined absorption band with λ_{max} = 645 nm in electron spectrum, allowing to control the reaction course by spectrophotometer.

All investigated copper NP react with acetic acid yielding basic copper acetate (Table 1).

Table 1. Conditions of production and physicochemical properties of the copper NP

Sample	Medium & method	Specific surface S	T_1, °C	T_2, °C	Q, J
Cu7	Nitrogen EW	7,8	20	?	2,52
Cu8	– " –	8,7	90	140	2,71
Cu16-2	– " –	>4	40	150	2,73
Cu18-2	– " –	9,7	20	80	1,58
Cu19	– " –	5,6	90	105	2,92
Cu13	Argon EW	2,2	60	120	2,16
Cu11	Xenon EW	6,0	105	160	3,18
Chem. reagent			- " -		1,33

T_1 is a reaction time with acetylacetonate, T_2 is a reaction time with acetic acid, *and* Q is a heat released in the reaction of 1 mg of copper with an excess of acetic acid. S is the area of specific surface of powder, m^2/g.

The reaction time is varied for powders produced by varying methods. Investigation of this reaction by the method of microcalorimetry emerges also distinctions in formation heats of based copper acetate even for copper NPs produced by the exploding wire (EW) method under various conditions.

Acetylacetone involving hydrogen atom replaceable in its enole form by metal and carbonyl oxygen locking the chelate ring can be assigned to organic acids milder than acetic one.

It is known that Cu (II) reacts readily with acetylacetone forming acetylacetonate of copper (II), Cu $(AA)_2$, which are exhibited as needle-shaped blue crystals. There is not an information about reaction between acetylacetone and copper to zeroth power of oxidation in literature. As a rule, Cu $(AA)_2$ is formed from acetates or carbonates of Cu (II) [4]. On boiling copper NP (chemical) with acetylacetone the powder is no dissolved distinctly.

In electron absorption spectra for reaction mixture a widespread intense band is within region 400 – 500 nm with an arm in region ~ 640 nm. Trace amounts of Cu $(AA)_2$ recorded by electron spectra can be occurred on Cu $(AA)_2$ formation from hydrocarbonate film coating a surface of copper. Copper NP produced by the method of evaporation – condensation (EC) reacts in a similar way.

The electroexplosive copper NP under the same conditions within ~ 0.5 – 5 min forms at the bottom a green solution with a reddish-brown trace amount identified by the complex formation reaction with ammonia (formation of blue crystals of the complex salt of $CuNH_4OH$) as cuprous oxide. In time, from this solution blue needles precipitate with a characteristic absorption band at 640 nm identifying that as Cu $(AA)_2$. The conditions of the reaction are shown in Table 1. Cu 18 (2) and Cu 7 exhibit a high reactivity as in reaction with acetic acid.

Attempts to bind a chemical activity of the copper NP with its physical properties have failed. But electroexplosive Cu NP reacts readily when compact copper is inert. It is supposable that this NP is like molecules in behavior. The last hypothesis is supported by complexation reaction of free base of tetraphenylporphin (TPP) with copper NP produced by the EW method.

3. Synthesis of metal tetraphenylporfins

Synthesis of complex compounds of porphyrins is based on complexation reaction with salts, namely, carbonyls or metal oxides in various organic solvents [6]. A mechanism of these reactions implies that a system porphyrin – salt reacts bimolecularly in one stage and following its transition state (2):

$$H_2P + \{MX_2S_{n-2}\} \rightarrow \{H_2P \cdot MX_2S_{n-4}\} + 2S, \qquad (2)$$

where H_2P is a free base of porphyrin, M is a metal, X is an anion, S is a solvent, and n is a charge, that is turned into a metalloporphyrin after removing $2H^+$.

In transition state by activation, a loss of two molecules of a solvent from coordination range of a salt [MX_2S_{n-2}] and stretch of all tearing bonds N–H_2, M–X, and M–S occur [6]. Copper tetraphenylporphin can be produced using the electroexplosive copper NP in one of solvents of clearly defined electron-donor or electron-acceptor nature as pyridine, nitrobenzene or dimethylformamide. Synthesis of Cu TPP occurs in each solvent with various rates.

Probably, severe acceptor nitrobenzene drawing off to itself an electron density of the Cu NP and forming a charged complex acts onto unstable structure of Cu NP. Charge structure of copper substitutes partially hydrogen in porphyrin-ligand, and copper TPP is formed. The reaction time is 5 min. Severe electron donor pyridine forms a complex when transferring a charge with porphyrin-ligand drawing off a proton to itself and vacating place for copper atom. The reaction time is 10 min. Dimethylformamide is weaker proton-acceptor. The reaction time is 20 min.

Synthesis of copper TPP using the electroexplosive Cu NP in chloroform has been performed to compare. No reaction goes really, copper TPP is formed as traces.

Reaction of Cu TPP formation uses the Cu electroexplosive nanopowder needs in finishing. High reactivity of copper and cobalt nanopowders in studied reactions allows one to suppose also their catalytic activity.

4. Oxidation of isopropylbenzene

Catalytic activity of the metal nanopowders was investigated in the model reaction of isopropyl-benzene (IPB) [6]. Cu nanopowders produced by the EW method in argon and nitrogen atmosphere and by the EC method in argon, nitrogen and CO_2 were taken for investigation. In Table 2 some properties of Cu NP are given.

Oxidation of IPB was performed on the gasometric setup [7]. 0.07 mole of IPB as added up to 0.35–0.5 % by mass of Cu NP, was introduced into the reactor. The experiment temperature was varied in the range of 30-60 °C. Because of a low activity of copper produced in argon by the EC method an oxidation was achieved adding azoisobutyronitril (AIBN) as the initiator.

Table 2. Conditions of production and some properties of copper NP

Method, sample, surroundings	Specific surface, m^2/g	Composition, %
EW, Cu8, nitrogen	8,7	85%Cu, 10% Cu_2O, 3,1% CuO
EW, Cu13, argon		
EC, nitrogen		
EC, argon		
EC, CO_2		

Liquid products of the reaction were analyzed by the GLC (gas-liquid chromatography) method under conditions of temperature programming as follows: initial temperature of the thermostat was 80 °C, its elevation was conducted with rate 3 °C/min, final temperature was 180 °C. Helium has been carrier gas. The calculations were performed using n-hexane as the standard.

Table 3.Influence of temperature and amount of copper NP produced by various methods on process of oxidation of IPB

Sample	Mass *m*, %	*T*, °C	AP yielding, mass %	DMPC yielding, mass %	*W*, %	*V***, %
EW, Cu8	0,35	30	0,031	0,09	0,12	4,85
EW, Cu8	0,35	45	0,07	0,61	0,68	9,48
EW, Cu8	0,35	60	No analyzed		–	9,79
EW, Cu8	0,5	60	No analyzed		–	9,83
EW, Cu13	0,5	60	0,2	0,33	0,53	9,36
EC, argon	0,5	30	No process goes			
EC, argon	0,5	45	Trace amount		–	0,76
EC, argon*	0,5	45	0,06	0,1	0,16	1,99
EC, argon*	0,5	60	0,04	0,19	0,20	6,18
AIBN	–	60	–	–	–	2,60

* – Process was performed in the presence of initiator AIBN,
** – Body of absorbed oxygen, W is the conversion of IPB.

Temperature and copper amount influence and an effect of conditions of production of copper nanopowders on oxidation process of IPB were also studied. An efficiency of one powder type or another follows from the rate of oxygen absorption by IPB in combination with copper NP as compared with the rate of that by IPB with AIBN. Data for influence of temperature and amount of copper nanopowders are given in Table 3 and in Figures 1 and 2. Acetophenone (AP) and dimethylphenylcarbinol (DMPC) have been identified in products of isopropylbenzene oxidation.

Copper NP Cu8 shows a catalytic activity even at $T = 30$ °C and 0.35 % of total copper mass (see Table 3). With increasing temperature a rate of oxygen absorption and a conversion of IPB increase. When Cu NP ($m = 0.5$ % by mass) produced by EC method in argon using, IPB is not oxidizing at 30 °C. With increasing temperature up to 45 °C the process occurred at a low rate of oxygen absorption and the reaction products were found in trace amounts. To initiate the oxidation process the reaction has been carried out in the presence of the radical initiator AIBN. It should be noted that AIBN initiates the IPB oxidation at $T = 60$ °C and with Cu NP at 45 °C.

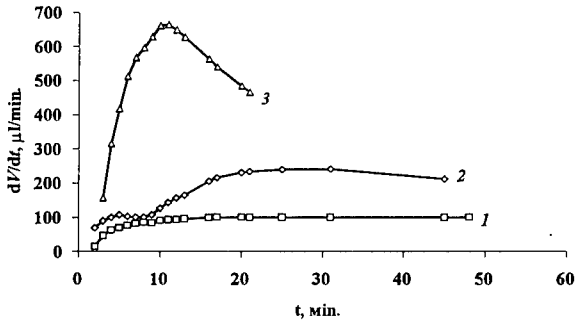


Fig. 1 Kinetic curves for IPB oxidation in the presence of 0.35 % of mass of Cu 8 NP at various temperatures: *1* – 30 °C, *2* – 45 °C, and *3* – 60°C.

With increase in temperature up to 60 °C a rate of oxygen absorption and conversion of IPB increase. Thus, it has been clarified that increasing of temperature and amount of copper NP results in a rate of oxygen absorption for all investigated powders.

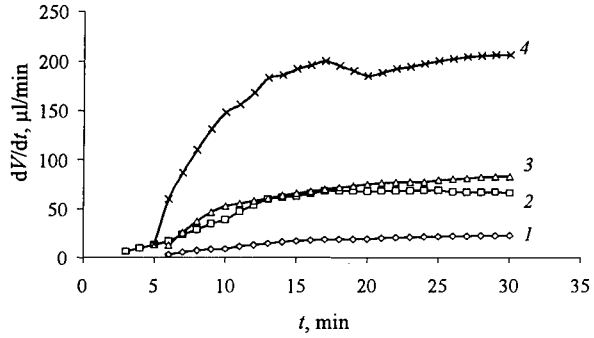


Fig. 2. Kinetic curves for absorption of IPB oxygen in the presence of copper NP produced by the EC method: *1* – Cu (Ar), 45 °C; *2* – Cu (Ar), AIBN, 45 °C; *3* – IPB + AIBN, 60 °C; *4* – Cu (Ar), AIBN (T = 60 °C, Cu mass is 0.5 % of total mass)

Table 4. Influence of the conditions of EC Cu NP production on the oxidation process of IPB at 60 °C with Cu mass = 0.5 %.

Surroundings	AP yield, mass %	DMPC yield, mass %	W, %	$V(O_2)$, ml
Argon	Trace amount		–	0,8
CO_2	No oxidation			
Argon*	0,04	0,19	0,2	6,18
CO_2 *	Trace amount		–	4,96
Nitrogen	0,055	0,31	0,395	7,56

*– Process proceeded in the presence of the AIBN initiator.

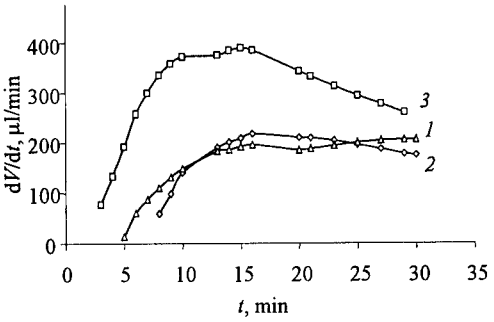


Fig. 3. Kinetic curves for IPB oxidation in the presence of Cu NP produced by the EC method (T = 60°C, Cu mass is 0.5 %) *1* – Cu (Ar), *2* – Cu (CO_2) + AIBN, *3* – Cu (N_2)

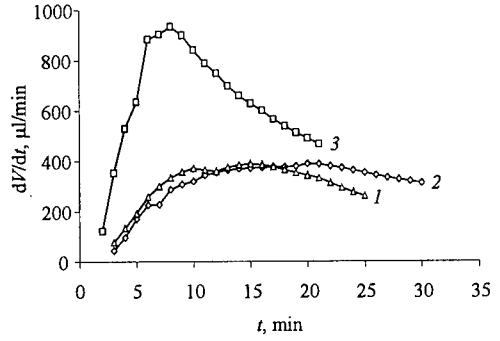


Fig. 4. Kinetic curves for oxidation of IPB in the presence of copper NP (T = 60 °C, Cu mass is 0.5 % of total mass): *1* – Cu (N_2), EC method; *2* – Cu 13 (Ar), EW method; *3* – Cu 8 (N_2)

It was of interest to compare activities of copper NP, produced by the EW and EC methods according to production medium in model oxidation reaction of IPB under the identical conditions. There are investigation results in Table 4 and in Fig. 3.

Of copper NP produced by the EC method the Cu nanopowder produced in nitrogen surroundings is most active one (Table 4). The electroexplosive NP produced from Cu 8 in nitrogen surroundings has the highest activity in oxidation reaction of IPB.

The cobalt nanopowder produced by EW method in nitrogen surroundings (S_{spec} = 8.3 m^2/g) has the similar behavior (Fig. 5). In the presence of this NP the reaction proceeds with a high rate but after 5–10 min a rate of oxygen absorption decreases already and a catalyze loses irreversibly its activity. An attempt to regenerate the catalyze washing out with various solutions has failed. As the X-ray diffraction and thermogravimetric analyses shown, no oxidation of CO NP under the reaction condition proceeded.

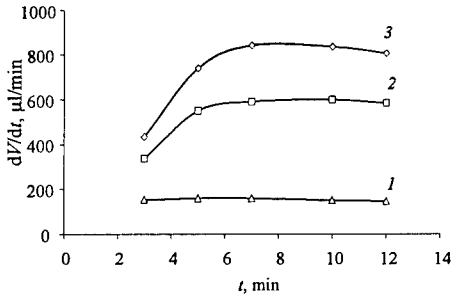


Fig. 5. Kinetic curves for oxidation of IPB in the presence of Co NP at various temperature (Co NP mass = 0.15 % of total that): *1* – T = 30 °C, *2* – 45 °C, *3* – 60 °C

It remains unclarified, why NP of Cu and Co fast lose their catalytic activity and what kind of oxidation mechanism of IPB in the presence of NP. This matter is the purpose for further investigation.

In study of reactivity, important data to solve both fundamental problems and applied that are received. The nanopowders have a unique reactivity.

Acknowledgement

This work was performed with support in part under Russian Foundation for Basic Research (grant 01-03-32027) and NATO Collaborative Linkage Grant No. 976783.

REFERENCES

1. E.E. Sirotkina, T.A. Fedushchak. The method of preparation of copper phthalocyanine in polymorphous form / Patent RF 2087475. BI No 23. – 1997.
2. E.E. Sirotkina, N.S. Kobotaeva, N.V. Svarovskaya, V.S. Sedoi. The method of production of indiumacetate tetraphenylporphin / Patent RF 2157373. BI No 28. – 2000.
3. Ripan R., Chetyanu I. Inorganic chemistry. Vol. 2. Metal chemistry. – M.: Mir, 1972. – 692 p.
4. Grinberg A.A. Introduction into chemistry of complex compounds. – M.: Goskhimizdat, 1957. – 385 p.
5. Berezin B.D., Lomova T.N. // Koordinatsionnaya khimia. 1993. – Vol. 19, No 3.
6. Berezin B.D. Coordination compounds of porphyrins and phthalocyanines. – M.: Nauka, 1978. – 28 p.
7. Emanuel N.M., Gladyshev G.P., Denisov E.P. Procedure of testing of chemical compounds as stabilizers for polymer materials. – Chernogolovka, 1986. – 76 p. (Preprint).

CHARACTERIZATION OF ULTRA-FINE POWDERS PRODUCED BY THE EXPLODING WIRE METHOD

V.S. SEDOI AND V.V. VALEVICH

Institute of High Current Electronics RAS, 634055 Tomsk, Russia

Abstract

This paper presents a new approach to the producing powders by the exploding wire method. The influence of initial conditions on the properties of powders is discussed. The basic factors are as follows: the level and the uniformity of the energy, dissipated in the exploding wire metal; the density and the chemical activity of surrounding gas; the initial radius of wire. The Electron Microscopes (Transmission and Scanning) and the Surface BET Method have been used for analyses. The production of ultra-fine powders based on such metals as *Al, W, Cu, Fe, Ag, Co, In, Pt* has been investigated.

Different surrounding passive gases (nitrogen, argon, xenon, and helium) were used for producing powders of pure metals. Samples were studied by chemical methods. The X-ray Diffraction and the Electron Diffraction methods were used for determination of the phase compositions. Characterization included also the Differential Scanning Calorimetry and the Thermogravimetry in air or argon with the heating velocity of 5 and 10^0/min. The fresh powders and the old powders (with long time after performing) have been tested.

In summary, it was shown that exploding wire method allows producing ultra-fine powders of various metals. The results obtained can be applied directly to the production of powders with specify characteristics. In any cases powders are of high activity.

1 Introduction

Compared to other methods of vaporization, the electrical explosion of wires has the advantage of the direct conversion of electrical energy into heat. It is well known, that the heating level, the uniformity of heat, and the pressure and type of the surrounding gas (inert or active) are the most important factors in the formation of particles, irrespective of the heating mode. Depending on the explosion conditions, the products can be in liquid, vapor-droplet, vapor, or vapor-plasma state. The velocity of expansion of the wire material and its temperature may exceed 1000 m/s and 10,000 K, respectively. When the input energy is of the

order of the sublimation energy, nanosized powders with the particle diameter below 100 nm are formed.

On the other hand, the physicochemical properties of nanophase materials and their behavior in chemical reactions and under physical actions essentially depend on the size of particles [1]. A limitation of the exploding wire method is that a distribution of powder sizes may be too wide and contain some amount of large particles [2].

The goal of the present work is to study the physical mechanism of the formation of powders and to investigate their physico-chemical properties. From the above it should be clear that particle formation is a complex process. Under specific conditions it is possible to produce the powder having narrow particle size distribution and small mass of large-sized fraction. Research along this line is both of scientific and engineering interest.

2 Production of ultra-fine powders by the electrical explosion of wires

2.1 Particle sizes and the specific energy input

The energy introduced in an exploding wire is one of the most important parameters. It is clear that the mean particle size d and the particle size distribution function will vary with increasing the energy introduced. This has been demonstrated by a number of researchers [3,4]. For low input energies, the particle size distribution function has a maximum in the range $10^{-7} - 10^{-6}$ m and the particles are formed from liquid drops. For higher input energy densities w the distribution has a single maximum which shifts to smaller sizes with increasing w/w_s (w_s is the sublimation energy). In this case, the particles are formed from the vapor phase prevail.

Figure 1 presents the particle diameter as a function of the energy, $d = f(w/w_s)$, constructed from the data's given by a variety of pu' lications. The above function has two distinct regions. There is no clear boundary between these regions. In the first region, the particle diameter varies by more than an order of magnitude while the energy content only doubles. This is related to the liquid-drop-to-condensation transition in the mechanism for the particle formation.

In the second region, particles are formed only on the condensation nuclei. It should be additionally mentioned that in the input energy density range $w/w_s \geq 1 \div 2$, the condensation centers are ions. An increase in input energy density results in an increase in the ions and in the expansion velocity. This leads to a decrease in the final size of the particles.

Magnetohydrodynamic calculations [5] show that even with w/w_s = 1 inner layers in the material wire change from liquid to plasma state during explosion. But in this region the particle sizes are variable and the distribution can have two maximums. The uniformity of the energy across the wire radius and length also play an important role.

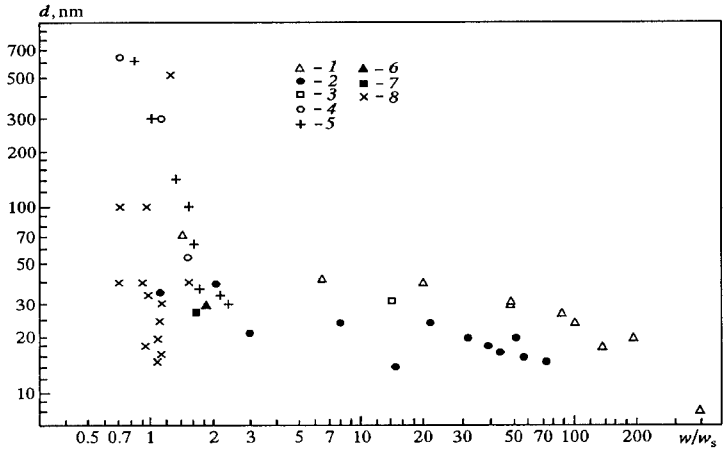


Figure 1. Particle diameter versus w/w_s. *1*, *2*, *3* from Ref. 3: *1* is count median diameter (CMD), Ag in air (Phalen); *2* – Cu in air, crystal size (Barkov); *3* – CMD for Cu in air (Vomela and Whytby); *4* – CMD for W in air; *5* – CMD for Cu in air; *6* – CMD for W in air; *8* – surface median diameter for Al in air.

2.2 The region of uniform heating

An electrical explosion of wires can be accompanied by various processes leading to a nonuniform current distribution over the wire length l and radius r. These are the breakdown of the liquid metal into drops under the action of surface tension forces, the development of magnetohydrodynamic (MHD) instabilities, the current skinning. The nonuniform heating leads to the powder polydispersion: the size distribution of the particles can have a several maximums (e.g., in the size regions below 10 nm, 10-100 nm, and over 0.1 μm).

The processes under consideration can influence the wire heating if their characteristic times compared with the Joule heating time in the order of magnitude. The heating time t_h can be evaluated if the heating current density is known, and the notion of "integral of specific current action" $h = \int j^2 dt \approx j^2 t$ [6, 7] is used:

$$t_h \approx h/j^2. \qquad (1)$$

The time of the action of capillary forces is $t_c = \gamma r^3/\alpha)^{0.5}$; the MHD instabilities develop within the time $t_{MHD} = 6(\gamma r^2/H^2_0)^{0.5}$; the current skinning time is $t_{sk} = \mu_0 r^2/\rho$, where γ is the density of the liquid wire, α is the coefficient of surface tension, H_0 is the magnetic field on the wire surface, μ_0 is the magnetic constant, and ρ is the resistivity.

For the condition where the characteristic time for a given process is of the order of the heating time (1), it should be expected that the Joule heating would be nonuniform. To compare these times, the corresponding similarity criteria can be formulated [7]:

$$\tau_c=(\gamma/\alpha)^{0.5} j^2 r^{1.5}/h_1, \quad (2)$$

$$\tau_{MHD}=12\gamma^{0.5} j/h_1 \quad (3)$$

$$\tau_{sk}=\mu_0 j^2 r^2/(\rho h_1). \quad (4)$$

Here, h_1 is the integral of specific current action corresponding to the material heating from the melting point to the onset of the explosion as such. From criteria (2)-(4) it can be seen that the current density j and the wire radius r are essential factors in the explosion of a given metal. In Fig. 2 the regions of uniform heating are shown. The capillary and MHD instabilities are effective below the j_c and j_{MHD} curves, respectively, and the current is skinned above the j_{sk} curves. In Fig. 2, the region of uniform heating of Al wires is crosshatched. Here, wire is not divided into drops by constrictions and the powder fineness becomes significantly higher because a number of the particles in size of more than 100 nm decrease. Preliminary investigations implemented at the Institute of High Current Electronics confirm this fact [8].

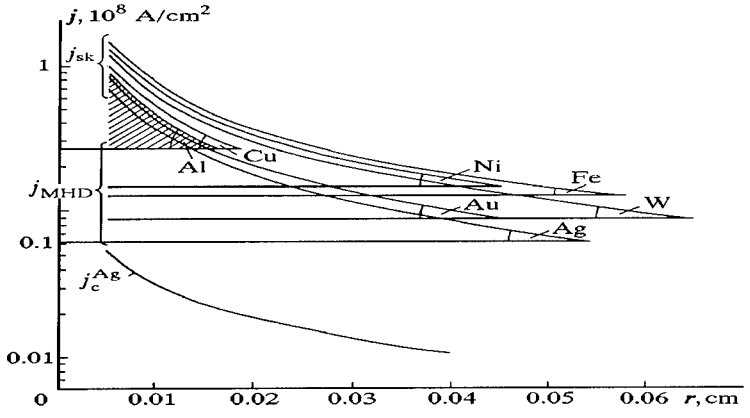


Figure 2. Conditions of uniform heating for various metals.

2.3 Effect of the current density on the powder fineness

As seen from criteria (2)-(4) and Figure 2, the current density j defines a uniformity of Joule heating and is essential factor for the powder production. If $j < j_{MHD}$ the sausage-type MHD instabilities develop and the wire is divided into drops along its length.

In Table 1, the data for the indium and aluminum powders with various specific energy introduced, w/w_s, and current density, j/j_{MHD}, are given as an example. Here, the powder fineness is characterized by the magnitude of the specific surface area, S. From Table 1, it can be seen that to control only the thermal energy introduced is deficient, and the current density is also significant factor. For instance, with equal introduced energies ($w/w_s = 0.8$), the specific surface area is more for the powder produced at the higher current density (see NN. 2 and 3 for In and NN. 5, 6 for Al powders). The uniform Joule heating allows producing powder with a higher fineness with lower energy expenditure (No 1 and No 3).

Table 1. Action of the current density on a fineness of the powder

No	Metal	w/w_s	j/j_{mhd}	S, m^2/g
1	Indium	0.6	1.33	3.6
2	- „ -	0.8	1.33	4.5
3	- „ -	0.8	0.47	3.0
4	- „ -	0.9	2.45	5.8
5	Aluminum	0.8	1.4	26
6	- „ -	0.8	1.0	14

2.4 Synthesis of ultra-fine metal powders in a low-pressure gas

G.P. Glazunov and others [9] investigated the formation of powders by the electrical explosion in an inert elevated-pressure gas, P = 1-600 atm. It has been shown that as a gas pressure increases, the medium size of the particles is increased and the function of the size distribution becomes wider. With decreasing of a surrounding gas density, a decrease of size of particles produced and narrower their size distribution can be expected.

Wire during the electrical explosion has some time-varying impedance and a time-varying voltage is applied to the gap with wire when the current passes. The electrical strength of a surrounding gas is bound to provide the required heat energy density in the wire. Otherwise, a discharge will develop within the gas shunting the wire and restricting its heating.

The experiments were implemented in the absence of the shunting discharge and the control was performed by the current oscillograms. To exclude an influence of heat effects of chemical reactions, inert gases and nitrogen were used (as shown below, molecular nitrogen is

inert at the lower pressure). In Table 2 and 3, the results are given; here, S is the specific surface area determined by the BET. An influence of the introduced energy density (the particle size is more for the lesser energy) and that of density of the surrounding medium (the particle size decreases with decreasing of the gas density, other factors being the same), are seen. Using of low-pressure nitrogen has allowed decreasing the particle size.

Table 2. Results of analyses for the copper powders

No	w/w_s	Gas	S, m^2/g
1	0.8	N_2	7.8
2	0.8	Ar	6.2
3	0.8	Xe+He	5,8
4	1.0	N_2	8.9
5	1.0	Ar+He	6.3
6	1.0	Xe+He	6.0

Table 3. Results of analyses for the aluminum powders

No	w/w_s	Gas	S, m^2/g	T, °C	Δm, %
1	0.75	N_2	22	520	5.5
2	0.75	Ar	18	516	9.8
3	0.75	Xe	9.3	525±3	14.3±1
4	1.0	N_2	24	516±3	19±4
5	1.0	Ar+He	-	523	15.8
6	1.0	Xe	16.1	530	16

2.4.1 Phase Analyses

A phase analysis of the samples was performed by the X-ray diffraction and electron diffraction methods. If the sample was produced in nitrogen, a quantity of fixed nitrogen was determined via decomposition of the sample in boiling sulfuric acid and in boiling concentrated alkali by the Kjeldal method.

The experiment [10] have shown that molecular nitrogen is chemically inert at lower pressure. Nitrides in the powders of investigated metals are either absent versus the pressure or found as a trace amount. Both the chemical and X-ray methods confirm this fact (see Figs. 3 and 4). As the figures suggest, the phase constitution is slightly depend on surroundings. The energy for dissociation of nitrogen molecule (53.7 kJ/mole) is far in excess of the sublimation energy of aluminum (18.8 kJ/mole). The synthesis of the nitride requires an additional activation. Disturbances in stoichiometric contents of nitrogen in the reaction region at the pressure reducing and a short time of the process are also of considerable importance.

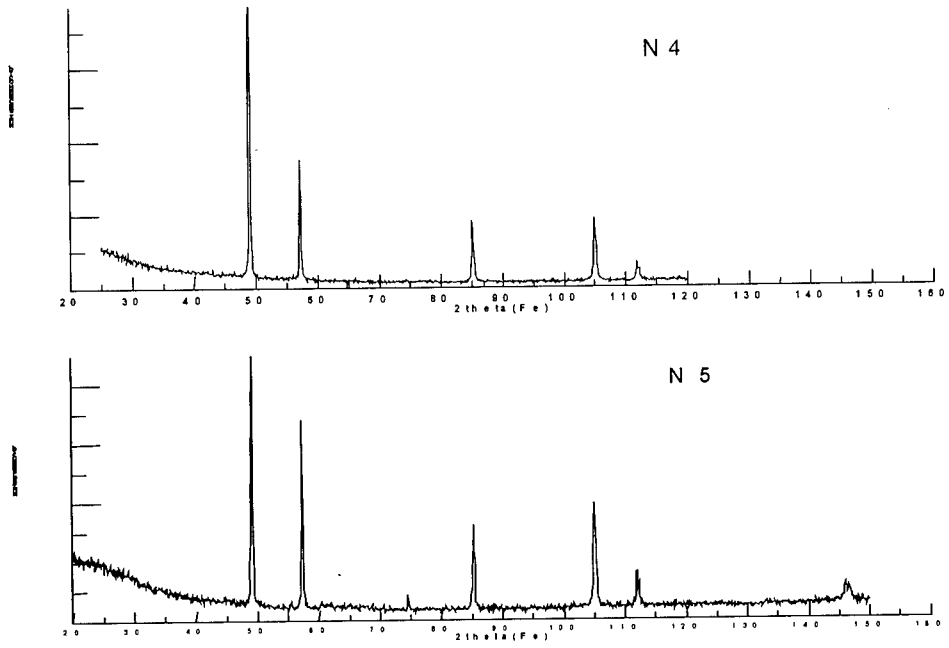


Figure 3. X-ray diffraction patterns for the Al powder (No.4 and No.5 in Table 3)

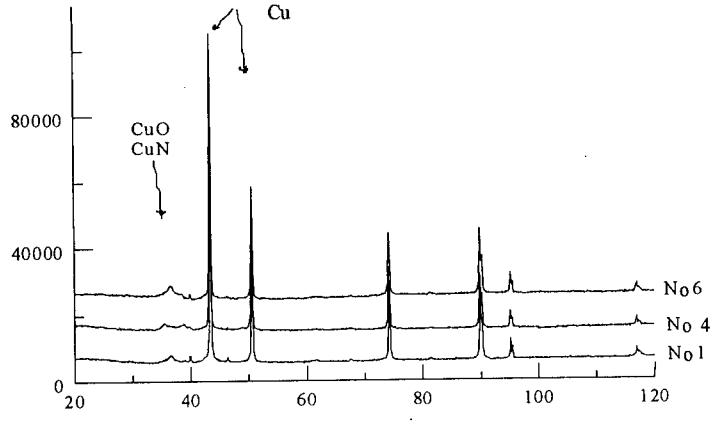


Figure 4. X-ray diffraction patterns of the copper powders (NoNo.1, 4, and 6Table 2);

2.4.2 Differential Thermal Analysis

To compare chemical activities of the powder samples, the differential thermal analysis (DTA) was used. In this analysis, magnitudes of the temperature of onset of intense oxidation, the temperature corresponding to peak of exothermic effect (Fig. 6), and enhancement of mass, Δm, when oxidizing before the melting point, have been compared.

The samples produced in nitrogen with the low density of the introduced energy denoted as No 1 in Table 3 begin intensely to oxidize at lower temperature compared to the samples produced in inert gases with the same energy density. On the other hand, a passivation of the samples produced with higher introduced energy density in nitrogen is observed. The powders produced in low-pressure gas are high active. It can be seen from comparison of the temperature corresponding to peak of exothermic effect (Fig. 6) - T_{peak} = 520 °C - with published analysis: 553 °C and 573 °C [11], 580 °C [12], 605 °C [13].

Another important question is the stability of the powder energetic characteristics during the time. Although this study is in progress, some results are presented in Table 4.

Table 4. The temperature of exopeak (T_{peak}) as a function of storage time (in months)

Sample	2	3	6	19	39
N60 (N_2)		520			530
N62 (Xe)		525±3			555
N95 (N_2)	550		520 (Fig. 6)	527	

3 Conclusion

A combined method of study of the metal nanopowders beginning from condition for production, investigation of their physico-chemical properties, and reactivity has allowed to formulate the conditions for the production and certification of the powders for various purposes.

The following results have been achieved.

The particle formation is a complex process dependent on several parameter such as the energy introduced into the wire, current density, and the ambient gas pressure. A detailed parametric study is necessary to optimize these variables.

The current density and radius of wire are essential factors in the electrical explosion. They determine a uniformity of Joule heating and a minimum size of the particles.

It has been first demonstrated that it is possible to produce powders of pure metals in nitrogen at low pressures. Nitrogen is a promising gas since it has a higher electric strength and a lower mass density than those of inert gases, and this allows one to increase the powder fineness, and that the metal powders produced in nitrogen exhibit a rather high and time-stable chemical activity.

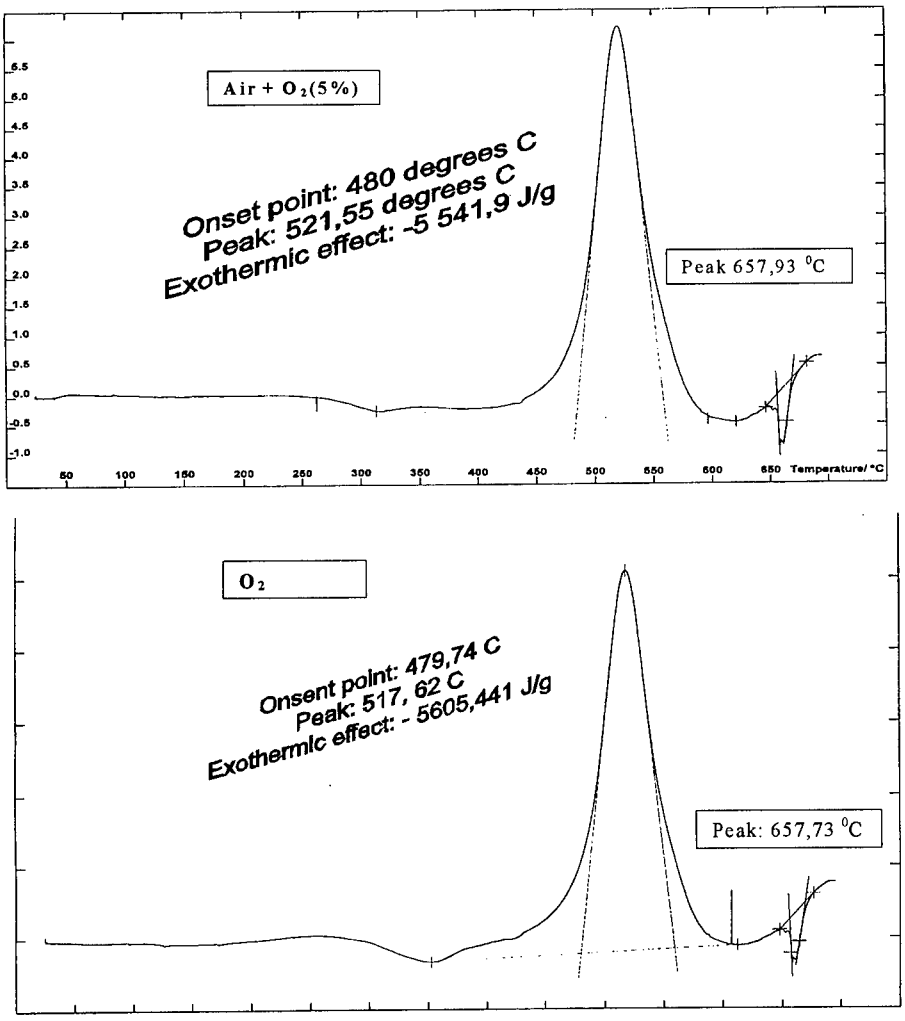


Figure 5. DTA of AL powder (S=18 m^2/g). Data's observed in DGA, France.

Acknowledgement

This work was performed with partial financial support under Russian Foundation for Basic Research (grant 01-03-32027) and NATO Collaborative Linkage Grant No. 976783. The authors would also like to thank researchers of Tomsk State University, Institute of Strength Physics and Material Sciences for performance of the X-ray analyses (Tomsk), and DGA, (France) for DTA tests.

References

1. V.N. Simonenko, V.E. Zarko. *Comparative studying the combustion behavior of composite propellants containing ultra fine aluminum.* Energetic materials, 30th Int. Annual Conf. of ICT, Karlsruhe, Germany, pp. 21(1-14).
2. S.G. Savage and O. Grinder. *Ultra-fine powder production methods: an overview.* Advances in powder metallurgy & particulate materials – 1992, volume 7, pp. 1-17.
3. R.F. Phalen. *Evaluation of an exploded-wire aerosol generator for use in inhalation studies.* Aerosol science, 1972, Vol. 3, pp. 395-406.
4. Yu.A. Kotov, N.A. Yavorsky. *Investigation of particles formed in the electrical explosion of wires*, Physics and Chemistry of the Material Treatment, no. 4, 1978, pp. 24-29.
5. V.V. Oreshkin, V.S. Sedoi, L.I. Chemezova. *A study of plasma of the exploding wires by MHD simulation method.* In: Research and application of plasmas (Proc.), Ed. by M. Sadovsky and H. Rothkaehl, Jarnoltovek near Opole (1997), Vol. 1, pp. 309-312.
6. G.W. Anderson and F.W. Neilson. *Use of the "Action Integral" in exploding wire studies".* Exploding Wires, Vol. 1, Chace and Moore, (eds.) New York: Plenum Press, 1959, pp. 97-103.
7. V.S. Sedoi, G.A. Mesyats, V.I. Oreshkin, V.V. Valevich, L.I. Chemezova. *The current density and the specific energy input in fast electrical explosion*, IEEE Transactions on Plasma Science, vol. 27, no. 4, 1999, pp. 845-850.
8. V.V. Valevich, V.S. Sedoi. *Production of the ultra-fine powders in the fast electrical explosion*, Russian Physics Journal, vol. 41, no. 6, 1998, pp. 70-76.
9. G.P. Glazunov, V.P. Kantzedal, L.A. Kornienko, N.A. Kosik, R.V. Mitin, A.P. Shevstusev. *Some properties of the dispersed powders produced by the electrical explosion of conductors in gas under the high pressure*, Voprosy Atomnoi Nauki i Tekhniki: Atomn. Materialovedenie, no. 1(1), 1978, pp. 21-24.
10. V.S. Sedoi and V.V. Valevich. *Obtaining of ultra-fine metal powders by the method of exploding wires in the low-pressure nitrogen*, Letters in J. of Tech. Phys., Vol. 25, No 14, July 1999, P.81-84.
11. G. Baudin, A. Lefrancois, D. Bergues, Y. Champion. *Combustion of nanophase aluminum in the detonation products of nitromethane.* 11th Symp. Int. on Detonation, Snowmass Village, Colorado, 1998.
12. M.M. Mench, C.L. Yeh, K.K. Kuo. *Propellant burning rate enhancement and thermal behavior of ultra-fine aluminum powders (ALEX).* Energetic materials. Production, Processing and Characterization. 29th Int. Annual Conf. of ICT. June 30-July 3, 1998, Karlsruhe, Federal Republic of Germany, pp. 30 (1-15).
13. Roland Sanden. *Characterization of electro-exploded aluminum (Alex).* Ref. 12, pp. 77-(1-10).

DETONATION BEHAVIOR OF EMULSION EXPLOSIVES

Yoshikazu Hirosaki, Kenji Murata, Yukio Kato

NOF Corporation

61-1 Kitakomatsudani, Taketoyo-cho, Chita-gun, Aichi 470-2398, JAPAN

and

Shigeru Itoh

Shock Wave and Condensed Matter Research Center, Kumamoto University

2-39-1 Kurokami, Kumamoto 860-8555, JAPAN

ABSTRACT

Ammonium nitrate - based industrial explosives show non-ideal detonation behavior. To study the effect of size and quantity of voids involved in heterogeneous explosives, some experiments have been carried out using emulsion explosives sensitized with plastic balloons of five different sizes ranging from 0.05mm to 2.42mm in the average diameter.

Detonation velocity and detonation pressure of the emulsion explosives containing plastic balloons of different size and quantity were determined for the charge diameter of 50mm. The explosives containing large (0.5mm or larger) balloon showed large difference between the measured and calculated detonation velocity and detonation pressure. The fraction of ammonium nitrate reacted in the reaction zone was estimated to be significantly low.

INTRODUCTION

Explosives for civil use, such as emulsion explosives or ANFO (Ammonium Nitrate-Fuel Oil), are usually ammonium nitrate (AN)-based. Those explosives are well known to show non-ideal detonation behavior due to its slow reaction rate compared to high explosives for military use. The "non-ideal" detonation wave propagates steadily but its characteristics are significantly affected by the conditions such as charge diameter and confinement. Detonation pressure and detonation velocity are much lower than those for infinite charge diameter. This behavior is depending on the long reaction zone length due to slow reaction rate of AN. Lateral rarefaction wave cools down the reaction zone and lower the reaction rate.

To study the effect of size and quantity of voids included in the heterogeneous explosive, the emulsion explosives were used because these explosives can be easily prepared by blending emulsion matrix and balloons to obtain desired explosive density. To study the detonation characteristics of the emulsion explosives, plastic balloons of various sizes were used as void material, whose average diameter is ranged from 0.05mm to 2.42mm.

EXPERIMENTALS

Samples

The formulation of the emulsion matrix used in this study is ammonium nitrate /sodium nitrate /water /wax and emulsifier = 77.66/4.68/11.22/5.40 in weight ratio. The oxygen balance of the emulsion matrix is 0.4g/100g, and the density of it is 1.39g/cm^3. A certain amount of plastic balloons of mono-cell or multi-cell structure shown in Table 1 were added into the emulsion matrix to achieve the desired explosive density. Five different sizes of balloons were used. PB-1 is the smallest balloon of mono-cell structure with the average diameter of 0.05mm, and others are the balloons of multi-cell structure with an average diameter ranging from 0.47 to 2.42mm.

Table 1 Characteristics of plastic balloons used in this study

	Average diameter (mm)	Standard deviation (mm)	Particle density (g/cm^3)	Structure	Material
PB-1	0.053	0.023	0.027	Mono-cell	Acrylonitrile / vinylidene chloride
PB-2	0.472	0.062	0.051	Multi-cell	Polystyrene
PB-3	0.795	0.129	0.077	Multi-cell	Polystyrene
PB-4	1.728	0.273	0.032	Multi-cell	Polystyrene
PB-5	2.420	0.403	0.064	Multi-cell	Polystyrene

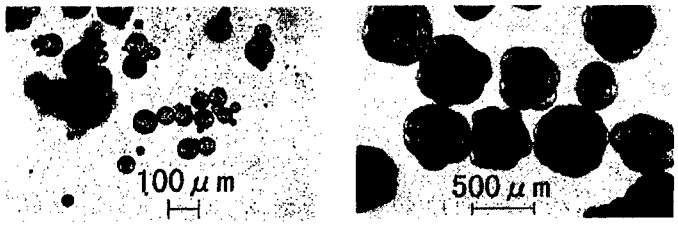


Fig.1 Microscopic photographs of plastic balloons PB-1 (left) and PB-2 (right)

Microscopic photographs of both structures are shown in Fig.1 as examples. The particle density of each balloon was determined from the densities of explosives that contain different amount of balloons. The size of balloon was optically measured.

Detonation Velocity Measurement

The emulsion explosive was loaded into a plastic film tube of 50mm in diameter and 300mm or longer in length. Steady detonation velocity was determined at 20°C by measuring the duration between the two ion gaps placed at the last part of the explosive with a distance of 100mm.

Detonation Pressure Measurement

The emulsion explosive loaded into PVC pipe of 51mm in inner diameter and 200mm in length was placed on a PMMA block as shown in Fig.2. A PVDF (polyvinylidenefluoride) film of 10 microns in thickness and 5mm squares was sandwiched with polyimide films together with electrodes made of copper foil. The PVDF gauge was put onto a PMMA block and then covered and glued with a PMMA plate of 1mm in thickness. The emulsion explosive loaded into a PVC (polyvinyl chloride) pipe (VP50) of 51mm in inner diameter, 60mm in outer diameter and 200mm in length was initiated with an electric detonator. Additional 30grams of emulsion explosive was also used as a booster explosive, if necessary. The output

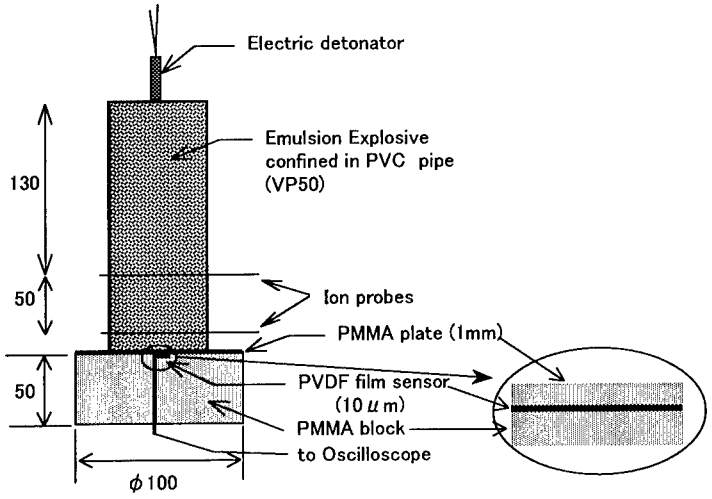


Fig.2 Experimental setup for detonation pressure measurements

of the pressure gauge was recorded with a digital oscilloscope at sampling interval of five nanoseconds. Calibration of PVDF pressure gauge was carried out by measuring electric charge created under hydraulic pressure and by comparing with the pressure measured with a manganin pressure gauge that has preliminary been calibrated. The pressure profile observed by PVDF pressure gauge is that transmitted into PMMA plate, which exists among the explosive and PVDF gauge.

Detonation velocity was also measured with ionization gaps that were placed at points 130mm and 180mm apart from the upper end of the charge.

RESULTS AND DISCUSSIONS

Detonation Velocity

Detonation velocity in the emulsion explosives of 50mm in diameter is shown in Fig.3. Voidage ϕ is void volume fraction in the explosive, and is defined as follows.

$$\phi = 1 - (\rho - \rho_B)/(\rho_E - \rho_B)$$

where, ρ, ρ_B and ρ_E are the densities of the explosive, plastic balloon and emulsion matrix respectively. The theoretical detonation velocity Dcj, calculated with a hydro-thermodynamic calculation code KHT, is also plotted in the figure for comparison. The plastic balloons were treated as reactive in the calculation. The emulsion explosives containing larger balloon present lower detonation velocity for the same explosive density. The emulsion explosives sensitized with the balloons of about 2mm in diameter give steady detonation velocity as low as 2500-3000 m/s at the voidage of 0.2-0.6. The detonation wave fails to propagate at higher voidage when the explosive contains voids of larger size. The fraction of AN reacted in the reaction zone was evaluated based on the measured and calculated detonation velocities. Ingredients other than AN were assumed to be 100 percent reactive in the calculation. The results are shown in Fig.4. The fraction of AN reacted in the reaction zone is as high as 80-90 % for the explosives sensitized with voids of 0.05mm at the voidage of 0.1-0.3. On the other hand, the fraction of AN reacted is as low as 30% or lower for the large voids of 2.42mm at the voidage of 0.2-0.3. It is considered that such poor reactivity of AN produces less energy in the reaction zone that leads longer reaction zone length.

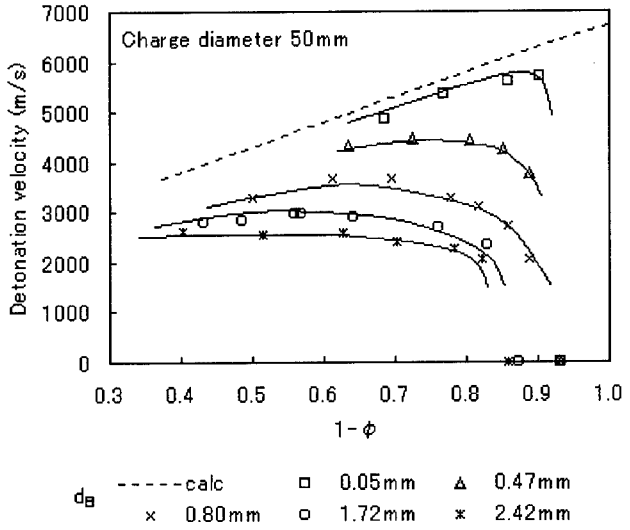


Fig.3 Detonation velocity of emulsion explosives sensitized with various size and quantity of plastic balloons. Voidage ϕ of zero refers to the emulsion matrix of density 1.39g/cm^3.

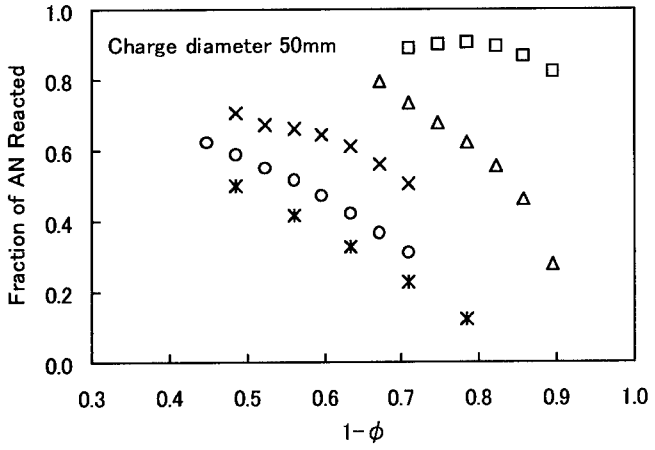


Fig. 4 Fraction of ammonium nitrate reacted in the reaction zone for the explosive of 50mm in diameter. The symbols are the same as those in Fig.3.

Detonation Pressure

The Effect of Void Size on Detonation Pressure

Fig.5 indicates pressure profiles observed for the emulsion explosives of density 1.05g/cm^3 (voidage 0.25) sensitized with balloons of five different sizes. The pressure rises up sharply to reach its peak pressure within about 75 nanoseconds in the explosives sensitized with balloons smaller than 1mm in diameter: PB-1, PB-2 and PB-3. The pressure rise time of about 75 nanoseconds can be explained by the detonation front curvature measured by optical observation [1] and shock transition time in PVDF film of 10 microns thick. Pressure decrease in the reaction zone behind leading shock and following decay in Taylor wave can be observed in the explosives sensitized with balloons PB-1 and PB-2. Whereas the explosive sensitized with larger balloons such as PB-4 or PB-5 requires longer time to reach its peak pressure. This is probably due to important irregularity of detonation front of the explosive that contains large balloons. The peak pressure is fairly low compared with that for smaller balloons. The pressure observed in this experiment is that transmitted into PMMA plate of 1mm in thickness. The pressure of detonation products, namely the detonation pressure was therefore determined from

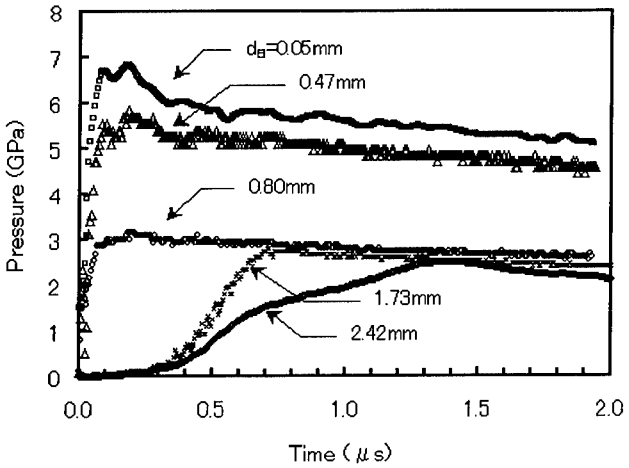


Fig.5 Pressure-time curves observed with PVDF gauge for the detonation of emulsion explosives of density 1.05g/cm^3 (voidage of 0.25) sensitized with various balloon sizes

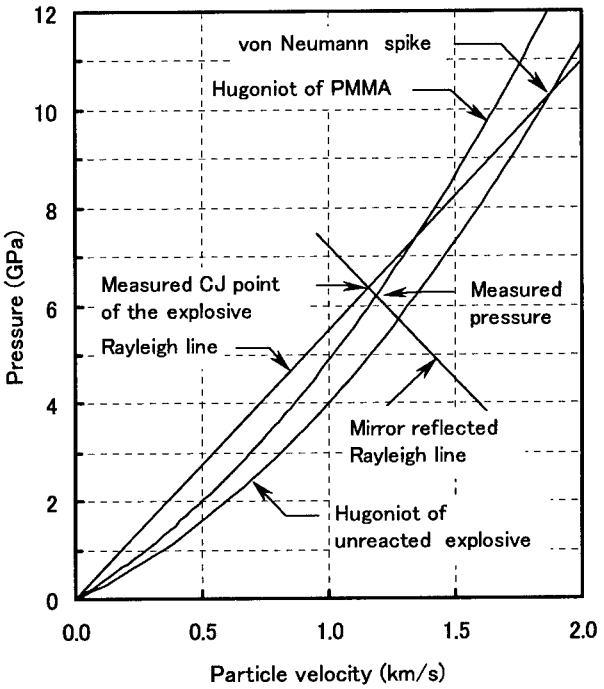


Fig.6 Impedance matching to determine the detonation pressure in the emulsion explosive of density 1.05g/cm^3 sensitized with balloons of 0.05mm in diameter A Rayleigh line of reaction product is used as a mirror reflected Hugoniot curve for the detonation product.

Table2 The effect of balloon size on the detonation properties of emulsion explosives of 51mm in diameter

Balloon diameter d_B(mm)	0.05	0.47	0.80	1.73	2.42
Explosive density (g/cm^3)	1.05	1.05	1.05	1.03	1.06
Voidage ϕ	0.25	0.26	0.26	0.25	0.26
Detonation velocity (m/s)	5230	4480	3510	3360	2960
Measured pressure (GPa)	6.3	5.5	3.2	2.8	2.5
Measured detonation pressure P (GPa)	6.4	5.1	2.8	2.5	2.1
Calculated CJ pressure P_{CJ} (GPa)	8.21	8.21	8.21	8.21	8.21
Adiabatic exponent γ_{CJ}	3.4	3.1	3.5	3.7	3.4
Fraction of AN reacted at C-J state estimated from pressure P	0.84	0.69	0.42	0.39	0.33
Fraction of AN reacted at C-J state estimated from detonation velocity	0.87	0.68	0.43	0.39	0.30

the impedance match method shown in Fig.6 as an example for the explosive sensitized with PB-1. The Hugoniot of PMMA was based on the reference [2], and that of the unreacted emulsion explosive was supposed to be same as Universal Hugoniot [3) 4)] for AN solution in this experiment. The Hugoniot of the detonation products of the emulsion explosive was approximated by a Rayleigh line in the vicinity of detonation pressure. The detonation pressure of 6.4GPa is obtained from the measured pressure of 6.3GPa in PMMA as in Fig.6.

The detonation pressures calculated and observed are summarized in Table 2 and graphically shown in Fig.7 as a function of balloon diameter. The bigger the balloon diameter is, the lower the observed detonation pressure is.

The fraction of AN reacted in the reaction zone was estimated from these data assuming that the ingredients other than AN be completely reactive. The results are shown in Fig.8. Detonation velocity was also measured in each experiment and the results are also shown in Table 2. The fraction of AN reacted was estimated from this measured detonation velocity. It is obvious that large balloons give lower reactivity in the explosive. This is probably due not only to the lateral rarefaction wave of the explosive but also to the rarefaction wave from the balloon itself that reduces pressure and temperature of the explosive in the reaction zone.

The fraction of AN reacted within the reaction zone estimated from the pressure agree considerably well with that estimated from detonation velocity.

The Effect of Voidage on Detonation Pressure

The density of the emulsion explosive was adjusted to 0.90g/cm^3 (voidage of around 0.37) and 1.19g/cm^3 (voidage of 0.14) with PB-1 or PB-2 to measure detonation pressure and detonation velocity. Pressure profiles are indicated in Fig.9 and Fig.10 respectively for the emulsion explosives containing balloons PB-1 and PB-2.

The results of detonation pressures measurements are summarized in Table 3 and Fig.11. The ideal detonation pressures P_{CJ} calculated with KHT code are also shown for comparison. The fraction of AN reacted within the reaction zone estimated from the measured detonation pressure and velocity is illustrated in Fig.12. The values of detonation velocity measured in this experiment are slightly higher compared with those shown in Fig.2 for the explosives of lower voidage and larger void size. This is due to stronger confinement of PVC pipe used in

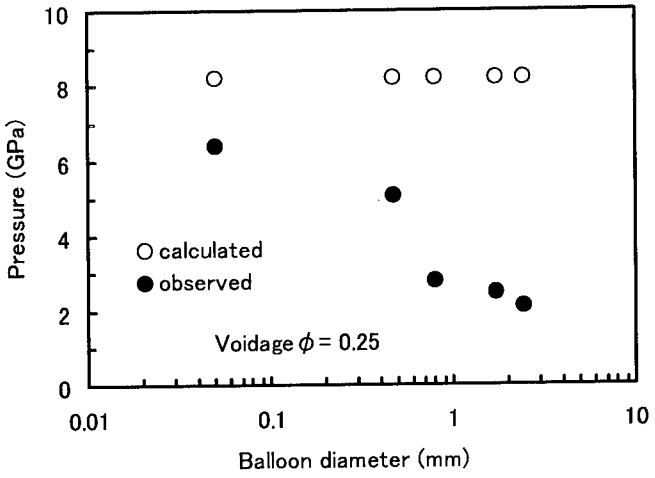


Fig.7 Detonation pressure of emulsion explosives as a function of void size

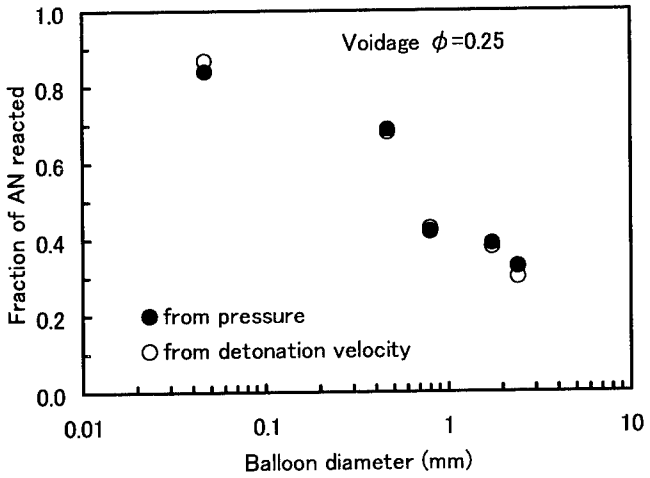


Fig.8 Estimated fraction of ammonium nitrate reacted in the reaction zone

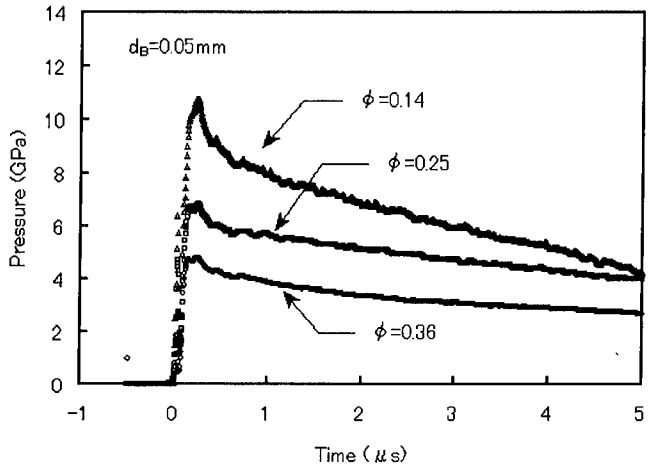


Fig.9 Pressure-time curves observed for the emulsion explosives at various voidage ϕ sensitized with balloons of 0.05mm in diameter

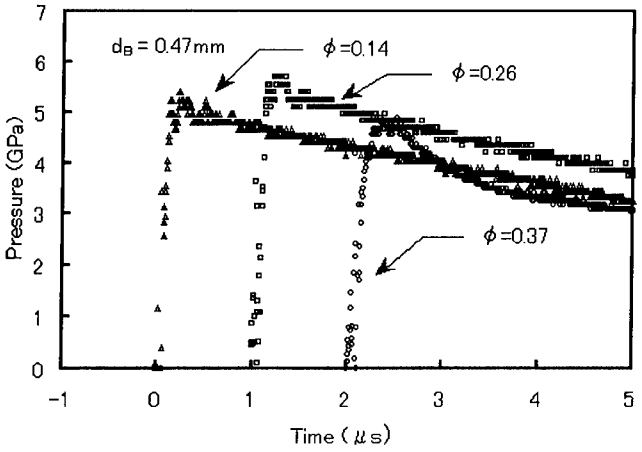


Fig.10 Pressure-time curves observed for the emulsion explosives sensitized with balloons of 0.47mm in diameter

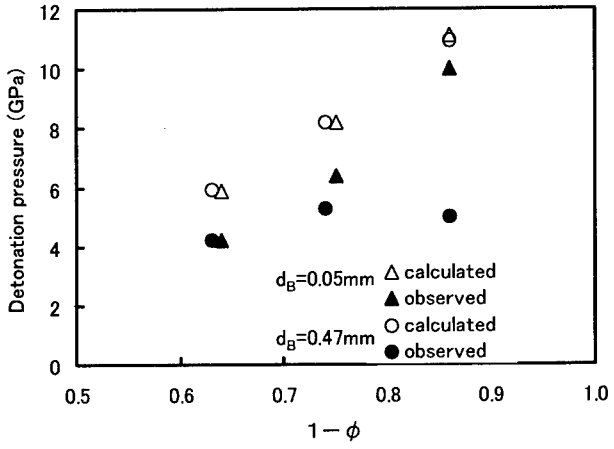


Fig.11 Detonation pressures of the emulsion explosives sensitized with different amount of balloons of 0.05mm and 0.47mm in diameter

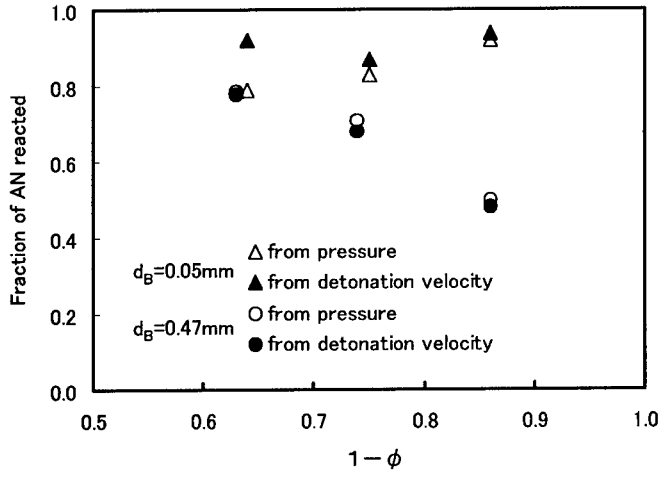


Fig.12 Fraction of ammonium nitrate reacted in the reaction zone estimated from the detonation pressure and detonation velocity of the emulsion explosives

Table3 The effect of voidage on detonation properties of the emulsion explosive sensitized with balloons of 0.05mm or 0.47mm in diameter

Balloon diameter d_B(mm)	0.05			0.47		
Explosive density (g/cm^3)	0.90	1.05	1.20	0.90	1.05	1.19
Voidage ϕ	0.36	0.25	0.14	0.37	0.26	0.14
Detonation velocity (m/s)	4720	5130	5890	4260	4480	4300
Measured pressure (GPa)	4.5	6.2	9.0	4.8	5.5	5.0
Measured detonation pressure P (GPa)	4.2	6.4	10.0	4.2	5.3	5.0
Calculated CJ pressure P_{CJ} (GPa)	5.87	8.21	11.12	5.93	8.21	10.94
Adiabatic exponent γ_{CJ}	3.8	3.0	3.1	2.9	3.0	3.4
Fraction of AN reacted at C-J state estimated from pressure P	0.79	0.83	0.92	0.78	0.71	0.50
Fraction of AN reacted at C-J state estimated from detonation velocity	0.92	0.87	0.94	0.78	0.68	0.48

pressure measurement than that of plastic film used in the previous experiment.

The explosive containing small balloon size of 0.05mm reacts fairly ideally and the detonation pressure observed is close to P_{CJ} at lower voidage. On the other hand, the explosive sensitized with larger balloons of 0.47mm in diameter shows large deviation between observed and calculated detonation pressures even at lower voidage. This is probably due to small number of balloons which act as hot spots, and this leads poor reactivity of the explosive that gives lower detonation pressure.

CONCLUSIONS

To examine the effects of size and volume fraction of voids in heterogeneous explosive, detonation velocity and detonation pressure were measured for the emulsion explosives sensitized with plastic balloons of five different sizes ranging from 0.05mm to 2.42mm in average diameter. Detonation pressure was measured with a PVDF film gauge.

When the size and volume fraction of voids were increased, the difference between the measured and calculated values was increased both for detonation velocity and pressure. The fraction of AN reacted in the reaction zone was higher than 80% for the emulsion explosives sensitized with voids of 0.05mm at voidage of 0.1-0.3. On the other hand, the fraction of AN reacted is as low as 30% for the large voids of 2.42mm at voidage of 0.2-0.3.

In the case of the emulsion explosives sensitized with voids smaller than 0.47mm, pressure decrease behind leading shock and following decay in Taylor wave were observed. Whereas,

in the case of emulsion explosives sensitized with voids larger than 1.73mm, detonation pressure rise time is larger than 0.5 microseconds due to important irregularity of detonation front.

REFERENCES

1) Hirosaki,Y., Sawada,T., Kato,Y., Hamashima,H., Itoh,S., J. Explosives Society Japan, Vol.62, 23-32, 2001

2) Marsh,S.P., "LASL SHOCK HUGONIOT DATA", University of California Press, 1980

3) Woolfork,R.W., Cowperthwaite,M., Robert Shaw, Thermochimica Acta, 5, 409, 1973

4) Hirosaki,Y., Ishida,T., Tokita,T., Mori,N., Hattori,H., Sakai,S., J. Explosives Society Japan, Vol.46, 376-383, 1986

32nd International Annual Conference of ICT: ENERGETIC MATERIALS - Ignition, Combustion and Detonation
(July 3 - July 6, 2001, Karlsruhe, Federal Republic of Germany)

Mathematical Modeling of the Long Tubular Solid-Propellant Element Anomalous Ignition in the Semi-Closed Volume

Dr. Alexander N. LUKIN
Physics-Chemical Mechanics Department, Institute of Applied Mechanics,
Ural Branch of the Russian Academy of Sciences,
Bldg. 222, Gorky Str., Izhevsk, Udmurt Republic, 426000, Russia
Tel: +7 (3412) 75 2731
Fax: +7 (3412) 43 1713
E-Mail: lukin@udm.ru

Important direction of the modern solid-propellant gas generators (SPGG) characteristics improvement is development of methods of prediction of the anomalous physical-chemical processes development on the SPGG initial stage operation with the purpose of exclusion of the ignition and combustion anomalous modes.

The numerical investigations were executed for the SPGG design scheme, which contained long tubular solid-propellant element (SPE) (ratio of the channel length to diameter L/d = 10 - 20), executed from the not metallized ballistite powder or composite propellant. The mass content of the combustion stabilizer in the propellant does not exceed 0.6 %. The igniter was installed at the SPGG non-flowing end-face. Diameter of SPGG combustion chamber throat approximately in 2 times more than the diameter of the SPE central channel. And the ring circumferential channel cross-sectional area more than SPE central channel cross-sectional area in 12 times. The SPGG is equipped with a nozzle cover. This design scheme was used for the fire stand tests (FST) execution. The FST have demonstrated that without use of the nozzle cover the SPE is not ignited. During the FST the SPE intermittent combustion mode was observed many times. The channel in the long SPE can be considered as a cylindrical pipe-resonator opened with one or from both ends. As a rule, in the narrow pipes the acoustic oscillations have an one-dimensional character.

At the mathematical model development was supposed, that the source of oscillatory process is in the SPE long central channel. One-dimensional gas-dynamic equations of the combustion products mixture motion along the SPE central and ring circumferential channels are written for the multicomponent biphase mixture of ideal gases. The peculiarities of the

boundary conditions definition in the course of the gas-dynamic task solution are considered. The equations, describing the gas-dynamic processes, are solved numerically by the large particles method, developed by Yuriy M.Davydov of Russia. For description of the SPE surfaces temperature state, as well as to find the moment of the SPE surfaces inflammation, was used the model, composed in accordance with approximate technique of Prof. R.Ye.Sorkin for solution of the heat conduction equation. Integral dependencies suggested by Prof. V.P.Bobrishev are used in account for the possible erosive effect in SPE burning. In the basis of this procedure is the solution of the asymptotic equations of heat conduction and diffusion in the gas phase of the burning propellant. For complex check-up of the developed mathematical model of physics-chemical processes, the numerical calculation results have been compared with the SPGG FST results. The numerical results have shown the SPE central long channel surface essentially nonuniform ignition, which results in appearance of the combustion products directional flow and in appearance of intensive shock waves. The numerical investigation of the wave processes development in the SPGG casing at various ratios of the ring circumferential and the central channels cross-sections areas also is conducted. Specially was investigated the SPE central channel ignition process, when the SPE lateral surface is armored. Obtained numerical results have confirmed the determining influence of the intensive wave processes in the SPE central channel on the anomalous ignition and combustion processes development in the SPGG casing.

Keywords: solid-propellant gas generator, anomalous ignition and combustion, mathematical model, numerical results, intensive wave processes

32nd International Annual Conference of ICT: ENERGETIC MATERIALS - Ignition, Combustion and Detonation
(July 3 - July 6, 2001, Karlsruhe, Federal Republic of Germany)

New Method of Prevention of the Anomalous Combustion Regimes Development in the Large-Sized SPRM

Dr. Alexander N. LUKIN
Physics-Chemical Mechanics Department, Institute of Applied Mechanics,
Ural Branch of the Russian Academy of Sciences,
Bldg. 222, Gorky Str., Izhevsk, Udmurt Republic, 426000, Russia
Tel: +7 (3412) 75 2731
Fax: +7 (3412) 43 1713
E-Mail: lukin@udm.ru

The important direction of the large-sized solid propellant rocket motors (SPRM) improvement is investigation of methods of optimal organization of the intrachamber processes development of the SPRM initial stage operation with the purpose of reduction of impact and vibrational loads on the rocket and its systems.

The main peculiarity of the structural diagrams of modern SPRM is that the firmly fastened internal channel charge has a partially non-fastening and unarmored end-face surfaces in the vicinity of the front bottom. In these conditions the end-face combustion surface can make up to 50 % and more of the whole combustion surface. The engine case has a "cocoon" type design and is manufactured from the organic plastic materials. For such conditions, the thickness of the non-flowing clearance between the SPRM case front bottom internal surface and the charge end-face surface can increase in 20 - 100 times at the operating pressures in the combustion chamber (5 - 10) MPa.

Operation of such engine can occur in abnormal mode. In a number of cases, listed peculiarity of the considered SPRM can cause the increased sensitivity of the SPRM initial stage operation to various kinds of the non-estimated actions. The intraballistic parameters in the initial stage of the large-sized SPRM operation in many respects are determined by the physics-chemical processes proceeding in the pyrotechnic ignition system (IS) and subsequent heat effect of the IS charge combustion products (CP) on the motor main charge. In the considered situation, the reason of an anomalous mode of ignition and combustion in the SPRM combustion chamber beginning can serve the non-estimated action from the pyrotechnic IS. Such non-calculated effect results in non-monotonicity of the working processes course during the propellant charge ignition. In the course of filling the intrachamber volume with CP coming from the IS and from the already ignited part of the charge, joint elastic deformations of the propellant charge and the organic plastic engine case may occur. However, the elongated deaf end-face clearance has no time to be expanded to the necessary size. In the result, close to the interface of the end-face clearance with the boot, which fastens the charge end-face with the rocket engine bottom, the powerful local dynamic loads may arise, caused by the gradually increased compression wave propagation phenomenon. Development of the above-mentioned phenomenon results in the boot breaking off from the engine case and from the charge.

The numerical study of the physics-chemical processes subsequent to the boot breaking off is conducted. The gas dynamics equations are solved numerically by Yu. M. Davydov's large particles method. For the complex check-up of the developed mathematical

model of the physics-chemical processes, the numerical calculation results have been compared with the fire stand tests results.

Calculation results show, in particular, the appearance of strong rarefaction waves, resulting in either extinction of the propellant charge (complete or temporary) or transition to a mode of the unsteady burning.

Realization of the described above, or similar, anomalous mode ignition, (which is accompanied by intensive shock waves rise in the large-sized SPRM combustion chamber) shows they are extremely dangerous. The beginning of the non-estimated vibrational and impact loads in the engine chamber can call the anomalous resonant effects in the whole system which result in damage of its various units and elements.

Executed calculations demonstrate that the described above ignition in an abnormal mode appearance in the SPRM can be prevented. The appropriate method for prevention of the solid propellant charge anomalous ignition regimes was developed. This method provides monotony of the SPRM operation during the start period by means of the CP selection, coming from the IS, both in space orientation and in time. For practical realization of new ignition method, special SPRM IS design scheme were elaborated.
This design scheme has increased reliability, as does not contain any mobile elements of design.

Keywords: large-sized SPRM, ignition system, anomalous ignition regimes, numerical study, new ignition method

IGNITION AND COMBUSTION STUDIES ON FORMALAZINE

Mohan Varma and Ramakant Singh*
Department of Space Engineering & Rocketry
Birla Institute of Technology
Mesra : 835215, Ranchi, India

Abstract

The catalytic and synergistic ignition and combustion behaviour of formalazine, a potential hybrid fuel for rocket engines, has been investigated. The fuel obtained by reaction of hydrazine with formaldehyde, as a white amorphous polymeric material was characterized and found to sustain combustion under ambient conditions without leaving any residue or soot. The ignition behaviour of the fuel was investigated using Red fuming nitric acid (RFNA) as oxidant. The results show that though the fuel is not hypergolic with RFNA, a copious amount of gases emanate with a very exothermic reaction. Subsequently, efforts were made to incorporate additives like potassium permagnate, potassium dichromate, ammonium vanadate and vanadium pentoxide (3 wt%) in RFNA and the hypergolic ignition of the fuel could be achieved in a wide range of O/F ratio. The fuel also showed synergistic hypergolic ignition when admixed with Mg or Mg : Al blends in different ratios. A plausible explanation for this behaviour is offered.

The thermal degradation results obtained using DTA, TGA and DSC for formalazine, provide positive indicators for its efficacy as a hybrid fuel. The results reveal that the decomposition process is endothermic under inert ambient conditions but becomes highly exothermic at higher pressures. The kinetic parameters for the process have been computed. The heat of combustion has also been evaluated using a bomb calorimeter and a comparison is presented with respect to other known hybrid fuels. An effort has also been made to blend the novel fuel (up to 40 wt%) in PVC plastisol and port burning tubular grains were test fired in a hybrid rocket motor under stream of gaseous oxygen, maintaining a constant oxidiser injection pressure. The regression rate of the fuel along the grain length was estimated after a firing duration of 10 sec ± 0.2 sec. It has been observed that formalazine enhances the regression rate of PVC plastisol up to a certain level beyond which it decreases.

---

* Presently Project Officer, DGCA, New Delhi.

1. Introduction

The potential capabilities of the hybrid rocket engines during the last three decades of their development could not be fully realized due to principal problems like poor fuel utilization, low regression rates, low combustion efficiency, low recovery of theoretical specific impulse and uneven burnout of the fuel along the length of the combustion chamber. In this backdrop, the task of development of advanced fuel systems with substantially high regression rates to achieve total fuel utilization attains paramount importance. It is recognized that the rate of consumption of the fuel is dependent upon primarily the rate of heat input and the energy available to cause fuel vaporization. Therefore, the important consideration is that an ideal fuel should have the lowest possible latent heat of decomposition or vaporisation and should be able to promote nearly self - sustaining chemical rection on the surface to produce reactable gases.

Many studies[1-6] have been attempted in the past, with an objective to develop highly energetic and fast regressing fuels for hybrid rocket engines. Most of these studies are aimed to get solid fuels which are generally the condensation products of aromatic amines and a suitable aldehyde or ketone. These fuels leave behind a large amount of carbon on combustion and show poor ignition characteristics with known storable liquid oxidants. Since hybrid combustion is a diffusion controlled phenomena which takes place within a turbulent boundary layer just above the pyrolysing fuel, the formation of carbonaceous products above the regressing fuel surface reduces the heat transfer rates from the combustion zone resulting in lower regression rates of such fuels and at times the problem of engine shut-down is also encountered due to inadequate injection of fuel vapours in the reaction zone.

In the present investigation, efforts have been made to synthesise formalazine (FA) which is expected to be useful as a hybrid fuel. The high energy material which leaves no residue or soot behind on burning, may also find application in explosive formulations and even modify ballistic properties of composite solid propellants or ignition characteristics of pyrotechnic igniters. The thermal decomposition, ignition and combustion behaviour of the novel fuel has been studied under different conditions with an aim to assess its suitability for diversed applications.

2. Experimental

2.1 Preparation and characterisation of fuel

Hydrazine hydrate (80%, density = 1.028 at 20^0 C) of Loba-Chemie Co. Mumbai was added drop by drop to a cold formaldehyde solution (35%, density = 1.080 at 20^0 C) of E.Merck in a ratio of 1:2 mol. respectively with constant stirring. The white creamy precipitate obtained was dried and pulverised into a fine powder which was later purified. The infra-red spectra of the prepared fuel was recorded on a double-beam Perkin-Elmer spectrophotometer by using nujol mull technique.

2.2 Thermal degradation studies

The thermal degradation studies of FA were carried out by recording its differential thermal analysis (DTA) and thermogravimetric analysis (TGA) curves on a NETZSCH simultaneous thermal analyser model - STA 409 under a flowing air atmosphere and at a heating rate of 10^0 C min^{-1}. The differential scanning calorimetric (DSC) results were also acquired on a Mettler - TA 4000 system using a DSC27HP measuring cell and TA72.5 graphware to determine kinetic parameters. The heating rate of 10^0 C min^{-1} was maintained and nitrogen gas was purged at a constant flow rate of 80 ml/min. A bomb calorimeter was used to measure the heat of combustion of FA at a oxygen pressure of 300 psi.

2.3 Ignition delay studies

Ignition delay, the time elapsed between the contact time of fuel and oxidiser and appearance of the flame, was measured employing RFNA (13.4 wt% NO_2) as oxidant, with the help of a suitable experimental set-up. A fixed average particle size of 200 μm of the fuel and metal powders (Mg and Al) was selected for ignition delay studies, conducted at 25^0 C ± 2^0 C. All additives were dissolved individually in RFNA at a concentration level of 3 wt%, just before the injection of oxidant on the fuel surface.

2.4 Regression rate studies

A head-end injection hybrid test motor comprising of an injector, a combustion chamber and a nozzle was used to investigate the regression behaviour of FA. The test motor was mounted on a flexural type thrust stand. The provision for injection of oxygen gas at high pressure was made at the head-end of the motor through an adapter and a single hole injector. The fuel grains were prepared by homogeneously mixing the pre-weighed quantities of polyvinyl chloride (PVC) resin and FA (upto 40 wt%) in dibutyl pthalate in instalments. The mix was then cast in a suitable mould and cured at a temperature of 130^0 C for four hours to get a tubular grain of 100 mm length , 50 mm outer dia and a central

port dia of 10 mm. Each fuel grain was weighed and then cast in the combustion chamber after applying an inhibitor coating on the surfaces not designated for burning. The cast motor was again kept in an oven at 130^0 C for 1 hour. A pyrotechnic igniter was used to initiate the combustion. The oxygen injection pressure was maintained at 300 psi for all the tests. After each test firing of 10 sec ± 0.2 sec duration, the local regression rate was determined by measuring the unburnt web thickness at regular interval of distance along the length of grain.

3. Results and Discussion

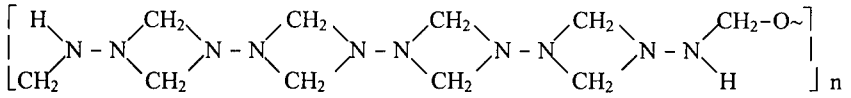
3.1 Characterisation of fuel

It is well known[7] that the reaction of hydrazine with formaldehyde proceeds quite unexpectedly beyond the hydrazone stage and results in formation of either tetraformal trisazine, or a polymeric white gelatinous precipitate if excess of formaldehyde is used. The infra-red spectra of the fuel prepared is shown in Fig. 1 and the assignments ascribed to different characteristic peaks are presented in Table 1.

Table 1 : Analysis of IR Spectra of Formalazine

Peak Frequency	Assignment
3450 (m)	N-H Stretching vibration
2980 (s)	C-H Stretching vibration
2860 (s)	
1640 (w)	C-O Stretching vibration, NH deformation vibration indicating free - NH group
1475 (m)	$-CH_2$ bending vibration
1440 (m)	
1350 (s)	$-CH_2$ Wagging Vibration, Methylene rocking indicating a $-CH_2$ aliphatic group
1196 (s)	$-CH_2$ twisting vibration
1090 (s)	alkyl- NH-R
970 (w)	Ring vibration,- NH out-of-plane deformation
830 (w)	C-N Stretching vibration
720 (w)	- CH_2 Stretching vibration, in-plane rocking

It is obvious from the nature and chemical structure of the reactants that the product will have C, H , O and N elements only. Based on the available spectral inputs and physico-chemical tests of the fuel, the following structure is confirmed :



3.2 Thermal degradation studies

The DTA and TG curves for FA in an atmosphere of air are shown in Fig.2. The DTA trace is seen to have an enormously exothermic peak in a temperature range between 240 - 330°C. The initial and maximum peak temperatures are observed to be 240°C and 286°C respectively. The TG profile, however, indicates three inflexion points at 120 °C, 200 °C and 290 °C. It may be noticed that a weight loss of the order of 11.41 wt % and 76.14 wt% occurs corresponding to 200 °C and 290 °C respectively. Visual observations on decomposition of FA at high temperatures reveal that the compound transforms from solid to gas phase almost instantaneously. However, when subjected to slower heating rates, the melting preceeds the decomposition.

Table 2 summarises the kinetic results obtained from DSC at ambient and higher pressures under inert atmoshpere. The DSC thermogram recorded under ambient conditions (Fig.3) shows a sharp endothermic peak with a peak temperature of the order of 287.3 °C.

Table 2 : Kinetic Results at Different Pressures under Flowing Nitrogen Atmosphere

Pressure (psi)	Temp.range (° C)	Peak Temp. (°C)	Activation Energy (kJ/ mol)	ΔH J/g	ln K_o
14.3	214 - 305	287.3 (endo)	244.14	788.0	48.04
300	255 - 305	277.7 (exo)	552.45	1103.8	117.38
600	235 - 295	268.6 (exo)	384.80	1291.3	81.75

The activation energy for the decomposition process is computed to be 244.14 kJ/ mol which is in excellent agreement with the reported value[8] under similar conditions. Efforts were also made to study the thermal degradation process at higher pressures viz. 300 psi and 600 psi.. The DSC trace is presented in Fig.4. It is interesting to note that the decomposition process of FA becomes highly exothermic and the peak temperature shifts to a significantly lower value. The onset temperature of decomposition peak is observed to be 265.9 °C and 253.8 °C at 300 psi and 600 psi respectively and the decomposition process follows the first order rate law.

Table 3 : Heat of Combustion of Various Hybrid Fuels

Sl.No.	Fuel	Heat of combustion* (kcal/mole)	
		Experimental	Theoretical
1.	Formalazine	1511.53	1645.33
2.	Benzaldehyde thiocarbonohydrazone	810.92	1179.52
3.	p-Dimethylaminobenzaldehyde thiocarbonohydrazone	1132.86	1549.98
4.	p-Chlorobenzaldehyde thiocarbonohydrazone	552.97	1165.35
5.	2-Furfuraldehydethiocarbonohydrazone	684.48	934.72
6.	Formaldehydethiocarbonohydrazone	434.24	515.66
7.	Acetonethiocarbonohydrazone	713.94	817.60
8.	Cyclohexanonethiocarbonohydrazone	980.22	1179.24
9.	Aniline Formaldehyde	894.83	-
10.	o-Toluidine Formaldehyde	887.14	-
11.	m- Toluidine Formaldehyde	1014.12	-
12.	o- Anisidine Formaldehyde	900.81	-
13.	PVC Plastisol	609.57	618.15

* Sl.No. 2-8 Ref. 9, Oxidizer - WFNA: Sl.No. 9 - 12 Ref. 10 , Oxidizer - FNA;
Sl. No. 1 and 13, Oxidizer - Oxygen gas

Table 3 summarises the experimental and theoretical heat of combustion values for various hybrid fuels which have been developed in the past. It is clear from the results that FA is by far the most superior fuel as far as the energetics is concerned. The results also show that nearly 92% of the theoretical value of heat of combustion can be obtained experimentally in case of this fuel.

3.3 Ignition delay studies

The ignition characteristics of FA have been investigated by igniting it with electrical igniter and red fuming nitric acid with and without additives like ammonium vanadate (AV), vanadium pentoxide (VP), potassium dichromate (PD) and potassium permagnate (PP). The effect of metal powders like Al and Mg on synergistic ignition of FA has also been studied at varying oxidiser - fuel ratios.

It has been found that FA fuel in powder or pellet form sustains the combustion under ambient conditions when ignited with the help of an electrical igniter. A non-luminous blue flame is observed and no residue is left. The burning rates of the fuel (without oxidant) though not measured were apparently of the order of a slow burning solid propellant. This suggests that the use of this fuel in hybrid rocket engines would facilitate

much better fuel utilization as compared to other hybrid fuels which are presently employed. The thermal degradation results clearly show that the fuel decomposition takes place in a narrow temperature range (260^0 C - 290^0 C) with a sharp weight loss supporting the excellent fuel consumption rate view point.

The hypergolicity of the fuel with RFNA oxidant has also been checked in a wide range of oxidizer - fuel ratio. It has been found that the fuel shows erratic ignition behaviour with RFNA though a copious amount of gases emanate with a very exothermic reaction in all the cases but the mixture does not always ignite. It is felt that a fine fuel particle size, higher concentration of nitrogen oxide in RFNA and a suitable oxidizer injection pressure may bring about self- ignition of FA - RFNA system.

The incorporation of additive (3 wt%) in RFNA facilitates self-ignition of FA. The study using the catalysed RFNA has been conducted in a wide range (0.5 - 5, by wt.) of O/F ratio and the results are summarised in Table 4.

Table 4 : Effect of Additives on Ignition Delay of FA - RFNA System

O/F ratio (by wt)	Ignition delay (sec)			
	Ammonium Vanadate	Vanadium Pentoxide	Potassium Dichromate	Potassium Permagnate
0.5	1.4	No Ignition	1.5	0.8
1.0	1.3	1.8	1.2	< 0.5
1.5	1.0	2.0	< 0.5	< 0.5
2.0	1.1	2.5	0.5	< 0.5
2.5	1.1	No Ignition	0.8	< 0.5
3.0	1.4	No Ignition	0.8	0.5
4.0	1.5	No Ignition	1.0	0.7
5.0	2.0	No Ignition	1.5	0.7

The order of additive effectiveness in bringing down the ignition delay of the system is PP > PD > AV >VP. All the additives used are well known oxidizing agents and release oxygen in nascent form on interaction with highly reactive RFNA. It may be anticipated that this would enhance the rate of oxidative degradation of the fuel molecule resulting in shorter ignition time. The entire process may take a rather complicated reaction route involving free radical mechanism but it is likely that an important initial step may be the scission of N - N bond in FA.

The additives tried in the present study had also been used in another investigation[3] related to ignition studies on aromatic amine - formaldehyde condensate/ FNA system and

AV had emerged as the most effective additive. The reason for better performance of AV was tentatively assigned to its capability to bring about oxidation of the benzene ring of the aromatic fuel faster. The ignition delay values obtained for these fuel systems were reported to be much higher than FA and in some cases the additives had increased the ID of the system. The surprising revelation in the present study is the effectiveness of vanadium pentoxide in a very narrow range of O/F ratio.

The data recorded in Fig. 5 on the effect of additives like VP, AV, PP and PD on ignition delay of FA - RFNA system clearly show that with the increase in O/F ratio ID first decreases and then increases to give a minimum ID value at a certain mixture ratio. The critical oxidiser - fuel ratio corresponding to minimum ID for the latter three additives lies in the vicinity of 1.75. The critical O/F ratio for VP containing system could not be obtained because the system fails to ignite beyond a very narrow range.

The process of ignition of a bipropellant system is directly dependent on the rate of chemical reaction and consequent heat liberation. The rate of heat liberation is expected to go on increasing at least upto the stoichiometric point at which minimum ID should be obtained. Beyond this ratio, ID should increase as a part of thermal energy out of the maximum heat liberated would be taken away by the excess of oxidiser for its vaporization. However, the results indicate that minimum ID is obtained around a critical O/F ratio equal to 1.75, which is far less from stoichiometric value. The significant divergence in critical O/F ratio from that of stoichimetry has also been observed in our another study[11].

Fig.6 depicting the effect of Mg content in the hybrid fuel on the synergistic hypergolic ignition of FA-RFNA system clearly indicates that the incorporation of the metal in the organic fuel makes the system spontaneously igniting which otherwise is non-hypergolic without an additive in the oxidant. The efficiency of oxidant, RFNA containing additives, goes drastically down with time. Thus, the exercise of blending Mg with fuel not only alleviates the above problem but also makes the system practically more useful. Further, it is also seen that with the incorporation of increasing amount of Mg powder in FA, ignition delay goes on decreasing to give its minimum value corresponding to 40 wt % of metal content. Exactly similar results have been observed with other organic fuels[6] also. The most probable reason that can be put forward for this behaviour seems to be the in-phase enormous increase in the exothermicity of the reaction at a faster rate via the formation of hydrated magnesium nitrate ($Mg(NO_3)_2 .6H_2O$) removing the water formed from the reaction site. On the other hand, it is quite surprising to note that incorporation of Al powder does not lead to ignition of the fuel - probably due to enveloping of its particles

by an impervious passive layer of oxide. It may be anticipated that blending of Al powder with FA would act as a diluent. In accordance with this apprehension, one can expect an increase in ignition delay when in a ternary fuel mixture (FA+Mg+Al), the larger proportions of Al powder is incorporated. The data recorded in Table 5 showing the effect of blending of increasing proportions of Al powder to the 1:1 (by wt.) binary mixture of FA and Mg, on ignition delay clearly support the above view.

Table 5 : Effect of Metal Content on Synergistic Ignition of FA with RFNA

Fuel composition FA : Metal ratio	Ignition delay (sec)	Fuel composition FA : Mg : Al ratio	Ignition delay (sec)
Magnesium			
10 : 1	1.0	5 : 5 : 1	0.8
5 : 1	0.8	5 : 5 : 2	0.9
5 : 2	0.5	5 : 5 : 3	1.4
5 : 4	< 0.5	5 : 5 : 4	1.8
5 : 6	< 0.5	1 : 1 : 1	2.2
5 : 8	0.9	5 : 1 : 5	1.2
1 : 2	1.2	5 : 2 : 5	1.1
Aluminium			
5 : 1	No Ignition	5 : 4 : 5	2.0
5 : 2	No Ignition	1 : 1 : 1	2.2
5 : 3	No Ignition	2 : 1 : 1	0.8
1 : 1	No Ignition	4 : 1 : 1	0.6

3.4 Regression rate studies

The schematic layout of the experimental set - up used in the present study is shown in Fig. 7. The results on local regression rate along the length of the fuel grain for varying FA content in the fuel composition have been presented in Fig. 8. The local regression rates obtained for the virgin PVC plastisol fuel are also plotted in the same figure in order to have a comparative view of its variation with FA loading.

A close examination of the curves reveal very interesting results of the variation of regression rate along the length of the fuel grain. The regression rate, in general , is seen to decrease steadily along the length from the leading edge but for the fuel compositions containing 10 and 20 wt% of FA. In these two cases, the regression rate is found to first increase upto a certain distance from the leading edge and then follows the course like other compositions.

The regression rate of the hybrid fuel grain is well known to be governed by a boundary layer combustion model in which the combustion is diffusion controlled and

dependent on the amount of fuel and oxidizer mass being injected into the flame zone from the opposite directions[12]. The mass of fuel vapours entering the combustion region is dependent on the heat transfer from the flame zone and in turn the pyrolysis rate of the regressing solid fuel. Again the total heat flux along the length of the fuel grain would vary and will be dependent on the amount of flowing gas and its velocity. As the oxygen passes down stream, it gets used up and diluted with the distance along the length of the grain. However, the total mass flux goes on increasing with distance from the head end as the combustion products are constantly added into the flowing gas. The regression rate at a particular locus thus depends on the predominance of the governing factor and if the depletion in oxygen available for the gas phase reaction overweighs the effect of increased total mass flux, the net result would be the decrease in regression rate downstream, as observed.

References

1. G.E. Moore and K. Berman, Jet Propulsion, (1956) 965.
2. U. Magnusson, World Aerospace System, 2 (1966) 50.
3. N.L. Munjal and M.G. Parvatiyar, J. Spacecraft and Rockets, 2 (1974) 248.
4. S.P. Panda and S.G. Kulkarni, Combustion and Flame, 28 (1977), 25.
5. G. Rajendran and S.R. Jain, Fuel, 63 (1984) 709.
6. S.R. Jain, R. Rao and K.N. Murthy, Combustion and Flame, 71 (1988) 233.
7. E.W. Schmidt, Hydrazine and its Derivatives, John Wiley & Sons, NY, (1984), 313.
8. P.R. Nambiar, Propellant, Explos. & Pyrotech., 10 (1985) 39.
9. S.R. Jain and G. Rajendran, J. Spacecraft and Rockets, 23 (1986) 120.
10. M.G. Parvatiyar, Ph.D. Thesis, Birla Inst.of Tech. (Ranchi Univ.) India,1975.
11. B.L. Gupta and Mohan Varma, Ind. J. of Engg. & Mat. Sc., 6 (1999) 13.
12. G.A. Marxman and M. Gilbert, IXth Symposium (Int.) on Combustion (1962) 371.

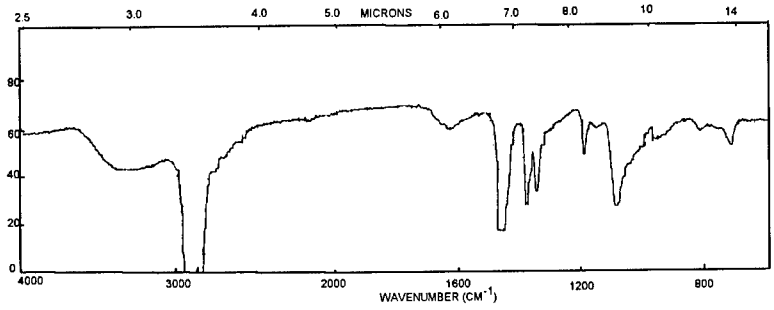


Fig. 1 IR spectra of formalazine

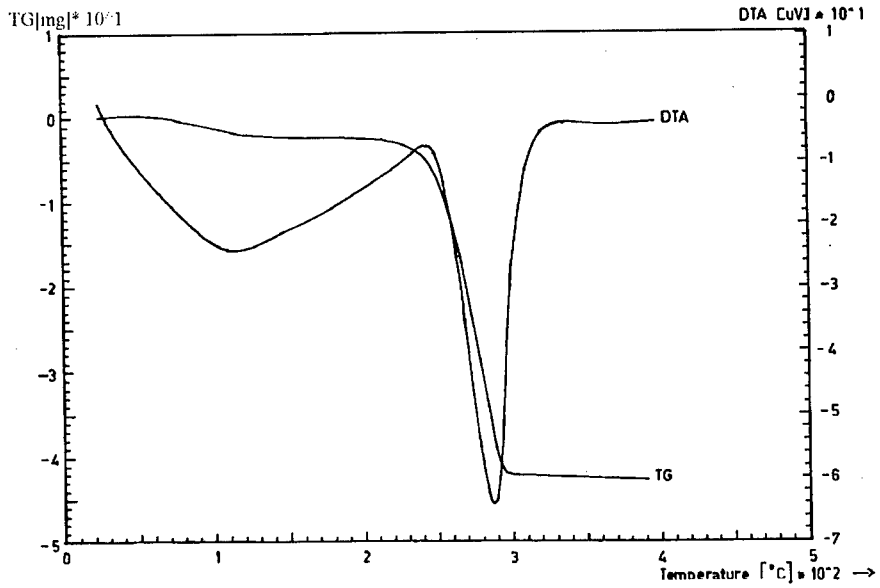


Fig. 2 DTA and TG traces of FA in flowing air atmosphere

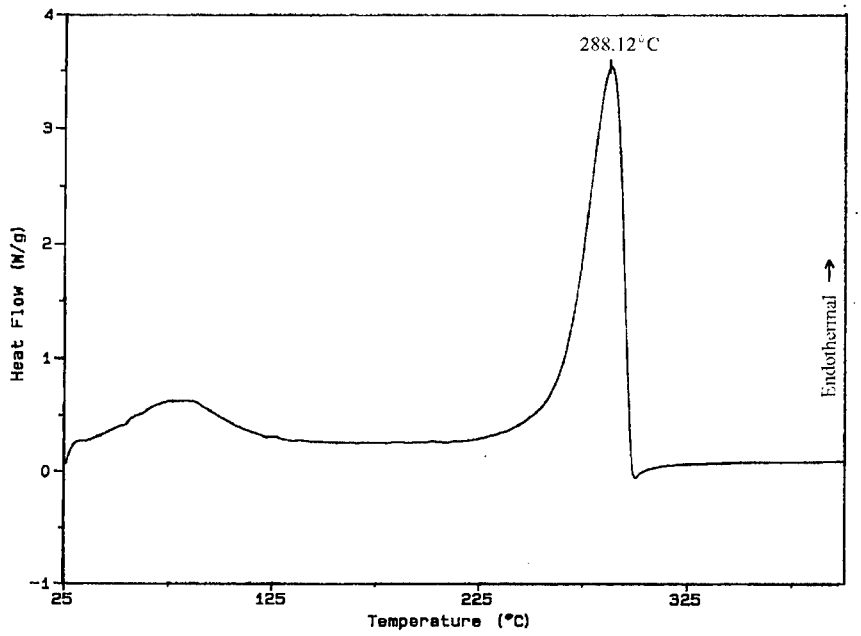


Fig. 3 DSC thermogram of FA at ambient pressure

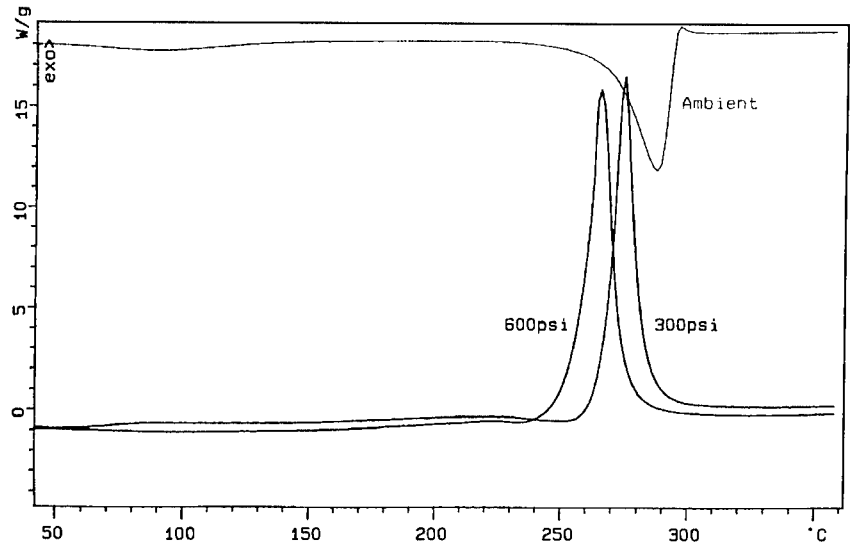


Fig. 4 DSC thermogram of FA at higher pressures

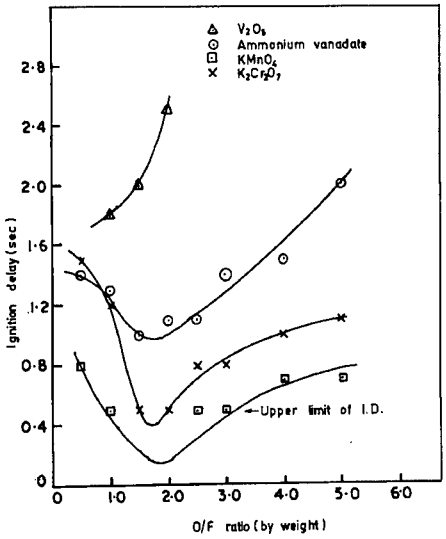


Fig. 5 Effect of additives on ignition delay of FA – RFNA system

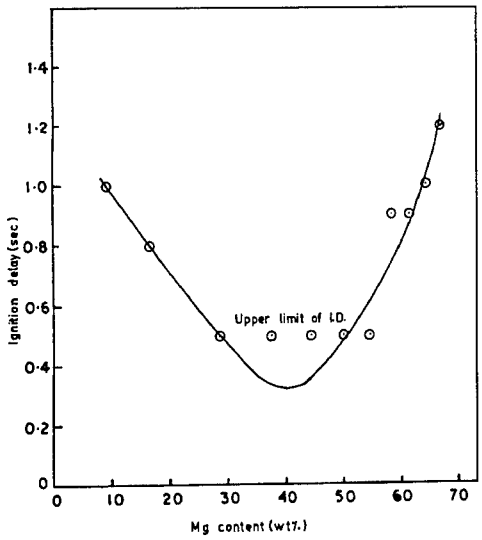


Fig. 6 Effect of magnesium content on synergistic ignition of FA – RFNA system

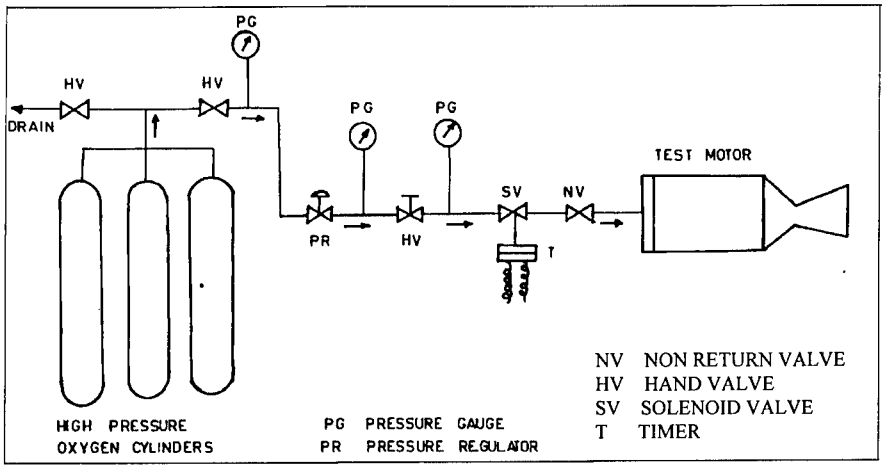


Fig. 7 Schematic diagram of experimental set - up

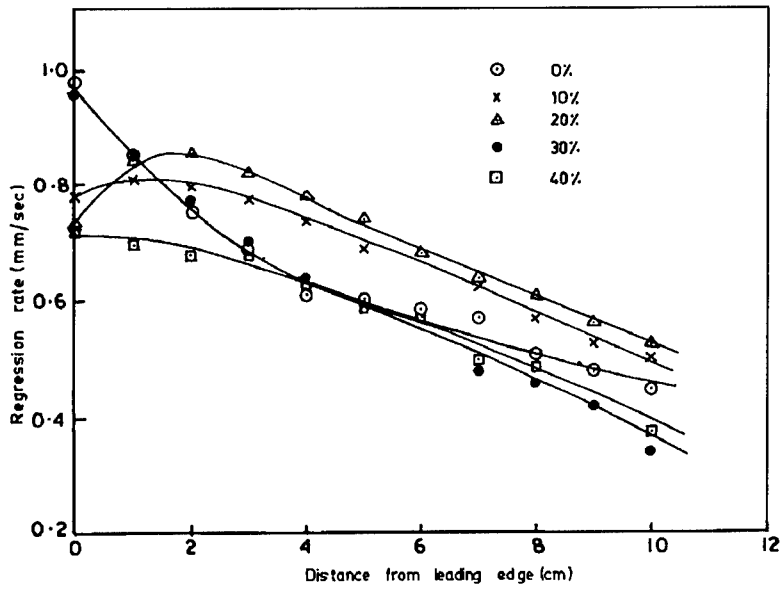


Fig. 8 Variation of regression rate at different FA loadings in PVC plastisol grain

Structure investigation of energetic substances by $^{14}N/^{15}N$ NMR spectroscopy

Yuri A. Strelenko

Zelinsky Institute of Organic Chemistry, Russian Academy of Sciences
Leninsky prospect 47, Moscow, Russia 117913
Fax: 007 095 135 5328; e-mail: strel@ioc.ac.ru

Keywords: NMR, nitrogroup, chemical shifts, coupling constants, line width.

Abstract: Some classes of energetic substances consist of a lot of nitrogen atoms. NMR spectroscopy ^{1}H, ^{13}C, ^{14}N and ^{15}N can provide the detailed evidence of chemical structure. Direct and long-range coupling constant ^{1}H-^{15}N can be measured at the natural ^{15}N isotope abundance. Fast relaxation time of quadrupole ^{14}N nuclei can be slowed down in some circumstances and sharp NMR signals ^{14}N can be observed. The influence of nitrogen atoms to ^{1}H and ^{13}C spectra can be caclulated and analysed to provide additional information about chemical structure. Quantum chemical *ab initio* calculation of NMR chemical shifts and relaxation times can help in NMR signals assignment of crowed spectra.

NMR evidence of the structure of potassium salt of dinitramid were resently made with ^{15}N enriched sample[1]. Triplet of central nigrogen atom with intensity one and doublet of nitrogroups with intensity two are observed in ^{15}N NMR spectrum (fig.1). This spectrum proves the topology and symmetry of dinitramide anione in solution.

Sometimes it is not so needed to enrich the investigated substance with ^{15}N isotope as ^{14}N NMR spectrum show arbitrary sharp sygnals. Spectrum of nitrous oxide in acetonitrile demonstrates two narrow sygnals of the terminal and middle atoms of nitrogen[2] (fig. 2). Both signals are triplets with 1:1:1 intensities due to spin-spin coupling of nuclei with spin 1. The outer components of triplets are slightly broadened due to fast relaxation of ^{14}N nucleus, this quadrupole effect can be theoretically calculated as it is shown at fig. 2.

The relaxation rates of quadrupole nuclei are strongly dependent from symmetry of electon density around nucleus[3]. The lone electons pair of nitrogen is the source of large of electronic field gradient at ^{14}N nucleus and it's fast relaxation, so that it is difficult to observe very wide signals in ^{14}N NMR spectrum of amines and amides. Otherwise, the line of symmetric $NH4^{+}$ cation is sharp enough to observe ^{1}H-^{14}N spin-spin

coupling splitting. The electronic field gradient of nitro- and azoxy-groups has arbitrary low values and ^{14}N signals with line width 1-200 Hz are well observed. As two substituens of nitrogen atom in this groups are fixed the rate of relaxation and line width ^{14}N signal depends from electron withdrawing ability of theird substituent: the higher the narrow. High natural abundance of ^{14}N isotope fortunates the use of ^{14}N NMR as fast analitical method to check availability of nitro- and azoxy-groups in investigated molecules. On the other hand, friquently it is difficult or impossible to observe ^{13}C signals of the directly connected to nitrogroup carbon atom due to ^{13}C-^{14}N spin-sping splitting. Calculated ^{13}C spectra of hypotetic nitro-compound are shown in the figure 3. For most realistic cases, when line width of ^{14}N signal of nitrogroup is 20-100 Hz, ^{13}C signal is so broad that can be lost in the noise (fig. 4, botton spectrum). Selective decoupling experiments $^{13}C\{^{14}N\}$ (fig. 4, middle and top) for both nitro and azoxy signals at ^{14}N frequencies (fig. 5) can help not only to observe such ^{13}C signals, but provide powefull tool for ^{13}C signals assignment[4].

The progress in the computers power, theory of quantum chemistry and fast algorithms open new abilities. For example, the accuracy of $^{14}/^{15}N$ chemical shift calculations provided by Gaussian-98[5] ~4 ppm is enouth to use in daily practice of NMR spectroscopy (fig. 4).

Literature

1. Shlyapochnikov V.A., Tafipovsky M.A., Tokmakov I.V., Baskir E.S., Anikin O.V., Strelenko Yu.A., Luk'yanov O.A., Tartakovsky V.A., "On the structure and spectra of dinitramide salts", J.Mol.Struct. (2001), 559(1), p. 147.
2. Strelenko, Yu. A.; Sergeyev, N. M.,"Isotope effect due to $^{15}N/^{14}N$ substitution on 14N-14N coupling constants in nitrous oxide",J. Mol. Struct. (1996), 378(1), p. 61.
3. Akitt J.W., McDonald W.S., "Arrangements of ligands giving low electric field gradients", (1984), 58, p.401.
4. Sheremetev, A. B.; Kulagina, V. O.; Aleksandrova, N. S.; Dmitriev, D. E.; Strelenko, Yu. A.; Lebedev, V. P.; Matyushin, Y. N., «Dinitrotrifurazans with oxy, azo, and azoxy bridges», Propellants, Explos., Pyrotech. (1998), 23(3), p. 142.
5. Gaussian 98, Revision A.3, M. J. Frisch, G. W. Trucks, H. B. Schlegel, G. E. Scuseria, M. A. Robb, J. R. Cheeseman, V. G. Zakrzewski, J. A. Montgomery, Jr., R. E. Stratmann, J. C. Burant, S.

Dapprich, J. M. Millam, A. D. Daniels, K. N. Kudin, M. C. Strain, O. Farkas, J. Tomasi, V. Barone, M. Cossi, R. Cammi, B. Mennucci, C. Pomelli, C. Adamo, S. Clifford, J. Ochterski, G. A. Petersson, P. Y. Ayala, Q. Cui, K. Morokuma, D. K. Malick, A. D. Rabuck, K. Raghavachari, J. B. Foresman, J. Cioslowski, J. V. Ortiz, B. B. Stefanov, G. Liu, A. Liashenko, P. Piskorz, I. Komaromi, R. Gomperts, R. L. Martin, D. J. Fox, T. Keith, M. A. Al-Laham, C. Y. Peng, A. Nanayakkara, C. Gonzalez, M. Challacombe, P. M. W. Gill, B. Johnson, W. Chen, M. W. Wong, J. L. Andres, C. Gonzalez, M. Head-Gordon, E. S. Replogle, and J. A. Pople, Gaussian, Inc., Pittsburgh PA, 1998.

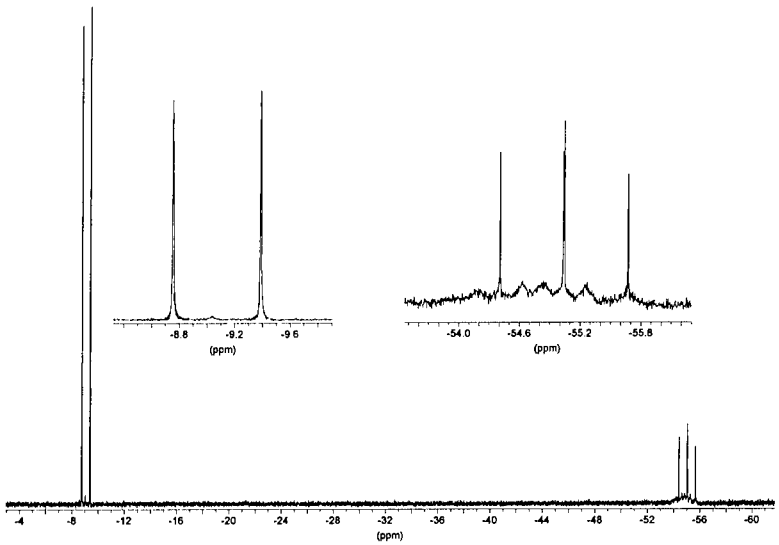


Fig. 1, ^{15}N NMR spectrum of the mixture of isotope species if dinitramide.

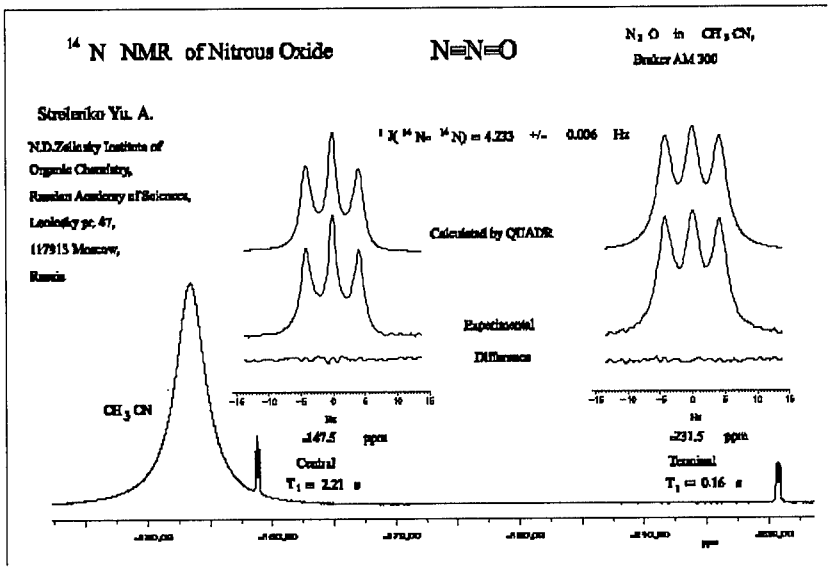


Fig. 2. ^{14}N NMR spectrum of nitrous oxide measured in acetonitrile at room temperature. The two insets shown above are the signals off two nitrogen atoms central at –147 ppm and terminal –231 ppm In both insets the upper trace is the best calculated spectrum, the middle trace is the experimental spectrum and the lower trace is the difference between experimental and calculated spectrum.

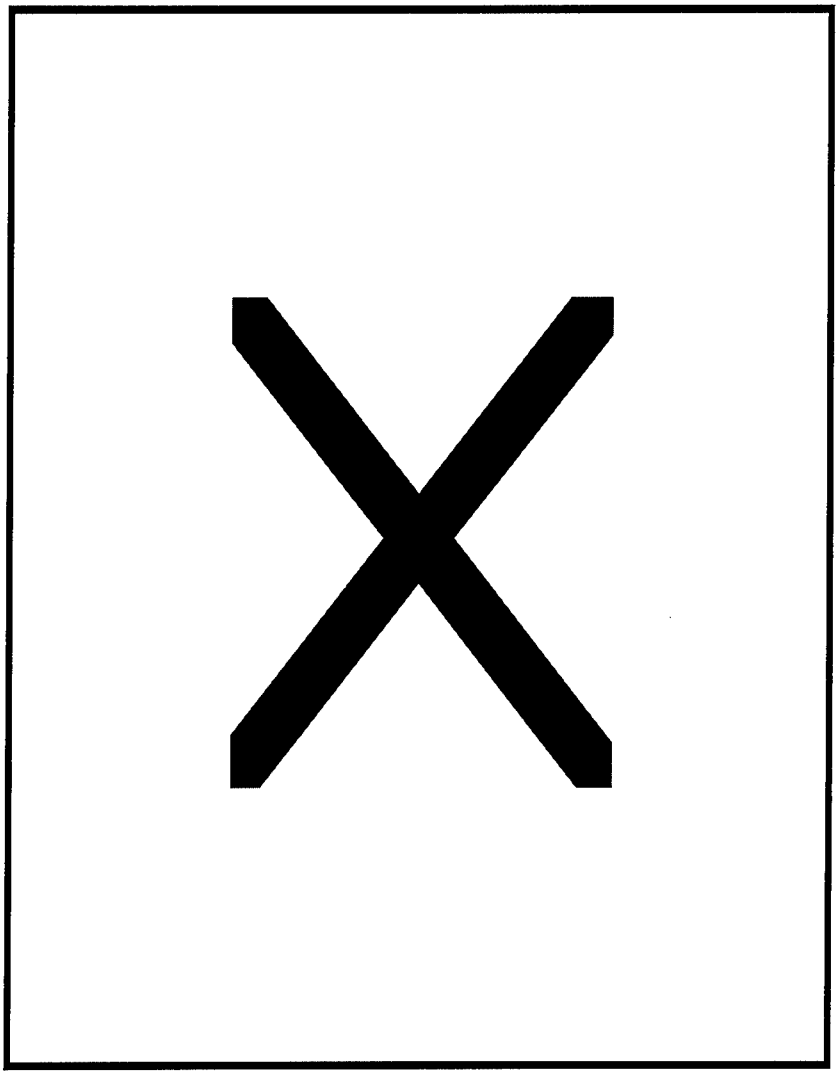


Fig. 3. Calculated ^{13}C NMR spectra (left) for hipothetic nitro compound with fixed to 20 Hz one bond ^{13}C-^{14}N spin-spin copling constant depending on line width of ^{14}N signal of nitro group in ^{14}N NMR spectrum (right).

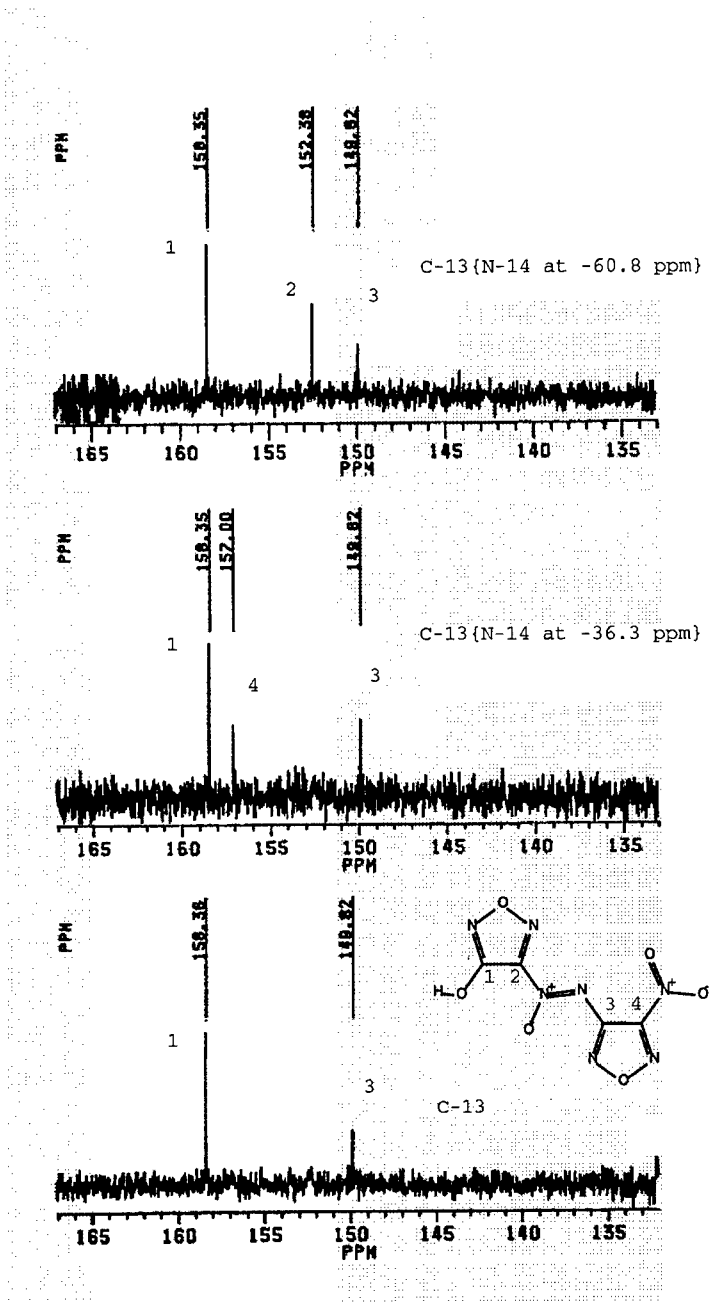


Fig.4. ^{13}C NMR spectra with selective decoupling ^{14}N signals of nitro- (middle) and azoxy-group (top) in ^{14}N NMR spectrum shown in fig.5.

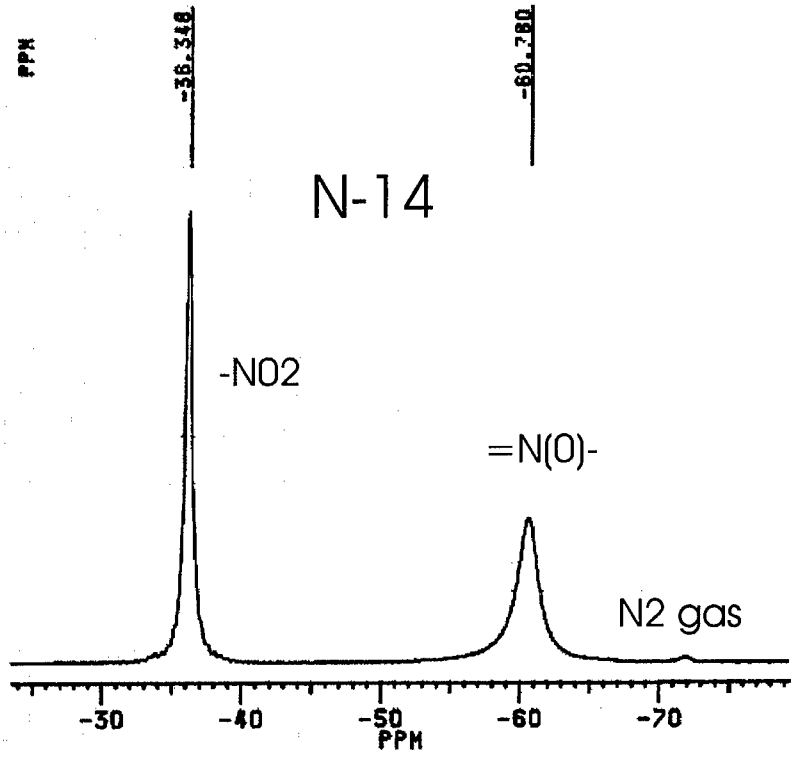


Fig. 5. ^{14}N NMR spectrum of compound shown in fig.4. Note small sharp signal of dissolved gas nitrogen from air at –72 ppm.

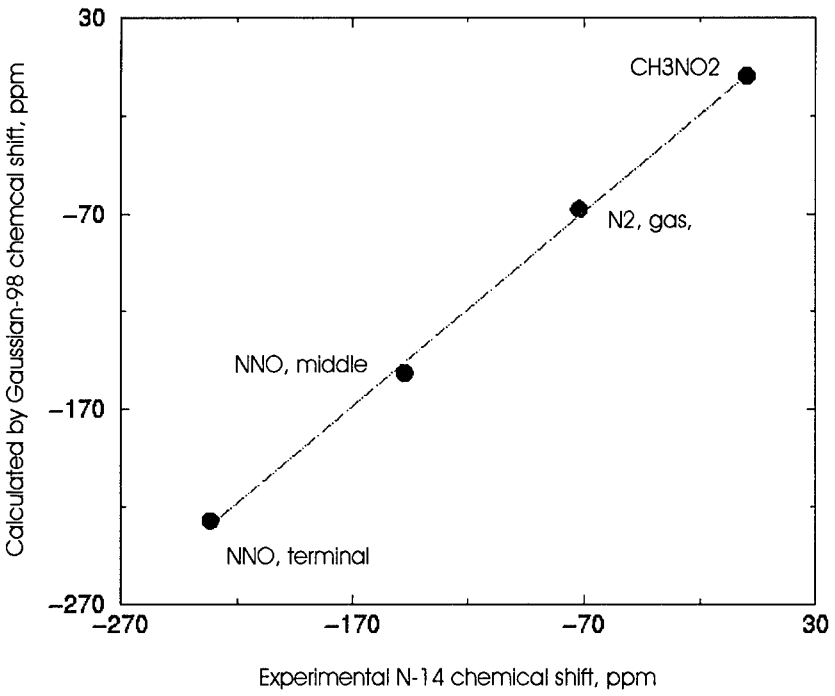


Fig. 6. Correlation of experimentaly measured chemical shifts ^{14}N NMR signals some small molecules and calculated by Gaussian-98 values. Calculations were performed at PC.

COMPUTER MODELING OF DECOMPOSITION REACTIONS OF HEXANITROHEXAAZAISOWURTZITANE (CL-20)

Aleksei Porollo, Tatyana Petukhova, and Victor Ivshin

Mari State University, Lenin square 1, Yoshkar-Ola 424000, Mari El Republic, Russia

Tatyana Pivina*

N.D. Zelinsky Institute of Organic Chemistry RAS, Leninsky prospect 47, Moscow 119992, Russia; e-mail: tsp@cacr.ioc.ac.ru

Boris Korsunskii and Oleg Golovanov

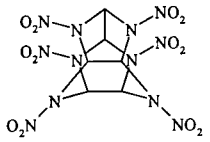
N.N. Semenov Institute of Chemical Physics RAS, Kosygin str. 4, Moscow 117977, Russia

ABSTRACT

Combinatorial enumeration as an approach to modeling of thermal decomposition of organic compounds has been developed on the basis of *Recombination Reaction Networks* (RRN). Its main idea is to consider every particle (molecule, ion, or radical) as potential reagents. As a result of multiple interactions a RRN is built, where one kind of nodes corresponds to generated particles, and another kind — to reaction descriptors, whereas directed edges represent relations of intermediates in particular reaction. Generation of intermediate particles is carried out using heuristic rules, developed by us after generalization of experimental data on decomposition mechanisms for major classes of energetic compounds. At the present study we have applied this approach to modeling of thermal decomposition reactions for hexanitrohexaazaisowurtzitane (CL-20).

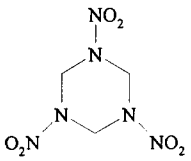
BACKGROUND

The high energy density nitroamine, CL-20 (Hexanitrohexaazaisowurtzitane (**HNIW**)) is a relatively new polycyclic caged nitramine that was synthesized in 1987 by T.A. Nielsen.[1] Structure of HNIW (chemical name is 2,4,6,8,10,12-hexanitro-2,4,6,8,10,12-hexaazatetracyclo-[5.5.0.$0^{5,9}$.$0^{3,11}$]dodecane) consists of isowurtzitane cage and nitro groups connected to the bridged nitrogens. Four modifications of HNIW were found to be stable at usual conditions, but ε-modification has the highest density only (2.04 g/cm^3).

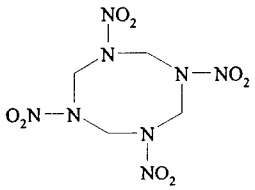


ε-HNIW (CL-20)

Inspite of HNIW similarity to well-known monocyclic nitramines (**RDX** and **HMX**), it has some advantages due to its caged structure. So constrained cycles in HNIW yield dramatically increase of heat of formation: $\Delta H^{\circ}_{RDX} = 70kJ/mol$, $\Delta H^{\circ}_{HMX} = 88kJ/mol$, and $\Delta H^{\circ}_{HNIW} = 415kJ/mol$.



RDX



HMX

Application of ε-HNIW as a component in high energetic composition demands details concerning its properties such as thermal stability and energetic characteristics. Since 90-s systematic investigation of new approaches to synthesis of HNIW[2-6] is conducted as well as thermolysis mechanism and kinetics determination.

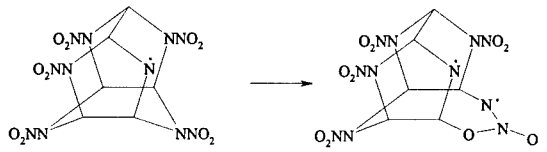
D.G. Patil and T.B. Brill determined kinetics of HNIW thermal decomposition using TGA and IR spectroscopy.[7,8] NO_2 revealed to be the main decay product followed by NO formation. Secondary HNIW cage decomposition is represented by competitive reactions. It was shown, homolysis of N–NO_2 bond is the dominant pathway of HNIW decomposition. The most portion of NO_2 produced is gaseous, but when temperature increased it reacts with nitramine cage. Reactions (1–3) explain NO formation as well as >C=O, >C=N– bonds determined in final products:

$$N\cdot + NO_2 \rightarrow N\text{–}O + NO \qquad (1)$$

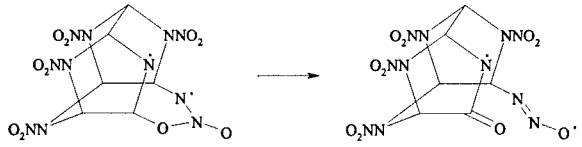
$$HC\cdot + NO_2 \rightarrow HC\text{–}O\cdot + NO \qquad (2)$$

$$HC\cdot + NO_2 \rightarrow HONO \rightarrow \tfrac{1}{2}NO + \tfrac{1}{2}NO_2 + \tfrac{1}{2}H_2O \qquad (3)$$

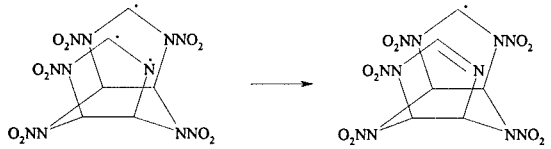
C–N bond believes to be weaken in HNIW after NO_2 loss by analogy with RDX and HMX thermolysis, bringing to the intramolecular rearrangements (4–6).



(4)



(5)

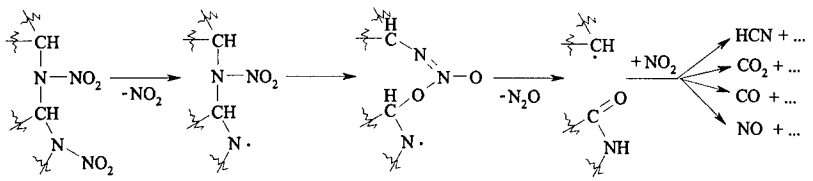


(6)

Wan X. and co-authors carried out determination of thermal stabilities of ε-CL-20 and HMX using accelerating rate calorimeter.[9] Velocities of self-heating and pressure increase have been calculated as a function versus self-heating temperature. The self-heating speed was used to determine the activation energy of HNIW decomposition. Self-heating temperature leap was found to be always much lower then at the corresponding explosive combustion temperature without detonation. Besides, this leap in HNIW case was lower then at HMX decomposition.

Ryzhkov L.R. and McBride J.M. studied a low-temperature photolysis of α-HNIW generating three $^{15}NO_2/^{15}NO_2$ radical pairs that were studied by single-crystal ESR spectroscopy at 80 K.[10] They traced radical pairs behavior increasing temperature up to 294°K. Implications for the mechanism of solid-state HNIW decomposition and the limited mobility of small molecules in lightly damaged crystals were discussed.

Löbbecke S. *et al.* investigated HNIW thermal decomposition products using rapid scan FTIR spectroscopy technique.[11,12] The main final products were determined CO_2, N_2O, NO_2 and HCN. Whereas NO and CO were slightly traced. Reaction scheme below was proposed to explain final products observed:

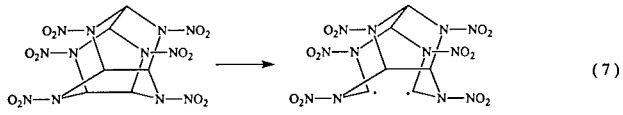


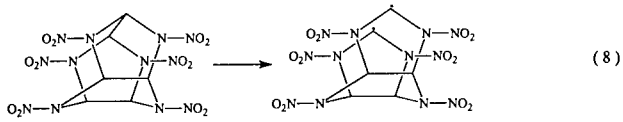
B. Korsounskii with co-workers studied kinetics of thermal decomposition of HNIW in solid state and in solution by thermo-gravimetry, manometry, optical microscopy, and IR.[13,14] A condensed residue formed during thermolysis of HNIW and its ignition at heating was found by IR spectroscopy to contain NO_2, NH_2 groups and none of C–H bonds. Thus, it was concluded that during these processes 5 of 6 NO_2 groups presenting in a HNIW molecule are lost. The isothermal decomposition of HNIW in solid state was determined to proceed with a self-acceleration. Kinetics of the reaction is described by the equation of the 1st-order autocatalysis. Activation energy of initial stage thermolysis corresponds to the calculated one of N–NO_2 homolysis.

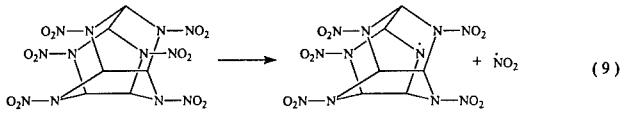
RESULTS AND DISCUSSION

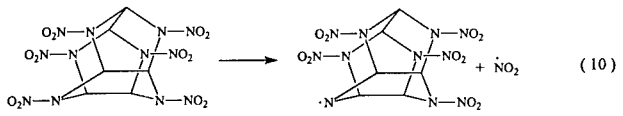
Program CASB[15] has been used to generated hypotheses about HNIW thermolysis mechanism. Reactions were generated by special rules as previously formed as new introduced taking into account functional and structural features of target compound.

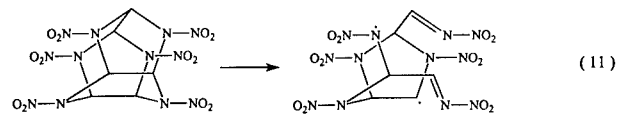
At the first stage possible primary products were generated by NO_2 group lost, C–C homolysis and concerted scission of three C–N bonds by analogy with thermal decomposition of RDX and HMX (Reactions 7–11).


(7)


(8)

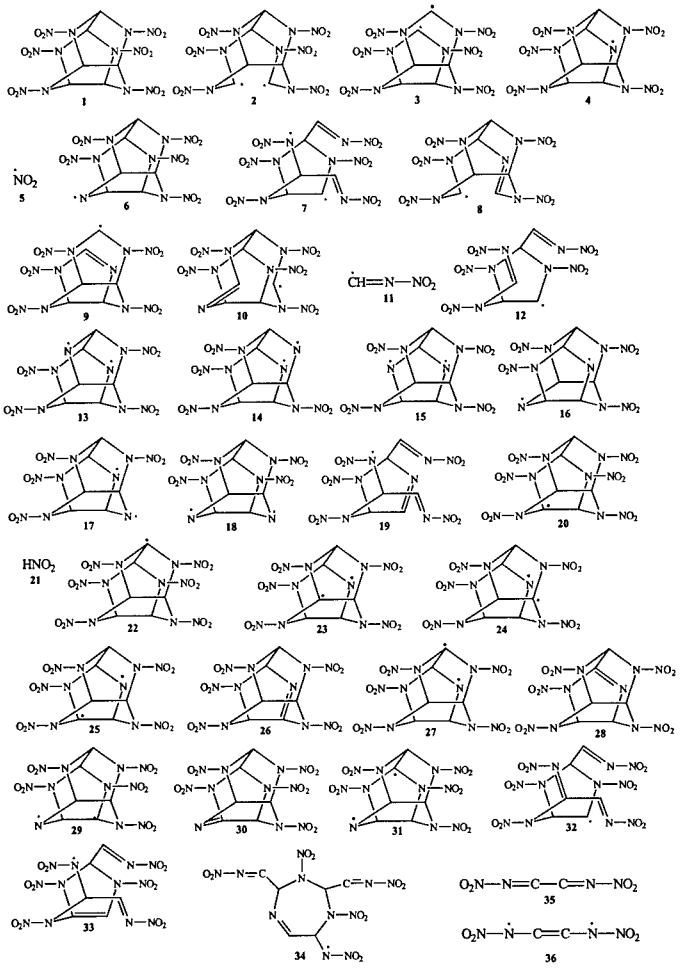

(9)

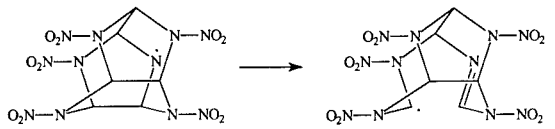

(10)


(11)

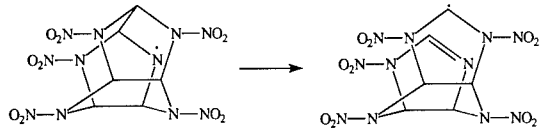
Activation energies of these reactions estimated by PM3 showed the similarity for NO_2 elimination from various nitrogens (72.226 kJ/mol and 70.742 kJ/mol for reactions 9 and 10, correspondingly). These initial stages of decomposition are believed to be equiprobable and dominating over other possible pathways of thermolysis.

Further decomposition of HNIW represents a very complex reaction recombination network including numerous intermediates. Below are structures produced on the first free stages of generation and some first reactions leading to them.

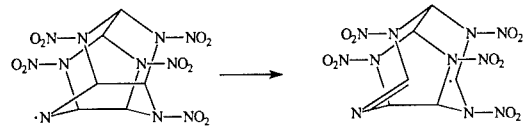




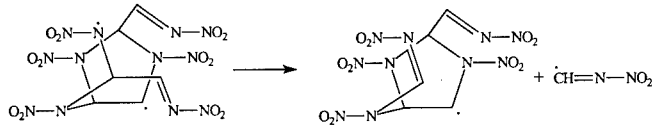
(12)



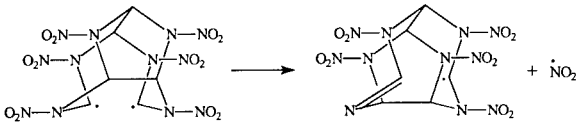
(13)



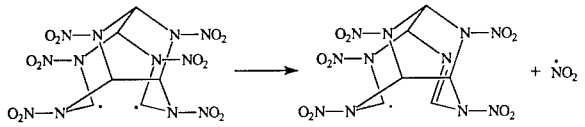
(14)



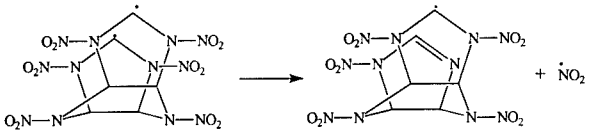
(15)



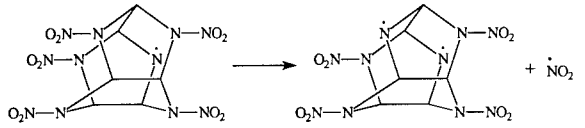
(16)



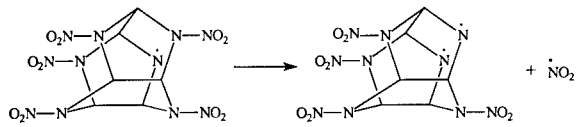
(17)



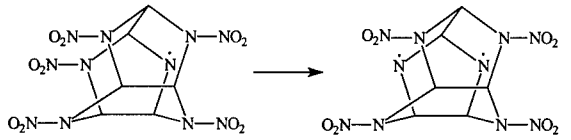
(18)



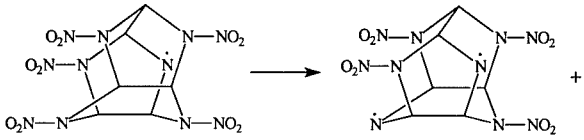
(19)



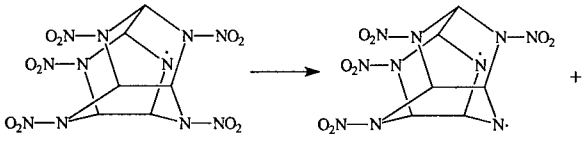
(20)



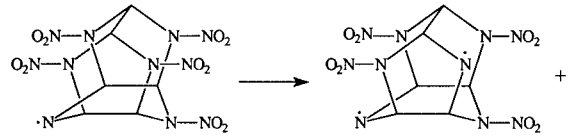
(21)



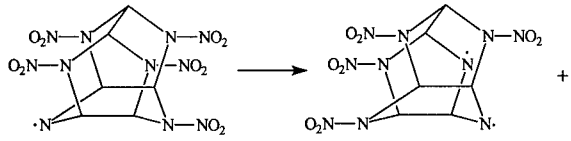
(22)



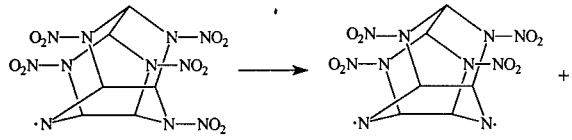
(23)



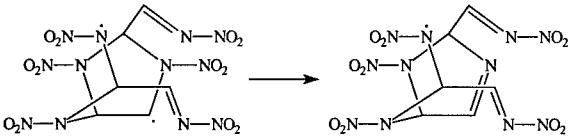
(24)



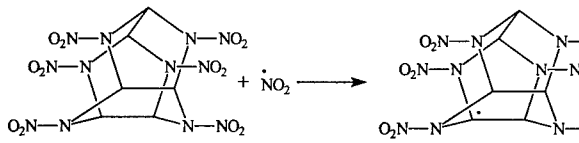
(25)



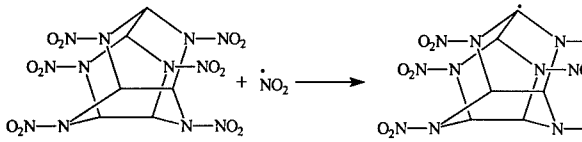
(26)



(27)



(28)



(29)

Complete reaction network of the HNIW thermal decomposition lets theoretically trace and investigate the pathways of experimentally observed final products. The first stages of the HNIW homolysis are needed to be estimated by *ab initio* activation energy calculations to evaluate precisely their kinetic preferences.

REFERENCES

1. T.A. Nielsen, R.A. Nissan, D.J. Vanderah, C.L. Coon, R.D. Gilardi, C.F. George, J. Flippen-Anderson, *J. Org. Chem.*, 1990, **55**, 1459.
2. A.J. Bellamy, *Tetrahedron*, 1995, **51**, 4711.
3. R.B. Wardle, J.C. Hinshaw, P. Braithwaite, M. Rose, G. Johnston, R. Jones, K. Poush, *Proc. of 27th Int. Annu. Conf. ICT.*, 1996, 27.1.
4. H. Bazaki, S. Kawabe, H. Miya, T. Kodama, *Proc. of 23rd Int. Pyrotech. Semin.*, 1997, 88.
5. R.B. Wardle, J.C. Hinshaw, *Brit. UK Pat. Appl.*, 1999, GB 2333292 A1, 31 p.
6. Y. Ou, H. Jia, Y. Xu, B. Chen, G. Fan, L. Liu, F. Zheng, Z. Pan, C. Wang, *Sci. China, Ser. B: Chem.*, 1999, **42**, 217.
7. D.G. Patil, T.B. Brill, *Combust. and Flame.*, 1991, **87**, 145.
8. D.G. Patil, T.B. Brill, *Combust. and Flame.*, 1993, **92**, 456.
9. X. Wan, Y. Ou, B. Chen, C. Feng, *Proc. of 3rd Beijing Int. Symp. Pyrotech. Explos.*, 1995, 520.
10. L.R. Ryzhkov, J.M. McBride, *J. Am. Chem. Soc.*, 1997, **119**, 4826.
11. S. Löbbecke, M.A. Bohn, A. Pfeil, A. Krause, *Proc. of 29th Int. Annu. Conf. ICT (Energetic Materials)*, 1998, 145.1.
12. S. Löbbecke, *Marburg, Univ., Diss.*, 1999.
13. B. Korsounskii, V. Nedelko, N. Chukanov, T. Larikova, F. Volk, *Proc. of 30th Int. Annu. Conf. ICT.*, 1999, 64/1.
14. V. Nedelko, N. Chukanov, A. Raevskii, B. Korsounskii, T. Larikova, O. Kolesova, F. Volk, *PEP*, 2000, **25**, 255.
15. A.A. Porollo, D.E. Lushnikov, T.S. Pivina, V.P. Ivshin, N.S. Zefirov, *Russ. Chem. Bull.*, 1999, **48**, 1845.

BURN RATE STUDIES OF COMPOSITE PROPELLANTS CONTAINING ULTRA-FINE METALS

P. Lessard, F. Beaupré and P. Brousseau,

Emerging Energetic Materials Section
Defence Research Establishment, Valcartier
2459 Pie-XI Blvd North, Val-Bélair, QC, Canada G3J 1X5

ABSTRACT

This paper discusses the effect of the incorporation of nano-powders in rocket propellants and gun propellants. Defence Research Establishment Valcartier (DREV) has initiated studies on the subject. The powders were added to an experimental minimum smoke rocket propellant, to a low smoke rocket propellant and to a LOVA-type gun propellant. Burn rate measurements were carried out in a strand burner for rocket propellants and in a closed vessel for gun propellants. Nanometric silicon, aluminium (ALEX) and a magnesium-aluminium alloy were tested at percentages up to 10% in GAP/AN (Glycidyl Azide Polymer/Ammonium Nitrate) propellants. The burn rate results were then compared to those of formulations containing micron-size silicon and aluminium. Ultrafine aluminium (ALEX) was added in HTPB/AP (Hydroxyl-Terminated PolyButadiene/Ammonium Perchlorate) propellants until the limit of processability was reached at 30% aluminium. It was also added at 3% and 5% in gun propellant formulations. Formulations of GAP/AN propellants containing nanometric aluminium showed very little improvement in burn rate, and the best results were obtained with silicon metal. Burning rate values of HTPB/AP mixes with ALEX increased at all pressures, a behaviour consistent with observations from other researchers. In gun propellant formulations it did not show an increase in the burn rate. In fact, larger micron-size aluminium promoted higher burn rates.

INTRODUCTION

There has been a lot of interest in recent literature for the use of ultra-fine aluminium powder (Refs. 1-2). These powders are being studied for potential applications in both propellants and explosives. About two years ago, the Defence Research Establishment, Valcartier (DREV) has initiated studies on the subject. While studying the incorporation of nano-powders into energetic materials such as explosives and rocket propellants, their possible application to gun propellants was also considered, earlier studies having shown that the incorporation of aluminum powders into LOVA-type gun propellant formulations (Ref. 3) had a beneficial effect on the burning rates. However, in these studies, the aluminum incorporated in the formulations had a particle size in the micron range. Based on that, the use of nano-powders was expected to give similar or even better results.

One of the objectives of the present work is to assess the consequences of the inclusion of ultra-fine metals on propellant performances. Preliminary results on the effect of the nature, particle size and concentration of various metal powders on the burn rate of composite propellants, both gun and rocket propellants, are reported in this paper.

EXPERIMENTAL

Both rocket and gun propellant formulations were considered. The approach and results for each will be reported in separate sections.

Rocket Propellants

Formulations

Both an experimental minimum smoke GAP/AN and a low smoke HTPB/AP propellant formulation in development were chosen. The selected GAP/AN propellant formulation is based

on earlier studies (Ref. 4). The binder is based on GAP cured by a mixture of IPDI and N-100. The system is plasticized , in a polymer/plasticizer ratio of 3/1, with a mixture of 2/3 BTTN and 1/3 BDNPA/F. DBTDL at very low concentration is used as a curing rate catalyst. The oxidizer consist of 65% by weight of a bimodal mixture (20/80) of prilled PSAN containing 3% ZnO and FEM ground NSAN. The formulation also included 0.75% by weight DPA and 0.25 % MgO as chemical stabilisers. Metal additives were added at the expense of the nitrate blend.

Silicon metal has been used previously as an additive for GAP/AN propellant (Ref. 5). It has been demonstrated that it can be included up to a level of 3% by weight apparently without jeopardising the minimum smoke qualification of the propellant (Ref. 5). While slightly improving the burn rate and being theoretically beneficial to the specific impulse, silicon metal generally shows a poor burning efficiency. For this reason it was felt desirable to experiment with much finer material. Consequently, an experimentally produced lot of nano-sized silicon metal was procured for comparison with the standard 7.4 μm material previously used at DREV. A similarly produced sample of magnesium-aluminium alloy containing 25% Mg was available for testing. ALEX nano aluminium from Argonide was also included in the study along with other aluminium grades for comparisons: ATA-7300 leafing flakes, Valimet H-2 and H-15. All were tested at 3% in the propellant and some (Nano Si, ALEX and H-2) up to 10% to assess concentration effects.

For the HTPB/AP propellant, a formulation developed in a previous project (Ref. 6) on high burn rate (HBR) propellants for nozzleless boosters, was selected as a starting point. The derived base formulation has a solid loading of 85%, consisting of a blend of 55% 200 μm and 45% 3.5 μm AP, and 0.5% hydrated ferric oxide (FeOOH) as burn rate catalyst. The binder is composed of the well-known R-45M hydroxyl-terminated polybutadiene (HTPB) mixed with a plasticizer (isodecyl pelargonate, IDP) and cured with dimeryl diisocyanate (DDI). The ALEX nano aluminium was added at the expense of the AP blend up to 30% by weight of the formulation. Two regular grades of aluminium, the Valimet H-2 and H-15, were also incorporated, up to 20%, in propellant formulations as a reference.

Processing

All propellants were processed in a Helicone 4CV (capacity 0.5 USgal) from Atlantic Research Corporation at a batch size of 500g.

Burning Rates

Burning rates measurements were performed in a strand burner at an initial propellant temperature of 25°C. GAP/AN formulations were fluid enough to be cast in fireproof polyethylene tubes. HTPB/AP propellants strands were cut from blocks and inhibited with latex paint.

Gun Propellants

Formulations

LOVA-type, nitramine-based, gun propellant formulations containing ALEX were processed and compared to an XM-39 type formulation which did not contain any aluminum powder and to formulations including regular grades of aluminum. Table I describes the different grade of aluminum powders that were used.

Processing

All formulations were processed in a 1 USgal capacity sigma blade mixer at a batch size of 1000g using a typical solvent-based process at a temperature of 50°C and a typical 7 perforations grain extruded.

Burning Rates

The formulations were submitted to a ballistic evaluation in a 700 cm^3 closed vessel at a loading density of 0.15 g/cm^3.

TABLE I

Aluminum Powders Included In Gun Propellant Formulations.

Grade	Average Particle Size
MDX-65	7.5 µm
MDX-75	54 µm
MDX-90	35.5 µm
ALEX	150 nm

RESULTS AND DISCUSSION

Rocket Propellants

GAP/AN Propellant

Table II summarises the effect of 3% metal on the burn rate of GAP/AN propellants. Results for three reference batches and duplicate results for one are reported. All values fall roughly between ± 4% of the average values.

Best results overall are obtained with silicon metal, independently of particle size. Nanosized silicon metal is showing better values at higher pressures thus resulting in an increased exponent. Aluminium, even nanometric, shows very little significant effect on burn rate, H-2 turning out the best improvement at all pressures while ALEX reduce the burn rate at 6.9 MPa and increase

it at 20.69 MPa thereby increasing the already high pressure exponent. Magnalium produce no change in burn rate. Even when there is an increase, in general all formulations are showing very little improvement in burn rate.

TABLE II

GAP/AN Propellant - Effect of 3% Metal on Burn Rate

		Burn Rate (cm/s)		
Additives	Grade	6.9 MPa	13.79 MPa	20.69 MPa
Nil	w/o	0.55	0.96	1.35
		0.56	0.95	1.25
		0.55	0.95	1.29
		0.58	1.00	1.36
	Average	***0.56***	***0.97***	***1.31***
Si Metal	7.4 μm	0.63	1.06	1.46
	290 nm	0.59	1.10	1.54
Aluminum	ATA-7300 flakes	0.53	0.95	1.35
	H-15 (12 μm)	0.58	1.03	1.41
	H-2 (2 μm)	0.62	1.04	1.40
	ALEX (150 nm)	0.53	0.96	1.40
MgAl	25% Mg (80 nm)	0.56	0.95	1.37

Table III summarizes the effect of metal content on the burn rate of GAP/AN propellants. Nanometric silicon metal shows the best significant improvement overall (7-19%) of all additives at higher pressures (13.79 and 20.69 MPa) in the 1-5% metal content range.

This is illustrated in Figure 1 where the relative burn rates of nanometric silicon metal containing GAP/AN propellant formulations are plotted against the percentage of metal incorporated in the formulation. Valimet H-2 aluminium produces modest (10% at best) but significant increases in burn rate at all pressures and concentrations (1-10%) with nearly constant pressure exponents. Nanometric aluminium shows a different behaviour, with reduced burn rates at low pressures and low metal concentration and increased burn rates at high pressure / high concentration and thus increased pressure exponents. Again a 10% increase in burn rate is the best result obtained.

TABLE III

GAP/AN Propellant - Effect of Metal Content on Burn Rate

		Burn Rate (cm/s)		
Additives	Content	6.9 MPa	13.79 MPa	20.69 MPa
Reference	0%	0.55	0.96	1.35
	0%	0.56	0.95	1.25
	0%	0.55	0.95	1.29
	0%	0.58	1.00	1.36
Average	***0%***	***0.56***	***0.97***	***1.31***
Nanometric	1%	0.58	1.09	1.41
Silicon	3%	0.59	1.10	1.54
Metal	5%	0.60	1.04	1.56
	10%	0.55	0.93	1.37
Aluminum	1%	0.64	1.00	1.39
H-2	3%	0.62	1.04	1.40
	5%	0.59	1.05	1.43
	10%	0.61	1.05	1.47
ALEX	1%	0.50	0.92	1.32
	3%	0.53	0.96	1.40
	5%	0.55	1.00	1.44
	10%	0.60	1.06	1.49

HTPB/AP Propellant

Table IV summarises the effect of aluminium content and type on the burn rate of HTPB/AP propellants. In the case of regular aluminium, Valimet H-2 (2μm) tends to only slightly increase burn rates, the larger increase being observed at 5% metal content and accompanied by a higher pressure exponent at low pressures. As for the H-15 (12μm) from the same source, burn rates is reduced at all pressures and exponents tend to decrease as well. Burn rate curves for ALEX are illustrated at Figure 2.

TABLE IV

HTPB/AP Propellant - Effect of Al Content.

		Burn Rate (cm/s)				
Additives	Content	6.9 Mpa	10.3 Mpa	13.79 Mpa	20.69 Mpa	27.59 Mpa
Reference	0%	1.04	1.12	1.29	1.72	2.62
ALEX	5%	1.46	1.68	1.85	2.79	3.97
	10%	2.00	2.71	2.78	3.47	5.04
	20%	2.22	2.78	3.23	3.79	4.96
	30%	2.16	2.74	3.18	3.80	4.73
H-2	5%	0.89	1.18	1.43	2.02	2.59
	10%	1.09	1.23	1.41	1.85	2.37
	20%	1.05	1.17	1.32	1.62	2.06
H-15	5%	1.04	1.17	1.24	1.62	2.26
	10%	0.89	1.02	1.14		2.09
	20%	0.76	0.82	0.92	1.09	1.42

Burning rate values drastically increase at all pressures up to a 10% metal content, a behaviour which is consistent with previous observations (Refs. 1-2). Although it needs to be confirmed, there seems to be a platonization effect, in the 10-15 MPa range, between 5 and 10% ALEX content. Burn rates reach their maximum values of approximately 2-2.5 times the reference propellant burn rate at a 20% metal content. Increasing the ALEX content to 30% does not result in a further increase, but drastically affects the propellant castability.

Gun Propellants

Ballistic data for the gun propellants formulations is given in Table V, including the parameters of a Vieille's burning rate law fitted through the results. The actual curves are shown in Figure 4 where the evolution of the burning rates of the six formulations is illustrated as a function of pressure.

TABLE V

Ballistic Data For Gun Propellant Formulations

Formulation	Aluminium Grade	Content (%)	P_{max} (Mpa)	Pression (Mpa)	Coefficient $(Mpa\text{-}s)^{exp}$	Exponent	r^2
XM - 39	-	-	182	20 - 180	1.09E-01	0.776	0.9890
LOVA - 297	ALEX	3	174	20 - 174	2.45E-02	0.995	0.9916
LOVA - 299	ALEX	5	187	20 - 180	3.62E-02	0.963	0.9909
LOVA - 298	MDX - 65	3	184	20 - 180	1.61E-01	0.607	0.7786
LOVA - 301	MDX - 90	3	182	20 - 180	2.01E-01	0.575	0.7547
LOVA - 300	MDX - 75	3	183	20 - 180	1.31E-01	0.753	0.9390

Only formulation LOVA-300 which contains MDX-75, the coarser particle size Al powder, exhibits an increase in burning rates over the formulation of reference, propellant XM-39 wich does not contain any metal powder. In fact, the two formulations with ALEX (LOVA- 297 and 299) have burn rates lower than all the other formulations tested. This is in contradiction to previously published results involving a double-base (NC/DINA) propellant (Ref. 7) wich seems to demonstrate the effect of the different type of propellant. Close examination of the pressure-time curves (not shown) reveal a slower pressure rise with ALEX containing formulations.

CONCLUDING REMARKS

In GAP/AN propellant,

- at 3% metal content, in general very little improvement in burn rate is observed.
- the best results are obtained with silicon metal, independently of particle size.
- nanosized Si metal shows significant improvement in the 1-5% metal content at high pressure (≤13.79 MPa).
- ALEX is modestly effective only at high metal content and high pressure.

In HTPB/AP propellants,

- fine aluminium (H-15, 12 μm) lowers burn rates.
- very fine aluminuim (H-2, 2μm) slightly increases the burn rate and pressure exponent.
- nanosized ALEX increases substancially the burn rates (100-125%) and a maximum is reached at a 20% metal content. There could be a platonization effect, in the 10-15 MPa range, between 5 and 10% ALEX content.

In LOVA gun propellants,

- the use of nano-powders in formulations has not proven to be effective from a burn rate standpoint as preliminary evaluation do not show an increase when ALEX is present.
- formulations containing aluminum of larger particle size exhibit higher burn rate values than those containing ALEX.
- only the formulation including the coarser particle size aluminium (MDX-90, 35.5 μm) had a burn rate faster than the reference XM-39 propellant.

Results demonstrate that the presence of nanosized metals in propellants does not necessarily translate into an improved burn rate, depending on the type of propellant and most probably the burning mechanism involved.

REFERENCES

1. Mench, M.M., Yeh, C.L. and Kuo, K.K., "Propellant Burning Rate Enhancement and Thermal Behavior of Ultra-fine Aluminum Powders (ALEX)", 29th International Annual Conference of ICT, Karlsruhe, Federal Republic of Germany, 1998, pp. 30-1,15.

2. Simonenko, V.N. and Zerko,V.E., "Comparative Studying the Combustion Behavior of Composite Propellants Containing Ultra Fine Aluminum", 30th International Annual Conference of ICT, Karlsruhe, Federal Republic of Germany, 1999, pp. 21-1,14.

3. ARDEC, private communication.

4. Lessard, P., Villeneuve, S. and Benchabane, M., "Insensitive, Minimum Smoke, Ammonium Nitrate Propellants", Proceedings of the 1993 Spring Technical Meeting of The Combustion Institute, Canadian Section, Université Laval, 10-12 May 1993, pp. 47-1 to 47-4.

5. Warren, L.C. and Asaoka, L.K., "Silicon as High Performance Fuel Additive for Ammonium Nitrate Propellant Formulations", U.S. Patent 5,500,061, Mar. 19, 1996.

6. Farinaccio, R. and Lessard, P., "Experimental Investigation of High Burn Rate Propellant for use in Nozzleless Boosters", AIAA 2000-3320, 36th AIAA/ASME/SAE/ASEE Joint Propulsion Conference & Exhibit, July 17-19, 2000, Huntsville, Alabama

7. Baschung, B., Grune, D., Licht, H., and H. Samirant., "Combustion Phenomena of a Solid Propellant Based on Aluminium Powder", 5th International Symposium on Special Topics in Chemical Propulsion (5-ISICP), Stressa, Italy, June 19-22, 2000

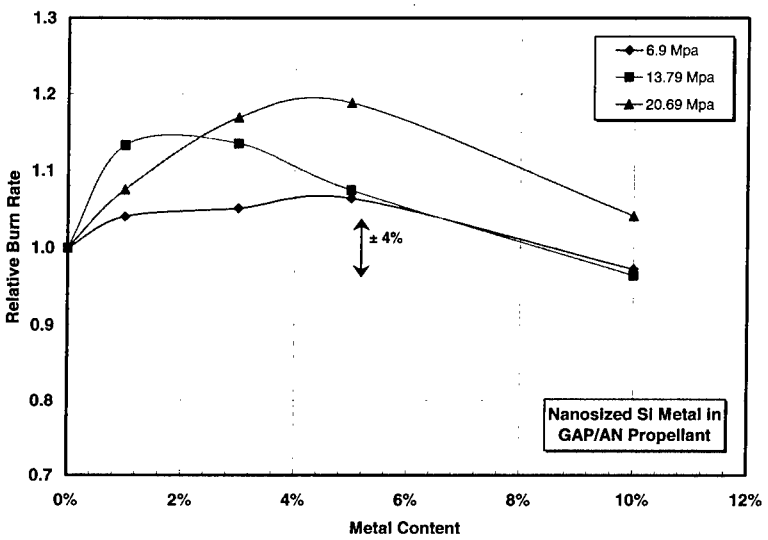


FIGURE 1 – Relative burn rates of nanometric silicon metal containing GAP/AN propellant formulations.

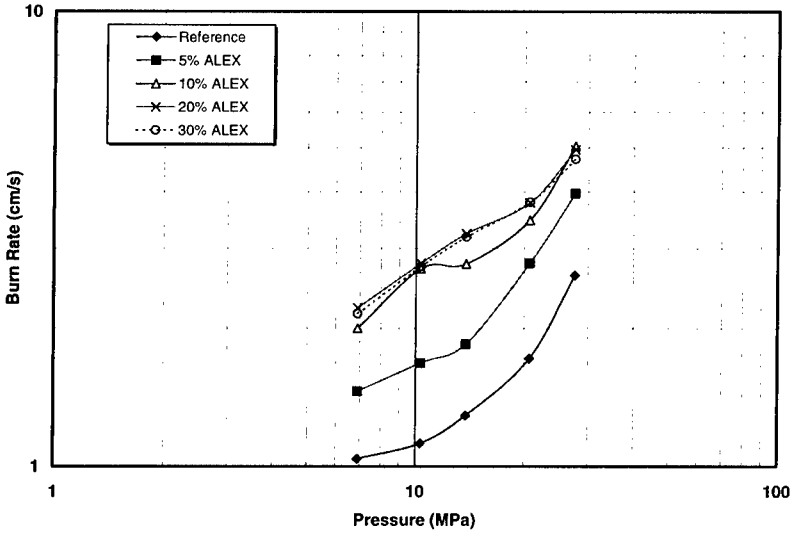


FIGURE 2 – Effect of ALEX content on burn rate-pressure relationship of HTPB/AP propellants

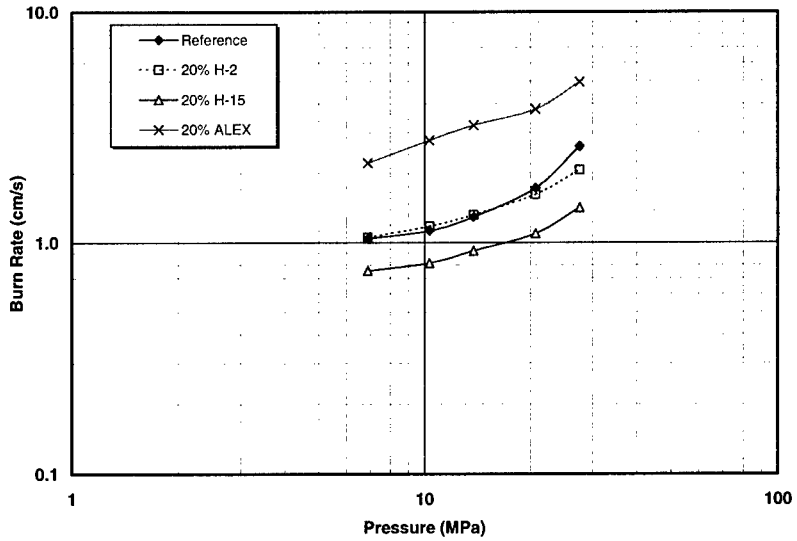


FIGURE 3 – Effect of aluminium type on the burn rate of HTPB/AP propellant at 20% metal content.

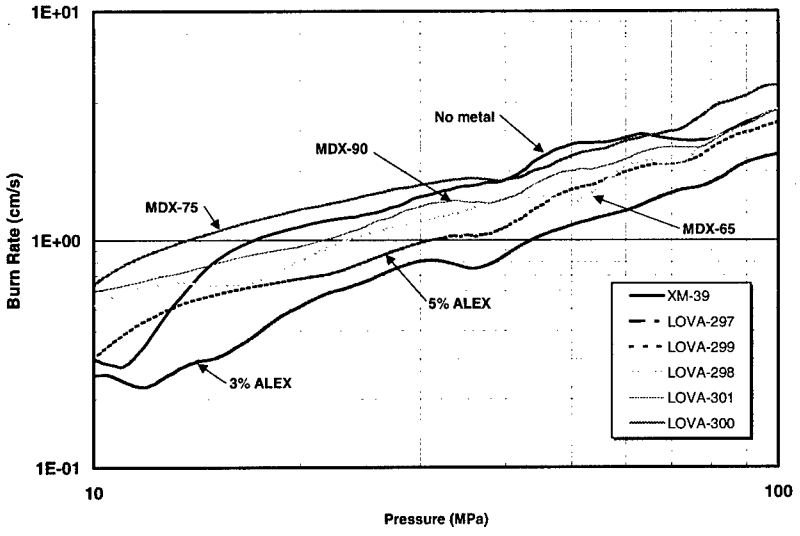


FIGURE 4 - Effect of aluminium type on the burn rate of gun propellant

NEW MELT-CAST EXPLOSIVES BASED ON ENERGETIC THERMOPLASTIC ELASTOMERS

Patrick Brousseau, Guy Ampleman and Sonia Thiboutot
Defence Research Establishment Valcartier
2459 Pie-XI Blvd. North
Val-Belair, QC
Canada G3J 1X5

and

Emmanuela Diaz
BCR Polysyntech Inc.
1524 Des Impératrices
Val-Bélair, Québec, Canada

ABSTRACT

A new class of melt-cast explosives was developed at Defence Research Establishment Valcartier (DREV) that incorporates energetic thermoplastic elastomers. In these new explosives, an energetic polymer is mixed with existing melt-cast compositions to reduce their vulnerability to external threats. This paper describes the first mixes of the new explosives and the tests performed on them. The tests were carried out to assess the potential of the new formulations. They include basic safety tests such as BAM Impact and Friction sensitivity tests and Vacuum Stability Tests. The DREV Gap Test was also carried out to assess the shock sensitivity of the mixes. The performance was evaluated through measurements of the detonation velocity. The results of Rifle Bullet Tests, which are a scale-down version of the bullet impact tests, are reported. The new explosives were stable, had performances between 81 and 95 % of Comp. B and showed a reduction of up to 27 % in shock sensitivity compared to Octol. The worst reaction observed in Rifle Bullet Tests at 10% and 20% polymer was a burning reaction. It was also demonstrated that the products are completely recyclable through simple procedures. The explosives showed a good potential that warrants additional investigations.

INTRODUCTION

Most new explosives developed for insensitive munitions are cast-cured plastic-bonded explosives. Their manufacturing process is very different from the one used in melt-cast operations. For a munitions industry, it means major capital investments for new equipment and acquisition of new processing methods. Another major disadvantage is the cumbersome disposal of the non-recyclable cured explosive at the end of its life cycle. Consequently, there is a strong need for a melt-cast explosive with a reduced vulnerability. The objective of this study was to obtain data on a new insensitive melt-cast explosive to assess its sensitiveness. Four main goals were sought with the new product:

- To achieve a significant reduction of vulnerability compared to Composition B.
- To match the performance of Composition B in terms of detonation velocity and pressure.
- To use existing melt-cast equipment for processing.
- To obtain a recyclable product.

There were some attempts in the past at developing a less-sensitive melt-cast explosive, but they all had drawbacks. Either the performance was too low, or the sensitivity was too high. Two good examples are the American AFX-644/645 [1] and the French XF 13 153 [2], which are based on TNT and NTO. They show good IM characteristics but have performances significantly lower than Composition B. A recent study by Cliff and Smith [3] also presented TNT/NTO formulations with detonation velocities and pressures down by approximately 7% and 21% respectively compared to Composition B. More work is needed to improve the performance of those products.

The approach proposed in the current study is innovative. An energetic thermoplastic elastomer (ETPE) is included in melt-cast TNT-based formulations. The idea of adding polymers to melt-cast explosives is not new. Various polymers were added to melt-cast formulations in the past [4 to 8]. However, the polymers were often

inert and a significant reduction in performance was observed. In the case of this study, the polymer is energetic and was developed at DREV [9]. It is unique and so far, it has shown great promise in our formulations. The polymer is rubbery in nature and transmits this behaviour to the melt-cast mixture. For this reason and because melt cast explosives contain TNT, the new explosives were named XRT for eXperimental Rubbery TNT. The incorporation of the polymer gives a very different behaviour to the melt-cast explosives. The mechanical properties were improved significantly. The approach taken was simply to add the polymer to existing well-known melt-cast explosives such as Octol and Composition B. Other approaches are possible and will be studied later.

EXPERIMENTAL

Polymer

The polymers used in this study are energetic thermoplastic elastomers (ETPEs) created at DREV [9]. Glycidyl azide polymer (GAP) having a functionality of two or less was used as a macromonomer and was polymerised with diphenylmethane-4,4'-diisocyanate (MDI) at a NCO/OH ratio of 1, to produce a linear copolyurethane thermoplastic elastomer which was not chemically crosslinked. This was only obtained using highly controlled conditions. The NCO/OH ratio must be about 1 to avoid chemical crosslinking between the chains and to obtain the best reproducible copolymer. In this copolymer, the elastomeric segment is provided by the amorphous glycidyl azide polymer, and the thermoplastic segment is provided by the urethane moieties. Each urethane group within the copolymer is capable of forming hydrogen bonds with the oxygen of another urethane or with the oxygen of an ether. Moreover, it is known that aromatic rings have a great tendency to align, therefore bringing together the urethane groups promoting hydrogen bond formation. By doing so, physical crosslinks are obtained between the chains and, as a result, an energetic copolyurethane thermoplastic elastomer is obtained (Figure 1). It should be mentioned that this process is not restricted to GAP but can be applied to any dihydroxyl-terminated telechelic energetic polymer having a functionality of two or less such as poly 3-azidomethyl-3-methyloxetane (AMMO), poly bis 3,3-azidomethyloxetane (BAMO), poly 3-nitratomethyl-3-

methyloxetane (NIMMO) or poly glycidyl nitrate (GLYN). The same polymers were used in gun propellant formulations in the past and showed good results [10].

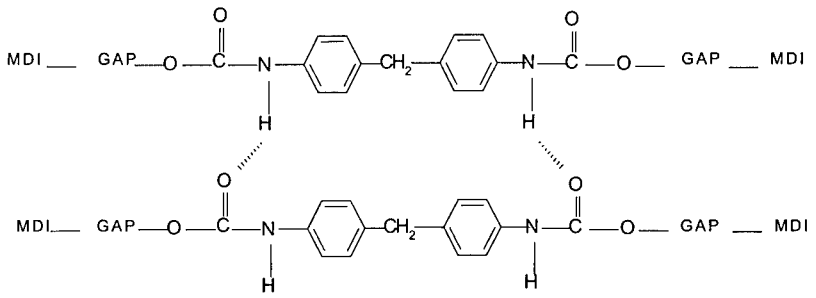


Figure 1: Illustration of a hard segment in a copolyurethane thermoplastic elastomer

Mixing

The polymer was included directly into regular melt-cast explosives such as TNT, Composition B, and Octol. Octol type II came from Holston Company and its batch number was HOL-505-655. Octol type II is an HMX/TNT mix at a ratio 70/30 whereas composition B is a mixture of RDX and TNT in the proportion of 60/40. The mixtures were prepared at the laboratory scale and pilot scale. In the laboratory, the quantity could vary between 10g and 50 g, whereas at the pilot plant it varied between 500 and 2500 g. The XRT formulations discussed in this paper are mixes of 10-20 % of ETPE in Octol type II or in Composition B. In addition, some 50/50 mixtures were made to study the compatibility of the ingredients. For the preparation of small-scale mixtures, all ingredients, e.g. 8 g of Octol II and 2 g of ETPE 2000C, were put in a flask and in an oil bath at a temperature of 100°C. When the TNT was melted, the agitation was started. After one or two hours, depending of the quantity of ETPE, the mixture was homogeneous and it was ready to be cast. At the pilot plant, the preparation of large-scale mixtures consisted in melting the Octol (or Comp. B) with steam in a jacketed vessel. The ETPE was added in three or four increments, depending on the percentage of

ETPEs in the final mixture, and each addition weighted 50g. The process lasted approximately two hours. At the end, the mixture was cast into various moulds.

Test Methods

The stability of pure compounds and the compatibility with other products were verified by the Vacuum Stability Test based on STANAG 4479 [11]. One modification has been made on that procedure: the duration of the analysis was extended to 48 hours at 100°C. A gassing of more than 2 ml/g of sample indicates an incompatibility.

Julius Peter impact and friction apparatuses were used to test the sensitivity of mixtures [12]. The minimum amount of energy necessary to have a sample reacting (explosion or decomposition) was measured. In addition, the viscosity was evaluated using a Brookfield apparatus model RVF. For each mixture, the measure was taken at four different rates (2, 4, 10 and 20 Rotations Per Minute - RPM).

The detonation velocity of the experimental compositions was measured on cylinders of explosives using ionisation probes. The cylinders were 2.54 cm in diameter and 20 cm long, and they were fired vertically. Initiation was made at the top using a pellet of RDX/wax (98.5/1.5) 3.18 cm in diameter by 2.54 cm long. A length of three diameters was left at the top to stabilise the detonation wave. Three probes were placed, separated by about 5.1 cm from each other, starting at 7.6 cm from the top. A small metal witness plate (7.6 cm x 7.6 cm x 0.65 cm) was placed underneath the cylinder to confirm the detonation of the cylinder. A small length (2.54 cm) was left at the bottom of the cylinder to avoid reflections off the witness plate. The distance between the probes was measured exactly and a counter recorded the time between each activation of the probes. Two velocities were then recorded. The reported value is the total distance between the first and the third probe divided by the time. The two numbers are used to verify that the velocity is constant and to evaluate the error on the measurement. All the cylinders measured for that study had a constant velocity at a diameter of 2.54 cm.

The shock sensitivities of two XRT formulations and of Octol were evaluated using the DREV Gap Test [13]. Samples 3.1 cm in diameter by 7.6 cm long were cut

from long cylinders and tested unconfined. The shock was provided by two pressed Tetryl pellets having a diameter of 1.572 cm and a length of 1.68 cm. These were initiated by an electrical bridge wire detonator. The barrier material was 1100-0 aluminium. A witness plate made of mild steel was placed at the bottom of the charge to confirm a detonation.

Rifle Bullet Tests were performed on two XRT formulations, Composition B and Octol according to the US Bullet Impact Method found in reference 14. The explosives were cast in standard 2-inch (5.1 cm) steel pipes (1/8 inch nominal) that were 7.6 cm long and fitted at both ends with standard screwed caps for 2-inch pipes. Each pipe contained approximately 250 g of explosives. Five samples of each explosive were tested. Bullets of calibre 7.62 mm were fired from a precision NATO tube placed at 27.5 meters from the charge. The pipes were placed in an upright position and held on a wooden 2x4 using plastic tie wraps. Five tubes were tested for each explosive. Ball C21 bullets were used. After it was realised that the bullets did not have enough energy to pierce the back wall of the filled pipes, two tests were made with Belgium armour-piercing bullets, one for each type of XRT formulation. A radar recorded the velocity of the bullets and a sonometer was placed at a distance of about 50 meters.

RESULTS AND DISCUSSION

Stability and Compatibility

The compatibility of the products was verified using Vacuum Stability Tests (VST). Mixtures containing 50 % of ETPE and 50 % of other explosives were made. The results are reported in Table 1. Since there was no gas evolved at levels superior to 2 ml/cm^3, the products were assessed as compatible.

Impact and Friction Sensitivity

The results of BAM impact and friction tests are presented in Table 2. It is clear from the results that the polymer is less sensitive to friction and reduces the sensitivity of all the mixes. It was a good indication that the polymer had a positive effect on melt-cast explosives, at percentages of 15 and 20%.

Table 1. Gassing (ml/g) of pure compounds and mixtures

SAMPLE	GASSING
	(ml/cm^3 ± 0.1)
TNT	0
ETPE	0.6
HMX (class III)	0.1
TNT/ETPE (50/50)	0.8
HMX class III/TNT/ETPE (50/25/25)	0.3
Comp.B/ETPE (50/50)	0.7
Octol/ETPE (50/50)	0.6

Table 2. Impact and friction sensitivity of mixes.

SAMPLE	IMPACT	FRICTION
	N.m	*N*
TNT	10	80
ETPE	15	> 360
Composition B	5	240
Octol	7.5	120
TNT/ETPE (50/50)	15	>360
Octol/ETPE (80/20)	20	>360
Octol/ETPE (85/15)	20	360
Comp. B/ETPE (80/20)	20	240
Comp. B/ETPE (85/15)	15	360

Viscosity

The addition of polymer increased the viscosity of the mixes. A factor of five was observed when the level of polymer was 20%. It indicates that it may be difficult to cast the product using current melt-cast processing equipment. However, the viscosity of

those Octol/ETPE mixes was still very much lower than the viscosity of plastic-bonded explosives, which is in the kP range.

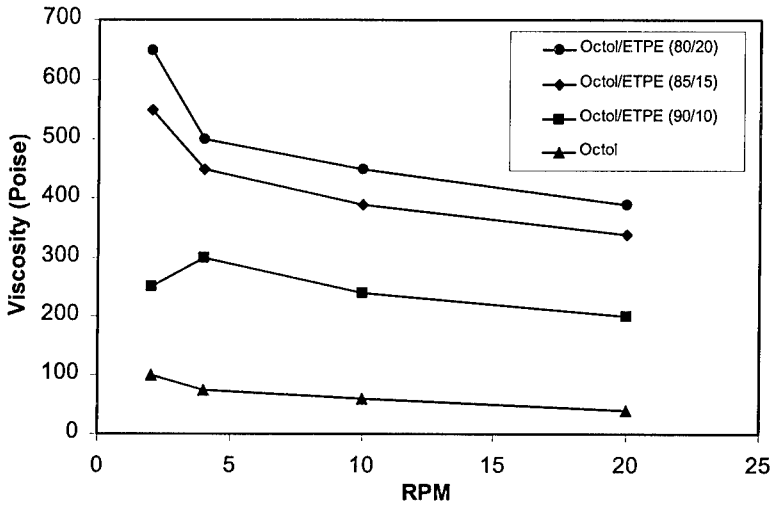


Figure 2: Viscosity of the mixes.

Performance

The measured detonation velocities of the formulations are reported in Table 3, along with the measured densities. Since one of the objectives of the project was to match the performance of Composition B, the velocities were also compared to selected values for the latter taken from the literature [15].

The detonation pressure is actually a better measurement of the energy of an explosive than the detonation velocity alone. No measurements of the detonation pressure were made on the products. However, an approximation [15] may be calculated with the simple equation:

$$P_{CJ} = \frac{1}{4}\rho\, D_v^2$$

where P_{CJ} is the Chapman-Jouguet pressure, ρ is the density of the explosive and D_v is the detonation velocity. The results are presented in Table 3.

The only product that had a performance equivalent to Comp. B was the product with 10% of ETPE. The products had theoretical detonation pressures equivalent to 81-95 % of the value for Composition B.

Table 3: Performance of the products

MIX	DENSITY	D_V	RELATIVE D_V	P_{CJ}	RELATIVE P_{CJ}
	g/cm³	*m/s*	*%*	*GPa*	*%*
Composition B[1]	1.69	7840	100	26.75	100
Octol/ETPE 80/20	1.59	7390	94	21.71	81
Octol/ETPE 85/15	1.64	7614	97	23.75	89
Octol/ETPE 90/10	1.67	7783	99	25.29	95
Octol	1.80	8388	107	31.70	119

1- From reference 15

Shock sensitivity

Gap Test results revealed a significant decrease of the shock sensitivity with the increase of ETPE content in the mixes. Only two formulations were tested, 10% ETPE and 20% ETPE in Octol. They were compared to Octol alone. The results are given in Table 4. Octol/ETPE (80/20) had the lowest sensitivity. It was substantially (27%) lower than Octol 70/30 and it was lower than Octol/ETPE (90/10). It is difficult to know whether the cause of this lower sensitivity is the lower percentage of HMX in the mix, the addition of the polymer or both. However, the quality of the charges was lower for the products with polymer. Since an increase of the percentage of polymer translates into an increase of the viscosity, Octol/ETPE (80/20) contained more defects (air bubbles). It is well known that the presence of defects increases the shock sensitivity of the explosives. Therefore, it should be possible to reduce this sensitivity through improvements in the casting methods.

Table 4. GAP Test results

PRODUCT	NITRAMINES	GAP THICKNESS	PEAK PRESSURE
	%	*Mm*	*GPa*
Octol	70	15.3	8.06
Octol/ETPE (90/10)	63	12.8	9.80
Octol/ETPE (80/20)	56	11.2	11.12

Recycling

This section describes the method used to separate nitramines, TNT and ETPEs in the final mixtures. To observe the influence of the compounds on the efficiency of the method, two types of nitramines (RDX and HMX) were tested.

The process started with nitramines decantation and was followed by separation of TNT and ETPE by solid-liquid extraction. The mixtures, composed of 6 g of nitramines, 2 g of TNT, and 2 g of ETPE, were put in ethyl acetate. TNT and ETPE were dissolved, whereas nitramines were insoluble. Finally, the HMX or RDX was filtered and a yield of 99% was obtained in both cases. Ethyl acetate was evaporated to give back the TNT/ETPE mixture.

Subsequently, the TNT/ETPE mixture was placed in a soxhlet. TNT was dissolved first, leaving the ETPE in the extraction timble. The solvent was evaporated and TNT was recuperated. The recycled TNT was analysed by NMR ^{1}H liquid spectroscopy to look for traces of ETPE. The spectrum showed only two peaks corresponding to pure TNT. No traces of ETPEs were found.

Afterwards, the extraction apparatus was charged with ethyl acetate to recover the ETPEs inside the timble. Yields obtained for the first extraction indicated that the ETPE contained a small percentage of trapped TNT. The recuperated ETPE was analysed by NMR ^{1}H liquid spectroscopy to determine the amount of TNT present. The NMR analyses showed 4% of TNT was present in the TNT/ETPE 2000C mixture. These

results corresponded in both cases to the missing quantity of TNT from the TNT dissolution step. More work is needed to completely clean the ETPE.

Rifle Bullet Tests

The Rifle Bullet Test results are summarised in Table 5. The results for Octol and Composition B were easily predictable. All the tests produced violent reactions. However, there were no complete detonations since the cylinders were always recovered. The caps were usually broken through and some of the material remained in the pipes after the tests.

Table 5. Rifle Bullet Test results

EXPLOSIVE	PARTIAL DETONATION	COMPLETE BURNING	NO REACTION
Octol	100 %	-	-
Octol/ETPE (90/10)	-	80 %	20 %
Octol/ETPE (80/20)	-	80 %	20 %
Composition B	100 %	-	-
CX-84[1]	-	50 %	50 %

1- From reference 16

The reactions for the XRT products were very interesting. The bullet penetrated the outer skin and ignited the material in the tube. For each composition, there was one tube for which no reaction occurred. The results of tests done in the past on a Canadian RDX-based PBX (CX-84) are given for comparison.

CONCLUSIONS

The objective of this study was to collect data on a new type of melt-cast explosive containing an energetic thermoplastic elastomer. The data showed that:

- The mixes were stable in the vacuum stability tests.

- The impact and friction sensitivities were significantly reduced compared to Comp. B and Octol.
- The viscosity of the mixes was higher than the viscosity of a regular melt-cast explosive and lower than the viscosity of a PBX. Processing at atmospheric pressure introduced large voids in the mixes but will still be possible for low concentrations of ETPEs.
- The detonation velocities of the studied mixes were between 94% and 99% of the value for Comp. B, while the calculated detonation pressures were between 81% and 95% of the pressure of Comp. B. It is still possible to match the performance of Comp. B with small adjustments to the formulation.
- The shock sensitivity as measured by the DREV Gap Test can be reduced by up to 27% compared to Octol. However, the quality of the samples has to be improved to get better data on the shock sensitivity.
- Recycling of all the products was demonstrated at a small scale with excellent yields.
- The new compositions behaved well in the Rifle Bullet Test and the worst reaction observed was a burning reaction.

The Rifle Bullet Test results indicated that the first goal of the product, which was to reduce the sensitivity, has a good possibility to be met. The second goal was to match the performance of Comp. B. From the detonation velocity tests, it seems that the percentage of polymer will have to be lower or equal to 10% in Octol in order to meet this requirement. Other possibilities still exist such as an increase of the density through vacuum casting or addition of a dense element such as aluminium powder. The third goal was to use existing melt-cast equipment. This goal will be more difficult to reach. The data suggested that the best formulation will contain 10% or less of ETPE. At these concentrations, it will still be possible to process the products. Nevertheless, while compared to cast-cured explosives, the processing of the XRT products will show great

advantages such as no pot life, no curing period and a recyclable product. Some modifications to existing equipment, such as the addition of vacuum mixing and casting, will probably have to be made because of the high viscosity of the products. Finally, the last goal, which was to have a recyclable product, was shown to be possible with excellent yields.

ACKNOWLEDGEMENTS

The authors wish to thank MM. André Marois and Serge Trudel and Ms. Mélanie Bouchard for performing the mixes and the tests required and for their active contribution to the generation of new ideas and solutions. The help of Dr. Charles Dubois in preparing the polymer at a larger scale is also acknowledged.

REFERENCES

1. *Air Force Views on Insensitive Munitions*, Proceedings of the Insensitive Munitions and Energetic Materials Technology Symposium, Tampa, Fl., October 1997.

2. Vaullerin, M., Morand, P., and Espagnacq, A., *Compositions explosives peu vulnérables mises en oeuvre par coulé-fondu*, 7e Congrès international de pyrotechnie, Brest, France, 1999.

3. Cliff, M.D., and Smith, M.W., *Assessment of Melt-Castable NTO/TNT Formulation*, DSTO-TR-0998, DSTO Aeronautical and Maritime Research Laboratory, Melbourne, Australia, July 2000.

4. Baroody, E.E., Gotzmer, C., Adolph, H.G., US Patent, No. 5,949,016, *Energetic Melt Cast Explosives*, Sept.7, 1999.

5. Voigt, H.W. Jr, US Patent, No. 4,284,442, *Castable TNT Compositions Containing a Broad Spectrum Performed Thermoplastic Polyurethane Elastomer Additive*, Aug., 18, 1981.

6. Stanton, H. D., Reed, R. Jr., US Patent, No. 4,445,948, *Polymer Modified TNT Containing Explosives*, May 1, 1984.

7. Johnson, N.C., Gill, R.C., Leahy, J.F., Gotzmer, C. Jr., Fillman, H.T., US Patent, No. 4,978,482, *Melt Cast Thermoplastic Elastomeric Plastic Bonded Explosive*, Dec. 18, 1990.

8. Voigt, H.W. Jr., Banker, B.R., US Patent, No. 4,325,759, *Preparation of TNT Thermoplastic Polymer Granules Readily Soluble in a TNT Melt*, Apr.20, 1982

9. Ampleman, G., Marois, A., Désilets, S., Beaupré, F., *Synthesis of Copolyurethane Thermoplastic Elastomers for use in Helova Gun Propellant Formulations*, DREV Report 9716, February 1998, UNCLASSIFIED.

10. Beaupré, F., Ahad, E. and Ampleman, G., *Preliminary Studies of HELOVA-Type Gun Propellant Containing Energetic Binders*; Proceedings of the American Defense Preparedness Association (ADPA) International Symposium on Energetic Materials Technology, Meeting 450, Orlando, Florida. 1994.

11. Explosifs: Essai de stabilité sous vide, NATO STANAG 4479, Edition 1, 1995.

12. BICT, *Sensitivity to impact : BAM Impact test, test description and procedure*, June 25, 1982.

13. Farinaccio, R., Hooton, I., Bélanger, C. and Jacques, P., *DREV Gap Test Calibration and Explosive Results*, DREV Report 4657/92, January 1992, UNCLASSIFIED.

14. Fedoroff, B.T., Sheffield, O.E., *Encyclopedia of Explosives and Related Items*, PATR 2700, Volume 2, Picatinny Arsenal, Dover, NJ USA, 1960.

15. Cooper, P.W., *Explosives Engineering*, Wiley-VCH, New York, 1996.

16. Drolet, J.F., Lavertu, R.R., Bélanger, C., Walker, G.R., *Castable Plastic-Bonded Explosive CX-84 A*, DREV M-2564/81, Octobre 1981, UNCLASSIFIED.

LABORATORY TESTING OF TNAZ MIXTURES

Pavel MAREČEK[a], Kamil DUDEK[a], Pavel VÁVRA[b]

[a] AliaChem, division Synthesia, Research Institute of Industrial Chemistry, CZ-532 17, Pardubice - Semtín, Czech Republic

[b] Department of Theory and Technology of Explosives, University of Pardubice, CZ-532 10 Pardubice, Czech Republic

Abstract

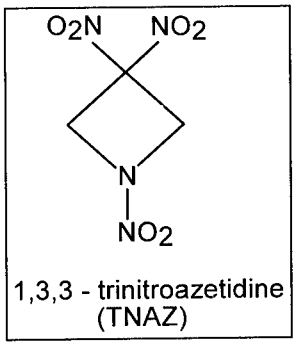
Preliminary testing of TNAZ mixtures with active components (HMX, RDX) has been performed in laboratory scale.

The evaluated parameters were shock sensitivity, detonation velocity and also compatibility. The results especially with regard to utilization of TNAZ as a component of explosives charge, are discused.

Introduction

Nitramines continue to be a source of new explosives characterised by high energy content. One of the substances of this type that has been given attention in systematic and practical ways since 1990 is 1,3,3-trinitroazetidine (TNAZ)[1].

1,3,3-Trinitroazetidine (TNAZ) is a relatively new explosive, which was first synthesised by two chemists of Naval Research Laboratory USA, T. G. Archibald and K. Baum, in 1984[2].



Chemically this is a cyclic nitramine containing geminal nitro groups. Owing to its effectiveness and sensitivity parameters (which are comparable with those of RDX), low melting temperature, and stability in liquid phase within a broad temperature interval, TNAZ has been suggested for use as an explosive suitable for casting either alone or as a casting matrix for other explosives.

TNAZ is thermally more stable than RDX, but more reactive than HMX[3,4]. The results of detonation calorimetry indicate that TNAZ possesses 96% of HMX energy and 150% of TNT energy[3]. TNAZ may offer 30-40% improvements in detonation pressure and velocity as a replacement for TNT-based formulations such as Composition-B[5]. It is suitable for

application as castable explosive or as an ingredient in solid rocket and gun propellants can be comparable with that of HNIW[4].

Compatibility, sensitivity and some other properties have been measured at the selected TNAZ mixtures with cyclotrimethylene trinitramine (RDX), cyclotetramethylene tetramine (HMX), Hytemp/Dioctyladipate and compared with analogous TNT based mixtures (Comp. B-3).

Experimental

TNAZ was prepared in our laboratory by modification method according to Coburn[6], melting point - 101°C. TNAZ cast charges were prepared under laboratory conditions, volume contraction of TNAZ mixtures was eliminated by means of stirring. TNAZ pellets of various density were prepared by vacuum pressing of phlegmatized TNAZ at ambient temperature.

Compatibility test

The TNAZ compatibility with HMX, RDX in mixtures has been tested by means of vacuum test at 110 °C for 20 hours. As the reference mixture has been used TNT mixtures (Comp. B-3). The results are given in Table 1.

Table 1 : Vacuum test of TNAZ mixtures at 110 °C for 20 hours.

	TNAZ	TNT	RDX	HMX
Density ($g.cm^{-3}$)	1.84	1.65	1.80	1.90
Volume of gas (cm^3)	0.01	0.01	0.03	0.06

	RDX/TNT 60/40	RDX/TNAZ 60/40	HMX/TNAZ 60/40	TNAZ/Hyt/DOA 98/1/1
Density ($g.cm^{-3}$)	1.72	1.78	1.85	1.78
TMD (%)	99.0	98.0	98.7	98.2
Volume of gas (cm^3)	0.13	0.10	0.04	0.03

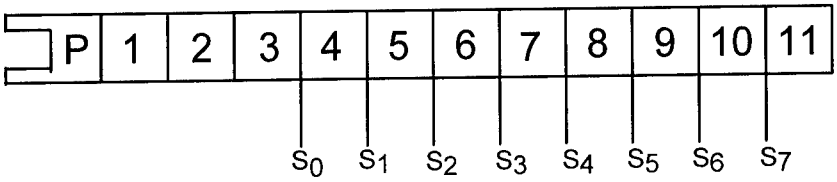
Detonation velocity measurement

Standard sensitivity and performance tests require large amounts of energetic material, usually kilograms at the very least. New small-scale test - PolyRho test - was developed at Los Alamos[7]. This test require a total of 100 - 150 grams of material - a quantity that is able to be synthesized in a laboratory.

PolyRho test is a performance test for measuring the detonation velocity over a range of densities. In our laboratory we were provided PolyRho test of TNAZ (TNAZ/Hytemp4454/DOA - 98/1/1%wt., Hytemp 4454- polyacrylate, DOA - dioctyladipate).

Pellets, 21 mm in diameter and approximately 21 mm in length were pressed to different densities. A rate stick is assembled from these pellets where the pellets were placed in the rate stick according to their density. The first pellet is next to the detonator and is the least dense and the last pellet is the most dense. Foil switches were placed between the pellets and an oscilloscope was used to record the arrival times of the detonation wave at each of these switches(Figure 1).

From this data and the heights of the individual pellets one can calculate the detonation velocity over each of the pellets and hence obtain detonation velocity as a function of density. Results of PolyRho test are shown in Table 2 and Figure 2.

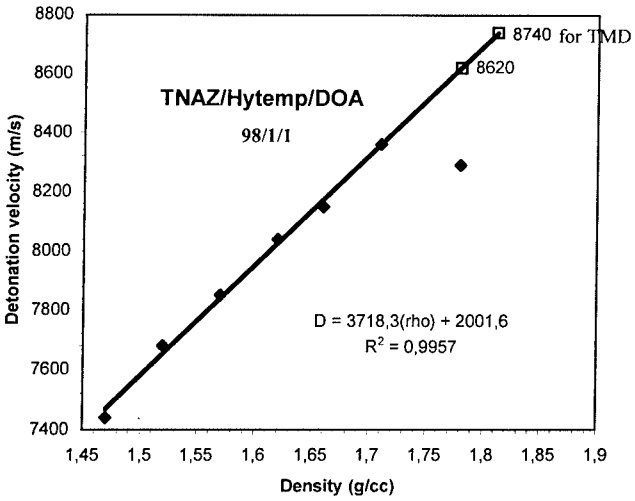


P - pentritol charge ∅ 21mm x 30 mm length
1,2,3.4 - number of TNAZ pellets (∅ 21mm) with the same densities (ρ = 1.47 g.cm^{-3})
5,6,7,8,9,10 - number of TNAZ pellets (∅ 21mm) with different densities
S_0,S_1,.. - number of switches

Figure 1: *Scheme of rate stick of TNAZ (TNAZ/Hytemp4454/DOA - 98/1/1%wt.).*

Table 2 - *Comparison of measured and calculated values of TNAZ detonation velocities (TNAZ/Hytemp4454/DOA - 98/1/1%wt.).*

Pellets number	Density ($g.cm^{-3}$)	$D_{MEASURED}$ ($m.s^{-1}$)	$D_{CALC.}$ (Kamlet) ($m.s^{-1}$)	$D_{CALC.}$ D=3718.3(rho)+2001.6 ($m.s^{-1}$)
4	1.47	7440	7650	7470
5	1.52	7680	7820	7650
6	1.57	7850	8000	7840
7	1.62	8040	8170	8030
8	1.66	8150	8320	8170
9	1.71	8360	8480	8360
10	1.78	8290	8700	8620



◆ - measured detonation velocity values

□ - calculated detonation velocity values from equation of straight line

TMD - theoretical maximum density (1.812 $g.cm^{-3}$)

Figure 2. *Detonation velocity as a function of density produced in a single PolyRho test of TNAZ (TNAZ/Hytemp4454/DOA - 98/1/1%wt.).*

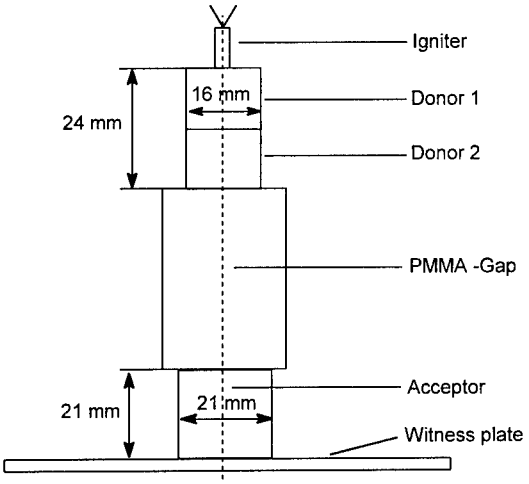
Detonation velocities of casting TNAZ mixtures (Ø 21 mm) is given in Table 3.

Table 3 - *Detonation velocities of TNAZ mixtures*

	Density ($g.cm^{-3}$)	TMD (%)	$D_{measured}$ ($m.s^{-1}$)	$D_{calculated}$ ($m.s^{-1}$)
RDX/TNAZ 60/40	1.780	98.0	8730	8730
HMX/TNAZ 60/40	1.851	98.7	8980	8970
RDX/TNT[7] 60/40	1.720	99.0	7890	8000

Shock sensitivity test

Sensitivity to shock wave has been determined by means of the so called „small" GAP-Test (Ø 21 mm).



Donor: 1. Ø16 mm x 13 mm long phlegmatized PETN 10%wax
2. Ø16 mm x 11 mm long phlegmatized RDX 5%wax

Acceptor: Ø 21 mm x 21 mm long

Spacer: Ø 25 mm PMMA cards of different thickness

Figure 3 - *Small - Scale Gap Test*

Table 4 - *Sensitivity to shock of TNAZ mixtures*

Pressed charge ∅21 mm

	Density ($g.cm^{-3}$)	TMD (%)	p_i^* (GPa)
HNIW/Hytemp/DOA 96/1/3	1.901	98.3	2.60
HMX/Hytemp/DOA 96/1/3	1.792	98.0	3.56
TNAZ/Hytemp/DOA 96/1/3	1.703	95.6	2.57

Cast charge ∅21 mm

	Density ($g.cm^{-3}$)	TMD (%)	p_i^* (GPa)
RDX/TNT[A] 50/50	1.71	99.0	2.9
PETN[B] 5% wax	1.60	94.4	1.1
RDX/TNAZ 60/40	1.78	98.0	1.0
HMX/TNAZ 60/40	1.85	98.7	1.1

$^*p_i$ - initiation pressure

A - ref. 9

B - ref. 10

Discussion

The data from vacuum test confirmed good TNAZ compatibility with both two nitramines (RDX, HMX) and a binder (Hytemp, DOA). As above given[11], relatively high TNAZ vapour tension resulted in a slight deposit of this substance on cool parts of the equipment and this property has to be considered when TNAZ is utilized.

Measured of detonation velocity by means of PolyRho test confirmed compliance between experimental and calculated values. We suppose that the deviation at the highest density value (3 measurements were performed) is likely to be caused by prevailing initiation

micromechanism (vacuum pressing) and hence insufficient charge diameter. As indirect confirmation, detonation velocity values of TNAZ mixtures with RDX and HMX can serve that comply well with calculation based on additivly rule.

Interesting results were obtained when sensitivity to shock wave was measured. Initiation pressures for TNAZ pressed charges are in accordance with values of HNIW and HMX pressed charges and, at the same time, they vary within applicable limits. On the contrary, the initiation pressure values of TNAZ cast charges with nitramines are on the same level as these of phlegmatized PETN. We suppose that sensitivity of these mixtures would by lowered using vacuum casting and for practical purposes it would probably be necessary to use desensitizing additives.

Conclusion

In compliance with the assumptions, the results showed TNAZ to be a substance with high performance parameters, applicable for preparation of castable mixtures. At present, high price, higher sensitivity (compared to TNT) and considerable vapour tension cause that this substance cannot be utilized more widely. Future works should be aimed at removal of these drawbacks of TNAZ with high performance parameters being retained.

Acknowledgement. The authors would like to thank V. Dusík and J. Těšitel for preparing TNAZ pellets, and V. Sejkora for measuring TNAZ detonation velocities.

References

1. Borman, *Chem. Eng. News* **72,** 18-22(1994)
2. T.G.Archibald, K.Baum: „Synthesis and X-ray Crystal Structure of 1,3,3-trinitroazetidine", J. Org. Chem. **55**, 2920-2924(1990).
3. Simpson, R. G. Garza, M. F. Foltz, D. I. Ornellas, *Characterization of TNAZ*, Rep. UCRL-ID-119572, Lawrence Livermore Lab., 1994.
4. K. Schmid and D. Kaschmieder, „Synthesis and Properties of TNAZ", *Proc. 31st Int. Annual Conf. ICT*, Karlsruhe, June 2000, p. 10/1-10/12..
5. Coburn, M. A. Hiskey, and T. G. Archibald, *Waste Manag.* ***47***, 143-146(1973).
6. D.Coburn, M.A.Hiskey: „Synthesis and Spectra of some ^{2}H-, ^{13}C-, and ^{15}N-Labeled Isomers of 1,3,3 - trinitroazetidine and 3,3 - dinitroazetidinium nitrate", J. Energet. Mat. **16**, 73-99(1998).
7. Stine, in: *Structure and Properties of Energetic Materials ,MRS* Symposium Proceedings **296**, Boston 1992, p. 3-12.
8. B.M.Dobratz, LLNL Explosives Handbook - Properties of Explosives and Explosive Simulants, UCRL - 52997, Lawrence Livermore Lab, 1981.
9. J.Majzlík, V. Dusík, DETPAR - The Catalogue of Detonation Parameters, Synthesia, Research Institute of Industrial Chemistry, Pardubice - Semtín, 1998.
10. S.Brebera, „Citlivost trhavin ke kompresní vlně - GAP Test", VZ - 201, 1972.
11. K.Dudek, P. Mareček and P. Vávra, „Laboratory testing of HNIW mixtures", *Proc. 31st Int. Annual. Conf. ICT*, Karlsruhe , June 2000, p.110/1-110/6.

GRUPPE RÜSTUNG
GROUPEMENT DE L'ARMEMENT
AGGRUPPAMENTO DELL'ARMAMENTO
DEFENCE PROCUREMENT AGENCY

Relationship Between Crystal Shape and Explosive Properties of K-6

H. Ritter, S. Braun, M. Schäfer
Institut Franco-Allemand de Recherches de Saint-Louis (ISL)
5 rue du Général Cassagnou
F-68301 Saint Louis

H.R. Aerni, H.R. Bircher, B. Berger, J. Mathieu

Swiss Defence Procurement Agency (DPA)
Weapons Systems and Munition Test Center
Feuerwerkerstrasse 39
CH-3602 Thun

A. Gupta

Wehrwissenschaftliches Institut für Werk-, Explosif- und Betriebsstoffe (WIWEB)
Großes Cent
D-53913 Swisttal

Abstract

2-Oxo-1,3,5-trinitro-1,3,5-triazacyclohexane (K-6) was synthesized according to the two step pathway over 2-oxo-5-tert-butyl-1,3,5-triazacyclohexane. Checking different nitrating agents, the best yields (61 %) have been achieved with nitronium tetrafluoroborate (NO_2BF_4) in acetonitrile. Different recrystallisation procedures from ethyl acetate resulted in two types of crystals K-6-D and K-6-I, with differering behaviour. Both products show very similar IR, MS and NMR spectra; by means of NMR spectroscopy the hydrolysis reaction of K-6 in d_6-DMSO and subsequent disproportion of the intermediate formed was shown. Thermoanalytical methods (DTA/TG, DSC and Hot Stage Microscopy HSM) showed a two-step decomposition at about 200°C for both types and some reactions of the K-6-D crystals due to crystal phase changes or tension effects. The NO_x development of K-6 at 90°C detected by Chemiluminescence (CL) did not exceed the range of known explosives.

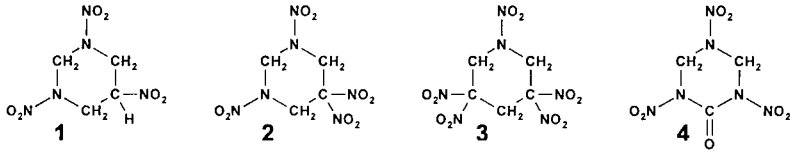
Some differences in the behaviour during handling safety testing were also found. BAM friction sensitivity testing of K-6-I results in a reaction threshold of 48 N load, whereas in two trials the reaction was violent enough to break the porcelain plate. K-6-D already reacts at 36 N, but its reaction is only moderate. In the BAM impact testing all K-6 samples except one coarse crystal fraction reveals a pronounced sensitivity of 2.0 Nm, which approaches primary explosive behaviour. Only the large crystals from DPA (4.5 Nm) are in the sensitivity area of HMX. The explanation of this fact can be found in different crystal shapes. Whereas X-ray diffraction investigations showed an orthorhombic elementary cell of the same size for both K-6 types, clear differences in the shape of the crystals could be shown with scanning electron microscopy (SEM). Whereas K-6-D consists of well built flat crystals, K-6-I has the structure of agglomerated thin plates.

The explosive properties of K-6 have been assessed by comparing its measured detonation velocity and brisance with other explosives. K-6 exceeds obviously the performance area of TNT or PETN, but a level higher than HMX cannot be achieved.

1. Introduction

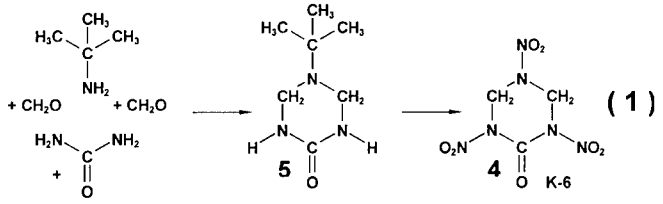
New energetic material based on the cyclic nitramine structure of hexogen or octogen can be expected to have a high performance, if the elemental composition is only marginally modified. There are examples, described in literature, such as **1** [1], **2** [2] or **3** [3], where nitramino units of the six-membered hexogen ring structure are replaced by geminal C-nitro groups (figure 1). The topic of interest in this paper is 2-oxo-1,3,5-trinitro-1,3,5-triaza-cyclohexane **4** (keto-RDX, K-6), where one hexogen methylen unit is replaced by carbonyl, what finally results in a cyclic urea structure. The synthesis of this material was independently performed in two different labs, one at ISL, the other at DPA. Depending on the origin of the material, we realized obvious differences in handling properties and thermal behaviour. This was the starting point for an intense investigation with the main objective to find out relationships between explosive properties and macroscopic structure.

fig. 1: Energetic molecules based on cyclohexane ring structures



2. Synthesis of 2-oxo-1,3,5-trinitro-1,3,5-triazacyclohexane K-6

The first step in the synthesis of 2-oxo-1,3,5-trinitro-1,3,5-triazacyclohexane (K-6) **4** is the cyclisation of formaldehyde, tert-butylamine and urea to 2-oxo-5-tert-butyl-1,3,5-triazacyclohexane **5** [4] (scheme 1). Whereas tert-butyl groups are generally easily nitrolysed, the nitration of secondary amines RR'NH with mixtures of nitric and sulfuric acid often suffers from low yields. Better results are obtained, if more reactive and selective reagents, like nitronium salts or dinitrogen pentoxide (N_2O_5), are used.



(1)

To obtain the trinitrated product K-6, **4**, we tested different nitration methods. Nitric acid (HNO_3) / acetic acid anhydride (Ac_2O, $(CH_3CO)_2O$) gave a relatively pure product. The addition of urea (H_2N-CO-NH_2) to this nitrating medium resulted in decreased yield and purity. The use of the three component nitration agent nitric acid (HNO_3)/ trifluoroacetic acid anhydride (TFAA $(CF_3CO)_2O$) / dinitrogen pentoxide (N_2O_5) led to significant higher yields. Finally, with nitronium tetrafluoroborate (NO_2BF_4) in acetonitrile, the published nitration yield of about 40% [4] was clearly exceeded (table 1).

tab. 1: Yield and melting point of K-6 obtained by different nitration methods

nitrating agent	yield [1] (%)	m.p. [1] (°C)	yield [2] (%)	m.p. [2] (°C)
HNO_3 / Ac_2O	25	180.8	18	183.7
HNO_3 / Ac_2O / H_2N-CO-NH_2	12	163.2	--	--
HNO_3/ TFAA / N_2O_5	37	173.2	18	181.0
NO_2BF_4	61	177.3	37	184.0

[1] raw material [2] after recrystallization from ethyl acetate

Larger quantities of 2-oxo-5-tert-butyl-1,3,5-triazacyclohexane **5** have been nitrated to K-6 with a mixture of acetic acid anhydride and nitric acid. In both labs (ISL and DPA) the crude product was recrystallized from boiling ethyl acetate, whereas the temperature control was slightly different. Due to these different procedures two types of crystals could be recovered. For further investigations, the material named as K-6-D (for K-6 from DPA) and K-6-I (for K-6 from ISL), was sieved to get a fine and a coarse crystal fraction:

K-6-D (fine) $\varnothing < 1.2$ mm and K-6-D (coarse) 1.2 mm $< \varnothing <$ 2.0 mm
K-6-I (fine) $\varnothing < 0.4$ mm and K-6-I (coarse) 0.4 mm $< \varnothing <$ 1.2 mm

3. Thermal behaviour

The thermal behaviour of energetic material, such as phase transitions or decompositions can be measured by simultaneous Differential Thermal Analysis/Thermogravimetry DTA/TG. The experiments have been performed with a sample amount in the range between 2.24 mg and 3.89 mg in an open alumina crucible, using a heating rate of 6 K/min and an inert gas flow (nitrogen) of 50 ml/min. As figures 2 and 3 show, the **fine K-6 crystal fractions** of either origin (DPA or ISL) show no endothermic signal, which could be related to a phase transition. The strongly exothermic decomposition reaction takes place in two steps for both samples. As shown in figure 4 and 5, the main DTA peak for the exothermal decomposition covers a preceeding exotherm. This fact is strongly confirmed by considering the derivated DTA curve (DDTA). In some of our measurements this effect was even more pronounced. The max exotherm was reached at 202°C for DPA's K-6 and 198°C for the ISL's material. Observing the thermal behaviour with Differencial Scanning Calorimetry (DSC), using aluminum crucibles with a triple perforated lid and a heating rate of 5 K/min, gave essentially the same results, especially regarding the two decomposition steps of K-6.

Investigating the two types of crystals with thermogravimetry (TG) shows unambiguously their different behaviour. While the weight loss of the fine K-6-I material starts at 159 °C and proceeds afterwards continously accelerating, the fine crystal fraction of K-6-D shows a two step weight loss. The starting temperature is about the same. A comparable TG behaviour of K-6 has already been observed by STAWINSKI [5] who explained the first weight loss step due to a beginning hydrolysis reaction of K-6 with ambient moisture.

When the **coarse crystal fractions** were analysed by DTA/TG, DTA signals were found again with maxima at 200°C. Surprisingly, the TG signal of the K-6-D sample exhibited several sharp weight losses without simultaneous measurable heat flow

variations, obviously not due to decomposition reactions (figure 6a). This sample decomposes in the same way as the fine crystal fraction of K-6-D in a closed crucible (figure 2, figure 6b); we explain this by a vigorous breaking of large crystals and fragments leaving the crucible. The coarse K-6-I material however gave the same TG signal (figure 7) as the corresponding fine crystal fraction. From these results, a certain crystal tension is supposed to exist in the DPA material. This prompted us to perform further tests with HSM.

fig. 2: DTA/TG trace of 3.89 mg K-6-D (fine) (temp. 25 – 285°C)

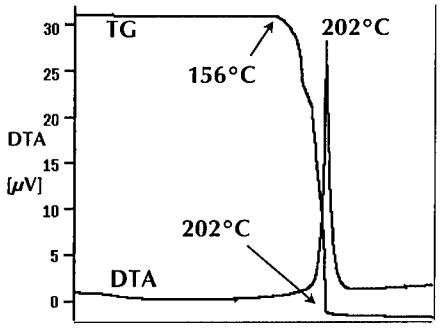


fig. 3: DTA/TG trace of 3.83 mg K-6-I (fine) (temp. 25 – 285°C)

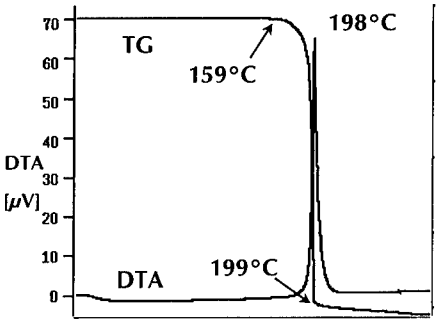


fig. 4: DTA/DDTA trace of 3.89 mg K-6-D (fine) (temp. 145 – 240°C)

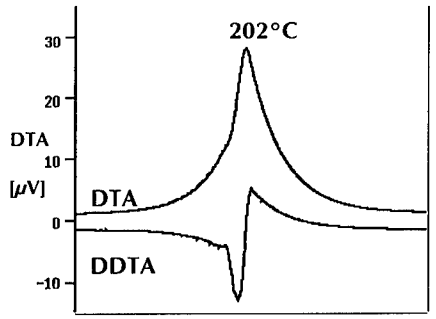


fig. 5: DTA/DDTA trace of 3.83 mg K-6-I (fine) (temp. 140 – 235°C)

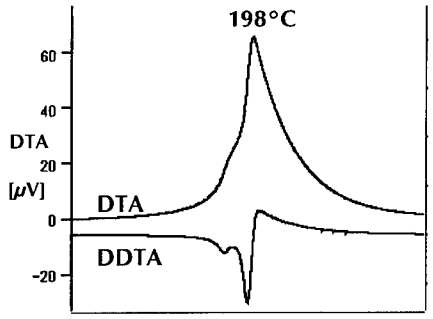


fig. 6: TG traces of K-6-D (coarse) (temp. 30 – 305°C)
a) 2.42 mg, crucible open
b) 2.24 mg, crucible closed

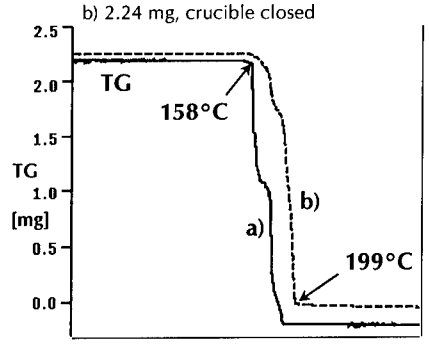
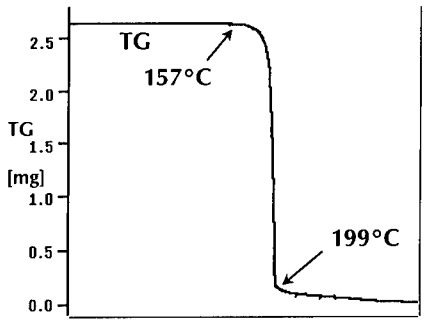
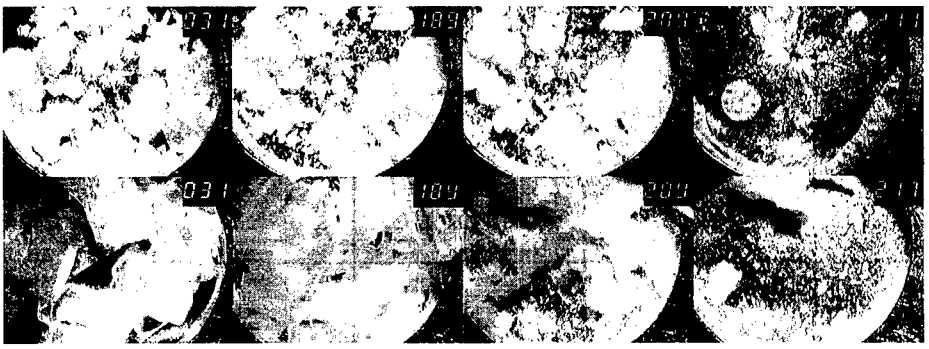


fig. 7: TG trace of 2.65 mg K-6-I (coarse) (temp. 30 – 305°C)



Hot Stage Microscopy can be considered as a visualized thermal analysis. A sample (about 2 mg) is heated up at a constant heating rate. The change in state of the sample, such as phase changes or chemical reactions (decompositions), can be observed under a microscope and recorded on a tape. HSM allows the observation of overlapping endothermic and exothermic effects or other effects, which are connected to an energy exchange rate below the detection limit of a DSC instrument [6].

fig. 8: Hot Stage Microscopy of K-6-I (top) and K-6-D (bottom)



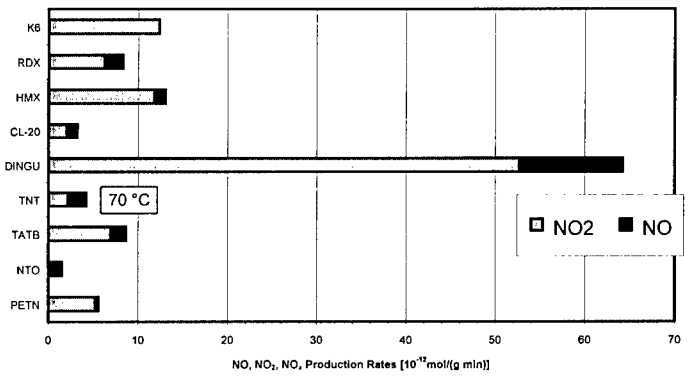
In the case of K-6, a quite obvious difference in the shape of the material can be seen at the beginning of the experiment (figure 8). Whereas the crystals, which have been produced in the DPA labs, show an regular structure, the ISL material is much finer and a morphological structure is hard to recognize. Up to 170°C both K-6 types seem to be absolutely stable. The crystals then start to move and a slight change of light refraction can be observed. The bulky DPA crystals seem to become more glassy. It is highly probable, that the movement of the crystals can be attributed to a crystal phase change, which is clearly not observable in DSC. It is important to notice that this effect occurs in both K-6 samples, whereas the larger DPA crystals start to move at some lower temperature. Starting at 195°C decomposition phenomena can be observed unambiguously. HSM has the drawback, that an exact starting point of a phase transition or decomposition reaction cannot be assigned. Both samples behave about the same way. At 209°C can be seen, that the bulky DPA-crystals have partially desintegrated, some of the material has already decomposed. At 217°C the HSM pictures show, that the reaction of K-6-I tends to finish off in liquid phase, whereas the DPA material remains as a solid for some time longer.

The overall thermal behaviour of both K-6 samples can be considered as very similar. The minor differences towards the end phase of the reaction could be attributed to different amount and type of sample impurities (melting process) or different interactions between the heating source and fine or bulky material.

Chemiluminescence detection was used to measure the NO_x production rate of different energetic material [7], [8]. The basic principle of this method is the conversion of NO to an excited NO_2^* by ozonisation and detection of the light at a characteristic wavelength, emitted due to the corresponding relaxation process to ground state. The use of a two chamber detector, one chamber being equipped with a Molybdenum converter for the chemical reduction of NO_2 to NO, allows the simultaneous detection of NO and and the total NO_x content.

NC propellants show NO_x production rates, which are two orders of magnitude higher as such of most high explosives. Due to the high chemical stability of most secondary high explosive molecules, a sample amount of 50 g was used at temperatures of about 90°C. Artificial preconditioned air was used to pass the samples and to carry NO_x produced by them to the detection system. The air flow rate was 190 ml/min. The values given in the corresponding graph (figure 9) are taken after 48 h, when all samples have reached a constant NO_x production rate.

fig. 9: NO and NO_x production rates of explosives at 90°C



The data show, that the NO_x production rate of K-6 at 90°C is in the range of most well established high explosives whereas hardly no NO is produced. Compared to Dinitroglycolurile (DINGU), whose ring structure contains also urea units, the thermal stability seems to be much better. In case of K-6, the well known deficit in thermal stability of urea based nitro compounds [9] could not be confirmed by chemiluminescence measurements.

4. Sensitivity

The handling properties of an explosive are essentially influenced by its sensitivity to friction, impact and electrostatic discharge. Measured data often suffer from poor comparability, when different test procedures are used and crystal size – an important factor in these tests – is not indicated. Some of the differing published data on K-6 sensitivity are given here:

Impact sensitivity (50%) 15 cm (32 cm HMX) [4]
(50 %) 1.5 ± 0.5 Nm (2 kg) [10]
Kasta hammer 5 kg weight: 11-27 cm upper and lower explosion limit [5]

Friction sensitivity (50%) 4.8 kp (12.8 kp HMX) [4]
(50 %) 10.8 ± 2.4 kp [10]
BAM friction sensitivity apparatus: 9.6 and 16 kg upper and lower explosion limit [5]

Electrostatic discharge sensitivity: 0.09 J (2.0 J at 500 Ω ; HMX 0.30 J) [4]

Using the **BAM impact machine** (1 kg weight) and the **BAM friction machine**, we found the following reaction thresholds (table 2) for at least one positive reaction in six tests :

tab. 2: Sensitivity to friction and impact of energetic materials (first reaction indicated)

	K-6-D coarse	K-6-D fine	K-6-I coarse	K-6-I fine	HMX fine	RDX fine	PETN fine
sensitivity to friction (kp)	3,6	3,6	4,8	4,8	12	12	6
sensitivity to impact (Nm)	4,5	2,0	2,0	2,0	4,0	4,5	3,5

The results of friction sensitivity testing show a somewhat higher sensitivity for the K-6-D material, but for both K-6 samples the order of magnitude and the comparison to HMX data agrees well with published data [4]. Two remarks must be given here: 1) We found for some samples reaction thresholds as high as 8 kp or 10 kp, but were not able to reproduce K-6 material with this property. 2) The reaction of the K-6-I material was often very violent, and despite the small sample quantity of 40 mm^3 the porcelain plate broke in two trials.

All K-6 samples, with the exception of DPA's coarse crystal fraction, reveal a pronounced impact sensitivity. With a value of 2 Nm, as measured for these samples, the sensitivity behaviour of primary explosives is approached. These data correspond to the 50% values of 15 cm (HMX 32 cm) [4] and 1.5 ± 0.5 Nm [10]. Only the coarse crystals of K-6-D are in the sensitivity area of HMX.

Electrostatic Discharge Sensitivity was tested with a inhouse-built apparatus [11], allowing the determination of this parameter between 1 μJ up to 1 Joule. The energy which is stored in corresponding capacitors is released between a pin with a well defined tip (electrode 1) and a brass plate (electrode 2), containing the sample in a small bore. The values given in the following table 3 correspond to the lower energy limit released between the two electrodes, where at least one event was detected in six trials.

tab. 3: Sensitivity to electrostatic discharge of energetic materials (in mJ, first reaction indicated)

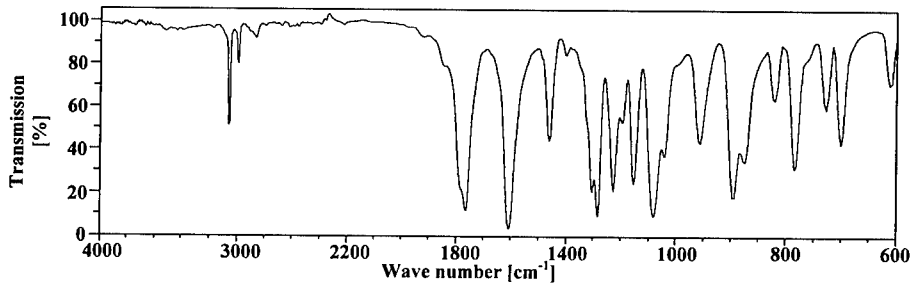
	K-6-D	K-6-I	PETN	RDX	TNT	TAGN	HMX	CL-20
Sensitivity (mJ)	> 1000	> 1000	56	320	320	1000	> 1000	> 1000

Based on the assumption that a human body with a capacity of 500 pF can build up a potential of about 30 kVolts, an electrostatic energy release of about 40 mJ is possible by simply touching grounded material. Therefore these 40 mJ are considered as the lower limit for handling safety in lab scale without taking any precautions. As expected for a secondary explosive, based on a nitramine structure, such as K-6, the sensitivity towards electrostatic discharge does not seem to be a critical parameter for handling safety.

5. Spectroscopy

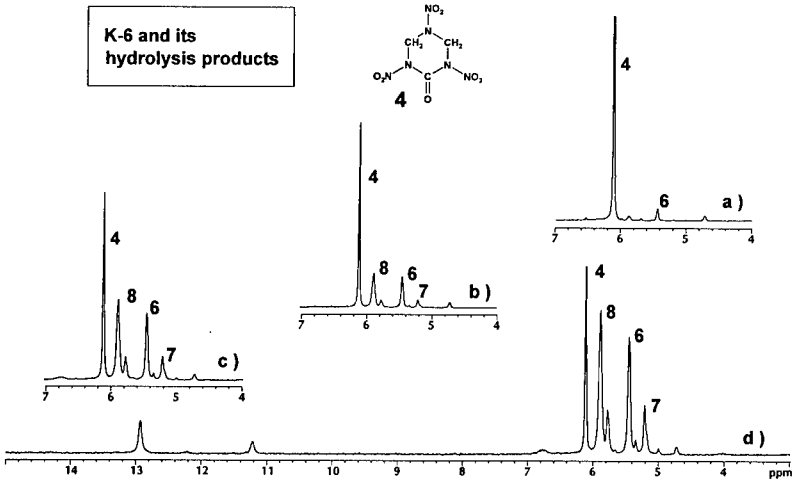
To verify the possible presence of different crystal modifications of K-6, which could be responsible for the unusual sensitivity differences of the K-6 samples, we applied **Infrared Spectroscopy IR**, a method especially suitable for the distinction of crystalline modifications. However the K-6-samples from DPA and ISL gave the same IR-spectra (figure 10) which were in accordance with other published data.

fig. 10: Infrared spectrum of K-6-I (KBr pellet)

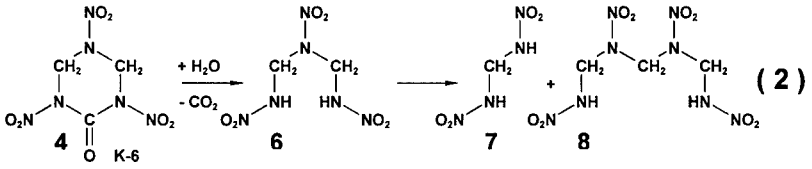


By means of **^{1}H and ^{13}C NMR Spectroscopy** the structural elements of a compound can be identified, but also the presence of impurities – another possible source for differing behaviour of energetic materials – can be detected. Again, both samples were not distinguishable; they gave – in d_3-acetonitrile solution at 25°C – the same signals at 6.01 ppm (^{1}H-NMR) and 62.85 ppm (^{13}C NMR). Due to poor solubility, the expected C=O signal was not detected. If d_6-DMSO, a better solvent for K-6 at 25°C, is used, all expected signals are found: 6.11 ppm (CH_2), 61.82 ppm (CH_2) and 142.67 ppm (C=O). Surprisingly, in this solvent the formation of several new signals takes place, and after some hours the signals of K-6 decreased considerably, as shown in figure 11.

fig. 11: ^{1}H NMR spectra of K-6-I in d_6-DMSO a) freshly prepared solution b) after 1 hour c) after 2 hours d) after 3 hours



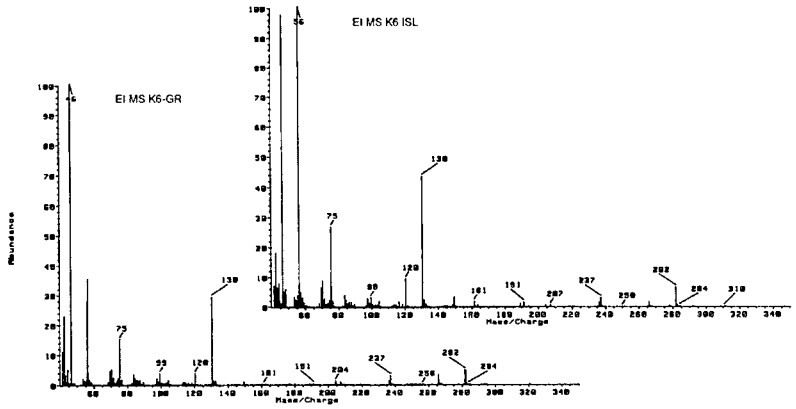
The chemical shift of these signals allows an unambigous assessment of the CH_2 and NH groups of the known primary nitramines 1,3,5-trinitrazapentane **6** (5.45 ppm), 1,3-dinitrazapropane **7** (5.20 ppm) and 1,3,5,7-tetranitrazaheptane **8** (5.45 ppm, 5.88 ppm). Obviously the hydrolysis reaction of K-6 in this solvent with water-traces yields the trinitramine **6** [12], followed by the known [13] disproportion reaction of compound **6** to give the open-chained nitramines **7** and **8** (scheme 2). In this case the aprotic-dipolar solvent d_6-DMSO compensates the rather small tendency of K-6 to hydrolysis at 25°C under neutral conditions [4][5].



(2)

Based on **Mass Spectroscopy** it can be concluded that the K-6 samples from DPA and ISL are chemically identical, because both mass spectra (figure 12) look very similar. The characteristic $(M+1)^+$ peak of K-6 which corresponds to 237 m/e is clearly visible in both EI-MS spectra. The mass at 282 m/e can be assigned to a K-6 structure with an additional nitro group. The peaks at 130 m/e, 120 m/e and 75 m/e are also visible in both mass spectra with the same pattern of magnitude. 46 m/e is characteristic for nitro and 56 m/e can be assigned to the ring fragments (CO)N(CH2) and N(CO)N.

fig. 12: EI mass specta of K-6-D and K-6-I

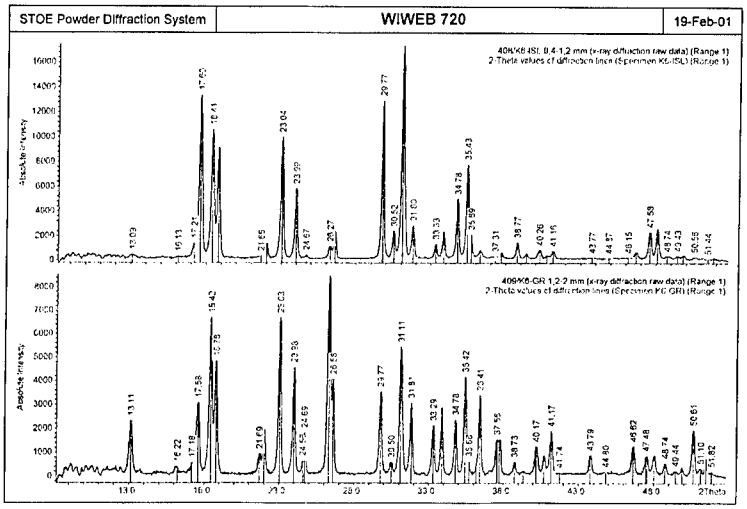


A detailed analysis of the crystal structure of the samples K-6-D and K-6-I was realized by **X-Ray Diffraction** using an automatic STOE transmission diffractometer. The powder diffraction patterns in figure 13 display nearly identical signals. Varying intensities of some diffraction lines are due to the preferred orientation of the crystallites positioned between mylar foils of the sample holder. The diffraction lines were indexed and the unit cell parameters refined. For both samples an orthorhombic crystal structure with an unit cell volume of 816.8 $Å^3$ was found.

tab. 4: Refined parameters of the unit cell

sample	system	a_0 (Å)	b_o (Å)	c_o (Å)	vol (Å^3)
K-6-D	orthorhombic	13,516 (3)	10,088 (22)	5,990 (12)	816,8 (4)
K-6-I	orthorhombic	13,528 (3)	10,0596 (22)	6,0024 (12)	816,8 (2)

fig. 13: Powder diffraction patterns of K-6-I (top) and K-6-D (bottom)



By **Scanning Electron Microscopy SEM** the size and surface of the K-6-D and K-6-I crystals was analyzed. Large differences between both coarse crystal fractions become clear by this method. The figures 14a and 14b show for K-6-D well built flat crystals with smooth surfaces whereas the smaller K-6-I crystals consist of agglomerates of very thin plates (fig. 15a and 15b).

fig.14a, 14b: Scanning electron microscopy of coarse K-6-D crystals

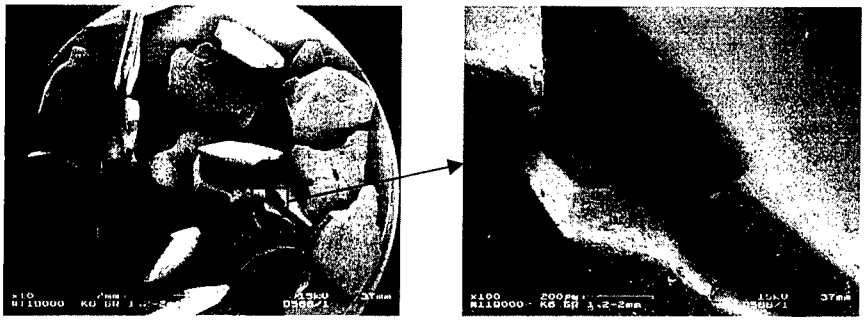


fig.15a, 15b: Scanning electron microscopy of coarse K-6-I crystals



6. Performance

The **detonation velocity** of K-6 was calculated using different codes and empirical formulas. The values vary between 8788 m/s and 8899 m/s (table 5). We prepared cylindrical charges of 10 g weight, containing 96% K-6-D and 4% of a binder (used in the HMX formulation Oktastit VIII [14]), pressed to a density of 1.853 g/cm^3 (95.8% of the theoretical maximal density TMD of 1.932 g/cm^3 [4]). The detonation velocity of 8790 ± 35 m/s measured on a 80 g charge corresponds well to the published value of 8814 m/s [4] (measured at d = 1.85 g/cm^3). It is noteworthy that Oktastit VIII with the same binder content and d =1.82 g/cm^3 (92.9 % of TMD) reaches only 8682 ± 19 m/s.

tab. 5: Detonation velocity of K-6 and HMX formulations
(calculated and measured data)

formulation	density (g/cm^3)	detonation velocity (m/s)	remarks
K-6	TMD	8788	[15] calcd
K-6	1.853	8899	[16] calcd
K-6	1.853	8789	[17] calcd
K-6	1.85	8814	measured [4]
K-6 / binder 96 / 4	1.853	8790	measured (this work)
Oktastit VIII	1.82	8682	measured (this work)

We used the test procedure of KAST [18] (compression of a copper cylinder by a test charge) to measure the **brisance** of different explosives. The data presented in table 6 show clearly that K-6 has a higher brisance than TNT or Pentastit (a formulation based on PETN and wax) and reaches nearly the brisance of octogen.

tab. 6: Brisance of explosives according to KAST [18]

explosive	sample mass [g]	sample height [cm]	sample diameter [cm]	density sample [g/cm^3]	compression of copper cylinder [mm]
Oktastit VIII *	9,9753	2,140	1,532	1,810	4,72
TNT	10,0091	2,138	1,738	1,604	3,75
Pentastit	9,9781	2,136	1,692	1,646	4,45
K-6 **	10,0075	2,121	1,532	1,858	4,66

* average of three tests
** average of two tests

7. Summary

2-Oxo-1,3,5-trinitro-1,3,5-triazacyclohexane (K-6) was synthesized according to the two step pathway over 2-oxo-5-tert-butyl-1,3,5-triazacyclohexane as described in the literature. Checking different nitrating agents, the best yields (61 %) have been obtained with nitronium tetrafluoroborate (NO_2BF_4) in acetonitrile. Due to the costs of NO_2BF_4 larger quantities have been synthesized by nitration with a mixture of acetic acid anhydride and nitric acid. Using this nitration agent, this synthesis was performed independently in the labs of DPA and ISL. A different temperature program during the recrystallisation process resulted in two types of crystals, named K-6-D (DPA) and K-6-I (ISL). For further investigations, each of these individually prepared products was separated into a fine and a coarse crystal fraction by dry-sieving.

Both K-6 products show very similar IR-, MS- and NMR-spectra. By means of NMR spectroscopy the hydrolysis of K-6 in d_6-DMSO and subsequent disproportion of the intermediate formed, was shown. DTA and DSC investigations indicate a two-step decomposition at about 200°C for both types. However, obvious differences can be seen in the thermogravimetric behaviour. The DPA material shows a weight loss in two steps, which was not detected for ISL's K-6. As observed by hot stage microscopy (HSM), the material tends to get glassy and starts to move at about 170°C. This effect is more obvious for the larger K-6-D crystals. Herewith an indication for an endothermal phase conversion that overlaps the beginning of the decomposition is given. The chemical stability was checked by chemiluminescence detection at 90°C. The formation of NO_x was in the range of other well established high explosives, such as HMX or RDX.

Some differences in the behaviour during handling safety testing were also found. BAM friction sensitivity testing of K-6-I results in a reaction threshold of 48 N load (at least one positive reaction in six trials). However in two tests the reaction was violent enough to break the porcelain plate. K-6-D already reacts at 36 N, but its reaction is only moderate. A major problem for almost all K-6 samples is the pronounced impact sensitivity, approaching the area of primary explosives. Using the BAM impact method, a threshold value (at least one reaction in six trials) of 2.0 Nm was determined. There was only one exception, the K-6-D coarse crystal fraction, that showed an impact sensitivity as HMX. It has been demonstrated that large crystals are more sensitive to impact. But in case of

our K-6 samples the effect of crystal size is surpassed by differences in the crystal shape. As we have shown with scanning electron microscopy (SEM), there are obvious differences in the shape of the crystals. Whereas K-6-D samples consist of well built crystals with smooth surfaces, K-6-I has the structure of agglomerated thin plates. Nevertheless, it was shown by X-ray diffraction investigations, that both K-6 types have an orthorhombic elementary cell of the same size.

The performance of K-6 was assessed by comparing the measured detonation velocity D = 8790 m/s (d = 1.853 g/cm^3) and brisance (compression of copper cylinder 4.66 mm) with other explosives like Oktastit VIII. K-6 exceeds obviously the performance range of TNT or PETN, but a level higher than HMX cannot be achieved. Despite its simple preparation, K-6 will not be a promising candidate to replace well established material such as HMX, mainly due to its tendency to hydrolysis with moisture and its pronounced sensitivity against impact and friction.

8. Bibliography

[1] H. RITTER, H.H. LICHT
Prop.Expl.Pyrotechn. **10**, 147 (1985)

[2] D.A. LEVINS, C.D. BEDFORD, S.J. STAATS
Prop.Expl.Pyrotechn. **8**, 74 (1983)

[3] D.A. CICHRA, H.G. ADOLPH
J.Org.Chem. **47**, 2474 (1982)

[4] A.R. MITCHELL, P.F. PAGORIA et al.
Prop.Expl.Pyrotechn. **19**, 232 (1994)

[5] H. BONIUK, W. PILECKI, T. STAWINSKI, M. SYCZEWSKI
Proc. **31th** Int. Symp. ICT, 46-1 (2000)

[6] E.L. CHARSLEY, T.T. GRIFFITHS, B. BERGER,
Proc. **24th** Int. Pyrotechnic Seminar, Monterey (1998)

[7] O. YUXIANG, W. YUKAI, Y. QIFANG
Proc. **8th** Symp. Chem. Probl. Conn. Stab. Expl., 347 (1988)

[8] B. VOGELSANGER, P. BEER, R. SOPRANETTI, M. MULDER
Internal Report SIG BP 2697 (1998)

[9] I.J. DAGLEY, M. KONY, G. WALKER
J.Energetic Mat. **13**, 35 (1995)

[10] H. ÖSTMARK, H. BERGMAN, K. EKVALL, A. LANGLET
Thermochim. Acta **260**, 201 (1995)

[11] B. BERGER, J. GYSELER,
Proc. **18th** Int. Symp. ICT, 55-1 (1987)

[12] P.F. PAGORIA, A.R. MITCHELL, E.S. JESSOP
Prop.Expl.Pyrotechn. **21**, 14 (1996)

[13] L.T. EREMENKO, V.V. ARAKCHEEVA et al.
Bull.Acad.Sci USSR **1984**, 2202

[14] P. ARNI, US Patent 4,428,786 (1984)

[15] L.R. ROTHSTEIN, R. PETERSEN
Prop.Expl., **4**, 56 (1979)

[16] M.J. KAMLET, S.J. JACOBS
J.Chem.Phys. **48**, 23 (1968)

[17] B.N. KONDRIKOV,
Shock and Detonation, Version 4.5, Mendeleev University of Chemical Technology, Moscow (1994)

[18] H.R. BIRCHER, H.R. AERNI
Forschungsbericht FA 26 Reg. Nr. 1175 (1994)

9. Acknowledgments

Gratitude is expressed to Nitrochemie Wimmis AG (NCW) where the chemiluminescence measurements have been performed and to the Swiss Department of Defence, Civic Protection and Sports, the German Ministry of Defense and the French Ministry of Defense who have funded the presented work.

Determination of new values of enthalpies of formation of nitrogen-containing organic radicals

Yurii D. Orlov

Tver State University
33 ul. Zhelyabova, 170000, Tver, Russian Federation.
Fax: +7 (082-2) 33-12-74. E-mail: Yurij.Orlov@tversu.ru

Interest in the chemistry of free radicals ($R^{\bullet}$) is associated with their important role in processes of combustion, polymerization, pyrolysis, aging of polymeric materials, atmospheric changes, metabolism in living organisms, and others. Experimental studies of thermochemical properties of R' are related to great methodological and technical difficulties due to the high chemical activity of ($R^{\bullet}$).

Available databases and methods for calculation of thermochemical characteristics of organic free radicals are reviewed in [1]. An automated databank on thermochemical properties of organic free radicals [1,2], which collected in the systematized form all known values from reference books [3,4], reviews [5,6], and calculation-analytical works [7,8], has been developed. This databank contains methods for calculation of thermochemical properties of organic radicals [7,9-12]. These methods were also used for analysis and systematization of the parameters.

The progress achieved during the past two decades is related to a considerable extent to the development of methods for experimental determination of enthalpies of formation ΔH_f^0 ($R^{\bullet}$).

Many of these methods make it possible to determine the dissociation energy of chemical bonds $D(R_1—R_2)$ in molecules R_1R_2. The D values are related to ΔH_f^0 ($R^{\bullet}$) and ΔH_f^0 (R_1R_2) by the correlation

$$D(R_1—R_2)=\Delta H_f^0(R_1^{\bullet})+\Delta H_f^0(R_2^{\bullet})-\Delta H_f^0(R_1R_2). \qquad (1).$$

The absence of necessary values of ΔH_f^0 of molecules is a factor impeding

calculations of new $\Delta H_f^0(R^\bullet)$ values.

For a number of years the author carries out a cycle of researches which purpose is development of quantitative base of thermochemistry of organic free radicals. This development consists in expansion of a database $\Delta H_f^0(R^\bullet)$, specification of known values $\Delta H_f^0(R^\bullet)$, studying of laws of correlation structure - property for new classes $R^\bullet$, creation enough simple and reliable methods of quantitative calculation of $\Delta H_f^0(R^\bullet)$. Our approach is based on selection of literary values of bond dissociation energies R-X in molecules RX for which are absent appropriate $\Delta H_f^0(R^\bullet)$. In this case the problem of finding $\Delta H_f^0(R^\bullet)$ basically is reduced to definition of enthalpies of formations of molecules $-\Delta H_f^0(RX)$. In the offered report there are described results by definition of new values $\Delta H_f^0(R^\bullet)$ for the organic free radicals containing of one or more atoms of nitrogen.

The basic sources of the information on bearing values D(R-X) for us were the data of D(R-H) received by an electrochemical method in solution DMSO (Bordwell F.G. with coll.), and also results of definition of values D from experimental values of constants of speed and energies of activation of reactions radical separation of atom X ($R^\bullet + R_iX \longrightarrow RX + R^\bullet_i$) with use of parabolic model of a transitive condition for the given reactions (Denissov E.T. with coll.). Last years these methods determine overwhelming majority of values D.

For definition of $\Delta H_f^0(RX)$ of molecules the different calculation methods were utilised: mainly method of macroincremental thermochemical simulation (MTS), also additive-group (AG) and substitution methods. The available experimental (E) data were also utilised. The carried out work is illustrated with table 1. It presents starting values D, used values $\Delta H_f^0(RX)$, and found values $\Delta H_f^0(R^\bullet)$. The origin of the data on $\Delta H_f^0(RX)$ - experimental (E) or calculated (C) value there is specified. For the last the method of calculation is given. Details of these calculations are given in work [28]. In the table references to the used literature are submitted also.

In total were determined new values ΔH_f^0 for 64 nitrogen-containing radicals, among them radicals of an aspect $R_1N^{\bullet}R_2$, where R_1 and R_2 are Ph or Np, derivatives of a pyridine, other nitrogen-containing cyclical radicals, C=N-containing radicals, derivatives of amides of an aspect $R_1C(O)N^{\bullet}R_2$ and $R_1C^{\bullet}HC(O)NR_2R_3$, oximyl-radicals of an aspect $R_1R_2C{=}NO^{\bullet}$ and $HON{=}C^{\bullet}R$, NO_2-containing radicals, and also series of other nitrogen-containing radicals and nitrenes (at multiplet S=1). All data are classified and tabulated.

For obtained values $\Delta H_f^0(R^{\bullet})$ the quantitative correlation structure-property is learnt, the arguments of this correlation and also some energetic performances, such as energy of a stress of a cycle, and energy of conjugate of an unpaired electron are determined. This approach is described in our work [28].

Table 1.

Determination of enthalpies of formation of nitrogen-containing radicals
(all values are in kJ/mol)

N	$R^{\bullet}$	X	D(R-X)	Ref.	$\Delta H_f^o(RX)$	Source $\Delta H_f^o(RX)$	$\Delta H_f^o(R^{\bullet})$
1	2-pyridylmethyl	CH_3	316	[13]	78,7	C,MTS	248
2	3- pyridylmethyl	CH_3	309	-//-	85,9	-//-	248
3	4- pyridylmethyl	CH_3	312	-//-	83,6	-//-	249
4	pyridin-2-yl	H	407	[14]	140,4±0,7	E[26]	329
5	pyrrol-1-yl	H	404,2	[15]	108,3±0,4	-//-	294,5
6	Indole-1-yl	H	392,5	-//-	156,5±1,1	-//-	331,0
7	$C^{\bullet}H(CN)_2$	H	377	[16]	265,5±1,5	-//-	424
8	$C_6H_5C^{\bullet}(CN)_2$	H	322±4	-//-	374,2	C,MTS	478
9	$C_6H_5C^{\bullet}HCN$	H	342,7±1,2	-//-	187,3	C,MTS	312,0
10	$(C_6H_5)_2C^{\bullet}CN$	H	324,3	[15]	284,9	-//-	391,2
11	$C_6H_5CH{=}N^{\bullet}$	R	220,9	[15]	432,6±13,8	E[26]	326,7
12	$(C_6H_5)_2N^{\bullet}$	H	365,7	[15]	226,8±3,0	-//-	374,5
	$(C_6H_5)_2N^{\bullet}$	C_6H_5	372±17	[17]	326,8±4,2	E[17]	369,9

13	carbazole-9-yl	H	387,8	[15]	209,6±3,7	E[26]	397,4
14	2-naphtalylphenylamyl	H	362,4	[18]	273,5	C,MTS	417,9
15	di-2-naphtalyl-phenylamyl	H	359,7	-//-	320,2	-//-	461,9
16	1-naphtalylphenylamyl	H	356,6	-//-	297,3	-//-	435,9
17	2-pyridylbenzyl	H	343	[16]	205,7	C,MTS	331
18	3-pyridylbenzyl	H	351	-//-	212,9	-//-	346
19	4-pyridylbenzyl	H	347	-//-	210,6	-//-	340
20	$CH_3CH{=}NO^{\bullet}$	H	410,9	[19]	-32,2	C,AG	160,7
21	$(CH_3)_2C{=}NO^{\bullet}$	H	400,8	[19]	-64,8	C,AG	118,0
22	$C_2H_5CH{=}NO^{\bullet}$	H	410,4	-//-	-51,9	-//-	140,5
23	$(C_2H_5)_2C{=}NO^{\bullet}$	H	386,2	-//-	-104,6	-//-	63,6
24	$(C_6H_5CH_2)_2C{=}NO^{\bullet}$	H	372,8	-//-	167,9	-//-	322,7
25	$(C_6H_5)_2C{=}NO^{\bullet}$	H	372,4	-//-	196,6	-//-	351,0
26	$C_6H_5CH{=}NO^{\bullet}$	H	377,4	-//-	95,3	-//-	254,7
27	$4\text{-}CH_3C_6H_4CH{=}NO^{\bullet}$	H	372,4	-//-	63,0	-//-	217,4
28	$C_6H_5C(CH_3){=}NO^{\bullet}$	H	381,2	-//-	57,1	-//-	220,3
29	$C_6H_5CH{=}CHCH{=}NO^{\bullet}$	H	370,7	-//-	167,1	-//-	319,8
30	$OHN{=}C^{\bullet}CH_3$	H	410	[20]	-32,2	-//-	160
31	$OHN{=}C^{\bullet}C_6H_5$	H	377	-//-	95,3	-//-	254
32	$H_2NC(O)N^{\bullet}H$	H	464	[21]	-245,8±2,1	E[26]	1
33	$H_3CC(O)N^{\bullet}H$	H	448	-//-	-238,3±0,8	-//-	9
34	$H_3CC(O)N^{\bullet}CH_3$	H	448	-//-	-233,9	C, MTS	-4
35*	$C_6H_5C(O)N^{\bullet}H$	H	448	[21]	-107,8	C, MTS	122
36	$CH_3C(O)N^{\bullet}C_6H_5$	H	414	-//-	-128,5±1,7	E[26]	68
37	$CH_3C(O)N^{\bullet}OH$	H	368	-//-	-344,6	C,MTS	-195
38	$C_6H_5C(O)N^{\bullet}OH$	H	368	-//-	-214,4	-//-	-64
39	$CH_3C(O)N^{\bullet}OCH_3$	H	377	-//-	-327,5	-//-	-169
40	$CH_3C(O)N^{\bullet}OCH_2C_6H_5$	H	372	-//-	-96	-//-	-59
41	$CH_3C(O)N^{\bullet}NH_2$	H	343	-//-	-161,7	-//-	-37
42	$C_6H_5C(O)N^{\bullet}NH_2$	H	339	-//-	-31,1	-//-	90
43	$C_6H_5C(O)N^{\bullet}N(CH_3)_2$	H	343	-//-	-42,4	-//-	83
44	$H_2NC(S)N^{\bullet}H$	H	389	[21]	-25,1	E[27]	146
45	$CH_3C(S)N^{\bullet}H$	H	381	[21]	-17,6	C, MTM	145
46	$C_6H_5C(S)N^{\bullet}H$	H	377	-//-	112,9	-//-	271

47	$3\text{-}NH_2\text{-}C_6H_4^{\bullet}$	NO_2	295,0	[22]	58,4±1,4	E[26]	320,4
48	$4\text{-}NH_2\text{-}C_6H_4^{\bullet}$	NO_2	302,0	-//-	58,8±1,5	-//-	327,8
49	$3\text{-}NO_2\text{-}C_6H_4^{\bullet}$	NO_2	278,2	-//-	53,8±1,8	-//-	299,0
	$3\text{-}NO_2\text{-}C_6H_4^{\bullet}$	NO_2	306,3±10,0	[23]	-//-	-//-	327,1
50	$4\text{-}NO_2\text{-}C_6H_4^{\bullet}$	NO_2	280,7	[22]	55,0	E[27]	302,7
51	$2\text{-}CH_3\text{-}4\text{-}NO_2C_6H_3^{\bullet}$	NO_2	295,4±8,4	[23]	24,3	E[27]	286,7
52	$3,5\text{-}(NO_2)_2C_6H_3^{\bullet}$	NO_2	276,0	[22]	62,4±2,2	E[26]	305,4
53	$CH_3N^{\bullet}NO_2$	NO_2	115,6	-//-	53,5±0,8	E[28]	136,1
54	$C_2H_5N^{\bullet}NO_2$	NO_2	121,5	-//-	27,6	C[28]	116,1
55	$н\text{-}C_3H_7N^{\bullet}NO_2$	NO_2	129,7	-//-	6,8	-//-	100,7
56	$н\text{-}C_4H_9N^{\bullet}NO_2$	NO_2	123,8	-//-	13,8	-//-	74,2
57	CH_3N:	N_2	174,4	[24]	307,2	C,AG[30]	481,6
58	C_2H_5N:	N_2	159,0	[24]	284,4	C,AG[30]	443,0
59	C_6H_5N:	N_2	153,9	[25]	376,6	-//-	530,5
60	$C_6H_5CH_2N$:	N_2	159,7	-//-	416,3	-//-	575,7
61	$Cyclo\text{-}C_6H_{11}N$:	N_2	159,7	-//-	226,8	-//-	386,5
62	$CH_3C(O)CH_2N$:	N_2	158,1	-//-	152,7	-//-	310,8
63	$C_2H_5C(O)OCH_2N$:	N_2	159,0	-//-	-60,7	-//-	119,3
64	$4\text{-}NO_2C_6H_4CH_2N$:	N_2	161,5	-//-	376,6	-//-	538,1

References

1. Yu. D. Orlov and Yu. A. Lebedev, *Zh. Khim. Termodinamiki I Termokhimii* [*J. Chem. Thermodynamics and Thermochemistry*], 1992, 131 (in Russian).

2. Al. G. Krestov, Yu. A. Lebedev, A. S. Ocheretovyj, and Yu. D. Orlov, *13th IUPAC Conf. On Chemical Thermodynamics*, Clermont-Ferrand, France, July 17-22, 1994, 330.

3. V. I. Vedeneev, L. V. Gurvich, V. N. Kondrat`ev, V. A. Medvedev, and E.L. Frankevch, *Energii razryva khimicheskikh svyazei. Potentsialy I srodstvo k elektronu* [*Energies of Chemical Bond Cleavage. Ionisation Potentials and Electron Affinity*], Izd. Akad. Nauk SSSR, Moscow, 1962 (in Russian).

4. L. V. Gurvich, G. V. Karachevtsev, V. N. Kondrat'ev, Yu.A. Lebedev, V.

A. Medvedev, V. K. Potapov, and Yu. S. Khodeev, *Energii razryva khimicheskikh svyazei. Potentsialy ionizatsii i srodstvo k elektronu*[*Energies of Chemical Bond Cleavage. Ionization Potentials and Electron Affinity*], Nauka, Moscow, 1974 (in Russian).

5. H. E. O'Neal and S. W. Benson, in *Free Radicals,* Ed. K. Kochi, Wiley-Interscience, New York, 1973, 2, 275.

6. D. McMillen and D. Golden, *Ann. Rev. Phys. Chem.,* 1982, 33, 493.

7. Yu. D. Oriov and Yu. A. Lebedev, *Zh. Fiz. Khim.,* 1991, **65,** 289 [*Russ. J. Phys. Chem.,* 1991, **65** (Engl. Transl.)].

8. Yu. D. Oriov and Yu. A. Lebedev, *Zh. Fiz. Khim.,* 1993, **67,** 925 [*Russ. J. Phys. Chem.,* 1993, 67 (Engl. Transl.)].

9. Yu. D. Oriov and Yu. A. Lebedev, *Izv. Akad. Nauk SSSR, Ser. Khim.,* 1984, **33,** 1074 [*Bull. Acad. Sci. USSR, Div. Chem. Sci.,* 1984, **33**, 377 (Engl. Transl.)].

10. Yu. D. Oriov and Yu. A. Lebedev, *Izv. Akad. Nauk SSSR, Ser. Khim.,* 1984, **33,** 1335 [*Bull. Acad. Sci. USSR, Div. Chem. Sci.,* 1984, **33**, 1227 (Engl. Transl.)].

11. Yu. D. Oriov, Yu. A. Lebedev, and B. L. Korsunskii, *Izv. Akad. Nauk SSSR, Ser. Khim.,* 1984, **33**, 1550 [*Bull. Acad. Sci. USSR, Div. Chem. Sci.,* 1984, **33**, 1424 (Engl. Transl.)].

12. Yu. D. Oriov and Yu. A. Lebedev, *Izv. Akad. Nauk SSSR, Ser. Khim.,* 1986, **35**, 1121 [*Bull. Acad. Sci. USSR, Div. Chem. Sci.,* 1986, **35**, 1016 (Engl. Transl.)].

13.B.D. Barton, S.E. Stein, *J. Chem. Soc. Far. Trans I.,* 1981, **77**, N 8, 1755-1762.

14.H. Leidreiter, H.G. Wagner, *Z. Phys. Chem. (BRD),* 1987, **153**, N 1-2, 99-108.

15.F.G. Bordwell, X. Zhand, Z.-P. Chend, J. *Org. Chem.,* 1991, **56**, N 10, 3216-3218.

16.F.G. Bordwell, J.-P. Cheng, G.-Z. Ji, A.V. Satish, X. Zhang, *J. Amer. Chem. Soc.*, 1991, **113**, N 26, 9790-9795.

17.W.V. Steele, *J. Chem. Thermodyn.* 1978, **10**, N 5, 441-444.

18.V.T. Varlamov, E.T. Denissov, *Izv. Akad. Nauk SSSR, Ser. Khim.,* 1980, 29,

N 4, 743-749. [*Bull. Acad. Sci. USSR, Div. Chem. Sci.,* 1980, **29**, 1227 (Engl. Transl.)]

19.F.G. Bordwell, G.-Z. Ji. *J., Org. Chem,.* 1992, **57**, N 11, 3019-3025.

20.F.G. Bordwell, G.-Z. Ji, X. Zhang, *J. Org. Chem.,* 1991, **56**, N 18, 5254-5256.

21.F.G. Bordwell, J.A. Harrelson, T.-Y. Lynch, *J. Org. Chem.*, 1990, 55, N 10, 3337-3341.

22.V.G. Matveev, G.M. Nasin, *Izv. Akad. Nauk SSSR, Ser. Khim.,* 1975, **24**, 774 [*Bull. Acad. Sci. USSR, Div. Chem. Sci.,* 1975, **24** (Engl. Transl.)].

23.A.C. Gonzalez, C.W. Larson, D.F. McMillen, D.M. Golden, *J. Phys. Chem.,* 1985, 89. N 22, 4809-4814.

24.G. Geischer, W.Z. Konig, *Phys. Chem.,* 1964. **227**, 81.

25.R.S. Stepanov, L.A. Kruglyakova, E.S. Buka, *Kinet. Catal.,* 1986, **27**, 479 [*Kinet. Catal.,* 1986, **27** (Engl. Transl.)].

26.J.B.Pedley, R.D. Naylor, S.P. Kirby, *Thermochemical data of organic compounds.*, L., N.-Y.: Chapman and Hall. 1986.

27.D. R. Stull, E. F. Westrum, Jr., and G. C. Sinke, *The Chemical Thermodynamics of Organic Compounds,* J. Wiley and Sons, New York, 1969.

28.Yu. D. Orlov *Regularities of correlation structure-property and quantity database in thermochemistry of organic free radicals.* // Thesis for a Doctor's of Chemistry degree. Tver. Tver State University, 1996, -325 p.

29.H. M. Rosenstock, J. Dannachin, and J. F. Liebman, *Radial. Phys. Chem.,* 1982, **20**, 7.

30.N. Cohen and S.W. Benson, *Chem. Rev.* 1993, **93**, 2419.

The modern database on enthalpies of formation of nitrogen-containing organic radicals

Yurii D. Orlov

Tver State University
33 ul. Zhelyabova, 170000, Tver, Russian Federation.
Fax: +7 (082-2) 33-12-74. E-mail: Yurij.Orlov@tversu.ru

Introduction

Interest to chemistry of free radicals ($R^{\bullet}$) is connected to their important role in processes of burning, polymerization, pyrolysis, ageing of polymeric materials, changes in an atmosphere, a metabolism in alive organisms and other. Nitrogen-containing organic $R^{\bullet}$ represent special interest as intermediates of processes of transformations of power-intensive compounds. Thermochemical quantities, main among which is enthalpy of formations ΔH_f^0, concern to the major characteristics of substances.

The experimental researches of thermochemical properties of $R^{\bullet}$ are conjugate to severe difficulties of methodological and engineering nature because of high reactivity $R^{\bullet}$. Therefore, a number of organic radicals that characterized by values of ΔH_f^0 is ten times less than number of appropriate molecules. On the base of selection and expertise the author has formed quantity database of ΔH_f^0 of organic intermediates including $R^{\bullet}$.

Criteria of examination

In the present section the basic criteria of processing of the initial data, acceptance of recommended magnitudes and estimations of their reliability are generalized. The analysis of the initial data should be as a whole multilevel and multifactorial inside each level. According to the given division it is possible to allocate the following basic levels and factors of the analysis of the initial data on thermochemistry of organic free radicals.

1. The analysis of the separate primary source.

At the given level it is necessary to consider as the basic following factors:

a) A technique of the experimental research, the used equipment, conditions of realization of experience.

b) A way of reception (recalculation) of $\Delta H_f^0(\mathrm{R}^\bullet)$ and - or D from the observably data.

c) Quality of the auxiliary (accompanying) magnitudes used at recalculation of $\Delta H_f^0(\mathrm{R}^\bullet)$.

d) The account by authors of results of other works by definition of same magnitude.

e) Authority and an operational experience of authors on the given area.

2.The analysis of the primary source as unit of a database.

At this stage the data for which there are some (two or more) independent estimations of magnitudes are investigated. Thus it is consideredassembly of the specified magnitudes in comparison, and it is necessary to consider the following factors:

a) A degree of the coordination of magnitudes in aggregate and in view of their quality and an origin (methods of reception, authors, laboratories).

b) Evolution of data in aggregate

3.A coordination of value of $\Delta H_f^0(\mathrm{R}^\bullet)$ with other related thermochemical values: D, $\Delta H_f^0(\mathrm{RX})$, $\Delta H_f^0(\mathrm{R}^+)$, $\Delta H_f^0(\mathrm{R}^\bullet)$, IP(R), EA(R).

Such coordination is checked by recalculation of the named magnitudes from considered value of $\Delta \mathrm{H}_\mathrm{f}^0(R^\bullet)$ with attraction of the additional data.

4. The analysis of magnitudes from the point of view of known laws structure - property. Thus it is necessary, that parameters of researched correlation structure - property were determined independently.

The estimation of quality given bases was made on the basis of these criteria. The data were classified on categories of severity on the basis of classification in which the data are qualified on four following categories (ctg):

1. Recommended (rec).

The independent magnitudes, confirmed with two or more researches.

2. Preliminary (pre).

The data of individual researches.

3. Questebly (ques).

Here are concerned the inconsistent data of various measurements, and also the data of individual researches for which all necessary details (a method, the equipment, conditions, the auxiliary data) or which do not correspond to reliable quantitative correlations structure - property.

4. Unacceptable (unac).

These are the data obviously contradicting to known laws structure - property, and also the data not found out or very doubtful (for example, taken off diagrams) origins.

Recommended values of ΔH_f^0 nitrogen-containing organic radicals

The report of values ΔH_f^0 of the specified radicals recommended on the basis of carried out by us and described above examination is submitted in table 1. Apparently, only results of expert estimations (one figure on each connection) here are submitted. Except for it, it is specified, on the basis of what number of experimental values the given one is recommended. In our disposal there are comments for each of figures and expert estimations, and also all initial experimental values and the appropriate bibliographic data. We also carry out the analysis of the submitted data on the basis of search of quantitative correlation structure - property within the framework of the additive - group approach. Parameters of such correlation are determined and the method of calculation of ΔH_f^0 of organic free radicals is offered . All this, together with the given table makes a modern database on ΔH_f^0 of nitrogen-containing radicals. However the volume of this material leaves for frameworks of given article. As of 1996 this material is given in our work [1].

Errors of the submitted values.

By consideration of a question on errors of recommended values ΔH_f^0 of intermediates we shall note the following. Errors of thermochemical magnitudes depend on many factors. Practically each of the factors considered in criteria of examination, and also a number of others are bringing the contribution in total values of errors. The difficulties arising at expert estimations of errors of thermochemical magnitudes on the basis of experimental works, are rather significant. For intermediates owing to specificity of objects and their researches these difficulties are repeatedly increased. The estimations of errors spent by authors in original works, as a rule, do not maintain serious criticism. In such conditions it is impossible to determine values of errors $\Delta H_f^0(\mathrm{R}^\bullet)$ correctly , and the majority of the values offered by us are appointed on the basis of the approached estimations. Many of them determine only top limit of a possible error. The appointed values of errors were estimated to within 1 kJ/mol, and the sign of their tenth shares has conditional character. In some cases we have refrained from estimations of errors of value $\Delta H_f^0(\mathrm{R}^\bullet)$ at all because of absence of objective criteria. We recommend to users of base at realization of thermodynamic calculations on the basis $\Delta H_f^0(\mathrm{R}^\bullet)$, Not characterized by an error, to take as the last ±13,0 kJ/mol. It corresponds by our estimation on the average to the top limit of an error of the appropriate values $\Delta H_f^0(\mathrm{R}^\bullet)$.

The quantitative data

Table 1.

Enthalpies of formation of nitrogen-containing organic radicals.

№	R•	$\Delta H_f^0(\mathrm{R}^\bullet)$ kJ/mol	±Δ [1] kJ/mol	ctg	NIE [2]
1	N≡C•	440,2	5,0	rec	10

2	$C^{\bullet}H_2NH_2$	150,6	6,0	rec	8
3	$CH_3N^{\bullet}H$	169,7		rec	6
4	$C^{\bullet}H_2C{\equiv}N$	244,8	9,2	rec	6
5	$CH_3CH{=}N^{\bullet}$	143,9		pre	1
6	$H_2C{=}N\text{-}C^{\bullet}H_2$	264	13	pre	1
7	$CH_3C^{\bullet}HNH_2$	108,8	7,0	rec	2
8	$CH_3NHC^{\bullet}H_2$	125		rec	2
9	$(CH_3)_2N^{\bullet}$	133,8		rec	6
10	$CH_3CH_2N^{\bullet}H$	138		pre	1
11	$N{\equiv}CC{\equiv}C^{\bullet}$	629	17	pre	1
12	$CH_3C^{\bullet}HCN$	209,6	9,6	pre	1
13	$(CH_3)_2NC^{\bullet}H_2$	109		ques	4
14	$(CH_3)_2C^{\bullet}NH_2$	71		pre	1
15	$C_2H_5NHC^{\bullet}H_2$	155		pre	1
16	pyrrol-1-yl	294,5		pre	1
17	$(CH_3)_2C^{\bullet}CN$	166,5		rec	2
18	$(C_2H_5)_2N^{\bullet}$	159		ques	2
19	pyridin-2-yl	351,8		ques	2
20	piperidine-1-yl	98,3		pre	1
21	$(C_2H_5)_2NC^{\bullet}H_2$	96		pre	1
22	2-$C^{\bullet}H_2$- pyridin	248		ques	2
23	3- $C^{\bullet}H_2$- pyridin	248		ques	1
24	4- $C^{\bullet}H_2$- pyridin	248		ques	1
25	3-NH_2-$C_6H_4^{\bullet}$	320,4		pre	1
26	4- NH_2-$C_6H_4^{\bullet}$	327,8		pre	1
27	$C_6H_5N^{\bullet}H$	230,5		rec	2
28	$C_6H_5N^{\bullet}CH_3$	222,6		rec	2
29	$C_6H_5CH{=}N^{\bullet}$	326,7		pre	1
30	Indole-1-yl	331,0		pre	1
31	$C_6H_5C^{\bullet}HCN$	312,0		pre	1

32	$C_6H_5C^{\bullet}CH_3(CN)$	227,6		pre	1
33	carbazole -9-yl	397,4		pre	1
34	$(C_6H_5)_2N^{\bullet}$	374,5		rec	2
35	$(C_6H_5)_2C^{\bullet}CN$	391,2		pre	1
36	2- pyridylbenzyl	331		pre	1
37	3- pyridylbenzyl	346		pre	1
38	4- pyridylbenzyl	340		pre	1
39	1-naphtalylphenylamyl	435,9		pre	1
40	2- naphtalylphenylamyl	417,9		pre	1
41	di-2- naphtalylamyl	461,9		pre	1
42	$CH_3N=N^{\bullet}$	213,0		ques	1
43	$C_2H_5N=N^{\bullet}$	236,4		pre	1
44	$(CH_3)_2CHN=N^{\bullet}$	213,0		pre	1
45	$CH_3(CH_2)_3N=N^{\bullet}$	195,0		pre	1
46	$(CH_3)_2CHCH_2N=N^{\bullet}$	189,5		pre	1
47	$CH_3CH_2CH(CH_3)N=N^{\bullet}$	195,4		pre	1
48	$(CH_3)_3CN=N^{\bullet}$	184,5		pre	1
49	$C_6H_5N=N^{\bullet}$	343,9		pre	1
50	$C_6H_5CH_2N=N^{\bullet}$	378,2		pre	1
51	$C^{\bullet}H(CN)_2$	424		pre	1
52	$C_6H_5C^{\bullet}(CN)_2$	478		pre	1
53	$C_6H_5N^{\bullet}N=C(CH_3)_2$	306,3		pre	1
54	$C_6H_5N=NC^{\bullet}(CH_3)_2$	220,5		pre	1
55	$CF_3N=N^{\bullet}$	-322,6		pre	1
56	$O=C=N^{\bullet}$	≤ 144,8		rec	3
57	$CH_3CH=NO^{\bullet}$	160,7		pre	1
58	$(CH_3)_2C=NO^{\bullet}$	118,0		pre	1
59	$C_2H_5CH=NO^{\bullet}$	140,5		pre	1
60	$(C_2H_5)_2C=NO^{\bullet}$	63,6		pre	1
61	$C_6H_5CH=NO^{\bullet}$	254,7		pre	1

62	4-$CH_3C_6H_4CH{=}NO^{\bullet}$	217,4		pre	1
63	$C_6H_5C(CH_3){=}NO^{\bullet}$	220,3		pre	1
64	$C_6H_5CH{=}CHCH{=}NO^{\bullet}$	319,8		pre	1
65	$(C_6H_5)_2C{=}NO^{\bullet}$	351,0		pre	1
66	$(C_6H_5CH_2)_2C{=}NO^{\bullet}$	322,7		pre	1
67	$OHN{=}C^{\bullet}CH_3$	160		pre	1
68	$OHN{=}C^{\bullet}C_6H_5$	254		pre	1
69	4-$N{\equiv}C$-$C_6H_4O^{\bullet}$	181,6		pre	1
70	$H_2NC(O)N^{\bullet}H$	1		pre	1
71	$CH_3C(O)N^{\bullet}H$	9		pre	1
72	$CH_3C(O)N^{\bullet}CH_3$	-4		pre	1
73	$C_6H_5C(O)N^{\bullet}H$	122		pre	1
74	$CH_3C(O)N^{\bullet}C_6H_5$	68		pre	1
75	$CH_3C(O)N^{\bullet}OH$	-195		pre	1
76	$C_6H_5C(O)N^{\bullet}OH$	-64		pre	1
77	$CH_3C(O)N^{\bullet}OCH_3$	-169		pre	1
78	$CH_3C(O)N^{\bullet}OCH_2C_6H_5$	-59		pre	1
79	$CH_3C(O)N^{\bullet}NH_2$	-37		pre	1
80	$C_6H_5C(O)N^{\bullet}NH_2$	90		pre	1
81	$C_6H_5C(O)N^{\bullet}N(CH_3)_2$	83		pre	1
82	$C_6H_5C(O)C^{\bullet}HN(CH_3)_2$	35		pre	1
83	$C^{\bullet}H_2NO_2$	103,5		pre	1
84	$CH_3C^{\bullet}HNO_2$	62,0		pre	1
85	$C_2H_5C^{\bullet}HNO_2$	52,9		pre	1
86	$(CH_3)_2C^{\bullet}NO_2$	36,4		pre	1
87	н-$C_3H_7C^{\bullet}HNO_2$	21,5		pre	1
88	$C^{\bullet}H(NO_2)_2$	139,1		pre	1
89	$CH_3C^{\bullet}(NO_2)_2$	90,9		pre	1
90	$C_2H_5C^{\bullet}(NO_2)_2$	65,8		pre	1
91	н-$C_3H_7C^{\bullet}(NO_2)_2$	44,4		pre	1

92	$C^{\bullet}(NO_2)_3$	201,2		pre	1
93	$(NO_2)_3CC^{\bullet}(NO_2)_2$	276,5		pre	1
94	$FC^{\bullet}HNO_2$	-65,3	7,9	pre	1
95	$FC^{\bullet}(NO_2)_2$	-41,4	7,1	ques	2
96	$F_2C^{\bullet}NO_2$	-238,5	11,3	rec	2
97	$(NO_2)_2FCC^{\bullet}(NO_2)_2$	33,0	13,0	rec	2
98	$(NO_2)_2FCC^{\bullet}F(NO_2)$	-209	9	pre	1
99	$ClC^{\bullet}(NO_2)_2$	160,0		pre	1
100	$BrC^{\bullet}(NO_2)_2$	120,7		pre	1
101	$3\text{-}NO_2\text{-}C_6H_4^{\bullet}$	299,0		rec	2
102	$4\text{-}NO_2\text{-}C_6H_4^{\bullet}$	302,7		pre	1
103	$2\text{-}CH_3,4\text{-}NO_2\text{-}C_6H_3^{\bullet}$	286,7		pre	1
104	$4\text{-}NO_2\text{-}C_6H_4C^{\bullet}H_2$	126		pre	1
105	$4\text{-}NO_2C_6H_4O^{\bullet}$	18,5		pre	1
106	$4\text{-}NO_2C_6H_4OC^{\bullet}H_2$	55		pre	1
107	$3,5\text{-}(NO_2)_2C_6H_3^{\bullet}$	305,4		pre	1
108	$F_2C^{\bullet}NF_2$	-270,3		pre	1
109	$FC^{\bullet}(NF_2)_2$	-37,2		pre	1
110	$C^{\bullet}(NF_2)_3$	131,4		pre	1
111	$CH_3C^{\bullet}(NO_2)NF_2$	78,7		pre	1
112	$FC^{\bullet}(NO_2)NF_2$	-54,8		pre	1
113	$(NO_2)_2C^{\bullet}NF_2$	187,9		pre	1
114	$(NO_2)_3CC^{\bullet}(NO_2)NF_2$	251,4		pre	1
115	$CH_3N^{\bullet}NO_2$	136,1	5,0	pre	1
116	$C_2H_5N^{\bullet}NO_2$	116,0	5,0	pre	1
117	$CH_3(CH_2)_2N^{\bullet}NO_2$	100,7	5,0	pre	1
118	$CH_3(CH_2)_3N^{\bullet}NO_2$	74,2	5,0	pre	1
119	$C^{\bullet}H_2ONO_2$	63		pre	1
120	$2,2,6,6\text{-}(CH_3)_4$-piperidine-4-on-1-oxyl	-213	13,0	pre	1

121	2,2,6,6-$(CH_3)_4$-piperidine-4-ol-1-oxyl	-291,2	13,0	pre	1
122	[4-CH_3O-C_6H_4]$_2$NO$^\bullet$	-13,8		pre	1

[1] Errors of the submitted values.
[2] Number of independent estimation.

The conclusion

The database of values ΔH_f^0 nitrogen-containing R$^\cdot$ is important and big (about 20%) a component of full database of the quantitative data on ΔH_f^0 of organic intermediates. This database now contains values ΔH_f^0 for more than 600 free radicals, carbenes, nitrenes, biradicals. For the majority of values $\Delta H_f^0(\mathrm{R}^\bullet)$ the described database quantitative correlations structure - property are investigated, parameters of these correlations, and also some power characteristics, such as energy of a tension of cycles, and energy of interface not coupled electron are determined. In process of occurrence new data the author will carry out updating and expansion of the described base. We also conduct work on creation of the automated computer databank on thermodynamic properties organic intermediates, and bond dissociation energies in molecules of organic compounds.

References

1. Orlov Yu. D./ Regularities of correlation structure-property and quantity database in thermochemistry of organic free radicals. // Thesis for a Doctor's of Chemistry degree. Tver. Tver State University, 1996, -325 p.

CATALYTIC OXIDATION OF UDMH FOR SOLUTION OF ENVIRONMENTAL PROBLEMS OF MISSILERY

Oxana P. Pestounova, Galina L. Elizarova, Mikhail A. Kerzhentsev, Zinfer R. Ismagilov, Valentin N. Parmon

Boreskov Institute of Catalysis, Siberian Branch of the Russian Academy of Sciences, Prospekt Akademika Lavrentieva, 5, Novosibirsk 630090, Russia
E-mail: oxanap@catalysis.nsk.su

For the last decade, neutralisation of highly toxic propellant-containing waters appeared to be a serious problem attracting a lot of attention. One of the main propellants for missiles 1,1-dimethylhydrazine (UDMH) is a highly toxic substance, which threshold permitted concentration in water is 0.01 p.p.m. At present there are no efficient methods for the UDMH removal from its diluted aqueous solutions. The main problem is that most of oxidative processes (such as oxidation with Cl-containing oxidant, radiolysis etc.) yield more than 10% of 1,1-dimethylnitrosoamine (DMNA), which is more toxic and stable substance, than UDMH.

We suggested to use catalysts based on Cu, Fe, Mn hydroxides to oxidize UDMH in aqueous solutions by oxygen [1, 2] and hydrogen peroxide [3]. In the present study we investigated the influence of reaction conditions on the UDMH oxidation rate and composition of products.

The hydroxide compounds of Cu, Fe supported on catalyst supports such as SiO_2, Al_2O_3, TiO_2 or zeolites (NaA, ZSM-5) with active component content not exceeding 2 wt.%, as well as bulk iron hydroxides and oxides, were used as the catalysts. The supported catalysts were prepared via addition of NaOH to a suspension of carrier in aqueous solutions of a nitrate or chloride of the active metal under vigorous stirring to adjust pH 7-8 [4, 5]. The procedure resulted in the fast quantitative deposition of hydroxide on the support. The oxidizable solutions contained 1-3wt. % UDMH. Air oxygen or hydrogen peroxide of the concentration 1-3 wt.% were used as the oxidizer.

The UDMH oxidation was carried out in a vessel with a reflux condenser at intensive stirring at various pH, temperatures 298-323 K and atmospheric pressure. Gas-liquid chromatography and UV-VIS spectroscopy were used to control the oxidation process. The reaction of UDMH with formaldehyde was used for spectrophotometric analysis of UDMH.

We have studied the influence of various factors such as the catalyst nature, the oxidant nature, the oxidant-to-substrate ratio, the catalyst weight, pH (7-9.5) and temperature (20-75 °C) on the reaction kinetics and the yields of the products. In a series of the catalysts studied, the copper-containing catalysts supported on silica and zeolites as well as iron-containing catalysts supported on zeolites appear to be the most active ones.

In Table 1 we compare the half times of the UDMH decomposition at its oxidation by hydrogen peroxide or air in the presence of the Cu- and Fe-containing catalysts. Apparently, the half-times of the UDMH decomposition demonstrate a many-fold decrease, when hydrogen peroxide is used instead of air. Without the catalysts, the oxidation of UDMH with hydrogen peroxide occurs slower by two orders of magnitude.

Table 1.
Half-times of UDMH decomposition ($\tau_{1/2}$) at its oxidation by hydrogen peroxide or air with no catalyst (No 1) or with various catalysts (No 2-7) at temperature 25°C.

No.	oxidizer	pH	catalyst	cat. weight, g	$\tau_{1/2}$, min
1	H_2O_2	7	-	-	618
2	"	7	2%Cu/SiO_2	0.25	0.9
3	"	9.5	"	0.25	0.8
4	air	7	"	1	49
5	"	9.5	"	1	46
6	H_2O_2	7	2%Fe/ZSM-5	1	3
7	air	7	2%Fe/NaA	1.5	70

UDMH concentration 0.25 M; H_2O_2 concentration 0.5 M, 25°C.

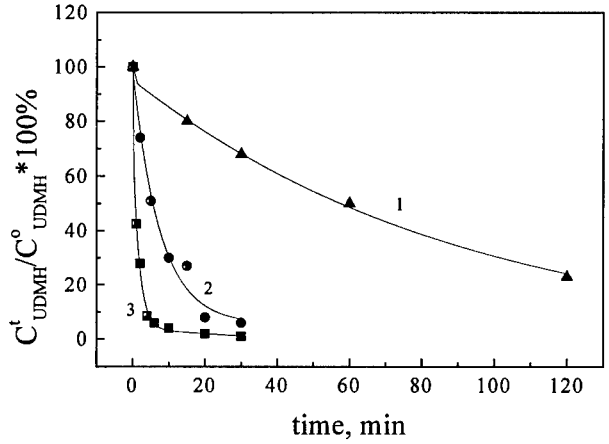
The pH has no substantial effect on the rate of the reaction (see table 1). The reaction rate increases essentially with increasing the temperature. The kinetic curves of the UDMH disappearance under different temperatures in the presence of the Fe-containing catalyst is shown in Figure 1. When the Cu-containing catalysts were used, the UDMH is totally oxidized in 5 minutes or less at 75 °C.

The composition and yield of the reaction products strongly depend on catalysts, pH and temperature. The main products for different reaction conditions are shown in Table 2.

When the oxidation of UDMH with H_2O_2 is carried out without catalysts approximately 10 products were observed irrespective of pH and temperature. The main products are methanol (5-15%), dimethylformamide (DMFA) (5-10%) and

dimethylnitrosamine (5-15%) (Table2, No.1-2). Such nonselectivity could be explained by the free radical mechanism of the reaction.

Figure 1.
Kinetic curves of the UDNH disappearance under different temperatures (1- 25°C, 2-



50°C, 3- 75°C).Catalytic oxidation with oxygen and hydrogen peroxide at pH 9-11 also yields 10-15% of DMNA (No. 4, 6, 9, 11). However if the catalytic oxidation is carried out at pH 7 or less the yield of DMNA does not exceed 1%.

At ambient temperature with Cu-containing catalysts and air as the oxidizing agent at pH 7 the main product is non-toxic formazane derivative (1,1,5,5-tetramethylformazanium cation) (~30-60%) (see No. 7). In the gas phase, methane and nitrogen were detected. Total toxicity of solutions in this case decreases more than by 10000 times.

When hydrogen peroxide is used, the yield of DMNA does not exceed 1%. In this case, the toxicity decreases about 100 times.

All presented results show that the detoxication of the aqueous solutions of UDMH has to be performed in the presence of catalysts at pH 7 or less. At that, if the initial concentration of UDMH in a solution is high, one has to use Cu-containing catalysts, at ambient temperature with air as the oxidant.

This process is developed for cleaning scrubbing waters from UDMH in a technology for catalytic UDMH destruction, elaborated under Project No. 959 of the International Science and Technology Center (ISTC). It can be also applied effectively for purification of industrial waste waters containing UDMH.

Table 2.

The main products of the oxidation UDMH without catalysts (No. 1-2), with Cu-containing catalyst (No. 3-7) and with Fe-containing catalyst (No. 8-11).

No.	catalyst	oxidizer	tempe-rature, °C	pH	products yield, %			
					CH_3OH	DMNA	DMFA*	F^+ or F^0 **
1	-	H_2O_2	75	7	16	4	4	6
2	"	"	"	9	7	13	3	4
3	2%Cu/SiO_2	"	"	7	10	0.7	2	0.4
4	"	"	"	9	3	13	6	0.1
5	"	"	25	7	1	0.9	6	31
6	"	"	"	9	3	10	13	11
7	"	air		7	1	-	0.05	30
8	2%Fe/ α-Al_2O_3	H_2O_2	75	7	4	1	-	23
9	"	"	"	9	4	12	-	10
10	"	"	25	7	4	2	-	25
11	Fe_2O_3	"	75	9	2	12	5	8

*- DMFA-dimethylformamide

**- F^+ - 1,1,5,5-tetramethylformazanium cation (under pH 7), F^0 – 1,1,5-trimethylformazane

ACKNOWLEDGEMENT - to the ISTC for financial support.

REFERENCES

1. G.L.Elizarova, L.G.Matvienko, O.P.Pestunova, etc, Kinet. Catal. Engl. Tr., ***39*** (1998), 44-50.

2. G.L.Elizarova, L.G.Matvienko, V.N.Parmon, Patent Russian Federation No. 2063385 (1998).

3. O.P.Pestunova, G.L.Elizarova, V.N.Parmon, Russian Journal of Applied Chemistry, ***72*** (1999), 1209.

4. G.L.Elizarova, L.G.Matvienko, V.L.Kuznetsov, D.I.Kochubey, V.N.Parmon, J.Mol.Cat., ***103*** (1995) 43.

5. G.L.Elizarova, L.G.Matvienko, O.L.Ogorodnikova, V.N.Parmon, The role of peroxo complexes in the catalitic decomposition of H_2O_2 in the presence of Cu(II) hydroxides, Kinet. Catal. Engl. Tr., ***41*** (2000) 332.

MONO- AND BISDIAZIRIDINES WITH HIGH FORMATION ENTHALPHY

Nina N. Makhova, Nailya Z. Kamalova, Tatyana V. Chabina,
Vera Yu. Petukhova, and Tatyana S. Pivina
N. D. Zelinsky Institute of Organic Chemistry, Russian Academy of Sciences,
47 Leninsky pr., 119992, Moscow, Russian Federation
Tel: 007 095 135 5326; Fax: 007 095 135 5328; e-mail:mnn@cacr.ioc.ac.ru

ABSTRACT

This study includes the synthesis of a series of mono- and bisdiaziridines with acetylene, azide and cyclopropyl substituents, investigation of of some their properties (boiling or melting points, density) and calculation of their formation enthalpy (ΔH_o) by different methods: (1) additive-groups and (2) semi-empirical quantum chemistry (PM3) and Atom-Atom Potential Functions (AAPF) methods. Among the synthesized compounds there are structures with record ΔH_o - more than 1300 Kcal/kg.

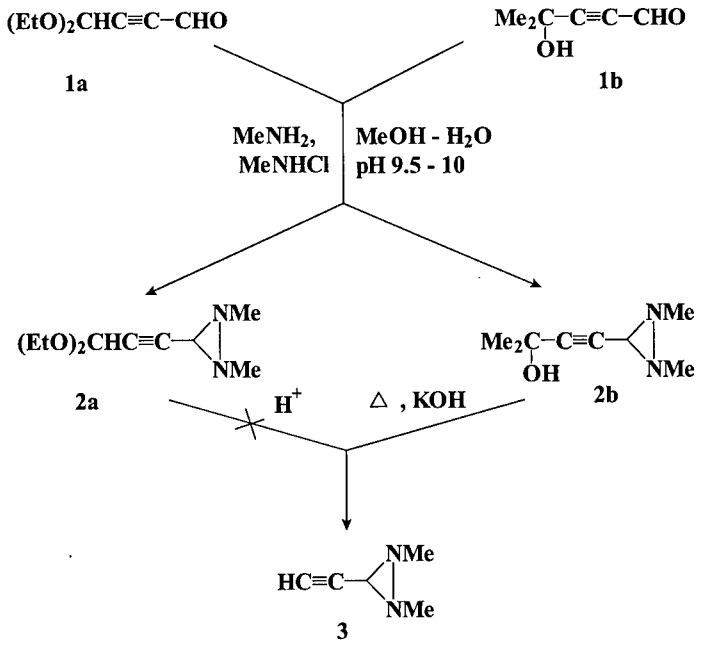
INTRODUCTION

Diaziridine derivatives (saturated three-member heterocycles with two nitrogen atoms) possess high formation enthalpy due to a strain of the three-membered cycle and a hydrazine fragment included in the molecule and, therefore, they are of high interest as potential components of rocket propellants. Formation enthalpy of diaziridine derivatives may be increased by introducing other groups with high formation enthalpy, e.g. acetylene, azide or cyclopropane into their molecules. Earlier[1] we described the synthesis and thermochemistry of diaziridines with aliphatic, nitro, nitrates and allylic substituents. This work incorporates the development of methods for including the above substituents into mono- and bisdiaziridine molecules.

Synthesis of mono- and bisdiaziridines with acetylene substituents

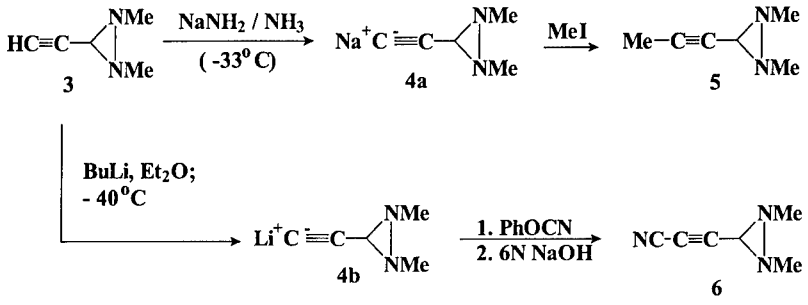
Theoretically the acetylene groups could be inserted in target diaziridines molecules both as fragments of initial carbonyl compounds and of amines. However all compounds with free acetylene groups should be excluded due to their susceptibility to Bu^tOCl or NaOCl usually used in the synthesis of diaziridines. The most convenient initial compounds for our aims would be structures with protected acetylene groups with the following protection removal. In this work we selected two accessible α-acetylene aldehydes **1a,b**, in which acetylene fragments were protected by acetalic and 1,1-dimethylhydroxymethylene groups, accordingly. The first protecting group is usually removed under acidic conditions and the second protecting group - under basic conditions. For the synthesis of corresponding 1,2-dimethyl-3-ethynyldiaziridines **2a,b** we used a developed earlier method[2,3] based on the interaction of carbonyl compounds, amines and aminating reagents (e.g. N-chloroalkylamines) in the MeOH-H_2O mixture at pH_{opt} 9.5-10. An attempt to remove acetalic protection in formed diaziridine **2a** in acidic medium failed - the main direction of this process was decomposition of **2a** under reaction conditions. However, the 1,1-dimethylhydroxymethylene group in diaziridine **2b** was successfully removed by pyrolysis under melting KOH in vacuum 140-150 mm Hg. The yield of obtained 1,2-dimethyl-3-ethynyldiaziridine **3** was 30% (Scheme 1).

Scheme 1



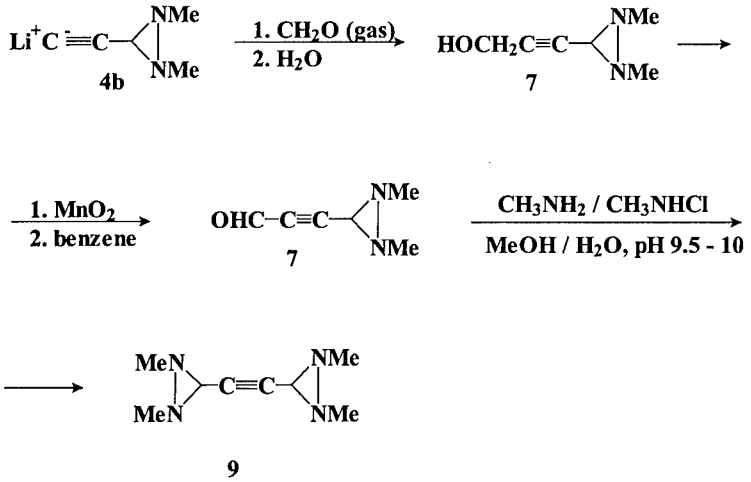
1,2-Dimethyl-3-ethynyldiaziridine **3** served as an initial compound for the synthesis of a wide scope of diaziridines with one or two acetylene fragments in the molecule. The one of typical transformation of compound **3** was metallation of the end acetylene group followed by the interaction of obtained salt **4** with the corresponding electrophylic reagent. Sodium salt **4a** was synthesized by reaction of diaziridine **3** with sodium amide in liquid ammonia and lithium salt - with BuLi at low temperature in ether. Alkylation of sodium salt with CH_3I resulted in 1,2-dimethyl-3-mehtylethynyldiaziridine **5** (Scheme 2). The interaction of lithium salt **4b** with phenoxycyan followed by the treatment with 6N NaOH gave 1,2-dimethyl-3-cyanoethynyldiaziridine **6** (Scheme 2).

Scheme 2



Lithium salt **4b** also served as an initial compound for the synthesis of hydroxymethylethynyl derivative **7**, which was prepared by passing of gaseous formaldehyde in solution of **4b** in ether at low temperature followed by the treatment of the reaction mixture with water. Oxidation of the hydroxymethyl group in compound **7** with MnO_2 in benzene at room temperature resulted in aldehyde **8.** On the basis of the latter compound was synthesized 3,3'-ethynylbisdiaziridine **9** by the interaction with MeNHCl and $MeNH_2$ in the $MeOH/H_2O$ mixture at pH 9.5-10, similar to the synthesis of diaziridines **2a,b** (Scheme 3).

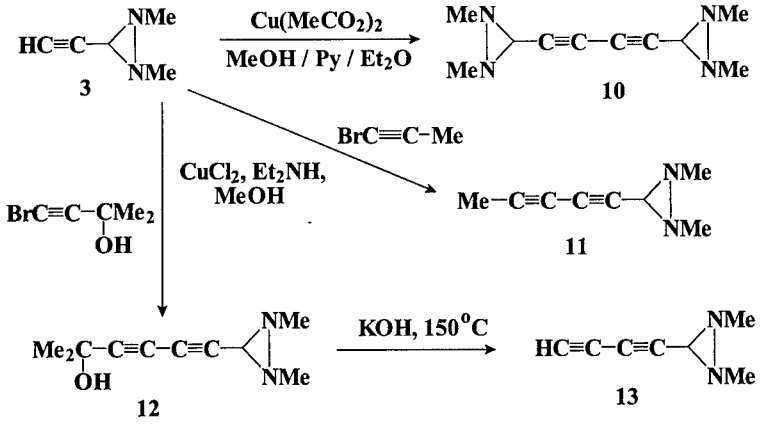
Scheme 3



Several approaches were developed for the synthesis of diaziridines with the diacetylene fragment. The preparation of such compounds was based on the oxidizing

doubling reaction (Glazer reaction[4]) or some of its modifications. The first example of such kind of a reaction was the synthesis of diaziridine **10** by oxidizing doubling of 1,2-dimethyl-3-ethynyldiaziridine **3** in the MeOH/Pyridine/Et_2O mixture in the presence of a catalytic amount of $Cu(MeCOO)_2$. One of the modifications of Glaser reaction is addition of bromoacethylenes to other acetylene compounds[5]. This reaction was used for the oxidizing doubling of diaziridine **3** with 1-bromo-2-methylacetylene and 1-bromo-2-(1,1-dimethylhydroxymethyl)acetylene. Both reactions were carried out in the presence of organic bases and a catalytic amount of CuCl and resulted in two diaziridines with diacetylene fragment **11** and **12,** accordingly. 1,1-Dimethylhydroxymethyl protection in compound **12** was removed by pyrolysis under melting KOH at 150° C with the formation of 1,2-dimethyl-3-diacethylenenyldiaziridine **13** (Scheme 4).

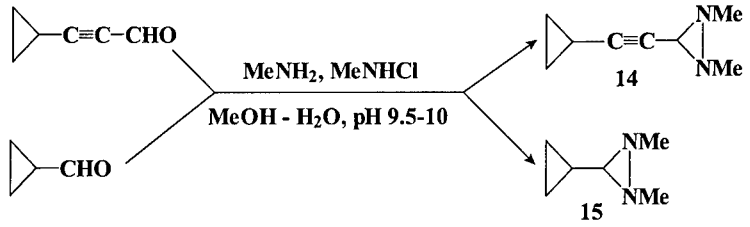
Scheme 4.

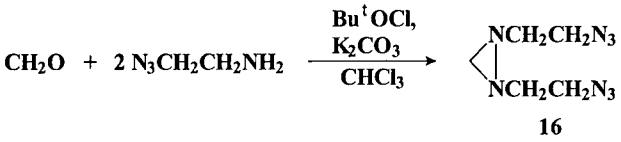


Synthesis of diaziridines with cyclopropyl, azide and diaziridinyl substituents

The synthesis of diaziridines with cyclopropyl substituents was performed from corresponding aldehydes - formylcyclopropane and cyclopropylethynylcarboxaldehyde. The latter aldehyde contains cyclopropyl and acetylene fragments simultaneously. Corresponding diaziridines **14** and **15** were prepared by the above method at pH 9.5-10. The introduction of two azides groups into diaziridine molecule (compound **16**) was carried out in one step from formaldehyde, β-azidoethylamine and Bu^tOCl in $CHCl_3$ in the presence of K_2CO_3 according to our method [6] (Scheme 5).

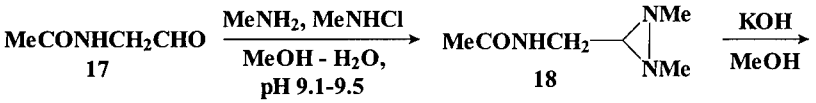
Scheme 5





A three-step approach was used for the synthesis of compound **20** containing three diaziridine cycles in the molecule. Acetaminoacetaldehyde **17** served as an initial compound for this aim. The first step consisted of the synthesis of diaziridine **18** from aldehyde**17**, methylamine and N-chloromethylamine at pH 9.1-9.5. Then acetyl protection in compound **18** was removed by heating with KOH/MeOH, and the interaction of formed 1,2-dimethyl-3-aminomethyldiaziridine **19** with formaldehyde and Bu^{t}OCl in $CHCl_3$ in the presence of K_2CO_3 resulted in 1,2-bis(1,2-dimethyldiaziridin-3-yl)methyldiaziridine **20** (Scheme 6).

Scheme 6



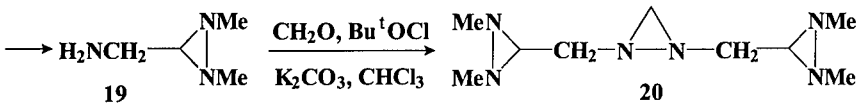
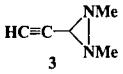
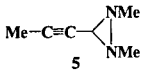
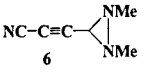
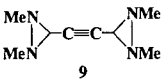
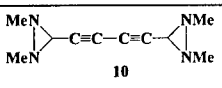
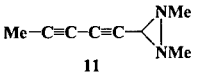
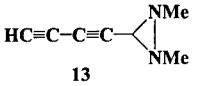
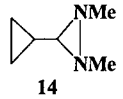
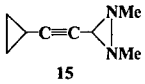
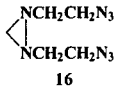
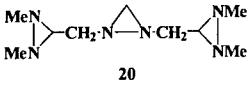


Table. Synthesized diaziridines

1	Compounds	d g/cm^3		m.p. °C	b.p. °C (Torr)	ΔH_o kcal/kg	
		Calc.	Exp.			Calc. (1)	Calc. (2)
1.	 3	0.89	0.90	0	108 (760)	1071.36	1092.50
2.	 5	0.89	0.91	-35	144 (760)	835.32	865.04
3.	 6	1.05	1.03	--	50 (8)	1071.83	1094.80
4.	 9	1.02	--	39	--	926.00	904.00
5.	 10	1.02	1.09	92-95	--	1076.40	1098.18
6.	 11	0.94	0.94	0-1	62 (3)	1155.13	1205.33
7.	 13	0.95	0.96	-3	67 (20)	1348.40	1397.04
8.	 14	0.90	0.92	--	117 (760)	532.45	502.54
9.	 15	0.94	0.93	--	40-41 (1)	828.90	802.16
10.	 16	1.17	1.167		95 (1.5)	1088.00	1034.04
11.	 20	1.03	1.01		90 (1)	710.50	690.00

So over the whole cycle of investigations a wide range of compounds with one, two and three diaziridine cycles in the molecule were synthesized and additional energetic groups - acetylene, azide and cyclopropyl were introduced into these structures. The study of some

physico-chemical properties of the synthesized substances (density, boiling and melting points) showed that most of the obtained compounds were liquids with density of about 1 g/cm^3 and higher (see Table). Calculation of their formation enthalpy was carried out by different methods: (1) additive-groups method (Semenov Institute of Chemical Physics) and (2) semi-empirical quantum chemistry (PM3)[7] and Atom-Atom Potential Functions (AAPF)[8,9] methods.

ACKNOWLEDGEMENT

This work was partially supported by Collaborative Linkage Grant SA (SST.CLG.977566) from the NATO.

REFERENCES

1. N. N. Makhova, V. Yu. Petukhova, V. V. Kuznetsov, L. I. Khmel'nitskii, V. P. Lebedev and V. I. Pepekin, Proceeding of 29th Int. Ann. Conf. of ICT, 1998, 10 (1-13).
2. V. V. Kuznetsov, N. N. Makhova, Yu. A. Strelenko and L. I. Khmel'nitskii, Izv. Acad. Nauk SSR, Ser. Khim., 1991, 2861 (Bull. Acad. Sci. USSR, Div. Chem. Sci., 1991, **40**, 2496).
3. V. V. Kuznetsov, N. N. Makhova and L. I. Khmel'ntskii, Izv. Acad. Nauk, Ser. Khim., 1997, 1410 (Russ. Chem. Bull., 1997, **46**, 1354).
4. R. J. Tedeschi and A. E. Brown, J. Ogg. Chem.,1964, **29,** 2051.
5. W. Chodkiewicz, Ann. Chim. (Paris), 1957, **2**, 819.
6. N. N. Makhova, A. N. Mikhailyuk, V. V. Kuznetsov, S. A. Kutepov and P. A. Belyakov, Mendeleev Commun., 2000, 182.
7. T. Clark. A Handbook of Computational Chemistry, John Wiley and Sons, Inc., 1985.
8. A. I. Kitaigorodsky, Organic Chemical Crystallography, Consultant Bureau, New York, 1961.
9. A.V. Dzyabchenko, T.S. Pivina, E.A. Arnautova. Journal of Molecular Structure, 1996, **378**, 67.

SOLID PROPELLANT COMBUSTION UNDER SHOCK WAVE LOADING

Alexander Yu. Dolgoborodov, Vladimir N. Marshakov

Institute of Chemical Physics RAS, 117977 Moscow, Russia, aldol@chph.ras.ru

ABSTRACT

The purpose of this work was to develop a laboratory technique, which would allow investigating stability of propellant burning under shock wave loading in the pressure range 100 - 300 MPa. For experimental investigation of stability of composite propellant combustion we used the combustion chamber. The explosive generator was used for shock waves formation in the propellant samples. The experiments were conducted in the combustion chamber at the products pressure range 1 - 12 MPa. The induction gauge was used for measuring of pressure variation of combustion products. HE charge was initiated in 1-1.5 seconds after ignition of the propellant. For shock pressure in a sample less than 150 MPa, the experimental results have shown that the steady combustion regime is retained. The small pressure decay was observed immediately after shock wave entered at a burning surface and then the previous parameters were restored. The shock pressure increasing up to 230 MPa results to product pressure rise and consequent combustion chamber breakage. The analysis of possible causes of observed differences in regimes of burning was performed.

INTRODUCTION

In operation on the ground and in flight, a solid-propellant rocket engine may be subjected to shock loading caused by external shock wave, impacts of fragments generated by explosions, and directed high-intensity energy fluxes [1-3]. Duration of these loads varies from 10^{-6} to 10^{-2} s, depending on the source, and the representative pressure pulses range from 0.1 kPa*s to 5 kPa*s. Effect of shock wave impulse on the operating rocket engine can result to disastrous consequences. Sometimes fire bench tests are carried out for determination of safe load levels of operating engine [4]. However realisation of such tests requires significant costs. The purpose of our work was to develop a rather cheap laboratory technique, which would allow investigating the stability of propellant burning under shock wave loading in the pressure range 0.1 to 0.3 GPa.

EXPERIMENTAL

For experimental investigation of stability of composite propellant combustion we used the combustion chamber. We investigate the samples of propellant on the base of polybutadiene rubber filled by ammonium perchlorate and HMX with a characteristic size of particles of 100-300

μm and fine aluminium particles (5-10 μm). Earlier the structure of shock wave was investigated for this propellant in work [5]. For shock wave formation in samples we used the explosive generator similar described in this work. The scheme of combustion chamber with explosive generator (EG) is displayed in Fig.1.

The combustion camera was made by the way of thick-walled vessel with volume about 2 litres. The shock wave impulses with maximum pressure 0.1-0.3 GPa formed by EG. EG consist of a composite charge of RDX (lens by a diameter of 40 mm and weight 15 g and intermediate charge with detonator in weight 5 g) and thin-walled copper barrel with water by a diameter of 85 mm. The HE charge was installed above at centre of a barrel. The barrel was fixed on a cover of the combustion chamber. The parameters of a shock wave were adjusted by variety of height of the barrel with water. The shock wave from water passed in a propellant sample through the organic-plastic insert in a cover of the combustion chamber. The diameter of the organic-plastic insert constituted 90 mm, width of 14 mm. Propellant samples were produced as truncated cones by a thickness of 40 mm and diameters of the basis 50 and 57 mm. Samples are located inside the chamber and nestled on the organic-plastic insert by a conic cartridge clip. Ignition of samples was made from the lower end face by burning products of powder charge of weight 5 g. On a lateral area of the chamber there were landing places under the nozzle block, block of a safety valve and reducing coupling under the inductive gauge DD-10. The products of burning were assigned from the chamber through a nozzle block. The pressure in chamber was registered by gauge DD-10 with the pressure indicator ID-2I on the oscilloscope N-117. The initiation of a HE charge was made in 1-2 second after ignition of a propellant with the help of synchronization scheme.

The experiments on determination of a shock wave structure in propellant samples without burning were previously conducted. For a measurement of shock wave pressure in samples were used piezoelectric film PVDF - gauges made and calibrated in laboratory by Yakushev V.V. (IPCP RAS, Chernogolovka). PVDF gauges were placed in two planes: on the contact boundary of the organic-plastic insert of the chamber and propellant sample and in a sample on depth of 20-22 mm. The scheme of experiments is shown in Fig. 2. In order to prevent of influence of air inclusions on a structure of a wave of an irregularity between the insert and sample were filled in with an epoxy resin ED-20.

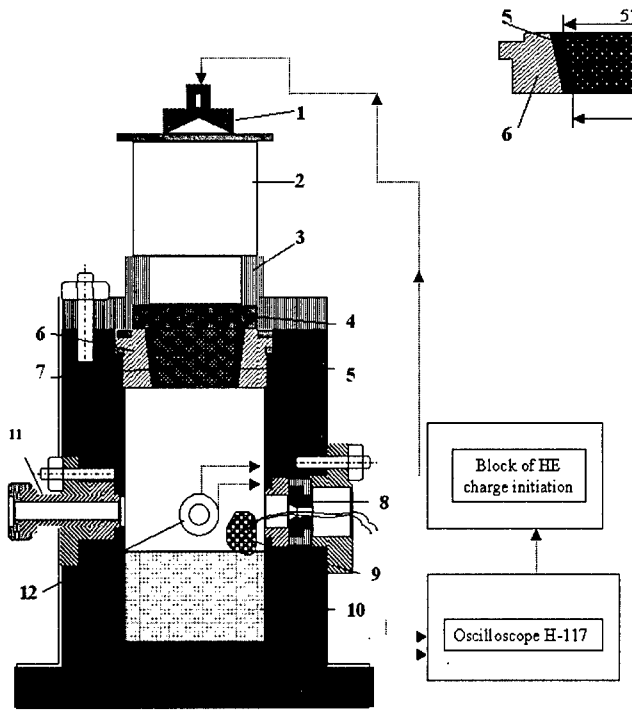


Fig. 1. Combustion chamber with explosive generator
1 - explosive charge,
2 - copper cylinder with water
3 - cover of chamber case
4 - organoplastic insert
5 - propellant sample
6 - conical cartridge
7 - protecting cover
8 - nozzle
9 - ignition powder charge
10 - additional insert of chamber
11 - block of safety diaphragm
12 - orifice in the chamber to adapter and pressure gauge DD-10

EXPERIMENTAL RESULTS

The trial tests were made without combustion of samples. Samples subjected to shock compression and were visually studied after a shock loading. Fastening of samples was carried out by two ways. In the first case the sample was retained against organic-plastic insert by the plexiglas screen. The screen had the holes of different diameter. In the second case the sample was consolidated only on a lateral area by a special conical cartridge from duralumin, thus also was given to a sample the conical form. In the latter case it was possible to achieve absence of separation of a sample from the insert after shock wave loading, and hereinafter this manner of fastening utilised for researches at combustion.

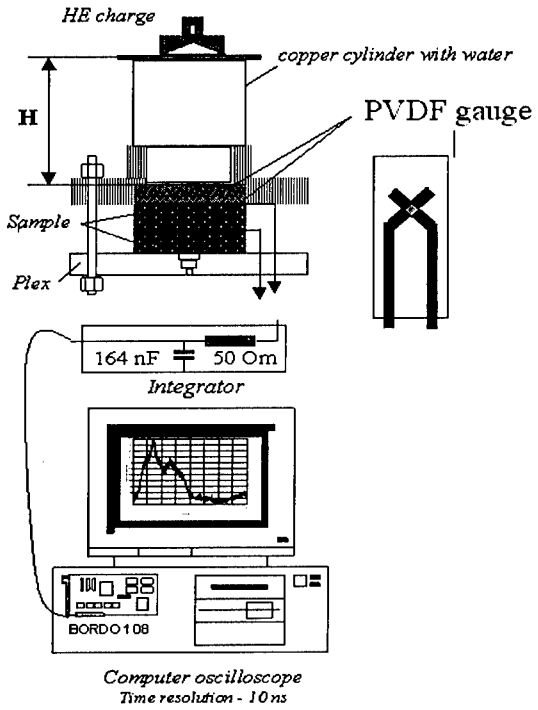


Fig. 2. Experimental set-up for pressure measurement in propellant samples

PVDF- piezoelectric film gauges made of polarized polyvinylidene-fluoride with sensing area 5.06 mm^2 formed by electric polarization at the crossing site (dynamic calibration by Yakushev V.V. (IPCP RAS) $0.01 < P < 0.34$ GPa $P=2.86^{-5} + 0.4415\ q + 1.027\ q^2 - 0.541\ q^3$, charge q is in $\mu C/cm^2$ and pressure in GPa. $\delta P \approx 10\%$

Visual research of samples in all cases has shown, that the large fragments of a filling material (HMX and ammonium perchlorate) from a near-surface layer take off from a sample, and the free surface of a sample gains spongy structure (see Fig. 3-4). In case of availability of holes in the screen in samples the destructions are observed. Thus the size of destructions decreases with growth of diameter of holes. So at diameter of a hole of 5 mm and shock wave pressure 0.135 GPa there was a full separation of spalling element by depth up to 2.5 mm. At diameter of a graduated hole of 18 mm there was a loosening of a sample in the field of a hole. Inside a propellant the spalling flaws have appeared. In case of a pressure increment till 0.23 GPa propellant lost

durability and the corrupting were considerably magnified, though complete spallation does not happen.

The experiments on measurement of the profile of pressure have shown the following. At a stratum of water of height 148 mm the pressure profile on contact boundary with the insert was close to the triangular form. The maximum pressure constituted 0.18 GPa. On depth of 21 mm in a sample the main features of a structure were saved. The maximum pressure has decreased up to 0.135 GPa. At decrease of a stratum of water on 50 mm the maximum pressure on depth of 21 mm inside a sample has increased till 0.23 GPa. The pressure profiles are shown at Fig. 4.

The experiences with burning were conducted at pressure inside the combustion chamber of 1 - 12 MPa. The pressure was regulated by selection of a nozzle diameter. In Fig. 5 four records of pressure are indicated at shock wave amplitudes - 0.135 and 0.23 GPa. The conducted experiences at a shock load by amplitude 0.135 GPa as a whole display saving stability of combustion. After shock wave exit on a shining surface happens small (approximately up to 0.2 MPa) pattern null of pressure and through 70 - 100 ms restoring of a former level. A reason of a pattern null of pressure can be break-up of a part of a warmed-over stratum from burning surface after shock wave passing.

At build-up of shock wave pressure up to 0.230 GPa there is a sharp rise of pressure. From the diagram in Fig. 5-4 it is visible, that the enlarged shock load has caused a steep of pressure, and at 12 GPa the organic-plastic insert was squeezed out from the chamber. There was corrupting the camera and, naturally, break-up of burning. The sharp pressure boost can be in this case caused at the expense of several reasons: increase of common burning square at the expense of a loosening and outbreak of a flame inside of a sample; separation of a heated stratum of sample with the subsequent afterburning in the chamber; spalling phenomenon inside a sample etc.

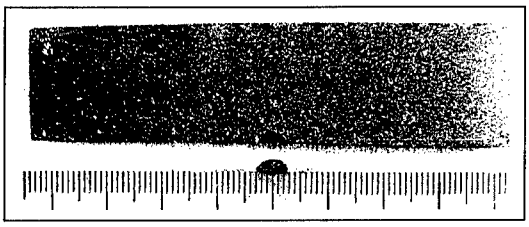
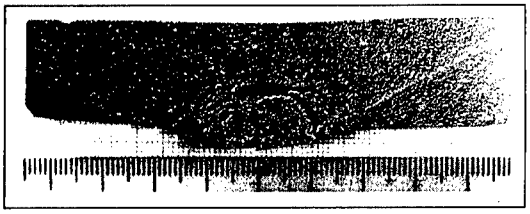


Fig. 3. Fracture of samples after shock wave loading 1-3 - propellant samples pressed from below by plexiglas plate with a hole

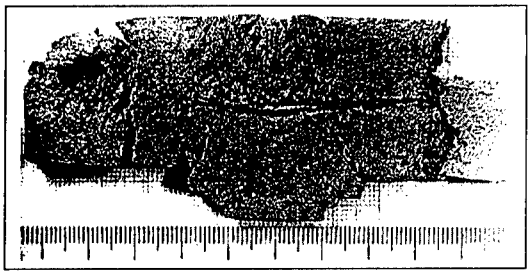
1- Plexiglas plate with 5 mm hole.

P_{sw} = 0.135 GPa



2- Plexiglas plate with graduated hole.

P_{sw} = 0.135 GPa

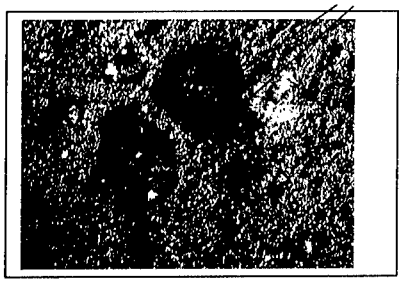


3- Plexiglas plate with graduated hole. P_{sw} = 0.23 GPa

4 - Sample is not fractured under shock loading when placed into the conical cartridge and fixed on the lateral surface. The large particles of HMX and ammonium perchlorate escape from a surface layer and free surface of the sample takes on a spongy texture.

sample free surface before shock loading and after shock loading

particles *holes*



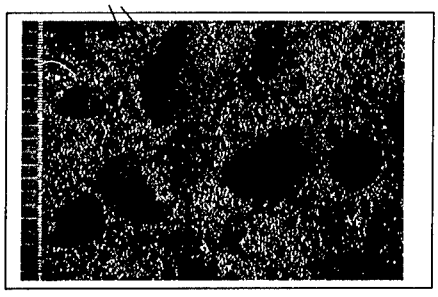
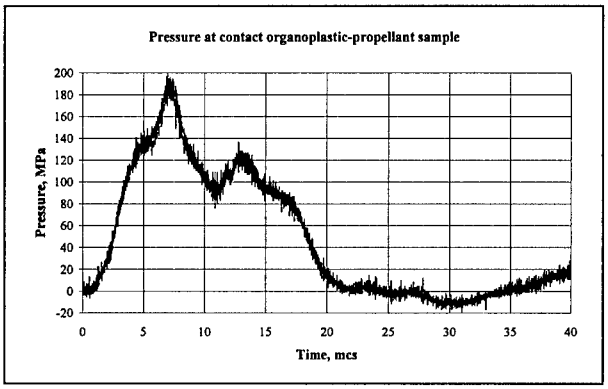


Fig. 4. Shock pressure records in propellant samples. (H - height of a stratum of water in the explosive SW generator)

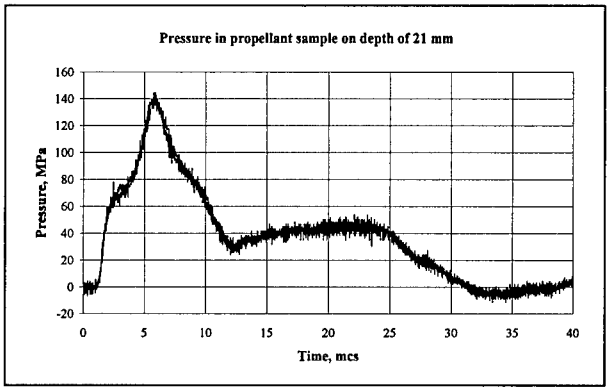
1 - H=148 mm
Pressure profile on the contact boundary organic-plastic insert - propellant

P_{max}=0.18 GPa



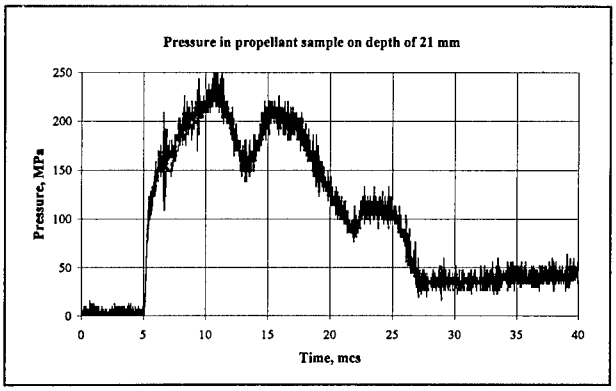
2 - H=148 mm
Pressure on the depth of 21 mm in sample

P_{max}=0.135 GPa



3 - H=88 mm
Pressure on the depth of 21 mm in sample

P_{max}=0.23 GPa



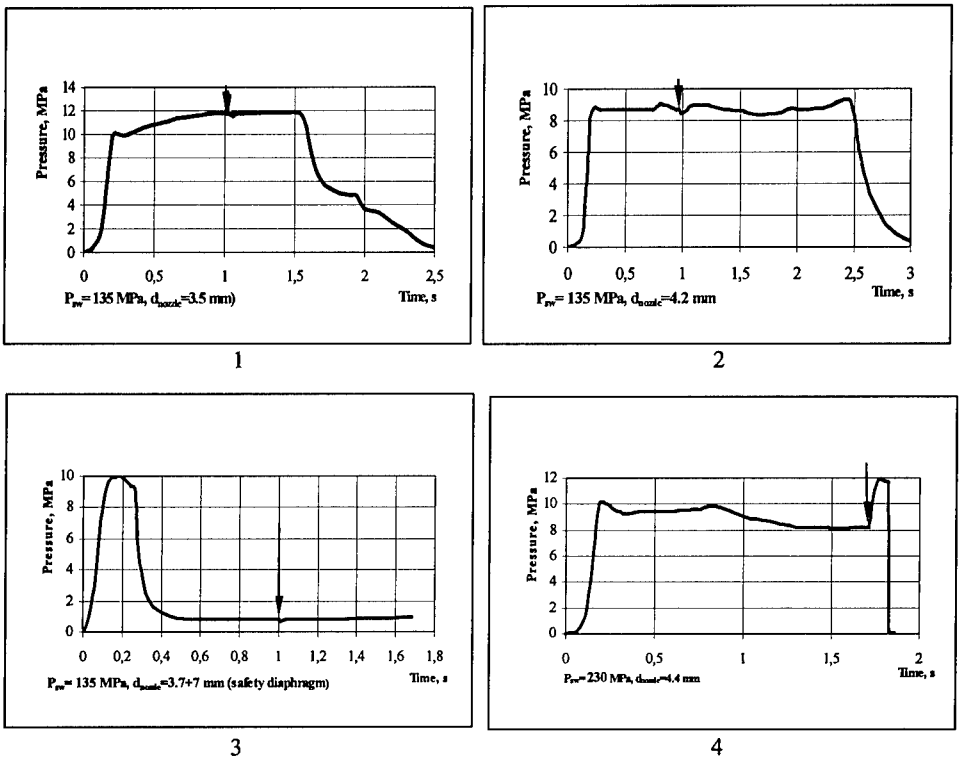


Fig. 5. Pressure variation in combustion chamber (vertical arrow shows a moment of shock loading)

1, 2, 3 – shock wave pressure = 0.135 GPa, 4 - P_{SW} = 0.23 GPa. Shock wave with pressure of 0.135 GPa leads to small pressure decay without violation of propellant burning stability at various operational modes of chamber. SW with pressure 0.23 GPa results in sharp pressure rise and chamber destruction.

CONCLUSIONS

The experimental procedure for conducting the laboratory tests on stability of propellant combustion under shock wave loading has been developed. There were manufactured and developed explosive generator, model testing unit, and combustion chamber for studying combustion of propellants under shock wave loading in the pressure range 0.1 – 0.3 GPa.

There were conducting the tests on combustion of the composite propellant in the chamber under shock wave with amplitude from 0.13 to 0.23 GPa. The experiments conducted in the combustion chamber under the pressure ranged from 1 to 12 MPa showed the following:

- The shock wave loading of the propellant sample with the amplitude 0.135 GPa did not cause the combustion failure and resulted only in insignificant (0.15 – 0.20 MPa) short-acting (20 – 70 ms) pressure decrease after which the previous pressure level restored. This means that steady state combustion regime was retained.
- Under the same conditions, shock-wave pulse with pressure amplitude of 230 MPa resulted in abrupt pressure increase and emergency conditions in the chamber.

In the last case, the abrupt pressure rise could be caused by several reasons that may be summarised as following: increasing of total burning area at the coast of surface disintegration and flame breaking into the sample; separation of heated-up layer with it consequent afterburning in the chamber; spalling fracturing of the sample etc.

The analysis of the pressure diagram suggests that, as the result of shock wave loading, separation of burning layer approximately from one third of total burning surface took place. Burning of this layer and ignition of the liberated surface caused the pressure increase in the chamber. More detail analysis of the phenomenon occurring under shock wave loading calls for further investigation.

REFERENCES

1. A.M. Sinyukov, L.I. Volkov, A.I. L'vov, and A.M. Shoshkevich. *Ballistic Solid-Propellant Rockets.* Voenizdat MO SSSR, Moscow, 1972. (in Russian)
2. *Space Weapons: Dilemma of Security.* E.P. Velikhov, R.E. Sagdeev, and A.A. Kokoshin, Eds.. Mir, Moscow, 1986. (in Russian)
3. S.P. Anisimov, A.M. Prokhorov, and V.E. Fortov. *Usp. Phys. Nauk.* **142**, issue 3, p.395 (1984)
4. A.V. Ostrik, and V.P. Petrovskii. *Chemical Physics Reports.* **14** (1-3) p. 10 (1995).
5. B.R. Gafarov, A.V. Utkin, C.V. Razorenov, A.A. Bogach, E.S. Yushkov. *Applied Mechanics and Technical Physics.* **40** (3), p.161 (1999).

EXPLOSION HEAT AND METAL ACCELERATION ABILITY OF HIGH EXPLOSIVES

M.N. Makhov

N.N. Semenov Institute of Chemical Physics, Russian Academy of Sciences.
4 Kosygin Street, Moscow, 117977, Russia. E-mail: makhov@polymer.chph.ras.ru

Abstract

The dependence of metal acceleration ability on the energy content of high explosives is considered in the paper. A semi-empirical method for evaluating explosive performance in metal acceleration applications is suggested. This method has been developed on the basis of the assumption that the amount of explosive energy, transferred to the driven metal, depends on the volumetric number of moles of gaseous products. The results of calculations, performed for some well-known and new explosives, are presented in the paper.

Introduction

The explosion heat (EH) is the fundamental parameter, defining the potential ability of explosion products (EP) to do work. The Hugoniot adiabate equation and the equation for the adiabatic work are written:

$$E_{CJ} - E_0 = P_{CJ}(V_0 - V_{CJ})/2 + Q; \quad (1)$$

$$A = E_{CJ} - P_{CJ}(V_0 - V_{CJ})/2 - E_1 \approx Q - E_1; \quad (2)$$

where: E_{CJ}, P_{CJ}, V_{CJ} - respectively the internal energy of products, the pressure and the specific volume of products at the C-J state; E_0, V_0 - the internal energy and the specific volume of an explosive at the initial state; Q - the heat effect, E_1 - the internal energy of products at the considered stage of adiabatic expansion; A - the adiabatic work.

As is seen from equations (1) and (2), the explosion work depends on EH. The latter defines the explosion work at the large degree of EP expansion ($E_1 \to 0$).

One of the most important characteristics of high explosives (HE) is the metal acceleration ability (MAA). Measurements of MAA are conducted using a series of experimental methods. These methods simulate various conditions of explosive applications in practice. Furthermore the results of these measurements allow one not only to determine MAA, but to study the law of EP expansion as well. Different approaches are taken to solving the problem of prior estimation of MAA.

Hydrodynamic calculations require a description of the shape of EP isentrope. The equation $P = A\rho^{\gamma}$ is often used for this purpose. As a rule, the isentropic exponent γ is assumed to be a constant. However γ can be considered as a constant only near the C-J point. Furthermore in contrast to the detonation velocity the C-J pressure is measured with relatively high error, and γ is not precisely predictable. The authors of [1,2] suggested the procedure for determining the effective value of γ over the range of EP expansion observed in Cylinder Test.

The Jones-Wilkins-Lee equation is widely used for description of EP isentrope:

$$P = Ae^{-R_1V} + Be^{-R_2V} + CV^{-(1+\omega)}; \qquad (3)$$

where: V is the relative volume and A, B, C, R_1, R_2, R_3 and ω are constants for a given explosive. These constants are usually selecteded to obtain the closest agreement with Cylinder Test results [2-4]. One of the most extensively used equations of state of EP is Becker-Kistiakowsky-Wilson equation of state with generalized parameters [3,5-8].

MAA of explosives is often estimated using some criteria, containing detonation wave parameters. For example, the kinetic energy of an accelerated cylindrical tube is considered as a function of the C-J pressure: $P_{CJ} = \rho D^2/(\gamma + 1)$, where: D - the detonation velocity, ρ - the initial charge density [9]. In [10] the relative detonation impulse is estimated as a function of the quantity:$\rho D/\gamma$. In [11] the velocities of accelerated plates and cylinder walls are evaluated from the contact boundary velocity. The similar approach is used in [12] where the velocity of

the accelerated plate is considered to be proportional to the initial velocity of the contact boundary. Such approach requires the knowledge of shock Hugoniot of the accelerated material, detonation parameters and γ of the explosive considered.

The authors of [13] proposed the unified form of explosive performance potential to characterize "strength" and "brisance" of HE. The results of following tests were considered: Lead Block, Ballistic Mortar, Cylinder Test, Kast Brisance Meter and Plate Dent Test. The potential involves three parameters: the number of moles of gaseous products, produced by a unit volume of an explosive, EH per unit volume of an explosive and the detonation velocity. However the approach, associated with using the unified performance criterion, is not quite correct, because the extent to which the explosion work is affected by each of the above-listed parameters depends on test conditions. In particular, as already noted, the explosion work depends mainly upon EH at the large degree of EP expansion.

The results of detonation impulse measurements, performed on modified Kast Brisance Meter for a number of solid and liquid explosives, are presented in [14]. Taking into account that EP composition changes with expansion, the authors of [14,15] did not use the values of detonation pressure or detonation velocity for evaluating the relative impulse. They proposed the empirical equation, containing the calorimetric value of EH and the average molecular weight of gaseous EP. This equation also accounts for negative influence of solid carbon, which can be present in EP of HE with negative oxygen balance.

As early as 1943 Gurney correlated fragment velocity data by assuming that a given explosive could deliver a characteristic value of specific energy in the form of the kinetic energy of EP and driven metal [16]. His model also assumed the linear velocity profile in products. Using this approach one can write an energy balance for any symmetric configuration. The metal velocity therewith may be expressed as: $U = (2E_G)^{0.5} f(\mu)$; where: E_G - the Gurney energy, $(2E_G)^{0.5}$ - the Gurney velocity, and μ - the ratio of metal mass to explosive mass.

The authors of [17] attempted to determine Gurney energies for a number of HE by thermodynamic calculations using Tiger Code and JCZ3 equation of state. However, in order to improve an agreement between calculations and experiments the authors used the effective value of the degree of EP expansion. The values of E_G, calculated at threefold EP expansion, corresponded to those, determined from experimental Cylinder Test data at sevenfold expansion. In [6] thermodynamic calculations were carried out with the use of BKW equation of state. In this calculations the values of E_G, obtained from experimental data at sevenfold EP expansion, corresponded to the values calculated at the expansion degree equal to 2.5.

Kamlet and co-workers estimated detonation velocities and pressures using the parameter: $\phi = NM^{0.5}Q^{0.5}$; where: Q and N are EH and the number of moles of gaseous EP per unit weight of an explosive, M is the average molecular weight of these products [18-20]. Values of N, M and Q were calculated from the H_2O-CO_2 arbitrary assumption of EP composition (the rule of maximum heat effect). In [21] the semi-empirical equation for predicting explosive performance in Cylinder Test was suggested. This equation involves the parameter ϕ and takes the form:

$$U_c\,(mm/\mu s) = 0.368\phi^{0.54}\rho^{0.84}(R - R_0)^{0.212 - 0.065\rho}; \qquad (4)$$

where: U_c - the radial cylinder wall velocity, ρ- the initial charge density, R_0 and R - initial and instantaneous values of the radius.

It should be noted that N, M and Q, calculated by the rule of maximum heat effect, remain hypothetical quantities, which are not realistic in many cases, especially for HE with negative oxygen balance.

To predict EH and EP composition of HE thermodynamic computation methods are often used. These calculations are usually based on the assumption that detonation products of C-H-N-O explosives are frozen on the C-J isentrope within the temperature range: 1500 – 2100 K [3,8,22-26]. Unfortunately, thermodynamic calculations overestimate EH values for HE with strongly negative oxygen balance (e.g., TNT). To reduce thermodynamically calculated values of EH for

explosives of this type some authors use various positive values of enthalpy of formation of carbon [5,8,24]. However, there is not a rigorous verification of the validity of this assumption. Nowadays the question of carbon behavior in detonation wave still remains unanswered.

In the present paper the method for predicting MAA of HE, based on the dependence of MAA on explosive energy content, is suggested. To calculate EH the semi-empirical method, proposed in [27], was applied. The equation for EH calculation was found to represent calorimetric data, obtained for 16 explosives at variable charge density [28]. This equation specifies the dependence of the coefficient of maximum heat realization on the initial charge density, the ratio of hydrogen content to carbon content and the oxygen factor of an explosive. EP compositions were estimated using the method suggested in [29]. Despite of simplicity, the methods used for calculating EH and EP composition show a good agreement between experiments and calculations over a wide range of explosive oxygen balances.

An important feature of the calorimetric technique employed in [28,30] is the use of the massive casing for charge confinement (the charge diameter and the thickness of the copper casing were 20 and 7 mm respectively). The role of the casing is to increase the extent of completeness of reactions in outer layers of charges. Furthermore, it is known, that EP of unconfined charges are shocked considerably by reflections from calorimetric bomb walls, causing new equilibrium of products to be frozen under conditions of low pressure. The casing attenuates the secondary heating of EP, as the energy of EP of heavily confined charges is largely converted to the kinetic energy of the casing [22-24,31,32]. It is shown in [31,32], that for pure explosives, such as TNT and HMX, re-equilibration of EP does not take place if the mass ratio: casing/explosive is more than 4. The value of EH, obtained under these conditions, does not depend on the thickness of the casing, corresponds to the EP composition, frozen on the C-J isentrope, and can serve as a measure of the energy content of an explosive. This value is a function only of the

loading density. If the mixture tested consists of high explosives with particle sizes of several tens μm, above mentioned values of the charge diameter and the thickness of the copper casing, as a rule, ensure the completion of reactions on the stage of EP expansion, preceding the freeze-out temperature range.

Results

In earlier work [27] semi-empirical relations for evaluating the explosive performance in Cylinder Test were suggested. The approach used was based on the dependence of the kinetic energy of the copper cylindrical tube on the value of EH per unit volume of an explosive. The coefficient of conversion of the chemical energy to the kinetic energy of the cylinder was considered to be a function of the volumetric number of moles of gaseous EP. The latter quantity influences not only the position of EP isentrope on P-V diagram but the slope of the isentrope as well. The greater the volumetric number of moles of gases, the "steeper" is the isentrope. The equation for the kinetic energy of the cylinder (E_c) was found in the form:

$$E_c = K(Q\rho). \qquad (5)$$

Here, K is the energy conversion coefficient, which is calculated by the equation:

$$K = K_1(N\rho)^{\alpha}; \qquad (6)$$

where: N – the number of moles of gaseous EP per unit weight of an explosive;ρ - the initial charge density.

Since K_1 and α have been found as functions of the outer radius of the cylinder, the energy conversion coefficient depends on the degree of EP expansion. The expression for α takes the form:

$$\alpha = 1.5\exp(-0.54R/R_0). \qquad (7)$$

The equation (7) was obtained by processing the total body of experimental data [21,33]. It should be emphasized that the accuracy of MAA calculation by equations (6-7) depends to a large measure on the correctness of EH determination.

The method described above should be used with care when mixtures are to be considered. Composite explosives, in particular mixtures, containing inorganic

oxidizers and fuel additives (e. g., Al), release their chemical energy over a much longer time scale than pure HE. In this case, the cylinder wall velocity can depend on the charge diameter and particle sizes of components [34].

A well-known experimental method for measuring MAA is the projection of a metal plate from the end of a charge. According to this method, the cylindrical charge, 40 x 40 mm, with the steel plate, 40 mm in diameter and 4 mm in thickness, are placed in the steel casing, 25 mm in wall thickness. The plate velocity on the distance of 40 mm from the initial position of the plate is chosen as a criterion of MAA.

In developing the method for predicting the plate projection ability of HE the same approach as previously [27] may be used, that is, the kinetic energy of the plate may be assumed to be dependent on the explosive energy content ($Q\rho$). The energy conversion coefficient may be considered as a function of the number of moles of gaseous EP ($N\rho$). It is found by processing the experimental data [35-37] that in this case α (equation (6)) is equal to 0.55. Calculated values of plate projection ability in comparison with experimental results are presented in Table 1.

In Table 1: HMX - cyclotrimethylenetrinitramine; BFADEN - bis(2-difluoramine-2,2-dinitroethyl)nitramine; BTEN - bis(2,2,2-trinitroethyl)nitramine; BTF - benzotrifuroxan. Two BTEN-based mixtures consist of carbon black and ultra-fine diamond. The quantity η_p is the relative value of plate velocity. The value of plate velocity of HMX, expressed in km/s, is given in brackets.

The compound BFADEN contains fluorine. At calculations the only fluorine-containing substance - HF is assumed to be present in EP. The results of thermodynamic calculations show that in the case of fluorine-containing explosives CF_4 should be present in EP close to the C-J point, but with EP expansion the content of CF_4 rapidly decreases whereas the content of HF increases [7]. Indeed, it has been found by calorimetric investigations and analyses of EP of bis(2,2-

dinitro-2-fluoroethyl)formal (FEFO) that all of fluorine of FEFO is present as HF rather than CF_4 in frozen EP [23].

Table 1. Calculated and experimental values of plate projection ability.

Explosive	ρ, g/cm^3	Q, kJ/kg	N, mol/kg	η_p, %	$\eta_{p,\,exp.}$, %
HMX	1.875	5650	37.14	100.0	100.0 [35] (2,185)
HMX	1.810	5610	37.37	97.1	97.5 [36]
BFADEN	2.033	6420	32.71	109.6	107.2 [37]
BFADEN/HMX, 60/40	1.973	6560	34.61	110.0	110.8 [37]
BTEN	1.92	5230	30.92	93.2	95.4 [35]
BTEN	1.844	5230	30.92	90.4	92.8 [35]
BTEN/HMX, 30/70	1.91	6110	35.36	104.0	103.0 [35]
BTEN/BTF, 60/40	1.861	6740	29.98	102.4	102.6 [35]
BTEN/C, 93/7	1.883	6300	30.29	100.2	100.0 [35]
BTEN/diamond, 93/7	1.982	6320	30.24	104.4	101.7 [35]

As is seen from Table 1, a reasonable agreement between calculated and experimental values of the plate projection ability has been obtained (the root-mean-square error is 1.7 %.). This is true even for the mixtures BTEN/C and BTEN/diamond, containing ultra-fine powders of combustible substances (in small amounts). Nonetheless, composite explosives, for instance, containing metal additives and inorganic oxidizers (Ammonium Nitrate, Ammonium Perchlorate, Potassium Perchlorate and so on), should be treated separately. On the other hand, the relationships presented above permit estimating the extent of interaction of mixture components by comparison of calculation results with experimental data.

From the obtained value of α it follows that the plate projection ability (in per-unit) in the experimental configuration considered corresponds to the tube acceleration ability in Cylinder Test at the degree of EP expansion approximately equal to 4.5. As an example, the results of calculations, performed for a number of explosives, differing significantly in oxygen balance and energy content, are presented in Table 2.

Table 2. Calculated values of MAA.

Explosive	ρ, g/cm^3	Q, kJ/kg	N, mol/kg	η_p, %	η_c, %	
					$V/V_0 = 2$	$V/V_0 = 7$
HMX	1.875	5650	37.14	100.0	100.0	100.0
DNDAF	2.002	7230	28.75	111.0	108.9	112.1
CL-20	2.04	6220	33.35	108.8	108.6	109.0
HNB	2.00	6830	26.78	105.7	103.1	107.2
TNAZ	1.84	6230	34.68	101.6	100.8	102.1
PETN	1.77	5940	34.02	95.8	94.4	96.5
K-56	1.975	4990	33.96	95.5	95.2	95.7
HNF	1.86	5050	36.90	93.8	93.7	93.9
DADNE	1.885	4590	36.50	90.2	90.0	90.3
2,4-DNI	1.763	4620	33.12	83.6	82.2	84.4
TATB	1.938	3970	32.48	82.9	82.1	83.4
HNS	1.74	4640	29.85	80.6	78.3	81.9
TNT	1.654	4440	31.56	76.9	74.8	78.1

In Table 2: η_c is the relative radial velocity of the copper tube in Cylinder Test, V/V_0 – the degree of EP expansion. The results have been obtained for following explosives: DNDAF – 4,4'-dinitro-3,3'-diazenofuroxan, CL-20 – 2,4,6,8,10,12-hexanitro-2,4,6,8,10,12-hexaazaizowurtzitane, HNB – hexanitrobenzene, TNAZ – 1,3,3-trinitroazetidine, PETN – pentaerythritol tetranitrate, K-56 – tetranitro-bicyclo-nonanone, HNF – hydrazinium nitroformate, DADNE – 1,1-diamino-2,2-dinitroethylene; 2,4-DNI – 2,4-dinitroimidazole, TATB – 1,3,5-

triamino-2,4,6-trinitrobenzene, HNS – 2,2',4,4',6,6'-hexanitrostilbene, TNT – 2,4,6-trinitrotoluene.

The semi-empirical equations suggested allow one to evaluate MAA of a given explosive not only in Cylinder Test, but in the steel plate acceleration test as well. The computation method has been developed on the basis of the assumption that the coefficient of conversion of chemical energy to the kinetic energy of the driven metal is a function of the number of moles of gaseous EP per unit volume of an explosive. There is reason to hope that this approach can be used for developing the method of MAA prediction in the case of other metal/explosive configuration.

References

1. Maranda A., Cudzilo S., Trzcinski W., and Nowaczewski J. Behaviour of Aluminum and TNT in the Detonation Waves of Ammonium Nitrate Explosives. Proc. 27th Intern. Annual Confer. of ICT. Karlsruhe. FRG. 1996. P. 43 (1 – 10).
2. Cudzilo S., and Trzcinski W.A. A Study on Detonation Characteristics of Pressed NTO. Proc. 31th Intern. Annual Confer. of ICT. Karlsruhe. FRG. 2000. P. 77 (1 – 14).
3. Finger M., Lee F., Helm F.H., Hayes B., Hornig H., McGuire R., Kahara M., and Guidry M. The Effect of Elemental Composition on the Detonation Behavior of Explosives. Proc. 6th Symp. (Intern.) on Detonation. ONR. ACR-221. 1976. P. 710.
4. Hornberg H. Determination of Fume State Parameters from Expansion Measurements of Metal Tubes. Propellants, Explosives, Pyrotechnics. 1986. V. 11. No 1. P. 23.
5. Mader C.L. Numerical Modeling of Detonation. Los Alamos Series in Basic and Applied Sciences. University of California Press. B. – L. – A. - L. 1979.
6. Gubin S.A., Odintsov V.V., Pepekin V.I. Thermodynamic Calculations of Detonation in Condensed Matters. Preprint. Chernogolovka. 1986. (in Russian).
7. Gubin S.A., Odintsov V.V., Pepekin V.I., Schargatov V.A. Khim. Fiz. 1990. V. 9. No 5. P. 673 (in Russian).
8. Suceska M. Calculation of Detonation Heat by EXPLO5 Computer Code. Proc. 30th Intern. Annual Confer. of ICT. Karlsruhe. FRG. 1999. P. 50 (1 – 13).
9. Baum F.A., Oreshko L.P., Stanyukovich K.P. et al. Physics of Explosion. Nauka Publ., Moscow. 1975. P. 358 (in Russian).
10. Apin A.Ya., Bardin E.P., Velina N.F. Vzryvnoe Delo. No 52/9. Gosgortekhizdat, Moscow. 1963. P. 90 (in Russian).
11. Kiryushkin A.N., Voskoboinikova N.F. Acceleration of Metal Plates by Explosion Products. Physics of Pulse Pressures. Trudy VNIIFTRI. Moscow. 1979. P. 77 (in Russian).
12. Voskoboinikov I.M., Voskoboinikova N.F. Assessment of Plate Projection Ability of High Explosives. Proc. 2th All-Union Conference on Detonation ("Detonation"). Chernogolovka. 1981. P. 64 (in Russian).
13. Mohan V.K., and Tang T.B. Propellants, Explosives, Pyrotechnics. 1984. V. 9. P. 30.
14. Eremenko L.T., Nesterenko D.A., Strukov G.V., and Garanin V.A. Relationship Between the Relative Detonation Impulse and Chemical Composition of an Explosive. Proc 5th All-union

Symposium on Combustion and Explosion ("Detonation"). Chernogolovka. USSR. 1977. P. 76 (in Russian).
15. Eremenko L.T., Nesterenko D.A. Khim Fiz., 1997. V. 16. No 9. P. 119 (in Russian).
16 Gurney R.V. The Initial Velocities of Fragments from Bombs, Shells and Grenades. BRL. Report 405. 1943.
17. Hardesty D.R., Kennedy J.E. Combustion and Flame. 1977. V 28. P 45.
18. Kamlet M.J., and Jacobs S.J. J. Chem. Phys. 1968. V. 48. P.23.
19. Kamlet M.L., and Ablard J.E. J. Chem. Phys. 1968. V. 48. P. 36.
20. Kamlet M.L., and Dickinson C. J. Chem. Phys. 1968. V. 48. P. 43.
21. Short J.M., Helm F.H., Finger M., Kamlet M.J. Combustion and Flame. 1981. V. 43. P. 99.
22. OrnellasD.L., Carpenter J.H., and Gun S.R. Rev. Sci. Instrum. 1966. V. 37. No 7. P. 907.
23. Ornellas D.L., J. Phys. Chem., 1968. V. 72. No 7. P. 2390.
24. Ornellas D.L., Combustion and Flame, 1974. V. 23. No 1. P. 37.
25. Cudzilo S., Trebinski R., Trzcinski W.A., and Wolanski P. Comparison of Heat Effects of Combustion and Detonation of Explosives in A Calorimetric Bomb. Proc. 29th Intern. Annual Confer. of ICT. Karlsruhe. FRG. 1998. P. 149 (1 – 14).
26. Volk F., Bathelt H., Schedlbauer F., and Wagner J. Preprint, 8th International Symposium on Detonation. Albuquerque. New Mexico. 1985. V. 1. P. 330.
27. Makhov M.N., Arkhipov V.I. Fiz. Goreniya i Vzryva, 1989. V. 25. No 3. P. 87 (in Russian).
28. Pepekin V.I., Makhov M.N., Lebedev Iu.A. Dokl. Akad. Nauk SSSR. 1977. V. 232. No 4. P. 852 (in Russian).
29. Makhov M.N., Pepekin V.I. Polish Journal of Chemistry. 1981. V. 55. P. 1381.
30. Makhov M.N. The Heat and Products of Explosion of Aluminized High Explosives. Proc. 31th Intern. Annual Confer. of ICT. Karlsruhe. FRG. 2000. P. 42 (1 – 11).
31. Makhov M.N., Pepekin V.I. To Calorimetric Determination of the Explosion Heat of High Explosives. Proc. 9th All-union Symposium on Combustion and Explosion ("Detonation"). Chernogolovka. USSR. 1989. P. 23 (in Russian).
32. Makhov M.N. Khim. Fiz. 2000. V. 19. No 6. P. 52 (in Russian).
33. Kamlet M.J., Short J.M., Finger M., Helm F., McGure R.R., and Akst I.B. Combustion and Flame. 1983. V. 51. P. 325.
34. Finger M., Hornig H.C, Lee E.L., Kury J.W. Metal Acceleration by Composite Explosives. Proc. 5th Symp. (Intern.) On Detonation. ONR. ACR-184. 1970. P. 55.
35. Arkhipov V.I., Makhov M.N., Pepekin V.I. Khim Fiz., 1993. V. 12. No 12. P. 1640 (in Russian).
36. Arkhipov V.I., Makhov M.N., Pepekin V.I., and Schetinin V.G. Khim Fiz., 1999. V. 18. No 12. P. 53 (in Russian).
37. Pepekin V. Development of High Efficiency Energetic Explosives. Proc. 27th Intern. Annual Confer. of ICT. Karlsruhe. FRG. 1996. P. 19 (1 – 7).

PECULIARITIES OF SOLID PROPELLANTS IGNITION BY CO_2-LASER RADIATION

B.N. Kondrikov, S. Cristoforetti
Mendeleev University of Chemical Technology, Moscow, Russia

L.T. DeLuca
Politecnico di Milano, Milano, Italy

Ignition of a solid propellant by externally applied thermal radiation is considered usually a process of formation of a heat layer with a temperature T_S at the irradiated gas/solid interface sufficient to induce the fast heat generation at the expense of the propellant ingredients decomposition reactions. This simple model was found to be reliable at investigation of double-base propellants ignition by CO_2-laser radiation at ambient pressure on the order of several MPa. At a lower pressure, say 0.1-0.5 MPa, this model does work only at low heat fluxes. At a high flux the irradiation time necessary to induce steady state burning of a propellant may be several tens times as big as the heating time defined above. During this time gap the induced gasification of the propellant is observed. The critical condition of burning wave generation is formulated in terms of a model that takes into account some way of decrease a flux as a result of the gasification process till the necessary critical flux be reached. Some additive proposal could be also required, say formation of a solid particle layer over the surface that in light of Kondrikov-Novozhilov (1976) approach is a powerful factor of the condensed substances burning stabilization. The main objective of this presentation is to develop a model of solid propellant ignition in the area of experimental conditions where ignition time essentially outreaches the time of the propellant heating to the temperature where its gasification begins.

The model is constructed on the assumption that a layer of carbonaceous particles formed on the propellant surface at gasification decreases the intensity of flux at the surface due to light scattering and absorption. When this intensity reaches a critical value, q_*, corresponding to the critical temperature gradient, dT_S/dx at $x=0$, the propellant acquires capability of burning which is preserved also when the flux is interrupted. This assumption corresponds to the linear $log\ q$ vs. t^*_{gas} dependence really observed in the case of double-base propellants (t^*_{gas} is the critical gasification time when ignition at implementation of so called "go-no go" technique takes place). In the case of composite propellants this model is also valid but the heterogeneity of the substance is the essential factor of the process and is considered independently.

Propellants, Burning, Gasification, CO_2-laser, Ignition

THERMAL DECOMPOSITION OF LIQUID POLYNITROESTERS IN A BROAD RANGE OF TEMPERATURES AND PRESSURES

B.N. Kondrikov and E.K. Alyoshkina

Mendeleev University of Chemical Technology, Moscow, Russia

Thermal decomposition of Nitroglycerin (NG), *bis*-Nitroxyethylnitramin (DINA) and Diethyleneglycoldinitrate (DGDN) are investigated in a temperature range of about 80 to 700^{0}C (higher than the melting points of all of the three substances studied) at pressures from subatmospheric to about one hundred thousand atmospheres. The kinetic constants are derived from the works carried out in Mendeleev Institute and from other publications. At low pressures and moderate temperatures ($\leq$1 atm and 80-200^{0}C) the results of usual kinetic experiments using the manometric method are employed. Slightly higher temperature region (180-300^{0}C) is encompassed by determination of induction period of auto-ignition of the substances at atmospheric pressure. Comparison of the results of our measurements and investigations of J. Zinn and R. Rogers, carried out seemingly at quite different operating conditions, has shown that they are suggested to be located in time-temperature plane very close to each other. The results of investigations by the late Dr. Joseph Venograd in syringes heated electrically are used to increase the temperature region at low and moderate pressures to about 800 K. The data derived from determinations of critical (failure) diameter of high velocity detonation of NG and DGDN are employed to obtain kinetic constants at 8-10 GPa and 800-1000 K.

The main result of the study consists in that the polynitroesters as opposed to some of the C-nitrocompounds, say TNT and Nitromethane, appear to be capable of preserving their kinetic features within the entire area of experimental conditions studied, ranging from 0.01 MPa to 10 GPa and from about 350 to 1000 K. The energies of activation and preexponential factors of Arrhenius equation for the first stage of the thermal decomposition reaction of these nitrocompounds are calculated. Particularly, for NG and DGDN they appear to be absolutely identical numbers in the whole range of the operating conditions studied.

Nitric esters, Thermal decomposition, Kinetics of detonation reactions, Auto-ignition

UNCONVENTIONAL PROPERTIES OF ULTRAFINE ENERGETIC MATERIALS

Michael John Gifford, Avic Chakravarty, Martin Greenaway, Stuart Watson,
William Proud & John Field.
Cavendish Laboratory, University of Cambridge, Madingley Rd., Cambridge, U.K.

Abstract

Sub-micron grain size energetic materials have been extensively researched within this laboratory. Sensitivity studies have shown not only decreased sensitivity to conventional stimuli, but also in the way they respond once reaction is initiated. This paper aims to provide an insight into the unusual behaviour displayed by these materials and to draw some conclusions regarding the role of different hot-spot mechanisms in the initiation and propagation of reaction in these novel materials.

Results of research into the deflagration-to-detonation transition and the shock-to-detonation transition resulting from different shock regimes will be presented.

1. Introduction

The development of manufacturing techniques capable of producing explosives such as cyclotrimethylene trinitramine (RDX) and pentaerythritol tetranitrate (PETN) in a form where the grain size is sub-micron has extended the study of grain size effects into new regimes.

It has long been known that the particle size of a charge has an effect on properties such as sensitivity, critical diameter, run-to-detonation length and mechanical characteristics. The experiments reported here show that it is not only the rates and scales of events that are altered by changes in particle size, but also in some cases the nature of the event is fundamentally changed. This paper describes the changes that occur in the shock-to-detonation transition (SDT) and the deflagration-to-detonation transition (DDT) when ultrafine charges are used.

A. Shock-to-Detonation Studies

When a shock-wave is incident on an energetic charge, a number of parameters determine whether detonation results. The natures of both the charge and the shock-wave are important.

In simple terms, a shock can be described by its pressure and duration (we ignore shock profile at this stage). For a shock to cause initiation it must be capable of creating sufficient chemical reaction to sustain the shock. Acting against this chemical reaction, to weaken the shock, are rarefactions due to the lateral expansion of material which may reach the detonation front and cause adiabatic cooling. The relationship between the required pressure and duration for initiation is such that the pressure must be high enough to cause sufficient reaction to sustain the shock in the time before the stimulus decays. If this criteria is met then a detonation will propagate in the charge.

The magnitude and duration of a shock required for a particular charge to be initiated are dependent on both the microstructure and chemistry of the charge. Microstructural discontinuities are important in the case of heterogeneous charges due to their role in hot-spot formation as the shock arrives. Bowden and Yoffe's[1] concept of hot-spots has been extensively used to explain the changes in shock sensitivity of explosives with changes in quantities such as porosity and particle size. As the shock wave propagates through the charge the energy of the shock-wave is to some extent localised by heterogeneities which subsequently become centres of exothermic chemical reaction.

B. Deflagration-to-Detonation Transition

Over the past 40 years, research into DDT in columns of solid explosives has concentrated on densities of above 60% of theoretical maximum density (TMD). These studies [2-6] have shown that the initial conductive burning that occurs following ignition gives off gases which then serve to propagate the burning along the column by convective mechanisms. The next stage in the mechanism, that has been observed is that un-reacted material is pushed along the column ahead of the reaction front. This un-

reacted material forms a plug which prevents any further gaseous flow through the column.

The compaction within the plug causes hot-spots due to collapse of gas spaces and friction between grains and the confinement. The reaction front accelerates as the compressed material burns by this compressive mode. After some distance the pressure and velocity of the downstream face of the plug reaches a point where detonation can break out and proceed along the remainder of the column.

Some research has been carried out in Russia and the United States using low density columns consisting of fine grain tetryl[7], picric acid [8-10] and high energy propellants [11,12]. This showed that a different mechanism mediated the transition to detonation. The principle difference between this mechanism and the one outlined above is that the outbreak of detonation is preceded by a rapid build-up of pressure in a region localised at the point where the detonation breaks out. This type of transition has been referred to as a type II DDT.

2. Materials Used

The PETN used in this study was in powder form with three different grain sizes. The conventional grain material came in standard sieve sizes 85 and 135 with mean grain sizes of 180 μm and 106 μm respectively.

The ultrafine PETN was made using a proprietary process and is composed of secondary clusters made up of many sub-micron primary particles. The secondary particles are sponge-like in appearance. Their high porosity gives a loose powder density of around 15% TMD.

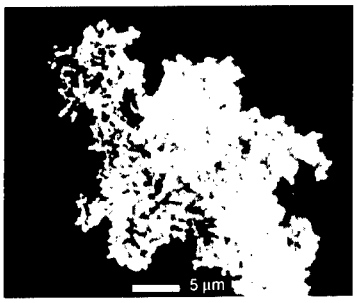


Figure 1. A secondary agglomeration of ultrafine PETN. The primary particles can be seen to be smaller than 1 micron.

The RDX was used in just two principle grain sizes. The conventional powder had a mean grain size of approximately 100 µm and although less angular than the PETN, the grains were still irregular. The ultrafine material again had a sponge-like morphology and a correspondingly high porosity although the secondary particles were weaker than those of PETN.

The PETN and the ultrafine RDX were supplied by ICI Nobel Enterprises (Ardeer). The conventional RDX was supplied by DERA Fort Halstead

3. Experimental

A. Charge preparation

The charges used in these studies were incrementally pressed into confinements. The increments used were small by comparison with the diameter of the charges. In the case of the shock-initiation studies the confinements used were 25 mm long, 25 mm diameter polymethylmethacrylate (PMMA) cylinders with a bore of 5mm.

For the studies of the DDT, the columns were also incrementally pressed. In order that the pressure was able to build up sufficiently for DDT to occur thick-walled metal was required. Copper cylinders were used for post event analysis and square section steel bar with polycarbonate windows were used if photographic access was required. The bore was 5mm for all of the experiments but the length of the charge varied between 60 and 100 mm.

B. Shock Initiation Studies.

Shock initiation studies were carried out in two different regimes. The aim of the studies was to determine the relative sensitivities of the different grain sizes for the same material when subjected to shocks of very different duration. PETN was used for this part of the study.

(i) Laser-driven flyer plates

A technique has been developed within this laboratory for producing 3μm thick aluminium flyers travelling at velocities between 3 and 8 mm μs^{-1}. A Lumonics YM800 Nd:YAG laser operating at the fundamental wavelength of 1064 nm is used to create a plasma at the interface of a fused silica substrate and an aluminium film. The expansion of the plasma causes the remainder of the film to be launched away from the substrate. Details of flyer characterisation and performance and of the experimental techniques used to launch the flyers have been described previously [13-15].

The pressed charges of PETN were placed at a distance of approximately 100 μm from the substrate in order to ensure that the flyer had been fully launched without having started to deteriorate in terms of either shape or velocity. The shock wave imparted by a 3 μm thick flyer can be calculated from the Hugoniot of the aluminium and an estimate of Hugoniot of granular PETN to have a duration of around 1 ns.

A Hadland Imacon 790 image converter camera was used to record the high-speed events that occurred during the flyer impact. The camera was used in streak mode to give continual records of the events that occurred on the surface of the charges.

(ii) Long duration shocks

In order to investigate the sensitivity of the pressed charges to initiation by long-duration shocks C8 detonators were used in a gap-test type configuration. The gaps used were PMMA. It was found that the geometry shown in figure 2 produced extremely reproducible results providing both the surface finish and the increment size of the charge

was carefully controlled. For the purposes of this study, a reproducible finish was achieved by pressing onto a smooth brass plate.

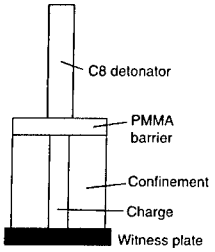


Figure 2. The configuration of the gap-tests

In order to measure the profile of the pressure pulse in this gap test geometry a number of shots were fired using calibrated piezoelectric PVDF gauges to measure the pressure history.

C. Deflagration-to-detonation transition

High-speed photography and post-mortem examination have been used to study DDT in charges of RDX and PETN in both the conventional and ultrafine forms. The charges were ignited using a nichrome wire through which an electric current is passed in a pyrotechnic consisting of 80% potassium dichromate and 20% boron. This gives few gaseous products and as a result does not significantly pre-pressurise the charge. The other components of the fuse system are designed to prevent rear-wards venting of the charge. The confinements are clamped at both ends in order to prevent any release of pressure during the event except by deformation of the confinement itself.

4. RESULTS

A (i) Short duration shocks

The results from these experiments are shown in figure 3. It can be seen that no charges of conventional PETN were initiated using the laser-driven flyers though some limited reaction was observed. In contrast the ultrafine material was readily initiated at flyer velocities of around 5 mm μs^{-1}.

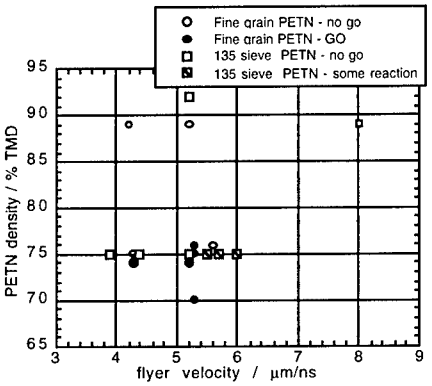


Figure 3. Scatter plot of the laser-driven flyer plate results

(ii) Long duration shocks

The gap testing has shown that the ultrafine material is significantly less sensitive to initiation by this form of stimulus than conventional grain size material. For columns pressed to 90% TMD (check this) the pressure required to initiate the conventional material has been found to be around 2.1 GPa while the ultrafine material is initiated at a pressure of approximately 4.1 GPa.

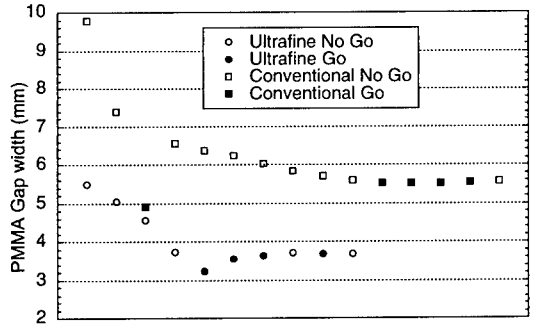


Figure 4. Results of gap testing of PETN

B. DDT results

(i) Ultrafine PETN results

Experiments carried out on columns of ultrafine PETN pressed to densities greater than 50% TMD showed that the columns would either undergo a type I DDT or not make the transition to detonation at all and simply deflagrate. A streak record of a typical type I

DDT event is shown in figure 5 After the initial conductive burn (which occurred prior to the camera being triggered) a convective burning (A) proceeds at a velocity of 0.15 ± 0.01 mm μs^{-1}. At A it can be seen that the compressive burning is already occurring downstream of the front. The velocity of the compressive burning accelerates from 0.49 ± 0.02 mm μs^{-1} to 0.93 ± 0.03 mm μs^{-1} prior to the formation of the critical plug that causes detonation to break out at 'D'

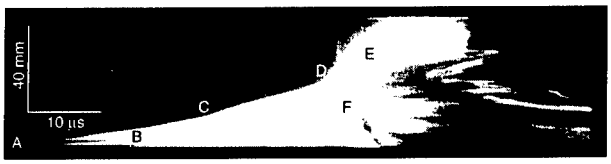


Figure 5. A type I DDT event in ultrafine PETN.

The detonation wave (E) then proceeds along the remainder of the column at a steady velocity of 3.6 ± 0.2 mm μs^{-1}. Also emanating from the point at which the detonation breaks out is a retonation wave (F). This travels back through the unreacted plug and the partially reacted material behind it at a velocity of 5.0 ± 0.2 mm μs^{-1}.

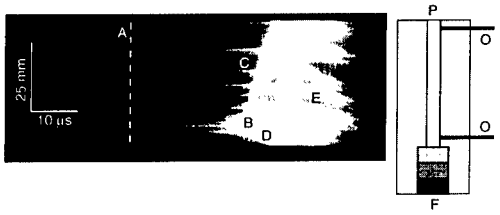


Figure 6. Streak photograph of a type II DDT event in ultrafine PETN. A schematic of the column configuration is shown to scale to the right of the photograph. P - PETN column; O - optical fibres; F - Fuse.

Figure 6 shows a streak record of type II DDT process occurring in a charge of ultrafine PETN pressed to a density of 29 ± 1% TMD. A schematic of the confinement is shown next to the streak record at the same scale as the photograph. The camera was triggered 50 µs after reaction reached the downstream optical fibre, which was some 600 µs after the burning reached the upstream fibre.

At the time indicated by the dashed line 'A', it can clearly be seen that reaction is taking place at a number of points which appear stationary on the time scale of the streak record. As the camera can only image the surface of the column it can be surmised that these reaction sites are in the part of the charge in contact with the window. The luminosity of the reaction at these sites continues to increase until at site 'B' the conditions reach the

critical parameters for initiation. There appears to be no shock wave associated with the build up to the initiation event. A detonation wave (C) then propagates downstream (relative to the ignition site) at an average velocity of 5.4 ± 0.2 mm μs^{-1}. There is also an upstream retonation wave (D), that propagates from the point 'B', but the proximity of the initiation to the upstream end of the column makes any calculation of the velocity of this wave difficult.

A reflected shock (E) travelling at 2.23 ± 0.09 mm μs^{-1} can also be seen propagating upstream from the point at which the detonation (C) reached the witness plate at the downstream end of the column.

(ii) Conventional PETN results

The studies on the conventional grain size PETN showed that only type I DDT events occurred even at the loose powder density of 31 ± 1 % TMD. The run-to-detonation distance varied with initial density. Previous studies[16] have shown that this distance is dependent on the initial density of the column as well as the grain size of the powder in question. Figure 7 shows the run-to-detonation distances against initial density from the research reported here. The results from the ultrafine material are also shown with the density region in which type II DDT events occur shaded.

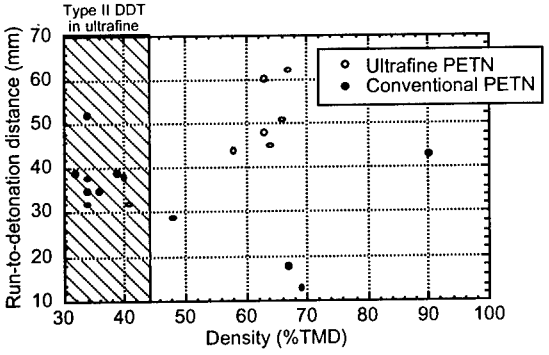


Figure 7. Run-to-detonation distances for ultrafine and conventional PETN at varying densities.

(iii) Ultrafine RDX results

The results from the experiments carried out on ultrafine RDX closely resemble those described above for ultrafine PETN. As with the PETN it was found that dense columns (in the case of RDX this was over 50 % TMD) did not undergo a DDT transition of either type in the lengths of column used in this study.

Columns pressed to below 50% TMD underwent a type II DDT. This has all the major features of the type II DDT as described for PETN. The streak record in figure 8 shows a typical event in a column of ultrafine RDX pressed to 37% TMD. As with the PETN, a conductive burning stage rapidly gives way to a convective burn as product gases are given off during reaction. This proceeds to the end of the column. The luminous regions in the streak record (A) do not appear to be as stationary as they were in the PETN charges. This is due to pressure and release waves reflecting along the column and carrying with them the material or gas that is causing the light emission. The detonation waves break out at 'B" and then travel along the column in both directions at slightly different speeds. The wave travelling downstream 'C' propagates at 2.1 ± 0.3 mm μs^{-1} whilst the upstream wave travels at 'D' 1.8 ± 0.3 mm μs^{-1}.

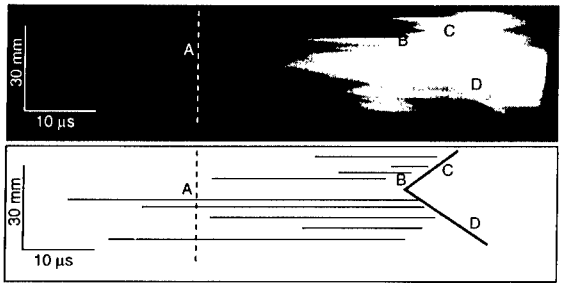


Figure 8. Streak record of a type II DDT event in a column of ultrafine RDX. A schematic of the photograph is given for clarity.

No type I DDT events were observed in columns of ultrafine RDX during this study.

(iv) Conventional RDX

The charges of conventional RDX either deflagrated when they were at a density above 75% TMD or underwent a type I DDT when the density was below this level. In none of the experiments involving conventional RDX was a type II DDT observed.

5. Discussion

It has been shown that despite being chemically the same, the ultrafine and conventional forms of both PETN and RDX have extremely different responses to stimuli. It must be remembered that in changing the grain size of the material there is also a marked change in both its mechanical properties and the distribution of voids within the system.

With regards the sensitivity to shock initiation it has clearly been shown that the ultrafine material is more sensitive than the coarse powder to the short duration high-pressure shocks imparted by the laser-driven flyers. The opposite is true for the relatively long lived shocks that were used in the gap testing. There are a number of possible contributory factors that could explain these differences.

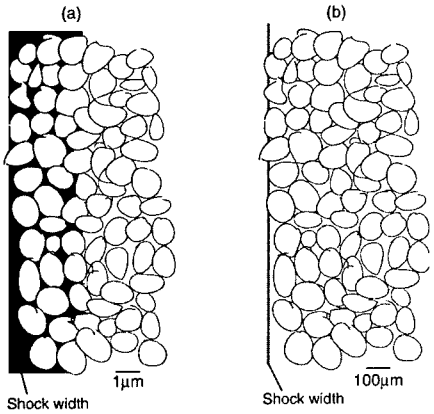


Figure 9. The shock from a laser-driven flyer will cover whole grains and pores in the case of the ultrafine material (a). In the case of the coarser conventional material (b) the shock will not cover whole grains and initially will only be incident on the pieces of material that are high on the surface.

Although a large amount of research has been carried out on the interaction of shocks with bubbles and gas spaces[17-23], there has been little interest in the regime of very thin shocks travelling over gas spaces that are far larger than the thickness of the shock itself. In the commonly investigated case of a shock whose duration is far longer than the collapse time of the bubble, the temperature reached by the gas within the bubble is higher for larger bubbles, but the speed of the jet impacting on the downstream face is higher for smaller bubbles. The relative importance of the gas compression and the jetting changes as shock pressures rise. For lower pressure shocks a large pore would be more effective for creation of high temperature hot-spots and for higher shocks, smaller pores would be more effective as the jetting becomes the dominant mechanism.

In both materials it is assumed that the voids will collapse rapidly and produce hot-spots by gas heating and jet impact. However the increased distance between the surface and the bulk of the grains in the coarse material acts to slow down the rate at which the temperature of the bulk can be raised and reaction can take place. A calculation of thermal transfer times based on inert spheres[24] shows that the dependence on particle size varies as the square of the radius. Thus even if the temperatures in the hot-spots in the ultrafine material doesn't get as high as that in the coarse there is still like to be more reaction due to the greater specific surface are of the grains.

In the case of the DDT results that have been obtained during this study, it appears that when low density columns of ultrafine material are used, it is possible to lose the compressive burning regime. This is thought to be due to the ultrafine material being composed of collections of primary particles held together by weak inter-granular bonds. When only lightly pressed, it remains easy for gaseous flow to take place either around the secondary agglomerations or by breaking through them. The channel does not become choked as in the type I case because the material lacks the bed strength to build up a coherent compaction wave.

The sequence of events in the type II DDT mechanism is thought to be a conductive burn, followed by a convective burn as gases are given off. The convective burn does not consume all of the material as it proceeds to the end of the column. Reaction continues along the column whilst the temperature and pressure continue to rise. Once a critical temperature and pressure have been reached, a thermal explosion occurs and a detonation wave consumes the remaining un-reacted material.

In the columns of PETN, the detonation wave has been shown to travel at velocities significantly in excess of those that would be expected for columns pressed to the initial densities that these columns started at. In the case of the columns of RDX, the opposite is the case. The factors that could be affecting the detonation velocity are; the increased pressure and temperature prior to the arrival of the detonation wave; compaction of the

material during the convective burning phase; the creation of channels within the charge; and the reduction in the available material due to the initial burning. Only the last of these acts to retard the velocity whilst the first three would act to increase it.

In the denser columns of ultrafine PETN it has been shown that the run-to-detonation distance for the type I DDT events is considerably longer than that in the conventional grain size charges. This effect is caused by the same factors that act to reduce the sensitivity of the charges to the long duration shocks. The compressive burning phase is primarily driven by compression of gas spaces rather than jetting. This means that the ultrafine material will require a greater build-up of pressure than the conventional material and hence longer run-to-detonation distances.

6. Conclusions

The studies to date have identified significant differences in the behaviour of ultrafine energetic materials when compared to their conventional counterparts. These differences make the ultrafine materials extremely interesting as substitutes for conventional materials where less sensitivity to accidental initiation is required for the same power output. A route to reliable initiation of these materials has also been identified in the case of the very thin high pressure shocks imparted by the laser-driven flyer systems.

Acknowledgements

Dr. Leach, Dr. Cook and Dr. Philbin of DERA (Fort Halstead) are thanked for their support of this work. ICI (Ardeer) are thanked for supplying the materials used in these studies and for their support of the project. M.J.G. was supported through this work on an EPSRC studentship. EPSRC are also thanked for their funding of the cameras used during the experiments.

References

1 F. P. Bowden and A. D. Yoffe, *Initiation and Growth of Explosion in Liquids and Solids (republ. 1985)* (Cambridge University Press, 1952).

2 N. Griffiths and J. M. Groocock, J. Chem. Soc. **11,** 4154-4162 (1960).

3 A. V. Obmenin, A. I. Korotkov, A. A. Sulimov, and V. F. Dubovitskii, Combust. Explos. Shock Waves **5,** 317-322 (1969).

4 A. I. Korotkov, A. A. Sulimov, A. V. Obmenin, V. F. Dubovitskii, and A. I. Kurkin, Combust. Explos. Shock Waves **5,** 216-222 (1969).

5 A. W. Campbell, "Deflagration-to-Detonation Transition in Granular HMX," Report No. 80-2016 (1980).

6 M. R. Baer, R. J. Gross, J. W. Nunziato, and E. A. Igel, Combust. Flame **65,** 15-30 (1986).

7 R. R. Bernecker, D. Price, J. O. Erkman, and A. R. Clairmont Jr., in *Proc. Sixth Symposium (Int.) on Detonation*, edited by D. J. Edwards (Office of Naval Research, Arlington, Virginia, 1976), p. 426-435.

8 B. S. Ermolaev, A. A. Sulimov, V. A. Okunev, and V. E. Khrapovskii, Combust. Explos. Shock Waves **24,** 59-62 (1988).

9 V. E. Khrapovskii, Combust. Explos. Shock Waves **29,** 129-134 (1993).

10 V. E. Khrapovskii and A. A. Sulimov, Combust. Explos. Shock Waves **31,** 23-29 (1995).

11 D. Price and R. R. Bernecker, Combust. Flame **42,** 307-319 (1981).

12 R. R. Bernecker and D. Price, Combustion & Flame **48,** 219-231 (1982).

13 S. Watson, Thesis, University of Cambridge, 1998.

14 S. Watson and J. E. Field, J. Phys. D: Appl. Phys. **33,** 170-174 (2000).

15 S. Watson and J. E. Field, J. Appl. Phys. **88,** 3859 (2000).

16 P. E. Luebcke, PhD Thesis, Cambridge, 1995.

17 F. P. Bowden and M. P. McOnie, Proc. R. Soc. Lond. A **298,** 38-50 (1966).

18 G. D. Coley and J. E. Field, Proc. R. Soc. Lond. A **335,** 67-86 (1973).

19 M. M. Chaudhri and J. E. Field, Proc. R. Soc. Lond. A **340,** 113-128 (1974).

20 R. B. Frey, in *Proc. Eighth Symposium (Int.) on Detonation*, edited by J. M. Short (Naval Surface Weapons Center, White Oak, Silver Spring, Maryland, 1985), p. 68-80.

21 J. P. Dear, J. E. Field, and A. J. Walton, Nature **332,** 505-508 (1988).

22 N. K. Bourne and J. E. Field, Proc. R. Soc. Lond. A **435,** 423-435 (1991).

23 J. E. Field, Accounts Chem. Res. **25,** 489-496 (1992).

24 C. D. H. Williams, New Scientist (1998).

PHASE TRANSFORMATIONS IN HEXANITROHEXAAZAISOWURTZITANE

N.V.Chukanov, N. I. Golovina, V.V.Nedelko, V. V. Dubikhin, S. A. Voschikova, O. A. Anan`ina, T.S.Larikova, G. M. Nazin, S. M. Aldoshin, B.L.Korsounskii

Institute of Problems of Chemical Physics

Russian Academy of Sciences

142432 Moscow Region Chernogolovka Russia

F.Volk

Fraunhofer-Institut für Chemische Technologie (ICT),

D-76318 Pfinztal BRD

Abstract

With the use of IR spectroscopy, calorimetry, and X-ray analysis the structure and phase transitions of α- and ε-modifications of hexanitrohexaazaisowurtzitane into γ-form have been studied. The transition α → γ proceeds with self-acceleration. Apparently, this is caused by topochemical nature of the process, including nucleation and frontal propagation. The poor reproducibility of the results is characteristic for the transition ε → γ in polycrystalline sample. The process has essentially discrete nature, which may be explained by the dependence of the ability of the crystals to undergo phase transition on their morphology, particularly, on the defects in the crystals. Cooperative effect is characteristic for this process. This effect is caused by the ability of phase transition in one crystal to induce the respective transitions in the whole cluster of adjacent crystals.

Six polymorphous modifications of hexanitrohexaazaisowurtzitane (HNIW) – from α to ζ - were described till now. α, β, γ, ε-polymorphs were investigated in most details [1-4]. Theory of the kinetics of phase transitions has been developed since end of XIXth century, and now this field of knowledge is elaborated profoundly [5], but experimental data on the phase transitions kinetics are very scanty, especially for the molecular crystals [6]. HNIW is a suitable substance for experimental investigation of the kinetics of phase transitions. On the other hand, quantitative description of the kinetics of phase transitions in HNIW is very useful for the technology of preparation of the HNIW-bearing formulations.

In the present communication the data on the phase transitionsα → γ and ε → γ are given.

The raw α-HNIW was synthesized in Institute of Organic Chemistry (Moscow). The crystals of α-HNIW have been prepared as follows. The raw (yellowish, fine-grained) α-HNIW has been converted into γ-form in the process of heating at 162^0C during 20 min and thereafter dissolved in ethylacetate up to saturation. After slow (during one month) evaporation of the solvent through a small opening, large (2 – 3 mg) well-formed crystals of α-HNIW were formed.

Crystal-structure analysis of α-HNIW was performed using 4-cyrcle diffractometer "Kuma-diffraction". α-HNIW is orthorhombic, space group Pbca, unit cell parameters are a = 9.603 (3), b = 13.304 (3), c = 23.653 (4) Å, z = 8. The coordinates of all atoms including H were refined using 2481 independent reflections up to R = 0.079. In Figure 1 a fragment of crystal structure of the α-HNIW is shown. One can see large cavities formed by the nitro groups. Three sites of H_2O were found within each cavity. The distances between these sites are short and water molecules cannot occur in all the sites at the same time. Therefore, the mean

occupancy of the sites of H_2O varies from 0 for the anhydrous form of α-HNIW up to 1/3 for the H_2O-saturated form.

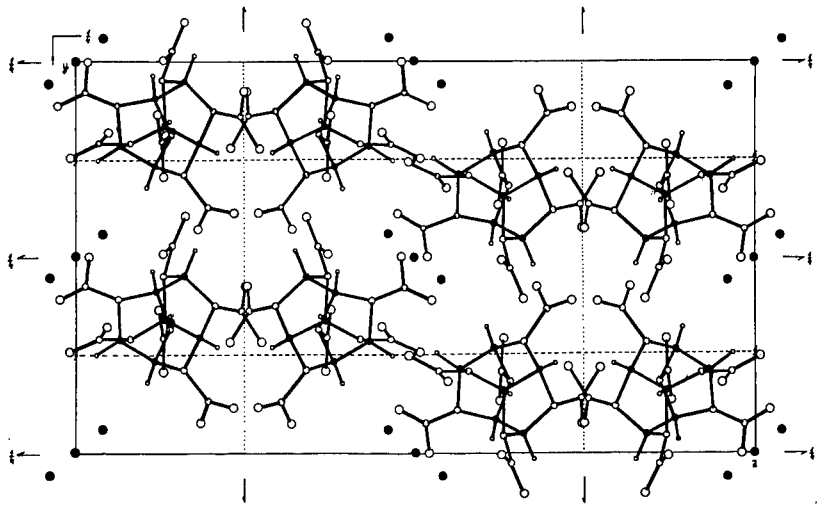


Figure 1. Crystal structure of α-HNIW

The calculated density for α-HNIW is 1.925 g/cm^3 for the anhydrous crystal and 1.965 g/cm^3 for the real occupation of H_2O-sites in the investigated crystal.

The kinetics of $\alpha \rightarrow \gamma$ phase transition has been investigated at 119^{0}C. In each experiment a single crystal of α-HNIW was heated in air during certain time interval, than grinded in a mortar to prepare a pellet with KBr for the subsequent IR spectrophotometric measurements. The results of the measurements are presented in the Figure 2. The phase transition proceeds with a pronounced induction period, after which the rate of the phase transition is approximately constant. This result can be treated as follows. Phase transitions mechanisms in solids are known to include nucleation as the initial stage [5]. The observed induction period and self-acceleration may correspond to this stage. On the second stage, the phase transition proceeds as linear movement of the phase boundary, which corresponds to approximately constant rate in Figure 2.

In the experiments on ε to γ transitions HNIW produced by Thiocol Corp. (USA) was used, with crystal sizes about 150μ. In this case (unlike α-HNIW) all experiments have been performed with polycrystalline samples.

The reproducibility of the kinetic data obtained by IR spectroscopy is very bad. In particular, in parallel performed experiments at the same

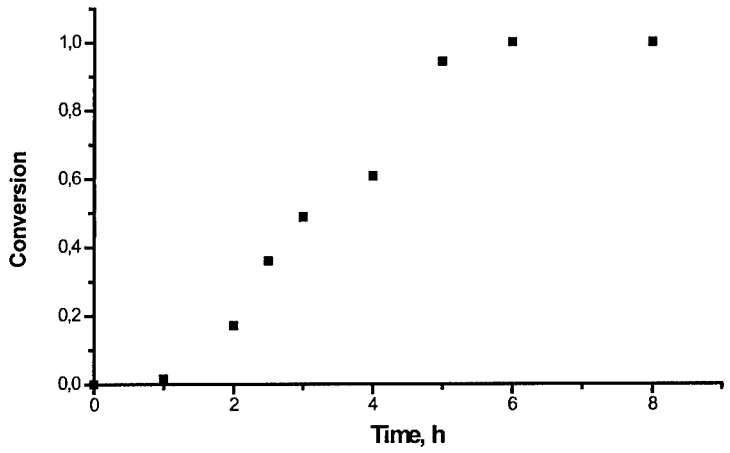


Figure 2. Kinetics of α → γ phase transition in HNIW at 145^{0}C

conditions over time can correspond to higher conversion. Some sets of these experiments are given below (η = conversion).

Set 1. 130^{0}C, HNIW sample 5 mg, 9 days, η = 0.

Set 2. 135^{0}C, HNIW sample 5 mg, consequent measurements (a few samples were placed into the thermostat for a different time). 1 day, η = 0; 3 days, η = 0.11.

Set 3. 140^{0}C, HNIW sample 5 mg, consequent measurements. 1 day, η = 0.38; 2 days, η = 0.54.

Set 4. 145^{0}C, independent measurements (different samples 5.5 – 5.8 mg). 5 experiments. η = 0.40, 0.36, 0.40, 0.34, and 1.00.

Set 5. 145^{0}C, independent measurements, 1 day. Sample variation. 0.5 mg, η = 0.84; 0.5 mg, η = 0.86; 2 mg, η = 0.93; 10 mg, η = 0.90; 20 mg, η = 0.94.

Set 6. 150^{0}C, HNIW sample 5 mg, independent measurements. 20 min, η = 0.21; 40 min, η = 0.47; 1 h, η = 0.60; 1.5 h, η = 0.53; 2 h, η = 0.55.

Set 7. 150^{0}C, HNIW sample 5 mg. independent measurements. 1 h, η = 0.21; 2 h, η = 0.70; 16 h, η = 0.88; 24 h, η = 1.00.

Set 8. 150^{0}C, consequent measurements. For each experiment total sample was cooled to the room temperature. The part of this sample (5 mg) we used for the spectral measurements and the sample was heated at 150^{0}C further. 0.5 h, η = 0; 1 h, η = 0; 2 h, η = 0; 3 h, η = 0.21; 4 h, η = 0.21.

Set 9. 160^{0}C, HNIW sample 5 mg, consequent measurements. 5 min, η = 0.03; 10 min, η = 0.08; 20 min, η = 0.90; 40 min, η = 1.00; 1 h, η = 1.00; 2 h, η = 1.00; 3 h, η = 1.00.

Additional information on the kinetics of ε to γ phase transition was obtained using isothermal calorimetry. The experiments have been performed by the differential calorimeter designed at the Institute of Problems of Chemical Physics (Chernogolovka). The typical kinetic curves of phase transition at 145^{0}C are presented in Figure 3. The lower curve corresponds to the phase transitions in a sample with the mass of 100 mg. The process proceeds extremely irregularly, as a set of endothermal peaks. The upper curve corresponds to a sample with the mass of 20 mg. In this case endothermal peaks are observed in combination with a smooth curve, corresponding to an exothermal process. The endothermal

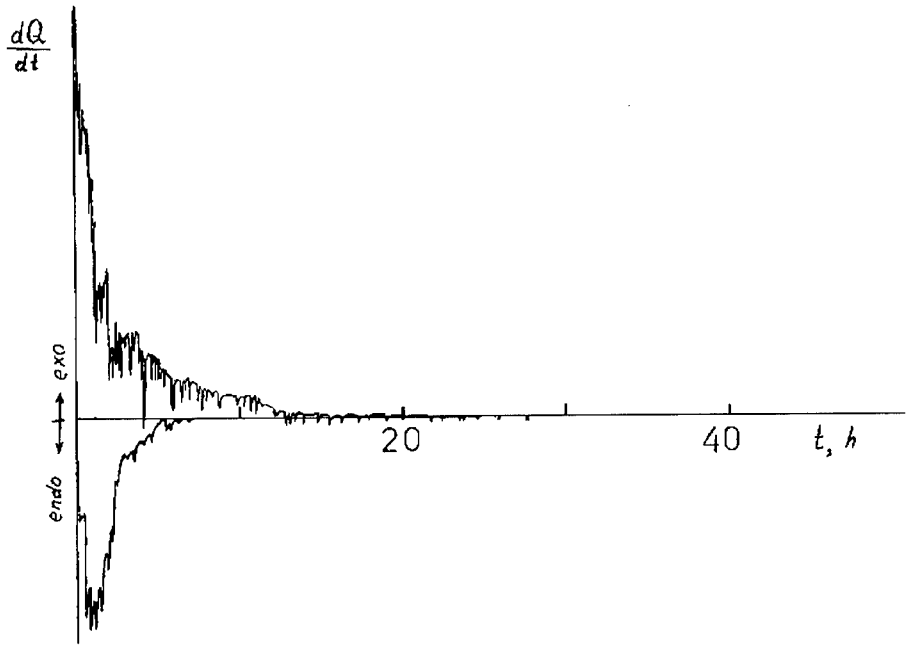


Figure 3. Calorimetric data on kinetics of phase transitionε → γ at 145^{0}C. Differential curves.

peaks do not correspond to formation of any intermediate phases. By IR spectroscopic data, only ε and γ polymorphs of HNIW are present in the sample at intermediate stages of the process. In Figures 4, 5 integral kinetic curves of endo- and exothermal processes presented (sample masses 100 and 17 mg respectively). The nature of the observed self-acceleration for 100 mg sample is probably the same as for α to γ transition.

The results observed can be explained by the effect of differences in phase transition stability of different crystals present in the sample. On the other hand, phase transitions in the single crystals are not fully mutually independent. Indeed, the sample with the mass 20 to 100 mg contains several thousand crystals, whereas the number of endothermal peaks does

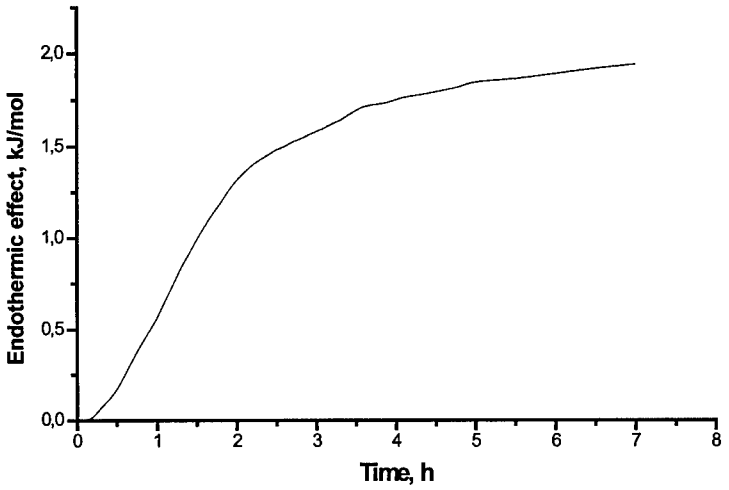


Figure 4. Calorimetric data on kinetics of phase transitionε → γ at 145^{0}C. Integral curve.

not exceed several tens. Very likely, in this system a cooperative effect takes place. It means that phase transition in a single crystal promotes such transitions in the neighboring crystals. As a result,ε to γ transition proceeds in a short time in a cluster containing a large number of single crystals. This conclusion has been confirmed in the special experiment, when a sample of ε-HNIW was diluted by a glass pulver. As a result, enhancement of a number of endothermic peaks and lowering of their intensities were observed. We explain this effect as a result of lowering of the cooperative effect owing to dissociation of the crystal clusters.

The observed non-reproducibility can be explained by independent behavior of separate clusters resulting in a distribution on the values of induction periods for the clusters.

The results described above make clear the non-isothermal phase transition data. In [4] it was shown that in the course ofε to γ transition a

series of endothermic peaks is observed. The authors explained it as a result of formation of intermediate metastable phases, whereas really only phase transitions $\varepsilon \rightarrow \gamma$ take place.

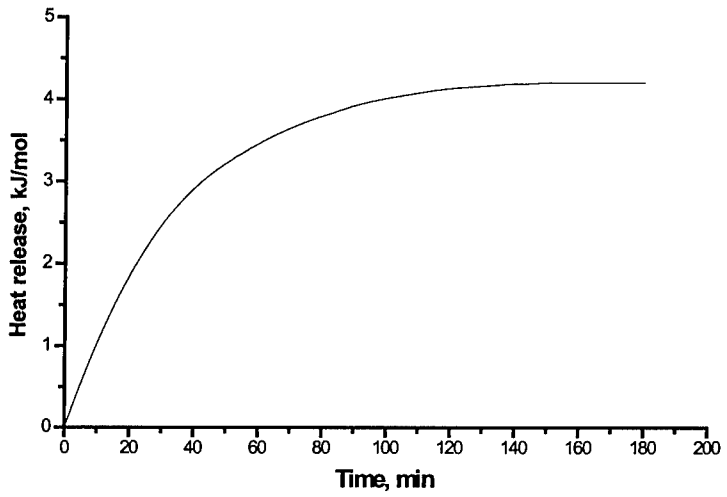


Figure 5. Kinetics of exothermic process, accompanying the phase transition at 145^{0}C, by calorimetric data. Integral curve.

The nature of the attendant exothermic effect remains unclear. The exothermic process proceeds in accordance with the first order kinetic law with the rate constant $5 \cdot 10^{-4}$ s^{-1} at 145^{0}C, whereas HNIW decomposes at this temperature with much lower rate constant $7 \cdot 10^{-9}$ s^{-1}.

The total heat release in the exothermic process depends crucially on the sample mass (see Table).

On the base of crystal structure refined by single-crystal diffraction we identified a number of different impurities, including dinitroimidazolidine, 1,6-diphenyl-1,2,5,6-dioxo-3,4-diazahexene-3,4, and, probably, salt of N-nitropyridinium. Exothermal effect dependence on the sample mass we explain as a result of exothermal process suppression by the

Table

Sample mass, mg	100	100	20	20	17	17*
Exothermic effect, kJ/mol	no	no	3,67	3,69	4,21	8,08
Sum of endothermic effects, kJ/mol	1,57	2,11	1,80	1,71	1,62	not measured

*- in the presence of glass pulver

gaseous products of impurity decomposition. However, this problem should be confirmed experimentally.

REFERENCES

1. T. P. Russell, P. J. Miller, G. J. Piermarini, S. Block, *"High-Pressure Phase Transition in γ-Hexanitrohexaazaisowurtzitane", J. Phys. Chem.*, 96, 5509 – 5512 (1992).
2. T. P. Russell, P. J. Miller, G. J. Piermarini, S. Block, *"Pressure/Temperature Phase Diagram of Hexanitrohexaazaisowurtzitane", J. Phys. Chem.*, 97, 1993 – 1997 (1993).
3. M. F. Foltz, C. L. Coon, F. Garcia, A. L. Nichols III, *"The Thermal Stability of the Polymorphs of Hexanitrohexaazaisowurtzitane, Part I", Propel., Expl., Pyrotechn.*, 19, 19 – 25 (1994).
4. M. F. Foltz, C. L. Coon, F. Garcia, A. L. Nichols III, *"The Thermal Stability of the Polymorphs of Hexanitrohexaazaisowurtzitane, Part II", Propel., Expl., Pyrotechn.*, 19, 133 – 144 (1994).
5. A. R. West, *"Solid State Chemistry and its Applications", John Wiley and Sons, Chichester e. a.*, 1984.
6. S. Flandrois, *"Cinetique de Changements de Phase a L`Etat Solide", J. Chim. Phys.*, 71, 979 – 991 (1974).

THE ENERGY PROPERTIES OF THE NITRO- AND NITRATEDERIVATIVES ADAMANTANES

Matyushin Yuriy N., Lebedev Vyacheslav P., Miroshnichenko Evgeniy A., Kostikova Larissa M., Inosemzev Yaroslav O.

Semenov Institute of Chemical Physics, Russian Academy of Sciences
117977 Kosygin Str. 4, Moscow, RUSSIA
Fax: (095) 938 2156. E-mail: ynm@polymer.chph.ras.ru

ABSTRACT

The enthalpies of combustion were measured by the method of bomb calorimetric and enthalpies of formation of the row nitro- and nitrate derivative adamantanes were calculated. The enthalpies of evaporation nitro- and nitrate derivative adamantanes were determined on the temperature dependency of pressure a pair, and their enthalpies of formation in the gas phase were received. The energetic effects of functional groups interaction in the molecule adamantane were calculated. The enthalpy of formation of the radicals 1-adamantane and 1-oxyladamantane and the dissociation energy of bonds in the derived adamantane were calculated.

INTRODUCTION

Polycyclic hydrocarbons and, especially, their derivatives are of interest for structural chemistry and for manufacture of medicinal preparations. There is a number of works on research of the thermochemical characteristics of polycyclic compounds, including, adamantane and its alkyl derivatives in the literature [1-5].

EXPERIMENT

Enthalpies of combustion are measured and enthalpies of evaporation for the oxygen and for nitroderivatives of adamantane are determined in this work. Enthalpies of combustion were determined with using semi-microcalorimetrical technique of the combustion in the bomb in the atmosphere of oxygen. The technique of the measurement and of the corrective actions is detailed stated in work [6]. Enthalpies of sublimation (all investigated compounds were crystal) were determined both by direct calorimetrical method of measurement in Calve's calorimeter, and on temperature dependence of the saturated pair pressure. Dimer of nitrosoadamantane was investigated by Knudsen's effusion method with using the techniques, which are stated in work [7].

The content of the basic component in samples was determined by the method of gas-liquid chromatographic. The substances were resublimed in vacuum at 10^{-3} Pa after two - three multiple recrystallisations from alcohol. The additional clearing 1-nitrateadamantane was executed by the method of zoned fusion. Absence of the moisture in samples was controlled by Fisher's method. The residual quantity of admixture in the samples did not exceed 0.1- 0.2 mass. %. The resuits of measurements are given in Table 1.

The following designations are entered in Table 1:

$\Delta_c H°(c)$ - enthalpy of combustion of compounds in a standard condition, $kJ \cdot mol^{-1}$;

$\Delta_f H°(c)$ - enthalpy of formation in a standard condition, $kJ \cdot mol^{-1}$;

$\Delta_{sub} H°$ – enthalpy of sublimation of compounds, $kJ \cdot mol^{-1}$;

$\Delta_f H°(g)$ - enthalpy of formation of compounds in a gas phase, $kJ \cdot mol^{-1}$.

The quantity of the burning experiments is given in brackets. The errors of measurements were estimated according to the recommendations of work [8].

Table 1.

Thermochemical characteristics of the adamantane derivatives, 298 K, $kJ \cdot mol^{-1}$

Compound	$-\Delta_c H°(c)$	$-\Delta_f H°(c)$	$\Delta_{sub} H°$	$-\Delta_f H°(g)$
Adamantane	6028,3±1,2 (8)	193,3±0,3	59,4±0,2	133,9±0,4*
Adamantanone	5615,1±1,2 (5)	319,7±1,2	76,1±1,5	243,6±1,9
1-adamantanole	5832,5±2,0 (6)	389,1±2,0	82,0±1,5	307,1±2,5
1-nitro-adamantane	5822,0±1,0 (6)	256,6±0,9	81,2±2,0	175,4±1,7*
1,3-dinitro-adamantane	5622,0±1,2 (5)	313,4±1,2	103,8±1,5	209,6±1,9
2,2-dinitro-adamantane	5685,2±2,2 (5)	250,6±0,9	89,1±1,5	161,5±1,7*
1-nitrate-adamantane	5773,9±2,0 (6)	305,0±2,0	79,9±1,5	225,1±2,5
1,3-dinitrate-adamantane	5522,0±2,0 (5)	413,8±2,0	105,9±1,7	307,9±2,6
1,3,5,7-tetranitrate-adamantane	5043,8±2,5 (4)	607,5±2,5	150,2±2,0	457,3±3,2
1-trinitromethyl-3-nitrate-adamantane	5989,4±2,5 (4)	340,0±2,5	125,0±2,0	215,0±3,2
1-nitroso-adamantane (dimer)	11951,2±2,5 (5)	206,3±2,5	97,5±1,8	108,8±3,1

*- from the text

RESULTS AND DISCUSSION

The experimental data for enthalpies of combustion of crystal adamantane $\Delta_c H°(c)$, lay in an interval from -6024.5 up to –6033.4 kJ·mol^{-1} [2-5]. The enthalpy of combustion adamantane in a standard condition (-6028.3±1.2 kJ·mol^{-1}), satisfactorily agreed with by the data from the most carefully executed works (-6024.5 ± 0.7 [2] and -6029.2 ± 0.4 kJ·mol^{-1} [4]), was received in this work.

The average value, received from all data, has made -6028.4± 0.3 kJ·mol^{-1}. Proceeding from this, the enthalpy of formation of crystal adamantane was received equal –193.3 ± 0.3 kJ·mol^{-1}. The average value for enthalpy of sublimation of adamantane (59.4 ± 0.2 kJ·mol^{-1}) was similarly received. These values are recommended for use in accounts connected with adamantane and its derivatives. The recommended values of the enthalpy of formation of adamantane in a standard condition, of the enthalpy of sublimation and of the enthalpy of formation in a gas phase (-133.9 ± 0.4 kJ·mol^{-1}) are given in Table 1. The experimental data on $\Delta_c H°(c)$ for 1-nitroadamantane (-5824.1 ± 2.2 kJ·mol^{-1}) and 2,2-dinitroadamantane (-5685.2 ± 1.0 kJ·mol^{-1}) from work [9] will be coordinated to the values, received in the given work. The averageweighted values of enthalpy of formation in a standard condition for these compounds $\Delta_f H°(c)$ are given in Table 1. They, together received by us, $\Delta_{sub} H$, have given $\Delta_f H°(g)$.

The enthalpies of formation of adamantane and of its derivative in a gas phase are given in Table 2. The enthalpies of replacement of hydrogen atoms on functional

groups in the adamantane molecule, $\mathbf{P_f}$, were determined and the energy effects of interaction of functional groups, Δ, are appreciated.

Table 2.

The enthalpies of replacement and the effective energies of interaction of the functional groups in adamantane derivatives in the gas phase, 298 K, kJ·mol^{-1}

Compound	$-\Delta_f H°(g)$	$-\Delta P_f$	Δ
Adamantane	133,9	-	-
Adamantanone	243,1	109,2	-
1-adamantole	307,1	173,2	-
1-nitroadamantane	175,4	41,5	-
1,3-dinitro-adamantane	209,6	75,7	7,3
2,2-dinitro-adamantane	161,5	27,6	44,4
1-nitrateadamantane	225,1	91,2	-
1,3-dinitrate-adamantane	307,9	174,0	8,4
1,3,5,7-tetranitrate-adamantane	457,3	323,4	41,4 (6,9)
1-trinitromethyl-3-nitrateadamantane	215,0	45,3 (81,1)	-

The replacement of group $\mathbf{CH_2}$ in adamantane on ketone group **CO** in a gas phase gives the energy of replacement equal -102.2 kJ·mol^{-1}. The similar value for acetone ($\Delta_f H°(g)$ = -216.5 [10]), concerning propane ($\Delta_f H°(g)$ = -103.8 kJ·mol^{-1} [10]),

has made -112.7 kJ·mol^{-1}, and for cyclohexanone ($\Delta_f H°(g)$ = -226.1 kJ·mol^{-1} [10]) concerning cyclohexane ($\Delta_f H°(g)$ = -123.0 kJ·mol^{-1} [10]) it turns out equal -103.1 kJ·mol^{-1}.

The substitution effect of group **CH** in adamantane in the situation 1 on group the **COH** has the value equal -173.2 kJ·mol^{-1}. It will be satisfactorily coordinated with $\mathbf{P_f}$ equal -178.0 kJ·mol^{-1} for 2-metyl-2-propyl alcohol ($\Delta_f H°(g)$ = -312,7 kJ·mol^{-1} [10]). For 2-butylalcohol, 3-amylalcohol and cyclohexylalcohol the substitution effects were appreciated on the basis of the data from the directory [10]. They have made accordingly -168.6, -168.6 and -163.2 kJ·mol^{-1}.

The replacement of hydrogen on nitrogroup in 1-nitroadamantane gives effect equal -41.5 kJ·mol^{-1}. For nitroalkanes the corresponding value $\mathbf{P_{f3}}$ (1) (the replacement of atom hydrogen at tertiary carbon on nitrogroup) is -41.0 kJ·mol^{-1} [6]. The values will be satisfactorily coordinated with each other. For 1,3-dinitroadamantane the substitution effect has made -75.7 kJ·mol^{-1}. On interaction nitrogroup, Δ, in the situation 1-3, which is equal $\mathbf{P_f}$ (1,3-dinitroadamantane) and -$\mathbf{2P_f}$ (1-nitroadamantane), it is necessary 7.3 kJ·mol^{-1}. The corresponding value for nitro- alkanes, $\Delta_{1,3}$, is received equal 8.4 kJ·mol^{-1} [6], that also will be satisfactorily coordinated to the value of effective energy of interaction, $\Delta_{1,3}$, in 1,3-dinitroadamantane.

In 2,2-dinitroadamantane the substitution effect has made -27.6 kJ·mol^{-1}, the corresponding value for 2,2-dinitroalkanes was received equal -29.7 kJ·mol^{-1} [6]. Both values are within the limits of measurement error of the formation enthalpy of 2,2-dinitroadamantane. Thus, it is evident, that energy effects of introduction of nitrogroup in nitroderivatives of adamantane are practically the same, as for nitro- derivatives of alkanes. Accepting the substitution effect of hydrogen in the

2-situation in adamantane same as in alkanes, where $\mathbf{P_{f2}}$ (1) is 36.0 kJ·mol^{-1}, and the effective energy of interaction of nitrogroup equal 42.3 kJ·mol^{-1}, we shall receive energy of interaction of nitrogroup in 2,2-dinitroadamantane: $\Delta_{2,2}$ = 44.4 kJ·mol^{-1}.

The energy of replacement of hydrogen atom in adamantane on nitrategroup in 1-nitrateadamantane has made -91.2 kJ·mol^{-1}. This value for 2-nitratepropane ($\Delta_f H°(g)$ = -190.8 ± 1.5 kJ·mol^{-1} [10]) was estimated from comparison with propane ($\Delta_f H°(g)$ = -103.9 ± 0.2 kJ·mol^{-1} [10]) and was received equal –86.9 kJ·mol^{-1}. These values of energy of replacement of hydrogen on nitrategroup, taking into account errors of measurement of properties of nitrates, will be satisfactorily coordinated among themselves.

For 1,3-dinitrateadamantane the substitution effect concerning adamantane has made -174.0 kJ·mol^{-1}, that, taking into account energy of introduction of nitrategroup (-91.2 kJ·mol^{-1}), results in effective energy of interaction of nitrategroups, which is 8.4 kJ·mol^{-1}. The corresponding value will be coordinated to energy of interaction of nitrogroups $\Delta_{1,3}$ = 8.4 kJ·mol^{-1} [6].

In 1,3,5,7-tetranitrateadamantane the enthalpy of replacement has made -323.4 kJ·mol^{-1}, and the energy of interaction of all groups has made 41.4 kJ·mol^{-1}. In recalculation on one interaction (all them 6) it results 6.9 kJ·mol^{-1} (value in brackets).

The size of energy of replacement in 1-trynitrometyl-3-nitrateadamantane concerning adamantane has made -81.1 kJ·mol^{-1}. The difference of formation enthalpies of nitroalkane in the gas phase was accepted as energy of replacement for nitrocompounds and corresponding derivatives, i.e. the group **C-H** was replaced with group **C – NO_2** [6]. In such case the 1-trynitrometyladamantane is necessary

to compare with 1-metyladamantane, which the enthalpy of formations in a gas phase can be taken from work [5] (-169.7 ± 1.4 kJ·mol^{-1}). Concerning this value the energy of replacement will make -45.3 kJ·mol^{-1}, therefore the value (-81.1 kJ·mol^{-1}) is put in brackets in Table 2. The energy of introduction in the molecule of adamantane by one of nitrategroup has made -91.2 kJ·mol^{-1}. The substitution effect of three hydrogen atoms on 3 nitrogroups at one atom of carbon was received equal 44.4 kJ·mol^{-1} [6], calculated thus the enthalpy of formation of 1-trinitromethyl-3-nitrateadamantane in a gas phase (-216.5 kJ·mol^{-1}) will be coordinated to experimental value (-215.0 ± 3.2 kJ·mol^{-1}).

The analysis of the formation enthalpy of adamantane derivatives in the gas phase has shown, in particular, for nitroderivatives and nitrates, that the energy effects of substitution and of interactions of these groups are congruent with the corresponding values of the characteristics for nitroalkanes. There are the kinetics data of thermodestruction for 1-nitroadamantane [11], which have shown, that this compound, as well as mononitroalkanes, destruction on the radical mechanism with the splitting of nitrogroup at the first stage and with the formation of the radical of 1-adamantane. Proceeding from the identity of energy properties of nitroderivatives of adamantane and of alkanes, and also from the identity of their primary act of the thermodestruction, it is possible to accept, that the energy of dissociation of bond **C – NO_2** in 1-nitroadamantane will be same, as in tertiary alkanes (246.0 kJ·mol^{-1} [12]). The enthalpies of formation of molecules and of radicals are connected with the energy of dissociation of bonds,**D**, by the correlation:

$$\mathbf{D(R_1 - R_2) = \Delta_f H°(g)(R_1) + \Delta_f H°(g)(R_2) - \Delta_f H°(g)\,(R_1R_2)} \qquad (1)$$

The enthalpy of formation NO_2 is equal 33.5 kJ·mol^{-1} [13], and the enthalpy of formation of 1-nitroadamantane in the gas phase was recommended -175.4± 1.7 kJ·mol^{-1} (Table 1). These values allow to determine the enthalpy of formation of the radical of 1-adamantane 37.1 kJ·mol^{-1}.

The enthalpy of formation of the radical of 1-adamantane has allowed to determine the energy of dissociation of the in 1-replaced derivatives of adamantane. The **D** values, given in Table 3, were received with the use of the formation enthalpies of adamantane derivatives, taken from Table 1. Data for 1-metyladamantane (-169.7 ± 1.4 kJ·mol^{-1}) taken from work [5], for 1-ethyladamantane (-190.4 ± 3.0 kJ·mol^{-1}) from work [14], for alkanes, alcohol and isopropylnitrate (tertbuthylnitrate is not investigated) from the reference book [10], the data on the enthalpies of formation radicals – from work [13], and for CH_3 – from work [15].

Table 3.

The energies of dissociation of bonds in the adamantane monoderivatives and the corresponding alkanes, 298 K, kJ·mol^{-1}

Compound	**D**	**Compound**	**D**
$C_{10}H_{15}$-NO_2	246,0	$(CH_3)_3C$-NO_2	246,0 [6]
$C_{10}H_{15}$-H	389,0	$(CH_3)_3C$-H	390,1
$C_{10}H_{15}$-CH_3	345,3	$(CH_3)_3C$-CH_3	343,2
$C_{10}H_{15}$-C_2H_5	335,9	$(CH_3)_3C$-C_2H_5	331,6
$C_{10}H_{15}$-OH	383,3	$(CH_3)_3C$-OH	389,2
$C_{10}H_{15}$-ONO_2	333,3	$(CH_3)_2CH$-ONO_2	335,6
$C_{10}H_{15}O$-H	431,5	$(CH_3)_3CO$-H	434,2

The satisfactory consent of the energies of dissociation of the various nature bonds in adamantane derivatives with the corresponding energy of bondsin hydrocarbon analogues, most likely is not casual. It proves the rightness and reliability of the enthalpy of formation of the radical of 1-adamantane determined in this work (37.1 kJ·mol^{-1}). The errors of the enthalpies of formation of known now radicals lay in an interval 5 ÷10 kJ·mol^{-1}, (except for $\mathbf{CH_3}$, for which the error was recommended less than 1 kJ·mol^{-1}). Taking into account insignificance of values of the divergence of energies of dissociation of bonds in 1-replaced adamantane and in hydrocarbon analogues, it is possible to assume, that recommended us the enthalpy of formation of the radical 1-adamantane has the error which is taking place in an interval of errors of hydrocarbon radicals, i.e. it does not exceed 5÷10 kJ·mol^{-1}.

The research of the initial stage of decomposition of the nitroesters has shown, that primary reaction is the hemolytic separation of group$\mathbf{NO_2}$ [16]. Thus by the most essential result was the same, that the energy of activation practically does not depend on the structure and on the phase condition of substance and it is in an interval 160 ÷170 kJ·mol^{-1}. Proceeding from these data and taking into account the fact, that, as was shown, the energetic parameters of the derivative adamantanes are identical to the corresponding characteristics of the derivative alkanes, it is possible to offer, that the energy of activation of separation of the group$\mathbf{NO_2}$ from 1-nitrateadamantane is the same, as for alkylnitrates. Proceeding from this, the energy of dissociation $\mathbf{C_{10}H_{15}O - NO_2}$ in 1-nitrateadamantane can be accepted of equal average energy of activation of reaction of thermodestruction of alkylnitrates (165 kJ·mol^{-1}) and, according to the equation (1), to receive the enthalpy of

formation of the radical 1-oxyladamantane equal -93.6 kJ·mol^{-1}. The energy of dissociation of the bond **O – H**, calculated on the formula (1), has made 431.5 kJ·mol^{-1}, whereas the corresponding value in 2-methyl-2-propylalcohol is 434.2 kJ·mol^{-1}.

This research was supported by the Russian Fund of Fundamental Investigation (project № 00-03-32196-a).

REFERENCES

1. Kizin A.N., Zaripov R.H., Lebedev V.P. et al. *Izv. Akad. Nauk RF, Ser. Khim* , **1996**, № 11, P. 2676 (in Russian).

2. Mansson M., Rapport N., Westrum E. *J. Am. Chem. Soc.,* **1970**, V. 92, № 25, P. 7296.

3. Boyd R., Sanwal S., Shary-Tehrany S., McNally D. *J. Phys. Chem.,* **1971,** V. 75, № 9, P. 1264.

4. Butler R., Carson A., Laye P., Steele W. *J. Chem. Thermodynamics.*, **1971,** № 3, P. 277.

5. Clark T., Mc O. Knox T., McKervey M. et al. *J. Am. Chem. Soc.*, **1979**, V. 101, № 9, P. 2404.

6. Miroshnichenko E.A., Vorob'eva V.P. *Zh. Fiz. Khimii,* **1999**, V. 73, № 3, P. 419 (in Russian).

7. Lebedev Y.A., Miroshnichenko E.A. Thermochemistry and Equilibria of Organic Compounds. Ed. M. Frenkel, VCH, **1993**, P. 165-375.

8. Oleinik B.N. .Precise Calorimetry. M.: Ed-n Standard, **1973**, 208 p.

9. Fritzsche K., Dogan B., Beckhaus H.-D. et al. *Thermochimica Acta*, **1999**. V. 160, P. 147.

10. Pedley J., Naylor R., Kirby C. Thermochemical Data of Organic Compounds. L., N.-Y.: Chapman and Hall. **1986**, 792 p.

11.Feinstein A., Fields E. *J. Org. Chem.*, **1971**, V. 36, № 7, P. 1996.

12. Miroshnichenko E.A., Vorob'eva V.P., Matyushin Y.N. *Khim Fizika.*, **1998**, V. 17, № 8, P. 29 (in Russian).

13. Gurvich L.V., Karachevcev G.V., Kondrat'ev B.N. et al. Energy of Chemical Bonds. Potentials of Ionization and Affinity to Elektron. M.: Nauka, **1974**, 351 p.

14. Melkhanova S., Pimenova S., Kolesov V. et al. *J. Chem. Thermodynamics*. **2000**. V. 32, № 10, P. 1311.

15. McMille D., Golden D. Hydrocarbon bond dissociation energies. Ann. Review
of physical chemistry. A.P. **1982**. V. 32, P. 493-532.

16. Lur'e B.A., Svetlov B.S. *Kinetika i kataliz,* **1994**, V. 35, № 2, P. 165

ENTHALPY CHARACTERISTICS OF THE POLYNITROAMINES

Evgeniy A.Miroshnichenko, Larissa M.Kostikova, Jaroslav O.Inozemtcev, Yuriy N.Matyushin,

Semenov Institute of Chemical Physics, Russian Academy of Sciences
117977 Kosygin Str. 4, Moscow, RUSSIA
Fax: (095) 137-8297. E-mail: ynm@polymer.chph.ras.ru

ABSTRACT

The energies of combustion and the enthalpies of vaporization of the number of compounds, containing in the molecule nitro-, nitroamine and nitrozoamine groups are measured. Their enthalpies of formation in the standard condition and in the gas phase are calculated. The energies of interaction nitro-, nitroamine and nitrozoamine groups in polynitronitroamines and polynitronitrozoamines are evaluated. The method of determination of the enthalpies of formation polynitronitroamine and polynitronitrozoamine radicals is offered. The energies of dissociation **N – NO_2, N – NO, C – N, C – C** and **C – H** bonds in polynitronitroamines are calculated.

INTRODUCTION

Inadditive part enthalpies of formation - an efficient energyinvalency interactions functional groups renders an essential influence upon the physical-chemical characteristics of compounds. Introduction to the molecule and accumulation in her functional groups brings about arising the energy of interaction between them and growing an inadditive part enthalpies of formation. Reason study, bring about the appearance of this energy, its quantitative evaluation, searching for regularities

of its change will allow effectively to decide problems of prediction and creating the substansces with set characteristics. Efficient energy invalency interactions depends on numbers, place of joining and chemical nature of functional groups. As far as the efficient energy of interaction of functional groups is constituent part of formation enthalpies of the compound, it will be realize at the decomposition of molecule in reactions of combustion or explosive conversion. The value of surplus energy render influence on stability and steadity of compound to different physical and chemical influences, their chemical behaviour, in many defines strength of chemical bonds, particularly strength of the most weak bond in the molecule. The efficient energy of interaction possible to present as a difference of two levels of potential energy of molecule - is experimental measured the formation enthalpies of the compound and calculated for the hypothetical condition, when interaction of functional groups is absent.

EXPERIMENT

The energies of combustion are measured on the hermetic calorimeter with the magnetic stirrer developed in ICP RAS specially for researches of energetic materials [1]. The calibration of the calorimeter is executed on burning the reference standard - benzoic acid of the mark K-1, certificated in D.I.Mendeleev Institute of Metrology. The absence of the systematic error of the measurements on the given calorimeter is confirmed by burning of the secondary reference standard – succinic and hippuric acids. The calorimeter allows to measure the thermal effects of the combustion reactions of the substances with the error 0.02 - 0.03%. The bases of a technique of burning of energetic materials are stated in work [2].

The enthalpies of vaporization for compounds were received from experimental data on saturated steam pressure and temperature relationship [3]. The condensed

phase volume was ignored at calculation. The vapor at low pressure was considered as ideal.

RESULTS AND DISCUSSION

Data on thermochemical properties of polynitroderivative nitroamines and nitrozoamines are presented in Table 1. The following designations are entered in Table 1:

$\Delta_f H°(c)$ - enthalpy of formation in a standard condition, $kJ \cdot mol^{-1}$;

$\Delta_{sub} H°$ – enthalpy of sublimation of compounds, $kJ \cdot mol^{-1}$;

$\Delta_f H°(g)$ - enthalpy of formation of compounds in a gas phase, $kJ \cdot mol^{-1}$.

Table 1.

Enthalpy characteristics of polynitronitroamines and polynitronitrozoamines, 298 K, $kJ \cdot mol^{-1}$

Compound	$\Delta_f H°(c)$	$\Delta_s H°$	$\Delta_f H°(g)$
$[(NO_2)_3CCH_2]_2NNO_2$	-27.6±2.1 [4]	117.6±0.9	90.0±2.3
$[(NO_2)_3CCH_2]_2NNO$	50.2±2.8 [4]	97.9±0.9	148.1±2.9
$[H(NO_2)_2CCH_2]_2NNO_2$	-160.7±2.9	133.1±1.2	-27.6±3.1
$(NO_2)_3CCH_2NNO_2(CH_2)_2C(NO_2)_3$	-87.9±2.9	117.2±1.1	29.3±3.1
$[(NO_2)_3CCH_2NNO_2CH_2]_2$	-35.5±2.8	150.2±1.2	111.7±3.0
$[(NO_2)_3CCH_2NNOCH_2]_2$	100.0±3.0	139.3±1.1	239.3±3.2
$[H(NO_2)_2CCH_2NNO_2CH_2]_2$	-169.0±3.0	164.0±1.2	-5.0±3.2
$[(NO_2)_3CCH_2NNO_2CH_2]_2CH_2$	-70.7±2.8	152.7±1.2	82.0±3.0

Energies of interaction of functional groups innitroderivative nitroamines and nitrozoamines in the gas phase possible to calculate from thecomparison of the atomization enthalpies $\Delta_a H°$ (or enthalpies of formation in the gas phase), received from experimental data, $\Delta_a H°exp$, and calculated on group contributions, $\Delta_a H°cal$,

take from work [5]. On the base given on nitroamine compounds [4] contribution nitrozoamine groups **N – $(C)_2(NO)$** in the enthalpy of formation in the gas phase and the enthalpy of atomization was calculated.

The contribution nitrozoamine groups in the enthalpy of atomization has form at the average 1051.0 kJ·mol^{-1}, and in enthalpy of formation in the gas phase is received equal 142.3 kJ·mol^{-1}.

In the Table 2 are brought results of comparision of the enthalpy of atomization nitroderivative of nitroamines and nitrozoamines, received from experimental data and from calculation values. In the Table 2 values Δ corresponds to energies of interaction of all functional groups. In work [5] was shown that interaction nitroamines groups, divided between itself more, than one group **CH_2**, possible neglect. Therefore value Δ is refer to the interaction of nitroamine and nitrozoamine groups with nitrogroups. In this case Δ_1 corresponds to an interaction nitroamine or nitrozoamine groups with one nitrogroup. From Tables 2 is seen that interactions of nitroamine and nitrozoamine groups with nitrogroups (position 1,3) are little differentiated between itself and form at the average 10.0 ± 0.4 kJ·mol^{-1}. Value Δ_1 close to energy of interaction nitrogroups in positions 1, 3 in the nitroalkanes (8.4 kJ·mol^{-1}) [6].

Table 2.

Enthalpy of atomization of nitroderivatives nitroamines and nitrozoamines, 298 K, kJ·mol^{-1}

Compound	$\Delta_a H^\circ$exp	$\Delta_a H^\circ$cal	Δ	Δ_1
$[(NO_2)_3CCH_2]_2NNO_2$	10913.1	10976.3	63.2	10.5
$[(NO_2)_3CCH_2]_2NNO$	10606.0	10659.2	53.2	8.9
$[H(NO_2)_2CCH_2]_2NNO_2$	9524.0	9569.6	45.6	11.4
$(NO_2)_3CCH_2NNO_2(CH_2)_2C(NO_2)_3$	12.123.6	12148.2	24.6	8.2
$[(NO_2)_3CCH_2NNO_2CH_2]_2$	14637.7	14700.5	62.8	10.5
$[(NO_2)_3CCH_2NNOCH_2]_2$	14011.4	14066.2	54.8	9.1
$[H(NO_2)_2CCH_2NNO_2CH_2]_2$	13247.8	13293.8	46.0	11.5
$[(NO_2)_3CCH_2NNO_2CH_2]_2CH_2$	15818.0	15872.4	54.4	9.1

In work [5] was shown that induction interaction nitrogroups, entered into nitroamine group, does not get through amine atom of nitrogen. It is possible to suppose that in molecules nitroderivative nitroamines and nitrozoamines an nitroalkyl groups interact with amine atoms of nitrogen.

Table 3.

Enthalpies of formation of radicals, 298 K, $kJ \cdot mol^{-1}$

Radical	$\Delta_f H^o(g)$
$(NO_2)_3CC^{\bullet}H_2$	150.6
$H(NO_2)_2CC^{\bullet}H_2$	103.3
$(NO_2)_3CCH_2C^{\bullet}H_2$	133.9
$(NO_2)_3CCH_2N^{\bullet}NO_2$	163.2 (220.5)
$H(NO_2)_2CCH_2N^{\bullet}NO_2$	115.9
$(NO_2)_3CCH_2NNO_2C^{\bullet}H_2$	173.6 (231.0)
$H(NO_2)_2CCH_2NNO_2C^{\bullet}H_2$	126.4
$(NO_2)_3CCH_2NNO_2(CH_2)_2NNO_2C^{\bullet}H_2$	197.5 (325.1)
$(NO_2)_3CCH_2N^{\bullet}(CH_2)_2C(NO_2)_3$	163.6
$H(NO_2)_2CCH_2NNO_2(CH_2)_2NNO_2C^{\bullet}H_2$	150.2
$H(NO_2)_2CCH_2NNO_2(CH_2)_2N^{\bullet}CH_2C(NO_2)_2H$	129.3
$(NO_2)_3CCH_2NNO_2(CH_2)_2\ N^{\bullet}CH_2C(NO_2)_3$	246.0 (316.3)
$(NO_2)_3CCH_2NNO_2CH_2C^{\bullet}HNNO_2CH_2C(NO_2)_3$	196.2 (323.8)
$H(NO_2)_2CCH_2NNO_2CH_2C^{\bullet}HNNO_2CH_2C(NO_2)_2H$	101.7
$(NO_2)_3CCH_2NNO_2CH_2C^{\bullet}H_2$	168.6 (225.9)
$[H(NO_2)_2CCH_2]_2N^{\bullet}$	129.7
$[(NO_2)_3CCH_2]_2N^{\bullet}$	224.3
$H(NO_2)_2CCH_2NNO_2CH_2C^{\bullet}H_2$	121.3

For getting of the dissociation bond energies in polinitroderivative nitroamines and nitrozoamines enthalpies of formation the radicals from work [5] and enthalpies of formation the radicals, calculated on the method of substituting (Table 3),are used.

In the Table 3 enthalpies of formation corresponding of the nitrozoamine radicals are presented in parenthesis.

The dissociation bond energies in nitroderivative nitroamines and nitrozoamines are provided in the Table 4. In the Table 4 indexes 1 and 2 of **C – C** bonds are indicated on the structural formules of compounds and on corresponding value of the dissociation energy. Values of the dissociation bond energy C^{1}–C, being between nitroamine and nitrozoamine groups, significantly below dissociation bond energies, located near di- or trinitromethyl groups (C^{2}–C). The energy bonds C^{1}–C are also below than this bond in 1,1,1,3,6,6,6-heptanitro-3-azahexane (compound 3 in Table 4). Value of the dissociation bond energy C^{2}–C in this compound noticeably exceeds the energy bond **C – CH_3** in n-hexane (343.1 kJ·mol^{-1}), that is determinated by the influence an trinitromethyl group. Values of the dissociation bond energies **C – N** in nitroderivative nitroamines and nitrozoamines significantly below values of energy an dissociation these bonds in methylamines, which are changed from 331.8 kJ·mol^{-1} in trimethylamine before 359.8 kJ·mol^{-1} in methylamine.

Table 4.

Energies of dissociation bonds in nitroamines and nitrozoamines, 298 K, kJ·mol^{-1}

Compound	N – N	C – N	C – C	C – H
$[(NO_2)_3CCH_2]_2NNO_2$	167.4	223.8	309.6	-
$[H(NO_2)_2CCH_2]_2NNO_2$	190.4	246.9	332.6	-
$(NO_2)_3CCH_2NNO_2CH_2{}^{1}\!-\!CH_2{}^{2}\!-\!C(NO_2)_3$	167.4	267.8	295.0[1] 365.3[2]	-
$(NO_2)_3CCH_2NNO_2CH_2{}^{1}\!-\!CH_2NNO_2CH_2{}^{2}\!-\!C(NO_2)_3$	167.4	220.1	235.6[1] 311.7[2]	302.5
$H(NO_2)_2CCH_2NNO_2CH_2{}^{1}\!-\!CH_2NNO_2CH_2{}^{2}\!-\!C(NO_2)_2H$	167.4	242.3	257.7[1] 333.9[2]	324.7
$[(NO_2)_3CCH_2]_2NNO$	163.2	223.0	308.8	-
$(NO_2)_3CCH_2NNOCH_2{}^{1}\!-\!CH_2NNOCH_2{}^{2}\!-\!C(NO_2)_3$	167.4	207.1	222.6[1] 311.7[2]	302.5

Values of the dissociation bond energies **C – H** in the Table 4 are refer to atoms of carbon, located between nitroamine and nitrozoamine groups. Values of energy an dissociation these bonds sighnificantly below **D(C – H)** in CH_2 groups in n-alkanes (395.0 $kJ \cdot mol^{-1}$) [7].

Values of the dissociation bond energies **C – N, C – H** and **C – C**, situated in immediate nearness to the nitroamines and nitrozoamines groups, significantly less, than in nitroamines, presented in work [5].

Thus, entering of the nitroalkyl groups in alkylnitroamines and nitrozoamines significantly increase energy of molecules relatively to additive values (Table 2). Here values of dissociation energy of more strong bonds are reduced, but values of energy an dissociation most weak bonds **N – NO_2** and **N – NO** do not decrease. Groups **N – $(NO_2)(C)_2$** and **N – $(NO)(C)_2$** in these compounds either as in polynitroamines (nitrozoamines), are characterized unchangeable energetic characteristics. This is determinated by particular characteristics amine atoms of nitrogen, as was it already note, not conductedinduction interaction. At the same time, we saw [5], that modification of nearest surrounding a group**N – $(NO_2)(C)_2$** (changing an atom of carbon on the hydrogen or nitrogroup) greatly changes values of energy an dissociation bond **N – NO_2**.

This research was supported by the Russian Fund of Fundamental Investigation (project № 00-03-32196-a).

REFERENCES

1. Matyushin Yu. N; Vorobev A. B; Konkova T. S et al., *Pat USSR 1221568*, **1986** (in Russian).

2. Lebedev Y. A.; Miroshnichenko E. A.; Knobel Y. K. *Thermochemistry of the Nitro Compounds*, Nauka, Moscow, **1970**, 168. (in Russian).

3. Lebedev Y.A., Miroshnichenko E.A. Thermochemistry and Equilibria of Organic Compounds. Ed. M. Frenkel, VCH, **1993**, P. 165-375.

4. Pepekin V.I., Matuyshin Y.N., Apin A.Y. *Izv. Akad. Nauk USSR, Ser. Khim.*, **1974**, № 8, P. 1786 (in Russian).

5. Kostikova L.M., Miroshnichenko E.A., Matyushin Y.N. *Energetic Materials.* 31th *International Annual Conference of ICT,* **2000**, Karlsruhe, FRG, P. 50.

6. Miroshnichenko E.A., Vorob'eva V.P. *Zh. Fiz. Khimii,* **1999**, V. 73, № 3, P. 419 (in Russian).

7. Gurvich L.V., Karachevcev G.V., Kondrat'ev B.N. et al. Energy of Chemical Bonds. Potentials of Ionization and Affinity to Elektron. M.: Nauka, **1974**, 351 p.

EFFICIENT ENERGIES OF INTERACTION OF FUNCTIONAL GROUPS AND ENERGIES OF DISSOCIATION BONDS IN ALKYLNITRATES

Larissa M.Kostikova, Evgeniy A.Miroshnichenko, Jaroslav O.Inozemtcev, Yuriy N.Matyushin,

Semenov Institute of Chemical Physics, Russian Academy of Sciences
117977 Kosygin Str. 4, Moscow, RUSSIA
Fax: (095) 137-8297. E-mail: ynm@polymer.chph.ras.ru

ABSTRACT

The enthalpies of formation of mono- and polyalkylnitrates in the standard condition are recommend on the base received by us experimental data and analysis of literary values. The contributions of the nitrates groups in the enthalpy characteristics of the alkylnitrates are received. The energy effects of interaction of nitrate groups in the gas phase are determined. The energy an dissociation bonds in the alkylnitrates in the comparison with corresponding to alcohols are calculated.

INTRODUCTION

An nitrates of alcohols (O-nitrocompounds) be of interest as energetic materials. Nitroethers are one of the component smokeless powders and powerful missile fuel. Some from them are capable plasstificate nitrate of cellulose and are used in the highenergy ballistic powder production. One of the most known and broadly used nitrates are a nitroglycerine (**NGC**), dinitrateethyleneglycol (**DNEG**), tetranitratepentaerythritol (**TEN**).

Nitrates of alcohols have more low energy of bond **O – NO_2** in contrast with bond **C – NO_2** in the nitrocompounds. Presents undoupted interest a study of the dissociation energy of **O – NO_2** groups and their efficient energy of

interaction depending on constructions of molecules and amounts ofnitrate groups.

EXPERIMENT

Sample of **NGC** was synthesized from the glycerine and nitric acid. Amount of admixtures formed less 0.1 %. The product purity dried in the vacuum 10^{-3} Pa on curve meltings has form 99.92 ± 0.05 mol %.

Enthalpy of evaporation **NGC** was measured on Kalve microcalorimeter in the interval from 313 before 393 K. Dependency to enthalpies of evaporation from the temperature has looking like that

$\Delta_v H^o = 98.37 - 0.22(T-273)$,

where $\Delta_v H^o$ – an enthalpy of evaporation **NGC**, kJ·mol^{-1}; T – a temperature, °K.

From this dependencies an enthalpy of evaporation **NGC** under 298 K is received equal 92.9 kJ·mol^{-1}.

Sample **DNEG** cleaned by evaporation in the vacuum 10^{-3} Pa and its purity on curve meltings has form 99.9± 0.1 mol %. Enthalpy of evaporation **DNEG** was measured on Kalve microcalorimeter. Growed monocrystals are grinded and dried in the vacuum 10^{-3} Pa. As of chromatographical analysis the sample did not contain admixtures.

Other crystalline compounds cleaned by a frequentative re-crystallization and fractional sublimation in the deep vacuum, and liquids - rectification in the vacuum 10^{-3} Pa. Enthalpy to sublimations **TEN** is defined by the method Lengmyur [1].

Enthalpies of combustion of the nitrates were determined with using semi-microcalorimetrical technique of the combustion in the bomb in the atmosphere of oxygen [2]. The technique of the measurement and of the corrective actions is detailed stated in work [3].

RESULTS AND DISCUSSION

In the Table 1 are brought literary given on thermochemical characteristics of mononitrates, and thermochemical data received in this work for number of polynitrates. Following indications are accepted in the Table 1:

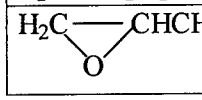
$\Delta_f H^\circ$ - the enthalpy of formation compounds in the standard condition;

$\Delta_{v,s} H^\circ$ - the enthalpy of vaporization;

$\Delta_f H^\circ(g)$ - the enthalpy of formation of the compounds in the gas phase.

Table 1.

Thermochemical properties nitrates, 298 K, $kJ \cdot mol^{-1}$

Compound	$-\Delta_f H^\circ$	$\Delta v,s H^\circ$	$\Delta_f H^\circ(g)$
CH_3ONO_2 (l)	156.1±1.2*	34.1±0.4*	122.0±1.3
$C_2H_5ONO_2$ (l)	190.4±1.2*	36.3±0.4*	154.1±1.3
n-$C_3H_7ONO_2$ (l)	214.6±1.2*	40.6±0.4*	174.0±1.3
iso- $C_3H_7ONO_2$ (l)	229.7±1.2*	38.8±0.4*	190.9±1.3
$(O_2NOCH_2)_2$ (l)	260.2±1.2	61.6±0.8	198.6±1.4
$(O_2NOCH_2)_2CHONO_2$ (l)	371.1±1.1	92.9±0.8	278.2±1.4
$(O_2NOCH_2)_4C$ (c)	556.8±2.0	150.6±1.8	406.2±2.7
$C_6H_8(ONO_2)_6$ (c) mannitol hexanitrate	706.7±4.2	-	-
$C_6H_8(ONO_2)_6$ (c) sorbitol hexanitrate	668.2±4.2	-	-
trans-$(O_2NOCH_2)_2(CH=CH)$ (l)	202.5±3.8	-	-
$O_2NOCH_2\ O_2NOC=CHCH_3$ (l)	215.1±3.5	-	-
 (l)	219.2±3.3	-	-

* - data from reference [4].

In the Table 2 are brought enthalpies of atomization, $\Delta_a H^\circ$, alkylmononitrate and corresponding alcohols and hydrocarbons, take from reference [4]. In this Table are brought enthalpies of substituting the atoms of hydrogen in the al-

kanes on the alcohol group or nitrate, **P**, as well as enthalpies of substituting an alcohol group on nitrate, P_I. From Table 2 is seen that values of effects of change **P** for alcohols and nitrates are greatly changed depending on constructions of hydrocarbon part of molecules. At the some time, values P_I turn out to be equal for all four nitrates, i.e. contribution the proper nitrogroups and its bonds with the oxygen in the enthalpy of atomization molecule of nitrate are equal and does not depend on hydrocarbon part.

Table 2.

Enthalpies of atomization of alkylmononitrates and corresponding alkanes and alcohols, 298 K, kJ·mol^{-1}

Compound	$\Delta_f H^o(g)$	$\Delta_a H^o$	P	P_I
CH_4	74.9	1661.9	-	-
CH_3OH	201.1	2037.2	375.3	-
CH_3ONO_2	122.0	2711.2	1049.3	674.0
C_2H_6	84.7	2822.5	-	-
C_2H_5OH	235.3	3222.5	400.0	-
$C_2H_5ONO_2$	154.1	3894.5	1072.0	672.0
C_3H_8	103.9	3992.8	-	-
n-C_3H_7OH	255.9	4394.0	401.2	-
n-$C_3H_7ONO_2$	174.0	5065.2	1072.4	671.2
Iso- C_3H_7OH	272.5	4410.8	418.0	-
iso-$C_3H_7ONO_2$	190.9	5082.3	1089.5	671.5

From enthalpies of atomization of the alkylnitrates, provided in the Table 2, it is possible select a contribution to the enthalpy of atomization group **O – NO_2**, which forms 1299.8 from methylnitrate, 1298.4 from ethylnitrate, 1297.9 from propylnitrate, and 1297.2 kJ·mol^{-1} from iso-propylnitrate. At the calculation contributions of groups in the enthalpy of atomization were used from work [4]. Average value of contribution **O – NO_2**, has form 1298.3 ± 0.6 kJ·mol^{-1}, and contribution to the enthalpy of formation in the gas phase is received equal -78.0 kJ·mol^{-1}. These values present itself own a contribution of the nitrate

group in the enthalpy of atomization (formation) without the bond **C – O**. Within error of experimental data a contribution of the nitrate group does not depend on energy of interaction of alcohol group oxygenwith hydrocarbon part of molecules. Separation of the nitrate fragment from the general contribution amount to the enthalpy of atomization (formation) is render useful on two reasons. First, this has allow to select from the general contribution own contribution of group **O – NO_2**. Secondly, it is render possible to describe with the smaller amount of parameters the whole row of monoalkylnitrates, begining with methylnitrate, the enthalpy characteristic which will agreed with other nitrates. In the initial calculation method [4] except contributions of ethereal groups **C – (O)$(H)_3$** and **C – (O)(C)$(H)_2$**, separate contributions on groups **C – (NO_3)(C)$(H)_2$** and **C – $(NO_3)(C)_2$(H)** are incorporated, at that first member of row (methylnitrate) does not account.

Identity of the nitrate group contribution in the enthalpy of formation monoalkylnitrates allows to suppose that induction interaction of hydrocarbon part of molecules spreads on the bond **C – O** groups **C – ONO_2** only and does not get through the atom of oxygen on other bonds of this group. In this case the energy of dissociation **O – NO_2** bond must not depend on hydrocarbon part of molecules, as this was in the case with bond **N – NO_2** in the nitroamines [5].

Review data on the kinetics of termodecomposition of the alkylnitrates, provided in work [6], has show that nitrates decompose monomolecular. Primary stage of the decomposition is a take-off of group **NO_2**. The most significante by the result was that energy to activations practically does not depend on constructions, amounts of the nitrate groups and phase condition of the compounds and be located in the interval 160 -170 $kJ \cdot mol^{-1}$.

The dissociation energy of **O – NO_2** bonds is taken an equal energy of thermodecomposition activation. Thus, thermochemical calculations and kinetic data bring about the alike conclusion: the energy of dissociation **O – NO_2** bond does not depend on the hydrocarbon radical.

In the Table 3 are brought the atomization enthalpies of polynitrates. In the Table 3 are accepted following marking:

Δ_a**Hexp** – the enthalpy of atomization, received on the base of enthalpies of formation of the compound in the gas phase;

Δ_a**Hcal** – the enthalpy of atomization, calculated on contributions of groups;

Δ – the full efficient energy of interaction in polynitrates;

$\Delta_{1,2}$ – the efficient energy of interaction of the nitrate groups, attached to nearby atoms of carbon;

$\Delta_{1,3}$ – the efficient energy of interaction of the nitrate groups, attached to atoms of carbon in positions 1,3. At the calculation of atomization enthalpies contribution the nitrate group, received in this work equal to 1298,3 kJ·mol^{-1}, is used.

Table 3.

Efficient energies of interaction of nitrate groups in polynitrates, 298 K, kJ·mol^{-1}

Compound	Δ_a**Hexp**	Δ_a**Hcal**	Δ	$\Delta_{1,2}$	$\Delta_{1,3}$
$(O_2NOCH_2)_2$ (l)	4941.6	4965.6	24.0	24.0	-
$(O_2NOCH_2)_2CHONO_2$ (l)	7174.3	7226.6	52.3	22.7	6.9
$(O_2NOCH_2)_4C$ (c)	10606.8	10646.6	39.8	-	6.6

The data provided in the Table 3 show that unlike polynitroamines, in polynitrates in positions 1,2 and 1,3 is observe sighnificant interaction nitrate groups. Interaction nitrate groups beside nearby atoms of carbon in **DNEG** has form 24.0 kJ·mol^{-1}. Interaction nitrate groups, join in the position 1,3, possible calculate from energy of interaction in 1,3-dinitrateadamantane (on one interaction happens to 8.4 kJ·mol^{-1} [7]), in 1,3,5,7-tetranitrateadamantane (on 6 interactions happens to 41.4 kJ·mol^{-1} [7]), and in **TEN** (on 6 interactions happens to 39.8 kJ·mol^{-1}). The averageweighted value $\Delta_{1,3}$ is received equal 6.9

$kJ \cdot mol^{-1}$. Coming from this values efficient energy of interaction$\Delta_{1,2}$ in **NGC** is received equal 22.70 $kJ \cdot mol^{-1}$. The averageweighted efficient energy of interaction $\Delta_{1,2}$ from **DNEG** and **NGC** forms 23.1 $kJ \cdot mol^{-1}$.

Consider a changing the energy of dissociation **C – O** bond in mono- and polynitrates. In the Table 4 the values of these energy are compare with corresponding to values in alcohols. The formation enthalpies of the radicals from [8], and the formation enthalpies of nitrates and alcohols from Table 1 and work [4] are used for calculations.

Table 4.

Dissociation energies of C – O bonds in nitrates and alcohols, 298 K, $kJ \cdot mol^{-1}$

Compound	D(C – O)
CH_3ONO_2	338.9
CH_3OH	388.3
$C_2H_5ONO_2$	332.6
C_2H_5OH	381.6
n-$C_3H_7ONO_2$	333.0
n-C_3H_7OH	382.0
iso-$C_3H_7ONO_2$	335.6
iso-C_3H_7OH	385.3
$O_2NOCH_2CH_2ONO_2$	307.4
$HOCH_2CH_2OH$	338.9
$O_2NOCH_2CH^{1}(ONO_2)CH_2^{2}ONO_2$	291.2^1; 323.0^2
$HOCH_2CH^{1}(OH)CH_2^{2}OH$	335.6^1; 333.0^2
$(O_2NOCH_2)_3CCH_2 - ONO_2$	310.5
$(HOCH_2)_3CCH_2 - OH$	335.6

From Table 4 is seen that the values of the dissociation energyof **C – O** bond in alcohols well above, than in corresponding to nitrates.The values of the dissociation energy of **C – O** bond in mononitrates on 20 $kJ \cdot mol^{-1}$lower, than in the ethers.

For the evaluation of the values of the dissociation energy of **C – O** bond in polynitrates the formation enthalpies of row of radicals on the method of substituting is calculated. Received enthalpies of forming the radicals have form in $kJ \cdot mol^{-1}$:

Radical	$\Delta_f H^0$	Radical	$\Delta_f H^0$
$O_2NOCH_2C^{\bullet}H_2$	37.7	$(O_2NOCH_2)_2C^{\bullet}H$	-57.3
$O_2NOCH_2CH(ONO_2)C^{\bullet}H_2$	-25.5	$(O_2NOCH_2)_3CC^{\bullet}H_2$	-158.2

As a whole possible note that nitrates groups have practically nonchanging the most weak **O – NO_2** bonds also, as nitroamine bonds **N – NO_2** and nitrozoamine bonds **N – NO** [9]. The values of the dissociation energy of these bonds stay constant and form near 165 $kJ \cdot mol^{-1}$. Energies of interaction of groups are distributed between other bonds, having more high the values of the dissociation energies (**N – C, C – C, C – H, C – O**). By these properties, **constancy of the values of the dissociation energy of bond of heteroatom with nitrogroup** (if heteroatom is connected with alkyl groups) **and reduction of values of of the dissociation energy for more strong bonds of nearest surrounding**, nitroamines, nitrozoamines and nitrates is principle are distinguish from **C**-nitrocompounds. As us was earlier shown [10], in polynitroalkanes the values of the dissociation energy of **C – NO_2** bond changes over a wide range, bond **C – H** stay constant, and bond **C – C** are increased are weaken depending on amounts and places of joining of nitrogroups. Probably, specifics of energy behaviour **N**- and **O**-nitrocompounds is defined by presence at atoms **N** and **O** nondivide electronic pairs, which are to enter in the interaction with nitrogroup, stabilizing fragments **N – NO_2 N – NO** and **O – NO_2**, and efficient energies of intergroup interactions are distributed on other bonds.

This research was supported by the Russian Fund of Fundamental Investigation (project № 00-03-32196-a).

REFERENCES

1. Lebedev Y.A., Miroshnichenko E.A. Thermochemistry and Equilibria of Organic Compounds. Ed. M. Frenkel, VCH, **1993**, P. 165-375.

2. Matyushin Yu. N; Vorobev A. B; Konkova T. S et al., *Pat USSR 1221568*, **1986** (in Russian).

3. Miroshnichenko E.A., Vorob'eva V.P. *Zh. Fiz. Khimii,* **1999**, V. 73, № 3, P. 419 (in Russian).

4. Cox J.D.; Pilcher G. *Thermochemistry of organic and metalloorganic* compounds. London – New-York: Acad. Press, **1970**, 643 p.

5. Kostikova L.M., Miroshnichenko E.A., Matyushin Y.N. *Energetic Materials.* 31th *International Annual Conference of ICT,* **2000**, Karlsruhe, FRG, P. 50.

6. Lur'e B.A., Svetlov B.S. *Kinetika i kataliz,* **1994**, V. 35, № 2, P. 165

7. Matyushin Y. N., Lebedev V. P., Miroshnichenko E.A.,Kostikova L.M., Inosemzev Y.O. THE ENERGY PROPERTIES OF THE NITRO- AND NITRATEDERIVATIVES ADAMANTANES, 32th *International Annual Conference of ICT,* **2001**, Karlsruhe, FRG.

8. Gurvich L.V., Karachevcev G.V., Kondratjev V.N. et al. *The Energies of Chemical Bonds. Ionization Potentials and Affinity to Electron.* Moscow, Nauka, **1974**, 351 p, (in Russian).

9. Miroshnichenko E.A., Kostikova L.M., Inozemtcev Y.O., Matyushin Y.N., ENTHALPY CHARACTERISTICS OF THE POLYNITROAMINES, , 32th *International Annual Conference of ICT,* **2001**, Karlsruhe, FRG.

10. Miroshnichenko E.A., Vorob'eva V.P., Matyushin Y.N., *Khim. Fizika,* **1998,** V. 17, № 8, P. 29.

THERMOCHEMICAL CHARACTERISTICS OF SALTS MEDINA AND EDNA

Yuriy N.Matyushin, Tatjana S.Konkova, Evgeniy A.Miroshnichenko

Semenov Institute of Chemical Physics, Russian Academy of Sciences
117977 Kosygin Str. 4, Moscow, RUSSIA
Fax: (095) 137-8297. E-mail: ynm@polymer.chph.ras.ru

ABSTRACT

The energies of combustion and enthalpies of solutionmethylnitroamine (**MNA**), methylenedinitroamine (**MEDINA**), ethylenedinitroamine (**EDNA**), hexamethyl-enedinitroamine (**GMDNA**) and their hydrazine salts are measured by precizion methods combustion and solution calorimetry. Enthalpies of formation the explored compounds are calculated on the grounds of received experimental data. The enthalpies of formation of the ions**MNA**, **MEDINA**, **EDNA** and **GMDNA** in infinitely dilution water dissolutons are calculated from two groups independent given on the enthalpies of formation and solutions of these compounds and their salts. Determination of the values of the enthalpies of formation the ions has allow get the enthalpies of formation of sodium and potassium salts **MEDINA** and **EDNA** on measured their the enthalpies of solution.

INTRODUCTION

Nitroamines and their derived to date are one of interesting in the applied plan of classes of polynitrous compounds. Salts of the nitroamine compounds are interesting in the plan highenergy polynitrous oxidizers,and ions nitroamines - intermediate products in the syntheses of compounds. Obtaining of bench marc thermochemical characteristics for first members of homologous row nitroamines - **MEDINA** and **EDNA** and their hydrazine, sodium and potassium salts was aim of this work, as far as just first members of homologous rows are powerfullydiffer-

ended on its characteristics. This fact necessary to take account into the development of methods of calculation of thermochemical values.

Primary aliphatic nitroamines present itself light-meltable crystalline substances. Dinitroamines - solid substances, melting temperature which depends on amounts and multiple of methylene groups in the molecule.

Measurement of enthalpies of combustion of energetic materials is connected with greater difficulties, since these compounds are high explosives, sensitive to heat and mechanical influences. Their energy of combustion significantly lower, than at hydrocarbons, but using the greater amounts of sample dangerously because of possible turning a combustion in the explossion.

As far as enthalpy of formation presents itself small a difference of two greater values - enthalpies of combustion and enthalpy amount of formation of the combustion products. The error in enthalpies of combustion defines error received of formation enthalpies.

To reduce error of the formation enthalpy it is necessary to use precision calorimetric equipment, have a greater amount of highclean materials and carefully perfect strategies of experiment. If under investigation compound is an electrolyte (acid, base, salt), dissociating at the dissolution in water on ions, its enthalpy of formation possible to define on the base of enthalpies of dissolution. Enthalpies of dissolution in difference with enthalpies of combustion are small values, so even greater relative errors in enthalpies of dissolution contribute small errors in the formation enthalpies of the electrolytes.

At the salt structure study by most important characteristics, along with enthalpies of combustion and dissolutions, enthalpies of formation the ions are, in particular, organic anions in infinitely dilute water solutions. Using combustion and dissolution calorimetry methods it is possible to define enthalpies of formation the new ions, as well as correct measured earlier values. As far as enthalpy of formation the salt compound is uniquely connected with enthalpies of formation its

ions in infinitely dilute watersolution through the enthalpy of dissolution (equation 1), the identity of values of enthalpies of formation an ion, received on the base given for two or more compounds, containing this ion, is a reliable warranty of correctness of determination of enthalpies of formation the under investigation substances.

$$\Delta_f H^\circ(Cat^+ \cdot An^-)_c + \Delta_{sol} H^\circ (Cat^+ \cdot An^-)_c = \Delta_f H^\circ(Cat^+)_{aq} + \Delta_f H^\circ(An^-)_{aq} \qquad (1)$$

where

$\Delta_f H^\circ(Cat^+ \cdot An^-)_c$ and $\Delta_{sol} H^\circ(Cat^+ \cdot An^-)_c$ - enthalpies of formation and dissolutions salts in the crystalline condition;

$\Delta_f H^\circ(Cat^+)_{aq}$ and $\Delta_f H^\circ(An^-)_{aq}$ - enthalpies of formation cation and anionof salt in condition infinitely dilute water solution.

Thus, for the study of electrolytes the most complex study of enthalpies of combustion and dissolutions is reliably, successfully used by us for the determination of thermochemical characteristics ofrow energetic materials of the salt structure [1-3].

Primary nitramines in difference trinitromethane [1], are weak electrolytes. Values **pKa** of the water dissolves of **MNA** and **GMDNA** form 6.2, **MEDINA** – 4.8 and **EDNA** – 5.9. For weak electrolytes complex thermo-chemical study except measurements of enthalpies of combustion and dissolutions measurements of enthalpies of diluting and conductivity requires. This required forcontrol a fullness of disinteration of salt compound molecules on ions and calculation of enthalpies of formayion the ions in condition infinitely dilute water solution.

EXPERIMENT

The enthalpies of formation of compounds from the energies of their combustion in the calorimetric bomb at large excess of oxygenwere determined. The energy of combustion was measured using specially designed (in ICP RAS) hermetic

calorimeter with magnetic stirrer for the energetic material test [4]. The calibration of the calorimeter was performed by combustion of benzoic acid as the standard (certified in Mendeleev Institute of Metrology, Sankt-Peterburg). The absence of systematic errors of the measurements was confirmed by experiments with combustion of other standards, namely succinic and hippuric acids. The calorimeter errors were equal only to 0.02 - 0.03%. The procedure of typical measures was described in detail earlier [5].

Calculation of the combustion enthalpies incorporates the amendments on heat exchange in the calorimeter, on the ignition and the combustion energy of auxiliary substance, on the thermal effect of formation of the nitric acid, Washburn, and work of expansion of gases.

To calculate the standard enthalpies of formation the following enthalpies of formations of combustion products were used

$$\Delta H^{\circ}_{f}\,[CO_2]_g = -393.51\ kJ\cdot mol^{-1}\ [6]$$
$$\Delta H^{\circ}_{f}\,[H_2O]_l = -285.83\ kJ\cdot mol^{-1}\ [6]$$

Enthalpies of solution are measured using a moving bomb calorimeter with a hermetic calorimetric vessel and isothermal jacket [7]. Calibration of calorimeter carried out by passing an electrical current through a heater located inside of calorimetric vessel. The accuracy of the reaction calorimeter is checked with help of the solution heat of **KCl** in water. The solution heat of **KCl** is obtained to equal $17531 \pm 9\ kJ\cdot mol^{-1}$ at **KCl** concentration of 1:1100 $\mathbf{H_2O}$, which matches well the recommend value of $17535 \pm 9\ kJ\cdot mol^{-1}$ [8]. Inaccuracy here and hereinafter is expressed in the manner of the duplicated standard deviation from the average value under the confidential interval 0.95. Calibration of calorimeter conducted by electrical current before and after dissolving of substance. An average value of energy equivalent are used in calculations.

The substance before the dissolution placed in preliminarily weighted thin-wall glass ampoules with the ground joint. Ampoules attached to high vacuum ap-

paratus and placed in thermostatic heater. After drying substances at corresponding temperature the ampoules sealed by fine blaze of gas burner with help of the special protector which prevents the substance from the influence of high temperature. The substances were weighted on Bunge weight with accuracy of 2.10^{-6} g.

For **MNA**, **GMDNA** and their hydrazine salt enthalpies the dissolution measured on the microcalorimeter Kalve. Enthalpies of diluting are measured on theflowing microcalorimeter PDMK-1.

Individuality **MNA** (99.86±0.08 мол. %) and **GMDNA** (99.89±0.03 мол. %) are defined by a method melting curves. Fullness of combustion of under investigation compounds defined on the analysis on CO_2, which has form (99.96-99.98)±0.03 %. Element analysis on C,H,N is carry out on the analyzer "Carlo-Erba", results of the analysis have form 100.00±0.03 %. Conductivity of thewater solution of nitroamines and their salts is measured on "Conductolyzer LKB-5300B" (errorof measurements 0.2 %).

RESALTS AND DISCUSSION

Results of conductivity measurements have show that undermolality 0.01 hydrazine salts stay partly associate. So calculation of enthalpies of dissolutionbefore condition infinitely dilute water solution realized with take account of data on dependencies integral heats dilution Φ_L from concentration **m** on the following equation

$$\Delta_{sol}H^{\circ}(\infty) = \Delta_{sol}H^{\circ}(m) - \Phi_L \qquad (2)$$

Heats of dilution measured in the interval ofmolality concentrations from $3 \cdot 10^{-2}$ before $2 \cdot 10^{-5}$ under 298 K with subsequent extrapolation to the infinitely dilution.

In the Table enthalpies of formation primary nitroamines and their hydrazine salts are presented. This enthalpies of formation received from enthalpies of combustion, $\Delta_f H^{\circ}(c)$.

Table.

Enthalpies of formation, dissolutions and dilution primary nitroamines and their salts, 298 K, kJ·mol^{-1}

Соединение	$-\Delta_f H^o$(c)	$\Delta_{sol} H^o$(m)	Φ_L	$-\Delta_f H^o$(rec)
CH_3NHNO_2 (c)	73.39±0.25	16.36±0.13	-1.38	73.24±0.28
$CH_3NNO_2 \cdot N_2H_5$ (c)	74.43±0.42	21.63±0.42	1.38	77.2 ±1.2
$CH_2(NHNO_2)_2$ (c)	62.22±0.42	23.68±0.08	-7.91	62.07±0.44
$CH_2(NNO_2)_2 \cdot 2N_2H_5$ (c)	51.80±1.25	59.62±0.08	38.36	54.7 ±1.6
$CH_2(NNO_2)_2 \cdot 2Na$ (c)		9.83±0.04		520.91±0.44
$CH_2(NNO_2)_2 \cdot 2K$ (c)		8.91±0.04		543.67±0.44
$(CH_2)_2(NHNO_2)_2$ (c)	103.76±0.42	40.38±0.08	-3.64	103.68±0.43
$(CH_2)_2(NNO_2)_2 \cdot 2N_2H_5$ (c)	94.14±0.85	49.92±0.13	15.48	95.3 ±1.6
$(CH_2)_2(NNO_2)_2 \cdot 2Na$ (c)		7.15±0.04		547.41±0.43
$(CH_2)_2(NNO_2)_2 \cdot 2K$ (c)		8.95±0.08		572.89±0.43
$(CH_2)_6(NHNO_2)_2$ (c)	211.8 ±1.1	51.4 ±1.2	-0.92	211.9 ±2.2
$(CH_2)_6(NNO_2)_2 \cdot 2N_2H_5$ (c)	207.74±0.75	61.50±0.85	16.31	207.7 ±2.6

The dissolution enthalpies before concentrations **m**, $\Delta_{sol} H^o$(m), heats of dilution, Φ_L, and in the last column – recommended values of formation enthalpies, calculated from enthalpies of dissolution and enthalpies of formation the ions,$\Delta_f H^o$(rec), also are presented . In this Table enthalpies of dissolution and formation of sodium and potassium salts **MEDINA** and **EDNA** also are presented. Values molality of solutions lay in the interval $10^{-2} - 2 \cdot 10^{-3}$. Formation enthalpies of the ions **CH_3-NNO_2, CH_2(-NNO_2)$_2$, (CH_2-NNO_2)$_2$** and **(CH_2)$_6$(-NNO_2)$_2$** have form -50.50 ± 0.25, -30.48 ± 0.43, -59.66 ± 0.42 and -159.6 ±1.9 kJ·mol^{-1} accordingly. Formation enthalpy of the ion hydrazine at calculations is accepted equal -1,46±1.05 kJ·mol^{-1} [1].

From Table is seen that enthalpies of dilution the weak electrolytes and their salts be able to form significant values and it is impossible neglect them in calculations formation enthalpies of the ions.

The salts of alkaline metals easy break up on ions. Therefore enthalpies of dissolution of metallic salts in condition infinitely dilute watersolution possible to define coming from enthalpies of dissolution of these salts under end concentrations. Enthalpies of dissolution disodium and dipotassium salts of **MEDINA** and **EDNA** measured under molality of solution 0.01 – 0.02. Within error of the measurements the dissolution enthalpies do not depend from concentrations of the solutions. Enthalpies of formation the ions **Na** and **K** are accepted equal -240.300 ± 0.065 and -252.14 ± 0.08 $kJ \cdot mol^{-1}$ [6].

This research was supported by the Russian Fund of Fundamental Investigation (project № 00-03-32196-a).

REFERENCE

1. Kon'kova T. S., Matyushin Y.N. *Izv. Akad. Nauk RF, Ser. Khim.*, **1998**, № 12, P. 2451 (in Russian).

2. Matyushin Y.N., Kon'kova T.S., Titova K.V., Rosolovskiy V.Y. *Bull. Acad. Sci. USSR, Div. Chem. Sci.*, **1985**, V. 34, P. 713 (Engl. Transl.).

3. Miroshnichenko E.A., Vorob'eva V.P., Matyushin Y.N. *Khim. Fizika*, **2000**, V. 19, № 6, P. 40 (in Russian).

4. Matyushin Yu. N; Vorobev A. B; Konkova T. S et al., *Pat USSR 1221568*, **1986** (in Russian).

5. Lebedev Y. A; Miroshnichenko E. A; Knobel Y. K. Thermochemistry of the Nitro Compounds, Nauka, Moscow, **1970**, 168. (in Russian).

6. Cox J. D; Vagman D. D; Medvedev V. A. (Eds.) Codata Key Values for Thermodynamics, New-York - Washington, **1989**.

7. Matyushin Yu. N., Vorobev A. B., Konkova T. S. et al. *Pat USSR* 726442, **1980** (in Russian).

8. Montjomery R.L. *J. Chem. Thermodynamics*, **1977**, vol. 9, P. 915.

Damage models for Service Life prediction

C Hobman, B Downes, D Tod
DERA, Fort Halstead, Sevenoaks, Kent, TN14 7BP, UK

Abstract

The accurate Service Life prediction of rocket motors is essential to maximise cost savings in weapon systems.

A material cumulative damage model can be used when a stress based analysis is to be undertaken for the Service Life prediction of rocket motors. This model determines the failure stress of a propellant at a given time. It is dependent on such factors as: a constant stress (σ_f) to which a component has been subjected; the time-to-failure (t_f) of the component under stress (σ_f); a temperature shift factor (α_T); and a cumulative damage factor (β).

The time-temperature dependency of a visco-elastic material such as rubbery propellant can be described using the Williams-Landel-Ferry (WLF) temperature shift factor (α_T). However, the response of a propellant under load may also have a humidity dependency.

This work covers endurance testing conducted on a rubbery composite propellant. The effect of different humidity levels on the mechanical fatigue of ammonium perchlorate composite propellant under load was studied.

Cumulative damage factors at various humidities were calculated and compared to a value which had previously been used in a Service Life prediction programme. The equivalent damage factors were found to be higher than this previous factor, for all tested humidities. This finding would then equate to an extension in the predicted Service Life for this type of propellant.

In addition, a discussion concerning the validation of the temperature shifts factor (α_T) for this particular propellant is included.

Introduction

A cumulative damage model has been used to estimate the effects of the stress loading history on a propellant. This is based on Bills linear cumulative damage model and assumes a power law dependence in the time-to-failure/stress relationships:

$$D(t,T) = 1 - \frac{1}{\sigma_f^{\beta} t_f} \int_0^t \sigma^{\beta} \frac{dt}{\alpha_{T_0}(T)}$$

Equation 1:

where $\sigma(t)$ is the stress loading history, t_f is the time to failure at a specified endurance stress levelσ_f, $\alpha(T)$ is the Williams-Landel-Ferry (WLF) shift factor and β is the cumulative damage index.

Under a prolonged constant load polymers typically have a definite lifetime which is a function of both the load level and of the intrinsic material properties. Due to the visco-elastic nature of rubbery composite propellants the mechanical properties are time-dependent. Under a constant load the material will have a time-to-failure which is dependent on the initial stress level. Creep is a time-dependent deformation which occurs when a material is subjected to load and becomes more evident with prolonged periods of time.

A basic power law creep relationship can be described by:

$$t_f = C\sigma^{-n}$$

Equation 2:

where C and n are constants. The gradient of the linear logarithmic stress versus logarithmic time to failure relationship gives the power law term, n. This can be related to the cumulative damage model, Equation 1, where it can be shown that the cumulative damage index, β, is in the fact the negative reciprocal of this gradient. Simple endurance testing can therefore give information about the cumulative damage index, β. By conducting endurance testing at different humidity levels any dependency that β may have on humidity can be investigated.

This cumulative damage model is also strongly temperature dependent. Differences in the thermal history of the grain are accounted for by using the WLF shift factor which is temperature dependent. This accounts for the time-temperature dependent nature of the visco-elastic propellant. The use of

stress relaxation experiments to better define a temperature dependent shift factor, as opposed to the traditional WLF equations, is described later in this paper.

Experiment - endurance testing for calculation of cumulative damage factor, β

Time-to-failure experiments (endurance testing) were conducted on a typical UK Service rubbery composite propellant at different humidities. Material was subjected to different initial stress levels and the subsequent time-to-failure noted. Failure times range from a few minutes to two years.

The different humidities were controlled using saturated salt solutions. A saturated salt solution is one that is in equilibrium with excess of solute at a given temperature. The solution can be either undersaturated, more commonly, or supersaturated with increasing temperature. This is unlikely to be of concern in our system, as the laboratories concerned are air conditioned with a maintained temperature of 21 ± 2°C.

Five different salts were used. These were selected on the basis that they gave an adequate range of humidities which were stable with respect to changes in temperature. Table 1 gives the salts used together with nominal values for the humdities of the saturated solutions.

Salt	Nominal relative humidity
Silica gel	< 0.05
KO.Ac	0.23
K_2CO_3	0.43
$Na_2Cr_2O_7$	0.52
$Na_2Cr_2O_7$*	0.60
NaCl	0.75

Table 1: nominal relative humidites of saturated salt solutions used

A digital NAMAS calibrated probe was used to check that the salt solutions made produced relative humidities close to the nominal values.

All tests were conducted at a constant temperature throughout so that the temperature-time dependency is effectively negated.

Maximum stress values from tensile testing were used as a guide for choosing the loads for endurance testing. A typical stress-strain curve for the propellant used is shown in Figure 1

* initial value for sodium dichromate saturated salt solution

Freely supported dumbbells of propellant were loaded to different stress levels in cabinets containing the saturated salt solutions. For long term testing visual inspection on a twice daily basis was considered adequate, as the errors involved over this timescale are small. Shorter term testing was monitored using a video camera and video recorder system.

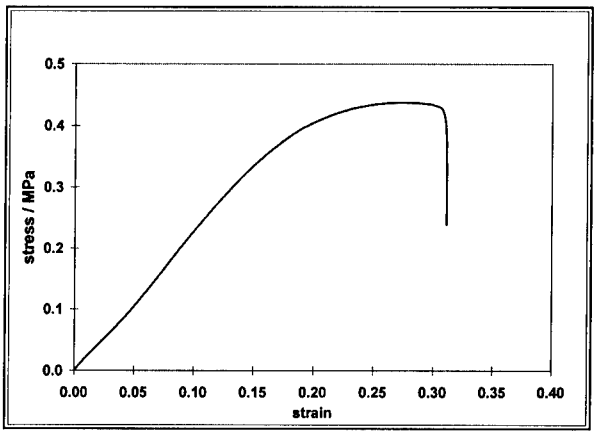


Figure 1: tensile test on composite propellant

Results of the endurance testing and general discussion

The time-to-failure values, as a function of initial stress, are shown in Figure 2.

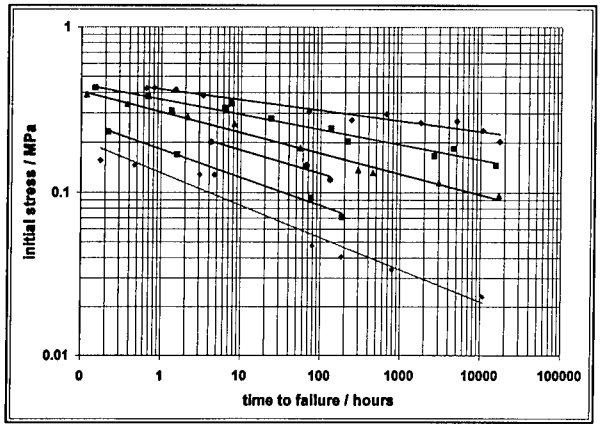


Figure 2: time-to-failure data

The humidity dependency of the time-to-failure is clearly seen; with time-to-failure decreasing with increasing humidity for any given initial stress value. A power law fit was applied to each set of data and a cumulative damage index, β, calculated for each humidity. The humidity dependency of the cumulative damage index is tabulated in Table 2. A graph also showing this dependency is given in Figure 3.

humidity / %	power law term	β
5	0.06366	15.7
23	0.09110	11.0
43	0.12480	8.0
52	0.14193	7.0
60	0.16908	5.9
75	0.19655	5.1

Table 2: cumulative damage index as a function of humidity

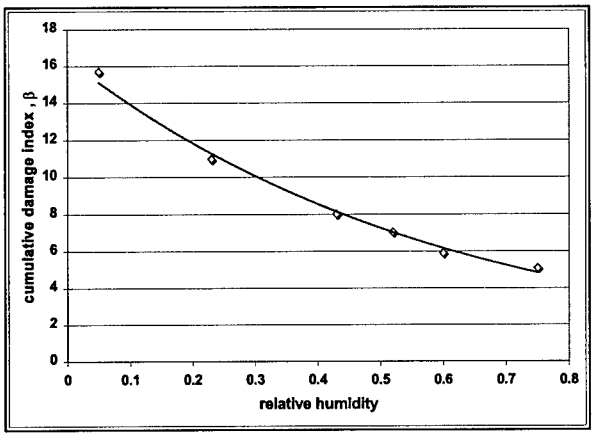


Figure 3: cumulative damage index as a function of humidity

The power and constant terms from each of the power law fits were also plotted as a function of humidity, see Figure 4. Further fits were performed on this data; a linear fit made with the power term, n, and a second order polynomial made with the constant, C.

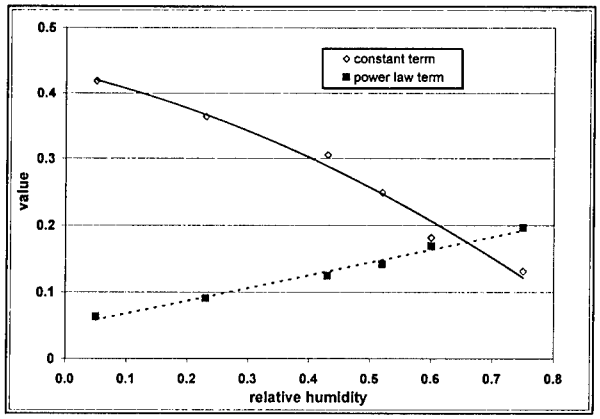


Figure 4: dependency of power and constant terms on humidity

From this a relationship predicting the time-to-failure characteristics over magnesium chloride saturated salt solution (RH $\approx$ 0.33) was made. Two samples were tested over saturated magnesium chloride solution. Figure 5 shows the results of the endurance testing compared to the predicted performance. There is good agreement between prediction and experiment.

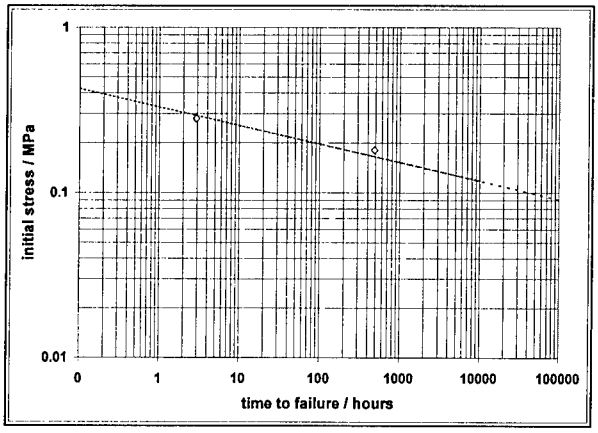


Figure 5: comparison between time-to-failure prediction over magnesium chloride and real failure

Another important consideration when using a cumulative damage model based on Equation 1 is the time-temperature dependent nature of the visco-elastic propellant. The Williams-Landel-Ferry shift factor is a parameter which is included in this stress based analysis. The original WLF equation describing the temperature dependency of the shift factor holds for the range of temperatures from just above the T_g to approximately 100K above the T_g. For a typical UK composite propellant the T_g falls around -85°C and so the traditional WLF shift factors are not

appropriate to describe propellant under typical storage conditions. The WLF equation also uses the T_g as the reference temperature and is therefore not particularly useful.
The two constant terms in the original WLF equation can be modified for different reference temperatures and there are equations for reference temperatures of about room temperature. Other work has also shown that the addition of an Arrhenius term is useful for temperatures which are 100K or more greater than the T_g.

The temperature dependency of the shift factor for the rubbery composite propellant has also been studied by DERA. Stress relaxation experiments were conducted at a variety of test temperatures and a form of horizontal shift procedure performed. The information gained from this was used on stress-strain data gathered form tensile tests conducted at different temperatures and different strain rates. The temperature-time dependency enabled the strain rate experimental window to be extended.

Figure 6 shows the temperature dependency of the shift factor as calculated from information from stress relaxation experiments and from a WLF equation for room temperature. The manual shift appears to describe an Arrhenius dependency, as shown by the linear fit in the log a_T against 1/T plot.

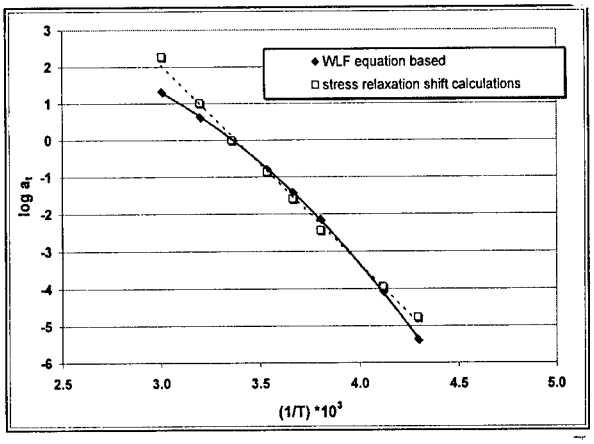


Figure 6: traditional WLF equation compared to DERA shift procedure

Reduced maximum stress data from tensile tests conducted at a variety of test temperatures and strain rates is shown in Figure 7.

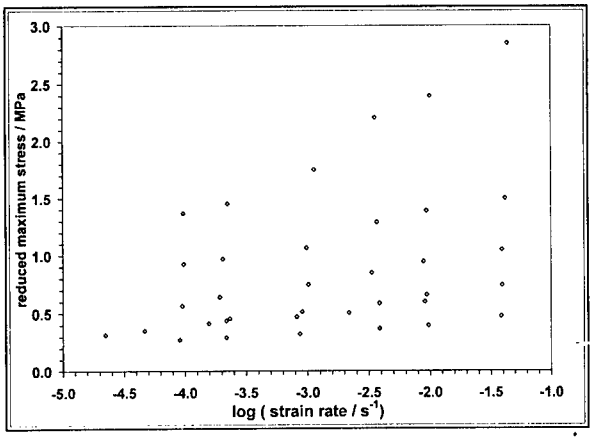


Figure 7: unshifted stress-strain data

The temperature-time dependency was then used to shift the strain rate to the reference temperature, in this case +25°C.

Figure 8 shows the shifted maximum stress data as described by the WLF type equation, whilst Figure 9 shows the shift as described by the DERA manual shift procedure.

The WLF shift procedure does appear to bring the data into line but the DERA procedure produces a much tighter group of shifted data.

Whilst this does not necessarily invalidate the traditional use of WLF type equations to modify test data, it does suggest that if we want to accurately use Service Life prediction programmes we must be sure that our input data is from the most valid data available.

Thus for Service Life prediction using the cumulative damage model as described in Equation 1, both the cumulative damage index, β, and the time-temperature shift factor, $\alpha(T)$, need to be well described. If these are not sufficiently described then any prediction may be well off the mark.

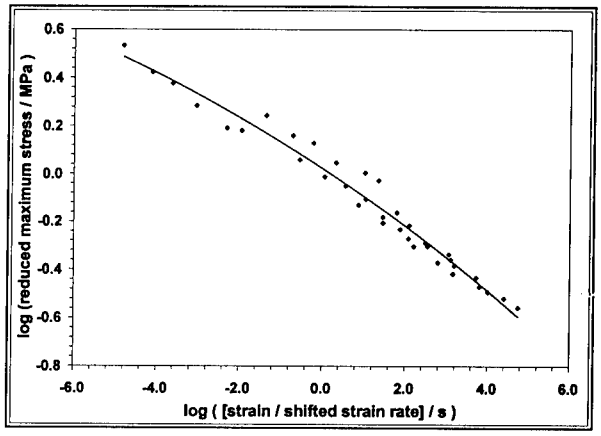


Figure 8: shifted maximum stress data as described by the WLF equation

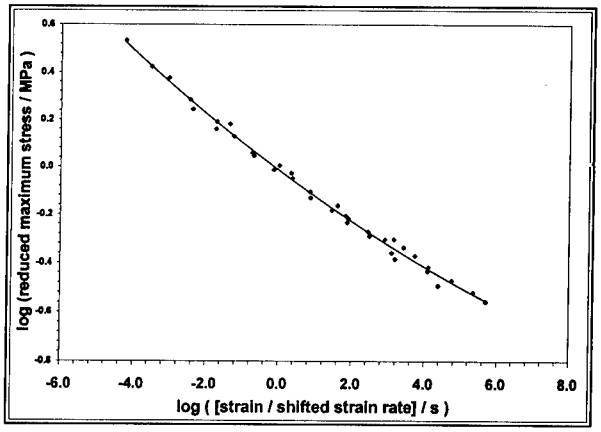


Figure 9: shifted maximum stress data as described by DERA procedure

Conclusions

The humidity dependence of the time-to-failure as a function of initial stress has been shown. An empirical relationship was developed linking the humidity, initial stress levels and the associated time-to-failure for this particular propellant. This relationship was tested for a chosen humidity and was found to satisfactorily predict the time-to-failure response at two chosen loads.

Increasing the humidity has the effect of reducing the time-to-failure of rubbery composite propellant when subjected to the same load. Although a propellant would not be expected to be subjected to high humdities, the humidity dependency should be accounted for and therefore modifications to any damage laws should be made.

A cumulative damage factor may be defined as the inverse gradient of the log stress log time-to-failure curves. A damage factor of 3.5 has been used in previous studies to estimate the life of a typical composite propellant. The equivalent damage factors shown here are higher than this value of 3.5 at all humidities tested. This equates to an extension in the predicted life of the material.

Care needs to be taken when using the temperature shift factor (α_T) and the limitations of using a WLF type equation should be known.

Recommendations

The linear relationship implies that for a uniaxial stress state the cumulative damage increases linearly with time. It has been suggested that damage is better described by a non-linear cumulative damage approach. Intuitively this would make more sense. After all, creep curves under constant load are often a complex mix of primary, secondary and tertiary stages for many materials. The strain response may also be quite different at different load levels.

There is a need to understand the effects of cumulative mechanical damage more thoroughly as better understanding of cumulative damage effects is vital for the progress of Service Life Prediction models. Experiments are needed to provide a link between the cumulative effects of micro-mechanical damage and the ultimate mechanical failure in energetic materials.

As a material undergoes deformation the accumulation of micro-mechanical damage causes debonding between the filler-binder matrix, called dewetting, and the formation of microvoids at certain areas, for example around particulates. The effect of this microstructural damage can have a distinct effect on the mechanical performance of a material. One way to try to quantify the effects of cumulative damage is to measure dilitation. Dilitation experiments are related to the accumulation of microstructural damage.

A combination of dilatation experiments together with information from endurance testing may help therefore in quantifying damage within a propellant material under load.

Development of Very Energetic Binder System Ingredients (PGN and DGTN)

Andrew J. Sanderson, Louis F. Cannizzo, Robert M. Hajik,
Thomas K. Highsmith, Laura J. Martins
Thiokol Propulsion
PO Box 707, M/S 244
Brigham City, UT 84302
USA
Phone: (435)-863-3708
Fax: (435)-863-2271
E-mail: Andrew.Sanderson@thiokol.com

Abstract

For many applications, high energy-density, oxygen-rich binder systems are necessary for performance and sensitivity improvements over the current state of the art. We have been actively investigating several ingredients for such binders systems. Two ingredients that are particularly promising are poly(glycidyl nitrate) (PGN), and diglycerol tetranitrate (DGTN).

PGN has been studied in a number of laboratories in the past 40 years. However its preparation has involved either very hazardous or very expensive synthetic routes. We have developed a new route to PGN that is attractive both from economic and safety considerations. This route is being scaled-up, and the aging and sensitivity characteristics of the product are being tested in formulations.

DGTN is an energetic plasticizer that has been known for many decades but its attractive properties for modern applications seem to have been overlooked. It was originally used to depress the freezing point of nitroglycerin (NG), but it was difficult to make and it does not swell nitrocellulose (NC). We have modified the synthesis of DGTN to obtain a quantitative yield from a readily available starting material. DGTN is iso-energetic with BTTN but it has many preferable characteristics, including a lower vapor pressure, no freezing point and lower cost. It also appears to improve sensitivity in some applications. Although it does not gelatinize NC, even in admixture with other plasticizers, we have found that it is an effective plasticizer of synthetic polymers such as PGN, polyethylene glycol (PEG) and polypropylene glycol (PPG), giving binder systems with very attractive properties. As with PGN, the synthesis is being scaled-up, and the aging and sensitivity characteristics of the product are being tested in formulations.

This paper discusses our recent findings on PGN and DGTN synthesis and characterization.

The Synthesis of PGN

PGN has been known for several decades, but despite its many attractive attributes, it has not been widely used. In a previous paper we presented improvements to the synthesis of the monomer, glcidyl nitrate (GN), that will enable it to be made safely and at a reasonable cost[1].

©2001 Thiokol Propulsion, a division of Cordant Technologies, Inc. Distribution authorized for public release.

Glycidyl Nitrate Synthesis

Using the fact that the ring closure of dinitroglycerin (DNG) with a strong base has been a long known though little practiced reaction, together with the relatively simple synthesis of DNG itself by the careful partial nitration of glycerin, we developed an overall synthesis that gives high purity GN in high yield from glycerin, nitric acid and sodium hydroxide (figure 1). The product is contaminated with up to 2% DNG and also up to 5% NG. These contaminants can be removed, or the synthetic procedure modified so that they do not occur. However, we have found that they do not interfere with the polymerization and are easily separated from PGN during the polymer isolation procedure.[2]

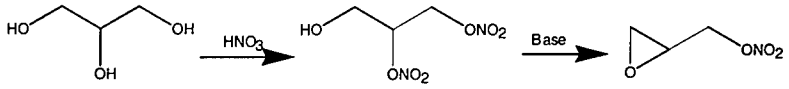


Figure 1. Glycidyl Nitrate from Glycerin

Polymerization of GN

The original polymerization of GN to give PGN by the US Navy[3] has been further developed by Desai and by Willer. GN is quite unreactive to standard cationic ring opening polymerization condition and so most polymerizations have been conducted with cationic polymerization under active monomer conditions, where the instantaneous monomer concentration is very low. Using this method, molecular weights of 3000-4000 for difunctional polymers have been reported. We have reproduced this work using essentially the same chemistry and found that under carefully controlled conditions we can obtain molecular weights in excess of 5000. Analysis of the ^{13}C nmr internal methylene peaks at 27ppm shows that we have very good initiation of the butane diol we use to make difunctional polymer (figure 2).

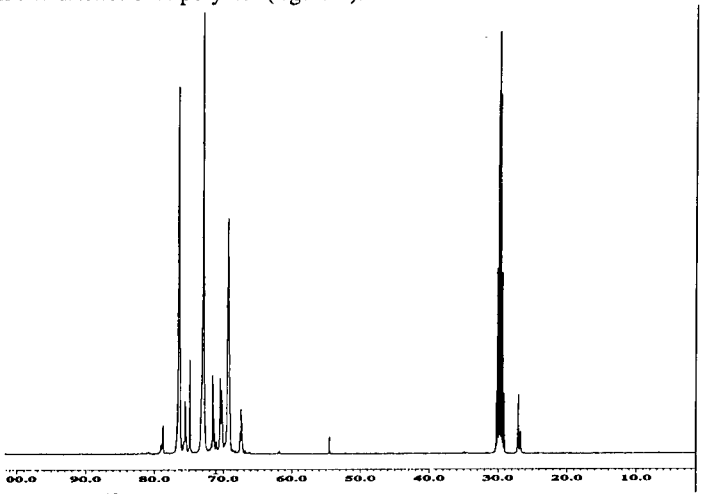


Figure 2. ^{13}C nmr of Butanediol Initiated PGN Before Removal of NG/DNG

We have used this difunctional product to make random block copolymers with crystalline polyBAMO as the hard block. The synthetic method to link the blocks has been discussed in detail elsewhere[4]. It basically consists of reacting the two homopolymers with two equivalents of toluene diisocyanate and then linking the isocyanate end capped polymers with butane diol. We noticed that this linked material was thermally stable and showed no tendency to unlink on ageing. Whereas it has been reported that when cross-linked with isocyanates, PGN ages poorly, fairly rapidly reverting to a liquid state[5].

In order to study this observation we conducted ageing studies similar to those reported by Leeming. In it we also tested the ICI end modified PGN. We were able to confirm that the cured end modified PGN withstands storage at elevated temperature whereas under these conditions our PGN and PGN previously made by a different route at our Elkton Division softened rapidly. For conventional PGN, on storage at 145°F after curing, a Shore A decrease can be observed after just a few days (figure 3, Elkton, and figure 4) whereas the Shore A of this cured end modified material remains constant over at least 30 days (figure 3, DERA/ICI fixed).

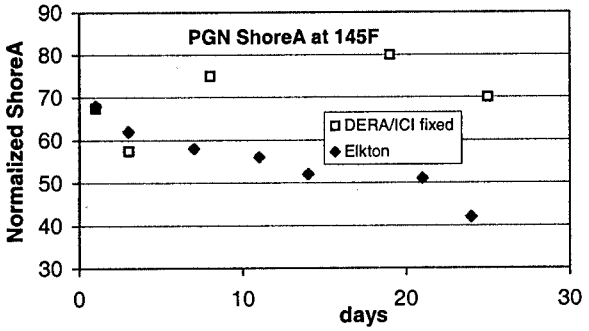


Figure 3. Aging of a Cured PGN-Based Propellant

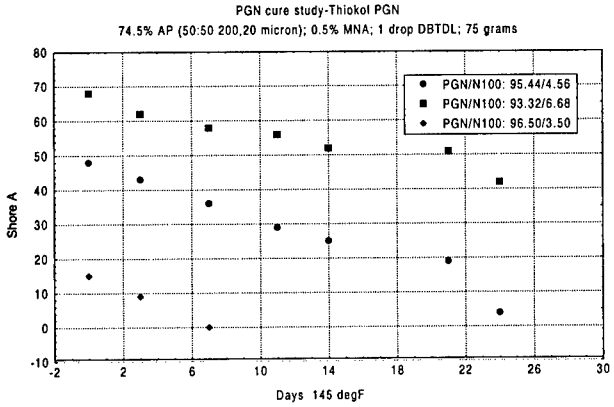


Figure 4: Ageing of PGN/N100 propellant samples at 145F

The principle difference between the samples for this ageing study and those TPEs that were observed not to decure was the curative, the aromatic diisocyanate TDI as opposed to aliphatic curatives. However we could not repeat the ageing studies using TDI as both it and the non-end-modified PGN are difunctional. To test the stability of cured PGN with TDI we thus made polyfunctional PGN using triol and tetraol initiators with the same polymerization technique.

In the proton nmr of trimethylol propane initiated PGN, the initiator can be clearly seen to be incorporated. This and the tetraol initiated PGN were found to cure easily to tough, flexible rubbers using TDI and an organotin cure catalyst. When these were aged, it was found that the TDI cured polyfunctional PGN is as stable as the end modified PGN (figure 5).

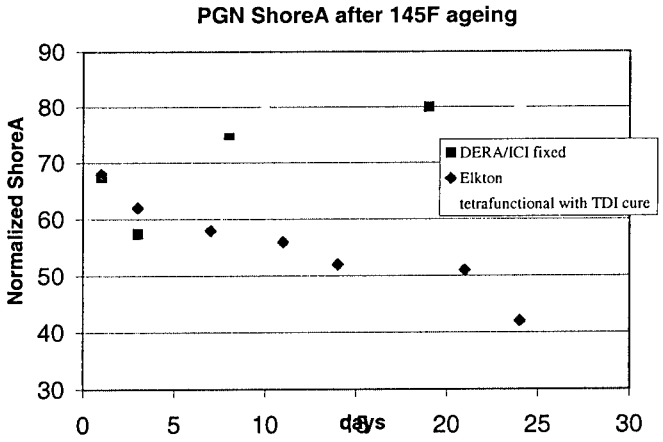


Figure 5: Comparison of the stability of end modified and conventional difunctional PGN cured with N100 with tetrafunctional PGN cured with TDI.

This can be rationalized on considering the nature of the urethane linkages in the cured polymers. The decure of PGN and aliphatic urethanes was postulated to be due to a rearrangement involving a "McLafferty type" 6-membered transition state[6] or proton transfer from the carbon adjacent to the nitrate ester to the urethane nitrogen (figure 6). If the latter type of mechanism is correct then the base strength of the urethane nitrogen is key to the rate at which the decomposition occurs. As a nitrogen directly attached to an aromatic ring is a very much weaker base than an aliphatic nitrogen, one would expect to see a substantial reduction in the rate of decomposition of the aromatic urethane, and this is observed in our ageing studies. This observation indicates against the "McLafferty type" rearrangement as in this case the effect of the R group and the base strength of the urethane nitrogen would have little or even a slight destabilizing effect[7].

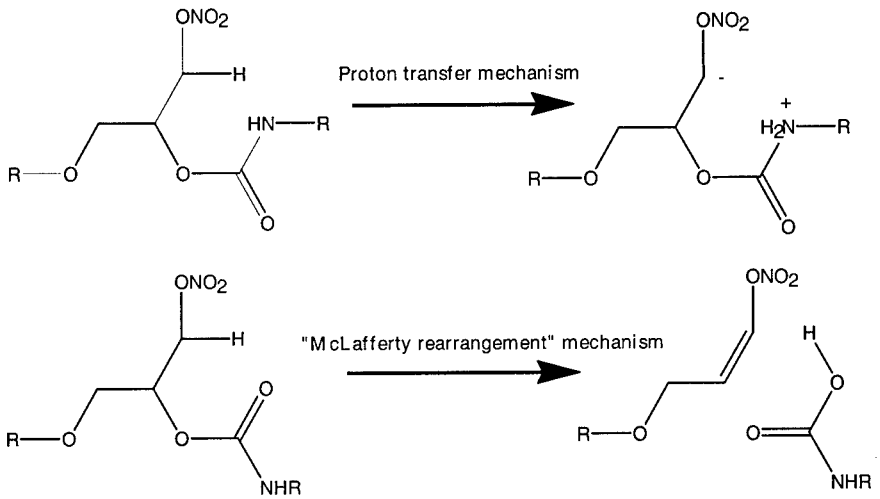


Figure 6: Potential mechanisms for the urethane decure of PGN

Synthesis of DGTN

Diglycerol tetranitrate (DGTN) is a high energy nitrate ester plasticizer that can be made from readily available starting materials. It is approximately iso-energetic with the commonly used plasticizer 1,2,4-butanetriol trinitrate (BTTN). It was produced and used in the UK prior to WWII in admixture with nitroglycerine to make low-freezing dynamites. It has also been made in the US, but again its production ceased by 1940[8]. There has been little published literature refering to DGTN in the last 50 years.

One of the reasons that stop the synthesis of DGTN was the somewhat difficult nitration of diglycerol (DG). Diglycerol is extremely viscous, and it was found that it had to be warmed in order to flow into conventional nitrate ester nitration reactors. The nitration with mixed acid was conducted in the same way as NG but having got the warmed DG into the reactor the reaction has to be cooled aggressively in order to prevent fume-off. In addition, after completion of the nitration, it was found that DGTN tended to form emulsions with the spent acid that were slow to break. Long contact with the spent acid, as with DEGDN and TEGDN nitration, readily lead to violent fume-offs, and even when the emulsion was made to break, it was difficult to isolate the pure product and the yield tended to be low (ca. 80% at best) due to some material being oxidized and some remaining in the spent acid.

There are however several reasons for reinvestigating DGTN. The first is cost. BTTN is significantly more expensive due in large part to the cost of the starting butanetriol. In contrast, diglycerol is a much lower cost starting material. The second reason is that DGTN is reported as having no freezing point, in contrast to the other high energy plasticizers, BTTN and TMETN. It also has a very low vapor pressure.

In order to investigate DGTN, we developed a modification to the synthesis of DGTN that gives an almost quantitative yield of DGTN from the nitration of DG in the presence of an organic solvent. The new synthesis procedure solves the safety problems

reported in the literature in the nitration of DG, a further benefit being that the yield is increased from the literature value of ca.80% to ca.100%.

DG is not at all miscible with solvents commonly used to dilute nitrations, such as methylene chloride. However, we found that we could stir the mixed acid for the nitration with an inert organic solvent and add the neat DG to this two phase mixture. The DG goes into and reacts with the acid phase. However the product being soluble in the organic solvent does not have a long time dissolved in the nitrating acid before it is extracted out into the organic phase of the reaction even if the DG addition is relatively slow. On completion of the nitration the organic phase rapidly forms a separate layer from the acid in which all of the DGTN is dissolved.

Characterization of DGTN

Surprisingly, considering the molecule nominally contains two secondary nitrate esters, DGTN has been demonstrated to have significantly better safety handling properties than comparable energetic plasticizers (e.g. BTTN).

Compatibility studies have been conducted and new minimum-smoke propellant formulations have been made with DGTN that show improved processing safety, propellant safety and mechanical property characteristics (especially at low temperatures) over iso-energetic compositions made with traditional plasticizers. Table 1 shows the small scale safety test results and tensile properties at low temperature of a DGTN formulation and a comparable BTTN formulation. The DGTN formulation has better strain and much better stress properties.

TABLE 1. Properties of Isoenergetic Minimum Smoke Formulations Changing BTTN for DGTN*

	Safety properties				Tensile properties @ -45F 2.0 ipm					
	TC impact (in)	ABL friction (lbs)	TC ESD (J)	SBAT onset (F)	E(2.7) (psi)	ε_{mt} (%)	ε_{ft} (%)	σ_m (psi)	σ_{mtc} (psi)	Shore A (ambient)
BTTN propellant	15.0	800 @ 8ft/s	>8	257	1032	455	456	274	1519	12
DGTN propellant	13.9	800 @ 8ft/s	>8	246	6379	508	510	516	2835	7

*TC impact values were obtained on a Thiokol-built impact test machine and are 50% values. ABL friction values are threshold numbers for 20 no fires. The TC ESD test was performed on a Thiokol designed instrument. Simulated Bulk Autoignition Test (SBAT) onsets were recorded for 1-gram samples heated at 24°F/hr.

The primary reason for the excellent low temperature behavior of DGTN formulations is that the pure material has no detectable freezing point. This seems to be because DGTN is not a single chemical substance. The standard way of making DG is by heating glycerin in the presence of a base (figure 4). The product is thus a mixture of the three structural isomers.

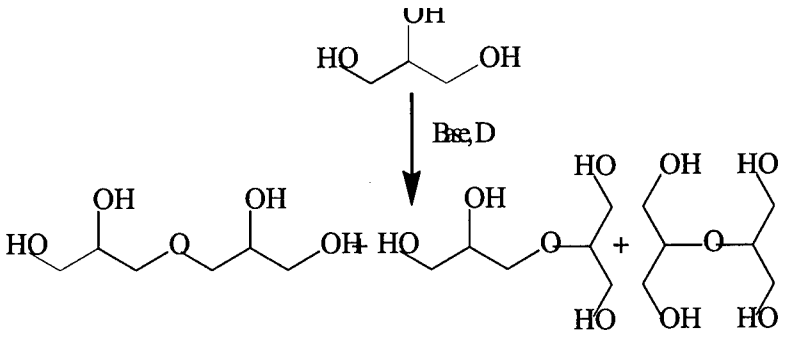


Figure 4. Synthesis of Diglycerol

Alternatively, glycerin can be heated with a substituted or otherwise activated glycerine derivative to improve reaction rate and yield. Obviously if the substitution is in the 1 position only the end to center and end to end isomers will be made. Alternatively, the 2 position can be activated and then only or primarily the end to centre and centre to centre isomers will predominate. These isomer mixtures are carried through in the nitration and thus DGTN from commercial DG is a mixture of three distinct structural isomers. The DGTN that we have made from DG containing all three isomers has been characterized by all the standard analytical techniques. In the ^{1}H nmr all of the peaks from all of the isomers are multiplets and in the same region, and thus it is not a useful technique for characterization of the product mixture.. However, ^{13}C nmr separates all of the different carbons. Careful quantitative ^{13}C nmr (figure 5) allows most of the peaks to be assigned as the relative isomer ratios can be assumed from the synthesis of the DG. In addition, the three isomers can be separated by HPLC (figure 6).

Conclusions

Both DGTN and PGN have been prepared at the kilo scale from readily available low cost starting materials and reagents. Initial formulation efforts have shown that they have significant advantages over currently used binder ingredients in terms of energy density, processability and sensitivity. We are continuing the scale-up, characterization and formulation work on both these promising materials in order to develop the next generation of high performance reduced sensitivity propellants and explosives.

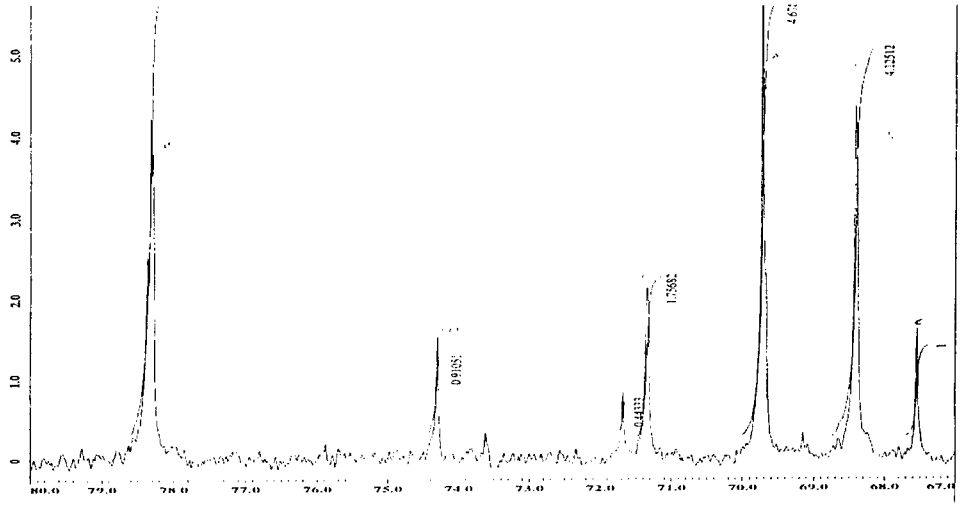


Figure 5. ^{13}C nmr of the Three DGTN Isomers

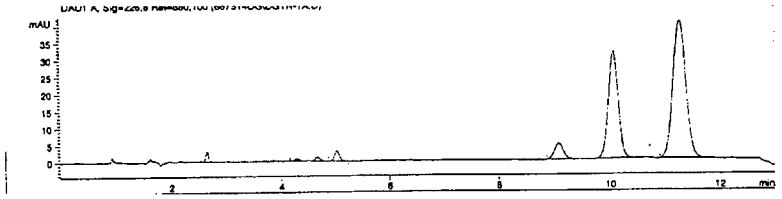


Figure 6. HPLC of the Three DGTN Isomers (Reverse Phase 50:50 Acetonitrile:Water)

References

[1] A. J. Sanderson et al, paper 36, Proceedings of the 31st International Conference of ICT, Fraunhofer ICT, 2000.
2. A. J. Sanderson et al, paper 36, Proceedings of the 31st International Conference of ICT, Fraunhofer ICT, 2000.
3 . W. J. Murback, W.R. Fish, R. W. Van Dolah, "Polyglycidyl Nitrate: Part 2, Preparation and Characterization of Polyglycidyl Nitrate," NAVORD Report 2028, Part 2 (NOTS 686), May 7, 1953.
[4] R. B. Wardle, U. S. Patent 4,806,613, Feb 1989.
5. W. B. H. Leeming et al, paper 99, Proceedings of the 27th International Conference of ICT, Fraunhofer ICT, 1996.
[6] N. C.Paul, M. E. Colclough, N. Chauhan, A. V. Cunliffe and W. B. H Leeming, Proceedings of the ADPA IM Technology Symposium, San Diego, 1996.
[7] Can. J. Chem., 56, 2582, 1978.
8. a) T. Urbanski "Chemistry and Technology of Explosives", vol. 4, Pergamon Press, 1964. b) Ph. Naom, "Nitroglycerin u. Nitroglycerinspregstoffe", Springer, Berlin 1924.

Development of an Alternate Process for the Synthesis of CL-20*

Louis Cannizzo, Scott Hamilton, Andrew Sanderson, Robert Wardle, Scott White
Thiokol Propulsion
P.O. Box 707, M/S 244
Brigham City, Utah, U.S.A.

Abstract

Development of novel ingredients has been demonstrated to be a lengthy and costly process. An entire spectrum of pitfalls threaten the steady progress of a material. To date, two general routes to the synthesis of CL-20 have been explored. One by Thiokol and another by essentially all other investigators. Each route has shown advantages and disadvantages. In this paper, a third route which has distinct differences from the previous routes will be described. This route still uses as a fundamental starting material the hexabenzyl compound, discovered by Nielson, and a hydrogenolysis. The by-products from this process differ somewhat from the two previous and will be described. A cooperative effort between Thiokol Propulsion and Asahi Chemical has led to significant scale-up and will be reported. It is interesting to note that a complete description of all the various isowurtzitane-derived species was achieved with a single analytical technique although some isomeric questions remain.

As a second aspect of the paper, we will report on the application of much vaunted model based control systems to the study of the nitration of this intermediate for the synthesis of CL-20.[1] To be able to use a model based control system, a detailed and highly accurate database of the process must be available. This study was designed to provide such an accurate model for a future model based control system. The responses of yield, purity, and kind of impurities to a range of reaction conditions were determined. The specific functions led to prediction of the best reaction conditions to ensure optimal reaction output. They also suggest remedies to in-process reaction upsets to minimize the likelihood of off-spec product being manufactured. The data from this study will be reported.

* © 2001, Thiokol Propulsion, a division of Cordant Technologies.
Grateful acknowledgment is made of financial support of this work by the U.S. Army Research, Development and Engineering Center at Picatinny Arsenal (see further acknowledgement in endnote 1).

Introduction

Since the initial discovery of CL-20 by Nielsen and co-workers[2] two general routes to the synthesis of CL-20 have been explored. Both start with the precursor hexabenzylhexaazaisowurtzitane (HBIW) which is synthesized by the acid catalyzed condensation of glyoxal with benzylamine. In the first method (Figure 1), HBIW is submitted to hydrogenolysis/acetylation to yield tetraacetyldibenzylhexaazaisowurtzitane (TADB). This intermediate is allowed to react with a nitrosation agent such as nitrogen tetroxide, giving tetraacetyldinitrosohexaazaisowurtzitane (TADN), which upon nitration is converted into the final product. The scale up of this route has proven problematic, specifically in the nitrosation step. However, very high purities of CL-20 have been reported.[3] In the second process (Figure 2), HBIW is again converted into TADB. A second hydrogenolysis reaction in the presence of formic acid yields tetraacetyldiformylhexaazaisowurtzitane (TADF) which is directly nitrated to produce CL-20. This method has been scaled to multi-hundred pound batches of CL-20 at Thiokol and has given over 10,000 pounds of product to date. Purities of 97-98% have routinely been obtained with the monoformyl analog of CL-20 as the main impurity.

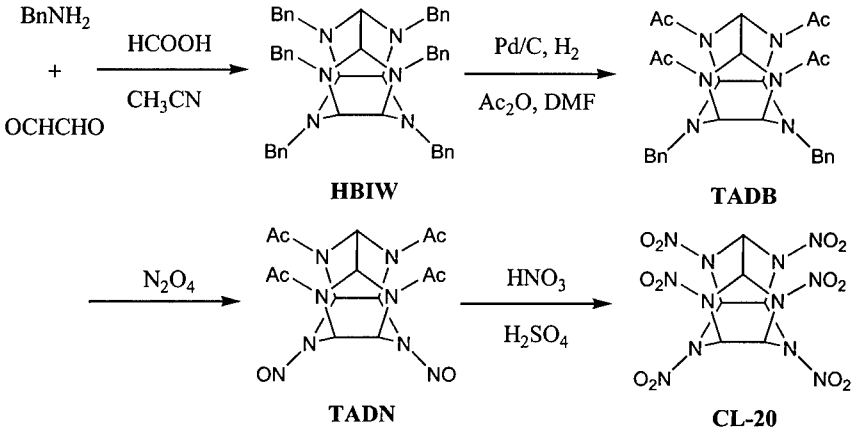
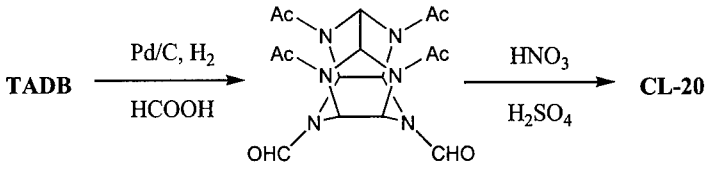


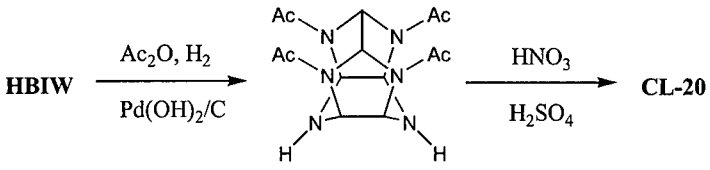
Figure 1. Four Step Synthesis of CL-20 Involving Intermediate Hydrogenolysis and Nitrosation Steps



TADF

Figure 2. Last Two Steps of the Four Step Synthesis of CL-20 Involving Two Intermediate Hydrogenolysis Steps (see Figure 1 for synthesis of TADB)

A third method of CL-20 synthesis has recently emerged (Figure 3).[4] In contrast to the first two methods, a modified hydrogenolysis/acetylation procedure developed by Asahi Chemical[5] directly gives in high yields (as a high purity material) the nitrolyzable precursor tetraacetyldiaminehexaazaisowurtzitane (TADA). The reduction of the number of synthetic steps from four to three is an obvious improvement of this last method over the first two. Furthers details on the continuing development and scale up of this last method are given in the following sections.



TADA

Figure 3. Last Two Steps of the Three Step Synthesis of CL-20 Involving One Intermediate Hydrogenolysis Step (see Figure 1 for synthesis of HBIW)

Results

Laboratory Scale Nitrations

Results from an initial set of sixteen of laboratory scale mixed acid nitrations of TADA at Thiokol were reported recently.[6] The critical parameters studied were concentration of sulfuric acid in nitric acid for the mixed acids (-10%, baseline, +10%,

+20%), loading of TADA in mixed acids (nominal, -25% acids), and amount of moisture in the acids (nominal, +4%). Changes in the yield and purity of CL-20 were correlated to the different conditions listed above. Purity analysis by high performance liquid chromatography (HPLC) also permitted the matching of impurity type and amounts to reaction conditions (see later section on HPLC analysis). A number of important observations were made:

1) The concentration of sulfuric acid was inversely proportional to the yield of CL-20, potentially due to decomposition of the starting material and/or product during the nitration process. The yields ranged from 86% to 94%. In general, intermediate concentrations of sulfuric acid gave the highest purities of CL-20. At the lowest and highest concentrations, the purity could be adversely impacted by the loading of TADA and/or the moisture level. Purities varied from 96.6% to 99.3%.
2) The loading of TADA was directly proportional to the yield of CL-20 in seven of eight parallel experiments. Also in parallel experiments, the higher loading of TADA always gave increased purities of CL-20 at the lower level of moisture and decreased purities at the higher level of moisture.
3) The amount of moisture present in the acids was directly proportional to the yield of CL-20 in six of eight parallel experiments. It can be postulated that water was able to mitigate the adverse effect of sulfuric acid concentration on yield since the six experiments with the observed correlation were all at higher sulfuric acid concentrations. Moisture level was inversely proportional to purity at the higher loading of TADA. At the lower loading, the correlation was much more complex. The two lower concentrations of sulfuric acid gave a direct correspondence of moisture to purity while at the two higher concentrations an inverse relationship was noted.

These observations prompted the initial selection of the third and fourth lowest sulfuric acid concentrations, higher TADA loading, and lower moisture level as the optimum values for each parameter that gave the best combination of yield and purity. Specifically, these conditions gave 93-94% yields of CL-20 with purities of 99.3-99.4%.

Two additional small sets of experiments were performed to maximize the loading of TADA (with the goal of increasing reactor capacity) and to minimize the reaction period (leading to a shorter overall process time). It was observed that at a slightly higher loading (-38% acids) very similar yields and purities were obtained. Still higher loadings (-50% acids) gave similar yields, but significant drops in purity. The process time could also be reduced to half of that employed in the original matrix. However, under these conditions, the lowest concentration of sulfuric acid (-10%) gave unacceptable drops in purity unless the moisture level was kept to a minimum.

Pilot Scale Nitrations

The information obtained during laboratory work was utilized to design a matrix of experiments to measure process robustness at the 20 gallon reactor scale. The key product property evaluated was purity. The required minimum value was 99%, giving a safe margin over the minimum STANAG value of 98%.[7] These experiments would also confirm that the effects of process parameters observed in the laboratory experiments will transition to larger scales. Process parameters varied included those from before (sulfuric acid concentration, TADA loading, moisture in acids) with the added value of process time. The matrix and purity results are presented in Table 1. Based upon the previous experiments, it was predicted to obtain the lowest purity using the simultaneous conditions of higher TADA loading, lower sulfuric acid concentration, higher moisture level, and shorter process time (run #5) and the highest purity with nominal conditions and minimum moisture (run #9). Gratifyingly, the results agreed with prediction. As expected, in the other experiments the process variations counterbalanced each other to give intermediate purities. In addition, the magnitude of these different effects were apparent. For example, in run #3 the adverse effects of increased moisture and shorter process time were effectively mitigated by the increased sulfuric acid content.

Table 1. Twenty Gallon Reactor Nitration Matrix*

RUN #	TADA LOADING	SULFURIC ACID CONCENTRATION	MOISTURE	PROCESS TIME	PERCENT PURITY
1	Nominal	-10%	+2%	+50%	98.94
2	Nominal	-10%	minimum	-50%	99.19
3	Nominal	+10%	+2%	-50%	99.42
4	Nominal	+10%	minimum	+50%	99.40
5	+5%	-10%	+2%	-50%	95.88
6	+5%	-10%	minimum	+50%	98.70
7	+5%	+10%	+2%	+50%	98.92
8	+5%	+10%	minimum	-50%	98.93
9	Nominal	nominal	minimum	Nominal	99.51

*The nominal TADA loading corresponds to the slightly higher loading (-38% acids) listed in the previous section. The nominal process time was reduced in half from the time used in the laboratory scale nitrations.

More importantly, the optimal conditions appear robust enough to allow for the expected minor process variations in the moisture level present in the mixed acids, sulfuric acid concentration and time/temperature profile while still reliably achieving the targeted purity. Near term plans are to scale the process up to a 500 gallon reactor scale and again verify acceptable purity within expected process limits.

HPLC Analysis

During the laboratory and pilot plant nitration studies, HPLC analysis was employed to determine the relative purity of the CL-20 samples obtained. The five impurities identified were:

1) 2,6,8,12-tetraoxa-4,10-dinitro-2,4,6,8,10,12-hexaazaisowurtzitane (tetraoxa)
2) 2,6-diacetyl-4,8,10,12-tetranitro-2,4,6,8,10,12-hexaazaisowurtzitane (diacetyl)
3) 2,12-dioxa-4,6,8,10-tetranitro-2,4,6,8,10,12-hexaazaisowurtzitane (dioxa)
4) 2-acetyl-4,6,8,10,12-pentanitro-2,4,6,8,10,12-hexaazaisowurtzitane (monoacetyl)
5) 2-oxa-4,6,8,10,12-pentanitro-2,4,6,8,10,12-hexaazaisowurtzitane (monooxa).

The chemical structures for these compounds are presented in Figure 4. Correction factors were applied to the peak integrations of each impurity as specified in Edition 1, 7th draft of STANAG 4566. Figure 5 illustrates the peak separation that was obtained. The peak assignments were confirmed by HPLC/mass spectrum analysis and high field (400 MHz) proton NMR of selected CL-20 samples. In the HPLC traces the peaks elute in the following order: tetraoxa (2.48 min), diacetyl (3 min), dioxa (4.6 min), monoacetyl

(5.25 min), monooxa (6.8 min), and CL-20 (9 min).

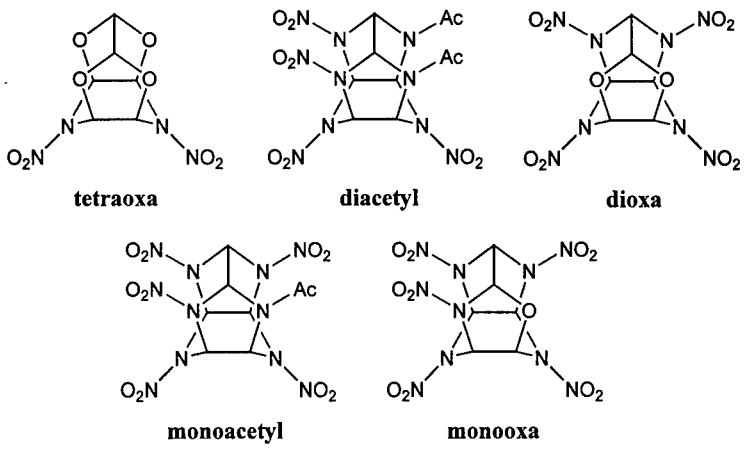


Figure 4. Impurities Formed During the Mixed Acid Nitration of TADA

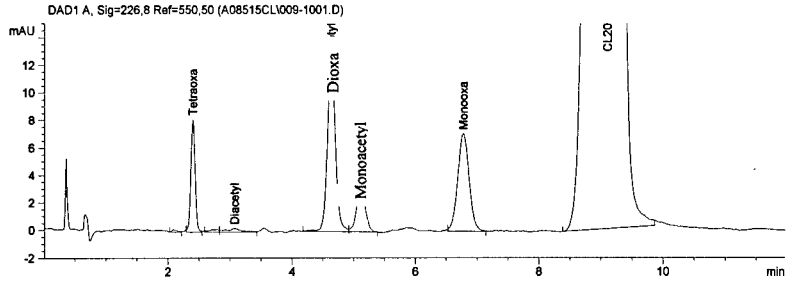


Figure 5. HPLC Chromatogram of CL-20 Produced From TADA

With identification and quantification of the impurities established, the previously mentioned process parameters could be correlated to impurity type and amount. The data for three representative samples from the laboratory nitrations is shown in Table 2. In experiment #1 it was observed that a significantly higher concentration of sulfuric acid gave higher amounts of oxa-based impurities compared to experiments with lower

concentrations. This agrees with the earlier postulate that higher concentrations of sulfuric acid will lead to decomposition of the starting material and/or product under the reaction conditions as evidenced by lower yields of CL-20 and increased amounts of oxa impurities. In experiment #2 a minimal amount of sulfuric acid gave very low levels of oxa-based impurities, but much larger quantities of acetyl-based compounds. The presence of these under nitrated impurities can be attributed to a less effective nitration, a common observation made when employing lower concentrations of sulfuric acid in mixed acids. In regards to the future CL-20 manufacturing process at Thiokol using TADA as a starting material, changes in the types and quantities of impurities will now give clear evidence to any process drift.

Table 2. Correlation of Process Parameters to Types and Quantities of Impurities*

Exper-ment	Sulfuric acid conc.	TADA loading	Moisture level	Wt% tetraoxa	Wt% diacetyl	Wt% dioxa	Wt% mono-acetyl	Wt% mono-oxa	Wt% CL-20
1	+20%	Nominal	Nominal	0.95	0.02	0.36	0.21	0.38	98.1
2	-10%	-25% acids	+ 4%	0.00	0.41	0.08	2.89	0.06	96.6
3	Nominal	-25% acids	Nominal	0.00	0.03	0.24	0.34	0.14	99.3

* Nominal conditions are those employed in laboratory scale nitrations.

Conclusions

A third route utilizing TADA as the precursor for CL-20 synthesis has been optimized in laboratory studies and scaled to the 20 gallon reactor. This methods appears to be very attractive with purities of >99% and yields of > 92% routinely achieved. In addition, the process can tolerate the variability normally encountered in production mixed acid nitrations (sulfuric acid concentration, TADA loading in mixed acids, moisture content of mixed acids, time/temperature profile). Finally, an excellent understanding of the cause and effect between nitration conditions and impurities produced has been achieved and will prove invaluable in monitoring and optimizing the future production of CL-20.

[1] A coordinated team effort led by ARDEC is pursuing utilization of a model-based control system for CL-20 production. The team includes ARDEC, Geocenters, Stevens Institute of Technology and Thiokol. Related programs include the TIME effort. General direction on the effort is provided by Tom McWilliams whose specific leadership is acknowledged. Specific assistance of Mark Mezger and Steve Nicolich is particularly noted.

[2] Nielsen, A. T.; Chafin, A. P.; Christian, S. L.; Moore, D. W.; Nadler, M. P.; Nissan, R. A.; Vanderah, D. J. "Synthesis of Polyazapolycyclic Caged Polynitramines," *Tetrahedron* **1998**, *54*, 11793-11812.

[3] Jacob, G.; Lacroix, G.; Destombes, V.; Cagnon, G.; Dumas, S. "Chemical and Polymorphic Characterization of CL-20," 2000 Insensitive Munitions and Energetic Materials Technology Symposium, November 27-30, 2000.

[4] (a) Hamilton, R. S.; Sanderson, A. J.; Wardle, R. B.; Warner, K. F. "Studies of the Synthesis and Crystallization of CL-20," 31st International Annual Conference of the ICT, June 27-30, 2000 (b) Kodama, et. al. EP 0753519, January 15, 1997.

[5] Kodama et. al. U.S. Patent 6,153,749, November 28, 2000.

[6] R. Wardle, S. Hamilton, L. Cannizzo, A. Sanderson, S. White "Scale-up of Energetic Materials Using Principles of Model-Based Control," 2000 Insensitive Munitions and Energetic Materials Technology Symposium, November 27-30, 2000.

[7] STANAG 4566, Edition 1, Draft 7.

COOK-OFF RESEARCH AT THE TNO PRINS MAURITS LABORATORY, PART II

Gert Scholtes, Richard Bouma, John Makkus, Marco Boers and Albert van der Steen
TNO Prins Maurits Laboratory
P.O. Box 45, 2280 AA Rijswijk
The Netherlands

ABSTRACT

At the TNO Prins Maurits Laboratory, considerable effort has been put into the research of energetic materials and their responses to a thermal stimulus (Cook-off). In 1998, the first overview on the cook-off research at TNO-PML was presented. Part II is presented in this paper. The cook-off research at TNO-PML is heading in several directions. Instrumented tests have been performed with several explosives to explore the mechanisms controlling the cook-off response. Temperature, pressure are measured as a function of time for the entire duration of the experiment, while the strain (optically and electrically) and pressure are measured at the end phase of the cook-off process. In addition computer models are under development to simulate the cook-off process. To know the chemical kinetics/crystal phase changes more precisely, fitting models in combination with experiments have been developed and performed. Also, several thermal and mechanical parameters of the energetic materials have been measured as a function of temperature up to the decomposition temperatures. The results of this research over the last several years will be presented.

EXPLO5 – COMPUTER PROGRAM FOR CALCULATION OF DETONATION PARAMETERS

Muhamed Sućeska

Brodarski institut – Marine Research & Special Technologies, Av. V. Holjevca 20, 10000 Zagreb, Croatia, E-mail: suceska@brod.hrbi.hr

Abstract

The computer program for the calculation of detonation parameters of an explosive, named EXPLO5, is based on the chemical equilibrium, steady-state model of detonation. The program uses Becker-Kistiakowsky-Wilson's (BKW) equation of state for gaseous detonation products and Cowan-Fickett's equation of state for solid carbon. The calculation of equilibrium composition of detonation products is done in the program by applying modified White, Johnson, and Dantzig's free energy minimisation technique.

The program is designed so that it enables the calculation of detonation parameters at the CJ point, as well as parameters of state along the expansion isentrope. Up to now the program has been tested on a series of explosives by the comparison of the experimental and calculated values of detonation velocity, pressure, temperature, heat, energy, and composition of detonation products. Generally, a satisfactory agreement was obtained for the detonation velocity and pressure, while the accuracy of calculation of the detonation heat and temperature is considerably affected by values of empirical constants in the BKW equation of state.

The analysis of applicability of different sets of constants in the BKW equation of state showed that the best overall agreement between the calculated and experimental values of detonation parameters obtains when the following set of constants, named BKWN set, was used: $\alpha = 0.5$, $\beta = 0.176$, $\kappa = 14.71$, and $\theta = 6620$.

1. Introduction

EXPLO5 is computer program for the calculation of detonation parameters of an explosive that is based on the chemical equilibrium, steady-state model of detonation [1]. The program uses the Becker-Kistiakowsky-Wilson (BKW) equation of state based upon a repulsive potential applied to the virial equation of state, to express the state of gaseous detonation products. The BKW equation of state in the following form is used [2]:

$$\frac{pV}{RT} = 1 + xe^{\beta x} \tag{1}$$

where: $x = \dfrac{\kappa \sum X_i k_i}{\left[V(T+\theta)\right]^{\alpha}}$

X_i – mol fraction of i-th gaseous product

k_i – molar covolumes of i-th gaseous product

α, β, κ, and θ – empirical constants

The state of solid carbon is described by the Cowan and Fickett's equation of state in the form [3]:

$$p = p_1(V) + a(V)T + b(V)T \tag{2}$$

The polynomial constants according to Cowan and Fickett [3,2] are used for the calculation of $p_1(V)$, $a(V)$ and $b(V)$.

The free energy minimisation technique, developed by White, Johnson and Dantzig [4], and modified by Mader [2], is applied for the mathematical expression of the equilibrium state of detonation products. The system of equations, formed according to this technique, is solved applying modified Newton's method of the following approximations [5].

The program EXPLO5 calculates the parameters of state of the products along the shock adiabate, starting from a density of a given explosive (ρ_0) and then increasing

it in an arbitrary chosen step up to the density of about $1.5 \cdot \rho_0$. Then, it determines the CJ point as a point on the shock adiabate at which the detonation velocity has minimum value. Ones the CJ point was determined the detonation parameters have been calculated applying the well-known relationships between them [1,2].

The program EXPLO5 also calculates the parameters of state along the expansion isentrope, starting from the CJ point and then increasing specific volume by a selected step up to some desired value (usually 15 times greater than the volume at the CJ point) [6].

Up to now the program was tested on a series of explosives having different composition and different densities [1,6,7]. Generally, it was found out that a satisfactory agreement exists between the calculated and experimental values of the detonation velocity and pressure. However, it is found that the calculated values of the detonation heat and temperature are strongly affected by the values of constants used in the BKW equation of state [8].

Typically, the constants α, β, κ, and θ in the BKW equation of state are adjusted to fit measured detonation properties. Cowan and Fickett showed that, for a given α and β, one may adjust κ to give experimental detonation velocity for a single explosive at a single density. The slope of $D = f(\rho_0)$ curve may be changed by changing β. With successive iteration on β and κ one can reproduce the experimental detonation velocity at two different densities for a single explosive [2].

In the computer program named Fortran BKW, C. Mader used two sets of the constants: the RDX set for most explosives, and the TNT set for explosives having large amount of solid carbon in detonation products, Table 1 [2].

Finger et al. attempted to determine the constants using measured detonation properties and calorimety data. The resulting data fit is the basis for the BKWR set of constants (Table 1).

M. Hobbs and M. Bear have recalibrated the constants in the BKW equation of state by comparing measured and calculated values of the detonation velocity, pressure, and temperature for 62 explosives. The set of constants they obtain in this way was assigned as the BKWS set (Table 1) [9].

I the previous paper [8] I have tried to recalibrate the BKWS set of constants taking into account an overall agreement, i.e. agreement between the calculated and

experimental values of the detonation velocity, pressure, temperature, heat, and composition of detonation products. In this work the values of α and θ are taken to be according to the BKWS set since they give the best agreement for the detonation temperature. The value of β is taken to be according the BKWR set since it gives the most acceptable slope of the detonation velocity-density curve. The value of κ is then allowed to vary until the best overall agreement is obtained. The result of such recalibration was the set of constants named BKWN set (Table 1).

Table 1. Values of constants in BKW equation of state and covolumes of gaseous detonation products

Set of constants	β	κ	α	θ
RDX	0.160	10.91	0.50	400
TNT	0.096	12.68	0.50	400
BKWR	0.176	11.80	0.50	1850
BKWS	0.298	10.50	0.50	6620
BKWN	0.176	14.71	0.50	6620

The applicability of EXPLO5 for the calculation of the detonation parameters, and the influence of the constants in the BKW equation of state on the calculated values of the detonation parameters is discussed in this paper.

2. Results and discussion

Several high explosives, for which experimental data for detonation parameters have been reported in literature, were chosen for the study in this paper. The detonation parameters are calculated for these explosives applying different sets of the constants: the RDX/TNT, BKWR, and BKWN set. The results of calculation are given in Table 2, along with the results obtained experimentally.

Table 2. Comparison of calculated and experimental values of some detonation parameters

Explosive	Density (g/cm^3)	Set of const.	D (mm/μs)	p (GPa)	T (K)	Q_{CJ} (kJ/kg)	Q_{1800} (kJ/kg)
HMX	1.89	**Experim.**	**9.11**	**39.0**	–	–	**5719**
		RDX	9.11	38.9	2359	6263	6245
		BKWR	9.10	38.4	2338	6214	6081
		BKWN	9.21	37.8	4286	6030	5818
	1.60	**Experim.**	**7.91**	**28.0**	**4300**	–	–
		RDX	7.98	26.3	2930	6218	6058
		BKWR	8.07	26.7	3611	6082	5816
		BKWN	8.22	26.7	4357	5809	5533
	1.20	**Experim.**	**6.58**	**16.0**	–	–	**5116**
		RDX	6.64	14.8	3416	5898	5548
		BKWR	6.96	15.4	3553	5199	5272
		BKWN	7.01	15.1	4264	5194	5284
HNS	1.655	**Experim.**	**7.03**	**21.5**	–	–	**4432**
		TNT	6.87	20.6	3237	5665	5303
		BKWR	7.17	21.4	3573	5526	5044
		BKWN	7.23	21.2	4079	5239	4794
	1.00	**Experim.**	**5.10**	**7.3**	–	–	**4550**
		TNT	5.18	7.9	3455	4924	4468
		BKWR	5.27	7.8	3607	4630	4230
		BKWN	5.33	7.8	3885	4341	4070
PETN	1.763	**Experim.**	**8.27**	**31.5**	–	–	**5739**
		RDX	8.65	32.7	2353	5900	5912
		BKWR	8.63	32.2	3355	5898	5919
		BKWN	8.66	31.1	4349	5889	5932
	1.60	**Experim.**	**7.75**	**26.6**	**4400**	–	–
		RDX	7.99	26.2	2701	5899	5915
		BKWR	8.02	25.8	3543	5898	5925
		BKWN	8.05	25.2	4425	5883	5935
	1.503	**Experim.**	**7.48**	**24.0**	–	–	**5824**
		RDX	7.63	22.8	2895	5899	5919
		BKWR	7.67	22.6	3653	5897	5929
		BKWN	7.69	22.1	4468	5876	5937
	1.263	**Experim.**	**6.59**	**16.0**	–	–	**5817**
		RDX	6.76	15.8	3339	5899	5934
		BKWR	6.81	15.7	3911	5893	5938
		BKWN	6.83	15.3	4553	5850	5944
NM	1.13	**Experim.**	**6.28**	**12.0**	**3430**	–	**4482**
		RDX	6.34	12.2	2901	5594	5306
		BKWR	6.37	12.4	3253	5421	5073
		BKWN	6.40	12.0	3583	5137	4650

TNT	1.64	**Experim.**	**6.95**	**21.0**	–	–	–
		TNT	6.94	20.5	2925	5435	5203
		BKWR	7.19	20.8	3275	5325	4950
		BKWN	7.15	20.2	3744	5087	4710
	1.632	**Experim.**	**7.07**	**20.5**	–	–	**4270**
		TNT	6.92	20.4	2937	5431	5197
		BKWR	7.16	20.7	3284	5320	4943
		BKWN	7.13	19.5	3718	5074	4670
	1.533	**Experim.**	**6.81**	**17.1**	–	–	**4382**
		TNT	6.62	17.7	3011	5391	5097
		BKWR	6.83	17.9	3322	5247	4830
		BKWN	6.81	17.1	3719	4982	4538
	1.00	***Experim.***	***5.00***	***6.7***	***3400***	–	–
		TNT	5.13	7.7	3209	4878	4455
		BKWR	5.20	7.2	3317	4596	4180
		BKWN	5.22	7.2	3550	4322	3998
RDX	1.80	**Experim.**	**8.75**	**34.7**	–	–	**5610**
		RDX	8.75	34.6	2585	6320	6265
		BKWR	8.79	34.6	3463	6246	6069
		BKWN	8.92	34.5	4354	6033	5810
	1.66	**Experim.**	**8.24**	**29.3**	**4320**	–	–
		RDX	8.21	28.7	2857	6297	6169
		BKWR	8.29	28.8	3585	6177	5940
		BKWN	8.44	28.8	4376	5922	5655
	1.20	**Experim.**	**6.77**	**15.2**	**4610**	–	–
		RDX	6.66	14.7	3441	5949	5596
		BKWR	6.79	15.2	3858	5726	5360
		BKWN	7.04	15.3	4314	5256	5346
	1.00	**Experim.**	**6.10**	–	**4600**	–	–
		RDX	6.07	10.7	3576	5654	5356
		BKWR	6.21	11.0	3910	5425	5363
		BKWN	6.31	10.7	4389	5255	5252
NGl	1.60	**Experim.**	**7.70**	**25.3**	**4260**	–	–
		RDX	7.71	24.8	3113	6295	6312
		BKWR	7.76	24.6	3841	6244	6312
		BKWN	7.77	23.8	4596	6073	6312

Notes: - Values of detonation temperature are according to Y. Kato (Ref. 1)
- Values of detonation heat are recalculated values from D. Ornellas (Ref. 12) and I. Akst (Ref. 12), taking water to be gaseous.
- Values of detonation velocity and pressure are according to M. Hobbs abd M. Bear (Ref. 9)

Two values of the detonation heat are given in Table 2. The value assigned as Q_{CJ} is the detonation heat at the CJ point, while the value assigned as Q_{1800} is the heat that corresponds to the state on the expansion isentrope at temperature 1800 K. This temperature is usually taken as the temperature at which all chemical reactions in the detonation products stop and composition of the detonation products freezes (freeze point) [10]. The value of detonation heat at the freeze point is comparable with calorimetricaly determined detonation heat [7].

The results given in Table 2 are further analysed in order to judge the applicability of individual sets of constants for the calculation of detonation parameters. The results of analysis are given in the following text.

2.1. Detonation velocity and pressure

The comparison between calculated and experimental values of detonation velocity for explosives given in Table 2, is presented graphically in Fig. 1.

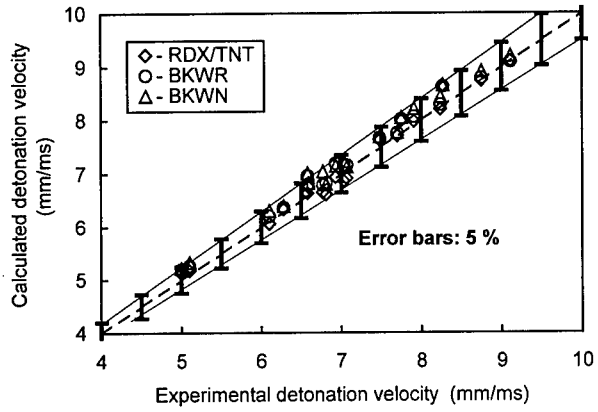


Figure 1. Comparison of experimental and calculated values of detonation velocity

It was found out by the linear regression analysis that the RDX/TNT set of constants gives the best agreement between the calculated and experimental values of detonation velocities, while the BKWN set of constants gives the worst agreement (Eq. 3):

$$\begin{aligned} &\text{RDX/TNT}: D_c = 0.0353 + D_e \quad (r = 0.9919,\ S = 0.142\ \text{mm/}\mu\text{m}) \\ &\text{BKWR} \quad : D_c = 0.1474 + D_e \quad (r = 0.9946,\ S = 0.112\ \text{mm/}\mu\text{m}) \\ &\text{BKWN} \quad : D_c = 0.2068 + D_e \quad (r = 0.9514,\ S = 0.109\ \text{mm/}\mu\text{m}) \end{aligned} \tag{3}$$

One can also note that any set of the constants gives consistently slightly greater values of detonation velocity: the RDX/TNT set for about 35 m/s, and the BKWN set for about 207 m/s. However, it should be stressed that the difference between the calculated and experimental values of detonation velocity is less than 5% in all cases (see Fig. 1).

The calculated values of detonation pressures for explosives given in Table 2 may differ up to about 12 % from those obtained experimentally (Fig. 3).

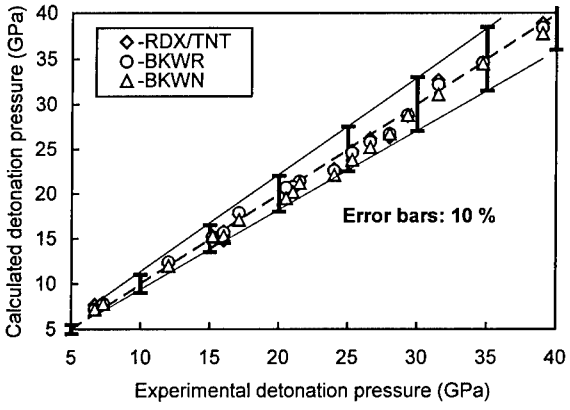


Figure 2. Comparison of experimental and calculated values of detonation pressure

From the results obtained by the linear regression analysis (Eq. 4) it follows that the BKWR set of constants gives the best agreement between the calculated and experimentally obtained detonation pressure (the mean error up to 4.5%). At the same time the BKWN set of constants gives the worst agreement (the mean error up to 12%).

$$\begin{aligned} &\text{RDX/TNT}: p_c = -0.2440 + p_e \quad (r = 0.9962,\ S = 0.7687\,\text{GPa}) \\ &\text{BKWR} \quad : p_c = -0.1944 + p_e \quad (r = 0.9972,\ S = 0.6439\,\text{GPa}) \\ &\text{BKWN} \quad : p_c = -0.6111 + p_e \quad (r = 0.9967,\ S = 0.6953\,\text{GPa}) \end{aligned} \tag{4}$$

The calculated values of detonation pressure are constantly slightly less than those obtained experimentally (from 0.19 up to 0.61 GPa) in all cases.

2.2. Detonation temperature and detonation heat

The calculated values of detonation temperature at the CJ point are compared to values determined experimentally by Y. Kato [11] for several explosives (see Table 2). The results of comparison are presented in Fig. 3, and by Eq. 5.

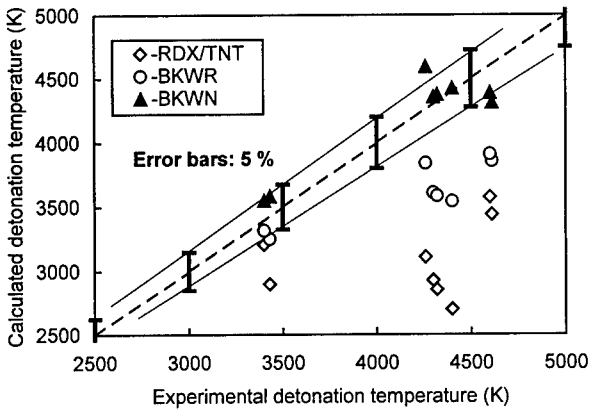


Figure 3. Comparison of experimental and calculated values of detonation temperature

$$\begin{aligned}
&\text{RDX/TNT}: T_c = -1074 + T_e \quad (r = 1.2993,\ S = 496.0\,\text{K}) \\
&\text{BKWR} \quad : T_c = -550 + T_e \quad (r = 0.6139,\ S = 288.8\,\text{K}) \\
&\text{BKWN} \quad : T_c = -33.75 + T_e \quad (r = 0.8608,\ S = 203.3\,\text{K})
\end{aligned} \tag{5}$$

It is obvious from Fig. 3, and from the results obtained by the linear regression analysis (Eq. 5) that the BKWN set of constants gives the best agreement between the calculated and experimentally obtained values of detonation temperature. It follows from Fig. 3 that values of detonation temperature calculated applying the BKWN set of constant differ less than 5% from those experimentally obtained. Values of detonation temperature calculated applying the BKWR set of constants are lower that those obtained experimentally for about 550 K (mean difference), i.e. nearly 20%. The worst agreement was obtained if the RDX/TNT set of constants is used: the calculated values of detonation temperature are lower than those obtained experimentally for about 1074 K (mean difference), i.e. nearly 40%.

The heat of detonation and composition of detonation products cannot be measured in a calorimeter. The values of the heat of detonation determined calorimetricaly by Ornellas [12] are not values at the CJ point, but values over the freeze-out region on the expansion isentrope.This experimental limitation causes difficulties in the understanding the detonation process more precisely, and consequently in judging the applicability of thermochemical computer programs calculation.

The temperature of 1800 K is usually taken as the freeze point, i.e. point on the expansion isentrope at which all chemical reactions stop and composition of detonation products freezes. EXPLO5 is designed in the way that enables to halt all chemical reactions and freeze the products composition at 1800 K (or some other selected temperature). The heat of detonation corresponding to this temperature, assigned as Q_{1800}, should be thus comparable with Ornellas' calorimetricaly determined heat of detonation. The same conclusion is valid for the composition of detonation products.

The results of comparison of calorimetricaly determined detonation heats for several explosives (see Table 2), and detonation heats at the chemical equilibrium freeze point are presented graphically in Fig. 4. By the linear regression analysis it was found out that the best agreement between these two values of detonation heats exists if the

BKWN set of constants is used:

$$\begin{aligned}
&\text{RDX/TNT}: Q_{1800} = 586.5 + Q_{\text{Ornellas}} \quad (r = 0.8100,\ S = 322.69\ \text{kJ/kg}) \\
&\text{BKWR} \quad : Q_{1800} = 398.8 + Q_{\text{Ornellas}} \quad (r = 0.9318,\ S = 226.00\ \text{kJ/kg}) \\
&\text{BKWN} \quad : Q_{1800} = 227.8 + Q_{\text{Ornellas}} \quad (r = 0.9805,\ S = 136.48\ \text{kJ/kg})
\end{aligned} \tag{6}$$

It follows from Eq. 6 that the BKWN set of constants gives the heats of detonation that differ up to 10% from the heats determined calorimetricaly. The RDX/TNT set of constants gives the largest error.

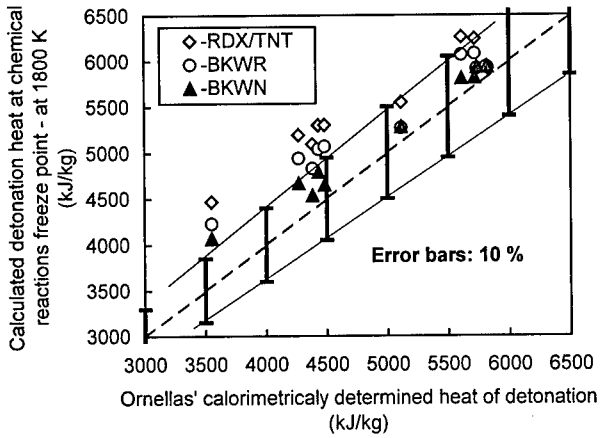


Figure 4. Comparison of experimental and calculated values of detonation heat

The comparison of calculated composition of detonation products at the freeze point at 1800 K with the composition determined by Ornellas from detonation calorimetry measurements [12], shows that the BKWN set of constants gives very acceptable agreement between them. At the same time the RDX/TNT type of constants gives the worst agreement.

Table 3. Composition of detonation products at the freeze point at 1800 K and composition determined experimentally from detonation calorimetry measurements [12]

Product	HMX, ρ_0 = 1.89 g/cm^3				PETN, ρ_0 = 1.73 g/cm^3				TNT, ρ_0 = 1.64 g/cm^3			
	Experim.	RDX	BKWR	BKWN	Experim.	RDX	BKWR	BKWN	Experim.	TNT	BKWR	BKWN
H_2O	**3.18**	3.99	3.88	3.44	**3.50**	3.92	3.84	3.73	**1.60**	2.26	1.98	1.61
H_2	**0.30**	–	0.065	0.26	**0.45**	0.023	0.14	0.26	**0.46**	0.14	0.30	0.50
CO_2	**1.92**	1.97	1.75	1.59	**3.39**	3.08	3.16	3.27	**1.25**	1.37	1.21	1.06
CO	**1.06**	0.069	0.62	1.39	**1.69**	1.92	1.83	1.73	**1.98**	0.99	1.61	2.27
NH_3	**0.39**	–	0.013	0.03	**0.038**	0.041	0.016	0.007	**0.16**	0.01	0.014	0.017
CH_4	**0.039**	–	0.019	0.13	**0.003**	–	–	–	**0.099**	0.041	0.099	0.18
N2	**3.68**	3.99	3.99	3.98	**2.00**	1.98	1.99	2.00	**1.32**	1.49	1.49	1.49
C_s	**0.98**	1.96	1.61	0.90	–	–	–	–	**3.65**	4.59	4.05	3.48

3. Conclusion

On the basis of the results presented it follows that the RDX/TNT set of constants gives the best agreement between the calculated and experimental values of detonation velocity, giving also very poor agreement for the detonation temperate and heat. The BKWR set of constants gives the best agreement for the detonation pressure but also poor agreement for the detonation temperature. An own set of constants, assigned as BKWN set (α = 0.5, β = 0.176, κ = 14.71 and θ = 6620), gives the best agreement for the detonation temperature, detonation heat, and composition of detonation products at the chemical equilibrium freeze point, but slightly less agreement for the detonation pressure and velocity. The above mentioned is summarised in Table 4.

Table 4. Error in predicting detonation properties

Set of constants	Mean absolute error (%)				Total* (%)
	D (in respect to D = 7 mm/s)	p (in respect to p = 22 GPa)	T (in respect to T = 4000 K)	Q (in respect to Q = 4500 kJ/kg)	
RDX/TNT	0.50	1.11	26.85	13.03	6.92
BKWR	2.11	0.89	13.75	8.86	4.71
BKWN	2.95	2.77	0.84	5.06	3.00

* Weighted by number of data. There are 19, 18, 8, and 11 D, p, T, and Q data

Taking into accounts all detonation parameters studied in this work the conclusion is that the BKWN set of constants gives the best overall agreement. It enables prediction of the detonation parameters with the error less than 10 %.

4. References

1. M. Sućeska, Calculation of Detonation Properties of C-H-N-O Explosives, Propellants, Explosives, Pyrotechnics 16, (1991) 197-202.
2. C. L. Mader, Numerical Modeling of Explosives and Propellants, CRC Press, Boca Raton, 1998, pp. 377-407.
3. R. D. Cowan, W. Fickett, Calculation of Detonation Properties of Solid Explosives with Kistiakowsky-Wilson Equation of State, J. Chem. Phys. 24 (1956) 932-939.
4. W. B. White, S. M. Johnosn, G. B. Dantzig, Chemical Equilibrium in Complex Mixtures, J. Chem. Phys. 28 (1958) 751-755.
5. L. A. Suris, Termodinamika visokotemperaturnih procesov, Moscow, Metalurgija, 1970, pp. 1-15.
6. M. Sućeska, Evaluation of Detonation Energy from EXPLO5 Computer Code Results, O Explosives, Propellants, Explosives, Pyrotechnics 24, 1-6 (1999).
7. M. Sućeska, Calculation of Detonation Heat by EXPLO5 Computer Code, Proc. of the 30 International Annual Conference of ICT, June 29 – July 2, Fraunhofer Institut Chemische Technologie, Karlsruhe, 1999, pp. 50/1-50/14.
8. M. Sućeska, Which Constants to Use in Becker-Kistiakowsky-Wilson Equation of State, Proc. of 3rd Seminar "New Trends in Research of Energetic Materials", Pardubice, Czech Republic, April 11-12, 2000, pp. 205-216.
9. M. L. Hobbs, M. R. Baer, Calibration of the BKW-EOS With a Large product Species Data Base and Measured C-J Properties, Proc. of the 10th Symp. (International) on Detonation, ONR 33395-12, Boston, MA, July 12 - 16, 1993. pp. 409-418
10. P. C. Souers, J. W. Kury, Comparison of Cylinder Data and Code Calculations for Homogeneous Explosives, Propellants, Explos., Pyrotechn. 18, 175-183 (1993).
11. Y. Kato, N. Mori, H. Sakai, K. Tanaka, T. Sakurai, T. Hikita, Detonation Temperature of Nitropmetane and Some Solid High Explosives, Proc. of the 8th Symp. (International) on Detonation, NSWC-MP 86-14, Albuquerque, NM, July 15 – 19, 1985, pp. 558-566.
12. D. L. Ornellas, Calorimetric Determinations of the Heat and Products of Detonation for Explosives: October 1961 to April 1982, Report UCRL-52821, Lawrence Livermore National Laboratory, Livermore, CA, USA (1982).
13. I. B. Akst, Heat of Detonation, the Cylinder Test, and Performance in Munitions, Proc. of the 9th Symp. (International) on Detonation, OCNR 113291-7, Portland, Oregon, August 28 – September 1, 1989, pp. 478-488

Luminosity of shock waves in perfluoroalkanes, perfluoroalkylamines and perfluorotoluene. *

I. M. Voskoboinikov.

Semenov Institute of Chemical Physics, Russian Academy of Sciences,
ul. Kosygina 4, Moscow, 117977 Russia,

Luminosities of shock fronts and substances at contact boundaries of perfluorotributylamine $N(C_4F_9)_3$, perfluorotriethylamine $N(C_2F_5)_3$, perfluorodecalin $C_{10}F_{18}$, perfluorotoluene C_7F_8 and perfluored transformer oil with contents of carbon 0.25 on weight (double carbon – carbon bonds are absent in structure of molecules of components, but there are cyclic fragments) with a window material retaining transparency upon compression to desired pressures are measured. We compared the temperatures, which are consistent with these lumenosities, with temperatures, which were calculated in suggestions of the conservation and decomposition of initial compound behind front of the wave. Decomposition of perfluoroalkanes and perfluoroalkylamines behind shock front was observed at temperatures near 2000 – 2100 K. As this takes place, temperature of front are less than temperature of substance behind front.

Behind fronts of sufficiently strong shock waves all liquid and solid organic compounds undergo chemical conversions. If these reactions change the specific volume, the Hugoniots are taking some peculiarities in their behavior at wave amplitudes exceeding certain value. If the specific volume changes insignificantly in the course of reaction, it can go unheeded, when Hugoniot only is determined experimentally, as it is common for majority of published works. Additional information about conversions behind the shock front can be gained, as it takes place, from analysis of measurements of other quantities. Among these are temperatures of front and substance at their contact surface with a window material retaining transparency upon compression to desired pressures, and some other. Since

* The work was supported by the Russian Foundation for Basic Research (project 00-03-32162a)

mentioned measurements were taken least rare, data for critical wave amplitudes are often absent in respect of some groups of compounds. A similar statement is true for perfluoroalkanes and particularly perfluoroalkylamines. When wave amplitude is more critical initial, compound undergoes chemical conversions behind front.

Attention is drawn to the fact that at decomposition of liquid carbon disulphide, acetonitrile and benzene behind front of the shock wave the temperatures of the front and substance at boundary with the window material differ on 400 – 500 K under one pressure. This is accounted for by shielding, on the front side, of radiation issuing from final state of the decomposition products by layers with incomplete conversion. The existence of chemical reactions in carbon disulphide and benzene behind shock front which are accompanied by decrease in the specific volume is established unequivocally by peculiarities of the behaviour of Hugoniot as the pressure increases above 6 and 12.5 GPa, respectively.

Noted difference of temperatures of the front and substance at decomposition of initial compound has been decided to use for the determination of critical intensities of waves, at the excess which exists decomposition of liquid perfluoroalkanes and perfluoroalkylamines behind front. Perfluorotributylamine $N(C_4F_9)_3$, perfluorotriethylamine $N(C_2F_5)_3$, perfluorodecalin $C_{10}F_{18}$, perfluorotoluene C_7F_8 and perfluored transformer oil with contents of carbon 0.25 on weight (double carbon – carbon bonds are absent in structure of molecules of components, but there are cyclic fragments) are used as the basis for investigation.

From results of computations it has been expected the absence of particularities in the course of Hugoniot for listed compounds because of decompositions behind front, exception represents toluene. This has conformity with the course of Hugoniot for Teflon , polyvinylidenefluoride and telomeric alcohols [1-3]

1. Experimental.

The schematic of the experimental rig is shown in Fig. 1. A detonation wave propagating through charge *1* in direct contact with assembly of liquid layers has

been harnessed to generate shock wave. Luminosity of shock wave in its passage though assembly was recorded with photomultipliers and displayed on oscilloscopes. The time resolution of the recording system is about 50 ns. The bottom of the assembly cell *2* containing liquids was made of aluminum foil whose presence did not affect the records. Layer *3* contained compound under test and layer *5* contained liquid served as a window material have been separated with a thin polypropylene film *4* retaining its transparency behind shock front. Variations in dynamic compressibility of the liquid in layer *5* enabled us to obtain different states of the shocked material at the interface between it and the window material. These measurements could be extrapolated in terms of pressure to the state in the incident shock wave. When thickness of polypropylene film *4* was more 0.2 mm, in one experience registered luminosities associated with two states in isentropic wave across substance behind shock front.

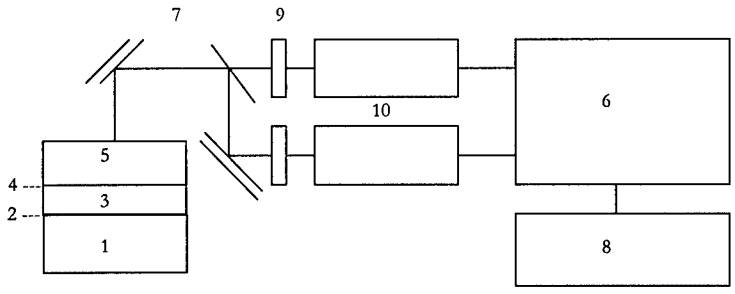


Fig. 1. Schematic of the experimental setup: (1) explosive charge, (2) bottom of assemble cell, (3) test liquid, (4) polypropylene film, (5) liquid window material, (6) recording unit, (7) mirrors, (8) synchronizing unit, (9) light filters, (10) photomultipliers.

This variant was marketed, when shock wave created by detonation of explosive charge with pressure $P_J = 36.8$ GPa and mass velocity $U_J = 2.3$ mm/mcs behind front. For shock wave in perfluorotributylamine a 20 % decrease in luminosity at contact boundary with polyethylene and a 10 % increase after reflection from glycerol are observed relative to luminosity of front. For shock wave in perfluorotriethylamine a 15 % decrease in luminosity at contact boundary

with polyethylene and a 5 % increase after reflection from glycerol takes place at wavelength 740 nm. Passage of a shock wave through the contact boundary of perfluorodecalin, perfluorotoluene and perfluored transformer oil with glycerol did not cause an observable changing its luminosity.

The situation is reversed if shock wave created by detonation of explosive charge with pressure P_J = 26.4 GPa and mass velocity U_J = 2.07 mm/mcs. Approximately 4-fold and 3-fold increases in luminosity at contact boundary of perfluorotributylamine with glycerol and with decane are observed relative to luminosity of front. At contact boundary of perfluorotoluene with decane luminosity remains essentially unchanged (at contact boundary with glycerol it must be expected increase in several times).

Thus for these liquids under smaller intensities of the shock wave and for all perfluored liquids under greater intensities of the wave luminosity on the contact border with the glycerol or increase, or nearly not changed. Hugoniots for all perfluored liquids on the diagram a pressure – a mass velocity are situated greatly above Hugoniots of glycerol, polyethylene and of course decane. Temperature of material on contact boundary which is extrapolated to pressure behind front of passing wave exceeds noticeably temperature of shock front.

Under smaller intensities of the wave, contrastingly, luminosity at contact boundary of perfluorodecalin and perfluored transformer oil with the glycerol is halved. Temperature of material on contact boundary which is extrapolated to pressure behind front of passing wave agrees closely with temperature of shock front. The most plausible hypothesis is that perfluorodecalin and perfluored transformer oil does not undergo chemical transformation behind shock front. There are bases to consider that initial compounds are decomposed behind shock fronts in all other cases.

Unexpected in comparison with the preceding was a following observation. When shock wave created by detonation of charge with P_J = 26.4 GPa and U_J = 2.07 mm/mcs, lumenosity at contact boundary of perfluorotriethylamine with glycerol and decane lowers by factor equal around 3 and more 5 accordingly from

luminosity of front. At the same time lumenosity at contact boundary of perfluorotributylamine with glycerol and decane increased by factor equal around 4 and 3 accordingly from luminosity of front. The end lumenosities are closely related in both cases however luminosity of shock front in perfluorotriethylamine seems as anomalous high.

2. Calculation procedures.

When organic compounds undergo no chemical transformation in condensed phase behind the shock front, their Hugoniots can be predicted with a good accuracy using, e.g., die generalized dependence proposed in [4] $U_S = C_0 + 2\ U_P - 0.1\ U_P^2/C_0$. Here U_S is shock velocity, C_0 is the bulk velocity of sound in the initial state which depends on the material compressibility, and U_P is the particle velocity behind the shock front. The temperatures behind shock waves are calculated from the energy conservation equation written assuming that $\Gamma/V = \Gamma_0/V_0$ [5]

$$c_V(dT/dU_P) = U_P - (C_0 + a\ U_P^2)(U_P - c_{VI}\ \Gamma_0\ T/U_S)/U_S$$

where Γ_0 is the initial value of the Gruneisen coefficient equal to 3 for organic compounds in condensed phase, V is the specific volume, and c_V and c_{VI} is the total specific heat and its fraction associated with intermolecular interactions, respectively. The velocity of sound behind the shock front C is calculated by the formula

$$C^2 = (U_S - U_P)^2[U_S + (U_S - C_0 - a\ U_P^2)(1 - (c_{VI}\ \Gamma_0/c_V)U_P)/U_S]/(C_0 + a\ U_P^2)$$

with Hugoniot written as $U_S = C_0 + 2\ U_P - a\ U_P^2$.

Shock wave parameters at high U_P values can be calculated with an acceptable accuracy by the procedure suggested in [6]. It is suggested that methane and carbon (for hydrocarbons), water (for alcohols and other compounds containing oxygen atoms in their molecules), and molecular nitrogen (for amines and other compounds) are formed as the degradation products. The specific volumes and internal energies of the products are supposed additive functions of the appropriate quantities of the components at the same pressures and temperatures.

The temperatures of shocked components were written by formula $T_{Hi} = k_i P_{Hi} + T_{0i}$ (in the general case the use of this formula is not a necessity, here we selected it as one of the simplest and illustrative expressions). The following set of equations was solved:

$P_{Hi} = [P - c_{V1i}\,\Gamma_{0i}(T - T_{0i})/V_{0i}]/(1 - c_{V1i}\Gamma_{0i}k_i/V_{0i})$, $P_{Hi} = U_{Si}U_{Pi}/V_{0i}$,

$V_i = V_{0i}(1 - U_{Pi}/U_{Si})$, $T_{Hi} = k_i P_{Hi} + T_{0i}$, $\Gamma_i/V_i = \Gamma_{0i}/V_{0i}$,

$(\partial V_i/\partial P)_H = -V_{0i}^2 (C_{0i} + a_i U_{Pi}^2)/(C_{0i} + 2 b_i U_{Pi} - 3 a_i U_{Pi}^2)/U_{Si}^2$,

$(\partial V_i/\partial P)_T = (\partial V_i/\partial P)_H / (1 - c_{V1i}\Gamma_{0i}k_i/V_{0i})$,

$(\partial V_i/T)_P = -(\partial V_i/\partial P)_H\, c_{V1i}\, k_i\Gamma_{0i}/V_{0i}/(1 - c_{V1i}\Gamma_{0i}k_i/V_{0i})$,

$(\partial V_i/\partial P) = \sum_{i=1}^{n}\alpha_i(\partial V_i/\partial P)_T$, $V = \sum_{i=1}^{n}\alpha_i V_i$, $(\partial V/\partial T)_P = \sum_{i=1}^{n}\alpha_i(\partial V_i/T)_P$,

$(\partial V_i/\partial P)_T = \sum_{i=1}^{n}\alpha_i(\partial V_i/\partial P)_T$,

$0.5P(V_0 - V) + Q = 0.5\sum_{i=1}^{n}\alpha_i P(V_{0i} - V_i) + \sum_{i=1}^{n}\alpha_i c_{Vi}(T - T_{Hi})$,

$-C^2/V^2 = (\partial P/\partial V)_S = (\partial P/\partial V)_T[1 - T/c_V(\partial V/\partial T)_P^2/(\partial V/\partial P)_T]$

$c_v = \sum_{i=1}^{n}\alpha_i c_{Vi}$, $U_S^2 = V_0^2 P/(V_0 - V)$, $U_P^2 = P(V_0 - V)$,

For the chosen P value one can find the T value and, then, all the other values in question. Here, α_i is the weight fraction of the i-th component, n is the number of components.

Hugoniots of tetracosane, ethanol and toluene (curves *2, 4,* and *6* in Fig. 2) and temperatures of substances behind front (T in table 1), for instance, calculated by this procedure at high particle velocities agree satisfactorily with their measured values (T_2 in table 1) for benzene and acetonitrile. The fact that temperature of front T_F less than temperature of substance behind front T_2, is explained by the partial shielding, on the front side, of radiation issuing from the final state of the degradation products by layers with the incomplete conversion. This allows us to hope that we would be able to successfully assess shock wave parameters of fluorinated compounds, provided the degradation products are properly chosen.

One of the most probable components of degradation of fluorinated compounds, particularly perfluorinated hydrocarbons, is tetrafluoromethane CF_4.

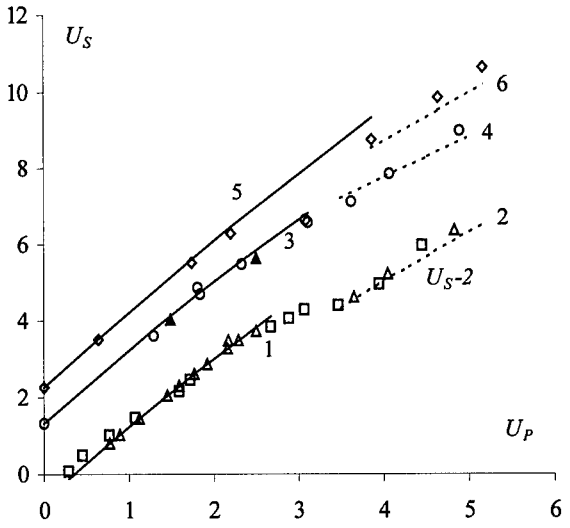


Fig. 2. Comparison results calculated Hugoniots of tetracosane (curves 5 and 6), ethanol (curves 3 and 4), and toluene (curves 1 and 2) with experiment (symbols).

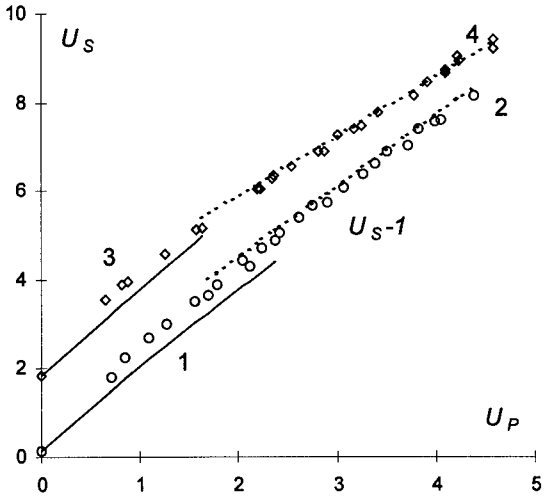


Fig. 3. Comparison of calculated Hugoniots of Teflon (curves 1 and 2) and polyvinilidene (curves 3 and 4) with experiment (symbols).

Table 1.

Compound	P, ГПа	T_F, K	T_2, K	T, K
Benzene	15.7	1840	2000	2100
	19.0	2080	2250	2400
	20.5	2150	2400	2500
Acetonitrile	17.0	2350	2800	2700
	18.6	2500	3000	2900

We failed to find in the literature experimental data on its shock compression and on sound velocity, e.g., in liquid phase at atmospheric pressure. For this reason, the shock Hugoniot of liquid CF_4 is calculated by the generalized dependence [4] for an initial state at a density of 1.96 g/cm^{3}and T_0 = 89 K. C_0 was found to be 1.1 mm/mcs by Rao's rule $C_0^{1/3} M/ d_0 = \Sigma b_i z_i$, where M is the molecular weight, d_0 is density, z_i is the contribution of the ith chemical bond, and b_i is the number of same bonds. $C - F$ bond contribution is taken to be 113. The calculated shock parameters of CF_4 then are used in assessing the state of the material behind shock waves in fluorinated compounds when their decomposition is supposed to occur.

Figure 3 compared the measured shock wave velocities in Teflon with their counterparts calculated with and without degradation of the original material behind die shock front (curves 1 and 2, respectively). The composition of the degradation products was formulated according to die formula $(CF_2)_n = n\ CF_4 + n\ C$. Carbon, as judged from the phase diagram, is in the diamond phase in the temperature and pressure range of interest (the same is true for decomposition of hydrocarbons). Agreement between the experimental and calculated values at particle velocities below 2 km/s is fairly good (curve 1 in Fig. 3). At lower particle velocities, the shock velocities calculated by the generalized dependence with no decomposition tend to the measured velocities remaining below the measurements.

The composition of the degradation products formed behind shock waves in polyvinylidenefluoride and telomeric alcohols is defined by the following formulas: $(C_2F_2H_2)_n \rightarrow 0.5\ n\ CF_4 + 0.5\ n\ CH_4 + n\ C,$

$C_3H_4OF_4 \rightarrow CF_4 + H_2O + 0.5\ CH_4 + 1.5\ C,$

$C_5H_4OF_8 \rightarrow 2\ CF_4 + H_2O + 0.5\ CH_4 + 2.5\ C,$

$C_5H_4OF_8 \rightarrow 3\ CF_4 + H_2O + 0.5\ CH_4 + 3.5\ C.$

The shock wave velocities calculated with and without regard for material decomposition to (he above products by the generalized dependence from [4] are displayed in Figs. 3 and 4. The measured values borrowed from [2,3] are shown by symbols. As in the case of Teflon, the experimental shock Hugoniots of polyvinylidene fluoride and telomeric alcohols at particle velocities exceeding 2.5 km/s are adequately described by calculations allowing for decomposition to CF_4 and carbon (curve *4* in Fig. 3 and curves *2,4,* and *6* in Fig. 4). At particle velocities below 2.0 km/s calculations by the generalized formula for the initial compounds (curves *1,3* in Fig. 3, and curves *1,3* and *5* in Fig. 4) provide better fit to experiment, though at lower pressures the deviation is greater than for the majority of organic compounds containing no fluorine.

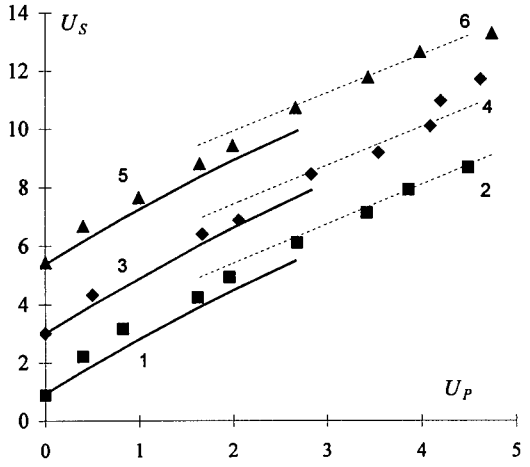


Fig. 4. Comparison of calculated Hugoniots of trihydrotetrafluoropropanol (curves 5 and 6), trihydrooctafluoropentanol (curves 3 and 4), and trihydrodecafluoroheptanol (curves 1 and 2) with experiment (symbols).

From the above discussion it appears that the suggested procedures for assessing shock wave parameters of fluorinated compounds enable to be predicted shock wave velocities with a satisfactory accuracy within a wide range of wave intensities. The formulas will be helpful in further more comprehensive studies of shock compression of these compounds with measuring other parameters.

3. Results and discussion.

In the table 2 the temperature T_H on the contact boundary with the window material, which were extrapolated on the pressure to the condition in passing wave, are compared with calculated temperatures T. Upper line 1 for each intensity is assigned to suggestion about conservation of initial compound before the front of the wave. Bottom line 2 for each intensity is assigned to suggestion of decomposition to CF_4 and carbon. As one would expect from the relation of luminosities of front and material on contact boundary with window material, temperatures T_H of perfluorodecalin and perfluored transformer oil under smaller intensity of wave alone are close to temperatures of compression of initial compounds. In other than that situation the temperatures T_H agree nicely with temperatures which were calculated to suggestion of decomposition to CF_4 and carbon.

In right columns measured temperatures of fronts T_F are compared with temperatures T_3 of initial compound, which are calculated behind front of wave spreading at the speed U_S. The luminosity of the shock wave in the compound, which suffers a conversion behind front, is dependent on several factors.Firstly, we must point to mentioned above the partial shielding, on the front side, by layers with the incomplete conversion of radiation issuing from the final state of the degradation products in liquid carbon disulphide, benzene and acetonitrile. Secondly, it is possible increase of luminosity of the final state by supplementary luminosity of initial compound with more high temperature directly behind front, as happens in dissociation of halogen derivatives of methane [7].

Table 2.

Compound	Density g/ml	**P** GPa	**U_s** mm/mcs	**T** K	**T_h** K	**T_3** K	**T_f** K
$(C_4F_9)_3N$	1.869 (1)	21.8	4.8	2010	2700		
	(2)	23.5	5.42	2900	2700	2600	2450
	(1)	28.5	5.35	2570	3450		
	(2)	30.5	5.87	3600	3450	3170	3350
$(C_2F_5)_3N$	1.745 (1)	20.0	4.55	2200	2750		
	(2)	22.2	5.26	3140	2750	3050	3100
	(1)	26.3	5.0	2700	3550		
	(2)	29.0	5.83	3700	3550	3800	3450
C_7F_8	1.776 (1)	22.0	5.16	1910	2750		
	(2)	23.0	5.51	3000	2750	2200	2500
	(1)	29.0	5.73	2400	3600		
	(2)	30.5	6.24	3500	3600	2860	3500
$C_{10}F_{18}$	1.965 (1)	22.0	4.82	2000	2050		2050
	(2)	24.0	5.43	2600	2050		
	(1)	29.0	5.18	2620	3000		
	(2)	31.5	6.05	3300	3000	3700	2900
$(C_{2.11}F_4)$	1.942 (1)	22.0	4.72	1980	1950		1950
	(2)	23.7	5.35	2700	1950		
	(1)	29.0	5.26	2500	2950		
	(2)	31.2	5.95	3300	2950	3400	2850

This variant, probably, there is at registrations of the luminosity of the shock wave of the smaller intensity in perfluorotriethylamine $N(C_2F_5)_3$. Will in addition notice, that time profile of the pressure for the front of the wave is like profile for the front of detonation wave, with Neumann's peak. With the growing of intensity of the wave the time, for which occurs decomposition of the compound behind the front, is noticeably diminished. This brings about the smaller difference between temperatures of the front T_F and temperatures of decomposition products T_H. Observed differences between them in 100 K are comparable with inaccuracies of extrapolation of temperatures of the matter on the contact boundary with the window material to the state in the passing wave, which are connected with accuracy of the prediction of Hugoniots under investigation compounds.

Relying on results of measurement and of calculation possible come to a conclusion that perfluoroalkanes and perfluoroalkylamines undergo the conversions behind the front of the shock wave at the temperatures above 2000 - 2100 K. Using kinetic data on decomposition of vapors of an alkanes through breaking $C - C$ bonds at temperatures before 1700 K, it is possible to make an estimate of time of the conversion of perfluoroalkanes and perfluoroalkylamines behind shock front smaller than 0.1 mcs.

REFERENCES.

1. C. E. Morris, J. N. Fritz, and R.G. McQueen, *J. Chem. Phys.* **80,** № 10, 5203 (1984).
2. *LASL Shock Hugoniot Data* (California, 1981).
3. R. F. Trunin, M. V. Zhernokletov, N. F. Kuznetsov, et. al., *Khim. Fiz.* **11**, № 3, 424 (1992).
4. A. N. Afanasenkov, V. M. Bogomolov, and I . M. Voskoboinikov, *Zh. Prikl. Mekhan. Fiz.* № 4, 137 (1969).
5. I. M. Voskoboinikov and M. F. Gogulya, *Fiz. Goreniya Vzryva* № 3, 105 (1978).
6. I. M. Voskoboinikov, *Khim. Fiz.* **10**, № 5, 672 (1991).
7. A. Yu. Dolgoborodov, I. M. Voskoboinikov, I. K. Tolstov, *Khim. Fiz.* **10**, № 5, 679 (1991).

THE LIMITS OF SHOCK – INITIATED EXPLOSION IN LIQUID BISFLUORODINITROETHYLFORMAL (FEFO) AND 1,6-DIAZIDO-2-ACETOXYHEXANE. CRITICAL DIAMETERS OF DETONATION OF BISFLUORODINITROETHYLFORMAL SOLUTIONS.

I. M. Voskoboinikov, S. A. Dushenok, and A. A. Kotomin

The limits of shock – initiated explosion and states along Hugoniots are measured for liquid bisfluorodinitroetylformal and 1,6-diazido-2-acetoxyhexane. The possibility of calculating the explosion limits using the kinetic parameters gained by studies on thermal decomposition of these classes of compounds in gas phase is demonstrated.

This study shows that changes in the critical diameters of detonation of liquid bisfluorodinitroethylformal (FEFO) with acetone, dibutylphthalate, ethanol, or diazide additives dissolved in it can be predicted with a reasonable accuracy using a value of 48 kcal/mol for the activation energy for unimolecular FEFO decomposition in gas phase. Predictions for FEFO diluted with cyclohexanol and with ethanol, at its low concentration, are somewhat poorer, presumably because of small temperature variations behind the shock front leading the detonation wave generated by faster decomposition of minor admixtures in the basic compound. The critical detonation diameters of FEFO solutions with nitromethane and isopropyl nitrate are controlled by faster decomposition of the diluents behind the shock front.

Measurements of the limits of a shock-initiated explosion in liquid explosives furnish information about the macrokinetics of their decomposition at temperatures and densities far exceeding their values achievable in conventional kinetic studies. The relevant data are available for relatively few compounds, some of which, e.g., nitromethane, exhibit certain macrokinetic peculiarities of their decomposition behind the shock wave front, associated with isomerization of the molecular structure at high densities (conversion into the aci-form [1, 2]). Therefore, it is

desirable to pursue investigation into the limits of shock-initiated explosion of liquid explosives differing in molecular structure. The objects of our investigation were 1,6-diazido-2-acetoxyhexane $N_3CH_2CH(OCOCH_3)CH_20CH_2CH_2N_3$ (referred to as diazide; initial density 1.198 g/cm^3) and bisfluorodinitroethylformal (abbreviated to FEFO; initial density 1.60 g/cm^3). The purity of the reagents analyzed by means of liquid chromatography was 99%.

1. Explosion limits.

The schematic of the experimental setup used previously to measure the limits of shock-initiated explosion of liquid azidoethanol [3] is pictured in Fig. 1. The shock wave was generated by detonation of a charge *1*; the test liquid layer *4* and the nonexplosive liquid layer with intense luminosity of the shock front (CCl_4 or $CHBr_3$) *2* were separated by a thin polypropylene film *3* which retained its transparency, as the wave passed through it. Because of its small thickness the film introduced no visible distortions in the process under observation at the time resolution of the detecting system of approximately 50 ns.

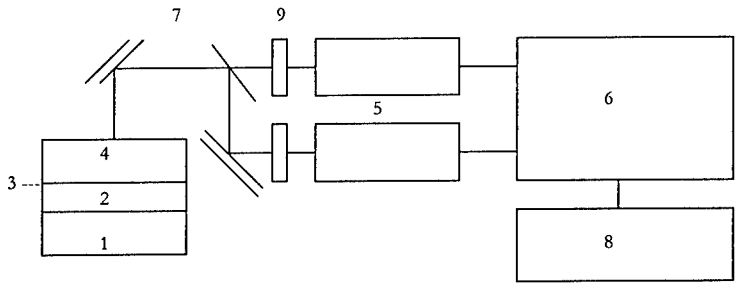


Fig. 1. Fig. 1. Schematic of the experimental setup: (1) explosive charge, (2) liquid indicator, (3) polypropylene film, (4) test explosive liquid, (5) photomultipliers, (6) recording unit, (7) mirrors, (8) synchronizing unit, (9) light filters.

CCl_4 and $CHBr_3$ were chosen as liquids 2, because their Hugoniots, temperature – vs – pressure dependences at the shock front, and variation of temperature with pressure along the isentrope of the shock-compressed material were known (e.g., see [4-6]). On initiation of explosion in the test liquid 4 the

luminosity of the shock front in CCl_4 (or $CHBr_3$), then variation in the luminosity at CCl_4 (or $CHBr_3$) – test liquid boundary, and finally, the luminosity due to adiabatic explosion and detonation were measured in succession (see Fig. 2).

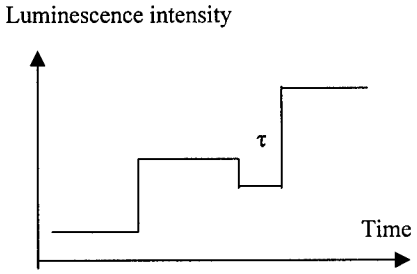


Fig. 2. Conventionalized record of luminosity made during initiation of diazide explosion.

Hugoniots of CCl_4 and $CHBr_3$ were taken in the form $Us = C_0 + b\,U_P - a\,U_P^2 = C_0 + 2\,U_P - 0.1\,U_P^2/C_0$ (Us is the wave propagation velocity, C_0 is the acoustic velocity in the initial state (0.96 mm/mcs for CCl_4 and 0.923 mm/mcs for $CHBr_3$). The temperature-pressure dependence at the shock front was approximated by $T_1 = 1530 + 135(P - 10)$ for CCl_4 and by $T_1 = 1570 + 125(P - 10)$ for $CHBr_3$ at temperatures below 2600 and 2000 K, respectively (here, pressure is in GPa, and temperature, in K). The temperature along the isentrope of shock-compressed $CCl4$ (or $CHBr_3$) was assumed to vary approximately as $\Delta T/T = (c_{V1}\,\Gamma/c_V)\,\Delta U_P/C$ (here, ΔU_P is the variation in the particle velocity in the wave propagating from the interface). The acoustic velocity behind the shock wave front, denoted by C, was calculated from equation

$$C^2 = (U_S - U_P)^2\{U_S + (U_S - C_0 - a\,U_P^2)[1 - (c_{V1}\,\Gamma/c_V)\,U_P/U_S]\}/(C_0 + a\,U_P^2)$$

derived within the framework of the molecular crystal model.

To determine $(c_{V1}\,\Gamma/c_V)$ and to refine the C value, we measured variation in the luminosity of a shock wave of nearly boundary between CCl_4 (or $CHBr_3$) and a liquid with a known Hugoniot, which retained its transparency behind the shock wave front (window material). For example, in experiments with CCl_4, this liquid was water; the luminosity of CCl4 at its contact with water reduced 1.5-fold at the chosen shock wave intensity. A plausible procedure for calculating $(c_{V1}\,\Gamma/c_V)$ from the variation in the luminescence intensity of a shock-compressed material, as the

shock wave traverses the interface with the window material, is set out, e.g., in [3]. It is also possible to draw on the fact that small relative variations in the temperature are proportional to variations in the particle velocity in an isentropic wave propagating from the interface.

All the parameters of a shock wave in CCl_4 (or $CHBr_3$) are to be determined from the luminosity of the shock front. Unless test liquid loses its transparency immediately behind the incident-wave front, as most liquids do, state in the Hugoniot are to be calculated from the variation in the luminosity at the contact boundary. In the pressure (P)-vs-particle velocity *(Up)* coordinates it coincides with the state in the isentrope of shock-compressed CCl_4 (or $CHBr_3$). The instant of drastic variation of the luminosity due to explosion of the test liquid corresponds to the delay of its adiabatic explosion behind the front of the incoming wave. In Table 1, P_1 is the pressure behind the shock wave front in CCl_4 or $CHBr_3$, and $d = (T_1 - T_2)/T_1$ is the relative variation in the temperature of these liquids, when the wave traverses the contact interface between them and the test liquid. T_1 is the temperature behind the shock front, and T_2 is the temperature in the wave reflected from the contact interface. P is the state in the isentropic wave propagating from the contact boundary with CCl_4 (or $CHBr_3$), and U_P is the state behind the shock front in the test liquid; τ is the adiabatic explosion delay.

Table 1.

Liquid	P_1, GPa	d	P, GPa	U_P, mm/mcs	τ, mcs
Diazide	15.2	0.036	13.2	2.23	0.35
	13.8	0.024	12.5	2.03	0.85
FEFO	15.0	0.032	13.0	1.60	0.1

The luminosity at the *CCl4* – diazide boundary changes approximately 1.25-fold in the event of a less intense wave and 1.6-fold in the event of a more intense

wave. These variations corresponded to the following states in the diazide Hugoniot: 12.5 GPa – 2.03 mm/mcs and 13.2 GPa –2.23 mm/mcs, respectively. The shock compression parameters of diazide listed in Table 2 were calculated in much the same way as in [I], using the acoustic velocity in the initial state C_0 = 1.25 mm/mcs. The calculated values of P and U_P agree closely with the results of measurements.

Table 2.

Liquid	U_P, mm/mcs	U_S, mm/mcs	T, K	P, GPa	C, mm/mcs
Diazide	2.0	4.93	1022	11.82	6.47
	2.1	5.10	1082	12.83	6.67
	2.2	5.27	1144	13.88	6.85
	2.3	5.43	1208	14.96	7.03
FEFO	1.6	4.45	894	11.38	
	1.7	4.62	972	12.57	
	1.8	4.8	1034	13.82	

The measured adiabatic explosion delays (0.85 mcs at 12.5 GPa and 0.35 mcs at 13.2 GPa) for diazide are an order of magnitude longer than their theoretical counterparts calculated at E = 40 kcal/mol, $z = 10^{14}$ 1/s [7], 1065 and 1105 K, and initiation pressures indicated in Table 2. On the other hand, the initiation pressures calculated from the measured adiabatic explosion delays at the above values of E and z appearing in the Arrhenius law equal 11 and 12 GPa. They differ from the measured pressures by 1.5 GPa — by the value only slightly exceeding the error of measurements. There is agreement between the limits of shock-initiated explosion of diazide and azidoethanol (τ = 0.12 mcs, P = 11.8 GPa, T = 1270 K) [I], and all

the measured values are reproduced in calculations with equal precision at the chosen values of E and z.

At an explosion delay of 0.1 /is, the luminosity of $CHBr_3$ at the boundary between $CHBr_3$ and FEFO reduced approximated 1.5-fold, while at the boundary between $CHBr_3$ and nitromethane, it reduced almost 3-fold at a slightly lower shock wave intensity [8]. The measured variation of the luminosity (see Table 1) corresponds to the pressure of 13 GPa at the shock wave front propagating in FEFO at U_P = 1.6 mm/mcs. This pressure is somewhat higher than that calculated at the same particle velocity from the $U_S = C_0 + 2\ U_P - 0.1\ U_P^2/C_0$ dependence, where C_0 = 1.43 mm/mcs was assessed from the Rao's relationship (see Table 2).

In studying thermal decomposition of polynitrocompounds [9-11] it was noticed that the kinetic parameters of the gas phase closely approximated their values for the liquid phase, and depended only slightly on the structure of alkyl radicals of heme-nitroalkanes. In the $CH_3(CH_2)_nC(NO_2)_3$ (n = 0,1,2) series, the activation energies and logarithms of the preexponential factors equal 43.2; 42.3; 43.6 kcal/mol and 17.18; 16.86; 17.17, respectively. With F in place of NO_2, the energy of the $C - N$ bonds increases by 4-6 kcal/mol, and therefore, the above parameters for, e.g., $CH_3CF(NO_2)_2$ equal 47.7 kcal/mol and 17.0, respectively. Extending the aforesaid to FEFO we obtain the activation energy of $E \approx 48$ kcal/mol and logarithm of the preexponential factor of $z \approx 17$.

As revealed by calculations at an adiabatic explosion delay of 0.1 mcsand the aforesaid values of the kinetic parameters, the temperature of 970 K is achieved behind the shock front at a pressure of 12.5 GPa. This value agrees reasonably closely with the initiation pressure of 13 GPa assessed from the variation in the luminescence intensity of $CHBr_3$ at the $CHBr_3$ – FEFO interface. For reference, the pressures of 12 and 13 GPa correspond to 930 and 990 K, and the adiabatic explosion delays calculated together with the pressures differ from the measured delay by not more than a factor of 3 – 4.

The aforesaid justifies the possibility of using the kinetic parameters of gas-phase thermal decomposition of diazide and FEFO at much lower temperatures (below 400 K) in calculations of the limits of their shock-initiated explosion.

2. Critical diameters of detonation.

Investigations of changes in the critical detonation diameters (d_c) of liquid explosive solutions may furnish, apart from solution of some practical problems associated with storing and transportation of these products, additional information about the macrokinetics of conversions in detonation waves and states of the material behind shock fronts. Owing to homogeneity of liquids transformations of the energetic material behind the shock front in detonation waves spreading through them proceed in the form of an adiabatic explosion. The reaction times in these waves are controlled by preheating of the material bulk.

Of course, one could attempt to assess the effective kinetic parameters controlling decomposition of the starting material behind the shock front, however in many investigations changes in critical detonation diameters do not exceed a factor of ten. This corresponds to relatively small changes in the material temperature behind the wave front (up to 20%), and what is more, the temperature is calculated rather than measured. Switching over from critical detonation diameter values to reaction times behind the shock front is not unique. Even in the works where the nature of critical-diameter is qualitatively accounted for no procedure capable of predicting its value has been suggested because of the complexity of the flow pattern arising behind the wave front.

Keeping in mind the aforesaid, it is expedient to explore feasibility of using the reaction kinetic parameters determined under conditions utterly different from those existing behind the shock front of a detonation wave rather than to extract these kinetic parameters from measured critical diameters of detonation of liquid explosive solutions. This check should be performed for various compounds, because one can not rule out in advance various situations (mechanisms) in different explosive systems. For instance, critical diameters for detonation of solutions of liquid alcohol nitrates can be assessed using the activation energy

values determined in experiments on their decomposition in gas phase. This is impractical in the case of nitromethane because of its decomposition in the aci-form with a much lower activation energy at high densities and pressures.

We undertook this investigation of critical diameters of detonation of explosive solutions to gain data on the ratio of decomposition times of compounds of a different chemical structure at temperatures around 2000 K. As follows from calculations, these temperatures are observed behind the shock front of detonation wave. Solutions of bisfluorodinitroethylformal $CH_2(OCH_2C(NO_2)_2F)_2$ (hereinafter FEFO), *1, 6* -diazido-2-acetoxyhexane $N_3CH2CH(OCOCH_3)CH_20CH_2CH_2N_3$ (diazide), nitromethane CH_3N0_2, nitroethane $C_2H_5NO_2$, isopropylnitrate $CH_3CH(ON0_2)CH_3$ (IPN), nitroglycerine $CH_2(ONO_2)CHCH_2(ONO_2)$ (NGC), and propyleneglycol dinitrate $CH_2(ON0_2)CH_2CH_2(ON0_2)$ (PGDN). We explore the possibility of assessing the critical diameters for detonation of solutions of the above-mentioned compounds and also of FEFO solutions with ethanol, dibutylphthalate, acetone, and cyclohexanol with the aid of activation energies for decomposition of polynitrocompounds and alcohol nitrates in gas phase. The temperatures in these researches were significantly lower than the temperatures behind the detonation front.

Critical diameters for detonation of solutions in thin-walled paper casings the inner surface of which was coated with polyethylene were measured using the traditional procedure. The length of charges was no less than 200 mm and exceeded their diameter by no less than ten times. Detonation was initiated with a specially designed intermediate booster charge. Tested charges were mounted with a small gap on a witness metal plate. The conversion degree in the initiated charge was assessed from the dent in the plate. The error of d_c measurement is 0.5 mm at $d_c < 5$ mm and 0.5 or 1.0 mm at d_c exceeding 10 mm. At charge diameters smaller than the indicated critical diameter by 0.5 or 1.0 mm detonation waves did not propagate to the charge end. The detonation velocity was measured in streak photographs taken with a rotating mirror camera SFR in runs with charge

diameters significantly greater than the critical diameter. The measurement error was less than 0.1 mm/mcs.

For each component we calculated the temperature T_F – pressure P_F dependences behind the shock front of the detonation. To simplify further computations, the calculated dependences were approximated within the pressure range of interest by the following formula: $T_F = T_0 + k P_F$. Then we calculated the temperature versus pressure dependence at the shock front of detonation waves spreading through the solutions tested (the calculation procedure can be found above).

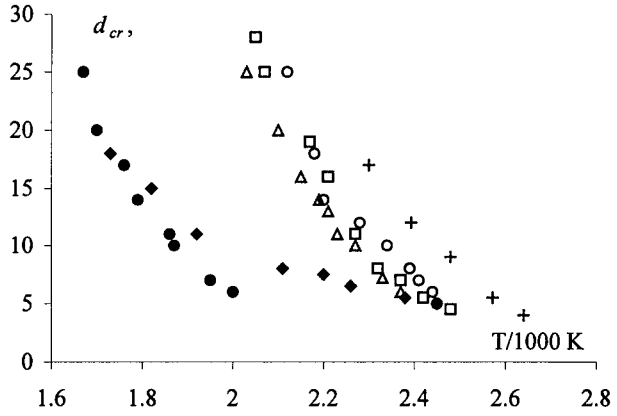


Fig. 3. Critical diameter d_c versus T_F for FEFO solutions. Painted by badges are inflicted given for solutions with nitromethane (rhombuses) and isopropylnitrate, light - for solution with diazide (triangles), dibutylphthalate and ethanol, crosses - for solution with nitroethane.

In the first place, we emphasize that the approximately equal d_c values measured in FEFO and NGC solutions with nitromethane, FEFO with isopropylnitrate and PGDN with nitromethane correspond to close values of the calculated T_F values. At the same d_c values measured in FEFO solutions with diazide, ethanol, dibutylphthalate, acetone, nitroethane, and cyclohexanol the calculated temperatures T_F are somewhat higher, but they are consistent fairly well with each other within this group of solutions (see Fig. 3). This suggests that in FEFO solutions with a high content of nitromethane and isopropylnitrate the rate

controlling reaction stage behind the wave front is decomposition of the diluents. In FEFO solutions with nonexplosive diluents, nitroethane and diazide the rate controlling reaction stage is FEFO decomposition. The possibility of predicting critical diameters of detonation of FEFO solutions with these diluents using one and the same activation energy 48 kcal/mol and logarithm of preexponential factor $z \approx 17$.

We used kinetic parameters of the decomposition in the gas phase of nitroethane $k = 10^{15.9} \exp(-28684/T)\ s^{-1}$, diazide $k = 10^{14} \exp(-20000/T)\ s^{-1}$ and FEFO $k = 10^{17} \exp(-24000/T)\ s^{-1}$. Values $\lg k$ for nitroethane, diazide, FEFO and propylnitrate are equal at the temperature 2000 K 9.67, 9.657, 11.788 and 12.129, but at the temperature 2600 K accordingly 11.11, 10.64, 12.991 and 12.54. For nitromethane with the gas kinetics are equal 9.86 and 11.33.

Thus, by way of example of FEFO we have demonstrated that the use in predicting the critical diameters of detonation of the activation energies assessed for the thermal decomposition reaction in gas phase at significantly lower temperatures is quite justified. Hopefully, the suggested approach to assessment of critical diameters of detonation will be helpful in studies of the reaction kinetics of other compounds behind the detonation front. The feasibility of detecting the component controlling the decomposition rate behind the detonation wave front in solutions of two explosive materials and of comparing, based on that, the values of the decomposition times of the components at temperatures in the shocked material is demonstrated.

REFERENCES

1. R. Engelke, W. L .Earl, and C. McM. Rohlfing, J. *Chem.* Phys., No. l, 142 (1986).
2. G. J. Piermarini, S. Block, and P. J. Miller, *J. Phys. Chem.*, **93**, No. l, 457 (1986).
3. I. M. Voskoboinikov, *Khim. Fiz.*, **10**, No. 12, 1705 (1991).
4. R. D. Dick, J. *Chem. Phys.*, **52**, No. 12, 6021 (1970).
5. I. M. Voskoboinikov, V. M. Bogomolov, A. N. Afanasenkov, and V. N. Shevelev, *Dokl. Akad. Nauk SSSR*, 182, No. 4, 807 (1968).
6. A. Yu Dolgoborodov, I. M. Voskoboinikov, and I. K. Tolstov, *Khim Fiz* **10**, No. 5, 679 (1991).
7. G. Geiseler and W. Konig, Z. *Phys. Chem.*, **227**, No. 1-2, 81 (1964)

8. I. M. Voskoboinikov and I. V. Bulanov, *Doklady 4 Vsesoyuznogo Soveshchaniya po Detonatsii* (Reports at the 4th USSR Conference on Detonation) (OIKhF AN SSSR, Chernogolovka, 1998), **1**, p. 134.

9. G. M. Nazin, G. B. Manelis, and F. I. Dubovitskii, *Izv. Akad. Nauk SSSR Ser. Khim.*, No. 11, 389 (1968).

10. G. M. Nazin, G. B. Manelis, and F. I. Dubovitskii, *Izv. Akad Nauk SSSR Ser. Khim.*, No. 11, 2631 (1968).

11. G. M. Nazin, G. B. Manelis, and F. I. Dubovitskii, *Izv. Akad. Nauk SSSR Ser. Khim.*, No. 11, 2628 (1968).

The temperatures of shock fronts at some liquid hydrocarbons with chemical composition C_5H_8.

I.M. Voskoboinikov, M. F. Gogulya.

Semenov Institute of Chemical Physics, Russian Academy of Sciences

117977 Kosygin Str. 4, Moscow, RUSSIA

Fax: (095) 938 2156. E – mail : voskob @ chph. ras. ru

The temperatures of shock fronts at some liquid hydrocarbons with equally chemical composition C_5H_8 but various density and enthalpy of formation were measured by optical technique. For one of a number, piperylene, Hugoniot has been defined more accurately. The possibility of the predictions of temperatures of shock compressed matter and Hugoniots has been demonstrated by results of computer simulations taking on the assumptions that initial compound polymerises or decomposes to CH_4 and carbon. In the context of model of molecular crystal it was executed evaluations some thermodynamic values with revision of chemical composition.

THE IGNITION OF ETHANOL AZIDE INDIVIDUAL DROPS

V.V.Golovko, A.K.Kopeyka, E.A.Nikitina

The Institute of Combustion & Advanced Technologies, Odessa National University, Dvoryanskaya 2, Odessa, 65026, UKRAINE, e-mail: vov@ictg.intes.odessa.ua

ABSTRACT

The results of investigation of individual drops ignition process of ethanol azide (EA) are presented. It has been found three regimes of ignition, that differ in kinetic of chemical reaction. The first it was obtained the experimental evidence of existence of temperature interval where the reaction oxidation and decomposition occurred simultaneously at ignition process of EA.

Introduction

The processes, which precede complete development of a burning zone of organic azide drops, become very important because of high values of burning rate of drops of these substances[1,2]. As the object for investigations was consider ethanol azide ($C_2H_5ON_3$).

The investigation of behaviour of ethanol azide (EA) drop at sudden influence of heated oxidize gas was the purpose of present paper. The dependence of a delay time of drops ignition on an initial temperature of surroundings $\tau_{del}(T_0)$ and the dependence of ignition temperature on an initial diameter of drops $T_{ign}(d_0)$ were studied in experiments .

Experiment

The construction of the electrical furnace with length 8 cm and diameter 1 cm allowed it to move about a drop. The drop was placed on fixed holder of the thermocouple. The initial diameter of EA drops changed in an interval from 1 to

2,5mm. The transference time of the furnace is equal 0,1c. The temperature of a drop ignition was determined as temperature of surroundings at the moment of ignition start. This temperature was measured by the second thermocouple, which was placed inside the furnace.

Results and discussion

The sharp explosive process of EA ignition was observed on interval of surroundings temperature from 470 to 560K. It was accompanied by sonic effect. The temperature of a drop at the moment of explosion wasn't more 370K. This temperature is lower than boil temperature of EA (433K at $1{,}013 \cdot 10^5$ Pa).

The EA drop was ignited as hydrocarbon fuel into interval of temperature from 560 to 630K. The flame of yellow colour was formed. The temperature of EA drop at the moment of ignition obtained 350K.

The decomposition of EA without a flame was observed at temperature 630K and above. The temperature of a drop was 320K at decomposition.

Thus, the character of ignition process of EA drops differed for three intervals of temperatures.

On fig.1 the dependence of the logarithm of ignition delay time on back temperature of surrounding $\ln\tau_{del}(1/T)$ in an interval of temperature from 470 to 560K for drops with a diameter d_0=1,32mm is shown.

The linear law features this dependence. The activation energy of chemical reaction, which limited of ignition process of EA drops, was determined.

$$E_1 = (14000 \pm 1000)\text{kal/mole}$$

It is known[3], that an activation energy of reaction of EA thermal decomposition is equal E_2=37800kal/mole. If to assume, that reaction, which limits process of ignition of EA drop in a temperature interval from 470 to 560K is reaction of EA vapor oxidizing by oxygen from air:

$$C_2H_5ON_3 + O_2 \rightarrow H_2O + CO_2 + N_2 + q_1$$

Then, for such reaction it is possible to use a formula for definition of activation energy as in works[4,5]:

$$\ln\left[\frac{d_0^2}{4T_{ign}^3} C_{O_2}^2\right] = const - \frac{E}{R}\frac{1}{T_{ign}} \qquad (1)$$

Where, d_0 - initial diameter of a drop, T_{ign} - temperature of ignition, C_{O_2} - weight concentration of oxygen. The results of calculation of chemical reaction activation energy on expression (1) allow to obtained value E=14300±1700kal/mole (fig. 2).

This value is very close to value of activation energy, which was obtained from dependence $\ln\tau_{del}$ $(1/T)$. Therefore it is possible, that ignition of EA drop proceeds on gas-phase mechanism in a temperature interval from 470 to 560K. And the ignition is limited by oxidizing reaction of EA vapor.

The results of experiments for ignition of EA drops in temperature interval from 560 to 600K are shown in a fig. 3.

The value of activation energy for this interval of temperature was received.

$$E_3 = (16000 \pm 1000)\text{kal/mole}$$

This value is more than one for gas-phase reaction of EA oxidizing, but it is less than the activation energies of thermal decomposition reaction of EA vapor. Obviously, the rate of a heat release during ignition is determined by the kinetic of parallel gas-phase reactions of oxidation and thermal decomposition of EA on this temperature interval.

1) $C_2H_5ON_3 + O_2 \rightarrow H_2O + CO_2 + N_2 + q_1$
2) $C_2H_5ON_3 \rightarrow C_2H_5ON + N_2 + q_2$

The first reaction has high value of thermal effect (q_1=2200kal/g), but smaller value of activation energy (E_1=14000kal/mole). The second reaction is poorly exothermic (q_2=550kal/g), but it has higher value of an activation energy (E_2=37800kal/mole).

In work[6] also it was indicated an opportunity of existence of thermal explosion with parallel reactions. An effective value of an activation energy E_*, which corresponds to gas-phase reactions of an oxidation and thermal decomposition of EA vapor it is possible to calculate according to results of these investigations:

$$E_* = \frac{q_1 k_1 E_1 C_{O_2}^2 + q_2 k_2 E_2}{q_1 k_1 C_{O_2}^2 + q_2 k_2} \qquad (2)$$

Where k_1 and k_2 - are constants of chemical reaction rate of thermal decomposition and gas-phase oxidation of EA vapor. The obtained value of E_* from the formula (2) is equal 15000kal/mole at the temperature 600K. This value is in good agreement with experimental value E_3=16000kal/mole. Such accordance is confirmed of existing opportunity of parallel reactions in a narrow interval of temperatures from 560 to 630K at gas-phase ignition of EA drops.

The process of ignition is degraded at values of temperature above than 630K. In this case flame-less decomposition of EA was observed.

Conclusion

Thus, the ignition of EA drops is occurred on gas-phase regime because of oxidation reaction of EA vapour. The reaction oxidation and decomposition of EA can occur simultaneously in a narrow interval of temperature from 560 to 600K.

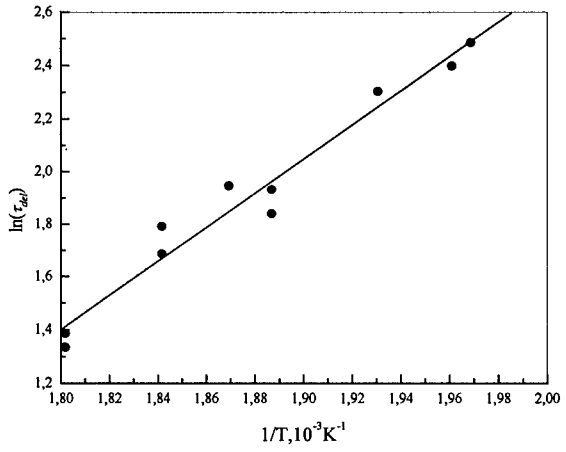


Fig.1 The dependence of the logarithm of ignition delay time on back temperature of surrounding $\ln\tau_{del}(1/T)$ in an interval of temperature from 470 to 560K (d_0=1,32mm).

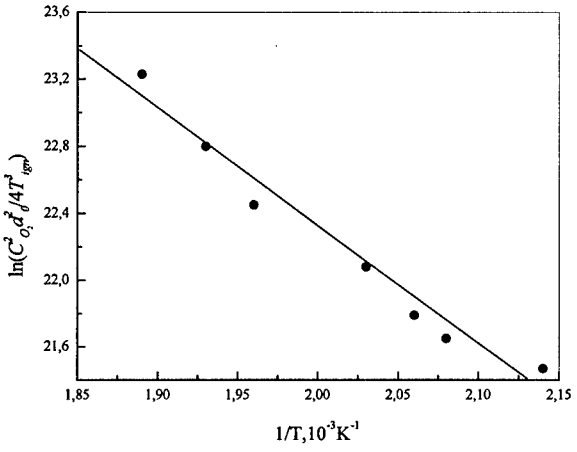


Fig.2 The dependence of the logarithm of ratio $\frac{d_0^2}{4T_{ign}^3}C_{O_2}^2$ on back temperature of surrounding in an interval of temperature from 470 to 560K (d_0=1,32mm).

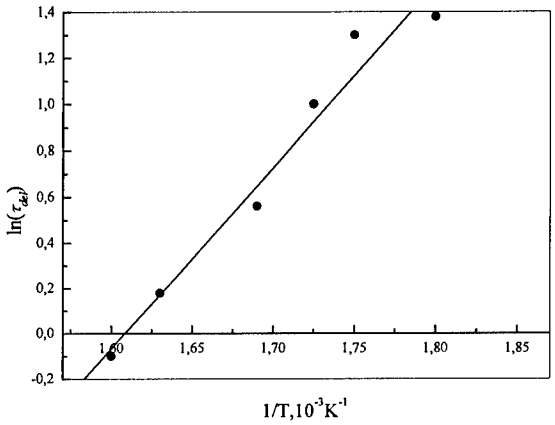


Fig.3 The dependence of the logarithm of ignition delay time on back temperature of surrounding $\ln\tau_{del}(1/T)$ in an interval of temperature from 560 to 600K (d_0=1,32mm).

References:

1. Golovko V.V., Kanashin S.P., Florko A.V., Ohrimenko N.A., The combustion of β-azidoethanole drop at atmospheric and reduced pressure. Physics of combustion and explosion 26, 61-64 (1990)
2. Golovko V.V., Kopeyka A.K., Kanashin S.P., Zolotko A.N., The combustion of ethanol azide drop into various surrounding. Proc. International Pyrotechnics Seminar XXI. - Moscow (Russia). –1995. -P.1110-1114
3. Kanashin,S.P., Kozhukh,M.S., Kulagin,A.N., Tokarev,N.P. The limiting conditions of combustion of β-ethanol azide. Physics of combustion and explosion 17,3:22-26(1981)
4. Bloshenko V.N., Merganov A.G., Peregudov N.N., Haykin B.I. About theory of gas-phase ignition of drop. Proc. Third All-Union Symposium on combustion and explosion. Science, Moscow, p.227 (1972)
5. Grigoriev Yu.M. The vaporization and ignition N-geptane into oxidation surrounding. Proc. Third All-Union Symposium on combustion and explosion. Science, Moscow, p.221 (1972)
6. Abramov V.G.,Vaginov D.A., Samoylenko N.G. The heat explosion of reacting systems with parallel reactions. Physics of combustion and explosion 13,1:48 (1977)

STUDY OF THE EFFECT OF POLYMER COATING ON ALUMINUM AGGLOMERATION

O. G. Glotov, V. E. Zarko, V. A. Shandakov, D. A. Yagodnikov*

INSTITUTE OF CHEMICAL KINETICS AND COMBUSTION,

Siberian Branch of Russian Academy of Sciences, Novosibirsk 630090, Russia

*) *BAUMAN MOSCOW STATE TECHNICAL UNIVERSITY, Moscow, 107005, Russia*

ABSTRACT

The effect of coating the aluminum particles with different polymers on the agglomerate characteristics was studied for 6 propellant formulations. All propellants were manufactured using well characterized ingredients and included 18 % Al, 18 % AP 160-315 μm, 9 % AP S=6700 cm^2/g, 35 % HMX 100-800 μm and 20% an energetic binder (polyvinyl tetrazole polymer plasticized with nitroester).

The following Al powders have been used. Commercial non-coated aluminium powder A1 (size D_{43} ~ 10 μm) was chosen as the basic one. The powders A2...A6 were obtained by coating the powder A1 with different polymer materials. Mass fraction of the in powders A2...A6 did not exceed 1%.

Most of coating materials are fluorine containing:

A2 - $Si[OCH_2(CF_2\text{-}CF_2)_3H]_4$

A3 - $Cl_2Si[OCH_2(CF_2\text{-}CF_2)_2H_2]_2$

A4 - $(CH_2{=}CH_2\text{-}O)_2Si[OCH_2(CF_2\text{-}CF_2)_2H_2]_2$

A5 - $CH_2\text{-}C(CH_3)(COOCH_3)$ polymethyl methacrylate (PMMA)

A6 - $CH_2{=}CF(COOCH_3)$ polymethyl fluorineacrylate (PMFA).

The propellants were fired at pressure about 4.6 MPa with freezing the condensed combustion products near the burning surface via mixing the flow of the combustion products with co-current nitrogen flow blowing through the bomb. The results on size distribution of agglomerates as well as the data on unburned aluminum content in sampled particles are presented.

All propellants have burning rate in the range 1.4-1.6 cm/s and exhibit weak agglomeration trend. It was found that several coating materials slightly reduce the agglomeration intensity via decreasing the agglomerate mass.

INTRODUCTION

Agglomeration of metal in the combustion wave of composite propellants as one of the main processes that control the efficiency of aluminum conversion into oxide still remains insufficiently studied problem [1]. It is known that the promising way to modify the metal particles ignition and combustion behavior is the coating of their surface with different materials - oxide, other metal, oxidizer, polymer, etc. [2-6]. For instance, some fluorine-containing polymers provide an increase in the flame propagation velocity for heterogeneous system *aluminum particles + gaseous*

oxidizer [3-4]. There is no detailed information concerning the mechanism of action of the coating. One may suppose that the atomic fluorine released during thermal decomposition of the coating matter reacts with the initial oxide film that usually preserves the aluminum particles against the oxidation. Thus, it is expected that fluorine-containing coating may affect an agglomeration process during combustion of solid propellant containing the coated aluminum via improvement of the flammability of the aluminum powder used in the propellant formulation. Due to great complexity of the physicochemical processes and the lack of the input data it is impossible at present time to predict theoretically the behavior of metal particles under fast heating in the combustion wave and to calculate the agglomerate parameters, i. e. agglomerates mass, their size distribution and extent of conversion of the aluminum into oxide. Therefore, the experiment remains the sole source of necessary information. The objective of the present work was to evaluate particle size distribution and free aluminum content for agglomerate particles formed in the combustion at elevated pressure of AP/HMX based propellants that contained commercial aluminum and aluminum coated with 5 different polymer materials.

EXPERIMENTAL TECHNIQUE

Propellant formulations

Totally six model propellants have been studied in the present work. All propellants were of the same global formulation (% mass): 9% AP1 S=6700 cm^2/g, 18% AP2 D=160÷315 μm, 35% HMX D>315 μm, 18% Al, and 20% energetic binder based on polyvinyl tetrazole polymer plasticized with nitroester [7]. The only difference was the type of aluminum powder used.

Mixing of the components was performed in the teflon mortar. Firstly, the non-metalized mixture was prepared and divided into portions about 40 g each. Then the aluminum powders with different coating were added to each batch. Aluminum powder A1 was used in the propellant Y1; A2 in Y2; and so forth, see Table 1. To manufacture the A2...A6 powders, the same aluminum A1 coated with different substances was used. Mass fraction of the coating material did not exceed 1%. Curing of cylindrical propellant samples was performed under heating in teflon forms (individual for each sample) with open ends. All samples were cured simultaneously,

i. e. at the same temperature regime. These arrangements were done in order to provide the identity of specimen's characteristics. Samples for the firing tests had cylindrical shape with diameter equal approximately 8 mm and length of 17 mm. The values of the propellant density (last column in Table 1) were estimated via measuring the weight and sizes of cured samples.

Table 1. Propellant density and aluminum powder used

Propellant ID	Aluminum powder	Coating matter	ρ, g/cm^3
Y1	A1	Commercial non-coated powder "ASD-4"	1.74±0.02
Y2	A2	$Si[OCH_2(CF_2\text{-}CF_2)_3H]_4$	1.71±0.01
Y3	A3	$Cl_2Si[OCH_2(CF_2\text{-}CF_2)_2H_2]_2$	1.72±0.01
Y4	A4	$(CH_2{=}CH_2\text{-}O)_2Si[OCH_2(CF_2\text{-}CF_2)_2H_2]_2$	1.72±0.05
Y5	A5	$CH_2\text{-}C(CH_3)(COOCH_3)$	1.72±0.02
Y6	A6	$CH_2{=}CF(COOCH_3)$	1.70±0.03

Propellant ingredients

All heterogeneous components (AP, HMX, and Al) used in the propellant manufacturing were thoroughly characterized by grain-size. The particle size analysis of each aluminum powder was performed using two techniques: 1) commer-cial automated granulometer Malvern 3600E, and 2) optical microscope. In the case of aluminum A1 the home made Coulter-like conductometric counter was used instead of the microscopic method. In the cases when the Malvern 3600E sizer was employed, a suspension of particles in the carrier liquid was subjected to ultrasound treatment during 30 second before measurement and the mechanical mixer was in action during the measurement procedure. The type of the carrier liquid used in Malvern measurements as well as the particle size distribution data in the form of mean diameters D_{mn} is presented in Table 2. The analysis of AP and HMX powders was performed using only of two methods depending on the grain size. The error of particle size measurement under use of optical microscope can be estimated as a half histogram size interval. This value was equal 0.5 μm for all studied aluminum powders and 17 μm for AP2 and HMX powders.

The size measurement results obtained with different methods for aluminum powders are in a good agreement. The only exclusion is the case of aluminum A5 that is caused by secondary coagulation of the particles in the carrier liquid observed for this powder. All aluminum powders have similar particle size distribution. This fact indicates that there is no aggregation of the particles after coating. The chemical analysis shows that in all powders A1÷A6 the free (metallic) aluminum content is 96.8÷98.0 % and the total aluminum content is 98.6÷99.8 % that means that the mass fraction of coating matter is small (< 1%).

Table 2. Mean sizes D_{nm} (μm) for propellant ingredients

Com-ponent	Analysis method, carrier liquid	D_{10}	D_{20}	D_{30}	D_{21}	D_{32}	D_{43}	D_{53}
A1	Malvern, water+ethanol	4.6	5.1	5.7	5.6	7.3	9.3	10.2
A1	conductometric counter	4.5	5.5	5.3	6.6	5.1	7.9	8.7
A2	Malvern, water+ethanol	4.8	5.2	5.7	5.7	6.8	8.1	8.9
A2	optical microscope	4.5	5.0	5.5	5.6	6.7	7.9	8.4
A3	Malvern, water+ethanol	4.8	5.2	5.6	5.6	6.6	7.9	8.5
A3	optical microscope	4.6	5.1	5.6	5.6	6.8	7.9	8.4
A4	Malvern, water+ethanol	5.5	5.9	6.4	6.4	7.6	8.9	9.5
A4	optical microscope	5.6	6.0	6.5	6.5	7.5	8.4	8.9
A5	Malvern, water+ethanol	6.0	6.7	7.6	7.5	9.5	12.1	13.5
A5	optical microscope	5.4	6.0	6.6	6.7	8.0	9.0	9.4
A6	Malvern, water+ethanol	5.5	6.0	6.6	6.6	8.1	9.9	10.7
A6	optical microscope	4.9	5.6	6.2	6.3	7.8	9.1	9.7
AP1	Malvern, hexane	4.5	5.4	6.6	6.5	9.6	13.1	14.8
AP2	optical microscope	282	285	288	288	294	301	304
HMX	optical microscope	211	236	264	265	330	402	434

The experimental procedure and data treatment

The original technique for studying the condensed combustion products (CCP) of solid propellants has been described previously [8-10]. It is based on sampling the particles followed by size distribution and chemical analyses. Typical features of the technique are: 1) continuously blowing of a special design bomb with inert gas, 2) freezing the particles at various distances from the burning surface via mixing the combustion products with inert gas in spatially localized area, 3) catching total

amount of the fine oxide particles (using the aerosol filter) and the agglomerates (using the set of wire mesh screens).

Below we present specific features of approach used in this work.

• Extinction of particles was reached near the burning surface via mixing with co-current flow of nitrogen blowing through the bomb. Nitrogen mass flow was typically 2 g/s that resulted in the gas velocity (directed along propellant specimen from the cold to the hot end) about 1 cm/s.

• Each experimental series consisted of firing 4 propellant samples with total mass about 5.7 g which were consecutively tested under identical conditions that provided generation of 1.4 g of CCP used for subsequent analyses. The lateral surface of the propellant specimen was inhibited with Solpren®.

• The thin (~ 1 mm) layer of uncured non-metalized propellant was attached to the ignited butt end of studied propellant specimen to make easier its ignition.

• The initial pressure in all experiments was 41 atm. The maximum rise of pressure during the combustion run was 10 atm. As characteristic pressure in the individual run was taken a half of sum of initial and final pressures. The characteristic pressure and burning rate for given series were taken as arithmetical mean values for characteristic pressure and burning rate in individual runs.

• The nominal mesh sizes of wire screens in the stack installed inside the bomb were 130, 160, 280, and 480 μm.

• The sampled particles were divided into fractions via dry and wet sieving in acetone by using sieves with the mesh sizes 130, 160, 280, 480, 600, and 880 μm. The particles caught by the filter were included into the sieve fraction <130 μm. All sieved fractions of particles were weighed and subjected to the particle size and chemical (permanganatometric) analyses to determine the free aluminum content [11].

• The fine (D < 130 μm) particles were analyzed by Malvern 3600E sizer using acetone as the carrier liquid after 30 seconds treatment with ultrasound and with continuous mechanical mixing of suspension.

• Particle size analysis for fractions with size D>130 μm was performed using optical microscope. The accuracy of size measurement estimated as a half of histogram sub-range was equal to 9 μm for fractions in the size range 130-300 μm, and 22 μm for fractions 300-450 μm. These values can be treated as an estimate for the accuracy of the data on the mean diameters reported below.

Based on the results of particle size analysis and chemical analysis of sieved fractions particles, the mass size distribution functions and the set of parameters that characterize the CCP particles were calculated using original computer codes.

The definitions of calculated functions and parameters are as follows:

Mass size distribution function for CCP particles, $f(D)$, or distribution of relative mass of CCP, is defined as $f_i(D) = m_i / (M_{prop} \cdot \Delta D_i)$, where m_i is the mass of CCP in the i-th histogram sub-range, and ΔD_i is the width of i-th size interval.

Mass size distribution function for unburned aluminum in CCP, $f_i^{Al}(D)$, is defined as $f_i^{Al}(D) = f_i(D) \cdot \varepsilon_j^{Al}$, where $f_i(D)$ is the histogram of relative mass of CCP and ε_j^{Al} is the mass content of aluminum in the j-th sieve fraction. Index i is omitted below.

Left bound size D_L of agglomerates. The whole population of CCP can be treated as consisting of **coarse** (**agglomerate**, $D>D_L$) and **fine** (**oxide**, $D<D_L$) particles. For propellants under study bound size D_L was determined as a local minimum of the mass size distribution function for unburned aluminum $f^{Al}(D)$. Such approach was suggested previously in [10]. Using the function $f^{Al}(D)$ instead of the function $f(D)$ allows determination of the effective bound size D_L even for propellants with weak agglomeration because there is the size interval in the range of 20÷120 μm, where $f^{Al}(D) \approx 0$. For propellants Y1÷Y3 and Y5÷Y7 it was found D_L=55 μm, and for propellant Y4 D_L = 24 μm.

Right bound size D_R of agglomerates was determined as the right end of the monotonous tail of the $f(D)$ curve normally filled with CCP particles. With $D>D_R$, the most histogram intervals are empty and only some of them contain 1÷2 particles. Actually, a limited number (1÷8) of the particles with the size greater than D_R were excluded from consideration when calculating the integral characteristics for the mass distribution function. The formation of extra large particles in each test is caused by destroying the igniting nichrome wire in the flow of hot combustion products. These particles can be recognized by abnormal high value of their density (ρ = 4÷8 g/cm^3 instead of ρ = 2.2÷3.2 g/cm^3 for "normal" agglomerates). Thus, the agglomerate characteristics were calculated in the size range $D_L<D<D_R$ with $D_R \neq D_{max}$ (where D_{max} is maximal diameter of sampled particles).

The set of *dimensionless integral characteristics of CCP* was calculated for fine and agglomerate particles on the basis of experimental mass size distribution

functions $f(D)$ and $f^{Al}(D)$. These characteristics are scaled by the total mass of propellant burned, M_{prop} (for example, $m_f = M_f/M_{prop}$, where M_f is the mass of fine particles). Calculated parameters are listed below:

m_f – dimensionless mass of fine particles,

m^{Al}_f – dimensionless mass of free aluminum in fine particles,

m_{ag} – dimensionless mass of agglomerates,

m^{Al}_{ag} – dimensionless mass of free aluminum in agglomerates,

m_{ccp} – total dimensionless mass of CCP,

m^{Al}_{ccp} – total dimensionless mass of aluminum in CCP,

$\eta = m^{Al}_{ccp}/m^{Al}_{prop}$ - total incompleteness of aluminum combustion,

where $m^{Al}_{prop} = 0.18$ – dimensionless initial mass of aluminum in propellant.

EXPERIMENTAL RESULTS

The intensity of agglomeration process during aluminized propellant combustion can be described by several characteristic parameters which are discussed below.

The **agglomerate size** is one of the main parameters that characterizes a consolidation of the aluminum particles in the combustion wave. Mean sizes of agglomerates D_{mn} are presented in Table 3 along with the burning rate. The propellants Y2 and Y5 have minimal agglomerate sizes. Their values are close to those for propellant Y1 which contains non-coated aluminum.

The points in coordinates $\{r - D_{43}\}$ are grouped into two sets: propellants Y1, Y2, Y5 and Y4, Y3, Y6, see Fig. 1.

The mass size distribution functions $f(D)$ for sampled CCP particles corresponding to agglomerate size range 55-600 μm are plotted in Figs. 2a and 2b for these propellant groups.

Table 3. Burning rate r at pressure 46 atm and agglomerate mean size D_{mn} in the range (D_L- D_R)

Propellant ID	r mm/s	D_L - D_R μm	D_{10} μm	D_{20} μm	D_{30} μm	D_{21} μm	D_{32} μm	D_{43} μm	D_{53} μm
Y1	15.8	55 - 500	87	90	95	93	105	127	145
Y2	14.8	55 - 525	90	94	99	98	111	133	152

Y3	16.0	55 - 625	156	162	169	167	186	219	242
Y4	16.4	24 - 525	151	155	159	158	168	184	196
Y5	13.9	55 - 650	86	89	95	92	106	140	173
Y6	13.9	55 - 600	138	149	163	161	196	249	280

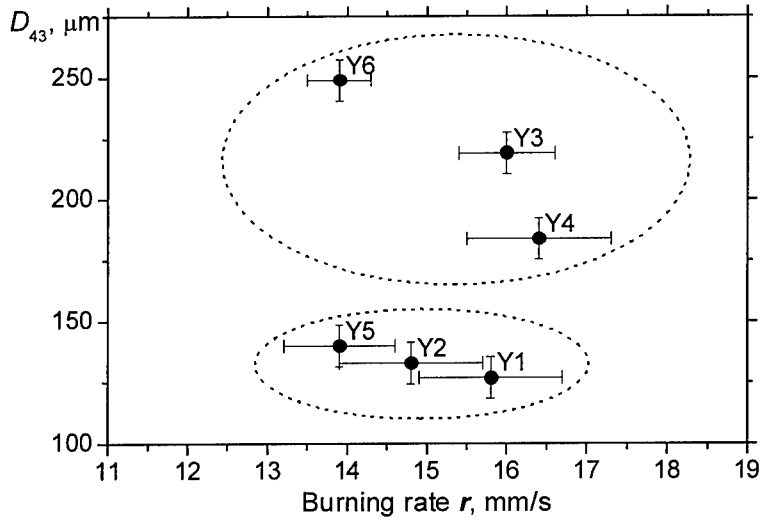


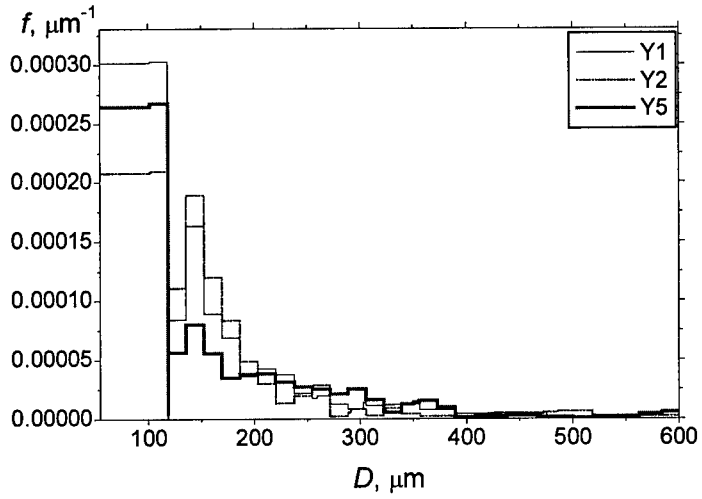
Fig. 1. Propellant burning rate and agglomerate mean size.

Analyzing Figs. 2a and 2b one can see that:

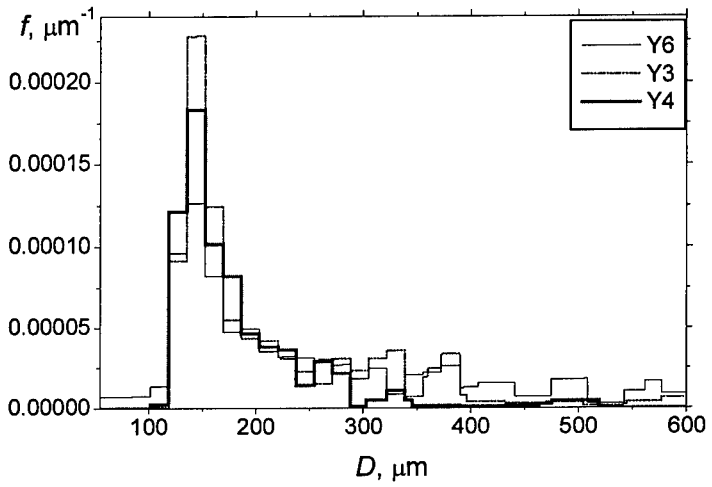
- The shape of curves for mass distribution functions in size range 118-300 μm is similar. They have maximum in histogram interval 136-153 μm and right-side asymmetry. One may assume that the formation of this portion of distribution curve is caused by the propellant geometrical structure, i. e. by size distribution of coarse propellant ingredients AP2 and HMX, through the "pocket" mechanism of agglomeration [12-13].

- Propellants Y3 and Y6 have relatively high mass contribution of particles with size D > 300 μm as compared with other propellants. It can be attributed to the action of multi-pocket mechanism of agglomeration [14]. Since the propellants under study are differ only in aluminum type, one may suppose the coating matters 3 and 6 produce some additional aggregation of aluminum particles that increases their agglomeration in the combustion wave.

Distinguishing feature of mass distribution function for propellants Y1, Y2, Y5 as compared with Y3, Y4, Y6 is heavy filling the size interval 55-118 μm. It means that the mass of particles is re-distributed from the size range 118-300 μm to the size range 55-118 μm that results in decrease of the mean sizes. It permits to divide the propellants onto two groups. In other words in the case of propellant group Y1, Y2, Y5 there is considerable proportion of agglomerates that formed inside the pocket but accumulate only part of aluminum contained within the pocket ("under-pocket" mechanism).



a)



b)

Fig. 2.
Mass size distribution function for agglomerates sampled at pressure 46 atm.
a) Propellants Y1, Y2, Y5. b) Propellants Y3, Y4, Y6.

Let us consider now other parameters characterizing the agglomeration intensity – dimensionless **agglomerate mass m_{ag}** that stands for the propellant's tendency to form a slag residue in the motor chamber, and **incompleteness of the aluminum combustion** η that stands for the propellant's capability to release a heat during aluminum conversion into oxide, see Table 4.

Table 4. Integral mass characteristics of CCP and of aluminum in CCP

Propt ID	m_{ccp}	m^{Al}_{ccp}	m_f	m^{Al}_f	m_{ag}	m^{Al}_{ag}	η
Y1	0.210	0.006	0.178	0.003	0.030	0.003	0.034
Y2	0.242	0.007	0.214	0.003	0.025	0.003	0.038
Y3	0.236	0.009	0.219	0.005	0.015	0.004	0.048
Y4	0.233	0.007	0.219	0.004	0.012	0.003	0.037
Y5	0.230	0.008	0.201	0.005	0.029	0.003	0.043
Y6	0.240	0.007	0.216	0.004	0.014	0.003	0.040

Indexes: Upper: Al – aluminum.
Lower: ccp – total CCP in size range 0.5 μm < D <D_{max}.
f – fine (oxide) particles in size range 0.5 μm < D <D_L.

ag – agglomerate particles in size range $D_L < D < D_R$.

Note: $m_{ccp} \geq m_f + m_{ag}$ and $m^{Al}_{ccp} \geq m^{Al}_f + m^{Al}_{ag}$ because of excluding the particles with size $D > D_R$ when processing the experimental data.

Figure 3 shows a comparison of agglomerate mass for different propellants. One can see that the agglomerate mass for the propellants Y3, Y6, Y4 is approximately twice less as compared with the reference propellant Y1. Propellant Y4 has minimal value of m_{ag}.

Incompleteness of aluminum combustion is plotted in Fig. 4 *versus* agglomerate mass. Taking into consideration the experimental error one may conclude that the propellants Y4, Y6, Y2 and Y1 have approximately the same aluminum combustion efficiency and it is slightly better than that for the propellants Y3 and Y5. Note that there is no direct correlation between m_{ag} and η.

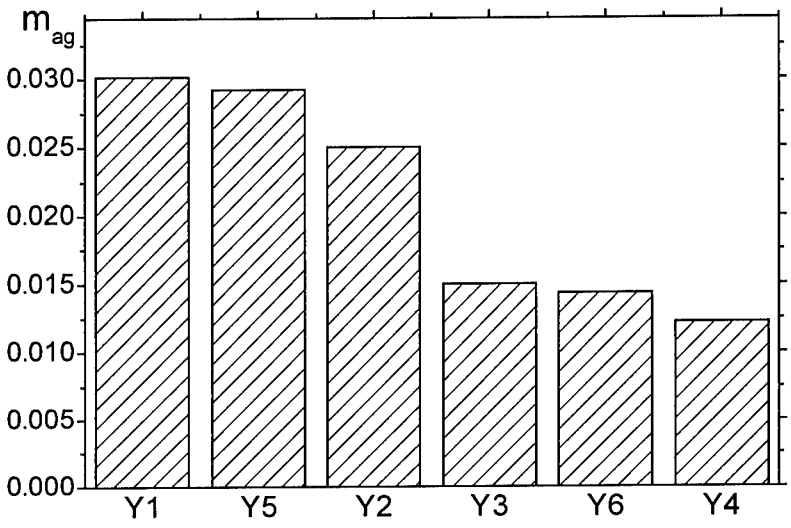


Fig. 3.
Dimensionless agglomerate mass for propellants under study at P = 46 atm.

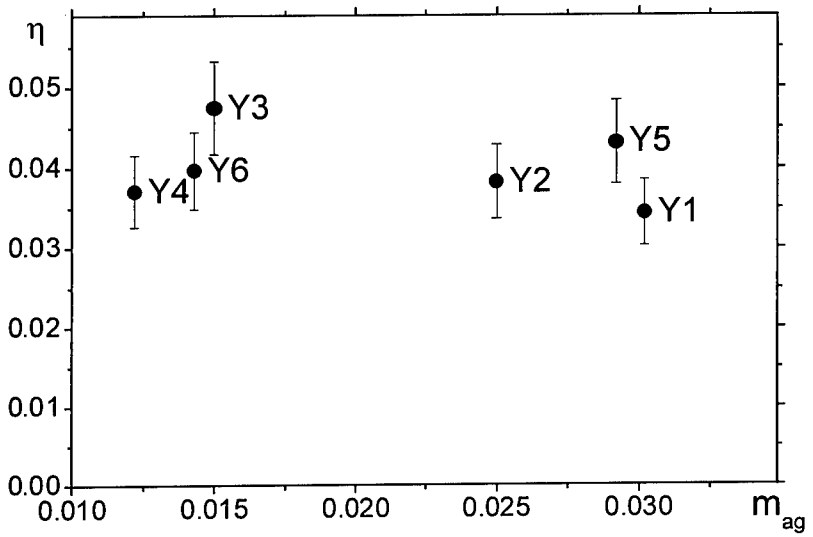


Fig. 4.
Incompleteness of aluminum combustion *vs* agglomerate mass (P = 46 atm).

CONCLUSIONS

The experimental estimation of the effect of aluminum particle coating on agglomeration parameters in solid propellant combustion has been performed.

The experiments were carried out under fixed experimental conditions: the propellants of given formulation type were tested using sampling technique at pressure 46 atm. Note that the particle size distribution for all coated aluminum powders used in propellant formulations were close to the reference non-coated aluminum powder.

It was found that a variation of only aluminum coating material leads to modification of the combustion characteristics - burning rate, agglomerate size distribution, combustion incompleteness of aluminum.

For aluminum coated with fluorine containing polymers A3, A4, and A6 the dimensionless agglomerate mass became approximately twice less in value as compared with the reference propellant containing non-coated aluminum. Here A3 is $Cl_2Si[OCH_2(CF_2\text{-}CF_2)_2H_2]_2$, A4 is $(CH_2{=}CH2\text{-}O)_2Si[OCH_2(CF_2\text{-}CF_2)_2H_2]_2$, and A6 is $CH_2{=}CF(COOCH_3)$.

Maximal effect was achieved in the case of A4-aluminum. Use of this aluminum also caused the increase in the burning rate (from 14 mm/s to 16.4 mm/s) while another coatings caused decreasing the burning rate. The effect of coatings studied on incompleteness of the aluminum combustion is relatively weak.

The results obtained demonstrate principal possibility for use of the coated aluminum to modify the solid propellant combustion characteristics. One may expect that the effect may become more sizable for the propellant formulations which are characterized with strong agglomeration trend.

ACKNOWLEDGMENTS

Experimental work has been sponsored in part by Russian Foundation for Basic Research (Grant No 99-15-96112). Partial support via NATO Linkage Grant No. 976783 is acknowledged.

The authors are grateful to Zhitnitskaya O. N., Bizyaev V. L., Fedotova T. D., Kir'yanova A. G. for the assistance in particle size and chemical analyses, and especially to Simonenko V. N. for manufacturing the propellants.

REFERENCES

1. Price E. W. "Combustion of Metalized Propellants", In: *Fundamentals of Solid Propellant Combustion,* Progress in Astronautics and Aeronautics, 1984, Vol. 90, pp. 479-514.

2. Breiter A. L., Maltsev V. M., Popov E. I. "Modification ways of condensed system metal fuels". *Combustion, Explosion and Shock Waves*, 1990, Vol. 26, No. 1.

3. Yagodnikov D. A., Voronetskii A. V., Maltsev V. M., Seleznev V. A. "On a possibility to increase the flame propagation velocity of aluminum suspension in air". *Combustion, Explosion and Shock Waves*, 1992, Vol. 28, No. 2.

4. Yagodnikov D. A., Voronetskii A. V. "Experimental and theoretical studies of ignition and combustion of capsulated aluminum-particle aerosuspension". *Combustion, Explosion and Shock Waves*, 1997, Vol. 33, No. 1.

5. Tai-Kang Liu, Song-Ping Luh, Huey-Cherng Perng. "Effect of boron particle surface coating on combustion of solid propellants for ducted rockets". *Propellants, Explosives, Pyrotechnics, 16*, 156-166 (1991).

6. Ing-Ming Shyu, Tai-Kang Liu. "Combustion characteristics of GAP-coated boron particles and the fuel rich solid propellant". *Comb. & flame 100:*634-644 (1995).

7. Kizhnyaev V. N., Suchanov G. T., Smirnova A. I. "The effect of the residual halogenous groups on hydrodynamic properties of the methylated poly-5-vinyl tetrazole". *High-molecular compounds. Series B,* 1991, Vol. 33, No 9, pp. 681-684. [In Russian].

8. Glotov O. G., Zyryanov V. Ya. "The Effect of Pressure on Characteristics of Condensed Combustion Products of Aluminized Solid Propellant". *Archivum Combustionis,* 1991, Vol. 11, No. 3-4, pp. 251-262.

9. Glotov O. G., Zyryanov V. Ya. "The Condensed Combustion Products of Aluminized Solid Propellants. I. The Method of Quenching at Various Distances from Burning Surface for Studying the Evolution of Particles". *Combustion, Explosion and Shock Waves*, 1995, Vol. 31, No. 1.

10. Glotov O. G., Zarko V. E., Karasev V. V., Beckstead M. W. "Aluminum Agglomeration in Solid Propellants: Formulation Effects". In*: Propellants, Explosives, Rockets, and Guns.* Proceedings of the 2nd Int. High Energy Materials Conference and Exhibit, December 8–10, 1998, IIT Madras, Chennai, India, pp. 131-137.

11. Fedotova T. D., Glotov O. G., Zarko V. E. "Chemical Analysis of Aluminum as a Propellant Ingredient and Determination of Aluminum and Aluminum Nitride in Condensed Combustion Products". *Propellants, Explosives and Pyrotechnics,* 2000, Vol. 25, No. 6, pp. 325-332.

12. Grigor'ev V. G., Zarko V. E., Kutsenogii K. P. "Experimental Investigation of the Agglomeration of Aluminum Particles in Burning Condensed Systems". *Combustion, Explosion and Shock Waves*, 1981, Vol. 17, No. 3.

13. Cohen N. S. "A Pocket Model for Aluminum Agglomeration in Composite Propellants", *AIAA Journal*, 1983, Vol. 21, No. 5, pp. 720-725.

14. Babuk V. A., Belov V. P., Khodosov V. V., Shelukhin G. G. "Investigation of the Agglomeration of Aluminum Particles During the Combustion of Metallized Composite Condensed Systems". *Combustion, Explosion and Shock Waves*, 1985, Vol. 21, No. 3.

THERMISCHE CHARAKTERISIERUNG VON TREIBLADUNGSPULVERN

P. Mäder, H.R. Bircher, B. Berger, P. Folly

Gruppe Rüstung, Fachabteilung Waffensysteme und Munition
Feuerwerkerstrasse 39, CH-3602 Thun

Abstract

Single base-, double base-, seminitramin- and nitramin-propellants were tested to characterize their thermal behaviour. Differential Scanning Calorimetry (DSC) analyses with different heating rates, KOENEN- and Slow Cook-off-tests were carried out. A possible influence of different grain geometries and formulations in respect of the thermal behaviour was investigated. An Arrhenius model was used to establish thermal activation energy values from DSC data. Relationships between chemical composition, start of decomposition and activation energies are shown.

Slow Cook-off-tests resulted in unexpected low start of decomposition temperatures for all nitrocellulose based propellants. Under confinement (according STANAG 4382) moderate reactions were seen. Nitramin propellants (LOVA) withstood thermal stress for a longer time and reacted at higher temperatures.

When conducting KOENEN-tests, for the various propellant types significant differences in the limiting diameter of the orifice plate were found.

1. Einleitung

Einbasige-, Zweibasige-, Seminitramin- und Nitramin-Treibladungspulver wurden in Bezug auf auf ihr thermisches Verhalten geprüft.

Mit drei grundsätzlich verschiedenen Testanordnungen (Differential Scanning Calorimetry, KOENEN-Test und Slow Cook-off-Test) wurde versucht, das thermische Verhalten der verschiedenen Treibladungspulver-Typen zu charakterisieren und Zusammenhänge zwischen Zusammensetzung, Korngeometrie, Treibladungspulver-Masse, Verdämmung und Aufheizgeschwindigkeit aufzuzeigen.

2. Untersuchungskonzept

2.1 Wahl der Treibladungspulver

In die Untersuchung wurden Einbasige- (SB), Zweibasige- (DB) und Seminitramin (SN) Treibladungspulver der Firma Nitrochemie Wimmis AG, sowie Nitramin-Treibladungspulver mit einbezogen. Die ausgewählten Pulvertypen wiesen 1-, 7- und 19- Loch Geometrien auf. Die nachfolgenden Tabellen geben einen Überblick über die Zusammensetzung und die Geometrie der untersuchten Treibladungspulver.

Tabelle 1: Zusammensetzung der untersuchten Treibladungspulver

TLP Typ	NC	NGL	Nitramin	Polymer	Weichmacher	Stabilisator
Einbasig (SB1, SB2, EI)	X				X	X
Doppelbasig (DB1, DB2)	X	X				X
Seminitramin (SN1, SN3)	X		X			X
LOVA (LOVA1, LOVA2)			X	X		X

NC = Nitrocellulose, NGL = Nitroglyzerin, Nitramin = Hexogen, Polymer = Cellulose Acet at Butyrat (inert) und Glizidyl Azid Polymer (energetisch), Weichmacher = herkömmliche, Stabilisator = herkömmliche

Tabelle 2: Geometrie der untersuchten Treibladungspulver

TLP Typ	Loch Anzahl	Länge [mm]	Durchmesser [mm]	Lochdurchmesser [mm]	Abbrand *	Volumen Korn [cm^3]	Oberfläche Korn [mm^2]	Gewicht Korn [g]
SB1	1	2.10	1.95	0.14	0	0.0062	19.731	0.0087
SB2	19	10.61	9.08	0.30	++	0.6728	619.472	1.0356
EI	7	4.42	4.27	0.14	+	0.0628	101.325	0.1025
DB1	1	3.40	2.67	0.97	0	0.0165	48.600	0.0265
DB2	19	10.87	9.63	0.18	++	0.7865	590.350	1.2422
SN1	7	2.96	2.71	0.12	+	0.0168	44.390	0.0249
SN3	7	3.05	3.80	0.14	+	0.0343	68.268	0.0332
LOVA1	7	2.90	3.60	0.16	+	0.0291	63.078	0.0480
LOVA2	7	7.00	3.30	0.30	+	0.0564	134.870	0.0775

* 0 = Plateau Abbrand + = progressiver Abbrand ++ = sehr progressiver Abbrand

2.2 Untersuchungsmethoden

Differential Scanning Calorimetry (DSC)

Bei der DSC wird der Wärmestrom (Wärmeleistung in Milliwatt) zur Kompensation einer Temperaturdifferenz zwischen Probe und Referenzsubstanz gemessen. Die von uns verwendete Aufheizrate beträgt **5°C/min**. Die Aktivierungsenergie wurde gemäss [1] bestimmt. Dazu wurden auch DSC Messungen mit Aufheizraten von 10°C/min und 20°C/min durchgeführt.

Für die DSC-Messungen wurden zirka 2mg der Prüfsubstanz in einen Aluminiumtiegel eingewogen und dann mit einem perforierten Deckel (Verdämmung gering) verschlossen. Die Onset-Temperaturen sowie die Temperaturen der Peak Maxima wurden ausgewertet.

Stahlhülsen Test (KOENEN)

Mit diesem Test kann die Empfindlichkeit von Feststoffen und Flüssigkeiten gegenüber intensiver Hitze (**Aufheizrate 3.3°C/sec**) unter verschiedenen Verdämmungsbedingungen untersucht werden.

Die Durchführung des Versuchs erfolgte gemäss STANAG 4491, Annex C1, sowie dem "Orange Book" [2], UN Test 1(b) oder 1(a).

Vor dem Beginn einer Experimentreihe ist es erforderlich, denjenigen Propangasfluss für die Brenner zu ermitteln, bei dem im Temperaturbereich von 50°C bis 250°C das in der Stahlhülse eingefüllte Dibutylphtalat mit 3.3 ± 0.3°C pro Sekunde erhitzt wird. Die Eichung wird mit einer 3mm Düsenplatte durchgeführt.

Die Probe wird in eine Stahlhülse von 75mm Länge und 24mm Innendurchmesser in drei Schritten eingefüllt und jeweils mit einer Kraft von 80N komprimiert. Für das Anbringen dieser Presskraft wird eine spezielle Vorrichtung mit Stempel verwendet. Pro Versuch werden zirka 25g Treibladungspulver benötigt. Nach dem Anzünden der Gasflammen wird einerseits die Zeit bis zur ersten sichtbaren Reaktion der Substanz und andererseits die Zeit bis zum Reaktionsende gemessen. Zusätzlich wird der Durchmesser des Loches in der Düsenplatte festgehalten.

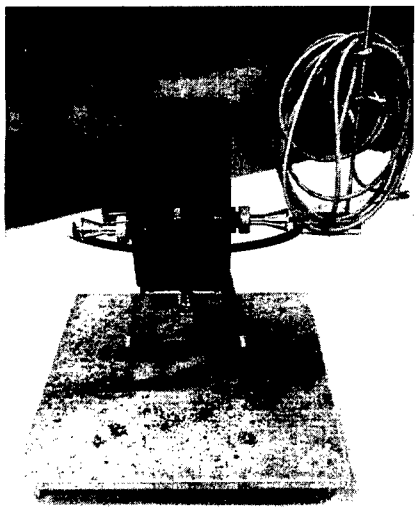


Abbildung 1: Stahlhülsentest Aufbau (KOENEN)

Hauptkriterium für die Beurteilung der Heftigkeit der Reaktion ist die Zerlegungsart der Stahlhülse. Dabei werden die folgenden Zerlegungszustände unterschieden:

0: Hülse unverändert

A: Hülsenboden aufgebläht

B: Hülsenboden und Wandung aufgebeult

C: Hülsenboden abgerissen

D: Hülse aufgerissen

E: Hülse in zwei Teile zerrissen

F: Hülse in drei oder mehr, hauptsächlich grosse Stücke zerlegt

G: Hülse in viele, hauptsächlich kleine Stücke zerlegt, Verschraubung aufgeweitet oder zerlegt

Beim KOENEN-Test wird der minimale Durchmesser, bei dem in drei Versuchen nie eine Reaktion der Heftigkeit "F" oder "G" beobachtet werden konnte, als Grenzdurchmesser bezeichnet.

Slow Cook-off-Test

Beim Slow Cook-off-Test wird die Umsetzungstemperatur und die Heftigkeit der Reaktion einer Substanz unter definierter Verdämmung bei einer kontinuierlichen **Aufheizrate von 3.3°C/h** bestimmt.

Der "EIDS Slow Cook-off-test" (EIDS = Extremely Insensitive Detonating Substances) wird gemäss "Orange Book" [2] der UNO, als Test 7(f) durchgeführt. Die Verdämmungsverhältnisse sind wie folgt definiert:

Die zu prüfende Substanz wird in ein nahtloses Stahlrohr von 200mm Länge, einem Innendurchmesser von 47.0mm und einer Wandstärke von 4.0mm eingefüllt. Die beidseitigen Verschlusskappen aus Stahl haben eine minimale Dimensionierung die der Wandstärke des Rohres entspricht. Das Drehmoment, mit dem die Stahlkappen aufgeschraubt werden, beträgt 204Nm.

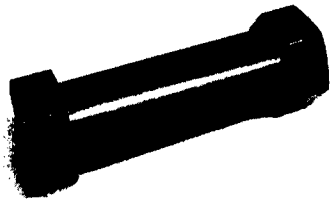


Abbildung 2: UN Stahlrohr

In einem Ofen wird ein einzelner Prüfkörper nach einer Konditionierungsphase (40°C/8h) mit einer Heizrate von 3.3°C/h kontinuierlich bis zum Eintreten eines Ereignisses aufgeheizt. Dabei wird die Temperatur aufgezeichnet und basierend auf den resultierenden Splittern des UN Stahlrohres und des Ofens die Heftigkeit des Ereignisses bestimmt. Es werden zirka 350g Treibladungspulver in das UN Stahlrohr eingefüllt.

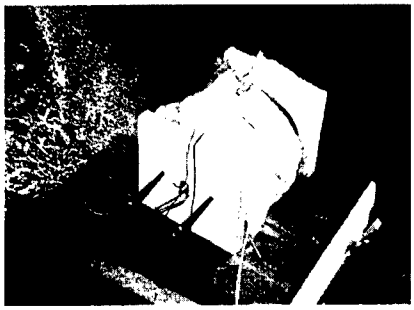


Abbildung 3: Slow Cook-off Ofen

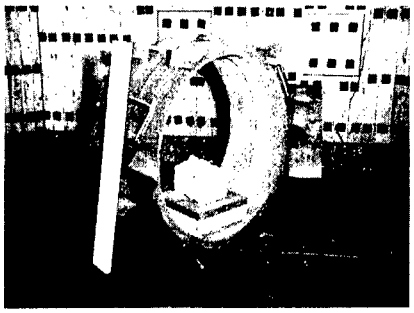


Abbildung 4: Slow Cook-off Versuchsaufbau

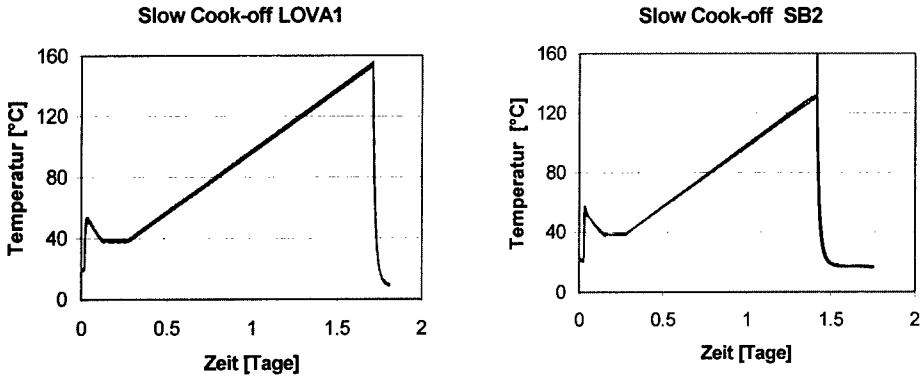


Abbildung 5: Slow Cook-off Temperaturverlauf

Beurteilung der Heftigkeit einer Reaktion

Obwohl im "Orange Book" [2] nicht explizit vorgesehen, wurde beim EIDS „Slow Cook-off-Test" die Heftigkeit einer Reaktion aufgrund der im MIL STANDARD 2105B definierten Reaktionsniveaus beurteilt.

Das Fragmentierungsmuster eines UN-Stahlrohrs kann mit Hilfe eines Referenzschemas dem entsprechenden Reaktionstyp zugeordnet werden.



Abbildung 6: Zuordnung von Splitterbildern zu Reaktionstypen

3. Ergebnisse

3.1 DSC

Zur Bestimmung der Temperatur des Zersetzungsbeginns (Onset) und der Temperatur der maximalen Exothermie wurden die verschiedenen Treibladungspulver Typen zwischen 30°C und 400°C mit einer Heizrate von 5°C/min aufgeheizt. Zur Berechnung der Aktivierungsenergie [3] wurden zudem Untersuchungen mit Aufheizraten von 10°C/min und 20°C/min durchgeführt.

Damit die berechneten Aktivierungsenergien überprüft werden konnten, wurde nach dem gleichen Verfahren die Aktivierungsenergie von Nitrocellulose bestimmt und mit Literaturangaben [5] verglichen.

Tabelle 3: Thermische Daten und Aktivierungsenergien von Nitrocellulose (NC)

Heizrate [°C/min]	**Onset** [°C]	**Peak Maximum** [°C]	**Peak extrapoliert** [°C]	**E_a bestimmt** [kJ/mol]	**E_a Literatur** [kJ/mol]
5	194.24	202.49	199.31	185	180 - 193
10	200.64	209.54	208.30		
20	207.96	213.36	213.15		

Die mittels DSC Messungen bestimmte Aktivierungsenergie stimmt mit den Literaturangaben überein [5].

Tabelle 4: Thermische Daten und Aktivierungsenergien verschiedener Treibladungspulver

TLP Typ	**Heizrate** [°C/min]	**Onset** [°C]	**Peak Maximum** [°C]	**E_a** [kJ/mol]
Einbasig, 1-Loch (SB1)	5	191.9	195.1	193
	10	195.8	200.4	
	20	200.5	207.9	
Einbasig, 19-Loch (SB2)	5	192.6	196.7	223
	10	197.6	201.2	
	20	199.3	207.7	
Einbasig, 7-Loch (EI)	5	191.5	198.3	251
	10	197.6	205.5	
	20	197.1	207.1	
Doppelbasig, 1-Loch (DB1)	5	179.9	189.9	101
	10	182.1	191.9	
	20	191.4	209.9	
Doppelbasig, 19-Loch (DB2)	5	172.6	194.2	131
	10	177.0	202.4	
	20	183.7	213.1	
Seminitramin, 7-Loch , (SN1) 20%RDX	5	191.7	199.8	195
	10	194.7	199.5	
	20	196.4	209.0	
Seminitramin, 7-Loch, (SN3) 40%RDX	5	189.5	196.7	203
	10	194.7	196.8	
	20	200.0	205.8	
LOVA 1, Polymer Inert, 75%RDX	5	210.2	232.6	136
	10	202.0	243.5	
	20	204.8	254.1	
LOVA 2, Polymer energetisch, 75% RDX	5	200.6	226.9	117
	10	221.0	238.6	
	20	231.8	251.5	

Stahlhülsen Test (KOENEN)

Die erhaltenen Grenzdurchmesser und die Zerlegungsarten der untersuchten Treibladungspulver sind in Tabelle 5 dargestellt.

Tabelle 5: Treibladungspulver-Masse, Geometrie und Reaktions-Charakteristik

TLP Typ	Loch Anzahl	TLP Masse [g]	TLP Körner pro Hülse [Stk]	Oberfläche Hülsenladung [mm^2]	Reaktions-zeit [s]	Grenz-durchmesser [mm]	Fragmen-tation
SB1	1	27.28	3136	61876	6	8	B
SB2	19	21.45	21	13008	7	12	B
EI	7	26.58	259	26243	8	12	B
DB1	1	23.45	885	43011	7	12	B
DB2	19	23.48	19	11216	7	20	B
SN1	7	26.49	1046	46431	8	12	B
SN3	7	26.70	804	54887	8	8	B
LOVA1	7	27.14	565	35639	13	5	B
LOVA2	7	21.20	274	36954	11	8	B

Die unterschiedlichen Treibladungspulver Massen zur Füllung der Stahlhülse sind auf die verschiedenen Geometrien zurückzuführen.

Slow Cook-off-Test

Die gemessenen Reaktionszeiten, Zersetzungstemperaturen und Reaktionstypen sind in Tabelle 6 dargestellt.

Tabelle 6: Treibladungspulver Masse, Geometrie und Reaktions-Charakteristik

TLP Typ	Loch Anzahl	TLP Masse [g]	Gravi-Meter [g/dm^3]	TLP Körner pro Rohr [Stk]	Oberfläche Rohrladung [cm^2]	Reaktions-zeit [h]	Reaktions-temperatur [°C]	Reaktions-typ
SB1	1	363	955	55357	10922	27	129	V
SB2	19	330	1051	505	3128	27	131	V
EI	7	367	1063	5485	5557	33	126	V
DB1	1	307	1127	18237	8863		124	III-IV
DB2	19	332	1044	439	2591	25	125	IV
SN1	7	355	975	20334	9026	27	129	IV
SN3	7	357	971	10037	6852	28	132	III-(IV)
LOVA1	7	359	1034	11761	7418	41	154	V
LOVA2	7	291	1192	2734	3687	41	152	IV

Fragmentierung des UN Stahlrohrs nach dem Slow Cook-off-Test

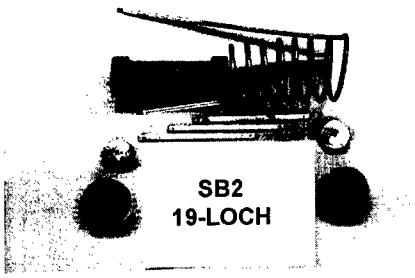


Abbildung 7: Reaktionstyp V

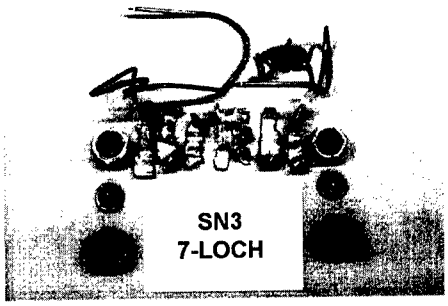


Abbildung 8: Reaktionstyp III-(IV)

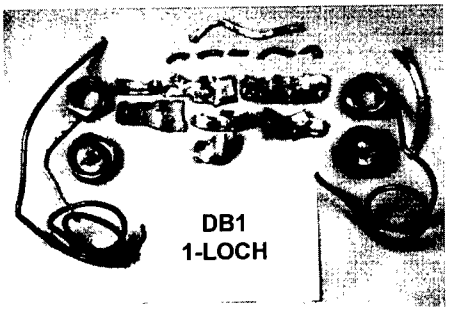


Abbildung 9: Reaktionstyp III-IV

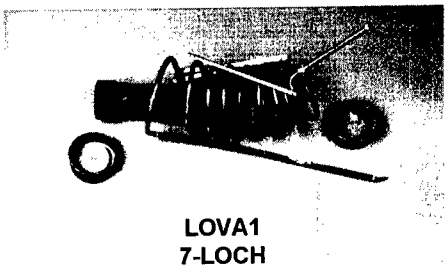


Abbildung 10: Reaktionstyp V

4. Diskussion

Die Untersuchung der Treibladungspulver mit Hilfe der Differential Scanning Calorimetry (DSC) zeigt, dass der Beginn der thermischen Zersetzung primär von der chemischen Zusammensetzung abhängig ist. So wird bei einbasigen Treibladungspulvern und bei Seminitraminpulvern auf der Basis von RDX die chemische Zersetzung durch die Nitrocellulose ausgelöst. Doppelbasige Pulver hingegen zeigen, aufgrund der geringeren thermischen Stabilität von Nitroglycerin (NGL: 162°C bei 4K/Min) einen früheren Zersetzungsbeginn. Interessant ist das thermische Verhalten des sogenannten EI Pulvers, welches trotz der inhomogenen Konzentrationsverteilung des zu 5% vorhandenen Sprengöls, sich in Bezug auf den thermischen Zersetzungsbeginn wie ein einbasiges Pulver verhält. Ein grundsätzlich anderes Verhalten zeigen bei den DSC-Untersuchungen die auf dem Energieträger RDX basierenden Nitramin-Treibladungspulver. Einerseits wird der Beginn der thermischen Zersetzungsreaktion bei bedeutend höheren Temperaturen detektiert (ca. 200°C), andererseits ist der Anstieg des Wärmeflusses bis zu den Peakmaxima

(227°C) bedeutend flacher. Dabei spielt es keine Rolle ob ein energetisches (GAP) oder inertes (CAB) Polymer verwendet wird. Offenbar wird die chemische Zersetzungsreaktion der beiden untersuchten Nitramin-Treibladungspulver durch den Energieträger RDX (207°C, 5°C/Min, Onset) ausgelöst, da die thermische Zersetzung der Binderpolymere erst bei höheren Temperaturen einsetzt (z.B. GAP gehärtet: 226°C, 5°C/Min, Onset).

Auch in Bezug auf die thermischen Aktivierungsenergien können drei Gruppen unterschieden werden. Da bei hohen Temperaturen RDX (ΔE_a = 189 kJ/Mol [4]) und NC (ΔE_a = 180-193 kJ/Mol [5]) ähnliche Aktivierungsenergien haben, liegen diese sowohl für einbasige-, wie auch Seminitraminpulver im Bereich zwischen 193 und 223 kJ/Mol. Die Aktivierungsenergien doppelbasiger Pulver sind, aufgrund der destabilisierenden Wirkung von Nitroglycerin (ΔE_a = 90 bis 134 kJ/Mol [6]) erwartungsgemäss bedeutend niedriger.

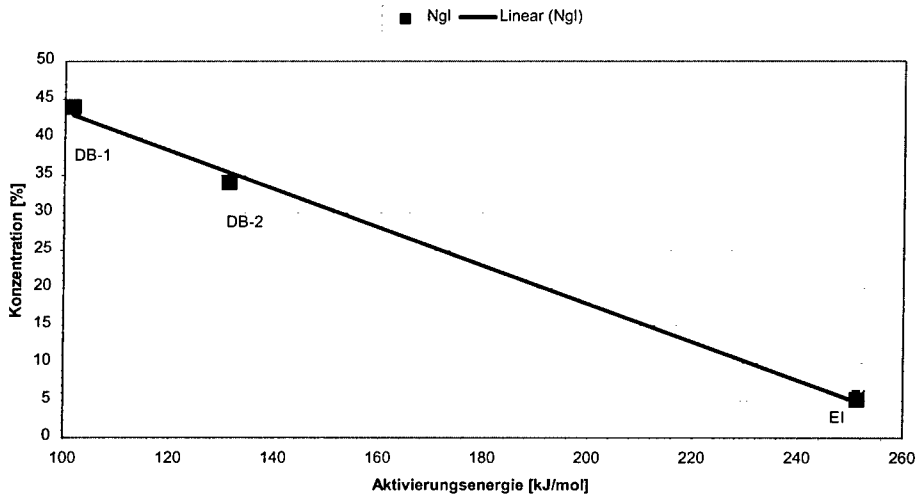


Abbildung 10: Korrelation von Aktivierungsenergie und Nitroglyceringehalt

Im gleichen Bereich liegen die Aktivierungsenergien der Nitramin-Treibladungspulver, welche jedoch bei Temperaturen >200°C ermittelt wurden. Es wird in der Literatur mehrfach darauf hingewiesen, dass Aktivierungsenergien eine starke Temperaturabhängigkeit zeigen können. Deshalb dürfen thermische Aktivierungsenergien, welche im Bereich der Zersetzungstemperaturen ermittelt wurden, nicht mit der chemischen Stabilität von Stoffen bei Umgebungstemperatur in Verbindung gebracht werden. Bei doppelbasigen Treibladungspulvern scheinen die Aktivierungsenergien durch die Nitroglycerinkonzentration, bei Nitramin-Pulvern durch die Art des Binderpolymers (inert oder energetisch) beeinflusst zu werden.

Bei der Interpretation der Daten aus dem KOENEN-Test muss neben der chemischen Zusam-

mensetzung der Treibladungspulver auch die Korngeometrie und die damit verbundene Progressivität des Abbrandes berücksichtigt werden. Wie unsere Versuche zeigen, ist der Grenzdurchmesser der Düsenplatte nicht primär von der ursprünglichen Gesamtoberfläche des getesteten Treibladungspulvers oder von dessen Schüttdichte abhängig.
Vergleicht man die beiden einbasigen Pulver SB1 und SB2 miteinander, stellt man fest, dass eine hohe Abbrandprogressivität einen grösseren Grenzdurchmesser zur Folge hat. Den gleichen Effekt stellt man auch bei doppelbasigen Pulvern (DB1 und DB2) fest, wobei diese aufgrund ihres Nitroglyceringehaltes grundsätzlich brisanter reagieren als Einbasige. Ein 7-Loch EI-Pulver verhält sich beim KOENEN-Test wie ein konstant brennendes (1-Loch) doppelbasiges oder ein sehr progessiv brennendes (19-Loch) einbasiges Pulver. Seminitraminpulver mit 7-Lochgeometrie (mittlere Progressivität) sind bezüglich ihres Verhaltens beim KOENEN-Test mit EI-Pulvern vergleichbar. Ein erhöhter RDX Gehalt scheint sich jedoch positiv auf den Grenzdurchmesser auszuwirken (vgl. SN1 und SN3). Das gutmütigste Verhalten zeigen erneut die beiden Nitramin-Treibladungspulver. Dabei sind aber wiederum klare Unterschiede feststellbar, welche auf die Verwendung von inerten oder energetischen Binder Polymeren zurückzuführen sind.

Die Resultate der Slow Cook-off-Tests zeigen ein anderes Bild. Mit Ausnahme der Nitramin-Treibladungspulver reagieren alle untersuchten Proben zwischen 124°C und 132°C. Diese überraschend tiefen Reaktionstemperaturen zeigen keine Abhängigkeit von der Oberfläche der Pulverkörner oder von der Abbrandprogressivität. Tendenziell reagieren doppelbasige Pulver bei tieferen Temperaturen. Die Unterschiede zwischen den Onset-Temperaturen, welche mit DSC (5°C/Min, 2mg, keine Verdämmung) ermittelt wurden und den Daten aus den Slow Cook-off-Tests (3.3°C/h, 300 - 360g, 4mm Stahlverdämmung), sind in der Regel grösser als 60°C (vergl. Abbildung 10).
Die Heftigkeit der Reaktion hingegen, kann bei Slow Cook-off-Tests wiederum fast ausschliesslich auf die Rezeptur zurückgeführt werden. So reagieren einbasige und EI-Pulver sehr moderat (Typ V), währenddem doppelbasige- und Seminitramin-Treibladungspulver durchwegs heftiger reagieren (Typ III und IV). Dabei scheint bei steigender Nitroglycerin- bzw. RDX-Konzentration die Reaktion heftiger zu werden. Wiederum fällt die moderate Reaktion des Nitramin-Treibladungspulvers mit inertem Binder auf (Typ V). Die Verwendung von GAP als energetisches Bindermaterial erhöht zwar die Gesamtenergie des Systems, zeigt aber in Bezug auf die Heftigkeit der Reaktion beim Slow Cook-off-Test eindeutige Nachteile.

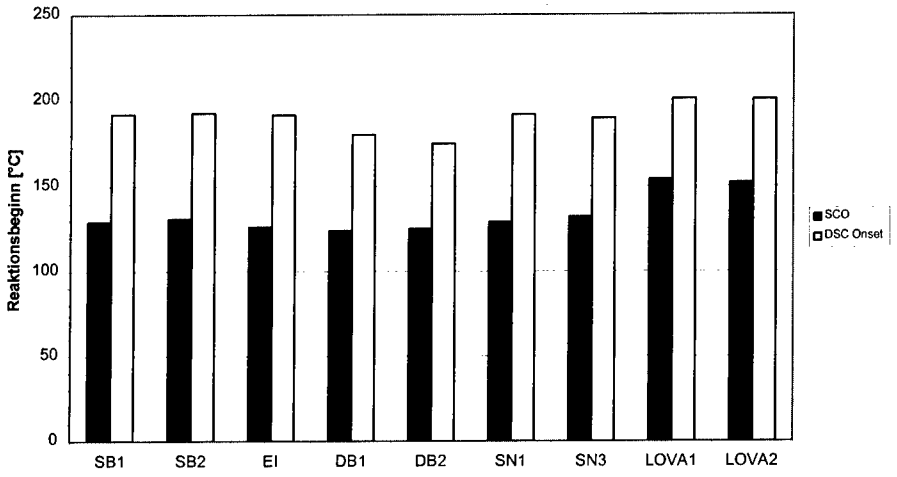


Abbildung 10: Vergleich der Onset Temperaturen aus DSC und Slow Cook-off (SCO)

Unsere Untersuchungen zeigen, dass Nitramin-Treibladungspulver mit inertem Binder bezüglich dem thermischen Verhalten klare Vorteile aufweisen. Es ist jedoch klar, dass auch unter Einbezug des energetischen Binders höchstens das Leistungsspektrum von einbasigen Pulvern erreicht werden kann. Doppelbasige Pulver, welche die höchsten Explosionswärmen aufweisen, haben eindeutig das schlechteste thermische Verhalten. Seminitraminpulver ergeben ein durchzogenes Bild. Währenddem ihr Verhalten in der DSC-Untersuchung demjenigen von einbasigen Pulvern ähnlich ist, kummulieren sich beim Slow Cook-off-Test sowohl die Nachteile der Nitrocellulose (tiefe Reaktionstemperatur), wie auch diejenigen des Hexogens (Heftigkeit der Reaktion).

Verdankungen

Für die Durchführung der DSC Messungen und Mithilfe bei den Slow Cook-off-Tests wird der Einsatz der Herren G. Reinhard (FS261) und J. Gyseler (FS264) verdankt. Herr R. Winkler (SM Thun) führte die KOENEN-Tests mit grossem Engagement durch. Herrn S. Engel (FS261) danken wir für die Hilfe bei der grafischen Gestaltung der Illustrationen.

5. Literatur

[1] American Society for Testing Materials (ASTM), Standard Test Method for Arrhenius Kinetic Constants for Thermally Unstable Materials, Annual Book of ASTM Standards, 1979, p 457

[2] UN ST/SG/AC.10/11/Rev.2, Recommendations on the Transport of Dangerous Goods

[3] T.Ozawa, Kinetic Analysis of Derivative Curves in Thermal Analysis, J. Thermal Analysis, 1970, Vol 2, p 301-324

[4] T. Urbanski, Chemistry and Technology of Explosives, 1986, Vol III, p 83

[5] T. Urbanski, Chemistry and Technology of Explosives, 1986, Vol II, p 308

[6] T. Urbanski, Chemistry and Technology of Explosives, 1986, Vol IV, p 298

THERMAL DECOMPOSITION AND COMBUSTION OF 2-METHYL-5-NITROTETRAZOLE

Vasily I. Kolesov, Valery P. Sinditskii, Viacheslav Y. Egorshev, Boris A. Lurie, Michail Y. Soloviev

Mendeleev University of Chemical Technology, 9 Miusskaya Square, 125047, Moscow, Russia

ABSTRACT

The combustion behavior and thermal decomposition kinetics of 2-methyl-5-nitrotetrazole (MNT) have been studied. Temperature profiles in the MNT combustion wave were measured using thin tungsten-rhenium thermocouples embedded in the strands. Analyses of gaseous and condensed combustion products as well as thermolysis products were carried out by means of chromatography, IR-, UV- and mass-spectrometry.

Combustion of the endothermic MNT molecule containing the oxidizing nitro group as well has been shown to proceed in the gas phase in accordance with the mechanism of burning of volatile explosives. MNT monomolecular decomposition reaction is the rate-controlling one and determines the burning rate. Incorporation of the nitro group into the tetrazole molecule increases not only the final combustion temperature, but temperature of the zone where the rate-controlling reaction occurs, thus affecting the burning rate.

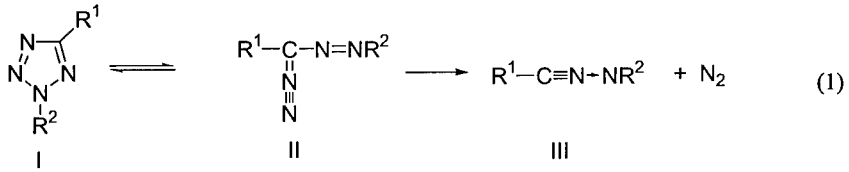
INTRODUCTION

The tetrazole chemical class comprises high-energy polynitrogen compounds that are of interest as propellant ingredients in the gas generator application. Besides, certain of tetrazoles possess the ability to modify the burning behavior of double base and composite propellants.

The burning rate of most endothermic substances is defined by the thermal decomposition kinetics [1]. This is the main distinctive feature of these compounds as compared to conventional redox systems, which burning rate is governed by not only the decomposition kinetics but essentially the subsequent secondary exothermic reactions of low activation energy. From scientific and practical standpoints, it is important to study the combustion behavior of compositions that would comprise both an endothermic compound and a redox system as the ingredients. This approach can be realized in studying combustion of an endothermic substance, which in addition contains an oxidizing group. Such a substance was chosen for the present investigation to be 2-methyl-5-nitrotetrazole (MNT), comprising both the endothermic tetrazole cycle and the nitro group. To attain the set goal it was necessary to investigate not only the combustion behavior but the thermal decomposition kinetics and mechanism also.

The stationary-state combustion of the 5-substituted tetrazoles was investigated previously [2,3,4,5] and some of the peculiar features were revealed. The main feature of tetrazole burning lies in the fact that, in the absence of oxidizing agents, the combustion process is accomplished by formation of thermostable high-energy nitrile derivatives rather than thermodynamic equilibrium composition of the combustion products. This results in incomplete heat release during combustion, even at high pressures. In studying combustion of 5-substituted tetrazoles, the electronic properties of the substituent have been shown to strongly affect the burning rate [3], whiles slightly influence the thermal stability of the tetrazole cycle [6]. This discrepancy is accounted for [5] by different ratio of 1H and 2H tetrazole tautomeric forms in the gas phase, where the burn rate controlling reactions occur and in the condensed phase, where the slow thermal decomposition is commonly investigated at 150-250°C [6,7].

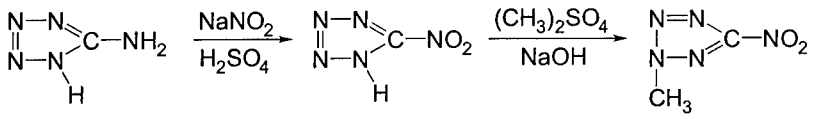
The structure of 2,5-disubstituted tetrazoles (I), to which MNT belongs, excludes the possibility of proton tautomeric transformations, resulting in more selective thermolysis than in the case of 5-substituted tetrazoles [7, 8]. The main transformation pathway is the monomolecular decomposition with liberation of nitrogen and formation of nitrilamine (III):



Further eliminating of RCN molecule is similar to liberation of HCN in the case of tetrazole. Impossibility of proton tautomeric transformations for 2,5-disubstituted tetrazoles permits more correct extrapolation of slow thermal decomposition data to the high-temperature combustion zone. The presence of the nitro group in the MNT molecule is believed to prevent from incomplete heat release typical for tetrazole combustion in the absence of the oxidizer.

EXPERIMENTAL

MNT Preparation and Properties. 2-Methyl-5-nitrotetrazole was prepared by the diazotization of 5-aminotetrazole in the excess of $NaNO_2$ followed by methylation with dimethylsulphate:



On the methylation, some amount of 1-methyl-5-nitrotetrazole is formed as an impurity which can be removed for the most part by recrystallization.

MNT is white plate-like crystals with density of 1.64 g/cc and melting point 86°C [9]. The enthalpy of formation was obtained to be 264.0 kJ/mole*). It is a rather sensitive explosive material with ignition temperature 263°C and detonation velocity 7800 m/s at its maximum density [10].

Burn Rate and Temperature Measurements. The combustion behavior of MNT at elevated pressures was studied in a window constant-pressure bomb. Investigation in the sub-atmospheric region was carried out in a vacuum chamber of 40 l volume. The whole pressure range was 0.005-36 MPa. A slit camera was used to determine a character of the combustion process as well as burning rate values. Samples to test were prepared by pressing the powdered substance into transparent acrylic tubes to the relative density of 0.9-0.95. The burn rate measurement accuracy was 3%.

Temperature profiles in the MNT combustion wave were measured using Π-shaped micro-thermocouples embedded in the pressed strands. The thermocouples were welded from 25 μm diameter tungsten—5% rhenium and tungsten—20% rhenium wires and rolled in bands to obtain 7 μm bead size.

Thermal Decomposition. The kinetics of MNT thermal decomposition have been studied in the both condensed and gas phases. Burdon-type compensation manometers with the reaction volume of about 10cc were used for monitoring the gas evolution during the course of the thermal decomposition as well as for obtaining the temperature dependence of MNT vapor pressure

Analysis. A gas chromatograph (ΛXM-8DM) and a Specord UV-VIS spectrophotometer were used for quantitative analyses of the gaseous products of MNT decomposition and combustion at sub-atmospheric pressures.

The condensed combustion and decomposition products were analyzed with a Nicolet mod. Magna Fourier spectrometer and a gas-liquid chromatograph combined with a mass-analyzer

*) The enthalpy of MNT formation was determined by Dr. T.S. Kon'kova and Dr. Yu.N. Matyushin of Institute of Chemical Physics of Russia

module. The concentration of HCN in the combustion products was measured with an accuracy of 0.1 mg/l by using an industrial detector.

RESULTS AND DISCUSSION

Burning behavior of MNT

The first studies of MNT combustion are presented in works [2,3]. It possesses elevated burning rates, which are several times higher than those of HMX and nitroesters (Fig. 1). The pressure dependence of MNT burning rate can be divided into three sections represented by the following equations:

Burning rate law, cm/s	Pressure range, MPa
$1.30p^{0.836}$	0.005 - 5.5
$2.25p^{0.54}$	5.5 -14
$0.446p^{1.15}$	14 -35

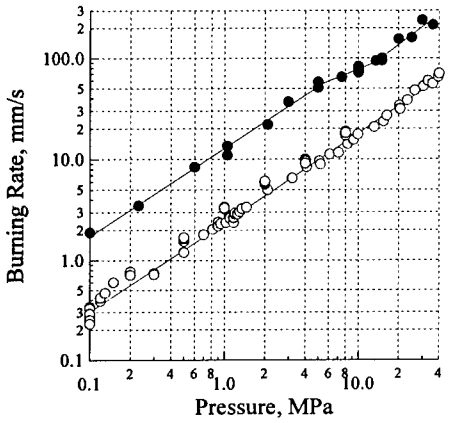


Fig. 1. Comparison of the combustion characteristics of MNT (black circles) and HMX (light circles).

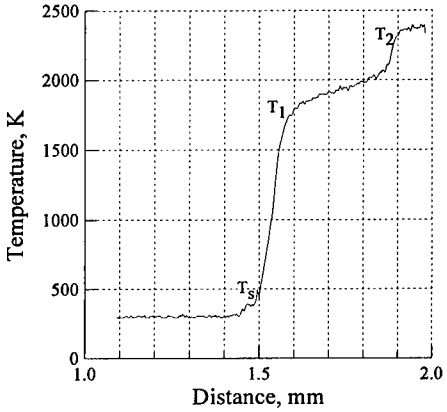


Fig. 2. Typical temperature profile on MNT combustion at 0.3 MPa.

Thermocouple-aided measurements were carried out within the pressure range of 0.01-1.1 MPa. A typical temperature profile of MNT combustion at 0.3 MPa is shown in Fig. 2. All results obtained are given in Table 1 and Fig. 3, which include the surface temperature (T_s), the temperature gradient above the surface (φ), temperatures of the onset and the ending of the first flame (T_1 and T_{1max}), and temperatures of the onset and the ending of the final flame (T_2 and T_{max}).

In the low-pressure range (0.01-0.02 MPa), there is a large molten layer at the MNT burning surface. Adhering of the liquid to the thermocouple horizontal section followed by a sharp springing out of the thermo-junction to the high-temperature gas zone leads to the apparent broadening of the molten layer and overstated values of the temperature gradient above the surface. In this connection, data of Table 1 on the temperature gradient should be considered as estimated ones.

Table 1. Characteristic temperatures of MNT combustion wave.

P, MPa	T_s, K	$\varphi*10^{-7}$, K/m	T_1, K	T_{1max}, K	T_2, K	T_{max}, K
0.01	440 ± 10	1	1200 ± 20	1250 ± 20		1250 ± 20
0.02	490 ± 10	3	1280 ± 20	1420 ± 20		1530 ± 20
0.10	535 ± 10	5 ± 1	1370 ± 15	1530 ± 20		1620 ± 10
0.23	550 ± 20	3 ± 1	1415 ± 15	1660 ± 20	2116 ± 20	2274 ± 20
0.3	500 ± 40	3 ± 1	1600 ± 50	1800 ± 20	2340 ± 20	2390 ± 20
0.7	580 ± 50	3 ± 1	1700 ± 50	1880 ± 60	2400 ± 20	2580 ± 10
1.1	600 ± 50	3 ± 1	1800 ± 50	2040 ± 50	2420 ± 20	2580 ± 10

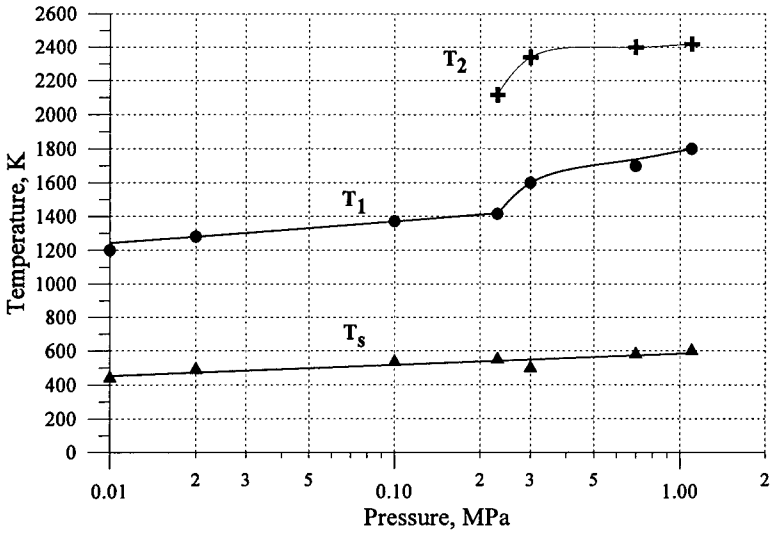


Fig. 3. Pressure dependence of characteristic temperatures of MNT combustion wave.

Two-flame structure of the MNT combustion wave is clearly noticeable in the profiles at pressures from 0.2 to 0.7 MPa (see Fig. 2 and Fig. 3). It should be noted however that the luminous secondary flame is visible even at sub-atmospheric pressures as low as 0.03 MPa, but it

stands 3 to 4 cm off the surface and cannot be recorded by thermocouples. Only at 0.2 MPa it approaches to the surface so close that comes within reach of the thermocouples.

To gain a detailed understanding of the combustion mechanism the composition of MNT combustion products at low pressures, i.e. when the reactions are far from the completion, has been determined. On burning at 0.01 to 0.02 MPa pressure range, 4.1±0.2 mole of gaseous products per one mole of MNT was found to be formed. Results of spectrometric analyses indicated 1.0±0.1 mole of NO while NO_2 and formaldehyde are entirely absent. Test for HCN gave 0.4-0.5 mole of HCN produced in combustion of one mole of MNT.

The condensed residue after burning of MNT sample pressed into quartz tubes was formed in small quantities (1-2 mg of 300-400 mg of initial MNT) and was identified as a polymeric substances of $(-CH_3NCO-)_n$ structure.

***Thermal Decomposition** of MNT*

Since MNT is a quite volatile substance, its thermal decomposition has been studied in both the condensed and gas phases. The temperature dependence of MNT vapor pressure is shown in Fig. 4. It follows the equation lnP (in Pa) = 24.8338 -7077/T in the temperature range of 393-513 K (120-240°C). The enthalpy of MNT vaporization can be derived from it as 58.84 kJ/mole (14.06 kcal/mole).

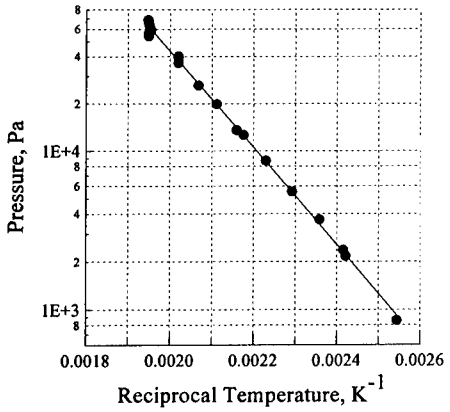


Fig. 4. Relationship between vapor pressure and temperature for MNT.

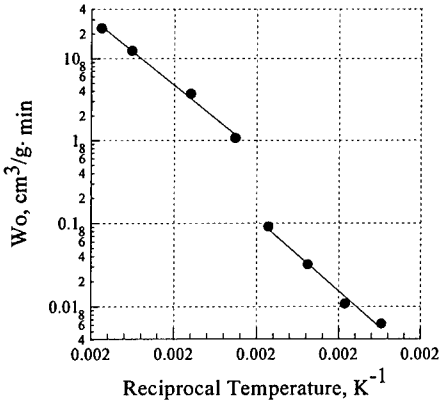


Fig. 5. Relationship between initial rate of gas evolution and temperature for MNT thermolysis in the gas phase (black points) and condensed phase (light points).

Based on MNT vapor pressure figures, load densities (the ratio of the sample weight to the vessel volume, M/V) were calculated for the thermal decomposition study in the gas phase (Table 2).

Table 2. Gas -phase thermal decomposition test conditions and results

T_o, °C	M/V, mg/cc	W_0, cc/g·min	V_∞, cc/g	G_{cond}, %
209	0.69	1.07	568.2	10.2
222	1.02	3.70	-	-
240	1.00	12.5	606.2	12.4
250	0.45	23.5	598.0	10.3

In the course of the experiments, the following parameters were measured: the initial rate of gas evolution (W_0), the final volume of gases evolved in the complete decomposition (V_∞), and the fraction of gases condensed upon cooling to room temperature (G_{cond}).

In the case of MNT thermal decomposition in the condensed phase (in the melt), the experiments were carried out at the considerably more load density, 47.8 mg/cc, and reduced temperatures to diminish influence of gas-phase decomposition. The initial rate of the full gas evolution (W_0) and the initial rate of gas evolution at the expense of condensed-phase decomposition only, corrected for both vapor pressure and gas-phase decomposition (W_{0cond}), were calculated. The results of Table 3 indicate that contribution of the gas-phase decomposition (D_g) accounts for not more than 8% of total gas evolution. The final gas volume after cooling to room temperature (V_{end}) allows estimation of the degree of MNT decomposition. It ranged from 0.8 to 1.3 %.

Table 3. Test conditions and results of MNT thermal decomposition in the condensed phase.

T_o, °C	$W_0 \cdot 10^3$, cc/g·min	$W_{0cond} \cdot 10^3$, cc/g·min	V_{end}, cc/g	D_g, %
170	6.44	6.23	1.43	3.2
180	11.5	10.81	2.49	6.0
190	34.21	31.98	4.42	6.5
200	98.56	90.92	7.90	7.7

The temperature dependencies of the initial gas evolution rate are presented in Fig. 5. In the $\ln W_o$ *vs.* reciprocal temperature, the experimental points fall on two straight lines described by corresponding equations $\ln W_o = 39.26\text{-}18854/T$ and $\ln W_o = 45.83\text{-}22804/T$. The activation energy of decomposition is 156.75 kJ/mole (37.46 kcal/mole) in the gas-phase and 189.59 kJ/mole (45.31 kcal/mole) in the condensed phase. The pre-exponential factors have been calculated for the reaction (1), assuming that only one nitrogen molecule evolves in the initial stage, to give expressions for the rate constant (in s^{-1}) as $k = 1.075 \cdot 10^{13} \cdot \exp(-18854/T)$ for the gas

phase and $k = 7.693 \cdot 10^{15} \cdot \exp(-22804/T)$ for the condensed phase. The kinetic parameters of the gas-phase decomposition proved to be very close to those observed in the gas-phase decomposition of MNT structural analog, 2-acetonyl-5-nitrotetrazole ($k = 1.55 \cdot 10^{13} \cdot \exp(-18470/T)$, s^{-1}) [11].

The chromatographic analysis of gaseous decomposition products using argon as a carrier gave the proportion of the main products as listed in Table 4.

Table 4. Composition of the gaseous products of MNT complete decomposition (%).

N_2	CO_2	CO	H_2	N_2O	NO_2	NO
70.4±1	21.6±0.6	7.0±0.2	less than 1	less than 1	no	no

On cooling to low temperatures, the decomposition gases reveal condensation of a substance within the range of -23 to -63°C, which has been identified as ammonium carbamate, NH_2COONH_4. Calculations showed that ammonia and carbon dioxide in the ratio 2:1 were present among the products in the amount of 14.45 % by volume. The condensation reaction on cooling can be represented as follows:

$$2NH_3 + CO_2 = NH_2COONH_4\downarrow$$

The condensed residue after decomposition of MNT formed as a thin brownish film on the inner wall of the device was identified as a mixture of trimethyl ether of isocyanuric acid and polymer of $(-CH_3NCO-)_n$ structure.

Thus, on the basis of determined decomposition products and material balance, the following reaction of MNT thermal decomposition in the gas can be proposed with an accuracy of 2-3%:

$$C_2H_3N_5O_2 = 0.32\ NH_3 + 1.96\ N_2 + 0.55\ CO_2 + 0.21\ CO + 0.07\ N_2O + 0.09\ H_2 + \\ + 0.62/x\ (CH_3NCO)_x,$$

where x = 1, 3, and more, i.e. methyl isocyanate can be monomer, trimer, or polymer. The whole set of data counts in favor of predominant trimer and, to a less degree, polymer.

Combustion mechanism of MNT

Based on the literature data on thermolysis of the tetrazoles and data on MNT combustion products obtained in this work, one can suggest the following overall reaction of its combustion at low pressures:

$$C_2H_3N_5O_2 = 1.3\ N_2 + 0.6\ CH_3NCO + 0.4\ H_2O + NO + 0.2\ C_2N_2 + 0.4\ HCN,$$

$$\Delta H° = -193.7\ \text{kJ/mole}$$

Thermodynamic calculations for this composition of combustion products give a temperature of 1200 K which is very close to the measured firs flame temperature (1250 K at pressure of 0.01 MPa).

Considering high volatility of MNT, it is logically believed that the MNT surface temperature is determined by its evaporation. Indeed, experimental data plotted as shown in Fig. 6 are in a good agreement with the temperature dependence of equilibrium vapor pressure.

The low decomposition rate in the condensed phase on burning of MNT (estimated degree of the decomposition is 0.05%) allows us to suggest that the burn rate-controlling reaction proceeds in the gas. The reaction order was assumed to be equal to unity as in the case of MNT thermal decomposition. Using a combustion model of volatile explosives [12], one can easily calculate the formal kinetics of a gas-phase reaction which is responsible for heat generation in the gas and controls the burning rate. The combustion model employed links the kinetics of the dominant reaction under flame conditions with the rate of burning:

$$m = \sqrt{\frac{2\lambda\mu}{c_p(T_f - T_0)} \cdot \frac{RPT_f^3}{(T_f - T_{01})} \cdot A\exp(-E/RT_f)}, \qquad (2)$$

where $\dot{m}$ is the mass burning rate; T_f is the flame temperature, in this instance, the first flame temperature, T_1 (see Table 1); μ is the molecule weight of MNT; p is pressure; E and A are the activation energy and preexponential factor of the controlling reaction, and c_p and λ are the average specific heat and thermal conductivity of the gas phase. The value of $T_{01} = T_0 - (L_m + L_v)/c_p$ stands for initial temperature, T_o, with allowance for the heat consumed for melting, L_m, and evaporation, L_v.

The product $A\exp(-E/RT_f)$ of Eq.2 represents the rate constant of the controlling reaction at flame temperature and can be derived from the equation by substituting the experimental burn

rate and first flame temperature into it. The rate constants of the controlling reaction in combustion of MNT at different pressures have been calculated in this way, assuming the first-order reaction of MNT decomposition in the flame and using the corresponding value of the activation energy. The results obtained have been plotted in the Arrhenius coordinates along with apparent first-order rate constants of MNT decomposition reaction (Fig. 7). Four points for pressures from 0.01 to 0.23 MPa lie parallel to the rate constant line of MNT decomposition. The slop of the line through these four points gives the ratio $E_a/R = 19240$ that corresponds to the activation energy E_a = 160 kJ/mole (38.2 kcal/mole). The last value closely matches the activation energy of MNT thermolysis in the gas phase (157 kJ/mole or 37.5 kcal/mole). A value of the pre-exponential factor, $A_0 = 3.33 \cdot 10^{13}$ (s^{-1}), is also close to A_0 of the gas-phase thermal decomposition.

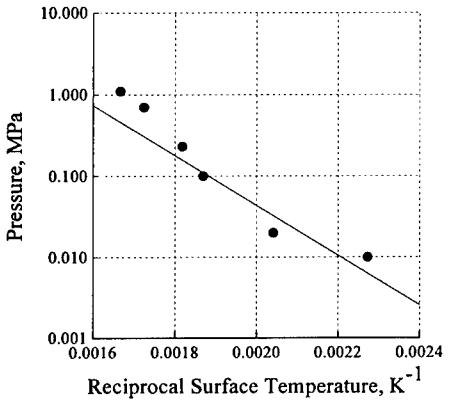


Fig. 6. Relationship between MNT vapor pressure and surface temperatures (points). The solid line is the extrapolated temperature dependence of MNT vapor pressure.

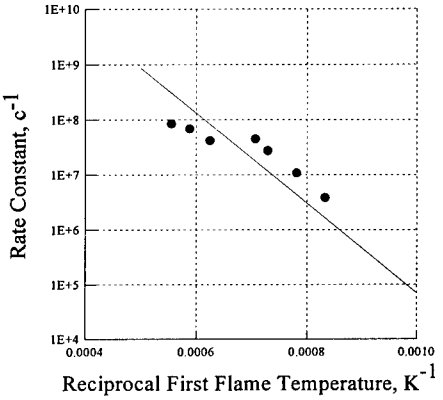


Fig. 7. The rate constants of the burn rate-controlling reaction in combustion of MNT (points). The solid line is the extrapolated temperature dependence of the rate constant of MNT thermolysis in the gas phase.

A departure of kinetic data obtained in combustion study at pressures above 0.23 MPa (the other three point of 0.3 to 1.1 MPa pressure range) from the thermal decomposition kinetics may be caused by a systematic overstatement of the results of thermocouple-aided measurements of first flame temperatures because of proximity effect of the second high-temperature flame (see Fig. 3).

A Beliayev-Zeldovich combustion model presumes the pressure exponent, ν, to be equal one half of the reaction order providing the temperature is invariable with pressure. In the case of MNT, ν is equal to 0.83 in the range of 0.01 to 5 MPa. This may be connected with a gradual

growth of T_1 with pressure. In the range of 5 to 14 MPa, the pressure exponent is only 0.54, that may be explained by cessation of temperature growing because of burning-out the most reactive fuel, in all probability HCN, in its reaction with NO. At higher pressures, the rate-limiting reaction is likely to shift to the high-temperature secondary flame.

It should be noted that in the case of MNT combustion the secondary flame appears at far less pressures and with a considerably less time delay than for combustion of C- and O-nitrocompounds. This indicates in favor of much more reactivity of fuel products in the MNT first flame (mainly such cyanic compounds as CH_3CNO, HCN, C_2N_2, etc.) in comparison to the reactivity of fuel in the first flame of the conventional C- and O-nitrocompounds.

The secondary flame involves reactions of complete reduction of NO to form practically the thermodynamic equilibrium of the combustion products:

$$C_2H_3N_5O_2 \rightarrow 2.5\ N_2 + 2\ CO + 1.5\ H_2 \qquad \Delta H^\circ = -485\ kJ/mole$$

The combustion temperature calculated for this composition, 2645 K, proved to be quite close to the experimental one, 2580 K.

CONCLUSION

Combustion of MNT, the endothermic tetrazole molecule, which contains in addition the oxidizing nitro group has been shown to proceed in the gas phase in accordance with the mechanism of burning of volatile explosives, with the decomposition reaction being the rate-limiting one. Incorporation of the nitro group into the tetrazole molecule, in contrast to the aryl azide molecule [1,13], increases not only the final combustion temperature, but also the temperature of the zone in which the rate-controlling reaction occurs, thus increasing the burning rate. Such behavior is likely to be conditioned by simultaneous formation of NO_2 radical and reactive species produced in the tetrazole decomposition.

ACKNOWLEDGEMENT

The authors express their gratitude to Dr. S.P.Smirnov for the help in conducting experiments on MNT thermal decomposition.

REFERENCES

1. Sinditskii V.P., Fogelzang A.E., Egorshev V.Yu., Serushkin V.V., and Kolesov V.I. "Effect of Molecular Structure on Combustion of Polynitrogen Energetic Materials," in *Solid Propellant Chemistry, Combustion, and Motor Interior Ballistics*, edited by V. Yang, T.B. Brill, and W.Z. Ren, Vol. 185, Progress in Astronautics and Aeronautics, American Institute of Aeronautics and Astronautics, Reston, VA, 2000, pp. 99-128.

2. Fogelzang, A.E., Egorshev, V.Y., Sinditskii, V.P., Dutov, M.D., and Solov'ev, M.Y., "Research of Combustion of Tetrazole and its Derivatives," *Proceedings of the 9th All-union Symposium on Combustion and Explosion. Combustion of Condensed System,* Institut Khimicheskoi Fiziki, Chernogolovka, 1989, pp. 3-5, 129-131 (in Russian).

3. Fogelzang, A.E., Egorshev, V.Y., and Sinditskii, V.P. "Influence of Chemical Nature of Substituent on the Burning Rate of 5-Substituent Tetrazoles," *Proceedings of 17th International Pyrotechnic Seminar Combined with 2nd Beijing International Symposium on Pyrotechnics & Explosives,* Vol. 2, Beijing Institute of Technology Press, Beijing, China, 1991, pp. 618-623.

4. Sinditskii V.P., Egorshev V.Y., Fogelzang A.E., Serushkin V.V., Kolesov V.I. "Combustion Behavior and Flame Structure of Tetrazole Derivatives," *Proc. 29 Inter. Annual Conf. of ICT*, Karlsruhe, FRG, 30 June -July 3, 1998, paper 171, pp. 1-14.

5. Sinditskii V.P., Egorshev V.Y., Fogelzang A.E., Serushkin V.V., Kolesov V.I. "Combustion Mechanism of Tetrazole Derivatives," *Khemicheskaya Fizika*, 1999, Vol.18, No. 8, pp.87-94 (in Russian).

6. Prokudin, V.G., Poplavsky, V.S., Ostrovsky, V.A. The Mechanism of Monomolecular Thermal Decomposition of Tetrazole and its 5-Substituted Derivatives. *Izvestia Akademii Nauk. Seria khim.*, 1996, N 9, pp.2216-2219 (in Russian).

7. Shurukhin Yu.V., Kluyev N.A., Grandberg I.I. Analogies in thermolysis and mass-spectral fragmentation of tetrazoles, *Khimia Geterocyklicheskikh Soedinenii*, 1985, Vol. 6, pp.723-741 (in Russian).

8. Prokudin, V.G., Poplavsky, V.S., Ostrovsky, V.A. The Mechanism of Monomolecular Thermal Decomposition of 1,5- and 2,5- Disubstituted Tetrazoles. *Izvestia Akademii Nauk. Seria khim.*, 1996, N 9, pp.2209-2215 (in Russian).

9. Henry R.A., Finnigan W.G. "Mono-Alkylation of Sodium 5-Aminotetrasolate in Aqueous Medium," *J. Amer. Chem. Soc.*, 1954, Vol.76, p.923.

10. Tarver C., Goodale M., Shaw R., Cowperthwaite M. "Study of Combustion to Detonation Transition for Two Isomeric Cast Primary Explosives," *Proc. 6th Symposium (Int.) on Detonation*, August 24-27, 1976, Colorado, CA.

11. Manelis G.B., Nazin G.M., Rybzov Yu.I., Strunin V.A. Thermal Decomposition and Combustion of Explosives and Propellants, Moscow, Nauka, 1996, 223 p.

12 Zeldovich, Y.B., and Frank-Kamenetskii, D.A., "The Theory of Thermal Propagation of a Flame," *Zhurnal Fizicheskoi Khimii (Russian Journal of Physical Chemistry),* Vol. 12, No. 1, 1938, pp. 100-105 (in Russian).

13. Fogelzang, A.E., Egorshev, V.Y., Sinditskii, V.P., and Dutov, M.D., "Combustion of Nitro Derivatives of Azidobenzenes and Benzofuroxans," *Combustion and Flame*, Vol. 87, No. 2, 1991, pp. 123-135.

INSTABILITY IN PROPELLANT CHANNEL INFLAMMATION

Igor G. Assovskiy & Oleg A. Kudryavtsev***
*Semenov Institute of Chemical Physics, RAS; Moscow 117977;
**Penza Institute of Artillery Engineering , Penza 440005, Russia.

Summary

This paper presents an experimental study of inflammation and subsequent unsteady combustion of a propellant channel. Tubular grains of double-base propellant were the subjects for these experiments. Emphasis is on inflammation of semi-closed cylindrical channels, started from the closed end. The ignition front propagation was monitored concurrently with pressure drop along the channel, igniting gas velocity and other characteristics of the process. The method of short inert insets into the channel was used to locate the ignition front during the channel inflammation. Influence of gas pressure in combustion chamber, the propellant initial temperature, and the channel sizes on the inflammation dynamics is demonstrated. It is found that pressure pulsations of large-amplitude attend the final stage of inflammation and subsequent combustion, if the channel length exceeds the critical one. Basically these pressure pulsations have two explicit modes. The amplitude of the low-frequency fluctuations is much more than amplitude of high frequency pressure-oscillations. Pressure increasing in combustion chamber suppresses the high frequency oscillations and also decreases the low frequency pulsations in the channel. These results are treated in framework of the L^* instability of combustion in nozzleless solid rocket motor.

Introduction

Knowledge on flame penetration into a channel of porous energetic material is important as for interior ballistics as for fire hazard of explosives. The channel inflammation is governed by thermo-chemical processes attending the material combustion, and depends on igniting gas-flow over the channel surface [1-6]. Therefore any experimental determination of the inflammation characteristics requires simultaneous measuring of many parameters influencing the flame spread along the channel. This requirement brings about some significant difficulties for experimental study of the inflammation of narrow channels, pores or cracks.

Previous investigations of the inflammation process could be devided on two groups. First are the works devoted to the critical conditions of flame penetration into a crack of propellant (see,.for example, [3-6]). Correlation between the critical sizes of crack or hole, gas pressure and temperature, propellant combustion law, and other characteristics of the process was studied in those works. The second group is the papers devoted to determination of rate and other dynamic characteristics of the flame penetration (see, for example, [2,6-13]). Majority of both group have studied the flame propagation in low gas-permeable material (a semiclosed channel or crack [3,4,11], low-porosity material [6,9,10,12,13]).

The ignition front is most difficult to locate during the inflammation, especially in a case of fast or non-steady flame penetration. Such a situation is typical for the starting transient of rocket

and gun systems [2,14]. Solid Propellant Rocket Motors with High Internal Gas Velocities sMost of published data on the flame spread were obtained optically [2-11,15]. For this reason, the question on correlation between positions of the gas-radiation front (flame front) and the ignition front (Fig. 1) is very important for diagnostics of the inflammation process. That is why this paper pays certain attention to methodological problems of the flame-spread optical study.

Theoretical Background

Distribution of integral intensity of gas luminescence J(x, t) in the channel (Fig. 1) depends, above all, on gas-temperature T(x, t) according to the Stephan-Boltzmann low: $J = \varepsilon\sigma T^4$. Here the extent of emissivity $\varepsilon=\varepsilon(PLj)$ is a function of product of the gas-pressure P and the ray's stroke Lj (Beer's low); the constant σ is equal to 5.67 10^{-8} W/(m^2K^4).

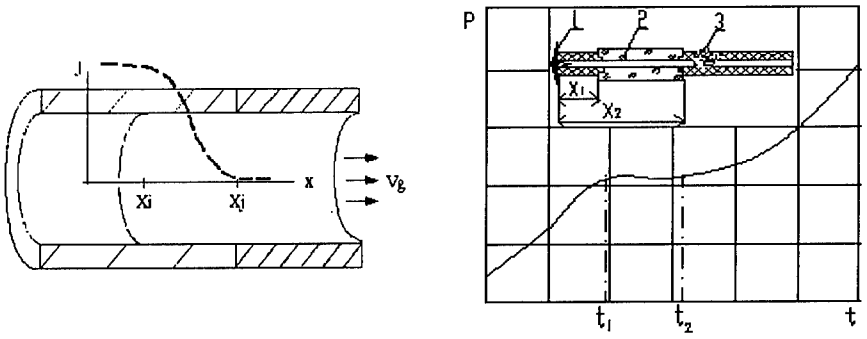


Fig.1. Schematic diagram of the gas-radiation distribution along a flammable channel. Xi and Xj are locations of ignition and radiation fronts.

Fig. 2. Segment of the pressure-time curve at the closed end of channal, corresponding to the ignition front passage throw the inert insertion. (Constant pressure in combustion chamber P=5.4 MPa, the channel length L=180 mm, and diameter d=2 mm). 1-plug; 2-inert insertion; 3- tubular grain of propellant; X_1-and X_2- distances up to the leading and trailing edges of insertion.

The luminescence front (the flame-front) position $Xj(t)$ corresponds to the critical value of radiation intensity $J^{\sim}$ registered by photographic material: $J(Xj, t)=J^{\sim}$. Using this equation, we can present the flame propagation rate R_f (relative to the material's surface) as a function of distribution of radiation intensity J:

$$R_f = dX_j/dt = -(\partial J/\partial t)/(\partial J/\partial x) . \qquad (1)$$

The flame rate R_f correlates also with a gas-particle velocity Vg and can be presented in form:

$$R_f = V_g + V_p , \qquad (2)$$

where Vp is the phase velocity of radiation front propagation relative to gas. The flame front position (relative to gas-flow and to ignition front position Xi) depends on temperature and pressure distributions along the channel, as it follows from Eqs.(1) and (2).

In a limit case of rest-gas, $Vg=0$, the radiation front can move if gas temperature distribution changes with time. On the other hand, difference between rates Rf and Vg is negligible if Vp is relatively small. It takes place when the temperature gradient dT/dx near the radiation front is great enough. Such conditions are quite typical for filtrational flame propagation in the low gas-permeabale materials (low porosity). In this case flame rate is equel approximately to the gas filtration rate. That is why the sensors of gas-flow rate can be used for determination of flame penetration rate [6,12,13]. In this paper the radiation front rate was used to estimate the the gas flow rate.

Significant leading of the luminescence front over the ignition front is typical for gas-permeable materials. The contact of hot gas with material leads to ignition only after a time delay ti. During this delay the luminescence front travels a distance: $l=Vg*ti$. The value of l defines the discrepancy between luminescence front and ignition front $(Xf-Xi)$. The error of optical registration of the ignition front location increases with increasing of gas flow rate and ignition time-delay. The data presented in this paper as in [4,6,8] confirm the leading of flame front over ignition front.

If a semi-closed channel was ignited at the closed end, the gas-flow rate is a function of total gas evolution from the ignited surface, and of pressure drop in the channel. Whether two of three mentioned above values are known we can evaluate the third [16]. The pressure drop in the channel was measured directly. The problem was to determine the ignition front location and its correlation with flame rate.

To solve this problem, we used the tubular samples with short inert insertions, see Fig. 2. These insets allowed us to separate the ignition front from the flame front when the ignition front passages through the boundary between flammable and inflammable materials. The ignition front passage through such a boundary (in contrast with the flame passage) induces an inflection point on the pressure-time curve measured at the closed end of channel (Fig. 2). One insertion induces two inflection points corresponding to leading and trailing boundaries of the insertion: X_1-and X_2: passaged at the moments t_1 and t_2.

$$X_1 = X_i(t_1), \quad X_2 = X_i(t_2). \tag{3}$$

Presetting the boundaries' coordinates X_1 and X_2 and defining the moments t_1 and t_2 on the

pressure-time curve we can evaluate a local rate *Ri* of the ignition front propagation:

$$R_i = (X_2 - X_1) / (t_2 - t_1). \quad (4)$$

It was supposed here, that the insertion is short enough to neglect its influence on the inflammation process..

Along with the local rate R_i (4), it is possible to evaluate the time-average rate R_i^ of the ignition front propagation up to the moment t_1:

$$R_i \hat{} = (X_1 - X_0) / (t_1 - t_0) = X_1 / (t_1 - t_0), \quad (5)$$

where t_0 is a moment of start of the ignition front propagation along the channel. Varying the inset's position in the channel it is possible to evaluate the change of Ri during the channel inflammation. Details of the method have been done elsewhere [1].

Experiments

The DB-propellant (62%-NC, and 35%-NDG) was used for investigations of the channel inflammation and subsequent combustion. The tubular grains were produced by pressing method. They had up to 360 mm in length and the channel's diameter from 1 to 3 mm. The web thickness was equal to 1.6 mm for all tubes. Such a web is transparent for movie-taking of the channel inflammation. Two 1.5 mm ports (11 and 14 on Fig.3) were bored in each of the propellant tubes to measure the pressure distribution inside the channel. The effect of the gas pressure in combustion chamber, the initial temperature of propellant, and the channel sizes on the inflammation characteristics have been studied

The tubular sample prepared for experiment was placed in the chamber opposite to the inspection window 9 protected by replaceable glass 13. The picture frequency of filming was not less than 5000 frame/sec. The flame front positions *Xj* were received projecting each frame on a special screen with scales. The labels of a time on the film were used to determine the function *Xj(t)* and the rate of flame front propagation (1).

Special experiments have been done to research the influence of initial temperature To on the inflammation process. For this purpose the assembled setup was controlled thermostatically during 8 hours. Results of measurements of flame and ignition fronts' rates are presented in Figs. 4 and 5. Typical pressure-time curves in the channels are presented in Figs. 6-8. The processing of oscillograms was made using a comparator. The total error in definition of pressure did not exceed 10 %. More information on experimental set-up, preparation of samples, and data processing is available in [1].

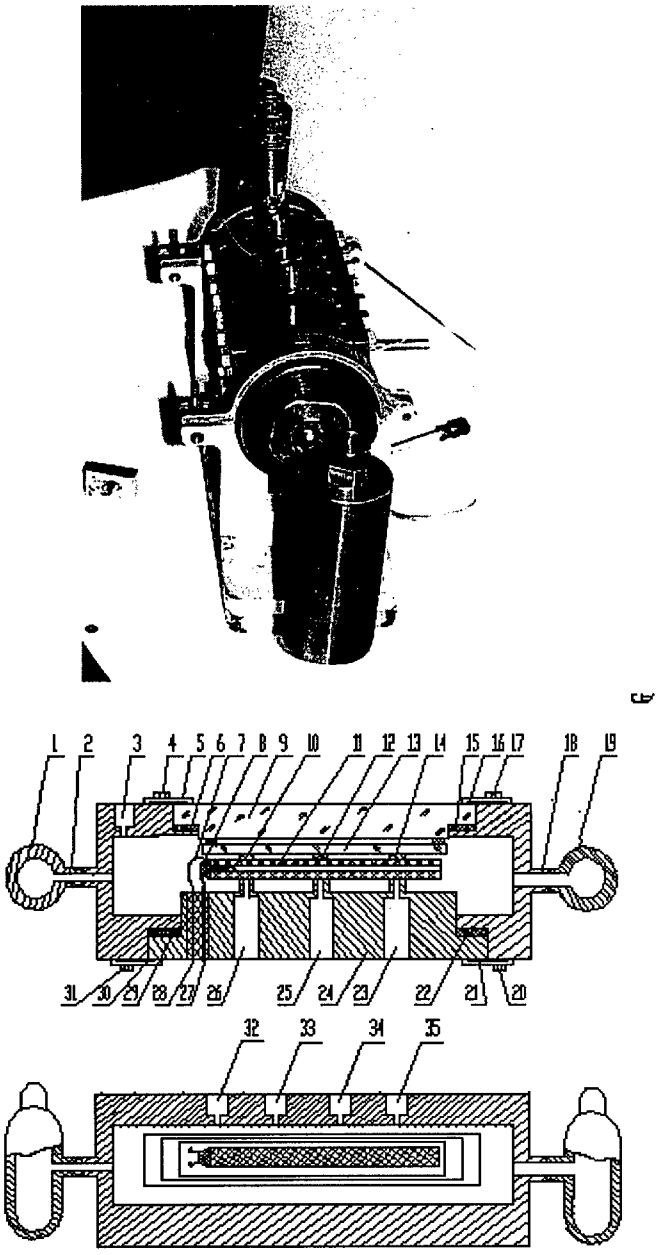


FIg.3. Photo and schematic diagram of experimental setup with a tubular propellant grain: 1,19-additional vessels; 2,18-connecting pipes, 3,23,15,26,32-holes for pressure sensors; 4,17,20,31-bolts; 5,16,21,30-stowed lock pieces; 6,25,22,29-sealing rings, 7-- nichrom spiral for ignition; 8-end plug; 9-porthole; 10,12,14-clamps; 11-propellant grain; 13-shift glass; 24-gate; 27,28-electro contacts; 33,35-holes for pressure release; 34-valve hole..

Discussion of Results

Flame and Ignition Fronts Propagation

The film study points to continuous passage of flame front through the inert inset.. This fact means that radiation front position at a cross-section $x=Xj$ does not depend on the channel surface state at this section. So, the radiation front (or flame front) position does not correspond to the ignition front, but represents itself only the hot gas front.

Typical values of the rate of flame propagation from the closed to open end of channel are presented in Fig.5. Appropriate values of the ignition-front propagation rate R_i estimated using Eqs. (4) and (5) have the same order as R_f. Appropriate values of the time-average rate $Ri^{\wedge}$ are slightly less than values of local rate Ri. So, for inflammation of 180 mm channel, the values of Ri at coordinates x=70 and 100 mm are equal to 50 and 100 m/s accordingly. At the same time the averaged rate $Ri^{\wedge}$ at the cross-section x=40 mm is equal to 20 m/s. It must be mentioned that a diagram of the ignition front propagation $Xi(t)$ from closed to open end of the 180 mm-channel coincides with initial part of the diagram for the 360 mm-channel.

Knowledge on correlation between the inflammation rate of propellant grains and pressure is needed for estimations of interior ballistics characteristics. Figure 4 presents local values of the ignition front rate and appropriate values of gas pressure in the channel (at the closed end). The calculated curve is the approximation of experimental points by the function

$$R_i = aP^{\vartheta}, \qquad (6)$$

where the pressure scale is 0.1 MPa, the rate scale is 1 m/s, and the constants values are a=3.77 10^{-5} and ϑ=3.32 (derived by the method of least squares).

Initial Temperature Influence on Flame Spread

Influence of initial temperature of propellant on the flame spread rate is one of the practically important but least investigated aspects of the inflammation process. To estimate experimentally this influence we studied the inflammation of long grains (L=360 mm, d=2.0 mm) at initial temperatures T_o = + 20 and -20 °C. The rate of flame propagation and the pressure-time curve at the closed end of channel were registered during the inflammation. Results of experiments are presented in Fig. 5.

The inflammation at low initial temperature, T_o = -20 °C, has distinctive characteristics in comparison with normal initial temperature. First is increase of ignition time delay t_o (the interval from the moment of voltage submission on the heating spiral prior to the luminescence appearance from the section close to the spiral). For example, t_o increases from 100 ms at T_o=+ 20 °C up to 400 ms at -20 °C. However, local values of the flame propagation rate at T_o = -20 °C essentially exceed appropriate values at +20 °C, especially on the initial stage of flame

propagation (see Fig.5). For example, the flame propagates from the point x/L = 0.2 up to the channel end x/L = 1.0 during 2.44 ms at + 20 °C, but it takes only 1.4 ms at T_o = -20 °C . At the open end of channel the flame rate achieves the maximum value 300 m/s. This maximum does not significanly depend on the initial temperature.

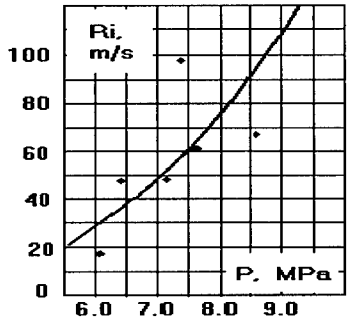


Fig.4. Correlation between the ignition front propagationa rate and pressure in the channel. ♦ - experiments; — -approximation (6).

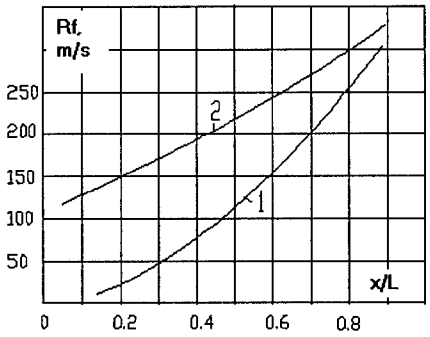


Fig.5. Initial temperature influence on the flame propagation rate. P_k = 5.6 MPa; d = 2.0 mm; -T_o = +20 (1), -20 (2)- °C.

Thus, the experiments show that decrease of initial temperature leads not only to increase of ignition time delay, but also to increase of the flame propagation rate. Such an acceleration of the flame spread is rather unexpected.

Effect of Accelerated Inflammation at Low Initial Temperate. In tested semi-closed channals the flame propagation rate is a direct function of gas-release rate from ignited surface of the channel. Dynamics of the flame propagation reflects the dynamics of the propellant combustion after ignition. Apparently, the effect of accelerated inflammation at low initial temperatureis associated with the effect of accelerated transient combustion after ignition [17]. At low initial temperatures the propellant needs for ignition much deeper preheating than that one at normal conditions.

Inflammation Instability

Experiments show that gas pressure n short semi-closed channels increases monotonically during the flame propagation from the closed to open end of channal. Such an inflammation picture changes if the channel length exceeds a critical one, see Fig. 6. The critical value of channal lengh depends on pressure in combustion chamber.The inflammation and subsequent combustion of quite long channals can be accompanied by pressure pulsations of high intensity, see Figs.6-8.

These pulsations have two modes of frequency. The order of low-frequency is 10 Hz, and high-frequency is about 0.5-1.0 KHz. The amplitude of low-frequency fluctuations is much bigger than amplitude of high frequency oscillations, and can exceed twice the pressure level in the chamber. The low-frequency pulsations correlate with radiation pulsations of hot gas in the channel. The channal length and the chamber pressure are among the main factors influencing the pressure pulsations in the channal, Figs. 6-8. The amplitude of low-frequency pulsations increases with increasing the channal length, Fig. 6, but frequency depends significantly on the chamber pressure, Fig.7.

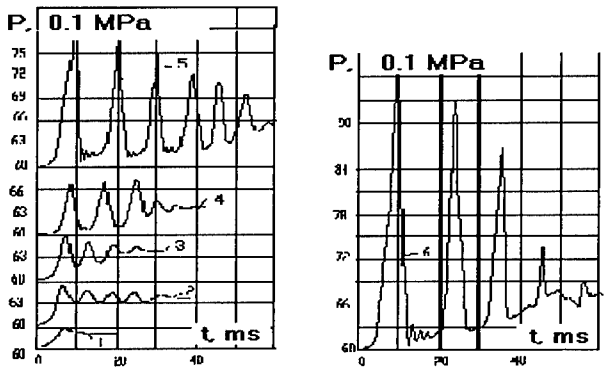


Fig. 6. Pressure pulsations in channal vs channal length (chamber pressure P_o = 6.0 MPa; channel diameter d = 2.0 mm): L = 90 (1); 100 (2); 110 (3); 120 (4); -150 (5); 180 mm (6).-

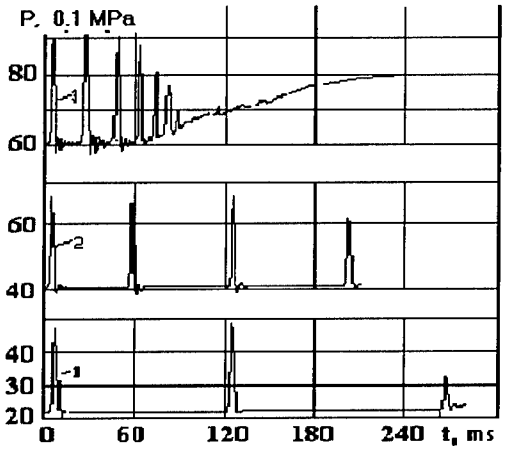


Fig. 7. Influence of constant pressure in combustion chamber P_c on pressure pulsations in the channel (L = 180 mm, d =2.0 mm). P_c =2.0 (1); 4.0 (2); 6.0 MPa (3).

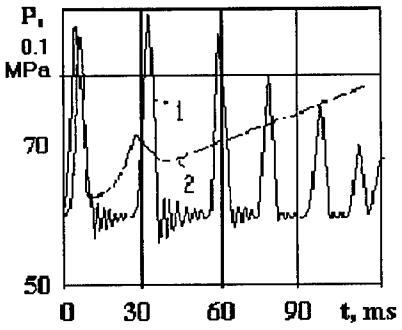


Fig. 8. Influence of growing up pressure in combustion chamber on pressure pulsations in the channel (L=180 mm, d=2.0 mm). dPc/dt = 0 (1); 20.0 MPa/s (2).

Pressure increase in combustion chamber leeds to stabilization of the pressure-time curve in the channel, Fig.8, decreasing the amplitude and frequency of low-frequenct pulsations, and rejecting the high frequency oscillations.

A preliminary analysis of these pressure pulsations shows their connection with L*-instability of solid rocket motors with long tubular charges [18-20]. The Pobedonostsev criterion Po = $4L/d$ [18] for the tested channals has values more than 200. It means that sound choking in the channel can take place. Therefore it can be expected, that unstable inflammation and subsequent combustion of long channels is similar to unstable combustion in solid rocket motor. Actually the channal combustion is similar to combustion in nozzleless solid rocket motors [21,22].

Conclusion

There is a critical length of semi-closed channel in propellant above which intensive pressure pulsations arise in the channal during its inflammation and subsequent combustion under constant external pressure..These pressure pulsations have two modes of frequency (order of 10 and 1000 Hz). The amplitude of the low-frequency pulsations is much bigger than amplitude of high frequency oscillations, and can exceed twice the external pressure.. Level of external pressure correlate with pulsations frequency. The amplitude and period of low-frequency pulsations increase with increasing length of the channel.

NOMENCLATURE

Symbols

D	diameter of channel, m
J	intensity of radiation, W/m^2
ε	absorbing ability of gas, 1
L	length of channel or optical path length, m
l	space scale, m
P	pressure, MPa
R	combustion rate, m/s
T	temperature, K
t	time, s
V	velocity, m/s
X	front position, m
x	space variable, m
DB	double-base
NC	nitrocellulose
NDG	nitrodiglycol
PMMA	polymethylmetacrylate

Subscripts

c	chamber
f	flame
g	gas
i	ignition front
j	radiation front
o	initial value
p	phase value

Superscripts

~	critical value
^	averaged value

REFERENCES

1. Assovskii I. G., and Kudryavtsev O. A., "A Method for Determining the Velocity of Channel Surface Ignition in a Propellant Charge", Chem. Phys. Reports, 1995, Vol.14(7), pp.1037-1047.
2. Peretz A., Kuo K.K., Caveny L.H., Summerfield M., "Starting Transient of Solid Propellant Rocket Motors with High Internal Gas Velocities", AIAA Journal, 1873, vol. 11, No. 12, pp. 1719-1727.
3. Andoh E., and Kubota N. "Flame Penetration into Propellant Holes", Propellants and Explosives, 1981, Vol. 6, pp: 166-169.
4. Andreev K. K., Thermal Decomposition and Combustion of Explosives, Nauka, Moscow, 1966.
5. Margolin A.D., Margulis V.M., "On Burning Penetration in Single Pore", Combustion, Explosion and Shock Waves, 1969, Vol. 5, No 1, pp. 15-16.
6. Belyaev A. F., Bobolev V. K., Korotkov A.I., Sulimov A.A., Chuiko S.V., Transition of Combustion to Explosion for Condensed Systems, Nauka, Moscow, 1973 (in Russian); Jerusalem, 1975 (in English).
7. Krasnov Yu. K., Margulis V.M., Margolin A. D., Pokhil P.F., "The Burning Penetration Velocity into Pores of an Explosive Charge", Combustion, Explosion and Shock Waves, 1970, vol. 6, No. 3, pp. 290-295.
8. Marchenko V.V., Romanov O.Ya, Shelukhin G.G., "On Inflammation and Starting Period of Combustion of a Channal in Double Base Propellant" Combustion, Explosion and Shock Waves, 1975, Vol. 11, No.4, pp. :519-530.
9. Krier H., Rajan S., Van Nassel W.F., "Flame Spreading and Combustion in Packed Beds of Propellant Grains", AIAA J, Voi. 14, No.3, pp. 301-309, 1976.
10. Horst F.W., Nelson C.W. ahd May I.W., "Flame Spreading in Granular Propellant. Comparison of Theory to Experiments", AIAA Journal, 1978, Vo.16, No.8, pp.769-770.

11. Kumar M., Kovacic S.M., Kuo K.K., "Flame Propagation and Combustion Processes in Solid Propellant Cracks", AIAA J., 1981, Vol.19, No. 6, pp.610-618.
12. Roman'kov A.V., Sulimov A.A., Sukoyan M.K. and Biryukov M.S., "Pressure distribution in convective combustion vawe propagating in porous propellant charge", Sov. J. Chemical Physics, 1992, Vol. 11, No. 7, pp. 983-990.
13. Wildegger-Gaissmaier A.E., Jons I.R., "Ignition of a Grannular Propellant Bed", Combustion and Flame, 1996, Vol. 106, pp. 219-230.
14. Gun Propulsion Technology. AIAA Progress in Astronautics and Aeronautics, 109, AIAA, Washington, 1988
15. Special Issue on Flame Spread over Solid Combustibles, Comb. Scien. and Technol., 32/1-4 (1983).
16. Assovskii I.G., "Method to Derive Solid Propellant Erosive Burning Rate Using Reactive Motor Pressure Diagram", in "Non-Intrusive Combustion Diagnostics", The Third Int. Symp. on Special Topics in Chemical Propulsion, TNO, The Netherlands, 1993, pp.85-86.
17. Assovskii I.G., "Phenomenological Theory of Propellants Ignition and Subsequent Unsteady Combustion in High Pressure Chambers", in book "Challenges in Propellants and Combustion. 100 Years after Nobel", edit. by Kuo K.K., N.Y.: Begell House Inc., 1997, pp. 1035-1045.
18. Zel'dovich Ya. B., Leipunskii O.I., and Librovich V.B., Theory of Non-Stationary Combustion of Solid Propellant, Moscow, "Nauka", 1975, p.79
19. Svetlichniy I.B., Margolin A.D., Pokhil P.F., "Low-Frequency Instability of Solid Propellant Combustion", Combustion, Explosion and Shock Waves , 1971, Vol. 7, № 2, pp. 186-194.
20. Assovskiy I.G., Rashkovskiy S.A., "Charge Design and Non-Acoustic Instability of Solid Rocket Motors", in "Combustion of Energetic Materials", The Fifth Int. Symp. on Special Topics in Chemical Propulsion, Streza, Italy, 2000, pp. 215-216.
21. Nahon S., "Nozzleless Solid-Propellant Rocket Motors: Experimental and Theoretical Investigations", AIAA Paper, 84-1312, June 1984.
22. Gany A., Aharon I., "Internal Ballistics Considerations of Nozzleless Rocket Motors", AIAA J. of Propulsion and Power, 1999, Vol. 15, No. 6, pp. 866-873.

Porous Graphitic Carbon (PGC) - A Convenient Column Packing Material for the HPLC Analysis of FOX-7.

Erik Holmgren, Patrick Goede and Nikolaj Latypov
FOI, Swedish Defence Research Agency, Department of Energetic Materials,
S-147 25 Tumba, Sweden.

Carlo Crescenzi and Håkan Carlsson
Department of Analytical Chemistry, Stockholm University
S-106 91 Stockholm Sweden

Summary

An HPLC method for the analysis of FOX-7 has been developed. Several different column packing materials were evaluated. FOX-7 has shown relevant affinity only for the graphitized carbon surface of the Hypercarb column. With this column, and with a suitable eluent phase, bulk FOX-7 and some possible byproducts were separated and analyzed by PDA-UV.

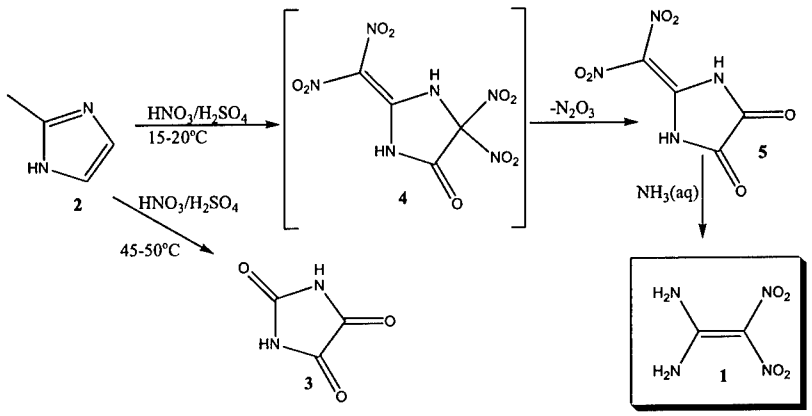
Keywords: FOX-7, HPLC, porous graphitic carbon, Hypercarb, Explosives.

1. Introduction

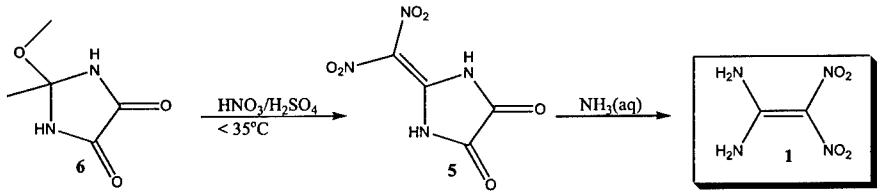
2,2-Dinitro-ethene-1,1-diamine (FOX-7) (**1**) is a thermally stable impact insensitive explosive with a calculated performance close to RDX. The sensitivity of FOX-7 (**1**) to physical constraints (impact, friction, heat, etc...) has been quite extensively studied[1,2], these studies support our belief that FOX-7 (**1**) is a prime candidate as a filler in insensitive munitions.

FOX-7 (**1**) was first synthesized in 1998 by Latypov et al[3]. Since then different synthetic methods have been developed and FOX-7 (**1**) is now synthesized in a pilot-plant on a kilogram scale. According to the procedures of Latypov et al FOX-7 (**1**) was prepared from 2-methylimidazole (**2**) in a two step process, according to scheme **1** and from 2-methoxy-2-methyl-4,5-imidazolidinedione in a two step process

according to scheme **2**. The aim of the present study was to develop a convenient HPLC method for purity analysis of the produced FOX-7 (**1**). Due to the extremely high polarity of the compound it was impossible to use conventional reversed phase HPLC conditions. After several attempt with different column packings we found that the graphitized carbon of the Hypercarb columns had the desired chromatographic properties.



Scheme 1



Scheme 2

2. Experimental.

2.1 Chemicals and Reagents

The chemicals and reagents used were: water (purified by a system from Continental Modulab type II Reagent grade water system), acetonitrile (HPLC Isocratic grade,

J.T.Baker), trifluroacetic acid (TFA) (normal grade, APOLLO Scientific limited) and ammonia (water solution, 25% analytical grade, Riedel-de Haen).

2.2 High-performance Liquid Chromatography

2.2.1 Analyte stock solutions:

FOX-7 was dissolved in acetonitrile to a concentration of 0.50 mg (3.4 µmol)/ml. 10 microliters of this solution were injected.
Analyte mix stock solution. FOX-7 29.2 µg (198 nmol)/ml, 2-(dinitromethylene)-4,5-imidazolidinedione (**5**), 34.6 µg (171,2 nmol)/ml, 2-methylimidazole (**2**) 71.1 µg (864 nmol)/ml, parabanic acid (**3**) 39.9 µg (350 nmol)/ml. 20 microliters of this solution were injected.

2.2.2 Gradient Systems

Neutral systems (**A1**)
A : 100% water B : 100% acetonitrile (V/V)
Gradient range: 3 min 0% B, 0-100% B in 7 min, 100% B in 12 min. Flow rate 0.8ml/min.

Acidic System (**A2**)
A : water 99%/1% TFA (V/V)
B : acetonitrile 99%/1% TFA (V/V)
Gradient range: 3 min 0% B, 0-100% B in 7 min, 100% B in 12 min. Flow rate 0.8ml/min

A different gradient range was used for the C 18, C 8 and Cyano columns. (**A3**)
Gradient range: 3 min 10% B, 10-100% B in 7 min, 100% B in 12 min. Flow rate 0.8ml/min.

Basic systems
A : water 99%/1% ammonia (**B1**) or water 99.9%/0.1% ammonia (**B2**) (V/V)

B : acetonitrile 96%/3% water/1% ammonia (**B1**) or acetonitrile 99.6%/0.3% water/0.1% ammonia (**B2**) (V/V)
Gradient range: 3 min 0% B, 0-100% B in 7 min, 100% B in 12 min. Flow rate 0.8ml/min.

Analyte mix: Acidic system (**A4**)
A : water 99%/1% TFA (V/V)
B : acetonitrile 99%/1% TFA, (V/V)
Gradient range: 2-100% B in 20 min, 100% B in 25 min. Flow rate 0.8ml/min.

2.2.3 HPLC system:
Waters HPLC pump Model 510, Waters Autosampler Model 717 plus, Waters UV Detector Model 996 photodiode array detector (190-390 nm). Waters System interface module (Millipore), Waters Software Millenium 32, Uniflows degassys DG-2410. All printed spectra show the absorption at 280 nm, except the basic FOX-7 analysis which is shown at 360 nm and the analyte mix which is shown at 215 nm and 330 nm.

Columns: Hypercarb 100x3 mm, 5 µm particles (Thermo Hypersil), Zorbax SB-C18 150x3, 3.5 µm particles(Agilent), Zorbax SB-C8 150x3, 3.5 µm particles (Agilent), Zorbax SB-CN 150x3, 3.5 µm particles (Agilent).

3. Results and Discussions

3.1 Retention Behaviour of FOX-7

FOX-7 is an extremely polar compound, which is virtually insoluble in many organic solvents (except dimethylsulfoxide, dimethylformamide, γ-butyrolactone and N-methyl-2-pyrrolidone). Compounds like these are usually very difficult to retain in conventional reversed phase conditions without the addition of ion pair salts. As expected, when using a C18 column under standard conditions FOX-7 eluted with the front (**figure 1, A1**). By adding 1% of TFA we achieved an improved peak-shape but the overall retention behaviour of the compound was still the same (**figure 2, A3**).

Similar results were obtained when using a C8 (**figure 3** and **4**) and cyano column (**figure 5** and **6**).

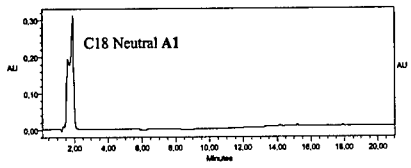


figure 1

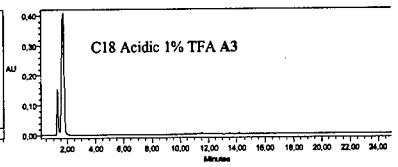


figure 2

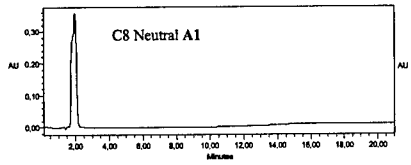


figure 3

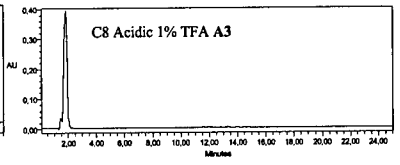


figure 4

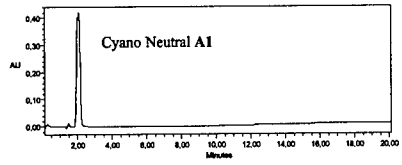


figure 5

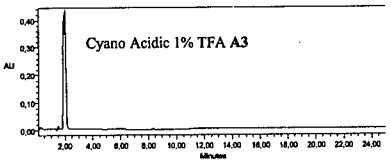


figure 6

During the last years there has been a great interest in porous graphitic carbon (PGC) as a column packing material [4,5]. The unique characteristic of this material is the ability of to interact, in reversed phase condition, with a polar molecule via an induced electrostatic dipole, (the so-called polar retention effect on graphite[Knox, 1997 #89]). In this way the retention time often increase with the polarity of the analyte. The advantage of higher retention times for polar molecules suggested us to use this stationary phase to separate and analyze the extremely polar explosive FOX-7. To our knowledge, the only other explosive which has been analyzed on the PGC column is the similarly polar 5-nitro-1,2,4-triazol-3-one (NTO)[6]. However, owing to strong interactions with the hypercarb, it was not possible to elute FOX-7 with an acceptable retention time and peak shape, even with 100% of acetonitrile. When 1% TFA was added to the buffer as a competitive eletronic modifier the polar retention

was reduced and the analyte eluted after 14 minutes with a nice peak shape (**figure 7, A2**). The suppression of polar interaction was also possible using a basic modifier in the eluant phase. In this case the retention time was 11 minutes (**figure 8, B1**). When FOX-7 was analyzed under basic conditions a relevant difference in the PDA-UV-spectra of the analyte depending on if the spectra was run with 1% ammonia (**B1**) or 0.1% ammonia (**B2**)(or 1% TFA (**A1**)) was observed (figure **9,10**). The absorption peak at 278 nm disappeared and was replaced by a much smaller peak at 272 nm, this can probably be attributed to a proton abstraction where the compound at a buffer concentration of 1% ammonia exists as a salt. Further investigations are underway to understand the zwitterionic nature of FOX-7.

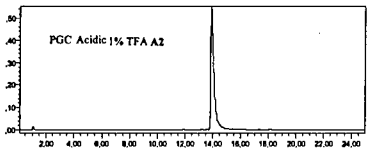


figure 7

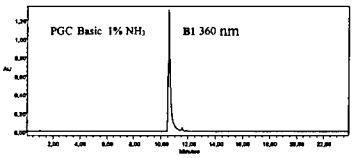


figure 8

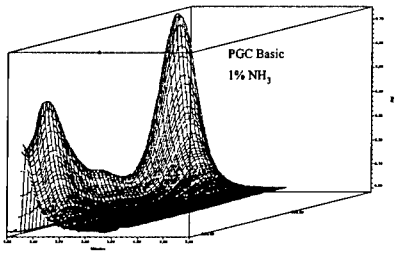


figure 9

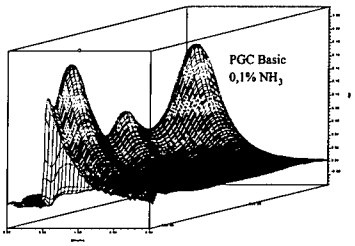
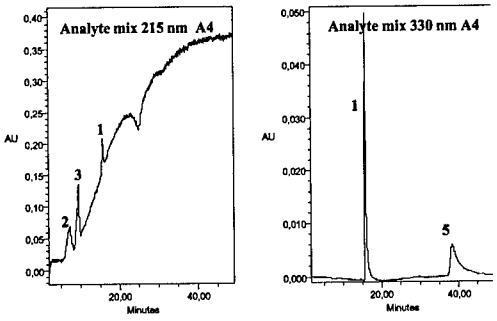


figure 10

3.2 Analysis of Possible Byproducts

FOX-7 can be prepared according to two routes as illustrated in **scheme 1** and **2**[3]. Nitration of 2-methylimidazole (**2**) gives 2-(dinitromethylene)-4,5-imidazolidinedione (**5**) which after addition of aqueous ammonia produces the desired FOX-7 (**1**). However, if the conditions of the nitration are not carefully controlled large amounts of parabanic acid (**3**) will be formed as a byproduct. When following the synthetic

route outlined in **scheme 2**, 2-methoxy-2-methyl-4,5-imidazolidinedione (**6**) is nitrated to produce 2-(dinitromethylene)-4,5-imidazolidinedione (**5**) which is transformed to FOX-7 (**1**) by the addition of ammonia. These compounds were considered possible byproducts from the synthesis of FOX-7 (**1**). We have analyzed all of them, except (**6**) which is hydrolytically instable even in water, by HPLC on the PGC column. An analyte mix containing (**1**), (**2**), (**3**) and (**5**) was run under acidic conditions (**A4**). FOX-7 and the possible byproducts could all be detected in the chromatogram (figure **11**). (**1**), (**2**) and (**3**) were clearly visible at 215 nm while (**1**) and (**5**) were visible at 330 nm.



1 Fox-7
2 1-Methylimidazole
3 Imidazolidin-2,4,5-trione, parabanic acid
5 2-Dinitromethyleneimidazolidine-4,5-dione

figure 11

4. Conclusions

The method presented (**A4**) is suitable for the for purity analysis of FOX-7. Due to differences in absorption maxima the use of programmed wavelength analysis or PDA-UV detector is suggested for trace analysis of impurities. Further studies are underway to understand the hydrolysis of **5** to FOX-7, these may of-course change our perception of which byproducts are plausible. HPLC analyses, on actual batches of FOX-7, have shown no traces of the expected or other impurities.

Acknowledgements

The authors would like to thank the Swedish Defence Forces and the Swedish Defence Materiel Administration for giving financial support to this project.

References

(1) H. Bergman, H. Östmark, A. Pettersson, M.-L. Pettersson, U. Bemm, M. Hihkiö, "Some Initial Properties and Thermal Stability of FOX-7" *1999 Insensitive Munitions and Energetic Materials Technology Symposium* Tampa, 1999.

(2) H. Östmark, H. Bergman, U. Bemm, P. Goede, E. Holmgren, M. Johansson, A. Langlet, N. V. Latypov, A. Pettersson, M.-L. Pettersson, C. Vörde, H. Stenmark, L. Karlsson, M. Hihkiö, "2,2-Dinitro-ethene-1,1-diamine (FOX-7) - Properties, Analysis and Scale Up" *2001 Insensitive Munitions and Energetic Materials Technology Symposium* Bordeaux, 2001.

(3) N. V. Latypov, J. Bergman, A. Langlet, U. Wellmar, U. Bemm, "Synthesis and Reactions of 1,1-Diamino-2,2-dinitroethylene": Tetrahedron 54, 11525-11536, (1998).

(4) J. H. Knox, P. Ross In *Advances In Chromatography*; Brown, P. H., Grushka, E., Eds.; Marcel Dekker Inc.: New York, 1997; Vol. 37, p 73-119.

(5) J. H. Knox, P. Ross In *Advances In Chromatography*; Brown, P. H., Grushka, E., Eds.; Marcel Dekker Inc.: New York, 1997; Vol. 37, p 120-161.

(6) L. Le Campion, A. T. Adeline, J. Ouazzani, "Separation of NTO Related 1,2,4-Triazole-3-one Derivatives by a High Performance Liquid Chromatography and Capillary Electrophoresis": Propellants, Explosives and Pyrotechniques 22, 233-237, (1997).

2,2-DINITRO-1,3-BIS-NITROOXY-PROPANE (NPN): A NEW ENERGETIC PLASTICISER

Niklas Wingborg and Carina Eldsäter
Swedish Defence Research Agency, FOI
SE-147 25 Tumba, SWEDEN. .

Abstract

A new energetic plasticiser, 2,2-dinitro-1,3-bis-nitrooxy-propane (NPN), has been characterised. Its high oxygen balance, +12.5%, and low glass transition temperature, -81.5°C (midpoint), makes it very attractive as an energetic plasticiser in solid propellants. The ability of NPN to lower the glass transition temperature and viscosity of uncured polyNIMMO has been studied and compared to other energetic plasticisers, such as BDNPA/F and Butyl-NENA. To increase the poor thermal stability of NPN, several conventional nitrocellulose/nitroglycerine stabilisers were evaluated. An effective stabiliser has, however, not yet been found.

Introduction

By using energetic polymers, such as poly(3-nitratomethyl-3-methyl oxetane) (polyNIMMO), it is possible to increase the specific impulse of a solid rocket propellant, compared to the current state of the art HTPB-propellants, by approximately 10%. PolyNIMMO has a glass transition temperature, T_g, at approximately –30°C and in general it increases by 10°C when cured.[1] The glass transition temperature must be lower than the minimum service temperature (usually –40 to –55°C depending on the application), especially when the propellant is case-bonded, to avoid failure of the motor during firing. The glass transition temperature of polyNIMMO can be depressed by using a suitable plasticiser. A plasticiser is also added to lower the viscosity of the uncured propellant to improve processing, since the solid loading, and thus the specific impulse, often are limited by processing ability.

To obtain a high specific impulse it is desirable to use energetic plasticisers. The optimum energetic plasticiser should have a low glass transition temperature, a low viscosity, a low ability to migrate, a high oxygen balance, be thermally stable and have a low impact sensitivity. These demands are in many cases contradictory and it is thus not easy to find the ultimate energetic plasticiser. Several energetic plasticisers, such as nitratoethyl nitramines (NENAs), nitrate esters (*e.g.* nitroglycerine, BTTN, TMETN), azido compounds, BDNPA/F, nitroaromatic compounds (*e.g.* K10) and nitrato oligomers (GlyN and NIMMO oligomers), have been developed world wide for use in solid propellants and PBX.[1,2,3,4,5,6] 2,2-dinitro-1,3-bis-nitrooxy-propane (NPN) has been proposed as a plasticiser for double-base propellants, but no experimental data has been published.[7] This paper presents results from the characterisation and evaluation of NPN as a potential energetic plasticiser in an energetic binder formulation.

Experimental

Materials

Polymer

PolyNIMMO BX PP880 , Poly(3-nitratomethyl-3-methyl oxetane), 2-functional, (Nobel Enterprises, UK.)

Plasticisers

Bu-NENA, N-n-butyl-N-(2-nitroxy-etyl)nitramine, (DYNO Industrier ASA, Norway).

BDNPA/F, Bis(2,2-dinitropropyl)acetal/Bis(2,2-dinitropropyl)formal (1:1), (Aerojet, USA).

Stabilisers

2-NDPA, 2-nitro diphenyl amine, puriss (Fluka AG, Switzerland).

Centralite I, 1,3-diethyl-1,3-diphenylurea (NEXPLO/Bofors, Sweden).

NQ, nitroguanidine (Fluka AG, Switzerland).

Akardite II, 1,1-diphenyl-3-methylurea (NEXPLO/Bofors, Sweden).

DPA, diphenyl amine, 98% (Merck, Germany).

Methods

The glass transition temperature, T_g, was measured using a Mettler DSC 30, differential scanning calorimeter, equipped with a ceramic sensor. Every test as well as the calibration was performed in a nitrogen atmosphere (50 ml/min) at a heating rate of 10°C/min. The samples were put in 40 µl aluminium cups with a pierced lid. The sample weight was between 10 and 20 mg. Calibration was made with indium (T_m= 156.6°C) and anhydrous *n*-octane *(Aldrich 29,698-8)* (T_m= -57°C). All tests were performed in duplicate.

The density of NPN was measured at room temperature by using a precision syringe (50 µl) and a micro balance.

The viscosity of the binder formulations was measured by a Stresstech HR Melt Rheometer at a constant shear rate of 1.0 s^{-1}. The viscosity measurements were done at 30 and 60°C.

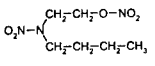
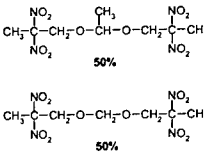
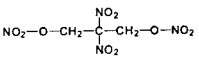
The thermal stability of NPN was determined by measuring the heat flow from approximately 0.5 grams of each sample. The measurements were done isothermally in a Thermal Activity Monitor, TAM 2277, heat flow (micro)calorimeter at 65°C. The samples were put in 3 ml glass ampoules and hermetically sealed with aluminium caps.

The impact sensitivities were determined according to the BAM standard which conforms to the UN guideline ST/SG/AC.10/11,[8] with two exceptions. First, the impact sensitivity was measured with a 2 kg drop weight and second the impact testing was done by using an up-and-down method on both sides of the 50 % probability level. For liquid explosives, the gap between the two steel cylinders was 2 mm.

Results and Discussion

A new energetic plasticiser, 2,2-dinitro-1,3-bis-nitrooxy-propane (NPN) have been synthesised at FOI and evaluated as a potential plasticiser in polyNIMMO. Some of the properties of NPN is presented in Table 1.

Table 1 Properties of energetic plasticisers used in this study.

	Bu-NENA	BDNPA/F	NPN
	$C_6H_{13}N_3O_5$	$C_{10}H_{17.3293}N_{5.341}O_{13.3528}$	$C_3H_4N_4O_{10}$
			
Mol. Weight (g/mol)	207	426	256
Oxygen balance[a] (%)	-104.3	-57.5	+12.5
Density (g/cm^3)	1.22[a]	1.39[a]	1.66[b]
Melting point (°C)	-9[a]	-15[a]	---
Enthalpy of formation[a] (kJ/g)	-930	-1940	---

a) Values from ref. 9.
b) Values measured by FOI.

Lowering of the glass transition temperature

All reported experimental values of glass transitions in this study are based on the temperature in the middle of the transition. This glass transition temperature is called the midpoint, T_{gMid}. Thus T_g in this study are equal to T_{gMid} and is calculated according to equation 1:

$$T_g = T_{gMid} = \frac{T_{gOn} + T_{gEnd}}{2} \qquad 1.$$

where the onset, T_{gOn}, and the endset, T_{gEnd}, of the transition were evaluated at the intercept of the extrapolated tangents as seen in the DSC curve for pure NPN in Figure 1.

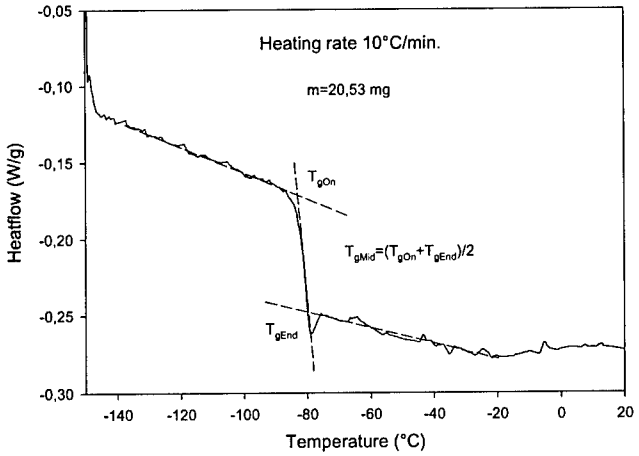


Figure 1 DSC glass transition curve of pure NPN.

In order to study the plasticising effect of NPN on uncured polyNIMMO, the glass transition on respective substance and on mixtures of the two, containing 25, 33 and 50wt% NPN, was measured. The results are presented in Figure 2 and in Table 2.

To calculate the glass transition temperature for a binary (single phase) mixture of a polymer and a plasticiser, many empirical equations have been proposed.[10,11] One of the more commonly used is the Fox equation:[12]

$$\frac{1}{T_g} = \frac{w_1}{T_{g1}} + \frac{w_2}{T_{g2}} \qquad 2.$$

where w is the weight fraction and the indices *1* is for the polymer and *2* is for the plasticiser. Observe that the temperature must be denoted in Kelvin when using the Fox equation. The equation is very useful when only the T_g for respective pure substance is known. The interaction between the polymer and the plasticiser is, however, not taken in to account.

To obtain a better fit to the experimental data in this study, the following equation has been used:

$$T_g = T_{g1} w_1 + T_{g2} w_2 + I w_1 w_2 \qquad 3.$$

This equation was introduced by Jenckel and Hensch[13] and have been successfully used by Chi to describe uncured and cured mixtures of polymers and energetic plasticisers.[14] I is called the interaction parameter and it will roughly correspond to the molecular flexibility of the plasticiser,[14] based on its molecular structure, and thus a value of the plasticisers ability to lower T_g is obtained. If I is equal to zero, equation 3 will describe a straight line in a T_g versus w_2 plot. In Figure 2 the experimental T_g (midpoint) data for polyNIMMO/NPN mixtures are shown. Equation 3 can be rewritten as:

$$I = \frac{T_g - T_{g1} w_1 - T_{g2} w_2}{w_1 w_2}. \qquad 4.$$

By using equation 4 the interaction parameter was calculated for each binary composition. Since all tests were performed in duplicate, six values were obtained. The interaction parameter for polyNIMMO/NPN was then calculated by taking the mean value of the six and was found to be –28.3°C with a standard deviation, s, of 3.3°C. A standard deviation of 3.3°C might seem large but the maximum influence in equation 2 will only be 0.8°C when $w_1 = w_2 =$ 0.5. The curve described by equation 3 was plotted in Figure 2 by using the calculated interaction parameter.

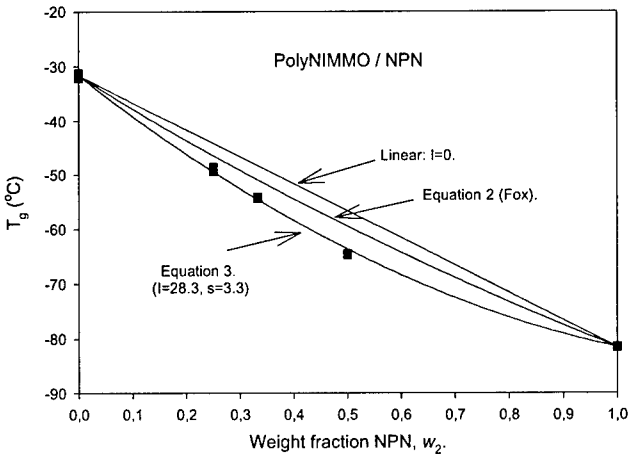


Figure 2 Glass transition temperature of uncured PolyNIMMO plasticised with NPN.

To compare the plasticising effect of NPN in polyNIMMO with other energetic plasticisers the same procedure was repeated with the energetic plasticisers Bu-NENA and BDNPA/F in combination with polyNIMMO. The results are presented in Figure 3 and in Table 2.

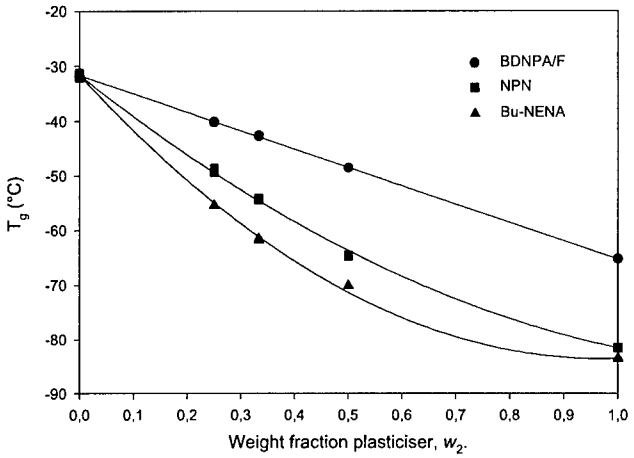


Figure 3 Glass transition temperature of uncured PolyNIMMO with different plasticisers.

Table 2 Glass transition temperatures of the pure materials and of 50/50 polyNIMMO/plasticiser mixtures and their calculated interaction parameter.

Substance	T_g (°C)	T_g (°C) w_2=0.5	I (°C)	s^a (°C)
PolyNIMMO	-31.6	-----	-----	----
NPN	-81.5	-64.6	-28.3	3.3
Bu-NENA	-83.5	-70.1	-54.9	3.7
BDNPA/F	-65.2	-48.5	-0.1	0.8

a) Standard deviation for the calculated interaction parameter.

Lowering of the viscosity

The ability of a plasticiser to lower the viscosity of the polymer was measured on 50/50 mixtures of polyNIMMO and plasticiser. It was shown that NPN was almost equally effective in lowering the viscosity of polyNIMMO as Bu-NENA (Table 3), which is considered to be very effective in this respect.[1]

Table 3 The viscosity of uncured 50/50 mixtures of polyNIMMO and different plasticisers at 30 and 60°C.

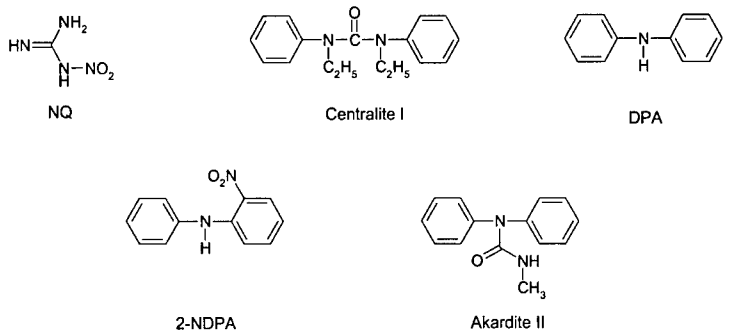
Polymer	Plasticiser	Viscosity (Pa·s)	
		30°C	60°C
PolyNIMMO	-	45	3.6
PolyNIMMO	Bu-NENA	0.5	0.2
PolyNIMMO	BDNPA/F	3.1	0.5
PolyNIMMO	NPN	0.8	0.3

Measured at a constant shear rate of 1.0 s^{-1}.

Thermal Stability of NPN

The thermal stability of NPN was measured by microcalorimetry. Pure NPN decomposed within one day at 65°C. In order to stabilise NPN, different conventional nitrocellulose/nitroglycerine stabilisers were tested (

Scheme **1**) in combination with NPN at 65°C.



Scheme 1 Stabilisers used in this study. Nitroguanidine (NQ), 1,3-diethyl-1,3-diphenylurea (Centralite I), diphenyl amine (DPA), 2-nitro-diphenyl amine (2-NDPA), 1,1-diphenyl-3-methylurea (Akardite II).

Figure 4 shows the effect of different stabilisers on the thermal stability of NPN. Akardite II and DPA have proven to be good stabilisers for nitroglycerine,[15] but they had no stabilising effect on NPN. NQ has shown to be effective in stabilising NENA compounds in the presence of ammonium perchlorate.[16] NQ was, however, not useful as a NPN stabiliser likely due to its insolubility in NPN. Centralite I and the derivative of DPA, 2-NDPA, was on the contrary to DPA the most effective in stabilising NPN. NPN/Centralite I was stable for one day at 65°C, whereas NPN/2-NDPA was stable for a minimum of 2 days. Autocatalytic reaction occurred, however, in less than four days.

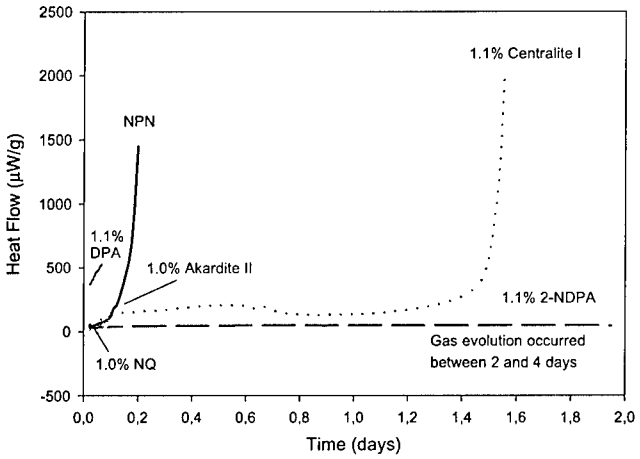


Figure 4 Heat flow evolved during isothermal microcalorimetry of NPN, stabilised with 1% of different stabilisers. Nitroguanidine (NQ), 1,3-diethyl-1,3-diphenylurea (Centralite I), diphenyl amine (DPA), 2-nitro-diphenyl amine (2-NDPA), 1,1-diphenyl-3-methylurea (Akardite II). Temperature: 65°C.

Impact sensitivity

It was found that the impact sensitivity of NPN was lower than 0.2 J which is considered as very sensitive[8]. Due to the high sensitivity of pure NPN the sensitivity of a 50/50 polyNIMMO/NPN mixture was studied as well, to se if the sensitivity could be improved. The impact sensitivity of the mixture was 2 J (evaluated at 50% probability) which is a substantial improvement but it should still be considered as sensitive.

Conclusions

A new energetic plasticiser, NPN, has been syntesised at FOI and it has a similar plasticising effect on polyNIMMO as Bu-NENA. The glass transition temperature of uncured polyNIMMO was depressed from -32 to -65°C by adding 50% NPN. NPN was also effective in lowering the viscosity of uncured polyNIMMO. A drawback of NPN is its thermal instability. Attempts to stabilise NPN with conventional nitrocellulose/nitroglycerine stabilisers have been made, but none of the substances were able to stabilise NPN for more than 2-4 days at 65°C.

Acknowledgements

The authors wish to gratefully acknowledge Dr Latypov at FOI, for inventing the synthesis route and synthesising the NPN material. The authors would further like to thank the Swedish Defence Forces and the Swedish Defence Materiel Administration for giving financial support to this project.

References

1. Bunyan P., Cunliffe A., Honey P. (1998). Plasticisers for new energetic binders. *29th International Annual Conference of ICT*, p. 86/1.
2. Ou Y., Chen B., Yan H., Jia H., Li J., Dong S. (1995). Development if energetic additives for propellants in China. *Prop. Power* 4, 838.
3. Rindone R.R., Huang D-S., Hamel E.E. (1996). Eneretic azide plasticizer. *US Patent* No. 5,532,390.
4. Drees D., Löffel D., Messmer A., Schmid K. (1999). Synthesis and characterization of azido plasticizer. *Prop. Expl. Pyrotech.* 24, 159.
5. Desai H.J., Cunliffe A.V., Hamid J., Honey P.J., Stewart M.J., Amass A.J. (1996). Synthesis and characterisation of α,ω-hydroxy and nitrato telechelic oligomers of 3,3-(nitratomethyl) methyl oxetane (NIMMO) and glycidyl nitrate (GLYN). *Polymer* 37, 3461.
6. Licht H-H., Ritter H., Wanders B. (1996). NENA-sprengstoffe. *27th International Annual Conference of ICT*, p. 21/1.
7. Baumgartner W.E., Butts P. G. (1975). Propellant composition containing beryllium hydride, nitrocellulose and nitrate co-plasticizers. *US Patent* No. 3,861,970.
8. United Nations. "Recommendation on the Transport of Dangerous Goods. Manual of Tests and Criteria" ST/SG/AC.10/11/Rev. 2.
9. ICT thermochemical database, 1999.
10. Nielsen L.E. (1994). *Mechanical properties of polymers and composites*. 2nd Ed. p. 519.
11. Gedde U.W. (1995). *Polymer Physics*. 1st Ed. p. 81.
12. Fox. T.G. (1956). Influence of diluent and of copolymer composition on the glass temperature of a polymer system. *Bull. Am. Phys. Soc.* 1, 123.

13. Jenckel E., Hensch R. (1950). *Kolloid Z.* 118, 56.

14. Chi M-S. (1981). Compatibility of cross-linked polymers with plasticizers by glass transition temperature measurement and swelling tests. *J. Polymer Sci. (Chem.)* 19, 1767.

15. Wilker S., Pantel G., Ticmanis U., Kaiser M. (2000). Compatibility investigations of nitrate esters. *31th International Annual Conference of ICT*, p.24/1.

16. Mullay J.J., Johnson R.A., van Norman J.F. (1996). Stabilized munitions containing a NENA compound. *US Patent* No. 5,507,893.

Some Characteristics of the Potassium 4,6-Dinitrobenzofuroxan Thermal Decomposition

Boris Lurie, Mohamed Dobbagh
Mendeleev University of Chemical Technology, Russia, Moscow
lurie@rctu.ru

Kinetics of the thermal decomposition of powdery substance have been studied under isothermal conditions (t= 140 - 180°C) by measuring gas evolution. Gaseous products were analysed by chromatography. The degree of the vessel filling by the substance (m/v) was altered from 0,001 to 0.016 g/cm^3. Under these conditions the KDNBF thermal decomposition proceeds with acceleration. The kinetic curve has a S-type form. The maximum rate is observed at the ~ 50% extent of the transformation. The total amount of the gaseous products formed in the decomposition is 2.25 mole/mole. One-half the gases condense on cooling to 20°C. Very likely this is water. The main part of the non-condensing gases are CO_2 (0.75 mole/mole) and N_2 (0.5 mole/mole). The amounts of NO and N_2O are 0.15 and 0.1 mole/mole respectively. Only traces of CO have been detected. One-half of nitrogen-containing products is present in the condensed phase.

The decomposition acceleration (W_{max}/W_o) slightly rises as the temperature decreases and the m/v value increases. This ratio is equal to 10 at 140°C. The temperature dependence of the KDNBF thermal decomposition rate (calculated for the initial stage) is described by the expression:

$$\lg k = 16.95 - 43500/2.3RT\ , [s^{-1}].$$

The magnitude of the activation energy is presented in kcal/mole. The activation energy of the process is practically invariable over the whole chemical transformation. The acceleration of decomposition is preceded by an initial "induction" period with a constant rate. Its formal dependencies on temperature and m/v ratio are presented.

The obtained results are compared with the experimental data of other authors and also with DNBF kinetics of decomposition. Mechanism of KDNBF chemical transformation in the thermal decomposition and characteristics of its combustion are discussed.

EFFECT OF ALEX AND BORON ADDITIVES ON IGNITION AND COMBUSTION OF AL-KNO_3 MIXTURE

Simonenko V.N., Zarko V.E., and Kiskin A.B.

Institute of Chemical Kinetics and Combustion, Novosibirsk, Russia

Sedoi V.S.* and Biryukov Yu.A.**

*Institute of High Currency Electronics, **State University, Tomsk, Russia

ABSTRACT

The effect of ultra fine Al and B additives on the ignition delay and burning rate of basic Al-KNO_3 pyrotechnic mixture has been studied. For comparison the mixture with $Ba(NO_3)_2$ as oxidizer was investigated. Three types of initiation stimulus with different energy supply intensity (Xenon lamp, electric squib and igniting capsule) were used. Experiments at atmospheric pressure and in the closed vessel were performed. A qualitative examination of condensed combustion products was made. Investigations showed that introduction of Alex in basic formulation decreases ignition delay time by 4 – 20 times depending on the Alex content. Addition of amorphous B demonstrated lower efficiency. The replacement of commercial Al (15 μm) with fine Al (3 μm) resulted in 6 – 9 times shorter ignition delay time. Replacement of KNO_3 by $Ba(NO_3)_2$ resulted in decrease of ignition delay time.

INTRODUCTION

The ignition of the main charge in different gas generators is reached by using a booster charge, which provides intense heating the main charge surface. One of the first and simplest formulations of the booster charge was black powder based on char and KNO_3. The formulations of the modern booster charges include various metals that results in increase in the maximal combustion temperature and amount of condensed combustion products. Typical metals used are Mg and Zr, and only rarely Al because of highly protective properties of Al_2O_3 that prevents interaction of pure Al with oxidizer (e.g., with oxygen). Fortunately, contemporary technology allows obtaining ultra fine (submicron) Al powders [1] whose ability for oxidation is much higher than that of the ordinary (10-30 μ in size) Al powder. This property makes ultra fine Al powder attractive for use in the newly developed booster charge formulations.

It is known fact that commercial pyrotechnic mixtures are based on relatively cheap chemical compounds. However, in order to meet specific technical demands it is sometimes needed to introduce small amount of non-traditional components into formulation of a booster charge. The objective of the present work was comparative analysis of ultra fine Al and amorphous B additives effect on ignition and combustion characteristics of the mixture of KNO_3 and ordinary Al powder. The same experiments were performed also with the mixtures based on $Ba(NO_3)_2$.

EXPERIMENTAL TECHNIQUE

Investigation of the ignition and combustion behavior was conducted on pressed and free packed powder samples. In experiments with pressed samples the Xenon lamp generating radiant flux 16 cal/cm^{2}s has been used. The signals of the recoil force and flame luminosity of ignited samples were recorded. Details of the technique are described in Ref. [2]. The pressed samples were manufactured by compacting powders under P = 900 atm and had the shape of cylinder with 0.8 cm length and 1.0 cm diameter. 2% mass of iditol was added in excess of 100% for binding the mixture. To increase the radiation absorption coefficient the ignited surface was covered with thin layer of the lamp soot.

Experiments with free packed (poured) mixtures were conducted in the air and in the closed vessel of 68 cm^3 volume. In the experiments, 0.5 g of tested material was freely placed into small plastic bag and electric squib was initiated by electrical current. A photodiode mounted at the distance 40 cm from the plastic bag recorded the intensity of radiation emitted by the ignited booster charge. When conducting experiments in the closed vessel, the signal of the pressure gauge was recorded.

In selected series of experiments the action of ignition stimulus was enhanced by use of powerful igniting capsule of KV-21 type. The more powerful initiation was undertaken in order to achieve an explosion type of the reaction regime in the booster charge. When using KV-21 capsule, 1g of the booster charge mixture was freely packed into brass cartridge case of 2 cm length and 1.5 cm diameter. The booster charge was fixed inside cartridge with the paper plug. After initiation of capsule the jet of the combustion products reached the paper target

mounted at the distance of 30 cm. The "prints" of different formulation booster charges then were compared.

For preparing the booster charges the powders of oxidizer KNO_3 (100-250 μ) or $Ba(NO_3)_2$ (100-300 μ) were used. Commercial fraction of Al powder with mean particle size 15 μ was taken as the basic one. In several experiments the narrow Al fraction with mean particle size 3 μ (Al fine) was employed which was obtained by processing the commercial Al powder in pneumatic jet unit [3]. As the additives, we used Alex, which is ultra fine Al with mean particle size 0.15-0.20 μ obtained by electroexplosion in nitrogen [1], and amorphous boron, B_{am}, with particle size less than 1 μ. To facilitate the ignition of pressed samples, the powder of Mg (70-300 μ) was introduced in the formulation in amount of 10%.

EXPERIMENTAL RESULTS

The first series of experiments was conducted with radiative heating of the pressed samples. Experiments on heating the pressed mixture of KNO_3 and ordinary Al powder showed impossibility of reaching normal ignition regime with luminous flame and self-sustaining combustion after cutting off the radiant flux. Upon heating, the surface of the samples started to melt and form the drops of liquid oxidizer that felt down from the vertical sample surface. On the contrary, pressed samples based on $Ba(NO_3)$ ignited easily under action of the same in magnitude radiant flux. It is worse to note that the above mixture with KNO_3 as oxidizer was successfully ignited after partial replacement of Al by Alex or B_{am}.

Table 1. Physicochemical properties of oxidizers [5,6].

	Density, g/cm^3	T melting, ^0C	T intense decomposition, ^0C	Active oxygen, %
KNO_3	2.11	336	600-700	40
$Ba(NO_3)_2$	3.24	592	600	30

Table 2. Physicochemical properties of metals [6,7].

	Density, g/cm^3	T melting, ^0C	T boiling, ^0C	T melting of oxide, ^0C
Al	2.7	660	2327	2050
B_{am}	2.34	2037	3860	450
Mg	1.74	650	1120	2800

In order to perform comparative analysis of the effect of additives on the combustion characteristics of pressed samples a proper part of Al powder was replaced by 10% of Mg in all formulations studied. Table 3 represents the composition of the pressed mixtures and experimental data on ignition delay and burning rate. It is seen that in the mixtures with KNO_3 the burning rate increases by 30% with addition of 5% of Alex and becomes doubled with addition of 5% of B_{am}. The ignition delay time becomes shorter by 25% in the case of Alex and thrice shorter in the case of B_{am} additive. Qualitatively, these trends remain the same for the mixtures based on $Ba(NO_3)_2$ but the magnitude of the effect is less.

Table 3. Composition and ballistic parameters of pressed samples.

KNO_3	65	65	65	65	-	-	-	-
$Ba(NO_3)_2$	-	-	-	-	65	65	65	65
МПФ-3	10	10	10	10	10	10	10	10
АСД-1	25	-	20	20	25	-	20	20
Al, fine	-	25	-	-	-	25	-	-
Alex	-	-	5	-	-	-	5	-
B_{am}	-	-	-	5	-	-	-	5
Iditol (in excess of 100%)	2	2	2	2	2	2	2	2
t_{ign}, s	2	1.5	1.5	0.7	1.8	1.6	1.3	1.2
r_b, cm/s	0.17	0.16	0.22	0.35	0.33	0.33	0.38	0.42

In the second series of experiments, studying the effect of additives on ignition and combustion of freely packed booster charges was conducted on the

mixtures which do not contain Mg. In the experiments the intensity of the flame radiation, when firing the charge in the air, and pressure rise, when firing in the closed vessel, were recorded.

Figure 1 shows the initial part of experimental records of the flame radiation for different type mixtures ignited in the air. The solid line represents radiation intensity of electrically heated igniting wire coated with the pyrotechnic lacquer. The first peak on this curve represents the glowing of the wire itself and the second peak represents combustion of the lacquer.

Summary of the results on the flame radiation intensity is presented in Table 4. The radiation emitted by flame has been measured in arbitrary units under fixed locations of the receiver and plastic bag with an ignited mixture.

To treat objectively the data on ignition delays, two methods of the processing the photodiode signal were employed. According to the 1st method the ignition delay time corresponded to the moment of reaching fixed amplitude of the flame radiation intensity. It equals 40 arbitrary units of radiation intensity, which was measured by the gauge used in our experiments. This value is designated as t_{40} in Table 4.

According to the 2nd method the ignition delay time corresponded to the moment of reaching 50% of the maximal amplitude signal of the flame radiation.

This value is designated as $t_{0.5}$ and also included in Table 4. As one can see, both methods give similar results in terms of qualitative description of the experimental trends for the intensity of reacting for different formulations initiated by the electrical squib. In addition the time of reaching maximal intensity of radiation t_{max} and the magnitude of maximal radiation intensity in arbitrary units are presented in Table 4.

According to the data of Table 4 the inclusion of B_{am} in the KNO_3+Al mixture results in decrease of ignition delay time by 1.3-1.8 fold and increase of the combustion completeness. The mixture with totally replaced ordinary Al by pneumatically ground Al (fine) is characterized by much shorter (approximately by 6-8 times) ignition delay time. Successive introduction of 5% and 15% of Alex into charge formulation and total replacement of ordinary Al by Alex lead to reducing the ignition delay time and increasing the intensity of radiation.

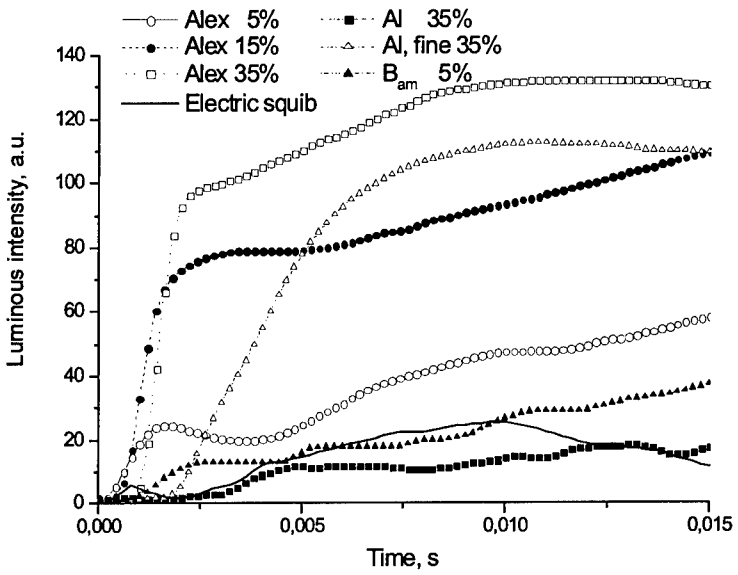


Fig. 1. Temporal behavior of the flame luminosity for the booster charges based on KNO_3 ignited in the air.

Table 4. Characteristic times and radiation intensity for the booster charges ignited in the air.

N	$t_{0.5}$, s	t_{40}, s	t_{max}, s	I_{max}, a.u.	Type of mixture
1	0.026	0.028	0.07	67	KNO_3(65%)+Al(35%)
2	0.014	0.0076	0.045	106	KNO_3(65%)+Al(30%)+Alex(5%)
3	0.0014	0.0011	0.032	122	KNO_3(65%)+Al(20%)+Alex(15%)
4	0.0016	0.0014	0.012	132	KNO_3(65%)+Alex(35%)
5	0.0041	0.0034	0.01	112	KNO_3(65%)+Al(Fine, 35%)
6	0.02	0.016	0.07	106	KNO_3(65%)+Al(30%)+B_{am} (5%)
7	0.052	0.052	0.23	80	$Ba(NO_3)_2$(65%)+Al(35%)
8	0.011	0.007	0.055	102	$Ba(NO_3)_2$(65%)+Al(30%)+Alex(5%)
9	0.0008	0.0006	0.023	104	$Ba(NO_3)_2$(65%)+Al(20%)+Alex(15%)
10	0.0004	0.0005	0.026	105	$Ba(NO_3)_2$(65%)+Alex(35%)
11	0.011	0.009	0.028	103	$Ba(NO_3)_2$(65%)+Al(Fine,35%)
12	0.014	0.013	0.1	108	$Ba(NO_3)_2$(65%)+Al(30%)+B_{am} (5%)

Within the second series of experiments the firings of the booster charge in the closed vessel were also conducted. Table 5 summarizes experimental data on maximal pressure rise in the closed vessel resulted from burn out of the booster charge and corresponding to this pressure the instant of time calculated from the moment of initiation of the electrical squib. It is seen that the basic mixture of KNO_3 and ordinary Al powder produces a relatively small maximal pressure (about 3 atm only). Examination of the combustion residue on the vessel bottom revealed noticeable amount of unburned components of the mixture after firing test.

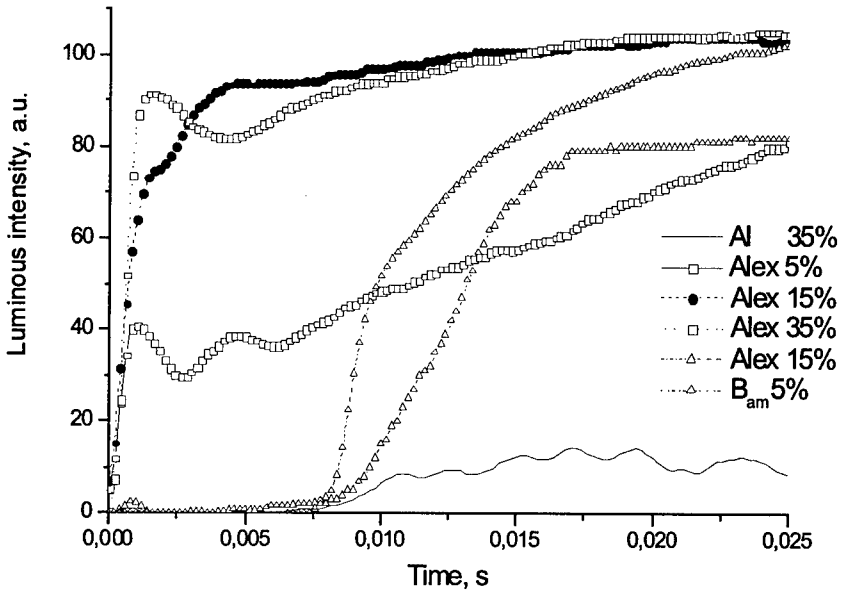


Fig. 2. . Temporal behavior of the flame luminosity for the booster charges based on $Ba(NO_3)_2$ ignited in the air.

The mixtures containing additives of Alex or B_{am} burn 2-3 times faster than the basic mixture and maximal pressure rise for such mixtures is 5-8 times higher. On the bottom of vessel relatively thick layer of fine oxide particles has been revealed.

When replacing oxidizer KNO_3 by $Ba(NO_3)_2$, all effects of additives on the ignition and combustion behavior of the booster charge remain qualitatively the same. As expected from thermodynamics, the maximal pressure in closed vessel

slightly decreases. The ignition delay time under firing in the air becomes slightly shorter.

Table 5. Characteristic time of reaching maximal pressure for different mixtures fired in the closed vessel.

N	t_{max}, s	P_{max}, atm	Type of mixture
1	0.44	2.9	KNO_3(65%)+Al(35%)
2	0.23	20.3	KNO_3(65%)+Al(30%)+B_{am} (5%)
3	0.44	8.8	KNO_3(65%)+Al(30%)+Alex(5%)
4	0.18	23.3	KNO_3(65%)+Al(20%)+Alex(15%)
5	0.16	16.7	KNO_3(65%)+Alex(35%)
6	0.2	18.0	KNO_3(65%)+Al(Fine, 35%)
7	0.51	8.4	$Ba(NO_3)_2$(65%)+Al(35%)
8	0.2	18.0	$Ba(NO_3)_2$(65%)+Al(30%)+B_{am} (5%)
9	0.16	17.2	$Ba(NO_3)_2$(65%)+Al(20%)+Alex(15%)

In the third series of experiments some qualitative observations were made in the experiments with firing the booster charge capsulated into brass cartridge case in conditions of initiation by powerful capsule KV-21. Only mixtures based on KNO_3 were tested. The appearance of the residue inside the brass cap and "print" of the combustion products jet on the paper target are different for different formulations.

After firing the basic mixture (KNO_3 + ordinary Al) the internal wall of the brass cartridge case has thin layer of particles consisting of unreacted original components. The target is covered by a layer of melted oxidizer with metallic particles inserted. After firing the charge containing 5% Alex, on the internal case wall small amount of aggregates is fixed consisting of sintered particles of oxidizer and metal. The target is covered with aggregates of 200-500 μm in size. The largest aggregates (up to 800 μm) are found on periphery of print.

When increasing the Alex content up to 15%, the amount of residue in the form of the metal agglomerates with maximal size reaching 3 mm increases

essentially. The temperature of jet is increased and in the center of target the agglomerate's size reaches 250-600 μm, but on periphery it amounts about 2000 μm. Even higher temperature in jet is realized in the case of total replacement of Al by Alex that is indicated by brown color of the target print. The size of the metal agglomerates in the center of print does not exceed 400 μm and it is less than 1000 μm on periphery.

When using B_{am} additive, the amount of the residue particles in the brass cartridge case is relatively small and their largest size does not exceed 1500 mm. The print on the target contains some amount of unreacted Al particles and agglomerates with size up to 300 μm.

DISCUSSION

Analysis of data on heating the pressed samples shows that the reason for impossibility of normal ignition of KNO_3 based mixture is relatively low melting point of oxidizer (336°C, Table 1). It is difficult to provide at this temperature sufficient reaction rate for oxidation of Al covered with thick oxide film. Observed formation of melted oxidizer drops and their motion along the vertical surface of pressed sample result in degeneration of thermal ignition. Ignition of $Ba(NO_3)_2$ based mixture in the same conditions of radiative heating occurs successfully that can be explained by relatively small temperature difference between the melting point of oxidizer (592°C) and that of metal (660°C). Probably, heating by higher radiant fluxes may result in normal ignition of KNO_3 based mixture but we had no powerful energy source available.

As expected, addition of Alex or B_{am} in the charge formulation decreases the ignition delay time and increases the burning rate of pressed samples. Visual observations made with photo camera indicate decreasing the size of agglomerates (length and width of burning particle track) in the flame of samples containing Alex or B_{am}. It is supposed that such an effect of additives results from the higher intensity of exothermic chemical reaction in the condensed phase in presence of Alex or B_{am}. It is known that Alex starts to oxidize readily at the temperature 350-400°C [8,9] and boron starts reacting after melting of oxide film at the temperature 450°C [4].

In experiments on ignition of the booster charge in the air it was established that the completeness of the basic mixture (KNO_3 and ordinary Al powder) combustion is relatively low. This has been indicated by low intensity of the flame luminosity and by examination of the combustion residues which contained partially melted and non-decomposed original components. Obviously, such behaviour is caused by relatively short time of heating and low reactivity of the metal. It should be noted that in conditions of our experiments the measured flame intensity did not correspond directly to the intensity of the flame reactions. Some variation of intensity of radiation can be attributed to the variation of the shape of the flame ball. In the case of fast ignition and intense reaction of the mixture, the source of radiation is compact and receiver records total radiation. In the case of low intensity ignition and mechanical failure of the plastic bag some part of charge may escape through the holes and receiver records reduced radiation signal.

Data presented in Figs.1 and 2 and Table 4 show that introduction of Alex in the basic formulation leads to significant increase in the flammability of the mixtures that exhibits itself in essential reducing the ignition delay time. Obviously, the reason for that is enhanced reactivity of Alex. The very developed surface of Alex due to its small particle size provides high energy release rate resulting in high completeness of combustion (minimal time of reaching a maximal radiation intensity). The interesting finding of this work concerns the high reactivity of pneumatically ground Al (fine) powder. According to experimental data (Table 4) the mixture with fine Al starts igniting after some delay as compared with the Alex containing mixture, but the time of reaching maximal flame radiation intensity is practically the same for both types of mixture. An enhanced reactivity of ground Al particles can be attributed not only to relatively small particle size but also to the possible mechanical defects and impact induced reaction sites on the particle surface.

Measurement of the pressure rise in experiments on the booster charge ignition in the closed vessel gave similar results on inflammability of the mixtures tested. Some complementary data on the combustion completeness brought examination of the combustion residue collected from the vessel bottom. The volume of the residue is higher in the case of firing the basic mixture when unburned components have been revealed on the vessel bottom.

In the case of ignition by powerful energy stimulus (capsule KV-21) it was revealed that variation of the Alex content leads to essential changing the appearance and component's content of the residue on the wall of the brass cartridge case. This shows principal possibility to control the extent of the mixture decomposition when changing the formulation of the booster charge. It should be noted that the total replacement of Al by Alex does not result in complete depletion of the mixture components in combustion at atmospheric pressure because of decreasing the charge density loading and increasing the length of change. Therefore, the charge totally based on Alex gives print on the paper target with traces of undecomposed particles of oxidizer.

CONCLUSIONS

In the course of this study technical difficulties have been revealed of reaching reliable ignition of free packed mixture of KNO_3 and ordinary Al (15 μ) powder initiated by electrical squib. A noticeable amount of unburned original components in the combustion residue and relatively small pressure rise in the closed vessel indicate incomplete combustion of such mixture in described conditions of testing. Partial replacement of ordinary Al by Alex or B_{am} leads to reducing the ignition delay time and increasing the combustion completeness. The most pronounced effect is observed for the mixture with total replacement of Al by Alex. It is wondering that the mixtures with totally replaced ordinary Al by fine Al (3 μ) powder exhibit very similar behavior to the mixtures totally based on Alex. The causes of such behavior should be explored in the future studies.

The ignition and combustion behavior of the mixture of $Ba(NO_3)_2$ and ordinary Al in terms of the effect of additives is qualitatively similar to that for KNO_3 based mixture. The ignition delay time is slightly shorter but maximal pressure rise in the closed vessel is less than for KNO_3 based mixture.

Partial support of the NATO Linkage Grant # 976783 is acknowledged.

REFERENCES

1. Sedoi V.S, Valevich V.V., "Obtaining of ultra-fine powders by the method of exploding wires in the low pressure nitrogen". Letters in Journal of Technical Physics (1999), V. 25, N 14, pp. 81-84.
2. Zarko, V.E., Simonenko, V.N., and Kiskin, A.B.,"Radiation-Driven, Transient Burning: Experimental Results". In: Progress in Astronautics and Aeronautics (De Luca, L., Price, E.W., Summerfield, M., Eds.) V. 143, Ch.10, 1992.
3. Biryukov Yu., Vorozhtsov A., Bogdanov L.. "Obtaining submicron abrasive powders by pneumatic processing of electric corundum and products of solid rocket propellants combustion". Energetic materials: Production, Processing and characterisation. Proceedings of the 29th International Annual Conference of ICT, FRG, 1998, pp. 162.1-162.9.
4. Shidlovskii A.A., Fundamentals of pyrotechnics. Moscow, Mashinostroenie, 1973, pp. 320, (in Russian).
5. Nikolaev N., Pyrotechnist – amateur. St – Peterburg, Publishing house of V.I. Gusinskii, 1899, pp. 360.
6. Pokhil P.F., Belyaev A.F., Frolov Yu.V., Logachev V.S., Korotkov A.I., "Combustion of Powdered Materials in Active Media", Nauka, Moscow 1972. (In Russian). See also: Air Force Systems Command Report FTD-MT-24-551-73, 1973.
7. Breiter A.L., Mal'tsev V.M., Popov E.I., "Models of Metal Inflaming", Fizika Goreniya i Vzryva, v. 13, N 4, 1977, pp. 558 – 570.
8. Il'in A.P., and Proskurovskaya L.T., "Two-Stage Combustion of Ultra-Fine Aluminum Powder in Air", Combustion, Explosion, and Shock Waves, v. 26, N 2, 1990, pp. 71 - 72.
9. Simonenko V.N., Zarko V.E., "Comparative studying the combustion behavior of composite propellants containing ultra fine aluminum", Energetic materials: Proceedings of the 30th International Annual Conference of ICT, FRG, 1999, 21.1- 21.14.

STUDY OF COMBUSTION CHARACTERISTICS OF THE ADN -BASED PROPELLANTS

Oleg P. Korobeinichev, Alexander A. Paletsky,
Alexander G. Tereshenko, Evgeny N. Volkov
Institute of Chemical Kinetics and Combustion SB RAS,
630090 Novosibirsk, Russia.

J. Michael Lyon, James G. Carver, Robert L. Stanley
Department Research and Development,
Al 35898, Redstone Arsenal, USA.

Keywords:
ammonium dinitramide, composite propellant, high pressure, combustion characteristics

ABSTRACT

This paper is devoted to the investigation of the main combustion characteristics of a model composite solid rocket propellant based on ammonium dinitramide (ADN) and polycaprolactone in the pressure range of 4.0 to 8.0 MPa. Polycaprolactone with molecular weight (MW) of 10.000, pCLN(10.000), and polycaprolactone diol with MW of 1.250, pCLN(1250), were used. Experimental data on the dependence of burning rate on pressure for an ADN/pCLN propellant of stoichiometric composition and for this propellant with different additives are presented in paper. Oxides of copper and lead in the range of 1-2% were used as catalytic additives. Another oxidizers (ammonium perchlorate, ammonium nitrate), cyclic nitramines (RDX, HMX) and aluminum in the amount of 10% were used as energetic additives. The dependence of the propellant burning rate on the initial temperature has been investigated. Composition of the combustion products of the propellant with and without aluminum at pressures of 4.0 and 8.0 MPa has been determined. Temperature of the final combustion products of the propellant without an additive and for some propellants with an additive has been determined by a thermocouple method.

INTRODUCTION

Ammonium dinitramide is a powerful chlorine-free oxidizer which can replace ammonium perchlorate (AP) in rocket propellants. Since the combustion products of ADN-based propellants are not toxic, these propellants are environmentally friendly and investigation of them is of great interest. Important physicochemical properties of ADN and ADN-based propellants were published for the first time in paper [1]. ADN has a higher heat of formation than the common solid rocket propellant oxidizer, AP. ADN-based propellants have higher specific impulse than AP-based propellants [1, 2]. At present there are only a few published papers which are devoted to the study of the combustion characteristics of the ADN-based propellants. Paper [3] is of great interest. This paper is devoted to the investigation of the safety characteristics (sensitivity to impact, friction and electrostatic discharge), thermal stability and burning rate (in a wide pressure range of 6.9-68 MPa) of cured propellants on the based on ADN, pCLN and nitrate ester (NE).

The most important combustion characteristics of a rocket propellant in terms of practical application are specific impulse, burning rate (r_b), parameter ν in dependence of burning rate on pressure ($r_b=A\times P^{\nu}$) and initial temperature, composition and temperature of combustion products. It is not known at present which factor determines the burning rate of ADN-based propellants. For pure ADN, combustion instability takes place in the pressure range of 2-10 MPa [4]. However, even small amounts of organic additives result in a reduction of both burning rates and their scatter in this pressure range [5, 6]. The burning rate and pressure exponent for ADN-based propellants depend on the type of binder used and the oxidizer/binder ratio. For example, model two-component propellants of ADN/paraffin (90/10) [7] and ADN/PBAN (87.5/12.5) [8] are characterized by parameter ν, which is equal to ~0.6 and ~0.8 respectively in the pressure range of 5.5-7.0 MPa. For cured a propellant of ADN(60%)/pCLN/NE [3] over a wide pressure range of 6.9-68 MPa the parameter ν=0.65. ADN-based propellants have high burning rates. However, they do not exceed the burning rate of pure ADN due to the inhibiting effect of organic additives. For example, the typical burning rate of a cured propellant based on ADN/pCLN at a pressure of 10.0 MPa is equal to ~23 mm/s, which is ~1.7 times less than the burning rate of pure ADN. Additionally, the burning rate and parameter ν for ADN-

based propellants depend on the shape of ADN particles. The effect of shape of ADN particles on parameter ν for an ADN/polybutadiene polymer propellant was studied by Ramaswamy [9] and it was shown that parameter ν in the case of spherical oxidizer particles in pressure range of 3.4 – 5.1 MPa can achieve value of 0.11. The catalytic effect of Cu_2O additives on the burning rate of pure ADN is described in paper [6].

The main objective of this research is the investigation of the main combustion characteristics such as: burning rate dependence on pressure, initial temperature, presence of energetic and catalytic additives; temperature and final combustion product composition in the pressure range of 4.0-8.0 MPa i.e. under conditions typical for the combustion chamber of a rocket motor.

EXPERIMENTAL

Experiments investigating the burning rate of strands of a model solid propellant based on ADN/pCLN were conducted in a combustion chamber of constant volume in an inert gas atmosphere. In experiments aimed at the determination of combustion product compositions, helium was used, and in other cases argon or nitrogen were used. ADN was synthesized at the Institute of Organic Chemistry RAS. It contains an impurity of ammonia nitrate (AN) in the amount of less than 3%. For some experiments ADN was purified from AN by a coal column method [10]. ADN crystals had a plate–type shape with longitudinal/transversal ratios of ~7:1. Ground ADN powder with an average particle size of ~40 μm was used for preparation of composite propellants. The melting point of ADN used in this investigation was determined to be 92-94°C. Non-cured strands of ADN/pCLN propellant of stoichiometric composition were prepared by mixing the ingredients in a dry cell at a temperature slightly exceeding melting point of the polymer (60°C for pCLN(10.000) and 36-48°C for pCLN(1250)). At room temperature the first polymer is a flake, and the second is a waxy solid. ADN/pCLN propellant of stoichiometric composition (St_b) consists of 89.08% ADN and 10.92% pCLN (percent by mass). Strands with diameter of 6 mm and length of 10-12 mm were pressed at a pressure of ~1400 MPa. To inhibit burning on the sides of the strands, they were coated with high vacuum silicone grease. In all cases different ingredients (Add) were added to the

stoichiometric propellant composition (St_b), i.e. xSt_b+yAdd means that in this propellant mass fractions of St_b and Add are equal to x% and y% respectively.

Measurement of the burning rate of a composite rocket propellant at high pressures (4.0÷8.0MPa) was conducted by two methods: by pressure control during the combustion process and by videotape recording of movement of the burning surface through combustion chamber windows.

Sampling of combustion products of propellant St_b(10.000) was carried out at pressures of 4.0 MPa and 8.0 MPa using probes, made of stainless steel with an internal angle of 40° and inlet orifice diameters of 170 μm and 130 μm. Combustion products were sampled to a bulb for subsequent gas chromatographic (GC) analysis. GC-analysis allowed determination of the content of gaseous combustion products such as N_2, CO_2, CO, H_2, NO and O_2. In the case of aluminized propellants, the strands were situated perpendicularly to the probe axis. Such strand location allowed sampling of combustion products before clogging of the inlet orifice by condensed combustion products.

Temperature of final the combustion products was measured by bare WRe(5%)-WRe(20%) thermocouples, made of wire with a diameter of 100 μm. The thermocouples had a Π-shaped form with a shoulder length of around 3 mm and were situated in the gas phase at a distance of ~2-5 mm from strand surface. Temperature distributions in condensed and gas phases were measured by flat WRe(5%)-WRe(20%) thermocouples (pressed in strand) with thickness of 13-15 μm and width of about 140-150 μm.

For investigation of St_b burning rate dependence on initial temperature, a system which allows the strand temperature to vary from –50°C to +50°C was used. Accuracy of the initial strand temperature was ±2°C.

For investigation of St_b burning rate dependence on initial temperature, a system which allows the strand temperature to vary from –50°C to +50°C was used. Accuracy of the initial strand temperature was ±2°C.

RESULTS AND DISCUSSION

Burning rate

Data on the dependence of burning rate (r_b) on pressure for baseline propellants ADN/pCLN (89.08/10.92) of stoichiometric composition (St_b) with two types of polymer, pCLN(1250) and pCLN(10.000), over a pressure range of 4.0-8.0 MPa are shown in Fig.1. Parameters of the dependence of burning rate on pressure $r_b=A\times P^{\nu}$ (r_b in mm/s, P in MPa) are given Table 1.

a. Effect of polymer properties

Stoichiometric propellants using pCLN with a molecular weight of 10.000 have a high dependence of burning rate on pressure with parameter ν having a value equal to 1.0. Replacement of this binder in the propellant by a polymer with the same structure and chemical composition, but with lower molecular weight (1250) and lower melting point (36-48°C in comparison with 60°C for pCLN(10.000)) led to a decrease of parameter ν to 0.7 (Fig.1, Table 1). But the absolute value of the burning rate increased by 1.5 times at a pressure of 4.0 MPa and by 1.2 times at 8.0 MPa.

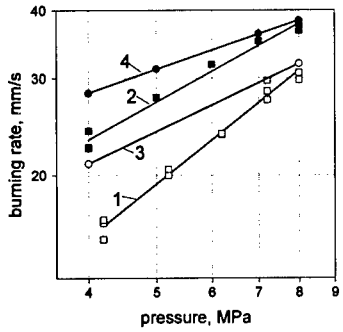


Fig.1. Effect of additive 2%CuO on dependence of burning rate on pressure: 1 (□) - St_b(10.000); 2 (■)- St_b(1250); 3 (O) - 98% St_b(10.000) +2% CuO; 4 (●) - 98% St_b(1250)+2% CuO.

b. Effect of small additives of catalysts CuO, PbO, PbO_2

Addition of 2%CuO to propellants St_b(1250) and St_b(10.000) increased the burning rate of these propellants at pressure of 4.0 MPa (Fig.1). With an increase of the initial pressure from 4.0 MPa to 8.0 MPa the effect of CuO on burning rate decreased. Qualitatively the effect of CuO on the burning rate of the propellant does not depend on the properties of the polycaprolactone used. Quantitatively the effect of an additive on the burning rate is characterized by parameter Z, which is defined as the ratio of the burning rates of propellant with and without an additive. Addition of 2%CuO resulted in an increase of the absolute value of the burning

rate of $St_b(1250)$ by 1.23 times and of $St_b(10.000)$ by 1.38 times at an initial pressure of 4.0 MPa (Table 2). Addition of 2%CuO to the propellant also effected parameter ν. Parameter ν decreased by 1.6 times: to 0.44 for propellant $St_b(1250)$ and to 0.60 for propellant $St_b(10.000)$ (Table 1).

Additionally, propellants with additives of 2%PbO and 2%PbO_2 have been investigated. The effect of 2%PbO on the burning rate of $St_b(10.000)$ at an initial pressure of 4.0 MPa is less than the effect of 2%CuO. Addition of PbO to $St_b(1250)$ in the amounts of 1 and 2% resulted in nonsteady combustion at the initial pressure of 4.0 MPa. The burning rate at that pressure varied ~2 times during the combustion of one strand.

Table 1.
Dependence of burning rate on pressure for propellants on the basis of St_b.

Propellant	Parameters	
	A	ν
100%$St_b(1250)$*	8.74	0.70
100%$St_b(10.000)$**	3.79	1.00
98%$St_b(1250)$+2%CuO	15.30	0.44
98%$St_b(1250)$+2%Pb_3O_4	12.92	0.42
98%$St_b(10.000)$+2%CuO	9.10	0.60
98%$St_b(10.000)$+2% Pb_3O_4	6.22	0.64

* - 89.08% ADN + 10.92% pCLN(1250)
** - 89.08% ADN + 10.92% pCLN(10.000)

Table 2.
Values of parameter Z depending on type of propellant and additive concentration.

Additive, %	2%PbO		1%CuO		2%CuO		2%Pb_3O_4	
pressure, MPa	4.0	8.0	4.0	8.0	4.0	8.0	4.0	8.0
Z, $St_b(1250)$	*	*	1.15	1.0	1.23	1.0	1.0	0.82
Z, $St_b(10.000)$	1.21	1.0	1.26	1.0	1.38	1.0	1.0	0.77

* - nonsteady combustion

The main component (89.08%) of the investigated propellants is ADN, therefore experiments investigating the addition of CuO on ADN combustion have been conducted. Combustion of ADN over the pressure range of 2.0-8.0 MPa is unstable [4]. Our investigation confirmed this fact. However, addition of 2%CuO to pure ADN resulted in stabilization of ADN combustion. It is noticeable, that the absolute burning rate values of a mixture 98%ADN+2%CuO are less than the lower boundary of observed scatter of the

burning rate of pure ADN. Burning rate of this mixture decreased with an increase of pressure from 4.0 to 8.0 MPa. So additive CuO influenced the burning rates of ADN-based propellants and pure ADN in opposite directions. This fact indicates that the mechanism of CuO influence on the combustion of these two systems is different.

Usually the effect of additives on propellant combustion has a complicated character. Combustion chemistry of double-based propellants is closer to that of ADN-based propellants than to that of other types of propellants. In both cases reactions of nitrocompounds in the condensed phase and the gas phase play an important role. According to [11] in the case of double-based propellants a significant catalytic effect of CuO and PbO_2 appears only when formation of a carbonaceous skeleton and the accumulation of catalyst on the burning surface take place. As skeleton contains a large amount of agglomerates with catalyst, the coefficient of thermal conductivity of this skeleton at the burning surface is higher than that of the propellant without additive. As a result additional heat release appears near the burning surface. This heat release accelerates reactions in both condensed phase and also gas-phase reactions close to burning surface and as a consequence the burning rate increases. In our case pyrolysis in the combustion wave of polymer pCLN(10.000) with higher melting point and larger MW proceeds less intensively. Therefore a carbonaceous skeleton on the burning surface of pCLN(10.000) is more developed in comparison with pCLN(1250). It was determined in experiments that an increase of the burning rate after addition of 1 and 2%CuO to baseline propellants is higher in the case of St_b(10.000) (Table 2). This corresponds with the mechanism of influence of catalysts on burning rate of double-based propellants described above.

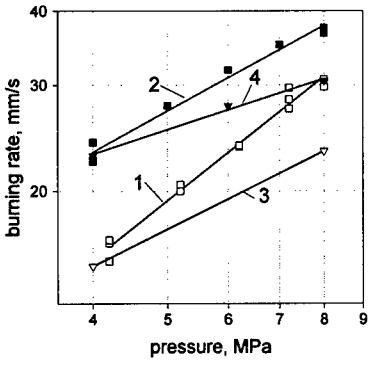


Fig.2. Effect of additive 2%Pb_3O_4 on dependence of burning rate on pressure: 1 (□) - St_b(10.000); 2 (■)- St_b(1250); 3 (▽) - 98% St_b(10.000) +2% Pb_3O_4; 4 (▼) - 98% St_b(1250)+2% Pb_3O_4.

c. Inhibition of propellant combustion by small additive of catalyst Pb_3O_4

As it is shown in Fig.2 a decrease in the burning rate of both baseline propellants took place at an initial pressure of 8.0 MPa upon addition of 2%Pb_3O_4. When the initial pressure was decreased

from 8.0 MPa to 4.0 MPa the influence of Pb_3O_4 on burning rate decreased. Addition of a mixed catalyst, 2%Pb_3O_4+2%CuO, did not result in the expected combined effect of the individual catalysts: increase of burning rate at 4.0 MPa (CuO) and decrease of burning rate at 8.0 MPa (Pb_3O_4). The effect of this composite additive turned out to be very close to that of 2%CuO. In this case Pb_3O_4 played a passive role.

d. Effect of addition of cyclic nitramines, another oxidizers and aluminum

The effect of different additives in the amount of 10% to propellant St_b(10.000) has been studied. In Table 3 the parameters of the dependence of burning rate on pressure over a pressure range of 4.0-8.0 MPa for propellants based on St_b(10.000) are shown.

Addition of 10% AN or 10% AP to St_b(10.000) resulted in a decrease of the burning rate at a pressure of 8.0 MPa and had almost no effect at 4.0 MPa, parameter ν decreased to 0.84 (AN) and 0.73(AP). Addition of 10% RDX or 10% HMX led to an increase of burning rate at 4.0 MPa pressure and did not effect the burning rate at 8.0 MPa. Addition of cyclic nitramines decreased ν to 0.62 (HMX) and 0.54 (RDX). It is noteworthy that propellants with additives of AN and AP have a positive oxygen balance and propellants with additives of RDX or HMX have a negative one. Addition of 10% Al (particles size ~15 μm) to St_b(10.000) did not change the dependence of burning rate on pressure but resulted in worse reproducibility of the data on the burning rate.

Table 3.
Dependence of burning rate on pressure for propellants based on St_b(10.000).

Propellant	Parameters	
	A	ν
90% St_b(10.000) + 10% RDX	9.63	0.54
90% St_b(10.000) + 10% HMX	7.66	0.62
90% St_b(10.000) + 10% AP	5.62	0.73
90% St_b(10.000) + 10% AN	4.60	0.84
St_b(10.000)	3.79	1.00

e. Effect of initial temperature

Burning rate dependence on the initial temperature (t_o, °C) for propellants St_b(1250) and St_b(10.000) at pressures of 4.0 and 8.0 MPa is presented in Table 4. The minimum temperature studied for both propellants was -50°C, and the maximum ones were +30°C

for $St_b(1250)$ and +50°C for $St_b(10.000)$ which did not exceed the melting point of the corresponding polymers. Temperature sensitivity of the propellants (β, %/K) was defined using the formula $\beta=d(\ln(r_b))/dT$. Absolute error in the measurement of β was ±0.15%/K. Temperature sensitivity of burning rate over different temperature ranges for pressures of 4.0 and 8.0 MPa is presented in Table 5.

Table 4.
Burning rate (r_b, mm/sec) at different initial temperatures (t_o, °C).

Propellant	P, MPa	t_o, °C				
		-50	-20	+20	+30	+50
$St_b(1250)$	4.0	18.9	18.4	23.0	24.1	-
	8.0	31.1	31.3	37.5	39.1	-
$St_b(10.000)$	4.0	-	11.5	15.2	-	19.9
	8.0	21.9	21.9	30.3	-	29.6

Table 5.
Temperature sensitivity (β, %/K) over different temperature ranges.

Propellant	P, MPa	temperature range, °C			
		-50 ÷ -20	-20 ÷ +20	+20 ÷ +30	+20 ÷ +50
$St_b(1250)$	4.0	≤0.15	0.56	0.47	*
	8.0	≤0.15	0.45	0.42	*
$St_b(10.000)$	4.0	*	0.69	*	0.89
	8.0	≤0.15	0.81	*	≤0.15

* - did not measure in experiment

A decrease of the initial temperature from -20°C to -50°C did not change burning rates of the propellants under investigation at pressures of 4.0 and 8.0 MPa (Table 4). Besides, at -50°C temperature, combustion instability took place, i.e. possibly these conditions are close to the combustion limit of the composite propellant ADN/pCLN. In the temperature range of -20°C to +20°C β for $St_b(10.000)$ is larger than β for $St_b(1250)$ and is equal to 0.7-0.8 and 0.5-0.6 %/K respectively (Table 5). A further increase of temperature of $St_b(1250)$ to +30°C had little change on β at pressures of 4.0 and 8.0 MPa. With an increase of initial temperature of propellant $St_b(10.000)$ to +50°C β slightly increased to ~0.9%/K at 4.0 MPa pressure and decreased to practically zero at 8.0 MPa. It is noteworthy that over the pressure range of 4.0-6.0 MPa and temperature range of –50 to +20°C β for pure ADN is less than that for propellant ADN/pCLN and is equal to 0.3-

0.4%/K. But β for pure ADN is larger than for the ADN/pCLN based propellant over the range of +20 to +80°C and is equal to 1.5-1.6%/K [12]. So, while ADN is the main ingredient in the model propellant St_b, nevertheless, there is no correlation between temperature sensitivity for ADN and the model propellant.

f. Effect of particles size of aluminum

Aluminum with particles size of ~15 μm and electro-exploded aluminum (ALEX) with particles size of ≤0.1 μm were used. Specific surface area of ALEX powder was ~12m^2/g, and the mass fraction of oxide film on the surface of ALEX was ~6%. Parameters of the dependence of burning rate of St_b(1250) propellant with additives of 10%Al (or ALEX) and 2% CuO are presented in Table 6.

Table 6.
Parameters of pressure dependence of burning rate
of aluminized propellants based on St_b(1250).

Propellant	Parameters	
	A	n
100%St_b(1250)	8.74	0.70
90%St_b(1250)+10%Al	11.67	0.50
90%St_b(1250)+10%ALEX	6.16	0.71
88%St_b(1250)+10%ALEX+2%CuO	12.0	0.49

Addition of aluminum particles with a size of 15 μm slightly decreased the burning rate of the propellant at 8.0 MPa pressure and did not effect it at 4.0 MPa. At the same time addition of ALEX in the same amount (10%) to the propellant St_b(1250) strongly decreased burning rate over the pressure range of 4.0-8.0 MPa and did not change parameter ν. Use of fine aluminum (ALEX) in propellants is necessary to achieve more complete oxidation and enlargement of specific impulse. Subsequent addition of 2%CuO resulted in a significant increase of the burning rate up to the burning rate of the propellant with 10%Al (15μm) additive. So, simultaneous addition of ALEX and CuO to the propellant may allow one to reach the optimal characteristics of the propellant (high burning rate, more completeness of combustion, low ν).

Temperature and composition of final combustion products

In Table 7 experimental values for the temperature (T_{exp}) of the final combustion products of propellant St_b(10.000) with and without additives at 4.0 MPa pressure are presented in comparison with the calculated thermodynamic equilibrium values ($\Delta T=T_{calc}-T_{exp}$). The thermodynamic equilibrium composition of the combustion products and temperatures (T_{calc}) were calculated with the computer code "Astra" [13]. We could not measure the temperature of the final combustion products for propellants with additives of 2%CuO and 10%Al using uncovered thermocouples. Data presented in Table 7 were corrected for heat loss by radiation [14]. In our case this radiation correction for cylindrical thermocouples with a diameter of 0.1 mm was equal to ~190K.

Table 7.
Temperature of the final combustion products of St_b(10.000) - based propellants at 4.0 MPa.

Propellant	T_{calc}, K	T_{exp}, K	ΔT,K
St_b	3148	2870	278
98%St_b+2%PbO_2	3139	2915	224
98%St_b+2%Pb_3O_4	3139	2910	229
90% St_b+10%AN	3057	2785	272
90% St_b+10%AP	3092	2870	222

Final combustion temperatures for the baseline propellant and propellant with additives of AN, AP and lead oxides are less than the corresponding calculated thermodynamic equilibrium temperatures by 220-280K. Small additives of PbO_2 and Pb_3O_4 increased experimental temperature values for the baseline propellant by ~50K. Temperature distribution (not taking into consideration radiation correction) in the combustion wave of St_b(10.000) was obtained with the aid of flat W-Re thermocouple with a thickness of 13-15 μm which is shown in Fig.3. In this case radiation correction at final temperature was equal to ~30K. Temperature of the propellant burning surface was determined by a method of "slope break" on the temperature profile [15] and was equal to 280-300°C. Temperature of the propellant surface was 70K less than the temperature of the burning surface of pure ADN at 4.0 MPa pressure, estimations of which are contained in paper [12]. So, the temperature of the propellant burning surface is not defined by

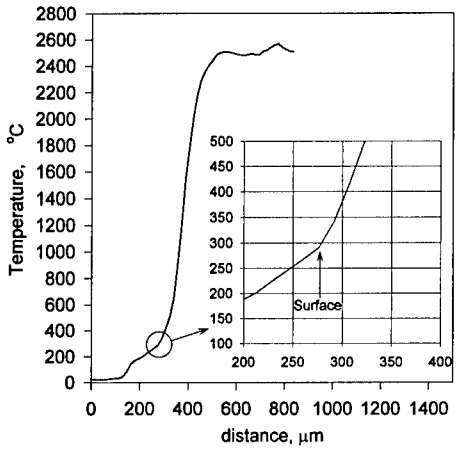


Fig.3. Temperature distribution in combustion wave of propellant St_b(10.000) at pressure of 4.0 MPa.

combustion of the main propellant ingredient - ADN. Width of the zone of heating in the condensed phase was ~180 μm, and width of the reaction zone in the gas phase for propellant St_b(10.000) was ~200 μm. The temperature gradient near the surface was ~11000 K/mm. Temperature of the final combustion products measured by different thermocouples is equal to 2870K. An increase of the initial pressure to 8.0 MPa did not change the temperature of the final combustion products of St_b(10.000). This is evidence of the completeness of reactions in the flame at pressures of 4.0 and 8.0 MPa. Formation of carbon-containing particles in the condensed phase is a possible explanation of the observed fact, that experimental temperatures did not achieve the calculated thermodynamic equilibrium temperatures. Thermodynamic equilibrium combustion products do not contain such particles. Equilibrium was not achieved because of the slow rate of oxidation of these particles by gaseous combustion products.

Table 8.
Compositions of the combustion products of St_b(10.000) - based propellants at 4.0 MPa pressure.

	H_2O	N_2	CO_2	CO	O_2	NO	H_2	OH	H:N:O:C
St_b, calc	0.41	0.339	0.088	0.05	0.025	0.013	0.03	0.034	0.91:0.69:0.73:0.14
St_b, exp	0.48	0.358	0.109	0.013	0.017	0.006	0.011	*	0.98:0.72:0.64:0.12
90%St_b+10%Al, calc	0.315	0.335	0.038	0.099	0.011	0.013	0.099	0.048	0.88:0.68:0.57:0.14
90%St_b+10%Al, exp	0.41	0.37	0.067	0.067	0.014	0.005	0.062	*	0.94:0.75:0.64:0.13

* - not measured in experiment

Compositions of the combustion products of propellants St_b(10.000) and 90%St_b(10.000)+10%Al at 4.0 MPa pressure are presented in Table 8. Increase of pressure to 8.0 MPa did not effect much on composition of combustion products. Chemical analysis of condensed combustion products showed that ~93% of the initial Al oxidized to Al_2O_3.

This fact was taken into account in calculations of the composition of gaseous combustion products of aluminized propellant. Content of H_2O in the combustion products was calculated with aid of material balance equations using the ratio of elements H:N:O:C in the initial propellant.

ACKNOWLEDGMENT

This work was supported by the US Army Aviation and Missile Command under Contract DAAHO1-98-C-R151.

REFERENCES

1. Z. Pak, "Some Ways to Higher Environmental Safety of Solid Rockets Propellant Application," AIAA Paper 93-1755, 1993.
2. M.L. Chan, R. Reed, D.A. Ciaramitaro, "Advances In Solid Propellant Formulations", Solid Propellant Chemistry, Combustion, and Motor Interior Ballistics, 2000, V.185, pp.185-206.
3. M.L. Chan, R. Reed, A. Turner, A. Atwood, and P.Curran, "Properties of ADN Propellants", 5-th International Symposium on Special Topics in Chemical Propulsion, Combustion of Energetic Materials, June 18-22, 2000, Stresa, Italy, pp.131-132.
4. A.E. Fogelzang, V.P. Sinditskii, V.Y. Egorshev, et al., "Combustion Behavior and Flame Structure of Ammonium Dinitramide", 28-th International Annual Conference of ICT, June 24-27, 1997, Karlsruhe, Federal Republic of Germany, pp.99(1-14).
5. V.P. Sinditskii, A.E. Fogelzang, V.Y. Egorshev, et al., "Combustion Peculiarities of ADN and ADN-Based Mixtures", 5-th International Symposium on Special Topics in Chemical Propulsion, Combustion of Energetic Materials, June 18-22, 2000, Stresa, Italy, pp.133-134
6. V.A. Strunin, A.P. D'yakov, G.B. Manelis, "Combustion of Ammonium Diniramide", Combustion and flame, 1999, V.117, pp.429-434.
7. A.E. Fogelzang, personal communication.
8. Ed. Price, personal communication.

9. A.L. Ramaswamy, "Issledovanie goreniya energeticheskih materialov na toplivnyh sostavah, soderghashchih granulirovanny ADN ", Fizika Goreniya i Vzryva, 2000, v.36, №1 c.131-137.
10. H. Ostmark, personal communication.
11. A.P. Denisjuk, L.A. Demidova, V.I.Galkin, "Vedushchaya zona goreniya ballistitnyh porohov s katalizatorami", Fizika Goreniya i Vzryva, 1995, v.31, №2 c.32-40.
12. A. A. Zenin, V. M. Puchkov, S.V.Finjakov, "Physics of ADN combustion" AIAA Paper 99-0595, 1999
13. B. Trusov, ASTRA Code, ver. 2/24, 1990.
14. R. M. Fristrom, A. A. Westenberg, "Flame Structure" Moscow, Metallurgia, 1969, p.139 (in Russian).
15. A. A. Zenin, "Thermophysics of stable combustion waves of solid propellants", Nonsteady Burning and Combustion Stability of Solid Propellants, L.De Luca, E.W.Price, M.Summerfild (Eds), NY, Academy Press, pp197-231.

Microparticle Formation of 1,3,5,7-tetranitro-1,3,5,7-tetraazacyclooctane by crystallizations with Ultrasound

Kwang-Joo Kim*, Kap-Mo Kim, Jung-Min Lee

Korea Research Institute of Chemical Technology, P.O.BOX 107, Yusung, Taejeon 305-600, South Korea
(* Corresponding author)

Abstract

Microparticle formation and crystallization kinetics of 1,3,5,7-tetranitro-1,3,5,7-tetraazacyclooctane (HMX) in solutions using sono-recrystallization were studied. Water, acetone and N-methylpyrrolidone were used as solvents. The mechanisms of crystallization using ultrasound were compared with those of stirred mixing crystallization. The results show that the recrystallized HMX with narrow size distribution microparticle with coefficient of variance of 0.35 and average particle size of 2 to 10 micron, which can be controlled by the operating conditions, was obtained. Shape of crystal was near to being spherical. Eventually microparticle of β-HMX was formed by the recrystallization with ultrasound.

Introduction

The crystallization and characterization of explosives, generally referred to as energetic materials has gained more and more attention recently. Especially microparticles of explosives are required for reducing the sensitivity toward an unintentional shock and by increasing the explosion performance.

1,3,5,7-Tetranitro-1,3,5,7-tetraazacyclooctane (HMX) is a high explosive energetic material[1]. HMX exists in four different polymorphic forms, i.e., α, β, γ and δ. β-HMX is the most stable and insensitive form and so is useful. The particle size and size distribution of HMX produced in industrial processes are frequently not those desired for subsequent use of this material. HMX crystals in different sizes are desired for the highest possible degree of packing for the HMX. Therefore the recrystallization of HMX needs to prepare HMX crystals with specific particle size distribution. HMX crystals of less than 5 micron is not easy to be formed in manufacturing process. Commination by special grinding process causes the danger of explosion during work and produces the shape pointed particles, which are very sensitive to unintentional shock[2]. Recrystallization using supercritical fluid faces on high energy cost and scale-up difficulties[3]. In this study, crystallization using ultrasound was presented to obtain narrow size

distribution microparticles of HMX.

Ultrasound can be used beneficially in field of crystallization. Ultrasound influences the nucleation behavior of the crystallization by initiating the nucleation at a relatively low supersaturation[4]. Ultrasound influences the crystal growth by disturbing the stagnant boundary layer which exists between the solid surface of the crystal and bulk of the solution. The influence of ultrasound in crystallization upgrades the particle properties like shape, size and size distribution.

In this study, microparticle formation and crystallization mechanisms of 1,3,5,7-tetranitro-1,3,5,7-tetraazacyclooctane (HMX) in solutions using sono-recrystallization were studied. Water, acetone and N-methylpyrrolidone were used as solvents. Crystallization conditions investigated were temperature, intensity of ultrasound, solvent compositions, agitation rate, etc.

Experimentals

HMX was from Hanwha Corp. The water used in this work was triple distilled. NMP was from Aldrich, 99.9 mol%. The experiments were performed in a batchwise operated crystallizer. The crystallizer was set with ultrasound system with 1/4 inch titanium horn and variable frequency of 0-70 kHz. The power of ultrasound dissipated by the crystallization system was 150 W. The crystallizer was a 300 ml vessel with 60 mm diameter and was equipped with the horn and an agitator. Thermostatic fluid was circulated from a refrigerated thermostat, with accuracy of 0.05K through the outer jacket of crystallizer. The analysis of CSD, shape and mean crystal size were carried out by image analysis system(VIDAS, Karl Zeiss) with optical and electron microscopes.

Mixture of HMX-NMP was prepared and a total of about 300 ml was charged into the feed. The temperature was adjusted to the desired initial value. Experiments were carried out various compositions of ternary mixture and frequency of ultrasound. Crystal slurry was withdrawn from the crystallizer to the crystal analysis system in order to measure crystal size, shape, and crystal size distribution. At the same time, samples were taken for analyzing purity and yield. The sampled crystals were filtered from the residual solution. The instruments of scanning electron microscopy, XRD, on-line crystal measurement system and IR were used to analyze particle size, particle size distribution, shape and crystallinity. Operating conditions investigated were temperature, intensity of ultrasound, solvent compositions, agitation rate, etc.

Results and discussion

Fig. 1 shows the solubilities of HMX in water + NMP. When the solubilities of HMX in NMP-water mixture are compared, it can be seen that in ternary mixture the addition of the water reduces the HMX solubility and the dependence of temperature on solubility increases with increasing the fraction of water. HMX is crystallized by adding appropriate amount of water in NMP-HMX solution or by cooling the solution of HMX-NMP-water, the proportions being determined from the phase diagram.

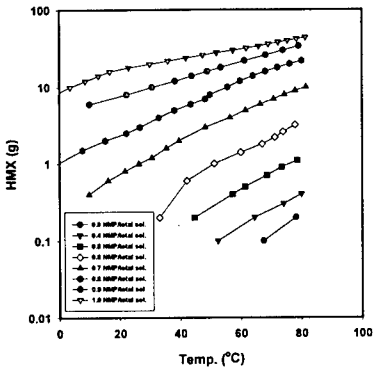
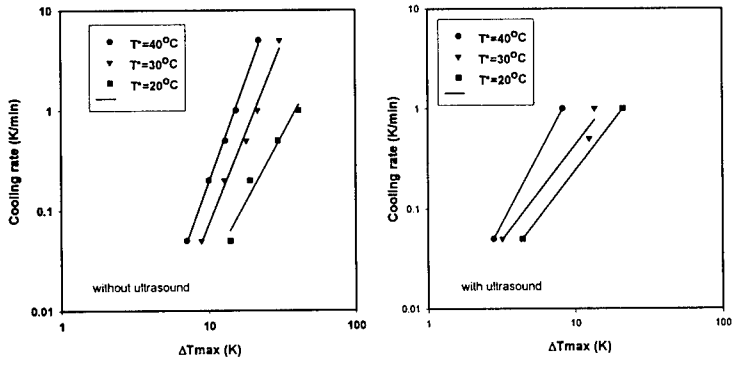


Fig. 1. Solubilities of HMX in water+NMP

Nucleation kinetic is characterized by relationship between the metastable zone width and cooling rate[5]. The maximum allowable undercooling was taken as the difference between the equilibrium temperature and the temperature at which nuclei were detected for each particular cooling rate.

Fig. 2 shows plots of cooling rate versus maximum undercooling for saturation temperature and ultrasound intensity in log-log coordinates.

Fig. 2. Effect of ultrasound on metastable zone width



They are found to give a good straight line. These results show that the metastable zone width of the HMX in solutions increases with the cooling rate for all the experimental conditions explored. The width of the metastable zone also increases with decreasing the water/NMP ratio and decreasing ultrasound intensity. The inverse dependence between metastable zone width and ultrasound intensity explains that

the probability of nucleus formation increases with the ultrasound. This may be considered due to the contribution of ultrasound as an accelerator for nucleation.

Figure 3 shows effect of ultrasound intensity on the mean crystal size. Comparing ultrasound intensity with agitation rate is presented. The mean crystal size decreases with increasing the ultrasound intensity. The number of cavitation bubbles increases with ultrasound intensity. If nucleation occurs in cavitation area, the degree of cavitation leads to homogenous dispersion of nuclei formed by micromixing effect. As the number of nucleus increases with ultrasound intensity, crystal size of final products decreases. Another possibility is that ultrasound leads to breakage of crystals and thus to a reduction of the mean size. However, analysis of SEM photographs didn't find the evidence of breaking particle and has very narrow size distributions compared to crystallization using ultrasound.

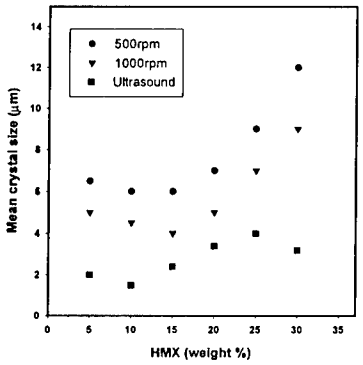


Fig. 3. Effect of ultrasound on crystal size

It suggests that the primary nucleation rate, characterized by considering the probability of formation of a critical nucleus corresponding to the maximum free energy change, can be expressed as[6]:

$$J = A\exp\left[\frac{-16\pi\gamma^3 v^2}{3\kappa^3 T^3 (\ln S)^2}\right] \quad (1)$$

Where S, γ, ν and κ means relative supersaturation, interfacial energy, molecular volume and Boltzmann constant, respectively.

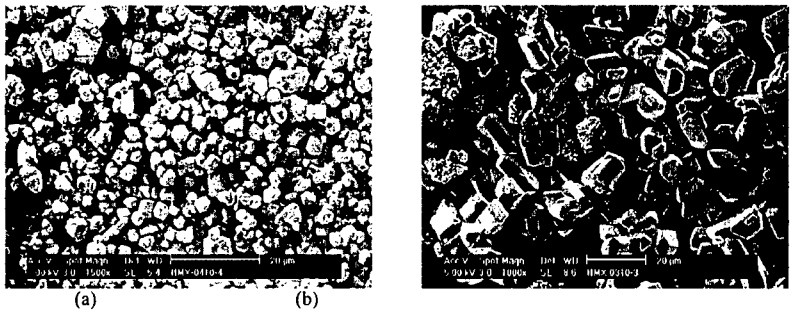
Generally speaking, the number of nuclei formed decreases with decreasing supersaturation. In no attrition and no agglomeration process, the decrease in the number of nuclei results in increase in crystal size of products. It was found in his study that crystal size decreased with ultrasound although ultrasound decreases the supersaturation. It suggests that local supersaturation in cavitation area of bubbles would be very high due to high mixing and high temperature in localized hot spot. Eventually high supersaturation in cavitation area is due to enhancing the nucleation rate.

The crystal growth rate depends on mass transfer coefficient, surface area and supersauration[6], as shown by

$$R_G = k_g A \Delta c \qquad (2)$$

Where k_g, A and Δc means overal crystal growth constant, surface area and supersaturation, respectively. Crystal growth rate in ultrasound was 4 times higher than that in the absence of ultrasound. The cavitation is responsible for the decrease in time for growth of crystals. Cavitation makes large shock waves which produce the micromixing. The micromixing is the localized turbulance of solid-liquid layer which accerelates the mass transfer rate through the layer by increasing the mass transfer coefficient. The cavitation makes a higher supersaturation in micromixing area.

Fig. 4 shows the SEM photographs of HMX crystals obtained in various crystallization modes. Crystals obtained by ultrasound shows more uniform shape. Crystallization with ultrasound improves crystal morphology by uniform crystals with lower aspect ratios compared to crystallization without ultrasound.



(a) (b)

Fig. 4. SEM photographs of HMX crystals obtained in:
(a) crystallization using ultrasound, (b)stirred crystallization

Conclusions

Microparticle formation of HMX in water+NMP mixture was carried out by the crystallization using ultrasound. The mechanisms of sono-crystallization were compared with those of stirred crystallization. The results show that the recrystallized HMX with narrow size distribution microparticle with coefficient of variance of 0.35 and average particle size of 2 to 10 micron, which can be controlled by the operating conditions. Shape of crystal was near to being spherical. Eventually microparticle of β-HMX was formed by the recrystallization with ultrasound.

Refrences

1. L. Svenssion, J. O. Nyqvist and L. Westling, J. Hazardous Materials, 13, 103(1986)
2. K.J. Kim, KRICT report, IG-9846(1999).
3. J. G. Cai, X. C. Liao and Z. Y. Zhou, The 4th Int, Sym. on Supercritical Fluid, 23(1997).
4. J. Lee and J. K. Synder, J. Am. Chem. Soc., 111, 1522(1989).
5. K.J. Kim and S.K. Ryu,. *Chem. Eng. Comm.*, 159, 51(1997).
6. J.W. Mullin, *Crystallization*, 3rd ed., p 60, Butterworth, Oxford, 1993.

Seeded Batch Cooling Crystallization of 3-nitro-1,2,4-triazol-5-one

Kwang-Joo Kim[1]*, Jung-Min Lee[1], Hyoun-Soo Kim[2], Bang-Sam Park[2]

1. Chemical Process & Engineering Center, Korea Research Institute of Chemical Technology, P.O.BOX 107, Yusung, Taejeon 305-600, Korea
2. Agency for Defense Development, P.O.BOX 35, Taejeon, Korea

(* Corresponding author)

Spherulitic crystallization using co-solvent for producing spherical 3-nitro-1,2,4-triazol-5-one(NTO) crystals was carried out in two laboratory-scale and bench-scale crystallizers. The effect of scale-up of crystallizers on mean size of crystals of NTO at batch cooling crystallization with seeds was explored. The simplified model based on the crystallization kinetics was established to the estimation of mean crystal size during the scale-up of crystallizer. It resulted from that the supersaturation was estimated theoretically and experimentally. Comparison of the crystals obtained from the laboratory-scale and from the bench-scale operations showed that the model can be successfully correlated with the mean crystal size. Eventually, the mean crystal size was estimated if composition of co-solvent was set optimally and the scale-up of crystallizer was reasonable.

Introduction

In manufacturing explosives, recrystallization of explosives from organic solvent and mixtures of solvents is used. Especially batch cooling crystallization using co-solvent is commonly used in control of size and shape of explosives[1,2].

For scale-up of crystallization process, the relationships among crystal growth, nucleation kinetics and composition of solution, and their effect on the crystallizer performance must be unveiled. These relationships are complicate and are not easy to be generalized. Therefore the models that simulate the crystallization process are limited in specific systems and crystallization methods like cooling and evaporation. More consideration for scale-up of crystallizer was given to control supersaturation level by cooling modes[3]. The models are turned for a simple configuration, so that extrapolation to other scales of operation or other geometries has limited validity.

Formation of spherulitic 3-nitro-1,2,4-triazol-5-one(NTO) crystals depends on kind of solvent, crystallization methods and solvent composition. We reported previously novel spherulitic crystallization techniques that produced the spherulites of NTO by rapid cooling crystallization with co-solvent in a laboratory-scale crystallizer[1]. It resulted that spherically spherulitic crystals had insensitivity toward sudden shock, high performance, and high packing density compared to polygonal crystals. However, scale-up effect on the crystallization kinetics in a cooling crystallization using co-solvent was never considered. Scale-up on crystallization of explosive compounds was never reported. Especially spherically spherulitic crystallization that made the limitations in solvent composition and operating conditions was not tried to its scale-up.

In this study, batch cooling crystallization tests were conducted with linear cooling mode by using a bench-scale draft-tube-baffled(DTB) crystallizer equipped with marine propeller agitator. The results are compared with those of laboratory-scale test using crystallizer equipped with a geometrically similar stirrer. A simplified model to predict crystal size during the scale-up of crystallizer was established.

Experiment

NTO was from Hanwha Corp., 99.5 mol% pure. The water used in this work was triply distilled. NMP was from Aldrich, 99.9 mol%. Before use, NTO was purified further by recrystallization in an analytical grade of methanol supplied from Merck. Purity of the NTO purified was above 99.93 mol%.

The laboratory jacketed crystallizer(300 ml, inner diameter 0.09m, height 0.12m) was made of Pyrex and is equipped with a stainless-steel marine stirrer(SUS 304) and sensors. Draft tube(diameter 0.06m, height 0.06m) and 4 inner baffles are included. Agitation speed was fixed at 600 min^{-1} (tip speed 1.9 m/s) to ensure well-mixed crystal suspension.

The bench-scale-jacketed crystallizer(50l, inner diameter 0.4m, height 0.5m) used was made of stainless steel(SUS 304), and is equipped with a geometrically similar marine propeller stirrer(SUS 304, diameter 0.12m, blade width 0.035m, blade angle 25°) and temperature sensors. Draft tube(inner diameter 0.27m, height 0.27m), 4 inner baffles(length 0.23m, width 0.12m) and 4 outer baffles(length 0.34m width 0.037m) are included. Agitation speed was fixed at 300 min^{-1} to ensure well-mixed crystal suspension. The required minimum agitation speed satisfied to particle size of 200 micron and suspension density of 0.2 was 140

rpm[22]. Therefore, agitation speed set in bench-scale crystallizer were enough to make well-suspended crystal in crystallizer.

Mixture of NTO-NMP-water was prepared, charged into the crystallizer. Composition was in the range of water/NMP ratio from 1.8 to 8.0 and NTO/NMP ratio from 0.25 to 1.0. The solution was maintained at 10°C above the saturation temperature for 30 min. The temperature was adjusted to the desired initial value and then the solution was cooled according to a constant cooling rate. Experiments were carried out with various compositions of ternary mixture at the constant cooling rate and the constant agitation speed. After crystallization, the resultant crystals were collected by filtration, washed with the saturated NTO solution and dried in an oven at 80 °C for 5hrs. Crystal slurry was withdrawn from the crystallizer to the crystal analysis system(Lasentec 400L) in order to measure crystal size, shape, and crystal size distribution. At the same time, samples were taken for analyzing purity and yield.

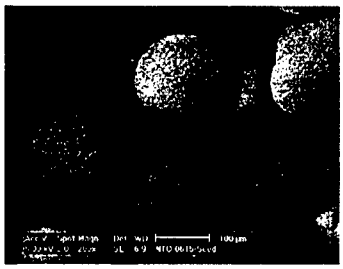


Fig. 1. Seed crystals

Fig. 1 shows SEM photograph of the seed crystals obtained. The seed size ranged from 75 μm to 115 μm. It was observed that the prepared NTO seed crystals were a type of sphere. Thus, value of the overall shape factor F was considered as 2. The crystals were sized by microscope with an image analyzer(VIDAS, Karl Zeiss).

Results and discussion

Effect of NMP on morphology

In order to get an understanding of growth process, crystals grown from different solvent mixture at the several levels of supersaturation, were inspected by scanning electron microscopy and compared. NTO crystals obtained from aqueous solution(i.e., NTO-water) belongs to be cubic system, as were shown in our previous works[2,3]. This cubic crystal of NTO grows invariantly in the binary solution but transforms into spherulitic form during the growth in the ternary system. The habit modification of NTO crystals is due to the presence of NMP in the ternary system. NTO crystals were obtained from various solvent mixtures by seeded cooling crystallization.

Fig. 2 shows SEM photographs of NTO crystals, which spherical seed crystals were grown in water+NMP solution. Figs. 2a, 2b and 2c show SEM photographs of NTO crystals, which spherical seed crystals were grown in solutions with water/NMP ratios of 1.8, 3.0 and 8.0, respectively. Crystallizations were carried out at crystallization temperature of 293 K, cooling rate of 1K/min and saturation temperature of 318 K. Figs. 2d, 2e and 2f shows SEM photographs of NTO crystals, which spherical seed crystals were grown at the same conditions except cooling rate of 10 K/min. In growth of the spherulitic crystals, it was found that crystals grow radially from center and hence have spherically spherulitic morphology. In order to investigate solvent effect on morphology, seed crystals were grown in aqueous solution.

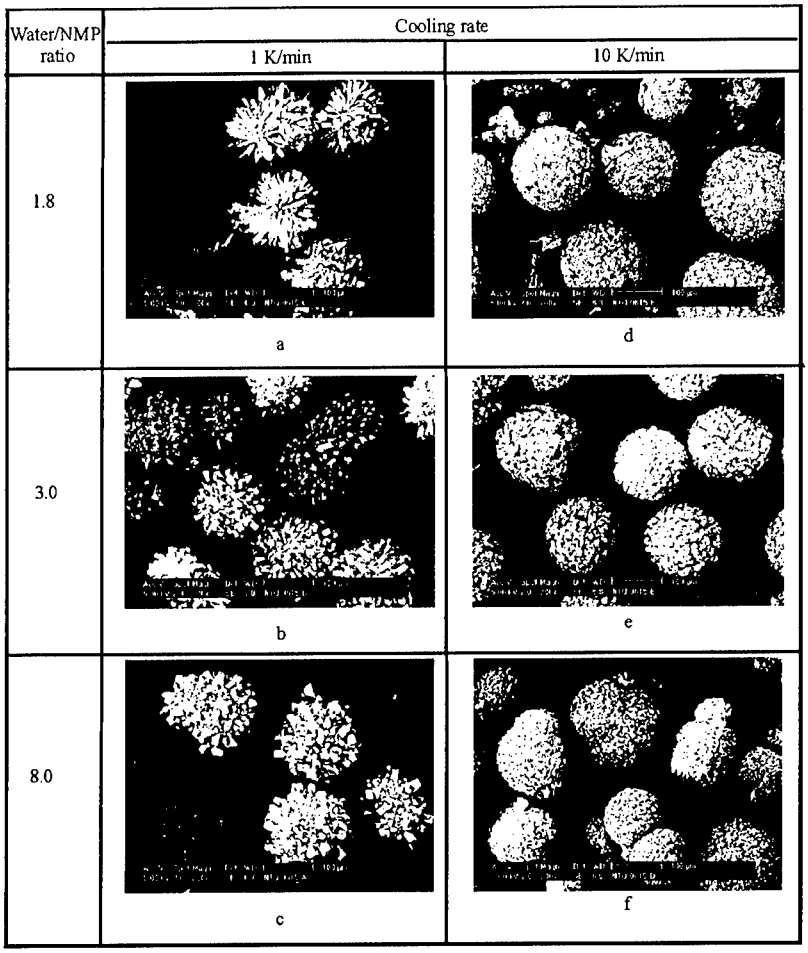
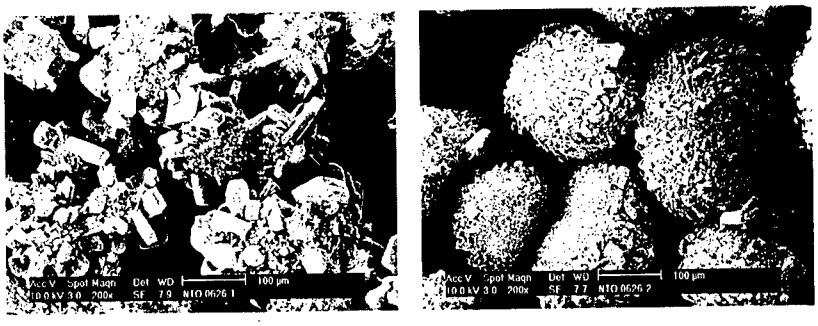


Fig.2. SEM photographs of NTO crystals

Fig. 3a and 3b show the SEM photographs of NTO crystals obtained in the cooling rate of 1 K/min and 10 K/min, respectively. Crystals grown from the aqueous solution present faces covered with larger cubes, which the edges shows a large number of irregular needles with no regular orientation. It was found that the crystals formed in water were not spherulites but agglomerates. As the content of NMP in the solvent is augmented, the number of crystallites adhering to the faces and corners of the needles increases. An increased tendency to the formation of aggregates toward radial direction parallels content of NMP in solvent. From the comparison between NTO morphologies obtained at two cooling rates, it is found that increase of cooling rate in cooling crystallization increases the compactness and the sphericity of NTO

crystals. Thickness of needled crystals aggregated in the seed crystals increases with decreasing cooling rate and with increasing water content in solvents.



a b

Fig. 3. SEM photographs of NTO crystals obtained in different cooling rates

In the previous works[1,4], it was found that the presence of NMP increases the metastable zone width of the NTO-water systems. The slow deposition of solute, together with a low production rate of nuclei, enables the formation of spherulitic crystals with quite smooth surfaces. As can be shown in Fig. 2, the crystals grown in lower ratio of water/NMP were found to be more spherical and compact. The reasoning strongly suggests that formation of spherulitic crystals is indeed determined by the nucleation process, while rate of spherulite growth can be controlled by rate of aggregation. The formation and growth of NTO spherulites in water-NMP-NTO solutions can be affected by several factors such as concentration and the type of solvent used. Solvation, selective solvation, and self-association of solute may also influence. From crystal growth behavior observed in the NTO-water-NMP, water roles as an accelerator, promoting a spherulitic morphology by enhancing NTO growth.

Crystal size

Crystal size depends mainly on the kinetics of nucleation and growth, which are functions of process variables such as agitation rate, feed composition, and production rate. These functions are eventually related to the degree of supersaturation. The supersaturation is a main parameter for controlling crystal growth and nucleation rates. Therefore, crystal size depends on the growth rate G, the nucleation rate B, and holdup of crystal φ_s[5].

$$L = f\left(\frac{G\varphi_s}{B}\right) \tag{1}$$

This relation results from the fact that the mean crystal size increases with an increasing growth rate and holdup of crystal and a decreasing nucleation rate.

The following simple correlation for the mean crystal size can be expressed.

$$L = K_N \varphi_s \Delta c^{g-n} \quad (2)$$

where

$$K_N = \frac{k k_G}{k_n} \quad (3)$$

K_N is a system constant comprising the kinetic parameters of crystallization such as k_g and k_n. As the rate constants k_n and k_G in Eq. (3) are in a ratio and their changes with temperature or other parameters are similar, the system constant K_N is relatively speaking, not too sensitive either to temperature or to intensity of mixing and to other parameters. It is therefore suitable for design calculations when changing the scale of crystallizer.

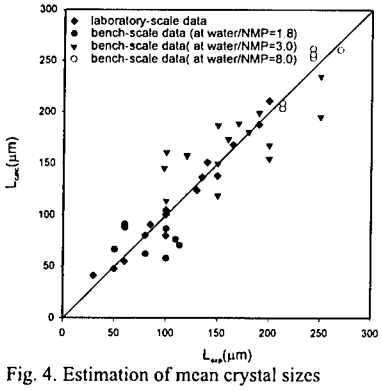


Fig. 4. Estimation of mean crystal sizes

Fig. 4 shows comparison between the calculated and experimental mean crystal sizes obtained in laboratory-scale and bench-scale tests. It is obvious that the results of experiments are reasonably well approximated by Eq. (3). The results show that Eq. (3) with the parameters K_N and g-n is satisfactory for representing the data from both series of measurements which differ in scale of the equipment used by more than two orders of magnitude

Eventually, it might be estimated that further scale-up based on the above equations would be sufficiently reliable, and that constitute an adequate starting point for the crystallizer design.

Conclusion

The size of the NTO crystals was strongly dependent on the composition of co-solvent during the scale-up of crystallizer. Comparison of the crystals obtained from the laboratory-scale and from the bench-scale operations showed that the hydrodynamic condition in crystallizer affects slightly CSD. No scale-up effect was observed in terms of CSD and average size if the composition of co-solvent is set optimally in ternary system. The mean size of crystals in cooling crystallization using co-solvent can be estimated by the simplified model based on the system constant of crystallization K_N.

Nomenclature

B nucleation rate, kg/m^3 s

Δc supersaturation, kg/kg

f function defined in Eq. 7

g growth order

G crystal growth rate, m/s

k_G overall growth rate coefficient, kg/m^2 s

L average crystal size

φ_s hold-up of crystals, kg/kg

References

[1] K.J. Kim, Spherulitic Crystallization of 3-nitro-1,2,4-triazol-5-one in water N-methyl-2-pyrrolidone, *J. Crystal Growth*, 208(2000) 569-578

[2] K.J. Kim, M.J. Kim, J.M. Lee, Development of Process for Controlling Morphology of NTO Crystals, KRICT report, Taejeon, 1998.

[3] K.J. Kim, M.J. Kim, J.M. Lee, H.S. Kim, S.H. Kim, B.S. Park, Control of size and shape of nto crystals by cooling crystallization, Int. Symposium CGOM, Bremen, Germany, 1997, 169-174.

[4] K.J. Kim, Nucleation Kinetics in Spherulitic Crystallization of Explosive Compound : 3-Nitro-1,2,4-triazol-5-one, Powder Technology, in print

[5] A. Mersmann, *Crystallization Technology Handbook*, Marcel Dekker, Inc., New York, 1994.

OBTAINING of SUBMICRON PARTICLES of SILICON and STUDY of THEIR INTERACTION with NITROGEN and CARBON

Yuri Biryukov, Alexander Roslyak, Leonid Bogdanov, Mansur Ziatdinov

Tomsk State University

36, Lenin pr, Tomsk 634050, Russia,

tel. (73822) 410-706, fax (73822) 417-264

E-mail: powder@niipmm.tsu.ru

Abstract

In the present work the results of experiments on producing of silicon submicron powders for different purposes including synthesis of nitrides and carbides are submitted. For obtaining of submicron powders of metals, alloys, organic and inorganic compounds the authors devised a pneumatic circulation unit combining processes of size reduction, classification, drying, mixing, and granulation of powders. Silicon nitrides and carbides were produced by the method of Self- Propagating High-Temperature synthesis (SHS-method). In trials it was determined, that the synthesis of nitrides and carbides for submicron powders goes faster and at lower temperatures, than for coarse powders. Besides there are very good premises for obtaining of submicron fractions of carbides and nitrides.

1. Introduction

Submicron materials, in particular powders of silicon and its compounds, recently attract the increasing attention of researchers because of a unique combination of their physical-chemical and technological characteristics. Chemically pure silicon is the basis for production of solar batteries and the cost reduction of its processing could be a break-through in production of ecological pure electrical energy. Carbides and nitrides of silicon are distinguished by high refractoriness, hardness, wear resistance, small coefficient of thermal expansion, stability to thermal impact and chemical resistance. They are applied successfully in the most various branches of engineering both civil, and military purpose.

To obtain high-quality constructional ceramics it is recommended to use high-pure homogeneous powders of nano and submicron size and monofraction structure with the equilibrium form of particles having identical activity to sintering. However production of such powders in large amounts and with the economically justified cost still is the challenging scientific and technical problem.

The paper gives the outcomes of researches into production of silicon powders with the sizes of particles about 1 micron and less than 1 micron by the use of pneumatic circulation unit, developed by the authors. The fractions with the various sizes of particles were tested at high-temperature synthesis of silicon nitrides and carbides. The influence of silicon particles sizes on velocity and temperature of the reaction of carbides and nitrides synthesis are discussed.

2. Experimental procedure

For producing of submicron powders of metals, alloys, organic and inorganic compounds the authors deviced a pneumatic circulation unit combining processes of size reduction, classification, drying, mixing, and granulation of powders. [1]. The design and principle of an operation of the unit has been detailed in [2]. Here we can do no more than describe some advantages of our method over other related methods for powder processing [3]:

- our principle of operation is realized as continuous - periodic, when the feed - material is loaded periodically, and the milled fractions are removed continuously;
- we have refused from contrary directed working jet streams of air and fluidization of the whole bed of a material;
- during a single refinement act the several fractions on the size of particles can be produced;
- in our mill re-circulation (inside the size reduction chamber and on external circuits of the unit) of gas with particles flows are organized in such a way that allows continuous removal of the final product from a refinement zone and return the coarser fractions in the zone.

As a consequence the mentioned unit has high capacity (up to 20 kg / h) and low production cost for powders with the particles sizes of 1 micron and less.

Researchers into refinement of metallurgical-grade silicon have been conducted on the experimental unit permitting to load up to 500 kg of initial raw material, and having capability to change weight of loading, coarseness of an initial material, pressure and consumption of working gas (air), rotation rate of the built-in separator. Classification of grinded material and collecting of the end fractions have been performed on two vortex separation devices and on a fabric filter. The aim of the study have been to select optimum conditions of silicon refinement and to produce experimental batches with various coarseness of particles for consequent synthesis of nitrides and carbides of silicon.

The synthesis of silicon nitride was conducted in a sealed chamber by the method of Self - Propagating High-Temperature synthesis (SHS)[4]. The powder of silicon was loaded in gas-permeable cup 30 mm in diameter and 70 mm in height. The cup were placed in the chamber. The chamber was filled in with nitrogen up to pressure 4,0 MPa after evacuation of air. The

samples were warmed up to temperature , when reaction of nitration begins by special electrical device. Thereafter the process proceeds as self-sustaining layer-by-layer combustion owing to exothermal reaction of silicon nitride formation. Thus fixed time and temperature of a reaction. On a final chamber pressure quantity of nitrogen absorbed by silicon was determined.

The synthesis of silicon carbide consists in preparation of a blend representing a silicon and carbon (gas soot) mixture in stoichiometric ratio. Then again the sample was pressed and was placed in the chamber, from which air was evacuated. The sample warmed up till the beginning of synthesis reaction. Time and temperature of the reaction were fixed.

Obtained carbide and nitride of silicon at first were crushed in a cone crusher, and then were loaded into the pneumocirculating unit with small initial volume of loading (up to 10 kg) to study processes of production of nitrides and carbides silicon submicron powders.

3. Results and Discussion

The study of influence of the unit operational modes on the mean size of produced fractions, output and specific grinding of energy for silicon size reduction were conducted on a pneumocirculating unit with charge up to 500 kg of raw material. As the purpose of researches was the obtaining of submicron fractions of silicon operating pressure and gas flow rate were installed on maximum value for realization of the most heavily process of a refinement. The output and size of finished particles were adjusted by rotation speed of a rotor in the built-in centrifugal separator. The results are shown in the table 1.

Table 1.Influence of the unit operational modes on the mean size of fractions, output and specific grinding of energy for silicon size reduction (δ_{50} - mean size of particles in each fraction)

№	Pressure of working gas, MPa	Volume of working gas, m^3/h	Rotation speed of rotor, ppm	δ_{50} for produced fractions , μm	Output kg/h	Specific grinding of energy, kWh/kg
1	0,65-0,7	500	1000	12	52,0	2,1
2			4000	8	18,0	6,1
3			5000	7	21,6	5,1
4			6000	6	15,0	7,3
5			6500	5	9,8	11,2

The table shows that the mean size of silicon particles decreases with increase of rotation speed of the rotor. As this take place the capacity decreases, and specific grinding of energy grows. The presented data do not contradict to results obtained on other mills of a pneumatic type [3] as to specific grinding of energy and, at the same time, over performs them in output for silicon with the sizes of particles about 1 μm.

As noted above, the grinded material is subjected additional classification in vortex separators and is caught on the filter. In result some fractions of grinded silicon, including in submicron range of the particles sizes of are obtained. Table 2 presents the data on output including relative outputs of fractions with the mean particles size δ_{50} = 5 μm, 1,5 μm, 0,7 μm and 0,5 μm. The influence of the silicon particles size of the raw material on output related to various fractions was analysed. Table 2 shows, that the maximum output of the fraction with the mean size-of 0,5 μm is achieved, if the mean size of particles in the raw material makes 20 μm.

Table 2. Influence of the particles size in loaded silicon to output to size-distribution of end products (δ_{50} - mean size of particles in each fraction)

№	δ_{50} for feed silicon, μm	Size-reduction output, Kg/h	δ_{50} for fractions, μm	Output on fractions, Kg/h	Relative output, %
1	800	16,05	5	15,0	93,5
			1,5	0,75	4,7
			0,7	0,3	1,8
2	150	18,0	5	16,7	92,6
			1,5	1,0	5,6
			0,7	0,3	1,8
3	100	14,2	7	13,0	91,6
			1,5	0,6	4,2
			0,7	0,6	4,2
4	60	29,5	5	28,0	94,9
			1,5	0,7	2,4
			0,5	0,8	2,7
5	30	67,3	5	62,9	93,4
			1,5	3,0	4,5
			0,5	1,4	2,1
6	20	96,1	5	88,5	92,1
			1,5	5,1	5,3
			0,5	2,5	2,6
7	10-15	68,8	5	59,4	86,3
			1,5	7,2	10,5
			0,5	2,2	3,2

For synthesis of silicon nitride 3 fractions with the mean sizes of particles 0,5 μm, 1 μm and 5 μm were used. It was noted the significant distinction in the reaction speed in quantity of

absorbed nitrogen and exterior appearance to the burned down samples. If samples from the powder of mean size 1 μm and 5 μm are good sintered and partially fused, the sample from silicon with mean particles sizes 0,5 μm crumbles readily and do not bear evidence of a sintering and fusing.

Fig.1 presents the rate of samples combustion as function of the mean sizes of initial silicon particles. From this figure we notice that the rate of combustion for mean particles size 0,5 μm differ dramatically from the rate of combustion for particles with the mean sizes 1 μm and 5 μm (in 1,5 and in 2 times accordingly).

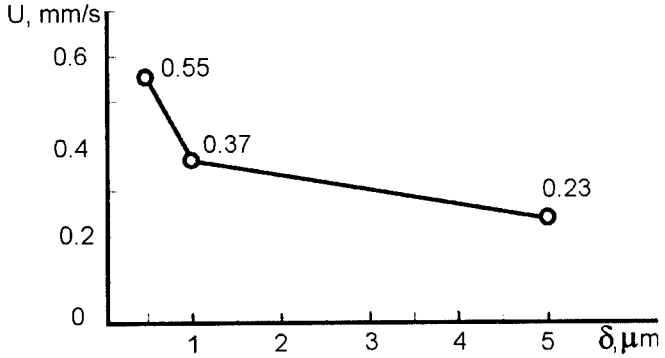


Fig.1. Rate of samples combustion depending on the mean sizes of initial silicon particles

The visual observations through sight glass also have shown significant changes of a combustion picture for silicon 0,5 μm particles. Fig 2 shows the nitrogen quantity of products of the reaction depending on the mean particles sizes.

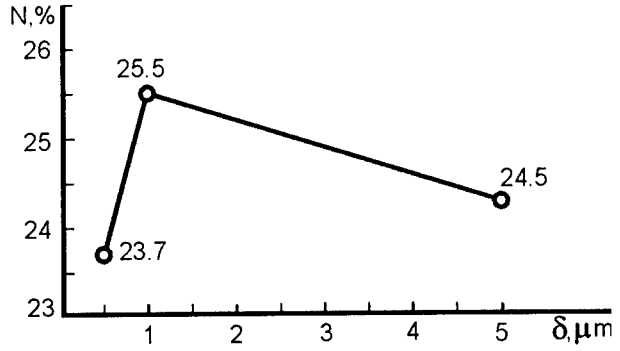


Fig.2. Weight percentage of Nitrogen in products of the reaction depending on the mean particles size of Silicon

. The consequent processing in the pneumocirculating unit has shown, that the size reduction of silicon nitride obtained by synthesis of powders with the sizes of particles about order to 1 μm, goes much more effective. The output of submicron particles is increased, and are reduced specific grinding energy.

On fig.3 the photos of powders of silicon and silicon nitride processed on the same unit are adduced. It is visible, that the sizes of silicon nitride particles are twice than silicon particles from which they were synthesized.

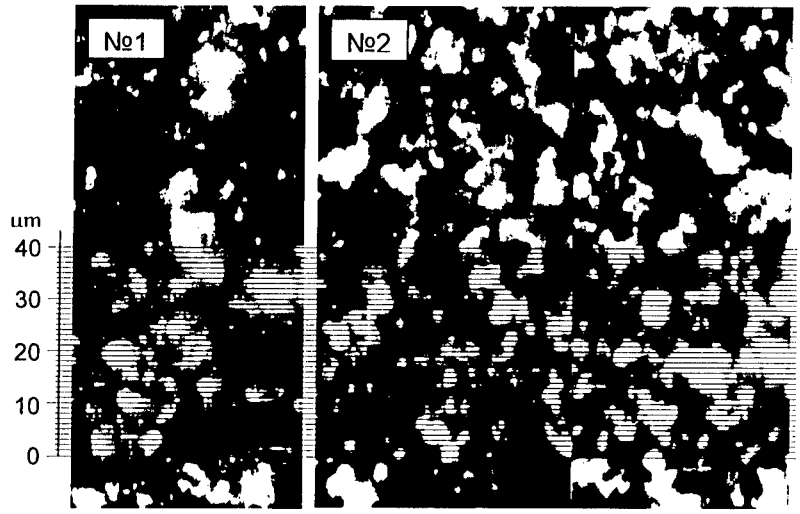


Fig. 3. Microscope and Computer image of Silicon (No 1, δ_{50} = 6 μm) and Silicon nitride (No 2, δ_{50} = 3 μm)

Risults submitted in the present report, and other our researches show, that the method of pneumatic processing of powders with the help of gas jets flooded in a bulk layer of a material, provides production of submicron silicon particles, of silicon carbide and silicon nitride of silicon and in combination with SHS - process can be laid in the foundation of the new highly performance technologies for new materials.

The work was supported by NATO Science Program (Collaborative Linkage Grant No.976783) and Russian Foundation of Fundamental Investigations (Grant No 01-01-00821)

References

[1]. Roslyak A, Biryukov Y, Pachin V. Pneumatic methods and units of powder technology (in Russian) Tomsk State University: Tomsk, 1990, 273 p.

[2] Yuri Biryukov, Alexander Vorogtsov, Alexander Roslyak, Leonid Bogdanov "Submicron Powders By Pneumatic Processing of Electric Corundum and Combustion Products Solid Propellant". Second International High Energy Materials Conference and Exhibit, Chenai, India, 1998.

[3]. Peter M. Silverberg, Stephen Miranda Sharon, Homing In On the Best Size Reduction Method, Chemical Engineering, November,1998, v. 105, No.12; P.102.

[4]. Merzhanov A.G., Nonequilibrium Theory of Flame Propagation, Proc. of the Zel'dovich Memorial, International Conference on Combustion, September 12-17, 1994, Moscow, p. 20-44.

ANALYSIS OF REACTION PRODUCTS OF CENTRALITE I IN PROPELLANTS

J. Petržílek[□], J. Skládal[□], F. Zrcek[•], M. Pražák[•], L. Janoušková[•]

[□] AliaChem a.s., Div. Synthesia, Research Institute for Industrial Chemistry, CZ-532 17 Pardubice-Semtín, Czech Republic

[•] Police of Czech Republic, Institute of Criminalistics, CZ-170 89, Praha, Czech Republic

Abstract

It was proven that possibility of oxygen access to the propellant sample plays an important role in its ageing processes. Increase of CI depletion rate and changes of prevailing decomposition products by oxygen influence were demonstrated. In the case of propellant containing high CI concentration (6.1 %) only very small amounts of nitrocentralites (less than 0.2 %) were found among the reaction products of CI. As the prevailing reaction product was found N-nitroso-N-ethylaniline, so the reactions leading to splitting the urea skeleton of CI are mostly taking place. This fact was valid for both experimental setups – ageing in vacuum or under oxygen. From 14 reaction products found by HPLC joust four of them could be positively identified with previously published compounds (N-nitroso-N-ethylaniline, 2-nitrocentralite, 4-nitrocentralite and 4-nitro-N-nitroso-N-ethylaniline). Two others were identified by us (N-ethyl-N-phenylformamide and N-phenyl-ethylcarbamate) and next three were identified as some oxidation products of CI. However concentrations of all found reaction products were very small compared to drop of CI concentration and their concentration did not change significantly in most cases, thus these products are considered as intermediate products which are further reacting and forming volatile products.

List of abbreviations

DPA	diphenylamine
NODPA	N-nitrosodiphenylamine
CI	Centralite I; N,N'-diethyl-N,N'-diphenylurea
2-NCI	N,N'-diethyl-N-fenyl-N'-(2-nitrophenyl)urea
4-NCI	N,N'-diethyl-N-fenyl-N'-(4-nitrophenyl)urea
2,4'-DNCI	N,N'-diethyl-N-(2-nitrophenyl)-N'-(4-nitrophenyl)urea
4,4'-DNCI	N,N'-diethyl-N-(4-nitrophenyl)-N'-(4-nitrophenyl)urea
NOEA	N-nitroso-N-ethylaniline
2-NEA	2-nitro-N-ethylaniline
4-NEA	4-nitro-N-ethylaniline
NO-4-NEA	N-nitroso-4-nitro-N-ethylaniline
NO-2-NEA	N-nitroso-2-nitro-N-ethylaniline

1. Introduction

Centralite I is used as stabilizer mainly of double based and triple based propellants. There is not as much information about CI acting in propellants as about DPA. This is given above all by the difficulties accompanying identification and quantification of CI daughter products in a propellant. By analysing of CI daughter products in experimental propellant subjected to accelerated ageing, Volk[1,2] identified two main groups of compounds by means of thin-layer chromatography. Partly, they are CI nitroderivatives (2-NCI, 4-NCI, 2,2'-DNCI, 2,4'-DNCI) partly the products of urea skeleton break up (NOEA, 2-NEA, 4-NEA, NO-2-NEA, NO-4-NEA, 2,4-DNEA, nitrobenzene and dinitrobenzene). Quantitative analyses of CI stabilized single base and double base propellant subjected to accelerated ageing are given in ref.[3,4]. Analysis of CI daughter products by means of HPLC and mass spectroscopy combination has been carried out by authors of work[5].

Analyses of several types of CI stabilized double base and triple base propellants subjected to accellerated ageing have been conducted by Curtis[6]. It follows from the results that with increasing initial CI concentration in the propellant the ratio of CI monoaromatic daughter products increases in comparison with urea derivatives. Possible mechanisms of reactions of this stabilizer are discussed by Curtis. He supposes CI splitting to be preceded with formation of intermediate - nitrosoammonium ion. This ion is capable of being subject to hydrolysis to NOEA and N-ethylaniline under formation of carbon dioxide molecule.

Mutual proportions of CI reactions products[7-9]

Curtis[6] presents that proportion of monoaromatic derivatives compared to CI nitroderivatives increases with increase in CI initial concentration. The results of analyses of CI stabilized propellants subjected to accelerated ageing that have been published in Ref.[3-6] have been recalculated by us to the number of moles of phenyl groups bonded in CI molecule and its daughter products. It follows from the data published that a considerable molar quantity of CI exists that is not identified in the propellant in the form of any CI derivative (total number of moles of phenyl groups belonging to CI and its daughter products in a defined time decreases with the time of conditioning). Quantity of such unidentified products of CI reactions is higher in the cases when splitting of urea skeleton is preferred to its nitration, which is in the cases when the initial CI concentration in the propellant is high (3 %). It is obvious from the comparison of MRP3a (single base propellant) and MRP7 (double base propellant with 24 % nitroglycerine content) that nitroglycerine increases quantity of 4-NCI and decreases quantity of NOEA in the propellant. In both cases, however, the total proportion of unidentified CI daughter products at the moment when zero CI concentration in the propellant is measured is high (92 % in case of MRP3a propellant and 80 % in case of MRP7a). Under this situation 4-NCI, NOEA and NO-4-NEA cannot be considered the main products of CI reactions because analyses of the products are incomplete. From this viewpoint 2-NEA, 4-NEA, 2,4-DNEA, NO-2-NEA daughter products the concentration of which in the propellant does not exceed 0.06 % can be considered either as products of reactions that proceed to small extent (probably the case of NO-2-NEA), or reactive intermediates that lead rapidly to NO-4-NEA or to unidentified products.

Analysis of M9 propellant (with initial concentration of CI 0.9 %) published in ref.[6] leads to a conclusion that in this case the predominant CI reactions are nitrations of its phenyl groups to *para* positions. The total proportion of unidentified CI products at the moment when CI has been spent is 31 %, which is lower value than that found in cases of propellants with initial CI quantity of 3 %.

Analysis of model propellants prepared by us[7,9] with initial CI concentrations of 0.8 %, 2.8 % and 6.4 % subjected to accelerated ageing has confirmed Curtis's conclusions[6] on increasing of preferences of urea skeleton splitting with increase in the initial CI concentration in the propellant. Also in cases of model propellants increasing of CI loss has been obvious given by the rise of quantity of unidentified products with increasing of initial CI concentration in the propellant.

Effect of access of oxygen in the course of conditioning of CI stabilized propellants

HPLC analysis of model propellants prepared by us[7,9] stabilized with CI (6.1 %) after accelerated ageing in inert atmosphere or under access of air oxygen has proven that a considerable number of peaks exists belonging to unidentified products and that response intensities of some of them exceed 4-NCI level. Obvious is also the fact that intensity of individual peaks differ considerably dependent on the environment of conditioning of propellant. It can be stated that overwhelming mechanisms of reactions proceeding in CI stabilized propellant depend on CI initial concentration but to a considerable extent also on a possibility of air access into the space above the propellant. Havránková[10] gives, on the basis of pressure measurement in vacuum test apparatus, that at temperature of 125 °C decrease in oxygen pressure occurs above the sample of pure CI. Measuring of oxygen pressure above the samples of double base CI stabilized propellants has proven a decrease in pressure (consuming of oxygen). It can be presumed that CI behaves also as an antioxidant capable of reacting directly with oxygen or with nitrogen dioxide that is formed by nitric oxide oxidation by oxygen. As the products of such oxidation reactions e.g. compounds with quinoidal structure can be supposed. Apart from oxidation products we can, by analogy with DPA reactions, presume formation of formamides (e.g. N-ethyl-N-phenylformamide) in the propellant[7,11]. From the viewpoint of the reactions proceeding it is not possible to consider nitrations and nitrosations only.

Effect of gelatinization of propellants on prevailing mechanisms of CI reactions in the propellant

The proven effect of initial CI concentration on the prevailing mechanisms of CI reactions can be in connection with a change in propellant structure. The ability of CI to gelatinize nitrocellulose is generally known[12]. It has been proven in[13] by means of measuring of the heat released in the course of gelatinization that CI forms a stable complex with nitrocellulose. Gelatination of model propellants with CI content of 3 % and more is obvious also by a mere sight on such a propellant - grains are of glassy structure. A change in propellant structure will lead also to changes in permeability for gases and changes in mobility of other compounds taking part in chemical reactions can also be supposed. To verify this hypothesis the propellant has been prepared containing CI (1 %) and dibutylphtalate (5.3 %) that is considered to be a compound that is not able to react neither with nitroesters nor with the products of their decomposition, but similarly to CI it gelatinizes nitrocellulose thus changing the propellant structure. The results of analyses of CI daughter products in this propellant after conditioning[7,9] both under air access and in inert atmosphere lead to a finding that dibutylphtalate slows down CI reactions in the propellant and changes the 4-NCI - NOEA ratio in a similar way as increase in CI concentration. These conclusions support the hypothesis of influencing the mechanisms of CI reactions by a change of propellant structure.

Possible causes of incompatibility of CI with nitroesters[7,9]

With a change in preferences of CI reaction mechanisms and with increase in proportion of products of urea skeleton splitting at higher initial CI concentrations in the propellant also an increased rate of weight loss of such propellants[14,15], higher heat flows[15], increased rate of gas release under vacuum test conditions[16,17] and, above all, a vigorous increase in gas

release rate under conditions of this test at propellants subjected to accelerated ageing. The preference of urea skeleton splitting is probably also the cause of increasing of the results of Bergmann-Junk tests[16,18-19] when CI has been concentrated in a thin surface layer of propellant grains where its concentration in this layer can be estimated of 15 – 25 %.

2. Experimental part

These work continues with analysis of experimental spherical model propellant sample STAB-309[7,9,15] stabilized by 6.09 % CI, containing approximately 14 % of nitroglycerine.

Sample ageing

Propellant was artificially aged under strictly controlled conditions – in STABIL apparatus for performing the vacuum stability tests. Aging was performed at 89 °C 6, 10 and 14 days. Two grams of the sample were heated in a hermetically sealed ampoule (of volume about 18 cm^3) and the pressure above the sample measured automatically. First set of samples was aged under conditions of vacuum stability test (measurement started in vacuum and the pressure gradually raised during the measurement up to the normal pressure by gas products evolved from the sample; no air oxygen could enter the ampoule), the second set started ageing in the ampoule filled by pure oxygen. For comparison purposes 2 g of pure CI were heated in oxygen also under the same conditions.

HPLC analysis

One gram of a sample was extracted by dichloromethane and analysed by HPLC (Hewlett-Packard HP 1050 with DA detection, equipped by HYPERSIL BDS-C18 5 μm 250×4 mm colon). Methanol-water (63.5 / 36.5 volume %) was used as the mobile phase. Retention times and UV spectra (in the range of 190-600 nm) of detected peaks were compared with consequent list of pure chromatographic standards:

CI; 2-NCI; 4-NCI; 2,4'-DNCI; 4,4'-DNCI; 2,2',4-trinitrocentralite I; 2,4,4'-trinitrocentralite I; 2,2',4,4'-tetranitrocentralite I; N-ethylaniline; NOEA; 2-NEA; 4-NEA; NO-2-NEA; NO-4-NEA; 2,4-dinitro-N-ethylanilin; 2,4,6-trinitro-N-ethylanilin; N-ethyl-N-phenylform-amide, N-phenyl-ethylcarbamate.

GC-MS

Individual peaks were separated by HPLC, concentrated and analysed by gas chromatography followed by mass spectroscopy in order to identify structures of unknown products found in the aged samples. Three systems were used for GC-MS analysis:

1. Varian 3400 gas chromatograph with colon DB-5MS (length 30 m, diameter 0.25 mm, film 0.25 μm, injector 200 °C, splitless mode, inlet 0.3 μl). The chromatograph was equipped by Finnigan ITD-800 MAT MS detector (ion trap type).
2. Varian GCQ gas chromatograph with Thermoquest GCQ, MS detector (ion trap type) with possibility of consequent framentation in MS/MS mode.
3. HP 6890 gas chromatograph with ITD screen colon (HP-5MS, 30 m, diameter 0.25 mm, film 0.25 μm, injector 200 °C, split mode, inlet 1 μl). Finnigan MAT MS ITD-800 with MS detector (quadrupole type).

Headspace analysis

Solid sample of propellant was heated to 50 °C ten minutes in a vial of 1.8 ml volume, gas above the sample was analysed by the equipment no. 1.

3. Results and Discussion

Results of HPLC analysis are summarized in Tables I-II and Figures 1-2. Individual HPLC peaks in range 3.5 to 12.5 minutes are described in the Figure 3. Bar graphs presented at Figures 4 and 5 show intensities of HPLC peaks respecting to products of ageing in vacuum or oxygen.

Identification of observed HPLC peaks

It is obvious from the results that the rate of CI depletion is higher in presence of oxygen than that under vacuum. Decrease of CI to 1.69 % from original concentration 6.09 % was observed after 14 days of ageing in oxygen and the decrease to 3.44 % after the same time in vacuum.

In spite of the fact that we compared the retention times and UV spectra of all HPLC peaks with chromatographic standards of compounds mentioned in literature as decomposition products of CI, only NOEA, NO-4-NEA, 2-NCI and 4-NCI were identified. At least ten more peaks remained, which were not identified with published compounds. From the analysis of aged propellants stabilized by DPA, where we have identified N,N'-diphenylformamide as one of products of DPA[7,11], we expected the possibility of N-ethyl-N-phenylformamide by analogy. The pure compound was synthesized and retention time and UV spectra agreed with the peak No. 2. The structure was also confirmed by mass spectra. The relatively intensive peak No. 3 (which could be observed in the case of samples aged in oxygen only) was identified by mass spectra as N-phenyl-ethylcarbamate. The structure was consequently confirmed by the agreement of retention times and UV spectra of prepared pure compound.

We proposed formation of oxidation products of CI and anilines in reference[7,9], oxidation of CI was also proven in reference[10]. Thus we performed test, were pure CI was heated under oxygen at the same conditions as the propellant was aged. The sample of CI contained traces of three other compounds after ageing which were positively identified with the peaks No. 8, 11 and 14 of chromatograms obtained for aged propellant. Thus we can say that these peaks are caused by some oxidation products of CI.

Concentrations of found products of ageing

The most clear result of the performed testing is the fact, that only small part of CI formed nitrated product (2-NCI or 4-NCI) and the product with highest concentration was found NOEA. This result is valid for both experiment setups - in oxygen and in vacuum.

The other conclusion is clear that the concentrations of found products are very small compared to the decrease of CI concentration (this is valid for both experimental setups again). Such conclusion is in compliance with results[7,9] previously published by us and also with data presented in references[3,6]. The other fact can be perceived from data presented on Figures 4 and 5 – only NOEA concentration is increasing significantly in the samples with increased duration of ageing. Intensities of the other peaks are changing only little. Such behaviour is more remarkable in the case of ageing under oxygen. Thus we may expect all the found decomposition products as intermediate products which concentrations are low and which undergo further reactions. Products of such reactions were not identified by HPLC thus

we can expect products with very high polarity with very low retention times or mostly volatile products. The later possibility is more probable, because high gas evolution rate or weight loss rate is observed at the measured sample[7,9,15] (and generally for samples containing higher amount of CI).

Results of the headspace analysis

Expecting the volatile decomposition products a qualitative headspace analysis was performed which identified ethylacetate, ethylformiate, benzene and methylnitrate as main organic products in gasses above heated propellant sample.

4. Conclusions

It comes from previously published results[6], that higher amount of CI in the propellant leads to the preference of reactions leading to splitting the urea skeleton of CI. Such reaction pathway is accompanied by heat generation, gas evolution and hence higher rate of weight loss. On the other hand, presence of CI is able to prevent the sample from accelerated decomposition and this ability increases with higher original CI concentration in propellant[7,15]. There are at least 14 of intermediate products of CI reactions in propellant (which were observed before all the CI in the sample had been depleted), six of them were identified, three are the same products which were formed by reaction of pure CI with oxygen, the other products were not identified. Concentration of all the products is very low, what is most probably caused by some further reactions of discussed compounds. The final reaction products are probably leaving the propellant sample as volatiles. The reaction mechanism of urea skeleton splitting starts probably according to reference[6] by formation of nitrosoammonium ion which can undergo to nucleophilic attack (as hydrolysis) or radical attack. Besides NOEA some other products which are more reactive than CI are formed and further reacting with oxygen, nitrogen dioxide and other propellant decomposition products. Such compounds can act as antioxidants and thus reduce the possibility of oxidative reactions of main components of a propellant. It was showed in references[15,20] that such oxidation reactions contribute significantly to the accelerated decomposition. The question is how effective are such compounds in trapping nitrogen oxides. It results from reference[21] that when CI or CII react with nitrogen dioxide, nitrogen oxide is one of the reaction products. Such situation can be also true in the case of CI stabilized propellant.

Table I Results of HPLC analysis of fresh and aged samples in vacuum

Peak No.	RT [min]	Compound	0 days [AU]	6 [AU]	10 [AU]	14 [AU]	0 [%]	6 [%]	10 [%]	14 [%]
1	3.56	internal standard					nd	nd	nd	nd
2	3.86	N-ethyl-N-fenylformamid	0.0	6.4	7.4	7.6	0.00	<0.03	<0.03	<0.03
3	4.62	N-phenyl-ethylcarbamate	0.0	0.0	0.0	0.0	0.00	0.00	0.00	0.00
4	4.83	NGL	133.6	123.4	123.8	138.9	nd	nd	nd	nd
5	5.04	NOEA	0.0	30.8	48.2	67.8	0.00	0.24	0.41	0.54
6	5.61	?	0.0	12.0	12.5	18.6	na	na	na	na
7	5.68	NO-4-NEA	0.0	0.0	0.0	0.0	0.00	0.00	0.00	0.00
8	6.13	?	0.0	2.1	3.1	3.8	na	na	na	na
9	6.94	?	0.0	1.6	3.5	4.3	na	na	na	na
10	7.10	?	0.0	2.1	3.6	3.0	na	na	na	na
11	7.79	?	0.0	5.9	5.5	3.8	na	na	na	na
12	9.00	?	0.0	2.4	1.6	1.2	na	na	na	na
13	10.15	2-NCI	0.0	4.2	3.2	2.2	0.00	0.07	0.06	0.03
14	10.44	?	0.0	1.0	1.0	1.5	na	na	na	na
15	11.38	4-NCI	0.0	8.7	7.8	3.9	0.00	0.13	0.13	0.06
16	11.93	?	0.0	6.1	5.7	4.2	na	na	na	na
17	18.78	CI	244.1	189.9	160.4	151.6	6.09	4.52	4.14	3.44

Table II Results of HPLC analysis of fresh and aged samples in oxygen

Peak No.	RT [min]	Compound	0 days [AU]	6 [AU]	10 [AU]	14 [AU]	0 [%]	6 [%]	10 [%]	14 [%]
1	3.56	internal standard					nd	nd	nd	nd
2	3.86	N-ethyl-N-fenylformamid	0.0	13.8	14.3	12.7	0.00	<0.03	<0.03	<0.03
3	4.62	N-phenyl-ethylcarbamate	0.0	26.9	29.8	28.8	0.00	0.07	0.07	0.07
4	4.83	NGL	133.6	146.4	143.2	139.6	nd	nd	nd	nd
5	5.04	NOEA	0.0	86.0	96.9	100.0	0.00	0.69	0.81	0.84
6	5.61	?	0.0	0.0	0.0	0.0	na	na	na	na
7	5.68	NO-4-NEA	0.0	14.0	19.6	16.5	0.00	0.14	0.17	0.15
8	6.13	?	0.0	5.8	5.9	6.3	na	na	na	na
9	6.94	?	0.0	4.7	4.2	4.6	na	na	na	na
10	7.10	?	0.0	4.0	3.6	3.5	na	na	na	na
11	7.79	?	0.0	10.6	3.4	4.0	na	na	na	na
12	9.00	?	0.0	1.6	2.6	0.0	na	na	na	na
13	10.15	2-NCI	0.0	3.0	3.0	2.7	0.00	0.05	0.05	0.05
14	10.44	?	0.0	9.5	9.4	8.9	na	na	na	na
15	11.38	4-NCI	0.0	12.0	12.3	11.8	0.00	0.19	0.19	0.18
16	11.93	?	0.0	1.6	1.2	0.8	na	na	na	na
17	18.78	CI	244.1	127.6	97.2	69.1	6.09	3.04	2.34	1.69

na result is not available due to not standard, nd value vas not determined

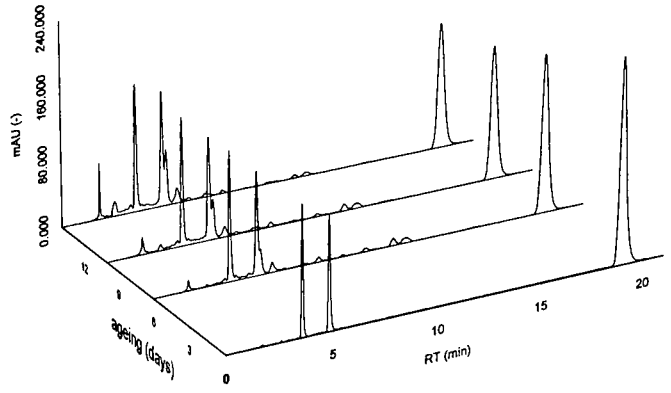


Figure 1 Results of HPLC analysis of fresh and aged samples in vacuum (response at 230 nm)

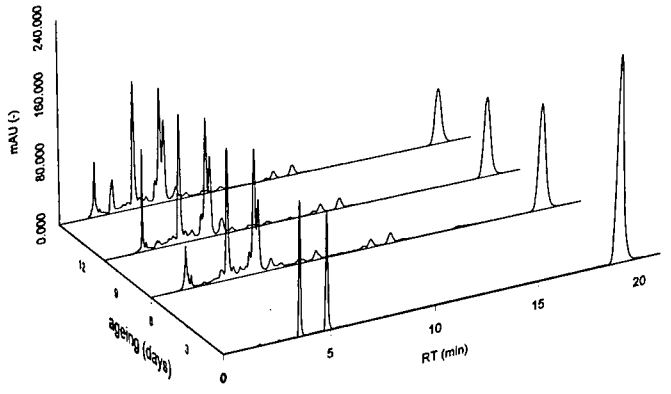


Figure 2 Results of HPLC analysis of fresh and aged samples in oxygen (response at 230 nm)

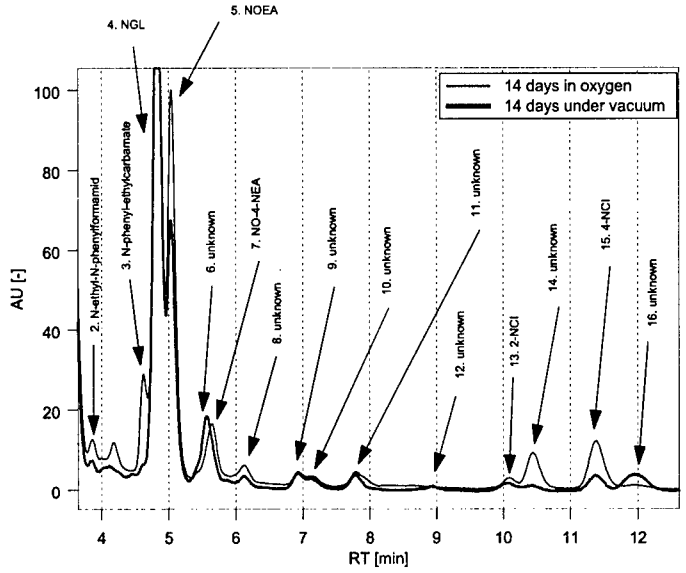


Figure 3 Results of HPLC analysis of samples aged in vacuum or oxygen 14 days at 89 °C (230 nm)

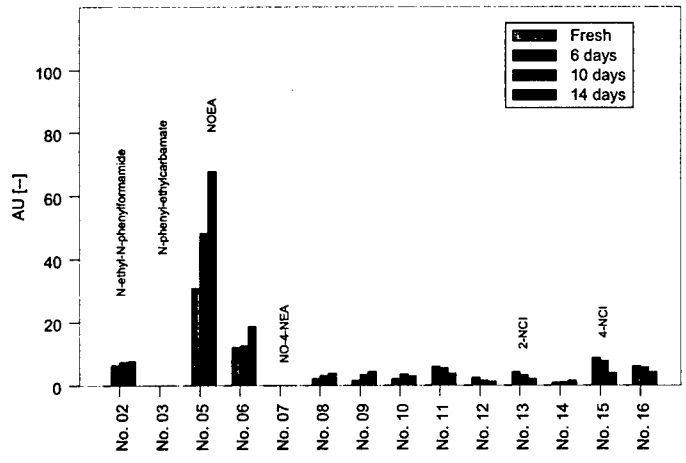


Figure 4 Peak heights (at 230 nm) of decomposition products in the samples aged in vacuum

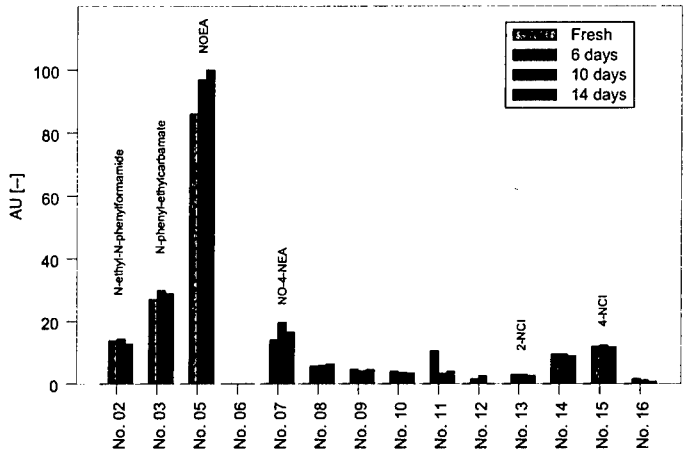


Figure 5 Peak heights (at 230 nm) of decomposition products in the samples aged in oxygen

5. References

1) Volk F., Bohn M., Wunsch G.: "Determination of chemical and mechanical properties of double base propellants", Propellants Expl. 12, 81, **(1987)**.

2) Volk F.: "Determination of the lifetimes of gun propellants using thin-layer chromatography", Propellants Expl. 1, 90, **(1976)**.

3) Wunsch G.: „Anwendungen der Hochdruck-Flüsichkeits-Chromatographie auf die Untersuchung der Alterung von Äthylcentralit", Int. Annu. Conf. ICT **(1977)**, 79.

4) Amman A..: Symp. Chem. Probl. Connected Stab. Explos. (Proc.) **(1976)**, 4th, 9.

5) Druet L., Angers J.: "LC/MS Studies of Ethyl Centralite Stabilized Propellants", Propellants Expl. 13, 87, **(1988)**.

6) Curtis N.J., Berry P.: "Derivatives of ethyl centralite in australian gun propellants", Propellants Expl. 14, 260, **(1989)**.

7) Jan Petržílek, "Relations between chemical stability and composition of smokeless powders", Annotations to Doctoral Thesis, Pardubice **(2000)**.

8) Skládal J., Petržílek J.: "Sledování rozkladu bezdýmných prachů pomocí HPLC", New trends in research of Energetic Materials, Pardubice **(1999)**, University of Pardubice, 258.

9) Skládal J., Petržílek J.: "Vliv podmínek urychleného stárnutí na reakce Centralitu I v bezdýmném prachu", New Trends in Research of Energetic Materials, Pardubice **(2000)**, University of Pardubice.

10) Havránková E., Pilná "Manometric stability tests of double-base propellants in vacuum, air, and oxygen", B.: Propellants Expl. 14, 118, **(1989)**.

11) Petržílek J., Skládal J.: "Vliv podmínek urychleného stárnutí na reakce difenylaminu v bezdýmném prachu", New Trends in Research of Energetic Materials, Pardubice **(2000)**, University of Pardubice.

12) Quinchon J., Trachant J., Nicolas M.: "Les poudres, propergols et explosives", vol. 3, Technique et Documentation, Paris **(1982)**.

13) Ksiazczak A., Ksiazczak T.: "Thermochemistry of the binary system nitrocellulose-s-diethyldiphenylurea", J. Therm. Anal. 54, **(1998)**, 323.

14) Volk F.: "Determining the shelflife of solid propellants", Propellants Expl. 1, 59-65, **(1976)**.

15) Wilker S., Petržílek J., Skládal J., Pantel G., Stottmeister L.: "Stability analysis of propellants containing new stabilisers", Int. Annu. Conf. ICT **(2000)**.

16) Petržílek J.: "Vacuum stability test of aged spherical propellants", Symp. Chem. Probl. Connected Stab. Explos., **(1998)**, 11 th.

17) Petržílek J.: "Vliv chemického složení sférických prachů na výsledky vysokoteplotních stabilitních zkoušek", Nové směry ve výzkumu výbušin, Pardubice **(1998)**, VÚPCH, 31.

18) Petržílek J.: "Relationships between results of high-temperature stability tests and chemical composition of spherical propelants", Int. Pyrot. Seminar 23, **(1997)**, 684.

19) Petržílek J.:Symp. "Relationships between results of stability tests obtained on the basis of large data sets", Chem. Probl. Connected Stab. Explos., **(1995)**, 10 th.

20) Wilker S., Petržílek J., Skládal J., Ticmanis U., Pantel G., Stottmeister L.: "Stability analyses of double base propellants in dependence of their DPA and NGL content", New Trends in Research of Energetic Materials, Pardubice **(2001)**, University of Pardubice.

21) Wallace I.G., Westlake S.: "The use of a chemiluminiscence Nox analyser to study the reactions of propellant stabilisers and their derivatives", Symp. Chem. Probl. Connected Stab. Explos. 7th (Proc.), **(1986)**, 19.

Thermal Decomposition of Cellulose Nitro Ethers in Ultra-Thin Layers on Metal Surfaces

V. A. Malchevsky, O. F. Pozdnyakov

Mendeleev Russian Chemical Technological University, Moscow
Physical Technical Institute, St. Petersburg

Advanced energetic formulations are marked with an extensive use of crystalline fillers, such as metals and metal oxides. It dramatically increases a role and importance of the surface in the research and formation of their physical-chemical parameters, e.g. combustion catalysis, thermal and mechanic stability. A specific feature of this research, as opposed to numerous known investigations on nitrocellulose thermal degradation, is a study of the kinetics and composition of nitrocellulose thermal decomposition products in monomolecular layers, starting with ~5 - 10Å on metal surfaces (Fe, Cu, Ni, Ta). NC with the nitrogen content of ~12.0 % was chosen as a research subject. It was prepared in a film form from acetone solutions with the volumetric concentration of 10^{-2} - 10^{-3} %. The process kinetics and decomposition products were studied by means of time-of-flight mass spectrometry using a direct flash technique. The specimen supported on the metal surface decomposed at 100 - 250 ^{0}C, rate of the specimen heat-up - 4 - 6 ^{0}C/sec.

The conducted investigations show that the nature of the metal surface produces notable effect on the process kinetic parameters. Among the studied metals, Fe manifested the highest activity. NC decomposition in the layers close to monomolecular proceeds much faster and with less activation energies than NC decomposition in a normal state. Rate constants of NC decomposition in films, ~6Å and 200Å at 162 ^{0}C, differ by about two orders of magnitude. In the isokinetic temperature region of ~260 - 280 ^{0}C, regardless k and E parameters in Arrenius equation, NC decomposition proceeds at high rates in layers of different thickness on metal surfaces.

The attained experimental results bridge a certain gap in the data on thermal stability formation, combustion, and adhesive and physical-mechanical characteristics of filled polymeric energetic formulations.

EFFECT OF AGING ON THERMAL DECOMPOSITION OF AMMONIUM PERCHLORATE

MOHAMED A. SADEK, MOHAMED H. MOEEN, MOSTAFA A. RADWAN, AND HAMDY H. AMEEN

Egyptian Armed Forces.

ABSTRACT

Effects of accelerated aging at 75°C on thermal decomposition properties of Ammonium Perchlorate (AP) was studied in this paper. Differential scanning calorimetry DSC, thermogravimetric analyzer TG/DTG and Fourier transformation infrared spectroscopy FTIR techniques was used to evaluate the aging process. DSC thermogram of AP shows endothermic peak at 246.9°C attributed to phase transition of AP from orthorhombic to cubic form and two exothermic peaks the first at 288.5 °C (weak) and the second at 423.9°C (sharp) referring to the decomposition of AP. After 120 days of aging DSC thermogram shows two distinguished endothermic peaks at 322.7°C and at 431.2 °C attributed to the decomposition of AP in two stages. Also, FTIR show a new peak at wave number 800cm^{-1} assign to the fragment of chlorate ion. Thermal decomposition mechanism of AP before and after 120 days of aging was proposed. Using, TG/DTG isothermal data and 1st order rate equation method the activation energy "E" of decomposition was calculated.

INTRODUCTION

Among current composite solid propellant oxidizers, AP has the highest oxidation potential and is the most widely used for high-energy applications. There is an important to study the thermal decomposition process of AP. This importance is arising from the significant effect of AP in the thermal decomposition process of composite solid rocket propellants. To study the rate of deterioration and the changing of the properties at short time, accelerated aging program is carried out at elevated temperatures higher than those expected at the practical service.

In this study accelerated thermal aging program of AP was carried out at 75^0C for 140 days. The DSC, TG/DTG and FTIR were done at different periods of time 20,40,80,120 and 140 days of aging.

EXPERIMENTAL

The DSC thermogram of AP obtained by using NETZSCH model DSC-200 differential scanning calorimeter. DSC-200 is calibrated using indium and zinc standards. The TG/DTG thermogram of AP was recorded from NETZSCH model TGA-209 thermogravimetric analyzers .A sample of 1-2mg (AP) have particle size of 7-11μm , a heating rate of 15°C/min and nitrogen gas as a protective gas at rate of 20ml/min was applied. Isothermal runs in TGA experiments are carried out by heating the samples to the required temperature at a heating rate of 40°C /min, then the temperature is kept constant for different periods of time. The infra red spectra of AP was carried out in the wave number range from $4000cm^{-1} - 500cm^{-1}$ by Mattson Infinity FTIR series using the potassium bromide (KBr) disc technique.

RESULTS AND DISCUSSIONS

Figure (1) and figure (2) illustrate the DSC and TG/DTG thermograms of AP before aging process respectively. In figure (1) the endothermic peaks observed at 246.9 ^{0}C has been assigned to the phase transition of AP from orthorhombic to cubic form. While the two exothermic peaks, the first at 288.5^0C (weak) and the second is at 423.9^0C (sharp) are due to decomposition of AP in two stages [1]. There is no endothermic peak attributed to melting of AP, thus AP decomposes without melting [1,2]. The DTG measurements indicate exactly the temperature of the beginning, the maximum rate, and the end of the change. Moreover the peak temperature represents the temperature at which the rate of mass-change is at a maximum and it is clearly not the temperature at which the sample begins to lose mass. In figure (2) the TG/DTG trace of AP shows two stages of mass loss. The first is given at 305.8^0C with 20% mass loss and the second is obtained at 384.5^0C with 80% mass loss. The gaseous products at the first stage of mass loss

up to a temperature 300^{0}C were found to be oxygen, chlorine, chlorine dioxide, hydrochloric acid, perchloric acid and water. It is shown to occur in the solid phase within the AP particle [2,3,4]. The second stage of mass loss includes the decomposition of AP to $NH_4^+ + ClO_4^-$.The decomposition process of AP occurs over the entire temperature range of decomposition, but only becomes dominant at temperature above those for solid-phase decomposition.

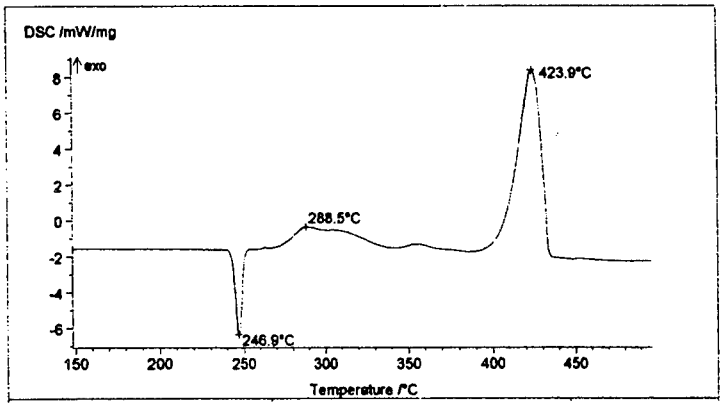


Figure (1) Dynamic DSC of AP (15 ^{0}C /min heating rate) before aging study

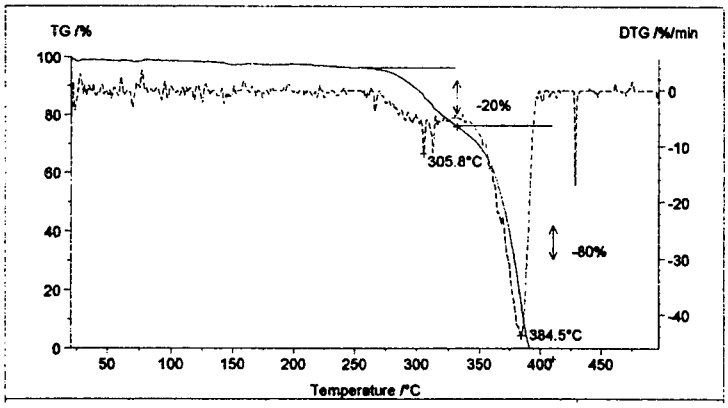


Figure (2) Dynamic TG/DTG of AP (15 ^{0}C /min heating rate) before aging study

Figure (3) shows the spectral structure of AP before aging study. Ammonium perchlorate has the simplest spectral structure. Where, absorption peaks occur at 3300cm^{-1}, 1400cm^{-1}, 1100cm^{-1} and at 600 cm^{-1}. These peaks reveal the structure and bonding present in AP. The peaks at 3300cm^{-1} and 1400cm^{-1} are the fundamental frequencies of ammonium ion in the infrared region [5]. The peak at 1400cm^{-1} is narrow but very strong and corresponds to NH_4^+ deformation. The peak at 3300cm^{-1} is broad and corresponds to asymmetric stretching of NH_4^+. The peaks at 1100cm^{-1} and 600cm^{-1} are also narrow and broad peaks. These peaks were corresponding to asymmetric stretching and bending modes of ClO_4^- respectively [6].

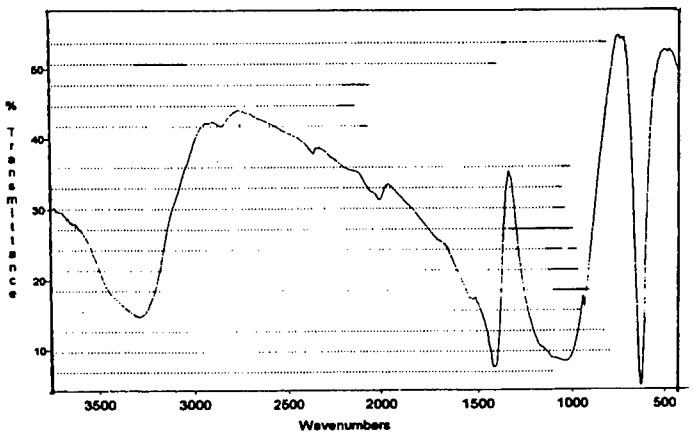


Figure (3) spectral structure of AP at zero time before aging study

The mechanism of AP before aging study can be proposed to follow the next mechanism [2,7].

$$NH_4ClO_4 \longrightarrow NH_4^+ + ClO_4^-$$

$$NH_4^+ + ClO_4^- \longrightarrow NH_3 + HClO_4$$

The principal evidence for this mechanism is that, the fragments of NH_4^+ and ClO_4^- ions are shown in IR spectrum.

Figure (4,5) illustrates the DSC thermograms of AP after 80 and 120 days of aging. These figures reveal that, the phase transition of AP from orthorhombic to cubic form was still evident over the entire range of aging time. The temperature variation of this phase change was found to be about ±2°C.The first exothermic decomposition temperature (weak peak) which located in figure (1) at 288.5 °C was shifted towards the higher temperature with increasing aging time. This peak was found to be 322.7°C and becomes broad and sharp at 120 days of aging time. The second exothermic peak (sharp peak) which located at 423.9 °C was also shifted towards the higher temperature with increasing aging time. At 120 days of aging this peak was found to be 431.2°C. Figures (6,7) illustrate the TG/DTG of AP at 120and 140days of aging time. In these figures the first stage of mass loss shows an increase in the amount of mass loss. This increase was found to be about 20% and it was on the expense of the second stage of mass loss. These results were confirmed with the previous DSC results at 120 days of aging .It was clearly that the mechanism of AP decomposition start to change after 120days of aging. Spectral structure of AP after 120 days and 140 days of aging was given in figure (8) and (9) respectively. These figures showed that, a new peak at 800 cm^{-1} was obtained in both figures. This peak was assigned to the fragments of chlorate ion [5]. This result also indicates that the decomposition mechanism of AP was changed after 120days of aging.

The mechanism of AP decomposition, after 120 days of aging, may be proposed as in the following mechanism:

$$NH_4ClO_4 \longrightarrow NH_4^+ + ClO_4^-$$

$$NH_4^+ + ClO_4^- \longrightarrow NH_3 + HClO_4$$

$$2\,HClO_4 \longrightarrow ClO_3^- + ClO^- + 2H^+ + 2O_2$$

$$ClO_3^- + ClO^- + 2H^+ + 2O_2 \longrightarrow H_2O + Cl_2O_7$$

$$2Cl_2O_7 \longrightarrow 2Cl_2 + 7O_2$$

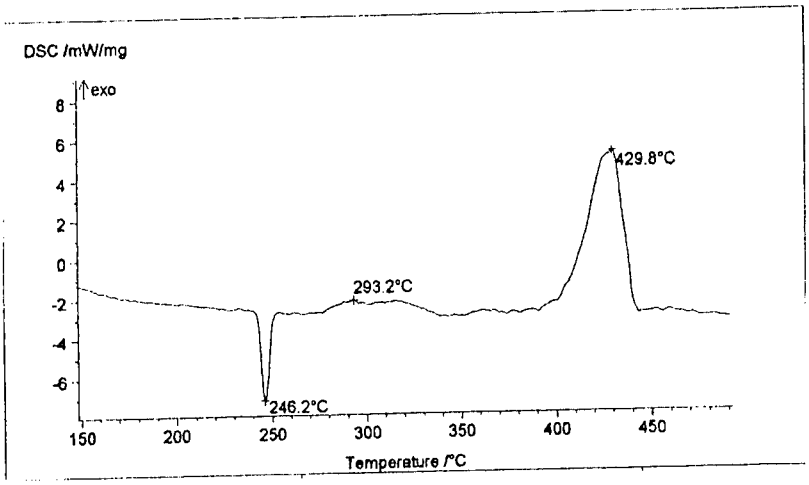


Figure (4) Dynamic DSC of AP (15 ^{0}C /min heating rate) after 80 days of aging time.

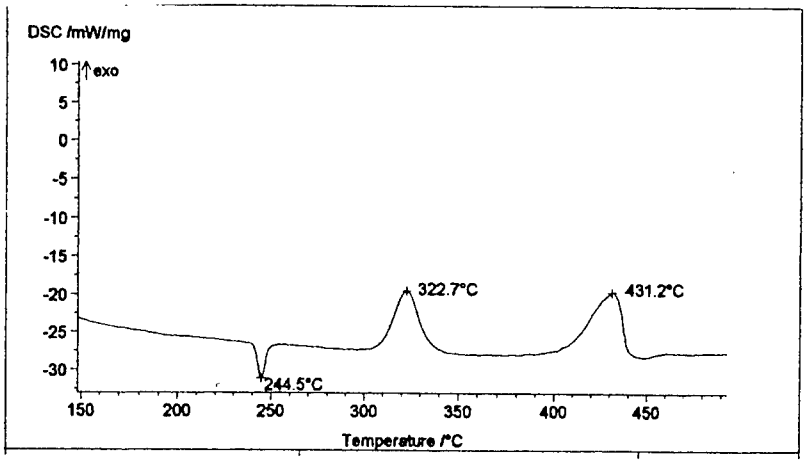


Figure (5) Dynamic DSC of AP (15 ^{0}C /min heating rate) after 120 days of aging time.

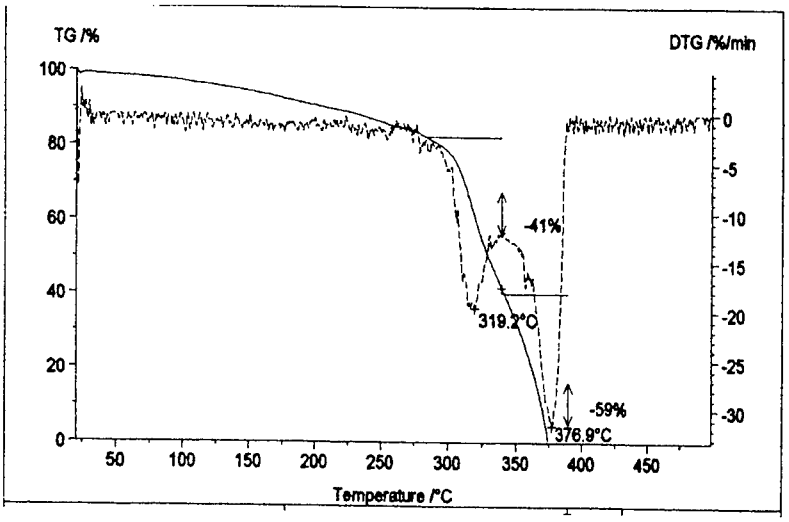


Figure (6) Dynamic TG/DTG of AP (15 ^{0}C /min heating rate) after 120 days of aging time.

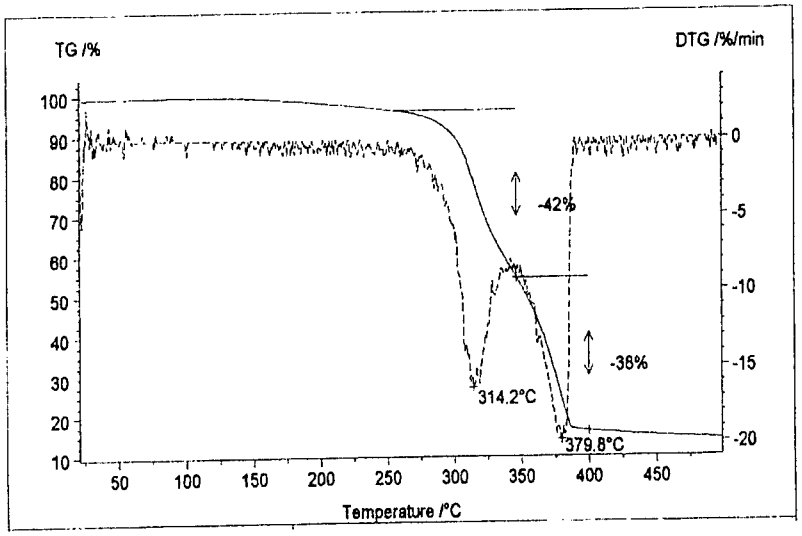


Figure (7) Dynamic TG/DTG of AP (15 ^{0}C /min heating rate) after 140 days of aging time.

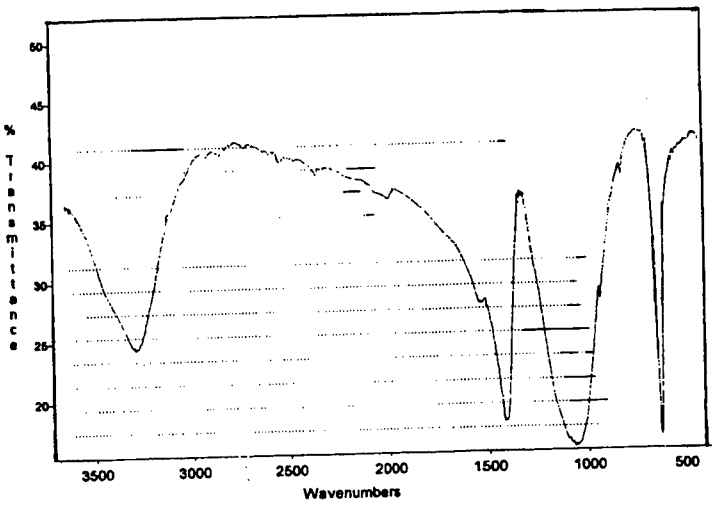


Figure (8) spectral structure of AP after 120 days of aging time.

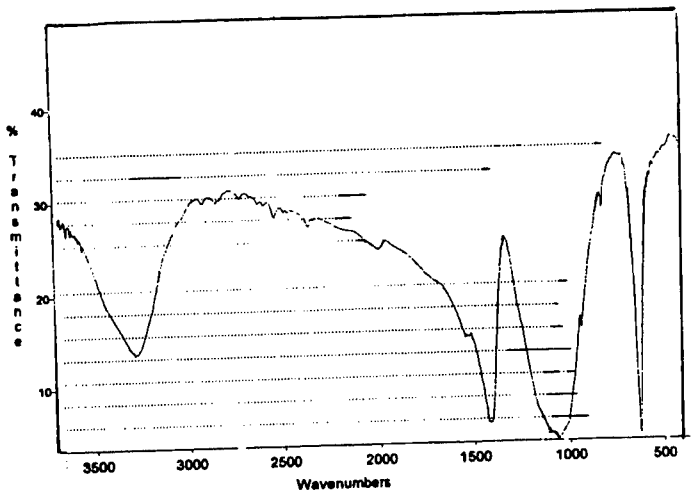


Figure (9) spectral structure of AP after 140 days of aging time.

Activation energy of thermal decomposition of AP was calculated by measuring the weight loss versus time to evaluate the first –order rate coefficients [8]. The integrated form of first order rate equation is,

$$\ln(C_A/ C_{Ao}) = -kt \qquad (1)$$

Where C_{Ao} is the initial mass, C_A is the mass at time (t), (k) is the first- order rate coefficient and, (t) is the time. A plot of $\ln(C_A/ C_{Ao})$ versus (t) will give a straight line with slope = (–k). Different (k) values were estimated at different temperature and the kinetic parameters were calculated from Arrhenius plots,

$$\ln k = \ln A - E/RT \qquad (2)$$

Where plot of ln (k) versus (1/T) will give a straight line with slope = (–E/R), (A) is the pre-exponential factor, (E) is the activation energy, (R) is the universal gas constant (1.98 cal/mole k) and (T) is the temperature in K. Figure (10) illustrate the isothermal TG for AP at different temperature before aging study. The convenient TG isothermal temperature range for studying the thermal decomposition of AP was found to be (240-270) °C. Table (1) show the estimated "k" values for AP at different temperatures. The values of E (Kcal/mole) for AP at different periods of aging time using isothermal technique- 1st order rate equation method were illustrated in table (2).

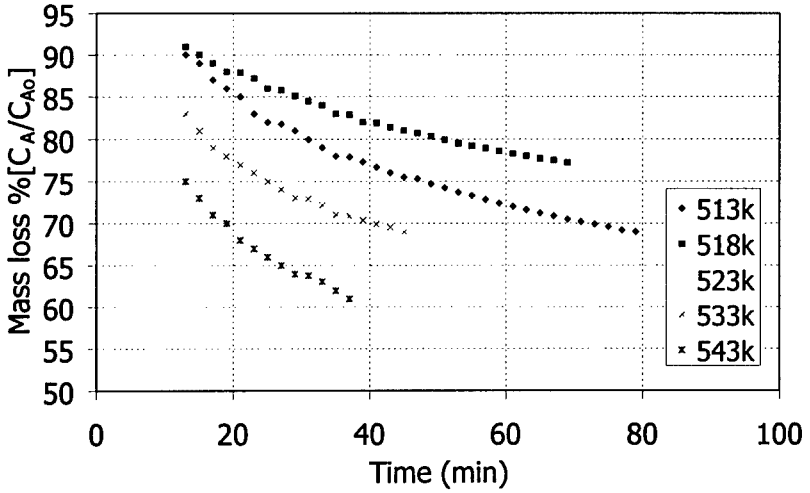


Figure (10) Isothermal TG for AP at different temperature before aging study

Table (1) the estimated "k" values for AP at different temperatures

Initial mass(mg) "C_{Ao}"	T (K)	$(1/T).10^3$	total mass loss %	-k (slope)	$k.10^3$	Ln k
4.265	513	1.94	21.4	-0.0038	3.8	1.3350
5.516	518	1.93	25.5	-0.0028	2.8	1.0296
4.296	523	1.91	28.0	-0.0052	5.2	1.6486
3.800	533	1.87	35.1	-0.0054	5.4	1.6863
4.021	543	1.84	33.8	-0.0081	8.1	2.0918

Table (2), the values of E (Kcal/mole) for AP at different periods of aging time using Isothermal technique- 1st order rate equation method

E (Kcal/mole)	Aging time (days)
16.708	zero
12.6	20
7.32	40
7.1	80
21.68	120
13.085	140

Figure (11); represents the dependence of the activation energy of AP on aging time. In this figure as the time increase a slight decrease in activation energy occurs till 80 days of aging. After this, a rapid increase occurs in the values of E till 120 days of aging. Then, a rapid decrease can be noticed till 140 days of aging. The previous results show that, The decrease in the E value indicates that, sever deterioration was occurred in AP after 120 days of aging. Therefore, in order to obtain an estimation of service lifetime from aging data, it is necessary to know the acceptable range of the activation energy value for the propellant and the AP oxidizer. Hence, a relation between deterioration of mechanical properties and the appearance of new peaks in the DSC thermogram of AP is required in order to estimate the service life of the propellants.

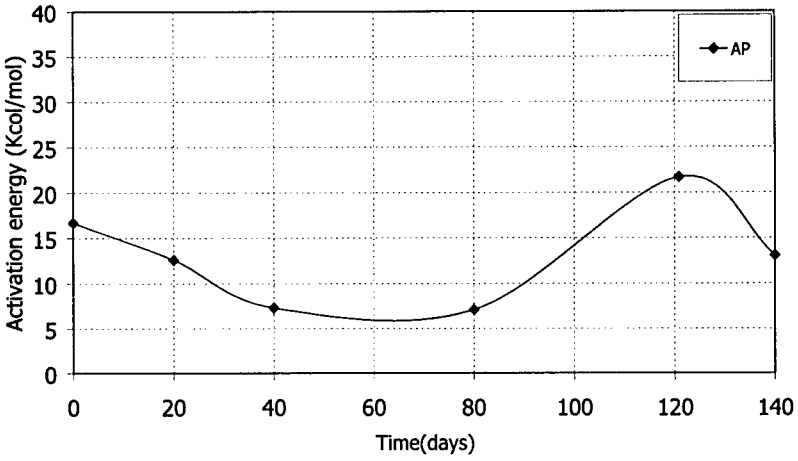


Figure (11) dependence of the activation energy of AP on aging time

Conclusions

The convenient TG isothermal temperature range for studying the thermal decomposition of AP was found to be (240-270) °C. After 120 days of aging at 75°C, DSC thermogram of AP showed two distinguished exothermic peaks (at 322.7°C and 431.2 °C) and was attributed to the decomposition of AP in two stages. Also, spectral structure of AP after 120 days and 140 days of aging time show a new peak at 800 cm^{-1} assigned to the fragments of chlorate ions. In order to obtain an estimation of service lifetime from aging data, it is necessary to know the acceptable range of the activation energy values for the propellant and the AP oxidizer. Also, a relation between deterioration of mechanical properties and the appearance of new peaks in the DSC thermogram of AP is required in order to estimate the service life of the propellants.

REFERENCES

[1] G.Hussain and G.J.Rees, Combustion of Ammonium Perchlorate Based Mixture with and without Black Powder, Studied by DSC and TG/DTG, Fuel, V.71, 471-473,1992.

[2] T. Urbanski, Chemistry and Technology of Explosives, V.4, pp.444-446, Pergamon Press Ltd. Headington Hill Hall, England, 1985.

[3] T. Urbanski, Chemistry and Technology of Explosives, V.2, pp.476-483, Pergamon Press Ltd. Headington Hill Hall, England, 1990.

[4] Behrens, Richard, and Leanna Minier, The thermal Decomposition Behavior of Ammonium Perchlorate and of an Ammonium Perchlorate Composite Propellant, 33rd JANNAF Combustion Meeting, Monterey, California, V.2, p.1-19, 1996.

[5] R. A. Isbell and M .Q. Brewster, Optical Properties of Energetic Materials: RDX, HMX, AP, NC/NG, and HTPB, Propellants, Explosives, Pyrotechnics, 23, pp.218-224, 1998.

[6] Keiichi Hori and A. Iwama, FTIR Spectroscopic Study on the Interaction Between Ammonium Perchlorate and Bonding Agents, Propellants, Explosives, Pyrotechnics, 15, pp.99-102, 1990.

[7] Yoshio Oyumi, Eishu Kimura, and Kiyokazu Nagayama, Accelerated Aging of Plateau Burn Composite Propellant, Propellants, Explosives, Pyrotechnics, 22,pp.263-268, 1997.

[8] H. H. Ameen, M. A. Sadek, M.H.Moeen, M. A. Radwan and H. A. Abd El Meged , Activation Energy of HMX Via Thermal Decomposition ,Twenty-Seventh International Pyrotechnics Seminar , Colorado ,USA, July 16-21,2000

Poster

THE DEVELOPMENT OF ENVIRONMENTAL LOGGING DEVICES FOR MUNITION LIFE ASSESSMENT

John Theobald & David A. Tod
DERA, Fort Halstead, Sevenoaks, Kent, TN14 7BP, UK
Steve Kilvington
DOSG, Ensleigh, Bath, BA1 5AB

ABSTRACT

The prediction and extension of service life has significant cost saving potential. DERA started monitoring the real environmental conditions experienced by munitions (initially temperature and humidity) approximately 10 years ago as a means of improving this prediction.

The historical development of devices specifically designed for munitions is presented, together with some of the data that has been generated from various climatic zones. A novel sub-miniature temperature logger has recently been tested for its suitability in this work and the results of this evaluation are presented.

The application of environmental monitoring to munition life assessment and extension, coupled with an understanding of ageing mechanisms and rates, offers significant advantages over conventional surveillance trials. Savings can be made in both time and a reduction in the number of expensive assets that must be destroyed.

Keywords: Environment
Temperature
Humidity
Service life
Surveillance

INTRODUCTION

The accompanying oral presentation "The Advantages of Environmental Monitoring for Munition Life Assessment" discusses the background to this subject and illustrates the principle by presenting work that has been carried out with a specific munition. For that particular munition, it has been possible to extend the storage life from 10 up to 15 years, when maintained in deep storage.

This poster focuses on some of the more recent development work that has been carried out to provide environmental logging devices, which are safe and suitable for close proximity to energetic materials.

TEMPERATURE LOGGER REQUIREMENT

The complexity of temperature data that needs to be recorded depends greatly on the likely failure mechanism expected for the munition being monitored. These failure mechanisms can generally be grouped into three generic classes:

- Mechanical degradation
- Chemical degradation
- Physical change (phase change)

Mechanical degradation can occur as a result of temperature cycling of the munition. This happens for instance to an air-launched missile, which may experience very high temperatures when the aircraft is on the tarmac and very low temperatures at high altitude. If the process is repeated, cracking and de-bonding of the rocket motor charge may occur, which can lead to catastrophic failure on ignition, due to increased burning

surface. Alternatively, this type of temperature cycling may lead to other forms of mechanical damage in the non-energetic parts of the munition. For mechanical degradation, a complete temperature / time log is required so that the magnitude and rate of change of temperature is available for analysis.

An example of chemical degradation is the loss of stabiliser or antioxidant in a rocket motor propellant as a function of time and temperature. However, the critical ageing mechanism could also be the degradation of a simple 'O' ring. In either case, this is often modelled using the Arrhenius equation, although other models may also be used. To obtain an effective life of the munition, the cumulative time spent at each temperature is required, but this does not of necessity require a detailed temperature / time log.

Physical change (phase change) is typified by the melting of a high explosive filling at elevated temperature. This can cause problems of exudation of material into unintended areas and can be potentially very serious. From a temperature monitoring standpoint, all that needs to be recorded is any temperature deviation outside of predefined limits.

NOVEL TEMPERATURE LOGGER

A miniature temperature logger has been evaluated for its potential to monitor the conditions experienced by munitions. It addresses the three generic requirements explained above in a small rugged package (figure 1). The device is constructed from a stainless steel case with a stainless steel lid, joined by a polypropylene seal. Electrical contact to the unit, for

programming and downloading of data, is achieved by connecting two wires, one to the case and the other to the lid.

The key features of this device are given below:

- Temperature range –30°C to +85°C at 0.5°C resolution
- Accuracy ± 1°C, in the range –20°C to +70°C
- Programmable measurement interval 1 to 255 minutes
- Expected service life – 10 years or 1,000,000 measurements (at 50°C or less)
- Logs up to 2048 consecutive temperature / time measurements
- Records a long-term temperature histogram with 2°C resolution into separate memory
- Records time and duration when temperature leaves a user defined range (max 12 high and 12 low excursions)
- 512 bytes of general purpose memory available for user information

The histogram storage is of particular interest as it provides a simple method of collecting large quantities of temperature data in a compact format. The temperature range of the device is divided into 2°C intervals (or temperature slots) and two bytes of memory allocated to each slot. For example the 20°C slot is used to count any reading where the temperature measured is either 20.0°C, 20.5°C, 21.0°C or 21.5°C.

Each time one of these temperatures is recorded, the count held in the corresponding two bytes of memory is incremented by one. With two bytes of memory, up to 65,536 readings can be recorded for each temperature slot, which provides a very high logging capacity. If the device is set to log at 60 minute intervals and it is maintained in a stable

environment so that all temperatures recorded lie in the same temperature slot, then the memory will only be filled after 7.5 years.

An example of a temperature histogram recorded at 1 minute interval for 6 months is given in figure 2. The maximum count corresponding to the 14°C slot (14.0, 14.5, 15.0 and 15.5°C) is approximately 33,000 while the total count for all slots is greater than 250,000.

This particular temperature logging device is unusually small in size, being approximately 16mm diameter by 6mm high. This should make the device eminently suitable for deployment within munitions. The use of stainless steel and polypropylene is expected to give good chemical compatibility with energetic materials, although further work needs to be carried out in this area.

Several tests have been carried on the device to simulate harsh conditions, including extreme cold and extreme heat. To date, the device has successfully withstood the abuse it has received with little effect on its calibration or accuracy of its real-time clock.

CONCLUSIONS

A novel temperature logging device is being evaluated which shows great promise for use in the military environment. Currently, a number of other safety aspects are being addressed concerning the deployment of this device in explosive magazines and munitions. It is intended that the latest available data will be displayed on the poster presentation.

REFERENCES

1 Environmental data logging for weapon life assessment, J S Dodds, D A Tod, J Theobald in Sensors for the Detection & Analysis of Energetics, Explosives & Pyrotechnics Symposium, Washington January 25 –26, 1999.

2 Environmental data logging, J Theobald in TEEMAC Open Workshop on Prediction of Life and Life Extension for Munitions, RMCS Shrivenham, 30 – 31st October 2000.

3 NATO STANNAG 2895, Extreme climatic conditions and derived conditions for use in defining design/test criteria for NATO forces materiel, February 1990.

Figure 1 – Miniature temperature logger

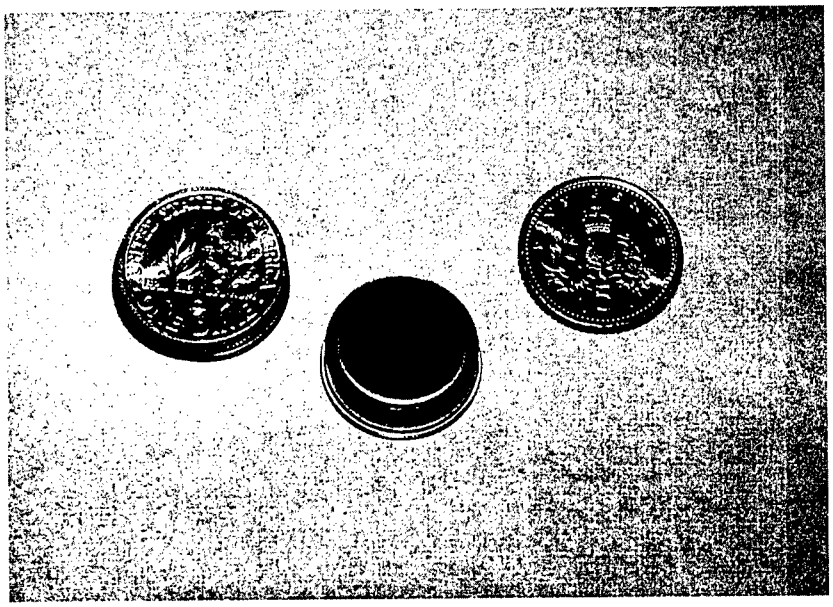
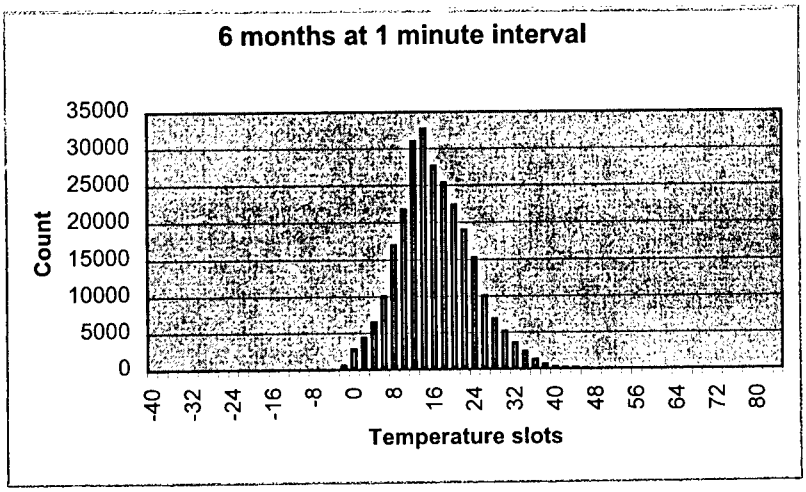


Figure 2 – Histographic storage of temperature data



FEASIBILITY STUDY TO USE A LASER SYSTEM FOR AN INSENSITIVE MUNITION DEFLAGRATION TEST

Murk van Rooijen
TNO Prins Maurits Laboratory, P.O. Box 45, 2280 AA Rijswijk, The Netherlands

Emmanuel Lapebie, Fréderic Peugeot

DGA ETBS, P.O. Box 712, 18015 Bourges Cedex, France

Frédéric Opdebeck, Phillippe Gillard
LEES, UPRES EA 1205, 63. Av. de lattre de Tassigny, 18020 Bourges Cedex, France

ABSTRACT

When applying impact tests on explosive materials it is possible to predict a violent response (type I, II) using theories of shock initiation mechanisms. It is much more complex to predict lower responses, for example explosion or deflagration (type III-IV). One of the reasons is that there is no test that determines the specific energy needed for an explosive to ignite. For many years the Laboratory of Energetic Explosions Structures has built up experience with igniting pyrotechnics with a laser diode. Because a laser diode has a well defined pulse amplitude and length, this system delivers a well defined energy to an explosive materials. Using a laser to ignite high explosives is more complex due to the low absorption of the laser energy by the explosives. This article describes a test set-up for igniting explosive with a special laser energy transfer mechanism that was tested using B/KNO_3 compositions. The results of a series of tests performed at DGA-ETBS on several HMX based explosives are being discussed. Although these tests did not result in a complete explosion of the test vehicles, experience on combustion ignition has been built up in order to develop a deflagration threshold test. From these results, it is possible to plan new tests which be performed at TNO-PML.

SENSITIVITY OF AMMONIUM PERCHLORATE AND AP-BASED MICSTURE TO MECHANICAL ACTION

G.T.Afanas'ev', V.M.Makharinskiy, S.M.Muratov, D.P.Trebunskikh

Samara State Technical University, Galaktionovskaya st.141, Samara 443010 Russia
† Semenov Institute of Chemical Phisics RAS, Kosygin st. 4, Moscow 117977 Russia

The sensitivity to mechanical actions of systems, opposite on properties, is investigated: Ammonium Perchlorate (AP), unable to combustion under normal conditions, and well shining mixtures AP with combustible. The outcomes of development of a method of an evaluation of Energetic Material (EM) sensitivity are showed, an operating duty of which transformation is the combustion. The propagation of combustion for limits of zone of action on surrounding EM considers as the positive test data.

Keywords: ammonium perchlorate, impact, shear, pressure, upper and lower limits.

BALLISTIC PROPERTIES OF HNF/Al/HTPB BASED PROPELLANTS

A.E.D.M. van der Heijden [1], *H.L.J. Keizers* [1], *L.D. van Vliet* [1], *M. van Zelst* [1], *W. Groenewegen* [1], *F. Lillo* [2] *and G. Marcelli* [2]

[1] *TNO Prins Maurits Laboratory, P.O. Box 45, 2280 AA Rijswijk, The Netherlands*
[2] *Fiat Avio, Corso Garibaldi 22, 00034 Colleferro, Italy*

Abstract

At TNO Prins Maurits Laboratory the development of HNF and HNF based propellants started in the early nineties. Recently HNF/HTPB based propellants were re-investigated and the experimental characterization of the thermal, stability, mechanical, hazardous and ballistic aspects appear promising, although in particular the thermal stability and burn rate exponent (~ 1) need further optimization. In this paper special attention is given to the identification of burn rate modifiers (BRM's) which should lower the burn rate exponent from ~ 1 to a range of 0.4-0.6. As a next step, motor firings are planned at 1 (TNO) and finally at 5 kg scale (Fiat Avio) with the most promising propellants.

In this paper the results of ballistic tests with HNF/Al/HTPB propellant formulations are presented and discussed. In cooperation with Fiat Avio the development of HNF/HTPB based propellants is studied in which a part of the HNF is replaced by ammonium perchlorate (AP). The ballistic properties of a selection of these propellants is included in this paper. Furthermore, typical mechanical, thermal stability and hazard characteristics of these propellant families will be presented.

1. Introduction

Since the 90's, the use of HNF as a new high performance oxidiser is being reinvestigated for space propulsion applications. Within European development programmes, significant improvements have been achieved over the last 10 years, with respect to the oxidiser itself as well as possible propellant formulations. Being more energetic, the newly developed formulations have the potential of significantly lowering the launch costs per kilogram weight.

Parallel to and harmonised with the developments in The Netherlands, Italy, Norway and UK contributed to the HNF based propellant developments the last few years. At the moment TNO Prins Maurits Laboratory and Fiat Avio collaborate on the development of HNF based propellants. Previous results have shown that, contrary to US patent literature [1], currently produced HNF combined with an HTPB binder leads to thermally stable propellant formulations [2,3]. The ballistic properties of HNF/HTPB propellants have been addressed in reference [3]. The burn rate at 7 MPa is ~ 15-25 mm/s and the burn rate exponent n is ~ 1. In particular the burn rate exponent must be reduced to approximately 0.6 or below before such a propellant can be applied in actual rocket motors. It is well-known that the burn rate exponent may be modified by using burn rate modifiers (BRM's). Different BRM's are currently under investigation at TNO and some typical results are presented in the current paper. Furthermore, preliminary ballistic properties (strand burner tests) of HNF/AP/Al/HTPB propellants in which part of the HNF is replaced by AP, are shown (activities mainly performed at Fiat Avio). Also several mechanical, thermal stability and hazard properties of this family of propellants will be presented.

2. Experimental

A series of potential BRMS's has been tested. Prior to the assessment of the ballistic properties, the stability of these compositions had to be verified, since ballistic modifiers may also affect the thermal stability of these energetic compositions. These data are not reported here.

2.1 Preparation of samples

The ballistc properties have been assessed by means of Chimney burner tests (strand burner). Samples for the chimney burner tests at TNO are prepared in a mechanical mixer (horizontal mixing blades) with a capacity of ~ 300 g propellant per batch. The mixer can be depressurized and heated in order to remove residual air in the propellant and to decrease the viscosity of the binder,

respectively. Solid loads up to 80 wt% have been reached. The amount of aluminium (14 wt%) has been determined on the basis of maximum theoretical performance with a total solid load of 80 wt%. The compositions of the propellants discussed in this paper are summarized in table 1. After obtaining a homogeneous mixture and the addition of the curing agent (isocyanate), a block of propellant is cast into a mould. After curing the propellant is cut resulting in the following specimens:

- 8-10 strands of ~ 7×7×100 mm^3 for chimney burner testing,
- 2-5 cylindrical samples 10 mm diameter and 10 mm high, for compression tests,
- 1-2 slabs of ~ 30×30×5 mm^3 for Shore A tests,
- remaining material for thermal stability (TG/DTA, VST, DSC), hazard testing (impact/friction) and ageing assessment.

Table 1: Composition of the propellant batches.

Batch code	HNF [wt%]	Al [wt%]	AP [wt%]	Stabilizers [wt%]	BRM [wt%]	Binder [d] [wt%]	Remarks
TNO							
HHU-2	72.5	–	–	2.5	–	25.0	Bimodal mix of HNF-C15 and HNF-S16 (70/30 wt%); non-aluminised
HHU-3	76.0	–	–	2.2	–	21.8	HNF-C18; non-aluminised
HHU-4	70.0	–	–	2.0	4.0	24.0	HNF-E8; non-aluminised
HHU-5	64.0	14.0 [a]	–	2.0	–	20.0	HNF-C24
HHU-6	64.0	14.0 [b]	–	2.0	–	20.0	HNF-C24
HHU-7	61.0	14.0 [b]	–	2.0	3.0	20.0	HNF-C24
Fiat Avio							
CC22-1	46.8	20.0 [c]	25.2	–	–	28.0	HNF-C18; HNF/AP ratio = 65/35
CC22-2	46.8	20.0 [c]	25.2	–	–	28.0	HNF-C18; HNF/AP ratio = 65/35
CC22-3	46.8	20.0 [c]	25.2	–	–	28.0	HNF-C18; HNF/AP ratio = 65/35
CC22-4	46.8	20.0 [c]	25.2	–	–	28.0	HNF-C18; HNF/AP ratio = 65/35
CC22-5	46.8	20.0 [c]	25.2	–	–	28.0	HNF-C18; HNF/AP ratio = 65/35

a Mean size of Al: 20 μm.
b Mean size of Al: 6 μm.
c Mean size of Al: 15 μm.
d Binder composition: HTPB/isocyanate/plasticiser.

Fiat Avio prepared several series of HNF/AP/Al/HTPB based samples on 150-200 g scale in a mechanical mixer for ballistic and mechanical testing. For these formulations no BRM was applied. A systematic screening of the influence of macro-components (like HNF/AP ratio, Al content, total solid loading) and process parameters was carried out. A selection of these batches and their

characteristics are included in this paper (see also table 1). The mean particle size of the AP used in these samples is 80 μm. The HNF/AP ratio is 65/35 wt%.

2.2 Chimney burner

In a chimney burner (strand burner) the burn rate of propellant can be determined as a function of pressure and temperature. From the observed burn rates at the different pressure levels, the ballistic behaviour of the propellant can be assessed. All tests have been performed at room temperature. TNO generally performs 7-10 tests per formulation to determine the burn rate law. For the screening tests of Fiat Avio, 2 tests per formulation have been carried out. Fiat Avio used a Crawford bomb, which is similar to a chimney burner. The burn rate was determined at two pressure levels, 4.5 and 6.0 MPa.

2.3 Mechanical properties

In order to obtain an indication of the mechanical properties of the propellant batches (300 g batches), compressive tests on 10 mm diameter propellant cylinders (height/diameter ratio = 1, strain rate 10 mm/min, 20 °C) and Shore A measurements have been performed. The Shore A value after 0 and/or 15 s loading is reported.

The samples produced by Fiat Avio were mechanically characterised by means of tensile tests on dog bones (strain rate 25 mm/min, 25 °C) and by means of Shore A hardness tests (0 and 15 s loading).

2.4 Thermal stability and hazard properties

Generally, the thermal stability can be assessed either by means of TG/DTA, DSC or VST tests. Usually a combination of two analytical techniques is chosen, *e.g.* TG/DTA and VST. The conditions during testing with the TG/DTA are:

Equipment	: Seiko TG/DTA 320
Temperature range	: 25 – 250 or 350 °C
Heating rate	: 2.5 or 10 °C/min
Atmosphere	: Nitrogen
Flow rate	: ~ 50 ml/min
Sample	: Open aluminium cup
Reference	: Empty open aluminium cup
Sample size	: ~ 5 – 10 mg

The vacuum stability was determined on ~ 1 g propellant samples in duplicate or triplicate during 48 hrs at 60 °C. For some specimens, a period of 100 hrs at 60 °C has been applied in order to determine the stability for prolonged periods of time. For safety reasons, an isothermal TG is performed at the same conditions as the VST prior to the VST test. In this manner a situation is prevented during which a high gas evolution rate occurs during a VST test, since this might lead to an undesired ignition of the sample and possible damaging of the equipment. The VST test uses either a mercury column to measure the gas evolution of the sample or a pressure transducer which measures the pressure increase as a function of time as a result of the gases evolving from the sample due to *e.g.* sublimation, decomposition or other chemical reactions. The set-up with the pressure transducers allows a continuous monitoring of the pressure as a function of time.

The hazard properties are determined according to the BAM impact and friction sensitivity standards ('one out of six').

3. Results and Discussion

3.1 Theoretical calculations

In figure 1 the results of theoretical calculations are shown, illustrating that when AP is replaced by HNF in an HTPB based binder, an increase in performance of ~ 3-4% is found. Typical state-of-the-art AP based propellants posess a 86-88 wt% solid load (a space booster and a missile application, respectively).

3.2 Chimney burner

Several HNF/HTPB formulations with and without aluminium have been analysed by means of chimney burner testing. The observed burn rates versus pressure level for HHU-6 are shown in Figure 2. The test results are summarised in Table 2. A typical example of a propellant strand is shown in Figure 3. The HHU-2, 3 and 6 are un-catalysed, but the latter formulation contains aluminium whereas the former two are non-aluminised. These tests show that the burn rate exponent is ~ 1. The difference in r_7 for HHU-2 and HHU-3 (both non-aluminised) can be attributed to a higher solid load of HNF in the latter case. The batches HHU-4 and 7 are catalysed by means of 3 wt% burn rate modifier. In particular the catalyst used in HHU-7 shows that the burn rate exponent can be lowered from ~ 1 to 0.85. Further improvements may be possible by changes in the

burn rate modifier content and type or by the addition of co-oxidisers. These tests are planned in the near future.

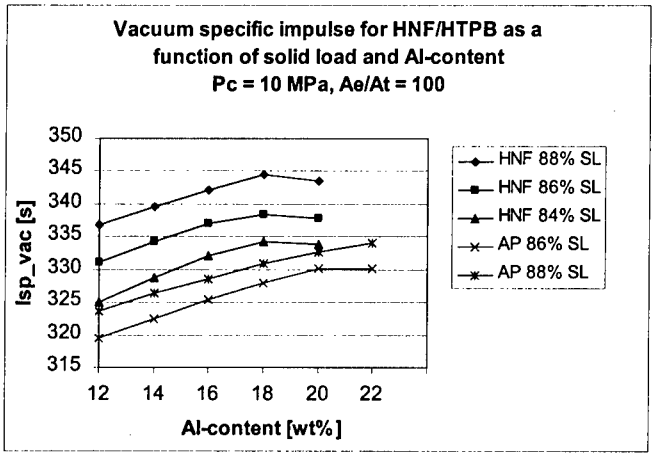


Figure 1: Vacuum specific impulse (in s) of different AP/HTPB and HNF/HTPB based aluminised propellants. The calculations have been performed as a function of Al-content and total solid load. This total solid load is indicated in the figure. The use of HNF replacing the conventional oxidizer AP leads to a significant increase in theoretical performance.

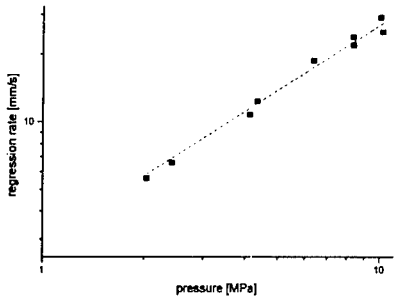


Figure 2: Typical example of chimney burner test results (HHU-6).

The burn rate exponents as determined by Fiat Avio show some scattering, which is either due to inhomogeneities in the samples (*e.g.* sedimentation effects) or due to the fact that the calculation of n is based on two data points, determined at two different pressure levels.

Table 2: Ballistic parameters as determined by chimney burner testing. For the tests by Fiat Avio the burn rate has been determined at two pressure levels; from the slope of the line connecting these two data points, the burn rate exponent n has been calculated.

Formulation	a	n	r_7 [mm/s]
TNO			
HHU-2	2.00	1.12	17.7
HHU-3	2.84	1.12	25.1
HHU-4	1.97	1.05	15.2
HHU-6	2.95	0.96	19.1
HHU-7	3.20	0.85	16.7
Fiat Avio			
CC22	–	1.07	–
CC22-1	–	1.22	–
CC22-2	–	1.27	–
CC22-3	–	1.06	–
CC22-4	–	1.24	–
CC22-5	–	1.26	–
CC22-6	–	1.28	–

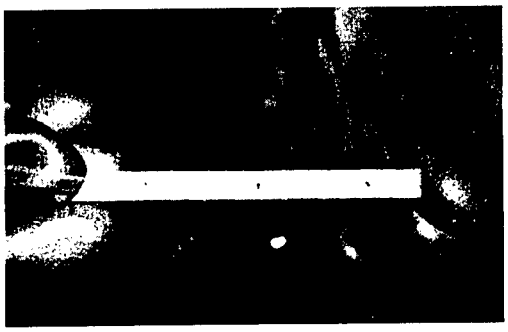


Figure 3: Typical example of an HNF/HTPB (non-aluminised) propellant strand, as used at TNO for determining the ballistic properties in a chimney burner test set-up.

3.3 Mechanical properties

The mechanical properties of several of the TNO and Fiat Avio samples have been determined by means of compression (TNO) or tensile tests (Fiat Avio) and Shore A hardness tests (both TNO and Fiat Avio). The results are presented in Table 3.

Note that the strain capacity, ε, and the strength, σ, cannot directly be compared between the TNO and Fiat Avio samples since these parameters have been determined under either compressive or tensile conditions. However, when comparing the results of the CC series of propellants, the results

are consistent and show a reasonable to good reproducibility. Observed differences in the mechanical properties of the HHU series are due to different solid loads and possible catalysing effects of the BRM's on the curing reaction. The latter was in particular observed forr HHU-7, which also had a significantly shorter pot-life during processing compared to the non-catalysed batch, HHU-6.

Table 3: Mechanical properties and Shore A values of a selection of propellants. Note: TNO compression tests, Fiat Avio uniaxial tensile tests.

Batch code	ε_{σ} max [%]	E_0 [MPa]	σ max [MPa]	Shore A @ 0 s / 15 s
TNO				
HHU-2	17.4	8.4	0.82	– / 52
HHU-3	13.6	8.2	0.73	– / 62
HHU-4	–	7.1	2.37 [a]	– / –
HHU-6	12.5	7.4	0.62	46 / 31
HHU-7	29.0	11.5	1.96	61 / 50
Fiat Avio	ε [%]	E_0 [MPa]	σ [MPa]	Shore A @ 0 s / 15 s
CC22	18.5	4.4	0.38	70 / 63
CC22-1	15.9	6.6	0.45	75 / 68
CC22-2	16.0	7.8	0.48	82 / 72
CC22-3	12.0	7.3	0.48	76 / 64
CC22-4	14.6	6.0	0.45	67 / 56
CC22-5	18.5	4.3	0.52	77 / 60
CC22-6	18.7	4.8	0.42	64 / 48

[a] σ at 60% strain.

When cutting the different propellant samples it was noticed that the bonding between the HNF particles and the binder is not very good: crystals are easily removed from the binder matrix. This indicates that bonding agents might be required to improve the binder/filler interaction. In spite of the bonding issue, the mechanical properties found sofar are considered reasonable, especially since no optimisation has been performed yet of *e.g.* the failure properties. The Shore A hardnesses observed, are comparable to state-of-the-art AP/HTPB composite propellants. See also reference [3] for more details.

3.4 Thermal stability and hazard properties

In table 4 the thermal stability and hazard characteristics of a selection of propellants is summarised. For reference purposes, some typical characteristic properties of HNF are included in this table as well.

The thermal stability data indicate that the use of specific BRM's may lead to an increase of the VST value as compared to a non-catalysed propellant, see *e.g.* HHU-2 (non-catalysed) and the catalysed propellants HHU-4 and HHU-7. This can also be concluded from the TG/DTA data, in particular for HHU-4 showing an onset temperature for decomposition of ~ 104 °C which is approximately 20-25 °C below the onset temperature found for a non-catalysed propellant (HHU-6) or pure HNF.

The friction sensitivity of the HNF/HTPB propellants shows higher values (less sensitive) than typical values of pure HNF (the results of grade HNF-C18 have been added for comparison). This is probably due to fixation of the HNF crystals in the binder matrix, herewith preventing direct contact with one another and reducing the sensitiveness of the propellant. The impact sensitivity of HNF/HTPB propellants is apparently determined by the impact sensitivity of HNF, since similar values for the propellant and the pure HNF samples have been found. No significant differences in the hazard properties of the non-aluminised and aluminised propellants have been observed.

Table 4: Thermal stability and hazard properties. For comparison some data on pure HNF are included.

Batch code	TG/DTA (scanning)				VST [ml/g]	Friction [N]	Impact [Nm]
HHU-2	No data				2.42 [a]	42	3
HHU-3	DTA		TG		5.36 [b]	36	2
	T onset dec.	124 °C	*T* onset dec.	125 °C			
	T peak dec.	131 °C	*T* extrapol onset	129 °C			
	Enthalpy dec.	-372 µVs/mg	Total mass loss	82 wt%			
HHU-4	DTA		TG		4.70 [c]	–	–
	T onset dec.	104 °C	*T* onset dec.	126 °C			
	T peak dec.	124 °C	*T* extrapol onset	–			
	Enthalpy dec.	–	Total mass loss	68 wt%			
HHU-6	DTA		TG		0.52 [c]	48	4
	T onset dec.	124 °C	*T* onset dec.	121 °C			
	T peak dec.	124 °C	*T* extrapol onset	124 °C			
	Enthalpy dec.	-507 µVs/mg	Total mass loss	70 wt%			
HHU-7	No data				1.20 [d]	–	–
HNF-C18	No data				0.19 [e]	16	2
HNF-C24	No data				0.15 [e]	–	–

[a] VST with mercury column, 100 hrs at 60 °C, duplicate measurement; after ~ 48 hrs: 1.10 ml/g.

[b] VST with mercury column, 100 hrs at 60 °C, duplicate measurement.

[c] VST with pressure transducers, 48 hrs at 60 °C, triplicate measurement.

[d] VST with mercury column, 48 hrs at 60 °C, duplicate measurement.

[c] VST with mercury column, 48 hrs at 60 °C (APP data, single measurement).

4. Conclusions

HNF based propellants are under study for their improved performance compared to state-of-the-art propellants. Recently, TNO and Fiat Avio prepared several series of HNF/HTPB propellant batches where the focus of TNO was on burn rate modification of an HNF/Al/HTPB propellant using BRM's whereas Fiat Avio characterised the use of the co-oxidiser AP to modify the ballistic properties of an HNF/Al/HTPB propellant. Based on the work perfromed, it can be concluded that it is possible to modify the burn rate properties with the help of a BRM (both the burn rate and the pressure exponent). The work performed on AP as a co-oxidiser did not yet lead to a conclusive statement about the quantity AP required in HNF/AP formulations in order to be a suitable alternative to reduce the pressure exponent of this family of propellants.

Acknowledgements

Part of the work presented here has been carried out by TNO-PML as subcontractor to Aerospace Propulsion Products (APP) under a European Space Agency's Contract Ref. 13239/98/NL/PA(SC).

List of abbreviations

AP	Ammonium Perchlorate
APP	Aerospace Propulsion Products
BRM	Burn Rate Modifier
ESA	European Space Agency
HNF	Hydrazinium NitroFormate
HTPB	Hydroxy-Terminated PolyButadiene
PML	Prins Maurits Laboratory
TNO	Netherlands Institute of Applied Scientific Research

References

[1] G.M. Low and V.E. Haury, *Hydrazinium nitroformate propellant with saturated polymeric hydrocarbon binder*, US Patent 3,708,359, January 2, 1973

[2] J. Louwers and A.E.D.M. van der Heijden, *Hydrazinium nitroformate based high performance solid propellants*, EP 0 959 085, May 20, 1998

[3] A.E.D.M. van der Heijden, H.L.J. Keizers and W.H.M. Veltmans, *HNF/HTPB based composite propellants*, presented at the 5-ISICP conference, June 2000, Stresa, Italy; to be published in an edited book entitled 'Combustion of Energetic Materials'

Explosive and Ballistic deactivating techniques for neutralizing of military ordnance and high explosive devices in the typical IEDD scenario.

by

Salem Al Ketbi, Ahwad Barshaid, and Saeed Alsaabi
Ordnance Training Center
Private Bag X1254
POTCHEFSTROOM 2531
Republic of South Africa
Fax Number: +27 (0)18 299 8729

Poster Presentation

Abstract:

Bomb disposal technology, in all its many forms, is used for identifying, neutralising and ultimately disposing of military ordnance and terrorist incendiary and explosive devices. Certain specialised devices and technical procedures enable the bomb disposal engineer to complete his delicate mission at minimum risk to life and limb.

Ballistic opening techniques using on-board firing devices like a single-shot disruptor or a water cannon provide the operator with a safe and effective weapon. The use of X-ray photography enables conclusions to be drawn concerning the interior composition of suspicious objects, providing vital decision making data.

Bombs and explosive devices may be neutralised using water disruptors minimising the danger to people and property and reducing the risk of breaking windows. A variety of

specialised disruptors are available, all designed for ease of operation and quick deployment.

The disruptors are able to disrupt or de-arm a wide range of hazardous objects. Thin-walled items as well as soft-walled objects can easily be penetrated by means of water or sand charges whilst thick-walled items, such as military ordnance, are de-armed by steel slugs.

The Pigstick Disruptor (EOD) is an established and well-proven piece of equipment developed as a means of disrupting thin walled improvised explosive devices (IEDD). It has been extensively used and has a high probability of avoiding detonation or explosion of the suspect device. The Pigstick (comprising a barrel mounted in a stand) is positioned using an anti-roll clamp to ensure accurate positioning. The equipment is initially loaded and then positioned adjacent to the IEDD. It can be tilted and finely adjusted. In operation an electrically detonated bridge-wire cap cartridge fires a slug of water at the mine case and explosives filling to disrupts the mine before it can explode.

The paper describes an experimental investigation into the detonation phenomena where an inert material is projected and accelerated by the explosives (in a closed system) to hydraulically disarm or disrupt a potentially dangerous explosive charge in the so-called "render safe" scenario.

Investigations were carried out to determine optimized pressure, and was then correlated to theoretical modeling predictions. Good correlation was obtained. Advantages are that the weapon is easy and simple to use, it is point-directed, and can be used against military and commercial explosives. It is being loaded with standard military ammunition. The weapon is 98% effective if used against the correct targets.

Precision required for parameters in thermal safety simulations

Uldis Ticmanis, Gabriele Pantel, Stephan Wilker, Manfred Kaiser

WIWEB, ASt Heimerzheim, Großes Cent, 53913 Swisttal (Germany)

Abstract

Thermal safety simulation of ammunition requires the input of **explosive data** (heat generation, heat conductivity, loading density, geometry), **system data** (heat transfer to the environment) and **ambient data** (temperature, time). The influence of these parameters on the **critical conditions** of **thermal explosion** (diameter, temperature, time) was examined by varations in relevant ranges. The resulting go / no go-curves were used for the assessment of total errors in simulation of real systems.

Kurzfassung

Simulation der thermischen Sicherheit von Munition erfordert die Eingabe von Daten des **Explosivstoffs** (Wärmeproduktion, Wärmeleitfähigkeit, Ladedichte, Geometrie), des **Systems** (Wärmetransfer an die Umgebung) und der **Umgebung** (Temperatur, Zeit). Der Einfluss dieser Parameter auf die **kritischen Bedingungen** der **Wärmeexplosion** (Durchmesser, Temperatur, Zeit) wurde durch Variieren in relevanten Bereichen untersucht. Die erhaltenen go / no go-Kurven ermöglichen die Abschätzung der Gesamtfehler bei der Simulation realer Systeme.

1 The relevance of thermal safety simulations

Resulting from many calculations our assessment is, that regularly produced gun propellants are safe, even in the largest diameter applications and under considerable thermal stress [1, 2, 3, 4]. Only low stability double base gun and rocket propellants which are used in large diameter ammunitions are worth being considered in thermal safety simulations. A further relevance remains for extreme storage conditions on a battlefield or for emergency situations like fire.

If, however, a simulation is felt to be necessary, one should know which precision is required for the input parameters to achieve reliable results.

2 Simulation software

For the simulations we used a commercially available program based on the heat transfer model of THOMAS [5] in an extended version of OPFERMANN [3, 6], allowing to formulate the heat generation of the explosive (decomposition kinetics), realistically by up to four reactions.

3 Definition of a standard cartridge and of the variation ranges

The parameter values selected as standard are listed in table 1.

TABLE 1. Parameter values for a standard cartridge

Parameter	Value	Meaning
Maximum heat generation [µW/g]	1500 at 89°C	Characteristic for a propellant with a moderate autocatalytic decomposition
Heat conductivity [W/(cm·K)]	0.001	Typical of grain propellants
Loading density [g·cm^{-3}]	1	Typical of grain propellants
Specific heat [J/(g·K)]	1.2	Characteristic for NC/NG based propellants
Heat transfer [W/(cm^2·K)]	0.01	Corresponding to a cartridge in a thermally insulated package

The kinetics were modelled by three independent reactions. The equations and parameter values are listed in Appendix 1. Figure 1 shows the simulation of a heat flow measurement of the propellant in a calorimeter at 89°C (small diameter, high heat transfer). The lines are representing the temperatures in different distances from the centre (upper line = 0 %, then 20%, 40%, 60%, 80%, 100% (= surface) and ambient temperature).

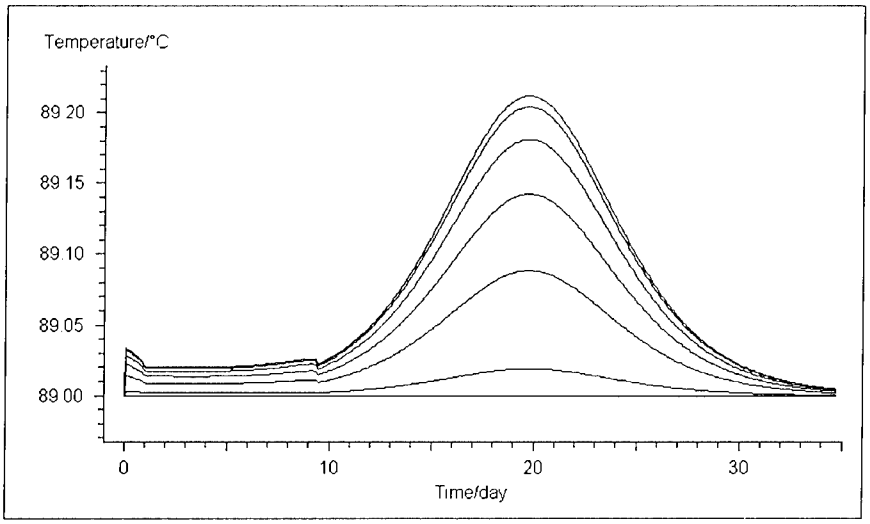


Figure 1. Simulation of a 10 mm cartridge at 89°C in a calorimeter

The maximum heat generation was modified by covariation of the frequency and the autocatalytic factor in reaction 3 keeping the reaction heat and time to maximum rate constant.

The chosen parameter variations are summarized in table 2.

TABLE 2. Variation ranges of the parameters

Parameter	Range	Meaning of lower limit	Meaning of upper limit
Maximum heat generation [µW/g]	500 - 5500 (at 89°C)	Propellant with a soft autocatalytic decomposition	Propellant with a relatively strong autocatalytic decomposition
Heat conductivity [W/(cm·K)]	0.0005 – 0.0080	Porous propellant	Rocket propellant containing conductive materials like boron
Loading density [g·cm^{-3}]	0.4 – 1.8	Porous propellant	High density rocket propellant
Specific heat [J/(g·K)]	0.9 – 2.5	Value at low temperatures	Possible value at high temperatures
Heat transfer [W/(cm²·K)]	0.001 – 10	Cartridge in a highly insulating package	Small calibre cartridge in a thin metallic shell

4 Simulation series

In every single simulation only one parameter was modified, whereas the others were kept constant at the values of table 2.

In series A the cartridge was set momentarily at 71°C, the temperature commonly used for testing long time stability of explosives [7]. The critical diameter in dependence of the parameter values was determined within a tolerance of 10 mm. The figures 2 and 3 illustrate the simulation of the „standard cartridge" shortly below and above the critical diameter. The results are presented in figure 4, where for a better comparison the diameter axes were kept equal. The upper points in the graphs mark an explosion, the lower a non explosion.

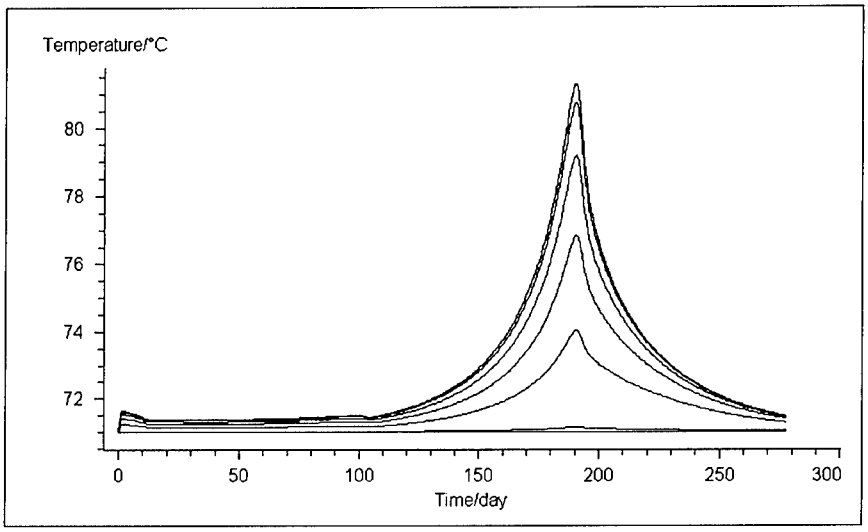


Figure 2. Simulation of a 210 mm cartridge at 71°C

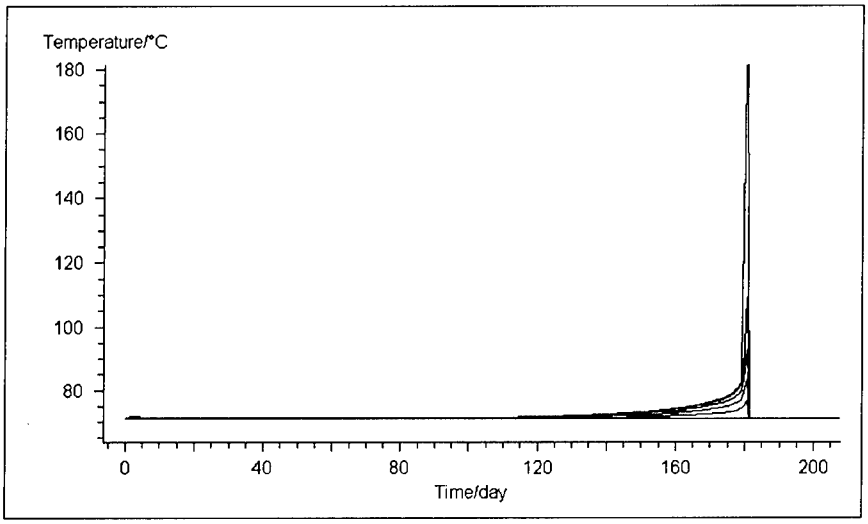


Figure 3. Simulation of a 220 mm cartridge at 71°C

In series B the diameter was fixed at 100 mm and the critical temperature in dependence of the parameter values was determined with a precision of at least 1°C. The results are shown in figure 5.

Finally, in series C the results of series B are plotted against the corresponding critical time (Figure 6). Since higher temperatures lead to shorter times the slopes of the curves are inverted.

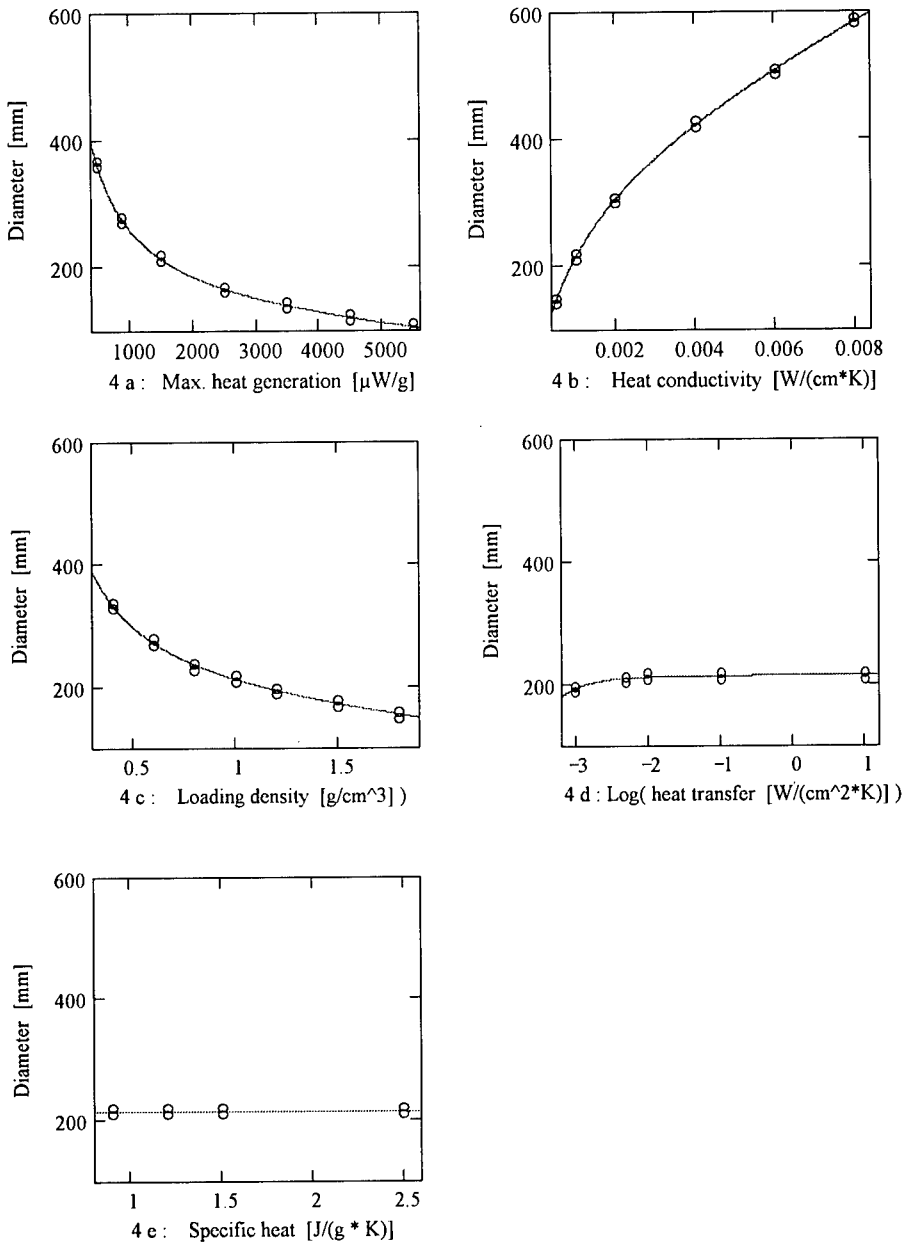


Figure 4. Critical diameter at 71 °C (series A)

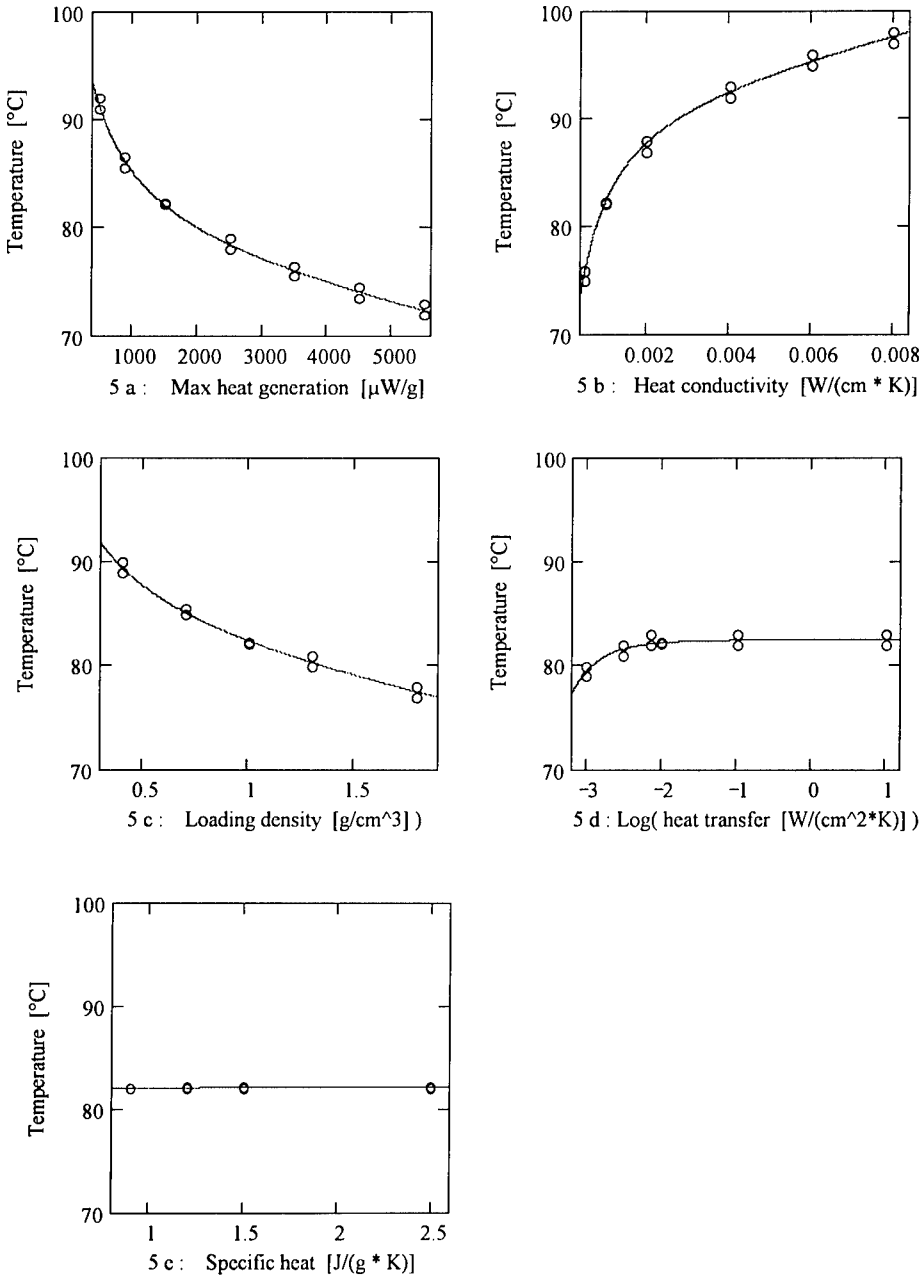


Figure 5. Critical temperature of a 100 mm cartridge (series B)

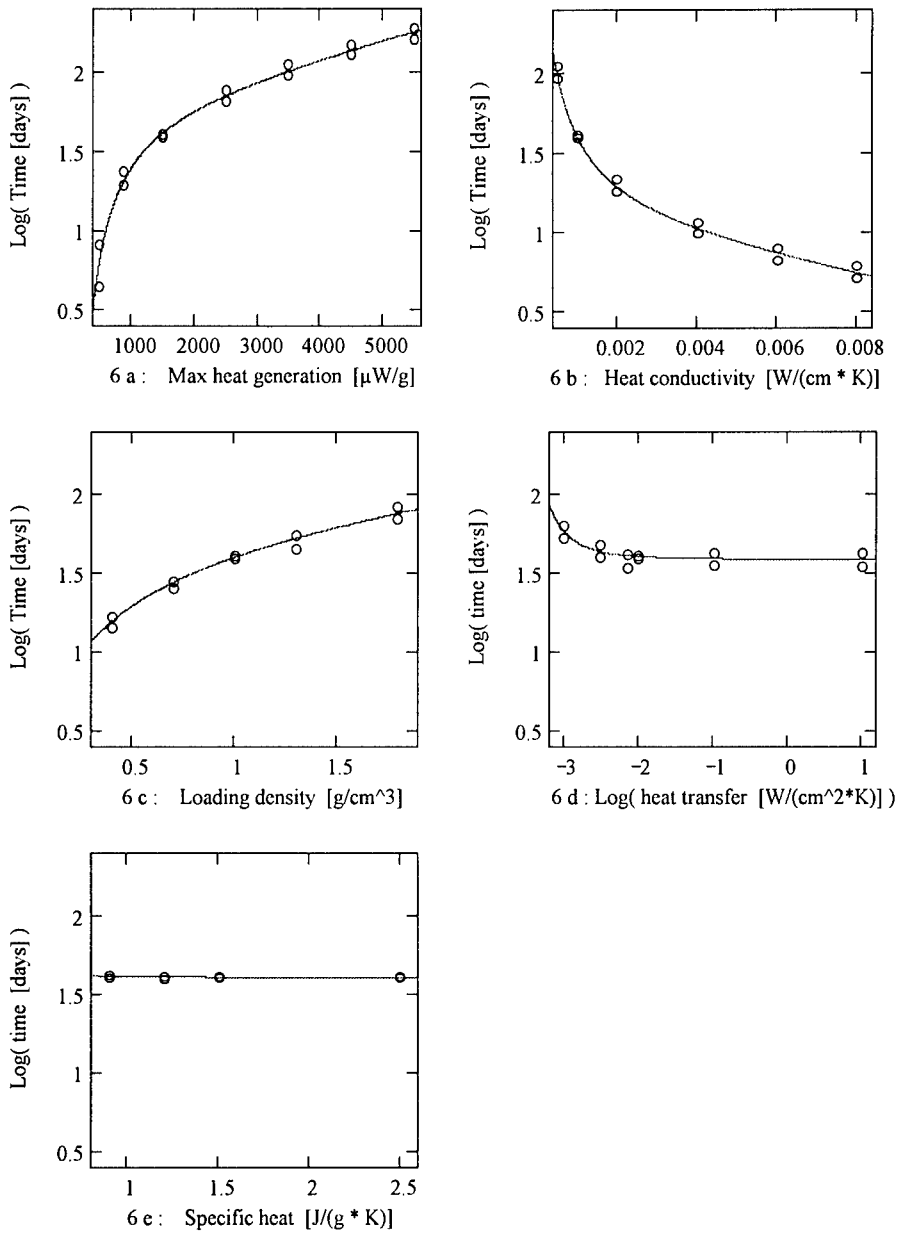


Figure 6. Critical time of a 100 mm cartridge (series C)

5 Qualitative summary of the results

Comments on the influence of the parameters on the critical conditions are given in table 3. Of course, they are valid only within the tested ranges (Table 2). The importance of the maximum heat generation is strongly underestimated because at the moment our program is unable to calculate really existing extremely autocatalytic reactions like those of some propellants containing high amounts of NG [1] (at moderate temperatures these propellants are nevertheless stable for very long periods).

TABLE 3. Influence of the parameters on critical conditions

Parameter	Influence
Maximum heat generation [µW/g]	Strong
Heat conductivity [W/(cm·K)]	Strong
Loading density [g·cm^{-3}]	Moderately strong
Heat transfer [W/(cm^2·K)]	Weak
Specific heat [J/(g·K)]	Negligible

The specific heat is as long of very low influence on the critical diameter and temperature as the total decomposition heat (about 2000 J/g) is considerably larger than the heat needed to increase the temperature up to explosion conditions (less than 200 J/g). The equally low variation of the critical time is due to the relatively short autocatalytic acceleration period and the assumed starting situation of the simulations where the cartridge was set momentarily at test temperature. If a simulation starts at room temperature the „warm up" time is considerably influenced by the specific heat.

6 Assessment of simulation errors

The curves in the figures 4, 5 and 6 are derived from data fitting using hyperbolic functions (Appendix 2). From these and the corresponding inverted functions we calculated relative parameter errors causing 1 % errors in critical diameter, (Celsius) temperatures and time (table 4). The smaller the tolerable parameter error is, the more precision is required for the parameter value.

TABLE 4. Relative parameter errors $F_{r,x}$ causing 1% errors of critical diameter, temperature and time

Critical quantity	Parameter x	Value	$F_{r,x}$ [%]	Value	$F_{r,x}$ [%]	Value	$F_{r,x}$ [%]
Diameter [mm]	Max. heat generation [µW/g]	500	2.18	1500	2.03	5500	1.36
	Heat conductivity [W/(cm·K)]	0.0005	1.73	0.001	1.84	0.008	2.01
	Loading density [g·cm^{-3}]	0.4	1.91	1.0	2.06	1.8	1.58
	Heat transfer [W/(cm²·K)]	0.001	8.91	0.01	149	10	32000
Temperature [°C]	Max. heat generation [µW/g]	500	9.71	1500	11.1	5500	7.92
	Heat conductivity [W/(cm·K)]	0.0005	7.44	0.001	9.27	0.008	11.14
	Loading density [g·cm^{-3}]	0.4	11.4	1.0	10.5	1.8	9.07
	Heat transfer [W/(cm²·K)]	0.001	22.6	0.01	330	10	80300
	Specific heat [J/(g·K)]	0.9	596	1.2	849	2.5	3700
Time [d]	Max. heat generation [µW/g]	500	0.354	1500	0.886	5500	0.686
	Heat conductivity [W/(cm·K)]	0.0005	0.709	0.001	0.840	0.008	0.912
	Loading density [g·cm^{-3}]	0.4	0.974	1.0	0.962	1.8	0.856
	Heat transfer [W/(cm²·K)]	0.001	1.82	0.01	32.2	10	3300
	Specific heat [J/(g·K)]	0.9	13.8	1.2	55.6	2.5	2510

It is obvious that in all three simulation series the sequence of the parameter influence is the same and as mentioned in table 3.

Comparing the series the required precision of the parameters generally increases from critical temperature to diameter and time.

Finally an example for calculation of the total errors in critical conditions may demonstrate the unsafeness when simulating a real system. Neglecting the ‚low influence' parameters (heat transfer and specific heat) and the easily calculable loading density, let us assume that both maximum heat generation and the heat conductivity are determined within an error of 5 %. Taking the lower values from table 4 the calculation results are listed in table 5.

TABLE 5. Typical total errors of simulations

Caused by	Error in critical diameter [%]	Error in critical temperature [%]	Error in critical time [%]
Error of max. heat generation	5/1.36 = 3.68	5/7.9 = 0.63	5/0.35 = 14.29
Error of heat conductivity	5/1.73 = 2.89	5/7.4 = 0.68	5/0.71 = 7.04
Max. total error	6.6	1.3	21

Practically the assumed experimental precision is hard to reach. This means that the errors in simulating critical conditions of thermal explosion may even be considerably larger.

References and Notes

[1] U. Ticmanis, S. Wilker, G. Pantel, M. Kaiser, P. Guillaume, C. Balès, N. v.d. Meer, „Principles of a STANAG for the estimation of the chemical stability of propellants by heat flow calorimetry", *ICT-Jahrestagung* 31, 2 (**2000**).

[2] MIL-STD 331B, „Environmental and Performance Tests for Fuze and Fuze Components", Ed. **1989**.

[3] STANAG 4582, „Explosives, Single and Double Base Propellants, Stability Test Procedure and Requirements using Heat Flow Calorimetry", WG Draft (**9/00**).

[4] U. Ticmanis, G. Pantel, M. Kaiser, „Simulation der chemischen Stabilität eines zweibasigen Kugelpulvers", *2. Int. Workshop Mikrokalorimetrie WIWEB*, p. 182-195 (**1999**).

[5] U. Ticmanis, G. Pantel, L. Stottmeister, „Stabilitätsuntersuchungen einbasiger Treibladungspulver – Mikrokalorimetrie im Grenzbereich", *ICT-Jahrestagung* 29, 27 (**1998**).

[6] P.H. Thomas, *Trans.Faraday Soc.* 54, 60-65 (**1942**).

[7] J. Opfermann, Manual for the Computer Program „Netzsch Thermal Safety Simulation", Edn. **2001**.

APPENDIX 1. Kinetics for modelling propellant decomposition

n - order reaction $$P = \Delta H * k * 10^6 * [1 - (1-n) * kt]^{\frac{n}{1-n}} \quad (1)$$

1st order with autocatalysis $$P = \Delta H * a^2 * k * 10^6 * \frac{e^{akt}}{(e^{akt} - 1 + a)^2} \quad (2)$$

Arrhenius equation $$k = A * e^{\frac{-E}{RT}} \quad (3)$$

P	=	Heat generation rate	[µW/g]
t	=	Reaction time	[s]
T	=	Temperature of reaction	[K]
k	=	Reaction rate constant	[s^{-1}]
A	=	Frequency factor	[s^{-1}]
R	=	Gas constant	0,0083143 kJ/(K·mol)
E	=	Activation energy	[kJ/mole]
n	=	Reaction order	-
a	=	Accelerating factor	-

Parameter values of the three independent reactions

Reaction N°	Equation N°	log A	E	n	log a	ΔH
1	1	15.4782	140	0.4	-	4.995
2	1	24.4050	140	0.25	-	88.367
3	2	11.7946	140	-	3	1499.638
total						1593.000

APPENDIX 2. equations used for fitting the go / no go points

$$y = a + \frac{b}{x^n} \qquad (1)$$

$$y = a + \frac{b}{(x+c)^n} \qquad (2)$$

$$y = a + bx + \frac{c}{x+d} \qquad (3)$$

Series	y	x	equ.	a	b	c	d	n
A	diameter	P_m	3	1.157E+2	-8.130E-3	1.963E+5	2.75E+2	
		λ	3	3.940E+2	3.048E+4	-5.100E-1	1.43E-3	
		S	3	1.715E+2	-3.196E+1	7.679E+1	3.50E-2	
		lg D	2	2.155E+2	-2.564E+7	7.07E+0		10
		C	const					
B	temp.	P_m	3	7.744E+1	-1.302E-3	1.226E+4	3.36E+2	
		λ	3	9.249E+1	8.747E+2	-1.554E-2	3.94E-4	
		S	3	7.833E+1	-2.770E+0	8.977E+0	3.30E-1	
		lg D	2	8.253E+1	-1.441E+6	6.695E+0		10
		C	1	8.2326E+1	-1.3433E-1			1
C	lg time	P_m	3	1.799E+0	9.900E-5	-4.794E+2	-4.90E+1	
		λ	3	1.019E+0	-4.711E+1	8.658E-4	3.57E-4	
		S	3	1.788E+0	1.756E-1	-4.734E-1	3.10E-1	
		lg D	2	1.590E+0	5.111E-1	4.300E+0		4
		C	1	1.6106E+0	3.9201E-3			5

P_m = maximum heat generation at 89°C [µW/g]

λ = heat conductivity [W/(cm·K)]

S = loading density [$g \cdot cm^{-3}$]

D = heat transfer [$W/(cm^2 \cdot K)$]

C = specific heat [J/(g·K)]

FORMATION OF STRUCTURAL AND PHYSICOCHEMICAL CHARACTERISTICS OF CELLULOSE NITRATES

Valerii I. Kovalenko, Eugeny L. Matukhin, Grigorii M. Khrapkovskii

Kazan state technological university
K. Marx st. 68, Kazan 420015. Russia. E-mail: koval@iopc.kcn.ru

Abstract. New quantitative data on kinetics of changes of the basic physicochemical properties of nitrates in the course of their synthesis: nitrogen content, molecular mass, degree of structural and chemical heterogeneity, chemical stability are given. The regularities of esterification processes in various media, destruction and denitration under the influence of various physicochemical factors, such as treatment in subacid, subalkali and neutral media, radiations *ets*, have been investigated in considerable detail. Major attention is given to the influence of physical cellulose treatment on the formation of basic physicochemical properties of nitrocellulose. It is noted, that the selection of modes of esterification, removal of used acids and stabilization, which takes into account the conditions of physical modification, makes it possible to obtain the materials with predetermined characteristics on the molecular mass magnitude and even, in a number of cases, to achieve the prescribed parameters of chain-length distribution.

Recently, a number of detailed investigations of cellulose and including CN [1], have been carried out. The major reason for this lies in the growing range of CN application, in particular, in their extensive use for the production of selective sorbents, biological membranes, detectors of ionizing radiations.

The investigations of cellulose fine molecular structure have been recently stimulated by the development of high-informative methods of molecular spectroscopy, such as the method of nuclear magnetic resonance with high resolution on nuclei C^{13} and N^{15} and infra-red Fourier spectroscopy method [2].

Novel interesting data were obtained while investigating kinetics and mechanism of cellulose nitration by various acid mixtures on the basis of nitric acid [2]. At present, there are also quite detailed data on kinetics of thermal decomposition, acid, basic and neutral CN hydrolysis [2-4].

However, there is still a considerable lack of both theoretical and applied researches, related to the study of changes in obtaining CN, its structural parameters and physico-chemical characteristics determining the consumer properties, such as thermal

decomposition rate, magnitude of molecular mass and other parameters of chain-length distribution, solubility etc. .

In the present communication the authors analyse some results obtained on studying the changes of CN molecular heterogeneity under various conditions of synthesis, as well as the quantitative data on thermal decomposition rate and change of molecular mass in the process of CN stabilization. The obtained results are of a certain interest, in particular, for stimulating further researches in this perspective and important direction.

Considerable spread of physico-chemical CN parameters, such as solubility, plasticizability at identical substitution directly points to the influence of molecular-structural heterogeneity. The composite heterogeneity of CN can be calculated on the data of C^{13} NMR-spectroscopy of high resolution. In works [1,5-8] the concept of CN molecular-structural heterogeneity, allowing to compare CN, obtained in various nitration conditions has been proposed. The suggested approach is based on determining Δ_i^e deviations of the experimentally calculated parts of each type of elementary α_i^e CN links from calculated α_i^0 for hypothetical extreme homogeneous CN of the same substitution degree, namely $\Delta_i^e = | \alpha_i^e - \alpha_i^0 |$, where α_i is a part of glucopyranose links, the index i = 0, 1, 2, 3 designates a type of an elementary link: not substituted, mono-, di-, trisubstituted accordingly. The sum of $\Sigma\Delta_i^e$ for CN of the given substitution degree is the measure of composite heterogeneity.

It is convenient to consider not absolute, but relative composite heterogeneity $N_r=\Sigma\Delta_i^e/\Sigma\Delta_i^c$, where $\Sigma\Delta_i^c$ is a composite heterogeneity in the case of homogeneous nitration, which is calculated in the same way.

The comparison of the results with the data on the composition of nitrating acids [1] shows, that the composite heterogeneity regularly decreases in full conformity with the content of nitronium ions in acid mixtures.

The maximum NO^+_2 content is observed in nitronium salt solution in sulfolane, the concentration NO^+_2 in the subsequent mixtures gradually decreases up to 1 % in anhydrous nitric acid and further in other mixtures, from aqueous HNO_3 the ion of

nitronium being absent [1]. Cellulose nitration process can be considered [2] as a combination of three parallel-serial proceeding processes:

1. diffusion of nitrating mixtureture in a polymeric matrix
2. formation of active pairs
3. interaction of active pairs (actual nitration)

These processes are followed by cross diffusion of particles (molecules, ions) and low-molecular products of reaction from microzones of nitrating cellulose. Since the rate of actual nitration (process 3) is higher than the rate of the former two processes 1 and 2, the composite heterogeneity of CN obtained will depend on the ratio of these rates. In mixtures $HNO_3 + N_2O_5$ и $HNO_3 + N_2O_5 + N_2O_4$ there is a plenty of N_2O_5 (up to 3 mol/l [5]) and, consequently, the heterogeneity, close to the maximum, is quite explanable (Nr varies from 2.0 to 1.3).

In mixtures $HNO_3 + H_2SO_4 + H_2O$ there is a considerable spread of composite heterogeneities, reflecting the change of nitronium ion content depending on the structure of nitrating mixtures. Topochemical character of nitration process by mixture $HNO_3 + H_2SO_4 + H_2O$ clearly demonstrates X-ray diffraction data: at the achievement of substitution degree (DS) 1.4 there appear indications of CN crystalinity, whereas the crystalinity of unnitrated cellulose disappears only at DS $\approx$ 2.0. At the use of anhydrous acid mixturetures CN crystalinity on X-rayograms appear at DS $\approx$ 1.0, at which level the crystalinity of unnitrated cellulose is still preserved.

Nitration of anhydrous nitric acid in dichlorethane results in the production of homogeneous CN, irrespective of the ratio of mixture components. According to the spectral data, in this system nitronium cation is absent [1]. The relative uniformity of these CN variate around unitity. The process of quasi-homogeneous nitration takes place [8]. In contradistinction to nitration by systems containing a significant amount of nitronium ions, the similar process in system $HNO_3 + H_2SO_4 + H_2O$ even at DS $\approx$ 0.1 results in utter annihilation of crystalline cellulose reflexes, whereas the occurance of CN crystallinity is observed at DS $\approx$ 1.0 for structure 70% HNO_3 + 30% CH_2Cl_2.

It should be noted that there undoubtedly exists a relationship between ion-molecular structure and morphology of cellulose matrix: in the presence of a significant amount of nitronium ions in initial nitrating mixture the structural changes of nitrating cellulose matrix are insignificant (system cellulose + HNO_3 + H_2SO_4 + H_2O) and, on the contrary, the molecular form of nitric acid substantially "homogenates" cellulose matrix, facilitating the process of nitrating mixture diffusion and thereby creating the preconditions for quasi-homogeneous nitration by means of occurrence of active pairs (system cellulose + HNO_3 + CH_2Cl_2). A variation of nitration conditions, which can influence not only the formation of active pairs, but also the diffusion rate of nitrating mixture at the expense of parameter changes of polymer matrix, can at other equal conditions considerably change CN heterogeneity.

Cellulose nitration usually proceeds in two stages: the first goes on quickly and the second appreciablly slower [1,8]. It is obvious, that the first stage occurs on the mechanism caused by the presence (or absence) of nitronium ions in initial nitrating mixture. It accordingly determines a level of composite heterogeneity of the produced cellulose nitrate. As to the second, slow stage, here situation is less certain: the change of structure of the reaction mixture can cause the change of the nitration mechanism, as well as the change of the rates of nitrating agent diffusion. It is obvious, that the process of diffusion of the particular nitrating agent in molecular matrix should be an obligatory constituent of unhomogeneous cellulose nitration model. The creation of such a model needs, first of all, a prolonged analysis of ion-molecular composition of nitrating mixtures to know by what ways the initial stage will proceed (quasi-homogenious or topochemical nitration). Secondly, it is important to know, if the mechanism of nitration is preserved or changes on the second, slower stage, when in microzones there appear low-molecular products of reaction, it is also important to know how they diffuse from microzones. Thirdly, it is necessary to control the variations of the morphology of the polymer matrix at the increase of substitution degree of the forming nitrate matrix. The solution of these three tasks will allow to create strict model of diffuse-kinetic nitration of cellulose. Now

available are only the first, though very interesting results realized by the model, diffusion stages of nitration process being audibly taken into account [9,10].

The cellulose nitrates purified from admixtures are chemically steady compounds irrespective of substitution degree. The study of the kinetics of thermal decomposition of samples with substitution degree varying from 1.9 to 2.7 (this interval contains practically all kinds of commercially used CN) shows, that they differ poorly in the magnitude of thermal decomposition activation energy, measured at the initial (non-catalytic) stage of the process. At the same time it has been noted, that the value of activation energy decreases with the growth of substitution degree. As it is known, the similar dependence is observed for nitroesters of polyatomic spirits having primary and secondary nitrate groups [3,4]. In works [4,11] it has been shown, that the value of O-N-bond dissociation energy in nitroesters at the transition from mononitro- to trinitroesters decreases by 3 kcal/mol, which is in good agreement with the available experimental data [4].

The magnitude of CN activation energy is effected by chemical structure of elementary link, in particular, by the change of substitution degree. In work [1] it has been shown, that in a wide interval of nitrogen contain change (from 11.8 to 13.8 %) there is a linear reduction of activation energy with the growth of substitution degree, which is observed with satisfactory preciseness. By extrapolating the experimental dependence we have obtained the estimation of activation energy for 6-mononitrate of cellulose in 45 kcal/mol. Experimental [12] and calculated [4] data indicate significant distinctions in rate of thermal decomposition in primary and secondary CN nitrate groups. That is why the initial event of thermal decomposition of all CN samples (with the exception of 6-mononitrate) is obviously connected with the opening of $O\text{-}NO_2$ at C_2, which is indicated by the data of CN thermodestruction study with the use of NMR spectroscopy of high resolution on C^{13} nuclei, as well as the result of theoretical research with the use of quantum-chemical methods [4].

Basing on the data of the study of the kinetics of thermal decomposition it is possible to assert, that CN is a stable enough compound capable of decomposing with appreciable rate at the temperature range 100 - 120 °C and higher [3,13]. At the same

time, the unstable admixtures of various nature getting into the sample in the process of synthesis, substantially increase the rate of CN thermal decomposition and cause the need for carrying out additional stage of stabilization within the framework of CN production technological process.

At present, the admixtures increasing the rate of CN decomposition are established and characterized: they are, first of all, sulfuric and nitric acid, nitrates absorbed during manufacturing, sulfoesters of cellulose, which can easily be formed as side products of interaction of cellulose and sulfuric acid, present in significant amounts in threefold mixture $HNO_3 + H_2SO_4 + H_2O$. Cellulose sulfoesters are to differ substantially by a much higher rate of thermal decomposition, as compared to CN. Using various methods, including X-ray electron spectroscopy, we have defined the content of cellulose sulfoesters in CN with different substitution degrees. It is noted that at the increase of nitrogen content in CN, the amount of sulfoesters is reduced, however at that the content of absorbed sulfuric acid in samples substantially grows. As a result the rate of thermal decomposition of CN samples is increased, the same process taking place at the initial nonautocatalytic stage.

For a long time in literature there was practically no information about the changes of the rate of thermal decomposition in the prosess of stabilization except for the data on the final stage of this process. In the last 10 - 15 years there appeared the first quantitative data, which allow to discuss some general regularities of the formation of chemical stability. Further we give the results obtained in the investigation of CN with identical substitution degree (≈2.4), prepared from cotton cellulose (sample 1) and wood cellulose differing in density of fibres in the material (samples 2 and 3). After synthesis the major bulk of the residual acid mixture was replaced from the samples. The content of absorbed acid present in samples was close enough (0.7 - 1.0 %). Samples were stabilized in identical conditions according to standard modes including the treatment in weakly acidic, wealky alkaline media.The study of thermal destruction was carried out in the interval 75 - 140 °C under the control of total gas release, heat release (calorimetry), and by chromatographic method, with the use of which the major results were obtained. The

content of CO_2, CO, NO, N_2O, N_2 was analyzed in the products of decomposition. Gaseous products were replaced from the reaction zone in 5 - 10 minutes. For calculation of kinetic parameters the volumes of analyzed gaseous products evolved at the complete decomposition of samples were determined [14-16].

Fig. 1 shows the kinetic curves of CO_2 evolving at the initial stages of the sample made from wood cellulose (sample 3). Of the similar character are the curves obtained in the investigation of CN, which have gone through the identical stabilization cycle and from other sorts of cellulose (samples 1 and 2).

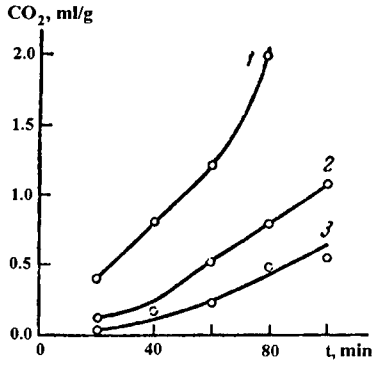


Fig. 1. Kinetic of decomposition of CN at 90 °C after processing in weakly acidic medium: *1* - 1.5h, *2* – 10h, *3* – 15h.

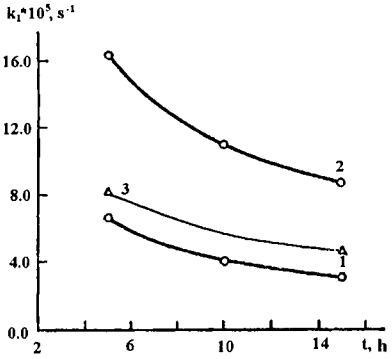


Fig. 2. Change of a constant of speed of decomposition at 90 °C depending on duration of processing in weakly acidic medium (sample **1** – cotton cellulose, samples **2** and **3** – wood).

Thermal destruction of CN samples, which have been treated in weakly acidic media up to the depth of η decomposition about 10 %, is satisfactorily described by autocatalysis equation of the second order:

$$\frac{d\eta}{dt} = k_1(1-\eta) + k_2(1-\eta)\,\eta^2$$

The initial rate of decomposition of CN samples drops with the increase of duration of their treatment in weakly acidic media. The samples made of wood cellulose

(2, 3) decomposed more quickly and those made from cotton (1) did it more slowly (fig. 2).

The values of constants obtained on accumulation of various final gaseous products, somewhat differ. At the same time, the activation energy found from the temperature dependences (fig. 3), is practically identical in the evolving processes for all analyzed gaseous thermal destruction products. After 5 hours of treatment in weakly acidic medium it makes up 24 kcal/mol and with the increased duration of treatment up to 15 hours it grows to 29 kcal/mol. The increase of the duration of treatment is accompanied by a substantial (approximately doublefold) reduction of the initial rate of decomposition (fig. 2).

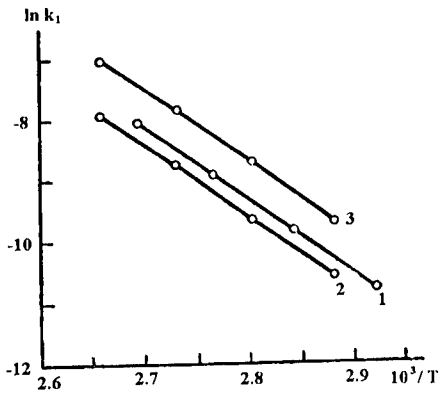


Fig. 3. Dependence of a constant of speed of an initial stage of decomposition CN after five-hour processing in weakly acidic medium from temperature (sample **1** – cotton cellulose, samples **2** and **3** – wood).

The value of activation energy of thermal decomposition of samples, treated in weakly acidic medium for 5 hours practically coincides with the activation energy of acid nitroester hydrolysis and neutral CN hydrolysis[13]. That is why it is thus obvious, that the thermal destruction of the sample at the initial stage of stabilization is exclusevely caused by acidic hydrolysis, occurring at the expense of sulfuric acid, not removed from fibres [14]. The differences of the constants of rates of thermal decomposition of CN, made from various sorts of cellulose (samples 1 - 3) are coused both by unequal amount

of residual acid, and by the various rate of its removal in the process of stabilization. Judging from the obtained data, the removal of sulfuric acid at the treatment of samples made from cotton cellulose in weakly acidic medium takes place more intensively, than in the case of samples made from wood cellulose (samples 2, 3). It should be noted, that this assumption is proved by the results of the direct analysis of changes of residual acid content in the process of stabilization [17]. In work [14] it has been shown, that basing on the data of the kinetics of thermal decomposition at the first stage of stabilization caused by acid hydrolysis and using available information about the content of residual acid and material dementions, it is possible to estimate the coefficient of diffusion of sulfuric acid from CN, which, for example, was found to be equal to 2.1×10^{-9} sm^2/sec.

The subsequent treatment in weakly alkiline acid essentially reduces the rate of CN thermal decomposition. This is coused first of all by the substantial reduction of sulfuric acid concentration. In this case, alongside with acidic hydrolysis the increasing contribution to the magnitude of activation energy of the initial (noncatalytic) stage of decomposition is made by the radical decomposition related to the opening of NO_2-bond at the destruction of secondary HCO-NO_2-group at C_2.

At the final stage of stabilization (after grounding) the process of thermal decomposition at the initial stages is satisfactorily described by the equation of the first order. Some data on the changes of decomposition rate in the prosess of stabilization are given in tab. 1.

Tab. 1 Basic kinetic characteristics of thermal decomposition rate of CN samples at various stages of stabilization

The samples investigated	lg k_1, s^{-1}	E_1, kcal/mol	lg k_2, s^{-1}	E_2, kcal/mol
5 hours in weakly acidic medium				
Sample 1	10.14	23.78	4.5	12.98
Sample 2	10.4	23.97	4.5	12.64
Sample 3	10.56	23.78	6.2	15.18
10 hours in weakly alkaline medium				
Sample 1	12.60	30.11	4.4	12.91
Sample 2	12.82	30.11	4.5	12.91
Sample 3	12.95	30.11	4.6	12.91

The samples investigated	lg k_1, s^{-1}	E_1, kcal/mol	lg k_2, s^{-1}	E_2, kcal/mol
	10 hours in the process final stabilization			
Sample 1	16.68	41.11	-	-
Sample 2	16.88	41.11	-	-
Sample 3	16.94	41.11	-	-

It should be noted, that the destruction of nitroesters and sulfonitroester of cellulose is obviously not the only reason for the reduction of thermal stability of CN. It has been established, for example, that the rate of thermal decomposition of CN can essentially differ in the cases when, according to the data of the analysis there is no sulfuric acid in samples. Under these conditions negative influence can be exerted by low-molecular CN, in which there is a significant amount of oxidated groups of different nature. At the same time it is known, that the presence of nitrocompounds (including nitroesters) of carbonyl groups in molecules can result in substantial reduction of dissoiciation energy C-N-bond , as well as the dissociation energy of $O-NO_2$-bond [4]. This factor of the reduction of thermal stability can become very important while carrying out the high-temperature stabilization of colloxylines, used for manufacturing various paintwork materials. The material given in this part shows, that now there is an opportunity to describe quantitatively the change of chemical stability at CN stabilization, using the data on the kinetics of thermal decomposition and changes of acid content. These data can be used for the creation of modern diffuse model of CN stabilization.

If the homogeniety of CN is basically formed in the process of synthesis, and the chemical stability, which is quantitatively measured by the rate of thermal decomposition, increases in the process of stabilization, then the viscosity of the solutions and the parameters of chain-length distribution of CN depend not only on modes of nitration and stabilization, but also (to a substantial degree) on the peculiarities cellulose used, on the conditions of its preparation and subsequent treatment [4,18].

The essential change of chain-length distribution is known to be observed in the process of cellulose esterification, coefficient of CN polydispercity M_w/M_n can amount the value of 4 and more.

The experimental data on the study of polydispercity in the process of cellulose esterification штвшсфеуы selective character of destruction, which disproves the casual character of openings. At the same time, the quantitative description of experimental data on hydrothermal CN destruction in the process of stabilization, namely at the temperature range 120-140 °C can be carried out on the basis of statistical analysis of the molecular mass reduction process (fig. 4 and fig. 5). The applicability of this approach is related to the absence of possibility of monomer formation at the investigated stages of the reaction, and to insignificant structural changes in the process of stabilization and, first of all, to kinetic peculiarities of the destruction process at high-temperature stabilization.

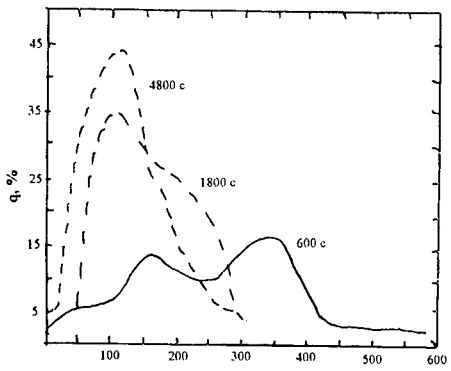


Fig. 4. Curve molecule-mass distribution of samples CN.

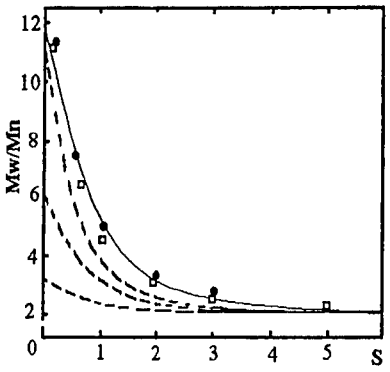


Fig. 5. Dependence Mw/Mn from number of the broken off bonds S (● - sample 1, □ - sample 2, --- - theoretical results, — - experimental).

CN destruction rate constant can be calculated from the known equation:

$$\frac{1}{DP_{n,t}} - \frac{1}{DP_{n,0}} = k\tau ,$$

where $DP_{n,t}$ and $DP_{n,0}$ - number-average polymerization degree of the initial and destructured sample. While processing the experimental data, obtained by the authors, it has been found out, that inverse value of average viscosity polymerization degree at the

investigated range of temperatures (120 - 140 °C) is satisfactorily described by linear time function (fig. 6). In this case constant of CN desstruction rate can be determined from tangentof inclination angle of the dependence of 1/DP from duration of processing.

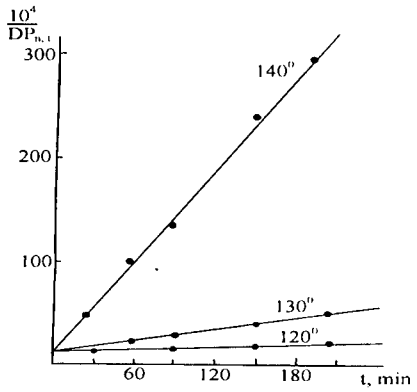


Fig. 6. Dependence 1/DP from d duration hydrolysis.

The analysis of the obtained results shows, that with the increase of treatment temperature there is a significant growth of CN destruction rate constant value (tab. 3).

Tab. 3 Some parameters hydrothermal decomposition.

$k \times 10^{-4}$, min^{-1}	T, °C	τ, min
0.14	120	180 – 210
0.4	130	210
3.0	140	210

At the same time at constant temperature in investigated time interval the rate practically does not change.

In carrying out the high-temperature CN treatment it is necessary to take into account both initial values of DP, and the peculiarities of chain-length distribution in the process of esterification. Thus, the regulation of CN solution viscosity, the magnitude of which is mainly determined by the magnitude of molecular mass of the polymer, involves the use of the suitable quantitative dependences on the changes of DP and other characteristics of chain-length distribution at two major stages of CN obtaining.

The methods of cellulose destruction, specially developed by the authors, allow to decrease the molecular mass of polymer with preservation of morphological structure of fibres, which provides normal conditions for esterification and stabilization. Thus there appeares a basic opportunity for obtaining cellulose nitrates with extremely low viscosity.

The data, presented in this communication, show, that now as a result of studying physico-chemical regularities of processes proceeding at the main stages of nitrocellulose production (nitration, stabilization) principally novel methods can be developed for regulating the structural characteristics of CN. It is worth noting the importance of the preliminary stage of cellulose preparation (including the use of various methods of physical treatment). The study of physico-chemical regularities of the processes of nitrocellulose production and the obtaining of the appropriate quantitative dependences opens an opportunity of the directed regulation of properties and manufacture of the materials with the given physico-chemical characteristics, including those of molecular mass and basic parameter of CN chain-length distribution.

References

[1] Kovalenko V. I. Uspekhi khimii. T. 64. 1995. p.803. (in Russian)

[2] Eremenko L. T., Korolev A. M., Berezina L. I. Nitrocellulosa I ee ispolzovanie v technike. Chernogolovka, ICP AN USSR. 1978. (in Russian)

[3] Lurye B. A., Svetlov B. S. Trudu MKHTI imeni D. I. Mendeleeva. Vup. 112. 1980. p.5. (in Russian)

[4] Khrapkovskii G. M., Marchenko G. N., Shamov A. G. Vliyanie stroeniya molekul na kineticheskie parametru monomoleculyarnogo raspada C- i O-nitrosoedinenii. Kazan, FEN. 1997. (in Russian)

[5] Kovalenko V. I. Vusokomolelulyarnue soedineniya. Ser. A. T. 37. 1995. p. 911. (in Russian)

[6] Kovalenko V. I. Struktura I dinamika molekulyarnukh system. Ioshkar-Ola. Part 1. 1995. p. 182. (in Russian)

[7] Kovalenko V. I. Struktura I dinamika molekulyarnukh system. Ioshkar-Ola-Kazan-Moskva. Part 2. 1996. p. 110. (in Russian)

[8] Kovalenko V. I. Rossiiskii Khimicheskii Jurnal. T. 41. N. 4. p.42. (in Russian)

[9] Popov S. P., Isgirov A. A., Kargin U. M. Khimiya I reakcionnaya sposobnost cellulozu i ee proizvodnukh. Izv. AN USSR. 1989. p. 55. (in Russian)

[10] Popov S. P., Popova E. V., Kargin U. M. Khimiya I reakcionnaya sposobnost cellulozu i ee proizvodnukh. Izv. AN USSR. 1991. p. 158. (in Russian)

[11] Khrapkovskii G. M., Shamov A. G., Shamov G. A., Shlyapochnikov V. A. Rossiiskii Chimicheskii Jurnal. T. 41. N 4. p. 14. Shamov A. G. (in Russian)

[12] Tranina E. A., Rafeev V. A., Corokin T. V., Rubinov U. I. Izv. AN, Ser. chim. 1990. p.1273. (in Russian)

[13] Lure B. A., Valimina Z. T., Avromenko E. N., Svetlov B. S. X Vsesouznoe soveshanie po kinetike i mekhanizmu chimicheskikh reakcii v tverdom tele. Chernogolovka. T. 1. 1989. p. 59. (in Russian)

[14] Khrapkovskii G. M., Philipov A. S., Garifzyaniv G. G., Rafeev V. A., Rubinov U. I. Izv. AN, Ser. chim. 1991. p.2744. (in Russian)

[15] Khrapkovskii G. M., Marchenko G. N., Rafeef. B. A, Rubtihov Iu. J. Proc. Of the 17-th International Semium Pyrotechnics and Explosiven. Beijing. V.2. 1991. p. 221. (in Russian)

[16] Khrapkovskii G. M., Philipov A. S., Rafeev V. A., Rubinov U. I. X Vsesouznoe soveshanie po kinetike i mekhanizmu chimicheskikh reakcii v tverdom tele. Chernogolovka. T. 2. 1989. p. 62. (in Russian)

[17] Khrapkovskii G. M., Rakhmankulov Sh. M., Akhmadieva G. K. II Vserossiiskaya konferenciya po ionnoi khromatographii. Moscow. 1989. p. 29. (in Russian)

[18] Matukhin E. L., Khrapkovskii G. M., Iarullin R. N. Dinamika molekulyarnukh system. Kazan. 2000. p.111. (in Russian)

THEORETICAL STUDY OF THE MECHANISM OF NITROALKANE GAS PHASE MONOMOLECULAR DECOMPOSITION[1]

Grigorii M. Khrapkovskii, Ekaterina V. Nikolaeva,

Denis V. Chachkov, Alexander G. Shamov

Kazan State Technological University, 420015, the Russian Federation, Kazan

Fax: (8432) 36 75 42, E-mail: shamov@kstu.ru

Abstract: With the use of non-empirical methods (MP2/6-31G(d), MP4/6-31G(d), QCISD/6-31G(d), CASSCF(2×2, 4×4, 6×6, 8×8)/6-31G(d), B3LYP/6-31G(d) and B3LYP/6-311++G(df,p)) the basic alternative mechanisms of gas-phase monomolecular decomposition of nitroalkanes, such as radical decomposition, HNO_2 elimination, nitro-nitrite rearrangement (NNR), formation of aci-nitrocompounds have been considered. The further development of the reactions up to the experimentally observable products has been studied in detail. For the reactions of radical decomposition, using the example of nitromethane and its derivatives, the characteristic points on the surface of potential energy in CN-bond stretching from equilibrium values of ~ 1.5 Å to ~5Å have been proved to be missing. The obtained data theoretically substantiate the possibility of the calculation of activation enthalpies (energies) and dissociation energies of CN-bond through enthalpies of parent compounds and formed radicals. The structure of transition state has been determined and the peculiarities of influence of substituents on HNO_2 elimination reaction have been revealed. On the basis of calculation of the geometry of transition state and kinetic parameters the possibility of competition of NNR with other mechanisms of initial event is discussed. It is noted, that the barrier of NNR is much higher than D(C-N) (the exception should be only made for fluoronitromethane), that is why there is practically no opportunity for experimental detection of this reaction in gaseous state. The processes of formation and destruction of aci-nitroalkanes are of interest for studying the peculiarities of liquid-phase decomposition. In addition, it is noted that the accumulation of nitrogroups essentially reduces the activation enthalpy of the formation of aci-nitroalkanes in gaseous state. Even starting with aci-dinitromethane the suitable value hardly differ from CN-bond dissociation energy, and for aci-trinitromethane this value is even a little bit less than that. The obtained data on geometry, electronic structure of molecules and transition states of more than 50 reactions of nitroalkanes allow to consider in detail the competition of various mechanisms of gas-phase decomposition. The results of this work could also be of interest for the discussion of general regularities of the influence of molecular structure on the reactivity of aliphatic nitrocompounds as a whole.

The study of thermal decomposition is one of the most important directions of researches in the field of nitrocompound chemistry [1,2]. The results obtained during the research of the kinetics of thermal decomposition are the basic source of information about dissociation energies of bonds and enthalpies of radical formation [3, 4]. Presently, gas-phase nitroalkane decomposition has been experimentally investigated in most detail: over 70 reactions have been analyzed, for which reliable kinetic parameters have been found. In many cases a solid set of data has been obtained on the structure of products at initial stages of decomposition [2, 5]. In recent years a considerable attention has been paid to the

[1] The work is carried out by means of the financial support of the Russian Fund of Fundamental Researches, the Grant № 00-03-33039, and the Competitive centre of fundamental natural sciences of Ministry of education of Russia, the Grant №E00-5.0-311.

theoretical study of the kinetics and mechanism of gas-phase decomposition of nitrocompounds with the use of quantum-chemical methods [4,6-10]. At the same time, a great number of fundamental problems of gas-phase decomposition of aliphatic nitrocompounds are not fully investigated. There are no data on the transition state structure of the basic experimentally proved mechanisms of nitroalkane monomolecular decomposition, which are accordingly connected with homolytic opening of C-N-bond and β-elimination of nitrogen acid [4,5]. There are significant discrepancies in the results of theoretical study of other alternative mechanisms of gas-phase decomposition using various quantum-chemical methods [4]. In many cases the calculation results considerably differ from experimental data, which does not allow to make any certain conclusions about the competition of various mechanisms of gas-phase monomolecular decomposition initial event and influence of molecular structure on the changes of kinetic parameters in series. In this work we give the results of studying the mechanism of nitroalkane gas-phase decomposition with the use of different non-empirical methods, as well as the methods of density functional (DFT) with B3LYP parameterization (13-14).

It was demonstrated with the reactions of nitromethane (NM) and nitroethylene gas-phase decomposition, that the use of methods B3LYP/6-31G (d) and B3LYP/6-311++G (df,p) in studying the reactions of monomolecular decomposition aliphatic nitrocompounds provides the least mean deviation of calculated and experimental values of formation enthalpy of parent compounds and reaction products (for reactions nitromethane and nitroethane the maximum deviation does not exceed 14.6 - 16.7 kJ/mol, a mean-square value in the sample consisting of 50 compounds makes up 7.3 kJ/mol) [15,16]. That is why it is by these methods that the greater part of the results was obtained. The calculations have been carried out with the use of software packages Gaussian 94 and Gaussian 98 [17, 18]. In all cases the conformity of found stationary points to minima or transition state (TS) was substantiated by the calculation of force constants. The presence of TS was confirmed by the presence of one negative value in Hessian matrix, and its belonging to investigated process was substantiated by the descents to reagents and products along reaction coordinate.

While studying the reactions of nitrocompound radical decomposition of major interest are the problems of transition state structure of the reaction and recombination barrier of the radicals formed at thermal decomposition. In figure 1 the energy curve of nitromethane at C-NO_2-bond stretching from 0.0015 to 0.005 pm is given.

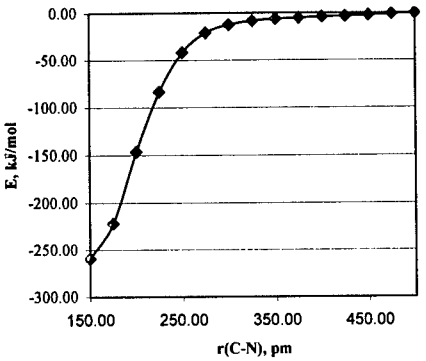


Figure 1. Energy change at C-N-bond stretching in nitromethane.

The monotone curve amply illustrates the asymptotic of decomposition process, when the energy of molecule at 0.005 pm coincides, accurate to 0.2 kJ/mol, with the sum of energies of formed radicals. The given data, proving the absence of characteristic points on the surface of potential energy of radical decomposition reaction and a barrier of recombination reaction of the radicals, indicate that C-NO_2-bond (D (C-N)) dissociation energy can be rightfully calculated as the difference of energies of radicals and NM. The calculated value of D(C-N) for NM, nitroethane (NE), nitropropane are close to experimental data obtained on the basis of studying the kinetics of gas-phase decomposition (tab. 1). At the radical mechanism of the initial event, D(C-N) practically coincides with the magnitude of gas-phase decomposition activation energy:

$$D(C\text{-}N) = E - RT$$

Table 1. C-NO_2-bond dissociation energies of some nitroalkanes.

Compound	D(C-N), kJ/mol[a]		Compound	D(C-N), kJ/mol[a]	
	B3LYP/ 6-31G(d)	Experiment		B3LYP/ 6-31G(d)	Experiment
CH_3NO_2	236.1	237.5	$CH_3CH_2NO_2$	235.9	228.8
CH_2FNO_2	229.7	-	CH_3CHFNO_2	233.4	-
CHF_2NO_2	216.8	-	$CH_3CF_2NO_2$	224.7	-
CF_3NO_2	212.7	-	$CH_3CHClNO_2$	216.2	-
CH_2ClNO_2	199.4	-	$CH_3CCl_2NO_2$	194.3	-
$CHCl_2NO_2$	163.6	-	$CH_3CFClNO_2$	159.6	-
CCl_3NO_2	130.5	153.2	$CH_2FCH_2NO_2$	191.6	-
$CHFClNO_2$	193.4	-	$CHF_2CH_2NO_2$	228.2	-
CF_2ClNO_2	189.8	-	$CF_3CH_2NO_2$	223.3	-
$CFCl_2NO_2$	164.5	-	$CF_3CF_2NO_2$	208.3	-
$CH_3CH_2CH_2NO_2$	238.5	238.9	$CH_3CH_2CH_2CH_2NO_2$	233.8	-
$CH_3CH(NO_2)CH_3$	230.1	220.1			

[a]The experimental values of D(C-N) are obtained from the kinetics of gas-phase thermal decomposition. [5]

Thus, the independent theoretical estimations of D(C-N) can be used for reliability control of available experimental data, as well as when there are no suitable results. The results of theoretical study of D(C-N) and E are of special interest when the radical decomposition is not the basic path of monomolecular decomposition (for example, at HNO_2 elimination from mononitroalkanes) and the

process is aggravated by the appearance of severe difficulties for experimental determination of the kinetic parameters.

The correlations, connecting the length of opening C-NO2-bond and the energy of radical gas-phase decomposition (and D(C-N)) was established in works [4,10,11] to be in the series of polynitro- and fluoropolynitroalkanes. The similar correlations are also observed for atomic charges of C-NO_2-group [4]. In most cases the parameters of geometrical and electronic structure of molecules were calculated with the use of semi-empirical quantum-chemical methods MINDO/3 and PM3. However, semi-empirical methods do not allow to estimate with due reliability the energy barriers of reactions. For this purpose it is more reasonable to use modern non-empirical and DFT-methods, in particular, B3LYP hybrid method.

In table 1 the results obtained by this method for fluoro-, chloronitromethanes are given. There are practically no experimental data on the kinetics of thermal decomposition for these compounds. Until recently there have been no data on D(C-N) magnitudes, formation enthalpies of compounds and radicals. For mononitrocompounds the main factors of influence of the substituents on D(C-N) and activation energy of the reaction of radical gas-phase decomposition should appear to be most demonstrative.

Table 2. Formation enthalpies of some nitroalkanes and radicals formed at the detachment ofNO_2-group, which have been obtained by B3LYP/6-31G(d) method[a].

Compound	ΔH_f^{298}, kJ/mol	ΔH_f^{298}, kJ/mol (experiment)	Radical	ΔH_f^{298}, kJ/mol	ΔH_f^{298}, kJ/mol (experiment)
CH_3NO_2	-68.0	-74.9	$CH_3^{\bullet}$	145.2	140.1
CH_2FNO_2	-242.04	-	$CH_2F^{\bullet}$	-32.8	-33.5
CHF_2NO_2	-452.96	-	$CHF_2^{\bullet}$	-256.7	-242.7
CF_3NO_2	-685.51	-	$CF_3^{\bullet}$	-493.3	-493.7
CH_2ClNO_2	-52.22	-	$CH_2Cl^{\bullet}$	126.7	121.3
$CHCl_2NO_2$	-27.28	-	$CHCl_2^{\bullet}$	115.9	100.4
CCl_3NO_2	10.38	-	$CCl_3^{\bullet}$	120.5	82.4
$CHFClNO_2$	-235.39	-	$CHFCl^{\bullet}$	-62.4	-
CF_2ClNO_2	-447.90	-	$CF_2Cl^{\bullet}$	-278.6	-280.3
$CFCl_2NO_2$	-216.56	-	$CFCl_2^{\bullet}$	-72.6	-92.1

[a] ΔH_f^{298} (NO_2) = 23 kJ/mol (ΔH_f^{298} (NO_2) (experiment) = 33.5 kJ/mol)

The substitution of hydrogen atom for fluorine atom in NM molecule exerts relatively weak influence on D(C-N) magnitude. For fluoronitromethane (FNM) and trifluoronitromethane (TFNM) the reduction of D(C-N) is less than 4.2 kJ/mol. The data of table 2 allows us to arrive to the conclusion that some minor reduction of C-NO_2-bond dissociation energy for fluoronitromethanes is explained by the fact that the decrease of formation enthalpies of the compounds at the introduction of fluorine at-

oms into the molecules is practically completely compensated by the analogous changes of the enthalpies of fluoromethyl radicals. The results of table 2 show, that the effect is connected with add stabilization of difluoromethyl radicals formed in the process of monomolecular decomposition. The analysis of the geometry of fluoromethyl radicals allows to assume, that the abnormal increase of stability of difluoromethyl radical can be explained on the basis of taking into account the tendencies of angle changes at the exit from fluorine atom plane.

Methyl radical is known to be flat, which follows from the results of experimental works and non-empirical calculations [4]. In fluoromethyl radicals the pyramidal structure itself is different, and the angle of exit from the atom plane increases with the accumulation of fluorine atom. However the greatest change (more than by 25°) in the series occurs in the case of difluoromethyl radical.

With the replacement of hydrogen for chlorine atoms significant growth of enthalpy of compounds has been marked, at the same time the enthalpy of radicals changes weakly. As a result, in the series of NM, chloropnitromethane (ChNM), dichloronitromethane (DChNM), trichloronitromethane (TChNM) there is a considerable reduction, more than by 83.7 kJ/mol, of D(C-N), which is in agreement with the experimental data on kinetics of radical gas-phase decomposition obtained for NM and ChNM.

In mixed fluorochloronitromethanes the magnitude of D(C-N) is determined by the presence of chlorine atoms in molecules and radicals. The values, calculated for these compounds, are close to the magnitudes, obtained for chloronitromethanes with identical number of chlorine atoms. The presence of fluorine causes but very weak (less than 4.2 kJ/mol) decrease of D(C-N). The attention should be paid to the fact that the magnitude of D(C-N) in dichloronitromethane, according to the calculation data, is even somewhat higher (by 0.8 kJ/mol), than in DChNM. This result, from our point of view, especially convincingly shows, that at the presence of two volumetric substituents (chlorine atoms) the influence of fluorine on D(C-N) is practically completely neutralized [19].

The analysis of results obtained for halogen nitroethanes shows, that both the change trends in the series, and the absolute magnitudes of D(C-N) for them are close to the characteristics obtained for analogous halogen nitromethanes. It still should be noted, that D(C-N) reduction of fluoronitroethanes is more effected by the hydrogen-to-fluorine replacement than fluoronitromethanes. It is worth noticing, that the presence of fluorine atom in 1-fluoro-1-chloronitroethane weakly influences D(C-N) magnitude. The similar effect was also marked above for halogen nitromethanes. The calcu-

lated D(C-N) reduction for fluoronitroethanes, in which fluorine atoms and nitrogroups are spatially remoted, seems to be rather unexpected.

Presently we have also estimated D(C-N) for many other nitroalkanes and the list of molecules in table 1 could be considerably extended [20]. We have decided, however, to be confined by the given results, which, as we see it, are quite sufficient for illustrating the potentialities of B3LYP method to estimate C-NO_2-bond dissociation energies and activation energy of gas-phase radical decomposition. It is noteworthy, that we have recently obtained the estimations of C-H-, C-F-, C-Cl-, C-C-bond dissociation energies [21], which are in quite good agreement with the available experimental data (though these data are not numerous). The potentiality for activation energies of aliphatic nitrocompound radical decompositions to be reliably estimated is of interest not only for independent control of available experimental data but also, first of all, for discussing the competition of different mechanisms of the initial event of decomposition.

The other experimentally proved mechanism of nitroalkane monomolecular decomposition, along with homolytic opening of C-NO_2-bond, is the process of β-elimination of nitrogen acid [2,5]. On this mechanism mononitroalkanes, α-halogennitrocompounds such as RCH_2CHXNO_2 (X = Hal), as well as many (α-nitroolefins are decomposed. Presently, only in gaseous state there have been investigated about 50 reactions, for which the kinetic parameters have been reliable determined [5]. For analyzing the experimental data and, in particular, for discussing the influence of substituents on the activation energy of HNO_2 gas-phase elimination in the series of nitroalkanes the modified MacCol-Benson theory [2,5], postulating the polar transition state, was previously used.

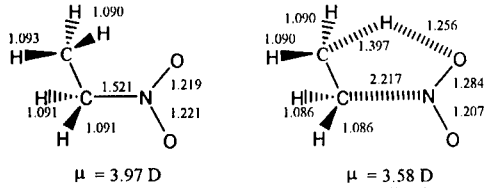
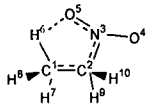


Figure 2. The geometrical parameters and dipole moments of nitroethane and TS of HNO_2 elimination, calculated by B3LYP/6-311++G(df,p) method

However the results of theoretical study of the mechanism of HNO_2 elimination from nitromethane, nitropropanes, nitrobutanes and a number of other mononitrocompounds, obtained with the use of semi-empirical (MINDO/3, PM3 [4,6]), non-empirical (MP2 [4], DFT[22]) methods rather consistently reject the conclusion about the polar TS of reaction. For all above-mentioned compounds the dipole moment of a molecule is higher, than TS. HNO_2 molecule in transition state is charged positively, hence, there is a component of dipole moment oppositely directed to intrinsic dipole moment of nitroalkane [6]. In figure 2

the basic geometrical parameters and magnitudes of NE dipole moments and TS of HNO_2 elimination from nitroethane, obtained by B3LYP/6-311++G(df, p) method, are given.

Table 3. Geometrical parameters of transition state (TS) of HNO_2 β-elimination, obtained by PM3 method [bond lengths in pm, angles in degrees, E kJ/mol]



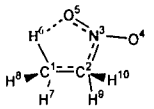
Compound	Geometrical parameters of a transition state								The power characteristics of reaction	
	C^1H^6	C^1C^2	C^2N	NO^5	NO^4	C^1C^2N	C^2NO^5	$C^2C^1H^6$	E [5]	$\Delta H^{\neq}$
1-st group										
$C_2H_5NO_2$	157.67	141.75	173.55	128.97	118.68	100.06	111.85	93.96	188.5	245.6
$C_3H_7NO_2$	159.48	142.63	171.43	129.21	118.66	100.50	112.40	43.27	187.9	238.5
$C_4H_9NO_2$	159.47	142.58	171.37	129.12	118.68	100.50	112.45	93.36	181.6	238.1
$C_5H_{11}NO_2$	159.60	142.59	171.36	129.15	118.67	100.53	112.45	93.31	181.6	238.1
$C_6H_{13}NO_2$	159.63	142.59	171.33	129.15	118.67	100.29	112.46	93.31	181.2	240.2
2-d group										
CH_3CHCH_3 | NO_2	154.76	142.49	176.57	128.48	118.76	98.85	111.54	94.89	182.0	247.3
$CH_3CHC_2H_5$ | NO_2	156.82	143.47	174.12	128.71	118.73	99.33	112.16	94.11	181.2	231.4
$C_2H_5CC_2H_5$ | NO_2 (CH3 above C)	154.26	143.35	176.63	128.29	118.82	98.28	111.99	94.84	170.3	220.5
3-d group										
CH_3CHFNO_2	153.22	143.00	176.85	128.06	118.57	99.12	111.19	94.63	184.1	234.3
$C_2H_5CHClNO_2$	157.07	142.91	171.32	128.64	118.58	110.4	112.23	93.55	165.7	226.8
$C_2H_5CHBrNO_2$	161.59	141.34	164.43	129.90	118.44	102.57	112.54	92.90	169.5	230.5

In TS of HNO_2 elimination from nitroalkanes, according to the data of semi-empirical methods (MINDO/3, PM3), C-H-bond length, formed by hydrogen atoms, participating in the reaction, is increased. The magnitudes of r(C-N), r(N-O) and r(C-C) in transition state change relatively less. Taking into account the above-mentioned data and the data on distribution of electronic density in molecules and TS, the conclusion can be made, that the process of HNO_2 elimination from nitroethane and a number of other mononitroalkanes, as it was for the first time marked in work [6], probably begins with intramolecular transfer of hydrogen (table 3).

However the results of the study with the use of non-empirical and DFT methods predict somewhat different picture [4,22]. According to these methods, the most considerable changes in the process of the reaction are observed for C-N-bond, which becomes practically completely opened in TS; C-H-bond is stretched somewhat less; relatively small changes in TS are predicted for N-O and C-C-bonds. As a whole, these results are in bad agreement with the assumption that intramolecular

transfer of hydrogen is the initial stage of HNO_2 elimination. At the same time they correspond to the conception about synchronous elimination, when there is a significant change of several bonds and angles [4,23].

Table 4. Geometrical parameters of transition state of HNO_2 β-elimination, obtained by B3LYP/6-31G(d) method [bond lengths in pm, angles in degrees, E kJ/mol]



Compound	Geometrical parameters of a transition state								The power characteristics of reaction	
	C^1H^6	C^1C^2	C^2N	NO^5	NO^4	C^1C^2N	C^2NO^5	$C^2C^1H^6$	E [5]	$\Delta H^{\neq}$
$CH_3CH_2NO_2$	138.7	139.0	221.7	128.4	120.7	95.3	100.7	93.3	188.5	190.1
CH_3CHFNO_2	135.4	139.0	227.7	128.6	120.9	92.4	100.8	96.5	184.7	179.0
$CH_2FCH_2NO_2$	137.5	138.7	221.8	128.1	120.6	95.0	100.8	93.2	-	200.1
$CH_3CF_2NO_2$	136.4	139.2	225.0	129.3	120.6	92.2	101.7	97.1	-	175.3
$CHF_2CH_2NO_2$	138.0	139.1	224.6	128.0	120.4	94.1	100.8	93.4	-	236.4
$CH_3CHClNO_2$	135.1	139.3	229.0	128.5	120.7	92.2	100.4	96.4	-	174.3
$CH_3CFClNO_2$	135.2	139.5	228.9	128.9	120.6	91.2	101.1	97.7	-	172.7
$CH_3CH(NO_2)_2$	137.8	138.6	220.0	127.6	120.2	95.4	100.7	94.0	-	172.0
$CH_3CH_2CH_2NO_2$	135.9	139.3	223.5	128.1	120.8	95.5	100.1	92.1	188.1	177.7
$CH_3CH(NO_2)CH_3$	135.8	139.6	229.4	128.6	121.1	92.6	100.2	95.3	182.3	187.0
$CH_3CH_2CH_2CH_2NO_2$	135.9	139.3	223.5	128.1	120.8	95.5	100.1	92.1	181.8	186.7

In table 4 the basic parameters of TS of HNO_2 β-elimination reaction and its energy characteristics for a number of nitroalkanes, calculated by B3LYP/6-31G(d) method are given. For NE the calculated values are very close to theoretical estimations. At the same time the results of MINDO/3, PM3, MP2/3-21G and MP2/6-31G(d) methods considerably overestate the reaction barrier (by 60-70 kJ/mol [23]), which is probably connected with the underestimation of the effect of electronic correlation, which results in overstating TS enthalpy (miscalculation of enthalpies of mononitrocompounds formation with the use of these methods does not practically exceed 10-15 kJ/mol [3]).

At the same time, the change trends in the series of activation energy are quite satisfactorily conveyed by these methods. This can be seen from the results given in table 4. For the compounds, given in table 4, the range of changes of experimental and calculated magnitudes of activation energy (enthalpy) makes up 26.4 and 22.6 kJ/mol. Weak changes in activation energy are relevant to the stability of bond lengths and angles of the reaction centre. However, it should be noted, that the geometrical parameters of TS reactions of primary and secondary nitroalkanes still considerably differ. In their turn, the magnitudes for α-halogennitroalkanes differ substantially from the latter ones. It allows for the sake of convenience of the analysis to divide mononitroalkane molecules into three groups.

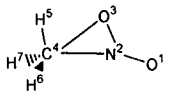
Above we have already pointed out, that according to the data of PM3 and MINDO/3 the greatest changes in transition state of HNO_2 β-elimination take place in C-H-bonds. It is interesting, that C-H bond lengthening for the compounds of 1-st group is accompanied by cymbate reduction of activation enthalpy. The most substantial growth of mobility of hydrogen atom, participating in the reaction, takes place at the introduction of halogens and NO_2 groups into β-position. So, for example, according to the estimations of MINDO/3 the magnitude of C-H-bond in 1,2-dinitroethane is by 2 pm higher, than in nitroethane (112.8 and 110.8 pm accordingly). Thus, due to the calculation data, β-elimination activation energy for 1,2-dinitroethane is by 80 kJ/mol lower, than for nitroethane [6]. The similar effect (relatively less expressed) is also observed for acceptor substituents in α-position. In particular in accordance with MINDO/3 data, the activation enthalpy of HNO_2 β-elimination from 1,1-dinitroethane as compared to nitroethane is by 25 kJ/mol lower. Accordingly, the differences of r(C-H) magnitudes in these molecules make up 3 pm, i.e. they are also much less, than in the case of 1,2-dinitroethane.

For the compounds with NO_2 groups at secondary or tertiary carbon atom, participating in HNO_2 β-elimination neither simple dependence between the changes of activation enthalpy and C-H-bond length in the basic and transition states nor the changes in the series of Δr(C-H) have been observed. At the same time it should be noted that for the compounds of this group the reduction of activation enthalpy proceeds monotonously with the increase of the magnitude of C=C double bond forming in the transition state. It is obvious, that the greater the length of this bond, the less energy is spent for rearrangement of transition state. It should be noted, that the greatest r(C=C) magnitude in the series in the transition state of 3-methylnitropentane reaction corresponds the lower magnitude of activation enthalpy as compared to 2-nitropropane. For transition states of the reaction with participation of halogen-substituted nitroalkanes the greatest changes have been experimentally observed in geometrical parameters [more than 8 pm for r(C-H)] and activation energy (about 19 kJ/mol). The change trends of activation enthalpy calculated values in most cases correspond to the change in the series of experimental values of gas-phase decomposition activation energy.

Along with the above considered two basic mechanisms of nitroalkane gas-phase decomposition a number of other alternative mechanisms of initial event have been discussed in literature [2,4]. Among them nitro-nitrite rearrangement (NNR), is undoubtedly of the greatest interest, in recent years it has repeatedly been investigated with the use of various quantum-chemical methods [4,8,9]. The attempts of experimental study of this process have also been undertaken [4]. However, despite of the

fact that the published results are of doubtless interest, all the attempts to draw unequivocal conclusions on their basis have ended in failure. So, for example, the data of quantum-chemical researches of nitromethane NNR were in poor agreement both in geometrical parameters of transition state, and in the magnitude of the reaction barriers [24]. With the use of mass-spectrometry it has been established, that intensive 30 m/z (NO) line was present in the products of high-vacuum NM pyrolysis [24]. However numerous researches on the kinetics of NM gas-phase decomposition and the analysis of products at initial stages of decomposition indicate the radical mechanism of the initial event [2,5].

Table 5. The basic geometrical parameters of transition state (TS) of the reaction of nitromethane nitro-nitrite rearrangement (bond lengths in pm, angles in degrees).



Method	Basis	C^4N^2	N^2O^3	N^2O^1	O^3C^4	$C^4N^2O^3$	$N^2O^3C^4$	$O^3C^4N^2$	$O^3N^2O^1$
PM3		183.5	128.5	118.9	188.9	72.1	67.56	40.34	120.36
HF	6-31G(d)	193.8	125.1	118.1	201.7	75	68.16	36.82	119.94
B3LYP	3-21G	191.1	139.0	124.8	201.8	73.4	65.23	41.32	119.55
	6-31G(d)	194.8	129.8	120.5	200.7	73.33	68.38	38.29	118.72
	6-311++ G(df,p)	197.1	129.3	119.4	201.5	72.9	69.24	37.83	119.32
QCISD	6-31G(d)	193.8	130.4	120.8	208.3	75.6	69.31	37.9	115.71
CASSCF (2×2)	6-31G(d)	191.0	128.0	118.9	198.9	74.23	67.53	38.25	117.7
CASSCF (4×4)	6-31G(d)	187.3	129.5	120.0	203.7	77.68	63.91	38.41	116.97
CASSCF (6×6)	6-31G(d)	186.0	134.2	119.7	202.1	76.36	63.46	40.18	116.82
CASSCF (8×8)	6-31G(d)	189.6	129.1	121.7	204.1	77.04	64.91	38.05	117.84
MP2	6-31G(d)	181.7	135.4	122.1	190.9	72.4	65.08	42.52	118.05
	6-311++ G(df,p)	180.1	132.8	120.4	187.4	71.79	65.93	42.29	118.95
MP4	6-31G(d)	187.8	131.4	121.1	196.6	73.67	66.44	39.89	118.97
MINDO/3 [8]		151.6	129.9	143.8	158.4	68	-	49.5	-
MP2 [9]	6-31G(d)	192.8	125.1	118.1	203.9	-	-	-	-
CASSCF(4×4) [9]	6-31G(d)	361.7	137.1	115.5	370.0	-	-	-	113.0

We undertook a comprehensive theoretical study of the transition state structure and the mechanism of gas-phase NNR for nitromethane with the use of different non- empirical and DFT methods, as well as semiempirical PM3 method [25].

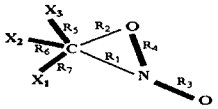
Geometrical parameters of TS, obtained with the use of different methods, and the reaction barriers are given in tables 5 and 6 accordingly. The analysis of the obtained results shows, that the data of various non-empirical methods are in good agreement. As the most reliable estimations of the barrier we consider the interval 272-275.5 kJ/mol, predicted by B3LYP/6-311++G(df, p) and B3LYP/6-31G(d) methods accordingly [21]. As the upper limit of the barrier there can be used 284.7 kJ/mol,

obtained by QCISD/6-31G(d) method. All these values are much higher than D(C-N) in NM, that is why the possibility of experimental detection of this reaction is practically excluded.

Table 6. Barrier height and thermal effect of the reaction of nitromethane nitro-nitrite rearrangement (kJ/mol).

Method	Basis	$\Delta H^{0\neq}$	$\Delta H^{298\neq}$	ΔH^{0}	ΔH^{298}
PM3		331.41	334.59	-22.55	-26.23
HF	6-31G(d)	330.87	331.29	15.56	14.60
B3LYP	3-21G	244.39	244.43	31.34	30.67
	6-31G(d)	277.52	279.11	-5.73	-6.57
	6-311++G(df,p)	271.96	272.71	-11.38	-12.47
QCISD	6-31G(d)	284.68	286.10	7.36	6.15
CASSCF (2×2)	6-31G(d)	332.46	332.46	22.01	21.21
CASSCF (4×4)	6-31G(d)	356.81	357.27	-2.47	-3.93
CASSCF (6×6)	6-31G(d)	321.08	321.50	-5.86	-7.24
MP2	6-31G(d)	297.32	297.11	-19.71	-20.63
	6-311++G(df,p)	-	-	-24.69	-25.90
MP4	6-31G(d)	296.85	297.11	3.26	2.18
MINDO/3 [8]		-	199.16	-	-17.15
MP2 [9]	6-31G(d)	-	307.52	-	26.11
CASSCF (4×4) [9]	6-31G(d)	-	287.02	-	-96.65
Experiment		-	-	-	36.07 [3]

Table 7. Geometrical parameters of NNR transition state of some nitroalkanes, obtained by B3LYP method (pm, degrees)



Method	Basis	X_1	X_2	X_3	R_1	R_2	R_3	R_4	R_5	R_6	R_7	∠ONO
CH_3NO_2	6-31G(d)	H	H	H	194.9	200.8	120.3	129.9	108.5	108.4	108.4	118.8
	6-311++G(df,p)				197.1	201.5	119.4	129.3	108.4	108.2	107.9	118.8
$CH_3CH_2NO_2$	6-31G(d)	H	H	CH_3	201.9	207.1	120.9	129.7	108.5	108.6	148.7	118.3
CH_2FNO_2	6-31G(d)	F	H	H	197.8	197.9	120.4	129.6	108.2	108.2	132.8	118.8
	6-311++G(df,p)				200.7	199.8	119.3	129.0	108.2	108.0	131.9	118.8
CHF_2NO_2	6-31G(d)	F	F	H	196.7	199.4	120.3	129.2	108.2	131.1	131.8	119.4
CF_3NO_2	6-31G(d)	F	F	F	192.2	196.0	119.8	129.3	131.3	132.0	130.2	119.9
CH_2ClNO_2	6-31G(d)	Cl	H	H	195.2	206.3	120.4	128.3	108.1	108.1	174.9	119.5
$CH_2(NO_2)_2$	6-31G(d)	NO_2	H	H	180.7	191.1	119.8	129.1	155.5	108.4	108.5	121.15

Table 8. NNR activation enthalpy and CN-bond dissociation energies of some nitroalkanes, obtained by B3LYP/6-31G(d) method (kJ/mol) [25].

Method	$\Delta H^{0\neq}$	$\Delta H^{298\neq}$	D(C-N), 0 K	D(C-N), 298 K	$D(C-N)^{exper.}$ [5]
CH_3NO_2	278.4	279.1	229.2	233.7	237.5
$CH_3CH_2NO_2$	261.0	262.5	229.5	235.9	228.8
CH_2FNO_2	211.5	212.6	226.4	229.7	-
CHF_2NO_2	233.5	234.0	214.9	216.8	-
CF_3NO_2	246.1	246.5	211.5	212.7	-
CH_2ClNO_2	263.4	264.9	196.1	199.4	-
$CH_2(NO_2)_2$	256.8	262.5	-	-	-

The influence of substituents in NNR reaction has been studied for four simple halogen nitromethanes: fluoronitromethane (FNM), difluoronitromethane (DFNM), trifluoronitromethane

(TFNM) and chloronitromethane (ChNM), as well as for NE and dinitromethane. The geometrical parameters of NNR transition state for these compounds and nitromethane are given in table 7. The energy characteristics are given in table 8.

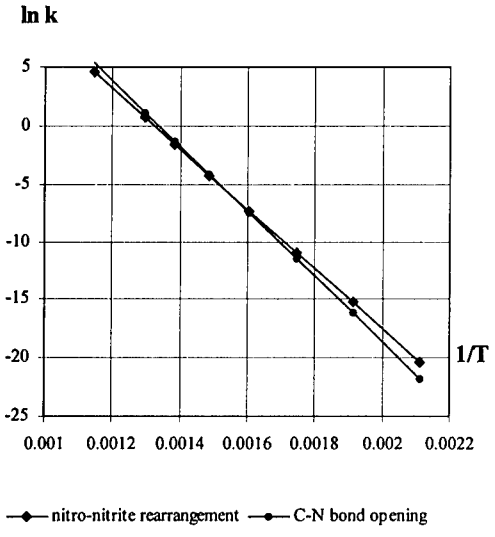


Figure 3. The dependence of reaction constant of nitro-nitrite rearrangement and radical decomposition on temperature.

For fluoronitromethanes and chloronitromethane NNR activation enthalpies are much lower, than for NM. It is of fundamental importance that D(C-N) in fluoronitromethane is higher than NNR barrier. Though predicted distinction of these values is insignificant (15-17 kJ/mol), this result indicates a theoretical possibility to detect NNR experimentally. To this end it is necessary to investigate the kinetics of thermal decomposition at a lower possible temperature, since at high temperatures the radical decomposition prevails because of the higher magnitude of preexponential factor. The data on the competition of NNR and radical FNM decomposition in a wide range of temperatures are presented in Fig. 3.

For chloronitromethanes NNR cannot make a competition to radical decomposition. Firstly, with the accumulation of chlorine atoms D(C-N) reduces sharply (by 34 kJ/mol in ChNM in comparison with NM), whereas the activation energy of NNR reduces much less (by 15 kJ/mol in ChNM in comparison with NM). Secondly, they are uncompetitive because of the higher magnitude of preexponential factor for radical reactions.

The secondary processes of gas-phase decomposition of nitroalkanes, connected with NNR, do not hamper the development of the reaction. We have studied one of the feasible decomposition processes of formed nitrites:

$CH_3ONO \rightarrow CH_2O + HNO$ (1)

$CH_2FONO \rightarrow CHFO + HNO$ (2)

According to the calculated data the reaction barrier (2) at 298.15 K makes up 130.5 kJ/mol, which is almost by 41.8 kJ/mol lower, than for the reaction (1). Thus, the analyzed process can be considered as one of the potential ways of fluoronitromethane decomposition. The data on TS geometry of the investigated reactions are given in figure 4.

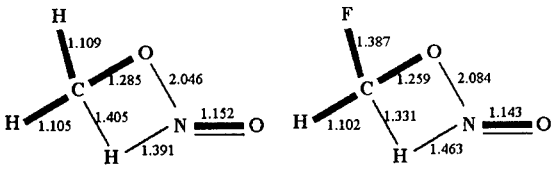


Figure 4. The structures of transition state of HNO elimination reaction

The above mentioned results show, that NNR can compete with the reactions of aliphatic nitrocompound radical decomposition only in rare cases, for example, at the destruction of fluoronitromethane. However the role of this mechanism considerably grows in the processes of liquid-phase decomposition, as well as gas-phase decomposition at high pressures. The considerable volume of activation of radical reactions can decrease their competitiveness as compared to the processes of molecular decomposition, for which the smaller magnitude of activation volume is observed [4].

The rigid limitations of the report length do not allow to present the results of theoretical research of other mechanisms of nitroalkane gas-phase decomposition, including the processes connected with the formation and subsequent decomposition on various aci-form channels. Well-known dinitromethane abnormality, which has long been discussed in literature [4], can be explained by this mechanism, as it was first shown in work [26]. Novel results obtained in the research of this mechanism with the use of non-empirical and DFT methods are given in works [27-28].

References:

1. K.K. Andreev, *Termicheskoe razlozhenie I gorenie vzryvnykh veshchestv (Thermal Decomposition and Combustion of Explosives)*, Nauka, Novosibirsk, 1966 (in Russian).
2. G.B. Manelis, G.M. Nasin, Yu.I. Rubtsov and V.A. Strunin, *Termicheskoe razlozhenie I gorenie vzryvnykh veshchestv (Thermal Decomposition and Combustion of Explosives)*, Nauka, Moscow, 1996 (in Russian).
3. Yu.A. Lebedev, E.V. Miroshnichenko, Yu.K. Knobel, *Termokimiya nitrosoedinenii*, Nauka, Moscow, 1970 (in Russian).
4. G.M. Khrapkovskii, G.N. Marchenko and A.G. Shamov, *Vliyanie molekulyarnoi struktury na kineticheskie parametry monomolekulyarnogo raspada C- i O-nitrosoedinenii (The Influence of Molecular Structure on the Kinetic Parameters of the Unimolecular Decomposition of C- and O-Nitro Compaunds)*, FEN, Kazan, 1997 (in Russian).

5. G.M. Nasin, G.B. Manelis, *Usp. Khim.*, 1994, **63**, 327 (*Russ. Chem. Rev.*, 1994, **63,** 313) (in Russian).
6. V.I. Faustov, S.A. Shevelev, N.A. Anikin, S.S. Yufit, *Izv. Acad. Nauk, Ser. Khim.*, 1979, 2800 (in Russian).
7. A.G. Turner, L.R. Devis, *J. Am. Chem. Soc.*, 1986, **103**, *19*, 5447.
8. M.J.S. Dewar, P. Ritchie, J. Alster, *J. Org. Chem.* 1985, **50**, 1031.
9. M.L. McKee, *J. Am. Chem. Soc.*, 1986, **108,** 5784; M.L. McKee, *J. Phys. Chem.*, 1989, **93,** 7365.
10. G.M. Khrapkovskii, Yu. I. Rutsov, V.A. Rafeev, G.N. Marchenko, G.B. Manelis, *I Processing of the International Pirotechnics Seminar, V.1, Beiying of Technology Press,* 1991, p.424.
11. G.M. Khrapkovskii, A.G. Shamov, G.A. Shamov and V.A. Shlyapochnikov, *Izv. Acad. Nauk, Ser. Khim.*, 1996, **10**, 2438 (in Russian).
12. G.M. Khrapkovskii, A.G. Shamov, G.A. Shamov and V.A. Shlyapochnikov, *Ros. Khim. Jurn.*, 1997, **XL1**, *4*, Vip.2, p. 14 (in Russian).
13. Baker J., *J. Comp. Chem.*, 1986, **7**, 385; *J. Comp. Chem.*, 1987, **8**, 563.
14. Baker J., *J. Chem. Phys.*, 1993, **98**, 5648; C. Lee, W. Yang, R.G. Parr, *Phys. Rev.*, 1988, **B37**, 785; B. Mierhlich, A. Savin, H. Stoll, H. Preuss, *Chem. Phys. Lett.*, 1989, **157**, 200.
15. A.G. Shamov, G.M. Khrapkovskii, *V kn. Struktura i dinamika molekulayrnych system.* 1999, p. 347 (in Russian).
16. A.G. Shamov, G.M. Khrapkovskii, *Mendeleev Commun.* 2001 (in press.).
17. Head-Gordon M., Gonzalez C., Pople J.A . and etc. Gaussian 94// Gaussian Inc. -Pittsburgh PA, 1995.
18. Head-Gordon M., Replogle E. S., Pople J. A. and etc. Gaussian 98// Gaussian Inc. -Pittsburgh PA, 1998.
19. G.M. Khrapkovskii, D.V. Chachkov, A.G. Shamov, *Zh. Obch. Khim.*, 2001 (in press, in Russian).
20. G.M. Khrapkovskii, D.V. Chachkov, A.G. Shamov, *V kn. Struktura i dinamika molekulayrnych system.* 2000, p. 451 (in Russian).
21. D.V. Chachkov, L.A. Stabrovskaya, A.G. Shamov, G.M. Khrapkovskii, *Isd. Tverskogo GU, Tver,* 2001 (in press, in Russian).
22. A.G. Shamov, G.M. Khrapkovskii, G.A. Shamov, *V kn. Struktura i dinamika molekulayrnych system.* 1998, p. 183 (in Russian).
23. G.M. Khrapkovskii, A.G. Shamov, G.A. Shamov and V.A. Shlyapochnikov, *Zh. Org. Khim.*, 1999, **35**, 891 (In Russian).
24. V.D. Kolosov, G.K. Klimenko, Yu.A. Pankrushev, G.A. Osipov. *V kn. IV Vsesoyusnogo simposiuma po goreniyu i vzryvu.* Nauka, 1977, p. 549 (in Russian).
25. G.M. Khrapkovskii, E.V. Nikolaeva, D.V. Chachkov, A.G. Shamov, *New Tends in Research of Energetic Materials. Pardubice*, 2001, **P17**, 1-22.
26. G.M. Khrapkovskii, A.G. Shamov, A.M. Rozin, *Dokl. Acad. Nauk SSSR*, 1988, **298**, *4*, 921.
27. G.M. Khrapkovskii, A.G. Shamov, G.A. Shamov and V.A. Shlyapochnikov, *Mendeleev Commun.*, 1997, 169.
28. G.M. Khrapkovskii, A.G. Shamov, G.A. Shamov and V.A. Shlyapochnikov, *Izv. Acad. Nauk, Ser. Khim.*, 2001 (in press, in Russian).

Synthesis and Characterization of Hydrazinium Azide Hydrazinate

Anton Hammerl, Thomas M. Klapötke* and Holger Piotrowski

Department of Chemistry, University of Munich, Butenandtstr. 5-13 (D), D-81377 Munich, Germany

Gerhard Holl and Manfred Kaiser

Wehrwissenschaftliches Institut für Werk-, Explosiv- und Betriebsstoffe, Großes Cent, D-53913 Swisttal, Germany

Received January , 2001

Most high energetic materials, such as TNT, RDX, HMX and CL-20 derive their energy from the oxidation of the carbon backbone. Modern compounds such as CL-20 [1] or the recently reported hepta- and octanitrocubanes [2] possess very high densities and utilize the cage strain of the molecules. They have high detonation velocities and, unfortunately, also high flame temperatures. Therefore, high nitrogen materials were investigated in recent years where the energy is derived from the high positive heat of formation of the compound. These compounds are often insensitive to electrostatic discharge, friction and impact like the recent 3,3'-azobis(6-amino-1,2,4,5-tetrazine). [3]

The detonation velocity correlates to $\sqrt{(Q/\mu}$ (Q: heat of explosion, μ: average molecular weight of products). Therefore, it is possible to reach high detonation velocities with

* to whom correspondence should be addressed: Fax: +49-89-2180-7492. E-mail: tmk@cup.uni-muenchen.de.

[1] Simpson, R. L.; Urtiew, P. A.; Ornellas, D. L.; Moody, G. L.; Scribner, K. J.; Hofman, D. M. *Propellants, Explos. Pyrotech.* **1997**, *22*, 249 and references therein.

[2] Zhang, M.-X.; Eaton, P. E.; Gilardi, R. *Angew. Chem.* **2000**, *112*, 422; *Angew. Chem. Int. Ed. Engl.* **2000**, *39*, 409.

[3] Chavez, D. E.; Hiskey, M. A.; Gilardi, R. D. *Angew. Chem.* **2000**, *112*, 1861; *Angew. Chem. Int. Ed. Engl.* **2000**, *39*, 1791.

explosives that have low weight explosion products. It was shown that the detonation velocity of hydrazinium azide at similar densities is faster than the detonation velocity of RDX, due to the formation of hydrogen during the explosion. [4] Unfortunately, hydrazinium azide is hygroscopic and volatile and, therefore, not in commercial use. We investigated several derivatives of hydrazinium azide, [5] but could not improve the characteristics to satisfy commercial standards.

Here, we present our studies on the hydrazine adduct of hydrazinium azide, which is after hydrazinium azide and ammonium azide the solid with the third highest nitrogen content.

The first indication for a hydrazine adduct of hydrazinium azide was found by Rieger, who isolated a colourless solid from a solution of hydrazinium azide in a mixture of ethanol and hydrazine that had a different melting point than hydrazinium azide. [6] While hydrazinium azide hydrazinate was mentioned in the literature, [7] the compound was never characterized or examined thoroughly.

((Equation 1))

Hydrazinium azide hydrazinate **1** [8] was synthesized in a straightforward, quantitative synthesis from equimolar amounts of hydrazinium azide and hydrazine in an evacuated

---

[4] Yakovleva, G. S.; Kurbangalina, R. Kh.; , Stesik, L. N. *Fiz. Goreniya Vzryva*, **1974**, *10(2)*, 270–274.
[5] a) Habereder, T.; Hammerl, A.; Holl, G.; Klapötke, T. M.; Knizek, J.; Nöth, H. *Eur. J. Inorg. Chem.* **1999**, *5*, 849–852. b) Habereder, T.; Hammerl, A.; Holl, G.; Klapötke, T. M.; Mayer, P.; Nöth, H. *Int. Annu. Conf. ICT*, **2000**, *31st*, 150-1. c) Hammerl, A.; Holl, G.; Hübler, K.; Klapötke, T. M.; Mayer, P. *Eur. J. Inorg. Chem.*, in press. d) Hammerl, A.; Holl, G.; Kaiser, M.; Klapötke, T. M.; Mayer, P.; Nöth, H.; Warchhold, M. *Z. Anorg. Allg. Chem.*, in press.
[6] Rieger, H. D. Ph.D. Thesis: *Hydronitric acid and hydrazine trinitrate*, Cornell University, Ithaca, New York, 1910
[7] a) Dresser, A. L.; Browne, A. W. *J. Am. Chem. Soc.* , **1933**, *58*, 261. b) Kirpichev, E. P.; Alekseev, A. P.; Rubtsov, Y. I.; Manelis, G. B.; *Russian Journal of Physical Chemistry*, **1973**, *47*, 1654.
[8] m.p.: 65 °C. ^{1}H NMR ([D6]DMSO): δ = 5.07 (s, N*H*). ^{14}N NMR ([D6]DMSO): δ = –133 (N*N*N), –278 (*N*N*N*), –321 (*N*H$_2$N*H*$_3$, *N*H$_3$N*H*$_2$). ^{15}N NMR ([D6]DMSO): δ = –133.4 (N*N*N), –278.2 (*N*N*N*), –332.5 (*N*H$_3$N*H*$_2$, *N*H$_2$N*H*$_2$). IR (KBr): ν/cm^{-1} = 3451 w, sh, 3356 m, 3285 m, 3168 m, 3063 m, 2958 m, 2603 m, sh, 2029 s($\nu_{as}(N_3^-)$), 1603 m, 1530 w, sh, 1342 w, 1260 w, 1096 m, 1016 w, sh, 949 w, 798 w, 649 w, 621 w, 552 w. – Raman (100 mW): ν/cm^{-1} = 3272 w, 3187 m, 1643 w, 1337 s($\nu_s(N_3^-)$), 1250 w, 1143 w, 961 w, 942 w, 439 w, 325 w, 233 m, 195 m, 154 m, 129 m. DSC: 16 °C, 65 °C (m.p.), 151.5°C. – N_7H_9: (107.12): Calc.: H 8.5 %, N 91.5 %; found: H 8.9 %, N 90.2 %.

schlenk vessel by heating the vessel for two days to 50 °C. **1** is a colorless solid that is, in contrast to hydrazinium azide, not volatile and not hygroscopic. The vibrational spectra show a larger number of absorptions than for hydrazinium azide, the signals of the azide group are observed at 2029 cm^{-1} (IR) and 1337 cm^{-1}, which are typical values for ionic azides.

The resonance of all protons in the ^{1}H NMR spectrum is found as a singlett at δ = 5.07, which is between the range of the protons signals for a hydrazinium ion (hydrazinium azide: δ = 6.97) and hydrazine (δ = 3.23). The azide atoms display two signals in the nitrogen NMR spectra, at δ = –133/–133.4 ($^{14/15}N$) for the central nitrogen atom and at δ = –278/–278.2 ($^{14/15}N$) for the two terminal nitrogen nitrogen atoms. The hydrazine nitrogen atoms give a signal at δ = –331/–332.5 ($^{14/15}N$) that has the same shift as the signal of the hydrazine nitrogen atoms in hydrazinium azide (δ = –331/–332.8 ($^{14/15}N$)).

The bonding parameters [9] of the hydrazinium ion and the hydrazine molecule agree with known compounds. [10,11]]

((**Figure 1:** Azide ion and molecules connected via hydrogen bonds in **1** as ORTEP-plot (thermal ellipsoids represent 25% probability); selected bond lengths [Å] and angles [°] of **1**: N(1)-N(2) 1.180(2), N(2)-N(3) 1.174(2), N(4)-N(5) 1.453(2), N(6)-N(7) 1.453(2), N(3)-N(2)-N(1) 179.5(2); hydrogen bonds: N-N distances [Å] (N-H···N angles [°]), H···N distances are given in the picture: N(4)-H(41)···N(6) 2.875(2) (167(2)), N(4)-H(42)···N(7) 2.747(2) (175(2)), N(4)-H(42)···N(6) 3.479(2) (144(1)), N(4)-H(43)···N(1) 2.945(2) (161(2)), N(5)-H(51)···N(1)

---

[9] Crystal data for **1** were recorded on a NONIUS KAPPA CCD diffractometer, Mo K_α radiation, λ = 0.71073, graphite monochromator: N_7H_9 (107.14), colorless rod, 0.30 x 0.07 x 0.06, monoclinic, $P\,2_1/c$, a = 6.3704(2) Å, b = 12.1111(4) Å, c = 6.9940(2) Å, β = 91.8666(2) °, V = 539.32(3) Å^3, Z =4, ρ_{calc} = 1.320 g/cm, μ = 0.106, $F(000)$= 232, T = 200(2) K, $-8 \le h \le 8$, $-15 \le k \le 15$, $-9 \le l \le 8$, reflections collected: 9191, independent reflections: 1226 (R_{int} = 0.0637), observed reflections: 895 [$I > 2\sigma(I)$]; structure solution SIR97 (Cascarano et al. *Acta Cryst. Sect. A* **1996**, *C79*); structure refinement SHELXL-97 (Sheldrick, G. M. University of Göttingen, Germany, **1997**), directs method, free refinement of all hydrogen atoms; final R indices [$I > 2\sigma(I)$]: R_1 = 0.0457, wR_2 = 0.0980; all data: R_1 = 0.0723, wR_2 = 0.1106

[10] a) Chiglien, P. G.; Etienne, J.; Jaulmes, S.; Laruelle, *P. Acta Cryst. Sect. B*, **1974**, *30*, 2229–2233. b) Holfter, H.; Klapötke; T. M.; Schulz, A. *Eur. J. Solid State Inorg. Chem.*, **1996**, *33*, 855.

[11] Collin, R. L.; Lipscomb, W. N. *Acta Cryst.* **1951**, *4*, 10.

3.111(2) (171(2)), N(5)-H(52)···N(3) 3.070(2) (156(2)), N(6)-H(61)···N(1) 3.133(2) (156(2)), N(6)-H(62)···N(3) 3.135(2) (173(2)), N(7)-H(71)···N(3) 3.126(2) (166(2)), N(7)-H(72)···N(5) 3.127(2) (160(2)).))

The azide ion of **1** is connected via six hydrogen bonds to three hydrazinium and three hydrazine molecules. The N-N distances of NH_2···N hydrogen bonds range between 3.070(2) and 3.135(2) Å and are longer than the N-N distance of the NH_3···N hydrogen bond with 2.9425(2) Å due to the positive charge on the NH_3 group.

((**Figure 2:** molecules connected via hydrogen bonds to hydrazinium and hydrazine molecules in **1** as ORTEP-plot (thermal ellipsoids represent 25% probability)))

The hydrazinium and hydrazine molecules are connected by two short hydrogen bonds (N-N distance 2.747(2) and 2.875(2) Å) between the hydrogen atoms of the NH_3 group of the hydrazinium ion and the lone pairs of the nitrogen atoms of the hydrazine molecule. The bond lengths of the azide ion show a slight difference (1.180(2) and 1.174(2) Å) due to different hydrogen bonding on both ends of the azide ion.

The explosion, initiated by electrical resistance heating in an evacuated steel bomb, gave dinitrogen, ammonia and dihydrogen. Compared to hydrazinium azide, **1** produces larger amounts of ammonia in the explosion. **1** showed no sensitivity to an electrical discharge of 20 kV (electrostatic), in a drop hammer test (5kg/50cm) [12] (shock) and to grinding in a mortar (friction). Like hydrazinium azide, **1** does not explode when heated slowly (10 °/min), but on contact with a hot metal surface.

We are currently studying hydrazine adducts of other hydrazinium salts with high nitrogen anions.

---

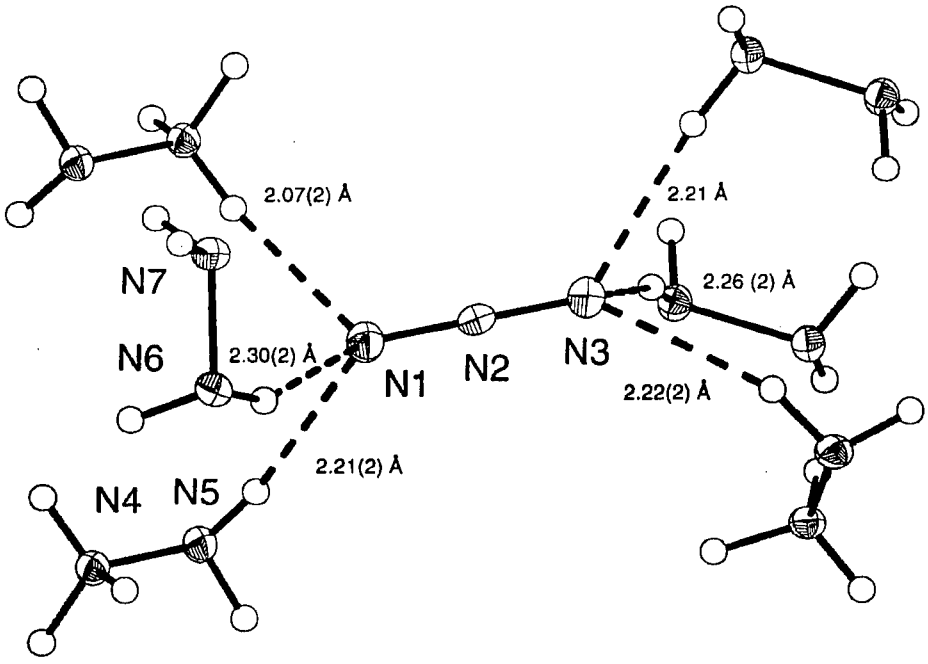
[12] Klapötke, T. M.; Rienäcker, C. M., *Propellants, Explos. Pyrotech.*, in press.

Acknowledgments. Financial support of this work by the University of Munich (LMU), the Deutsche Forschungsgemeinschaft (DFG, KL 636/7-1) and the German Federal Office of Defense Technology and Procurement (BWB) is gratefully acknowledged.

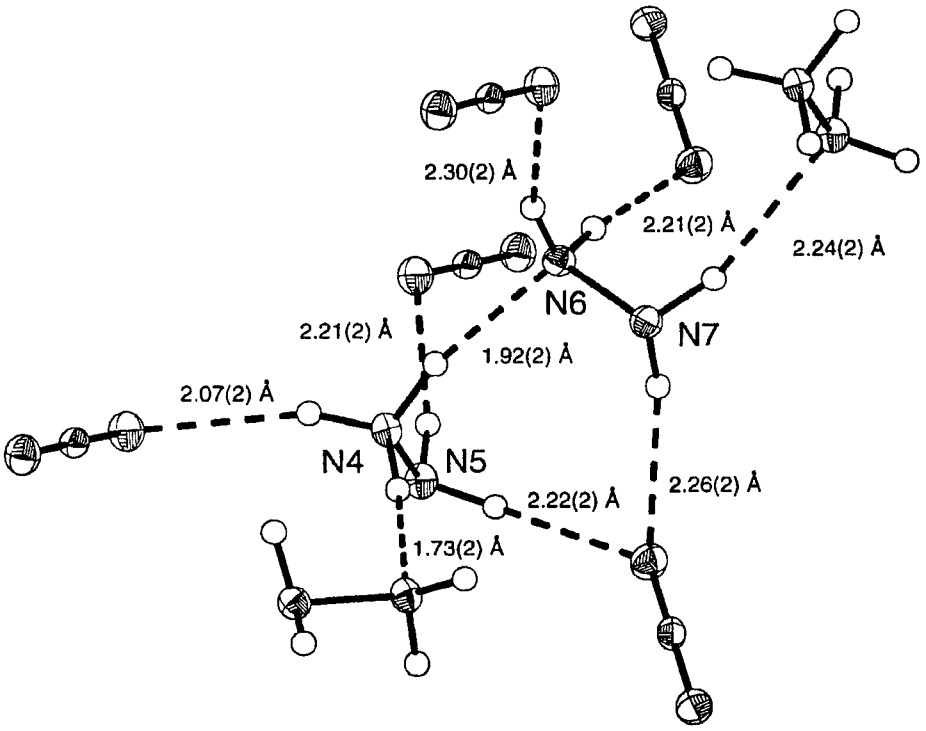
((Equation 1))

$$[H_2NNH_3]^+[N_3]^- + H_2NNH_2 \longrightarrow [H_2NNH_3]^+[N_3]^- \cdot H_2NNH_2$$

((**Figure 1:** Azide ion and molecules connected via hydrogen bonds in **1** as ORTEP-plot (thermal ellipsoids represent 25% probability); selected bond lengths and angles of **1**: N(1)-N(2) 1.180(2), N(2)-N(3) 1.174(2), N(4)-N(5) 1.453(2), N(6)-N(7) 1.453(2), N(3)-N(2)-N(1) 179.5(2); hydrogen bonds: N-N distances [Å] (N-H N angles [°]), H N distances are given in the picture: N(4)-H(41) N(6) 2.875(2) (167(2)), N(4)-H(42) N(7) 2.747(2) (175(2)), N(4)-H(43) N(1) 2.945(2) (161(2)), N(5)-H(51) N(1) 3.111(2) (171(2)), N(5)-H(52) N(3) 3.070(2) (156(2)), N(6)-H(61) N(1) 3.133(2) (156(2)), N(6)-H(62) N(3) 3.135(2) (173(2)), N(7)-H(71) N(3) 3.126(2) (166(2)), N(7)-H(72) N(5) 3.127(2) (160(2)).))



((**Figure 2:** molecules connected via hydrogen bonds to hydrazinium and hydrazine molecules in **1** as ORTEP-plot (thermal ellipsoids represent 25% probability)))



NEW 1,2,4-TRIAZOLYL AND TETRAZOLYL DERIVATIVES OF NITROGUANIDINE

Alexander M. Astachov[1], Irina V. Gelemurzina[1], Alexander D. Vasiliev[2], Andrey A. Nefedov[1], Ludmila A. Kruglyakova[1], Rudolf S. Stepanov[1]

[1]Siberian State Technological University,
660049, Krasnoyarsk, prosp. Mira, 82, Russia
[2]Institute of Physics RAS (Sib. Div.)
660036, Krasnoyarsk, Russia

ABSTRACT

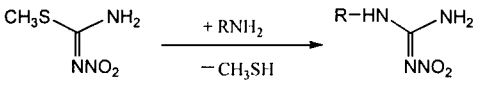
New energetic compounds, 1-(tetrazol-5-yl)-2-nitroguanidine and 1-nitroguanyl-1,2,4-triazole derivatives, were synthesized by reaction between 1-nitro-2-methylisothiourea and aminoheterocycle (5-aminotetrazole, 3,5-diamino-1,2,4-triazole and 5-amino-1,2,4-triazole). Structure and some physical and chemical properties of the compounds obtained are discussed.

INTRODUCTION

Undoubtedly, both the derivatives of five-member high nitrogen-containing heterocycles (1,2,4-triazole and tetrazole) [1–3], and various nitroguanidines [4] are of interest for use as energetic compounds, such as explosives, components of powders and solid rocket propellants. It is possible to expect that joining nitroguanyl fragment with 1,2,4-triazole and tetrazole cycles in one molecule would lead to new highly energetic compounds, which would possess positive properties of both classes, thus combining high density and thermal stability with low impact sensitivity.

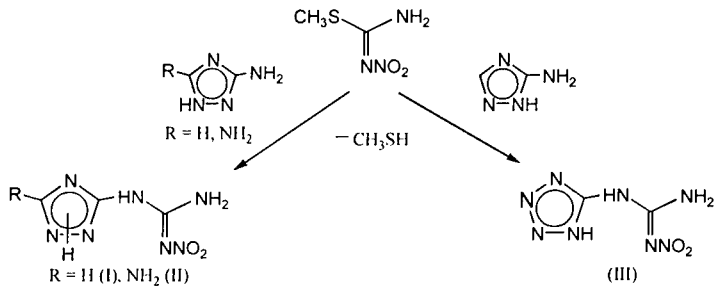
One of known methods to synthesize derivatives of nitroguanidine is the reaction of amines with 1-nitro-2-methylisothiourea [5] (scheme 1).

Scheme 1



A large number of various aliphatic and benzoaromatic substituted nitroguanidines synthesized by this method is described in the literature. At the same time, we found no references that heterocycle compounds, such as 1,2,4-triazole and tetrazole, have ever been used in this reaction between aminoderivatives. In the present work we originally proposed to synthesize appropriate tetrazolyl and 1,2,4-triazolyl derivatives of nitroguanidine proceeding from 5-aminotetrazole, 3,5-diamino-1,2,4-triazole and 5-amino-1,2,4-triazole (scheme 2) and to study their physical-chemical properties.

Scheme 2

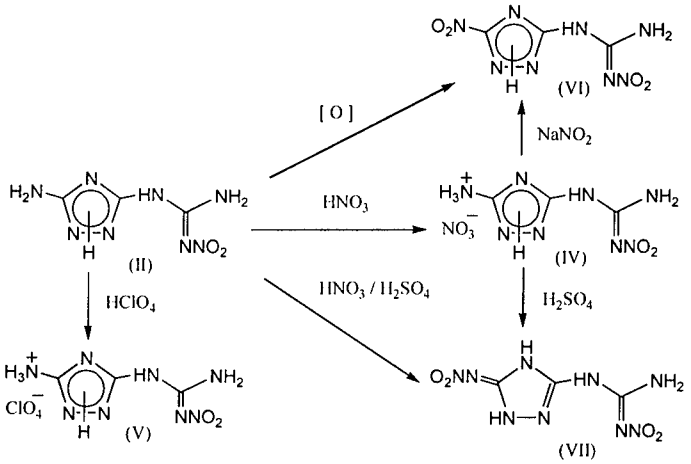


The presence of reaction-able primary aminogroup (directly bonded with heterocycle)[1] in compound (II) allowed to expect other energetic compounds to be obtained (scheme 3).

Appropriate chemical transformations were carried out and their products seemed to correspond to the proposed reaction schemes 2 and 3. That notion was supported by the results of elementary analysis, UV- and FTIR-spectroscopy. For a long time, we considered compounds obtained by us to correspond to the formulas (I-VII).

[1] Being involved in conjugation with nitroguanyl system must deactivate the other primary aminogroup in nitroguanyl fragment of molecule.

Scheme 3

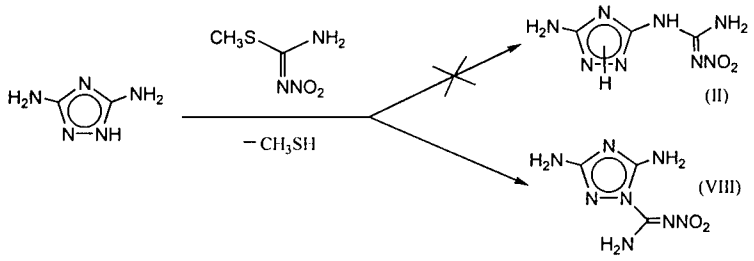


However, it was later discovered by X-ray structure investigation that one obtains different products of isomeric structure by starting with aminoderivatives of 1,2,4-triazole. Unfortunately, these products contain similar molecular fragments, and, therefore, elementary analysis, UV and FTIR spectroscopic data were not capable to determine structure.

RESULTS AND DISCUSSION

The X-ray structure investigation interprets unambiguously the product of interaction of 1-nitro-2-methylisothiourea with 3,5-diamino-1,2,4-triazole as 1-nitroguanyl-3,5-diamino-1,2,4-triazole (VIII). Thus, reaction does not proceed by one of the aminogroups, as was expected, but by atom of nitrogen in position one of the triazole cycle (scheme 4)!

Scheme 4



X-ray molecular structure of 1-nitroguanyl-3,5-diamino-1,2,4-triazole is shown on Fig. 1. Nitroguanyl fragment, triazole cycle, and aminogroups, bonded with heterocycle, are all located practically in one plane. The dashed line on figure shows intramolecular hydrogen bonded.

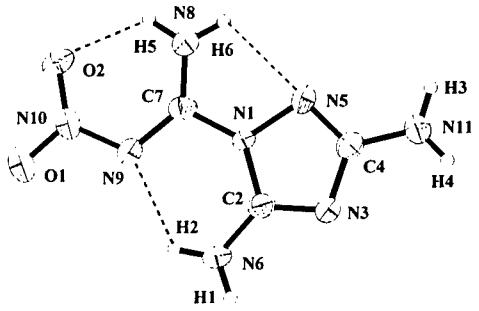


Figure 1. X-ray molecular structure of 1-nitroguanyl-3,5-diamino-1,2,4-triazole.

Crystal data (at 20°C):

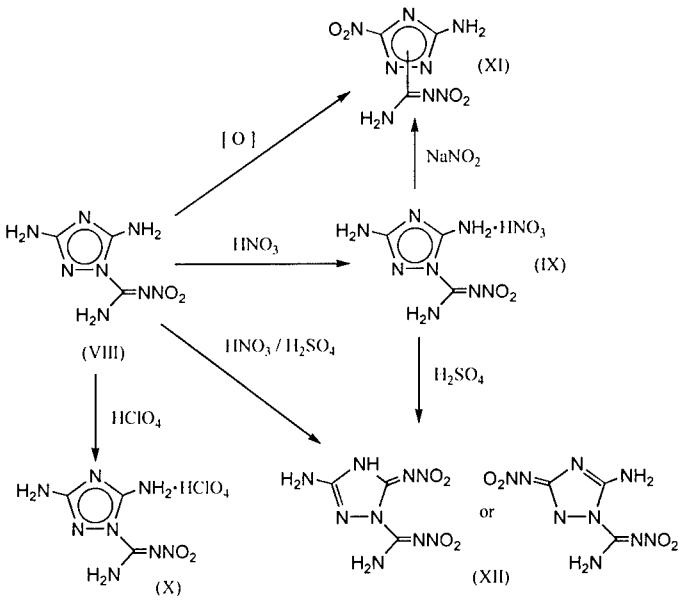
a=20.678(1)Å, b=7.2493(5)Å, c=19.251(1)Å, α=β=γ=90°, V=2885.74(29)Å^3, Z=16, $d_{x\text{-}ray}$=1.714 г/см^3, space group Pbca.

Consequent chemical transformations of compound (VIII) are shown in scheme 5 (instead of the previously suggested scheme 3).

Despite two free aminogroups present in compound (VIII), it was possible to obtain only monosalts such as nitrate (IX) and perchlorate (X) when reacting with strong mineral acids. Before X-rays were done, we considered the fact that only monosalts have been formed in the acid's excess to be an additional indication of suggested structure (II) that contains one free aminogroup. Salts (IX) and (X) are stable in usual conditions but proved to be unstable hydrolytically. When attempting

to re-crystallize these salts from water, full hydrolysis occurs and initial substances, compound (VIII) and acid solution, are formed.

Scheme 5



Low basicity of aminogroup of compound (VIII) is possibly due to a through conjugation between aminogroups, triazole cycle and nitroguanyl fragment in a molecule. This conjugation results in reducing electron density of aminogroups and displacing electron density towards electron-acceptor, that is, nitroguanyl fragment.

We cannot unambiguously claim that aminogroup is protonized when salts are formed as compound (VIII) reacts with acids. It may be that triazole cycle is protonized instead, as it happens with 5-amino-1,2,4-triazole [1].

Similarly to nitrimines known earlier, the electronic spectra of the compounds obtained show peaks for $n \rightarrow \pi^*$ transition in nitrimine fragment (Fig. 2). It was not possible to obtain UV spectra for compounds (XI) and (XII) due to their low solubility. Due to full hydrolysis of salts (IX) and (X) in water solutions their spectra proved to be identical to the spectrum of compound (VIII) (Fig. 2).

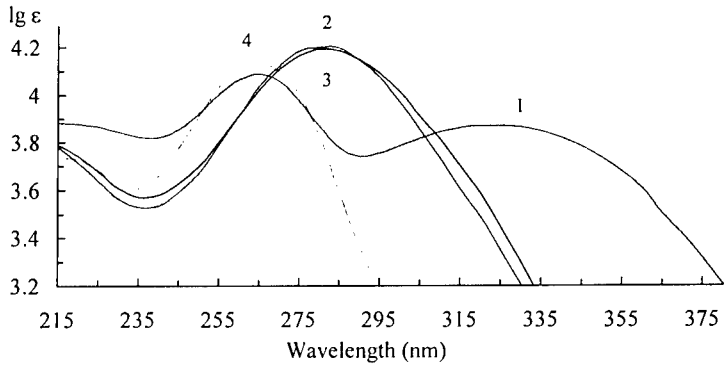


Figure 2. UV spectra water solution: 1-nitroguanyl-3,5-diamino-1,2,4-triazole, 1-nitroguanyl-3,5-diamino-1,2,4-triazole nitrate, 1-nitroguanyl-3,5-diamino-1,2,4-triazole perchlorate (1), 1-nitroguanyl-3(5)-amino-1,2,4-triazole (2), 1-(tetrazol-5-yl)-2-nitroguanidine monohydrate (3) and nitroguanidine (4).

Currently, only compound (VIII) structure is established by X-ray analysis. This is because of difficulty in deriving compounds' single-crystalline samples except for salts (IX) and (X). X-ray powder diffraction analysis does not allow determining parameters of unit cells. This is possibly because each particular compound is simultaneously present in several different forms (polymorphic modifications, tautomers etc).

For example, one can obtain at least three products with the same elementary composition and identical UV spectra in water solutions (Fig. 2) for 1-nitroguanyl-3(5)-amino-1,2,4-triazole (XIII) just by changing crystallization conditions. These products, however, show different X-ray powder diffraction and FTIR spectra (Fig. 3). FTIR spectra for the other compounds are shown on Fig. 4.

All the compounds obtained have no melting point (endothermic peak on thermograms DTA is absent). Their thermal decomposition progresses in a solid phase at temperatures above 200°C.

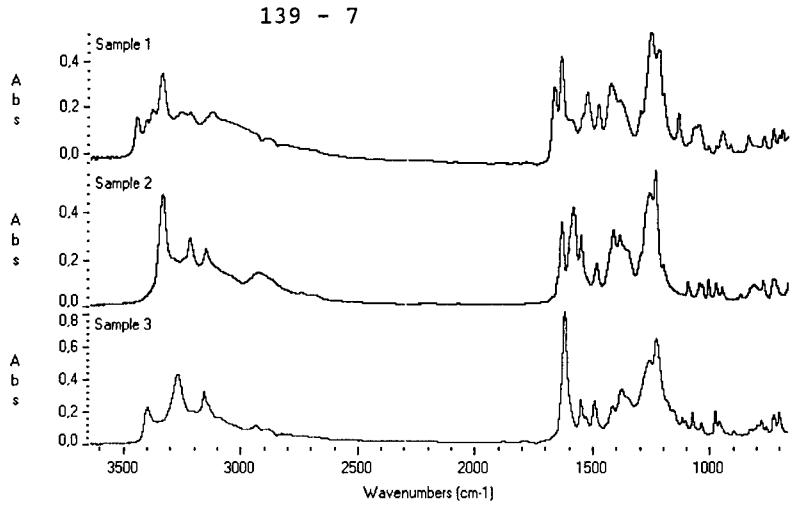


Figure 3. FTIR spectra samples of 1-nitroguanyl-3(5)-amino-1,2,4-triazole obtained by various crystallization conditions.

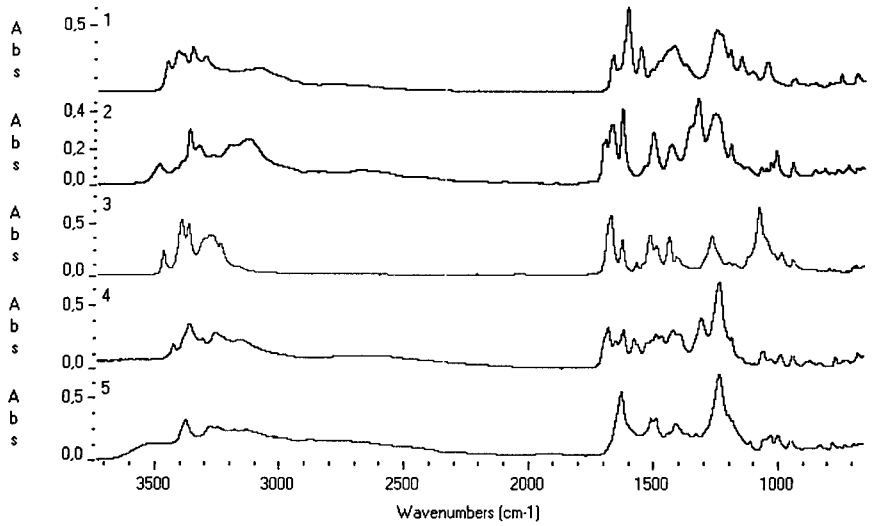


Figure 4. FTIR spectra: 1-nitroguanyl-3,5-diamino-1,2,4-triazole (1), 1-nitroguanyl-3,5-diamino-1,2,4-triazole nitrate (2), 1-nitroguanyl-3,5-diamino-1,2,4-triazole perchlorate (3), 1-nitroguanyl-3(5)-amino-5(3)-nitrimino-1,2,4-triazol (4), 1-(tetrazol-5-yl)-2-nitroguanidine monohydrate (5).

Interaction of 5-amino-1,2,4-triazole with 1-nitro-2-methylisothiourea proceeds on nitrogen heterocycle, same as for 3,5-diamino-1,2,4-triazole. The reaction product chemical properties, such as high solubility in acids and the fact that solubility in an alkaline medium is practically unchanged when compared with neutral water solution, support this. To the contrary, originally suggested compound (I), if obtained, would form salts in an alkaline medium or, at least, would be well soluble. This is because of a non-replaced hydrogen atom in a nitrogen triazole cycle for compound (I).

At the same time, interaction of 5-aminotetrazole with 1-nitro-2-methylisothiourea most likely yields 1-(tetrazol-5-yl)-2-nitroguanidine (III) as reaction product. This is supported, in particular, by formation of salts for compound (III) in alkaline medium. The difficulty of deriving single-crystalline samples of the reaction product in this case has not allowed us making X-ray structure analysis. However, for potassium salts of compound (III) it was possible to determine unit cell parameters by powder diffraction data (at 20°C):

a=7.036(1)Å, b=11.417(1)Å, c=4.6810(7)Å, α=93.17(1)°, β=106.77(1)°, γ=83.48(1)°

V=357.64(5)Å^3, Z=2, $d_{x\text{-}ray}$=1.952 г/см^3, space group $P\bar{1}$.

In principle, relatively small number of atoms in a unit cell allows establishing structure of potassium salts for compound (III) by powder diffraction data. This work is currently under way.

Confronted with difficulties of determining structure experimentally for compounds obtained, we carried out structural analysis through computational methods of quantum chemistry. Semiempirical quantum-chemical calculations were carried out for optimal molecular geometries in MNDO, AM1 and PM3 approximations. Compound (VIII), with certain geometrical parameters determined experimentally, served as an etalon substance that allowed evaluating adequacy of computational methods used for compounds under consideration.

Calculated geometry for 1-nitroguanyl-3,5-diamino-1,2,4-triazole molecule is close to experimental (Fig.5). Standard deviations of calculated geometrical

parameters from experimental values were 0.069-0.073Å for bond lengths and 2.5-4.6° for bond angles, depending on calculation method. This reasonably good result correspondence made us hope that structure of the other compounds could also be predicted by computational methods.

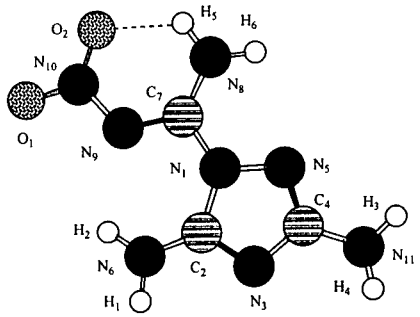


Figure 5. Computational geometry of a molecule 1-nitroguanyl-3,5-diamino-1,2,4-triazole.

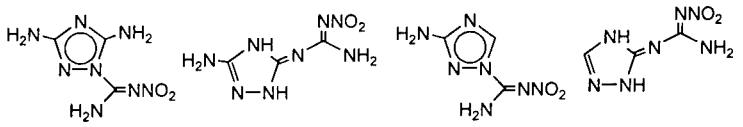
For 1-nitroguanyl-3(5)-amino-1,2,4-triazole with a minor difference (0.02 kJ/mole)[2] preferences are given to a structure of 1-nitroguanyl-3-amino-1,2,4-triazole. In practice, this small difference in energy for 3- and 5-aminoderivatives means that both isomers may be present simultaneously in a compound.

For compound (XII), 1-nitroguanyl-3-amino-5-nitrimino-1,2,4-triazole is chosen based on calculations of structure. The primary nitramine structure with a minimum heat of formation differs from the nitrimine structure by only 3.4 kJ/mole. Any other possibilities for a different structure are less preferable.

For nitrocompound (VI) the most favorable disposition of the substituents proved to be that of 1-nitroguanyl-5-amino-3-nitro-1,2,4-triazole proved. The 1-nitroguanyl-3-amino-5-nitro-1,2,4-triazole structure is less favorable by 14.8 kJ/mole.

[2] Hereafter, the calculated energy parameters of molecules are obtained by method PM3, which proved to be the most preferable for this purpose.

The calculations have shown that originally suggested reaction products (I, II) are far more preferable thermodynamically than compounds (VIII, XIII), that are actually formed:



277.08 (VIII) 264.56 (II) 297.60 (XIII) 276.57 (I)

The significances ΔH^{0}_{f} (kJ/mole) for most energetically favorable conformations are indicated.

This suggests that it is possible to synthesize these products in the future, may be by modifying conditions of reaction or by rearrangement.

Research of physical-chemical properties is currently under way. The study of thermal stability, sensitivity to mechanical impact and performances of substances (III-VIII) is being conducted as well. We keep trying to obtain single-crystal samples of the compounds to determine their structure unambiguously by X-ray analysis.

REFERENCES

[1] **Pevzner M.S.** "The 1,2,4-triazole derivatives – high-energetic compounds". *Russ. Chem. J.* (*Ross. Khim. Zh.*) **1997**. Vol. 41. N 2. P. 73–83 (in Russian).

[2] **Licht H.H., Braun S., Schäfer M., Wanders B., Ritter H.** "Nitrotriazole: chemische struktur und explosive eigenschaften". *Energetic Materials – Production, Processing and Charakterization. 29th Intern. ICT-Conference.* **1998**. Karlsruhe. FRG. 47/1–47/15.

[3] **Ostrovskii V.A., Koldobskii G.I.** "Energetic tetrazoles". *Russ. Chem. J.* (*Ross. Khim. Zh.*) **1997**. Vol. 41. N 2. P. 84–98 (in Russian).

[4] **McKay A.F.** "Nitroguanidines". *Chem. Rev.* **1952**. Vol. 51. N 2. P. 301–346.

[5] **Fishbein L., Gallaghan J.A.** "The preparation of 2-alkyl-1(or 3)-nitro-2-thiopseudourea. Part I. Reactions with amines". *J. Am. Chem. Soc.* **1954**. Vol. 76. N 7. P. 1877–1879.

HEATS OF FORMATION OF ENERGETIC OXETANE MONOMERS AND POLYMERS

Robert D. Schmidt

Energetic Materials Center, Lawrence Livermore National Laboratory,
P.O. Box 808 (Mail Stop L-282), Livermore, California 94551 USA

Gerald E. Manser

Propellant Technology and Development, Aerojet Corporation, PO Box 13222
Sacramento, California 95813-6000 USA

ABSTRACT

Energetic oxetane polymers have shown promise as performance-enhancing ingredients in gun and missile propellants. In order to correctly predict the performance of energetic materials containing these polymers, it is important to have accurate, experimentally determined values for the polymer heats of formation (ΔH_f). In support of a theoretical study on gun propellant performance, heats of combustion were experimentally determined for a series of oxetane polymers and monomers (see below) using combustion calorimetry, and from these, ΔH_f values were calculated. Polymers included BAMO/AMMO, BAMO/NMMO (polyol and TPE), and BNMO/NMMO mixtures. In order to calculate the ΔH_f of the polymers from heat of combustion data, a number of assumptions were made regarding the polymer structure and molecular weight. A comparison of the ΔH_f values for the monomers and polymers were made, and these values were compared to heats of formation measured elsewhere.

INTRODUCTION

Energetic binders made from oxetanes have been investigated for use in gun propellants and in other applications where an energetic binder would be useful. In order

to predict the performance of an energetic material, it is important to have accurate, experimentally determined values for the material's heat (enthalpy) of formation (ΔH_f). While there are reports in the literature[1-4] of measured ΔH_f values for energetic oxetanes, these are generally limited to monomers and single-component polymers. In this study, heats of formation were determined for a series of oxetane monomers (including two previously unreported), as well as polymers and polymer mixtures, using combustion calorimetry. The compounds studied were based on the energetic monomers azidomethylmethyloxetane (AMMO), *bis*-azidomethyloxetane (BAMO), nitratomethylmethyloxetane (NMMO) and *bis*-nitratomethyloxetane (BNMO), and the non-energetic monomers ethoxymethylmethyloxetane (EMMO) and *bis*-ethoxymethyloxetane (BEMO). Samples of these materials were prepared at the Aerojet Corp. in Sacramento, California. Chemical structures of the monomers are shown in figure 1.

The following equation relates the heat of formation (ΔH_f) of a material to its heat of combustion (ΔH_c):

$$\Delta H_{f\,(material)} = \Delta H_{f(combustion\ products)} - \Delta H_{c(material)}$$

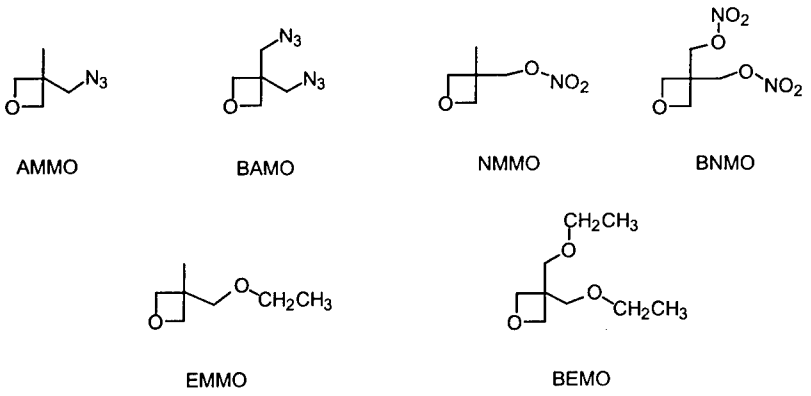


Figure 1. Oxetane monomer structures.

The value for $\Delta H_{c(material)}$ is determined directly by combustion calorimetry. The material is ignited and burned in a sealed pressure bomb which contains pure oxygen atmosphere. The bomb is immersed in a water bath during combustion, and the resulting temperature rise of the bath is measured and used to calculate the value for $\Delta H_{c(material)}$. A value for $\Delta H_{f(combustion\ products)}$ is then calculated. In the case of CHNO compounds, the combustion products are N_2, CO_2, H_2O and small amounts of HNO_3. Since the heat of formation of nitrogen gas is zero (by definition for the elemental form), it does not contribute to the product heat of formation. The amount of nitric acid produced during combustion is measured by performing an acid-base titration of the liquid water remaining in the bomb. A correction for this HNO_3 is then calculated using the standard heat of formation of the acid. (In practice, these data are entered into the calorimeter computer, which then automatically includes this correction in the reported $\Delta H_{c(material)}$.) The heats of formation of CO_2 and H_2O are determined by calculating the moles of these species produced during combustion (which is based on the C and H content of the material), and multiplying by their respective standard heats of formation:

ΔH_f (CO_2) = -94.051 kcal/mol

ΔH_f (H_2O) = -68.315 kcal/mol

So, for example, complete combustion of the AMMO monomer produces 5 moles of CO_2 and 4.5 moles of H_2O per mole of AMMO, which gives a $\Delta H_{f(combustion\ products)}$ = -777.67 kcal/mol. The measured ΔH_c of AMMO was -6384.09 cal/g (which includes the correction for HNO_3). This is multiplied by the molecular weight of AMMO (127.147 g/mol)) to give a molar ΔH_c of -811.72 kcal/mol. Therefore:

$\Delta H_{f(AMMO)}$ = (-777.67) – (-811.72) = +34.04 kcal/mol (or +0.2677 kcal/g).

RESULTS

Table 1 summarizes the experimental heats of formation determined by this study. For comparison, values measured elsewhere are given in the right column, if available. In general, our results agreed well with those values reported elsewhere, which gives us confidence that our values for previously unreported materials are accurate.

Table 1. Summary of Heat of Formation Measurements.

Material	**Measured Heats of Formation**		
(ingredient wt. %, if mixture)	kcal/mol	kcal/g	lit. (kcal/mol)
AMMO	+34.04	+0.2677	+43.00[a]
BAMO	+103.60	+0.6161	+124.00[a]; +102.039[b]
BEMO	-151.17	-0.8680	-
BNMO	-89.82	-0.4316	-75.90[c]
EMMO	-113.38	-0.8709	-
NMMO	-79.99	-0.5437	-79.67[d]
Poly-BAMO	+88.79	+0.5280	+89.12 to +124.00[c]
Poly-BEMO	-289.69	-1.6626	-164.00[d]
Poly-NMMO (polyol)	-82.78	-0.5626	-94.00 to -73.90[c]
Poly-BAMO(50%)/AMMO (50%) (TPE)	+41.16	+0.2842	-
Poly-BAMO(73%)/NMMO (27%) (polyol)	+46.09	+0.2848	-
Poly-BAMO(73%)/NMMO (27%) (TPE)	+35.55	+0.2196	-
Poly-BNMO(66%)/NMMO (34%) (TPE)	-101.26	-0.5548	-

Notes: (a) from reference 1, p. 22-10; (b) from reference 2, p. IIB-2-10; (c) from ICT Thermochemical Data Base; (d) from reference 3, pp. 87-4 & 87-5

A. General Experimental Notes. A Parr Instruments 1261 combustion calorimeter was used to conduct all experiments. Samples were burned in a 250 ml platinum-lined Parr bomb (Model 1105), using a platinum combustion crucible and platinum igniter wire. Sample sizes ranged between 0.3 and 1 gram, depending on burn characteristics. For volatile liquid samples, a tape seal was made over the sample combustion crucible to prevent evaporation prior to ignition. (The heat of combustion of this tape is known, and

was accounted in the calculations. See results for AMMO for complete description, below.) Solid samples were pressed into pellets (if in powdered form) or, if in chunk form, were cut to the appropriate weight. In some cases, benzoic acid in pellet form was added to the combustion crucible along with the sample to facilitate complete combustion. Accuracy of material weight is ± 0.1 mg (not accounted for in error figures below). Post-burn gases were tested for presence of CO (which indicates incomplete combustion), and any runs where CO was detected were discarded. After each combustion, the inner bomb surfaces were rinsed with deionized water, and these washings were titrated for nitric acid using a 0.0709 sodium carbonate solution and methyl orange indicator. The titration data were entered into the calorimeter and heats of combustion were corrected automatically for nitric acid by the calorimeter software.

B. Oxetane Monomer Heat of Formation Results and Calculations.

1. **AMMO Monomer**. Aerojet lot # C923-64, liquid. AMMO does not burn cleanly in the oxygen bomb without a burn enhancer. Therefore, benzoic acid was added to each burn run, resulting in clean burns. Since AMMO is a liquid with significant volatility, the combustion crucible was sealed with cellophane tape to prevent mass loss due to evaporation. The liquid was added to the crucible with a syringe, by piercing the tape seal with the syringe needle. (The ΔH_c of the tape is known from separate measurements, and is deducted from the measured ΔH_c of AMMO.) Result: $\Delta H_c = 6384.09 \pm 13.63$ cal/g (average of 3 runs), which gives $\underline{\Delta H_f = +34.04 \pm 1.73}$ $\underline{\text{kcal/mol} = +0.2677 \pm 0.0136 \text{ kcal/g.}}$
2. **BAMO Monomer**. Aerojet SRR 70881, lot # 072798. BAMO burned fairly well without burn enhancers. However, each run left approximately 1 mg of an unburned, brown residue that, when washed with water, partially dissolved. No correction was made for this. Result: $\Delta H_c = 5037.63 \pm 7.71$ cal/g (average of 5 runs), which gives $\underline{\Delta H_f = +103.60 \pm 1.30 \text{ kcal/mol} = +0.6161 \pm 0.0077 \text{ kcal/g.}}$
3. **BEMO Monomer**. Burned cleanly on each run, using tape seal method to avoid evaporation errors (as with AMMO). Result: $\Delta H_c = 7522.11 \pm 8.77$ cal/g (average of 5 runs), which gives $\underline{\Delta H_f = -151.17 \pm 1.52 \text{ kcal/mol} = -0.8680 \pm 0.0088 \text{ kcal/g.}}$

4. **BNMO Monomer**. Aerojet lot # CR3 RX2. Burned as pressed pellets, this compound burned very well. Results: ΔH_c = 3140.82 ± 8.58 cal/g (average of 5 runs), which gives ΔH_f = -89.82 ± 1.79 kcal/mol = -0.4316 ± 0.0086 kcal/g.
5. **EMMO Monomer**. Lot # 957-44K, liquid. EMMO is the most volatile of all the monomers analyzed, so experiments were conducted using tape-seal method (see AMMO, above). EMMO burns cleanly by itself, so no burn enhancers were needed. Results: ΔH_c = 7859.28 ± 15.23 cal/g (average of 4 runs), which gives ΔH_f = -113.38 ± 1.98 kcal/mol = -0.8709 ± 0.0152 kcal/g.
6. **NMMO Monomer**. Burned cleanly with benzoic acid burn enhancer. Results: ΔH_c = 4741.86 ± 11.47 cal/g (average of 5 runs), which gives ΔH_f = -79.99 ± 1.69 kcal/mol = -.5437 ± 0.0115 kcal/g.

C. Oxetane Polymer Heat of Formation Results and Calculations.

The following calculations use the assumption that the average molecular weight of the polymer is large in comparison to the monomer (i.e., the average number of repeating units, *n*, is greater than about 20). In effect, this neglects the weight of the "additional" – H and -OH groups at the chain ends, and it is then an excellent approximation that the polymer chain molecular weight is an integral multiple of the monomer molecular weight.

1. **Poly-NMMO (polyol)**. Lot # 727-64, viscous liquid. Burned fairly well with benzoic acid burn rate enhancer. Result: ΔH_c = 4722.87 ± 4.89 cal/g (average of 4 runs). Using the above assumption, one gram of poly-NMMO will burn to produce 1.496 grams of CO_2 and 0.5510 grams of H_2O. This gives a product ΔH_f = -5.286 kcal/g poly-NMMO. This gives ΔH_f = -82.78 ± 0.72 kcal/mol = -0.5626 ± 0.0049 kcal/g.
2. **Poly-BEMO**. Lot # C647-91. Burned cleanly without burn enhancers. Result: ΔH_c = -6723.89 ± 19.42 cal/g (average of 6 runs), which gives ΔH_f = -289.69 ± 3.38 kcal/mol = -1.6626 ± 0.0194 kcal/g.
3. **Poly-BAMO/AMMO (TPE)**. Lot # C923-58. Weight ratio of BAMO:AMMO = 0.50 : 0.50. This was a difficult material on which to obtain satisfactory combustion.

Burned as pressed pellets, the material tended to leave relatively large amounts of unburned residue. Combustion was slightly cleaner using benzoic acid as a burn enhancer, but unburned residue remained after each run. This residue was combusted separately (using benzoic acid to complete the combustion), and a correction for unburned material was determined. Result: ΔH_c = -5552.72 ± 15.29 cal/g (average 3 runs, corrected for unburned material). Based on a polymer empirical formula of $C_5H_{8.5694}N_{4.2917}O_1$, calculated ΔH_f = +41.16 ± 2.22 kcal/mol = +0.28422 ± 0.0153 kcal/g.

4. **Poly-BAMO/NMMO (polyol).** Lot # 927-44A, sticky, highly viscous liquid. Ratio of BAMO:NMMO = 0.73 : 0.27. Burned very well using benzoic acid as a burn enhancer. Result: ΔH_c = -4941.35 ± 2.41 cal/g (average of 3 runs). Based on a polymer empirical formula of $C_5H_{8.2971}N_{4.5144}O_{1.8914}$, calculated ΔH_f = +46.09 ± 0.39 kcal/mol = +0.28479 ± 0.0024 kcal/g.
5. **Poly-BAMO/NMMO (TPE).** Aerojet lot # ETPE-21, in the form of 1-2 cm rubbery chunks, with light conglomerations of finer particles. Ratio of BAMO:NMMO = 0.73 : 0.27. Burned fairly well without burn enhancers, although small amounts of soot remained after each burn (generally < 0.3 mg). The soot was occasionally found outside the crucible in a 1-2 cm patch on the inner wall of the combustion bomb, indicating possible ejection of the material from the combustion crucible. Use of burn rate enhancers resulted in combustion of bomb gasket, even with small amounts of sample. Result: ΔH_c = -4876.19 ± 9.57 cal/g (average of 4 runs, no correction for unburned residue). Based on a polymer empirical formula of $C_5H_{8.2971}N_{4.5144}O_{1.8914}$, calculated ΔH_f = +35.55 ± 1.55 kcal/mol = +0.21963 ± 0.0096 kcal/g.
6. **Poly-BNMO/NMMO (TPE).** Lot # C965-167B, rubbery chunks. Ratio of BNMO:NMMO = 0.66 : 0.34. Generally good burns, although some had unburned residue. Some runs were burned with benzoic acid as a burn enhancer, with slightly better results. No correction for unburned material was made. (Attempts to quantify heat of unburned material gave inconsistent results. In any case, the correction is probably insignificant, due to relatively small weight of unburned residue.) ΔH_c = -3597.86 ± 7.70 cal/g (average of 5 runs). Based on a polymer empirical formula of

$C_5H_{8.4215}N_{1.5785}O_{5.7354}$, calculated ΔH_f = -101.26 ± 1.41 kcal/mol = -0.55479 ± 0.0077 kcal/g.

7. **Poly-BAMO**. Lot # 979-205, solid powder pressed into pellets. Burned in a similar fashion to poly-BAMO/NMMO (TPE), leaving a small amount of soot in the crucible and on bomb wall. (No correction was made for this, but was estimated to be <5cal/g.) Result: ΔH_c = -4949.47 ± 12.21 cal/g (average of 3 runs), which gives ΔH_f = +88.79 ± 2.05 kcal/mol = +0.5280 ± 0.0122 kcal/g.

ACKNOWLEDGEMENT

This work was performed under the auspices of the U. S. Department of Energy by the Lawrence Livermore National Laboratory under contract No. W-7405-ENG-48.

REFERENCES

1. Simmons, R. L. *Energetic Materials-Technology, Manufacturing and Processing*, Proc. 27th Int. Annual Conf. of ICT, Karlsruhe, Germany, **1996**.
2. Harris, L. E., *et. al.* Proceedings--1998 Insensitive Munitions and Energetic Materials Technology Symposium, Nov. 17-19, 1998, San Diego, CA, p. IIB-2-1.
3. Wallace, I. A; Braithwaite, P. C.; Haaland, A. C.; Rose, M. R.; Wardle, R. B. *Energetic Materials-Production, Processing and Characterization*, Proc. 29th Int. Annual Conf. of ICT, Karlsruhe, Germany, **1998**.
4. ICT Database of Thermochemical Values, Version 2.0, **1999**.

Molecular Mechanics Force field calculation to predict explosive properties of organic nitrocompounds

M Karthikeyan[1], MB Talawar[2] and PN Gadhikar[1]

Abstract

In the present investigation attempt is made to predict the properties of organic molecules especially explosives using in-house developed software Computer Generated Automatic Chemical Structure Data Base (CG-ACS-DB). The program utilizes the combinatorial techniques to Generate molecular diversity, and screen them for best fit. The program was supplemented with BKW Equation of state to calculate explosive properties from the elemental analysis (C,H,N and O) of Molecular structures. A Case study on plannar and other strained ring systems are analysed using MMX Force field modelling. The effect of nitrogroups and ring strain in molecular energy and their Linear relationship with explosive performance is presented.

Introduction

Designing new molecules possing deisred qualities is an important activity in chemical research in the areas such as polymers, explosives, drugs, pesticides and so on. The requirements of an ideal high energetic composition for modern warheads are highly demanding. They should fulfill the requirements of better thermal stability and better mechanical properties. Formal substance qualification is the final steps in making a composition available to weapons designers. The traditional approach to this problem often requires a search involving a combinatorially large number of potential candidate molecules or compositions. Accurate chemical modelling reduces the cost of developing new molecules and also provides detailed understanding on them.

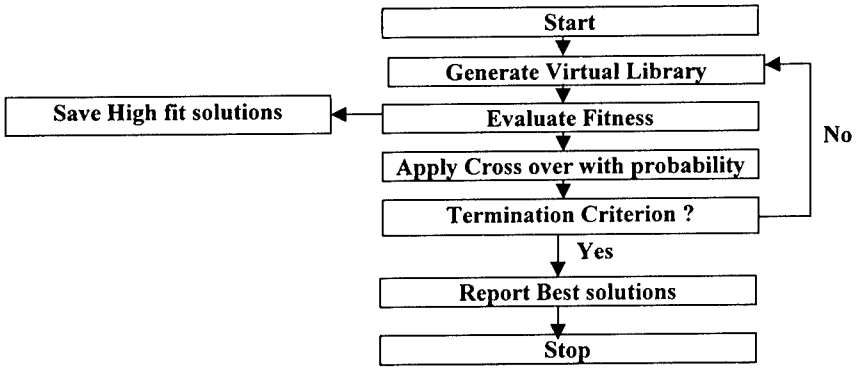
Need for numerical modelling of explosives

Recent efforts towards more powerful explosive have focussed research on the synthesis of new classes of high energy and high-density explosives[1]. These include compact, strained ring and three dimensional cage compounds containing optimum number of nitrogroups as determined by thermo-hydrodynamic calculations [2-3]. Selection of candidate energetic material projected for synthesis to satisfy performance criteria is becoming an advanced scientific activity with time. The use of modelling as a predictive tool is likely to increase with an increased reliance on simulation for synthesis, performance and vulnerability prediction of high-energy materials. Developments over the next few years promise to lead to new materials with predicted properties prior to synthesis.

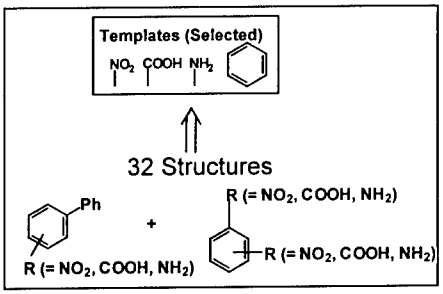
1 Armament Research Development Establishment, Pune, India
2 High Energy Material Research Laboratory, Pune, India

Genetic Algorithms

A Genetic Algorithm (GA) approach is implemented in the in-house developed computer program[4-6] for generating new structures by combinatorial means. The various phases of GA based modelling are initialization, fitness evaluation, selection policy and generic operations as shown in Fig. 1. to produce the report of best solutions [7].



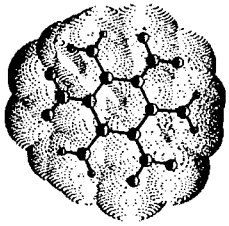
This program generated organic nitro molecules from selected sub-structural units Fig. 2. The starting molecules were modified in two different ways: crossover and mutation. The control process, which determines which molecules proceed to the next generation, depends on the fitness to satisfy the proposed properties. Only the most likely structures with fitness will be propagated forward.



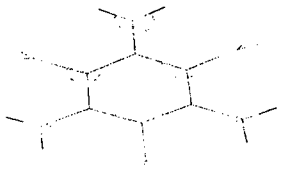
The most used and best-calibrated BKW equation of state is used to calculate detonation properties assuming steady state and chemical equilibrium. Additionally the density, detonation velocity and detonation pressure at crystal density were calculated using these equations.

Molecular Modelling Techniques

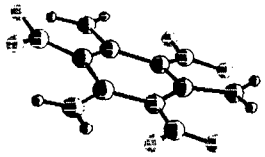
Given input of sub-structural units or fragments such as Phenyl, Nitro, Carboxylic , Amino functional groups etc., the property data of offspring molecular structures were analysed for fitness. The associated 3D structure files in SMD format was analysed for energy (MMX), Heat of formation (Hf), Strain Energy (SE) and Molecular Volume etc.



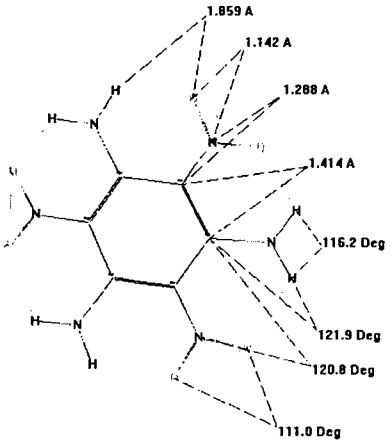
TATB (3D Model)
Molecular Volume = 231 A^3
Total Surface = 214.279
Unsaturated Area = 43.285
Polar Area = 170.993



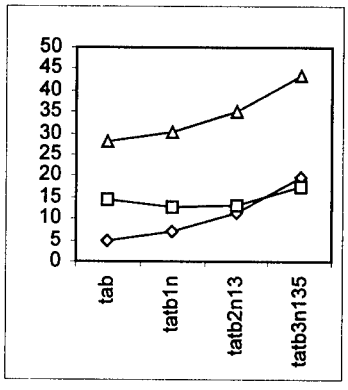
TATB (Electron Density Map – HOMO)



TATB (3D Ball-Stick Model)



TATB (H- bonding with
Bond length and Bond angles)



TATB (Effect of Nitrogroup
In Molecular energy, Hf and SE)

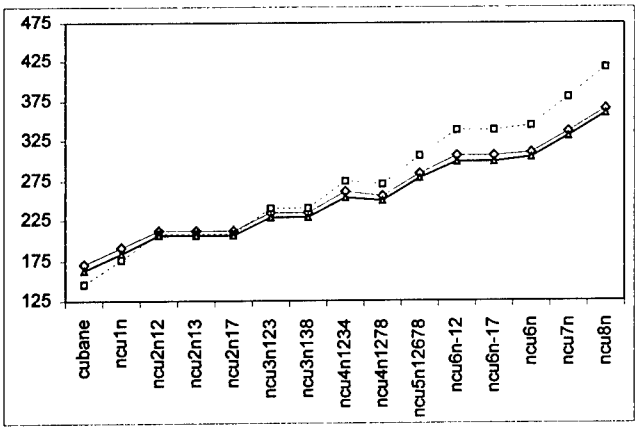
△ SE
◇ MMX
□ Hf

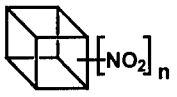
The other relevant data such as molecular formula, sub-structure information (cyclic, aromatic, strained systems etc.,) were used for predicting explosive properties at various densities.

Force Field Calculations

For the past five decades, the quantum chemical calculations were performed on small molecules to predict their properties. In the present technological scenario, it is now feasible to computationally analyse the large number of molecules with dozens of atoms, which inturn revolutionized nearly all branches of molecular chemistry. In the present investigation we are summarising the computational results obtained on TATB, RDX, HMD and strained nitrocubanes.

ID	Code	MMX	Hf	SE
1	ncu1n	190.9	176.95	184.4
2	ncu2n12	212.5	207.89	206.0
3	ncu2n13	212.8	208.24	206.4
4	ncu2n17	212.4	207.82	206.0
5	ncu3n123	235.4	240.17	229.1
6	ncu3n138	235.3	240.03	229.0
7	ncu4n1234	260.6	274.63	254.3
8	ncu4n1278	255.8	269.84	249.5
9	ncu5n12678	283.7	307.09	277.5
10	ncu6n-12	306.1	338.84	300.0
11	ncu6n-17	306.0	338.70	299.9
12	ncu6n	310.9	343.62	304.8
13	ncu7n	337.6	379.57	331.5
14	ncu8n	366.1	417.47	360.2
15	cubane	169.8	146.55	163.2



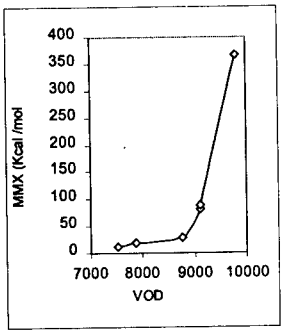


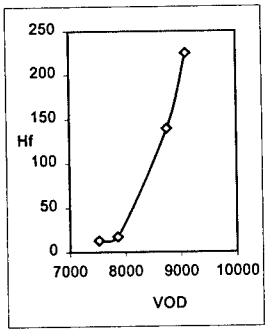
Nitro cubanes (Effect of Nitrogroup In Molecular energy, Hf and SE)

△ SE
◇ MMX
□ Hf

Explosive	MMX	Hf	SE	VOD(E)	BKW(R)	BKW(T)	Density
DATB	11.500	13.24	34.9	7520	7959	7559	1.788
TATB	19.911	17.49	43.3	7860	8411	7848	1.895
RDX	29.161	139.37	28.7	8754	8754	8263	1.800
HMX	81.645	224.95	81.0	9100	9159	8556	1.900

The experimental VOD and other computational data such as MMX energy, Heat of formation (Hf), Strain Energy (SE) and Density of all these explosives were plotted. The plots are self-explanatory with linear relationship.





As the number of nitrogroups increases in a molecular framework of explosives with increase in molecular energy that in turn reflected in the improved explosive properties.

Hardware and Modelling software

All these calculations were performed in IBM-390. In house developed CG-ACS-DB computer program was used to generate database of virtual molecules and their properties data files. PCMODEL for windows was used to perform force field calculations. The MOPAC and OrbDraw Programs were used for viewing the molecular orbitals and electron density data.

Conclusion

In the present investigation, an attempt was made to integrate quantum chemical computation with detonation properties of explosives. The compounds were simulated and computed which are having structural similarity with popular explosives such as RDX, HMX, TATB and strained nitrocubanes. The presented theoretical prediction results with experimental data displayed a linear relationship in terms of explosive performance. Further work is in progress in this field.

References

1. Singh H, "High explosives-Past, Present and Future", Propellants and Explosives technology, Course notes of the Professional Development Short Term Course, IIT Madras, India, December 6 & 7, 1998, 244-270.
2. Mader CL, "Numerical Modeling of Explosives and Propellants", Second Ed. CRC Press, New York, 1998.
3. Persson P-A, Holmberg R and Lee J. "Rock Blasting and Explosives Engineering". CRC Press, New York, 1994.
4. Karthikeyan M, Gadhikar PN and Salwan SK, "Computer search for high energetic organic compounds from the automatically generated chemical structure database", 5th intl. Conf. On Chem Str. June 6-10, 1999 The Netherlands.
5. Karthikeyan M, Gadhikar PN and Salwan SK, "CG-ACS-DB: Computer Generated Automatic Chemical Structure Database", Copyright @ DRDO, 1999, New Delhi, India.
6. Karthikeyan M, Gadhikar PN and Salwan SK, " Algorithm for Compact Storage and Retrieval of Chemical Structures as Intelligent Pixels", ChemInt'99, September 27-29,1999 Washington DC, USA.
7. Venkatasubrarmanian V, Chan K and Caruthers JM, Computers Chem Engng Vol.18, 833-844, 1994.

HIGH ENERGY PROPELLANTS, SINTERED BORON BASED

J.M. Mota*, M.A. Martinez*, F. Velasco*, A.J. Criado**

* Dpto. Ciencia de Materiales e Ingeniería Metalúrgica. Universidad Carlos III de Madrid.

**Dpto. Ciencia de Materiales e Ingeniería Metalúrgica. Universidad Complutense de Madrid.

ABSTRACT

A high energy propellant for motor rockets has just been developed. It is constituted by a base of boron plus a chemical reductor.

Boron was chosen as fuel in view of its excellent thermodynamic values for combustion per unity of volume[1,2], confronted with traditional fuels.The problem of the boron in combustion process is the formation of a surface layer of oxide, which delays the ignition process, reducing the perfomance of the rocket engine (some part of the boron may burn in the outer side of the engine)[3].

The solutions given in this project are based on the incorporation of the reducing elements such as aluminium, magnesium, etc. into the net of the boron so that the layer of oxide can be avoid in the first stage of the combustion (ignition). The manufacturing method was by using those crucibles which are specially designed for the controlled reactive sintering (another version of metallothermic techniques) with thermic shock conditions.

The obtained sintered fuel is a vitreous Boron-aluminum, free of oxide and with a great combustion rate, superior to the propellants joining in its formulation amorphous boron mixed with aluminum.

INTRODUCTION

The incorporation of reducing elements to amorphous boron was achieved by using the powder technology. The choice of proper elements were in function of the Ellingham diagram (figure 1) and the thermodinamic data (table I).

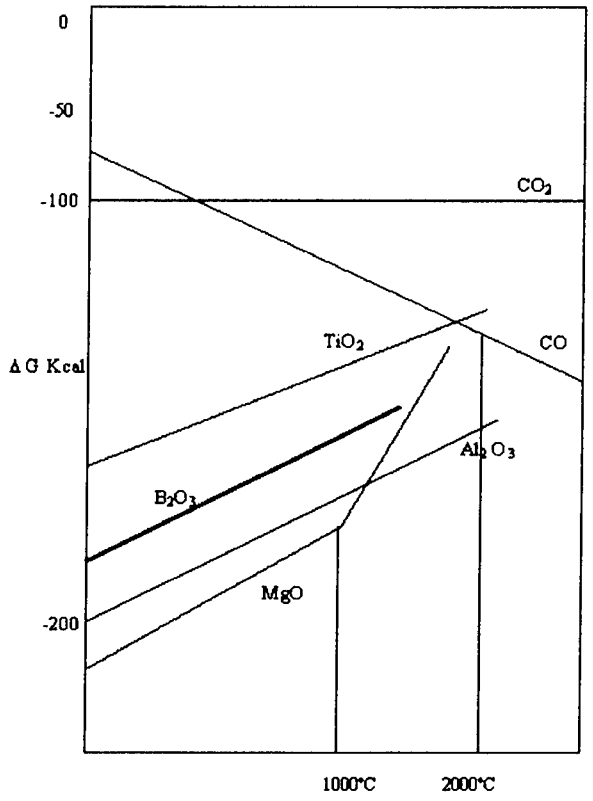


Figure 1. Ellingham diagram[4]

The suitable working conditions were designed in order to obtain an amorfhous sintered boron free of oxide. The crystallization was avoided working in state solid condition (in a few cases, transitory liquid phase appears). The suitable working conditions were designed leaning on the phase diagram of Al-B system[3,4] (figure 2).

Table I. Heats of formation of inorganic oxides[5]

REACTION	cal/mol	KJ/mol
2 Al (s) + 3/2 O_2 (g) = Al_2O_3 (s)	- 404.080	- 1.691,5
Mg (s) + ½ O_2 (g) = Mg O (s)	- 144.090	- 603,0
Ti (s) + O_2 (g) = Ti O_2 (s)	- 288.360	- 955,9
Zr (s) + O_2 (g) = Zr O_2 (s)	- 262.980	- 1.100,9
C (graphite) + O_2 (g) = CO_2 (g)	-93.690	- 392,0

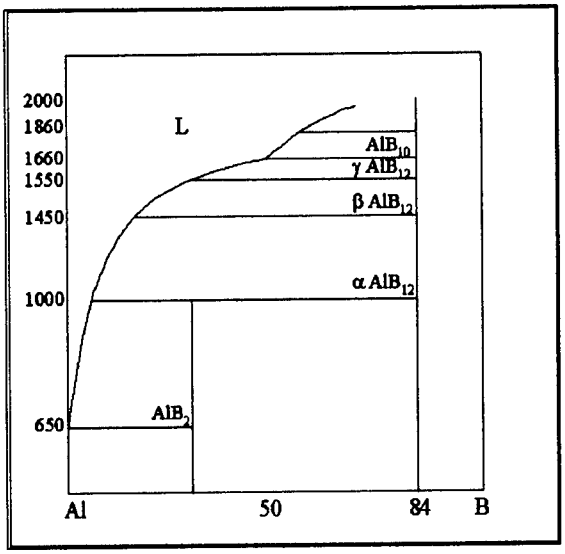


Figure 2. Phase diagram of Al-B system[6,7]

EXPERIMENTAL DETAILS.

Sucessive cycles of compactión-sintering-milling and thermal shock were suitable procedures for preparing borides and especially vitreous boron-aluminum. These procedures supply to aluminum high activation energy. It is very considerable in the sintering process and the especially form in the reaction between boron and a chemical reductor like aluminum. The best way for the incorporation of reducing elements into the boron in an amorphous state was achieved by using the powder technology.

The green compact sintering process was possible for the used crucibles, specially designed for this process. These crucibles were chosen because leave supply

thermic shock, coating and controlled atmosphere (and all nonequilibrium conditions).

The procedure of manufacturing the composite (in particular the mixing and homogenization) is favoured whenever the sintered boron is preferred to the amorphous boron, since the former has no possibility of becoming agglomerated (the first step before the sintering process is the utilization of organic solves and ultrasounds techniques.

Once obtained, it was mixed with an oxidizer plus a polymer which together with the action of another metallic fuel, constitute the propellant in a composite form. Two series of the test tubes were made, one with amorphous boron and another one with sintered boron. The results of both controlled combustions were the following (table II).

Table II. Tested propellants.

PROPELLANT TYPE 1	PROPELLANT TYPE 2
Sintered (B-25Al) 40 %	Boron 30 %
Ammonium nitrate 20 %	Ammonium nitrate 20 %
HTPB 40 %	HTPB 40 %
	Aluminum 10 %

The obtained composite was subjet to trials to controlled combustion in Crawfor bomb. The results were compared to the ones obtained from the combustion of a propellant with an identical composition but incorporating amorphous boron.

RESULTS

1) Nonreactive sintering.

Current crucibles cause oxides and borides as we see in figures 3 and 4. Crucibles specially designed for this work promote the formation of vitreous B-Al, free of oxides, as figures 5, 6 and 7 show. These figures represent the more important steps in the sintering process.



Figure 3. B-50 Al %; 15 min. 1373 K

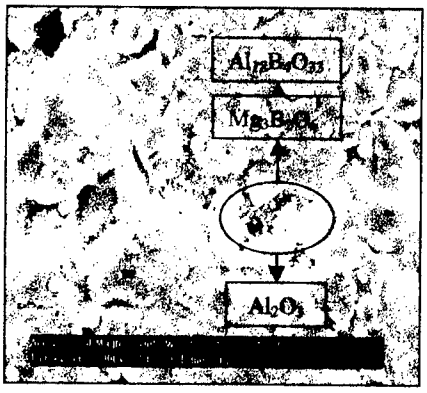


Figure 4. B-50 Al % ; 15 min. 1373 K

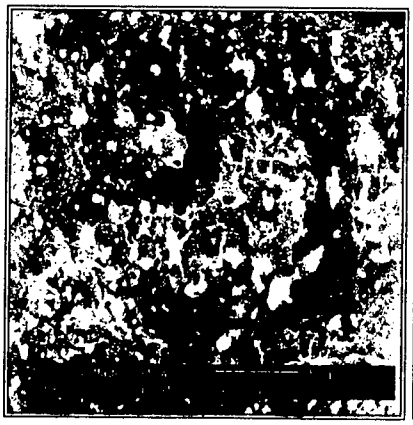


Figure 5. Start of sintering.
B-10Al %; 5min.1373 K



Figure 6. B-10Al %; Intermediate step.
Sintering neck formation; 10min.1373 K



Figure 7. B-10 Al %; 15 min. 1373 K
End step of sintering

The oxides identificated in figure 4, $Al_{18}B_4O_{33}$ and $Mg_3B_2O_3$. $Al_{18}B_4O_{33}$ was obtained in the preheating[8] of sintering:

$$2Al_2O_3 + 2B_2O_3 \rightarrow 2Al_2O_3\ B_2O_3$$

$$9(2Al_2O_3\ B_2O_3) \rightarrow 2(9\ Al_2O_3\ 2B_2O_3) + 5B_2O_3$$

The preheating in the sintering can be avoided with the special crucibles developed. All the samples were tested, studied by means of techniques like X-Ray difraction (XR), scanning electron microscopy (SEM) and micro-analysis by EDS.

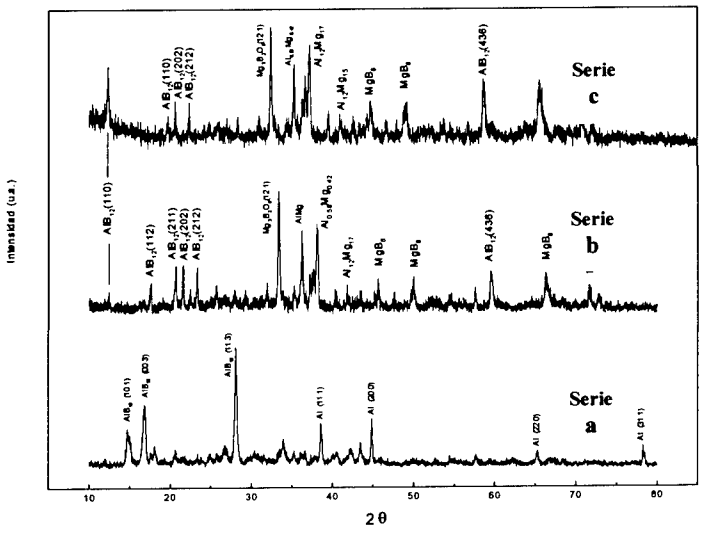


Figure 8. Difractogram for the samples to the series a, b and c. B-25Al % in weight.

In figure 8 we can see difractograms to the series (a), (b) and (c) of composition B-25Al % in weith. The serie (a) has been prepared in oxidizing atmosphere and low temperature, causing no much oxidation. The series (b) and (c) have been obtained in nonoxidizing atmosphere and high temperatures, causing many borides and mixed oxides.

2) Sintermetallothermic techniques

Sintermetallothermic techniques were suitable procedure for preparing boride and vitreous boron (controlled reactive sintering). As raw material for boron, boron acid and boron oxide were use. Isostatic and gravity were the main ways for obtain the compaction. The results obtained are in the following block diagram of figure 9.

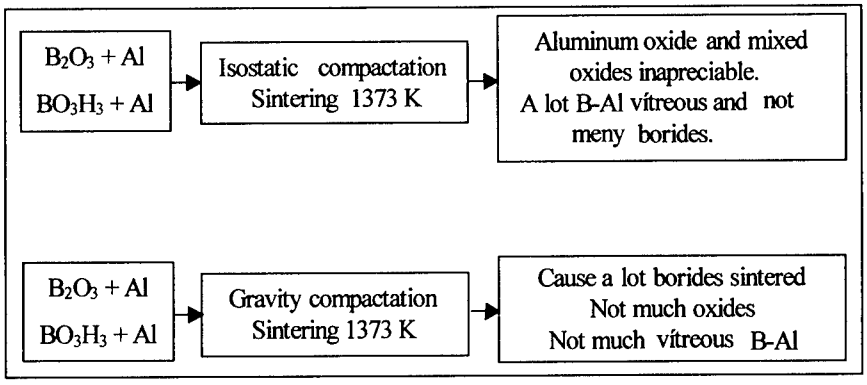


Figure 9. Sintermetallothermic block diagram.

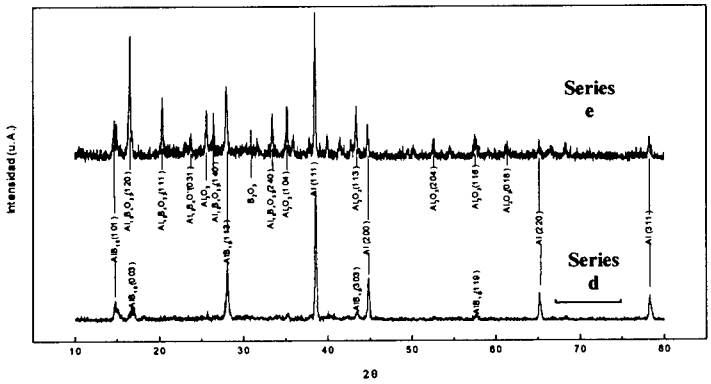


Figure 10. Difractograms to the series (d) and (e).
Metallothermic B_2O_3-Al. 30-45 min. 1373 K.

The procedure of sintering using isostatic compactation (serie e) at 1373 K during 45 min., favoured oxide and vitreous B-Al formation (figure 10). Sintering using gravity compactation at 1373 K during 30 min.(serie d), favoured aluminum borides sintering (figure 10).

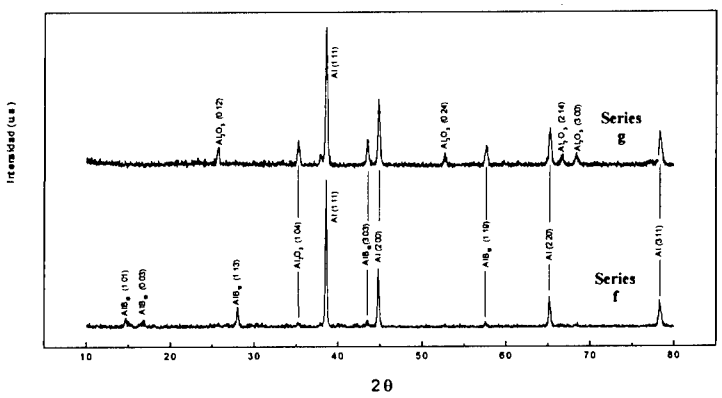


Figure 11. Difractograms to the samples of the series (f) and (g).Metallothermics from BO_3H_3-Al; 30 min. 1373 K

Sintering in nonoxidizire atmosphere with energic isostatic compaction (serie g) at 1373 K promote a lot of oxides (figure 11). Sintering in nonoxidizing atmosphere with gravity compactation (serie f) at 1373 K, forms aluminum borides (figure 11).

COMBUSTION CHAMBER

Once obtained the sintered fuel, it was mixed and homogeneized. In a second step it was joined to HTPB plus polymeritation catalizador to form the terminate propellant.

Two series of the test tubes were made, one with amorphous boron and another one with sintered boron. The results of both controlled combustions are the following (figure 12 and table III):

1. The combustion speed of the propellant which incorporate sintered boron is superior in a 40 % to the one with amorphous boron.

2. The weight of the ash obtained in the combustion is inferior in a 20 % in the propellant that contains sintered boron.

Table III. Combustion chamber results for two series of propellants at 295 K y 27 Kg/cm^2 pressure

PROPELLANT	SAMPLE	SPEED COMBUSTION mm/s	ASH (% weight)
TYPE 1	Serie 1 (vitreous sintered)	1,06 ± 0,01	55
	Serie 2 (vitreous sintered)	0,99 ± 0,01	55
	Serie 3 (AlB_{10} sintered)	1,02 ± 0,01	56
	Serie 4 (AlB_{10} sintered)	1,04 ± 0,01	54
TYPE 2	Serie 5 (amorphous boron)	0,73 ± 0,01	69
	Serie 6 (amorphous boron)	0,74 ± 0,01	60
	Serie 7 (amorphous boron)	0,68 ± 0,01	64
	Serie 8 (amorphous boron)	0,72 ± 0,01	60

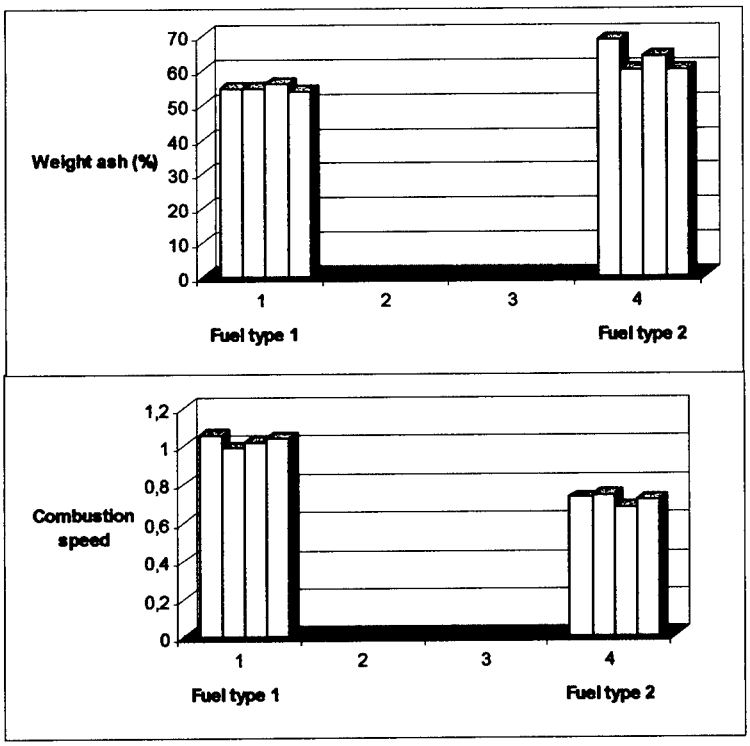


Figure 12. Combustion characteristics of two series of propellants.

CONCLUSIONS

1. A high energy propellant for motor rockets has just been developed. It is constituted by a base of boron plus a chemical reductor.

2. The incorporation of reducing elements into boron in an amorphous state was achieved by using the powder technology. The suitable working conditions were designed in order to obtain an sintered amorphous boron free of oxide.

3. Sucessive cycles of compactión-sintering-milling and thermic shock were suitable procedures to preparing boride sintering and especially vitreous boron-aluminum.

4. The preheating in the sintering can be avoid with the special crucibles developed for this work.. These crucibles were chosen because leave supply all nonequilibrium conditions.

5. As raw material for boron, boron acid and boron oxide were use. Isostatic and gravity were the main ways for obtain the compaction. The results obtained are as good as the amorphous boron sintering.

6. The combustion speed of that propellant which incorporate sintered boron is superior in a 40 % to the one with amorphous boron.

7. The weight of the ash obtained in the combustion is inferior in a 20 % in the propellant that contains sintered boron.

REFERENCES

1. King M. K., "Ignition and Combustion of Boron Particles and Clouds", Atlantic Research Corporation, Alexandria, V.a. J. Spacecraft. 19, 4 (1982) 294.

2. Gany A., Netzer D.W. "Fuel Perfomance Evaluation for the Solid-Fueled Ramjet", Int. J. Turbo Jet Engines. 2, 2 (1985) 157-168.

3 Jarymowyed T.A., Yang V., Kuo K.K. "Analisys of Boron Particle Ignition Above a Burning Solid Fuel In a High-Velocity Environment". Boron.Based Solid Propellant and Solid Fuel. Kuo K.K. CRC Press Inc. (1993) 326.

4. Ellingham H.J.T., J. Soc. Chem. Ind. Trans. 63, 125, 144 y Cottrell A. H. "An Introduction to Metallurgy" Christ's College, Cambridge. London 1967.

5. Powder Metal Tech. Appl. A.S.M. Handbook. 7 (1988) 1088.

6. Serebryanskii V.T., Epelbaum V.A., zhdanov G.S.,"Phase Diagram of Al-B System" Dokl. Akad. Nauk SSSR, 141, (1961) 884-886; Proc. Acad. Sci. USSR, Chem. Sect. 141 (1961) 1244-1246.

7. Rodney P.E. "Constitution of binary Alloys (First Supplement)". McGraw-Hill, Inc.(1965) 26.

8. Yonghe L., Sheng Y., Zhimeng G., Lai H. "Aluminum Borate in the Combustion Synthesis of Aluminum Boride Composite". J.Materials Research. 13, 7 (1988)1750.

DESTRUCTION OF TNT BY OXIDATION WITH OZONE

M.E. Rabanal*, B. Oquillas*, M.A. Martínez,*, A.J. Criado**, N. Braojos***, A. Pérez de Diego***.

* Materials Science and Engineering Department. Escuela Politécnica Superior. Universidad Carlos III de Madrid. Avda. de la Universidad 30, 28911-Leganes. Spain.

** Materials Science and Engineering Department. Facultad de Ciencias Químicas. Universidad Complutense de Madrid. Ciudad Universitaria s/n, 28030-Madrid. Spain.

*** Laboratorio Químico Central de Armamento. La Marañosa, 28330-San Martín de la Vega. Spain.

ABSTRACT

The main objective of this project is the development of a process for the TNT elimination. Because of its high stability, TNT molecule is impossible to destroy by the biochemical degradation processes, usually used in the depurification of residual effluents. A new oxidation process, using an emergent technology such as oxidation with ozone, will carry out their elimination.

Industries like petrol, or process for fertiliser production, or anodizing of aluminium, are interested in the elimination of their nitrated organic wastes without diluting them in big amounts of water. This interest is imposed by environmental reasons and by the strict European Union normative as well as countries normative regarding the reduction of wastes. So the proposed subject is on plain actuality.

The analysis of samples taken a different time of the oxidation process by means of COD test and DSC analysis have confirmed the almost complete elimination of TNT molecule.

1.- Introduction

In the area of study of new technologies, our work group is carrying out experiments for the deactivation of propellants, in particular, 2,4,6-nitrotoluene (TNT) and other propellants very stable and many quantities. These propellants can not be destroyed either by simple combustion or by means of biochemical process, used in the cleanliness of residual waste. In this experimental work, we try to give an easy way for the elimination of propellants by oxidation process, with a new technology as oxidation process with ozone (1, 2).

The reactions of TNT removal and other nitrade aromatic organic compounds by oxidation with ozone have been studied broadly (3, 4, 5, 6, 7).

Besides of military industry, the oil industry, fertilising manufactures and others are very interesting in the elimination of organic waste without necessity to dilute in big quantity of water. Then, the optimisation of this process, in our case elimination of TNT, also will be applicatied in civil industry.

The experiments carried out in the previous stage a project (8, 9, 10) have supplied some knowledge about the removing of organic aromatic compounds by oxidation process, in particular with the TNT.

The nitroaromatic propellers are compounds with high stability chemistry. For example, the 2,4,6-trinitrotoluene (TNT), is a crystalline solid (monoclinic system with axial ratio a:b:c:1.64047:1:0.61936). It is yellow with a of melting point 80.6ºC, although it depends on purity and presence of isomers.

The big stability of TNT molecule requires a strong oxidation in concentrated acid environment:

$$CH_3\text{-}C_6H_2(NO_2)_3 + 8\ H_2O ===> 7\ CO_2\,(g) + 1.5\ N_2\,(g) + 21H^+ + 21e^-$$

TNT is not soluble in water and soluble in sulphuric acid (Table I) (11). In order to oxidize TNT it is better that the solvent has a low viscosity because it increases the transport of mass and decreases the energetic consumption. The use of sulphuric acid decreases the viscosity of mixture.

Table I - Solubility of TNT in sulphuric acid at different temperature (11).

T (°C)	CONCENTRATIONS (%)						
	70	75	80	85	90	95	100
	SOLUBILITY (%)						
0	---	0.3	0.4	0.6	2.0	3.5	13.0
10	---	0.3	0.4	0.7	2.2	4.0	13.5
20	---	0.3	0.5	0.8	2.5	4.8	15.0
30	---	0.3	0.5	0.9	2.6	5.2	15.5
40	---	0.3	0.6	1.0	2.7	6.0	16.5
50	0.2	0.4	0.6	1.3	3.0	7.0	18.0
60	0.2	0.4	0.7	1.7	3.5	8.5	21.0
70	0.2	0.5	1.0	2.3	5.2	11.0	24.8
80	0.3	0.7	1.6	3.3	7.0	13.5	29.0
90	0.6	1.3	2.4	4.8	10.0	18.0	26.5

2.- The ozone as oxidant

The ozone has been applied during decades in potable water treatment, but due to the development of new ozone generator equipments with greater yields, this method has been used in other areas (12).

Among the main advantages about the use of ozone confronted with other oxidants that have chlorine, it must be pointed out the absence of organichlorine compounds. In this reaction, also the rusty product, only appears oxygen, which is not a contaminant.

Nowadays, there are very applications such as:

- Treatment of potable water.- It is the traditional application of ozonation process, because of removing organic compound, solids in suspension, seaweeds, iron, heavy metals and other contaminants presents in the water (13). Also, the ozone has an effect of sterilisation and an improvement in the separation of solid-liquid.
- Treatment of waste water.- the effect of ozone is the elimination of tensoactives, phenols, cyanides, heavy metals, pesticides, etc.
- Treatment of residuals water.-the ozone has a effect of removing of phenols, cianures, phosphites, heavy metals, and organic compounds with double and triple

binding. The high ozone powder in oxidation process and its sterilization effect permit that the residual water can be reused in gardens, to clean streets, etc (14, 15, 16).

- Water of industry process- The use of ozone in paper mill wears not out fibre and produces not residues. The principal difficulty consists on having a good contact between liquid and gaseous phases, or between liquid and solid phases (17, 18, 19, 20, 21, 22, 23, 24).
- Treatment of water of cooling system.- For removing biologic contamination (25).

3.- Experimental Equipment

The ozone is obtained in a "SANDER 301.7" generator. By means of an oxygen current, the ozone is generated by an electric discharge a high voltage. The generated ozone is carried out to reactor, where there is a TNT solution in sulphuric acid (figure 1).

The ozone in acid environment attacks the nucleofiles positions of TNT, destroying the aromaticity of TNT quickly and efficiently.

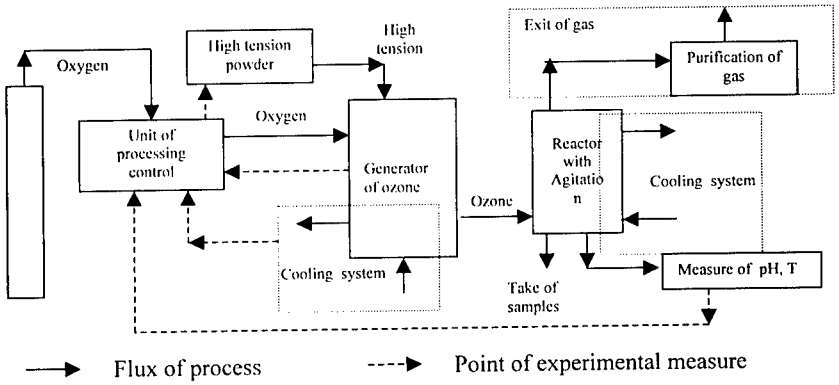


Figure 1: Scheme of ozone generator used in the experiments carried out in the oxidation process.

It is known that the ozone solubility in water decreases with temperature. Still, there are not studies about solubility of ozone in sulphuric acid solution, but we think that it will have a similar behaviour. Initially we will work at low temperatures increasing the stay time of ozone in the solution, but when the TNT concentration increases then will be necessary high temperatures for total solubility.

The reactor characteristics are very important because there is a heterogeneous reaction between the ozone and organic compounds and it is very critic the time of staying of ozone in the reactor (26). We will optimise the stay time and finally we will change the reactor type (figure 2).

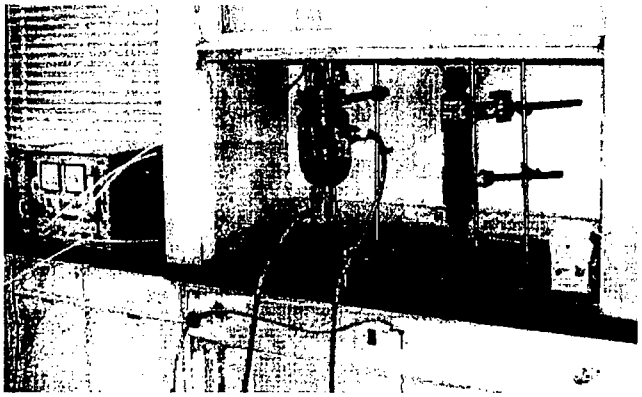


Figure 2: Reactor used in the first experiments.

The elimination of TNT was evaluated by means of Chemistry Oxygen Demand (COD) (27), that is a measure of quantity of emaciated oxygen for the total oxidation of organic compounds in order to turn in inorganic compounds.

In order to potenciometrics titration the equipment used were Titroprocesador 726 of Metrohm, the work electrode is a combinate electrode Pt/Ag-AgCl.

4.- First experimental results

At different times we took samples beginning for initial time. Parallelment we carried out the DSC analysis in order to evaluate the performance of oxidation process. (Figure

3). A summary of results is presented in Table II.

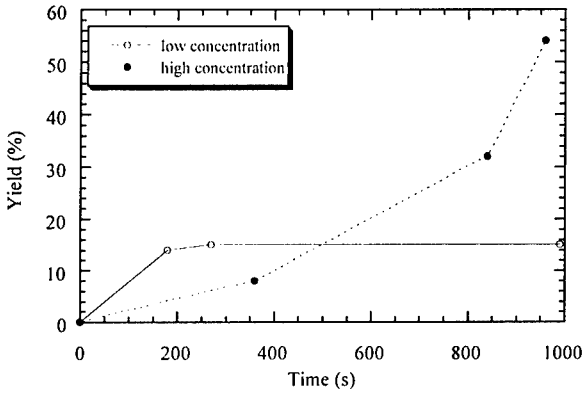


Figure 3: Yield vs. Time.

Table II.- Results obtained by ozonation process.

Test	COD_0 (g/l)	COD_f (g/l)	R (%)
Low concentration	31.53	26.25	15
High concentration	68.14	31.53	54

By differential scanning calorimetry of the samples collected at different times of oxidation process, we can evaluate the reaction, because between 80-90ºC it appears a big endothermic peak corresponding to TNT. At longer times this peak decreases until total disappearance. Therefore we can conclude that this oxidation process has eliminated TNT.

5.- Conclusions

The principal initial conclusions of this experimental work are:

1.- By means of oxidation process with ozone we have reduced the organic matter in a 80%. These results have been obtained with solutions of 40-50 g/l of TNT in concentrated sulphuric acid and using ozone flux of 8 a 10 g/m^3 at 25ºC.

2.- The best condition for the removal of TNT has been using solution a 80% in sulphuric acid, but the only problem was that are necessary high temperatures been more difficult the taking of samples and decrease the stay time of ozone in the solution.

3.- By means of DSC analysis carried out, the total elimination of TNT after ozonation process is confirmed.

6.- Future work

We have to optimise the influence of parameters in oxidation process with ozone as:

- Concentration of solutions of TNT-sulphuric acid.
- Flux of ozone.
- TNT concentration initial.
- Temperature, stirring speed, type of reactor, etc...
- Time of ozone stay.
- Addition of catalyst, and the use of ultraviolet wave.

Also, it is very important the identification and quantification of intermediate and final compounds due to oxidation process.

7.- References

1) L. Gutiérrez. Situación actual desde la perspectiva medioambiental de la industria internacional y nacional de la desmilitarización de los explosivos. Memorial de Ingeniería y Armamento. 147(1997) pp. 323-329.

2) J.L. Bueno, H. Sastre, A.G. Lavin. Contaminación e ingeniería ambiental. Vol.III:Contaminación de aguas. Ed. FICYT, Oviedo (1977) pp. 575-596.

3) P.S. Lang, W.K. Ching, D.M. Willberg, M.R. Hoffmann. Oxidative degradation of TNT by ozone in an electrohydraulic discharge reactor. Environ. Sci. Technol., 32,20 (1998) pp. 3142-3148.

4) R.J. Spanggord, D. Yao, T. Mill. Kinetics of aminodinitrotoluene oxidations with ozone and hydroxyl radical. Environ. Sci. Technol., 34,3 (2000) pp. 450-454.

5) C.H. Kuo, M.E. Zappi, S.M. Chen. Peroxone oxidation of toluene and TNT. Ozone Sci Engineering, 22,5 (2000) pp. 519-534.

6) J. Baraza, S Esplugas. Descomposición del ácido fórmico con O_3/H_2O_2 Afinidad. 57, 486 (2000) pp. 88-92

7) M.S. Elovitz, U.von-Gunten, H.P. Kaiser. Hydroxyl radical/ozone ratios during ozonation processes. II. The effect of temperature, pH, alkalinity, and DOM properties. Ozone Sci. Engineering. 22,2 (2000) pp. 123-150.

8) M.E. Rabanal, M.A. Martinez, A.J. Criado, N. Braojos, A. Perez de Diego. TNT destruction by electrochemical way. Int. Annu. Conf. ICT, 28th (Combustion and Detonation), (1977) pp.100.1-100.6. Fraunhofer Institut fuer Chemische Technologie.

9) M.E. Rabanal, M.A. Martinez, A.J. Criado, N. Braojos, A. Perez de Diego. Optimization of experimental conditions for the TNT elimination by electrochemical process. Int. Annu. Conf. ICT, 30th (Combustion and Detonation), (1999) pp. 73.1-73.10. Fraunhofer Institut fuer Chemische Technologie.

10) M. Acedo, M.E. Rabanal, M.A. Martinez. "Destrucción de residuos aromáticos nitrados". Ing. Química, 367 (2000) pp. 227-229.

11) T. Urbannski. Chemistry and technology of explosives. Vol. I. Pergamon Press 1964.

12) F. Santiago. "Oxidación avanzada de efluentes líquidos con oxigeno, ozono y agua oxigenada". Tratamiento 2 (1993) pp. 47-51.

13) X. Oliver. "Oxidación avanzada mediante ozono". Ing. Química 10 (1991) pp. 181-184.

14) J. Pardo, E. Chamarro, S. Esplugas. "Tratamientos de aguas residuales con ozono y radiación UV". Tecnología del agua (artículos técnicos) 93 (1992) pp. 26-32.

15) L. B. Wiart. Empleo del ozono en la depuradora de aguas residuales. Medio Ambiente-RETEMA Mayo-junio (1990) pp. 65-69.

16) J. Sarasa, M.P. Roche, M.P. Ormad, M.S. Muteburría, J.L. Ovelleiro. "Caracterización y tratamiento de las aguas residuales procedentes de la fabricación de colorantes azóicos". Tecnología del agua (artículos técnicos) 116 (1993) pp. 17-23.

17) M.A. Sevener. "El ozono: un plan de investigación de la oxidación de compuestos orgánicos sintéticos en agua". Ing. Química 1 (1990) pp. 239-245.

18) M. C. Prat, M. Vicente, S. Esplugas. "Decoloración de las aguas de blanqueo de la industria papelera mediante ozono". Ing. Química 4 (1988) pp. 141-145.

19) G. Sánchez. "Tecnología electroquímica para tratamiento de efluyentes industriales". Ing. Química. 11 (1995) pp. 113-122.

20) J.F. Tortosa, O. Leclerc, L. Petit.. "Ozonización de materiales lignocelulósicos". Ing. Química 307 (1994) pp. 47-52.

21) L.C. Chen. "Effects of factors and interacted factors on the optimal decolorization process of methyl orange by ozone". Water-research. 34, 3 (2000) pp. 974-982.

22) L. Kos, J. Perkowski. "Simultaneous application of H_2O_2/UV or O_3/H_2O_2/UV in textile wastewater treatment". Fibres and textiles in Eastern Europe. 7,3 (1999) pp. 57-61.

23) C.P. Yu, Y.H. Yu. "Identifying useful real-time control parameters in ozonation process". Water Sci Technol.. 42,3-4 (2000) pp. 435-440

24) L. Kos, J. Perkowski. "Advanced oxidation process in the technology of textile wastewater treatment". Fibres and textiles in Eastern Europe. 8, 1 (2000) pp. 66-70.

25) M. Baresel, W. Wenzel, O. Leitzke, K. Schwämmlein, C. Beseler. Ozonización en circuitos de agua de refrigeración. Ing. Química 303 (1994) pp. 81-85.

26) Z.Do Quang, C.C. Ramirez, M. Roustan. "Influence of geometrical characteristics and operating conditions on the effectiveness of ozone contacting in fine-bubbles conventional diffusion reactors". Ozone Sci. Engineering. 22,4 (2000) pp. 369-378.

27) Norma UNE 77-004-89. Determinación de la Demanda química de Oxígeno (DQO). Método del dicromato.

Geschäumte Treibladungen mit energetischen Bindern: Abbrandcharakteristik

Foamed Propellants with Energetic Binders: Burning Characteristics

Angelika Meßmer, Thomas S. Fischer

Fraunhofer Institut Chemische Technologie, Joseph-von-Fraunhoferstr. 7
76327 Pfinztal, Deutschland

Abstract

Foamed propellants based on polymer bonded nitramines show high burning rates due to their porous structure. Using different explosive fillers, energetic binders and porous structures foamed propellants with high energy and variable burning and material characteristics can be realised. Because of this variability foamed propellants can be adjusted to manifold applications. The performance of the propellants depends on the formulation and mainly on the porous structure. In order to examine the effect of different porous structures on burning rate and material behaviour closed vessel tests and vulnerability tests with foamed propellants with varied density and porosity have been performed.

Kurzfassung

Geschäumte polymergebundene Treibladungen besitzen aufgrund ihrer porösen Struktur gegenüber kompakten Treibladungen eine hohe Abbrandgeschwindigkeit. Durch den Einsatz verschiedener explosiver Füllstoffe und energetischer Binder sowie durch Einstellung unterschiedlicher Porosität lassen sich Treibladungen mit hohem Energieinhalt und variablen Material- und Abbrandeigenschaften realisieren. Aufgrund dieses vielfältigen Leistungsprofils können geschäumte Treibladungen an unterschiedlichste Anforderungen angepaßt werden und besitzen damit ein breites Anwendungsspektrum. Neben dem Einfluß der Formulierung werden die Eigenschaften der geschäumten Treibladungen hauptsächlich durch die Porenstruktur beeinflußt. Um den Einfluß der Porosität zu untersuchen, wurden Ladungen mit variierter Dichte und Porengröße hergestellt und in der ballistischen Bombe sowie in verschiedenen Empfindlichkeitstests untersucht.

1 Einleitung

Geschäumte Treibladungen auf der Basis polymergebundener Nitramine zeigen eine Reihe von Vorteilen wie hoher Energieinhalt und variable Material- und Abbrandeigenschaften [1, 2]. Durch die große innere Oberfläche der Porenstruktur brennen geschäumte Treibladungen mit hoher Abbrandrate, so daß auch großvolumige Treibladungsformkörper ausreichend schnell abbrennen können. Aufgrund dieser Abbrandcharakteristik sowie der guten mechanischen Eigenschaften der polymergebundenen Systeme können neue Ladungskonfigurationen wie zum Beispiel verbrennbare Hülsen oder hülsenlose Munition realisiert werden [3, 4]. Die Einstellung des geforderten innenballistischen Leistungsprofils erfolgt dabei durch Formulierung und innere Porenstruktur, so daß die äußere Ladungsgeometrie konstant gehalten werden kann.
Geschäumte Treibladungsformkörper lassen sich durch das Verfahren des Reaktionsschaumgusses auf einfache Weise herstellen - auch in sehr komplexer Geometrie [5]. Weitere Anwendungen wie das Umschäumen bzw. Fixieren oder Verbinden von Ladungskomponenten mit verbrennbaren Schichten, das Ausfüllen von Leerräumen oder den Gradientenaufbau von Treibladungen sind daher vorstellbar.
Um das Leistungsprofil geschäumter Treibladungen zu untersuchen, wird im Fraunhofer ICT umfangreiche Grundlagenforschung betrieben, darüber hinaus werden in verschiedenen entwicklungsnahen Projekten mögliche Anwendungen getestet. Die Arbeiten umfassen die Entwicklung von Formulierungen und Ladungskonfigurationen sowie die Charakterisierung von Material- und Abbrandeigenschaften. Da das Leistungsprofil geschäumter Treibladungen neben der Formulierung hauptsächlich durch die innere Porenstruktur bestimmt wird, liegt ein Schwerpunkt auf der Untersuchung der Herstellung und der Auswirkungen der Schaumstruktur auf das Eigenschaftsprofil der geschäumten Treibladungen. Im folgenden werden einige Ergebnisse dieser Arbeiten vorgestellt.

2 Abbrandcharakteristik geschäumter Treibladungen: Experiment und Simulation

2.1 Herstellung der Porenstruktur

Geschäumte Treibladungen können nach dem Prinzip des Reaktionsschaumgusses hergestellt werden. Dabei werden aus dem polymeren Binder und Energieträgern wie Nitraminen und Nitraten gießfähige Mischungen hergestellt. Diese Mischungen werden in geschlossene Gießformen gefüllt, wo sie aufschäumen und aushärten. Die Porenstruktur der Ladungen kann dabei durch Herstellparameter wie Temperatur und Druck sowie durch Additive wie Treibmittel und Schaumstabilisatoren variiert werden [6].

Da geschäumte Systeme im allgemeinen keine einheitliche Porengröße aufweisen, sondern ein Ensemble aus Poren mit unterschiedlicher Größe vorliegt, wird die tatsächliche innere Oberfläche der Treibladung durch die vorliegende Porengrößenverteilung, d. h. Größe und Anzahl der Poren, festgelegt. Somit kann durch Variation der Porosität bei gleicher Gesamtdichte der Ladung ein unterschiedliches Verhalten eingestellt werden. Aufgrund der starken Abhängigkeit der Material- und Abbrandeigenschaften von Gesamtdichte und Porenstruktur müssen Ladungsgewicht und Porengrößenverteilung mit hoher Reproduzierbarkeit einstellbar sein. Um das Herstellungsverfahren dahingehend zu prüfen, wurden Wiederholungschargen verschiedener geschäumter Treibladungen hergestellt und charakterisiert. Werden Formulierung und Herstellparameter konstant gehalten, kann eine bestimmte Porenstrukur reproduzierbar hergestellt werden (siehe Abbildung 1).

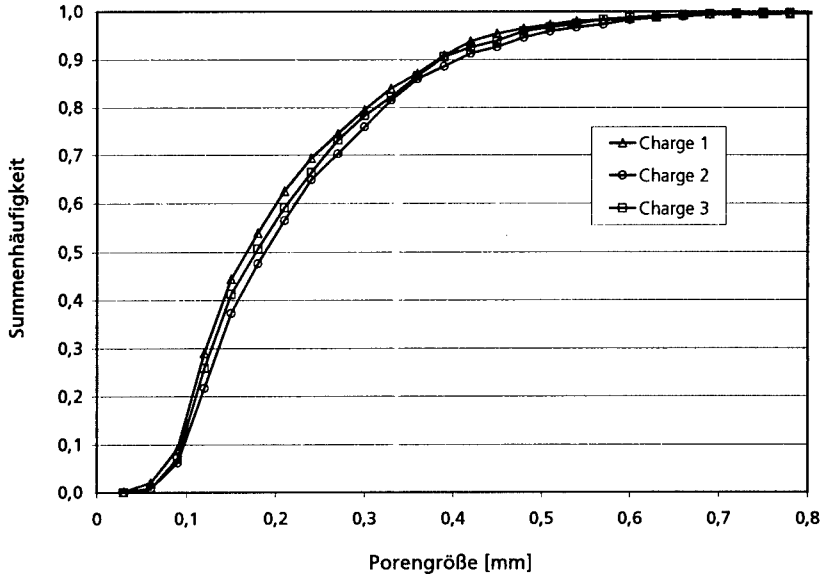


Abb. 1 : Reproduzierbarkeit der Porenherstellung bei geschäumten Treibladungen: Porengrößenverteilung von Wiederholungschargen bei konstanter Formulierung und konstanten Herstellparametern (65% RDX, 35% Polyurethan, 0,765 g/cm³).

2.2 Untersuchung in der ballistischen Bombe

Um das Abbrandverhalten geschäumter Treibladungen zu untersuchen, werden Versuche in der ballistischen Bombe durchgeführt. Dazu werden aus dem geschäumten

Material Würfel mit einer Kantenlänge von 10 mm hergestellt. Im Gegensatz zum Treibladungsformkörper kann hier die Ladedichte durch die Anzahl der Würfel eingestellt werden, ein Einfluß der Ladungsgeometrie wird damit ausgeschaltet. Bei konstanter Porosität (siehe Abbildung 1) zeigen die Ladungen in der ballistischen Bombe ein entsprechend reproduzierbares Abbrandverhalten (siehe Abbildung 2).

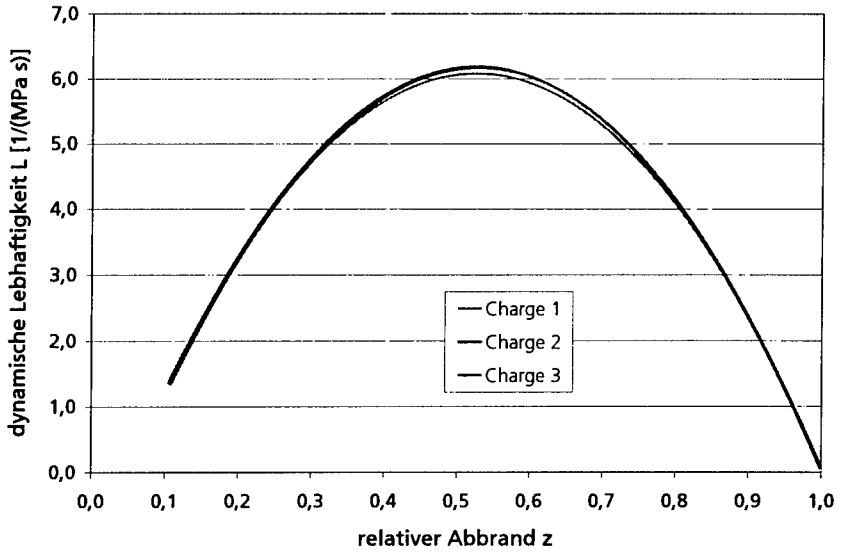


Abb. 2: Reproduzierbarkeit der Abbrandeigenschaften geschäumter Treibladungen: Lebhaftigkeit von Wiederholungschargen bei konstanter Formulierung und konstanten Herstellparametern (65% RDX, 35% PU, 0,765 g/cm³; ballistische Bombe mit Einsatz, 112 ml, Δ = 0,2 g/cm³, 21°C).

Um den Einfluß der Porengröße auf den Abbrand näher zu untersuchen, wurden Treibladungen mit konstanter Materialdichte und variierter Porengrößenverteilung hergestellt. Dazu wurde bei konstanter Ladungsmasse bzw. Materialdichte die Menge an Treibmittel variiert. Bei erhöhter Treibmittelmenge werden größere Poren erzeugt, d. h. die Porengrößenverteilung verschiebt sich nach rechts (Abbildung 3). Die mittlere Porengröße d_{50} ändert sich dementsprechend (0,07 mm / 0,09 mm / 0,11 mm).
Die Untersuchung dieser Ladungen in der ballistischen Bombe zeigt, daß Abbrandrate und Lebhaftigkeit steigen, je kleiner die Poren sind bzw. je größer die daraus resultierende innere Oberfläche der Ladung ist (siehe Abbildung 4 und 5).

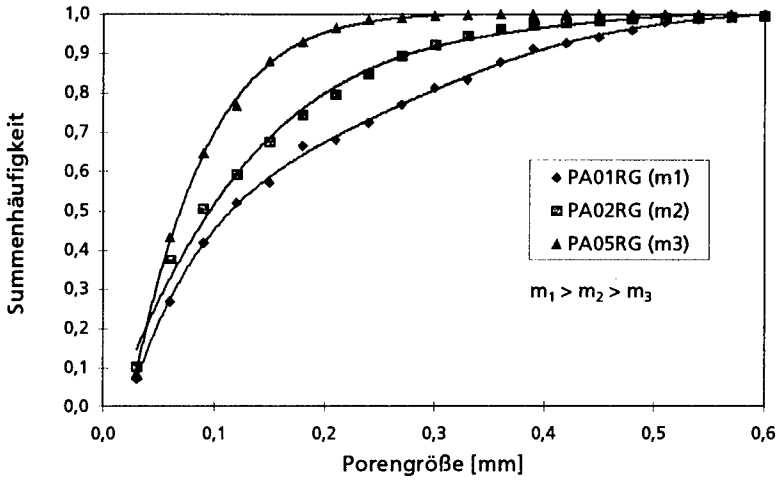


Abb. 3: Porengrößenverteilung geschäumter Treibladungen bei konstanter Materialdichte und variierter Treibmittelmenge m_i (70% RDX, 30% Polyurethan, 0,88 g/cm³).

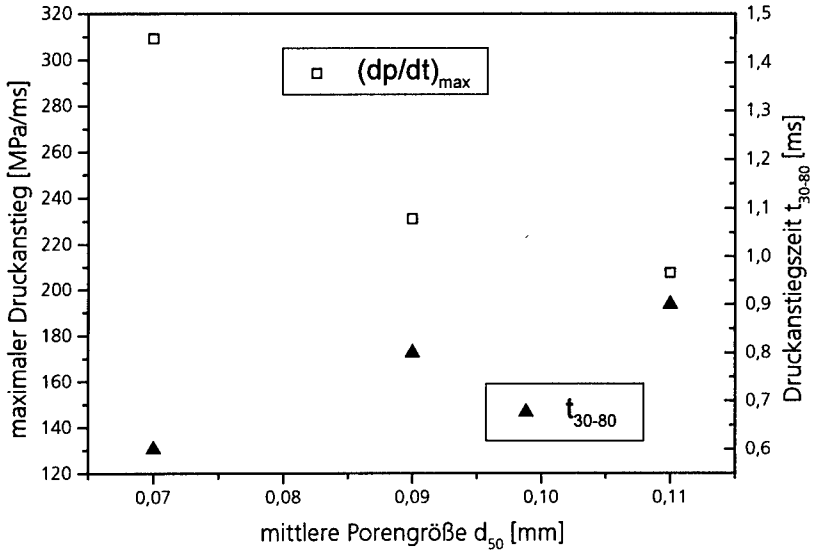


Abb. 4: Abbrandgeschwindigkeit geschäumter Treibladungen bei variierter mittlerer Porengröße d_{50}: maximaler Druckanstieg dp_{max} und Druckanstiegszeit t_{30-80} (70% RDX, 30% Polyurethan, 0,88 g/cm³; ballistische Bombe mit Einsatz, 106 ml, Δ = 0,2 g/cm³, 21°C).

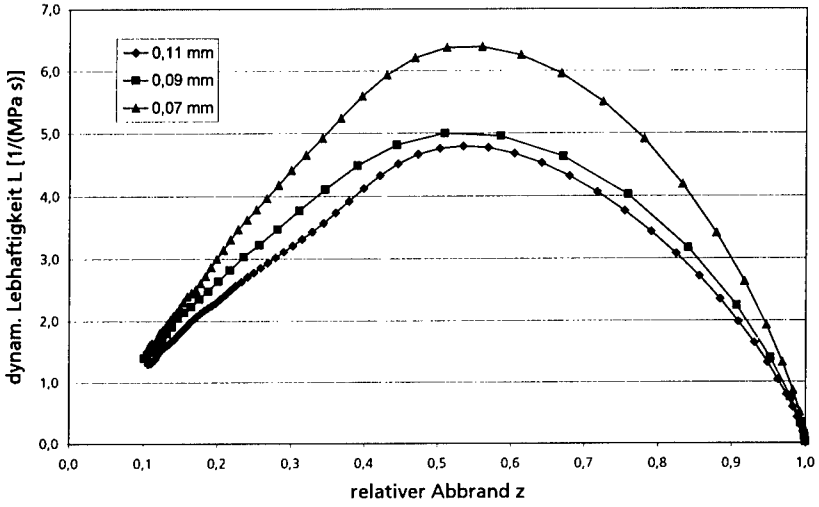


Abb. 5: Lebhaftigkeit geschäumter Treibladungen bei variierter mittlerer Porengröße d_{50} (70% RDX, 30% Polyurethan, 0,88 g/cm³; ballistische Bombe mit Einsatz, 106 ml, Δ = 0,2 g/cm³, 21°C).

2.3 Modellierung des Abbrandes geschäumter Treibladungen

Für die Auslegung einer Ladung auf der Basis innenballistischer Simulationen werden treibladungsspezifische Daten wie die lineare Abbrandrate oder die Massenproduktionsrate benötigt. Diese Daten können aus Experimenten in der ballistischen Bombe bestimmt werden, für konventionelle Treibladungspulver kann die Abbrandrate dabei mit Hilfe der Formfunktion des Pulvers ermittelt werden. Bei geschäumten bzw. porösen Ladungen ist eine Formfunktion dagegen nicht einfach herleitbar. Wird bei der Auswertung der Schußdaten die innere Struktur vernachlässigt und nur mit der äußeren Ladungsgeometrie gerechnet, zeigt die Abbrandgeschwindigkeit im Gegensatz zu kompakten Treibladungen eine Abhängigkeit von der Ladedichte [7] und ist somit keine Stoffkenngröße mehr. Eine formale Auswertung der Ergebnisse aus der ballistischen Bombe nach Vieille ist zwar möglich, liefert aber für jede Ladedichte unterschiedliche Koeffizienten. Eine Übertragung auf andere Geometrien und Ladedichten, z. B. für die Simulation des innenballistischen Verhaltens in der Waffe, ist auf Basis der nach dem Vieille'schen Gesetz ermittelten Abbrandkoeffizienten daher nicht ohne weiteres möglich.

Deshalb wurde im Fraunhofer ICT ein phänomenologisches Modell entwickelt [8, 9], das durch die explizite Berücksichtigung der inneren Struktur eine qualitative Beschreibung der Abbrandcharakteristik aus Experimenten ermöglicht. Darüber hinaus lassen sich mit dem Modell bereits qualitative Aussagen über den Einfluß von Dichte und Porengröße auf die Abbrandcharakteristik machen. Im Gegensatz zu kompakten Treibladungen ist die Reaktionszone bei porösen Treibladungen vergrößert. Hot spots und in die Poren eindringende heiße Gase führen zu Entzündung und Verbrennung nicht nur der aktuellen äußeren Oberfläche, sondern auch in der Tiefe der porösen Ladungen. Abbrandunterbrechungsexperimente zeigen, daß die Reaktionszone in der Größenordnung von 100 µm liegen kann. Wegen des großen Einflusses der Tiefe der Reaktionszone auf den Druckanstieg sind quantitative Voraussagen noch nicht möglich [9]. Durch Experimente mit systematischen Parametervariationen und Modifizierungen wird das Simulationsmodell dahingehend weiterentwickelt.

2.4 Empfindlichkeit geschäumter Treibladungen

Bei geschäumten Treibladungen stellt sich die Frage, ob durch die poröse Struktur die Empfindlichkeit der Formkörper gegenüber äußeren Einflüssen wie Stoß- und Schockbelastung negativ beeinflußt wird, z. B. aufgrund von hot spots. Deshalb wurden mit geschäumten Treibladungen verschiedene Empfindlichkeitstests durchgeführt. Entgegen üblicher Konventionen wurden bei den hier beschriebenen Tests nicht die vorgegebenen Probenabmessungen gewählt, sondern es wurden reale Treibladungsformkörper verwendet, um den Einfluß der jeweiligen Ladungsgeometrie wie z. B. der Wandstärke zu berücksichtigen.
Bei Beschuß einer verbrennbaren Hülse (Länge 230 mm, Wandstärke ca. 7 mm) mit schwerem MG Kal. 0.5 wurde das Hülsenmaterial mechanisch zerstört, aber nicht entzündet (siehe Abbildung 7). Auch bei Beschuß durch Anzündeinheit und Beiladung oder auf das Projektil erfolgte keine Reaktion. Bei Hohlladungsbeschuß auf 5 hintereinander aufgereihte Hülsenabschnitte (Höhe 45 mm, Wandstärke ca. 10 mm) wurde eine schnelle Deflagration, aber keine Detonation ausgelöst. Ein entsprechendes Ergebnis brachte die Untersuchung einer verbrennbaren Hülse (Länge 230 mm, Wandstärke ca. 7 mm) im BAM 50/60 Stahlrohrtest. Nach Initiierung der Boosterladung deflagrierte das Hülsenmaterial, eine Detonationsfront wurde nicht weitergeleitet (siehe Abbildung 6). Ein Ansteigen der Empfindlichkeit aufgrund der Porosität konnte bei diesen Ladungsgeometrien bzw. Formulierungen nicht festgestellt werden.



Abb. 6.: BAM 50/60 Stahlrohr-Test mit einer verbrennbaren Hülse (Länge 230 mm, Wandstärke ca. 7 mm, 65% RDX, 35% energetischer Binder auf GAP-Basis).

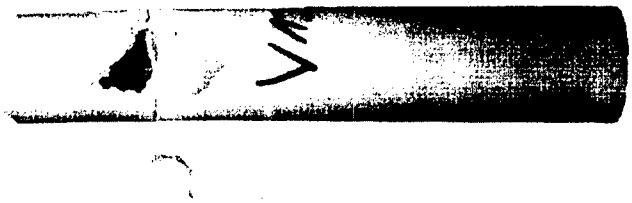


Abb. 7.: Beschuß mit Kal. 0.5 auf eine verbrennbare Hülse (Länge 230 mm, Wandstärke ca. 7 mm, 65% RDX, 35% energetischer Binder auf GAP-Basis).

3 Zusammenfassung und Ausblick

Nach dem Prinzip des Reaktionsschaumgusses hergestellte geschäumte Treibladungen können je nach Formulierung und Herstellparametern mit unterschiedlicher Porenstruktur hergestellt werden, dementsprechend können die Material- und die Abbrandeigenschaften bei konstanter Formulierung und Gesamtdichte variiert werden. Um den Einfluß der Porenstruktur zu untersuchen, wurden geschäumte Treibladungen mit variierter Porosität und Dichte hergestellt und in der ballistischen Bombe getestet. Bei konstanten Inhaltsstoffen und Herstellparametern zeigen die Ladungen eine reproduzierbare Porosität und Abbrandcharakteristik. Durch Veränderung der Porengröße wird auch die Abbrandcharakteristik beeinflußt. Je kleiner die Poren bei konstanter Gesamtdichte sind, um so größer ist die daraus resultierende innere Oberfläche, dementsprechend steigen Abbrandrate und Lebhaftigkeit an.

Da für geschäumte Treibladungen wie für konventionelle Treibladungspulver bisher keine Formfunktion vorliegt, können experimentelle Ergebnisse aus der ballistischen Bombe nicht mit üblichen Simulationsprogrammen ausgewertet werden. Deshalb wurde im Fraunhofer ICT ein neues phänomenologisches Modell entwickelt, das durch explizite Berücksichtigung der inneren Porenstrukur die qualitative Beschreibung der in Experimenten gefundenen Abbrandphänomene ermöglicht. Dies umfaßt Änderungen von Dichte, Formulierung, Geometrie, Porengröße und Porengrößenverteilung aber auch Einflüsse experimenteller Parameter wie der Ladedichte. Auf dieser Basis sind Vorhersagen des speziellen ballistischen Verhaltens geometrisch komplexer poröser Ladungen möglich.

Empfindlichkeitstests wie Hohlladungsbeschuß und Stahlrohrtest an geschäumten Treibladungsformkörpern mit energetischem Binder zeigen, daß die Unempfindlichkeit durch die poröse Struktur nicht beeinträchtigt wird.

In anschließenden Arbeiten wird neben der Weiterentwicklung von Formulierung und Materialeigenschaften die Untersuchung der Wechselwirkung zwischen Porenstruktur und Abbrandcharakteristik vertieft. Da polymergebundene Nitramin-Treibladungen eine vergleichsweise hohe Anzündenergie benötigen, werden darüber hinaus neue Anzündkonzepte untersucht. Geplant sind z. B. mehrschichtige Ladungsaufbauten und der Einsatz unterschiedlicher Anzündmittel. Durch einen mehrschichtigen Aufbau soll einerseits die Anzündung optimiert werden, andererseits kann durch Kombination von Treibladungsschichten mit unterschiedlicher Abbrandrate das innenballistische Leistungsprofil gesteuert werden.

Literatur

[1] A. Meßmer, A. Pfatteicher, K. Schmid, W. Kuglstatter, Foamed propellants with energetic binders, Proceedings of the 31th International Annual Conference of ICT, Karlsruhe, Germany, P111/1-13, 2000

[2] T. S. Fischer, A. Meßmer, G. Langer, Geschäumte polymergebundene Treibladungen, 23. Wehrtechnisches Symposium - Innenballistik der Rohrwaffen, BAkWVT Mannheim, 25.-27.05.1999

[3] F. Schedlbauer, A. Meßmer, U. Steffens, I. Reuter, Combustible Cases for RMK 30, Proceedings of the 29th International Annual Conference of ICT, Karlsruhe, Germany, P103/1-9, 1998

[4] A. Meßmer, A. Pfatteicher, F. Schedlbauer, Herstellung und Charakterisierung von geschäumter hülsenloser Munition, Bericht 10/98, Fraunhofer Institut für Chemische Technologie, 1998

[5] A. Meßmer, F. Schedlbauer, Konzeption einer Herstellungsanlage für geschäumte polymergebundene Treibladungen, Bericht 12/97, Fraunhofer Institut für Chemische Technologie, 1997

[6] J. Schwörer, J. Böhnlein-Mauß, Untersuchung des Einflusses von Verfahrensparametern auf die Schäumungsstruktur von gefüllten Kunststoffen, Bericht 3/96, Fraunhofer Institut für Chemische Technologie, 1996

[7] T. S. Fischer, N. Eisenreich, S. Kelzenberg, G. Langer, A. Meßmer, Abbrandmodelle für Rohrwaffentreibmittel: Abbrandverhalten des Rohrwaffentreibmittels JA2 und Abbrandphänomene poröser Ladungen, 31st International Annual Conference of ICT, Karlsruhe, Federal Republic of Germany, P143, 2000

[8] T. S. Fischer, W. Koppenhöfer, G. Langer, M. Weindel, Modellierung von Abbrandphänomenen bei porösen Ladungen, 30th International Annual Conference of ICT, Karlsruhe, Federal Republic of Germany, P98, 1999

[9] T. S. Fischer, A. Meßmer, Burning Characteristics of foamed polymer bonded propellants, Proceedings of the 19th International Symposium on Ballistics, Interlaken, Switzerland, 7. – 11.05.2001

Thermal Analysis of Hydrazinium Nitroformate (HNF)

S. Löbbecke, H. Schuppler, W. Schweikert

Fraunhofer Institut für Chemische Technologie ICT,
Joseph-von-Fraunhofer Strasse 7, D-76327 Pfinztal, Germany

Introduction

In recent years new chlorine-free oxidizers like ammonium dinitramide (ADN) and hydrazinium nitroformate (HNF, fig. 1) have received an increasing interest as a substitute for amonium perchlorate (AP) in various propellant formulations.

A reduced rocket exhaust signature and environmental benefits due to the absence of chlorine as well as an improved theoretical and experimental performance of HNF based composite propellants are known from literature [1-5]. However, besides these advantageous properties of HNF, stability, compatibility and sensitivity of HNF are still discussed in a controversial way [6-8].

As part of a joint research program on new oxidizers between the TNO Prins Maurits Laboratory (The Netherlands) and the Fraunhofer Institute ICT (Germany) a physicochemical characterization of HNF has been carried out at ICT.

This paper focuses on the thermoanalytical investigation of HNF describing both the decomposition exothermicity and the time-resolved detection of thermal decomposition products. The latter allows the identification of the main decomposition pathway of HNF.

Typical properties of HNF measured at ICT are summarized in table 1.

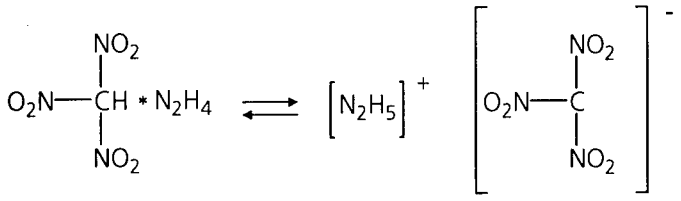


Fig. 1: hydrazinium nitroformate (HNF)

Tab. 1: selected properties of hydrazinium nitroformate (HNF)

molecular formula	$N_2H_5C(NO_2)_3$
sum formula	$CH_5N_5O_6$
molecular weight	183.08 g/mole
appearance	yellow needle-like crystals of 1 - 2 mm length
particle size distribution	d (0.1) = 99.95 µm, d (0.5) = 241.90 µm, d (0.9) = 483.26 µm
water content	0.18%
ΔH_f	-72 kJ/mole [9]
oxygen balance	+13.11%
density	1.846 g/cm³
impact sensitivity	2 Nm
friction sensitivity	16 N

Experimental

HNF was synthesized by Aerospace Propulsion Products (APP), The Netherlands, and supplied in cooperation with TNO Prins Maurits Laboratory, The Netherlands.

The thermoanalytical characterization was carried out by applying DSC (TA Instruments, MDSC 2920), TGA (TA Instruments, HIRES-TGA 2950), TG-MS (Balzer Thermostar) and fast infrared spectroscopic Evolved Gas Analysis (EGA) based on a self constructed heatable optical cell adapted to a rapid scan FTIR spectrometer (Nicolet 60 SX).

Samples weighing between 0.200 mg and 2.500 mg (for DSC measurements: up to 1.000 mg) were analyzed as received under argon atmosphere by applying heating rates between 0.5 K/min and 10.0 K/min, resp. up to 2.0 K/min for DSC experiments, which were carried out in sample pans with pierced lids made of aluminum.

For statistical reasons all experiments were repeated up to eight times. Stepwise variation of heating rates ensures that characteristic temperatures (e.g. onset temperature, maximum heat flow temperature) can be extrapolated to a formal heating rate of zero.

Results

Figure 2 shows a characteristic DSC spectrum of HNF (heating rate: 2.0 K/min) consisting of a sharp exothermicity with two heat flow maxima.

The onset temperature of the exothermic decomposition is at aprox. 125°C, the exothermicity itself is spread over a relatively narrow temperature range. A complete listing of all relevant DSC data obtained at different heating rates can be found in Tab. 2.

Heating rates higher than 2.0 K/min resulted in an uncontrolled decomposition of HNF with no reproducable heat flow peaks.

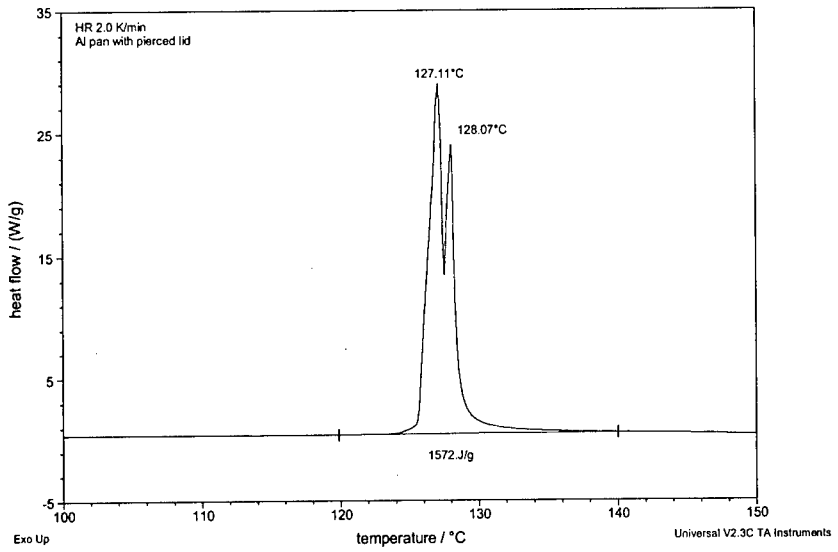


Fig. 2: DSC curve of HNF

Surprinsingly, the DSC curves obtained are in two points different from those reported so far in open literature [10-12].

In some references a small endothermal peak explained as the melting of HNF is reported just before the exothermic decomposition is detected [10-12], whereas such endothermicity could not be observed in our measurements although DSC experiments were repeated up to eight times at each heating rate. Furthermore, in [11] it is reported that such missing endothermic peak was only observed for aged and thus chemically modified HNF samples.

However, an aging of the HNF sample investigated in this study can be excluded. The FTIR spectra of the HNF sample (fig. 3) are in excellent accordance with reference spectra of pure HNF reported in [11] and [13]. No evidence for aging, like the broadening of the 964 cm^{-1} and 954 cm^{-1} peaks (N-N stretch) to a single peak or the disappearance of the 1242 cm^{-1} shoulder (NH_2 rock, NO_2 sym. stretch), could be found. Therefore, the absence of the endothermic "melting" peak can not be explained by an aged or otherwise unpure sample.

Tab. 2: characteristic DSC data of HNF

heating rate	onset temperature of exothermic decomposition T_{onset} (HR 0)	maximum heat flow temperature T_{max1} (HR 0)	maximum heat flow temperature T_{max2} (HR 0)	decomposition enthalpy ΔH_{decomp}
0.5 K/min	118.53 ± 0.21°C	119.67 ± 0.17°C	120.60 ± 0.19°C	1297 ± 72 J/g 237.5 ± 13.2 kJ/mole
1.0 K/min	121.86 ± 0.23°C	123.61 ± 0.18°C	124.44 ± 0.17°C	1522 ± 50 J/g 278.6 ± 9.2 kJ/mole
2.0 K/min	125.11 ± 0.31°C	127.11 ± 0.15°C	128.10 ± 0.16°C	1566 ± 16 J/g 286.7 ± 2.9 kJ/mole

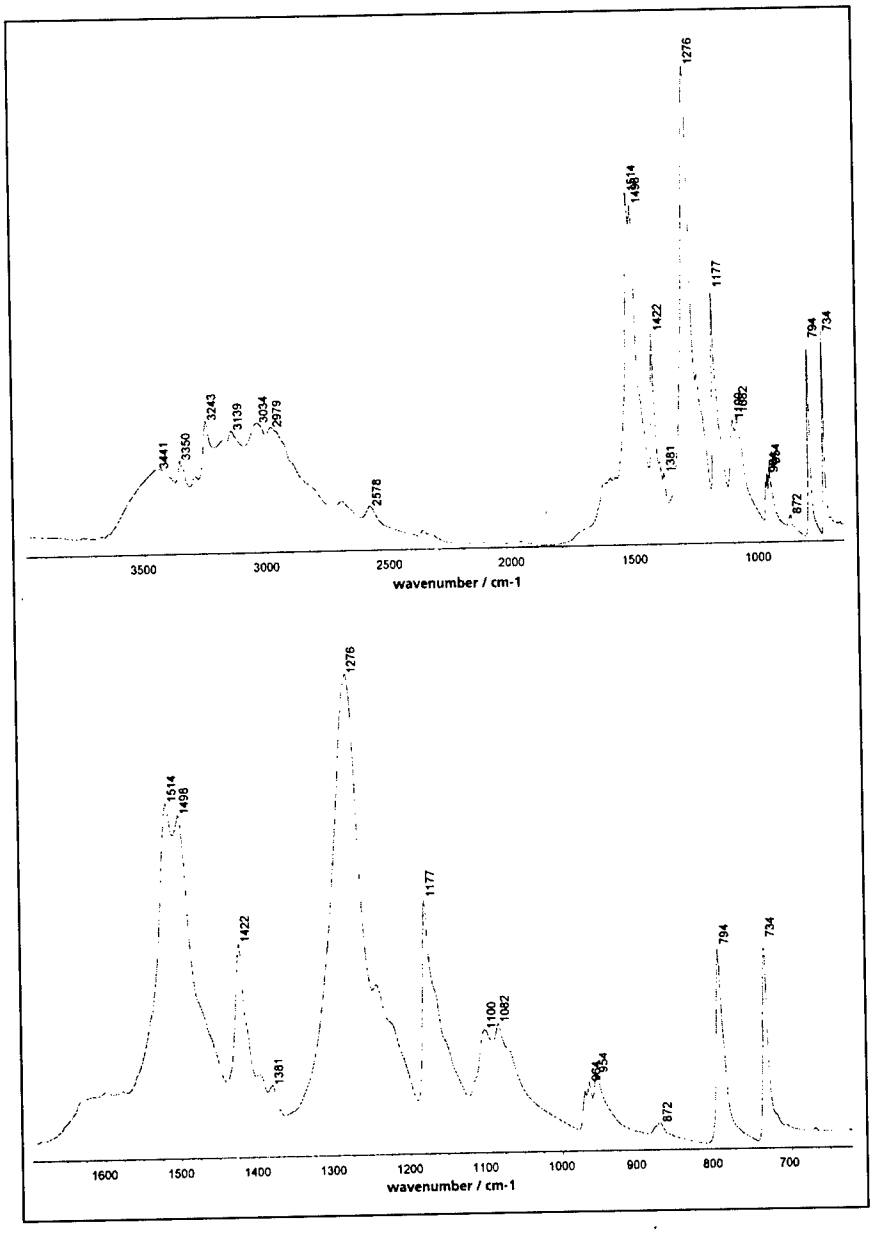


Fig. 3: infrared spectra of HNF

A second difference between the measured DSC curves and reference DSC measurements of HNF [10-12] is the resolution of the exothermicity in two heat flow peaks.

This difference could be explained by the relatively high heating rate of 10 K/min applied in [10-12] causing a joint appearance of the two close exothermic steps. A two-step exothermicity is also reported by Hatano et al. [14] but, unfortunately, the applied heating rate is not mentioned.

However, a two step decomposition of HNF could also be confirmed by thermogravimetric analysis applying higher heating rates like 10.0 K/min (fig. 4).

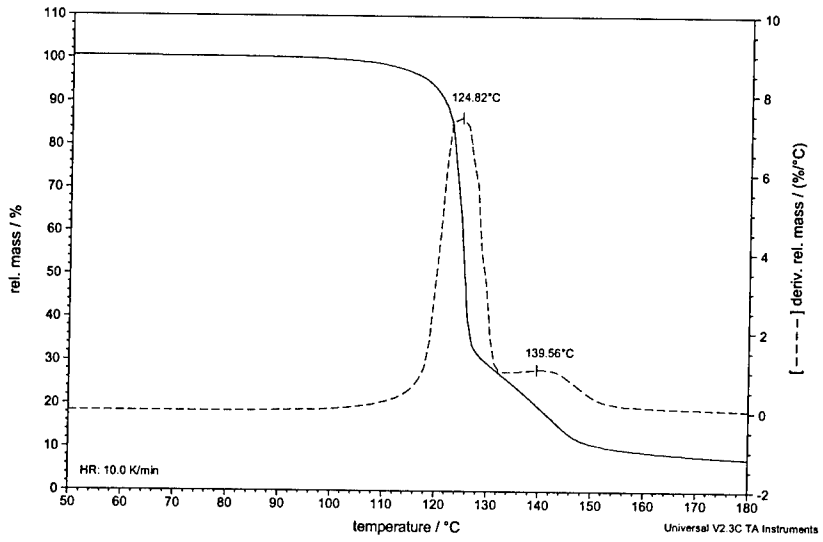


Fig. 4: TGA curve (and its derivative) of HNF

A more closer view on the two-step exothermicity reveals that with increasing heating rate the relative (heat flow) intensity of the first step increases continually while that of the second step decreases in the same way (fig. 5). This trend continues when heating rates higher than 2.0 K/min are applied like in TGA measurements (see fig. 4).

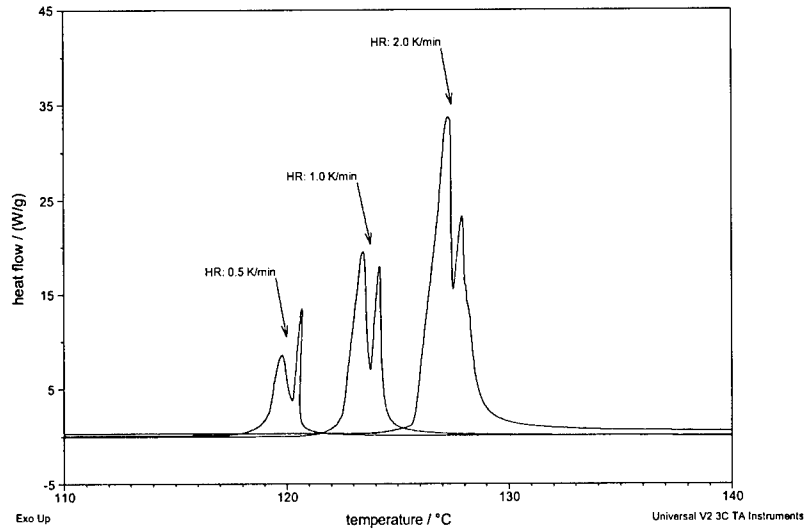


Fig. 5: DSC curves of HNF at different heating rates (0.5, 1.0 and 2.0 K/min)

The result of the infrared spectroscopic EGA (Evolved Gas Analysis) during the thermal decomposition of HNF is shown in fig. 6 as a waterfall plot. Again, two main decomposition steps could be observed. At first, the release of a product possessing an IR spectrum which is - on a first view - not very unlike the spectrum of HNF (see fig. 3), followed by the decomposition of this product forming carbon dioxide (CO_2) and dinitrogen oxide (N_2O) as main decomposition gases.

A closer view on the IR spectrum of the intermediate product reveals significant differences compared with the IR spectrum of HNF. Fig. 7 shows the appearance of a characteristic ammonium functionality in the spectrum (NH_4^+, centered at 3237 cm^{-1}). Furthermore, the N-N stretch absorption bands around 950 cm^{-1} of the hydrazinium group in the HNF spectrum have disappeared, indicating again the transformation of the hydrazinium group to an ammonium group. Further differences between the spectra of HNF and the intermediate product can be observed in the 1400 - 1600 cm^{-1} spectral range (NH_3^+ bend, NH_3^+ deformation) which can be also explained as a changed counter

ion of the $[C(NO_2)_3]^-$ anion. Hence, the EGA experiments indicate clearly the formation of ammonium nitroformate (ANF) as a (first) intermediate product during slow thermal HNF decomposition as already suggested by Brill et al. [13].

Besides ANF, further decomposition products could be detected at the transition from the first stage of HNF decomposition to the second one: small amounts of CO_2 and N_2O as well as ammonia (NH_3, double peak at 965 cm^{-1} and 930 cm^{-1}) and trinitromethane $HC(NO_2)_3$ with its characteristic sharp IR absorption bands at 1610 cm^{-1}, 1300 cm^{-1} and 778 cm^{-1} (fig. 8). It has to be pointed out that the concentration of $HC(NO_2)_3$ increases continually while ANF is already decomposing (see fig. 6).

Finally, at temperature above 220°C only carbon dioxide and dinitrogen oxide (besides traces of water) could be detected as the final (IR active) decomposition products (fig. 9). NO_2 was not detected during the entire decomposition process.

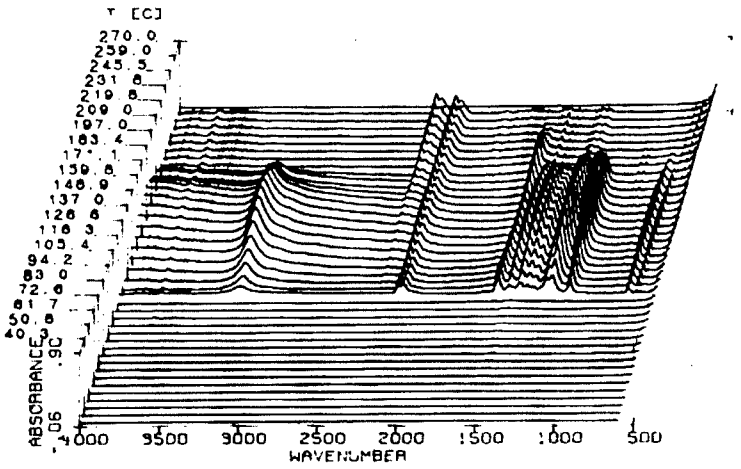


Fig. 6: infrared spectroscopic Evolved Gas Analysis of HNF (heating rate: 5.0 K/min)

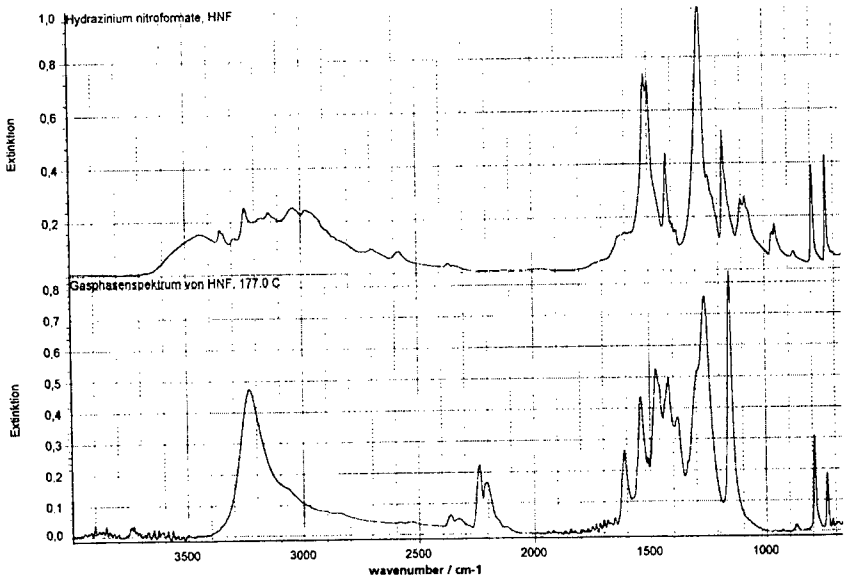


Fig. 7: IR spectra of HNF and the intermediate product (underneath) detected at 177°C (ANF)

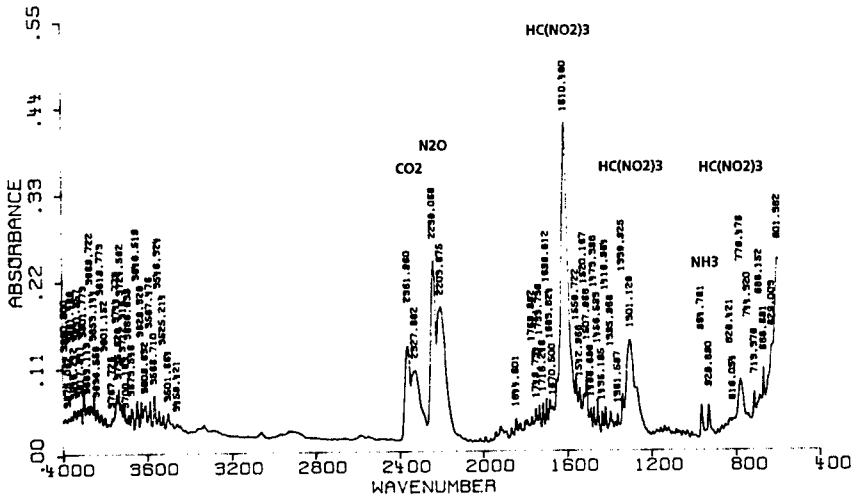


Fig. 8: IR spectrum detected at 220°C during EGA experiment

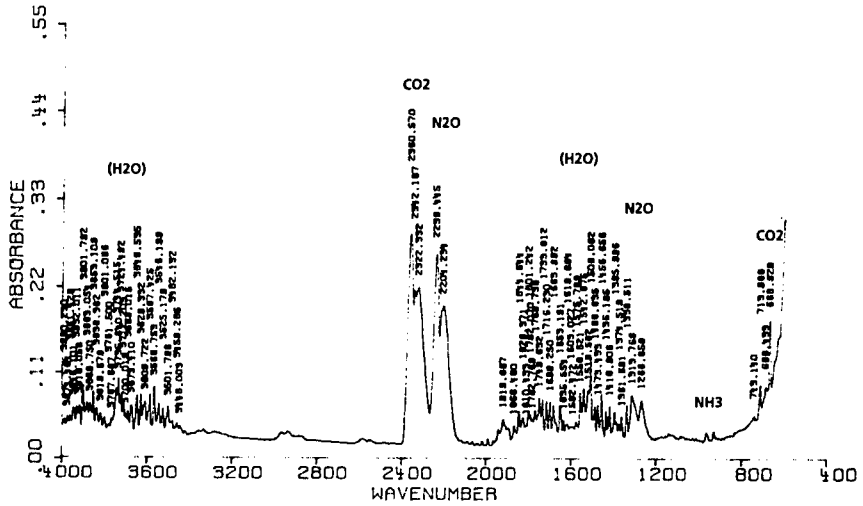


Fig. 9: IR spectrum detected at 270°C during EGA experiment

The infrared spectroscopically analyzed decomposition pathway and products of HNF could be confirmed by TG-MS measurements. Fig. 10 shows a characteristic plot of online detected ion masses scanned in the range of m/z 1 to m/z 50 during a TGA experiment applying a heating rate of 5.0 K/min.

Both the two-step mechanism and the main decomposition gases detected by IR-EGA like CO_2, N_2O, NH_3 and traces of water were mass spectrometrically observed. Furthermore, also the IR inactive decomposition gases N_2 (m/z 14, 28) and O_2 (m/z 16, 32) could be detected in both decomposition steps.

At the very beginning of the thermal decomposition TG-MS measurements applying ion mass scans up to m/z 200 have also indicated the presence of HNF (m/z 185, MH^+) and ANF (m/z 169, MH+) in the gas phase. Fig. 11 shows the corresponding mass spectrum detected at 110°C under isothermal conditions.

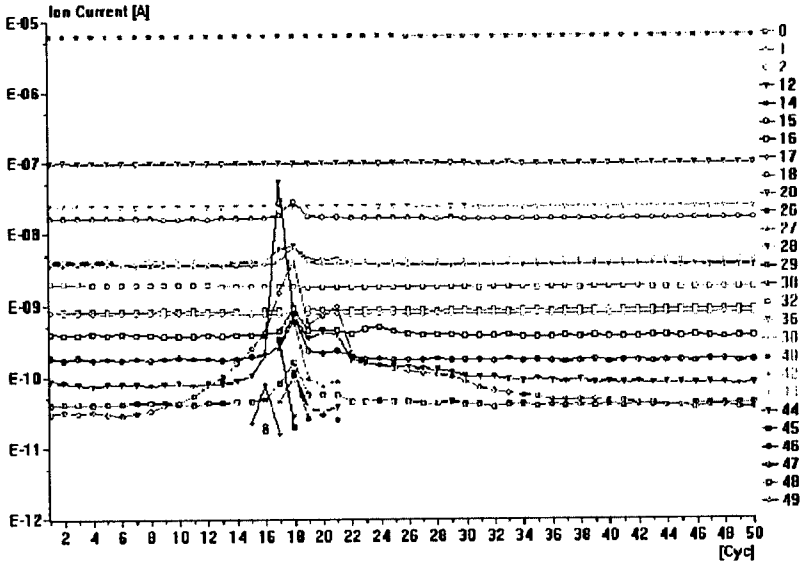


Fig. 10: TG-MS measurement of HNF (heating rate: 5.0 K/min)

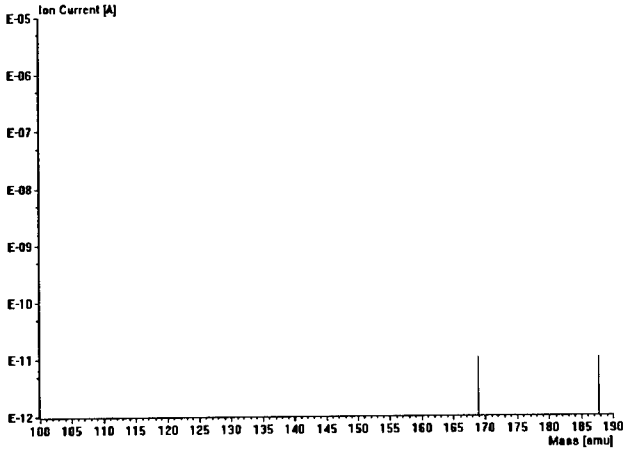


Fig. 11: mass spectrometric detection of HNF and ANF at the very beginning of thermal decomposition

References

[1] J.N. Godfrey, U.S. Patent 3,196,059, **1965**

[2] H. Johnson, P.D. Oja, U.S. Patent 3,213,609, **1965**

[3] J.R. Lovett, U.S. Patent 3,378,594, **1968**

[4] H.F.R. Schoyer, A.J. Schnorhk, P.A.O.G. Korting, P.J. van Lit, AIAA Paper 97-3131, **1997**

[5] H.F.R. Schoyer, A.J. Schnorhk, P.A.O.G. Korting, P.J. van Lit, J.M. Mul, G.M.H.J.L. Gadiot, J.J. Meulenbrugge, *J. Prop. Powder* 11, **1995**, 856

[6] W.H. Jago, U.S. Patent 3,307,985, **1967**

[7] G.M. Low, V.E. Haury, U.S. Patent 3,658,608, **1972**

[8] G.M. Low, V.E. Haury, U.S. Patent 3,708,359, **1973**

[9] S.F. Sarner, *Propellant Chemistry*, Reinhold Publishing Corporation, New York, **1966**

[10] M. van Zelst, A.E.D.M. van der Heijden, 31st Int. Annu. Conf. ICT: Energetic Materials - Analysis, Diagnostics and Testing, 8, 27 - 30 June **2000**, Karlsruhe, Germany

[11] J.M. Bellerby, C.S. Blackman, M. van Zelst, A.E.D.M. van der Heijden, 31st Int. Annu. Conf. ICT: Energetic Materials - Analysis, Diagnostics and Testing, 104, 27 - 30 June **2000**, Karlsruhe, Germany

[12] W.P.C. de Klerk, A.E.D.M. van der Heijden, W.H.M. Veltmans, 12th Int. Congress on Thermal Analysis and Calorimetry, 14 - 18 August **2000**, Copenhagen, Danmark

[13] G.K. Williams, T.B. Brill, *Combust. and Flame* 102, **1995**, 418

[14] H. Hatano, T. Onda, S. Kiname, S. Suzuki, Proceed. 20th Int. Pyrotechnics Seminar **1994**, 397

Acknowledgements

Supply of HNF samples by TNO and scientific co-operation with the colleagues from The Netherlands is gratefully acknowledged.

Application of Microreactors for the Nitration of Ureas

J. Antes, T. Türcke, J. Kerth, E. Marioth, F. Schnürer,
H.H. Krause, S. Löbbecke*

Fraunhofer Institut für Chemische Technologie ICT,
Joseph-von-Fraunhofer Strasse 7, D-76327 Pfinztal, Germany

Introduction

The nitration reaction is both one of the oldest and most common industrial reactions and one of the most hazardous. The nitration of organic compounds is a highly exothermic reaction [1] and give rise to products that have a propensity to be thermally unstable at elevated temperatures. Thermal runaways of nitrations have been responsible for a number of industrial accidents [2].
Furthermore, strong exothermicities in combination with short reaction times cause large numbers of secondary, consecutive and decomposition reactions due to hot spots and accumulated reaction heat. The occasional result is a wide spectrum of products with correspondingly low selectivity, yield and purity.

One way to greatly reduce the potential hazard of highly exothermic or explosive nitrations is to miniaturize the synthesis apparatus and auxiliary equipment by employing microreactors [3 - 6]. Furthermore, the high surface to volume ratio in microreactors provides much better temperature control than that in macroscopic batch or flow-through reactors. Microreactors thus not only permit safe operation, but also suppression of secondary and consecutive reactions due to isothermal processing, short retention times (continuous processing) and intensive mixing of the reactants.

This paper reports on the application of microreactors for the exothermic nitration of N,N'-dialkyl substituted ureas which is probably the most difficult reaction step in the synthesis of the energetic plastiziser DNDA (fig.1).
From macroscopic batch reactions it is known that always both the mono- and dinitro-substituted products are obtained. With respect to a further processing of the nitroureas

to the final DNDA plastiziser a quantitative synthesis of N,N'-dialkyl-N,N'-dinitro-urea is preferably wanted to achieve improved energetic properties of the final product.

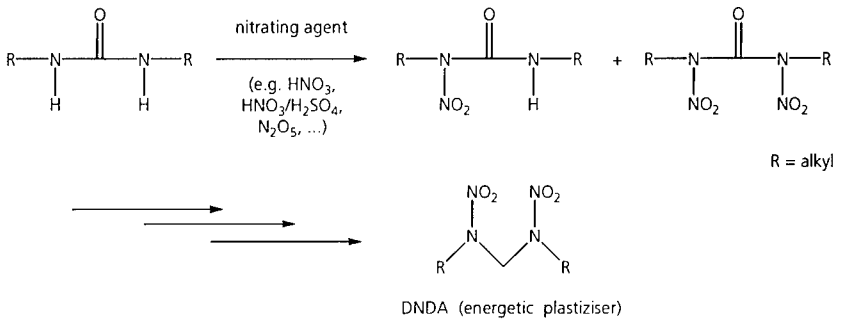


Fig. 1: Nitration of N,N'-dialkyl substituted ureas for the synthesis of DNDA

However, until now a deliberate synthesis of mononitro resp. dinitro substituted ureas has not been achieved, so that in conventional DNDA synthesis both derivatives are immediately processed to the final product.

Detailed information about a deliberate control of the nitration degree (number of introduced nitro groups), selectivity and yield of urea nitration products are not available so far. Hence, to improve yield and product quality of the entire DNDA synthesis the nitration step has to be investigated and analyzed in detail. For this reason microreactors have been applied.

Experimental

Two different types of microreactors have been used for the nitration experiments. A commercially available silicon micromixer based on a microfluidic split-and-recombine structure (MiMoCo GmbH, Ilmenau/Germany; fig. 2) and a microreactor array made of glass containing 20 reaction channels in parallel with integrated educt mixing zones and cooling structure (own development in cooperation with mgt mikroglas technik AG, Mainz/Germany; fig. 3) [4, 5].

Both types of microreactors have been well characterized with respect to their mixing quality (by applying modified Villermaux/Dushman reactions [5]), their fluidic dynamics

(by applying CFD calculations) and their heat transfer characteristics [5, 6]. CFD simulations were also used to optimize process conditions (e.g. educt input, flow rates, temperature).

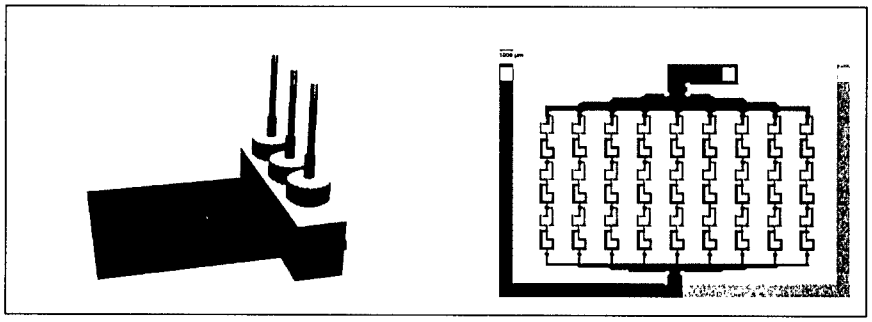


Fig. 2: micromixer made of silicon in a PEEK housing (mixing principle: split-and-recombine of fluid streams; see scheme on the right)

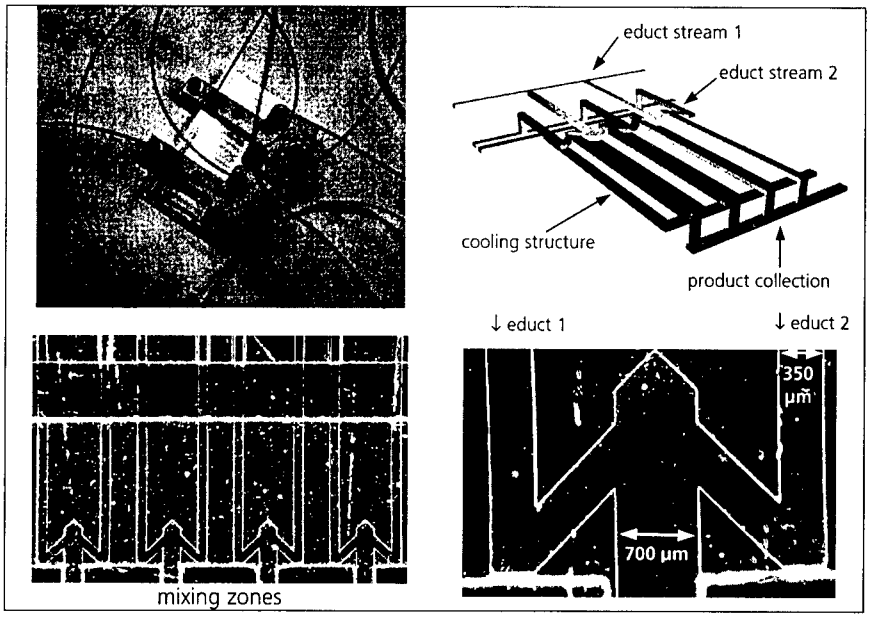


Fig. 3: microreactor made of glass consisting of 20 reaction channels in parallel and an integrated cooling structure

Since nitrating agents are highly corrosive media only resistant materials can be applied for such reactions. Silicon, glass and titanium have been proved to be suitable for nitration processes. Microstructured devices made of stainless steels did not withstand such corrosion processes.

Different nitrating agents have been used for the microreaction experiments. Besides concentrated and fuming nitric acid (65% resp. conc. HNO_3), nitrating acid ("mixed acid": HNO_3/H_2SO_4 = 1:1 to 6:1) and dinitrogen pentoxide (N_2O_5) as a less acid nitrating agent were used. N_2O_5 was either dissolved in CH_2Cl_2 or used as a gaseous reactant (in-situ production: $N_2O_4 + O_3$). Nitrating agents have been used in up to 6-fold excess.

Ureas (dissolved in dichloromethane) and nitrating agents (liquid or dissolved) have been supplied by pulsation-free pumps, mixed inside the microreactors (resp. micromixers) and then passed through reaction capillaries (e.g. PTFE tubes) of different lengths representing different retention times (0.6 s - 82 s).

Nitrations have been carried out in a continuous mode at defined temperatures between 0°C and 20°C. The reaction mixture eluting out of the microreaction system has been quenched in ice water and/or cold dichloromethane, extracted and passed to NMR, MS, IR, HPLC or GC-MS for analysis.

FTIR microscopy has been applied for the online monitoring of nitrations in silicon microreactors. Due to a high spatial resolution of this analytical method (≥ 10 µm) educts and products of nitrations can be identified and distinguished at different positions inside the microreactor [7]. Both intermediates and final products of nitrations can be IR spectroscopically detected by focusing the IR beam consecutively on different reaction zones. Hence, the progress of nitrations can be monitored online in microreactors which helps analyzing and understanding the entire nitration process.

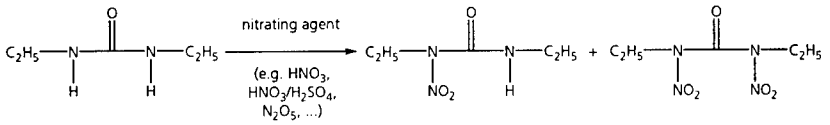
Nitration in microreactors have been performed by systematic variation of the process conditions (e.g. temperature, flow rate resp. retention time, nitrating agent, stoichiometry, etc.). Since educts like diethyl urea are very expensive precursors for the DNDA synthesis alternative educts like the corresponding thiourea (diethyl thiourea is 35 times cheaper) have been also investigated in microreaction processes.

Furthermore, the specific features of microreactors allow also to carry out nitrations under new process conditions, e.g. at room temperature (in contrast to minus 20°C in macroscopic batch reactors) due to the good heat and mass transfer performance of the microreactors combined with the short retention times of the reactants.

Microreaction experiments were accompanied by calorimetric investigations of the nitrations applying a RC 1 heat flow reaction calorimeter (2 L glass reactor, Mettler-Toledo, Switzerland). Reactions have been carried out at temperatures between -30°C and 0°C. Ureas were continously added to the reactor containing different nitrating agents (e.g. HNO_3, N_2O_5). Electrical calibrations have been carried out before and after the reactions to register changes in heat capacity and heat transfer properties of the entire reaction system.

Exemplary results

The nitration of N,N'-diethyl-urea in macroscopic batch reactors led to mixtures of mono- and dinitro derivatives, which were chromatographically separated and clearly identified by NMR, MS and IR spectroscopy (fig. 4 and 5). Yields of up to 75% could be achieved for N,N'-diethyl-N,N'-dinitro-urea.



Experiments in microreactors carried out so far did not show significant differences in the product spectrum compared with macroscopic experiments. Despite of ensuring short retention times and isothermal conditions to a great content yields and selectivities for the dinitro resp. mononitro derivative could not be dramatically enhanced, although a tendency for higher yields of N,N'-diethyl-N-nitro-urea have been be observed.
Furthermore, there were no convincing evidences to clear up whether the mononitro derivative is a key intermediate for the synthesis of the dinitro substituted product.
Calorimetric data from the RC 1 show that the reaction proceeds instantaneously and is very exothermic. The mass flow rate seems to have a strong influence on the reactor temperature. The measured reaction enthalpy of the nitration of N,N'-dialkyl-urea and N,N'-dialkyl-thiourea (see below) under various mass flow rates and nitrating conditions corresponds to an adiabatic temperature increase between 40 and 280 K calculated by considering the reaction mass and the heat capacity of the reactants. The temperature and the nitrating conditions have a strong influence on the stability of the N,N'-dialkyl-

N,N'-dinitro-urea. Above 0°C in strong acids, like fuming nitric acid, decomposition reactions of the N,N'-dialkyl-N,N'-dinitro-urea takes place in the reaction mixture.

A new approach to a quantitative synthesis of N,N'-diethyl-N,N'-dinitro-urea was investigated by using the much cheaper N,N'-diethyl-thiourea as starting material.
In macroscopic batch reactors four products were obtained, two - at that time - unidentified products of 90% yield as well as small amounts of N,N'-diethyl-N-nitro-urea and the target compound N,N'-diethyl-N,N'-dinitro-urea (10%). Surprisingly, no C=S functionality was found in the products anymore.

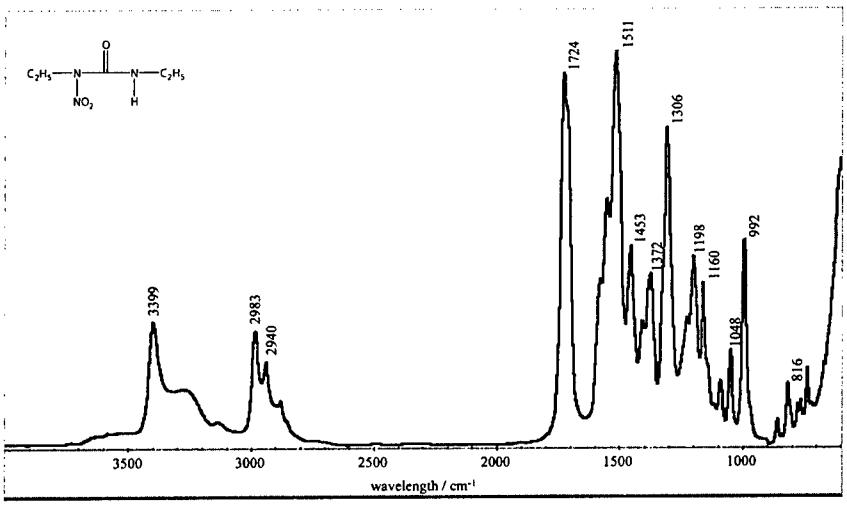


Fig. 4: IR spectrum of N,N'-diethyl-N-nitro-urea

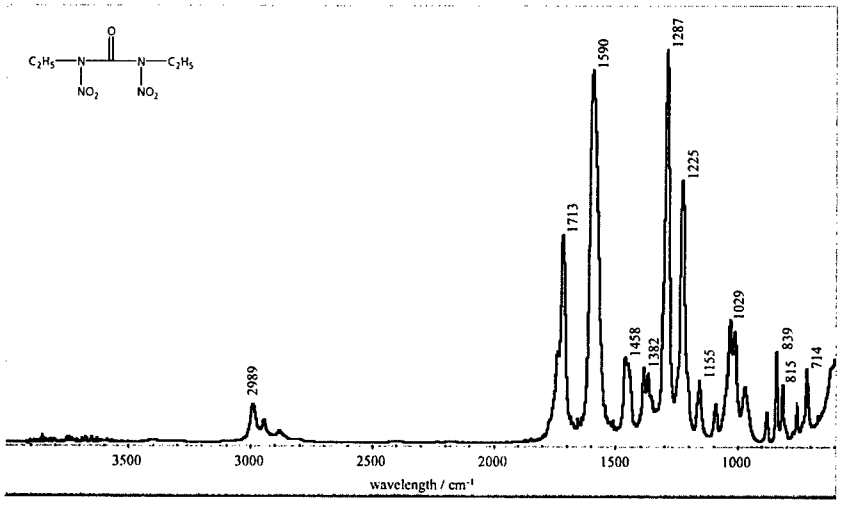
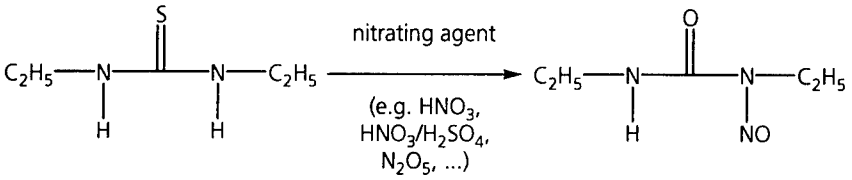


Fig. 5: IR spectrum of N,N'-diethyl-N,N'-dinitro-urea

The nitration of N,N'-diethyl-thiourea was repeated by applying microreactors under systematic variation of process parameters and conditions.

Even under mild conditions (e.g. weak nitrating agents) only one product with approx. 100% selectivity was obtained in all microreaction experiments, which could be easily isolated and identified by MS (fig. 6) and IR (fig. 7) as N,N'-diethyl-N-nitroso-urea:



On the basis of these experiments the main products of the macroscopic experiments could be also identified as N,N'-diethyl-N-nitroso-urea and probably N,N'-diethyl-N,N'-dinitroso-urea.

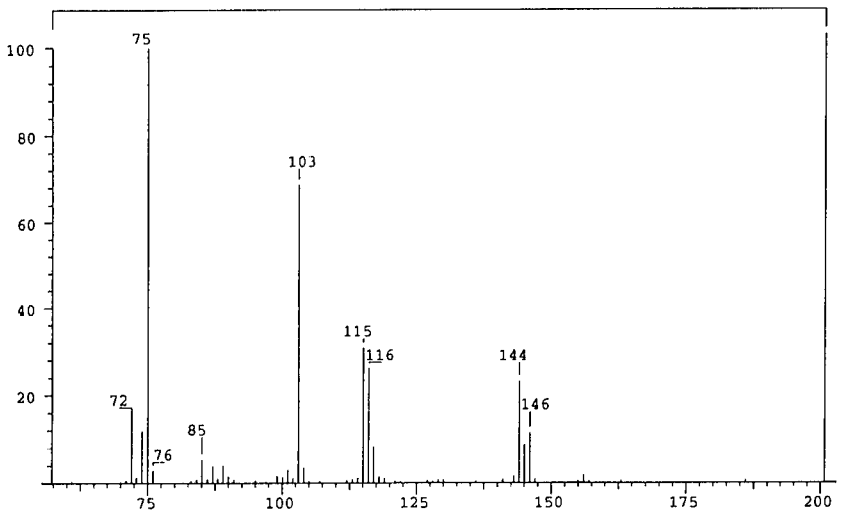


Fig. 6: MS spectrum of N,N'-diethyl-N-nitroso-urea (MH^+: m/z = 146)

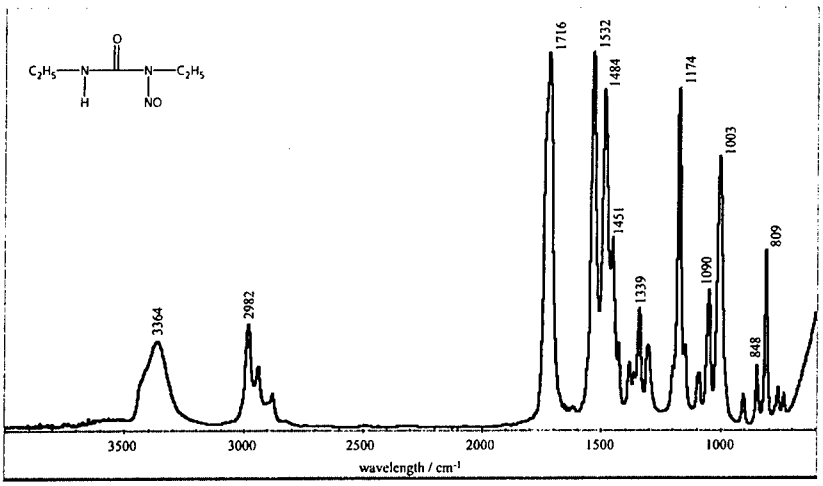
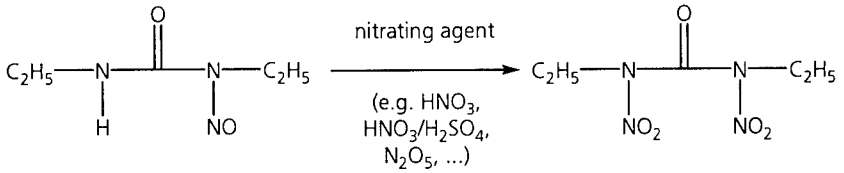


Fig. 7: IR spectrum of N,N'-diethyl-N-nitroso-urea

It could be shown that microreactors turned out to be suitable tools for the safe and highly selective synthesis of N,N'-diethyl-N-nitroso-urea. A selective synthesis and isolation of this stable product made also a consecutive nitration step possible. For this reason N,N'-diethyl-N-nitroso-urea was nitrated again in microreactors under similar conditions as described above:



The product obtained with approx. 100% selectivity could be identified as N,N'-diethyl-N,N'-dinitro-urea, the target product for the further DNDA synthesis!

This result, obtained by performing the nitration of N,N'-diethyl-thiourea in microstructured reactors under systematic and controlled process variation, is of significant importance for a better understanding and subsequent optimization of the entire DNDA synthesis. A promising new synthetic route was discovered based on the nitrosation of N,N'-diethyl-thiourea and subsequent nitration of the formed nitroso derivative.
Furthermore, for the first time a successful "step-by-step" nitration process was carried out by applying microreaction technology.

From the mechanistic point of view the reactions could be explained as follows:
The sulphur of the thiourea functionality is oxidized by the nitrating agent (e.g. HNO_3) forming simultaneously amounts of nitrous acid (HNO_2) which acts as an nitrosation agent. Furthermore, in an excess of HNO_3, HNO_2 exists essentially as N_2O_4, which is nearly completely ionized as $NO^+ + NO_3^-$ [8].
Such nitroso compounds are excellent precursors for the introduction of nitro groups as evidenced by the second nitration step.

Very similar results were obtained for the nitration of N,N'-dimethyl-urea and N,N'-dimethyl-thiourea, respectively, confirming the described reaction pathway via the corresponding nitroso derivatives.

Hence, these experiments show the great potential of microreaction technology as a suitable tool for process development, process analysis and process engineering.
The results obtained by applying microreactors can now be transfered to the synthesis of N,N'-diethyl-N,N'-dinitro-urea on a macroscopic scale. First experiments have already shown that the macroscopic nitrosation of the dialkyl substituted thioureas can be also achieved by conventional nitrosation agents like $NaNO_2/H_2SO_4$. However, the excellent heat transport properties of microreactors makes it more easier to achieve high selectivities, since it has to be considered that the oxidation resp. nitrosation step is the most exothermic step of the entire process.

References

[1] T. Urbanski, *Chemistry and Technology of Explosives*, Vol. 1, Pergamon Press, Oxford, 1983, p.139

[2] J. Barton, R. Rogers, *Chemical Reaction Hazards*, Institution of Chemical Engineers, UK, 1997, p. 7

[3] J.R. Burns, C. Ramshaw, *A Microreactor for the Nitration of Benzene and Toluene*, 4th Int. Conference on Microreaction Technology (IMRET 4), 5-9 March 2000, Atlanta, GA, USA

[4] J. Antes, T. Tuercke, E. Marioth, K. Schmid, H. Krause, S. Loebbecke, *Use of Microreactors for Nitration Processes*, 4th Int. Conference on Microreaction Technology (IMRET 4), 5-9 March 2000, Atlanta, GA, USA

[5] S. Loebbecke, J. Antes, T. Tuercke, E. Marioth, K. Schmid, H. Krause, *The Potential of Microreactors for the Synthesis of Energetic Materials*, 31st Int. Annu. Conf. ICT: Energetic Materials - Analysis, Diagnostics and Testing, 33, 27 - 30 June 2000, Karlsruhe, Germany

[6] E. Marioth, S. Loebbecke, M. Scholz, F. Schnuerer, T. Tuercke, J. Antes, H.H. Krause, *Investigation of microfluidics and heat transferability inside a microreactor array made of glass*, 5th Int. Conference on Microreaction Technology (IMRET 5), 27-30 May 2001, Strasbourg, France

[7] T. Tuercke, W. Schweikert, F. Lechner, J. Antes, H.H. Krause, S. Loebbecke, *Monitoring of Chemical Processes in Microreactors by Adapting FTIR Microscopy and HPLC*, 5th Int. Conference on Microreaction Technology (IMRET 5), 27-30 May 2001, Strasbourg, France

[8] G.A. Olah, R. Malhotra, S.C. Narang, *Nitration*, VCH New York, 1989, p. 129

WinMOPAC - A helpful Tool for the Simulation of New Energetic Molecules

Paul Bernd Kempa and Jochen Kerth

Fraunhofer-Institut für Chemische Technologie (ICT), J.-von-Fraunhofer-Str. 7, D-76327 Pfinztal-Berghausen, Germany

Abstract

The development of new energetic substances is not easy. Therefore it is desirable to receive certain data as stability, energy content, possible reactions etc. before the synthesis. A helpful tool for this is the semiempirical molecule orbital program WinMOPAC. Some of the capabilities are shown with the three constitutional isomers of diamino-dinitro-pyrazine of the sum formula $C_4N_6O_4H_4$.

Introduction

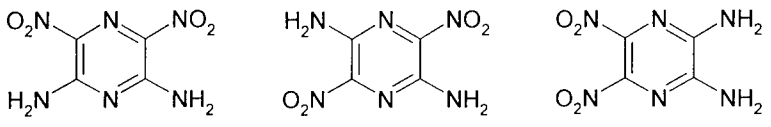
The development of better explosives and propellants for military and civil targets needs new or modified energetic materials. Their synthesis is often difficult, moreover time consuming and expensive. Achievement values, like stability, energy content, chemical and physical behavior, distribution of charges and orbitals, and structural specifics, as symmetry and spectroscopic data, can be determined. On the basis of these values, an evaluation of this new or modified energetic material is possible. To reduce costs, time and to avoid the synthesis of less effective substances in advance, it is helpful to have the possibility of predicting some values of the synthesized compound. So you can avoid inefficient synthesis right from the start. The semiempirical molecule orbital program WinMOPAC enables us to do this.

Description of the program WinMOPAC

WinMOPAC is a graphical user interface and full Windows implementation of the semiempirical molecular orbital package MOPAC. It has been designed for the study of molecular structures and reactions. MOPAC was developed over the last 30 years by J. Stewart [1]. The semiempirical Hamiltonians MINDO/3 [2], MNDO [3], AM1 [4], PM3 [5], and MNDO/d [6] are used in the electronic part of the calculation to obtain molecular orbitals, the heat of formation and its derivative with respect to molecular geometry. Using these results MOPAC calculates the vibrational spectra, thermodynamic quantities, isotopic substitution effects and force constants for molecules, radicals, ions and polymers. For studying chemical reactions, a transition state location routine [7] and two transition state optimizing routines [8, 9, 10] are available.

Application of WinMOPAC for pyrazine isomers

The program was tested for the simulation of energetic compounds. Diamino-dinitro-pyrazine with the formula $C_4N_6O_4H_4$ exists in three constitutional isomers and serves as an example to demonstrate the possibilities of WinMOPAC. The first is 2,6-diamino-3,5-dinitro-pyrazine (1) [11], a precursor for the synthesis of LLM-105 (NPEX-1) [12,13]. The second is 2,5-diamino-3,6-dinitro-pyrazine (2) [14] and the third isomer the hypothetical and yet not synthesized 2,3-diamino-5,6-dinitro-pyrazine (3). The choice of these molecules enables us to test how WinMOPAC simulates and distinguishes different molecules of the same molecular formula.



1 2 3

Fig. 1: The constitutional isomers of diamino-dinitro-pyrazine.

Optimization of the geometry

Starting with given values or in this case rough conception of the molecules, models of the isomers are developed. After choosing a suitable Hamiltonian an energetic optimization of the geometry was performed. All the following calculations are done with the PM3 Hamiltonian. The geometry optimization reveals heat of formation, dipole momentum, ionization energy, orbital energies, bond lengths, bond angles, torsion angles, bond order and charges. Fig. 2-4 show the optimized geometries of the three pyrazine isomers. The calculated molecule data are summarized in Table 1.

Compound	2,6-diamino-3,5-dinitro-pyrazine (1)	2,5-diamino-3,6-dinitro-pyrazine (2)	2,3-diamino-5,6-dinitro-pyrazine (3)
	ICT	DERA	not synthesized
HEAT OF FORMATION	14.577022 kcal	23.251167 kcal	25.923945 kcal
ELECTRONIC ENERGY	-14074.565902 EV	-13945.983373 EV	-14084.533625 EV
CORE-CORE REPULSION	11396.522425 EV	11268.316043 EV	11406.982197 EV
DIPOLE	7.69316 DEBYE	1.50424 DEBYE	9.94655 DEBYE
SYMMETRY	C2v	C2	C1
IONIZATION POTENTIAL	9.950643 EV	9.605906 EV	9.738843 EV
HOMO / LUMO ENERGIES (EV)	-9.951 / -1.373	-9.606 / -2.214	-9.739 / -1.995
MOLECULAR WEIGHT	200.113	200.113	200.113

Table 1: Results of the geometry optimization of the three pyrazine isomers.

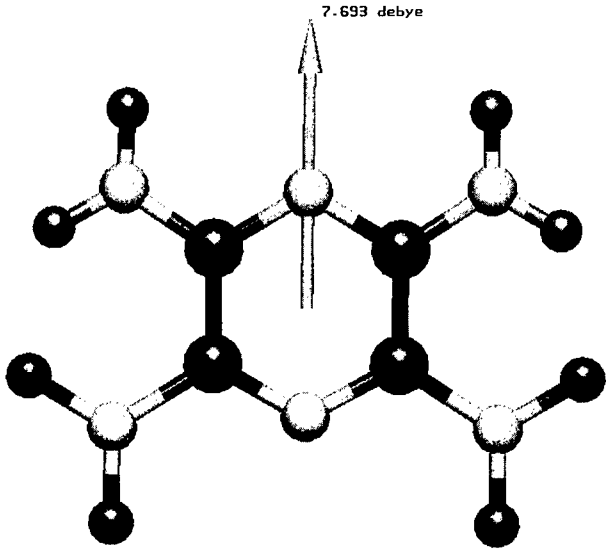


Fig. 2: Molecule of 2,6-diamino-3,5-dinitro-pyrazine (1).

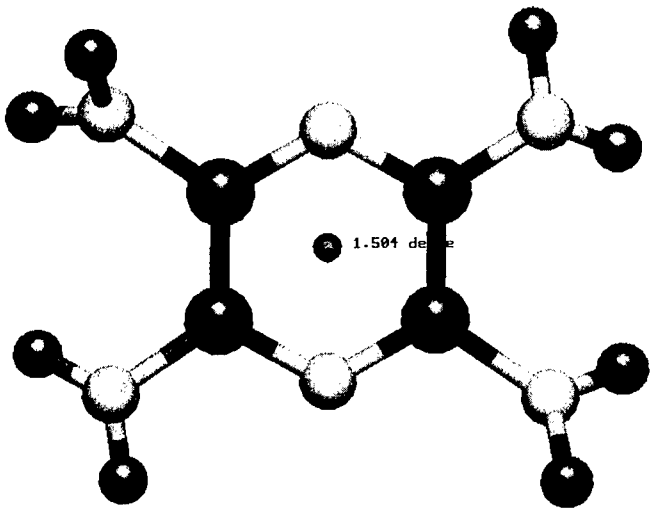


Fig. 3: Molecule of 2,5-diamino-3,6-dinitro-pyrazine (2).

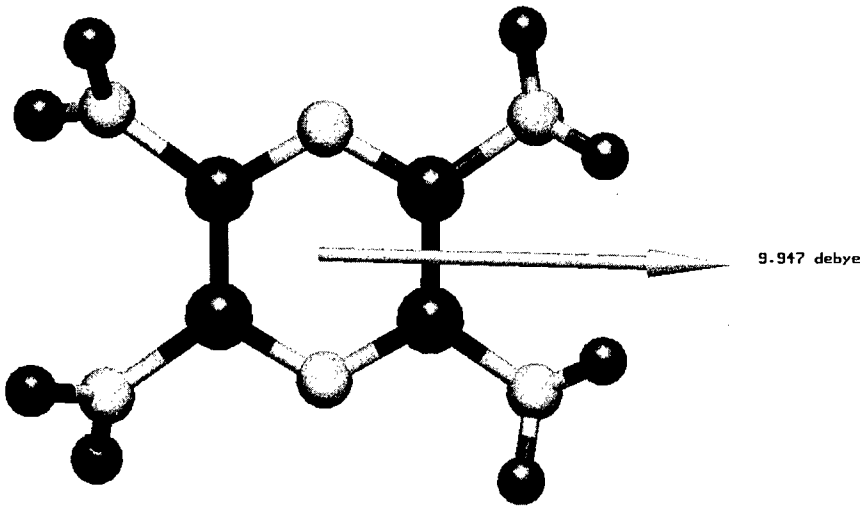
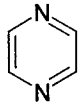


Fig.4: Molecule of 2,3-diamino-5,6-dinitro-pyrazine (3).

The ring geometries of these isomers, including the bond order and the charges, was compared with the parent compound pyrazine (4), which was also calculated. The results are summarized in Table 2. Fig 7 - 9 show the graphic distribution of the charges (positive charge = light gray; negative charge = dark gray). It can be seen, that the charges are mainly located over the nitro-groups.



4

Fig.5: Pyrazine (4)

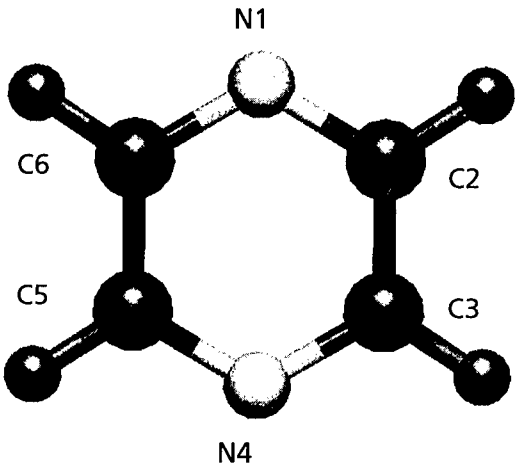


Fig. 6: Molecular structure of pyrazine (4).

Bond	pyrazine	2,6-diamino-3,5-dinitro-pyrazine (1)	2,5-diamino-3,6-dinitro-pyrazine (2)	2,3-diamino-5,6-dinitro-pyrazine (3)
N1 – C2	1.353	1.372	1.367	1.354
C2 – C3	1.400	1.447	1.417	1.439
C3 – N4	1.353	1.346	1.348	1.354
N4 – C5	1.353	1.346	1.367	1.362
C5 – C6	1.400	1.447	1.417	1.395
C6 – N1	1.353	1.372	1.348	1.362
Bond order				
N1 – C2	1.4400	1.2979	1.3488	1.4323
C2 – C3	1.3851	1.1035	1.2685	1.1658
C3 – N4	1.4400	1.4397	1.4493	1.4313
N4 – C5	1.4400	1.4398	1.3480	1.3589
C5 – C6	1.3851	1.1036	1.2686	1.4041
C6 – N1	1.4400	1.2984	1.4486	1.3583
Angles				
C6 – N1 - C2	119.0	118.6	120.3	120.2
N1 – C2 -C3	120.5	120.5	118.8	119.5
C2 – C3 - N4	120.5	119.4	120.9	119.5
C3 – N4 - C5	119.0	121.5	120.3	120.2
N4 – C5 - C6	120.5	119.4	118.8	120.3
C5 – C6 - N1	120.5	120.5	120.9	120.3

Table 2: Geometric values of pyrazine, compared with the geometric values of the rings of the three isomers.

The optimized geometry of pyrazine shows a symmetric ring without torsion. All C - N bonds are equal with a bond length of 1.353 Å and a bond order of 1.44, for C - C bonds 1.4 Å and 1.385. The bond angles in the ring are 119° and 120.5°. For the atoms, where the nitro- or the amino-groups are located, a change in these values can be observed as summarized in Table 2. Furthermore a small torsion in the rings is observed. The torsion angel is ± 1.0° for the first, ± 1.8° for the second and ± 2.3° for the third isomer.

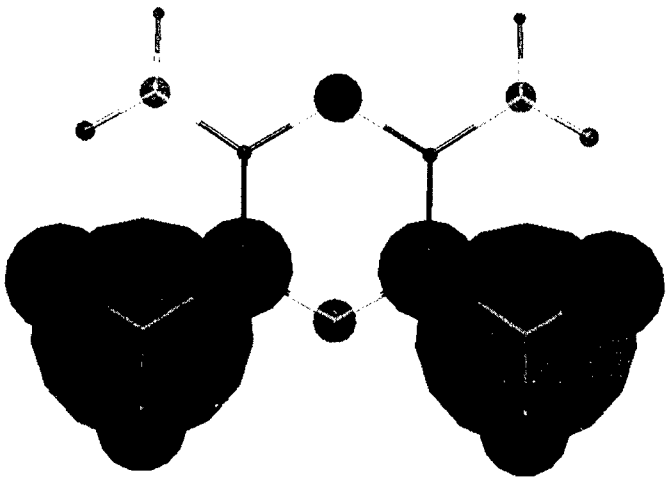


Fig.7: Charge distribution over the molecule of 2,6-diamino-3,5-dinitro-pyrazine.

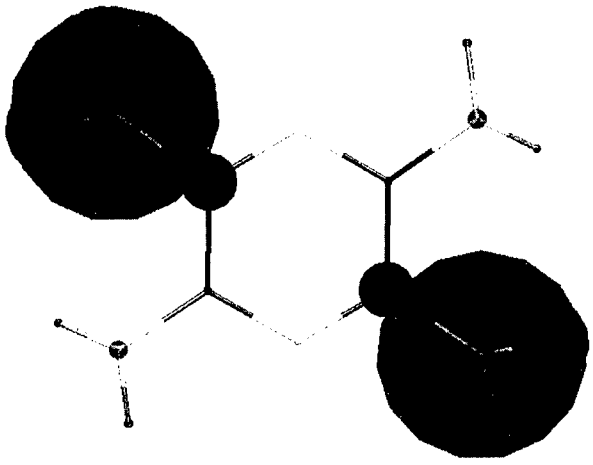


Fig.8: Charge distribution over the molecule of 2,5-diamino-3,6-dinitro-pyrazine.

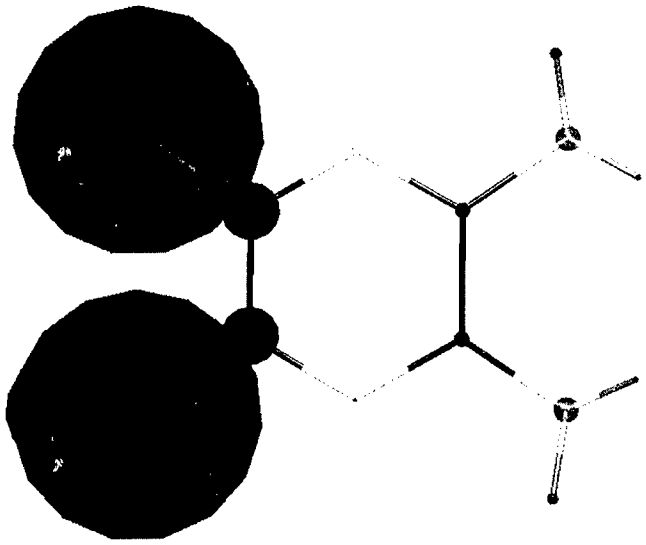


Fig.9: Charge distribution over the molecule of 2,3-diamino-5,6-dinitro-pyrazine.

IR-Spectra

Based on the optimized molecule structures WinMopac calculates the normal modes of a molecule and generates simulated IR-spectra. Fig. 10 shows the calculated IR-spectra of pyrazine for comparison and Fig. 11,12 show those of the pyrazine isomers (2) and (3). A measured IR-Spectrum exists for the isomer (1). For comparison with the simulated one in Fig. 13 it is shown in Fig. 14.

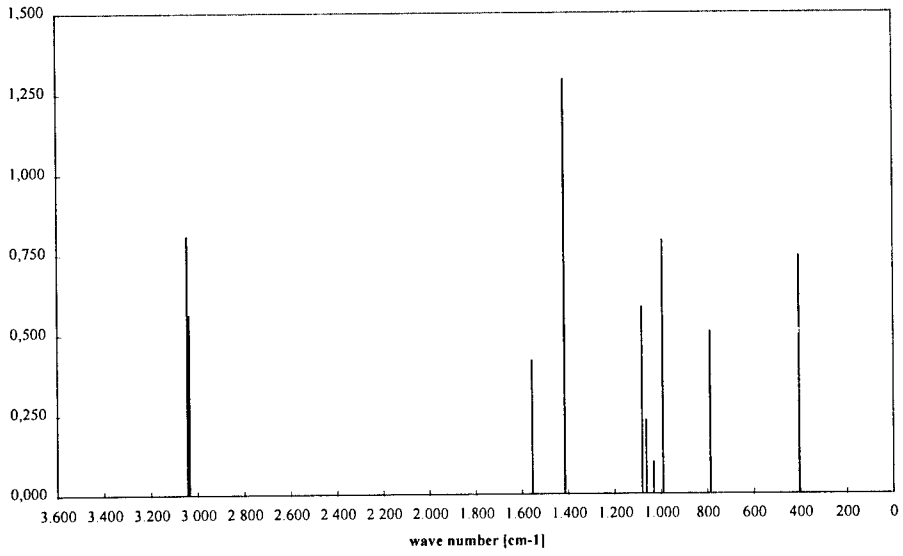


Fig.10: Simulated IR-Spectrum of pyrazine (4).

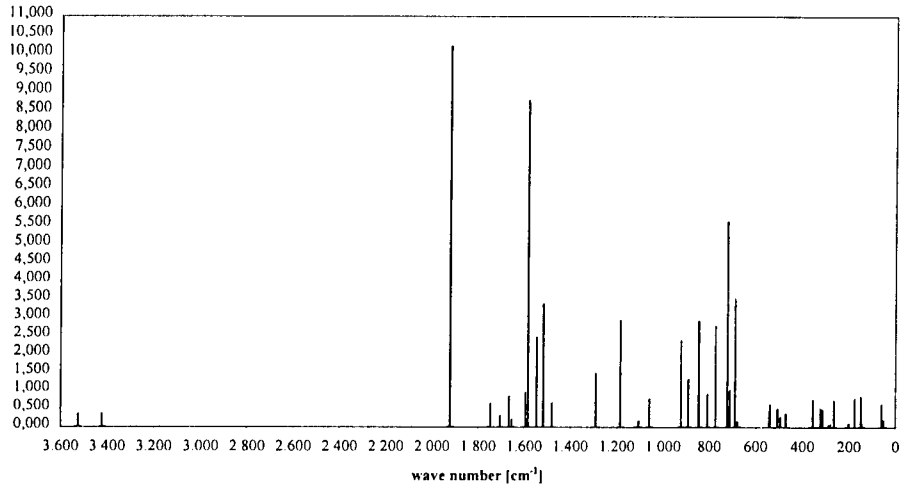


Fig. 11: Simulated IR-Spectrum of 2,5-diamino-3,6-dinitro-pyrazine (2).

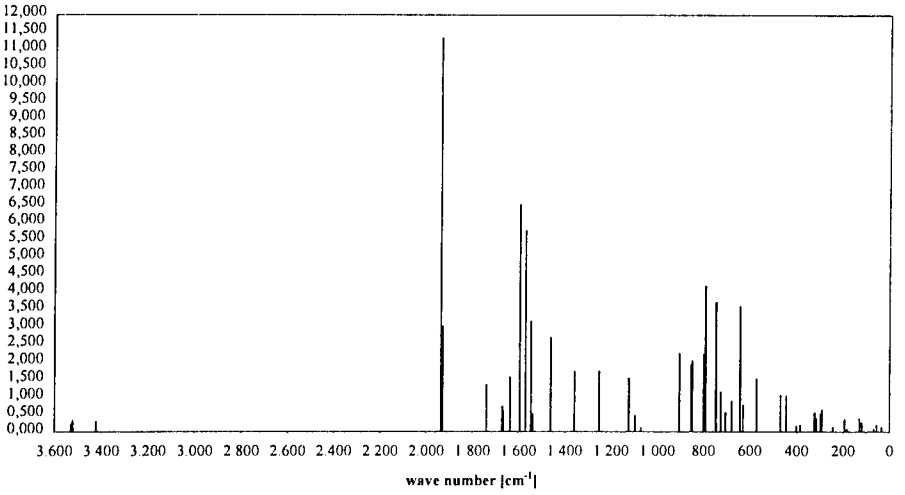


Fig. 12: Simulated IR-Spectrum of 2,3-diamino-5,6-dinitro-pyrazine (3).

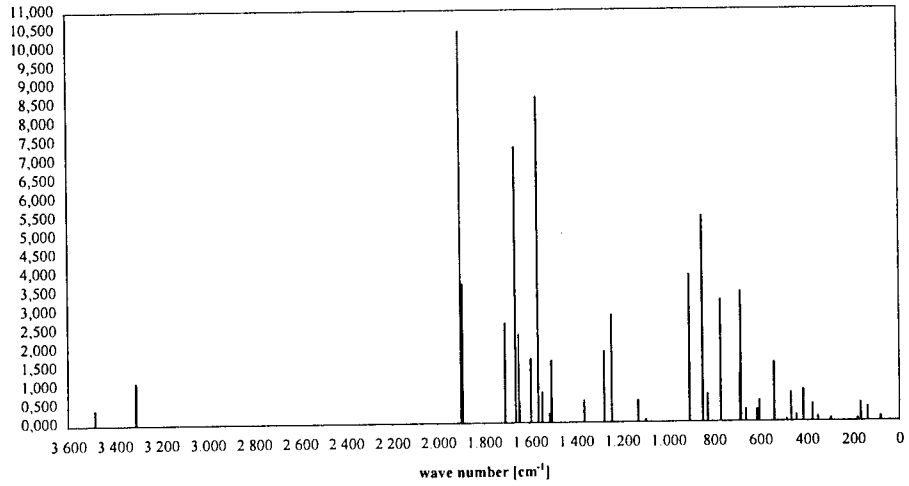


Fig. 13: Simulated IR-Spectrum of 2,6-diamino-3,5-dinitro-pyrazine (1).

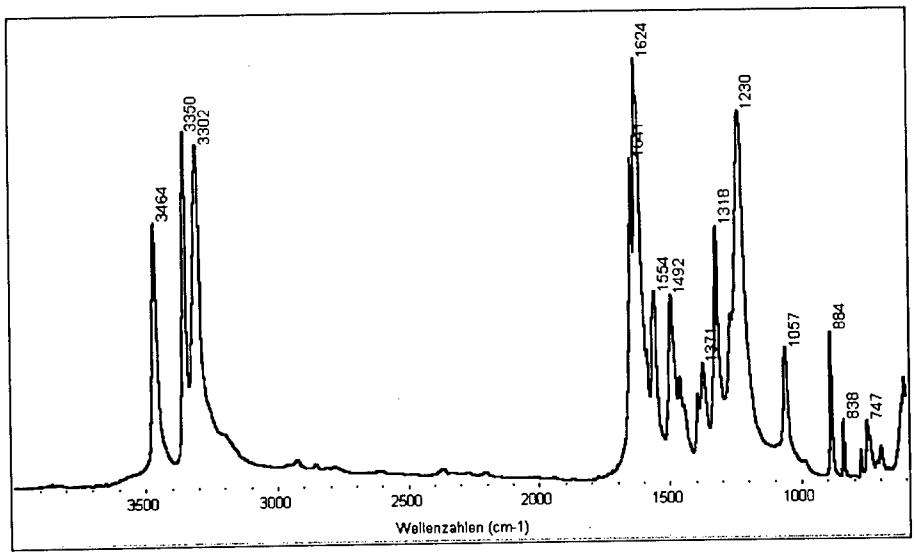


Fig. 14: Measured IR-Spectrum of 2,6-diamino-3,5-dinitro-pyrazine (1).

The calculated data can help us to identify a compound by comparison of a calculated IR-Spectrum with a measured one of a synthesized compound. A difference between both IR-Spectra can occur, because the calculated one is for the ideal molecule symmetry and the measured one is performed with the molecule incorporated in the crystal. This is clearly shown in the comparison of the simulated and the measured IR-Spectra of isomer (1).

Conclusion

This example shows some of the capabilities of WinMOPAC and how this program can be used for the development of new energetic materials. The isomers (1) and (2) show a good thermal stability, that is probably due to hydrogen bonding. In the case of the third isomer it was assumed that fewer or no hydrogen bonds are formed, so that a less stable or instable product was expected. Yet the simulation shows a heat of formation of 25 kcal per mol for the third isomer, so that the synthesis of this energetic substance, so far not yet synthesized, seems possible.

Literature

[1] J. J. P. Stewart: MOPAC: A General Molecular Orbital Package. Quant. Chem. Prog. Exch.,10:86, 1990.

[2] R. C. Bingham, M. J. S. Dewar, and D. H. Lo: Ground States of Molecules. XXV. MINDO/3. An Improved Version of the MINDO Semiempirical SCF-MO Method. J. Am. Chem. Soc., 97:1285–1293, 1975.

[3] M. J. S. Dewar and W. Thiel: Ground States of Molecules, 38. The MNDO Method. Approx-imations and Parameters. J. Am. Chem. Soc., 99:4899–4907, 1977.

[4] M. J. S. Dewar, E. G. Zoebisch, E. F. Healy, and J. J. P. Stewart: AM1: A New General Purpose Quantum Mechanical Model. J. Am. Chem. Soc., 107:3902–3909, 1985.

[5] J. J. P. Stewart: Optimization of Parameters for Semi-Empirical Methods I-Method. J. Comp. Chem., 10:209–220, 1989.

[6] W. Thiel and A. Voityuk: Extension of MNDO to d-Orbitals -Parameters and Results for the 2nd Row Elements and for the Zinc Group, J. Phys. Chem., 1996, 100, 616-629 (1996).

[7] J. Baker: An Algorithm for the Location of Transition States. J. Comp. Chem., 7:385, 1986.

[8] R. H. Bartels: Report CNA-44. University of Texas and Center for Numerical Analysis, 1972.
[9] A. Komornicki and J. W. McIver: Rapid Geometry Optimization for Semiempirical Molecular Orbital Methods. Chem. Phys. Lett, 10:303, 1971.
[10] A. Komornicki and J. W. McIver: Structure of Transition States in Organic Reactions. General Theory and an Application to the Cyclobutene-Butadiene Isomerization using a Semiempirical Molecular Orbital Method. J. Am. Chem. Soc., 94:2625–2633, 1972.
[11] D. S. Scott: US 3,808,209.
V. A. Tartakowsky, O. P. Shitov, I. L. Yudin, V. A. Myasnikov: SU 1,703,645.
[12] R.A. Hollins, R.A. Nissan, W.S. Wilson: 2,6-Diamino-3,5-dinitro-pyridine-1-oxide - A New Insensitive Explosive Report, NAWC-WPNS-TP-8228, AD-A29799/5GAR, August 1995.
[13] R.L. Atkins, W. Bauer: A Partnership of National Laboratories, MWD DEA-A-76-G-1218-Meeting: Energ. Mat. for Munitions, 1997.
[14] S.P. Philbin, R.W. Millar, R.G. Coombes: Preparation of 2,5-Diamino-3,6-Dinitropyrazine (ANPZ-i): A Novel Candidate High Energy Insensitive Explosive, Propellants, Explosives, Pyrotechnics 25, 2000, 302-306.

Kinetic Model for the Polymerization Reaction Of Toluene Diisocyanate with HTPB

*S. A. Shokry**

* Prof. Dr. Shokry Abd El – Sami Shokry
Head of quality control and quality assurance sections, AZC, Cairo, Egypt

ABSTRACT

The kinetic model of the urethane formation reaction between toluene diisocyanate and hydroxyl – terminated polybutadiene has been derived.
The polymerization reaction was carried out in toluene solution at four different temperatures (30,40,50 and 60 C), and the used catalyst was dibutyltin dilaurate. It was found that the polymerization reaction exhibited second order kinetics for both the ortho and para isocyanate and the increase in temperature enhanced the reactivity of the isocyanate. Activation energies were calculated from Arrhenius equation and their values were (6200 and 7160) cal./mole. The preceding results give the evidences to derive an expected mechanism for the urethane formation reaction. The relative simplicity of the derived model gives it the potential for application in the design of industrial polymerization facilities.

Introduction

The unsaturated polymers of hydroxyl-terminated polybutadiene (HTPB) and toluene diisocyanate (TDI) was theorized to be used as a binder for composite solid propellant and plastic bonded explosives which meet the current criteria for thermal and ballistic properties. This binder offers the best properties of increasing the solid loading due to its low viscosity. It also gives the propellant system high specific impulse due to the relatively high combustion flame temperature, results from the relatively high level of hydrogen in the system at a given oxidizer loading (1,2).

The major drawback to these binders is their low pot live during manufacture (3). These types of polymer are also used in polyurethane industry, for synthesis of polyurethane elastomers. They can offer the produced elastomers, the combined properties of polyethers, ester urethanes and conventional rubber as well (4).

On the survey of pervious work in the predication of the kinetic model of the polybutadiene- urethane formation reaction, one can find that comparatively little information had been published in this field, and the reported work was not complete, and mostly unsatisfactory.

So the objective of this work is to develop complete kinetic model for the HTPB-TDI *Polymerization reaction. The reaction was carried out according to the operating conditions reported in earlier study and aided by the results from recent studies. Following that line of reasoning which was supported by a considerable amount of early and recent results, we study the polymerization reaction in toluene solution as a solvent at different reaction temperatures of 30,40,50 and 60 ^{o} C. The used catalyst was dibutlytin dilaurate.*

Experimental

Polymerization experiments were carried out for different time intervals and at different reaction temperatures.

Apparatus

The used apparatus as shown from figure (1) is a glass reactor of double jacket fitted with glass stirrer, the temperature of the circulating water is controlled using an efficient thermostat.

Materials and Procedure

The used materials are:

- HTPB from Philips Petroleum company (USA) under trade name Butarez-HTS-polymer with hydroxyl number of 0.95 mg. equivalent (OH) Per gm. of polymer, as determined by acetyliation with acetic anhydride in pyridine solution (5).

- Tolylene 2,4 diisocanate (TDI), from Bayer company with isocyanate number of 11.4426 mg. equivalent (NCO) pert gm. of TDI, as determined by Malec and David method (6).

The glass reactor was charged by 5 gm. of HTPB in 10 ml. of toluene, the temperature was controlled with accuracy equal 1 °C using controlled thermostat. The mixture was stirred under continuos evacuation (5-10mm.Hg.) to remove air bubbles and humidity was mixed with the catalyst (and then the mixture was added to the previously stirred HTPB. Stirring was continued under vacuum (30-50 mm. Hg.), till the decided time. The concentration was 0.2M and the ratio of (-NCO/ -OH) was unity. After each decided reaction time (0.5,1,1.5,....,4 h), the reaction mixture was removed to another flask and 5 mol.of 2M-dibutylamine solution was added. The flask was kept for 24 h to insure complete reaction between the unreacted isocyanate and dibutylamie. The excess amine was back titerated with 0.5M HCL, using the method of Baker and Holdsworth (7).

Results and Discussion

Linear polyurethane is formed in polyaddition reaction of isocyanate group (-NCO) and alcoholic hydroxyl groups.

$$R\text{-}N{=}C{=}O + R`\text{-}OH \longrightarrow R\text{-}N(H)\text{—}C(=O)\text{-}OR`$$

The obtained polymer contains the characteristic urethane link

$$\text{-}[\text{--}N(H)\text{—}C(=O)\text{—}O]\text{—}$$

The reaction of isocyanate and alcohol was investigated to be second order reaction (8). But reactivity of the two isocyanate groups in TDI molecule are different, the –NCO group in para position is more reactive than the isocyanate in ortho position (9). That means pronounced discontinuity must

be observed in the conversion time relation. So for the complete kinetic model for this reaction, the following demands must be satisfied.

1. Order of the reaction must be determine for both the two position Isocyanate groups.
2. Derivations of the mathematical relation involving the conversion with time before and after the distinct break in continuity.
3. Making the empirical equation relating rate constants of each reaction with the controlling factors.

The polymerization reaction of HTPB with TDI were carried out at four different temperatures (30,40,50,and 60 ^{0}C). By the application of the differential method for determining the order of reaction on the resultant conversions,

$$\text{Ln } (dx/dt)=\text{Ln}k+n\text{Ln}(a-x)$$

Where x is the conversion, k is the rate constant, a is the initial concentration, t is the time, and n is the order of reaction.

Figures (1,2) show the plot of Ln (dx/dt) versus Ln (a-x) at each temperature. It was seen from the figures that the assumed very distinct breaks appeared beyond the 35 % conversion. It also seen that the above relation was represented by a sires of straight lines, their slops assured that the order of reaction of both isocyanate groups are second order.

To determine the rate constants as a function of temperatures for the reaction of the ortho and para position isocyanates groups, we apply the second order rate equation,

$$dx/dt = ka\,(1-x)^2$$

By integration,

$$x / a\,(a-x) = kt$$

Through the fitting of the relation of (x/a (a-x)) and time at each temperature. The slops of the resulting straight lines determine the rate constant of the reaction at that temperature. Figure (3) and table (1) show the results of that fitting. It is also clear from the figure that the increase in temperature enhances the reactivity of the isocyanate groups. To determine which isocyanate group enhanced selectively, the more reactive para or the less reactive ortho, we calculate the ratio between the rate constants for the two groups as shown in table (1). From the table it is observed that the less reactive ortho isocyanate group more selectively increased by the effect of the increase in the reaction temperature.

Activation energies and frequency factors were also determined from the Arrhenius equation,

$$k = A\, e^{-E/RT}$$

$$\text{Ln } k = \text{Ln } A - (E/RT)$$

Figure (4) is the plot of the logarithmic rate constant versus the reciprocal of temperature, which is a straight line; its slop indicates the value of E/R. Table (1) shows the values of the activation energies and frequency factors. It is clear that the activation energy for the reaction of the ortho group (7160) cal.mol.$^{-1}$ is higher than that of the para group (6200) cal.mol.$^{-1}$ this is normal case because of the inductive effect of the methyl group in the 1 position.

Mechanism of the Reaction:

From the preceding results we can get the evidences to derive the following mechanism for the polymerization reaction:

a. The catalyst Dibutyltin dilaurate (D) react with HTPB to form active hydroxyl:

$$D + HO\text{-}R^{\cdot}\text{-} \xrightarrow{k1} D\ldots HO\text{-}R^{\cdot}\text{-} \quad \text{(fast reaction)} \qquad (1)$$

$$D\ldots HO\text{--}R^{\cdot} + HO\text{-}R^{\cdot}\text{-} \underset{}{\overset{K}{\rightleftharpoons}} \begin{matrix} D\ldots O - R^{\cdot} \\ H\ldots HO - R^{\cdot}\text{-} \end{matrix} \quad \text{(complex1)} \qquad (2)$$

b. Active hydroxyl react with NCO to form urethane which is rate controlling step:

$$\text{Complex1} + RNC{=}O \xrightarrow{k2} \text{complex2} \quad \text{(fast reaction)} \qquad (3)$$

$$\text{Comlex2} \xrightarrow{k3} \text{comlex3} + R^{\cdot}\text{-OH} \quad \text{(fast)} \qquad (4)$$

$$\text{Complex3} \xrightarrow{k4} \text{- R COONH-} + D \quad \text{(fast)} \qquad (5)$$

Since step (1) is fast,

$$[\,D\ldots HO\text{-}R^{\cdot}\text{-}] = [\,D\,] = [\,D]o$$

$$K = \frac{[\text{complex1}]}{[\,OH\,]\,[\,D\ldots HO\text{-}R^{\cdot}\text{-}\,]}$$

[complex1] $= K\,[OH]\,[\,D...HO\text{-}\,R^{\cdot}\,-\,]$

$= K\,[OH\,]\,[\,D\,]_o$

From step (3) we have,

$$\frac{d\,[\,NCO\,]}{d\,t} = -k3\,[\,NCO\,]\,[\,complex1\,]$$

$$= -\,k3K\,[\,NCO\,][\,OH\,][\,D\,]_o$$

Since [NCO] = [OH]

Therefor,

$$\frac{d\,[NCO\,]}{d\,t} = \frac{d\,[OH\,]}{d\,t}$$

$$= -\,k3K\,[\,OH\,][\,NCO\,][\,D\,]_o$$

$$= -k\,[\,OH\,][\,NCO\,] \qquad [\,D\,]_o = \text{constant}$$

$$= -k[\,OH\,]^2$$

$$= -\,k[\,NCO\,]^2$$

Conclusions

A detailed kinetic model has been developed to describe the polymerization reaction between toluene diisocyanate and HTPB. Based on this model the significant effect of the temperature on the reaction has been determined. This model is simple and easy to be used in the industrialization activity in urethane production. The used technique of the experimental work could be used to guide and corroborate other researchers for modeling of similar reaction systems.

Literature Cited

1. Bottaro, .J.C. " Recent advances in explosives and solid propellants" , Chemistry and Industry, April, 1996.
2. Borman, Stu., "Advanced energetic materials for military and space applications", C&EN, January, 17, 1994, Washington.
3. Mark, H.F. and Gaylard, .G., "Encyclopedia o polymer science and technology", vol. 2, Interscience publishers, NewYork, 1970.
4. Eatan, P.E." Starting materials for chemistry of 1990's and new century." , Chemistry and Int. Ed. Engl. 31, 1421-1436, 1992.
5. Lyubomilove, V.I. and Useich, T.D. , Plast. Massy, 2,67,1961.
6. David, D.J. and Staley, H.B., " High polymer, vol. XVI, " Analytical chemistry of polymers , part 3", Wiely Interscience,New York,357,1969.
7. Baker, J.W. and Holdsworth, J.B., J. Chem. Soc., 713,1947.
8. Coutinho, L.C. and Cavalheiro, J. Appl. Polym. Symp., 49,29,1991.
9. Sauders, J.H. and Frich, K.C." Polyurethane chemistry ad technology, part 1", Chemistry Interscience Publications, NewYork, 1962.

Table 1 Rate Constants and Activation Energies for The Polymerization Reaction.

Temperature (^{o}C)	Rate Constants ($cm^3 mole^{-1} s^{-1}$)		k_1/k_2	Activation Energies ($cal. mole^{-1}$)	
	k_1(4-NCO)	k_2(2-NCO)		E_1(4-NCO)	E_2 (2-NCO)
30	1.3	0.67	1.94		
40	2	1.12	1.76		
50	2.6	1.54	1.69	6200	7160
60	3.2	1.92	1.97		

Figure 1 Apparatus for polymerization reaction
(1. Heating water in 2. Heating water out 3. Heating jacket 4. Glass reactor 5. stirrer 6. To vacuum pump).

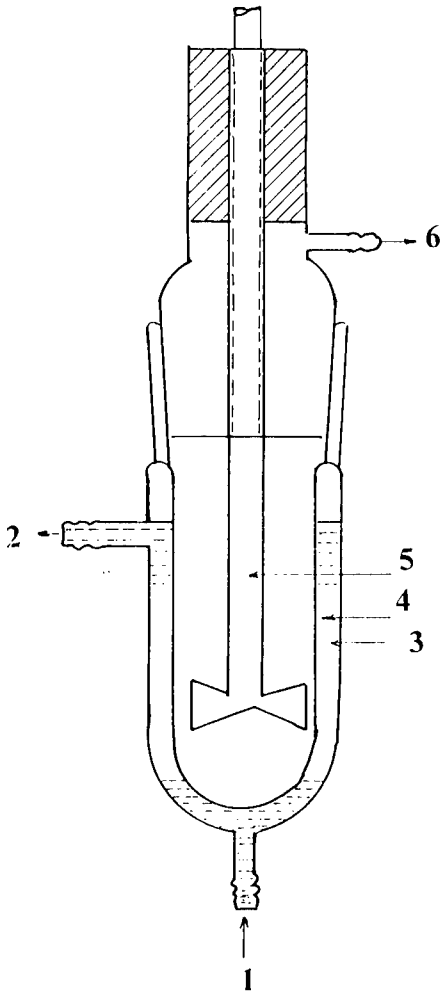


Figure 2 Determination of the reaction order at temperatures of 30 C, 40 C and 50 C

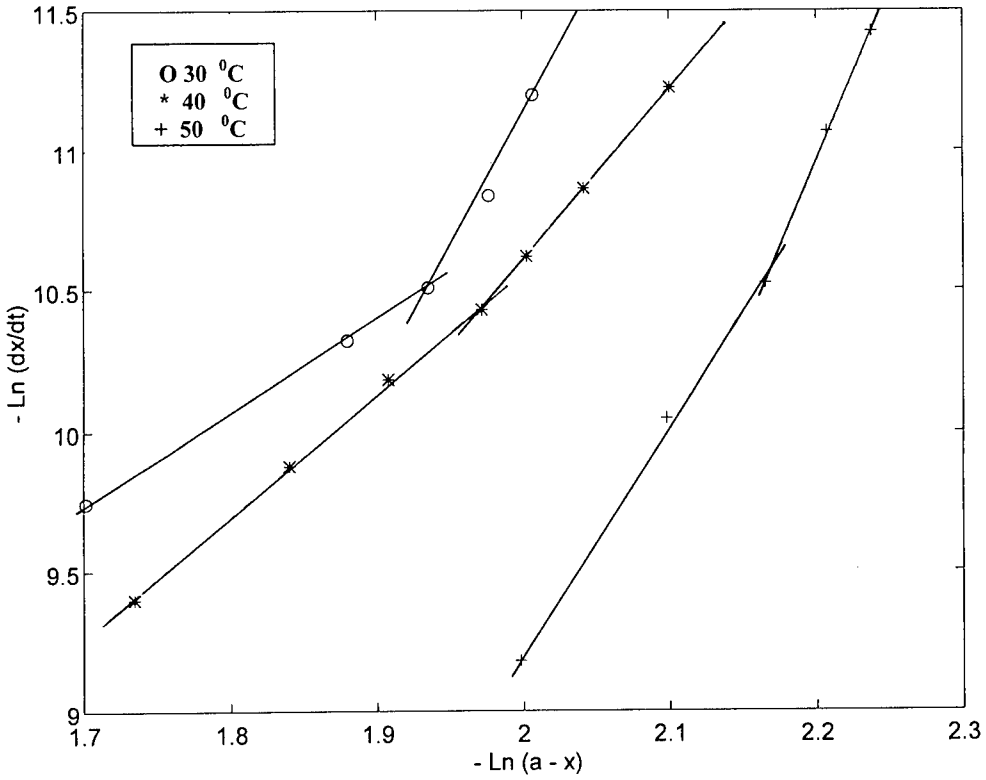


Figure.3 Determination of the reaction order at 60 C

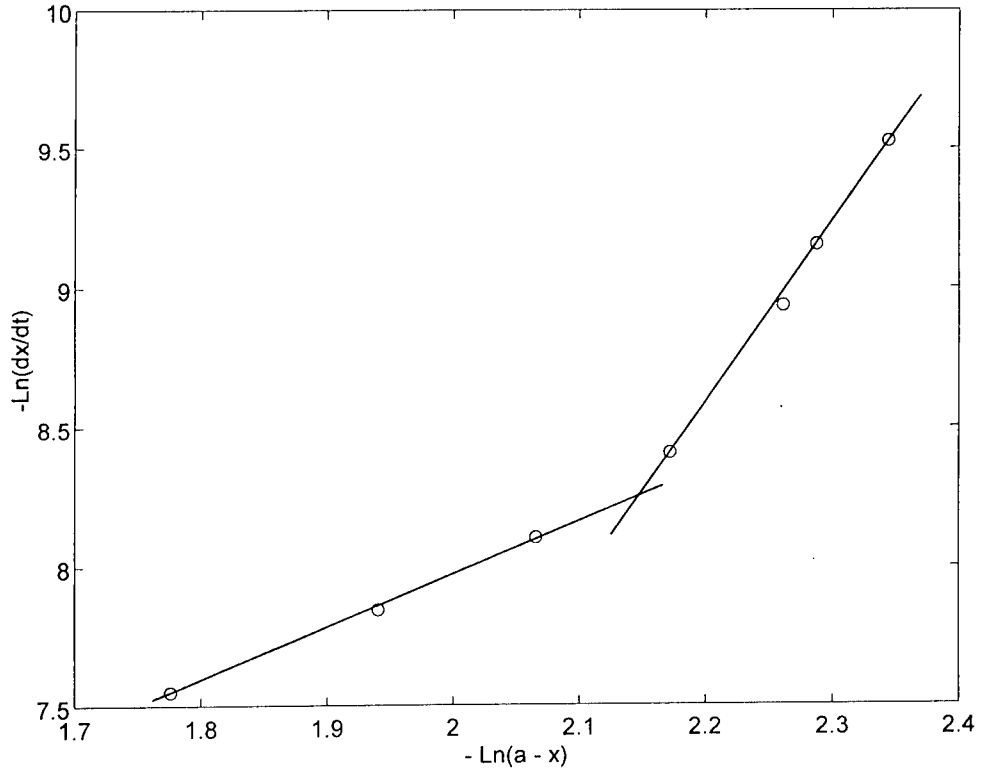


Figure.4 Determination of the reaction rate constants at different temperatures

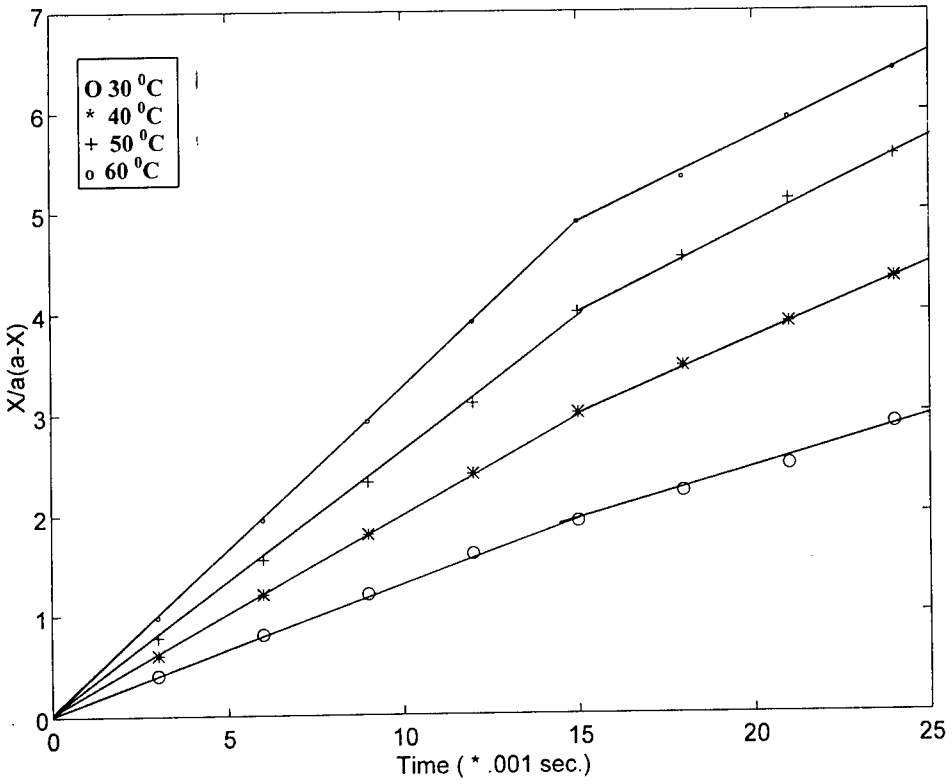
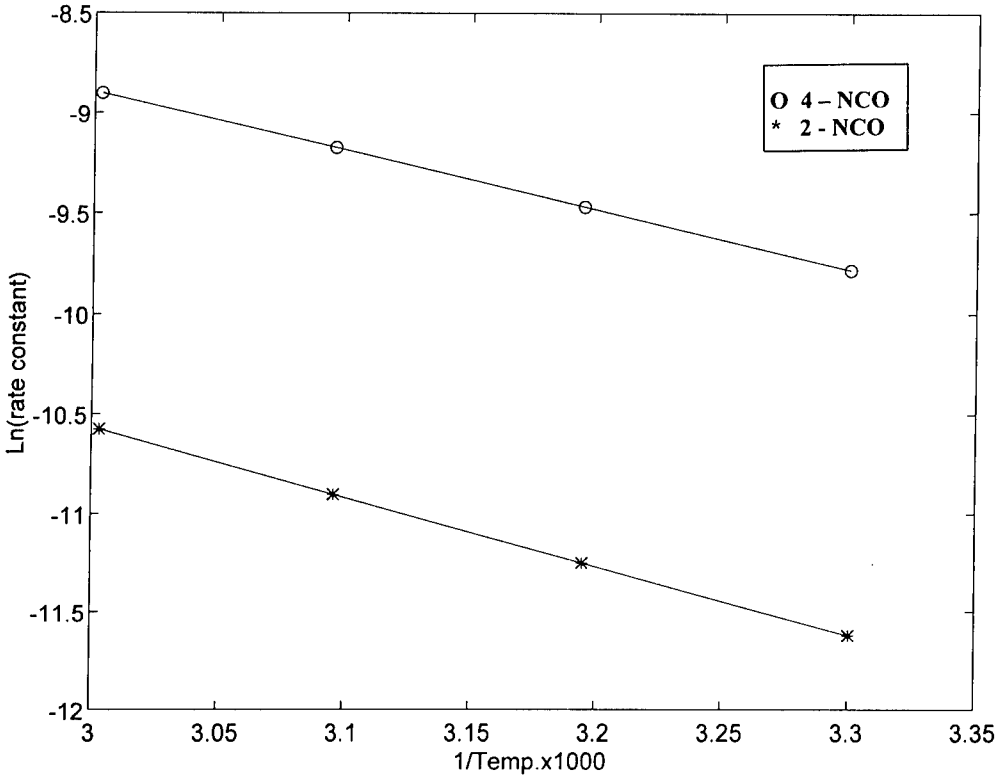


Figure 5 Arrhenius plot for the polymerization reaction



ABOUT THE BURNING BEHAVIOUR AND OTHER PROPERTIES OF SMOKE REDUCED COMPOSITE PROPELLANTS BASED ON AP / CL20 / GAP

Siegfried Eisele, Klaus Menke

Fraunhofer-Institut für
Chemische Technologie
- ICT -
Joseph-von-Fraunhofer-Straße 7
76327 Pfinztal

Abstract

AP/CL20/GAP propellants with only 20 % AP and energetic plasticizers based on BTTN/TMETN/GAPA exhibit some unique properties which are not covered by the existing solid rocket propellants. Together with a significantly reduced exhaust signature obeying to AB AGARD signature classification, they are endowed with a high specific impulse up to I_{SPEQ} = 2500 Ns/kg and 4400 Ns/dm³ < $I_{SPEQ} \cdot \rho$ < 4500 Ns/dm³ for 70 : 1 expansion ratio, burning rates up to 50 mm/s at 10 MPa and pressure exponents from 0,3 < n < 0,5 in the pressure range 4 to 25 MPa.

Together with these outstanding properties they combine good processibility, good chemical stability and good mechanical properties. Although according to Gap tests their safety classification belongs to class 1.1, their sensitivity to detonation is lower than for pressed explosives or than for high energetic doublebase or composite doublebase propellants.

With these properties AP/CL20/GAP propellants recommend themselves for application in rocket motors for actively guided highly accelerating tactical missiles (HVMs or HFKs) or for high performance end burning grains for missiles which require improved camouflage and a hardly detectable trajectory.

Zusammenfassung

Treibstoffsysteme auf der Basis von AP/CL20/GAP, die nur 20 % AP und energetische Weichmacher in Gestalt von TMETN/BTTN/GAPA enthalten, besitzen ein Eigenschaftsspektrum, das von keinem anderen bisher existierenden Raketentreibstoff eingenommen wird. Zusammen mit einer deutlich reduzierten Abgasstrahlsignatur, die der AGARD-Klassifizierung AB zugeordnet ist, sind sie mit einem hohen spezifischen Impuls bis zu I_{SPEQ} = 2500 Ns/kg und 4400 Ns/dm³ < $I_{SPEQ} \cdot \rho$ < 4500 Ns/dm³ für ein Entspannungsverhältnis von 70 : 1 ausgestattet, Abbrandgeschwindigkeiten bis zu 50 mm/s bei 10 MPa und Druckexponenten von 0,3 < n < 0,5 im Druckbereich von 4 bis 25 MPa.

Zusammen mit diesen herausragenden Eigenschaften verbinden sie gute Verarbeitbarkeit, gute chemische Stabilität und gute mechanische Eigenschaften. Obwohl sie nach den Ergebnissen von Gap Tests in Klasse 1.1 sicherheitsklassifiziert sind, ist ihre Empfindlichkeit gegenüber Detonation geringer als von gepreßten Explosivstoffen oder von hochenergetischen Doublebase- oder Composit Doublebase Festtreibstoffen.

Mit diesen Eigenschaften empfehlen sich AP/CL20/GAP Treibstoffe zur Anwendung in Raketenmotoren von aktiv gelenkten, hoch beschleunigenden taktischen Flugkörpern (HVMs oder HFKs) oder für Hochleistungsstirnbrennerantriebe von Flugkörpern, die verbesserte Tarnung und eine schwer zu detektierende Flugbahn verlangen.

1. Introduction

Formulations based on CL20/GAP have been taken into consideration as a new upcoming minimum smoke propellant system[1]. It is endowed with a high composite like specific impulse and exhibits considerable higher burn rates compared to other minimum smoke doublebase- or nitramine propellants.
Formulations based on AP/HMX/GAP were presented some years before as promising candidates for reduced smoke and possible substitute for AP/HTPB propellants[2]. Due to the limited burnrates and high pressure exponents they still have disadvantages and couldn't reach the performance and application profile of fast burning composite propellants based on AP/Al/HTPB and AP/HTPB.

In specialized formulations, the conventional composite propellants are applied for HVM or HFK - highly accelerating hypervelocity missile systems – to be used for the defence against incoming missiles, ICBMs, helicopters with high agility and tanks.
Their disadvantages are the production of large amounts of hydrogen chloride in the exhaust. Together with aluminiumoxide and substantiate air humidity they create large amounts of smoke and an easy detectable trajectory.

To overcome these disadvantages our goal was the development of a new propellant system which should combine minimum or reduced smoke behaviour with a high thermodynamic performance and burn rates being comparable to the best fast burning composite propellants based on AP/HTPB and AP/Al/HTPB. Due to the promising features of CL20/GAP formulations[1)] and our experiences with the AP/HMX/GAP system we looked for formulations based on AP/CL20/GAP with energetic plasticizers and limited amounts of 20%AP.

A propellant with only 20 % AP will fall into the AGARD classification B for secondary signature[3)] thus producing an almost invisible trail under most environmental conditions. Together with an improved launcher camouflage active guidance by laser beam riding or trajectory control by radar appear to be possible in that case.
For HVM-application, however, the propellant must fulfil a lot of requirements which are not so easy to achieve together:

- → high specific impulse $I_{SP} \geq 250$ s (1000 psi, 68,9 : 1 expansion ratio)
- → high burning rates $r_{10MPa} \geq 30$ mm/s
- → low pressure exponents $n \leq 0,5$
- → high mechanical strength together with viscoelastic properties in full application range from –54 °C to +72 °C
- → good thermal stability and service life
- → low sensitivity to detonation and impact

2. Propellant System

To achieve high thermodynamic performance together with high burning rates and significantly reduced signature the propellant system of AP/CL20/GAP was designed. The propellant compositions are:

20 %	AP
42 %; 47 %	CL20
35 %; 30 %	GAP binder polymer together with energetic plasticizers like:
	➢ TMETN
	➢ TMETN / GAPA
	➢ TMETN / BTTN / GAPA
3 %	Additives

Like CL20, TMETN/BTTN are most convenient to achieve a good internal energy and oxygen balance together with good chemical and thermal stability[4]. GAP and GAPA contribute not only to an increased thermodynamic performance but significantly to increased burning rates and improved combustion behaviour. Last but not least about 3 % burning rate modifiers like 1,5 % iron-III-oxide and 1,5 % zirconium carbide are applied for further adjustment of burning rates and combustion behaviour. In this contribution the properties of three propellant formulations based von AP/CL20/ GAP are compared with another fast burning smoke reduced propellant system based von AP/PU/TMETN[5]. The last one contains 58 % AP and produces large amounts of secondary signature. The binder is a non energetic Polyesterurethane of the Desmophene® type which often has been used for nitrate ester plastified EMCDB and NEPE-propellants[6].

3. Thermodynamic Performance

Thermodynamic performance calculations were applied with the ICT thermodynamic code and data base developed by Volk and Bathelt[7]. The most significant parameters for an expansion ratio of 70 : 1 from three AP/CL20/GAP formulations and the AP/PU/ TMETN reference system are put up in table 1 together with the calculated reaction

products at nozzle. Values of the specific impulse I_{SPEQ} and the volumetric one: $I_{SPEQ} \cdot \rho$ are plotted in figures 1 and 2. Spec. impulse values from formulations with mixed TMETN/GAPA plasticizers can be pointed out by interpolation. The lines present the I_{SP} dependence towards the amount of plasticizer in the binder and the mass percentage of CL20 respectively the total amount of solids in the propellant.

Preferred formulations are: 20 % AP, 3 % burning rate modifier (Fe_2O_3 + ZrC) and a binder polymer based on 82,2 % GAP and 17,8 % N100. Formulations with pure TMETN exhibit a strong, formulations with pure GAPA a moderate increase of I_{SP} with the increase of CL20 concentration. An increase of I_{SP} is observed too with increasing amounts of plasticizer in the binder portion. With 70 % solids loading and major amounts of nitrate ester I_{SP} values of 2500 Ns/kg and 4500 Ns/dm^3 are quite realistic to achieve. Table 1 gives an impression about the thermodynamic values of formulations which were made in the lab scale and which are discussed further.

4. Processibility and Mechanical Properties

The casting viscosity and mechanical properties of several formulations with 65 % and 70 % solid loading are presented in the tables 2, 3 and 4 together with other data. Viscosity measurements were performed with a Brookfield spindle viscosimeter at 50 °C casting temperature. Mechanical properties have been determined using a Zwick uni-axial tensile tester with 50 mm/min drawing speed at different temperatures. Glass transition temperatures and thermal expansion koefficients were measured by TMA with a heating rate of 10°/min.

All CL20 formulations even with 70 % solids are easy processible. Very convenient for this purpose appears to be the high density of CL20 and the applied AP/CL20 particle size distribution. The casting viscosity is about two times better compared to corresponding AP/HMX/GAP formulations[2].

If the binder formulation is focussed on one GAP diol and N100 specification and if curing time, temperature and curing catalyst are kept constant, the mechanical proper-

ties mainly depend on the mass percentage of solids, on the polymer plasticizer ratio and on the NCO/OH equivalent ratio.
There is no change of modulus and elongation if TMETN is replaced by GAP-A (182 – 181), however, a slight softening in E modul and increase in elongation occurs if TMETN is partly replaced by BTTN (182 – 189). Remarkable softening is observed with high amounts of plasticizer and low NCO/OH equivalent ratios. By analyzing the mechanical data from 11 formulations it is shown, that the plots of E-modul versus elongation and tensile strength versus modulus obey exponential laws independently of different formulation parameters (see figures 3 and 4). The best fit to HVM requirements, which demand high modulus and tensile strength, is made with 70 % solid loading and 60 % energetic plasticizer being part of the binder. The mechanical properties of propellant No. 189 at high and low temperatures in table 4 and the glass transition points in table 2 and 3 indicate that there is no freezing at low and no significant softening at high application temperatures.

5. Chemical Stability and Sensitivity

The results of short term tests and subsequent storage at 90 °C for determination of chemical stability are pointed out in figure 5 together with tables 2 and 3. Dutch tests were performed by heating a propellant sample of 2 g in a loosely fitted stopper tube at 105 °C. Weight loss was determined from 8 – 72 h heating. The test fails if more than 2 % weight loss are obtained. Vacuum stability tests were performed by heating 2,5 g propellant sample for 40 h at 100 °C stored under a pressure of less than 1 mm Hg. The test fails if there is more than 2 ml/g gas production during the heating period. Autoignition points were determined by heating a sample of 200 mg in an open test tube with a heating rate of 20°/min. Dutch tests and vacuum stability tests show that all formulations are sufficiently stable even without nitrate ester stabilizers. By replacing TMETN by GAPA the stability is slightly improved, with BTTN the weight loss at 90 °C is a little bit higher. All results indicate that chemical stability of the formulations are better than those of conventional Doublebase- or nitroglycerine containing EMCDB propellants. For a detailed discussion see also the paper of M. Bohn and S. Eisele (No. 152 in these proceedings)[8].

Some data about mechanical and detonation sensitivity are pointed out in table 5 additionally to the data in the tables 2 and 3. Impact and friction sensitivity were determined by BAM impact and friction apparatus manufactured by Julius Peters Co. Due to the incorporation of AP the mechanical sensitivity of the formulations is high, but comparable to conventional fast burning composite propellants.

Gap tests were only performed according to WIWEB test with 21 mm Gap Ø, using a PMMA block as Gap material. Gap distances of 50 mm Ø and initiation pressures were estimated from former tests. The results of 4 different AP/CL20/GAP formulations have been put up in table 7 in comparison to a pressed booster charge consisting of 94,5 % RDX, 4,5 % wax and 1 % graphite (HWC).
Independently of solid loading and plasticizer amounts all formulations are sensitive to detonation and clearly belong to 1.1 classification. Compared to HWC, however, the detonation sensitivity is much lower.

6. Burning behaviour

Burning rates of the propellants were determined at 20 °C from 2 to 25 MPa by Crawford measurements. Coated strands with 5 mm square section and 150 mm length with two 50 mm measuring distances were used. The results are exhibited in figures 6 and 7 showing four logarithmic plots of burning rates and pressure exponents versus pressure. In figure 6 the difference of propellant 182 with pure TMETN is pointed out in comparison to propellant 181 with a mixture of TMETN/GAPA. Burning rates and mainly the pressure exponents are strongly influenced by incorporating GAP-A. If only nitrate esters are applied the pressure exponent tends to increase from n = 0,5 to 0,8, with GAPA the pressure exponent remains constant between $0,4 < n < 0,5$. Compared to analogue AP/HMX/GAP formulations the burning rates are higher and their pressure depedence is quite more convenient for application in a fast burning propellant grain.

In figure 7 burning rates and pressure exponents of the fast burning propellant 189 with GAPA/BTTN/TMETN are presented in comparison to the fast burning formulation 130 with AP/PU/TMETN. Although the burning rates are similar the AP/CL20/GAP propellant promises more benefit according to the decrease of pressure exponent from 0,5 to 0,3

and to the higher mechanical modulus which should fit more to a highly perforated grain geometry (see part 4).

7. Summary and Conclusion

Propellants based on AP/CL20/GAP meet most of the requirements which are demanded for a propellant to be used for HVM application. They are endowed with a high specific impulse, the maximum going up to I_{SPEQ} = 2500 Ns/kg (255 sec) and 4400 Ns/dm³ < $I_{SPEQ} \cdot \rho$ < 4500 Ns/dm³. This is quite more than for any other rocket propellant which belongs to the class with minimum or reduced smoke behaviour.

With only 3,7 mol% (5,3 mass%) the HCL content in the exhaust is significantly lower than for the reference system based on AP/PU/TMETN (13,4 mol%, 18,0 ma%) and for reduced smoke propellants based on AP/HTPB (18,8 mol%, 25,3 ma%). It conforms clearly to the B classification of secondary signature according to Nato AGARD standardization.

With only 20 % AP burning rates up to r = 50 mm/s at 10 MPa are achieved which are pretty high even for metallized or reduced smoke composite propellants[6]. According to the reference system all fast burning propellants have been incorporated more than 50 % AP up to now, fast burning HTPB based composite ones even 70 % to 88 % AP.

CL20 in combination with GAP, nitrate ester and GAP-A appear to be one of the best burn rate promoting ingredient combinations for this type of propellant. High molecular energy and kinetic reactivity are connected to good oxygen balance. With only 20 % AP a maximum of system performance can be achieved.

From our former work it is known that Type "B" signature AP/HMX/GAP formulations enable maximum burning rates of 25 mm/s < r < 30 mm/s at 10 MPa and I_{SP} values which are ≈ 3 % lower than the corresponding CL20 propellants. Their major disadvantages, however, are high pressure exponents (n = 0,5 – 0,7) preventing their application in high perforated grain geometries. With burning rates up to 50 mm/s and pressure exponents approaching n = 0,3 at high pressures AP/CL20/GAP propellants recommend

themselves for this purpose. They recommend themselves too for high performance sustainers with an end burning grain and a minimum smoke trajectory. Although not optimized their mechanical properties are quite sufficient for this application. Especially for the perforated grain geometry of a HVM propellant a little bit more toughness including an increase in tensile strength and modulus will be convenient. It should be achievable by optimizing the GAP binder specification, properties and curing conditions.

AP/CL20/GAP formulations are sensitive to detonation and fall below the 1.1 classification. Their initiation pressure, however, is higher than for a conventional pressed explosive formulation based on RDX/Wax/Graphite. It is higher too, than for a conventional high energetic doublebase or composite doublebase propellant. Although the hazards in manufacturing CL20 are not completely known, it is shown that the AP/-CL20/GAP propellant system combines some unique properties which are not covered by the existing rocket propellants: reduced signature, high performance and high burning rates together with low pressure exponents. It is obvious that these propellants will become promising candidates for high accelerating boosters or high performance end burners to be used in actively guided missiles.

8. References

1) Yves Longevialle M.Golfier, H. Graindorge;
"New Generation of Propellants for High Performance Solid Rocket Motors"
AVT Conference Proceedings about "Small Rocket Motors and Gas Generators" pp 25-1 to 25-11, Corfu 1999

2) Klaus Menke, Siegfried Eisele;
"Rocket Propellants with Reduced Smoke and high Burning Rates"
Prop. Explos. Pyrot. 22, 112 – 119 (1997)

3) P.A. Kessel in
"Rocket Motor Plume Technology"
AGARD LS 188 1993 pp 3-1 to 3-9

4) F.Volk, H. Bathelt;
"Thermochemical Data Base of Energetic Materials"
Last Update 04/2001, Fraunhofer Institut für Chemische Technologie, Pfinztal

5) Propellant Nr. 130 in reference 2

6) A. Davenas;
"Solid Rocket Propulsion Technology"
Pergamon Press, Oxford 1993

7) F. Volk, H. Bathelt;
"Application of the Virial Equation of State in Calculating Interior Ballistic Quantities" Prop. Explos. 1, 7-14 (1976)

8) M. Bohn, S. Eisele;
"Ageing and Service Time Period Assessment of Novel Solid Rocket Propellant Formulations containing CL20, AP and Energetic Plasticizers"
32th Intern. Ann. ICT Conf. 2001 (Proc.) pp 152-1 ff.

Abbreviations and Symbols

AGARD	Advisitory Group for Aerospace Research and Development
Al	Aluminium
AP	Ammoniumperchlorate
BTTN	Butantrioltrinitrate
CL20	Hexanitrohexaazaisowurzitane
EMCDB	Elastomer Modified Composite Double Base
GAP	Glycidylazidopolymer
GAPA	Glycidylazidopolymerazide
HFK	Hyperschallflugkörper
HTPB	Hydroxyterminated Polybutadiene
HVM	Hypervelocity Missile
I_{SPEQ}	Specific Impulse (Equilibrium Flow)
$I_{SPEQ} \cdot \rho$	Volumetric Specific Impulse (Equilibrium Flow)
NEPE	Nitric Ester Plastified Elastomer
PU	Polyurethane
RDX	Cyclotrimethylenetrinitramine
TMETN	Trimethylolethanetrinitrate
WIWEB	Wehrwissenschaftliches Institut für Werk-, Explosiv- und Betriebsstoffe

Acknowledgement

The authors want to express their thanks to the German Ministry of Defense for financial support of this work

Table 1 Calculated thermodynamic values of AP/CL20/GAP formulations (Expansion ratio 70:1)

	Nr 182		Nr 181		Nr 189		Nr 130	
AP	20,0 %		20,0 %		20,0%		58,0 %	
CL20	47,0 %		47,0 %		47,0 %		-	
GAP/N 100 + Plasticizer	30,0 %		30,0 %		30,0 %		-	
PU+ Plasticizer	-		-		-		40,5 %	
Plasticizer	TMETN		GAP-A / TMETN		GAP-A / BTTN /TMETN		TMETN	
Additives	3,0 %		3,0 %		3,0 %		1,5 %	
Expansion Ratio 70:1								
Spec. Impulse $I_{SP,EQ}$ (Ns/kg)	2504		2456		2468		2435	
Spec. Impulse $I_{SP,EQ}$ (s)	249,6		247,0		247,8		249,9	
Vol. spec. Imp. $I_{SP,EQ}$ ρ (Ns/dm^3)	4522		4353		4382		3970	
Comb. Temperature (K)	3201		3027		3066		2865	
Char. Velocity c* (m/s)	1549		1540		1544		1491	
Density $\rho_{theor.}$ (g/cm^3)	1,81		1,77		1,77		1,63	
Adiabatic Coeff.	1,234		1,247		1,245		1,217	
Mean Mol.Weight (g/mol)	25,38		24,11		24,32		25,21	
Oxygen Balance (%)	-21,6		-28,6		-27,4		-16,93	
REACTION PRODUCTS NOZZLE	Mol%	Ma%	Mol%	Ma%	Mol%	Ma%	Mol%	Ma%
CO_2	13,88	23,41	9,33	16,67	9,87	17,47	20,01	32,94
H_2O	20,13	13,89	14,96	10,94	15,50	11,23	38,20	25,27
N_2	26,03	27,94	27,17	30,91	27,49	30,98	11,83	12,18
CO	22,98	24,68	27,20	30,95	26,51	29,87	9,59	9,87
H_2	12,19	0,94	16,89	1,38	16,12	1,30	6,29	0,47
HCL	3,91	5,47	3,64	5,38	3,68	5,34	13,43	18,00
OTHERS	0,61	3,57	0,81	3,77	0,83	3,81	0,65	1,27

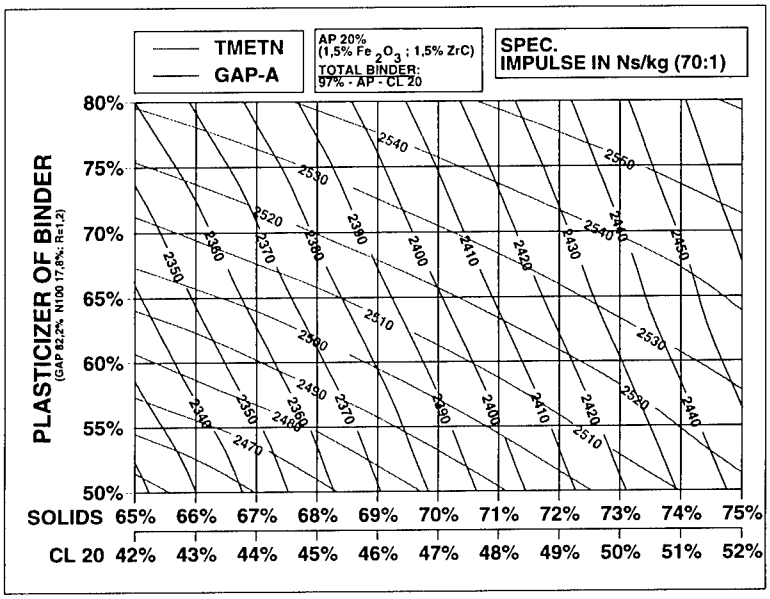


Figure 1: Thermodynamic Optimisation of AP/CL20/GAP formulations:
Change of the specific impulse I_{SPEQ} upon solid loading and plasticizer ratio

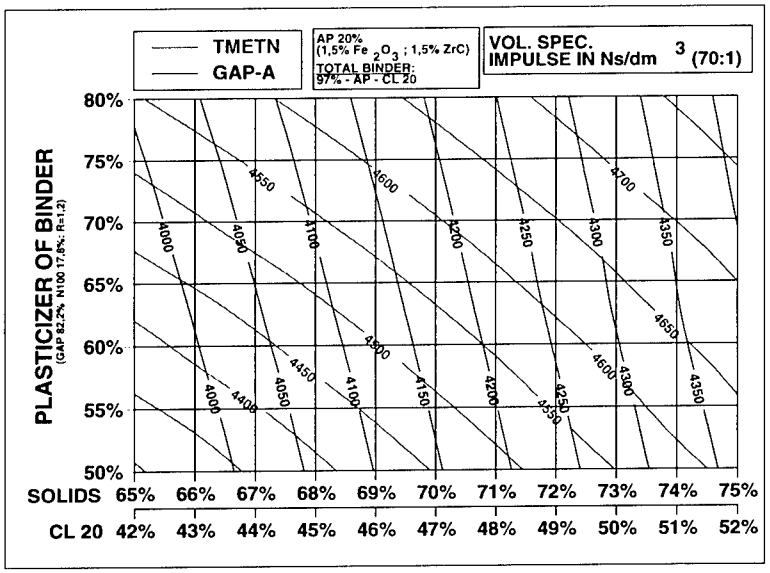


Figure 2: Thermodynamic Optimisation of AP/CL20/GAP formulations:
Change of $I_{SPEQ}*\rho$ upon solid loading and plasticizer ratio

Table 2: Basic Properties of some AP/CL20/GAP Propellants

	Nr.182	Nr 181
AP	20,0 %	20,0 %
CL20	47,0 %	47,0 %
GAP / N 100 + Plasticizer	30,0 %	30,0 %
Plasticizer	TMETN	GAP-A / TMETN
Additives	3,0 %	3,0 %

NATO - AGARD SECONDARY SIGNATURE CLASS	B	B
$I_{SP,EQ}$ (70:1) (Ns/kg)	2508	2450
$I_{SP,EQ} \sphericalangle \rho$ (70:1) (Ns/dm^3)		4342
Burning Rate at 10 MPa in mm/s	34,8 ± 0,7	38,0 ± 0,7
Pressure Exponent	0,5 → 0,8	≤ 0,45
Tensile strength σ (N/mm^2)	0,58 ± 0,01	0,59 ± 0
Elongation ε (%)	19,8 ± 0,6	19,2 ± 1,6
Elastic Modulus (N/mm^2)	5,72 ± 0,03	5,78 ±0,06
Dutch Test Weight Loss (%) (105°C/8-72h)	0,90	0,66
Deflagrationtemp. (°C)	185	189
Vacuum stability (ml/g) (40h / 100°C)	1,74	1,32
Processing Viscosity (Pas) (30°C)	148	152
Friction Sensitivity (N)	40	40
Impact Sensitivity (Nm)	3	4
Glass Transition Temperature (TMA) (°C)	-	-52
Thermal Expansion Coefficient (TMA) (1/K)	-	$8,75*10^{-5}$

Table 3: Basic Properties of an AP/CL20/GAP Propellant compared to an AP/PU/TMETN NEPE - Propellant

	Nr 189	Ref: Nr 130
AP	20,0 %	58,0 %
CL20	47,0 %	-
GAP / N 100 + Plasticizer	30,0 %	-
PU + Plasticizer	-	40,5 %
Plasticizer	GAP-A / BTTN / TMETN	TMETN
Additives	3,0 %	1,5 %

NATO - AGARD SECONDARY SIGNATURE CLASS	B	C
$I_{SP,EQ}$ (70:1) (Ns/kg)	2472	2435
$I_{SP,EQ} \prec \rho$ (70:1) (Ns/dm^3)	4391	3970
Burning Rate at 10 MPa in mm/s	45,3 ± 0,7	51,8 ± 0,3
Pressure Exponent	0,6 → 0,3	≤ 0,5
Tensile strength σ (N/mm^2)	0,54 ± 0,06	0,63 ± 0,03
Elongation ε (%)	24,9 ± 1,4	> 300
Elastic Modulus (N/mm^2)	4,46 ± 0,19	0,57
Dutch Test Weight Loss (%) (105°C/8-72h)	0,75	0,33
Deflagrationtemp. (°C)	190	185
Vacuum stability (ml/g) (40h / 100°C)	1,54	1,04
Processing Viscosity (Pas) (30°C)	144	84
Friction Sensitivity (N)	32	40
Impact Sensitivity (Nm)	4	4
Glass Transition Temperature (TMA) (°C)	-58	-61
Thermal Expansion Coefficient (TMA) (1/K)	8,50 *10^{-5}	-

Table 5: Mechanical Properties of AP/CL20/GAP propellants in the temperature range from –40° to +50°C

Batch Nr / Curing time		**191 / 2d**			**189 / 1d**		
AP		20,00 %			20,00 %		
CL20		42,00 %			47,00 %		
GAP / N 100 (R=1,05) + PLASTICIZER		35,00 %			30,00 %		
PLASTICIZER		**TMETN /GAP - A**			**TMETN /GAP - A /BTTN**		
ADDITIVES		3,00 %			3,00 %		
Mech. Properties (50 mm/min)		**-40°C**	**+20°C**	**+50°C**	**-40°C**	**+20°C**	**+50°C**
σ_{max}	**(N/mm²)**	**4,40**	**0,54**	**0,39**	**4,35**	**0,60**	**0,40**
ε at σ_{max}	(%)	17,0	25,4	22,2	17,1	21,7	23,3
σ at ε_{max}	(N/mm²)	3,14	0,46	0,33	2,60	0,54	0,37
ε_{max}	**(%)**	**18,9**	**28,2**	**22,8**	**28,1**	**24,9**	**25,7**
E modulus	**(N/mm²)**	**80**	**2,7**	**2,3**	**116**	**4,5**	**3,5**

Table 6: Mechanical and detonation sensitivity of AP/CL20/GAP formulations

TOTAL SOLIDS	HWC	65%	65%	70%	70%
AP		20%	20%	20%	15%
CL20		42%	42%	47%	47%
ADDITIVES		3,0%	3,0%	3,0%	3,0%
GAP / N100 + PLASTICIZER		35%	35%	30%	30%
PLASTICIZER		TMETN / GAP-A	BDNPF-A / GAP-A	TMETN / GAP-A	TMETN / GAP-A
RDX WAX GRAPHITE	94,5% 4,5% 1,0%				
Friction Sensitivity (N)	216	32	36	24	32
Impact Sensitivity (Nm)	7,5	5,0	4,0	4,0	5,0
GAP-Distance (Ø21mm) (mm PMMA)	18+/19-	11+/12-	12+/13-	11+/12-	12+/13-
GAP - Distance (estim.; Ø 50 mm)	≈ 53	≈ 44	≈ 45	≈ 44	≈ 45
Initiation Pressure	≈ 21 kbar	≈ 34 kbar	≈ 31 kbar	≈ 34 kbar	≈ 31 kbar

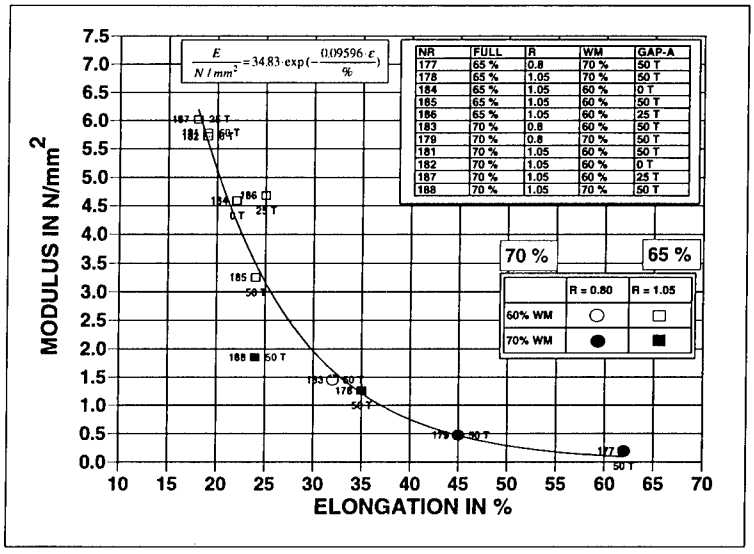


Figure 3: Elastic modulus versus elongation of different AP/CL20/GAP formulations

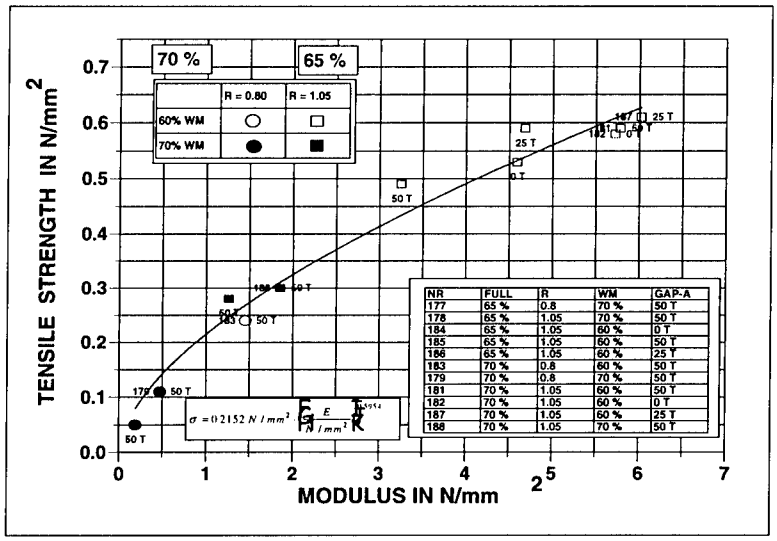


Figure 4: Tensile strength versus elastic modulus of different AP/CL20/GAP formulations

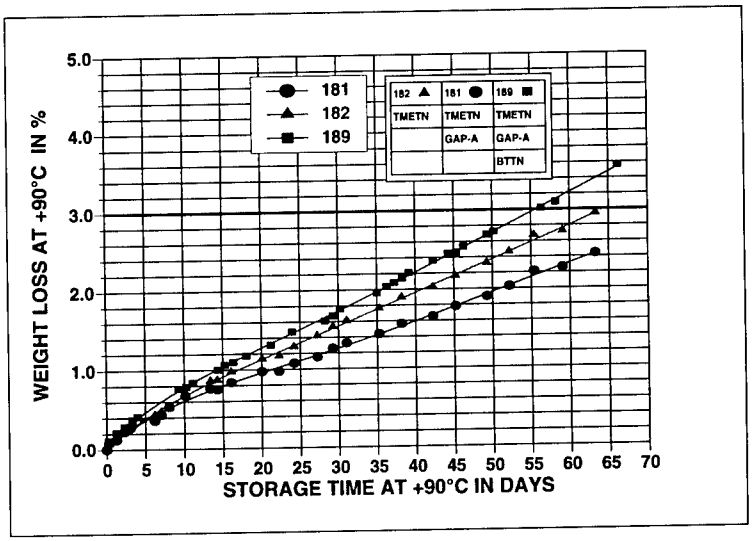


Figure 5: Weight loss of AP/CL20/GAP propellant samples during storage at 90°C

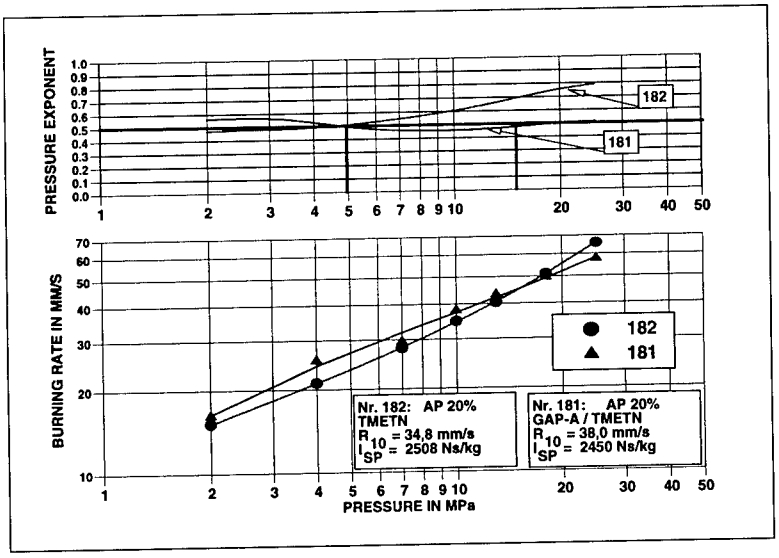


Figure 6: Burnrates and Pressure exponents determined by Crawford Measurements for formulation 182 with TMETN and 181 with TMETN/GAP-A

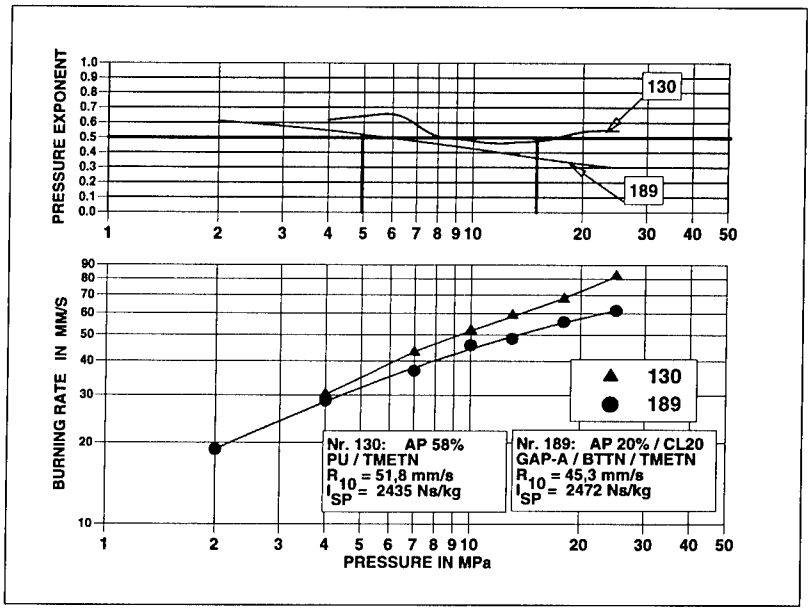


Figure 7: Burnrates and Pressure exponents determined by Crawford Measurements for formulation 189 with BTTN/TMETN/GAP-A and reference propellant 130

New Aspects for Determination of Aging Behaviour of Energetic Materials

Geißler, Egon; Eisenreich, Norbert; Geißler, Adam; Hübner, Christof

Fraunhofer-Institut für Chemische Technologie ICT
Joseph-von-Fraunhofer-Str. 7
D-76327 Pfinztal

Summary

Service life prediction of energetic materials is correlated with aging behaviour. The aging process leads to a change in mechanical properties e. g. to a change in stiffness and an embrittlement of the material. Background of the aging process are chemical micromechanical phenomena. Therefore the characterisation and understanding of micromechanical phenomena like matrix-filler detachment, crosslinking and chain scission are the key to the understanding of aging behaviour of energetic materials. These micromechanical phenomena influence both the mechanical behaviour and the sensitivity to impacts of energetic materials. In this paper different methods to study the aging behaviour of energetic materials and the correlation to micromechanical phenomena are described. Furthermore the influence on the macroscopic observable mechanical properties and the service life time is discussed.

1. Introduction

Modern solid rocket propellants, gun powder or special kinds of explosives are composite materials. These energetic materials are composed principally in the same way: relative hard particles are dispersed in a relatively soft matrix material. The matrix material has to fulfil two main tasks: (1) it burns during the service of the propellant and (2) it gives the mechanical stability to the compound. The particles deliver the oxygen for the burning and contribute to the production of energy by containing burnable substances. Therefore the composition of the energetic material is strongly influenced by the demand of their energetic properties. On the other hand side a suitable mechanical stability of the system is

necessary for proper service. Mechanical failure of energetic materials can cause catastrophic failures of rocket motors or guns.
During service life the rocket propellant, the gun powder or other kinds of explosives have to survive the rigors of the environmental loads through mechanical and climatic conditions. The energetic material in the system is loaded by impacts, vibrations, temperature cycles and humidity.

These loads can lead to a change in the microscopic structure of the energetic material. Matrix-filler debonding happens. These causes an increase in surface due to cracks or matrix-filler-debonding which could lead to an unwanted extreme increase in burning rate. This increase in burning rate causes a pressure rise and could lead to a catastrophic failure.

2. Mechanism of Aging in Energetic Materials

Energetic materials like solid propellants and gun powders are composed of a large percentage of energetic materials. Additives like ballistic modifiers, plasticizers and stabilizers are added to improve the performance of the material. Various ingredients interact with each other or with the atmosphere during lifetime. These interactions produce irreversible changes in the energetic material which can have a serious effect on both the ballistic and mechanical properties. Aging of energetic materials is influenced by the mechanism.

The change in mechanical properties such as modulus or tensile strength indicate that aging in the energetic material has happened. Loss of plasticizer leads to a higher modules. Long time storage at high temperature may cause embrittlement by changes in the binder material. On the other hand side binder chain scission and crosslink degradation may happen. This leads to a counter effect the softening of the material.

An important phenomena which can cause severe problems during the service of energetic materials is the detachment of the matrix and filler surface [8,17,18]. This detachment does not only lead to a weakening of the material, a decrease of

the modulus and an increased inclination to break, but can also produce vacuoles in the material. Breakage which occur when the propellants or the gun powder burn can cause an immediate pressure rise and therefore lead to a catastrophic failure in the system.

The vacuoles which are formed by a detachment increase the impact sensitivity even if no breakage occur. They are filled with gases which sort from the matrix or the filler e. g. absorbed humidity. At the event of a strong mechanical impact due to rough handling or a projectile, these gases are very rapidly compressed and as a consequence heat up to temperatures which can ignite the energetic material.

In the filler alone, breakage of filler particles can take place, especially at high compressions due to impacts. Agglomerates of single filler particles break. This leads to a decrease of stiffness of the material and to formation of vacuoles with their negative influence on the impact sensitivity as explained above.

Due to this facts, the matrix material itself and the interface of matrix and filler deserves special attention. Therefore in the next chapter, modern methods for the analysis of aging are reported and discussed in view of their applicability for energetic materials.

3. Methods for the Analysis of Aging Behaviour

3.1. Detection of Matrix-Filler Debonding by Measurement of the Mechanical Properties

The process of aging is correlated to a change in material properties. Cracks can be detected in a standard tensile test due to their weakening of the material. Whether the weakening is really due to cracks, has to be determined by separate methods.

In the Fraunhofer ICT the Poisson Ratio was measured with a non contact laser optical system. In this experiments composite propellants which were predamaged

by matrix-filler detachment where tested. The specimen with matrix-filler detachment show a decrease in Poisson Ratio [23,24,25,26,27].

3.2. Microscopy

Microscopy is a classic method for the detection of cracks in composite materials [21]. The materials must be prepared for the detection of the failures which in many cases causes artefacts. Especially in the case of elastomeric materials, cracks which occurred between filler and matrix during loading can close again when the material is unloaded again. Furthermore in most cases, the investigation is only possible on the surface of the material.

3.4. NMR Imaging of Energetic Materials

NMR imaging has become a common method in medical diagnostics for years. The application of NMR imaging in material science is very new. NMR allows a view through the surface into the material. If these method is coupled with tomography, a 3-D picture of the bulk material is possible in special cases. Nowadays the spatial resolution of NMR imaging (10μm and more) is limited compared to other imaging and microscopic methods.

Figure 1 shows the NMR-image of the distribution of glass beads in a polymer matrix. The diameter of the glass beads is 1 mm. In figure 2 the distribution of carbon black in a polyurethane matrix is shown. The average particle size of the carbon black is 20 nm. In this case the single particle could not be resolved. But it is possible to observe agglomerates of filler particles.

In figure 3 NMR-images of polyurethane probes with different crosslinking densities are shown. The crosslinking density is influenced by the isocyanate index. The properties of the polyurthane is influenced by the amount of isocyanate component, e. g. by under- or overcrosslinking. Undercrosslinking, isocyanate index less than 100, means free hydroxyl groups. Overcrosslinking means that the

polyurethane moieties undergo consecutive reactions, i. e. the formation of allophanates. Therefore if the isocyanate index is increased the crosslinking density increases too.

The examined polyurethane probes have an isocyanate index of 12.5, 25, 50 and 100. In the NMR-experiment the mobility of the molecule is measured. This means that in the case of increasing crosslinking density the mobility of the molecules decreases. All four probes were excited by the same NMR-pulse sequence. The intensity of the echo signal was measured at the same echo time for all four probes. The intensity of the echo signal is a measure for the crosslinking density of the polyurthane structure. In the case of low crosslinking density the molecules are very mobile. Therefore the intensity of the echo signal is high. On the other hand side in the case of high crosslinking density the molecules are less mobile the intensity of the echo signal is low.

The crosslinking density is shown in figure 3 in form of a grey scale. Light pictures means the intensity of the echo signal is high the molecules are mobile. Dark pictures mean the intensity of the echo signal is low the molecules are less mobile. The crosslinking degree is high. It can be shown that the grey scale corresponds with the crosslinking density.

Figure 4 shows the NMR-image of uncrosslinked and crosslinked polyurethane. The uncrosslinked part of the probe is uncured polyurethane. This figure shows a similar result as figure 3. The darker area in the probe is the region of high crosslinking density. In this region is the mobility of molecules low.

In figure 5 a polyurethane probe with inhomogeneous crosslinking density is shown. The probe was prepared as a non-homogeneous mixture of polyol and diisocyanate. The gray value shows the local crosslinking density. Dark regions have a high crosslinking density and light region have a low crosslinking density.

NMR-Imaging can bring useful information about aging mechanism in energetic materials. It is possible to observe the agglomerates of the filler particles. NMR

imaging is extremely useful to map local variations in composition, matrix filler interaction and cross-link density. With NMR the aging mechanism could be separated.

5. Conclusions

The measurement of material properties is a quick simple and valuable method to examine the aging behaviour of energetic materials [10]. Especially the determination of Poisson's Ratio is a powerful method for the determination of dewetting in energetic materials. It is relatively simple to perform and gives additional information for the use of FEM methods for the development of energetic systems.

NMR imaging and microscopy deliver valuable information of the morphology of energetic material during aging.

Especially NMR imaging offers new aspects of examining aging behaviour. With this method the different aging mechanism like change in crosslinking density and molucular degradation could be separated by the determination of the mobility of the molecules.

References

[1] Eisenreich, Norbert; Geißler, Adam; Geißler, Egon; Hübner, Christof
Analysis and Test Methods for Service Life Prediction of Energetic Materials.
Fraunhofer-Institut Chemische Technologie, Pfinztal, D-76327, Germany, 31th International Annual Conference of ICT 2000, p 149.1-149.11, 2000.

[2] Geißler, Egon; Hübner, Christof
Einsatz der Methode der Finiten Elemente zur Berechnung des Deformationsverhaltens von gefüllten Polymeren.
MARC Benutzertreffen, 28.-29. Oktober 1999, München, Paper 16, 1999.

[3] Hübner, Christof; Geißler, Egon
Finite element modelling of matrix-filler debonding of energetic materials.
Fraunhofer-Institut Chemische Technologie, Pfinztal, D-76327, Germany, 30th International Annual Conference of ICT 1999, p 99.1-99.15, 1999.

[4] Hübner, Christof; Geißler, Egon; Elsner, Peter; Eyerer, Peter
The importance of micromechanical phenomena in energetic materials.
Propellants, Explosives and Pyrotechnics, (1999), 24(3), 119-125, 1999.

[5] Geißler, Egon; Hübner, Christof
A finite element based unit cell model to analyse the deformation behaviour of filled polymers.
International Union of Pure and Applied Chemistry, 1998 Prague Meetings on Macromolecules, 18th Discussion Conference, Paper PC 7, 1998.

[6] Geißler, E.; Hübner, C.
Finite-element simulation of the micromechanics of solid propellants and gun propellants.
Fraunhofer-Institut Chemische Technologie, Pfinztal, D-76327, Germany, 29th International Annual Conference of ICT 1998, p 83.1-83.11, 1998.

[7] Geißler, Egon; Hübner Christof
Finite Elemente Modellierung der Mikromechanik von gefüllten Polymeren.
MARC Benutzertreffen, 28.-29. Oktober 1999, München, Paper 9, 1998.

[8] Lohrmann, M.; Hübner, Ch.
The influence of the matrix-filler-interaction on the mechanical properties of filled elastomers.
Fraunhofer-Inst. Chemische Technologie (ICT), Pfinztal-Berghausen, D-76327, Germany, 27th International Annual Conference of ICT 1996, p140.1-140.12, 1996.

[9] Hübner, Christof
Ermittlung eines zweidimensionalen zeit- und deformationsabhängigen Materialgesetzes für gefüllte Elastomere unter Berücksichtigung von Phasengrenzflächenphänomenen.
Diss., Universität Karlsruhe (T. H.), 1994.
In wissenschaftlicher Schriftenreihe des ICT, Bd. 10, Pfinztal, 1994.

[10] Husband, D. Mark
Use of dynamic mechanical measurements to determine the aging behaviour of solid propellant.
Propellants, Explosives and Pyrotechnics, v 17 n 4 Jul 1992, p 196-202, 1992.

[11] Geißler, Adam; Geißler, Egon
Dynamic behavior of composites under preloading.
Propellants, Explosives and Pyrotechnics, v 17 n 4 Jul 1992, p 211-213, 1992.

[12] Geißler, Egon
Anwendungung eines speziellen Stoffgesetzes für nichtlinear viskoelastische Werkstoffe in einem Finite Elemente Programm.
Diss., Universität Karlsruhe (T. H.), 1992.
In wissenschaftlicher Schriftenreihe des ICT, Bd. 3, Pfinztal, 1992.

[13] Geißler, Adam
Dynamisches Verhalten von compoundierten Kunststoffen unter Vorbelastung, dargestellt am Beispiel eines geschlossenzelligen Schaumstoffes und eines hochgefüllten Kunststoffes.
Diss., Universität Karlsruhe (T. H.), 1991.
In wissenschaftlicher Schriftenreihe des ICT, Bd. 2, Pfinztal, 1992.

[14] Geißler, E.; Geißler, A.; Weber, H.
Ein Stoffgesetz für nichtlinear viskoelastische Werkstoffe unter großer statischer und überlagerter dynamischer Belastung.
ZAMM – Z. angew. Math. Mech. 71 (1991) 4, T 248- T251.

[15] Weber, H.; Geißler, E.
Safe Cushion Design for sensitive products.
6th IAPRI World conference on Packaging '89, Hamburg 27.-29. September 1989.

[16] Geißler, Egon; Weber, Herbert
Constitutive equations for dynamically loaded polymer solids and their application in a finite element program.
3rd European Rheology Conference and Golden Jubilee Meeting of the British Society of Rheology, Edinburgh, UK, 3.-7. September 1988, p 171-173, 1988.

[17] Hübner, Ch.; Stacer, R. G.
Recovery of strain-induced damage in filled and unfilled elastomers.
3rd European Rheology Conference and Golden Jubilee Meeting of the British Society of Rheology, Edinburgh, UK, 3.-7. September 1988, p 226-228, 1988.

[18] Stacer, R. G.
Autohesion in the presence and absence of interfacial mass transfer.
3rd European Rheology Conference and Golden Jubilee Meeting of the British Society of Rheology, Edinburgh, UK, 3.-7. September 1988, p 465-467, 1988.

[19] Geißler, Adam; Weber, Herbert
Dynamic material properties of a closed-cell polyethylene foam.
3rd European Rheology Conference and Golden Jubilee Meeting of the British Society of Rheology, Edinburgh, UK, 3.-7. September 1988, p 552-554, 1988.

[20] Weber, H.; Geißler, A.; Kugler, H.-P.
Einsatz der experimentellen Mechanik in der statischen und dynamischen Prüfung unverstärkter Kunststoffe.
Experimentelle Mechanik in Forschung und Praxis. Düsseldorf: VDI-Verlag, VDI-Bericht 679, 1988

[21] Geißler, Adam; Schmitt, Waltraud
Investigations of a closed-cell foam with scanning electron microscopy.
3rd European Rheology Conference and Golden Jubilee Meeting of the British Society of Rheology, Edinburgh, UK, 3.-7. September 1988, p 555-557, 1988.

[22] Eisenreich, N.; Fabry, C.; Fischer, R.; Geißler, A.; Kugler, H.P.; Sinn, F.
Strain distribution in the uniaxial tensile test up to high strain rates.
Propellants, Explosives and Pyrotechnics, v 12 n 3 Jun 1987, p 101-104, 1987.

[23] Geißler, A.; Schmitt, D.; Ziegahn, K.-F.
Materials science and environmental qualification applied on solid chemical energetics.
Propellants, Explosives and Pyrotechnics, v 12 n 3 Jun 1987, p 92-96, 1987.

[24] Eisenreich, Norbert; Geißler, Adam; Kugler, H. Peter; Weinkötz, Christoph
Volume change measurements of filled polymers due to humidity changes.
Proc. - Inst. Environ. Sci. (1986), 32nd, 141-4, 1986.

[25] Eisenreich, N.; Geißler, A.; Fabry, K.; Kugler, H. P.
Tensile test of solid propellants by the use of optical techniques.
1985 Proceedings, 31st Annual Technical Meeting - Institute of Environmental Sciences: Improve Your Odds with Sound Basic Science and Creative Engineering.
Inst. of Environmental Sciences, Mount Prospect, IL, USA, Las Vegas, NV, USA
30 Apr 1985-02 May 1985, Proceedings, Annual Technical Meeting - Institute of Environmental Sciences 31st.Publ by Inst. of Environmental Sciences, Mount Prospect, IL, USA, p 452-457, 1985.

[26] Eisenreich, N.; Fabry, K.; Geißler, A.; Kugler, H.-P.
Messung der Querkontraktionszahl an Kunststoffen im Hinblick auf die Beurteilung der Füllstoffhaftung.
Deutscher Verband für Materialprüfung E. V., Vortag in der Tagung Werkstoffprüfung 1985,
3.-4- Dezember 1988, Bad Nauheim, S. 391-398, 1988.

[27] Kugler, H.-P.; Eisenreich, N.; Pielka, C.; Geißler, A.
Messung der Querkontraktionszahl unter einachsiger dynamischer Beanspruchung.
Vorträge der Tagung Werkstoffprüfung 1984, DVM.

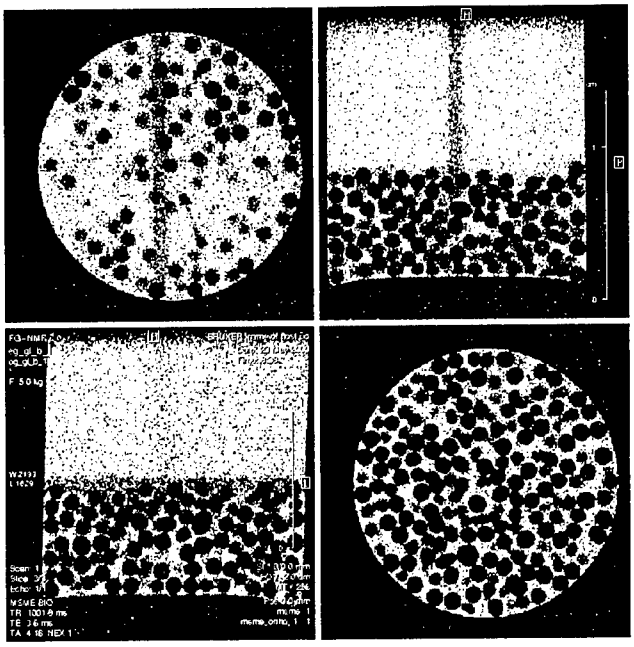
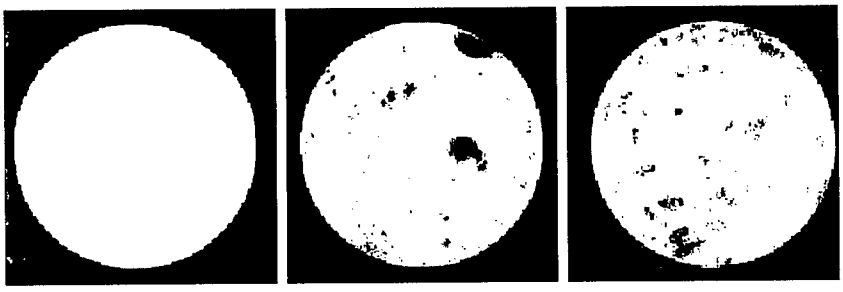


Figure 1: NMR-Image of the distribution of glass beads in a polymer matrix



0 weight-% Carbon black 15 weight-% Carbon black 30 weight-% Carbon black

Figure 2: NMR-image of elastomer matrix with different content of carbon black

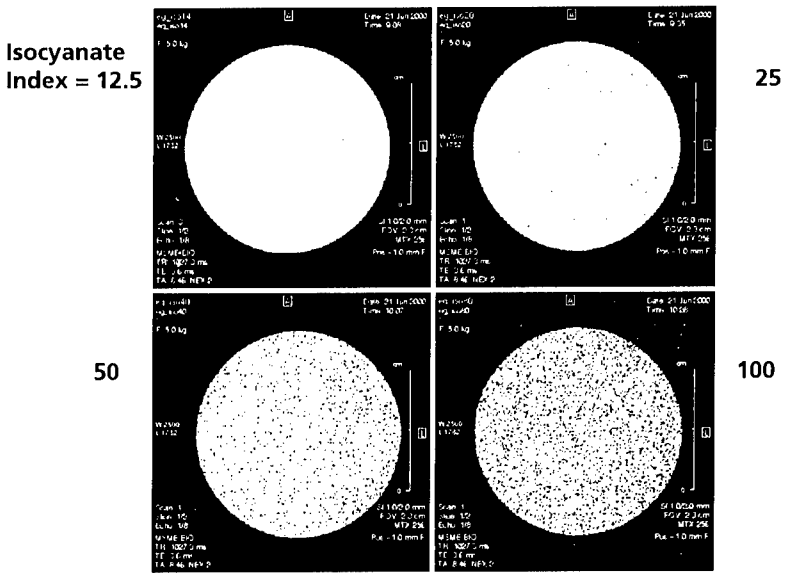


Figure 3: NMR-images of polyurethane with different isocyanate index

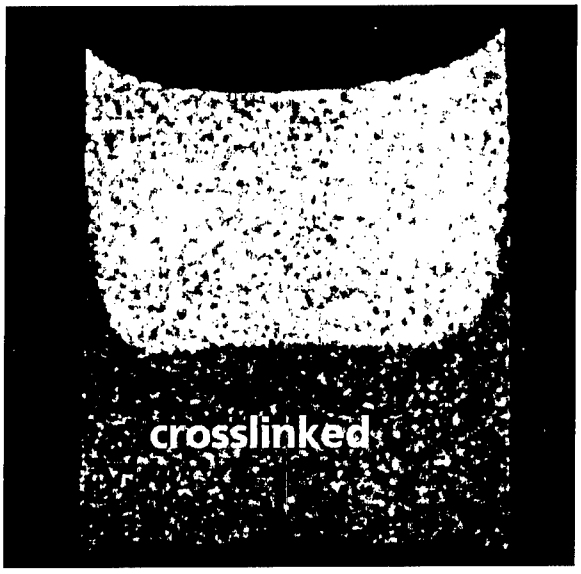


Figure 4: NMR-image of polyurethane with different degree of crosslinking

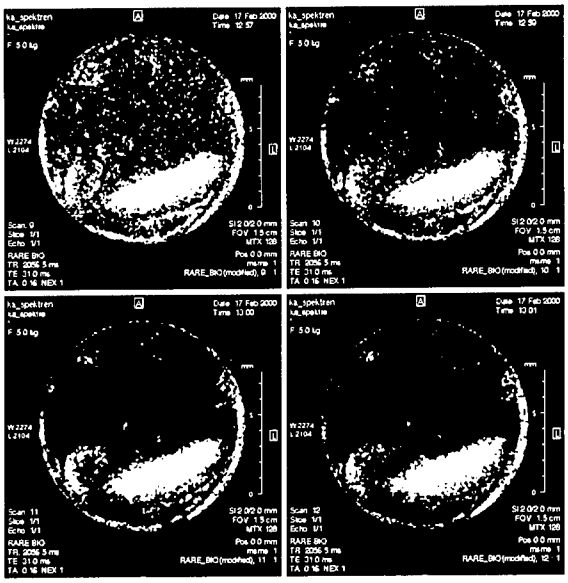


Figure 5: Polyurethane with inhomogeneous crosslinking density

Erzeugung schneller gerichteter Ringwirbel für den Impulstransport über mittlere Distanzen

Jörg Backhaus

Fraunhofer Institut für Chemische Technologie, ICT
Joseph-von-Fraunhofer-Str. 7
76327 Pfinztal

Abstract

In the topic of nonlethal weapons the intention consists to implement a physically clearly notable impulsetransfer by means of shot ring eddies over middle distances up to 100 m. The study informes about different procedures of vortex ring generation and points out the advantages of the applied method concerning the task. Favorable generation geometries are discussed on the basis of simulations and first experimental results for formation and propagation of vortex rings in air are introduced.

1. Einführung

Im Zusammenhang mit der Entwicklung Nichtletaler Wirkmittel (NLW) laufen am Fraunhofer Institut für Chemische Technologie Studien im Bereich der Erzeugung von propagierenden Ringwirbeln. Dabei interessiert, in wie weit sich diese Strömungsstrukturen eignen, zielgerichtet Impuls über nennenswerte Distanzen zu übertragen und bei welchen Entfernungen gegebenenfalls auf diese Weise noch ein nutzbarer Impulseintrag nachgewiesen werden kann. Als Fernziel wird dabei eine Distanz von bis zu 100 m angestrebt.

2. Stand der Forschung

Die eigenständige Fortbewegung von Ringwirbeln ist in der Literatur von zahlreichen Autoren untersucht worden. Das Bildungsprinzip ist bei den meisten dieser Arbeiten ähnlich, und besteht prinzipiell im kolbengetriebenen Ausstoßen eines Fluidvolumens aus einem Rohr in die freie ungestörte Umgebung (Kolbenrohrmethode). In der Scherschicht zwischen bewegtem und ruhendem Medium rollt das ausgestoßene Fluidvolumen pilzförmig einen Wirbelring auf, der sich dann stetig entlang der

verlängerten Rohrachse fortbewegt. Je nach Gestalt, Verhalten und Reynoldszahl der beobachteten Wirbelringe wird zwischen laminaren und turbulenten unterschieden, wobei große Ringdurchmesser zu größerer Stabilität führen [Lu79]. Während bei kleineren Austrittsgeschwindigkeiten laminare Ringe gebildet werden, die jedoch bei kleinsten Störungen in der Umgebung leicht zerfallen [go92], entstehen turbulente bei schnellerem Ausstoß des Fluidvolumens und können sich auch bei Außenturbulenz weiter fortbewegen [Arn75].

Im Gegensatz zu der idealisierten Wirbelbewegung im reibungsfreien Medium, ist die Fortbewegung realer Wirbelringe in viskosem Fluid Reibungseinflüssen unterworfen. Deshalb vergrößert sich der reale turbulente Wirbelring mit der Zeit und verliert an Geschwindigkeit.

Untersuchungen an der ETH Zürich [go92], bei denen die Eignung von Wirbelringen zur Raumbelüftung mit Frischluft überprüft wurde, zeigten dass im gewählten Geschwindigkeitsbereich der Wirbelerzeugung (Fluidgeschwindigkeit am Austritt U_{F0} = 1.2 m/s) die turbulente Durchmischung in den Randzonen des erzeugten Wirbelringes so groß ist, dass der Transport von Frischluft über Strecken von mehreren Metern praktisch unmöglich war. Das Hauptproblem dabei liegt in dem vom turbulenten Wirbelring erzeugten Nachlauf, der sich bei der Umströmung des Wirbelringes durch das Umgebungsmedium bildet, und welcher ständig Fluid aus den inneren Bereichen des Ringes erhält. Auch in früheren Untersuchungen [Arn75] in Wasser wurde beobachtet, dass die zur Sichtbarmachung des Wirbelringes in den Bildungsbereich eingebrachte Farblösung nur zu sehr geringen Prozentsätzen von den erzeugten Ringen mittransportiert wurde.

Neuere Untersuchungen von Gharib [gh98] zeigen aber, dass sich auch bei hohen Reynoldszahlen Wirbelringe ohne Nachlauf erzeugen lassen, wenn die Menge der in der Scherschicht erzeugten Vorticity (Winkelgeschwindigkeit in einem Raumpunkt) einen Grenzwert – die Bildungszahl - nicht übersteigt.

Neben der Menge an erzeugter Vorticity ist außerdem der Verlauf ihrer Erzeugung von entscheidender Bedeutung für die Wirbelbildung. Ergebnisse aus unterschiedlichen Studien [go92], [Didd] legen nahe, dass ein impulsartiger Ausstoß des Fluid Volumens mit abfallendem Geschwindigkeitsprofil bezüglich der Energieübertragung in den Wirbelring besonders vorteilhaft ist.

Die Lauflänge ist vor allem eine Frage der Stabilität des Wirbelringes und dessen Anfangsimpuls. Um diesen zu maximieren, sollte die Ausschussgeschwindigkeit und die den Wirbelring bildende Fluidmasse möglichst groß sein. Große Austrittsdurchmesser

zur Erzeugung großer Wirbelringe scheinen daher sinnvoll. Je höher die Ausschussgeschwindigkeit des Luftvolumens, um so im Verhältnis weniger stark sollte sich die Viskosität der Luft auswirken, was auch von verschiedenen Autoren ([gh98], [Max1]) für hohe Reynoldszahlen festgestellt wird. Arnold[Arn75] weist außerdem darauf hin, dass erst durch große Fortpflanzungsgeschwindigkeiten ab ca. 30 m/s die Störwirkung der Außenturbulenz signifikant herabgesetzt werden kann. Dies ist eine Voraussetzung zur Erreichung der gewünschten geradlinigen Fortbewegung.

Damit lassen sich die Anforderungen an das Erzeugungssystem zur Bildung weitlaufender Wirbelringe wie folgt zusammenfassen:

- großer Austrittsdurchmesser D
- möglichst hohe Fluidaustrittsgeschwindigkeit U_{F0}
- Impulsartiger Fluidausstoß
- Einstellbarkeit von Austrittsfluidvolumen bzw. Austrittsverlauf $U_{F0}(t)$

3. Realisierungsmöglichkeiten

Ein großes Problem liegt in der Übertragbarkeit der bisherigen experimentellen Studien auf die oben beschriebene Aufgabenstellung, da deren überwiegender Teil Laboruntersuchungen in Wassertanks bei vergleichsweise kleinen Reynoldszahlen darstellt. Nur wenige beschäftigen sich explizit mit der turbulenten Wirbelringbewegung ([max77],[GleCo90], [go92]), wobei hier Reynoldszahlen bis ca. 48000 erreicht und die Bewegung lediglich über einige 10 Durchmesser hinweg beobachtet werden.

Legt man die von Arnold angegebene Fortbewegungsgeschwindigkeit U_R von 30 m/s zu Grunde, bei der Ringwirbel noch weitgehend ungestört durch Luft laufen, so muss das Austrittsfluid nach Gottschalk mechanischer Analogie [go92] mindestens mit doppelter Geschwindigkeit U_{F0} das Rohr verlassen. Geht man zusätzlich noch wie z.B. Maxworthy [max77] von einem exponentiellen Abfall von U_R beim turbulenten Ring aus, so muss U_{F0} noch weitaus höher liegen, damit überhaupt weitere Strecken zurückgelegt werden können. Damit kommt man schnell auf Austrittsgeschwindigkeiten $U_{F0} > 100$ m/s. Geht man von einem Zylinderdurchmesser von z.B. 0.2 m aus, so ergeben sich Reynoldszahlen von weit über 10^6, die sich nicht ohne weiteres mit der bei den Laborversuchen üblichen Kolbenrohrmethode erreichen lassen. Gerade die geforderten großen Austrittsdurchmesser der verwendeten Rohre gehen mit mechanischen Problemen einher, da sich große Kolben kaum ausreichend schnell bewegen lassen. Deshalb wurde bei der Projektierung des Versuchsgerätes die Kolbenmethode verworfen.

Anstatt dessen soll das benötigte schnell aus dem Rohr zu pressende Fluidvolumen durch eine kontrolliert ausgeführte Gasexplosion erzeugt werden. Dieses im folgenden als Stoßrohr bezeichnete Erzeugungsprinzip ist in einigen älteren Arbeiten beschrieben worden ([Arn75], [Lu79]). Allerdings kamen dort Erzeugungsgeometrien mit mehreren Metern Durchmesser und vertikaler in den Himmel gerichteter Abschussrichtung zum Einsatz. Wenngleich die so erzeugten Wirbelringe weit über 1000 m vertikal zurückgelegt haben, so weisen die Autoren auch darauf hin, dass der Auftrieb als Antriebskraft für diese minutenlange Fortbewegung eine entscheidende Rolle spielt. Diese Ergebnisse lassen sich daher nicht direkt auf den angestrebten Einsatzzweck übertragen.

4. Bildungszahlkonzept

Ein wichtiger Punkt zur Erreichung großer Distanzen ist die Verminderung von Impulsverlusten bei der Translation der Ringwirbel. Es stellt sich nun die Frage, ob sich das Gharib *et. al.* [gh98] eingeführte Konzept der Bildungszahl N_K für Ringwirbel mit Zylinder-Kolben-Anordnung auf die hier skizzierte Stoßrohrmethode übertragen lässt. Dabei spielt die Justierbarkeit des Systems und die Reproduzierbarkeit einmal eingestellter Parameter eine entscheidende Rolle.

Die Bildungszahl N_K bezeichnet das Verhältnis des Kolbenweges L_K zum Zylinder- bzw. Austrittsdurchmesser D, an dem die Ringwirbelbildung in der Scherschicht zwischen dem ruhendem Umgebungsmedium und dem mit einer Geschwindigkeit U_{F0} aus dem Zylinder austretenden Fluid einsetzt. Der Kolbenweg L_K stellt hier eine integrale Größe dar, die sich vom Bewegungsverlauf des Kolbens $U_K(t)$ ableitet:

$$L_k = \int_0^t U_K(t)\,dt \qquad (1)$$

Vereinfachend gehen wir zunächst von einer Propfenströmung am Zylinderaustritt aus womit die Fluidgeschwindigkeit nur noch von der Kolbenbewegung abhängt. Beim Aufrollen des Wirbelrings erhöht sich dessen Zirkulation durch den Vorticitystrom aus der Scherschicht bis sich der Ring ablöst. Gharib et. al. konnte nun zeigen, dass es einen vom der Bildungszahl N_K abhängigen Grenzwert an Zirkulation gibt, den der Ring aufnehmen kann. Wird dieser überschritten, so bildet sich hinter dem abgelösten Ring eine Nachlaufzone aus, die ihm wieder Zirkulation entzieht und seine Bewegung verlangsamt. Ein nachlauffreier Wirbelring lässt sich nach obiger experimentellen Studie bei $L_K/D = 4$ erzeugen. Theoretische Untersuchungen von Linden und Turner [LiTu01] bestätigen diese Beobachtungen.

Für den Fall eines inkompressiblen Fluids wie Wasser ist die Austrittsgeschwindigkeit U_{F0}

des Fluids praktisch gleich der des Kolbens U_K, so dass in diesem Fall L_K auch durch Integration von U_{F0} ermittelt werden kann. Bei den geforderten Austrittsgeschwindigkeiten > 100 m/s kann für Luft die Kompressibilität jedoch nicht mehr vernachlässigt werden. Für ein kompressibles Medium ist $U_K(t)$ einer von mehreren Parametern, die in funktionellem Zusammenhang mit der Austrittsgeschwindigkeit U_{F0} stehen. Integriert man diese über der Zeit nach

$$L_F = \int_0^t \bar{U}_{F0}(t)\,dt \qquad (3),$$

so erhält man analog zu Gharib eine Ausschublänge L_F. Setzt man diese zum Durchmesser D des Rohres ins Verhältnis, so kann man auch für die Wirbelerzeugung mittels Stoßrohr eine Bildungszahl

$$N_S = \frac{L_F}{D} \qquad (4)$$

angeben, die aber nicht direkt mit der von Gharib entwickelten vergleichbar ist und daher im folgenden als Stoßzahl bezeichnet wird.

Die Berechnung dieser Stosszahl setzt jedoch die Kenntnis von $U_{F0}(r,t)$ voraus, welche nur durch Simulation oder aufwändige Strömungsmesstechnik ermittelt werden kann. Eine erste thermodynamische Abschätzung macht daher Sinn:

Geht man von einem festen Rohrdurchmesser D aus, so besteht die Aufgabe darin, eine Vergleichsgröße für den oben abgeleiteten Kolbenweg L_K zu finden. Dies ist leicht möglich, wenn man Kolben- und Stoßrohr auf ihre eigentliche Funktion hin betrachtet, nämlich innerhalb einer vorgegebenen Zeit ein bestimmtes Fluidvolumen V durch einen kreisförmigen Querschnitt A mit dem Durchmesser D in die Umgebung zu pressen. Für beide ist

$$V_{F0} = AL_K \qquad (5)$$

und bereits vor dem Ausschub im Zylinder vorhanden. Während V_{F0} im Kolbenrohr durch den Kolben vorgetrieben wird, übernimmt diese Funktion im Stoßrohr das in Folge der Verbrennung expandierende Abgasvolumen V_A. Idealisiert man die Grenzfläche zwischen diesem und dem bei Umgebungsbedingungen im Rohr befindlichen V_{F0} als eben im Sinne einer Pfropfenströmung, so kann auch hier von einer „Kolbenbewegung" mit Geschwindigkeitsverlauf $U_P(t)$ und Kolbenweg L_P gesprochen werden. Während U_P von der Verbrennungskinetik abhängt, folgt L_P aus der adiabaten Verbrennungstemperatur des verwendeten Brenngases T_{ad} und kann daher auch ohne Integration angegeben werden. Soll also ein Fluidvolumen V_{F0} aus dem Rohr verdrängt werden, so muss das davor in der Brennkammer befindliche Brenngasvolumen V_B direkt nach der Verbrennung zur Zeit t' gerade so weit expandiert werden, dass gilt:

$$V_{P0} = V_A(t') - V_B(t_0) \tag{6}$$

bzw. bei gleichem Querschnitt von Brennkammer und Rohr:

$$L_P = L_A(t') - L_B \tag{7}$$

Die Ausdehnung eines vollständig umgesetzten Brenngasvolumens im Verhältnis zum Ausgangsvolumen ist durch das Expansionsverhältnis ε gegeben. Mit dem idealen Gasgesetz folgt daraus

$$\epsilon = \frac{V_A}{V_B} = \frac{T_{ad}}{T_0} = \frac{L_A}{L_B} \rightarrow L_A = \epsilon L_B \tag{8}$$

, wobei T_{ad} für stöchiometrische Mischung eines Brenngases mit Luft aus Tabellen (z. B. [Wa97]) entnommen werden kann. Damit folgt für L_P :

$$L_P = \epsilon L_B - L_B = L_B(\epsilon - 1) \tag{9}$$

Mit den oben genannten Idealisierungen läßt sich damit die Bildungszahl N_K für ein Kolbensystem auch auf das Stoßrohr anwenden:

$$N_K = \frac{L_K}{D} \approx \frac{L_P}{D} = \frac{L_B}{D}(\epsilon - 1) \tag{10}$$

Für ein bestimmtes Brenngas, einen konstanten Brennkammer- bzw. Rohrdurchmesser D und die Bildungszahl N läßt sich so die erforderliche Brennkammerlänge ableiten. Ein solches System wäre jedoch sehr unflexibel, da nur eine Bildungszahl voreingestellt werden könnte. Außerdem liegt der adiabaten Verbrennungstemperatur die ideale Mischung sämtlicher Komponenten zu Grunde, die sich in der Praxis oft nur unter Luftüberschuss realisieren lässt. Zusätzlich nimmt diese Darstellung keine Rücksicht auf die Kinetik der Verbrennungsreaktion, welche neben der Rohrgeometrie für den Geschwindigkeitsverlauf $U_P(t)$ am Rohrauslass verantwortlich und für die Wirbelringbildung sehr bedeutsam ist. Es stellt sich somit die Frage, wie die Gasexpansion gesteuert werden kann. Dazu bietet sich der ohnehin erwünschte Luftüberschuss (innerhalb der Explosiongrenzen des Brennstoffes) an, denn durch einen erhöhten Anteil von Inertkomponenten sinkt die Verbrennungstemperatur T_M des Gesamtgemisches, sowie mittelbar auch die Flammgeschwindigkeit.

Teilt man das Abgasvolumen V_A gedanklich in eines mit stöchiometrischem abreagiertem Brennstoff-Luft-Gemisch V_1 mit T_{ad} und eines mit Überschussluft V_2 mit T_0 entsprechend $V_2 = l V_1$ auf, so kann man mit $m_i = \rho_i V_i$, T_M aus einer Enthalpiebilanz nach:

$$T_M = \frac{\sum_i m_i c_{pi} T_i}{\sum_i m_i c_{pi}} \quad \text{bzw.} \quad T_M = \frac{T_{ad}\rho_A c_{pa} + l T_0 \rho_{l.} c_{pl.}}{\rho_A c_{pa} + l \rho_{l.} c_{pl.}} \qquad (11)$$

und damit zu

$$\epsilon_M = \frac{T_M}{T_0} = \frac{T_{ad}\rho_A c_{pa} + l T_0 \rho_{l.} c_{pl.}}{T_0(\rho_A c_{pa} + l \rho_{l.} c_{pl.})} \qquad (12)$$

abschätzen. Eingesetzt ergibt sich so für die Stoßzahl im Stoßrohr:

$$N_S = \frac{L_B}{D} = \frac{T_{ad}\rho_A c_{pa} + l T_0 \rho_{l.} c_{pl.}}{T_0(\rho_A c_{pa} + l \rho_{l.} c_{pl.})} - 1 \quad . \qquad (13)$$

Es besteht damit die begründete Hoffnung, dass sich das Konzept der Bildungszahl auch auf die Erzeugung turbulenter Wirbelringe in Luft übertragen läßt. Nachlauffreie Ringwirbel könnten sich dann sehr viel weiter fortbewegen, als man bisher angenommen hat.

5. Versuchsaufbau

Als Ausgangspunkt für die Untersuchungen der Stoßrohrmethode wurde ein einfacher Ringwirbelerzeuger entworfen, um das gewählte Erzeugungsprinzip in Simulationen und ersten Experimenten auf seine Erfolgsaussichten zu testen.

Das Gerät besteht aus einer zylinderförmigen Brennkammer mit der Länge L_B und dem Durchmesser D, in der das Brenngasgemisch über eine an der konvexen Rückwand angebrachten Zündkerze gezündet wird. Durch eine Ringblende mit dem Radius R_B gelangen die Abgase nach erfolgter Verbrennung in das Expansionrohr („Rohr") der Länge L_E und gleichem Durchmesser D und verdrängen die dort befindliche Luft in die Umgebung. In Folge des so erzeugten Fluidausstoß' am Rohrauslass mit der Fluidgeschwindigkeit $U_{F0}(t,r)$ rollt sich der Wirbelring in der Scherschicht auf.

Die Einstellbarkeit dieses Geschwindigkeitsverlaufs bzw. des ausgestoßenen Fluidvolumens soll über die in die Kammer eingebrachte Brenngasmenge realisiert werden. Dazu muss das Gemisch aber sicher und schnell durchzünden, damit sich die Abgasexpansion überhaupt innerhalb bestimmter Grenzen reproduzieren lässt. Für das Gasgemisch lassen sich daraus folgende verbrennungstechnische Anforderungen ableiten:

- großer Explosionsbereich bzw. niedrige und hohe Explosionskonzentrationen in Luft bei Standard-Umgebungsbedingungen. (Justierbarkeit)

- sichere bzw. leichte Zündung bzw. niedriger Flammpunkt und Zündtemperatur bei Standardbedingungen (Reproduzierbarkeit)
- hoher volumenbezogener Energieinhalt bzw. Heizwert (Anfangsimpuls)
- hohe laminare Flammgeschwindigkeit in breitem Mischungsbereich (Anfangsimpuls, Justierbarkeit)
- einfaches Handling
- Ungiftigkeit von Gasgemisch und Verbrennungsprodukten

Diese Anforderungen werden z. B. von Acetylen (C_2H_2) gut erfüllt, weshalb es als Brenngas für die praktische Realisierung ausgewählt wurde.

6. SIMULATIONEN

Die obigen Abschätzungen zeigen, dass sich das Bildungszahlkonzept prinzipiell auch auf die Stossrohrmethode übertragen lässt. Sie basieren aber lediglich auf Gleichgewichtsthermodynamik und tragen dem instationären Ablauf einer Explosivreaktion nicht Rechnung. Weiterhin führt die praktische Ausführung des bisher nur schematisch beschriebenen Stossrohres zu strömungsmechanischen Eigenschaften, die ebenfalls bisher vernachlässigt wurden:

Brennkammer und Expansionsrohr sind durch eine Ringblende voneinander getrennt, welche eine Durchmischung von einströmendem Brenngasgemisch und im Expansionsrohr ruhender Luft vor der Zündung verhindern soll. Sie dient außerdem dem Druckaufbau in der Brennkammer direkt nach der Zündung, womit ein sicheres Durchzünden erst gewährleistet werden kann. Die Folge ist eine Einschnürung der in das Expansionrohr schießenden Abgasströmung. Die oben vorausgesetzte Propfströmung kann sich daher erst nach einer ausreichend langen Strecke l_{an} wieder ausbilden, welche zu der für die Expansion notwendigen Rohrlänge hinzuaddiert werden muss.

An Hand von Verbrennungs- bzw. Strömungsimulationen wurde daher untersucht, wie sich die instationäre Verbrennung in der stöchiometrisch mit C_2H_2-Luftgemisch befüllten Brennkammer auf das Austrittsprofil der Fluidgeschwindigkeit $U_{f0}(r,t)$ auswirkt und welcher Geschwindigkeitsbereich dabei erreicht wird.

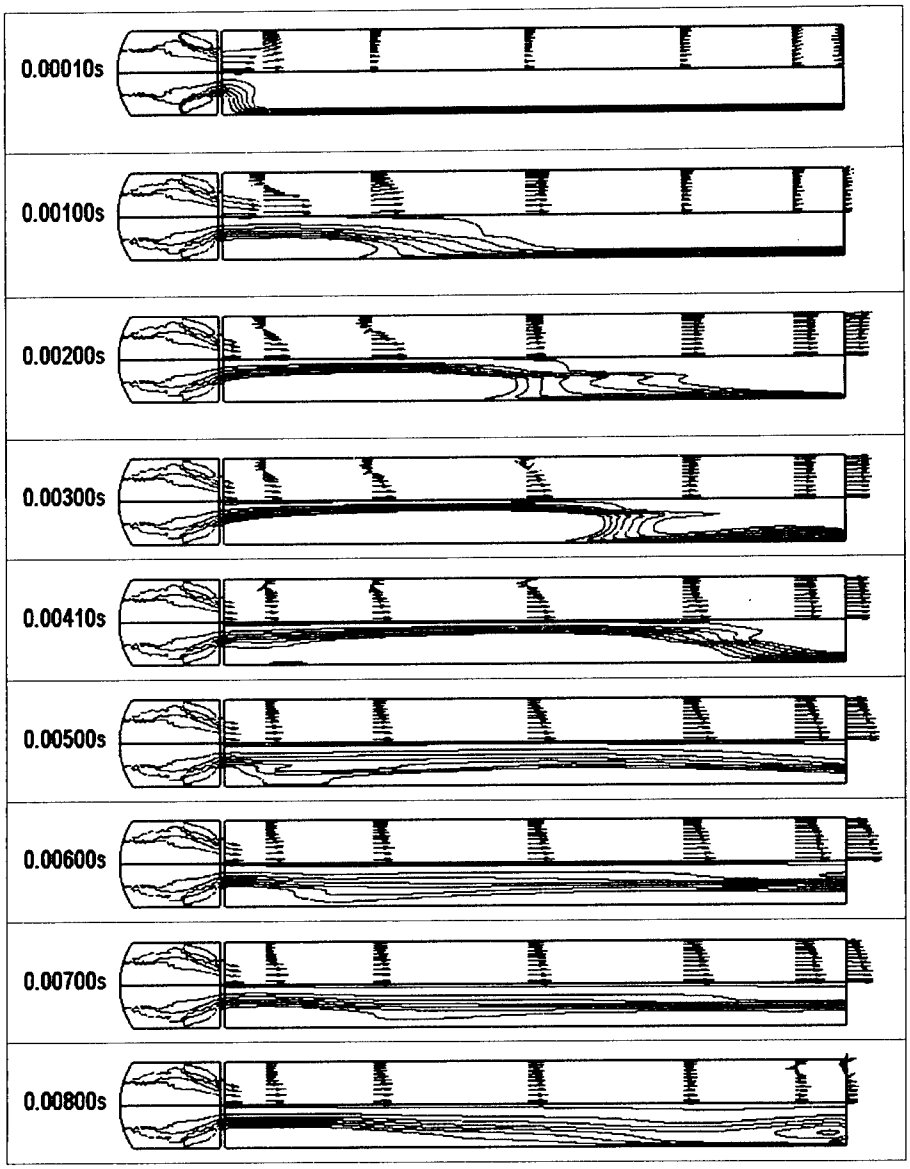


Bild 1: Simulation von Geschwindigkeit(oben) und Stromfunktion(unten)

An Hand der negativen Geschwindigkeitsvektoren lässt sich die maximale Ausdehnung des an der Ringblende auftretenden Rezirkulationswirbels bei t=0.0041 s ablesen. Das letzte Rohrdrittel wird dabei jedoch nicht erreicht, die Länge des Expansionsrohres kann also in erster Nährung als ausreichend bezeichnet werden.

Es zeigt sich, dass am Rohraustritt bei x/D = 6 sich bereits 1 ms nach der Zündung ein über dem Rohrradius r nahezu konstantes Profil der axialen Austrittsgeschwindigkeit $u_r(r)$ ausbildet (Bild 1). Ab t= 5 ms nimmt die Geschwindigkeit im Kernbereich deutlich

zu und erreichen nach 6 ms ihr Maximum (Bild 2). Nach ca. 8 ms hat sich die Strömung dann wieder deutlich verlangsamt, womit die Austrittsphase beendet ist.

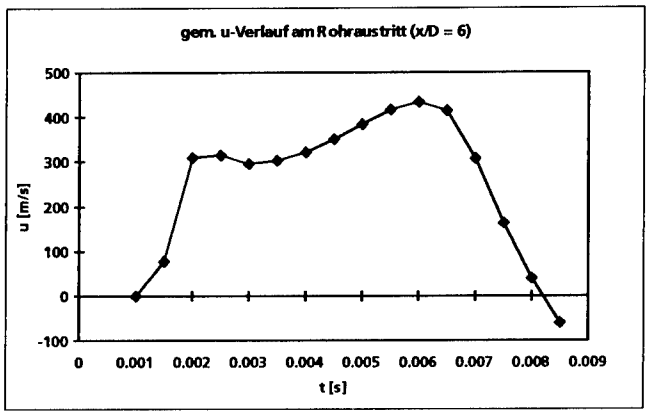


Bild 2: simulierter Austrittsgeschwindigkeitsverlauf

Die Forderung nach hohen Austrittsgeschwindigkeiten kann damit als erfüllt gelten. Für den in Bild 2 aufgetragenen Verlauf ergibt sich mit D=0.2 m eine Stoßzahl N_S von 10.

7. EXPERIMENTE

Für die Detektion der erzeugten Wirbelringe wurde entlang der verlängerten Rohrachse in regelmäßigen Abständen Wasserregner angebracht. Durchschlägt ein Wirbelring ein solches Wasserstränenfeld, so zerstäubt er sämtliche Wassertropfen in seiner Flugbahn und stanzt somit seine eigene Kontur als gut sichtbarer Aerosolring aus dem Stränenfeld heraus. Mittels per Zündimpuls getriggerter Videoaufzeichnungen lassen sich dann Position, Abmessung und Fortbewegungsgeschwindigkeit eines durchtretenden Ringwirbels ermitteln. Dabei muss jedoch berücksichtigt werden, dass die Ringe bei jedem Durchtritt an Impuls verlieren. Für unverfälschte Geschwindigkeitsmessungen können daher nur freie Flugdistanzen zwischen Generator und erstem Stränenfeld ausgewertet werden.

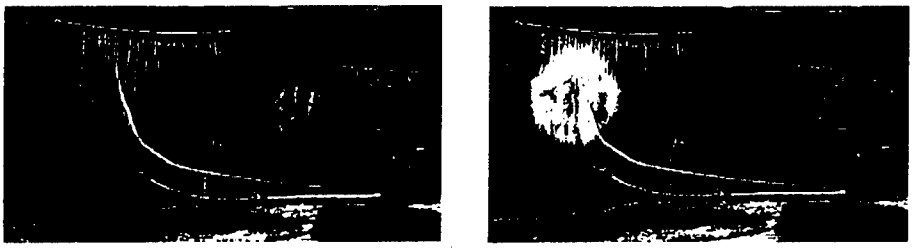


Bild 3 Vermessung der Wirbelringbewegung mittels Stränenfeldmethode

Erste Versuche ergaben Lauflängen von maximal 35 m , wobei die detektierten Ringe noch eine durchschnittliche Fortbewegungsgeschwindigkeit von 27 m/s hatten. Der Durchmesser betrug dabei im Mittel 1.2 m.

Betrachtet man den Geschwindigkeitsabfall zwischen zwei Messpunkten mit 10 m Abstand, so halbiert sich die Translationsgeschwindigkeit über diese Strecke von 56 m/s auf 27 m/s. Bezogen auf Bewegungsgeschwindigkeit und Radius des Wirbelrings ergibt sich somit eine Reynoldszahl von maximal $1.8\ 10^9$. Allerdings wurden an noch nicht ausreichend vielen Distanzen gemessen, so dass noch keine eindeutige Proportionalität abgeleitet werden konnte. Die von Arnold gemachten Prognosen bezüglich einer Mindestgeschwindigkeit für die Fortbewegung in turbulenter Außenströmung können damit jedoch in erster Nährung bestätigt werden.

8. Zusammenfassung und Ausblick

Die Nutzung von Ringwirbeln für den Impulstransport in Luft stellt an das Erzeugungssystem Anforderungen, die sich mit dem klassischen Kolben-Zylinder-Aufbau nur schwer realisieren lassen. Impulsartig ansteigende hohe Austrittsgeschwindigkeiten bei gleichzeitig großem Rohrdurchmesser lassen sich jedoch mittels eines Stoßrohres realisieren, bei dem das Fluidvolumen explosionsgetrieben aus dem Erzeugungsrohr verdrängt wird. Mit Hilfe numerischer Simulationen konnte die Eignung eines dementsprechend konzipierten Versuchsaufbaus überprüft und bei ersten praktischen Experimenten nachgewiesen werden. Die erzeugten Wirbelringe erlauben dabei einen eindeutig messbaren Impulstransport über eine Distanz von bis zu 35 m. Die Optimierung der Erzeugungsgeometrie im Sinne einer möglichst nachlauffreien Ringerzeugung soll die Reichweite weiter erhöhen. Entsprechende Simulationen und Strömungvermessungen sind Gegenstand aktueller Arbeiten.

Literatur

go92: G. J. Gottschalk, Intermittant ventilation by moving vortex rings, 1992

Didd: Didden, Norbert, Untersuchung laminarer, instabiler Ringwirbel mittels Laser-Doppler-Anemome, 1977

gh98: M. GHARIB, E. RAMBOD, K. SHARIFF, A universal time scale for vortex ring formation, 1998

Arn75: O. Arnold, Verhalten von Wirbelringen in turbulenzarmer und turbulenter Grundströmung, 1975

Lu79: H. J. Lugt, Wirbelströmung in Natur und Technik, 1979

Max1: t. Maxworthy, Turbulent vortex rings, 1974

GleCo90: A. Glezer, D. Coles, An experimental study of a turbulent vortex ring, 1990

max77: t. Maxworthy, Some experimental studies of vortex rings, 1977

LiTu01: Linden P.F.; Turner J.S, The formation of 'optimal' vortex rings, and the efficency of propulsion de, 2001

Wa97: J. Warnatz, Verbrennung, 1997

gle88: A. Glezer, The formation of vortex rings, 1988

Stabilitäts- und Nutzungsdauerbewertung von neuartigen Festtreibstoff-Formulierungen mit CL20, AP und energetischen Weichmachern

Stability and Service Time Period Assessment of Novel Solid Rocket Propellant Formulations Containing CL20, AP and Energetic Plasticizers

Manfred A. Bohn, Siegfried Eisele

Fraunhofer-Institut für Chemische Technologie (ICT)
Postfach 1240, D-76318 Pfinztal-Berghausen, Germany

Abstract

To achieve higher burning rates with rocket propellants some batches have been formulated, for which the main ingredients are the energetic plasticizers GAP-A, TMETN (trimethylolethane trinitrate) and BTTN (1,2,3-butanetriol trinitrate), the energetic substances ammonium perchlorate (AP) and ε-CL20 (ε-HNIW). The binder was GAP-N100. From the view of stability, the interesting fact is that the formulations contain no typical stabilizer for the nitric acid ester components TMETN and BTTN, although their contents range up to 21 mass-%. One reason to do this is to increase the content of the high energy substances. To assess the stability and ageing a series of tests and investigations was performed. These have been Dutch Mass Loss Test (DMLT), Vacuum Stability Test (VST), mass loss as function of time at the temperatures of 80°C and 90°C, and heat generation rate measurements as function of time at 80°C with the TAM (Thermal Activity Monitor) of Thermometric AB, Sweden. The evaluation of the measurements is based on kinetic models.

1. Einleitung

Für den Antrieb von schnellfliegenden Flugkörpern bis zu Mach ≥ 4 sind schnell brennende Festtreibstoffe nötig. Ein Weg dies zu erreichen sind Formulierungen mit hochenergetischen und von vornherein schnellbrennenden Komponenten und die geeignete Korngrößeneinstellung kristalliner Energiestoffe. Weiters dazu siehe den Beitrag P 149 dieser Tagung /1/. Als Oxidatoren wurden Ammoniumperchlorat und ε-CL20 (ε-HNIW, Hexanitro-hexaaza-isowurtzitan) gewählt. Der Binder ist mit GAP-N100 energetisch. Zum Erreichen einer genügend niedrigen Glasübergangstemperatur werden energetische Weichmacher zugesetzt. Neben GAP-A wurden zur Verbesserung der Sauerstoffbilanz auch die Salpetersäureester TMETN (Trimethylolethantrinitrat) und BTTN (1,2,3-Butantrioltrinitrat) verwendet.

Paper 152 (pages 152-1 to 152-13) presented on the 32nd International Annual Conference of ICT, July 3 to 6, 2001, Karlsruhe, Germany. Fraunhofer-Institut für Chemische Technologie (ICT), Postfach 1240, D-76318 Pfinztal, Germany.

Um den Energiegehalt zu maximieren, wurden keine typischen Stabilisatoren für Salpetersäureester zugesetzt, obwohl deren Gehalte bis zu 21 Mass.-% reichen. Ziel der Untersuchung ist, die stabilisatorfreien Formulierungen als einsatzfähig zu begründen und Unterschiede in der Stabilität und im Alterungsverhalten auf die Zusammensetzung zurückzuführen.

2. Vorgehen zum Erreichen einer Nutzungsdauerbewertung

Mit Daten aus der Stabilitätsprüfung ist eine Alterungs- und Nutzungsdauervoraussage noch nicht zu erhalten. Dies gilt einmal prinzipiell, da dazu Zeit-Temperaturdaten bei verschiedenen Temperaturen nötig sind /2,3/. Zweitens werden diese Tests bei sehr hohen Temperaturen nur als schnelle Sichtungsprüfung durchgeführt. Der übliche Temperatureinsatzbereich von Munition ist nach STANAG 2895 /4/ mit maximal 71°C weit tiefer gelegen. Drittens sind es noch unbekannte Formulierungen, so daß für die Anwendung vereinfachter, meßdatenreduzierter Voraussageverfahren wie 'Erfüllen einer Prüfzeit' oder 'Zeit bis zum Ereignis' noch die erforderliche Datenbasis fehlt und solche Verfahren daher nicht anwendbar sind.

Zum Erstellen dieser Datenbasis werden zunächst Massenverlustdaten (MV) als Funktion der Zeit und Temperatur bestimmt. Da bei noch unbekannten Formulierungen eine Meßgröße allein noch nicht eine gesicherte Beurteilung erlaubt, werden auch die Wärmeentwicklungsraten (WER) mit einem Mikrokalorimeter, Typ TAM (Thermal Activity Monitor) von Thermometric AB, Schweden, bestimmt.

Tabelle 1: Rahmenzusammensetzung der untersuchten Formulierungen.

		178	180	181	182	184	185	189
WM GAP-A	[M.-%]	12,25	14	9	-	-	10,5	9
WM TMETN	[M.-%]	12,25	14	9	18	21	10,5	2,25
WM BTTN	[M.-%]	-	-	-	-	-	-	6,75
GAP-N100	[M.-%]	10,5	7	12	12	14	14	12
ε-CL20	[M.-%]	42	42	47	47	42	42	47
AP	[M.-%]	20	20	20	20	20	20	20
Zusätze	[M.-%]	3	3	3	3	3	3	3
O_2-Bilanz	[%]	-28,7	-27,8	-27,1	-20,0	-22,9	-31,2	-25,8
I_{SP} (70:1, Gl.str.)	[Ns/N]	251	252	253	258	255	249	254
I_V (70:1, Gl.str.)	[Ns/l]	4290	4330	4420	4580	4450	4240	4440
Q_{EX} (gasf. Was.)	[J/g]	4840	4940	4960	5370	5200	4750	5020

WM: Weichmacher M.-%: Massenprozent

3. Zusammensetzung der Formulierungen

Die Rahmenzusammensetzung der sieben untersuchten Formulierungen ist in der Tabelle 1 zusammengestellt. Mit angegeben sind die Daten für die Sauerstoffbilanz, die thermodynamisch berechneten Daten für den gewichtsstrombezogenen spezifischen Impuls I_{sp} und den treibstoffvolumenstrombezogenen spezifischen Impuls I_v, beide bei sog. Gleichgewichtsströmung in der Düse und einem Brennkammerdruck-zu-Enddruck-Verhältnis von 70 bar zu 1 bar, sowie die thermodynamisch berechnete Explosionswärme Q_{EX}. Alle thermodynamischen Berechnungen wurden mit dem ICT-Thermodynamik-Programm durchgeführt.

4. Ergebnisse

4.1 Selbstentzündungstemperatur, Holland-Test und Vakuumstabilität

In der Tabelle 2 sind die Daten aus der Stabilitätsprüfung zusammengestellt. Die Selbstentzündungstemperatur (SET) wurde mit dem Wood-Metallbad bei einer Aufheizrate von 5°C/min und 0,2g Einwaage bestimmt. Der Holland-Test (HT) wurde bei 105°C durchgeführt. Er bestimmt den Massenverlust (MV) über 72 Stunden, wobei der MV der ersten 8 h von dem bei 72 h abgezogen wird. Für den Vakuumstabilitätstest (VST) wurde der übliche Aufbau mit dem Quecksilbermanometer verwendet. Der VST-Test wurde bei 100°C durchgeführt. Die Werte für die SET und den HT erfüllen die üblichen Grenzwerte. Die Werte des VST liegen alle etwas über dem Grenzwert, was jedoch auf die etwas zu hohe Prüftemperatur zurückgeführt werden kann. Insgesamt sind die Daten der Stabilitätsprüfung noch als gut zu bewerten.

Tabelle 2: Ergebnisse der Stabilitätsprüfung der Formulierungen.

	Grenzwert	178	180	181	182	184	185	189
Selbstentzündungstemperatur, 5°C/min [°C]	≥ 170	172	173	175	172	170	176	177
Massenverlust im Holland-Test, 105°C, 4g [%]	≤ 2	0,78	0,75	0,68	0,90	1,11	0,80	0,75
Vakuumstabilität, 100°C, 40h, 2,5g [ml/g]	≤ 1,2	1,55	1,56	1,32	1,74	2,06	1,49	1,54

4.2 Massenverlust als Funktion der Zeit und Temperatur

Beispielhaft für alle HFK-Ansätze sind die Massenverlustdaten als Funktion der Zeit des Formulierungsansatzes HFK 178 in Abb. 1 bei 90°C gezeigt. Die Daten der beiden Parallelproben liegen sehr gut zusammen. Dies gilt für alle sieben untersuchten Ansätze bei allen Meßtemperaturen.

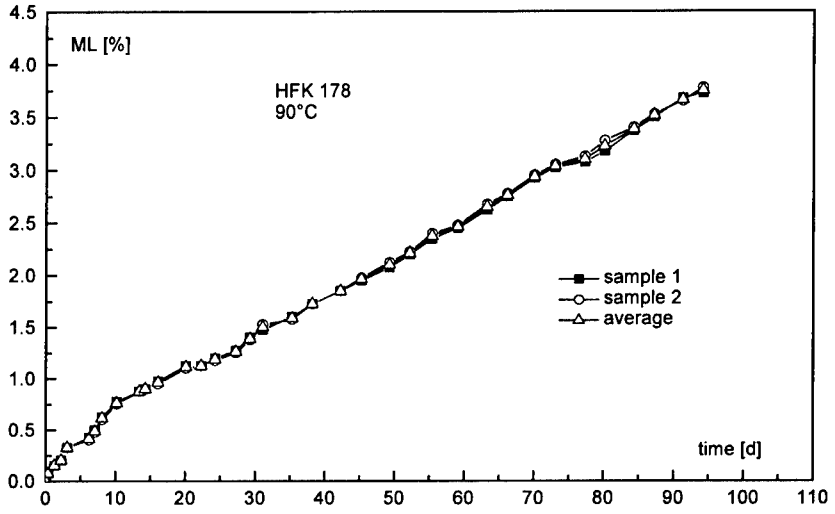


Abb. 1: Massenverlustmeßdaten des HFK 178 bei 90°C. Die Daten beider Parallelproben liegen sehr gut zusammen.

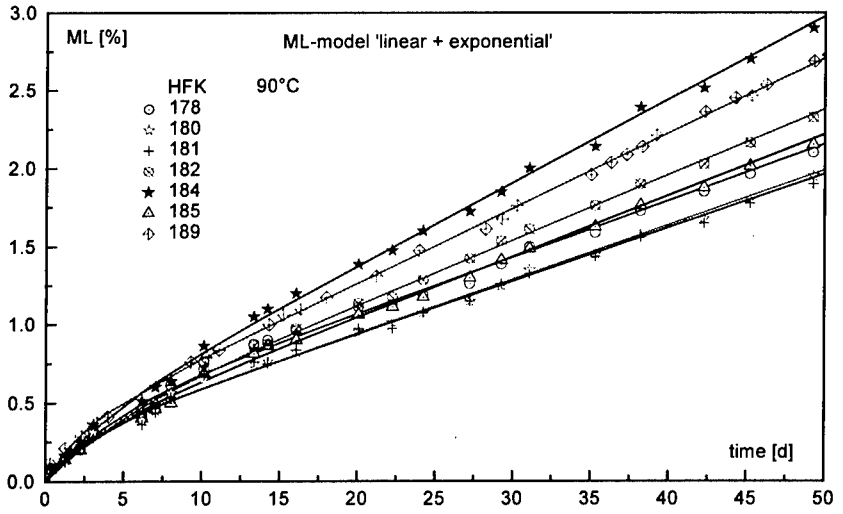


Abb. 2: MV-Meßdaten der sieben HFK-Ansätze bei 90°C. Die durchgezogenen Kurven sind das MV-Model 'linear+exponentiell'.

In Abb. 2 sind die MV-Meßdaten aller sieben HFK-Ansätze gezeigt. Die Daten wurden über die jeweiligen Parallelproben gemittelt. Der HFK 184 mit 21 Mass.-% TMETN als einzigem Weichmacher zeigt die höchste Zersetzungsrate k_{ML}, gefolgt von HFK 189 mit TMETN+BTTN und GAP-A. Danach kommt HFK 182 mit 18 Mass.-% TMETN. HFK 182 liegt schon nahe dem Feld der anderen Formulierungsansätze mit GAP-A und TMETN. HFK 180 und 181 haben die niedrigste Zersetzungsrate. In Abb. 2 sind auch die Kurven des MV-Modells eingetragen. Alle Beschreibungen sind sehr gut. Alle MV-Kurven zeigen anfangs einen gekrümmten Anstieg, dann ein lineares Zunehmen. Das lineare Zunehmen des MV bedeutet reaktionskinetisch ein globale Zersetzungsreaktion von 0. Ordnung. In der Regel findet man solches Reaktionsverhalten nur bei kleinen Umsätzen wie sie hier zur Beurteilung von Bedeutung sind. Höhere Umsätze machen bei Treibmitteln aus praktischer Sicht keinen Sinn, da dann ihr Energieverlust schon zu hoch ist und auch andere Eigenschaftsänderungen das Treibmittel unbrauchbar machen. Im Gesamtverlauf ist die Zersetzungsreaktion komplexer, daher wird diese Zesetzungreaktion im folgenden pseudo-0. Ordnung genannt.

4.3 Wärmeentwicklungsrate und Wärmeentwicklung

Die Wärmeentwicklungsrate (WER) dQ/dt des Ansatzes HFK 180 zeigt die Abb. 3. Durch Integration über die Zeit erhält man daraus die Wärmeentwicklung (WE) Q, welche mitdargestellt ist, für sie gilt die rechte Ordinatenachse. Die WE zeigt einen zum MV analogen Verlauf: den Anfangsbereich und danach den linearen Anstieg, was wiederum eine Zersetzung nach pseudo-0. Ordnung bedeutet.

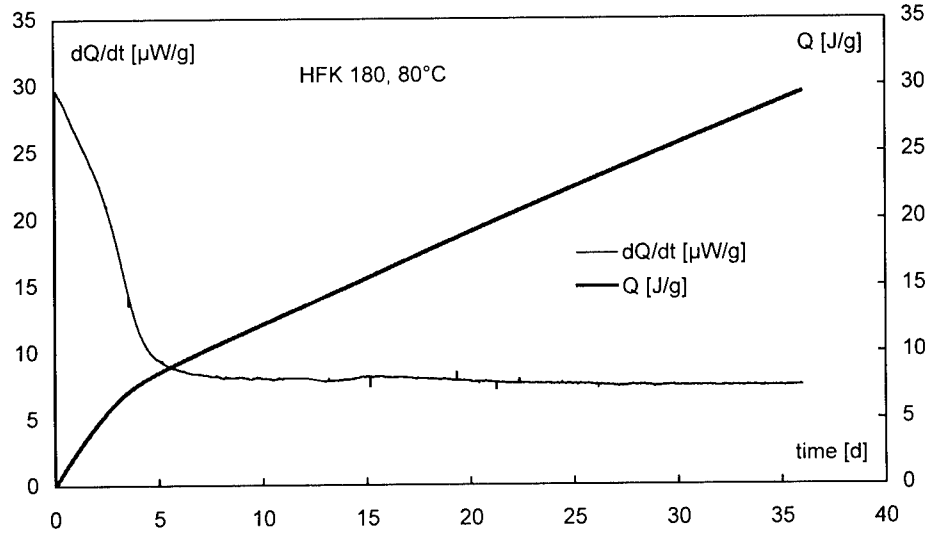


Abb. 3: Anfangs- und Langzeitverhalten des HFK 180 bei 80°C in der Wärmeentwicklungsrate (WER) dQ/dt. Die nahezu konstante WER ab etwa 10 Tagen entspricht einer Reaktion pseudo-0. Ordnung. Die zum MV analoge Wärmeentwicklung (WE) Q ist daher linear ansteigend.

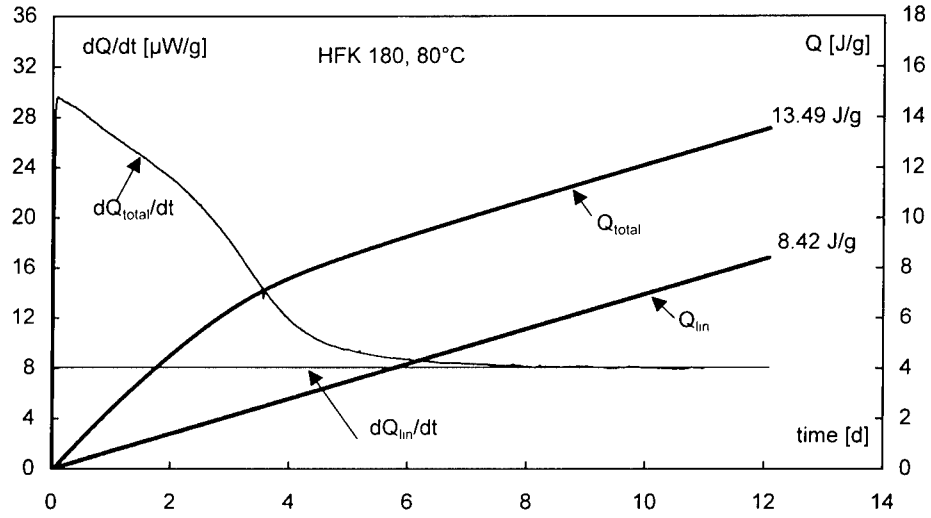


Abb. 4: Abtrennung des Anfangsverhaltens vom Langzeitverhalten in der WER und WE beim Ansatz HFK 180.

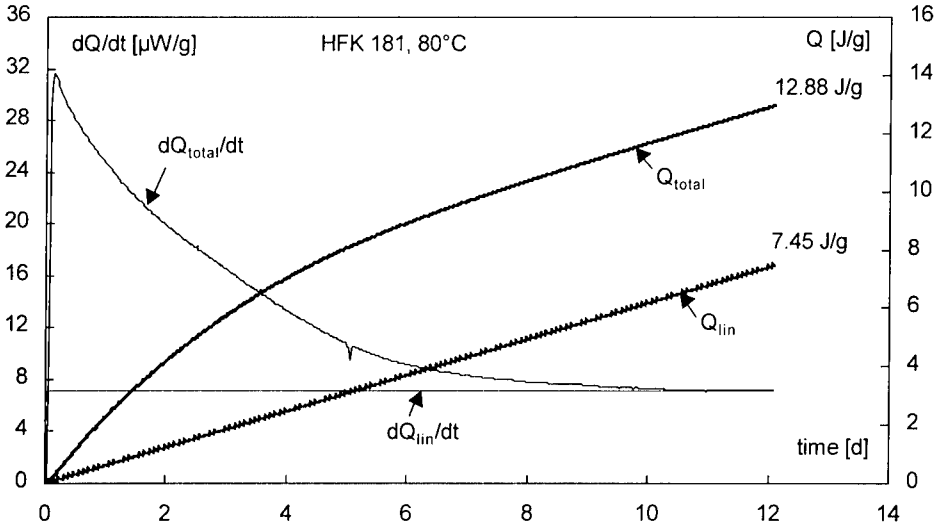


Abb. 5: Abtrennung des Anfangsverhaltens vom Langzeitverhalten in der WER und WE beim Ansatz HFK 181.

Beide Meßgrößen, Massenverlust und Wärmeentwicklungsrate, lassen die gleiche Interpretation der Daten zu. Dies ist eine gute Absicherung der darauf aufbauenden Nuztungsdauervoraussage. Abb. 4 und Abb. 5 zeigen die Auftrennung der

WER in den Anfangsbereich und den für die Beurteilung zu verwendenden 'linearen' Teil, der jeweils mit dem Index 'linear' gekennzeichnet ist.

5. Diskussion

Die Massenverlustdaten werden mit dem MV-Modell 'linear + exponentiell' bzw. '0. Ordnung + 1. Ordnung' analysiert. Das Reaktionschema ist in Gl.(1) angegeben, es ist in molaren Konzentrationen der einzelnen Komponenten formuliert.

(1) $A \xrightarrow{k_A} B + C + S$

$V \xrightarrow{k_V} V_-$

Das Schema enthält die Hauptkomponente A, welche sich in die gasförmigen Stoffe C (steht für alle), in die festen Reaktionsprodukte S (steht für alle) und in das Produkt B zersetzt. B kann gasförmig oder fest sein und kann als autokatalytisch wirksame Komponente in der Beschreibung verwendet werden /5/. Die Nebenkomponente V kann verdampfen oder sich nach einer Reaktion 1. Ordnung völlig in gasförmige Produkte umsetzten. Für die Hauptkomponente A wird unten eine Zersetzung nach 0. Ordnung angesetzt.

Für die gemessene Masse M(t,T) gilt Gl.(2).

(2) $M(t,T) = M_A(t,T) + M_B(t,T) + M_S(t,T) + M_V(t,T) + M_N$

$M_A(t,T)$ ist die Masse der Hauptkomponente, $M_C(t,T)$ steht für die Massen der entweichenden gasförmigen Produkte, $M_B(t,T)$ ist die Masse des Zersetzungsprodukts B, $M_S(t,T)$ ist die Masse der festen Zersetzungsprodukte, M_N ist die Masse nichtreagierender Stoffe, $M_V(t,T)$ ist die Masse der verdampfenden oder sich völlig gasförmig zersetzenden Stoffe V. Zur Zeit t = 0 gilt für M(0) die Gl.(3).

(3) $M(0) = M_A(0) + M_B(0) + M_S(0) + M_V(0) + M_N$

Eine weitere Bestimmungsgleichung für M(t,T) ist die Gl.(4).

(4) $M(t,T) = M(0) - M_C(t,T) - \left(M_V(0) - M_V(t,T)\right)$

Der letzte Term der Gl.(4) gibt die bis zur Zeit t verdampfte oder sich gasförmig zersetzte Masse von V an. Für die Verdampfung /Zersetzung des Stoffs V wird eine Reaktion 1. Ordnung angesetzt, Gl.(5).

(5) $M_V(t,T) = M_V(0) \cdot \exp(-k_V \cdot t)$

Für $M_C(t,T)$ gilt die Gl.(6) /2,3,5/.

(6) $M_C(t,T) = C(t,T) \cdot m_C \quad = \frac{m_A - m_B - m_S}{m_A} \cdot (M_A(0) - M_A(t,T))$

Die Massen m_i sind die Molmassen der einzelnen Stoffe. Damit folgt für die Meßgröße M(t,T) die Gl.(7) und für die mit M(0) normierte Masse $M_r(t,T)$ = M(t,T)/M(0) die Gl.(8). Die Molmasse m_C ist gleich der Molmassendifferenz m_A-m_B-m_S.

$$(7) \qquad M(t,T) = M(0) - \frac{m_C}{m_A} \cdot (M_A(0) - M_A(t,T)) - M_V(0) \cdot (1 - \exp(-k_V \cdot t))$$

$$(8) \qquad M_r(t,T) = 1 - \frac{m_C}{m_A} \cdot \frac{M_A(0)}{M(0)} (1 - M_{Ar}(t,T)) - \frac{M_V(0)}{M(0)} \cdot (1 - \exp(-k_V \cdot t))$$

Für $M_V(0)$ wird ein Massenanteil a an M(0) angesetzt, $M_V(0)$ = a·M(0). Damit gilt für $M_A(0)$ die Gl.(9).

$$(9) \qquad M_A(0) = M(0) \cdot (1-a) - \left(M_B(0) + M_S(0) + M_N\right)$$

Die Gl.(8) wird damit zur anwendbaren Gl.(10).

$$(10) \quad M_r(t,T) = 1 - \frac{m_C}{m_A} \cdot \left((1-a) - \frac{M_B(0) + M_S(0) + M_N}{M(0)} \right) \cdot \left(1 - M_{Ar}(t,T)\right) - a \cdot \left(1 - \exp(-k_V \cdot t)\right)$$

Für $M_{Ar}(t,T)$ wird der Ausdruck des zugehörigen Zersetzungsschemas für die Komponente A eingesetzt. Für den Massenverlust MV(t,T) gilt die Gl.(11).

$$(11) \qquad MV(t,T) = OF_{ML} + 100\% \cdot (1 - M_r(t,T))$$

Mit OF_{ML} wird ein eventueller MV-Offset berücksichtigt, der nicht von den Zersetzungen verursacht wird.

Im folgenden wird angenommen, daß $M_B(0)$ und $M_S(0)$ für die HFK-Ansätze gleich null sind. Eventuell vorhandenes M_N sei so klein, daß $M_N/M(0)$ gegenüber (1-a) vernachlässigt werden kann. Die Hauptkomponente A (A ist eine zusammengesetzte Größe, daher auch hier als globale Zersetzung behandelt) der HFK-Ansätze zeigt eine Zersetzung nach pseudo-0. Ordnung (linearer Anstieg im MV) mit der Reaktionsgeschwindigkeitskonstanten k_A bzw. umformuliert für den Massenverlust mit k_{ML}. Der Zusammenhang zwischen beiden Reaktionsgeschwindigkeitskonstanten ist in Gl.(12) mit angegeben.

$$(12) \qquad MV_A(t,T) = OF_{ML} + 100\% \cdot \left(\frac{m_C}{m_A} \cdot k_{ML}(T) \cdot t \right)$$

$$\text{mit} \qquad k_{ML}(T) = k_A(T) \cdot \frac{m_A}{M_A(0)} \qquad M_{Ar}(t,T) = 1 - k_{ML}(T) \cdot t$$

Die Verunreinigung oder die Nebenkomponente V zersetzt sich nach einer Reaktion 1. Ordnung mit der Reaktionsgeschwindigkeitskonstanten k_V, wobei a der Massenanteil der Nebenkomponente an der Gesamtmasse ist.

(13) $MV_V(t,T) = OF_{ML} + 100\% \cdot a \cdot (1 - \exp(-k_V(T) \cdot t))$

Für die Gesamtbeschreibung MV(t,T) = MV_A(t,T) + MV_V(t,T) erhält man Gl.(14)

(14) $$MV(t,T) = OF_{ML} + 100\% \cdot \left(\frac{m_C}{m_A} \cdot (1-a) \cdot k_{ML}(T) \cdot t + a \cdot (1 - \exp(-k_V(T) \cdot t)) \right)$$

Das Verhältnis m_C/m_A wird näherungsweise zu 1 gesetzt. In den Messungen war OF_{ML} immer null. Die Anpaßparameter des Modells sind somit a, k_V und k_{ML}. Die Anwendung des MV-Modells ist in der Abb. 6 am Beispiel des Formulierungsansatzes HFK 178, gealtert bei 90°C, zu sehen. Die Punkte sind die Meßwerte, gemittelt über zwei Proben. Die drei Linienkurven sind das Modell in der Gesamtdarstellung und mit den beiden separierten Anteilen. Die Korrelationskoeffizienten R sind für alle sieben Formulierungsansätze hoch, Tabellen 3 und 4, alle HFK-Ansätze zeigen qualitativ gleiches Verhalten, siehe Abb. 2. In den Tabellen 3 und 4 sind die Reaktionsgeschwindigkeitskonstanten als $k_{ML} \cdot 100\%$ angegeben.

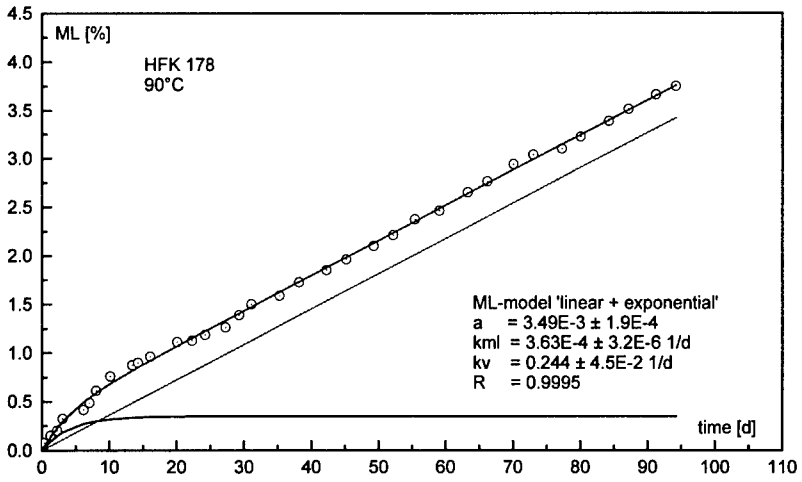


Abb. 6: Anwendung des Modells '0. Ordnung + 1. Ordnung' oder 'linear + exponentiell' zur Beschreibung der MV-Daten. Bei allen sieben untersuchten Formulierungsansätzen war die Beschreibung mit dem Modell mit der gleichen Güte möglich. Die Auftrennung der Summenkurve in die beiden Modellanteile '0. Ordnung' und '1. Ordnung' ist dargestellt.

Die zu den Gln. (12) und (13) analogen Gleichungen der Wärmeentwicklung Q sind Gl.(15) und Gl.(16). Die Größen $(-\Delta H_{R,i})$ sind die zu den Einzelreaktionen gehörigen Reaktionswärmen. OF_Q ist wie OF_{ML} ein berücksichtigbarer Offset.

(15) $Q_A(t,T) = OF_Q + (\cdot k_Q(T) \cdot t)$ mit $k_Q(T) = k_A(T) \cdot (-\Delta H_{R,A})$

(16) $Q_V(t,T) = OF_Q + (-\Delta H_{R,V}) \cdot a \cdot (1 - \exp(-k_V(T) \cdot t))$

In den WER-Kurven ist allerdings noch ein weiterer Anteil enthalten, die Exothermie der Nachhärtung des Binders GAP-N100. Folglich sind mindestens drei Terme zur Beschreibung der WER-Kurven nötig.

Tabelle 3: MV-Werte bei 90°C bestimmt mit dem MV-Modell und dessen Parameter k_{ML}, k_V und a, sowie der Korrelationskoeffizient der Modellanpassung. Der erste MV-Wert ist der Gesamt-MV, der zweite ist der MV nur von der Zersetzung 0. Ordnung.

		178	180	181	182	184	185	189
MV nach 18d	[%]	1,1 / 0,7	0,9 / 0,6	0,9 / 0,6	1,1 / 0,8	1,3 / 1,0	1,0 / 0,7	1,2 / 0,9
MV nach 40d	[%]	1,9 / 1,5	1,7 / 1,4	1,7 / 1,4	2,0 / 1,7	2,5 / 2,2	1,9 / 1,6	2,2 / 1,9
MV nach 60d	[%]	2,6 / 2,2	2,4 / 2,1	2,4 / 2,1	2,8 / 2,5	3,5 / 3,2	2,7 / 2,4	3,2 / 2,9
k_{ML}·100%	[%/d]	0,036	0,035	0,034	0,042	0,054	0,039	0,048
k_V	[1/d]	0,24	0,41	0,34	0,22	0,24	0,25	0,43
a	[%]	0,35	0,25	0,26	0,29	0,31	0,27	0,30
Korrel.koeffiz.	[-]	0,9995	0,9996	0,9995	0,9993	0,9993	0,9996	0,9997

Tabelle 4: MV-Werte bei 80°C bestimmt mit dem MV-Modell und dessen Parameter k_{ML}, k_V und a, sowie der Korrelationskoeffizient der Modellanpassung. Der erste MV-Wert ist der Gesamt-MV, der zweite ist der MV nur von der Zersetzung 0. Ordnung.

		178	180	181	182	184	185	189
MV nach 60d	[%]	0,90 / 0,55	0,76 / 0,51	0,76 / 0,52	0,89 / 0,60	1,07 / 0,77	0,87 / 0,61	1,26 / 0,96
MV nach 80d	[%]	1,08 / 0,74	0,93 / 0,68	0,95 / 0,68	1,09 / 0,80	1,34 / 1,03	1,08 / 0,81	1,58 / 1,28
MV nach 100d	[%]	1,27 / 0,92	1,10 / 0,85	1,12 / 0,86	1,29 / 1,00	1,60 / 1,29	1,28 / 1,01	1,90 / 1,60
k_{ML}·100%	[%/d]	0,0106	0,0089	0,0093	0,0114	0,0145	0,0111	0,0160
k_V	[1/d]	0,244	0,297	0,352	0,275	0,322	0,419	0,23
a	[%]	0,24	0,22	0,21	0,18	0,17	0,19	0,30
Korrel.koeffiz.	[-]	0,997	0,995	0,996	0,997	0,999	0,999	0,9994

Die Reihenfolge der Alterungsrate der HFK-Ansätze ausgedrückt mit den Zersetzungsraten k_{ML} der Reaktion pseudo-0. Ordnung ist:

90°C: $184 > 189 > 182 > 185 > 178 > 180 \approx 181$

80°C: $189 > 184 > 182 > 185 > 178 > 181 \approx 180$

Diese Reihenfolge ist im wesentlichen durch den Sprengölanteil und den Sprengöltyp erklärbar. Bei 90°C zersetzt sich HFK 184 mit dem höchsten TMETN-Anteil am schnellsten, gefolgt von HFK 182. Jedoch liegt HFK 189 in der Zersetzungsrate höher als HFK 182, da sich BTTN schneller als TMETN zersetzt. Bei 80°C zersetzt sich HFK 189 am schnellsten. Die Reihenfolge der anderen HFK-Ansätze wird wahrscheinlich durch reaktive Wechselwirkungen zwischen GAP und CL20 mitbestimmt /6/.

Tabelle 5: Arrhenius-Parameter der HFK-Ansätze bestimmt aus den MV-Daten bei 80°C und 90°C, linearer MV-Teil.

	178	180	181	182	184	185	189
Ea [kJ/mol]	130	146	138	139	140	134	117
lg(Z [%/d]) [-]	17,3	19,6	18,4	18,6	18,9	17,9	15,5

In der Tabelle 5 sind die Arrhenius-Parameter für den linearen Teil der MV-Daten angegeben, berechnet aus den Daten für 80°C und 90°C. Es wurden die mit dem MV-Modell ermittelten MV-Daten dazu verwendet. Mit diesen Daten können die zur Nutzungsdauervoraussage zu verwendenden Reaktionsgeschwindigkeitskonstanten $k_{ML}(T)$ bei anderen Temperaturen berechnet werden, Gl.(17). Damit können dann die zu erwartenden MV-Daten z.B. bei 40°C nach Gl.(18) bestimmt werden, welche in Tabelle 6 angegeben wurden. Der MV-Anteil der Verunreinigung oder der Anfangsphase bei 90°C wurde zum MV-linear Wert bei 40°C addiert und nach oben gerundet.

(17) $$k_{ML}(T) \cdot 100\% = Z[\%/d] \cdot \exp(-Ea/RT)$$

(18) $$MV_A(t,T) = 100\% \cdot k_{ML}(T) \cdot t$$

Die Beurteilung mit den WE-Daten ist für fünf HFK-Ansätze ebenfalls in Tabelle 6 angegeben. Es wird der Energieverlust bezogen auf die Explosionswärme Q_{EX} als Kriterium verwendet, welcher maximal gleich 3% von Q_{EX} betragen darf. Die prozentualen Energieverluste bei 80°C haben nahezu die gleichen Werte wie die Massenverluste bei 80°C. Zur Bewertung wurden die WE-Werte nach 12 Tagen Meßzeit verwendet und auf 60 Tage umgerechnet. Die Zersetzungsreaktionen verlaufen somit im Massen- und Energieverlust kongruent, d.h. beide Meßmethoden liefern übereinstimmende Aussagen. Der Ansatz HFK 189 hat die kleinste Aktivierungsenergie und altert daher bei niedrigeren Temperaturen am schnellsten.

Tabelle 6: Bewertung des Zeit-Temperatur-Verhaltens der sieben HFK-Ansätze.

	Grenzwert	178	180	181	182	184	185	189
MV, 90°C	≤ 3% von M(0) nach 18 Tagen	1,1%	09%	0,9%	1,1%	1,3%	1,0%	1,2%
MV, 80°C	≤ 3% von M(0) nach 60 Tagen	0,9%	0,8%	0,8%	0,9%	1,1%	0,9%	1,3%
WE, 80°C	≤ 3% von Q_{EX} nach 60 Tagen	0,86%	0,85%	0,75%			0,90%	1,4%
MV, 40°C	≤ 3% von M(0) nach 13,3 Jahren	0,6%	0,4%	0,4%	0,5%	0,6%	0,5%	0,8%
Q_{EX} [J/g]		4940	4940	4960	5370	5200	4750	5020

6. Schlußfolgerung

Die Wärmeentwicklung (WE) ist die zum Massenverlust (MV) analoge Größe, sie hat bei den HFK-Ansätzen qualitativ die gleiche Kurvenform wie die MV-Kurven. Der nach einer Anfangsphase linear zunehmende Meßwert sowohl im MV als auch in der WE ist als Zersetzung nach einer globalen Reaktion pseudo-0. Ordnung zu interpretieren. Nach den Anfangsphasen wird die WER ab etwa 10 Tagen nahezu konstant, was in dieser Meßgröße auch der Reaktion pseudo-0. Ordnung entspricht. Allerdings ist ein leichter Abfall der WER-Kurve zu erkennen, so daß autokatalytisches Zersetzungsverhalten der Salpetersäureester TMETN und BTTN in diesen Formulierungsansätzen im bewertungsrelevanten Zeitraum nicht zu erwarten ist. Beide Meßgrößen stimmen in der Aussage über das Alterungsverhalten überein. Mit den berechneten Arrhenius-Parametern für k_{ML} aus den 80°C- und 90°C-Daten wurde eine Alterungsvoraussage für 40°C durchgeführt und mit den zulässigen Grenzwerten (für NC-Treibstoffe aufgestellte Erfahrungswerte) für Massen- und Energieverlust verglichen. Die Grenzwerte '3% von der Anfangsmasse M(0)' für den maximal zulässigen MV und '3% von Q_{EX}' für den maximal zulässigen Energieverlust werden weit unterschritten. Das chemisch-thermische Alterungsverhalten dieser Formulierungsansätze ist sehr günstig, obwohl kein TMETN- bzw. BTTN-Stabilisator zugesetzt wurde.

7. Literatur

/1/ S. Eisele, K. Menke
About the Burning Behaviour of Smoke Reduced Composite Propellants based on AP / CL20 / GAP
Proceed. 32nd International Annual Conference of ICT, paper 149, July 3-6, 2001, Karlsruhe, Germany.
Fraunhofer-Institut für Chemische Technologie (ICT), Postfach 1240, D-76318 Pfinztal-Berghausen, Germany.

/2/ M.A. Bohn
Systematische Darstellung der Alterung von Rohrwaffentreibmitteln und Raketenfesttreibstoffen
Proceed. 28th International Annual Conference of ICT, pages 109-1 to 109-46, June 24-27, 1997, Karlsruhe, Germany.
Fraunhofer-Institut für Chemische Technologie (ICT), Postfach 1240, D-76318 Pfinztal-Berghausen, Germany.

/3/ M.A. Bohn
Kinetic Modelling of the Ageing of Gun Propellants and Rocket Propellants for the Improved And Time-Extended Prediction of Their Service Lifetime
Proceed. of the 4th Conference on 'Life Cycles of Energetic Materials' pages 188 to 225, March 29 to April 1, 1998, Fullerton, California, USA.
Editor: J.A. Sanchez, Los Alamos National Laboratory, Los Alamos, NM, USA.

/4/ STANAG (Standardization Agreement) 2895
Extreme climatic conditions and derived conditions for use in defining design and test criteria for NATO forces material
1990, NATO Headquarters, Military Agency for Standardization, Bruxelles, Belgium.

/5/ M.A. Bohn
Modelling of the stability, ageing and thermal decomposition of energetic components and formulations using mass loss and heat generation
Proceed. 27th International Pyrotechnics Seminar, pages 751 to 770, July 16-21, 2000, Grand Junction, Colorado USA.
International Pyrotechnics Seminars USA, Inc., IIT Research Institute Chicago, Illinois, 60616-3799, USA.

/6/ V. Thome, P.B. Kempa, M.A. Bohn
Erkennen von Wechselwirkungen der Nitramine HMX und CL20 mit Formulierungskomponenten durch Computersimulation
Proceed. 31st International Annual Conference of ICT, pages 63-1 to 63-20, June 27-30, 2000, Karlsruhe, Germany.
Fraunhofer-Institut für Chemische Technologie (ICT), Postfach 1240, D-76318 Pfinztal-Berghausen, Germany.

ABBRAND VON SANDWICH-STRUKTUREN MIT WECHSELWEISE ANGEORDNETEN OXIDATOR BRENNSTOFF-PAAREN

S. Poller, V. Weiser, S. Hötzeldt, S. Kelzenberg, F. Hidalgo
Fraunhofer-Institut Chemische Technologie (ICT)
Joseph-von-Fraunhoferstr. 7
D-76327 Pfinztal (Berghausen), Germany

Zusammenfassung

Der Abbrand von wechselweise angeordneten gefrorenen Oxidator/Brennstoff-Paaren wurde in einer Linearbrennkammer untersucht. Dabei diente ein heißer Gasstrom zur Verdampfung der ersten beiden CSP-Module und zur Verbrennungsunterstützung. Als Brennstoffe wurden verschiedene Polymere eingesetzt, Oxidator war 85%iges H_2O_2. Es zeigte sich, dass HTPB in dieser Versuchsanordnung der geeignetste Brennstoff war. Die Abbrandraten der Oxidatormodule stiegen bei einsetzender Reaktion der Treibstoffe deutlich an. Außerdem zeigte sich ein wesentlich gleichmäßigerer Abbrand bei größerer Anzahl kleinerer Module.

Abstract

COMBUSTION OF OXIDIZOR-FUEL SANDWICHES

The combustion of frozen oxidiser/fuel Sandwiches in a linear combustion chamber was analysed. A hot gas stream was used to vaporise the first two CSP-modules and to sustain the combustion. Polymers were used as fuels and the oxidiser was H_2O_2(85%). The most suitable fuel in these experiments was HTPB. The burning rates of the oxidiser modules increased during the reaction of the components. It was shown that the combustion was getting more even with a higher number of small modules.

1 EINLEITUNG

Raketentriebwerke mit festen Treibstoffen zeichnen sich durch große Zuverlässigkeit und hohe volumenspezifische Leistungsdaten aus. Wegen der sehr beschränkten Auswahl an geeigneten festen Oxidatoren und Bindern erreichen Feststofftriebwerke nur vergleichsweise niedrige spezifische Impulse, die erheblich unter jenen von Flüssigkeitsantrieben liegen. Bei Flüssigkeitsraketenantrieben besteht dagegen eine große Vielfalt verfügbarer Brennstoffe und Oxidatoren, sie erfordern jedoch eine deutlich aufwendigere Verfahrenstechnik beim Antrieb. Die spezifischen Impulse reichen bis in den hochenergetischen Bereich von 4000 Ns/kg und mehr. [1], [2]

Ein Ansatz diese günstigen Eigenschaften von festen Treibstoffen mit denen von flüssigen zu kombinieren sind Kryofesttreibstoffe (Cryo Solid Propellants „CSP"). Die Idee der CSP beruht auf folgendem Prinzip:

Alle Treibstoffe und ihre Komponenten werden durch entsprechende Kühlung ausschließlich im festen Aggregatzustand eingesetzt

Die Treibstoffe können gemischt eingefroren werden und bilden dann ein Monergol. Eine Untersuchung über monergole CSPs ist in [6], [11] beschrieben. Eine weitere Idee der Nutzung von CSPs besteht darin die Treibstoffe modular getrennt einzufrieren. Dadurch wird die Sicherheit erhöht, da sich die Komponenten getrennt voneinander im Triebwerk befinden und notfalls auch eine Isolation an den Grenzflächen möglich ist. Außerdem bestimmt die Anordnung der Treibstoffkomponenten neben der Treibstoffauswahl das Abbrandverhalten des Treibsatzes.

Eine wesentliche Besonderheit der hier untersuchten CSPs ist die Möglichkeit analog zu einem Hybridsystem Oxidator und Brennstoff getrennt vorzulegen [9], [2]. Dabei sind unterschiedliche geometrische Anordnungen denkbar. Im einfachsten Fall ist der modulare CSP-Treibsatz aus wechselweise angeordneten Oxidator/Brennstoff-Paaren angeordnet.

Um zu verhindern, dass nach der Anzündung geometriebedingte Wärme- und Stoffaustauschprozesse zu unkontrollierten Abbrandprozessen führen, soll ein heißer Gasstrom das Abbrandverhalten maßgeblich regulieren, in dem er die Verdampfung des ersten, stromaufwärts liegenden Moduls erzwingt. Im Idealfall kann bei tiefgekühlten CSP durch Abschalten des Stützgasstroms der Abbrand sogar unterbrochen werden.

Da diese Treibstoffanordnung bisher noch nicht realisiert wurde, sollten die im folgenden beschriebenen Versuche dazu dienen erste Erfahrungen mit dieser Anordnung zu erzielen und das Abbrandverhalten von solchen Sandwich-Strukturen zu untersuchen.

2 EXPERIMENTELLES

2.1 Konstruktion und Aufbau einer Testbrennkammer mit Stützbrenner

Die Testbrennkammer bestand aus einen Aluminiumgehäuse mit einem Innenraum von 100 mm Länge, 50 mm Breite und 13 mm Tiefe. An der Frontseite war über die gesamte Kammerfläche ein Sichtfenster aus Thermoglas angebracht. An der Oberseite befand sich seitlich versetzt der Brennereingang an der unteren Seite gegenüber die Auslassdüse. Seitlich der Gaskanals wurden die CSP-Module eingesetzt. Abbildung 1 skizziert den Aufbau der Testbrennkammer. Die Versuche wurde in Analogie zur Anordnung beim Raketenstart Top-Down durchgeführt. Ein Spiraleinsatz diente als Glühwendel und erlaubte die Brennerflamme in der unterkühlen Kammer zu stabilisieren. Brennergas war ein leicht unterstöchiometrisches Propan-Luft-Gemisch mit einem Volumenstrom von 12 l/min. Einige Versuche wurden mit einem geringeren Gasstrom von 6 l/min gefahren.

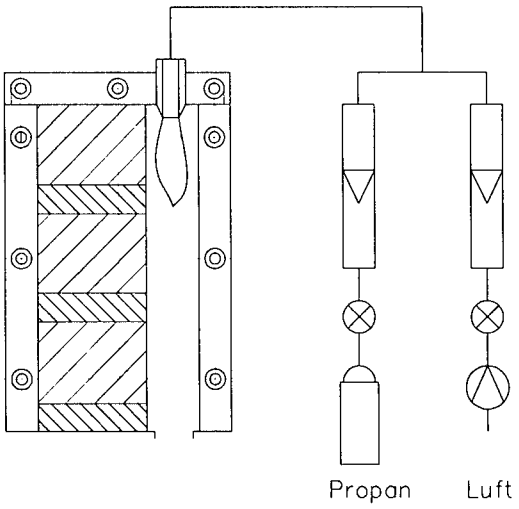


Abbildung 1 Aufbau der Testbrennkammer

2.2 Abbrandtests

Untersucht wurden die Brennstoffe HTPB, GAP, HDPE, LDPE und 2-Propanol. Als Oxidator diente H_2O_2(85%). Zur Untersuchung der Wärmeabgabe des Brenners über der Kammerlänge wurden Dummyversuche mit Eis durchgeführt. Die Eignung der Brennstoffe wurde in Versuchen mit jeweils 2 oder 3 Paaren von Oxidator- und Brennstoffblöcken untersucht. Bei allen Versuchen befand sich in Strömungsrichtung gesehen zuerst ein Oxidatorblock. Die Modulbreite war jeweils so gewählt, dass sich in der Brennkammer etwa ein stöchiometrisches Brennstoff/Oxidator-Gemisch befand. Bei den Versuchen hat sich HTPB als geeignetster Brennstoff erwiesen. Mit ihm wurden weitere Versuche bei verschiedenen Geometrien und Brennereinstellungen gefahren. Bei einigen Versuchen wurde der Brenner zeitweise ausgeschaltet.
Tabelle 1 gibt eine Übersicht über die durchgeführten Versuche und Parameter.

Das Propan wurde am Rotameter-Ventil auf die Zündungseinstellung aufgedreht, es musste sofort die Zündung der Propanflamme an der Glühwendel erfolgen. Die Luft am Rotameter-Ventil wurde aufgedreht und der Durchfluss beider Gase auf die jeweilige Versuchseinstellung gestellt. Die Glühwendel wurde mindestens 20 s aufgeheizt.
Die vorbereitete Brennkammer mit Treibsatz wurde so über die Wendel geschoben, dass die Glühende Wendel direkt neben dem ersten Oxidatormodul platziert war. Die Düse befand sich unten. Der Stützbrenner musste bei Bedarf erneut gezündet werden, die Flamme stabilisierte sich aber schnell an der Glühwendel. Am Stützbrenner-Kopf wurde eine Dichtung aus Knetmasse angebracht, um ein Ausströmen heißer Gase oben aus der Brennkammer zu verhindern.
Im weiteren Verlauf brannte der CSP infolge der Einwirkung der Brennerflamme ab.

Die Versuche wurden mit einer digitalen Videokamera beobachtet. Die Beobachtung erschwerte sich durch Eisbildung an der äußeren und Rußanlagerung an der inneren Fensterseite, so dass nicht aller Versuche vollständig ausgewertet werden konnten.
Untersucht wurde das Verhalten der CSP-Module, die Flammenform und das Ausbilden von Reaktionszentren.
Gemessen wurde die Regression der Modulblöcke durch Auswertung der Videofilme.

Brennstoff	Oxidator	Modulzahl	Brenner	Bemerkung
Brennertest				
Wasser	-	1	groß	
Wasser	-	1	klein	
Vorversuche				
HTPB	H_2O_2(85%)	3+3	groß	Plexiglasscheibe verkokt, erste CSP-Entzündung
HTPB	H_2O_2(85%)	2+2	groß +aus	Drahtgitter an Glasinnenseite, stabiler Abbrand über Brennstoffmodulen brennt auch ohne Stützbrenner
HTPB	H_2O_2(85%)	5+5	groß +aus	stabiler Abbrand an Brennstoffmodulen brennt auch ohne Stützbrenner
Brennstoffversuche				
2-Propanol	H_2O_2(85%)	2+2	groß	2-Propanol schmilzt und läuft aus
2-Propanol	H_2O_2(85%)	2+2	groß	dito
LDPE	H_2O_2(85%)	3+3	groß	Flamme sehr instabil, geringe Intensität LDPE fliest aus der Düse Regression: H_2O_2 >> LDPE
HDPE	H_2O_2(85%)	2+2	groß	Flamme stabil, geringe Intensität kein HDPE fliest aus der Düse Regression: H_2O_2 >> HDPE
HDPE	H_2O_2(85%)	3+3	groß	Flamme stabil, geringe Intensität kein HDPE fliest aus der Düse Regression: H_2O_2 >> HDPE
GAP	H_2O_2(85%)	2+2	groß	Flamme instabil; Verpuffungen, Intensität hoch Flamme meist hinter GAP-Stäben Regression: H_2O_2 >> GAP
Versuche zur Regressionsratenmessung				
HTPB	H_2O_2(85%)	2+2	groß	stabiler Abbrand über Brennstoffmodulen
HTPB	H_2O_2(85%)	3+3	groß	stabiler Abbrand an Brennstoffmodulen Regression: H_2O_2 >> HTPB
HTPB	H_2O_2(85%)	4+4	groß	stabiler Abbrand über gesamte CSP-Oberfläche, solange HTPB nicht weit übersteht Regression: H_2O_2 > HTPB
HTPB	H_2O_2(85%)	4+4	groß	stabiler Abbrand über gesamte CSP-Oberfläche, solange HTPB nicht weit übersteht Regression: H_2O_2 > HTPB
HTPB	H_2O_2(85%)	5+5	groß	sehr stabiler Abbrand über gesamte CSP-Oberfläche, solange HTPB nicht weit übersteht Regression: H_2O_2 > HTPB
HTPB	H_2O_2(85%)	4+4	groß +aus	Erlöschen oder Intensitätsabsenkung bei Ausschalten des Stützbrenners Regression: H_2O_2 > HTPB
HTPB	H_2O_2 (85%)	2+2	klein	mäßig stabiler Abbrand an Brennstoffmodulen Regression: H_2O_2 >> HTPB

Tabelle 1 Übersicht über die in der Testbrennkammer durchgeführten Versuche und Parameter

3 ERGEBNISSE

Brennertest

Die Auswertung der Eisabbrände ergab bei großer Brennereinstellung eine maximale Wärmeabgabe des Stützbrenners etwa 15 bis 20 mm hinter der Brennerdüse. Darüber sank die Wärmeabgabe etwa linear mit der Kammerlänge ab. Die Regressionsrate des Eises am Maximum war etwa 3 bis 5 mal höher als an der Ausgangsdüse der Kammer. Mit zunehmendem Abstand der Eisoberfläche von der Brennerflamme sank die Regressionsrate erheblich ab. Da bei diesen Versuchen an der Feststoffoberfläche keine Verbrennung mit Flammenbildung stattfand, konnte aufgrund der Eisbildung am Glasfenster die Regression nicht genau abgelesen werden. Eine Abschätzung des Energiestroms war auch deshalb nicht möglich, weil das geschmolzene Wasser teilweise nach unten abfloss und teilweise verdampfte. Für die hauptsächlich qualitativ verstandenen Versuche war eine genauere Abschätzung nicht notwendig. Bei den Versuchen mit Brennstoff und Oxidator wurde der erste Oxidatorblock im Bereich der maximalen Wärmeabgabe angebracht.

Bei kleiner Brennereinstellung verlief die Regression über der gesamten Brennkammerlänge etwa halb so schnell, wie bei der großen Einstellung. Das Maximum der Wärmeabgabe lag näher an der Brennerdüse.

Vorversuche

Die Vorversuche wurden mit HTPB durchgeführt. Etwa 30 bis 60 s nach dem Einschalten des blau brennenden Brenners, zeigten sich erste rotgelbe Flammen an der stromaufwärts gelegenen Grenzfläche zwischen H_2O_2 und HTPB. Daraus bildete sich einige Zeit lang eine homogene Verbrennungsfront entlang der CSP-Oberfläche. Die Regression von H_2O_2 war höher als die des Brennstoffes. Einzelne Tropfen an der Düse der Brennkammer deuten darauf hin, dass das H_2O_2 teilweise unverbraucht abfloss und verdampfte. Dadurch standen die Brennstoffblöcke aus der CSP-Oberfläche heraus. Die Flamme riss auf und es bildeten sich einzelne, unstetig aber z. T. sehr intensiv brennende Flammenzentren an der stromaufwärts gelegenen Grenzfläche zwischen H_2O_2 und HTPB.

Verschiedene Brennstoffe

Wie bei konventionellen Raketentreibstoffen sind nicht alle CSP-Komponenten in jeder Konfiguration und jedem Druckbereich einsetzbar. Die Versuchsreihe sollte Ansatzpunkte geben, welche Brennstoffe für schichtweise aufgebaute Modulkonfigurationen wie beispielsweise dem Diskstack geeignet sind.

Der im Normalzustand flüssige Brennstoff 2-Propanol, der sich in früheren Versuchen als brauchbarer Rod-In-Matrix-Brennstoff erwiesen hatte [4], lies sich in der hier untersuchten Konfiguration nur schwer anzünden. Er schmolz sehr schnell und floss aus der Brennkammer, bevor er mit dem noch festen H_2O_2 reagieren konnte. Dies führte dazu, dass die Oxidatorblöcke nicht mehr fixiert waren und ebenfalls nach unten fielen. Bei diesem Druck eignet sich 2-Propanol nicht für Diskstackanordnungen. Um dieses Problem zu umgehen, wurde beschlossen für die weiteren Versuche in der Linearbrennkammer nur noch feste Brennstoffe einzusetzen. Sie vereinfachten die Versuchsdurchführung erheblich, da der Oxidator in einem Schritt um den Brennstoff herum gefroren werden konnte.

Auch Low-Density-Polyethylen (LDPE) erwies sich in der vertikal angeordneten Linearbrennkammer als ungeeignet. Es ließ sich sehr schwer entzünden und brannte dann mit einer wenig intensiven Flamme. Die Regression des LDPE war wesentlich langsamer, als die von H_2O_2. D.h. Unter den untersuchten Bedingungen reagiert LDPE langsamer als H_2O_2 schmilzt und verdampft. Nach einiger Zeit schmolz das LDPE und floss aus der unteren Brennkammerdüse. Dabei bestand die Gefahr einer Düsenverstopfung.

High-Density-Polyethylen (HDPE) eignet sich besser für den Einsatz in der Brennkammer. Es zeigte keinen Schmelzfluss und brannte deutlich stabiler als LDPE. Eine relativ schwach brennende Flamme stabilisierte sich dabei an der Oberseite der PE-Stäbe. Sie reagierte hier mit der über die Stäbe fließenden H_2O_2-Schmelze. Allerdings war die Regression des H_2O_2 erheblich höher als der Umsatz der HDPE-Stäbe. Doch scheint HDPE für den Einsatz in einer Druckbrennkammer durchaus geeignet. Da man hier bessere Wärmeübergänge und damit eine höhere Pyrolysenrate des Kunststoffs erwarten kann.

GAP ist ein energetischer Kunststoff, der gerne als Binder von Festtreibstoffen eingesetzt wird. Es ist über Azidogruppen vernetzt, die beim Abbrand unter Freisetzung von Energie- und elementarem Stickstoff aufbrechen. Diese Stickstoffproduktion ist zumindest bei niedrigen Drücken für den Abbrand in der untersuchten Linearbrennkammer ungünstig. Bei den Versuchen brannte die intensive Flamme am GAP sehr unregelmäßig und es kam sogar zu kleineren Verpuffungen an den Enden der Brennstoffstäbe. Dieses Verhalten führt auch bei

Festtreibstoffen zu einem unregelmäßigen Niederdruckabbrand. Bei einem Druck über 1 MPa verschwindet es gewöhnlich. GAP könnte für eine CSP-Druckbrennkammer durchaus geeignet sein.

Hydroxiterminiertes Polybutatien (HTPB), das ebenfalls oft als Festtreibstoffbinder eingesetzt wird zeigte das geeignetste Abbrandverhalten in der atmosphärischen Linearbrennkammer. Es entzündet sich relativ bald nach dem Anzünden des Stützbrenners. Dabei bildete sich, zumindest solange die Längenunterschiede zwischen den Brennstoff- und Oxidatorblöcken nur wenige Millimeter betrugen, eine schichtweise aufgebaute Flamme homogen über die gesamte Brennkammerlänge, parallel zur CSP-Oberfläche. Trotzdem war auch hier die Regression des Oxidators wesentlich höher als die des HTPB.
Nach dem Anzünden des CSP verdoppelte sich die Regressionsrate des H_2O_2 in etwa. Die Regression wurde also wesentlich vom CSP-Abbrand bestimmt und nicht nur vom Stützbrenner. Abbildung 2 zeigt den Verlauf des Abbrandes eines CSP aus HTPB und H_2O_2 mit je 3 Modulen. Es sind deutlich die Reaktionszonen zu erkennen. Eine starke Rußbildung behinderte eine genaue Lokalisation der CSP-Oberfläche und verhinderte dadurch eine genauere Analyse.



Abbildung 2 Verlauf des Abbrandes eines 2*3-HTPB/H_2O_2-CSP.

Versuche zur Abbrandunterbrechung

Bei einigen Versuchen wurde der Stützbrenner nach einer Anzündzeit von 60 s abgeschaltet. Dabei verringerte sich die Verbrennungsintensität immer sehr stark. Oft erlösch der Abbrand vollständig. Wenn der Brenner ausgeschalten war verringerte sich die Regression der H_2O_2-Module erheblich. Mit dem Stützbrenner kann man also den Abbrand beeinflussen. Unter

welchen Bedingungen der Abbrand komplett abbricht konnte mit dem einfachen Versuchsaufbau nicht festgestellt werden.

Versuche mit unterschiedlicher Brennerleistung

Bei großer Brennerstufe zündete der CSP nach ca. 45 s an. Dabei war die Regression des H_2O_2 noch nicht weit fortgeschritten und es bildete sich noch eine geschlossene Flammenfront parallel zur CSP-Oberfläche aus. Dagegen zündete bei kleiner Brennerstufe der CSP erst nach 150 s, als die HTPB-Brennstoffstäbe schon deutlich hervorstanden. Hier bildeten sich nur kleine stark flackernde Flammen direkt hinter den Brennstoffmodulen aus. Bei kleiner Brennerstufe war die Regression aller H_2O_2-Module wesentlich geringer als bei großer Brennerstufe. Abbildung 3 zeigt die über die gesamte Versuchsdauer gemittelten Regressionszeiten jeweils zweier H_2O_2-Module. Die Regression des oberen Moduls war jeweils höher als die des unteren (Zählung beginnt beim ersten Modul nahe der Brennerdüse). Bei kleiner Brennerstufe hatten die schwachen Flammen nur einen unwesentlichen Einfluss auf den Verlauf der Regressions-Zeit-Kurve. Der Abbrand war maßgeblich vom Stützbrenner bestimmt.

Der Stützgasstrom bestimmt also wesentlich die Anzündzeit und das Abbrandverhalten in der untersuchten Linearbrennkammer.

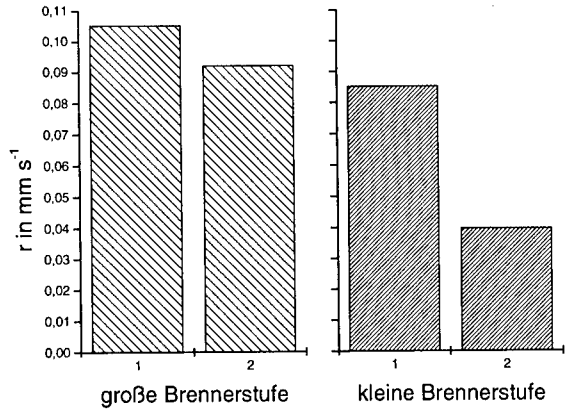


Abbildung 3 Über die gesamte Versuchsdauer gemittelten Regressionszeiten jeweils zweier H_2O_2-Module bei großer und kleiner Brennereinstellung

Versuche zur Regression bei unterschiedlicher Modulgeometrie

Die Anzahl der Module pro Brennerlänge übt einen großen Einfluss auf das Anzünd- und Abbrandverhalten aus. Je mehr Moduleinheiten im Brenner waren, desto kürzer waren die Anzündzeiten (vgl. Tabelle 2).

Modulzahl	2*2	2*3	2*4	2*4	2*5
Anzündzeit	45-50 s	25-30 s	15-20 s	10-15 s	5-10 s

Tabelle 2 Zeit bis zur ersten Flammenbildung über dem CSP-Treibstoff nach Anzünden der Stützbrennerflamme. Treibstoffkombination: H_2O_2(85%)/HTPB

Kleine Moduleinheiten ergeben auch eine gleichmäßigere Flammenfront über der CSP-Oberfläche. Abbildung 4 zeigt den Vergleich des Abbrands bei Variation der Modulzahl.



Abbildung 4 Vergleich der CSP-Abbrände unterschiedlicher Modulzahlen jeweils zu Beginn des CSP-Abbrands (oben) und im weiteren Verlauf (unten). Von links nach rechts: 2*2-, 2*3-, 2*4- und 2*5-Module. Jeweils bei großer Brennereinstellung.

Die Unterschiede zwischen der Regression von H_2O_2 und HTPB waren allerdings bei allen Versuchen zu beobachten. Sie führten bei einem Längenunterschied zwischen H_2O_2 und HTPB von etwa 10 mm zum Abreisen der Flammenfront und es bildeten sich Reaktionszentren nahe der Brennstoffstäbe aus.

Abbildung 5 zeigt die über die gesamte Versuchszeit gemittelten Regressionsraten der einzelnen H_2O_2-Module. Sie liegen alle in einem Bereich von etwa 0.1 bis 0.2 mm s^{-1}, zeigen aber keine eindeutigen Tendenzen bzgl. Modulzahl und Modulposition.

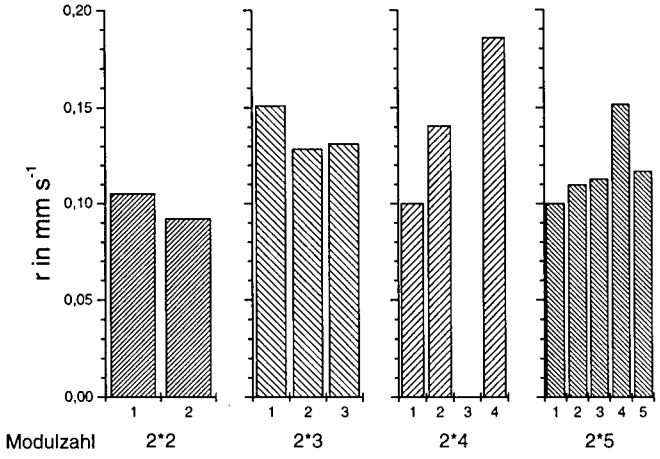


Abbildung 5 Über die gesamte Versuchszeit gemittelten Regressionsraten der einzelnen H_2O_2-Module bei verschiedenen Modulzahlen.

4 DISKUSSION

Die unterschiedlichen Abbrandraten von den Oxidator und Brennstoffmodulen ist eine direkte Folge der Stoffeigenschaften der Treibstoffkomponenten. Durch Lösung der Wärmeleitungsgleichung im Feststoff (vgl. z. B. [7]) ergibt sich für die stationäre Regressionate r:

$$r = \frac{Q}{\rho\left(c_{ps}\left(T_m - T_0\right) + L_m + c_{pl}\left(T_{l->g} - T_m\right) + L_{l->g}\right)} \qquad \text{Gl. 1}$$

(ρ Dichte, c_p spezifische Wärmekapazität, T Temperatur, L Phasenumwandlungswärme

Indizes: s fest, l flüssig, g gasförmig, m schmelzen, l→g beim vergasen, pyrolysieren bzw. sieden)

Nimmt man vereinfachender Weise an, daß der vom Stützbrenner übertragene Wärmestrom Q über jedem Modul gleich sei, was zumindest für nebeneinanderliegende Modulblöcke gegeben ist, verhalten sich nach Gl. 1 die Regressionsraten r_i zweier unterschiedlicher Materialien wie

$$\frac{r_1}{r_2} = \frac{\rho_2\left(c_{ps2}\left(T_{m2} - T_0\right) + L_{m2} + c_{pl2}\left(T_{l->g,2} - T_{m2}\right) + L_{l->g,2}\right)}{\rho_1\left(c_{ps1}\left(T_{m1} - T_0\right) + L_{m1} + c_{pl1}\left(T_{l->g,1} - T_{m1}\right) + L_{l->g,1}\right)} \qquad \text{Gl. 2}$$

Gl. 2 gibt auch eine Hilfestellung für die Auswahl von geeigneten Stoffpaaren.

5 LITERATUR

[1] Lo R., Eisenreich N., „Modulare und kryogene Festtreibsätze- eine neue Klasse chemischer Raketenantriebe", Deutscher Luft- und Raumfahrtkongress, Bremen, Oktober 1998

[2] Lo R. E., „A Novel Kind of Solid Rocket Propellant", Aerospace Science and Technology, Elsevier, 1998.

[3] Eisenreich N., Lo R. E., Adirim H., Kelzenberg S., Weiser V.: „Kryofeststoff-triebwerkstechnologie, Phase II: Experimentelle Machbarkeitsstudie und Vorbereitung der nächsten Phase", Abschlußbericht 15.4.1999

[4] Lo R., Adirim H., Voronetzky A., Weiser V., Eisenreich N., Kelzenberg S., Poller S., „Weiterführende und ergänzende Untersuchungen zur Kryofeststoff Triebwerks-technologie"; BMBF-Bericht zu Projekt PA-FA/RD-JR 50 TT 9812; März 2000

[5] Lo R., Adirim H., Poller S., Eisenreich N., Weiser V., Kelzenberg St., „Advances in cryogenic solid rocket propulsion", 31st International Annual Conference of ICT, 2000, Karlsruhe, Paper 15

[6] Weiser V., Poller S., Kelzenberg St., Eisenreich N., Lo R., Adirim H., „Abbrandverhalten von Kryofesttreibstoffen"; 31th International Annual Conference of ICT, June 27-30, 2000, Karlsruhe, pp. 145-(1-14)

[7] Eckl W., Kelzenberg S., Weiser V., Eisenreich N., „Einfache Modelle der Anzündung von Festtreibstoffen"; 29th International Annual Conference of ICT, 1998, Energetic Materials; Karlsruhe, pp. 154-1 – 154-2

[8] Lo, R.; Adirim, H.; Weiser, V.; Laßmann, J.; „Developing Cryogenic Solid Rocket Motor Technology for Space Propulsion"; 2nd Conference on Academic and Industrial Cooperation in Space Research, 15-17 November 2000, Graz, Austria

[9] Weiser, V.; Kelzenberg, S.; Poller, S.; Eisenreich, N.; Lo, R.; Adirim H.; „Theoretical and Experimental investigations on combustion of cryogenic solid propellants"; 51st international Astronautical Congress; 2-6 Oct 2000/Rio de Janeiro, Brazil; Paper IAF-00-s.3.05

[10] Kelzenberg, St.; Weiser, V.; Poller, S.; Eisenreich, N.; Lo, R.; Adirim, H.; „Theoretische und Experimentelle Untersuchungen zur Technologie der Kryofeststoffantriebe"; Deutscher Luft- und Raumfahrtkongress 2000; Leipzig; DGLR-JT2000-34

[11] Weiser V., Besnard C., Kelzenberg S., Poller S.; „Modellierung und Experiment von gefrorenen H_2O_2/Methanol-Mischungen"; 32th International Annual Conference of ICT, July 3-6, 2001, Karlsruhe, pp. 154-(1-6)

MODELLIERUNG UND EXPERIMENT VON GEFRORENEN H_2O_2/METHANOL-MISCHUNGEN

V. Weiser, C. Besnard, S. Kelzenberg, S. Poller
Fraunhofer-Institut Chemische Technologie (ICT)
Joseph-von-Fraunhoferstr. 7
D-76327 Pfinztal (Berghausen), Germany

Abstract

The complete simulation of solid propellant burning requires the knowledge of all reaction steps and physical properties of the energetic material. This is only possible for some simple fluid species. Experiments have been realised with mixtures of methanol and H_2O_2. To simulate a solid phase behaviour the mixtures had been frozen. The reaction mechanism of this mixtures was modelled using isothermal calculations with Chemkin and simplified to a degradations reaction of 1. order. With this one step reaction and using a 1D transient burning model satisfying agreement of pressure depending burning rates and temperatures could be found.

Zusammenfassung

Die Simulation eines Festtreibstoffabbrands setzt voraus, daß alle reaktionskinetischen und stoffspezifischen Daten der Ausgangskomponenten bekannte sind. Dies ist nur für einige einfache Flüssigkeiten oder Gase möglich. So wurden Experimente mit gefrorenen Methanol/H_2O_2-Mischungen durchgeführt. In diesem Zustand verhält sich die Mischung physikalisch wie ein Festtreibstoff. Der elementare Reaktionsmechanismus ist bekannt. Mit Hilfe von isothermen Chemkin-Rechnungen konnte eine einfacher Zersetzungsreaktion 1. Ordnung ermittelt werden. Damit gelang die Abbrandsimulation des Feststoffes mit einem eindimensionalen Berechnungsmodell. Es liefert eine befriedigende Übereinstimmung mit den gemessenen Abbrandraten.

Einleitung

Die Simulation des Abbrandes von festen Treibstoffen wird durch die Komplexität der Vorgänge erschwert. Neben der Reaktionchemie müssen auch Wärme- und Stoffübertragungsvorgänge in der festen, flüssigen und gasförmigen Phase, sowie die Strömungsmechanik in der Gasphase berücksichtigt werden. Eine besondere Herausforderung ist die Modellierung der Kopplung von Flamme und der Vergasung des kondensierten Materials. Bei vielen festen Energetischen Materialien ist im besonderen keine detaillierte Reaktionschemie bekannt. Besser ist dies bei niedermolekularen flüssigen oder gasförmigen Substanzen wie Methan, Methanol, N_2O_4 oder H_2O_2 erfüllt. Hier liegen detaillierte Mechanismen von Elementarreaktionen inkl. derer Arrheniusparameter vor [1,2]. Flüssige und gasförmige Systeme zeigen wiederum ein anderes Phasenübergangsverhalten als Festtreibstoffe. Will man ein System mit bekannter Reaktionskinetik als Festtreibstoff modellieren und gleichzeitig experimentell untersuchen, kann man auf Kryofesttreibstoffe (Cryogenic Solid Propellants, CSP) zurückgreifen.

Diese neue Technologie wird derzeit als zukunftsträchtiges Raketenantriebssystem höherer Leistung entwickelt [3,4]. Sie beruht auf der Idee hochenergetische Flüssigtreibstoffe durch gefrieren in Festtreibstoffe umzuwandeln. Der selbstregulierte Abbrand von Festtreibstoffen erfordert keine schwere und aufwendige Fördertechnik, wie konventionelle Flüssigtriebwerke. Dadurch könnten Raketenbuster in der Größe eines Adriane 5 Triebwerks konstruiert werden, die bei gleichem Gewicht bis zu 40% mehr Nutzlast ins All befördern [4,5].
Thermodynamische Rechnungen zeigen, daß durch das Einfrieren auch auf sehr tiefe Temperaturen nur wenige Prozent der Leistungsfähigkeit der Ausgangssubstanzen verloren geht.
Aus der Sicht des Modellierers verhält sich ein CSP wie ein gewöhnlicher Festtreibstoff bekannter Reaktionskinetik mit allen für FTS-Abbrände charakteristischen Phasenübergängen wie Schmelzen, Pyrolysieren und Verdampfen.

Experimentelles

Untersucht wurden Mischungen von Methanol mit 85%-igen Wasserstoffperoxid. Diese Komponenten sind flüssig mischbar. Die Mischung zeigt eine für den Experimentator ausreichende Stabilität und Anzündbarkeit. Die Komponenten sind Basischemikalien deren Reaktionschemie und Stoffeigenschaften weitreichend untersucht wurden [1,2]. Die Komponenten wurden im stöchiometrischen Verhältnis von 0.9, 1 und 1.1 gemischt und in kleine Reagenzgläser (Länge: 70 mm; Durchmesser: 5 mm) eingefüllt. Durch langsames Eintauchen in flüssigen Stickstoff wurden sie zonenweise gefroren. Es ergaben sich optisch homogene Proben mit reproduzierbaren Verbrennungseigenschaften.
Sie wurden in einer Optischen Bombe auf Abbrandgeschwindigkeit, Flammengeometrie und Temperatur untersucht. Dazu wurde ein Digitalcamcorder und ein schnelles NIR-Spektrometer eingesetzt. Der Versuchsaufbau, die Meßtechik und die Ergebnissse sind in [6] detailliert beschreiben.

Theorie

Reaktionskinetik in der Gasphase

Die Entwicklung der Rechenleistung ermöglicht es heute in der Gasphase kompliziertere kinetische Mechanismen mit mehreren hundert Reaktionen zu berechnen [1,2]. Z. B. erlaubt der Code CHEMKIN II die isobare, isochore, adiabate oder isotherme Berechnung des Temperatur-Zeit- und Konzentrations-Zeit-Verlaufs von beliebig vielen Elementarreaktionen. Derzeit stehen umfangreiche Algorithmen für Reaktionen mit Stoffen der Elemente C, H, N, O, Cl zur Verfügung. Dabei werden alle wichtigen gasförmigen Verbindungen in Flammen abgedeckt. Das Programm ist mit einer thermodynamischen Datenbank verknüpft, die gegebenenfalls durch Daten der ICT-Thermodynamik-Datenbank ergänzt werden kann.
Im untersuchten Fall wurden isothermen Rechnungen für stöchiometrische Mischungen von H_2O_2 (85%) und Methanol bei Temperaturen zwischen 800 und 4000 K durchgeführt. Dabei wurde der GRI-Mechanismus mit 279 Elementarreaktionen eingesetzt [1]. Abbildung 1 zeigt eine Beispiel mit dem zeitlichen Verlauf der wichtigsten Reaktionskomponenten. Man sieht wie sich sehr schnell, aber etwa zeitgleich die Ausgangkomponenten fast vollständig zersetzen. Dabei werden hauptsächlich H_2, O_2,

CO und OH bebildet, die im weiteren zu CO_2 und H_2O aufoxidiert werden. Die Bildung des zweiten Endprodukts Wasser beginnt schon mit der Zersetzung des H_2O_2.

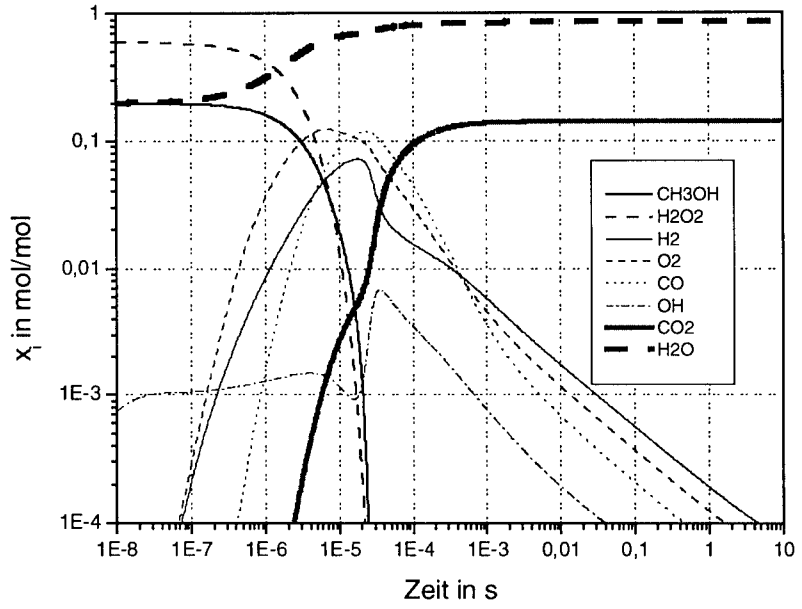


Abbildung 1 Verlauf der wichtigsten Reaktionsprodukte bei der Zersetzung einer stöchiometrischen Mischung von H_2O_2 (85%) und Methanol. Isotherm berechnet mit CHEMKIN II.

Abbrand von festen und flüssigen Treibstoffen

Mit finiten CDF-Rechnungen gelingt es auch komplexe Zusammenhänge von Fluiddynamik, Wärme-/Stofftransport, Phasenumwandlung und Reaktion beim Abbrand von Festtreibstoffen zu erfassen. Das ICT arbeitet an dem Modell CTEM (Combustion Transients of Energetic Materials). Es dient zur eindimensionalen mathematischen Simulation der instationären Verbrennung energetischer Materialien (EM). Dabei können die Wärmeströme und Druckbedingungen zeitabhängig variiert werden. Das ursprünglich feste EM schmilzt und verdampft an der Oberfläche. Der Strahlungswärmestrom wird in der Tiefe des EM absorbiert. Die Eindringtiefe variiert mit den optischen Eigenschaften des EM. Die chemische Umwandlung wird sowohl in der kondensierten als auch der Gasphase mit insgesamt 4 Reaktionsschritten n-ter Ordnung berücksichtigt. An der Abbrandoberfläche wird der Phasenübergang nach dem Verdampfungsgesetzt von Clausius-Clapeyron formuliert. Eingabeparameter sind Stoffwerte wie Wärmeleitfähigkeit, Wärmekapazität, Dichte, Molmasse, Verdampfungswärme, Schmelzwärme, Schmelztemperatur, Absorptionskoeffizienten für Strahlung; Reaktionsparameter wie Aktivierungsenergie, Präexponentialfaktor, Reaktionswärme und Umgebungsbedingungen bzw. Startwerte wie Anfangstemperatur, Druckvariation, Zusammensetzung, externer Wärmefluß. Als Ergebnisse erhält man in zeitabhängiger Form:

- Regressionsgeschwindigkeit
- Oberflächentemperatur

- Wärmeflüsse
- Dicke der Schmelzschicht
- Temperaturverteilung und Konzentrationsverläufe in der festen, flüssigen und gasförmigen Phase

Vereinfachter Reaktionsmechanismus

CTEM erlaubt nur Berechnungen mit einer einfachen Reaktionschemie, die aus den Chemkin-Rechnungen gewonnen werden sollte.
Der Abbrand eines kondensierten Treibstoffes wird hauptsächlich durch die aus der Flammenzone rückgeführten Reaktionswärme geprägt. Dabei liefern die oberflächennahen Reaktionen den wesentlichen Wärmebeitrag. Im untersuchten Fall ist das die Zersetzung der verdampften Ausgangsprodukte. Wie Abbildung 1 zeigt erfolgt sie praktisch zeitgleich. Die Konzentrationen von H_2O_2 und Methanol wurden addiert und aus den Halbwertszeiten der gemeinsamen Zersetzung die jeweilige Reaktionsgeschwindigkeit berechnet. Dabei wurde eine einfache Reaktions 1. Ordnung angenommen. Abbildung 2 zeigt den Arrheniusplot bei unterschiedlichen Temperaturen und die dabei gefundenen Reaktionsparameter. Im interessanten Bereich zwischen 800 und 2500 K ergibt sich eine gute Übereinstimmung.
Die bei der Reaktion freigesetzten Wärmemenge wurde mit 7100 kJ kg^{-1} so gewählt, daß sich in der Verbrennungszone die in [6] gemessene Verbrennungstemperatur von 1700 bis 2000 K einstellte.

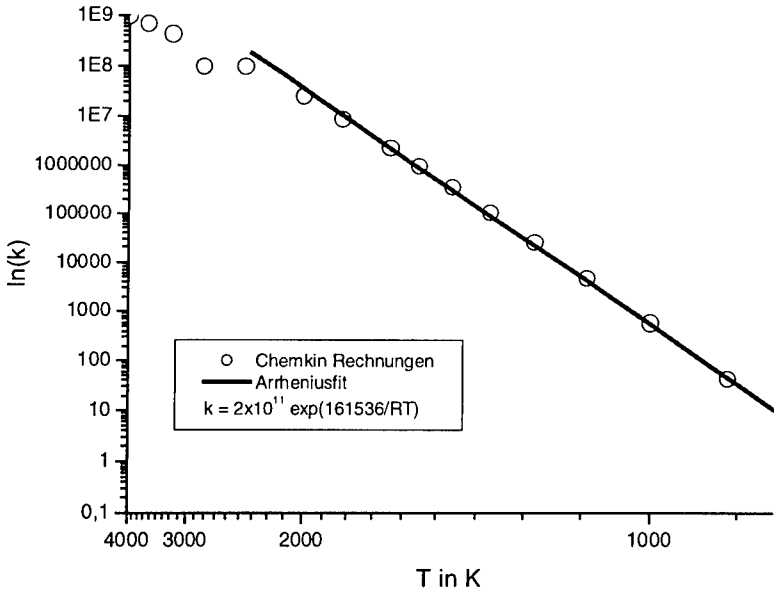


Abbildung 2 Zersetzung von H_2O_2 (85%) /Methanol als 1-stufigen Reaktion 1. Ordnung. Arrheniusplot mit den gefundenen Reaktionsparameter.

Ergebnisse

Mit diesen Parametern und den in Tabelle 1 aufgeführten Stoffeigenschaften wurden CTEM-Rechnungen mit verschiedene Anfangstemperaturen zwischen 150 bis 230 K durchgeführt. Dieser Temperaturbereich entsprach dem Intervall bei dem die o. g. Experimente durchgeführt wurden. Untersucht und berechnet wurde Abbrandraten im Druckbereich zwischen 1 und 20 bar. Die experimentellen Werte (Symbole) und die berechneten Abbrandraten sind in Abbildung 3 zusammengefaßt. Man findet eine zufriedenstellende Übereinstimmung. Dabei muß man bedenken, daß bei der Berechnung starke Vereinfachungen durchgeführt wurden und im untersuchten Temperaturbereich weder die Stoffeigenschaften der Ausgangskomponenten noch deren Mischung genau bekannt sind.

Tabelle 1 Stoffeigenschaften

	Methanol	H_2O_2 (85%)
spez. Wärmekapazität	180,4 J $mol^{-1}K^{-1}$	87 J $mol^{-1}K^{-1}$
Verdampfungswärme	35.2 kJ mol^{-1}	44.3 kJ mol^{-1}
Schmelzwärme	3.2 kJ mol^{-1}	11.4 kJ mol^{-1}
Dichte (flüssig)	0,788 g cm^{-3}	1.38 g cm^{-3}
Siedepunkt	337.7 K	420 K
Schmelzpunkt	175 K	253,6 K
Molmasse	32.0 g mol^{-1}	31.6 g mol^{-1}

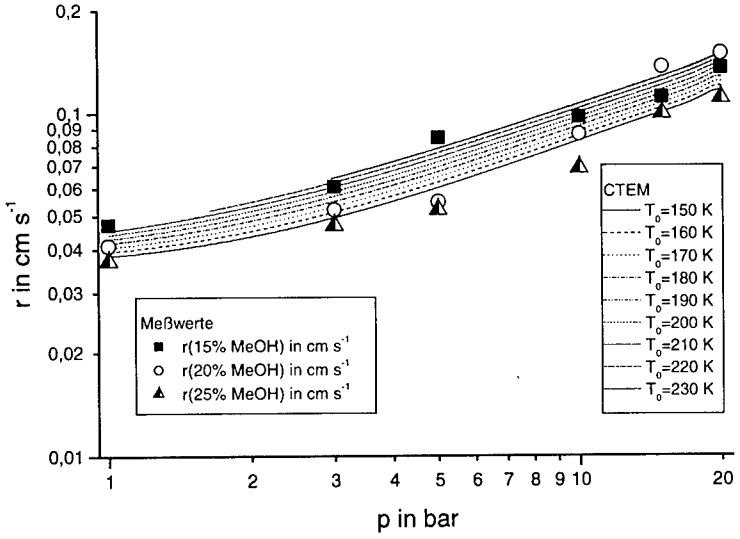


Abbildung 3 Abbrandrate unter Druck von gefrorenen H2O2 (85%)/Methanol-Mischungen. Gemessen in einer Optischen Bombe (Symbole) und berechnet mit CTEM (Linien).

Literatur

[1] M. Frenklach, H. Wang, C.T. Bowman, R.K. Hanson, G.P. Smith, D.M. Golden, W.C. Gardiner and V. Lissianski An Optimized Kinetics Model for Natural Gas Combustion, 25th Int. Symp. Comb., Irvine, California, Work-In-Progress Poster Session 3, Number 26., 1994

[2] Miller, J.A.; Bowman, C.T.; Mechanism and modeling of nitrogen chemistry in combustion; Prog. Energy. Combust. Sci. 1989, Vol. 15. pp. 287-338

[3] Lo, R. E.; „A Novel Kind of Solid Rocket Propellant", Aerospace Science and Technology, Elsevier, 1998.

[4] Lo, R.; Adirim, H; Poller, S.; Eisenreich, N.; Weiser; V.; Kelzenberg. St; Advances in cryogenic solid rocket propulsion; 31st International Annual Conference of ICT, 2000, Karlsruhe, Paper 15

[5] Weiser, V.; Kelzenberg, S.; Poller, S.; Eisenreich, N.; Lo, R.; Adirim H.; Theoretical and Experimental investigations on combustion of cryogenic solid propellants; 51st intenational Astronautical Congress; 2-6 Oct 2000/Rio de Janeiro, Brazil; Paper IAF-00-s.3.05

[6] Eckl, W.; Weiser, V.; Besnard, C.; Bestimmung der Temperatur von H_2O_2/Brennstoff-Flammen aus den Emittierten NIR-Wasserbanden; 31th International Annual Conference of ICT, June 27-30, 2000, Karlsruhe, pp. 137-(1-10)

Modellierung des Einflusses thermischer Stoffeigenschaften auf das Abbrandverhalten fester Treibstoffe

V. Weiser, S. Kelzenberg, N. Eisenreich, C. Moya
Fraunhofer-Institut für Chemische Technologie (ICT), Pfinztal, Germany
vw@ict.fhg.de

Abstract

MODELLING OF THE INFLUENCE OF THERMAL PROPERTIES ON THE BURNING BEHAVIOUR OF SOLID PROPELLANTS
The burning behaviour of a solid propellant is strongly controlled by all fluxes of heat, mass and impulse via a complex feedback mechanism. The characteristic parameter is given with the surface temperature. This paper investigates the influence of the properties of the solid material: density, heat capacity, latent heat of evaporation and heat conductivity to the burning rate by calculations with 3 different models. Under steady state conditions heat conductivity exert no practical influence to the burning behaviour. The other properties show an inverse influence. The burning simulation of an energetic material requires an exact knowledge of phase changing energies and a realistic model to describe the heat transfer.

Zusammenfassung

Beim Abbrand eines energetischen Materials ist die Abbrandrate mit der Flammenzone über die Wärme-, Stoff- und Impulsströme verknüpft. Dabei spielt die sich einstellende Oberflächentemperatur eine entscheidende Rolle. Untersucht wird der Einfluß der Stoffparameter des Festtreibstoffs Dichte, Wärmekapazität, Verdampfungswärme und Wärmeleitfähigkeit auf das Abbrandverhalten. Untersucht werden 3 verschiedene theoretische Modelle. Im stationären Verbrennungszustand wirkt sich die Wärmeleitfähigkeit nicht auf die Rechnungen aus. Die anderen Stoffeigenschaften weisen einen reziproken Einfluß auf die Abbrandrate aus. Bei Modellrechnungen ist es besonders wichtig die Umwandlungswärme und Temperatur an der Oberfläche zu kennen. Dies setzt ein entsprechend gutes Modell für die Wärmebilanz voraus.

Einleitung

Beim Abbrand eines Festtreibstoffes vergast energetisches Material unter Einwirkung der aus der Verbrennungszone rückgeführten Wärme. Stabilisiert sich der Abbrand verbrennt der Treibstoff mit einer konstanten Abbrandrate. Das entstandene Gleichgewicht ist nur noch von technischen Randparametern wie dem Brennkammerdruck oder der Treibstofftemperatur abhängig. Dieses Gleichgewicht ist wesentlich geprägt vom Temperaturprofil in der Verbrennungszone senkrecht zur Treibstoffoberfläche, das den Wärmerücktransport bestimmt. Es ist durch die Reaktionszeiten in der Gasphase, der freigesetzten Wärme und der Geschwindigkeit der abströmenden Gase bestimmt. Die Vergasungsrate ist zusätzlich von der Oberflächentemperatur abhängig, die neben der auftreffenden Flammenwärme von physikalisch-thermischen Eigenschaften der kondensierten Phase wie Wärmeleitfähigkeit, Wärmekapazitäten und Phasenumwandlungen beeinflußt wird [1-3]. Die Einwirkung dieser Stoffeigenschaften auf das

Abbrandverhalten ist äußerst komplex. Doch wäre ein tieferes Verständnis der Zusammenhänge eine große Hilfe bei der Entwicklung und Optimierung neuer Festtreibstoffe. Die Untersuchung ist experimentell nur schwer oder gar nicht zu realisieren, da es normalerweise nicht gelingt einzelne Stoffeigenschaften zu variieren ohne gleichzeitig andere mit zu beeinflussen. So ist man auf Modellrechnungen angewiesen, bei denen leicht einzelne Parameter geändert werden können.
Oft sind die benötigten Stoffeigenschaften nur vage bekannt, so gibt eine solche Untersuchung mit Modellrechnungen wichtige Hinweise welche Stoffparameter genau bekannt sein sollten und bei welchen ungefähre Schätzwerte akzeptabel sind.

Modelle

Das einfachste Modell, das den Einfluß der Stoffeigenschaften des festen energetischen Materials beschreibt läßt sich direkt aus der Wärmleitungsgleichung im Feststoff unter Annahme einer konstanten, externen Wärmequelle herleiten [4,5].

$$\rho c_p \frac{\partial T}{\partial t} - \lambda \Delta T = Q[\bar{x},t] \qquad \text{Gl. (1)}$$

(ρ Dichte, c_p spezifische Wärmekapazität, T Temperatur, t Zeit, λ Wärmeleitfähigkeit, x Ortskoordinate)
Mit der Transformation $\bar{x} = x - rt$ wird aus:

$$\frac{\partial T[\bar{x},t]}{\partial t} = \frac{\partial T[x,t]}{\partial t} - r\frac{\partial T[x,t]}{\partial x} \qquad \text{Gl. (2)}$$

Für den stationären Fall lässt sich daraus die bekannte Formel für die Abbrandrate r ableiten:

$$r = \frac{\dot{Q}}{\rho\left(c_p\left(T_{i\to g} - T_0\right) + L\right)} \qquad \text{Gl. (3)}$$

Dabei beschreibt $T_{i\to g}$ die Oberflächentemperatur, die sich aufgrund des Wärmeeintrags von der Flammenzone Q bei der Vergasung einstellt. L ist die bei der Vergasung auftretende Umwandlungswärme.
Bei diesem einfachen Modell ist die stationäre Abbrandrate von der Wärmeleitfähigkeit λ unabhängig.
Dieses Modell berücksichtigt nicht die Kopplung zwischen vergastem Treibstoff und Wärmerückführung aus der Gasphase. Dazu sind deutlich aufwendigere Modelle [6,7] notwendig. Für die hier beschriebenen Untersuchungen wurde das Modell CTEM (Combustion Transients of Energetic Materials) [5,8,9] eingesetzt, das in Zusammenarbeit zwischen dem ICT und Wissenschaftler der Russischen Akademie der Wissenschaften in Novosibirsk (Sibirien) entwickelt wird. Es dient zur mathematischen Simulation der instationären Verbrennung energetischer Materialien (EM). Dabei können die Wärmeströme und Druckbedingungen zeitabhängig variiert werden. Das ursprünglich feste EM schmilzt und verdampft an der Oberfläche. Der Strahlungswärmestrom wird in der Tiefe des EM absorbiert. Die chemische Umwandlung findet in der kondensierten und der gasförmigen Phase statt. An der Abbrandoberfläche wird der Phasenübergang nach dem Verdampfungsgesetz von Clausius-Clapeyron formuliert. Diese Beschreibung gilt für den Fall der Verbrennung sublimierender oder schmelzender und verdampfender EM. Eingabeparameter sind Stoffwerte wie Wärmeleitfähigkeit, Wärmekapazität, Dichte, Molmassen, Verdampfungswärme, Schmelzwärme, Schmelztemperatur, Absorptionskoeffizienten für Strahlung; Reaktionsparameter wie Aktivierungsenergie, Präexponentialfaktor, Reaktionswärme und Umgebungs-

bedingungen bzw. Startwerte wie Anfangstemperatur, Druck, Zusammensetzung, externer Wärmefluß. Als Ergebnisse erhält man in zeitabhängiger Form:

- Regressionsgeschwindigkeit
- Oberflächentemperatur
- Wärmeflüsse
- Dicke der Schmelzschicht

Darüberhinaus werden Temperaturverteilung und Konzentrationsverläufe in der festen, flüssigen und gasförmigen Phase ortsaufgelöst eindimensional berechnet.

Rechnungen

Im folgenden werden Rechnungen an einem System beschrieben, dessen chemische und physikalische Stoffeigenschaften HMX nachempfunden sind (Tabelle 1). Ausgehend von diesem Referenzzustand wurden stufenweise einzelne Stoffeigenschaften um jeweils etwa eine Zehnerpotenz nach oben und unten variiert und die Abbrandrate berechnet.
In einer ersten Reihe wurde die auf die Treibstoffoberfläche transportierte Wärme fest definiert. Ihr Betrag wurde mit 500 cal $cm^{-2}s^{-1}$ so gewählt, daß sich im Referenzzustand die experimentell bestimmte Abbrandrate bei 70 bar einstellte.
In einer zweiten Reihe wurde eine durch Arrheniusparameter kontrollierte Gasphasenreaktion vom Typ A $\rightarrow$ B $\rightarrow$ C erlaubt. Die Reaktionsparameter wurden so gewählt, daß sich im Referenzzustand das gleiche Druckverhalten bei der Abbrandrate ergab, wie bei experimentell bestimmten Werten. Abbildung 2 zeigt die recht gute Übereinstimmung in der Druckkurve. Die Parameter wurden durch intuitive Variation bestimmt. Dabei ergab sich, daß der erste Reaktionsschritt A $\rightarrow$ B im wesentlichen für die absolute Höhe der Abbrandrate verantwortlich ist und der zweite Reaktionsschritt B $\rightarrow$ C hauptsächlich den Druckexponenten des Abbrands beeinflußt.
Bei den Rechnungen mit Gasphasenreaktion wurde Treibstoff mit einem in 3 ms von 500 auf 35 cal $cm^{-2}s^{-1}$ abnehmenden Wärmestrom angezündet. Die Rechnungen wurden jeweils solange durchgeführt bis ein stationärer Zustand der Abbrandrate, Oberflächentemperatur und des Temperaturprofils über dem Feststoff erreicht war. Meist reichten dafür 10 ms. In einigen Fällen konvergierte die Rechnung nicht oder der Abbrand erlosch. So konnten keine Abbrandraten bestimmt werden. Bei allen Rechnungen betrug der Brennkammerdruck 70 bar bei einer Anfangstemperatur von 300 K.
Sofern möglich wurden die Rechnungen ebenfalls nach dem einfachen Modell von Gl. (3) durchgeführt.

Ergebnisse

Zur Auswertung der Rechnungen wurden der Endwert der Abbrandrate r durch Division mit dem Wert beim Referenzzustand (Index 0, Tabelle 1) entdimensioniert und über der ebenso entdimensionierten Stoffeigenschaft aufgetragen. Abbildung 3 bis 1 zeigt die Ergebnisse nach Gl. (3) und Serie 1 und 2 der Rechnungen mit CTEM. Diese Auftragung veranschaulicht den unter den oben beschriebenen Bedingungen gefundenen Einfluß der Stoffeigenschaften.
Wie die Lösung der Wärmeleitungsgleichung Gl. (3) nahe legt, beeinflußt die Wärmeleitfähigkeit λ der kondensierten Phase auch bei den numerisch untersuchten Serien die Abbrandrate praktisch nicht, auch wenn sie um mehr als eine Größenordnung vom Referenzwert abweicht. Dies hat sowohl für theoretische als auch praktische Arbeiten

eine große Bedeutung. Da die Wärmeleitfähigkeit für viele Treibstoffe nicht bekannt ist, kann für Modellrechungen ein grober Schätzwert eingesetzt werden. Einige Treibstoffentwickler und Patente schlagen vor die Abbrandrate durch eine bessere Wärmeleitfähigkeit wie z.B. eingebettete Kupferdrähte zu erhöhen. Die Modellrechnungen bestärken diese Überlegungen nicht.
Die Wärmekapazität c_p der kondensierten Phase weist einen etwas höheren Einfluß auf. Geringere Wärmekapazitäten erhöhen die Abbrandrate, größere erniedrigen sie. Bei den numerischen Rechnungen ist der Einfluß niedrigerer Wärmekapazitäten stärker als der hoher. Die Reaktion in der Gasphase verstärkt den Effekt. c_p-Werte sind allerdings kalorimetrisch leicht und genau zu bestimmen, so daß sie für die meisten Modellierungsaufgaben hinreichend genau bekannt sind.
Einen starken Einfluß übt die Feststoffdichte aus. Sie geht nach Gl. (3) umgekehrt proportional in die Abbrandrate ein. Die numerischen Rechnungen bestätigen diesen Effekt. So brennt ein stärker verdichteter Treibstoff langsamer ab. Auch die Dichte läßt sich normalerweise sehr genau bestimmen oder oft z.B. durch das arithmetische Mittel der Einzelkomponenten abschätzen. So sind auch hier wenig Probleme bei Modellrechnungen zu erwarten.
Schwieriger ist der Einfluß der Umwandlungswärme L und der Oberflächentemperatur $T_{l\to g}$ zu beschreiben.
Bei Gl. (2) haben die Parameter tendenziell den gleichen Einfluß wie c_p und die Dichte. Die Kurven von T und ρ fallen nur scheinbar aufeinander. T hat eine etwas größere Steigung. In diesem Modell werden L und $T_{l\to g}$ als voneinander unabhängige Stoffkonstanten angenommen. Beim numerischen CTEM-Modell sind die beiden Werte über das Verdampfungsgesetz nach Clausius-Clapeyron verbunden nach

$$p_D = C_T \, exp\left(-\frac{LM}{RT_{l\to g}}\right) \qquad A_T = ln(C_T) \qquad \text{Gl. (4)}$$

(p_D Dampfdruck, M Molmasse der Kondensierten Phase, R idelale Gaskonstante, $T_{l\to g}$ Siedepunkt)
Der separate Eingabeparameter A_T in CTEM erlaubt die unabhängige Variation von L und $T_{l\to g}$. So konnte 1) L so variiert werden, dass sich bei gleichem Verdampfungsgesetz $T_{l\to g}$ automatisch einstellte, 2) L so variiert werden, daß $T_{l\to g}$ konstant blieb und 3) $T_{l\to g}$ bei konstantem L variiert wurde. Die Variation 1 übt einen sehr großen Einfluß auf die Rechnungen aus. Dies liegt daran, daß durch L gleichzeitig T variiert wird. Beim Abbrand führt eine kleinere Verdampfungswärme zu einer höheren Vergasungsrate gleichzeitig aber kühlt der verdampfte Massenstrom die Oberfläche stärker ab, so daß das System recht unvorhersehbar reagiert. Dies gilt besonders im Fall mit Gasphasenreaktion. Wird bei 2) die Oberflächentemperatur konstant gehalten, wirkt sich die Verdampfungswärme bei den numerischen Rechnungen kaum auf die Abbrandrate aus. Auch die Rechnungen zu 3) verdeutlichen den starken Einflluß der Oberflächentemperatur auf die Abbrandrate, bei der bei den unterschiedlichen Modellrechnungen nicht einmal die Tendenz übereinstimmt. Dies spiegelt die Bedeutung der Oberflächentemperatur als eine Kenngröße des Kopplungsmechanismus zwischen Wärmerückführung aus der Flammenreaktion und Vergasung des Feststoffes wieder. Die Oberflächentemperatur ist also keine Stoffeigenschaft, sondern wird durch die Wärme-, Stoff- und Impulsbilanzen im gesamten Abbrandsystem bestimmt.

Literatur

[1] DeLuca L. Pagani C.D., Verri M.; A Review of Solid Rocket Propellant Combustion, ISTS paper No 94-a-30v, Int. Symp. Space Techn. Sci. Yokohama, Japan 15-24 may 1994

[2] Eisenreich N.; Theoretische Untersuchungen über den Abbrand von Festtreibstoffen ICT-Bericht 5/76, Pfinztal 1976.

[3] Eisenreich N.; Vergleich Theoretischer und Experimenteller Untersuchungen über die Anfangstemperaturabhängigkeit der Abbrandgeschwindigkeit von Festtreibstoffen ICT-Bericht 8/77, Pfinztal 1977.

[4] Eckl, W.; Kelzenberg, S.; Weiser, V.; Eisenreich, N.; Einfache Modelle der Anzündung von Festtreibstoffen; 29th International Annual Conference of ICT, 1998, Energetic Materials; Karlsruhe, pp. 154-1 – 154-2

[5] Weiser, V.; Eckl, W.; Fischer, Th.; Kelzenberg, St.; Langer; G.; Phenomena of the Combustion of the Gun Propellant JA2; Norbert Eisenreich, 5th International Symposium on Special Topics in Chemical Propulsion: Combustion of Energetic Materials; 19-22 June 2000; Stresa, Italy; paper 5-ISICP-017-9-OP-VW

[6] Blomshield, F. S.; Nitramine Composite Solid Propellant Modelling; Naval Weapon Center, China Lake; CA 93555-6001, July 1989

[7] Beckstead, M. W.; Overview of Combustion Mechanisms and Flame Structure for Advanced Solid Propellants; Progress in Astronautics and Aeronautics; Vol. 185; AIAA Inc. Reston,Virginia; Chap. 2.1, p. 287-285

[8] V. E. Zarko, L. K. Gusachenko, and A. D. Rychkov, "Simulation of Combustion of Melting Energetic Materials" Defence Science Journal; Vol. 46 No.5, pp. 425 - 433, (1996).

[9] L. K. Gusachenko, V. E. Zarko, and A. D. Rychkov, "Modeling of Gasification of Evaporated Energetic Materials under Irradiation" INTAS Workshop, Milan, July (1996).

Tabelle 1 Referenzparameter für die Rechnungen von Serie 2

Parameter	Einheit	Wert
Wärmeleitfähigkeit λ	cal $cm^{-1}s^{-1}K^{-1}$	5e-4
Wärmekapazität c_p	cal $g^{-1}K^{-1}$	0.35
Dichte ρ	g cm^{-3}	1.9
Anfangstemperatur T_0	K	300
Druck p	bar	70
Wärmestrahlung auf Treibstoff Q_r	cal $cm^{-2}s^{-1}$	35
Verdampfungswärme L	cal g^{-1}	100
Clausius-Clapeyron-Parameter A_T		20.42
Schmelzwärme Q_m	cal g^{-1}	0
Schmelzpunkt T_m	K	0
Frequenzfaktoren Arrheniusgesetze A_g		13.0; 12.5
Reaktionsordnungen N_g		1; 2
Aktivierungsenergien E_{Ag}	cal mol^{-1}	37000, 40500
Reaktionswärmen Q_g	cal g^{-1}	300; 430
Molmassen M_i	g mol^{-1}	222; 35, 30

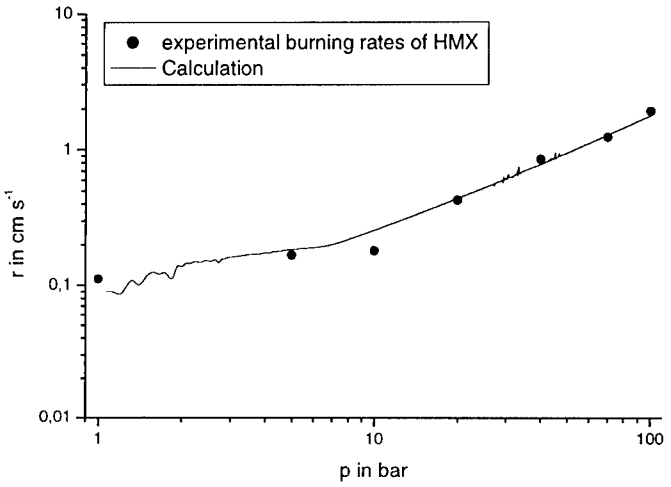


Abbildung 2 Abbrandraten von HMX im Vergleich mit CTEM-Rechnungen

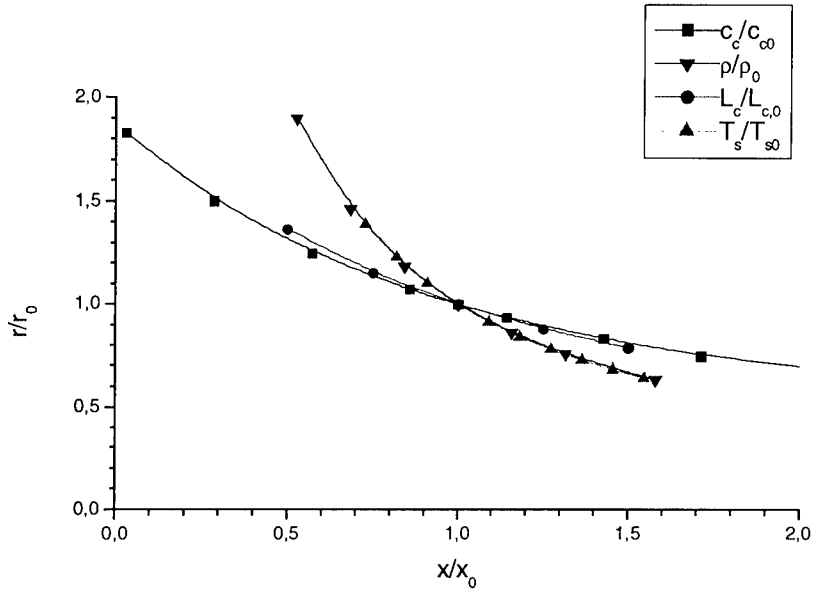


Abbildung 3 Abhängigkeit der Abbrandrate von den Stoffeigenschaften der kondensierten Phase nach Gl. (3)

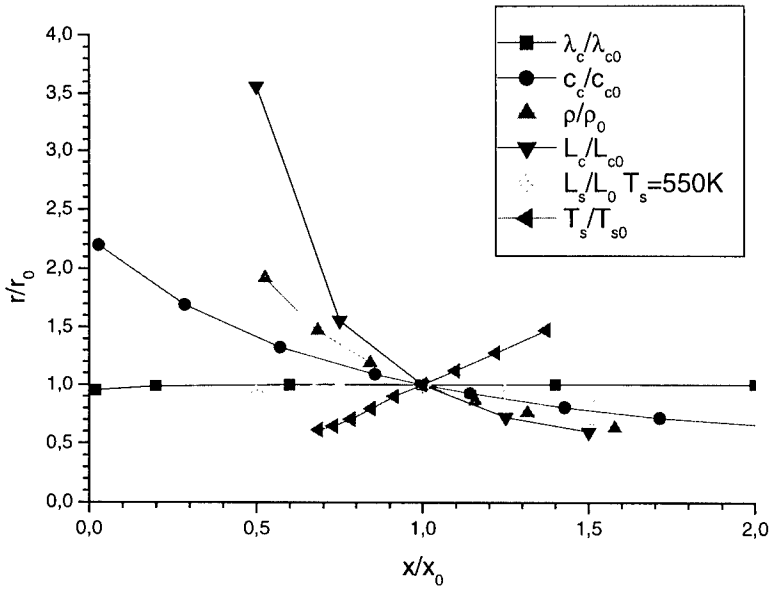


Abbildung 4 Abhängigkeit der Abbrandrate von den Stoffeigenschaften der kondensierten Phase; ermittelt mit CTEM bei festem Wärmeeintrag auf die Oberfläche (Serie 1)

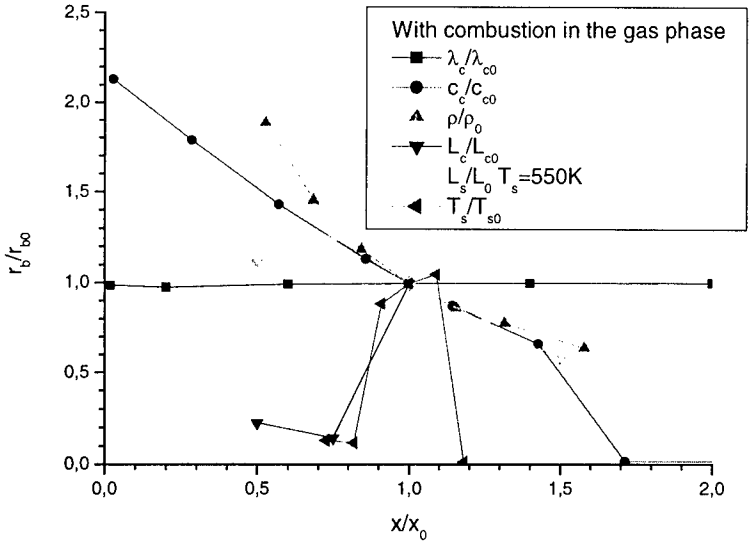


Abbildung 5 Abhängigkeit der Abbrandrate von den Stoffeigenschaften der kondensierten Phase ermittelt mit CTEM mit 2-stufiger Gasphasenreaktion (Serie 2)

„SOLVENT EFFECTS ON THE MORPHOLOGY OF ε-CL-20 CRYSTALS"

Thome, Volker; Kempa, Paul Bernd; Herrmann, Michael

Fraunhofer ICT, Joseph v. Fraunhoferstr.7, 76327 Pfinztal (Berghausen)

Abstract:

A number of solvents were tested on influencing the morphology of ε-CL-20 crystals. The examples of di-i-propyl ether, methyl-i-butyl ketone, nitrobenzene and water show that different morphologies of ε-CL-20 are found after recrystallization. Solvents affect crystal growth of CL-20 from solution and change the morphologies of ε-CL-20. This fact is very important for handling CL-20 like filtrating, grinding or storage, because the mechanical stability depends on the shape of the crystals. X-ray diffraction patterns of the crystals were analyzed with Rietveld refinement to find out the texture of the faces and the preferred growth directions of the crystals. SEM pictures show that in some cases the blocking of energetically favourable sites by solvent molecules creates oddlooking morphologies.

Introduction:

A solvent interacts with the solute in many ways, originating phase transitions, decomposition, or complexation of the solute. This paper presents solvents, in which ε-CL-20 crystallizes without inclusions. Solvents influence the morphology of growing crystals, because removing a solvent molecule from a crystal surface requires a definite amount of energy, which depends on the affinity of a solvent molecule to the different surfaces of a crystal and determines the attachment energy. The attachment energy is defined as the energy release on the attachment of a growth slice to a growing crystal surface. The growth rate of a crystal face is proportional to its attachment energy. Faces with low attachment energies possess the most morphological importance.

In this work we want to show that the combination of Rietveld refinement with computer simulations and crystallographic considerations is suited to explain some solvent effects on the morphology of ε-CL-20 crystals. For this reason the morphologies of ε-CL-20 are simulated with and without solvents. The results are compared with materials crystallized from different solvents. For determining the preferred crystal planes an effect is used occurring with the preparation of samples to be measured with x-ray powder diffractometers. The preferred crystal planes tend to be positioned parallel to the sample holder surface, creating

higher intensities of the reflection peaks than the other planes. Rietveld refinement calculates the theoretical intensities. Comparing with the measured intensities determines the preferred planes.

Experimental:

ε-CL-20 crystals were recrystallized in different solvents in a glass bottle. The solutions were evaporated at room temperature. Powder diffraction patterns were recorded with an x-ray diffractometer D8000 of Bruker-AXS. The patterns were evaluated by Rietveld refinement with the programm „BGMN" [1]. A computer simulation on a SGI workstation with the program Cerius 4.2 from MSI was performed to obtain the morphology of ε-CL-20 without solvent effects and to visualize the growth directions of the crystals.

Results and discussion:

The morphology of ε-CL-20 calculated with the attachment energy method with the UFF (Universal Force Field) [2] agreed well with the simulated crystals in nitramines like HMX [3]. A setup of QEq charges and a spline function were used to sum the Coulomb and Van der Waals forces within a cutoff radius of 14 $\mathring{A}$. Fig.1 shows the simulated crystal shape of ε-CL-20. The predominating growth forms are {011} with 42.5% and {110} with 30% of total surface area. It means that without solvent effects ε-CL-20 crystallizes in a prismatic shape.

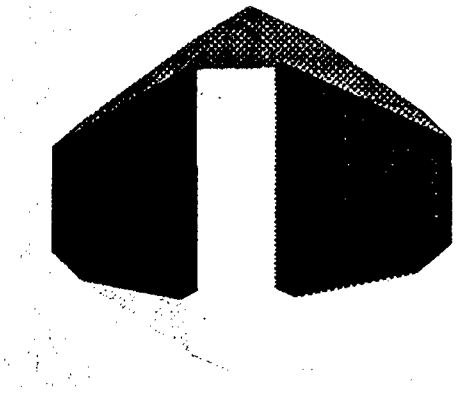


Fig. 1: Morphology of ε-CL-20, simulated after the attachment energy method with UFF and a spline on function. The black surface area shows the predominating {011} growth form

From a di-i-propyl ether solution we obtained ε-CL-20 crystals with smooth surfaces. The Rietveld refinement shows that the crystals grow with a preferred orientation along the b-direction, because the (h0l) faces, which are parallel to the b-direction, are inhibited by solvent molecules and therefore possess more morphological importance.



Fig. 2: SEM picture of ε-CL-20 crystallized from a di-i-propyl ether solution

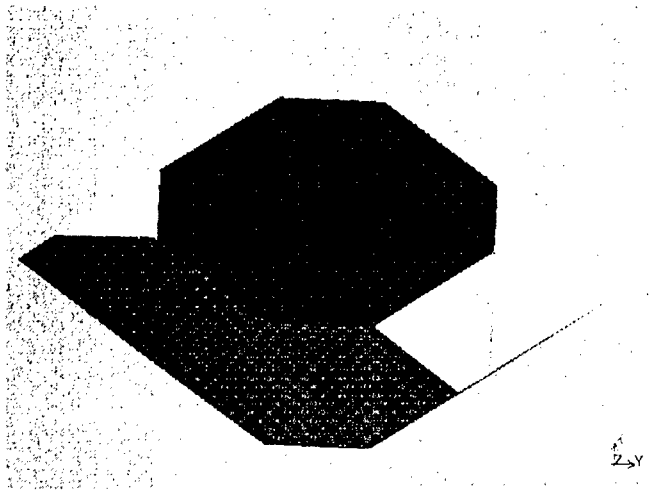


Fig. 3: Blocking of (h0l) faces by solvent molecules affects crystals growing preferred in b-direction by increase of the (10-1) surface (black). This morphology is derived from the original one (Fig.1) by shortening the center to face distance of (10-1).

From a methyl-i-butyl ketone solution ε-CL-20 crystals grow in a so-called „cauliflower-structure", consisting of hollow needles.

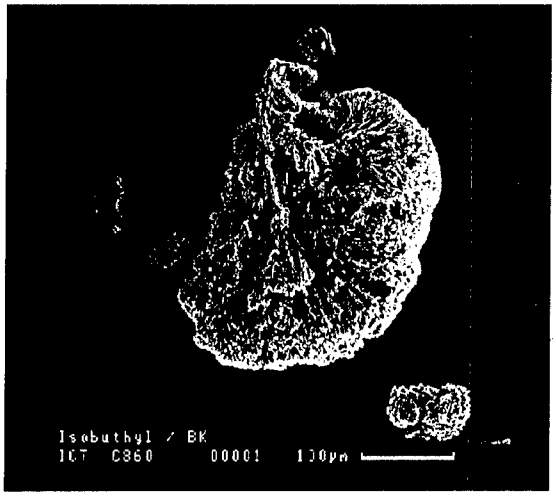


Fig. 4: „cauliflower-structure" of ε-CL-20 crystallized from a methyl-i-butyl ketone solution

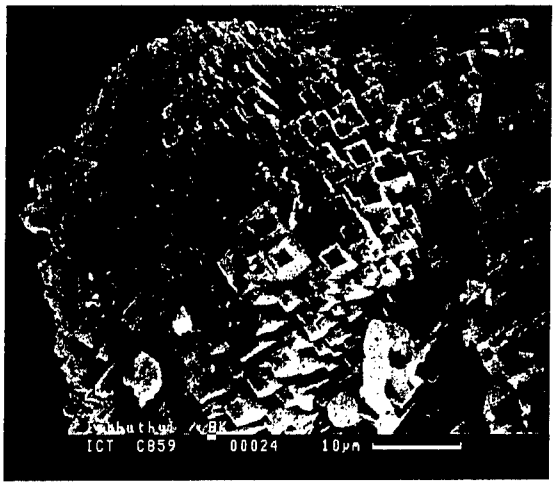


Fig. 5: CL-20 crystals formed as hollow needles

A possible explanation of this growth mechanism is given by Kleber et al.[4]: If solvent molecules are inhibiting the transport of material from the edges and corners to the inner area of a growing surface, where the energetically most favourable sites are situated, only the edges are completely developed. If the sites of the edges are also blocked by solvent molecules, only

crystal growth in a longitudinal direction is possible, for example along a given screw axis. By symmetry of space group P21/c ε-Cl-20 possess such a screw axis in b-direction [Fig.7] and from a nitrobenzene solution so-called whiskers or hair crystals were detectable. They were generated by suppressed crystallization processes or by removal of potential differences.

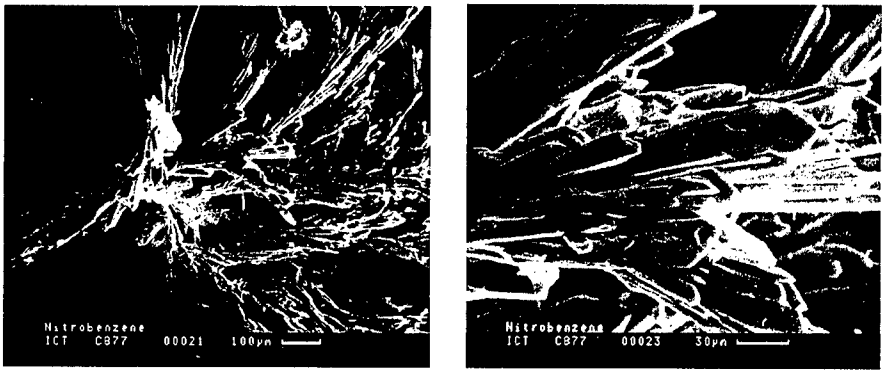


Fig. 6: hair crystals of ε-CL-20 from a nitrobenzene solution

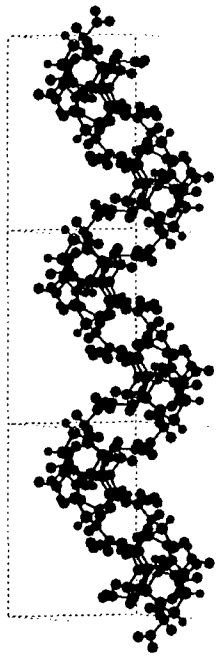


Fig. 7: screw axis in b-direction in ε-CL-20 builded of 1x3x1 unit cells

From a water solution we obtained crystals with a prismatic morphology similar to the calculated one, but the crystals were agglomerated and subparticles grew up on rough surfaces.

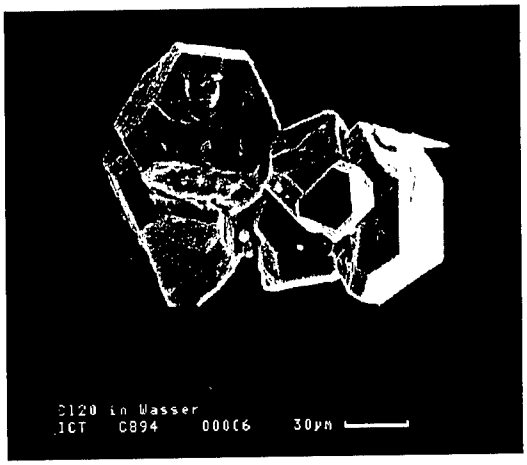


Fig. 8: ε-CL-20 recrystallized from a water solution

After Rietveld refinement we observed that the (0k0) faces are textured, the crystals grew in a preferred orientation perpendicular to the b-direction. The explanation for this effect is that the exposed nitro-group on the top of the screw-axis [Fig.7] interacts with the -OH groups of water, inhibiting crystal growth in b-direction. Tab.1 shows the 5 main x-ray diffraction peaks in ε-CL-20 in comparison to crystals from a di-i-propyl ether and a water solution.

Tab. 1: Calculation of the most textured faces after a Rietveld refinement

	ORIGINAL	DI-I-PROPYL ETHER			WATER		
h k l	Int. [%]	Texture	Int. [%]	text. faces	texture	Int. [%]	text. faces
1 1 0	100	0,88	100		0,7323	100	
1 1 –1	31,03	0,64	32,23		1,1746	38,2	
0 0 2	46,09	0,82	49,53		0,6647	89,87	
2 3 0	30,26	0,97	36,78		1,1012	24,14	
3 0 –1	37,82	0,88	20,77		1,8544	24,22	
		2,2994	8,42	-204	2,0669	0,28	020
		2,1975	0,45	-305	2,0669	10,46	040
					2,4033	1,31	150
					2,0669	1,07	060

Conclusions:

1.) The Rietveld refinement with the BGMN program detects preferred crystal planes, which have been influenced by solvents and growth directions in ε-CL-20 from different solutions.

2.) Computer simulations calculating crystal morphologies provide informations about the crystal growth with or without solvent effects.

3.) Understanding the crystal growth mechanism in ε-CL-20 by crystallographic considerations, crystallization of ε-CL-20 crystals with smooth surfaces, higher qualities and improved processability should be possible.

In future work an eventual correlation between textured faces and the mechanical or thermal stability of the ε-CL-20 crystals shall be investigated.

References:

[1] User manual BGMN © 1999 by Dr. J. Bergmann, Dresden Germany

[2] Rappe, A.K. et al.; „UFF, a full periodic table force field for molecular mechanics and molecular dynamics simulations", *J. Am. Chem. Soc.* **1992**, *114*, 10024-10035

[3] Thome, V.; Kempa, P. B.; Herrmann, M.; „Molecular simulations of the morphology of energetic materials", 31st International Conference of ICT, **2000** Karlsruhe

[4] Kleber, W.; Bautsch, H. J.; Bohm, J.; „Einführung in die Kristallographie", Verlag Technik GmbH Berlin **1990**, p.213-215

High Speed Mechanical Testing of Solid Polymeric Materials

O. Jedicke; C. Hübner; A. Moreno Martín; N. Eisenreich; A. Herzog; K. Zilly

Fraunhofer Institute of Chemical Technology (ICT)

Postfach 12 40, 76318 Pfinztal-Berghausen

Germany

Abstract

In modern applications, especially in the use of polymeric materials as matrix material for explosives and propellants, these materials are subjected to extreme mechanical stresses in short time scales during their use. The prevention of injuries during an application, but also transportation and storage, is one of the most important questions in research and development of modern energetic materials. Neither the mechanical behaviour nor the material properties of most applied polymeric materials are well known under these extreme conditions of deformation and concrete constitutive laws and material principles do virtually not exist. Consequently, the measurement of material data under similar conditions is necessary to expand data bases and support material descriptions. The mechanical testing requires a sophisticated measurement technique. Strain rates from 1 m/s up to 100 m/s make the measuring of relevant material-parameters difficult. A special problem arises when measuring the local deformation rate and the energy flow through the material. The digital`"High Speed Video Technique" makes the necessary data for the image processing immediately availability. Combined with a special software for the visualisation of flow phenomena in a vector field, such a measurement-system allows to determine the material parameters Poisson´s Ratio and Young `s modulus.

1.0 Measurement – Technique

The mechanical testing of polymeric materials under high deformation rates requires a sophisticated measurement technique. Strain rates from 1 m/s up to 100 m/s require digital "High Speed Video Technique". In this way, it is important to observe special points which must not necessarily exist in a regular pattern. The comparison of the patterns of two successive frames, allows to determine the flow of moving points. Thus it is possible to derive the superficial flow field of the test sample. Regarding time, the limiting factor is the used High Speed Video Technique, which provides about ~ 40.000 frames/s, a restricting resolution with respect to space and time. The complete system consists in the calibration set-up, the high speed tensile test machine, the monitoring system and the software to process the data. The main part of the complete measurement system is the high speed tensile test machine. The construction principle is based on a hydraulic geared piston connected with the sample through a piston rod. The vent is placed horizontally and the maximal reachable force is about 10 kN. Possible local speeds can grow up to 100 m/s and depend on the tested polymeric material. The force measurement is made with the help of a load cell and a transient recorder, in connection with the high speed camera in order to start the measurement of the force together with the camera by means of a trigger signal. To get the material data of the main mechanical parameter which characterise the material also at high deformation rates it is necessary to combine both, the elongation and the force signals and analyse this coupling in detail. A further problem is the sample preparation out of polymeric materials which have to been tested. Material data must be comparable otherwise no material selection can be done and subsequent development becomes difficult. Material structure and orientation, especially in regard to fibre reinforced materials must be well investigated and have to be considered in the analyse of measured data. In all cases, the main interest according to the correlation between the in coupled force and the mechanical behaviour of the polymeric materials is to find a relation which describes the behaviour of polymeric material under high deformation rates and elongation.

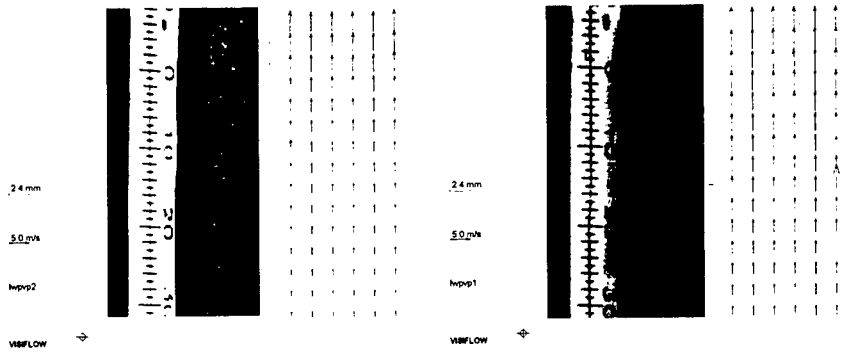
2.0 Evaluation of the Data and Results

The speed of the crossbar can be assumed to be directly proportional to the sample elongation when stretching the sample. A simple expression which relates both parameters is as following [1]:

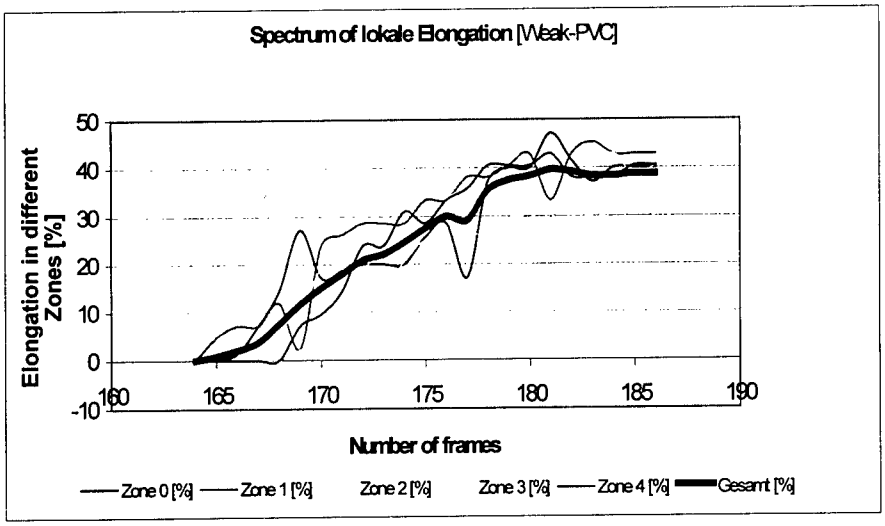
$$\dot{\varepsilon}_w = \frac{1}{(1+\varepsilon_N)(l_0 + A_0 kM)} v_{Traverse} \qquad [2.0]$$

The factor "k" corresponds to the total yielding of the testing system, the inverse ratio of the spring constant. "M" represents the slope of the curve Stress-Elongation, and it is a measurement of the stiffness or rigidity of the material. In the elastic domain "M" is named Elasticity Modulus. To identify both, the rate of elongation and the speed of elongation, the correlation program VISIFLOW has been used. The digital pictures are detected and compared with the help of this special software. Coupling these results with the time difference between two consecutive pictures it is possible to get information about the magnitude of the deformation

speed, and the direction of it. Soft PVC has been tested and the results are showed below. In figure 2 the local rate of elongation vs. image sequence (frame) is shown. The correlation between image sequence and time is done directly.

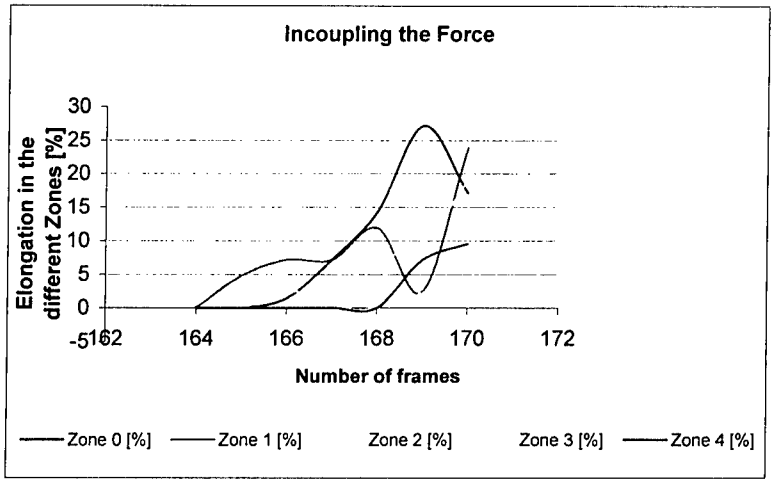


[Fig 1] Two successive frames during a high speed tensile test. The time between both frames is 0.14 ms. Comparing both frames, the vector field is obtained with a cross correlation program. The result discernible is the pattern of the pigments and also the lateral movement of the single points in the upper part of the frames. The upper part represents the accelerated part of the sample, the down part the fixed end of the sample.



[Fig 2] Spectrum of locale Elongation in different sample zones.

The actual beginning of the stress for the Soft PVC takes place at 165-180 image sequence. With a frequency of 6028 Hz (by use of an analogous High Cam technique) this phase takes only 2.5 ms. For a high resolution it is necessary to get a appropriate number of frames in this experimental time window. Two phenomena have to be taken into account. At first, the in coupled force on the moved side of the sample is not equal along the complete sample up to the fixed sample end, because of the energy losses through the sample by transforming mechanical energy into thermal energy and due to inertia. The second point is, that the material behaviour can not considered as homogenous along the complete length of the sample, because different deformation speeds along the sample arise and the material behaviour depend on the deformation speed. In that case, as well the calculation as the interpretation must be done carefully and in any case only partial.



[Fig 3] The in coupling of the force signal for different ranges or zones marked over the sample. It needs 0.7 ms time till the force signal reaches the fixed part of the sample and can be measured.

That means, that the measured force is not directly correlated to the deformation of the sample and must be corrected to get the Young's Modulus. Simultaneous measurements with a thermo-camera can show more information about the energy flow through the sample. In this case is discernible, that mostly the in coupled force is also caused to thermal processes inside the material. Sources of friction can be located and get as well visible within the material as the thermal energy transfer during a breaking process of a sample. The arise of thermal energy in both breaking zones (left and right one) can be set more or less equal to the breaking of chemical boundaries in this part of the sample.

Summary

With the presented measurement system, based an video equipment, one is able to get a set of mechanical properties like Elasticity Modulus, Poisson's Ratio and the elongation to describe the behaviour of polymeric materials under high deformation rates. One advantage of this experiment is the possibility of measure the typical mechanical properties at a different speed range during one single experiment. A further advantage is, that the experimental work, stored on data carrier in digital modus, is available at any time and thus different utilisation can be done to get more and accurate results by one single tensile test. As well, material production and preparation can be saved especially in the case of prototyped material samples. Further and possible ways to continue this innovative development of measurement technique will be a deeper study in field flow considering the embedment in the analytic and numeric simulation and modelling of the material behaviour under special conditions of deformation.

Literature

[2] **E. Roeder, N. Achten, M. Arens, H.G. Hilpert;** Materialprüfung 21 [1979] 10, S.345

[3] **G. Jacoby, G. Mall;** Berg- und Hüttenmännisches Monatsheft 122 [1977] 2, S.264

[4] **C. G'Sell and J.J. Jonas;** Journal of Material Science, 14, 583 [1979]

[5] **C. G'Sell, N.A: Aly-Helal, and J.J. Jonas;** Journal of Material Science, 18, 1731 [1983]

[6] **C. G'Sell, J.M. Hiver, A. Dahoun, and A. Souahi;** Journal of Material Science, 27,5031 [1992]

[7] **F. R. Schwarzl;** Polymermechanik, Springer-Verlag, [1990]

[8] **J. D. Ferry;** Viscoelastic Properties of Polymers, John Wiley & Sons, [1970]

[9] **Hans Batzer;** Polymere Werkstoffe in Bd.1 Chemie und Physik, Georg Thieme Verlag [1982] ISBN 3-13-648101-1

[10] **O. Jedicke, N. Eisenreich;** Optische Messung der Geschwindigkeitsverteilung bei Deformationsversuchen unter hohen Belastungsgeschwindigkeiten; 30th International Annual Conference of ICT, Karlsruhe, pp. 111-(1-10) [1999]

[11] **O. Jedicke, A. Baier;** Messung der thermischen Energieverteilung in der Bruchzone polymerer Materialien; Proceedings of 7-tes Problemseminar Deformation und Bruchverhalten von Kunststoffen, Institut für Polymerwerkstoffe e. V. Fachbereich Ingenieurwissenschaften, Martin – Luther - Universität, Halle – Wittenberg; [1999]

[12] **O. Jedicke, N. Eisenreich, I. Alvarez Ortega;** Visualisierung der Deformationsgeschwindigkeiten polymerer Materialien in einem Vektorfeld; Proceedings of 7-tes Problemseminar Deformation und Bruchverhalten von Kunststoffen, Institut für Polymerwerkstoffe e. V. Fachbereich Ingenieurwissenschaften, Martin – Luther - Universität, Halle – Wittenberg; [1999]

[13] **O. Jedicke, N. Eisenreich, I. Álvarez Ortega, A. Baier;** Speed Distribution and Energy Flow in High Rates Deformation Experiments (1 m/s – 100 m/s), Proceedings of International Workshop on Video-Controlled Materials Testing and In-Situ Microstructural Characterization; Nancy (France); [1999]

[14] **O. Jedicke, N. Eisenreich;** Thermo-mechanical Testing of Polymeric Materials under Rates of Deformation between 10^{-2} m/s – 10^{+2} m/s, Proceedings of 3rd International Conference and Exhibition Berlin (Germany); [2000]

[15] **O. Jedicke, N. Eisenreich;** Mechanische Materialuntersuchung polymerer Werkstoffe unter Deformationsgeschwindigkeiten von 10^{-2} bis 10^{+2} m/s, ACHEMA Frankfurt am Main (Germany) Prodeedings Werkstofftechnik und Materialprüfung [2000]

[16] **O. Jedicke, N. Eisenreich, I. Álvarez Ortega, A. Baier;** Speed Distribution and Energy Flow in High Rates Deformation Experiments (1 m/s – 100 m/s), Proceedings of 4-th EUROMECH in Metz (France); [2000]

Thermo-mechanical Properties of Special Polymeric Materials

O. Jedicke; A. Moreno Martín; N. Eisenreich

Fraunhofer Institute of Chemical Technology (ICT)

Postfach 12 40, 76318 Pfinztal-Berghausen

Germany

Abstract

The objectives of mechanical testing of polymeric materials by uniaxial tensile tests is conventionally the investigation of the mechanical properties and material behaviour. Properties and material behaviour are not independence from stretching rates as well as material temperature during the uniaxial tensile test. Thus, instructions are given for the mechanical testing and temperatures of the polymerisation of any kind of polymeric material have been registered in literature to guarantee the comparison of results. However, no concrete model of interaction between dynamical demand and its thermal effects exist to describe the material behaviour more completely. Still there exist low information about, how the mechanical loads affect the material temperature. This is a point of interest for the producers and users of propellant and explosive materials, which use thermoplastic materials as a matrix for highly filled polymers. Especially these materials are subjected to high loads in shorts scales of time, and the knowledge of its thermal behaviour under these circumstances is not only a matter of interest, but of safety. An spontaneous increase of the interior temperature or local hot spots can lead to different material-failures and thus to a risk in acting with explosive and propellant materials. The following work will introduce in the measurement technique and first results, in regard to the thermo-mechanical behaviour of polymeric materials, applied to the conventional material testing of polymeric materials. The recording of the material temperature during a uniaxial tensile test requires measurement technique which distinguishes from the measurement techniques used to acquire only mechanical parameters such as stress, elongation, Young's modulus or Poisson's ratio. Of course, both mechanical and thermal information would be desired to obtain, and this task involves the combination of all measurement methods.

1.0 Influence of the Mechanical Demands on the Interior Material Temperature

Especially the thermo-mechanical properties and even the mechanical behaviour of polymeric materials, are not easily to describe. The interaction between both is not described through a single material model for all kinds of polymeric materials and no closed form in mathematical calculation exist. Therefore, investigations of polymeric materials must depend on experimental work and its results. To direct experimental work, it is necessary to set a starting point. In the case of thermo-mechanical behaviour it can be the First Law of Thermodynamics:

$$dU = Q - W \qquad [1.0]$$

where "**U**" is the internal energy, "**dU**" the total differential , "**Q**" the heat flux absorbed by the system and "**W**" the work made by the system. In this law both are included, the thermal effects and the mechanical ones. Equation [1.0] is independent from the selected material and thus general valid. A more detailed description of the variables "**Q**" and "**W**" leads to the following expression:

$$\rho \cdot c_p \cdot \left(\frac{dT}{dt}\right) + \left(\frac{dQ_a}{dt} + \frac{dQ_\kappa}{dt}\right) = \frac{dW}{dt} + \frac{dU}{dt} \qquad [1.1]$$

and further to:

$$\rho \cdot c_p \cdot \left(\frac{dT}{dt}\right) + \left(\frac{dQ_a}{dt} + \frac{dQ_\kappa}{dt}\right) = \left(\sigma + \frac{dU}{d\varepsilon}\right) \cdot \frac{d\varepsilon}{dt} \qquad [1.2]$$

where the left side of the equation corresponds to the heat flux Q and the right side represents the difference between the internal energy flux and the power made by the system. However, to find out the temperature field in the sample is not a simple task.

The sample is heated by the action of stretching force. In order to solve the heat transfer through and within the sample, we must consider conduction and convection. The conduction heat transfer is ruled by the Fourier equation, which has the following expression for an isotropic and homogeneous material:

$$\frac{\partial T}{\partial t} = \frac{k}{\rho \cdot c_p} \cdot \nabla^2 T + \frac{q'}{\rho \cdot c_p} \qquad [1.3]$$

where,

T is the local temperature [K]

k is the thermal conductivity [W/m·K]

ρ is the density [kg/m^3]

$\mathbf{c_p}$ is the specific heat [J/kg·K]

q' is the heat source [W/m^3]

Some difficulties occur when trying to solve the equation [1.3]. These difficulties are:

- The sample stretches, and we have not any more an isotropic and homogeneous material through the complete sample length.
- The observed domain has not a simple three-dimensional geometry. In addition this geometry changes in time, while mostly a neck is produced on the sample and this neck enlarges in time.
- The structure within the neck is orientated.
- Due to internal heat sources, generated probably within the sample by:
  - Friction
  - Broken molecular linkages

Because of it, our Fourier equation [1.3] becomes a non linear equation. As it will be shown later, the heat sources move in time and through the sample at a rate different from the strain rate. This fact must be taken into account! In addition, the evaluation of the heat source values are difficult to estimate.

The convection heat transfer involves the Navier Stokes equation. We would be interested in correlation that provide a simple calculus of the Nusselt number in order to derive the local Newton film coefficient h(x, y, z). In that case, it is possible to write the convection heat transfer in the following form:

$$q' = h(x,y,z,t)\cdot(T(x,y,z,t)-T_{\infty}) \qquad [1.4]$$

Of course, no correlation for the Nusselt number exists in regard to the geometry and boundary conditions of the problem, as well as the non steady character of the problem makes all the approaches quite inaccurate.

Because of these reasons, it is really difficult to evaluate a closed form of thermal solution. Only with the help of numerical simulations it is possible to receive some results, to improve the understanding of the heat flow through and out of the sample during a tensile test. However, these numerical approach cannot be made without the calculation of the heat sources generated within the sample. To investigate the nature of these heat sources is one of the main aims of the research work.

2.0 Experimental Work and Measurement-Technique

As mentioned before, only one heat sources was generated and splits during the test into two different heat sources [fig.1]. This fact was determined with the help of a digital "Thermo-camera", which works with:

3.500 frames/s

in a temperature range of:

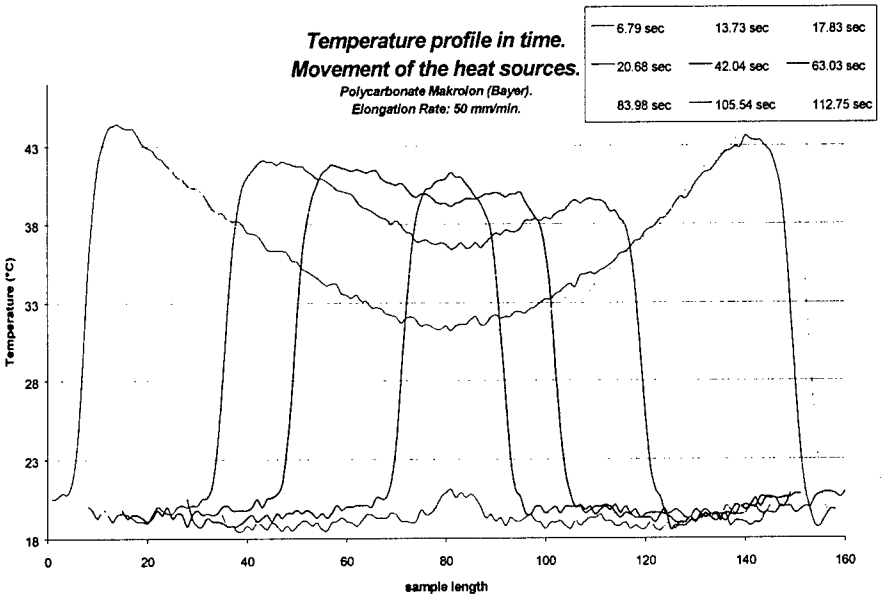
−10 °C up to +2.000 °C.

Two different modes of the Thermo-camera can be used, a line mode in measuring the temperature distribution along one single axis, the sample length axis in a thin expansion, and one modus to measure the temperature distribution completely over the sample surface. Whereas the line modus deliver 3.500 frames/s and therefore can also be used to calculate elongation and deformation speed with approximately useful results. The full modus cannot be used for those calculation because of recording only a few frames/s.

The interesting time-phase of most high deformation rates experiments in regard to polymeric materials be situated in the range of only a few ms. In that case, with 3.500 frames/s in the line modus it is almost possible to observe the appearance of thermal energy and the transportation of it through the material during a tensile test under various stretching rates by measuring the temperature distribution on the sample surface. The measurement of the temperature distribution completely through the tested sample or even inside a breaking zone (Gradient of temperature) contains the information of the conversion of mechanical energy into thermal energy and the release of chemical energy during a breaking process referring the chemical linkages, the throw off of the polymeric chains and also information related to the material behaviour depending on thermo-mechanical aspects, that means friction between single layers. In all cases, the main interest according to the correlation between the in coupled energy and the thermo-mechanical behaviour of the polymeric materials is, to find an approximately relation which describes the interaction within the polymeric structures and the appearances of different mechanical behaviour of polymeric materials under high dynamical demands.

In the full modus, the surface temperature was recorded, and the existence of the moving heat sources was observed. As it is shown in the figure sequence, only one single heat source was generated at first, while stretching the sample. This one occurs nearly in the middle of the sample, which is not necessarily always in the middle of the sample, up to a maximum temperature, and then splits into two, while a sample-neck came into existence.

The temperature profile on the complete sample surface can be obtained, so that it is possible to compare how fast both heat sources move forward the specimen edges. In [fig.1] an overview of the evaluation of the effect is given. Shown is the evolution in time of the temperature profile.



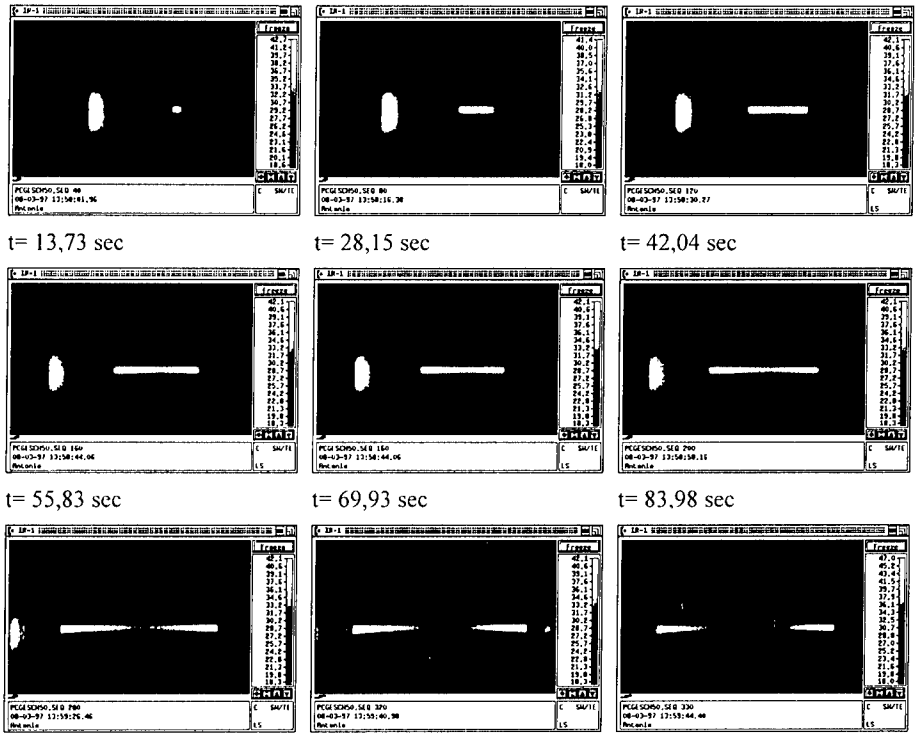
[Fig 1] The Evaluation of the temperature profile on the sample surface during a tensile test. Shown is the evaluation over 112.75 seconds.

The middle point of the diagram (where the first heat source is originated at the sample length 80) is not a heat source any longer, since it can be measured, how is the cooling down of it, and compared with the free cooling down of a single hot point. The expression of the temperature profile in time of this cooling process has the following equation:

$$T(t) = T_{\infty} + (T_0 - T_{\infty}) \cdot e^{-t/\tau} \qquad [2.0]$$

where τ is the constant time, which depends on the density of the material, the volume, the heat capacity, the observed area and Newton film coefficient "**h**". For this equation, the following assumption was done, that the heat transfer due to conduction from the hotter surrounding points is negligible compared to the heat transfer due to convection. Experimental results confirm the assumption, so that it can be affirmed that the heat source is divided in two and it moves towards the sample-ends.

The following figure [fig.2] shows an original recorded sequence, set together from single frames, measured with the above described Thermo-camera. In the displayed photos, the splitting of the first single heat source into two, as well as the displacement of both single heat source towards the sample-ends can be seen.



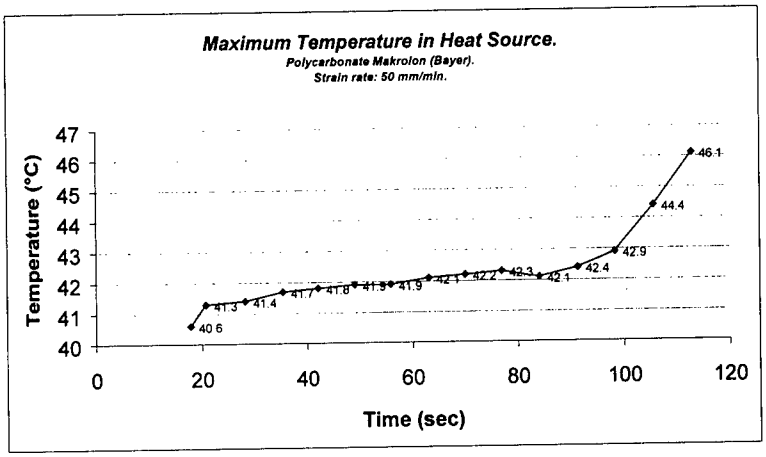
t= 13,73 sec t= 28,15 sec t= 42,04 sec

t= 55,83 sec t= 69,93 sec t= 83,98 sec

t= 98,23 sec t= 112,75 sec t= 127,94 sec

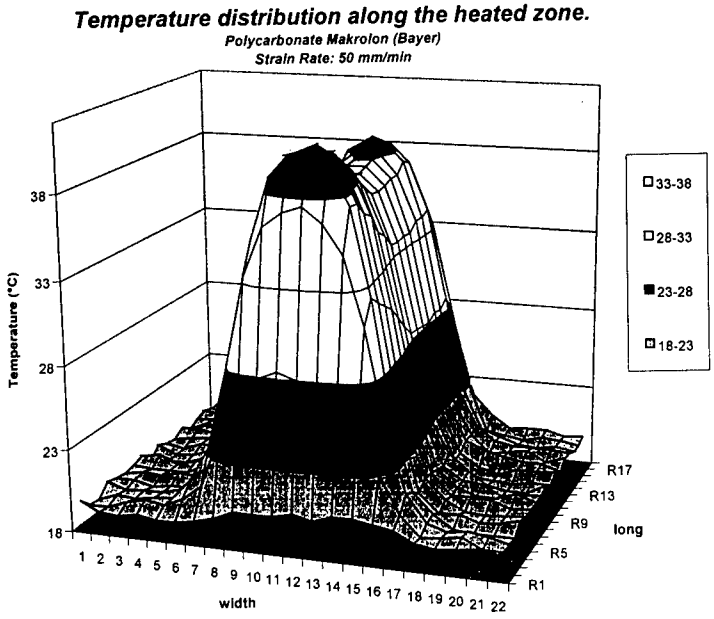
[Fig 2] Recorded sequence of a tensile test of a polymeric material Polycarbonat. The elongation rate was 50mm/min. Lighter colours represents high temperature. Observed was the presence of two heating sources moving forward to samples end as the test proceeds.

These both heat sources move along the length of the sample, reaching higher temperatures. Figure [fig.3] gives a temporal distribution of the maximum temperatures reached in the heat sources.



[Fig 3] Temperature evolution in the heat sources. Though an increasing tendence is observed, it is only near the sample-ends (clamp).

So far, only longitudinal profiles were analysed. A more detailed study can provide us a three dimensional plot of temperature as a function of x and y. This are the sample temperature profiles measured on the sample surface.



[Fig 4] Temperature distribution of the surface of the sample in two dimensions. Only the heated zone is represented.

Another point of interest is the dependence of this phenomena on the strain rate. Three different strain rates were used to test a PC -sample:

50 mm/min

150 mm/min

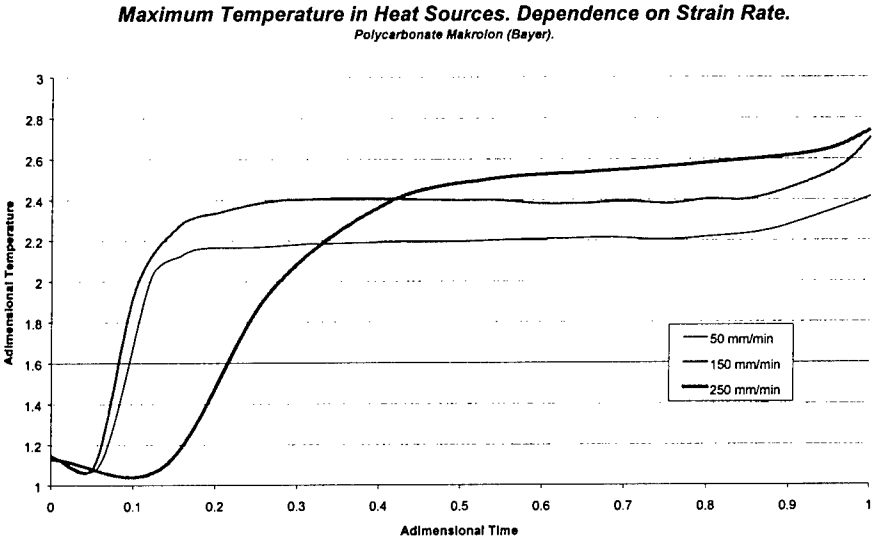
250 mm/min.

To improve the understanding of the thermal behaviour of the tested polymer under different strain rates, adimensional results are shown together in Figure [fig.5]. The adimensional temperature "θ" is calculated dividing the surface temperature per room temperature (20 °C), and the adimensional time "τ" is obtained dividing the time per testing time (until the sample breaks).

$$\theta = \frac{T(t)}{T_{\infty}} \qquad [2.1]$$

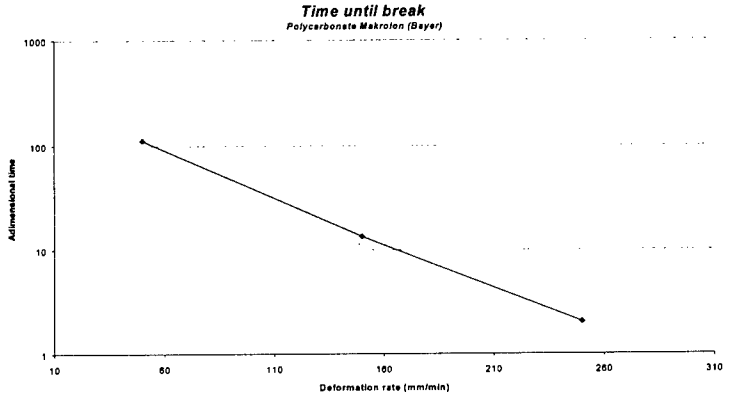
$$\tau = \frac{t}{t_{final}} \qquad [2.2]$$

This is a first approach to a non dimensional study of our problem.



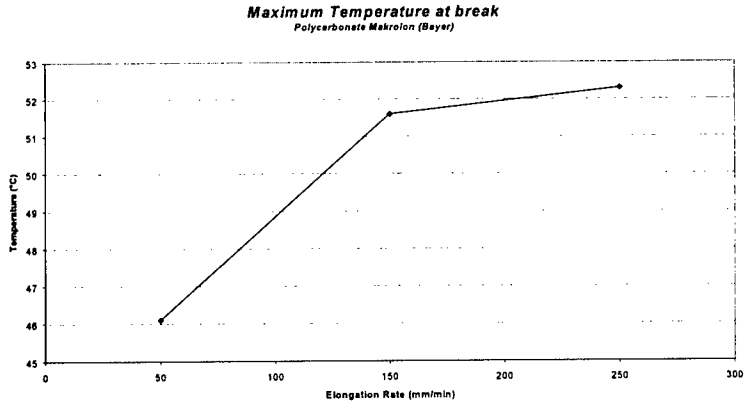
[Fig 5] Maximum temperature in the heat sources. Characteristically temperature: Room temperature 20°C. Characteristically time: testing time. An inertial behaviour is noticed at higher strain rates.

The sample break takes different times for each deformation rate. Figure [fig.6] shows the dependence of this effect as a function of the strain rates.



[Fig 6] Time until sample breaking as a function of the deformation rate. A linear tendence can be noticed between log(t) and the deformation rate.

The maximum temperature is reached within the sample when breaking. Higher temperatures are reached in the sample at break. The accuracy of the thermo-camera is not high enough to detect peaks of temperature in small areas neither the outer or the transversal surfaces. However, it is a fact that at break, the sample reaches a peak of temperature due to the break of chemical linkages in the micro-structure of the polymeric material. The following figure [fig.7] gives an expression of the maximum temperature measured by the thermo-camera, though a deeper work must be performed in order to detect higher temperatures. Electron microscopy can be used for this purpose. We can get aware of reaching melting temperatures at breaking point, which would give us a clue about the minimum temperature in the breaking-surface of the sample.



[Fig 7] Maximum temperature at the breaking point. Higher temperatures can be obtained when increasing the strain rate. These values are obtained from the thermo-camera data sheet, which is an relative data sheet, and can thus not be considered as the real maximum.

3.0 Summary

The aim of the presented research is to sort out the quality and quantity of the thermal energy released during the tensile tests. Several mechanisms are the cause of the warming up process when stretching the sample or set under mechanical stress. Namely, frictions among polymer chains (or layers), breaking and disconnection of different chemical linkages which bound the chains each other, are involved in the physical phenomena. Higher levels of temperature are obtained at the breaking point. Thus, the existence of the breaking of covalent bonds within the polymers must be considered.

The comprehension of the mechanical and chemical behaviour of the micro-molecular structures obtained under mechanical loads is fundamental in order to elaborate a consistent description of the thermo.-mechanical processes within polymeric materials under dynamical loads. Under dynamical demands there may be some aspects to describe yet, and a different influence of each may change with the strain rate.

The measurement techniques available provide us the chance to combine a set of mechanical data (like Young's modulus, Poisson's ratio and elongation) with the thermal state caused by the mechanical loads, in such a way that we can have a more general knowledge of the material behaviour under mechanical demands.

Literature

[1] **Yuli K. Godovsky;** Thermophysical Properties of Polymers, Springer Verlag [1992] ISBN 3-540-54160-8

[2] **Gerhard Kluge, Gernot Neugebauer;** Grundlagen der Thermodynamik, Spektrum Akademischer Verlag [1994] ISBN 3-86025-301-8

[3] **Hans Dieter Baehr, Karl Stephan;** Wärme- und Stoffübertragung, Springer Verlag [1996] ISBN 3-540-60374-3 2-te Auflage

[4] **Hans Batzer;** Polymere Werkstoffe in Bd.1 Chemie und Physik, Georg Thieme Verlag [1982] ISBN 3-13-648101-1

[5] **Heinz Schmiedel;** Handbuch der Kunststoffprüfung, Carl Hanser Verlag [1992] ISBN 3-446-16336-0

[6] **Gottfried W. Ehrenstein, Gabriela Riedel, Pia Trawiel;** Praxis der Thermischen Analyse von Kunststoffen, Carl Hanser Verlag [1998] ISBN 3-446-21001-6

[7] **O. Jedicke, N. Eisenreich;** Optische Messung der Geschwindigkeitsverteilung bei Deformationsversuchen unter hohen Belastungsgeschwindigkeiten; 30th International Annual Conference of ICT, Karlsruhe, pp. 111-(1-10) [1999]

[8] **O. Jedicke, A. Baier;** Messung der thermischen Energieverteilung in der Bruchzone polymerer Materialien; Proceedings of 7-tes Problemseminar Deformation und Bruchverhalten von Kunststoffen, Institut für Polymerwerkstoffe e. V. Fachbereich Ingenieurwissenschaften, Martin – Luther - Universität, Halle – Wittenberg; [1999]

[9] **O. Jedicke, N. Eisenreich, I. Álvarez Ortega, A. Baier;** Speed Distribution and Energy Flow in High Rates Deformation Experiments (1 m/s – 100 m/s), Proceedings of International Workshop on Video-Controlled Materials Testing and In-Situ Microstructural Characterization; Nancy (France); [1999]

[10] **O. Jedicke, N. Eisenreich;** Thermo-mechanical Testing of Polymeric Materials under Rates of Deformation between 10^{-2} m/s – 10^{+2} m/s, Proceedings of 3rd International Conference and Exhibition Berlin (Germany); [2000]

[11] **O. Jedicke, N. Eisenreich, I. Álvarez Ortega, A. Baier;** Speed Distribution and Energy Flow in High Rates Deformation Experiments (1 m/s – 100 m/s), Proceedings of 4-th EUROMECH in Metz (France); [2000]

Characterisation and Development of Gas Generators for Fire Extinguishing Systems

Neutz, J.; Fischer, Th.; Ebeling, H.; Klemenz, M.; Weiser, V.

Fraunhofer Institut für Chemische Technologie, Joseph von Fraunhofer Strasse 7, D-76327 Pfinztal

Abstract:

Chemical gas generators produce gas on the basis of a combustion process. It is very useful to observe this combustion reaction during the whole development of a new gas generator. This is especially true for the burning rate, because of its important role for design. This paper describes the characterization of the interior ballistic behaviour and the determination of the burning temperature of several gas generator compositions. They are based on the two fuels, an oxidizer and several additives.

The linear burning rate was measured at pressures of 10, 20, 40 and 70 bar in an optical bomb. In parallel, experimental investigations on gas generator strand combustion were performed applying NIR emission spectroscopy to study temperature and concentration profiles.

The results showed a high sensitivity and reproducibility of the spectrometer system combined with a fast data analysis. Besides the vibrational temperature and the concentration of water, particle temperatures and concentrations are obtained, which is very useful in the investigation of gas generator propellants. The determined flame temperatures are significantly lower than calculated adiabatic values but mainly in the expected range.

Kurzfassung:

Chemische Gas Generatoren erzeugen die Gase auf der Basis eines Verbrennungsprozesses. Dabei ist es sinnvoll, während des gesamten Entwicklungszeitraumes einer neuen Gas-Generator-Formulierung, das Abbrandverhalten zu überwachen. Dieser Beitrag beschreibt die Charakterisierung des Abbrandverhaltens und der Abbrandtemperatur einiger Gas-Generator-Formulierungen. Die Formulierungen bestehen aus zwei Brennstoffen, einem Oxidator und unterschiedlichen Zusatzstoffen.

Die lineare Abbrandrate wurde in einer optischen Bombe bei 1, 2, 4 und 7 Mpa gemessen. Parallel zu diesen Untersuchungen wurden Untersuchungen zur Abbrandtemperatur und Gaskonzentrationen mittels NIR Emissions-Spektroskopie durchgeführt.

Die Ergebnisse zeigten eine hohe Sensitivität und Reproduzierbarkeit des Spektrometersystems kombiniert mit einer schnellen Messwerterfassung. Neben den Abbrandtemperaturen und den Wasserkonzentrationen wurden Partikeltemperaturen und Konzentrationen bestimmt. Die gemessenen Flammentemperaturen sind zwar signifikant niedriger als die berechneten adiabatischen Temperaturen, jedoch im erwarteten Bereich.

1 Introduction:

The application of gas generators in security technology, especially as airbags in automotive applications, increased in the last ten years tremendously. In all cases the basic feature of a gas generator is to produce a high amount of gas per mass unit.

One of the important points of interest for further application of a new gas generator composition is the characterization of the interior ballistic behaviour. Especially for the design and development of new gas generator systems the detailed knowledge of the interior ballistic behaviour of the gas generator composition is needed. There are three possibilities for characterization of the interior ballistic behaviour – Crawford Bomb, Ballistic Bomb and Optical Bomb. Crawford and ballistic bombs are systems, where only the burning rate can be determined. The optical bomb provides several opportunities of optical and non-intrusive measuring methods, e.g. UV/Vis and NIR spectroscopy, for characterization of the flame structure of the propellant and determination of the linear burning rate. Another advantage of the optical bomb is a reduction of experiments due to the possibility to use two measuring methods within on experiment.

Nearly every combustion process is producing water and the absorption coefficient in the near infrared is in a range where on the one side hot emission (e.g. in flames) shows a strong signal and on the other side cold absorption (e.g. in air) can be neglected in the data analysis.

Therefore, spectroscopic investigation of near infrared water bands seems to be an ideal optical flame diagnostic e.g. as a method for non-intrusive temperatures determination of flames and hot gases. An additional advantage is the simple experimental setup combined with a fast data analysis allowing even an online temperature monitoring.

2 Interior Ballistic Behaviour:

The interior ballistic behaviour of propellants is affected by various factors like e.g. chemical compositon, temperature and geometric shape. Generally the interior ballistic behaviour is described by the burning rate r. The burning rate relates the velocity of the reaction zone to the system parameters like pressure and temperature. The most used relation for the pressure dependence of the burning rate r is Vieille´s law described below.

$$r = \alpha \cdot \left(p / p_0 \right)^{\beta}$$

It is an experimentally derived relation, which fits to the burning behaviour of nearly all homogeneous solid gas generators. The obtained linear burning rates as a function of pressure were fitted with a non linear curve fit to obtain the two parameters of Vieille's law.

The tested mixtures are based on the fuels Di-Guanidinium-5,5'-Azotetrazolat (GZT) and Guanidinium-Aminotetrazolat (GA), an oxidizer and additives. The fuel composition changed from pure GZT (MGO 40101) to pure GA (MGO 44601) with different amounts of GZT and GA in the other mixtures (MGO 44201 – MGO 44501) to show the influence of the new fuel GA on the burning behaviour. The mixtures were processed and pressed into a shape of 40x4x4 mm – so called strands – for the measurements. The strands are epuipped with ignition paste and a thin wire at the top to provide ignition by electrical power.

Composition	α	β
MGO 40101	0.34	0.94
MGO 44201	0.58	0.64
MGO 44301	0.54	0.59
MGO 44401	0.44	0.66
MGO 44501	0.49	0.60
MGO 44601	0.51	0.56

Tab. 1: Vieille's law parameters of some gas generator compositions

The burning behaviour of the different mixtures were characterized in an optical bomb with interior volume of 1,5 dm^3. A principle sketch of the setup is shown in. The strands are fitted into a rag in a way, that they are visible through the two windows. The pressure inside the bomb is adjusted with compressed nitrogen and a little flow of nitrogen prevents fogging of the windows. The linear burning rate was measured at 10, 20, 40 and 70 bar.

The burning rates were measured with a CCD camera, which enables sampling rates up to 300 pictures per second. The CCD camera is connected to a personal computer via a framegrabber and the calibration is done by a transparent reference grid with known grid distance. Every picture is treated with a mathematical picture analysis to detect the proceeding of the burning front. Even faulty measurements due to formation of slag droplets or with only temporary linear burning behaviour can be evaluated.

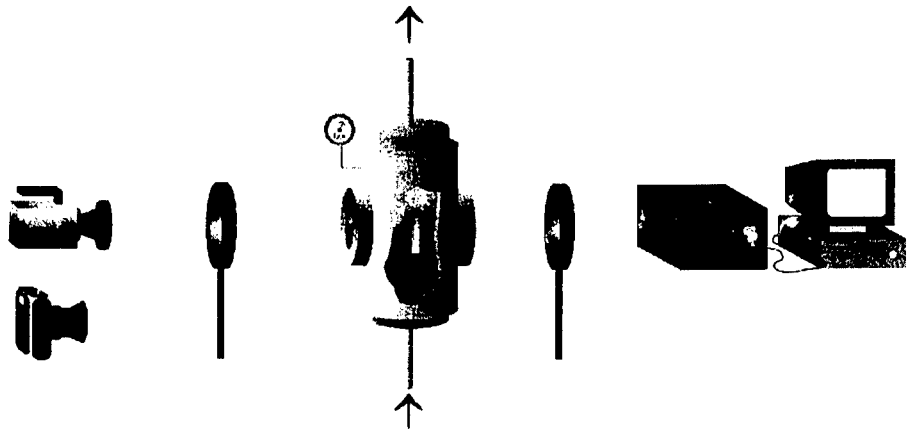


Fig. 1: Experimental Setup of Optical Bomb

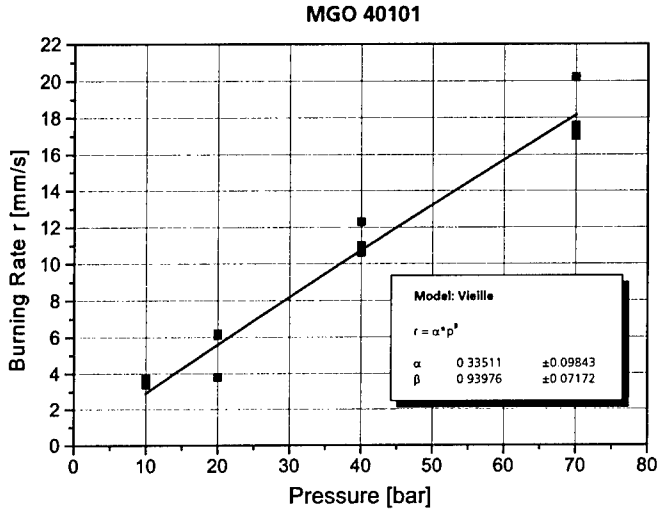


Fig. 2: Measured Burning Rates (Dots) of MGO 40101 with Fit (Line)

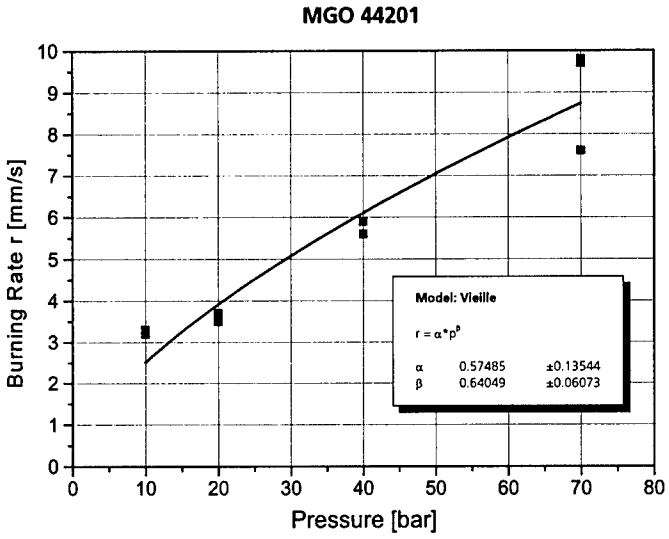


Fig. 3: Measured Burning Rates (Dots) of MGO 44201 with Fit (Line)

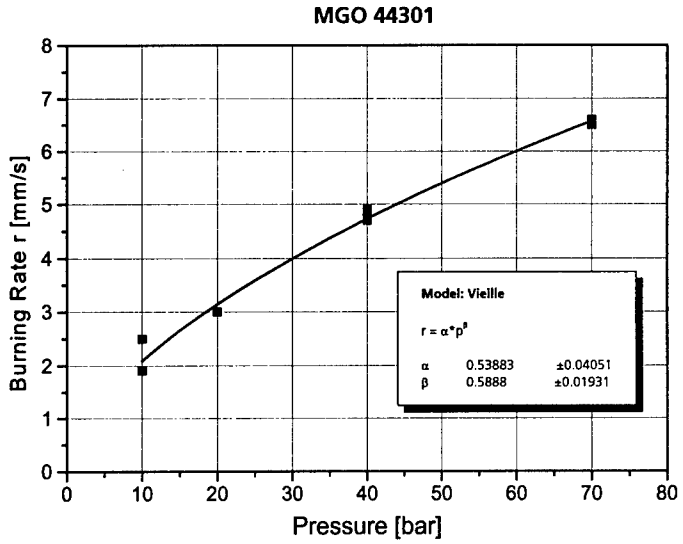


Fig. 4: Measured Burning Rates (Dots) of MGO 44301 with Fit (Line)

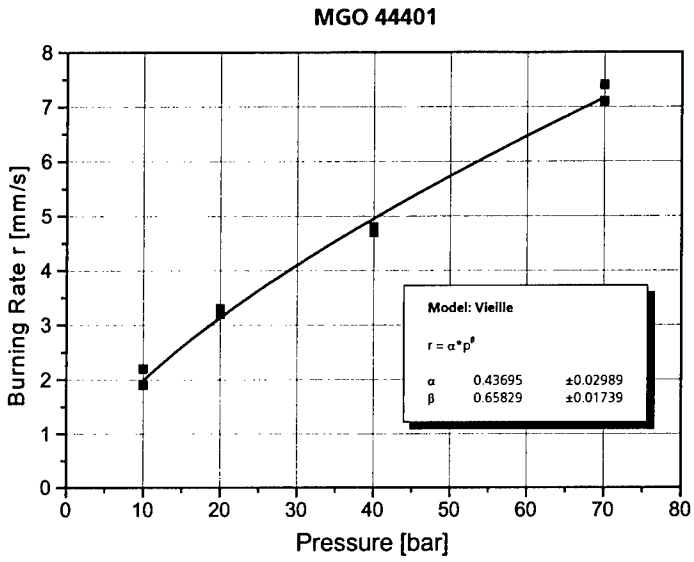


Fig. 5: Measured Burning Rates (Dots) of MGO 44401 with Fit (Line)

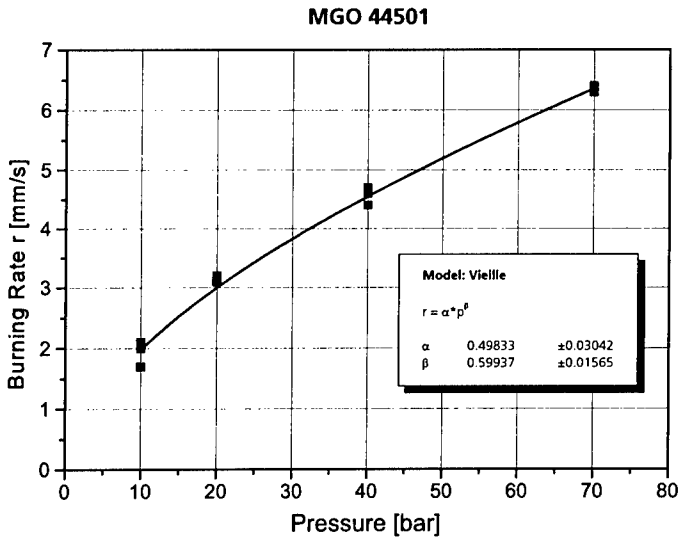


Fig. 6: Measured Burning Rates (Dots) of MGO 44501 with Fit (Line)

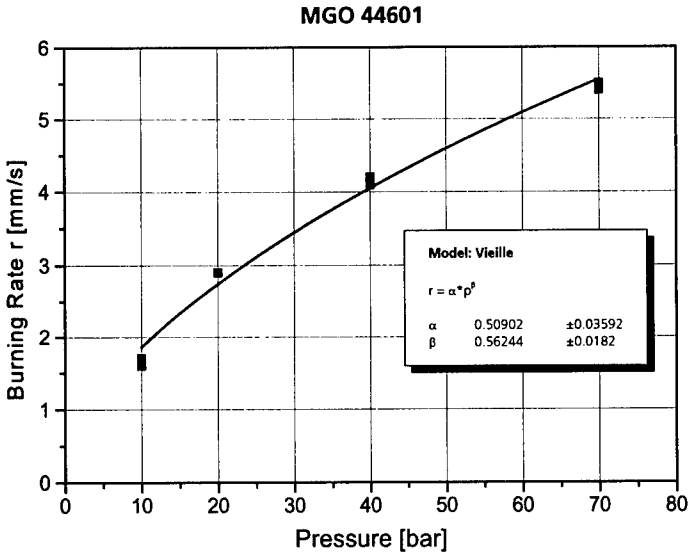


Fig. 7: Measured Burning Rates (Dots) of MGO 44601 with Fit (Line)

3 Temperature Measurements:

3.1 Experimental

The near infrared emission spectra were recorded using a HGS 1700. The system is based on a Zeiss MCS 511 grating spectrometer equipped with a 256 element InGaAs diode array as detector (spectral range 0.9 to1.7 micron). The spectral resolution is about 15 nm at the maximum scan rate of 300 spectra per second[1,2].

A 600 µm glass fiber is used as optical entrance. To allow a defined spatial resolution, a 100 µm pin aperture has been positioned 7 mm in front of the fiber. Taking into account the aperture to flame distance, a circular view field of 5 mm diameter results which allows only a very raw distinction of different flame zones.

We applied this system to the combustion of different gas generator propellant strands under pressure conditions. The experiments were performed in an optical bomb, a cylindrical high pressure vessel (maximum pressure 30 MPa, 70 mm diameter) equipped with two opposite quartz windows allowing the application of several non-intrusive combustion diagnostics like pyrometry, spectroscopy and cinematography at the same time. The experimental setup is described in detail in other publications[3,4] as well as the concept to obtain burning rates

simultaneously from video data[3], which were used to correlate time history with the local position on the flame axis above the burning surface.

3.2 Data Analysis

To determine a physical property like the temperature from spectroscopic data, the frequency resolved intensity distribution has to be modeled and compared to experimental spectra[5].

The calculation of molecular emission and transmission spectra needs the knowledge of the frequency and wavelength resolved absorption coefficient. Non-linear polyatomic molecules like water have lots of spectral lines in the infrared which can not be calculated applying a simple analytical model[6]. Therefore, a band model, based on tabulated data must be used considering profile, half width and distribution of spectral lines[7].

At high temperatures, the ‚Random Band Model' with a combined Doppler and Lorentz profile is approved. Additionally, each molecule is compressed in a line group (Single-Line-Group-Model). The Curtis-Godson-Approximation is used to get the ‚Curve of Growth'.

The here applied modeling code of the near infrared water band spectra is based on the data published in the 'Handbook of Infrared Radiation from Combustion Gases'[7]. It allows the calculation of the emission and transmission spectra of H_2O in a temperature range from 600 to 3500 K taking into account self absorption, pressure broadening and soot. The calculated intensity distributions are compared to experimental spectra by a least-squares fit routine with the parameter temperature and concentration length. An example for the data analysis is shown in Fig. 8. A more detailed description of the band modeling theory is given elsewhere[5].

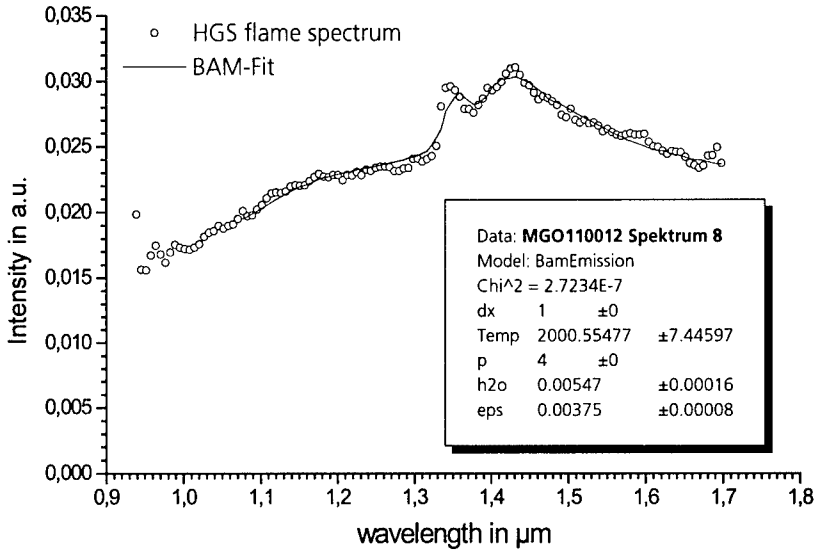


Fig. 8: Characteristic spectra of some investigated energetic materials

3.3 Results

The application of the HGS 1700 is very easy. After calibrating the spectrometer system with a black body radiator as reference emitter, the fiber optic was simply fixed in front of the quartz window of the optical bomb and the emission spectra were recorded. The system showed an excellent sensitivity. Even at low temperatures a high signal to noise ratio is observed. The data analysis needs only a few seconds.

In the investigated NIR range all energetic materials emit more or less strong continuum radiation due to bulk materials. This continuum is overlapped by clear water bands systems at 1.3 µm and very weak water bands at 1.1 µm. The continuum system can be satisfying fitted using the a constant emissivity (grey body radiation). The calculated spectra with combined water and continuum radiation fit well to the experimental data (see Fig. 8) and the reproduction of the experiments and measurements were excellent (see Fig. 9). Additional test measurements on a black body radiator and a tungsten strip lamp at different temperatures (1200 to 2000 K) with the same calibration file resulted in a very high accuracy in a range of ±20 K.

In the experimental setup, the flame front of the burning propellant strand is passing the detector with a constant burning rate if a steady combustion is assumed. In spite of the low spatial resolution of the spectrometer optics different reaction zones are observable at the adjusted exposure time of 100 ms. On typical observed flame length of 10 to 50 mm the spatial resolution of the optics is 2 to 10 times smaller than the total reaction zone.

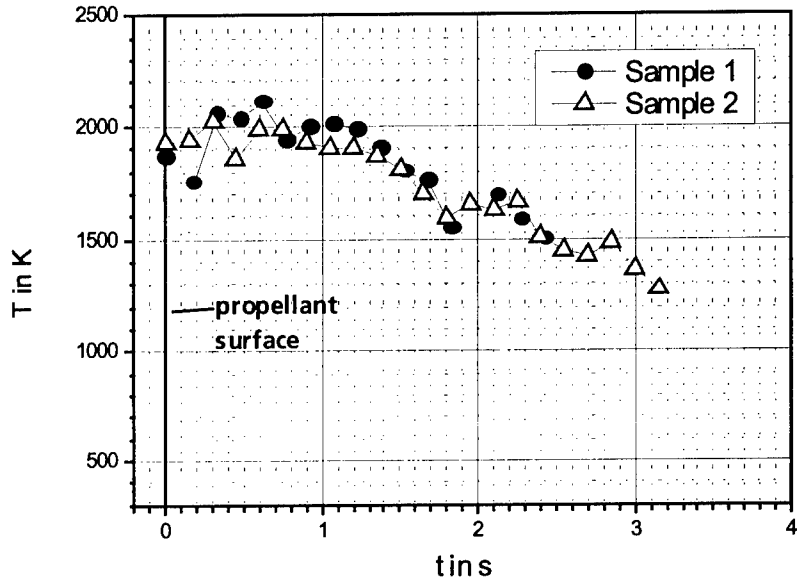


Fig. 9: Comparison of two MGO11001 at 4 MPa

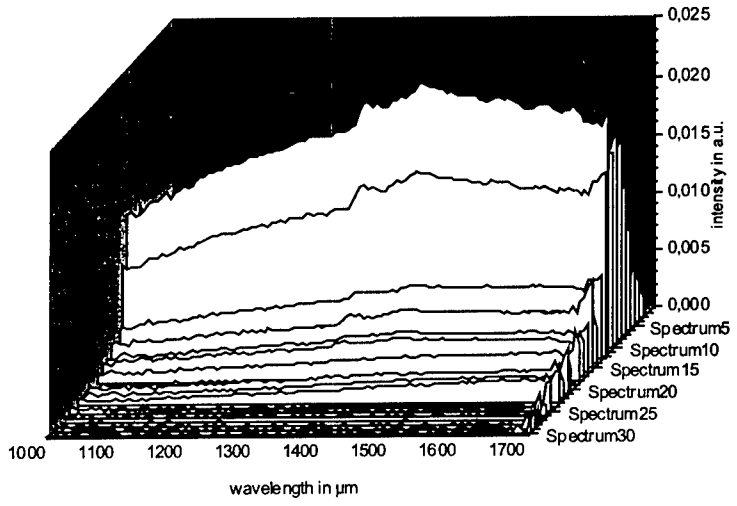


Fig. 10: Waterfall plots of spectra series, when combustion front passed the detector field

energetic material	Pressure in Mpa	mean temperature in K	min. T in K	max. T in K	ICT-Code in K
MGO11001	4	2000	1700	2100	2880
MGO14201	4	1800	1500	2000	2900
MGO14301	4	1850	1500	2100	2920
MGO14401	4	1900	1600	2000	2940
MGO14601	4	1850	1600	2050	2840

Tab. 2: Measured and calculated temperatures for some gas generator compositions

Temperature and concentration fluctuations of water and soot in the flame front are monitored. At typical burning rates of 5 to 20 mm/s about 20 to 100 single shots per experiment are acquired. This allows a reliable statistical data analysis.

The determined main, minimum and maximum temperatures of the investigated samples are listed in Tab. 2. Additionally, the adiabatic flame temperatures calculated from the ICT code[8] are given. All measured temperatures a significantly lower than the adiabatic ones.

Experiences from previous experiments using other diagnostic systems like mid infrared emission spectroscopy[3,4,9], 2-color-pyrometry[10,11], line reversal[12] or CARS showed, that temperatures 300 to 700 K below the adiabatic value are realistic. Reasons are radiation losses, incomplete reaction and cooling by cold nitrogen used as inert pressure medium in the optical bomb.

4 Conclusions:

The data analysis showed, that this method is suitable for monitoring of energetic material flames. Advantages of the optical bomb are the simple experimental setup and the fast data analysis (possible online monitoring of gas temperatures). Besides the burning rate, the vibrational temperature and the concentration of water, particle temperatures and concentrations are obtained, which is very useful in the investigation of composite propellants.

5 References

[1] Eckl, W.; Weiser,V.; Weindel; M.; Determination of the Temperature in an Isopropanol Diffusion and a Premixed Propane-Air Flame; Application Note - HGS-1700 der Fa. WMM Sensorik Gmbh & Co.KG

[2] Weiser, V.; Eckl, W.; Eisenreich, N.; Langer, G.; Weindel, M.; Analyzing Molecular IR-Emission Spectra of Deflagrating Methane Air Mixtures at Different Pressures; 17th International Colloquium on the Dynamics of Explosions and Reactive Systems (ICDERS); July 25-30,1999; Heidelberg, Germany; Presentation 90; http://reaflow.iwr.uni-heidelberg.de/~icders99/program.htm

[3] Weiser, V.; Eisenreich, N.; Baier, A.; Eckl, N.; Burning Behaviour of ADN Formulations; Propellants, Explosives, Pyrotechnics 24; 163-167 (1999)

[4] Eckl, W.; Eisenreich, N.; Liehman, W.; Menke, K.; Rohe, T.; Weiser, V.; Combustion Phenomena of Boron Containing Propellants; Challenges in Propellants and Combustion – 100 Years after Nobel; Begell House, New York, 1997, pp. 896 – 905

[5] Eckl, W.; Weiser, V.; Weindel, M.; Eisenreich, N.; Auswertemodelle zur Bestimmung der Temperatur- und Molekülverteilung in Festtreibstoffen; 30th International Annual Conference of ICT, 1999, Karlsruhe, pp. 112-(1-10)

[6] G. Herzberg, 'Molecular Spectra and Molecular Structure II. Spectra of Polyatomic Molecules', D. van Nostrand Company Inc., Princeton, New Jersey, 1950

[7] Ludwig, C.B.; Malkmus, W.; Reardon, J.E.; Thomson, J.A.L.; Handbook of Infrared Radiation from Combustion Gases, NASA SP-30980 (1973)

[8] F. Volk, H. Bathelt, "User's Manual for the ICT-Thermodynamic Code; Vol. 2", ICT-Bericht 1/1991

[9] Eckl, W.; Weiser, V.; Langer, G.; Eisenreich, N.; Burning Behaviour of Nitramine Model Formulations; Propellants, Explosives, Pyrotechnics 22; 148-151 (1997)

[10] Weiser, V.; Eckl, W.; N. Eisenreich; Spektroskopische und Pyrometrische Untersuchungen des Abbrandverhaltens von AN/GAP-Mischungen mit verschiedenen Phasenstabilisatoren; 25th International Annual Conference of ICT, 1994, Karlsruhe, pp. 25-(1-15);

[11] Eckl, W.; Eisenreich, N.; Liehmann, W.; Schneider, H.; Weiser, V.; Emission Spectroskopy and Pyrometry of Propellant Flames and Rocket Plumes; Non-Intrusive Combustion Diagnostics; (Kuo K. K., Parr T. P. ed.), Begell House, Inc. New York, 1994

[12] M. Hund, N. Eisenreich, and F. Volk, "Determination of Interior Ballistic Parameters of Solid Propellants by Different Methods", Proc. 6th Int. Symp. on Ballistics, Orlando 1981, pp. 77-84.

[13] Eisenreich, N.; Eckl, W.; Fischer, Th; Weiser, V.; Phenomena of the combustion of the gun propellant JA2; (this symposium)

[14] Neutz, J.; Schmid, H.; Klemenz, M.; Interior ballistic behaviour of a new gas generator fuel for fire extinguishing purpose; 5th International Symposium an Exhibition on Sophisticated Car Occupant Safety Systems (Airbag 2000+); 2000; 36-1 to 36-7

THE EFFECTS OF COLOR CHANGING ON THERMAL STABILITY AND COMPATIBILITY OF TATB

Huang Yi-gang Wang Xiao-chuan Li Guang-lai Wang Lin

(Institute of Chemical Materials of China Academy of Engineering Physics)

Abstract: in this paper, the thermal stability of green and yellow TATB was investigated by eudiometer, calorimeter, explosion point and differential thermal analysis. The results indicate that the color-changing of TATB mainly appears on it's surface. The thermal stability and the compatibility of green and yellow TATB were good, with color changing after 360 days of natural light illumination. The thermal stability and the compatibility of yellow TATB were better than that of green TATB.

Keywords: TATB structure thermal stability

INTRODUCTION

TATB is currently used as insensitive high explosive. After being illuminated, the color of the explosive will change, from yellow to green, to black. Because TATB has many uses, during the process of development, application and storage, the effects of color changing on it's thermal stability and compatibility of TATB and other materials contacting with it are becoming more important.

Britt[1] and David[2] had investigated the reason of color changing of TATB and molecular structure of green TATB produced after color change. The results indicate that the main reason of color changing lies in the illuminated molecular on its surface, which absorbed energy, and turn them into excited molecular. And thus cause electron transition and form free radical. We had also studied the reason and get the same result [3]. In order to develop color-changed TATB extendedly, we simulate the processes of application and storage of TATB by using natural light illumination. We investigated the thermal stability of color-changed TATB, and provide theoretical basis for the development, application and storage of insensitive explosive.

l. PREPARATION OF GREEN TATB

The color-changing of TATB appears on it's surface. Although it changes quickly under illumination, it is relatively difficult to gain high-content TATB. We increased it's specific surface area to exposure it under natural light sufficiently, so that we can increase the content of color-changed TATB. The content of green TATB is approximate 1%, exceeding the content of natural color-changed TATB obtained from normal application and storage.

2. INVESTIGATION OF THERMAL STABILITY AND COMPATIBILITY

In order to the thermal stability and compatibility of green and yellow TATB, we used the normal standard method (including vacuum stability, thermogravimetry, differential thermal analysis. explosion point, Bourdon type glass manometer test (eduiometer and calorimeter)) of judging thermal stability and compatibility of explosive. The results were compared with that of yellow TATB. The samples were put in constant temperature field, the weight of gas produced by samples, the amount of weight-loss, and the height of heat-release peaks were measured after a limited period. The results were used to assess the thermal stability and compatibility of green and yellow TATB.

2.1 VACUUM STABILITY TEST (VST)

Put 0.6g samples of yellow TATB and green TATB into the experimental instruments respectively. Keep 48h at 120□ . Heat 0.2g sample for 2h at 260□ , the measured amount of weight-loss was used to assess it's thermal stability(see table 1).

2.2 THERMOGRAVIMETRY

Put 0.6g samples of yellow TATB and green TATB into experimental instruments respectively keep 48h at 120□. Measure the amount of their weight-loss(see table 1).

2.3 DIFFERENTIAL THERMAL ANALYSIS (DTA)
Rise temperature of 200mg samples of yellow TATB and green TATB at the rate of 20□/min respectively. Record the endothermic change and exothermic change of the two samples (see table 1).

2.4 EXPLOSION POINT
Put 50mg samples of yellow TATB and green TATB into 8" detonator respectively. Exert pressure to 50kg. Keep both the samples in constant temperature fields. Record the time of explosion caused by thermal effect. Measure the explosion delay time near the heat explosion point, the results were used to calculate the explosion point of 5s explosion delay time, which is called explosion point (see table 2).

2.5 BOURDON TYPE GLASS MANOMETER TEST
Put 3g samples of yellow TATB and green TATB into experimental instruments

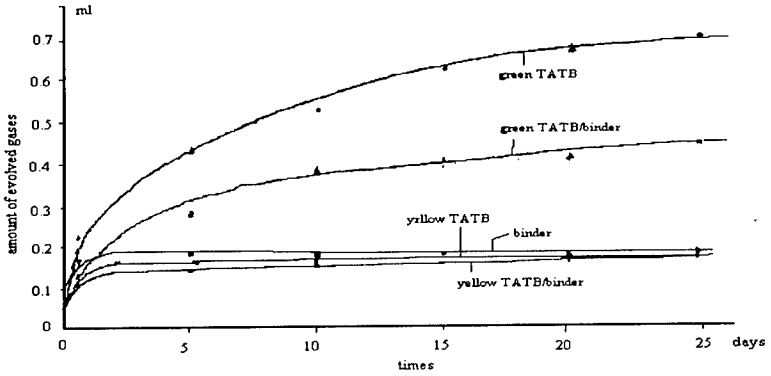
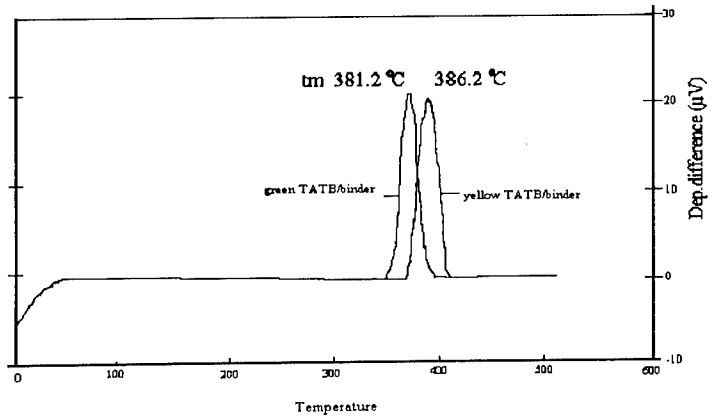


Figure 1 the result of vacuum stability

respectively. Heat 25 days at 120□. Measure the amount of gas-releasing at different period (figure 1).

3 RESULTS AND DISCUSSION
Thermal stability is defined as the capability of keeping the physical and chemical properties of explosives and relative materials no significant change under thermal energy. The experimental results of yellow TATB and green TATB are shown in figure 2.

figure 2 the scheme of DTA of yellow and green TATB/binder



Because we have not yet absolute assess method for the stability of explosives, according to the normal analytic method, we obtained the following results: among all explosives, the yellow TATB and green TATB are the most stable, and their stability meet the needs of weapons. But, the amount of gas-releasing of green TATB, measured by VST, Bourdon type glass manometer test, is greater than that of yellow TATB. After keep 48h at 120□, weight-loss of green TATB is greater than that of yellow TATB.

Table I The experimental results of compatibility of yellow TATB and green TATB

	Yellow TATB	Green TATB
VST(5.0g/120□/48h)	0.13ml	0.97ml
VST(0.2g/260□/2h)	0.58ml	1.56ml
TG(120□/48h)	0.13%	0.15%
Bourdon test(g/120□/25days)	0.182ml	0.710ml
DTA(□)	380.8□ 404.5□	373.3□ 399.1□
Explosion point(□)	437.4□	432.8□

Two exothermic peaks of green TATB are 7□ lower than that of yellow TATB, which is mainly caused by the structure changing of TATB. And the explosion point of green TATB decrease 4.6□ than that of the yellow TATB. The above results are mainly caused by structure changing of green TATB[1]. After been illuminated, free radicals appeared on the molecular structure of yellow TATB. The -NO2 group is excited, and activation energy decrease, which lead to reduction of fusing point, decomposition point and the explosion point.

We also observed from experiments that the color-changing of TATB occurs only after illumination. And it's color keep the same after 48h at 120□ basicly. After 2h at 200□, it's color changes from yellow to light brown. The color of green TATB becomes deeper, which indicates that the high-temperature will cause color change of TATB. Using the sample which has been heated 2h at 260□. We conducted differential thermal analysis and found the exothermic peak increase about 5□,which indicates that the substances which are unstable at high temperature have volatilized.

The experimental results of compatibility of yellow TATB and green TATB with binder resin(1:1) is shown in table 2 and table 3 measured by eudiometers and calorimeters.

Table 2 The results of compatibility of yellow TATB and green TATB with binder measured by eudiometers

	VST		Boutdon test		TG	
	120□/48 h	reactivity	120□/48h	reactivity	120□/48 h	reactivity
Yellow TATB(2.5g)	0.07ml		0.130ml		0.13%	
Green TATB(2.5g)	o.45ml		0.338ml		0.15%	
binder	0.26ml		0.183ml		0.20%	
Yellow TATB/ binder	0.23ml	-0.10	0.139ml	-0.0017	0.07%	-0.09%
Green TATB/ binder	0.65ml	-0.06	0.251ml	-0.010	0.10%	-0.07%

From the results of VST□TG and Bourdon type glass manometer test, the amounts of gas-releasing of yellow TATB and green TATB mixed with binder (1:1) is less than that of single explosive sample, the reactivity is shown negative, which is no interaction with TATB and binder.

Table 3 The results of compatibility of yellow TATB and green TATB with binder measured by calorimeters

	DTA(□)	Reactivity	Explosion	Reactivity

			point(□)	
Yellow TATB	380.4 404.5		437.4	
Green TATB	373.3 399.1		432.8	
Yellow TATB/ binder	386.2	5.4	438.2	0.8
Green TATB/ binder	381.2	7.9	437.7	4.9

From the table 3, we know that the decomposition temperatures of yellow TATB□green TATB each mixed with binder have raised. Two exothermic peaks merge to one peak, the temperature of yellow TATB/ binder is 386.2□ and that of green TATB/ binder is 381.2□. The temperatures of explosion of 5s explosion delay time of yellow TATB/ binder and green TATB/ binder is higher than pure explosive, but that of yellow TATB/ binder is higher 5□ than green TATB/ binder. So, binder is better as a binder of TATB explosive, and no interactivity with TATB. The compatibility of yellow TATB was better than that of green TATB.

4. CONCLUSION

The experimental results indicate that the thermal stability of green TATB and yellow TATB, the molecular compatibility of TATB with binders were good. And the thermal stability and the compatibility of yellow TATB were better than that of green TATB.

Reference

1 Brit A, et al. Propellant and Explosive. 1981,6,94
2 David W. Firsich, et al. Journal of Energetic materials, 1984, 2(3)
3 Huang Yiguang, et al. GF-B ZW-C-990071

The Contacted Compatibility of PBX and Polyurethane

Luo Xuemei Zuo Yufen Xu Ruijuan
(China Academy of Engineering Physics,610003)

Abstract:We have studied the compatibility of PBX and polyurethane through Bruton method ,and have studied the interaction mechanism through TG-IR and VST-MS analysis as well.Basing on all data we have got, we think that the contaction between them has accelerated themselves' decomposition .As to the reason ,we think,NO_2 ,the intermediate product of PBX's decomposition,has combined with H_2O to produce inorganic acid which can catalyze the hydrolysis of polyurethane;on the other hand,the depletion of NO_2 would promote the decomposition of PBX .

Keywords: PBX TG-IR MS compatibility

1 Introduction

The compatibility of explosives and related material is very important to components' storage reliability.In previous work we have studied the compatility of PBX and many kinds of related material through accelerated aging test,long term stockpile and structural analysis etc., and found there is some kind of action between PBX and polyurethane.

At elevated temperature of 80,100,120□,we have tested the gas release of PBX,polyurethane,PBX/polyurethane mixed system in Bruton tube related to different duration.Combining with VST-GC/MS method,TG-IR analysis we have studied the interaction mechanism of PBX/polyurethane as well.

2 Experiments

2.1 material

PBX moulding powder ,PBX cylinder(Φ15×5),aluminium, steel,polyurethane

2.2 apparatus

(1) Bruton method instrument

(2) Vaccum-Stability-testing instrument

(3) Organic Mass Spectrum Instrument:MAT95S,Finnigan MAT Co.,German,combined with GC.Maximum resolution 6000,maximum mass number detectable 3500aum

(4) TG-IR Instrument:TG, IR

2.3 experiments

2.3.1 Bruton method

PBX moulding powder,polyurethane,PBX/polyurethane samples are sealed into Bruton tubes under 80,100,120□ repectively,with a 0.1g/ml packed density.Heating duration ranges from 24 to 264 hours.Evaluate the gas release at different interval.

2.3.2 VST-GC/MS combined analysis

Seal PBX moulding powder (2.5g),polyurethane(2.5g),PBX/polyurethane(2.5/2.5g) into vaccum stability testing tubes separately,then heat the tubes under 100□ for 48 hours,finally,inlet gas release into GC/MS system for evaluation.GC state:sample inlet temperature 100□,column temperature 30□,constant .MS state:ionization pattern EI.POS,resolution 3760,mass range 5~200aum.

2.3.3 TG-IR

TG-IR experiments are applied to PBX moulding powder ,polyurethane and PBX/ polyurethane respectively, sample amount:11mg,scanning rate 20□/min,carrier gas N_2,the volume of flow 100ml/min.

3 Results and discussion

3.1 Bruton method results

Gas release-duration of several kind of material (ml/g)

duration (hr)	80□			100□			120□		
	PBX	Polyureth -ane	PBX/poly- urethane	PBX	Polyur -ethane	PBX/poly -urethane	PBX	Polyur -ethane	PBX/poly -urethane
0.083	0.000	0.065	0.006	0.009	0.176	0.143	0.000	0.343	0.349

0.167	—	—	—	—	—	—	—	—	0.442
0.5	0.000	0.177	0.123	0.027	0.361	0.170	0.026	0.435	0.613
1	0.000	0.177	0.142	0.046	0.361	0.287	0.078	0.635	0.706
2	0.000	0.205	0.180	0.046	0.379	0.323	0.078	0.669	0.851
4	0.000	0.205	0.199	0.046	0.388	0.385	0.078	0.719	0.987
8	0.000	0.224	0.199	0.046	0.397	0.457	0.078	0.753	1.208
12	—	—	—	—	—	—	—	—	1.387
24	0.000	0.224	0.284	0.082	0.432	0.681	0.112	0.819	1.659
48	0.000	0.224	0.360	0.109	0.467	0.860	0.156	0.861	—
72	0.000	0.242	0.379	0.118	0.511	0.986	0.156	0.920	—
96	0.000	0.242	0.436	0.128	0.529	1.093	0.182	1.037	—
120	0.000	0.242	0.493	0.137	0.555	1.165	0.199	1.087	—
144	0.038	0.242	0.521	0.146	0.573	1.219	0.216	1.162	—
168	0.038	0.261	0.531	0.155	0.573	1.282	0.234	1.221	—
192	0.038	0.261	0.540	0.164	0.591	1.317	0.234	1.271	—
216	0.038	0.261	0.606	0.164	0.617	1.389	0.277	1.305	—
240	—	—	0.625	—	—	—	—	1.346	—
264	—	—	—	—	—	—	—	1.397	—

From fig.1~3,we find that the contaction between PBX and polyurethane has increased both the gas release amount and the rates of releasing.The higher the temperature,the larger the increment.

Regressing these data through ORIGIN software,we find an apparent first exponential decay relationship exiting between duration and gas release of mixed system(PBX/polyurethane).The empirical equations are listed as followed:

80□ $y = 625 - 511.85669\exp(-x/84.48367)$

100□ $y = 1364.99047 - 1129.10858\exp(-x/60.50597)$

120□ $y = 1659 - 1192.83492\exp(-x/7.11936)$

y—gas release amount(μl) x—duration(hr)

3.2 VST-GC/MS results

Based on fig.4,the GC/MS spectrum of PBX' gas release,peak intensity of O_2(m/z:32) is 7.230E+07,of CO_2(m/z:44) is 4.260E+05,of H_2O(m/z:18) is 7.612E+05,of NO(m/z:30) is 1.562E+04.CH_3,the fragment of CH_4,has a peak intensity 3.123E+03 at m/z:15.

Based on fig.6,the GC/MS spectrum of polyurethane's gas release,peak intensity of O_2 (m/z:32) is 8.640E+07,of H_2O(m/z:18) is 8.461E+05,of CO_2(m/z:44) is 1.869E+05,of HCOOH(m/z:46) is 4.060E+03,of CH_3(m/z:15.) is 8.745E+03.

Based on fig.5, the GC/MS spectrum of PBX/polyurethane' gas release, peak intensity of O_2(m/z:32) is 7.341E+07, of CO_2(m/z:44) 2.063E+06,of N_2O 4.126E+05, of H_2O 1.134E+06,of NO(m/z:30) 3.523E+05,of HCOOH(m/z:46) 3.779E+04, of CH_3(m/z:15.) 1.062E+04.In one word,there are three phenomena in mixed system:first,the release of CO_2,the common decomposing product of PBX and polyurethane,is far more greater than that of simple superimposing of two separate systems;second,the release of HCOOH,a gaseous phase product of polyurethane,has increased when contacted with PBX;third, N_2O is a product in PBX's decomposition[1,2],but in single PBX system it is undetectable due to its extremely low intensity, while in mixed system it can be detected.

3.3 TG-IR analysis

In fig.7,PBX starts to decompose at 271.09□.At 275.42□,4.28% of it has decomposed.When at 286.56□,decomposition has finished.

In fig.9,polyurethane starts to decompose at 353.57□.At 447.63□,99.15% of it has decomposed.When at 471.04□,decomposition has finished.

In fig.11,6.66% of the mixed system has already decomposed at 265.86□.When temperature is up to 277.8□,43.42% has decomposed.It means most explosive has finished decomposing before that point.When at 482.56□,decomposition of the whole system has finished.

From above,we can say that the contaction of polyurethane to PBX has lowered PBX's beginning decomposing temperature.

The gaseous phase products of each system at any stage of decomposition can be detected on line through IR analysis.

In fig.8,products detectable of PBX include CO_2, N_2O,NO_2,HCHO,NO.

In fig.10, H_2O,carbonyl group,-CH_3, CO_2,CO can be detected at the initial stage of polyurethane's decomposing.Along with the deepening of reaction,peak intensity of CO_2 is getting more and more strong while CO more and more weak.

In fig.12,NO, CO_2, N_2O, NO_2 can be detected at the initial stage (6~9min).At the later stage(19~28min), NO_2 is almost undetectable and CO_2 and NO make up the most part of gas products.We also find the peak intensity of NO_2 at 1302cm^{-1} has experienced a weak-strong-weak-diminish period.

We have also applied storage tests to these material at ambient temperature 5~30□,relative humidity 60~90%. The way of storage :(1) related material alone (2) PBX mixed with related material(3) PBX alone.

From mass loss-duration curves of PBX cylinders in different storing ways,we find three of them are almost overlapped.These overlapped curves stand mass loss-duration of cylinders stored alone,contacted with steel,or with aluminium respectively.The curve showing that of cylinders contacted with polyurethane is high above other cnes.After a long time contaction with PBX,polyurethane has become light red from previous colorless.It doesn't fade even vacuum-pumped in dry oven for 4 hours at room temperature.

IR spectrum of polyurethane in different storing ways are listed in fig.14.The characteristic peak of –COOH at 1720cm^{-1} is due to the hydrolysis of polyurethane.The strengthening of this peak in lower part of fig.14 means a deeper hydrolysis of polyurethane when contacted with PBX.

The dimensions of cylinders stored in varied ways have kept unchanged after 46 months .

4 Mechanism of the interaction between PBX and polyurethane

Based on all the results above, we can infer that:

(1) The contaction between PBX and polyurethane has accelerated the decomposition of each own.

(2) NO_2 is a intermediate product in PBX's decomposition.

Following equations show us some reactions possiblely happening in the mixed system.

HMX is the major composition in PBX.

$$HMX \xrightarrow{\Delta} NO + N_2O + N_2 + CO + CO_2 \qquad (1)$$

NO_2 is its intermediate product[2].

Polyurethane's thermal decomposition:

$$polyurethane \xrightarrow{\Delta} \sec ondary - a\min e + CO_2 \qquad (2)$$

Polyurethane's hydrolysis:

$$polyurethane \xrightarrow{H_2O} HO - R - COOH + CO_2 \qquad (3)$$

The reaction between NO_2 and H_2O:

$$NO_2 + H_2O \rightarrow HNO_2 + NO \qquad (4)$$

HNO_2 may catalyse reaction (3).

So,we think the interactionn mechanism is as follow,on one hand, NO_2,as an intermediate product of explosive's decomposition ,has not only joined the continuing decomposition,but also combined with H_2O to produce HNO_2 which can catalyze reaction(3);on the other hand,the equation balance of explosive's decomposition could be broken and move toward right because of the depletion of NO_2.

5 Conclusions

5.1 The contaction between PBX and polyurethane has accelerated the decomposition of each own.

5.2 NO_2 could combine with H_2O to produce HNO_2 which can catalyze hydrolysis of polyurethane;the decomposition of explosive has been promoted due to the depletion of NO_2.

5.3 The interaction can be restrained if lowering moisture content in material.

Reference

1.Chu Shijin. Explosive thermal analysis. Science Republication Agency,Beijing,1994

2. Explosive thermal decomposition.Андреев,1965.

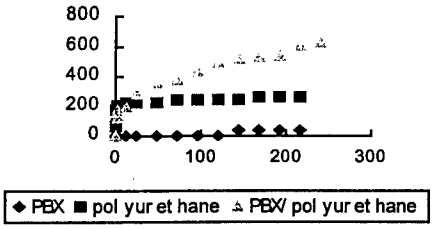


Fig1. Gas release-duration curve under 80□(X-hr,Y-ul)

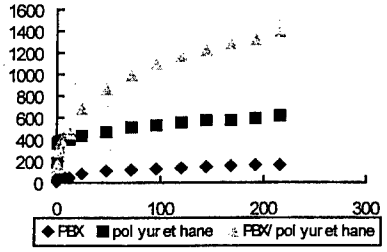


Fig.2 Gas release-duration curve under 100□(X-hr,Y-μl)

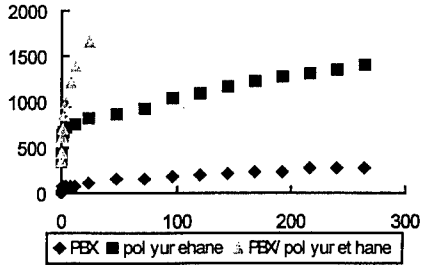


Fig.3 Gas release-duration curve under 120□(X-hr,Y-μl)

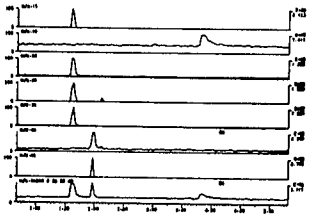


Fig.4 PBX GC/MS analysis

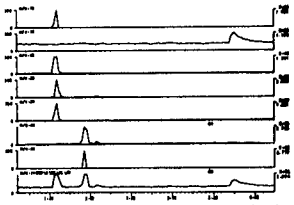


Fig.5 PBX /polyurethane GC/MS analysis

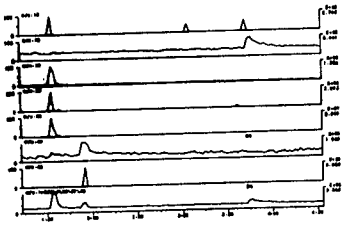


Fig.6 polyurethane GC/MS analysis

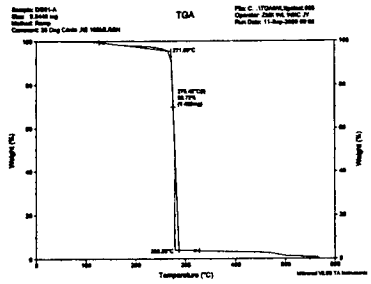


Fig.7 PBX TG analysis

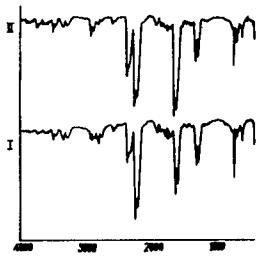


Fig.8 PBX TG-IR analysis
□-15~16 min □-27~29min

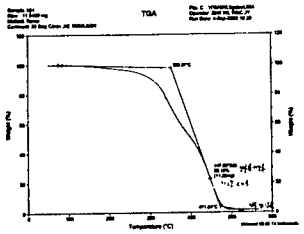


Fig.9 Polyurethane TG analysis

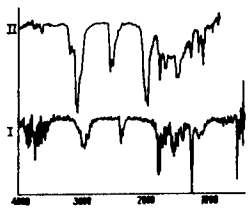
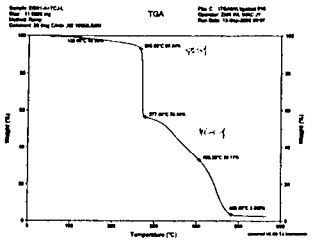


Fig.10 Polyurethane TG-IR analysis

□-6~9 min □-17~19min



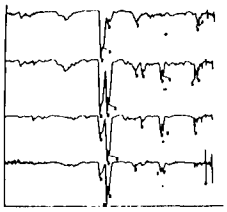


Fig.11 PBX/ Polyurethane TG analysis Fig.12 PBX/Polyurethane TG-IR analysis
□-6~9 min □-9~12min □-12~19min
□-19~28min(from down to up)

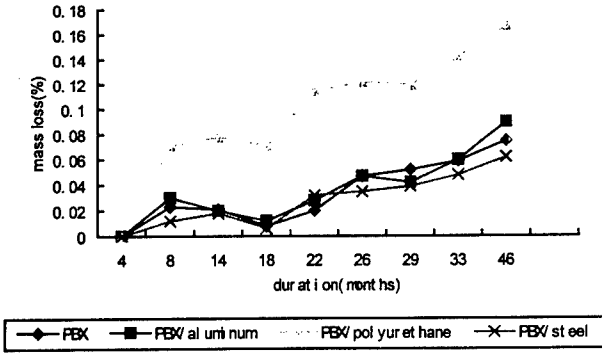


Fig.13 mass loss-duration of storaged PBX cylinders

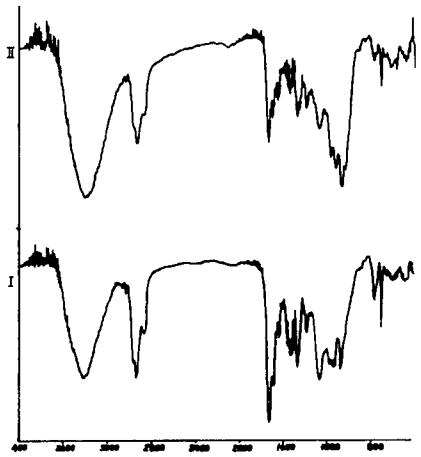


Fig.14 IR spectrum of long term stockpiled polyurethane
□-contacted with PBX □-stored anlone

EMISSIONSSPEKTREN BRENNENDER METALLE

E. Roth, Y. Plitzko, V. Weiser, W. Eckl, H. Poth, M. Klemenz

Fraunhofer-Institut Chemische Technologie (ICT)
Joseph-von-Fraunhoferstr. 7
76327 Pfinztal (Berghausen), Germany

Abstract

EMISSIONSPEKTRA OF BURNING METALLS
Burning Al, Mg, Ti and B strongly contributes to rocket plume signature. An application of this emission spectra is given in flares. The elements have been burned in air and oxygen. Emission spectra are received with UV/Vis, NIR and IR spectrometers. In the visible range wellknown emission lines and bands are found. In NIR and IR range only grey body radiation can be observed with temperatures of 1800 to 2000 K (Al), 1900 to 2400 K (Mg), 1800 to 2200 K (Ti) and 1200 to 1400 K (B).

Kurzfassung

Die Verbrennung von Aluminium, Magnesium, Titan und Bor trägt maßgeblich zur Signatur des Raketenabgasstrahls bei. Die Strahlungsemission wird bei Leucht- oder Täuschkörpern gezielt ausgenutzt. Die Substanzen wurden unter Luft und Sauerstoff spektrokopisch im UV/Vis, NIR und MIR-Bereich untersucht. Im sichtbaren Strahlungsbereich zeigen die Elemente die bekannten charakteristischen Emissionsbanden und -linien. Die Emission im NIR und IR ist weniger dokumentiert. Hier finden sich vornehmlich Kontinuumsspektren, die zumindest im NIR-Bereich von 1000 bis 1700 nm sehr gut mit einem grauen Strahler beschrieben werden können. Dabei ergeben sich Temperaturen von 1800 bis 2000 K (Al), 1900 bis 2400 K (Mg), 1800 bis 2200 K (Ti) und 1200 bis 1400 K (B).

Einleitung

Metalle wie Aluminium, Magnesium und Titan verbrennen mit hohen Temperaturen. Deshalb werden manchmal zur Leistungssteigerung feinste Metallpartikel zu Composite-Festtreibstoffen beigegeben. Bor ist ein viel diskutierter Sekundärtreibstoff für luftatmende Triebwerke. Alle diese Elemente emittieren Strahlung im gesamten Wellenlängenbereich des elektromagnetischen Spektrums und tragen so zur Signatur des Abgasstrahls bei. In Leucht- oder Täuchkörpern (MTV-Flares) werden diese Komponenten gezielt eingesetzt, um eine emissionsstarke Strahlung bestimmter Charakteristik zu erzeugen.
Die Strahlungsemission dieser Elemente im UV/Vis ist gut untersucht [3,11]. Es zeigen sich vornehmlich charakteristische Linien und Banden der angeregten Atome oder Oxide. Die Emission im NIR und IR ist weniger dokumentiert [5].
Im folgenden wurden Emissionspektren von reinem Aluminium, Magnesium, Titan und Bor unter Luft oder Sauerstoff im UV/Vis, NIR und MIR Bereich zusammengestellt, um ihren Beitrag zur Strahlung des Abgasstrahls oder in Leuchtkörpern abzuschätzen. Die Spektren erlauben eine Temperaturbestimmung durch mathematischen Vergleich mit theoretischen Gas- und Graustrahlerspektren. Als Referenz für Anzündflammen wurden auch die Spektren eines Kohlenwasserstoffs (n-Heptan) aufgenommen, die von den Banden der Verbrennungsprodukte Wasser, Kohlendioxid und Ruß dominiert werden [1].

Experimentelles

Spektrometer

UV/Vis-Spektrometer

Zur Aufnahme der Spektren im ultravioletten (UV) und sichtbaren (Vis) Spektralbereich wurde ein Gitterspektrometer der Firma LOT mit 250 mm Brennweite verwendet. Die eingesetzten Gitter erlaubten Messungen im UV bei 230 bis 570 nm (Auflösung 300 Linien/mm) und im Vis von <400 bis 880 nm (Auflösung 150 Linien/mm). Ein UV-sensibilisierter Silicium-CCD (ANDOR) mit einer Auflösung von 1024 Punkten detektiert die Intensitätsverteilungen mit einer minimalen Belichtungszeit von 10 ms pro Spektrum.

Die Wellenlängenkalibrierung erfolgt über geeichte Bandenstrahler (Neon, Quecksilber). Zur quantitativen Kalibrierung im Vis-Bereich dienen Wolframbandlampenspektren definierter temperaturabhängiger Strahlungsleistung, die unter den jeweils gleichen optischen Bedingungen aufgenommenen werden. In UV-Bereich erschien eine Intensitätskalibrierung als nicht sinnvoll, da das Emissionsspektrum von Wolfram unter 400 nm zu schwach ist, um eine definierte Kalibrierung zu gewährleisten.

NIR-Spektrometer

Zur Aufnahme der Spektren im nahen Infrarot wurde ein Gitterspektrometer HGS 1700 basierend auf dem Zeiss System MCS 511 verwendet, das speziell für Flammgasmessungen modifiziert wurde. Dieses Gerät ist mit einem InGaAs Diodenarray (256 Elemente) ausgestattet und deckt den Spektralbereich von 0.9 bis 1.7 µm ab. Die erreichbare spektrale Auflösung liegt bei 15 nm bei einer Scanrate von 300 Spektren pro Sekunde [6]. Als Eingangsoptik wurde eine spezielle Sonde verwendet, die auf das Glasfaserbündel nur Licht aus einem engen Öffnungswinkel von etwa 5° einkoppelt und auf den Spektrometerbaustein lenkt. Dadurch erhält man im vorliegenden Fall eine relativ gute Ortsauflösung von 4 bis 5 mm (Abstand 50 bis 100 mm).

IR-Spektrometer

Zur Erfassung der IR-Strahlungsemission stand ein Filterradspektrometer zur Verfügung, das speziell für den Einsatz an realen Flammen und Verbrennungssystemen entwickelt wurde [7,8]. Hinter dem Öffnungsspalt (1.5 mm) wird das eintreffende Licht über zwei Hohlspiegel auf den Detektor abgebildet. Im Strahlengang befindet sich der Monochromator. Als Monochromator dient eine rotierende Aluminiumscheibe mit drei Filtersegmenten. Die Segmente weisen kontinuierlich variierende Interferenz- und Blockungsschichten auf, die je nach Winkelgradstellung eng begrenzte Wellenlängenintervalle von etwa 2% der nominalen Wellenlänge transmittieren.

Der Wellenlängenbereich des IR-Spektrometers erstreckt sich von 2.4 - 14 µm. Das Filterrad wird mit einem Präzessions-Schrittmotor angetrieben, der es ermöglicht das Filterrad bis 130 Mal pro Sekunde zu drehen, wobei jeweils der komplette Spektralbereich durchfahren wird. Die Wellenlängenzuordnung erfolgt über die Winkelstellung. Das ausgefilterte Licht trifft auf einen InSb/HgCdTe-Sandwichdetektor. Die Empfindlichkeit der Indium-Anitimonid-Diode erstreckt sich von 1 - 5.5 µm. Längerwellige Strahlung passiert die Detektorschicht und wird von der darunterliegenden HgCdTe-Schicht detektiert. Für ein gutes Signal/ Rausch-Verhältnis benötigt das System eine Betriebstemperatur von 77 K, die durch Kühlung mit Flüssigstickstoff erreicht wird. Zur Wellenlängenkalibrierung wird das bandenreiche Transmissionsspektrum einer Polystyrolfolie eingesetzt. Der detektierte Datenstrom wird in einem Transputer System (HYDRA der Fa. Kinzinger) online gepuffert und nach der Messung auf Festplatte abgespeichert [9,10].

Bestimmung der Flammentemperatur

Zur Modellierung von Spektren heißer Gase im Infrarotbereich wurde in Zusammenarbeit mit der Fa. WISPRO ein Programm entwickelt, das auf einem Bandenmodell und dem Datenmaterial des „Handbook of Infrared Radiation from Combustion Gases„ [2] beruht. Das Datenmaterial umfaßt den Temperaturbereich von 600 K bis 3000 K und wurde zusammen mit dem Modell der NASA durch vielfältige Experimente validiert. Berücksichtigt werden dabei die wichtigsten Banden von H_2O (1.3, 1.8, 2.7 und 6.2 µm), CO_2 (2.7 und 4.3 µm), CO (4.65 µm), NO (5.3 µm) und HCl (3.5 µm). Zusätzlich kann Emission bzw. Absorption von Rußpartikeln in die Berechnung mit einbezogen werden. Daneben berücksichtigt es die Selbstabsorption und Druckverbreiterung.

Das Programm kann Absorptionskoeffizienten, Emissions- und Transmissionsspektren von inhomogenen Gasgemischen im Infrarot-Bereich von 1 µm bis 10 µm berechnen. Da die Berechnung eines Spektrums durch die Benutzung eines Bandenmodells nur Bruchteile einer Sekunde benötigt, kann auch ohne großen Zeitaufwand durch Anpassung berechneter Bandenprofile an experimentelle Spektren auf Temperatur und Konzentrationen rückgeschlossen werden.

Untersuchte Materialien

- Bor, amorph
- leichtentzündliches Nanopulver von Aluminium (ALEX Nanopartikel)
- Magnesiumpulver (Ø≤100 µm)
- Titanpulver (Ø≤50 µm)
- n-Heptan (Kohlenwasserstoffrefernz für Anzündflamme mit CO_2 und H_2O Banden)

Durchführung

Die Brennstoffe wurden in einem Abzug offen als Pool Fire abgebrannt. Die Metallpulver wurden auf einer Stahlplatte als Haufwerk mit ca. 40 mm Basisdurchmesser frei abgebrannt. Nur die UV/Vis-Messungen von Bor und Titan wurden in einer optischen Bombe unter reinem Sauerstoff durchgeführt. Der flüssige Kohlenwasserstoff n-Heptan wurde in einen Porzellantiegel (Ø=40 mm) gefüllt. Entzündet wurden die Brennstoffe mit einem Lötbrenner.
Das Zentrum der Abbrandoberfläche wurde auf den Öffnungsspalt der Spektrometer abgebildet. Für den UV/Vis-Bereich wurde dazu eine Quarzglaslinse (f=125 mm) und im IR eine CaF_2-Linse verwendet (f=85 mm). Am HGS-NIR-Spektrometer ist ein Quarzlichtleiter mit einer Blendenöffnung von 200 µm angebracht, die etwa 100 mm vor dem Flammenzentrum justiert war.
Bei den Metallbränden wurden Spektren über den gesamten Verbrennungszeitraum aufgenommen. Bei der flackernden Kohlenwasserstoffflamme wurde nach Erreichen einer stabilen Flamme über mehrere Fluktuationsphasen zeitaufgelöste Folgen von Einzelspektren gezogen. Die Belichtungszeit betrug je nach Strahlungsintensität 10 bis 200 ms. Bei jeder Messung wurde zusätzlich ein Dunkelspektrum gezogen.

Auswertung

Die IR-Spektrometer wurden unter den gleichen Abbildungsbedingungen mit einem Schwarzstrahler bei 1773 K kalibriert. Dazu wurde durch Division des Kalibrierspektrums durch ein gerechnetes Schwarzstrahlerspektrum gleicher Temperatur eine wellenlängenabhängige Kalibrierfunktion erstellt. Allen Spektren wurde zuvor das jeweilige Dunkelspektrum abgezogen. Die Kalibrierung ergibt eine wellenlängenunabhängige Empfindlichkeit des Sensors. Bei Einhaltung der optischen Bedingungen erhält man theoretisch eine Intensitätskalibrierung in Leistung pro Wellenlänge, Fläche und Raumwinkel. Allerdings ist zu beachten, daß die untersuchten Flammen stark flackerten und sich aus Intensitätsgründen keine Blende im Strahlengang befand. So waren die Flammen nicht immer vollständig auf dem Detektor

abgebildet. Die Voraussetzungen für eine qualitative Leistungskalibrierung waren deshalb nur teilweise erfüllt. Dies gilt speziell für die NIR-Messungen.

UV/Vis-Spektren

Metallflammen weisen im ultravioletten und sichtbaren Strahlungsbereich eine Vielzahl charakteristischer Linienemissionen auf. Dabei handelt es sich sowohl um Atom- als auch Molekülspektren [3]. Kohlenwasserstoffe zeigen im gleichen Bereich zahlreiche Bandensysteme 2-atomiger Moleküle [11].

Bor
Im UV erkennt man zahlreiche Banden, die BO oder BO_2 zugeschriebn werden können (Abbildung 1). So können die Linien bei 459-461 und 504 nm BO und die Banden bei 453, 471, 492, 518 und 548 nm BO_2 zugeordnet werden [3].
Im sichtbaren Strahlungsbereich zeigt die untersuchte Borflamme die für BO_2 typischen Banden (Abbildung 2). Dokumentierte Liniengruppen befinden sich bei 453, 471, 492, 518, 548, 580, 603, 620 und 640 nm [3].

Aluminium
Im UV emittiert ein bandenähnliches Spektrum bei 400 bis 480 nm (Abbildung 3). Es wird dem Aluminiumatom zugeschrieben. Eine ebenfalls dokumentierte Liniengruppe bei 370 nm konnte nicht aufgelöst werden. Bei 460 bis 510 nm finden sich zahlreiche Linien die AlO zugeordnet werden können. In diesem Bereich emittiert auch AlH.
Im sichtbaren Strahlungsbereich wird das Spektrum der Aluminiumflamme von einem ansteigenden Kontinuum dominiert (Abbildung 4). Starke Linien vom Natriumduplett (589 und 589.5 nm) und den Kaliumlinien bei 766,5 und 769.9 nm findet man in fast allen Flammen. Sie werden schon von kleinsten Verunreinigungen mit diesen Elementen verursacht. Bei 670 nm ist eine schwache Aluminiumlinie dokumentiert [4], die im gemessenen Spektrum unerwartet stark emittiert.

Magnesium
Im UV emittieren zwischen 340 und 410 nm zahlreiche Linien, die sowohl MgO als auch MgOH zugeschrieben werden können (Abbildung 5). Bei 420 bis 460 nm werden Mg-Atomlinien angeregt. Bei 500, 515 und 570 nm emitterien weitere MgO-Liniengruppen.
Im Vis zeigt die untersuchte Magnesiumflamme nur ein schwaches Kontinuum (Abbildung 6). Dokumentierte Liniengruppen von MgO finden sich bei 495, 595, 610 und 620 nm sowie Mg-Linien bei 520 und 770 nm. Das System bei 650 bis 710 nm konnte nicht zugeordnet werden.

Titan
Das Titan-Spektrum zeigt im UV/Vis-Bereich einige typische Banden, die sich TiO zuordnen lassen (Abbildung 7). Dokumentierte Liniengruppen finden sich bei 476-490 (schwach), 495, 517, 545, 559-563, 616, 621, 708-712, 767 nm [3]. Auch hier sieht man wieder Die Na-Linie bei 589 nm.

n-Heptan
Das UV-Spektrum der untersuchten n-Heptanflamme zeigt vor allem im unteren Flammenbereich zahlreiche 2-atomige Radikalspektren im UV-Bereich (Abbildung 8):

- OH bei 306 nm,
- CN bei 350 und 390 nm (schwach ausgeprägt),
- CH bei 390 und 430 nm (nicht sicher detektiert),
- C_2 bei 430, 470, 515 und 560 nm.

Die Bandensysteme liegen auf einem Rußkontinuum.
Im sichtbaren Strahlungsbereich überdeckt die Rußemission alle Banden (Abbildung 9).

NIR-Spektren

Bor
Die schwerentzündlichen Bor-Proben brannten mit einer leuchtend grünen Flamme ab. Im hier untersuchten Wellenlängenbereich wurden Kontinuumsspektren gefunden, deren Strahlungsmaximum bei etwa 2 µm lag (Abbildung 10). Außerdem deutet sich bei 1.35 µm die Wasserbande an.

Aluminium
Die hellleuchtende Korona der Aluminiumflamme ergab praktisch keine detektierbare Strahlung im NIR. Deshalb wurde auf die glühende Oberfläche fokusiert. Hier findet sich ausschließlich eine Kontinuumsstrahlung, deren Maximum im untersuchten NIR Bereich liegt. Linien oder Banden wurden nicht beobachtet (Abbildung 11).

Magnesium
Die Proben ließen sich mit dem Lötbrenner nur schwer und unreproduzierbar anzünden. Manchmal entstand eine weißleuchtende Flammenkorona, sonst glühte die Mg-Schüttung. In beiden Fällen wurden Kontinuumsspektren gefunden (Abbildung 12). Das Strahlungsmaximum der Glut lag etwa bei 2 µm. In der Flammenkorona liegt das Maximum bei 1µm. Hier deutet sich zusätzlich die Wasserbande bei 1.4 µm an. Das Wasser stammt vermutlich aus der Feuchtigkeit der Verbrennungsluft.

Titan
Bei den NIR-Spektren von Titan wurde ausschließlich eine Kontinuumsstrahlung gefunden, deren Maximum bei etwa 1.35 µm liegt (Abbildung 13). Linien oder Banden konnten nicht beobachtet werden.

n-Heptan
n-Heptan zeigt ein Rußkontinuum, bei dem die Wasserbande bei1.4 µm zu sehen ist. Bei 10 mm Flammenhöhe ist die Bande jedoch stärker ausgeprägt als bei 50 mm (Abbildung 14 und Abbildung 15).

Flammentemperaturen

Mit dem HGS ließen sich die Temperaturverläufe der einzelnen Abbrände ermitteln. Die Auswertung der Metallspektren erfolgt durch anfitten der Kontinuumsstrahlung, da Wasserbanden meist nicht detektiert werden konnten. Beim Kohlenwasserstoff ist der Wasserbande eine Kontinuumsstrahlung überlagert. Hierbei wird dann neben der Wasserbande auch der Absorptionskoeffizient von Ruß mitberücksichtigt. Abbildung 16 zeigt Beispiele für angefittete Banden. Die Fitgüte war unter Annahme eines grauen Strahlers mit konstantem Emissionsgrads sehr gut.

Die Kurvenverläufe der Metallabbrände ähneln sich alle. Zunächst war mehr oder weniger lang eine helleuchtende Strahlung der Flamme zu beobachten, was sich in den hohen Temperaturen zwischen 2000 und 2300 K je nach Metall wiederspiegelt. Anschließend glühte nur noch die Metallschüttung und die Temperaturen sanken um mehrere hundert Kelvin auf 1000 bis1200 K bei Aluminium und Magnesium (Abbildung 18 und Abbildung 19) und auf etwa 1700 K bei Titan (Abbildung 20). Nur bei Bor war dieser Effekt nicht zu sehen. Die Temperatur sank hier langsam von etwa 1400 K auf 1200 K (Abbildung 17). Wahrscheinlich war die Flamme nicht direkt im Fokus des Spektrometers.

Der Temperaturverlauf der n-Heptanflamme (Abbildung 21) unterscheidet sich deutlich von dem der Metalle. In beiden Flammenhöhen spiegelt sich das periodische Flackern in den Temperaturverläufen wieder. Auch sieht man deutlich, daß die Temperatur im Flammenfuß (10

mm) mit 1760-1920 K höher ist als im oberen Flammenbereich (50 mm), wo nur 1640-1780 K erreicht werden.

IR-Spektren

Bor
Emittiert im IR hauptsächlich Kontinuumsstrahlung an der glühenden Oberfläche (Abbildung 22). Spezielle Banden konnten nicht beobachtet werden. Die Wasserbanden bei 2.9 µm und 6 µm sowie die CO_2-Emission bei 4.4 µm stammen von RDX, das zu besseren Anzündung untergemischt wurde.

Aluminium
Auch die Aluminiumflamme zeigt nur ein Kontinuum (Abbildung 23). Man erkennt schwache Wasserbanden bei 2.9 µm und 6 µm sowie eine schwache CO_2-Emission bei 4.4 µm. Beide Stoffe werden aus der Verbrennungsluft in die Flamme getragen und zur Emission angeregt.

Magnesium
Die Spektren unterscheiden sich wenig von der Al-Flamme (Abbildung 24). Die etwas andere Wölbung des Kontinuums deutet auf eine etwas niedrigere Temperatur hin.

Titan
Die Spektren unterscheiden sich nicht von denen der Aluminiumflamme (Abbildung 25).

n-Heptan
Die Flamme emittiert Wasserbanden bei 2.9, 6 und 7 µm. Die CO_2-Bande bei 4.4 µm ist stark ausgeprägt (Abbildung 26). Zusätzlich deutet sich bei manchen Spektren das Rußkontinuum an.

Literatur

[1] Eckl, W., Eisenreich, N., 1991, Temperaturbestimmung in Flammen chemischer Energieträger durch Analyse 2- und 3-atomiger Molekülspektren, ICT-Bericht 12/91

[2] Ludwig, C.B., Malkmus, W., Reardon, J.E., Thomson, J.A.L., „Handbook of Infrared Radiation from Combustion Gases„, NASA-SP-3080, 1973.

[3] Pearce, R. W. B.; Gaydon, A. G.; The Identification of Molekular Spectra; Capman & Hall Ltd., London

[4] NIST Chemestry WebBook; http://webbook.nist.gov/chemistry/

[5] Morrison, M. E.; Scheller, K.; Spectral Characteristics of Hydrogen-Air Flames Containing Aluminium, Magnesium and Boron; Combustion and Flame; Vol. 13, 1969; pp. 93-97

[6] Eckl, W.; Weiser,V.; Weindel; M.; Determination of the Temperature in an Isopropanol Diffusion and a Premixed Propane-Air Flame; Application Note - HGS-1700 der Fa. WMM Sensorik Gmbh & Co.KG

[7] Blanc, A., Eisenreich, N., Kull, H., Liehmann, W., Charakterisierung von Verbrennungs-prozessen mittels zeitaufgelöster IR-Spektroskopie im Bereich 1 - 14 µm, 19th International Annual Conference of ICT, 1988, Karlsruhe, pp. 74-(1-13);

[8] Deimling, L., Eckl, W.; Eisenreich, N.; Liehmann, W.; Schneider, H.; Weiser, V.; Non-Intrusive Combustion Diagnostics of Propellant Flames and Rocket Plumes; 24th International Annual Conference of ICT, 1993, pp. 63-(1-9)

[9] Baier, A.; Infrarotspektroskopische in-situ Untersuchungen von Verbrennungsvorgängen mit Hilfe eines neuen Filerradspektrometers; Diplomarbeit Fachhochschule Mannheim Dezember 1995

[10] Baier, A.; Weiser, V.; Eisenreich, N.; Halbrock, A.; IR-Emissionsspektroskopie bei Verbrennungsvorgängen von Treibstoffen und Anzündmitteln; 27th International Annual Conference of ICT, 1996, Karlsruhe, pp. 84-(1-12)

[11] Mavrodineanu, R. and Boiteaux, H., 1965, Flame Spectroscopy, J. Wiley & Sons, Inc, New York

Abbildungen

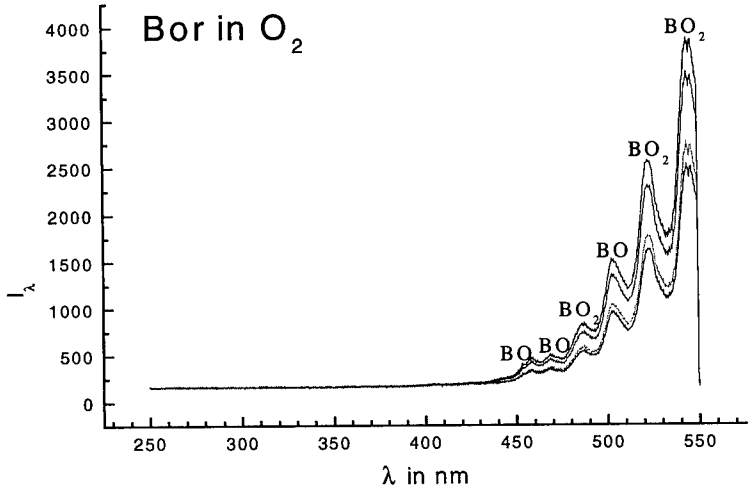


Abbildung 1 **UV-Spektrum einer Borflamme**

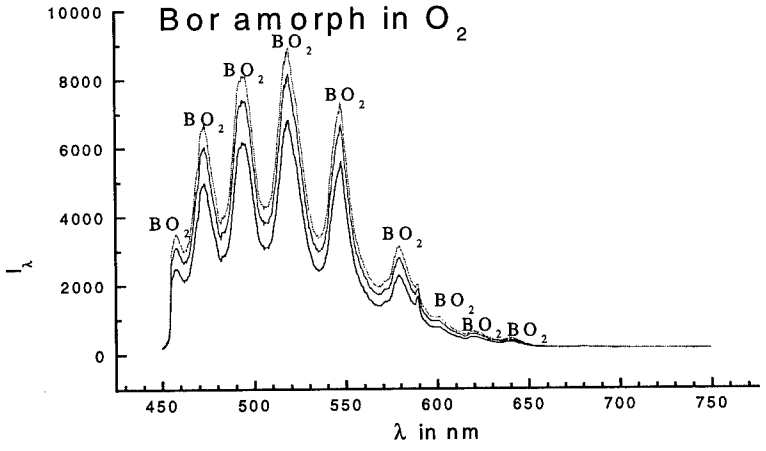


Abbildung 2 **Vis-Spektrum einer Borflamme**

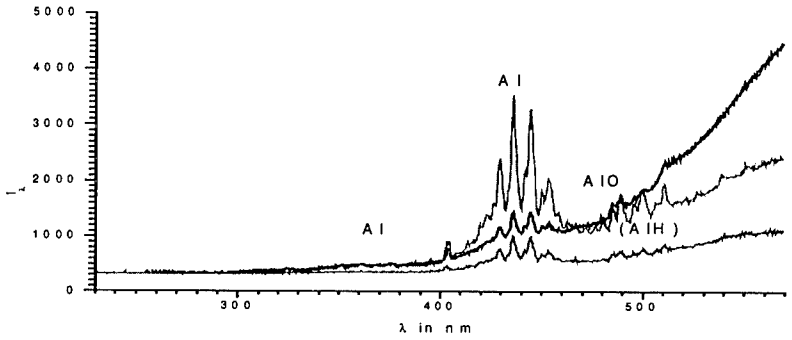


Abbildung 3 **UV-Spektrum einer Aluminiumflamme**

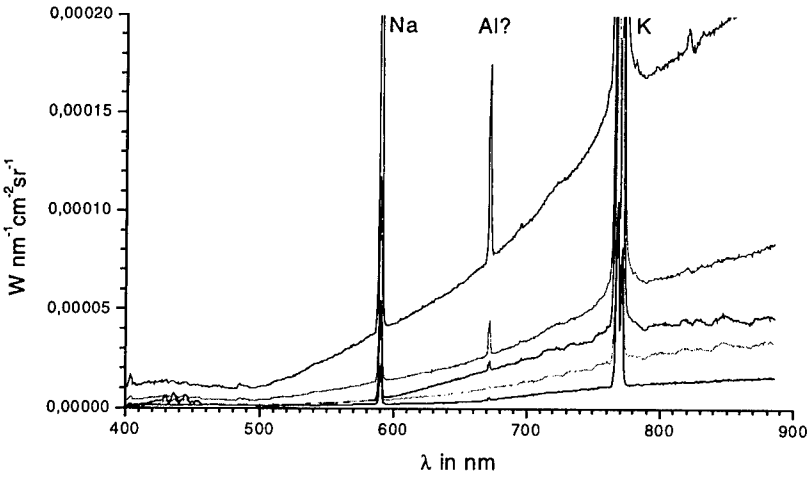


Abbildung 4 **Vis-Spektrum einer Aluminiumflamme**

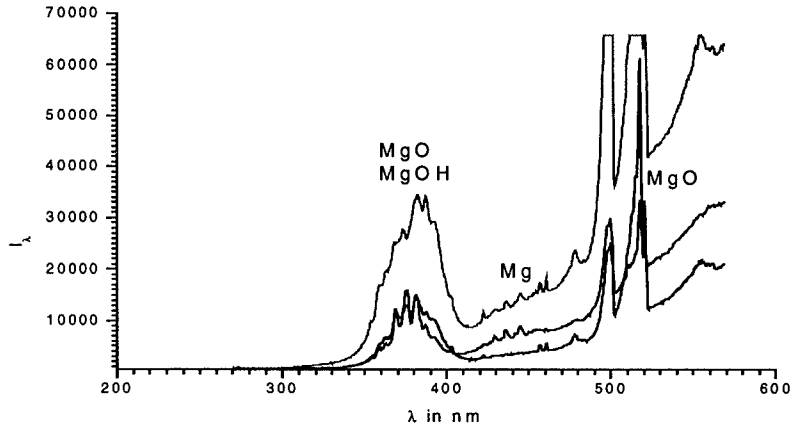


Abbildung 5 **UV-Spektrum einer Magnesiumflamme**

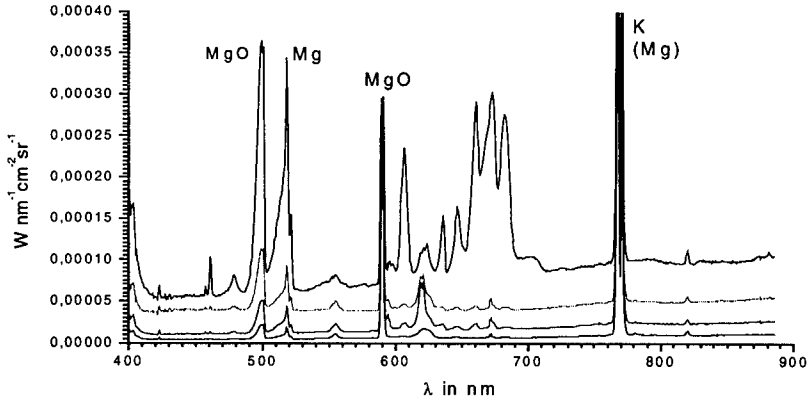


Abbildung 6 **Vis-Spektrum einer Magnesiumflamme**

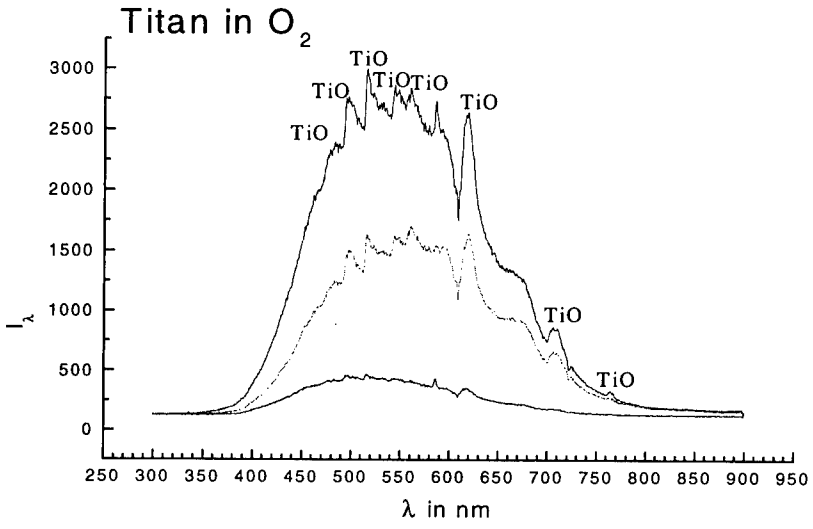


Abbildung 7 **UV/Vis-Spektrum einer Titanflamme**

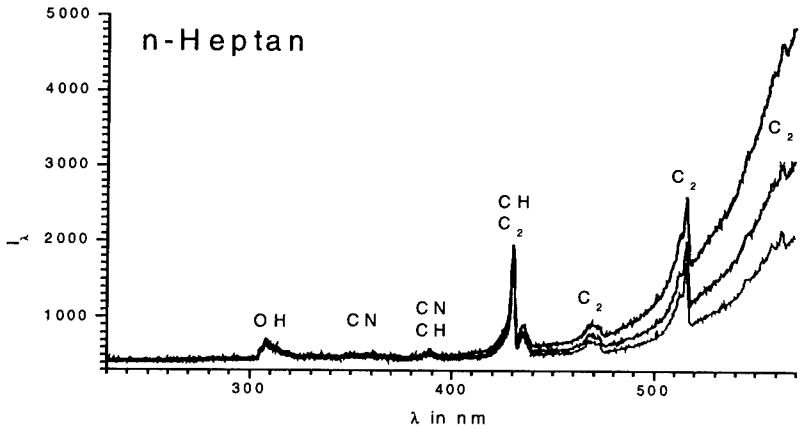


Abbildung 8 **UV-Spektrum einer n-Heptanflamme**

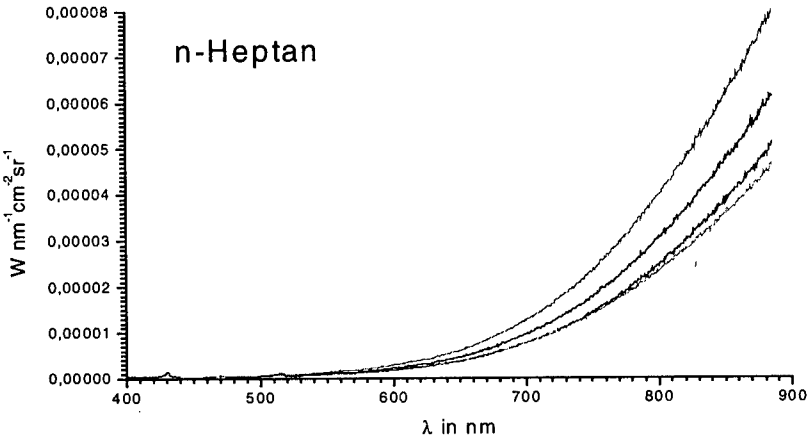


Abbildung 9 **Vis-Spektrum einer n-Heptanflamme**

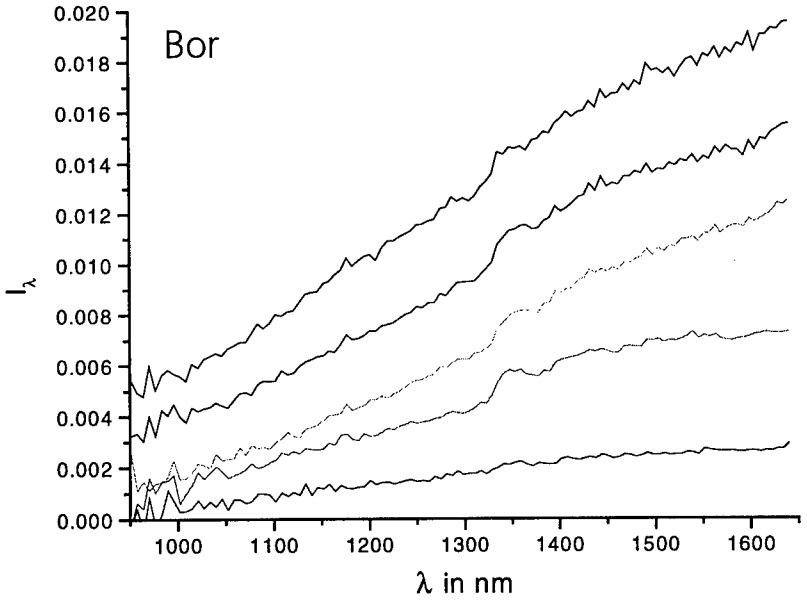


Abbildung 10 **NIR-Spektrum einer Borflamme**

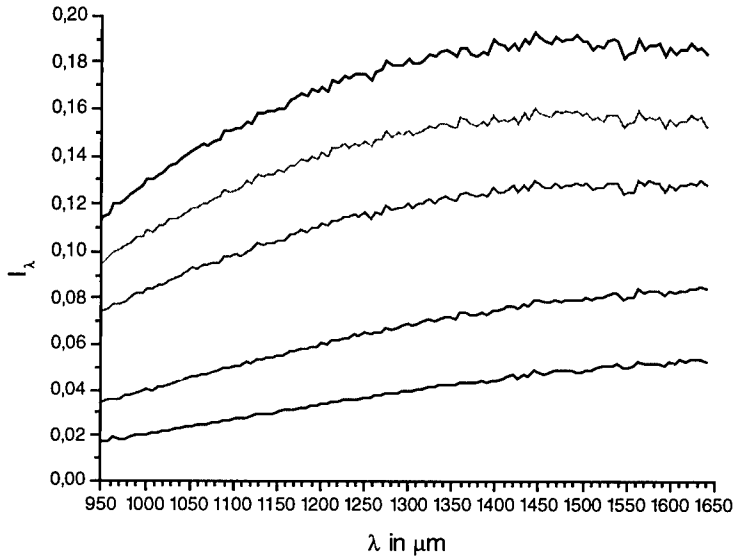


Abbildung 11 **NIR-Spektrum einer Aluminiumflamme (Fokus auf Schüttung)**

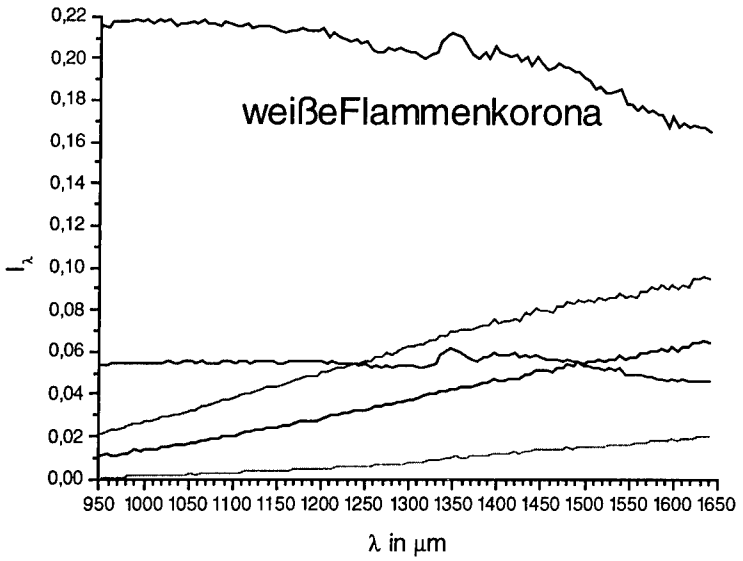


Abbildung 12 **NIR-Spektrum einer Magnesiumflamme**

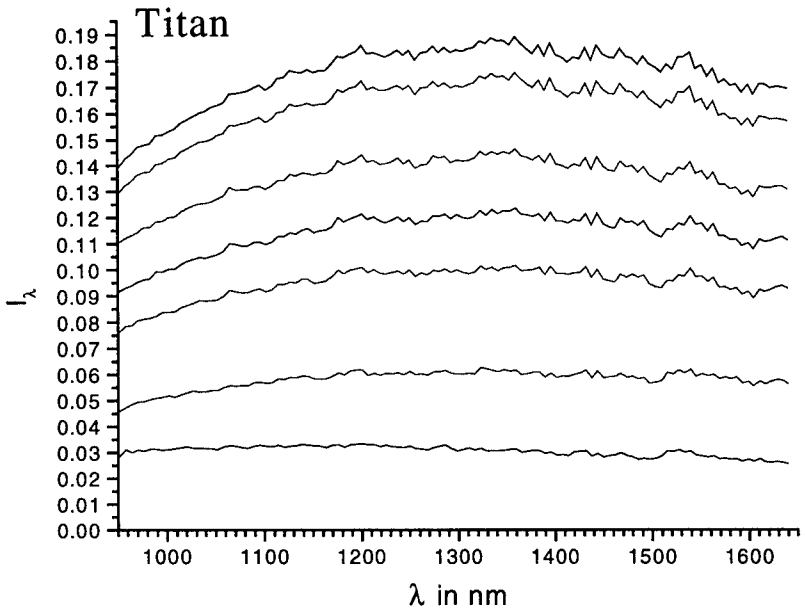


Abbildung 13 **NIR-Spektrum einer Titanflamme**

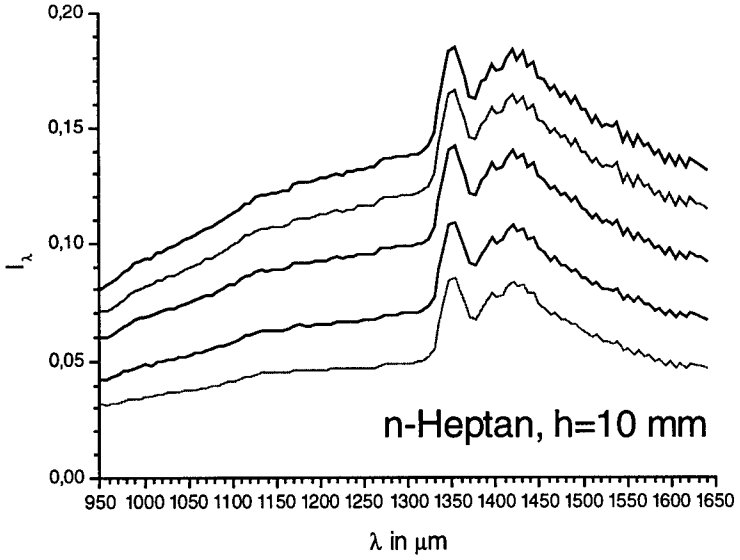


Abbildung 14 **NIR-Spektrum einer n-Heptanflamme (Fokus im unteren Flammenbereich)**

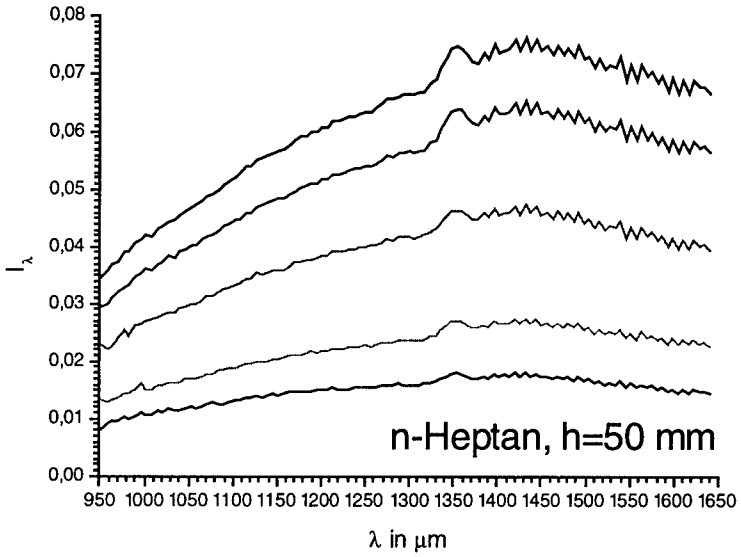


Abbildung 15 **NIR-Spektrum einer n-Heptanflamme (Fokus im oberen Flammenbereich)**

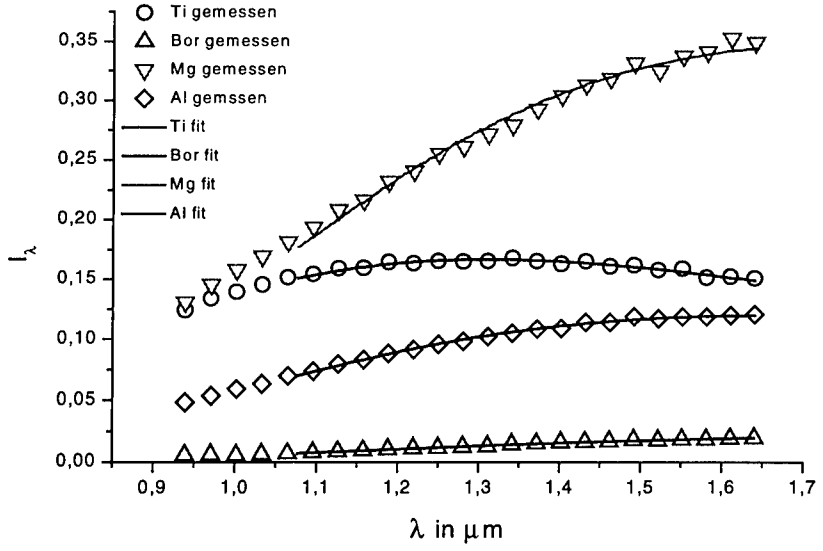


Abbildung 16 **Vergleich gemessene und angefittete Spektren**

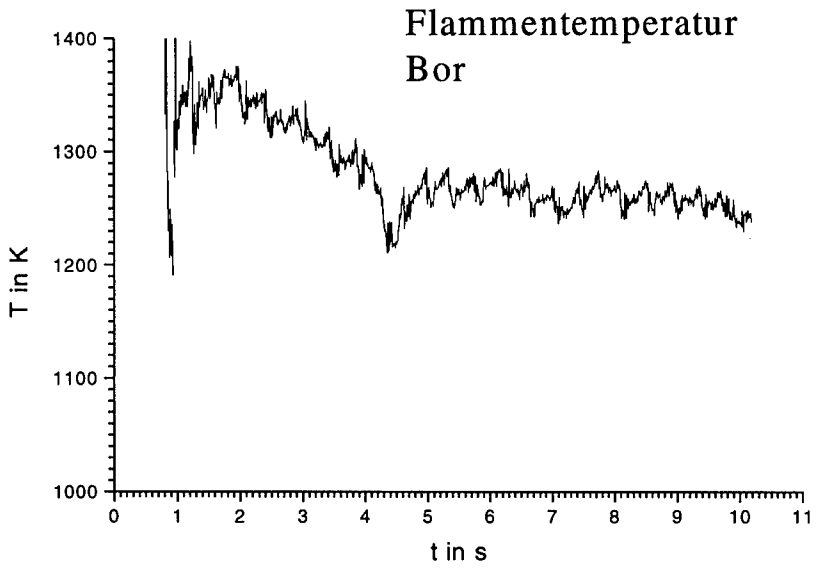


Abbildung 17 **Flammentemperatur von Bor**

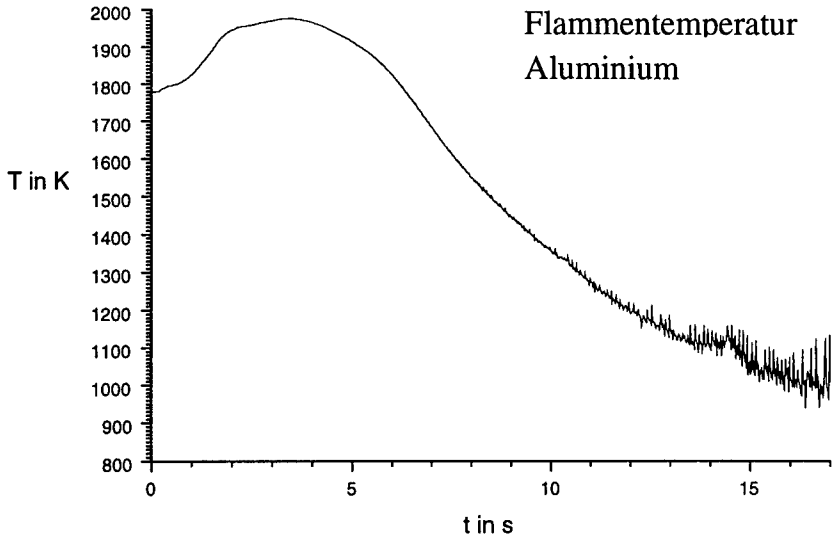


Abbildung 18 **Flammentemperatur von Aluminium**

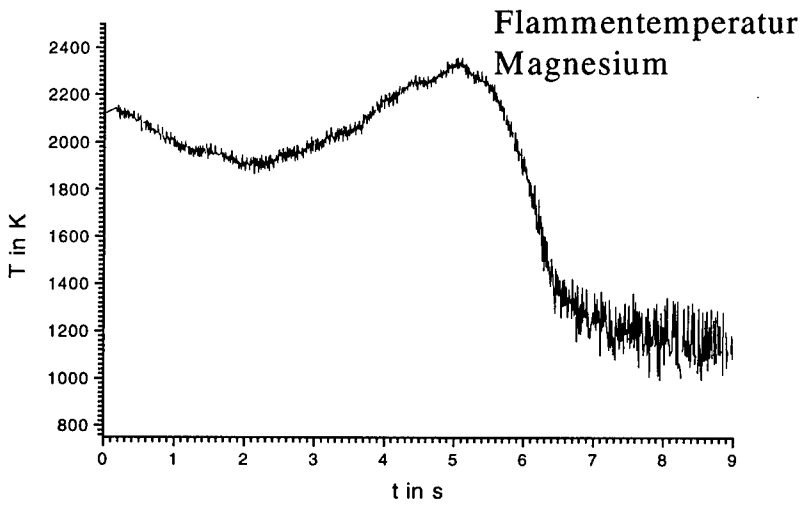


Abbildung 19 **Flammentemperatur von Magnesium**

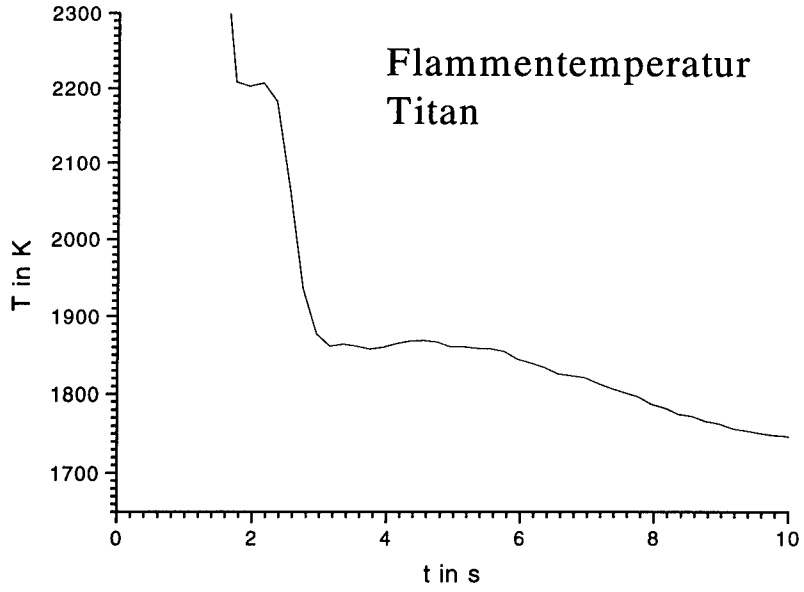


Abbildung 20 **Flammentemperatur von Titan**

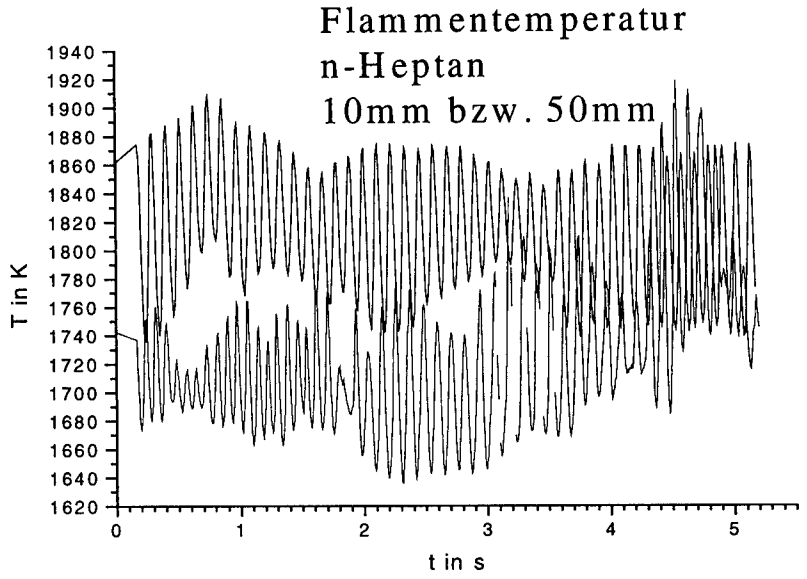


Abbildung 21 **Flammentemperatur von n-Heptan in 10 bzw. 50 mm Flammenhöhe**

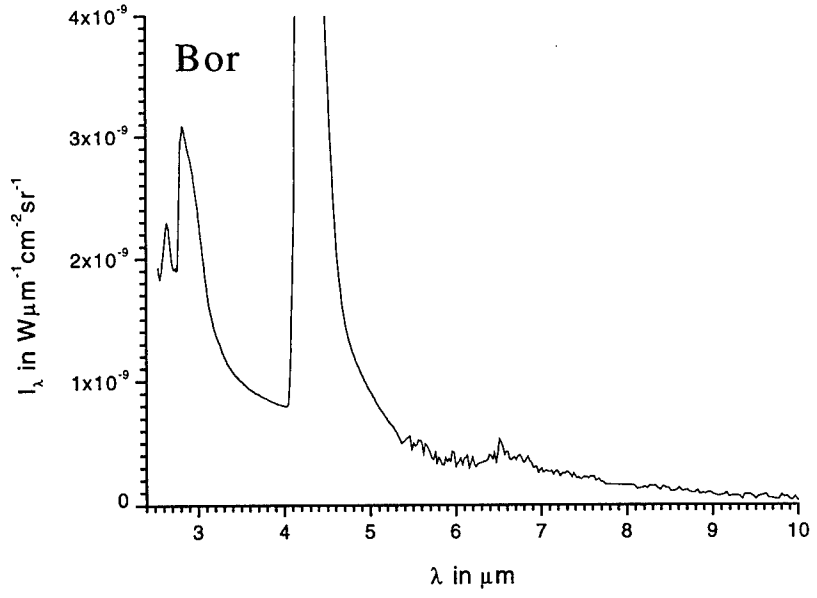


Abbildung 22 **IR-Spektrum einer Borflamme**

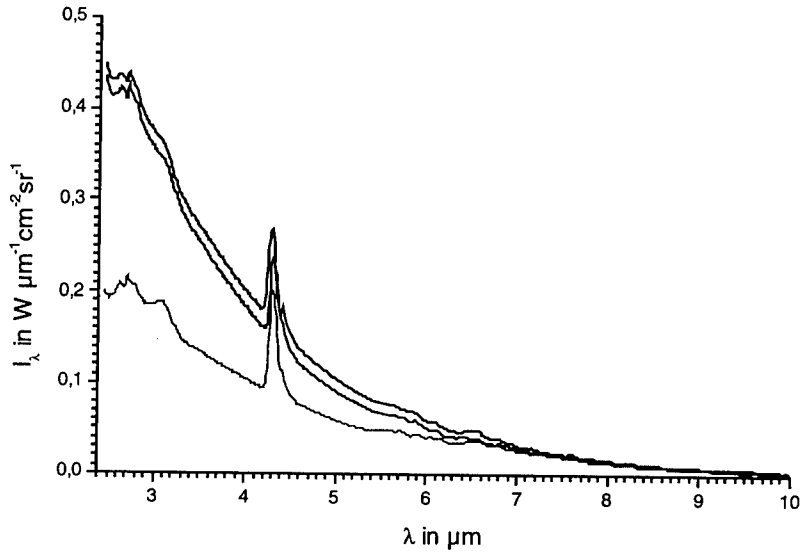


Abbildung 23 **IR-Spektrum einer Aluminiumflamme**

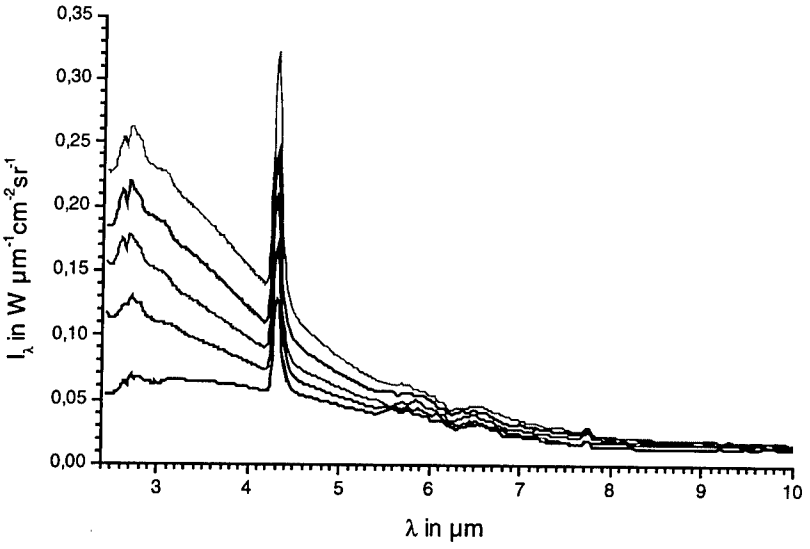


Abbildung 24 **IR-Spektrum einer Magnesiumflamme**

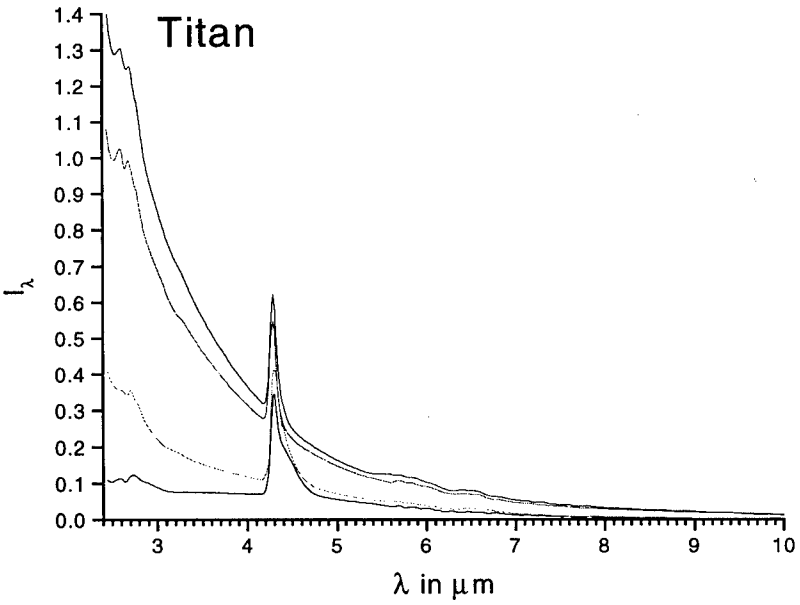


Abbildung 25 **IR-Spektrum einer Titanflamme**

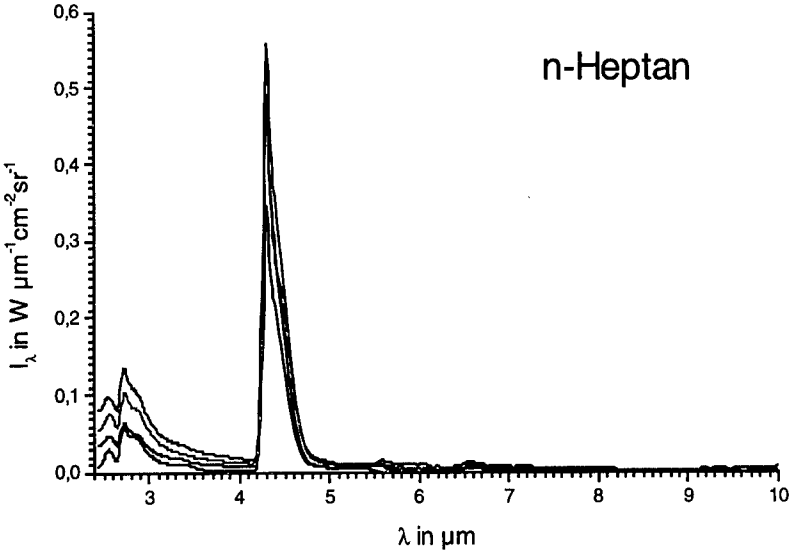


Abbildung 26 IR-Spektrum einer n-Heptanflamme

ABBRANDUNTERSUCHUNGEN AN FLÜSSIGEN UND GELFÖRMIGEN MISCHUNGEN VON NITROMETHAN UND H_2O_2

V. Weiser, F. Hidalgo, Y. Plitzko

Fraunhofer-Institut Chemische Technologie (ICT)
Joseph-von-Fraunhoferstr. 7
D-76327 Pfinztal (Berghausen), Germany

Abstract

COMBUSTION OF LIQUID AND GELLED MIXTURES WITH NITROMETHAN AND H_2O_2

Gelled rocket propellants are insensitive and gives the opportunity of trust controlled propulsion. The combustion of different liquid and gelled mixtures of nitromethane in H_2O_2 (85%) is investigated in a pressurised window bomb. Video frames, burning rates and flame temperatures are presented and discussed.

Einleitung

Gelförmige Raketentreibstoffe bieten die Möglichkeit Raketenantriebe mit variabler Schubstärke, Schubregelbarkeit und –unterbrechung in Kombination mit Signaturarmut, hoher spezifischer Leistung sowie geringer Empfindlichkeit und Verwundbarkeit herzustellen. Auch wenn ein Teil der in Frage kommenden Brennstoffe und Oxidatoren mit hohem Leistungspotential gefährlich und gesundheitsschädlich sein können, wird das Kontaminationsrisiko jedoch durch die Gelierung deutlich verringert.

Gelierte Treibstoffe sind unter normalen Umgebungsbedingungen fest. Unter Druck- und Scherspannungseinfluß werden sie fließfähig und erlauben eine Förderung vom Tank in die Brennkammer und somit eine entsprechende Durchsatzsteuerung zur Schubvariation. Die gelförmige Konsistenz läßt gute Insensitivitätseigenschaften und ein gefahrloses Handling erwarten. Ihre Leistung, d. h. der spezifische Impuls von gelierten Brennstoff / Oxydatorsystemen ist häufig größer, als der der entsprechenden Festtreibstoffe.

Obwohl der Wunsch nach unverwundbaren Treibstoffen diergole Systeme favorisiert, sprechen Gründe der Systemvereinfachung dafür auch monergole Systeme zu untersuchen. Zu den reologischen Eigenschaften, Systemüberlegungen und dem Handling wurden schon einige Untersuchungen angestellt [1-10]. Verbrennungseigenschaften wurden bisher nur bei mit Nanoaluminum (ALEX) vergelten Treibstoffen untersucht [2, 4]. Diese Treibstoffe haben allerdings den Nachteil einer hohen Abgasstrahlsignatur. Bei anderen Geltreibstoffen konnten noch keine Untersuchungen der Verbrennungseigenschaften gefunden werden.

Im folgenden werden erste Abbranduntersuchungen von vergelten und flüssigen Nitromethan/Wasserstoffperoxid-Mischungen zusammenfassend beschrieben.

Experimentelles

Das untersuchte Modellsystem Nitromethan/H_2O_2 ermöglicht spezifische Impulse über 2500 ms^{-1} bei Verbrennungstemperaturen um 3000 K [11]. Bei den Versuchen wurden Wasserstoffperoxid mit 85% Reinheit eingesetzt. Das Massenverhältnis Nitromethan/ H_2O_2(85%) betrug 20/80 und 40/60. Zur Vergelung wurden 5% Aerosil zugegeben. Zur Referenz dienten unvergelte Mischungen. Die beiden Komponenten reagieren nicht hypergol, trotzdem stehen noch Stabilitätsuntersuchungen aus. Deshalb wurden die Proben jeweils direkt vor dem Abbrand hergestellt, um reproduzierbare Ergebnisse zu erlangen.

Die Mischungen wurden in Reagenzgläser (Ø, 5 mm, Länge 70 mm) eingefüllt und durch einem mit Glühdraht initiierten Treibstoffstückchen angezündet. Die Untersuchungen fanden in einer optischen Bombe bei 0.1 bis 4 MPa Stickstoffdruck statt. Die Apparatur ist in [12] detailliert beschrieben.
Mit einem digitalen Camcorder wurden das Erscheinungsbild der Verbrennungsreaktion und die Abbrandrate untersucht [12]. Zur Temperaturmessung und Charakterisierung der Wasserbildung wurde ein NIR-Spektrometer eingesetzt. Das Verfahren ist in [13] genau beschrieben.

Ergebnisse

Flammenbilder

Abbildung 1 zeigt einige Fotos der Verbrennungszonen beim Druckabbrand. Mit steigendem Druck leuchtet die Flammenzone heller. Dies deutet auf eine intensivere Reaktion hin. Unter der Reaktionstemperatur schmilzt bei den vergelten Treibstoffen das Aerosil an der Abbrandoberfläche zu Glasschuppen zusammen, die nach Erreichen einer bestimmten Größe mit dem Gasstrom ausgetragen werden. Der Abbrand der flüssigen Proben unterscheidet sich prinzipiell von dem der Gelförmigen. Bei den vergelten Proben ist eine hellleuchtende Zone an der Phasengrenzfläche und eine Flammenzone über dem Treibstoff zu beobachten. Im Innern des Gels etwa 5 mm unter der Oberfläche bilden sich einzelne Blasen. Vermutlich handelt es sich um Sauerstoff von sich zersetzendem H_2O_2. DSC-Messungen zeigen das die Zersetzungstemperatur von Nitromethan weitaus höher ist, als die von Wasserstoffperoxid. Besonders bei niedrigem Druck ist die leuchtende Reaktionszone an der Abbrandoberfläche nicht eben, sondern frißt sich wurmförmig in die kondensierte Phase hinein. Bei den flüssigen Proben ist die Oberfläche eben und es bilden sich ebenfalls kleine Bläschen. Darüber erkennt man druckunabhängig eine intensiv blau leuchtende Zone von etwa 2 mm Höhe. Erst darüber findet man die gelbleuchtende Flammenzone. Mit steigendem Druck scheint die Flamme länger zu werden.

Abbrandraten

Die gemessenen Abbrandraten sind in Abbildung 2 in druckabhängiger Form zusammengestellt. Die Punkte zeigen einzelne Messungen. Es wurden bei jeder Druckstufe mindestens 3 Messungen vorgenommen. Die Linien verbinden die Mittelwerte. Die Gele brennen reproduzierbarer als die flüssigen Proben. Dies gilt besonders für die Mischung 20/80. Die Abbrandraten steigen mit dem Druck an. Die meisten Mischungen deflagrierten ab einem Druck von 0.5 bis 1 MPa. Hier waren keine Messungen möglich. Die Bestimmung eines Druckexponenten erschien als sinnlos. Bei einem Mischungsverhältnis

von 40/60 brennt die gelförmige Probe etwa doppelt so schnell wie die flüssige Vergleichsprobe. Beim Mischungsverhältnis 20/80 liegen die Abbrandraten beider Proben zumindest im unteren Druckbereich in der gleichen Größenordnung.

Flammentemperaturen

Die gemessenen Flammentemperaturen sind in Tabelle 1 zusammengefaßt. Die Temperaturen basieren wesentlich auf der Messung der Wasserbande bei 1.6 µm, die fast ausschließlich im Nahen Infrarot emittiert. Bei den Gelproben ist ein leichtes Untergrundspektrum, das vermutlich vom Aerosil herrührt zu beobachten. Die Auswertung erschwert sich, da dieses Untergrundspektrum eine niedrigere Temperatur aufweist als die Wasserbande. So sind die Temperaturen mit Vorsicht zu bewerten [13].

Die Temperaturen der Mischungen 20/80 liegen unabhängig vom Reaktionsdruck zwischen 1650 und 2200 K. In diesem Bereich liegt auch die adiabate Verbrennungstemperatur dieser Mischungen [11]. Dabei liegen die Temperaturen der flüssigen Mischungen um etwa 100 K höher als die der Gele.

Die Mischungen 40/60 sind mit 2500 bis 2900 K deutlich heißer. Sie korrelieren gut mit der adiabaten Verbrennungstemperatur von 2900 K. Bei diesem Mischungsverhältnis liegt die gemessene Temperatur der Flüssigkeit etwa 200 K niedriger als die des Gels. Dies könnte u.U. die in diesem Fall deutlich höhere Abbrandrate erklären. Eine genauere Analyse dieser Phänomene steht noch aus.

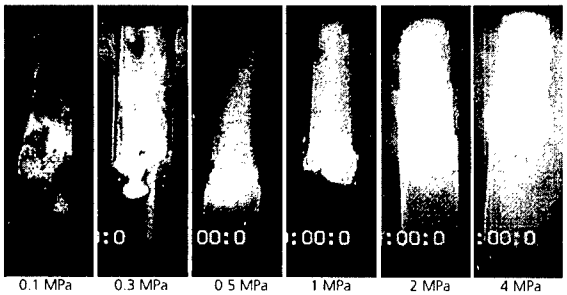
Literatur

1. Natan, B.; Rahimi, S.; The status of gel propellants in year 2000; 5th International Symposium on Special Topics in Chemical Propulsion: Combustion of Energetic Materials; 19-22 June 2000; Stresa, Italy; paper
2. Palaszewski, B.
   "Metallized Gelled Propellants: Oxygen/RP-1/Aluminium rocket engine calorimeter heat transfer measurements and analysis", AIAA 97-2974, 33rd AIAA Joint Propulsion Conference, July 6-9, 1997, Seattle, WA, USA
3. Rahimi, S., Natan, B.
   "Atomization Characteristics of Gel Fuels", AIAA 98-3230, 34th AIAA Joint Propulsion Conference, July 13-15, 1998, Cleveland, OH, USA
4. Sirignano, W.A., Delplanque, J.-P., Liu, F.
   Selected Challenges in Jet and Rocket Engine Combustion Research, AIAA97-2701, 33rd AIAA Joint Propulsion Conference, July 6-9 1997, Seattle, WA, USA
5. Hodge, K.F., Crofoot, T.A.
   "Gelled Propellants for Tactical Missile Applications", AIAA99-2976, 35th AIAA Joint Propulsion Conference, June 20-23, 1999, Los Angeles, CA, USA
6. Ivancic, B., Mayer, W.
   "Experimental and Numerical Investigation of Atomization in LOX/GH2-Rocket Combustors", Proceedings, 15th ILASS-Europe '99, Toulouse, pp. 81-82, July 5-7, 1999
7. Ivancic, B., Mayer, W., Krülle, G., Brüggemann, D.
   "Experimental and Numerical Investigation of Time and Length Scales in LOX/GH2-Rocket Combustors", 35th AIAA Joint Propulsion Conference, AIAA 99-2211, June 20-24, 1999, Los Angeles, CA, USA

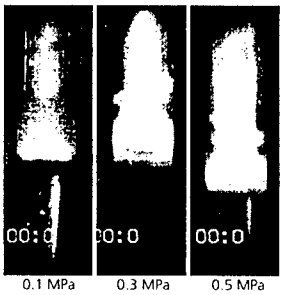
8. Mayer, W., Schik, A., Vieille, B., Chaveau, C., Gökalp, I., Talley, D., Woodward, R.;"Atomization and Breakup of Cryogenic Propellants under High-Pressure Subcritical and Supercritical Conditions", Journal of Propulsion and Power, Vol. 14, No. 5, pp. 835-842, 1998
9. Pein, R., Ciezki, H.K., Eicke, A.
"Instrumental Diagnostics of Solid Fuel Ramjet Combustor Reaction Products Containing Boron", 31st AIAA Joint Propulsion Conference, July 10-12, 1995, San Diego, CA, USA
10. Hallit, R.E., Allan, B.D., Logan, N.
Compatibility of 1100 and 2014 Aluminum Alloys with Several Gelled IRFNA Systems, AIAA-95-2533, 31st AIAA Joint Propulsion Conference, July 10-12, 1995, San Diego, CA, USA
11. Volk, F.; Bathelt, H.; Rechenprogramm zur Ermittlung thermochemischer und innenballistischer Größen, sowie von Gasdetonationsparametern; ICT-Bericht 3/82, 1982
12. Weiser, V.; Eisenreich, N.; Baier, A.; Eckl, N.; Burning Behaviour of ADN Formulations; Propellants, Explosives, Pyrotechnics 24; 163-167 (1999)
13. Eckl, W.; Weiser, V.; Eisenreich, N.; Spectroscopic Flame Diagnostics by Analyzing NIR Water Bands; 5th International Symposium on Special Topics in Chemical Propulsion: Combustion of Energetic Materials; 19-22 June 2000; Stresa, Italy; paper 5-ISICP-007-9-OP-VW

Tabelle 1 Zusammenfassung der mit einem NIR-Spektrometer gemessenen Temperaturen

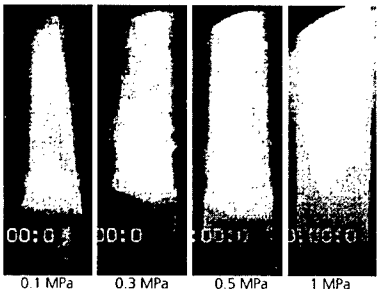
	0.1 MPa	0.3 MPa	0.5 MPa	1 MPa	2 MPa	4 MPa
20/80 Gel	1650-1800K	1650-1850K	1650-1800K	1700-1800K	1700-1800K	1700-1900K
20/80 Flüss.	1850-1950K	2000-2100K	1900-2200K	(2700K)	--	--
40/60 Gel	k.A.	2800-2900K	k.A.	2650-2700K	--	--
40/60 Flüss.	k.A.	2600-2900K	2500-2800K	2100-2800K	1900-2300K	--



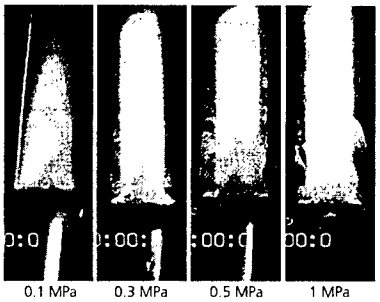
0.1 MPa 0.3 MPa 0 5 MPa 1 MPa 2 MPa 4 MPa
Nitromethan/H2O2 (85%) 20/80 (Gel: 5% Aerosil)



0.1 MPa 0.3 MPa 0.5 MPa
Nitromethan/H2O2 (85%) 20/80 (flüssig)



0.1 MPa 0.3 MPa 0.5 MPa 1 MPa
Nitromethan/H2O2 (85%) 40/60 (Gel: 5% Aerosil)



0.1 MPa 0.3 MPa 0.5 MPa 1 MPa
Nitromethan/H2O2 (85%) 40/60 (flüssig)

Abbildung 1 Fotos beim Abbrand in der Optischen Bombe

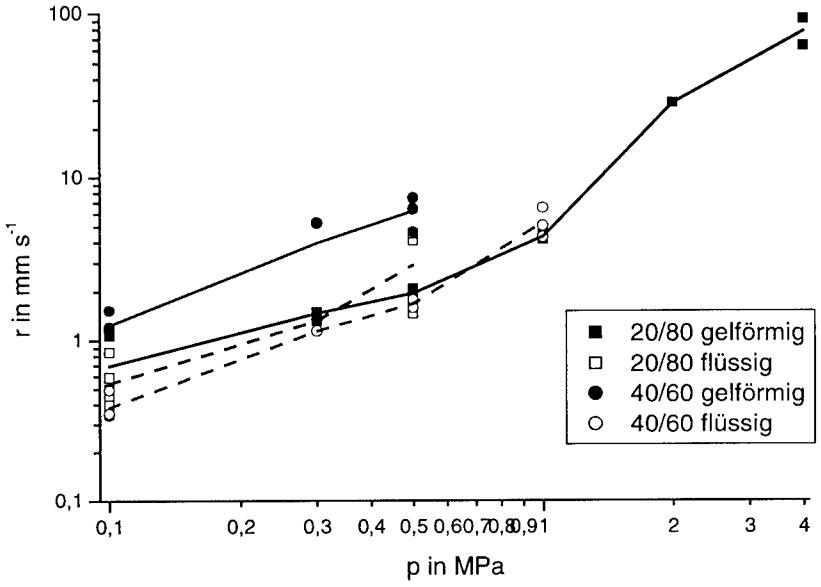


Abbildung 2 **Abbrandrate unter Druck**

Verbrennungsmodellierung mit Hot Spots

S. Kelzenberg, N. Eisenreich, T.Fischer, A. Kolezcko

Fraunhofer Institut Chemische Technologie (ICT), Pfinztal, Germany

Kurzfassung

Es wird ein Programm vorgestellt, das es erlaubt, den Abbrand poröser Treibstoffe zumindest qualitativ zu simulieren. Dem Programm liegt ein Algorithmus zugrunde, der den Abbrand mit Hilfe von Hot Spots beschreibt. Die Ergebnisse des Programmes werden mit Messungen bei Experimenten mit elektrothermisch-chemischer Anzündung verglichen. Dabei zeigt sich eine recht gute qualitative Übereinstimmung, die bei der Interpretation der Messergebnisse behilflich ist.

Abstract

A computer code is presented that allows the simulation of the burning of a porous propellant at least at a qualitative level. The code uses an algorithm that describes the burning by hot spots. The results of the calculations are compared with measurements from experiments for the electrothermal-chemical ignition. The good qualitative correspondance between measurements and calculations helps with the interpretation of the experiment.

1. Einleitung

Verschiedene Phänomene im Bereich der Anzündung sind charakterisiert durch das kurzzeitige Auftreten von punktförmigen oder räumlich eng begrenzten heißen Zonen englisch Hot Spots. Beispiele sind die Anzündung durch heiße Partikel, die den überwiegenden Teil ihrer Energie dort abgeben, wo sie zur Ruhe kommen, oder die Wirkung von Poren, in die heißes Gas aus der Reaktionszone eindringen und das umgebende Material entzünden kann. Im Unterschied zu vielen anderen festen Treibmitteln gehorcht der Abbrand poröser Treibmittel nicht dem Vieille'schen Gesetz. Porosität kann gezielt auf mindestens zweierlei Arten erzeugt werden, entweder durch Aufschäumen des Materials oder durch Vorbehandlung bei der elektrothermisch-chemischen Anzündung.

2. Theoretische Beschreibung von Hot Spots

Ausgangspunkt der theoretischen Beschreibung ist die Differentialgleichung für die Wärmeleitung im Feststoff:

$$\rho c_p \frac{\partial T[\vec{x},t]}{\partial t} - \lambda \cdot \Delta T[\vec{x},t] = \dot{Q}[\vec{x},t] \qquad (1)$$

Für die rechte Seite der Differentialgleichung ist die Beschreibung der Wärmequellen und –senken einzusetzen.

Hot Spots können auf zwei Arten beschrieben werden, entweder mit Hilfe von Dirac'schen Deltafunktionen:

$$\dot{Q}[\vec{x},t]=Q_0\cdot\delta[\vec{x}-\vec{x}_0]\cdot\delta[t-t_0] \tag{2}$$

oder mit Gaussfunktionen:

$$\dot{Q}[\vec{x},t]=\frac{Q_0}{(2\pi)^{3/2}\sigma_x\sigma_y\sigma_z}\cdot e^{-\left(\frac{(x-x_0)^2}{2\sigma_x^2}+\frac{(y-y_0)^2}{2\sigma_y^2}+\frac{(z-z_0)^2}{2\sigma_z^2}\right)}\cdot\frac{1}{(2\pi)^{1/2}\sigma_t}\cdot e^{\frac{(t-t_0)^2}{2\sigma_t^2}} \tag{3}$$

Auf die Beschreibung mit Gaussfunktionen muss vor allem bei numerischen Rechnungen zurückgegriffen werden oder wenn explizit ausgedehnte Bereiche als Wärmequelle berücksichtigt werden sollen. Demgegenüber erlauben die Deltafunktionen eine einfachere Darstellung, solange die Differentialgleichung analytisch gelöst werden kann.

3. Chemische Reaktionen

Eine weitere Wärmequelle ist die chemische Umsetzung des Basismaterials. Zur Beschreibung müssen verschiedene Annahmen getroffen werden. Insbesondere muss entschieden werden, ob die Temperaturabhängigkeit der Reaktion dem Arrhenius-Ansatz entspricht und welches Reaktionsgeschwindigkeitsgesetz man zugrunde legt [1]. Der Arrhenius-Ansatz legt fest wie die Reaktionskonstante k von der Temperatur abhängt:

$$k[T]=Z\cdot e^{-\frac{E}{RT}} \tag{4}$$

Das Reaktionsgeschwindigkeits-Gesetz gibt an wie die Reaktionsgeschwindigkeit von den Konzentrationen der beteiligten Stoffe abhängt:

$$\frac{\partial[A]}{\partial t}=k[T]\cdot f[[A],[B],\cdots] \tag{5}$$

Der einfachste Fall ist das Reaktionsgesetz 0-ter Ordnung. Zusammen mit dem Arrhenius Ansatz ergibt sich:

$$\frac{\partial[A]}{\partial t}=Z\cdot e^{-\frac{E}{RT}} \tag{6}$$

4. Poröser Abbrand

Der Umsatz von porösen Treibmitteln liegt deutlich über der linearen Abbrandrate von kompaktem energetischem Material und gehorcht nicht dem Vieille'schen Gesetz. Einige theoretische Ansätze gehen davon aus, dass heißes Gas aus der Flamme in das poröse Material eindringt. Nach dem Darcy'schen Gesetz ist die Eindringgeschwindigkeit

der Gase proportional zum Druckgradienten und der Permeabilität des Materials (bzw. umgekehrt proportional zum Strömungswiderstand k_d)

$$\nabla P = -k_d v_{hg} \tag{7}$$

Die Gase wirken in den Poren wie Hot-Spots, die sich zu sphärischen Abbrandzonen entwickeln und eine wesentlich größere Oberfläche besitzen, als eine ebene Abbrandfront. Berücksichtigt man den Mindestabstand der Flamme zur Oberfläche, der druckabhängig ist [2]-[4], so findet man, dass ein poröser Abbrand nur stattfinden kann, wenn die Poren größer sind als der Mindestabstand [5].

$$\frac{dP}{dt} \propto \frac{dm}{dt} = 4\pi\rho \sum_{i,j,k} r_{i,jk}^2(t) \frac{dr_{i,j,k}}{dt} \qquad r_{i,j,k} \text{ kleiner als die Eindringtiefe} \tag{8}$$

Heißes Gas, das sich mit der Geschwindigkeit v_{hg} ausbreitet, erzeugt Hot Spots zur Zeit t_n eventuell unter Einschluß einer Verzugszeit t_R (hier = t_R 0):

$$t_n = t_{n-1} + \frac{x_{n,j,k} - x_{n-1,j,k}}{v_{hg}} + t_R \tag{9}$$

5. Numerische Simulation

Aus dem in den vorhergehenden Abschnitten gesagten ergibt sich folgende Differentialgleichung mit einer gemischten Darstellung für die Hot-Spots:

$$\rho c_p \frac{\partial T[\vec{x},t]}{\partial t} - \lambda \cdot \Delta T[\vec{x},t] = \rho \cdot q \cdot Z \cdot e^{-\frac{E}{RT}} + Q_0 \cdot \sum_{i=1}^{n} \left(\frac{1}{(2\pi)^{3/2}\sigma_x\sigma_y\sigma_z} \cdot e^{-\left(\frac{(x-x_i)^2}{2\sigma_x^2} + \frac{(y-y_i)^2}{2\sigma_y^2} + \frac{(z-z_i)^2}{2\sigma_z^2}\right)} \cdot \delta[t-t_i] \right) \tag{10}$$

Dabei wird für die chemische Reaktion des Abbrandes des Basismaterials ein Reaktionsgeschwindigkeitsgesetz 0-ter Ordnung angenommen. Die n Hot-Spots haben hier alle denselben Energieinhalt Q_0 und werden zu verschiedenen Zeiten t_i an den Orten x_i initialisiert. Der Lösungsalgorithmus, der in diesem Programm zur Anwendung kommt, macht zunächst vom Green'schen Lösungsverfahren Gebrauch. Ausgehend von der Lösung der homogenen Differentialgleichung mit räumlichen Grenzen im unendlichen (Gleichung (11)),

$$g[\vec{x}-\vec{x}',t-t'] = \left(\frac{\rho c_p}{4\pi\lambda(t-t')}\right)^{3/2} \cdot e^{\frac{\rho c_p(\vec{x}-\vec{x}')^2}{4\lambda(t-t')}} \tag{11}$$

erhält man eine Lösung für die inhomogene Differentialgleichung durch Faltung der homogenen Lösung mit den Quelltermen (Gleichung (12)).

$$T[\vec{x},t]=\int g[\vec{x}-\vec{x}',t-t']\cdot\frac{\rho\cdot q\cdot Z}{\rho\cdot c_p}\cdot e^{-\frac{E}{RT}}dt'dx'dy'dz'$$
$$+\int g[\vec{x}-\vec{x}',t-t']\cdot\sum_{i=1}^{n}\left(\frac{Q_0}{\rho c_p(2\pi)^{3/2}\sigma_x\sigma_y\sigma_z}\cdot e^{-\left(\frac{(x'-x_i)^2}{2\sigma_x^2}+\frac{(y'-y_i)^2}{2\sigma_y^2}+\frac{(z'-z_i)^2}{2\sigma_z^2}\right)}\cdot\delta[t'-t_i]\right)dt'dx'dy'dz' \quad (12)$$

Für das erste Integral in Gleichung (12) lässt sich keine geschlossene Lösung angeben, da die Temperatur in der e-Funktion selbst wieder von x und t abhängt. Deshalb wählt man für die Integration über die Zeit folgende Näherung:

$$T_{reak}[\vec{x},t]=\int\left(\frac{\rho c_p}{4\pi\lambda\Delta t}\right)^{3/2}\cdot e^{-\frac{\rho c_p(\vec{x}-\vec{x}')^2}{4\lambda\Delta t}}\cdot\frac{q\cdot Z}{c_p}\cdot e^{-\frac{E}{RT}}\cdot\Delta t\cdot dx'dy'dz' \quad (13)$$

Für das zweite Integral in Gleichung (12) lässt sich für die Integration über die Zeit eine geschlossene Lösung angeben. Sie ist für $t > 0$, wenn alle Hot-Spots bei $t = 0$ initiiert werden:

$$T_{hs}[\vec{x},t]=\int\left(\frac{\rho c_p}{4\pi\lambda\Delta t}\right)^{3/2}\cdot e^{-\frac{\rho c_p(\vec{x}-\vec{x}')^2}{4\lambda\Delta t}}$$
$$\cdot\sum_{i=1}^{n}\left(\frac{Q_0}{\rho c_p(2\pi)^{3/2}\sigma_x\sigma_y\sigma_z}\cdot e^{-\left(\frac{(x'-x_i)^2}{2\sigma_x^2}+\frac{(y'-y_i)^2}{2\sigma_y^2}+\frac{(z'-z_i)^2}{2\sigma_z^2}\right)}\right)dx'dy'dz' \quad (14)$$

Ausgehend von den beiden Integralen (13) und (14) wird folgender Algorithmus entwickelt.

Im ersten Schritt wird durch die Initiierung der Hot-Spots eine Anfangstemperaturverteilung bestimmt:

$$T_1[\vec{x},t]=\sum_{i=1}^{n}\left(\frac{Q_0}{\rho c_p(2\pi)^{3/2}\sigma_x\sigma_y\sigma_z}\cdot e^{-\left(\frac{(x'-x_i)^2}{2\sigma_x^2}+\frac{(y'-y_i)^2}{2\sigma_y^2}+\frac{(z'-z_i)^2}{2\sigma_z^2}\right)}\right) \quad (15)$$

Ausgehend von $T_1[x,t]$ wird im zweiten Schritt der Reaktionsfortschritt berechnet:

$$T_2[\vec{x},t]=T_1[\vec{x},t]+\Delta t\cdot\frac{q\cdot Z}{c_p}\cdot e^{-\frac{E}{R(T_1[\vec{x},t]+T_0)}} \quad (16)$$

Dabei ist T_0 die Anfangs- oder Umgebungstemperatur vor der Initiierung der Hot-Spots.

Im dritten Schritt wird die räumliche Entwicklung der Temperaturverteilung $T_2[x,t]$ durch Faltung mit der Green'schen Funktion berechnet. Dabei können sowohl adiabate als auch nicht adiabate Randbedingungen gewählt werden. Wird eine Wand als adiabat angenommen so werden die Temperaturwerte an dieser Wand gespiegelt und bei der Berechnung des Faltungsintegrals entsprechend berücksichtigt.

$$T_3[\vec{x},t]=\int\left(\frac{\rho c_p}{4\pi\lambda\Delta t}\right)^{3/2}\cdot e^{\frac{\rho c_p(\vec{x}-\vec{x}')^2}{4\lambda\Delta t}}\cdot T_2[\vec{x},t]\cdot dx'dy'dz' \qquad (17)$$

Im nächsten Schritt nimmt $T_3[x,t]$ den Platz von $T_1[x,t]$ in Gleichung (12) ein und so weiter. Die Schritte 2 und 3 werden solange wiederholt bis die Summe der Δt gleich der gewünschten Gesamtzeit ist. Damit die chemische Reaktion nicht bis ins unendliche läuft wird die weitere Reaktion bei Erreichen einer Maximaltemperatur abgebrochen.

Sollen zu einem späteren Zeitpunkt weitere Hot-Spots initiiert werden, so kann der Schritt 1 erneut eingefügt werden.

Die tatsächliche Temperaturverteilung nach dem Durchlaufen eines vollständigen Zyklus ergibt sich durch $T_3[x,t]+T_0$.

6. Ergebnisse

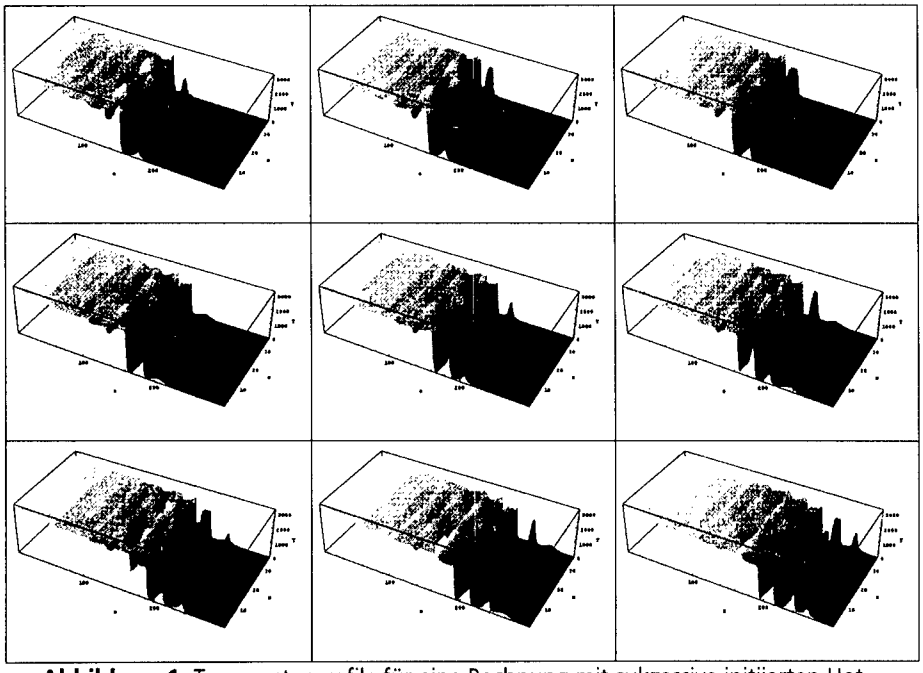


Abbildung 1: Temperaturprofile für eine Rechnung mit sukzessive initiierten Hot Spots

Der oben beschriebene Algorithmus wurde in ein Fortran Programm implementiert. Eingabeparameter für das Programm sind Stoffeigenschaften des Treibmittels wie Dichte Wärmekapazität und Wärmeleitfähigkeit, Angaben zur chemischen Reaktion, Angaben zur Größe und Struktur des Rechengitters und Angaben zu Größe und Anzahl der Hot Spots. Als Ergebnisse liefert das Programm für jeden Zeitschritt den Stoffumsatz in normierter Form, die Umsatzrate, die Temperaturverteilung für eine bestimmte Ebene

und die Größe der Abbrandoberfläche. Abbildung 1 zeigt Temperaturprofile für eine Rechnung, bei der nacheinander immer neue Hot Spots in kurzem Abstand vor der Abbrandfront initiiert wurden. Die Bilder haben jeweils gleichen zeitlichen Abstand. Dabei beschleunigt sich der Abbrand.

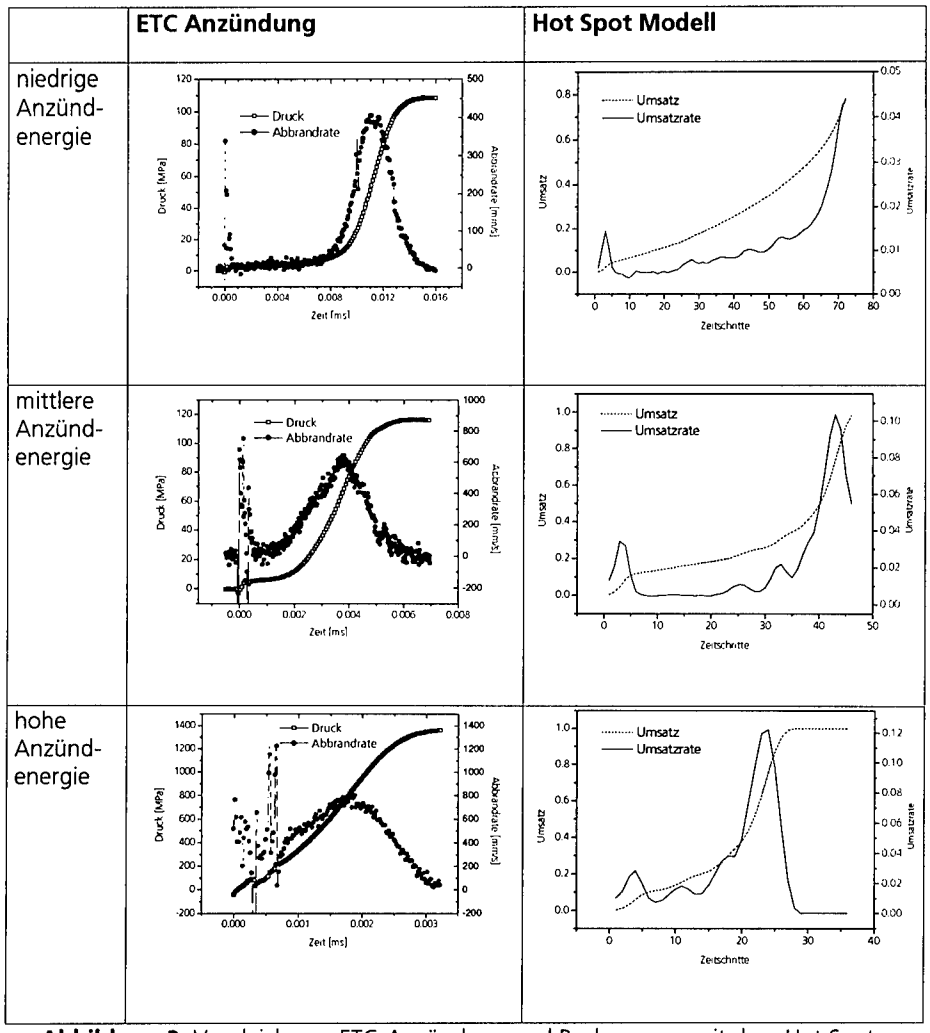


Abbildung 2: Vergleich von ETC-Anzündung und Rechnungen mit dem Hot Spot Modell. Dabei zeigt sich eine qualitative Übereinstimmung zwischen dem Druck und der Abbranrate im Experiment (links) und dem Umsatz und der Umsatzrate in den Rechnungen (rechts)

Einen qualitativen Vergleich zwischen Experiment und Theorie zeigt Abbildung 2. Links sind jeweils die Ergebnisse von Messungen eines Experimentes zur elektro-thermisch-chemischen Anzündung dargestellt [6]. Von oben nach unten wurden dabei immer höhere Anzündenergien verwendet. Bei niedriger Anzündenergie findet man

zunächst einen normalen Abbrand. Nach dem Überschreiten eines bestimmten Druckwertes erfolgt jedoch ein beschleunigter Abbrand. Die Erklärung dafür ist, dass ab einem bestimmten Druck heißes Gas in die Poren eindringen und die Innenseiten der Poren anzünden kann. Durch entsprechende Wahl der Eingabeparameter läßt sich dieses Verhalten mit dem hier vorgestellten Programm zumindest qualitativ simulieren.

Höhere Anzündenergien führen zu einem früheren Erreichen des notwendigen Gasdruckes für das Eindringen in die Poren, bis irgendwann dieser Wert schon bei der Anzündung überschritten ist. Durch Veränderung der entsprechenden Eingabeparameter kann auch dieses Verhalten simuliert werden.

7. Literatur

[1] Peter W. Atkins, Physikalische Chemie; 2. Aufl.; VCH, Weinheim; 1996.

[2] T. Fischer, G. Langer, N. Eisenreich, "Burning Rate Models of Gun Propellants", European Forum on Ballistics of Projectiles, EFBP'2000, Saint-Louis, France, April 11-14, 2000, 117-127.

[3] S. Kelzenberg, N. Eisenreich, W. Eckl, V. Weiser, "Modelling Nitromethane Combustion", Propellants, Explosives, Pyrotechnics. 24, (1999) 189-194.

[4] N. Kubota, T. J. Ohlemiller, L. H. Caveny and M. Summerfield, 15th Symposium (International) on Combustion, Tokyo 1974, pp. 529.

[5] N. Eisenreich, "A Photographic Study of the Combustion Zones of Burning Double Base Propellant Strands", Propellants and Explosives 5, 141-146 (1978).

[6] A. Koleczko, W. Ehrhardt, S. Kelzenberg, N. Eisenreich, " Plasma Ignition and Combustion", Propellants, Explosives, Pyrotechnics 26, 75-83 (2001)

Synthesis and Characterization of 2,6-Diamino-3,5-dinitropyrazine-1-oxide (NPEX-1)

J. Kerth, W. Kuglstatter

Fraunhofer Institut Chemische Technologie ICT
Joseph-von-Fraunhofer-Straße 7
D-76327 Pfinztal, Germany

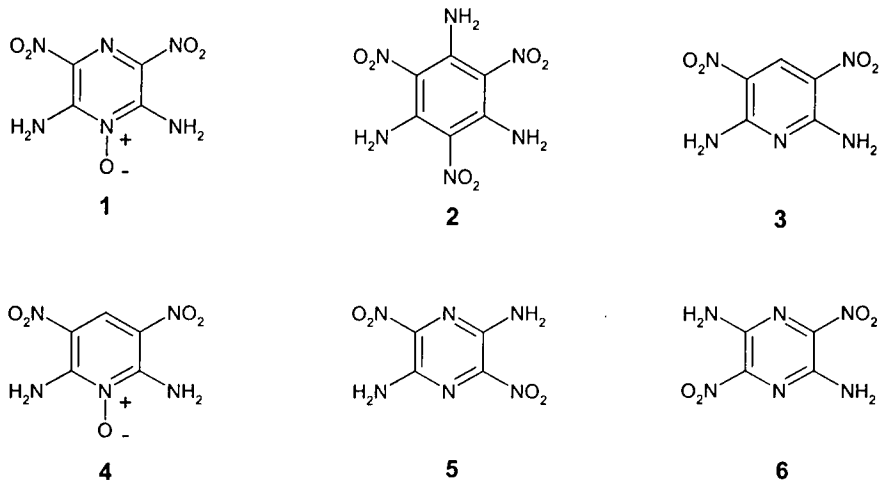
Abstract

The synthesis and characterization of 2,6-Diamino-3,5-dinitropyrazine-1-oxide (NPEX-1), an insensitive nitrogen-rich energetic heterocycle, was performed at ICT in order to enable independent investigations. The substance was synthesized in four steps with an overall yield of 41% and fully characterized by IR, NMR, DSC, TG, ARC and BAM impact and friction sensitivity tests.

Introduction

Nitrogen-rich substances have received an increasing interest as components for high energetic materials (explosives, propellants, gas generators, etc.). In particular, heterocyclic compounds are considered to be ideal to get powerful energetic materials because of their high molecular density, low volatility and mostly positive enthalpy of formation. Additional functionalization with nitro and amino groups impart power and insensitivity to the molecules. One such compound recently developed is 2,6-Diamino-3,5-dinitropyrazine-1-oxide **1**, also known as LLM-105. It was first synthesized in 1993 by Pagoria at LLNL[1]. It belongs to the group of thermally very stable and insensitive explosives. 1,3,5-Triamino-2,4,6-trinitrobenzene (TATB) **2** is currently the benchmark of this class. Further well known examples of nitrogen heterocycles with alternating nitro and amino groups are DADPy **3** and DADPyOx **4**

developed by Licht and Ritter at ISL[2]. Very recently Philbin reported the synthesis of ANPZ-i **5**, an isomer to the precursor ANPZ **6** of LLM-105[3].



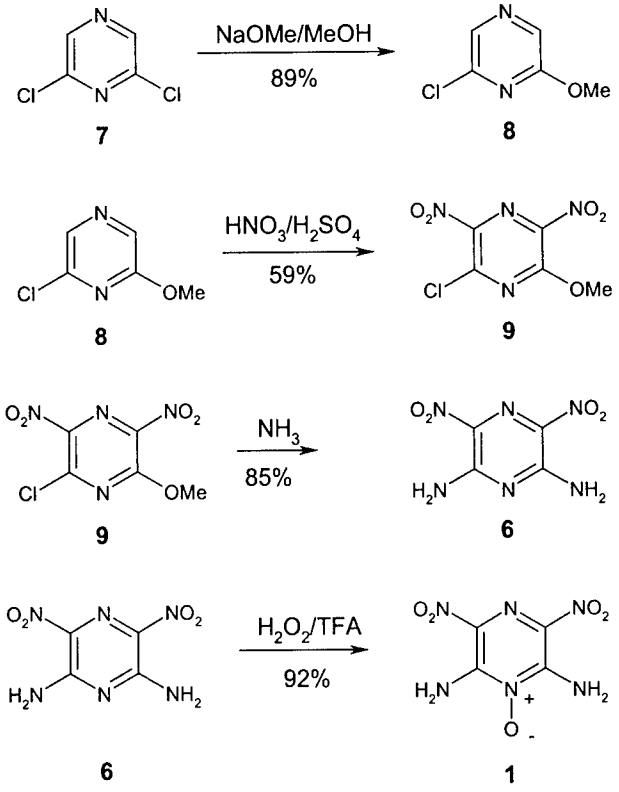
1 **2** **3**

4 **5** **6**

Scheme 1: Some insensitive high explosives

Synthesis

In order to enable independent investigations of 2,6-Diamino-3,5-dinitropyrazine-1-oxide **1** (ICT-name is NPEX-1) we were interested in the synthesis of this promising compound. To date three different synthetic routes to **1** are known. All three pathways lead to the immediate precursor of NPEX-1, 2,6-diamino-3,5-dinitropyrazine (ANPZ) **6**. The original route is a five step reaction sequence developed by Donald at DuPont[4] which suffers from low yields and a long reaction sequence. An alternative way described in the literature[5] could not be reproduced according to Pagoria[1]. The third route to ANPZ is disclosed in a Russian Patent[6] and starts from commercially available 2,6-Dichloropyrazine. We decided to carry out the last mentioned reaction sequence which leads within four steps to NPEX-1.



Scheme 2: Synthesis of NPEX-1

The first step is the nucleophilic displacement of one chlorine from the commercially available 2,6-Dichloropyrazine **7**. The reaction is performed with sodium methoxide (75 % excess) in refluxing methanol. 2-Chloro-6-methoxypyrazine **8** is obtained as a pale-yellow solid in 89% yield. The nitration step is conducted with a mixture of 20% fuming sulfuric acid and 100% nitric acid under careful control of the reaction temperature. After conventional work-up 2-Chloro-6-methoxy-3,5-dinitropyrazine **9** is obtained as a yellow solid in 59% yield. Subsequent treatment of this product with aqueous ammonia (25%) in acetone at 40-60°C furnished 2,6-Diamino-3,5-dinitropyrazine **6** as an orange solid in 85% yield. The last step is the oxidation of ANPZ to it's N-oxide with trifluoroacetic acid and hydrogen peroxide (60%). NPEX-1 is finally obtained as a yellow powder in 92% yield. The purity of this material is 93% according to ^{1}H NMR. The product still contains small amounts of ANPZ as a by-

product, which is still present even after prolonged reaction time. Due to it's very low solubility in common organic solvents, it is difficult to purify the product via crystallization. Therefore we performed the analytical testing with this material.

Characterization

IR-spectroscopy

Hydrogen-bonding of the amino-group to the neighbouring nitro group lead to four signals for the NH_2-vibrations. The NO_2-vibrations can be found at 1567cm^{-1} (asymmetric) and 1338 cm^{-1} (symmetric) respectively.

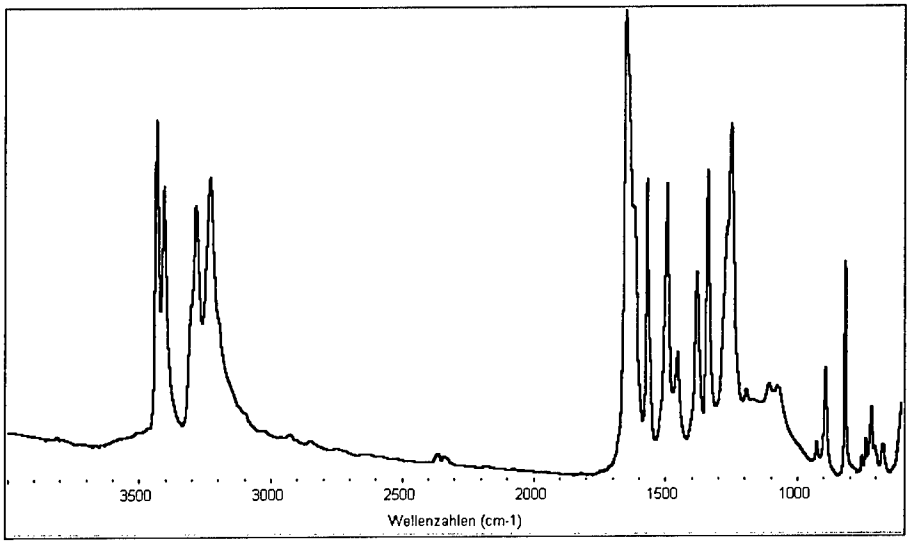


Figure 1: IR-spectrum of NPEX-1 (KBr)

NMR-spectroscopy

The ^1H NMR spectra of NPEX-1 shows two signals at 8.76 and 9.05 ppm for both amino groups which demonstrates their hindered rotation around the C-N bond on the NMR time-scale. This shows the known effect of hydrogen-bonding to the neighbouring nitro groups. The little impurity at 8.21 and 8.59 ppm is the precursor-compound ANPZ which shows the same effect.

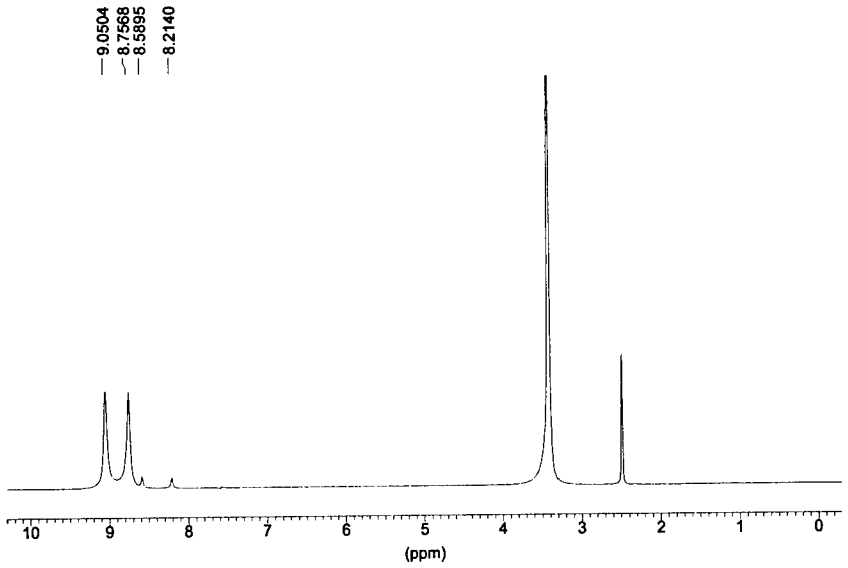


Figure 2: ^1H NMR spectra of NPEX-1 (DMSO-d_6, 400.1 MHz)

The ^{13}C NMR spectra is characterized by an up-field shift to 125.0 ppm of the carbon-atoms attached to the nitro groups. The C-NH_2 absorbs at 144.7 ppm.

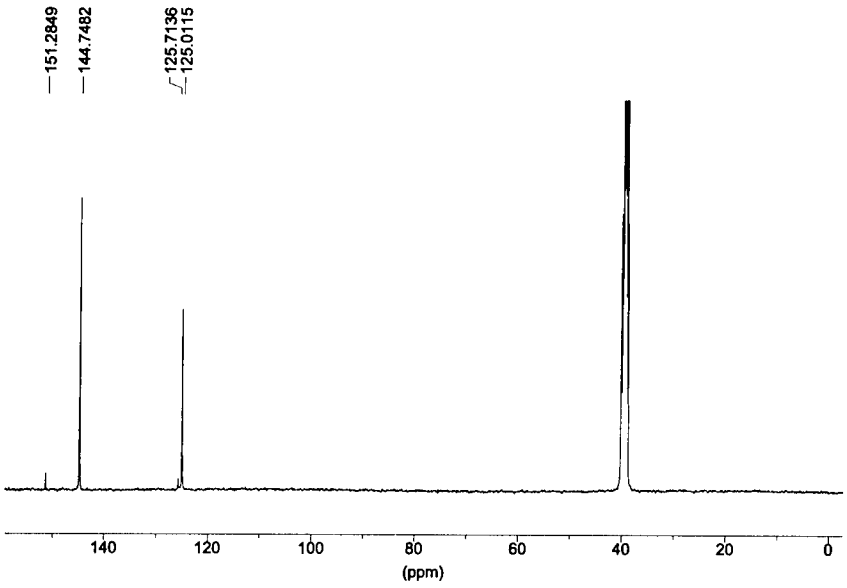


Figure 3: ^{13}C NMR of NPEX-1 (DMSO-d_6, 100.6 MHz)

In the ^{15}N NMR spectra four different signals can be observed. The highfield signal at –292.1 ppm belongs to the amino groups. The N-oxide function absorbs at –139.8 ppm. The signal at -106.6 ppm can be attributed to the second ring-nitrogen and the nitro groups can be found at –16.2 ppm.

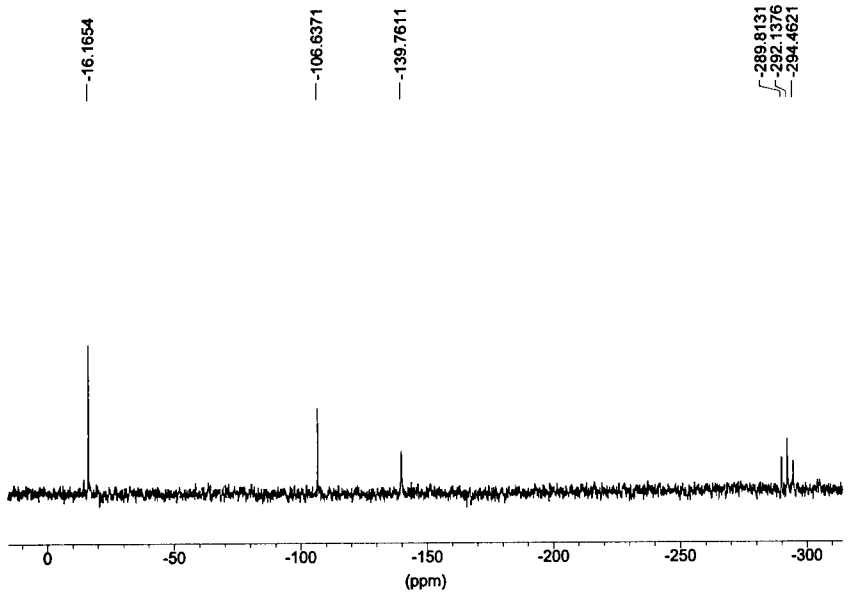


Figure 4: ^{15}N NMR spectra of NPEX-1 (DMSO-d_6, 40.6 MHz)

Differential Scanning Calorimetry, DSC

The analysis demonstrates the very high thermal stability of NPEX-1 in a wide temperature range. The decomposition starts above 300 °C. Two decomposition exotherms at 343 °C and 350 °C can be observed.

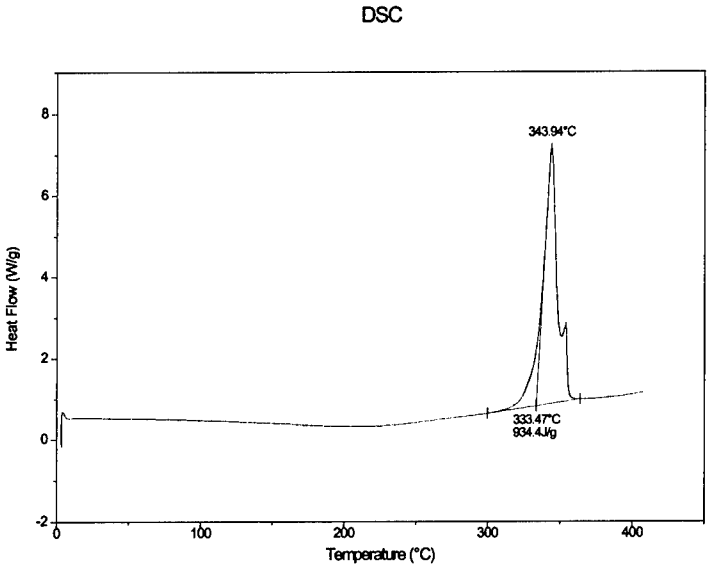


Figure 5: DSC (sample pans with pierced lids)

Thermo Gravimetry, TG

The test was performed at a heating rate of 5°C/minute. The result of the measurement is shown in figure 6.

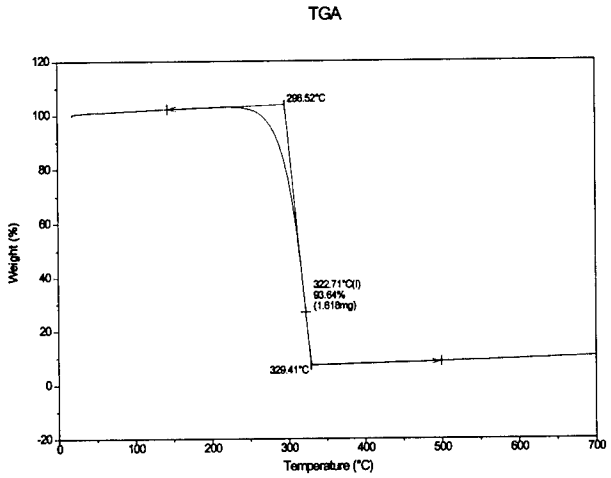


Figure 6: TG plot of NPEX-1 at a heating rate of 5 °C/min

As can be seen , the weight started to decrease between 220 and 230 °C followed by a mass loss between 260 and 330 °. In contrast to the two heat flow maxima which can be observed in the DSC experiment the TG curve of NPEX-1 shows only one continual mass loss step during decomposition.

Accelerating Rate Calorimeter-measurement

The experiment determined a remarkable adiabatic self heating only at about 280°C. In comparison to the nitramines RDX and HMX this indicates an increased thermo-stability. Furthermore the deflagration of NPEX-1 extends on a longer period as these nitramines used to do. This is a significant benefit of NPEX-1.

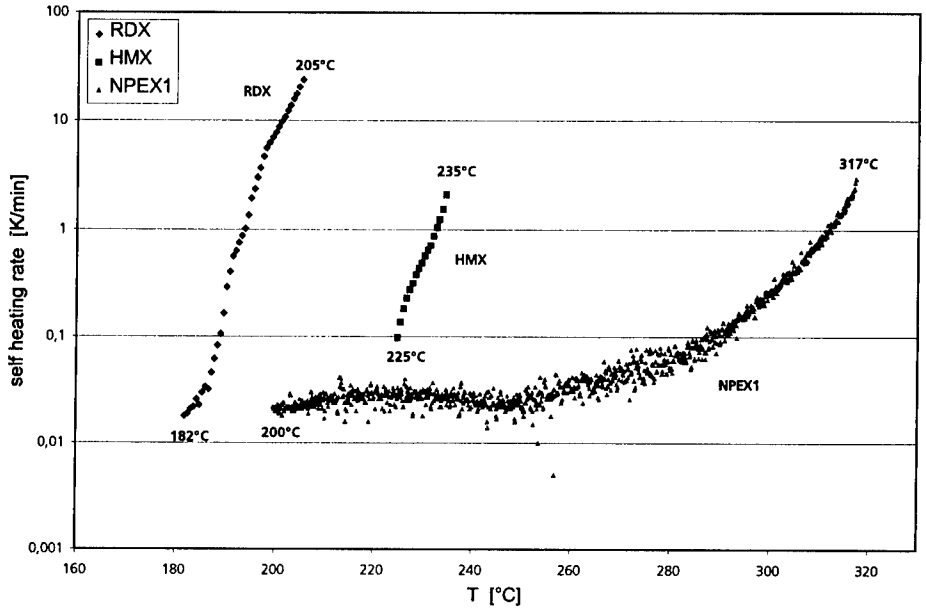


Figure 7: ARC-measurement of NPEX-1

Sensitivity

The impact and friction sensitivities were determined according to the BAM standard. The impact sensitivity was measured with a 1 kg drop weight. The results are shown in Table 1.

Impact energy (Nm)	6
Friction load (N)	240

Table 1: Sensitivity data evaluated at 16.7 % probability

According to the results shown above NPEX-1 is very insensitive to friction. The impact sensitivity is higher and lies in the area of common high explosives like RDX and HMX.

Summary and Conclusions

NPEX-1 has been synthesized at ICT in an overall yield of 41%. It is a thermally very stable compound and shows low sensitivity towards friction. Due to the high price of the starting material 2,6-Dichloropyrazine alternative synthetic routes have to be investigated in order to get greater quantities of this promising compound.

Acknowledgement

We like to thank Dr. M. Kaiser from the WIWEB for the recording of the NMR-spectra and helpful discussions.

References

1) P. F. Pagoria et al., DEA-A-76-G-1218, Energetic Materials for Munitions, **1998**; R.L. Atkins, W. Bauer, MWD DEA-A-76-G-1218, Energetic Materials for Munitions, **1997**; R. M. Doherty, R. L. Simpson, 28th Int. Annual Conference of ICT, pp.10.1–12, **1997**.
2) H. H. Licht, B. Wanders, H. Ritter, ISL-Report, 101/89, **1989**; H. H. Licht, B. Wanders, ISL-Technical Report, 510/89, **1989**.
3) S. P. Philbin, R. W. Millar, R. G. Coombes, *Propellants, Explosives, Pyrotechnics* **2000**, *25*, 302.
4) D. S. Donald, US Patent 3,808,209.
5) E. C. Taylor, C. K. Cain, H. M. Loux, *J. Am. Chem. Soc.* **1954**, *76*, 1874; E. C. Taylor, H. M. Loux, E. A. Falco, G. H. Hitchings, *J. Am. Chem. Soc.* **1955**, *77*, 2243.
6) V. A. Tartakovskii, O. P. Shitov, I. L. Yudin, V. A. Myasnikov, SU Patent 1,703,645.
7) R.A. Hollins, R.A. Nissan, W.S. Wilson, Report, NAWC-WPNS-TP-8228, AD-A29799/5GAR, **1995**.